Cover Picture



David S. Ginger, Hua Zhang, and Chad A. Mirkin*

Dip-Pen Nanolithography makes possible rapid patterning of surfaces on the nanometer scale. The cover picture clearly shows the principles of this technique: the deposition of dye molecules from an atomic force microscopy tip onto a substrate. Feymans 1960 dictum on miniturization, shown in nanometer-sized type in the background, is proving to be once again applicable. C. A. Mirkin et al. summarize in their Review on page 30 ff. the current status of dip-pen lithography and predict possible future developments.

Nothing Stands Still

Jean Tinguely

"Jean Tinguely is one of the most important artists of the 20th century. With his kinetic objects … he played a fundamental role in helping to shape the appearance of art in the second half of the century." This is how the foreword of a book "Tinguely" begins (Prestel Verlag, Munich, 2002), and a similarly formulated statement would be appropriate for this journal: *Angewandte Chemie* is one of the most important scientific journals of the 20th century. With its innovation it played a fundamental role in helping to shape the appearance of chemistry in the second half of the century. This is the essence of a speech given by Professor K. C. Nicolaou in his function as a member of the International Advisory Board of *Angewandte Chemie* at a reception that took place during the ACS Meeting in New York in September 2003 in celebration of the change to weekly publication. See the facing page for the speech and a few photos from the event.

International Edition available electronically from issue 1/1962

For most of the second half of the 20th century an English edition of *Angewandte Chemie* also appeared, and all issues of this International Edition will be available electronically from January 2004. The so-called backfiles (1962–1997; later issues are already available online) contain almost 2000 Reviews, many of which are legendary. More than 13000 short Communications and approximately 400 Highlights, complete with links to references and other features, will make these backfiles a treat for librarians and readers alike—and orders for the backfiles received by the end of January will qualify for a considerable discount (see back cover).

In 2003, 48 issues were published, with a total of 6158 pages, which is 1253 pages more than in 2002 (+25%)! This growth resulted in part from the 6% more Communications published, but in part from the significant increase in the number of Minireviews, Highlights, Essays, and News items: In the revamped *Angewandte Chemie* the axiom "it's all in the mix" is truer than ever. The time had certainly come to place more emphasis on other features—alongside the unchanged very important Communications section, which has grown substantially over the last decade.

The concern expressed by readers that doubling the publication frequency would lead to a decline in the quality/rejection rate, has proved unjustified. In the first 11 months of 2003 we received 2560 Communications (+16%), and in the first half of 2003 the rejection rate was 64% (2002: 62%). Table 1 gives information about the origins of the Communications. A distinct growth in manuscript submissions from the USA, Japan, the UK, and Germany is noticeable; phenomenal has been the increase in the number of manuscripts submitted from the People's Republic of China (see also Figures 1 and 2). Other journals have observed the same phenomenon, which reflects the rapidly growing research activities in China and the desire of scientists to publish in internationally renowned journals.

アンゲバンテ・ヘミー
Angewandte Chemie in Japanese

Growth brings with it not only gratification, but also more challenges. It has certainly not escaped the attention of the readers of *Angewandte Chemie* that we have published a significant number of Corrigenda and Apologies during the last year. The Apologies in particular result from misconduct, for example, the failure to cite directly related own publications or (self-)plagiarism. Too many references to one's own work can, of course, also be embarrassing, but it is worse when this accompanies failure to cite the work of other authors. On the subject of citing the literature: In Communications (and Highlights) in

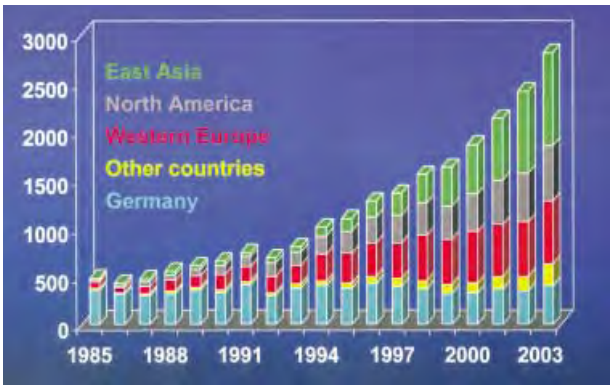


Figure 1. Regional origins of Communications submitted between 1985 and 2003.

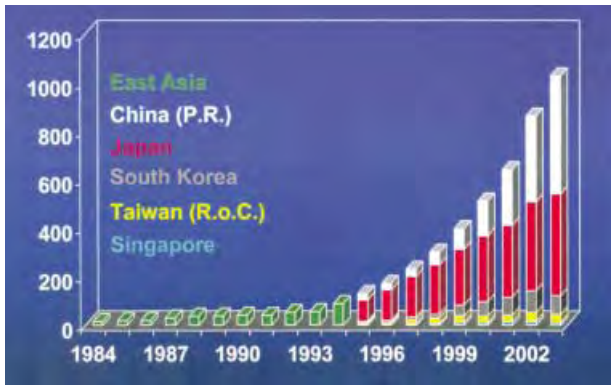


Figure 2. Origins of Communications submitted from East Asia between 1995 and 2003.

© 2004 Wiley-VCH Verlag GmbH & Co. KGaA, Weinheim

Table 1: Country of origin of Communications submitted between January and November 2001, 2002, and 2003 (percentages in brackets). Manuscripts with authors from several countries are assigned to the country of the submitting author.

Country	2001	2002	2003[a]
USA	401 (19)	448 (19)	512 (18)
China (P.R.)	213 (11)	356 (15)	486 (17)
Japan	296 (14)	366 (15)	420 (15)
Germany	359 (17)	349 (14)	400 (14)
Great Britain	112 (5)	127 (5)	173 (6)
France	105 (5)	98 (4)	116 (4)
Spain	74 (3)	86 (4)	90 (3)
India	68 (3)	75 (3)	84 (3)
South Korea	71 (3)	82 (4)	77 (3)
Switzerland	55 (3)	55 (2)	61 (2)
Canada	52 (2)	51 (2)	55 (2)
Netherlands	32 (2)	32 (1)	54 (2)
Italy	65 (3)	65 (3)	50 (2)
Taiwan (R.C.)	27 (1)	36 (1)	32 (1)
Israel	27 (1)	27 (1)	25 (1)
Sweden	13 (1)	14 (1)	14 (1)
Poland	11 (1)	16 (1)	11 (0)
Russia	9 (0.5)	11 (1)	12 (0)
Singapore	14 (1)	14 (1)	11 (0)
Greece	8 (0.5)	14 (1)	8 (0)
Others	97 (4)	97 (4)	125 (4)
Total	2109	2419	2818

[a] Projected figures for 2003 based on available data for 10 months.

Angewandte Chemie all seminal and very important original work on which a contribution is based should be cited, but not much more. Rather than citing in detail every single publication on the topic discussed, it is better to include a reference to a review article, for example, from *Angewandte Chemie*: All Reviews published in the journal since 1962 are collected in a freely accessible register on our homepage (and the backfiles mentioned above offer the full texts). Since the middle of last year we have explicitly asked referees whether the results are described in the context of previous publications, and whether this previous work is cited appropriately. Nevertheless, a Communication appeared at the end of last year, in issue 46, in which a complex was claimed to be new, although it had already been described in detail in 1970 (see p. 14)

Reading referee reports is one thing that can annoy authors; however, even a bad or inaccurate report, which in the worst case can also be off the mark in its tone, should merely prompt an author to consider whether the article could not

Serving Science

In gathering my thoughts and deciding what to say, I could not help but admire the many things that publishers do for science and technology. They are the communicators of what happens in the minds and laboratories of scientists to the outside world and, as such, they play a crucial role in the dissemination of knowledge around the world, which, in turn, translates, or should translate, into the spread of technology and wealth among those who have it and those who struggle to survive.

But I do want to single out Wiley-VCH on this occasion as a pioneer organization in publishing, particularly in chemistry. For those of us who watch the pulses of our science through the journals and the latest books, we notice the originality and imagination that the Wiley-VCH team injects into their products, and the aggressive pursuit of distinction and professionalism by which they define the gradient of publishing in chemistry and related disciplines. Importantly, not only do they execute in the most professional and timely manner the tasks put in front of them by authors, but they initiate and shape ideas which they implement or suggest for implementation to potential authors. Their leadership *shows*, as we move into the 21st century, with the new weekly image of *Angewandte Chemie* and the several new journals they launched over the last few years, as well as the many irresistible books they stimulated, adopted, beautifully designed, illustrated, and published. When I was a student I hardly knew what *Angewandte Chemie* was! And there was the time, of course, when they rejected one of our first and most influential papers on the total synthesis of taxol! But that was the distant past. As we all know, *Angewandte Chemie* has come a long way, and I am proud to serve on its International Advisory Board. Today, it is the first journal I reach for on my desk among the many that land there every week. They must have many secrets for their successes, but I will tell you one that I know! They reach out and respect their readers and authors alike.

K. C. Nicolaou
The Scripps Research Institute, La Jolla and Department of Chemistry, University of California, San Diego


K. C. Nicolaou, La Jolla (left) and J. D. Roberts, Pasadena.


Sarah and Sam Danishefsky with P. Gölitz


E.-E. Wille (Wiley-VCH) and K. Nakanishi, New York; left: D. Bergbreiter, College Station.


R. Boese, Essen (left), H. B. Bürgi, Bern, and R. F. W. Bader, Hamilton, Ontario (right).


P. Stang, Salt Lake City (left) and K. Christe, Edwards, California.

 © 2004 Wiley-VCH Verlag GmbH & Co. KGaA, Weinheim

perhaps be presented somewhat more clearly. Reading the edited manuscript (or more precisely, the galley proofs) is the other. *Angewandte Chemie* is one of the few scientific journals in which all contributions are still edited by technically highly qualified editors, for whom clarity has priority over all else. In an Editorial in *Analytical Chemistry* (2003, issue 13, p. 2774) Roger W. Murray covered the essential under the heading "Clarity First: Language in Research Articles". The attempt to increase clarity through the editing process can, of course, also lead to errors, but the same applies here as to referee reports: Authors are asked to consider the changes, even if they are occasionally incorrect, simply as a suggestion. *Angewandte Chemie* has a very wide, heterogeneous readership around the world, and these are the people for whom the editors work.

Furthermore, *Angewandte Chemie* is a journal that should not only be used for specific searches—it offers the opportunity to find something that one is not even looking for, and this is indispensable for creative scientific work. Essential for a good overview of the developments in chemistry are certainly the Reviews. The German Chemical Society (Gesellschaft Deutscher Chemiker, GDCh), to which *Angewandte Chemie* belongs, has announced a competition to find out which were the best and most important Reviews in *Angewandte Chemie* in 2003. We are already excited about the outcome and shall report on the results in a future issue.

Back to where we started: With weekly publication, its new structure, and its more modern layout, *Angewandte Chemie* is presenting itself in such a way as to continue to shape the appearance of chemistry in this new century. This first issue of volume 43 (volume 116 of the German edition) demonstrates our ambition to meet the challenge: Two Reviews by outstanding chemists of the younger generation, Professor Chad Mirkin (Northwestern University) and Professor Stuart Schreiber (Harvard University), deal with chemistry and nanotechnology on the one hand, and chemistry and life sciences on the other—"angewandte Chemie" (applied chemistry) in the best sense of the term. The name *Angewandte Chemie* will continue to be the agenda, in so far as the foundations for the application of the chemistry of tomorrow and the future are to be found in this journal. Nothing stands still!



Peter Gölitz

PS: At the end of 2003 Prof. Wolfram Saenger (Freie Universität Berlin) and Prof. Konrad Sandhoff (Rheinische Friedrich-Wilhelms-Universität, Bonn) finished their terms as members of the Editorial Board of *Angewandte Chemie*. Four new Board members have been appointed: Prof. Rainer Metternich (Schering AG, Berlin), Prof. Hartmut Michel (Max-Planck-Institut für Biophysik, Frankfurt), Dr. Hans Ulrich Stilz (Aventis Pharma Deutschland GmbH, Frankfurt), and Prof. Rolf Thauer (Max-Planck-Institut für terrestrische Mikrobiologie, Marburg), and they will help to shape the future of this journal. You can read more about these scientists on the News page (p. 18).

PPS: Hard to believe, but true: *Chemistry—A European Journal* is already in its 10th year of publication in 2004, and is expected to publish about 6650 pages; *ChemBioChem* and *ChemPhysChem* are already in their 5th year with well over 1500 pages each. *ChemPhysChem* has established itself as a leading physical chemistry/chemical physics journal, and *ChemBioChem* shines, for example, with outstanding special issues, the most recent of which was on RNA (issue 10/03). The European sister journals of *Angewandte Chemie* now all work with the editing system "manuscriptXpress"; *Angewandte Chemie* plans to follow their lead soon.

 © 2004 Wiley-VCH Verlag GmbH & Co. KGaA, Weinheim

Angewandte EarlyView

The following articles are available online (in Wiley InterScience). You can find them at www.angewandte.org, under Full Text, Early View.

R. A. Böckmann, H. Grubmüller:*
Multistep Binding of Divalent Cations to Phospholipid Bilayers: A Molecular Dynamics Study
DOI: 10.1002/anie.200352784
Published online: December 4, 2003

A. Evers, G. Klebe:*
Ligand-Supported Homology Modeling of G-Protein-Coupled Receptor Sites: Models Sufficient for Successful Virtual Screening
DOI: 10.1002/anie.200352776
Published online: December 2, 2003

Articles judged by the referees or the editor as being either very important or very urgent are immediately edited, proof-read, and electronically published once the manuscript has arrived in the editorial office in final form. As long as there is no page number available these articles should be cited in the following manner:

Author(s) *Angew. Chem. Int. Ed.*, online publication date, DOI.

News

Four New Members of the Editorial Board ____ 18

Books

Classics in Total Synthesis II ____ 20 Kyriacos C. Nicolaou, Scott A. Snyder *reviewed by A. Fürstner*

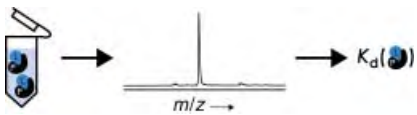
Highlights

Mass Spectrometry

K. Breuker* ____ 22 – 25

New Mass Spectrometric Methods for the Quantification of Protein–Ligand Binding in Solution

At first sight, it is not immediately discernible how molecular-weight measurements can be used for the determination of binding constants for protein–ligand complexes. Nevertheless, successful strategies have been developed for the quantitative analysis of protein–ligand binding by mass spectrometry (see

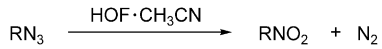


scheme), which offers the distinct advantages of speed and the potential for automation.

Oxidation

G. K. S. Prakash,* M. Etzkorn ____ 26 – 28

Direct Oxidation of Azides to Nitro Compounds



The "tamed" hypofluorous acid complex $HOF \cdot CH_3CN$ has been found to be a convenient reagent for the expedient oxidation of azides to their corresponding nitro compounds. The method is quite versatile with both aromatic and aliphatic azides.

© 2004 Wiley-VCH Verlag GmbH & Co. KGaA, Weinheim

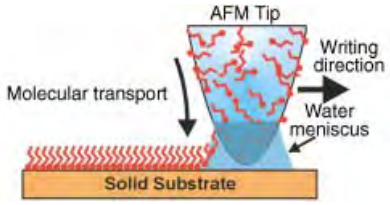
Contents

Reviews

Nanolithography

D. S. Ginger, H. Zhang, C. A. Mirkin* ——— **30–45**

The Evolution of Dip-Pen Nanolithography

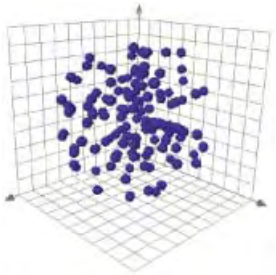


More than scratching the surface: Dip-pen nanolithography (DPN) is a new scanning-probe-based direct-write tool for generating surface-patterned chemical functionality on the sub-100-nm length-scale (see picture). This article introduces DPN and reviews the rapid growth of the field of DPN-related research and its impact on areas ranging from biological nanoarrays to patterned magnetic media to microelectromechanical systems (MEMs).

Discovery of Small Molecules

M. D. Burke, S. L. Schreiber* ——— **46–58**

A Planning Strategy for Diversity-Oriented Synthesis



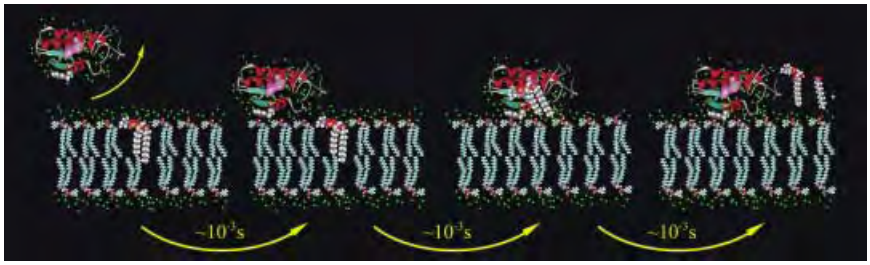
Space—the final frontier: A complementary approach to retrosynthetic analysis has been used to develop forward-synthetic analysis which forms the basis of diversity-oriented synthesis (see scheme). The goals of diversity-oriented synthesis include the development of pathways leading to the efficient (three- to five-step) synthesis of collections of small molecules having rich skeletal and stereochemical diversity.

Communications

Hydration Dynamics

L. Zhao, S. K. Pal, T. Xia, A. H. Zewail* ——— **60–63**

Dynamics of Ordered Water in Interfacial Enzyme Recognition: Bovine Pancreatic Phospholipase A_2



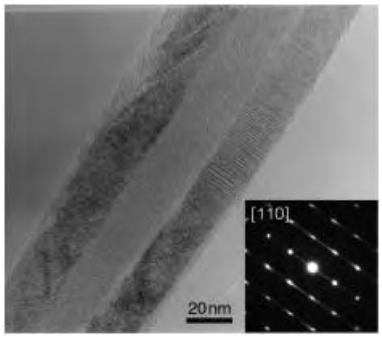
Slippery when wet: Water molecules at the interface between a protein (e.g. bovine pancreatic phospholipase A2) and a micellar substrate act as a lubricant and facilitate movement and binding of the protein at the surface (see picture). Studies of the hydration dynamics before and after complexation reveal that these interactions are crucial for enzymatic function.

Silicon Tubular Nanostructures

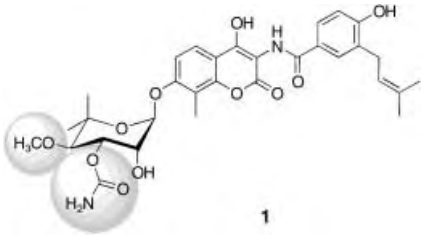
J. Hu,* Y. Bando, Z. Liu, J. Zhan, D. Golberg, T. Sekiguchi ——— **63–66**

Synthesis of Crystalline Silicon Tubular Nanostructures with ZnS Nanowires as Removable Templates

Silicon epitaxy on ZnS nanowires results in the formation of ZnS/Si core/shell nanowires; chemical removal of the zinc blende nanowire templates produces monocrystalline silicon tubular nanostructures with outer diameters of about 60–180 nm, wall thicknesses of about 20–60 nm, and lengths of several micrometers (see picture). The electron diffraction pattern of an individual nanostructure (inset) confirmed the presence of single-crystalline silicon.



© 2004 Wiley-VCH Verlag GmbH & Co. KGaA, Weinheim



Two steps forward: The glycosylated aminocoumarin antibiotic novobiocin (**1**) is produced by *Streptomyces spheroides* and inhibits the bacterial type II topoisomerase DNA gyrase. The sugar-tailoring enzymes NovP and NovN that catalyze the final two steps in novobiocin biosynthesis were overproduced in *Escherichia coli* and characterized as a methyltransferase and carbamoyltransferase, respectively.

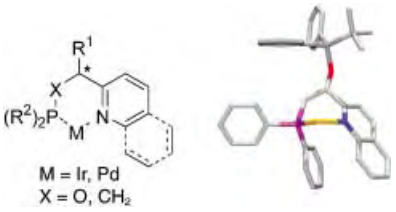
Biosynthesis of Antibiotics

C. L. Freel Meyers, M. Oberthür, H. Xu, L. Heide, D. Kahne, C. T. Walsh* **67 – 70**

Characterization of NovP and NovN: Completion of Novobiocin Biosynthesis by Sequential Tailoring of the Noviosyl Ring

---

Potent transition-metal complexes for asymmetric catalysis are formed from readily accessible N,P ligands constructed from basic N-heteroaryl building blocks (see structure). Their simple assembly should not be misconstrued: they posses several handles by which to tune both steric and electronic parameters. The potential of these ligands is demonstrated by the high levels of enantioselection they induce in such divergent processes as



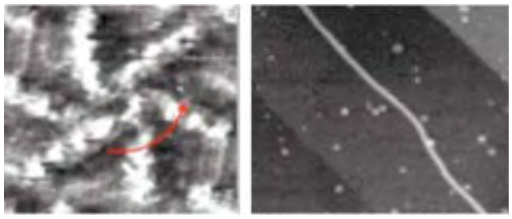
asymmetric hydrogenation and the Heck reaction.

Chiral N,P Ligands

W. J. Drury III, N. Zimmermann, M. Keenan, M. Hayashi, S. Kaiser, R. Goddard, A. Pfaltz* **70 – 74**

Synthesis of Versatile Chiral N,P Ligands Derived from Pyridine and Quinoline

---



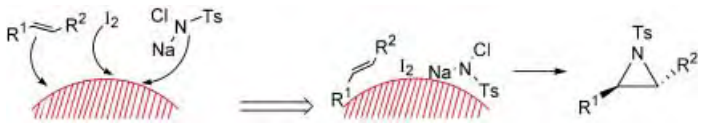
Hierarchical self-assembly: Oligo(*p*-phenylenevinylene)s with pendant diamino triazine moieties can self-assemble through hydrogen-bonding interactions to give hexameric rosettes (see picture, left). These rosettes further organize into large supramolecular tubules (right) with perfect space filling.

Hydrogen-Bonded Assembly

P. Jonkheijm, A. Miura, M. Zdanowska, F. J. M. Hoeben, S. De Feyter,* A. P. H. J. Schenning,* F. C. De Schryver,* E. W. Meijer* **74 – 78**

π-Conjugated Oligo(*p*-phenylenevinylene) Rosettes and Their Tubular Self-Assembly

---



Olefins can be converted into aziridines by using a chloramine-T/I_2 system, and silica and water as the reaction medium (see picture). Moreover, the ring-opening reaction of the resulting aziridine with an azide or a cyanide ion proceeds in the same medium.

Reaction Media

S. Minakata,* D. Kano, Y. Oderaotoshi, M. Komatsu* **79 – 81**

Silica–Water Reaction Media: Its Application to the Formation and Ring Opening of Aziridines

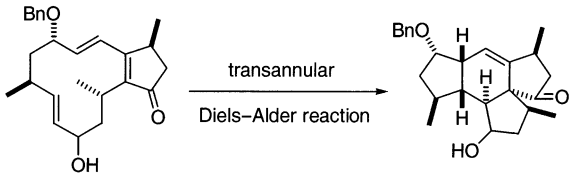
 © 2004 Wiley-VCH Verlag GmbH & Co. KGaA, Weinheim

Contents

Spirotetracycle Synthesis

K. Araki, K. Saito, H. Arimoto, D. Uemura* ——— **81 – 84**

Enantioselective Synthesis of the Spirotetracyclic Carbon Core of Mangicols by Using a Stereoselective Transannular Diels–Alder Strategy



"TADA!" is not the trumpet fanfare but the transannular Diels–Alder reaction concluding the synthesis of the tetracyclic core of the mangicols, a family of marine sesterterpenes. Further highlights in the synthesis include a novel chlorination and an intramolecular Nozaki–Hiyama–Kishi coupling reaction. Bn = benzyl.

Kinetic Resolution of Epoxides

M. Bandini, P. G. Cozzi,* P. Melchiorre, A. Umani-Ronchi* ——— **84 – 87**

Kinetic Resolution of Epoxides by a C–C Bond-Forming Reaction: Highly Enantioselective Addition of Indoles to *cis*, *trans*, and *meso* Aromatic Epoxides Catalyzed by [Cr(salen)] Complexes



The high reactivity of indoles has led to a new approach for the kinetic resolution of epoxides. [Cr(salen)] efficiently catalyzes a new C–C bond-forming reaction that allows the kinetic resolution of *cis* and *trans* aromatic epoxides (see scheme). By employing the same catalytic system, different indolyl derivatives were obtained in high enantiomeric excesses (up to 98%) by asymmetric ring opening of *meso*-stilbene oxide.

Cluster Expansion

A. Mukherjee, M. Nethaji, A. R. Chakravarty* ——— **87 – 90**

Cubane $\{Cu^{II}_4\}$ Cluster as a Precursor for the Preparation of a Mixed-Valent $\{Cu^{II}_{12}Cu^{I}_2\}$ Core

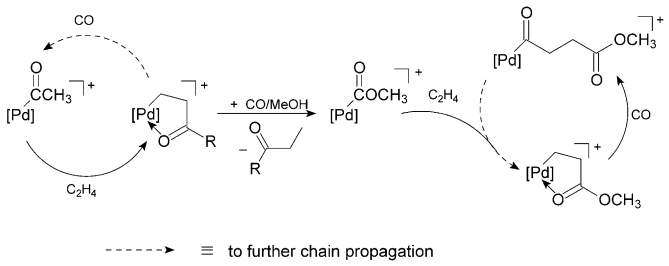


A molecular octopus: A ferromagnetic cubane cluster $[\{Cu^{II}(HL)\}_4]$, which has eight vacant coordination sites on its pendent arms, undergoes metal-driven self-assembly to form an antiferromagnetic mixed-valent tetradecanuclear complex with a prismatic propeller-shaped $\{Cu^{II}_{12}Cu^{I}_2\}$ core (see scheme).

Reaction-Mechanism Elucidation

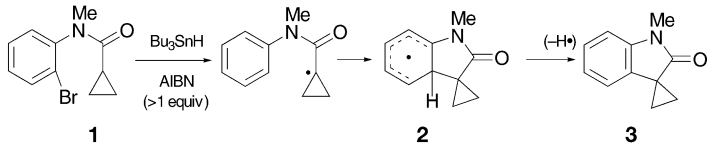
J. Liu, B. T. Heaton, J. A. Iggo,* R. Whyman ——— **90 – 94**

The Complete Delineation of the Initiation, Propagation, and Termination Steps of the Carbomethoxy Cycle for the Carboalkoxylation of Ethene by Pd–Diphosphane Catalysts



An elegant model: The intermediates in both the hydride and carbomethoxy cycles, and in chain transfer for carboalkoxylation of ethene and CO–alkene copolymerization have been characterized for a highly active cationic palladium–diphosphane catalyst (see scheme). In contrast to previous reports on model systems, alkene insertion into the Pd–C(O)OMe and Pd–C(O)Me bonds is found to occur at comparable rates.

© 2004 Wiley-VCH Verlag GmbH & Co. KGaA, Weinheim



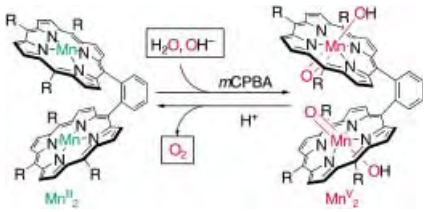
1 2 3

The fate of intermediate π radicals is crucial in Bu_3SnH-mediated cyclization by homolytic aromatic substitution, for example, of bromo compound **1** via radical **2** to give oxindole **3** (AIBN = azobisisobutyronitrile). The results indicate that the mechanism requires the abstraction of a hydrogen radical from the intermediate π radical by the radical initiator or a product of initiator breakdown, and also that arene solvents are not always the best solvents for radical reactions.

Radical-Reaction Mechanism

A. L. J. Beckwith,* V. W. Bowry, W. R. Bowman,* E. Mann, J. Parr, J. M. D. Storey* ——— **95 – 98**

The Mechanism of Bu_3SnH-Mediated Homolytic Aromatic Substitution

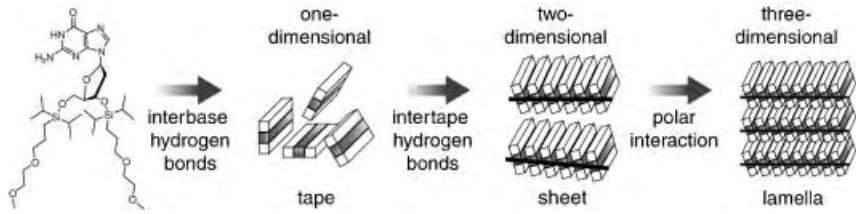


A high valent Mn^V=O porphyrin dimer is prepared by peracid oxidation of an Mn^{III} dimer under basic conditions at room temperature (see scheme; mCPBA = *m*-chloroperbenzoic acid). The addition of an acid to a solution of the Mn^V=O complex results in quantitative dioxygen evolution. Water and/or hydroxide ions are the sources of both the oxo ligand and the evolved dioxygen.

Oxygen Evolution from Water

Y. Shimazaki, T. Nagano, H. Takesue, B.-H. Ye, F. Tani, Y. Naruta* ——— **98 – 100**

Characterization of a Dinuclear Mn^V=O Complex and Its Efficient Evolution of O_2 in the Presence of Water

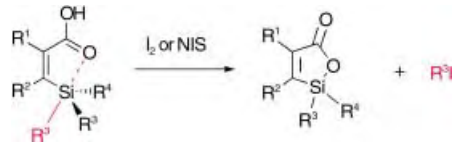


A super film: 2D sheet assemblies of alkylsilylated deoxyguanosine derivatives were formed by double intertape hydrogen bonding between hydrogen-bonded 1D tape motifs. Introduction of polar oxyethylene units at the sheet surface allowed the fabrication of a flexible, self-supporting supramolecular film (see figure) with a well-defined structural hierarchy.

Supramolecular Materials

I. Yoshikawa, J. Li, Y. Sakata, K. Araki* ——— **100 – 103**

Design and Fabrication of a Flexible and Self-Supporting Supramolecular Film by Hierarchical Control of the Interaction between Hydrogen-Bonded Sheet Assemblies



Dealkylation of trialkylvinylsilanes: The direct electrophilic cleavage of one silicon–carbon bond of tetraorganosilanes activated by the intramolecular pentacoordination of a slightly nucleophilic ester or carboxylic acid group provides a novel route to silalactones (see scheme).

Synthesis of Silalactones

M. Shindo,* K. Matsumoto, K. Shishido ——— **104 – 106**

Electrophilic Cleavage of One Silicon–Carbon Bond of Pentacoordinate Tetraorganosilanes: Synthesis of Silalactones

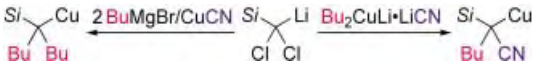
 © 2004 Wiley-VCH Verlag GmbH & Co. KGaA, Weinheim

Contents

Organocuprates

J. Kondo, Y. Ito, H. Shinokubo,*
K. Oshima* ——— 106 – 108

Consecutive Double 1,2-Migration of Two Different Groups in Silyl(dichloromethyl)-cuprates

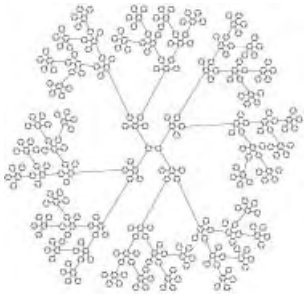


Very different reactivity of two types of cuprates: Treatment of a silyldichloromethyllithium compound with a copper reagent prepared from BuMgBr and CuCN gives the product of consecutive dibutylation. On the other hand, $Bu_2CuLi{\cdot}LiCN$ affords the butylation/cyanation product (see scheme, *Si* = Ph_2MeSi).

Dense-Shell Dendrimers

S. Rosenfeldt,* N. Dingenouts, D. Pötschke, M. Ballauff, A. J. Berresheim, K. Müllen, P. Lindner ——— 109 – 112

Analysis of the Spatial Dimensions of Fully Aromatic Dendrimers

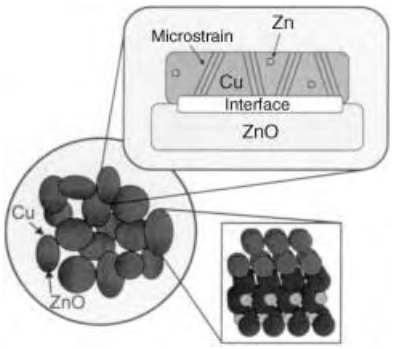


Do dendrimers in solution have a dense shell or a dense core? This question can be answered with the help of small-angle neutron scattering. The fully aromatic dendrimer G4-M shown here displays the expected rigid structure in solution and represents the first example of a real dense-shell dendrimer.

Structure-Activity Relationships

B. L. Kniep, T. Ressler,* A. Rabis, F. Girgsdies, M. Baenitz, F. Steglich, R. Schlögl ——— 112 – 115

Rational Design of Nanostructured Copper–Zinc Oxide Catalysts for the Steam Reforming of Methanol

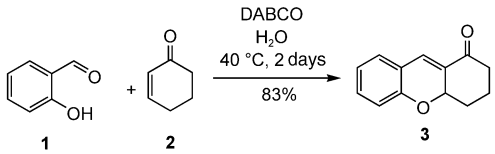


Getting under the surface of aging: The bulk structure of copper nanoparticles can be tailored during the preparation by exploiting known structure–activity relationships. Ageing of freshly precipitated precursors leads to characteristic phase transitions and enables control of microstrain and particle size (see picture) properties which influence catalytic activity.

Privileged Structures

B. Lesch, S. Bräse* ——— 115 – 118

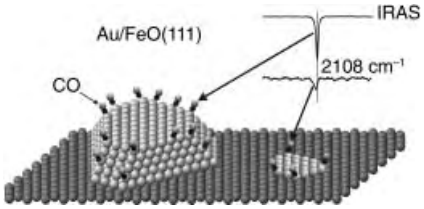
A Short, Atom-Economical Entry to Tetrahydroxanthenones



1 2 3

A reaction that takes to water: The domino Michael addition/aldol condensation of salicylic aldehydes like **1** as the nucleophile and 2-cyclohexen-1-one (**2**) as the Michael acceptor provides 2,3,4,4a-tetrahydroxanthen-1-ones such as **3** in good yields. DABCO = 1,4-diazabicyclo[2.2.2]octane.

© 2004 Wiley-VCH Verlag GmbH & Co. KGaA, Weinheim



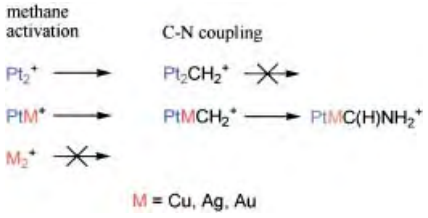
Monolayer gold islands with a thickness of one or a few monolayers on an FeO(111) substrate are found to exhibit identical CO adsorption behavior as large gold particles (see picture). This result suggests that particle thickness does not play a significant role in CO adsorption, and therefore size effects seen for the low-temperature CO oxidation reaction are not related to quantum size effects.

Surface Chemistry

C. Lemire, R. Meyer, Sh. Shaikhutdinov, H.-J. Freund* ——— 118 – 121

Do Quantum Size Effects Control CO Adsorption on Gold Nanoparticles?

And they all do it! Like $PtAu^+$, the lighter dinuclear platinum–coinage-metal clusters $PtCu^+$ and $PtAg^+$ also mediate the C–N coupling of methane and ammonia. As the homonuclear clusters Pt_2^+, Cu_2^+, Ag_2^+, and Au_2^+ are inactive (see scheme), the particular electronic situation of the bimetallic clusters appears to be crucial for the outcome of this intriguing reaction.



Methane Activation

K. Koszinowski, D. Schröder, H. Schwarz* ——— 121 – 124

Coupling of Methane and Ammonia by Dinuclear Bimetallic Platinum–Coinage-Metal Cations PtM^+

Communications labeled with this symbol have been judged by two referees as being "very important papers".

The publication of Communications labeled with this symbol has been accelerated because of their topical or highly competitive nature.

The issues for December 2004 appeared online on the following dates
Issue 45: November 18. · Issue 46: November 25. · Issue 47: December 8. · Issue 48: December 10.

Sources

Product and Company Directory

You can start the entry for your company in "Sources" in any issue of *Angewandte Chemie*.

If you would like more information, please do not hesitate to contact us.

Wiley-VCH Verlag – Advertising Department
Tel.: 0 62 01 - 60 65 65
Fax: 0 62 01 - 60 65 50
E-Mail: MSchulz@wiley-vch.de

Service

Keywords ——— 126

Authors ——— 127

Sources ——— A1

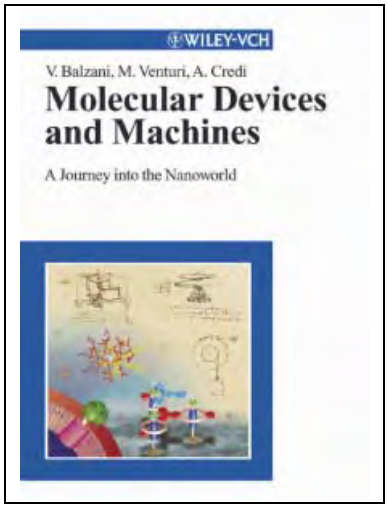
Preview ——— 129

 © 2004 Wiley-VCH Verlag GmbH & Co. KGaA, Weinheim

Apology

In the Communication "$[Ni_6(SCH_2CH_2OH)_{12}]$: A Double Crown [12]Metallacrown-6 Nickel(II) Cluster" by **F.–F. Jian**, **K. Jiao**, **Y. Li**, **P.–S. Zhao**, **L.–D. Lu** (*Angew. Chem. Int. Ed.* **2003**, *42*, 5722) the crystal structure of the main compound has already been reported: "Nickel and Palladium Complexes of 1-Hydroxyethane-2-thiol and Analogues. Part 1. Crystal Structure of Cyclohexakis[bis-(μ-1-hydroxyethane-2-thiolato)-nickel(II)]" R. O. Gould, M. M. Harding, *J. Chem. Soc.* (A) **1970**, 875–881. The authors also missed several important references to related species, these include: "A New Type of Cyclic Transition Metal Complex, $[Ni(SC_2H_5)_2]_6$" P. Woodward, L. F. Dahl, E. W. Abel, B. C. Crosse, *J. Am. Chem. Soc.* **1965**, *87*, 5251–5253; "The Structure of a Toroidal, Neutral, Homoleptic Ni(II) Complex with a Chelate Dithiolate Ligand, $[Ni_6(SCH_2CH_2CH_2S)_6]$" J. Sletten, J. A. Kovacs, *Acta Chem. Scand.* **1994**, *48*, 929–932; "Cyclo-$[Ni(\mu_2\text{-}SPh)_2]_9$ and Cyclo-$[Ni(\mu_2\text{-}SPh)_2]_{11}$: New Oligomeric Types of Toroidal Nickel(II) Thiolates Containing Geometrically Unprecedented 9- and 11-Membered Ring Systems" S. A. Ivanov, M. A. Kozee, W. Alex Merrill, S. Agarwal, L. F. Dahl "*J. Chem. Soc. Dalton Trans.* **2002**, 4105–4115. The authors apologize for these oversights.

Key-Technologies of the Future



ISBN 3-527-30506-8
€ 99,-* / sFr 146,-

*The Euro price is only valid for Germany.

VINCENZO BALZANI, Italy, ALBERTO CREDI, and MARGHERITA VENTURI, all of University of Bologna, Italy

Molecular Devices and Machines
A Journey into the Nanoworld
2003. XVII, 494 pp Hbk

The miniaturization of bulky devices and machines is a process that confronts us on a daily basis. However, nanoscale machines with varied and novel characteristics may also result from the enlargement of extremely small building blocks, namely individual molecules. This bottom-up approach to nanotechnology is already being pursued in information technology, with many other branches about to follow.
Written by Vincenzo Balzani and his team of co-authors, this book provides a comprehensive overview of this fascinating and multifarious topic, offering newcomers and experts alike a wealth of information.

- Most important new technologies for a broad audience
- Unifying, critical, and stimulating overview of red-hot topics

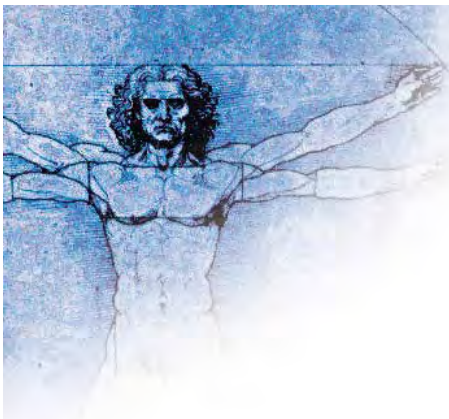
Wiley-VCH Verlag
Fax: +49 (0)6201 606 184
e-Mail: service@wiley-vch.de
www.wiley-vch.de

Register now for the free
WILEY-VCH Newsletter!
www.wiley-vch.de/home/pas

WILEY-VCH

50303032_kn

 © 2004 Wiley-VCH Verlag GmbH & Co. KGaA, Weinheim



New Editorial Board Members

The Editorial Board of *Angewandte Chemie* advises the editors on matters regarding the content and presentation of the journal. Its members represent the broad spectrum of chemistry in universities, research institutes, and industry. A. Kleemann (Asta Medica) and B. Wetzel (Boehringer Ingelheim) have just finished their terms, and four new members have accepted the invitation of the German Chemical Society's Board to take up a four-year term from January 1, 2004.

Hartmut Michel received the Nobel Prize in Chemistry (1988) together with J. Deisenhofer and R. Huber for the determination of the three-dimensional structure of a photosynthetic reaction center.[1] At the Max-Planck-Institut (MPI) für Biophysik in Frankfurt/M. (Germany) he now studies membrane-protein gene expression and the mode of action of cytochrome *c* oxidase, which plays an essential role as the terminal enzyme in aerobic metabolism.



H. Michel

Michel studied biochemistry at the Universität Tübingen (Germany) and in 1977 completed his PhD with D. Oesterhelt in Würzburg (Germany) on proton gradients at the cell membranes of halobacteria. Shortly afterwards he began attempts to crystallize membrane proteins, in which he succeeded in 1979. He moved with Oesterhelt to the MPI für Biochemie (Martinsried, Germany) and in 1981 succeeded in crystallizing a photosynthetic reaction center. In 1987 he became director at the MPI für Biophysik (Frankfurt/M.).

Rudolf K. Thauer studied medicine (Frankfurt/M.) and biochemistry (Tübingen). He completed his PhD (with K. Decker) and his habilitation at the Universität Freiburg (Germany). Following postdoctoral research at the Case Western Reserve University (Cleveland, OH, USA) he became professor at the Universität Bochum (Germany) in 1973. In 1976 he moved to the Universität Marburg (Germany) and has been director of the MPI für terrestrische Mikrobiologie in Marburg since 1991.



R. Thauer

His research is focused on the biochemistry of methanogens and the structures and reaction mechanisms involved in enzymatic methane production. His contribution on the stereospecificity of hydrogenases was the cover-picture article in *ChemBioChem* 7–8/2001.[2] Thauer is a member of the Editorial Advisory Board of *ChemBioChem*.

Hans Ulrich Stilz completed his chemistry studies with D. Seebach at the Universität Freiburg and the ETH Zürich (Switzerland) with a dissertation on hyperconjugation in activated ketones.[3a] He completed his PhD in 1990 with D. Oesterhelt at the MPI für Biochemie (Martinsried) on structure–property relationships of photosynthetic reaction centers.[3b] During this period he spent six months with H. Michel at the MPI für Biophysik (Frankfurt/M.). After his PhD studies he spent two years at the California Institute of Technology (Pasadena, USA) with P. Dervan, where he carried out research into the sequence-specific recognition of C–G base pairs and the formation of triple helices.



H. U. Stilz

Stilz started at Hoechst AG in 1992 and has contributed to the development of several drug candidates. Since 1999 he has been head of chemistry research at Aventis in Germany. He is involved with international chemistry management at Aventis and has been head of the GDCh medicinal chemistry section since 2003.

Rainer Metternich has led the European Research Center of Schering AG in Berlin since 2001. Between 1986 and 1997 he moved up the ranks in pharmaceutical research at Sandoz AG in Basel from laboratory to division leader. From 1997 to 2000 he was senior chemistry expert and member of the global research-management committee at Novartis.



R. Metternich

Metternich studied chemical engineering in Jülich (Germany), then chemistry at the Universität Marburg, where he also completed his PhD in 1985 with R. W. Hoffmann on topics including the configurational stability of chiral organometallic reagents.[4] During a postdoctoral period with D. A. Evans at Harvard University in Cambridge, MA (USA) he worked on stereoselective synthesis and the total synthesis of natural products. In 2001 he was made Honorary Professor of Organic Chemistry at the Technische Universität Berlin (Germany). Metternich has also been a member of the GDCh Board since 2004.

[1] J. Deisenhofer, H. Michel, *Angew. Chem.* **1989**, *101*, 872; *Angew. Chem. Int. Ed. Engl.* **1989**, *28*, 829.

[2] S. Bartoschek, G. Buurman, R. K. Thauer, B. H. Geierstanger, J. P. Weyrauch, C. Griesinger, M. Nilges, M. C. Hutter, V. Helms, *ChemBioChem* **2001**, *2*, 530.

[3] a) T. Laube, H. U. Stilz, *J. Am. Chem. Soc.* **1987**, *109*, 5876; b) W. Holzapfel, U. Finkele, W. Kaiser, D. Oesterhelt, H. Scheer, H. U. Stilz, W. Zinth, *Proc. Natl. Acad. Sci. USA* **1990**, *87*, 5168

[4] R. W. Hoffmann, J. Lanz, R. Metternich, G. Tarara, D. Hoppe, *Angew. Chem.* **1987**, *99*, 1196; *Angew. Chem. Int. Ed. Engl.* **1987**, *26*, 1145.

 © 2004 Wiley-VCH Verlag GmbH & Co. KGaA, Weinheim

Mass Spectrometry

New Mass Spectrometric Methods for the Quantification of Protein–Ligand Binding in Solution**

*Kathrin Breuker**

Keywords:
analytical chemistry · binding assays · mass spectrometry · protein–ligand binding

Mass spectrometry (MS) has recently been reported as an alternative technique for the quantitative characterization of protein–ligand interactions in solution, that is, the determination of equilibrium constants for protein–ligand association (K_a) or dissociation ($K_d = 1/K_a$). Three such approaches are considered here.[1–3,4] Common to all approaches is that products from protein–ligand binding assays are analyzed by mass spectrometry, thereby taking advantage of inherent MS capabilities such as speed and sensitivity. However, the different strategies have individual advantages, limitations, and potentials. Two of the methods, SUPREX (stability of unpurified proteins from rates of H/D exchange)[1] and PLIMSTEX (protein–ligand interactions in solution by MS, titration, and H/D exchange),[2] involve H/D exchange of amide protons of the protein backbone in solution.[5] The third method, termed by the authors "competitive MS binding assay",[3] is similar to competitive radioligand binding assays, but uses MS for quantification.

SUPREX utilizes the MALDI (matrix-assisted laser desorption/ionisation) technique,[6] a method with relatively high tolerance for buffers, salts, and contaminations by small molecules,[7] so that further sample clean-up was either not necessary or, in critical cases, limited to the use of chromatographic pipette tips (ZipTip).[1b] PLIMSTEX and the competitive MS binding assay use ESI (electrospray ionization),[8] for which samples were cleaned-up by on-line reversed-phase chromatography. Thus all three methods can handle buffers, salts, and other molecules typically present in biological assays that could otherwise interfere with the MS analysis.

SUPREX[1] effectively measures the stability of proteins against chemical denaturation, both in the absence and presence of one or more ligands. This is achieved by monitoring the change in H/D exchange induced by the addition of urea or guanidinium chloride; the exposure of initially buried amide protons of the backbone upon denaturation makes them accessible for H/D exchange. The increase in protein mass resulting from H/D exchange was plotted against the concentration of the denaturant. The SUPREX curve obtained was fitted with sigmoidal functions to extract the $C^{1/2}_{SUPREX}$ values (the concentration of the denaturant at the midpoint of the transition, Figure 1a). The $C^{1/2}_{SUPREX}$ values for protein–ligand complexes were higher than the corresponding values for the protein by itself, which is indicative of binding-induced stabilization. The free energies of folding ΔG_f were determined from the $C^{1/2}_{SUPREX}$ values at various exchange times (between a few minutes and several hours); the difference in the free energies of protein folding in the absence and presence of ligand(s) was then used to calculate the K_d values. The data treatment assumes that protein H/D exchange proceeds under so-called EX2 conditions (unfolding rate $\ll$ refolding rate $\gg$ H/D exchange rate),[5a] and that unfolding is a two-state process (that is, there are no folding intermediates). Within these limitations, SUPREX can be used for the determination of the free energies ΔG_f of both protein and protein complex folding, as well as the dissociation constants of the protein complex. Unknown complex stoichiometries can potentially be determined in SUPREX experiments with various ligand concentrations.[1] SUPREX binding constants generally agree with values obtained by other methods within a factor of 3, with some higher values of up to about 16 obtained in 4 out of 13 cases (Table 1).

PLIMSTEX[2] relies on a change in H/D exchange upon equilibrium titration of the protein with the ligand, which is monitored by position shifts in the mass spectrum (change in the m/z values of the protein). A PLIMSTEX curve is then generated by plotting the deuterium uptake versus total ligand concentration (normalized to the fixed total protein concentration, Figure 1b). Typically, these uptake values decrease with increasing ligand concentration, which reflects an increased protection of the backbone amide protons on formation of the protein–ligand complex. The data was fit by the authors using their newly developed "1:n protein:ligand sequential binding model",[2b] which assumes stepwise binding of up to n identical ligands to a protein and that H/D exchange of individual amide protons are independent from each other. The relative concentrations of the species involved and the associated deuterium uptake were computed, and equilibrium binding constants obtained by iterative-

[*] Dr. K. Breuker
Institute of Organic Chemistry
Innsbruck University
Innrain 52a, 6020 Innsbruck (Austria)
Fax: (+43) 512-507-2892
E-mail: kbreuker@gmx.net

[**] The author acknowledges the Austrian Science Foundation for generous funding (FWF grant P15767).

 © 2004 Wiley-VCH Verlag GmbH & Co. KGaA, Weinheim DOI: 10.1002/anie.200301695

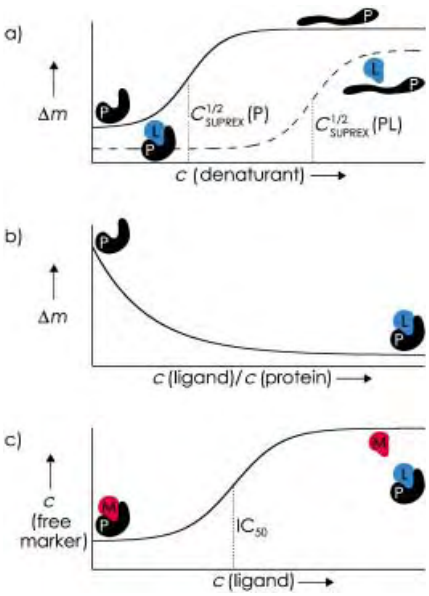


Figure 1. Schematic illustration of SUPREX, PLIMSTEX, and the competitive MS binding assay. a) For the SUPREX analysis, the increase in mass (Δm) resulting from amide H/D exchange of the protein (P, solid line) and protein–ligand complex (PL, dashed line) after a specific exchange time is plotted versus the concentration of the denaturant. The transition from lower to higher Δm values reflects the transition from folded to unfolded protein or protein–ligand complex in solution, as more amide protons become accessible for H/D exchange with increasing denaturant concentration. b) For the PLIMSTEX analysis, the increase in mass (Δm) resulting from amide H/D exchange of the protein (P) is plotted versus total ligand (L) concentration (normalized to the fixed total protein concentration). Here, H/D exchange was continued for up to several hours until it reached a near steady state. Typically, the Δm values decrease with increasing ligand concentration as a result of an increased protection of the backbone amide protons on forming the protein–ligand complex. c) In the competitive MS binding assay, the competitive binding of ligand (L) to the protein (P) releases marker (M) from the protein–marker complex. The free marker is separated from the assay by centrifugation and quantified by MS using a calibration curve from another experiment performed without protein.

ly minimizing the deviation between the experimental and calculated data. Unlike SUPREX, PLIMSTEX can also monitor intermediate binding states.[2a] PLIMSTEX binding constants agreed within a factor of 3.5 with values obtained from other methods, as long as the total protein concentration did not exceed about $10\,K_a$ ($50\,K_a$ gave a factor of 6.1). PLIMSTEX does not yield reliable K_a values for very high protein concentrations (ca. $5000\,K_a$), but such curves can nevertheless be used for the determination of the complex stoichiometry.

In the competitive MS binding assay[3] a marker molecule which addresses the desired binding site of the target protein with high affinity and selectivity is first selected. In contrast to conventional binding assays, the mass-spectrometric approach generally allows for the use of native (that is, unmodified, nonlabeled) markers. Next, the protein–marker complex is exposed to varying amounts of ligand whose binding to the protein is under study. The competitive binding of the ligand to the protein releases the marker, which is separated from the assay by centrifugation and quantified by MS using a calibration curve determined from another experiment without protein. To obtain detectable changes in the concentration of the free marker during titration with ligand, the competitive MS binding assay was performed under conditions where "marker depletion" was substantial, that is, the concentration of released marker was substantial relative to the concentration of the free marker in the absence of competing ligands.[9] Equilibrium concentrations of the unbound marker were plotted versus concentrations of the ligand (Figure 1c), and the data fitted with a sigmoidal function to extract IC_{50} values (the ligand concentration that inhibits 50% of specific protein–marker binding). Finally, the K_d values were calculated from the IC_{50} values according to Goldstein and Barrett;[9] this data treatment assumes a simple competitive equilibrium and that the concentration of free ligand is not significantly affected by competitive binding. Binding constants obtained with the competitive MS binding assay agree within a factor of 2 with values obtained from radioligand binding assays.

In summary, the K_d values from all the above methods agree reasonably well with reference values determined by other methods.[1–3] The K_d values obtained from the SUPREX experiments were the least accurate, with a mean error of 36% (Table 1), but good agreement with reference values was nevertheless obtained in most cases. The competitive MS binding assay gave, on average, the best agreement with reference values. However, the systems studied by this method were very similar (1:1 binding of different inhibitors to the same protein), while SUPREX and PLIMSTEX were also applied to systems of more complex stoichiometry and a larger variety of binding partners (Table 1). A major advantage of SUPREX and PLIMSTEX is that these methods *detect proteins* after H/D exchange. The analysis of partially deuterated proteins by MS/MS, or protein digests followed by MS, potentially allows for the characterization of structural changes induced by the binding of ligand(s) and identification of ligand binding sites.[5] On the other hand, a major advantage of the competitive MS binding assay is that it *does not rely on protein detection* by mass spectrometry: the strategy can use membrane-bound and higher mass proteins not amenable to MS analysis because only the marker and not the protein is subjected to mass spectrometry. A major limitation of the competitive MS binding assay is the need for a marker that binds to the target protein with high affinity and selectivity; this restricts the method to ligand variants of some well-characterized systems. Moreover, quantification of the marker by mass spectrometry requires linear MS response within the concentration range studied, and the marker separation procedure prior to MS may perturb the equilibrium. A major limitation of SUPREX and PLIMSTEX is the upper mass limit for which changes in protein mass arising from H/D exchange can be resolved by MS. Although MS can detect protein complexes with mass values exceeding 2 MDa,[10] most mass spectrometers do not generally provide sufficient mass-resolving power and accuracy for the analysis of H/D exchange in high-molecular-weight proteins; protein studied in the systems by SUPREX and PLIMSTEX had masses below 20 kDa. However, the use of ultrahigh resolution Fourier transform mass spectrometers (FTMS) that are capable of resolving isotopic peaks for proteins as large as 112 kDa considerably increases this upper mass limit.[11]

 © 2004 Wiley-VCH Verlag GmbH & Co. KGaA, Weinheim

Table 1: Protein–ligand systems studied by SUPREX, PLIMSTEX, and the competitive MS binding assay.[a]

Method	Complexes	System	K_d (exp) [nm]	Error [%]	Factor[b]
SUPREX[c]	protein–protein, protein–peptide, protein–amino acid–DNA duplex	TrpR + W + DNA, 1:2:1	0.16	±56.3	1.6
		S protein + S peptide (1:1)	2.4	±25	2.2
		S protein + S peptide (1:1)	34	±35.3	5.4
		S protein + Sp8 (1:1)	400	±17.5	9.8
		B1 domain + Fc frag (1:1)	520	±26.9	2.2
		FIV Pr + TL3 (1:1)	520	±63.5	12.7
		ablSH3 + prp4 (1:1)	5.2×10^3	±46.2	1.1
		S protein + Sp7 (1:1)	9.7×10^3	±30.9	1.4
		ablSH3 + prp3 (1:1)	25×10^3	±32	1.0
		ablSH3 + prp2 (1:1)	28×10^3	±28.6	1.0
		ablSH3 + prp1, 1:1	57×10^3	±43.9	2.1
		TrpR + W (1:2)	130×10^3	±15.4	3.1
		S protein + Sp6 (1:1)	250×10^3	±44	15.6
				av: ±35.8	av: 4.6
PLIMSTEX[d]	protein–small molecule, protein–metal ions, protein–metal ions–peptide	Apo-CaM + Ca^{2+}, K_3K_4	0.2	±8	2.5
		holo-CaM + melittin (1:1)	18.4	±0.6	6.1
		I-FABP + potassium oleate (1:1)	385	±7.7	1.1
		apo-CaM + Ca^{2+} (K_4)	11.1×10^3	±11.1	3.5
		apo-CaM + Ca^{2+} (K_3)	18.5×10^3	±9.3	1.4
		ras-GDP + Mg^{2+} (1:1)	25×10^3	±7.5	1.7
				av: ±7.4	av: 2.7
competitive MS binding assay[e]	protein–inhibitor	dD_1r + SKF83566, 1:1	1.9	±15.8	1.4
		dD_1r + (+)-butaclamol (1:1)	11	±9.1	2.0
		dD_1r + haloperidol (1:1)	220	±27.3	2.0
		dD_1r + trifluoperazine (1:1)	460	±8.7	2.1
		dD_1r + chlorpromazine (1:1)	620	±1.6	2.0
		dD_1r + pimozide (1:1)	4.7×10^3	±4.3	1.9
				av: ±11.1	av: 1.9

[a] TrpR: Trp repressor, W: L-tryptophan, DNA: 25-base pair DNA duplex containing TrpR cognate DNA sequence. S protein: S protein component of bovine RNase S (residues 21–124 of RNase A), S peptide: S peptide component of bovine RNase S (residues 1–20 of RNase A), Sp6–Sp8: truncated S peptide mutants, B1 domain: B1 domain of protein G, Fc frag: Fc portion of mammalian IgG antibody, FIVPr: feline immunodeficiency virus protease, TL3: small-molecule inhibitor, ablSH3: Src homology domain 3 of Abelson tyrosine kinase, prp1–prp4: variants of proline-rich decameric peptides, CaM: porcine calmodulin, I-FABP: rat intestinal fatty acid binding protein, ras-GDP: GDP-bound human $p21^{H-ras}$ protein, dD_1r: dopamine D_1 receptor from porcine striatal membrane. [b] Factor within which the measured K_d value agrees with that from other methods. [c] From Ref. [1a,b]. [d] From Ref. [2]. [e] From Ref. [3].

All three methods rely on sophisticated data analysis, and the individual models for fitting the data should be critically evaluated with respect to experimental conditions and the complexity of the system studied. For example, SUPREX assumes EX2 exchange kinetics; however, EX1 kinetics may apply instead for some systems, which would be apparent from bimodal H/D exchange profiles.[5a] The protein and ligand concentrations in the assay are highly critical for PLIMSTEX and the competitive MS binding assay.[2a,9] However, an appropriate data analysis and careful adjustment of experimental parameters are required with any binding study, not just those based on mass spectrometry. The high throughput and potential for automation together with low sample consumption make mass spectrometry an indispensable tool in proteomics research[12] and an attractive choice for quantitative protein–ligand binding studies.

[1] a) K. D. Powell, M. C. Fitzgerald, *Biochemistry* **2003**, *42*, 4962–4970; b) K. D. Powell, S. Ghaemmaghami, M. Z. Wang, L. Ma, T. G. Oas, M. C. Fitzgerald, *J. Am. Chem. Soc.* **2002**, *124*, 10256–10257.

[2] a) M. M. Zhu, D. L. Rempel, Z. Du, M. L. Gross, *J. Am. Chem. Soc.* **2003**, *125*, 5252–5253; b) a detailed description of the model can be found in: M. M. Zhu, D. L. Rempel, M. L. Gross, *J. Am. Chem. Soc.*, in press.

[3] G. Höfner, K. T. Wanner, *Angew. Chem.* **2003**, *115*, 5393–5395; *Angew. Chem. Int. Ed.* **2003**, *42*, 5235–5237.

[4] Not discussed here are MS-based methods for the determination of equilibrium binding constants that rely on the detection of intact gaseous protein–ligand complexes; see, for example, S. W. Bligh, T. Haley, P. N. Lowe, *J. Mol. Recognit.* **2003**, *16*, 139–147.

[5] a) J. R. Engen, D. L. Smith, *Anal. Chem.* **2001**, *73*, 256A–265A; b) L. Wang, H. Pan, D. L. Smith, *Mol. Cell. Proteomics* **2002**, *1*, 132–138; c) J. J. Englander, C. Del Mar, W. Li, S. W. Englander, J. S. Kim, D. D. Stranz, Y. Hamuro, V. L. Woods, *Proc. Natl. Acad. Sci. USA* **2003**, *100*, 7057–7062; d) J. G. Mandell, A. M. Falick, E. A. Komives, *Anal. Chem.* **1998**, *70*, 3987–3995.

[6] a) M. Karas, D. Bachmann, U. Bahr, F. Hillenkamp, *Int. J. Mass Spectrom. Ion Processes* **1987**, *78*, 53–68; b) M. Karas, F. Hillenkamp, *Anal. Chem.* **1988**, *60*, 2299–2301; c) M. Karas, U. Bahr, A. Ingendoh, F. Hillenkamp, *Angew. Chem.* **1989**, *101*, 805–806; *Angew. Chem. Int. Ed. Engl.* **1989**, *28*, 760–761.

 © 2004 Wiley-VCH Verlag GmbH & Co. KGaA, Weinheim

[7] D. N. Nguyen, G. W. Becker, R. M. Riggin, *J. Chromatogr. A* **1995**, *705*, 21 – 45.
[8] J. B. Fenn, M. Mann, C. K. Meng, S. F. Wong, C. M. Whitehouse, *Science* **1989**, *246*, 64 – 71.
[9] A. Goldstein, R. W. Barrett, *Mol. Pharmacol.* **1987**, *31*, 603 – 609; erratum: A. Goldstein, R. W. Barrett, *Mol. Pharmacol.* **1988**, *33*, 720.
[10] a) F. Sobott, C. V. Robinson, *Curr. Opin. Struct. Biol.* **2002**, *12*, 729 – 734; b) S. Sanglier, E. Leize, A. V. Dorsselaer, F. Zal, *J. Am. Soc. Mass Spectrom.* **2003**, *14*, 419 – 429.
[11] a) A. G. Marshall, C. L. Hendrickson, S. D. H. Shi, *Anal. Chem.* **2002**, *74*, 252A – 259A; b) A. G. Marshall, C. L. Hendrickson, G. S. Jackson, *Mass Spectrom. Rev.* **1998**, *17*, 1 – 35; c) N. L. Kelleher, M. W. Senko, M. M. Siegel, F. W. McLafferty, *J. Am. Soc. Mass Spectrom.* **1997**, *8*, 380 – 383.
[12] R. Aebersold, M. Mann, *Nature* **2003**, *422*, 198 – 207.

Particles From Every Angle

2003. Volume 20.
6 issues per year.
ISSN Print 0934-0866
ISSN Online 1521-4117

Have a glance at one of the most vital sources in the field.

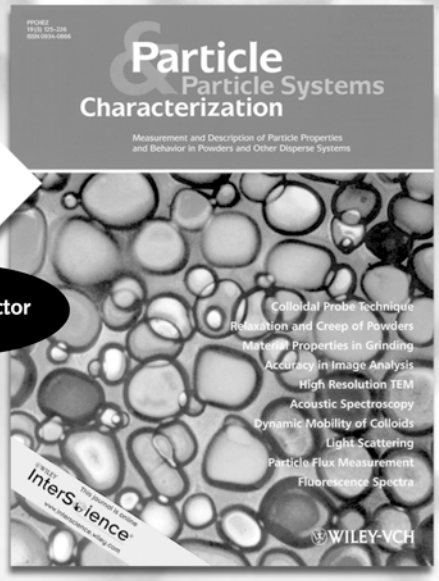
New Impact Factor 0.633

WILEY InterScience DISCOVER SOMETHING GREAT

Download a sample copy at:
www.interscience.wiley.com

More information available at:
www.wiley-vch.de/home/particle

3803011_bu



Highlights in 2003

Congress issues:

- **"Application of Laser Techniques to Fluid Mechanics"** Lisbon 2002, selected articles covering special fields of the characterization of disperse systems
- **"World Congress of Particle Technology"** Sydney 2002, selected articles covering particle characterization

Special issue:

- **"Characterization of Pore Size Distributions"** by guest editors M. Thommes and A. Neimark

New in 2003:

- Book Reviews and Conference Calendar

John Wiley & Sons, Inc. • Fax: 1-201-748-5915
e-Mail: subinfo@wiley.com • www.wiley.com

John Wiley & Sons, Ltd. • Fax: +44 (0) 1243-843232
e-Mail: cs-journals@wiley.co.uk • www.wileyeurope.com

Wiley-VCH • Fax: (49) 6201 606-184
e-Mail: service@wiley-vch.de • www.wiley-vch.de

WILEY

WILEY-VCH

 © 2004 Wiley-VCH Verlag GmbH & Co. KGaA, Weinheim

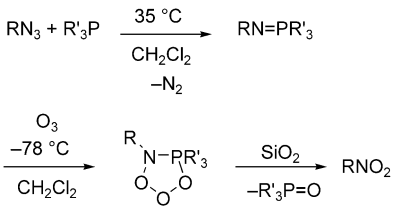
Oxidation

Direct Oxidation of Azides to Nitro Compounds

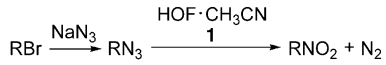
G. K. Surya Prakash and Markus Etzkorn*

Keywords:
azides · fluorine · nitro compounds · oxidation · synthetic methods

Nitro compounds[1] are one of the fundamental classes of substances in organic chemistry: Historically, they have been important as explosives and precursors for azo dyes. Today, they play a key role as synthetic intermediates or targets in the preparation of dyes, plastics, perfumes, and pharmaceuticals.[2] Besides their tremendous value for synthetic chemists, nitro compounds have also played an important role in the development of mechanistic concepts.[3] They can be obtained by direct nitration of aromatic and aliphatic hydrocarbons under certain conditions, activated hydrocarbons via anionic intermediates, alkenes, alkyl halides, and ketones (α-nitration).[4] For these transformations, a broad variety of nitrating reagents (electrophilic, radical, and nucleophilic) have been investigated. The oxidative approach[4] to nitro compounds is well-established for amines and oximes, whereas the oxidative multistep sequence developed by Corey and co-workers with primary or secondary azides produces the corresponding nitro products in only moderate yields (Scheme 1).[5]



Scheme 1. Synthesis of nitro compounds from azides by Corey and co-workers: The ozone adduct decomposes to the product during the chromatographic workup.



Scheme 2. Direct oxidation of azides to nitro compounds.

A new method to obtain nitro compounds directly from aliphatic and selected aromatic azides in excellent yields was recently introduced by Rozen and Carmeli (Scheme 2).[6] The convenient oxidation protocol, which makes use of the well-established HOF·CH_3CN complex **1**, is a useful tool for the straightforward and expedient synthesis of nitro compounds.

Particularly Rozen and his group have introduced complex **1** as potent oxygen-transfer reagent for a variety of reactions, some of which are occasionally difficult for certain substrates: They applied this reagent in the synthesis of epoxides from various olefins,[7] ketones from methyl ethers,[8] esters by the Baeyer–Villiger reaction,[9] sulfones from sulfides,[10] nitro compounds from amines[11] and amino acids,[12] *N*-oxides from tertiary amines,[13] and other conversions.[14] Another interesting application is the use of labeled $H^{18}OF{\cdot}CH_3CN$ as the reagent of choice for the synthesis of $H^{16}O^{18}OH$ and $^{16}O^{18}O$.[15]

Hypofluorous acid (HOF) itself has quite an interesting history and exhibits complex chemical properties.[16] Despite the first experimental claims in 1932,[17] the official year of its birth is 1968, when Noble and Pimentel unequivocally characterized the compound in a solid nitrogen matrix by IR spectroscopy.[18] Neat HOF proved to be a hazardous material.[19] Its synthetic potential thus slumbered for several years before Rozen and his group ultimately introduced a convenient and practical method to obtain "tamed" HOF by passing elemental fluorine through wet acetonitrile.[20] Both water and acetonitrile are necessary to obtain the strong oxidizing and hydroxylating complex **1**. The exact structure of the active reagent has not yet been determined; nevertheless a 1:1 hydrogen-bonded complex that is in equilibrium with its components is a reasonable description.[16] The "tame" but still powerful HOF·CH_3CN complex **1** in aqueous acetonitrile has been investigated intensively, is quite easy to handle, and is of great synthetic value and potential.

The new application of complex **1** for the direct oxidation of azides to nitro compounds in CH_2Cl_2 at 0 °C is quite remarkable. The reactions of aliphatic azides proceed smoothly within a few seconds in excellent yields (80–98 %). Side reactions are prevented by the short reaction times, which also prevent any slow substitution of the adjacent hydrogen atoms. This advantageous difference in reactivity also allows the conversion of benzyl azide without any concomitant reaction of the aromatic ring and tolerates, for example, an acetate group in the preparation of 5-nitropentyl acetate. Furthermore, it is noteworthy that no Nef reaction was observed with any secondary or primary substrates! Insight into the mechanism was obtained after studies with labeled $H^{18}OF$ and with differently *para*-substituted aromatic azides. The ^{18}O label was found on both oxygen atoms of the nitro group, thus establishing the intermediacy of substituted nitrosobenzenes. The reaction of the aromatic azides is rather sluggish (10 min–1 h) and does not oc-

[*] Prof. Dr. G. K. S. Prakash, Dr. M. Etzkorn
Loker Hydrocarbon Research Institute and Department of Chemistry
University of Southern California
837 Bloom Walk
Los Angeles, CA 90034-1661 (USA)
Fax: (+1) 213-740-6270
E-mail: gprakash@usc.edu

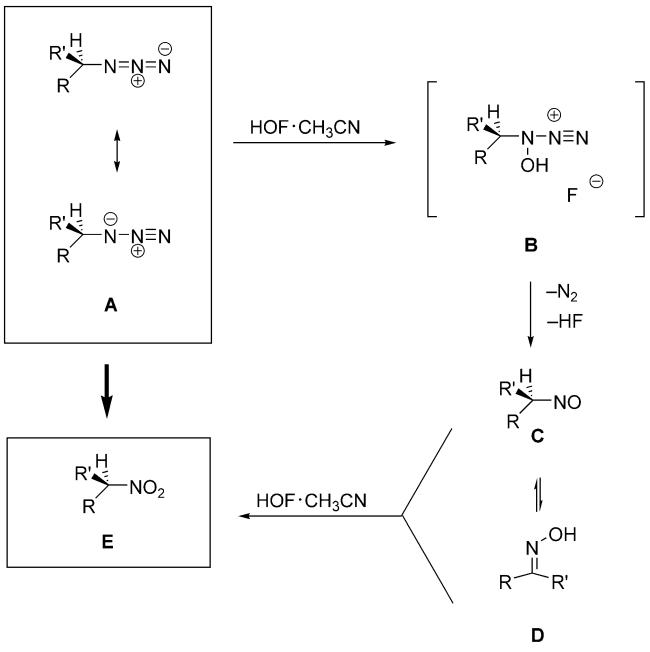
© 2004 Wiley-VCH Verlag GmbH & Co. KGaA, Weinheim
DOI: 10.1002/anie.200301710

cur with electron-poor substrates (e.g. *p*-$NO_2(C_6H_4)N_3$). In a control experiment, nitrosobenzene reacted instantaneously to give the nitro derivative. Based on these observations the following mechanism was proposed (Scheme 3):

HOF·CH_3CN (**1**) reacts in a rate-limiting step with the electron-rich nitrogen atom of the azide **A** to form the nitroso compound **C** after elimination of N_2 and HF from the ion pair **B**, whose exact nature was not specified further. A second molecule of HOF finally oxidizes the nitroso intermediate **C** in a fast step to the target nitro compound **E**. Particularly for aliphatic azides that bear a hydrogen atom at the α position, one might consider an alternative pathway: As nitroso compounds can easily rearrange to oximes **D** (nitroso–isonitroso (nitroso–oxime) tautomerism) under a variety of conditions,[21] the latter could actually be oxidized to the target nitro compound **E**. Such oxidations of oximes are well-documented in the literature. For example, the reaction of aldoximes with the urea·H_2O_2 complex and trifluoroacetic anhydride in acetonitrile at 0 °C yield their corresponding nitro compounds, whereas ketoximes were further transformed into ketones, thus demonstrating the susceptibility of secondary nitro compounds to the Nef reaction.[22] Olah, Prakash, and co-workers improved this latter oxidation and obtained nitro compounds from aldoximes and ketoximes in moderate to good yields in the presence of sodium perborate tetrahydrate/acetic acid at 55–60 °C.[23]

In summary, the oxidation of azides with HOF·CH_3CN (**1**) by Rozen and Carmeli is the first direct conversion of azides into nitro compounds in excellent yields. This new method for the preparation of nitro compounds could eventually develop into a standard procedure. Considering the commercial availability of premixed fluorine/nitrogen mixtures (e.g. Matheson Tri-Gas) even "non-fluorine" chemists should be encouraged to apply the synthetically valuable complex **1** as a convenient reagent. The method is superior to Corey's oxidative multistep sequence.[5]

Furthermore, azides are easily prepared, and, despite their negative aura as notoriously dangerous and friction-sensitive compounds, many groups including ours have worked with them safely.[24] Sharpless and co-workers recently demonstrated the synthetic potential of azides on a multimolar scale (click chemistry), for example, in combinatorial chemistry, without encountering any hazards.[25] Time will tell, whether Rozen's new azide oxidation method will "click" in a standard laboratory setting.



Scheme 3. Proposed mechanism for the oxidation of azides with HOF·CH_3CN.

[1] a) *Houben-Weyl: Methoden der Organischen Chemie*, *Vol. 10/1* (Ed.: E. Müller), Thieme, Stuttgart, **1971**; *Houben-Weyl: Methoden der Organischen Chemie*, *Vol. E16D/1* (Ed.: E. Müller), Thieme, Stuttgart, **1992**; b) *The Chemistry of the Nitro and Nitroso Group* (Ed.: H. Feuer), Wiley Interscience, New York, **1969**, Part 1, **1970** Part 2, and **1982** Supplement F.

[2] a) N. Ono, *The Nitro Group in Organic Synthesis*, Wiley-VCH, New York, **2001**; b) H. Feuer, A. T. Nielson, *Nitro Compounds: Recent Advances in Synthesis and Chemistry*, VCH, New York, **1990**; c) K. B. G. Torssell, *Nitrile Oxides, Nitrones, and Nitronates in Organic Synthesis: Novel Strategies in Synthesis*, VCH, New York, **1988**.

[3] a) G. A. Olah, R. Malhotra, S. C. Narang, *Nitration: Methods and Mechanisms*, VCH, New York, **1989**; b) K. Schofield, *Aromatic Nitrations*, Cambridge University Press, Cambridge, **1980**.

[4] For individual conditions and reagents, see references [1–3] and references therein.

[5] E. J. Corey, B. Samuelsson, F. A. Luzzio, *J. Am. Chem. Soc.* **1984**, *106*, 3682–3683.

[6] S. Rozen, M. Carmeli, *J. Am. Chem. Soc.* **2003**, *125*, 8118–8119.

[7] a) S. Dayan, I. Ben-David, S. Rozen, *J. Org. Chem.* **2000**, *65*, 8816–8818; b) S. Rozen, Y. Bareket, S. Dayan, *Tetrahedron Lett.* **1996**, *37*, 531–534.

[8] S. Rozen, S. Dayan, Y. Bareket, *J. Org. Chem.* **1995**, *60*, 8267–8269.

[9] S. Rozen, Y. Bareket, M. Kol, *Tetrahedron* **1993**, *49*, 8169–8178.

[10] a) S. Rozen, Y. Bareket, *J. Org. Chem.* **1997**, *62*, 1457–1462; b) A. Toyota, Y. Ono, J. Chiba, T. Sugihara, C. Kaneko, *Chem. Pharm. Bull.* **1996**, *44*, 703–708.

[11] a) S. M. Dirk, E. T. Mickelson, J. C. Henderson, J. M. Tour, *Org. Lett.* **2000**, *2*, 3405–3406; b) S. Rozen, M. Kol, *J. Org. Chem.* **1992**, *57*, 7342–7344; c) M. Kol, S. Rozen, *J. Chem. Soc. Chem. Commun.* **1991**, 567–568.

[12] S. Rozen, A. Bar-Haim, E. Mishami, *J. Org. Chem.* **1994**, *59*, 1208–1209.

[13] a) S. Dayan, M. Kol, S. Rozen, *Synthesis* **1999**, 1427–1430; b) D. E. Chavez, M. A. Hiskey, *J. Energ. Mater.* **1999**, *17*, 357–377.

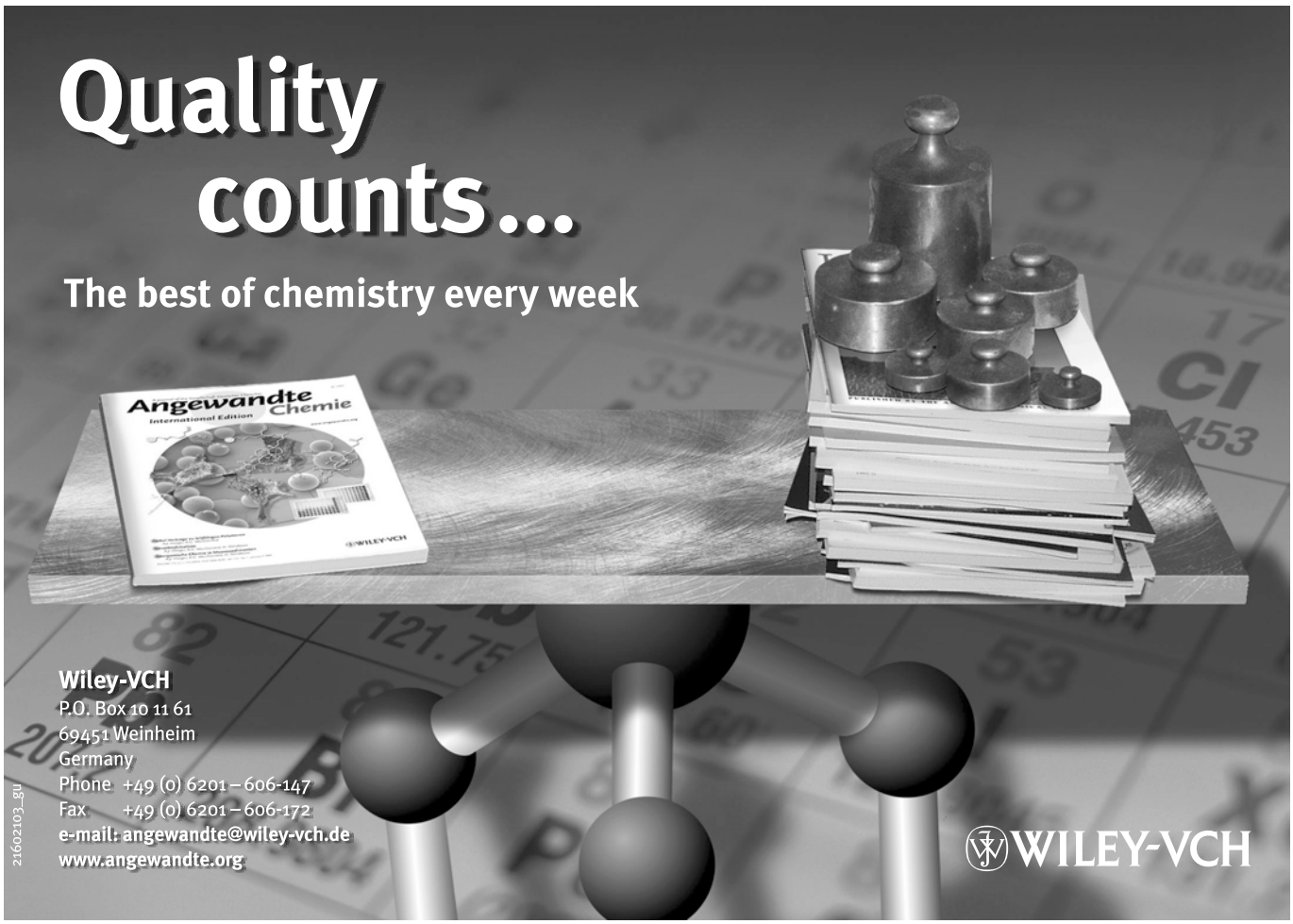
[14] a) S. Rozen, *Acc. Chem. Res.* **1996**, *29*, 243–248; b) S. Rozen, *Pure Appl. Chem.* **1999**, *71*, 481–487.

[15] E. H. Appelman, R. C. Thomson, A. G. Engelkemeir, *Inorg. Chem.* **1979**, *18*, 909–911.

[16] a) E. H. Appelman, *Acc. Chem. Res.* **1973**, *6*, 113–117; b) E. H. Appelman,

 © 2004 Wiley-VCH Verlag GmbH & Co. KGaA, Weinheim

O. Dunkelberg, M. Kol, *J. Fluorine Chem.* **1992**, *56*, 199 – 213.
[17] L. M. Dennis, E. G. Rochow, *J. Am. Chem. Soc.* **1932**, *54*, 832 – 833; b) L. M. Dennis, E. G. Rochow, *J. Am. Chem. Soc.* **1933**, *55*, 2431 – 2434.
[18] P. N. Noble, G. C. Pimentel, *Spectrochim. Acta Part. A* **1968**, *24*, 797 – 806.
[19] R. C. Thomson, E. H. Appelman, J. C. Sullivan, *Inorg. Chem.* **1977**, *16*, 2921 – 2926.
[20] S. Rozen, M. Brand, *Angew. Chem.* **1986**, *98*, 565; *Angew. Chem. Int. Ed. Engl.* **1986**, *25*, 554 – 555.
[21] M. B. Smith, J. March, *March's Advanced Organic Chemistry*, 5th ed., Wiley, New York, **2001**, p. 76.
[22] R. Ballini, E. Marcatoni, M. Petrini, *Tetrahedron Lett.* **1992**, *33*, 4835 – 4838.
[23] G. A. Olah, P. Ramaiah, C.-S. Lee, G. K. S. Prakash, *Synlett* **1992**, 337 – 339.
[24] a) *Houben-Weyl: Methoden der Organischen Chemie*, *Vol. 10/3* (Ed.: E. Müller), Thieme, Stuttgart, **1965**, *Houben-Weyl: Methoden der Organischen Chemie*, *Vol. E16A/2* (Ed.: E. Müller), Thieme, Stuttgart, **1990**; b) *The Chemistry of the Azide Group* (Ed.: S. Patai), Wiley Interscience, New York, **1971** and Supplement D, Parts 1,2, **1983**; c) *Azides and Nitrenes* (Ed.: E. F. V. Scriven), Academic Press, Orlando, Florida, **1984**; d) *The Chemistry of Halides, Pseudo-Halides, and Azides* (Eds.: S. Patai, Z. Rapaport), Wiley Interscience, New York, **1995**, Parts 1 and 2; e) G. K. S. Prakash, J. J. Struckhoff, K. Weber, A. Schreiber, B. Bau, G. A. Olah, *J. Org. Chem.* **1997**, *62*, 1872 – 1879.
[25] V. V. Rostovtsev, L. G. Green, V. V. Fokin, K. B. Sharpless, *Angew. Chem.* **2002**, *114*, 2708 – 2711; *Angew. Chem. Int. Ed.* **2002**, *41*, 2596 – 2599.



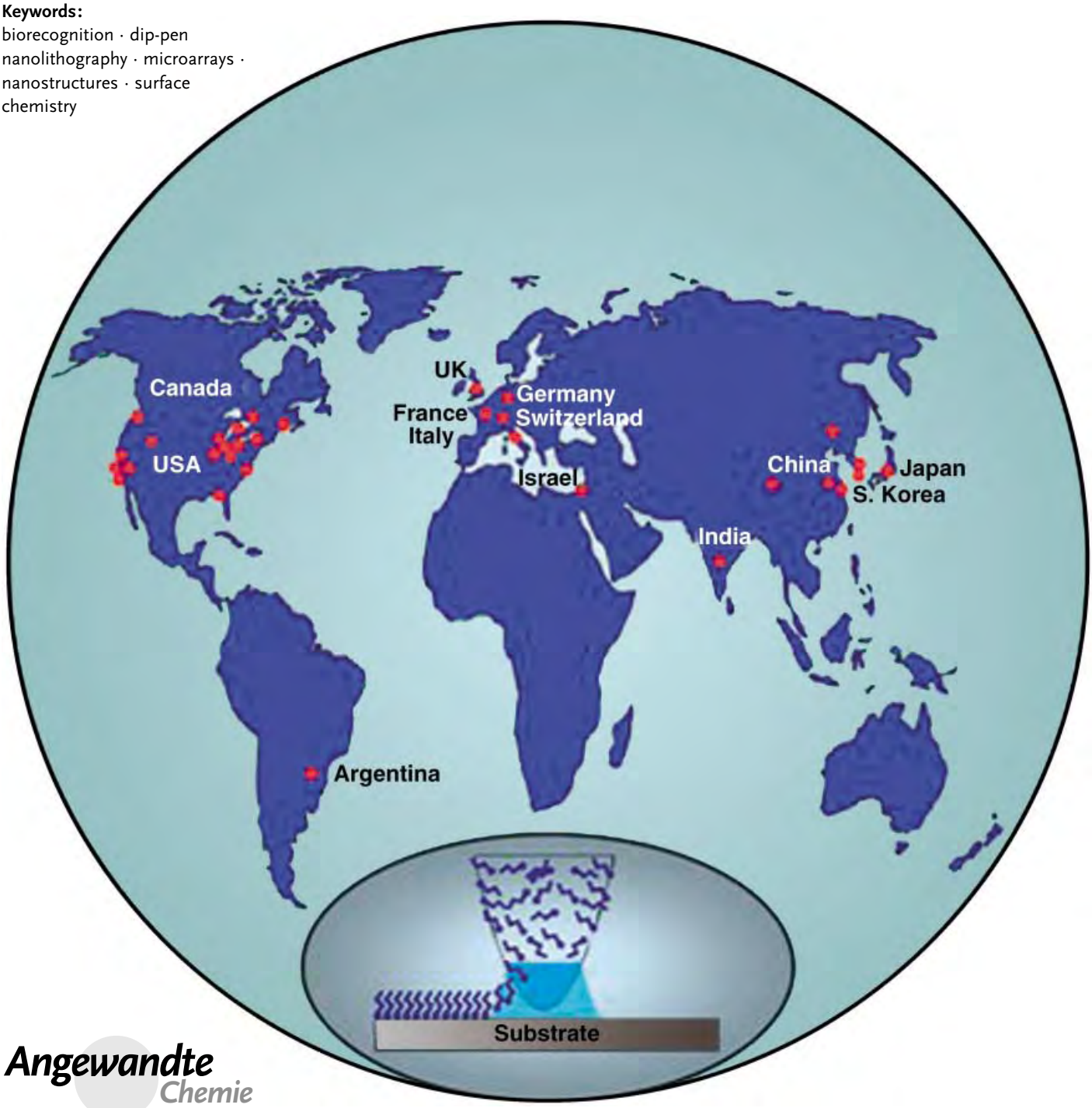
 © 2004 Wiley-VCH Verlag GmbH & Co. KGaA, Weinheim

Nanolithography

The Evolution of Dip-Pen Nanolithography

*David S. Ginger, Hua Zhang, and Chad A. Mirkin**

Keywords:
biorecognition · dip-pen nanolithography · microarrays · nanostructures · surface chemistry



© 2004 Wiley-VCH Verlag GmbH & Co. KGaA, Weinheim
DOI: 10.1002/anie.200300608

The ability to tailor the chemical composition and structure of a surface on the 1–100 nm length scale is important to researchers studying topics ranging from electronic conduction, to catalysis, to biological recognition in nanoscale systems. Dip-pen nanolithography (DPN) is a new scanning-probe based direct-write tool for generating such surface-patterned chemical functionality on the sub-100 nm length-scale, and it is a technique that is accessible to any researcher who can use an atomic force microscope. This article introduces DPN and reviews the rapid growth of the field of DPN-related research over the past few years. Topics covered range from the development of new classes of DPN-compatible chemistry, to experimental and theoretical advances in the understanding of the processes controlling tip–substrate ink transport, to the implementation of micro-electro-mechanical system (MEMS) based strategies for parallel DPN applications.

From the Contents

1. Introduction 31

2. Applications for DPN 33

3. Ink Transport: Experiment and Theory 39

4. Development of High-Throughput Parallel Dip-Pen Nanolithography 42

5. Summary and Outlook 43

1. Introduction

Developing methods that allow the chemistry of surfaces to be controlled on the 1–100 nm length scale is a fundamental and exciting challenge in nanoscience and nanotechnology because it opens new possibilities in fields ranging from molecular electronics to biomedicine to catalysis. This challenge has motivated numerous researchers since the invention of the scanning tunneling microscope (STM) and its descendents (including atomic force microscopy (AFM)). Elegant structures have been painstakingly crafted—one molecule at a time—with serial STM systems operating under ultrahigh vacuum (UHV) and at low temperatures. Other groups have used STM- and AFM-based methods to oxidize, scrape, or etch nanostructures onto surfaces. Such techniques have important applications but are generally limited to the growth of thin oxides on select metal and semiconductor surfaces, or to multistep etch-and-backfill procedures that cannot be easily generalized to the parallel patterning of multicomponent nanostructures.

In 1999 dip-pen nanolithography (DPN) was introduced to the research community as a new tool for fabricating nanostructures on surfaces.[1] DPN is a direct-write scanning-probe-based lithography in which an AFM tip is used to deliver chemical reagents directly to nanoscopic regions of a target substrate (Figure 1). Early results showed that DPN could be used to pattern alkanethiol self-assembled monolayers (SAMs) onto gold surfaces with high-resolution and registration (Figure 2 A, B).[1–3] Importantly, it was also shown that this technique offered the ability to pattern multiple chemical species with sub-100-nm alignment. It was also shown that DPN-defined SAMs were of high-quality (crystalline in the case of 1-octadecanethiol (ODT) and 16-mercaptohexadecanoic acid (MHA; thiohexadecanoic acid)) and could be used as etch resists so that both metal and semiconductor nanostructures could be generated using DPN,[4] a technique which has been refined to produce a variety of high-resolution metal and semiconductor features with controllable surface chemistry.[5,6] More

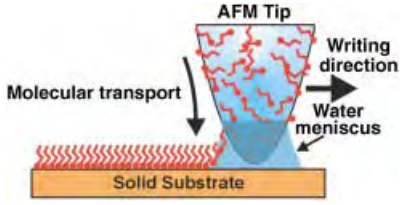


Figure 1. Schematic representation of the DPN process. A water meniscus forms between the AFM tip which is coated with "ink" molecules and the solid substrate. Reproduced with permission from ref. [1].

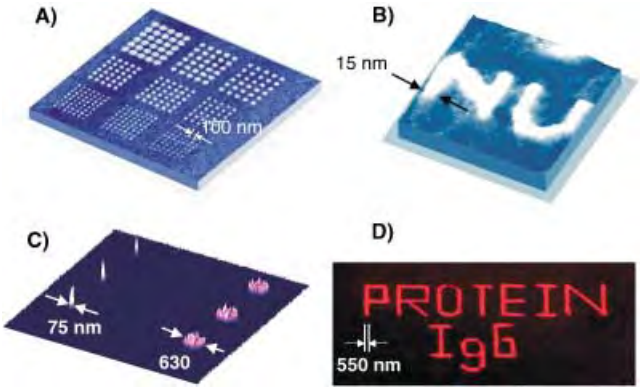


Figure 2. A) Nanoscale dot arrays written on a polycrystalline Au surface with mercaptohexadecanoic acid (MHA; thiohexadecanoic acid) by DPN[56] and B) nanoscale letters written on an Au(111) surface with MHA by DPN.[2] C) TM-AFM image of 25- and 13-nm gold nanoparticles hybridized to surface DNA templates generated with direct-write DPN (unpublished). D) Fluorescence image of direct-write DPN patterns of fluorescently labeled immunoglobulin G (IgG) on SiO_x.[46]

[*] Prof. D. S. Ginger, Dr. H. Zhang, Prof. C. A. Mirkin
Department of Chemistry
Northwestern University
2145 Sheridan Road, Evanston, IL 60208-3113 (USA)
Fax: (+1) 847-467-5123
E-mail: camirkin@chem.northwestern.edu

DOI: 10.1002/anie.200300608

© 2004 Wiley-VCH Verlag GmbH & Co. KGaA, Weinheim

Table 1: Overview of the various DPN ink–substrate combinations that have been reported.

Ink	Substrate	Notes	References
Alkylthiols (e.g. ODT and MHA)	Au	15 nm resolution with sharp tips on single crystal surfaces, <50 nm on polycrystalline surfaces	[1–7, 22, 23, 33, 87, 92, 110, 111]
Ferrocenylthiols	Au	redox active nanostructures	[59]
Silazanes	SiO_x, GaAs	patterning on oxides	[81, 111]
Proteins	Au, SiO_x	both direct write and indirect assembly	[3b, 10, 11, 30, 34, 46, 47, 67, 77, 111]
Conjugated polymers	SiO_x	polymer deposition verified spectroscopically and electrochemically	[8–10]
DNA	Au, SiO_x	sensitive to humidity and tip-silanization conditions	[12, 64]
Fluorescent dyes	SiO_x	luminescent patterns	[10, 68]
Sols	SiO_x	solid-state features	[17, 18, 112]
Metal salts	Si, Ge	electrochemical and electroless deposition	[14–16]
Colloidal particles	SiO_x	viscous solution patterned from tip	[13, 31, 65]
Alkynes	Si	C—Si bond formation	[66]
Alkoxysilanes	SiO_x	humidity control important	[109, 111]
ROMP materials	SiO_x	combinatorial polymer brush arrays	[108]

recently, DPN has been developed to pattern a variety of "ink–substrate" combinations. DPN is compatible with many inks, from small organic molecules[1–7, 109–111] to organic[8–10] and biological[11,12] polymers (Figure 2C, D), and from colloidal particles[13,31,65] to metal ions[14–16] and sols.[17,18,112] DPN can be used to pattern surfaces ranging from metals to insulators and to pattern on top of functional monolayers adsorbed on a variety of surfaces. We have even shown that DPN can be used to feed monomers to a living-polymerization reaction in a site-specific fashion, thus opening the possibility of creating and screening combinatorial arrays of polymer features.[108] An overview of the various chemistries used and the systems in which they have been applied are presented in Table 1. Many of these systems are discussed in more detail in Section 2.

As perhaps the only lithographic technique that offers high resolution and registration with direct-write printing capabilities (Figure 3), DPN is a particularly attractive tool for patterning biological and soft organic structures onto surfaces. These molecules can be deposited in either ambient or inert environments without exposing them to ionizing UV or electron-beam radiation. Furthermore, several different kinds of molecules can be deposited without exposing the substrate to harsh solvents or chemical etchants, and without risking cross-contamination—the desired chemistry is carried out exactly, and only, where it is needed.[7]

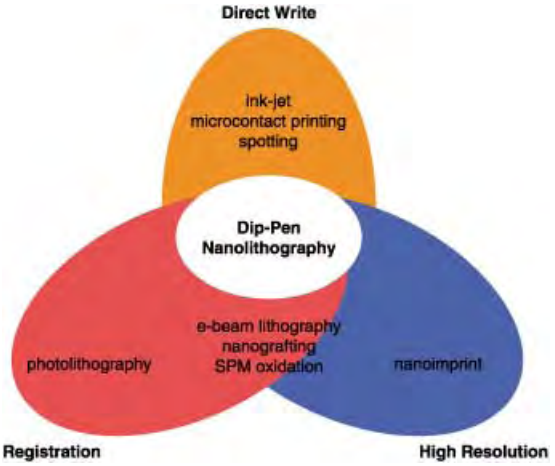


Figure 3. Comparison of the capabilities of DPN with various other lithographic tools. SPM = scanning probe microscopy.

Because of these advantages, many groups have started contributing to the development of DPN. At present, dozens of laboratories around the world have begun to study, develop, or use DPN as a tool in their own research.[8,10,11,13,15,16,19–32] The topics these workers have studied range from the fundamentals of tip-substrate ink transport,[21–23,33] to the direct deposition of metallic structures



Chad A. Mirkin earned his B.S. at Dickinson College (1986) and a Ph.D. from the Pennsylvania State University (1989). After an NSF Postdoctoral Fellowship at MIT, he joined the faculty of Northwestern University where he is currently the George B. Rathmann Professor of Chemistry and Director of the Institute of Nanotechnology. He leads a multidisciplinary research program focusing on the chemistry and physics of nanoscale solution and surface architectures. His numerous awards include the Feynman Prize, the ACS Award in Pure Chemistry, the Sackler Prize from Tel Aviv University, and the Wilson Prize from Harvard University.



David S. Ginger earned dual B.S. degrees in chemistry and physics at Indiana University in 1997. He received a British Marshall Scholarship and NSF Graduate Fellowship and completed his Ph.D. in physics in the Optoelectronics Group at the University of Cambridge (UK) in 2001. He then joined Prof. Mirkin's group as an NIH Postdoctoral Fellow and a DuPont Fellow at Northwestern University. He is presently an Assistant Professor of Chemistry at the University of Washington in Seattle. His research interests center on the physical chemistry of nanoscale materials.

 © 2004 Wiley-VCH Verlag GmbH & Co. KGaA, Weinheim

and development of electrochemical DPN,[8,15] to the deposition of biomolecules[12,30,34] and the effects of DPN on the organization of biopolymers.[11]

2. Applications for DPN

It is often difficult to predict the path of development that an emerging technology will follow. However, a survey of the recent literature suggests several scientific and technological areas where DPN is likely to have an important impact (although there are certainly other uses waiting for a researcher to perform the proof-of-concept and development experiments). In this section we focus on four areas in which we believe the unique capabilities of DPN are particularly likely to make an impact: patterning biomolecular micro- and nanoarrays (Section 2.1), building tailored chemical surfaces for studying and controlling biorecognition processes from the molecular to cellular level (Section 2.2), generating chemical templates for the controlled orthogonal assembly of materials on surfaces (Section 2.3), and the use of DPN as a rapid prototyping tool for generating hard nanostructures using chemical etching on a length-scale comparable, or even superior, to that obtainable with e-beam lithography (Section 2.4). The use of DPN for in situ studies of surface reactivity and exchange chemistry is discussed separately in Section 3.

2.1. Biomolecular Micro- and Nanoarrays

As a direct-write technique, DPN is particularly well-suited for patterning biological molecules on surfaces. With a resolution limit orders of magnitude better than any alternative robotic spotting or photolithographic technology, DPN has the potential to revolutionize the technology of surface-based biomolecular assays, including array-based DNA, small molecule, and protein detection. Such chip-based array-format detection systems, or "microarrays," have become ubiquitous in almost all areas of health-related research.[35–41] The power of cDNA and oligonucleotide arrays to quantify both gene expression and genomic structure (e.g. through single-nucleotide-polymorphism (SNP) detection), has led to their use in among others oncology,[38] infectious-disease pathology,[39] neurology,[40] and pharmaco-genomics,[39,41] to cite a handful of examples. Although less mature and technically more challenging than their DNA-based counterparts, protein microarrays are also under academic and industrial development.[42] In terms of array fabrication and screening technology, the resolution advantage that DPN brings to this field (Figure 4) is fundamentally exciting for two reasons: The first advantage comes from the 10000 to 100000-fold increase in areal density that could be achieved with the use of DPN. With an appropriate readout scheme, such densities would allow an assay to screen for a correspondingly larger number of targets, or, of even greater immediate impact—would allow a fixed number of targets to be screened with a correspondingly smaller sample volume, and in a shorter amount of time. In the future, one could imagine screening an entire human genome for single-nucleotide polymorphisms on a single chip using tiling methods.[36] Such an application would require a large number of conventional gene chips (over 10000 of today's state-of-the art chips (with 20-μm features)), which would require the printing and screening of an area approximately the size of a large car space in a parking lot. However, such an ambitious experiment would be feasible with a single 2×2-cm^2 chip with a spot size of 150 nm. Although major strides in bioinformatics would be required both to design as well as interpret the data from such an array, it is worth pointing out that such an application could not even be addressed with existing micron-scale technologies owing to the large chip areas and sample volumes required. The second advantage of such high-resolution patterning is that it would not only require, but also greatly facilitate, the development of high-throughput, high-resolution screening tools. While present-day detection methods may be inadequate for screening such high-density arrays, miniaturization on the scale accessible with DPN will allow the development of screening methods that are suitable for such nanoscale structures. There are many opportunities in this regard: when a feature composed of receptors is miniaturized to the scale of the biological analytes or their attached labels, almost every mechanical, electrical, and chemical property of the receptor feature is changed upon

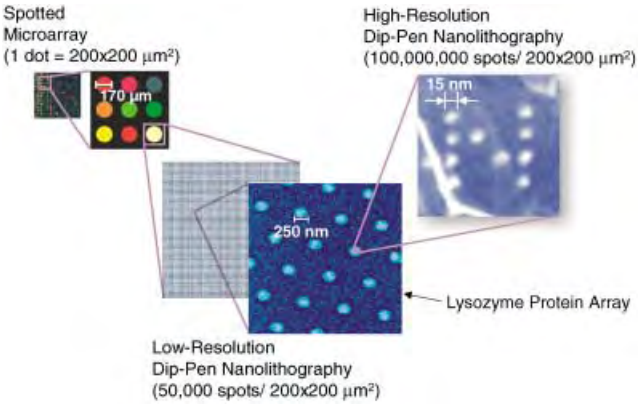


Figure 4. Schematic illustration of the power of DPN resolution in the context of biomolecular nanoarray fabrication.



Hua Zhang earned his B.S. (1992) and M.S. (1995) in chemistry at Nanjing University (China), and his Ph.D. in physical chemistry at Peking University in 1998 under the supervision of Profs. Zhongfan Liu and Xiaojie Xu. After time as a research associate using AFM to study single dendrimers in Prof. De Schryver's group in Leuven (Belgium), he joined Prof. Mirkin's group at Northwestern University as a postdoctoral fellow in 2001, where he worked on dip-pen nanolithography for fabricating solid-state metallic nanostructures by wet chemical etching. He now works at NanoInk Inc.

© 2004 Wiley-VCH Verlag GmbH & Co. KGaA, Weinheim

reaction with the analyte. These properties, which include size, shape, electrical conductivity, and hydrophilicity, all can be monitored in situ with an AFM or with on-chip electronic circuitry. In the long term, it may even be possible to direct the attachment of proteins and virus particles in specific orientations and thus to study reactivity as a function of structural configuration.

To proceed along such a path towards miniaturization will require obstacles to be overcome along the way. However, the potential rewards clearly justify the effort. One potential difficulty comes from cross-reactivity and nonspecific binding (NSB) of analyte or other species to the array spots. Although NSB is a problem for any surface-based assay, NSB is likely to become more problematic for screening on the nanoscale: on a nanoscale receptor spot it would be possible for a few nonspecifically bound particles to completely overwhelm the intended signal. Fortunately, moving to the nanoscale offers new possibilities to alleviate the NSB problem. On one hand, for a small sacrifice in information density, redundancy and "error checking" can be built into any array. On the other hand, controlling (and screening) the chemical environment with nanoscale precision could offer the opportunity both to reduce the frequency of NSB events, and to more readily identify them when they do occur. Finally, because DPN is a direct-write technology, cross-contamination of the patterned array features is entirely eliminated.

Before any of the advantages of high-resolution array patterning can be realized, it is essential to identify and develop patterning methods for particular classes of biomolecules. To demonstrate the power of DPN-based patterning and screening, we and our colleagues have used indirect adsorption techniques (Figure 5) to generate arrays of both proteins and oligonucleotides. Although it is difficult to generalize indirect techniques such as these to the fabrication of complex multicomponent arrays, single-component structures can provide powerful demonstrations as well as useful tests of array-screening performance (and can be used to investigate scientific problems in their own right, see Section 2.2). Although the patterning method depicted in Figure 5 relies on electrostatic interactions to immobilize the proteins on a surface, Zauscher, Chilkoti, and co-workers have recently demonstrated that a similar indirect approach can be used to immobilize proteins through covalent coupling.[19]

Figure 6 shows how such a DPN-fabricated protein array could potentially be used as a label-free protein-screening tool. An array of rabbit IgG protein is deposited as depicted in Figure 5. The dimensions of a single IgG molecule are $14.5 \times 8.5 \times 4$ nm, and the height of the array features after protein adsorption, (measured with AFM), are consistent with these values. Treating the array with rabbit anti-IgG leads to a 1:1 binding of the antibody–antigen IgG pairs, which results in a doubling of the average feature height, as observed in the micrographs. Perhaps more significantly, the control array (Figure 6C) which was exposed to a solution containing lysozyme, retronectin, goat/sheep anti-IgG, and human anti-IgG (without any rabbit anti-IgG) shows no change in feature height, which indicates that the patterned proteins retain their specificity. Although the orientation of

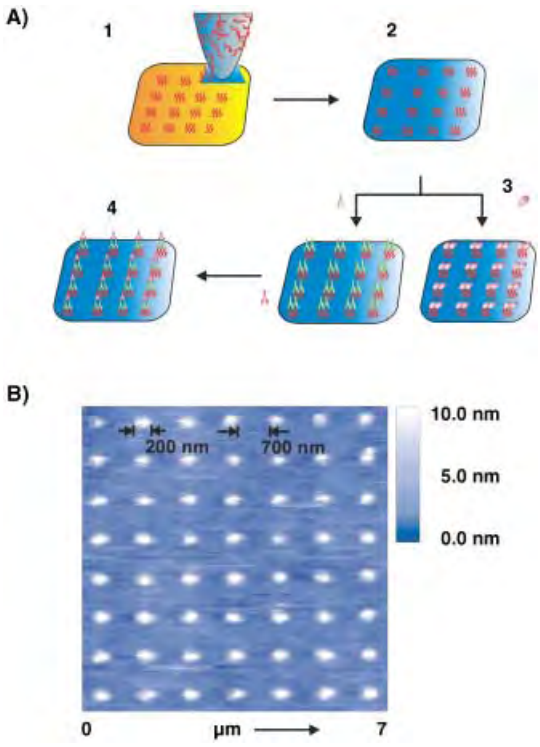


Figure 5. A) Diagram of proof-of-concept experiments, in which proteins were adsorbed on DPN-generated MHA patterns 1) MHA deposited from AFM tip onto surface, 2) passivation, 3) protein adsorption, 4) antibody recognition. The resulting protein arrays were then characterized by AFM. B) Topography image (contact mode AFM) of the retronectin protein array (reproduced with permission from ref. [34]).

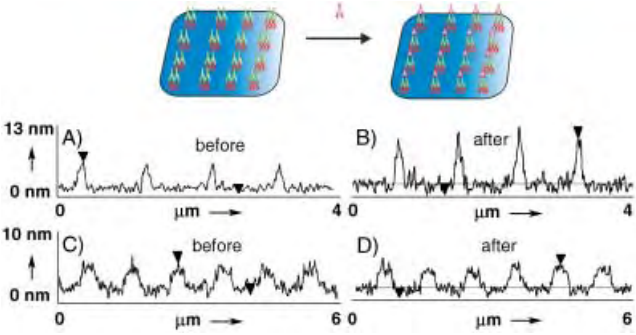


Figure 6. Height profiles of TM-AFM images: rabbit IgG assembled on an MHA dot array generated by DPN before (A) and after (B) treatment with a solution containing lysozyme, goat/sheep anti-IgG, human anti-IgG, and rabbit anti-IgG; a rabbit IgG nanoarray before (C) and after (D) exposure to a solution containing lysozyme, retronectin, goat/sheep anti-IgG, and human anti-IgG. (Portions reproduced with permission from ref. [34].)

the surface-bound IgG protein is not controlled in this experiment, a sufficient fraction of the population provides the solution-borne antibodies with access to the relevant binding domains of the protein.

Ideally, one would like to use the direct-write capabilities of DPN to fabricate biomolecular arrays with spots of many different types. Meeting this challenge requires the development of methods to coat tips reliably, the identification of

 © 2004 Wiley-VCH Verlag GmbH & Co. KGaA, Weinheim

conditions for reproducible tip–substrate transport and ink–substrate coupling, and ultimately the implementation of parallel-pen and integrated-inking systems. Because the MEMs challenges of parallel-pen and integrated-inking systems are covered more fully in Section 4, this section will focus instead on the chemistry involved.

We have used direct-write DPN to pattern oligonucleotides on both metal and insulating surfaces.[12] To transfer DNA to a surface in a controlled fashion, several factors were found to be important, these include precise control of the ambient humidity and careful functionalization and inking of the AFM tips. DNA patterns could be written on gold surfaces using hexanethiol-modified oligonucleotides, and acrylamide-modified (Acrydite) oligonucleotides could be coupled with oxidized silicon wafers that had been modified with 3′-mercaptopropyltrimethoxysilane layers. The resulting patterns could be hybridized to both fluorophore-labeled oligonucleotides as well as to DNA-functionalized gold nanoparticles (Figure 7). Nanoparticle labels[43–45] are particularly promising tags for nanoscale detection applications. They exhibit a wide variety of properties—from their high molar extinction coefficients, to their physical shapes—which can be used to encode information. Indeed Figure 7B shows how a property as simple as nanoparticle size could conceivably be used as a tag in an AFM-based screening procedure, much in the way different colored fluorophores are used in optical screening. In this regard, nanoparticle labeling can serve as a bridge between the development of micro- and nanoscale detection technologies as their unique optical properties also make nanoparticles suitable for more conventional optical screening methods: Figure 7D shows an image

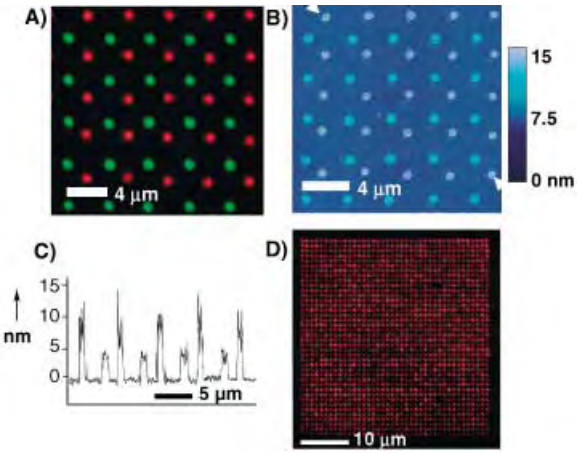


Figure 7. Direct patterning of multiple-DNA inks by DPN. A) Combined red–green fluorescence image of two different fluorophore-labeled sequences (Oregon Green 488-X and Texas Red-X) simultaneously hybridized to a two-sequence array deposited on a silanized SiO_x substrate by DPN. B) Tapping-mode AFM image of 5-nm (dark) and 13-nm (light) diameter gold nanoparticles assembled on the same pattern after dehybridization of the fluorophore-labeled DNA. C) The line plot was taken diagonally through both nanoparticle patterns, and the start and finish are indicated by the arrows in (B). D) Darkfield opitcal image showing scattering from densely packed 13-nm diameter DNA-functionalized nanoparticles hybridized to a 1600-dot DNA array patterned on SiO_x by direct-write DPN. (A–C reproduced with permission from ref. [12], D, unpublished).

of a DNA microarray with 1600 spots captured by optical microscopy.

In addition to oligonucleotides, several papers have described the formation of nanoscale protein patterns by using DPN techniques. In the first report of direct biomolecular patterning, Kaplan, Mirkin and co-workers described the deposition of thiolated collagen and collagen-like peptides onto gold surfaces using tapping-mode AFM.[11] The deposited collagen was observed to assemble into helical structures with the 65-nm periodicity that is characteristic of native collagen fiber, and fluorescence-mode near-field scanning optical microscopy (NSOM) imaging was used to confirm that the deposited structures reacted with collagen-specific antibodies. Together, these two pieces of information strongly suggest that the DPN deposition process allows, or even facilitates, the formation of native collagen structures. This result is encouraging as it provides evidence that it is possible to preserve the native/active structures of at least some types of proteins during the DPN process.

More recently, De Yoreo's group has shown that it is possible to generate nanoscale patterns of human chorionic gonadotropin antibody by direct-write DPN onto 3-glycidoxypropyltrimethoxysilane-modified glass surfaces.[10] They used proteins tagged with tetramethylrhodamine dye to facilitate imaging of the resulting patterns with confocal fluorescence microscopy. However, they did not report characterization of the biological activity of the protein patterns after deposition, so it is unknown whether the antibody retained its structure and function after the deposition and surface coupling processes. Although DPN is an extremely gentle lithographic technique, surface interactions, though apparently favorable for collagen, could potentially serve to denature other classes of proteins. Indeed, recent studies have been aimed at investigating the complex issues involved in preserving the biological activity of immunoproteins, such as IgG, during a DPN experiment and have demonstrated that it is indeed possible to deposit active immunoproteins, but that specific conditions must be maintained.[46,47]

2.2. Controlling Biorecognition Processes from the Molecular to the Cellular Level

It is fair to say that the past two years have witnessed an explosion in the types of compounds that have been patterned using DPN. Among these, biological molecules, including oligonucleotides, peptides, and proteins, have been patterned on glass and metal surfaces, generating much excitement. These advances have opened the door for research into nanoscale array-based screening technologies, as well as highlighted areas of research into DPN processes that should prove fruitful. Topics such as the preservation of protein activity and the mitigation of nonspecific binding have already been discussed in the previous section. Another important topic for future research will be improving DPN resolution. Although most of the biomolecular DPN papers published have shown high-resolution (≈ 100 nm) patterns, none have yet taken biomolecular lithography to the reso-

 © 2004 Wiley-VCH Verlag GmbH & Co. KGaA, Weinheim

lution obtainable at the cutting-edge of DPN technology (currently ≈15 nm for alkanethiol inks on single-crystal gold surfaces).[2] Such sizes are commensurate with the size of individual biological macromolecules, which offers the tantalizing possibility that DPN could be used to position individual structures with molecular resolution to create tailored chemical surfaces that would allow the investigation of a variety of biological recognition processes spanning the molecular to the cellular level. The development of even higher-resolution DPN techniques may require the use of high aspect ratio AFM tips (such as carbon nanotubes[48]) or the combination of DPN with techniques such as nanografting. The DPN–nanografting combination was described by G.-y. Liu and co-workers in a method they call the "nanopen-reader-writer" (NPRW) (Figure 8).[20,49] NPRW employs a

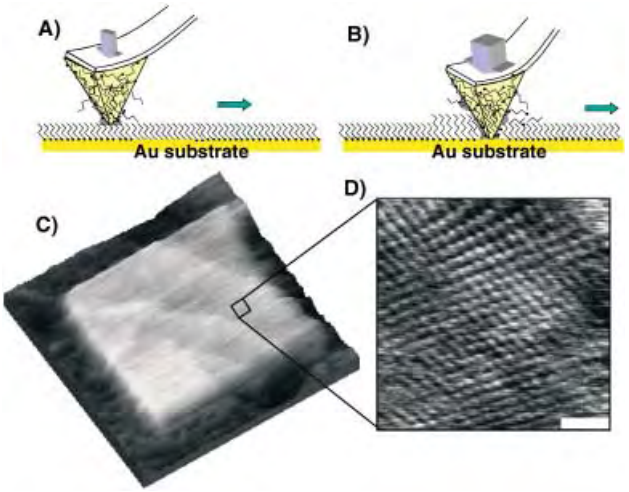


Figure 8. DPN can be combined with other scanning-probe lithography techniques, such as nanografting, to retain the advantages of each. A) In the "nanopen-reader–writer" (NPRW) system, the surface is first passivated with a bulk self-assembled monolayer. B) By applying a high contact force the tip shaves away some of the passivating molecules, which allows the ink from the tip to generate patterns in direct-write fashion. C) A 200×200 nm^2 square with sharp corners prepared using NPRW by depositing C_{18} thiol in a C_{10} monolayer. D) A high-resolution topograph of the patterned region, scale bar is 2 nm. Images courtesy of G.-y. Liu.

bulk SAM passivation layer to inhibit writing except under conditions of high applied contact force, thus decreasing the sensitivity of DPN to ambient conditions and ink-diffusion rates while bringing the direct-write and ambient-compatibility of DPN to the nanografting community. Electrochemical modification of SAM patterns provides another route towards feature-size reduction.[50] By controlling the electrochemical potential of a patterned substrate, it is possible to selectively address different regions of a pattern with distinct desorption potentials. Because thiols at the edge of a surface feature are less stable than those in its center, DPN patterned structures can be shrunk in an electrochemical "whittling" process that allows the feature sizes of an entire array of patterns to be reduced in parallel (Figure 9).[50]

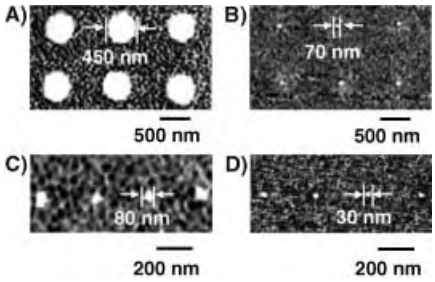


Figure 9. Electrochemical "whittling" of DPN patterns. Lateral force microscopy (LFM) images of MHA patterns before and after electrochemical desorption. A) and C) an MHA dot pattern. B) The pattern in (A) after 6 min desorption at −750 mV (Ag/AgCl reference electrode). D) The pattern in (C) after 1 min desorption at −750 mV (Ag/AgCl reference electrode). (Reproduced with permision from ref. [50].)

Even without special modifications, the length scales accessible to DPN have already opened new possibilities in studying cellular adhesion processes. Many types of cells have evolved a complex system of ligand–receptor interactions through which they recognize and interact with their external environment.[51] The ability to pattern these ligands on surfaces on the micron, nanometer, and potentially even molecular scale, is allowing the investigation of cell–receptor interactions in entirely new experiments. To demonstrate the potential of this method, our group and the Mrksich group fabricated nanoarrays of retronectin (a recombinant cellular adhesion protein based on fibronectin) using DPN.[34] Cells adhere to retronectin through the binding of integrin receptors.[51] As a cell adheres to and spreads across a surface, the integrin receptors associate into clusters comprising several other proteins to form a focal adhesion complex. Previously, lithographic methods capable of varying the size and spacing of retronectin features on surfaces had been limited to micron-scale resolution, which makes them incapable of probing the typical distribution of focal adhesion sizes (50–500 nm).[51] Using DPN, it was possible to pattern 200 nm Rectronectin features and demonstrate that cells were able to adhere to and to spread on the DPN patterns (though not as much as on unpatterned retronectin-coated surfaces). Because the sizes of the focal adhesion complexes are believed to be 50–500 nm, DPN provides a particularly powerful tool to study the distribution of focal adhesion sizes, and the effects of retronectin domain size and spacing on cellular adhesion. With direct-write DPN, it should even be possible to study interactions between cells and surfaces patterned with multiple ligands on multiple length-scales. Such an experiment would be extremely difficult if not impossible to perform with conventional lithographic or stamping processes, which are inherently indirect or single-ink processes.

As the methods for depositing both small organic molecules and large biomolecules using DPN are refined, additional opportunities for tailoring surface-bound ligand–receptor interactions will certainly present themselves. Eventually, it may even be possible to control the attachment of individual entities—such as large proteins or viruses—to surfaces in specific locations, and with well-controlled ori-

 © 2004 Wiley-VCH Verlag GmbH & Co. KGaA, Weinheim

entations. As a step towards this goal, the immobilization of both native and genetically engineered cow pea mosaic virus (CPMV) particles on DPN patterns has been studied.[52,53] In that work, CPMV particles were used which had been engineered to express cysteine groups at the vertices of the icosohedral virus capsid.[54,55] These particles can be selectively immobilized onto bifunctional linkers that have been patterned via DPN.[54,55] De Yoreo and co-workers demonstrated that molecules with a thiol on one end, and an amine on the other, could be patterned at very high ($\approx$50 nm) resolution (Figure 10).[53] A heterobifunctional linker can then be used to couple the exposed amine groups on the pattern with the exposed cysteine groups on the engineered CPMV.[53]

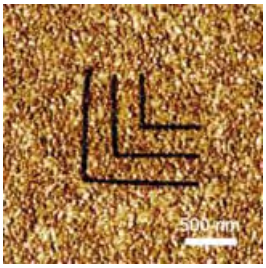


Figure 10. Fifty-nanometer wide lines of a bifunctional amine-thiol linker molecule deposited on gold by DPN. The patterns were used to mediate the adhesion of virus particles to the surface. Reproduced with permission from ref. [53].

Smith et al. also demonstrated that DPN could be used to deposit mixed monolayers to finely tune CPMV immobilization.[52] Although monolayers of 100% maleimide will covalently bind engineered CPMV particles, under certain conditions they can also nonspecifically adsorb non-engineered wild type CPMV (as well as a large number of proteins) owing to hydrophobic interactions. Thus, the selective immobilization of specifically engineered virus particles on DPN-generated patterns is aided by the deposition of mixed monolayers from coated AFM tips. With improvements in the resolution of DPN, or through the use of larger virus particles, it should be possible to control the distribution of particles on the surface and even to immobilize individual particles in specific locations. A number of proteins and viruses possess characteristic dimensions which are tantalizingly close to the resolutions obtainable with DPN, and it is anticipated that controlling the attachment and orientation of such particles on surfaces for studies of biorecognition processes on a variety of length scales will provide a fruitful area of study.

2.3. Building Nanostructured Materials with DPN: Templates for Orthogonal Assembly

Outside of biology, the surface-templated assembly of particles with sub-micrometer to sub-100-nanometer dimensions is of interest to researchers working in fields ranging from colloidal crystallization to magnetic information storage, and from photonics to nanoscale electronics. As DPN offers a rapid method of structuring the surface chemistry of a variety of substrates on these length-scales, it can provide a powerful approach to investigating problems in these fields.

We have developed a number of DPN-based methods for controlling the immobilization of particles with diameters ranging from 5 nm to nearly 1 μm onto surfaces. Electrostatic interactions between MHA and amine- or amidine-coated polystyrene spheres can control the immobilization of 190 nm to 930 nm diameter particles with single-particle precision.[56] Although others have used techniques ranging from microcontact printing to optical tweezers to position similarly sized particles on surfaces,[57,58] the flexibility and relatively high throughput of DPN allowed templates to be screened for particle adsorption in a combinatorial fashion. By preparing a large number of test templates on a single substrate, DPN could be used to quickly identify the optimal conditions for immobilizing single particles in a single experiment.[56] Furthermore, we have shown that electrostatic particle assembly can be used to form arrays of magnetic nanostructures.[110]

One limitation of electrostatically directed particle assembly is the binary nature of the interaction pairs—surfaces can be programmed only with positive or negative charges, thereby limiting the information content of a particular pattern and the complexity of the particle-based structures which can be assembled with such a technique. To increase the complexity of structures that can be generated with electrostatic DPN templates, we turned our attention to redox-active ferrocenylalkylthiol inks.[59] By choosing inks with differing redox potentials, the oxidation state and surface charge of the patterned molecules can be tailored by controlling the electrochemical potential of the substrate. This approach allows finer control over electrostatically directed particle assembly, thus allowing the orthogonal assembly of different sizes of nanoparticles.

In terms of information content, biological molecules offer the potential to encode vastly more information than synthetic chemical systems. Indeed, billions of years of evolution have resulted in a highly efficient biochemical information-storage system based on nucleic acids, and we and others have studied the use of DNA to direct the assembly of a variety of nanoparticle-based systems over the past few years.[60–63] The potential to imprint a surface with a virtually limitless quantity of information (a 15-mer of DNA offers 4^{15} different possibilities, and working with longer sequences extends this range even further) and the possibility of doing so with the exceptional resolution of DPN has motivated the development of DPN-based DNA patterning techniques. The first approach used to control the orthogonal assembly of nanoparticles relied on the indirect patterning of DNA: MHA was patterned using DPN, and then carbodiimide chemistry was used to link amine-functionalized oligonucleotides to the surface.[64] While multiple sequences can be deposited using indirect methods, each additional sequence requires its own additional patterning and coupling steps, which can ultimately lead to cross-contamination of the patterns, which highlights the disadvantage of indirect lithographic processes. It was for these reasons that direct-write

 © 2004 Wiley-VCH Verlag GmbH & Co. KGaA, Weinheim

DPN strategies were developed for depositing DNA onto surfaces using chemically modified AFM tips and precisely controlled environmental conditions (Section 2.1).[12] Using such a strategy, sequence-specific interactions can be used to direct the assembly of DNA-functionalized particles into a number of predefined nanopatterns (see Figure 7). In some respects, DNA is the ideal molecule for DPN-based template generation: although considerable effort was required to prepare cantilevers and identify conditions amenable to direct-write DNA patterning, the virtually limitless range of DNA sequences available means that an enormous number of ligand–receptor pairs can now be patterned using nearly identical experimental conditions.

Although the focus of this Review has so far been on generating templates for particle assembly, it is also possible to use DPN to directly place nanoparticles, or generate solid nanostructures, in specific locations on surfaces. For instance, Brust, Ondarcuhu, and co-workers inked an AFM tip with a concentrated liquid solution of alkanethiol-capped gold colloid.[13] By controlling the contact force they were then able to deposit 5 nm diameter particles in clusters of 50–200 nm in diameter depending on the contact force used,[13] and a similar method was recently reported by G.-y. Liu and co-workers.[65]

In another direct-patterning approach for hard-nanostructure fabrication, J. Liu and co-workers have used both electrochemical and electroless versions of DPN to deposit metal nanostructures on surfaces.[14,15] By using the water meniscus not only as a transport medium, but also as a nanoscale electrochemical cell, they were able to deposit Pt, Au, Ge, Ag, Cu, and Pd through electrochemical reduction onto a Si surface in a technique they termed E-DPN (electrochemical-DPN).[14] Significantly, they also showed that the deposited features were not the result of anodic oxidation of the Si, but rather arose from metal reduction. Later, they were able to demonstrate that metals could also be deposited without an applied bias. In that work DPN was used to deliver $HAuCl_4$ to an HF etched Si surface. There, Au^{3+} ions can be reduced to Au^0 in electroless fashion to produce nanoscale Au lines (Figure 11 A).[15] Buriak and co-workers have used DPN to draw Au and Pd wires on Ge(100) surfaces based on a similar electroless surface reduction process.[16] They also generated nanopatterns on Si by applying a bias while using DPN to deliver alkynes to a H–passivated Si wafer (Figure 11 C,D).[66] Electrically driven DPN processes have even been used to pattern biomolecules onto surfaces. Stone and co-workers have demonstrated high-resolution patterning of several different proteins on nickel using this method (Figure 11 B).[67]

Sols can be patterned by direct-write DPN, which allows the generation of solid-state dielectric and magnetic nanostructures.[17,18] For applications which do not require the chemical complexity afforded by DNA-directed orthogonal assembly, or where the final target is a fluorescent material[10,68] or conducting polymer,[8–10] such approaches can provide a direct route to complex nanostructures with potentially useful magnetic or optical properties.

A variety of DPN-based methods for the generation of templates that can direct the assembly of functional nanostructures have been developed. It is anticipated that the next generation of experiments will focus on using DPN as a rapid prototyping tool to fabricate arrays of nanostructures with interesting and potentially useful optical or electrical properties. At the same time, others will continue to pioneer DPN-related techniques that will make the pattern-generation process even more routine, especially at very high resolutions (< 20 nm).

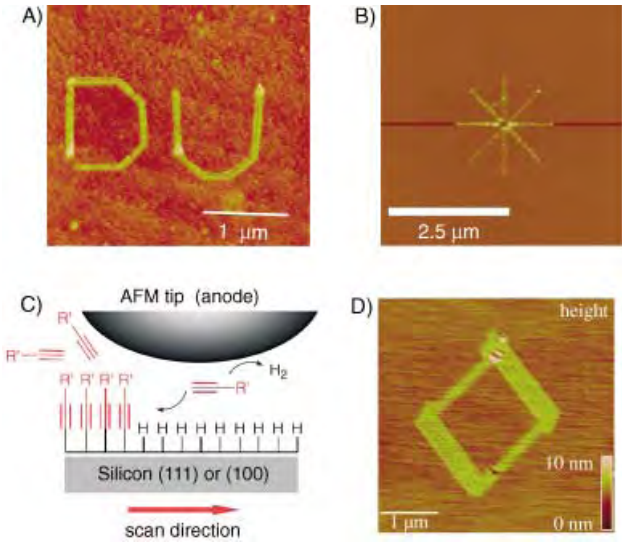


Figure 11. Electroless and electrical DPN techniques. A) $HAuCl_4$ was deposited from the DPN tip and plated by electroless deposition onto a silicon surface (reproduced with permission from ref. [15]). B) TIPA-8 protein filaments deposited on nickel under −2 V bias (reproduced with permission from ref. [67]). C) Scheme and D) results of nanopatterning by delivering alkynes to a hydrogen-passivated surface using DPN while applying an electrical bias (reproduced with permission from ref. [66]).

2.4. DPN-Patterned Etch Resists

Several methods, including electron-beam lithography,[69] photolithography,[69] micro-contact printing,[70,71] nanoimprint lithography,[72] ion-beam lithography,[73,74] and some forms of scanning-probe lithography[75] can be used to pattern inorganic materials. However, very few of these techniques offer the ability to work routinely in the sub-50-nm regime with control over feature size and interfeature distance, especially when such features are made of both hard and soft materials. Furthermore, the vast majority of these techniques, require elaborate and expensive instrumentation and are inherently single-ink processes. In this section we describe how the combination of DPN with wet chemical etching,[76] can be used to fabricate both metal and semiconductor nanostructures without requiring any hardware other than an AFM with closed-loop scanning.

DPN-generated MHA or ODT SAMs can be used as resists for creating three-dimensional (3D) multilayered solid-state structures by standard wet-etching techniques (Figure 12). A scanning electron microscopy (SEM) image of a portion of a 40000-dot array (Figure 12 A) shows the

 © 2004 Wiley-VCH Verlag GmbH & Co. KGaA, Weinheim

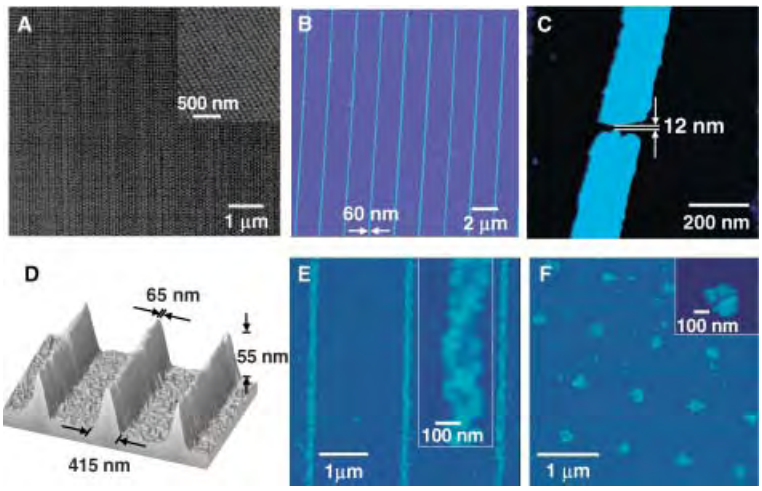


Figure 12. Etched nanostructures. A) SEM image of 45-nm gold nanodots (reproduced with permission from ref. [6]), B) TM-AFM image of 60-nm gold nanolines (reproduced with permission from ref. [77]) and C) 12-nm gold nanogap (reproduced with permission from ref. [6]) on a Si/SiO_x surface. D) 3D Si(100) nanostructures[4]). TM-AFM image of DNA-modified line (E), and dot (F), features after hybridization with complementary DNA-modified nanoparticles; insert: high-resolution TM-AFM images.[5]

regularity of the feature size and interfeature distance. The actual dot diameter as measured by SEM is approximately 45 nm. The uniformity of the nanostructures is quite good, which demonstrates the ability to fabricate high quality sub-50-nm features using the DPN process. At present, the smallest-diameter dot structures that have been made with this method are 25 ± 5 nm.[6] By using this method, we have been able to generate complex features including lines, circles, triangles, and dots. Figure 12B shows a typical etched gold nanoline array with line widths of 60 nm.[77] Importantly, because DPN can be used to deliberately make almost any sort of feature regardless of shape and size (up to the many-micrometer length scale), the technique also can be used to generate nanoelectrode gaps in the range of 12 to 100 nm (Figure 12C).[6] The ability to generate gold features also provides a route to generate structured semiconductor surfaces. By using the gold of the etched features as a resist, nanoscale patterns can be etched into an underlying silicon substrate. By removing the residual gold with aqua regia, nanofeatures composed of silicon can thus be produced (Figure 12D).[4]

Gold surface features can be treated with other inorganic (e.g., gold nanoparticles) and/or biological materials (e.g., DNA, proteins, viruses, peptides) to form hybrid bioinorganic nanoarrays. After etching, the nanostructures are still coated with MHA or ODT, and it is difficult to conduct subsequent gold-thiol modifications on the features that make up the array. However, by irradiating the array with a UV lamp and subsequently rinsing it with Milli-Q H_2O, the oxidized monolayer of MHA can be removed[78–80] to generate gold nanostructures that are easily modified with other thiol-containing molecules. As one example, it was shown that the freshly prepared gold nanopatterns can be functionalized with a disulfide-functionalized oligonucleotide.[5] To demonstrate that the oligonucleotides were, in fact, adsorbed onto the gold patterns and not on the other areas of the array, their hybridization properties were studied with 30-nm gold particles functionalized with complementary DNA by a three-strand system.[5] TM-AFM images of the arrays show that the particles hybridize to the oligonucleotide-functionalized gold nanofeatures but not the areas surrounding these features (Figure 12E and F).[5] High-resolution images of the dots and lines clearly show the individual particles on the nanofeatures.

DPN-generated etch resists provide a straightforward way of creating arrays of inorganic nanostructures (e.g., Au, Ag, Pd) on a semiconducting or an insulating surface. The ease of use and accessibility of AFM systems (as compared to electron-beam lithography/SEM systems for instance) are major advantages of the DPN-based approach to hard-nanostructure fabrication. Furthermore, the resulting structures can be selectively modified with adsorbates that provide additional and desirable functionality. By combining these etching approaches with direct-write deposition of molecular and biomolecular inks described above, it will be possible to generate an even wider variety of functional nanostructures.

3. Ink Transport: Experiment and Theory

Developing an understanding of the tip–substrate ink transport process not only is a fundamental issue, but also is important to the further development of DPN as a workhorse nanofabrication technique. A better understanding of ink-transport processes would facilitate efforts to develop more rapidly and optimize new ink–substrate combinations, help efforts to improve the resolution of DPN (which is presently in the 15-nm range under optimum conditions),[2] and guide efforts to fabricate custom tips, integrated inking systems and parallel cantilever arrays for high-throughput patterning (see Section 4).

Tip–substrate molecular transport is a complicated process and likely to be influenced by numerous parameters. These include the chemical makeup (and purity) of both the ink and surface, the tip shape, composition, and surface chemistry, the distribution and mobility of ink on the tip, and the temperature under which the experiment is carried out. Furthermore, except under UHV conditions, some form of full or partial water adlayer will be present on the patterning surface. Under ambient conditions, a water meniscus can condense between the tip and the surface. Under most conditions then, it seems apparent that the presence of ambient moisture will influence the DPN process, just as it affects the imaging resolution of contact-mode AFM in air. Given these facts, the humidity at which the patterning is carried out, and the water solubility of the ink will influence the DPN deposition process. Because of the influence of humidity on the transport of various inks, it is prudent to encase AFM instruments used for DPN in a humidity-

 © 2004 Wiley-VCH Verlag GmbH & Co. KGaA, Weinheim



Figure 13. An AFM (Park Scientific AutoProbe CP Research) encased in a humidity-controlled glove box (PlasLabs) for temperature- and humidity-controlled DPN experiments.

controlled glove box (Figure 13) or environmental chamber. This system provides a controllable and reproducible environment for performing DPN experiments, and allows a user to switch samples and conduct multiple experiments with the same environmental parameters.

Over the past year, several experiments have quantified the effects of humidity and temperature on the DPN patterning of various inks. De Yoreo and co-workers studied the deposition of MHA on gold substrates as a function of contact time and humidity.[22] They observed faster deposition at higher humidities and interpreted their results as a combination of the kinetics of ink dissolution into the meniscus and of the size of the meniscus. On the other hand, Sheehan and Whitman conducted a similar study on ODT and found only a negligible dependence of the writing speed on the ambient humidity.[23] In parallel with these groups, we conducted a systematic study of the DPN deposition of both MHA and ODT as a function of varying humidity and temperature.[33] Consistent with the results of both De Yoreo and Sheehan and Whitman, MHA was found to exhibit an increase in deposition rate at elevated humidity, while ODT showed little if any dependence. As noted above, however, molecular transport from the AFM tip to the surface depends on many variables, and our results showed that the magnitude of the humidity dependence could depend on the temperature at which the experiment was carried out (and vice versa).[33] Such results underscore the need for careful control over experimental conditions to facilitate valid comparisons between studies being conducted in the multiparameter space of a typical DPN experiment (and certainly help account for some of the variability in the early data). The differences in behavior between ODT and MHA can be explained in terms of their different solubilities in the water meniscus. This interpretation is consistent with the temperature dependence of the deposition rates as well as their humidity dependence. Such an interpretation is also supported by our data which showed that the deposition of DNA oligomers (one of the most hydrophilic inks studied to date) was extremely sensitive to the ambient humidity (with faster deposition occurring at higher humidities, and no observable transport at low humidity ($<30\,\%$)).[12]

One surprising result from these initial experiments has been that for the DPN deposition of molecules ranging from simple alkanethiols[33] to oligonucleotides,[12] and from silazanes[81] to conducting polymers,[9] the growth of feature size with contact time exhibits an extremely similar functional form (although the "rate constants" for each molecular class can vary widely). For the patterning of dots (by holding the AFM tip in stationary contact with the surface) this functional form was first fit as a linear dependence of dot area, a, with contact time, t (square-root dependence of dot diameter with contact time) [Eq. (1)] with k serving as a (ink, temperature,

$$a = k\,t + b \tag{1}$$

humidity, etc. dependent) fitting parameter, and b corresponding to a tip size/coating dependent parameter.

This fit is consistent with the AFM tip serving as a source of constant ink flux, and has been modeled by Schatz, Ratner, and co-workers in terms of two-dimensional (2D) diffusion with a source.[82] More recently, Sheehan and Whitman have challenged the assumption of a constant ink flux from the AFM tip, and have suggested that the tip be modeled as a source of constant ink concentration.[23] Their results yield an expression for the surface ink concentration as a function of both deposition time and distance from the AFM tip. Their calculations appear to match their data slightly better than those with Equation (1) over the range of contact times studied. However, to date, neither model has been tested systematically over a large range (several orders of magnitude) of contact times. Such an experiment would serve to differentiate more clearly between the assumptions of the tip serving as a source of constant flux and constant concentration. It is possible that under different conditions (type of molecule, scan speed, temperature, humidity, etc.) the tip may be more accurately modeled by one assumption over the other. In this regard, it is worth noting that De Yoreo and coworkers were able to fit their data in terms of Equation (1),[22] but with two different rate constants at different times. These two rates were attributed to the regimes in which the kinetics of ink detachment from the tip (at short contact times/high scan speeds) and ink diffusion (at long contact times/slow scan speeds), respectively, limit the growth kinetics. Underscoring the importance of molecular properties, some types of molecules can also exhibit "anomalous" diffusion properties in DPN experiments and produce fractal-like rather than circular features (Figure 14).[21]

It seems natural that the effects of temperature and humidity will vary depending on the nature of the molecules

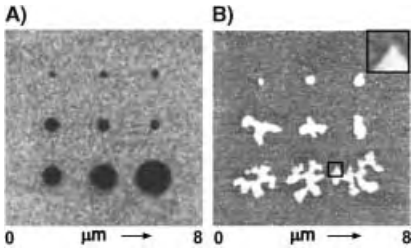


Figure 14. "Normal" diffusion (A) observed for ODT on gold, and "anomalous" diffusion (B) observed for 1-dodecylamine on mica, inset: higher-resolution image. Reproduced with permission from ref. [21].

 © 2004 Wiley-VCH Verlag GmbH & Co. KGaA, Weinheim

used, and this is indeed consistent with most experience. It is even possible that different molecules are transported to the surface by fundamentally different mechanisms. Comparing the transport properties of an aliphatic thiol, such as ODT with those of DNA provides a particularly vivid demonstration of these issues. Several groups have demonstrated that the deposition rate of ODT is only slightly affected by humidity. In contrast, it was found that with oligonucleotide inks, the area of spots generated at constant contact times could be varied by nearly an order of magnitude by a change in relative humidity of less than 20 percent. DNA is difficult to pattern at either very low humidities (where no deposition was observed) or very high humidities (where the rapid flow of DNA from the cantilever to the surface prevented the generation of nanoscale patterns). For different molecules, it is possible that similar phenomena could arise from effects ranging from variations in the viscosity of hygroscopic ink solutions as they equilibrate with the ambient environment, to the size of the water meniscus formed between the tip and the surface.

On the theoretical side, Schatz, Ratner, and Jang recently studied the condensation of a liquid meniscus between an AFM tip and a surface using a grand canonical Monte Carlo simulation of a 2D lattice gas.[83] They included a variety of effects in their model (such as the wettability and curvature of the AFM tip) that should be important to the DPN process. These studies provide important insights, and make qualitative predictions on the dependence of DPN feature sizes on ambient humidity—at least under the assumption that deposition is under thermodynamic control and related to the size of the meniscus.

Although these studies provide a promising start, much work remains to be done (in terms of both experiment and theory). On the theory side, it is likely that a complete simulation of the DPN process will require models which combine the thermodynamics of meniscus formation with the dynamic effects of ink desorption, transport through the meniscus, and self-assembly. On the experimental side, more direct comparisons of transport properties for a wider range of inks under a wider range of carefully controlled conditions are needed.

Because the patterns that are deposited during DPN can be imaged in situ using AFM/LFM as they are formed, DPN itself provides a unique opportunity to study the dynamics of the monolayer nucleation and growth process. Although scanning-probe methods have been applied previously to obtain molecular-resolution images of SAM structure, formation, and growth,[84–86] DPN brings a new level of experimental control to such studies. In particular, the serial nature of such an experiment allows the monolayer growth to be modulated in both a *site*-specific and time-controlled fashion, which facilitates a step-by-step imaging of the surface modification process, and side-by-side comparisons of a continuous gradient of conditions on a single surface. In conjunction with Hong, we first applied this approach to the study of ODT and MHA monolayer formation.[87] Rather than holding the AFM tip in a single location to form dots, coated tips were raster-scanned rapidly across a substrate while acquiring a series of images (note that a complete theory of DPN deposition will ultimately need to explain deposition in this rapid-scan mode as well as dot formation at long dwell times). Under ambient conditions of 30% relative humidity, it was observed that the formation of an ODT monolayer followed a nucleation and growth process, with small crystalline domains of ODT appearing at even low surface coverages. In contrast, MHA monolayers exhibited quite different growth kinetics, and were observed to coat gold terraces uniformly until saturation coverage was reached. Again, these differences were interpreted in terms of the presence of the water meniscus and the relative hydrophilicities of the ink molecules. It would be particularly informative to conduct similar studies on a systematic series of adsorbates.

In another application, we have applied DPN as a tool for the in situ study of monolayer exchange processes—another area of fundamental scientific interest as well as industrial importance.[7] DPN-initiated site-selective exchange can potentially be used to produce a variety of complex nanostructures, and is important to understand, especially in terms of the deposition of mixed monolayers, (as have been used in the controlled adsorption of virus particles discussed in Section 2.2). To study the relative rates of exchange, a series of adsorbates, including ODT, MHA, ferrocene (11-mercaptoundecyl), and ferrocene (11-mercapto-1-oxoundecyl), were patterned by DPN into a series of identical "nanolibraries" (Figure 15 A and B). This arrangement facilitates the side-by-side comparison of the exchange properties of a series of adsorbates under identical conditions as a function of feature size and composition. Furthermore, the site-selective and serial nature of the DPN initiated exchange experiment provides a way to extract kinetic data on a large number of

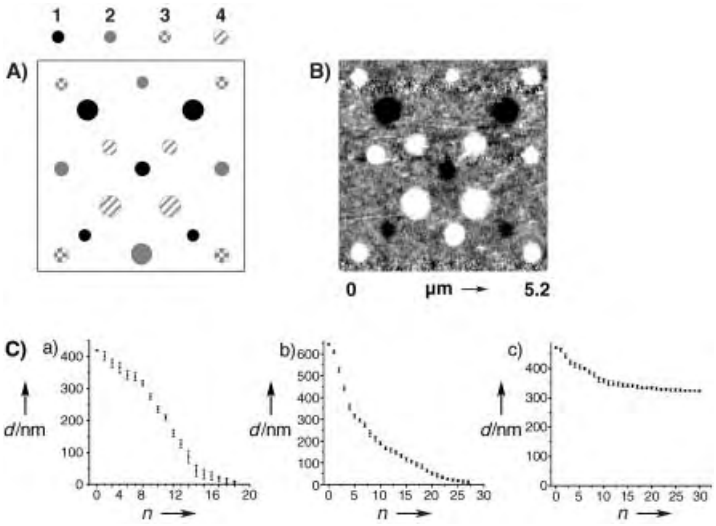


Figure 15. Studying site-selective monolayer exchange using DPN. A) Schematic representation of a combinatorial library design containing the four different molecular inks. B) LFM image of the library described in (A), collected with a clean tip at 4 Hz and contact force of 0.5 nN (24 °C, 40% relative humidity). C) Plot of dot diameter *d* as a function of number of scans *n* at 3 Hz with an ODT coated tip for a) **3**, b) **4**, and c) **2**. The library studied is in (B). **1** ODT, **2** MHA, **3** ferrocene (11-mercapto-1-oxoundecyl), **4** ferrocene (11-mercaptoundecyl). In all cases, the scan size was 5.4×5.4 µm. Reproduced with permission from ref. [7].

 © 2004 Wiley-VCH Verlag GmbH & Co. KGaA, Weinheim

nearly identical nanostructures (Figure 15C). Using this method, the relative stabilities of monolayers formed from the adsorbates were deduced to be, in order of decreasing stability: MHA, ODT, ferrocene (11-mercaptoundecyl), and ferrocene (11-mercapto-1-oxoundecyl). Furthermore it was observed that the nanostructures exchanged preferentially from the outside inward, consistent with the electrochemical whittling experiments[50] described in Section 2.2, and providing evidence for a defect-mediated exchange process. This hypothesis was confirmed by experiments conducted on single-crystal gold surfaces which showed that monolayers were dramatically more stable to DPN-initiated exchange on single-crystal surfaces than on polycrystalline gold surfaces.

These experiments have only scratched the surface of what could prove to be a rich series of DPN-based ink transport, surface kinetics, and exchange studies. For instance, DPN can be used to pattern monolayer-thick diffusion barriers (corrals) on surfaces, and then selectively deposit inks within such a structure.[3] Understanding the patterns that are formed as a result requires an understanding not only of the thermodynamics of meniscus formation in the vicinity of such structures, but also the kinetics of ink diffusion across native and modified surfaces, as well as of the stability and time evolution of the surface chemistry under conditions where monolayer exchange can occur.

4. Development of High-Throughput Parallel Dip-Pen Nanolithography

Up to this point the focus of this Review has been on the progress and technology of "single-pen" DPN, which can serve as a powerful tool by enabling researchers to fabricate and study structures which would be difficult, if not impossible, to create and study with other techniques. However, like all scanning-probe-based imaging and lithographic systems, DPN is inherently a serial process. To increase the throughput and area accessible to scanning-probe techniques, several groups are pursing the development of parallel-probe cantilever arrays. In collaboration with us,[3] C. Liu and co-workers have developed MEMs-based parallel-probe strategies designed specifically with the constraints of DPN applications in mind.[92,94,95]

Among the best known parallel probe research is that conducted at IBM,[88,89] and also at Stanford University.[90,91] The primary aim of the IBM group has been in the area of high-density data storage. Towards this end they have implemented an independently addressable 32×32 probe array as part of IBM's "millipede" project. The 1024-cantilever array measures approximately 3 mm per side, and each cantilever is assigned to read and write its own approximately 100×100 μm area. The data-storage medium itself is actually a very thin film of polymer. To write a bit of data, a tip is heated to over 400 °C allowing it to sink into the polymer. Reading of data is accomplished by operating the tips at slightly lower temperatures. Those tips that fall into contact with a written bit of data are cooled more rapidly than those resting on the polymer surface. In addition, Quate and co-workers at Stanford have developed a number of 1D and 2D probe arrays for both imaging and lithographic applications. With regard to lithographic applications, their principle approach to patterning has been current-induced lithography, and they have thus developed schemes for regulating the current emitted from the tip by regulating the tip–substrate bias.[90,91]

The requirements of thermal data-transfer and current-induced lithographic methods distinguish themselves from the requirements of DPN-based applications. Because patterning in a DPN experiment occurs whenever a coated tip is held in contact with a surface, independent control of the on/off state of each cantilever in an array requires independent actuation of the force applied to, and height of, the cantilever on/above the surface—an engineering challenge that is distinct from controlling the temperature or bias applied to a cantilever. Furthermore, the goal of making parallel-probe DPN systems wide-spread and easily accessible makes fabrication costs and integration with standard AFM systems important design considerations.

The simplest implementation of parallel-pen DPN is thus a passive probe array. In this case, the pens are not actuated independently but are simultaneously brought into contact with the surface and scanned together, which allows the duplication of a single pattern a number of times equal to the number of probes in the array. The first experiments in this area used commercially available cantilevers with an inter-tip spacing of 1.4 mm.[3] Recently, the group of C. Liu has produced cantilever arrays composed of up to 10000 pens (Figure 16A). In conjunction with C. Liu and co-workers we have demonstrated writing with arrays of 32 parallel probes; images of eight 60-nm features that were written in parallel are shown in Figure 16B.[92] Since active feedback is applied to only a single cantilever in the array, and the others are allowed to track the topography passively, specific constraints on the registration between the array and the surface, as well as the flexibility of the cantilevers must be met.[92] A commercial entity, NanoInk, has begun producing prototype passive arrays with as many as a million pens (Figure 16C and D).[93] For patterning large areas in high-throughput DPN applications without sacrificing the registration capabilities of DPN, along with C. Liu, we have developed DPN tips made of polydimethylsiloxane (PDMS), we call this technique scanning-probe contact printing (SP-CP).[94]

Independent control of each probe tip is the next step, and can be accomplished using piezoelectric, capacitive, or thermoelectric actuation. In the first generation of active parallel-probe DPN arrays, thermoelectric actuation has been used: resistive heating of a multilayer cantilever results in differential expansion of the components, which leads to bending of the probe. Using this approach, a range of complex patterns can be generated at high speed because the contact between each tip and the writing surface is independently controlled. C. Liu and co-workers have also developed strategies capable of independently verifying the "on/off" state of each probe in a highly parallel array based on electrical conduction.[95]

The final challenge of complete MEMs integration of DPN technology is the automation of tip coating and ink delivery. It is proposed that custom microfluidic systems will

 © 2004 Wiley-VCH Verlag GmbH & Co. KGaA, Weinheim

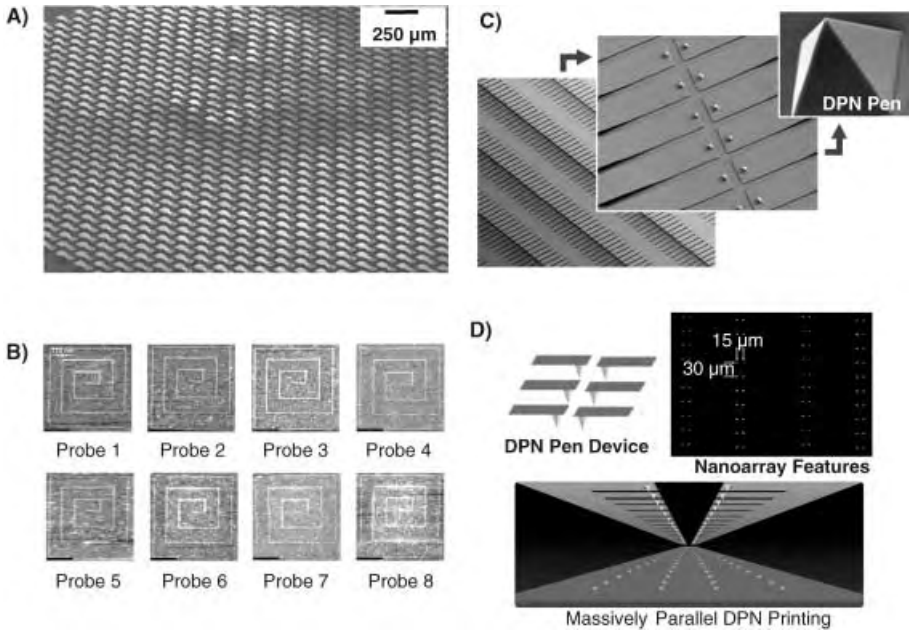


Figure 16. Parallel-probe DPN. A) SEM image of a high-density, 2D array of passive DPN probes (courtesy of Chang Liu UIUC) B) Contact-mode AFM topographic images of eight copies of ODT patterns generated by using a parallel probe array of AFM cantilevers (reproduced with permission from ref. [92]). C) SEM images of a commercial "Massively Parallel Pen" (MPP) array (courtesy of NanoInk, Inc). D) Fluorescence micrograph of spots written with the MPP array (courtesy of NanoInk, Inc.).

ultimately be used to control the inking of individual cantilevers in a parallel probe array. The realization of such systems will depend on the development and adaptation of a number of technologies. Large-scale integration of microfluidic technologies is still challenging, and arrays of 1000 individually addressable wells represent the current state-of-the-art.[96] Thus, to meet the inking needs of parallel probe arrays (with an ultimate goal of being able to deliver a different ink to each probe in a 10000-pen array), new microfluidic arrays of addressable ink wells must be implemented. Such systems are already under development.[97] In addition to microfluidic ink wells into which tips can be "dipped," integrating the microfluidics directly into the tips themselves offers another attractive possibility for MEMs engineers interested in DPN. In an extension of the DPN technique that some have likened to a "fountain pen",[98] both micro- and nanopipettes have been used as scanning-probe tips with hollow cores through which inks ranging from chemical etchants[98] to photoresist[99] and even biomolecules,[26,100] can be pumped directly to a surface for site-specific lithography. Although nanopipette-DPN work is presently restricted by the hand-fabrication of pulled glass capillaries, Espinosa and co-workers are lifting this limitation by using advances in microfabrication technology to generate massively parallel fountain-pen arrays.[101] In this regard, it is striking to note how the evolution of DPN—from a quill pen to a fountain pen to a multiple-pen plotter—has emulated the blueprint provided by the evolution of modern macro-scale writing and printing technologies. Indeed, this evolution has followed very closely the path proposed at the initial invention of DPN.[60,102–107]

5. Summary and Outlook

DPN is a unique scanning-probe-based lithographic tool for generating high-resolution patterns of chemical functionality on a range of surfaces. The combination of resolution, registration, and direct-write capability offered by DPN distinguishes it from any alternative lithographic strategy and makes DPN a promising tool for patterning soft organic and biological nanostructures. Many other recent lithographic tools that have been developed, such as microcontact patterning (μCP) and nanoimprint lithography (NIL), have been driven by the desire to create tools that can compete with existing techniques in the semiconductor arena on the basis of cost and, in the case of NIL, by offering higher resolution. An attractive feature of DPN is that it is both a tool for scientific discovery as well as an engineering advance that allows useful multicomponent nanostructures to be printed at a resolution that is superior to any conventional lithographic tool. In an age of nanotechnology, where being able to fabricate nanostructures of a certain composition, size, and shape is essential, DPN in its current state of development is already a tool that will allow for rapid advances in the science and technology of highly miniaturized structures. If the efforts to transform it into a massively parallel process are successful, it will become a powerful production tool in both the life sciences and the semiconductor industry.

This Review has covered several areas of current DPN research, including the generation of biomolecular nanoarrays for diagnostic applications as well as fundamental studies of ligand–receptor interactions. Other particularly attractive areas of DPN research include the generation of templates for assembling (and also for directly depositing) colloidal particles, as well as the creation of a variety of hard nanostructures through direct deposition as well as etching. While much remains to be learned about the DPN deposition process, particularly in the area of tip-substrate ink transport and diffusion, several studies published over the past year have begun to help clarify things. The transport of two molecules as similar as ODT and MHA can exhibit different sensitivities to their environmental conditions, and a complete theory of DPN deposition will need to combine the effects of meniscus formation as well as the kinetics of ink transport in a manner that can account for the specific chemistry of an individual ink. Finally, we have described the ongoing development of both passive and active parallel-pen DPN arrays. Although predicting the future is troublesome, it is nevertheless fascinating and fun to speculate on the possibil-

 © 2004 Wiley-VCH Verlag GmbH & Co. KGaA, Weinheim

ities that would be opened when such highly parallel DPN systems are realized. High-throughput deposition of biomolecular arrays is one application that comes to mind. Today, scientists use robotic spotting systems (with only 4–16 parallel pins) to generate custom DNA and protein chips. Even modestly parallel DPN systems could compete with these systems in terms of throughput, thereby allowing the fabrication and screening of entire chips using AFM-based systems. One could imagine that similar parallel DPN systems could be applied to combinatorial studies of catalysis, as well as to the patterning of molecule-based electronic materials with high levels of registration. Finally, with respect to semiconductors, the ability to add and remove solid-state materials from an underlying substrate makes DPN a very attractive potential tool for lithographic mask fabrication, inspection, and repair. It is clear that DPN has a bright future in both its single- and multi-pen incarnations.

The Air Force Office of Scientific Research (AFOSR), Defense Advanced Research Projects Agency (DARPA), Army Research Office (ARO), and National Science Foundation (NSF) are all acknowledged for support. D.S.G. thanks the National Institutes of Health (NIH) and DuPont for postdoctoral fellowship support.

Received: May 22, 2003 [A608]

[1] R. D. Piner, J. Zhu, F. Xu, S. H. Hong, C. A. Mirkin, *Science* **1999**, *283*, 661.
[2] S. H. Hong, J. Zhu, C. A. Mirkin, *Science* **1999**, *286*, 523.
[3] S. H. Hong, C. A. Mirkin, *Science* **2000**, *288*, 1808.
[4] D. A. Weinberger, S. G. Hong, C. A. Mirkin, B. W. Wessels, T. B. Higgins, *Adv. Mater.* **2000**, *12*, 1600.
[5] H. Zhang, Z. Li, C. A. Mirkin, *Adv. Mater.* **2002**, *14*, 1472.
[6] H. Zhang, S.-W. Chung, C. A. Mirkin, *Nano Lett.* **2003**, *3*, 43.
[7] A. Ivanisevic, K. V. McCumber, C. A. Mirkin, *J. Am. Chem. Soc.* **2002**, *124*, 11997.
[8] B. W. Maynor, S. F. Filocamo, M. W. Grinstaff, J. Liu, *J. Am. Chem. Soc.* **2002**, *124*, 522.
[9] J. H. Lim, C. A. Mirkin, *Adv. Mater.* **2002**, *14*, 1474.
[10] A. Noy, A. E. Miller, J. E. Klare, B. L. Weeks, B. W. Woods, J. J. De Yoreo, *Nano Lett.* **2002**, *2*, 109.
[11] D. L. Wilson, R. Martin, S. Hong, M. Cronin-Golomb, C. A. Mirkin, D. L. Kaplan, *Proc. Natl. Acad. Sci. USA* **2001**, *98*, 13660.
[12] L. M. Demers, D. S. Ginger, S. J. Park, Z. Li, S. W. Chung, C. A. Mirkin, *Science* **2002**, *296*, 1836.
[13] M. Ben Ali, T. Ondarçuhu, M. Brust, C. Joachim, *Langmuir* **2002**, *18*, 872.
[14] Y. Li, B. W. Maynor, J. Liu, *J. Am. Chem. Soc.* **2001**, *123*, 2105.
[15] B. W. Maynor, Y. Li, J. Liu, *Langmuir* **2001**, *17*, 2575.
[16] L. A. Porter, H. C. Choi, J. M. Schmeltzer, A. E. Ribbe, L. C. C. Elliott, J. M. Buriak, *Nano Lett.* **2002**, *2*, 1369.
[17] L. Fu, X. G. Liu, Y. Zhang, V. P. Dravid, C. A. Mirkin, *Nano Lett.* **2003**, *3*, 757.
[18] M. Su, X. G. Liu, S. Y. Li, V. P. Dravid, C. A. Mirkin, *J. Am. Chem. Soc.* **2002**, *124*, 1560.
[19] J. Hyun, S. J. Ahn, W. K. Lee, A. Chilkoti, S. Zauscher, *Nano Lett.* **2002**, *2*, 1203.
[20] N. A. Amro, S. Xu, G.-y. Liu, *Langmuir* **2000**, *16*, 3006.
[21] P. Manandhar, J. Jang, G. C. Schatz, M. A. Ratner, S. Hong, *Phys. Rev. Lett.* **2003**, *90*, 115505.
[22] B. L. Weeks, A. Noy, A. E. Miller, J. J. De Yoreo, *Phys. Rev. Lett.* **2002**, *88*, 255505.
[23] P. E. Sheehan, L. J. Whitman, *Phys. Rev. Lett.* **2002**, *88*, 156104.
[24] G. Agarwal, L. A. Sowards, R. R. Naik, M. O. Stone, *J. Am. Chem. Soc.* **2003**, *125*, 580.
[25] R. McKendry, W. T. S. Huck, B. Weeks, M. Florini, C. Abell, T. Rayment, *Nano Lett.* **2002**, *2*, 713.
[26] A. Bruckbauer, L. M. Ying, A. M. Rothery, D. J. Zhou, A. I. Shevchuk, C. Abell, Y. E. Korchev, D. Klenerman, *J. Am. Chem. Soc.* **2002**, *124*, 8810.
[27] S. Matsubara, H. Yamamoto, K. Oshima, E. Mouri, H. Matsuoka, *Chem. Lett.* **2002**, 886.
[28] Y. M. Jung, S. J. Ahn, E. R. Kim, H. Lee, *J. Korean Phys. Soc.* **2002**, *40*, 712.
[29] X. Hong, L. Wei, W. Guo, J. Li, W. L. Song, Y. B. Bai, T. J. Li, *Chem. J. Chin. Univ.* **2002**, *23*, 1778.
[30] L. Wei, X. Hong, W. Guo, Y. B. Bai, T. J. Li, *Chem. J. Chin. Univ.* **2002**, *23*, 1386.
[31] J. H. Liao, L. Huang, N. Gu, *Chin. Phys. Lett.* **2002**, *19*, 134.
[32] H. L. Zhang, Y. Guo, H. L. Li, D. Q. Yang, *Chem. J. Chin. Univ.* **1999**, *20*, 1460.
[33] S. Rozhok, R. Piner, C. A. Mirkin, *J. Phys. Chem. B* **2003**, *107*, 751.
[34] K. B. Lee, S. J. Park, C. A. Mirkin, J. C. Smith, M. Mrksich, *Science* **2002**, *295*, 1702.
[35] S. P. A. Fodor, *Science* **1997**, *277*, 393.
[36] E. S. Lander, *Nat. Genet.* **1999**, *21*, 3.
[37] D. R. Walt, *Science* **2000**, *287*, 451.
[38] A. Schulze, J. Downward, *Nat. Cell Biol.* **2001**, *3*, E190.
[39] M. Kato-Maeda, Q. Gao, P. M. Small, *Cell. Microbiol.* **2001**, *3*, 713.
[40] P. G. Marciano, J. H. Eberwine, R. Raghupathi, T. K. McIntosh, *Restor. Neurol. Neurosci.* **2001**, *18*, 105.
[41] F. F. Bier, F. Kleinjung, *Fresenius J. Anal. Chem.* **2001**, *371*, 151.
[42] D. S. Wilson, S. Nock, *Angew. Chem.* **2003**, *115*, 510; *Angew. Chem. Int. Ed.* **2003**, *42*, 494.
[43] R. C. Jin, Y. W. Cao, C. A. Mirkin, K. L. Kelly, G. C. Schatz, J. G. Zheng, *Science* **2001**, *294*, 1901.
[44] R. Elghanian, J. J. Storhoff, R. C. Mucic, R. L. Letsinger, C. A. Mirkin, *Science* **1997**, *277*, 1078.
[45] T. A. Taton, C. A. Mirkin, R. L. Letsinger, *Science* **2000**, *289*, 1757.
[46] J. H. Lim, D. S. Ginger, K. B. Lee, J. Heo, J. M. Nam, C. A. Mirkin, *Angew. Chem.* **2003**, *115*, 2411; *Angew. Chem. Int. Ed.* **2003**, *42*, 2309.
[47] K. B. Lee, J. H. Lim, C. A. Mirkin, *J. Am. Chem. Soc.* **2003**, *125*, 5588.
[48] H. J. Dai, N. Franklin, J. Han, *Appl. Phys. Lett.* **1998**, *73*, 1508.
[49] G.-Y. Liu, N. A. Amro, *Proc. Natl. Acad. Sci. USA* **2002**, *99*, 5165.
[50] Y. Zhang, K. Salaita, J. H. Lim, C. A. Mirkin, *Nano Lett.* **2002**, *2*, 1389.
[51] M. Mrksich, *Curr. Opin. Chem. Biol.* **2002**, *6*, 794.
[52] J. C. Smith, K.-B. Lee, Q. Wang, M. G. Finn, J. E. Johnson, M. Mrksich, C. A. Mirkin, *Nano Lett.* **2003**, *3*, 883.
[53] C. L. Cheung, J. A. Camarero, B. W. Woods, T. W. Lin, J. E. Johnson, J. J. De Yoreo, *J. Am. Chem. Soc.* **2003**, *125*, 6848.
[54] Q. Wang, T. W. Lin, J. E. Johnson, M. G. Finn, *Chem. Biol.* **2002**, *9*, 813.
[55] Q. Wang, E. Kaltgrad, T. W. Lin, J. E. Johnson, M. G. Finn, *Chem. Biol.* **2002**, *9*, 805.
[56] L. M. Demers, C. A. Mirkin, *Angew. Chem.* **2001**, *113*, 3159; *Angew. Chem. Int. Ed.* **2001**, *40*, 3069.
[57] J. P. Hoogenboom, D. L. J. Vossen, C. Faivre-Moskalenko, M. Dogterom, A. van Blaaderen, *Appl. Phys. Lett.* **2002**, *80*, 4828.
[58] J. Aizenberg, P. V. Braun, P. Wiltzius, *Phys. Rev. Lett.* **2000**, *84*, 2997.

 © 2004 Wiley-VCH Verlag GmbH & Co. KGaA, Weinheim

[59] A. Ivanisevic, J. H. Im, K. B. Lee, S. J. Park, L. M. Demers, K. J. Watson, C. A. Mirkin, *J. Am. Chem. Soc.* **2001**, *123*, 12424.
[60] C. A. Mirkin, *MRS Bull.* **2000**, *25*, 43.
[61] N. C. Seeman, A. M. Belcher, *Proc. Natl. Acad. Sci. USA* **2002**, *99*, 6451.
[62] C. M. Niemeyer, *Angew. Chem.* **2001**, *113*, 4254; *Angew. Chem. Int. Ed.* **2001**, *40*, 4128.
[63] A. P. Alivisatos, K. P. Johnsson, X. G. Peng, T. E. Wilson, C. J. Loweth, M. P. Bruchez, P. G. Schultz, *Nature* **1996**, *382*, 609.
[64] L. M. Demers, S. J. Park, T. A. Taton, Z. Li, C. A. Mirkin, *Angew. Chem.* **2001**, *113*, 3161; *Angew. Chem. Int. Ed.* **2001**, *40*, 3071.
[65] J. C. Garno, Y. Y. Yang, N. A. Amro, S. Cruchon-Dupeyrat, S. W. Chen, G.-Y. Liu, *Nano Lett.* **2003**, *3*, 389.
[66] P. T. Hurley, A. E. Ribbe, J. M. Buriak, *J. Am. Chem. Soc.* **2003**, *125*, 11334.
[67] G. Agarwal, R. R. Naik, M. O. Stone, *J. Am. Chem. Soc.* **2003**, *125*, 7408.
[68] M. Su, V. P. Dravid, *Appl. Phys. Lett.* **2002**, *80*, 4434.
[69] G. M. Wallraff, W. D. Hinsberg, *Chem. Rev.* **1999**, *99*, 1801.
[70] Y. N. Xia, J. A. Rogers, K. E. Paul, G. M. Whitesides, *Chem. Rev.* **1999**, *99*, 1823.
[71] Y. Xia, G. M. Whitesides, *Angew. Chem.* **1998**, *110*, 568; *Angew. Chem. Int. Ed.* **1998**, *37*, 550.
[72] S. Y. Chou, *MRS Bull.* **2001**, *26*, 512.
[73] M. Albrecht, C. T. Rettner, A. Moser, M. E. Best, B. D. Terris, *Appl. Phys. Lett.* **2002**, *81*, 2875.
[74] Y. S. Kim, W. Hong, H. J. Woo, H. W. Choi, G. D. Kim, J. H. Lee, S. Lee, *Jpn. J. Appl. Phys. Part 1* **2002**, *41*, 4141.
[75] G. Y. Liu, S. Xu, Y. L. Qian, *Acc. Chem. Res.* **2000**, *33*, 457.
[76] Y. N. Xia, X. M. Zhao, E. Kim, G. M. Whitesides, *Chem. Mater.* **1995**, *7*, 2332.
[77] H. Zhang, K.-B. Lee, Z. Li, C. A. Mirkin, *Nanotechnology* **2003**, *14*, 1113.
[78] M. J. Tarlov, D. R. F. Burgess, G. Gillen, *J. Am. Chem. Soc.* **1993**, *115*, 5305.
[79] J. Y. Huang, J. C. Hemminger, *J. Am. Chem. Soc.* **1993**, *115*, 3342.
[80] J. Y. Huang, D. A. Dahlgren, J. C. Hemminger, *Langmuir* **1994**, *10*, 626.
[81] A. Ivanisevic, C. A. Mirkin, *J. Am. Chem. Soc.* **2001**, *123*, 7887.
[82] J. K. Jang, S. H. Hong, G. C. Schatz, M. A. Ratner, *J. Chem. Phys.* **2001**, *115*, 2721.
[83] J. K. Jang, G. C. Schatz, M. A. Ratner, *J. Chem. Phys.* **2002**, *116*, 3875.
[84] G. E. Poirier, E. D. Pylant, *Science* **1996**, *272*, 1145.
[85] G. E. Poirier, M. J. Tarlov, *Langmuir* **1994**, *10*, 2853.
[86] C. A. Widrig, C. A. Alves, M. D. Porter, *J. Am. Chem. Soc.* **1991**, *113*, 2805.
[87] S. H. Hong, J. Zhu, C. A. Mirkin, *Langmuir* **1999**, *15*, 7897.
[88] P. Vettiger, M. Despont, U. Drechsler, U. Durig, W. Haberle, M. I. Lutwyche, H. E. Rothuizen, R. Stutz, R. Widmer, G. K. Binnig, *IBM J. Res. Dev.* **2000**, *44*, 323.
[89] W. P. King, T. W. Kenny, K. E. Goodson, G. L. W. Cross, M. Despont, U. T. Durig, H. Rothuizen, G. Binnig, P. Vettiger, *J. Microelectromech. Syst.* **2002**, *11*, 765.
[90] E. M. Chow, G. G. Yaralioglu, C. F. Quate, T. W. Kenny, *Appl. Phys. Lett.* **2002**, *80*, 664.
[91] T. Sulchek, R. J. Grow, G. G. Yaralioglu, S. C. Minne, C. F. Quate, S. R. Manalis, A. Kiraz, A. Aydine, A. Atalar, *Appl. Phys. Lett.* **2001**, *78*, 1787.
[92] M. Zhang, D. Bullen, S. W. Chung, S. Hong, K. S. Ryu, Z. F. Fan, C. A. Mirkin, C. Liu, *Nanotechnology* **2002**, *13*, 212.
[93] L. M. Demers, G. della Cioppa, *Genet. Eng. News* **2003**, *23*, 32.
[94] X. Wang, K. S. Ryu, D. A. Bullen, J. Zou, H. Zhang, C. A. Mirkin, C. Liu, *Langmuir* **2003**, *19*, 8951.
[95] J. Zou, D. Bullen, X. F. Wang, C. Liu, C. A. Mirkin, *Appl. Phys. Lett.* **2003**, *83*, 581.
[96] T. Thorsen, S. J. Maerkl, S. R. Quake, *Science* **2002**, *298*, 580.
[97] D. Banerjee, J. Fragala, T. Duenas, R. Shile, B. Rosner in *Proceedings of the Seventh International Symposium on Miniaturized Chemical and Biochemical Analysis (micro-TAS 2003)* (Squaw Valley, October 5–9, 2003), **2003**, *1*, 58.
[98] A. Lewis, Y. Kheifetz, E. Shambrodt, A. Radko, E. Khatchatryan, C. Sukenik, *Appl. Phys. Lett.* **1999**, *75*, 2689.
[99] M. H. Hong, K. H. Kim, J. Bae, W. Jhe, *Appl. Phys. Lett.* **2000**, *77*, 2604.
[100] A. Bruckbauer, D. J. Zhou, L. M. Ying, Y. E. Korchev, C. Abell, D. Klenerman, *J. Am. Chem. Soc.* **2003**, *125*, 9834.
[101] K.-H. Kim, C. Ke, N. Moldovan, H. D. Espinosa in *Proceedings of the Society of Experimental Mechanics Annual Conference* (Charlotte, NC, 2.–4. June 2003), **2003**, 235.
[102] C. A. Mirkin, *Inorg. Chem.* **2000**, *39*, 2258.
[103] C. A. Mirkin, R. D. Piner, S. Hong, U.S. Patent App. No. 20020063212, May 24, **2001**.
[104] C. A. Mirkin, S. Hong, V. P. Dravid, U.S. Patent App. No. 20020122873, Jan. 28, **2002**.
[105] C. A. Mirkin, G. della Cioppa, L. Demers, K.-B. Lee, S.-J. Park, U.S. Patent App. No. 20030068446, Oct. 2, **2002**.
[106] C. A. Mirkin, V. P. Dravid, M. Su, X. Liu, U.S. Patent App. No. 20030162004, Dec. 17, **2002**.
[107] C. A. Mirkin, R. Piner, S. Hong, U.S. Patent App. No. 20030157254, Nov. 22, **2002**.
[108] X. G. Liu, S. W. Liu, C. A. Mirkin, *Angew. Chem.* **2003**, *115*, 4785; *Angew. Chem. Int. Ed.* **2003**, *42*, 4933.
[109] H. Jung, R. Kulkarni, C. P. Collier, *J. Am. Chem. Soc.* **2003**, *125*, 12096.
[110] X. G. Liu, L. Fu, S. H. Hong, V. P. Dravid, C. A. Mirkin, *Adv. Mater.* **2002**, *14*, 231.
[111] D. J. Pena, M. P. Raphael, J. M. Byers, *Langmuir* **2003**, *19*, 9028.
[112] M. Su, S. Y. Li, V. P. Dravid, *J. Am. Chem. Soc.* **2003**, *125*, 9930.

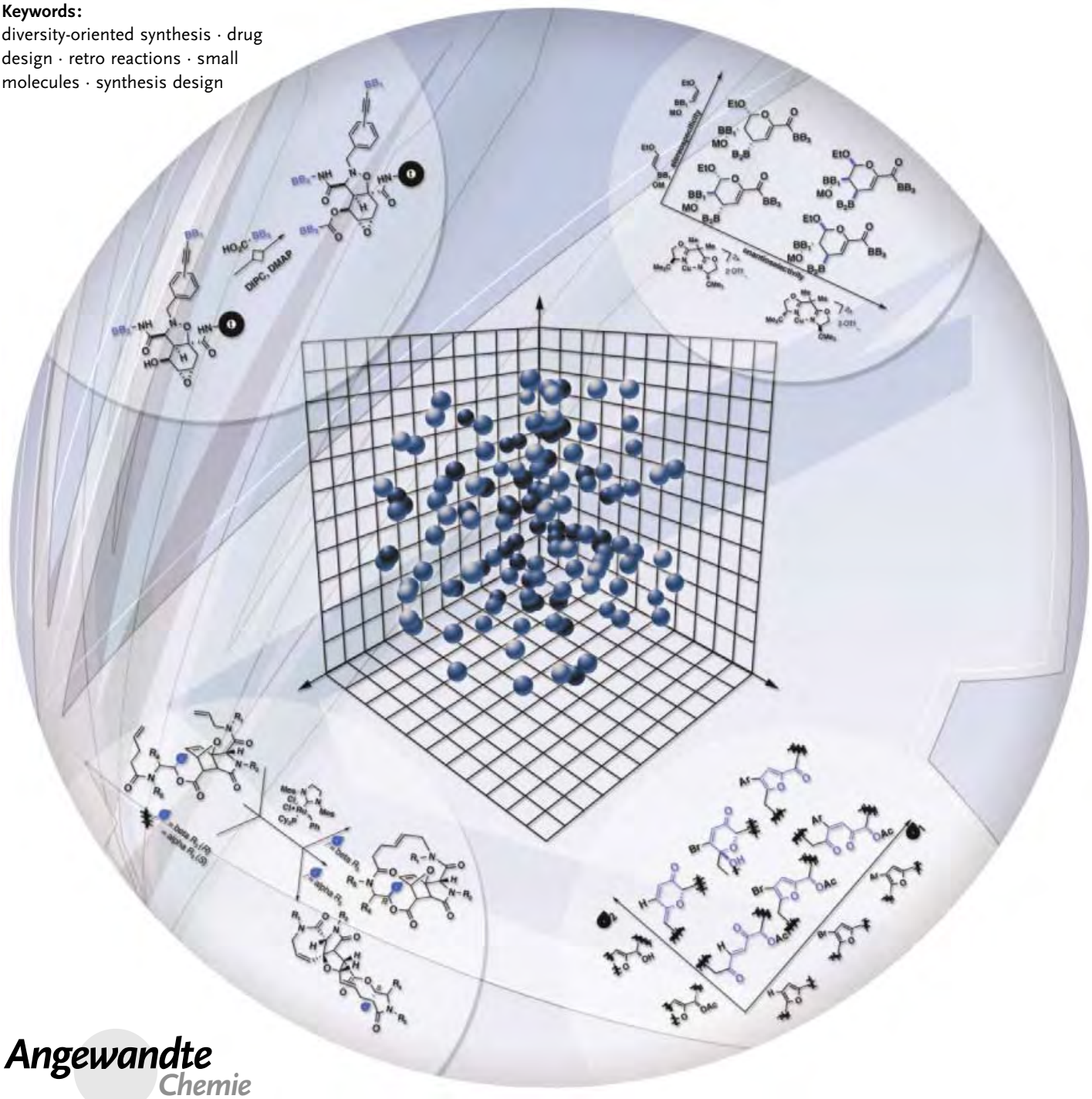
 © 2004 Wiley-VCH Verlag GmbH & Co. KGaA, Weinheim

Discovery of Small Molecules

A Planning Strategy for Diversity-Oriented Synthesis

*Martin D. Burke and Stuart L. Schreiber**

Keywords:
diversity-oriented synthesis · drug design · retro reactions · small molecules · synthesis design



© 2004 Wiley-VCH Verlag GmbH & Co. KGaA, Weinheim

DOI: 10.1002/anie.200300626

In contrast to target-oriented synthesis (TOS) and medicinal or combinatorial chemistry, which aim to access precise or dense regions of chemistry space, diversity-oriented synthesis (DOS) populates chemical space broadly with small-molecules having diverse structures. The goals of DOS include the development of pathways leading to the efficient (three- to five-step) synthesis of collections of small molecules having skeletal and stereochemical diversity with defined coordinates in chemical space. Ideally, these pathways also yield compounds having the potential to attach appendages site- and stereoselectively to a variety of attachment sites during a post-screening, maturation stage. The diverse skeletons and stereochemistries ensure that the appendages can be positioned in multiple orientations about the surface of the molecules. TOS as well as medicinal and combinatorial chemistries have been advanced by the development of retrosynthetic analysis. Although the distinct goals of DOS do not permit the application of retrosynthetic concepts and thinking, these foundations are being built on, by using parallel logic, to develop a complementary procedure known as forward-synthetic analysis. This analysis facilitates synthetic planning, communication, and teaching in this evolving discipline.

From the Contents

1. Introduction 47
2. Retrosynthetic Analysis and Forward-Synthetic Analysis 48
3. Complexity-Generating Reactions and their Use in DOS To Generate Complex Products Efficiently (Simple→Complex) 49
4. Diversity-Generating Processes and their Use in DOS To Generate Diverse Products Efficiently (Similar→Diverse) 50
5. Integrated Forward-Synthetic Analysis for Generating Both Complexity and Diversity (Simple and Similar→Complex and Diverse) 55
6. A Challenge for Synthesis in the Future. 55
7. Summary 57

1. Introduction

Small-molecules can exert powerful effects on the functions of macromolecules that comprise living systems. This remarkable ability makes them useful, both as research tools for understanding life processes and as pharmacologic agents for promoting and restoring health. Synthetic organic chemists aim to gain access to these compounds using three general approaches.

The first approach uses target-oriented synthesis (TOS) and relies primarily on nature to discover small-molecules with useful, macromolecule-perturbing properties. Natural compounds can be identified in screens of extract mixtures, isolated, and then structurally characterized by using a variety of spectroscopic techniques. Once such a structure has been identified, it can become a target for chemical synthesis. The aim of the synthesis effort in TOS is to access a precise region of chemical space,[1] which is often defined by a complex natural product known to have a useful function (Figure 1 A).

The second approach uses either medicinal chemistry or combinatorial chemistry and aims to explore a dense region of chemistry space in proximity to a precise region known to have useful properties (Figure 1 B). The source of the starting or lead compounds can vary and may include a natural product, a known drug, or a rationally designed structure developed from a mechanistic hypothesis and/or a crystal structure of a macromolecule of interest.

Synthetic chemists' ability to access precise or dense regions of chemistry space defined by natural products or known drugs have led to major advances in the chemical and life sciences. Nevertheless, the following question remains unanswered: Are the regions of chemistry space defined by natural products and known drugs, which have been so intensely scrutinized to date, the best or most fertile regions for discovering small-molecules that modulate macromolecular function in useful ways? Given the extraordinary potential for such small molecules to promote the understanding and betterment of human health, it is urgent that organic chemists begin to answer this basic question. One aim of diversity-oriented synthesis[2] (DOS) is to meet this challenge.

The synthesis effort in DOS aims to create a broad distribution of compounds in chemistry space, including currently poorly populated (or even vacuous) space, and in the future, in space found empirically to correlate best with desired properties (Figure 1 C). The first step toward achieving this aim is to recognize that the problem of accessing broad regions of chemistry space is different than the problem of accessing precise or dense regions. These problems are different and, therefore, present distinct challenges and require distinct solutions.

[*] Dr. M. D. Burke, Prof. S. L. Schreiber
Department of Chemistry and Chemical Biology
Howard Hughes Medical Institute
ICCB, Harvard University
12 Oxford Street, Cambridge, MA 02138 (USA)
Fax: (+1) 617-495-0751
E-mail: sls@slsiris.harvard.edu

 DOI: 10.1002/anie.200300626 © 2004 Wiley-VCH Verlag GmbH & Co. KGaA, Weinheim

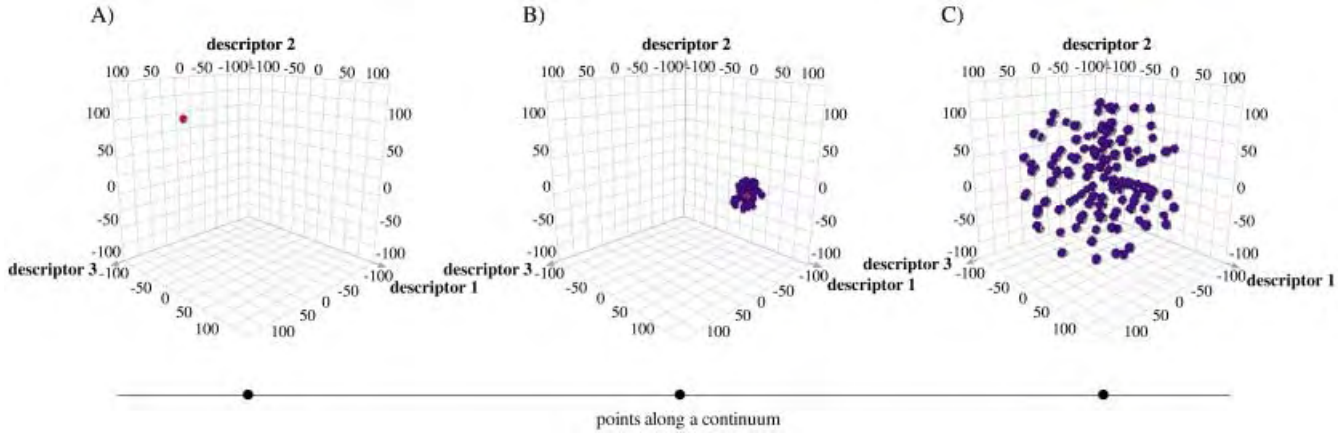


Figure 1. Comparison of TOS (A), medicinal and combinatorial chemistry (B), and DOS (C). Each three-dimensional plot is meant to represent the chemical product or collection of products derived from a single synthesis pathway. Each axis plots a calculable or measurable property of a small molecule (for example, molecular weight, solubility). A) The aim in TOS is to synthesize a single target structure having known or predicted properties (red sphere). B) The goal in medicinal and combinatorial chemistry is to synthesize a collection of analogues (blue spheres) of a target structure having known or predicted properties (red sphere). C) The aim in DOS is to populate chemistry space broadly with complex and diverse structures having unknown properties (blue spheres) as a first step in the small molecule discovery process. In some ways, these three approaches to synthesizing small-molecules represent points along a continuum.

TOS as well as medicinal and combinatorial chemistries have been advanced by the development (beginning over 40 years ago) of a general planning strategy known as retrosynthetic analysis,[3] in which a complex target is transformed into a sequence of progressively simpler structures by formally performing chemical reactions in the reverse-synthetic direction. Prior to this, strategic solutions to the problems of synthesizing different target structures were developed on a case-by-case basis. The introduction of a general planning strategy had a revolutionizing impact on these fields in at least three ways: by assisting chemists in planning efficient synthesis pathways that access complex target structures, by creating a language and defining concepts to facilitate communication between colleagues, and by providing a framework for teaching this field to new generations of organic chemistry students.

Retrosynthetic concepts and thinking depend on the existence of a defined target structure. Retrosynthetic analysis cannot be effectively applied in DOS because there is no single target structure. However, the foundations of retrosynthetic analysis are being used (by applying parallel logic) to develop a complementary strategy to facilitate synthetic planning, communication, and teaching within the realm of DOS.

2. Retrosynthetic Analysis and Forward-Synthetic Analysis

Synthesis pathways in TOS are linear and convergent, and they are planned in the reverse-synthetic direction by using retrosynthetic planning, which aims to move in the direction of complex→simple. In contrast, in DOS, where the structural complexity of the individual compounds and the structural diversity of the overall collection are maximized, synthesis pathways are branched and divergent, and they are planned in the forward-synthetic direction[4] by using forward-synthetic analysis. Forward-synthetic planning aims to move in the direction of simple and similar→complex and diverse. (Maximizing diversity and correlating structure with activity are inherently computational challenges. This article will not focus on these elements of DOS despite their critical nature;



Stuart L. Schreiber was born in Virginia, USA in 1956. He received his BA at the University of Virginia in 1977, completed his PhD at Harvard University under the supervision of R. B. Woodward and Y. Kishi, and joined the faculty at Yale University in 1981. In 1988 he returned to Harvard and is now an Investigator at the Howard Hughes Medical Institute, and Morris Loeb Professor and Chair of the Department of Chemistry and Chemical Biology. His research interests focus on developing systematic ways to explore biology and medicine using small molecules.



Martin D. Burke was born in 1976 in Maryland, USA. He graduated in chemistry from Johns Hopkins University in 1998 and recently completed his PhD thesis in synthetic organic chemistry under the supervision of Prof. Schreiber at Harvard University.

 © 2004 Wiley-VCH Verlag GmbH & Co. KGaA, Weinheim

here we simply note the recent launching of ChemBank on the Internet[5] as a first step towards providing the requisite tools to the chemical community.)

The basic subunit of retrosynthetic planning is the transform, that is, the theoretical transformation of a product into a substrate by formally performing a chemical reaction in the reverse-synthetic direction. To make use of a transform in retrosynthetic analysis one must first identify the corresponding "retron", that is, the enabling structural subunit ("keying element") that permits its application, in the chemical target. In contrast, the basic subunit of forward-synthetic planning is the process, namely, the transformation of a collection of substrates into a collection of products by performing a number of chemical reactions together in the forward-synthetic direction. The key element for implementing a process is common reactivity, that is, the inherent chemical reactivity common to a collection of compounds that makes them all potential substrates for the same reaction(s). To plan efficient DOS pathways containing iterative processes, it is critical to identify products-equals-substrates relationships, such that the products of one process have some common inherent chemical reactivity that makes them all potential substrates for another process.

TOS and DOS share the aim of accessing complex structures efficiently. Structurally simplifying transforms are critical in TOS when devising a retrosynthesis for a complex target structure, and iterative application of these transforms can lead to a plan for an efficient synthesis.[6] In contrast, when planning a diversity-oriented synthesis in the forward direction, complexity-generating reactions are most valuable for accessing complexity in an efficient manner. Moreover, identification of pairwise relationships, where the product of one complexity-generating reaction is the substrate for another, can lead to highly complex products with just a few synthetic steps.

TOS does not share the aim of accessing diversity. The aim in medicinal and combinatorial chemistry is to access diversity to some degree, and usually involves synthesizing analogues of a given target structure. This can be accomplished efficiently using solid-phase synthesis[7] to append different sets of building blocks to a common molecular skeleton.[8] Retrosynthetic planning is used in this context to devise pathways to a target structure that permit the addition of diverse sets of building blocks during the actual synthesis. If this common skeleton contains multiple reactive sites with potential for orthogonal functionalization, the powerful technique of split-pool synthesis[9] can be used to access all possible combinations of building blocks (namely, the complete matrix) efficiently. In DOS, where there is no one target structure, the problem of diversity is subdivided into three diversity elements: appendages (for example, building blocks and "σ elements"; see below), stereochemistry, and molecular skeletons. Forward-synthetic planning aimed at accessing these diversity elements relies on the use of diversity-generating processes, which is defined as the transformation of a collection of relatively similar substrates into a collection of more diverse products. In an ideal DOS pathway all of the products of one diversity-generating process are substrates for another, thus making it possible to use split-pool synthesis to access combinatorially matrices of building blocks, stereochemical isomers, and even molecular skeletons.

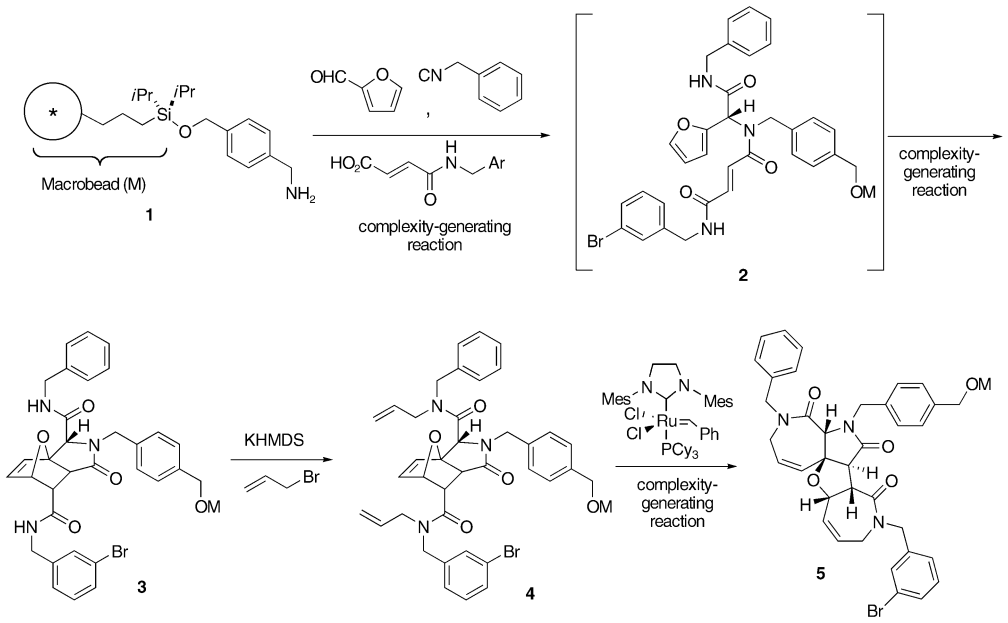
3. Complexity-Generating Reactions and their Use in DOS To Generate Complex Products Efficiently (Simple→Complex)

The structures and functions of natural products suggest that structural complexity may be positively correlated with macromolecule-perturbing function and specificity of action. This correlation is particularly striking in small molecules known to disrupt protein–protein interactions. Therefore, it is a goal of DOS to access small molecules with complex molecular skeletons,[10] and forward-synthetic planning aims to proceed in the direction of simple→complex. Moreover, in contrast to the relatively flat molecular skeletons often used in medicinal and combinatorial chemistry that tend to project appendages outward along the perimeter of a circle, the aim in DOS is to access more globular or spherical molecular skeletons to which substituents can be potentially appended along the surface of a sphere during a post-screening, optimization stage.

To maximize efficiency and, in the case of researchers affiliated with ICCB,[11] to be compatible with one-bead/one-stock solution technology platforms, synthesis pathways in DOS should be no more than three to five steps (which leaves no room for protective-group manipulations). Therefore, to achieve skeletal complexity in DOS it is critical to identify and to implement complexity-generating reactions that rapidly assemble complex molecular skeletons. Moreover, the identification in the forward direction of pairwise relationships, where the product of one complexity-generating reaction is the substrate for another,[12] can lead to high levels of molecular complexity in a very efficient manner.

For example, as shown in Scheme 1, the Ugi four-component coupling reaction[13] can be used to assemble a complex product from simple starting materials in a single step. If those simple starting materials are selected to include both a diene and a dienophile, then the product of this first complexity-generating reaction **2** is a substrate for another, namely an intramolecular Diels–Alder reaction.[14] The identification of this pairwise relationship made it possible to generate complex molecular skeleton **3** from simple starting materials in a single synthetic step. Moreover, it was recognized that the product **3** is almost a substrate for an additional complexity-generating reaction, namely a ring-opening/ring-closing metathesis,[15] and can be transformed into such a substrate (**4**) by bisallylation with KHMDS and allyl bromide. (This type of forward-synthetic planning is analogous to the identification of partial retrons and the use of functional-group manipulations to make the application of structurally simplifying transforms possible in retrosynthetic analysis.) Treatment of **4** with the Grubbs catalyst[16] resulted in a complexity-generating ring-opening/ring-closing metathesis reaction to generate product **5**, which has a highly complex 7-5-5-7 polycyclic molecular skeleton.

 © 2004 Wiley-VCH Verlag GmbH & Co. KGaA, Weinheim



Scheme 1. Three-step synthesis of a complex 7-5-5-7 polycyclic ring system using complexity-generating reactions having the product-equals-substrate relationship. KHMDS = potassium 1,1,1,3,3,3-hexamethyldisilazine, Mes = 2,4,6-trimethylphenyl, Cy = cyclohexyl.

4. Diversity-Generating Processes and their Use in DOS To Generate Diverse Products Efficiently (Similar→Diverse)

DOS pathways aim to proceed in the direction of similar structures→diverse structures to gain access to broad regions of chemistry space efficiently. To achieve this requires planning (in the forward direction) a series of products-equals-substrates relationships, that is, the products of one diversity-generating process should share some common inherent chemical reactivity. This common reactivity serves as a keying element that makes the products collective substrates for a subsequent diversity-generating process. The goal of achieving diversity can be simplified by considering three distinct diversity elements: appendages, stereochemistry, and skeletons.

4.1. Appendage Diversity

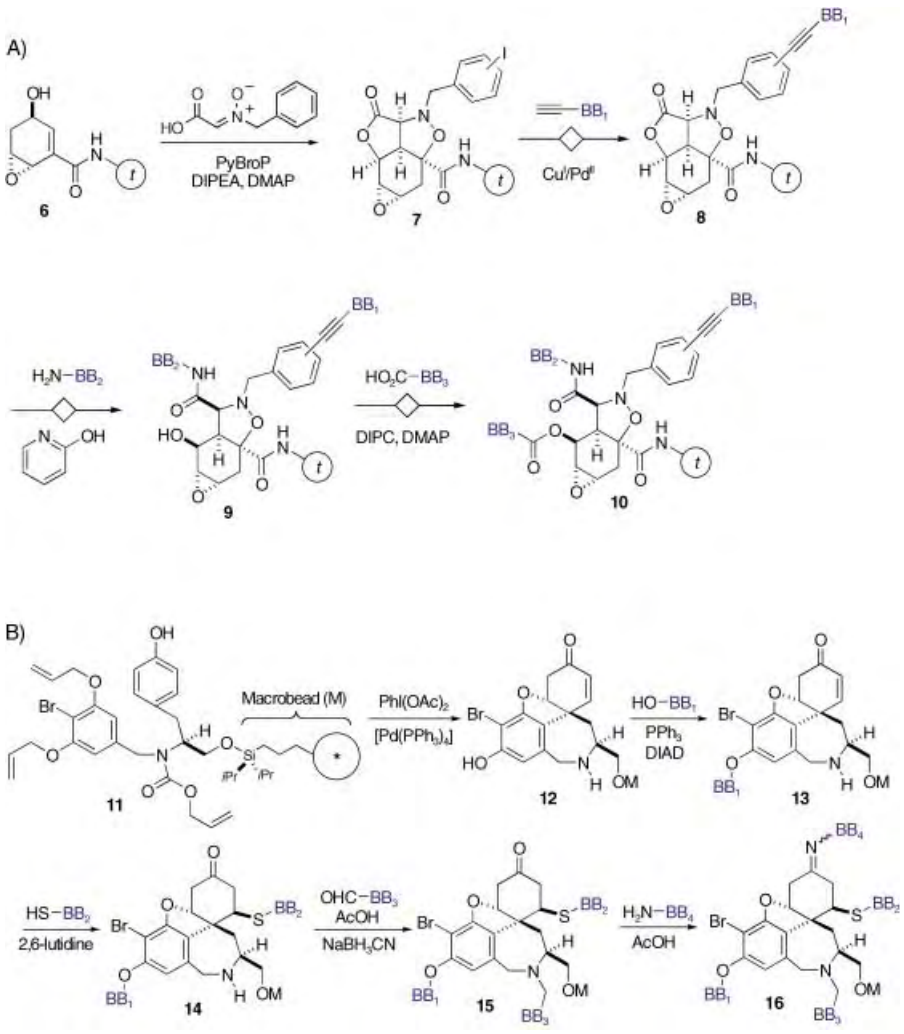
The simplest diversity-generating process is the central feature of combinatorial chemistry and involves the use of coupling reactions to attach different appendages to a common molecular skeleton. In forward-synthetic analysis these are referred to as appending processes. If a molecular skeleton has multiple reactive sites with potential for orthogonal functionalization, then the technique of split-pool synthesis can be used to harness the power of combinatorics (a multiplicative increase in the number of products with an additive increase in the number of reaction conditions), and thereby generate all possible combinations of appendages (that is, the complete matrix) efficiently.

The origins of DOS were combinatorial chemistry efforts that simply used increasingly sophisticated organic transformations. These efforts began with a complexity-generating reaction to yield a single, complex molecular skeleton having several attachment points followed by a series of diversity-generating appending processes (potentially in split-pool format) to attach all possible combinations of building blocks to this common skeleton. This one-synthesis/one-skeleton approach has proven to be highly general and capable of generating hundreds, thousands, or even millions of distinct small molecules in just three to five steps.[8,17,18]

For example, a complexity-generating, consecutive transesterification–cycloaddition reaction was used to generate, in one step, the tetracyclic skeleton **7** with potential for functionalization through a series of diversity-generating appending processes (Scheme 2A).[17] A Sonogashira coupling reaction was first used to append a diverse collection of alkyne building blocks (BB_1) to the iodoaryl moiety of **7** and thereby to generate the collection of more diverse products **8**. Although these products differ in the identity of BB_1, they all have a common electrophilic lactone moiety. This common reactivity makes this collection of products **8** of the first diversity-generating appending process a collection of potential substrates for another appending process, namely, an amine-mediated lactone-opening reaction that generated a collection of new products **9**. Similarly, while members of this new collection of products **9** differ in the identity of both BB_1 and BB_2, they all share a common nucleophilic secondary hydroxy group, thus making them all substrates for a third appending process that resulted in their coupling with a collection of carboxylic acid building blocks (BB_3). This series of products-equals-substrates relationships made it possible to carry out this four-step synthetic pathway by using split-pool synthesis and thereby generate the complete matrix of building blocks **10** in a highly efficient manner.

A second example that vividly illustrates the power of a complexity-generating reaction is shown in Scheme 2B. In this case, a biomimetic, complexity-generating oxidative

 © 2004 Wiley-VCH Verlag GmbH & Co. KGaA, Weinheim



Scheme 2. Building-block diversity generated combinatorially. See text for details. A) Split-pool synthesis of compounds derived from Shikimic acid. The encircled "*t*" represents a solid support of tentagel. The diamond-filled arrow is used to represent an appending process carried out in split-pool format. B) Diversity-oriented synthesis of galanthamine-related compounds. PyBroP = bromotris(pyrrolidino)phosphonium hexafluorophosphate, DIPEA = *N*,*N*-diisopropylethylamine, DMAP = 4-dimethylaminopyridine, DIPC = diisopropylcarbodiimide, DIAD = diisopropylazodicarboxylate.

cyclization reaction was used to transform acyclic precursor **11** into the rigid skeleton **12**, which has four sites of potential reactivity (two nucleophilic and two electrophilic) that can each be orthogonally functionalized by a series of diversity-generating appending processes.[18] In the first of these appending process, a Mitsunobu reaction was used to couple a diverse collection of building blocks derived from primary alcohols to the phenolic alcohol of **12**. The products **13** of this process share a common cyclic enone functionality, which was selectively functionalized by the conjugate addition of a collection of thiols (BB_2). While the products of this second appending process differ in terms of the identities of BB_1 and BB_2, they all share a common nucleophilic secondary amine, which makes them all substrates for a third appending process involving coupling to a diverse collection of aldehyde, acid chloride, and isocyanate building blocks (BB_3, only the aldehydes are shown). The resulting collection of products **15** represents all possible combinations of a three-dimensional matrix of building blocks, yet they all share a common electrophilic ketone. This common moiety imparts common reactivity to all the members of this collection, and made it possible to carry out a final appending process with a diverse collection of hydrazine and hydroxylamine building blocks (BB_4). In this example a consecutive series of four products-equals-substrates relationships enabled the efficient generation of a four-dimensional, combinatorial matrix of building block diversity elements appended to a complex molecular skeleton **16**.

This one-synthesis/one-skeleton approach has proven to be general and highly efficient;[8] however, its impact in the academic and pharmaceutical realms has thus far been limited.[19] This may be because compounds having a common molecular skeleton display chemical information similarly in three-dimensional space, thus limiting the pool of potential binding partners to only those macromolecules with a complementary three-dimensional binding surface. Thus, an important (and intellectually challenging) aim in DOS is to develop efficient synthesis pathways that yield products that represent many diverse displays of chemical information in three-dimensional space. To achieve this goal it is necessary to gain efficient access to stereochemical and skeletal diversity.

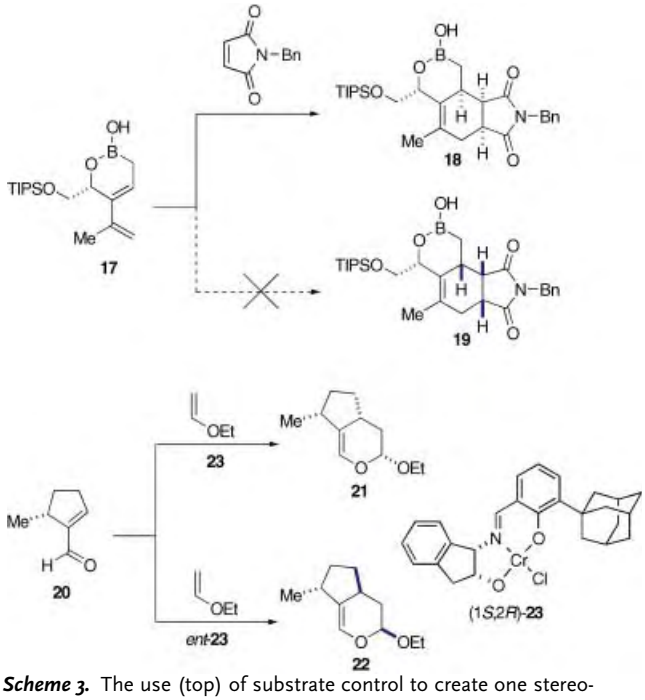
4.2. Stereochemical Diversity

Stereochemical diversity increases the number of relative orientations of potential macromolecule-interacting elements in small molecules. It can best be achieved by using stereospecific reactions that proceed with enantio- or diastereoselectivity. The corresponding transforms for these types of processes are well-known in the context of retrosynthetic planning. Since diversity-generating processes involve the transformation of a collection of substrates into a collection of products, it is critical that the processes used to generate new stereogenic centers are both selective and general.[20] The collective transformation of chiral substrates into products having increased stereochemical diversity (namely, diaster-

 © 2004 Wiley-VCH Verlag GmbH & Co. KGaA, Weinheim

eoselective diversity-generating processes) requires powerful reagents that can override substrate bias and deliver diastereomeric products with very high selectivity.[21]

For example, a diastereoselective intermolecular Diels–Alder reaction was used to transform the chiral dialkenylboronic acid **17** into the cycloadduct **18**, with the selective formation of three new stereogenic centers (Scheme 3).[22]



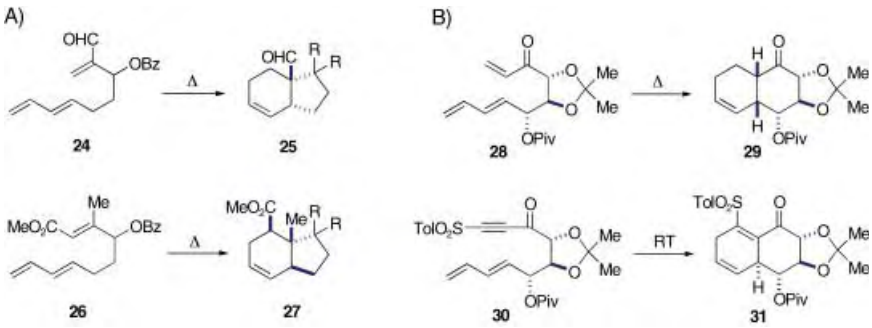
Scheme 3. The use (top) of substrate control to create one stereoisomer selectively and (bottom) of a chiral reagent **23** to override the stereochemical bias of a chiral substrate—a possible solution to the challenge of stereochemical diversity in DOS. TIPS = triisopropylsilyl, Bn = benzyl.

This reaction and its relatives represent a promising development for application to DOS pathways. It also illustrates the double-edged sword of highly stereoselective reactions. Since the diastereoselectivity of this transformation is under a powerful substrate control (steric interactions with the TIPS-protected hydroxymethyl group direct cycloaddition to the less sterically hindered face of the diene) it may prove challenging to generate the opposite diastereomeric product **19**.

Clues for progress come from advances made in double (more generally, multiple) diastereoselection reactions.[23] For example, Jacobsen and co-workers have demonstrated the use of chiral catalyst **23**, which can override the stereochemical bias of a chiral substrate and generate diastereomeric products with high selectivity.[24,25] Since transformations with such a catalyst are reagent-controlled, it is possible to use both enantiomers of **23** in a diastereoselective stereochemical diversity-generating process and thereby transform a common, chiral substrate into a collection of products having increased stereochemical diversity. For example, (1*S*,2*R*)-**23** was used to transform chiral enal **20** into dihydropyran **21** through a catalyst-controlled inverse-electron-demand diastereoselective hetero-Diels–Alder reaction.[25] Alternatively, it was possible to override the stereochemical bias of the chiral substrate and generate the diastereomeric dihydropyran **22** using the enantiomer of this catalyst, (1*R*,2*S*)-**23**. The discovery of these types of powerful reagents is critical to achieving stereochemical diversity in DOS. While catalysts such as **23** are capable of controlling the face selectivity of one coupling partner (in this case the chiral enal substrate), the development of double-diastereoselective reagents that can override the face selectivity of both coupling partners, for example, to achieve *exo* versus *endo* selectivity in the Diels–Alder reaction, would be highly valuable. For example, chemists have succeeded in discovering highly effective catalysts to yield the *endo*-Diels–Alder product of cyclopentadiene and acrolein enantioselectively. It remains as a formidable challenge, however, to develop an effective catalyst for the same reaction that yields the *exo* product enantioselectively.

While certain types of stereochemical flexibility (for example, the ability to achieve both *exo* and *endo* relative face selectivity in a Diels–Alder reaction process) are sometimes difficult to achieve in intermolecular reactions, there are a number of examples of this type of stereochemical control in intramolecular transformations. In the Diels–Alder example, Alder's "*endo* rule" is often not obeyed when the reaction is performed in the intramolecular mode.[26] In this case, subtle changes in the structure of substrates can exert powerful effects on the stereochemical outcome of intramolecular reactions that produce new stereogenic centers.[26–28] Such controlling elements may prove to be valuable for achieving stereochemical diversity in DOS.

For example, Roush and co-workers found that the position of the activating carbonyl group of the dienophile in substrates such as **24** and **26** can control *exo* versus *endo* selectivity for intramolecular Diels–Alder reactions (Scheme 4 A).[26] Substrate **24**, with an activating aldehyde group on the internal position of the dienophile, yields predominantly the *cis*-fused perhydroindan ring system (*exo* product). Alter-

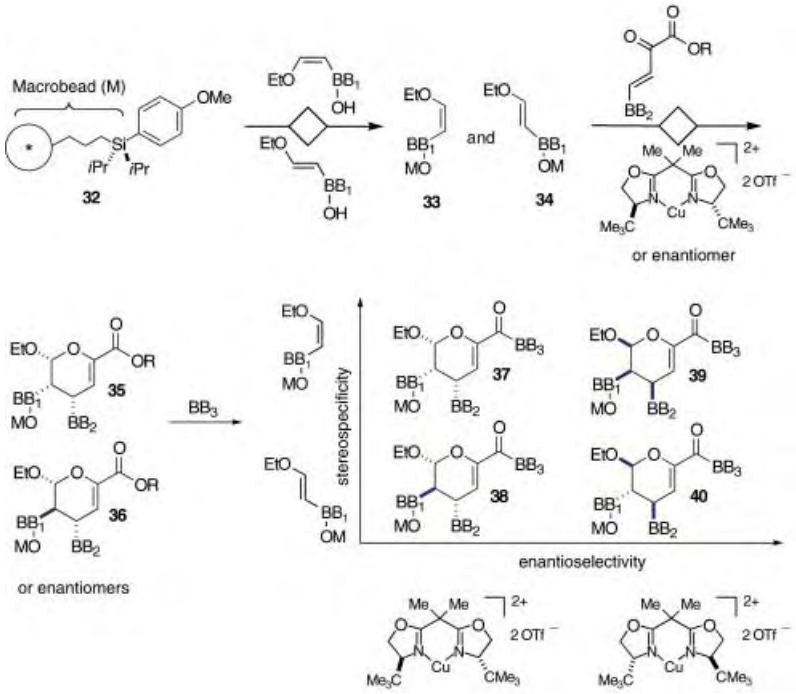


Scheme 4. Subtle changes in substrate structure can dictate distinct stereochemical outcomes for intramolecular reactions that generate new stereogenic centers. Bz = benzoyl, Tol = tolyl, Piv = trimethylacetyl.

 © 2004 Wiley-VCH Verlag GmbH & Co. KGaA, Weinheim

natively, the terminally activated substrate **26** undergoes an intramolecular Diels–Alder reaction to yield the *trans*-fused (*endo*) cycloadduct as the major product. Sulikowski and coworkers reported that intramolecular Diels–Alder cycloaddition with vinyl ketone **28** and alkynone **30** led to cycloaddition adducts with opposite diastereoselectivity (Scheme 4B).[28] It is conceivable that these types of stereochemical diversity-generating transformations could be carried out with spatially segregated, pooled substrates under common reaction conditions.

Forward-synthetic planning that incorporates multiple stereochemical diversity-generating processes into a single pathway should also make it possible to generate stereochemical diversity in a combinatorial fashion, analogous to the ability of appending processes to generate building-block diversity in a combinatorial manner. An early example of this is shown in the DOS pathway in Scheme 5, in which both stereospecific and enantioselective stereochemical diversity-generating processes were used to generate a combinatorial matrix of four stereoisomeric products.[29]



Scheme 5. Combinatorial stereochemical diversity: both stereospecific and enantioselective stereochemical diversity-generating processes were used to generate a combinatorial matrix of four stereoisomeric products. Tf = trifluoromethanesulfonyl.

4.3. Skeletal Diversity

DOS pathways that yield collections of products with many distinct molecular skeletons are particularly effective at achieving a diverse display of chemical functionality in three-dimensional space. There are, at present, two different strategies for planning DOS pathways that generate skeletal diversity.

The first strategy involves using different reagents to transform a common substrate with the potential for diverse reactivity into a collection of products having distinct molecular skeletons (Figure 2A).[2,30] This approach is analogous to the natural process of cell differentiation in which a

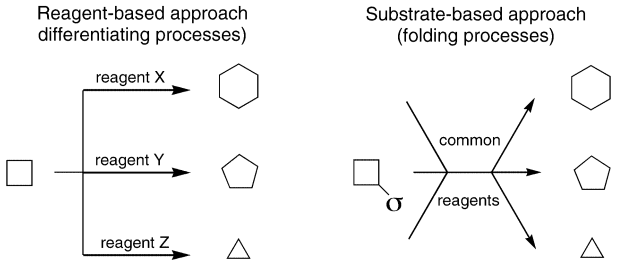


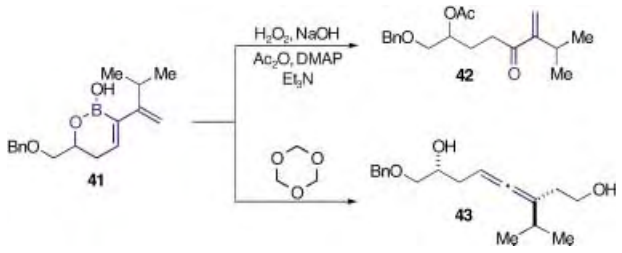
Figure 2. Two general approaches for planning synthesis pathways that generate skeletal diversity. See text for details.

pluripotent stem cell is transformed into different cell types on exposure to distinct differentiation factors. These reagent-based skeletal diversity-generating transformations are, therefore, also referred to as differentiating processes. For example, the unsaturated, cyclic dialkenylboronic ester **41** has potential for diverse reactivity, and thus, different reagents can be used to transform this common, pluripotent substrate into different products (Scheme 6; two are shown), each having a distinct molecular skeleton.[31] Treatment of **41** with hydrogen peroxide and sodium hydroxide effects an oxidation which leads to enone **42**. Alternatively, treatment of the same substrate with 1,3,5-trioxane effects transformation into the trisubstituted allene **43**.

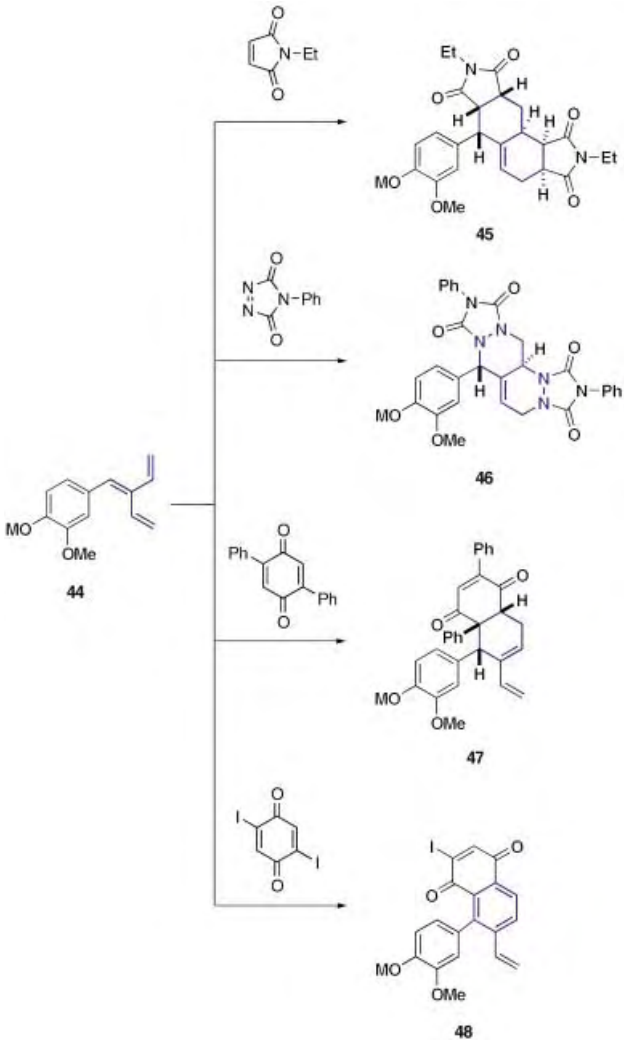
Another example of this reagent-based approach for generating skeletal diversity is shown in Scheme 7. It was determined that the Fallis-type[32] triene **44** is another pluripotent substrate that can be transformed into a collection of products with distinct molecular skeletons by the actions of different reagents.[33] For example, treatment of **44** with highly reactive, cyclic disubstituted dienophiles such as ethyl maleimide led to double cycloaddition reactions and yielded unsaturated decalin skeletons functionalized with maleimide-derived building blocks (for example, **45**). Treatment of the same substrate **44** with a different reagent, specifically a substituted triazol-3,5-dione, produced an unsaturated tetraazadecalin skeleton **46** through a hetero-Diels–Alder reaction. Treatment of **44** with less-reactive tri- and tetrasubstituted dienophiles resulted in single cycloaddition reactions and yielded functionalized cyclohexene derivatives such as **47**. Alternatively, treatment of **44** with halogenated quinones resulted in cycloaddition followed by spontaneous dehydrohalogenation and aromatization to yield benzene derivatives such as **48**.

In contrast to appending processes, these differentiating processes have not (as of yet) been used to generate skeletal

 © 2004 Wiley-VCH Verlag GmbH & Co. KGaA, Weinheim



Scheme 6. A differentiating process: the use of different reagents to transform a common, pluripotent substrate into a collection of products having distinct molecular skeletons.



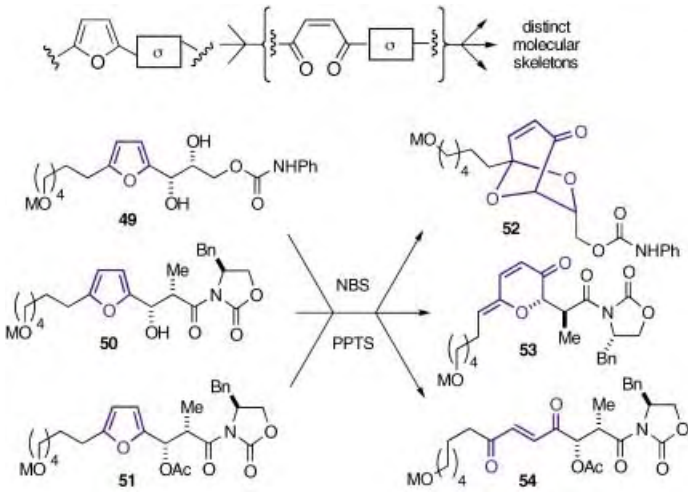
Scheme 7. The transformation of a common, pluripotent substrate into products having distinct skeletons by the actions of different reagents.

diversity combinatorially. Doing so will require the identification of differentiating processes having the products-equals-substrates relationship, that is, all of the skeletally distinct products of one differentiating process must share a common chemical reactivity that makes them all potential substrates for another differentiating process. This type of forward-synthetic planning is challenging, and will require nonmutually exclusive approaches to the two, potentially conflicting, goals of maximizing structural diversity and maintaining common reactivity.

An alternative synthesis strategy circumvents this potential conflict. In this case, diverse skeletons of small molecules can be accessed combinatorially by transforming a collection of substrates having different appendages that pre-encode skeletal information (called σ elements) into a collection of products having distinct molecular skeletons using common reaction conditions (Figure 2B).[34] This strategy is analogous to the natural process of protein folding,[35] in which different structural information pre-encoded in primary amino acid sequences is transformed into structurally diverse macromolecules using a common folding buffer. Thus, these substrate-based skeletal diversity-generating transformations are referred to as folding processes in forward-synthetic analysis. An advantage of this approach is that sets of σ elements can be identified that act in combination, that is, a matrix of σ elements can pre-encode all combinations of distinct skeletal outcomes.

These folding processes can be planned by first identifying a relatively unreactive core structure that can be transformed into a more reactive intermediate upon treatment with mild reagents. Distinct skeletal outcomes can then be pre-encoded into a collection of substrates by attaching to this common core different appendages (σ elements) having complementary reactivity with the latent, reactive intermediate. Mild conditions can then be used to liberate the reactive intermediate and to realize the pre-encoded, complementary reactivity, thus resulting in the formation of different skeletons.

The aromatic furan ring, for example, is a relatively unreactive core structure that, upon treatment with a mild oxidant, can be transformed into a more reactive, electrophilic *cis*-enedione intermediate.[36] As shown in Scheme 8, by appending three distinct two-carbon side chains containing



Scheme 8. A skeletal diversity-generating folding process: the transformation of substrates having different σ elements (that is, appendages that pre-encode skeletal information) into products having different skeletons under a common set of reaction conditions.

 © 2004 Wiley-VCH Verlag GmbH & Co. KGaA, Weinheim

two, one, or zero nucleophilic hydroxy groups to a common furan core, it was possible to transform three structurally similar substrates into three products having distinct molecular skeletons through a common set of oxidative and acidic reaction conditions (NBS and PPTS, respectively). Furan derivative **49**, with a side chain containing two nucleophilic hydroxy groups, underwent NBS-mediated oxidative ring expansion and subsequent ketalization[37] to yield the [3.2.1]bicyclic ketal **52.** Alternatively, the Evans aldol product **50**, with a single hydroxy group on its side chain, underwent oxidative ring expansion and acid-catalyzed dehydration to yield the alkylidene pyran-3-one **53**. Finally, treatment of furan derivative **51**, with no nucleophilic hydroxy groups on its two-carbon side chain, under the same reaction conditions resulted in oxidative opening of the furan ring followed by olefin isomerization[38] to yield the *trans*-enedione **54**.

The use of this substrate-based approach to generate skeletal diversity combinatorially (namely, achieving a multiplicative increase in skeletons with an additive increase in appendages) requires at least two sets of σ elements that can be appended at different sites and function in combination to pre-encode a matrix of distinct skeletal outcomes. For example, it was determined that different appendages at the 4-position of the furan core can also pre-encode distinct molecular skeletons. Moreover, a combinatorial matrix of these two different σ elements (H, Br, or aryl at the 4-position of furan combined with OH or OAc on the α carbon atom; a 3×2 matrix) can pre-encode a complete, combinatorial matrix of six distinct skeletal outcomes that were realized in a one-pot reaction under common conditions (Scheme 9).

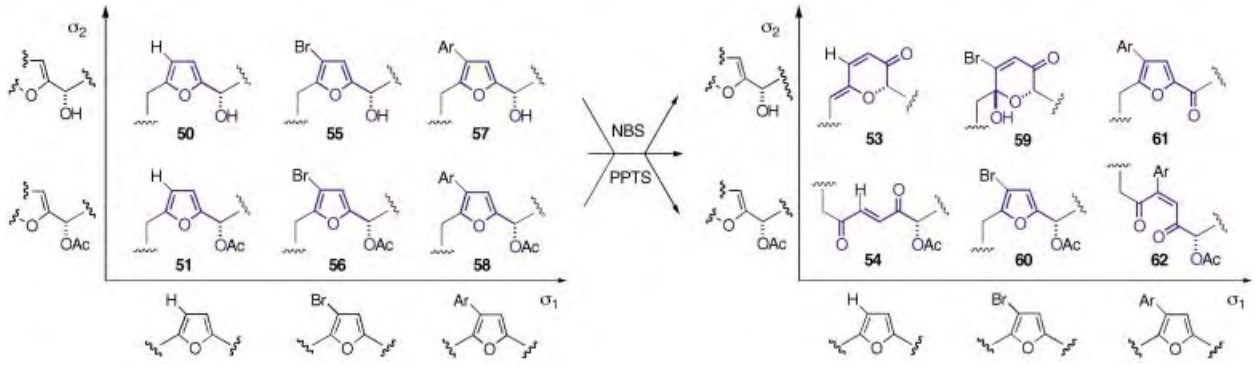
In contrast to the one-synthesis/one-skeleton approach (which typically involves forming a single molecular skeleton early in a synthesis), a folding process can be used to generate new skeletons at the end of a synthesis pathway. This approach facilitates the generation of functionalized skeletons that might otherwise be difficult to access, such as those having building blocks coupled through carbon–carbon bonds at stereogenic quaternary carbon centers (for example, **59**) and/or potentially unstable structural elements (for example, enediones **54** and **62**). Additionally, σ elements can be attached to a common molecular skeleton by using appending processes (similar to the way building blocks are appended in the one-synthesis/one-skeleton approach). The maintenance of structural similarity and, therefore, common reactivity until late in the synthesis pathway facilitates the realization of this approach using the split-pool technique. These potential advantages were realized in the context of a five-step, fully encoded, split-pool synthesis which yielded a collection of products representing overlapping, combinatorial matrices of molecular skeletons and appended building blocks in both enantiomeric and diastereomeric forms (Scheme 10).

5. Integrated Forward-Synthetic Analysis for Generating Both Complexity and Diversity (Simple and Similar→Complex and Diverse)

As described in the previous sections, two goals of DOS (namely, generating structural complexity and structural diversity in an efficient manner) can be considered independently, and different strategies have been developed to address each of these distinct challenges. However, achieving high levels of both complexity and diversity in the context of a single DOS pathway will require integrated forward-synthetic planning. One logical approach is to incorporate complexity-generating reactions into stereochemical and skeletal diversity-generating processes. This is another challenging frontier—however, some recent progress suggests that this approach can be effective (Scheme 11).[39]

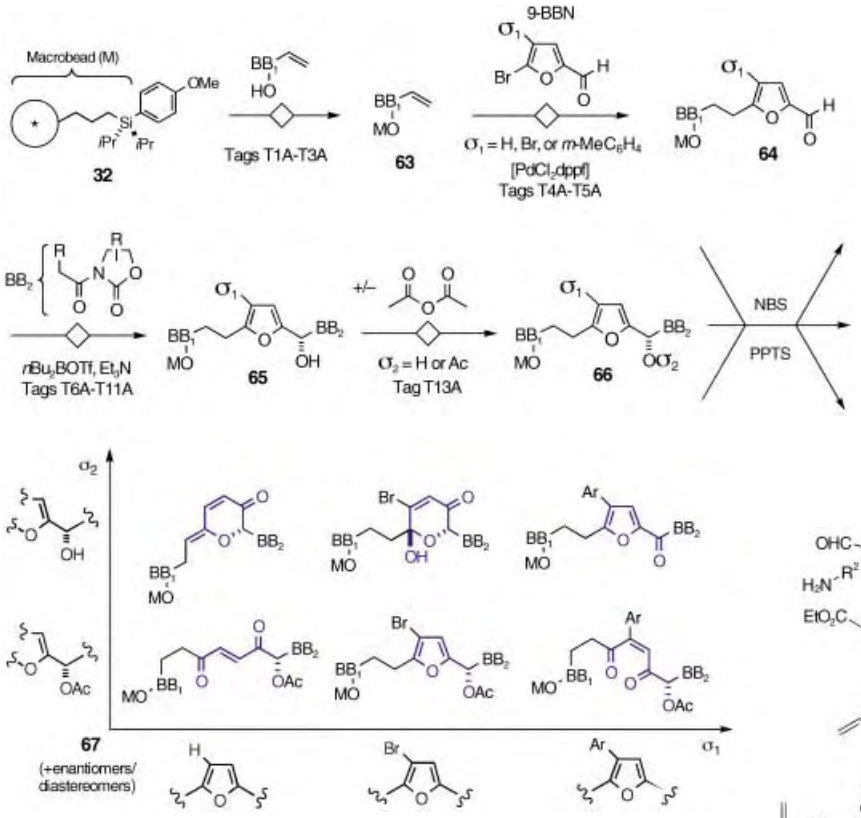
6. A Challenge for Synthesis in the Future.

DOS, as it has evolved in 2004, entails the development of pathways leading to the efficient (3–5 step) synthesis of collections of small molecules having rich skeletal and stereochemical diversity and, we propose here, the potential to attach appendages (during a post-screening, maturation stage) site- and stereoselectively to several attachment sites (Scheme 12). In contrast to earlier efforts in DOS, as well as to past and present efforts in medicinal and combinatorial chemistry, we suggest that appending processes involving building blocks (as distinct from σ elements) should be of less importance in the original synthesis. Incorporating untapped



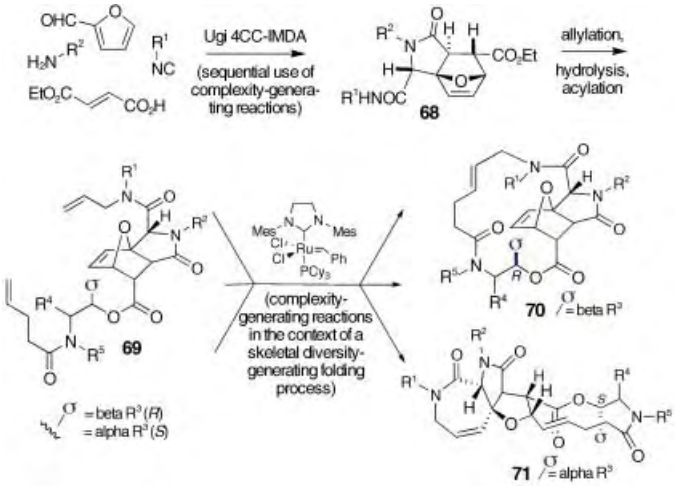
Scheme 9. Combinatorial skeletal diversity: the transformation of a collection of substrates having a combinatorial matrix of σ elements appended to a common molecular skeleton into a collection of products that represents a complete, combinatorial matrix of distinct skeletal possibilities. NBS = *N*-bromosuccinimide, PPTS = pyridinium *p*-toluenesulfonate.

 © 2004 Wiley-VCH Verlag GmbH & Co. KGaA, Weinheim



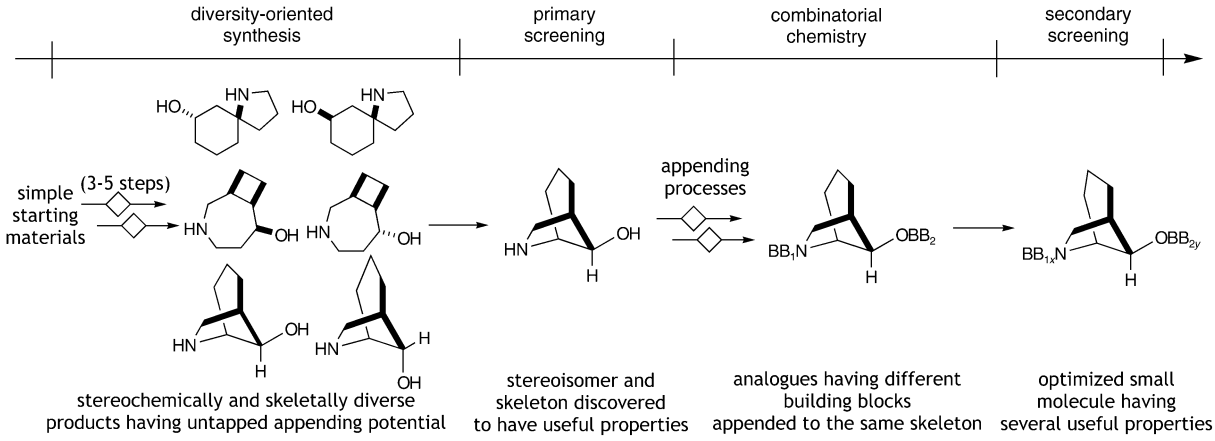
Scheme 10. Split-pool synthesis of a collection of compounds representing all possible combinations of building block, stereochemical, and skeletal diversity elements. 9-BBN = 9-borabicyclo[3.3.1]nonane, dppf = 1,1′-bis(diphenylphosphanyl)ferrocene.

synthetic chemistry. By including this consideration into future DOS pathways, the possibility for an overall discovery process illustrated in Scheme 12 is made possible, one that creates synergistic links between the strengths of DOS and combinatorial chemistry. Finally, subsets are selected from the large collection of potential products from any given DOS pathway for synthesis with guidance from computations of molecular descriptors, analyses of these descriptors relative to reference small-molecules previously annotated, and the application of filters to minimize undesired properties, especially poor solubility.



Scheme 11. The generation of both skeletal complexity and skeletal diversity through the incorporation of complexity-generating reactions into a skeletal diversity-generating folding process. It was determined that a single stereocenter in otherwise similar substrates **69** pre-encodes the formation of highly complex products **70** and **71**, which have very different molecular skeletons, under a common set of reaction conditions. This example also illustrates the potential of using folding processes to link stereochemical diversity to skeletal diversity.

appending potential into products of DOS pathways ensures the possibility for facile, post-screening appending processes that can ease the optimization of properties not examined in primary, "discovery" screens. In this way, synthetic planning anticipates the likely need for optimization and provides a unique and general solution for it—something not yet addressed, to our knowledge, in other applications of



Scheme 12. A potentially general approach for discovering small molecules with useful properties that begins with the efficient synthesis of collections of small molecules having structural complexity, stereochemical and skeletal diversity, and untapped appending potential.

 © 2004 Wiley-VCH Verlag GmbH & Co. KGaA, Weinheim

7. Summary

Achieving the goals of DOS requires new advances in strategic thinking. Although the logic of diversity-oriented synthesis is still evolving, some guiding principles have emerged that provide the basis for a forward-synthetic analysis. Structural complexity can be most efficiently accessed using complexity-generating reactions, ideally in series, where the product of one complexity-generating reaction is the substrate for another. Structural diversity can be accessed using diversity-generating processes, and planning efficient DOS pathways depends on the identification of such processes where the products of one diversity-generating process are the substrates for another. It is necessary to gain efficient access to both stereochemical and skeletal diversity to achieve a diverse display of chemical information in three-dimensional space. Stereochemical diversity can be generated by using stereospecific and stereoselective diversity-generating processes, with the latter relying heavily on the development of powerful reagents that can override substrate bias to generate, ideally, all possible diastereomeric products with a high degree of selectivity. Skeletal diversity can be achieved by using both reagent-based (differentiating) and substrate-based (folding) strategies, with the latter having a demonstrated potential for generating skeletal diversity combinatorially. Achieving both complexity and diversity in an efficient manner requires integrated forward-synthetic planning, for example, the incorporation of complexity-generating reactions into stereochemical and skeletal diversity-generating processes.

The answer to the question: "Are the regions of chemistry space defined by natural products and known drugs, which have been so intensely scrutinized to date, the best or most fertile regions for discovering small-molecules that modulate macromolecular function in useful ways?" is not known. However, we believe that the answer to this question is likely to be "no", that is, the vast, previously unexplored regions of chemistry space likely contain small molecules having extraordinary properties that can contribute in unprecedented ways to the understanding and betterment of human health. Fortunately, this hypothesis can be tested with experiment, although doing so will require synthetic organic chemists to gain broad access to these as-of-yet unexplored regions of chemistry space in a highly efficient manner,[40] and thereby bring these extraordinary small molecules into existence. DOS aims to achieve this objective, and, although the challenge is daunting, synthetic organic chemists have a history of rising to such challenges.

Glossary of terms

Chemical space: n-dimensional space defined by the value of *n* descriptors; these descriptors can be of a chemical or biological nature and are either computed or measured.

Molecular skeleton: the combination of rigidifying elements (covalent bonds, non-covalent bonds, and non-bonding interactions) that define a molecule's overall three-dimensional shape; a complex molecular skeleton is one that is defined by a large number and/or variety of rigidifying elements.

Target-oriented synthesis
Retrosynthetic analysis: A problem-solving technique for transforming the structure of a synthetic target molecule to a sequence of progressively simpler structures along a pathway which ultimately leads to simple or commercially available starting materials for a chemical synthesis.
Transform: The exact reverse of a synthetic reaction.
Retron: The enabling structural subunit that permits the application of a transform.

Diversity-oriented synthesis
Forward-synthetic analysis: A problem-solving technique for transforming a collection of simple and similar starting materials into a collection of more complex and diverse products.
Process: The transformation of a collection of substrates into a collection of products.

Colleagues at Harvard University's Department of Chemistry and Chemical Biology and ICCB, especially M. D. Shair, E. J. Corey, D. Brittain, and G. Lalic are gratefully acknowledged for helpful discussions. M.D.B. is an HHMI predoctoral fellow. We thank Eric Keller for creating the frontispice for this Review.

Received: August 19, 2003 [A626]

[1] Chemistry space is multidimensional, with each dimension defined by a value of a descriptor; descriptors can be of a biological or chemical nature and are either computed or measured.
[2] S. L. Schreiber, *Science* **2000**, *287*, 1964; S. L. Schreiber, *Chem. Eng. News* **2003**, *81*(9), 51.
[3] E. J. Corey, X.-M. Cheng, *The Logic of Chemical Synthesis*, Wiley, New York, **1995**; E. J. Corey, *Angew. Chem.* **1991**, *103*, 469; *Angew. Chem. Int. Ed. Engl.* **1991**, *30*, 455 *(Nobel Lecture)*; E. J. Corey, *Pure. Appl. Chem.* **1967**, *14*, 19; E. J. Corey, W. T. Wipke, *Science* **1969**, *166*, 178; E. J. Corey, *Q. Rev. Chem. Soc.* **1971**, *25*, 455.
[4] M. R. Spaller, M. T. Burger, M. Fardis, P. A. Bartlett, *Curr. Opin. Chem. Biol.* **1997**, *1*, 47.
[5] http://chembank.med.harvard.edu/.
[6] For reviews, see "Cascade Reactions": *Tetrahedron Symposium in Print*, No. 62 (Ed.: R. Grigg), Elsevier, New York, **1996**; F. E. Ziegler in *Comprehensive Organic Synthesis*, *Combining C-C π-Bonds*, *Vol. 5* (Ed.: L. A. Paquette), Permagon, Oxford, **1991**, chap. 7.3; T.-L. Ho, *Tandem Organic Reactions*, Wiley, New York, **1992**.
[7] R. B. Merrifield, *J. Am. Chem. Soc.* **1963**, *85*, 2149; C. C. Leznoff, J. Y. Wong, *Can. J. Chem.* **1972**, *50*, 2892; F. Camps, J. Castells, M. J. Ferrando, J. Font, *Tetrahedron Lett.* **1971**, *12*, 1713; F. Camps, J. Castells, J. Pi, *An. Quim.* **1974**, *70*, 848; A. Patchornik, M. A. Kraus, *J. Am. Chem. Soc.* **1970**, *92*, 7857; J. I. Crowley, H. Rapoport, *J. Am. Chem. Soc.* **1970**, *92*, 6363; V. Yedida, C. C. Lexnoff, *Can. J. Chem.* **1980**, *58*, 1140; M. J. Farrall, J. M. J. Fréchet, *J. Org. Chem.* **1976**, *41*, 3877; J. M. J. Fréchet, *Tetrahedron* **1981**, *37*, 663.
[8] B. A. Bunin, J. A. Ellman, *J. Am. Chem. Soc.* **1992**, *114*, 10997; R. J. Simon, K. S. Kania, R. N. Zuckermann, V. D. Huebner,

 © 2004 Wiley-VCH Verlag GmbH & Co. KGaA, Weinheim

D. A. Jewell, S. Banville, S. Ng, L. Wang, S. Rosenberg, C. K. Marlowe, D. C. Spellmeyer, R. Tan, A. D. Frankel, D. V. Santi, F. E. Cohen, P. A. Bartlett, *Proc. Natl. Acad. Sci. U.S.A.* **1992**, *89*, 9367; S. H. Dewitt, J. S. Kiely, C. J. Stankovic, M. C. Schroeder, D. M. R. Cody, M. R. Pavia, *Proc. Natl. Acad. Sci. U.S.A.* **1993**, *90*, 6909; P. H. H. Hermkens, H. C. J. Ottenheijm, D. Rees, *Tetrahedron* **1996**, *52*, 4527; P. H. H. Hermkens, H. C. J. Ottenheijm, D. Rees, *Tetrahedron* **1997**, *53*, 5643; R. E. Dolle, K. H. Nelson, Jr., *J. Comb. Chem.* **1999**, *1*, 235; R. E. Dolle, *J. Comb. Chem.* **2000**, *2*, 383; R. E. Dolle, *J. Comb. Chem.* **2001**, *3*, 477; R. E. Dolle, *J. Comb. Chem.* **2002**, *4*, 369.

[9] A. Furka, F. Sebestyén, M. Asgedom, G. Dibó, in *Highlights of Modern Biochemistry, Proceedings of the 14th International Congress of Biochemistry, Prague, Czechoslovakia* (VSP, Utrecht, Netherlands), **1988**, *13*, 47; A. Furka, F. Sebestyén, M. Asgedom, G. Dibó, *Int. J. Pept. Protein Res.* **1991**, *37*, 487; R. A. Houghten, C. Pinilla, S. E. Blondelle, J. R. Appel, C. T. Dooley, J. H. Cuervo, *Nature* **1991**, *354*, 84; K. S. Lam, S. E. Salmon, E. M. Hersh, V. J. Hruby, W. M. Kazmierski, R. J. Knapp, *Nature* **1991**, *354*, 82.

[10] It is useful to describe the molecular skeleton of a small molecule as the combination of rigidifying elements (covalent bonds, noncovalent bonds, and nonbonding interactions) that define its overall three-dimensional shape. In that vein, a complex molecular skeleton is one that is defined by a large number and/or variety of rigidifying elements.

[11] http://iccb.med.harvard.edu/.

[12] For a review of such transformations, see L. F. Tietze, U. A. Beifuss, *Angew. Chem.* **1993**, *105*, 137; *Angew. Chem. Int. Ed. Engl.* **1993**, *32*, 131.

[13] I. Ugi, A. Dömling, W. Hörl, *Endeavour* **1994**, *18*, 115.

[14] K. Paulvannan, *Tetrahedron Lett.* **1999**, *40*, 1851; D. Lee, J. K. Sello, S. L. Schreiber, *Org. Lett.* **2000**, *2*, 709.

[15] W. J. Zuercher, M. Hashimoto, R. H. Grubbs, *J. Am. Chem. Soc.* **1996**, *118*, 6634; W. J. Zuercher, M. Scholl, R. H. Grubbs, *J. Org. Chem.* **1998**, *63*, 4291; R. Stragies, S. Blechert, *Tetrahedron* **1999**, *55*, 8179; O. Arjona, A. G. Csákÿ, M. C. Murcia, J. Plumet, *J. Org. Chem.* **1999**, *64*, 9739.

[16] M. Scholl, S. Ding, C. W. Lee, R. H. Grubbs, *Org. Lett.* **1999**, *1*, 953; A. K. Chatterjee, R. H. Grubbs, *Org. Lett.* **1999**, *1*, 1751.

[17] D. S. Tan, M. A. Foley, M. D. Shair, S. L. Schreiber, *J. Am. Chem. Soc.* **1998**, *120*, 8565.

[18] H. E. Pelish, N. J. Westwood, Y. Feng, T. Kirchhausen, M. D. Shair, *J. Am. Chem. Soc.* **2001**, *123*, 6740.

[19] R. Breinbauer, I. R. Vetter, H. Waldmann, *Angew. Chem.* **2002**, *114*, 3002; *Angew. Chem. Int. Ed.* **2002**, *41*, 2878.

[20] W. S. Knowles, M. J. Sabacky, *Chem. Commun.* **1968**, 1445; T. P. Dang, H. B. Kagan, *Chem. Commun.* **1971**, 481; W. S. Knowles, M. J. Sabacky, B. D. Vineyard, D. J. Weinkauff, *J. Am. Chem. Soc.* **1975**, *97*, 2567.

[21] K. B. Sharpless, *Chem. Scr.* **1985**, *25*, 71; S. Masamune, W. Choy, J. S. Petersen, L. R. Sita, *Angew. Chem.* **1985**, *97*, 1; *Angew. Chem. Int. Ed. Engl.* **1985**, *24*, 1; S. Masamune, *Heterocycles* **1984**, *21*, 107; S. Y. Ko, A. W. M. Lee, S. Masamune, L. A. Reed III, K. B. Sharpless, F. J. Walker, *Science* **1983**, *220*, 949; B. A. Harisson, G. L. Verdine, *Org. Lett.* **2001**, *3*, 2157; T. M. Gierasch, Z. Shi, G. L. Verdine, *Org. Lett.* **2003**, *5*, 621.

[22] G. C. Micalizio, S. L. Schreiber, *Angew. Chem.* **2002**, *114*, 160; *Angew. Chem. Int. Ed.* **2002**, *41*, 152.

[23] O. I. Kolodiazhnyi, *Tetrahedron* **2003**, *59*, 5953.

[24] A. G. Dossetter, T. F. Jamison, E. N. Jacobsen, *Angew. Chem.* **1999**, *111*, 2549; *Angew. Chem. Int. Ed.* **1999**, *38*, 2398; G. D. Joly, E. N. Jacobsen, *Org. Lett.* **2002**, *4*, 1795; K. Gademann, D. E. Chavez, E. N. Jacobsen, *Angew. Chem.* **2002**, *114*, 3185; *Angew. Chem. Int. Ed.* **2002**, *41*, 3059.

[25] D. E. Chavez, E. N. Jacobsen, *Org. Lett.* **2003**, *5*, 2563.

[26] W. R. Roush, S. M. Peseckis, *J. Am. Chem. Soc.* **1981**, *103*, 6696.

[27] J. W. Coe, W. R. Roush, *J. Org. Chem.* **1989**, *54*, 915; F. K. Brown, K. N. Houk, *Tetrahedron Lett.* **1985**, *26*, 2297; J. D. White, B. G. Sheldon, *J. Org. Chem.* **1981**, *46*, 2273; D. F. Taber, C. Campbell, B. P. Gunn, C. I. Chiu, *Tetrahedron Lett.* **1981**, *22*, 5141; for a review on diastereofacial selection in ring-closing reactions, see T. Tokoroyama, *Chem. Eur. J.* **1998**, *4*, 2397.

[28] K. Kim, U. S. M. Maharoof, J. Raushel, G. A. Sulikowski, *Org. Lett.* **2003**, *5*, 2777.

[29] R. A. Stavenger, S. L. Schreiber, *Angew. Chem.* **2001**, *113*, 3525; *Angew. Chem. Int. Ed.* **2001**, *40*, 3417.

[30] D. Lee, J. Sello, S. L. Schreiber, *J. Am. Chem. Soc.* **1999**, *121*, 10648.

[31] G. C. Micalizio, S. L. Schreiber, *Angew. Chem.* **2002**, *114*, 3406; *Angew. Chem. Int. Ed.* **2002**, *41*, 3272.

[32] S. Woo, N. Squires, A. G. Fallis, *Org. Lett.* **1999**, *1*, 573.

[33] O. Kwon, S. B. Park, S. L. Schreiber, *J. Am. Chem. Soc.* **2002**, *124*, 13402.

[34] M. D. Burke, E. M. Berger, S. L. Schreiber, *Science* **2003**, *302*, 613.

[35] C. B. Anfinsen, *Science* **1973**, *181*, 223.

[36] N. Clauson-Kaas, P. Dietrich, J. T. Nielson, *Acta Chem. Scand.* **1953**, *7*, 845; N. Elming, *Adv. Org. Chem.* **1960**, *2*, 67.

[37] O. Achmatowicz, Jr., P. Bukowski, B. Szechner, Z. Zwierzchowska, A. Zamojski, *Tetrahedron* **1971**, *27*, 1973; J. M. Harris, G. A. O'Doherty, *Tetrahedron Lett.* **2000**, *41*, 183.

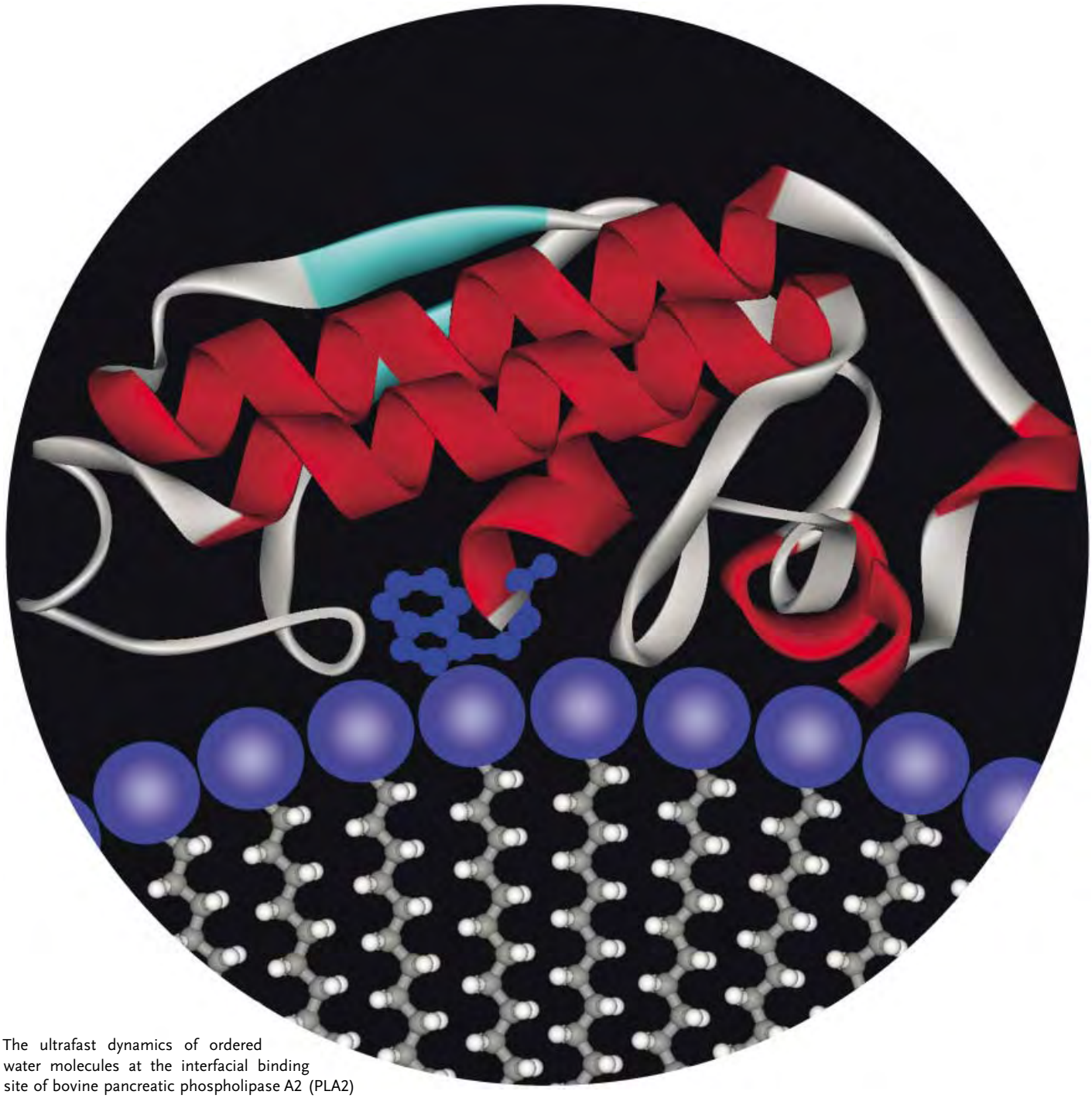
[38] Y. Kobayashi, M. Nakano, G. B. Kumar, K. Kishihara, *J. Org. Chem.* **1998**, *63*, 7505.

[39] J. K. Sello, P. R. Andreana, D. Lee, S. L. Schreiber, *Org. Lett.* **2003**, *5*, 4125.

[40] Realizing the goals of DOS will require organic chemists to adopt computational tools from computer and information science, since the complexities of multidimensional (chemical and biological) descriptor space can only be tackled using these tools.

 © 2004 Wiley-VCH Verlag GmbH & Co. KGaA, Weinheim

Communications



The ultrafast dynamics of ordered water molecules at the interfacial binding site of bovine pancreatic phospholipase A2 (PLA2) have been investigated. The timescales of hydration were established by selectively exciting the tryptophan residue at the substrate-recognition site and probing the motion of water molecules by rotational and translational diffusion. The dynamic role of water as a "lubricant" and in binding is presented by A. H. Zewail et al. on the following pages.

DOI: 10.1002/anie.200352961
© 2004 Wiley-VCH Verlag GmbH & Co. KGaA, Weinheim

Hydration Dynamics

Dynamics of Ordered Water in Interfacial Enzyme Recognition: Bovine Pancreatic Phospholipase A_2**

*Liang Zhao, Samir Kumar Pal, Tianbing Xia, and Ahmed H. Zewail**

The bovine pancreatic phospholipase A_2 (PLA2) protein consists of a single polypeptide chain with 123 residues. It belongs to a family of calcium-dependent lipolytic enzymes that hydrolyze the 2-acyl ester bond of phospholipids to release fatty acids and lysophospholipids. These proteins are unique prototypes in interfacial enzymology.[1,2] Two structural features of PLA2 are of functional interest: the catalytic site with a conserved Asp–His pair and Ca^{2+} as obligatory cofactor, and the interfacial binding region (i-face, ≈ 1700 Å^2), which determines the interface preference for the membrane-binding equilibrium (Figure 1). The surface wall of the interfacial binding site is covered with hydrophobic and some polar residues.[2]

It is known that PLA2 proteins are activated by aggregated substrates in the form of micelles or vesicles.[3] The mechanism behind the phenomenon of interfacial activation, however, has been a subject of debate, and two models have been proposed.[2] In the "enzyme model", it has been suggested that the conformational changes of the enzyme upon binding play a role in interfacial activation. Conformational changes have been observed by NMR spectroscopy.[4,5] In reference [5], it was demonstrated that PLA2 is not denatured by the anionic surfactant sodium dodecyl sulfate (SDS) at a much higher concentration (50 mM) than its critical micellar concentration (≈ 1 mM)—protein–micelle complexes are formed. The study also indicated that when bound to the micelle, the overall protein structure remains intact, although a more-ordered helical conformation is observed at the N-terminus of the protein. In the "substrate model", the activation was attributed to the orientation, conformation, or hydration sites of the phospholipid molecules in the aggregates, facilitating substrate diffusion from the interfacial binding surface to the catalytic site.[6]

Hydration of these biomolecules must be important for the stability of the structure and the function.[7–10] As discussed in a series of publications from our group, ordered water has a unique role in the dynamics of protein[11–13] and DNA[14] recognition. The PLA2 system serves as a model protein–substrate complex to study the role of intrinsic interfacial hydration dynamics in enzyme activity. A high-resolution X-ray crystallographic investigation[15] of bovine PLA2 showed that at least one tightly bound water molecule is crucial during catalysis. However, most of the water molecules are located 2.5–3.0 Å away from the protein surface and form hydrogen bonds to the protein atoms.[15] A single tryptophan at position 3 (Trp3) is part of the interfacial binding site[16] and is significantly exposed to the solvent environment.[17] Upon binding to the SDS micelle, the Trp3 residue is sandwiched at the interface and partially protected from bulk solvent.

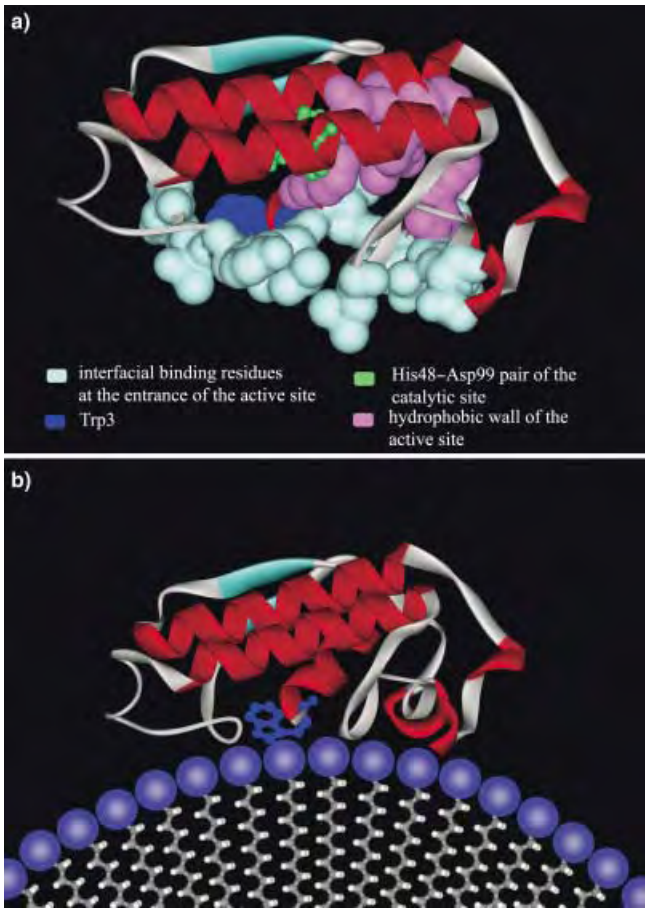


Figure 1. a) X-ray crystal structure of bovine pancreatic phospholipase A_2 (PLA2). Trp3 is part of the interfacial binding site and the catalytic site is away (15 Å) from the interface.[2] The assignment of different groups of amino acid residues follows reference [16]. The structure was downloaded from Protein Data Bank (ID code 3BP2). b) A simplified model of protein–micelle complex, indicating the location of Trp3 of the protein at the interface.

Herein we present our first studies on the hydration dynamics at the binding site of PLA2, for free protein and for the complex (Figure 1). We observed dynamically ordered water at the interface and we were able to determine the role of substrate hydration from the distinct timescales of the complex. We also determined the rigidity of Trp in this interface region. The importance of these results to the recognition and activity of the enzyme is discussed.

Because of its unique location in the protein, Trp3 serves as an excellent intrinsic probe to study the hydration

[*] L. Zhao, S. K. Pal, T. Xia, Prof. Dr. A. H. Zewail
Laboratory for Molecular Sciences
Arthur Amos Noyes Laboratory of Chemical Physics
California Institute of Technology
Pasadena, CA 91125 (USA)
Fax: (+1) 626-796-8315
E-mail: Zewail@caltech.edu

[**] Financial support from the National Science Foundation is acknowledged.

 © 2004 Wiley-VCH Verlag GmbH & Co. KGaA, Weinheim DOI: 10.1002/anie.200352961

dynamics at the interfacial binding site. After the indole chromophore of tryptophan is excited with a femtosecond pulse, a large dipole moment is created and the surrounding water molecules must reorganize to reach the new equilibrated state. This process is manifested as the dynamic shift of the fluorescence spectrum (Stokes shift). The hydration process can therefore be followed in real time by recording the transient at different wavelengths—on the blue side one observes a decay, whereas on the red side a rise replaces the decay. The shift of the fluorescence peak is then used to construct the hydration correlation function, $C(t) = [\tilde{\nu}(0) - \tilde{\nu}(t)]/[\tilde{\nu}(0) - \tilde{\nu}(\infty)]$, in which $\tilde{\nu}(t)$ is the spectrum maximum position at a given time (e.g., see reference [11]). A study of the time-dependent behavior of $C(t)$ thus provides direct information on local solvation dynamics around the tryptophan probe.

The steady-state fluorescence spectra of PLA2 in water and with the micelle are shown in Figure 2 A. The tryptophan emission maximum in the complex (339 nm) was blue shifted by 9 nm relative to that on the protein surface (348 nm), indicating a more hydrophobic environment upon micelle binding. The emission of free tryptophan in bulk water is shown for comparison. The absorption peak of tryptophan remains nearly the same in all cases; one complete absorption spectrum of the protein–micelle complex is shown. Note that as our excitation wavelength 297 nm is close to the apparent 0–0 transition (295 nm)[18] of tryptophan, the excess vibrational energy is relatively insignificant.

To investigate the nature of hydration dynamics at the protein surface and in the interface between the protein and substrate micelle, we obtained fluorescence upconversion femtosecond transients when using the technique described previously.[11] Representative fs-resolved transients for PLA2 and PLA2–SDS complex in water are shown in Figure 2 B. Fourteen transients at different wavelengths covering the blue and red sides were obtained. The constructed hydration correlation function, $C(t)$,[11,13,19] for the PLA2 surface and PLA2–SDS interface is shown in Figure 3. For PLA2 in water,

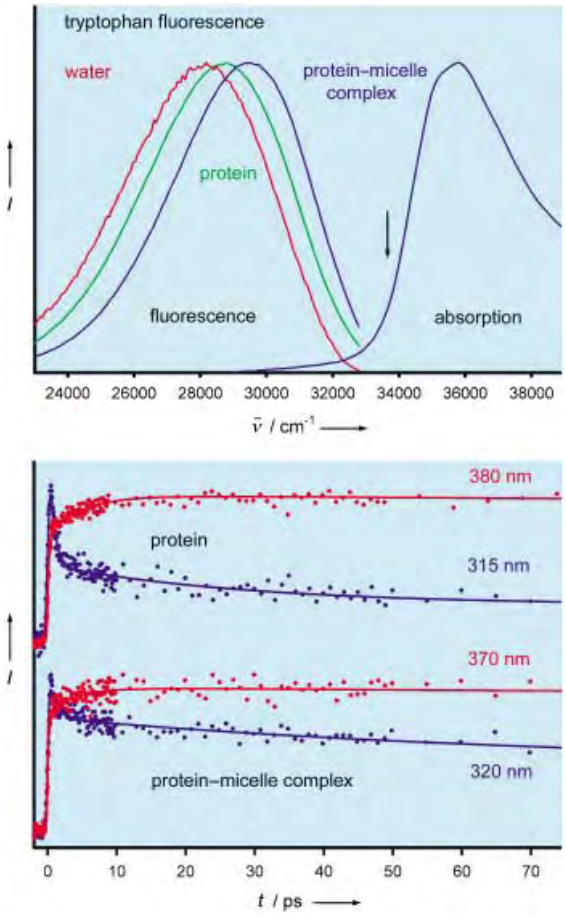


Figure 2. a) Normalized steady-state fluorescence spectra of Trp3 at the protein surface (green) and for the protein–micelle complex (blue). The fluorescence spectrum of free tryptophan in bulk water is shown (red) for comparison. The absorption spectrum for protein-micelle complex is also shown; the arrow indicates excitation (297 nm) (see text). B) Representative femtosecond-resolved fluorescence upconversion transients for Trp3 at the protein surface and in the protein–micelle complex. The excitation wavelength was 297 nm. Fourteen such transients were recorded (see text).

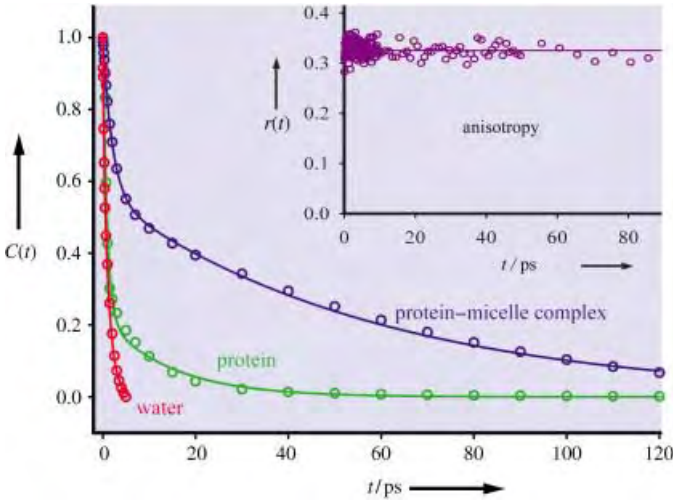


Figure 3. Comparison of the hydration correlation function, $C(t)$, for the protein surface and protein–micelle complex. We also include the result from tryptophan in bulk water for comparison. Inset: Time-resolved anisotropy, $r(t)$, of the PLA2–SDS complex.

$C(t)$ is the sum of two exponentials with time constants 0.9 ps (78 %) and 14.6 ps (22 %), indicating that relaxation in the hydration shell of PLA2 occurs through two types of water trajectories: bulk type (0.9 ps) and surface-bound type (14.6 ps); any sub-100-fs components in these dynamics are unresolved. For the free enzyme, the results are consistent with previous hydration times for other proteins.[11–13] For the PLA2–SDS complex, $C(t)$ gives two well-separated timescales: 2.0 ps (44 %) and 59 ps (56 %). The contribution of the faster component to the total spectral shift significantly decreased from 78 % to 44 %. Remarkably, the increase in hydration time from $\approx$15 ps to 59 ps parallels the slowness observed for water at the surface of cationic CTAB micelle.[19]

To study the motion of the probe tryptophan, we measured the time-resolved anisotropy decay, $r(t)$, at 350 nm. For both PLA2 and PLA2–SDS complex, $r(t)$ is

 © 2004 Wiley-VCH Verlag GmbH & Co. KGaA, Weinheim

persistent up to 200 ps (Figure 3, inset) except for a small (10%) 40-ps decay component for PLA2. These results indicate that our probe Trp3 is mostly restricted in motion during the timescale of surface hydration.

The bimodality observed in the hydration at the protein surface is understood, as dynamic processes between surface and bulk water lead to the formation of an ordered layer with a thickness in the nanometer range.[20] At the surface of PLA2, the exposure of the Trp3 to the aqueous environment is apparent from the dominance (78%) of bulk-type hydration (0.9 ps), but the presence of the 14.6 ps (22%) component must reflect the contribution of the layered water. Molecular dynamics simulation studies,[17] which have considered solvation at the surface of PLA2 as manifested in the spectral shifts by both water and residues of the protein (internal Stark effect), showed that $\approx 95\%$ of the shift is due to water. The domination of the bulk-type water at the surface interfacial binding site—in the absence of substrate micelle—affords flexibility and efficiency for the recognition process. Upon complexation with the micelle, the hydration dynamics at the interface become fourfold slower (59 ps), replacing a major portion of water with those ordered on the substrate micelle (typically 60 ps).[19] However, to maintain equilibrium, a fraction of mobile (bulk type) water is still present.

Generally the PLA2 binding to the substrate surface is diffusion-controlled, with subpicomolar to micromolar dissociation constants, depending on the exact nature of the aggregates and the source of the enzymes.[21,22] Once bound to the interface, the dissociation of the enzyme is generally very slow relative to the timescale of the catalytic turnover. In a complete characterization of the interfacial catalysis by bovine pancreatic PLA2, analysis of the integrated Michaelis–Menten reaction progress was carried out for the hydrolysis of a 1,2-dimyristoyl-sn-glycero-3-phosphomethanol vesicle in a highly "scooting" mode.[22] In this particular system, the enzyme binds to the vesicle with subpicomolar affinity ($\Delta G° \approx 15$ kcal mol^{-1}). On the vesicle, the enzyme-substrate association occurs on a millisecond timescale, with subsequent catalytic turnover within a few milliseconds. Figure 4 presents a simplified picture of kinetic pathway of the enzyme PLA2 and associated timescales.

In the PLA2–SDS complex system, it has been found that the binding releases almost 40 kcal mol^{-1} of heat ($\Delta H°$), consistent with high-affinity binding.[5] The lateral movement of the enzyme on the surface should be facilitated by the presence of water molecules, with fast mobility (ps) at the interface, which act as lubricant. For the enzymatic reaction to take place in a biologically relevant enzyme–membrane system, individual substrate lipid molecules must be transported at least 15 Å away from its position within the membrane to reach the catalytic center.[2] The role of the water molecules is important in this process.[10,23] The more-rigidly ordered water molecules characterized by their slower dynamics of ≈ 60 ps would maintain a network of hydrogen bonds that stabilizes the interfacial binding and the structure of the transporting channel, hence facilitating the movement to the catalytic site. In this case, the coincidence of the hydration time at the interface with that of micelle substrate suggests the importance of the "substrate model". Moreover, the hindered motion of Trp3 upon micelle binding, from the anisotropy, indicates that structural rigidity is important for substrate recognition of the enzyme.

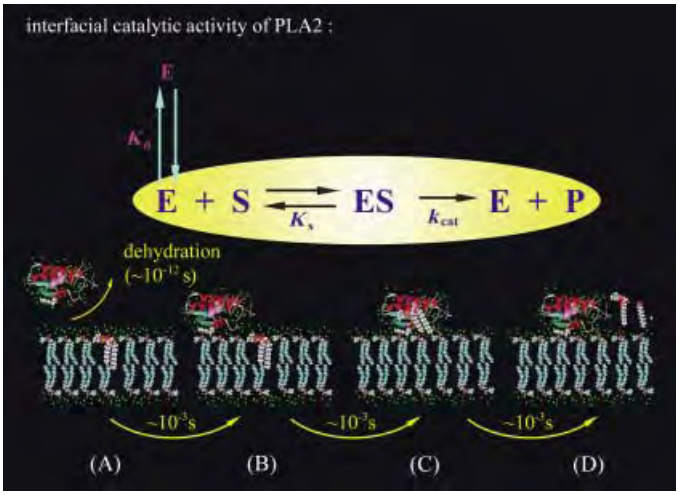


Figure 4. Reaction pathways in the catalytic activity of the protein PLA2. K_d indicates the equilibrium dissociation constant of the enzyme to the membrane. K_s and k_{cat} denote the equilibrium dissociation of the enzyme–substrate complex and catalytic rate constant (see text). Schematic representation of the catalytic steps of the enzyme: A) The enzyme and the host that contains the substrate. B) The complex of the enzyme with the host. C) The complex of the enzyme with the membrane-bound substrate. D) The products. The timescales represent an estimate for the different processes involved.[2]

Experimental Section

Fluorescence upconversion: A detailed experimental setup for the fs-resolved fluorescence upconversion technique can be found elsewhere.[11] The tryptophan residue was excited at 297 nm with a pulse energy of 250–300 nJ. A total of 14 transients were taken for the free PLA2 and PLA2–SDS complex system at various wavelengths.

Samples: Ultrapure tris (ICN Biomedicals, Ohio), calcium chloride (Mallinckrodt, Kentucky), hydrochloric acid (J. T. Baker, New Jersey), sodium dodecyl sulfate (SDS, Fluka BioChemika, $\geqslant 99\%$), L-α-phosphatidylcholine (Sigma), and PLA2 (Sigma) were purchased and used without further purification. The purity of PLA2 was checked by several techniques, including MALDI and ESI mass spectrometry and tryptophan fluorescence spectrum. The biological function of the enzyme was confirmed by enzymatic assays with L-α-phosphatidylcholine as substrate following the titrametric protocol utilized by Sigma-Aldrich Corporation.

The protein solution (357 μM) was made by dissolving the PLA2 sample (lyophilized powder, approximately 20% protein in tris buffer salt) in water (Nanopure Infinity Ultrapure Water System, Barnstead/Thermolyne), followed by exhaustive dialysis against a pH 7.5 buffer solution (50 mM Tris/5 mM $CaCl_2$) in the molecular porous membrane tubing (Spectrum Laboratories, Inc.). To make the protein–SDS micelle complex, SDS is dissolved in the dialyzed PLA2 solution described above to a concentration of ≈ 50 mM.

Received: September 26, 2003 [Z52961]
Published Online: December 8, 2003

Keywords: enzymes · femtochemistry · hydration dynamics · lipases · surfactants

 © 2004 Wiley-VCH Verlag GmbH & Co. KGaA, Weinheim

[1] O. G. Berg, M. K. Jain, *Interfacial Enzyme Kinetics: Turnover, Processivity, and Replenishment*, Wiley, London, **2002**.
[2] O. G. Berg, M. H. Gelb, M. D. Tsai, M. K. Jain, *Chem. Rev.* **2001**, *101*, 2613.
[3] J. J. Volwerk, G. H. de Haas, *Lipid-Protein Interactions*, *Vol. 1*, Wiley, New York, **1982**.
[4] C. Yuan, I. L. Byeon, Y. Li, M. D. Tsai, *Biochemistry* **1999**, *38*, 2909.
[5] P. M. Kilby, W. U. Primrose, G. C. K. Roberts, *Biochem. J.* **1995**, *305*, 935.
[6] D. L. Scott, S. P. White, Otwinowskiz, W. Yuan, M. H. Gelb, P. B. Sigler, *Science* **1990**, *250*, 1541.
[7] J. A. Kornblatt, M. J. Kornblatt, *Int. Rev. Cytol.* **2002**, *215*, 49.
[8] J. A. Rupley, G. Cateri, *Adv. Protein Chem.* **1991**, *41*, 37.
[9] Y. Pocker, *Cell. Mol. Life Sci.* **2000**, *57*, 1008.
[10] P. W. Fenimore, H. Frauenfelder, B. H. McMahon, F. G. Parak, *Proc. Natl. Acad. Sci. USA* **2002**, *99*, 16047.
[11] S. K. Pal, J. Peon, A. H. Zewail, *Proc. Natl. Acad. Sci. USA* **2002**, *99*, 15297.
[12] S. K. Pal, J. Peon, B. Bagchi, A. H. Zewail, *J. Phys. Chem. B* **2002**, *106*, 12376, and references therein.
[13] J. Peon, S. K. Pal, A. H. Zewail, *Proc. Natl. Acad. Sci. USA* **2002**, *99*, 10964.
[14] S. K. Pal, L. Zhao, A. H. Zewail, *Proc. Natl. Acad. Sci. USA* **2003**, *100*, 8113.
[15] B. W. Dijkstra, K. H. Kalk, W. G. J. Hol, J. Drenth, *J. Mol. Biol.* **1981**, *147*, 97.
[16] B. W. Dijkstra, J. Drenth, K. H. Kalk, *Nature* **1981**, *289*, 604.
[17] J. T. Vivian, P. R. Callis, *Biophys. J.* **2001**, *80*, 2093.
[18] X. H. Shen, J. Knutson, *J. Phys. Chem. B* **2001**, *105*, 6260.
[19] S. K. Pal, J. Peon, A. H. Zewail, *Proc. Natl. Acad. Sci. USA* **2002**, *99*, 1763.
[20] S. M. Bhattacharyya, Z.-G. Wang, A. H. Zewail, *J. Phys. Chem. B* **2003**, *107*, 13218.
[21] L. S. Jung, J. S. Shumaker-Parry, C. T. Campbell, S. S. Yee, M. H. Gelb, *J. Am. Chem. Soc.* **2000**, *122*, 4177.
[22] O. G. Berg, B. Z. Yu, J. Rogers, M. K. Jain, *Biochemistry* **1991**, *30*, 7283.
[23] G. Zaccai, *Biophys. Chem.* **2000**, *86*, 249.

 © 2004 Wiley-VCH Verlag GmbH & Co. KGaA, Weinheim

Silicon Tubular Nanostructures

Synthesis of Crystalline Silicon Tubular Nanostructures with ZnS Nanowires as Removable Templates**

Junqing Hu, Yoshio Bando, Zongwen Liu, Jinhua Zhan, Dmitri Golberg, and Takashi Sekiguchi*

Since the discovery of carbon nanotubes in 1991,[1] a large number of inorganic solids with layered or nonlayered crystal lattices have been found to form stable and energetically viable nanotubes (composed of molecular layers) or tubular nanostructures.[2] Nowadays, inorganic nanotubes and tubular nanostructures with interesting properties and potential applications constitute an important domain of the nanostructural family. In particular, one-dimensional Si nanostructures are of special interest due to the key role of Si in the modern semiconductor industry. Different methods have been developed for the fabrication of Si nanowires, for example, the laser-ablation metal-catalytic method,[3] the oxide-assisted method,[4] and the solution technique.[5] There have also been reports on the synthesis of Si nanotubes, but these tubular forms of Si are either polycrystalline or amorphous.[6] Although the existence of stable monocrystalline Si nanotubes and tubular nanostructures has been predicted theoretically,[7] they have never been observed experimentally.

Among the many routes for synthesizing nanostructured materials, template-based methods offer various advantages.[8] Recently, monocrystalline GaN nanotubes were prepared by "epitaxial casting", in which hexagonal ZnO nanowires were used as templates for epitaxial overgrowth of thin GaN sheaths, and the ZnO nanowire templates were subsequently removed by thermal reduction and evaporation with formation of GaN tubular nanostructures.[9] We believed that this template process could be exploited to prepare monocrystalline Si tubular nanostructures. It is known that diamondlike cubic Si and zinc blende ZnS have similar crystal structures and very close lattice constants (ZnS: $a = 0.5431$ nm, Si: $a = 0.5420$ nm).[10] In accordance with lattice-matching theory, effective epitaxial growth of Si on ZnS substrates should be possible, since the growth of ZnS thin films on Si substrates has already been demonstrated.[11] Here we report on the growth of crystalline Si tubular nanostructures. A novel template process generates crystalline Si

[*] Dr. J. Hu, Dr. Y. Bando, Dr. Z. Liu, Dr. J. Zhan, Dr. D. Golberg, Dr. T. Sekiguchi
Advanced Materials Laboratory and Nanomaterials Laboratory
National Institute for Materials Science (NIMS)
Namiki 1-1, Tsukuba, Ibaraki 305-0044 (Japan)
Fax: (+81) 298-51-6280
E-mail: hu.junqing@nims.go.jp

[**] This work was supported by the Japan Society for the Promotion of Science (JSPS) Fellowship tenable at the National Institute for Materials Science, Tsukuba, Japan.

Supporting information for this article is available on the WWW under http://www.angewandte.org or from the author.

 DOI: 10.1002/anie.200352483 © 2004 Wiley-VCH Verlag GmbH & Co. KGaA, Weinheim

tubular nanostructures with outer diameters of about 60–180 nm, wall thicknesses of about 20–60 nm, and lengths of several micrometers. Zinc blende ZnS nanowires were used as one-dimensional templates for epitaxial growth of thin monocrystalline Si sheaths, which led to the formation of ZnS/Si core/shell nanowires. Crystalline Si tubular nanostructures were formed by chemical removal of the ZnS nanowire cores.

The X-ray diffraction pattern of a sample of Si tubular nanostructures is shown in Figure 1. The reflections can be indexed to diamondlike cubic Si with a lattice constant of $a = 5.428$ Å, consistent with the standard value (JCPDS file 27-1402: $a = 5.430$ Å) within experimental error.

The TEM images (Figure 2a–c) reveal that the product consists of relatively straight tubular structures. Typically, the lengths of the as-synthesized tubular structures can reach several micrometers. Most of them (Figure 2a) have outer

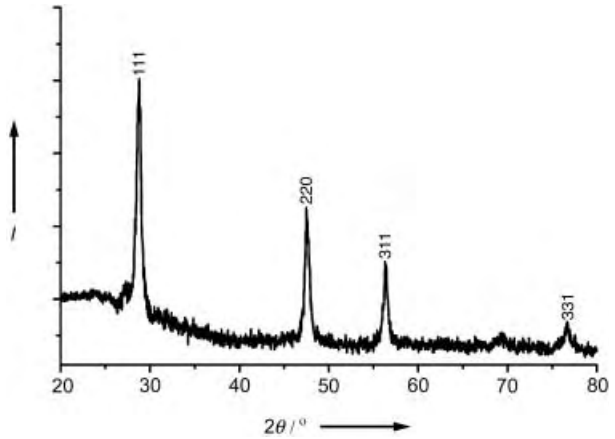


Figure 1. XRD pattern recorded from as-synthesized Si tubular nanostructures.

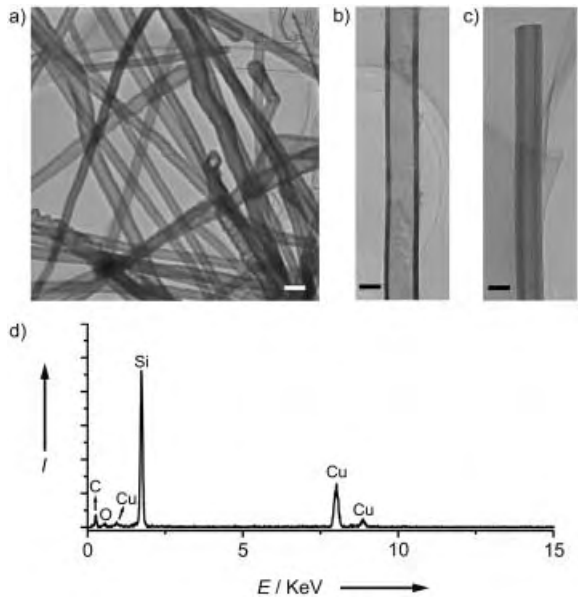


Figure 2. a) TEM image of Si tubular nanostructures. Scale bar: 200 nm. b) TEM image displaying an Si nanotube with a thin wall. c) TEM image displaying the open end of a Si nanotube. Scale bars in b) and c): 100 nm. d) EDS spectrum taken from an individual Si tubular nanostructure.

diameters of about 120–180 nm, and a small fraction of the tubes have smaller outer diameters of about 60–70 nm. The majority of tubes have wall thicknesses of about 40–60 nm, and a small number have thinner walls with thicknesses of about 20 nm (Figure 2b). Some tubes have one closed end (Figure 2a), while others are open-ended (Figure 2c). Analysis by energy-dispersive X-ray spectroscopy (EDS, Figure 2d) confirmed that the nanotubes are made of Si with a minimal content of O. Together with the XRD data, these results show that the obtained sample consists of crystalline Si tubular nanostructures.

Figure 3a shows a high-magnification TEM image of a segment of a straight Si tubular structure with an outer diameter and wall thickness of about 60 and 20 nm, respectively. The electron diffraction (ED) pattern (Figure 3a, inset) can be indexed to the [110] zone axis of crystalline Si, in which the streaking along the [111] direction originates from the stacking faults on the {111} planes, as suggested by the streaklike contrasts on the corresponding faces in TEM images. Figure 3b depicts the high-resolution TEM image of this crystalline tubular nanostructure, in which the (111) fringes with a d spacing of about 0.31 nm are aligned perpendicular to the longitudinal direction of the tube, suggesting a [111] growth orientation of the monocrystalline Si tubular domains. The thin sheath of amorphous SiO_2 that was noticed on the surface was attributed to unavoidable surface oxidation and/or surface adsorption of oxygen on the tubes during sample processing. Figure 3c and d respectively show a TEM image and its corresponding Si elemental map for a thin Si tubule. Line-scanning elemental profiles across the Si nanotube (white line in Figure 3c) representing the spatial distribution of the atomic species are shown in Figure 3e. The Si profile displays two peaks with a gap in the center. Both the elemental map and spatially resolved elemental profile show the tubular shape of the Si nanomaterial.

In the template-based growth of the crystalline Si tubular nanostructures, ZnS/Si core/shell nanowires were initially obtained, as shown in the TEM image in Figure 4a, in which the shell is a Si thin layer, and the core is a ZnS nanowire. As seen in Figure 4b, residual segments (nanorods) of the ZnS nanowire template remains in an open-ended Si tubular nanostructure after treatment of the ZnS/Si core/shell nanowires with HCl solution, owing to incomplete decomposition of the ZnS nanowire, which suggests that the Si tubular nanostructure is an extension of the thin Si sheath of the ZnS/Si core/shell nanowire. Figure 4c shows an HRTEM image of the interfacial domain between the Si shell and the ZnS core of a ZnS/Si core/shell nanowire. The well-defined epitaxial relationship ($(111)_{Si}//(111)_{ZnS}$; $[111]_{Si}//[111]_{ZnS}$) between the Si shell and ZnS core that is clearly observed is due to the similar crystal structure and the close lattice-matching of Si and ZnS. Line-scanning elemental profiles across a ZnS/Si core/shell nanowire (white line in Figure 4a) are shown in Figure 4d. The profile of Si shows two peaks, on the right- and left-hand sides, with lower intensity in the center, whereas the profiles of Zn and S both show a broad peak at the center; this verifies the core/shell nature of the ZnS/Si nanowires. It is noteworthy that polycrystalline Si nanotubes and microtubes were

 © 2004 Wiley-VCH Verlag GmbH & Co. KGaA, Weinheim

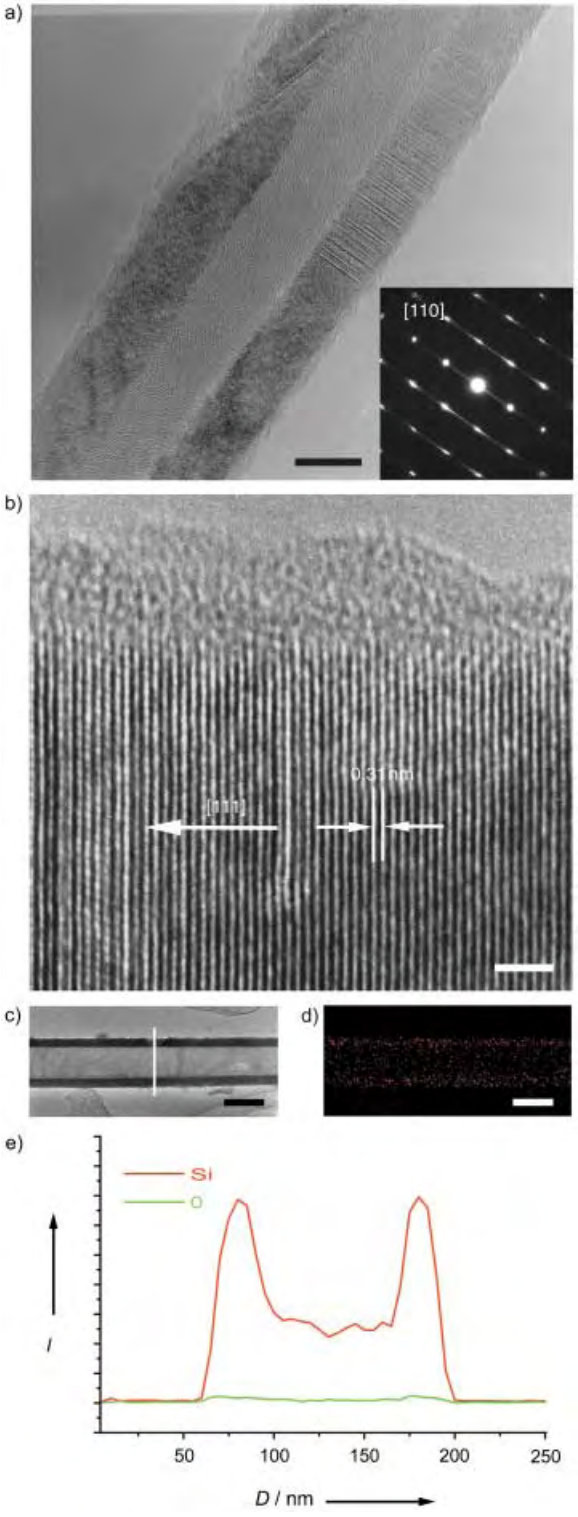


Figure 3. a) High-magnification TEM image depicting a segment of a Si nanotube, and an ED pattern (inset) corresponding to the [110] zone axis of a Si single crystal. Scale bar: 20 nm. b) HRTEM image of a Si nanotubular structure, in which the (111) (d_{111} = 0.31 nm) fringes are aligned perpendicular to the axis direction of the tube, which suggests a [111] growth direction of this tubular nanostructure. Scale bar: 2 nm. c) TEM image of a segment of a Si nanotube. d) Si elemental map as further evidence for a tubular structure. Scale bars in c) and d): 100 nm. e) Line-scanning (indicated by a line in c)) elemental mapping highlighting the spatial Si elemental profile across the tube.

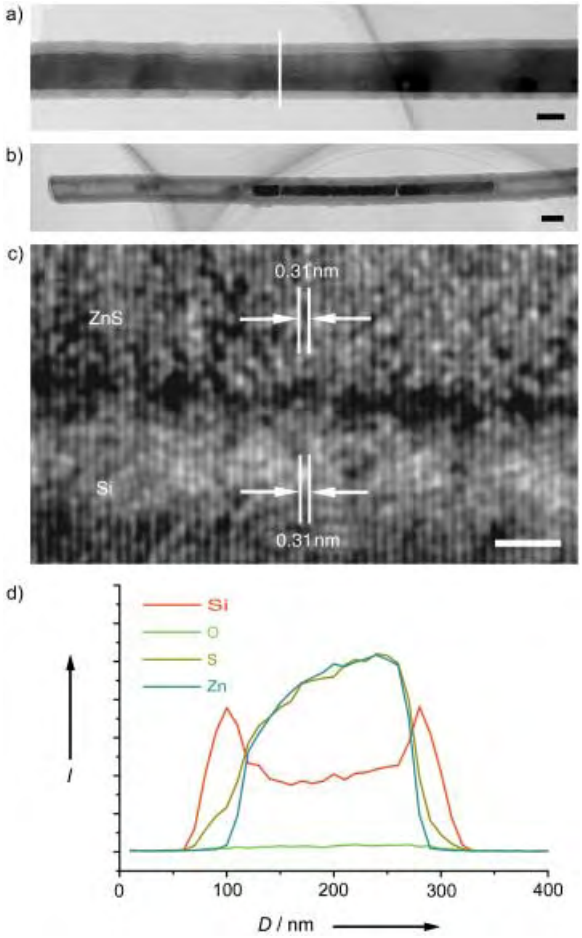


Figure 4. a) TEM image of a segment of a ZnS/Si core/shell nanowire. b) TEM image showing the residual segments of the ZnS nanowire template in the open-ended Si nanotube after treatment of the ZnS/Si core/shell nanowires with HCl solution. Scale bars in a) and b): 100 nm. c) HRTEM image taken from the interfacial domain between the Si shell and ZnS core of a ZnS/Si core/shell nanowire, revealing an epitaxial relationship ($(111)_{Si}//(111)_{ZnS}$; $[111]_{Si}//[111]_{ZnS}$) between the Si shell and the ZnS core. Scale bar: 2 nm. d) Line-scanning (indicated by a white line in a)) elemental mapping displaying Si, Zn, and S spatial elemental distribution profiles across the ZnS/Si core/shell nanowire.

obtained from similar synthetic processes in the absence of ZnS nanowire templates. This implies that the ZnS nanowires formed during the first stage of synthesis play the key role in producing monocrystalline Si tubular structures in the two-stage ZnS-nanowire-templated process.

Figure 5 shows a room-temperature cathodoluminescence (CL) spectrum of the Si tubular nanostructures. One broad and weak emission peak at about 450 nm was detected. Compared with the photoluminescence behavior of bulk Si nanowires (emission band centered at $\approx$624 nm (N_2 carrier gas) or $\approx$783 nm (Ar carrier gas)),[12] the peak position of the Si tubular nanostructures is shifted dramatically to lower wavelengths; this may be attributable to some intrinsic point defects and impurities in these Si nanostructures.

Monocrystalline Si tubular nanostructures are distinctly different from previously reported Si nanowires and other Si-based nanostructures,[13] due to the characteristic internal

 © 2004 Wiley-VCH Verlag GmbH & Co. KGaA, Weinheim

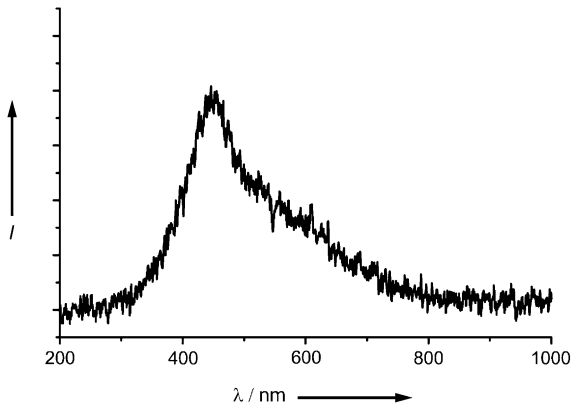


Figure 5. Room-temperature CL spectrum of the as-synthesized Si tubular nanostructures.

cavity peculiar to a tubular shape. This cavity could be filled with different semiconducting materials with various band gaps to give interesting electrical and optical nanodevices, for example, nanoscale lasers and/or light emitting devices with tunable wavelengths. In addition, theoretical predictions have indicated that Si nanotubes (or tubular nanostructures) have a semiconducting band gap, which in contrast to carbon nanotubes, is independent of the tube diameter or chirality.[7b] We believe that the present discovery of Si crystalline tubular nanostructures will promote further experimental studies on their physical properties and applications.

Experimental Section

ZnS/Si core/shell nanowires were grown by thermal evaporation of ZnS and SiO powders under controlled conditions in a vertical induction furnace, as described in detail elsewhere.[14] Briefly, the furnace consisted of a fused-quartz tube and an inductively heated cylinder made of high-purity graphite coated with a thermally insulating layer of carbon fiber. A graphite crucible containing ZnS powder was placed in the central cylindrical zone. After evacuation of the quartz tube to about 0.2 Torr, a stream of pure Ar was passsed through the tube at a flow rate of 120 $cm^3 s^{-1}$ and ambient pressure, and evaporation was conducted at 1200 °C (measured by an optical pyrometer with an estimated accuracy of ± 10 °C). Numerous ZnS nanowires with diameters of 20–60 nm had grown on the carbon-fiber layer after 1.5 h of evaporation. They were directly used as templates for the growth of ZnS/Si core/shell nanowires in the following stage of synthesis: The crucible containing SiO powder was rapidly heated to 1450 °C and maintained at this temperature for 1 h (the pressure in the tube and Ar flow rate in this stage were kept unchanged). The disproportionation of SiO led to the formation of Si vapor. A thin layer of Si grew by condensation of the Si vapor on the ZnS nanowire templates, and ZnS/Si core/shell nanowires formed. Finally, the ZnS nanowire templates were removed from the ZnS/Si core/shell nanowires with HCl solution. This final step resulted in the formation of crystalline Si tubular nanostructures. The collected products were characterized and analyzed by X-ray diffraction (XRD, RINT 2200), transmission electron microscopy (TEM, JEM-3000F and JEM-3100FFF), and energy-dispersive X-ray spectroscopy (EDS). Cathodoluminescence (CL) spectroscopy was carried out with a high-spatial-resolution, low-energy CL (HRLE-CL) system and a thermal field-emission scanning electron microscope (TFE-SEM, Hitachi S4200).

Received: July 28, 2003
Revised: September 12, 2003 [Z52483]

Keywords: crystal growth · epitaxy · nanostructures · nanotubes · silicon

[1] S. Iijima, *Nature* **1991**, *354*, 56.
[2] See, for example a) R. Tenne, L. Margulis, M. Genut, G. Hodes, *Nature* **1992**, *360*, 444; b) E. J. M. Hamilton, S. E. Dolan, C. M. Mann, H. O. Colijn, C. A. Mcdonald, S. G. Shore, *Science* **1993**, *260*, 659; c) Y. Feldman, E. Wasserman, D. J. Srolovitz, R. Tenne, *Science* **1995**, *267*, 222; d) N. G. Chopra, R. J. Luyken, K. Cherrey, V. H. Crespi, M. L. Cohen, S. G. Louie, A. Zettl, *Science* **1995**, *269*, 966; e) P. Hoyer, *Langmuir*, **1996**, *12*, 1411; f) R. Tenne, M. Homyonfer, Y. Feldman, *Chem. Mater.* **1998**, *10*, 3225; g) L. Pu, X. M. Bao, J. P. Zou, D. Feng, *Angew. Chem.* **2001**, *113*, 1538; *Angew. Chem. Int. Ed.* **2001**, *40*, 1490; h) E. J. Mele, P. Kral, *Phys. Rev. Lett.* **2002**, *88*, 056803-1; i) M. Nath, C. N. R. Rao, *Angew. Chem.* **2002**, *41*, 3601; *Angew. Chem. Int. Ed.* **2002**, *41*, 3451; j) J. H. Jung, H. Kobayashi, K. J. C. van-Bommel, S. Shinkai, T. Shimizu, *Chem. Mater.* **2002**, *14*, 1445.
[3] a) A. M. Morales, C. M. Lieber, *Science* **1998**, *279*, 208; b) Y. Cui, L. J. Lauhon, M. S. Gudiksen, J. F. Wang, C. M. Lieber, *Appl. Phys. Lett.* **2001**, *78*, 2214.
[4] a) N. Wang, Y. H. Tang, Y. F. Zhang, C. S. Lee, S. T. Lee, *Phys. Rev. B* **1998**, *58*, R16024; b) S. T. Lee, Y. F. Zhang, N. Wang, Y. H. Tang, I. Bello, C. S. Lee, Y. W. Chung, *J. Mater. Res.* **1999**, *14*, 4503; c) W. S. Shi, H. Y. Peng, L. Xu, N. Wang, Y. H. Tang, S. T. Lee, *Adv. Mater.* **2000**, *12*, 1927; d) J. L. Gole, J. D. Stout, W. L. Rauch, Z. L. Wang, *Appl. Phys. Lett.* **2000**, *76*, 2346.
[5] J. D. Holmes, K. P. Johnston, R. C. Doty, B. A. Korgel, *Science* **2000**, *287*, 1471.
[6] a) J. Sha, J. J. Niu, X. Y. Ma, J. Xu, X. B. Zhang, Q. Yang, D. R. Yang, *Adv. Mater.* **2002**, *14*, 1219; b) S. Y. Jeong, J. Y. Kim, H. D. Yang, B. N. Yoon, S.-H. Choi, H. K. Kang, C. W. Yang, Y. H. Lee, *Adv. Mater.* **2003**, *15*, 1172.
[7] a) S. B. Fagan, R. J. Baierle, R. Mota, A. J. R. da Silva, A. Fazzio, *Phys. Rev. B* **2000**, *61*, 9994; b) G. Seifert, T. Köhler, H. M. Urbassek, E. Hernández, T. Frauenheim, *Phys. Rev. B* **2001**, *63*, 193409; c) A. S. Barnard, S. P. Russo, *J. Phys. Chem. B* **2003**, *107*, 7577.
[8] See, for example a) W. Liang, C. R. Martin, *J. Am. Chem. Soc.* **1990**, *112*, 9666; b) C. J. Brumlik, C. R. Martin, *J. Am. Chem. Soc.* **1991**, *113*, 3174; c) R. Parthasarathy, C. R. Martin, *Nature* **1994**, *369*, 298; d) C. R. Martin, *Science* **1994**, *266*, 1961; e) M. Nishizawa, V. P. Menon, C. R. Martin, *Science* **1995**, *268*, 700; f) P. M. Ajayan, O. Stephan, P. Redlich, C. Colliex, *Nature* **1995**, *375*, 564; g) B. B. Lakshmi, P. K. Dorhout, C. R. Martin, *Chem. Mater.* **1997**, *9*, 857; h) J. C. Hulteen, C. R. Martin, *J. Mater. Chem.* **1997**, *7*, 1075.
[9] J. Goldberger, R. R. He, Y. F. Zhang, S. Lee, H. Q. Yan, H.-J. Choi, P. D. Yang, *Nature* **2003**, *422*, 599.
[10] S. M. Sze, *Physics of Semiconductor Devices*, Wiley-Interscience, New York, **1981**.
[11] a) L. T. Romano, R. D. Bringans, X. Zhou, W. P. Kirk, *Phys. B* **1995**, *52*, 11201; b) X. H. Zhou, S. Jiang, W. P. Kirk, *J. Appl. Phys.* **1997**, *82*, 2251; c) N. H. Tran, A. J. Hartmann, R. N. Lamb, *J. Phys. Chem. B* **2000**, *104*, 1150.
[12] Y. F. Zhang, Y. H. Tang, H. Y. Peng, N. Wang, C. S. Lee, I. Bello, S. T. Lee, *Appl. Phys. Lett.* **1999**, *75*, 1842.
[13] W. S. Shi, H. Y. Peng, N. Wang, C. P. Li, L. Xu, C. S. Lee, R. Kalish, S. T. Lee, *J. Am. Chem. Soc.* **2001**, *123*, 11095.
[14] a) D. Golberg, Y. Bando, L. Bourgeois, K. Kurashima, T. Sato, *Carbon* **2000**, *38*, 2017; b) D. Golberg, Y. Bando, W. Q. Han, K. Kurashima, T. Sato, *Chem. Phys. Lett.* **1999**, *308*, 337; c) W. Q. Han, Y. Bando, K. Kurashima, T. Sato, *Appl. Phys. Lett.* **1998**, *73*, 3085.

 © 2004 Wiley-VCH Verlag GmbH & Co. KGaA, Weinheim

Biosynthesis of Antibiotics

Characterization of NovP and NovN: Completion of Novobiocin Biosynthesis by Sequential Tailoring of the Noviosyl Ring**

*Caren L. Freel Meyers, Markus Oberthür, Hui Xu, Lutz Heide, Daniel Kahne, and Christopher T. Walsh**

Novobiocin, clorobiocin, and coumermycin A_1 are members of the aminocoumarin family of natural products and exert their antibacterial effects by inhibiting the bacterial type II topoisomerase DNA gyrase. Specifically, the aminocoumarins are competitive inhibitors of adenosine triphosphate (ATP) binding and hydrolysis, which are essential for the catalysis of topoisomer interconversion during bacterial DNA replication.[1,2] The aminocoumarins novobiocin (**1**) and clorobiocin (**2**; Figure 1a) have three structural elements: the central 3-amino-7-hydroxycoumarin is linked at the 3-amino moiety to a prenylated 4-hydroxybenzoic acid component, and at the 7-position to an L-noviosyl sugar component. The noviosyl ring of both compounds can be methylated at the 4′-hydroxy group and carbamoylated (novobiocin) or acylated (clorobiocin) at the 3′-hydroxy group.

X-ray crystallographic studies of novobiocin and clorobiocin with their target protein (Figure 1b–d) suggest that the noviosyl sugar component has several key interactions with the ATP binding site of the DNA gyrase subunit GyrB.[1] In particular, the cocrystal structure of novobiocin with GyrB reveals a hydrogen-bonding interaction between the 3′-*O*-carbamoyl moiety and an ordered water molecule in the ATP binding site (Figure 1c). The larger 5-methylpyrrolyl acyl moiety of clorobiocin displaces this water molecule and makes hydrophobic contacts with the enzyme side chains (Figure 1d). This structural alteration leads to a 10-fold increase in antibacterial potency,[2] which suggests that the substituent at the 3′-position of the aminocoumarin antibiotics controls antibacterial activity to a significant extent.

For this reason, it is of particular interest to introduce structural diversity at the 3′-position of the noviosyl ring and generate novel aminocoumarin variants by chemoenzymatic

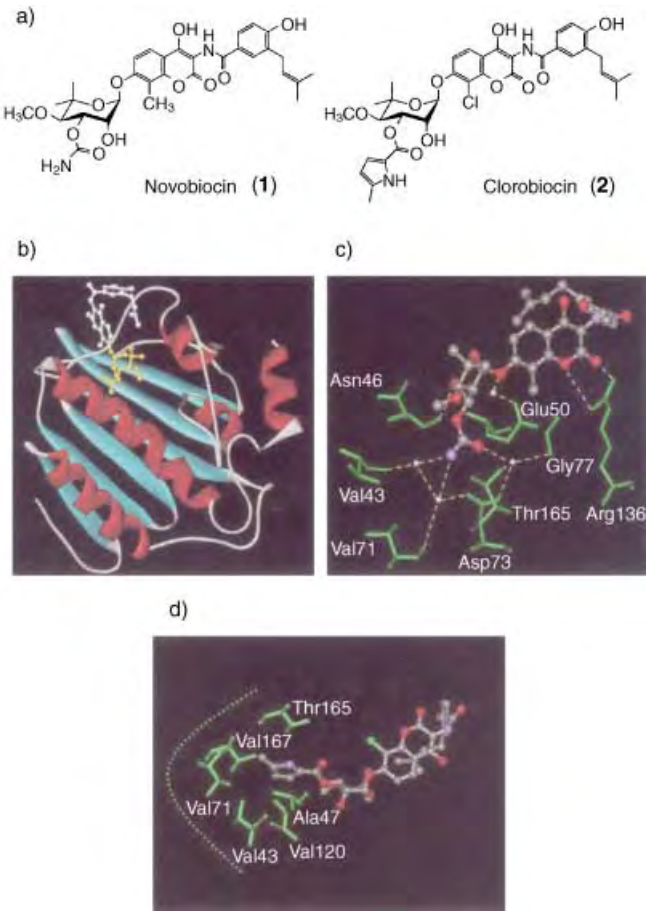


Figure 1. a) Novobiocin and clorobiocin structures; b) novobiocin bound to GyrB; c) side view of novobiocin bound to GyrB; d) clorobiocin bound to GyrB.

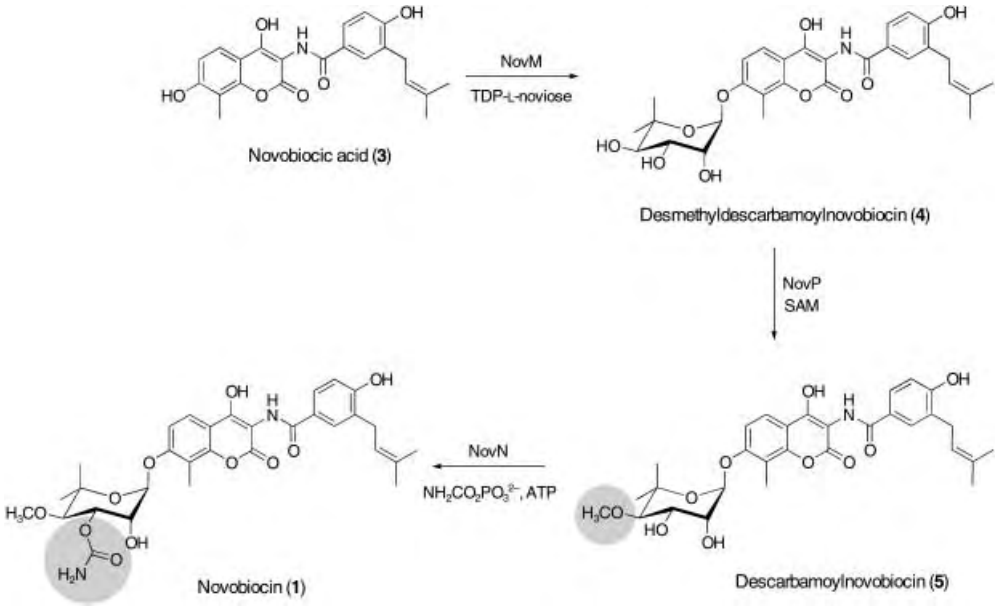
routes. Our research group is interested in the characterization of glycosyltransferases dedicated to antibiotic assembly and maturation. Our work includes the use of glycosylation in chloroeremomycin and vancomycin biosynthesis to generate novel analogues.[3,4] In addition, we recently reported the heterologous overproduction of the L-noviosyl transferase NovM in *Escherichia coli* and its purification in a soluble, active form, and we have characterized NovM as a catalyst for the conversion of novobiocic acid (**3**) into desmethyldescarbamoylnovobiocin (**4**; Scheme 1). The transfer of noviose from thymidine-5′-diphosph-β-L-noviose (TDP-β-L-noviose) to novobiocic acid occurs with a catalytic rate constant of $k_{cat} > 300\ min^{-1}$.[5] Desmethyldescarbamoylnovobiocin (**4**) is presumably the substrate for regiospecific methylation at the 4′-position followed by carbamoylation at the 3′-position. These transformations are the final enzymatic steps in novobiocin biosynthesis[6] and have been predicted to be catalyzed by the enzymes NovP and NovN, respectively, in the novobiocin biosynthetic cluster.[7]

We report herein the cloning and overproduction of the 30-kDa *Streptomyces spheroides* NovP in *E. coli*, and its purification in soluble form as an *N*-His_6-tagged protein (Figure 2, Lane 1). The catalytic activity of NovP as a methyltransferase in the conversion of desmethyldescarba-

[*] Dr. C. L. Freel Meyers, Prof. C. T. Walsh
Department of Biological Chemistry
and Molecular Pharmacology
LHRRB 309, Harvard Medical School
Boston, MA 02115 (USA)
Fax: (+1) 617-432-0556
E-mail: Christopher_walsh@hms.harvard.edu
Dr. M. Oberthür, Prof. D. Kahne
Department of Chemistry, Princeton University
Princeton, NJ, 08544 (USA)
Dr. H. Xu, Prof. L. Heide
Pharmaceutical Institute, Tuebingen University
72076 Tuebingen (Germany)

[**] We gratefully acknowledge the National Institutes of Health Grants 49338 (to C.T.W.), 66174 (to D.K.), and AI054007-01 (to C.L.F.M.). The contribution of X.H. and L.H. was supported by a grant from the Deutsche Forschungsgemeinschaft.

 DOI: 10.1002/anie.200352626 © 2004 Wiley-VCH Verlag GmbH & Co. KGaA, Weinheim



Scheme 1. The final steps in novobiocin biosynthesis. SAM, *S*-adenosylmethionine.

S. spheroides NovN (75 kDa) was cloned and overproduced in *E. coli*, and purified as a C-His_8-tagged protein (Figure 2, Lane 2) following extensive optimization of the procedure. The catalytic activity of NovN as a carbamoyltransferase was confirmed by HPLC results showing the conversion of precursor **5** into novobiocin (**1**) in the presence of the enzyme (Figure 3b). Incubation of desmethyldescarbamoylnovobiocin (**4**) with NovN in the presence of carbamoyl phosphate and ATP did not result in the formation of desmethylnovobiocin, which confirms the observation of Kominek and Sebek[6] that NovN acts after NovP in the synthetic sequence. Further confirmation of novobiocin formation was obtained by mass spectral analysis (calcd:

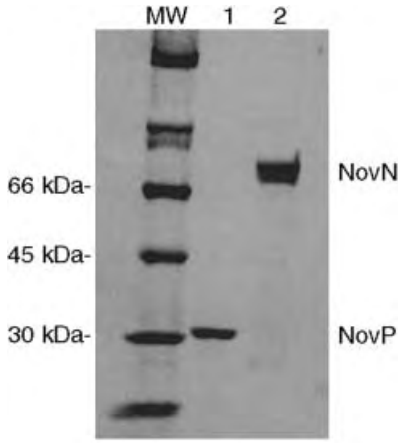


Figure 2. 4–15% tris(hydroxymethyl)aminomethane (Tris)/HCl SDS-PAGE of purified NovP and NovN.

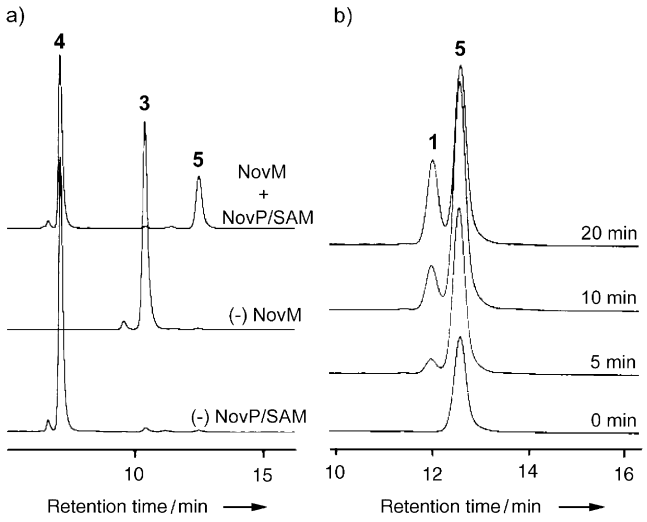


Figure 3. a) Overnight tandem incubation of novobiocic acid (**3**) with NovM/TDP-L-noviose, then NovP/SAM, pH 8, RT; b) conversion of descarbamoylnovobiocin (**5**) into novobiocin (**1**) in the presence of NovN/$NH_2CO_2PO_3^{2-}$/ATP, pH 7.5, RT.

moylnovobiocin (**4**) into descarbamoylnovobiocin (**5**; Scheme 1) was initially confirmed in tandem incubations of novobiocic acid (**3**) with NovM/TDP-L-noviose and NovP/SAM. A new compound whose formation was dependent upon the presence of NovP/SAM was detected by HPLC (Figure 3). Analysis of the reaction mixture by LCMS confirmed that this compound was descarbamoylnovobiocin (**5**; calcd: m/z 570.23 [M+H^+]; found: 570.20). The kinetic characterization of NovP was then undertaken by using purified **4** obtained from a large-scale NovM incubation. NovP catalyzes 4′-*O*-methylation of **4** with $k_{cat} = 0.400 \pm 0.006\ min^{-1}$ and $K_M = 9.5 \pm 3\ \mu M$ (K_M, Michaelis constant), which is a low but usable catalytic efficiency. The enzymatic methylation of compound **4** provided quantities of **5** sufficient for assay of the last enzyme in the biosynthetic pathway of novobiocin.

m/z 613.23 [M+H^+]; found: 613.15). Novobiocin generated from novobiocic acid and TDP-L-noviose in the presence of the three purified enzymes NovM, NovP, and NovN and the cosubstrates SAM, carbamoyl phosphate, and ATP is identical to commercially available novobiocin (Sigma Aldrich) according to HPLC results. However, novobiocin undergoes isomerization to isonovobiocin (the 2′-*O*-carbamoyl isomer of novobiocin) in dilute alkali;[8] isonovobiocin is also known to be a side-product obtained during fermentation/purification of novobiocin.[9] It is therefore important to establish the position of the carbamoyl group in the product of the NovN-catalyzed reaction. Novobiocin can easily be distinguished

 © 2004 Wiley-VCH Verlag GmbH & Co. KGaA, Weinheim

from isonovobiocin by ^{1}H NMR spectroscopy. The ^{1}H NMR spectrum (500 MHz, [D_6]dimethyl sulfoxide (DMSO), 23 °C) obtained for the NovN product was identical to the spectrum of novobiocin and showed peaks at the chemical shifts characteristic for noviose resonances ($\delta = 5.16$ (dd, $J_{2,3} = 3.1$, $J_{3,4} = 9.8$ Hz, 1H; 3-H), 4.08 ppm (m, 1H; 2-H)), which are distinctly different from those recorded in the literature for isonovobiocin ($\delta = 4.18$ (3-H), 4.93 ppm (2-H)).[10]

Further confirmation of novobiocin formation was obtained by comparison of the antibiotic potencies of the NovN reaction product and commercially available novobiocin. The minimum inhibitory concentrations (MICs) of each compound against two bacterial strains (*Enterococcus faecium* and *Staphylococcus aureus*) were determined and found to be comparable (data not shown). Previous reports have established that the 3′-*O*-carbamoyl moiety is essential for antibiotic activity;[11] loss of activity is observed with the descarbamoylnovobiocin precursor. We also observed an MIC for descarbamoylnovobiocin (**5**) that was more than 100-fold higher than that determined for novobiocin.

Kinetic parameters were determined for NovN by using purified descarbamoylnovobiocin (**5**) obtained from a large-scale tandem NovM/NovP incubation. NovN catalyzes the carbamoylation of **5** with $k_{cat} = 4.1 \pm 0.2$ min^{-1}. K_m values of 4.6 ± 1.3 μM and 5.1 ± 0.4 μM were measured for the substrates descarbamoylnovobiocin and carbamoyl phosphate, respectively.

Surprisingly, the carbamoyltransferase activity of NovN is dependent upon Mg-ATP. The regulatory role of ATP in the activation of the aspartate *N*-carbamoyltransferases in a number of bacterial systems has been well studied.[12–16] Activation of *O*-carbamoyltransferases by ATP in secondary metabolite biosynthesis has been reported in only one case: *O*-carbamoylation of 3-hydroxymethylcephem in *Streptomyces clavuligerus*.[17] The role of ATP in the activation of carbamoyltransferase CmcH was investigated in this study, but the authors were unable to conclude whether ATP acts as an effector or as a substrate in the transfer of a carbamoyl moiety to 3-hydroxymethylcephem. In general, regulation of late-stage transformations by ATP in secondary metabolite biosynthesis is not well documented. The role of ATP activation in this final step of novobiocin biosynthesis remains to be elucidated.

The availability of the last three enzymes in the novobiocin biosynthetic pathway, NovM, NovP, and NovN, in purified, active forms through *E. coli* expression will allow evaluation of the possibility of generating an aminocoumarin library in which variation of each component, as well as sugar decoration results in novobiocin analogues that can be evaluated for antibiotic activity. Moreover, tandem NovM/NovP incubations have been carried out on a 30-mg scale, which provides sufficient material to study the regioselective chemical carbamoylation and/or acylation of descarbamoyl novobiocin (**5**) at the 3′-position. We anticipate that variation of the 3′ moiety will provide insight into the structural requirements for gyrase inhibition and antibiotic activity.

Materials and Methods

Preparation of pNovP-pET28a and pNovN-pET37b overexpression constructs: The genes encoding NovP and NovN were amplified from *Streptomyces spheroides* (ATCC23965) genomic DNA and pXHN,[18] respectively. Amplification of *novP* was accomplished by using the foward primer 5′-GCGTATCATATGGCACCTATCGTGGAAACCGCG-3′ and the reverse primer 5′-GCCATTAAGCTTTTACCGGGTGCGTTGCCAG TAG-3′, which include *Nde*I/*Hind*III restriction sites. Amplification of *novN* was accomplished by using the foward primer 5′-CCGAATCA TATGCTCATTCTTGGCCTGAACGGG-3′ and the reverse primer 5′-GCGTTACTCGAGTCACGGTGCGGATCCGGCACC-3′, with *Nde*I/*Xho*I restriction sites. The amplified genes were inserted into pET28a (*novP*) and pET37b (*novN*) vectors after restriction digests, and pNovP-pET28a and pNovN-pET37b were expressed in *E. coli* TOP10 competent cells.

Overproduction and purification of NovP and NovN: Purified pNovP-pET28a and pNovN-pET37b plasmids were transformed into BL21 (DE3) competent *E. coli* cells. Transformants harboring the pNovP-pET28a and pNovN-pET37b constructs were grown in Luria–Bertani (LB) medium supplemented with kanamycin (50 μg mL^{-1}). NovP was overproduced and purified as described for NovM.[5] For the overproduction of NovN, cells were grown at 25 °C to an optical density of around 0.35. The temperature was reduced to 20 °C and the cells were shaken for 1 h. NovN production was induced with isopropyl-β-D-thiogalactopyranoside (60 μM) and the cells were shaken overnight at 20 °C. NovN was isolated from cell extracts as described for NovM.[5]

Characterization of NovP: Reactions were carried out at ambient temperature and reaction mixtures contained desmethyldescarbamoylnovobiocin (**4**) and SAM in tricine (75 mM, pH 8.5), NaCl (100 mM), bovine serum albumin (BSA; 1 mg mL^{-1}), and DMSO (5%). Reactions were initiated by the addition of NovP and terminated at specified time points by quenching in methanol (2× reaction volume) at 4 °C. For the determination of K_m and k_{cat}, NovP and SAM were added to final concentrations of 500 nM and 500 μM, respectively, and the concentration of desmethyldescarbamoylnovobiocin was varied (2.5–50 μM). The reaction was terminated after 10 and 20 min for each concentration. Each experiment was carried out in triplicate.

Quenched aliquots were incubated at −20 °C for 30 min and then centrifuged (5 min at 13000 rpm) to remove precipitated protein. The supernatant was analyzed by analytical reverse-phase HPLC (CH_3CN/H_2O (60:40), 0.1% TFA, 1 mL min^{-1}) monitored at 340 nm. Product formation was confirmed by LCMS (**5**: calcd for $C_{30}H_{35}NO_{10}$: *m/z* 570.23 $[M+H]^+$; found: 570.20) on a Shimadzu LCMS-QP8000α instrument. The desmethyldescarbamoylnovobiocin (**4**; $R_t = 7.0$ min) and descarbamoylnovobiocin (**5**; $R_t = 12.5$ min) HPLC peak areas were measured and the product concentration was calculated as a percent of the total peak area.

Characterization of NovN: Reactions (75 μL total volume) were carried out at ambient temperature and reaction mixtures contained descarbamoylnovobiocin (**5**), carbamoyl phosphate, and ATP (4 mM) in Tris (75 mM, pH 9.0), $MgCl_2$ (10 mM), BSA (1 mg mL^{-1}), and DMSO (5%). Reactions were initiated by the addition of NovN (200 nM) and terminated by quenching the reaction mixture with methanol (150 μL) at 4 °C. K_m and k_{cat} were determined with descarbamoylnovobiocin (**5**) and carbamoyl phosphate as the variable substrates. The determination of the K_m value for descarbamoylnovobiocin (**5**) was accomplished at a constant concentration of carbamoyl phosphate (500 μM) and over a range of descarbamoylnovobiocin (**5**) concentrations (5–50 μM). The reaction was quenched after 5 min for each concentration. The determination of the K_m value for carbamoyl phosphate was accomplished at a constant concentration of descarbamoylnovobiocin (**5**; 50 μM) and over a range of carbamoyl phosphate concentrations (1–14 μM). The reaction was quenched after 10 min for each concentration. Each experiment was carried out in triplicate.

 © 2004 Wiley-VCH Verlag GmbH & Co. KGaA, Weinheim

Quenched aliquots were analyzed as described above (HPLC: CH_3CN/H_2O (20:80), 0.1% trifluoroacetic acid (TFA), 15 min, 1 mL min^{-1}; after 15 min, 20–100% CH_3CN gradient over 10 min). Product formation was confirmed by LCMS (calcd for $C_{31}H_{36}N_2O_{11}$: 613.23 $[M+H]^+$; found: 613.15). The concentrations of descarbamoylnovobiocin (**5**; $R_t = 12.5$ min) and novobiocin (**1**, $R_t = 11.9$ min) were determined as described for NovN.

Large-scale NovM,P,N reactions and purification of enzymatic reaction products: A large-scale NovM incubation was carried out with novobiocic acid (**3**; 30 mg) and TDP-L-noviose. Reaction progress was monitored by HPLC. Upon completion, the crude reaction mixture was loaded onto a C18 sep pak column (900 mg bed, Alltech) conditioned with β-morpholinoethanesulfonic acid (75 mM, pH 6). The sep pak cartridge was washed with water (15 mL) to remove salts and by-products. Desmethyldescarbamoylnovobiocin (**4**) was eluted in acetonitrile/water (60:40) and concentrated by lyophilization. The enzymatic reaction products from NovP and NovN incubations were purified by using this protocol. Further purification of the NovP reaction product **5** by preparatory HPLC was necessary to remove *S*-adenosyl-L-homocysteine.

Received: August 12, 2003 [Z52626]

Keywords: antibiotics · biosynthesis · enzymes · novobiocin · transferases

[1] R. J. Lewis, O. M. Singh, C. V. Smith, T. Skarzynski, A. Maxwell, A. J. Wonacott, D. B. Wigley, *EMBO J.* **1996**, *15*, 1412.
[2] M. Gellert, M. H. O'Dea, T. Itoh, J. Tomizawa, *Proc. Natl. Acad. Sci. USA* **1976**, *73*, 4474.
[3] H. C. Losey, J. Jiang, J. B. Biggins, M. Oberthür, X.-Y. Ye, S. D. Dong, D. Kahne, J. S. Thorson, C. T. Walsh, *Chem. Biol.* **2002**, *9*, 1305.
[4] H. C. Losey, M. W. Peczuh, Z. Chen, U. S. Eggert, S. D. Dong, I. Pelczer, D. Kahne, C. T. Walsh, *Biochemistry* **2001**, *40*, 4745.
[5] C. L. Freel Meyers, M. Oberthür, J. W. Anderson, D. Kahne, C. T. Walsh, *Biochemistry* **2003**, *42*, 4179.
[6] L. A. Kominek, O. K. Sebek, *Dev. Ind. Microbiol. Ser.* **1974**, *15*, 60.
[7] M. Steffensky, A. Mühlenweg, Z. X. Wang, S. M. Li, L. Heide, *Antimicrob. Agents Chemother.* **2000**, *44*, 1214.
[8] J. W. Hinman, E. L. Caron, H. Hoeksema, *J. Am. Chem. Soc.* **1957**, *79*, 3789.
[9] I. V. Gracheva, V. A. Severina, *Antibiotiki* **1966**, *11*, 45.
[10] F. W. Crow, W. K. Duholke, K. A. Farley, C. E. Hadden, D. A. Hahn, B. D. Kaluzny, C. S. Mallroy, G. E. Martin, R. F. Smith, T. J. Thamann, *J. Heterocycl. Chem.* **1999**, *36*, 365.
[11] D. C. Hooper, J. S. Wolfson, G. L. McHugh, M. B. Winters, M. N. Swartz, *Antimicrob. Agents Chemother.* **1982**, *22*, 662.
[12] P. Chen, F. Van Vliet, M. Van De Casteele, C. Legrain, R. Cunin, N. Glansdorff, *J. Bacteriol.* **1998**, *180*, 6389.
[13] R. Cunin, C. S. Rani, F. Van Vliet, J. R. Wild, M. Wales, *J. Mol. Biol.* **1999**, *294*, 1401.
[14] L. Fetler, P. Vachette, *J. Mol. Biol.* **2001**, *309*, 817.
[15] J. B. Sakash, A. Tsen, E. R. Kantrowitz, *Protein Sci.* **2000**, *9*, 53.
[16] J. F. Vickrey, G. Herve, D. R. Evans, *J. Biol. Chem.* **2002**, *277*, 24490.
[17] S. J. Brewer, P. M. Taylor, M. K. Turner, *Biochem. J.* **1980**, *185*, 555.
[18] H. Xu, Z. X. Wang, J. Schmidt, L. Heide, S. M. Li, *Mol. Genet. Genomics* **2002**, *268*, 387.

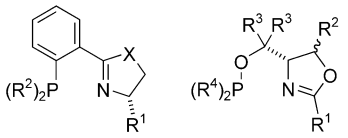
 © 2004 Wiley-VCH Verlag GmbH & Co. KGaA, Weinheim

Chiral N,P Ligands

Synthesis of Versatile Chiral N,P Ligands Derived from Pyridine and Quinoline**

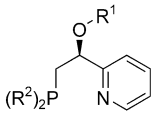
*William J. Drury III, Nicole Zimmermann, Martine Keenan, Masahiko Hayashi, Stefan Kaiser, Richard Goddard, and Andreas Pfaltz**

Chiral phosphanyl oxazolines **1** (PHOX)[1] and related compounds such as **2**[2] and **3**[3] have established themselves as highly versatile, readily accessible ligands for controlling the stereochemistry of metal-catalyzed reactions. The success of

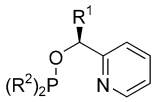


1 X = O
2 X = NR

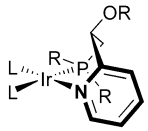
3



4



5



6

these ligands in the Ir-catalyzed hydrogenation of olefins[2–4] and imines,[5] and the intention to mimic the coordination sphere of Crabtree's catalyst ($[(Cy_3P)(pyridine)Ir(cod)]PF_6$)[6] (Cy = cyclohexyl, cod = 1,5-cyclooctadiene) with a chiral bidentate ligand, motivated us to prepare chiral pyridyl phosphanes having the general structure **4**.[7] On the basis of simple force-field calculations carried out with a fixed standard geometry for the P-Ir-N core and the known propensity of 2-(oxymethyl)pyridines to adopt an antiperiplanar conformation of the N-C-C-O fragment,[8] we anticipated that these ligands would form a rigid chelate ring in a

[*] Dr. W. J. Drury III, Dr. N. Zimmermann, Dipl.-Chem. S. Kaiser,[+]
Prof. Dr. A. Pfaltz
Department of Chemistry
University of Basel
St. Johanns-Ring 19, 4056 Basel (Switzerland)
Fax: (+41) 61-267-1103
E-mail: andreas.pfaltz@unibas.ch
Dr. M. Keenan, Dr. M. Hayashi, Dr. R. Goddard[+]
Max-Planck-Institut für Kohlenforschung
Kaiser-Wilhelm-Platz 1
45470 Mülheim an der Ruhr (Germany)

[+] X-Ray analyses.

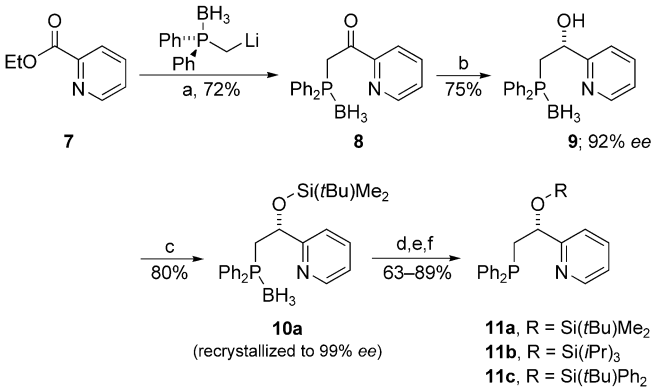
[**] Financial support for this work from the American and Swiss National Science Foundations is gratefully acknowledged. N.Z. thanks the Fonds der Chemischen Industrie for a Kekulé fellowship. The authors kindly thank Dr. Thomas Lectka (The Johns Hopkins University) for helpful discussions.

Supporting information for this article is available on the WWW under http://www.angewandte.org or from the author.

 © 2004 Wiley-VCH Verlag GmbH & Co. KGaA, Weinheim DOI: 10.1002/anie.200352755

boat conformation (**6**), thus generating a similar steric environment around the Ir atom as the PHOX ligands. However, as oxazoline and pyridine ligands are expected to have different electronic effects on a coordinated metal, we thought that pyridine-derived ligands, such as **4**, could induce new patterns of reactivity and selectivity. We report here the synthesis and application of a series of pyridyl phosphanes **4** along with the analogous quinoline derivatives and pyridyl phosphinites **5**.

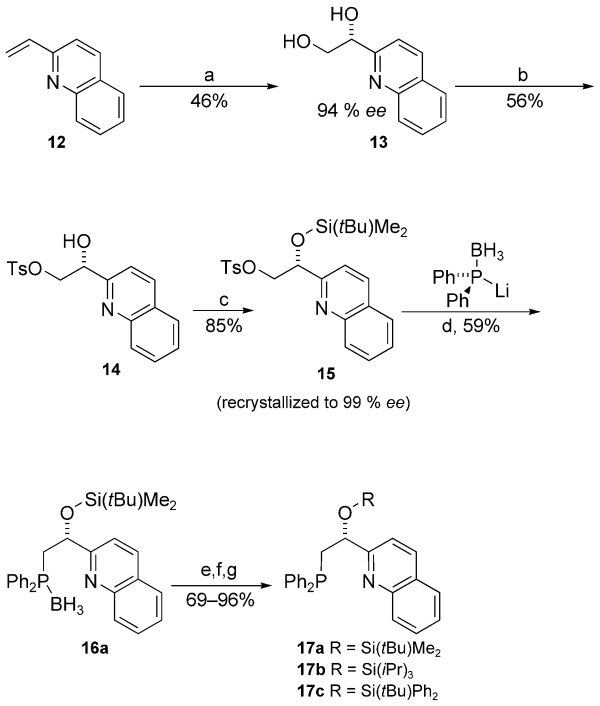
We felt that the ready availability of all starting materials was of utmost importance. With this in mind, we chose ethyl picolinate (**7**) as an appropriate entry point (Scheme 1). This



Scheme 1. Synthesis of pyridyl phosphanes **11a–c**. a) $Ph_2PCH_3{\cdot}BH_3$ (1 equiv), TMEDA (1.1 equiv), *s*BuLi (1.1 equiv), −78 °C, 2 h, then **7** (1.1 equiv), −78 °C to RT, 18 h; b) (−)-Ipc$_2$BCl (2.5 equiv), THF, 0 °C, 19 h; c) *t*BuMe$_2$SiOTf (1.4 equiv), 2,6-lutidine, CH_2Cl_2, RT, 2 h, (after recrystallization, 59%); d) $(Bu_4N)F$ (2 equiv), THF, RT, 4 h, 99%; e) $(iPr)_3SiOTf$ (1.4 equiv), 2,6-lutidine, CH_2Cl_2, RT, 18 h, 94%; or *t*BuPh$_2$SiCl (1.25 equiv), imidazole (4.3 equiv), CH_2Cl_2, 80%; f) diethylamine, RT, 12 h, **11a** (63%), **11b** (81%), **11c** (89%). TMEDA = *N*,*N*,*N*′,*N*′-tetramethylethylenediamine, Tf = trifluoromethanesulfonyl.

was readily alkylated by lithiated BH_3-protected methyldiphenylphosphane to yield ketone **8**.[9] This material could be reduced to **9** by (−)-chlorodiisopinocampheyl borane [(−)-Ipc$_2$BCl],[10] in good yield and high enantioselectivity. As this product is an oil, we directly carried it forward in hopes of recrystallizing a later intermediate. We capped the benzyl alcohol by straightforward protection with *t*BuMe$_2$SiOTf to provide **10a**, in which the ethereal oxygen atom has been rendered noncoordinating. As this material could be obtained enantiomerically pure after recrystallization, it was chosen as the common intermediate for the construction of all other analogues. At this point, it was unclear what role the silane might play during catalysis. To gain insight, we cleaved the silyl group and reprotected the alcohol with either $(iPr)_3$-SiOTf (**10b**) or *t*BuPh$_2$SiCl (**10c**). Finally, the free phosphanes **11a–c** were obtained by stirring the corresponding boranes in diethylamine overnight, and filtering the reaction mixture through silica gel.[11]

To increase the steric bulk of the coordinating N-heterocycle, we wanted to replace the pyridine ring by a quinoline unit. However, the enantioselective reduction of the quinoline analogue of **8** with Ipc$_2$BCl was sluggish and gave only 70% *ee*. Therefore, an alternative route based on the Sharpless dihydroxylation[12] of 2-vinylquinoline[13] (**12**) was devised (Scheme 2).



Scheme 2. Synthesis of quinolyl phosphanes **17a–c**. a) $K_2OsO_4{\cdot}H_2O$ (1 mol%), $(DHQD)_2PHAL$ (1 mol%), $K_3[Fe(CN)_6]$ (3 equiv), K_2CO_3 (3 equiv), *t*BuOH/H_2O (1:1), 0 °C to RT; b) TsCl (1 equiv), pyridine, −10 °C, 4 h; c) *t*BuMe$_2$SiCl (1.3 equiv), imidazole (2.5 equiv), CH_2Cl_2, RT, 5 h, (after recrystallization, 74%); d) $Ph_2PH{\cdot}BH_3$ (1.2 equiv), *n*BuLi (1.2 equiv), THF, −78 °C to 0 °C, 1 h, then **15**, THF/DMF (3:2), RT, 24 h; e) $(Bu_4N)F$ (2 equiv), THF, RT, 4 h, 99%; f) $(iPr)_3SiOTf$ (1.4 equiv), 2,6-lutidine, CH_2Cl_2, RT, 18 h, 99%; or *t*BuPh$_2$SiCl (1.25 equiv), imidazole (4.3 equiv), CH_2Cl_2, 79%; g) diethylamine, RT, 12 h, **17a** (69%), **17b** (86%), **17c** (96%). $(DHQD)_2PHAL$ = hydroquinidine-1,4-phthalazinediyl diether, Ts = toluene-4-sulfonyl.

The oxidation of **12** reproduciblity provided diol **13** in acceptable yield and high *ee* value on a multigram scale (46%, 94% *ee*).[14] Selective tosylation of the primary alcohol, followed by silylation provided enantiomerically pure **15** after recrystallization from ethyl acetate/hexanes. Sulfonate displacement by $LiPPh_2{\cdot}BH_3$ gave the protected ligand **16a**. At this point, the overall diversity of the ligand set can be expanded by judicious choice of nucleophile, and we have obtained similar results with di-*o*-tolyl, di-*m*-xylyl, and dicyclohexylphosphane–borane complexes.[15] As outlined for the pyridyl phosphanes, the free ligands **17a–c** were obtained by exchange of the silyl group and deborination.

Cationic Ir complexes were made from *N*-heteroaryl phosphanes **11a–c** and **17a–c**. Heating a dichloromethane solution of the appropriate ligand in the presence of 0.5 equivalent of $[Ir(cod)Cl]_2$ for 2 h followed by counterion exchange with sodium tetrakis[3,5-bis(trifluoromethyl)phenyl]borate ($NaBAr_F$)[16] (1.6 equiv), in the presence of water,

 © 2004 Wiley-VCH Verlag GmbH & Co. KGaA, Weinheim

provided the complexes as orange solids. These are generally air and moisture stable, as well as being amenable to chromatography on silica gel (dichloromethane/pentanes).[17]

We were able to obtain crystals of (*S*)-**19a** suitable for X-ray analysis.[18] The crystal structure confirmed the absolute configuration originally assigned to ligands **17a–c** and **11a–c**, based on heuristic rules for Ipc_2BCl reduction[10] and asymmetric dihydroxylation.[12] It also showed the expected boat conformation of the chelate ring (see structure **6**). We also determined the crystal structures of racemic PF_6^- analogues of **19b** and **19c**,[18] which show a much higher tendency to crystallize than the corresponding enantiomerically pure BAr_F salts. The chelate ring and the silyloxy groups in these two complexes, and in complex (*S*)-**19a**, adopt virtually the same geometry. The chiral equatorial/axial arrangement of the two *P*-phenyl groups is very similar to that found in Ir–PHOX complexes (see Figure 1).[5] Moreover, space-filling models show that the quinoline and the isopropyloxazoline moieties occupy similar regions in space. The striking similarity between the chiral coordination spheres in the quinolyl phosphane and PHOX complexes suggests that, although the ligand structures are distinctly different, they should allow comparable levels of enantiocontrol.

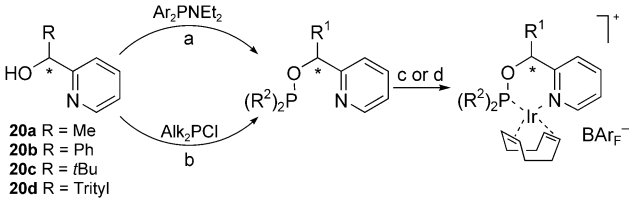
In the three crystal structures mentioned above, the silyl groups are bent toward the coordination sphere. As shown in Figure 1, one of the Si-phenyl groups is located above the Ir atom (distance between the essentially parallel Ph and P-Ir-N planes ca. 3.7 Å), close enough to interact with the active



Figure 1. Comparison of [Ir(**1**)(cod)]PF_6 (R^1 = *i*Pr, R^2 = Ph) and the PF_6^- analogue of *rac*-**19c**. Hydrogen atoms, cod, and PF_6^- ions in both structures have been omitted for clarity.

site of the catalyst. Therefore, it is not surprising that in catalytic studies the enantioselectivity was found to depend on the structure of the silyl group (see below).

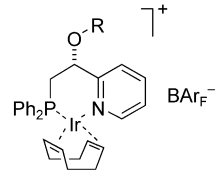
The success with phosphinite ligands **3**[3] prompted us to replace the R_2PCH_2 fragment in ligands **4** by a R_2PO group (Scheme 3). The requisite alcohols were readily prepared by reduction of commercially available ketones (**20a**, **b**) with sodium borohydride or alkylating the appropriate aldehyde with 2-lithiopyridine (**20c**, **d**). By this route, a diverse set of ligands with many different R groups, ranging from simple methyl to colossal trityl, could be readily prepared. The racemic alcohols were then resolved into their component enantiomers by chiral HPLC (see Supporting Information).[19] To our surprise, all attempts to react chlorodiarylphosphanes with pyridyl alkoxides were unsuccessful. However, *N*,*N*-diethylaminodiaryl phosphanes in the presence of acidic heterocycle salts[20] led to the desired phosphinites in all but



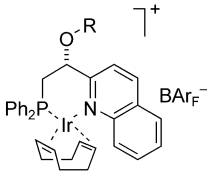
21a R^1 = Me, R^2 = Ph, (*S*), 71%
21b R^1 = Me, R^2 = *o*Tol, (*S*), 65%
21c R^1 = Ph, R^2 = Ph, (*R*), 67%
21d R^1 = Ph, R^2 = *o*Tol, (*S*), 70%
21e R^1 = Ph, R^2 = Cy, (*S*), 65%
21f R^1 = Ph, R^2 = *t*Bu, (*R*), 58%
21g R^1 = *t*Bu, R^2 = Ph, (*S*), 78%
21h R^1 = *t*Bu, R^2 = *o*Tol, (*R*), 90%
21i R^1 = *t*Bu, R^2 = Cy, (*S*), 86%
21j R^1 = *t*Bu, R^2 = *t*Bu, (*S*), 79%
21k R^1 = Trityl, R^2 = Ph, (*R*), 95%

Scheme 3. Synthesis of pyridyl phosphinite complexes **21a–k**. a) Ar_2PNEt_2/4,5-dichloroimidazole/triethylamine (1:1:1; 1.5—3.0 equiv), CH_2Cl_2, RT, 1–3 d; b) Alk_2PCl (1 equiv), KH (1.1 equiv), Et_2O/DMF (9:1), 0 °C to RT, 18 h; c) $[Ir(cod)Cl]_2$ (0.5 equiv), CH_2Cl_2, 50 °C, 2 h, then $NaBAr_F$ (1.5 equiv), 50 °C, 30 min; d) $[Ir(cod)Cl]_2$ (0.5 equiv), CH_2Cl_2, 0–50 °C, 2 h, then $NaBAr_F$ (1.5 equiv), 50 °C, 30 min.

the most congested systems.[21] The products were then isolated by column chromatography, under argon, in greater than 97% purity (^{31}P NMR). In contrast to their aryl conjoiners, dialkyl chlorophosphanes readily react with pyridyl alkoxides. The instability of the resultant phosphinites meant that it was imperative to carefully control reagent stoichiometry, and when this was done simple filtration of the reaction mixture through degassed silica provided >90% pure material. The corresponding Ir complexes were made by a slightly modified procedure, because of the higher ligand sensitivity. Again, the resultant complexes are stable red to orange solids that can be purified by chromatography or crystallization.



18a R = Si(*t*Bu)Me_2
18b R = Si(*i*Pr)$_3$
18c R = Si(*t*Bu)Ph_2

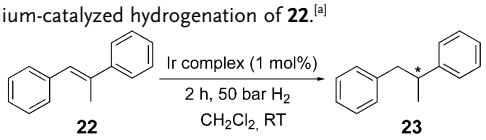


19a R = Si(*t*Bu)Me_2
19b R = Si(*i*Pr)$_3$
19c R = Si(*t*Bu)Ph_2

The iridium complexes synthesized above were used to hydrogenate several representative alkenes. The efficacy of the complexes in the hydrogenation of *trans*-α-methylstilbene (**22**) are summarized in Table 1. In general, the phosphinites are superior in terms of both enantioselectivity and conversion. In the case of the pyridyl phosphanes (**18a–c**) the nature of the silane seems to play a disproportionately large role. This can be rationalized in light of the crystal structures discussed above. High enantioselectivity was also obtained with other substrates such as monoaryl alkenes **24** and **25**,

 © 2004 Wiley-VCH Verlag GmbH & Co. KGaA, Weinheim

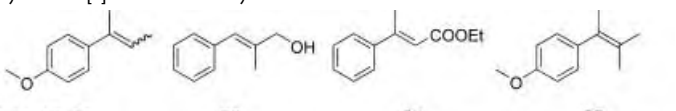
Table 1: Iridium-catalyzed hydrogenation of **22**.[a]



(1)

Catalyst	Configuration	Conv. (%)[b]	*ee* (%)[c]
18a	*R*	93	88 (*R*)
18b	*R*	>99	57 (*R*)
18c	*R*	>99	4 (*R*)
19a	*R*	80	45 (*R*)
19b	*R*	92	45 (*R*)
19c	*R*	69	56 (*R*)
21a	*S*	>99	90 (*S*)
21b	*S*	>99	93 (*S*)
21c	*R*	>99	94 (*R*)
21d	*S*	>99	95 (*S*)
21e	*S*	>99	87 (*S*)
21f	*R*	>99	96 (*R*)
21g	*S*	>99	90 (*S*)
21h	*R*	>99	96 (*R*)
21i	*S*	>99	96 (*S*)
21j	*S*	>99	97 (*S*)
21k	*R*	44	38 (*R*)

[a] Conditions: see Equation (1); experimental procedures: see Ref. [3]. [b] Determined by GC.[3] [c] Determined by HPLC.[3]

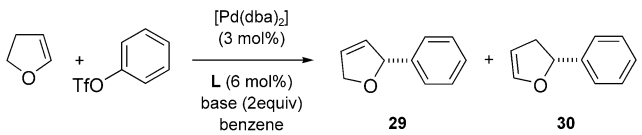


(*E*)-**24**; (*Z*)-**25** **26** **27** **28**

24: **21c**; 87% *ee*, >99% **21h**; 96% *ee*, >99% **21f**; 95% *ee*, >99% **21j**; 81% *ee*, >99%
25: **21c**; 90% *ee*, >99%

allylic alcohol **26**, and ethyl 2-methylcinnamate **27**. Of particular note is the tetrasubstituted alkene **28**, a substrate that gives low conversion and poor enantioselectivity with most catalysts. Overall, the complexes rival the best catalysts developed so far, and in some cases match the highest reported *ee* values.

To further demonstrate the generality and utility of N-heteroaryl phosphanes and phosphinites we tested the ligands as catalyst precursors for several palladium-catalyzed processes. While the phosphinites formed rather unselective complexes in this regard, the phosphanes proved to be far superior, especially in the enantioselective Heck reaction (Scheme 4). While the product mixtures contain slightly more of isomer **30** than when PHOX complexes are used, the enantiomeric excess equaled the highest reported values.[22]



L = **11a** (proton sponge, 60 °C, 3 days): 87% *ee* (**29**), **29/30** = 97:3, 97% conv.
L = **11b** (EtN*i*Pr$_2$, 60 °C, 3 days): 92% *ee* (**29**), **29/30** = 98:2, 83% conv.
L = **17a** (EtN*i*Pr$_2$, 50 °C, 2 days): 97% *ee* (**29**), **29/30** = 83:17, 100% conv.
L = **17b** (proton sponge, 50 °C, 2 days): 99% *ee* (**29**), **29/30** = 95:5, 48% conv.

Scheme 4. Enantioselective Heck reaction. dba = *trans*,*trans*-dibenzylideneacetone, proton sponge = 1,8-bis(dimethylamino)naphthalene.

The results presented indicate considerable potential for these structurally simple and readily available heteroaryl phosphanes and phosphinites. Their modular nature, which enables easy tuning of steric and electronic properties, suggests that these ligands should be widely applicable in asymmetric catalysis.

Received: September 1, 2003 [Z52755]

Keywords: asymmetric catalysis · Heck reaction · hydrogenation · ligand design · N,P ligands

[1] a) G. Helmchen, A. Pfaltz, *Acc. Chem. Res.* **2000**, *33*, 336.
[2] a) F. Menges, M. Neuburger, A. Pfaltz, *Org. Lett.* **2002**, *4*, 4713; for related ligands, see: b) C. A. Busacca, D. Grossbach, R. C. So, E. M. O'Brien, E. M. Spinelli, *Org. Lett.* **2003**, *5*, 595.
[3] a) J. Blankenstein, A. Pfaltz, *Angew. Chem.* **2001**, *113*, 4577; *Angew. Chem. Int. Ed.* **2001**, *40*, 4445; b) F. Menges, A. Pfaltz, *Adv. Synth. Catal.* **2002**, *344*, 40.
[4] A. Pfaltz, J. Blankenstein, R. Hilgraf, E. Hörmann, S. McIntyre, F. Menges, M. Schönleber, S. P. Smidt, B. Wüstenberg, N. Zimmermann, *Adv. Synth. Catal.* **2003**, *345*, 33.
[5] P. Schnider, G. Koch, R. Prétôt, G. Wang, F. M. Krüger, A. Pfaltz, *Chem. Eur. J.* **1997**, *3*, 887.
[6] R. H. Crabtree, *Acc. Chem. Res.* **1979**, *12*, 331.
[7] For other chiral pyridine and quinoline derived N,P ligands, see: a) T. Bunlaksananusorn, K. Polborn, P. Knochel, *Angew. Chem.* **2003**, *115*, 4071; *Angew. Chem. Int. Ed.* **2003**, *42*, 3941; b) P. Espinet, K. Soulantica, *Coord. Chem. Rev.* **1999**, *293*, 499; c) J. M. Brown, D. I. Hulmes, P. J. Guiry, *Tetrahedron* **1994**, *50*, 4493; d) B. Wolfe, T. Livinghouse, *J. Am. Chem. Soc.* **1998**, *120*, 5116; e) K. Ito, R. Kashiwagi, K. Iwasaki, T. Katsuki, *Synlett* **1999**, *10*, 1563; f) G. Franciò, F. Faraone, W. Leitner, *Angew. Chem.* **2000**, *112*, 1486; *Angew. Chem. Int. Ed.* **2000**, *39*, 1428; g) A. V. Malkov, M. Bella, I. G. Stará, P. Koèovský, *Tetrahedron Lett.* **2001**, *42*, 3045.
[8] C. Moberg, H. Adolfsson, K. Wärnmark, P. O. Norrby, K. M. Marstokk, H. Møllendal, *Chem. Eur. J.* **1996**, *2*, 516.
[9] See, for example, a) T. Imamoto, T. Kusumoto, N. Suzuki, K. Sato, *J. Am. Chem. Soc.* **1985**, *107*, 5301; b) T. Imamoto, T. Oshiki, T. Onozawa, T. Kusumoto, K. Sato, *J. Am. Chem. Soc.* **1990**, *112*, 5244.
[10] H. C. Brown, J. Chandrasekharan, P. V. Ramachandran, *J. Am. Chem. Soc.* **1988**, *110*, 1539.
[11] a) R. Ewalds, E. B. Eggeling, A. C. Hewat, P. C. J. Kamer, P. W. N. M. van Leeuwen, D. Vogt, *Chem. Eur. J.* **2000**, *6*, 1496 .
[12] H. C. Kolb, M. S. VanNieuwenhze, K. B. Sharpless, *Chem. Rev.* **1994**, *94*, 2483.
[13] 2-Vinylquinoline is commercially available from Acros Chemical, or alternately, can be prepared from quinoline in one step, see: M. A. Fakhfakh, X. Franck, A. Fournet, R. Hocquemiller, B. Figadère, *Tetrahedron Lett.* **2001**, *42*, 3847.
[14] Dihydroxylation of 2-vinylpyridine afforded the corresponding diol in only 15% yield (94% *ee*).
[15] N. Zimmermann, Dissertation, University of Basel, **2001**.
[16] D. L. Reger, T. D. Wright, C. A. Little, J. J. S. Lambda, M. D. Smith, *Inorg. Chem.* **2001**, *40*, 3810. See also: J. L. Leaser, Jr., R. Cvetovich, F.-R. Tsay, U. Dolling, T. Vickery, D. Bachert, *J. Org. Chem.* **2003**, *68*, 3695.

 © 2004 Wiley-VCH Verlag GmbH & Co. KGaA, Weinheim

[17] For long-term storage (> 2 weeks), complexes were kept under argon at −25 °C.

[18] CCDC-217683 (**19a**), CCDC-218218 (*rac*-**19b**), CCDC-218219 (*rac*-**19c**) contains the supplementary crystallographic data for this paper. These data can be obtained free of charge via www.ccdc.cam.ac.uk/conts/retrieving.html (or from the Cambridge Crystallographic Data Centre, 12, Union Road, Cambridge CB21EZ, UK; fax: (+44) 1223-336-033; or deposit@ccdc.cam.ac.uk). *rac*-**19c**: crystallized from CH_2Cl_2/Et_2O, $C_{47}H_{50}F_6Ir_1N_1O_1P_2Si_1$, $M_r = 1041.16$, orange block $0.20 \times 0.22 \times 0.24$ mm, triclinic, space group $P\bar{1}11$, $a = 10.9930(8)$, $b = 12.8619(7)$, $c = 15.8814(12)$ Å, $\alpha = 98.936(9)$, $\beta = 104.955(6)$, $\gamma = 95.555(7)°$, $V = 2120.9(3)$ Å^3, $\rho_{calcd} = 1.630$ g cm^{-3}, $\mu = 3.316$ mm^{-1}, $F(000) = 1044.000$, $Z = 2$, $Mo_{K\alpha}$ radiation ($\lambda = 0.71073$ Å, graphite monochromator), $T = 173$ K, Θ scan range $3.168 < \Theta < 33.000°$. 108123 reflections collected ($\pm h$, $\pm k$, $\pm l$), 15971 independent reflections, 12910 observed reflections [$I > 3\sigma(I)$], 532 refined parameters. $R = 0.0345$, $Rw = 0.0242$, max. residual electron density −2.55(3.06) e$^-$ Å^{-3}, located near the metal center. There were no restraints applied. Hydrogen atoms were calculated and refined as riding atoms. Data collection was performed with a Kappa CCD diffractometer. Programs used: structure solution: SIR79 (A. Altomare, M. C. Burla, M. Camalli, G. L. Cascarano, C. Giacovazzo, A. Guagliardi, A. Grazia, G. Moliterni, G. Polidori, R. Spagna, *J. Appl. Crystallogr.* **1999**, *32*, 115), structure refinement: CRYSTALS (D. J. Watkin, *Crystals*, *Issue 11*, Chemical Crystallography Laboratory, Oxford, **2001**), weighting scheme: Chebychev polynomial (J. R. Carruthers, D. J. Watkin, *Acta Crystallogr. Sect. A* **1979**, *35*, 698). We thank Markus Neuburger for assistance in solving the crystal structures of *rac*-**19b** and *rac*-**19c**.

[19] While we have chosen to separate the enantiomers on expediency grounds, this is by no means necessary as enantioselective routes to all but one are known. **20a**: a) B. Lipshutz, L. Asher, K. Noson, *Org. Lett.* **2002**, *4*, 4045; b) R. Seemayer, M. P. Schneider, *Tetrahedron: Asymmetry* **1992**, *3*, 827; c) M. D. Garret, R. Scott, G. N. Sheldrake, *Tetrahedron: Asymmetry* **2002**, *13*, 2201; **20b**: d) A. G. Davies, J. Kenyon, K. Thaker, *J. Chem. Soc.* **1956**, 3394; e) N. A. Salvi, S. Chattopadhyay, *Tetrahedron* **2001**, *57*, 2833; **20c**: f) C. Bolm, M. Zehnder, D. Bur, *Angew. Chem.* **1990**, *102*, 206; *Angew. Chem. Int. Ed. Engl.* **1990**, *29*, 205; g) C. Bolm, M. Ewald, M. Felder, G. Schlingloff, *Chem. Ber.* **1992**, *125*, 1169; g) G. Cheulucci, F. Soccolini, *Tetrahedron: Asymmetry* **1992**, *3*, 1235.

[20] E. E. Nifantiev, M. K. Grachev, S. Y. Burmistrov, *Chem. Rev.* **2000**, *100*, 3755.

[21] We were unable to prepare the pyridyl phosphinite (R^1 = trityl, R^2 = *o*-Tol) even in the presence of a large excess of reagents.

[22] a) O. Loiseleur, P. Meier, A. Pfaltz, *Angew. Chem.* **1996**, *108*, 218; *Angew. Chem. Int. Ed. Engl.* **1996**, *35*, 20; b) O. Loiseleur, M. Hayashi, N. Schmees, A. Pfaltz, *Synthesis* **1997**, 1339; c) O. Loiseleur, M. Hayashi, M. Keenan, N. Schmees, A. Pfaltz, *J. Organomet. Chem.* **1999**, *576*, 16.

 © 2004 Wiley-VCH Verlag GmbH & Co. KGaA, Weinheim

Hydrogen-Bonded Assembly

π-Conjugated Oligo-(*p*-phenylenevinylene) Rosettes and Their Tubular Self-Assembly**

Pascal Jonkheijm, Atsushi Miura, Magdalena Zdanowska, Freek J. M. Hoeben, Steven De Feyter, Albertus P. H. J. Schenning,* Frans C. De Schryver,* and E. W. Meijer**

Artificial cylindrical and tubular aggregates of specifically programmed molecules are of interest as sensing, transport, and bioactive systems. An important design to form these aggregates is via ring stacking and most of these stacks are composed of single-molecule rings, for example, cyclic oligopeptides.[1] Hydrogen-bond interactions between molecules are attractive candidates for obtaining well-defined supramolecular cyclic structures due to their spatial arrangement and directionality.[2] Multiple examples of these cyclic structures exist that are based on hydrogen-bonding building blocks.[3] Further aggregation of cyclic supramolecular structures into extended aggregates is, however, scarce.[4] Recently, Stupp and co-workers described an elegant example of the self-assembly of dendron rod–coil molecules into tetrameric hydrogen-bonded rosettes that further organize into nanoribbons by additional hydrogen bonding and π--π interactions.[5] Nanohelices of cadmium sulfide were made by the mineralization of these aggregates. Fenniri et al. demonstrated the formation of rosette nanotubes in which the helicity could be tuned by using amino acids.[6]

We and others have used noncovalent interactions to design π-conjugated oligomers that organize hierarchically over several length scales.[7] Self-assembled supramolecular structures of conjugated molecular building blocks are a

[*] P. Jonkheijm, F. J. M. Hoeben, Dr. A. P. H. J. Schenning, Prof. Dr. E. W. Meijer
Laboratory of Macromolecular and Organic Chemistry
Eindhoven University of Technology
P.O. Box 513, 5600 MB Eindhoven (The Netherlands)
Fax: (+31) 40-2451036
E-mail: a.p.h.j.schenning@tue.nl
e.w.meijer@tue.nl

Dr. A. Miura, M. Zdanowska, Dr. S. De Feyter, Prof. Dr. F. C. De Schryver
Department of Chemistry
Laboratory of Photochemistry and Spectroscopy
Katholieke Universiteit Leuven
Celestijnenlaan 200-F, 3001 Leuven (Belgium)
Fax: (+32) 16-327990
E-mail: Steven.DeFeyter@chem.kuleuven.ac.be
frans.deschryver@chem.kuleuven.ac.be

[**] The authors would like to thank Dr. R. Kleppinger and Dr. P. Strunz for providing SANS beam time. This work was supported by the Council for Chemical Research of the Netherlands Organization for Scientific Research (CW-NWO), the Royal Dutch Academy of Sciences (KNAW), the DWTC (through IUAP-V-03), the IWT and a fellowship of the Fund for Scientific Research—Flanders (Belgium).

Supporting information for this article is available on the WWW under http://www.angewandte.org or from the author.

 © 2004 Wiley-VCH Verlag GmbH & Co. KGaA, Weinheim DOI: 10.1002/anie.200352790

promising class of materials to improve the solid-state organization of future optoelectronic devices.[8] Thorough research has allowed control of the photophysical properties through precise choice of the chemical structure.[9] Up to now most, if not all, π-conjugated oligomers self-assemble through the stacking of rods. To create cylindrical or, even more exciting, tubular aggregates with perfect space filling, requires another hierarchical assembly process. Here, we report on a unique and unexpected process to construct hexameric π-conjugated rosettes that self-assemble into chiral tubular objects.

In our research of quadruple-hydrogen-bonded dimeric oligomers,[7d] we analyzed two oligo-(*p*-phenylenevinylene) (OPV) precursors bearing a diamino triazine moiety (**OPVT3**, **OPVT4**; Figure 1) with scanning tunneling micro-

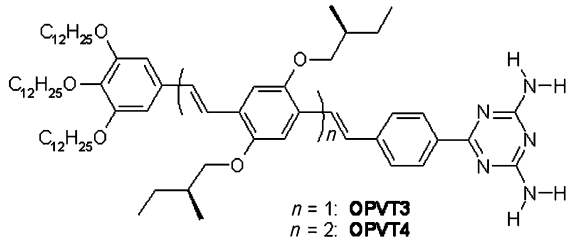


Figure 1. Molecular structures of **OPVT3** and **OPVT4**.

scopy (STM) to obtain detailed information about self-assembly at surfaces. Unexpectedly, the STM images showed chiral hexameric rosette structures lying flat on the surface, with the diamino triazine moieties pointing to the center forming hydrogen bonds (Figure 2).[10] The trimer and tetramer are next to the diamino triazine motif, and are equipped with a tridodecyloxy "wedge" end group and substituted with two or four enantiomerically pure (*S*)-2-methylbutoxy side chains on the OPV backbone. Being the precursors for oligomers studied earlier, their syntheses were published elsewhere.[7d,11] The STM images were acquired at the solid–liquid interface using graphite as substrate and 1-phenyloctane as solvent.[12] The lengths of the bright rods correspond to the conjugated backbone of OPV, in which individual phenyl rings are sometimes resolved. Similarly, as observed before, two out of three dodecyloxy chains reside in the darker areas.[13] The rosettes are ordered in rows and form a hexagonal two-dimensional (2D) crystal lattice with alkyl chains interdigitating with adjacent rosettes. The cavity of the rosette has an estimated diameter of approximately 0.7 nm. The packing parameters (Figure 2e and f) were determined as follows: $a_1 = 55.4 \pm 0.7$ Å, $a_2 = 56.3 \pm 0.8$ Å, $\alpha = 60 \pm 5°$ for **OPVT3**, and $a_1 = 60.3 \pm 0.5$ Å, $a_2 = 61.5 \pm 0.6$ Å, $\alpha = 60 \pm 4°$ for **OPVT4**. Although **OPVT3** and **OPVT4** appear to order in a similar way—oblique unit cells, rosette structure, specific orientation of alkyl chains and OPV backbone with respect to graphite symmetry axes, a comparable angle between the OPV backbone and the dodecyloxy chain—the organization of the molecules within a single rosette surprisingly differs (Figure 2c and d). The rosettes of **OPVT3** and **OPVT4** have different "rotation directions", as shown by the orientation of

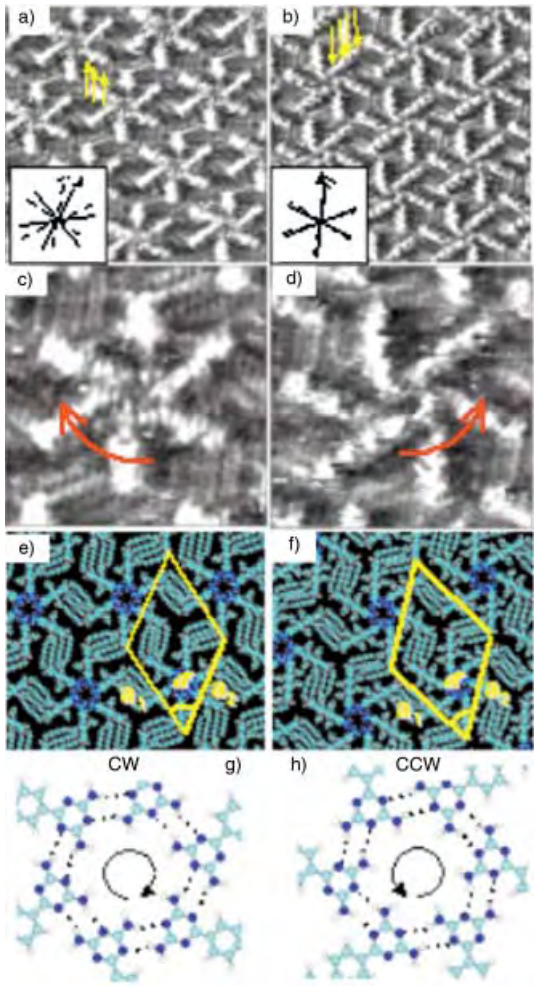


Figure 2. a, b) STM images of **OPVT3** (14.4×14.4 nm^2, $V_{set} = -0.50$ V, $I_{set} = 0.50$ nA), and **OPVT4** (18.4×18.4 nm^2, $V_{set} = -0.50$ V, $I_{set} = 0.45$ nA) monolayers at the solid–liquid interface using graphite as the substrate and 1-phenyloctane as the solvent. Yellow arrows point to intramolecularly resolved phenyl rings of the OPV backbone. Insets show the propagation direction of rosette lattices (solid line) and the main symmetry axes of graphite substrate (dashed line); c, d) close-up images of **OPVT3** and **OPVT4** rosettes. Red arrows indicate the "rotation direction" of the rosette; e, f) molecular models of an **OPVT3** and **OPVT4** monolayer; g, h) Representation of clockwise (CW) and counterclockwise (CCW) rosette structures showing the respective hydrogen-bonding patterns. Experimentally, the CCW rosette is observed for **OPVT4** and the CW rosette for **OPVT3**.

the OPV backbones, although they only differ in length and, hence, the number of stereocenters. In addition, the relative orientation of rows of rosettes with respect to the main crystallographic axes of graphite shows opposite 2D chirality ($+17.7 \pm 1.7°$ and $-2.3 \pm 0.8°$ for **OPVT3** and **OPVT4**, respectively). Calculations show that the free volume of the **OPVT4** rosettes is a minimum in the case of counterclockwise (CCW) helical rosettes and therefore expected to be more stable, which is observed experimentally. However, a CCW rosette of **OPVT3** would be destabilized by the steric interactions of the OPV and dodecyloxy chains; hence the clockwise (CW) rosette structure can be explained.

 © 2004 Wiley-VCH Verlag GmbH & Co. KGaA, Weinheim

With the STM results in hand, it is intriguing to study the behavior of the molecules in solution and to search for the self-assembly of the rosettes into well-defined space-filling tubules. The UV/Vis absorption spectra of **OPVT3** and **OPVT4** in chloroform show structureless bands at $\lambda_{max} =$ 408 and 430 nm, respectively. The fluorescence maxima are positioned at $\lambda_{em\,max} = 470$ and 501 nm, respectively. The absorption and fluorescence data are characteristic for molecularly dissolved oligomers and the maxima are red-shifted when the conjugation length increases.[14] The UV/Vis absorption spectrum in heptane (5×10^{-5} M) shows a blue shift of the main band to $\lambda_{max} = 421$ nm for **OPVT4** (Figure 3a) and a red shift on the onset of the absorption. This behavior is typical for aggregated OPV derivatives.[7d] Similar spectral changes were observed in other apolar alkanes like pentane and dodecane. A similar shift in the onset of the absorption band is only observed for **OPVT3** at higher concentrations, while the absorption maximum remains unchanged.[15] The fluorescence intensity of **OPVT3** and **OPVT4** in heptane (Figure 3b) is reduced and strongly red-shifted to $\lambda_{max} = 510$ and 530 nm, respectively.

A bisignated circular dichroism (CD) effect for **OPVT4** (Figure 3c) is observed exhibiting a positive Cotton effect [+] at higher energy ($\lambda_{max,[+]} = 387$ nm) and a negative Cotton effect [−] at lower energy ($\lambda_{max,[-]} = 428$ nm). The zero-crossing lies at $\lambda = 400$ nm, which is not related to a maximum in absorption for **OPVT4** in heptane. Surprisingly, the bisignated CD spectrum of **OPVT3** (Figure 4a) is opposite to **OPVT4** ($\lambda_{max,[-]} = 380$ and $\lambda_{max,[M+]} = 428$ nm). The zero-crossing of the Cotton effect of **OPVT3** is positioned at $\lambda =$ 405 nm, which is close to the absorption maximum of the chromophore indicating strong exciton coupling. It is tempting to compare the opposite CD effects for the two molecules with the opposite chirality of the two molecules at the graphite surface. However, for **OPVT4** we found an inversion of the Cotton effect with time (Figure 4c). At 288 K, an almost complete conversion was obtained within 80 min ($\lambda_{max,[-]} = 410$ and $\lambda_{max,[+]} = 448$ nm) accompanied by a shifted zero-crossing to 422 nm, which is in close proximity of the absorption maximum. Annealing of **OPVT3** did not lead to sign reversal, only an increase of the Cotton effect was observed, while the zero-crossing is even closer to the absorption maximum. The sign reversal of **OPVT4** shows first-order kinetics with a rate constant of $k = 5.6 \times 10^{-4}\ s^{-1}$ (Figure 4c, inset). The helix that is initially present is presumably the kinetically controlled aggregate, while the helix that is finally formed is the thermodynamically stable form.[16] Hence, the exciton-coupled CD spectra for **OPVT3** and **OPVT4** are the same in the thermodynamically stable structures.

The aggregation process was further studied by temperature-dependent measurements (Figure 3). For **OPVT4** in heptane, the fluorescence maximum shifts from $\lambda_{max} = 530$ to 495 nm upon heating while the absorption maximum shift from $\lambda_{max} = 420$ to 430 nm. The values at high temperature are close to those found in chloroform, which indicates molecularly dissolved species. The melting transition temperature from the aggregated state to molecular dissolved species lies

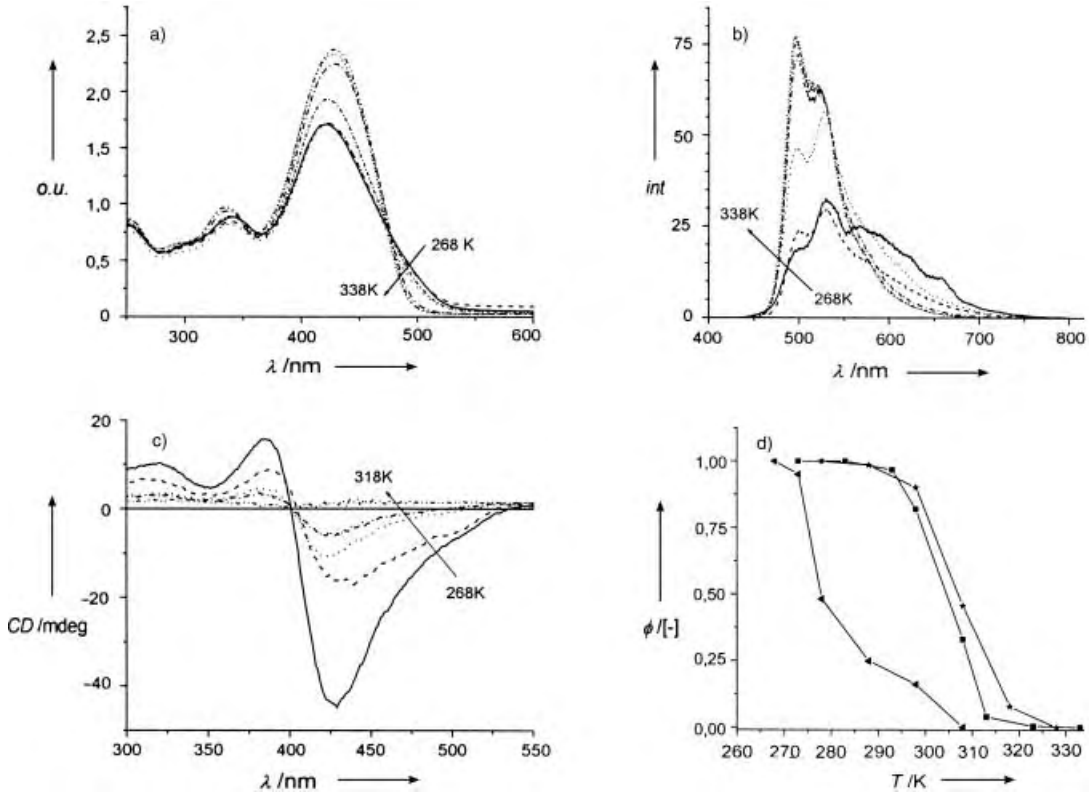


Figure 3. Temperature-variable a) UV/Vis, b) fluorescence, and c) CD spectra of **OPVT4** in heptane solution (5×10^{-5} M); d) melting-transition curves with fraction of aggregated species versus temperature based on CD (◂), fluorescence (⋆), and UV/Vis (■) data for **OPVT4**.

 © 2004 Wiley-VCH Verlag GmbH & Co. KGaA, Weinheim

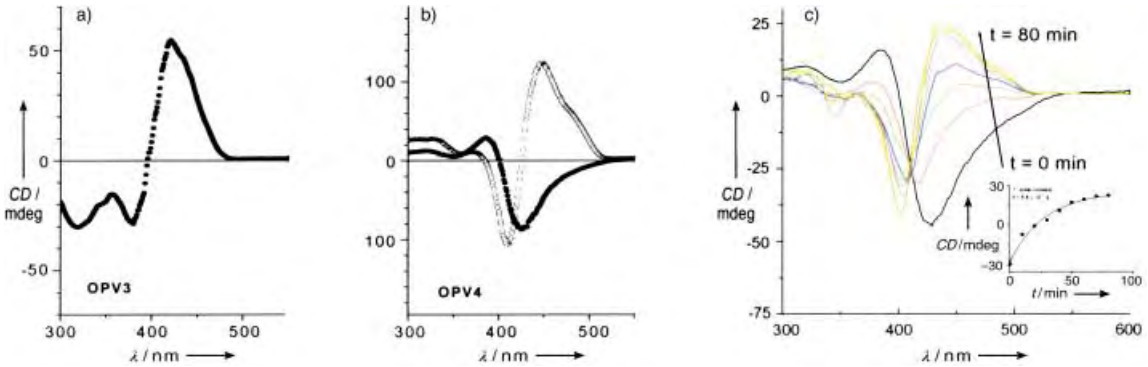


Figure 4. CD spectra of a) **OPVT3** (2.5×10^{-4} M) and b) **OPVT4** (5×10^{-5} M) in annealed heptane solutions recorded after maintaining at 293 K for 10 min (●) and for 24 hr (○); c) time-dependent CD spectra of **OPVT4** in steps of 10 min at 288 K. The inset shows the change of the CD intensity at $\lambda = 450$ nm versus time fitted to first-order kinetics.

at $T_m = 305$ K (Figure 4d). Remarkably the Cotton effect disappears earlier ($T_m = 280$ K, Figure 4d) than the disassembly. This behavior indicates a two-step aggregation process; first a transition from molecular dissolved species into achiral stacked structures that further develop into helical stacks. This aggregation process is distinct from our earlier findings on related OPVs.[7d] Hence, it is proposed that several secondary interactions act independently in the self-assembly process, as often seen in the assembly processes in aqueous media.[17]

Small-angle neutron scattering (SANS) and atomic force microscopy (AFM) measurements of **OPVT4** assemblies were used to study the shape of the supramolecular aggregates in solution, and as transferred from solution to a graphite surface. SANS data of **OPVT4** (5×10^{-4} M in dodecane, $T = 288$ K) showed a linear slope of -1 with a side maximum in the plot of the scattering vector versus the scattering intensity (Figure 5d) that is representative of cylindrical aggregates. The scattering data at low angles do not show a change in slope, which indicates that the persistence length of the aggregates reaches at least 185 nm at minimum experimental Q. From the position of the side maximum at high angles, the radius of the cross section can be estimated as 7 nm. AFM experiments were performed on drop-cast films from heptane solutions (5×10^{-5} M) of **OPVT4** on graphite.[18] Isolated cylindrical aggregates were revealed with lengths up to 10 μm (Figure 5a and b). Presumably during the transfer process the stacks present in solution further self-assemble in the stack direction yielding longer aggregates in the solid state. Crossovers of separate fibers are often observed. The width of the stacks is uniformly ~40 nm. Corrected for broadening of the lateral dimensions due to tip-convolution effects, the actual width is about 10 nm.[19] The heights of the stacks was determined to be ~6.4 nm from the height profile (Figure 5c), which is more reliable since soft tapping conditions were applied. This thickness is in agreement with the SANS data and corresponds well to the diameter of the hydrogen-bonded hexamers found by STM pointing to fibers consisting of stacked rosettes. The measured length and diameter show that the aspect ratio of the aggregates can be as high as 1500. We did not observe helicity in the stacks. Helicity might still be present due to a pitch length that is too small to be detected or that the dodecyloxy tails that shield the stacks are not helically ordered.

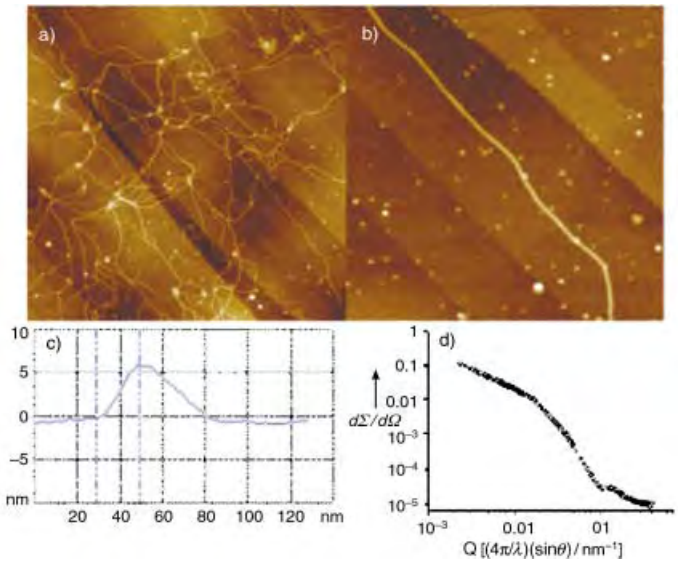


Figure 5. AFM images of drop-cast **OPVT4** solutions in heptane (5×10^{-5} M) on graphite: a) 6.3×6.3 μm² (z range: 30 nm) and b) 804×804 nm² (z range: 20 nm); c) height profile of a fibril; d) SANS data revealing columnar structures in dodecane solutions of **OPVT4**.

Despite the temptation to relate the rotational direction or supramolecular chirality of the chiral rosettes as detected by CD and STM, it is in our view impossible at the present time. CD spectroscopy probes primarily rosette–rosette interactions whereas in STM the packing of rosettes is predominantly determined by rosette–graphite interactions. The formation of the tubules, however, can be proposed based on the earlier work of other supramolecular aggregates.[20] The OPVs with diamino triazine moieties self-assemble hierarchically; first forming hexameric rosettes by hydrogen-bond formation, which subsequently develops into stacks aided by π–π interactions of the phenylenevinylene groups. Once organized into stacks that are highly space-filled as compared to self-assembled rods, the chiral side chains induce

 © 2004 Wiley-VCH Verlag GmbH & Co. KGaA, Weinheim

supramolecular helicity. It is proposed that the cyclic hexameric rosettes are not fully planar at the triazine terminus, which results in a propeller arrangement that allows interplanar hydrogen-bond interactions form rosette to rosette, thus locking the rosettes within the tubules.[4d,17] Upon heating, these hydrogen bonds are broken, which results in a loss of the Cotton effect. Time-dependent CD measurements show that the locking of rosettes is a very delicate process.

This work demonstrates guidelines for programming π-conjugated molecules into self-assembled tubular aggregates in solution and in the solid state.[21] Weak interactions that determine the packing of molecules in a crystal can be applied to the supramolecular organization in solution. The tubules of 6.4 nm in diameter and with perfect space filling are still soluble due to the apolar shell that surrounds the stacks. Since the cavity of the rosettes contains amines and has a diameter of nearly 1 nm this seems an ideal channel for transportation. Current research focuses on studying the behavior of the interior of the tubular stacks and their possible connection with the well-defined and ordered π-conjugated periphery.

Received: September 4, 2003 [Z52790]

Keywords: helices · hydrogen bonds · noncovalent interactions · self-assembly · supramolecular chemistry

[1] For a recent review and references therein: D. T. Bong, T. D. Clark, J. R. Granja, M. R. Ghadiri, *Angew. Chem.* **2001**, *113*, 1016; *Angew. Chem. Int. Ed.* **2001**, *40*, 988.

[2] G. A. Jeffrey, *An Introduction to hydrogen bonding*, Oxford University, Oxford, **1997**.

[3] For example: a) J. A. Zerowski, G. M. Whitesides, *J. Am. Chem. Soc.* **1994**, *116*, 4298; b) A. Ranganathan, V. R. Pedireddi, C. N. R. Rao, *J. Am. Chem. Soc.* **1999**, *121*, 1752; c) L. J. Prins, F. De Jong, P. Timmerman, D. N. Reinhoudt, *Nature* **2000**, *408*, 181; d) G. M. Whitesides, E. E. Simanek, J. P. Mathias, C. T. Seto, D. N. Chin, M. Mammen, D. M. Gordon, *Acc. Chem. Res.* **1995**, *28*, 37; e) M. L. Highfill, A. Chandrasekaran, D. E. Lynch, D. A. Hamilton, *Cryst. Growth Des.* **2002**, *1*, 15; f) S. V. Kolotuchin, S. C. Zimmerman, *J. Am. Chem. Soc.* **1998**, *120*, 9092; g) A. Marsh, M. Silvestri, J.-M. Lehn, *Chem. Commun.* **1996**, 1527.

[4] For example: a) N. Kimizuka, S. Fujikawa, S. Kuwahara, T. Kunitake, A. Marsh, J.-M. Lehn, *Chem. Commun.* **1995**, 2103; b) H. Schönherr, V. Paraschiv, S. Zapotoczny, M. Crego-Calama, P. Timmerman, C. W. Frank, G. J. Vancso, D. N. Reinhoudt, *Proc. Natl. Acad. Sci. USA* **2002**, *99*, 5025; c) G. Gottarelli, E. Mezzina, G. P. Spada, F. Carsughi, G. di Nicola, P. Mariani, A. Sabaticci, S. Bonazzi, *Helv. Chim. Acta* **1996**, *79*, 220; d) W. Yang, X. Chai, L. Chi, X. Liu, Y. Cao, R. Lu, Y. Jiang, X. Tang, H. Fuchs, T. Li, *Chem. Eur. J.* **1999**, *5*, 1144.

[5] a) E. D. Sone, E. R. Zubarev, S. I. Stupp, *Angew. Chem.* **2002**, *114*, 1781; *Angew. Chem. Int. Ed.* **2002**, *41*, 1706; b) E. R. Zubarev, M. U. Pralle, E. D. Sone, S. I. Stupp, *J. Am. Chem. Soc.* **2001**, *123*, 4105.

[6] H. Fenniri, B.-L. Deng, A. E. Ribbe, *J. Am. Chem. Soc.* **2002**, *124*, 11064.

[7] a) F. S. Schoonbeek, J. H. van Esch, B. Wegewijs, D. B. A. Rep, M. P. de Haas, T. M. Klapwijk, R. M. Kellog, B. L. Feringa, *Angew. Chem.* **1999**, *111*, 1486; *Angew. Chem. Int. Ed.* **1999**, *38*, 1393; b) F. Würthner, C. Thalacker, A. Sautter, *Adv. Mater.* **2000**, *12*, 562. c) A. P. H. J. Schenning, A. F. M. Kilbinger, F. Biscarini, M. Cavallini, H. J. Cooper, P. J. Derrick, W. J. Feast, R. Lazzaroni, Ph. Leclère, L. A. McDonell, E. W. Meijer, S. C. J. Meskers, *J. Am. Chem. Soc.* **2002**, *124*, 1269; d) A. P. H. J. Schenning, P. Jonkheijm, E. Peeters, E. W. Meijer, *J. Am. Chem. Soc.* **2001**, *123*, 409; e) R. B. Prince, L. Brunsveld, E. W. Meijer, J. S. Moore, *Angew. Chem. Int. Ed.* **2000**, *112*, 234; *Angew. Chem. Int. Ed.* **2000**, *39*, 228; f) A. Ajayaghosh, S. J. George, V. K. Praveen, *Angew. Chem.* **2003**, *115*, 346; *Angew. Chem. Int. Ed.* **2003**, *42*, 332; g) A. P. H. J. Schenning, J. van Herrikhuyzen, P. Jonkheijm, Z. Chen, F. Würthner, E. W. Meijer, *J. Am. Chem. Soc.* **2002**, *124*, 10252; h) H. Engelkamp, S. Middelbeek, R. J. M. Nolte, *Science* **1999**, *284*, 785; i) V. Percec, M. Glodde, T. K. Bera, Y. Mlura, I. Shlyanovskaya, K. D. Singer, V. S. K. Balagurusamy, P. A. Helney, I. Schnell, A. Rapp, H.-W. Spiess, S. D. Hudson, H. Duan, *Nature* **2002**, *417*, 384.

[8] U. Mitschke, P. Bäuerle, *J. Mater. Chem.* **2000**, *10*, 365; b) H. Sirringhaus, P. J. Brown, R. H. Friend, M. M. Neilsen, K. Bechgaard, B. M. W. Langeveld-Voss, A. J. H. Spiering, R. A. J. Janssen, E. W. Meijer, P. Herwig, D. M. de Leeuw, *Nature* **1999**, *401*, 685; c) L. Schmidt-Mende, A. Fechtenkötter, K. Müllen, E. Moons, R. H. Friend, J. D. MacKenzie, *Science* **2001**, *293*, 1119.

[9] R. E. Martin, F. Diederich, *Angew. Chem.* **1999**, *111*, 1440; *Angew. Chem. Int. Ed.* **1999**, *38*, 1350.

[10] Interestingly, the formation of hydrogen-bonded hexameric structures of melamines was previously proposed in literature: C. Thalacker, F. Würthner, *Adv. Funct. Mater.* **2002**, *12*, 209.

[11] The synthesis of **OPVT3** will be published elsewhere: P. Jonkheijm, F. J. M. Hoeben, R. Kleppinger, J. van Herrikhuyzen, A. P. H. J. Schenning, E. W. Meijer, *J. Am. Chem. Soc.*, in press.

[12] For a recent review and references therein: S. De Feyter, F. C. De Schryver, *Chem. Soc. Rev.* **2003**, *32*, 139.

[13] A. Gesquière, P. Jonkheijm, A. P. H. J. Schenning, E. Mena-Osteritz, P. Bäuerle, S. De Feyter, F. C. De Schryver, E. W. Meijer, *J. Mater. Chem.* **2003**, *13*, 2164.

[14] E. Peeters, A. Marcos, S. C. J. Meskers, R. A. J. Janssen, *J. Chem. Phys.* **2000**, *112*, 9445.

[15] Concentration-dependent UV/Vis measurements in dodecane also show that **OPVT4** starts to aggregate at 5×10^{-6} M whereas **OPVT3** starts at 2.5×10^{-5} M.

[16] M. M. Bouman, E. W. Meijer, *Adv. Mater.* **1995**, *7*, 385.

[17] L. Brunsveld, H. Zhang, M. Glasbeek, J. A. J. M. Vekemans, E. W. Meijer, *J. Am. Chem. Soc.* **2000**, *122*, 6175.

[18] With STM and AFM we observe different types of structures on graphite. This might be the result of the different solvents applied. Another possibility could be that in case of the AFM studies, a monolayer of rosettes is initially formed, and that on top of this layer fibers are present. We have not investigated this in detail.

[19] The broadening can be estimated by using a simple model based on a spherical tip apex (radius R) and a rectangular cross section of the fiber (height H) with 2(H(2R-H))/0.5 as in P. Samori, V. Francke, T. Mangel, K. Müllen, J. Rabe, *Opt. Mater.* **1998**, *9*, 390. For the present height and a terminal radius of commercial tips of 20 nm the broadening is about 29 nm. Therefore, the "true" width is obtained by subtracting the broadening from the apparent width and is about 10 nm.

[20] L. Brunsveld, B. J. B. Folmer, E. W. Meijer, R. P. Sijbesma, *Chem. Rev.* **2001**, *101*, 4071.

[21] J.-M. Lehn, *Chem. Eur. J.* **2000**, *6*, 2097.

 © 2004 Wiley-VCH Verlag GmbH & Co. KGaA, Weinheim

Reaction Media

Silica–Water Reaction Media: Its Application to the Formation and Ring Opening of Aziridines**

Satoshi Minakata, Daisuke Kano, Yoji Oderaotoshi, and Mitsuo Komatsu**

In recent years, the demand for environmentally benign organic-chemical processes has increased and this issue must be considered, from the ecological point of view, in the future design and implementation of new synthetic methodologies.[1] Organic reactions in aqueous media have been the subject of considerable attention in terms of achieving more environmentally friendly synthetic transformations.[2] On the other hand, aziridines[3] are useful synthetic intermediates for a variety of organic syntheses and they are frequently present as important substructures of biologically active compounds. Thus, the development of an efficient synthetic route to aziridines represents an attractive task for organic chemists and, as a result, a variety of methodologies have been exploited.[4]

We recently reported on the iodine-catalyzed formation of aziridines from olefins by using chloramine-T (CT)[4k] in aqueous media by the addition of a phase-transfer catalyst (PTC).[4l] The use of PTC to permit the reaction in aqueous media is a general method because of the ionic character of CT. An alternative potential process in water was devised based on the adsorptive nature of silica gel. Although the application of silica gel to organic synthesis has been widely investigated,[5] to the best of our knowledge its use in organic reactions in aqueous media has not been exploited.[6] Silica would be effective as organic reaction media in water because the organic molecule as a substrate would be expected to be adsorbed to the silica by hydrophobic interactions between the surface of the silica and the organic molecule (Figure 1). Herein we report on the iodine-catalyzed formation of aziridines from olefins by using CT and the ring opening of the resulting product in a silica–water system, in which the use of silica (silica gel or MCM-41) showed unique results.

Although the reaction of styrene with CT in the presence of K_2CO_3 and a catalytic amount of I_2 in water did not proceed at all, the addition of silica gel to the system led to the production of the desired aziridine (Table 1). For example, when styrene (1.0 mmol) was treated with CT (2.0 mmol), K_2CO_3 (2.0 mmol), and I_2 (10 mol%) in the presence of silica gel 60[7] (0.25 g) in water, *N*-(*p*-toluenesulfonyl)-2-phenylaziridine was obtained in 32% yield (entry 1). An increase in the amount of the silica gel used to 0.5 g improved the yield of the product (entry 2), but additional amounts failed to improve the efficiency of the reaction. The use of four equivalents of CT under the conditions of entry 2 gave the best result, an 85% yield of the aziridine (entry 3). From the difference in efficiency of the reactions (entry 1 versus entry 2), the product yield appears to be dependent on the specific surface area of the silica gel. Recently, mesoporous materials have attracted considerable attention in organic synthesis as solid acids or supports.[8] MCM-41,[9] one of such mesoporous silicas with a hexagonal array of uniform mesopores, was evaluated in the present aqueous system to synthesize aziridines. The use of MCM-41 led to a positive result, even when the reaction was carried out with two equivalents of CT and 0.25 g of silica (entry 4). A reaction using MCM-41 might proceed effectively because of its larger specific surface area, which is nearly double that of silica gel 60.

A variety of olefins were examined for this silica-mediated preparation of aziridines in water by using the iodine catalyst-CT system (Table 2). In the presence of MCM-41 (0.25 g), K_2CO_3 (2.0 mmol), and an iodine catalyst (20 mol%), 1,2-dihydronaphthalene was reacted with CT (2.0 mmol) to afford the corresponding aziridine in 75% yield. Other

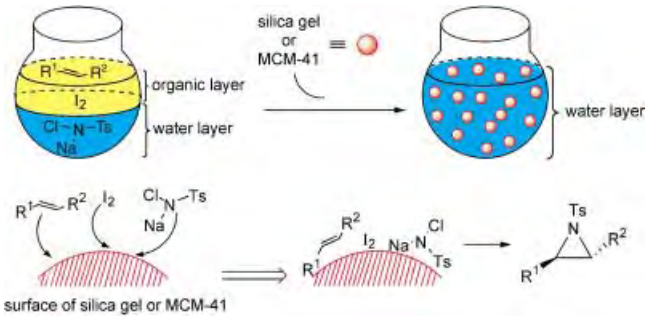
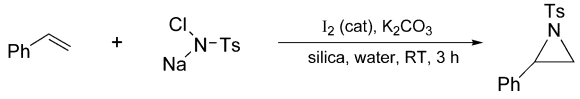


Figure 1. Proposed path for the formation of aziridines in a water–silica system.

Table 1: A comparison of silica gel 60 and MCM-41 as surface media for the formation of aziridine from styrene by using CT in Water.[a]



Entry	Silica [g]	CT [mmol]	Specific surface area [$m^2 g^{-1}$]	Yield [%]
1	silica gel 60 (0.25)	2.0	640	32
2	silica gel 60 (0.5)	2.0	640	55
3	silica gel 60 (0.5)	4.0	640	85
4	MCM-41 (0.25)	2.0	1060	80

[a] Reaction conditions: styrene (1.0 mmol), CT (2.0 or 4.0 mmol), I_2 (10 mol%), K_2CO_3 (2.0 mmol), silica (0.25 or 0.5 g), H_2O (1.5 mL), RT, 3 h. Ts = *p*-toluenesulfonyl.

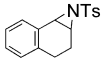
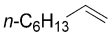
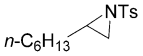
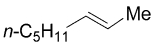
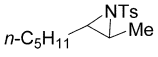
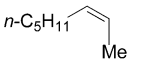
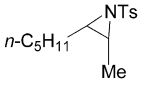
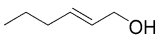
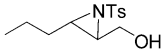
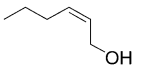
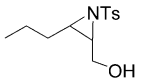
[*] Dr. S. Minakata, Dr. D. Kano, Dr. Y. Oderaotoshi, Prof. Dr. M. Komatsu
Department of Applied Chemistry
Graduate School of Engineering, Osaka University
Yamadaoka 2-1, Suita, Osaka 565-0871 (Japan)
Fax: (+81) 6-6879-7402
E-mail: minakata@chem.eng.osaka-u.ac.jp
komatsu@chem.eng.osaka-u.ac.jp

[**] This work was partially supported by a Grant-in Aid for Scientific Research from the Japan Society for the promotion of Science.

Supporting information for this article is available on the WWW under http://www.angewandte.org or from the author.

DOI: 10.1002/anie.200352842
© 2004 Wiley-VCH Verlag GmbH & Co. KGaA, Weinheim

Table 2: Silica–water-mediated formation of aziridines from various olefins.[a]

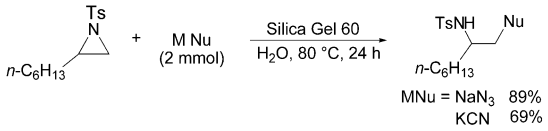
olefin	aziridine	yield [%] MCM-41	Silica gel 60	
		75	68	
		75	68	
		64	53	
		7	26[b] 49	
		4[c]	42[c]	
		27[d]		70[d]
		56[c]		58[c]
		72[d]	59[d]	61[b,d]

[a] Reaction conditions: olefin (1.0 mmol), CT (2.0 mmol), I_2 (20 mol%), K_2CO_3 (2.0 mmol), silica (MCM-41; 0.25 g or silica gel 60; 1.0 g), H_2O (1.5 mL), RT, 3 h. [b] Silica gel 60 (0.5 g). [c] *Trans* only. [d] *Cis* only.

cyclic olefins such as cyclohexene and cyclopentene were also used with the MCM-41 system resulting in the formation of aziridines in good yields. When these reactions were carried out with silica gel 60 (1.0 g), aziridines were also obtained in good yields. In spite of the fact that a larger amount of silica gel 60 (1 g; surface area: 640 m^2) was employed, compared to that of MCM-41 (0.25 g; surface area: 265 m^2), better results were achieved when the latter system was used, thus indicating that specific properties of MCM-41, which is a mesoporous solid and has an hexagonal array, may have played a role in these reactions. Although the formation of aziridines from acyclic olefins mediated by MCM-41 proceeded with a low yield, the same reactions with silica gel 60 gave the desired aziridines in moderate to good yields. The origin of this might be differences of the pore sizes of the MCM-41 and silica gel 60. As the average pore size of the MCM-41 used in this system is 25 Å, about half that of silica gel 60 (60 Å), we assume that the high degree of freedom of acyclic olefins suffers from difficulty in interacting with the surface of the MCM-41. On the other hand, allylic alcohols gave the corresponding aziridines in good yields with either MCM-41 or silica gel 60. It is possible that the hydroxyl group of these olefins may assist in the adsorption of olefins to the surface of the silicas.[10] This prediction is supported by the fact that the aziridination of *trans*-2-hexene scarcely proceeded under the same conditions.

To understand the different efficiencies for the aziridination, the amount of cyclohexene and 1-octene adsorbed to the two types of silicas were investigated in MeOH. Although there was little difference between silica gel 60 and MCM-41 in terms of the amount of cyclohexene adsorbed, a remarkable difference was observed for 1-octene.[11] As a result, the efficiency of the reaction is dependent on the extent of adsorption of olefins to the silicas, strongly suggesting that the reaction occurs on the surface of the silicas.

To show the generality of this media in organic synthesis, the ring opening of *N*-(*p*-toluenesulfonyl)-2-*n*-hexylaziridine with NaN_3 or KCN was examined. The reaction of the aziridine with NaN_3 or KCN in water in the absence of silica did not proceed. When silica gel 60 was added, however, the reaction proceeded to afford the regioselective ring-opening products (Scheme 1).



Scheme 1. Application of silica–water system to the ring opening of 2-hexyl-*N*-(*p*-toluenesulfonyl)aziridine with NaN_3 or KCN.

In summary, a new organic transformation in water by exploiting the adsorptive nature of silica is demonstrated; the formation of aziridines and their ring opening are used as examples. Applications of the present system to other organic reactions are now in progress, as the use of this system represents an environmentally benign organic synthesis.

Received: September 11, 2003 [Z52842]

Keywords: aziridines · cyclization · nitrogen heterocycles · silicates · water chemistry

[1] P. T. Anastas, T. C. Williamson in *Green Chemistry, Designing Chemistry for the Environment* (Eds.: P. T. Anastas, T. C. Williamson), American Chemical Society, Washington, DC, **1996**, pp. 1–17.

[2] C.-J. Li, T.-H. Chan, *Organic Reactions in Aqueous Media*, Wiley, Chichester, **1997**.

[3] a) D. Tanner, *Angew. Chem.* **1994**, *106*, 625–646; *Angew. Chem. Int. Ed. Engl.* **1994**, *33*, 599–619; b) W. H. Pearson, B. W. Lian, S. C. Bergmeie in *Comprehensive Heterocyclic Chemistry II*, *Vol. 1A* (Ed.: A. Padwa) Pergamon, Oxford, **1996**, pp. 1–60; c) K. M. L. Rai, A. Hassner in *Comprehensive Heterocyclic Chemistry II*, *Vol. 1A* (Ed.: A. Padwa) Pergamon, Oxford, **1996**, pp. 61–96.

[4] Representative examples of direct aziridination of olefins, see a) H. Kwart, A. A. Kahn, *J. Am. Chem. Soc.* **1967**, *89*, 1951–1953; b) J.-E. Bäckvall, *J. Chem. Soc. Chem. Commun.* **1977**, 413–414; c) J. T. Groves, T. Takahashi, *J. Am. Chem. Soc.* **1983**, *105*, 2073–2074; d) D. Mansuy, J.-P. Mahy, A. Dureault, G. Bedi, P. Battioni, *J. Chem. Soc. Chem. Commun.* **1984**, 1161–1163; e) R. S. Atkinson, B. J. Kelly, *J. Chem. Soc. Chem. Commun.* **1988**, 624–625; f) V. F. Rudchenko, S. M. Ignatov, R. G. Kostyanovsky, *J. Chem. Soc. Chem. Commun.* **1990**, 261–262; g) M. Barani, S. Fioravanti, M. A. Loreto, L. Pellacani, P. A. Tardella, *Tetrahedron* **1994**, *50*, 3829–3834; h) D. A. Evans, M. M. Faul, M. T. Bilodeau, *J. Am. Chem. Soc.* **1994**, *116*, 2742–2753; i) T. Ando, S. Minakata, I. Ryu, M. Komatsu, *Tetrahedron Lett.* **1998**, *39*, 309–312; j) J. U. Jeong, B. Tao, I. Sagasser, H. Henniges, K. B. Sharpless, *J. Am. Chem. Soc.* **1998**, *120*, 6844–6845; k) T. Ando, D. Kano, S. Minakata, I. Ryu, M. Komatsu, *Tetrahedron*

 © 2004 Wiley-VCH Verlag GmbH & Co. KGaA, Weinheim

1998, *54*, 13485 – 13494; l) D. Kano, S. Minakata, M. Komatsu, *J. Chem. Soc. Perkin Trans. 1* **2001**, 3186 – 3188; m) S. Minakata, D. Kano, R. Fukuoka, Y. Oderaotoshi, M. Komatsu, *Heterocycles* **2003**, *60*, 289 – 298.

[5] For reviews, see a) I. W. C. E. Arends, R. A. Sheldon, M. Wallau, U. Schuchardt, *Angew. Chem.* **1997**, *109*, 1190 – 1211; *Angew. Chem. Int. Ed. Engl.* **1997**, *36*, 1144 – 1163; b) B. Pugin, H.-U. Blaser in *Comprehensive Asymmetric Catalysis*, *Vol. 3* (Eds.: E. N. Jacobsen, A. Pfaltz, H. Yamamoto), Springer, Berlin, **1999**, pp. 1367 – 1386; c) R. A. Sheldon, H. van Bekkum, *Fine Chemicals Through Heterogeneous Catalysis*, Wiley-VCH, Weinheim, **2001**.

[6] Although quite recently a similar concept was revealed, it needs a complicated system including the requirement of a surfactant. R. Abu-Reziq, D. Avnir, J. Blum, *Angew. Chem.* **2002**, *114*, 4306 – 4308; *Angew. Chem. Int. Ed.* **2002**, *41*, 4132 – 4134.

[7] Silica gel 60 was purchased from Nacalai Tesque.

[8] For examples, See a) K. R. Kloetstra, H. van Bekkum, *J. Chem. Res. Synop.* **1995**, 26 – 27; b) A. Cauvel, G. Renard, D. Brunel, *J. Org. Chem.* **1997**, *62*, 749 – 751; c) F. Fajula, D. Brunel, *Microporous Mesoporous Mater.* **2000**, *48*, 119 – 125; d) S. Jun, R. Ryoo, *J. Catal.* **2000**, *195*, 237 – 243; e) V. R. Choudhary, S. K. Jana, N. S. Patil, *Tetrahedron Lett.* **2002**, *43*, 1105 – 1107; f) J. H. Clark, *Acc. Chem. Res.* **2002**, *35*, 791 – 797.

[9] a) C. T. Kresge, M. E. Leonowicz, W. J. Roth, J. C. Vartuli, J. S. Beck, *Nature* **1992**, *359*, 710 – 712; b) J. S. Beck, J. C. Vartuli, W. J. Roth, M. E. Leonowicz, C. T. Kresge, K. D. Schmitt, C. T.-W. Chu, D. H. Olson, E. W. Sheppard, S. B. McCullen, J. B. Higgins, J. L. Schlenker, *J. Am. Chem. Soc.* **1992**, *114*, 10834 – 10843; c) M. Grün, K. K. Unger, A. Matsumoto, K. Tsutsumi, *Microporous Mesoporous Mater.* **1999**, *27*, 207 – 216.

[10] Although substrates that have only an olefin moiety are adsorbed to the surface of silica in water by hydrophobic repulsion, the substrates with functional groups such as a hydroxy group have an ability to interact with the surface (terminal) of silica (HO–Si), if they are not highly soluble in water.

[11] See Supporting Information.

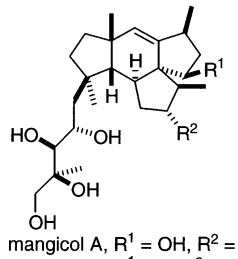
 © 2004 Wiley-VCH Verlag GmbH & Co. KGaA, Weinheim

Spirotetracycle Synthesis

Enantioselective Synthesis of the Spirotetracyclic Carbon Core of Mangicols by Using a Stereoselective Transannular Diels–Alder Strategy**

*Keisuke Araki, Keiji Saito, Hirokazu Arimoto, and Daisuke Uemura**

The synthesis of complex natural products has been investigated extensively by chemists, but the construction of architecturally novel carbon frameworks remains a challenging problem. Of particular importance is the effective synthesis of extremely complex carbocycles incorporating quaternary carbons and consecutive asymmetric centers.[1] Mangicols isolated from the marine fungus *Fusarium heterosporum* by Fenical and co-workers in 2000 are new sesterterpenoids with a novel carbon framework (Figure 1) that exhibit



1: mangicol A, R^1 = OH, R^2 = H
2: mangicol B, R^1 = H, R^2 = OH
3: mangicol C, R^1 = H, R^2 = H

Figure 1. Structure of the mangicols.

cytotoxic and antiinflammatory activities.[2] The highly complex spirotetracyclic skeleton of the mangicols was recognized as an attractive target for total synthesis, since its stereoselective construction, especially at the quaternary carbons, should be quite challenging.

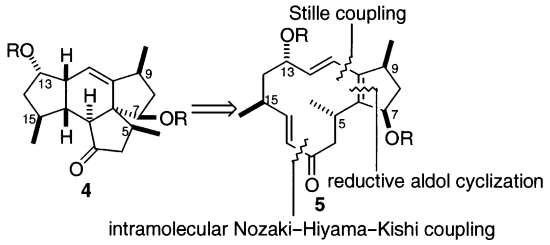
We hypothesized that the stereoselective synthesis of the tetracyclic framework of mangicols, including the spiro carbon core, would be efficiently accomplished by employing a transannular Diels–Alder (TADA) reaction. TADA reactions are powerful tools for the construction of polycyclic frameworks and have often been used as the key step in the total synthesis of natural products.[3] The first report of a TADA reaction was that by Deslongchamps et al., who employed a 13-membered cyclic triene.[3b–d] Thereafter, this research group extensively investigated the TADA reactions of a 14-membered cyclic triene. Roush et al. investigated TADA reactions of 12-membered cyclic trienes for the

[*] K. Araki, K. Saito, Prof. Dr. H. Arimoto, Prof. Dr. D. Uemura
Graduate School of Science, Nagoya University
Furo-cho, Chikusa, Nagoya 464-8602 (Japan)
Fax: (+81)52-789-3654
E-mail: uemura@chem3.chem.nagoya-u.ac.jp

[**] This work was supported in part by Grants-in-Aid (Nos. 11175101 and 12045235) for Scientific Research from the Ministry of Education, Culture, Sports, Science and Technology, Japan.

 DOI: 10.1002/anie.200351750 © 2004 Wiley-VCH Verlag GmbH & Co. KGaA, Weinheim

synthesis of spinosyn A;[3e] however, only poor stereoselectivity was achieved. The difficulties in controlling the stereochemistry of TADA reactions arise from the small differences in energy among the possible transition states. Thus, the careful design of the triene intermediate is essential for the stereoselective construction of the framework. As shown in Scheme 1, we chose trienone **5** as the key intermediate; the stereochemistry of the substituted positions—C5, C7, C9, C13, and C15—is such that trienone **5** would be in the desired conformation.

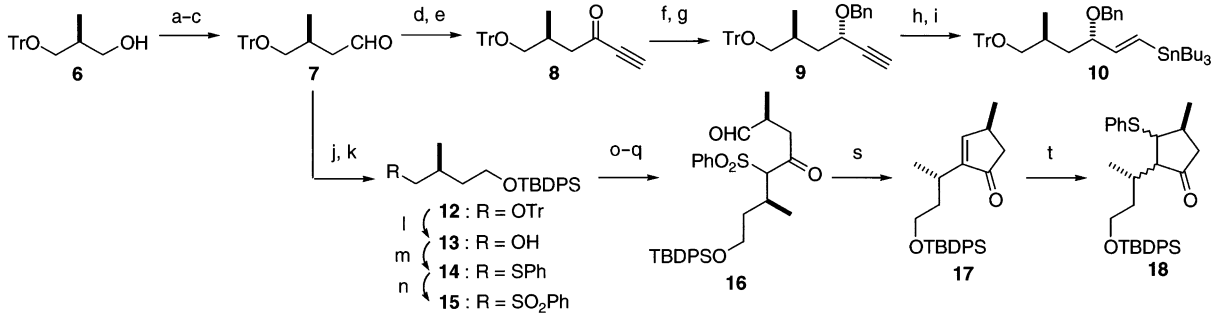


Scheme 1. Retrosynthetic analysis of tetracyclic compound **4**.

Our synthesis commenced with the tosylation of alcohol **6**,[4] derived from methyl (*R*)-3-hydroxy-2-methylpropionate in two steps (Scheme 2). Substitution of the tosylate with sodium cyanide gave the nitrile quantitatively. The resulting nitrile was reduced with DIBAL-H and the product then hydrolyzed to give the common intermediate aldehyde **7**. The addition of ethynylmagnesium bromide to aldehyde **7** afforded secondary alcohols in a diastereomeric mixture (1:1), which were then oxidized with MnO_2 to give ynone **8**. After the diastereoselective reduction of **8** was achieved by Corey's method,[5] protection with benzyl bromide gave benzyl ether **9**. Transformation of benzyl ether **9** to vinylstannane **10** was carried out in two steps: first, conversion to bromoalkyne by treatment of benzyl ether **9** with *N*-bromosuccinimide (NBS) and $AgNO_3$,[6] and then hydrostannation[7] of the bromoalkyne. β-Chlorocyclopentenone **11** was also derived from the common intermediate aldehyde **7**. Aldehyde **7** was reduced with $NaBH_4$, followed by formation of the TBDPS ether **12**. Subsequent acidic removal[8] of the Tr group gave alcohol **13**. Elaboration to the sulfide **14** was followed by oxidation of **14** with *m*CPBA to give sulfone **15**. The Julia coupling reaction[9] between the carbanion generated from sulfone **15** and the common intermediate aldehyde **7** gave a diastereomeric mixture of hydroxy sulfones. The Tr group was removed under acidic conditions, and the resulting diol was oxidized with Dess–Martin periodinane[10] to afford ketoaldehyde **16**. Several attempts at an intramolecular aldol cyclization reaction of **16** failed. However, a reductive aldol cyclization reaction with SmI_2 proceeded smoothly, and subsequent treatment with Al_2O_3 gave cyclopentenone **17**. The Michael addition of thiophenol to cyclopentenone **17** afforded β-thiophenylcyclopentanone **18** as a mixture of diastereomers (13:1).

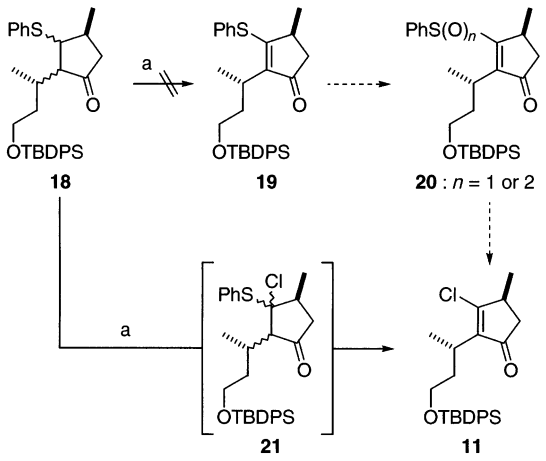
The conversion of β-thiophenylcyclopentanone **18** into β-chlorocyclopentenone **11**, a Stille coupling precursor, was then examined (Scheme 3). We initially thought that this conversion would take several steps, namely, 1) conversion of β-thiophenylcyclopentanone **18** into vinylsulfide **19** by a published procedure,[11] 2) oxidation of vinylsulfide **19**, and 3) a Michael addition–elimination reaction with a chloride ion to the intermediate **20** to give β-chlorocyclopentenone **11**. We found, however, that β-chlorocyclopentenone **11** could be generated from β-thiophenylcyclopentanone **18** directly in a novel one-pot process through oxidative chlorination. When β-thiophenylcyclopentanone **18** was oxidized with trichloroisocyanuric acid, β-chlorocyclopentenone **11** was obtained in good yield. We considered the possibility that this type of oxidative chlorination proceeds via the Pummerer-type intermediate **21**. There are no published procedures for the direct β-halogenation of cyclopentenones, and thus this reaction was regarded as a promising strategy for the β-chlorination of enones.

Stille coupling[12] between intermediates **10** and **11** was then examined (Scheme 4). The coupling reaction was con-

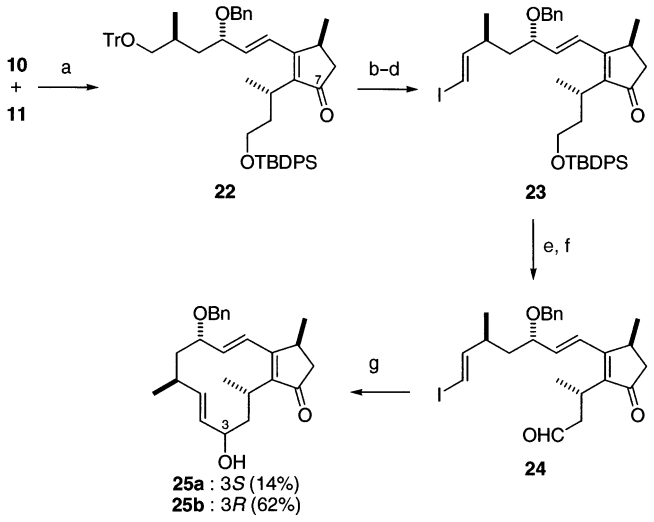


Scheme 2. Synthesis of **10** and **18**. a) TsCl, pyridine, RT, 20.5 h; b) NaCN, DMSO, 60 °C, 21 h; c) DIBAL-H, CH_2Cl_2, −78 °C, 30 min; then aq. NH_4Cl, 98% in 3 steps; d) ethynylmagnesium bromide, THF, 0 °C, 1 h; e) MnO_2, CH_2Cl_2, RT, 3 h, 64% in 2 steps; f) (*S*)-2-methyl-CBS-oxazaborolidine, BH_3·SMe_2, toluene, −40 °C, 30 min, 95%, >98:2 d.r.; g) BnBr, NaH, DMF, 0 °C, 2 h, 100%; h) NBS, $AgNO_3$, acetone, RT, 1 h, 100%; i) Bu_3SnH, [$Pd(PPh_3)_4$], THF, 0 °C, 30 min, 76%; j) $NaBH_4$, EtOH, 0 °C, 30 min; k) TBDPSCl, imidazole, DMF, RT, 1 h, 74% in 2 steps; l) TFAA, TFA, CH_2Cl_2, RT, 1 h; then MeOH, NEt_3, 0 °C, 1.5 h, 85%; m) PhSSPh, PBu_3, DMF, RT, 1.5 h; n) *m*CPBA, $NaHCO_3$, CH_2Cl_2, RT, 1.5 h, 89% in 2 steps; o) **15**, *n*BuLi, THF, −78 °C, 30 min; then **7**, THF, −78 °C, 1.5 h; p) HCOOH, Et_2O, RT, 5.5 h; q) aq. NH_3, MeOH, RT, 1.5 h, 75% in 3 steps; r) Dess–Martin periodinane, CH_2Cl_2, RT, 1 h, 67%; s) SmI_2, THF, RT, 1 h; then Al_2O_3, 73%; t) PhSH, NEt_3, THF, RT, 7 h, 71%. BnBr = benzyl bromide, CBS = Corey–Bakshi–Shibata, DIBAL-H = diisobutylaluminum hydride, DMF = dimethylformamide, DMSO = dimethyl sulfoxide, *m*CPBA = *m*-chloroperbenzoic acid, NBS = *N*-bromosuccinimide, RT = room temperature, TBDPSCl = *tert*-butyldiphenylsilyl chloride, TFA = trifluoroacetic acid, TFAA = trifluoroacetic anhydride, Tr = triphenylmethyl, TsCl = *p*-toluenesulfonyl chloride.

 © 2004 Wiley-VCH Verlag GmbH & Co. KGaA, Weinheim



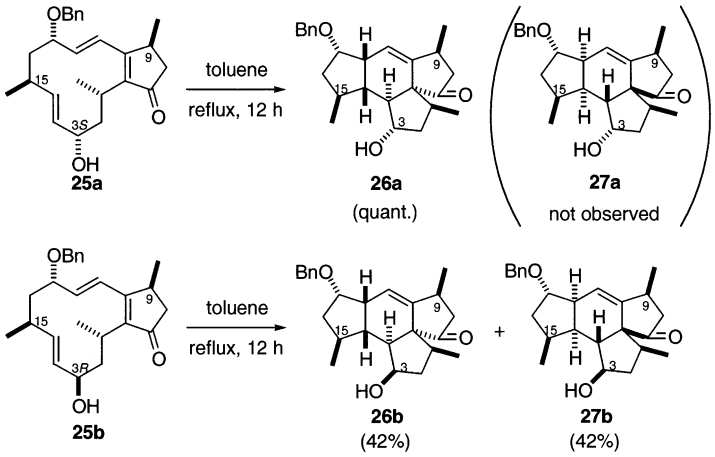
Scheme 3. Synthesis of **11**. a) Trichloroisocyanuric acid, benzene/Et_2O (2:1 v/v), 0 °C, 21 h, 79 %.



Scheme 4. Synthesis of **25**. a) $[Pd(PPh_3)_4]$, NMP, 100 °C, 22 h, 98 %; b) $ZnBr_2$, CH_2Cl_2, RT, 1.5 h, 94 %; c) Dess–Martin periodinane, CH_2Cl_2, RT, 1.5 h, 92 %; d) CHI_3, $CrCl_2$, THF, RT, 40 min, 90 %; e) TBAF, THF, RT, 6 h, 88 %; f) PDC, CH_2Cl_2, RT, 1 h, 86 %; g) $CrCl_2$, cat. $NiCl_2$, DMSO, 24 h, 50 °C. NMP = 1-methyl-2-pyrrolidinone, PDC = pyridinium dichromate, TBAF = tetrabutylammonium fluoride.

ducted with $[Pd(PPh_3)_4]$ as the catalyst and at a high temperature (100 °C) to afford dienone **22** in excellent yield. However, a subsequent Luche reduction of dienone **22** was low-yielding due to the instability of the reduced product. Thus, we avoided reducing C7s carbonyl group in order to stabilize the diene. After the Tr group of dienone **22** was removed with $ZnBr_2$,[13] subsequent oxidation of the primary alcohol gave an aldehyde, which was converted by a Takai reaction[14] into vinyliodide **23**. The TBDPS group of **23** was removed with TBAF to give an alcohol, which was oxidized to afford the aldehyde **24**. Because the 12-membered cyclic trienone was expected to be unstable, mild reaction conditions for the macrocyclization were thought necessary. Macrocyclization of **24** was accomplished by an intramolecular Nozaki–Hiyama–Kishi (NHK) coupling reaction.[15a] Although the intramolecular NHK coupling reactions reported to date have given poor yields,[15c] intramolecular cyclization of aldehyde **24** proceeded nicely to afford two diastereomers of the desired trienones **25a** (6 %) and **25b** (38 %), which were then easily separated by column chromatography. Moreover, when this coupling reaction was carried out at 50 °C, even higher yields of **25a** (14 %) and **25b** (62 %) resulted.

With the cyclic triene precursor in hand, we attempted TADA reactions of both **25a** and **25b** (Scheme 5). When either trienone was heated in toluene at reflux, the TADA



Scheme 5. Transannular Diels–Alder reactions of **25a** and **25b**.

reaction proceeded smoothly to give the desired tetracyclic compound. The stereochemistry of each tetracyclic compound was determined by NOE experiments and NOESY correlations in the ^1H NMR spectra. Surprisingly, we found that the stereoselectivity of the TADA reaction was primarily dependent on the stereochemistry of the hydroxy group at C3. The TADA reaction of trienone **25a** afforded predominantly the desired tetracyclic compound **26a**, whereas reaction of trienone **25b** gave both the desired isomer **26b** and the undesired isomer **27b** in a ratio of 1:1.

The diastereoselectivity of the TADA reaction can be accounted for by the energy differences for the possible conformations of the transition states (Figure 2). Obviously, products **26** and **27** are formed by an *exo* approach. The possibility of two *endo* approaches is excluded by severe ring strain in the transition states. Although transition state **A** shows allylic repulsion between the methyl group at C5 and the hydrogen atom at C12, transition state **B** has severe transannular interactions between the hydrogen atom at C11 and the methyl group at C15. As a result, transition state **A** is formed prior to transition state **B**, and **26a** is obtained as the sole product. However, in the transition state for the 3*R* alcohol **25b**, small difference in energy between transition state **C** and transition state **D** lead to dramatic changes in stereoselectivity. Unlike transition state **B**, transition state **D** does not have allylic repulsion between the hydrogen atom at C1 and the hydroxy group at C3. At the same time, transition state **C** has relatively higher energy due to the allylic interaction with the C3 alcohol. Consequently, the energy of

 © 2004 Wiley-VCH Verlag GmbH & Co. KGaA, Weinheim

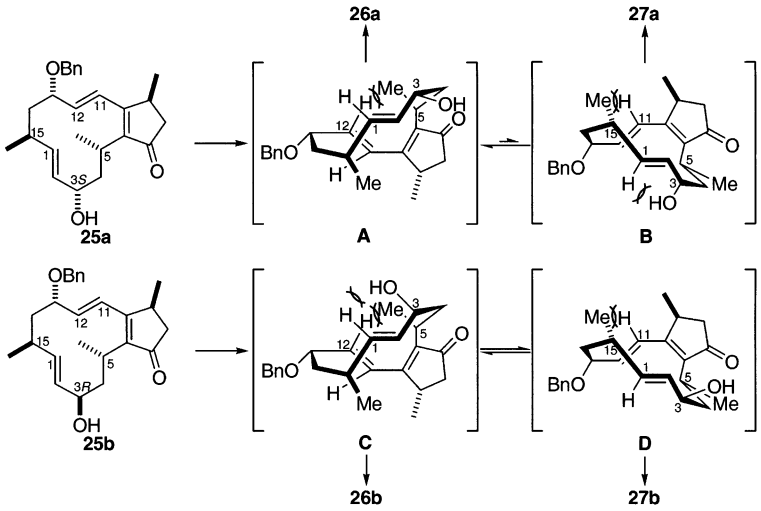


Figure 2. Transition states of the transannular Diels–Alder reactions of **25a** and **25b**.

transition state **C** is equal to that of transition state **D**, and thus **26b** and **27b** are produced in a ratio of 1:1.

In conclusion, we successfully completed the highly stereoselective synthesis of the spirotetracyclic carbon core of the mangicols. The present synthesis features a novel chlorination step, an intramolecular NHK coupling reaction, and the stereoselective construction of a tetracyclic compound through a TADA reaction. The steric repulsion of the hydroxy group of C3 was stereocontrolled in the TADA reaction to predominantly afford the desired tetracyclic compound. Compounds **26a** and **26b** are versatile intermediates for the synthesis of the mangicol family. Further studies on the total synthesis of mangicol A (**1**) are currently underway in our laboratory.

Received: April 25, 2003 [Z51750]

Keywords: cycloaddition · diastereoselectivity · natural products · spiro compounds · synthesis design

[1] a) E. J. Corey, A. Guzman-Perez, *Angew. Chem.* **1998**, *110*, 402–415; E. J. Corey, A. Guzman-Perez, *Angew. Chem. Int. Ed.* **1998**, *37*, 388–401; b) J. Christoffers, A. Mann, *Angew. Chem.* **2001**, *113*, 4725–4732; *Angew. Chem. Int. Ed.* **2001**, *40*, 4591–4597.

[2] a) M. K. Renner, P. R. Jensen, W. Fenical, *J. Org. Chem.* **2000**, *65*, 4843–4852; b) M. K. Renner, P. R. Jensen, W. Fenical, *J. Org. Chem.* **1998**, *63*, 8346–8354.

[3] a) E. Marsault, A. Toró, P. Nowak, P. Deslongchamps, *Tetrahedron* **2001**, *57*, 4243–4260; b) K. Baetting, C. Dallaire, R. Pitteloud, P. Deslongchamps, *Tetrahedron Lett.* **1987**, *28*, 5249–5252; c) K. Baetting, A. Marinier, R. Pitteloud, P. Deslongchamps, *Tetrahedron Lett.* **1987**, *28*, 5253–5254; d) G. Bérubé, P. Deslongchamps, *Tetrahedron Lett.* **1987**, *28*, 5255–5258; see also: e) S. A. Frank, A. B. Works, W. R. Roush, *Can. J. Chem.* **2000**, *78*, 757–771; f) F. Tureček, V. Hanuš, P. Sedmera, H. Antropiusová, K. Mach, *Tetrahedron* **1979**, *35*, 1463–1467.

[4] M. Nakata, M. Arai, K. Tomooka, *Bull. Chem. Soc. Jpn.* **1989**, *62*, 2618–2635.

[5] a) E. J. Corey, R. K. Bakshi, S. Shibata, *J. Am. Chem. Soc.* **1987**, *109*, 5551–5553; b) E. J. Corey, R. K. Bakshi, S. Shibata, C.-P. Chen, V. K. Singh, *J. Am. Chem. Soc.* **1987**, *109*, 7925–7926.

[6] H. Hofmeister, K. Annen, H. Laurent, R. Wiechert *Angew. Chem.* **1984**, *96*, 720–722; *Angew. Chem. Int. Ed. Engl.* **1984**, *23*, 727–729.

[7] H. X. Zhang, F. Guibé, G. Balavoine, *J. Org. Chem.* **1990**, *55*, 1857–1867.

[8] E. Krainer, F. Naider, *Tetrahedron Lett.* **1993**, *34*, 1713–1716.

[9] M. Julia, J.-M. Paris, *Tetrahedron Lett.* **1973**, *14*, 4833–4836.

[10] D. B. Dess, J. C. Martin, *J. Org. Chem.* **1983**, *48*, 4155–4156.

[11] P. Bakuzis, M. L. F. Bakuzis, *J. Org. Chem.* **1981**, *46*, 235–239.

[12] a) J. K. Stille, *Angew. Chem.* **1986**, *98*, 504–519; *Angew. Chem. Int. Ed. Engl.* **1986**, *25*, 508–524; b) J. K. Stille, B. L. Groh, *J. Am. Chem. Soc.* **1987**, *109*, 813–817.

[13] V. Kohli, H. Blöcker, H. Köster, *Tetrahedron Lett.* **1980**, *21*, 2683–2686.

[14] K. Takai, K. Nitta, K. Utimoto, *J. Am. Chem. Soc.* **1986**, *108*, 7408–7410.

[15] a) K. Takai, M. Tagashira, T. Kuroda, K. Oshima, K. Utimoto, H. Nozaki, *J. Am. Chem. Soc.* **1986**, *108*, 6048–6050; b) H. Jin, J.-i. Uenishi, W. J. Christ, Y. Kishi, *J. Am. Chem. Soc.* **1986**, *108*, 5644–5646; c) For a recent review of the intramolecular Nozaki–Hiyama–Kishi coupling reaction see: A. Fürstner, *Chem. Rev.* **1999**, *99*, 991–1045.

 © 2004 Wiley-VCH Verlag GmbH & Co. KGaA, Weinheim

Kinetic Resolution of Epoxides

Kinetic Resolution of Epoxides by a C–C Bond-Forming Reaction: Highly Enantioselective Addition of Indoles to *cis*, *trans*, and *meso* Aromatic Epoxides Catalyzed by [Cr(salen)] Complexes**

Marco Bandini, Pier Giorgio Cozzi, Paolo Melchiorre, and Achille Umani-Ronchi**

Epoxides are valuable intermediates in organic synthesis. Elaboration of optically active epoxides by selective ring-opening reactions with nucleophiles and radicals in the presence of Lewis acids or Lewis bases provides access to a variety of enantiomerically enriched compounds.[1] Currently, enantioenriched *cis* and *trans* epoxides can be efficiently

[*] Dr. M. Bandini, Prof. Dr. P. G. Cozzi, Dr. P. Melchiorre, Prof. Dr. A. Umani-Ronchi
Dipartimento di Chimica "G. Ciamician", Università di Bologna
Via Selmi, 2 40126 Bologna (Italy)
Fax: (+390) 51-2099456
E-mail: pgcozzi@ciam.unibo.it
umani@ciam.unibo.it

[**] We thank MIUR, Rome (FIRB funds), "Progetto Stereoselezione in Chimica Organica – Metodologie ed Applicazioni", and the University of Bologna (funds for selected research topics) for financial support of this research.

Supporting information for this article is available on the WWW under http://www.angewandte.org or from the author.

 © 2004 Wiley-VCH Verlag GmbH & Co. KGaA, Weinheim DOI: 10.1002/anie.200352073

prepared by catalytic epoxidation.[2] However, the ready accessibility of epoxides in racemic form renders kinetic resolution an attractive alternative route to optically active epoxides.[3] In particular, racemic terminal epoxides have been used as substrates in kinetic-resolution reactions promoted by [Cr(salen)Cl] and [Co(salen)OAc] (Figure 1) with

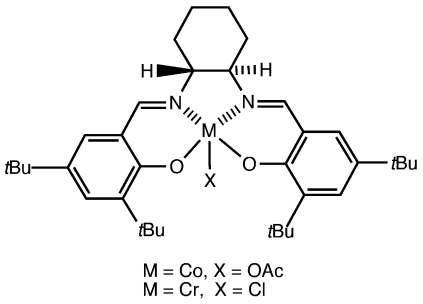
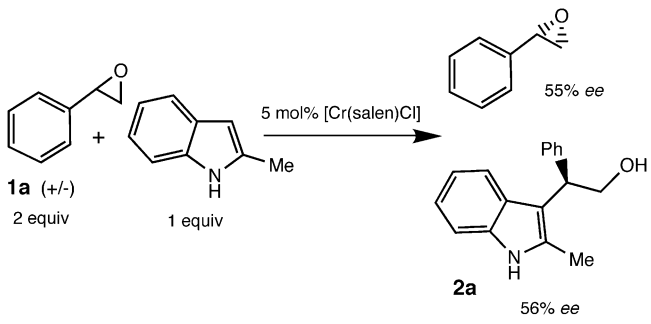


Figure 1. Metal salen complexes.

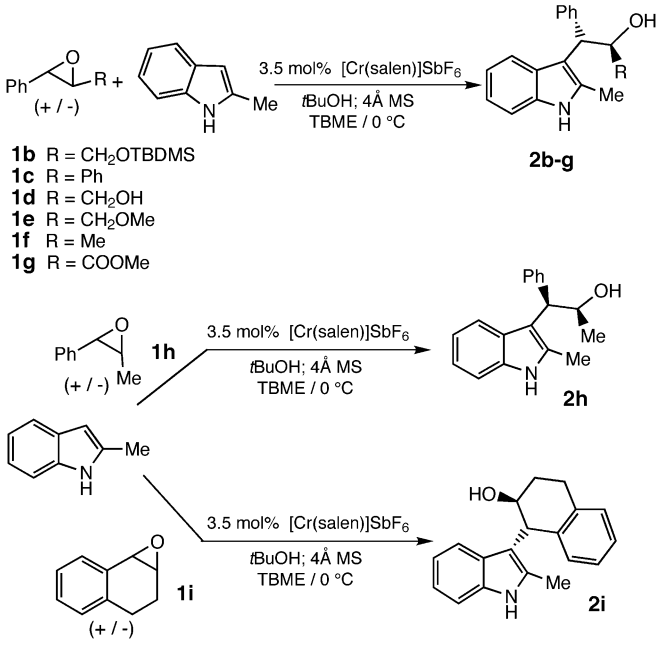
remarkable results.[4] However, 1,2-disubstituted epoxides are still challenging substrates for kinetic resolution,[5] and a general kinetic resolution of both *cis* and *trans* aromatic epoxides catalyzed by metal salen complexes has been not reported.[6] Here we present the first method for the catalytic kinetic resolution of both *cis* and *trans* aromatic epoxides, based on a C–C bond-forming reaction with indoles.[7] Moreover, the methodology is also effective in the desymmetrization of *meso* aromatic epoxides, which provides access to highly enantioenriched indolyl derivatives.[8]

During our studies on indium halides as Lewis acid catalysts we discovered that $InBr_3$ can promote ring opening of aromatic epoxides with indoles.[9] Considering the ability of [Cr(salen)Cl] (Figure 1, M = Cr, X = Cl) to generate a suitable chiral environment,[10] we tested the possibility of using this complex in the asymmetric ring opening of racemic styrene oxide derivatives with indoles. The reaction was performed at room temperature in noncoordinating solvents (CH_2Cl_2 or *tert*-butyl methyl ether (TBME), 0.3 M) with 5 mol% of (*R*,*R*)-[Cr(salen)Cl] as catalyst (Scheme 1) and commercially available 2-methylindole as the nucleophile.[11] Under these conditions, after complete consumption of 2-methylindole, the unconsumed styrene oxide and the indolyl



Scheme 1. Reaction of racemic styrene oxide with 2-methylindole catalyzed by [Cr(salen)Cl].

derivatives **2a** were isolated with enantiomeric excesses of 55 and 56%, respectively.[12] To apply this novel reaction to the kinetic resolution of 1,2-disubstituted epoxides, *trans*-1-[(*tert*-butyldimethylsilyloxy)]-3-phenyloxirane (**1b**) was chosen as a model substrate. Reaction of racemic epoxide **1b** (2 equiv) with 2-methylindole (1 equiv) was performed in the presence of [Cr(salen)Cl] (5 mol%) in TBME. Although the desired ring-opened product **2b** was isolated with high enantioselectivity (*ee* = 78%), the *trans* aromatic epoxide **1b** was in general rather unreactive (70% conversion over 5 days). To increase the reactivity of the system we used cationic [Cr(salen)] complexes, prepared by exchange with silver salts by following the protocol of Jacobsen et al.[13] We found that [Cr(salen)]SbF_6 in the presence of 4 Å molecular sieves (MS), TBME as solvent, and *t*BuOH (1 equiv relative to 2-methylindole) led to complete consumption of 2-methylindole over 16 h (Scheme 2). The unconsumed epoxide (*R*,*R*)-



Scheme 2. Kinetic resolution of *cis* and *trans* aromatic epoxides with 2-methylindole.

1b and the corresponding indolyl derivative **2b** were isolated with the same enantiomeric excess (77%). Then 1,2-disubstituted aromatic epoxides **1b–i** were treated with 2-methylindole under these optimized conditions. An excess of epoxide (3 equiv) and a reaction temperature of 0 °C ensured that the ring-opened product was obtained with high enantiomeric excess (Table 1). Both *cis* and *trans* aromatic epoxides reacted with complete regioselectivity to give the corresponding indolyl derivatives **2b–i** in high yields and with good enantioselectivity values (up to 91% *ee*; Table 1, entry 1).[14] *Cis* aromatic epoxides were more reactive than *trans* epoxides. It is noteworthy that the stereochemical outcome of this kinetic resolution is strictly dependent on the stereochemistry of the starting epoxides. In fact, the *trans* and *cis* β-methylstyrene oxides **1f** and **1h** gave the ring-opened

 © 2004 Wiley-VCH Verlag GmbH & Co. KGaA, Weinheim

Table 1: Kinetic resolution of aromatic epoxides with 2-methylindole.[a]

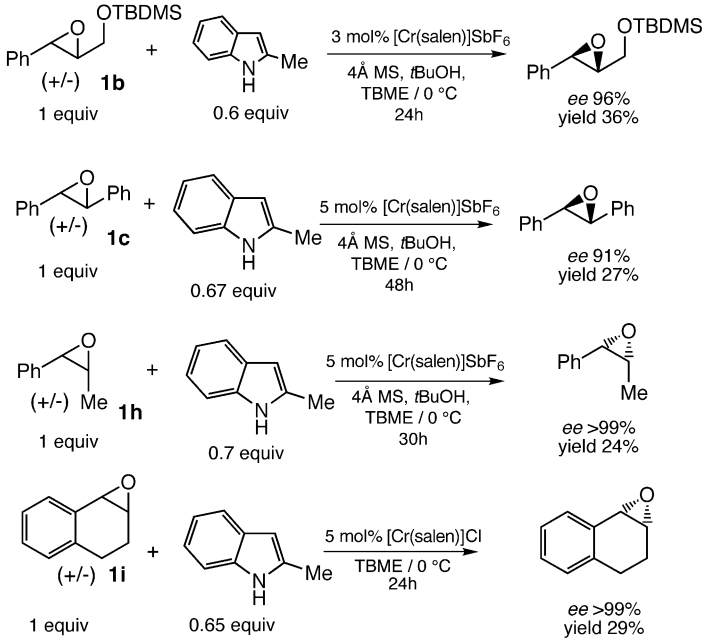
Entry	Epoxide	*t* [h]	Yield [%][b]	*ee* of **2** [%][c]	*s*[d]
1	**1b**	16	96	91	30
2	**1c**	48	82	86	15
3	**1d**	40	93	87	25
4	**1e**	24	98	86	23
5	**1f**	36	99	72	10
6	**1g**	30	85	80	13
7	**1h**	18	95	80	13
8	**1i**[d]	24	97	83	16

[a] Reactions were carried out with 1 equiv of 2-methylindole, 3 equiv of racemic epoxide, 1 equiv of *t*BuOH, and 3.5 mol% [Cr(salen)]SbF_6 relative to the racemic epoxide. [b] Yield of **2** after chromatographic purification. [c] Enantiomeric excesses were evaluated by HPLC analysis; see Supporting Information. [d] Selectivity factor. [e] [Cr(salen)Cl] (3.5 mol% relative to the epoxide) was used as catalyst.

products **2f** and **2h** with *S* and *R* absolute configuration of the benzylic stereocenter, respectively.

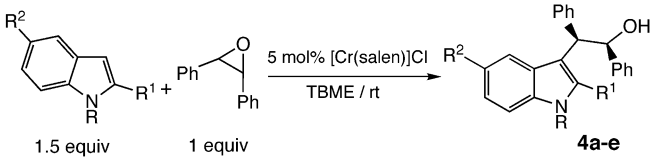
A useful feature of kinetic resolution is that the enantiopurity of the unconverted substrate can be enhanced through higher substrate conversion. Indeed, while reactions applied to prochiral substrates give products with constant enantioselectivity, the enantiomeric excesses obtained in kinetic resolutions are a function of conversion. Therefore, to obtain high enantiomeric excesses, the selectivity factor must be evaluated.[15]

In principle, this kinetic resolution could represent a general method for the preparation of both *cis* and *trans* aromatic epoxides with high *ee* values starting from racemic substrates. This concept was demonstrated by the reaction of selected *cis* and *trans* epoxides (Scheme 3). Table 1 lists the selectivity factors for treatment of the epoxides with 2-methylindole. By adjusting the amount of 2-methylindole on the basis of the selectivity factor, it was possible to isolate the unconverted epoxides with high enantioselectivity and in satisfactory yields (24–36%).[16] *Trans* epoxides **1b** and **1c** were isolated in high enantiomeric excesses (91 and 96%, respectively), while the more reactive *cis* epoxides **1h** and **1i** were isolated in enantiomerically pure form (*ee* > 99%). To the best of our knowledge this is the first example of kinetic resolution of both *cis* and *trans* aromatic epoxides by a C–C bond-forming reaction.[17]



Scheme 3. Highly enantioselective kinetic resolution of aromatic epoxides.

Finally, this [Cr(salen)]-catalyzed addition of indoles to epoxides was also applied to the asymmetric ring opening (ARO) of *meso*-stilbene oxide. In this case the commercially available [Cr(salen)Cl] (5 mol%) proved to be effective in catalyzing the highly selective ARO of *meso*-stilbene oxide in the presence of different substituted indoles (Scheme 4). The corresponding indolyl derivatives **4a–e** were isolated in excellent yield and high enantioselectivity (yield 95–98%; 90–98% *ee*, Table 2).



3a R = H, R^1 = H, R^2= H
3b R = Me, R^1 = H, R^2= H
3c R = H, R^1 = Me, R^2 = H
3d R = Me, R^1= Me, R^2 = H
3e R = H, R^1 = H, R^2 = OMe

Scheme 4. Asymmetric ring opening of *meso*-stilbene oxide with indoles.

Table 2: ARO of *meso*-stilbene oxide with indoles.

Entry	Indole	*t* [h]	Yield [%][a]	*ee* [%][b]
1	**3a**	36	98	93
2	**3b**	30	96	96
3	**3c**	36	98	98
4	**3d**	36	95	97
5	**3e**	36	95	90

[a] Yield of **4** after chromatographic purification; [b] Enantiomeric excesses were evaluated by HPLC; see Supporting Information.

In summary, we have developed a highly effective methodology for the kinetic resolution of 1,2-disubstituted aromatic epoxides, based on a C–C bond-forming reaction. The method uses 2-methylindole as the resolving agent, and both the indolyl derivatives and the unconverted epoxides are obtained in high enantiomeric excess. Further studies on the mechanistic and practical aspects of this new kinetic-resolution procedure are in progress.

Received: June 6, 2003 [Z52073]

Keywords: aromatic epoxides · asymmetric catalysis · indoles · kinetic resolution · N,O ligands

 © 2004 Wiley-VCH Verlag GmbH & Co. KGaA, Weinheim

[1] R. A. Johnson, K. B. Sharpless in *Catalytic Asymmetric Synthesis* (Ed.: I. Ojima), VCH, New York, **1993**, Chap. 4.1.

[2] K. B. Sharpless, *Angew. Chem.* **2002**, *114*, 2126 – 2135; *Angew. Chem. Int. Ed.* **2002**, *41*, 2024 – 2032. For important methodologies for the preparation of optically active aromatic epoxides, see T. Katsuki, *Coord. Chem. Rev.* **1995**, *140*, 189 – 214; b) Y. Tu, Z.-X. Wang, Y. Shi, *J. Am. Chem. Soc.* **1996**, *118*, 9806 – 9807.

[3] J. M. Keith, J. F. Larrow, E. N. Jacobsen, *Adv. Synth. Catal.* **2001**, *343*, 5 – 26.

[4] a) M. Tokunaga, J. F. Larrow, F. Kakiuchi E. N. Jacobsen, *Science* **1997**, *277*, 937 – 938; b) J. F. Larrow, S. E. Schaus, E. N. Jacobsen, *J. Am. Chem. Soc.* **1996**, *118*, 7420 – 7421; d) D. A. Annis, E. N. Jacobsen, *J. Am. Chem. Soc.* **1999**, *121*, 4147 – 4154; e) R. Breinbauer, E. N. Jacobsen, *Angew. Chem.* **2000**, *112*, 3750 – 3753; *Angew. Chem. Int. Ed.* **2000**, *39*, 3604 – 3607; f) J. M. Ready, E. N. Jacobsen, *J. Am. Chem. Soc.* **2001**, *123*, 2687 – 2688; g) J. M. Ready, E. N. Jacobsen, *Angew. Chem.* **2002**, *114*, 1432 – 1435; *Angew. Chem. Int. Ed.* **2002**, *41*, 1374 – 1377.

[5] Kinetic resolution of 2,2-disubstituted epoxides catalyzed by [Cr(salen)]: H. Lebel, E. N. Jacobsen, *Tetrahedron Lett.* **1999**, *40*, 7303 – 7306.

[6] Kinetic resolution of 1,2-disubstituted epoxides with enzymes: K. Faber, *Biotransformations in Organic Chemistry*, Springer, Berlin, **2000**, pp. 135 – 136.

[7] Kinetic resolution of epoxides via C–heteroatom bond-forming reactions: a) S. E. Schaus, E. N. Jacobsen, *Tetrahedron Lett.* **1996**, *37*, 7937 – 7940; b) S. E. Schaus, J. F. Larrow, E. N. Jacobsen, *J. Org. Chem.* **1997**, *62*, 4197 – 4199; c) L. E. Martinez, J. L. Leighton, D. H. Carsten, E. N. Jacobsen, *J. Am. Chem. Soc.* **1995**, *117*, 5897 – 5898; d) M. H. Wu, E. N. Jacobsen, *Tetrahedron Lett.* **1997**, *38*, 1693 – 1696; e) E. N. Jacobsen, *Acc. Chem. Res.* **2000**, *33*, 421 – 431; f) J. Gu, M. J. Dirr, Y. Wang, D. L. Soper, B. De, J. A. Wos, C. R. Johnson, *Org. Lett.* **2001**, *3*, 791 – 794.

[8] Important examples of ARO reactions of *meso* epoxides with carbon nucleophiles: a) M. B. Cole, K. D. Shimizu, C. A. Krueger, J. P. A. Harrity, M. L. Snapper, A. H. Hoveyda, *Angew. Chem.* **1996**, *108*, 1776 – 1779; *Angew. Chem. Int. Ed. Engl.* **1996**, *35*, 1668 – 1671; b) S. E. Schaus, E. N. Jacobsen, *Org. Lett.* **2000**, *2*, 1001 – 1004; c) M. Lautens, J.-L. Renaud, S. Hiebert, *J. Am. Chem. Soc.* **2000**, *122*, 1804 – 1805; d) M. Lautens, C. Dockendorff, K. Fagnou, A. Malicki, *Org. Lett.* **2002**, *4*, 1311 – 1314; e) M. Lautens, K. Fagnou, S. Hiebert, *Acc. Chem. Res.* **2003**, *36*, 48 – 58.

[9] M. Bandini, P. G. Cozzi, P. Melchiorre, A. Umani-Ronchi, *J. Org. Chem.* **2002**, *67*, 5386 – 5389.

[10] a) E. N. Jacobsen, *Acc. Chem. Res.* **2000**, *33*, 421 – 431; b) M. Bandini, P. G. Cozzi, A. Umani-Ronchi, *Chem. Commun.* **2002**, 919 – 927.

[11] Other indoles (indole; 1-methyl-, 5-methoxy-, 5-bromo-, 5-benzyloxy-, and 5-nitroindole) were less reactive than 2-methyindole.

[12] Interestingly, the absolute configuration of isolated **1a** was the opposite of that in other kinetic resolutions carried out with [Cr(salen)] and [Co(salen)] complexes, and this indicates that a different mechanism is probably operative in this case. For [Co(salen)]-catalyzed kinetic resolution, see S. E. Schaus, B. D. Brandes, J. F. Larrow, M. Tokunaga, K. B. Hansen, A. E. Gould, M. E. Furrow, E. N. Jacobsen, *J. Am. Chem. Soc.* **2002**, *124*, 1307 – 1315. For kinetic resolution employing [Cr(salen)], see ref. [7e].

[13] S. E. Schaus, J. Brånalt, E. N. Jacobsen, *J. Org. Chem.* **1998**, *63*, 403 – 405.

[14] Absolute configurations of products **2a**, **2f**, and **2i** were established by HPLC analysis by comparing the retention times with those of authentic samples; for all other products the absolute configuration was assigned by analogy.

[15] The lower limit of the selectivity factor s for the epoxides was estimated by using the equation $s = \ln[1-c(1+ee)]/\ln[1-c(1-ee)]$ in the reaction with 2-methylindole (*ee* is the percentage enantiomeric excess of the ring-opened products; yields of ring-opened products were used for conversion c.

[16] The amount of 2-methylindole was adjusted to obtain the maximum yield possible with the highest enantiomeric excess for the unconverted epoxides. As we use 0.6–0.7 equiv of 2-methylindole, the maximum theoretical yield is 30–40 %.

[17] Methylidene cyclohexene oxide could be resolved with a C–C bond-forming reaction: a) F. Baldassi, P. Crotti, F. Macchia, M. Pineschi, A. Arnold, B. L. Feringa, *Tetrahedron Lett.* **1998**, *39*, 7795 – 7798; b) F. Bertozzi, P. Crotti, F. Macchia, M. Pineschi, A. Arnold, B. L. Feringa, *Org. Lett.* **2000**, *2*, 933 – 936.

 © 2004 Wiley-VCH Verlag GmbH & Co. KGaA, Weinheim

Cluster Expansion

Cubane $\{Cu^{II}_4\}$ Cluster as a Precursor for the Preparation of a Mixed-Valent $\{Cu^{II}_{12}Cu^{I}_2\}$ Core**

*Arindam Mukherjee, Munirathinam Nethaji, and Akhil R. Chakravarty**

Current interests in the chemistry of high-nuclearity transition-metal complexes draw from their utility in the emerging science of nanomaterials,[1] as models for the multimetal active sites of metal-storage proteins,[2] and as single molecule magnets (SMMs).[3,4] In addition, such super-sized molecules often show a variety of supramolecular interactions.[5] The "self-assembly" process of generating a high-nuclearity cluster from a mono- or dimeric precursor generally involves low-dentate organic ligands.

Using a pentadentate Schiff base, *N*,*N*′-(2-hydroxypropane-1,3-diyl)bis(acetylacetoneimine) (H_3L), we have been successful in isolating a discrete tetranuclear copper(II) cubane cluster $[\{Cu^{II}(HL)\}_4]$ (**1**) which, unlike other clusters, has four pendant arms with eight donor sites (four imine nitrogen atoms and four hydroxy groups) available for binding to additional metal ions. Complex **1**, as a "molecular octopus", is a new precursor for high nuclearity copper clusters. This complex on reaction with copper(II) perchlorate in presence of KOH forms an octanuclear copper(II) species

[*] A. Mukherjee, M. Nethaji, Prof. A. R. Chakravarty
Department of Inorganic and Physical Chemistry
Indian Institute of Science
Bangalore-560012 (India)
Fax: (+91) 80-3600-683
E-mail: arc@ipc.iisc.ernet.in

[**] We thank the Department of Science and Technology, Government of India, for financial support (Grant SP/S1/F-01/2000) and for the CCD facility. We also thank the Convenor, Bioinformatics Center, IISc, for database search.

Supporting information for this article is available on the WWW under http://www.angewandte.org or from the author.

 DOI: 10.1002/anie.200352350 © 2004 Wiley-VCH Verlag GmbH & Co. KGaA, Weinheim

$[Cu_8L_4(OH)_3](ClO_4)$ that has already been prepared by us from a different reaction using a binuclear precursor.[6] The same metal-driven self-assembly process under different reaction conditions leads to the formation of a new discrete tetradecanuclear mixed-valent complex $[Cu^{II}_{12}Cu^{I}_{2}L_6(OH)_6](ClO_4)_2$ (**2**). Herein, we present the synthesis, crystal structures and magnetic properties of **1** and **2**. Complex **2** is a rare discrete molecular tetradecanuclear transition-metal complex with multidentate ligand system.[7] In addition two copper(I) atoms are encapsulated in a core containing twelve copper(II) atoms giving a prismatic propeller structure.

Complex $[\{Cu(HL)\}_4]$ (**1**), prepared from a reaction of $[Cu(H_2O)_6](ClO_4)_2$ with H_3L in presence of triethylamine in CH_2Cl_2/MeOH, crystallizes in the cubic space group $P\bar{4}3n$ with one copper center and one ligand along with one lattice water in the crystallographic asymmetric unit.[8] The structure consists of a tetranuclear core with the metal centers linked by μ_3 alkoxo oxygen atom, to form a cubic arrangement of the metal and the oxygen atoms (Figure 1). The copper centers

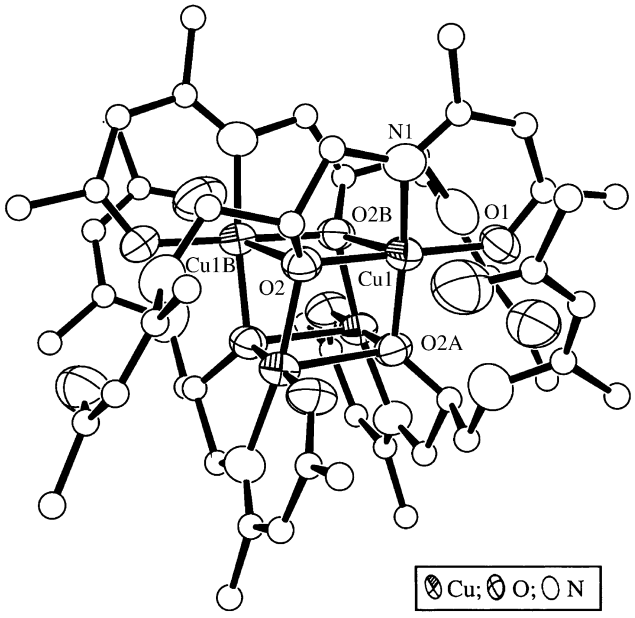


Figure 1. A perspective view of the complex in (**1**·4 H_2O) the thermal ellipsoids are set at 50% probability, the carbon atoms are shown as spheres with a reduced size for clarity. Selected interatomic distances [Å] and angles [°]: Cu1-O1 1.905(6), Cu1-O2 1.974(5), Cu1-O2A 1.971(5), Cu1-O2B 2.437(5), Cu1-N1 1.927(7); Cu1-O2-Cu1B 101.9(2), Cu1-O2-Cu1C 104.7(2), Cu1B-O2-Cu1C 89.61(19). Symmetry operations: A: $-x+3/2,z-1/2,-y+1/2$; B: $x,-y,-z+1$; C: $-x+3/2,-z+1/2,y+1/2$.

are in an essentially square-pyramidal (4 + 1) geometry with one bridging Cu–O bond being the axial group (2.437(5) Å). The Cu···Cu distances are 3.438(1) and 3.124(1) Å. The potentially pentadentate ligand (H_3L) binds in a dianionic tridentate form through one imine nitrogen, one enolized oxygen as the terminal, and the anionic alkoxo-oxygen atom as the bridging site. This leaves the remaining hydroxy group and the imine nitrogen atom as pendant, noncoordinating sites suitable for cluster expansion through metal-driven self-assembly process (Figure 2). The nonbonded shortest Cu···O and Cu···N separations involving the pendant donor sites are 3.6 and 3.2 Å, respectively.

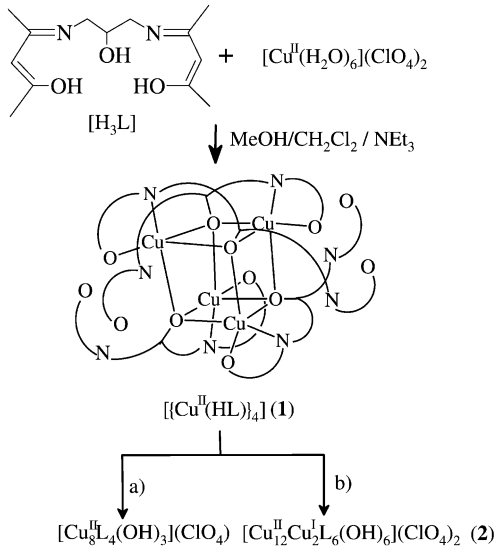


Figure 2. Reaction pathways in the self-assembly processes forming tetra-, octa-, and tetradecanuclear copper cores: a) $[Cu(H_2O)_6](ClO_4)_2$ and KOH in EtOH; b) $[Cu(H_2O)_6](ClO_4)_2$, H_3L, and piperidine in CH_2Cl_2/MeOH.

When **1** is treated with $[Cu(H_2O)_6](ClO_4)_2$ in a 1:4 molar ratio in presence of KOH in ethanol, the product is an octanuclear copper(II) complex $[Cu_8L_4(OH)_3](ClO_4)$, that has already been reported by us.[6] The reaction involves an addition of four copper(II) ions. Further addition of metal ions to **1** takes place on treatment of it with $[Cu(H_2O)_6](ClO_4)_2$ and H_3L in a 1:10:4 mole ratio in presence of piperidine in methanol and CH_2Cl_2 to form the tetradecanuclear mixed-valent complex $[Cu^{II}_{12}Cu^{I}_{2}L_6(OH)_6](ClO_4)_2$ (**2**). The cluster expansion process **1**→**2** involves the addition of ten copper atoms and two ligands to the cubane structure. Single crystals of **2**·3 H_2O, obtained by slow evaporation of the reaction mixture, belong to the trigonal space group $R\bar{3}c$ with six molecules in the unit cell.[8] The structure consists of six $\{Cu^{II}_{2}L\}^{+}$ units, each linked to two μ_3-OH groups attached to two copper(I) centers (Figure 3). The N_2O_3-donor Schiff base displays trianionic pentadentate mode of coordination. There are two central encapsulated copper(I) units that are presumably formed by the reduction of cupric ion owing to geometrical constraints within the core (see below). The Cu3 atom is bonded to three OH groups giving a threefold rotation axis with a propeller-shaped structure (see Supporting Information). In this essentially prismatic unit, the Cu3 atom has been assigned +1 oxidation state based on its trigonal-pyramidal structure in which the Cu3-O4 separation is 2.282(8) Å. The Cu3 atom is displaced 1.27(1) Å from the plane formed by three hydroxo oxygen atoms. The O-Cu3-O angle is 92.07(4)°. The deviation from the trigonal-planar structure could be due to the small size of the cavity accommodating the copper(I) atom. In addition, charge

 © 2004 Wiley-VCH Verlag GmbH & Co. KGaA, Weinheim

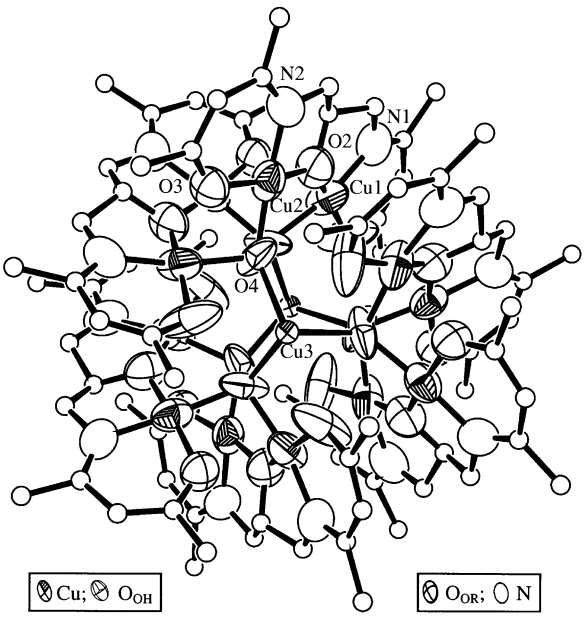


Figure 3. A perspective view of the complex in **2**·3 H_2O with the thermal ellipsoids set at 50% probability the carbon atoms are shown as spheres with a reduced size for clarity. Selected bond lengths [Å] and angles [°]: Cu1-O1 1.899(11), Cu1-O2 1.941(11), Cu1-O4, 1.957(9), Cu2-O2 1.915(9), Cu2-O3 1.888(9), Cu2-O4 1.966(11), Cu1-N1 1.887(14), Cu2-N2 1.941(13), Cu3-O4 2.282(8); Cu1-O2-Cu2 136.5(6), Cu1C-O4-Cu2 101.8(4), Cu1C-O4-Cu3 100.4(4), Cu2-O4-Cu3 127.5(6). The prismatic structure involving the Cu^{I} centers can be seen. Symmetry operations: C:$-x+y+2/3$, $-z+1/6$, $-x+4/3$.

neutrality of this discrete molecular species requires two copper centers in +1 oxidation state. The Cu···Cu distance of 3.583(3) Å within the $\{Cu_2L\}^+$ units in **2** is similar to that observed in $[Cu_2L(O_2CMe)]$ (3.502(2) Å).[9] The dicopper(II) units in **2**, however, resemble the dialkoxo-bridged dicopper(II) complexes.[10]

The cluster expansion process is associated with a significant change in the magnetic properties as shown by preliminary magnetic data. The temperature dependence of the magnetic susceptibility of **1** and **2** is shown in Figure 4. The cubane cluster **1** has a μ_{eff} value of 1.76 μ_B and 2.31 μ_B per copper(II) center at 300 and 18 K, respectively (μ_{eff} per molecule: 3.51 μ_B, 300 K; 4.63 μ_B, 18 K). The observed increase in the $\chi_M T$ value on lowering the temperature

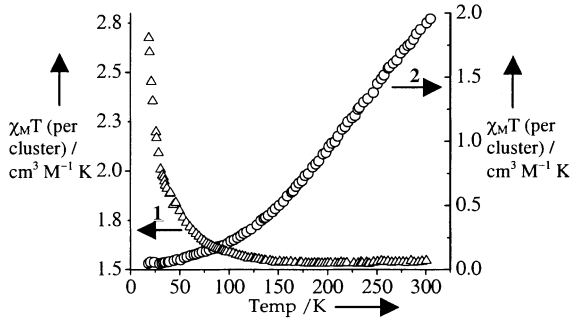


Figure 4. Plots of $\chi_M T$ (per molecule) versus T for complexes **1** (△) and **2** (○) in the temperature range 305–18 K.

suggests intracluster ferromagnetic interaction.[11] The contribution from the intercluster magnetic interaction should be negligible considering the large separation of the clusters from each other (intercluster Cu···Cu separation, ≈9.5 Å). The tetradecanuclear complex **2** shows, in contrast, strong antiferromagnetic (AF) behavior with singlet as a ground state. The magnetic moment values per copper(II) center are 1.12 and 0.17 μ_B at 300 and 18 K, respectively (μ_{eff} per molecule: 3.91 μ_B, 300 K; 0.62 μ_B, 18 K). Complex **2** has six $\{Cu_2L\}^+$ moieties with a Cu-O-Cu alkoxo bridge angle of 137°. Such an angle with a planar geometry of the alkoxo oxygen atom is likely to promote strong AF interactions within the dimeric unit.[10] The Cu1C-O4-Cu2 angle of 101.8(4)° with a pyramidal geometry of O4 atom (sum of angles 330°) is likely to promote weak AF interactions between two intracluster interdimer units.[12] Detailed magnetic studies are in progress.

In conclusion, the ferromagnetic cubane cluster **1** with eight pendant binding sites presents a reactive precursor for the synthesis of high-nuclearity copper clusters by metal-driven self-assembly processes. Isolation of discrete molecular octanuclear copper(II) and tetradecanuclear mixed-valent copper complex with a propeller-shaped $\{Cu^{II}_{12}Cu^{I}_{2}\}$ core shows that the cubane complex can be used as a new precursor for the preparation of high-nuclearity clusters of nanometric size.

Experimental Section

1 was prepared from a reaction of $[Cu(H_2O)_6](ClO_4)_2$ (2.96 g, 8.0 mmol) with H_3L[9] (3.79 g, 14.9 mmol) in CH_2Cl_2/MeOH mixture (1:1 v/v, 40 mL) in presence of triethylamine (3.9 mL, 28.03 mmol) under reflux for 30 min. Dark blue crystalline product in ≈87% yield was obtained on slow evaporation of the solvent at 25°C. Single crystals were obtained by slow diffusion of hexane to a CH_2Cl_2 solution of **1**. Complex **2** was prepared in ≈66% yield from a reaction of **1** (0.2 g, 0.16 mmol) in CH_2Cl_2 (10 mL) with $[Cu(H_2O)_6](ClO_4)_2$ (0.6 g, 1.6 mmol) in presence of H_3L (0.19 g, 0.64 mmol) and piperidine (0.15 mL, 1.5 mmol) in MeOH (10 mL). The octanuclear complex $[Cu_8L_4(OH)_3](ClO_4)$ was prepared from a reaction of **1** (0.21 g, 0.16 mmol) with $[Cu(H_2O)_6](ClO_4)_2$ (0.24 g, 0.64 mmol) and KOH (0.53 g, 0.94 mmol) in ethanol (15 mL) in 55% yield (0.14 g). The crystals of the octanuclear complex gave cell parameters similar to those reported earlier.[6] Elemental analysis (%) calcd for **1**: C 49.44, H 6.38, N 8.87; found C 49.21, H 6.54, N 9.02, (%) calcd for **2** C 34.72, H 4.48, N 6.23; found: C 34.88, H 4.68, N 6.33. UV/Vis in MeOH λ_{max},(ε, M^{-1} cm^{-1})]: 233 (22500), 310 (43000), 630 nm (280) for **1** and 281 (60000), 315 (91000), 620 nm (1000) for **2**. $\chi_M T$ (per molecule) $cm^3 M^{-1}$ K: 2.675 at 18.54 K and 1.551 at 305.31 K for **1**; 0.048 at 18.41 K and 1.954 at 304.73 K for **2** (Supporting Information).

Received: July 10, 2003 [Z52350]

Keywords: cluster compounds · copper · magnetic properties · mixed-valent compounds · self-assembly

[1] R. E. P. Winpenny, *Adv. Inorg. Chem.* **2001**, *52*, 1; V. G. Makhankova, O. Y. Vassilyeva, V. N. Kokozay, B. W. Skelton, J. Reedijk, G. A. Vanalbada, L. Sorace, D. Gatteschi, *New. J. Chem.* **2001**, *25*, 685.

[2] H. Oshio, N. Hoshino, T. Ito, M. Nakano, F. Renz, P. Gütlich, *Angew. Chem.* **2003**, *115*, 233; *Angew. Chem. Int. Ed.* **2003**, *42*,

 © 2004 Wiley-VCH Verlag GmbH & Co. KGaA, Weinheim

223; A. Caneschi, A. Cornia, S. J. Lippard, *Angew. Chem.* **1995**, *107*, 511; *Angew. Chem. Int. Ed. Engl.* **1995**, *34*, 467.
[3] D. Gatteschi, R. Sessoli, *Angew. Chem.* **2003**, *115*, 278; *Angew. Chem. Int. Ed.* **2003**, *42*, 268.
[4] W. Wernsdorfer, N. Aliaga-Alcalde, D. N. Hendrickson, G. Christou, *Nature* **2002**, *416*, 408.
[5] J.-M. Lehn in *Supramolecular Chemistry - Concepts and Properties*, VCH, Weinheim, **1995**; R. W. Saalfrank, E. Uller, B. Demleitner, I. Bernt, *Struct. Bonding (Heidelberg)* **2000**, *96*, 149; F. A. Cotton, C. Lin, C. A. Murillo, *Acc. Chem. Res.* **2001**, *34*, 759; M. Fujita, K. Umemoto, M. Yoshizawa, N. Fujita, T. Kusukawa, K. Biradha, *Chem. Commun.* **2001**, 509; G. J. E. Davidson, S. J. Loeb, *Angew. Chem.* **2003**, *115*, 78; *Angew. Chem. Int. Ed.* **2003**, *42*, 74; B. J. Holliday, C. A. Mirkin, *Angew. Chem.* **2001**, *113*, 2076; Angew. *Chem. Int. Ed.* **2001**, 40, 2022.
[6] K. Geetha, M. Nethaji, A. R. Chakravarty, *Inorg. Chem.* **1997**, *36*, 6134.
[7] C. J. Milios, E. Kefalloniti, C. P. Raptopoulou, A. Terzis, R. Vincete, N. Lalioti, A. Escuer, S. P. Perlepes, *Chem. Commun.* **2003**, 819; G. Aromi, A. Bell, S. J. Teat, A. G. Whittaker, R. E. P. Winpenny, *Chem. Commun.* **2002**, 1896.
[8] Crystal data for **1**·4 H_2O: $C_{52}H_{88}N_8O_{16}Cu_4$, $M_r = 1335.46$, blue prisms ($0.265 \times 0.18 \times 0.145$ mm), cubic, $P\bar{4}3n$, $a = b = c = 22.421(4)$ Å, $V = 11272(3)$ Å^3, $Z = 6$, $\rho_{calcd} = 1.180$ g cm^{-3}, $\mu = 1.174$ mm^{-1}, min/max trans. = 0.6341/0.8345, $2\theta_{max} = 48°$, λ(Mo-Kα) = 0.71073 Å, $T = 293(2)$ K, 2961 unique reflections [R(int) = 0.1554], $R1 = 0.0693$, $wR2 = 0.1805$ [$I > 2\sigma(I)$], $R1 = 0.0953$, $wR2 = 0.1915$ (all data), GoF (F^2) = 1.077, $N_0/N_v = 2960/180$. Crystal data for **2**·3 H_2O: $C_{78}H_{126}N_{12}O_{35}Cl_2Cu_{14}$, $M_r = 2752.37$, green prisms ($0.325 \times 0.185 \times 0.09$ mm), trigonal, $R\bar{3}c$, $a = b = 16.318(2)$, $c = 70.22(2)$ Å, $V = 16193(6)$ Å^3, $Z = 6$, $\rho_{calcd} = 1.693$ g cm^{-3}, $\mu = 2.824$ mm^{-1}, min/max trans. = 0.6133/0.8943, $2\theta_{max} = 50°$, λ(Mo-Kα) = 0.71073 Å, $T = 293(2)$ K, 3077 unique reflections [R(int) = 0.0781], $R1 = 0.0879$, $wR2 = 0.2634$ [$I > 2\sigma(I)$], $R1 = 0.1228$, $wR2 = 0.2908$ (all data), GoF (F^2) = 1.048, $N_0/N_v = 3077/205$. X-ray diffraction data were measured in frames with increasing ω (width of 0.3 deg./frame) and with a scan speed at 6 s/frame for **1** and at 12 s/frame for **2** on a Bruker SMART APEX CCD diffractometer, equipped with a fine focus 1.75 kW sealed tube X-ray source. Empirical absorption corrections were carried out using MULTISCAN (for **1**) and SADABS (for **2**) program: R. Blessing, *Acta Crystallogr. Sect. A* **1995**, *51*, 33. The structures were solved by the heavy atom method and refined by full matrix least-squares using SHELX system of programs: G. M. Sheldrick, SHELXS-97, Program for the Solution of Crystal Structures, University of Göttingen, Göttingen (Germany), **1997**. All non-hydrogen atoms were refined anisotropically. The hydrogen atoms attached to carbon atoms in the complex were generated and assigned isotropic thermal parameters, riding on their parent carbon atoms, and used for structure factor calculation only. CCDC 214522 and 214523 contain the supplementary crystallographic data for **1** and **2**, respectively. These data can be obtained free of charge via www.ccdc.cam.ac.uk/conts/retrieving.html (or from the Cambridge Crystallographic Data Centre, 12 Union Road, Cambridge CB21EZ, UK; fax: (+44) 1223-336-033; or deposit@ccdc.cam.ac.uk). ORTEP and packing diagrams in color for **1** and **2** are given as Supporting Information.
[9] Y. Nishida, S. Kida, *J. Chem. Soc. Dalton Trans.* **1986**, 2633.
[10] M. Handa, N. Koga, S. Kida, *Bull. Chem. Soc. Jpn.* **1988**, *61*, 6853.
[11] H. Oshio, Y. Saito, T. Ito, *Angew. Chem.* **1997**, *109*, 2789; *Angew. Chem. Int. Ed. Engl.* **1997**, *36*, 2673.
[12] O. Kahn, *Molecular Magnetism*, VCH, Weinheim, **1993**.

 © 2004 Wiley-VCH Verlag GmbH & Co. KGaA, Weinheim

Reaction-Mechanism Elucidation

The Complete Delineation of the Initiation, Propagation, and Termination Steps of the Carbomethoxy Cycle for the Carboalkoxylation of Ethene by Pd–Diphosphane Catalysts**

Jianke Liu, Brian T. Heaton, Jonathan A. Iggo, and Robin Whyman*

Drent and Budzelaar have proposed two catalytic cycles for cationic Pd–diphosphane complex catalyzed CO–alkene coupling reactions such as CO–ethene copolymerization and methoxycarbonylation of ethene.[1] The hydride cycle is initiated by alkene insertion into a Pd–hydride bond whilst the carbomethoxy cycle is initiated by CO insertion into a Pd–methoxy bond. The two cycles may operate in parallel, for example, CO–alkene copolymerization, or one cycle may dominate, for example, the Lucite process for the methoxycarbonylation of ethene to methylpropanoate. Where the two cycles operate in tandem there exists the possibility of crossover between the cycles which has been inferred from chain end-group analysis.[1,2] Product selectivity is determined in both the initiation and termination step(s).[3–5] The chain-propagation steps, insertion of CO into a metal–alkyl bond, and insertion of alkene into a metal–acyl, bond have been extensively investigated,[6–10] whilst van Leeuwen has recently discussed termination by alcoholysis of the Pd–alkyl[11] and Pd–acyl intermediates.[4] We have recently (1) fully characterized the intermediates in and (2) delineated the initiation process of the hydride cycle.[12–14] The hydride cycle is thus well established, however, a complete cycle for the Pd–carbomethoxy mechanism has not yet been demonstrated because of the absence of suitable Pd–carbomethoxy precursors.[15–18] We report herein a simple, general procedure for the preparation of the key cationic monocarbomethoxy Pd–diphosphane compounds and present an NMR study that characterizes, for the first time, all the intermediates in the carbomethoxy cycle. We also report (1) the delineation of the propagation steps of the hydride cycle for this catalyst, and (2) for the first time, characterization of all the complexes involved in termination of the hydride cycle with concomitant crossover and initiation of the carbomethoxy cycle. It should be noted that ligands of the type used in this work give highly active catalysts in this field of chemistry.[3]

[*] J. Liu, Prof. B. T. Heaton, Dr. J. A. Iggo, Dr. R. Whyman
Department of Chemistry, Donnan and
Robert Robinson Laboratories
University of Liverpool
P. O. Box. 147, Liverpool, (UK) L69 7ZD
Fax: (+44) 151-794-3588
E-mail: iggo@liv.ac.uk

[**] The financial support of the EPSRC, grant RG/R37685, is gratefully acknowledged.

Supporting information for this article is available on the WWW under http://www.angewandte.org or from the author.

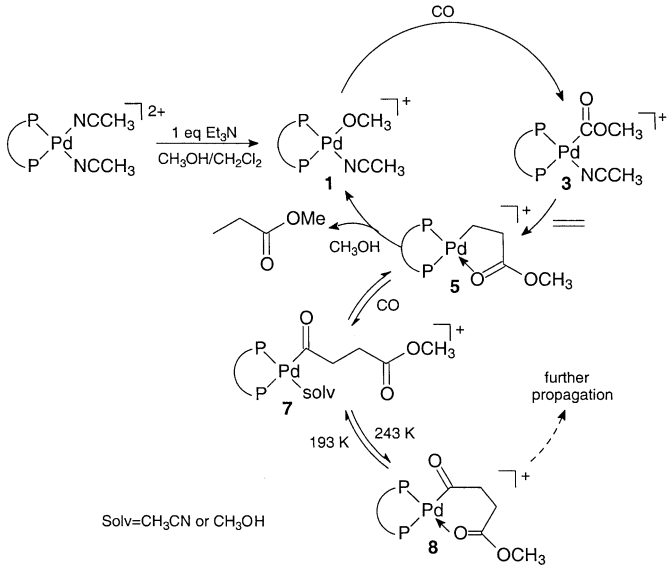
 © 2004 Wiley-VCH Verlag GmbH & Co. KGaA, Weinheim DOI: 10.1002/anie.200352369

The addition of one equivalent of triethylamine to a CO saturated solution of $[Pd(dibpp)(CH_3CN)_2][CF_3SO_3]_2$, (dibpp = 1,3-($iBu_2$P)$_2$-$C_3H_6$) in a 9:1 mixture of dichloromethane and methanol at −78 °C, gives two new doublets at $\delta = 3.7$ and, 17.0 ppm, $^2J(P,P) = 28$ Hz in the $^{31}P\{^1H\}$ NMR spectrum (Table 1). The NMR parameters of **1** are unchanged in the presence of excess CH_3CN, which indicates that the fourth coordination site in **1** is occupied by CH_3CN rather than methanol. Complex **1** is therefore assigned as the Pd–methoxy species $[Pd(dibpp)(OCH_3)(CH_3CN)]^+$, which is too unstable to be isolated and reacts readily with ^{12}CO to give **3** (Scheme 1; the putative intermediate $[Pd(dibpp)(OCH_3)(CO)]^+$, **2**, is not observed, see also Scheme 2). The $^{31}P\{^1H\}$ NMR spectrum of **3** shows two doublets at $\delta =$ 8.3 and −15.5 ppm, $^2J(P,P) = 47$ Hz. On using ^{13}CO, these resonances are further split by ^{31}P–^{13}C coupling, Table 1, and a corresponding doublet of doublets is observed in the $^{13}C\{^1H\}$ NMR spectrum at $\delta =$ 191.7 ppm, $^2J(P_{trans},C) = 167$ Hz, $^2J(P_{cis},C) = 9$ Hz, which is characteristic of the carbonyl of an ester group. Complex **3** can thus be formulated as $[Pd(dibpp)\{C(O)OCH_3\}(CH_3CN)][CF_3SO_3]$. The addition of a second equivalent of triethylamine leads to the formation of the Pd bis-carbomethoxy complex $[Pd(dibpp)\{C(O)OCH_3\}_2]$, **4**. The $^{31}P\{^1H\}$ and $^{13}C\{^1H\}$ NMR spectra of **4**, labeled with ^{13}CO, show second order AA′XX′ patterns, which have been simulated. The calculated chemical shifts and coupling constants for **4** are given in Table 1 and are similar to those found for **3**, thus substantiating the assignment of **3** and **4** as the mono and biscarbomethoxy complexes. In contrast to the ready reversibility of insertion of CO into Pd methyl bonds, **3** is stable towards decarbonylation; solutions of **3** can be taken to dryness in vacuo and extracted into dichloromethane with no change in the $^{31}P\{^1H\}$ NMR, that is, the insertion of CO into the Pd–methoxy bond is irreversible even though the fourth coordination site is occupied by CH_3CN.[19,20] The dppp (dppp = 1,3-bis(diphenylphosphinyl)propane) analogue can be prepared in a similar fashion, thus demonstrating the generality of the synthetic method (see Supporting Information).

Table 1: NMR spectroscopic data for the complexes involved in Scheme 1.

Complex	δ ^{31}P [ppm]	$J(P,P)$ [Hz]	$J(P,C)$ [Hz]	δ ^{13}C [ppm][a]
1 $[Pd(dibpp)(OCH_3)(CH_3CN)][CF_3SO_3]$	3.7 dd	28		
	17.0	28		
3 $[Pd(dibpp)\{C(O)OCH_3\}(CH_3CN)][CF_3SO_3]$	8.3 dd	47	9	191.7 dd
	−15.5 dd	47	167	
4 $[Pd(dibpp)\{C(O)OCH_3\}_2]$[b]	−8.2	45	152	203.0
	−8.2	45	12	203.0[c]
5 $[Pd(\overline{dibpp)\{CH_2CH_2C(O)}OCH_3\}][CF_3SO_3]$	13.3 d	46		193.3 d
	−12.0 dd	46	10	
6 $[Pd(dibpp)\{CH_2CH_2C(O)OCH_3\}(CH_3CN)][CF_3SO_3]$	12.7 dd	46	2	
	−12.6 dd	46	4	179.0 dd
7 $[Pd(dibpp)\{C(O)CH_2CH_2C(O)OCH_3\}(CH_3CN)][CF_3SO_3]$	4.1 dd	68	9	241.5 dd
	−18.6 dd	68	116	173.0 s
8 $[Pd(\overline{dibpp)\{C(O)CH_2CH_2C(O)}OCH_3\}][CF_3SO_3]$	17.9 dd	63	16	228.4 ddd[c]
	−14.3 dd	63	129	186.0 d

[a] $^{13}C\{^1H\}$ NMR spectroscopic data and $J(PC)$ were obtained from experiments using ^{13}CO. [b] AA′XX′, the chemical shifts and coupling constants were obtained from simulation of the experimental spectrum by using gNMR 4.1. [c] $J(CC) = 6$ Hz.



Scheme 1. The "carbomethoxy cycle" for Pd catalyzed CO–ethene coupling.

The stability of **3** makes it a promising starting point for a mechanistic NMR study of the carbomethoxy cycle (Scheme 1). On bubbling ethene through a dichloromethane solution of **3** at −78 °C, followed by warming to −30 °C for 1.5 hr, $^{31}P\{^1H\}$ and $^{13}C\{^1H\}$ NMR spectroscopy reveals complete conversion of **3** to a new complex **5**, $[Pd(\overline{dibpp)\{CH_2CH_2C(O)}OCH_3\}]^+$ (see Table 1). The observation of a doublet for the ester carbon at $\delta = 193.3$ ppm in the $^{13}C\{^1H\}$ NMR spectrum, $J(P,C) = 10$ Hz, indicates that a five-membered chelating structure is formed in which the oxygen atom of the ester carbonyl coordinates to the metal

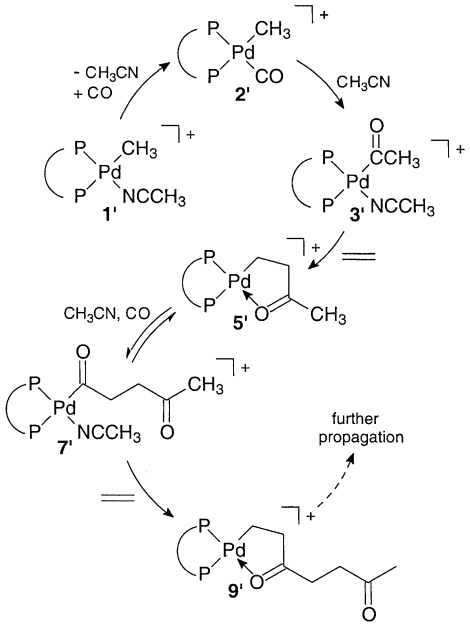
 © 2004 Wiley-VCH Verlag GmbH & Co. KGaA, Weinheim

center. This coupling is lost on addition of acetonitrile to the solution, which indicates cleavage of the chelate ring and coordination of CH_3CN to the Pd center, **6**. There are several reports of chelating structures, in which the oxygen of an acyl group coordinates to the Pd centre;[21–24] however, examples of similar chelating structures involving coordination of the oxygen atom of the ester group are rare,[11,24,25] and we believe this is the first example of such a chelating structure for a cationic diphosphane palladium system formed directly by the carbomethoxy cycle. A brief report exists of an analogous dppp compound synthesized by an alternative route.[11]

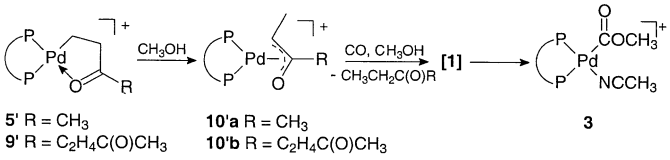
The reaction of **5** with ^{13}CO at −30 °C gives two new Pd acyl species **7** and **8** that are in equilibrium, Scheme 1. The $^{13}C\{^1H\}$ NMR spectrum of **7**, Table 1, comprises a doublet of doublets at $\delta = 241.5$ ppm, $^2J(P_{trans},C) = 116$, $^2J(P_{cis},C) = 9$ Hz, characteristic of an acyl carbonyl group coordinated to a square planar {Pd(dibpp)} fragment at δ 173 ppm, thus indicating the carbonyl group of the ester is not coordinated to the Pd center. Complex **7** can thus be formulated as the "open" acyl complex $[Pd(dibpp)\{C(O)CH_2CH_2C(O)OCH_3\}(Solv)]^+$. Complex **8** is formulated as the "chelating" acyl $[Pd(dibpp)\{C(O)CH_2CH_2C(O)OCH_3\}]^+$, on the basis of the downfield shift of the carbonyl of the ester group, $\delta =$ 186 ppm, compare with $\delta = 173$ ppm in **7**. Addition of methanol to a dichloromethane solution of **5** at room temperature releases one equivalent of methyl propanoate as the only organic product detected by $^{13}C\{^1H\}$ NMR. In the presence of CO, **3** is regenerated smoothly in situ and can be used to initiate a new catalytic cycle, Scheme 1.

Base was required to generate the Pd-methoxy species used in the work above, however, cationic Pd–diphosphane complex catalyzed CO–alkene coupling reactions such as CO–ethene copolymerization and methoxycarbonylation of ethene are normally performed in the presence of an excess of a strong acid such as CH_3SO_3H. The same chemistry as that outlined above can be accessed in the absence of base by chain crossover from the "hydride" cycle, Scheme 2 and 3. (Primes are used throughout this work to indicate analogous intermediates in the cycles shown in Schemes 1 and 2). Although attempts to prepare the Pd(dibpp)–hydride cation were unsuccessful, the methyl complex $[Pd(dibpp)(CH_3)(CH_3CN)][CF_3SO_3]$ **1′**, provides a clean entry point into the chemistry of the hydride cycle[4–7,11] (with the exception of the initial insertion of C_2H_4 into the Pd–H bond). **1′** was prepared in a manner similar to that described by Brookhart and co-workers.[26] Sequential insertions of CO and ethene were then monitored at low temperature (−78 °C to −30 °C) by $^{31}P\{^1H\}$ and $^{13}C\{^1H\}$ NMR spectroscopy, and gave the reaction sequence **1′**→**2′**→**3′**→**5′**→**7′**→**9′** (Scheme 2, Table 2) in agreement with reports on other diphosphane ligands.[6,7,12,14,15,26–31]

Importantly however, we have been able to characterize, for the first time, all the organometallic species involved in the methanolysis of the chelate complexes **5′** and **9′**, that is, **5′**→**10a′**→[**1**]→**3**, and **9′**→**10b′**→[**1**]→**3** with the exception of **1** (the involvement of which can be inferred from the work above; see Scheme 3). Van Leeuwen and co-workers have previously shown that methanolysis of the Pd-chelated alkyl



Scheme 2. The "hydride" cycle (initiated from $[Pd(dibpp)(CH_3)(CH_3CN)][CF_3SO_3]$ **1′**) for Pd-catalyzed CO–ethene coupling. (Primes indicate analogous complexes to those in Scheme 1.)



Scheme 3. Termination of the hydride cycle and crossover to the carbomethoxy cycle.

species proceeds via an enolate intermediate but were unable to characterize the organometallic products of solvolysis of the enolate.[11] Isomerization of the β-chelate complexes **5′** and **9′** to the enolates **10′a** and **10′b**, respectively, occurs in the presence of excess methanol (Scheme 3); in the absence of methanol decomposition of the β-chelate was observed. The methoxy species **1** was not observed presumably because of its instability and readiness to react with CO (see above)[32] to give **3**, from which we have been able to restart the carbomethoxy cycle described above.

All of the steps in both the hydride and carbomethoxy catalytic cycles for Pd-catalyzed CO–ethene coupling for a single, highly active catalyst have thus been fully characterized by NMR for the first time. The characterization of the active catalytic species resulting from chain termination through protonolysis of the Pd–alkyl intermediate in the hydride cycle has allowed the pathway from the hydride to the carbomethoxy cycle through a methanolysis chain-transfer step to be demonstrated for the first time. Termination of the carbomethoxy cycle by methanolysis of the alkyl intermediate also gives **3**. It has previously been noted that alcoholysis of the acyl intermediate gives ester product and a Pd–hydride

 © 2004 Wiley-VCH Verlag GmbH & Co. KGaA, Weinheim

Table 2: NMR spectroscopic data for the complexes involved in Scheme 2 and 3.

Complex	δ ^{31}P [ppm]	J(P,P) [Hz]	J(P,C) [Hz]	δ ^{13}C [ppm][a]
1′ [Pd(dibpp)(CH$_3$)(CH$_3$CN)][CF$_3$SO$_3$]	11.1 d	42		
	−15.6 d	42		
2′ [Pd(dibpp)(CO)(CH$_3$)][CF$_3$SO$_3$]	−0.5 dd	47	114	181.6 dd
	−12.3 dd	47	16	
3′ [Pd(dippp){C(O)CH$_3$}(CH$_3$CN)][CF$_3$SO$_3$]	5.4 dd	70	10	242.6 dd
	−19.6 dd	70	112	
5′ [Pd(dibpp){CH$_2$CH$_2$C(O)CH$_3$}][CF$_3$SO$_3$]	12.7 d	46		236.0 d
	−13.5 dd	46	10	
7′ [Pd(dippp){(C(O)CH$_2$CH$_2$C(O)CH$_3$)}(CH$_3$CN)][CF$_3$SO$_3$]	3.9 dd	69	10	240.3 dd
	−19.1 dd	69	114	
9′ [Pd(dibpp){CH$_2$CH$_2$C(O)CH$_2$CH$_2$C(O)CH$_3$}(CH$_3$CN)][CF$_3$SO$_3$]	14.7 d	47		237.4 dd
	−13.6 dd	47	10	
10a′ [Pd(dibpp){CH$_2$CH$_2$C(O) CH$_3$}][CF$_3$SO$_3$]	12.8 d	44		208.4 s
	−15.2 d	44		
10b′ [Pd(dibpp){CH$_2$CH$_2$C(O)CH$_2$CH$_2$C(O)CH$_3$}][CF$_3$SO$_3$]	12.5 d	52		206.3 s
	−16.5 d	52		
3 [Pd(dibpp){C(O)OCH$_3$}(CH$_3$CN)][CF$_3$SO$_3$]	7.8 dd	48	9	190.8 dd
	−15.7 dd	48	167	

[a] ^{13}C{^{1}H} NMR spectroscopic data and J(PC) were obtained from experiments by using ^{13}CO.

species "locking" the catalysis into the hydride cycle,[4,33] this work shows that methanolysis of the alkyl intermediate in both cycles gives a Pd–methoxy species, thus locking the catalysis into the carbomethoxy cycle.

Qualitatively, the rate of ethene insertion into the Pd–carbomethoxy bond in **3** is found to be similar to that of insertion into the Pd–acyl bond in **3′**, that is, insertion occurs at low temperature on the timescale of tens of minutes. This contrasts with literature precedent, in which insertion of alkene into the Pd–carbomethoxy bond is reported not to occur at room temperature on a timescale of days, if at all.[15,18] Although we cannot rule out that the high reactivity we observe is due to the different ligand used—dialkyl versus diaryl diphosphane—it seems likely that the low reactivity toward alkene insertion of Pd carbomethoxy complexes reported in previous work may reflect the presence of a strongly coordinating anion or ligand in the fourth coordination site rather than the intrinsic reactivity of the Pd–carbomethoxy bond.

The β-chelate has been proposed to be a resting state in catalytic cycle,[21] it is therefore interesting to compare the reactivity of [Pd(dibpp){CH$_2$CH$_2$C(O)OCH$_3$}]$^+$ **5** with that of the analogous β-chelate in the hydride cycle [Pd(dibpp){CH$_2$CH$_2$C(O)CH$_3$}]$^+$ **5′**. The chelate ring in **5** can be easily opened by the addition of acetonitrile to a dichloromethane solution of **5** to give **6** quantitatively. Complex **6** is formulated as the ring opened cation [Pd(dibpp){CH$_2$CH$_2$C(O)OCH$_3$}(CH$_3$CN)]$^+$ based on the upfield shift of the carbonyl carbon ($\delta = 179$ ppm) in **6** relative to that in **5**, and loss of the 10 Hz P,C coupling characteristic of a dative bond from the oxygen of the ester group to the Pd centre. This contrasts with the stability of **5′**, in which the chelating structure is preserved in the presence of strongly coordinating solvents (e.g. acetonitrile) or anions (e.g. trifluoroacetate). These results indicate that the ketonic group is a stronger Lewis base toward the metal centre than the ester carbonyl group in this system, compare Scheme 1 and 2.

Several six-membered chelates formed by coordination of the oxygen atom of a ketone to the metal centre have been reported during the stepwise insertion of alkenes and CO into metal–acyl compounds[34,35] and we report herein an analogous structure **8** involving coordination of an ester carbonyl group formed directly from successive insertions of ethene and CO into a Pd carbomethoxy species. The six-membered Pd–acyl chelates derived from the hydride cycle are reported

 © 2004 Wiley-VCH Verlag GmbH & Co. KGaA, Weinheim

to promote methanolysis relative to further ethene insertion,[3] however, our preliminary results show that further ethene insertion into **7** is preferred over methanolysis. These findings indicate that the oxochelates (**5** and **8**) formed in the carbomethoxy cycle are more susceptible to nucleophilic attack by substrates such as ethene, strong coordinating solvents, and anions, than their counterparts in the hydride cycle.

A Pd–carbomethoxy compound **3** has been synthesized by a simple methodology; this has allowed the Pd carbomethoxy cycle in CO–ethene coupling to be demonstrated for the first time and all important intermediates in both the carbomethoxy and hydride cycles to be characterized by ^{31}P and ^{13}C NMR spectroscopy. In contrast to previous reports, comparable reactivity towards ethene insertion was observed for the Pd carbomethoxy complex **3** and the Pd acetyl complex **3′** and is attributed to the absence of a strongly coordinating ligand in the fourth coordination site of **3**. In copolymerization and methoxycarbonylation reactions, the chain termination steps are as important as initiation and propagation since they can govern the product selectivity and regeneration of the catalytically active species. Methanolysis of the Pd β-chelate complexes occurs in both cycles regenerating the Pd–OCH_3 species **1** which, in the presence of CO, forms the Pd–$C(O)OCH_3$ species initiating a new catalytic cycle.

Received: July 14, 2003
Revised: October 6, 2003 [Z52369]

Keywords: carbonylation · copolymerization · homogeneous catalysis · palladium · polyketones · reaction mechanisms

[1] E. Drent, P. H. M. Budzelaar, *Chem. Rev.* **1996**, *96*, 663.
[2] *Catalytic Synthesis of Alkene-Carbon Monoxide Copolymers and Cooligomers, Vol. 27* (Ed.: A. Sen), Kluwer, Dordrecht, **2003**.
[3] R. I. Pugh, E. Drent, *Adv. Synth. Catal.* **2002**, *344*, 837.
[4] P. W. N. M. van Leeuwen, M. A. Zuideveld, B. H. G. Swennenhuis, Z. Freixa, P. C. J. Kamer, K. Goubitz, J. Fraanje, M. Lutz, A. L. Spek, *J. Am. Chem. Soc.* **2003**, *125*, 5523.
[5] Z. Freixa, P. W. N. M. van Leeuwen, *J. Chem. Soc. Dalton Trans.* **2003**, 1890.
[6] J. Ledford, C. S. Shultz, D. P. Gates, P. S. White, J. M. DeSimone, M. Brookhart, *Organometallics* **2001**, *20*, 5266.
[7] K. Nozaki, N. Sato, Y. Tonomura, M. Yasutomi, H. Takaya, T. Hiyama, T. Matsubara, N. Koga, *J. Am. Chem. Soc.* **1997**, *119*, 12779.
[8] C. Bianchini, A. Meli, *Coord. Chem. Rev.* **2002**, *225*, 35.
[9] G. Consiglio, *Chimia* **2001**, *55*, 809.
[10] C. Bianchini, A. Meli, W. Oberhauser, *J. Chem. Soc. Dalton Trans.* **2003**, 2627.
[11] M. A. Zuideveld, P. C. J. Kamer, P. W. M. N. van Leeuwen, P. A. A. Klusener, H. A. Stil, C. F. Roobeek, *J. Am. Chem. Soc.* **1998**, *120*, 7977.
[12] G. R. Eastham, B. T. Heaton, J. A. Iggo, R. P. Tooze, R. Whyman, S. Zacchini, *Chem. Commun.* **2000**, 609.
[13] G. R. Eastham, R. P. Tooze, M. Kilner, D. F. Foster, D. J. Cole-Hamilton, *J. Chem. Soc. Dalton Trans.* **2002**, 1613.
[14] W. Clegg, G. R. Eastham, M. R. J. Elsegood, B. T. Heaton, J. A. Iggo, R. P. Tooze, R. Whyman, S. Zacchini, *J. Chem. Soc. Dalton Trans.* **2002**, 3300.
[15] G. Dekker, C. J. Elsevier, K. Vrieze, P. W. N. M. van Leeuwen, C. F. Roobeek, *J. Organomet. Chem.* **1992**, *430*, 357.
[16] A. Dervisi, P. G. Edwards, P. D. Newman, R. P. Tooze, S. J. Coles, M. B. Hursthouse, *J. Chem. Soc. Dalton Trans.* **1999**, 1113.
[17] M. Sperrle, G. Consiglio, *J. Mol. Catal. A* **1999**, *143*, 263.
[18] G. Cavinato, L. Toniolo, *J. Organomet. Chem.* **1990**, *398*, 187.
[19] J. E. Byrd, J. Halpern, *J. Am. Chem. Soc.* **1971**, *93*, 1634.
[20] H. C. Clark, K. R. Dixon, W. J. Jacobs, *J. Am. Chem. Soc.* **1969**, *91*, 1346.
[21] W. P. Mul, H. Oosterbeek, G. A. Beitel, G. J. Kramer, E. Drent, *Angew. Chem.* **2000**, *112*, 1919; *Angew. Chem. Int. Ed.* **2000**, *39*, 1848.
[22] M. J. Green, G. J. P. Britovsek, K. J. Cavell, F. Gerhards, B. F. Yates, K. Frankcombe, B. W. Skelton, A. H. White, *J. Chem. Soc. Dalton Trans.* **1998**, 1137.
[23] P. Braunstein, C. Frison, X. Morise, *Angew. Chem.* **2000**, *112*, 2989; *Angew. Chem. Int. Ed.* **2000**, *39*, 2867.
[24] S. Mecking, L. K. Johnson, L. Wang, M. Brookhart, *J. Am. Chem. Soc.* **1998**, *120*, 888.
[25] E. G. Lundquist, K. Folting, W. E. Streib, J. C. Huffman, O. Eisenstein, K. G. Caulton, *J. Am. Chem. Soc.* **1990**, *112*, 855.
[26] C. S. Shultz, J. Ledford, J. M. DeSimone, M. Brookhart, *J. Am. Chem. Soc.* **2000**, *122*, 6351.
[27] I. del Rio, C. Claver, P. W. M. N. van Leeuwen, *Eur. J. Inorg. Chem.* **2001**, 2719.
[28] K. Vrieze, J. H. Groen, J. G. P. Delis, C. J. Elsevier, P. W. N. M. van Leeuwen, *New J. Chem.* **1997**, *21*, 807.
[29] C. Bianchini, A. Meli, G. Muller, W. Oberhauser, E. Passaglia, *Organometallics* **2002**, *21*, 4965.
[30] W. Clegg, G. R. Eastham, M. R. J. Elsegood, B. T. Heaton, J. A. Iggo, R. P. Tooze, R. Whyman, S. Zacchini, *Organometallics* **2002**, *21*, 1832.
[31] J. Wolowska, G. R. Eastham, B. T. Heaton, J. A. Iggo, C. Jacob, R. Whyman, *Chem. Commun.* **2002**, 2784.
[32] D. Milstein, *Acc. Chem. Res.* **1988**, *21*, 428.
[33] R. I. Pugh, E. Drent, *Catalytic Synthesis of Alkene-Carbon Monoxide Copolymers and Cooligomers, Vol. 27* (Ed.: A. Sen), Kluwer, Dordrecht, **2003**, chap. 2.
[34] R. A. M. Robertson, A. D. Poole, M. J. Payne, D. J. Cole-Hamilton, *Chem. Commun.* **2001**, 47.
[35] F. C. Rix, M. Brookhart, P. S. White, *J. Am. Chem. Soc.* **1996**, *118*, 4746.

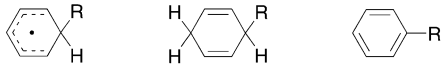
 © 2004 Wiley-VCH Verlag GmbH & Co. KGaA, Weinheim

Radical-Reaction Mechanism

The Mechanism of Bu_3SnH-Mediated Homolytic Aromatic Substitution

Athelstan L. J. Beckwith, Vincent W. Bowry, W. Russell Bowman,* Emma Mann, Jonathan Parr, and John M. D. Storey**

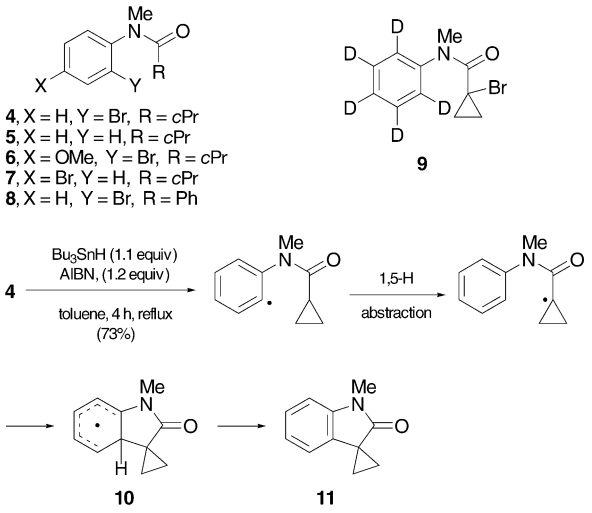
A large and growing number of Bu_3SnH-mediated cyclization reactions which proceed in modest to good yields[1–6] involve intramolecular homolytic aromatic substitution of arenes and heteroarenes. These and similar intermolecular reactions proceed by addition of the initial radicals R$^\bullet$, generated by $Bu_3Sn^\bullet$ radicals, to the aromatic rings (ArH) to yield intermediate substituted cyclohexadienyl radicals ArRH$^\bullet$ **1**. The mechanistic question is how the fully aromatic products ArR **3** are formed in what is formally an oxidation reaction.



1 **2** **3**

There are a number of possible mechanisms by which the conversion of a substituted cyclohexadienyl radical ArRH$^\bullet$ **1** into a substituted arene **3** might occur. Herein we report our attempts to distinguish between them. The first and most obvious possible mechanism involves disproportionation of **1** or hydrogen-atom transfer from Bu_3SnH to afford the intermediate $ArRH_2$ (e.g., **2**) and its isomers, which can then undergo oxidation by the initiator or oxygen on workup. Whilst oxidation during workup may be plausible, dihydro-type systems, such as **2**, are not oxidized rapidly in air.[7] The yields are also higher than 50%, and this rules out disproportionation as the main mechanism.

As a test for H transfer from Bu_3SnH to the π radical **1**, bromo compound **4** (Scheme 1) was converted into the spiro-oxindole **11** by treatment with Bu_3SnD. Under these circumstances any cyclohexadiene derivative formed would bear a



Scheme 1. Synthesis of oxindoles by homolytic aromatic substitution; AIBN = azobisisobutyronitrile.

deuterium substituent and would be expected to give at least some partially deuterated analogue of the product **11**. In the event, careful D NMR spectroscopy of the crude product showed no detectable signal for deuterium attached to an arene, a result that precludes the formation of a dihydro intermediate and suggests that homolytic aromatic substitution is not directly dependent on the use of Bu_3SnH as radical carrier. This conclusion agrees with that of Crich and Hwang,[7] who found that intermediate π radicals in Bu_3SnH-mediated cyclizations could be effectively intercepted by the efficient hydrogen-atom donor PhSeH (with the formation of a dihydro spiro-cyclized product) but not by Bu_3SnH.

Two possible mechanisms are characterized by the production of dihydrogen. One involves the induced decomposition of Bu_3SnH [Eq. (1)], a reaction which has no precedent but appears to be thermodynamically feasible. The other mechanism that we proposed earlier[1,2] involves Bu_3SnH acting as a hydride donor and ArRH$^\bullet$ as a protic acid to give the arene radical anion $[Ar{-}R]^{\bullet-}$ [Eq. (2)]. This can undergo single-electron transfer (SET) to the precursor halide to propagate the chain [Eqs. (3) and (4)], that is, a $S_{RN}1$-type mechanism. The possible occurrence of these reactions was probed by treating the deuterated radical precursor **9** (Scheme 1) with Bu_3SnH to give the corresponding tetradeutero analogue of **11** (66% yield). If the mechanism involves the reactions of either Equation (1) or (2), HD should be formed. However, careful examination of the gaseous products by mass spectrometry, NMR, and Raman spectroscopy failed to detect any HD. We therefore conclude that the mechanism does not involve either of the steps given in Equations (1) and (2).

$$ArRH^{\bullet} + Bu_3SnH \rightarrow Ar{-}R + Bu_3Sn^{\bullet} + H_2 \quad (1)$$

$$ArRH^{\bullet} + Bu_3SnH \rightarrow [Ar\text{-}R]^{\bullet-} + Bu_3Sn^{+} + H_2 \quad (2)$$

$$[Ar{-}R]^{\bullet-} + Ar{-}Br \rightarrow Ar{-}R + [Ar{-}Br]^{\bullet-} \quad (3)$$

$$[Ar{-}Br]^{\bullet-} \rightarrow Ar^{\bullet} + Br^{-} \quad (4)$$

[*] Prof. A. L. J. Beckwith, Dr. V. W. Bowry
Research School of Chemistry, Australian National University
Canberra, ACT 0200 (Australia)
Fax: (+61) 2-6253-0737
E-mail: beckwith@rsc.anu.edu.au
Prof. W. R. Bowman, Dr. E. Mann, Dr. J. Parr
Department of Chemistry, Loughborough University
Loughborough, Leicestershire LE11 3TU (UK)
Fax: (+44) 1509-223-925
E-mail: w.r.bowman@lboro.ac.uk
Dr. J. M. D. Storey
Department of Chemistry, Meston Building
University of Aberdeen, Old Aberdeen AB24 3UE (UK)
Fax: (+44) 1224-272-921
E-mail: j.storey@abdn.ac.uk

Supporting information for this article is available on the WWW under http://www.angewandte.org or from the author.

 DOI: 10.1002/anie.200352419 © 2004 Wiley-VCH Verlag GmbH & Co. KGaA, Weinheim

In a further test for the intermediacy of $[Ar-R]^{\bullet-}$ an equimolar mixture of **4** (X = H) and its *p*-methoxy derivative **6** was treated with 0.5 molar equivalents of Bu_3SnH in the usual way. If the reaction involves chain-propagating electron transfer from the intermediate arene radical anion $[Ar-R]^{\bullet-}$ to Ar–Hal [Eq. (3)], the more readily reduced substrate **4** should be preferentially consumed. In the event, GC analysis of the reaction mixture showed that the two substrates had been consumed to an equal extent. This experiment further confirms that these reactions do not involve the mechanism given in Equations (2)–(4).

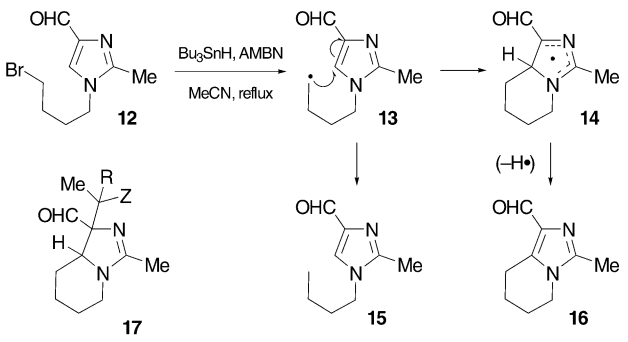
Hydrogen-atom transfer to other radicals present in the reaction mixture [Eq. (5)] is another possibility. If disproportionation between $Bu_3Sn^{\bullet}$ and $ArRH^{\bullet}$ occurs, the reaction should be catalytic in Bu_3SnH. However, when a series of experiments on the cyclization of **12** was conducted with a constant quantity of azobismethylisobutyronitrile (AMBN, 1.0 equiv) and decreasing amounts of Bu_3SnH, the yield of cyclized material dropped steadily (e.g., 2.2 equiv of Bu_3SnH: **16** (92%) and **12** (0%); 0.5 equiv of Bu_3SnH: **16** (0%) and **12** (75%)). These results clearly indicate that Bu_3SnH is not regenerated during the reaction.

$$ArRH^{\cdot} + X^{\cdot} \rightarrow Ar-R + XH \qquad (5)$$

Further experiments were conducted to determine whether radicals $X^{\bullet}$ formed directly from initiators can abstract hydrogen from $ArRH^{\bullet}$ [Eq. (5)]. One involved azobisisobutyronitrile (AIBN)-initiated conversion of the deuterated precursor **9** into the tetradeutero analogue of **11**. Examination of the reaction mixture by GC-MS and D NMR spectroscopy revealed the formation of Me_2CDCN in 23% yield. In another experiment involving di-*tert*-butyl peroxide as initiator and an excess of Bu_3SnH, D NMR spectroscopy of the mixture indicated the presence of both Bu_3SnD and *tert*-BuOD. Both $Bu_3Sn^{\bullet}$ radicals[8] and 2-cyanoprop-2-yl radicals (from AIBN)[9] rapidly quench any traces of oxygen present with formation of the corresponding peroxy radicals, $Bu_3SnOO^{\bullet}$ and $Me_2C(CN)OO^{\bullet}$, which might act as H abstractors. Although all the reaction mixtures were thoroughly deoxygenated with nitrogen gas, studies have shown that traces of oxygen remain unless very special conditions are used.[9] The conversion of **12** into the cyclization product **16** (see Scheme 2) in similar yields when di-*tert*-butyl peroxide or triethylborane (> 1 equiv) was used as the initiator in place of AIBN suggests that *tert*-butoxyl or ethyl radicals, respectively, can carry out the required H abstraction [Eq. (5)].

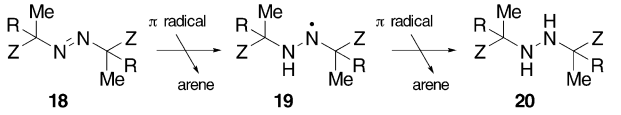
Intermediate π radicals (e.g., **14**) may also couple with other radicals (e.g., to give **17**). For cyclization onto indoles,[6] products from the addition of $Me_2C^{\bullet}CN$ from AIBN breakdown to the π radicals have been isolated and shown to undergo elimination to give the aromatic product.

Common to many[1–4] but not all[5,13] reactions involving radical addition to aromatic systems is the reported need for stoichiometric amounts of initiator. We also found this to be the case by conducting a series of experiments involving the cyclization of **12**[10] (Scheme 2), in which the amount of AMBN (**18**; R = Et, Z = CN; see Scheme 3) was varied while other conditions were kept constant. Analysis of the products by ^{1}H NMR spectroscopy with an internal standard revealed a clear relationship between the yield of cyclized product and the amount of AMBN used (e.g., AMBN: 1.0 equiv, **16** (92%), **12** (0%); 0.5 equiv, **16** (43%), **12** (53%); 0.25 equiv, **16** (8%), **12** (92%)).[10]



Scheme 2. Synthesis of bicyclic imidazole **16**.

Further confirmation of the role of the initiator was obtained when **4** was treated under the standard conditions (110 °C, 240 min) with Bu_3SnH/AIBN (1.2 equiv). The evolution of only 0.3 equivalents of nitrogen indicated that 0.9 equivalents of AIBN was not consumed by breakdown to nitrogen gas and 2-cyano-2-propyl radicals. Nevertheless, careful analysis of reaction mixtures of the Bu_3SnH/AMBN-mediated reaction of **12** by GC-MS and ^{1}H NMR spectroscopy showed no signs of the expected reduction product **20** (R = Et, Z = CN; Scheme 3). An explanation for the non-detection of **20** (R = Et, Z = CN) was obtained when independent synthesis showed it to be extremely unstable. The diester AIBMe (**18**; R = Me, Z = CO_2Me) was also used as initiator, but its reduced form **20** (R = Me, Z = CO_2Me), although a stable compound, also decomposed under our reaction conditions. Further studies on this problem are continuing. Recently the isolation of **20** (R = Me, Z = CO_2Me) from a Bu_3SnH-mediated cyclization onto pyrazole with AIBMe as initiator was reported.[3b]



Scheme 3. Reduction of azo initiators.

These results suggest that in these reactions (Schemes 2 and 3) the initiator is acting as the oxidizing agent. Curran et al.[11] previously reached the same conclusion. Furthermore, dialkyldiazenes (R–N=N–R) have been shown to abstract hydrogen from benzhydryl radicals to yield benzophenone and the corresponding hydrazines,[12] and this supports the possibility that AIBN/AMBN may have a similar role. The intimate details of the mechanism remain obscure. Possibly, a two-step process via an intermediate hydrazyl radical (Scheme 3) is involved, but an SET reaction between AMBN or AIBN and the intermediate cyclohex-

 © 2004 Wiley-VCH Verlag GmbH & Co. KGaA, Weinheim

adienyl π radical to yield the radical anion of AMBN or AIBN or AIBN and a π cation, which would rapidly aromatize with loss of a proton, cannot be ruled out.

The above results indicate that the mechanism of Bu_3SnH-mediated homolytic aromatic substitution does not involve the electron-transfer processes of Equations (3)–(4). It appears therefore that the predominant, although probably not the sole, reaction sequence[6,13] for processes initiated by azo compounds (R′−N=N−R′) is given by Equations (6)–(9)

$$R'' + Bu_3SnH \rightarrow R'H + Bu_3Sn^{\cdot} \quad (6)$$

$$Bu_3Sn^{\cdot} + R{-}Br \rightarrow Bu_3SnBr + R^{\cdot} \quad (7)$$

$$R^{\cdot} + ArH \rightarrow ArRH^{\cdot} \quad (8)$$

$$2\,ArRH^{\cdot} + R'{-}N{=}N{-}R' \rightarrow 2\,ArR + R'NHNHR' \quad (9)$$

When the reaction is initiated by RO$^{\cdot}$ radicals the last step is most likely replaced by that of Equation (5), where X$^{\cdot}$ = RO$^{\cdot}$. Both types of reaction involve the conversion of ArRH$^{\cdot}$ into product in a chain-terminating step.

If these sequences are correct then homolytic aromatic substitution reactions, both intra- and intermolecular, should retard alternative radical processes. This hypothesis was tested in a series of experiments involving stannane-mediated reduction of bromooctane in the presence of **8** (see Scheme 1), which undergoes cyclization. In the absence of other radical processes reduction of bromooctane is first-order in Bu_3SnH and half-order in initiator. However, kinetic analysis of the system involving both reduction of bromooctane and cyclization of **8** with chain termination according to the above mechanism indicated that the initial reaction rate should be proportional to $[\text{initiator}]_{\text{initial}}$ and inversely proportional to $[\mathbf{8}]_{\text{initial}}$. The results of a series of experiments involving mixtures of **8**, 1-bromooctane, Bu_3SnH, and di-*tert*-butyl hyponitrite (BONNOB) in cyclohexane at 45 °C were in full accord with this hypothesis. For example, when the concentrations of the other reactants were kept constant, reactions involving $[\text{BONNOB}]_{\text{initial}} = 4.5$ mM and 1.5 mM gave initial rates of formation of octane of 4.3 and 1.4 μM s^{-1}, respectively. However, when $[\text{BONNOB}]_{\text{initial}}$ was kept at 1.5 mM, initial concentrations of **8** of 11 and 22 mM gave initial rates of formation of octane of 2.8 and 1.5 μM s^{-1}, respectively. The conformity of the observed rates to those expected supports the notion that most, if not all, of the intermediate, substituted cyclohexadienyl radicals formed during the cyclization of **8** undergo termination directly with the initiator or with radicals derived from it.

Finally, the effect of substituted cyclohexadienyl-radical intermediates on the course of a typical stannane-mediated chain reaction was explored by determining the rates of reduction of two typical substrates with Bu_3SnH in benzene and cyclohexane. In the first series of experiments the progress of the AIBN-initiated ($[\text{AIBN}]_{\text{initial}} = 0.1$ mM) reduction of methyl *p*-bromobenzoate with Bu_3SnH at 70 °C in benzene was compared with that of the reaction under the same conditions in cyclohexane. The results revealed that the reaction rate was dramatically retarded in benzene. For example, after heating for 2 h in cyclohexane the yield of methyl benzoate was 97 %; in benzene the yield was 6.5 %. In a second series of experiments with $[\text{AIBN}]_{\text{initial}} = 0.5$ mM it was found that the reduction of 1-bromooctane also occurs more slowly in benzene than in cyclohexane. Thus, after 40 min at 70 °C the yields of octane in cyclohexane and benzene were 80 and 28 %, respectively.

These results, which indicate that the intermediacy of substituted cyclohexadienyl radicals results in chain termination, have implications concerning the choice of conditions for the use of Bu_3SnH and other radical carriers in synthesis. Reactions involving intramolecular homolytic substitution will require larger amounts of initiator and more forcing conditions than usual. More significantly, it appears that arenes, such as benzene, toluene, and *tert*-butylbenzene, are not necessarily the best solvents for reactions involving very low concentrations of substrate, under which conditions homolytic addition to the solvent may compete effectively with the desired chain-transfer processes. In such cases the use of alternative, nonaromatic solvents could be advantageous. Also, it should be noted that although relatively large amounts of initiator are required, the methods described in our earlier reports[1–3] provide efficient routes to compounds such as **11** and **16** that are not easily accessed by other means. In these reactions, the initiator should be regarded as an expendable reagent. Although good chain reactions are desirable, they do not necessarily equate with good synthetic methods. Initial studies with alternative hydride sources to Bu_3SnH, for example, tris(trimethylsilyl)silane and tributylgermanium hydride, implicate the same mechanistic considerations.

Received: July 21, 2003 [Z52419]

Keywords: azo compounds · cyclization · radical reactions · radicals · reaction mechanisms

[1] A. L. J. Beckwith, J. M. D. Storey, *J. Chem. Soc. Chem. Commun.* **1995**, 977–978.
[2] F. Aldabbagh, W. R. Bowman, E. Mann, A. M. Z. Slawin, *Tetrahedron* **1999**, *55*, 8111–8128; W. R. Bowman, H. Heaney, B. M. Jordan, *Tetrahedron* **1991**, *47*, 10119–10128.
[3] a) W. R. Bowman, E. Mann, J. Parr, *J. Chem. Soc. Perkin Trans. 1* **2000**, 2991–2999; b) S. M. Allin, W. R. S. Barton, W. R. Bowman, T. McInally, *Tetrahedron Lett.* **2002**, *43*, 4191–4193.
[4] A detailed list of references is supplied in the Supporting Information. Recent leading references include a) E. Bonfand, L. Forslund, W. B. Motherwell, S. Vázquez, *Synlett* **2000**, 475–478; C. Escolano, K. Jones, *Tetrahedron* **2002**, *58*, 1453–1464; J. Marco-Contelles, M. Rodríguez-Fernández, *Tetrahedron Lett.* **2000**, *41*, 381–384; A. Nunez, A. G. de Viedma, V. Martínez-Barrasa, C. Burgos, J. Alvarez-Builla, *Synlett* **2002**, 1093–1096; Review: A. Studer, M. Bossart in *Radicals in Organic Synthesis, Vol. 2* (Eds.: P. Renaud, M. P. Sibi), Wiley-VCH, Weinheim, **2001**, pp. 62–80.
[5] D. C. Harrowven, B. J. Sutton, S. Coulton, *Tetrahedron* **2002**, *58*, 3387–3400.
[6] M.-L. Bennasar, T. Roca, R. Griera, J. Bosch, *J. Org. Chem.* **2001**, *66*, 7547–7551; M.-L. Bennasar, T. Roca, R. Griera, M. Bassa, J. Bosch, *J. Org. Chem.* **2002**, *67*, 6268–6271.
[7] D. Crich, J.-T. Hwang, *J. Org. Chem.* **1998**, *63*, 2765–2770.

 © 2004 Wiley-VCH Verlag GmbH & Co. KGaA, Weinheim

[8] I. P. Beletskaya, A. S. Sigeev, V. A. Kuzmin, A. S. Tatikolov, L. Hevesi, *J. Chem. Soc. Perkin Trans. 2* **2000**, 107 – 109.
[9] W. K. Busfield, I. D. Jenkins, P. Van Le, *Polym. Bull.* **1997**, *38*, 149 – 155.
[10] See Table 1, Supporting Information.
[11] D. P. Curran, H. Liu, *J. Chem. Soc. Perkin Trans. 1* **1994**, 1377 – 1393; D. P. Curran, H. Yu, H. Liu, *Tetrahedron* **1994**, *50*, 7343 – 7366.
[12] P. S. Engel, W.-X. Wu, *J. Am. Chem. Soc.* **1989**, *111*, 1830 – 1835.
[13] The fact that reactions with iodoarenes[5] have been reported to proceed with substoichiometric amounts of AIBN indicates an alternative mechanism involving SET or possibly C–I homolysis.

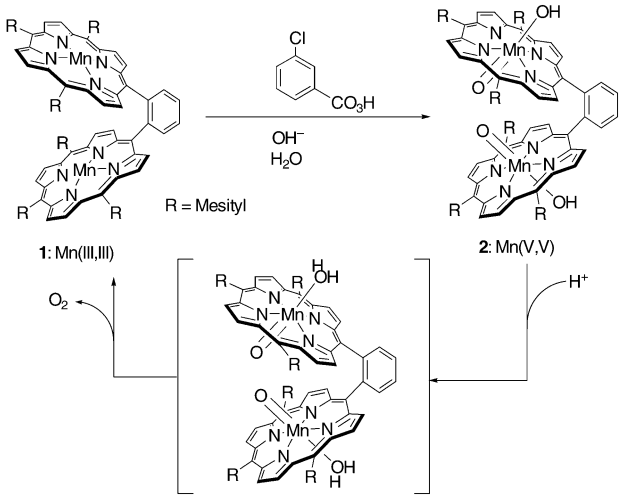
 © 2004 Wiley-VCH Verlag GmbH & Co. KGaA, Weinheim

Oxygen Evolution from Water

Characterization of a Dinuclear Mn^{V}=O Complex and Its Efficient Evolution of O_2 in the Presence of Water**

*Yuichi Shimazaki, Taro Nagano, Hironori Takesue, Bao-Hui Ye, Fumito Tani, and Yoshinori Naruta**

The oxidation of water in the process of dioxygen evolution is catalyzed by an oxygen-evolving complex (OEC) in photosynthesis, which is one of the most important and fundamental chemical processes in nature.[1–3] The active site in a photosynthetic OEC protein contains a tetramanganese cluster,[4] which adopts a Y-shaped geometry as revealed by recent X-ray structure analysis of photosystem II.[5] Though the mechanism of dioxygen evolution has not been determined, the stage of oxygen evolution would involve either a high valent terminal oxo manganese species[3,4,6] or the coupling of bridging oxo units.[2,3] Manganese complexes have been extensively studied as artificial OEC models in structural and functional investigations to understand the mechanism of oxygen evolution from water in photosynthetic OEC.[3] However, only a few Mn complexes that can catalyze homogeneous water oxidation have been reported.[7,8] We have previously reported dimanganese complexes of dimeric tetraarylporphyrins linked by 1,2-phenylene bridge (Scheme 1).[8] The anodic oxidation of an aqueous solution of acetonitrile (5% v/v H_2O in CH_3CN) with the dimanganese tetraarylporphyrin dimer evolved oxygen in the potential



Scheme 1. Structure of Mn_2–dimeric porphyrin complex $[Mn(DTMP)]^{2+}$ (**1**) and a reaction pathway for O_2 formation.

range >1.20 V versus Ag/Ag^+. The catalyst can also oxidize olefins such as cyclooctene to form epoxide with stoichiometric amounts of *m*-chloroperbenzoic acid (*m*CPBA).[9] We proposed that the oxidation of a dimanganese(III) tetraarylporphyrin dimer could give the corresponding high valent Mn=O complex, which is the active species in these oxidation. However, the mechanisms of oxygen evolution and epoxidation, especially the formation of a high-valent Mn=O intermediate have not been fully confirmed. Herein, we report on the oxidation of the dimanganese porphyrin dimer by employing *m*CPBA as an oxidant, and the characterization of the resulting Mn^{V}=O species by spectroscopic methods. Furthermore, oxygen evolution was observed from the Mn^{V}=O species when a small excess of trifluoromethanesulfonic acid (CF_3SO_3H) was added. To the best our knowledge, this is the first clear example of an O–O bond formation involving a Mn^{V}=O species.

The addition of two molar equivalents of *m*CPBA for each Mn ion to the Mn^{III}_2 porphyrin dimer $[Mn_2(DTMP)(OH)]$-$NO_3{\cdot}5H_2O$ (**1**) afforded the Mn^{V}_2 complex **2** (Scheme 1) in CH_2Cl_2/CH_3CN (1:1, v/v) solution that contained 35 equivalents of tetrabutylammonium hydroxide (Bu_4NOH) and 1.0% water at room temperature. Species **2** exhibited a very sharp Soret band centered at 423 nm (Figure 1). When one molar equivalent of 1,1-diphenyl-2-picrylhydrazine (DPPH—a one-electron reductant for each Mn ion) was added to **2**, a Mn^{IV}_2 species **3** was rapidly formed, which has a Soret band centered at 415 nm. Complex **3** was also prepared when one molar equivalent of *m*CPBA for each Mn ion was added to **1** in CH_2Cl_2/CH_3CN (1:4, v/v) solution in the presence of five equivalents of Bu_4NOH, confirmed by UV/Vis spectrum. When the solution of **2** was left stand at room temperature, the Soret band at 423 nm gradually disappeared and a 468 nm band accordingly appeared with isosbestic points indicating

[*] Dr. Y. Shimazaki, T. Nagano, H. Takesue, Dr. B.-H. Ye, Dr. F. Tani, Prof. Dr. Y. Naruta
Institute for Materials Chemistry and Engineering
Kyushu University, Higashi-ku, Fukuoka 812-8581 (Japan)
Fax: (+81) 92-642-2715
E-mail: naruta@ms.ifoc.kyushu-u.ac.jp

[**] This work was supported by Grants-in-Aids for COE Research (08CE2005) and for Scientific Research on Priority Areas (09235225 and 11228207) from MEXT and for Scientific Research (A) (14204073) from JSPS, partly by P&P project, Green Chemistry, of Kyushu University, and a postdoctoral fellowship from JSPS (B.-H. Y.) for which we express our thanks.

Supporting information for this article is available on the WWW under http://www.angewandte.org or from the author.

 © 2004 Wiley-VCH Verlag GmbH & Co. KGaA, Weinheim DOI: 10.1002/anie.200352564

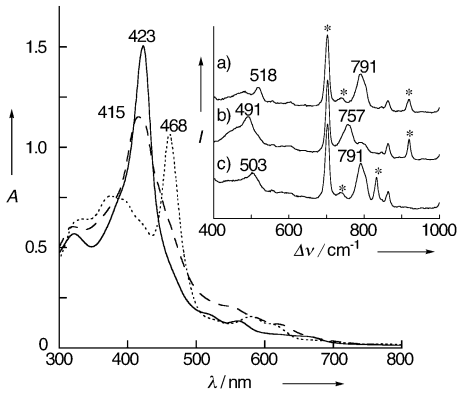


Figure 1. Comparison of the absorption spectra; $\mathbf{1}\cdot NO_3$, ••••; **2**, ——; **3**, – – –. Inset: resonance Raman spectra of **2** (5 °C, $\lambda_{ex} = 413.1$ nm, 20 mW). a) $Bu_4N^{16}OH$ in CH_2Cl_2/CH_3CN, b) $Bu_4N^{18}OH$ in CH_2Cl_2/CH_3CN, c) Bu_4NOD in CH_2Cl_2/CD_3CN. Incubation time of the isotopic experiment was 10 min before the Raman data was collected.

the direct reduction to an Mn^{III}_2 species. The change in absorbance over time at 423 nm at 20 °C showed that the decay of **2** is first-order. The half-life ($t_{1/2}$) of **2** was 3.1 h (the observed decay constant, $k_{obs} = 6.19 \times 10^{-5}\ s^{-1}$), thus implying that **2** was stable at 20 °C.[10–12] The Mn^V_2 species **2** was also stable under similar basic conditions in CH_2Cl_2/CH_3CN (1:3, v/v) solution with 10 % water ($k_{obs} = 3.38 \times 10^{-5}\ s^{-1}$). The stability of **2** is dependent upon the amount of Bu_4NOH. For example, in the presence of five equivalents of Bu_4NOH, the decay constant of **2** $k_{obs} = 5.47 \times 10^{-3}\ s^{-1}$ ($t_{1/2} = 2.1$ min) at 20 °C and furthermore, without the presence of Bu_4NOH, we did not observe the appearance of **2** under oxidation by *m*CPBA. Thus, highly basic conditions are necessary for the formation and the stabilization of **2**.

The ESR spectrum of **3** at 77 K showed $g = 4.5$ and 2.2 (g = the g factor), signals characteristic of a high-spin d^3 Mn^{IV} complex.[13,14] On the other hand, **2** was ESR inactive at 5 K. Though an oxo-bridged dinuclear Mn^{IV} porphyrin complex is ESR inactive,[15] the Mn centers of **1** could not be bridged intra/intermolecularly by an oxo or hydroxo group, because of the steric hindrance of the *meso* mesityl groups.[16] However, some examples of monomeric Mn^V=O complexes have been reported to be diamagnetic species.[10–12] On the basis of these chemical and magnetic studies, we assign the Mn centers of **2** as low-spin, d^2 Mn^V ions.

The resonance Raman spectrum of **2** exhibited two isotope-sensitive intense bands at 791 and 518 cm^{-1} (Figure 1, inset). By replacing $Bu_4N^{16}OH$ in $H_2{}^{16}O$ with $Bu_4N^{18}OH$ in $H_2{}^{18}O$, these bands shifted to 757 and 491 cm^{-1}, respectively. Furthermore, by replacing $Bu_4N^{16}OH$ in $H_2{}^{16}O$ with $Bu_4N^{16}OD$ in $D_2{}^{16}O$, the 518 cm^{-1} band shifted to 503 cm^{-1}, while the 791 cm^{-1} band did not shift. The observed isotopic shifts of 34 and 27 cm^{-1} with ^{18}O-substitution and 15 cm^{-1} with OD-substitution are in good agreement with the calculated values (^{18}O, 35 and 22 cm^{-1}; OD, 11 cm^{-1}) from the harmonic oscillator approximation of Mn^V=O and Mn^V–OH stretching vibrations. Therefore, the 791 and 518 cm^{-1} bands are assigned to $\nu(Mn^V{=}O)$ and $\nu(Mn^V{-}OH)$, respectively, thus indicating that each Mn center of **2** is six-coordinate HO–Mn^V=O. The observed Mn^V=O stretching frequency is higher than that of $[Mn^{IV}(O)(OH)(TMP)]^-$ (712 cm^{-1}; TMP = tetramesitylporphyrin),[14] thus indicating the Mn^V=O bond is stronger than Mn^{IV}=O. On the other hand, $\nu(Mn^V{\equiv}O)$ of a Mn tetraamide complex (979 cm^{-1}) is much higher than the present value,[12] which shows that the manganese–oxo bond of **2** is much weaker than that of the tetraamide complex, presumably because of the effect of the *trans*-hydroxo ligand in **2**. Although ^{16}O-*m*CPBA was used as an oxidant in the ^{18}O-labeled experiment, the isotopic shifts were observed, because of facile exchange of the oxo and hydroxo oxygen atoms with oxygen atoms of H_2O and OH^-. Oxo–hydroxo tautomerism, that is, conversion of oxo to the hydroxo moiety, would proceed through a hydrogen-bonded water molecule in a concerted fashion.[17] Consequently, oxo and hydroxo groups could exist both inside and outside of the cavity in the tautomeric process.

The monomeric Mn^V=O porphyrin species can exist only for a few seconds or minutes, whereas **2** is stable for several hours.[10–12] Actually, we could not observed a stable Mn^V=O(TMP) complex under the same conditions used for **2**. The higher stability of **2** than that of Mn^V=O(TMP) complex is due to its characteristic structure.[16] The present dimeric complex has a hydrophobic cavity surrounded by the porphyrin rings and the bulky *meso* mesityl groups, which could protect the inside oxo groups.

When 40 equivalents of CF_3SO_3H for each manganese ion was added to the HO–Mn^V=O species **2** in CH_2Cl_2/CH_3CN (1:3, v/v) solution that contained 10 % water, the Mn^V species was spontaneously reduced to Mn^{III} within a few seconds and O_2 evolution was observed under an Ar atmosphere. The yield of the evolved O_2 was determined by mass spectrometry to be 92 % with respect to complex **2**, based on the assumption that each $[Mn^V{=}O]_2$ complex gives one O_2 molecule (Figure 2). Upon ^{18}O-substitution of water and hydroxide,

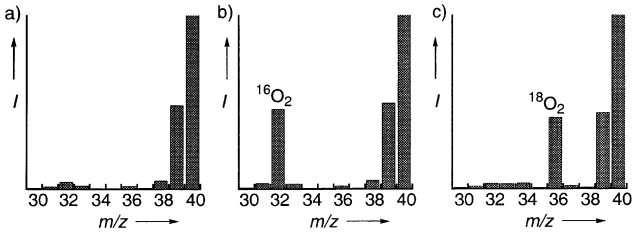


Figure 2. Mass spectrometric gas analysis upon the addition of CF_3SO_3H to **2** under an Ar atmosphere. a) Before addition of CF_3SO_3H to **2**, b) addition of 40 equiv CF_3SO_3H to **2** in $H_2{}^{16}O/{}^{16}OH^-$, c) addition of 40 equiv CF_3SO_3H to **2** in $H_2{}^{18}O/{}^{18}OH^-$.

$^{18}O_2$ was observed to evolve in a yield greater than 90 %. Furthermore, the mixture of $^{16}O_2$, $^{16}O^{18}O$, and $^{18}O_2$ was observed in a statistical distribution, when the mixture of $^{16}OH^-$ in $H_2{}^{16}O$ and $^{18}OH^-$ in $H_2{}^{18}O$ was employed. The ratio of $^{16}O_2$:$^{16}O^{18}O$:$^{18}O_2$ was in good agreement with the calculated value from the applied isotopic ratio of ^{16}O:^{18}O in water and hydroxide anion (for example, the observed ratio of $^{16}O_2$:$^{16}O^{18}O$:$^{18}O_2{}^{16}O = 4:42:54$, the calculated ratio of

 © 2004 Wiley-VCH Verlag GmbH & Co. KGaA, Weinheim

$^{16}O_2$:$^{16}O^{18}O$:$^{18}O_2{}^{16}O = 9:42:49$ from the applied isotopic ratio of ^{16}O:$^{18}O = 3:7$ in water and hydroxide anion). These results indicated quantitative incorporation of oxygen atoms from H_2O and OH^- into the evolved O_2. On the other hand, no O_2 evolution was detected on the controlled experiment with a $Mn^{IV}{}_2$ species **3**. It was reported that $H_2O{-}Mn^V{=}O$ can oxidize halide anion through an oxo-transfer reaction.[11] Indeed, upon protonation, **2** quantitatively oxidized Cl^- into ClO^- by an attack of the $Mn^V{=}O$ moiety on Cl^-, whereas without protonation, Cl^- oxidation could not be observed. Thus, the protonation on **2** could form a transient intermediate, such as $(H_2O{-}Mn^V{=}O)_2$. The O–O bond formation would occur by the attack of the $H_2O{-}Mn^V{=}O$ group on water, or by a coupling reaction between the oxo groups of each $Mn^V{=}O$ unit. Furthermore, as decomposition of the Mn complex was not detected in the stoichiometric reaction presented herein, the interconversion between **1** and **2** can be extended to a catalytic cycle.

In conclusion, we have characterized the $Mn^V{=}O$ porphyrin dimer as a key intermediate of the O_2 evolution in detail. The reaction of the $Mn^{III}{}_2$ complex **1** with *m*CPBA under strong basic conditions gave the stable diamagnetic $Mn^V{}_2$ intermediate **2**, which has oxo and hydroxo axial ligands derived from water and/or hydroxide ions. Addition of a small excess amount of acid to **2** rapidly afforded a $Mn^{III}{}_2$ species, and dioxygen was evolved quantitatively. Further studies on the mechanism of this oxygen evolution catalyzed by the dimanganese tetraarylporphyrin dimer are in progress in our laboratory.

Received: August 4, 2003 [Z52564]

Keywords: manganese · O ligands · oxidation · oxygen · porphyrinoids

[1] a) W. Ruettinger, G. C. Dismukes, *Chem. Rev.* **1997**, *97*, 1; b) R. Manchanda, G. W. Brudvig, R. H. Crabtree, *Coord. Chem. Rev.* **1995**, *144*, 1; c) T. J. Meyer, *Acc. Chem. Res.* **1989**, *22*, 163; d) A. J. Bard, M. A. Fox, *Acc. Chem. Res.* **1995**, *28*, 141.

[2] V. L. Pecoraro, M. J. Baldwin, A. Gelasco, *Chem. Rev.* **1994**, *94*, 807.

[3] M. Yagi, M. Kaneko, *Chem. Rev.* **2001**, *101*, 21.

[4] a) G. C. Dismukes, Y. Siderer, *Proc. Natl. Acad. Sci. USA* **1981**, *66*, 706; b) G. C. Dismukes, K. Ferris, P. Watnick, *Photobiochem. Photobiophys.* **1982**, *3*, 243.

[5] a) A. Zouni, H. T. Witt, J. Kern, P. Fromme, N. Krab, W. Saenger, P. Orth, *Nature* **2001**, *409*, 739; b) N. Kamiya, J.-R. Shen, *Proc. Natl. Acad. Sci. USA* **2003**, *100*, 98.

[6] a) C. W. Hoganson, G. T. Babcock, *Science* **1997**, *277*, 1953; b) J. Messinger, M. Badger, T. Wydrzynski, *Proc. Natl. Acad. Sci. USA* **1995**, *92*, 3209; c) V. L. Pecoraro, M. J. Baldwin, M. T. Caudle, W. Hsieh, N. A. Law, *Pure Appl. Chem.* **1998**, *70*, 925; d) M. L. Gilchrist, J. A. Ball, D. W. Randall, R. D. Britt, *Proc. Natl. Acad. Sci. USA* **1995**, *92*, 9545; e) P. E. M. Siegbahn, R. H. Crabtree, *J. Am. Chem. Soc.* **1999**, *121*, 117.

[7] a) J. Limburg, J. S. Vrettos, L. M. Liable-Sands, A. L. Rheingold, R. H. Crabtree, G. W. Brudvig, *Science*, **1999**, *283*, 1524; b) W. Ruettinger, M. Yagi, K. Wolf, G. C. Dismukes, *J. Am. Chem. Soc.* **2000**, *122*, 10353; c) J. Limburg, J. S. Vrettos, H. Y. Chen, J. C. de Paula, R. H. Crabtree, G, W, Brudvig, *J. Am. Chem. Soc.* **2001**, *123*, 423.

[8] Y. Naruta, M. Sasayama, T. Sasaki, *Angew. Chem.* **1994**, *106*, 1964; *Angew. Chem. Int. Ed. Engl.* **1994**, *33*, 1839.

[9] K. Ichihara, Y. Naruta, *Chem. Lett.* **1998**, 185.

[10] a) J. T. Groves, J. Lee, S. S. Marla, *J. Am. Chem. Soc.* **1997**, *119*, 6269; b) N. Jin, J. T. Gloves, *J. Am. Chem. Soc.* **1999**, *121*, 2923.

[11] N. Jin, J. L. Bourassa, S. C. Tizio, J. T. Groves, *Angew. Chem.* **2000**, *112*, 4007; *Angew. Chem. Int. Ed.* **2000**, *39*, 3849.

[12] a) T. J. Collins, R. D. Powell, C. Slebodnick, E. S. Uffelman, *J. Am. Chem. Soc.* **1990**, *112*, 899; b) F. M. MacDonnell, N. L. P. Fackler, C. Stern, T. V. O'Halloran, *J. Am. Chem. Soc.* **1994**, *116*, 7431; c) C. G. Miller, S. W. Gordon-Wylie, C. P. Horwitz, S. A. Strazisar, D. K. Periano, G. R. Clark, S. T. Weintraub, T. J. Collins, *J. Am. Chem. Soc.* **1998**, *120*, 11540; d) Z. Gross, G. Golubkov, L. Simkhovich, *Angew. Chem.* **2000**, *112*, 4211; *Angew. Chem. Int. Ed.* **2000**, *39*, 4045; e) B. S. Mandimutsira, B. Ramdhanie, R. C. Todd, H. L. Wang, A. A. Zareba, R. S. Czemuszewicz, D. P. Goldberg, *J. Am. Chem. Soc.* **2002**, *124*, 15170.

[13] Y. Naruta, M. Sasayama, K. Ichihara, *J. Mol. Catal. A* **1997**, *117*, 115.

[14] a) J. T. Groves, M. K. Stern, *J. Am. Chem. Soc.* **1988**, *110*, 8628; b) Y. Oliver Su, M. K. Stern, K. A. Macor, D. Kim, J. T. Groves, T. G. Spiro, *J. Am. Chem. Soc.* **1988**, *110*, 4158.

[15] J. A. Smegal, C. L. Hill, *J. Am. Chem. Soc.* **1983**, *105*, 3515.

[16] Since the metal complexes of DTMP ligand have a long metal-metal distance (> 6 Å) and a rigid framework against inward bending, the Mn cernters cannot be bridged by a coordinated oxo or hydroxo anion, see Y. Shimazaki, H. Takesue, T. Chishiro, F. Tani, Y. Naruta, *Chem. Lett.* **2001**, 538.

[17] J. Bernadou, B. Meunier, *Chem. Commun.* **1998**, 2167.

 © 2004 Wiley-VCH Verlag GmbH & Co. KGaA, Weinheim

Supramolecular Materials

Design and Fabrication of a Flexible and Self-Supporting Supramolecular Film by Hierarchical Control of the Interaction between Hydrogen-Bonded Sheet Assemblies**

*Isao Yoshikawa, Jun Li, Yuka Sakata, and Koji Araki**

Structural hierarchy is found in highly ordered protein structures and other biological systems, which offer excellent examples for the design and construction of macroscale supramolecular structures by self-assembly through formation of noncovalent bonds.[1] Relatively strong, directional intermolecular interactions, such as hydrogen bonding and

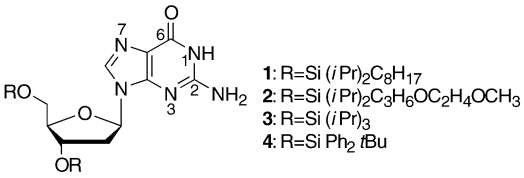
[*] I. Yoshikawa, J. Li, Y. Sakata, Prof. K. Araki
Institute of Industrial Science
University of Tokyo
4-6-1 Komaba, Meguro-ku, Tokyo 153-8505 (Japan)
Fax: (+81) 3-5452-6364
E-mail: araki@iis.u-tokyo.ac.jp

[**] This work was partly supported by a Grant-in-Aid for Scientific Research (grant nos. 14045211 and 14350482) from the Ministry of Education, Science, Sports, and Culture, Japan.

 © 2004 Wiley-VCH Verlag GmbH & Co. KGaA, Weinheim DOI: 10.1002/anie.200352641

coordination, have been effectively used for the construction of well-defined nanometer-scale or mesoscopic assemblies on the molecular level, and various patterns of nanoassemblies have been reported.[2] However, the self-association and self-organization of nanoassemblies into macroscale organized structures are not yet clearly understood since various thermodynamic and kinetic contributions are intricately intertwined in these processes. Therefore, the design and fabrication of materials as macroscale fibers[3] or films,[4] and in other three-dimensional shapes[2,5] with well-defined supramolecular structures are challenging targets and have been attracting much attention. Though supramolecular films can be assembled by stacking mesoscopic two-dimensional sheet assemblies, only a limited number of reports have appeared so far that relate to self-supporting and flexible films.[6] Herein, we report the fabrication of a self-supporting and flexible supramolecular film with a well-defined structural hierarchy through the design of alkylsilylated guanosine derivatives with appropriate molecular structures. Hierarchical control of the stacking of the mesoscopic sheetlike assemblies formed by multiple hydrogen bonds was achieved by tuning the interaction between the sheet assemblies.

In our efforts to develop artificial nucleoside-based supramolecular materials, we found that alkylsilylated guanosine derivative **1** (Scheme 1) showed excellent gelation



Scheme 1. Chemical structures of trialkylsilyl guanosine derivatives.

with alkanes through the formation of a unique sheetlike assembly[7] in which different hydrogen bonds operate on different hierarchical levels. Double interbase hydrogen bonds from 2-NH_2 to 6-C=O and 1-NH to 7-N lead to the formation of a one-dimensional tape motif (Figure 1a) commonly found for guanosine derivatives.[3c,8] Additional double hydrogen bonds between 2-NH_2 and 3-N connect these tapes to form the two-dimensional sheetlike assembly (Figure 1b). The intertape hydrogen bonds were cleaved selectively on heating, with a concomitant gel-to-liquid-crystal phase transition. The one-dimensional tape motif

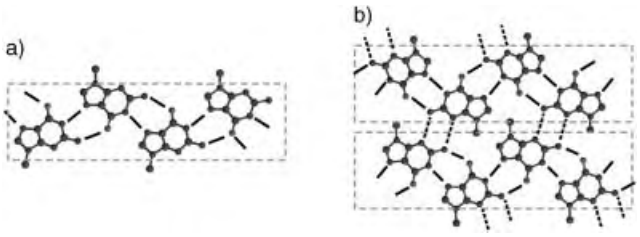


Figure 1. a) Tape motif and b) sheetlike hydrogen bond network structures.

formed by the intratape hydrogen bonds was preserved in the liquid-crystal state, which confirms the hierarchy of the intra- and intertape hydrogen bonds. Hierarchical control of the two-dimensional sheet assembly was thus achieved. Our next target was to construct a three-dimensional macroscale structure from the two-dimensional sheets by tuning the intersheet interactions. For this purpose we introduced oxyethylene groups at the ends of the alkylsilyl moieties to give guanosine derivative **2**. This molecular design was expected to result in situation of the oxyethylene groups at the sheet surface and an increase in the intersheet interaction.

Unlike **1**, nucleoside derivative **2** showed no ability to gelate with alkanes or other common solvents. However, the formation of a flexible translucent film was observed at an air–water interface when dimethylformamide (DMF)/water (1:19 (v/v)) was used as a solvent in the gelation test. Translucent films 0.02–0.10-mm thick were also obtained by casting methanol, ethyl acetate, chloroform, and benzene solutions of **2** (5% (wt/wt)) onto a flat and smooth teflon plate, with subsequent air-drying and removal from the teflon plate. Unlike Langmuir–Blodgett (LB) films or other films made from low-molecular-weight compounds, the films obtained by this method retained their shape without any support. The spectral and thermal properties of films prepared from different solvents were nearly identical. A similar translucent film was formed by casting onto a glass plate instead of the teflon plate, but it could not be removed from the glass surface. An attempt to fabricate a self-supporting film of **1** by the same procedure was unsuccessful and produced a waxy solid after complete evaporation of the solvent.

The tensile strength of the self-supporting films was 0.51 ± 0.03 MPa, with an average elongation at break of 2.1 ± 0.4% (20 samples). Although this tensile strength is smaller than that of common polymer films, the obtained films were sufficiently stable and flexible to allow bending (Figure 2). No

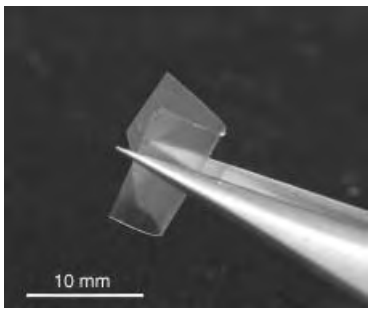


Figure 2. The self-supporting film of **2** produced from an ethyl acetate solution (5% wt/wt). The film thickness was about 0.03 mm.

crystallization was observed with time except when acetone was used as the cast solvent, and the films retained their flexible nature for at least six months at room temperature. No weight loss was observed by thermogravimetry differential thermal analysis below its decomposition temperature ($>200\,^{\circ}C$), which shows that solvent molecules are not incorporated in the films. Solvent peaks were not observed

 © 2004 Wiley-VCH Verlag GmbH & Co. KGaA, Weinheim

in the IR and ^{1}H NMR spectra of the films, which confirms the absence of solvent molecules within the structures.

Figure 3 shows differential scanning calorimetry (DSC) curves of a cast film. The first heating curve of the film (Figure 3a) shows an endothermic peak at 115 °C, at which

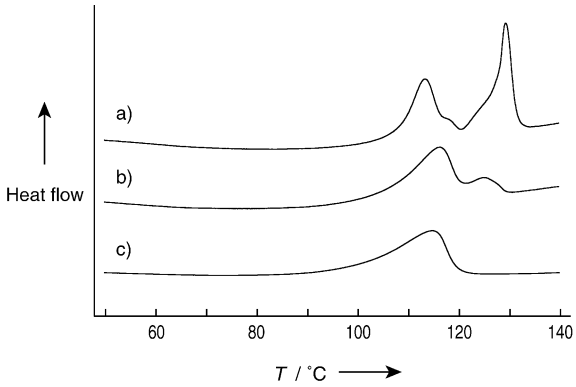


Figure 3. DSC curves of the cast film of **2** upon heating for a) the first, b) the second, and c) the fourth time.

temperature the film became turbid and fragile. The sharp endothermic peak observed at 130 °C is the melting point of the film, and the sample became a colorless isotropic liquid at this temperature. These peaks were not clearly separated in the second heating curve, and only a broad melting peak was observed at 110–120 °C after repeated heating/cooling cycles (Figure 3c).

The hydrogen-bonding pattern in the cast film was studied by temperature-controlled IR spectrometry. Crystals of **3** and **4**, whose structures were established by X-ray crystallography,[7] were used as the reference samples and have sheetlike two-dimensional (Figure 1b) and tapelike one-dimensional (Figure 1a) hydrogen bonding network structures, respectively. The spectrum of the film at room temperature (Figure 4b) was similar to that of **3**, with the 2-NH_2 deformation peak at 1648 cm^{-1} and no free-NH stretching peak at 3495 cm^{-1}. This observation indicates that the two-dimensional hydrogen-bonding network was the dominant structure in the film. Therefore, introduction of the oxyethylene units had little effect on the hydrogen-bonding pattern of the guanine moieties, and the hydrogen-bonded sheet assemblies were preserved in the cast film of **2**. A shift of the 2-NH_2 deformation peak from 1648 to 1630 cm^{-1} and a slight increase in the free-NH stretching peak at 3495 cm^{-1} were observed at around 110 °C (Figure 4c). These peaks are characteristic of the spectrum of **4** (Figure 4d), which suggests that selective cleavage of the intertape hydrogen bonds had occurred to some extent. This temperature corresponds to the first endothermic peak in the first DSC heating curve (Figure 3a). A similar endothermic peak was also observed at the temperature resulting in selective cleavage of the intertape hydrogen bonds for the **1**/dodecane system.[7]

Figure 5 shows the X-ray diffraction pattern of the cast film seen when the incident beam is parallel to the film surface. Fanlike diffraction was observed in the directions normal to the film surface (Figure 5b), which indicates the

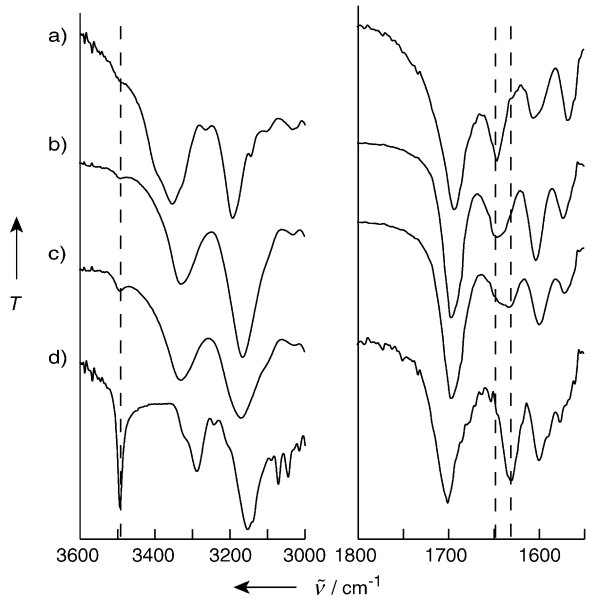


Figure 4. IR spectra of the cast film of **2** and two reference compounds. a) reference compound **3**; b) the cast film of **2** at room temperature; c) the cast film of **2** at 120 °C; d) reference compound **4**. The dashed lines highlight 3495, 1650, and 1629 cm^{-1}.

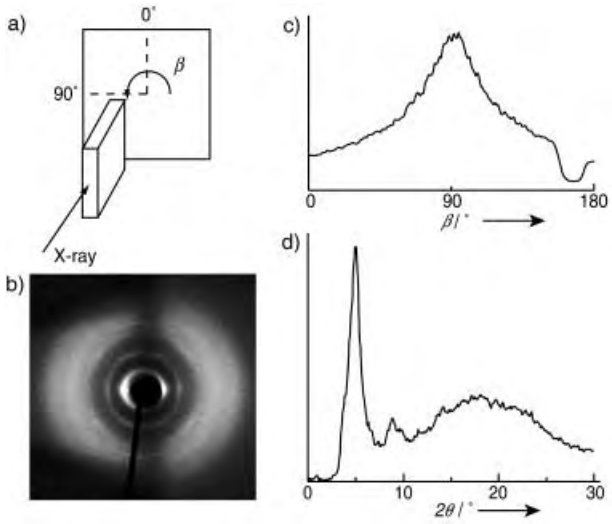


Figure 5. X-Ray diffraction pattern of the cast film of **2**. a) Schematic view of the sample set-up. b) Diffraction pattern collected at the imaging plate. The diffraction profiles along c) the β direction at $2\theta = 4.5$–$5.5°$ and d) the 2θ direction at $\beta = 90°$ are shown.

presence of a lamella-like structure aligned parallel to the film surface. A peak appeared at $2\theta = 4.45°$ ($d = 1.98$ nm), and no additional peak was observed in the smaller-angle range ($0.1° < 2\theta < 4.45°$). The thickness of the hydrogen-bonded sheet in the **1**/dodecane gel was measured by AFM to be 2.5 nm,[7] which corresponds to the sheet assembly with fully extended alkyl chains. In the case of the cast film of **2**, stronger intersheet interaction caused stacking of the sheets. Therefore, the alkylsilyl moieties at the sheet surface might be partially interdigitated with those of the adjacent sheets and/or highly tilted.

 © 2004 Wiley-VCH Verlag GmbH & Co. KGaA, Weinheim

The well-defined hierarchical structure in the supramolecular film of **2** was thus established. The one-dimensional tape motifs formed by interbase double hydrogen bonds are connected by double intertape hydrogen bonds to form two-dimensional sheet assemblies, and polar intersheet interaction allows fabrication of the flexible, self-supporting film.

Intersheet interaction between the nonpolar surfaces is likely to be limited to van der Waals interaction since the sheet assembly of **1** has its alkyl end groups at the sheet surface. The weak intersheet interaction allowed the penetration of solvent molecules between these sheets and the assembly showed excellent gelation with alkanes (Figure 6a).

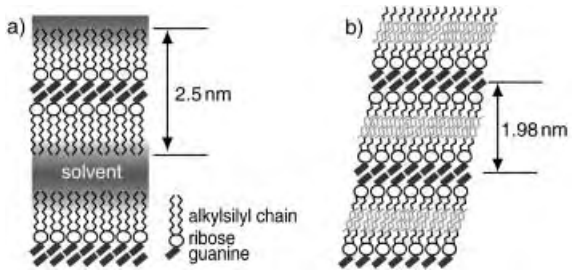


Figure 6. Schematic representation of a) the **1**/alkane gel and b) the cast film of **2**.

However, the intersheet interaction was not strong enough for the fabrication of a self-supporting film and only a waxy solid was produced. In the case of **2** (Figure 6b), stronger intersheet interaction resulted from the introduction of the polar oxyethylene groups at the sheet surface and contributed to the stacking of the sheets to form a lamella-like structure. Thus, a flexible, self-supporting film was obtained. Solvent molecules could no longer penetrate into the space between these sheets and **2** had no gelation ability. The introduction of the polar oxyethylene units had little effect on the hydrogen-bonded sheet assembly, which establishes the hierarchical structure of the film.

The hierarchical control of the interaction between well-defined nanometer-scale and mesoscopic assemblies can cause drastic changes in macroscale shape and properties and allows fabrication of a flexible and self-supporting film. This approach is therefore a promising example of the design and fabrication of supramolecular materials.

Experimental Section

2 was prepared according to the procedure reported previously for similar compounds.[9] 4,7-Dioxaoct-1-ene[9a] (8.12 g, 70 mmol) and a small amount of H_2PtCl_6 (< 1 mg) was heated to 100 °C in an N_2 atmosphere. Chlorodiisopropylsilane (10 mL, 59 mmol) was added dropwise and the mixture stirred overnight. After cooling the mixture, the products with low-boiling points were removed (75 Torr, 80 °C) and the residue (6.12 g) was used without further purification. 2′-Deoxyguanosine (1.22 g, 4.6 mmol), imidazole (3.12 g, 45 mmol), and DMF (4.6 mL) were added and the mixture was stirred overnight (N_2, RT). A chloroform solution of the mixture was washed three times with water and purified by column chromatography (Merck silica gel 60, ethanol/chloroform (1:30 v/v)) to give **2** as a white solid (1.08 g, 1.5 mmol). ^{1}H NMR (400 MHz, $CDCl_3$, 25 °C, tetramethylsilane): $\delta = 0.64$ (m, 4H), 0.9–1.2 (m, 28H), 1.68 (m, 4H), 2.38 (m, 1H), 2.56 (m, 1H), 3.3–3.7 (m, 18H), 3.80 (d, 2H), 4.01 (s, 1H), 4.65 (s, 1H), 6.24 (t, 1H), 6.31 (br s, 2H), 7.75 (s, 1H), 12.02 ppm (br s, 1H); elemental analysis: calcd for $C_{34}H_{65}N_5O_8Si_2$: C 56.09, H 9.00, N 9.62 %; found: C 55.95, H 8.72, N 9.94 %; HRMS (FAB): calcd for $C_{34}H_{66}N_5O_8Si_2$ $[M-H]^+$: 728.4449; found: 728.4436.

The ^{1}H NMR spectrum was recorded on a JEOL AL400 spectrometer operating at 400 MHz. The thermal properties were measured on a Rigaku TG8120 or a Perkin-Elmer Pyris 1 DSC instrument. A JEOL WINSPEC100 instrument with an IR-MAU300 infrared microscopy unit and a Mettler FP-800 thermosystem was used for temperature-controlled IR measurements. IP images of X-ray diffraction patterns were obtained with a MAC Science DIP Labo imaging-plate system. Small-angle X-ray scattering data were collected with a Rigaku RINT2500V diffractometer in the range $0.1° < 2\theta < 10°$. The tensile strength of the film was measured by a Tensilon model UTM-II instrument (Toyo Keisoku Kiki Co.) with a cross-head speed of 0.4 mm min^{-1}.

Received: August 13, 2003 [Z52641]

Keywords: hydrogen bonds · nucleosides · self-assembly · supramolecular chemistry · thin films

[1] a) J.-M. Lehn, *Supramolecular Chemistry*, VCH, Weinheim, **1995**; b) *Supramolecular Materials and Technologies* (Ed.: D. N. Reinhoudt), Wiley, Chichester, **1999**.

[2] a) G. R. Desiraju, *Angew. Chem.* **1995**, *107*, 2541; *Angew. Chem. Int. Ed. Engl.* **1995**, *34*, 2311; b) B. Moulton, M. J. Zaworotko, *Chem. Rev.* **2001**, *101*, 1629; c) T. Kato, N. Mizoshita, K. Kanie, *Macromol. Rapid Commun.* **2001**, *22*, 797; d) L. Brunsveld, B. J. B. Folmer, E. W. Meijer, R. P. Sijbesma, *Chem. Rev.* **2001**, *101*, 4071.

[3] a) C. B. St. Pourcain, A. C. Griffin, *Macromolecules* **1995**, *28*, 4116; b) R. K. Castellano, R. Clark, S. L. Craig, C. Nuckolls, J. Rebek, Jr., *Proc. Natl. Acad. Sci. USA* **2000**, *97*, 12418; c) K. Araki, R. Takasawa, I. Yoshikawa, *Chem. Commun.* **2001**, 1826; d) R. Takasawa, K. Murota, I. Yoshikawa, K. Araki, *Macromol. Rapid Commun.* **2003**, *24*, 335; e) V. Berl, M. Schmutz, M. J. Krische, R. G. Khoury, J.-M. Lehn, *Chem. Eur. J.* **2002**, *8*, 1227; e) T. Shimizu, *Macromol. Rapid Commun.* **2002**, *23*, 311.

[4] a) A. Ulman, *An Introduction to Ultrathin Organic Films: from Langmuir-Blodjett to Self-Assembly*, Academic Press, Boston, **1991**; b) A. Sautter, C. Thalacker, B. Heise, F. Würthner, *Proc. Natl. Acad. Sci. USA* **2002**, *99*, 4993; c) K. Ariga, J. Kikuchi, M. Naito, E. Koyama, N. Yamada, *Langmuir* **2000**, *16*, 4929; d) I. K. Iverson, S. M. Casey, W. Seo, S.-W. Tam-Chang, B. A. Pindzola, *Langmuir* **2002**, *18*, 3510.

[5] a) O. Ikkala, G. ten Brinke, *Science* **2002**, *295*, 2407; b) G. Ungar, Y. Liu, X. Zeng, V. Percec, W.-D. Cho, *Science* **2003**, *299*, 1208; c) C.-S. Lee, N. Kimizuka, *Proc. Natl. Acad. Sci. USA* **2002**, *99*, 4922.

[6] T. Kunitake, *Angew. Chem.* **1992**, *104*, 692; *Angew. Chem. Int. Ed. Engl.* **1992**, *31*, 709.

[7] T. Sato, M. Seko, R. Takasawa, I. Yoshikawa, K Araki, *J. Mater. Chem.* **2001**, *11*, 3018.

[8] a) U. Thewalt, C. E. Bugg, R. E. Marsh, *Acta Crystallogr. Sect. B* **1970**, *26*, 1089; b) C. C. Wilson, J. N. Low, P. Tollin, *Acta Crystallogr. Sect. C* **1985**, *41*, 1123; c) T. Giorgi, F. Grepioni, I. Manet, P. Mariani, S. Masiero, E. Mezzina, S. Pieraccini, L. Saturni, G. P. Spada, G. Gottarelli, *Chem. Eur. J.* **2002**, *8*, 2143.

[9] a) L. Boksányi, O. Liardon, E. Kováts, *Helv. Chim. Acta* **1976**, *59*, 717; b) K. K. Ogilvie, A. L. Schifman, C. L. Penny, *Can. J. Chem.* **1979**, *57*, 2230.

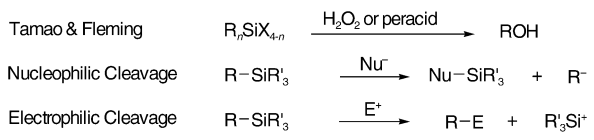
 © 2004 Wiley-VCH Verlag GmbH & Co. KGaA, Weinheim

Synthesis of Silalactones

Electrophilic Cleavage of One Silicon–Carbon Bond of Pentacoordinate Tetraorganosilanes: Synthesis of Silalactones**

Mitsuru Shindo, Kenji Matsumoto, and Kozo Shishido*

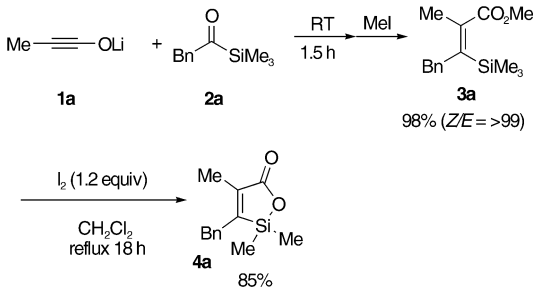
The cleavage of silicon–carbon bonds is an important process in synthetic organic chemistry.[1] The Tamao–Fleming oxidation[2] is one general method for peroxide oxidation of organosilicon bearing at least one heteroatom or aromatic group, sometimes with the aid of a fluoride ion. In addition to the several published reports on intramolecular nucleophilic attack of an oxyanion on silicone leading to demethylation[3] or dephenylation,[4] there have also been some examples of electrophilic cleavage under strongly acidic conditions or by using fluorosilicates.[5] However, the selective cleavage of one carbon–silicon bond, especially the C(sp^3)–Si bond, in a tetraorganosilane is a challenging problem that has yet to be solved. Herein, we describe the direct electrophilic cleavage of one silicon–carbon bond activated by intramolecular pentacoordination of carbonyl oxygen, thus leading to the novel synthesis of silalactones (Scheme 1).



Scheme 1. Cleavage of Si–C bonds.

In the course of our studies on ynolates (**1**),[6] we found that a highly stereoselective olefination of acylsilanes (**2**) afforded (*Z*)-β-trialkylsilylacrylates (**3**).[7] When the desilyliodination of the acrylic acid ester **3a** upon treatment with iodine was attempted, the desired β-iodoacrylate was not produced at all, but the unexpected 2*H*-[1,2]oxasilol-5-one (silalactone **4a**) was obtained in good yield (Scheme 2).

Silalactone **4a** was also obtained by using (*Z*)-β-trialkylsilylacrylic acid **5** as the substrate in the presence of iodine and pyridine under reflux in CCl_4 (Table 1). The fact that one equivalent of iodomethane was generated indicated that the



Scheme 2. The unexpected formation of silalactone **4a** by the cleavage of a Si–C bond.

silicon–carbon bond was cleaved electrophilically by iodine. This is one of only a few examples of direct electrophilic C(sp^3)–Si bond cleavage. These results prompted us to examine the generality of this oxidation reaction by using various types of (*Z*)-β-silyl-α,β-unsaturated acids.

As shown in Table 1, the silalactones were obtained in good to excellent yields using the acrylic acids bearing several types of substituents, including *o*-silylbenzoic acids. When *N*-iodosuccinimide (NIS) was used in place of iodine, the reaction proceeded faster at room temperature (entry 2, Method B), but in some cases, lower yields were obtained (entry 8). The ethyl, isopropyl, and phenyl groups, as well as the methyl group, were also cleaved (entries 4, 5 and 6). Since the substrate that have a terminal alkenyl group also furnished the silalactone **4h** (entry 10), the cleavage of the Me–Si bond proceeds faster than the iodination of the olefins. The methoxy and siloxy substituents were stable under these reaction conditions (entries 9 and 11). In the reaction of the substrate bearing the *tert*-butyldimethylsilyl group, the methyl group was selectively cleaved (entries 3 and 9). It is noteworthy that the methyl group rather than the phenyl group was selectively cleaved (entry 13).

The X-ray crystal structures[8] of (*Z*)-β-trimethylsilyl-α-methylcinnamic acid (**5f**) may explain why the carbon–silicon bonds are unusually activated (Figure 1). The distance between the silicon atom and the carbonyl oxygen (Si–O2) is 2.826 Å, which is shorter than the sum of the van der Waals radii (3.35 Å) for the silicon and oxygen atoms, and the bond length of C9–Si is longer than that of the C13–Si or C14–Si bonds. The angles of C9-Si-C5, C9-Si-C13, and C9-Si-C14 are all slightly smaller (105.2–105.8) than those of a tetrahedral structure. From these values, it would seem that in the crystal structure, a weak intramolecular coordination of the neutral carbonyl oxygen to the tetraorganosilane, probably due to the rigid geometry, gives rise to the hypervalent silicon structure,[9] in which O2 and C9 are at apical positions. In the $CDCl_3$ solution structure, however, the ^{29}Si NMR spectra did not show a significant upfield shift,[10] which would generally be seen in a pentacoordinate silane,[11] relative to that observed in the corresponding tetrahedral analogues. Since even at −90 °C in CD_2Cl_2 only one singlet was observed in the ^{1}H NMR spectrum for the Me_3Si group, the C5–Si bond rotates freely. As a result, these compounds are not a perfect trigonal-bipyramidal pentacoordinated structure,[12] corre-

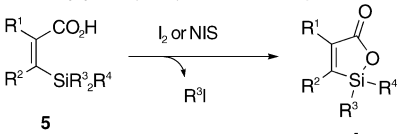
[*] Prof. Dr. M. Shindo, K. Matsumoto, Prof. Dr. K. Shishido
Institute for Medicinal Resources
University of Tokushima
Sho-machi 1, Tokushima 770-8505 (Japan)
Fax: (+81) 88-633-7294
E-mail: shindo@ph2.tokushima-u.ac.jp

[**] This work was supported in part by a Grant-in-Aid for Scientific Research in the Priority Area (A) "Exploitation of Multi-Element Cyclic Molecules" from the Ministry of Education, Culture, Sports, Science and Technology, Japan, and PRESTO, JST. K.M. thanks the Japan Society for the Promotion of Science (JSPS) for a research fellowship.

Supporting information for this article is available on the WWW under http://www.angewandte.org or from the author.

 © 2004 Wiley-VCH Verlag GmbH & Co. KGaA, Weinheim DOI: 10.1002/anie.200352705

Table 1: Cleavage of Si–C bonds of (*Z*)-β-silylacrylic acids **5** to provide silalactones **4**.



5 **4**

Entry	R^1	R^2	R^3	R^4	Method[a]	*t* [h]	**4**	Yield [%]
1	Me	Bn	Me	Me	A	29	**4a**	90[b]
2	Me	Bn	Me	Me	B	1	**4a**	96
3	Me	Bn	Me	*t*Bu	A	18	**4b**	81
4	Me	Bn	Et	Et	A	28	**4c**	94
5	Me	Bn	*i*Pr	*i*Pr	A	35	**4d**	74
6	Me	Bn	Ph	Ph	A	34	**4e**	87
7	Me	Ph	Me	Me	A	20	**4f**	95
8	Me	Ph	Me	Me	B	1.5	**4f**	65
9	Me	$MeOC_2H_4$	Me	*t*Bu	A	19	**4g**	85
10	Me	4-pentenyl	Me	Me	A	28	**4h**	65
11	PhCH(OTBS)	H	Me	Me	A	50	**4i**	64
12	*o*-silylbenzoic acid		Me	Me	A	28	**4j**	81
13	*o*-silylbenzoic acid		Me	Ph	A	23	**4k**	90

[a] Method A: I_2, pyridine in CCl_4 under reflux. Method B: NIS in CH_2Cl_2 at RT. Usually 0.1–0.5 mmol scale. [b] 82% yield for 10 mmol scale.

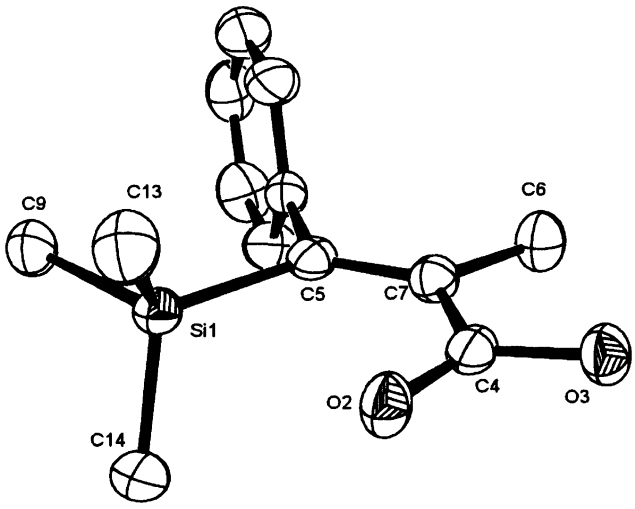


Figure 1. ORTEP drawing of the X-ray crystal structure of **5f** (thermal ellipsoids set at the 50% probability level) selected distances [Å] and angles [°]: Si1-O2, 2.826(1); Si1-C9, 1.875(2); Si1-C13, 1.862(2), Si1-C14, 1.865(2); Si1-C5, 1.922(2); C5-Si1-C9, 105.26(9); C9-Si1-C13, 105.8(1); C9-Si1-C14, 105.5(1).

sponding to an intermediate at the early stage of the S_N2 reaction at the silicon.

From this spectral information, the reaction mechanism can be elucidated based on the cooperative push–pull mechanism, which involves the double activation of the C9–Si bond mainly by the electrophilic iodine (pull) and secondarily by the nucleophilic oxygen (push). Since the methyl group was preferentially cleaved rather than the phenyl group, the electrophile would directly attack the $C(sp^3)$–Si σ bond bearing the higher HOMO energy rather than the $C(sp^2)$–Si σ bond, in contrast to *ipso* substitution.[13] And, the steric hindrance of the *t*Bu group would prevent its cleavage. Because the electron deficient alkene bears the ester group, the electrophilic iodine attacks only the R group, not the alkene (Figure 2).

The reactivity and synthetic utility of the silalactones are not well known.[14] Reduction by $LiAlH_4$ gave the cyclic silyl ether **6** in good yield. Grignard reagents attack the silicon selectively to afford the (*Z*)-β-silylacrylic acids (Scheme 3). Palladium catalyzed cross-coupling reactions (Hiyama coupling)[15] of the silalactone with aryl iodides furnishes the (*Z*)-β-arylacrylic acid in good yield without the use of a fluoride source. These transformations indicate the synthetic utility of the silalactones.

In conclusion, we have found a new methodology for the direct electrophilic cleavage of C–Si bonds activated by the formation of pentacoordinate organosilanes. This can be considered as an activation method for stable C–Si bonds. The silalactones would be useful for the preparation of multisubstituted alkenes and silicon-containing compounds.

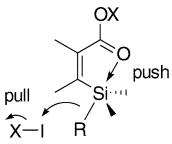
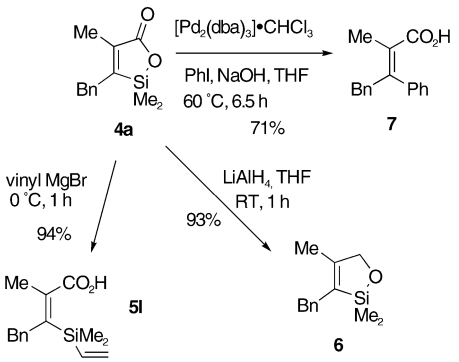


Figure 2. The push–pull mechanism.



Scheme 3. Transformations of silalactone **4a**.

Received: August 22, 2003 [Z52705]

Keywords: cleavage reaction · hypervalent compounds · iodine · silalactones · silanes

[1] For a review, see: G. R. Jones, Y. Landais, *Tetrahedron* **1996**, *52*, 7599-7662.

[2] a) K. Tamao, N. Ishida, M. Kumada, *J. Org. Chem.* **1983**, *48*, 2120–2122; b) I. Fleming, R. Henning, H. Plaut, *J. Chem. Soc.*

 © 2004 Wiley-VCH Verlag GmbH & Co. KGaA, Weinheim

Chem. Commun. **1984**, 29; c) M. A. Brook, *Silicon in Organic, Organometallic, and Polymer Chemistry*, Wiley, New York, **2000**.
[3] For examples, see: a) W. Kirmse, F. Söllenböhmer *J. Chem. Soc. Chem. Commun.* **1989**, 774–775; b) C. Eaborn, P. B. Hitchcock, *J. Chem. Soc. Perkin Trans. 2* **1991**, 1137–1141; c) P. F. Hudrlik, Y. M. Abdallah, A. M. Hudrlik, *Tetrahedron Lett.* **1992**, *33*, 6743–6746; d) H. Taguchi, K. Ghoroku, M. Tadaki, A. Tsubouchi, T. Takeda, *Org. Lett.* **2001**, *3*, 3811–3814; e) S. K. Tipparaju, S. K. Mandal, S. Sur, V. S. Puranik, A. Sarkar, *Chem. Commun.* **2002**, 1924–1925. For the report by Hudrlik et al on debenzylation and deallylation, albeit in moderate yields, see: f) P. F. Hudrlik, Y. M. Abdallah, A. M. Hudrlik, *Tetrahedron Lett.* **1992**, *33*, 6747–6750.
[4] M. Murakami, M. Suginome, K. Fujimoto, H. Nakamura, P. G. Andersson, Y. Ito, *J. Am. Chem. Soc.* **1993**, *115*, 6487–6498.
[5] For examples of the acidic or electrophilic C–Si bond cleavage, see: a) C. Eaborn, *J. Chem. Soc.* **1949**, 2755–2764; b) M. Ishikawa, M. Kumada, H. Sakurai, *J. Organomet. Chem.* **1970**, *23*, 63–69; c) K. Tamao, J. Yoshida, H. Yamamoto, T. Kakui, H. Matsumoto, M. Takahashi, A. Kurita, M. Murata, M. Kumada, *Organometallics* **1982**, *1*, 355–368; d) M. Demuth, G. Mikhail, *Synthesis* **1982**, 827; e) M. Bordeau, S. M. Djamei, J. Dunogues, R. Calas, *Bull. Soc. Chim. Fr.* **1982**, II159–160; f) K. Tamao, T. Hayashi, Y. Ito, *Bull. Soc. Chim. Fr.* **1995**, *132*, 556–558; g) M. Mutahi, T. Nittoli, L. Guo, S. McN. Sieburth, *J. Am. Chem. Soc.* **2002**, *124*, 7363–7375. See also: h) Y. Yamamoto, Y. Takeda, K. Akiba, *Tetrahedron Lett.* **1989**, *30*, 725–728; i) K. Itami, K. Terakawa, J. Yoshida, O. Kajimoto, *J. Am. Chem. Soc.* **2003**, *125*, 6058–6059.
[6] For reviews, see: a) M. Shindo, *Chem. Soc. Rev.* **1998**, *27*, 367–374; b) M. Shindo, *J. Synth. Org. Chem. Jpn.* **2000**, *58*, 1155–1166; c) M. Shindo, *Yakugaku Zasshi* **2000**, *120*, 1233–1246.
[7] M. Shindo, K. Matsumoto, S. Mori, K. Shishido, *J. Am. Chem. Soc.* **2002**, *124*, 6840–6841.
[8] CCDC-218067 (**5 f**) contains the supplementary crystallographic data for this paper. These data can be obtained free of charge via www.ccdc.cam.ac.uk/conts/retrieving.html (or from the Cambridge Crystallographic Data Centre, 12 Union Road, Cambridge CB21EZ, UK; fax: (+44) 1223-336-033; or deposit@ccdc.cam.ac.uk).
[9] For pentacoordinate tetraorganosilanes, see: a) K. Jurkschat, C. Mugge, J. Schmidt, A. Tzschach, *J. Organomet. Chem.* **1985**, *287*, C1-C4; b) M. Weinmann, A. Gehrig, B. Schiemenz, G. Huttner, B. Nuber, G. Rheinwald, H. Lang, *J. Organomet. Chem.* **1998**, *563*, 61–72. For selected reviews on extracoordinate silanes, see: c) C. Chuit, R. J. P. Corriu, C. Reye, J. C. Young, *Chem. Rev.* **1993**, *93*, 1371–1448; d) R. R. Holms, *Chem. Rev.* **1996**, *96*, 927–950.
[10] The chemical shift of compounds **5** in the ^{29}Si NMR is +4 ~ −8 ppm, like that of vinyltrimethylsilanes.
[11] A. I. Albanov, L. I. Gubanova, M. F. Larin, V. A. Pestunovich, M. G. Voronkov, *J. Organomet. Chem.* **1983**, *244*, 5–16.
[12] The pentacoordination character TBPa is 20% and TBPe 37% according to the Tamao equation: K. Tamao, T. Hayashi, Y. Ito, *Organometallics* **1992**, *11*, 2099–2114.
[13] The electrophilic selective cleavage of the Ph–Si bond would be an *ipso* substitution mechanism involving a cation intermediate.[2b,5f,g] The Tl^{III}-mediated direct cleavage of the Me–Si bond in preference to the Ph–Si bond was reported, see: F. Kakiuchi, K. Furuta, S. Murai, Y. Kawasaki, *Organometallics* **1993**, *12*, 15–16.
[14] For preparation of unsaturated silalactones, see: U. Wannagat, R. Schrader, *J. Organomet. Chem.* **1988**, *341*, 95–108.
[15] For a review, see: Y. Hatanaka, T. Hiyama, *Synlett* **1991**, 845–853.

 © 2004 Wiley-VCH Verlag GmbH & Co. KGaA, Weinheim

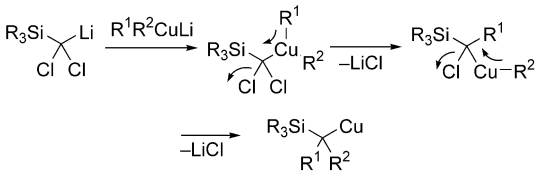
Organocuprates

Consecutive Double 1,2-Migration of Two Different Groups in Silyl(dichloromethyl)cuprates**

Junichi Kondo, Yuki Ito, Hiroshi Shinokubo, and Koichiro Oshima**

Organocuprates are among the most important classes of organometallic compounds that have a wide range of utility in organic synthesis.[1] There are several types of copper reagents, such as the classical Gilman cuprates, cyanocuprates, heterocuprates, and boron trifluoride complexes of alkylcopper compounds. Among them, cyano-Gilman cuprates prepared from copper cyanide and organolithium or organomagnesium reagents have been frequently employed in a number of reactions due to their high and reliable reactivity.[2] Here we report on the very different reactivity of cyanocuprates derived from organolithium and Grignard reagents.[3]

1,2-Migration of an alkyl group on the metal center in metal carbenoid reagents is a typical reaction of ate-type organometallic compounds.[4] This process has been successfully utilized in alkylation of α-haloalkylmetal compounds (metal = Zn, B, Al, Cu, Mn, etc.) and allows facile introduction of an alkyl group into organometallic reagents.[5] This process enables complex metal reagents to be prepared from relatively simple and easily accessible organometallic reagents. In this context, we expected that consecutive double migration of two different alkyl groups in α,α-dihaloalkylmetal compounds would afford a diversity of more complex organometallic reagents that can be easily manipulated (Scheme 1).



Scheme 1. Consecutive double alkylation of silyl(dichloromethyl)-cuprate.

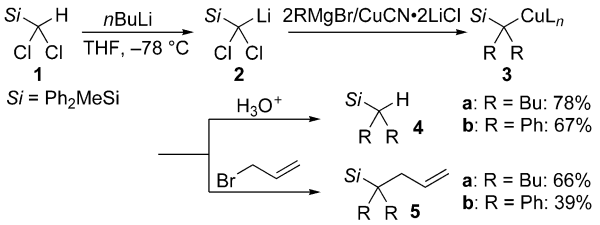
[*] J. Kondo, Y. Ito, Dr. H. Shinokubo, Prof. Dr. K. Oshima
Department of Material Chemistry
Graduate School of Engineering, Kyoto University
Kyoto Daigaku Katsura, Nishikyo-ku, Kyoto 615-8510 (Japan)
Fax: (+81) 75-383-2438
E-mail: hshino@kuchem.kyoto-u.ac.jp
oshima@fm1.kuic.kyoto-u.ac.jp

[**] This work was supported by Grants-in-Aid for Scientific Research and COE Research from the Ministry of Education, Culture, Sports, Science and Technology, Government of Japan. J.K. acknowledges JSPS for financial support.

Supporting information for this article is available on the WWW under http://www.angewandte.org or from the author.

 © 2004 Wiley-VCH Verlag GmbH & Co. KGaA, Weinheim DOI: 10.1002/anie.200352828

Addition of butyllithium to a solution of dichloromethyl(methyl)diphenylsilane (**1**)[6] in THF at −78 °C led to quantitative formation of silyl(dichloromethyl)lithium **2**, which was then treated with copper reagents derived from copper cyanide. As expected from Scheme 1, the copper reagent prepared by mixing butylmagnesium bromide with CuCN in a 2:1 ratio gave the dibutylated product **4a** by consecutive migration in good yield after aqueous workup (Scheme 2).[7] Using phenylmagnesium bromide instead of



Scheme 2. Dialkylation reaction of **1**.

BuMgBr gave the diphenylated product **4b** in 67% yield. Addition of allyl bromide before quenching resulted in trapping of the intermediate copper species to provide **5a**,**b**.[8]

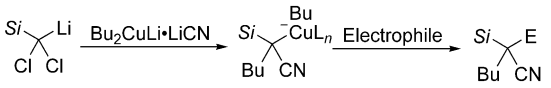
Surprisingly, the cyano-Gilman cuprate $Bu_2CuLi{\cdot}LiCN$ gave butylation/cyanation product **7a** in good yield without formation of dibutylated silane **4a** (Scheme 3).[9] The reaction with $sBu_2CuLi{\cdot}CuCN$ furnished α-cyanosilane **7b** in 56% yield. The intermediate copper species **6** reacted with a variety of electrophiles, such as allyl bromide, methyl iodide, acyl chlorides, and aldehydes (Table 1).[10] Reaction with aldehydes provided α,β-unsaturated nitriles by Peterson elimination of the initial adducts.[11]

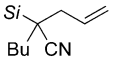
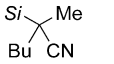
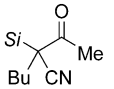
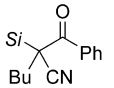
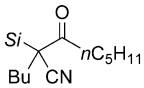
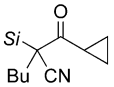
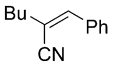
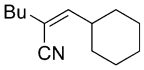
Alkylation/cyanation also occurred with the copper reagent derived from butylmagnesium bromide and CuCN in a 1:1 ratio (Scheme 4). However, the reactivity of the resulting copper species **8** in trapping reactions is very different from that of **6**. For example, treatment of **8** with allyl bromide gave none of the allylated product. On the basis of stoichiometry, the copper reagent is assumed to be an alkylcopper compound rather a cuprate. Hence, the reactivity of **8** is lower than that of the corresponding cuprate **6**.

In addition to alkylation/cyanation, consecutive butylation/phenylation was accomplished by sequential treatment of **2** with BuCu and PhMgBr (Scheme 5). The key here is the use of CuI not CuCN as the starting copper salt. Using CuCN instead of CuI led to a 1:1.1 mixture of **10** and **7a**, along with unidentified products. The intermediate copper compound **9** can be coupled with allyl bromide and acetyl chloride in moderate yield.

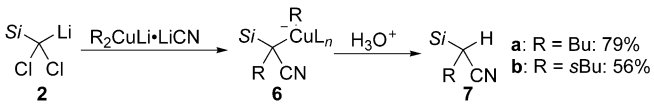
In conclusion, we have demonstrated very different reactivity between two types of cyanocuprates prepared from CuCN and Grignard or lithium reagents. Treatment of a silyl(dichloromethyl)lithium compound with the copper reagent prepared from 2 BuMgBr and CuCN gives the dibutylation product, whereas $Bu_2CuLi{\cdot}LiCN$ (cyano-Gilman cuprate) yields butylation/cyanation products. An EXAFS study indicated that these two cuprate reagents have

Table 1: Consecutive butylation/cyanation followed by C–C bond formation.[a]

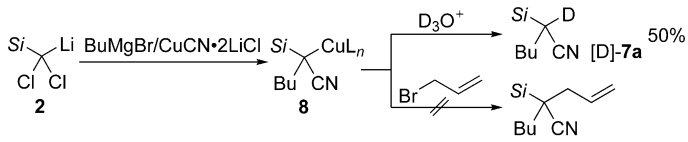


Entry	Electrophile	Product	Yield [%]
1	$CH_2{=}CHCH_2Br$		71
2	MeI		70
3	CH_3COCl		54
4	PhCOCl		57
5	$nC_5H_{11}COCl$		54
6	cC_3H_7COCl		48
7	PhCHO[b]		75 (Z/E = > 99/1)
8	$cC_6H_{11}CHO$[b]		57 (Z/E = 55/45)

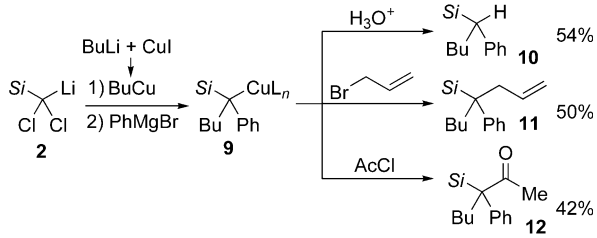
[a] Conditions: $Bu_2CuLi{\cdot}LiCN$ (1.1 equiv) and electrophile (2.0 equiv) were employed. $Si = Ph_2MeSi$. [b] $Bu_2CuLi{\cdot}LiCN$ (1.1 equiv), RCHO (3.0 equiv), and Me_3SiCl (4.5 equiv) were employed. Me_3SiCl was used as the Lewis acid.



Scheme 3. Alkylation/cyanation of **2**.



Scheme 4. Reaction of **2** with a cyanocuprate.



Scheme 5. Consecutive butylation/phenylation of **2**.

 © 2004 Wiley-VCH Verlag GmbH & Co. KGaA, Weinheim

very different structures, which may be responsible for the differing reactivity of these species.[3]

Experimental Section

7a: *n*BuLi (0.31 mL, 1.6 M in hexane, 0.50 mmol) was added to a solution of **1** (141 mg, 0.50 mmol) in THF (5 mL) dropwise at −78 °C, and the mixture was stirred for 30 min. To the resulting solution at −78 °C, a solution of nBu$_2$CuLi·LiCN, prepared by mixing *n*BuLi (0.78 mL, 1.6 M in hexane, 1.25 mmol) and CuCN·2 LiCl (0.55 mL, 1.0 M in THF, 0.55 mmol) at 0 °C, was added. After 5 min, the mixture was allowed to warm gradually to 0 °C. The mixture was stirred for 1 h at 0 °C and then poured into dilute aqueous HCl. The mixture was extracted with ethyl acetate, and the organic layers were dried over anhydrous Na_2SO_4. Concentration and purification gave 2-(methyldiphenylsilyl)hexanenitrile **7a** (116 mg, 0.39 mmol) in 79 % yield.

Received: September 9, 2003 [Z52828]

Keywords: alkylation · C—C coupling · carbenoids · copper · cyanation

[1] a) *Modern Organocopper Chemistry* (Ed.: N. Krause), Wiley-VCH, Weinheim, **2000**; b) *Organocopper Reagents* (Ed.: R. J. K. Taylor), Oxford University Press, Oxford, **1994**; c) E. Nakamura, S. Mori, *Angew. Chem.* **2000**, *112*, 3902; *Angew. Chem. Int. Ed.* **2000**, *39*, 3750.

[2] a) B. H. Lipshutz in *Organometallics in Synthesis* (Ed.: M. Schlosser), Wiley, Chichester, **2002**, p. 665; b) N. Krause, *Angew. Chem.* **1999**, *111*, 83; *Angew. Chem. Int. Ed.* **1999**, *38*, 79.

[3] Structural study on magnesiocyanocuprates by X-ray absorption: H. Huang, J. E. Penner-Hahn, *Book of Abstracts 210th ACS National Meeting*, **1995**.

[4] P. Kocienski, C. Barber, *Pure Appl. Chem.* **1990**, *62*, 1933.

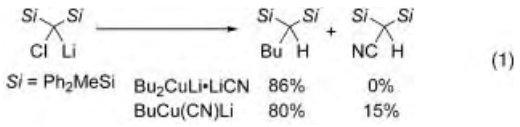
[5] For copper-mediated reactions, see: a) G. H. Posner, G. L. Loomis, H. S. Sawaya, *Tetrahedron Lett.* **1975**, 1373; b) K. Kitatani, T. Hiyama, H. Nozaki, *J. Am. Chem. Soc.* **1976**, *98*, 2362; c) K. Kitatani, H. Hiyama, H. Nozaki, *Bull. Chem. Soc. Jpn.* **1977**, *50*, 1600.

[6] Dichloromethylsilanes are easily prepared according to a reported procedure: a) C. Bacquet, D. Masure, J. F. Normant, *Bull. Soc. Chim. Fr.* **1975**, 1797; b) H. Shinokubo, K. Miura, K. Oshima, K. Utimoto, *Tetrahedron* **1996**, *52*, 503.

[7] The structures of copper species derived from Grignard reagents and CuCN are not well elucidated. Here we describe the reagent as 2 RMgBr/CuCN to indicate stoichiometry.

[8] Reactivity of α-silylalkylcuprates: S. H. Bertz, M. Eriksson, G. Miao, J. P. Snyder, *J. Am. Chem. Soc.* **1996**, *118*, 10906.

[9] We performed a preliminary experiment on the reaction of monochlorocuprate. Treatment of chlorodisilylmethyllithium with Bu$_2$CuLi·LiCN or BuCu(CN)Li provided predominantly butylated product [Eq. (1)]. However, the order of migration of



(1)

butyl and cyano groups in dichlorocuprates is not clearly elucidated and requires further investigation.

[10] The reaction with acetophenone resulted in a low yield of the desired α,β-unsaturated nitrile (14 %).

[11] For the formation of α,β-unsaturated nitriles by the Peterson reaction, see: a) Y. Yamakado, M. Ishiguro, N. Ikeda, H. Yamamoto, *J. Am. Chem. Soc.* **1981**, *103*, 5568; b) I. Ojima, M. Kumagai, *Tetrahedron Lett.* **1974**, 005; c) I. Matsuda, S. Murata, Y. Ishii, *J. Chem. Soc. Perkin Trans. 1* **1979**, 26.

 © 2004 Wiley-VCH Verlag GmbH & Co. KGaA, Weinheim

Dense-Shell Dendrimers

Analysis of the Spatial Dimensions of Fully Aromatic Dendrimers

Sabine Rosenfeldt, Nico Dingenouts, Dominic Pötschke, Matthias Ballauff, Alexander J. Berresheim, Klaus Müllen, and Peter Lindner*

Dendrimers present a fascinating class of molecules because of their regularly branched structure and their unusual properties.[1–4] Most of the dendrimers described so far are composed of flexible repeating units. Such a molecule can assume a vast number of conformations that are generated by rotation about the bonds between these units (Figure 1 b). In particular, the terminal groups can fold back into the interior of the molecule. A totally different situation arises when considering the stiff, fully aromatic dendrimer G4-M (Figure 1 a): In this case the benzene rings are either linear or form an angle of 60° or 120° to each other. Therefore, rotation about the bonds between the rings cannot change the structure of the molecule profoundly. Most importantly, no backfolding of the terminal groups is possible in such a molecule.

The structure shown in Figure 1 b suggests a "dense-shell" structure of flexible dendrimers, which consists of a hollow core closed by a densely packed shell of end groups. Such a dendritic box could be used, for example, as a molecular container. Hence, many ideas for possible applications of dendrimers originated from this picture.[1–3] These ideas were further encouraged by an early publication by de Gennes and Hervet in which the first theoretical treatment of such dense-shell structures was presented.[5] Subsequent theoretical work, however, has demonstrated convincingly that flexible dendrimers exhibit their maximum density in the core of the molecule ("dense-core model") and that there is a finite probability for the end groups to be located at any position within the molecule.[6–9] Experimental studies by small-angle neutron scattering (SANS[10]) have fully corroborated this result (see the review of this work in reference [11]). In particular, the distribution of end groups in a flexible fourth-generation dendrimer was determined experimentally for the first time by use of SANS.[12]

Thus a change of paradigm has occurred, as the previous assumption of the dense-shell model has been replaced by a model based on well-established results of polymer physics. Herein we elucidate this point further by analyzing the spatial structure of the stiff, fully aromatic dendrimer G4-M.[12–17] It has been demonstrated by SANS[11,18–22] that such a stiff dendrimer has a dense-shell structure as expected. In accordance with results obtained by NMR spectroscopy[17] it is shown that a high segment density must result in the periphery of the molecule if the number of generations is high enough.

The analysis employed herein consists of measuring the SANS intensities $I_0(q)$ at different contrast. This method, termed contrast variation, has been applied frequently to colloidal systems.[10,11] Hence, it suffices to delineate the main points of this analysis:[11,24] The intensity $I_0(q)$ of an isolated molecule dissolved in a suitable solvent is governed by the contrast $\bar{\rho}-\rho_m$, where $\bar{\rho}$ is the average scattering-length density of the molecule and ρ_m is the scattering-length density of the solvent. The scattering length defines the strength of the scattered radiation emanating from a given atom or segment. Since the scattering intensity is always related to the corresponding scattering volume, the scattering-length densities are the decisive quantities. The quantity q is the magnitude of the scattering vector and can be calculated from the scattering angle θ and the wavelength λ of the radiation employed ($q=(4\pi/\lambda)\sin(\theta/2)$).[10] The contrast in the SANS experiments can be changed by using mixtures of deuterated and nondeuterated solvents, because the scattering-length density of the solvent depends strongly on the degree of deuteration.[10]

The average scattering-length density $\bar{\rho}$ can be obtained directly from experimental data because $I_0(q)$ can be approximated by the Guinier law for small scattering angles, that is, small q values [Eq. (1)]. In this equation, N/V is the number of

$$I_0(q) \cong \frac{N}{V} V_p^2(\bar{\rho}-\rho_m)^2 \exp\left(-\frac{R_g^2}{3}q^2\right) \quad (1)$$

dissolved molecules, V_p their volume, and R_g the radius of gyration.[10,11] The volume V_p can be used to calculate the molecular weight M according to $M=N_L V_p \bar{\nu}$, where $\bar{\nu}$ is the partial specific volume determined experimentally.[18–20] First, however, the experimental scattering intensities must be extrapolated carefully to vanishing concentration, and the incoherent contribution always present in neutron scattering must be subtracted before Equation (1) is applied.[22]

Figure 2 shows the Guinier plot of the SANS data for the dissolved dendrimer G4-M according to Equation (1). The curves differ with respect to the contrast $\bar{\rho}-\rho_m$ obtained through mixtures of deuterated and nondeuterated toluene. It is evident that the extrapolation to $q=0$ provides no difficulty, so that V_p ($=30.3\ \mathrm{nm}^3$) and $\bar{\rho}$ ($=2.42\times10^{10}\ \mathrm{cm}^{-2}$) can be obtained. From these data and the measured specific volume the molecular weight M was determined to be $22250\ \mathrm{g\,mol}^{-1}$, which is in agreement, within experimental

[*] Dr. S. Rosenfeldt,[+] Dr. N. Dingenouts, D. Pötschke, Prof. Dr. M. Ballauff[+]
Polymer-Institut
Universität Karlsruhe
Kaiserstrasse 12, 76128 Karlsruhe (Germany)
Fax: (+49) 721-608-3153
E-mail: matthias.ballauff@uni-bayreuth.de
Dr. A. J. Berresheim, Prof. Dr. K. Müllen
Max-Planck-Institut für Polymerforschung
Postfach 3148, 55021 Mainz (Germany)
Dr. P. Lindner
Institut Laue-Langevin
B.P. 156X, 38042 Grenoble Cedex (France)
[+] Present Address:
Physikalische Chemie I
Universität Bayreuth
95440 Bayreuth (Germany)

 DOI: 10.1002/anie.200351810 © 2004 Wiley-VCH Verlag GmbH & Co. KGaA, Weinheim

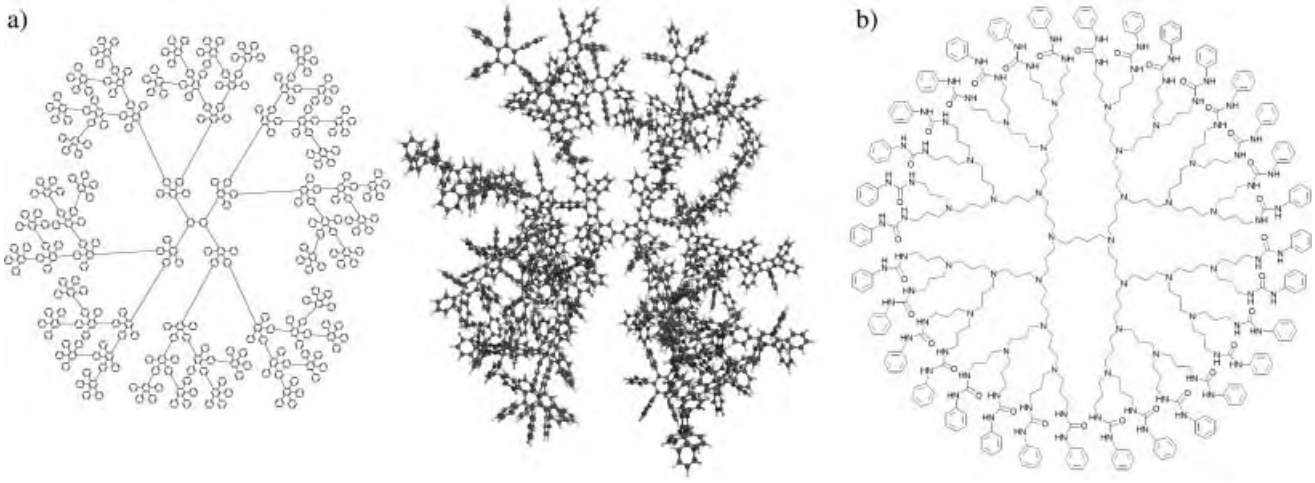


Figure 1. a) The stiff dendrimer G4-M.[12,13] b) A flexible dendrimer that has been studied by small-angle neutron scattering.[8,18,21–23]

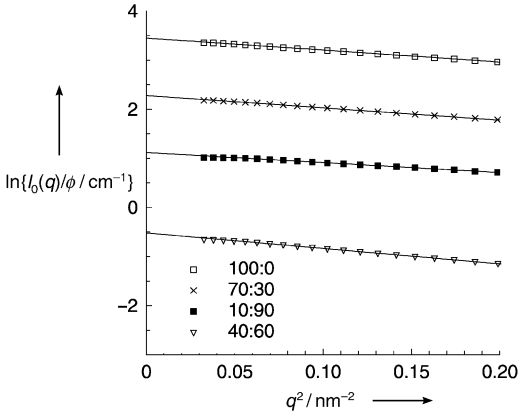


Figure 2. Guinier plot[10] [see Eq. (1)] of the scattering intensities obtained at different contrast. The contrast between the dissolved dendrimer G4-M and the solvent was adjusted through the use of mixtures of deuterated and nondeuterated toluene. The ratio of the deuterated to nondeuterated toluene is given. All data have been extrapolated to vanishing concentration, and the incoherent background has been removed.

error ($\pm 600\,\mathrm{g\,mol^{-1}}$), with the calculated value ($22\,927\,\mathrm{g\,mol^{-1}}$) and the value determined by mass spectrometry. Moreover, the radius of gyration R_g, which also depends on contrast, can be determined from this plot and extrapolated to infinite contrast by an appropriate procedure.[11] For the dendrimer G4-M R_g turns out to be 2.6 nm.

If $\bar{\rho}$ is known, the measured scattering intensity $I_0(q)$ can be expanded in powers of the contrast $\bar{\rho}-\rho_m$ [Eq. (2)],[11,18,20,21] which provides the partial intensities

$$I_0(q) = [\bar{\rho}-\rho_m]^2\, I_S(q) + 2\,[\bar{\rho}-\rho_m]\, I_{SI}(q) + I_I(q) \qquad (2)$$

$I_S(q)$, $I_{SI}(q)$, and $I_I(q)$. The first term $I_S(q)$ contains information on the spatial structure of the dissolved molecule. In contrast, the second and third terms are related to the variation of the scattering-length density within the molecule[25] and therefore cannot be used for analyzing the shape of the molecule. The resulting partial intensity $I_S(q)$ of the stiff dendrimer G4-M is displayed in Figure 3. A weak side maximum is visible at about 1.7 nm^{-1}, which already points to a well-defined structure of G4-M.

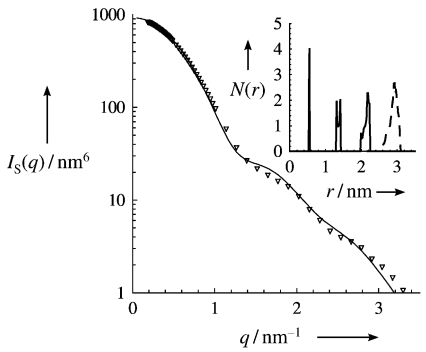


Figure 3. Modeling of the partial scattering intensity $I_S(q)$ (triangles) obtained from the experimental SANS data by contrast variation. Solid lines: fit obtained by the model described in Figure 4. Inset: number of spheres $N(r)$ located within the distance r from the center of the molecule. The distribution of the end groups is shown by a dashed line.

The transformation of $I_S(q)$ into real space can not be done by the method employed for flexible dendrimers as shown in Figure 1b. Simulations demonstrated that the direct Fourier transformation of $I_S(q)$ only leads to correct results for fully flexible dendrimers, that is, if the structure is averaged over a sufficiently high number of conformers.[8,9] The dendrimer G4-M under consideration in this case, however, hardly has any flexibility as a result of its rigid structure. Moreover, it has no radial symmetry.[26]

Therefore, $I_S(q)$ was analyzed by the model shown in Figure 4. In general, small-angle scattering does not have atomic resolution and parts of the molecule such as the benzene rings can be rendered in a suitably coarse-grained model when evaluating $I_S(q)$. Thus the central biphenyl unit is represented by two spheres, and each of the four dendrons emanating from this central unit is modeled by eight spheres

 © 2004 Wiley-VCH Verlag GmbH & Co. KGaA, Weinheim

(Figure 4). Hence, each sphere represents five benzene rings. The distance between the centers of these spheres must approximately be the dimensions of two benzene rings, and

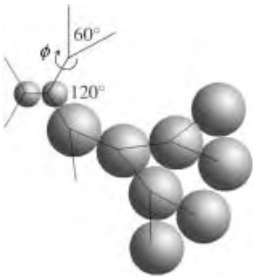


Figure 4. Model used to determine the partial scattering intensity $I_S(q)$ [Eq. (2)]. The molecular structure of the dendrimer is represented by spheres connected by freely rotating bonds. The central biphenyl unit is modeled by two small spheres (diameter: 0.4 nm). Each dendron emanating from this center is modeled by eight spheres whose distance (0.87 nm) and radius (0.8 nm) are treated as fit parameters in the simulation.

this parameter therefore determines the overall dimensions of the molecule. Since each sphere must provide the scattering power of five benzene rings, the diameter was increased appropriately. Hence, neighboring spheres overlap. For the sake of clarity, however, this overlap is not shown in Figure 4. Finally, the bonds between all spheres can be rotated freely.

The scattering intensity can now be calculated as follows: Different conformers are generated by a set of torsional angles chosen at random. If a given torsional angle leads to an overlap between two spheres that do not belong to the same dendron, this angle is dismissed and a new one is generated. To obtain sufficient accuracy, about 500 conformers were generated in this way. The scattering intensity $I_S(q)_{\text{conformer}}$ of each conformer results from the scattering contribution of all the spheres and their positions in the conformer according to Equation (3),[10] where d_{ij} denotes the distance between the

$$I_S(q)_{\text{conformer}} = \sum_{i,j} A_i(q)\, A_j(q) \frac{\sin q\, d_{ij}}{q\, d_{ij}} \qquad (3)$$

spheres i and j with radius R in the corresponding conformer. The scattering amplitudes $A_j(q)$ of the spheres are given by Equation (4).[10] The average over all conformations results

$$A_i(q) = \frac{4\pi}{3} R^3 \left(\frac{\sin q\, R - q\, R \cos q\, R}{q\, R^3} \right) \qquad (4)$$

from the arithmetic mean of all $I_S(q)_{\text{conformer}}$ values calculated in this way. The only fit parameters are the distance of the spheres and their radius R [see Eq. (4)].

From this modeling of $I_S(q)$ (optimal fit, solid line in Figure 3) the distance between the spheres d turns out to be 0.87 nm and the radius R is 0.8 nm. These values lead to full agreement between theory and experiment within the limits of error. The distance between the spheres corresponds approximately to the length of a biphenyl unit. The diameter of the spheres (1.6 nm) fits well to the average dimensions of the subunits, which consist of five benzene rings each.

The inset in Figure 3 shows the number $N(r)$ of spheres located within distance r from the center of the molecule. While the first generation is still strictly localized, higher generations are spread out over larger distances due to the averaging of different conformers. Therefore, SANS shows that the dendrimer G4-M has a stiff structure in which the segments have a well-defined distance from the center.

The above conclusions derived from SANS measurements were corroborated by an investigation by Saalwächter and coworkers[17] by using solid-state NMR spectroscopy. In this case the marked slowing of the terminal phenyl groups could be proved directly and traced back to their mutual steric hindrance. Moreover, this study demonstrated that the dendrons can not reorient even at high temperatures. This again points to a strong mutual steric hindrance between the dendrons.

The conclusions drawn from the present work are related to our basic understanding of dendrimers and their molecular shape: The dendrimer G4-M exhibits a molecular structure that can be described by the dense-shell model hitherto applied to all dendrimers. Such a stiff shape, however, in which all end groups are located in the periphery of the molecule (see Figure 3, inset) can only be realized by a concomitantly stiff chemical structure. Flexible dendrimers, on the other hand, are characterized by a segmental distribution that exhibits its maximum in the center of the molecule.[11,18–23] in such a structure the end groups can fold back easily.[18] Consequently, flexible dendrimers exhibit the dense-core structure discussed above that was predicted by theory quite some time ago. On the other hand, dense-shell dendrimers can only be formed from stiff units, as shown for the dendrimer G4-M.

Experimental Section

The dendrimer was synthesized as previously described.[12,13] Toluene (Merck, p.a.) and deuterated toluene (C_7H_8; Euriso-top, degree of deuteration: 99.96 %) were used as received. The specific volume ($(0.82 \pm 0.04)\ \text{cm}^3\,\text{g}^{-1}$) of G4-M was determined by using a DMA-60 densitometer (Paar, Graz, Austria). All SANS data were obtained by using the beamline D11 of the Institut Laue-Langevin in Grenoble. The data were corrected to obtain the absolute intensities by use of the software directly available at the beamline. The extrapolation of the data to vanishing concentration and the subtraction of the incoherent background were carried out as described in reference [22].

Received: May 6, 2003 [Z51810]

Keywords: dendrimers · small-angle neutron scattering · structure elucidation

[1] F. Vögtle, S. Gestermann, R. Hesse, H. Schwierz, B. Windisch, *Prog. Polym. Sci.* **2000**, *25*, 987 – 1041.
[2] S. M. Grayson, J. M. J. Fréchet, *Chem. Rev.* **2001**, 3819 – 3867.
[3] S. Hecht, *J. Polym. Sci. Part A* **2003**, *41*, 1047 – 1058.
[4] *Dendrimers and other Dendritic Polymers* (Eds.: J. M. J. Fréchet, D. A. Tomalia), Wiley-VCH, Weinheim, **2002**.

 © 2004 Wiley-VCH Verlag GmbH & Co. KGaA, Weinheim

[5] P. G. de Gennes, H. Hervet, *J. Phys. (Paris)* **1983**, *44*, L351 – L360. This much-cited publication has a problem, however, as was recently pointed out (T. C. Zook, G. T. Pickett, *Phys. Rev. Lett.* **2003**, *90*, 15502-1-015502-4): The method of de Gennes and Hervet leads to a maximum segment density in the core of the dendrimers if applied correctly.
[6] R. L. Lescanec, M. Muthukumar, *Macromolecules* **1990**, *23*, 2280 – 2288.
[7] D. Boris, M. Rubinstein, *Macromolecules* **1996**, *29*, 7251 – 7260.
[8] H. M. Harreis, C. N. Likos, M. Ballauff, *J. Chem. Phys.* **2003**, *118*, 1979 – 1988.
[9] I. Götze, C. N. Likos, *Macromolecules*, **2003**, *36*, 8189 – 8197.
[10] J. S. Higgins, H. C. Benoit, *Polymers and Neutron Scattering*, Clarendon Press, Oxford, England, **1994**; the radius of gyration is equal to the root mean square distance of the units from the center of mass of the dendrimer.
[11] "Structure and Dimensions of Polymer and Colloidal Systems": M. Ballauff, *NATO Sci. Ser. Ser. C* **2002**, *568*.
[12] K. Müllen, F. Morgenroth, *Tetrahedron* **1997**, *53*, 15349 – 15366.
[13] F. Morgenroth, C. Kübel, K. Müllen, *J. Mater. Chem.* **1997**, *7*, 1207 – 1211.
[14] K. Müllen, A. J. Berresheim, M. Müller, *Chem. Rev.* **1999**, *99*, 1747 – 1785.
[15] U.-M. Wiesler, A. J. Berresheim, F. Morgenroth, G. Lieser, K. Müllen, *Macromolecules* **2001**, *34*, 187 – 199.
[16] H. Zhang, P. C. M. Grim, P. Foubert, T. Vosh, P. Vanoppen, U.-M. Wiesler, A. J. Berresheim, K. Müllen, P. C. de Schryver, *Langmuir* **2000**, *16*, 9009 – 9014.
[17] M. Wind, K. Saalwächter, U.-M. Wiesler, K. Müllen, H. W. Spiess, *Macromolecules* **2002**, *35*, 10071 – 10086.
[18] S. Rosenfeldt, N. Dingenouts, M. Ballauff, N. Werner, F. Vögtle, P. Lindner, *Macromolecules* **2002**, *35*, 8098 – 8105.
[19] D. Pötschke, M. Ballauff, P. Lindner, M. Fischer, F. Vögtle, *Macromolecules* **1999**, *32*, 4079 – 4087.
[20] D. Pötschke, M. Ballauff, P. Lindner, M. Fischer, F. Vögtle, *Macromol. Chem. Phys.* **2000**, *201*, 330 – 339.
[21] N. Dingenouts, S. Rosenfeldt, N. Werner, F. Vögtle, P. Lindner, A. Roulamo, K. Rissanen, M. Ballauff, *J. Appl. Cryst.* **2003**, in press.
[22] S. Rosenfeldt, N. Dingenouts, M. Ballauff, P. Lindner, C. N. Likos, N. Werner, F. Vögtle, *Macromol. Chem. Phys.* **2002**, *203*, 1995 – 2004.
[23] C. N. Likos, S. Rosenfeldt, N. Dingenouts, M. Ballauff, P. Lindner, C. N. Likos, N. Werner, F. Vögtle, *J. Chem. Phys.* **2002**, *117*, 1869 – 1877.
[24] See M. Ballauff in reference [4], pp. 176–194.
[25] Both terms need to be subtracted carefully before evaluating the scattering intensity to deduce the spatial structure. This problem is of central importance when analyzing dendrimers, which are rather small objects. The analysis of $I_0(q)$ without this correction may lead to incorrect conclusions.[11,24]
[26] Central to this analysis is the description of flexible dendrimers by an average segment density termed $T(r)$, which is of central symmetry and leads to $I_S(q)$ upon Fourier transformation.[8] For stiff systems, however, the deviations of an averaged intensity would be too high, so that no meaningful description of $I_S(q)$ would be possible. This can be seen from the fact that the description through an averaged $T(r)$ would lead to pronounced minima (zeros) of $I_0(q)$. The experimental scattering intensity, however, exhibits only a weak side maximum (see Figure 3). Moreover, this demonstrates that G4-M does not have radial symmetry, and models that assume distributions with central symmetry can not be applied.

 © 2004 Wiley-VCH Verlag GmbH & Co. KGaA, Weinheim

Structure-Activity Relationships

Rational Design of Nanostructured Copper–Zinc Oxide Catalysts for the Steam Reforming of Methanol**

Benjamin L. Kniep, Thorsten Ressler, Annegrit Rabis, Frank Girgsdies, Michael Baenitz, Frank Steglich, and Robert Schlögl*

Copper–zinc oxide (aluminum oxide) catalysts are industrially used for methanol synthesis and the water gas shift reaction and, hence, have been investigated intensively in the last few decades in both academia and industry. In addition, Cu/ZnO catalysts are also known to be active for the steam reforming of methanol for the production of hydrogen.[1] Because methanol is one of the potential candidates for hydrogen production in fuel-cell applications, Cu/ZnO catalysts are of potential importance. Therefore, a detailed knowledge of the relationships between catalytic activity, and surface structure and bulk structure is desirable to prepare new and improved catalysts according to a knowledge-based (rational) catalyst design. Unfortunately, for the majority of heterogeneous catalysts the required structure –activity relationships are not sufficiently well known.

In contrast to the assumption that the activity of copper catalysts increases linearly with the copper surface area, copper nanoparticles have been shown to exhibit surfaces with different catalytic activities.[2] Recently, we reported that the catalytic activity of binary Cu/ZnO catalysts in methanol synthesis and methanol steam reforming correlates with the microstrain in the bulk of the copper particles.[3–5] However, for known structure–activity relationships the question arises, how can a particularly active "real structure" of a heterogeneous catalyst be rationally prepared and improved? Assuming a positive correlation between microstrain and the activity of copper nanoparticles on ZnO, then tailoring the microstrain in copper particles during the preparation of the catalyst precursors is the next step towards a rational catalyst design. Cu/ZnO catalysts are commonly prepared by precipitating mixed copper zinc hydroxycarbonates from copper- and zinc nitrate solutions. In principle, each step in the

[*] Dipl.-Chem. B. L. Kniep, Dr. T. Ressler, Dr. F. Girgsdies, Prof. Dr. R. Schlögl
Department of Inorganic Chemistry
Fritz-Haber-Institute of the MPG
Faradayweg 4–6, 14195 Berlin (Germany)
Fax: (+49) 308413-4401
E-mail: Ressler@fhi-berlin.mpg.de
Dr. A. Rabis, Dr. M. Baenitz, Prof. Dr. F. Steglich
Department of Solid-State Physics
Max Planck Institute for Chemical Physics of Solids
Nöthnitzer Strasse 40, 01187 Dresden (Germany)

[**] The authors acknowledge the ZEIT-Stiftung (nanotechnology for future automobile technology) and the Deutsche Forschungs Gemeinschaft, DFG (SP "bridge building in heterogeneous catalysis") for generous financial support. Bettina Bems and Michael Schur are thanked for the preparation of catalyst precursors.

 © 2004 Wiley-VCH Verlag GmbH & Co. KGaA, Weinheim DOI: 10.1002/anie.200352148

preparation of Cu/ZnO catalysts (i.e. ageing, washing, drying, calcining, reducing) affects the microstructural characteristics of the catalyst. The strong influence of ageing of the precursor on the catalytic activity of the resulting catalysts has been described in the literature.[6,7] For example, precipitated catalyst precursors aged for more than 30 min in the mother liquor showed a significant increase in activity compared to the non-aged catalyst precursors. However, the corresponding structure–activity relationships remained unclear.

Herein, we present correlations between the increase in activity of copper catalysts prepared from aged precipitates and the structure of the catalysts under working conditions. Moreover, appropriate ageing of the catalyst precursors enables a particular target structure for the resulting catalyst to be obtained. Copper–zinc oxide catalysts (Cu:Zn = 70:30) were prepared from differently aged precursors (0, 15, 30, 120 min). The microstructure of the reduced and activated catalysts was investigated by in situ X-ray diffraction (XRD) combined with mass spectrometry and NMR spectroscopy.

Figure 1 shows the X-ray diffraction patterns of two Cu/ZnO catalysts (0 and 120 min ageing) measured under methanol steam reforming conditions. Reduction of the

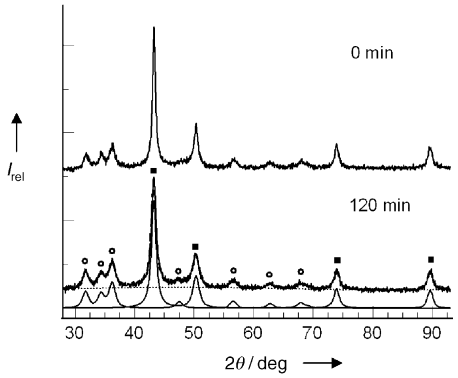


Figure 1. In situ X-ray powder diffraction patterns of two Cu/ZnO catalysts (■ Cu phase; ○ Zn phase) obtained from precursors aged for 0 and 120 min measured at 250 °C under methanol steam reforming conditions (I_{rel} = intensity). The disordered structure leads to a broadening of the signals for the Cu and ZnO phases. The Pawley method was employed to simulate the experimental patterns by a sum of profile functions and a background polynomial.

CuO/ZnO precursors in hydrogen leads to copper nanoparticles supported on ZnO with a quantitative composition of 68 mol % copper and 32 mol % zinc. No significant changes in the phase composition of the active Cu/ZnO catalysts were observed, however, the individual copper diffraction lines show significant deviations in their profiles as a function of ageing time. The catalytic activity in the steam reforming of methanol was monitored simultaneously with the XRD measurements and revealed an increase in activity between 15 and 30 min precipitate ageing (Figure 2).[8] Within the first minutes under reaction conditions all the catalysts exhibited a decrease in activity by about 5 % of the maximum activity. The hydrogen-production rates also displayed in Figure 2 were determined after no further decrease in activity was

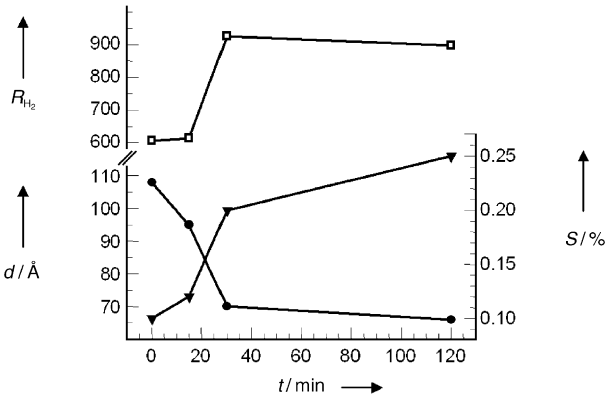


Figure 2. a) Hydrogen-production rate R_{H_2} [$\mu mol\,g^{-1}\,s^{-1}$], crystallite size d (●), and microstrain nanoparticles S ▼) of the copper (calculated from Cu 111 line measured at 250 °C) as a function of ageing time t of the corresponding precursors.

detectable. Figure 3 shows the dependence of the hydrogen-production rate on the specific copper surface area as determined by surface titration with N_2O and estimated by the XRD crystallite size.[9] Evidently, the sudden increase in hydrogen-production rate cannot be explained by a linear correlation between copper surface area and activity.

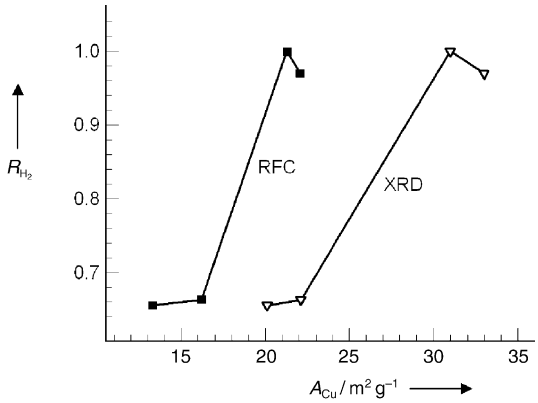


Figure 3. Normalized hydrogen-production rate R_{H_2} as function of specific copper surface area A_{Cu} calculated from the XRD data and measured by N_2O titration of the copper surface (RFC).

Microstructural changes of the active Cu/ZnO catalyst under working conditions were elucidated by a detailed line-profile analysis of the X-ray diffraction patterns (Figure 1). A uniform, oriented in one direction, compressive or tensile strain (macrostrain) results in a increase or decrease in the unit cell and thus a shift of the X-ray diffraction lines, whereas a statistical distribution of both tensile and compressive strain in different directions result in a broadening of the diffraction lines (microstrain). Both increased particle size and microstrain yield a symmetric line broadening in the X-ray diffraction pattern. The analysis of the Cu 111 diffraction line reveals a decrease in copper particle size from 110 Å (0 min) to 70 Å (120 min). In addition, an increase in the microstrain in the copper particles with increasing ageing

 © 2004 Wiley-VCH Verlag GmbH & Co. KGaA, Weinheim

time, from initially 0.09% after 0 min ageing to 0.26% after 120 min ageing, was observed. In comparison, nonsupported copper particles prepared by calcination and reduction of malachite ($Cu_2(OH)_2(CO_3)$) have a particle size of 300 Å and a microstrain of 0.06%.[10] The small degree of strain in the unsupported copper material clearly demonstrates that the role of ZnO is not only to disperse the copper and prevent the copper particles from sintering. An epitaxial orientation of Cu and ZnO, lattice imperfections caused by Zn incorporated in Cu, or an incomplete reduction of copper may be the origin of the strain in the supported copper nanoparticles. Furthermore, the analysis of the X-ray patterns of differently aged copper catalysts yields a distinct anisotropy in both particle size and microstrain, which may indicate changes in the morphology of the particles as a function of precipitate ageing.

To corroborate the in situ X-ray diffraction experiments, ex situ NMR spectroscopy investigations of the various Cu/ZnO catalysts were performed. Similar to X-ray diffraction line broadening, the line profile and breadth of the ^{63}Cu NMR signal is determined by the crystallite size and microstrain of the copper particles.[11] Large and highly ordered copper crystallites result in small and symmetric NMR signals. A decreasing copper crystallite size leads to symmetric broadening of the NMR signals, whereas an increasing microstrain (disorder of the copper) results in asymmetric signal profiles or even additional NMR signals. The ^{63}Cu NMR spectra of the differently aged Cu/ZnO catalysts are shown in Figure 4. The

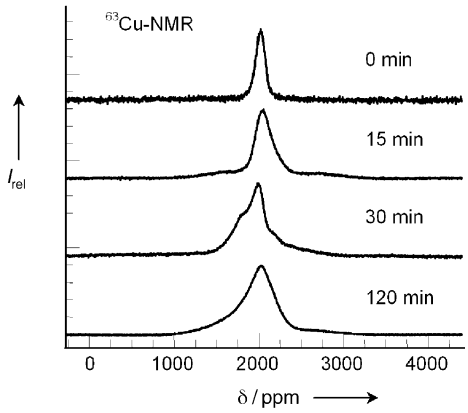


Figure 4. ^{63}Cu NMR spectra of four Cu/ZnO catalysts prepared from precursors aged for 0, 15, 30, and 120 min measured at 4.2 K (I_{rel} = intensity).

NMR spectra of the Cu/ZnO catalysts are in good agreement with the X-ray diffraction patterns. The NMR spectra of the catalysts obtained from precursors aged for 0 and 15 min have a symmetric and narrow line profile indicating large and well-ordered Cu particles. Conversely, the NMR spectra of the catalysts obtained from precursors aged for 30 and 120 min show board signal with an asymmetric line profile corresponding to small and strained Cu nanoparticles.

Previous investigations concerning structural changes of the precursors during ageing in the mother liquor revealed, that the initially amorphous precipitates (e.g. georgeite) transform after a certain time into crystalline rosasite and aurichalcite.[6] The point of crystallization of the precursors correlates well with the sudden increase in activity of the resulting Cu/ZnO catalysts. Calcinations of the amorphous, non-aged precursors may lead to the formation of separated CuO and ZnO crystallites and less active Cu/ZnO catalysts. Conversely, in the crystalline precursors, CuO and ZnO are ideally mixed and uniformly distributed leading, upon reduction, to small and highly disordered Cu/ZnO catalysts.

Figure 2 and 3 clearly indicate, the increase in activity of the copper catalysts correlates not only to the decreasing particle size, but also with the increasing microstrain in the copper nanoparticles. The analysis of the X-ray diffraction patterns and the NMR spectra confirm the structure–activity relationships for Cu/ZnO catalysts. The good correlation between the increase in the structural disorder in the copper nanoparticles and the increase in catalytic activity as a function of precursor ageing is revealed by both methods. The results of both solid-state techniques emphasize the importance of bulk structural investigations in heterogeneous catalysis. In addition, the relationships between the "real structure" of the Cu/ZnO catalysts and their activity in methanol steam reforming permits for the first time a rational explanation for the positive effect of precursor ageing on the active catalyst.

Our investigations have shown that the microstructural characteristics of Cu/ZnO catalysts can be tailored directly during the preparation, for instance, by an appropriate ageing procedure. The results presented clearly indicate, that the structure of the catalyst affects the activity more than variations in the chemical composition. The structure–activity relationship of Cu/ZnO catalysts described and the possibility to tailor the "real structure" of a catalyst during the preparation, are a step towards a rational design of improved catalysts.

Experimental Section

Preparation of Cu/ZnO catalysts: The copper zinc hydroxycarbonate precursors for the Cu/ZnO catalysts (molar ratio of copper to zinc = 70:30) were prepared by precipitation from metal nitrate solutions with sodium carbonate at constant pH (pH 7). The resulting precipitates were aged under continuous stirring in the mother liquor for 0, 15, 30, and 120 min, collected by filtration, and washed with deionized water (6 × 80 mL) under continuous stirring at 60 °C. Subsequently, the samples were dried at 120 °C for 10 h followed by calcination at 390 °C (heating ramp = 6 °C min^{-1}) in static air for 3 h. More details about the preparation conditions and the resulting precursor phases can be found in ref. [6].

X-Ray diffraction: In situ X-ray powder diffraction experiments were performed on a STOE Bragg-Brentano diffractometer (STADI P, $Cu_{K\alpha}$ radiation, secondary monochromator, scintillation counter). Reduction of the calcined CuO/ZnO precursors in 2 vol% H_2 in helium in a temperature range from 27–250 °C at a heating ramp of 6 °C min^{-1} was carried out in a Bühler high temperature cell (HDK S1). In situ XRD patterns were recorded at 250 °C under methanol steam reforming conditions (2.5 vol% CH_3OH, 2.5 vol% H_2O) (28.0–93.0° 2θ, step width 0.04° 2θ, counting time: 2 s/dp (dp = data point)). The catalytic activity was determined by measuring the gas-phase composition with a mass spectrometer.

X-ray powder diffraction patterns of the various Cu/ZnO catalysts under reaction conditions were analyzed by the Pawley

 © 2004 Wiley-VCH Verlag GmbH & Co. KGaA, Weinheim

method ("full pattern refinement").[12] Therefore, a sum of pseudo-Voigt-profile functions and an appropriate background function were refined for the experimental X-ray diffraction patterns. Free running parameters in the refinement were the lattice constants of Cu and ZnO, the intensities and the Gaussian and Lorentzian parts of the profile of the individual *hkl* lines, a linear zero shift in the 2θ scale, and four coefficients for the background polynomial. The crystallite size and microstrain corresponding to the broadening of each *hkl* line were determined from the Lorentzian and Gaussian part of the individual profile functions.[13] The specific copper surface areas as calculated from the crystallite size assuming a spherical particle ($\rho_{Cu} = 8.92\ g\,cm^{-3}$ [14]), are in good agreement with the results of the N_2O titration ("reactive frontal chromatography", RFC)[15] ($T = 40\,°C$, 0.5 vol% N_2O in Helium, Cu surface atom density: 1.47×10^{19} [16]).

NMR spectroscopy: After reduction of the copper oxides according to the conditions mentioned above, ^{63}Cu and ^{65}Cu NMR spectra of the Cu/ZnO catalysts were measured with a Bruker MSL 300 spectrometer at 79.618 MHz for ^{63}Cu and 85.288 MHz for ^{65}Cu at 4.2 K in an Oxford cryostat. Spin-echo experiments (90°–τ–180°) were performed with a 90° pulse of 5.5 μs, a "recycling delay" of 2 s and a τ value of 25 μs. The spectra shown are calibrated against $CuBr_{(s)}$ at −381 ppm.[17] The results obtained for ^{65}Cu correspond to those for ^{63}Cu.

Received: June 16, 2003 [Z52148]

Keywords: heterogeneous catalysis · NMR spectroscopy · structure–activity relationships · X-ray diffraction

[1] P. J. Wild, M. J. F. M. Verhaak, *Catal. Today* **2000**, *60*, 3.
[2] Y. Kanai, T. Watanabe, T. Futjitani, M. Saito, J. Nakamura, T. Uchijama, *Catal. Lett.* **1994**, *27*, 67; J. Nakamura, I. Nakamura, T. Uchijima, Y. Kanai, T. Wanabe, M. Saito, T. Fujitani, *Cata. Lett.* **1995**, *31*, 325.
[3] M. M. Günter, T. Ressler, B. Bems, C. Büscher, T. Genger, O. Hinrischsen, M. Muhler, R. Schlögl, *Catal. Lett.* **2001**, *71*, 37.
[4] M. M. Günter, T. Ressler, R. E. Jentoft, B. Bems, *J. Catal.* **2001**, *203*, 133.
[5] In addition to various experimental data, new theoretical studies based on DFT calculations have shown that strained copper particles exhibit modified adsorption energies and dissociation barriers, and, thus, different catalytic activities. S. Sakong, A. Groß, *Surf. Sci.* **2003**, *525*, 107.
[6] B. Bems, M. Schur, A. Dassenoy, H. Junkes, D. Herein, R. Schlögl, *Chem. Eur. J.* **2003**, *9*, 2039.
[7] D. M. Whittle, A. A. Mirzaei, J. S. J. Hargreaves, R. W. Joyner, C. J. Kiely, S. H. Taylor, G. J. Hutchings, *Phys. Chem. Chem. Phys.* **2002**, *4*, 5915; S. H. Taylor, G. J. Hutchings, A. A. Mirazaei, *Chem. Commun.* **1999**, 1373; D. Waller, D. Stirling, F. S. Stone, M. S. Spencer, *Faraday Discuss.* **1989**, *87*, 107.
[8] A similar increase in activity is also observed under methanol synthesis conditions. Thus, the structure–activity correlations revealed also hold for this reaction.
[9] The larger Cu surface area obtained from XRD crystallite size calculations compared to N_2O titration results (see Figure 3) may be because of interactions of the copper particles with ZnO or deviations from a spherical morphology.
[10] Another method to separate the contributions of crystallite size and microstrain to X-ray diffraction line broadening is described by Williamson and Hall (G. K. Williamson, W. H. Hall, *Acta Metall.* **1953**, *1*, 22) using the different dependencies of the two effects on the diffraction angle. The so-called "Willamson–Hall plot" works well for isotropic samples, however, because the samples analyzed here exhibit a strong anisotropy, the crystallite size and the microstrain had to be determined by analyzing individual lines.
[11] A. V. Chadwick, I. J. F. Popett, D. T. S. Maitland, M. E. Smith, *Chem. Mater.* **1998**, *10*, 864.
[12] G. S. Pawley, *J. Appl. Crystallogr.* **1981**, *14*, 357.
[13] J. I. Langford, *J. Appl. Crystallogr.* **1978**, *11*, 10.
[14] Handbook of Chemistry and Physics, 60th ed.
[15] G. C. Chinchen, C. M. Hay, H. D. Vandervell, K. C. Waugh, *J. Catal.* **1987**, *103*, 79.
[16] J. W. Ewans, M. S. Wainright, A. J. Bridgewater, D. J. Young, *Appl. Catal.* **1983**, *7*, 75.
[17] J. Mason, Multinuclear NMR, *Plenum Press*, New York, **1989**.

 © 2004 Wiley-VCH Verlag GmbH & Co. KGaA, Weinheim

Privileged Structures

A Short, Atom-Economical Entry to Tetrahydroxanthenones**

*Bernhard Lesch and Stefan Bräse**

Dedicated to Professor Burchard Franck

Heterocycles play an important role in the design and discovery of new physiologically active compounds.[1] In the field of modern medicine "privileged structures," groups of compounds whose members bind on different classes of receptors, have attracted much attention.[2] The best known examples are the benzodiazepines.[2]

The xanthones, which have more than 600 members, over 100 of which display a tetrahydroxanthone moiety, are among these privileged structures.[3] Secalonic acids (Scheme 1) and ergochromes are members of this group of natural products.[4] All secalonic acids are 2,2′-fused xanthone dimers, differing only with respect to the configuration of several C atoms in the framework. The secalonic acids exhibit toxic,[5] antibacterial,[6] and mutagenic[7] properties, along with fetotoxic and teratogenic actions.[8] Some derivatives of the secalonic acids were tested as cytostatics.[9] Secalonic acid D inhibits HIV protease[10] and several protein kinases,[11] while secalonic acid F is phytotoxic.[12]

Despite the potential of xanthones as privileged structures in the search for new pharmaceuticals, only one successful total synthesis of a member of this group is known, that of 10-methyl-10-demethoxycarbonylhemisecalonic acid A.[13] The

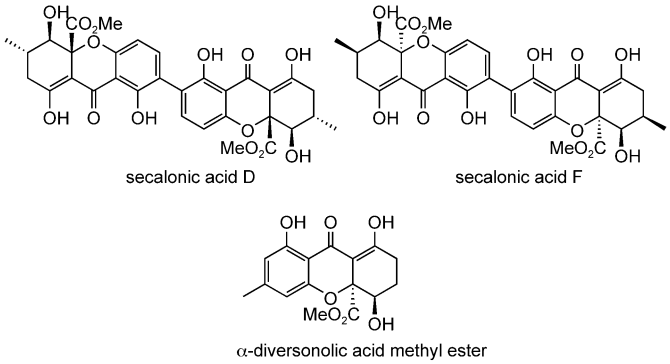
[*] Prof. Dr. S. Bräse
Institut für Organische Chemie
Universität Karlsruhe (TH)
Fritz-Haber-Weg 6, 76131 Karlsruhe (Germany)
Fax: (+49) 721-608-8581
E-mail: braese@ioc.uka.de

Dipl.-Chem. B. Lesch
Kekulé-Institut für Organische Chemie und Biochemie
Rheinische Friedrich-Wilhelms-Universität Bonn
Gerhard-Domagk-Strasse 1, 53121 Bonn (Germany)

[**] This work was supported by the Fonds der Chemischen Industrie and the Deutschen Forschungsgemeinschaft (DFG) (SFB 380).

Supporting information for this article is available on the WWW under http://www.angewandte.org or from the author.

 DOI: 10.1002/anie.200352154 © 2004 Wiley-VCH Verlag GmbH & Co. KGaA, Weinheim

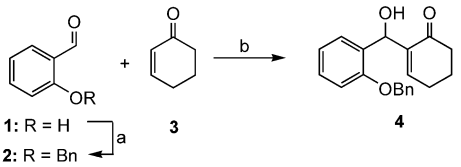


Scheme 1. Selected natural products with a tetrahydroxanthone moiety.

key step in this synthesis is the oxidative ring closure of a benzophenone derivative.[14] Several other routes to partially hydrogenated tetrahydroxanthones have also been described.[15]

From a retrosynthetic point of view, tetra- and hexahydroxanthones can be dissected into an arene and a cyclohexane. In order to sidestep C–O and C–C coupling reactions on the arene unit, the bridging carbon and the oxygen atoms must be derived from the arene, which sets fewer limitations on the substitution pattern of the arene unit. Based on these considerations we chose 2-hydroxybenzaldehyde as the arene core and 2-cyclohexen-1-none for the cyclohexane building block.

The attempted Baylis–Hillman reaction[16] of *O*-benzylated salicylic aldehyde (**2**) and 2-cyclohexen-1-one (**3**) gave the desired allylic alcohol **4** in poor yields (Scheme 2). In

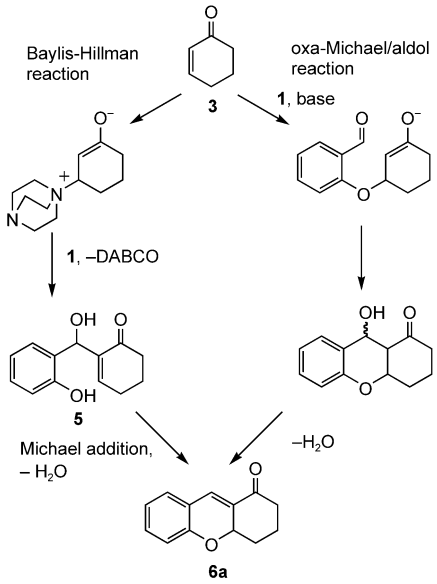


Scheme 2. a) K_2CO_3, BnBr, CH_3CN, reflux, 18 h, 89%; b) DABCO (1.0 equiv), dioxane/water 1:1, RT, 72 h, 13%. RT = room temperature.

contrast, the analogous reaction of unprotected salicylic aldehyde (**1**) with 2-cyclohexen-1-one did not result in the Baylis–Hillman adduct **5**, but rather the tetrahydroxanthone **6a** (Scheme 3) in good yields. The best results, 83% yield, were obtained when the reaction was conducted in degassed water, with 1,4-diazabicyclo[2.2.2]octane (DABCO) as a base, and with sonification.

Tetrahydroxanthone **6a** may be formed by two different routes (Scheme 3): The first route starts with a Baylis–Hillman reaction followed by an oxa-Michael addition and dehydration. In the second approach the sequence is initiated by the Michael addition of the phenol on the cyclohexenone and a subsequent aldol condensation provides the tetrahydroxanthone.

The synthesis of chromenes starting from 2-hydroxybenzaldehydes and acyclic Michael acceptors is a known reaction.[17] Typically it is performed in dioxane with potassium



Scheme 3. Reaction conditions: 0.5 equiv DABCO, water, RT, sonification, 48 h, 83%.

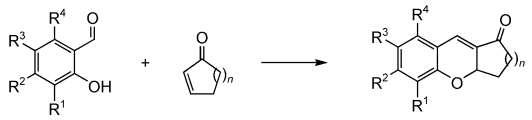
carbonate[17a] or potassium *tert*-butoxide in *tert*-butyl alcohol,[17b] which supports the domino oxa-Michael/aldol condensation pathway. However, when DABCO was used as a base, a sequence of the Baylis–Hillman reaction and a Michael addition was invoked.[17d,e] Furthermore, it is known that the Baylis–Hillman reaction is accelerated by sonification.[18] The reaction described in Scheme 3 can be performed with potassium carbonate as a base, while attempts with triphenylphosphane, a known catalyst for the Baylis–Hillman reaction, failed. The reaction presented should therefore be regarded as a domino oxa-Michael addition/aldol condensation reaction.[19] Using sonification instead of stirring ensured the effective mixture of the biphasic system.

To gain deeper insight into the scope and limitations of this method, several electron-rich and electron-poor *o*-hydroxybenzaldehydes were used as substrates, along with cyclohexenone and cyclopentenone. The products obtained are listed in Table 1. Since the starting materials are not soluble in water, dioxane/water mixtures were used as solvents without further optimization of the conditions. 2-Cyclohexen-1-one was superior to the more sensitive 2-cyclopent-1-one as a substrate, probably because the latter oligomerizes under basic conditions.[20] Substitution of C3 of the cyclohexenone is not tolerated under the tested conditions. Donor-substituted or benzoannelated tetrahydroxanthones could be isolated in reasonable yields. Only the acceptor-substituted product **6c** was obtained in moderate yield, probably due to the lower nucleophilicity of the corresponding phenolate anion.

The chemistry of the α,β-unsaturated system **6a** was examined with respect to the total synthesis of the secalonic acids. This required careful control of the oxidation states at C1, C9, and C9a. Since the direct osmium-catalyzed dihydroxylation of **6a** failed, the ketone was reduced with $NaBH_4$ to give the allylic alcohol **7** (Scheme 4). This was dihydroxylated using Upjohn conditions,[21] giving rise to the triol **8**,

 © 2004 Wiley-VCH Verlag GmbH & Co. KGaA, Weinheim

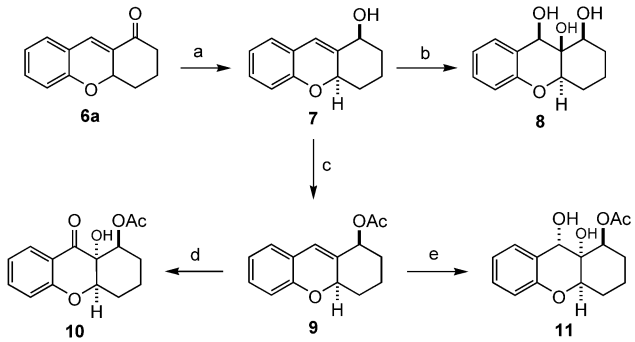
Table 1: Range of products from the domino oxa-Michael/aldol condensation between salicylic aldehydes and cyclohexenone and cyclopentenone.



6

R^1	R^2	R^3	R^4	*n*	Product	Yield [%]
H	H	H	H	2	**6a**	83
OH	H	H	H	2	**6b**	48
H	H	NO_2	H	2	**6c**	25
H	H	H	H	1	**6d**	23
OH	H	H	H	1	**6e**	19
H	H	OCH_3	H	2	**6f**	93
OCH_3	H	H	H	2	**6g**	63
H	OCH_3	H	H	2	**6h**	67
H	H			2	**6i**	70

while the acetylated derivative **9** yielded the hydroxyketone **10** when two equivalents of the oxidant were used. If only one equivalent was used, the diol **11** was isolated along with traces of the hydroxyketone **10** (Scheme 4).

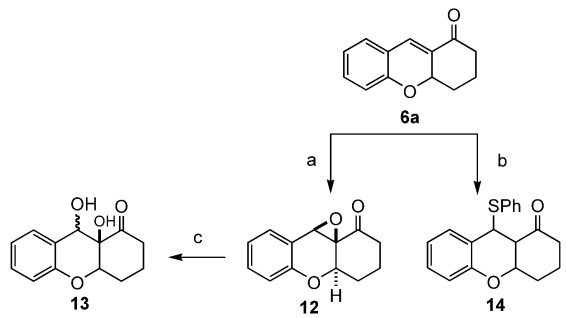


Scheme 4. a) $NaBH_4$, MeOH, RT, 4 h, 77%; b) K_2OsO_4, K_2CO_3, 1.1 equiv NMO, acetone/water 5:1, RT, 72 h, 51%; c) 2 equiv Ac_2O, pyridine, 0°C to RT, 4 h, 83%; d) K_2OsO_4, K_2CO_3, 2.2 equiv NMO, acetone/water 5:1, RT, 3 h, 74%, e) K_2OsO_4, K_2CO_3, 1.1 equiv NMO, acetone/water 5:1, RT, 3 h, 77% (based on recovered starting material). All relative configurations were suggested on the basis of NMR data. NMO = *N*-methylmorpholine *N*-oxide.

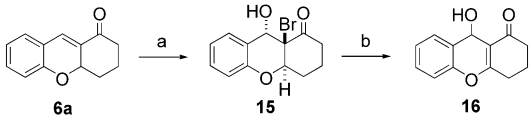
Treatment of the xanthenone **6a** with KOH/H_2O_2 in methanol gave the epoxide **12**, which could be hydrolyzed in quantitative yields (Scheme 5). The resulting diol **13** was isolated as a 3:1 mixture of diastereomers, probably due to epimerization at C9. The suitability of **6a** as a Michael acceptor could be demonstrated by the reaction with thiophenol as the nucleophile.

In order to introduce a substituent on C4a by a Michael addition,[13a] the olefin **6a** was converted into the bromohydrin **15** in good yield by reaction with NBS in DMSO/water. The elimination to give the allylic alcohol **16** proceeded cleanly in dioxane with DABCO as the base at room temperature (Scheme 6).

The described procedure provides rapid access to tetrahydroxanthones from readily available starting materials



Scheme 5. a) KOH, H_2O_2, MeOH, 0°C, 30 min, 61%; b) 0.1 equiv KOH, 1.1 equiv PhSH, 1 equiv NEt_3, THF/MeOH 4:1, RT, 1 h, 90% (NMR); c) aq phosphate buffer ($c = 0.1$ mol L^{-1}, pH 2.5), RT, 18 h, quant.



Scheme 6. a) NBS, H_2O, DMSO, 0°C to RT, 2 h, 80%; b) 3 equiv DABCO, dioxane, RT, 18 h, 73%. DMSO = dimethyl sulfoxide, NBS = *N*-bromosuccinimide.

under mild reaction conditions. This method provides an efficient route to this complex class of natural products. Studies on a possible asymmetric variant of the reaction are in progress. We are also examining the not-well-studied oxidative coupling of the monomeric xanthones[22] to give the secalonic acids.

Received: June 11, 2003 [Z52154]

Keywords: domino reactions · Michael addition · secalonic acids · xanthones

[1] a) L. Wang, K. W. Woods, Q. Li, K. J. Barr, R. W. McCroskey, S. M. Hannick, L. Gherke, R. B. Credo, Y.-H. Hui, K. Marsh, R. Warner, J. Y. Lee, N. Zielinski-Mozng, D. Frost, S. H. Rosenberg, H. L. Sham, *J. Med. Chem.* **2002**, *45*, 1697–1711; b) E. A. Couladouros, A. T. Strongilos, *Angew. Chem.* **2002**, *114*, 3829–3832; *Angew. Chem. Int. Ed.* **2002**, *41*, 3677–3680.

[2] a) B. E. Evans, K. E. Rittle, M. G. Bock, R. M. DiPardo, R. M. Freidinger, W. L. Whitter, G. F. Lundell, D. F. Veber, P. S. Anderson, R. S. L. Chang, V. J. Lotti, D. J. Cerino, T. B. Chen, P. J. Kling, K. A. Kunkel, J. P. Springer, J. Hirshfield, *J. Med. Chem.* **1988**, *31*, 2235–2246; b) J. S. Mason, I. Morize, P. R. Menard, D. L. Cheney, C. Hulme, R. F. Labaudiniere, *J. Med. Chem.* **1999**, *42*, 3251–3264, and references therein; c) K. C. Nicolaou, J. A. Pfefferkorn, A. J. Roecker, G.-Q. Cao, S. Barluenga, H. J. Mitchell, *J. Am. Chem. Soc.* **2000**, *122*, 9939–9953.

[3] a) M. U. S. Sultanbawa, *Tetrahedron* **1980**, *36*, 1465–1506; b) W. B. Turner, *J. Chem. Soc. Perkin Trans. 1* **1978**, 1621; c) J. S. Holker, T. E. O'Brien, T. J. Simpson, *J. Chem. Soc. Perkin Trans. 1* **1983**, 1365–1368; d) K. Hase, S. Kadota, P. Basnet, J. Li, S. Takamura, T. Namba, *Chem. Pharm. Bull.* **1997**, *45*, 567–569; e) K. Hase, J. Li, P. Basnet, Q. Xiong, S. Takamura, T. Namba, S. Kadota, *Chem. Pharm. Bull.* **1997**, *45*, 1823–1827.

[4] a) C. L. Barnes, R. Ubillas, R. S. Tempesta, *J. Chem. Crystallogr.* **1999**, *29*, 1031–1035; b) C.C Howard, R. A. Johnstone, T. J.

 © 2004 Wiley-VCH Verlag GmbH & Co. KGaA, Weinheim

King, L. Lessinger, *J. Chem. Soc. Perkin Trans. 1* **1976**, 1820; c) B. H. Wang G. M. Polya, *Planta Med.* **1996**, *62*, 111–114; d) R. S. Zeng, S. M. Luo, Y. H. Shi, M. B. Shi, C. Y. Tu, *Agron. J.* **2001**, *93*, 72–79.

[5] a) C. S. Reddy, A. W. Hayes, W. L. Williams, A. Ciegler, *J. Toxicol. Environ. Health* **1979**, *5*, 1159–1169; b) A. Ciegler, A. W. Hayes, R. F. Vesonder, *Appl. Environ. Microbiol.* **1980**, *39*, 285–287.

[6] A. Stoll, J. Renz, A. Brack, *Helv. Chim. Acta* **1952**, *35*, 2022–2034.

[7] a) F. C. Wehner, P. G. Thiel, S. J. Van Rensburg, I. P. C. Demasius, *Mutat. Res.* **1978**, *58*, 193–203; b) C. S. Reddy, R. V. Reddy, P. K. Chan, A. W. Hayes, *J. Environ. Pathol. Toxicol.* **1980**, *4*, 31–37.

[8] a) C. S. Reddy, R. V. Reddy, A. W. Hayes, A. Ciegler, *J. Toxicol. Environ. Health* **1981**, *7*, 445–455; b) K. Mayura, A. W. Hayes, W. O. Berndt, *Toxicology* **1982**, *25*, 311–322.

[9] a) T. Yamamoto (Asahi Chemical Industry Co., Ltd., Japan), JP 5404402 19790407, **1979**; b) T. Iwaguchi, H. Kitagawa, K. Hirose, T. Ishida, T. Yamamoto, *Gann* **1980**, *71*, 900–906; c) H. Kitagawa, M. Nakamura, Y. Kiuchi, T. Iwaguchi, *Gann* **1981**, *72*, 802–805; d) I. Kurobane, S. Iwahashi, A. Fukuda, *Drugs Exp. Clin. Res.* **1987**, *8*, 339–344.

[10] F. McPhee, P. S. Caldera, G. W. Bemis, A. F. McDonagh, I. D. Kuntz, C. S. Craik, *Biochem. J.* **1996**, *320*, 681–686.

[11] B. H. Wang, G. M. Polya, *Planta Med.* **1996**, *62*, 111–114.

[12] R. S. Zeng, S. M. Luo, Y. H. Shi, M. B. Shi, C. Y. Tu, *Agron. J.* **2001**, *93*, 72–79.

[13] B. Franck, J. Stöckigt, U. Zeidler, G. Franckowiak, *Chem. Ber.* **1973**, *106*, 1198–1220.

[14] B. Franck, U. Zeidler, *Chem. Ber.* **1973**, *106*, 1182–1197.

[15] a) C. D. Gabbutt, J. D. Hepworth, M. W. J. Urquhart, L. M. Vazquez de Miguel, *J. Chem. Soc. Perkin Trans. 1* **1997**, 1819–1824; b) S. Klutchko, M. von Strandtmann, J. R. Shavel, US Pat. 3862141, **1975**; c) C. K. Ghosh, S. Bhattacharyya, C. Ghosh, A. Patra, *J. Chem. Soc. Perkin Trans. 1* **1999**, 3005–3013; d) R. M. Letcher, T.-Y. Yue, K.-F. Chiu, A. S. Kelkar, K.-K. Cheung, *J. Chem. Soc. Perkin Trans. 1* **1998**, 3267–3276.

[16] a) A. B. Baylis, M. E. D. Hillman, DE-B 2155113, **1972** [*Chem. Abstr.* **1972**, *77*, 34174q]; b) V. K. Aggarwal, G. J. Tarver, R. McCague, *Chem. Commun.* **1996**, 2713–2714; c) M. Shi, Y.-S. Feng, *J. Org. Chem.* **2001**, *66*, 406–411.

[17] a) L. Rene, R. Roger, *Eur. J. Med. Chem.* **1975**, *10*, 72–78; b) Y. Satoh, J. L. Stanton, A. J. Hutchison, A. H. Libby, T. J. Kowalski, W. H. Lee, D. H. White, E. F. Kimble, *J. Med. Chem.* **1993**, *36*, 3580–3594; c) M. Shiraishi, Y. Aramaki, M. Seto, H. Imoto, Y. Nishikawa, N. Kanzaki, M. Okamoto, H. Sawada, O. Nishimura, M. Baba, M. Fujino, *J. Med. Chem.* **2000**, *43*, 2049–2063; d) P. T. Kaye, X. W. Nocanda, *J. Chem. Soc. Perkin Trans. 1* **2000**, 1331–1332; e) P. T. Kaye, X. W. Nocanda, *J. Chem. Soc. Perkin Trans. 1* **2002**, 1318–1324.

[18] F. Coelho, W. P. Almeida, D. Veronese, C. R. Mateus, E. C. S. Lopes, R. C. Rossi, G. P. C. Silveira, C. H. Pavam, *Tetrahedron* **2002**, *58*, 7437–7447.

[19] L. F. Tietze, *Chem. Rev.* **1996**, *96*, 115–136.

[20] R. Ehama, K. Inomata, *J. Tohoku Pharm. Univ.* **2001**, *48*, 69–76 [*Chem. Abstr.* **2001**, *138*, 321161].

[21] a) V. VanRheenen, R. C. Kelly, D. Y. Cha, *Tetrahedron Lett.* **1976**, *17*, 1973–1976; b) V. VanRheenen, D. Y. Cha, W. M. Hartley, *Organic Syntheses Collected Vol. VI*, Wiley, New York, **1988**, pp. 342–348.

[22] a) Review on aryl–aryl couplings: G. Bringmann, R. Walter, R. Weirich, *Angew. Chem.* **1990**, *102*, 1006–1019; *Angew. Chem. Int. Ed. Engl.* **1990**, *29*, 977–991; b) biomimetic aryl–aryl couplings: G. Bringmann, S. Tasler, *Tetrahedron* **2001**, *57*, 331–343; c) vgl: W. Tuckmantel, A. P. Kozikowski, L. J. Romanczyk (Mars Inc., USA), WO 0061547, **2000** [*Chem. Abstr.* **2000**, *133*, 309794].

 © 2004 Wiley-VCH Verlag GmbH & Co. KGaA, Weinheim

Surface Chemistry

Do Quantum Size Effects Control CO Adsorption on Gold Nanoparticles?**

*Celine Lemire, Randall Meyer, Shamil Shaikhutdinov, and Hans-Joachim Freund**

Size effects in adsorption and reactivity of supported metal particles have been observed for at least two decades.[1,2] In recent years, gold nanoparticles have received attention for their extraordinary catalytic activity for reactions such as low temperature CO oxidation.[3–5] A number of different theories have been advanced to explain this reactivity in terms of special reaction sites created by the metal–support interface.[3–5] Goodman's group invoked quantum effects to explain a maximum in CO oxidation activity[6,7] and suggested that particle thickness, in this case two atomic layers, may be the key parameter. Herein, through a combination of scanning tunneling microscopy (STM), temperature programmed desorption (TPD), and infrared reflection absorption spectroscopy (IRAS), we report the first experimental evidence that thin islands of gold in fact have the same CO adsorption behavior as large gold particles and extended gold surfaces. Therefore observed differences in reactivity of gold nanoparticles are proposed to arise from the presence of highly uncoordinated gold atoms.

We have previously found that palladium exhibits two-dimensional (2D) growth on a FeO(111) thin film, forming large monolayer islands,[8] which display CO adsorption behavior that is different from bulk palladium.[9] However, we have found in the case of gold that the transition from 2D- to 3D-growth occurs at a very low coverage (≈ 0.1 monolayers).[10] Therefore, in the present work, we re-examine the situation at these low coverages to determine whether 2D gold structures also show deviations in CO adsorption behavior from the bulk.

For coverage up to 0.1 Å (effective thickness), gold forms islands of monolayer height (Figure 1 a). The inset in Figure 1 a shows that these monolayer islands are well shaped. At further increasing coverage the nucleation density remains fairly constant and two-layer particles form. Finally, at highest coverage studied (≈ 2 Å), Au deposits of up to 7 nm in diameter and 4–5 layers in height are seen (Figure 1 b). Note that unlike many other cases of nucleation and growth on oxide films[11] the metal particles nucleate on regular sites of the FeO films.[8] This implies that one may study the role of layer thickness independently of the influence of defects.

[*] Dr. C. Lemire, Dr. R. Meyer, Dr. Sh. Shaikhutdinov, Prof. H.-J. Freund
Fritz-Haber-Institut der Max-Planck-Gesellschaft
Faradayweg 4–6, Berlin 14195 (Germany)
Fax (+49) 30-8413-4101
E-mail: freund@fhi-berlin.mpg.de

[**] We acknowledge financial support from the EU Networks "Catalysis by Gold" (AURICAT) and "Reactivity of Cöean and Modified Oxide Surfaces" (Oxide Surfaces). R.M. thanks the Alexander von Humboldt Foundation for a fellowship.

 © 2004 Wiley-VCH Verlag GmbH & Co. KGaA, Weinheim DOI: 10.1002/anie.200352538

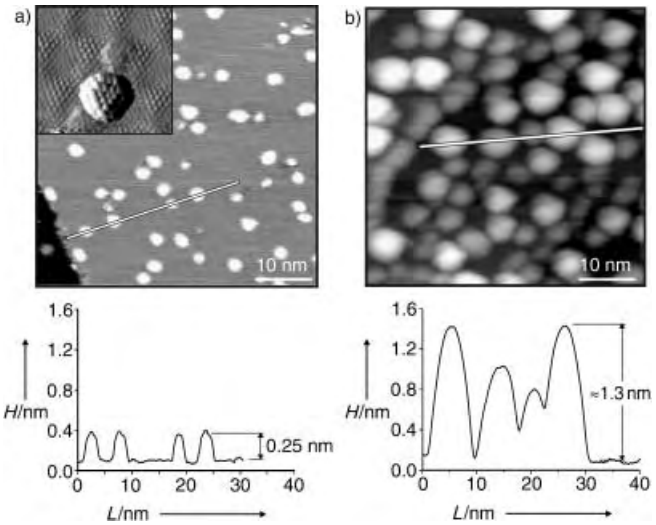


Figure 1. Room temperature STM images of Au deposited on FeO(111) and annealed to 500 K at different Au coverages: a) 0.1 Å, b) 2.0 Å. The line scans below the images clearly show islands of one atomic layer in height (in a) and 3D-particles up to five layers in height (in b). The inset in (a) shows a high-resolution STM image of the individual monolayer island (image size 7×7 nm^2). Tunneling parameters: $V_{tip}=200$ mV, $J=0.8$ nA.

Although particle size effects in CO adsorption have previously been observed for Au on other oxides,[10,12] the comparison of TPD spectra (Figure 2a) shows for thin islands of gold and large particles on FeO(111) that the desorption of CO is essentially independent of particle thickness. In all spectra, a low temperature feature at 130 K and a second feature at 200 K are observed, their relative intensities increase with increasing gold coverage.

The presence of two desorption peaks (at 140 and 185 K) in the CO TPD spectra has been observed for highly stepped Au(332) surfaces.[13] Gottfried et al. observed only a single peak at 140 K for CO chemisorption on Au(110),[14] a second, higher desorption-temperature feature grew after the surface was roughened by ion bombardment. This suggests that our low temperature feature may be associated with terrace sites while CO desorption at a higher temperature is associated with sites of lower gold coordination, such as the particle edges.

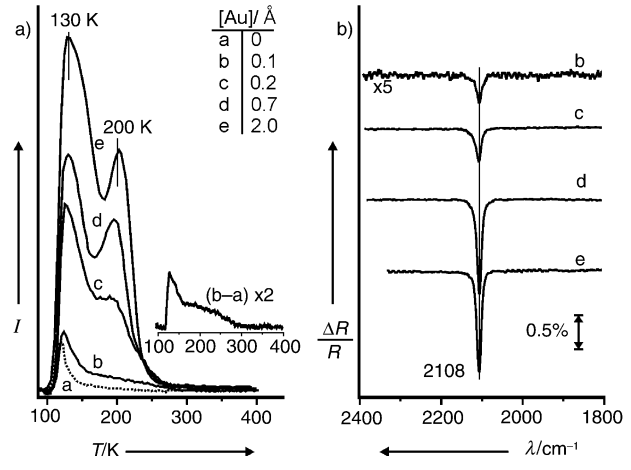


Figure 2. CO TPD (a) and IRAS (b) spectra comparing CO adsorption behavior for gold deposits as a function of Au coverage (in Å) following exposure of 1.5 Langmuir CO at 90 K. As FeO is inert to CO adsorption,[8,9] a small feature in the TPD detected at approximately 120 K is assigned to desorption from the sample holder. The difference spectrum is shown for the lowest coverage, for clarity.

A theoretical examination of the effects of dimensionality, has shown that unsupported gold monolayer islands should not adsorb CO at all.[15] However, it was noted that strain effects induced by an underlying support could lead to stronger adsorption behavior.[16,17] When grown on various substrates in an epitaxial manner gold has been found to exhibit both the lattice constant for Au(111)[18,19] and deformed-lattice constants[20,21]. Therefore, our observations could also be dependent upon the support. However, it seems unlikely that strain is playing a significant role in the adsorption of CO as the TPD spectra shown in Figure 2a are essentially identical not only to one another but also not significantly different from spectra obtained from CO desorption from single-crystal surfaces Au(332)[13] and from 3D gold particles on alumina.[10] In addition, the reactivity in real gold catalysts has been shown to be relatively independent of the support when the particles are properly dispersed.[3,4,22]

The IRAS spectra comparing CO adsorption states on thin Au layers and large Au particles on FeO(111) reveal only one signal at 2108 cm^{-1} regardless of the Au coverage (Figure 2b). Again, this result matches data previously obtained for "bulk" single-crystal gold surfaces[13,23,24] and large 3D particles.[25] However, particle size effects have been observed for varying gold coverages on alumina[25,26] and titania[12] which show red and blue shifts, respectively, of the CO signal as particle size is decreased. Although these shifts were only of the order of 10 cm^{-1}, for a system that is as notoriously insensitive as CO on Au, this represents evidence that the small particles supported on these supports may undergo changes in electronic structure as their size changes. As this is not the case for the monolayer islands observed here, one can conclude that issues of quantum confinement are not likely to be the determining factor.

To determine the origin of the two separate peaks in the TPD spectra (see Figure 2a), CO was dosed at 90 K on a sample with monolayer gold islands (0.1 Å coverage) which was subsequently examined by IRAS following heating to various temperatures (Figure 3). A thermal flash to 150 K revealed that the IRAS signal at 2108 cm^{-1} is not significantly reduced, although all CO from the low-temperature state of the TPD experiment must practically be desorbed. We continue to observe measurable IRAS intensity all the way up to 200 K with a slight blue shift of the band to 2115 cm^{-1}. As similar behavior was observed for larger gold particles (not shown), we assign the single IRAS peak observed (see Figure 2b) to the high-temperature desorption state (185 K) in TPD spectra (Figure 2a). This suggests that the quite intense desorption signal below 150 K in the TPD spectra for annealed samples is from CO molecules with no or low IRAS intensity.

 © 2004 Wiley-VCH Verlag GmbH & Co. KGaA, Weinheim

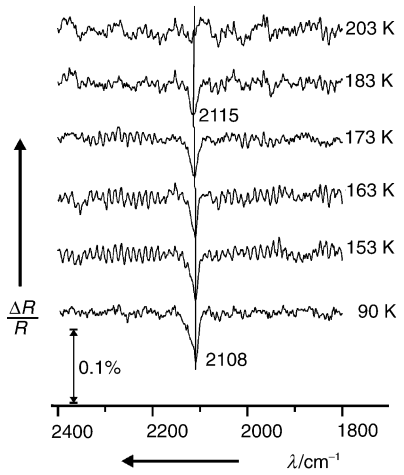


Figure 3. IRAS spectra for monolayer islands formed by deposition of 0.1 Å of gold. The sample was exposed to 1.5 Langmuir CO at 90 K and then heated to the listed temperature. All measurements were made at 90 K.

According to selection rules applied in an IRAS experiment,[27] only vibrations having a dipole moment perpendicular to the surface are excited. Therefore, it is probable that the low-temperature desorption state is due to CO weakly adsorbed parallel to the gold surface. This conclusion is supported by the observations of Dumas et al., whereby saturation of the IRAS signal at 2110 cm^{-1} was found at a CO coverage of 0.25 monolayers on a rough gold film. The appearance of signals for physisorbed CO was not seen until 0.6 monolayers, thereby suggesting adsorption of CO in this intermediate coverage regime occurred in a non-IR sensitive configuration.[24] Recent UV photoemission spectroscopy measurements of CO on Au(110) suggest that the majority of the chemisorbed CO may indeed be lying parallel to the surface.[14] The blue shift of the CO IR signal at increasing temperature (or decreasing CO coverage) is atypical of CO adsorption on other metal surfaces such as Pt or Pd.[28,29] However, this trend has been observed on other gold surfaces[13,25] and is generally attributed to the lack of back-donation of electrons from the metal to CO.[30]

Our data indicates that earlier hypotheses surrounding unusual adsorption/reaction properties of gold particles of particular thickness[6,7] are not valid for CO adsorption. It is possible to come to this conclusion because the gold particles nucleate on regular lattice sites of the FeO(111) film, unlike gold on other oxide surfaces, such as TiO_2, where gold exhibits a strong preference for defects.[31,32] Therefore, the influence of defects on the electronic structure of the particles may be excluded.

One could attribute the size effects observed to the interaction of such thin islands with oxygen. Campbell and co-workers[33] have reported that monolayer gold particles adsorb atomic oxygen with up to 40% higher binding energies than larger particles. However, as no detailed structural characterization of the particles was made, conclusions tied only to particle thickness are difficult.

From theoretical studies, the presence of highly uncoordinated gold atoms has been proposed to effect the strength of the adsorption of CO and oxygen,[15,34] and this has been demonstrated for the adsorption of CO on gold step and edge sites by using high resolution electron energy loss spectroscopy (HREELS) in an examination of Au films on Pd(111).[35,36] A single adsorption state at approximately 2120 cm^{-1} and the adsorption intensity could be correlated with the film deposition temperature and therefore the film roughness. That the desorption state extended to 300 K for CO from "as deposited" gold particles on an FeO(111) film[10] implies that in the process of annealing to 500 K, the highly uncoordinated atoms that are responsible for the presence of this high-temperature state are lost owing to sintering and restructuring effects. In turn, this indicates that the presence of defects in the substrate (which are absent in our system) may determine the reactivity and adsorption properties of gold, perhaps by stabilizing particles with a larger number of low-coordinated atoms.

In summary, using CO as a probe molecule we have found that monolayer islands of gold do not, in fact, have different adsorption properties to bulk gold. The exceptional activity of gold nanoparticles for the low-temperature CO oxidation reaction probably does not arise from quantum size effects as a result of particle thickness, but rather the presence of highly uncoordinated atoms.

Experimental Section

The work was performed in two separate ultrahigh vacuum (UHV) chambers (base pressure below 2×10^{-10} mbar) which were both equipped with differentially pumped quadrupole mass spectrometers (Hiden Analytical) for TPD measurements. The TPD spectra could be used for comparing and combining the STM structural data (measured in the first chamber) and spectroscopic (IRAS) data (measured in the second chamber).

Thin FeO(111) films were prepared on a Pt(111) single crystal by literature methods.[37–40] Gas exposures were performed with a directional doser. Gold was evaporatively deposited on the FeO film with a rate of ca. 0.1 Å min^{-1} (effective thickness) as calibrated by a quartz microbalance. A retarding potential was applied to the sample to avoid any sputtering caused by acceleration of the metal ions towards the sample. The Au coverage was measured in nominal thickness (in Å). For each measurement an Au/FeO sample, a new film was grown. After deposition of gold, the sample was heated to 500 K to thermally stabilize the system for TPD experiments. For CO desorption measurements, the sample was cooled to about 90 K, placed about 0.5 mm in front of the spectrometer shield (6 mm aperture) and heated with a rate of 5 $K\,s^{-1}$. IRAS data (Mattson RS-1 FTIR, spectral resolution 2 cm^{-1}) presented are transmission spectra in which the ratio of the signal with and without CO is given. All measurements were performed at 90 K. Exposure of the sample to CO did not result in any CO_2 formation and therefore there was no reduction of the oxide support. TPD and IRAS measurements could be repeated many times, which indicates that the surface did not undergo any changes.

Received: August 1, 2003
Revised: September 24, 2003 [Z52538]
Published Online: December 2, 2003

Keywords: carbon monoxide · gold · nanoparticles · oxide films · surface chemistry

 © 2004 Wiley-VCH Verlag GmbH & Co. KGaA, Weinheim

[1] G. C. Bond, *Surf. Sci.* **1985**, *156*, 966.
[2] M. Che, C. O. Bennett, *Adv. Catal.* **1989**, *36*, 55.
[3] M. Haruta, *CATTECH* **2002**, *6*, 102, and references therein.
[4] M. Haruta, *Chem. Rec.* **2003**, *3*, 75, and references therein.
[5] G. C. Bond, D. T. Thompson, *Catal. Rev. Sci. Eng.* **1999**, *41*, 319, and references therein.
[6] V. Valden, S. Pak, X. Lai, D. W. Goodman, *Catal. Lett.* **1998**, *56*, 7.
[7] M. Valden, X. Lai, D. W. Goodman, *Science* **1998**, *281*, 1647.
[8] Sh. K. Shaikhutdinov, R. Meyer, D. Lahav, M. Bäumer, T. Klüner, H.-J. Freund, *Phys. Rev. Lett.* **2003**, *91*, 076102.
[9] D. Lahav, T. Klüner, R. Meyer, Sh. K. Shaikhutdinov, H.-J. Freund, unpublished results.
[10] Sh. K. Shaikhutdinov, R. Meyer, M. Naschitzki, M. Bäumer, H.-J. Freund, *Catal. Lett.* **2003**, *86*, 211.
[11] M. Bäumer, H.-J. Freund, *Prog. Surf. Sci.* **1999**, *61*, 127.
[12] D. C. Meier, D. W. Goodman, *J. Am. Chem. Soc.*, submitted.
[13] C. Ruggiero, P. Hollins, *J. Chem. Soc. Faraday Trans.* **1996**, *92*, 4829.
[14] J. M. Gottfried, K. J. Schmidt, S. L. M. Schroeder, K. Christmann, *Surf. Sci.* **2003**, *536*, 206.
[15] M. Mavrikakis, P. Stoltze, J. Nørskov, *Catal. Lett.* **2000**, *64*, 10.
[16] M. Mavrikakis, B. Hammer, J. K. Nørskov, *Phys. Rev. Lett.* **1998**, *81*, 2819.
[17] M. Ø. Pedersen, S. Helveg, A. Ruban, I. Stensgaard, E. Laegsgaard, J. K. Nørskov, F. Besenbacher, *Surf. Sci.* **1999**, *426*, 395.
[18] F. Cosandey, T. Madey, *Surf. Rev. Lett.* **2001**, *8*, 73.
[19] S. Ferreo, A. Piednoir, C. R. Henry, *Nanoletters* **2001**, *1*, 227.
[20] S. Giorgio, C. Chapon, C. R. Henry, G. Nihoul, J. M. Penisson, *Philos. Mag. A* **1991**, *64*, 87.
[21] S. Giorgio, C. R. Henry, B. Pauwels, G. Van Tendeloo, *Mater. Sci. Eng. A* **2000**, *297*, 197.
[22] M. Okumura, S. Nakamura, S. Tsubota, T. Nakamura, M. Azuma, M. Haruta, *Catal. Lett.* **1998**, *51*, 53.
[23] Y. Jugnet, F. J. Cadete Santos Aires, C. Deranlot, L. Piccolo, J. C. Bertolini, *Surf. Sci.* **2002**, *521*, L639.
[24] P. Dumas, R. G. Tobin, P. L. Richards, *Surf. Sci.* **1986**, *171*, 579.
[25] D. R. Rainer, C. Xu, P. M. Holmblad, D. W. Goodman, *J. Vac. Sci. Technol. A* **1997**, *15*, 1653.
[26] C. Winkler, A. J. Carew, S. Haq, R. Raval, *Langmuir* **2003**, *19*, 717.
[27] T. Yates, T. E. Madey, *Vibrational Spectroscopy of Molecules on Surfaces*, Plenum, New York, **1987**.
[28] C. W. Olsen, R. I. Masel, *Surf. Sci.* **1988**, *201*, 444.
[29] J. Szanyi, W. K. Kuhn, D. W. Goodman, *J. Vac. Sci. Technol. A* **1993**, *11*, 1969.
[30] J. France, P. Hollins, *J. Electron Spectrosc. Relat. Phenom.* **1993**, *64*/65, 251.
[31] N. Lopez, J. K. Nørskov, *Surf. Sci.* **2002**, *515*, 175.
[32] L. Giordano, G. Pacchioni, T. Bredow, J. Fernández Sanz, *Surf. Sci.* **2001**, *471*, 21.
[33] V. A. Bondzie, S. C. Parker, C. T. Campbell, *J. Vac. Sci. Technol. A* **1999**, *17*, 1717.
[34] S. R. Bahn, N. Lopez, J. K. Norskov, K. W. Jacobsen, *Phys. Rev. B* **2002**, *66*, 081405.
[35] B. Gleich, M. Ruff, R. J. Behm, *Surf. Sci.* **1997**, *386*, 48.
[36] M. Ruff, S. Frey, B. Gleich, R. J. Behm, *Appl. Phys. A* **1998**, *66*, S513.
[37] G. H. Vurens, M. Salmeron, G. A. Somorjai, *Surf. Sci.* **1988**, *201*, 129.
[38] G. H. Vurens, V. Maurice, M. Salmeron, G. A. Somorjai, *Surf. Sci.* **1992**, *268*, 170.
[39] M. Ritter, W. Ranke, W. Weiss, *Phys. Rev. B* **1998**, *57*, 7240.
[40] W. Weiss, W. Ranke, *Prog. Surf. Sci.* **2002**, *70*, 1.

 © 2004 Wiley-VCH Verlag GmbH & Co. KGaA, Weinheim

Methane Activation

Coupling of Methane and Ammonia by Dinuclear Bimetallic Platinum–Coinage-Metal Cations PtM^+**

*Konrad Koszinowski, Detlef Schröder, and Helmut Schwarz**

Dedicated to Professor Lutz F. Tietze

The activation and functionalization of methane constitute continuing challenges for catalysis. One example of their industrial realization is given by the Degussa process for the large-scale production of hydrogen cyanide from methane and ammonia using platinum as heterogeneous catalyst [Eq. (1)].

$$CH_4 + NH_3 \xrightarrow{\langle Pt\rangle,\ 1500\,K} HCN + 3\,H_2 \qquad (1)$$

Our aim is the development of a gas-phase model for this process that may enhance the current mechanistic knowledge[1,2] and thus ultimately contribute to rational catalyst improvement. So far, atomic Pt^+, homonuclear clusters Pt_m^+ as well as small heteronuclear clusters $Pt_mAu_n^+$ ions have been studied.[3–7] Whereas all the homonuclear Pt_m^+ clusters investigated achieve CH_4 activation in the first reaction step,[8,9] the C–N coupling of the resulting carbene species $Pt_mCH_2^+$ with NH_3 only works for $m = 1$.[3–5] In contrast, the dinuclear cluster mediates C–N bond formation if one platinum atom is replaced by a gold atom.[6] This finding was ascribed to a particularly well-balanced binding situation in the $PtAuCH_2^+$ species. The bonding is strong enough to afford spontaneous activation of CH_4 on the one hand but does not prevent the CH_2 fragment from coupling with NH_3 on the other.[6] Recent results have shown, however, that the larger bimetallic $Pt_mAu_n^+$ clusters do not mediate the coupling step between the CH_2 moiety and NH_3, thus pointing to special features of $PtAu^+$.[10]

To further elucidate the remarkable role of the second metal in the dinuclear cluster, we have extended our studies to $PtCu^+$ and $PtAg^+$. The change from gold to its lighter congeners copper and silver is straightforward in view of their electronic and chemical similarities (note, however, that gold is distinguished from both copper and silver by the operation of much stronger relativistic effects[11]). As with $PtAu^+$, the reactions with CH_4, O_2, and NH_3 are investigated; for comparison, the reactivities of Cu_2^+ and Ag_2^+ are included

[*] Dr. K. Koszinowski, Dr. D. Schröder, Prof. Dr. H. Schwarz
Institut für Chemie, Technische Universität Berlin
Strasse des 17. Juni 135
10623 Berlin (Germany)
Fax: (+49) 30-314-21102
E-mail: Helmut.Schwarz@www.chem.tu-berlin.de

[**] Financial support by the Deutsche Forschungsgemeinschaft, the Fonds der Chemischen Industrie, and the Degussa AG is gratefully acknowledged. M = Cu, Ag, Au.

 DOI: 10.1002/anie.200352817 © 2004 Wiley-VCH Verlag GmbH & Co. KGaA, Weinheim

as well. Special attention is paid to the reactions of the metal carbenes with NH_3.

Similar to Pt_2^+ and $PtAu^+$,[7,9] both $PtCu^+$ and $PtAg^+$ efficiently activate CH_4 [Table 1 and Eq. (2)]. As the homonuclear coinage-metal dimers M_2^+ (M = Cu, Ag, Au) prove to be inert,[12] the platinum center appears essential for the reaction. This finding is as expected because a prerequisite for the spontaneous dehydrogenation of CH_4 is that the metal carbene formed is sufficiently thermochemically stable. Such a strong M_2^+–CH_2 interaction requires a double bond and, thus, at least two free valences at the metal core that are not available in the cases of Cu_2^+, Ag_2^+, and Au_2^+. Because promotion energies are rather high for the first- and second-row transition metals,[13] ds hybridization is not a viable option for the Cu_2^+ and Ag_2^+ dimers either.

Table 1: Bimolecular rate constants k and efficiencies (φ) for the reactions of the dinuclear cations $PtCu^+$, $PtAg^+$, $PtAu^+$, and Pt_2^+ as well as the corresponding carbene species.

Reaction	$k \times 10^{-10}$[cm^3 s^{-1}] (φ)			
	M = Cu	Ag	Au	Pt
$PtM^+ + CH_4 \rightarrow PtMCH_2^+ + H_2$	5.8 (0.59)	6.0 (0.63)	6.4[7] (0.67)	8.2[9] (0.85)
$PtM^+ + O_2 \rightarrow M^+ + PtO_2$	0.35 (0.064)	0.04 (0.01)	0[7]	1.3[9] (0.25)
$PtM^+ + NH_3 \rightarrow PtMNH^+ + H_2$	0	0	0	5.4[9] (0.27)
$\rightarrow MNH_3^+ + Pt$	8.5 (0.42)	3.9 (0.19)	0	0
$\rightarrow PtNH_3^+ + M$	0	0	2.8[10] (0.14)	0
$PtMCH_2^+ + NH_3 \rightarrow [Pt,M,C,H_3,N]^+ + H_2$	5.2 (0.26)	4.9 (0.24)	6.0[10] (0.30)	9.7[5] (0.49)

$$PtM^+ + CH_4 \rightarrow PtMCH_2^+ + H_2 \quad (2)$$

Exposure of $PtCu^+$ and $PtAg^+$ ions to O_2 results in cluster degradation [Eq. (3)]. Platinum's affinity for the +IV oxidation state encountered in PtO_2 is also well-known from classical solution chemistry; in contrast, copper and silver prefer lower oxidation numbers, in accordance with the product distribution observed.[14] The bias of copper and silver against high oxidation states also accounts for the lack of reactivity of Cu_2^+ and Ag_2^+ toward O_2.[12,15]

$$PtM^+ + O_2 \rightarrow M^+ + PtO_2 \quad (3)$$

The efficiency of cluster degradation decreases when changing M from Cu to Ag and completely vanishes for Au (Table 1).[7] Presumably, the high ionization energy of gold, IE(Au) = 9.23 eV, strongly disfavors the generation of Au^+ in comparison to Cu^+ and Ag^+ (IE(Cu) = 7.73 and IE(Ag) = 7.58 eV).[16] Moreover, the similar size and energy of the orbitals of Pt and Au are supposed to lead to a better overlap and a stronger binding that further hinders cluster degradation for $PtAu^+$. In contrast, the easier fragmentation of Pt_2^+ is attributed to the presence of open valences at the metal core that result in an increased interaction between the cluster ion and O_2.[9] Compared to PtM^+, the reaction of Pt_2^+ is also statistically favored because two reactive atoms are present.

A different kind of cluster degradation occurs upon reaction of $PtCu^+$ and $PtAg^+$ with NH_3 [Eq. (4)]. In this reaction type, the basic substrate substitutes one metal atom and yields MNH_3^+ complexes. Whereas neutral Pt is lost from $PtCu^+$ and $PtAg^+$, the analogous reaction of $PtAu^+$ gives $PtNH_3^+$ and Au; similar degradation processes are observed for the homonuclear M_2^+ coinage-metal clusters.[10,12]

$$PtM^+ + NH_3 \rightarrow MNH_3^+ + Pt \quad (4)$$

The product distributions found for the heteronuclear clusters can be explained by simple thermochemical considerations. An analysis of the heats of formation for the two alternative product combinations, $MNH_3^+ + Pt$ versus $PtNH_3^+ + M$, demonstrates that the former exit channel clearly lies lower in energy for M = Cu and Ag (Table 2), in agreement with experimental results.[16–21] For M = Au, the larger uncertainties of the thermochemical data available do not allow an unambiguous assessment. However, the tendency is for the relative stability of the $PtNH_3^+ + M$ product channel to be significantly enhanced compared to the situation for M = Cu and Ag, which is consistent with the different reactivities observed. In contrast, Pt_2^+ dehydrogenates NH_3 to form Pt_2NH^+.[9] This reaction again points to the high potential of platinum in terms of bond activation.

Table 2: Heats of formation $\Delta H_f^\ominus$ [kJ mol^{-1}] for the two alternative product pairs ($MNH_3^+ + Pt$ and $PtNH_3^+ + M$) observed in the reactions of PtM^+ with NH_3.[a]

M	$\Delta H_f^\ominus(MNH_3^+ + Pt)$	$\Delta H_f^\ominus(PtNH_3^+ + M)$	$\Delta\Delta H_f^\ominus$
Cu	1366 ± 15	1451 ± 12	85 ± 19
Ag	1365 ± 13	1398 ± 12	33 ± 18
Au	1479 ± 30	1479 ± 12	0 ± 32

[a] Calculated from $D_0(M^+\text{-}NH_3)$ (ref.[17–20]), $\Delta H_f^\ominus(M)$, $\Delta H_f^\ominus(NH_3)$ (ref. [21]) and IE(M) (ref. [16]).

The reactivity of the heteronuclear clusters towards NH_3 totally changes upon addition of the CH_2 fragment to the metal core. Instead of cluster degradation, dehydrogenation takes place exclusively [Table 1, Eq. (5)]. The dehydrogenation products formed from $PtAuCH_2^+$ and $Pt_2CH_2^+$, differ in their consecutive reactions. Thus, the homonuclear product ion, which was shown to have a $Pt_2C^+\cdot NH_3$ carbide structure, cannot activate NH_3 and only adds a second substrate molecule in a slow association reaction.[5,6] In marked contrast, $[Pt,Au,C,H_3,N]^+$ dehydrogenates another NH_3 molecule [Eq. 6 with M = Au (φ = 0.03)].[6,22]

$$PtMCH_2^+ + NH_3 \rightarrow [Pt,M,C,H_3,N]^+ + H_2 \quad (5)$$

$$[Pt,M,C,H_3,N]^+ + NH_3 \rightarrow [Pt,M,C,H_4,N_2]^+ + H_2 \quad (6)$$

 © 2004 Wiley-VCH Verlag GmbH & Co. KGaA, Weinheim

For both M = Cu and M = Ag, Equation (6) occurs as well, in the former case with rather high ($\varphi = 0.23$) and in the latter with low ($\varphi \approx 0.01$) efficiency. The fact that the primary product $[Pt,M,C,H_3,N]^+$ is still capable of NH_3 activation strongly suggests that also the first dehydrogenation step involves activation of NH_3. This issue was further probed by isotopic labeling.

For the reaction of $PtMCD_2^+$ with NH_3 three different product channels with distinct H/D distributions can in principle be expected [Eqs. (5a)–(5c)].

$$PtMCD_2^+ + NH_3 \rightarrow [Pt, M, C, H_3, N]^+ + D_2 \quad (5a)$$

$$\rightarrow [Pt, M, C, H_2, D, N]^+ + HD \quad (5b)$$

$$\rightarrow [Pt, M, C, H, D_2, N]^+ + H_2 \quad (5c)$$

In the case of the homonuclear $Pt_2CD_2^+$ carbene cluster, exclusively D_2 is lost [Eq. (5a) with M = Pt] which is only compatible with a $Pt_2C^+{\cdot}NH_3$ structure of the product ion.[5,6] In contrast, the reaction of $PtAuCD_2^+$ gives rise to all three possible products in a ratio of 70(±15):100:80 (±15) [Eqs. (5a)–(5c)].[6] Again, quite similar behavior is found for M = Cu and M = Ag. For M = Cu the ratio between the Reactions (5a)–(5c) amounts to 15(±10):100:25(±20) whereas it corresponds to ≤5:100:30(±5) for M = Ag. The rather high ranges of uncertainty assigned particularly to the product distribution for M = Cu mainly result from the complicating effect of D/H exchange reactions for the deuterium containing product ions which requires a determination of the branching ratios by extrapolation to zero reaction time.

The experimentally observed product ratios can be compared with two extreme cases. First, neglecting kinetic isotope effects, statistical H/D equilibration should yield a 17:100:50 distribution. Similarly, experiment finds larger fractions of H_2 [Eq. (5c)] than of D_2 [Eq. (5a)] elimination for M = Cu and Ag. In contrast, both product channels almost have equal probability for $PtAuCD_2^+$ which possibly indicates the presence of a second pathway leading to direct D_2/NH_3 exchange without NH_3 activation in this case.[6] Both $PtCuCD_2^+$ and $PtAgCD_2^+$ give a degree of HD loss that is higher than that expected from statistical scrambling. This behavior resembles the reactivity of mononuclear $PtCD_2^+$ that exclusively eliminates HD upon reaction with NH_3.[3] A quantum-chemical and experimental characterization of this process established an aminocarbene structure $PtC(D)NH_2^+$ for the product ion.[4] Given the similarity between the reactivities of $PtCD_2^+$ and $PtMCD_2^+$ (M = Cu and Ag) towards NH_3, analogous structures of the product ions appear likely. The partial H/D scrambling found for the dinuclear ions could point to a secondary interaction between the M atom and the attacking NH_3 molecule in the course of the reaction. In the case of $PtAuCD_2^+$, the enhanced scrambling observed is in line with a particularly favorable M–H binding for M = Au, which results from both the relatively high electronegativity of gold and the large spatial extension of its 6s orbital.

Further evidence for the formation of aminocarbene complexes is provided by the subsequent reactions of the labeled ions. In the case of mononuclear $PtC(D)NH_2^+$, exclusively HD is lost upon reaction with NH_3. This result is consistent with the theoretically predicted bisaminocarbene structure ($PtC(NH_2)_2^+$) for the secondary product.[3,4] Whereas H/D exchange reactions presumably compete with the inefficient subsequent reactions of the $[Pt,Ag,C,H_x,D_y,N]^+$ species ($x + y = 3$) and thus prevent an assessment of the label distribution in the products, the situation is more favorable for their faster reacting copper counterparts. Thus the products $[Pt,Cu,H_4,N_2]^+$ and $[Pt,Cu,H_3,D,N_2]^+$ are found in a ratio of 100:20(±10). This distribution fully agrees with the transformation of the aminocarbene structures into bisaminocarbene structures on substitution of the carbene H or D atom by an NH_2 group [Eqs. (6a)–(6c)].

$$PtCuC(H)NH_2^+ + NH_3 \rightarrow PtCuC(NH_2)_2^+ + H_2 \quad (6a)$$

$$PtCuC(D)NH_2^+ + NH_3 \rightarrow PtCuC(NH_2)_2^+ + HD \quad (6b)$$

$$PtCuC(D)NHD^+ + NH_3 \rightarrow PtCuC(NH_2)(NHD)^+ + HD \quad (6c)$$

In conclusion, we find that both $PtCu^+$ and $PtAg^+$ display reactivities much resembling that of $PtAu^+$. Particularly, all three dinuclear platinum–coinage-metal cluster ions PtM^+ mediate coupling of CH_4 and NH_3, whereas neither Pt_2^+ nor M_2^+ do so.[23] Given the considerable differences between Cu, Ag, and Au in terms of ionization energies, atomic radii, and orbital energies, the parallel reactivities of the PtM^+ cluster ions are quite surprising. Possibly, the specific electronic structure of the PtM^+ ions is essential for C–N bond formation between CH_4 and NH_3. An experimental verification of this hypothesis requires the investigation of further isoelectronic species, such as Pt_2^0 and $PtIr^-$. Moreover, though extremely demanding, computational methods could be helpful in answering this question as well.

Experimental Section

The dinuclear cluster ions Cu_2^+, Ag_2^+, $PtCu^+$, and $PtAg^+$ were generated by laser desorption/ionization from the corresponding solid metals (Cu, Ag, PtCu (2:1 weight ratio), and PtAg (2:1), respectively) followed by supersonic expansion.[24,25] After transfer of the ions into the cell of a CMS 47X Fourier-transform ion-cyclotron-resonance mass spectrometer,[26] the most abundant dimer ion ($^{63}Cu_2^+$, $^{107}Ag^{109}Ag^+$, $^{63}Cu^{196}Pt^+/^{65}Cu^{194}Pt^+$, and $^{107}Ag^{196}Pt^+/^{109}Ag^{194}Pt^+$; the latter two combinations of isotopomers are not resolved in the broadband detection-mode) was selected by means of the FERETS ion-ejection method.[27] After thermalization with pulsed-in Ar buffer gas, reactions with the leaked-in substrates were studied at variable reaction times. Bimolecular rate constants k (with estimated errors of ±30% for CH_4 and O_2[28] and ±50% for NH_3) were derived from the decline of the reactant ion and the increase of the product ions on the basis of the pseudo-first-order approximation. Reaction efficiencies $\varphi = k/k_{cap}$ were calculated according to capture theory.[29] For the investigation of the reactivity of the metal carbenes, these were produced by pulsing-in CH_4 to the mass-selected and thermalized dimer ions. Otherwise, consecutive reactions were analyzed by numerical routines (for details, see ref. [30,31]).

Received: September 8, 2003 [Z52817]
Published Online: December 5, 2003

 © 2004 Wiley-VCH Verlag GmbH & Co. KGaA, Weinheim

Keywords: C–H activation · cluster compounds · copper · gold · platinum · silver

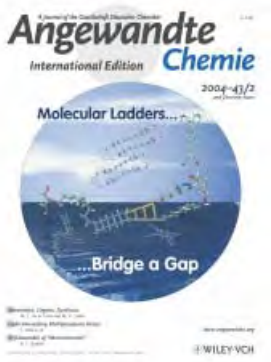
[1] D. Hasenberg, L. D. Schmidt, *J. Catal.* **1986**, *97*, 156.
[2] A. Bockholt, I. S. Harding, R. M. Nix, *J. Chem. Soc. Faraday Trans.* **1997**, *93*, 3869.
[3] M. Aschi, M. Brönstrup, M. Diefenbach, J. N. Harvey, D. Schröder, H. Schwarz, *Angew. Chem.* **1998**, *110*, 858; *Angew. Chem. Int. Ed.* **1998**, *37*, 829.
[4] M. Diefenbach, M. Brönstrup, M. Aschi, D. Schröder, H. Schwarz, *J. Am. Chem. Soc.* **1999**, *121*, 10614.
[5] K. Koszinowski, D. Schröder, H. Schwarz, *Organometallics* **2003**, *22*, 3819.
[6] K. Koszinowski, D. Schröder, H. Schwarz, *J. Am. Chem. Soc.* **2003**, *125*, 3676.
[7] K. Koszinowski, D. Schröder, H. Schwarz, *ChemPhysChem*, **2003**, *4*, 1233.
[8] U. Achatz, C. Berg, S. Joos, M. K. Beyer, G. Niedner-Schatteburg, V. E. Bondybey, *Chem. Phys. Lett.* **2000**, *320*, 53.
[9] K. Koszinowski, D. Schröder, H. Schwarz, *J. Phys. Chem. A* **2003**, *107*, 4999.
[10] K. Koszinowski, D. Schröder, H. Schwarz, *Organometallics*, in press.
[11] H. Schwarz, *Angew. Chem.* **2003**, *115*, 4580; *Angew. Chem. Int. Ed.* **2003**, *42*, 4442, and references therein.
[12] With regard to the reactivity of Ag_2^+, see also: P. Sharpe, C. J. Cassady, *Chem. Phys. Lett.* **1992**, *191*, 111.
[13] K. K. Irikura, J. L. Beauchamp, *J. Phys. Chem.* **1991**, *95*, 8344.
[14] A. F. Holleman, E. Wiberg, *Lehrbuch der Anorganischen Chemie*, 101st ed., Walter de Gruyter, Berlin, **1995**.
[15] M. P. Irion, A. Selinger, *Chem. Phys. Lett.* **1989**, *158*, 145.
[16] http://webbook.nist.gov/.
[17] R. Liyanage, M. L. Styles, R. A. J. O'Hair, P. B. Armentrout, *Int. J. Mass Spectrom.* **2003**, *227*, 47.
[18] D. Schröder, H. Schwarz, J. Hrušák, P. Pyykkö, *Inorg. Chem.* **1998**, *37*, 624.
[19] D. Walter, P. B. Armentrout, *J. Am. Chem. Soc.* **1998**, *120*, 3176.
[20] H. El Aribi, C. F. Rodriquez, T. Shoeib, Y. Ling, A. C. Hopkinson, K. W. M. Siu, *J. Phys. Chem. A* **2002**, *106*, 8798.
[21] M. W. Chase, Jr., C. A. Davies, J. R. Downey, Jr., D. J. Frurip, R. A. McDonald, A. N. Syverud, *J. Phys. Chem. Ref. Data* **1985**, *14*, Suppl. 1.
[22] In Reaction 6 with M = Au, an additional elimination of AuH yielding $[Pt,C,H_5,N_2]^+$ takes place as a competing process ($\varphi = 0.03$).[6,10] Apparently, this reaction is facilitated by the relatively strong binding in AuH, D_0(Au-H) = 300 kJ mol^{-1} (G. Herzberg, *Molecular Spectra and Structure*, *Vol. I*, reprint ed., Krieger, Malabar, **1989**).
[23] The homonuclear coinage-metal dimers fail to activate CH_4. $Au_2CH_2^+$ generated in other ways cannot be coupled with NH_3 either.[10] The analogous reactivities of $Cu_2CH_2^+$ and $Ag_2CH_2^+$ could not be probed because there are no practical gas-phase syntheses for these ions (e.g., reaction of M_2^+ with CH_3X, X = Cl, Br, and I, does not afford the desired result).
[24] M. Engeser, T. Weiske, D. Schröder, H. Schwarz, *J. Phys. Chem. A.* **2003**, *107*, 2855.
[25] C. Berg, T. Schindler, M. Kantlehner, G. Niedner-Schatteburg, V. E. Bondybey, *Chem. Phys.* **2000**, *262*, 143.
[26] K. Eller, W. Zummack, H. Schwarz, *J. Am. Chem. Soc.* **1990**, *112*, 621.
[27] R. A. Forbes, F. H. Laukien, J. Wronka, *Int. J. Mass Spectrom. Ion Processes* **1988**, *83*, 23.
[28] D. Schröder, H. Schwarz, D. E. Clemmer, Y.-M. Chen, P. B. Armentrout, V. I. Baranov, D. K. Böhme, *Int. J. Mass Spectrom. Ion Processes* **1997**, *161*, 175.
[29] T. J. Su, *J. Chem. Phys.* **1988**, *88*, 4102; T. J. Su, *J. Chem. Phys.* **1988**, *89*, 5355.
[30] U. Mazurek, H. Schwarz, *ICR Kinetics*, Technische Universität Berlin, **1998**.
[31] U. Mazurek, *Dissertation*, TU Berlin, D83, **2002**.

 © 2004 Wiley-VCH Verlag GmbH & Co. KGaA, Weinheim

Cover Picture

Xiuchun Gao,[+] Tomislav Friščić, and Leonard R. MacGillivray*

A supramolecular approach to covalent synthesis allows the photoconversion of polyenes into ladderanes, which are challenging synthetic targets discovered in the lipid membranes of the anammox bacteria that participate in the oceanic nitrogen cycle. In their Communication on page 232 ff. X. Gao, T. Friščić, and L. R. MacGillivray explain how solid-state synthesis directed by molecular templates can provide gram quantities of the ladderanes in quantitative yield. Thus, ladderanes bridge a gap between conventional synthesis, supramolecular chemistry, and biology.



Contents

Angewandte EarlyView

The following articles are available online (in Wiley InterScience). You can find them at www.angewandte.org, under Full Text, Early View.

D. Fenske, C. Persau, S. Dehnen, C. E. Anson:*
Syntheses and Crystal Structures of the Ag–S Cluster Compounds $[Ag_{70}S_{20}(SPh)_{28}(dppm)_{10}]$ $(CF_3CO_2)_2$ and $[Ag_{262}S_{100}(StBu)_{62}(dppb)_6]$
DOI: 10.1002/anie.200352351
Published online: December 9, 2003

T. Auletta, B. Dordi, A. Mulder, A. Sartori, S. Onclin, C. M. Bruinink, M. Péter, C. A. Nijhuis, H. Beijleveld, H. Schönherr, G. J. Vancso, A. Casnati, R. Ungaro, B. J. Ravoo, J. Huskens, D. N. Reinhoudt*:*
Writing Patterns of Molecules on Molecular Printboards
DOI: 10.1002/anie.200352767
Published online: December 9, 2003

J. Steiner, G. Stößer, H. Schnöckel:*
$[Ga_{51}(PtBu_2)_{14}Br_6]^{3-}$: An Elementoid Gallium Cluster with Metalloid and Nonmetalloid Structural Elements
DOI: 10.1002/anie.200352472
Published online: December 9, 2003

Articles judged by the referees or the editor as being either very important or very urgent are immediately edited, proof-read, and electronically published once the manuscript has arrived in the editorial office in final form. As long as there is no page number available these articles should be cited in the following manner:

Author(s) *Angew. Chem. Int. Ed.*, online publication date, DOI.

Meeting Reviews

Quantum Mechanics and Chemistry: The Relevance of Nonlocality and Entanglement for Molecules — **144 – 145** — *A. Chatzidimitriou-Dreismann and M. Arndt*

Books

Protein–Ligand Interactions — **146** — Hans-Joachim Böhm, Gisbert Schneider — *reviewed by G. Hessler*

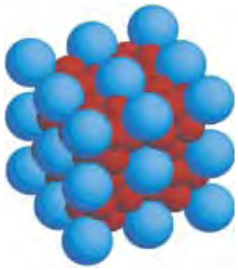
Drug Bioavailability — **146** — Han van de Waterbeemd, Hans Lennernäs, Per Artursson — *reviewed by S. Grüneberg, S. Güssregen*

Highlights

Functional Materials

A. L. Rogach* — **148 – 149**

Binary Superlattices of Nanoparticles: Self-Assembly Leads to "Metamaterials"



A simple bottom-up approach allows the aggregation of nanoparticles to a variety of superlattices with controlled collective properties. For example, monodisperse magnetic Fe_2O_3 nanocrystals (blue) and PbSe semiconductor quantum dots (red) form a binary three-dimensional AB_{13}-type superlattice by self-assembly (see picture).

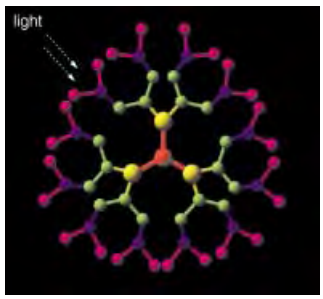
Minireviews

Artificial Photosynthesis

M.-S. Choi, T. Yamazaki, I. Yamazaki, T. Aida* — **150 – 158**

Bioinspired Molecular Design of Light-Harvesting Multiporphyrin Arrays

Coming to the point: Light-harvesting multiporphyrin arrays can be seen as molecular models for photochemical events in biological photosynthesis. This Minireview examines the structural parameters that enable the design of arrays with a large absorption cross-section for visible light and allow a vectorial transfer of the excitation energy to a designated point (see picture).



© 2004 Wiley-VCH Verlag GmbH & Co. KGaA, Weinheim

Reviews

Inspiration or imitation? A biomimetic strategy pursues the development of synthetic methodology that imitates a natural biogenetic process. Not all biosyntheses can be mimicked in vitro. A biomimetic route to a natural product is more likely to be successful when the involvement of enzymes in the biological route being mimicked is low.



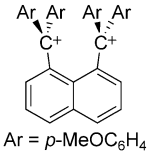
Biomimetic Synthesis

M. C. de la Torre,*
M. A. Sierra* ——— **160 – 181**

Comments on Recent Achievements in Biomimetic Organic Synthesis

Communications

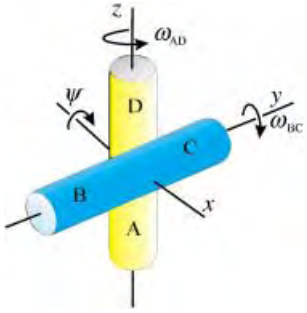
A voracious appetite for electrons is displayed by the 1,8-bis(methylium)naphthalenediyl dication (see picture). Cooperative effects arising from the proximity of the methylium centers intensify the electron affinity of this molecule and make it very sensitive to reduction.



Arene Electrochemistry

H. Wang, F. P. Gabbaï* ——— **184 – 187**

Synthesis and Reactivity of a 1,8-Bis(methylium)naphthalenediyl Dication



Only a small set of magnetic-field-induced residual dipolar couplings is required to determine the global structure of branched nucleic acids. This is demonstrated for the example of the Holliday junction (shown schematically) after ^{13}C labeling in the ribose of specific thymine residues. Accurate calculation of the magnetic-field-induced alignment tensor for any nucleic acid conformation allows the reduction in the required number of parameters.

Branched Nucleic Acids

B. N. M. van Buuren, J. Schleucher, V. Wittmann, C. Griesinger, H. Schwalbe, S. S. Wijmenga* ——— **187 – 192**

NMR Spectroscopic Determination of the Solution Structure of a Branched Nucleic Acid from Residual Dipolar Couplings by Using Isotopically Labeled Nucleotides

For the USA and Canada:
ANGEWANDTE CHEMIE International Edition (ISSN 1433-7851) is published weekly by Wiley-VCH PO Box 191161, D 69451 Weinheim, Germany. Air freight and mailing in the USA by Publications Expediting Inc. 200 Meacham Ave., Elmont, NY 11003. Periodicals postage paid at Jamaica NY 11431. US POSTMASTER: send address changes to *Angewandte Chemie*, Wiley-VCH, 111 River Street, Hoboken, NJ 07030. Annual subscription price for institutions: Europe € 3430.00/3118.00; outside Europe US$ 4499.00/4090.00 (valid for print and electronic/print or electronic delivery); for individuals who are personal members of a national chemical society, or whose institution already subscribes, or who are retired or self-employed consultants, print only: Europe € 248.00/outside Europe US$ 378.00. Postage and handling charges included. All Wiley-VCH prices are exclusive VAT.

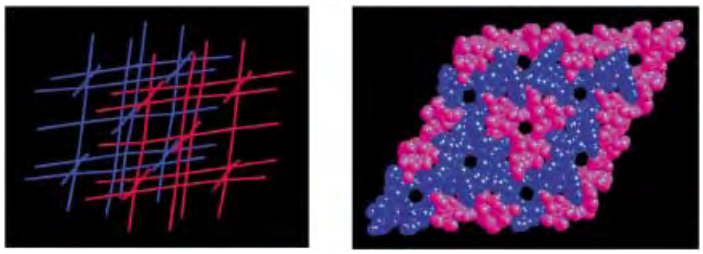
 © 2004 Wiley-VCH Verlag GmbH & Co. KGaA, Weinheim

Contents

3D Copper Coordination Polymer

X.-H. Bu,* M.-L. Tong, H.-C. Chang, S. Kitagawa,* S. R. Batten ____ **192 – 195**

A Neutral 3D Copper Coordination Polymer Showing 1D Open Channels and the First Interpenetrating NbO-Type Network



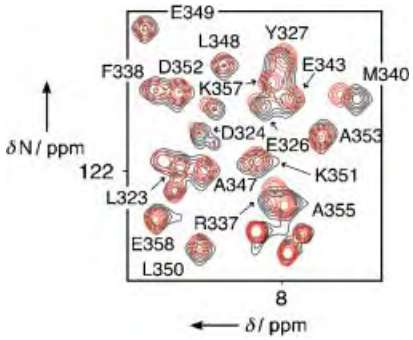
Being bulky is good: The use of a bulky multifunctional ligand is key to the successful construction of a neutral 3D copper coordination polymer that shows 1D open channels and the first interpenetrating NbO-type network (see picture). The absorption properties of the complex are investigated.

Molecular Recognition

X. Salvatella, M. Martinell, M. Gairí, M. G. Mateu, M. Feliz, A. D. Hamilton, J. de Mendoza, E. Giralt* ____ **196 – 198**

A Tetraguanidinium Ligand Binds to the Surface of the Tetramerization Domain of Protein P53

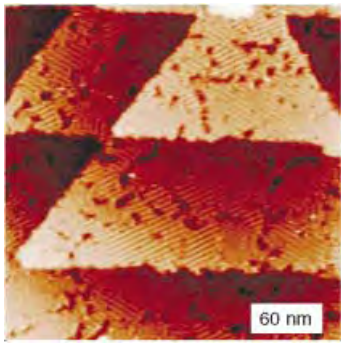
A key therapeutic target in the fight against cancer, the tetramerization domain of the tumor suppressor protein P53 binds a tetraguanidinium ligand at its surface. A specific interaction involving four salt bridges was detected by two NMR-based techniques (see figure). The design of protein-surface ligands is a major challenge because of competition between the ligand and water molecules.



DNA on Gold Surfaces

H. Wackerbarth, M. Grubb, J. Zhang, A. G. Hansen, J. Ulstrup* ____ **198 – 203**

Dynamics of Ordered-Domain Formation of DNA fragments on Au(111) with Molecular Resolution



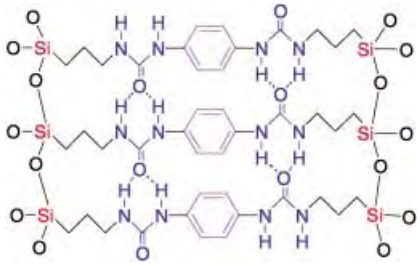
Binding of single-strand oligonucleotides with ten adenine bases to single-crystal Au(111) through hexamethylene thiol has been studied by cyclic voltammetry and in situ scanning tunneling microscopy. The high surface coverage is in keeping with adsorption in the upright position. Strongly negative potentials give long-range ordered-adsorbate domains, which are characterized to single-molecule resolution (see picture).

Hybrid Silica

J. J. E. Moreau,* B. P. Pichon, M. Wong Chi Man, C. Bied, H. Pritzkow, J.-L. Bantignies, P. Dieudonné, J.-L. Sauvajol ____ **203 – 206**

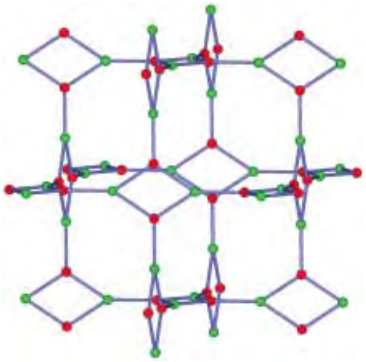
A Better Understanding of the Self-Structuration of Bridged Silsesquioxanes

The best solution? A highly crystalline hybrid silica has been obtained through the hydrolysis of a precursor in the solution phase. The self-organized structure of the lamellar material consists of diureido–phenylene bridging units (see picture); structural comparisons of this material and its molecular precursor show the existence of similar hydrogen-bonding interactions in both structures.



© 2004 Wiley-VCH Verlag GmbH & Co. KGaA, Weinheim

One-pot synthesis of 1,2,4-triazoles: Hydrothermal treatment of copper(II) ions, ammonia, and nitriles yielded two copper(I) triazolate coordination polymers, the structures of which have unearthed the unprecedented formation of triazolates through the cycloaddition of NH_3 and RC≡N. The polymers exhibit novel network topologies based on trigonal nodes (see picture).



Copper Triazolate Networks

J.-P. Zhang, S.-L. Zheng, X.-C. Huang, X.-M. Chen* ——— 206 – 209

Two Unprecedented 3-Connected Three-Dimensional Networks of Copper(I) Triazolates: In Situ Formation of Ligands by Cycloaddition of Nitriles and Ammonia

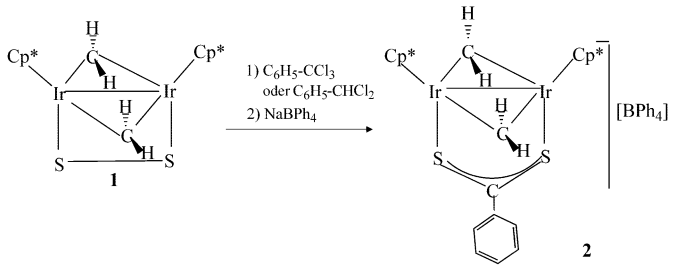
Clusters of magnets: The first examples of manganese single-molecule magnets (SMMs) consisting exclusively of trivalent metal centers are reported. These are hexanuclear clusters containing the $[Mn^{III}_6(\mu_3\text{-}O)_2(\mu_2\text{-}OR)_2]^{12+}$ core (see picture, Mn yellow, O red) and have an $S = 4$ ground state. Variation of the oxygen-containing ligands allows a potentially large family of SMMs to be prepared.



Magnetic Properties

C. J. Milios, C. P. Raptopoulou, A. Terzis, F. Lloret, R. Vicente, S. P. Perlepes,* A. Escuer* ——— 210 – 212

Hexanuclear Manganese(III) Single-Molecule Magnets

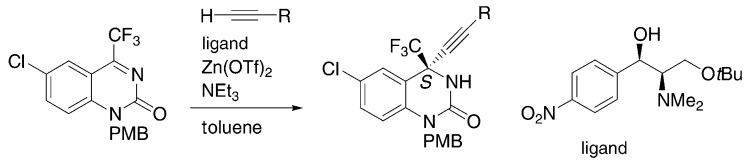


Cleaning up with sulfur: The multiple C–Cl bonds of toxic, polychlorinated organic compounds can be activated by the coordinated S_2 ligand of complex **1**. For example, reaction of **1** with C_6H_5-$CHCl_2$ or C_6H_5-CCl_3 in methanol forms a dithiobenzoate complex, which on addition of $NaBPh_4$ provides complex **2**; $Cp^* = C_5Me_5$.

Bond Activation

T. S. Lobana,* K. Isobe,* H. Kitayama, T. Nishioka, I. Kinoshita ——— 213 – 215

Activation of C–Cl and C–H Bonds by Ligated S_2^{2-} Ions: Conversion of Organic Chlorides into Organosulfur Compounds in *cis*-$[(IrCp^*)_2(\mu\text{-}CH_2)_2(\mu\text{-}S_2R)]^+$



Second-generation nonnucleoside reverse transcriptase inhibitors can now be efficiently prepared. Alkynylation of the ketimine (see scheme; PMB = *p*-methoxybenzyl) leads to the synthesis of tertiary amines in excellent yield and with high enantioselectivity. The ligand used in the reaction is a derivative of chloramphenicol base.

Enantioselective Synthesis

B. Jiang,* Y.-G. Si ——— 216 – 218

Highly Enantioselective Construction of a Chiral Tertiary Carbon Center by Alkynylation of a Cyclic *N*-Acyl Ketimine: An Efficient Preparation of HIV Therapeutics

 © 2004 Wiley-VCH Verlag GmbH & Co. KGaA, Weinheim

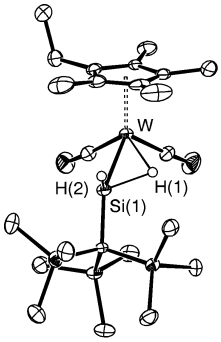
Contents

Silylene–Tungsten Complexes

T. Watanabe, H. Hashimoto, H. Tobita* ——— 218 – 221

Hydrido(hydrosilylene)tungsten Complexes with Strong Interactions between the Silylene and Hydrido Ligands

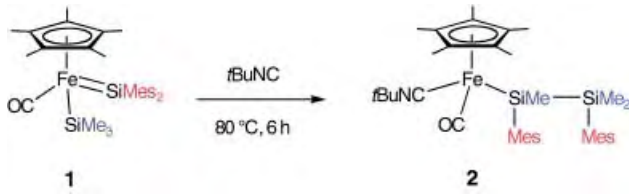
A hydrido ligand bridging a W=Si bond is present in a novel hydrido(hydrosilylene)–tungsten complex (see picture) and its η^5-C_5Me_5 analogue, which were synthesized by photolysis of $[Cp'W(CO)_3Me]$ ($Cp' = \eta^5$-C_5Me_4Et, η^5-C_5Me_5) in the presence of $H_3SiC(SiMe_3)_3$. This strong hydrido–silylene interligand interaction was revealed by NMR spectroscopic and X-ray structural analyses.



Silyl(silylene)–Iron Complexes

H. Tobita,* A. Matsuda, H. Hashimoto, K. Ueno, H. Ogino ——— 221 – 224

Direct Evidence for Extremely Facile 1,2- and 1,3-Group Migrations in an $FeSi_2$ System

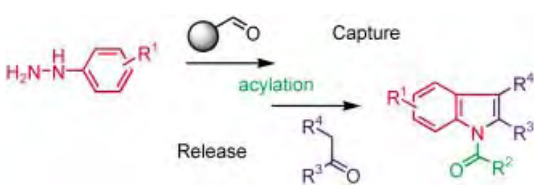


Facile 1,2- and 1,3-group migrations: The first donor-free silyl(silylene)–iron complex **1** has been prepared and structurally characterized (see scheme). This complex reacts with *t*BuNC under mild heating to give a disilanyl complex **2** through 1,3-alkyl and aryl migration and 1,2-silyl migration processes. Complex **2** is an example of how organosilicon species bound to transition-metal centers can change their form in a dynamic fashion (Mes = 2,4,6-trimethylphenyl).

Kinase Inhibitors

C. Rosenbaum, P. Baumhof, R. Mazitschek, O. Müller, A. Giannis,* H. Waldmann* ——— 224 – 228

Synthesis and Biological Evaluation of an Indomethacin Library Reveals a New Class of Angiogenesis-Related Kinase Inhibitors

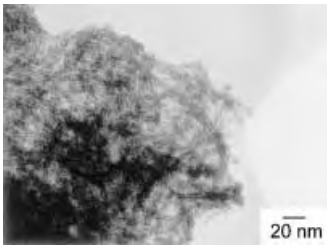


Capture and release: Indomethacin has served as a lead compound for the synthesis of a library that revealed a new class of kinase inhibitors. A synthetic approach termed "resin-capture-release" was developed (see scheme) that allowed a large library to be synthesized easily. Six of the library compounds were found to be inhibitors of angiogenesis-related receptor tyrosine kinases.

Nanotubular Materials

T. Kijima,* T. Yoshimura, M. Uota, T. Ikeda, D. Fujikawa, S. Mouri, S. Uoyama ——— 228 – 232

Noble-Metal Nanotubes (Pt, Pd, Ag) from Lyotropic Mixed-Surfactant Liquid-Crystal Templates



Platinum, palladium, and silver nanotubes of 6–7-nm outer diameters are synthesized by the reduction of metal salts confined to lyotropic mixed-surfactant liquid crystals (see picture). The lyotropic liquid crystals act as a template and are formed by the 1:1 combination of medium and large surfactant molecules into a hexagonal array of cylindrical rodlike micelles.

© 2004 Wiley-VCH Verlag GmbH & Co. KGaA, Weinheim

Steps in supramolecular chemistry: Molecules in the form of linear templates have been used to preorganize polyenes in the solid state through hydrogen-bonding interactions. The polyenes can then undergo [2+2] photocycloaddition reactions to produce [3]- and [5]ladderanes in gram quantities and 100% yield. (The picture shows the obtained [5]ladderane.)

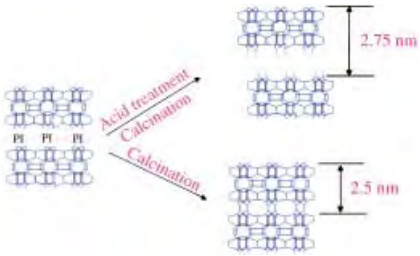


Ladderanes

X. Gao, T. Friščić, L. R. MacGillivray* ——— 232 – 236

Supramolecular Construction of Molecular Ladders in the Solid State

With an analogous structure to an MWW lamellar precursor, a titanosilicate (denoted Ti-YNU-1) has been developed by using a postsynthetic acid-treatment and calcination procedure (see scheme). The material behaves as a large-pore zeolite, showing high activity, selectivity, and stability towards the liquid-phase epoxidation of bulky cycloalkenes using H_2O_2 as an oxidant.

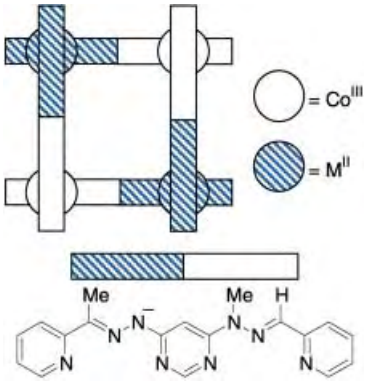


Zeolite Synthesis

W. Fan, P. Wu, S. Namba, T. Tatsumi* ——— 236 – 240

A Titanosilicate That Is Structurally Analogous to an MWW-Type Lamellar Precursor

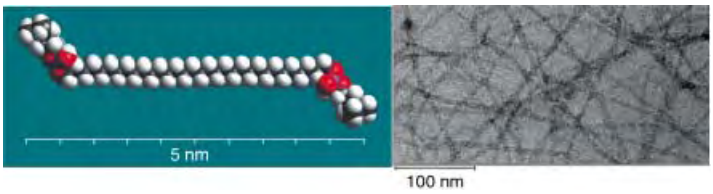
Regioselective, redox, and chiroselective features were used in a three-tiered synthesis to construct $Co^{III}_2M^{II}_2$ [2×2] grid-type arrays (M^{II} = Co^{II}, Zn^{II}, Fe^{II}; see picture). The assemblies are based on a bis(hydrazone) ligand containing ionizable and non-ionizable compartments. This route allows the cobalt oxidation state to be selectively modified according to the charge on the hydrazone moiety.



Metal-Directed Self-Assembly

L. H. Uppadine, J.-M. Lehn* — 240 – 243

Three-Level Synthetic Strategy Towards Mixed-Valence and Heterometallic [2×2] Gridlike Arrays



Nanomaterials

K. Köhler, G. Förster, A. Hauser, B. Dobner, U. F. Heiser, F. Ziethe, W. Richter, F. Steiniger, M. Drechsler, H. Stettin, A. Blume* ——— 245 – 247

Self-Assembly in a Bipolar Phosphocholine–Water System: The Formation of Nanofibers and Hydrogels

The bolaamphiphile PC-C32-PC with two phosphocholine headgroups and one long C_{32} alkyl chain (see the space-filling model, left) forms nanofibrils in aqueous solution at room temperature solely by hydrophobic interactions. The gels that result were studied by electron microscopy (image on the right), differential scanning calorimetry, and FT-IR spectroscopy. At higher temperatures the fibers "melt" and small aggregates form.

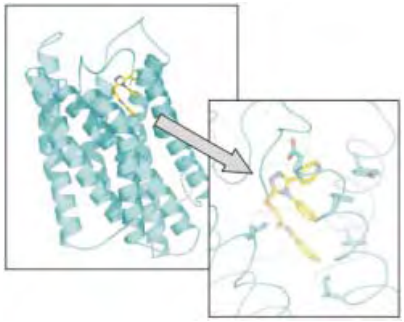
 © 2004 Wiley-VCH Verlag GmbH & Co. KGaA, Weinheim

Contents

Protein Models

A. Evers, G. Klebe* ——— 248 – 251

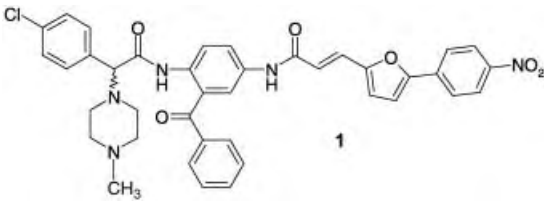
Ligand-Supported Homology Modeling of G-Protein-Coupled Receptor Sites: Models Sufficient for Successful Virtual Screening



Virtual proteins: A computer method is described that uses ligand information in the homology modeling of proteins. This method was used to construct a model of a G-protein-coupled receptor, which was successfully used as a basis for structure-based drug design by virtual computer screening (see picture).

Enzyme Inhibitors

J. Wiesner, K. Kettler, J. Sakowski, R. Ortmann, A. M. Katzin, E. A. Kimura, K. Silber, G. Klebe, H. Jomaa, M. Schlitzer* ——— 251 – 254



1

Farnesyltransferase Inhibitors Inhibit the Growth of Malaria Parasites In Vitro and In Vivo

The inhibition of farnesyltransferase was recently suggested as a new strategy for malaria therapy. A class of farnesyltransferase inhibitors such as **1** has been prepared which have in vivo activity in a murine malaria model. These inhibitors significantly reduce the farnesylation of parasite proteins.

Communications labeled with this symbol have been judged by two referees as being "very important papers".

The publication of Communications labeled with this symbol has been accelerated because of their topical or highly competitive nature.

Deadline for recruitment adverts

47/2003	November 14	Publication date:	December 8
48/2003	November 21	Publication date:	December 15

Angewandte Chemie International Edition
Advertising Sales Department:
Marion Schulz
Phone: 0 62 01 – 60 65 65
Fax: 0 62 01 – 60 65 50
E-Mail: MSchulz@wiley-vch.de

Place an advert in the printed version and have it made available online for 1 month, free of charge!

Service

Keywords ——— 256

Authors ——— 257

Preview ——— 259

Apology

In the communication "Anion–π Interactions: Do They Exist?" (*Angew. Chem.* **2002**, *114*, 3539–3542; *Angew. Chem. Int. Ed.* **2002**, *41*, 3389–3392) by A. Frontera, P. M. Deyà, et al. previous thematically related work was unintentionally not cited. H.-J. Schneider et al. published experimental evidence of π interactions between anions and aryl groups of several host–guest systems.[1–3] The term "anion–π interaction" was introduced by H.-J. Schneider et al. to describe the interaction of sulfate anions with aryl groups of a host–guest system.[4] The authors apologize for this oversight.

[1] H.-J. Schneider, *Angew. Chem.* **1991**, *103*, 1419; *Angew. Chem. Int. Ed. Engl.* **1991**, *30*, 1417.

[2] H.-J. Schneider, T. Blatter, B. Palm, U. Pfingstag, V. Rüdiger, I. Theis, *J. Am. Chem. Soc.* **1992**, *114*, 7704.

[3] H.-J. Schneider, F. Werner, T. Blatter, *J. Phys. Org. Chem.* **1993**, *6*, 590.

[4] H.-J. Schneider, A. Yatsimirsky, *Principles and Methods in Supramolecular Chemistry*, Wiley & Sons, Chichester, **2000**.

Corrigenda

In the Communication "Silynes (RC≡SiR′) and Disilynes (RSi≡SiR′): Why Are Less Bonds Worth Energetically More?" by S. Shaik et al. (*Angew. Chem.* **2001**, *113*, 4146–4150; *Angew. Chem. Int. Ed.* **2001**, *40*, 4023–4026) Table 2 included incorrect numerical data. The correct version of the table is given below.

Table 2. In situ bond energies for the linear and *trans*-bent isomers of HCSiH (**1**), HSiSiH (**2**), and HCCH (**3**) in the linear (**L**) and *trans*-bent (**B**) isomers.[a]

		Bond energies [kcal mol^{-1}]					
		HCSiH		HSiSiH		HCCH	
	Type	**1L**	**1B**	**2L**	**2B**	**3L**	**3B**[b]
1	$D(\pi_{out})$	57.7	56.5	45.5	34.0	88.2	74.1
2	$D(\pi_{in})$	57.7	∼35[c]	45.5	∼27[c]	88.2	∼44[c]
3	$D_{2\pi}$	∼105[c]	∼71[c]	∼80[c]	∼56[c]	169.8	∼110[c]
4	ΔE_σ[d]	−42.1		−53.0		−33.9	

[a] Calculated using the VB procedure described in ref. [17] with the 6-311G* basis set. The $D(\pi_{out})$ values are calculated with the BOVB method.[18] [b] The H-C-C angle was fixed at 124.6° (as in **2B**) and all other geometrical parameters were optimized. [c] These are estimated BOVB bond energies which were calculated by adding dynamic correlation increments obtained for the out-of-plane π bonds. For these cases BOVB calculations are too CPU-time demanding. [d] $\Delta E_\sigma = E_\sigma(\mathbf{B}) - E_\sigma(\mathbf{L})$. Obtained by comparing the total energy of the corresponding σ frames with all the π electrons uncoupled (Figure 3).

In the Communication by Abu-Lebdeh et al. (*Angew. Chem. Int. Ed.* **2003**, *42*, 4499–4501), the author list should appear in the following order: P.-J. Alarco, Y. Abu-Lebdeh, and M. Armand. On page 4499, column 2, line 6, the full sentence should read: "Most interestingly, when we doped this plastic crystalline phase with a lithium trifluoromethanesulfonimide salt to increase and possibly add a Li^+ ion contribution to the total conductivity, no new phases appeared." In the concluding paragraph on page 4500, the value 6.2×10^{-3} S cm^{-1} should be 6.2×10^{-4} S cm^{-1}, as in the discussion.

 © 2004 Wiley-VCH Verlag GmbH & Co. KGaA, Weinheim



Quantum Mechanics and Chemistry: The Relevance of Nonlocality and Entanglement for Molecules**

Aris Chatzidimitriou-Dreismann* and Markus Arndt*

The predictions of quantum physics often seem to contradict the intuitive, and apparently reasonable, assumptions about how the world should behave as described by classical physics. However, until now all quantum predictions could been confirmed on the microscopic scale. The main goal of the recently established EU research and training network QUACS[1] is to explore, to test, and to control the "strange" quantum properties of nonlocality, entanglement, and decoherence, and to apply these features to complex systems including large molecules and even condensed matter. Two topics of the workshop will be discussed herein.

Chemists adopted the notion of delocalized wave functions of electrons some decades ago, for example, in the description of molecular bonds. However, the relevance of quantum physics to chemistry goes far beyond what is generally taught in chemistry textbooks. The significance of nonlocality on the macromolecular scale was already demonstrated in a diffraction experiment with fullerene molecules in 1999.[2] The development of new matter-wave interferometers[3] has now allowed clear evidence of the de Broglie wave nature of meso-tetraphenylporphyrin (TPP) and of the fluorofullerene $C_{60}F_{48}$ to be obtained (Figure 1).[4] TPP ($C_{44}H_{30}N_4$, 614 g mol^{-1}) was the first organic molecule shown to have quantum wave nature. The porphyrin core is also found as a structural element of many complex biological structures, such as hemoglobin and chlorophyll. With respect to interferometry it is interesting to note that TPP has a very flexible structure with a low degree of symmetry, so that it might decohere more easily than the rigid and compact fullerenes. With 108 atoms $C_{60}F_{48}$ (1632 g mol^{-1}) is currently the most compact and most complex molecule for which the interference of matter waves could be shown.

Interference experiments are carried out in a vacuum chamber to avoid the loss of molecules and interference visibility.[3–5] The molecular beams are created by sublimation in an oven (TTP: 690 K, $C_{60}F_{48}$ 560 K). The molecules travel with velocities of 100–200 m s^{-1}, that is, with de Broglie wavelengths of about 2–5 pm, and traverse three gold gratings with a grating period of about 990 nm and open gaps of about 470 nm. Although every molecule may still be regarded as strictly localized before it enters the interferometer, the first grating prepares the transverse coherence required and delocalizes each molecule over more than 1 μm at the second grating, that is, over two grating periods or over more than 1000 times the diameter of the molecule. Interference behind the second grating then leads to a molecular density pattern (interference fringes), which can be scanned with the third grating. Interference persists as long as each interfering molecule is well isolated from the environment. However, collisions with background gases in the apparatus entangle the interfering molecules with the gas and thus lead to a gradual suppression of quantum interference.[5]

The second topic of the workshop to be discussed herein concerns the subfemtosecond entanglement of protons with adjacent particles, such as other protons or electrons. Entanglement is a purely quantum-mechanical phenomenon, which can not be accounted for by classical mechanics. It has been investigated with a new technique of neutron Compton scattering (NCS)[6–8] and, most recently, with electron–proton Compton scattering (ECS).[8,9] These novel experimental techniques open up the time window for investigation of the quantum dynamics of protons and thus reveal dramatic quantum effects on the attosecond scale.[5–8] Several years ago a surprisingly low proton-scattering intensity was observed in NCS experiments on water molecules.[6] This effect was also found in a great variety of materials, such as organic

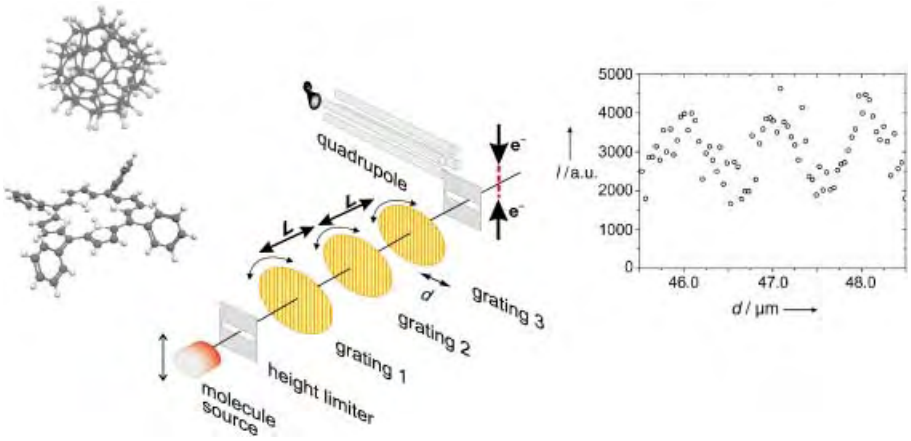


Figure 1. It can be shown with the aid of this interferometer that even large molecules have wave features. Grating 3 is moved by a distance *d* perpendicular to the beam.

[*] Prof. Dr. A. Chatzidimitriou-Dreismann
Institut für Chemie, Stranski-Laboratorium
Technische Universität Berlin
Strasse des 17. Juni 112, 10623 Berlin (Germany)
Ao. Univ. Prof. Dr. M. Arndt
Institut für Experimentalphysik
Universität Wien
Boltzmanngasse 5, 1090 Wien (Austria)

[**] The 2nd Workshop on "Entanglement and Decoherence of Complex Quantum Systems", Erwin Schrödinger Institute, Vienna, September 5–7, 2003. The workshop took place within the frame of the EU network QUACS (Quantum Complex Systems).

 © 2004 Wiley-VCH Verlag GmbH & Co. KGaA, Weinheim DOI: 10.1002/anie.200320079

liquids, polymers, amphiphiles, and metal hydrides. Apparently the hydrogen nuclei in all these compounds are sometimes "invisible" to the neutron probes. This effect on the attosecond scale could be confirmed by using an independent method, namely ECS. In the investigation of a solid polymer at room temperature, the electron experiments (Australian National University, Canberra, Australia) showed the same decreased intensity as complementary neutron experiments (ISIS neutron spallation source, UK).[8–9] The agreement of the results is surprising because the two projectiles (electrons and neutrons) interact with protons through fundamentally different forces—electromagnetic and strong interactions, respectively. As a result of the large energy transfer, these experiments can also be used to study elementary chemical reactions on the attosecond timescale, in particular cleavage of the covalent C–H bond.

The results described herein also imply that, in contrast to the popular view among chemists, atomic nuclei can not always be considered as classical mass points.

[1] Coordinator: G. Kurizki, Weizmann Institute, www.weizmann.ac.il/chemphys/gershon/quacs/quacs.html

[2] M. Arndt, O. Nairz, J. Voss-Andreae, C. Keller, G. van der Zouw, A. Zeilinger, *Nature* **1999**, *401*, 680.

[3] B. Brezger, L. Hackermüller, S. Uttenthaler, J. Petschinka, M. Arndt, A. Zeilinger, *Phys. Rev. Lett.* **2002**, *88*, 100404.

[4] L. Hackermüller, S. Uttenthaler, K. Hornberger, E. Reiger, B. Brezger, A. Zeilinger, M. Arndt, *Phys. Rev. Lett.* **2003**, *91*, 090408.

[5] K. Hornberger, S. Uttenthaler, B. Brezger, L. Hackermüller, M. Arndt, A. Zeilinger, *Phys. Rev. Lett.* **2003**, *90*, 160401.

[6] C. A. Chatzidimitriou-Dreismann, T. Abdul Redah, R. M. F. Streffer, J. Mayers, *Phys. Rev. Lett.* **1997**, *79*, 2839.

[7] C. A. Chatzidimitriou-Dreismann, T. Abdul-Redah, B. Kolarić, *J. Am. Chem. Soc.* **2001**, *123*, 11945.

[8] C. A. Chatzidimitriou-Dreismann, M. Vos, C. Kleiner, T. Abdul-Redah, *Phys. Rev. Lett.* **2003**, *91*, 057403.

[9] "Entangled Protons in a Solid Polymer", *Physics Today* **2003**, *56* (9), 9.

Meeting Reviews in *Angewandte Chemie* are meant to offer a view of the current state of a field rather than a comprehensive list of lectures. Authors are invited to describe what they feel were the most interesting contributions.

 © 2004 Wiley-VCH Verlag GmbH & Co. KGaA, Weinheim

Functional Materials

Binary Superlattices of Nanoparticles: Self-Assembly Leads to "Metamaterials"

*Andrey L. Rogach**

Keywords:
materials science · nanoparticles · self-assembly · superlattices

Recent efforts in colloidal chemistry have provided powerful tools for the gram-scale synthesis of nanoparticles of different materials with variable and precisely controlled size, shape, composition, and surface properties.[1] Currently available highly monodisperse semiconductor, noble metal, magnetic metal alloy, and oxide nanocrystals can be used as building blocks for the fabrication of 2D or 3D superstructures. The new collective properties of these artificial solids can then be investigated and harnessed. In superlattices formed this way, the individual nanoparticles can be considered as "artificial atoms".

The use of self-assembly strategies based on the dispersive attractions of nanoparticles was realized to be an attractive "bottom up" chemical approach to their superstructures.[1] An advantage of this approach is its simplicity: both 2D and 3D assemblies can be prepared simply by placing a drop of a colloidal solution of monodisperse nanoparticles on a suitable support and allowing the solvent to evaporate slowly. Self-assembled colloidal crystals can also be formed from semiconductor or magnetic metal nanoparticles by gentle destabilization of the colloidal dispersions.[2]

Twenty years ago, studies on colloidal crystals known from nature (gem opals) or grown synthetically from monodisperse microspheres with bimodal size distribution and selected size ratios[3] showed that the composition of the structures follows the composition of the atomic intermetallic alloys—AB, AB_2, AB_5, or AB_{13}—albeit on a much larger size scale. A question naturally arose recently as to whether the same rules would govern the formation of superlattices from nanometer-sized building blocks—that is, monodisperse nanoparticles with bimodal size distribution. The first examples of binary nanocrystal assemblies were 2D arrays built from noble metal nanoparticles.[4] Monodisperse Au or Ag and Au nanoparticles self-assembled into regular AB_2 or AB "alloy superstructures", depending on the relative amounts of nanocrystals and on the ratio of particle diameters. Later, a trilayer superlattice of magnetic $CoPt_3$ nanocrystals of two different sizes (4.5 and 2.6 nm) consistent with the AB_5 structure was reported (Figure 1).[5] In the first plane, each 4.5-nm $CoPt_3$ nanocrystal is surrounded by a hexagon of 2.6-nm nanocrystals. The second plane consists only of hexagons of small particles, which are rotationally shifted by 30° relative to the first plane. The third plane is a repeat of the first.

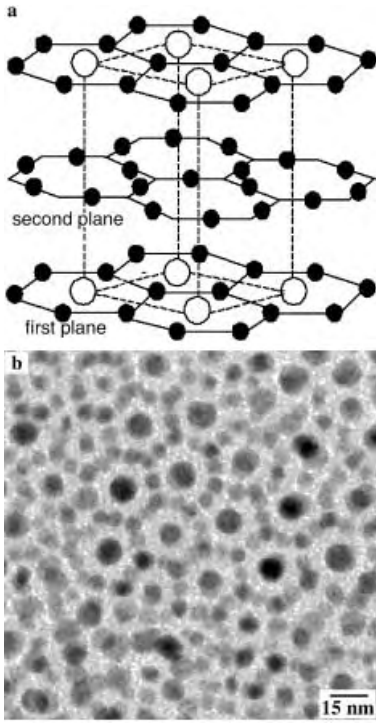


Figure 1. a) Schematic representation of the AB_5 superlattice (isostructural with intermetallic phase $CaCu_5$). b) TEM image of a trilayer structure of $CoPt_3$ nanoparticles of two different sizes (4.5 and 2.6 nm). Reprinted with permission from reference [5].

Murray and co-workers reported the next logical step in the development of nanoparticle-based binary superlattices: the use of materials with distinctly different properties (PbSe semiconductor quantum dots and Fe_2O_3 magnetic nanocrystals) to prepare 3D superstructures.[6] Precisely ordered, large single domains (up to 2 μm^2) of AB_2 and AB_{13} superlattices were obtained by simply allowing the solvent (dibutyl ether) to evaporate overnight. The starting liquor consisted of a diluted mixed dispersion of 11-nm Fe_2O_3 particles and a tenfold surplus of 6-nm PbSe nanoparticles. Figure 2 shows an example of the $\{100\}_{SL}$ projection of the AB_{13} superlattice, with each large Fe_2O_3 nanoparticle spaced with eight small PbSe nanocrystal to form a square array. A trilayer AB_5 structure similar to that in Figure 1 was also found, although only in smaller regions. The AB_2 and AB_{13} superlattices of the best quality were formed with an effective particle size ratio of 0.58, which is in a good agreement with the calcu-

[*] Dr. A. L. Rogach
Photonics & Optoelectronics Group
Physics Department & CeNS
Universität München
Amalienstrasse 54
80799 München (Germany)
Fax: (+49) 89-2180-3441
E-mail:
andrey.rogach@physik.uni-muenchen.de

© 2004 Wiley-VCH Verlag GmbH & Co. KGaA, Weinheim
DOI: 10.1002/anie.200301704

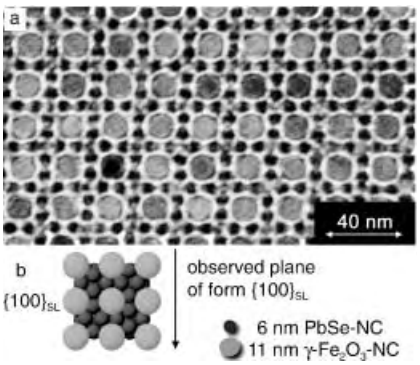


Figure 2. a) TEM image of a 3D superstructure of γ-Fe_2O_3 (11 nm) and PbSe nanoparticles (6 nm). b) Schematic representation of the AB_{13} superlattice (isostructural with intermetallic phase $NaZn_{13}$). Reprinted with permission from reference [6].

lated value for the assembly of micrometer-sized colloidal hard spheres.[7]

The binary superlattices formed by this simple chemical self-assembly approach were given the term "metamaterials" by Murray and co-workers. According to the authors,[6] metamaterials are materials with properties arising from the controlled interaction and mutual influence of their components, in this case, individual nanoparticles of different origin. Keeping in mind the large variety of high-quality monodisperse nanocrystals that is available, all with further adjustable parameters such as size and surface capping, the toolbox for the construction of these complex materials is indeed inexhaustible. Accordingly, many fundamental questions with respect to these samples need to be investigated. What happens after excitation of a regular binary supelattice comprising of two different semiconductor nanoparticles, or, in the simplest case, differently sized nanoparticles of one and the same semiconductor material? Does charge transfer or energy transfer takes place? How does the magnetic field created by the magnetic particle sublattice influence the optical properties of the semiconductor neighbors? Which is expected: quenching or enhancement of the luminescence of the semiconductor nanoparticles in a binary superlattice with metal counterparts? The spacing between nanocrystals in a superlattice can be fine tuned on the sub-nanometer scale by choosing different capping ligands—how do these measures influence the collective optical, magnetic, and electrical properties of the metamaterial?

Self-assembly of high-quality nanoparticles of different origin into complex ordered materials will provide samples for these studies and open the door to a new domain of bottom-up chemistry with enough potential to compete with the top-down approaches of nanolithography.

[1] a) C. B. Murray, C. R. Kagan, M. G. Bawendi, *Annu. Rev. Mater. Sci.* **2000**, *30*, 545 – 610; b) A. L. Rogach, D. V. Talapin, E. V. Shevchenko, A. Kornowski, M. Haase, H. Weller, *Adv. Funct. Mater.* **2002**, *12*, 653 – 664.

[2] a) C. B. Murray, C. R. Kagan, M. G. Bawendi, *Science* **1995**, *270*, 1335 – 1337; b) D. V. Talapin, E. V. Shevchenko, A. Kornowski, N. Gaponik, M. Haase, A. L. Rogach, H. Weller, *Adv. Mater.* **2001**, *13*, 1868 – 1871; c) E. V. Shevchenko, D. V. Talapin, A. Kornowski, F. Wiekhorst, J. Kötzler, M. Haase, A. L. Rogach, H. Weller, *Adv. Mater.* **2002**, *14*, 287 – 290.

[3] a) J. V. Sanders, *Philos. Mag. A* **1980**, *42*, 705 – 720; b) S. Youshimura, S. Hachisu, *Prog. Colloid Polym. Sci.* **1983**, *68*, 59 – 70.

[4] a) C. J. Kiely, J. Fink, M. Brust, D. Bethell, D. J. Schiffrin, *Nature* **1998**, *396*, 444 – 446; b) C. J. Kiely, J. Fink, J. G. Zheng, M. Brust, D. Bethell, D. J. Schiffrin, *Adv. Mater.* **2000**, *12*, 640 – 643.

[5] E. V. Shevchenko, D. V. Talapin, A. L. Rogach, A. Kornowski, M. Haase, H. Weller, *J. Am. Chem. Soc.* **2002**, *124*, 11 480 – 11 485.

[6] F. X. Redl, K.-S. Cho, C. B. Murray, S. O'Brien, *Nature* **2003**, *423*, 968 – 971.

[7] M. D. Eldridge, P. A. Madden, D. Frenkel, *Nature* **1993**, *365*, 35 – 37.

 © 2004 Wiley-VCH Verlag GmbH & Co. KGaA, Weinheim

Artificial Photosynthesis

Bioinspired Molecular Design of Light-Harvesting Multiporphyrin Arrays

*Myung-Seok Choi, Tomoko Yamazaki, Iwao Yamazaki, and Takuzo Aida**

Keywords:
dendrimers · energy transfer · light harvesting · photosynthesis · porphyrinoids

Recent progress in fundamental studies on multiporphyrin arrays has provided structural parameters for the molecular design of artificial light-harvesting antennae which mimic the wheel-like antenna complexes of photosynthetic purple bacteria. Covalent and noncovalent approaches have been employed for the construction of artificial light-harvesting multiporphyrin arrays. Such arrays are categorized into ring-shaped, windmill-shaped, star-shaped, and dendritic architectures. In particular, dendritic multiporphyrin arrays have been proven to be promising candidates for both providing a large absorption cross-section and enabling the vectorial transfer of energy over a long distance to a designated point. Such molecular and supramolecular systems are also expected to be potent components for molecular electronics and photonic devices.

1. Introduction

Biological photosynthesis is one of the most interesting photochemical events and converts solar energy into chemical potentials. The crystal structures of some of the light-harvesting antenna complexes present in purple photosynthetic bacteria show the presence of highly symmetric wheel-like supramolecular architectures involving a great number of bacteriochlorophyll pigments (Figure 1).[1] Such wheel-like chromophore arrays play an essential role in the efficient capturing of light energy and its subsequent funneling to the reaction center.[2] These structural features have motivated chemists to design artificial light-harvesting antennae consisting of multiple porphyrin units and to explore their photochemical properties so as to generate a general approach for achieving the vectorial transfer of energy over a long distance to a designated point. Such synthetic light-harvesting antenna molecules not only contribute to a better understanding of the photochemical events involved in biological photosynthesis, but also have a great potential as nanoscopic objects for molecular electronics and photonics involving photovoltaic cells, field-effect transistors, and light-emitting devices.[3]

Herein we focus on a recent development of covalent (molecular) and noncovalent (supramolecular) approaches to

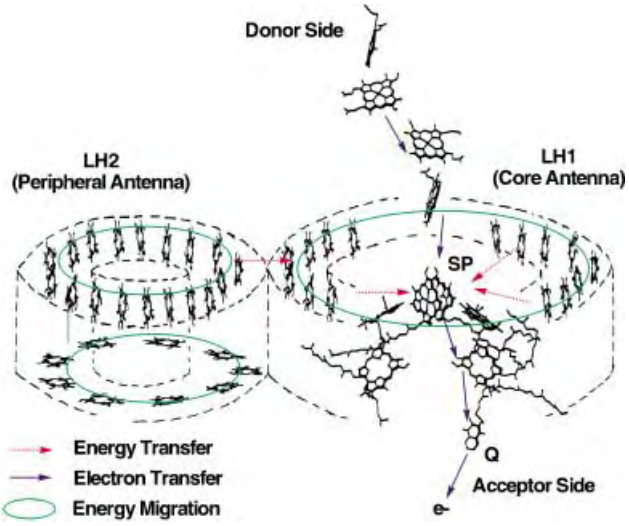


Figure 1. Schematic representation of the active site of purple photosynthetic bacteria.

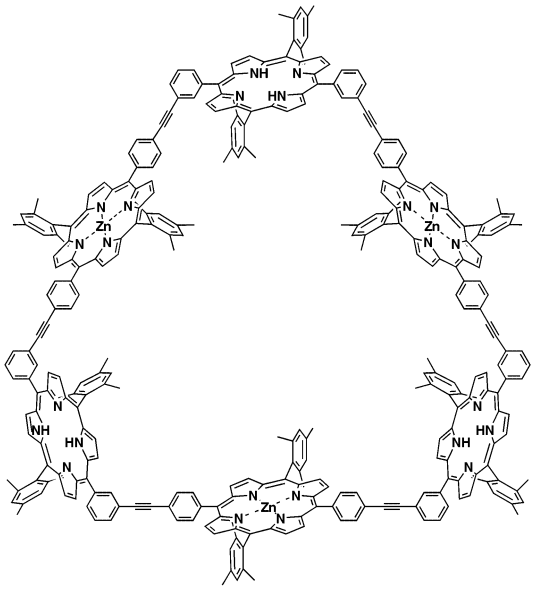
[*] Dr. M.-S. Choi, Prof. Dr. T. Aida
ERATO Nanospace Project
Japan Science and Technology Corporation (JST)
2-41 Aomi, Koto-ku, Tokyo 115-0064 (Japan)
Fax: (+81) 3-5841-7310
E-mail: aida@macro.t.u-tokyo.ac.jp
Dr. T. Yamazaki, Prof. Dr. I. Yamazaki
Department of Chemical Process Engineering
Graduate School of Engineering
Hokkaido University
Kita-13-Nishi-8, Kita-ku, Sapporo 060-8628 (Japan)

© 2004 Wiley-VCH Verlag GmbH & Co. KGaA, Weinheim
DOI: 10.1002/anie.200301665

the design of light-harvesting multiporphyrin arrays including 1) ring-shaped, 2) star-shaped, 3) windmill-shaped, and 4) dendritic architectures, where special emphasis is placed on their geometry-dependent photochemical properties.

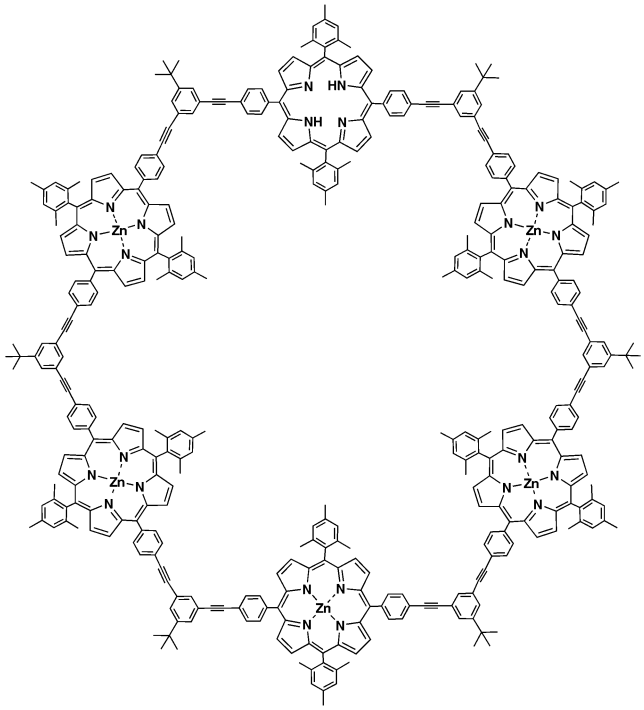
2. Ring-Shaped Light-harvesting Antennae

Ring-shaped multiporphyrin arrays[4] are interesting candidates for artificial light-harvesting antennae which are intended to mimic structural aspects of the wheel-like chromophore arrays in photosynthetic purple bacteria. Cyclic



1

hexamer **1**, which consists of an alternating arrangement of zinc and free-base porphyrins (P_{Zn} and P_{FB}), has been synthesized by a Pd-mediated coupling of a zinc complex of bis(4-ethynylphenyl)porphyrin and a free-base bis(3-iodophenyl)porphyrin in the presence of a template molecule.[5] Time-resolved spectroscopy has shown that the photoexcited singlet state of the P_{Zn} units has a lifetime (τ) of 17 ps, from which the P_{Zn}-to-P_{FB} energy transfer rate constant (k_{ENT}) and the quantum efficiency (Φ_{ENT}) have been evaluated to be $2.9 \times 10^{10}\ s^{-1}$ and 99%, respectively. In contrast, cyclic hexamer **2**, which consists of five P_{Zn} units and a single P_{FB} unit,



2

shows a Φ_{ENT} value of only 40%.[6] Although the advantages of such ring-shaped chromophore arrays over linear analogues in intramolecular energy transfer have been discussed in the literature,[7] the realization of vectorial energy transfer along the ring system still remains a challenge.

3. Star-Shaped Light-Harvesting Antennae

Star-shaped porphyrin pentamers consisting of a focal free-base porphyrin unit (P_{FB}) attached to four peripheral zinc



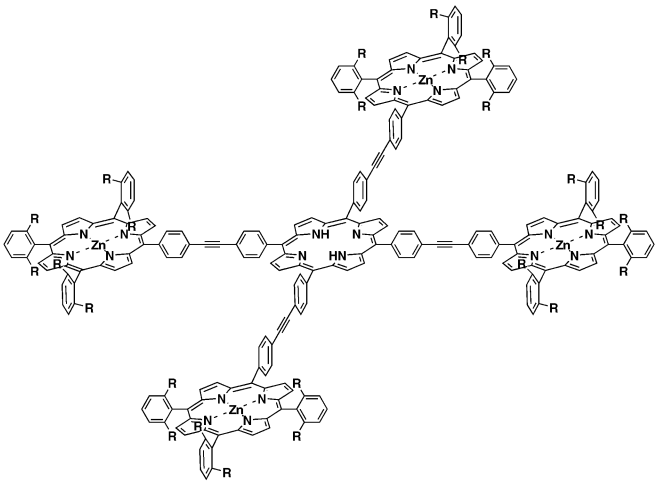
Takuzo Aida was born in 1956. He received his Ph.D. from the University of Tokyo in Polymer Chemistry in 1984, and then began an academic career at the University of Tokyo. In 1996, he was promoted to Full Professor at the Department of Chemistry and Biotechnology at the University of Tokyo. His research interests include controlled macromolecular synthesis with mesoporous inorganic materials, photo- and supramolecular chemistry of dendritic macromolecules, fabrication of nanoscopic materials, and bio-related molecular recognitions and catalyses. In 1996, he was appointed as a researcher of the JST PRESTO Project "Fields and Reactions", and in 2000 was the leader of the ERATO Project on "NANOSPACE".



Myung-Seok Choi was born in 1968 in Korea. He received his Ph.D. from the University of Tokyo in 2002. He then joined the ERATO Nanospace Project, Japan Science and Technology Corporation (JST). In 2003, he joined the Fusion Domain Laboratory of the SONY Cooperation. His research interests focus on the design of dendritic macromolecules by using molecular and supramolecular approaches.

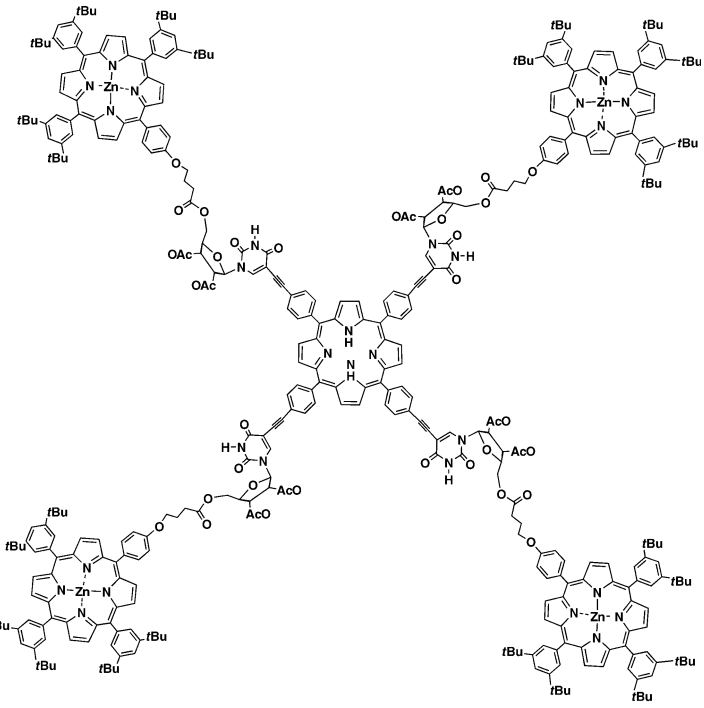
© 2004 Wiley-VCH Verlag GmbH & Co. KGaA, Weinheim

porphyrin units (P_{Zn}) have been extensively studied as simple models of biological light-harvesting antennae. Compound **3** is an early example of a multiporphyrin



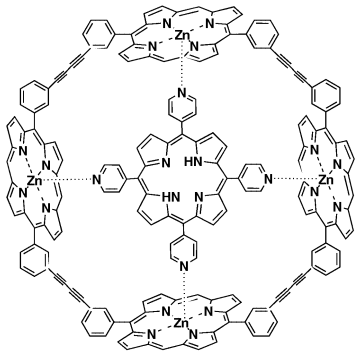
3 (R = OMe)

array that makes use of diphenylethyne spacers for the connection of P_{FB} and P_{Zn} units with a center-to-center distance of 20 Å.[8] The P_{Zn}-to-P_{FB} energy transfer efficiency (Φ_{ENT}) in **3** has been reported to be 90%, with a weak electronic donor–acceptor interaction at the ground state playing a role.[9] Compound **4** containing flexible nucleosidic spacers between energy donor and acceptor units has been synthesized. Interestingly, the flexible linkers allow the P_{Zn} units to wrap around and electronically shield the P_{FB} unit. Nevertheless, steady-state fluorescence spectroscopy studies have shown that compound **4** displays essentially identical P_{Zn}-to-P_{FB} energy-transfer characteristics as compound **3**.[10]



4

Inclusion complex **5**, which consists of a tetrakis(4-pyridyl)porphyrin free base (P_{FB}) surrounded by a rigid cyclic tetramer of zinc porphyrin (P_{Zn}) has been synthesized.[11,12] Photoexcitation of **5** at 411 nm results predominantly in electron transfer from the P_{Zn} units to the included P_{FB} molecule, where the fluorescence from the peripheral P_{Zn} units is quenched without any enhancement of the emission from the P_{FB} molecule. In sharp contrast, photoexcitation of the P_{Zn} units of inclusion complex **6**, which has a rigid coordina-



5

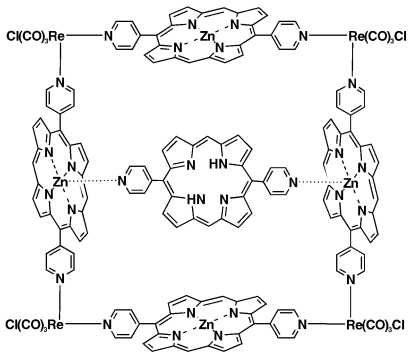


Iwao Yamazaki was born in 1942. He received his Ph.D. from Hokkaido University in Molecular Photophysics in 1972, and then joined Hokkaido University as an Assistant Professor. In 1980, he moved to the Institute of Molecular Science (Okazaki, Japan) as an Associate Professor, and then joined Hokkaido University in 1988 as a Full Professor at the Department of Chemistry. His research interests include ultrafast photochemical processes in organized molecular systems and their applications to quantum mechanical switching devices. In 1990 he received the Distinguished Research Award, Chemical Society of Japan in the field of time-resolved spectroscopy of molecular photophysics.



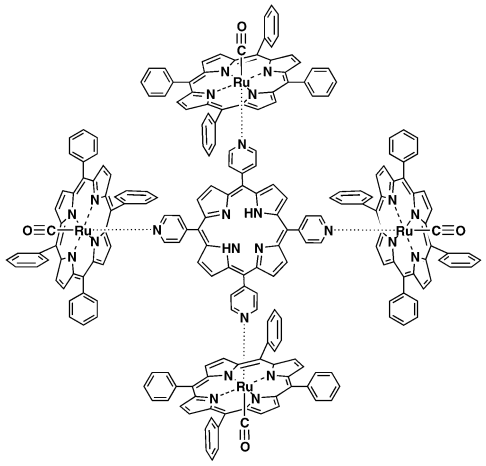
Tomoko Yamazaki was born in 1945. She graduated from Hokkaido University (Faculty of Pharmacy), and then joined the Research Institute of Applied Electricity at Hokkaido University as a Research Assistant. In 1980–1988 she was involved in time-resolved fluorescence studies on molecular assemblies at the Institute of Molecular Science. In 1988 she returned to Hokkaido University.

 © 2004 Wiley-VCH Verlag GmbH & Co. KGaA, Weinheim



6

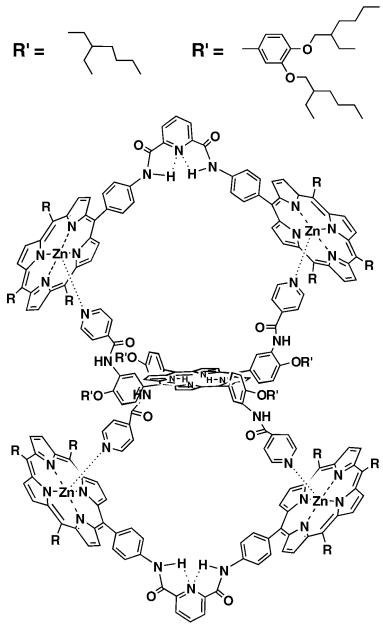
tion square consisting of four P_{Zn} units and an internal P_{FB} unit, shows an enhancement in the fluorescence from the P_{FB} unit at the expense of that from the P_{Zn} units. This effect occurs as a result of a P_{Zn}-to-P_{FB} energy transfer.[13] A ruthenium porphyrin (P_{Ru}) forms a side-to-face assembly **7**



7

with a tetrakis(4-pyridyl)porphyrin (P_{FB}) free base through axial coordination interactions.[14] The photoexcited singlet state of the P_{Ru} units is strongly perturbed by the heavy metal effect of the Ru atoms,[15] which results in a highly efficient intersystem crossing to the triplet state (100% efficiency). Excitation of compound **7** at 532 nm results in a P_{Ru}-to-P_{FB} energy transfer via the triplet state occurring with 100% efficiency and a k_{ENT} value in the range of 10^8–$10^9\ s^{-1}$.[16] Compound **8** is also an interesting multiporphyrin array because of its unique three-dimensional supramolecular architecture formed through cooperative coordination interactions.[17] The k_{ENT} and Φ_{ENT} values of **8** have been evaluated by time-resolved fluorescence spectroscopy to be $2\times10^9\ s^{-1}$ and 73%, respectively.

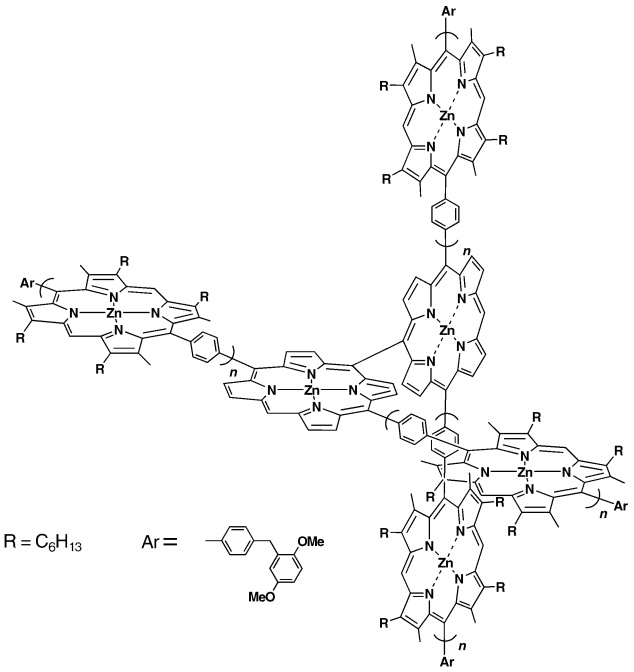
Star-shaped multiporphyrin arrays are therefore potent candidates for highly efficient energy transfer. However, the number of chromophore units that can be incorporated into those molecules is only small, thus, preventing the formation of a large absorption cross-section, which is essential for capturing low numbers of photons.



8

4. Windmill-Shaped Light-Harvesting Antennae

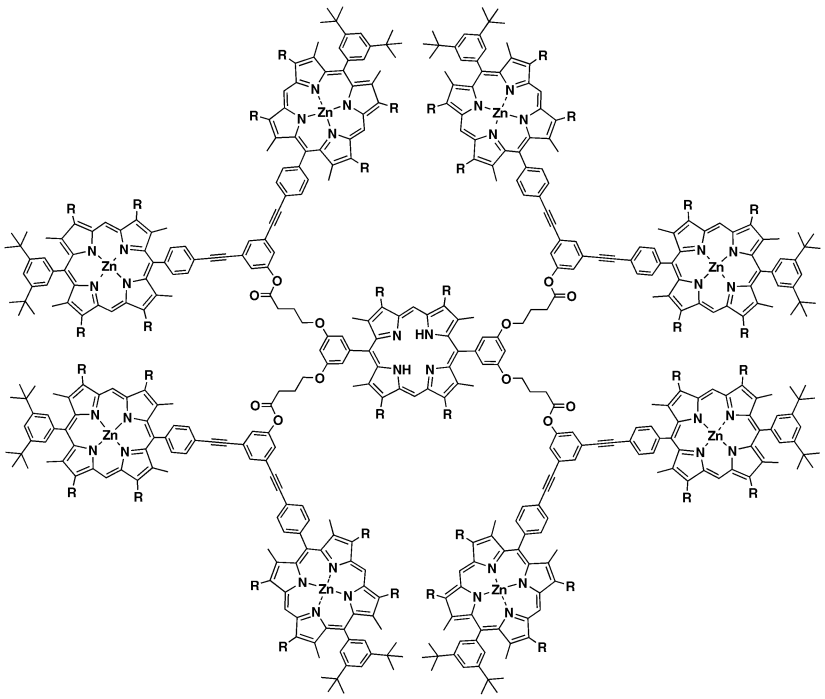
The synthesis and photochemical properties of windmill-shaped multiporphyrin arrays have been investigated; their molecular structures, though essentially similar to star-shaped architectures, possibly would allow incorporation of a larger number of chromophore units, thereby increasing the absorption cross-section. Windmill-like multiple zinc-porphyrin arrays with a *meso-meso*-coupled zinc porphyrin (P_{Zn}) dimer (**9**, $n = 1, 2$) at its center have been synthesized, as well as their



9 ($n = 1, 2$)

 © 2004 Wiley-VCH Verlag GmbH & Co. KGaA, Weinheim

polymeric homologues (gridlike architecture).[18,19] The focal P_{Zn} dimer in **9** has a slightly lower energy (2.08 eV) than those at the periphery (2.15 eV), thereby allowing the excitation energy to flow from the periphery to the central core. In fact, photoexcitation of **9** at 540 nm (nonselective excitation) results in an enhanced emission from the *meso-meso*-linked P_{Zn} units (651 nm) at the expense of the fluorescence from the peripheral P_{Zn} units (580 and 629 nm). Time-resolved spectroscopy has shown that **9** has biphasic fluorescence decay behavior, which is composed of two exponential components with lifetimes of 56 ps (73%) and 1.62 ns (27%) which are assignable to the decays of the peripheral and core P_{Zn} units, respectively. The time-resolved spectra at the initial stage consist predominantly of an emission from the peripheral P_{Zn} units which is then transformed rapidly to a broad emission from the focal P_{Zn} dimer. The photochemical properties of a novel electron-transfer relay system consisting of acceptor-appended **9** ($n=1$) have also been reported.[20]



10

5. Dendritic Light-Harvesting Antennae

In general, energy-transfer properties by a through-space (Förster) mechanism are dependent on the donor–acceptor (D-A) distance r, where the efficiency would decrease according to $1/r^6$.[21] Artificial light-harvesting antennae require a great number of chromophore units to obtain a large absorption cross-section.[22] Dendrimers are hyperbranched, three-dimensional macromolecules with regular treelike arrays of branch units,[23] and have attracted great attention as novel nanoscopic light-harvesting molecules.[24] Hence, dendritic architectures are interesting scaffolds for the three-dimensional positioning of a great number of chromophore units. However, if these chromophore units do not cooperate with one another, the acquired light energy is scattered and the excited states are lost before the energy is channeled to a designated functionality, which triggers, for example, electron-transfer reactions. Therefore, the molecular design of energy funnels should be considered for the vectorial transfer of energy over a large distance.

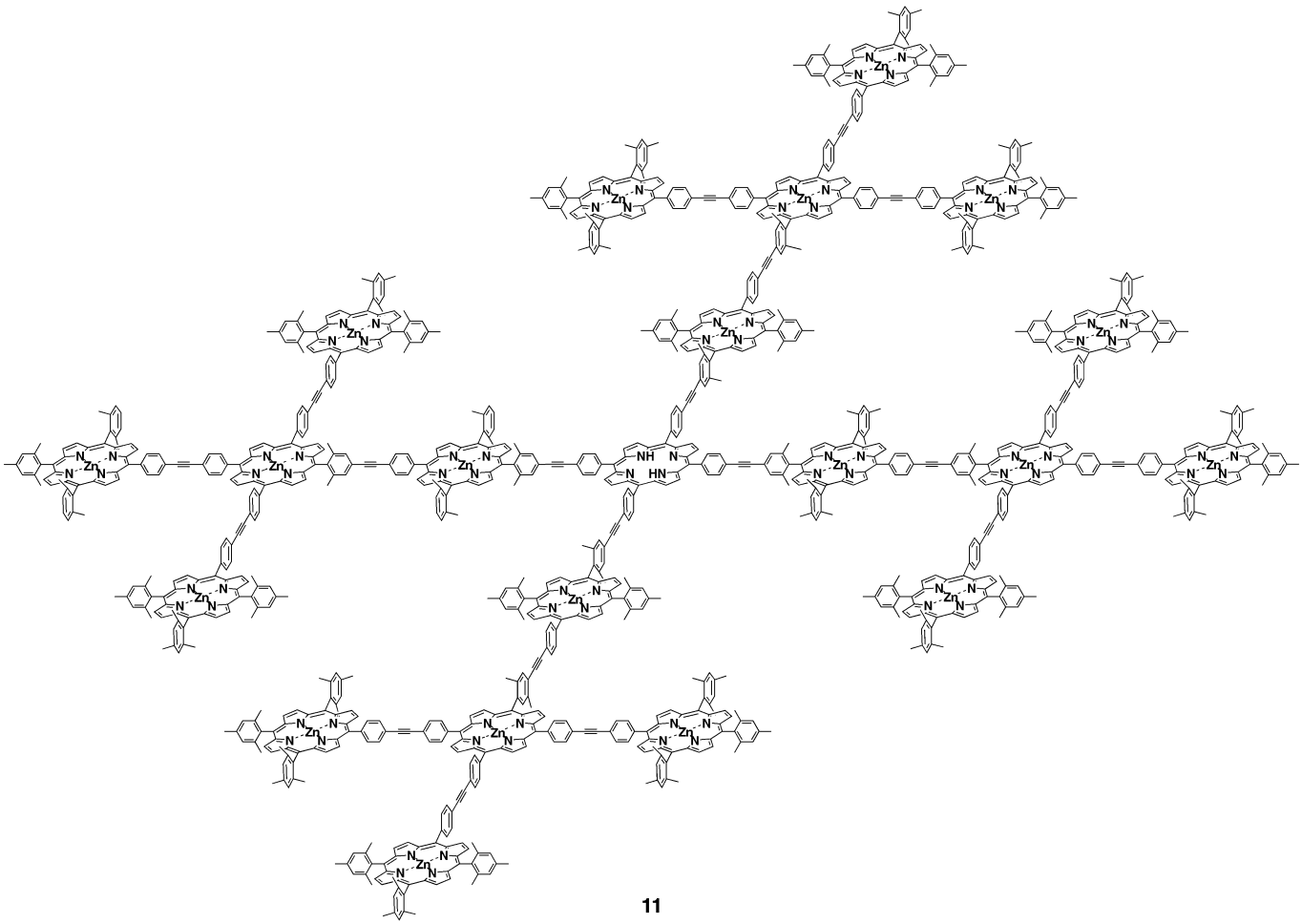
Examples of dendritic multiporphyrin arrays include a vinylene-linked nonameric dendritic nickel porphyrin array[25] and a nonameric dendritic zinc porphyrin array with ethynylene and ester spacers.[26] Compound **10**, which consists of an energy-accepting free-base porphyrin (P_{FB}) core decorated with eight energy-donating zinc porphyrin (P_{Zn}) units, was later synthesized for photochemical studies.[27] Excitation of the P_{Zn} units of **10** results in fluorescence emission from the P_{FB} focal core as a result of a P_{Zn}-to-P_{FB} energy transfer. Evaluation of the fluorescence decay profile of the P_{Zn} units shows that the energy transfer takes place rather slowly ($k_{ENT}=9\times10^8\ s^{-1}$) with a quantum efficiency (Φ_{ENT}) of 60%. The fluorescence quantum yield of the P_{FB} core in compound **10** is virtually identical to that of the model porphyrin monomer.

The synthesis of a metalloporphyrin array consisting of 21 nickel porphyrin units, referred to as mandala-patterned bandanna, has been reported, whose energy-transfer properties, however, were not investigated because of the photochemical inertness inherent to nickel porphyrin derivatives.[28] However, the photoactive dendritic multiporphyrin array **11**, which consists of 21 porphyrin units attached through diarylethyne linkers to a free-base porphyrin focal core, has been synthesized.[29] Time-resolved absorption spectroscopy of compound **11** has shown a decay of the excited singlet state of the P_{Zn} units, followed by an increase in the absorption of the P_{FB} core. The P_{Zn}-to-P_{FB} energy transfer has a Φ_{ENT} value of 92%.

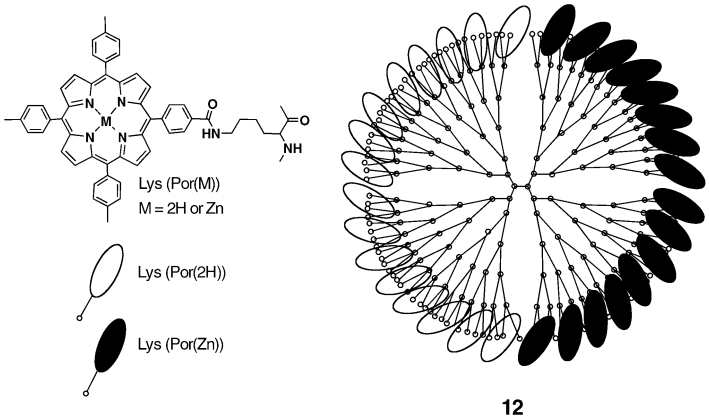
Energy-transfer events on the dendrimer surface are also interesting. This prompted the synthesis of dendritic poly(L-lysine) **12**, which bears two hemispherically segregated domains comprised of 16 free-base porphyrin (P_{FB}) units and 16 zinc porphyrin (P_{Zn}) units on the exterior surface. A steady-state fluorescence study has shown the occurrence of a two-dimensional P_{Zn}-to-P_{FB} energy transfer with a Φ_{ENT} value of 43%.[30] Here, photoexcitation of a certain P_{Zn} unit in compound **12** is followed by an energy migration within the P_{Zn} domain, and then the excitation energy is transferred to a P_{FB} unit at a boundary of the two domains.

The large dendritic multiporphyrin array **13a** has been synthesized. This array consists of four dendritic wedges of a zinc porphyrin heptamer ($7P_{Zn}$), which act as energy donating

 © 2004 Wiley-VCH Verlag GmbH & Co. KGaA, Weinheim



11

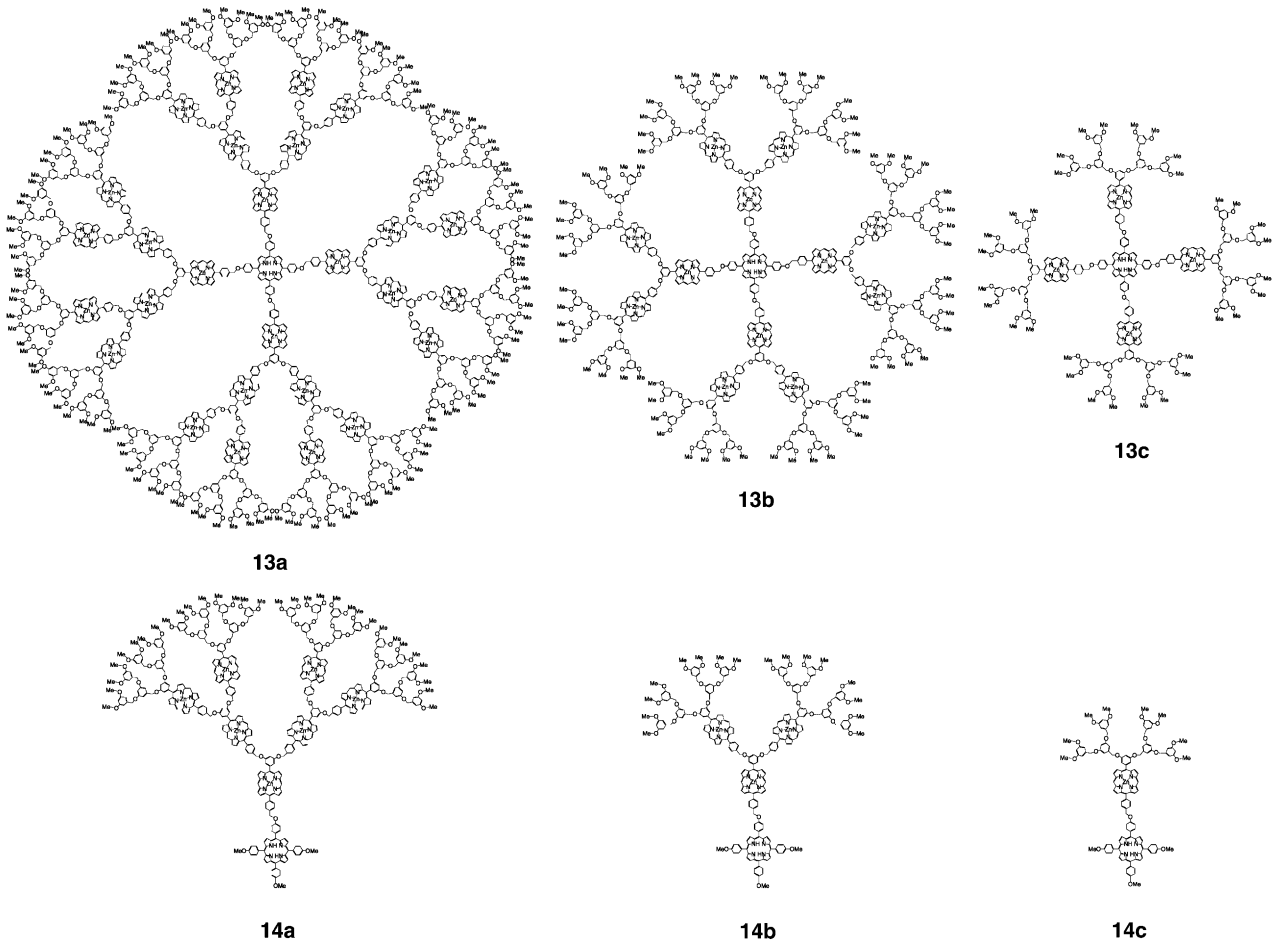


12

units, that are anchored by a free-base porphyrin (P_{FB}) focal core, which acts as the energy acceptor.[31] This molecule is intended to mimic the morphologies of wheel-like supramolecular assemblies of bacteriochlorophyll pigments in biological light-harvesting antennae. Excitation of the P_{Zn} units in compound **13a** results in a highly efficient P_{Zn}-to-P_{FB} energy transfer that generates an enhanced emission from the P_{FB} focal core. In sharp contrast, compound **14a**, a conical version of **13a**, displays an emission mostly from the P_{Zn} units, with only a weak emission from the P_{FB} focal core. Time-resolved fluorescence spectroscopy of **13a** initially shows an increase in the fluorescence from the P_{Zn} units (589 and 637 nm), which then decays progressively to allow the generation of a new fluorescence from the P_{FB} core. The average lifetime of the photoexcited P_{Zn} units in compound **13a** (680 ps) is much shorter than those in compound **14a** (1899 ps), despite the fact that **13a** has a large number of P_{Zn} units located away from the energy-accepting P_{FB} focal core. The energy transfer rate constant (k_{ENT}) for **13a** has been evaluated to be $1.04 \times 10^9\ s^{-1}$, which is one order of magnitude larger than that for **14a** ($0.10 \times 10^9\ s^{-1}$). The energy-transfer efficiencies (Φ_{ENT}), calculated from these k_{ENT} values, are 71 and 19% for **13a** and **14a**, respectively, which have very different structures. This observation indicates the important role of the morphology of the chromophore array in intramolecular energy transfer. A fluorescence depolarization study has shown that the energy transfer in **13a** is facilitated by a cooperative energy migration among the dendritic P_{Zn} units, a situation analogous to the photochemical events in bacterial light-harvesting antenna complexes.

Photochemical properties of two series of dendritic compounds **13a–c** and **14a–c** show very different depend-

 © 2004 Wiley-VCH Verlag GmbH & Co. KGaA, Weinheim



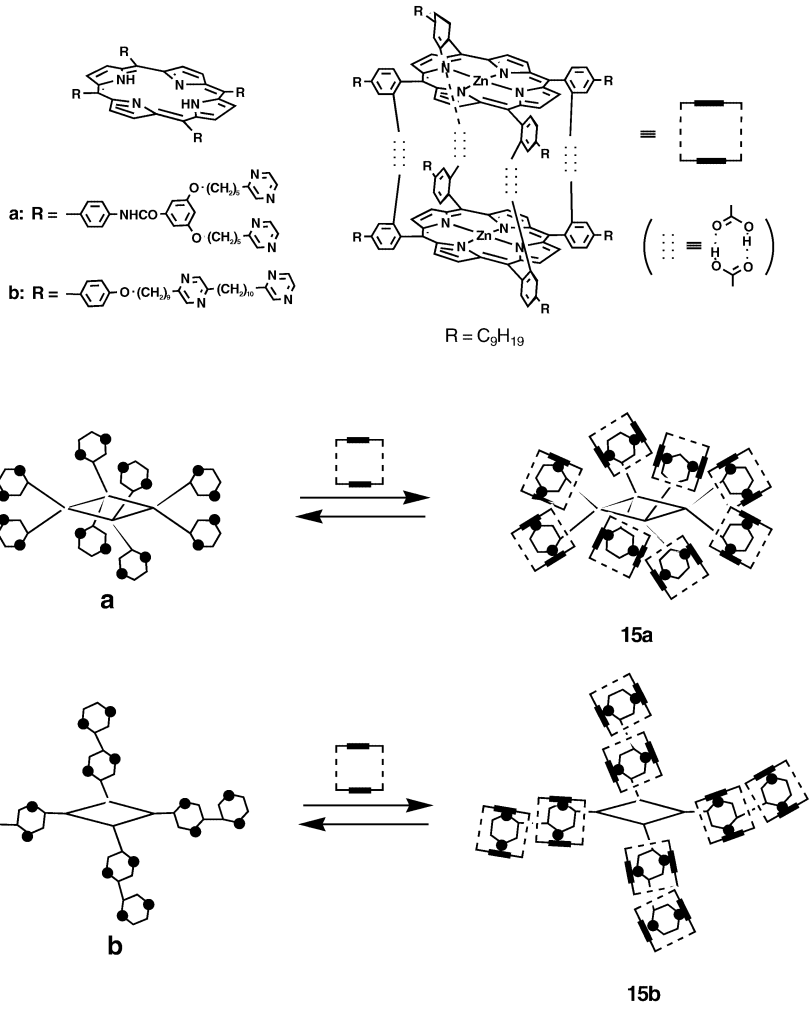
encies on the generation number.[32] The Φ_{ENT} value decreased from 86% (**14c**) to 66% (**14b**), and then to 19% (**14a**), while the energy-transfer properties of **13a–c** with four dendritic zinc porphyrin wedges exhibit a much smaller generation-number dependency: Φ_{ENT} value ranges from 87% (**13c**) to 80% (**13b**), and then to 71% (**13a**). Light-harvesting activities of the multiporphyrin arrays can be evaluated from the molar extinction coefficients (ε_{415}) of the Soret absorption band ($\lambda = 415$ nm) multiplied by the P_{Zn}-to-P_{FB} energy transfer efficiency (Φ_{ENT}). The light-harvesting activity of **13a–c** is considerably increased with increasing generation number of the dendritic wedges; the $\varepsilon_{415}\Phi_{ENT}$ value of **13a**, for example, is ten times as large as that of **14c**. In sharp contrast, those values for compounds **14a–c** are much lower and hardly dependent on the generation number. Dendritic light-harvesting antennae, like biological light-harvesting antennae, also require a certain molecular geometry to enhance the energy-transfer activities.

Supramolecular versions of dendrimer-like light-harvesting complexes have been reported. A hydrogen-bonded zinc porphyrin cyclic dimer ($^2P_{Zn}$) forms nonameric and heptadecameric multiporphyrin arrays (**15a**)[33,34] through metal–ligand coordination with a free-base porphyrin focal core bearing pyrazine arms (P_{FB}). Energy transfer takes place with a Φ_{ENT} value of 80% upon excitation of the $^2P_{Zn}$ units, which results in a fluorescence emission from the P_{FB} focal core.[34] On the other hand, serial-type compound **15b** shows a less-efficient energy transfer with a Φ_{ENT} value of only 55%. These contrasting values indicate an important role of the geometry of **15a** in the efficient transfer of energy.

6. Summary and Outlook

Artificial photosynthesis is one of the ultimate goals of science and technology for the 21st century. Artificial photosynthesis can be realized by the integration of light-harvesting antenna parts with an electron-transfer relay system that enables long-lived charge separation. Artificial light-harvesting antennae require a molecular design that allows incorporation of a great number of chromophore units to obtain a large absorption cross-section for capturing a low number of photons. At the same time, those chromophore units are required to cooperate efficiently with one another so as to channel the acquired light energy over a long distance to a designated point. A three-dimensional molecular design of chromophore arrays is essential for an efficient cooperation of chromophore units. The highlighted multiporphyrin arrays for capturing visible light are roughly classified into four categories, depending on their molecular geometries. Among those, dendritic scaffolds appear to be the most promising for the three-dimensional arrangement of a large number of

 © 2004 Wiley-VCH Verlag GmbH & Co. KGaA, Weinheim



chromophore molecules and also for an efficient cooperation of those chromophore molecules to act as energy funnels and allow vectorial energy transfer. Future research along this line would also involve integration of these artificial antennae into electron-transfer relay systems to achieve artificial photosynthesis. Furthermore, their potential applications also include solar cells, light-emitting materials, sensor systems, and many other electronic and photonic nanodevices that utilize the conversion of light energy into chemical potentials.

Received: May 2, 2003 [M1665]

[1] a) G. McDermott, S. M. Prince, A. A. Freer, A. M. Hawthornthwaite-Lawless, M. Z. Papiz, R. J. Cogdell, N. W. Isaacs, *Nature* **1995**, *374*, 517; b) S. Karrasch, P. A. Bullough, R. Ghosh, *EMBO J.* **1995**, *14*, 631; c) T. Pullerits, V. Sundström, *Acc. Chem. Res.* **1996**, *29*, 381.

[2] a) X. Hu, A. Damjanovic, T. Ritz, K. Schulten, *Proc. Natl. Acad. Sci. USA* **1998**, *95*, 5935; b) A. M. V. Oijen, M. Ketelaars, J. Köhler, T. J. Aartsma, J. Schmidt, *Science* **1999**, *285*, 400.

[3] a) M. R. Wasielewski, *Chem. Rev.* **1992**, *92*, 435; b) D. Gust, T. A. Moore, A. L. Moore, *Acc. Chem. Res.* **2001**, *34*, 40.

[4] a) G. M. Dubowchik, A. D. Hamilton, *J. Chem. Soc. Chem. Commun.* **1987**, 293; b) C. M. Drain, K. C. Russell, J.-M. Lehn, *Chem. Commun.* **1996**, 337; c) H. A. M. Biemans, A. E. Rowan, A. Verhoeven, P. Vanoppen, L. Latterini, J. Foekema, A. P. H. J. Schenning, E. W. Meijer, F. C. de Schryver, R. J. M. Nolte, *J. Am. Chem. Soc.* **1998**, *120*, 11054; d) K. Chichak, N. R. Brand, *Chem. Commun.* **2000**, 1211; e) R. Takahashi, Y. Kobuke, *J. Am. Chem. Soc.* **2003**, *125*, 2372.

[5] J. Li, A. Ambroise, S. I. Yang, J. R. Diers, J. Seth, C. R. Wack, D. F. Bocian, D. Holten, J. S. Lindsey, *J. Am. Chem. Soc.* **1999**, *121*, 8927.

[6] O. Mongin, A. Schuwey, M. A. Vallot, A. Gossauer, *Tetrahedron Lett.* **1999**, *40*, 8347.

[7] P. G. Van Patten, A. P. Shreve, J. S. Lindsey, R. J. Donohoe, *J. Phys. Chem. B* **1998**, *102*, 4209.

[8] S. Prathapan, T. E. Johnson, J. S. Lindsey, *J. Am. Chem. Soc.* **1993**, *115*, 7519.

[9] J. Seth, V. Palaniappan, T. E. Johnson, S. Prathapan, J. S. Lindsey, D. F. Bocian, *J. Am. Chem. Soc.* **1994**, *116*, 10578.

[10] N. Solladié, M. Gross, J.-P. Gisselbrecht, C. Sooambar, *Chem. Commun.* **2001**, 2206.

[11] S. Anderson, H. L. Anderson, J. K. M. Sanders, *Angew. Chem.* **1992**, *104*, 921; *Angew. Chem. Int. Ed. Engl.* **1992**, *31*, 907.

[12] S. Anderson, H. L. Anderson, A. Bashall, M. McPartlin, J. K. M. Sanders, *Angew. Chem.* **1995**, *107*, 1196; *Angew. Chem. Int. Ed. Engl.* **1995**, *34*, 1096.

[13] R. V. Slone, J. T. Hupp, *Inorg. Chem.* **1997**, *36*, 5422.

[14] E. Alessio, M. Macchi, S. Heath, L. G. Marzilli, *Chem. Commun.* **1996**, 1411.

[15] C. M. Drain, F. Nifiatis, A. Vasenko, J. D. Batteas, *Angew. Chem.* **1998**, *110*, 2478; *Angew. Chem. Int. Ed.* **1998**, *37*, 2344.

[16] A. Prodi, M. T. Indelli, C. J. Kleverlaan, F. Scandola, E. Alessio, T. Gianferrata, L. G. Marzilli, *Chem. Eur. J.* **1999**, *5*, 2668.

[17] R. A. Haycock, A. Yartsev, U. Michelsen, V. Sundström, C. A. Hunter, *Angew. Chem.* **2000**, *112*, 3762; *Angew. Chem. Int. Ed.* **2000**, *39*, 3616.

[18] A. Nakano, A. Osuka, I. Yamazaki, T. Yamazaki, Y. Nishimura, *Angew. Chem.* **1998**, *110*, 3172; *Angew. Chem. Int. Ed.* **1998**, *37*, 3023.

[19] A. Nakano, T. Yamazaki, Y. Nishimura, I. Yamazaki, A. Osuka, *Chem. Eur. J.* **2000**, *6*, 3254.

[20] A. Nakano, A. Osuka, T. Yamazaki, Y. Nishimura, S. Akimoto, I. Yamazaki, A. Itaya, M. Murakami, H. Miyasaka, *Chem. Eur. J.* **2001**, *7*, 3134.

[21] a) T. Förster, *Z. Naturforsch. A* **1949**, *4*, 321; b) T. Förster, *Discuss. Faraday Soc.* **1959**, *27*, 7.

[22] a) V. S.-Y. Lin, S. G. DiMagno, M. J. Therien, *Science* **1994**, *264*, 1105; b) R. W. Wagner, T. E. Johnson, J. S. Lindsey, *J. Am. Chem. Soc.* **1996**, *118*, 11166.

[23] a) D. A. Tomalia, H. Baker, J. Dewald, M. Hall, G. Kallos, S. Martin, J. Roeck, J. Ryder, P. Smith, *Polym. J.* **1985**, *17*, 117; b) G. R. Newkome, C. N. Moorefield, F. Vögtle, *Dendritic Molecules: Concepts, Syntheses, Perspectives*, VCH, Weinheim, **1996**.

[24] a) G. M. Stewart, M. A. Fox, *J. Am. Chem. Soc.* **1996**, *118*, 4354; b) C. Devadoss, P. Bharathi, J. S. Moore, *J. Am. Chem. Soc.* **1996**, *118*, 9635; c) A. Bar-Haim, J. Klafter, R. Kopelman, *J. Am. Chem. Soc.* **1997**, *119*, 6197; d) D.-L. Jiang, T. Aida, *Nature* **1997**, *388*, 454; e) S. Tretiak, V. Chernyak, S. Mukamel, *J. Phys. Chem. B* **1998**, *102*, 3310; f) V. Balzani, S. Campagna, G. Denti, A. Juris, S. Serroni, M. Venturi, *Acc. Chem. Res.* **1998**, *31*, 26; g) D.-L. Jiang, T. Aida, *J. Am. Chem. Soc.* **1998**, *120*, 10895; h) S. L. Gilat, A. Adronov, J. M. J. Fréchet, *Angew. Chem.* **1999**, *111*, 1519;

 © 2004 Wiley-VCH Verlag GmbH & Co. KGaA, Weinheim

Angew. Chem. Int. Ed. **1999**, *38*, 1422; i) A. Adronov, J. M. J. Fréchet, *Chem. Commun.* **2000**, 1701.
[25] D. L. Officer, A. K. Burrell, D. C. W. Reid, *Chem. Commun.* **1996**, 1657.
[26] C. C. Mak, N. Bampos, J. K. M. Sanders, *Angew. Chem.* **1998**, *110*, 3169; *Angew. Chem. Int. Ed.* **1998**, *37*, 3020.
[27] C. C. Mak, D. Pomeranc, M. Montalti, L. Prodi, J. M. K. Sanders, *Chem. Commun.* **1999**, 1083.
[28] K. Sugimura, H. Tanaka, T. Matsumoto, T. Kawai, Y. Sakata, *Chem. Lett.* **1999**, *28*, 1193.
[29] M. R. Benites, T. E. Johnson, S. Weghorn, L. Yu, P. D. Rao, J. R. Diers, S. I. Yang, C. Kirmaier, D. F. Bocian, D. Holten, J. S. Lindsey, *J. Mater. Chem.* **2002**, *12*, 65.
[30] N. Maruo, M. Uchiyama, T. Kato, T. Arai, H. Akisada, N. Nishino, *Chem. Commun.* **1999**, 2057.
[31] M.-S. Choi, T. Aida, T. Yamazaki, I. Yamazaki, *Angew. Chem.* **2001**, *113*, 3294; *Angew. Chem. Int. Ed.* **2001**, *40*, 3194.
[32] M.-S. Choi, T. Aida, T. Yamazaki, I. Yamazaki, *Chem. Eur. J.* **2002**, *8*, 2668.
[33] Y. Kuroda, K. Sugou, K. Sasaki, *J. Am. Chem. Soc.* **2000**, *122*, 7833.
[34] K. Sugou, K. Sasaki, K. Kitayama, T. Iwaki, Y, Kuroda, *J. Am. Chem. Soc.* **2002**, *124*, 1182.

 © 2004 Wiley-VCH Verlag GmbH & Co. KGaA, Weinheim

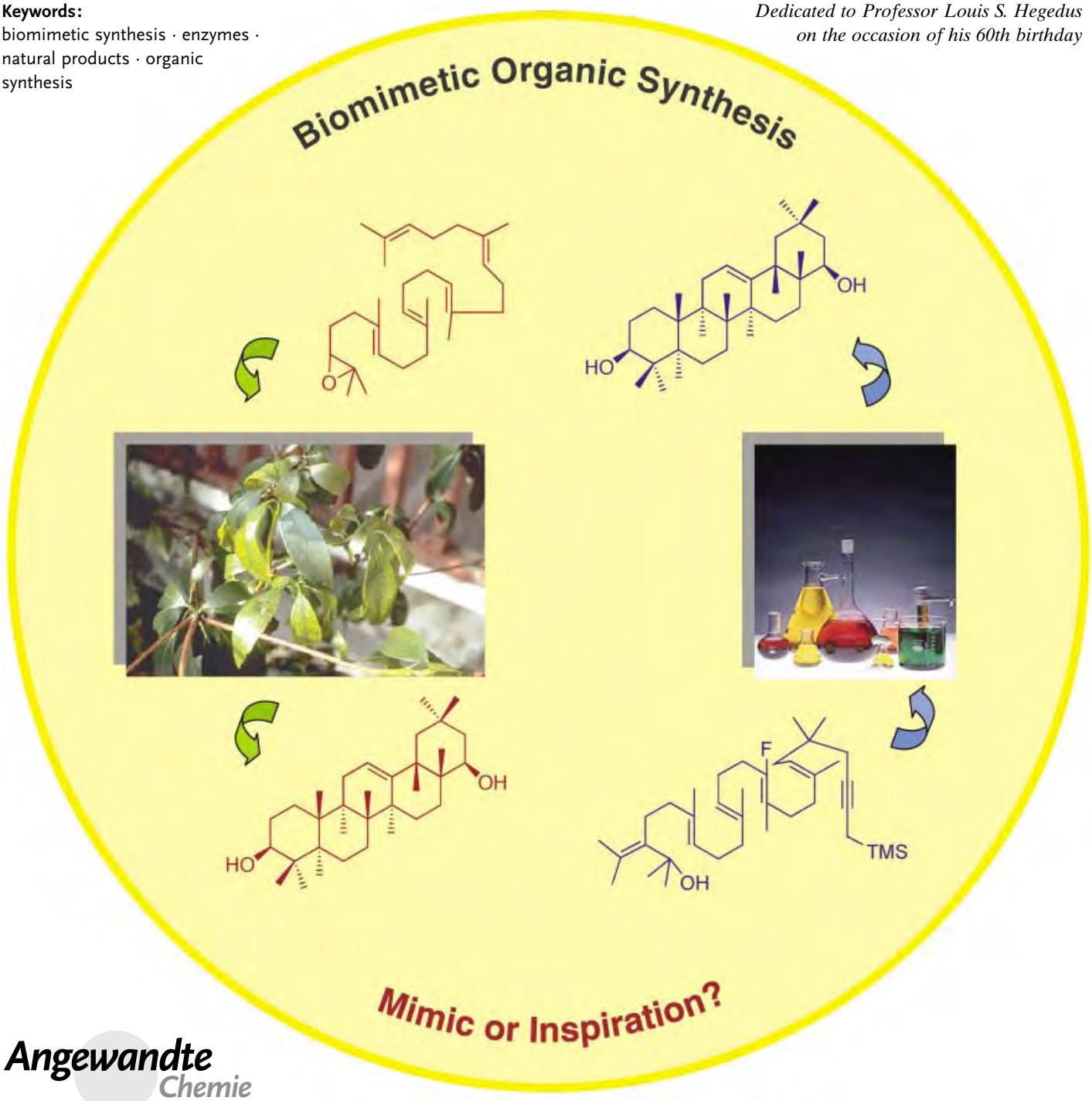
Biomimetic Synthesis

Comments on Recent Achievements in Biomimetic Organic Synthesis

María C. de la Torre and Miguel A. Sierra**

Keywords:
biomimetic synthesis · enzymes · natural products · organic synthesis

Dedicated to Professor Louis S. Hegedus on the occasion of his 60th birthday



© 2004 Wiley-VCH Verlag GmbH & Co. KGaA, Weinheim
DOI: 10.1002/anie.200200545

The appealing beauty of the routes that Nature uses to build natural products is breathtaking and the quest for laboratory syntheses that mimic these routes is longstanding. Since Robert Robinson introduced the concept of biomimetic synthesis in 1917, debates have been conducted about the participation of specific enzymes in every step of the biogenesis of every class of natural product. The successful synthesis of many natural products often follows routes analogous to processes that occur in the living cell with minimum enzyme participation. It should not be concluded, however, that we are only able to imitate biogenetic processes in which enzymes are not involved. Perhaps the most appealing facet of a biomimetic strategy is that it pursues the development of synthetic methodology inspired by biogenesis, even if the mimicked biogenetic route is only hypothetical. Improved biogenetic syntheses could be brought about by artificial enzymes that catalyze specific transformations.

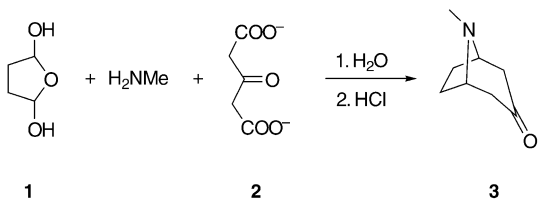
From the Contents

1. Introduction 161
2. Polyether Biomimetic Synthesis 163
3. The Diels–Alder Biomimetic Approach 165
4. The Jewel of the Biomimetic Synthesis: Cyclization of Isoprenoids 166
5. Biomimetic Synthesis with Rigid Substrates 171
6. The Biomimetic Oxidative Coupling of Phenols: The Closest to Reality? 173
7. Stepping Stones: Physiological-type Artificial Syntheses 176
8. Conclusions and Outlook 177

1. Introduction

"*For all natural products, there exists a synthesis from ubiquitous biomolecules. The inherent interconnectivity of natural products implies that a truly biomimetic total synthesis represents a general solution not to the preparation of a compound but to the preparation of all similarly derived natural products (discovered and undiscovered).*" These words were recently written by Skyler and Heathcock[1] to illustrate their work toward a general solution to the synthesis of the pyridoacridine family of alkaloids and summarize the general idea of biomimetic synthesis.[2] The concept of biomimetic synthesis was coined by Robinson, following his straightforward synthesis of tropinone (**3**) from glutaraldehyde (**1**), methylamine, and acetone dicarboxylic acid **2** reported in 1917 (Scheme 1).[3]

Van Tamelen systematized the different ideas and the philosophy underlying the terms biomimetic or biogenetic-type synthesis in his seminal work written in 1961.[4] The definitions and ideas collected in van Tamelen's work are still valid. Van Tamelen defined biomimetic synthesis as a specific reaction or a sequence of reactions that mimic a proposed biological pathway. The process being imitated usually has a solid biochemical background.[5]



1 2 3

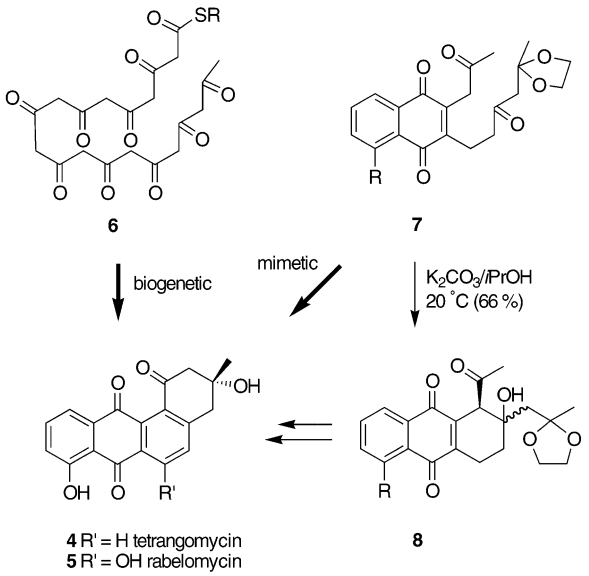
Scheme 1. Robinson's one-pot preparation of tropinone, the first example of a biomimetic synthesis.[3]

The synthesis of angucyclinone derivatives tetrangomycin (**4**) and rabelomycin (**5**) by Krohn et al. exemplifies this definition (Scheme 2).[6] The biogenetic route to these compounds is well-known. It involves the decaketide **6**, which is transformed into the angucyclinone skeleton by intramolecular aldol condensation. The cyclization process may occur either with concomitant or subsequent enzymatic oxidations and reductions.[7] To mimic the biogenetic process, severe restrictions have to be introduced in the starting material. The cyclization substrate, 1,4-naphtoquinone derivative **7**, lacks the quasi-benzylic carbonyl group. This group had been connected with preferential linear cyclization,[8] and was used to reduce the many unwanted aldol condensations to two cyclization modes: linear and angular. With these restrictive conditions in hand, compound **7** was prepared and cyclized in a stepwise fashion to the desired products via tricyclic intermediates **8**.

The term biomimetic synthesis is also used to describe a sequence of reactions carried out to support a biogenetic hypothesis. In this case, a reaction is effected on a putative substrate of the transformation under study. Should the reaction succeed, the biosynthetic route would be generally accepted. The synthesis of the indole alkaloid ervitsine (**9**) by

[*] Dr. M. C. de la Torre
Instituto de Química Orgánica
Consejo Superior de Investigaciones Científicas
C/Juan de la Cierva 3, 28006 Madrid (Spain)
Fax: (+34) 91-562-2900
E-mail: iqot310@iqog.csic.es
Prof. M. A. Sierra
Departamento de Química Orgánica
Facultad de Química, Universidad Complutense
28040 Madrid (Spain)
Fax: (+34) 91-394-4103
E-mail: sierraor@quim.ucm.es

 DOI: 10.1002/anie.200200545 © 2004 Wiley-VCH Verlag GmbH & Co. KGaA, Weinheim

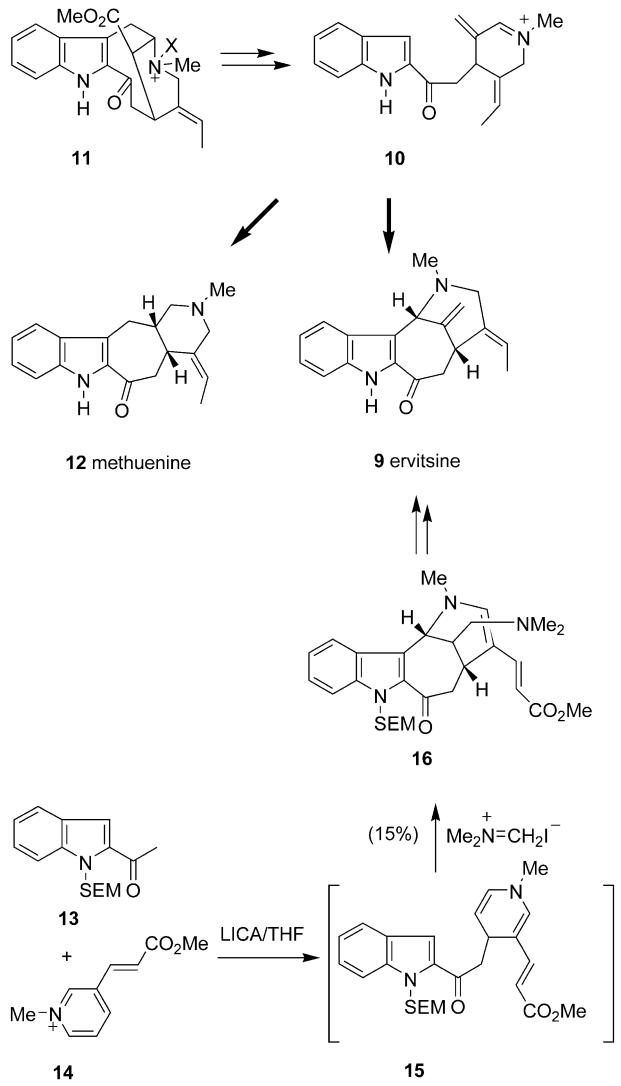


Scheme 2. Left: cyclization of polyketides to angucyclinone derivatives; right: biomimetic synthesis of tetrangomycin and rabelomycin by Krohn and co-workers.[6]

Bosch and co-workers exemplifies this meaning of biomimetic synthesis (Scheme 3).[9] The biogenetic pathway to this compound was proposed to involve the key intermediate **10**,[10] which is formed from a vobasine *N*-oxide equivalent **11**. Intermediate **10** would be transformed into ervitsine (**9**) by 1,2-addition of the indole nucleus to the α,β-unsaturated iminium group. The more favorable 1,4-addition would lead to the related alkaloid methuenine (**12**). In fact, both alkaloids **9** and **12** are biogenetically related.[11]

The key intermediate **16** was prepared by the nucleophilic addition of the enolate derived from **13** to the γ position of the pyridinium salt **14** (Scheme 3). The resulting 1,4-dihydropyridine **15** was trapped with the Eschenmoser salt ($Me_2N^+=CH_2I^-$), and adduct **16** was isolated under these conditions. Compound **16** was transformed into the desired alkaloid **9** by sequential Cope elimination, treatment with acid, and reduction with $NaBH_4$ (Scheme 3). The success of this approach was claimed to validate the proposed biogenetic pathway.

Sometimes the biomimetic synthesis fails and the biogenetic hypothesis remains unsupported. One such case involved the attempt to convert phorbol (**17**) into 12-hydroxydaphnetoxin (**18**; Scheme 4).[12] Evidence for the



Scheme 3. The synthesis of ervitsine by Bosch and co-workers supports the biogenetic hypothesis proposed for this alkaloid.[9] SEM = 2-(trimethylsilyl)ethoxymethyl, LICA = lithium isopropylcyclohexylamide.

biogenetic conversion of the tigliane (phorbol) skeleton into the daphnane skeleton rested on the isolation of compounds that had both structural types from a single plant species.[13] The biogenetic proposal suggests that the oxidation of the C16 methyl group would provide the necessary activation to trigger the C9-ester-assisted cyclopropyl-to-carbinyl rear-

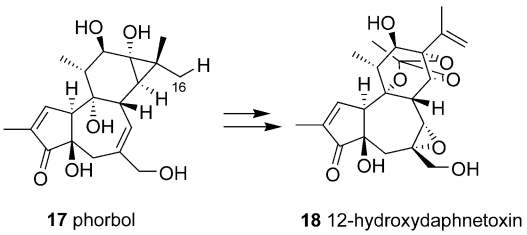


Maria C. de la Torre studied chemistry at the Universidad Complutense de Madrid (UCM) and received her PhD in 1986. After postdoctoral stays at Imperial College (Prof. Steven Ley) and Colorado State University (Prof. Albert Meyers), she returned to Madrid in 1989 as a Scientific Researcher at the Consejo Superior de Investigaciones Científicas. Her current research interest focuses on the chemistry of densely functionalized natural products, and in the preparation of natural product hybrids with mixed and/or complementary biological properties.



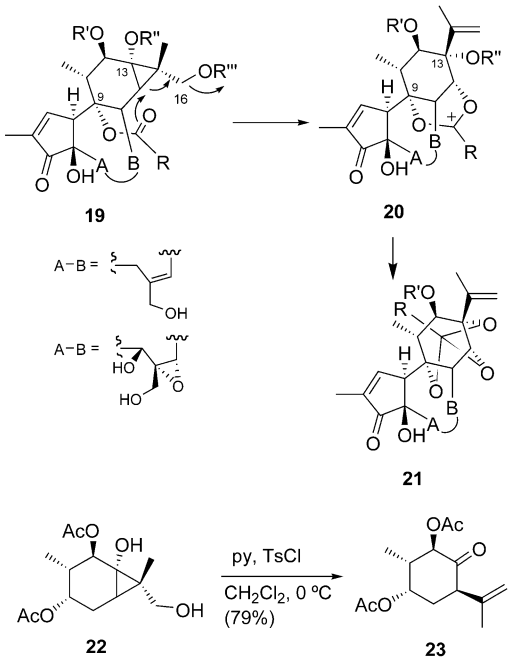
Miguel A. Sierra studied chemistry at the UCM (Madrid) and received his PhD in 1987, after which he was appointed to Assistant Professor. After a postdoctoral stay at Colorado State University (Prof. Louis Hegedus), he returned to Madrid where he was promoted to Professor in 1990. His research encompasses the development of new processes based on transition-metal complexes, the preparation of new bioorganometallic compounds tailor-made for specific applications in crop protection, and the study of environmental organic processes.

© 2004 Wiley-VCH Verlag GmbH & Co. KGaA, Weinheim



17 phorbol **18** 12-hydroxydaphnetoxin

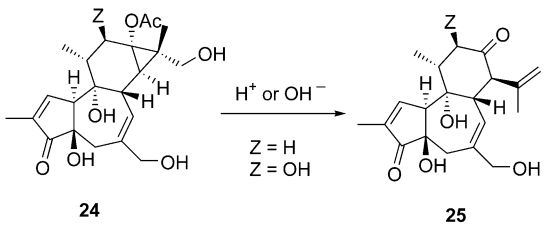
The tigliane to daphnane rearrangement



Scheme 4. The attempted biomimetic rearrangement of tigliane to daphnane was unsuccessful.[12] Ts = tosyl = 4-toluenesulfonyl; py = pyridine.

rangement (**19**→**21**). Bicyclic cyclopropane **22** was prepared and treated with 1 equivalent of tosyl chloride and pyridine to mimic the cyclopropyl–carbinyl rearrangement. The desired rearrangement did not occur (probably owing to the non-participation of the ester group). Instead, the β,γ-unsaturated ketone **23** was obtained as a result of the cleavage of the "wrong" cyclopropane bond. This bond cleavage is probably a consequence of assistance by the lone pair of electrons of the tertiary alcohol, which undergoes transformation to the π system of the incipient ketone. Different blocking groups were used to avoid the participation of this tertiary alcohol, without any success. Therefore, the biomimetic hypothesis remained unsupported.

It can be argued that in the case discussed above, the model was too simple to mimic the transformation that occurs in a considerably more complex structure. However, the analogous transformation was already tested in compound **24**, resulting again in the cleavage of the undesired cyclopropane bond to produce ketone **25** (Scheme 5).[14] However, we should remember that according to van Tamelen, "*It seems hardly necessary to add that the success of a 'biogenetic-type' synthesis by itself does not constitute evidence for the operation*



24 **25**

Scheme 5. The attempt to reproduce the tigliane to daphnane rearrangement in a complex molecule was also unsuccessful.[14]

of a particular chemical step in nature (although in a remarkable case, the temptation to draw such a conclusion will be great)."[4]

At this point it is worth discussing two coexisting, albeit antagonistic, ideas about the biosynthesis of natural products: The first idea is almost as old as the concept of biomimetic synthesis itself and was sketched by Robinson in the following way: "*Previous suggestions have no laboratory analogy. It has been assumed that plants have enormously powerful reagents that can cause substances, the properties of which have been investigated with considerable care, to undergo transformations that cannot be induced in the laboratory. To a certain extent, specially in regard to oxidation and reduction, this must be true, but it is probable that this aspect has been exaggerated and that an equally important cause of the variety and complexity of synthesis in plants resides in the highly reactive nature of the substances that function as reactive intermediates.*"[15]

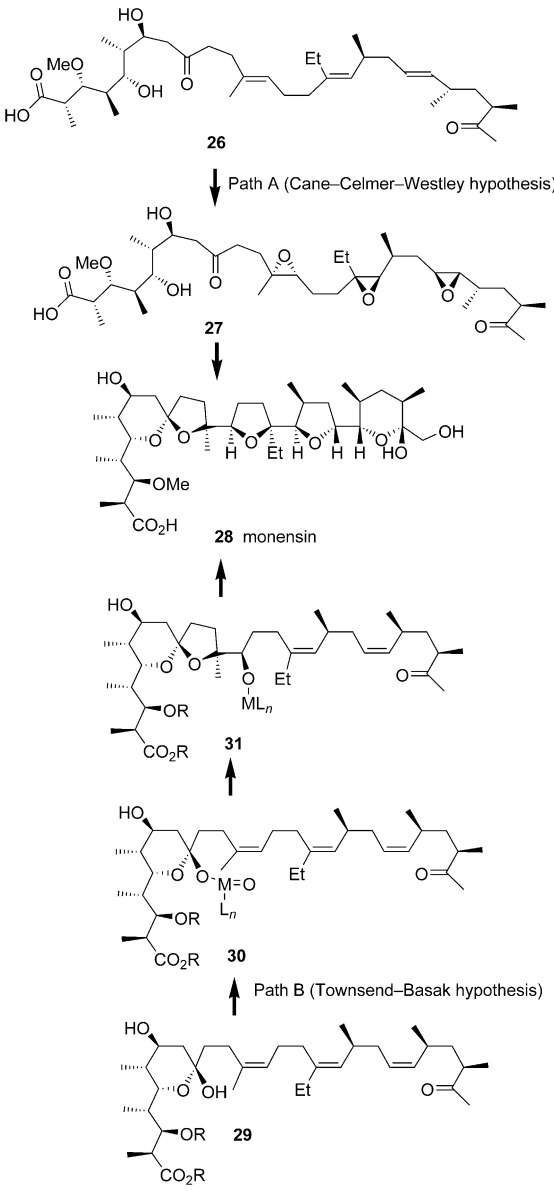
As an alternative, Heathcock defined Nature as the quintessential process development chemist. Thus "*…we think that the molecular frameworks of most natural products arise by intrinsically favorable chemical pathways—favorable enough that the skeleton could have arisen by a nonenzymic reaction in the primitive organism. If a molecule produced in this purely chemical manner was beneficial to the organism, enzymes would eventually have evolved to facilitate the production of this useful material. Further optimization of the biological activity might have been accomplished by cytochrome P450-mediated oxidations. Once again, those oxidation products that conferred an evolutionary advantage to the organism would have promoted selection of oxidase variants with appropriate binding selectivity.*"[16]

The two ideas are separated by almost one century, but, at the dawn of the new millennium, there is still no clear proof to tip the scales in either direction.

2. Polyether Biomimetic Synthesis

One of the most appealing controversies in the field of biomimetic synthesis involves the biosynthesis of polyethers.[17] Currently, two biogenetic hypotheses for these products coexist. The first hypothesis was postulated by Cane, Celmer, and Westley[18] in 1983 (CCW hypothesis) and proposes that the biosynthesis of polyethers is a two-step process involving the enzymatic polyepoxidation of an acyclic polyene precursor **26** to form polyepoxide **27** (Scheme 6,

 © 2004 Wiley-VCH Verlag GmbH & Co. KGaA, Weinheim



Scheme 6. The Cane–Celmer–Westley polyepoxide[18] and the Townsend–Basak oxidative cyclization[19a] hypotheses for the biogenesis of monensin.

path A). From **27**, a cascade of intramolecular epoxide-ring-opening reactions forms the polyether skeleton **28** (*anti* cyclization hypothesis). Townsend and Basak proposed[19] 10 years later that the polyether framework may be built through a *syn* oxidative polycyclization of an open-chain hydroxyolefin **29** (Scheme 6, path B). Premonensin triene **26** is the postulated starting material for the CCW hypothesis, whereas triene **29** is the postulated starting material in the Townsend–Basak proposal—neither of these trienes has yet been found as natural product. Moreover, synthetic radiolabeled (*E*,*E*,*E*)-premonensin triene derivatives failed to demonstrate isotopic incorporation in monensin (**28**).[20] Neither of these hypotheses have been proved, nor have the enzyme-induced transformations depicted in paths A or B been reported to date.

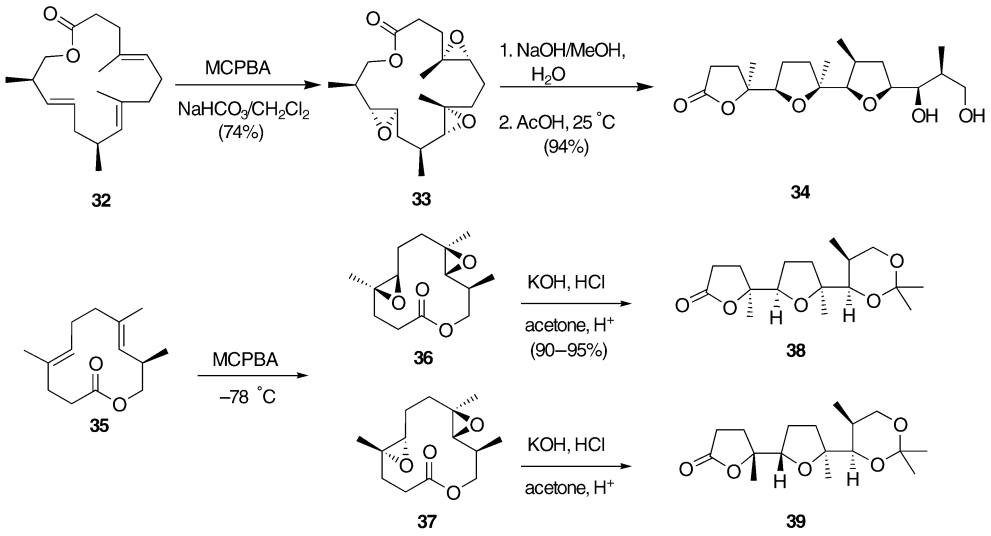
The CCW model gained rapid acceptance. In an impressive synthetic tour de force, the fundamental hypothesis depicted in path A in Scheme 6 was validated in different laboratories. For example, triepoxide **33** was prepared by treatment of macrocyclic lactone **32** with MCPBA (Scheme 7). Saponification of **33** and treatment with AcOH formed the tricyclic polyether **34**.[21] It was thence concluded that the polycyclization behavior of epoxide **33** provided strong support for the polyepoxide CCW biogenetic hypothesis. Simultaneously, diastereomeric polyepoxides **36** and **37** were prepared by oxidation of macrocyclic lactone **35** with MCPBA**.** Saponification and stereoselective cyclization of **36** and **37** led to the formation of polyethers **38** and **39**, respectively.[22]

Analogously, an approach to the C12–C21 bistetrahydrofuran moiety of monensin was reported soon after the Townsend–Basak hypothesis was formulated (Scheme 8).[23] Triene **40** was dihydroxylated with AD-mixβ to form 1,2-diol **41**. The *syn* oxidative cyclization of **41** to form tetrahydrofuranyl ketone **42** was induced with Collins reagent. Reduction of the ketone group of **42** occurred with complete Felkin–Ahn stereocontrol to provide **43**, which underwent oxidative cyclization in the presence of $(Cl_2CHCO_2)ReO_3$ to give the *trans*,*cis*-bistetrahydrofuranyl alcohol **44**. Alcohol **44** includes the C and D rings of monensin (**28**). The stepwise construction of **44** required three different metal–oxo reagents (Os for the dihydroxylation step, Cr for the first oxidative step, and Re for the second). McDonald and co-workers speculate that a single biosynthetic enzyme containing a metal–oxo site might catalyze all three transformations (in the presence of an external oxidizing agent, $NAD^+ \rightarrow NADH$).[24]

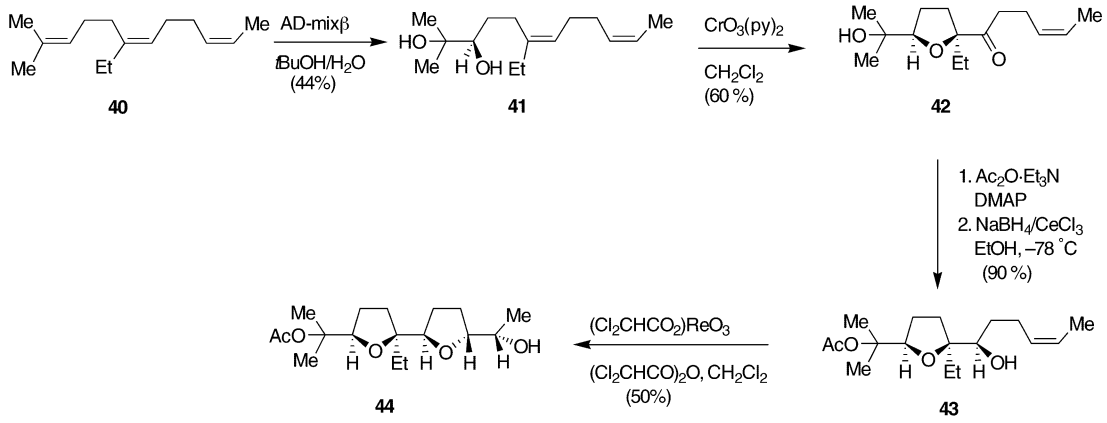
The oxidative cyclization cascade used in the preparation of goniocin (**45**), a fatty acid derivative isolated from *Goniothalamus giganteus*,[25] was devised to use only one metal reagent (Scheme 9)**.** The synthesis involved the tandem oxidative cyclization of an appropriate acyclic triene in the presence of Re_2O_7 as the key step.[26] In the context of the Townsend–Basak hypothesis, this approach to **45** would be a perfect biomimetic synthesis. The relative configuration of the six stereogenic centers in the trisfuran skeleton was derived from the single stereogenic center of **46**. Treatment of triene **46** with $CF_3CO_2ReO_3$ in TFAA resulted in the formation of a single tristetrahydrofuranyl product **47** in 48% yield (Scheme 9). Surprisingly, the product **47** has a *trans*,*threo*,*cis*,*threo*,*cis*,*threo* configuration instead of the desired *trans*,*threo*,*trans*,*threo*,*trans*,*threo*. The undesired stereochemical result was attributed to the absence of the butenolide moiety present in goniocin. The oxidative cyclization was repeated in triene **48**, which has much more elaborated skeleton. Triene **48** formed compound **49**, whose stereochemistry is identical to that of **47** (Scheme 9). The correct stereochemistry of the natural product could not be accessed in this way.

The successful approach to goniocin (**45**)[27] defined the correct stereochemistry on the first THF ring by treatment of diene **50** with $CF_3CO_2ReO_3$ in TFA to yield **51** (Scheme 10). Compound **51** was converted into tristetrahydrofuranyl **53** by asymmetric dihydroxylation and ring closure of bismesylate **52**. The same sequence of reactions was repeated with *ent*-**50**

 © 2004 Wiley-VCH Verlag GmbH & Co. KGaA, Weinheim



Scheme 7. Early successful synthetic routes developed to prove the CCW hypothesis for the biogenesis of polyether antibiotics.[21] MCPBA = *meta*-chloroperbenzoic acid.



Scheme 8. The stepwise building of bistetrahydrofuran **44** using three different metals supports the Townsend–Basak hypothesis for the biogenesis of polyether antibiotics.[23] DMAP = 4-(dimethylamino)pyridine.

to form *ent*-**53**, which was transformed into cyclogoniodenin T (**54**). The authors hypothesized that the coexistence of the two natural products **45** and **54** with different configurations in the same organism is the result of two alternative modes of tandem ring closures. Both routes would start from a common polyepoxide intermediate.

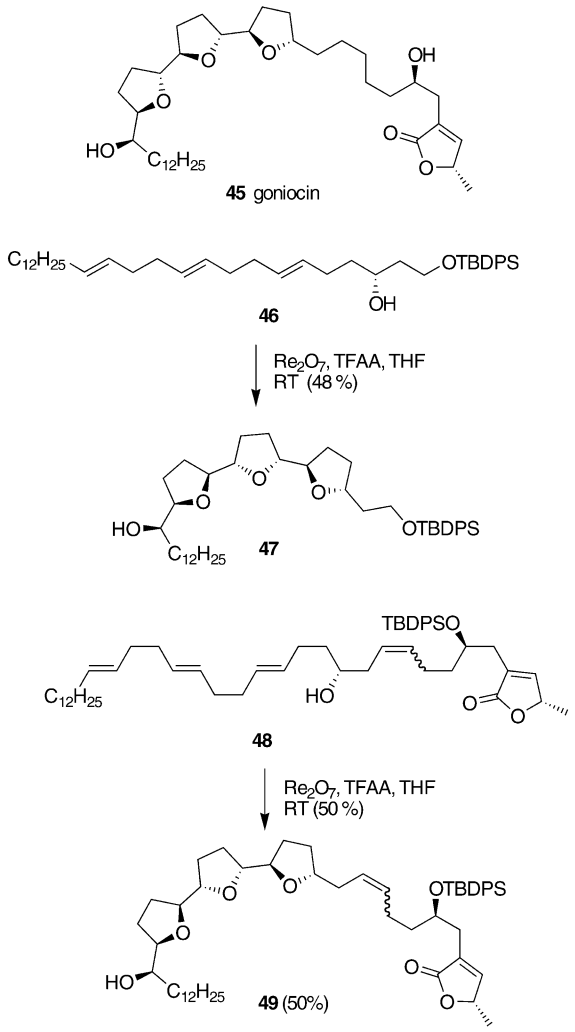
The fused polycyclic ethers of marine origin are closely related to the polyether antibiotics. For example, brevetoxin B (**55**) may, according to Nicolaou and Sorensen,[28] arise in one dramatic event from the polyepoxide precursors **56** or **57**. Clearly, biosynthetic path A (Scheme 11), originally proposed by Nakanishi and co-workers,[29] is closely related to the CCW hypothesis for the biosynthesis of polyether antibiotics. The event leading to brevetoxin B is initiated synchronously by attack of the carboxylate ion at the oxirane carbon atom at the left terminus (as drawn). The protonation of the unconjugated double bond on the right-hand side would occur either prior or simultaneously to the attack by the carboxylate group. Path B was also proposed in the context of the CCW hypothesis by Shimizu.[30] It involves the amphiphilic intramolecular attack of the hydroxy group (right-hand side of drawn structure) at the proximal oxirane carbon atom upon protonation of the carbonyl oxygen atom on the left-hand side of the polyepoxide **57**. Although modest advances to implement this methodology have been made,[31] it has not been successful in the syntheses of fused cyclic polyethers.[32]

The examples above show how two coexisting biogenetic hypotheses may trigger substantial efforts to achieve the synthesis of the classes of compounds involved.

3. The Diels–Alder Biomimetic Approach

Does nature know about the Diels–Alder reaction? The question posed by Laschat in a Highlight[33] was answered by stating that "*until now* [early 1996], *there is no case known where the corresponding enzyme system, that is the Diels–Alderase, could be detected*". And further in the same article,

 © 2004 Wiley-VCH Verlag GmbH & Co. KGaA, Weinheim



Scheme 9. The one-step oxidative cyclization approach to goniocin (**45**) to produce the wrong stereoisomer.[25,26] TFAA = trifluoroacetic anhydride; TBDPS = *tert*-butyldiphenylsilyl.

the author stated that "*in view of the difficulties in detecting and isolating Diels–Alderases, one might assume that there are no enzyme-catalyzed [4+2] cycloadditions involved in natural systems. However, this assumption seems to be incorrect!*" Timely and thorough reviews on the topic are available.[34] Therefore, we will limit our discussion to only two examples: One synthesis mimics a probable enzyme-catalyzed biogenetic process, and the other mimicks a possible uncatalyzed but spontaneous biogenetic process. It should be clear that current experimental evidence for enzyme involvement in the biological Diels–Alder reaction is circumstantial.[35]

The solanapyrones **58** and **59** are two phytotoxins produced by the fungus *Alternaria solani.* The hypothetical involvement of Diels–Alderases in these processes was reported by Oikawa et al.[36] based on the different *endo*/*exo* ratios obtained for adducts **58** and **59** when either a cell-free extract of *A. solani* (**58**/**59** 47:53) or water (**58**/**59** 97:3) were used in the synthesis of these compounds from precursor **60** (Scheme 12).

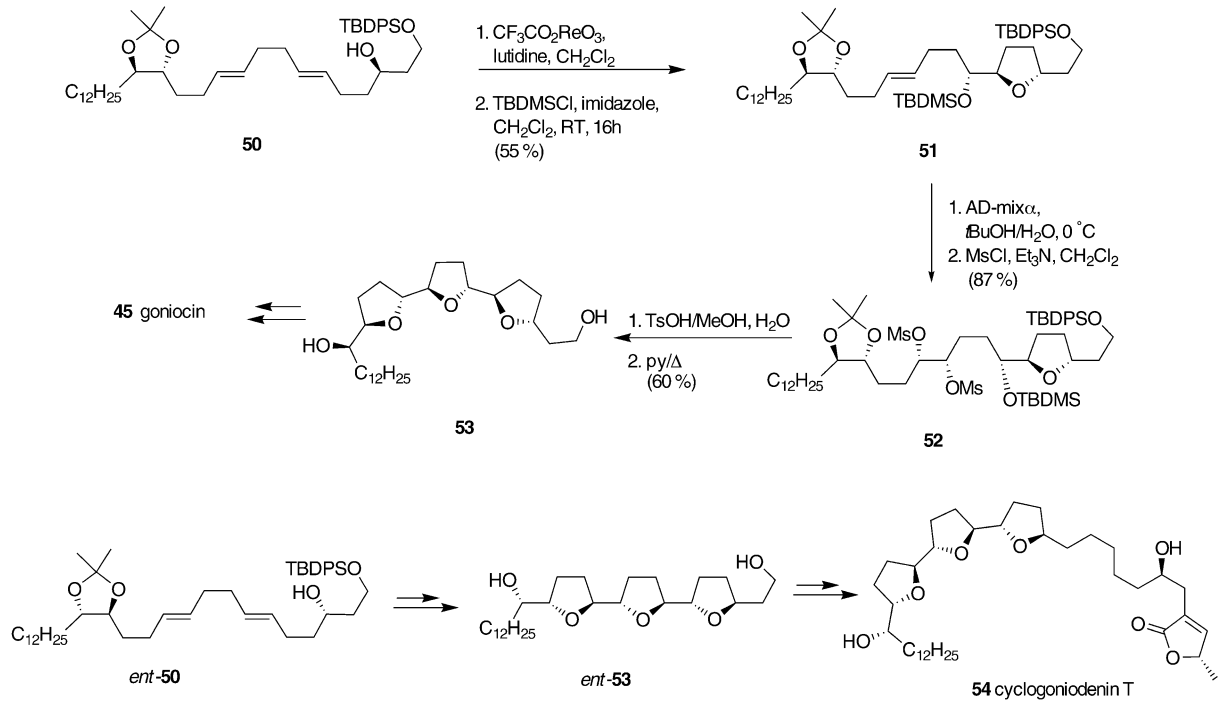
Although the involvement of Diels–Alderases in the biogenesis of the solanapyrones is a strong possibility, such enzymes may be excluded from the biosynthesis of the bisorcibillinols. Bisorcibillinoids[37] are structurally related dodecaketides, all of which potentially originate from the natural product sorbicillin (**61**). The proposed biosynthetic pathways (Scheme 13) for bisorbicillinol (**62**), bisorbibutenolide (**63**), and bisorbicillinolide (**64**) involved the initial regio- and stereospecific [4+2] dimerization of sorbicillin (**61**) and 2′,3′-dihydrosorbicillin after an enantioselective oxidation. From **62**, two successive anionic rearrangements and a final Michael addition provide **63** and **64**.[38] This biogenetic proposal was fully mimicked by Nicolaou and co-workers[39] starting from α-diacetoxy dienone **65**. Treatment of dienone **65** with base led to the Diels–Alder adduct **62** in 40% yield. The same reaction was repeated with (*S*)-**65**, and the optical rotation of the synthetic **62** was in good agreement with that reported for the natural product. This reaction provided four stereogenic centers, two of which are fully substituted, with complete region- and *endo* selectivity. Furthermore, the fully thermal reaction (heating of **65** in benzene or in AcOH for several hours) did not give any Diels–Alder product. The treatment with base should reveal a diquinolate system by hydrolysis of the acetyl group to form the reactive **66** after protonation. Therefore, it seems reasonable that the thermal reaction could not produce satisfactory results (Scheme 13). Afterwards, following the hypothesis of Abe et al., **62** was transformed into **63** by treatment with KHMDS. However, although treatment of **62** with KHMDS led smoothly to **63**, any other base failed to convert **62** or **63** into bisorbicillinolide (**64**). This is noteworthy since **63** is hypothetically a biogenetic intermediate of the anionic cascade for the formation of **64**.

The above syntheses mimicked a biogenetic hypothesis that involves the Diels–Alder reaction. The same chemical process may be used for different organisms to produce different secondary metabolites.[40] However, it is unusual to propose so many biotransformations based on a process for which an enzymatic system has not been unambiguously proved to exist. We use Williams's words to summarize this point: "*…despite the increasing number of natural products that have been identified and proposed to arise via a biological Diels–Alder reaction, a great deal of experimental and intellectual penetration into the mechanistic subtleties of putative biosynthetic Diels–Alder reactions need to be conducted*".[34a]

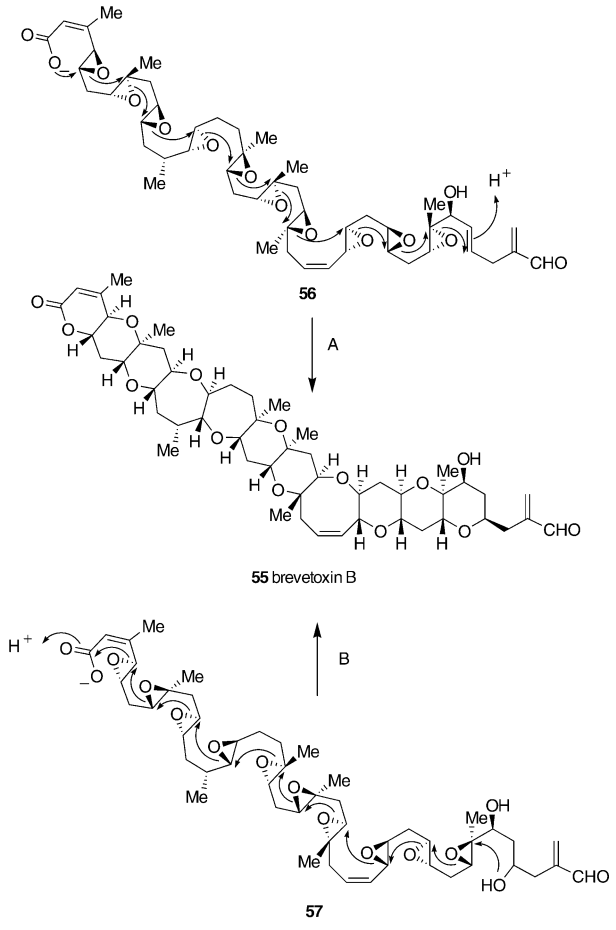
4. The Jewel of the Biomimetic Synthesis: Cyclization of Isoprenoids

The research behind the achievements in the field of isoprenoid biogenesis and the efforts to mimic their biosynthesis are fundamental milestones in the history of organic chemistry.[41,42] Isoprenoids have amazingly diverse structures whose construction are mediated by cyclases. Several polycyclic isoprenoids are generated from simple linear polyene substrates such as geranyl pyrophosphate (GPP, **68**) farnesyl pyrophosphate (FPP, **69**), or geranylgeranyl pyrophosphate (GGPP, **70**) (Figure 1).

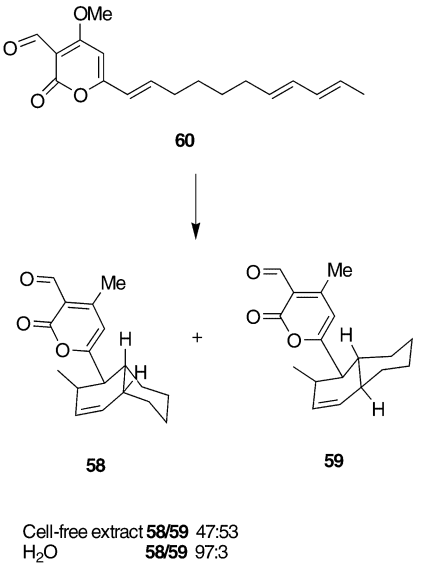
 © 2004 Wiley-VCH Verlag GmbH & Co. KGaA, Weinheim



Scheme 10. The sequential and successful approach to goniocin (**45**) and cyclogoniodenin T (**54**). TBDMS = *tert*-butyldimethylsilyl; DMF = *N*,*N*-dimethylformamide; Ms = mesyl = methanesulfonyl.[27]



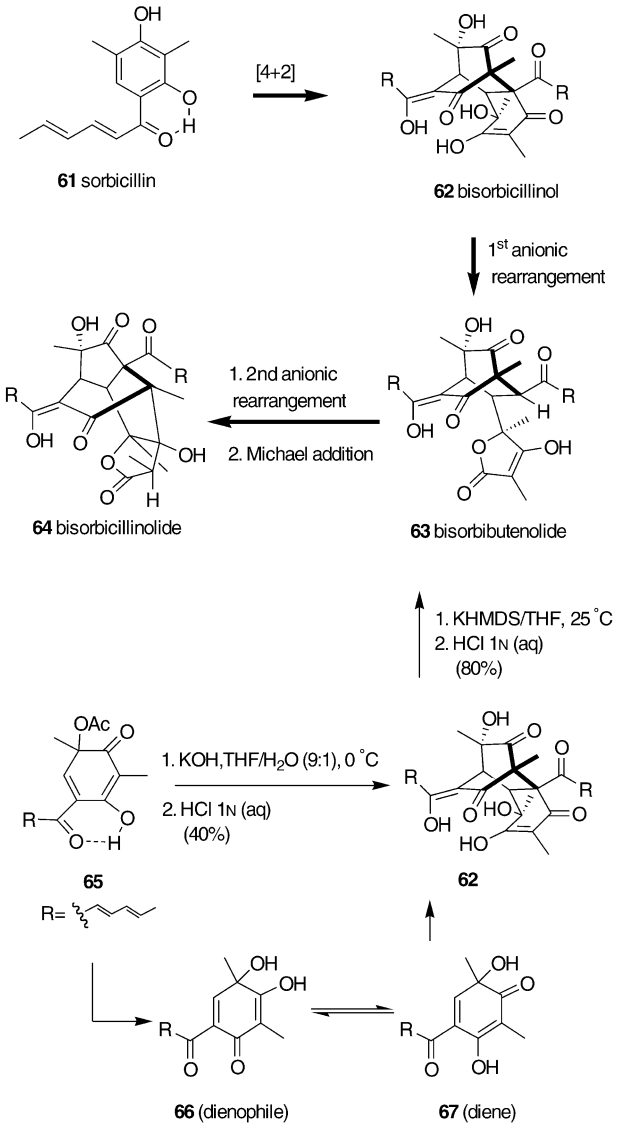
Scheme 11. Two alternatives to the cascade cyclization leading to brevetoxin B.



Scheme 12. A possible Diels–Alderase-catalyzed Diels–Alder reaction.[36]

The formation of polycyclic isoprenoids, which bear diverse stereocenters, is mediated by cyclases in a single enzyme-controlled asymmetric reaction (Figure 1).[43] The beauty of the process rests in the fact that the same substrate can form diverse families of isoprenoid structures which depend on the enzymes used. It is thought[44] that the specific cyclizations occur in a four-step sequence: 1) generation of a carbocation, 2) control of the conformation of the substrate, 3) stabilization of intermediates, and 4) quenching of the final

 © 2004 Wiley-VCH Verlag GmbH & Co. KGaA, Weinheim



Scheme 13. The biogenetic proposal for the biosynthesis of bisorcibillinols; synthesis by Nicolaou and co-workers. HMDS = bis(trimethylsilyl)amide.[39]

carbocation. Based on this scheme, the origin of the stereoselectivity of the polycyclic system rests on the generation of the carbocation.[44a] Two question arise: What is the level of involvement of cyclases in these processes? Can truly enantioselective biomimetic cyclization of isoprenoids be achieved in vitro?

The first question is addressed by the theory of "minimal enzymatic assistance".[43] This theory postulated the possibility that "*for the formation of novel and unexpected products by the cyclases, it is also possible that the active sites are simply permissive and therefore do not intervene completely in the folding and cyclization of substrates which they do not normally encounter. The role of the cyclase is most likely to involve initiation of cyclization and prevention of alternative modes of cyclization*".

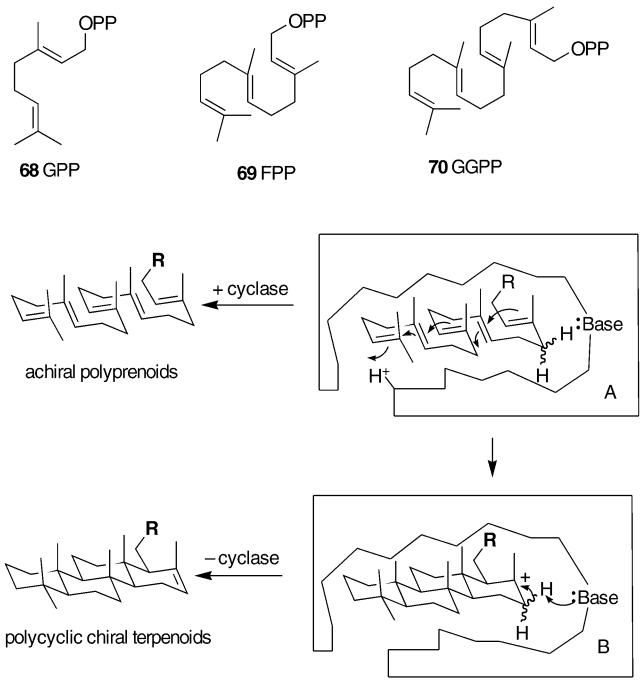
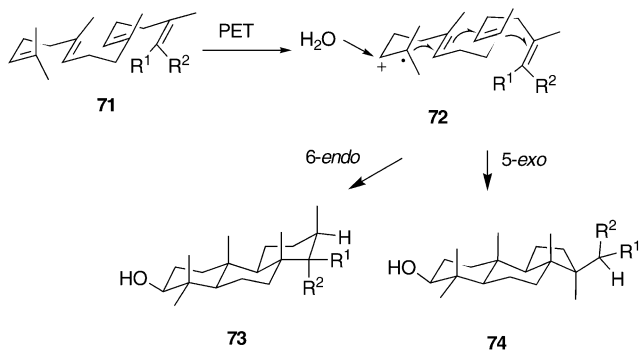


Figure 1. Cyclase cyclization of linear polyenes.

The second question has been addressed experimentally by using artificial cyclases based on the combined system of a Lewis acid and a chiral Brønsted acid (LBA) (see below).

An elegant illustration of the minimal-enzymatic-assistance hypothesis is the synthesis of a steroid nucleus reported by Demuth and Heinemann.[45] The philosophy of this approach parallels the ionic-cyclization process. The initial step is the regioselective oxidation of the terpenoid polyalkene **71** at the ω position by photoinduced electron transfer (PET). The oxidation process generates the parent radical cation **72**, which evolve in a productive way by trapping of a nucleophile (usually water). The trapping is followed by radical cyclization and termination by quenching of the resulting neutral radical (Scheme 14).[46] Ring closure (6-*endo*- or 5-*exo*-trig) could terminate the cyclization, leading to **73** or **74**, respectively.

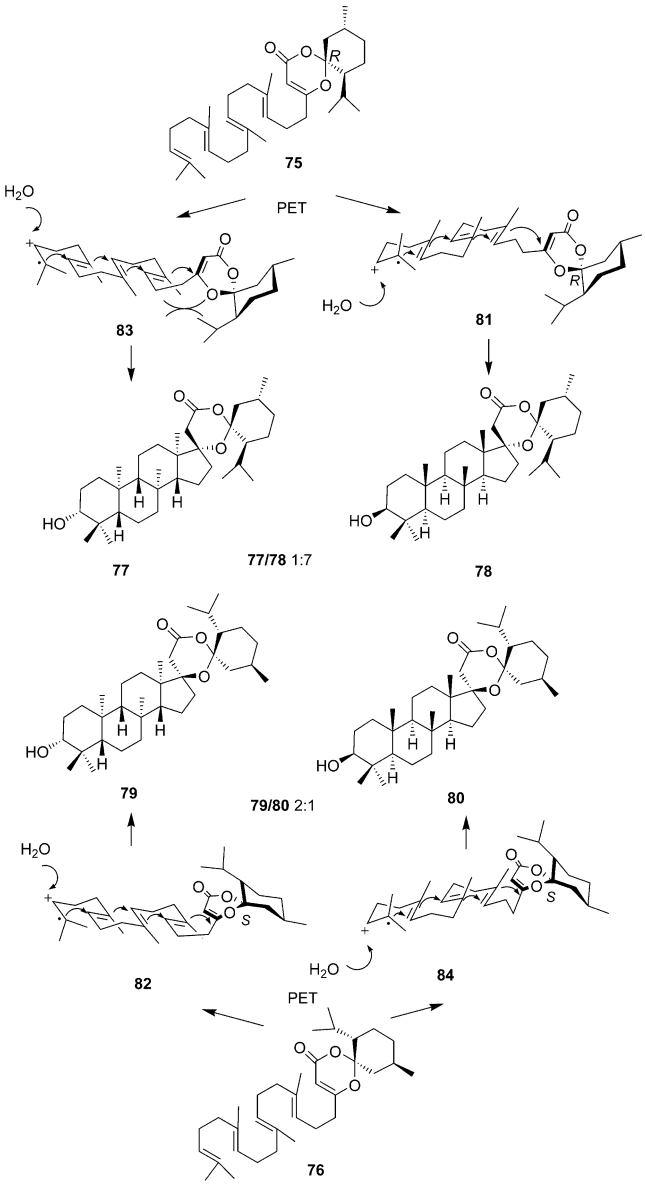
The enantiomerically pure (*E*,*E*,*E*)-geranylgeranylmethyldioxinones **75** and **76** were irradiated in the presence of



Scheme 14. Two alternatives for the photoinduced electron transfer (PET) cyclization of terpenoid polyalkene **71**.[46]

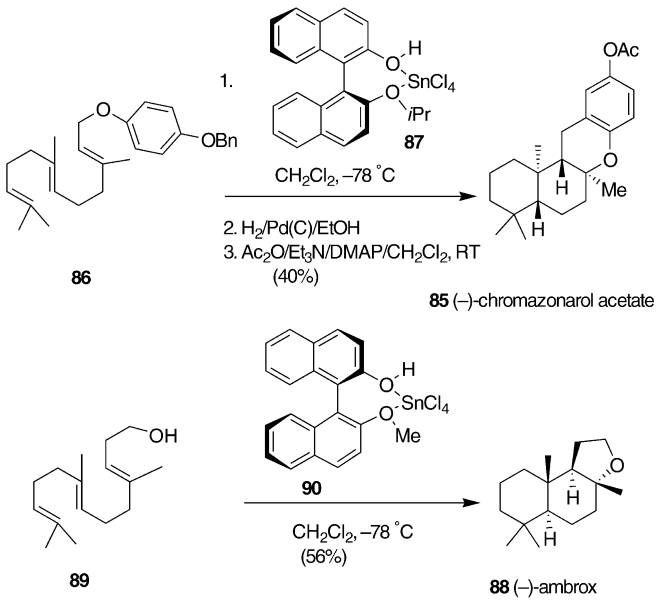
 © 2004 Wiley-VCH Verlag GmbH & Co. KGaA, Weinheim

catalytic amounts of 1,4-dicyanotetramethylbenzene (DCTMB) and biphenyl (BP) as the electron donor–acceptor couple (Scheme 15). The major photoproducts of **75** were **77** and **78** as a diastereomeric mixture (1:7). Analogously, irradiation of the diastereomer **76** led to a mixture (2:1) of cyclization products **79** and **80**. In both cases, the termination occurs exclusively in the 5-*exo*-trig mode. The degree of asymmetric induction observed in both cases is remarkable and is due to the geometry of the double bonds of **75** and the sequential formation of six-membered rings. The chiral auxiliary is remote from the initial radical cation center. This undoubtedly suggests a diastereoselective folding of the polyalkene chain immediately after the initial PET oxidation steps (it is not likely that such a preorganization exists before the PET). The main reaction paths proceed through the α folding of the polyalkene chain such as in intermediates **81** and **82**. The β-folded intermediates **83** and **84** are disfavored. This case of remote asymmetric induction supports the feasibility of effecting a highly selective cyclization of the polyene by anchoring a portion of the molecule in the enzyme (minimal enzymatic assistance). The covalently tethered chiral auxiliary plays the role of the enzyme center. Remarkably, the analogous transformation via cationic intermediates does not take place in vitro.



Scheme 15. The bias for α folding over β folding of the chiral polyalkenes **75** and **76** is shown in their PET cyclization.

The enantioselective polyene cyclization has been mimicked through an external chiral promoter. This shows that it is feasible to mimic the remote participation of the enzyme in the initial protonation of the polyene. Since the coordination of a Lewis acid to a Brønsted acid restricts directional access to the proton and increases the Brønsted acidity, chiral Lewis–Brønsted acids (LBAs) can be considered as "protons" surrounded by chiral environments, and hence have been used in enantioselective protonations.[47] As stated above, the generation of the carbocation is the key step in determining the absolute stereoselectivity of a polyene cationic cyclization.[44,47a] Therefore, LBAs may be used as surrogates in the enzymatic enantiodifferentiating protonation steps. Yamamoto and co-workers demonstrated this concept by synthesizing the acetate **85** of (−)-chromazonarol, a minor constituent of the brown Pacific seaweed *Dictyopteris undulata*, from the corresponding farnesyl derivative **86** (Scheme 16). Thus, 4-benzyloxyphenyl farnesyl ether (**86**) was treated with a stoichiometric amount of chiral LBA **87** for 24 h at −78 °C. Under these conditions, the tetracyclic derivative **85** was obtained with 44 % *ee*, after debenzylation and acetylation, in a process involving an initial Claisen rearrangement followed by cationic cyclization. Furthermore, the restrictive element introduced by the aromatic ring in **86** is not needed as (−)-ambrox (**88**), the main odorant component of ambergris, was

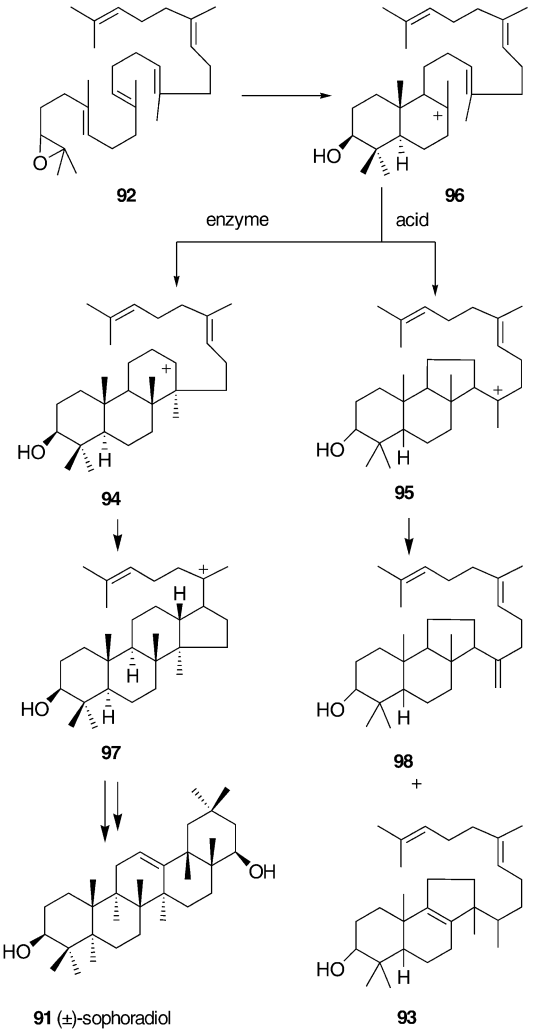


Scheme 16. Biomimetic enantioselective polyene cyclization using a chiral Lewis–Brønsted acid (LBA).

 © 2004 Wiley-VCH Verlag GmbH & Co. KGaA, Weinheim

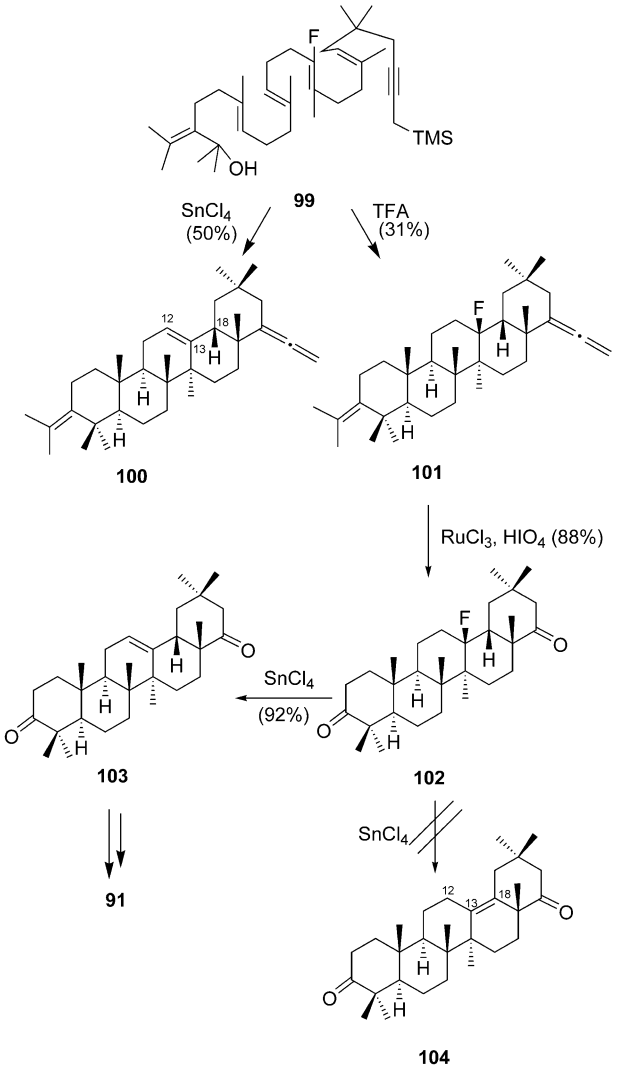
prepared by enantioselective cyclization of homofarnesol (**89**) promoted by **90** in 56% yield (42% *ee*) (Scheme 16).[47b]

The cyclization of polyenes by PET or LBAs demonstrates that it is feasible to mimic the biogenetic processes at least partially. Evidently, the number of cyclization modes and the diastereoselectivity are dependent on the spontaneous preorganization of substrates in the applied media at the temperatures used. A synthetic cyclase would need to solve the problem of the organization of the conformation of the substrates during the cyclization of the intermediates. Such additional cavities together with the use of catalytic amounts of chirality-transfer agents would undoubtedly lead to truly biomimetic processes. The synthesis of (±)-sophoradiol (**91**) by Johnson and Fish is a classical attempt to solve the problem (Scheme 17).[48] Whereas the enzymatic cyclization of oxidosqualene (**92**) leads to the pentacyclic triterpenoids of the oleanane series **91**,[49] the acid-catalyzed reaction of **92** leads instead to tricyclic products such as **93**. The premature termination of the acid-catalyzed reaction is rationalized by comparison of the relative stabilities of the cationic intermediates **94** and **95**. The initial cyclization of **92** generates bicyclic cation **96** both in acid or enzyme-catalyzed processes. However, whereas the enzymatic process leads to the anti-Markovnikov tricyclic cation **94**, the acid-induced process produces the favored cation **95**. Evolution of both cations leads to the observed penta- and tricyclic products **91** and **93**, respectively.



Scheme 17. The enzymatic cyclization of oxidosqualene leads to pentacyclic triterpenoids, whereas its acid-catalyzed cyclization forms tricyclic compounds.[48,49]

During the seminal work of Johnson and co-workers on the cyclization of polyenes,[50] a fluorine atom was introduced in the substrates as a cation-stabilizing auxiliary (Scheme 18).[51] The regiochemistry of the cyclization is controlled by the fluorine atom to give exclusively the six-membered ring, whereas the five-membered ring is formed in its absence. In this regard, the polyene cyclization substrate **99** was prepared and treated with $SnCl_4$ at $-78\,^{\circ}C$ for 10 min. Cyclization with loss of HF led to the formation of pentacyclic derivative **100** in 50% yield. Treatment of **99** with trifluoroacetic acid (TFA) gave fluorinated derivative **101** in 31%

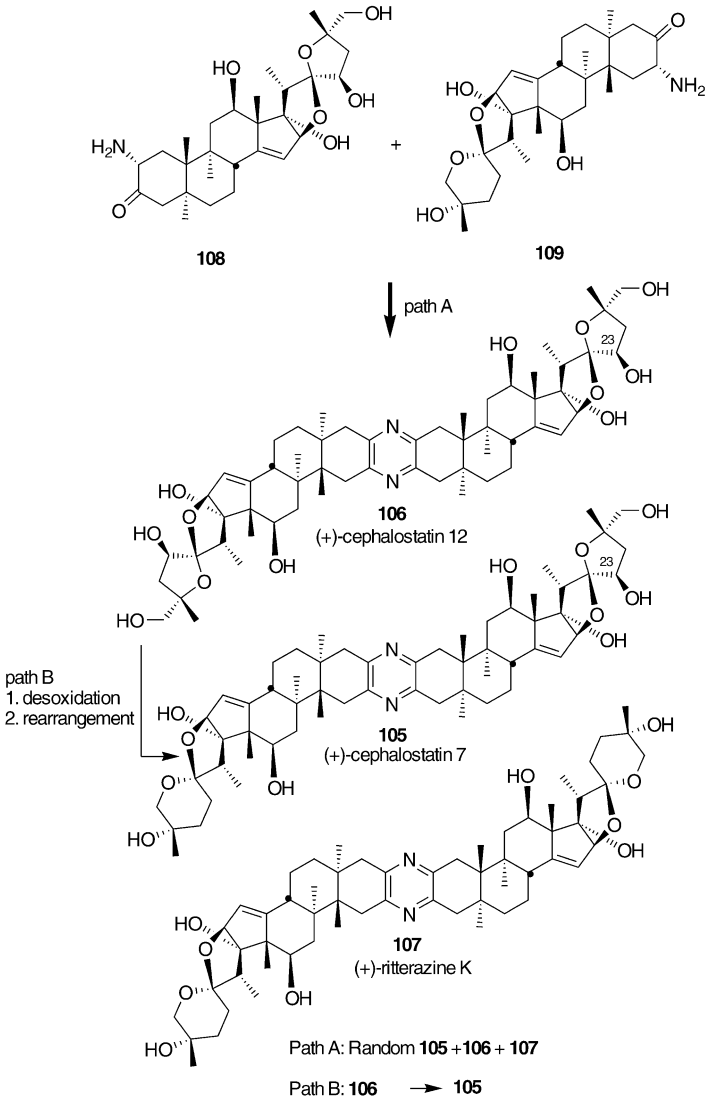


Scheme 18. The fluorine atoms acts as a cation-stabilizing auxiliary in the cyclization of polyenes. TFA = trifluoroacetic acid.[50,51]

yield. (±)-Sophoradiol (**91**) was prepared from **101** in four steps. The key step in this sequence was the dehydrodefluorination of intermediate **102**, which was obtained from **101** by oxidative cleavage of the allene and alkene functions. Derivative **103** is formed by treatment with $SnCl_4$ as a consequence of the strain within the structure of the fluoropentacyclic derivative. The Lewis acid facilitates dehydrofluorination and produces a planar sp^2-hybridized carbon center at C13, thus relieving the strain. The exclusive formation of **103** is due to the favored *anti* 1,2-diaxial elimination of HF (C13-F_{ax}, C12-H_{ax}); the disfavored *syn* 1,2-elimination (C13-F_{ax}, C18-H_{eq}) would lead to the isomer **104**. Therefore, the fluorine atom not only directs the polycyclization to the pentacyclic *all-trans* six-membered-ring system, but also defines the position of the double bond, either during the cyclization process (formation of compound **100**), or thereafter during the completion of the synthesis of **91** (**102**→**103**).

These syntheses mimic three different aspects of the biosynthesis of terpenes: 1) remote induction by an enzyme, 2) chiral discrimination promoted by a chiral proton source, and 3) stabilization of the carbocation intermediates. The remaining point to be mimicked is the conformational organization. It is foreseeable that processes in which the four key points of the action of cyclases are combined will be reported in a near future. Such a process would yield known structural types, but may also lead to new non-natural structures. Again, we can speculate that the combination of the three factors (in vitro) would lead to preorganization. The required folding of the cyclization substrates would emanate from the highly chiral surfaces in the cell. Johnson raised this question as early as 1968 in his review on nonenzymatic biogeneticlike olefin cyclizations: "*The theoretical question to be answered is, how important is the enzyme in directing the course of the cyclization? One popular view is that the enzyme plays an all-important role, i.e., it serves as template which holds the substrate in a single rigidly folded conformation with the olefinic bonds appropriately juxtaposed for cyclization. There are, on the other hand, some good a priori reasons for entertaining the hypothesis that squalene-like (*all-trans*) polyolefins should have an intrinsic susceptibility to cyclize stereoselectively to give a product having 'natural' configuration.*"[50e]

pyrazine core structure is assembled through dimerization and oxidation of steroidal α-aminoketones (Scheme 19).[54]



Scheme 19. Random formation versus biological oxidation in the biosynthesis of tridecacyclic pyrazines to form steroidal α-aminoketones.

5. Biomimetic Synthesis with Rigid Substrates

The required restriction of the conformational freedom of the cyclization substrates is a general cul de sac in designing cascade biomimetic synthesis (this is also true in conventional cascade syntheses). Therefore, the use of rigid substrates usually ensures the success of the biomimetic approach. The success in mimicking processes of dimerization of rigid substrates is seen in the appealing total synthesis of (+)-cephalostatin 7 (**105**), (+)-cephalostatin 12 (**106**), and (+)-ritterazine K (**107**) reported by Fuchs and co-workers.[52] Cephalostatins and other tridecacylic pyrazines were isolated from the marine tube worm *Cephalodiscus gilchristi* and from the tunicate *Ritterella tokioka*.[53] The biogenetic hypothesis for this kind of compounds is based on the premise that the

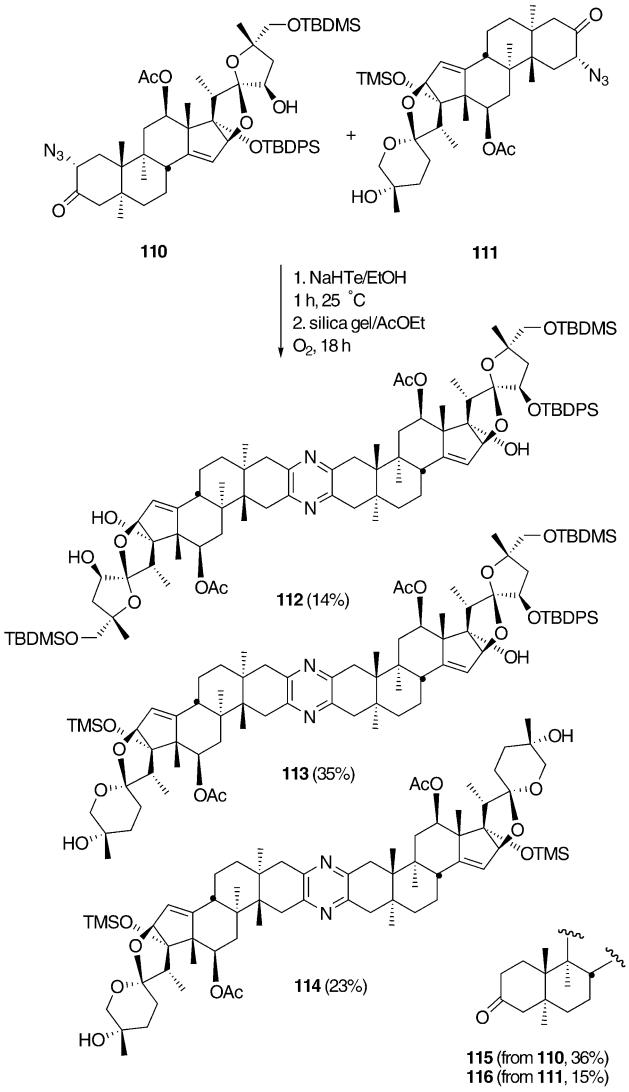
A fascinating question regards the timing of the dimerization step. It can be envisaged that a single precursor, steroid **108** or **109**, undergoes dimerization to produce the C_2-symmetrical dimers **106** or **107**, respectively, whereas unsymmetrical **105**, would be formed from a mixture of the α-aminoketones **108** and **109**. The result of this last scenario would be the formation of **106**, **105**, and **107** (1:2:1). In this case, the precursors **108** and **109** should be present in the same concentration, and the dimerization rates for all the α-aminoketones should be approximately the same. This appealing hypothesis that random coupling is responsible for the observed distribution of products falls apart, however, as the unsymmetrical **105** was isolated in 100-fold higher yield than the symmetrical **106** or **107** (Scheme 19).

 © 2004 Wiley-VCH Verlag GmbH & Co. KGaA, Weinheim

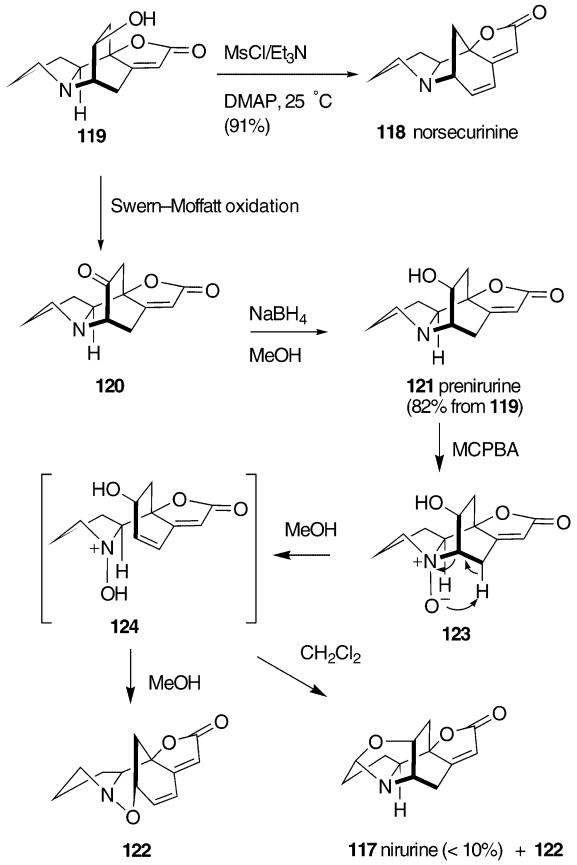
Therefore, a second pathway for biosynthesis of the cephalostatins must involve the biological deoxygenation of symmetrical **106** at C23, followed by acid-catalyzed rearrangement of the 5/5 spiroketal to the 6/5 spiroketal present in **105**.[55] This last transformation can be mimicked in the laboratory by the use of selective protecting groups to ensure differentiation of functional groups. It is necessary to indicate that the 5/5→6/5 spiroketal rearrangement does not require the participation of enzymes, as it occurs spontaneously in vitro.

The biomimetic approach used by Fuchs and co-workers[52] to prepare compounds **105**–**107** was the statistical combination of α-aminoketones **108** and **109**. A 1:1 mixture of α-azidoketones **110** and **111** was treated with NaHTe and then with mildly acidic silica gel. A mixture of pyrazines **112**, **113**, and **114** was obtained in 14, 35, and 23% yields, respectively (Scheme 20). The bias observed for compound **114** (as opposed to the expected 1:1 ratio of **112**/**114**) was explained by the reductive cleavage of azides **110** and **111**. This side reaction formed the reduced by-products **115** and **116** in 36% and 15% yields, respectively. As the reductive cleavage of **110** and **111** by NaHTe disturbed the 1:1 ratio of α-aminoketones derived from **110** and **111**, it is reasonable that the coupling reaction was biased toward the ritterazine K precursor **114.** The synthesis of pyrazine-derived alkaloids sketched in Scheme 20 shows that these compounds may be formed by dimerization of the appropriate α-aminoketone precursors without enzyme intervention. A synthesis that mimics the selective formation of unsymmetrical cephalostatins still remains open.[56]

The idea of mimicking the evolution of enzyme-generated precursors underlies the synthesis of the pentacyclic alkaloid (±)-nirurine (**117**) reported by Magnus et al.[57] Nirurine was isolated from *Phyllanthus niruri* L. and was thought to be biogenetically related to norsecurinine (**118**), which was also isolated from *Phyllanthus*. Towards the synthesis of (±)-**117**, alcohol **119** was cleanly rearranged to **118** via its mesylate (Scheme 21). Alternatively, alcohol **119** was oxidized to ketone **120**, which was reduced to prenirurine (**121**), the hypothetical precursor of **117**. Thus, **121** was treated with MCPBA to give the rearranged product **122**, presumably through a Cope elimination of the unstable *N*-oxide **123**. Optimization of the reaction conditions finally led to the use of dichloromethane as solvent to handle the *N*-oxide **123**. Small amounts of (±)-nirurine (**117**) were obtained, together with the main reaction product **122** (Scheme 21). The outcome of this synthesis led the authors to change the biogenetic



Scheme 20. Random approach to tridecacyclic pyrazines by Fuchs and Jeong.[55] TMS = trimethylsilyl.



Scheme 21. Synthesis of nirurine by Magnus et al.[57]

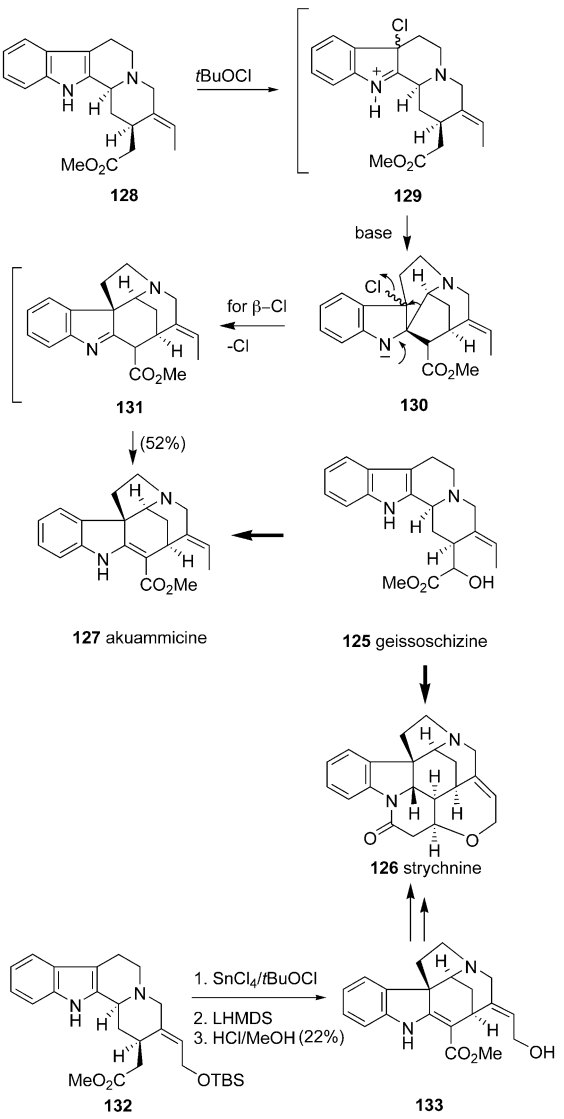
 © 2004 Wiley-VCH Verlag GmbH & Co. KGaA, Weinheim

proposal: "*…in view of the low yield of (±)-nirurine* ***117*** *because of the competing rearrangement, it seems likely that prenirurine* ***121*** *is not the biogenetic precursor to (±)-nirurine* ***117****, and that aminal formation (oxidation adjacent to nitrogen) takes place at an earlier stage*".

Within the scope of strychnine synthesis,[58] the approach to this alkaloid reported by Martin and co-workers[59] is an exceptional example of the successful application of an hypothetic biotransformation to obtain the synthetic target. The critical element in the design of this synthetic plan was inspired by the proposed biogenetic reorganization of the indole alkaloids based on the corynantheoid skeleton into the alkaloids of the *Strychnos* family.[60] The *Corynanthe* alkaloid geissoschizine (**125**) is the biosynthetic precursor of strychnine (**126**) and akuammicine (**127**). Several mechanistic pathways have been proposed to explain the extensive series of skeletal rearrangements involved in the transformation of one family of alkaloids into the other. Could these rearrangements be mimicked in the laboratory? Deformylgeissoschizine (**128**) was chlorinated with *t*BuOCl to form the epimeric chloroindolines **129** (Scheme 22). Reaction of **129** with lithium diisopropylamide produced a complex reaction mixture, which contained traces of **127**. Apparently, the epimeric chloroindolines **129** are deprotonated at the position α to the CO_2Me group. The resulting enolate cyclizes onto the iminium carbon atom to yield **130**. Skeletal reorganization of **130** into **131** followed by tautomerization yielded **127**.

Further experimentation demonstrated that only β-chloroindoleine (β-**129**) and not its α isomer, α-**129**, is involved in the rearrangement of **128** into **127**. The key, therefore, was to produce exclusively the β isomer. This problem was solved by the addition of a Lewis acid to the chlorinating mixture applied to **128**. The rearrangement **128** into **127** could be effected in 52% yield in the presence $SnCl_4$/*t*BuOCl followed by treatment with LHMDS base. The conditions were applied to tetracyclic derivative **132** to furnish 18-hydroxyakuammicine (**133**) in 22% yield (Scheme 22). Compound **133** was previously transformed into strychnine (**126**) by Overman and co-workers in four steps.[61]

Thus, even if we do not know the biogenetic mechanism, we can devise conditions to run successfully a feasible transformation in the laboratory. The mastery demonstrated by Martin and co-workers to effect the transformation of **128** into **127** shows how cytosollike conditions can be mimicked in the laboratory.

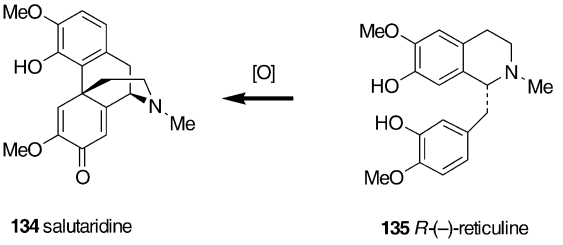


Scheme 22. Fine-tuning of the reaction conditions to effect the rearrangement of chloroindoline into akuammicine by Martin et al.[59]

6. The Biomimetic Oxidative Coupling of Phenols: The Closest to Reality?

The singular achievement by Barton[62] which demonstrated that the tetracylic skeleton of salutaridine (**134**) arises from oxidative coupling of (*R*)-(−)-reticuline (**135**) (Scheme 23), a proposal made by Robinson more than 30 years before,[63] and his subsequent synthesis of the salutaridine nucleus by biomimetic oxidation of a reticuline in 0.03% yield clearly demonstrated that this class of process could be mimicked in the laboratory.[64]

The fact that Nature provides a vast number of biaryl natural products with great structural diversity has made the topic of mimicking the phenol coupling an exceptionally active area or research.[65] The key point, regardless of the diverse hypotheses that may be postulated for each particular biogenetic route, is the laboratory oxidant used to mimic the



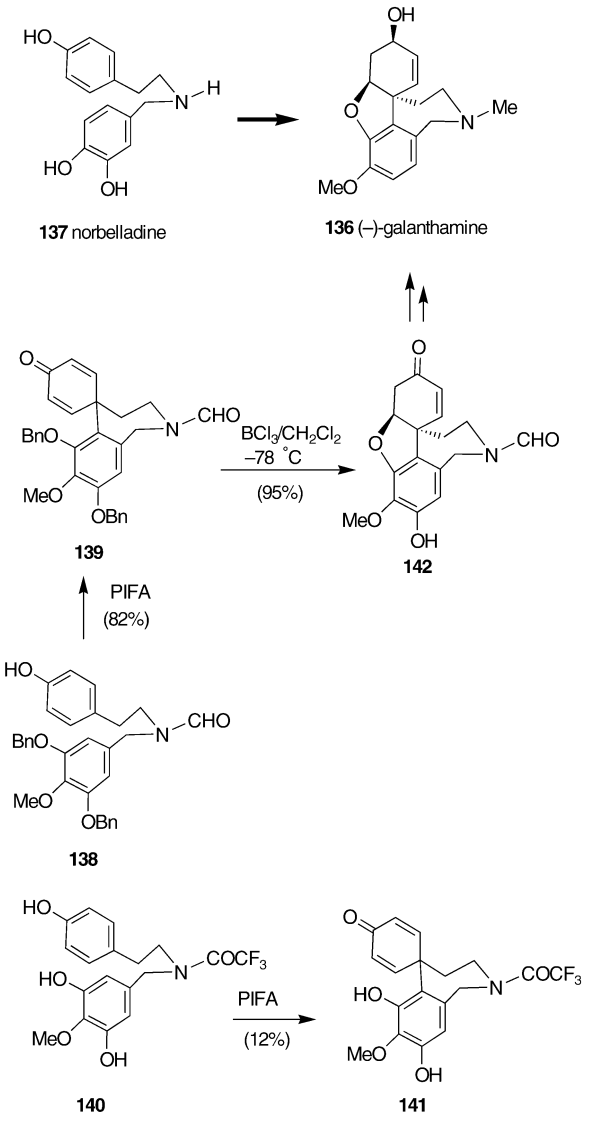
Scheme 23. Oxidative coupling of reticuline to form salutaridine, as proposed by Robinson[63] and effected by Barton 30 years later.[64]

 © 2004 Wiley-VCH Verlag GmbH & Co. KGaA, Weinheim

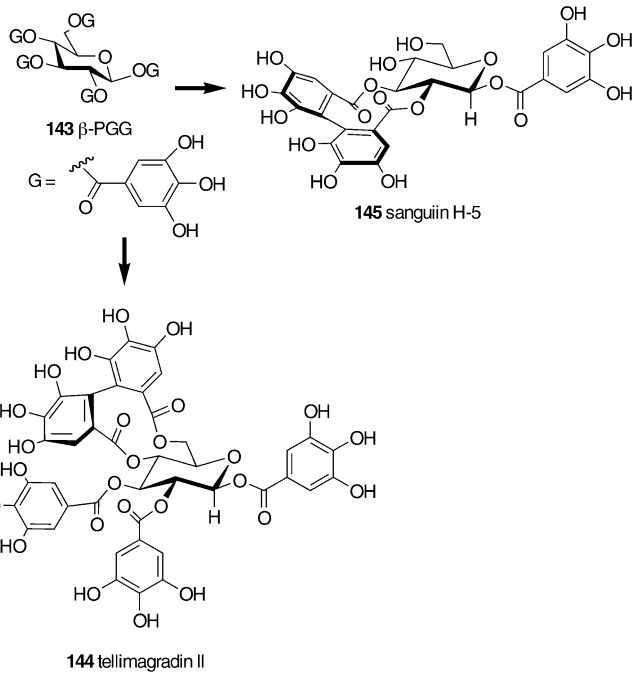
one-electron transfer that triggers the biaryl coupling in the biological media. The efficiency of the mimetic process is increased as the oxidant reagent used is finely tuned. The diverse routes for the preparation of (±)-galanthamine (**136**) developed through the years illustrate this point.

(−)-Galanthamine **136** is considered to be synthesized biologically by the phenolic oxidative coupling of norbelladine (**137**; Scheme 24).[66] Galanthamine was initially prepared by Barton and Kirby[67] by using $K_3[Fe(CN)_6]$ to effect the oxidative coupling. The process occurred in very low yield (0.92%), and during the following 40 years, several other oxidative methods to effect this coupling were published.[68] Yields of the pivotal oxidative step in the synthesis of galanthamine were consistently below 50%. Recently, the aromatic rings of norbelladine-like derivative **138** were coupled by using phenyliodine(III) bis(trifluoroacetate) (PIFA) to give the coupled product **139** in 82% yield. Remarkably, the ideal substrate **140** that yields the narwedine-type product **141** (the direct precursor of **136**) only gives a 12% yield in this transformation. (±)-Galanthamine (**136**) was accessed from **139**, debenzylation of which provided **142.** Deoxygenation of the extra phenol group of **142** was followed by transformation of the *N*-formyl into an *N*-methyl group (Scheme 24).[69] Analogous coupling with hypervalent iodine (in this case, the reagent of choice was $PhI(OAc)_2$) was used to prepare a library of galanthamine-like molecules[70] through *biomimetic diversity-oriented synthesis.* Although the diversity step was introduced once the biomimetic oxidative coupling was effected, the efficiency of the biomimetic coupling was beyond doubt (Scheme 24).[71]

The exquisite stereoselectivity observed in many oxidative couplings might be asserted as a certain proof of enzyme participation. However, this selectivity may in some cases be intrinsic to the oxidative coupling. The monomeric ellagitannins are members of the hydrolyzable tannin class of polyphenol extractives derived from the secondary metabolism of dicotyledonous species of Angiospermae.[72] Schmidt and Mayer[73] established that ellagitannins, which are derived from β-PGG (**143**) and have hexahydroxydibenzoyl residues at the 4,6- (e.g. **144**) and 2,3-positions (e.g. **145**) of the thermodynamically more stable $^4C_1$ glucose conformer, almost invariably contain the *S* atropisomer of the biaryl unit (Scheme 25). This hypothesis was made without knowing the enzymology of the biosynthesis of ellagitannins. The stereochemical outcome of the C–C oxidative biaryl coupling would be governed by the conformational preferences of the galloylated polyol core. Less-stable conformations of the glucose framework would allow bridging between galloyl groups at the 3,6-, 1,6-, and 2,4-positions of the six-membered sugar rings. However, in these cases, the stereochemistry is



Scheme 24. The oxidative approach to galathamine from norbelladine: a 40-year-old problem. PIFA = phenyliodine(III) bis(trifluoroacetate).



Scheme 25. The Schmidt–Mayer hypothesis for the configuration of the biaryl moiety of monomeric ellagitannins.[73] PGG = pyrogalloyl glucose.

 © 2004 Wiley-VCH Verlag GmbH & Co. KGaA, Weinheim

less predictable and in some cases both atropisomers are formed.[74]

The synthesis of sanguiin H-5 (**145**) by Feldman and Sambandan[75] was based on the hypothesis of Schmidt and Mayer.[73] Sugar **146** was esterified with acid **147** and the TBDMS groups of the product **148** were cleaved by treatment with TBAF to furnish free bisphenol **149** (Scheme 26). The oxidative coupling ($Pb(OAc)_4$) of the phenolic rings in **149** was effected, and a mixture of the three regioisomeric biphenyls **150**–**152** was obtained (Scheme 26). Notably, the three regioisomers maintain the *S* stereochemistry, which proves that the coupling was highly diastereoselective. The free phenol groups in the mixture were benzylated and the anomeric *O*-protecting group was cleaved photolytically. β-Selective galloylation with galloyl chloride (**153**) again furnished a regioisomeric mixture **154** as a single stereoisomer at C1 of the glucose ring. Cleavage of the remaining protecting groups yielded sanguiin H-5 (**145**). The formation of the *S* atropisomer with the exclusion of its *R* isomer is in full agreement with the Schmidt–Mayer hypothesis. This example can best be concluded in the words of Feldman and Sambandam: "*Implicit in the formation of only a single atropisomer through selective oxidation of the cyclization precursor* in vitro *is that diastereoselectivity in the* in vivo *oxidative process does not require enzymic intervention. Rather, the chirality of the biphenyl C–C bond may be governed by the conformational dictates of the polyol template* in vivo *as well as* in vitro."[75,76]

To end this section, the studies carried out by Evans et al.,[77] which resulted in the synthesis of the vancomycin aglycon **157**, are especially clarifying. Vancomycin (**158**) was isolated from *Amycolatopsis orientalis* and is a prototype for antibiotics that have arylglycine heptapeptide aglycons tethered with a range of sugar residues (Figure 2).[78] In spite of the tremendous importance of this class of antibiotics, the nature and sequence of many essential steps of their biosynthesis as well as the structure of biosynthesis intermediates

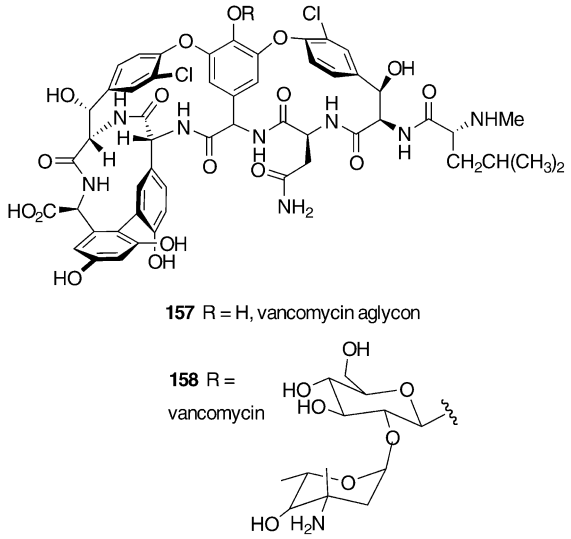
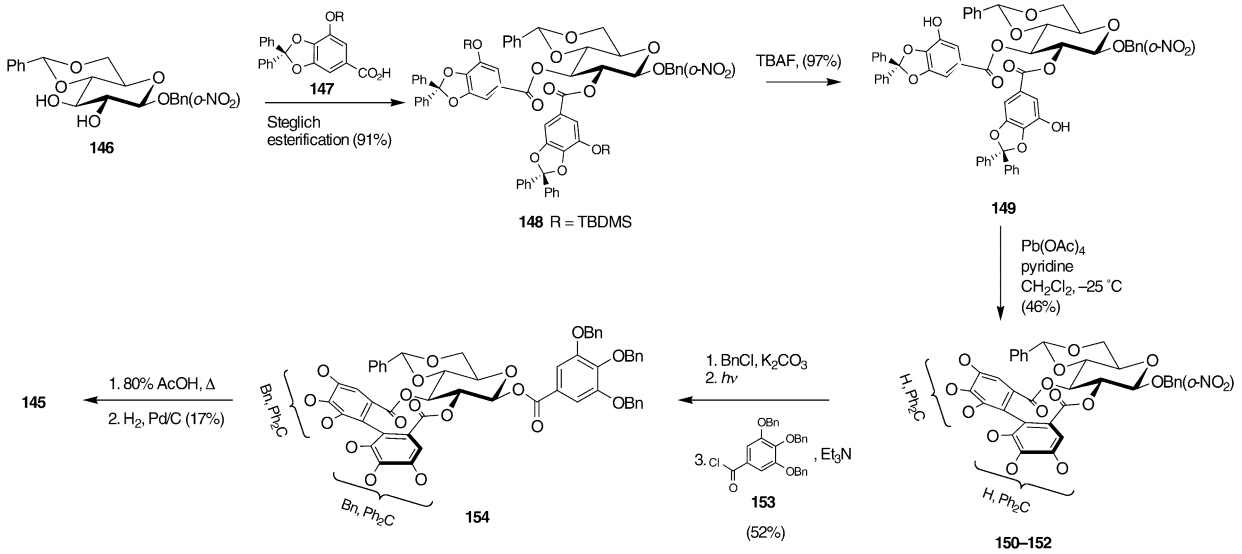


Figure 2. Vancomycin and the vancomycin aglycon.

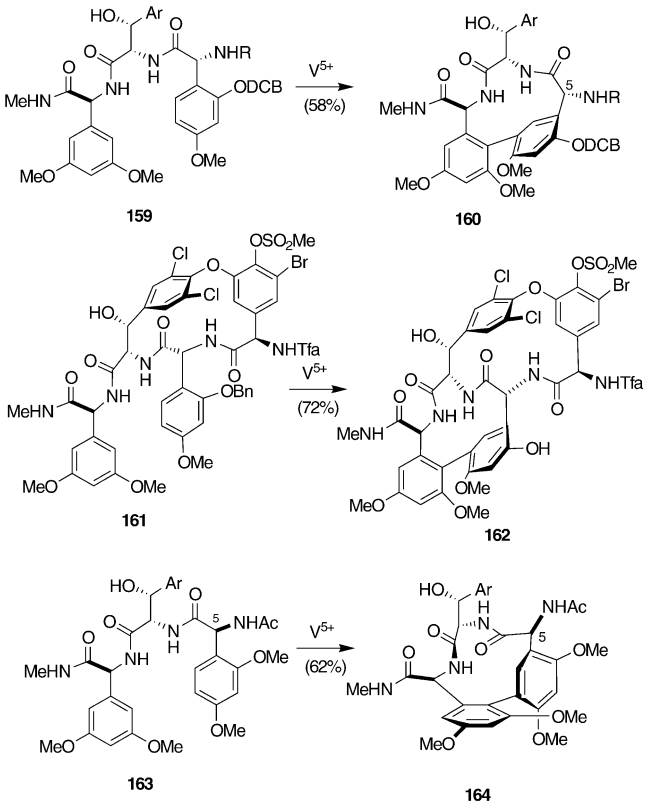
remain unknown. In fact, it was only recently that the sequence of cyclization steps to form the cyclic peptides was disentangled, and the C–C oxidative coupling of the biaryl moiety was proposed as the last step of the sequence.[79]

This step was carefully studied by Evans et al.[77b] The oxidative cyclization of tripeptides such as **159** has a clear kinetic bias for the non-natural atropisomer **160** (Scheme 27). The stereochemical bias is maintained in the more complex oxidative cyclization found in the cyclization of **161** to **162** (during the synthesis of orienticin C).[80] 1,3-Strain was claimed to be the key stereochemical control element in these cyclizations, as the tripeptide **163**, which is epimeric at C5 with respect to **159**, formed the natural atropisomeric product **164** (Scheme 27). Hence, the thermodynamic biaryl atropisomer bias in vancomycin should be due to the global structure and not to stereochemical elements proximal to the

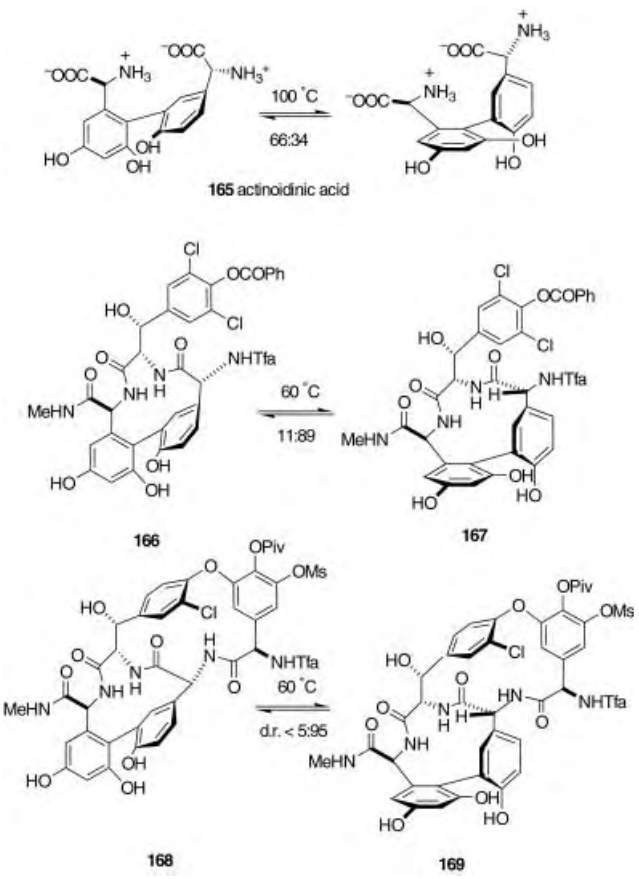


Scheme 26. Synthesis of sanguiin H-5 by Feldman and Sambandan proving the Schmidt–Mayer hypothesis.[75] TBAF = tetrabutylammonium fluoride.

 © 2004 Wiley-VCH Verlag GmbH & Co. KGaA, Weinheim



Scheme 27. Dissection of the C–C oxidative coupling of the biaryl moiety of vancomycin-related fragments by Evans and co-workers.[77] DCB = 3,4-dichlorobenzyl; Tfa = trifluoroacetyl.



Scheme 28. Equilibrium between natural (right) and non-natural (left) atropisomers of vancomycin-type compounds.[77a c 81a] Piv = pivaloyl.

biaryl link. The following results support and clarify this hypothesis: Both isomers of actinoidinic acid (**165**) equilibrate at 100 °C to afford a 2:1 equilibrium ratio favoring the non-natural isomer (Scheme 28). In contrast, thermal equilibration of cyclic tripeptide **166** favors the natural isomer **167** (89:11).[77c,81] This bias is even enhanced in the bicyclic tetrapeptides **168** and **169**.[77a]

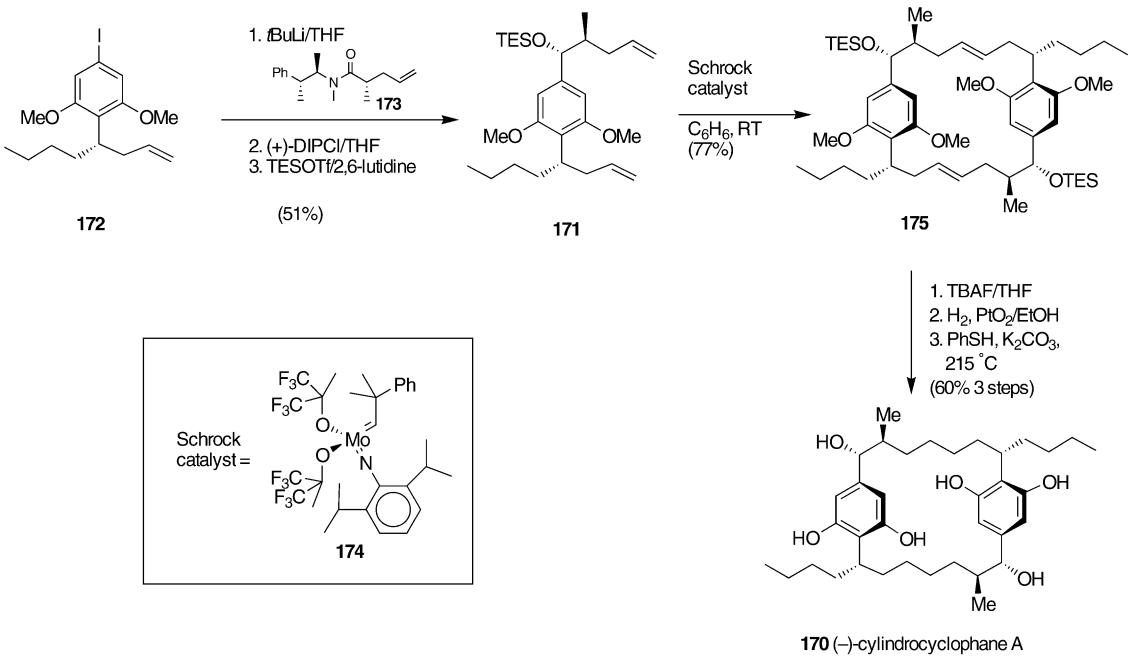
7. Stepping Stones: Physiological-type Artificial Syntheses

According to van Tamelen,[4] "*biogenetic-type syntheses are thus to be distinguished from physiological-type synthesis, in which not only plausible bio-organic substitutes are employed, but also specific conditions of temperature, pH, dilution, etc., which supposedly compare to those obtaining in a living cell are used*". In an ideal situation, the biomimetic synthesis should equal the physiological-type synthesis. This definition suggests that smoothness, efficiency, and elegance are intrinsic to physiological-type synthesis. Modern organic synthesis pursues the same goals, often mimicking neither biogenetic pathways nor physiological conditions. The following syntheses are only two of many examples, and they masterly combine smoothness, efficiency, and superb elegance.

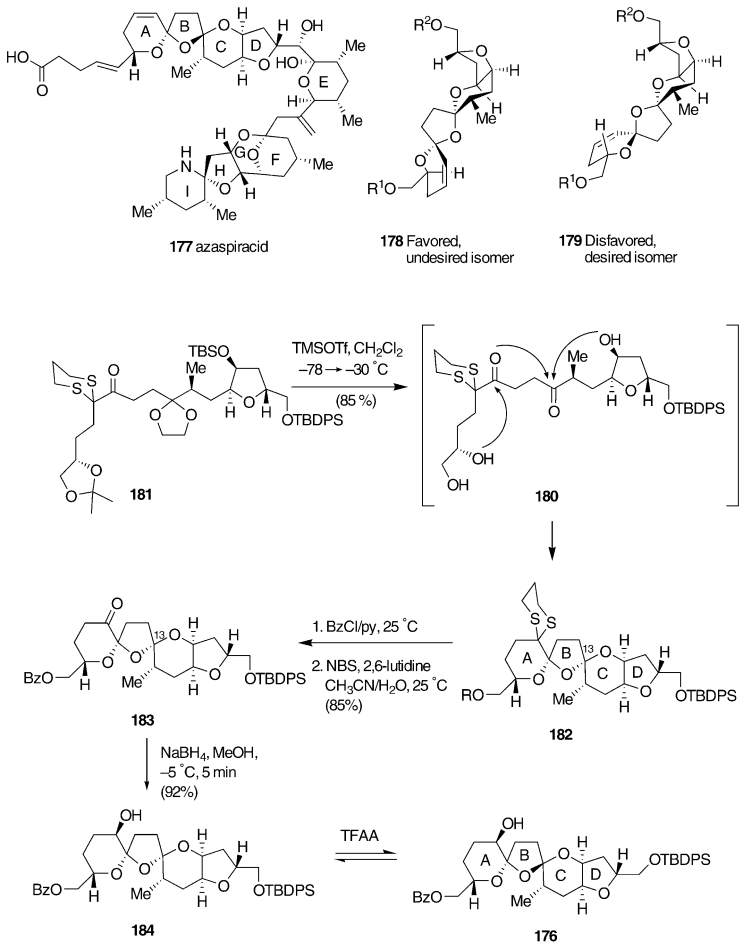
The synthesis of (−)-cylindrocyclophane A (**170**) by Smith et al.[82] was envisaged as a dimerization of two equal chiral moieties **171**, which in turn was obtained from iodide **172** by reaction with the alkoxide derived from the Myers amide **173**, reduction with (+)-DIPCl, and subsequent silylation (Scheme 29). Compound **171** was submitted to metathesis by using the Schrock catalyst **174** to furnish the desired [7,7]-paracyclophane **175** as a single isomer in high yield. Desilylation and hydrogenation produced the tetramethylated derivative of (−)-cylindrocyclophane A. Relatively harsh reaction conditions were required to cleave the methoxy groups (PhSH, K_2CO_3, 215 °C). The unexpected efficiency and selectivity in the dimerization reactions suggested that the [7,7]-paracyclophane skeleton is the thermodynamically more favored isomer. Therefore, a cascade of reversible olefin metatheses drives the reaction toward the formation of this compound.

One could get the wrong impression that only the thermodynamically favored products can be accessed in a physiological-like artificial synthesis. During the synthesis of the ABCD ring system **176**[83a] of azaspiracid (**177**), Nicolaou et al.[83] were confronted with problem that the unfavorable anomeric effects would lead to the favored epimer, (13*S*)-**178**, rather than to the natural product (13*R*)-**179** (Scheme 30). The mimetic formation of the ABCD azaspiracid core was achieved by the one-pot cyclization of ketotriol **180**, which

 © 2004 Wiley-VCH Verlag GmbH & Co. KGaA, Weinheim



Scheme 29. Synthesis of (−)-cylindrocyclophane A by Smith et al.[82] DIPCl β-chlorodiisopinocampheylborane; TES = triethylsilyl.



Scheme 30. Preparation of the ABCD ring system of azaspiracid by Nicolaou and co-workers.[83a] NBS = *N*-bromosuccinimide.

was generated in situ from **181**. The product **182** had, in fact, the wrong configuration at C13. However, it was reasoned that an equatorial free hydroxy group at C9 might invert the non-natural 13*S* configuration **182** to the natural 13*R* isomer by the effect of its hydrogen bonding, which would overcome the unfavorable anomeric effects. Thus, the hydroxy group was constructed from the masked carbonyl group on **182.** Treatment of **184** with acid smoothly epimerized the C13 center to form the desired epimer (13*R*)-**176** in 56% yield.

The two examples above resemble physiological conditions but neither is a biomimetic synthesis. The [7,7]-paracyclophane skeleton of cylindrocyclophane A (**170**) has been proposed to be biogenetically formed by dimerization of two identical resorcinol fragments, presumably involving electrophilic aromatic substitution, with an appropriate alkene side chain.[84] No biogenetic hypothesis for the formation of azaspiracid has been reported to the best of our knowledge.

8. Conclusions and Outlook

A biomimetic synthesis can be defined as the successful synthesis of a natural product by mimicking a proposed biological pathway. As the proposed biological pathway often parallels analogous organic processes, without further biochemical support, it is not surprising that such biomimetic syntheses are successful.

Which biogenetic processes are most likely to be mimicked successfully? The initial idea of

 © 2004 Wiley-VCH Verlag GmbH & Co. KGaA, Weinheim

Robinson that organisms produce few very reactive starting materials stands against the theory of evolution of enzymatic processes for the many natural products known. It is difficult to believe that specific enzymes have evolved to produce a specific transformation in a specific substrate that is usually produced in minute amounts. The enormous amount of secondary metabolites and their unimaginable structural diversity would make the number of enzymes involved in their production astronomical. Of course the intervention of multivalent and multifunctional enzymes, which are yet to be discovered, can always be proposed. These enzymes would have to be ubiquitous (and evasive), as is the distribution of secondary metabolites.[85]

The rules of the game are the same for cells as for the people working in the laboratory.[86] Hence, the lesson we can learn from biomimetic synthesis is that both ideas can be the extremes of the same process. The hypothesis of "minimum enzymatic participation" in the production of secondary metabolites could be the key. We have seen that a biomimetic synthesis is more likely to be successful if the involvement of enzymes in the mimicked processes is low. Once the enzyme initiates the biogenetic process, the resulting initial substrate has the structural requirements for the subsequent reactions, and the biosynthetic process proceeds without further involvement of the enzyme. Additional maturation of the metabolite may occur after that, with the participation of enzymes with a wide range of activities, as proposed by Heathcock.[16]

In this way, we can learn from biomimetic synthesis which steps are biogenetically non-enzymatic; such steps are fully reproducible because the reactivity of the substrate is intrinsic to its structure. Steps that require the intervention of external reagents to mimic the enzyme (for example, a chiral Lewis acid or a specific oxidant) would suggest an enzymatic process. The use of artificial enzymes designed to achieve specific transformations together with the use of the new technologies of surface- and micelle-directed synthesis[87] will probably lead to improved mimetic syntheses inspired by biogenetic processes.

Support for this work under grant BQU2001-1283 from the Ministerio de Ciencia y Tecnología (Spain) is gratefully acknowledged. We are indebted to Prof. Mar Gómez-Gallego and Dr. María José Mancheño (UCM) for continuous valued help, many valuable suggestions, and for patiently correcting the manuscript. We are grateful to Prof. Benjamín Rodríguez (CSIC), who, despite our different opinions, shared his invaluable knowledge about the chemistry of natural products. We thank Prof. R. M. Williams (Colorado State University) for kindly providing us with a copy of his review before publication. We also thank the reviewers of this Review for their invaluable critical discussions and suggestions.

Received: July 24, 2002 [A545]

[1] D. Skyler, C. H. Heathcock, *Org. Lett.* **2001**, *3*, 4323 – 4324.
[2] For selected reviews on the biomimetic synthesis some families of natural products, see: a) U. Scholz, E. Winterfeldt, *Nat. Prod. Rep.* **2000**, *17*, 349 – 366; b) C. H. Heathcock, *Angew. Chem.* **1992**, *104*, 675; *Angew. Chem. Int. Ed. Engl.* **1992**, *31*, 665 – 681; c) E. Magnier, Y. Langlois, *Tetrahedron* **1998**, *54*, 6201 – 6258; d) M. Arend, B. Westermann, N. Risch, *Angew. Chem.* **1998**, *110*, 1096 – 1122; *Angew. Chem. Int. Ed.* **1998**, *37*, 1044 – 1070.
[3] a) R. Robinson, *J. Chem. Soc.* **1917**, *111*, 762 – 768; b) R. Robinson, *J. Chem. Soc.* **1917**, *111*, 876 – 899; for additional early seminal work on "*model experiments on the question of biogenesis of natural products*", see: c) C. Schöpf, H. Bayerle, *Justus Liebigs Ann. Chem.* **1934**, *513*, 190 – 202; d) C. Schöpf, G. Lehmann, *Justus Liebigs Ann. Chem.* **1935**, *518*, 1 – 37; e) C. Schöpf, F. Oechler, *Justus Liebigs Ann. Chem.* **1936**, *523*, 1 – 29; f) C. Schöpf, K. Thierfelder, *Justus Liebigs Ann. Chem.* **1935**, *518*, 127 – 155, and references therein; for a detailed discussion of this topic, see: g) K. W. Bentley, *Nat. Prod. Rep.* **1987**, *4*, 13 – 23.
[4] E. E. van Tamelen, *Fortschr. Chem. Org. Naturst.* **1961**, *19*, 242 – 290.
[5] Strictly speaking, van Tamelen used the term *biogenetic-type* synthesis to describe an organic synthesis that follow, at least in its major aspects, biosynthetic pathways that have been proved proved or presumed to be used in the natural construction of the end product.; see reference [4], p. 245.
[6] a) K. Krohn, N. Böker, U. Flörke, C. Freund, *J. Org. Chem.* **1997**, *62*, 2350 – 2356; see also: b) K. Krohn, U. Flörke, C. Freund, N. Hayat, *Eur. J. Org. Chem.* **2000**, 1627 – 1632; c) K. Krohn, S. Bernhard, U. Flörke, N. Hayat, *J. Org. Chem.* **2000**, *65*, 3218 – 3222; d) K. Krohn, S. Bernhard, *Eur. J. Org. Chem.* **1999**, 3099 – 3103.
[7] a) T. J. Simpson, *Nat. Prod. Rep.* **1987**, *4*, 339 – 376; b) D. O'Hagan, *The Polyketide Metabolites*, Ellis Horwood, Chichester, **1991**; c) D. O'Hagan, *Nat. Prod. Rep.* **1995**, *12*, 1 – 32.
[8] a) K. Krohn, G. Schäfer, *Liebigs Ann.* **1996**, 265 – 270; b) K. Krohn, E. Roemer, M. Top, *Liebigs Ann.* **1996**, 271 – 277.
[9] M.-Ll. Bennasar, B. Vidal, J. Bosch, *J. Am. Chem. Soc.* **1993**, *115*, 5340 – 5341.
[10] M. Andriantsiferana, R. Besselièvre, C. Riche, H.-P. Husson, *Tetrahedron Lett.* **1977**, 2587 – 2590.
[11] a) A. Husson, Y. Langlois, C. Riche, H.-P. Husson, P. Potier, *Tetrahedron* **1973**, *29*, 3095 – 3098; b) C. Thal, M. Dufour, P. Potier, *J. Am. Chem. Soc.* **1981**, *103*, 4956 – 4957.
[12] S. S. Magar, R. C. Desai, P. L. Fuchs, *J. Org. Chem.* **1992**, *57*, 5360 – 5369.
[13] S. Zayed, A. Hafez, W. Adolf, E. Hecker, *Experientia* **1977**, *33*, 1554 – 1555.
[14] a) T. Okuda, T. Yoshida, S. Koike, N. Toh, *Phytochemistry* **1975**, *14*, 509 – 515; b) W. Adolf, E. Hecker, *Tetrahedron Lett.* **1975**, 1587 – 1590.
[15] Cited in reference [3g], p. 15.
[16] C. H. Heathcock, *Proc. Natl. Acad. Sci. USA* **1996**, *93*, 14323 – 14327.
[17] For an outstanding discussion of the two co-existing hypotheses for polyether biosynthesis (oxidative polycyclization and polyepoxide cascade), see: U. Koert, *Angew. Chem.* **1995**, *107*, 326 – 328; *Angew. Chem. Int. Ed. Engl.* **1995**, *34*, 298 – 300.
[18] D. A. Cane, W. D. Celmer, J. W. Westley, *J. Am. Chem. Soc.* **1983**, *105*, 3594 – 3600.
[19] a) C. A. Townsend, A. Basak, *Tetrahedron* **1991**, *47*, 2591 – 2602; b) F. E. McDonald, T. B. Towne, *J. Am. Chem. Soc.* **1994**, *116*, 7921 – 7922.
[20] a) D. S. Holmes, J. A. Sherringham, U. C. Dyer, S. T. Russell, J. A. Robinson, *Helv. Chim. Acta* **1990**, *73*, 239 – 259; b) "Chemical and Biochemical Aspects of Polyether-Ionophore Antibiotic Biosynthesis": J. A. Robinson, *Prog. Chem. Org. Nat. Prod.* **1991**, *58*, 1 – 81.
[21] W. C. Still, A. G. Romero, *J. Am. Chem. Soc.* **1986**, *108*, 2105 – 2106.

 © 2004 Wiley-VCH Verlag GmbH & Co. KGaA, Weinheim

[22] S. L. Schreiber, T. Sammakia, B. Hulin, G. Schulte, *J. Am. Chem. Soc.* **1986**, *108*, 2106 – 2108.

[23] a) F. E. McDonald, C. C. Schultz, *Tetrahedron* **1997**, *53*, 16435 – 16448; b) T. B. Towne, F. E. McDonald, *J. Am. Chem. Soc.* **1997**, *119*, 6022 – 6028.

[24] Reference [23] also contains an excellent discussion on the analogous epoxide-cyclization approach to monensin from (*all-E*)-premonensin. It is probable that the many ideas collected within this discussion may eventually lead to the completion of the synthesis of a polyether from the epoxidation of (*all-E*)-premonensin.

[25] Z.-M. Gu, X.-P. Fang, L. Zeng, J. L. McLaughlin, *Tetrahedron Lett.* **1994**, *35*, 5367 – 5368.

[26] S. C. Sinha, A. Sinha, S. C. Sinha, E. Keinan, *J. Am. Chem. Soc.* **1997**, *119*, 12014 – 12015.

[27] S. C. Sinha, A. Sinha, S. C. Sinha, E. Keinan *J. Am. Chem. Soc.* **1998**, *120*, 4017 – 4018.

[28] K. C. Nicolaou, E. J. Sorensen, *Classics in Total Synthesis*, VCH, Weinheim, **1996**, p. 748.

[29] a) M. S. Lee, D. J. Repeta, K. Nakanishi, *J. Am. Chem. Soc.* **1986**, *108*, 7855 – 7856; b) M. S. Lee, G.-W. Qin, K. Nakanishi, M. G. Zagorski, *J. Am. Chem. Soc.* **1989**, *111*, 6234 – 6241.

[30] Y. Shimizu, *Natural Toxins: Animal, Plant, and Microbial* (Ed.: J. B. Harris), Clarendon, Oxford, **1986**, p. 123.

[31] For a review, see: K. Fujiwara, N. Hayashi, T. Tokiwano, A. Murai, *Heterocycles* **1999**, *50*, 561 – 593.

[32] For the synthesis of halichondrin B, see: a) T. D. Aicher, K. R. Buszek, F. G. Fang, C. J. Forsyth, S. H. Jung, Y. Kishi, M. C. Matelich, P. M. Scola, D. M. Spero, S. K. Yoon, *J. Am. Chem. Soc.* **1992**, *114*, 3162 – 3164; b) J. J.-W. Duan, Y. Kishi, *Tetrahedron Lett.* **1993**, *34*, 7541 – 7544; c) D. P. Stamos, Y. Kishi, *Tetrahedron Lett.* **1996**, *37*, 8643 – 8646; for the synthesis of hemibrevetoxin B, see: d) K. C. Nicolaou, K. R. Reddy, G. Skokotas, F. Sato, X.-Y. Xiao, *J. Am. Chem. Soc.* **1992**, *114*, 7935 – 7936; e) K. C. Nicolaou, K. R. Reddy, G. Skokotas, F. Sato, X.-Y. Xiao, C.-K. Hwang, *J. Am. Chem. Soc.* **1993**, *115*, 3558 – 3575; for the synthesis of brevetoxin B, see: f) K. C. Nicolaou, C.-K. Hwang, M. E. Duggan, D. A. Nugiel, Y. Abe, K. Bal Reddy, S. A. DeFrees, D. R. Reddy, R. A. Awartani, S. R. Conley, F. P. J. T. Rutjes, E. A. Theodorakis, *J. Am. Chem. Soc.* **1995**, *117*, 10227 – 10238; g) K. C. Nicolaou, E. A. Theodorakis, F. P. J. T. Rutjes, M. Sato, J. Tiebes, X.-Y. Xiao, C.-K. Hwang, M. E. Duggan, Z. Yang, E. A. Couladouros, F. Sato, J. Shin, H.-M. He, T. Bleckman, *J. Am. Chem. Soc.* **1995**, *117*, 10239 – 10251; h) K. C. Nicolaou, F. P. J. T. Rutjes, E. A. Theodorakis, J. Tiebes, M. Sato, E. Untersteller, *J. Am. Chem. Soc.* **1995**, *117*, 10252 – 10263; i) K. C. Nicolaou, E. J. Sorensen, *Classics in Total Synthesis*, VCH, Weinheim, **1996**, p. 731 – 786; j) K. C. Nicolaou, *Angew. Chem.* **1996**, *108*, 644 – 664; *Angew. Chem. Int. Ed. Engl.* **1996**, *35*, 589 – 607; for the synthesis of brevetoxin A, see: k) K. C. Nicolaou, Z. Yang, G.-q. Shi, J. L. Gunzer, K. A. Agrios, P. Gärtner, *Nature* **1998**, *392*, 264; for the synthesis of hemibrevetoxin B, see also: l) I. Kadota, P. Jung-Youl, N. Koumura, G. Pollaud, Y. Matsukawa, Y. Yamamoto, *Tetrahedron Lett.* **1995**, *36*, 5777 – 5780; m) T. Nakata, S. Nomura, H. Matsukura, M. Morimoto, *Tetrahedron Lett.* **1996**, *37*, 217 – 220; n) M. Morimoto, H. Matsukura, T. Nakata, *Tetrahedron Lett.* **1996**, *37*, 6365 – 6368; o) Y. Mori, K. Yaegashi, H. Furukawa, *J. Am. Chem. Soc.* **1997**, *119*, 4557 – 4558.

[33] S. Laschat, *Angew. Chem.* **1996**, *108*, 313 – 315; *Angew. Chem. Int. Ed. Engl.* **1996**, *35*, 289 – 291.

[34] a) E. M. Stocking, R. M. Williams, *Angew. Chem.* **2003**, *115*, 3186 – 3223; *Angew. Chem. Int. Ed.* **2003**, *42*, 3078 – 3115; b) K. C. Nicolaou, S. A. Snyder, T. Montagnon, G. Vassilikogiannakis, *Angew. Chem.* **2002**, *114*, 1742 – 1773; *Angew. Chem. Int. Ed.* **2002**, *41*, 1668 – 1698; c) R. M. Williams, R. J. Cox, *Acc. Chem. Res.* **2003**, *36*, 127 – 139; d) for a recent commentary on the problem of the bio-Diels–Alder reaction, see: M. Johansson, B. Köpcke, H. Anke, O. Sterner, *Angew. Chem.* **2002**, *114*, 2262 – 2264; *Angew. Chem. Int. Ed.* **2002**, *41*, 2158 – 2160.

[35] For potential naturally occurring Diels–Alderases, see: a) K. Auclair, A. Sutherland, J. Kennedy, D. J. Witter, J. P. van den Heever, C. R. Hutchinson, J. C. Vederas, *J. Am. Chem. Soc.* **2000**, *122*, 11519 – 11520; b) K. Watanabe, T. Mie, A. Ichihara, H. Oikawa, M. Honma, *J. Biol. Chem.* **2000**, *275*, 38393 – 38401; for antibody catalysts, see: c) D. Hilvert, K. W. Hill, K. D. Nared, M. M. Auditor, *J. Am. Chem. Soc.* **1989**, *111*, 9261 – 9263; d) A. C. Braisted, P. G. Schultz, *J. Am. Chem. Soc.* **1990**, *112*, 7430 – 7431; For RNA catalysts, see: e) B. Seelig, S. Keiper, F. Stuhlmann, A. Jäschke, *Angew. Chem.* **2000**, *112*, 4764 – 4768; *Angew. Chem. Int. Ed.* **2000**, *39*, 4576 – 4579; f) B. Seelig, A. Jäschke, *Chem. Biol.* **1999**, *6*, 167 – 176; g) T. M. Tarasow, B. E. Eaton, *Cell. Mol. Life Sci.* **1999**, *55*, 1463 – 1472. A comprehensive compendium on natural products whose biogenesis has been proposed to involve Diels–Alderases can be found in reference [34a]. After submission of this Review, the crystal structure of a claimed natural Diels–Alderase, fungal macrophomate synthase (MPS), in a complex with pyruvate was reported.[35b] This extraordinary enzyme catalyzed a five-step transformation of pyrones to benzoates, including a Diels–Alder reaction; see: h) T. Ose, K. Watanabe, T. Mie, M. Honma, H. Watanabe, M. Yao, H. Oikawa, I. Tanaka, *Nature* **2003**, *422*, 185 – 189.

[36] H. Oikawa, K. Katayama, Y. Suzuki, A. Ichihara, *J. Chem. Soc. Chem. Commun.* **1995**, 1321 – 1322.

[37] The term bisorbicillinoids, which describes all dimeric sorbicillin-derived natural products, was recently introduced: K. C. Nicolaou, R. Jautelat, G. Vassilikogiannakis, P. S. Baran, K. B. Simonsen, *Chem. Eur. J.* **1999**, *5*, 3651 – 3665.

[38] a) N. Abe, T. Murata, A. Hirota, *Biosci. Biotechnol. Biochem.* **1998**, *62*, 2120 – 2126; a second fungal metabolite very similar to bisorbibutenolide (**63**), which differs only in the relative configuration at C9, was isolated in 1997 and named trichotetronine: b) O. Shirota, V. Pathak, C. F. Hossain, S. Sekita, K. Takatori, M. Satake, *J. Chem. Soc. Perkin Trans. 1* **1997**, 2961 – 2964; c) R. Andrade, W. A. Ayer, L. S. Trifonov, *Can. J. Chem.* **1996**, *74*, 371 – 379.

[39] a) K. C. Nicolaou, G. Vassilikogiannakis, K. B. Simonsen, P. S. Baran, Y.-L. Zhong, V. P. Vidali, E. N. Pitsinos, E. A. Couladouros, *J. Am. Chem. Soc.* **2000**, *122*, 3071 – 3079; b) K. C. Nicolaou, K. B. Simonsen, G. Vassilikogiannakis, P. S. Baran, V. P. Vidali, E. N. Pitsinos, E. A. Couladouros, *Angew. Chem.* **1999**, *111*, 3762 – 3766; *Angew. Chem. Int. Ed.* **1999**, *38*, 3555 – 3559; see also: c) D. Barnes-Seeman, E. J. Corey, *Org. Lett.* **1999**, *1*, 1503 – 1504.

[40] J. Mann, *Secondary Metabolism*, 2nd ed., Oxford University Press, New York, **1987**.

[41] "The Isoprenoids": P. Manitto, *Biosynthesis of Natural Products*, Ellis Harwood, Chichester, **1981**, pp. 215 – 313.

[42] Even the well-established sequence leading to the monomeric units in terpenoid biosynthesis is being fundamentally modified. Thus, the synthesis of isopentenyl pyrophosphate and dimethylallyl pyrophosphate, thought to occur exclusively from mevalonic acid, has been shown to proceed alternatively, by the methylerythritol phosphate pathway: a) M. Rohmer, *Nat. Prod. Rep.* **1999**, *16*, 565 – 574; b) M. Rohmer in *Comprehensive Natural Products Chemistry*, *Vol. 2* (Ed.: D. E. Cane), Elsevier, Oxford, **1999**, pp. 45 – 67; c) A. Fontana, M. T. Kelly, J. D. Prasad, R. J. Andersen, *J. Org. Chem.* **2001**, *66*, 6202 – 6206; d) P. M. Dewick, *Nat. Prod. Rep.* **1999**, *16*, 97 – 130.

[43] I. Abe, M. Rohmer, G. D. Prestwich, *Chem. Rev.* **1993**, *93*, 2189 – 2206.

[44] a) L. C. Tarshis, M. Yan, C. D. Poulter, J. C. Sacchettini, *Biochemistry* **1994**, *33*, 10871 – 10877; b) K. U. Wendt, K. Poralla, G. E. Schulz, *Science* **1997**, *277*, 1811 – 1815; c) C. M. Starks, K.

 © 2004 Wiley-VCH Verlag GmbH & Co. KGaA, Weinheim

Back, J. Chappell, J. P. Noel, *Science* **1997**, *277*, 1815 – 1820; d) C. A. Lesburg, G. Zhai, D. E. Cane, D. W. Christianson, *Science* **1997**, *277*, 1820 – 1824.

[45] C. Heinemann, M. Demuth, *J. Am. Chem. Soc.* **1999**, *121*, 4894 – 4895.

[46] a) U. Hoffmann, Y. Gao, B. Pandey, S. Klinge, K.-D. Warzecha, C. Krüger, H. D. Roth, M. Demuth, *J. Am. Chem. Soc.* **1993**, *115*, 10358 – 10359; b) K.-D. Warzecha, X. Xing, M. Demuth, R. Goddard, M. Kessler, C. Krüger, *Helv. Chim. Acta* **1995**, *78*, 2065 – 2076; c) K.-D. Warzecha, X. Xing, M. Demuth, *Pure Appl. Chem.* **1997**, *69*, 109 – 112; d) C. Heinemann, X. Xing, K.-D. Warzecha, P. Ritterskamp, H. Görner, M. Demuth, *Pure Appl. Chem.* **1998**, *70*, 2167 – 2176.

[47] a) S. Nakamura, K. Ishihara, H. Yamamoto, *J. Am. Chem. Soc.* **2000**, *122*, 8131 – 8140; b) K. Ishihara, S. Nakamura, H. Yamamoto, *J. Am. Chem. Soc.* **1999**, *121*, 4906 – 4907.

[48] P. V. Fish, W. S. Johnson, *J. Org. Chem.* **1994**, *59*, 2324 – 2335.

[49] a) S. Dev, A. S. Gupta, S. A. Patwardhan *CRC Handbook of Terpenoids*, *Vol. II* (Ed.: S. Dev), CRC, Boca Raton, **1989**, pp. 7 – 61, 326–489; b) J. D. Conolly, R. A. Hill, *Nat. Prod. Rep.* **1989**, *6*, 475 – 501.

[50] For reviews, see: a) P. A. Barlett in *Asymmetric Synthesis*, *Vol. 3* (Ed.: J. D. Morrison), Academic Press, New York, **1984**, pp. 341 – 409; b) J. K. Sutherland, *Chem. Soc. Rev.* **1980**, *9*, 265 – 280; c) W. S. Johnson, *Angew. Chem.* **1976**, *88*, 33 – 41; *Angew. Chem. Int. Ed. Engl.* **1976**, *15*, 9 – 17; d) W. S. Johnson, *Bioorg. Chem.* **1976**, *5*, 51 – 98; e) W. S. Johnson, *Acc. Chem. Res.* **1968**, *1*, 1 – 8; f) see also the following seminal paper: A. Eschenmoser, L. Ruzicka, O. Jeger, D. Arigoni, *Helv. Chim. Acta* **1955**, *38*, 1890 – 1904; this paper may, in part, have inspired Johnson's ulterior work in this area. For early work to assess the requirement for enzyme control in the biosynthesis of lanosterol, see: g) E. E. van Tamelen, *Acc. Chem. Res.* **1968**, *1*, 111 – 120; the following seminal papers compare enzyme versus chemical cyclization of squalenes: h) E. E. van Tamelen, G. M. Milne, M. I. Suffness, M. C. Rudler, R. J. Anderson, R. S. Achini, *J. Am. Chem. Soc.* **1970**, *92*, 7202 – 7204; i) E. E. van Tamelen, J. W. Murphy, *J. Am. Chem. Soc.* **1970**, *92*, 7204 – 7206; j) E. E. van Tamelen, J. H. Freed, *J. Am. Chem. Soc.* **1970**, *92*, 7206 – 7207; k) E. E. van Tamelen, J. P. McCormick, *J. Am. Chem. Soc.* **1968**, *91*, 1847 – 1848.

[51] a) W. S. Johnson, W. R. Bartlett, B. A. Czeskis, A. Gautier, C. H. Lee, R. Lemoine, E. J. Leopold, G. R. Luedtke, K. J. Bancroft, *J. Org. Chem.* **1999**, *64*, 9587 – 9595; for a discussion on the fluorine atom as a cation-stabilizing auxiliary, see: b) W. S. Johnson, B. Chenera, F. S. Tham, R. K. Kullnig, *J. Am. Chem. Soc.* **1993**, *115*, 493 – 497; c) W. S. Johnson, V. R. Fletcher, B. Chenera, W. R. Bartlett, F. S. Tham, R. K. Kullnig, *J. Am. Chem. Soc.* **1993**, *115*, 497 – 504; d) W. S. Johnson, R. A. Buchanan, W. R. Bartlett, F. S. Tham, R. K. Kulling, *J. Am. Chem. Soc.* **1993**, *115*, 504 – 515; e) W. S. Johnson, M. S. Plummer, S. P. Reddy, W. R. Bartlett, *J. Am. Chem. Soc.* **1993**, *115*, 515 – 521; f) P. V. Fish, W. S. Johnson, *J. Org. Chem.* **1994**, *59*, 2324 – 2335; g) P. V. Fish, W. S. Johnson, G. S. Jones, F. S. Tham, R. K. Kullnig, *J. Org. Chem.* **1994**, *59*, 6150 – 6152.

[52] J. U. Jeong, S. C. Sutton, S. Kim, P. L. Fuchs, *J. Am. Chem. Soc.* **1995**, *117*, 10157 – 10158.

[53] G. R. Pettit, M. Inoue, Y. Kamano, D. L. Herald, C. Arm, C. Dufresne, N. D. Christie, J. M. Schmidt, D. L. Doubek, T. S. Krupa, *J. Am. Chem. Soc.* **1988**, *110*, 2006 – 2007.

[54] a) G. R. Pettit, Y. Kamano, M. Inoue, C. Dufresne, M. R. Boyd, C. L. Herald, J. M. Schmidt, D. L. Doubek, N. D. Christie, *J. Org. Chem.* **1992**, *57*, 429 – 431; b) G. R. Pettit, Y. Ichihara, J. Xu, M. R. Boyd, M. D. Williams, *Bioorg. Med. Chem. Lett.* **1994**, *4*, 1507 – 1512.

[55] a) J. U. Jeong, P. L. Fuchs, *J. Am. Chem. Soc.* **1994**, *116*, 773 – 774; b) J. U. Jeong, P. L. Fuchs, *Tetrahedron Lett.* **1994**, *35*, 5385 – 5388.

[56] Three total syntheses of these unsymmetrical compounds have been reported; however, none can be described as biomimetic: a) M. Drögemüller, R. Jautelat, E. Winterfeldt, *Angew. Chem.* **1996**, *108*, 1669 – 1671; *Angew. Chem. Int. Ed. Engl.* **1996**, *35*, 1572 – 1574; b) C. H. Heathcock, S. C. Smith, *J. Org. Chem.* **1994**, *59*, 6828 – 6839; c) T. G. Lacour, C. Guo, S. Bhandaru, M. R. Boyd, P. L. Fuchs, *J. Am. Chem. Soc.* **1998**, *120*, 692 – 707; for the synthesis of analogues, see: d) W. Li, T. G. LaCour, P. L. Fuchs, *J. Am. Chem. Soc.* **2002**, *124*, 4548 – 4549.

[57] P. Magnus, J. Rodríguez-López, K. Mulholland, I. Matthews, *J. Am. Chem. Soc.* **1992**, *114*, 382 – 383.

[58] For an excellent account of the diverse approaches to strychnine and other *Strychnos* alkaloids, see: J. Bonjoch, D. Solé, *Chem. Rev.* **2000**, *100*, 3455 – 3482.

[59] a) M. Ito, C. W. Clark, M. Mortimore, J. B. Goh, S. F. Martin, *J. Am. Chem. Soc.* **2001**, *123*, 8003 – 8010; b) S. F. Martin, C. W. Clark, M. Ito, M. Mortimore, *J. Am. Chem. Soc.* **1996**, *118*, 9804 – 9805.

[60] a) E. Wenkert, B. Wickberg, *J. Am. Chem. Soc.* **1965**, *87*, 1580 – 1589; b) A. R. Battersby, E. S. Hall, *Chem. Commun.* **1969**, 793 – 794; c) A. I. Scott, P. C. Cherry, A. A. Qureshi, *J. Am. Chem. Soc.* **1969**, *91*, 4932 – 4933.

[61] a) S. D. Knight, L. E. Overman, G. Pairaudeau, *J. Am. Chem. Soc.* **1993**, *115*, 9293 – 9294; b) S. D. Knight, L. E. Overman, G. Pairaudeau, *J. Am. Chem. Soc.* **1995**, *117*, 5776 – 5788.

[62] D. H. R. Barton, *Pure Appl. Chem.* **1964**, *9*, 35 – 47.

[63] R. Robinson, S. Sugasawa, *J. Chem. Soc.* **1933**, 280 – 281. One reviewer provided us with an interesting history of the genesis of the oxidative work on biomimetic synthesis and the biogenesis of these alkaloids: In 1925, the oxidative dimerization of *p*-cresol was described, but the structure of the resulting product was assigned incorrectly (R. Pummerer, H. Puttfarcken, P. Schopflocher, *Ber. Dtsch. Chem. Ges. B* **1925**, *58*, 1808 – 1820). Robinson's early views on the biogenesis of morphine and its congeners were based on the flawed structure of that ketone. It was Barton who formulated the correct structure and elaborated a set of simple rules for oxidative phenolic radical coupling (D. H. R. Barton, T. Cohen, *Festschrift Prof. A. Stoll zum siebzigsten Geburtstag*, Birkhäuser, Basel, **1957**).

[64] a) D. H. R. Barton, G. W. Kirby, W. Steglich, G. M. Thomas, *Proc. Chem. Soc. London* **1963**, 203 – 204; b) D. H. R. Barton, D. S. Bhakuni, R. James, G. W. Kirby, *J. Chem. Soc. C* **1967**, 128 – 132.

[65] a) G. M. Kesrú, M. Nógrádi in *Studies in Natural Products Chemistry*, *Vol. 20* (Ed.: Atta-ur-Rahman), Elsevier, Amsterdam, **1998**, pp. 263 – 322; b) D. A. Whiting in *Comprehensive Organic Synthesis*, *Vol. 3* (Eds.: B. M. Trost, I. Fleming, G. Pattenden), Pergamon, Oxford, **1991**, pp. 659 – 703; c) W. Bauer, R. Stadler, M. H. Zenk, *Bot. Acta* **1992**, *105*, 370 – 374; d) R. Gerardy, M. H. Zenk, *Phytochemistry* **1993**, *32*, 79 – 86; e) R. Stadler, M. H. Zenk, *J. Biol. Chem.* **1993**, *268*, 823 – 831; f) T. Kametani, H. Nemoto, T. Kobari, S. Takano, *J. Heterocycl. Chem.* **1970**, *7*, 181 – 186; g) M. Sainsbury, *Tetrahedron* **1980**, *36*, 3327 – 3359; h) A. Varvoglis, *Tetrahedron* **1997**, *53*, 1179 – 1255; i) A. McKillop, A. G. Turrell, D. W. Young, E. C. Taylor, *J. Am. Chem. Soc.* **1980**, *102*, 6504 – 6512; j) G. Bringmann, R. Walter, R. Weirich, *Angew. Chem.* **1990**, *102*, 1006 – 1019; *Angew. Chem. Int. Ed. Engl.* **1990**, *29*, 977 – 991; k) R. Bringmann, R. Walter, R. Weirich in *Methods of Organic Chemistry (Houben Weyl)*, *4th ed.*, *1952–*, *Vol. E21a* **1995**, pp. 567 – 587.

[66] A. R. Battersby, W. I. Taylor, *Oxidative Couplings of Phenols*, Dekker, New York, **1967**.

[67] D. H. R. Barton, G. W. Kirby, *Proc. Chem. Soc. London* **1960**, 392 – 393.

 © 2004 Wiley-VCH Verlag GmbH & Co. KGaA, Weinheim

[68] a) T. Momose, T. Nakamura, K.-I. Kanai, *Heterocycles* **1977**, *6*, 277–280; b) K. Shimizu, K. Tomioka, S.-I. Yamada, K. Koga, *Chem. Pharm. Bull.* **1978**, *26*, 3765–3771; c) Y. Kita, M. Arisawa, M. Gyoten, M. Nakajima, R. Hamada, H. Tohma, T. Takada, *J. Org. Chem.* **1998**, *63*, 6625–6633; for the biomimetic synthesis of galanthamine, see: d) D. H. R. Barton, G. W. Kirby, *J. Chem. Soc.* **1962**, 806–817.

[69] M. Node, S. Kodama, Y. Hamashima, T. Baba, N. Hamamichi, K. Nishide, *Angew. Chem.* **2001**, *113*, 3150–3152; *Angew. Chem. Int. Ed.* **2001**, *40*, 3060–3062.

[70] H. E. Pelish, N. J. Westwood, Y. Feng, T. Kirchhausen, M. D. Shair, *J. Am. Chem. Soc.* **2001**, *123*, 6740–6741.

[71] For the earlier development of nonmetallic oxidative agents to effect the biomimetic oxidative phenolic coupling (during the synthesis of (−)-codeine), with a subsequent improvement in yield, see: J. D. White, G. Caravatti, T. B. Kline, E. Edstrom, *Tetrahedron* **1983**, *39*, 2393–2398.

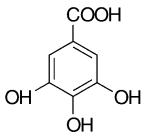
[72] For an excellent review on the chemistry of the ellagitannins, see: S. Quideau, K. S. Feldman, *Chem. Rev.* **1996**, *96*, 475–503.

[73] a) O. T. Schmidt, *Fortschr. Chem. Org. Naturst.* **1956**, *13*, 70–136; b) O. T. Schmidt, W. Mayer, *Angew. Chem.* **1956**, *68*, 103–115.

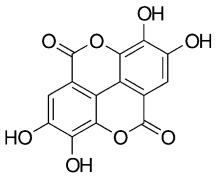
[74] a) G.-I. Nonaka, M. Ishimatsu, M. Ageta, I. Nishioka, *Chem. Pharm. Bull.* **1989**, *37*, 50–53; b) T. Tanaka, S. Kirihara, G.-I. Nonaka, I. Nishioka, *Chem. Pharm. Bull.* **1993**, *41*, 1708–1716.

[75] K. S. Feldman, A. Sambandam, *J. Org. Chem.* **1995**, *60*, 8171–8178.

[76] There is an additional interesting point related to the biosynthesis of the ellagitannins: In the oxidative aryl coupling hypothesis, the ellagitannins are derived from a fully galloylated glucose precursor. Therefore, those ellagitannins with unacylated hydroxy groups on the glucose frame would result from the hydrolysis of fully galloylated monomers or oligomers within the plant cell, with concomitant release of either gallic acid (**155**) or ellagic acid (**156**). According to Quideau and Feldman, (reference [72], p. 481): "*it is, however, possible that hydrolysis may also occur post mortem. This unfortunate ambiguity raises concerns when identifying isolates as* bona fide *natural products*".



155 gallic acid



156 ellagic acid

[77] a) D. A. Evans, M. R. Wood, B. W. Trotter, T. I. Richardson, J. C. Barrow, J. L. Katz, *Angew. Chem.* **1998**, *110*, 2864–2868; *Angew. Chem. Int. Ed.* **1998**, *37*, 2700–2704; b) D. A. Evans, C. J. Dinsmore, P. S. Watson, M. R. Wood, T. I. Richardson, B. W. Trotter, J. L. Katz, *Angew. Chem.* **1998**, *110*, 2868–2872; *Angew. Chem. Int. Ed.* **1998**, *37*, 2704–2708; c) D. A. Evans, C. J. Dinsmore, D. A. Evrard, K. M. DeVries, *J. Am. Chem. Soc.* **1993**, *115*, 6426–6427.

[78] For two excellent reviews on the chemistry and biology of vancomycin antibiotics, see: a) D. H. Williams, B. Bardsley, *Angew. Chem.* **1999**, *111*, 1264–1286; *Angew. Chem. Int. Ed.* **1999**, *38*, 1172–1193; b) K. C. Nicolaou, C. N. C. Boddy, S. Bräse, N. Winssinger, *Angew. Chem.* **1999**, *111*, 2230–2287; *Angew. Chem. Int. Ed.* **1999**, *38*, 2096–2152.

[79] a) D. Bischoff, S. Pelzer, B. Bister, G. J. Nicholson, S. Stockert, M. Schirle, W. Wohlleben, G. Jung, R. D. Süssmuth, *Angew. Chem.* **2001**, *113*, 4824–4827; *Angew. Chem. Int. Ed.* **2001**, *40*, 4688–4691; b) R. D. Süssmuth, S. Pelzer, G. Nicholson, T. Walk, W. Wohlleben, G. Jung, *Angew. Chem.* **1999**, *111*, 2096–2099; *Angew. Chem. Int. Ed.* **1999**, *38*, 1976–1979; c) D. Bishoff, S. Pelzer, A. Höltzel, G. J. Nicholson, S. Stocker, W. Wohlleben, G. Jung, R. D. Süssmuth, *Angew. Chem.* **2001**, *113*, 1736–1739; *Angew. Chem. Int. Ed.* **2001**, *40*, 1693–1696.

[80] For the synthesis of the orientincin C aglycon, see: a) D. A. Evans, C. J. Dinsmore, A. M. Ratz, D. A. Evrard, J. C. Borrow, *J. Am. Chem. Soc.* **1997**, *119*, 3417–3418; b) D. A. Evans, J. C. Barrow, P. S. Watson, A. M. Ratz, C. J. Dinsmore, D. A. Evrard, K. M. DeVries, J. A. Ellman, S. D. Rychnovsky, J. Lacour, *J. Am. Chem. Soc.* **1997**, *119*, 3419–3420.

[81] D. A. Evans, C. J. Dinsmore, *Tetrahedron Lett.* **1993**, *34*, 6029–6032.

[82] A. B. Smith III, C. M. Adams, S. A. Kozmin, D. V. Paone, *J. Am. Chem. Soc.* **2001**, *123*, 5925–5937.

[83] a) K. C. Nicolaou, W. Qian, F. Bernal, N. Uesaka, P. M. Pihko, J. Hinrichs, *Angew. Chem.* **2001**, *113*, 4192–4195; *Angew. Chem. Int. Ed.* **2001**, *40*, 4068–4071; b) K. C. Nicolaou, P. M. Pihko, N. Diedrichs, N. Zou, F. Bernal, *Angew. Chem.* **2001**, *113*, 1302–1305; *Angew. Chem. Int. Ed.* **2001**, *40*, 1262–1265; Corrigendum: K. C. Nicolaou, P. M. Pihko, N. Diedrichs, N. Zou, F. Bernal, *Angew. Chem.* **2001**, *113*, 1621; *Angew. Chem. Int. Ed.* **2001**, *40*, 1573

[84] a) B. S. Moore, J.-L. Chen, G. M. L. Patterson, R. E. Moore, L. S. Brinen, Y. Kato, J. Clardy, *J. Am. Chem. Soc.* **1990**, *112*, 4061–4063; b) B. S. Moore, J.-L. Chen, G. M. L. Patterson, R. E. Moore, *Tetrahedron* **1992**, *48*, 3001–3006.

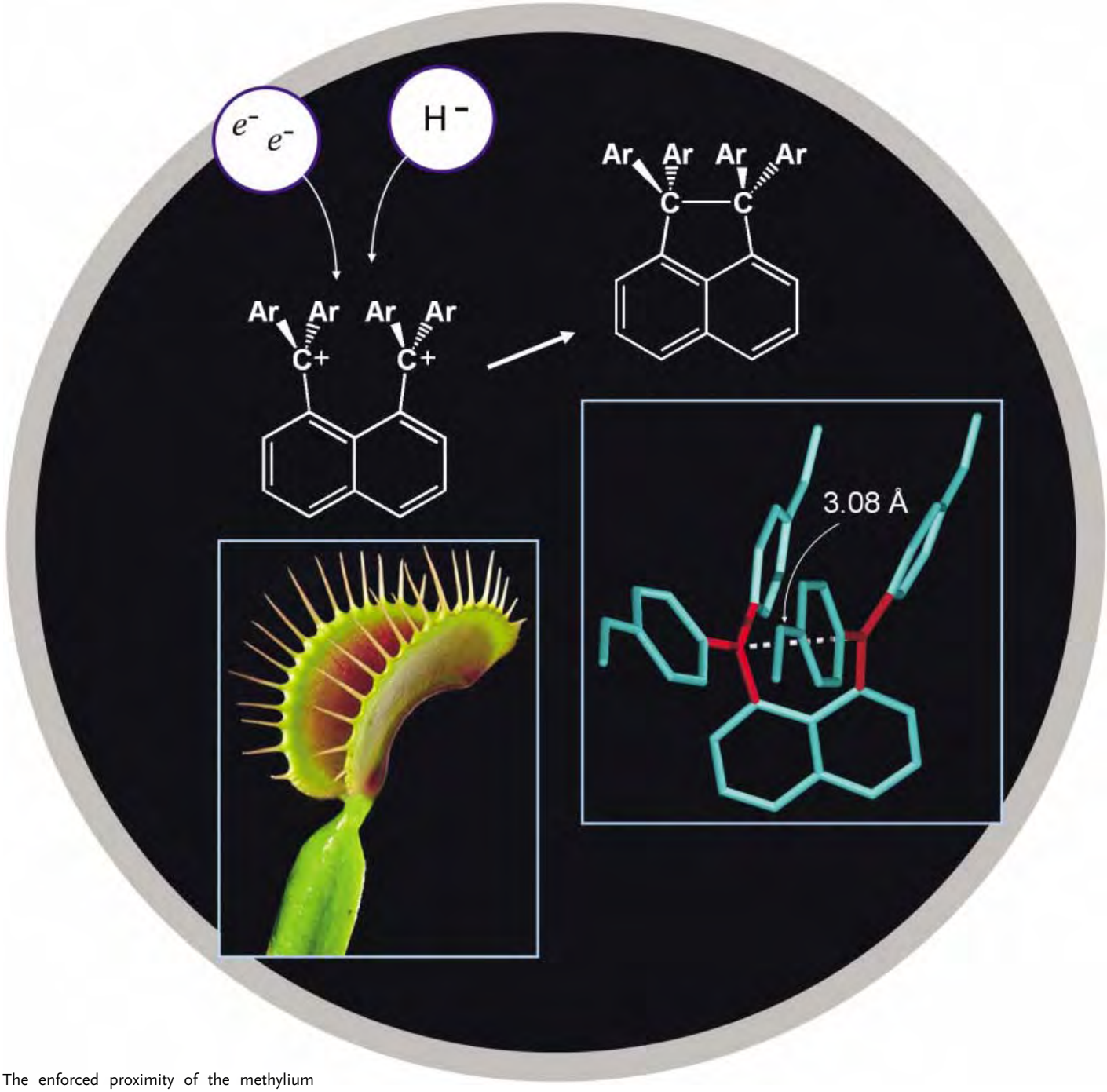
[85] Evidently, there is a different point of view. Based on a definition of a natural product as a substance that has no known role in the internal economy of the producing organism, Williams et al. "*…propose that all such structures serve the producing organisms by improving their survival fitness. We argue that this conclusion is necessitated by the fact that natural products are normally complex structures, whose biosynthesis is programmed by many kilobases of DNA. If it were otherwise, the pressures of Darwinian natural selection would have precluded the expenditure of so much metabolic energy in their construction and the development of such complexity.*" (D. H. Williams, M. J. Stone, P. R. Hauck, S. K. Rahman, *J. Nat. Prod.* **1989**, *52*, 1189–1208).

[86] See, for example, the excellent article about whether or not enzymes obey Baldwin's rules: J. A. Piccirilli, *Chem. Biol.* **1999**, *6*, R59–R64.

[87] For selected reviews, see: a) Y. Murakami, J. Kikuchi, Y. Hisaeda, O. Hayashida, *Chem. Rev.* **1996**, *96*, 721–758; b) R. Breslow, S. D. Dong, *Chem. Rev.* **1998**, *98*, 1997–2012; c) W. B. Motherwell, M. J. Bingham, Y. Six, *Tetrahedron* **2001**, *57*, 4663–4686.

 © 2004 Wiley-VCH Verlag GmbH & Co. KGaA, Weinheim

Communications



The enforced proximity of the methylium centers in 1,8-bis(bis(*p*-methoxyphenyl)methylium)-naphthalenediyl dication makes them cooperate and ultimately magnifies the electron affinity of this molecule. Like the carnivorous plant *Dionaea* traps flies, this dication readily captures electrons and then holds them in a newly formed carbon–carbon bond. For more information on this chemistry, see the following Communication by F. P. Gabbaï and H. Wang.

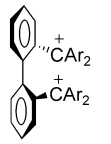
DOI: 10.1002/anie.200353011
© 2004 Wiley-VCH Verlag GmbH & Co. KGaA, Weinheim

Arene Electrochemistry

Synthesis and Reactivity of a 1,8-Bis(methylium)naphthalenediyl Dication**

*Huadong Wang and François P. Gabbaï**

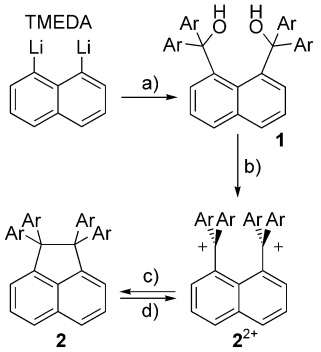
Triarylmethylium cations constitute one of the best studied classes of stable carbocations.[1,2] In addition to being used as dyes,[3] such species have become ubiquitous in the domain of olefin polymerization catalysis where they serve as activators.[4] Recent advances in the chemistry of these compounds focus on their incorporation in bifunctional derivatives. Among these,[5] a series of dicationic systems in which two triarylmethylium cations are linked by a biphenyl (as in $\mathbf{A}^{2+}$) or a binaphthyl backbone have been prepared and have been shown to display unique electrochromic properties.[6,7] Structural studies indicate that the methylium centers of these biphenyl- or binaphthyl-based systems are separated by only 3.5–3.7 Å. Owing to inherent coulombic repulsions, it can be assumed that the physical separation between the methylium centers governs the stability and reactivity of such derivatives. Hence, control over this separation could serve to fine-tune the electrophilic and Lewis acidic properties of such bifunctional molecules. Applying this paradigm to the synthesis of highly electrophilic and Lewis acidic bidentate molecules, we are now targeting bis(methylium) dications that feature short intercationic separation. Herein, we report on the synthesis, characterization, and reactivity of 1,8-bis(bis(*p*-methoxyphenyl)methylium) naphthalenediyl dication ($\mathbf{2}^{2+}$), which features two methylium centers separated by 3.076(2) Å.



$\mathbf{A}^{2+}$

Ar = *p*-MeOC$_6$H$_4$

The reaction of 1,8-dilithionaphthalene·TMEDA[8] with two molar equivalents of 4,4-dimethoxybenzophenone affords the corresponding diol, namely 1,8-bis[bis(*p*-methoxyphenyl)hydroxymethyl]naphthalene (**1**) (Scheme 1). Upon treatment with a mixture of aq [HBF_4] and $(CF_3CO)_2O$, this diol undergoes a double dehydroxylation reaction to afford the corresponding dication, $\mathbf{2}^{2+}$ (Scheme 1). The ^{1}H NMR spectrum of $\mathbf{2}^{2+}$ features the expected signals for a symmetrically *peri*-substituted naphthalene derivative: the signals for the hydrogen atoms at the 2- and 7-positions are shifted downfield by 1.05 ppm with respect to the analogous signals of **1**. The appearance of four distinct signals for the hydrogen



Scheme 1. Synthesis of $\mathbf{2}^{2+}$ and **2**. Ar = *p*-MeO(C$_6$H$_4$). a) Ar_2CO in THF at −78 °C; b) aq [HBF_4]/$(CF_3CO)_2O$; c) Li[BEt_3H] in THF; d) aq [HBF_4]/CF_3CO_2H. TMEDA = *N*,*N*,*N*′,*N*′-tetramethylethylenediamine.

attached to the aromatic core of the *p*-methoxyphenyl groups indicates restricted rotation of the latter. The ^{13}C resonance of the carbocationic centers appears at δ = 191.8 ppm, which is comparable to that observed for other carbocations such as bis(4-methoxyphenyl)phenylmethylium.[9]

A single-crystal X-ray analysis[10] revealed the existence of a sterically congested structure (Figure 1, top). The tight geometrical constraints present in the structure of $\mathbf{2}^{2+}$ induce distortions of the naphthalenediyl skeleton. Especially noteworthy are the C9-C8-C02 and C9-C1-C01 angles (125.36(16) and 126.60(15)°, respectively) which are larger than the ideal value of 120°. As indicated by the sum of the bond angles at C01 ($\Sigma_{(C\text{-}C_{01}\text{-}C)} = 359.6$) and C02 ($\Sigma_{(C\text{-}C_{02}\text{-}C)} = 359.8$), each methylium center adopts a trigonal-planar arrangement. The trigonal coordination planes of the C01 and C02 centers form relatively large dihedral angles with the plane containing the naphthalene backbone (59.7 and 59.6°, respectively), indicating that conjugation of the methylium center empty p_z orbital with the π-system of the naphthalene backbone can only be modest. By contrast, the *p*-methoxyphenyl groups strongly stabilize the methylium centers, as indicated by the small dihedral angles that they form with the trigonal coordination planes of the C01 and C02 centers (18.1–28.5°). This mesomeric stabilization is also reflected by the short C01−C11, C01−C21, C02−C31, and C02−C41 bonds. Finally, as a result of this unique molecular structure, the vicinal methylium centers are separated by 3.076(2) Å, which is the shortest such distance so far reported.[5–7]

The structure of $\mathbf{2}^{2+}$ was computationally optimized using DFT methods (B3LYP, 6-31 + G* for the methylium carbon centers, 6-31G for all other atoms).[11] The fully optimized geometry approaches that observed for the dication in [$\mathbf{2}^{2+}$][BF_4^-]$_2$. Most importantly, examination of the DFT orbitals reveals that the methylium p_z orbitals largely contribute to the LUMO and are oriented toward one another in a transannular fashion (Figure 1, bottom). Thus, $\mathbf{2}^{2+}$ is both structurally and electronically similar to 1,8-bis(diphenylboryl)naphthalene, which features an interboron separation of 3.002(2) Å and whose LUMO bears strong contributions from the converging 2p_z boron orbitals.[12]

[*] H. Wang, Prof. Dr. F. P. Gabbaï
Chemistry Department
Texas A&M University 3255 TAMU
College Station, TX 77843-3255 (USA)
Fax: (+1) 979-845-4719
E-mail: gabbai@mail.chem.tamu.edu

[**] This work was supported by the Welch Foundation (A-1423) and the National Science Foundation (CHE-9807975, purchase of the X-ray diffractometers; CHE-0077917 purchase of NMR instrumentation). We thank Lisa Perez for her help with the calculations.

Supporting information for this article is available on the WWW under http://www.angewandte.org or from the author.

 © 2004 Wiley-VCH Verlag GmbH & Co. KGaA, Weinheim DOI: 10.1002/anie.200353011

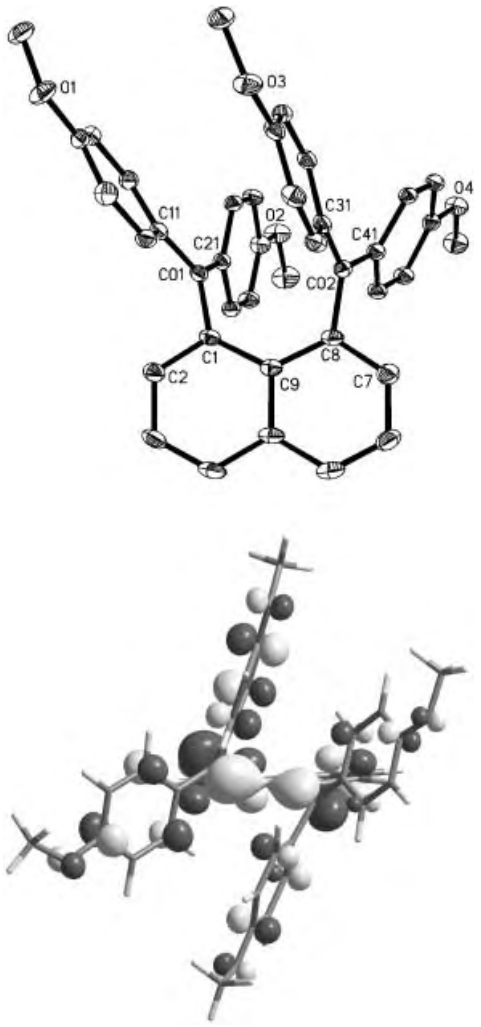


Figure 1. Top: ORTEP plot of the molecular structure of $\mathbf{2}^{2+}$ in $[\mathbf{2}^{2+}][BF_4^-]_2(MeCN)_2$ with thermal ellipsoids set at the 50% probability level. Hydrogen atoms are omitted for clarity. Selected bond lengths [Å] and bond angles [°]: C01-C02 3.076(2), C01-C11 1.418(2), C01-C21 1.440(2), C01 C1 1.483(2), C02-C41 1.430(2), C02-C31 1.432(2), C02-C8 1.482(2); C11-C01-C21 124.06(16), C11-C01-C1 117.59(15), C21-C01-C1 118.00(15), C41-C02-C31 123.65(15), C41-C02-C8 117.48(15), C31-C02-C8 118.64(15), C2-C1-C01 113.78(16), C9-C1-C01 126.60(15), C7-C8-C02 114.71(16), C9-C8-C02 125.36(16). Bottom: DFT orbital picture showing the LUMO in $\mathbf{2}^{2+}$.

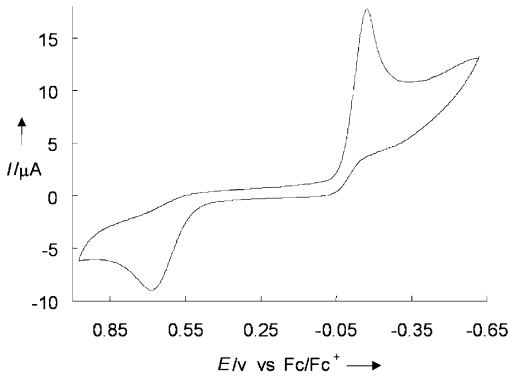
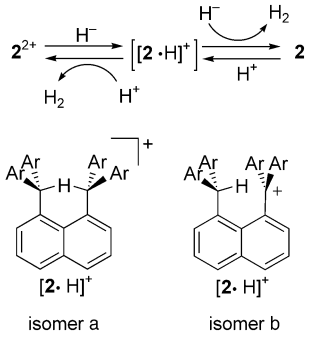


Figure 2. Cyclic voltammogram of $\mathbf{2}^{2+}$ in CH_2Cl_2 with a Pt working electrode; scan rate: 100 mVs^{-1}, 0.1 M NBu_4PF_6.

The cyclic voltammogram of $\mathbf{2}^{2+}$ shows a two-electron reduction wave at −0.17 V (vs Fc/Fc^+), corresponding to the formation of acenaphthylene **2** (Figure 2). As a confirmation, the same voltammogram is obtained when starting from pure **2** (vide infra). The reduction of $\mathbf{2}^{2+}$ does not meet the electrochemical criteria of reversibility, and reoxidation necessitates a more positive potential of 0.68 V (vs Fc/Fc^+). In comparison to 2,2′-bis(bis(*p*-methoxyphenyl)methylium)-biphenyl ($\mathbf{A}^{2+}$), whose reduction occurs at −0.28 V,[6a,13] reduction of $\mathbf{2}^{2+}$ appears remarkably facile as it is shifted by more than 0.11 V toward cathodic potentials. In turn, this difference provides a measure of the cooperative effects that result from the proximity of the neighboring methylium centers in $\mathbf{2}^{2+}$; it also reflects the increased electrophilicity of $\mathbf{2}^{2+}$. We also note that the oxidation of **2** into $\mathbf{2}^{2+}$ necessitates a less cathodic potential (0.68 V) than that observed for its biphenyl analogue (oxidation at 1.01 V).

It is well known that triarylmethylium cations add hydrides to afford the neutral triaryl methane derivatives.[14] In the present case, however, treatment of $\mathbf{2}^{2+}$ with $LiHBEt_3$, KH, or $(p\text{-}Me_2NC_6H_4)_3CH$ leads to reductive coupling and formation of **2**, which is accompanied by gas evolution (Scheme 1). Reaction with $LiDBEt_3$ does not lead to any deuterium incorporation, ruling out a mechanism in which the hydride would attack one of the aromatic rings. Hence, we propose that this reaction proceeds through formation of $[\mathbf{2}{\cdot}H]^+$, which undergoes rapid deprotonation (Scheme 2). By analogy with the reactivity of 1,8-diborylnaphathlene hydride sponges,[15] it is tempting to suggest that intermediate $[\mathbf{2}{\cdot}H]^+$ possesses a C–H–C 3c–2e bridge ($[\mathbf{2}{\cdot}H]^+$ isomer a).[16] However, we have not been able to confirm this formulation, and an unsymmetrical structure should also be considered ($[\mathbf{2}{\cdot}H]^+$ isomer b) (Scheme 2). In the presence of a substoichiometric amount of $LiHBEt_3$, only mixtures of **2** and $\mathbf{2}^{2+}$ are observed. This suggests that the proposed intermediate $[\mathbf{2}{\cdot}H]^+$ is labile and can revert to the dication $\mathbf{2}^{2+}$ by extrusion of a hydride.



Scheme 2. Proposed pathways for the reactions of $\mathbf{2}^{2+}$ with hydrides and of **2** with protons.

We have determined the crystal structure of **2**.[10] Remarkably, the bond of 1.670(3) Å linking the former methylium

 © 2004 Wiley-VCH Verlag GmbH & Co. KGaA, Weinheim

carbon centers constitutes one of the longest $C(sp^3)-C(sp^3)$ bonds so far reported.[17,18] Because of this lengthening, this bond can be anticipated to be inherently weak and therefore possibly reactive. As a matter of fact, **2** undergoes a slow oxidation reaction when treated with aq $[HBF_4]/CF_3CO_2H$ leading to the formation of $\mathbf{2}^{2+}$, which could be isolated in 55–70% yield (Scheme 2). While Brønsted acids are known to act as oxidants in the formation of carbenium ions,[19] formation of two methylium centers by oxidative protonolysis of a $C(sp^3)-(sp^3)$ bond remains unprecedented.[20] Moreover, we note that acid-induced C–C bond activations typically necessitate the use of superacidic media.[21] This oxidation reaction likely proceeds by protonation of **2**, which under acidic conditions extrudes a hydride to afford $\mathbf{2}^{2+}$. Once again, the intermediacy of $[\mathbf{2}\cdot H]^+$ can be invoked (Scheme 2). Theoretical investigations are currently underway to support this proposal.

In summary, we report the first stable compound featuring two methylium cation centers directly connected by a *peri*-substituted naphthalene backbone. The enforced proximity of the methylium centers in $\mathbf{2}^{2+}$ intensifies the electron affinity of this unusual molecule. In the presence of hydrides, this dication undergoes reductive coupling which also leads to the formation of **2**. The newly formed C–C bond of the latter is long and undergoes an oxidative protonolysis reaction which affords $\mathbf{2}^{2+}$.

Experimental Section

1: A solution of 4,4-dimethoxylbenzophenone (1.12 g, 4.52 mmol) in THF (15 mL) was added to a solution of 1,8-dilithionaphthalene (0.50 g, 1.95 mmol) in THF (5 mL) at −78 °C. The reaction mixture was stirred for 2 h at −78 °C and for another 12 h at room temperature. After addition of 5% aq NH_4Cl (20 mL) the organic phase was extracted with ether, dried with $MgSO_4$, and concentrated. Column chromatography on silica gel (*n*-hexane/ethyl acetate 6:1) afforded **1** (0.51 g, 43%) as a light yellow solid. ^{1}H NMR ($CDCl_3$, 500 MHz): $\delta =$ 3.73 (s, 12H, CH_3), 6.55 (d, $J = 8.8$ Hz, 8H, C_6H_4), 6.92 (d, $J = 7.3$ Hz, 2H, H_{Naph}), 6.97 (d, $J = 8.8$ Hz, 8H, C_6H_4), 7.37 (t, $J = 7.8$ Hz, 2H, H_{Naph}), 7.80 ppm (d, $J = 8.3$ Hz, 2H, H_{Naph}); ^{13}C NMR ($CDCl_3$, 125.9 MHz) $\delta = 55.3$, 85.1, 112.7, 113.2, 123.2, 129.0, 129.2, 131.0, 133.5, 141.9, 142.8, 158.4 ppm; Elemental analysis calcd (%) for $C_{40}H_{36}O_6\cdot 0.85\,CHCl_3$: C 68.70, H 5.20; found: C 68.82, H 5.10.

$[\mathbf{2}^{2+}][BF_4^-]_2$: A suspension of **1** (0.19 g, 0.31 mmol) in $(CF_3CO_2)O$ (5 mL) was treated with aq $[HBF_4]$ (48%, 0.20 mL, 1.5 mmol). The reaction mixture was stirred for 2 h before Et_2O (20 mL) was added to the mixture, which resulted in precipitation of the product as a dark-red solid. It was washed with small portions of Et_2O to afford a $[\mathbf{2}^{2+}][BF_4^-]_2$ (0.19 g, yield 79%). Single crystals of $[\mathbf{2}^{2+}][BF_4^-]_2\cdot(MeCN)_2$ were obtained by vapor diffusion of diethyl ether into a solution of $[\mathbf{2}^{2+}][BF_4^-]_2$ in acetonitrile. ^{1}H NMR ([D$_6$]acetone, 500 MHz): $\delta =$ 4.19 (s, 12H, CH_3), 6.97 (dd, $J = 2.2$, 9.0 Hz, 4H, C_6H_4), 7.17 (dd, $J = 9.0$, 2.7 Hz, 4H, C_6H_4), 7.27 (d, $J = 8.6$ Hz, 4H, C_6H_4), 7.67 (dd, $J =$ 1.2, 7.3 Hz, 2H, H_{Naph}), 7.89 (dd, $J = 2.4$, 9.2 Hz, 4H, C_6H_4), 8.03 (dt, $J = 0.9$, 7.8 Hz, 2H, H_{Naph}), 8.85 ppm (dd, $J = 1.2$, 8.3 Hz, 2H, H_{Naph}); ^{13}CNMR ([D$_6$]acetone, 125.9 MHz): $\delta = 57.7$, 117.8, 118.1, 127.3, 131.4, 135.2, 135.7, 136.9, 138.7, 142.8, 144.2, 145.6, 172.9, 191.8 ppm; Elemental analysis calcd (%) for $C_{40}H_{34}O_4B_2F_8\cdot 2\,CH_3CN$: C 62.25, H 4.98; found: C 61.71, H 4.75. UV/Vis (CH_3CN): $\lambda_{max}(\log(\varepsilon)) = 482$ (5.46).

2: A solution of $LiBEt_3H$ in THF (1.0 M, 0.5 mL, 0.5 mmol) was added to a stirred solution of $[\mathbf{2}^{2+}][BF_4^-]_2$ (53 mg, 70 μmol) in THF (10 mL) at room temperature. After 30 min the reaction mixture was quenched by adding 5% aq NH_4Cl (20 mL). The organic phase was extracted with ether, dried with $MgSO_4$, and concentrated. Column chromatography on silica gel (*n*-hexane/ethyl acetate 8:1) afforded **2** (30 mg, 74%) as a light yellow solid. Single crystals of **2** suitable for X-ray structural analysis were obtained by slow evaporation of the solvent from a solution of **2** in acetonitrile. ^{1}H NMR ([D$_6$]acetone, 500 MHz): $\delta = 3.67$ (s, 12H, CH_3), 6.50 (d, $J = 8.5$ Hz, 8H, C_6H_4), 6.84 (d, $J = 8.8$ Hz, 8H, C_6H_4), 7.23 (d, $J = 7.1$ Hz, 2H, H_{Naph}), 7.60 (t, $J =$ 7.3 Hz, 2H, H_{Naph}), 7.82 ppm (d, $J = 8.3$ Hz, 2H, H_{Naph}); ^{13}C NMR ([D$_6$]acetone, 125.9 MHz): $\delta = 54.6$, 73.4, 112.0, 112.5, 123.4, 128.3, 131.8, 136.9, 137.8, 150.8, 157.6 ppm; Elemental analysis calcd (%) for $C_{40}H_{34}O_4$: C 83.02, H 5.92; found: C 82.59, H 5.90.

Received: October 3, 2003 [Z53011]

Keywords: arenes · carbocations · cooperative effects · electrochemistry · Lewis acids

[1] H. H. Freedman in *Carbonium Ions*, *Vol. IV* (Eds.: G. A. Olah, P. von R. Schleyer), Wiley-Interscience, New York, **1973**, chap. 28.
[2] C. Herse, D. Bas, F. C. Krebs, T. Bürgi, J. Weber, T. Wesolowski, B. W. Laursen, J. Lacour, *Angew. Chem.* **2003**, *115*, 3270–3274; *Angew. Chem. Int. Ed. Engl.* **2003**, *42*, 3162–3166.
[3] D. F. Duxbury, *Chem. Rev.* **1993**, *93*, 381–433.
[4] For examples, see: a) E. Y.-X. Chen, T. J. Marks, *Chem. Rev.* **2000**, *100*, 1391–1434; b) W. E. Piers, G. J. Irvine, V. C. Williams, *Eur. J. Inorg. Chem.* **2000**, 2131–2142.
[5] J. Nishida, T. Suzuki, T. Tsuji, *J. Syn. Org. Chem. Jpn.* **2002**, *60*, 40–51, and references therein.
[6] a) T. Suzuki, J. Nishida, T. Tsuji, *Angew. Chem.* **1997**, *109*, 1387–1389; *Angew. Chem. Int. Ed. Engl.* **1997**, *36*, 1329–1331; b) T. Suzuki, J. Nishida, T. Tsuji, *Chem. Commun.* **1998**, 2193–2194.
[7] a) J. Nishida, T. Suzuki, M. Ohkita, T. Tsuji, *Angew. Chem.* **2001**, *113*, 3351–3354; *Angew. Chem. Int. Ed.* **2001**, *40*, 3251–3254; b) H. Higuchi, E. Ohta, H. Kawai, K. Fujiwara, T. Tsuji, T. Suzuki, *J. Org. Chem.* **2003**, *68*, 6605–6610.
[8] W. Neugebauer, T. Clark, P. von R. Schleyer, *Chem. Ber.* **1983**, *116*, 3283–3292.
[9] E. M. Arentt, R. A. Flowers II, R. T. Ludwig, A. E. Meekhof, S. A. Walek, *J. Phys. Org. Chem.* **1997**, *10*, 499.
[10] Crystal data: $[\mathbf{2}^{2+}][BF_4^-]_2\cdot(MeCN)_2$: $C_{44}H_{40}O_4B_2F_8N_2$, $M_r =$ 834.40, monoclinic, space group $P2(1)/n$, $a = 7.7412(17)$, $b =$ 30.885(7), $c = 16.494(4)$ Å, $\beta = 94.675(4)°$, $V = 3930.5(15)$ Å^3, $Z = 4$, $\rho_{calcd} = 1.410$ g cm^{-3}, $Mo_{K\alpha}$ radiation ($\lambda = 0.71073$ Å), $T =$ 110(2) K, 29394 measured reflections, 9351 unique, $R_{int} = 0.0729$, $R_1 = 0.0560$, $wR_2 = 0.1397$ (all data). **2**: $C_{40}H_{34}O_4$, $M = 578.71$, triclinic, space group $P\bar{1}$, $a = 10.0914(17)$, $b = 10.8633(19)$, $c =$ 15.308(3) Å, $\alpha = 101.893(3)°$, $\beta = 98.924(3)°$, $\gamma = 111.528(3)°$, $V = 1477.7(4)$ Å^3, $Z = 2$, $\rho_{calcd} = 1.301$ g cm^{-3}, $Mo_{K\alpha}$ radiation ($\lambda = 0.71073$ Å), $T = 110(2)$ K, 12635 measured reflections, 6539 unique, $R_{int} = 0.0424$, $R_1 = 0.0633$, $wR_2 = 0.1306$ (all data). The crystals ($0.23 \times 0.22 \times 0.11$ mm for $[\mathbf{2}^{2+}][BF_4^-]_2\cdot(MeCN)_2$ and $0.46 \times 0.27 \times 0.11$ mm for **2**) were mounted onto a glass fiber with Apiezon grease. All the structures were solved by direct methods, which successfully located most of the non-hydrogen atoms. Subsequent refinement on F^2 using the SHELXTL/PC package (version 5.1) allowed location of the remaining non-hydrogen atoms. CCDC-220813 and 220814 contain the supplementary crystallographic data for this paper. These data can be obtained free of charge via www.ccdc.cam.ac.uk/conts/retrieving.html (or from the Cambridge Crystallographic Data Centre, 12, Union Road, Cambridge CB2 1EZ, UK; fax: (+44) 1223-336-033; or deposit@ccdc.cam.ac.uk).
[11] Computational details have been assembled in the Supporting Information.

[12] a) J. D. Hoefelmeyer, F. P. Gabbaï, *J. Am. Chem. Soc.* **2000**, *122*, 9054 – 9055; b) J. D. Hoefelmeyer, M. Schulte, M. Tschinkl, F. P. Gabbaï, *Coord. Chem. Rev.* **2002**, *235*, 93 – 103.
[13] The potentials reported for $\mathbf{A}^{2+}/\mathbf{A}$ in ref. [6a] are: red. 0.18 V, ox. 1.47 V versus SCE. Versus Fc/Fc^{+}, these potentials can be calculated at −0.28 and 1.01 V by substraction of 0.46 V (see: N. G. Connelly, W. E. Geiger, *Chem. Rev.* **1996**, *96*, 877 – 910.
[14] T.-Y. Cheng, R. M. Bullock, *J. Am. Chem. Soc.* **1999**, *121*, 3150 – 3155.
[15] a) H. E. Katz, *J. Am. Chem. Soc.* **1985**, *107*, 1420 – 1421; b) F. P. Gabbaï, *Angew. Chem.* **2003**, *115*, 2318 – 2321; *Angew. Chem. Int. Ed.* **2003**, *42*, 2218 – 2221.
[16] J. E. McMurry, T. Lectka, *Acc. Chem. Res.* **1992**, *25*, 47 – 53.
[17] a) K. K. Baldridge, Y. Kasahara, K. Ogawa, J. S. Siegel, K. Tanaka, F. Toda, *J. Am. Chem. Soc.* **1998**, *120*, 6167 – 6168, and references therein; b) H. F. Bettinger, P. von R. Schleyer, H. F. Schaefer, *Chem. Commun.* **1998**, 769 – 770; c) K. Toda, Tanaka, M. Watanabe, K. Tamura, I. Miyahara, T. Nakai, K. Hirotsu, *J. Org. Chem.* **1999**, *64*, 3102; d) B. Kahr, D. V. Engen, K. Mislow, *J. Am. Chem. Soc.* **1986**, *108*, 8305; e) T. Suzuki, K. Ono, H. Kawai, T. Tsuji *J. Chem. Soc. Perkin Trans. 2* **2001**, 1798 – 1801.
[18] Long carbon–carbon bonding 4c–2e interactions are encountered in species such $[(TCNE)_2]^{2-}$. See a) J. J. Novoa, P. Lafuente, R. E. Del Sesto, J. S. Miller, *Angew. Chem.* **2001**, *113*, 2608 – 2613; *Angew. Chem. Int. Ed.* **2001**, *40*, 2540 – 2545; b) J.-M. Lü, S. V. Rosokha, J. K. Kochi, *J. Am. Chem. Soc.* **2003**, *125*, 12161 – 12171.
[19] a) R. K. Thauer, A. R. Klein, G. C. Hartmann, *Chem. Rev.* **1996**, *96*, 3031 – 3042; b) S. Sankararaman, W. Lau, J. K. Kochi, *J. Chem. Soc. Chem. Commun.* **1991**, 396 – 398; c) K. Komatsu, H. Akamatsu, S. Aonuma, Y. Jinbu, N. Maekawa, K. Takeuchi, *Tetrahedron* **1991**, *47*, 6951 – 6966.
[20] This reaction bears some analogy with the acid-induced formation of a monocationic ketocarbenium species. See: T. Suzuki, T. Nagasu, H. Kawai, K. Fujiwara, T. Tsuji, *Tetrahedron Lett.* **2003**, *44*, 6095 – 6098.
[21] G. A. Olah, G. K. S. Prakash, J. Sommer, *Superacids*, Wiley-Interscience, New York, **1985**.

 © 2004 Wiley-VCH Verlag GmbH & Co. KGaA, Weinheim

Branched Nucleic Acids

NMR Spectroscopic Determination of the Solution Structure of a Branched Nucleic Acid from Residual Dipolar Couplings by Using Isotopically Labeled Nucleotides**

*Bernd N. M. van Buuren, Jürgen Schleucher, Valentin Wittmann, Christian Griesinger, Harald Schwalbe, and Sybren S. Wijmenga**

Branched nucleic acids play important biological roles, and well-known examples such as the Hammerhead ribozyme, the all-RNA enzyme, a three-way junction (3H according to IUPAC nomenclature[1a]), and the Holliday junctions[1b] or DNA four-way junctions (J6, Figure 1a; 4H according to IUPAC nomenclature[1a]) have recently been reviewed.[2a–c] The Holliday junctions form the central intermediates in both homologous and site-specific recombination. In solution, in the presence of multivalent ions and thus under physiological salt conditions, their structure consists of two quasi-continuously stacked helices in an essentially canonical conformation (Figure 1c).[2b,c] Four recent crystal structures of 4H[2d–g] confirm these structural features, but no coherence is observed in the value of the interhelix angle ψ (defined in Figure 1b); three structures show right-handed interhelix

[*] Prof. Dr. S. S. Wijmenga
Laboratory of Physical Chemistry-Biophysical Chemistry
University of Nijmegen
Toernooiveld 1, 6225ED Nijmegen (The Netherlands)
Fax: (+31) 24-3652112
E-mail: sybrenw@sci.kun.nl

Dr. B. N. M. van Buuren
Unilever Research & Development
Olivier van Noortlaan 120, 3133AT Vlaardingen (The Netherlands)

Dr. J. Schleucher
Department of Medical Biochemistry and Biophysics
Umeå University, S-90187 Umeå (Sweden)

Dr. V. Wittmann
Johann Wolfgang Goethe-Universität Frankfurt/M.
Institut für Organische Chemie und Chemische Biologie
Marie-Curie-Strasse 11, 60439 Frankfurt/M. (Germany)

Prof. Dr. C. Griesinger
Max-Planck-Institut für biophysikalische Chemie
Am Fassberg 11, 37077 Göttingen (Germany)

Prof. Dr. H. Schwalbe
Johann Wolfgang Goethe-Universität Frankfurt/M.
Zentrum für Biomolekulare Magnetische Resonanz
Institut für Organische Chemie und Chemische Biologie
Marie-Curie-Strasse 11, 60439 Frankfurt/M. (Germany)

[**] This work was supported by grants from the Kempe Minne Foundation (BVB), the Swedish National Research Council (SW), Bioteknik Medel Umeå University (SW), the DFG (GR1211/2-4, En111/11-3) (C.G., H.S.), the Karl Winnacker foundation (H.S.), and the European LSF for Biomolecular NMR (ER-BCT950034). We thank Janny Hof for critical reading of the manuscript.

Supporting information for this article is available on the WWW under http://www.angewandte.org or from the author. Included are the fit results, the original J_{CH} values as a function of magnetic field, and the derived mRDCs.

 DOI: 10.1002/anie.200351632 © 2004 Wiley-VCH Verlag GmbH & Co. KGaA, Weinheim

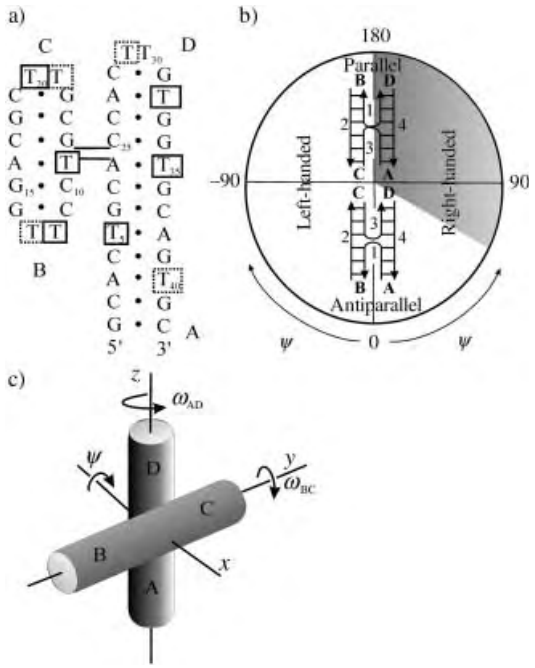


Figure 1. a) Sequence and arm designation for J6. The ^{13}C-labeled thymines in two samples are indicated as boxed residues (solid/dashed outline). b) The interhelix angle ψ, strand numbering, and conformation designations following 4H nomenclature. The parallel and antiparallel orientations of the AD and BC helices are defined by the corresponding drawings. Left-handed and right-handed indicate the orientation of the AD helix relative to the BC helix. The grey region was excluded for steric reasons. c) The chosen molecular axis frame and designation of the coaxially stacked helices.

angles,[2d–f] while the angle in the fourth structure is left-handed.[2g] In the solution structure[3] of the J6 model for a Holliday junction, based on NMR spectroscopy using NOE and *J* coupling constants, the quasi-continuously stacked helices AD and BC[3a] have a left-handed interhelix angle (Figure 1b). The determination of the relative helix orientations is the central question concerning the structure of branched nucleic acids.

Herein we describe how a relatively small set of long-range NMR restraints can be used to determine the global structure of branched nucleic acids. This is shown with the example of the Holliday junction, and the previous assignment of a left-handed interhelix angle is confirmed. The approach relies on the measurement of a set of residual dipolar couplings (RDCs) in a DNA sample with thymidine residues that are ^{13}C labeled in the deoxyribose moiety of the nucleotide[4] (Figure 1a). This chemical labeling strategy allows rapid determination of the overall conformation of branched nucleic acids.

In NMR spectra of liquid samples, RDCs contain information about long-range orientation and complement the local NMR restraints, NOEs, and *J* coupling constants. The RDCs are observed for molecules for which isotropic rotational tumbling is partially restricted.[5–7] This restriction can be induced by non-isotropic media such as liquid crystals or phages.[5a,e–h] However, partial alignment can also be conferred by the intrinsic properties of a molecule. For example, the anisotropy of the magnetic susceptibility,[8,9] a pronounced feature of double-stranded oligonucleotides, induces a partial alignment of a molecule in strong homogeneous magnetic fields and thereby gives rise to magnetic-field-induced RDCs (mRDCs).[5a–d,j–n,9]

The anisotropy of the molecular magnetic susceptibility tensor (χ_{mol}) is caused by the magnetic susceptibility of the individual nucleobases (χ_b). The latter are dominated by base ring currents with the long axis (z) of χ_b perpendicular to the base plane. Their principal components ($\chi_{b,xx}$, $\chi_{b,yy}$, $\chi_{b,zz}$) can be written as $(0,0,-13)\times10^{-34}$ m^3 in SI units. The average value of $\chi_{b,zz}$ per base can be calculated on the basis of the Cotton–Mouton effect[8] or from quantum mechanics[10] with good accuracy (Tables 1 and 2). χ_{mol} can be calculated as the tensor sum of the individual χ_b values as long as the structure of a nucleic acid molecule is known [Eq. (1)].

$$\chi_{mol} = \sum_{i=1}^{N} (\vec{\nu}_{b,i}^{T} \otimes \vec{\nu}_{b,i})\chi_{b,zz,i} \quad (1)$$

Table 1: Estimate of the base χ values.

	CG [-10^{-34} m^3]	AT [-10^{-34} m^3]
ElOPt[a]	−25.4	−19.9
JB[b]	−20.4	−26.2
HM[b]	−23.8	−30.4
GP[b]	−26	−36
Average all	-26 ± 5	
Average base	-13 ± 2.5	

[a] Value of χ from reference [8]; [b] JB: χ from ring currents with ring currents obtained using Johnson–Bovey equations from reference [10a]; HM: χ from ring currents with ring currents obtained using Haig–Mallion equations from reference [10a]; GP: χ from ring currents with ring currents obtained from reference [10b]. For a CG base pair the ring currents of C and G were added; an analogous method was used for an AT base pair. The values for the ring currents are relative to those for benzene and proportional to the magnetic susceptibility tensor. The χ values of the CG and AT base pairs were obtained by multiplying the ring current with χ for benzene (-12.7×10^{-34} m^3[9]). The GP ring currents were multiplied with a factor 1.7 to take into account the fact that GP used lower ring currents values, because part of the base susceptibility is attributed to bond magnetic susceptibility. The χ tensor is oriented perpendicular to the base. Consequently, its principal components can be written as $(0,0,\chi_{zz})$, where χ_{zz} indicates the z principal component. The average of all different base pair estimates leads to an average value χ_{zz} per base of $13\pm2.5\times10^{-34}$ m^3.

Table 2: Ring currents calculated for the four nucleic acid bases G, A, T, and C.[a]

	GP	JB	HM
G	0.94(0.62)	1.30(0.73)	1.51 (0.74)
A	1.56(1.00)	1.78(1.00)	2.04 (1.00)
T	0.11(0.07)	0.28(0.16)	0.35 (0.17)
C	0.28(0.18)	0.31(0.17)	0.37 (0.18)

[a] GP, JB, and HM are as defined in Table 1; the values in parentheses indicate the ring current values relative to that for adenine.

 © 2004 Wiley-VCH Verlag GmbH & Co. KGaA, Weinheim

Here, ν_b is a unit row vector perpendicular to the base plane i, N the number of bases in the molecule, and the symbol $\otimes$ represents the direct matrix product of the column and row vector.

When non-isotropic media[5a,e–h,6,7] are used to align molecules, the size (axial and rhombic component) and orientation (three Euler angles) of the alignment tensor in a molecular frame have to be derived from the experimental RDCs; this requires a minimum of five RDCs. The relative domain orientation in an n domain molecule with known domain structure is defined by three Euler angles for each pair of domains, so that in addition a minimum of three parameters (RDCs) are needed to derive the relative orientation of each domain.[5a,d,7] In the procedure proposed by Dosset et al.,[7f] for each domain an alignment tensor is first derived and the relative domain orientations are subsequently obtained by reorienting each domain such that all alignment tensors have the same common orientation. This procedure can be simplified in the case of magnetic-field-induced alignment, because the size and orientation of the alignment tensor can be calculated from each trial structure. Such reduction in complexity is also obtained if the size and shape of the alignment tensor can be predicted from the shape and/or charge distribution of the molecule.[7d,e]

Residual dipolar couplings $^1D_{CH}$ have been measured in the sugar moiety of ten thymine residues of the J6 model. The residual dipolar coupling $D_{CH,i}$ of a dipolar C–H vector i can be calculated in a chosen molecular reference frame by direct matrix multiplications of χ_{mol} and $\vec{\nu}_{CH,i}$, where the latter is the unit row vector pointing along the C–H vector i expressed in the chosen reference frame [Eq. (2)].

$$D_{CH,i} = -S\left[\frac{h}{2\pi^2}\gamma_C\,\gamma_H\,r_{CH}^{-3}\frac{1}{4\pi}\frac{1}{15\,k\,T}B_o^2\frac{3}{4}\right]\left[\left(\vec{\nu}_{CH,i}\,\vec{\vec{\chi}}_{mol}\,\vec{\nu}^{T}_{CH,i}\right) - \left(\frac{1}{3}\ \mathrm{Trace}\ \vec{\vec{\chi}}_{mol}\right)\right] \quad (2)$$

Here, h is Planck's constant, γ_C and γ_H are the gyromagnetic ratios of the ^{13}C and ^1H nuclear spins, r_{CH} is the distance between the directly bonded C and H nuclei, kT is the thermal energy, and B_o is the magnetic field strength in Tesla. The order parameter S[5a,d,11] takes into account the reduction in the size of $D_{CH,i}$ by intramolecular dynamics and has been assumed to be 1 here.

The relative orientation of the two semi-continuously stacked helices of 4H (Figure 1c) is defined by three parameters. In any axes frame, the AD helix orientation is specified by its three Euler angles, the polar angles, θ_{AD} and ϕ_{AD}, and the rotation around the helix axis ω_{AD} (BC helix orientation: θ_{BC}, ϕ_{BC}, and ω_{BC}). We defined a right-handed reference frame in which the AD helix lies along the z axis ($\theta_{AD}=0$, $\phi_{AD}=0$) and the x axis is perpendicular to the plane spanned by the AD and BC helix axes. The BC helix then rotates by definition in the yz plane ($\phi_{BC}=90$) and θ_{BC} equals the interhelix angle ψ ($\theta_{AD}=0$). In this molecular axis frame, the conformation of 4H is defined by the interhelix angle ψ, and the angles ω_{AD} and ω_{BC} indicate the rotation about their own axes. From a given set of RDCs (minimum of three required), two sets of solutions for the conformation of 4H can be derived. Thus, for the first set of two solutions (set 1), the 4H conformation is defined by the angles ω_{AD1} and ω_{BC1} with the interhelix angle equal to ψ_1 and $\psi_1+180°$. The second set of two solutions (set 2) is defined by the angles ω_{AD1} and $\omega_{BC1}+180°$ with the interhelix angle again equal to ψ_1 and $\psi_1+180°$. Set 2 is sterically disallowed, because strands 1 and 3 (Figure 1b) cross from the AD to the BC helix. Furthermore, $\omega_{AD1}+180°$ leads only to equivalent solutions involving rotation of the whole molecule. The two solutions of set 1 are reduced to one unique solution when $-60° \le \psi < -180°$, because the crossing strands intermingle for $60° \le \psi < 180°$[12] and thus exclude this region (Figure 1b). As shown below, we found a value close to $-90°$ and thus one unique solution was obtained.

For each conformation χ_{mol} was calculated and subsequently D_{CH}^{calcd} determined. The optimal conformation was found by comparing D_{CH}^{calcd} with D_{CH}^{exp} as the minimum root mean square difference (rmsd). In total 28 mRDCs were derived from least-squares fits of $^1J_{CH}$ coupling constants and measured[13] at four different magnetic fields (400–800 MHz; see Supporting Information). They are given in Table 3 as Δ^1J_{CH} between 400–800 MHz and denoted as D_{CH}. A variety of optimizations were performed with model helices or helices derived from two NOE-based experimental structures (Figure 2 and Supporting Information). Most striking is that ψ always has a well-defined minimum ($-88° < \psi_{opt} < -98°$, depending on the optimization, Figure 2a). This is more negative than the value of approximately $-70°$ in the NOE-

Table 3: Experimental dipolar couplings D of the model Holliday junction J6, as determined from measurements at four magnetic fields.[a]

Arm	Residue	D(C1′,H1′) [Hz]	D(C3′,H3′) [Hz]	D(C4′,H4′) [Hz]
A	T5	−1.7[b]	1.2	0.1
A	T35	0.6	−0.2	0.6
A	T40	0.6	0.0	1.4
D	T29	−1.2	0.7	2.1
D	T32	−3.0	−0.3	−0.6
B	T9	0.5	−0.7	3.1
B	T12	–	0.2	1.8
B	T13	0.5	1.1	2.3
C	T20	1.6	–	1.8
C	T21	1.0	1.6	2.3

[a] The dipolar couplings were determined from a least-squares fit of the magnetic field dependence of the $^1J_{CH}$ coupling constants of H1′-C1′, H3′-C3′, and H4′-C4′ at 400, 500, 600, and 800 MHz. The measured $^1J_{CH}$ value can be written as $^1J_{CH} = a\,B_o^2 + {}^1J_{CH}°$, where $^1J_{CH}°$ represents the $^1J_{CH}$ value at a magnetic field of zero and the slope a contains the D_{CH} information ($a = D_{CH}/B_o^2$). For the least-squares fit the above equation was used. The D_{CH} at a given field is then equal to ($a\,B_o^2$). The D_{CH} values were calculated from the slope as the difference ΔD_{CH} between values at 800 and 400 MHz. Thus, they correspond to D_{CH} measured at an effective magnetic field of $(64–16)^{0.5}\times 100$ MHz = 693 MHz. Two samples were used with ^{13}C labeling in the ribose; sample 1 was labeled at T5, T9, T12, T20, T32, and T35; and sample 2 at T13, T12, T29, and T40. [b] The uncertainty in the D_{CH} values is estimated to be ± 0.5 Hz.

 © 2004 Wiley-VCH Verlag GmbH & Co. KGaA, Weinheim

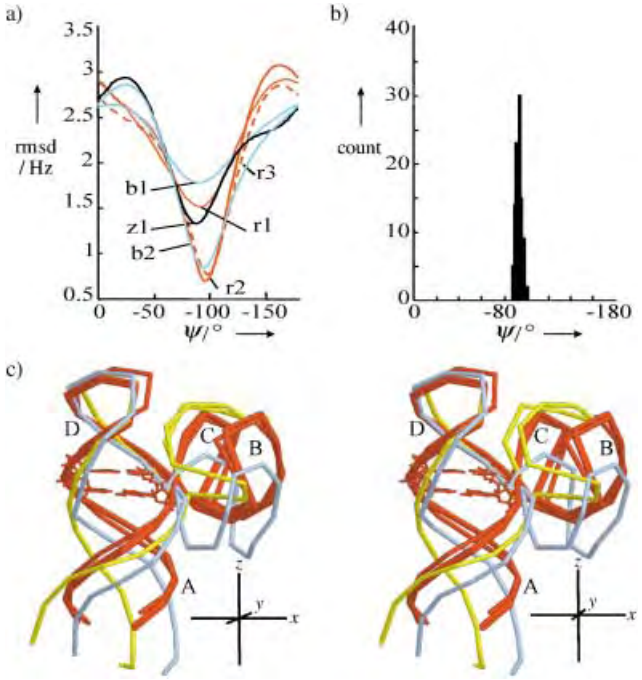


Figure 2. a) Plot of the rmsd of D_{CH}^{exp} and D_{CH}^{calcd} versus ψ. The AD and BC helices were modeled as B-DNA helices capped with a known stable CTTG loop[14] (red, r) or taken from the NOE-based structure set (blue, black, z: two structures close to average). Model helices (r): fit with 3 (r1) or 3+7 parameters (r2) or as r2 with base-specific $\chi_{b,zz}$ (r3; see Supporting Information). Experimental helices: fit with 3 (b1, z1) or 3+8 parameters (b2). b) Monte Carlo estimate of the spread in ψ of fit r1 (see the text). The fitting was repeated for 100 samples of the 28 mRDCs with random variation in their values according to normal distribution with $\sigma = 0.5$ Hz. c) Stereo views of the mRDC-optimized 4H (corresponding to fits r1–r3 and b2) and the NOE-based 4H (yellow, optimized is b2) with chosen axes frame (see the text). χ_{mol} essentially coincides with this chosen axes frame (see Supporting Information).

based structure. The Monte Carlo (MC) spread in ψ due to the 0.5-Hz experimental error on D_{CH} is small (rmsd 3–6°, Figure 2b and Supporting Information). The angles ω_{AD} and ω_{BC} also have well-defined minima, but their MC errors are somewhat larger (rmsd 6–15°; see Supporting Information). The use of base-specific values instead of one average value for $\chi_{b,zz}$ in the calculation of χ_{mol} hardly affects the fit results (Figure 2a). Similarly, increasing or decreasing the average $\chi_{b,zz}$ value by one standard deviation does not change the fit results (see Supporting Information). To verify these results, cross validation was carried out on the three-parameter fit M(3)_r1 (Figure 2) by randomly removing six of the 28 mRDCs in 100 different samples. For each sample the fitting was carried out and the MC spread determined to yield average values and deviations (rmsd) for ψ_{opt}, $\omega_{AD,opt}$, and $\omega_{BC,opt}$ of −93 (3)°, −159°(6°) and −182° (6°), respectively. The similarity of these values with those found for the other fit results (see Supporting Information) further confirms the conclusions.

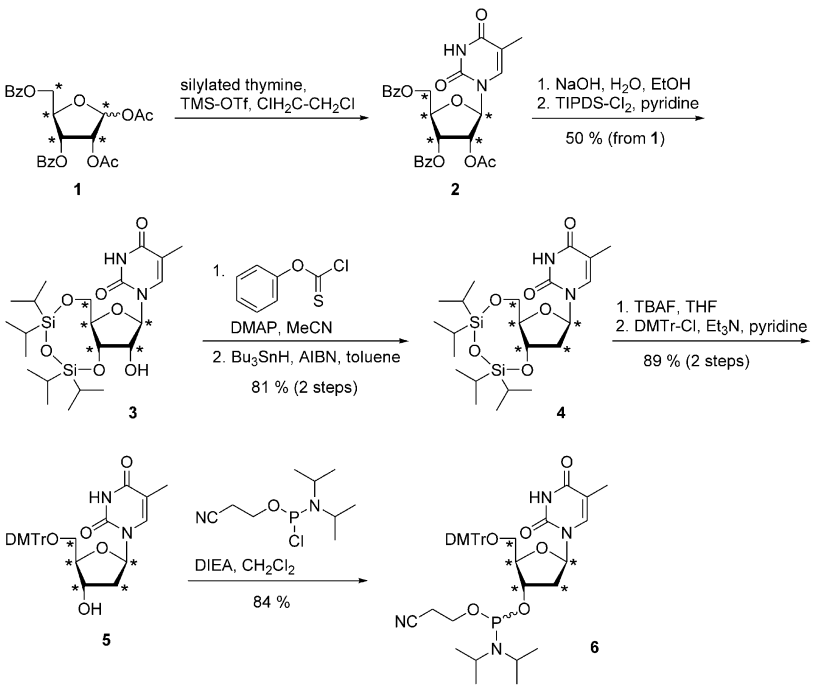
Although the fits with three adjustable parameters gave well-defined minima, the correlation between D_{CH}^{exp} and D_{CH}^{calcd} showed a systematic offset for the H3′-C3′ and H4′-C4′ mRDCs (see Supporting Information). Variation in sugar puckering and orientation may affect the orientation of these vectors (but not H1′-C1′). Note that in DNA the energy well for the S-puckered deoxyribose is relatively wide, and sugars are often not found to be 100% S-puckered even in regular helices. Furthermore, the ribose rings are oriented approximately parallel to the helix axis, so that the sugar pucker motion, repuckering, and reorientation will mainly affect the ω angles of these vectors. Therefore, we operationally included small additional ω rotations, where the H3′-C3′ and H4′-C4′ mRDCs were treated as separate groups in the A, B, C, and D helices, and found indeed improved fit results (see Supporting Information). However, the number of adjustable parameters (≤ 11) remains much smaller than the number of experimental mRDCs (28).

Model helices gave similar results and the best fits (Figure 2a, red curve), and the mRDC-optimized 4H structures nearly overlap (Figure 2c, red structure). Compared with the NOE-based structure, the main change, apart from the small change in ψ, is that the BC helix has rotated by about 40° around its own axis (Figure 2c, yellow versus red structure), leading to a net opening of the cavity formed by the facing major grooves. In the mRDC-optimized NOE-based structure (Figure 2c, blue structure), the BC helix has rotated approximately 40° further. Optimization of the other experimental structure leads to a smaller cavity opening, and the resulting structure is close to the yellow structure shown in Figure 2c. Generally, the fits using experimental helices are not as good (Figure 2a, red versus blue and black structures), thus leading to the larger uncertainty in the value of ω_{BC}. This can be attributed to the difficulty of using NOEs to define global features even within the regular helix domains.

We have assumed a single rigid structure for the calculation of χ_{mol} and D_{CH} [Eqs. (1) and (2)]. It is of interest to consider potential hinge motion, that is, motion of the BC helix with respect to the AD helix. Internal motion is usually taken into account by an order parameter S [Eq. (2)], which simply scales the mRDCs, and the optimized angles should be viewed as effective angles.[11] Assuming that the potential hinge motion can be accounted for in this way a rough estimate of its amplitude can be obtained. The errors in χ_{mol} and D_{CH} are about 10% and 15%, respectively, which correspond to an overall error of around 18% in the tensor and allows for an overall S value of about 0.82. If we further assume that the hinge motion can be described by axial wobbling in a cone according to $\frac{1}{2}\cos\varepsilon(1+\cos\varepsilon) = S$, the amplitude of this motion would imply an opening half-angle of about 28°. Thus, this would allow replacement of the model with a fixed orientation of the two helices with an interhelical angle of about −90° by a model in which the structure has an effective angle of −90° with a spread of around ±28°. It should be noted, however, that the effect of hinge motion is more complex than a simple scaling of the dipolar couplings, because the hinge motion differently affects the axial and rhombic components of χ_{mol} as well as its orientation with respect to the AD and BC helices (for certain C–H vectors hinge motion may even lead to an increase in D_{CH}). An accurate estimation of the effect of hinge motion would require simulation of these motions.

 © 2004 Wiley-VCH Verlag GmbH & Co. KGaA, Weinheim

In summary, we have shown with the example of the Holliday junction that the global orientation of branched nucleic acids can be derived from a small set of mRDCs by taking advantage of the reduction in required parameters, thus extending approaches based on phage-induced RDCs.[15] The same type of analysis can be extended to other branched nucleic acids in a relatively straightforward fashion. For instance, under physiological salt conditions, RNA and DNA 3H show coaxial stacking of two of the three arms. The global conformation is then defined by three angles that describe the relative helix orientations and would require the same minimum number of mRDCs as for the 4H discussed here. Similarly, for more strongly branched nucleic acids, such as 5H and 6H sometimes found in RNAs, the global conformation is defined by the relative orientation of three helices when coaxial stacking is present and would require a minimum of six mRDCs (six Euler angles define the relative helix orientations). The mRDC size, although sufficiently large here, can easily be increased by using larger magnetic fields or larger nucleic acids (e.g. extension of each of the 4H helices by four base pairs leads to ΔD_{CH}^{max} of 16 Hz for 900 vs. 400 MHz). Also, with present cryoprobe technology, magnetic-field-induced dipolar couplings can be determined at natural abundance.



Scheme 1. Synthesis of **6**. The asterisks indicate the ^{13}C-labeled positions. AIBN = azobisisobutyronitrile, Bz = benzyl, DIEA = *N*,*N*-diisopropylethylamine, DMAP = 4-dimethylaminopyridine, DMTr = 4,4′-dimethoxytriphenylmethyl, OTf = trifluoromethanesulfonate, TBAF = tetrabutylammonium fluoride, TIPDS = tetraisopropyldisilyl, TMS = trimethylsilyl.

Experimental Section

[$^{13}C_5$]-Thymidine phosphoramidite (**6**): Two J6 samples (Figure 1a) were synthesized according to Scheme 1 with thymidine residues ^{13}C-labeled in the deoxyribose moiety of the nucleotide[4] (see Figure 1a). [$^{13}C_6$]Glucose was converted into 1,2-di-*O*-acetyl-3,5-di-*O*-benzoyl ribofuranose (**1**) and glycosylated to give nucleoside **2** according to a published procedure.[4] 2′-Deoxygenation was carried out following a procedure described by Robins et al. for the synthesis of 2′-deoxyuridine.[16] Briefly, **2** was deprotected and treated with the Markiewicz reagent to give 3′,5′-protected nucleoside **3**, which was further converted into its 2′-*O*-phenoxythiocarbonyl derivative. Reductive deoxygenation with tri-*n*-butyltin hydride and the free-radical initiator AIBN in warm toluene provided the thymidine derivative **4**. Fluoride-induced removal of the silyl protecting group and treatment with dimethoxytrityl chloride gave **5**, which was phosphitylated to yield phosphoramidite **6**. The product was ready for use in automated DNA synthesis.

Received: April 10, 2003
Revised: September 30, 2003 [Z51632]

Keywords: Holliday junctions · isotopic labeling · NMR spectroscopy · nucleic acids · structure elucidation

[1] a) D. M. J. Lilley, R. M. Clegg, S. Diekmann, N. C. Seeman, E. von Kitzing, P. J. Hagerman, *Nucleic Acids Res.* **1995**, *23*, 3363–3364; b) R. Holliday, *Genet. Res.* **1964**, *5*, 282–304.

[2] a) A. Kuzminov, *Microbiol. Mol. Biol. Rev.* **1999**, *63*, 751–813; b) S. C. West, *Annu. Rev. Genet.* **1997**, *31*, 213–244; c) D. M. J. Lilley, *Q. Rev. Biophys.* **2000**, *33*, 109–159; d) J. Nowakowski, P. J. Shim, G. S. Prasas, C. D. Stout, G. F. Joyce, *Nat. Struct. Biol.* **1999**, *6*, 151–156; e) B. F. Eichman, J. M. Vargason, B. H. M. Mooers, P. S. Ho, *Proc. Natl. Acad. Sci. USA* **2000**, *97*, 3971–3976; f) M. Ortiz-Lombardía, A. González, R. Eritja, J. Aymamí, F. Azorín, M. Coll, *Nat. Struct. Biol.* **2000**, *6*, 913–917; g) J. Nowakowski, P. J. Shim, C. D. Stout, G. F. Joyce, *J. Mol. Biol.* **2000**, *300*, 93–102.

[3] a) B. N. M. van Buuren, J. Schleucher, S. S. Wijmenga, *J. Biomol. Struct. Dyn.* **2000**, *11*, 237–243; b) B. N. M. van Buuren, T. Herman, S. S. Wijmenga, E. Westhof, *Nucleic Acids Res.* **2002**, *30*, 507–514.

[4] S. Quant, R. W. Wechselberger, M. A. Wolter, K. Wörner, P. Schell, J. W. Engels, C. Griesinger, H. Schwalbe, *Tetrahedron Lett.* **1994**, *35*, 6649–6652.

[5] a) J. H. Prestegard, H. M. Al-Hashimi, J. R. Tolman, *Q. Rev. Biophys.* **2000**, *33*, 371–424; b) A. Bax, N. Tjandra, *Nat. Struct. Biol.* **1997**, *4*, 254–256; c) N. Tjandra, J. G. Omichinski, A. M. Gronenborn, G. M. Clore, A. Bax, *Nat. Struct. Biol.* **1997**, *4*, 732–738; d) J. H. Prestegard, *Nat. Struct. Biol.* **1998**, *5*, 517–522; e) A. Bax, N. Tjandra, *J. Biomol. NMR* **1997**, *10*, 289–292; f) M. R. Hansen, L. Mueller, A. Pardi, *Nat. Struct. Biol.* **1998**, *5*, 1065–1074; g) G. M. Clore, R. M. Starich, A. M. Gronenborn, *J. Am. Chem. Soc.* **1998**, *120*, 10571–10572; h) G. M. Clore, A. M.; Gronenborn, N. Tjandra, *J. Magn. Reson.* **1998**, *131*, 159–162; i) G. Cornilescu, L. J. Marquardt, M. Ottiger, A. Bax, *J. Am. Chem. Soc.* **1998**, *120*, 6836–6837; j) H. C. Kung, K. Y. Wang, I. Goljer, P. H. Bolton, *J. Magn. Reson. Ser. B* **1995**, *109*, 323–325; k) H. M. Al-Hashimi, A. Majundar, A. Gorin, A. Kettani, E.

 © 2004 Wiley-VCH Verlag GmbH & Co. KGaA, Weinheim

Skripkin, D. J. Patel, *J. Am. Chem. Soc.* **2001**, *123*, 633 – 640; l) H. M. Al-Hashimi, A. Gorin, A. Majumdar, D. J. Patel, *J. Am. Chem. Soc.* **2001**, *123*, 3179 – 3180; m) H. M. Al-Hashimi, Y. Gosser, A. Gorin, W. Hu, A. Majumdar, D. J. Patel, *J. Mol. Biol.* **2002**, *315*, 95 – 102; n) H. M. Al-Hashimi, J. R. Tolman, A. Majumdar, A. Gorin, D. J. Patel, *J. Am. Chem. Soc.* **2001**, *123*, 5806 – 5807; p) N. Sibille, A. Pardi, J. P. Simorre, M. Blackledge, *J. Am. Chem. Soc.* **2001**, *123*, 12135 – 12146.

[6] a) N. Tjandra, S. I. Tate, A. Ono, M. Kainosho, A. Bax, *J. Am. Chem. Soc.* **2000**, *122*, 6190 – 6200; b) A. Vermeulen, H. Zhou, A. Pardi, *J. Am. Chem. Soc.* **2000**, *122*, 9638 9647.

[7] a) M. W. F. Fischer, J. A. Losonczi, J. L. Weaver, J. H. Prestegard, *Biochemistry* **1999**, *38*, 9013 – 9022; b) N. R. Skrynnikov, N. K. Goto, D. Yang, W. Choy, J. R. Tolman, G. A. Mueller, L. E. Kay, *J. Mol. Biol.* **2000**, *295*, 1265 – 1273; c) E. T. Mollova, R. Hansen, A. Pardi, *J. Am. Chem. Soc.* **2000**, *122*, 11561 – 11562; d) C. A. Bewley, G. M. Clore, *J. Am. Chem. Soc.* **2000**, *122*, 6009 – 6016; e) M. Zweckstetter, A. Bax, *J. Am. Chem. Soc.* **2000**, *122*, 3791 – 3792; f) P. Dosset, J. C. Hus, D. Marion, M. Blackledge, *J. Biomol. NMR* **2001**, *20*, 223 – 231.

[8] G. Weill in *Molecular Electro-Optics* (Ed.: S. Krause), Plenum, New York, **1981**, pp. 473 – 483.

[9] A. A. Bothner-By in *Encyclopedia of Nuclear Magnetic Resonance* (Eds.: D. M. Grant, R. K. Harris), Wiley, Chicester, **1995**, pp. 2932 – 2938.

[10] a) D. A. Case, *J. Biomol. NMR* **1995**, *6*, 341 – 346; b) C. Giessner Prettre, B. Pullman, *Q. Rev. Biophys.* **1987**, *20*, 113 – 172.

[11] J. Meiler, J. J. Prompers, W. Peti, C. Griesinger, R. Brüschweiler, *J. Am. Chem. Soc.* **2001**, *123*, 6098 – 6107.

[12] E. von Kitzing, D. M. Lilley, S. Diekmann, *Nucleic Acids Res.* **1990**, *18*, 2671 – 2683.

[13] N. Tjandra, A. Bax, *J. Magn. Reson.* **1997**, *124*, 512 – 515.

[14] J. H. Ippel, H. Van den Elst, G. A. Van der Marel, J. H. Van Boom, C. Altona, *Biopolymers* **1998**, *46*, 375 – 393.

[15] K. Bondensgaard, E. T. Mollova, A. Pardi, *Biochemistry* **2002**, *41*, 11532 – 11542.

[16] M. J. Robins, J. S. Wilson, F. Hansske, *J. Am. Chem. Soc.* **1983**, *105*, 4059 – 4065.

 © 2004 Wiley-VCH Verlag GmbH & Co. KGaA, Weinheim

3D Copper Coordination Polymer

A Neutral 3D Copper Coordination Polymer Showing 1D Open Channels and the First Interpenetrating NbO-Type Network**

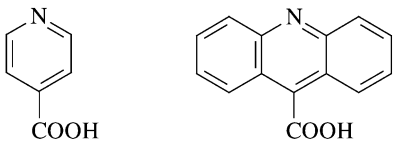
Xian-He Bu, Ming-Liang Tong, Ho-Chol Chang, Susumu Kitagawa,* and Stuart R. Batten*

The construction of coordination networks with novel topologies and porous structures that provide new sizes, shapes, and chemical environments is of great interest in recent years, due to their intriguing structural diversity and potential for many applications.[1,2] In recent years many porous metal–organic frameworks with unique structures have been obtained and their adsorption properties were widely investigated, however, those with specially shaped channels such as 1D helices are rare.[3] Metal–ligand coordination has been well used in the directed assembly of extended porous metal–organic networks, and one of the key points for such studies is the design or choice of components that organize themselves into desired patterns with useful functions. In this regard, considerable attention has been devoted to the networking ability of isonicotinic acid (**1**) and its derivatives,[4] which are multifunctional ligands potentially able to act as bridging ligands to produce open lattice species with various structural topologies and large pores. In this study, we choose an analogy of **1**, 9-acridinecarboxylic acid (HL), whose coordination chemistry has not been previously investigated, as a bridging ligand to construct new framework materials with novel structures and special properties based on combining its bridging coordination ability with its steric bulk. Although the coordination sites of HL and **1** are very similar, their coordination chemistry are found to be quite different due to the bulk of HL. We report herein a 3D twofold interpenetrating NbO-type network $[Cu_2(\mu_2\text{-}OMe)_2(\mathbf{L})_2\cdot(H_2O)_{0.69}]_n$ (**2**) with 1D channels.

[*] Prof. X.-H. Bu
Department of Chemistry
Nankai University
Tianjin 300071 (China)
Fax: (+86) 22-2350-2458
E-mail: buxh@nankai.edu.cn
Dr. M.-L. Tong, Dr. H.-C. Chang, Prof. S. Kitagawa
Department of Synthetic Chemistry and Biological Chemistry
Graduate School of Engineering
Kyoto University
Kyoto 606-8501 (Japan)
Fax: (+81) 75-753-4979
E-mail: kitagawa@sbchem.kyoto-u.ac.jp
Dr. S. R. Batten
School of Chemistry
Monash University
Victoria 3800 (Australia)

[**] This work was supported by the Outstanding Youth Foundation of NSFC (No. 20225101), a Grant-In-Aid for Creative Scientific Research (No.13GS0024) from the Ministry of Education, Culture, Sports, Science, and Technology, Japan, and the Australian Research Council (S.R.B.).

 © 2004 Wiley-VCH Verlag GmbH & Co. KGaA, Weinheim DOI: 10.1002/anie.200352024



1 HL

Black crystals of **2** were obtained by the reaction of $Cu(NO_3)_2 \cdot 3H_2O$ and HL in MeOH in the presence of Et_3N in fairly strong basic conditions. It is noteworthy that the amount of Et_3N used in the synthetic process is a key point for the formation of **2** because at weak basic or weak acidic conditions, a dinuclear[5a] or a trinuclear Cu^{II} complex[5b] would form.

2 crystallizes in the high symmetry trigonal space group $R\bar{3}$ and consists of $Cu_2(\mu_2\text{-}OMe)_2$ dimers bridged by two-connecting L ligands. Figure 1a illustrates the coordination environment of center Cu atoms and the fourfold connectivity of the bimetallic unit. Although there are two crystallographically different dimers in the structure, they are both chemically and topologically identical. In the context of the structure, the dicopper dimers constitute so-called secondary building units (SBUs).[6] The copper atoms in each SBU are bridged by two methanolato anions to give $[Cu_2(\mu_2\text{-}OMe)_2]^{2+}$ fragments in which the Cu···Cu distance is 2.992(2) Å. Each copper atom is four-coordinate, with two methanolato oxygen atoms, one carboxylic oxygen atom of L and one nitrogen atom from another L ligand. The Cu_2 unit, which acts as a node, is connected to four others through four bridging L ligands. Each Cu^{II} center coordinates to one L through the pyridyl nitrogen atom, and to another through the carboxylate functional group (Figure 1a). The coordination of the ligands is such that the pyridyl donors form a *trans* arrangement across the dimer, as do the carboxylate.

The bridging of the SBUs produces an overall 3D network which is spacious enough to contain a second, interpenetrating network. The structure of **2** can be described as two-fold interpenetrating nets with NbO topology, if the dimer is regarded as a four-connecting node (Figure 1b). To the best of our knowledge, this is the first example of interpenetrating NbO networks.[7] The lack of interpenetrating NbO networks in the literature has recently been attributed to the fact that, unlike other network topologies such as diamond or α-Po, NbO is not a self-dual—that is, it cannot interpenetrate in such a way that it is fully catenated.[7a,8] The interpenetration reported here is that of partially catenated nets, with two of the eight six-membered rings not catenated.[7a,8] The structure of **2** does show, however, that interpenetration is possible for this network topology.

Space-filling views of the structure reveal small channels that run parallel to the *z* axis (Figure 1c) which contain disordered water molecules (for which a reasonable refinement for the structure was not possible[9]). Calculations from the X-ray structural parameters show that the solvent-accessible void space in the channels is approximately 24%.[10] The smallest diameter of these channels, after taking into account van der Waals radii, is only about 2.8 Å. However, the observed porosity of the structure (see below) can perhaps be explained by the fact that the channels are not uniform, and are significantly more open in sections. Thus halfway between the narrow sections of the channels lay more open cavities with minimum diameters of about 5.3 Å (and, given its nonspherical shape, larger maximum diameters). No significant channels are observed in any other direction.

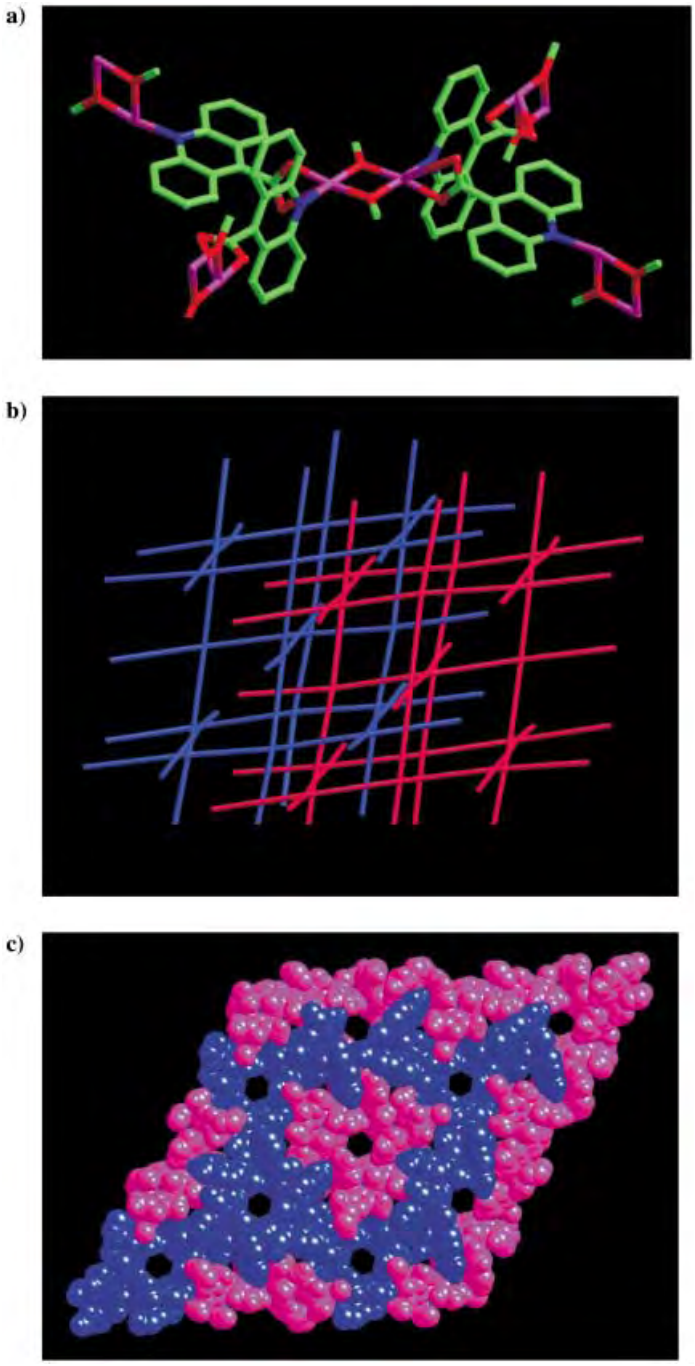


Figure 1. a) The structure of **2**, showing the local coordination geometry. Each $Cu_2(OMe)_2$ dimer is bridged by four L ligands to four other dimers. Green: C; blue: N; red: O; pink: Cu, hydrogen atoms are omitted for clarity. b) The two-fold interpenetrating NbO-type networks, with the nodes representing the $Cu_2(OMe)_2$ dimers, and the links the bridging L ligands. c) Space-filling diagram of the two-fold interpenetrating networks viewed down the *z* axis. Note the 1D channels apparent.

 © 2004 Wiley-VCH Verlag GmbH & Co. KGaA, Weinheim

The structure contains numerous intra- and internetwork CH···π and π···π supramolecular interactions that presumably help to stabilize the adopted structure. For example, the rings that form the narrowest part of the channels are stabilized by intranetwork CH···π interactions (Figure 2a). The structure also contains double helices, in which each strand is part of a separate network, which are again stabilized by numerous weak intermolecular interactions (Figure 2b). These double helices run parallel to both the z axis and the 1D channels, and pass through the midpoints of imaginary "triangles" whose corners are defined by the 1D channels (as can be seen in Figure 1c).

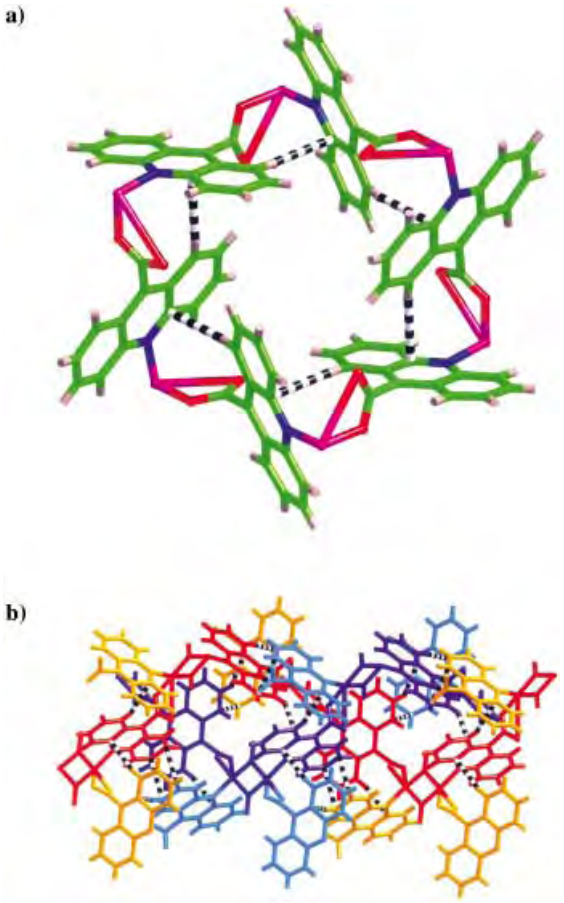


Figure 2. a) A view of the narrowest part of the 1D channels, emphasizing the intranetwork CH···π interactions (shown as black and white striped bonds). b) The double helix motif contained in the structure, with CH···π and π···π interactions depicted as black and white striped bonds. The two strands of the double helix are shown in purple and red, with L appendages to these strands shown in blue and yellow, respectively.

To examine the thermal stability and porous functionality of the synthetic material, the TG analysis and gas adsorption isotherms were carried out. The TG curve shows the release of water molecules below 70 °C. No further weight loss could be observed upon heating up to about. 200 °C, and after this point the compound starts to decompose. Figure 3 shows the isotherms of anhydrous **2** for the adsorption of N_2 and alcohols (EtOH and MeOH) at 77 and 298 K, respectively. A rapid increase in the amount of adsorbed gas is shown by an increase in pressure of up to $0.05\,P_0$, which indicates the diffusion of guest gas molecules into the channels. Approximately 6.0, 3.7 and 4.3 mmol of N_2, EtOH and MeOH, respectively, were adsorbed per 1.0 g of anhydrous sample at a pressure of $0.8\,P_0$. Moreover, adsorption and desorption experiments with MeOH trace the same isotherms, which indicates that the channel structure is retained through this process. Thus, these isotherms are of type **1** according to the IUPAC classification.[11]

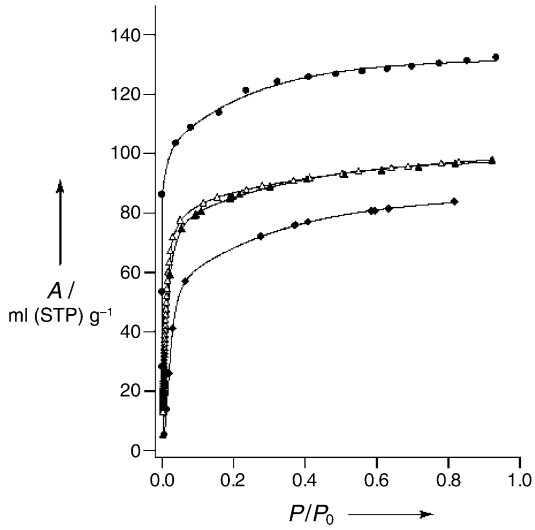


Figure 3. Isomers for the adsorption of N_2 (●) at 77 K and, EtOH (◆) and MeOH (▲) and desortion of MeOH (Δ) on **2** at 298 K. (A = absolute adsorption; STP = standard temperature and pressure).

In conclusion, we have successfully constructed a 3D Cu^{II} coordination polymer with 1D channels by using a unique bulky bridging ligand and the key point for the synthetic procedures has been well established. The structure of this complex provides the first two-fold interpenetrating NbO-type network and this result shows that interpenetration is possible for this network topology. The porous properties have been studied and we expect that this coordination polymer will find applications such as in gas separation.

Experimental Section

Synthesis of **2**: $Cu(NO_3)_2{\cdot}3H_2O$ (245 mg, 1 mmol) was added to a stirring colorless solution of HL (224 mg, 1 mmol) dissolved in MeOH (100 mL) in the presence of excess Et_3N. After a few minutes, the solution was then filtered and left to stand at room temperature. Black crystals of **2** suitable for X-ray analysis were obtained after several days in about 50 % yield. Elemental analysis calcd (%) for **2**: C 55.90, H 3.44, N 4.35; found: C 51.44, H 3.77, N 3.95. IR (KBr pellet): $\tilde{\nu}$ = 3415s, 2359w, 1615s, 1474w, 1386m, 1321m, 766m, 645m cm^{-1}.

Single-crystal X-ray structure determination on **2**: The data were collected at 298(2) K on a Rigaku mercury CCD diffractometer with graphite-monochromated Mo-K_α radiation. The structure was solved by direct methods by using SHELXS-97 and extended by using Fourier techniques. Crystal data: $C_{60}H_{44}Cu_4N_4O_{13.38}$, M_r = 1289.15, rhombohedral, space group $R\bar{3}$, $a = b = 53.643(7)$ Å, c = 11.920(10) Å, V = 29706(24) $Å^3$, Z = 18, μ = 13.30 cm^{-1}, ρ_{cald} =

 © 2004 Wiley-VCH Verlag GmbH & Co. KGaA, Weinheim

1.297 g cm^{-3}, $\lambda(Mo_{K\alpha}) = 0.71073$ Å, GOF = 1.157, $R1$ ($wR2$) = 0.0709 (0.1934) [10484 observed ($I > 2\sigma(I)$)] for 12944 ($R_{int} = 0.0973$) independent reflections out of a total of 51565 reflections with 761 parameters. CCDC-210834 (**2**) contains the supplementary crystallographic data for this paper. These data can be obtained free of charge via www.ccdc.cam.ac.uk/conts/retrieving.html (or from the Cambridge Crystallographic Data Centre, 12 Union Road, Cambridge CB2 1EZ, UK; fax: (+44) 1223-336-033; or deposit@ccdc.cam.ac.uk).

Gas adsorption measurements: The sorption isotherm measurements of nitrogen and alcohol (MeOH and EtOH) were performed at 77 and 298 K, respectively, by using BELSORP18 (BEL inc) automatic volumetric adsorption equipment. A known weight (100–200 mg) of the as-synthesized sample was placed in the quartz tube, then, prior to measurements, the sample was dried under high vacuum at 373 K for 10 h to remove the solvated water molecules. The adsorbate was dosed into the sample tube, then the change of the pressure was monitored and the amount of adsorption was determined by decrease in pressure at the equilibrium state.

Received: June 2, 2003 [Z52024]

Keywords: carboxylate ligands · coordination polymers · copper · microporous materials · N ligands

[1] For recent reviews, see: a) O. R. Evans, W. Lin, *Acc. Chem. Res.* **2002**, *35*, 511; b) L. H. Gade, *Acc. Chem. Res.* **2002**, *35*, 575; c) B. Moulton, M. J. Zaworotko, *Chem. Rev.* **2001**, *101*, 1629; d) M. Eddaoudi, D. B. Moler, H. Li, B. Chen, T. M. Reineke, M. O'Keeffe, O. M. Yaghi, *Acc. Chem. Res.* **2001**, *34*, 319; e) D. Braga, *J. Chem. Soc. Dalton Trans.* **2000**, 3705; f) R. Robson, *J. Chem. Soc. Dalton Trans.* **2000**, 3735; g) C. Piguet, J.-C. G. Bünzli, *Chem. Soc. Rev.* **1999**, *28*, 347; h) A. J. Blake, N. R. Champness, P. Hubberstey, W.-S. Li, M. A. Withersby, M. Schröder, *Coord. Chem. Rev.* **1999**, *183*, 117.

[2] For examples: a) G. J. Halder, C. J. Kepert, B. Moubaraki, K. S. Murray, J. D. Cashion, *Science* **2002**, *298*, 1762; b) R. Kitaura, S. Kitagawa, Y. Kubota, T. C. Kobayashi, K. Kindo, Y. Mita, A. Matsuo, M. Kobayashi, H.-C. Chang, T. C. Ozawa, M. Suzuki, M. Sakata, M. Takata, *Science* **2002**, *298*, 2358; c) M. Oh, G. B. Carpenter, D. A. Sweigart, *Angew. Chem.* **2003**, *115*, 2072; *Angew. Chem. Int. Ed.* **2003**, *42*, 2026; d) H. Zhao, M. J. Bazile, Jr., J. R. Galán-Mascarós, K. R. Dunbar, *Angew. Chem.* **2003**, *115*, 1045; *Angew. Chem. Int. Ed.* **2003**, *42*, 1015; e) L. Pan, H. Liu, X. Lei, X. Huang, D. H. Olson, N. J. Turro, J. Li, *Angew. Chem.* **2003**, *115*, 560; *Angew. Chem. Int. Ed.* **2003**, *42*, 542; f) L. Carlucci, G. Ciani, D. M. Proserpio, F. Porta, *Angew. Chem.* **2003**, *115*, 331; *Angew. Chem. Int. Ed.* **2003**, *42*, 317; g) M. Eddaoudi, J. Kim, M. O'Keeffe, O. M. Yaghi, *J. Am. Chem. Soc.* **2002**, *124*, 376; h) E. Lee, J. Kim, J. Heo, D. Whang, K. Kim, *Angew. Chem.* **2001**, *113*, 413; *Angew. Chem. Int. Ed.* **2001**, *40*, 399; i) X.-H. Bu, W. Chen, S.-L. Lu, R.-H. Zhang, D.-Z. Liao, W.-M. Bu, M. Shionoya, F. Brisse, J. Ribas, *Angew. Chem.* **2001**, *113*, 3301; *Angew. Chem. Int. Ed.* **2001**, *40*, 3201; j) T. J. Prior, D. Bradshaw, S. J. Teat, M. J. Rosseinsky, *Chem. Commun.* **2003**, 500.

[3] a) Y. Cui, S. J. Lee, W. Lin, *J. Am. Chem. Soc.* **2003**, *125*, 6014; b) O. R. Evans, H. L. Ngo, W. Lin, *J. Am. Chem. Soc.* **2001**, *123*, 10395; c) G. J. E. Davidson, S. J. Loeb, *Angew. Chem.* **2003**, *115*, 78; *Angew. Chem. Int. Ed.* **2003**, *42*, 74; d) S. Masaoka, S. Furukawa, H.-C. Chang, T. Mizutani, S. Kitagawa, *Angew. Chem.* **2001**, *113*, 3933; *Angew. Chem. Int. Ed.* **2001**, *40*, 3817.

[4] For recent examples: a) O. R. Evans, R.-G. Xiong, Z. Wang, G. K. Wong, W. Lin, *Angew. Chem.* **1999**, *111*, 557; *Angew. Chem. Int. Ed.* **1999**, *38*, 536; b) K. S. Min, M. P. Suh, *Eur. J. Inorg. Chem.* **2001**, 449; c) M. E. Chapman, P. Ayyappan, B. M. Foxman, G. Y. Yee, W. Lin, *Cryst. Growth Des.* **2001**, *1*, 159; d) L. R. MacGillivray, R. H. Groeneman, J. L. Atwood, *J. Am. Chem. Soc.* **1998**, *120*, 2676; e) J. Y. Lu, A. M. Babb, *Chem. Commun.* **2001**, 821; **2002**, 1340; f) R. Gheorghe, M. Andruh, A. Müller, M. Schmidtmann, *Inorg. Chem.* **2002**, *41*, 5314; g) S.-i. Noro, S. Kitagawa, M. Yamashita, T. Wada, *CrystEngComm* **2002**, *4*, 162.

[5] Crystal data: a) The dinuclear complex: $C_{58}H_{40}Cu_2N_4O_{10}$, $M_r = 1080.02$, triclinic, space group $P\bar{1}$, $a = 10.060(8)$ Å, $b = 10.676(8)$ Å, $c = 11.793(10)$ Å, $\alpha = 90.987(8)°$, $\beta = 110.288(11)°$, $\gamma = 94.560(9)°$, $V = 1182.9(16)$ Å^3, $Z = 1$, $\mu = 9.68$ cm^{-1}, $\rho_{cald} = 1.516$ g cm^{-3}, $\lambda(Mo_{K\alpha}) = 0.71073$ Å, GOF = 0.996, $R1$ ($wR2$) = 0.0506 (0.1288) [2667 observed ($I > 2\sigma(I)$)] for 3661 ($R_{int} = 0.0201$) independent reflections out of a total of 4129 reflections with 338 parameters; b) The trinuclear complex: $C_{90}H_{72}Cu_3N_6O_{18}$, $M_r = 1716.16$, cubic, space group $Pa\bar{3}$, $a = b = c = 19.990(2)$ Å, $V = 7988.0(14)$ Å^3, $Z = 4$, $\mu = 8.67$ cm^{-1}, $\rho_{cald} = 1.427$ g cm^{-3}, $\lambda(Mo_{K\alpha}) = 0.71073$ Å, GOF = 1.364, $R1$ ($wR2$) = 0.1129 (0.1996) [1941 observed ($I > 2\sigma(I)$)] for 2335 ($R_{int} = 0.1319$) independent reflections out of a total of 24814 reflections with 193 parameters. The data are not good enough due to the small size and poor quality of the crystal obtained. The data were collected at 298(2) K on a Rigaku mercury CCD diffractometer with graphite monochromated $Mo_{K\alpha}$ radiation. The structures were solved by direct method using SHELXS-97 and extended using Fourier techniques.

[6] M. O'Keeffe, M. Eddaoudi, H. Li, T. Reineke, O. M. Yaghi, *J. Solid State Chem.* **2000**, *152*, 3.

[7] a) O. D. Friedrichs, M. O'Keeffe, O. M. Yaghi, *Solid State Sci.* **2003**, *5*, 73; b) An earlier review on interpenetration (S. R. Batten, R. Robson, *Angew. Chem.* **1998**, *110*, 1558; *Angew. Chem. Int. Ed.* **1998**, *37*, 1460) incorrectly described the topology of the hydrogen bonded networks contained in the 1:1 cocrystal of cyanuric acid and biuret as being NbO-related, when in fact they have the $CdSO_4$ topology. Possibly as a result, a number of other papers have made the same error in topological assignment: c) K. N. Power, T. L. Hennigar, M. J. Zaworotko, *Chem. Commun.* **1998**, 595; d) S. S. Kuduva, D. C. Craig, A. Nangia, G. R. Desiraju, *J. Am. Chem. Soc.* **1999**, *121*, 1936; e) J. -H. Fournier, T. Maris, M. Simard, J. D. Wuest, *Cryst. Growth Des.* **2003**, *3*, 535. To our knowledge only a small number of non-interpenetrating NbO networks have been reported: f) T. Niu, X. Wang, A. J. Jacobson, *Angew. Chem.* **1999**, *111*, 2059; *Angew. Chem. Int. Ed.* **1999**, *38*, 1934; g) see ref. [8]. Since acceptance of this work for publication, another report of doubly interpenetrating networks has been published:B. Chen, F. R. Fronczek, A. W. Maverick, *Chem. Commun.* **2003**, 2166.

[8] M. Eddaoudi, J. Kim, M. O'Keeffe, O. M. Yaghi, *J. Am. Chem. Soc.* **2002**, *124*, 376.

[9] The exact number of water molecules in the crystallographic asymmetry unit cannot determined according to the Fourier electron-densities because of disorder.

[10] The accessible void volume was calculated with the program PLATON by using a probe with a radius of 1.2 Å. A. L. Spek, *Acta Crystallogr. Sect. A* **1990**, *46*, C34.

[11] IUPAC, *Pure. Appl. Chem.* **1985**, *57*, 603.

 © 2004 Wiley-VCH Verlag GmbH & Co. KGaA, Weinheim

Molecular Recognition

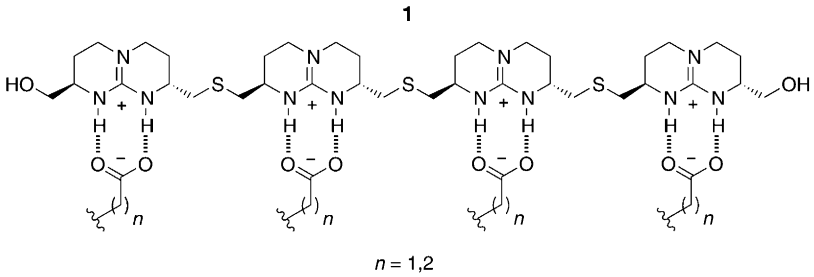
A Tetraguanidinium Ligand Binds to the Surface of the Tetramerization Domain of Protein P53**

*Xavier Salvatella, Marc Martinell, Margarida Gairí, Mauricio G. Mateu, Miguel Feliz, Andrew D. Hamilton, Javier de Mendoza, and Ernest Giralt**

Proteins often perform their functions as part of networks regulated by protein–protein interactions[1] and the design of specific inhibitors of these interactions will lead to new approaches for the treatment of important diseases.[2] However, the successful design of such binders to protein surface is difficult because of the physicochemical properties of protein–protein interfaces, which are very large, flat, and rich in well-solvated hydrophilic residues such as Asp, Glu, and Arg.[3] We showed previously that oligomers of chiral, bicyclic guanidines, which are known to interact effectively with anionic groups,[4] bind the surface of helical or partially helical tetraanionic peptides in alcoholic media.[5,6] We report herein that, in aqueous solution, the tetraguanidinium compound **1** (Scheme 1) binds to an anionic patch at the surface of the tetramerization domain of the tumor suppressor protein P53, a key therapeutic target for cancer treatment.[7]

The shape and charge complementarity of the helical secondary structures of tetraguanidinium compounds such as **1** with those of helical peptides containing four anionic residues at the *i* and *i*+3 relative positions enables these molecules to bind in 10% aqueous methanol.[5,6] To assess whether this supramolecular architecture can be applied to the recognition of such anionic sequences at the surface of a protein, we studied the binding of compound **1** with the tetramerization domain of P53. This particular domain was selected because it has two overlapping helical tetraanionic sequences on its surface, one formed by residues Glu336, Glu339, Glu343, and Glu346, and the other by Glu343, Glu346, Glu349, and Asp352 (Figure 1).[8] The main function of the tetramerization domain is to stabilize the overall structure of the protein. Since tetramerization is essential for P53 function,[7] small molecules that bind to this domain and affect its stability could potentially be used to modulate the antitumor activity of the protein.[9]

We examined this system by both chemical shift perturbation (CSP)[10] and saturation transfer difference (STD)



Scheme 1. Chemical structure of the tetraguanidinium ligand **1** and the model proposed for its interaction with aspartate ($n=1$) or glutamate ($n=2$) residues on peptide and protein surfaces.

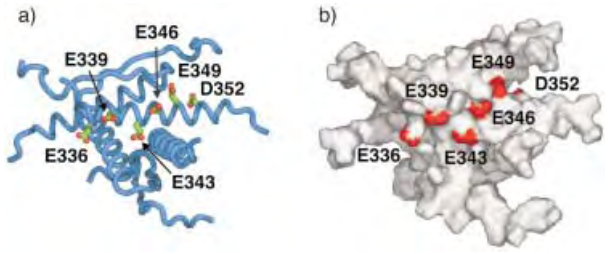


Figure 1. a) Ribbon representation of the tetramerization domain of protein P53.[8] For clarity, only the side chains of the residues Glu336, Glu339, Glu343, Glu346, Glu349, and Asp352 of one monomer are shown. b) Solvent-accessible surface of the domain. The surface corresponding to the side-chain oxygen atoms of the six anionic residues of one monomer is shown in red. The primary structure of the tetramerization domain in the region of interest (residues 335–355) is RERFEMFRELNEALELKDAQA.

[*] Dr. X. Salvatella,[+] M. Martinell, Prof. E. Giralt
Institut de Recerca Biomèdica de Barcelona
Parc Científic de Barcelona
Josep Samitier 1–5, 08028 Barcelona (Spain)
and
Departament de Química Orgànica
Universitat de Barcelona
Martí i Franqués 1–11, 08028 Barcelona (Spain)
Fax: (+34) 93-403-7126
E-mail: egiralt@pcb.ub.es
Dr. M. Gairí, Dr. M. Feliz
Servei de Ressonància Magnètica Nuclear
Serveis Cientificotècnics
Universitat de Barcelona
Josep Samitier 1–5, 08028 Barcelona (Spain)
Prof. M. G. Mateu
Centro de Biología Molecular
Universidad Autónoma de Madrid
Cantoblanco, 28049 Madrid (Spain)
Prof. A. D. Hamilton
Department of Chemistry, Yale University
P.O. Box 208107, New Haven, CT 06520 (USA)
Prof. J. de Mendoza
Departamento de Química Orgánica
Universidad Autónoma de Madrid
Cantoblanco, 28049 Madrid (Spain)
[+] Current address:
Chemical Laboratory, University of Cambridge
Lensfield Road, Cambridge CB2 1EW (UK)

[**] X.S. and M.M. acknowledge the Generalitat de Catalunya for a predoctoral fellowship. This work was partially supported by grants from the Ministerio de Ciencia y Technlogía-FEDER (Grant no. BIO2002-2301) and the Generalitat de Catalunya (Grup Consolidat 1999SGR0042 and Centre de Referència en Biotecnologia).

Supporting information for this article is available on the WWW under http://www.angewandte.org or from the author.

 © 2004 Wiley-VCH Verlag GmbH & Co. KGaA, Weinheim DOI: 10.1002/anie.200352115

spectroscopy[11,12] because these techniques use distinct physical mechanisms to report binding and provide complementary structural information about recognition. Binding was initially studied by comparing the [^{1}H,^{15}N]-HSQC spectrum of a ^{15}N-enriched sample of the P53 tetramerization domain with that of a second sample containing four equivalents of tetraguanidinium ligand **1** in addition to the ^{15}N-enriched protein domain. As shown in Figure 2, the binding of ligand **1** to the surface of the tetramerization domain caused significant changes in the ^{1}H and ^{15}N chemical shifts of residues Arg 337, Met 340, Leu 344, Ala 347, and Leu 350. To show that these changes were solely a result of the presence of ligand **1**, a solution of the P53 tetramerization domain was titrated with the ligand and the titration was monitored by [^{1}H,^{15}N]-HSQC spectroscopy. This titration afforded a dissociation constant of approximately 50 μM, which is similar to that for the binding of ligand **1** with shorter, flexible peptides in 10% aqueous methanol[6] and is particularly high given the more competitive conditions employed in the experiments described herein.

The highly efficient transfer of saturation within a macromolecular target–ligand complex is used in STD spectroscopy to selectively obtain the ^{1}H 1D spectrum of the ligand by recording the difference spectrum of a sample that also contains a substoichiometric amount of the macromolecular target.[11] Application of this technique to a solution of the P53 tetramerization domain and ligand **1** confirmed the results of the CSP experiment: the difference spectrum (Figure 3) shows signals from ligand **1** but the signals of a low-molecular-weight impurity cannot be observed, which demonstrates that ligand **1** is indeed bound to the surface of the domain.

STD spectroscopy can also be used to identify the functional groups of the ligand that interact with the macromolecular target through measurement of the relative saturation transferred to each proton.[12] As shown in Figure 3, the signals of higher normalized intensity in our system correspond to the protons closest to the binding site proposed in Scheme 1. The normalized intensity is maximal for the α_S protons, which are immediately adjacent to the nitrogen atoms involved in contacts with the anionic protein side chains. The intensity decreases gradually with increasing distance of the protons from the binding site (70% for protons CH_2S, 54% for protons β_S and 52% for protons γ_S).

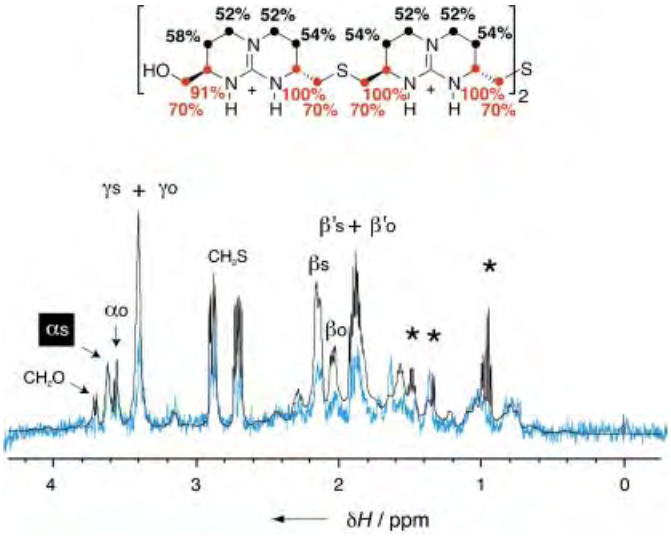


Figure 3. 1D ^{1}H spectrum of the sample used for the STD experiment (black) and its STD spectrum (blue). The relative saturation transferred to each proton is shown on the chemical structure of compound **1**. The color code used for the atoms of the ligand is based on a cut-off of 50% normalized saturation transfer. The signals labeled with * correspond to a low-molecular-weight impurity.

Although the chemical shift changes shown in Figure 2 are small, an analysis of the structural relationship between the residues whose chemical shifts change most significantly indicates that the anionic patch that interacts noncovalently with the tetraguanidinium ligand is most likely that formed by the four Glu side chains at positions 336, 339, 343, and 346 (Figure 4). These residues define a patch in which negative charges are placed at relative positions i, $i+3$, $i+7$, $i+10$ on the α helix. This pattern differs from the canonical i, $i+3$, $i+6$, $i+9$ arrangement that we showed to bind to the tetraguanidinium ligand in our previous work with tetraanionic peptides.[5,6] However, inspection of Figure 1 reveals that the anionic side chains of Glu 349 and particularly of Asp 352 at the C terminus of the canonical anionic patch are significantly less accessible than those of the first two residues of the noncanonical i,

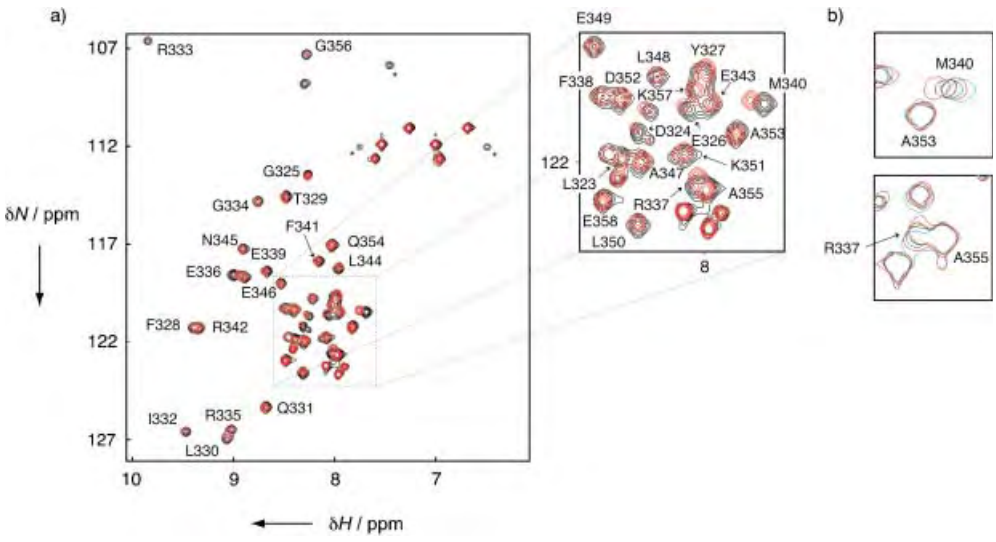


Figure 2. a) [^{1}H,^{15}N]-HSQC spectrum of the tetramerization domain of protein P53 in the absence (black contours) and in the presence (red contours) of ligand **1** (4 equiv). b) Titration results for residues Ala 353, Met 340, Arg 337, and Ala 355.

 © 2004 Wiley-VCH Verlag GmbH & Co. KGaA, Weinheim

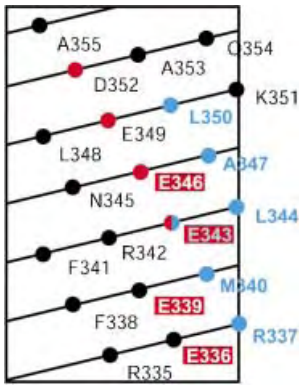


Figure 4. Projection of the surface defined by the helix (residues Ala 336 to Ala 355) of one of the monomers in the tetramerization domain of protein P53. Residues that form part of the canonical *i*, *i*+3, *i*+6, *i*+9 anionic patch are shown as red spheres, those which effectively bind the ligand are labeled with red boxes. The residues that experience the greatest changes in chemical shift upon binding of the protein to **1** are shown in blue.

i+3, *i*+7, *i*+10 patch (Glu 336 and 339). We showed in our previous study with tetraglutamate-containing peptides that the longer side chain of Glu, which has one more carbon atom than that of Asp, allows a significant increase in the plasticity of the tetraanionic binding site in terms of its secondary structure.[6] The results described herein indicate that the additional carbon atom in the Glu side chain may also allow significant relaxation of the topological constraints imposed by the *i*, *i*+3, *i*+6, *i*+9 interaction model. This apparent shift of the binding site highlights the importance of taking into account the plasticity of protein surfaces in the design of selective ligands, especially in cases such as this in which the binding motif is formed by long and flexible side chains.

In summary, the tetraguanidinium ligand **1** binds to an anionic patch on the surface of the P53 tetramerization domain with high affinity, as shown by CSP and STD spectroscopies. These results validate the structure-based approach to the design of nonpeptidic protein surface ligands that inhibit protein–protein interactions.

Received: June 11, 2003
Revised: October 2, 2003 [Z52115]

Keywords: host-guest systems · ligand design · molecular recognition · NMR spectroscopy · proteins

[1] H. Jeong, B. Tombor, R. Albert, Z. N. Oltval, A.-L. Barabási, *Nature* **2000**, *407*, 651 – 654.
[2] M. W. Peczuh, A. D. Hamilton, *Chem. Rev.* **2000**, *100*, 2479 – 2493.
[3] a) R. A. Laskowski, N. M. Luscombe, M. B. Swindells, J. M. Thornton, *Protein Sci.* **1996**, *5*, 2438 – 2452; b) F. B. Sheinerman, R. Norel, B. Hönig, *Curr. Opin. Struct. Biol.* **2000**, *10*, 153 – 159; c) W. L. DeLano, *Curr. Opin. Struct. Biol.* **2002**, *12*, 14 – 20.
[4] a) A. Echavarren, A. Galán, J.-M. Lehn, J. de Mendoza, *J. Am. Chem. Soc.* **1989**, *111*, 4994 – 4995; b) C. Seel, A. Galán, J. de Mendoza, *Top. Curr. Chem.* **1995**, *175*, 101 – 132; c) J. Sánchez-Quesada, C. Seel, P. Prados, J. de Mendoza, I. Dalcol, E. Giralt, *J. Am. Chem. Soc.* **1996**, *118*, 277 – 278; d) M. Berger, F. P. Schmidtchen, *J. Am. Chem. Soc.* **1999**, *121*, 9986 – 9993, and references cited therein.
[5] a) M. W. Peczuh, A. D. Hamilton, J. Sánchez-Quesada, J. de Mendoza, T. Haack, E. Giralt, *J. Am. Chem. Soc.* **1997**, *119*, 9327 – 9328; b) T. Haack, M. W. Peczuh, X. Salvatella, J. Sánchez-Quesada, J. de Mendoza, A. D. Hamilton, E. Giralt, *J. Am. Chem. Soc.* **1999**, *121*, 11813 – 11820; c) B. P. Orner, X. Salvatella, J. Sánchez-Quesada, J. de Mendoza, E. Giralt, A. D. Hamilton, *Angew. Chem.* **2002**, *114*, 125 – 127; *Angew. Chem. Int. Ed.* **2002**, *41*, 117 – 119.
[6] X. Salvatella, M. W. Peczuh, M. Gairí, R. K. Jain, J. Sánchez-Quesada, J. de Mendoza, A. D. Hamilton, E. Giralt, *Chem. Commun.* **2000**, 1399 – 1400.
[7] P. Chène, *Oncogene* **2001**, *20*, 2611 – 2617.
[8] G. M. Clore, J. Ernst, R. Clubb, J. G. Omichinski, W. M. P. Kennedy, K. Sakaguchi, E. Apella, A. M. Gronenborn, *Nat. Struct. Biol.* **1995**, *2*, 321 – 333.
[9] a) A. N. Bullock, A. R. Fersht, *Nat. Rev. Cancer* **2001**, *1*, 68 – 76; b) A. Friedler, L. O. Hansson, D. B. Veprintsev, S. M. V. Freund, T. M. Rippin, P. V. Nikolova, M. R. Proctor, S. Rüdiger, Alan R. Fersht, *Proc. Natl. Acad. Sci. USA* **2002**, *99*, 937 – 942.
[10] a) J. Kallen, C. Spitzfaden, M. G. M. Zurini, G. Wider, H. Widmer, K. Wüthrich, M. D. Walkinshaw, *Nature* **1991**, *353*, 276 – 279; b) P. J. Hajduk, R. P. Meadows, S. W. Fesik, *Science* **1997**, *278*, 497 – 499.
[11] a) M. Mayer, B. Meyer, *Angew. Chem.* **1999**, *111*, 1902 – 1906; *Angew. Chem. Int. Ed.* **1999**, *38*, 1784 – 1788; b) J. Klein, R. Meinecke, M. Mayer, B. Meyer, *J. Am. Chem. Soc.* **1999**, *121*, 5336 – 5337.
[12] M. Mayer, B. Meyer, *J. Am. Chem. Soc.* **2001**, *123*, 6108 – 6117.

 © 2004 Wiley-VCH Verlag GmbH & Co. KGaA, Weinheim

DNA on Gold Surfaces

Dynamics of Ordered-Domain Formation of DNA fragments on Au(111) with Molecular Resolution**

*Hainer Wackerbarth, Mikala Grubb, Jingdong Zhang, Allan G. Hansen, and Jens Ulstrup**

Molecular alignment or recognition between reacting biological molecules and macromolecules such as protein–protein and DNA–protein interactions, or DNA hybridization with electrostatic interactions as broadly controlling factors is

[*] Dr. H. Wackerbarth, M. Grubb, Dr. J. Zhang, Dr. A. G. Hansen, Prof. Dr. J. Ulstrup
Department of Chemistry, Building 207
Technical University of Denmark
2800 Lyngby (Denmark)
Fax: (+45) 4588-3136
E-mail: ju@kemi.dtu.dk

[**] Financial support from the Danish Technical Science Research Council is acknowledged. We also wish to acknowledge discussions with Dr. Richard J. Nichols, University of Liverpool and Rodolphe Marie, The Microelectronics Center, Technical University of Denmark.

Supporting information for this article is available on the WWW under http://www.angewandte.org or from the author.

 © 2004 Wiley-VCH Verlag GmbH & Co. KGaA, Weinheim DOI: 10.1002/anie.200352146

crucial both in natural biological processes and in biotechnological applications. This applies for example, to DNA-based biosensors, in which subtle control of probe immobilization is required to ensure suitable adsorbate oligonucleotide orientation and accessibility of complementary strands or other substrate molecules.[1] Electric fields caused by an electrochemical electrode in contact with the natural aqueous buffer media here offer a highly convenient tool.

However, efforts in DNA-based biosensor technology towards the nanoscale and single-molecule levels require: first that single-crystal, atomically planar electrode surfaces be the environment for biomolecular function. Second, chemical linking and some degree of supramolecular order must prevail, otherwise adsorbate structures are too conformationally labile for functional biomolecules to be imaged.[2,3] We have previously exploited the high sensitivity of single-crystal electrochemistry and the high resolution of scanning tunneling microscopy directly in aqueous buffer (in situ STM) to study assembled monolayers of several proteins.[2–6] These combined techniques disclosed dense monolayers of the proteins, which could be structurally mapped to single-molecule resolution in their full functional state. Herein, we report that single-crystal electrochemistry and in situ STM are introduced to characterize surface-bound thiol-modified short oligonucleotides. We have focused on single-strand oligonucleotides with ten adenine nucleobases (HS-10A) and with a single adenine base (HS-A) to which a hexamethylene thiol linker is covalently attached at the 5′-end. The oligonucleotide strand is short enough that details about interfacial structural and dynamic behavior can be obtained compared with the complex macromolecular structure of longer DNA-fragments. The strand is, however, long enough to offer insight into oligonucleotide collective properties and novel structural features compared with single-nucleotide bases.

The oligo- or mononucleotide was first adsorbed at open circuit potential by immersing the electrodes into the appropriate solution. Figure 1 A shows cyclic voltammograms (CV) of HS-10A and HS-A in the potential range from $+0.6$ to -0.9 V. All potentials are referenced to saturated calomel electrode (SCE). HS-10A (a) and HS-A (b) show a dominant peak at -0.671 V and -0.675 V, respectively. The latter peak has a shoulder at the negative side of the peak potential, which is also sometimes observed for HS-10A. With reference to the in situ STM data (see below) the shoulder can be assigned to the coexistence of ordered adsorbate domains separated by regions of disordered adsorption of variable abundance. We have also recently observed such a pattern for *N*-phenyl-mercaptoacetamide disulfide on Au(111).[4] Figure 1 B shows three consecutive scans of HS-10A. The -0.671 V peak has almost disappeared in the second and completely in the third scan. The data in Figure 1 point unambiguously to the strong -0.671 V peak being caused by reductive desorption of HS-10A, that is, a one-electron reduction of the Au–S bond and release of the adsorbed molecules.[7a] The formation of the Au–S bond is confirmed by X-ray photoelectron spectroscopy (XPS; see Supporting Information). The coverage of the thiol-linked oligonucleotide can be determined from the Faradaic charge associated

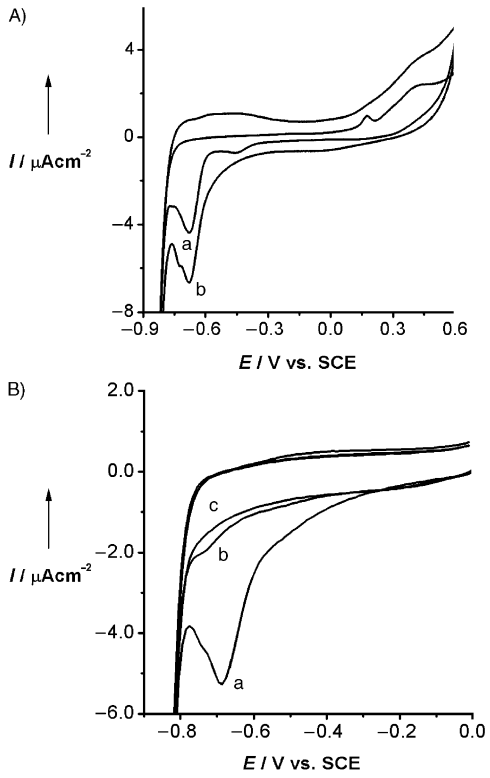


Figure 1. Cyclic voltammetry of reductive desorption in 0.1 M phosphate, pH 6.9. Scan rate 10 $mV s^{-1}$. (A) CV of HS-10A (a) and HS-A (b) adsorbed on Au(111). (B) First scan (a), second scan (b), and the third scan (c) of HS-10A reflect the desorption of the molecules from the surface.

with the voltammetric peak. Peak integration gives 27 ± 5 and 28 ± 4 $\mu C cm^{-2}$ for HS-10A and HS-A, respectively.

The reductive-current peak of organic-thiol layers has two components. The dominant component stems from interfacial charge transfer from the electrode to chemisorbed thiolate, but there is also a capacitive component caused by the formation of the aqueous double layer on the uncoated gold surface after thiol desorption.[7b,c] The non-Faradaic contribution can be estimated to be 1.9 $\mu C cm^{-2}$ for HS-10A by interfacial capacitance data (see Supporting Information). Hence, the resulting coverage is 260 ± 60 $pmol cm^{-2}$. The coverage is significantly higher than values reported by Tarlov and co-workers for longer single- and double-strand (25 bases or base pairs), who found coverages in the range 10–90 $pmol cm^{-2}$, and by Demers et al., who found values of ≈ 20 $pmol cm^{-2}$ for 12-base oligonucleotides.[1,8,9] The coverage is, however, determined by a variety of different parameters such as adsorption time, ionic strength, oligonucleotide length and base sequence, and electrode surface morphology. The research groups of Tarlov and Demers used Au-film substrates treated by "piranha solution", which is known to give a surface morphology quite different from the atomically planar Au(111) surface used in this work. A thiol-modified single-stranded oligonucleotide with 25 bases on Au(111)-surface gives similar coverages as HS-10A (unpublished results). The corresponding double-stranded oligonucleotide also provides a high coverage, which is in accordance with the coverage reported by Kelly et al.[10] We have focused

 © 2004 Wiley-VCH Verlag GmbH & Co. KGaA, Weinheim

on the oligonucleotide adsorption features on a well-defined Au(111) electrode surface and the effect of the electrode polarization on the adsorbate structural organization.

A simple estimate shows that densely packed oligonucleotides in an upright or tilted position, based on the assumption that a cylindrical geometry with a diameter of 10 Å gives a coverage very close to 210 pmol cm^{-2}. Recumbent or flat-lying oligonucleotides give significantly lower coverages, that is, between 40 and 80 pmol cm^{-2}. In an upright/tilted position the coverage would, moreover, be little affected by the number of adenines. The almost identical charges determined from reductive desorption of the gold–sulfur bond for HS-A and HS-10A therefore substantiate an upright or tilted position of the adsorbates, bound to the surface solely by the thiol-linker group.

In situ STM images show the electronic structure and electronic conductivity of the adsorbates.[5,11] The properties are also controlled by the molecular-adsorbate conformation. Packing constraints in the adlayer can, for example, impose molecular conformations with poor electronic conductivity unfavorable for in situ STM imaging.[12] Reliable imaging also requires that environmental conditions for the formation of monolayers of some lateral order are defined. Spatial constraint of the conformationally labile adsorbate molecules packed into dense, closely spaced layers or domains with long-range order by collective lateral interactions is hence essential for robust high-resolution imaging.

Figure 2 shows two representative in situ STM images of HS-10A adsorbed at open circuit potential on a Au(111)-electrode surface in contact with aqueous buffer. The open-circuit potential was measured to be 0.19 V. Extensive oligonucleotide adsorption is clearly apparent but with little or no long-range structural order at the sample potential −0.21 V (Figure 2A). Clearly ordered domains, however, appear when the sample potential for the same sample is lowered in situ to −0.61 V, Figure 2B. The sample electrochemical potential is thus a crucial determining factor in the adsorption dynamics and the resulting supramolecular two-dimensional HS-10A adsorbate organization on the Au(111)-surface.

Figure 3 shows high-resolution in situ STM images of other features of HS-10A domains adsorbed under potential control at −0.61 V and recorded at −0.21 V, still significantly lower than the open circuit potential. The character of the observed domains is unchanged in the potential range from −0.61 to −0.21 V but a better quality image is achieved at −0.21 V. A further increase to slightly positive potentials results in the slow disappearance of the domains leaving the adlayer in an entirely disordered state but with the same high overall coverage as in the ordered domains. When the potential was set back to −0.61 V, an ordered structure was reconstituted, thus demonstrating the reversibility of the potential-induced domain formation. Figure 3A shows long-range adsorbate order and pits typical for adsorbed organic-thiolate layers on Au(111) surfaces located at the domain boundary regions. The domains are oriented with an angle of almost 60° to each other and follow the triangular Au(111) structure, which is clearly seen underneath the adsorbate layer. The high resolution in Figure 3B displays bright spots organized in rows with lower contrast in between. The

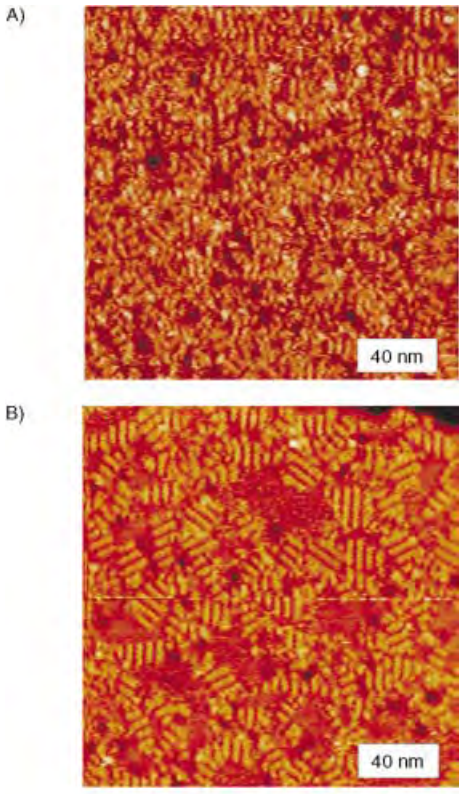


Figure 2. In situ STM images of HS-10A in 0.01 M phosphate buffer, pH 7.1, recorded in the constant-current mode, tunneling current 0.5 nA and bias voltage −0.15 V. The oligonucleotide was adsorbed under open circuit potential and scanned at the sample potential −0.21 V versus SCE. (A) By decreasing the sample potential to −0.61 V versus SCE (B) domain formation, displayed by areas with ordered structure, was observed.

distance between the spots along a row is about 5 Å and the spacing between the spots in parallel rows is 11 Å. This is clearly reflected by the height profiles along and orthogonal to the rows (Figure 3B insets). The rows form a $(\sqrt{3}\times 4)$R30° surface lattice, with a total coverage of 288 pmol cm^{-2}.[13] This is close to the coverage of 260 ± 60 pmol cm^{-2} determined by CV, especially in view that the coverage calculated from the surface lattice represents only the ordered structure inside the domains (50 nm^2 compared to the electrode surface 0.2 cm^2) and not the inter-domain region, pits, steps, and disordered areas. The close values of the coverage obtained by CV and in situ STM thus point to the overall highly uniform character of the electrode surface. The highly ordered-surface lattice of HS-10A was not observed for thiol-free 10-A oligonucleotide adsorption under electrochemical potential control. This emphasizes the fundamentally different adsorption modes for thiolated and thiol-free 10-A oligonucleotide forms.

The length of possible flat-lying oligonucleotides on the surface would affect the formation of the domains. The HS-A nucleotide adlayer was, therefore, also mapped by in situ STM. Potential-controlled adsorption of HS-A showed clearly ordered domains with the same $(\sqrt{3}\times 4)$R30° surface lattice as HS-10A (see Supporting Information). The same surface lattice for the thiolated mono- and oligonucleotide

 © 2004 Wiley-VCH Verlag GmbH & Co. KGaA, Weinheim

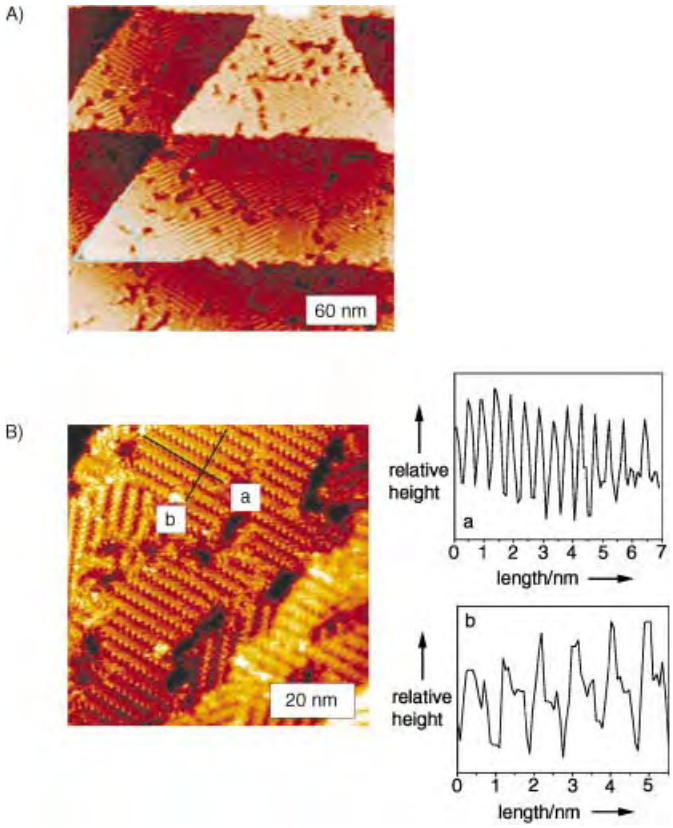
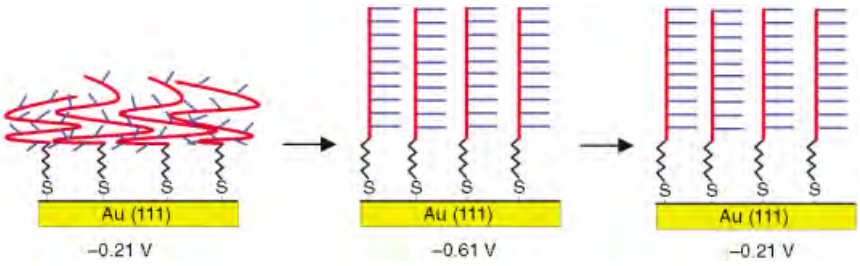


Figure 3. In situ STM images of HS-10A in 0.01 M phosphate buffer, pH 7.1, obtained in constant-current mode. The HS-10A layer was assembled at −0.61 V and scanned at −0.21 V sample potential versus SCE. The bias voltage was −0.15 V. A) The oligonucleotide adlayer follows the triangular Au(111) structure underneath (angle is indicated in blue), scan area 60×60 nm^2, tunneling current 0.3 nA. B) The bright spots represent single oligonucleotide molecular units, scan area 20×20 nm^2, tunneling current 0.8 nA. Relative height profiles along the lines a and b indicated in the image.[14]

can best be explained by perpendicular or tilted adsorption of both adsorbates, which are attached to the electrode surface solely through the thiol linker. The bright spots are likely to represent thiolate adsorbed on three-fold hollow sites, that is, in the "hole" between three adjacent surface Au-atoms. These holes are better conducting sites for STM for adsorbed thiolate than bridge states, that is, bridge sites between a pair of neighboring Au-atoms. The weaker contrasts represent the nucleotide part but the similarity between HS-10A and HS-A could imply that only residues close to the thiolate group are monitored.

Taken together the voltammetric data and the in situ STM images point unambiguously to a densely packed adlayer for thiolated mono- and oligonucleotides, linked to the gold surface solely through the thiol group. The organization of the oligonucleotides can be illustrated by the Scheme 1. Capacitance data suggest that the potential of zero charge of the Au(111)-electrode in 0.1M phosphate solution is about 0.3 V (see Supporting Information). Oligonucleotide adsorption either at the open-circuit potential or at controlled, more negative potentials is thus at a negatively charged electrode surface. Specific adsorption by thiolate linking is then likely to be favored over nonspecific adsorption because of electrostatic repulsion of the negatively charged oligonucleotide backbone from the electrode surface. Densely packed monolayers of HS-10A or HS-A with the 10-A backbone oriented towards the solution, which are not in direct contact with the Au(111)-surface are therefore expected, but the solvent-exposed backbone would still be disordered in random conformations close to the potential of zero charge. The electrochemical potential shifts to more negative values, thus increasing the electric field in the interfacial region. This would, first, push the oligonucleotide backbone further into the solution, and second, induce conversion from the coiled conformation towards an extended, more upright conformation. A potential-dependent orientation of thiol-modified double-stranded oligonucleotides has also been shown by electrochemical-potential-controlled atomic force microscopy.[15] In either case the intermolecular electrostatic repulsion between the strongly charged oligonucleotide anions would be screened by a network of counter ions, which can even be expected to stabilize the domain formation, analogous to cation-induced DNA aggregation (see below).[16] The strong collective intermolecular interaction would also induce Au–S bond breaking and reformation during the domain-ordering process. This would most likely involve Au–S bond labilization and some degree of adsorbate surface diffusion. The energies of the electrostatic backbone repulsion from the surface and the surface diffusion are comparable and would roughly cancel out each other.

Several other effects would reinforce this conversion. One is exposure of the negatively charged backbone phosphate groups, with favored solvation compared to the coiled conformation. Another effect would be stabilization of the extended orientation by hydrophobic stacking or hydrogen bonding between the adenines. Both thermodynamics and kinetics of the folding of a single-strand polyadenine with 16 adenines and short complementary sequences at each end into a roughly circular molecular beacon was also recently found to show molecular rigidity originating from base stacking. The stacking energy corresponding to ten adenine



Scheme 1. Orientation of HS-10A oligonucleotide adsorbed in ordered domains on the Au(111)-electrode. Repulsion between the phosphate backbone and the highly negatively polarized surface forces the oligonucleotide into an extended position. Hydrophobic base stacking and lateral hydrogen bonding between neighboring units stabilize the adsorption mode of the extented HS-10A.

 © 2004 Wiley-VCH Verlag GmbH & Co. KGaA, Weinheim

bases comes close to the surface-diffusion activation energy and therefore contributes significantly to the ordering process. Similar folding of polythymine showed no rigidity.[17]

A mechanistic view of the disorder–order transition therefore emerges where the thiol-modified oligonucleotides are first adsorbed specifically at high surface coverage but in random conformations on the solution side. Stacking, hydrogen-bond formation, and other interactions favorable for ordered-domain formation are kinetically hindered in this state. Subsequent backbone repulsion at large negative potentials ushers the adsorbed oligonucleotides into extended conformations in which stacking and other lateral interactions are much less hindered, thus leading to facile domain formation. Electrostatic triggering by the electrode-surface charge is thus a key feature in maintaining the ordered-surface adsorbate domains.

The results reported are the first case for the formation of domains of specifically adsorbed thiol-modified oligonucleotides with long-range order mapped to single-molecule or higher resolution. The basis for this novel observation is the use of high-quality single-crystal electrode surfaces and electrochemical-potential control of the adsorption process. Previous reports have mostly been based on polycrystalline electrodes or etched gold films[1,10,18] giving rough surface morphologies that are hard to reproduce.[19] A study based on annealed commercial Au-films disclosed a dense monolayer but not domain formation nor single-molecule resolution.[15] These results add to evolving high-resolution DNA-related science and biotechnology towards the nanoscale and single-molecule levels.[20–22] Single-molecule, *ss*- and *ds*-oligonucleotide molecular electronic-conductivity mechanisms is immediately one such area. Two-dimensional or columnar DNA-based molecular aggregation induced by transition-metal complexes, presently in intense focus, is another area in which single-molecule resolution by the comprehensive approach suggested could be within reach.[16] Systematic extension to longer and variable-base composition would finally offer novel nanoscale biotechnological importance to single-molecule hybridization of immobilized DNA-based molecules. This approach requires, however, that studies of the specific adsorption mode and the long-range domain-order phenomenon observed for the simple repetitive 10A sequence be extended to variable-length and base-sequence oligonucleotides. The thiol-modified 25-base pair oligonucleotide from the breast-cancer-susceptibility gene (BRCA1) has been shown by single-crystal voltammetry and XPS to display the same high-coverage binding mode as the shorter HS-A and HS-10A oligonucleotides.[23] In situ STM of this sequence is, however, not presently available.

Experimental Section

Hexanesulfonyl mono- and oligonucleotides modified at the 5′ end were obtained from TAG Copenhagen. The sample quality was checked by matrix-assisted laser desorption ionization time-of flight (MALDI-TOF) mass spectroscopy. K_2HPO_4, and KH_2PO_4 were of "superpure" quality. Millipore water (Milli-Q-Housing) was used throughout.

Single-crystal gold electrodes for electrochemistry were prepared as bead electrodes by the method of Clavilier and Hamelin.[24a,b] The hanging meniscus method was used in voltammetric measurements. Cyclic voltammograms were recorded by using an Autolab system (Eco Chemie, The Netherlands). A coiled bright platinum wire and a saturated calomel electrode were used as counter and reference electrode, respectively. The medium was 0.1M K_2HPO_4/KH_2PO_4 buffer, pH 6.9. The solutions were deoxygenated by purging the solutions with purified argon prior to use and an argon atmosphere was maintained above the solutions during experimental recordings.

In situ STM was recorded by a PicoSPM instrument (Molecular Imaging Co., USA) with a bipotentiostat for independent control of substrate and tip potential, and of the in-house built three-electrode KEL-F cells. The constant-current mode was used. The substrate was a Au(111)-disc prepared and checked as previously reported.[25] Reference and counter electrodes were platinum wires. 0.01M phosphate (pH about 7.0) was supporting electrolyte. Tungsten tips were prepared and coated as previously.[25] The disc or bead electrodes were immersed in buffer solution, 0.01M K_2HPO_4/KH_2PO_4, pH 6.9, containing 1 μM oligonucleotide, and soaked for three to five hours at room temperature. After completion of the surface immobilization, the samples were thoroughly rinsed with Millipore water. Glassware and other utensils were cleaned as previously reported.[6]

Received: June 16, 2003
Revised: August 29, 2003 [Z52146]

Keywords: adsorption · electrochemistry · oligonucleotides · scanning probe microscopy · self-assembly

[1] T. M. Herne, M. J. Tarlov, *J. Am. Chem. Soc.* **1997**, *119*, 8916.
[2] A. G. Hansen, A. Boisen, J. U. Nielsen, H Wackerbarth, I. Chorkendorff, J. E. T. Andersen, J. Zhang, J. Ulstrup, *Langmuir* **2003**, *19*, 3419.
[3] Q. Chi, J. Zhang, J. U. Nielsen, E. P. Friis, I. Chorkendorff, G. W. Canters, J. E. T. Andersen, J. Ulstrup, *J. Am. Chem. Soc.* **2000**, *122*, 4047.
[4] J. Brask, H. Wackerbarth, K. J. Jensen, J. Zhang, I. Chorkendorff, J. Ulstrup, *J. Am. Chem. Soc.* **2003**, *125*, 94.
[5] J. Zhang, Q. Chi, A. M. Kuznetsov, A. G. Hansen, H. Wackerbarth, H. E. M. Christensen, J. E. T. Andersen, J. Ulstrup, *J. Phys. Chem. B* **2002**, *106*, 1131.
[6] Q. Chi, J. Zhang, E. P. Friis, J. E. T. Andersen, J. Ulstrup, *J. Electrochem. Commun.* **1999**, *1*, 91.
[7] a) D. F. Yang, C. P. Wilde, M. Morin, *Langmuir* **1996**, *12*, 6570; b) D. F. Yang, C. P. Wilde, M. Morin, *Langmuir* **1997**, *13*, 243; c) M. J. Esplandiu, H. Hagenström, D. M. Kolb, *Langmuir* **2001**, *17*, 828.
[8] S. Y. Petrovykh, H. Kimura-Suda, L. J. Whitman, M. J. Tarlov, *J. Am. Chem. Soc.* **2003**, *125*, 5219.
[9] L. M. Demers, C. A. Mirkin, R. c. Mucic, R. A. Reynolds, R. L. Letsinger, R. Elghanian, G. Viswanadham, *Anal. Chem.* **2000**, *72*, 5535.
[10] S. O. Kelley, N. M. Jackson, M. G. Hill, J. K. Barton, *Angew. Chem.* **1999**, *111*, 991; *Angew. Chem. Int. Ed.* **1999**, *38*, 941.
[11] C. L. Claypool, F. Faglioni, W. A. Goddard, H. B. Gray, N. S. Lewis, R. A. Marcus, *J. Phys Chem. B* **1997**, *101*, 5978.
[12] J. Zhang, Q. Chi, J. U. Nielsen, E. P. Friis, J. E. T. Andersen, J. Ulstrup, *Langmuir* **2000**, *16*, 7229.
[13] The $(\sqrt{3}\times 4)$R30° notion implies that the adsorbate molecules are organised in a rectangular unit cell in which each molecule is separated by four Au atoms along the atomic rows of the face-centered cubic Au(111)-lattice (4×2.885 Å $= 11.54$ Å), and by $\sqrt{3}$ times a Au-atom diameter perpendicular to this direction.
[14] The height profile is shown as relative apparent heights along and perpendicular to the atomic rows of the Au(111)-surface.

 © 2004 Wiley-VCH Verlag GmbH & Co. KGaA, Weinheim

The absolute heights can only be obtained subject to details of the interfacial electronic tunneling mechanisms.
[15] S. O. Kelley, J. K. Barton, N. M. Jackson, L. D. McPherson, A. B. Potter, E. M. Spain, M. J. Allen, M. G. Hill, *Langmuir*, **1998**, *14*, 6781.
[16] a) A. A. Kornyshev, S. Leikin, *Proc. Natl. Acad. Sci. USA* **1998**, *95*, 13579; b) A. A. Kornyshev, S. Leikin, *Phys. Rev. Lett.* **1999**, *82*, 4138; c) V. A. Bloomfield, *Curr. Opin. Struct. Biol.* **1996**, *6*, 334.
[17] N. L. Goddard, G. Bonnet, O. Krichevsky, A. Libchaber, *Phys. Rev. Lett.* **2000**, *85*, 2400.
[18] S. O. Kelley, J. K. Barton, *Bioconjugate Chem.* **1997**, *8*, 31.
[19] M. Twardowski, R. G. Nuzzo, *Langmuir* **2002**, *18*, 5529.
[20] R. F. Service, *Science* **1998**, *282*, 396.
[21] E. Southern, K. Mir, M. Shchepinov, *Nat. Genet.* **1999**, *21*, 5.
[22] L. Chen, K. A. Haushalter, C. M. Lieber, G. L. Verdine, *Chem. Biol.* **2002**, *9*, 345.
[23] H. Wackerbarth, M. Grubb, J. Zhang. A. G. Hansen, J. Ulstrup, unpublished results.
[24] a) J. Clavilier, R. Faure, G. Guinet, R. Durand, *J. Electroanal. Chem.* **1980**, *107*, 205; b) A. Hamelin, *J. Electroanal. Chem.* **1996**, *407*, 1.
[25] A. G. Hansen, Ph. D. thesis, Technical University of Denmark **2002**.

 © 2004 Wiley-VCH Verlag GmbH & Co. KGaA, Weinheim

Hybrid Silica

A Better Understanding of the Self-Structuration of Bridged Silsesquioxanes**

Joël J. E. Moreau, Benoît P. Pichon, Michel Wong Chi Man, Catherine Bied, Hans Pritzkow, Jean-Louis Bantignies, Philippe Dieudonné, and Jean-Louis Sauvajol*

Sol–gel chemistry represents an interesting field of research for designing hybrid organic–inorganic materials.[1–3] Solid materials with new properties have been prepared in this way and in this context, bridged silsesquioxanes[4,5] rapidly developed as potentially applicable hybrid materials in many areas of interest, such as in heterogeneous catalysis,[6,7] solid-phase extraction,[8] and nonlinear optics.[9] The challenge for materials chemists is to direct the organization of these solids for an optimal accessibility of the organic functionalities. In this currently expanding area, the surfactant-mediated route for the structuration of silica[10] has successfully been extended to bridged silsesquioxanes.[11] Periodic mesoporous hybrid silicas have been synthesized from silyl organics, $(RO)_3Si\text{-}R'\text{-}Si(OR)_3$ with R′ acting as organic bridging units. In all cases, external templating macromolecules or supramolecular assemblies were employed as the main structuring agent. Moreover, it has been shown that weak interactions between aromatic units in the solid could afford anisotropic nanostructured materials.[11a,12] We recently introduced a novel and general approach for the organization of these hybrids based on hydrogen-bonding interactions that are provided by urea groups within the organic bridging fragment.[13] We took advantage of the auto-association properties of these organic units to self-direct and structure the final solid material. Accordingly, we succeeded in preparing hybrids with interesting morphologies such as helical fibers,[13a] hollow tubes and spheres,[13b] and also layered sheets exhibiting long-distance ordered structure.[13c] It is interesting to note that in the absence of these self-associative groups, the hydrolysis and condensation of organotrialkoxysilanes always led to amorphous solid materials.[4,5] However, self-organized hybrids formed through a heterogeneous solid/liquid hydrolysis–condensation reaction.[13–15] The mechanism of the structuration of the solid and its relation to the nature of the supramolecular assemblies arising from the self-association of the molecular precursor was unclear.

On this basis, we explored the possibility of forming a soluble urea-derived molecule which could self-assemble and lead to an organized hybrid via a homogeneous hydrolysis–condensation reaction. In this paper, we describe the synthesis of a convenient soluble silylated diureidophenylene derivative and its conversion to a self-organized, ordered hybrid material in a homogeneous fashion.

Compound **1** was synthesized by the reaction of γ-isocyanatopropyltriethoxysilane with 1,4-diaminobenzene. When subjected to acid hydrolysis with HCl in a 1:1 volume mixture of THF and water, **1** completely dissolved, and after 0.5 h a white precipitate appeared. The mixture was kept under static conditions at 65 °C for 3.5 days to afford **BS1** (Scheme 1).

Elemental analysis and solid-state ^{13}C and ^{29}Si NMR studies showed that the solid material **BS1** consists of a highly condensed siloxane network with organic fragments covalently bonded to the silica network. The solid-state ^{29}Si NMR exhibits T^2 (≈55 %) and T^3 (≈45 %) units and no Q units, which indicates that approximately one uncondensed OH group per two silicon atoms remain in the solid network.

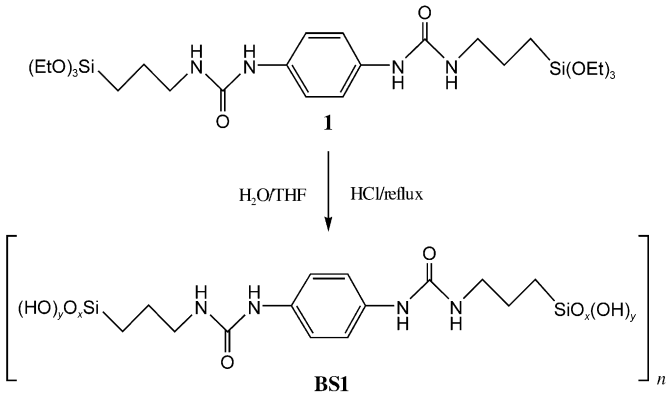
A scanning electron microscope (SEM) image shows **BS1** to consist of crystalline plates (Figure 1a; 1.5–-16 μm long, 0.5–3 μm wide and 70–120 nm thick), which is confirmed by the observed light extinction of the crystallites in optical polarized microscopy. Transmission electron microscope

[*] Prof. Dr. J. J. E. Moreau, Dipl. Arb. B. P. Pichon, Dr. M. Wong Chi Man, Dr. C. Bied
Hétérochimie Moléculaire et Macromoléculaire (UMR-CNRS 5076)
Ecole Nationale Supérieure de Chimie de Montpellier
8, rue de l'école normale, 34296 Montpellier cédex 5 (France)
Fax: (+33) 467-147-212
E-mail: jmoreau@cit.enscm.fr
Dr. H. Pritzkow
Anorganisch-Chemisches Institut, Universität Heidelberg
Im Neuenheimer Feld 270, 69120 Heidelberg (Germany)
Dr. J.-L. Bantignies, Dr. P. Dieudonné, Dr. J.-L. Sauvajol
Groupe de Dynamique des Phases Condensées (UMR-CNRS 5581)
Université de Montpellier II, Place Eugène Bataillon, 34095 Montpellier cédex 5 (France)

[**] We gratefully acknowledge the "Ministère de la Recherche de France" through the ACI 2002 Nanosciences-Nanotechnologies and the CNRS for financial supports. We thank Prof. Dr. Pierre Delord and Dr. Martin In for helpful discussions.

Supporting information for this article is available on the WWW under http://www.angewandte.org or from the author.

 DOI: 10.1002/anie.200352485 © 2004 Wiley-VCH Verlag GmbH & Co. KGaA, Weinheim



Scheme 1. Synthesis of compound **1** and of the lamellar-bridged silsesquioxane **BS1**.

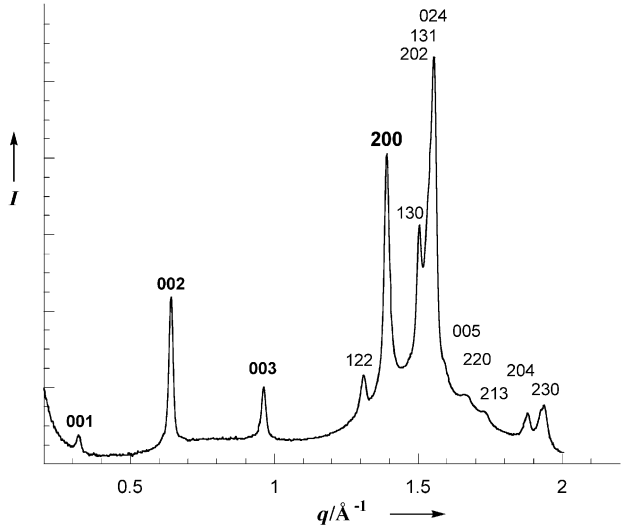


Figure 2. XRD profile of **BS1**.

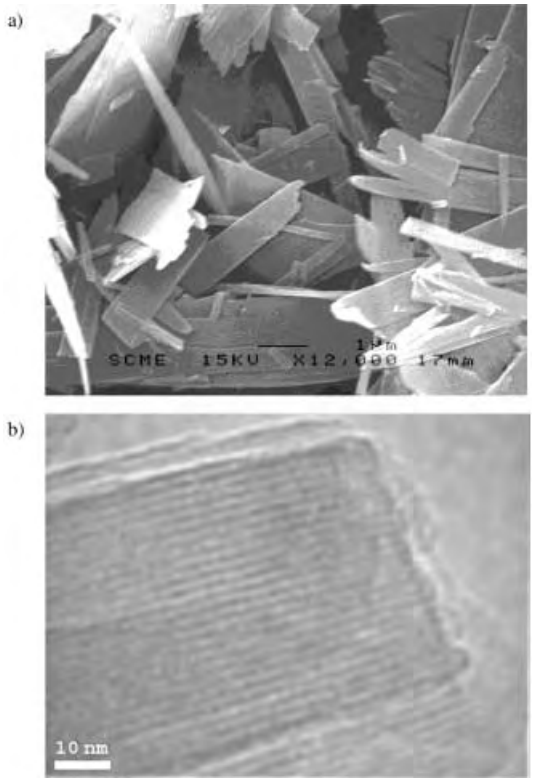


Figure 1. Electronic microscopy pictures of **BS1**; a) SEM image, and b) TEM image.

(TEM) analysis (Figure 1b) demonstrates the sheetlike structure of the solid with an interlamellar distance of ≈19.8 Å, which can be related to the length of the bridging organic unit as already reported for alkylene derivatives.[13c]

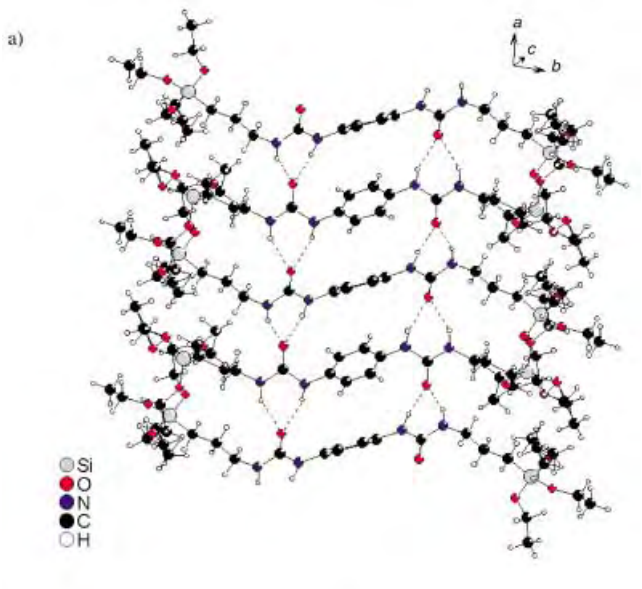
The X-ray powder diffraction pattern (XRD) of **BS1** exhibits sharp peaks that indicate a material with a long-range-ordered structure (Figure 2). Three orders of (00*l*) peaks are clearly assigned to the lamellar structure with *d* spacings (19.7 Å) in good agreement with the interlamellar distance observed from the TEM picture. This is the first time that a self-structured bridged silsesquioxane with long-range order is obtained in a homogeneous reaction from a solution of a completely dissolved molecular precursor. To clarify the mechanism of formation of the self-organized hybrids, we carried out a single-crystal X-ray structural study of **1**,[16] which allows an analysis of the organized hybrid **BS1** (Figure 3).

There are two independent centrosymmetric molecules in the cell, which are alternately bonded by intermolecular hydrogen bonds of the urea groups (N···O separations = 2.88–2.91 Å) forming sheets along the *a* axis (Figure 3a). The phenylene groups of neighboring molecules in the sheet are not coplanar (angle between the planes = 35.9°). The sheets adopt a herringbone packing motif in the direction of the *b* axis (Figure 3b).

The main observation that helps to interpret the lamellar structure of **BS1** is seen in Figure 3a: The intermolecular distance between two neighboring urea groups (4.5 Å) is consistent with the (200) peak found in the XRD profile of **BS1**. Taking into account the regular repetition of the two twisted phenylene units, a periodicity twice that length (9.0 Å) is observed and can clearly be assigned to hydrogen-bonding interactions between the urea groups.

We applied an X-ray profile-matching procedure (FullProf/WinPlotr software), to determine the structure of **BS1**. The results show that the diffraction spectrum of **BS1** fits with an orthorhombic crystal lattice with the following parameters: $a = 9.05$, $b = 14.06$, $c = 19.7$ Å. The *a* values are very close for both solids indicating that the periodicity in **1**, related to the hydrogen bonding between molecules, should be maintained in **BS1**. Moreover, the structure of **BS1** is characterized by a smaller volume than that of **1**. This is consistent with a closer packing of molecules in the *bc* plane with the loss of EtO groups by condensation and is presumably favored by siloxane-bond formation during polycondensation. The **BS1** lamellar distance observed across the crystal thickness in the TEM (Figure 1b) is of the same order of magnitude as *c*. This value appears to be associated to the lamellar character of this solid. These results indicate that the polycondensation of **1** in

 © 2004 Wiley-VCH Verlag GmbH & Co. KGaA, Weinheim



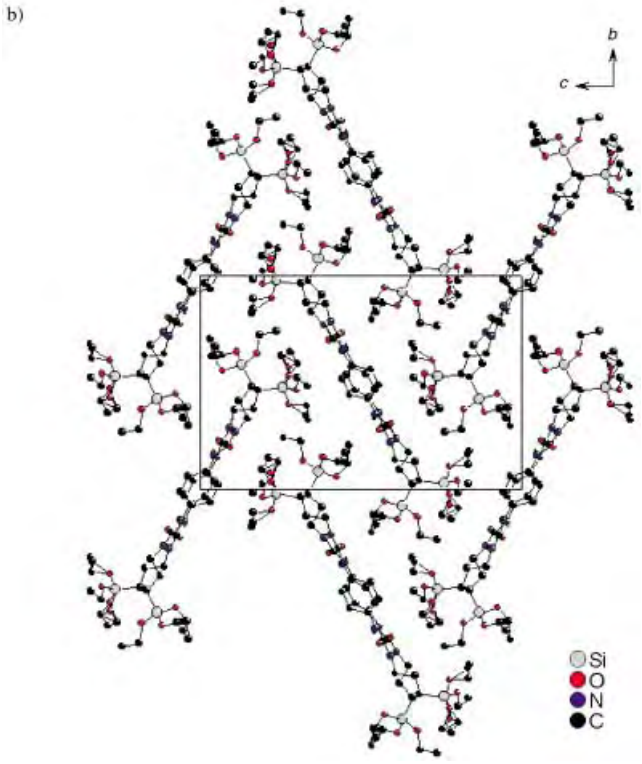


Figure 3. Single-crystal X-ray structure of **1**.

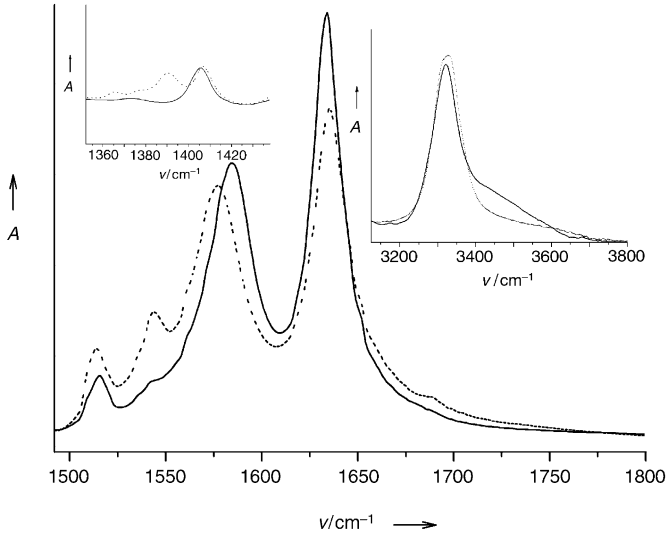


Figure 4. IR spectra of **1** (-----) and **BS1** (——).

THF/water induces the formation of a crystalline solid **BS1** with structural similarities which can be explained by the self-assembly of the molecules through hydrogen bonds for both cases.

The similarity of the structure of **1** with that of **BS1** can also be shown from their IR spectra (Figure 4). For comparison, they are normalized on one of the stretching ($\tilde{\nu}_{CC}$ = 1410 cm^{-1}) bands of the ring (left inset) as the number of rings is the same in both samples (note that the position of this band is the same for both compounds). Both samples are dominated by the amide modes, which are very sensitive to H-bonding (δ_{NH}, ν_{CO}, ν_{NH}).[17] The stretching frequencies ν_{CO} and ν_{NH}, centered at 1634 cm^{-1} and 3326 cm^{-1}, respectively, are at the same position for **1** and **BS1** (right inset) indicating that the strength of the H-bonding is similar. In contrast, the slight shift in the δ_{NH} mode around 1585 cm^{-1} is mainly related to structural differences between both samples.

Whereas in previous reports[13–15] organized solids were obtained upon hydrolysis of the precursor in the solid state, we have shown here for the first time that a highly crystalline hybrid material can be obtained upon hydrolysis of a completely solubilized precursor in solution. Its formation is due to the self-assembly properties of the molecular precursor, which direct the formation of the hybrid three-dimensional network. During the course of the reaction, the polycondensates organize via self-assembly of urea groups leading to a nanostructured hybrid material **BS1** in lamellar form. Relationships drawn from the single-crystal X-ray structural study of the crystalline molecular precursor allow significant progress in the interpretation of the structure of the resulting hybrid silica. The development of this method for the preparation of other hybrid silicas with new functionalities and targeted properties is currently in progress.

Experimental Section

1: 1,4-diaminobenzene (560 mg, 5.18 mmol) was dissolved in CH_2Cl_2 (40 mL) under a nitrogen atmosphere in a Schlenk tube. γ-Isocyanatopropyltriethoxysilane (2.69 mg, 10.9 mmol) was slowly added at room temperature and the mixture was stirred overnight. The solvent was evaporated and the white precipitate obtained was washed with pentane. The solution was filtered and the white solid was dried in vacuo.

Yield: 2.75 g, 88 %; m.p. 190 °C; IR ($CHCl_3$): $\tilde{\nu}$ = 1577(δ_{NH}), 1636 (ν_{CO}), 3322 cm^{-1} (ν_{NH}); ^{1}H NMR (200 MHz, $CDCl_3$, TMS): δ = 0.59 (t, 4H; CH_2Si), 1.20 (t, 9H; CH_3), 1.51 (qt, 4H; CH_2), 3.14 (m, 4H; NCH_2), 3.80 (qd, 12H; OCH_2), 6.44 (s, 4H; H_{ar}), 6.49 (m, 2H; NH), 7.60 ppm (m, 2H; NH); ^{13}C NMR (50 MHz, $CDCl_3$): δ = 7.8 (CH_2Si), 18.3 (CH_3), 23.8 (CH_2), 42.9 (CH_2N), 58.3 (CH_2O), 124.3 and 134.0

 © 2004 Wiley-VCH Verlag GmbH & Co. KGaA, Weinheim

(C_{ar}), 157.8 ppm (CO); ^{29}Si (50 MHz, $CDCl_3$): $\delta = -45.4$ ppm; MS (FAB): m/z (%): 602 (25) [M^+]; elemental analysis calcd (%) for $C_{26}H_{50}N_4O_8Si_2$: C 51.80, H 8.37, N 8.82; found: C 51.51, H 8.16, N 8.82.

BS1: Compound **1** (125 mg, 0.21 mmol) was dissolved in THF (1.4 mL) and water (1.4 mL) from which a white precipitate appeared. A solution of HCl (1M, 41.5 μL) was added and the mixture was heated to reflux. After 5 min complete solubilization was observed. Precipitation occurred after 0.5 h. The mixture was filtered after 3.5 days and the solid was washed with water and ethanol prior to vacuum drying for 12 h. **BS1** was obtained as a white powder. IR (KBr): $\tilde{\nu} = 1585$ (δ_{NH}), 1635 ($\tilde{\nu}_{CO}$) and 3329 cm^{-1} ($\tilde{\nu}_{NH}$); ^{13}C CPMAS NMR: $\delta = 13.8$, 25.0, 44.3, 125.3, 134.1, 158.6 ppm; ^{29}Si CPMAS NMR: $\delta = -57.1$, -66.2 ppm (T^2 and T^3 units).

Received: July 28, 2003 [Z52485]

Keywords: hydrogen bonds · nanostructures · organic–inorganic hybrid composites · self-assembly · silsesquioxanes

[1] C. Sanchez, F. Ribot, *New J. Chem.* **1994**, *18*, 1007 – 1047.
[2] D. Avnir, *Acc. Chem. Res.* **1995**, *28*, 328 – 334.
[3] a) *Organic/inorganic Hybrid Materials*, *MRS Symp. Vol. 628* (Eds.: R. M. Laine, C. Sanchez, C. J. Brinker, E. Giannelis), **2000**; b) *Organic/inorganic Hybrid Materials*, *MRS Symp. Vol. 726* (Eds.: R. M. Laine, C. Sanchez, C. J. Brinker, E. Giannelis), **2002.**
[4] K. J. Shea, D. A. Loy, O. W. Webster, *J. Am. Chem. Soc.* **1992**, *114*, 6700 – 6710.
[5] R. J. P. Corriu, J. J. E. Moreau, P. Thépot, M. Wong Chi Man, *Chem. Mater.* **1992**, *4*, 1217 – 1224.
[6] U. Schubert, *New J. Chem.* **1994**, *18*, 1049 – 1058.
[7] A. Adima, J. J. E. Moreau, M. Wong Chi Man, *Chirality* **2000**, *12*, 411 – 420.
[8] J.-C. Broudic, O. Conocar, J. J. E. Moreau, D. Meyer, M. Wong Chi Man, *J. Mater. Chem.* **1999**, *9*, 2283 – 2285.
[9] B. Lebeau, S. Brasselet, J. Zyss, C. Sanchez, *Chem. Mater.* **1997**, *9*, 1012 – 1021.
[10] C. T. Kresge, M. E. Leonowicz, W. J. Roth, J. C. Vartulli, J. S. Beck, *Nature* **1992**, *359*, 710 – 712.
[11] a) S. Inagaki, S. Guan, T. Ohsuna, O. Terasaki, *Nature* **2002**, *416*, 304 – 307; b) B. J. Melde, B. T. Holland, C. F. Blanford, A. Stein, *Chem. Mater.* **1999**, *11*, 3302 – 3308; c) T. Asefa, M. J. MacLachlan, N. Coombs, G. A. Ozin, *Nature* **1999**, *402*, 867 – 871; d) A. Sayari, S. Hamoudi, Y. Yang, I. L. Moudrakovski, J. R. Ripmeester, *Chem. Mater.* **2000**, *12*, 3857 – 3863; e) Y. Lu, H. Fan, N. Doke, D. A. Loy, R. A. Assink, D. A. LaVan, C. J. Brinker, *J. Am. Chem. Soc.* **2000**, *122*, 5258 – 5261.
[12] B. Boury, R. J. P. Corriu, *Chem. Commun.* **2002**, 795 – 802.
[13] a) J. J. E. Moreau, L. Vellutini, M. Wong Chi Man, C. Bied, *J. Am. Chem. Soc.* **2001**, *123*, 1509 – 1510; b) J. J. E. Moreau, L. Vellutini, M. Wong Chi Man, C. Bied, *Chem. Eur. J.* **2003**, *9*, 1594 – 1999; c) J. J. E. Moreau, L. Vellutini, M. Wong Chi Man, C. Bied, J.-L. Bantignies, P. Dieudonné, J.-L. Sauvajol, *J. Am. Chem. Soc.* **2001**, *123*, 7957 – 7958.
[14] a) N. Liu, K. Yu, B. Smarsly, D. R. Dunphy, Y.-B. Jiang, C. J. Brinker, *J. Am. Chem. Soc.* **2002**, *124*, 14540 – 14541; b) N. Liu, D. R. Dunphy, M. A. Rodriguez, S. Singer, C. J. Brinker, *Chem. Commun.* **2003**, 1144 – 1145.
[15] H. Muramatsu, R. J. P. Corriu, B. Boury, *J. Am. Chem. Soc.* **2003**, *125*, 854 – 855.
[16] Crystal data for **1**: $C_{26}H_{50}N_4O_8Si_2$, $M_r = 602.88$, monoclinic, $P2_1/n$, $a = 9.037(1)$, $b = 15.502(2)$, $c = 23.387(3)$ Å, $\beta = 92.837(2)°$, $V = 3272.4$ Å^3, $\rho_{calcd} = 1.224$ g cm^{-3}. Data collection: CCDarea detector, $Mo_{K\alpha}$ radiation, $T = -170\,°C$, 4690 unique reflections, 3362 observed ($I > 2\sigma 1$), $\Theta_{max} = 23.3°$. Structure solved by direct methods and refined by full-matrix least-squares on F^2 (SHELXTL NT 5.1, Bruker-AXS 1998), 405 parameters, $R1 = 0.085$, $wR2 = 0.187$, with disorder of some of the ethoxy groups. CCDC-215379 contains the supplementary crystallographic data for this paper. These data can be obtained free of charge via www.ccdc.cam.ac.uk/conts/retrieving.html (or from the Cambridge Crystallographic Data Centre, 12, Union Road, Cambridge CB2 1EZ, UK; fax: (+44) 1223-336-033; or deposit@ccdc.cam.ac.uk).
[17] G. Careri, U. Buontempo, F. Galluzzi, A. C. Scott, E. Gratton, E. Shyamsunder, *Phys. Rev. B* **1984**, *30*, 4689 – 4702.

 © 2004 Wiley-VCH Verlag GmbH & Co. KGaA, Weinheim

Copper Triazolate Networks

Two Unprecedented 3-Connected Three-Dimensional Networks of Copper(I) Triazolates: In Situ Formation of Ligands by Cycloaddition of Nitriles and Ammonia**

*Jie-Peng Zhang, Shao-Liang Zheng, Xiao-Chun Huang, and Xiao-Ming Chen**

Dedicated to Professor Hai-fu Fan on the occasion of his 70th birthday

Networked coordination polymers are of great current interest for potential applications as materials and because of their intriguing variety of architectures and new topologies.[1–3] It was suggested that, among numerous topological nets, the most important and plausible targets for designed synthesis are those with "simple, high-symmetry" structures.[4] However, only a very limited number of types of simple three-dimensional (3D) 3-connected[2] and 4-connected nets based solely on square-planar nodes, such as the cubic NbO ($6^4 8^2$),[3a,b] tetragonal $CdSO_4$ ($6^5 8$),[3c] "dense net" ($7^5 9$),[3d] and $4.4.8_4.8_4.8_8.8_8$[3e] nets have been reported so far, in contrast to the widely established 2D 3-connected honeycomb or brickwall (6^3) and 4-connected square grids (4^4).[1] Meanwhile, some 3-connected nets can be described as augmented 4-connected nets by substituting four adjacent 3-connected nodes for 4-connected nodes,[4,5] for example, 4.8^2 for 4^4, 4.12^2 for NbO ($6^4 8^2$), and 4.14^2 for diamond (6^6).[2c]

[*] J.-P. Zhang, Dr. S.-L. Zheng, X.-C. Huang, Prof. Dr. X.-M. Chen
School of Chemistry and Chemical Engineering
Sun Yat-Sen University
Guangzhou 510275 (China)
Fax: (+86) 20-8411-2245
E-mail: cescxm@zsu.edu.cn

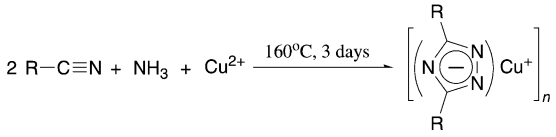
[**] This work was supported by NSFC (No. 20131020) and Ministry of Education of China via a Doctorate Program Fund (No. 20020558024) and a key project grant (No. 01134).

Supporting information for this article is available on the WWW under http://www.angewandte.org or from the author.

 © 2004 Wiley-VCH Verlag GmbH & Co. KGaA, Weinheim DOI: 10.1002/anie.200352627

On the other hand, novel coordination architectures with ligands generated in situ, (especially those that are inaccessible by direct preparation) are of great interest in coordination chemistry and organic chemistry for discovery of new organic reactions and understanding their mechanisms.[6–10] Nitriles are of major importance in the syntheses of many products by addition to the nitrile carbon atom, and such processes usually require activation of RCN, for example, by ligation of a metal. Some compounds not usually accessible by pure organic chemistry have been obtained by metal-mediated reactions such as cycloadditions of tetrazoles and oxadiazolines.[6–9]

In our continuing studies on hydrothermal ligand reactivity and new coordination architectures,[10] we established the hydrolysis of 1,10-phenanthroline (phen) to 1*H*-1,10-phenanthrolin-2-one in various copper complexes under hydrothermal conditions.[10a,b] We then carried out an analogous reaction using copper(II) nitrate, phen, ammonia, and acetonitrile, which yielded a small quantity of pale-yellow crystals of $[Cu(mtz)]_n$ (Hmtz = 3,5-dimethyl-1,2,4-triazole, **1**) and an unanalyzed mixture. As phen was not present in the product, we then used $Cu(OH)_2$ (or $Cu_2(OH)_2CO_3$), ammonia, and acetonitrile or butyronitrile to perform the reaction (Scheme 1) and obtained solid **1** or $[Cu(ptz)]_n$ (**2**) (Hptz = 3,5-



Scheme 1. Hydrothermal synthesis of **1** (R = Me) and **2** (R = *n*Pr).

dipropyl-1,2,4-triazole), respectively, in moderate yield (up to 40%). Similar reactions performed with nitriles bearing pyridyl and phenyl groups yielded copper(I) complexes of 3,5-dipyridyl- and 3,5-diphenyltriazolate.[11] The crystals of these compounds are stable toward air, and are insoluble in water and common organic solvents. However, their ready dissolution in aqueous HCl indicates that the triazole ligands can be liberated by acidification.

Based on the above observations, we suggest that the triazolates were derived from coupling of the nitriles and ammonia. The presence of Cu^I ions in the products indicates that Cu^{II} ions may act as an oxidant, in a similar manner as in our previous in situ hydrothermal reactions,[10] to assist the elimination of protons in the cycloaddition to give the final ligands. In contrast to the metal-mediated reductive coupling of nitriles to generate diimino-, enediimido-, or bis(imino)-amines, and the addition of two nitriles with another species to produce metallocycles, all of which have already been reported,[6,9] our one-pot, copper-mediated, hydrothermal reactions of nitriles and ammonia represent a novel, non-hydrazine synthetic route to 3,5-disubstituted 1,2,4-triazoles. 1,2,4-Triazole derivatives are of particular interest for their multifarious uses in agriculture, medicine, and industry. Continuous efforts have focused on the search for more efficient, simple, and green synthetic procedures for this useful class of heterocycles, although many methods have been known for decades. However, most 1,2,4-triazoles are still prepared by multistep procedures, which usually involve the use of hydrazine derivatives as starting materials or conversion of other ring systems.[12]

1,2,4-Triazoles are also unique ligands in coordination chemistry, especially in the synthesis of magnetic metal clusters, since they exhibit the coordination modes of both imidazoles and pyrazoles.[13] However, no crystal structure of a binary metal triazolate has been reported to date. Crystallographic studies on **1** and **2**[14] revealed that each triazolate binds in the μ_3-tridentate mode, and each Cu^I ion is coordinated in a trigonal-planar fashion (Cu···Cu 3.499(1) Å, Cu–N 1.963(1)–2.016(1) Å, and N-Cu-N 111.9(1)–134.3(1)° for **1**; Cu···Cu 3.422(1) Å, Cu–N 1.963(2)–1.973(3) Å, N-Cu-N 116.7(1)-121.6(1)° for **2**; see Supporting Information), and in each case a novel 3D 3-connected net results. A variety of intriguing 3D 3-connected nets were predicted by Wells decades ago,[5] but they have rarely been documented in coordination polymers.[2]

The framework of **1** consists of 1D helices in which the Cu^I ions are bridged by the triazolates in the imidazolate mode (Figure 1b). Each helical chain is further connected to four adjacent antiparallel chains through interchain Cu–N coordination bonds into a 3D net. The resulting 3-connected net (Figure 1a) for **1** can be symbolized as 4.8.16, which is unprecedented. This net is closely related to a series of other 3-connected nets such as 10^3-a, 10^3-d, 10^3-f, $8^2$10-a, $8^2$10-b, and 4.14^2, since they all can be projected as a planar 4.8^2 net, but differs in the arrangement and type of helices.[5] The network in **1** contains large 3D channels, which are fully occupied by an identical, translational net (see Supporting Information). A double-helical fragment (Figure 1c) of the entire structure may help to understand the interpenetration pattern in **1**. Note that the 4.8.16 net can be simplified as a $4.4.8_4.8_4.8_8.8_8$ net based on 4-connected square-planar nodes (see Supporting Information). In other words, the topology of **1** can also be rationalized as a 4-connected net by considering dimeric $\{Cu_2(mtz)_2\}$ subunits as 4-connected nodes. Of equal interest is that the 3-connected topological net in **2** exhibits a 4.12^2 net (Figure 2b) predicted by Wells,[5] which had also not yet been documented in coordination networks. The 4.12^2 net can also be simplified to an NbO net (Figure 2c) if each $\{Cu_2(ptz)_2\}$ subunit (Figure 2a) is considered as 4-connected node,[4] an example distinct from the rarely observed, true 4-connected NbO nets.[3a,b] Similar to other NbO nets, the network of **2** also contains channels, which are mainly occupied by the disordered propyl groups.

Very few 3D networks are based solely on square-planar nodes, since 2D square grids (4^4) are favored when square-planar building blocks self-assemble into extended structures.[1] The question arises why the similar dimeric building blocks in **1** and **2** extend not into a common 2D 4^4 net but into 3D $4.4.8_4.8_4.8_8.8_8$ and NbO nets. Examination of the related nets reveals differences in the dihedral angles between adjacent nodes in the networks based solely on square-planar nodes. These angles are all parallel for 4^4, all perpendicular for NbO, all acute for $4.4.8_4.8_4.8_8.8_8$, two parallel and two perpendicular for $CdSO_4$, and two parallel

 © 2004 Wiley-VCH Verlag GmbH & Co. KGaA, Weinheim

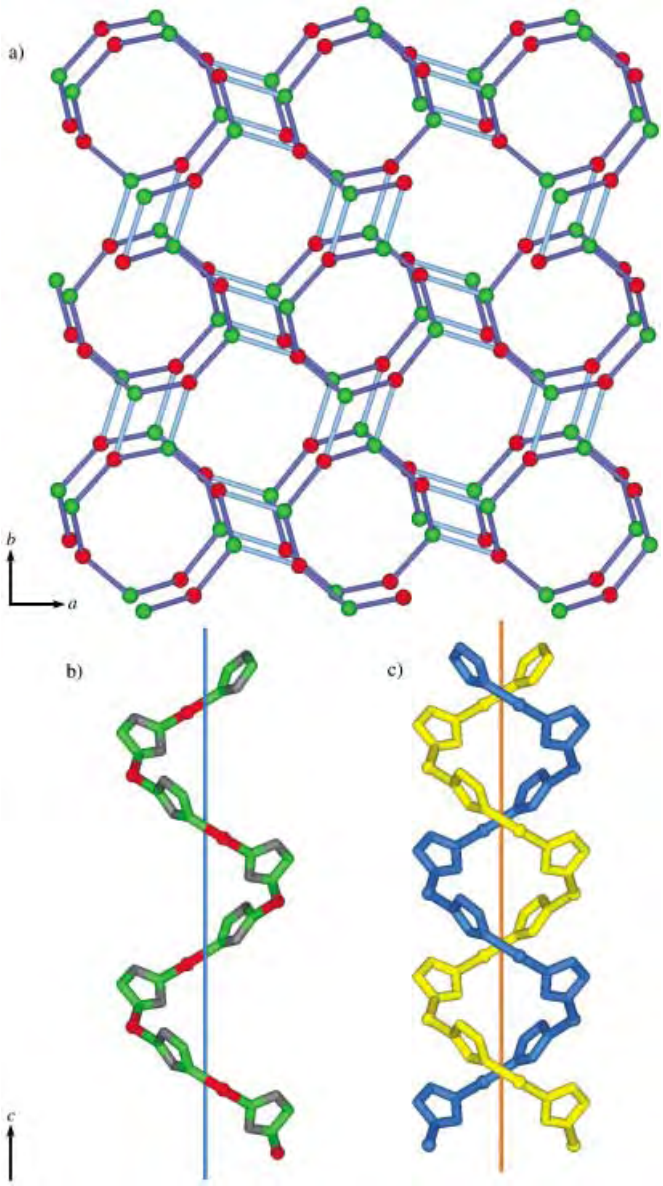


Figure 1. Compound **1**: a) A single 4.8.16 net projected along the *c* axis, b) a single left-handed helical fragment, and c) a double helical fragment. For clarity, the methyl groups are omitted, and the triazolate groups are represented by green spheres in a).

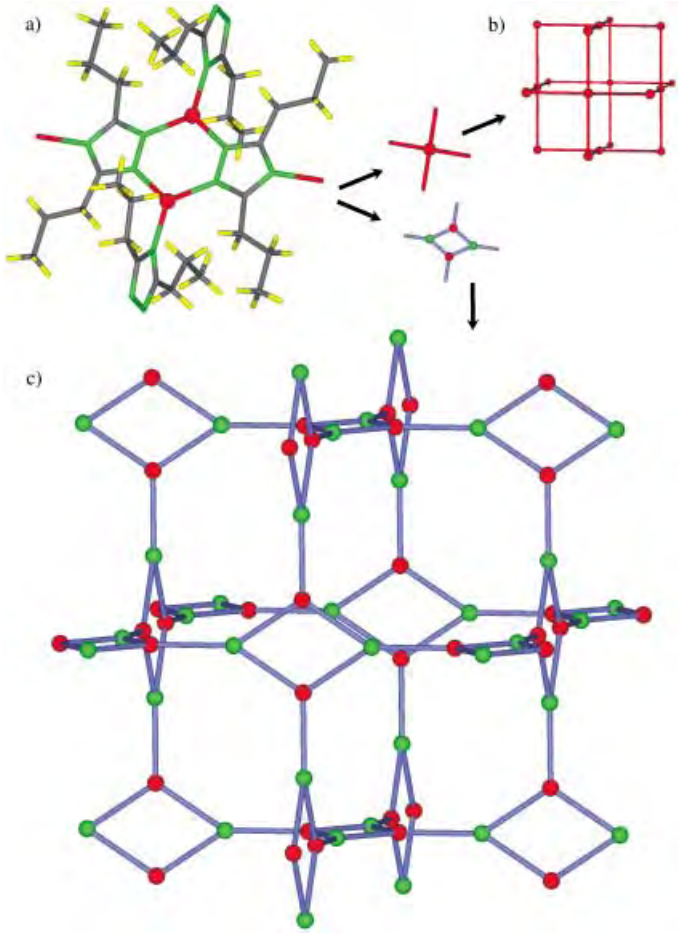


Figure 2. Compound **2**: a) Definitions of the 3- and 4-connected nodes, b) the 4-connected NbO net, and c) the 3-connected 4.12^2 net.

and two acute for USF-1 networks.[3g] These facts indicate that the topology of a network based solely on square-planar nodes depends strongly on the orientation of adjacent nodes; therefore, a specific network based solely on square-planar nodes can be assembled by control of the dihedral angles. A few structures have been successfully synthesized by directing rigid square-planar secondary building units (SBUs) with ligands of specific geometry.[4c] In contrast, the ligands in both **1** and **2** are very similar except for the substituents, and the dihedral angles are about 30° in the case of methyl groups and 90° in the case of the larger propyl groups, respectively. Consequently, we may suggest that steric repulsion of the substituents of these triazolates may enforce the dihedral angles between adjacent square-planar nodes. Since all such 4-connected nets can be augmented to related 3-connected nets, this work also illustrates an alternative strategy of using trigonal-planar building blocks to build such intriguing networks, rather than the usual methods involving square-planar units.

In summary, we have described two unprecedented copper(I) triazolate coordination polymers formed by unprecedented copper-mediated cycloadditions of nitriles and ammonia. These compounds form 3-connected networks with novel topologies that have implications for understanding the relationship between related nets, and the one-pot reaction may serve as a new synthetic approach for the synthesis of triazole derivatives.

Experimental Section

Synthesis of **1**: a) Hydrothermal treatment of $Cu_2(OH)_2CO_3$ (0.221 g, 1.0 mmol), aqueous ammonia (25%, 3.0 mL), and butyronitrile (5.0 mL) at 160°C for 3 days yielded pale-yellow needlelike crystals in 40% yield based on $Cu_2(OH)_2CO_3$. b) $Cu_2(OH)_2CO_3$ (0.221 g, 1.0 mmol) was replaced by $Cu(OH)_2$ (0.098 g, 1.0 mmol), and the yield was 20% based on $Cu(OH)_2$.

Synthesis of **2**: a) Hydrothermal treatment of $Cu_2(OH)_2CO_3$ (0.221 g, 1.0 mmol), aqueous ammonia (25%, 2.0 mL), and acetonitrile (2.0 mL) at 160°C for 3 days yielded pale-yellow blocklike

 © 2004 Wiley-VCH Verlag GmbH & Co. KGaA, Weinheim

crystals in 25% yield based on $Cu_2(OH)_2CO_3$. b) $Cu_2(OH)_2CO_3$ (0.221 g, 1.0 mmol) was replaced by $Cu(OH)_2$ (0.098 g, 1.0 mmol), and the yield was 10% based on $Cu(OH)_2$.

Elemental analysis (%) calcd for **1** ($C_4H_6CuN_3$): C 30.09, H 3.79, N 26.32; Found: C 30.05, H 3.83, N 26.28. Calcd for **2** ($C_8H_{14}CuN_3$): C 44.53, H 6.54, N 19.48; Found: C 44.60, H 6.50, N 19.39. IR (KBr): **1**: $\tilde{\nu}$ = 3425m, 2960s, 2919s, 1487vs, 1415vs, 1366vs, 1332vs, 1090m, 1040m, 974m, 768s, 693m, 624 cm^{-1} m; **2**: $\tilde{\nu}$ = 3440m, 2959vs, 2930vs, 2873vs, 1496vs, 1461vs, 1354vs, 1274s, 1224s, 1079s, 901m, 825m, 746 cm^{-1} m.

Received: August 12, 2003 [Z52627]

Keywords: copper · cycloaddition · hydrothermal synthesis · N ligands · triazoles

[1] a) M. Eddaoudi, D. B. Moler, H.-L. Li, B. Chen, T. M. Reineke, M. O'Keeffe, O. M. Yaghi, *Acc. Chem. Res.* **2001**, *34*, 319–330; b) P. J. Hagrman, D. Hagrman, J. Zubieta, *Angew. Chem.* **1999**, *111*, 2798–2848; *Angew. Chem. Int. Ed.* **1999**, *38*, 2639–2684; c) B. Moulton, M. J. Zaworotko, *Chem. Rev.* **2001**, *101*, 1629–1658; d) S. R. Batten, R. Robson, *Angew. Chem.* **1998**, *110*, 1558–1595; *Angew. Chem. Int. Ed.* **1998**, *37*, 1461–1494.

[2] a) B. F. Abrahams, S. R. Batten, M. J. Grannas, H. Hamit, B. F. Hoskins, R. Robson, *Angew. Chem.* **1999**, *111*, 1538–1540; *Angew. Chem. Int. Ed.* **1999**, *38*, 1475–1477; b) B. F. Abrahams, P. A. Jackson, R. Robson, *Angew. Chem.* **1998**, *110*, 2801–2804; *Angew. Chem. Int. Ed.* **1998**, *37*, 2656–2659; c) L. Carlucci, G. Ciani, D. M. Proserpio, S. Rizzato, *Chem. Commun.* **2001**, 1198–1199; d) J.-C. Dai, X.-T. Wu, Z.-Y. Fu, S.-M. Hu, W.-X. Du, C.-P. Cui, L.-M. Wu, H.-H. Zhang, R.-Q. Sun, *Chem. Commun.* **2002**, 12–13; e) L. Carlucci, G. Ciani, D. W. V. Gudenberg, D. M. Proserpio, *New J. Chem.* **1999**, *23*, 397–401, and references therein.

[3] a) M. Eddaoudi, J. Kim, M. O'Keeffe, O. M. Yaghi, *J. Am. Chem. Soc.* **2002**, *124*, 376–377; b) T.-Y. Niu, X.-Q. Wang, A. J. Jacobson, *Angew. Chem.* **1999**, *111*, 2059–2062; *Angew. Chem. Int. Ed.* **1999**, *38*, 1934–1937; c) S. A. Barnett, A. J. Blake, N. R. Champness, C. Wilson, *Chem. Commun.* **2002**, 1640–1641; d) L. Carlucci, G. Ciani, P. Macchi, D. M. Proserpio, *Chem. Commun.* **1998**, 1837–1838; e) B. Rather, B. Moulton, R. D. B. Walsh, M. J. Zaworotko, *Chem. Commun.* **2002**, 694–695; f) L. Carlucci, N. Cozzi, G. Ciani, M. Moret, D. M. Proserpio, S. Rizzato, *Chem. Commun.* **2002**, 1354–1355; g) B. Moulton, H. Abourahma, M. W. Bradner, J.-J. Lu, G. J. McManus, M. J. Zaworotko, *Chem. Commun.* **2003**, 1342–1343.

[4] a) M. O'Keeffe, M. Eddaoudi, H.-L. Li, T. Reineke, O. M. Yaghi, *J. Solid State Chem.* **2000**, *152*, 3–20; b) O. D. Friedrichs, M. O'Keeffe, O. M. Yaghi, *Acta Crystallogr. Sect. A* **2003**, *59*, 22–27; c) O. M. Yaghi, M. O'Keeffe, N. W. Ockwig, H. K. Chae, M. Eddaoudi, J. Kim, *Nature* **2003**, *423*, 705–714.

[5] A. F. Wells, *Three-Dimensional Nets and Polyhedra*, Wiley, New York, **1977**.

[6] a) E. C. Constable, *Metals and Ligand Reactivity*, VCH, Weinheim, **1996**; b) R. A. Michelin, M. Mozzon, R. Bertani, *Coord. Chem. Rev.* **1996**, *147*, 299–338; c) V. Y. Kukushkin, A. J. L. Pombeiro, *Chem. Rev.* **2002**, *102*, 1771–1802, and references therein.

[7] a) Z. P. Demko, K. B. Sharpless, *Angew. Chem.* **2002**, *114*, 2214–2217; *Angew. Chem. Int. Ed.* **2002**, *41*, 2110–2113; b) Z. P. Demko, K. B. Sharpless, *Angew. Chem.* **2002**, *114*, 2217–2220; *Angew. Chem. Int. Ed.* **2002**, *41*, 2113–2116, and references therein.

[8] R.-G. Xiong, X. Xue, H. Zhao, X.-Z. You, B. F. Abrahams, Z.-L. Xue, *Angew. Chem.* **2002**, *114*, 3954–3957; *Angew. Chem. Int. Ed.* **2002**, *41*, 3800–3803.

[9] M. N. Bochkarev, G. V. Khoroshenkov, H. Schumann, S. Dechert, *J. Am. Chem. Soc.* **2003**, *125*, 2894–2895.

[10] a) X.-M. Zhang, M.-L. Tong, X.-M. Chen, *Angew. Chem.* **2002**, *114*, 1071–1073; *Angew. Chem. Int. Ed.* **2002**, *41*, 1029–1031; b) X.-M. Zhang, M.-L. Tong, M.-L. Gong, H.-K. Lee, L. Luo, K.-F. Li, Y.-X. Tong, X.-M. Chen, *Chem. Eur. J.* **2002**, *8*, 3187–3194; c) J. Tao, Y. Zhang, M.-L. Tong, X.-M. Chen, T. Yuen, C. L. Lin, X.-Y. Huang, J. Li, *Chem. Commun.* **2002**, 1342–1343.

[11] J.-P. Zhang, X.-M. Chen, unpublished results.

[12] a) K. T. Potts, *Chem. Rev.* **1961**, *61*, 87–127; b) E. S. H. El Ashry, L. F. Awad, M. Winkler, *J. Chem. Soc. Perkin Trans. 1* **2000**, 829–834; c) C.-J. Liu, E. J. Iwanowicz, *Tetrahedron Lett.* **2003**, *44*, 1409–1411, and references therein.

[13] J. G. Haasnoot, *Coord. Chem. Rev.* **2000**, *200–202*, 131–185.

[14] Crystal data for **1**: tetragonal, $P4_2/n$ (no. 86), a = 13.470(2), c = 6.142(2) Å, V = 1114.6(5) Å^3, Z = 8, ρ_{calcd} = 1.903 g cm^{-3}, $F(000)$ = 640, $\mu(Mo_{K\alpha})$ = 3.796 mm^{-1}, 7811 reflections measured, 1593 unique reflections (R_{int} = 0.015), final R_1 = 0.0268, wR_2 = 0.0646, S = 1.082 for all data; **2**: cubic, $Im\bar{3}$ (no. 204), a = 14.923(2) Å, V = 3323.2(8) Å^3, Z = 12, ρ_{calcd} = 1.294 g cm^{-3}, $F(000)$ = 1344, $\mu(Mo_{K\alpha})$ = 1.928 mm^{-1}, 10034 reflections measured, 743 unique reflections (R_{int} = 0.020), final R_1 = 0.0513, wR_2 = 0.1516, S = 1.154 for all data. Data for **1** and **2** were collected with $Mo_{K\alpha}$ radiation (λ = 0.71073 Å) at 293 K on a Bruker SMART Apex CCD diffractometer by using frames of 0.3° oscillation ($4.3 \le 2\theta \le 60°$ for **1** and $3.9 \le 2\theta \le 55.9°$ for **2**). The structures were solved by direct methods, and all non-hydrogen atoms were subjected to anisotropic refinement by full-matrix least-squares on F^2 using the SHELXTL program.[15] CCDC-217202 and -217203 contain the supplementary crystallographic data for this paper. These data can be obtained free of charge via www.ccdc.cam.ac.uk/conts/retrieving.html (or from the Cambridge Crystallographic Data Centre, 12, Union Road, Cambridge CB2 1EZ, UK; fax: (+44) 1223-336-033; or deposit@ccdc.cam.ac.uk).

[15] SHELXTL 6.10, Bruker Analytical Instrumentation, Madison, Wisconsin, USA, **2000**.

 © 2004 Wiley-VCH Verlag GmbH & Co. KGaA, Weinheim

Magnetic Properties

Hexanuclear Manganese(III) Single-Molecule Magnets**

Constantinos J. Milios, Catherine P. Raptopoulou, Aris Terzis, Francesc Lloret, Ramon Vicente, Spyros P. Perlepes, and Albert Escuer**

Single-molecule magnets (SMMs)[1,2] are molecular species that can retain magnetization in the absence of a magnetic field below a blocking temperature. They represent the smallest possible magnetic storage device, which retains information in a single molecule rather than in a magnetic particle or array of particles. Furthermore, such molecules straddle the classical/quantum interface in also displaying quantum tunneling of magnetization and quantum phase interference. The SMM behavior derives from the intrinsic intramolecular properties of a high-spin ground state, and large and negative (easy axis type) magnetoanisotropy.[1,2] Experimentally, a SMM exhibits both a frequency-dependent out-of-phase alternating current (ac) magnetic susceptibility (χ'') signal and hysteresis loops in magnetization versus direct current (dc) field studies.[1] To date, the best and most extensively studied SMMs are the class of the dodecanuclear species $[Mn_{12}O_{12}(O_2CR)_{16}(H_2O)_x]^{n-}$ ($n=0,\ 1,\ 2;\ x=3,\ 4$; $Mn^{III}{}_8Mn^{IV}{}_4$ for $n=0$) and their derivatives,[1,2] but there are a number of other examples of SMMs containing manganese (at the oxidation states II/III, III/IV or II/III/IV), iron, cobalt, nickel, and vanadium.[1–3] Important to the future of the field of SMMs is the development of new synthetic schemes that can yield molecules with a large spin and/or anisotropy. Herein we report access to the first members of a new class of manganese-based SMMs consisting exclusively of Mn^{III} ions with T_B (T_B = blocking temperature) greater than 2 K.

[*] C. J. Milios, Prof. S. P. Perlepes
Department of Chemistry
University of Patras
265 00 Patras (Greece)
Fax: (+30) 2610-997118
E-mail: perlepes@patreas.upatras.gr
Dr. R. Vicente, Prof. A. Escuer
Departament de Química Inorgànica
Universitat de Barcelona
Martí Franqués 1–11, 08028 Barcelona (Spain)
Fax: (+34) 93-490-7725
E-mail: albert.escuer@qi.ub.es
Dr. C. P. Raptopoulou, Dr. A. Terzis
Institute of Materials Science
NCSR "Demokritos"
153 10 Aghia Paraskevi Attikis (Greece)
Prof. F. Lloret
Departament de Química Inorgànica
Universitat de València
Doctor Moliner 50, 46100 Burjassot (Spain)

[**] A.E. and R.V. thank the Ministerio de Ciencia y Tecnología (Spain), project BQU2003/0538, for financial support of this research.

Supporting information for this article is available on the WWW under http://www.angewandte.org or from the author.

Reaction of $Mn(O_2CMe)_2\cdot 4H_2O$ with salicylaldoxime (H_2salox, 1:1 molar ratio) in EtOH at room temperature led to a deep green solution from which the hexanuclear complex **1**·4 EtOH was isolated. The presence of the dianionic form of

$$[Mn_6O_2(O_2CMe)_2(salox)_6(EtOH)_4]\cdot 4\,EtOH \quad \mathbf{1}\cdot 4\,EtOH$$

the ligand ($salox^{2-}$) is a consequence of the 2:1 $MeCO_2^-$:H_2-salox ratio used in the reaction.

Another route to good yields of pure **1** involves a comproportionation reaction between nBu$_4$NMnO$_4$ and $Mn(O_2CMe)_2\cdot 4H_2O$ in the presence of H_2salox (3:1:3 molar ratio) in EtOH at room temperature.

In the crystal structure (Figure 1),[4] **1** lies on an inversion center and has a novel $[Mn^{III}{}_6(\mu_3\text{-}O)_2(\mu_2\text{-}OR)_2]^{12+}$ core, whose topology consists of six Mn ions arranged as two $\{Mn_3(\mu_3\text{-}O)\}$ subunits bridged by two oximato oxygen atoms (O11, O11′). The Mn2···Mn3 moiety is further bridged by one *syn*, *syn*-μ_2:η^1:η^1: $MeCO_2^-$ group. Four of the $salox^{2-}$ ligands show the common μ_2:η^1:η^1:η^1 coordination mode (**A**), while the other

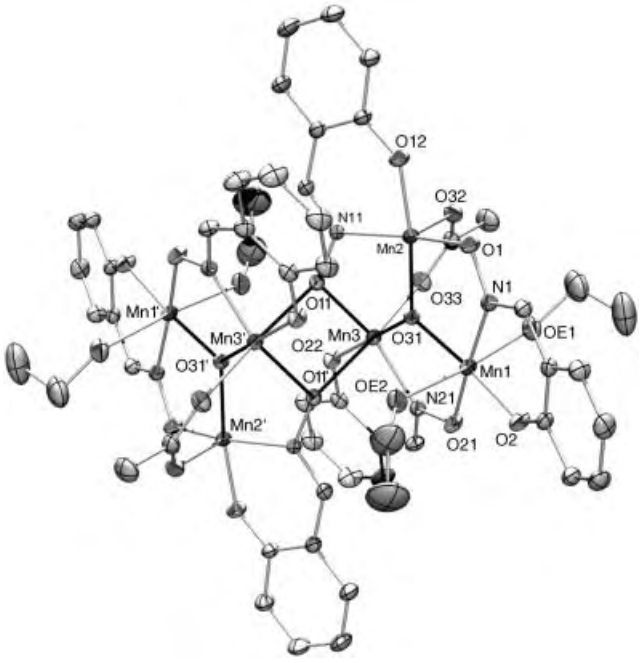
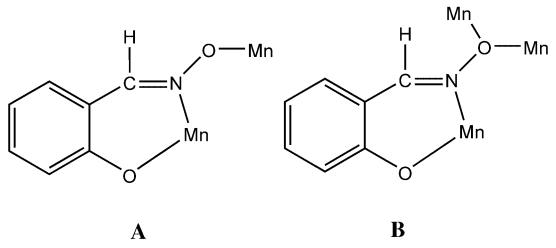


Figure 1. ORTEP plot of the molecular structure of **1** (the thermal ellipsoids are set at 20% probability). Primed and unprimed atoms are related by the crystallographic inversion center, OE1 and OE2 are the oxygen atoms of the crystallographically independent ethanol ligands.



A **B**

 © 2004 Wiley-VCH Verlag GmbH & Co. KGaA, Weinheim DOI: 10.1002/anie.200351079

two adopt the rare[5] μ_3:η^1:η^2:η^1 (**B**) mode. The two crystallographically independent EtOH ligands complete the six-coordination at Mn1. Ions Mn1 and Mn3 are bound to an O_5N set of donor atoms and display Jahn–Teller elongation, as expected for high-spin $3d^4$ ions in near octahedral geometry; the Jahn–Teller axes are OE1-Mn1-OE2 and O33-Mn3-O11′. Mn2 has a distorted square-pyramidal geometry, with the acetate oxygen O32 at the apical position. Complex **1** joins a very small family of Mn^{III}_6 clusters[6] and has a remarkably similar structure to $[Cr_6O_2(O_2CEt)_2(salox)_6(H_2O)_2(EtCN)_2]$.[7]

Complex $[Mn_6O_2(O_2CPh)_2(salox)_6(EtOH)_4]\cdot EtOH$ (**2**·EtOH) was prepared in a fashion very similar to that for **1** by using $Mn(O_2CPh)_2\cdot 2H_2O$. Disregarding the difference in RCO_2^- ligand and the fact that the structure of the benzoate cluster[4] contains two almost identical hexanuclear molecules, compounds **1** and **2** display similar molecular structures.

Solid-state dc magnetic susceptibility measurements were performed in the range 2.0–200 K under a field of 0.1 T (Figure 2). The data were fitted using a full-diagonalization treatment[8] based on the interaction pattern shown in Figure 3 and on the corresponding Hamiltonian [Eq. (1)].

$$\mathscr{H} = -2J_1(S_3\cdot S_{3'}) - 2J_2(S_2\cdot S_3 + S_{2'}\cdot S_{3'}) - 2J_3(S_1\cdot S_2 + S_1\cdot S_3 + S_{1'}\cdot S_{2'} + S_{1'}\cdot S_{3'}) - 2J_4(S_2\cdot S_{3'} + S_{2'}\cdot S_3) \quad (1)$$

Measurements below 15 K were omitted in the fitting because zero-field effects are likely to influence the data in this temperature range. The best fitting parameters obtained are $J_1 = +12.4\ cm^{-1}$, $J_2 = -3.5\ cm^{-1}$, $J_3 = -12.6\ cm^{-1}$, $J_4 = -0.45\ cm^{-1}$, $g = 2.00$ ($R = 2.1\times10^{-4}$, $R = \Sigma(\chi_M^{calcd} - \chi_M^{exp})^2/\Sigma(\chi_M^{exp})^2$). Interaction through the oximato bridges indicate antiferromagnetic (AF) coupling as usually observed for this kind of ligand and the positive J_1 value obtained is in agreement with magnetostructural correlations found in dinuclear Mn^{III} units containing the $\{Mn_2^{III}(\mu_2\text{-}OR)_2\}^{4+}$ subcore.[9] The system may be envisaged as two ferromagnetically coupled AF triangles. The competitive interactions (J_2 and J_3) and the fact that $J_3 \gg J_2$, clearly stabilize a local $S = 2$ ground state in each triangular unit.[10] The dominant ferromagnetic J_1 pathway (versus the very weak J_4 one) leads to an $S = 4$ ground state for the hexanuclear cluster.

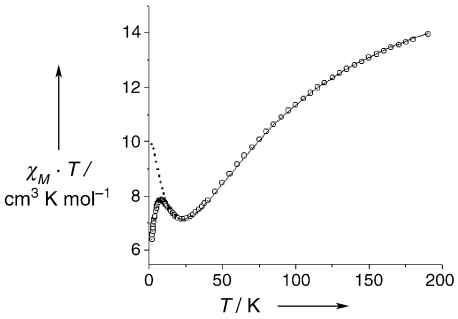


Figure 2. Plot of the $\chi_M T$ versus T for a solvated form of complex **1**. Solid line is a fit of the data down to 15 K. The dotted line below 15 K indicates the spin-only behavior that tends to reach a $\chi_M T$ value of 10 $cm^3\,K\,mol^{-1}$ ($S = 4$).

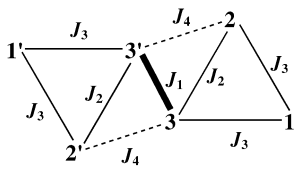


Figure 3. The exchange-interaction pattern for complex **1**. The numbering scheme used for the spin carriers is the same as that used in Figure 1.

A crucial requirement for the SMM response is parallel alignment of the anisotropy axes which generates a bulk cluster anisotropy. As has been pointed out,[2] anisotropic ions are a necessary (but not sufficient) condition to generate SMMs; an adequate topological arrangement of the local anisotropy tensors is also required. Compounds **1** and **2** with an $S = 4$ ground state, local anisotropic ions, and an adequate global topology (all the elongation axes are parallel), are good candidates to be SMMs. Thus, ac susceptibility experiments were performed to determine whether these complexes would exhibit a slow magnetization-relaxation phenomenon. The in-phase $\chi_M' T$ signal of a solvated form of **1** shows a frequency-dependent decrease at $T < 6$ K indicative of the onset of slow relaxation. This was confirmed by the concomitant appearance of an out-of-phase (χ_M'') signal (Figure 4) arising from

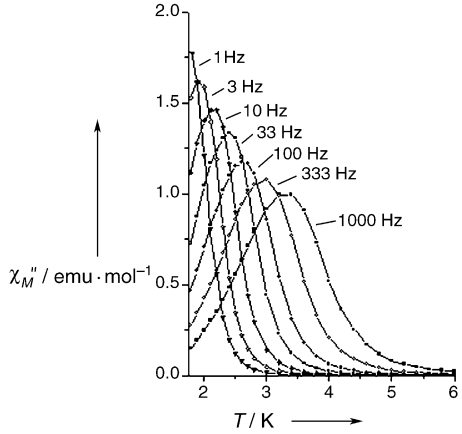


Figure 4. Plot of the out-of-phase (χ_M'') signal in ac susceptibility studies versus T under a field oscillating at the frequencies indicated for a solvated form of compound **1**.

the inability of **1** to relax sufficiently rapidly, at these temperatures, to keep up with the oscillating field. For the ac frequency range 1–1000 Hz, the χ_M'' peaks of solvated **1** occur between 1.96–3.30 K. The presence of an out-of-phase signal establishes[1–3] that **1** is a SMM. The magnetization relaxation rate data obtained from the ac data were fitted to the Arrhenius equation $\tau = \tau_0\cdot e^{-U_{eff}/(KT)}$, where τ is the relaxation time, U_{eff} is the energy barrier for the relaxation of the magnetization, k is Boltzmann's constant and τ_0 is the preexponential factor. From the fit, U_{eff} was found to be 28.0 K with $\tau_0 = 3.6\times10^{-8}$ s. For an integer spin system, the barrier to thermally activated magnetization relaxation is $S^2|D|$, where D is the axial zero-field splitting (ZFS) parameter. Thus, the experimentally determined kinetic

 © 2004 Wiley-VCH Verlag GmbH & Co. KGaA, Weinheim

energy barrier of 28.0 K (19.5 cm^{-1}) implies a minimum value of D of -1.22 cm^{-1}. In spite of the relatively large $|D|$ value and that τ_0 is comparable to that of manganese SMMs with higher nuclearities,[1,2] the relaxation is still fast at 2 K, owing to the moderate S value of the ground state. Further studies at lower temperatures are planned to investigate magnetization hysteresis loops (expected at $T < 1$ K) and the possible presence of quantum tunneling of the magnetization. Preliminary results show that **2** exhibits a comparable SMM response with τ_0, U_{eff}, and $|D|$ values of 2.3×10^{-8} s, 19.4 cm^{-1}, and 1.21 cm^{-1}, respectively.

Simulation of the reduced magnetization dependence upon H/T for solvated **1**, assuming the D value to be -1.22 cm^{-1} for $S = 4$ and $g = 2.00$, shows excellent agreement with the experimental data, which gives an independent confirmation of the ground state of the system and the energy-barrier value (Figure 5).

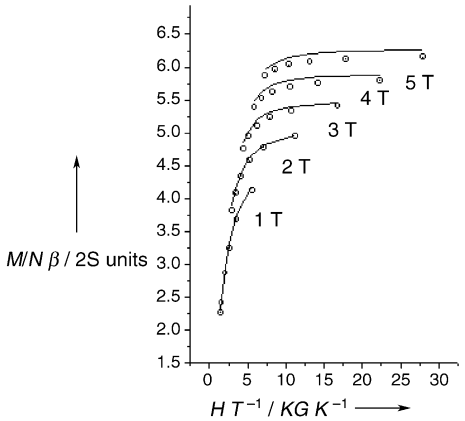


Figure 5. Plot of the reduced magnetization versus H/T for solvated **1** at 1, 2, 3, 4, and 5 T. The solid lines correspond to the simulation using the D and S values obtained from ac and dc independent measurements.

Work in progress reveals that substitution of the benzoate ligands present in **2** by various chlorobenzoates leads to products with similar structures and SMM properties. A full magnetic analysis of this potentially large family of SMMs will be reported elsewhere.[11]

Experimental Section

Treatment of a stirred colorless solution of $Mn(O_2CMe)_2{\cdot}4H_2O$ (0.073 g, 0.30 mmol) in EtOH (25 mL) with nBu_4NMnO_4 (0.036 g, 0.10 mmol) resulted in a dark red-brown solution. Solid H_3salox (0.041 g, 0.30 mmol) was slowly added to this solution and soon dissolved to give a dark green solution. This solution was stirred for a further 30 min, filtered, and the filtrated layered with Et_2O/*n*-hexane (40 mL, 1:1 v/v) to give X-ray quality, dark red-green crystals of the product, which were collected by filtration, washed with EtOH, and dried in air; the formulation **1**·4 EtOH was determined crystallographically, but the dried solid was analyzed as solvate EtOH-free. Yield 40–50%, elemental analysis (%) calcd for $C_{54}H_{60}Mn_6N_6O_{22}$: C 43.97, H 4.04, N 5.70; found for dried sample: C 44.27, H 4.11, N 5.61; selected IR data (KBr pellet): $\tilde{\nu} = 3424$ (br, m), 1598 (s), 1540 (m), 1472 (m), 1440 (s), 1282 (s), 1044 (s), 1028 (s), 918 (s), 754 (m), 680 (s), 652 (m), 476 cm^{-1} (m).

Received: February 3, 2003
Revised: July 14, 2003 [Z51079]

Keywords: cluster compounds · magnetic properties · manganese · N,O ligands · single-molecule magnets

[1] G. Christou, D. Gatteschi, D. N. Hendrickson, R. Sessoli, *MRS Bull.* **2000**, *25*, 66.
[2] For a recent review, see: D. Gatteschi, R. Sessoli, *Angew. Chem.* **2003**, *115*, 278; *Angew. Chem. Int. Ed.* **2003**, *42*, 268.
[3] a) C. Cadiou, M. Murrie, C. Paulsen, V. Villar, W. Wernsdorfer, R. E. P. Winpenny, *Chem. Commun.* **2001**, 2666; b) E. K. Brechin, M. Soler, J. Davidson, D. N. Hendrickson, S. Parsons, G. Christou, *Chem. Commun.* **2002**, 2252.
[4] Crystal structure data for **1**·4 EtOH : $C_{62}H_{84}Mn_6N_6O_{26}$, $M_r = 1658.99$, triclinic, space group $P\bar{1}$, $a = 11.794(7)$, $b = 14.50(1)$, $c = 12.652(8)$ Å, $\alpha = 107.81(2)$, $\beta = 114.00(2)$, $\gamma = 96.04(2)°$, $V = 1815(2)$ Å^3, $Z = 1$, $\rho_{calcd} = 1.518$ g cm^{-3}, $T = 298$ K, $\mu(Mo_{k\alpha}) = 1.094$ mm^{-1}, $F(000) = 856$, $2\theta_{max} = 48.5°$, 6182 reflections collected, 5884 unique ($R_{int} = 0.0322$), restraints/parameters = 0/533, $R1(F) = 0.0474$ and $wR2(F^2) = 0.1085$ using 4057 reflections with $I > 2\sigma(I)$. Crystal structure data for **2**·EtOH : $C_{66}H_{70}Mn_6N_6O_{23}$, $M_r = 1644.92$, triclinic, space group $P\bar{1}$, $a = 15.045(1)$, $b = 13.047(1)$, $c = 19.989(2)$ Å, $\alpha = 69.04(1)$, $\beta = 87.59(1)$, $\gamma = 82.84(1)°$, $V = 3635.5(5)$ Å^3, $Z = 2$, $\rho_{calcd} = 1.503$ g cm^{-3}, $T = 298$ K, $\mu(Cu_{k\alpha}) = 8.891$ mm^{-1}, $F(000) = 1684$, $2\theta_{max} = 121.5°$, 11282 reflections collected, 10918 unique ($R_{int} = 0.0683$), restraints/parameters = 0/1070, $R1(F) = 0.0560$ and $wR2(F^2) = 0.1487$ using 8837 reflections with $I > 2\sigma(I)$. CCDC 200455 (**1**·4 EtOH) and CCDC-200456 (**2**·EtOH) contain the supplementary crystallographic data for this paper. These data can be obtained free of charge via www.ccdc.cam.ac.uk/conts/retrieving.html (or from the Cambridge Crystallographic Data Centre, 12 Union Road, Cambridge CB2 1EZ, UK; fax: (+44) 1223-336-033; or deposit@ccdc.cam.ac.uk).
[5] J. M. Thorpe, R. L. Beddoes, D. Collison, C. D. Garner, M. Helliwell, J. M. Holmes, P. A. Tasker, *Angew. Chem.* **1999**, *111*, 1191; *Angew. Chem. Int. Ed.* **1999**, *38*, 1119.
[6] For example, see: X. Xia, M. Verelst, J.-C. Daran, J.-P. Tuchagues, *J. Chem. Soc. Chem. Commun.* **1995**, 2155.
[7] P. Chaudhuri, M. Hess, E. Rentschler, T. Weyhermüller, U. Flörke, *New J. Chem.* **1998**, *22*, 553.
[8] CLUMAG program, D. Gatteschi, P. Luca, *Gazz. Chim. Ital.* **1993**, *123*, 231.
[9] R. Clèrac, H. Miyasaka, M. Yamashita, C. Coulon, *J. Am. Chem. Soc.* **2002**, *124*, 12837.
[10] E. Libby, J. K. McCusker, E. A. Schmitt, K. Folting, D. N. Hendrickson, G. Christou, *Inorg. Chem.* **1991**, *30*, 3486.
[11] Details will be reported in a full paper.

 © 2004 Wiley-VCH Verlag GmbH & Co. KGaA, Weinheim

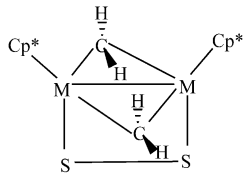
Bond Activation

Activation of C–Cl and C–H Bonds by Ligated S_2^{2-} Ions: Conversion of Organic Chlorides into Organosulfur Compounds in *cis*-[(IrCp*)$_2$(μ-CH$_2$)$_2$(μ-S$_2$R)]$^+$**

Tarlok Singh Lobana, Kiyoshi Isobe,* Hiroaki Kitayama, Takanori Nishioka, and Isamu Kinoshita*

Numerous organic halides, such as 1,1,1-trichloroethane, 1,2-dichloroethane, mono-, di-, and trichloromethylbenzenes, chloroform, dichloromethane, and carbon tetrachloride are used in chemical laboratories, industries, and electrical appliances. Most of these organic halides are toxic and some find their way into the atmosphere, thus posing health hazards. As a result, various investigators are engaged in the activation of carbon–chlorine bonds using chemical, microbial, or thermal methods for converting organic halides into either less toxic or industrially useful materials.[1–7]

The activation of C–Cl bonds by chemical methods essentially involves reactions at a metal surface[2] or oxidative addition at the metal center of complexes.[3,4,7] Thiolate anions S_n^{2-} ($n = 1, 2, 3$) can convert alkyl chloride into dialkyl oligosulfane by activation of the C–Cl bond.[8] However, there is no report of multiple C–Cl bond activation by a coordinated S_2 ligand.[1–9] The S_2 ligand in *cis*-[(MCp*)$_2$(μ-CH$_2$)$_2$(μ-S$_2$)] (**1**: M = Rh, **2**: M = Ir; Cp* = C$_5$Me$_5$) coordinates to the dinuclear metal unit in a parallel fashion and displays high nucleophilicity towards dioxygen.[10,11] With the electronically and structurally unique S_2 ligands in compounds **1** and **2**,[12] we have explored the multibond activation of C–Cl and C–H bonds in polychlorinated organic compounds. Herein we report the formation of dithiocarboxylate or related complexes by the reaction of **2** with a series of chlorinated organic substrates, namely, (1,1,1-trichloromethyl)benzene, (1,1-dichloromethyl)benzene, and (chloromethyl)benzene.



M = Rh (**1**), Ir (**2**)

Iridium compound **2** activates all three C–Cl bonds of C$_6$H$_5$-CCl$_3$ as well as the C–Cl and C–H bonds of C$_6$H$_5$-CHCl$_2$ to form the dithiobenzoate complex *cis*-[(IrCp*)$_2$(μ-CH$_2$)$_2$(μ-S$_2$C-C$_6$H$_5$)][BPh$_4$] (**3**; Scheme 1).[12,13] Furthermore, it activates the C–Cl bond of C$_6$H$_5$-CH$_2$Cl to produce the S-benzylated compound *cis*-[(IrCp*)$_2$(μ-CH$_2$)$_2$(μ-SS-CH$_2$-C$_6$H$_5$)][BPh$_4$] (**4**). This result shows that a decrease in the number of C–Cl bonds makes activation of C–H bonds more difficult, thus paving the way for the formation of **4**. Complexes **3** and **4** are stable and are not affected by air, moisture, or light under ambient conditions. This stability is in contrast to the active species **2**, which is sensitive to air. The formation of compound **4** can be described as an oxidative addition of C$_6$H$_5$-CH$_2$Cl at one S atom, while the reactions to produce **3** involve loss of either two Cl or one Cl and one H atoms. The exact mechanism of the reaction is not yet clear.

The ^{1}H and ^{13}C NMR spectra of compound **3** suggest that the dinuclear unit of {(IrCp*)$_2$(μ-CH$_2$)$_2$} remains intact in solution.[12,13] The characteristic S$_2$C signal of the dithiobenzoate carbon atom appears at $\delta = 210.8$ ppm. Interestingly, the S-benzyl compound **4** shows two signals for nonequivalent Cp* groups, four signals for asymmetric protons of the μ-CH$_2$ groups, and four signals (AB quartet) for S-CH$_2$ protons.[13] The ^{13}C NMR spectrum of **4** displays one signal for the S-CH$_2$ carbon atom at $\delta = 54.2$ ppm, two signals each for the CH$_3$ groups, C$_5$ ring, and μ-CH$_2$ carbon atoms.[13] ESI-mass spectrometry shows signals for the cations of **3** and **4**.[13]

The structures of the cations of **3** and **4** are shown in Figures 1 and 2.[14] Compound **3** has a five-membered ring of Ir$_2$S$_2$C consisting of an Ir–Ir single bond (2.6523(4) Å), two Ir–S single bonds (2.319(2), 2.304(2) Å), and two S–C bonds (1.667(9), 1.68(1) Å) that are intermediate between a single bond and a double bond. This framework clearly demonstrates that two iridium atoms coordinate to the dithiobenzoate which is formed by insertion of the "CC$_6$H$_5$" moiety from C$_6$H$_5$-CHCl$_2$ or C$_6$H$_5$-CCl$_3$ into the S–S bond of the original disulfide ligand. In contrast, compound **4** has a four-membered ring of Ir$_2$S$_2$ made up of an Ir–Ir single bond (2.6517(2) Å), two Ir–S single bonds (2.341(1), 2.368(1) Å), and a short S–S bond (2.091(2) Å). One of the two S atoms is bonded to the C$_6$H$_5$-CH$_2$ moiety which originates from C$_6$H$_5$-CH$_2$Cl.

The reaction of **2** with *p*-ClC$_6$H$_4$-CCl$_3$, with a chloride atom directly attached to the benzene ring, resulted in the formation of *cis*-[(IrCp*)$_2$(μ-CH$_2$)$_2$(μ-S$_2$C-C$_6$H$_4$-Cl-*p*)][BPh$_4$], which is similar to **3**.[15] From these reactions, it was noted that the ease of C–Cl or C–H bond cleavage varies in the following sequence: *p*-ClC$_6$H$_4$-CCl$_3$ ≈ C$_6$H$_5$-CCl$_3$ > C$_6$H$_5$-CHCl$_2$ > C$_6$H$_5$-CH$_2$Cl. The activation of C–Cl bonds in C$_6$H$_5$CCl$_3$ and *p*-ClC$_6$H$_4$CCl$_3$ using rhodium compound **1** formed the analogous complexes *cis*-[(RhCp*)$_2$(μ-CH$_2$)$_2$(μ-S$_2$C-C$_6$H$_5$)][BPh$_4$] and *cis*-[(RhCp*)$_2$(μ-CH$_2$)$_2$(μ-S$_2$C-C$_6$H$_4$-Cl-

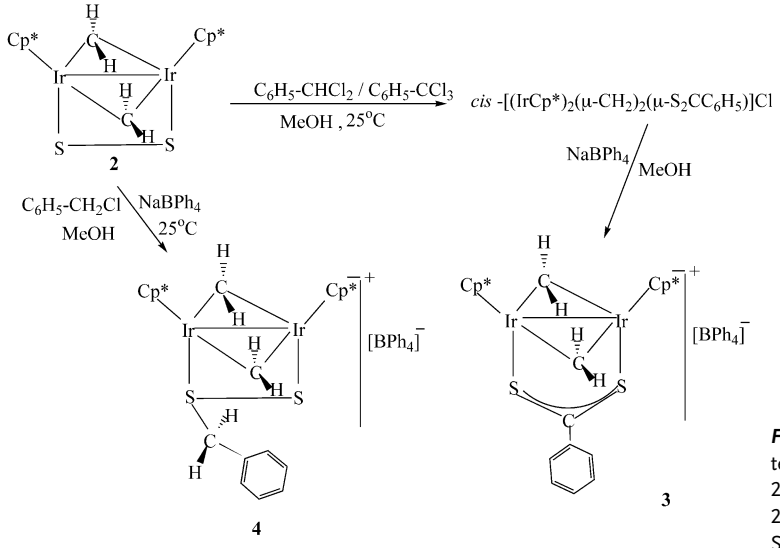
[*] Prof. Dr. T. S. Lobana,[+] Prof. Dr. K. Isobe, H. Kitayama, Dr. T. Nishioka, Dr. I. Kinoshita
Department of Materials Science
Graduate School of Science
Osaka City University
Sugimoto, Sumiyoshi-ku, Osaka 558-8585 (Japan)
Fax: (+81) 76-264-5742
E-mail: tarlokslobana@yahoo.co.in
isobe@cacheibm.s.kanazawa-u.ac.jp

[+] Current address: Department of Chemistry
Guru Nanak Dev University
Amritsar—143 005 (India)
Fax: (+91) 183-2-258820

[**] We gladly acknowledge the award of an Invitation Fellowship for Professor Lobana from the Japan Society for the Promotion of Science(JSPS) and sabbatical leave by the parent university in Amritsar. Cp* = C$_5$Me$_5$.

Supporting information for this article is available on the WWW under http://www.angewandte.org or from the author.

 DOI: 10.1002/anie.200351792 © 2004 Wiley-VCH Verlag GmbH & Co. KGaA, Weinheim



Scheme 1. Reactions of complex **2** with chlorinated organic substrates proceeds with C–Cl or C–H bond activation to provide products **3** and **4**.

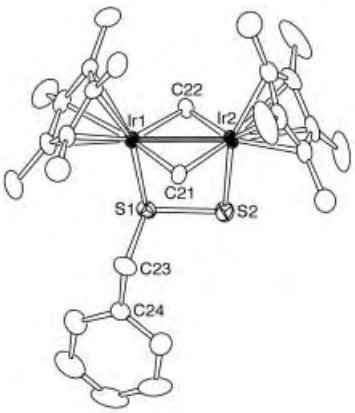


Figure 2. Structure of **4** (H atoms and the BPh_4^- counterion are omitted for clarity). Selected bond lengths [Å] and angles [°]: Ir1-Ir2 2.6517(2), Ir1-S1 2.341(1), Ir2-S2 2.368(1), S1-C23 1.849(6), S1-S2 2.091(2), C23-C24 1.505(8); Ir2-Ir1-S1 83.22(3), Ir1-Ir2-S2 83.07(3), Ir2-S2-S1 96.21(7), Ir1-S1-S2 97.45(6), S1-C23-C24 112.7(4), S2-S1-C23 103.9(2).

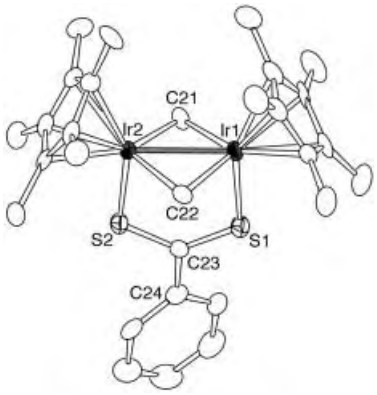


Figure 1. Structure of **3** (H atoms and the BPh_4^- counterion are omitted for clarity). Selected bond lengths [Å] and angles [°]: Ir1-Ir2 2.6523(4), Ir1-S1 2.319(2), Ir2-S2 2.304(2), S1-C23 1.667(9), S2-C23 1.68(1), C23-C24 1.47(1); Ir2-Ir1-S1 94.18(7), Ir1-Ir2-S2 94.20(7), Ir2-S2-C23 112.7(3), Ir1-S1-C23 112.4(4), S2-C23-S1 126.5(5).

p)][BPh_4].[15] The reaction of **2** with CCl_4 is more complex, and one of the products identified by ^{1}H NMR spectroscopy and ESI mass spectrometry is *cis*-[(IrCp*)$_2$(μ-CH_2)$_2$(μ-S_2CH)][BPh_4].[15] Finally, compound **2** activated all three C–Cl bonds of 1,1,1-trichloroethane to form *cis*-[(IrCp*)$_2$(μ-CH_2)$_2$(μ-S_2C-CH_3)]$^+$$Cl^-$. The ESR studies of a reaction mixture of **2** with $C_6H_5CCl_3$ have shown that cleavage of C–Cl bonds (as well as C–H bonds in other substrates) probably occurs with intermediate formation of paramagnetic species ($g = 2.046$), the exact nature of which is not yet understood.

The reactions described herein may lead to the development of catalytic cycles using *trans*-[(MCp*)$_2$(μ-CH_2)$_2$$Cl_2$] (M = Rh, Ir) as catalysts in the activation of organic chlorides via active species **1** or **2**. Further investigations are in progress.

Experimental Section

3: Methanol (5 mL) and (1,1,1-trichloromethyl)benzene (18 μL, 0.024 g, 0.123 mmol) dissolved in methanol (3 mL) were added to a flask containing solid **2** (0.060 g, 0.080 mmol).[12] The contents were stirred for 48 h at room temperature; the color of the solution changed from dark brown to dark red. The solvent was removed with a rotary evaporator in the open atmosphere. The ^{1}H NMR spectrum of a small sample in CD_3OD was recorded to confirm the formation of the cation of **3** (Cl^-).[13] The solid in the flask was redissolved in MeOH (5 mL), and an excess of $NaBPh_4$ (0.050 g, 0.160 mmol) dissolved in MeOH (5 mL) was added. The dark red precipitates formed were collected by filtration and washed with methanol (yield: 0.055 g, 60 %). The solid was redissolved in dichloromethane (5 mL), filtered, and the filtrate layered with an excess of dry toluene (50 mL). Orange crystals of **3** formed in a few days. M.p. 270–275 °C (decomp), elemental analysis calcd (%) for $C_{53}H_{59}BIr_2S_2$: C 55.10, H 5.15; found: C 54. 91, H 5.10.

4: Methanol (5 mL) and (chloromethyl)benzene (18 μL, 0.020 g, 0.160 mmol) dissolved in methanol (2 mL) were added to a flask containing solid **2** (0.060 g, 0.080 mmol). The contents were stirred for 72 h at room temperature; the color of the solution changed from dark brown to red-brown. The rest of the procedure was the same as described for compound **3**. Yield: 0.050 g, 54 %. The crystals of **4** were initially grown from CH_2Cl_2/toluene and subsequently regrown from CH_2Cl_2/methanol. M.p. 220–225 °C (decomp), elemental analysis calcd (%) for $C_{53}H_{61}BIr_2S_2$: C 54.99, H 5.31; found: C 54. 20, H 5.28.

Received: May 2, 2003
Revised: August 4, 2003 [Z51792]

Keywords: C–Cl activation · C–H activation · iridium · S ligands

[1] B. Sun, B. M. Griffin, H. L. Ayala-del-Rio, S. A. Hashsham, J. M. Tiedje, *Science* **2002**, *298*, 1023–1025.
[2] G. Zhou, A. J. Gellman, *J. Catal.* **2000**, *194*, 233–239.
[3] S. Iwamatsu, H. Kondo, K. Matsubara, H. Nagashima, *Tetrahedron* **1999**, *55*, 1687–1706.

 © 2004 Wiley-VCH Verlag GmbH & Co. KGaA, Weinheim

[4] E. Sola, V. I. Bakhmutov, F. Torres, A. Elduque, J. A. Lopez, F. J. Lahoz, H. Werner, L. A. Oro, *Organometallics* **1998**, *17*, 683 – 696.

[5] S. Ishida, T. Iwamoto, C. Kabuto, M. Kira, *Chem. Lett.* **2001**, 1102 – 1103.

[6] J. J. Difelice, E. R. Ritter, *Combust. Sci. Technol.* **1996**, *116*, 5 – 30.

[7] a) H. B. Friedrich,, J. R. Moss, *Adv. Organomet. Chem.* **1991**, *33*, 235 – 290; b) K. J. Bradd, B. T. Heaton, C. Jacob, J. T. Sampanthar, A. Steiner, *J. Chem. Soc. Dalton Trans.* **1999**, 1109 – 1112; c) H. F. Haarman, J. M. Ernsting, M. Kranenburg, H. Kooijman, N. Veldman, A. L. Spek, P. W. N. M. van Leeuwen, K. Vrieze, *Organometallics* **1997**, *16*, 887 – 900; d) K. Kashiwabara, A. Morikawa, T. Suzuki, K. Isobe, K. Tatsumi, *J. Chem. Soc. Dalton Trans.* **1997**, 1075 – 1081; e) H. Nishiyama, M. Horihata, T. Hirai, S. Wakamatsu, K. Itoh, *Organometallics* **1991**, *10*, 2706 – 2708; f) C. Tejel, M. A. Ciriano, J. A. López, F. J. Lahoz, L. A. Oro, *Organometallics* **2000**, *19*, 4977 – 4984; g) M. A. Ciriano, M. A. Tena, L. A. Oro, *J. Chem. Soc. Dalton Trans.* **1992**, 2123 – 2124; h) G. E. Ball, W. R. Cullen, M. D. Fryzuk, B. R. James, S. J. Rettig, *Organometallics* **1991**, *10*, 3767 – 3769; i) C. Tejel, M. A. Ciriano, L. A. Oro, A. Tiripicchio, F. Ugozzoli, *Organometallics* **1994**, *13*, 4153 – 4155; j) Y. W. Ge, P. R. Sharp, *J. Am. Chem. Soc.* **1990**, *112*, 3667 – 3668.

[8] a) N. Yamada, M. Furukawa, M. Nishi, T. Takata, *Chem. Lett.* **2002**, 454 – 455; b) T. Takata, D. Saeki, Y. Makita, N. Yamada, N. Kihara, *Inorg. Chem.* **2003**, *42*, 3712 – 3714.

[9] a) M. Nishio, H. Matszaka, Y. Mizobe, M. Hidai, *Angew. Chem.* **1996**, *108*, 979 – 981; *Angew. Chem. Int. Ed. Engl.* **1996**, *35*, 872 – 874; b) *Comprehensive Coodination Chemistry*, *Vol. 2* (Eds.: G. Wilkinson, R. D. Gillard, J. A. Mc Cleverty by, A. Müller, E. Diemann), Pergamon Press, Oxford, **1987**, chap. 16.1, p. 536.

[10] a) T. Nishioka, S. Nakamura, Y. Kaneko, T. Suzuki, I. Kinoshita, S. Kiyooka, K. Isobe, *Chem. Lett.* **1996**, 911 – 912; b) K. Isobe, S. Okeya, N. J. Meanwell, A. J. Smith, H. Adams, P. M. Maitlis, *J. Chem. Soc. Dalton Trans.* **1984**, 1215 – 1221; c) K. Isobe, Y. Ozawa, A. Vazquez de Miguel, T. W. Zhu, K. M. Zhao, T. Nishioka, T. Ogura, T. Kitagawa, *Angew. Chem.* **1994**, *106*, 1934 – 1935; *Angew. Chem. Int. Ed. Engl.* **1994**, *33*, 1882 – 1883; d) A. M. Mebel, K. Morokuma, K. Isobe, *Inorg. Chem.* **1995**, *34*, 1208 – 1211.

[11] K. Shiomi, B. K. Breedlove, H. Kitayama, T. Nishioka, I. Kinoshita, N. Koga, K. Isobe, *Chem. Commun.* **2002**, 1756 – 1757.

[12] Compound **2** was prepared by the reaction of *trans*- $[(IrCp^*)_2(\mu\text{-}CH_2)_2Cl_2]$ (0.120 g, 0.160 mmol) with Li_2S_2 (0.030 g, 0.385 mmol) in methanol (75 mL) (method A), or by the reaction of *trans*-$[(IrCp^*)_2(\mu\text{-}CH_2)_2Cl_2]$ (0.120 g, 0.160 mmol) with elemental sulfur (0.011 g, 0.344 mmol) in dry methanol (30 mL) and addition of $NaBH_4$ (0.024 g, 0.632 mmol) in 10 mL of dry THF (method B). In both cases the reactions were carried out under an atmosphere of N_2 and followed by removal of solvent under vacuum. ^{1}H NMR (300 MHz, CD_3OD): $\delta = 1.87$ (30 H, s, Cp*), 7.64 (2 H, s, μ-CH_2), 8.01 (2 H, s, μ-CH_2); ^{13}C NMR (75 MHz, CD_3OD): $\delta = 9.83$ (CH_3), 96.5 (C_5 ring of Cp*), 106.8 (μ-CH_2); MS(ESI), $m/z = 746$ [M^+]. Compound **1** was prepared by method A with *trans*-$[(RhCp^*)_2(\mu\text{-}CH_2)_2Cl_2]$ (0.060 g, 0.104 mmol) and Li_2S_2 (0.016 g, 0.205 mmol) in methanol (50 mL). ^{1}H NMR (300 MHz, CD_3OD): $\delta = 1.74$ (30 H, s, Cp*), 9.09 (2 H, s, μ-CH_2), 9.91 (2 H, s, μ-CH_2).[10a,11]

[13] Compound **3**: ^{1}H NMR (600 MHz, $CDCl_3$): $\delta = 1.80$ (30 H, s, Cp*), 7.60 (2 H, s, μ-CH_2), 8.50 (2 H, s, μ-CH_2), 7.71 (2 H, dd, $J =$ 8.4, 1.1 Hz, *o*-$PhCS_2$), 7.46 (1 H, tt, $J = 7.4$, 0.4 Hz, *p*-$PhCS_2$), 7.29 (2 H, tt, $J = 8.2$, 0.3 Hz, *m*-$PhCS_2$), 7.42 (8 H, s, br, *o*-Ph_4B), 7.03 (8 H, t, $J = 7.4$ Hz, *m*-Ph_4B), 6.87 (4 H, t, $J = 7.1$ Hz, *p*-Ph_4B); ^{13}C NMR (150 MHz, $CDCl_3$): $\delta = 9.41$ (CH_3), 99.8 (C_5 ring of Cp*), 100.8 (μ-CH_2), 140.2 (*i*-C, $PhCS_2$), 126.3 (*o*-C, $PhCS_2$), 128.5 (*m*-C, $PhCS_2$), 132.1(*p*-C, $PhCS_2$), 210.8 (CS_2), 164.3 (*i*-C, BPh_4), 136.3 (*o*-C, BPh_4), 125.4 (*m*-C, BPh_4) 121.5 (*p*-C, BPh_4); MS (ESI), $m/z = 835$ [M^+]. Compound **4**: ^{1}H NMR (300 MHz, $CDCl_3$): $\delta = 1.77$ (15 H, s, Cp*), 1.79 (15 H, s, Cp*), 3.89, 3.85, 3.73, 3.69 (2 H, S-CH_2), 7.87 (1 H, s, μ-CH_2), 7.514 (1 H, s, μ-CH_2), 7.509 (1 H, s, μ-CH_2), 7.410 (1 H, s, μ-CH_2), 7.29 (2 H, *m*, *o*-$PhCH_2$), 7.24 (1 H, *p*-$PhCH_2$- obscured by solvent peak), 7.12 (2 H, m, *m*-$PhCH_2$), 7.41 (8 H, s, br, *o*-Ph_4B), 7.01 (8 H, t, $J =$ 7.3 Hz, *m*-Ph_4B), 6.85 (4 H, t, $J = 7.1$ Hz, *p*-Ph_4B); ^{13}C NMR (75 MHz, $CDCl_3$): $\delta = 9.66$, 9.95 (CH_3), 97.2, 98.0 (C_5 ring of Cp*), 106.2, 109.3 (μ-CH_2), 132.9 (*i*-C, Ph-CH_2SS-), 129.1 (*o*-C, Ph-CH_2SS-), 128.9 (*m*-C, $PhCH_2$SS-), 128.8 (*p*-C, $PhCH_2$SS-), 54.2 (SS-CH_2), 164.2 (*i*-C, BPh_4), 136.3 (*o*-C, BPh_4), 125.4 (*m*-C, BPh_4), 121.5 (*p*-C, BPh_4); MS (ESI), $m/z = 837$ [M^+].

[14] Crystallography : The intensity data were collected on a Rigaku/MSC Mercury CCD diffractometer with graphite-monochromated $Mo_{K\alpha}$ radiation ($\lambda = 0.71070$ Å) at 193 K. All calculations were performed using SGI INDY. The structure was solved by direct methods using the program SIR 92 and refined by full-matrix least-squares techniques against F^2 using the SHELXL-97 and teXsan program as a graphical interface. Crystal data for **3** ($C_{53}H_{59}Ir_2S_2B$): red prism, $0.10 \times 0.20 \times 0.23$ mm, $M_r = 1155.42$, monoclinic space group, $P2_1$ (no. 4); $a = 9.892$ (2), $b = 21.841(3)$, $c = 11.990(2)$ Å, $\beta = 119.715(3)°$, $V = 2249.8(6)$ Å^3; $\rho_{calcd} = 1.705$ g cm^{-3}, $Z = 2$; $F(000) = 1136$, $\mu(Mo_{K\alpha}) = 6.054$ mm^{-1}; 21 941 reflections were collected, of which 8247 were unique ($R_{int} = 0.052$); $R_1 = 0.041$ (7210 reflections with $I > 2.0\sigma I$), $wR_2 = 0.080$ (all data). Crystal data for **4** ($C_{53}H_{61}BIr_2S_2$): orange prism, $0.15 \times 0.20 \times 0.20$ mm, $M_r = 1157.43$, monoclinic space group, $P2_1/a$ (no. 14); $a = 11.9872(5)$, $b = 28.281(1)$, $c = 13.9403(7)$ Å, $\beta = 94.231(3)°$, $V = 4713.0(4)$ Å^3; $\rho_{calcd} = 1.631$ g cm^{-3}, $Z = 4$; $F(000) = 2280.00$, $\mu(Mo_{K\alpha}) = 5.780$ mm^{-1}; 36 629 reflections were collected, of which 10 690 were unique($R_{int} = 0.037$); $R_1 = 0.037$ (9602 reflections with $I > 2.0\sigma I$), $wR_2 = 0.096$ (all data). Crystallographic data (excluding structure factors) for the crystal structures reported in this paper have been deposited with the Cambridge Data Centre as supplementary publication number: CCDC 208939 (**3**) and CCDC 216144 (**4**) contains the supplementary crystallographic data for this paper. These data can be obtained free of charge via www.ccdc.cam.ac.uk/conts/retrieving.html (or from the Cambridge Crystallographic Data Centre, 12 Union Road, Cambridge CB2 1EZ, UK; fax: (+44) 1223-336-033; or deposit@ccdc.cam.ac.uk).

[15] See the Supporting Information.

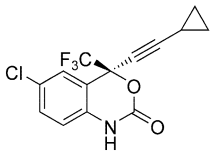
 © 2004 Wiley-VCH Verlag GmbH & Co. KGaA, Weinheim

Enantioselective Synthesis

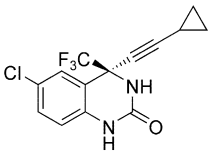
Highly Enantioselective Construction of a Chiral Tertiary Carbon Center by Alkynylation of a Cyclic *N*-Acyl Ketimine: An Efficient Preparation of HIV Therapeutics**

Biao Jiang and Yu-Gui Si*

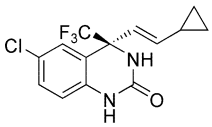
Recently great efforts have been made on developing methodology for generating secondary carbinols as well as secondary propargyl alcohol and propargyl amine by enantioselective alkynylation of aldehydes and aldimines.[1] However, the asymmetric synthesis of tertiary carbinols and carbinamines by addition of carbon nucleophiles to ketones and ketimines has experienced considerable frustration. Human immunodeficiency virus (HIV) is prone to mutation, which in turn leads to drug resistance. Dihydroquinazolines DPC 961 and DPC 083 are second-generation HIV non-nucleoside reverse transcriptase inhibitors (NNRTIs) with enhanced potency when compared to Efavirenz (Sustiva).[2] DPC 961 is currently undergoing clinical evaluation owing to its activity against wild-type HIV-1 and its increased potency toward the K103N-containing HIV as well as other NNRTI-resistant mutant viruses.[3]



Efavirenz (Sustiva)



DPC 961



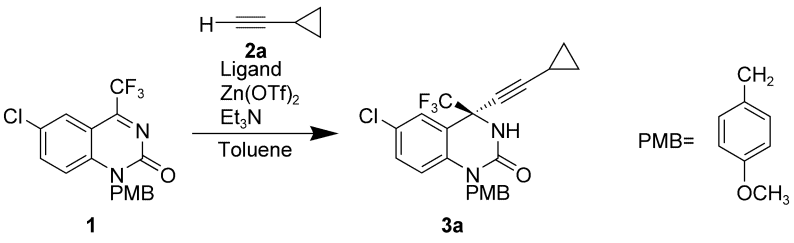
DPC 083

The challenge for synthesizing this class of NNRTIs is to form a tertiary carbinamine in an asymmetric manner. The syntheses of these compounds include diastereoselective 1,4-addition of a magnesium acetylide to 2(3*H*)-quinazolinone containing a chiral auxiliary substituent[4] or 1,2-enantioselective addition of a lithium acetylide to a cyclic *N*-acyl ketimines using lithium cinochona alkaloids[5] or lithium 4β-morpholinocaran-3α-ol as a chiral moderator.[6] The asymmetric addition step, for which the enantiomeric excess is consistently around 92% to 94%, requires the use of 3–5 equivalents of organometallic acetylide and low temperatures (−60 °C to −75 °C). In addition, the strongly basic conditions lead to decomposition of the product. Therefore, it is highly desirable to search for a practical asymmetric synthesis of this new class of dihydroquinazolinones which can then be scaled up to satisfy clinical demands.

The method involving a chiral additive appears to be the most advantageous because it avoids the step involving auxiliary attachment and removal and holds the potential for direct recovery and reuse of the unchanged chiral reagent. We have been developing a practical enantioselective preparation of chiral alchohols with C–C bond formation by alkynylation of a carbonyl group and activation of the C–H bond in terminal alkynes by a combination of zinc salt, tertiary amine, and a readily available chiral amino alcohol as the ligand.[7] We were interested in studying the enantioselective alkynylation of the cyclic *N*-acyl ketimine **1** (see Scheme 1) using a chiral amino alcohol as ligand by activation of the C–H bond in terminal alkynes.

To examine the possibility of alkynylation of ketimine **1** with a terminal acetylene, the reaction was carried out in the presence of zinc salts and triethylamine without a chiral amino alcohol as ligand. Treatment of **1** with one equivalent of cyclopropyl acetylene (**2a**), $Zn(OTf)_2$, and triethylamine gave the racemic adduct **3a** in 95% yield at room temperature after 10 h (Scheme 1). The use of $ZnCl_2$ instead of $Zn(OTf)_2$ could not promote the reaction. This result stimulated us to investigate the asymmetric alkynylation of the ketimine using a chiral ligand.

We examined the alkynylation of the ketimine with derivatives of ephedrine as ligands since *N*-methyl ephedrine (**4a**)[8] and (1*S*, 2*S*)-**5a**[7b] have been successfully used in the asymmetric alkynylation of aldehydes



Scheme 1. The alkynylation of ketimine **1** with cyclopropylacetylene. OTf = trifluoromethanesulfonate.

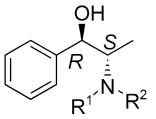
with a terminal acetylene. However, the derivatives of ephedrine ligands **4a** and **4b** (Bn = benzyl) gave very poor enantioselectivity and low yields in the alkynylation reaction, even when 1.1 equivalents of ligand and zinc triflate were used (Table 1, entries 1 and 2). In consideration of cost and availability, we decided to improve the enantioselectivity by using derivatives of chloramphenicol base. Both enantiomers of chloramphenicol bases are easily obtained from commercial chloramphenicol synthesis. In the subsequent investigations, a series of derivatives (**5a**–**5d**, **6**; TMDMS = *tert*-

[*] Prof. Dr. B. Jiang, Y.-G. Si
Shanghai Institute of Organic Chemistry
Chinese Academy of Sciences
354 Fenglin Road, Shanghai 200032 (P.R. China)
Fax: (+86) 21-6416-6128
E-mail: jiangb@mail.sioc.ac.cn

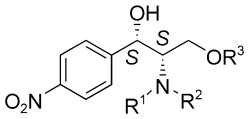
[**] This work was financially supported by the Science & Technology Commission of Shanghai Municipality and the National Natural Science Foundation of China.

Supporting information for this article is available on the WWW under http://www.angewandte.org or from the author.

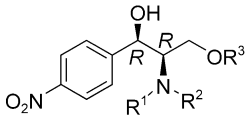
 © 2004 Wiley-VCH Verlag GmbH & Co. KGaA, Weinheim DOI: 10.1002/anie.200352301



4a: R^1=Me;R^2=Me
4b: R^1=Me; R^2=Bn



5a: R^1=Me; R^2=Me; R^3=TMDMS
5b: R^1=Me; R^2=Me; R^3=Tr
5c: R^1=Me; R^2=Me; R^3=*t*Bu
5d: R^1=Me; R^2=Bn; R^3=Tr



6

Table 1: Effect of the chiral ligand on the selectivity of the alkynylation of ketimine **1** with cyclopropylacetylene (see Scheme 1).[a]

Entry	Ligand (equiv)	$Zn(OTf)_2$ [equiv]	NEt_3 [equiv]	*T* [°C]	*t* [h]	Yield of **3a** [%][b]	*ee* **3a** [%][c]	Config. of **3a**[d]
1	**4a** (1.1)	1.1	2.5	25	14	34	44.1	(−)-*S*
2	**4b** (1.1)	1.1	2.5	25	10	24	23.5	(+)-*R*
3	(*S*,*S*)-**5a** (1.1)	1.1	2.5	25	10	95	99.1	(+)-*R*
4	(*S*,*S*)-**5b** (1.1)	1.1	2.5	25	10	93	98.0	(+)-*R*
5	(*S*,*S*)-**5c** (1.1)	1.1	2.5	25	10	91	99.3	(+)-*R*
6	(*S*,*S*)-**5d** (1.1)	1.1	2.5	25	10	90	42.1	(−)-*S*
7	(*S*,*S*)-**5c** (1.1)	1.1	1.5	60	10	64	99.0	(+)-*R*
8	(*S*,*S*)-**5c** (1.1)	1.1	2.5	25	6	95	99.3	(+)-*R*
9	(*R*,*R*)-**6** (1.1)	1.1	2.5	25	6	95	99.2	(−)-*S*

[a] All reactions were performed on 0.5-mmol scale. [b] Yield of isolated product. [c] Determined by HPLC on a chiral stationary phase, Chiralcel OD, *i*PrOH/hexane 10/90, 0.7 mL min^{-1}, 254 nm. [d] The absolute configuration is based on comparison with the literature.[4a, 9]

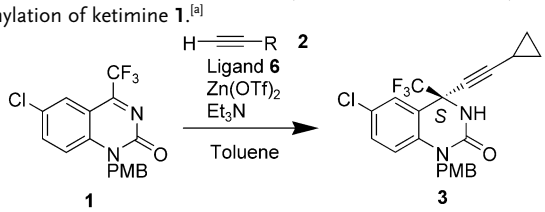
butyldimethylsilyl, Tr = triphenylmethyl) were evaluated as ligands in an effort to obtain more efficient enantioselective alkynylation.

The substituents on the 2-nitrogen and 3-oxygen atoms greatly affected the enantioselectivity of the reaction. The derivatives of chloramphenicol base with an amino group bearing two methyl groups and a C3-oxygen atom attached to a tertiary carbon atom gave excellent enantioselectivities and yields (Table 1, entries 3–5). When one of the amino substituents was changed to benzyl, the enantioselectivity was severely decreased (entry 6). The inexpensive yet effective chiral ligand **5c** and its enantiomer (1*R*, 2*R*)-**6** gave excellent enantioselectivities in the alkynylation reactions (entries 8 and 9). Thus treatment of the cyclic *N*-acyl ketimine **1** with 1.1 equivalents of cyclopropylacetylene, 1.1 equivalents of $Zn(OTf)_2$, 1.1 equivalents of (1*R*, 2*R*)-**6**, and 2.5 equivalents of Et_3N in toluene at room temperature for 6 h provided adduct **3a** (isolated in 95% yield with 99.2% *ee*). Reducing the amount of Et_3N to 1.5 equiv caused a decrease in the chemical yield (entry 7). Removal of the *p*-methoxybenzyl (PMB) group in (−)-**3a**[9] with ceric ammonium nitrate gave (−)-(*S*)-DPC 961 with a specific rotation of $[\alpha]_D^{20} = -63$ (c = 0.275, MeOH), which is identical to the reported value.[4a] Therefore, the stereochemistry of the adduct (−)-**3a** obtained using (1*R*, 2*R*)-**6** as the ligand was assigned the *S* configuration.

In a brief exploration of the scope of this novel asymmetric reaction, other acetylenes were studied by using (1*R*, 2*R*)-**6** as the ligand. All of the phenyl-, alkyl-, and silyl-substituted terminal alkynes gave excellent enantioselectivities (up to 99.5% *ee*) and high yields (Table 2). When the reaction was run on a 100-gram scale, **3a** was obtained in 96% yield and with 99.1% *ee* (Table 2, entry 1). Simple recrystallization from heptane afforded **3a** in 95% yield with over 99% *ee*. The chiral amino alcohol ligand **6** could be recovered unchanged (90% recovery) by basification of the acid aqueous extracts. The recovered ligand was of suitable purity to be recycled directly (entry 2). Acetylenes containing bulky substituents gave the adducts with up to 99.5% *ee* (entries 6–8).

In conclusion, a novel and highly enantioselective alkynylation of cyclic ketimine has been developed for the synthesis of tertiary amines in excellent yield and with high enantioselectivity. This approach has provided an efficient method for the synthesis of the important second-generation non-nucleoside reverse transcriptase inhibitors. The advantages of the enantioselective reaction include the following: 1) only 1.1 equivalents of acetylene is required; 2) the reaction is carried out under standard conditions, avoiding low temperatures and harmful reagents for generating organometallic acetylide; and 3) the chiral ligand based on a derivative of chloramphenicol is easily prepared from a pharmaceutical commodity source, and can be recovered and

Table 2: Effect of the terminal alkynes on the selectivity in the alkynylation of ketimine **1**.[a]



1 **3**

Entry	**2** (R=)	*T* [°C]	*t* [h]	Product **3** (yield [%])[b]	*ee* of **3** [%][c]
1	**2a** (cyclopropyl)	25	6	**3a** (96)	99.1[d]
2	**2a** (cyclopropyl)	25	10	**3a** (95)	99.1[e]
3	**2b** 2-phenylethyl)	25	12	**3b** (73)	98.2
4	**2c** (phenyl)	25	8	**3c** (88)	98.2
5	**2d** (*tert*-butyl)	30	15	**3d** (63)	98.5
6	**2e** (*n*-butyl)	25	6	**3e** (92)	>99.5
7	**2f** (trimethylsilyl)	25	8	**3f** (87)	>99.5
8	**2g** (cyclopentylmethyl)	25	6	**3g** (86)	>99.5

[a] All reactions were performed on 0.5-mmol scale, unless otherwise stated. [b] Yield of isolated product. [c] Determined by HPLC on a chiral stationary phase, Chiralcel OD or AD. [d] The reaction was performed on a 100-gram scale. [e] The chiral ligand was recycled for three runs.

 © 2004 Wiley-VCH Verlag GmbH & Co. KGaA, Weinheim

reused without decreasing enantioselectivity and chemical yield.

Experimental Section

In a typical experiment, cyclopropyl acetylene (**2a**; 73 mg, 1.1 mmol) was added under an argon atmosphere over 2 h at 25 °C to a solution of $Zn(OTf)_2$ (396 mg, 1.1 mmol), (1*R*, 2*R*)-**6** (326 mg, 1.1 mmol), and triethylamine (252 mg, 2.5 mmol) in dried toluene (1 mL). Then ketimine **1** (369 mg, 1 mmol) was added. After 6 h the mixture was cooled to 0 °C, and 6 N HCl (10 mL) was added. The mixture was extracted with EtOAc (3 × 5 mL; Ac = acetyl). The combined organic layer was washed with 6 N HCl (3 × 5 mL), saturated Na_2CO_3 aqueous, and brine and then dried with Na_2SO_4. After removal of solvent under vacuum, the residue was purified by flash chromatography on silica gel (hexane/EtOAc 6/1) to afford **3a** (412 mg, 95 % yield, 99.3 % *ee*). $[\alpha]_D^{20} = -74.1$ ($c = 0.6$ in methanol); ^{1}H NMR (300 MHz, [D$_6$]DMSO): $\delta = 9.00$ (s, 1H), 7.46 (br s, 1H), 7.41 (dd, $J = 2.8$ and 8.9 Hz, 1H), 7.13 (d, $J = 8.2$ Hz, 2H), 6.96 (d, $J = 8.7$ Hz, 1H), 6.87 (d, $J = 8.6$ Hz, 2H), 5.12 (d, $J = 16.4$ Hz, 1H), 4.93 (d, $J = 16.5$ Hz, 1H), 3.69 (s, 3H), 1.52 (m, 1H), 0.93–0.87 (m, 2H), 0.77–0.72 ppm (m, 2H); ^{19}F NMR (282 MHz, [D$_6$]DMSO): $\delta = -81.3$ ppm (s, 3F); ^{13}C NMR (75 MHz, [D$_6$]DMSO): $\delta = 158.3$, 151.2, 136.6, 130.8, 128.4, 127.6, 127.5, 125.8, 123.8 (q, $J = 289$ Hz), 117.1, 116.5, 114.0, 91.8, 68.0, 57.7 (q, $J = 32$ Hz), 54.9, 43.9, 8.3, 8.2, −1.2 ppm; MS (EI) $m/e = 434$ (M^+, 6.6), 365(13.8), 121(100); HR-EI-MS calcd for $C_{22}H_{18}ClF_3N_2O_2$: 434.1009, found: 434.0967.

Received: July 4, 2003 [Z52301]

Keywords: alkynes · amino alcohols · drug design · ketimines · zinc

[1] a) R. Fässler, D. E. Frantz, J. Oetiker, E. M. Carreira, *Angew. Chem.* **2002**, *114*, 3180 – 3182; *Angew. Chem. Int. Ed.* **2002**, *41*, 3054 – 3056; b) C. Fischer, E. M. Carreira, *Org. Lett.* **2001**, *3*, 4319 – 4321; c) D. E. Frantz, R. Fässler, C. S. Tomooka, E. M. Carreira, *Acc. Chem. Res.* **2000**, *33*, 373 – 381; d) C. Wei, C.-J. Li, *J. Am. Chem. Soc.* **2002**, *124*, 5638 – 5639.

[2] J. W. Corbett, S. S. Ko, J. D. Rodgers, L. A. Gearhart, N. A. Magnus, L. T. Bacheler, S. Diamond, S. Jeffrey, R. M. Klabe, B. C. Cordova, S. Garber, K. Logue, G. L. Trainor, P. S. Anderson, S. K. Erickson-Viitanen, *J. Med. Chem.* **2000**, *43*, 2019 – 2030.

[3] a) R. W. King, R. M. Klabe, C. D. Reid, S. K. Erickson-Viitanen, *Antimicrob. Agents Chemother.* **2002**, *46*, 1640 – 1646; b) J. W. Corbett, *Curr. Med. Chem. Anti-Infect. Agents* **2002**, *1*,119 – 140; c) J. W. Corbett, S. S. Ko, J. D. Rodgers, L. T. Bacheler, S. Diamond, C.-M. Lai, S. Jeffrey, R. M. Klabe, S. R. Rabel, J. A. Saye, S. P. Adams, G. L. Trainor, P. S. Anderson, S. K. Erickson-Viitanen, *Antimicrob. Agents Chemother.* **1999**, *43*, 2893 – 2897.

[4] a) N. A. Magnus, P. N. Confalone, L. Storace, M. Patel, C. C. Wood, W. P. Davis, R. L. Parsons, *J. Org. Chem.* **2003**, *68*, 754 – 761; b) N. A. Magnus, P. N. Confalone, L. Storace, *Tetrahedron Lett.* **2000**, *41*, 3015 – 3019.

[5] M. A. Huffman, N. Yasuda, A. E. DeCamp, E. J. J. Grabowski, *J. Org. Chem.* **1995**, *60*, 1590 – 1594.

[6] G. S. Kauffman, G. D. Harris, R. L. Dorow, B. R. P. Stone, R. L. Parsons, Jr., J. A. Pesti, N. A. Magnus, J. M. Fortunak, P. N. Confalone, W. A. Nugent, *Org. Lett.* **2000**, *2*, 3119 – 3121.

[7] a) B. Jiang, Z. L. Chen, X. X. Tang, *Org. Lett.* **2002**, *4*, 3451 – 3453; b) B. Jiang, Z. L. Chen, W. N. Xiong, *Chem. Commun.* **2002**, 1524 – 1525; c) Z. L. Chen, W. N. Xiong, B. Jiang, *Chem. Commun.* **2002**, 2098 – 2099.

[8] a) D. E. Frantz, R. Fässler, E. M. Carreira, *J. Am. Chem. Soc.* **2000**, *122*, 1806 – 1807; b) N. E. Anand, E. M. Carreira, *J. Am. Chem. Soc.* **2001**, *123*, 9687 – 9688.

[9] The specific rotation of **3a** {$[\alpha]_D^{25} = -31.6$ ($c = 0.6$, MeOH)} reported in reference [4a] was not corrected. The reaction with (1*R*, 2*R*)-**6** as ligand gave (−)-(*S*)-**3a** with a specific rotation $[\alpha]_D^{20} = -74.1$ ($c = 0.6$, MeOH), while using (1*S*, 2*S*)-**5c** gave (+)-(*R*)-**3a** with a specific rotation $[\alpha]_D^{20} = +74.3$ ($c = 0.6$, MeOH).

 © 2004 Wiley-VCH Verlag GmbH & Co. KGaA, Weinheim

Tungsten–Silylene Complexes

Hydrido(hydrosilylene)tungsten Complexes with Strong Interactions between the Silylene and Hydrido Ligands**

*Takahito Watanabe, Hisako Hashimoto, and Hiromi Tobita**

The chemistry of transition-metal–silylene complexes has been extensively studied owing to their hypothetically important roles in many catalytic processes.[1] Since the late 1980s a number of base-stabilized and base-free silylene complexes have been synthesized and characterized.[1–11] Among these complexes, those that bear H atoms on the silylene ligand are particularly interesting because the Si–H bond could diversify the reactivity of the M=Si bond through its possible reactions, such as α-elimination, oxidative addition, and hydrosilylation. However, donor-free silylene complexes of this type only became known quite recently. Youngs et al. reported the generation of the cationic silylene complex $[(Et_3P)_3(H)_2Ir{=}Si(H)(2,6\text{-}Mes_2C_6H_3)]B(C_6F_5)_4$ (Mes = 2,4,6-trimethylphenyl),[9] and Tilley et al. reported the formation of neutral $[\{PhB(CH_2PPh_2)_3\}(H)_2Ir{=}Si(H)(2,4,6\text{-}i\text{Pr}_3C_6H_2)]$ and its interesting reactivity.[11] The isolation and structural characterization of such complexes have not yet been achieved.

We previously reported that the photoreaction of $[Cp^*Fe(CO)_2SiMe_3]$ ($Cp^* = \eta^5\text{-}C_5Me_5$) with a relatively bulky H_3SiR' ($R' = t\text{Bu}$, $(CMe_2)_2H$) gave mononuclear dihydrosilyliron complexes $[Cp^*Fe(CO)_2SiH_2R']$.[12] We have now applied this methodology to tungsten complexes and the much bulkier $H_3SiC(SiMe_3)_3$ ligand to synthesize the hydrido(hydrosilylene) complexes $[Cp'(CO)_2(H)W{=}Si(H)\{C(SiMe_3)_3\}]$ (**1a**, $Cp' = Cp^*$; **1b**, $Cp' = \eta^5\text{-}C_5Me_4Et$). Here

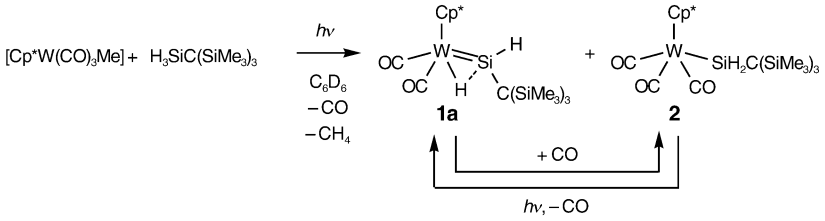
[*] T. Watanabe, Dr. H. Hashimoto, Prof. H. Tobita
Department of Chemistry
Graduate School of Science, Tohoku University
Aoba-ku, Sendai 980–8578 (Japan)
Fax: (+81) 22-217-6543
E-mail: tobita@mail.tains.tohoku.ac.jp

[**] This work was supported by the Ministry of Education, Culture, Sports, Science and Technology of Japan (Grants-in-Aid for Scientific Research Nos. 14204065, 14078202, and 14044010).

 © 2004 Wiley-VCH Verlag GmbH & Co. KGaA, Weinheim DOI: 10.1002/anie.200352383

we report the synthesis, isolation, and full characterization of **1a**, **1b**, a CO adduct of **1a**, namely $[Cp^*(CO)_3WSiH_2\{C(SiMe_3)_3\}]$ (**2**), and the stoichiometric hydrosilylation of acetone by **1a**. The X-ray crystal structure of **1b** and theoretical calculations on a model compound of **1** are also presented.

Irradiation (24 min) of a solution of $[Cp^*W(CO)_3Me]$ and $H_3SiC(SiMe_3)_3$ in C_6D_6 in a sealed pyrex NMR tube with a 450 W medium-pressure Hg lamp produced an approximately 1:1 mixture of silylene complex **1a** and silyl complex **2** in a photostationary state (Scheme 1). When this solution was kept in the sealed tube at room temperature, **1a** reacted with



Scheme 1. Photoreaction of $[Cp^*W(CO)_3Me]$ with $H_3SiC(SiMe_3)_3$.

CO that was produced during photolysis and was completely converted to **2** after 4 days. Complex **1a** was isolated as a single product in 62% yield when the irradiation was performed with periodic removal of CO gas from the irradiated solution. Similarly, the η^5-C_5Me_4Et analogue **1b** was isolated in 44% yield. Isolated **1a** reacted quantitatively with CO gas at room temperature to give **2**. Conversely, **2** was completely converted to **1a** by irradiation and periodic removal of CO gas.

The ^{29}Si NMR spectrum (C_6D_6) of **1a** exhibits two signals for the silylene and silyl ligands at $\delta = 275.3$ and -3.6 ppm, respectively. The large downfield shift of the silylene signal, which is comparable to that of reported hydrido(hydrosilylene) complexes such as $[(Et_3P)_3(H)_2Ir{=}Si(H)(2,6\text{-}Mes_2C_6H_3)]B(C_6F_5)_4$ ($\delta = 239.3$ ppm),[11] suggests that the silicon atom of the silylene ligand in **1a** is essentially sp^2 hybridized. The ^1H NMR spectrum (C_6D_6) of **1a** shows signals for SiH and WH groups at $\delta = 10.39$ ($^1J_{SiH} = 154.9$ Hz) and -10.67 ppm ($^1J_{WH} = 64.9$ Hz), respectively. The significant downfield shift of the SiH signal is consistent with sp^2 hybridization of the silicon atom. Importantly, the $^2J_{SiH}$ coupling constant (28.6 Hz) observed for the WH signal implies the existence of direct interaction between the hydrido and silylene ligands.[13] Note that there is no indication of such interaction for $[\{PhB(CH_2PPh_2)_3\}(H)_2Ir{=}Si(H)R]$,[9] $[(Et_3P)_3(H)_2Ir{=}Si(H)R']B(C_6F_5)_4$,[11] and the related tungsten complexes $[Cp^*(Me_2PCH_2CH_2PMe_2)(H)_2W{=}SiMe_2]B(C_6F_5)_4$[4] and $[Cp^*(CO)_2(H)W{=}SiPh_2(py)]$ (py = pyridine).[5] In the ^{13}C NMR spectrum, **1a** shows a single resonance for carbonyl groups at $\delta = 231.8$ ppm at room temperature, while two signals are observed at $\delta = 233.0$ and 235.3 ppm at 183 K in [D8]toluene ($\Delta G^{\ddagger}_{213\,K} = 41$ kJ mol^{-1}, determined by the coalescence-point method). This result indicates that rapid exchange of carbonyl groups occurs in **1a** at room temperature. In the IR spectrum, the ν_{CO} bands for **1a** (1928 and 1853 cm^{-1}) appear at higher energy than those of $[Cp^*(CO)_2(H)W{=}SiPh_2(py)]$ (1892 and 1806 cm^{-1}).[5] This is apparently attributable to stronger back-donation to the silylene ligand in **1a**, which leads to weaker back-donation to the carbonyl ligands. The ν_{SiH} band appears at 2052 cm^{-1}. A weak and broad absorption observed at 1589 cm^{-1} can be assigned to the WH group, interaction of which with the silylene ligand dramatically reduces the strength of the W–H bond.[14]

The solid-state structure of **1b** was determined by X-ray crystal structure analysis (Figure 1).[15] Selected bond lengths and angles are listed in Table 1. The tungsten atom in **1b** adopts a distorted four-legged piano-stool structure, in which the hydrido and silylene ligands occupy the mutually *cis* positions. The W–Si(1) bond length (2.3703(11) Å) is shorter than those of known silyltungsten complexes (2.469–2.653 Å).[16] This length is even shorter than that of the donor-free silyl(silylene)tungsten complex $[Cp^*W(CO)_2(=SiMes_2)(SiMe_3)]$ (2.3850(12) Å),[7] but somewhat longer than that of

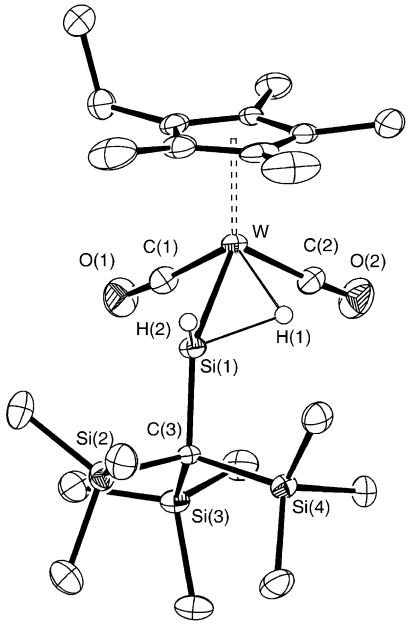


Figure 1. ORTEP plot of **1b**. Thermal ellipsoids are drawn at the 50% probability level.

cationic $[Cp^*(Me_2PCH_2CH_2PMe_2)(H)_2W{=}SiMe_2]B(C_6F_5)_4$ (2.358(2) and 2.354(3) Å).[4] The W–H bond is oriented toward the empty p orbital on the silicon atom of the silylene ligand. Although it is generally difficult to discuss M–H and Si–H interactions on the basis of X-ray structures, the W–H(1) and Si(1)–H(1) distances of 1.82(7) Å and 1.71(6) Å, respectively, in **1b** are both within the range in which a bonding interaction between two atoms exists.[13] The Si(1)-W-H(1) and W-Si(1)-H(1) angles are 46(2) and 50(2)°, respectively. These angles and the W–H and Si–H distances

 © 2004 Wiley-VCH Verlag GmbH & Co. KGaA, Weinheim

Table 1: Selected bond lengths [Å] and angles [°] for the X-ray crystal structure of **1b** and the energy-minimized structure of **1′**.

	1b	**1′**
W–Si(1)	2.3703(11)	2.377
W–H(1)	1.82(7)	1.85
Si(1)–H(1)	1.71(6)	1.71
Si(1)–H(2)	1.54(7)	1.50
W–C(1)	1.950(5)	1.97
W–C(2)	1.964(5)	1.98
Si(1)-W-H(1)	46(2)	46
W-Si(1)-H(1)	50(2)	51
W-Si(1)-C(3)	141.4(1)	135
W-Si(1)-H(2)	110(3)	121

in **1b** strongly indicate the existence of significant interligand interaction between the silylene and the hydrido ligands. Nevertheless, pyramidalization of the Si(1) atom is very small; the Si(1), W, H(2), and C(3) atoms are almost coplanar, and the sum of the valence angles around Si(1) excluding H(1) is 357(3)°. Therefore, **1** has an unprecedented structure in which a hydrido ligand bridges the W=Si bond.

This structural view of **1** was well reproduced by molecular orbital calculations. A DFT calculation at the B3LYP level was performed for model complex $[Cp(CO)_2(H)W{=}Si(H)\{C(SiH_3)_3\}]$ (**1′**).[17] The structural parameters of the energy-minimized structure of **1′** are in good agreement with those of the X-ray crystal structure of **1b** (Table 1). The overlap populations, Wiberg bond indexes,[18a] and NLMO/NPA bond orders[18b] all indicate a significant interaction between the H atom of the WH group and the Si atom of the silylene ligand; for example, NLMO/NPA bond orders: 1.518 for W–Si, 0.511 for W–μ-H, and 0.476 for Si–μ-H. These data are rationalized by the existence of two bonding interactions, that is, the normal two-centered, two-electron (2c–2e) W–Si bond and the 3c–2e W-H-Si bond in the W-H-Si moiety of **1′**, according to NBO analysis.[18c]

Complex **1a** reacted with one molar equivalent of acetone in C_6D_6 at room temperature over 1 h to give mainly the hydrosilylation product $[Cp^*(CO)_2(H)W{=}Si(OCHMe_2)\{C(SiMe_3)_3\}]$ (**3**) together with a few unidentified products. Complex **3** was characterized by ^1H, ^{13}C, and ^{29}Si NMR spectroscopy.[19] This result suggests a possible role of the hydrido(hydrosilylene) complex as an intermediate in the hydrosilylation of ketones with trihydrosilane. We are now investigating **1a** as a catalyst for hydrosilylation reaction.

In summary, **1a** and **b** are the first isolated and structurally characterized hydrido(hydrosilylene) complexes. They exhibit a strong interligand interaction between the hydrido and silylene ligands. Complex **1a** hydrosilylates acetone at room temperature to give **3**. Further studies on the reactivity of **1** are in progress.

Experimental Section

1a: A degassed solution of $[Cp^*W(CO)_3Me]$ (100 mg, 0.239 mmol) and $H_3SiC(SiMe_3)_3$ (70 mg, 0.27 mmol) in hexane in a pyrex sample tube with a teflon vacuum valve was irradiated with a 450 W medium-pressure Hg lamp for 2 h at 5 °C. The reaction mixture was degassed at 15 min intervals by a freeze–pump–thaw cycle on a vacuum line. The reaction mixture was filtered through a membrane filter, and volatile substances were removed from the filtrate. The residue was washed with cold hexane (0.3 mL × 3) and dried to give 98 mg (0.15 mmol, 64 %) of **1a** as orange crystals. ^1H NMR (300 MHz, C_6D_6): $\delta = -10.67$ (d, 1H, $^1J_{WH} = 64.9$, $^2J_{SiH} = 28.6$, $^3J_{HH} = 1.8$ Hz, WH), 0.37 (s, 27H, SiMe), 1.90 (s, 15H, C_5Me_5), 10.39 ppm (d, 1H, $^1J_{SiH} = 154.9$, $^2J_{WH} = 13.3$, $^3J_{HH} = 1.8$ Hz, SiH). $^{13}C\{^1H\}$ NMR (75.5 MHz, C_6D_6): $\delta = 3.9$ (SiMe), 11.4 (C_5Me_5), 24.0 ($CSiMe_3$), 102.7 (C_5Me_5), 232.4 ppm (CO). $^{29}Si\{^1H\}$ NMR (59.6 MHz, C_6D_6): $\delta = -3.6$ (SiMe), 275.3 ppm (WSi, $^1J_{WSi} = 109.9$ Hz). IR (C_6D_6): $\tilde{\nu} = 2052$ (ν_{SiH}), 1928, 1853 (ν_{CO}), 1589 cm^{-1} (ν_{WH}). Elemental analysis (%) calcd for $C_{22}H_{44}O_2Si_4W_1$: C 41.50, H 6.96; Found: C 41.32, H 6.86.

1b: Complex **1b** was obtained as orange crystals by a procedure similar to that for **1a** from $[(\eta^5\text{-}C_5Me_4Et)W(CO)_3Me]$ (240 mg, 0.555 mmol) and $H_3SiC(SiMe_3)_3$ (70 mg, 0.56 mmol). Yield: 160 mg (0.246 mmol, 44 %). ^1H NMR (300 MHz, C_6D_6): $\delta = -10.67$ (d, 1H, $^1J_{WH} = 65.0$, $^2J_{SiH} = 28.3$, $^3J_{HH} = 1.7$ Hz, WH), 0.38 (s, 27H, SiMe), 0.85 (t, 3H, $^3J_{HH} = 7.7$ Hz, $C_5Me_4CH_2CH_3$), 1.90 (s, 6H, C_5Me_4Et), 1.95 (s, 6H, C_5Me_4Et), 2.30 (q, 2H, $^3J_{HH} = 7.7$ Hz, $C_5Me_4CH_2CH_3$), 10.42 ppm (d, 1H, $^1J_{SiH} = 155.1$, $^2J_{WH} = 13.7$, $^3J_{HH} = 1.7$ Hz, SiH). $^{13}C\{^1H\}$ NMR (75.5 MHz, C_6D_6): $\delta = 3.8$ (SiMe), 10.9 (C_5Me_4Et), 11.2 (C_5Me_4Et), 16.4 (C_5Me_4Et), 20.0 (C_5Me_4Et), 23.9 ($CSiMe_3$), 102.0 (C_5Me_4Et), 103.1 (C_5Me_4Et), 108.4 (C_5Me_4Et), 232.1 ppm (CO). $^{29}Si\{^1H\}$ NMR (59.6 MHz, C_6D_6): $\delta = -3.6$ (SiMe), 275.1 ppm (WSi, $^1J_{WSi} = 109.9$ Hz). IR (C_6D_6): $\tilde{\nu} = 2052$ (ν_{SiH}), 1928, 1853 (ν_{CO}), 1589 cm^{-1} (ν_{WH}). Elemental analysis (%) calcd for $C_{23}H_{46}O_2Si_4W_1$: C 42.45, H 7.12; Found: C 42.43, H 7.01.

2: A solution of $[Cp^*W(CO)_3Me]$ (100 mg, 0.239 mmol) and $H_3SiC(SiMe_3)_3$ (70 mg, 0.266 mmol) in hexane was irradiated for 2 h at 5 °C in a sealed pyrex tube. After the sample tube had stood for 60 h at room temperature, the reaction mixture was filtered through a membrane filter, and volatile substances were removed from the filtrate. The residue was washed with cold hexane (0.3 mL × 3) and dried to give 79 mg (0.12 mmol, 50 %) of **2** as orange crystals. ^1H NMR (300 MHz, C_6D_6): $\delta = 0.49$ (s, 27H, SiMe), 1.58 (s, 15H, C_5Me_5), 4.37 ppm (s, 2H, SiH, $^1J_{SiH} = 179.3$ Hz). $^{13}C\{^1H\}$ NMR (75.5 MHz, C_6D_6): $\delta = -5.0$ ($CSiMe_3$), 5.43 (SiMe), 9.6 (C_5Me_5), 102.2 (C_5Me_5), 223.9 ppm (CO). $^{29}Si\{^1H\}$ NMR (59.6 MHz, C_6D_6): $\delta = -27.2$ (WSi), 0.80 ppm (SiMe). IR (KBr pellet): $\tilde{\nu} = 2096$ (ν_{SiH}), 1982, 1903, 1888 cm^{-1} (ν_{CO}). Elemental analysis (%) calcd for $C_{23}H_{44}O_3Si_4W_1$: C 41.55, H 6.67; Found C 41.85, H 6.69.

Received: July 15, 2003
Revised: September 22, 2003 [Z52383]

Keywords: hydrido ligands · hydrosilylation · silicon · silylene complexes · tungsten

[1] a) T. D. Tilley in *The Chemistry of Organic Silicon Compounds* (Eds.: S. Patai, Z. Rappoport), Wiley, New York, **1989**, pp. 1415–1477; b) M. S. Eisen in *The Chemistry of Organic Silicon Compounds*, *Vol. 2* (Eds.: Z. Rappoport, Y. Apeloig), Wiley, New York, **1998**, pp. 2037–2128.
[2] a) H. Ogino, *Chem. Rec.* **2002**, *2*, 291–305; b) M. Okazaki, H. Tobita, H. Ogino, *Dalton Trans.* **2003**, 493–506.
[3] J. C. Peters, J. D. Feldman, T. D. Tilley, *J. Am. Chem. Soc.* **1999**, *121*, 9871–9872.
[4] S. R. Klei, T. D. Tilley, R. G. Bergman, *J. Am. Chem. Soc.* **2000**, *122*, 1816–1817.
[5] H. Sakaba, M. Tsukamoto, T. Hirata, C. Kabuto, H. Horino, *J. Am. Chem. Soc.* **2000**, *122*, 11511–11512.
[6] B. V. Mork, T. D. Tilley, *J. Am. Chem. Soc.* **2001**, *123*, 9702–9703.
[7] K. Ueno, S. Asami, N. Watanabe, H. Ogino, *Organometallics* **2002**, *21*, 1326–1328.

 © 2004 Wiley-VCH Verlag GmbH & Co. KGaA, Weinheim

[8] S. R. Klei, T. D. Tilley, R. G. Bergman, *Organometallics* **2002**, *21*, 3376 – 3387.
[9] R. S. Simons, J. C. Gallucci, C. A. Tessier, W. J. Youngs, *J. Organomet. Chem.* **2002**, *654*, 224 – 228.
[10] B. V. Mork, T. D. Tilley, *Angew. Chem.* **2003**, *115*, 371 – 374; *Angew. Chem. Int. Ed.* **2003**, *42*, 357 – 360.
[11] J. D. Feldman, J. C. Peters, T. D. Tilley, *Organometallics* **2002**, *21*, 4065 – 4075.
[12] a) Y. Kawano, H. Tobita, H. Ogino, *J. Organomet. Chem.* **1992**, *428*, 125 – 143; b) L.-S. Luh, Y.-S. Wen, H. Tobita, H. Ogino, *Bull. Chem. Soc. Jpn.* **1998**, *71*, 2865 – 2871.
[13] J. Y. Corey, J. Braddock-Wilking, *Chem. Rev.* **1999**, *99*, 175 – 292.
[14] The calculated W–H stretching frequency (1525 cm^{-1}) is close to the experimental value. Accordingly, the ν_{SiD} and ν_{WD} bands of [Cp*(CO)$_2$(D)W=Si(D){C(SiMe$_3$)$_3$}] appear at 1481 and 1142 cm^{-1}, respectively.
[15] **1b**: monoclinic; $P2_1/n$; $a = 15.9541(5)$, $b = 11.8021(3)$, $c = 17.2847(5)$ Å, $\beta = 114.6906(14)°$, $V = 2957.02(15)$ Å^3, $Z = 4$; $C_{23}H_{46}O_2Si_4W$, $T = 150(2)$ K, 24833 reflections, 6358 independent reflections ($R_{int} = 0.0555$), $R1 = 0.0297$ ($I > 2\sigma(I)$), $wR2 = 0.0875$; $\mu = 4.085$ mm^{-1}; refinement by full-matrix least-squares methods on F^2. The positions of the hydrogen atoms of the SiH and the WH groups were located in the Fourier-difference electron-density map and were refined with isotropic thermal parameters. CCDC-214274 contains the supplementary crystallographic data for this paper. These data can be obtained free of charge via www.ccdc.cam.ac.uk/conts/retrieving.html (or from the Cambridge Crystallographic Data Centre, 12, Union Road, Cambridge CB2 1EZ, UK; fax: (+44) 1223-336-033; or deposit@ccdc.cam.ac.uk).
[16] Based on a search of the Cambridge Structural Database, CSD version 5.24 (November, **2002**).
[17] The detailed analysis will be presented elsewhere.
[18] a) K. Wiberg, *Tetrahedron* **1686**, *24*, 1083 – 1096; b) NLMO/NPA (Natural localized molecular orbital/natural population analysis); A. E. Reed, F. Weinhold, *J. Chem. Phys.* **1985**, *83*, 1736 – 1740; c) E. D. Glendening, A. E. Reed, J. E. Carpenter, F. Weinhold, NBO (natural bond orbital), NBO Version 3.1.
[19] Spectral data of **3**: ^{1}H NMR (300 MHz, C_6D_6): $\delta = -6.12$ (s, 1H, WH, $^1J_{WH} = 56.0$ Hz, $^2J_{SiH} = 34.0$ Hz), 0.46 (s, 27H, SiMe), 1.39 (d, $^3J_{HH} = 6.3$ Hz, 6H, OCH*Me*$_2$), 1.94 (s, 15H, C_5Me_5), 4.84 ppm (sept, $^3J_{HH} = 6.3$ Hz, 1H, OC*H*Me$_2$). ^{13}C{^{1}H} NMR (75.5 MHz, C_6D_6): $\delta = 6.8$ (SiMe), 11.5 (C_5*Me*$_5$), 25.8 (OCH*Me*$_2$), 33.6 (*C*SiMe$_3$), 68.7 (SiO*C*HMe$_2$), 100.9 (*C*$_5$Me$_5$), 225.6 (CO). ^{29}Si{^{1}H} NMR (59.6 MHz, C_6D_6): $\delta = -2.1$ (SiMe), 229.2 ppm (WSi, $^1J_{WSi} = 130.8$ Hz).

 © 2004 Wiley-VCH Verlag GmbH & Co. KGaA, Weinheim

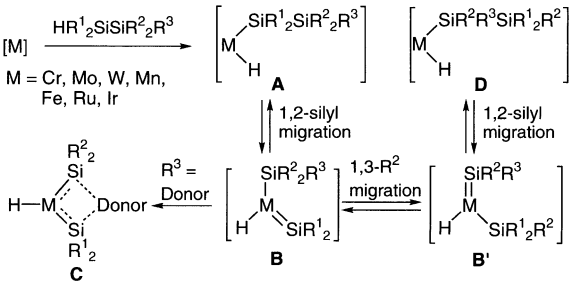
Silyl(silylene)–Iron Complexes

Direct Evidence for Extremely Facile 1,2- and 1,3-Group Migrations in an $FeSi_2$ System**

Hiromi Tobita, Akihisa Matsuda, Hisako Hashimoto, Keiji Ueno, and Hiroshi Ogino*

The formation and high reactivity of transition-metal–element multiple bonds plays an important role in transition-metal-catalyzed reactions, in particular, by facilitating the cleavage and formation of usually robust bonds. Olefin metathesis is a typical and very useful example of this type of reaction, in which carbene complexes, which have a metal–carbon double bond, are not only key intermediates but may also act as high-performance catalysts.[1] In contrast to metal–carbon multiple bonds, metal–element multiple bonds, where the element is from the third or subsequent row of the periodic table, have been much less widely investigated. Among them, silylene complexes, which possess a metal–silicon double bond, have been the most extensively studied,[2–9] but the mechanisms of their reactions remain rather unclear.

Both ourselves and Pannell's group have insisted, through the generation of silyl(silylene) complexes with transition metals from groups 6 to 9 and the preparation of their donor-stabilized forms, that 1,2- and 1,3-group migrations of these systems (Scheme 1) occur very easily under mild conditions, and cause the metal-catalyzed oligomerization/deoligomerization, isomerization, and redistribution of organosilicon



Scheme 1. Illustrating the 1,2- and 1,3-group migrations in silyl(silylene) complexes with metals of groups 6 to 9.

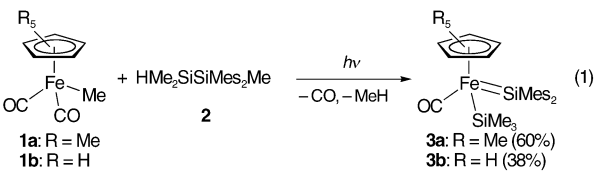
[*] Prof. H. Tobita, A. Matsuda, Dr. H. Hashimoto
Department of Chemistry, Graduate School of Science
Tohoku University, Sendai 980-8578 (Japan)
Fax: (+81) 22-217-6543
E-mail: tobita@mail.tains.tohoku.ac.jp
Prof. K. Ueno
Department of Chemistry, Faculty of Engineering
Gunma University, Kiryu 376-8515 (Japan)
Prof. H. Ogino
Miyagi Study Center, The University of the Air, Sendai 980-8577 (Japan)

[**] This work was supported by the Ministry of Education, Culture, Sports, Science and Technology, Japan [Grants-in-Aid for Scientific Research Nos. 13440193, 14204065, and 14078202]

 DOI: 10.1002/anie.200352519 © 2004 Wiley-VCH Verlag GmbH & Co. KGaA, Weinheim

compounds.[2,3,10–12] In fact, this mechanism was notably successful in explaining the redistribution reactions of various organosilicon, -germanium, and -phosphorus systems.[13–15] We have previously given direct experimental evidence for 1,2-silyl-migration from Si to the metal M (**A**→**B** or **D**→**B′**) via isolating complexes of the type **B′** or **C**, which are formed in reactions of complexes of type **A** or **D**.[2,3,16] Furthermore, we have observed fluxional behavior in the 1,3-migration of methyl groups on an externally donor-stabilized silyl(silylene)iron complex [Cp(CO)Fe(=$SiMe_2$←HMPA)$SiMe_3$] (HMPA = hexamethyl phosphoramide) by variable-temperature NMR spectroscopy.[17] In this process, we assumed that the coordinated HMPA dissociates at elevated temperatures to generate a donor-free silyl(silylene) complex. We now give direct evidence for 1,3-alkyl migration (**B**→**B′** and vice versa) and 1,2-silyl migration from M to Si (**B**→**A** or **B′**→**D**) by employing newly synthesized, donor-free silyl(silylene)iron complexes.

Photolysis of [Cp′$Fe(CO)_2Me$] (**1a**: Cp′ = η^5-C_5Me_5 (Cp*); **1b**: Cp′ = η^5-C_5H_5 (Cp)) in the presence of $HSiMe_2$-$SiMes_2Me$ (**2**; Mes = mesityl (2,4,6-trimethylphenyl)) produced the first donor-free silyl(silylene)iron complexes [Cp′Fe(CO)(=$SiMes_2$)$SiMe_3$] (**3a**: Cp′ = Cp*, 60%; **3b**: Cp′ = Cp, 38% yield, calculated by NMR spectroscopy [Eq. (1)]). Complex **3a** could be isolated as orange crystals in 40% yield, whereas isolation of **3b** was unsuccessful



because of its extreme instability. We have previously synthesized the tungsten analogue of **3a** by a similar method, but the chemistry has not been thoroughly investigated.[16]

The molecular structure of **3a** is shown in Figure 1.[18] The two mesityl groups are on the silylene ligand, while all of the three methyl groups are on the silyl ligand. The iron–silylene bond (Fe–Si(1) 2.154(1) Å) is about 9% shorter than the iron–silyl bond (Fe–Si(2) 2.343(2) Å) and is the shortest reported bond of this type.[19] The silylene silicon atom is tricoordinate and its geometry is almost planar (sum of the three bond angles around Si(1) = 359.3 (2)°). No intermolecular bonding interaction was found. The ^{29}Si NMR spectra of **3a** and **3b** show signals for the dimesitylsilylene ligand at extremely low field (365.8 ppm for **3a** and 372.0 ppm for **3b**), which is characteristic of the donor-free dialkyl- or diarylsilylene complexes.[5,16] Also present are the resonances for the trimethylsilyl ligand (28.4 ppm for **3a** and 31.0 ppm for **3b**). These data unambiguously demonstrate the donor-free silyl(silylene)iron structures. In each of the ^{1}H NMR spectra of **3a** and **3b**, all the four *o*-Me groups, four *m*-H atoms, and two *p*-Me groups in two mesityl groups are inequivalent at room temperature. Apparently, the extremely congested

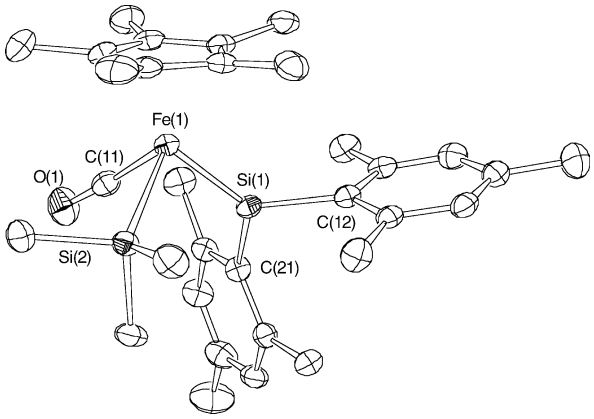
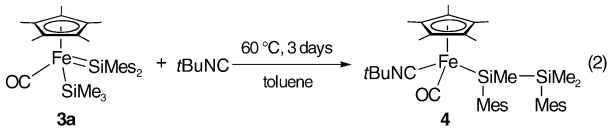


Figure 1. ORTEP drawing of **3a** showing thermal ellipsoids at the 50% probability level. Selected bond lengths [Å] and angles [°]: Fe(1)-Si(1) 2.154(1), Fe(1)-Si(2) 2.343(1), Fe(1)-C(11) 1.724(4); Si(1)-Fe(1)-Si(2) 93.15, Fe(1)-Si(1)-C(12) 127.8(1), Fe(1)-Si(1)-C(21) 127.2(1), C(12)-Si(1)-C(21) 104.3(2).

structures of **3a** and **3b** lead to hindered rotation around both the Fe=Si and the Si–C(mesityl) bonds.

Sharma and Pannell previously reported that the photolysis of linear oligosilanyl–[$Fe(CO)_2Cp$] complexes containing more than three silicon atoms produces highly branched, tris(silyl)silyl iron complexes in high yields, for example, [{$Me_3Si(Me_2Si)_3$}$Fe(CO)_2Cp$] is converted to [$(Me_3Si)_3Si$–$Fe(CO)_2Cp$] on irradiation.[12] In this reaction, the 1,2-silyl migration from the Fe center to the silylene silicon atom on the silyl(silylene) iron intermediates (corresponding to **B**→**A** or **B′**→**D**; Scheme 1) could play an important role.

To confirm this hypothesis, thermolysis of **3a** in the presence of several two-electron-donor ligands was carried out. As a result, when **3a** was heated to 80 °C for 6 h in the presence of *t*BuNC, a disilanyl complex [Cp*Fe(CO)(CN-



*t*Bu)SiMesMeSiMesMe_2] (**4**) was isolated as a main product in 25% yield [Eq. (2)]. The ^{29}Si NMR signals of **4** appear in the normal range of disilanyl iron complexes (9.5 ppm for Fe–Si and −11.2 ppm for terminal Si atoms). The molecular structure of **4** is shown in Figure 2.[18] A *t*BuNC molecule is terminally coordinated to the iron center, and each of the α- and β-Si atoms of the disilanyl ligand is coordinated to a mesityl group. The Fe–Si(1) and Si(1)–Si(2) bond lengths are 2.4107(7) and 2.4004(9) Å, respectively, which are normal values for single bonds.

A mechanism that can rationalize the reactions in Equations (1) and (2) is illustrated in Scheme 2. From **1a**, successive CO dissociation, oxidative addition of **1**, methane reductive elimination, 1,2-silyl migration, and 1,3-methyl migration occur to afford **3a**. Three isomeric donor-free silyl(silylene) complexes (**3a**, **3a′**, and **3a″**) are in rapid

 © 2004 Wiley-VCH Verlag GmbH & Co. KGaA, Weinheim

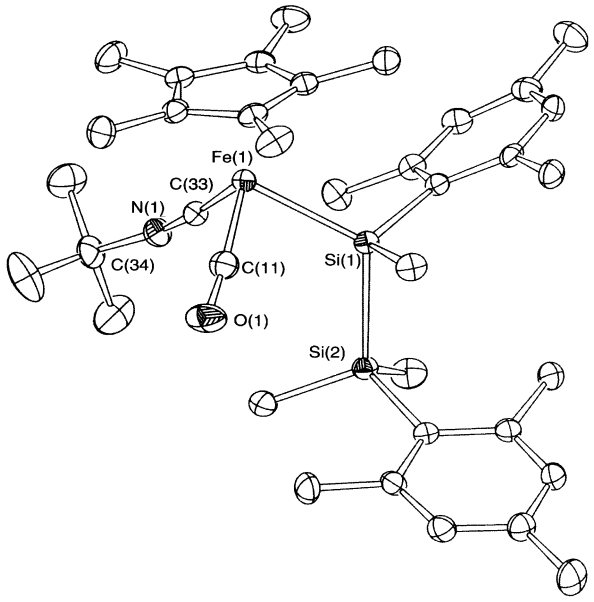
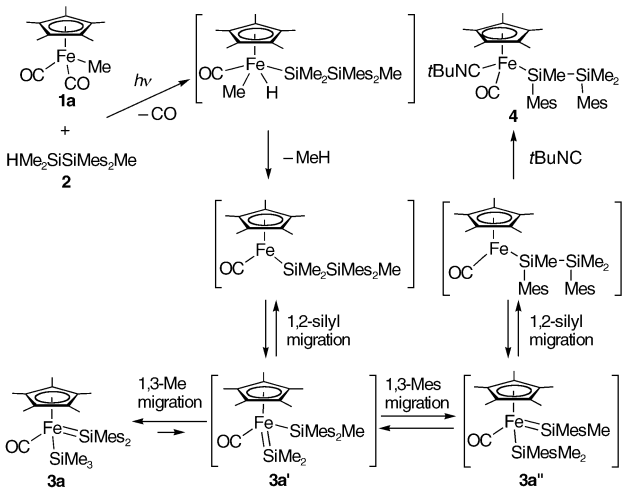


Figure 2. ORTEP drawing of **4** showing thermal ellipsoids at the 50% probability level. Selected bond lengths [Å] and angles [°]: Fe(1)-Si(1) 2.4107(7), Fe(1)-C(11) 1.732(2), Fe(1)-C(33) 1.808(2), Si(1)-Si(2) 2.4004(9), N(1)-C(33) 1.174(3); Fe(1)-Si(1)-Si(2) 118.74(3), Si(1)-Fe(1)-C(11) 84.23(9), Si(1)-Fe(1)-C(33) 94.92(7), C(11)-Fe(1)-C(33) 92.5(1), Fe(1)-C(33)-N(1) 173.4(2), C(33)-N(1)-C(34) 162.0(3).



Scheme 2. A mechanism for the formation of [Cp*Fe(CO)(=$SiMes_2$)-$SiMe_3$] (**3a**) and [Cp*Fe(CO)(CN*t*Bu)SiMesMeSiMesMe$_2$] (**4**).

equilibrium at room temperature, where **3a** is the major and only observable isomer. When this equilibrium mixture is heated in the presence of *t*BuNC, 1,2-migration of the silyl ligand onto the silylene ligand followed by coordination of *t*BuNC to the unsaturated iron center occurs to produce **4**. It should be noted that both **3a** and **4** take the structures that obviously minimize the steric repulsion between the bulky groups, namely, the two mesityl groups and a pentamethylcyclopentadienyl group. In other words, **3a** and **4** are the thermodynamically controlled products. Both the formation of **3a** and its conversion to **4** involves 1,2-silyl migration and 1,3-alkyl and/or aryl migration processes. These are considered to be concerted processes with low energy barriers.[20] Importantly, through the latter process, usually robust Si–C bonds readily cleave under extremely mild conditions: The typical bond dissociation energy of the Si–C single bond is 301 kJ mol^{-1}, which is comparable to that of the C–C single bond (346 kJ mol^{-1}).[21]

In this paper, we have provided the most straightforward evidence for extremely facile 1,2- and 1,3-group migrations in silyl(silylene) complex systems. These observations clearly show how organosilicon species bound to a transition-metal center can change their structures in an amazingly dynamic fashion through extremely facile Si–C and Si–Si bond fission and formation processes. A more detailed elucidation of the dynamic behavior is underway.

Experimental Section

3a: A pentane solution (3 mL) of [Cp*Fe(CO)$_2$Me] (**1a**; 1.02 g, 3.89 mmol) and $HSiMe_2SiMes_2Me$ (**2**; 1.01 g, 2.96 mmol) in a pyrex sample tube with a teflon vacuum valve was irradiated for 80 min with a 450 W medium-pressure Hg lamp immersed in a water bath (4 °C). The reaction mixture was degassed every 20 min by a conventional freeze-pump-thaw cycle on a vacuum line. The reaction mixture was filtered through a glass filter and volatiles were removed from the filtrate under reduced pressure. The residue was recrystallized from pentane at −30 °C to afford orange crystals of [Cp*Fe(CO)-(=$SiMes_2$)$SiMe_3$] (**3a**) in 40% yield (0.660 g, 1.18 mmol). ^{1}H NMR (300 MHz, [D$_6$]benzene): $\delta = 0.59$ (s, 9H, $SiMe_3$), 1.56 (s, 15H, C_5Me_5), 2.05 (s, 3H, *o*-Me), 2.10 (s, 3H, *o*-Me), 2.12 (s, 3H, *o*-Me), 2.15 (s, 3H, *o*-Me), 2.74 (s, 3H, *p*-Me), 3.05 (s, 3H, *p*-Me), 6.51 (s, 1H, *m*-H), 6.56 (s, 1H, *m*-H), 6.79 (s, 1H, *m*-H), 6.86 ppm (s, 1H, *m*-H); ^{13}C{^{1}H} NMR (75.5 MHz, [D$_6$]benzene): $\delta = 9.5$ ($SiMe_3$), 10.1 ($C_5\mathit{Me}_5$), 21.1 (*p*-Me), 23.7 (*o*-Me), 24.0 (*o*-Me), 24.7 (*o*-Me), 24.9 (*o*-Me), 93.7 (C_5Me_5), 128.7 ($C_6H_2Me_3$), 129.2 ($C_6H_2Me_3$), 138.7 ($C_6H_2Me_3$), 138.9 ($C_6H_2Me_3$), 139.2 ($C_6H_2Me_3$), 139.3 ($C_6H_2Me_3$), 142.5 ($C_6H_2Me_3$), 142.8 ($C_6H_2Me_3$), 145.3 ($C_6H_2Me_3$), 145.6 ($C_6H_2Me_3$), 220.2 ppm (CO); ^{29}Si{^{1}H} NMR (59.6 MHz, [D$_6$]benzene): $\delta = 28.4$ ($SiMe_3$), 365.8 ppm ($SiMes_2$); IR ([D$_6$]benzene solution): $\tilde{\nu} = 1905$ cm^{-1} (s, ν_{CO}); MS (EI, 70 eV) 558 (M^+, 8), 543 (M^+-CH_3, 30), 515 (M^+-CH_3-CO, 12), 73 ($SiMe_3$, 100); elemental analysis calcd (%) for $C_{32}H_{46}FeOSi_2$: C 68.79, H 8.30; found: C 69.07, H 8.41.

4: A toluene solution (5 mL) of **3a** (0.103 g, 0.184 mmol) and *t*BuNC (0.0730 g, 0.878 mmol) in a pyrex tube with a teflon vacuum valve was heated to 80 °C for 6 h. After removal of volatiles, the yellow residue was recrystallized from toluene/hexane to afford yellow crystals of [Cp*Fe(CO)(CN*t*Bu)SiMesMeSiMesMe$_2$] (**4**) in 25% yield (0.030 g, 0.047 mmol). ^{1}H NMR (300 MHz, [D$_6$]benzene): $\delta = 0.69$ (s, 3H, SiMesMe_2), 0.97 (s, 3H, SiMesMe_2), 1.09 (s, 3H, SiMesMe), 1.46 (s, 15H, C_5Me_5), 2.15 (s, 3H, *p*-Me), 2.23 (s, 3H, *p*-Me), 2.45 (s, 6H, *o*-Me), 2.52 (s, 3H, *o*-Me), 2.64 (s, 3H, *o*-Me), 6.78 (s, 2H, *m*-H), 6.84 (s, 1H, *m*-H), 6.88 ppm (s, 1H, *m*-H); ^{13}C{^{1}H} NMR (75.5 MHz, [D$_6$]benzene): $\delta = 6.4$ (SiMe), 6.7 (SiMe), 9.9 ($C_5\mathit{Me}_5$), 11.7 (SiMe), 21.1 ($C_6H_2\mathit{Me}_3$), 25.8 ($C_6H_2\mathit{Me}_3$), 26.8 ($C_6H_2\mathit{Me}_3$), 28.0 ($C_6H_2\mathit{Me}_3$), 31.2 ($C\mathit{Me}_3$), 56.3 (CMe$_3$), 92.7 (C_5Me$_5$), 128.9 (C_6H_2Me$_3$), 129.1 (C_6H_2Me$_3$), 129.3 (C_6H_2Me$_3$), 130.1 (C_6H_2Me$_3$), 136.3 (C_6H_2Me$_3$), 136.9 (C_6H_2Me$_3$), 137.2 (C_6H_2Me$_3$), 140.3 (C_6H_2Me$_3$), 144.5 (C_6H_2Me$_3$), 145.3 (C_6H_2Me$_3$), 176.6 (FeCN), 222.3 ppm (CO); ^{29}Si{^{1}H} NMR (59.6 MHz, [D$_6$]benzene): $\delta = -11.2$ ($SiMesMe_2$), 9.5 ppm (SiMesMe); IR ([D$_6$]benzene solution): $\tilde{\nu} = 1907$ cm^{-1} (s) (ν_{CO}); MS (EI, 70 eV) 641 (M^+, 0.3), 626 (M^+–Me, 0.6), 556 (M^+–CO–*t*Bu, 4), 515 (M^+–CO–CN*t*Bu–Me, 7), 464

 © 2004 Wiley-VCH Verlag GmbH & Co. KGaA, Weinheim

(M^+−CO−2Me−Mes, 100); elemental analysis calcd (%) for $C_{37}H_{55}FeONSi_2$: C 69.24, H 8.64, N 2.18; found: C 69.31, H 8.66, N 2.28.

Received: July 30, 2003 [Z52519]

Keywords: group migration · iron · ligands · rearrangement · transition metals

[1] T. M. Trnka, R. H. Grubbs, *Acc. Chem. Res.* **2001**, *34*, 18.
[2] H. Ogino, *Chem. Rec.* **2002**, *2*, 291.
[3] M. Okazaki, H. Tobita, H. Ogino, *Dalton Trans.* **2003**, 493.
[4] S. R. Klei, T. D. Tilley, R. G. Bergman, *Organometallics* **2002**, *21*, 3376, 4648.
[5] J. D. Feldman, J. C. Peters, T. D. Tilley, *Organometallics* **2002**, *21*, 4065.
[6] H. Sakaba, M. Tsukamoto, T. Hirata, C. Kabuto, H. Horino, *J. Am. Chem. Soc.* **2000**, *122*, 11511.
[7] T. A. Schmedake, M. Haaf, B. J. Paradise, D. Powell, R. West, *Organometallics* **2000**, *19*, 3263.
[8] S. H. A. Petri, D. Eikenberg, B. Neumann, H.-G. Stammler, P. Jutzi, *Organometallics* **1999**, *18*, 2615.
[9] B. Gehrhus, P. B. Hitchcock, M. F. Lappert, H. Maciejewski, *Organometallics* **1998**, *17*, 5599.
[10] K. H. Pannell, J. Cervantes, C. Hernandez, J. Cassias, S. P. Vincenti, *Organometallics* **1986**, *5*, 1056.
[11] H. Tobita, K. Ueno, H. Ogino, *Chem. Lett.* **1986**, 1777.
[12] H. K. Sharma, K. H. Pannell, *Chem. Rev.* **1995**, *95*, 1351.
[13] K. Tamao, G.-R. Sun, A. Kawachi, *J. Am. Chem. Soc.* **1995**, *117*, 8043.
[14] S. M. Katz, J. A. Reichl, D. H. Berry, *J. Am. Chem. Soc.* **1998**, *120*, 9844.
[15] P. Braunstein, M. Knorr, C. Stern, *Coord. Chem. Rev.* **1998**, *178–180*, 903.
[16] K. Ueno, S. Asami, N. Watanabe, H. Ogino, *Organometallics* **2002**, *21*, 1326.
[17] K. Ueno, K. Nakano, H. Ogino, *Chem. Lett.* **1996**, 459.
[18] **3a**: monoclinic; $P2_1/c$; $a = 10.4593(2)$, $b = 18.3566(6)$, $c = 16.0338(4)$ Å, $\beta = 96.5724(7)°$; $V = 3058.2(1)$ Å^3; $Z = 4$; $C_{32}H_{46}FeOSi_2$; $T = 150$ K, 26965 reflections, 6692 independent ($R_{int} = 0.043$); $R1 = 0.046$ ($I > 3\sigma(I)$), $Rw = 0.106$; $\mu = 5.93$ cm^{-1}; Full-matrix least-squares on F^2. **4**: monoclinic; $P2_1$; $a = 8.8296(2)$, $b = 20.6795(5)$, $c = 9.9852(2)$ Å, $\beta = 99.970(1)°$; $V = 1795.68(7)$ Å^3; $Z = 2$; $C_{37}H_{55}FeNOSi_2$; $T = 150$ K, 17660 reflections, 4233 independent ($R_{int} = 0.036$); $R1 = 0.027$ ($I > 2\sigma(I)$), $Rw = 0.063$; $\mu = 5.14$ cm^{-1}; Full-matrix least-squares on F^2. CCDC-215618 (**3a**) and CCDC-215619 (**4**) contains the supplementary crystallographic data for this paper. These data can be obtained free of charge via www.ccdc.cam.ac.uk/conts/retrieving.html (or from the Cambridge Crystallographic Data Centre, 12, Union Road, Cambridge CB21EZ, UK; fax: (+44) 1223-336-033; or deposit@ccdc.cam.ac.uk).
[19] Based on a search of the Cambridge Structural Database, CSD version 5.24 (November **2002**).
[20] K. Morokuma, private communication; Z. Liu, PhD Thesis, Emory University, **2000**, chap. 3. MO calculation (B3LYPLANL2DZ) for the 1,3-migration of a Me group from a silyl ligand to a silylene ligand in [CpFe(CO)(=SiMe$_2$)SiMe$_3$] showed that this is a concerted process with no intermediate and the activation energy of this process is 12.0 kcal mol^{-1}.
[21] J. Emsley, *The Elements*, 3rd ed., Oxford University Press, Oxford, **1998**.

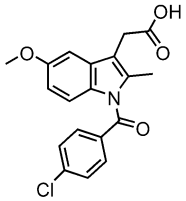
 © 2004 Wiley-VCH Verlag GmbH & Co. KGaA, Weinheim

Kinase Inhibitors

Synthesis and Biological Evaluation of an Indomethacin Library Reveals a New Class of Angiogenesis-Related Kinase Inhibitors**

Claudia Rosenbaum, Patrick Baumhof, Ralf Mazitschek, Oliver Müller, Athanassios Giannis, and Herbert Waldmann**

The combinatorial synthesis of small-molecule libraries on solid supports has emerged as a powerful and widely used method for the discovery of new biologically active compounds, in particular those for subsequent application in chemical biology and medicinal chemistry research. The choice of the underlying molecular framework of the individual library members is vital to the success of this approach. The hit rates in biochemical and cell biological assays, as well as the quality of the hits and the lead compounds derived from them are expected to be particularly high, even with relatively small libraries, if the compound class in question can be regarded as biologically prevalidated.[1] In this regard, indoles represent one of the most relevant structural classes. The plethora of indole-based biologically active natural products and indole-derived drugs spans an enormous range of biological activity. Consequently, the synthesis of indole-based compound libraries has received a great deal of attention, in particular in drug development.[2] Among the biologically active indole derivatives, indomethacin (**1**) is of particular interest. This compound belongs to the nonsteroidal antiinflammatory drugs (NSAIDs), which are widely applied in the treatment of, for example, pain, arthritis,[3] cardiovascular diseases,[4,5]



Indomethacin (**1**)

[*] Dipl.-Chem. P. Baumhof, Dr. R. Mazitschek, Prof. Dr. A. Giannis
Max-Planck-Institut für molekulare Physiologie
Abteilung Chemische Biologie
Otto-Hahn-Strasse 11, 44227 Dortmund (Germany)
and
Universität Dortmund, Fachbereich 3, Organische Chemie
Fax: (+49) 231-133-2499
E-mail: giannis@chemie.uni-leipzig.de

Dr. C. Rosenbaum, Prof Dr. H. Waldmann
Universität Leipzig
Institut für Organische Chemie
Johannisallee 29, 04103 Leipzig (Germany)
Fax: (+49) 341-9736-599
E-mail: herbert.waldmann@mpi-dortmund.mpg.de

PD Dr. O. Müller
Max-Planck-Institut für molekulare Physiologie
Abteilung Strukturelle Biologie

[**] This research was supported by the Max-Planck-Gesellschaft and the Fonds der Chemischen Industrie.

Supporting information for this article is available on the WWW under http://www.angewandte.org or from the author.

 © 2004 Wiley-VCH Verlag GmbH & Co. KGaA, Weinheim DOI: 10.1002/anie.200352582

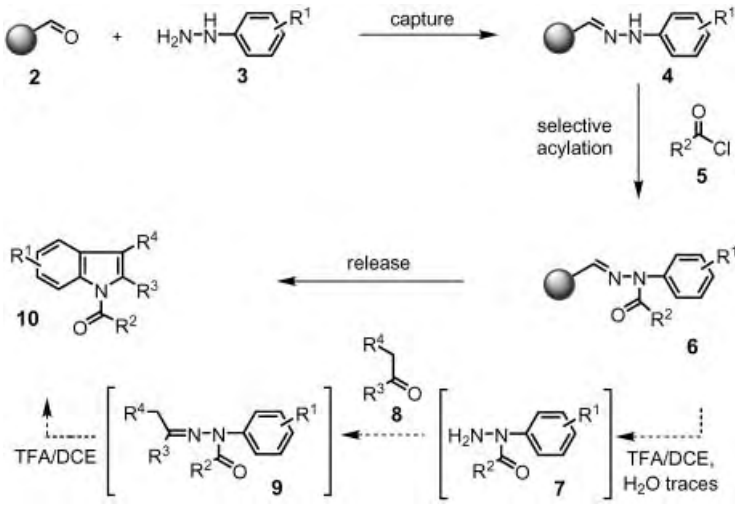
and Alzheimer's disease,[6,7] and in the treatment and prevention of cancer.[8,9]

It has been demonstrated that indomethacin induces G1 arrest and apoptosis of human colorectal cancer cells by influencing the Wnt signaling pathway,[10] downregulates the transcriptional activity of the peroxisome proliferation-activated receptor δ,[11] and inhibits the formation of new blood vessels from pre-existing ones (angiogenesis) through direct effects on endothelial cells mediated by the mitogen-activated protein (MAP) kinase signaling pathway.[9] Although the precise molecular targets of indomethacin in these processes have not been identified unambiguously, it is clear that indomethacin fulfils the criterium of biological prevalidation. In fact, its core may be regarded as a privileged structure.[12]

We have developed a synthesis of an indomethacin library and investigated the biological activity of the library compounds with respect to possible inhibition of receptor tyrosine kinases involved in angiogenesis. When planning the synthesis, we envisioned that application of the Fischer indole synthesis would allow a fairly diverse library to be built up from three readily available building blocks in a very short reaction sequence.[13] To establish a particularly practical and efficient method, we implemented a "resin-capture-release" strategy[14] that obviated the need for permanent attachment to and final detachment from the solid support, which would have required linker groups to be added and removed in two additional steps. The chosen strategy is summarized in Scheme 1. An aldehyde resin **2** is condensed with hydrazines **3** to yield polymer-bound hydrazones **4**. The polymer in intermediates **4** serves on the one hand as a reagent-capturing auxiliary, which allows easy removal of surplus reagent, and on the other hand as a temporary blocking function for the terminal NH_2 group of the hydrazine. Regioselective N-acylation of the second nitrogen atom in the subsequent step is thereby guaranteed. Surplus reagent is also readily removed from the selectively *N*-acylated hydrazones **6**. These intermediates are then subjected to treatment with acid and ketones **8** in the presence of traces of water to yield the desired indole derivatives **10**. In this reaction sequence, the water hydrolyzes the hydrazones and thereby releases selectively acylated hydrazines **7** into solution, where they condense with ketones **8** to give hydrazone intermediates **9**. These compounds then undergo a [3,3] sigmatropic rearrangement under the reaction conditions, which shifts the equilibrium between the hydrazones **6** and **9** irreversibly to the desired side. This strategy employs ketones, acid chlorides, and hydrazines as building blocks, all of which are either commercially available in great variety or readily prepared by numerous well-established synthesis methods. Use of these building blocks therefore allows ready construction of a fairly diverse compound collection.

The building blocks shown in Scheme 2 were subjected to this resin-capture-release indole synthesis reaction sequence (for experimental details, see the Supporting Information). The solid support was a polystyrene aldehyde resin (Advanced Chemtech) with a loading of 0.9 mmol g^{-1}. A library of 197 indomethacin analogues was synthesized (see the Supporting Information) in overall yields ranging from 4% to quantitative (see Table 1). For example, indomethacin **1** was obtained by this four-step process in an overall yield of 63% after purification by chromatography.

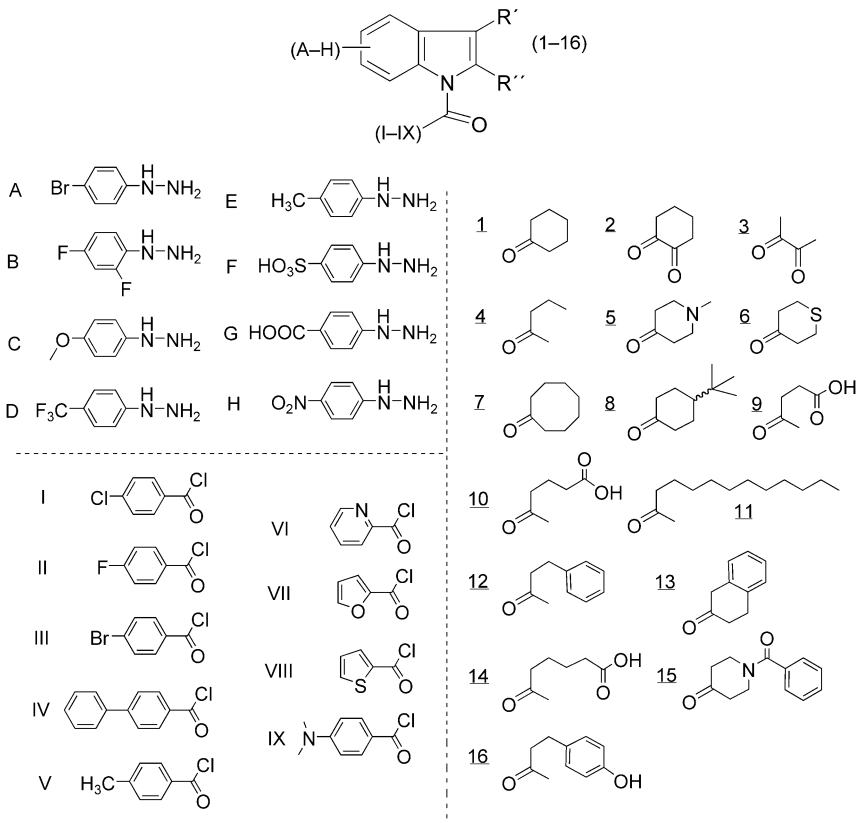
These results demonstrate that the synthesis is compatible with a variety of different functional groups in each building block. Electron-withdrawing and electron-donating substituents can be incorporated in the hydrazine and the acid chloride, and electron-poor and electron-rich heterocycles are tolerated as well. The ketones may also incorporate different heteroatom substituents. Not unexpectedly, the overall yield was highest if activating electron-donating substituents were present in the hydrazines. This result indicates the importance of having two hydrazone-formation reactions in the whole process. However, the synthesis of *N*-acylated indoles by the resin-capture-release strategy is successful even in the presence of deactivating SO_3H, COOH, and NO_2 groups. The crude reaction products were obtained with purities of approximately 70 to over 99%, depending on the ketone employed. All compounds were isolated in more than 99% purity by simple chromatography.



Scheme 1. Concept of the "resin-capture-release" indole synthesis. DCE = 1,2-dichloroethane, TFA = trifluoroacetic acid.

Our initial biochemical investigation of the indomethacin-derived compound library was directed by the intriguing ability of the parent compound to inhibit angiogenesis. Angiogenesis, the development of new blood vessels from preexisting ones, is central to wound repair, inflammation, and embryonic development. Furthermore, aberrant angiogenesis is considered to be a key step in tumor growth, spread, and metastasis.[15,16] Vascular development depends on endothelium-specific receptor tyrosine kinases, in particular the vascular endothelial growth factor receptors 1–3 (VEGFR1–3) and the Tie-2 receptor.[17] All these receptors have been implicated in tumor angiogenesis[18–22] and antagonization of Tie-2, VEGFR-2, or VEGF-D (a ligand of VEGFR-3) inhibits tumor growth and tumor metastasis in vivo.[21,23,24] The development of low-molecular-weight inhibitors of these receptor tyrosine kinases is among the most promising approaches to

 © 2004 Wiley-VCH Verlag GmbH & Co. KGaA, Weinheim



Scheme 2. Building blocks employed in the "capture-and-release" Fischer indole synthesis.

Table 1: Results of the library synthesis.

Building blocks	Yield[a] [%]	Building blocks	Yield[a] [%]
A-I	45–quant.	C-IX	20–47
A-V	9–26	D-I	47
A-VII	62–quant.	E-I	40–90
B-I	21–60	F-I	4–58
C-I	19–45	F-IV	4–52
C-II	16–63	F-VI	15–20
C-III	32–81	F-VII	7–55
C-IV	15–81	F-VIII	11–66
C-VI	17–49	F-IX	10–29
C-VII	9–99	G-I	4–26
C-VIII	21–46	H-I	11–29

[a] Yield ranges are given for the conversion of the respective *N*-acylated hydrazones by treatment with ketones 1–16. All yields are based on the initial loading of the aldehyde resin (0.9 mmol g^{-1}) and refer to purified products. The compounds were identified by LC-MS, GC-MS, NMR spectroscopy, and high-resolution mass spectrometry.

the development of new, alternative antitumor drugs, and several inhibitors of VEGFR-2 are in clinical trials.[25,26]

A high concentration (0.5 mM) of indomethacin inhibits angiogenesis in vitro after stimulation of endothelial cells with the angiogenic growth factors VEGF and basic fibroblast growth factor.[9] Analysis of the cells indicated that treatment with the drug led to reduced activity of MAP kinase, but it remained unclear whether this low activity was a result of direct inhibition of the enzyme or inhibition of a MAP-kinase-activating protein upstream in the signaling cascades that converge at MAP kinase.

Given the importance of the receptor tyrosine kinases mentioned above and the fact that they signal through MAP kinase, we speculated that the observed antiangiogenic effect of indomethacin might be mediated at least in part by inhibition of these kinases. This inhibiting effect appears to be relatively weak, since 0.5 mM indomethacin were required to inhibit angiogenesis in the cellular test system.[9] Screening of an indomethacin-derived compound library could therefore reveal analogues with higher biological activity.

To investigate this hypothesis, 134 compounds considered to be representative of the entire library were selected and assayed as possible inhibitors of VEGFR-2, VEGFR-3, Tie-2, and fibroblast growth factor receptor 1 (FGFR-1). In addition, insulin-like growth factor 1 receptor (IGF1R) was included in the screen. IGF1R affects cell mitogenesis, survival, transformation, and insulin-like activities by binding its ligands, IGF1 and IGF2. This receptor influences postnatal growth physiology and its activity has been associated with malignant disorders such as breast cancer.[27] The antiapoptotic effect induced by the IGF1/IGF1R system correlates with the induction of chemoresistance in various tumors.[28]

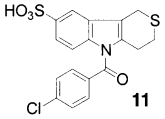
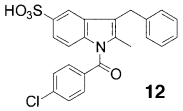
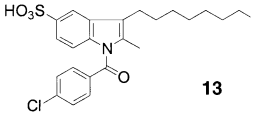
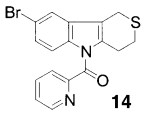
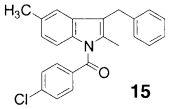
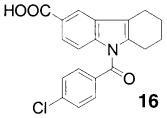
Of the 134 compounds investigated, 6 inhibit the kinases with IC_{50} values in the low-micromolar range (see Table 2).[29] Indomethacin itself does not inhibit any of the kinases at concentrations of up to 100 μM. Although a clear structure–activity relationship cannot be deduced from the limited number of compounds investigated, several preliminary conclusions may be drawn. A considerable degree of selectivity between the kinases can be achieved, and both selectivity and potency can be mediated by changing the substituents, in particular those on the indole ring. Among the *N*-acyl groups, the *p*-chlorobenzoic acid amide group appears to be particularly favorable, but not limiting. The presence of a polar substituent at the 3-position of the indole core structure is not beneficial for inhibitory activity. These initial findings indicate that it should be possible to develop more potent and selective inhibitors based on the molecular skeleton defined by indomethacin-type compounds.

Our data do not clearly prove a direct link between the antiangiogenic properties of indomethacin and inhibition of angiogenesis-related receptor tyrosine kinases. However, the finding that closely related analogues of the drug are active inhibitors of these kinases suggests that such a link might indeed exist. It is possible that, under the conditions of the cellular assay mentioned above, the fairly hydrophobic indomethacin concentrates in the plasma membrane and thereby creates local concentrations that are substantially higher than the overall concentration. These high local concentrations might lead to inhibition of the receptors.

The discovery that indomethacin-derived indole derivatives are inhibitors of angiogenesis-related receptor tyrosine

 © 2004 Wiley-VCH Verlag GmbH & Co. KGaA, Weinheim

Table 2: Inhibition of angiogenesis-related receptor tyrosine kinases by members of the compound library.

Compound	IC_{50} for receptor tyrosine kinase [μM][a] VEGFR-2	VEGFR-3	Tie-2	IGF1R	FGFR-1
 **11**	21 ± 8.8	n.d.	3 ± 1.8	9 ± 3.5	6 ± 2.2
 **12**	20 ± 8.8	17 ± 6.2	9 ± 2.7	17 ± 4.9	n.d.
 **13**	9 ± 11.4	6 ± 4.6	4 ± 1.5	15 ± 3.6	7 ± 1.2
 **14**	n.a.	11 ± 1.4	n.d.	n.a.	n.a.
 **15**	19 ± 2.8	11 ± 1.5	n.d.	n.a.	n.a.
 **16**	10 ± 0.3	21 ± 0.8	n.d.	n.a.	n.a.

[a] To assay the inhibitory activity the kinase-catalyzed phosphorylation of poly(Glu_4-Tyr) was measured in the presence of varying concentrations of inhibitor. The kinases were employed in the form of fusion proteins of glutathione-*S*-transferase and the respective kinase domain. The relative amount of phosphorylated substrate was quantified by means of an antiphosphortyrosine enzyme-linked immunosorbent assay with an antiphosphotyrosine-antibody-conjugated horseradish peroxidase (POD). The bound antibody was detected by the light emitted after addition of a chemiluminescence substrate for POD. All IC_{50} values were calculated from at least four independent determinations. IC_{50}: concentration required for 50% inhibition. n.d.: not determined. n.a.: remaining enzyme activity more than 50% at 50 μM inhibitor concentration.

kinases, in particular Tie-2, VEGFR-3, and FGFR-1, as well as the IGF1 receptor is of interest because only very few classes of inhibitors are known for Tie-2, VEGFR-3, FGFR-1, and IGF1R.[25,30,31] The structural framework defined by the indomethacin core and the ease of its synthetic variation, for example, by the "resin-capture-release" strategy described herein, open up new opportunities for the development of antiangiogenesis drugs and antagonists of the IGF1 receptor. Compounds **11**–**13** are not particularly cytotoxic; exposure of T98g brain cells to these compounds at a concentration of 10 μM for four days did not lead to an increase in cell mortality.

In addition to the opportunity for the development of antiangiogenesis drugs, the finding that the indomethacin core structure defines a new class of kinase inhibitors is of general relevance to medicinal chemistry and chemical biology.

Received: August 7, 2003 [Z52582]

Keywords: angiogenesis · combinatorial chemistry · indomethacin · kinase inhibitors · medicinal chemistry

[1] R. Breinbauer, I. R. Vetter, H. Waldmann, *Angew. Chem.* **2002**, *114*, 3002–3015; *Angew. Chem. Int. Ed.* **2002**, *41*, 2878–2890.

[2] For reviews on the indole ring as a privileged structure and combinatorial syntheses of indole-based compound libraries, see: a) D. A. Horton, G. T. Bourne, M. L. Smythe, *Chem. Rev.* **2003**, *103*, 893–930; b) S. Bräse, C. Gil, K. Knepper, *Bioorg. Med. Chem.* **2002**, *10*, 2415–2437.

[3] A. A. Schuna, *J. Am. Pharm. Assoc.* **1998**, *38*, 728–735.

[4] S. H. Goodnight, *Curr. Opin. Hematol.* **1996**, *3*, 355–360.

[5] L. A. Rodriguez, C. Varas, C. Patrono, *Epidemiology* **2000**, *11*, 382–387.

[6] P. D. Sloane, *Am. Fam. Physician* **1998**, *58*, 1577–1586.

[7] B. L. Flynn, K. A. Theesen, *Ann. Pharmacother.* **1999**, *33*, 840–849.

[8] S. J. Shiff, B. Rigas, *Gastroenterology* **1997**, *113*, 1992–1998.

[9] M. K. Jones, H. Wang, B. M. Peskar, E. Levin, R. M. Itani, I. J. Sarfels, A. S. Tarnawski, *Nat. Med.* **1999**, *5*, 1418–1423.

[10] G. Hawcraft, M. D'Amico, C. Albanese, A. F. Markhom, R. G. Pestell, M. A. Kull, *Carcinogenesis* **2002**, *23*, 107–114.

[11] T.-C. He, T. A. Chan, B. Vogelstein, K. W. Kinzler, *Cell* **1999**, *99*, 335–345.

[12] B. E. Evans, K. E. Rittle, M. G. Bock, R. M. DiPardo, R. M. Freidinger, W. L. Whitter, G. F. Lundell, D. F. Veber, P. S. Anderson, R. S. L. Chang, V. J. Lotti, D. J. Cerino, T. B. Chen, P. J. Kling, K. A. Kunkel, J. P. Springer, J. Hirshfield, *J. Med. Chem.* **1988**, *31*, 2235–2246.

[13] For Fischer indole syntheses on solid support, see: a) S. M. Hutchins, K. T. Chapman, *Tetrahedron Lett.* **1996**, *37*, 4869–4872; b) L. Yang, *Tetrahedron Lett.* **2000**, *41*, 6981–6984; c) L. C. Cooper, G. G. Chicchi, K. Dinnell, J. M. Elliott, G. J. Hollingworth, M. M. Kurtz, K. L. Locker, D. Morrison, D. E. Shaw, K.-L. Tsao, A. P. Watt, A. R. Williams, C. J. Swain, *Bioorg. Med. Chem. Lett.* **2001**, *11*, 1233–1236; d) J. Tois, R. Franzèn, O. Aitio, K. Huikko, J. Taskinen, *Tetrahedron Lett.* **2000**, *41*, 2443–2446.

[14] A. Kirschning, H. Monenschein, R. Wittenberg, *Chem. Eur. J.* **2000**, *6*, 4445–4450.

[15] a) J. Folkman, *Nat. Med.* **1995**, *1*, 27–31; b) A. Giannis, F. Rübsam, *Angew. Chem.* **1997**, *109*, 606–609; *Angew. Chem. Int. Ed. Engl.* **1997**, *36*, 588–590.

[16] a) J. Folkman, *N. Engl. J. Med.* **1971**, *285*, 1182–1186; b) P. Carmeliet, R. K. Jain, *Nature* **2000**, *407*, 249–257.

[17] a) G. D. Yancopoulos, S. Davis, N. W. Gale, J. R. Rudge, S. J. Wiegand, J. Holash, *Nature* **2000**, *407*, 242–248; b) P. C. Maisonpierre, C. Suri, P. F. Jones, S. Bartunkova, S. J. Wiegand,

 © 2004 Wiley-VCH Verlag GmbH & Co. KGaA, Weinheim

C. Radziejewski, D. Compton, J. McClain, T. H. Aldrich, N. Papadopoulos, T. J. Daly, S. Davis, T. N. Sato, G. D. Yancopoulos, *Science* **1997**, *277*, 55 – 60.
[18] S. Hiratsuka, Y. Maru, A. Okada, M. Seiki, T. Noda, M. Shibuya, *Cancer Res.* **2001**, *61*, 1207 – 1213.
[19] H. Kubo, T. Fujiwara, L. Jussila, H. Hashi, M. Ogawa, K. Shimizu, M. Awane, Y. Sakai, A. Takabayashi, K. Alitalo, Y. Yamaoka, S. I. Nishikawa, *Blood* **2000**, *96*, 546 – 553.
[20] A. Stratmann, T. Acker, A. M. Burger, K. Amann, W. Risau, K. H. Plate, *Int. J. Cancer* **2001**, *91*, 273 – 282.
[21] S. A. Stacker, C. Caesar, M. E. Baldwin, G. E. Thornton, R. A. Williams, R. Prevo, D. G. Jackson, S. Nishikawa, H. Kubo, M. G. Achen, *Nat. Med.* **2001**, *7*, 186 – 191.
[22] M. Skobe, T. Hawighorst, D. G. Jackson, R. Prevo, L. Janes, P. Velasco, L. Riccardi, K. Alitalo, K. Claffey, M. Detmar, *Nat. Med.* **2001**, *7*, 192 – 198.
[23] P. Lin, J. A. Buxton, A. Acheson, C. Radziejewski, P. C. Maisonpierre, G. D. Yancopoulos, K. M. Channon, L. P. Hale, M. W. Dewhirst, S. E. George, K. G. Peters, *Proc. Natl. Acad. Sci. USA* **1998**, *95*, 8829 – 8834.
[24] J. Drevs, I. Hofmann, H. Hugenschmidt, C. Wittig, H. Madjar, M. Muller, J. Wood, G. Martiny-Baron, C. Unger, D. Marme, *Cancer Res.* **2000**, *60*, 4819 – 4824.
[25] D. H. Boschelli, *Drugs Future* **1999**, *24*, 515 – 537.
[26] See, for example: G. Bold, K.-H. Altmann, J. Frei, L. Marc, P. W. Manley, P. Traxler, B. Wietfeld, J. Brüggen, E. Buchdunger, R. Cozens, S. Ferrari, P. Furet, F. Hofmann, G. Martiny-Baron, J. Mestan, J. Rösel, M. Sills, D. Stover, F. Acemoglu, E. Boss, R. Emmenegger, L. Lässer, E. Masso, R. Roth, C. Schlachter, W. Vetterli, D. Wyss, J. M. Wood, *J. Med. Chem.* **2000**, *43*, 2310 – 2323, and references cited therein.
[27] M. J. Ellis, S. Jenkins, J. Hanfelt, M. E. Redington, M. Taylor, R. Leek, K. Siddle, A. Harris, *Breast Cancer Res. Treat.* **1998**, *52*, 175.
[28] A. Grothey, W. Voigt, C. Schober, T. Muller, W. Dempke, H. J. Schmoll, *J. Cancer Res. Clin. Oncol.* **1999**, *125*, 166 – 173.
[29] The structure–activity relationship apparent from the selected 134 compounds and comparison with the structures of the remaining 63 compounds indicated that biochemical investigation of the latter would not reveal more potent inhibitors. Therefore, 63 of the library compounds were not screened.
[30] P. Cohen, *Nat. Rev. Drug Discovery* **2002**, *1*, 309 – 315; A. J. Bridges, *Chem. Rev.* **2001**, *101*, 2541 – 2571.
[31] L. Kissau, P. Stahl, R. Mazitschek, A. Giannis, H. Waldmann, *J. Med. Chem.* **2003**, *46*, 2917 – 2931.

 © 2004 Wiley-VCH Verlag GmbH & Co. KGaA, Weinheim

Nanotubular Materials

Noble-Metal Nanotubes (Pt, Pd, Ag) from Lyotropic Mixed-Surfactant Liquid-Crystal Templates**

Tsuyoshi Kijima, Takumi Yoshimura, Masafumi Uota, Takayuki Ikeda, Daisuke Fujikawa, Shinji Mouri, and Shinji Uoyama*

A lot of attention is currently focused on nanosized tubular materials because of their unique physical properties and potential applications as gas and fluid paths or reservoirs in catalysis, fuel cells, sensors, and separation systems.[1] Since the discovery of carbon nanotubes,[2] there have been reports on a variety of inorganic nanotubes based on boron nitride,[3] metal sulfides,[4] metal borates[5] and metal oxides.[6] Besides high-temperature processes,[2–5] another approach that makes use of solid or molecular templates[6] has been developed for the synthesis of such nanotubular materials. For metals important in catalysis and other nanotechnological fields, synthesis by using nanoporous polymer and anodic aluminum films as templates led to gold,[7a] nickel,[7b] and palladium[7c] nanotubes, but with inner diameters as large as 10–100 nm. Furthermore, no report has appeared on the fabrication of metal nanotubes by using a surfactant or other molecular templates, although mesoporous platinum was obtained by using the lyotropic liquid crystals (LCs) of nonionic surfactants.[8] In brief, the previous templating approaches to metals yielded only nanoporous materials or thick-walled tubular structures. This fact seems to suggest that thin-walled metal nanotubes with diameters below 10 nm might be unobtainable because of their extremely high surface energies, in spite of their potentially attractive functionalities, as expected by analogy with the magnetically and catalytically unique properties of platinum nanowires.[9] The previous surfactant templating process that was first applied to the synthesis of mesoporous silica MCM-4,[10] used almost exclusively a single ionic or nonionic surfactant. In contrast, our recent study revealed that the lyotropic nematic media of nonionic–cationic mixed surfactant are effective for the preparation of tin oxide microwires.[11] This motivated us to apply such a mixed surfactant template to the fabrication of nanostructured metals. Herein we demonstrate the first synthesis of platinum, palladium, and silver nanotubes, with inner diameters of

[*] Prof. Dr. T. Kijima, T. Yoshimura, M. Uota, T. Ikeda, D. Fujikawa, S. Mouri, S. Uoyama
Department of Applied Chemistry, Faculty of Engineering
Miyazaki University
Miyazaki, 889–2192 (Japan)
Fax: (+81) 985-58-2876
E-mail: t0g102u@cc.miyazaki-u.ac.jp

[**] Supported by Grant-in-Aids for the CREST of Japan Science and Technology Coorporation (JST) and Promotion of Evolutional Science and Technology in Miyazaki Prefecture. We thank Chiharu Hoshiyama for her assistance in TEM investigation.

Supporting information for this article is available on the WWW under http://www.angewandte.org or from the author.

 © 2004 Wiley-VCH Verlag GmbH & Co. KGaA, Weinheim DOI: 10.1002/anie.200352630

3–4 nm and outer diameters of 6–7 nm, by the reduction of metal salts confined to lyotropic mixed LCs of two different sized surfactants. The mechanism of formation of such metal nantubes is also proposed.

In the typical fabrication process, the liquid crystalline phase of hexachloroplatinic acid (H_2PtCl_6), nonaethylene glycol monododecyl ether ($C_{12}EO_9$), polyoxyethylene (20) sorbitan monostearate (Tween 60) and water at a molar ratio of 1:1:1:60 was treated with hydrazine. The transmission electron-microscope (TEM) image of the resulting black powders showed an aggregate of nanotubular materials (Figure 1 A). Energy-dispersive X-ray (EDX) analysis of the reduced powders confirmed the existence of platinum as the major component and the complete removal of chloride ions librated during the reduction of platinum ions into platinum metal. Hence, the tubular materials thus obtained can be identified as platinum nanotubes with inner and outer diameters of 3 and 6 nm, respectively. Some round spots with a diameter of about 6 nm are observed in the same image because some of the folded nanotubes are oriented parallel to the electron beam. The length of nanotubes is estimated to be much greater than 100 nm, but it is impossible to determine the total length of an isolated nanotube because the nanotubular materials are highly cohered into a dense aggregate. The X-ray-diffraction (XRD) pattern of the reduced solid also exhibited a broad shoulder at $2\theta = 0.5$–$2°$ that is presumably due to the nanotubular structure (Figure 2). The

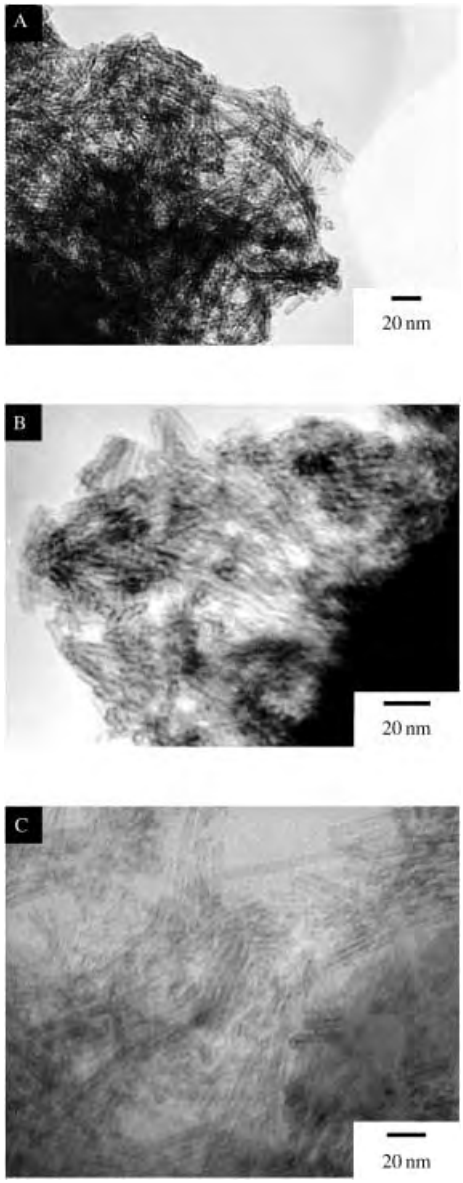


Figure 1. TEM images showing A) platinum, B) palladium, and C) silver nanotubes obtained by reducing their precursory mixed surfactant LC phases with hydrazine.

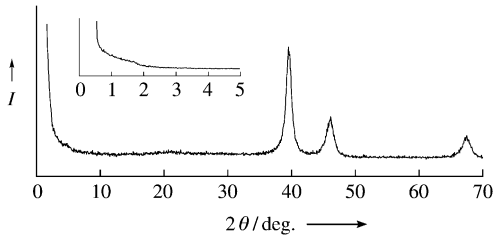


Figure 2. XRD pattern of the as-grown platinum nanotube obtained by the hydrazine treatment.

two broad peaks at $2\theta = 39.73°$ and 46.19° are assigned to the (111) and (200) reflections, respectively, of the fcc structure with a unit cell parameter of 0.3929 nm, which is very close to that of the bulk metal (0.3923 nm). Thermogravimetric analysis (TGA) and FTIR spectroscopy revealed that the solid contains ≈ 36 wt % of remaining surfactant species, which suggests that the nanotubular platinum particles are stabilized by the remaining organic species. An additional experiment showed that the organic content is further decreased to ≈ 13 wt % by treatment with an ethanol solution of sodium acetate. The catalytic activities of platinum nanotubes would not always be lowered by surfactant or other molecular protection, as various noble metal colloids stabilized by surfactants and solvents were demonstrated to be effective for hydrogenation[12] and use in the Heck reaction.[13]

A similar reaction by using $Pd(NO_3)_2$ in place of H_2PtCl_6 also yielded palladium nanotubes with inner and outer diameters of 3 and 6 nm, respectively (Figure 1 B). Another fabrication process that uses sodium dodecylsulfate (SDS) and Tween 60 as a mixed template with $AgNO_3$ resulted in the formation of an aggregate of silver nanotubes with inner and outer diameters 4 and 7 nm, respectively (Figure 1 C). It is noted throughout the above three systems that the metal nanotubes are highly cohered into a dense aggregate. This aggregation, together with the stability of electron-beam system, which was affected by the organic species evaporated from the metal samples placed in the vacuum chamber of TEM, led to difficulties in observing a higher resolution image of an isolated metal nanotube. According to TGA, palladium nanotubes washed with ethanol were three times less contaminated with remaining organic materials than the platinum nanotubes, and hence the former metal particles tended to form more dense aggregates. This may be the

 © 2004 Wiley-VCH Verlag GmbH & Co. KGaA, Weinheim

reason why the TEM image of palladium is a little less clear than that of platinum as observed in Figure 1.

In marked contrast to the above observations, no nanotubular metals were obtained when the reaction was performed by using any one of $C_{12}EO_9$, SDS, and Tween 60 as the sole templating agent. These facts clearly indicate that mixed-surfactant LCs based on Tween 60 are essential to the preparation of noble-metal nanotubes. It is therefore particularly intriguing to elucidate the pathway from the precursory mixture to the formation of nanotubes and the factor that determines their dimensions. For this report, we focused our attention on the characterization of the precursory LC in the $H_2PtCl_6/C_{12}EO_9$/Tween 60/H_2O system.

The XRD patterns of the $C_{12}EO_9$/Tween 60/H_2O mixtures at a molar ratio of 1:y:60 exhibited one major peak around $2\theta = 1.5°$ and a very weak broad band near $2\theta = 2.5°$ (Figure 3A). These two peaks are attributed to the 100 and 110 reflections for a hexagonal structure with $a \approx 7$ nm. Similarly to the $C_{12}EO_8/H_2O$[14] and $C_{16}EO_8/H_2O$[8a,14b] LCs, the $C_{12}EO_9/H_2O$ ($y = 0$) mixture also forms a hexagonal phase with $a = 6.82$ nm. No layered-phase characteristic of the binary Tween 60/H_2O system is observed for the $y = 0$–2 compositions. It is also remarked that even upon addition of much larger surfactant molecules, the hexagonal structure is maintained over a wide range of $y = 0$–1.6 while keeping the parameter a in the narrow range of 6.8–7.2 nm. More interestingly, the parameter a, which corresponds to the rod-to-rod distance in an array of cylindrical rodlike micelles, varies in a sine-wave with the Tween 60 content y and has a minimum of $a = 6.9$ nm at $y \approx 1$ (Figure 3C). These findings suggest that $C_{12}EO_9$ and Tween 60 surfactant molecules, which are very different in size, mix at the molecular level to form a hexagonal array of cylindrical micelles and that their equimolar composition may afford the most dense or stabilized phase. When H_2PtCl_6 was added to the $y = 1$ hexagonal composition, the XRD peaks of the resulting phases showed a marked tendency to decrease in intensity with increasing platinum content x (Figure 3B). Thus, the precursory 1:1:1:60 phase that contained the $PtCl_6^{2-}$ ion could be identified as an LC with a hexagonal but disordered array of mixed surfactant cylindrical micelles corresponding to $a =$ 6.9 nm.

On the basis of the above X-ray observations along with the structural parameters of surfactant molecules (Table 1), we proposed a structure model for the precursory 1:1:1:60 LC (Figure 4A). This model is based on a structural calculation done by assuming that equimolar amounts of $C_{12}EO_9$ and Tween 60 molecules are arranged side by side with their hydrophobic tail groups fully extended and tilted at the same angle to form a cylindrical rodlike micelle; their hydrophilic heads are assumed to be directed to the outside and the rodlike micelles further assembled into a hexagonal array with a rod-to-rod distance equal to the observed value of 6.9 nm.[15] Additionally, the hydrophilic head groups of both surfactant molecules were assumed to adopt a spherical conformation with the same packing coefficient of 0.681 as observed for a number of amorphous or poorly crystalline polymers.[16] The structural calculations also indicated that the surfactant molecules in the mixed surfactant LC are much less tilted with respect to the rod axis than those in the hexagonal LC of $C_{12}EO_9$ (Fig-

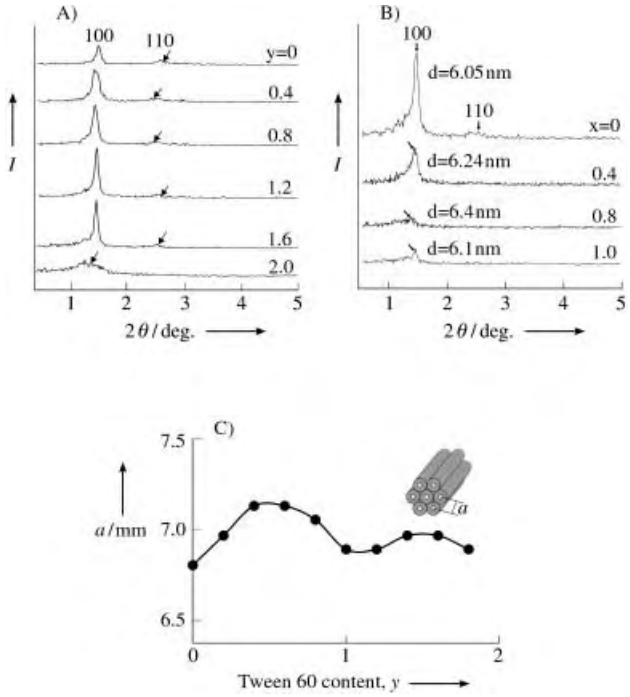
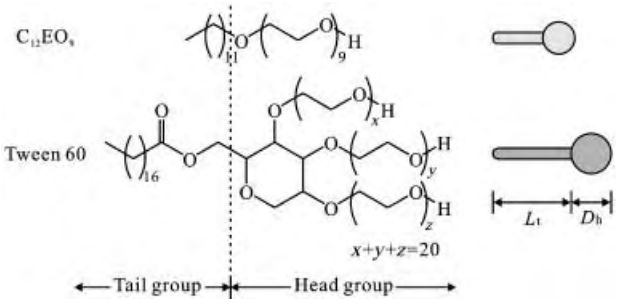


Figure 3. XRD patterns of A) the 1:y: 60 mixtures of $C_{12}EO_9$, Tween 60 and H_2O and B) the x:1:1:60 mixtures of H_2PtCl_6, $C_{12}EO_9$, Tween 60 and H_2O at ≈ 15 °C ($Cu_{K\alpha}$), and C) plots of the rod-to-rod distance, a, as a function of Tween 60 content, y, for the former ternary mixtures.

Table 1: Stuctural parameters of $C_{12}EO_9$ and Tween 60 molecules.[a]

Surfactant	Head group		Tail group		Molecule	
	Effect. Volume $V_{h,i}$ [nm^3][b]	Diameter $D_{h,i}$ [nm]	Volume $V_{t,i}$ [nm^3]	Length $L_{t,i}$ [nm]	Volume $V_{m,i}$ [nm^3]	Length $L_{m,i}$ [nm]
$C_{12}EO_9$	0.589	1.04	0.214	1.61	0.803	2.65
Tween 60	1.299	1.30	0.324	2.53	1.623	3.88

[a] The CO_2 group of Tween 60 molecules is assumed to be a part of the tail. [b] Effective volume is given by the van der Waals volume/0.681 according to Slonimskii et al. [16]



 © 2004 Wiley-VCH Verlag GmbH & Co. KGaA, Weinheim

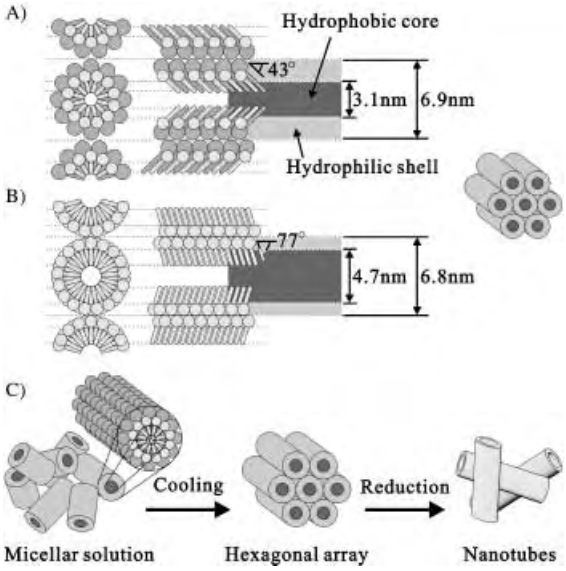


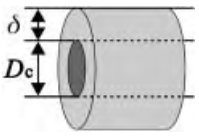
Figure 4. Schematic models for the formation of platinum nanotubes in the mixed surfactant templating system: A) Mixed ($C_{12}EO_9$/Tween 60) and B) single ($C_{12}EO_9$) surfactant cylindrical rodlike micelles. C) Pathway from micellar solution to metal nanotubes by the reduction of metals salts confined to the aqueous shell of mixed-surfactant cylindrical micelles. The metal salts and water molecules are omitted from the models.

ure 4B). Thus, we supposed that the present platinum nanotubes are formed by a mixed surfactant templating mechanism (Figure 4C). In this mechanism, the rodlike micelles of $C_{12}EO_9$ molecules in an aqueous medium are combined with much larger-sized sorbitan-based non-ionic surfactant molecules (Tween 60) to form an aqueous solution of the mixed surfactant cylindrical micelles as described above. On cooling the mixed micellar solution would be converted into a hexagonal LC with $a = 6.9$ nm. At the final stage, the platinum species confined to the aqueous region of the molecular assemblies are reduced into platinum atoms.

The observed inner diameter of 3 nm for both the platinum and palladium nanotubes agrees closely with 3.1 nm calculated for the diameter of the hydrophobic core of the mixed surfactant micelle (Table 2). This is because the reduced metal is stabilized at the interface between the hydrophobic and the hydrophilic domains, as Attard et al. explained the formation of H_I-platinum from a hexagonal LC of $C_{16}EO_8$.[8a] The subsequent process, however, is remarkably different between both systems. In the mixed-surfactant system, the reduced metal grows into nanotubes with a wall-thickness of 1.5 nm within the cylindrical micelle because the aqueous shell has a maximum thickness of 1.93 nm according to the calculation (Table 2). In contrast, the aqueous shells in the $C_{16}EO_8$ and the $C_{12}EO_9$ systems are as thin as 1.0 nm. The insufficient thickness for the separate growth of nanotubes would lead to mesoporous or bulk metals as a result of agglomeration and coalescence of metal clusters deposited within neighboring micelles, as observed for these single-surfactant systems. A similar mechanism would apply to the Ag-based system. A preliminary experiment showed that the 1:1:1:60 composition of $AgNO_3$/SDS/Tween 60/water is also a hexagonal LC with $a = 7.03$ nm close to that for the platinum system. The observed inner diameter of 4 nm for the silver nanotube (larger than 3 nm for the other two metals) may be due to an increase in the effective diameter of hydrophobic core by the coulomb-repulsive effect of the sulfate group bonded to the dodecyl chain.

In summary, the reduction of metal salts confined to lyotropic mixed surfactant LCs resulted in the first synthesis of platinum, palladium, and silver nanotubes of 6–7 nm outer diameter. Equimolar amounts of medium and large surfactant molecules are combined into a hexagonal array of cylindrical rodlike micelles ≈ 6.9 nm in diameter and the aqueous outer shell of the rodlike micelles is so thick that the reduced metal grows into nanotubes separately within the aqueous shell. This can be explained by a structure model constructed on the basis of the molecular parameters of surfactants along with X-ray observations. The uniformly sized platinum and the other two metal nanotubes are promising for potential applications as electrodes in batteries and fuel cells, environmental catalysts, and electronic nanodevices. The mixed surfactant templating method could also be extended to the synthesis of a wide range of nanotubular materials, inorganic or organic.

Table 2: Structural parameters of surfactant cylindrical rodlike micelles.



Surfactant	Number of molecules per cross section N	Diameter of core D_c [nm]	Thickness of shell δ [nm]
$C_{12}EO_9$	17	4.73	1.04
$C_{12}EO_8$	21	5.72	1.00
$C_{12}EO_9$/Tween 60	12/12	3.12	1.93

Experimental Section

A mixture of H_2PtCl_6, $C_{12}EO_9$, Tween 60, and H_2O in a 1:1:1:60 molar ratio was shaken at 60 °C, then cooled to between 15 and 25 °C and allowed to stand at that temperature for 30 min. Polarizing optical microscopy revealed that the homogeneous mixture was an isotropic solution at 60 °C and transformed around 28 °C into a LC phase. An excess amount of hydrazine was added to the cooled (25 °C) pasty material and then kept at that temperature for 24 h. The resulting solid was separated, washed with water and then repeatedly with ethanol prior to drying in air. Similar syntheses by using $Pd(NO_3)_2$, or $AgNO_3$, SDS, and in place of H_2PtCl_6 and $C_{12}EO_9$ were carried out to obtain palladium and silver nanotubes. To characterize the precursory LC phases, pasty mixed phases of $C_{12}EO_9$, Tween 60, and H_2O with different compositions were also prepared by using the same heating and cooling processes as above. All TEM images were taken with a Hitachi H-800 MU microscope operated at 200 keV. Wide-angle XRD patterns were measured by the reflectance method using $Cu_{K\alpha}$ radiation, and small angle ones for pasty or powdered samples were measured by the transmission

 © 2004 Wiley-VCH Verlag GmbH & Co. KGaA, Weinheim

method on a Shimadzu XRD-7000 diffractometer equipped with a glass plate of 1 mm thick with a slit of 1 mm wide filled with specimen.

Received: August 12, 2003 [Z52630]

Keywords: liquid crystals · mixed surfactant · nanotubes · platinum · template synthesis

[1] a) Issues in nanotechnology, *Science* **2000**, *290*, 1523; b) C. J. Brumlik, V. P. Menon, C. R. Mrtin, *J. Mater. Res.* **1994**, *9*, 1174; c) W. Tremel, *Angew. Chem.* **1999**, *111*, 2311; *Angew. Chem. Int. Ed.* **1999**, *38*, 2175; d) K. J. C. van Bommel, A. Friggeri, S. Shinkai, *Angew. Chem.* **2003**, *115*, 1010; *Angew. Chem. Int. Ed.* **2003**, *42*, 980.
[2] S. Iijima, *Nature* **1991**, *354*, 56.
[3] N. G. Chopra, R. J. Ruyken, K. Cherry, V. H. Crespi, M. L. Cohen, S. G. louie, A. Zettl, *Science* **1995**, *269*, 966.
[4] a) R. Tenne, L. Margulis, M. Genut, G. Hodes, *Nature* **1992**, *360*, 444; b) Y. Feldman, E. Wasserman, D. J. Srolovitz, R. Tenne, *Science* **1995**, *267*, 222.
[5] R. Ma, Y. Bando, D. Golberg, T. Sato, *Angew. Chem.* **2003**, *115*, 1880; *Angew. Chem. Int. Ed.* **2003**, *42*, 1836.
[6] a) M. E. Spahr, P. Bitterli, R. Nesper, M. Müller, F. Krumeich, H. U. Nissen, *Angew. Chem.* **1998**, *110*, 1339; *Angew. Chem. Int. Ed.* **1998**, *37*, 1263; b) C. N. R. Rao, B. C. Satishkumar, A. Govindaraj, *Chem. Commun.* **1997**, 1581; c) H.-P. Lin, C.-Y. Mou, S.-B. Liu, *Adv. Mater.* **2000**, *12*, 103; d) M. Adachi, T. Harada, M. Harada, *Langmuir* **1999**, *15*, 7097; e) M. Yada, M. Mihara, S. Mouri, M. Kuroki, T. Kijima, *Adv. Mater.* **2002**, *14*, 309.
[7] a) C. R. Martin, *Science* **1994**, *266*, 1961; b) J. Bao, C. Tie, Z. Xu. O. Ma, D. Sheng, *Adv. Mater.* **2002**, *14*, 44; c) M. Steinhart, Z. Jia, A. K. Schaper, R. B. Wehrspohn, U. Gosele, J. H. Wendorff, *Adv. Mater.* **2003**, *15*, 706.
[8] a) G. S. Attard, C. G. Goltner, J. M. Corker, S. Henke, R. H. Templer, *Angew. Chem.* **1997**, *109*, 1372; *Angew. Chem. Int. Ed. Engl.* **1997**, *36*, 1315; b) G. S. Attard, P. N. Bartlett, N. R. B. Coleman, J. M. Elliott, J. R. Owen, J. H. Wang, *Science* **1997**, *278*, 838.
[9] M. Sasaki, M. Osada, N. Sugimoto, S. Inagaki, Y. Fukushima, A. Fukuoka, M. Ishikawa, *Microporous Mesoporous Mater.* **1998**, *21*, 597.
[10] C. T. Kresge, M. E. Leonowicz, W. J. Roth, J. C. Vartuli, J. S. Beck, *Nature* **1992**, *359*, 710.
[11] T. Kijima, T. Ikeda, M. Yada, M. Machida, *Langmuir* **2002**, *18*, 6453.
[12] a) A. Henglein, B. G. Ershov, M. J. Malow, *J. Phys. Chem.* **1995**, *99*, 1419; b) N. Toshima, T. Takahashi, *Bull. Chem. Soc. Jpn.* **1992**, *65*, 400.
[13] M. T. Reetz, G. Lohmer, *Chem. Commun.* **1996**, 1921.
[14] a) G. S. Attard, J. C. Glyde, C. G. Goltner, *Nature* **1995**, *378*, 366; b) D. J. Mitchell, *J. Chem. Soc. Faraday Trans. 1* **1983**, *79*, 975.
[15] See Supporting Information.
[16] G. L. Slonimskii, A. A. Askadaskii, A. I. Kitaigorodskii, *Vysokomol. Soyed. A* **1970**, *12*, 494.

 © 2004 Wiley-VCH Verlag GmbH & Co. KGaA, Weinheim

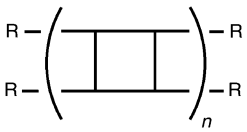
Ladderanes

Supramolecular Construction of Molecular Ladders in the Solid State**

*Xiuchun Gao,[+] Tomislav Friščić, and Leonard R. MacGillivray**

In memory of Xiuchun Gao

An [*n*]ladderane is a molecule that consists of *n* edge-sharing cyclobutane rings (where $n \geq 2$) that define a molecular equivalent of a macroscopic ladder.[1] Ladderanes are considered promising building blocks in optoelectronics[2] and, very recently, have been identified in biological systems ($n = 3$ and 5), in the form of ladderane lipids,[3,4] which are integral components in the microbiological conversion of ammonium and nitrite ions to dinitrogen gas.[3,4] In the simplest case, a *cis*-fused [*n*]ladderane ($n = 3, 5, 7\ldots$) can be constructed by photochemical dimerization of two all-*trans*-poly-*m*-enes ($m = 2, 3, 4\ldots$). Despite the apparent simplicity of this intermolecular process, however, such a transformation generally fails.[1] This can be attributed to the lack of a method that overcomes the energetic cost, due to solvent[5] and entropy[1,5] effects, of organizing two polyene molecules in a suitable geometry in the liquid phase for photoreaction, although a covalent linker that holds two polyene chains in a parallel orientation for a high-yield, intramolecular photoaddition to give a [*n*]ladderane ($n = 3$ and 5) has been reported.[6]



[*n*]ladderane

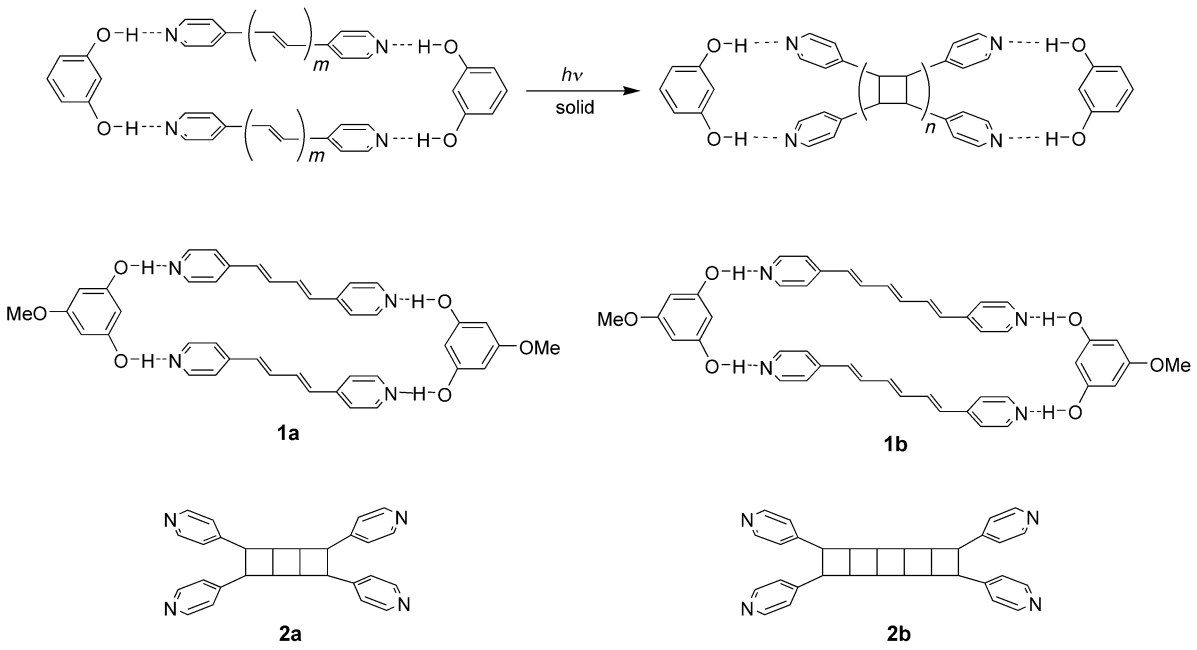
We believe that a supramolecular approach to covalent synthesis[7,8] in the organized, solvent-free environment of the solid state[8] can provide a solution to the problem of organizing two polyenes for an intermolecular reaction to give a ladderane. Specifically, by taking an approach to control reactivity in solids[9] by using molecules that serve as linear templates,[10–13] we have anticipated that the cocrystallization of resorcinol (1,3-benzenediol), or a derivative, with an all-*trans*-bis(4-pyridyl)poly-*m*-ene (4-pyr-poly-*m*-ene) would produce a four-component molecular assembly, 2(resorcinol)·2(4-pyr-poly-*m*-ene), in which each resorcinol preorganizes, through two O−H···N hydrogen-bonding interactions, two poly-*m*-enes for [2+2] photoaddition.[14] In this design, the two polyenes (Scheme 1) would be positioned by

[*] T. Friščić, Prof. L. R. MacGillivray
Department of Chemistry, University of Iowa
Iowa City, IA 52242–1294 (USA)
Fax: (+1) 319-335-1270
E-mail: len-macgillivray@uiowa.edu

[+] Deceased

[**] We are grateful to the National Science Foundation (CAREER Award, L.R.M., DMR-0133138) for funding. Acknowledgment is also made to the Research Corporation (Research Innovation Award) for financial support.

 © 2004 Wiley-VCH Verlag GmbH & Co. KGaA, Weinheim DOI: 10.1002/anie.200352713



Scheme 1.

the templates such that the C=C bonds of the olefins lie parallel and separated by < 4.2 Å, a position suitable for the photoreaction. UV irradiation of the solid would produce the targeted [*n*]ladderane, with the C=C bonds reacting to form the fused cyclobutane framework. Herein, we report the application of 2(5-OMe-res)·2(4-pyr-poly-*m*-ene) (where: $m = 2$ (**1a**) and 3 (**1b**); 5-OMe-res = 5-methoxyresorcinol) to construct [*n*]ladderanes (where $n = 3$ (**2a**) and 5 (**2b**)) in the solid state. The remarkable efficiency of this intermolecular process is exemplified by the fact that the polyenes are converted to the ladderanes stereospecifically, in gram quantities, and in 100% yield.[11]

In a typical experiment, one equivalent of 5-OMe-res[11] was co-crystallized with an equimolar amount of a 4-pyr-poly-*m*-ene[15] in methanol. Single crystals of **1a** and **1b** suitable for X-ray analysis formed in the methanolic solution within a period of approximately one day.

Single-crystal X-ray structure analyses of **1a** and **1b** reveal that the linear templates preorganize each polyene into a position for intermolecular photoaddition that is favorable for ladderane formation.[6]

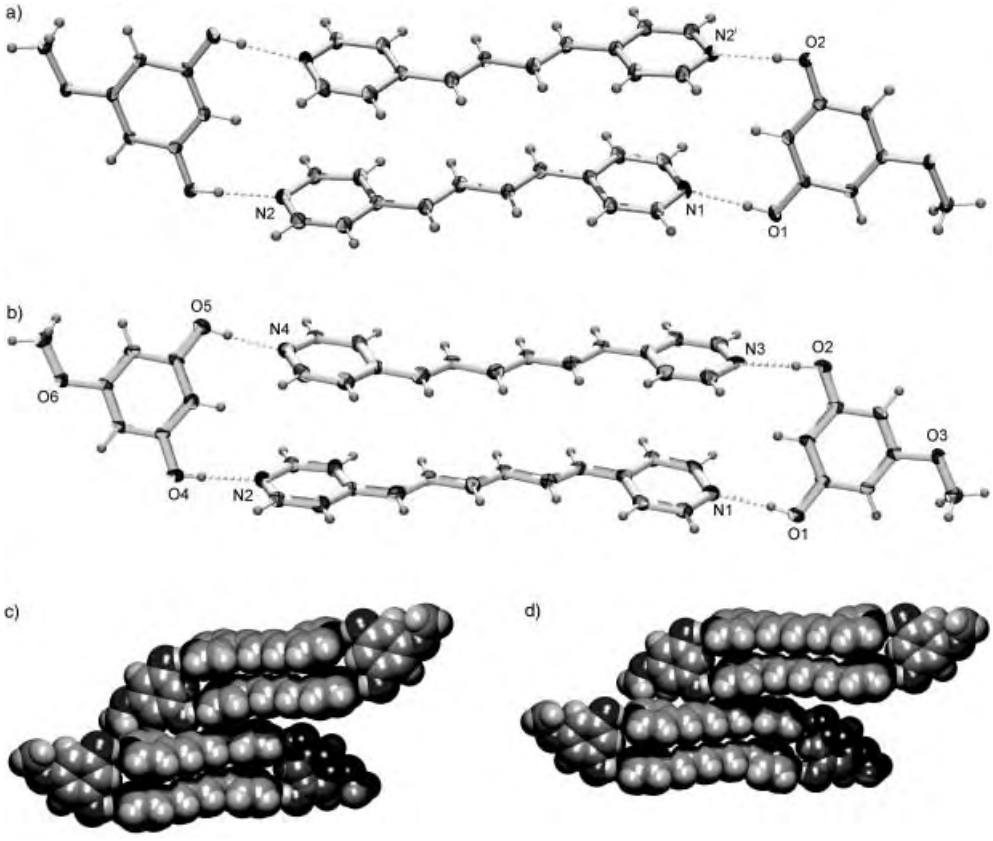


Figure 1. X-ray crystal structures of **1a** and **1b**: a) ORTEP view of **1a**, b) ORTEP view of **1b**, c) space-filling view of the packing of **1a**, and d) space-filling view of the packing of **1b**. Selected interatomic distances [Å] and angles [°]: a) O1···N1 2.761(3), O2···N2^{i} 2.736(3), O1-H1O···N1 175.5(2), O2-H2O···N2^{i} 171.4(2); b) O1···N1 2.792(5), O2···N3 2.777(6), O4···N2 2.782(6), O5···N4 2.756(6), O1-H1O···N1 173.6(3), O2-H2O···N3 173.4(3), O4-H4O···N2 176.6(3), O5-H5O···N4 175.1(3). Symmetry operator i: $-x+1$, $-y$, $-z+2$. The asymmetric unit of 2(5-OMe-res)·2(4-pyr-poly-2-ene) consists of one half assembly, which resides around a crystallographic center of inversion, whereas that of 2(5-OMe-res)·2(4-pyr-poly-3-ene) involves two full assemblies, which are virtually identical.

 © 2004 Wiley-VCH Verlag GmbH & Co. KGaA, Weinheim

In each case, the linear templates and polyenes form discrete, four-component molecular assemblies that are held together by four O–H···N hydrogen bonds (Figure 1a,b), wherein the templates orient the polyenes in a parallel arrangement. The separation between the stacked C=C bonds ranges from 3.78 to 3.82 Å and 3.69 to 3.97 Å in **1a** and **1b**, respectively. Nearest-neighbor assemblies of each solid pack in an antiparallel fashion so that the olefins of the hydrogen-bonded assemblies are the sole C=C bonds organized to undergo reaction (Figure 1c,d).

To evaluate the reactivity of the solid-state molecular assemblies, powdered crystalline samples of **1a** and **1b** were subjected to UV irradiation (broadband Hg lamp) for periods of approximately 120 and 72 h, respectively. As evidenced by ^{1}H NMR spectroscopy (in [D$_6$]DMSO), **2a** and **2b** formed stereospecifically and in 100% yield (Figure 2). Each ladderane is characterized by the complete disappearance of the olefinic protons and the emergence of cyclobutane protons in the $\delta = 3.0$–4.3 ppm range.[6,16] The three fused cyclobutane rings of **2a** produced two broad signals at $\delta = 3.49$ and 4.30 ppm (1:1 ratio), while the five fused cyclobutane rings of **2b** produced three broad signals at $\delta = 3.12$, 3.27, and 4.27 ppm (1:1:1 ratio).

To confirm the structures of the ladderanes, the reactions were repeated in gram quantities. The linear templates were then separated from each photoproduct by solvent extraction. Single-crystals of **2a** and **2b**·2(benzene) were grown, over a period of approximately three days, by way of slow solvent evaporation from ethanol and benzene, respectively.

Single-crystal X-ray structure analyses confirm the structures of **2a** and **2b** (Figure 3). Each photoproduct consists of a *cis*-fused cyclobutane framework with ends that are functionalized with four 4-pyridyl groups. The C–C bond lengths and C-C-C bond angles of the fused cyclobutane units compare well to both calculated and experimentally related structures.[6,16]

The ladderanes **2a** and **2b** appear to form within **1a** and **1b** through stepwise [2+2] photodimerizations. ^{1}H NMR spectra obtained 24 and 48 h into each reaction reveal that lower-order [*n*]ladderanes form during the generation of each

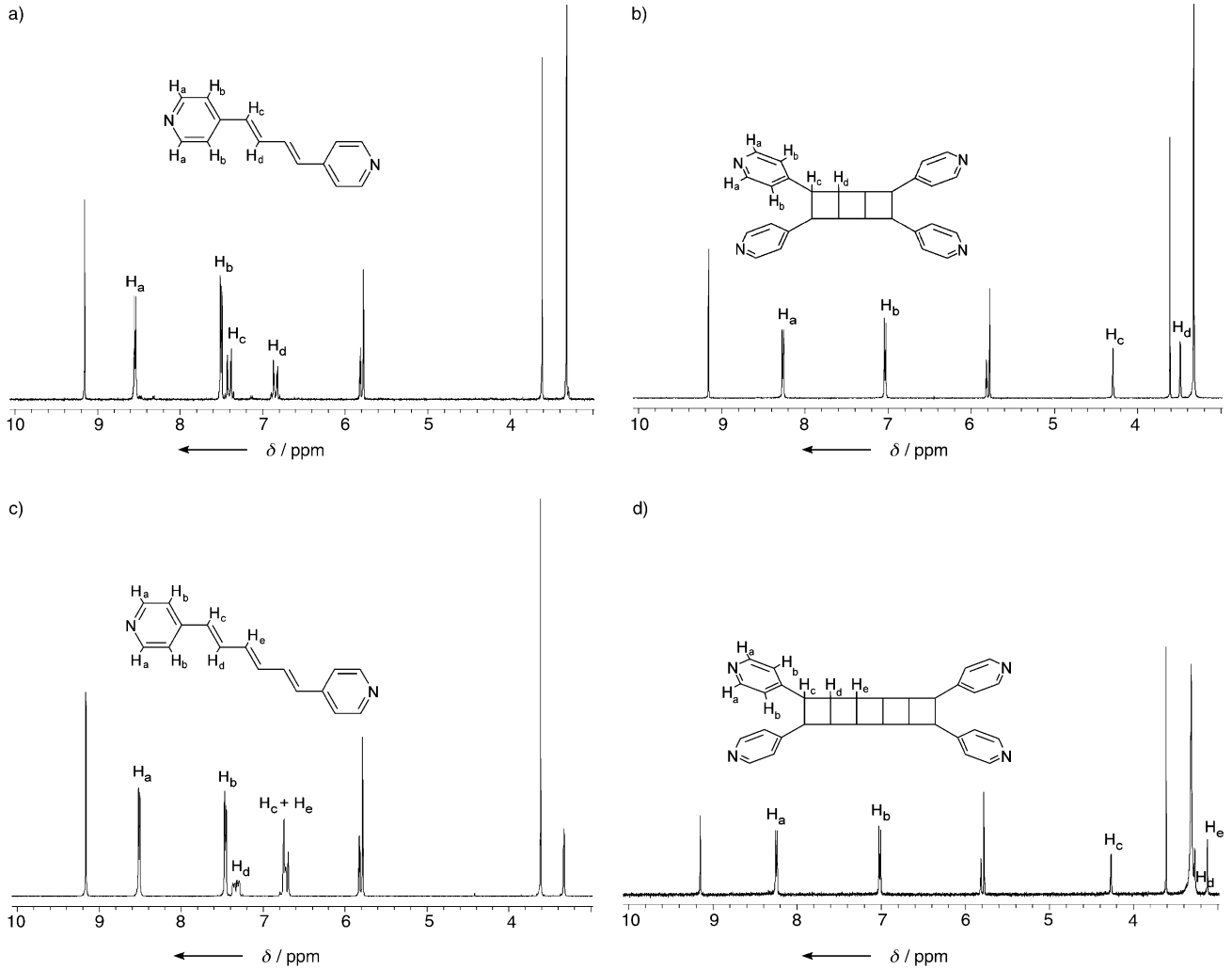


Figure 2. ^{1}H NMR spectra of the solid-state assemblies before and after photoreaction: a) **1a** (before), b) **1a** (after), c) **1b** (before), and d) **1b** (after).

 © 2004 Wiley-VCH Verlag GmbH & Co. KGaA, Weinheim

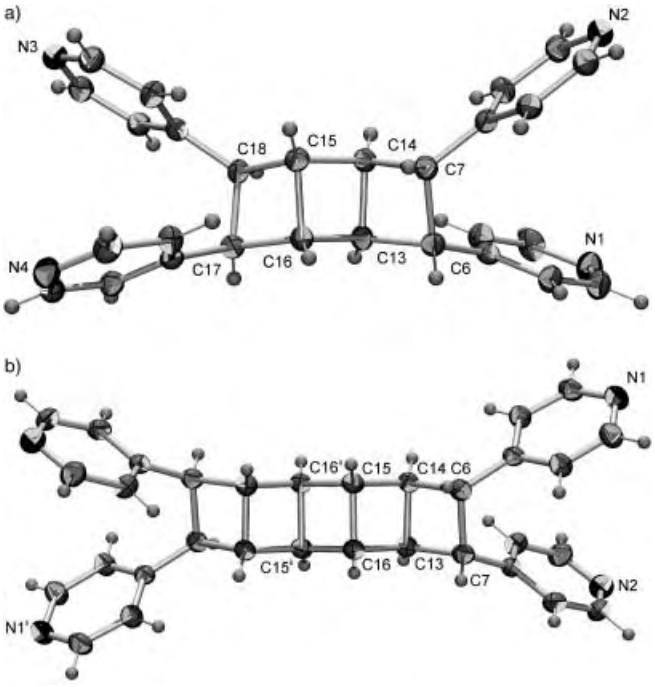


Figure 3. ORTEP perspectives of the ladderanes: a) **2a** and b) **2b**. Selected interatomic distances [Å] and angles [°]: C6-C7 1.593(5), C13-C14 1.566(5), C15-C16 1.575(5); b) C6-C7 1.585(3), C13-C14 1.567(3), C15-C16 1.585(3), C16-C15^{ii} 1.526(3). Symmetry operator ii: $-x+2$, $-y$, $-z+1$. The asymmetric unit of **2a** contains two full ladderanes, which are virtually identical, while that of **2b**·2(benzene) contains one half ladderane, which resides around a crystallographic center of inversion, and an included benzene molecule, respectively.

final product. Thus, a product consistent with a single cycloaddition (i.e., "[1]ladderane") precedes **2a** while products consistent with single and double cycloadditions (e.g., [3]ladderane) precede **2b**. Such observations contrast reactivity experiments involving 1,4-butadienes,[14,17] which exhibit similar packing in the solid state and react, via a single photodimerization, to produce *cis*-vinyl cyclobutanes and rearrange thermally, via a Cope rearrangement,[18] into *cis–cis* cyclooctadienes.[19] Here, the relatively strong O–H···N hydrogen bonds between the templates and reactants may serve to force divinyl groups from a first photoaddition into a conformation suitable for a second and third photoaddition, thus leading to each ladderane product.[20] In the case of **2b**, such stepwise transformations may occur either randomly or by way of a "zipper" process in the solid.[6] Experiments are underway to determine the structures of the lower-order ladderanes and the sequence by which the photocycloadditions occur.[21]

In this report, we have demonstrated that a linear template may be used to position two polyenes for an intermolecular reaction to produce [*n*]ladderanes ($n=3$ or 5). The template preorganizes the polyenes, through hydrogen-bonding interactions, for [2+2] photodimerizations in the solid state. By using the organized, solvent-free environment of the solid state[9] for reaction, the ladderanes can be formed in gram quantities and in 100% yield. We believe that these results illuminate the utility of applying concepts of supramolecular chemistry and self-assembly to address a problem of covalent synthesis[7,8] and we are now exploring whether such template molecules can be used to construct ladderanes of increasing size and complexity in the solid state.[8]

Experimental Section

1a and **1b**: 4-pyr-poly-2-ene and 4-pyr-poly-3-ene were prepared according to a literature procedure.[22] 5-OMe-res was commercially available. Cocrystals of **1a** were obtained by evaporation of a solution of 4-pyr-poly-2-ene (0.058 g, 0.28 mmol) and 5-OMe-res (0.039 g, 0.28 mmol) in hot methanol (3.0 mL). Co-crystals of **1b** were obtained in a similar manner using 4-pyr-poly-3-ene (0.030 g, 0.13 mmol) and 5-OMe-res (0.018 g, 0.13 mmol).

Solid-state photoreactions and isolation of **2a** and **2b**: UV irradiation of powdered crystalline **1a** (500 W Hg lamp) over a period of 120 h resulted in 100% conversion of poly-2-ene to [3]ladderane. In the case of **1b**, the quantitative formation of the [5]ladderane was achieved after 72 h. In both cases, the irradiation experiments were performed by placing finely ground samples of either **1a** or **1b** between two pyrex plates and turning each sample in eight-hour intervals to ensure uniform irradiation. The irradiated solids were stirred with 1M KOH solution, then extraction with methylene chloride and evaporation of the organic phase yielded the appropriate ladderane as a white solid in 85% yield. All procedures were readily scaled up to give the ladderanes in gram quantities. Single crystals of **2a** were grown from ethanol, while single crystals of **2b** were grown from benzene yielding a 1:2 benzene solvate. ^{1}H NMR of **1a** before irradiation (300 MHz, [D$_6$]DMSO): $\delta=9.15$ (br s, 2H), 8.54 (dd, 4H), 7.50 (dd, 4H), 7.40 (dd, 4H), (dd, 4H), 5.82 (br t, 1H), 5.78 (br d, 2H), 3.61 ppm (s, 3H). ^{1}H NMR of irradiated **1a** (300 MHz, [D$_6$]DMSO): $\delta=9.16$ (br s, 4H), 8.26 (dd, 8H), 7.04 (dd, 8H), (br t, 2H), 5.78 (br d, 4H), 4.30 (br s, 4H), 3.61 (s, 6H), 3.49 ppm (br s, 4H). ^{1}H NMR of **1b** before irradiation (300 MHz, [D$_6$]DMSO): $\delta=9.16$ (br s, 2H), 8.52 (dd, 4H), 7.46 (dd, 4H), 7.33 (m, 2H), 6.72 (m, 4H), 5.82 (br t, 1H), 5.79 (br d, 2H), 3.61 ppm (s, 3H). ^{1}H NMR of irradiated **1b** (300 MHz, [D$_6$]DMSO): $\delta=9.15$ (br s, 4H), 8.25 (dd, 8H), 7.02 (dd, 8H), (br t, 2H), 5.78 (br d, 4H), 4.27 (br s, 4H), 3.61 (s, 6H), 3.27 (br s, 4H), 3.12 ppm (br s, 4H).

Crystal data for **1a**: monoclinic, $P2_1/c$, $a=9.182(5)$, $b=13.381(5)$, $c=15.122(5)$ Å, $\beta=106.712(5)°$, $V=1779.5(13)$ Å^3, $Z=4$, $\rho_{calcd}=1.300\,g\,cm^{-3}$, $R_1=0.0441$ for 2324 reflections with $I>2\sigma(I)$. Crystal data for **1b**: triclinic, $P\bar{1}$, $a=9.081(3)$, $b=21.143(4)$, $c=21.308(18)$ Å, $\alpha=87.92(4)$, $\beta=79.47(6)$, $\gamma=78.91(2)°$, $V=3947(4)$ Å^3, $Z=2$, $\rho_{calcd}=1.260\,g\,cm^{-3}$, $R_1=0.0891$ for 6150 reflections with $I>2\sigma(I)$. Crystal data for the **2a**: triclinic, $P\bar{1}$, $a=12.534(5)$, $b=12.583(5)$, $c=14.787(5)$ Å, $\alpha=100.388(5)$, $\beta=106.555(5)$, $\gamma=89.945(5)°$, $V=2195.7(14)$ Å^3, $Z=2$, $\rho_{calcd}=1.260\,g\,cm^{-3}$, $R_1=0.0647$ for 4018 reflections with $I>2\sigma(I)$. Crystal data for **2b**·2(benzene): monoclinic, $P2_1/c$, $a=9.475(2)$, $b=15.048(3)$, $c=12.235(2)$ Å, $\beta=95.95(3)°$, $V=1735.0(6)$ Å^3, $Z=4$, $\rho_{calcd}=1.196\,g\,cm^{-3}$, $R_1=0.0438$ for 1625 reflections with $I>2\sigma(I)$. All crystal data were measured on a Nonius Kappa CCD single-crystal X-ray diffractometer at 77 K. After anisotropic refinement of all non-hydrogen atoms, aromatic, methine, and hydroxyl hydrogen atoms were placed in idealized positions and allowed to ride on the atom to which they were attached. The structure of **1b** was determined to be a rotational twin, the twinning law being a twofold rotation about the (011) reciprocal lattice direction. All crystallographic calculations were conducted using SHELXL-97.[23] CCDC-218101 (**1a**), CCDC-218102 (**1b**), CCDC-218103 (**2a**), and CCDC-218104 (**2b**) contain the supplementary crystallographic data for this paper. These data can be obtained free of charge via www.ccdc.cam.ac.uk/conts/retrieving.html (or from the Cambridge Crystallographic Data Centre, 12, Union Road, Cam-

 © 2004 Wiley-VCH Verlag GmbH & Co. KGaA, Weinheim

bridge CB2 1EZ, UK; fax: (+44) 1223-336-033; or deposit@ccdc.cam.ac.uk).

Received: August 25, 2003 [Z52713]
Published Online: November 5, 2003

Keywords: dimerization · ladderanes · self-assembly · supramolecular chemistry · topochemistry

[1] For a recent highlight on ladderanes, see: H. Hopf, *Angew. Chem.* **2003**, *115*, 2928 – 2931; *Angew. Chem. Int. Ed.* **2003**, *42*, 2822 – 2825.
[2] W. Li, M. A. Fox, *J. Am. Chem. Soc.* **1996**, *118*, 11752 – 11758.
[3] a) J. S. S. Damste, M. Strous, W. I. C. Rijpstra, E. C. Hopmans, J. A. J. Geenevasen, A. C. T. van Duin, L. A. van Niftrik, M. S. M. Jetten, *Nature* **2002**, *419*, 708 – 712; b) E. F. DeLong, *Nature* **2002**, *419*, 676 – 677.
[4] M. M. M. Kuypers, A. O. Sliekers, G. Lavik, M. Schmidt, B. B. Jørgensen, J. G. Kuenen, J. S. S. Damste, M. Strous, M. S. M. Jetten, *Nature* **2003**, *422*, 608 – 611.
[5] For discussions on organizing molecules in solution, see: a) D. H. Williams, E. Stephens, M. Zhou, *Chem. Commun.* **2003**, 1973 – 1976; b) M. Rekharsky, Y. Inoue, S. L. Tobey, A. Metzger, E. V. Anslyn, *J. Am. Chem. Soc.* **2002**, *124*, 14959 – 14967.
[6] H. Hopf, H. Greiving, P. G. Jones, P. Bubenitschek, *Angew. Chem.* **1995**, *107*, 742 – 744; *Angew. Chem. Int. Ed. Engl.* **1995**, *34*, 685 – 687.
[7] M. C. T. Fyfe, J. F. Stoddart, *Acc. Chem. Res.* **1997**, *30*, 393 – 401.
[8] a) J. Xiao, M. Yang, J. W. Lauher, F. W. Fowler, *Angew. Chem.* **2000**, *112*, 2216 – 2219; *Angew. Chem. Int. Ed.* **2000**, *39*, 2132 – 2135; b) J. J. Kane, R.-F. Liao, J. W. Lauher, F. W. Fowler, *J. Am. Chem. Soc.* **1995**, *117*, 12003 – 12005.
[9] a) K. Tanaka, F. Toda, *Chem. Rev.* **2000**, *100*, 1025 – 1074; b) V. Ramamurthy, K. Venkatesan, *Chem. Rev.* **1987**, *87*, 433 – 481.
[10] a) L. R. MacGillivray, *CrystEngComm* **2002**, *4*, 37 – 42; b) D. B. Varshney, G. S. Papaefstathiou, L. R. MacGillivray, *Chem. Commun.* **2002**, 1964 – 1965; c) L. R. MacGillivray, J. L. Reid, J. A. Ripmeester, G. S. Papaefstathiou, *Ind. Eng. Chem. Res.* **2002**, *41*, 4494 – 4497; d) G. S. Papaefstathiou, A. J. Kipp, L. R. MacGillivray, *Chem. Commun.* **2001**, 2432 – 2433; e) L. R. MacGillivray, J. L. Reid, J. A. Ripmeester, *J. Am. Chem. Soc.* **2000**, *122*, 7817 – 7818.
[11] We used "template switching" to identify a template that affords each [*n*]ladderane in 100% yield. See: T. Friščić, L. R. MacGillivray, *Chem. Commun.* **2003**, 1306 – 1307.
[12] For use of linear templates in the solid state, see also: a) Y. Ito, B. Borecka, J. Trotter, J. R. Scheffer *Tetrahedron Lett.* **1995**, *36*, 6083 – 6086; b) D. G. Amirakis, M. A. Garcia-Garibay, S. J. Rowan, J. F. Stoddart, A. J. P. White, D. J. Williams, *Angew. Chem.* **2001**, *113*, 4386 – 4391; *Angew. Chem. Int. Ed.* **2001**, *40*, 4256 – 4261; c) S. Phba, H. Hosomi, Y. Ito *J. Am. Chem. Soc.* **2001**, *123*, 6349 – 6352; d) D. G. Amirsakis, A. M. Elizarov, M. A. Garcia-Garibay, P. T. Glink, J. F. Stoddart, A. J. P. White, D. J. Williams, *Angew. Chem.* **2003**, *115*, 1158 – 1164; *Angew. Chem. Int. Ed.* **2003**, *42*, 1126 – 1132; e) N. Shan, W. Jones, *Tetrahedron Lett.* **2003**, *44*, 3687 – 3689.
[13] For use of linear templates in the liquid phase, see: a) T. R. Kelly, C. Zhao, G. J. Bridger, *J. Am. Chem. Soc.* **1989**, *111*, 3744 – 3745; b) R. J. Pieters, I. Huc, J. Rebek *Tetrahedron* **1995**, *51*, 485 – 498; c) D. M. Bassani, V. Darcos, S. Mahony, J.-P. Desvergne, *J. Am. Chem. Soc.* **2000**, *122*, 8795 – 8796; c) D. M. Bassani, X. Sallenave, V. Darcos, J.-P. Desvergne, *Chem. Commun.* **2001**, 1446 – 1447; d) H. Zitt, I. Dix, H. Hopf, P. G. Jones, *Eur. J. Org. Chem.* **2002**, 2298 – 2307.
[14] G. M. J. Schmidt, *Pure Appl. Chem.* **1971**, *27*, 647 – 678.
[15] S. Woitellier, J. P. Launay, C. W. Spangler, *Inorg. Chem.* **1989**, *28*, 758 – 762.
[16] a) G. Mehta, M. B. Viswanath, A. C. Kunwar, *J. Org. Chem.* **1994**, *59*, 6131 – 6132; b) R. N. Warrener, G. Abbenante, C. H. L. Kennard, *J. Am. Chem. Soc.* **1994**, *116*, 3645 – 3646; c) M. A. Miller, J. M. Schulman, *J. Mol. Struct.* **1988**, *163*, 133 – 141.
[17] a) A. Elgavi, B. S. Green, G. M. J. Schmidt, **1973**, *95*, 2058 – 2059; b) M. D. Cohen, A. Elgavi, B. S. Green, Z. Ludmer, G. M. J. Schmidt, *J. Am. Chem. Soc.* **1972**, *94*, 6776 – 6779.
[18] For a theoretical treatment of the Cope rearrangement in ladderanes, see: D. J. Tantillo, R. Hoffmann, *Angew. Chem.* **2002**, *114*, 1075 – 1078; *Angew. Chem. Int. Ed.* **2002**, *41*, 1033 – 1036.
[19] For oligomerizations and polymerizations of cyclobutanes in the solid state, see: a) L. Addadi, M Lahav, *J. Am. Chem. Soc.* **1978**, *100*, 2838 – 2844; b) M. Hasegawa, *Chem. Rev.* **1983**, *83*, 507 – 518.
[20] For movement in crystals, see: a) G. R. Desiraju, *Nature* **2003**, *423*, 485; b) I. C. Paul, D. Y. Curtin, *Acc. Chem. Res.* **1973**, *6*, 217 – 225.
[21] V. Enkelmann, G. Wegner, K. Novak, K. B. Wagener, *J. Am. Chem. Soc.* **1993**, *115*, 10390 – 10391.
[22] P. Carsky, S. Hünig, I. Stemmler, D. Scheutzow, *Liebigs Ann. Chem.* **1980**, 291 – 304.
[23] G. M. Sheldrick, SHELXL-97, Program for Refinement of Crystal Structure, University of Göttingen, Göttingen (Germany), **1997**.

 © 2004 Wiley-VCH Verlag GmbH & Co. KGaA, Weinheim

Zeolite Synthesis

A Titanosilicate That Is Structurally Analogous to an MWW-Type Lamellar Precursor**

*Weibin Fan, Peng Wu, Seitaro Namba, and Takashi Tatsumi**

Titanosilicate catalysts are of scientific and technological interest because of their ability to be applied to environmentally friendly chemical processes for the liquid-phase catalytic oxidation of a variety of organic compounds, by using H_2O_2 as a clean oxidant. The medium-sized pore

[*] Dr. W. Fan, Dr. P. Wu, Prof. T. Tatsumi
Division of Materials Science & Chemical Engineering
Graduate School of Engineering, Yokohama National University
Tokiwadai 79-5, Yokohama 240-8501 (Japan)
Fax: (+81) 45-339-3943
E-mail: ttatsumi@ynu.ac.jp
Prof. S. Namba
Department of Materials, Teikyo University of Science and Technology, Uenohara-machi, Yamanashi 409-0193 (Japan)

[**] This work was supported by Core Research for Evolutional Science and Technology of Japan Science and Technology Corporation. W.F. gratefully acknowledges Japan Society for Promotion of Science (JSPS) for a fellowship as a foreign researcher.

Supporting information for this article is available on the WWW under http://www.angewandte.org or from the author.

 © 2004 Wiley-VCH Verlag GmbH & Co. KGaA, Weinheim DOI: 10.1002/anie.200352723

openings of TS-1 render it inactive for the oxidation of lager molecules.[1] Therefore, many efforts have been made to develop large-pore titanosilicates to meet increasing demands for synthesizing fine chemicals in an environmentally friendly way. For this purpose, Ti-Beta, Ti-MTW, Ti-MOR, and Ti-ITQ-7, all with 12-membered-ring (12-MR) pores, as well as Ti-containing mesoporous materials have been prepared.[1–5] However, none of these catalysts are efficient enough in terms of intrinsic activity and stability. Recently, Ti-MWW has proved to be much more active than TS-1 and Ti-Beta in the epoxidation of linear alkenes with H_2O_2,[6] but unfortunately for the oxidation of bulky molecules, it is still inferior to Ti-Beta owing to severe steric restrictions. Actually, with respect to MWW-type materials, potential advantages are expected from their supercages and side pockets, but access to the supercages is seriously restricted by the openings of the elliptical 10-MR pores once the three-dimensional (3D) MWW crystalline structure is formed from the lamellar precursor. Thus, Corma et al. delaminated an MWW zeolite into isolated crystalline sheets by a rather complicated method, and then grafted on titanocene to obtain Ti/ITQ-2.[7] However, this material can only achieve high reactivity and epoxide selectivity with organic hydroperoxide oxidants under extremely harsh conditions (that is, the absence of water in the system), probably as a result of the presence of a large number of hydrophilic silanol groups that reside on the exterior surface. From the geometrical point of view, the retention of a lamellar structure with a layer spacing not less than that of an as-synthesized MWW precursor after calcination would be an alternative way for creating the open space required for reactions. Thus prepared materials not only make the active sites within the supercages more accessible to bulky molecules but are also endowed with the capability of promoting the oxidation reactions with an aqueous solution of H_2O_2 as an oxidant. This would open new possibilities for titanosilicates to be applied to fine-chemical industry. We have succeeded in preparing such a novel titanosilcate catalyst (denoted as Ti-YNU-1), and have found that this material shows substantially improved oxidation ability, epoxide selectivity, and stability in the liquid-phase epoxidation of cycloalkenes.

Figure 1 shows the XRD patterns of as-synthesized samples of 3D Ti-MWW and Ti-YNU-1. The as-synthesized sample had the structure of an MWW lamellar precursor, as evidenced by the presence of peaks due to the 001 and 002 reflections (Figure 1 a). A 3D MWW framework was formed upon direct calcination as a result of condensation of hydroxyl groups between the layers (Figure 1 b). In contrast, the layer structure was still retained when the as-synthesized material was refluxed in acid solution and further calcined (Figure 1 c and d). When compared with 3D Ti-MWW, the diffraction lines associated with the *c* crystallographic axis are all shifted to lower values of 2θ for Ti-YNU-1. This indicates that the unit-cell parameter *c* had increased.[8] Indeed, the *c* parameter of Ti-YNU-1 was 27.47 Å, in contrast to 24.98 Å for the corresponding 3D structure, while both samples showed similar *a* and *b* parameters. Since the crystalline structure within the layers is highly rigid, it is reasonable to suggest that the increase in the *c* parameter is mainly due to the expansion of the layer spacing by about 2.5 Å.

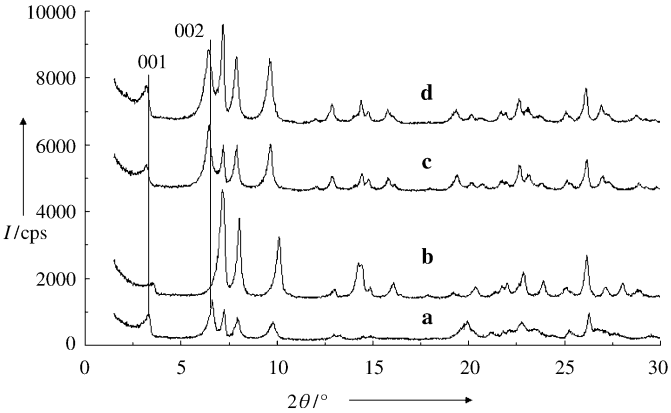


Figure 1. XRD patterns of a) the as-synthesized lamellar precursor of Ti-MWW, b) the directly calcined material (3D Ti-MWW), c) an acid-treated sample and d) the same sample after calcination (Ti-YNU-1).

Figure 2 shows high-resolution transmission electron micrograph (HRTEM) images of the edge-on view of the crystallites. The thickness of every 10 layers in Ti-YNU-1 is comparable to that of 11 layers in 3D Ti-MWW. Considering that the single-layer thickness for 3D MWW zeolites is about 25 Å, the TEM images visually demonstrate that Ti-YNU-1 has an interlayer spacing enlarged by about 2.5 Å, in agreement with the XRD characterization. This structure is totally

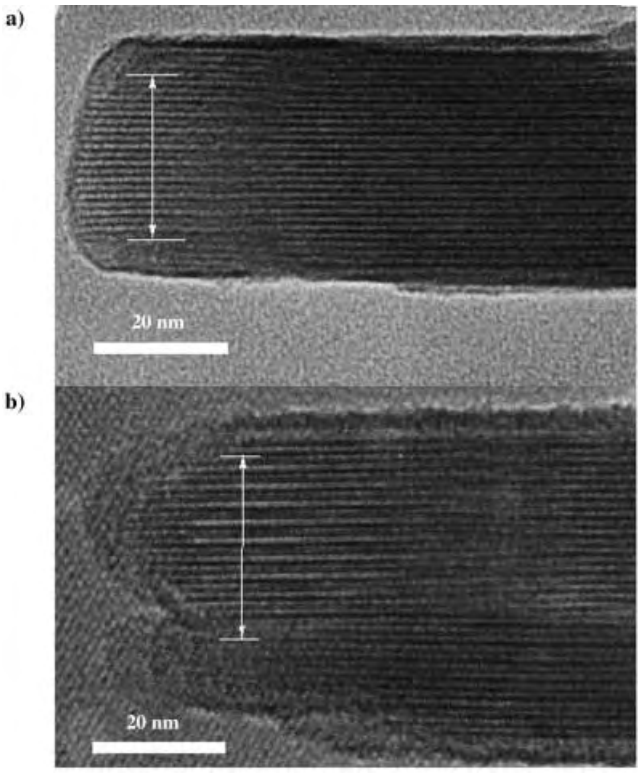


Figure 2. Edge-on TEM images of 3D Ti-MWW (a) and Ti-YNU-1 (b). (The arrow indicates the thickness of 10 layers.)

 © 2004 Wiley-VCH Verlag GmbH & Co. KGaA, Weinheim

different from ITQ-2, which is composed of separate layers.[9] In contrast, Ti-YNU-1 possesses a lamellar structure that is analogous to the MWW-type precursor although the linkage between the layers after removing the templating molecules is not fully determined at the moment. The possibility that the layers are pillared by a small amount of Ti that remains after acid treatment can be excluded because the lamellar structure (Si-YNU-1) was still formed under similar synthesis conditions even when titanium was not added to the synthesis gel. The diffraction lines of ITQ-2 are very weak in intensity and almost indiscernible,[9] whereas those of Ti-YNU-1 are similar to those of 3D Ti-MWW. This result shows that their structures are completely different. The former lacks long-range periodicity, while the latter completely retains this property. In addition, the delamination process also inevitably led to the partial destruction of the crystalline-sheet structure, and consequently affected the catalytic performance.

The formation of a lamellar structure depends heavily on the amount of Ti present in the synthesis gel. When the Si/Ti ratio in the synthesis gel was greater than 50, the lamellar structure appeared gradually with decreasing Ti content after acid treatment and subsequent calcination. In contrast, the 3D MWW structure was only formed at lower Si/Ti ratios (e.g., ≈ 30). The surface area and pore volume of Ti-YNU-1 are about 676 $m^2 g^{-1}$ and 0.202 $mL g^{-1}$, whereas those of 3D Ti-MWW are only 528 $m^2 g^{-1}$ and 0.154 $mL g^{-1}$, respectively. This supports the substantial expansion of the layer space. The N_2 adsorption/desorption isotherms show that Ti-YNU-1, like 3D Ti-MWW, displays typical behavior of microporous materials with an external surface area of about 61.4 $m^2 g^{-1}$, which confirms that it is a well-crystalline molecular sieve. In contrast, ITQ-2 shows a significantly high mesopore volume and an external surface area of about 700 $m^2 g^{-1}$.[9] This provides more evidence that Ti-YNU-1 possesses a structure different from that of ITQ-2 or Ti/ITQ-2.

Compared with the 3D Ti-MWW sample, Ti-YNU-1 showed a more intense band in the OH-vibration region of the FTIR spectrum (3728 cm^{-1}), which is probably ascribed to asymmetric hydrogen-bonded silanols.[10] Furthermore, the ^{29}Si MAS NMR spectrum of Ti-YNU-1 showed a signal at 88.6 ppm, which is characteristic of Q^2 ($Si(OH)_2(OSi)_2$) and/or $Si(OH)(OTi)(OSi)_2$ and was absent for 3D Ti-MWW. The presence of a large number of silanol groups in Ti-YNU-1 was also proved by H_2O adsorption at 298 K. The amount of the adsorbed water on Ti-YNU-1 was about four times as large as that on 3D Ti-MWW. Nevertheless, diffuse reflectance UV/Vis spectroscopy shows that all of the Ti atoms in Ti-YNU-1 are tetrahedrally coordinated, as evidenced by the presence of a band at ≈ 210 nm but no bands above 250 nm that could be attributed to octahedrally coordinated Ti and titanium oxides.[11] For Ti/ITQ-2, the grafted Ti is merely located at the external surface, but not in truly isomorphous substituted lattice sites; hence, it is similar to Ti-MCM-41, which is also prepared via the grafting method.[12] This probably accounts for the fact that epoxidation of cyclohexene can only be carried out without water present, while Ti/ITQ-2 serves as a catalyst.[7]

The reason for the formation of Ti-YNU-1 is not clear. The presence of silanol groups, related to defect sites not occupied by Ti at high Si/Ti ratios, is tentatively presumed to cause the stacking faults when the intercalated piperidine was removed by acid treatment, which then gives rise to a layered structure even after further calcination. With an increase in Ti content in the gel, more Ti atoms would be incorporated into the T_1 positions of the proposed structure.[13,14] The stacking faults would be thus eliminated since the Ti–OH bond (1.95 Å) is much longer than Si–OH bond (1.61 Å), and incorporation of Ti in T_1 sites constricts the T-O-T angle so that it is more acute than the Si-O-Si angle in pure silicates.[15] The scheme for the formation of Ti-YNU-1 is illustrated in Figure 3.

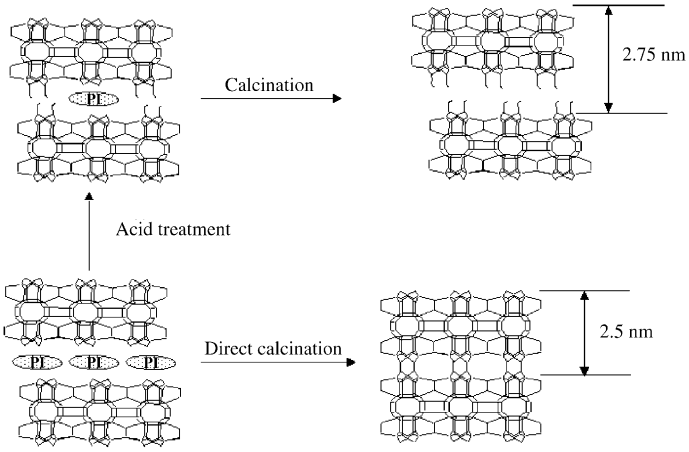


Figure 3. Possible scheme for the formation of Ti-YNU-1 and 3D Ti-MWW, as well as their structures. Direct calcination of the as-synthesized lamellar precursor burns off the organic species and subsequently leads to dehydroxylation between the layers and hence formation of 3D MWW structure. However, the acid treatment washes out most of the organic species, which causes stacking faults due to the presence of silanols on defect sites. Ti-YNU-1 with a lamellar structure is then obtained even after subsequent calcination.

Table 1 summarizes the catalytic results for the oxidation of cyclohexene over various titanosilicates. Compared with Ti-Beta, Ti-YNU-1 not only exhibited a higher activity but also gave much higher epoxide selectivity. 3D Ti-MWW showed a moderate conversion, whereas TS-1 and Ti-MOR were less active. This indicates that among the typical titanosilicates, Ti-YNU-1 is the most active and selective catalyst for the oxidation of cyclohexene irrespective of the lowest Ti content. The stability of the catalyst was investigated by repeating the reaction eight times. The used Ti-YNU-1 catalyst gave a cyclohexene conversion and an epoxide selectivity in the range of 31.5–34.5% and 87.5–92.8%, respectively, after being regenerated by calcination in air at 773 K. In contrast, the conversion on Ti-Beta decreased by 23% when subjected to only three repeated reaction runs.

The turnover number (TON) for the oxidation of different clycloalkenes catalyzed by various titanosilicate molecular sieves is depicted in Figure 4. TS-1 exhibited high activity for the oxidation of cylopentene, while the activity declined drastically in the case of cyclohexene, and even more severely with increasing molecular size of cycloalkenes, due to increasing steric restrictions. Although 3D Ti-MWW showed

 © 2004 Wiley-VCH Verlag GmbH & Co. KGaA, Weinheim

Table 1: Catalytic activity of various titanosilicates in the oxidation of cyclohexene.[a]

Catalyst	Si/Ti	Conv. [%]	Selectivity [%]		H_2O_2
			Epoxide	Others[b]	Selectivity [%]
TS-1	83	3.3	17.9	82.1	n.d.
3D Ti-MWW	45	8.1	35.0	65.0	74.8
Ti-MOR[c]	92	9.0	55.0	45.0	63.5
Ti-Beta	35	16.5	78.4	21.6	51.6
Ti-YNU-1	240	21.2	90.8	9.2	78.5

[a] Reaction conditions: catalyst (0.05 g) , acetonitrile (10 mL), cyclohexene (10 mmol), H_2O_2 (10 mmol; 31% aqueous solution), 333 K, 2 h. [b] Cyclohexanediol, 2-cyclohexen-1-ol and 2-cyclohexen-1-one. [c] Ti-MOR was post-prepared by treating the dealuminated sample (Si/Al = 468) with $TiCl_4$ vapor at 773 K for 1 h. 0.2 g of the catalyst was used; all the other conditions were identical. n.d. = not detected.

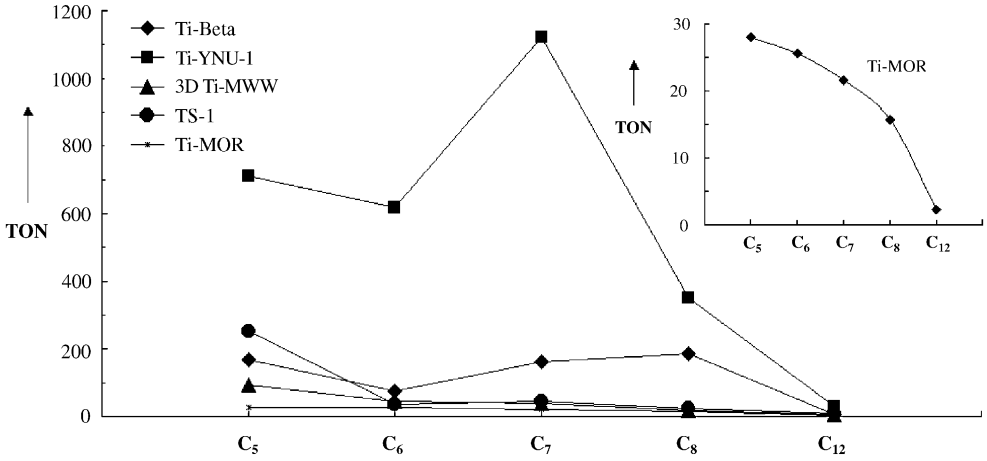


Figure 4. The turnover number (TON/(mol (mol Ti)$^{-1}$)) for the oxidation of cycloalkenes with 5–12 carbon atoms over various titanosilicate molecular sieves. For reaction conditions, see Table 1. The inset shows the TON of Ti-MOR.

much stronger intrinsic ability than TS-1 for the oxidation of linear alkenes,[6] it gave a lower TON for the oxidation of cyclopentene. This indicates that an increased steric restriction is exerted on 3D Ti-MWW, and is consequently indicative of a smaller opening in 3D Ti-MWW than in TS-1. In contrast, the catalytic activity of Ti-YNU-1 and Ti-Beta increased up to C_7 or C_8 cycloalkenes (except for cyclopentene), respectively, and then declined sharply. The activity is expected to increase with an increase in the number of carbon atoms in the cycloalkenes because of the increased number of electron-donating methyl groups on the coplanar conformation. The reason for a lower conversion of cyclohexene than that of cyclopentene on Ti-YNU-1 and Ti-Beta is probably that the reaction temperature in the oxidation of cyclopentene (333 K) is much higher than its boiling point (319 K). It can be reasonably deduced that the pore window of Ti-YNU-1 is slightly smaller than that of Ti-Beta from the fact that Ti-Beta exhibits the highest TON for cyclooctene among the cycloalkenes investigated while Ti-YNU-1 shows the highest TON for cycloheptene. For Ti-MOR, the conversion gradually declines as cycloalkenes increase in molecular size. It is reasonable to assume that the pore size of Ti-MOR is smaller than that of Ti-YNU-1 but larger than that of TS-1 since Ti-MOR shows comparable conversion for cyclopentene (10.2%) and cyclohexene (9.0%) but lower conversion for cycloheptene (7.5%). This result shows that the steric constraints become important for Ti-MOR with cycloheptene. Thus, it is concluded that the effective pore size of various titanosilicate molecular sieves decreases in the order Ti-Beta > Ti-YNU-1 > Ti-MOR > TS-1 > 3D Ti-MWW. This result is consistent with the XRD characterization that showed that the layer space of Ti-YNU-1 is enlarged by about 2.5 Å as compared with 3D Ti-MWW, since the effective pore openings of Beta and mordenite zeolites are 7.1×7.3 Å and 7.0×6.5 Å, respectively, whereas that of 3D MWW is 4.0×5.5 Å between the layers.[16]

In summary, a new titanosilicate Ti-YNU-1, with a lamellar structure analogous to a MWW precursor, has been synthesized. It exhibits the pore properties of 12-MR zeolite and proves to be a highly active, selective, and stable catalyst in the liquid-phase epoxidation of bulky alkenes with H_2O_2.

XRD patterns of samples prepared with a synthesis gel of differing Si/Ti ratios as well as OH-region IR spectra of Ti-YNU-1 and 3D Ti-MWW are presented as Supporting Information.

Experimental Section

The lamellar precursor of the MWW titanosilicate was synthesized from highly siliceous MWW zeolite, [Ti(OBu)$_4$], piperidine (PI), and deionized water following procedures reported elsewhere.[17] Typically, PI (7.24 g) and [Ti(OBu)$_4$] (0.29 g) were dissolved in 22.5 g of deionized water, then highly deboronated B-MWW (5 g) was added to the above solution. The resultant mixture was heated at 443 K for 5 days under rotation. The as-synthesized precursors were then refluxed in 2 M HNO_3 solution and further calcined at 823 K for 10 h to obtain a novel lamellar titanosilicate with a structure analogous to the MWW precursor, and denoted as Ti-YNU-1.

The liquid-phase oxidation of alkenes with H_2O_2 (31% in aqueous solution) was carried out at 333 K for 2 h while stirring in a round-bottomed flask equipped with a condenser. The temperature was controlled with a water bath. In a typical batch, catalyst (0.05 g), acetonitrile (10 mL; solvent), alkene (10 mmol; substrate), and H_2O_2 (10 mmol; oxidant) were employed. With respect to the investigation of catalytic stability, the reaction conditions were maintained for the repeat experiments, that is, reaction temperature = 333 K, reaction

 © 2004 Wiley-VCH Verlag GmbH & Co. KGaA, Weinheim

time = 2 h, cyclohexene/H_2O_2 = 1:1 molar ratio, 1 mL MeCN per mmol cyclohexene, 1 g catalyst per 100 mmol cyclohexene. After each run, the catalyst was centrifuge-washed with acetone and then distilled water for four times, respectively. The solid material was dried at 100 °C, and further calcined at 550 °C for 8 h before the next reaction run.

X-ray diffraction (XRD) patterns were recorded by a MAC Science M3X 1030 X-ray diffractometer with $Cu_{K\alpha}$ radiation (40 kV, 20 mA). The diffuse reflectance UV/Vis spectra (DRS) were measured on a Jasco V-550 UV/Vis spectrophotometer. OH-region infrared (IR) spectra were acquired on a PE-1600 FTIR spectrometer. Before recording the spectra in the OH region, the samples were first evacuated at 500 °C and 10^{-4} Torr for 2 h. ^{29}Si MAS NMR measurements were performed on a JEOL JNMECA 400 nuclear magnetic resonance spectrometer at ambient temperature. The chemical shift was referenced to an external standard of polydimethylsilane. The spin rate of the rotor was 5.0 kHz with a repetition time of 30 s. A pulse length of 7 μs was applied and approximately 3000 scans were accumulated. The spectra were deconvoluted with a Gaussian–Lorentzian mixed equation. The TEM images were obtained with a JEOL JEM-2000EX at 200 KV. N_2 adsorption (77 K) and H_2O adsorption (298 K) were carried out on Belsorp 28SCA and Belsorp 18SCA instruments, respectively. Thermogravimetric analysis was measured by an ULVAC-Riko TGD 9600 thermal analysis system. The chemical composition of the samples was determined with an inductively coupled plasma-atomic emission spectrometer (Shimadzu ICPS-8000E). The product was analyzed by a Shimadazu GC-14B gas chromatograph equipped with a 50 m OV-1 capillary column and a flame ionization detector. The amount of the unconverted H_2O_2 was determined by titrating with 0.1M $Ce(SO_4)_2$ aqueous solution.

Received: August 27, 2003 [Z52723]

Keywords: alkenes · epoxidation · heterogeneous catalysis · titanosilicates · zeolites

[1] G. Bellussi, M. S. Rigutto, *Stud. Surf. Sci. Catal.* **1994**, *145*, 151.
[2] M. A. Camblor, A. Corma, A. Martínez, J. Pérez-Pariente, *Chem. Commun.* **1992**, 589.
[3] A. Tuel, *Zeolites* **1995**, *15*, 236.
[4] P. Wu, T. Komatsu, T. Yashima, *J. Phys. Chem.* **1996**, *100*, 10316.
[5] M. J. Díaz-Cabañas, L. A. Villaescusa, M. A. Camblor, *Chem. Commun.* **2000**, 761; A. Corma, M. J. Díaz-Cabañas, M. E. Domine, F. Rey, *Chem. Commun.* **2000**, 1725.
[6] P. Wu, T. Tatsumi, T. Komatsu, T. Yashima, *J. Catal.* **2000**, *202*, 245.
[7] A. Corma, U. Diaz, V. Fornes, J. L. Jorda, M. Domine, F. Rey, *Chem. Commun.* **1999**, 779.
[8] R. Millini, G. Perego, W. O. Parker, Jr., G. Bellussi, L. Carluccio, *Microporous Mater.* **1995**, *4*, 221.
[9] A. Corma, V. Fornes, S. B. Pergher, T. L. M. Maesen, J. G. Buglass, *Nature* **1998**, *396*, 353.
[10] G. P. Heitmann, G. Dahlhoff, W. F. Hölderich, *J. Catal.* **1999**, *186*, 12.
[11] P. Wu, T. Tatsumi, T. Komatsu, T. Yashima, *J. Phys. Chem. B* **2001**, *105*, 2897.
[12] T. Maschmeyer, F. Rey, G. Sanker, J. M. Thomas, *Nature* **1995**, *378*, 159.
[13] M. E. Leonowicz, J. A. Lawton, S. L. Lawton, M. K. Rubin, *Science* **1994**, *264*, 1910.
[14] P. Wu, W. Fan, T. Tatsumi, unpublished results.
[15] M. E. Davis, C. Chen, S. L. Burkett, R. F. Lobo, *Mater. Res. Soc. Symp. Proc.* **1994**, *346*, 831.
[16] C. Baerlocher, W. M. Meier, D. H. Olson, *Atlas of Zeolite Framework types*, Elsevier, Amsterdam, **2001**, pp. 77, 191, 203.
[17] P. Wu, T. Tatsumi, *Chem. Commun.* **2002**, 106.

 © 2004 Wiley-VCH Verlag GmbH & Co. KGaA, Weinheim

Metal-Directed Self-Assembly

Three-Level Synthetic Strategy Towards Mixed-Valence and Heterometallic [2 × 2] Gridlike Arrays**

*Lindsay H. Uppadine and Jean-Marie Lehn**

The metal-directed self-assembly of polydentate ligands provides a convenient route to a variety of supramolecular architectures.[1] Examples to date that illustrate the versatility of the process include helicates,[2] cages,[3] ladders,[4] racks,[5] and grids.[6,7] Interest in these assemblies has also been fueled by their potential for a wide range of applications. For example, inorganic arrays have been used as hosts for neutral,[8] cationic,[9] and anionic species,[10] with the possibility of electrochemical[10d] or optical sensing.[11] Metal-based assemblies are also prospective candidates for the development of novel materials incorporating magnetic,[12] electronic,[13] or optical features.[11,14] In particular, gridlike arrays possessing two different metals could exhibit interesting physicochemical properties arising from the precise positioning of the metallic centers.[7b] For example, the possibility of addressing the metal ions individually through an external stimulus would allow information to be written and stored at specific sites within the array.[15]

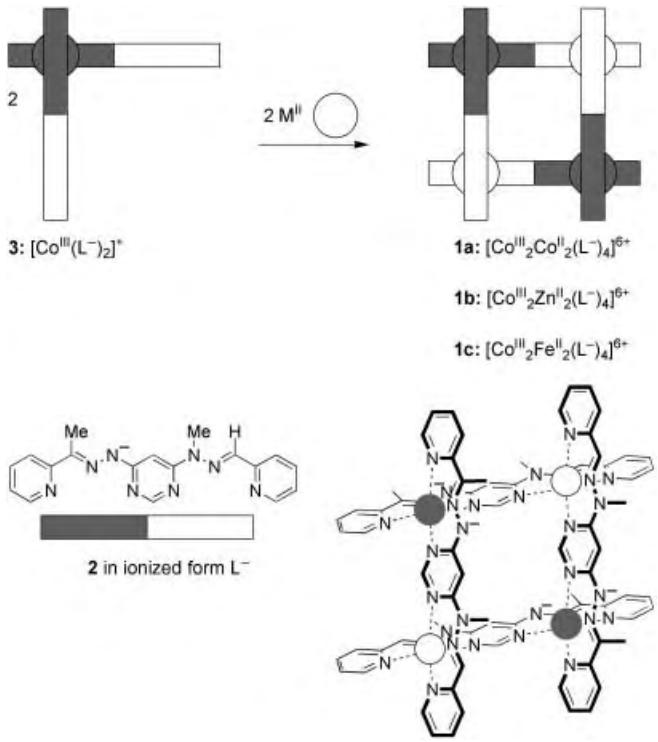
[2 × 2] Grids incorporating one type of metal center are easily constructed by one-step self-assembly reactions between the appropriate ditopic ligand and metal cation.[6a,7a] In contrast, the synthesis of heterometallic grids with precisely located metal ions is more problematic. One approach towards this type of grid has been described and involves sequential self-assembly coupled with a protection/deprotection step.[7b] We now report a novel methodology for the generation of mixed valence and heterometallic [2 × 2] grid-type architectures **1** based on a stepwise constructed bis(hydrazone) ligand **2** containing both an ionizable NH site and a non-ionizable NMe center (Scheme 1). This synthetic pathway utilises a three-level strategy involving 1) steric control of regioselectivity, 2) modulation of the redox state through protonation, and 3) chiroselective-toposelective self-assembly.

The key intermediate in the synthesis is the monometallic "corner-type" complex **3** (Scheme 1). It contains a substitutionally inert Co^{III} center to prevent scrambling when a second ion is introduced to assemble the grid. A stepwise, controlled route was employed to construct complex **3** (Scheme 2).

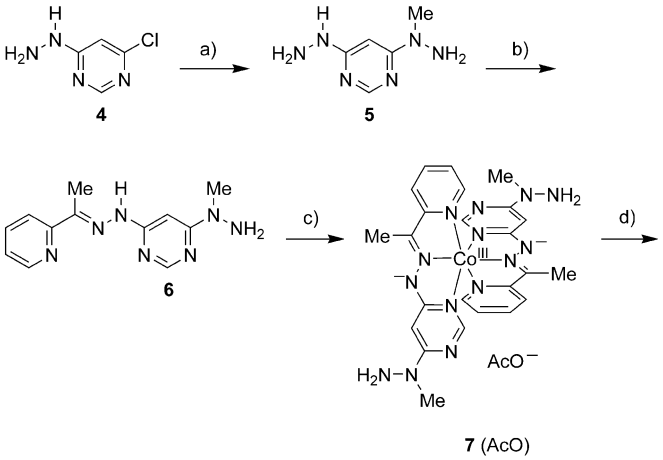
[*] Dr. L. H. Uppadine, Prof. Dr. J.-M. Lehn
Laboratoire de Chimie Supramoléculaire
ISIS/Université Louis Pasteur
8 allée Gaspard Monge
67083 Strasbourg (France)
Fax: (+33) 390-245140
E-mail: lehn@isis.u-strasbg.fr

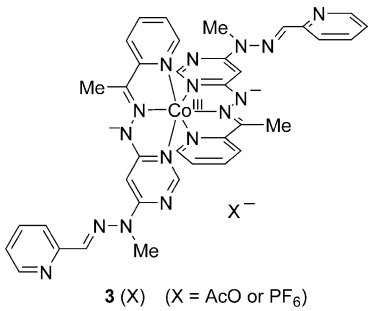
[**] This work was supported by a CNRS postdoctoral fellowship. We thank Dr. R. Graff, Dr. J.-P. Kintzinger, and Dr. P. Maltese for performing the two-dimensional NMR experiments.

 © 2004 Wiley-VCH Verlag GmbH & Co. KGaA, Weinheim DOI: 10.1002/anie.200352937



Scheme 1. Self-assembly of the [2×2] grid-type metallosupramolecular architectures **1** from the "corner" precursor **3** incorporating ligand **2**.





Scheme 2. Synthesis of complex $[Co^{III}(L^-)_2]^+$ (**3**): a) $MeNHNH_2$, MeOH; b) 2-acetylpyridine, MeOH; c) $Co(OAc)_2{\cdot}4H_2O$, MeOH; d) 2-pyridinecarboxaldehyde, MeOH.

First, the terdentate ligand **6** containing just one metal binding pocket was prepared by a regioselective synthetic approach. 4-Chloro-6-hydrazinopyrimidine (**4**)[16] was treated with *N*-methylhydrazine to give compound **5**, which was subsequently condensed with one equivalent of 2-acetylpyridine (Scheme 2). It was reasoned that the condensation reaction would occur preferentially at the hydrazino site possessing an ionizable NH hydrazone group. This site selectivity results from the fact that reaction with the *N*-methylhydrazine moiety involves an unfavorable 1,3-steric repulsion between its methyl group and that of the 2-acetylpyridine reagent. Indeed, the ratio of products from the condensation at the $NHNH_2$ and $NMeNH_2$ sites of **5** was 13.5:1.

Second, the pathway towards complex **3** takes advantage of the ionizable NH site of **6** to promote a redox reaction at a bound metal center (Scheme 2). Thus, $Co^{II}(OAc)_2{\cdot}4H_2O$ reacts with **6** to generate the Co^{III} complex **7** in a process promoted by the synergistic coupling between the deprotonation of ligand **6** by the acetate anion of $Co^{II}(OAc)_2{\cdot}4H_2O$, which acts as a base, and the aerial oxidation of cobalt(II) to cobalt(III) facilitated by its stabilization by two negatively charged ligands.[17] Thereafter, condensation of **7** with 2-pyridinecarboxaldehyde yields complex **3** containing two free metal-ion binding sites which cannot be deprotonated because they incorporate an *N*-methyl-protected hydrazone. This allows Co^{II} ions to be introduced at these sites without oxidation to Co^{III}.

The final step rests on a coupled chiro- and toposelective process to construct a heterometallic grid (Scheme 1). The [2×2] grid array is assembled from two corner complexes **3** of the *same* chirality; the connection of (*R*)- and (*S*)-**3** is geometrically prohibited.[7b] As a result, each assembly reaction yields one enantiomer of the chiral grid structure **1**.

Solubility problems in the self-assembly step hindered attempts to prepare **1a** from $Co(BF_4)_2{\cdot}6H_2O$ and **3** in MeCN. The counterion in **3** was therefore changed to the hexafluorophosphate salt **3**·PF_6. This complex reacts with $Co(BF_4)_2{\cdot}6H_2O$ in acetonitrile to afford the mixed valence array **1a** (Scheme 1). Evidence for the tetranuclear core was obtained from electrospray mass spectrometry. The spectrum reveals a series of peaks which can be attributed to sequential loss of PF_6^- and/or BF_4^- counterions $(\mathbf{1a}(PF_6)_2(BF_4)_4{-}x\,PF_6{-}y\,BF_4)^{(x+y)+}$ ($x = 0$–2, $y = 0$–4).

The ^1H NMR spectrum of grid **1a** displays several remarkable features consistent with the proposed mixed-valence structure (Figure 1 a, b). The very strongly shifted peaks at lowest field (138.5–213.7 ppm) possess the shortest relaxation times ($T_1 = 0.9$–2.1 ms) and are attributed to the three protons closest to the paramagnetic Co^{II} center (pyr6′, pym2, and H_{im}).[18] The remaining ten signals ($\delta = 6.9$–75.7 ppm) were assigned using a combination of COSY and ROESY experiments and are divided into two sets. Protons adjacent to the Co^{II} center exhibit shifted signals at $\delta = 18.2$–75.7 ppm (pyr3′, pyr4′, pyr5′, pym5) and at $\delta = 6.9$ ppm (NMe). In contrast, the cluster of five peaks in the high-field region (7.9–14.3 ppm) is assigned to pyridyl and CMe protons at the Co^{III} site. These protons belong to the coordination sphere of the low-spin, diamagnetic Co^{III} ion,

 © 2004 Wiley-VCH Verlag GmbH & Co. KGaA, Weinheim

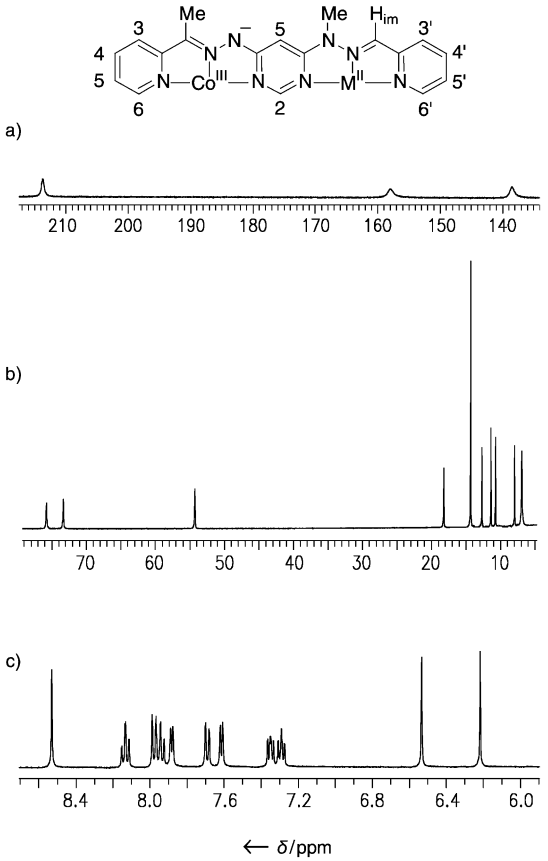


Figure 1. ^{1}H NMR spectra (400 MHz, CD_3CN) of grid **1a** in the low-field (a) and high-field (b) regions; low-field region of grid **1b** (c).

although the neighboring paramagnetic Co^{II} center clearly affects their chemical shifts and relaxation rates.

The generality of the synthetic strategy was demonstrated by preparing grids **1b** and **1c** from **3**·PF_6 and $M^{II}(BF_4)_2$ (M^{II} = Zn^{II}, Fe^{II}, respectively; Scheme 1). In contrast to grid **1a** the ^{1}H NMR spectra of these grids are restricted to the diamagnetic region (Figure 1c), which indicates that both iron(II) centers are low spin in complex **1c**.

In conclusion, a three-tiered synthetic strategy was used to construct a mixed valence [2×2] $Co^{II}_2Co^{III}_2$ grid as well as heterometallic analogues. This strategy, which encompasses regioselective, redox, and chiroselective features, implements the approach and procedures developed for the synthesis of complex organic molecules in the stepwise elaboration of inorganic architectures. The arrays are based on a heteroditopic ligand, which contains ionizable and non-ionizable compartments, thus allowing the oxidation state of the cobalt ions to be modified according to the charge on the hydrazone moiety. Such [2×2] grid motifs, in which the oxidation states can be locally manipulated and addressed by external effectors (for example, protons),[19] are of interest for future multistable molecular devices incorporating multilevel redox activity.[13] It is noteworthy that molecular spin ladders display grid-type arrays[20] and that cells presenting a four-dot [2×2]-type architecture have been considered as components of quantum-dot cellular automated devices.[21]

Experimental Section

1a$(PF_6)_2(BF_4)_4$: **3**(PF_6) (33.7 mg, 37.6 μmol) and $Co(BF_4)_2$·$6H_2O$ (12.8 mg, 37.6 μmol) were stirred in MeCN (2.5 mL) at room temperature for 18 h. The product was obtained as a dark-red solid by recrystallization from MeCN/Et_2O (33.3 mg, 75%). ^{1}H NMR (400 MHz, CD_3CN): δ = 213.7, 158.1, 138.5 (pyr6, pym2, H_{im}), 75.7 (pyr3′ or 5′), 73.3 (pym5), 54.3 (pyr3′ or 5′), 18.2 (pyr4′), 14.3 (CMe), 12.7 (pyr3), 11.4 (pyr6), 10.7 (pyr4), 7.9 (pyr5), 6.9 ppm (NMe); UV/Vis (MeCN): λ_{max} (ε in $mol^{-1}\,dm^3\,cm^{-1}$): 462 (123000), 364 (58000), 325 (62000), 277 nm (74000); MS (ES): m/z = 1040.2 $[M-2BF_4]^{2+}$, 1011.2 $[M-PF_6-BF_4]^{2+}$, 982.1 $[M-2PF_6]^{2+}$, 749.2 $[Co^{III}(L^-)_2]^+$, 672.2 $[Co^{II}(LH)(L^-)-C_5H_4N]^+$, 664.4 $[M-3BF_4]^{3+}$, 645.1 $[M-PF_6-2BF_4]^{3+}$, 625.8 $[M-2PF_6-BF_4]^{3+}$, 476.6 $[M-4BF_4]^{4+}$, 462.1 $[M-PF_6-3BF_4]^{4+}$, 447.6 $[M-2PF_6-2BF_4]^{4+}$, 352.3 $[M-PF_6-4BF_4]^{5+}$, 340.7 $[M-2PF_6-3BF_4]^{5+}$, 269.4 $[M-2PF_6-4BF_4]^{6+}$; elemental analysis (%) calcd for $Co_4C_{72}H_{68}N_{32}P_2B_4F_{28}$·$6H_2O$: C 36.6, H 3.4, N 19.0; found: C 36.6, H 3.2, N 18.7.

Received: September 23, 2003 [Z52937]

Keywords: cobalt · coordination modes · mixed-valent compounds · redox chemistry · self-assembly

[1] a) J.-M. Lehn, *Supramolecular Chemistry—Concepts and Perspectives*, VCH, Weinheim, **1995**; b) *Comprehensive Supramolecular Chemistry*, *Vol. 9* (Eds.: J. L. Atwood, J. E. D. Davies, D. D. MacNicol, F. Vögtle, J.-M. Lehn), Pergamon, Oxford, **1996**.

[2] a) C. Piguet, G. Bernardinelli, G. Hopfgartner, *Chem. Rev.* **1997**, *97*, 2005; b) E. C. Constable in *Comprehensive Supramolecular Chemistry*, *Vol. 9* (Eds.: J. L. Atwood, J. E. D. Davies, D. D. MacNicol, F. Vögtle, J.-M. Lehn), Pergamon, Oxford, **1996**, p. 213.

[3] a) P. N. W. Baxter in *Comprehensive Supramolecular Chemistry*, *Vol. 9* (Eds.: J. L. Atwood, J. E. D. Davies, D. D. MacNicol, F. Vögtle, J.-M. Lehn), Pergamon, Oxford, **1996**, p. 165; b) P. N. W. Baxter, J.-M. Lehn, G. Baum, D. Fenske, *Chem. Eur. J.* **1999**, *5*, 102; c) P. N. W. Baxter, J.-M. Lehn, B. O. Kneisel, G. Baum, D. Fenske, *Chem. Eur. J.* **1999**, *5*, 113; d) J. S. Fleming, K. L. V. Mann, C.-A. Carraz, E. Psillakis, J. C. Jeffrey, J. A. McCleverty, M. D. Ward, *Angew. Chem.* **1998**, *110*, 1315; *Angew. Chem. Int. Ed.* **1998**, *37*, 1279.

[4] a) W. Huang, S. Gou, D. Hu, S. Chantrapromma, H.-K. Fun, Q. Meng, *Inorg. Chem.* **2001**, *40*, 1712; b) P. N. W. Baxter, G. S. Hanan, J.-M. Lehn, *Chem. Commun.* **1996**, 2019.

[5] a) P. Ceroni, A. Credi, V. Balzani, S. Campagna, G. S. Hanan, C. R. Arana, J.-M. Lehn, *Eur. J. Inorg. Chem.* **1999**, 1409; b) G. S. Hanan, C. R. Arana, J.-M. Lehn, D. Fenske, *Angew. Chem.* **1995**, *107*, 1191; *Angew. Chem. Int. Ed. Engl.* **1995**, *34*, 1122.

[6] Examples of grids with tetrahedrally coordinated metal ions: a) M.-T. Youinou, N. Rahmouni, J. Fischer, J. A. Osborn, *Angew. Chem.* **1992**, *104*, 771; *Angew. Chem. Int. Ed. Engl.* **1992**, *31*, 733; b) P. N. W. Baxter, J.-M. Lehn, J. Fischer, M.-T. Youinou, *Angew. Chem.* **1994**, *106*, 2432; *Angew. Chem. Int. Ed. Engl.* **1994**, *33*, 2284; c) P. N. W. Baxter, J.-M. Lehn, B. O. Kneisel, D. Fenske, *Angew. Chem.* **1997**, *109*, 2067; *Angew. Chem. Int. Ed. Engl.* **1997**, *36*, 1978.

[7] Examples of grids with octahedrally coordinated metal ions: a) G. S. Hanan, D. Volkmer, U. S. Schubert, J.-M. Lehn, G. Baum, D. Fenske, *Angew. Chem.* **1997**, *109*, 1929; *Angew. Chem. Int. Ed. Engl.* **1997**, *36*, 1842; b) D. M. Bassani, J.-M. Lehn, K. Fromm, D. Fenske, *Angew. Chem.* **1998**, *110*, 2534; *Angew. Chem. Int. Ed.* **1998**, *37*, 2364; c) L. Zhao, Z. Xu, L. K.

 © 2004 Wiley-VCH Verlag GmbH & Co. KGaA, Weinheim

Thompson, S. L. Heath, D. O. Miller, M. Ohba, *Angew. Chem.* **2000**, *112*, 3244; *Angew. Chem. Int. Ed.* **2000**, *39*, 3114.
[8] a) M. Fujita, J. Yakaki, K. Ogura, *J. Am. Chem. Soc.* **1990**, *112*, 5645; b) K. Umemoto, H. Tsukui, T. Kusukawa, K. Biradha, M. Fujita, *Angew. Chem.* **2001**, *113*, 2690; *Angew. Chem. Int. Ed.* **2001**, *40*, 2620; c) P. N. W. Baxter, J.-M. Lehn, B. O. Kneisel, D. Fenske, *Chem. Commun.* **1997**, 2231.
[9] a) R. W. Saalfrank, R. Burak, A. Breit, D. Stalke, R. Herbst-Irmer, J. Daub, M. Porsch, E. Bill, M. Müthe, A. X. Trautwein, *Angew. Chem.* **1994**, *106*, 1697; *Angew. Chem. Int. Ed. Engl.* **1994**, *33*, 1621; b) D. L. Caulder, R. E. Powers, T. N. Parac, K. N. Raymond, *Angew. Chem.* **1998**, *110*, 1940; *Angew. Chem. Int. Ed.* **1998**, *37*, 1840.
[10] a) B. Hasenknopf, J.-M. Lehn, B. O. Kneisel, G. Baum, D. Fenske, *Angew. Chem.* **1996**, *108*, 1987; *Angew. Chem. Int. Ed. Engl.* **1996**, *35*, 1838; b) D. K. Chand, K. Biradha, M. Fujita, *Chem. Commun.* **2001**, 1652; c) C. S. Campos-Fernández, R. Clérac, J. M. Koomen, D. H. Russell, K. R. Dunbar, *J. Am. Chem. Soc.* **2001**, *123*, 773; d) P. D. Beer, N. Berry, M. G. B. Drew, O. D. Fox, M. E. Padilla-Tosta, S. Patell, *Chem. Commun.* **2001**, 199.
[11] R. V. Slone, K. D. Benkstein, S. Bélanger, J. T. Hupp, I. A. Guzei, A. L. Rheingold, *Coord. Chem. Rev.* **1998**, *171*, 221.
[12] a) O. Waldmann, J. Hassmann, P. Müller, G. S. Hanan, D. Volkmer, U. S. Schubert, J.-M. Lehn, *Phys. Rev. Lett.* **1997**, *78*, 3390; b) L. K. Thompson, L. Zhao, Z. Xu, D. O. Miller, W. M. Reiff, *Inorg. Chem.* **2003**, *42*, 128; c) E. Breuning, M. Ruben, J.-M. Lehn, F. Renz, Y. Garcia, V. Ksenofontov, P. Gütlich, E. Wegelius, K. Rissanen, *Angew. Chem.* **2000**, *112*, 2563; *Angew. Chem. Int. Ed.* **2000**, *39*, 2504.
[13] M. Ruben, E. Breuning, M. Barboiu, J.-P. Gisselbrecht, J.-M. Lehn, *Chem. Eur. J.* **2003**, *9*, 291.
[14] M. Ruben, J.-M. Lehn, G. Vaughan, *Chem. Commun.* **2003**, 1338.
[15] A. Semenov, J. P. Spatz, M. Möller, J.-M. Lehn, B. Sell, D. Schubert, C. H. Weidl, U. S. Schubert, *Angew. Chem.* **1999**, *111*, 2701; *Angew. Chem. Int. Ed.* **1999**, *38*, 2547.
[16] J. Chesterfield, J. F. W. McOmie, E. R. Sayer, *J. Chem. Soc.* **1955**, 3478.
[17] The coordination reaction between $Co^{II}(OAc)_2 \cdot 4H_2O$ and 2-pyridinecarboxaldehyde-2′-pyridylhydrazone also results in deprotonation of the ligand with concomitant oxidation of Co^{II} to Co^{III}: F. Lions, K. V. Martin, *J. Am. Chem. Soc.* **1958**, *80*, 3858.
[18] For a review on the NMR of paramagnetic substances, see I. Bertini, C. Luchinat, *Coord. Chem. Rev.* **1996**, *150*, 1.
[19] A detailed electrochemical study of these systems is now underway.
[20] C. Rovira, *Chem. Eur. J.* **2000**, *6*, 1723.
[21] a) M. Lieberman, S. Chellamma, B. Varughese, Y. Wang, C. Lent, G. H. Bernstein, G. Snider, F. C. Peiris, *Ann. N. Y. Acad. Sci.* **2002**, *960*, 225; b) C. S. Lent, B. Isaksen, M. Lieberman, *J. Am. Chem. Soc.* **2003**, *125*, 1056.

 © 2004 Wiley-VCH Verlag GmbH & Co. KGaA, Weinheim

Nanomaterials

Self-Assembly in a Bipolar Phosphocholine–Water System: The Formation of Nanofibers and Hydrogels

*Karen Köhler, Günter Förster, Anton Hauser, Bodo Dobner, Ulrich F. Heiser, Friederike Ziethe, Walter Richter, Frank Steiniger, Markus Drechsler, Heiko Stettin, and Alfred Blume**

Bipolar lipids with only one long alkyl chain and two polar headgroups at the ends are model compounds for the chemically more complicated bola lipids from *Archea* bacteria, for instance, the bis(diphytanyl) diglycerol tetraethers.[1] In *Irlbachia alata* and *Anthocleista djalonensis,* the bola lipid docosan-1,22-diyl-bis-[2-(trimethylammonio)ethylphosphate] (irlbacholine) has a C_{22} alkyl chain that connects two polar phosphocholine groups and has been used in plant medicine. It was found to be effective against the fungus *Trichophyton rubrum*, which affects the skin, and other fungal infections.[2]

In the course of studies on the possibility of using similar bola lipids with one long alkyl chain as membrane stabilizers, a bola phospholipid with a C_{32} alkyl chain was synthesized, namely the lipid dotriacontan-1,32-diyl-bis-[2-(trimethylammonio)ethylphosphate] (PC-C32-PC, **1**; Figure 1).[3] During the initial characterization of **1** we observed unusual aggregation behavior, which necessitated further physico-chemical investigations. To obtain sufficient quantities of **1** a more efficient synthetic route to long-chain bola compounds was necessary.

We prepared lipid **1** in gram quantities by a newly developed simple and effective procedure. The construction of the chain with 32 carbon atoms is possible in a one-step synthesis by a copper-catalyzed coupling of undec-10-en-1-ylmagnesium bromide with 1,10-dibromodecane in a molar ratio of 2:1 (see Experimental Section). Dotriacontan-1,31-diene is then converted into dotriacontan-1,32-diol by hydroboration with disiamyl borane and subsequent oxidative hydrolysis. The importance of the new reaction is underlined by the possibility of functionalizing the 1- and 32-positions. The phosphocholine moieties were introduced by the reaction of dotriacontan-1,32-diol with 2-bromoethyl phosphoric acid dichloride in chloroform. This classic phosphorylation reagent was more effective than more modern variants. The trimethylammonium groups in **1** were introduced by established procedures.[4]

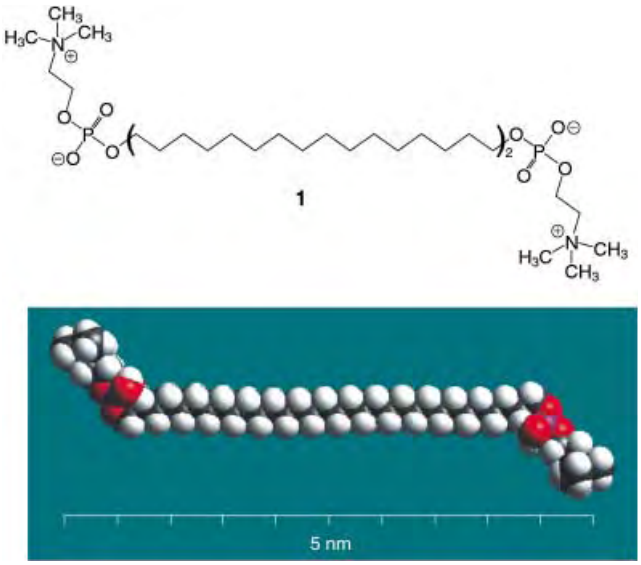


Figure 1. Structure of **1** with a bulky, polar phosphocholine headgroup at each end of the C_{32} hydrocarbon chain.

Because of the long alkyl chain and the large polar headgroups at both chain ends of **1,** it forms novel types of aggregate structures not observed previously. We investigated the self-assembly of the bipolar compound in aqueous solution using differential scanning calorimetry, electron microscopy, X-ray scattering, viscosity measurements, and FT-IR spectroscopy.

In highly dilute aqueous solution ($c < 0.5$ wt %), a very viscous, almost transparent gel is observed. The 0.1-wt % sample shown in Figure 2 has a water/**1** molar ratio of ca. 45000:1; we see that an enormous amount of water can be "immobilized" by the gel structure. At temperatures above 50 °C or through mechanical stress the gel character disappears and a fluid solution is obtained; the viscosity drops by about five orders of magnitude. Preliminary viscosity measurements at room temperature show an indication of a yield stress (τ_0*) of roughly 7.2 Pa for a 0.8-wt % solution (Figure 3). Temperature-dependent viscosity measurements indicate a viscosity of ca. 5×10^3 Pa s at room temperature which drops to values below 5×10^{-4} Pa s at temperatures above 70 °C, that is, values close to that of pure water at the same temperature. The rheological behavior found for this



Figure 2. Hydrogel of a solution of **1** (0.1 wt %) in water at room temperature.

[*] Dipl.-Chem. K. Köhler, Dr. G. Förster, Dr. A. Hauser, Prof. Dr. A. Blume
MLU Halle-Wittenberg
Institut für Physikalische Chemie
Mühlpforte 1, 06108 Halle/Saale (Germany)
Fax: (+49) 345-5527157
E-mail: blume@chemie.uni-halle.de
Prof. Dr. B. Dobner, Dr. U. F. Heiser, Dr. F. Ziethe
MLU Halle-Wittenberg
Institut für Pharmazeutische Chemie
Wolfgang-Langenbeck-Strasse 4, 06120 Halle/Saale (Germany)
Dr. W. Richter, F. Steiniger
FSU Jena, Institut für Ultrastrukturforschung
Ziegelmühlenweg 1, 07740 Jena (Germany)
Dr. M. Drechsler
FSU Jena, Institut für Pharmazie
Philosophenweg 14, 07743 Jena (Germany)
Dr. H. Stettin
Physica Messtechnik GmbH
Helmuth-Hirth-Strasse 6, 73760 Ostfildern (Germany)

 DOI: 10.1002/anie.200351731 © 2004 Wiley-VCH Verlag GmbH & Co. KGaA, Weinheim

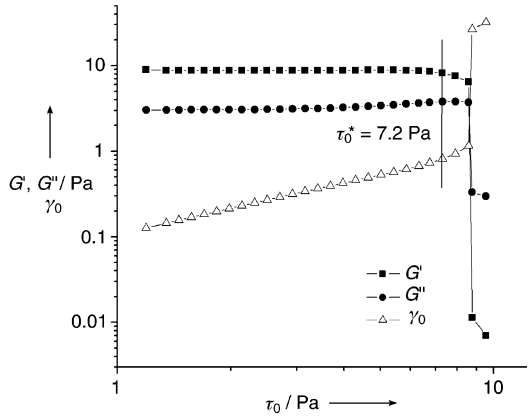


Figure 3. Rheological measurements on an aqueous solution of **1** with constant shear stress (controlled stress oscillation). The characteristic relation between the storage and loss moduli $G' > G''$ indicate the region of linear strain response; the shear stress amplitude γ_0 increases linearly up to the yield stress of $\tau_0^* = 7.2$ Pa. $T = 23\,^{\circ}C$, $\omega = 10$ Hz, $c = 0.8$ wt%.

system is complicated and in some way related to the behavior of other association colloids such as wormlike micelles.[5].

The gel state at room temperature can be explained by the existence of a dense three-dimensional network of fibrils, which can be found even in highly dilute aqueous suspensions (0.03 wt%) by cryo-transmission electron microscopy. All the fibrils are approximately 6–7 nm thick (Figure 4). This

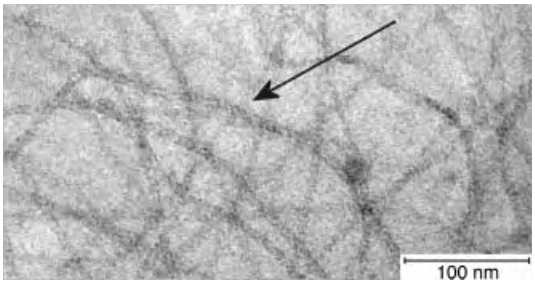


Figure 4. Cryo-TEM image of an aqueous suspension of **1** (0.03 wt%). A nanofiber with helical structure is marked with an arrow.

corresponds roughly to the length of **1**. The fibrils appear to have a helical structure, but the resolution of cryo-electron micrographs is notoriously poor, and an unequivocal description of the structure is not possible. Since **1** is not chiral there must be just as many right-handed as left-handed helices. Indeed, in some cryo-transmission electron micrographs fibrils with opposite handedness seem to be present. Because the fibers are so small in diameter, it is not possible to obtain quantitative statistics. The formation of helices could be explained by the following: two or more molecules are arranged side by side in one direction, but because of the bulky headgroups the chains cannot adopt a completely parallel packing in the direction perpendicular to the first one. To optimize the hydrophobic interaction the long axes of adjacent molecules twist relative to each other. This type of self-assembly would result in a helical structure with a thickness of roughly one molecular length.

The formation of gels in aqueous solution induced by organic molecules is well known, particularly in the polymer field. However, the type of gels formed by aggregating low-molecular-weight molecules can be quite different because the gel formation is connected to a self-assembly process. Gel formation has been observed for other bola compounds, such as nucleotide bolaamphiphiles and compounds containing bisurea dicarboxylic acid groups.[6] In these cases, the gel formation arises mainly through polar interactions, especially hydrogen bonds. As a consequence, the fibers formed are much thicker. In gels of **1**, however, intermolecular polar interactions do not play a role, and the aggregation process seems to be driven exclusively by hydrophobic effects, that is, the minimization of the hydrophobic surface area of the long alkyl chains.

Freeze-fracture electron microscopy was used to investigate the lipid self-assembly in more concentrated samples in the presence of glycerol (Figure 5). In a sample quick-frozen

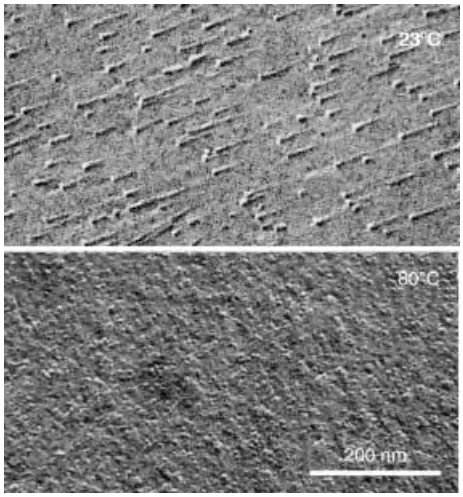


Figure 5. Freeze-fracture electron microscopic picture of a solution of **1** (2 wt%) in H_2O/glycerol (4:1). Top: Sample was kept for one day at 23 °C and then quick-frozen. Bottom: Sample was heated to 80 °C and then quick-frozen.

from room temperature to −196 °C the fracture faces show oriented fibrils 7 nm thick sticking out of the surface at a certain angle. In samples cooled from 45 °C this structure is still present, but when the samples are quenched from starting temperatures of 50 °C or even 80 °C the fibrillar structure has disappeared and only aggregates or smaller particles are seen with diameters in the range of 3–10 nm. We also investigated solutions quenched from 80 °C using dynamic light scattering (DLS). We found that the sample consists of both small monodisperse particles (radius 2–5 nm) as well as larger aggregates. When the samples were kept at room temperature for longer times, the viscosity increased strongly, again indicating the reformation of the gel, that is, the formation of nanofibrils.

 © 2004 Wiley-VCH Verlag GmbH & Co. KGaA, Weinheim

To detect the exact temperature for the transition of the nanofibrils into smaller aggregates DSC measurements were performed. Three endothermic peaks were seen upon heating and a strong hysteresis in the transition behavior was observed. After the first heating a defined annealing protocol had to be applied to reproduce the initial data. For all measured concentrations a main transition with the largest latent heat is found at $T \approx 48\,^{\circ}C$ along with a peculiar jump in the heat capacity. This could be a consequence of changes in the interactions of the chain region with water, that is, an increase in the wetting of hydrophobic surfaces. At this particular temperature the breakdown of the gel was also observed.

The largest heat for the main transition was observed when the sample had been kept at 2 °C for eight hours and the gel had fully developed. At room temperature apparently metastable states (smaller aggregates) can occur which only slowly convert into the equilibrium aggregation state (nanofibers). In the heating curves a further small endothermic transition at $T \approx 40\,^{\circ}C$ is seen, and at $T = 73\,^{\circ}C$ there is another very broad peak. In contrast to the other transitions the high-temperature peak does not change its position and shape under various experimental conditions (e.g. different heating rates or longer equilibration at low temperatures).

To find out if conformational changes in the chains occur at the different transition temperatures, FT-IR measurements were carried out. The symmetric and antisymmetric CH_2 stretching vibrations are reliable indicators of the order of the hydrocarbon chains of alkyl compounds. In FT-IR spectra recorded between 2 °C and 85 °C, two frequency increases of the stretching modes at $T = 47\,^{\circ}C$ and 72 °C indicate a stepwise formation of *gauche* conformers. These temperatures correspond to the temperature of the two upper peaks observed in the DSC experiment ($T \approx 48\,^{\circ}C$ and 72 °C).

It can be concluded that the bola architecture of **1** reduces the ability for formation of lamellar phases. In dilute aqueous solution at room temperature fibrils of **1** with rigid chain packing are formed solely by hydrophobic interactions and not by hydrogen bonds. The fibers can extend over several micrometers. As a consequence, the solution becomes gel-like. At higher concentrations the fibers seem to be arranged in a parallel fashion and form sheets consisting of parallel fibrils. The stability of the fibers is not very great, and changes in length may be induced by mechanical stress. At a defined main transition temperature of 48 °C the long chains of **1** become more disordered, and as a consequence the aggregate size and morphology change dramatically. The reformation of the fibrils at low temperature after cooling is time and concentration dependent.

Experimental Section

Dotriacontan-1,31-diene: A solution of 11-bromoundec-1-ene (14 g, 60 mmol) in dry ether (50 mL) was added dropwise to stirred magnesium turnings (2.1 g, 85 mmol) under an argon atmosphere. After the exothermic reaction had subsided, the mixture was heated at reflux for 2 h. The excess magnesium was removed, and the Grignard solution was concentrated under reduced pressure at 10 °C. Dry THF (180 mL) was added to the oily residue at a rate such that the temperature remained below 0 °C. A solution of 1,10-dibromodecane (6 g, 20 mmol) in dry THF (20 mL) was added in one portion. After the mixture had been stirred for 2 min, dilithium tetrachlorocuprate (3.5 mL, 1M solution in THF) was added dropwise at 0 °C. Within some minutes the reaction mixture became turbid. After 20 min at 0 °C the mixture was diluted with 20 mL of dry THF, and stirring was continued for a further 3 h at the same temperature. For the workup of the reaction 100 mL of ether were added and the resulting mixture was poured into a cold saturated solution of ammonium chloride. The organic layer was separated and the aqueous phase was extracted with ether (50 mL). The combined organic phases were washed with water, dried over sodium sulfate, and concentrated to dryness under reduced pressure. For purification the residue was dissolved in 100 mL of ether/THF (1:1). After addition of 70 mL of acetone, the precipitate was filtered off. This precipitation procedure was repeated to give the pure product as a waxy white solid. Yield: 7.8 g (87 %), m.p. 59–61 °C (uncorrected); ESI-MS: 446 [M^+]; ^{1}H NMR: ($CDCl_3$, 400 MHz, 298 K): $\delta = 1.18$–1.37 (m, 52 H, -CH_2-), 1.99–2.05 (m, 4 H, =CH-CH_2-), 4.89–4.99 (m, 4 H, CH_2=), 5.75–5.85 ppm (m, 2 H, =CH-); Elemental analysis calcd for $C_{32}H_{62}$: C 86.10, H 13.89; found: C 86.01, H 13.96.

The rest of the synthesis of **1** can be found in references [3, 4].

Received: April 23, 2003
Revised: July 28, 2003 [Z51731]

Keywords: amphiphiles · hydrogels · nanomaterials · phospholipids

[1] G. D. Sprott, *J. Bioenerg. Biomembr.* **1992**, *24*, 555 – 566; M. Kates, *The Biochemistry of Archaea* (Eds.: M. Kates, D. J. Kushner, A. T. Matheson), Elsevier, Amsterdam, **1993**, pp. 261 – 295; M. Nishihara, H. Morii, Y. Koga, *J. Biochem.* **1987**, *101*, 1007 – 1015.

[2] D. E. Bierer, R. E. Gerber, S. D. Jolad, R. P. Ubillas, J. Randle, E. Nauka, J. Latour, J. M. Dener, D. M. Fort, J. E. Kuo, W. D. Inman, L. G. Dubenko, F. Ayala, A. Ozioko, C. Obialor, E. Elisabetsky, T. Carlson, T. V. Truong, R. C. Bruening, *J. Org. Chem.* **1995**, *60*, 7022 – 7026; Q. Lu, R. P. Ubillas, Y. Zhou, L. G. Dubenko, J. M. Dener, J. Litvak, P.-W. Phuan, M. Flores, Z. J. Ye, R. E. Gerber, T. Truong, D. E. Bierer, *J. Nat. Prod.* **1999**, *62*, 824 – 828.

[3] F. Ziethe, Ph.D. Thesis, Martin-Luther-Universität Halle-Wittenberg, **2003**; U. F. Heiser, B. Dobner, *Chem. Commun.* **1996**, 2025 – 2026; U. F. Heiser, B. Dobner, *J. Chem. Soc. Perkin Trans. 1* **1997**, 809 – 815.

[4] H.-J. Eibl. A. Nicksch, BRD-Patent 23 45 060, **1975**.

[5] H. Rehage, H. Hoffmann, *Mol. Phys.* **1991**, *74*, 933 – 973.

[6] T. Shimizu, R. Iwaura, M. Masuda, T. Hanada, K. Yase, *J. Am. Chem. Soc.* **2001**, *123*, 5947 – 5955; R. Iwaura, K. Yoshida, M. Masuda, K. Yase, T. Shimizu, *Chem. Mater.* **2002**, *14*, 3047 – 3053; L. A. Estroff, L. Leiserowitz, L. Addadi, S. Weiner, A. D. Hamilton, *Adv. Mater.* **2003**, *15*, 38 – 42; I. W. Hamley, *Angew. Chem.* **2003**, *115*, 1730 – 1752; *Angew. Chem. Int. Ed.* **2003**, *42*, 1692 – 1712.

 © 2004 Wiley-VCH Verlag GmbH & Co. KGaA, Weinheim

Protein Models

Ligand-Supported Homology Modeling of G-Protein-Coupled Receptor Sites: Models Sufficient for Successful Virtual Screening**

*Andreas Evers and Gerhard Klebe**

Recent advances in the various genome-sequencing projects have opened the floodgates to thousands of protein sequences that are possibly new targets for drug discovery.[1] Accordingly, computer techniques are required for the reliable prediction of protein structures accurate enough to serve as a platform for structure-based drug design. We have developed a new approach that models proteins by homology. Because the bound ligand molecules serve as restraints, more relevant geometries of protein binding sites result.[2] Initial homology models of the target protein are optimized iteratively by including information about bioactive ligands as spatial restraints (Figure 1).

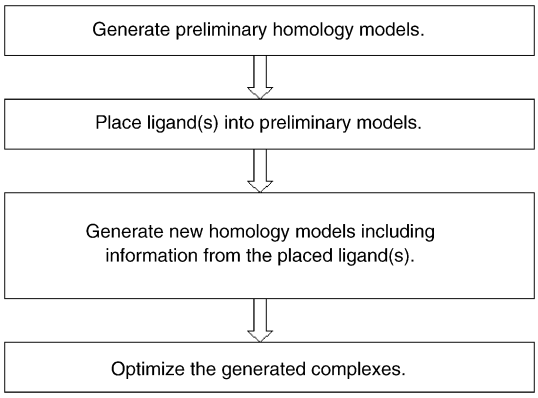


Figure 1. Schematic overview of the concept followed in our MOBILE approach. Starting with the structure of one or more template proteins, we generate several preliminary homology models of our target protein using MODELLER.[3] Next, one or more ligands known to bind to the target protein are placed into an averaged binding-site representation of the generated ensemble of superimposed models.[4] Improved protein models are then generated with MODELLER, now explicitly considering the docked ligand(s) as additional restraints. The ligands are considered in terms of knowledge-based pair potentials extracted from the protein–ligand scoring function DrugScore.[5] After the resulting generated complexes are scored with DrugScore, a final model is chosen from the individual models that best explains the observed ligand binding. This complex can be optimized further by selecting and combining portions from different models. Finally, the model is refined by optimizing the side-chain-to-ligand interactions using a common force field.[6]

[*] A. Evers, Prof. Dr. G. Klebe
Institut für Pharmazeutische Chemie der Universität Marburg
Marbacher Weg 6, 35032 Marburg (Germany)
Fax: (+49) 06421-28-28994
E-mail: klebe@mailer.uni-marburg.de

[**] The authors are grateful to Dr. Arne Svensson (AstraZeneca, Mölndal) for determining the binding affinities of the seven test compounds described in this report.

Our approach, MOBILE (*Mo*deling *B*inding Sites *I*ncluding *L*igand Information *E*xplicitly), has been parameterized and validated by reproducing binding-site models of proteins for which the structure is actually known. Subsequently, we applied this method to the discovery of neurokinin-1 (NK1) receptor antagonists. A ligand with binding affinity in the submicromolar range was found for this protein, which belongs to the family of G-protein-coupled receptors (GPCRs).

In structure-based drug design, knowledge of the three-dimensional structure of a target protein is of utmost importance. It is either determined by X-ray crystallography or by NMR spectroscopy. However, the rate at which protein sequences are presently being discovered exceeds by far the rate at which protein structures can be determined experimentally. Thus, for a considerable number of putative drug targets, the three-dimensional structure will not be readily available. In such cases the most reliable computer-based technique for generating a three-dimensional protein structure is homology modeling.[7] However, homology modeling only considers information available from the related protein structures. The model remains at a rather approximate level if in the target protein several amino acids of the active site are replaced with respect to those in the template protein(s). Usually, in a drug-design project, binding data about ligands become available, for example, from high-throughput screening, before the spatial structure is elucidated. In due course, ligand-based structure–activity relationships are established (by 3D QSAR methods)[8] to pinpoint features responsible for trends in the binding affinity. These methods generate some kind of a generalized blueprint of the putative binding pocket of the target protein without giving explicit information about its actual composition. These methods further support ligand optimization; however, they are limited with respect to the design of novel or alternative molecular skeletons. Our new method tries to combine the advantages of both homology modeling and ligand-based 3D QSAR analysis.

In a real-life test scenario we applied MOBILE to the neurokinin-1 (NK1) receptor belonging to the superfamily of GPCRs mediating responses to, for example, visual, olfactory, hormonal, and neurotransmitter signals. GPCRs are one of the most relevant target families in small-molecule drug design. Currently, 50% of all marketed drugs address GPCRs.[9] Since GPCRs are membrane-bound proteins, their expression, purification, crystallization, and structure determination remain difficult. So far, only the structure of bovine rhodopsin could be determined with sufficiently high resolution.[10] Its crystal structure serves as a template reference for homology modeling of all other members of the GPCR family. Because of the limited accuracy, drug discovery based on virtual screening with rhodopsin-based GPCR models has not yet been reported in literature. Instead, successful computer-aided drug discovery for GPCRs was achieved by applying ligand-based virtual screening techniques.[11]

A first step towards drug discovery with rhodopsin-based protein models was attempted by Bissantz et al.,[12] who recently demonstrated that their homology models of the dopamine D3, muscarinic M1, and vasopressin V1a receptors

 © 2004 Wiley-VCH Verlag GmbH & Co. KGaA, Weinheim DOI: 10.1002/anie.200352776

were reliable enough to retrieve known antagonists by virtual screening from a database, which also comprised randomly selected drug-like molecules. Another GPCR modeling technique that does not rely on the crystal structure of bovine rhodopsin is PREDICT.[13] In screening for novel binders based on their GPCR models, the authors report hit rates of 10 to 24%.

The NK1 receptor belongs to the series of tachykinin-binding receptors (NK1, NK2, and NK3). They selectively bind the peptide neurotransmitters substance P, neurokinin A, and neurokinin B, respectively. Substance P plays a role in the transmission of pain and is involved in inflammation and immune response. The probably best studied NK1 antagonist is CP-96345. Information on its bioactive conformation was obtained by several theoretical and experimental studies.[14] Through mutational studies[15] and comparative affinity determinations based on CP-96345 binding, the essential amino acids involved in ligand recognition could be identified and translated into a crude topographical interaction model (see Figure 3b). According to our homology model, the binding pocket of CP-96345 overlaps with the binding site of retinal in bovine rhodopsin.

The sequence identity between bovine rhodopsin and the NK1 receptor amounts to 21% (Figure 2). If only the transmembrane regions are considered, this increases to 27%. No sequence similarity can be detected to the retinal binding-site of bovine rhodopsin, which renders the homology modeling particularly challenging. With our approach, 100 preliminary homology models based on the crystal structure of rhodopsin were generated. Next, CP-96345 was docked rigidly into the modeled binding pockets with AutoDock using the ligand conformation observed in its crystal structure (CSD reference code LEWCUL; Figure 3a). From the set of docked ligand conformations, we selected the solution that best reproduced the key interactions depicted in the topographical model (Figure 3b). Subsequently, new homology models were generated explicitly considering bound CP-96345. The best-scored amino acids were merged in a combinatorial fashion, and finally a model without unfavorable van der Waals interactions was obtained.

Figure 3c shows the ligand-binding site of the resulting complex, which convincingly reproduces the proposed interactions in the 2D interaction model (Figure 3b).[14] The quality of the model was validated by probing its ability to accommodate other known NK1 antagonists from structurally diverse compound classes. Common chemical features of known NK1 antagonists and published mutation data identifying the key interaction points of the ligands with the NK1 receptor were used to establish a pharmacophore hypothesis (see Figure 3d). This model was used to retrieve ligands from seven databases containing a total of over 800000 compounds.

A search strategy similar to that reported previously by us for the search of enzyme inhibitors[17] was applied. We focused only on "leadlike" compounds with up to seven rotatable bonds and a molecular weight of less than 450 Da. A 2D filter was applied to extract compounds containing at least two phenyl rings and one hydrogen-bond acceptor. The program UNITY was then used to constrain the mutual spatial arrangement of the aromatic rings and the hydrogen-bond acceptor (Figure 3b and d), considering the protein environment in terms of excluded volume constraints. The remaining 11109 compounds were flexibly docked into the modeled NK1 binding pocket using the program FlexX-Pharm.[18] As a reference, the pharmacophore depicted in Figure 3d was used

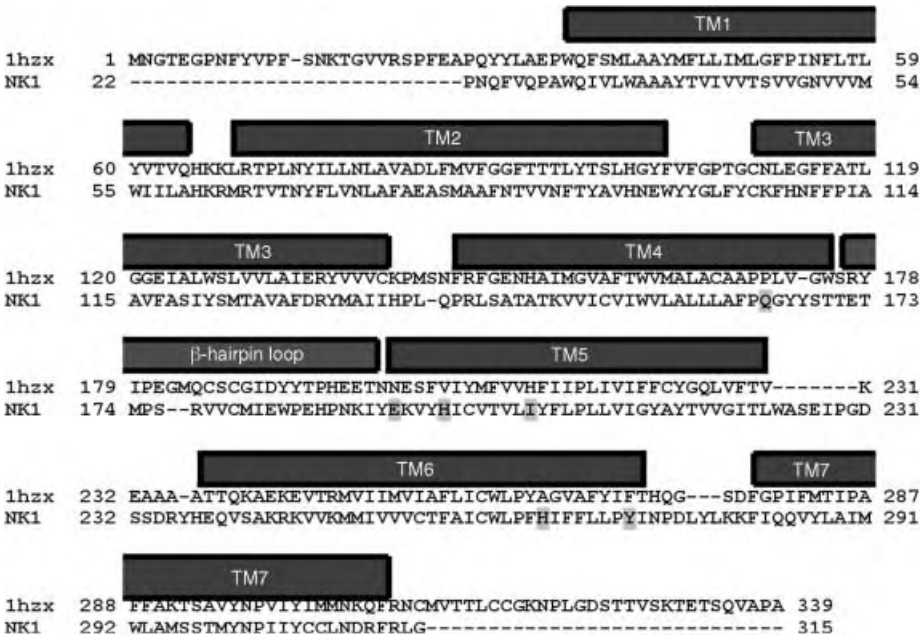


Figure 2. Sequence alignment of bovine rhodopsin and the NK1 receptor. All residues known from mutational studies to be involved in binding CP-96345 are marked in gray. These residues are Gln165 (according to the Ballesteros–Weinstein numbering scheme[16] 4.60), Glu193 (5.35), His197 (5.39), Ile204 (5.46), His265 (6.52), and Tyr272 (6.59).

 © 2004 Wiley-VCH Verlag GmbH & Co. KGaA, Weinheim

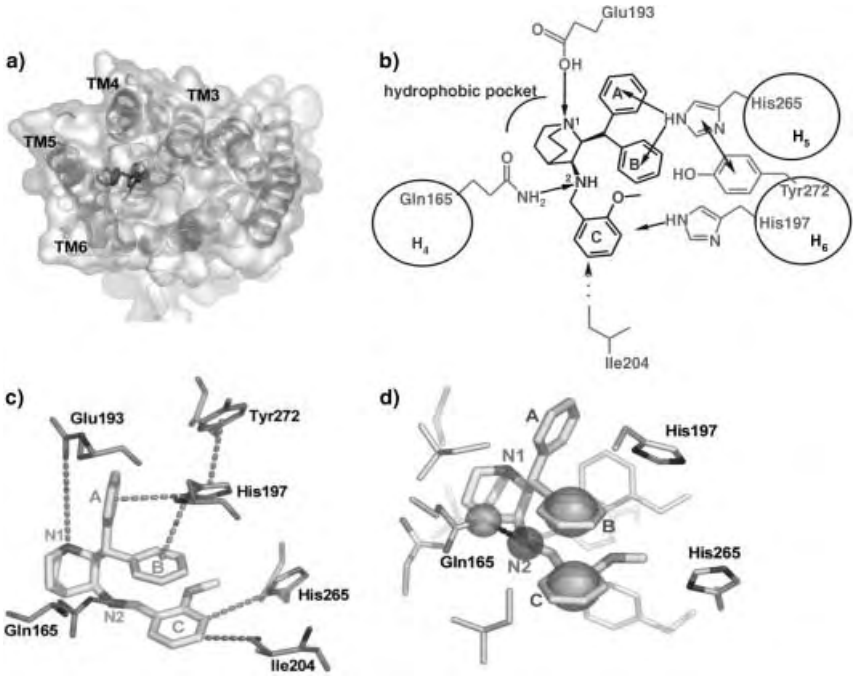
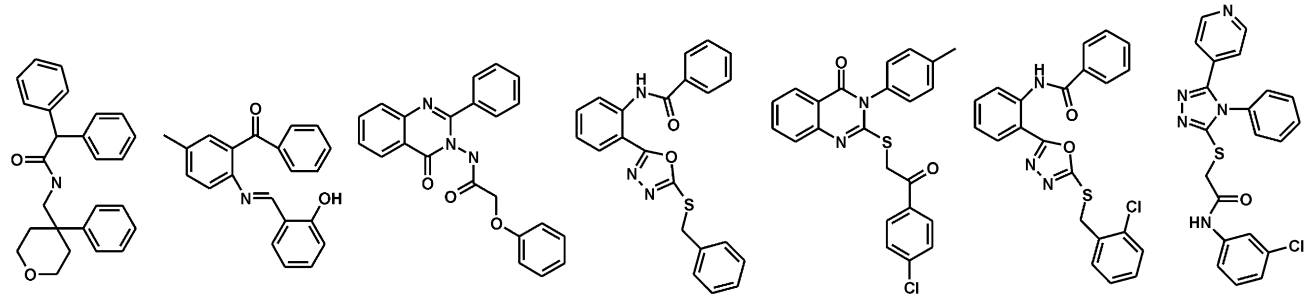


Figure 3. The NK1 receptor and its antagonist CP-96345. a) Top view (extracellular) of the NK1 receptor homology model complexed with CP-96345. b) Schematic representation of postulated interactions of the NK1 receptor with CP-96345, established by analyzing the published mutational data and affinity measurements of NK1 antagonists. The arrows indicate proposed key interactions between the receptor and the ligand. The most important interactions essential for the binding of NK1 antagonists are 1) the hydrogen bond between Gln165(4.60)-NH and a corresponding acceptor of the antagonist and 2) an amine–arene interaction established between His197 (5.39) and the the aromatic moiety B. Analysis of NK1 antagonists from structurally diverse classes reveals that the aromatic group C is also required for binding. c) Modeled complex of the NK1 receptor with CP-96345. The dashed lines indicate the key interactions proposed in the topographical interaction model depicted in part b. d) Structure-based pharmacophore hypothesis based upon data from known NK1 antagonists. The hypothesis is characterized by three major features: 1) a hydrogen bond between the Gln165(4.60)-NH and a corresponding acceptor (here, N2) of the ligand; 2) the aromatic moiety B which interacts with His197 (5.39) in amine–arene interactions; and 3) a further aromatic group C.

as an additional constraint within the docking process. Subsequently, binding affinities were estimated using DrugScore. After minimizing the produced complexes of the best-ranked solutions using MOLOC,[6] we inspected the best hits visually and analyzed their adopted binding modes, the agreement with the proposed 2D interaction model (Figure 3b), and the mutual surface complementarity between protein and accommodated ligand. In particular, highly flexible ligands and ligands having unsatisfied H-bond donors or acceptors and unoccupied voids along the interface were eliminated. Finally, seven compounds (Scheme 1) were selected for in vitro testing. We chose a radioligand binding assay on whole CHO (Chinese Hamster Ovary) cells (with substance P as the radioligand), which is sensitive enough to detect ligands with a binding affinity of at least 1 μM. Of the seven compounds, one showed affinity (ASN-1377642 from AEPC, see Figure 4) in the submicromolar range, exhibiting a K_i value of 251 nM. ASN-1377642 meets the criterion defined in our screening query.

We can conclude that our ligand-supported homology modeling produces binding-site models that successfully serve as a platforms for structure-based drug design. A major advantage is the fact that information about known ligands is not only included into the protein-modeling process but also considered in the subsequent screening: Structural features about known NK1 antagonists were used to establish the pharmacophoric elements that drive our hierarchical 2D and 3D screening strategy. In this way the protein model restrained the 3D screening process and guided the generation of ligand conformations in the binding pocket. Finally, these docking solutions were ranked by evaluating the interactions between the protein and the ligand. Considering that CP-96345 and ASN-1377642 have similar pharmacophore features, but distinctly different molecular frameworks, we believe that our hit would not have been one of the top hits in a solely ligand-based screening approach.

It should be noted that the success of this method depends on the sequence identity between the target and template protein in the ligand binding pocket. If this agreement is low,



Scheme 1. Compounds that were tested for antagonism of the NK1 receptor. ASN-1377642 has a K_i value of 251 nM.

 © 2004 Wiley-VCH Verlag GmbH & Co. KGaA, Weinheim

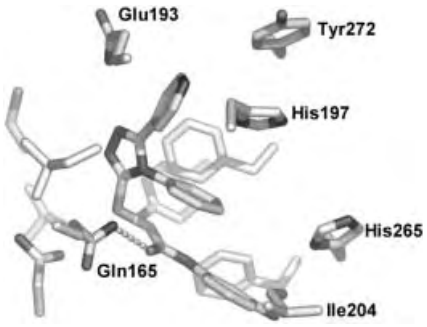


Figure 4. Modeled binding mode of ASN-1377642, which was discovered as a potent NK1 antagonist by virtual screening based on our homology model. The pharmacophore hypothesis is convincingly well matched. The essential hydrogen bond to Gln165(4.60)-NH is established through the carbonyl oxygen atom of an amide group.

additional information is required, for example, from mutational data, and from a high-affinity ligand conformation that is close to the bioactive one.

Received: September 3, 2003 [Z52776]
Published Online: December 2, 2003

Keywords: computer chemistry · G proteins · protein models · receptors

[1] a) A. L. Hopkins, C. R. Groom, *Nat. Rev. Drug Discovery* **2002**, *1*, 727–730; b) J. Drews, *Science* **2000**, *287*, 1960–1964.
[2] A. Evers, H. Gohlke, G. Klebe, *J. Mol. Biol.* **2003**, *334*, 327–345.
[3] A. Sali, T. L. Blundell, *J. Mol. Biol.* **1993**, *234*, 779–815.
[4] a) A. Schafferhans, G. Klebe, *J. Mol. Biol.* **2001**, *307*, 407–427; b) F. Osterberg, G. M. Morris, M. F. Sanner, A. J. Olson, D. S. Goodsell, *Proteins Struct. Funct. Genet.* **2002**, *46*, 34–40.
[5] H. Gohlke, M. Hendlich, G. Klebe, *J. Mol. Biol.* **2000**, *295*, 337–356.
[6] P. R. Gerber, *J. Comput.-Aided Mol. Des.* **1998**, *12*, 37–51.
[7] D. Baker, A. Sali, *Science* **2001**, *294*, 93–96.
[8] a) *3D QSAR in Drug Design. Ligand–Protein Complexes and Molecular Similarity.* (Eds.: H. Kubinyi, G. Folkers, Y. C. Martin), Kluwer/ESCOM, Leiden, **1998**; b) *3D QSAR in Drug Design. Recent Advances.* (Eds.: H. Kubinyi, G. Folkers, Y. C. Martin), Kluwer/ESCOM, Leiden, **1997**.
[9] T. Klabunde, G. Hessler, *ChemBioChem* **2002**, *3*, 928–944.
[10] a) D. C. Teller, T. Okada, C. A. Behnke, K. Palczewski, R. E. Stenkamp, *Biochemistry* **2001**, *40*, 7761–7772; b) K. Palczewski, T. Kumasaka, T. Hori, C. A. Behnke, H. Motoshima, B. A. Fox, I. Le Trong, D. C. Teller, T. Okada, R. E. Stenkamp, M. Yamamoto, M. Miyano, *Science* **2000**, *289*, 739–745.
[11] a) S. Flohr, M. Kurz, E. Kostenis, A. Brkovich, A. Fournier, T. Klabunde, *J. Med. Chem.* **2002**, *45*, 1799–1805; b) D. P. Marriott, I. G. Dougall, P. Meghani, Y. J. Liu, D. R. Flower, *J. Med. Chem.* **1999**, *42*, 3210–3216.
[12] C. Bissantz, P. Bernard, M. Hibert, D. Rognan, *Proteins Struct. Funct. Genet.* **2003**, *50*, 5–25.
[13] O. M. Becker, S. Shacham, Y. Marantz, S. Noiman, *Curr. Opin. Drug Discovery Dev.* **2003**, *6*, 353–361.
[14] a) Y. Takeuchi, E. F. B. Shands, D. D. Beusen, G. R. Marshall, *J. Med. Chem.* **1998**, *41*, 3609–3623; b) C. J. Swain, E. M. Seward, M. A. Cascieri, T. M. Fong, R. Herbert, D. E. MacIntyre, K. J. Merchant, S. N. Owen, A. P. Owens, V. Sabin, M. Teall, M. B. VanNiel, B. J. Williams, S. Sadowski, C. Strader, R. G. Ball, R. Baker, *J. Med. Chem.* **1995**, *38*, 4793–4805; c) G. J. Boks, J. P. Tollenaere, J. Kroon, *Bioorg. Med. Chem.* **1997**, *5*, 535–547.
[15] a) T. M. Fong, M. A. Cascieri, H. Yu, A. Bansal, C. Swain, *Nature* **1993**, *362*, 350–353; b) T. M. Fong, H. Yu, M. A. Cascieri, D. Underwood, C. Swain, C. D. Strader, *J. Biol. Chem.* **1994**, *269*, 14957–14961; c) T. M. Fong, H. Yu, M. A. Cascieri, D. Underwood, C. Swain, C. D. Strader, *J. Biol. Chem.* **1994**, *269*, 2728–2732.
[16] J. A. Ballesteros, H. Weinstein, *Methods Neurosci.* **1995**, *25*, 366–428.
[17] a) S. Gruneberg, B. Wendt, G. Klebe, *Angew. Chem.* **2001**, *113*, 404–408; *Angew. Chem. Int. Ed.* **2001**, *40*, 389–393; b) S. Gruneberg, M. T. Stubbs, G. Klebe, *J. Med. Chem.* **2002**, *45*, 3588–3602; c) R. Brenk, L. Naerum, U. Gradler, H. D. Gerber, G. A. Garcia, K. Reuter, M. T. Stubbs, G. Klebe, *J. Med. Chem.* **2003**, *46*, 1133–1143.
[18] S. A. Hindle, M. Rarey, C. Buning, T. Lengauer, *J. Comput.-Aided Mol. Des.* **2002**, *16*, 129–149.

 © 2004 Wiley-VCH Verlag GmbH & Co. KGaA, Weinheim

Cover Picture

Taolei Sun, Guojie Wang, Lin Feng, Biqian Liu, Yongmei Ma, Lei Jiang,* and Daoben Zhu



The yin and the yang represent the two opposing fundamental properties of nature and the universe in ancient Taiji Chinese philosophy. Superhydrophilicity and superhydrophobicity are fundamentally opposing properties of wettability. Reversible switching between these surface properties can be thermally induced through the combination of chemical modification of the surface, and surface roughness. For more information, see the Communication by L. Jiang and co-workers on page 357 ff.

Contents

Angewandte EarlyView

The following articles are available online (in Wiley InterScience). You can find them at www.angewandte.org, under Full Text, Early View.

M. J. Sever, J. T. Weisser, J. Monahan, S. Srinivasan, J. J. Wilker:*
Metal-Mediated Cross-Linking in the Generation of a Marine-Mussel Adhesive
DOI: 10.1002/anie.200352759
Published online: December 18, 2003

D. W. Kim, D. Y. Chi:*
Polymer-Supported Ionic Liquids: Imidazolium Salts as Catalysts for Nucleophilic Substitution Reactions Including Fluorinations
DOI: 10.1002/anie.200352760
Published online: December 18, 2003

Articles judged by the referees or the editor as being either very important or very urgent are immediately edited, proof-read, and electronically published once the manuscript has arrived in the editorial office in final form. As long as there is no page number available these articles should be cited in the following manner:

Author(s) *Angew. Chem. Int. Ed.*, online publication date, DOI.

Meeting Review

Highly Branched Macromolecules at the Interface of Chemistry, Biology, Physics, and Medicine — **272 – 273** — *Rainer Haag and Fritz Vögtle*

Books

Green Industrial Applications of Ionic Liquids — **274** — Robin D. Rogers, Kenneth R. Seddon, Sergei Volkov — *reviewed by B. Cornils*

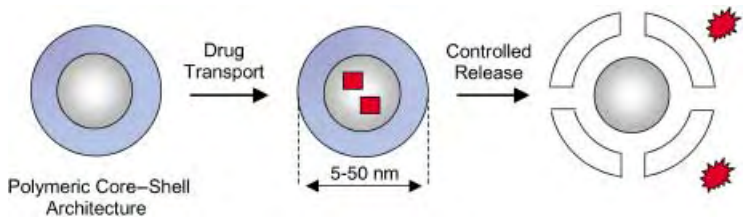
Handbook of Free Radical Initiators — **275** — E. T. Denisov, T. G. Denisova T. S. Pokidova — *reviewed by H. Fischer*

Highlights

Drug Delivery

R. Haag* — **278 – 282**

Supramolecular Drug-Delivery Systems Based on Polymeric Core–Shell Architectures

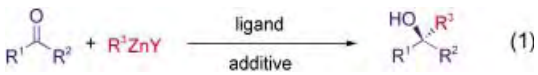


Hitting the target: Although the cellular uptake of supramolecular nanocarriers by endocytosis is not cell-specific, a high passive selectivity has been observed in porous tissues, such as tumor tissue. The encapsulated, often toxic, drug is efficiently shielded and can develop its activity by selective release from the nanocarrier upon a shift of the pH value in the tumor tissue or inside the cell (see scheme).

Organometallic Reactions

D. J. Ramón, M. Yus* — **284 – 287**

Chiral Tertiary Alcohols Made By Catalytic Enantioselective Addition of Unreactive Zinc Reagents to Poorly Electrophilic Ketones?

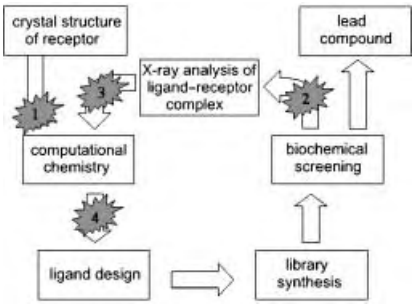


Ligands that activate both the starting ketone and the zinc reagent are essential in catalyzing enantioselective nucleophilic additions yielding tertiary alcohols [Eq. (1)]. Controlled generation of compounds with such quaternary stereogenic centers is one of the major challenges in synthetic organic chemistry.

© 2004 Wiley-VCH Verlag GmbH & Co. KGaA, Weinheim

Reviews

Tools for Speed: Whereas X-ray crystallography gives a static picture of a biomolecule, NMR spectroscopy provides information on dynamic processes. Recent developments in NMR spectroscopy for the determination of the structure, dynamics, and interactions of proteins with ligands hold great promise in structure-aided drug design (see scheme).

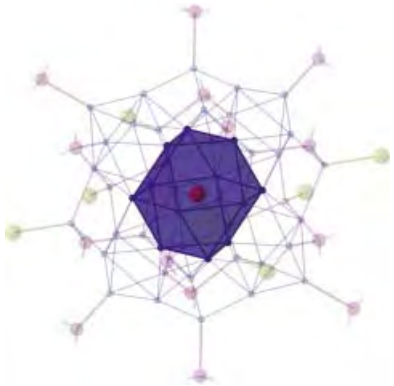


NMR Spectroscopy of Biomolecules

S. W. Homans* ——— **290 – 300**

NMR Spectroscopy Tools for Structure-Aided Drug Design

Communications



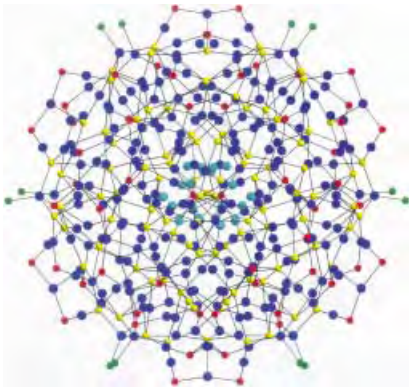
Metal or nonmetal? Gallium is a chameleon, both as an element and in a metalloid Ga_{51} cluster. The cluster consists of a central Ga_{13} unit with the same fcc topology as the high-pressure form of Ga-IV. A second shell of Ga atoms and GaBr and $GaPR_2$ groups binds the central core in a corset-like molecular structure (see picture).

Gallium Clusters VIP

J. Steiner, G. Stößer, H. Schnöckel* ——— **302 – 305**

$[Ga_{51}(PtBu_2)_{14}Br_6]^{3-}$: An Elementoid Gallium Cluster with Metalloid and Nonmetalloid Structural Elements

With a maximum diameter of 3.7 nm, $[Ag_{262}S_{100}(StBu)_{62}(dppb)_6]$ (dppb = 1,4-bis(diphenylphosphanyl)butane) is the largest structurally characterized metal chalcogenide cluster (see picture, P green, S yellow and red, Ag blue). The Ag–S substructure has a relationship to structural characteristics observed in binary Ag_2S phases: tetrahedral AgS_4 and AgS_3P units are linked by trigonal planar AgS_3 and approximately linear AgS_2 units. While the cluster periphery is well ordered, the Ag and S atomic sites in the center of the cluster are disordered. This observation is in accordance with macroscopic properties of Ag_2S.



Giant Silver–Sulfur Clusters VIP

D. Fenske,* C. Persau, S. Dehnen, C. E. Anson ——— **305 – 309**

Syntheses and Crystal Structures of the Ag–S Cluster Compounds $[Ag_{70}S_{20}(SPh)_{28}(dppm)_{10}](CF_3CO_2)_2$ and $[Ag_{262}S_{100}(StBu)_{62}(dppb)_6]$

For the USA and Canada:
ANGEWANDTE CHEMIE International Edition (ISSN 1433-7851) is published weekly by Wiley-VCH PO Box 191161, D 69451 Weinheim, Germany. Air freight and mailing in the USA by Publications Expediting Inc. 200 Meacham Ave., Elmont, NY 11003. Periodicals postage paid at Jamaica NY 11431. US POSTMASTER: send address changes to *Angewandte Chemie*, Wiley-VCH, 111 River Street, Hoboken, NJ 07030. Annual subscription price for institutions: Europe € 3430.00/3118.00; outside Europe US$ 4499.00/4090.00 (valid for print and electronic/print or electronic delivery); for individuals who are personal members of a national chemical society, or whose institution already subscribes, or who are retired or self-employed consultants, print only: Europe € 248.00/outside Europe US$ 378.00. Postage and handling charges included. All Wiley-VCH prices are exclusive VAT.

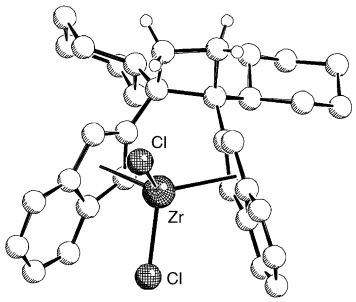
 © 2004 Wiley-VCH Verlag GmbH & Co. KGaA, Weinheim

Contents

Zirconocene Derivatives

W.-L. Nie, G. Erker,* G. Kehr, R. Fröhlich ——— **310 – 313**

Formation of a Unique *ansa*-Metallocene Framework by Intramolecular Photochemical [2+2] Cycloaddition of Bis(2-alkenylindenyl)zirconium Complexes

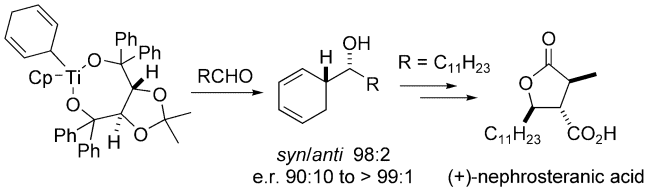


Complexes with backbone: Upon photolysis the title complexes undergo intramolecular [2+2] cycloaddition to yield unique cyclobutylene-bridged *ansa*-zirconocenes. The annelated phenylene rings of the indenyl ligand lie directly above and below the σ ligands of the bent metallocene wedge (see picture). Ligands that are introduced inside the resulting "phenylene π-electron box" display special chemical and spectroscopic features.

Asymmetric Synthesis

F. Schleth, A. Studer* ——— **313 – 315**

Desymmetrization of Metalated Cyclohexadienes and Application to the Synthesis of Nephrosteranic Acid



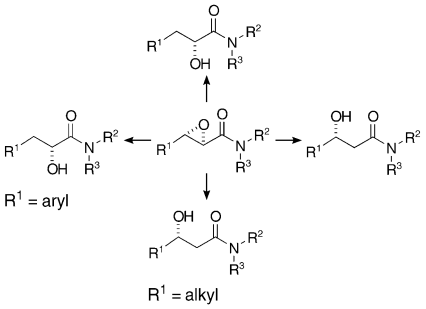
Chiral cyclohexadienyl Ti-TADDOLate reacts with aldehydes to provide the corresponding homoallyl alcohols in high yields with excellent diastereo- and high enantioselectivities (see scheme). The new method has been used as the key step in an efficient synthesis of nephrosteranic acid.

Regioselective Epoxide Opening

H. Kakei, T. Nemoto, T. Ohshima, M. Shibasaki* ——— **317 – 320**

Efficient Synthesis of Chiral α- and β-Hydroxy Amides: Application to the Synthesis of (*R*)-Fluoxetine

Four flavors for epoxide openings: The regioselective openings of epoxy amides obtained by asymmetric epoxidation yields all types of aryl- and alkyl-substituted hydroxy amides sometimes counter to the reactivity of the α- and β-positions.

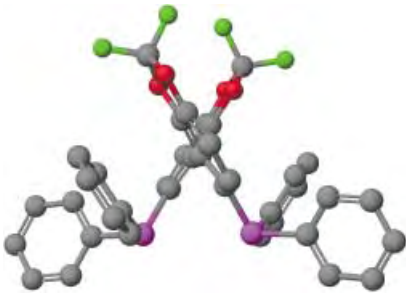


Asymmetric Hydrogenation

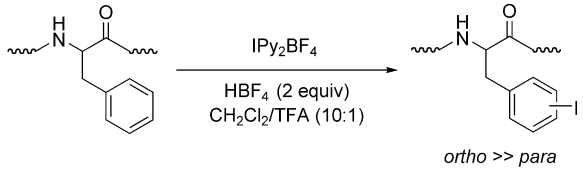
S. Jeulin, S. Duprat de Paule, V. Ratovelomanana-Vidal,* J.-P. Genêt,* N. Champion, P. Dellis* ——— **320 – 325**

Difluorphos, an Electron-Poor Diphosphane: A Good Match Between Electronic and Steric Features

The π acidity makes the difference: The fluorinated diphosphane, difluorphos, is synthesized (see structure: purple = P, red = O, green = F, gray = C) and its steroelectronic features are evaluated in theoretical and experimental studies. Its unusual π acidity explains the excellent results obtained with it in ruthenium-mediated asymmetric hydrogenation of fluorinated β-functionalized ketones. These results are better than those obtained with other biphenyl-based diphosphanes.



© 2004 Wiley-VCH Verlag GmbH & Co. KGaA, Weinheim

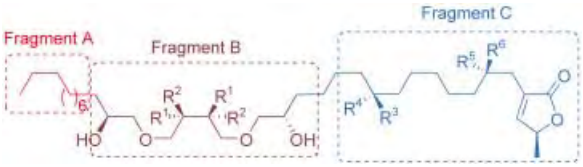


Iodination

G. Espuña, G. Arsequell, G. Valencia, J. Barluenga,* J. M. Alvarez-Gutiérrez, A. Ballesteros, J. M. González **325 – 329**

Regioselective Postsynthetic Modification of Phenylalanine Side Chains of Peptides Leading to Uncommon *ortho*-Iodinated Analogues

A convenient and direct iodination of Phe residues in peptide sequences was observed upon treatment with IPy_2BF_4. The experimental conditions were optimized (see scheme) and the role of the peptidyl fragment to drive the formation of the elusive *ortho*-iodo isomer as the major product was investigated.

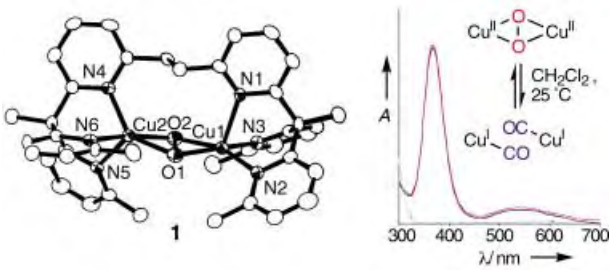


Natural Product Analogues

S. Jiang, Y. Li, X.-G. Chen, T.-S. Hu, Y.-L. Wu, Z.-J. Yao* **329 – 334**

Parallel Fragment Assembly Strategy Towards Multiple-Ether Mimicry of Anticancer Annonaceous Acetogenins

A small library of annonaceous acetogenin mimetics was established by a parallel fragment assembly strategy. Biological evaluation showed the diastereomeric analogues (see scheme) to have good selectivity between KB and Bel-7402 cells.



Bioinorganic Chemistry

M. Kodera,* Y. Kajita, Y. Tachi, K. Katayama, K. Kano, S. Hirota, S. Fujinami, M. Suzuki **334 – 337**

Synthesis, Structure, and Greatly Improved Reversible O_2 Binding in a Structurally Modulated μ-η^2:η^2-Peroxodicopper(II) Complex with Room-Temperature Stability

Facile O_2 release from an oxyhemocyanin model has been achieved for the first time, with the new room-temperature-stable μ-η^2:η^2-peroxodicopper complex $[Cu_2O_2(L2)]^{2+}$ (**1**). X-ray structural and spectroscopic studies on **1** show that elongation of the Cu–O bonds, induced by the bridgehead methyl groups of L2, is responsible for the ease of O_2 release. CO/O_2 binding by **1**, monitored by UV/Vis spectroscopy (see picture), is completely reversible.



Bio-Analytical Mass Spectrometry

H. R. Hansen, R. Pickford, J. Thomas-Oates, M. Jaspars, J. Feldmann* **337 – 340**

2-Dimethylarsinothioyl Acetic Acid Identified in a Biological Sample: The First Occurrence of a Mammalian Arsinothioyl Metabolite

Arsenic in sheep's clothing: the first characterization of a thio-organoarsenate compound (2-dimethylarsinothioyl acetic acid) isolated from a biological source (a rare breed of seaweed-eating sheep; see picture) is reported. The result indicates that mammalian arsenic metabolism is much more complex than has been claimed before, which opens up new questions about the toxicity of such organoarsenothio(y)l compounds.

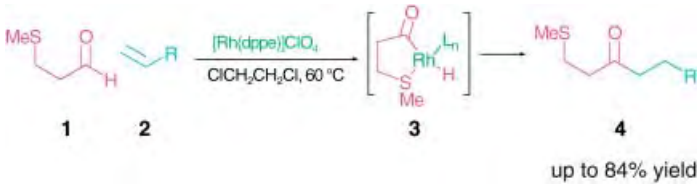
 © 2004 Wiley-VCH Verlag GmbH & Co. KGaA, Weinheim

Contents

Hydroacylation of Alkenes

M. C. Willis,* S. J. McNally, P. J. Beswick ——— 340 – 343

Chelation-Controlled Intermolecular Hydroacylation: Direct Addition of Alkyl Aldehydes to Functionalized Alkenes

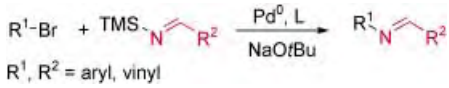


The pendant methylsulfanyl group of aldehyde **1** provides chelation stabilization (see **3**), thus allowing direct hydroacylation of functionalized electron-poor alkenes **2** in good yields under mild conditions. Electron-deficient alkynes can also be used as substrates. R = ester, amide, imide, sulfone; dppe = 1,2-bis(diphenylphosphanyl)ethane.

Cross-Coupling

J. Barluenga,* F. Aznar, C. Valdés ——— 343 – 345

N-Trialkylsilylimines as Coupling Partners for Pd-Catalyzed C–N Bond-Forming Reactions: One-Step Synthesis of Imines and Azadienes from Aryl and Alkenyl Bromides

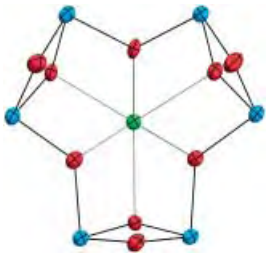


A good substitute: Imines, 1-azadienes, 2-azadienes, and even 2-azatrienes are prepared in one step from aryl and alkenyl bromides by palladium-catalyzed cross-coupling with *N*-trimethylsilylimines. The reaction introduces *N*-trimethylsilylimines as a synthetic equivalent for the R-CH=N moiety in C–N bond-forming reactions.

Magnetic Clusters

A. J. Tasiopoulos, T. A. O'Brien, K. A. Abboud, G. Christou* ——— 345 – 349

Mixed Transition-Metal—Lanthanide Complexes at Higher Oxidation States: Heteronuclear Ce^{IV}–Mn^{IV} Clusters



Wheels within wheels: A new family of mixed cerium(IV)–manganese(IV) clusters has been prepared spanning a range of Ce:Mn ratios from 3:2 to 1:6. The unusual core of the latter $CeMn_6$ complex is shown (Ce green, Mn blue, O red). All the compounds exhibit antiferromagnetic interactions between their constituent Mn^{IV} ions.

Nanostructures

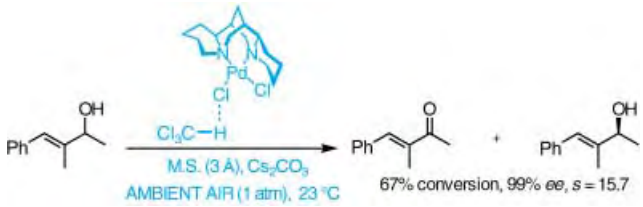
S. Leclair, P. Baillargeon, R. Skouta, D. Gauthier, Y. Zhao,* Y. L. Dory* ——— 349 – 353

Micrometer-Sized Hexagonal Tubes Self-Assembled by a Cyclic Peptide in a Liquid Crystal

Dissolved in nematic liquid crystals, rigid disk-shaped macrolactams may form large hexagonal hollow tubes. Computer modeling (see picture, O red, N blue, C gray, H white), Raman and infrared microspectroscopy reveal a hierarchical and self-similar-structured self-assembly of the cyclic peptide in the liquid-crystal medium.



© 2004 Wiley-VCH Verlag GmbH & Co. KGaA, Weinheim



Air is enough to mediate the highly enantioselective oxidation of secondary alcohols at room temperature with palladium(II) and sparteine in nonflammable solvents. Examination of the role of solvents capable of hydrogen bonding and their ability to solvate halide anions led to a novel set of conditions for the highly enantioselective oxidative kinetic resolution of secondary alcohols.

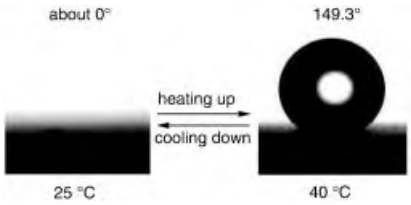
Kinetic Resolution

J. T. Bagdanoff, B. M. Stoltz* _ **353 – 357**

Palladium-Catalyzed Oxidative Kinetic Resolution with Ambient Air as the Stoichiometric Oxidation Gas

---

From soaking wet to bone dry: The concept of reversible switching between superhydrophilicity and superhydrophobicity of a surface (see picture) exploits the thermally responsive wettability of poly(*N*-isopropylacrylamide), and this property is enhanced by surface roughness.



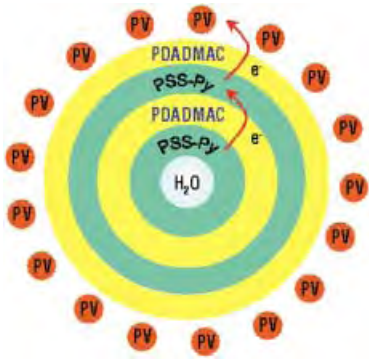
Surface Chemistry

T. Sun, G. Wang, L. Feng, B. Liu, Y. Ma, L. Jiang,* D. Zhu _____ **357 – 360**

Reversible Switching between Superhydrophilicity and Superhydrophobicity

---

Vectorial electron transfer between identical chromophores across the polyelectrolyte multilayer walls of hollow microcapsules can be photoinduced (see picture). This is achieved by inserting pyrene units in sufficiently high concentration into a film and setting up a polarity gradient over nanometer dimensions along which the charge transfer is directed. PV = polyviologen; PSS-Py = polystyrenesulfonic acid/pyrene; PDADMAC = poly(diallyldimethylammonium chloride).



Polymer Microcapsules

L. Li, H. Möhwald* _____ **360 – 363**

Photoinduced Vectorial Charge Transfer across Walls of Hollow Microcapsules

---

An anomalous transport effect has been found by neutron spin echo measurements on *n*-alkanes diffusing in a small-pore zeolite: the diffusivity decreases from C_1 to C_8, but rises for C_{10} and has a maximum at C_{12}, then decreases again. This confirms the existence of the "window effect" proposed thirty years ago by Gorring. The picture shows schematically how one end of a C_{12} chain extends through a zeolite window, lowering the barrier to diffusion.



Diffusion in Zeolites

H. Jobic,* A. Méthivier, G. Ehlers, B. Farago, W. Haeussler _____ **364 – 366**

Accelerated Diffusion of Long-Chain Alkanes between Nanosized Cavities

 © 2004 Wiley-VCH Verlag GmbH & Co. KGaA, Weinheim

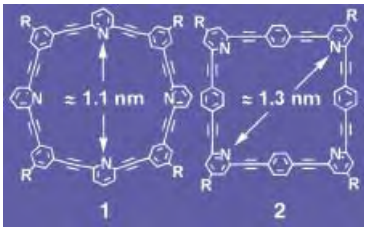
Contents

Light-Emitting Macrocycles

Y. Yamaguchi,* S. Kobayashi, S. Miyamura, Y. Okamoto, T. Wakamiya, Y. Matsubara, Z.-i. Yoshida* ——— **366 – 369**

Synthesis and Light-Emitting Characteristics of Doughnut-Shaped π-Electron Systems

Doughnut-shaped fluorescent molecules: Highly symmetrical, functionally and structurally interesting octakis-*m*-cyclynes **1** and octakis-*p*-cyclynes **2** are shown to be a new class of light-emitting materials (see scheme). A pentacoordinate Cu^{II} complex of **1** exhibits remarkably intense fluorescence, contrary to the behavior expected for Cu^{II} complexes, which suggests that other transition-metal complexes of **1** may also function as luminescent materials.

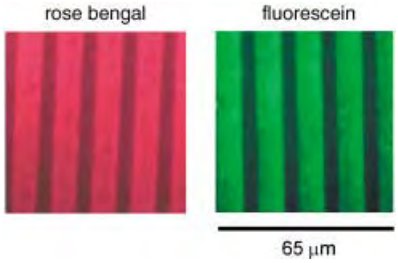


Microcontact Printing

T. Auletta, B. Dordi, A. Mulder, A. Sartori, S. Onclin, C. M. Bruinink, M. Péter, C. A. Nijhuis, H. Beijleveld, H. Schönherr G. J. Vancso, A. Casnati, R. Ungaro, B. J. Ravoo, J. Huskens,* D. N. Reinhoudt* ——— **369 – 373**

Writing Patterns of Molecules on Molecular Printboards

Self-assembled monolayers of cyclodextrin receptor molecules on gold or silicon oxide surfaces function as molecular printboards to which molecules with complementary recognition motifs can be transferred selectively by writing or printing. One example demonstrating the application of this methodology is the supramolecular microcontact printing of dendrimers loaded with fluorescent dyes (see confocal microscopy images after loading with rose bengal and fluorescein).



Communications labeled with this symbol have been judged by two referees as being "very important papers".

The publication of Communications labeled with this symbol has been accelerated because of their topical or highly competitive nature.

Looking for outstanding employees?

Do you need another expert for your excellent team?
...Chemists, PhD Students, Managers, Professors, Sales Representatives...

Place an advert in the printed version and have it made available online for 1 month, free of charge!

Angewandte Chemie International Edition
Advertising Sales Department: Marion Schulz
Phone: 0 62 01 - 60 65 65
Fax: 0 62 01 - 60 65 50
E-Mail: MSchulz@wiley-vch.de

Service

Keywords ——— *376*

Authors ——— *377*

Angewandte's Sister Journals *374 – 375*

Preview ——— *379*



Highly Branched Macromolecules at the Interface of Chemistry, Biology, Physics, and Medicine**

Rainer Haag* and Fritz Vögtle*

The interest in dendritic ("treelike") macromolecules has been growing exponentially, even though it is already 25 years since the first reports were published on this subject. This development is not only reflected by the increasing number of publications on dendrimers, but also by the increasing number of participants at the international dendrimer symposium (IDS). The IDS takes place every two years and was organized this year at the Freie Universität Berlin (FU Berlin) by A. D. Schlüter, E. W. Meijer, A. Hult, and F. Vögtle, together with DECHEMA.

With the transition from classical structural chemistry towards functional chemistry, this research area has undergone significant development in a very short time. This might also be the reason for the large increase in the number of young scientists who are fascinated by dendritic molecules and their application potential. The highly interdisciplinary nature of this field is striking, as became apparent in the opening lecture of J. M. J. Fréchet (University of California, Berkeley). Dendrimer chemistry branches out into biology, medicine, physics, and chemical engineering. It has very much been shaped by collaborations between inorganic, organic, physical, and polymer chemists, as well as synthetic, analytical, theoretical, and industrial chemists. For example, highly multidisciplinary lectures by synthetic chemists were detailed with spectroscopic and theoretical models put forward by experts in the respective fields. There is much interaction of this type between different research groups (e.g. those of Aida/Yamazaki, Ballauff/Vögtle/Müllen, Fréchet/Szoka, Müllen/De Schryver, Schlüter/Rabe, Vögtle/Balzani). The diversity of dendritic architectures shows the tremendous breadth of the field (Figure 1): from low-molecular-weight to high-molecular-weight structures, from functional dendrimers to hyperbranched and dendronized polymers or supramolecular core–shell architectures.

Since the dimensions of dendritic macromolecules are in the region of several nanometers, they can be analyzed and characterized with a range of modern analytical methods, including SANS (small-angle neutron scattering), single-molecule spectroscopy, STM, and AFM. Bigger complexes, such as those of dendronized polyamines and DNA, can also be visualized by AFM (Rabe, Schlüter, and co-workers, Berlin).[1] In the case of perfect dendrimers and supramolecular aggregates with defined building blocks, the mass-spectrometric characterization (by MS–MS coupling) can be valuable (Broeren, Meijer, and co-workers, TU Eindhoven).

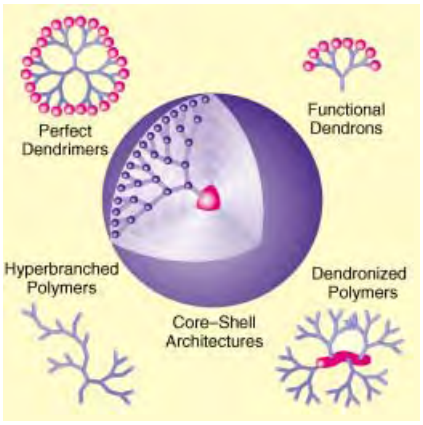


Figure 1. Overview of dendritic architectures and their nomenclature. With the kind permission of Dr. S. Hecht (FU Berlin).

The focus of the conference was on functional dendrimers. In the foreground were photoactivity, the manipulation of photons (Balzani), and glycodendrimers (Lindhorst), but also the functionalization of dendrons, for example, in combinations with C_{60} (Nierengarten) or porphyrins (Aida, Vinogradov), modern chemical analysis with multiple chromophors (Müllen, Josel), and applications, for example, as multifunctional supports for catalysts (Reek, Portnoy). A large variety of supramolecular aggregates with dendritic building blocks were also presented, including novel amphiphiles and defined micelles (Hirsch), supramolecular chirality and helicity (Percec), molecular imprinting (Zimmerman), self-assembled materials (Stupp), and metallodendrimers (Newkome).

Numerous potential biomedical applications of dendrimers,[2] as well as actual industrial applications, were presented: diagnostics (magnetic resonance imaging, electroluminescence), dendritic "glues" for eye surgery, dendritic polyamines as vectors for gene transfection and as additives for plastics and coatings. "Gadomer-24"[2] is a lysine dendrimer with 24 peripheral Gd complexes that has been designed for contrast-rich magnetic resonance angiography (MRA; Platzek, Schering AG). As a result of its high relaxivity and long intravascular retention a long-lasting high contrast is obtained for the imaging of blood vessels. This is extremely important for the imaging of the coronary arteries (Figure 2). For intravenous MRA application rapid and quantitative renal elimination of the dendrimer from the body is crucial. This dendritic MRA diagnostic is currently in the last stage of clinical trials and will be produced in quantities of $>1000\ \mathrm{kg\,a^{-1}}$ when it goes on the market. "Gadomer-24" is the first dendritic compound to come this far on the road towards in vivo application.

The sensitivity of luminescence and electroluminescence markers can be enhanced significantly with the use of dendritic labels. This is an important issue for future medical diagnostics (Josel, Roche Diagnostics). The use of different dendritic polyamines as vec-

[*] Prof. Dr. R. Haag
Organische Polymerchemie
Universität Dortmund (Germany)
Prof. Dr. F. Vögtle
Kekulé-Institut für Organische Chemie und Biochemie
Universität Bonn (Germany)

[**] The 3rd International Dendrimer Symposium, Berlin, September 17–20, 2003; www.ids-3.de

 © 2004 Wiley-VCH Verlag GmbH & Co. KGaA, Weinheim DOI: 10.1002/anie.200320082

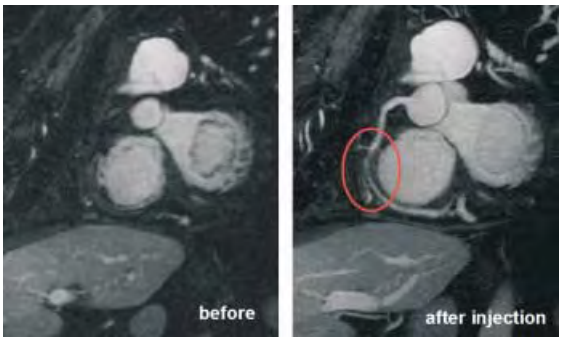


Figure 2. Magnetic resonance imaging of the right coronary artery (human heart), before and after injection of Gadomer-24. The imaging of the artery stenosis is remarkable (indicated with the red circle). With the kind permission of the Universität Essen.

tors for in vitro gene transfection, as commercialized by QIAGEN GmbH a few years ago,[3] was the subject of several talks and posters. F. Diederich (ETH, Zürich) presented a novel approach, which instead of large dendritic polyamines uses small oligoamine dendrons with a lipophilic tail.[4] These polyamine amphiphiles come together to form polycationic micelles suitable for the complexation and transport of DNA. An advantage is their lower toxicity as compared to high-molecular-weight vectors.

Besides the overall growing number of conference contributions, the number of presentations on hyperbranched polymers has increased in particular. In their lectures M. Antonietti (MPI Golm) and B. Voit (IPF Dresden) critically compared new routes, as well as the advantages and disadvantages of hyperbranched compounds. Several technical processes and applications were highlighted. For example, hyperbranched molecules are already used as additives in inks for inkjet printing. They also play a role in paper processing. B. Bruchmann (BASF) reported that hyperbranched poly(ethylene imine)s (PEI) have been a subject of research at BASF for more than 50 years. PEIs with molecular weights of up to 25000 g mol^{-1} are produced on a ton scale with narrow molecular-weight distributions and high degrees of branching. With new hyperbranched polyurethanes[5] as additives for plastics and coatings, hardness, flexibility, and hence scratch resistance can be improved dramatically.

A new approach to functional hyperbranched polymers was presented by Z. Guan. The dendritic structures are available from the cheapest monomer conceivable, ethene, and a small amount of a functionalized olefin by a catalytic process based on a "chain-walking" mechanism. Through this procedure it is also possible to generate novel core–shell architectures in a single step.[6]

In his after-dinner lecture J. Put (DSM) presented from an industrial viewpoint the history of dendrimer chemistry, which started in 1978 with cascade molecules. How important are dendrimers for chemistry, for research in general, for industry, and for the future? His answer: "very!" Dendrimers, despite their high structural variability, challenge the synthetic and analytical arsenals. Because of their multifunctionality they open up many future perspectives for covalent and supramolecular architectures. His conclusion: Dendrimers should receive much more attention, especially from industry, than they do currently. However, hyperbranched polymers are also suitable for large-scale applications in many cases, and DSM has its own successful candidate in "hybrane".

In general the dendrimer symposium reflected the refreshing mobility and activity of the dendrimer sector. It was future oriented and instructive for the large number of young scientists present. The possibility of selective functionalization but also certain problems in the synthesis of higher dendrimer generations were highlighted. Despite some new approaches, simple and highly efficient syntheses leading to higher generations are rare. An elegant approach was presented by C. Hawker (IBM). Perfect dendrimers have been obtained by a copper-catalyzed [3+2] cycloaddition in extremely high yields and purities (sometimes without purification). In this context, the question of when to use perfect dendrimers and when to use hyperbranched polymers was raised: Perfect dendrimers are certainly superior for pharmaceuticals and diagnostics, as well as for measurements of physicochemical effects, for example, dendritic effects in general or the evaluation of steric/electronic/chiral effects of dendrons. Hyperbranched polymers on the other hand are advantageous for larger particle sizes (high pseudogenerations) or for industrial applications (e.g. as coating additives), when the price dictates the choice of monomer.

Research into dendritic compounds has been successful, but to take full advantage of the opportunities offered by this evolving field further intensive studies are needed. Some major problems have already been solved in terms of synthesis, analysis, and applications. It has been demonstrated that dendrimers can be tailor-made for specific applications, with respect to their size, molecular topology, functionality, surface properties, and photoactivity. Further applications in the diverse areas of materials and life sciences are anticipated. The next international dendrimer symposium (IDS-4), organized by J. M. J. Fréchet and D. A. Tomalia, will take place in May 2005 in Mount Pleasant (Michigan, USA).

[1] I. Gössl, L. Shu, A. D. Schlüter, J. P. Rabe, *J. Am. Chem. Soc.* **2002**, *124*, 6860–6865.
[2] For a recent review, see: S.-E. Stiriba, H. Frey, R. Haag, *Angew. Chem.* **2002**, *114*, 1385–1390; *Angew. Chem. Int. Ed.* **2002**, *41*, 1329–1334.
[3] For further information, see: http://www.qiagen.com/transfectiontools.
[4] D. Joester, M. Losson, R. Pugin, H. Heinzelmann, E. Walter, H. P. Merkle, F. Diederich, *Angew. Chem.* **2003**, *115*, 1524–1528; *Angew. Chem. Int. Ed.* **2003**, *42*, 1486–1490.
[5] a) B. Bruchmann, U. Ehe, F. Wingerter, K. Stiefenhöfer, U. Treuling, EP1026185, **1999**; b) C. Gao, D. Yan, *Macromolecules* **2003**, *36*, 613–620; c) B. Bruchmann, W. Schrepp, *e-Polym.* **2003**, 14.
[6] G. Chen, X. S. Ma, Z. Guan, *J. Am. Chem. Soc.* **2003**, *125*, 6697–6704.

 © 2004 Wiley-VCH Verlag GmbH & Co. KGaA, Weinheim

Drug Delivery

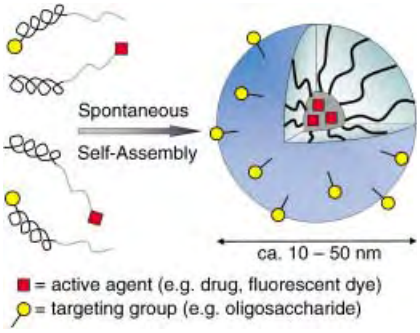
Supramolecular Drug-Delivery Systems Based on Polymeric Core–Shell Architectures**

*Rainer Haag**

Keywords:
block copolymers · dendrimers · drug delivery · micelles · supramolecular chemistry

The physicochemical properties of new drugs are important factors regarding whether they will be successful in vivo. A number of criteria have been empirically postulated based on numerous structure–activity profiles of successful and nonsuccessful drugs for the efficient cellular uptake of these small drug molecules by diffusion through the cell membrane.[1] However, many potent drug candidates fail in preclinical studies because of limited solubility, stability, and toxicity. Thus, a number of drug-delivery systems have been developed to overcome these transport problems.[2–4] These include physical aggregates of amphiphilic molecules, such as polymeric micelles[3–5] as well as stable unimolecular micelles,[6] which have been considered as powerful nanocarriers in the dawning era of polymer therapeutics.[7]

This highlight focuses on some recent developments of polymeric core–shell architectures (namely block-copolymer and unimolecular micelles) and the pathway of cellular uptake of such supramolecular drug-delivery systems. In contrast to micelles of small surfactant molecules, polymeric micelles (Scheme 1) are generally more stable and can retain the loaded drug for a longer period of time.[3] The block-copolymer micelles form spontaneously in water by self-assembly when the concentration of the amphiphilic block copolymer is above the critical micellar concentration (CMC). The driving forces can either be the hydrophobic interaction of the inner block, for example, a nonpolar poly(caprolactone) block (PCL), or ionic interactions of a cationic block, for example, a poly(aspartate) block (PAsp), complexed to a negatively charged polymer, such as DNA, which results in the formation of a polyion micelle.[4] The outer block consists in many cases of a polar poly(ethylene oxide) (PEO) block, which will form the shell of the nanocarrier and protect the core through steric stabilization. It has also been demonstrated that PEO prevents the adsorption of proteins[8] and hence forms a biocompatible polymeric nanocarrier shell. The size of these block-copolymer micelles is determined by thermodynamic parameters, although partial size-control is possible by variation of the block length. These block-copolymer micelles are typically several tenths of nanometers in diameter with a relatively narrow size distribution, and are therefore similar in size to viruses, lipoproteins, and other naturally occurring transport systems. A major obstacle for such nanocarrier systems is the nonspecific uptake by the reticuloendothelial systems (RES). The size and the surface properties of such block-copolymer-based nanocarriers require careful design to achieve long circulation times in blood and to reach their target.[9] The polarity and functionality of each block allows control over the spontaneously formed core–shell architecture. While terminal functionalities on the outer block ("the shell") control the biocompatibility and might also incorporate possible targeting functionalities of these nanocarriers, the inner block can be used to complex or covalently couple active drug molecules (see Scheme 1). This concept is frequently used to solubilize nonpolar drugs with a limited solubility in water (for example, pluronics: PEO-*b*-PPO).[10]



Scheme 1. Architecture of block-copolymer micelles which spontaneously form by self-assembly in water. The characteristic features are a pronounced core–shell architecture which can be controlled by the individual polymer blocks. Typical examples of block copolymers are PEO-*b*-PPO, PEO-*b*-PCL, and PEO-*b*-PAsp.

Cellular Uptake of Block-Copolymer Micelles by Endocytosis

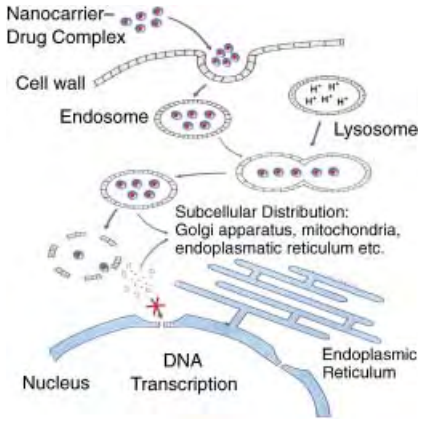
While the passive cellular uptake of small drug molecules occurs in most cases by simple diffusion through the cellular membrane, this bilayer is a barrier for most macromolecules and other nanoparticles. An alternative pathway for the cellular uptake of

[*] Prof. Dr. R. Haag
Organische Polymerchemie
Universität Dortmund
Otto-Hahn-Strasse 6
44227 Dortmund (Germany)
Fax: (+49) 231-755-6148
E-mail: haag@chemie.uni-dortmund.de

[**] The author thanks the Deutsche Forschungsgemeinschaft and Fonds der Chemischen Industrie for continuing financial support.

 © 2004 Wiley-VCH Verlag GmbH & Co. KGaA, Weinheim DOI: 10.1002/anie.200301694

macromolecules and nanoparticles (5–100 nm) proceeds by so-called endocytosis (Scheme 2), where bubblelike vesicles are separated from the cell membrane by folding inward and these so-called endosomes simultaneously ingest surrounding materials. The endosomes then fuse with lysosomes in which the pH value is significantly lower (ca. pH 4–5) than under normal physiological conditions (pH 7.4). This pH shift has also been used for selective drug delivery inside cells (see below). Although the mechanism of endocytosis has been studied by several research groups,[11] many details are not yet fully understood. The understanding of the subcellular distribution is essential for their application, particularly for the targeted delivery of hydrophobic drugs incorporated into water-soluble block-copolymer micelles.

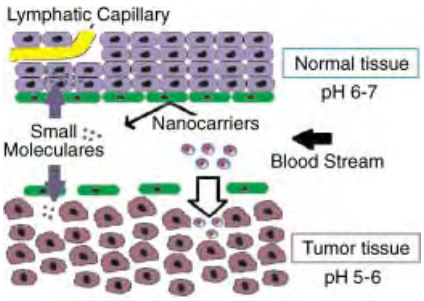


Scheme 2. Endocytotic pathway for the cellular uptake of macromolecules and polymeric nanocarriers for drug delivery.

Recently, Maysinger and co-workers prepared fluorescent-labeled block-copolymer micelles (40% fluorescent-labeled core, Scheme 1) and followed the cellular uptake of these nanocarrier systems by confocal microscopy of rat pheochromocytoma cells (PC12 cells).[12] Even though endocytosis could not be detected directly by optical microscopy, various interesting distribution phenomena were revealed by this study. Fluorescence from the fluorescent-labeled PCL-*b*-PEO micelles was detected in the cytoplasma but not in the cellular membrane or the nucleus (Scheme 2). Also, the entry of micelles into the cells was time- and concentration-dependent, and reached equilibrium between 16 and 24 h.[13] Even though some quenching of the fluorescence occurred as a result of the close packing of the dye inside the micelle, it was clearly demonstrated that these micellar nanocarriers with a PEO shell are internalized by cells and reside in the cytoplasma of the cell. Further localization of the micelles was achieved by labeling several cytoplasmic organelles with specific fluorescent probes and observing the different dyes with triple-labeling confocal microscopy. Partial co-localization was detected with dyes selective for various organelles, including lysosomes, the Golgi apparatus, mitochondria, and endoplasmatic reticulum. A similar subcellular distribution of the fluorescent-labeled PCL-*b*-PEO micelles was observed in NIH 3T3 cells, which suggests that these biocompatible micelles without targeting groups in their shell are suitable for drug delivery in multiple cytoplasmic regions of different cells. Finally the authors could demonstrate by internalization of 5-dodecanoylaminofluorescein (DAF, a toxic fluorescent probe) that DAF noncovalently incorporated into the micelle shows a higher cell toxicity than free DAF entering the cytosol through the membrane. This interesting observation indicates that the extent of cellular uptake of a drug within such polymeric nanocarriers by endocytosis can lead to higher local concentrations than that obtained by diffusion of the free drug through the membrane. This effect was demonstrated by decreased cell viability upon treatment with the toxic nanocarrier-encapsulated DAF.

Tumor-Specific Drug Delivery by Enhanced Permeation and Retention (EPR Effect)

Several concepts have been investigated for tissue-specific drug delivery and enhanced endocytosis using polymeric nanocarriers.[7] In addition to active delivery pathways through the use of targeting groups on the surface of these nanocarriers, such as oligosaccharides or antibodies (see Scheme 1),[11] passive accumulation into porous tissues, such as tumor tissue, is also of great importance.[3] The rationale for using macromolecules or other nanoparticles as efficient carriers for the delivery of antitumor agents has been strengthened by recent studies concerning the enhanced permeability of tumor blood vessels and their subsequent accumulation in solid tumors (Scheme 3).[14,15]



Scheme 3. Schematic representation of the enhanced permeation retention model (EPR effect), which explains the selective accumulation of nanocarriers in the porous tumor tissue. Reprinted with kind permission from Dr. F. Kratz (Clinic for Tumor Biology, Freiburg).

The mechanism by which macromolecules or other nanoparticles accumulate in tumor tissue has been termed enhanced permeability and retention (EPR effect),[16,17] and serves as a working model for explaining the targeting potential of polymers for solid tumors.

Blood vessels in most normal tissues have an intact endothelial layer which allows the diffusion of small molecules but excludes macromolecules or other nanoparticles from the tissue. In contrast, as a consequence of its fast growth, the endothelial layer of blood vessels in tumor tissue is often porous, and both small and large molecules have access to the malignant tissue. Tumor tissue does not generally have a lymphatic drainage system, and thus macromolecules are retained and can accumulate in solid tumors. The vascular permeability of human tumor xenografts in nude mice has been investigated for molecules of various size and it was demonstrated that even small liposomes (up to several hundered nanometers) can pass through the porous endothelial layer of tumor tissue and reach tumor cells.[15] The anatomical and physiological properties of tumor tissue, therefore, serve as a three-dimensional target for delivering anticancer drugs to the tumor by using

 © 2004 Wiley-VCH Verlag GmbH & Co. KGaA, Weinheim

macromolecular nanocarriers as drug-delivery systems (Scheme 3).[7,17]

Various biocompatible macromolecules and nanoparticles are attractive carrier systems because of their selective uptake in tumor tissue, their excellent water solubility, their synthetic diversity, and their low costs. One of the key issues which has been addressed in recent years regarding the pharmacological activity of macromolecular drug delivery systems is the significance of labile linker groups between the drug and the polymer ("Ringsdorf model").[18,19] Therefore, in many macromolecular carrier systems the drug is linked to the polymer through a spacer molecule, which incorporates a predetermined breaking point that allows the bound drug to be released at a given cellular site.[7,19] Two types of linker molecules have been investigated: 1) acid-labile linkers, such as, hydrazones,[20,21] and 2) peptide linkers which can be cleaved by lysosomal enzymes.[22] Both types of bonds exploit the cellular-uptake mechanism for macromolecules (endocytosis), which allows the polymer-bound drug to be released in intracellular compartments. A significant drop in the pH value takes place (Scheme 3) in tumor tissue from the physiological pH value (7.4) in the extracellular space to pH 6.0–5.0, and to around pH 4–5 in primary and secondary lysosomes (Scheme 2). In addition, a large number of lysosomal enzymes become active in the acidic environment of these vesicles, for example, phosphatases, nucleases, proteases, esterases, and lipases. Both, the low pH values in endosomes and lysosomes as well as the presence of lysosomal enzymes are, therefore, intracellular properties which can be used for the development of new polymeric nanocarriers which release the polymer-bound drug specifically in tumor cells.[7,23]

Block-Copolymer Micelles for the Delivery of Antitumor Agents

In addition to these polymer–drug conjugates, in which the cytostatic molecules are covalently attached to a single macromolecule chain, Kataoka et al. have recently reported a pH-sensitive supramolecular nanocarrier for adriamycin based on biocompatible block-copolymer micelles.[24] Adriamycin (ADR) is one of the most frequently used drugs in cancer therapy.[25] This very potent cytostatic was coupled through an acid-labile hydrazone linker to a PEO-*b*-PAsp copolymer (Figure 1).

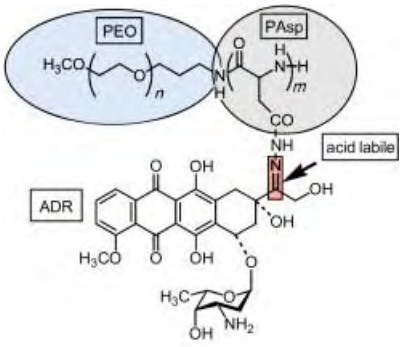


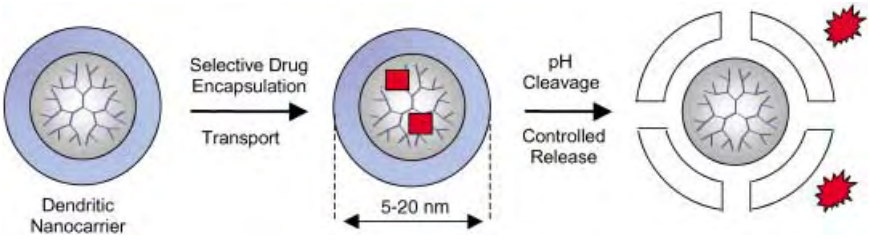
Figure 1. ADR-block-copolymer conjugate which self-assembles spontaneously to form block-copolymer micelles in water. The acid-labile hydrazone bond is cleaved at pH < 6 and ADR is released.

After spontaneous self-assembly of these drug-loaded supramolecular nanocarriers (see Figure 1), release kinetics clearly demonstrated the effective cleavage of the hydrazone bonds at pH ≤ 5 with release of the active drug (ADR). The release was, however, negligible under physiological conditions in the cell culture medium (pH ca. 7).

A human small-cell lung cancer cell line SBC-3 was incubated with the intact drug and the ADR-loaded block-copolymer micelles for in vitro studies. In the case of intact drugs, ADR molecules seemed to rapidly penetrate the cell wall by diffusion, while the micellar drug conjugate resulted in a time-dependent cellular uptake by endocytosis. The results revealed that the micelles were very effective against cancer cells SBC-3. In addition, the growth inhibition of the cells shifted as exposure time increased, which suggested that the drugs were in an active form and that cytotoxicity was delayed until the drugs were liberated from the micelles and intercalated in the DNA strands in the cell nucleus. Although the higher selectivity for tumor tissue has not yet been demonstrated in this case, the reduced in vivo toxicity and fewer side effects relative to the free toxic cytostatic have been reported for other cytostatic–nanocarrier conjugates.[21,26]

Dendritic Core–Shell Architectures for Drug Delivery

While physical aggregates of amphiphilic micellar structures are frequently used as drug-delivery systems, because of their noncovalent assembly, these physical aggregates can be unstable under shear force and other environmental effects, such as temperature and pressure, which are used for example in sterilization. An alternative approach is the covalent modification of dendritic macromolecules with an appropriate shell that results in stable micelle-type structures that are suitable for the noncovalent encapsulation of guest molecules (Scheme 4).[6,27] The size of these dendritic nanocarriers can be exactly defined in the range of 5–20 nm. Another advantage of these supramolecular host–guest systems over the covalent polymer–drug conjugate is their more general applicability.[27] The encapsulation of guest molecules is driven by noncovalent interactions (ionic, H-bonding, and van der Waals interac-



Scheme 4. Unimolecular dendritic nanocarrier for supramolecular encapsulation of biologically active compounds (for example, drugs and oligonucleotides). The drug load can be released selectively in acidic media (such as tumor tissue) when the acid-labile linkers (connecting the shell to the core) are cleaved.

 © 2004 Wiley-VCH Verlag GmbH & Co. KGaA, Weinheim

tions) and can be tailored for various drugs at the same time, while a polymer–drug conjugate has to be synthesized individually in an extensive multistep synthesis.

Although the encapsulation and the transport of guest molecules into these dendritic architectures have been studied by several research groups,[28] relatively little is known about the active release of the encapsulated guest molecules by pH-triggered cleavage of the shell in the physiological pH range (Scheme 4). In many cases the pH-dependent release from dendritic core–shell architectures has only been achieved under severe conditions[29] or by protonation of poly(propylene amine) dendrimers[30] and their derivatives.[31]

Recently, we reported a simple and general concept for the generation of core–shell-type architectures from readily accessible hyperbranched polymers was reported.[32] Several pH-sensitive nanocarriers have been prepared based on commercially available dendritic core structures (polyglycerol and poly(ethylene imine)) by attaching pH-sensitive shells through acetal or imine bonds (Figure 2). In some cases the pH-responsive nanocarriers showed extremely high transport capacities, which is another important criteria for efficient drug delivery. Various guest molecules, such as polar dyes, oligonucleotides, and cytostatic molecules have been encapsulated inside these dendritic core–shell architectures. In addition, the dendritic polyamine core structure with an imine-linked shell (Figure 2) shows the necessary release profile for tumor tissue: fast release at pH 6 and no (slow) release at pH 7.4.

In summary, the supramolecular nanocarrier systems described in this highlight have great potential for efficient drug delivery. The advantage of these polymeric core–shell architectures is their good size control (5–20 nm for dendritic core–shell architectures and 10–50 nm for block–copolymer micelles). The encapsulated, often toxic, drug is efficiently shielded and can develop its activity by selective release from the nanocarrier upon application of an external signal, such as pH change. While the cellular uptake of these nanocarriers (without specific targeting groups) by endocytosis is not cell-specific, a high passive selectivity has been observed for these nanocarriers in porous tissues, such as tumor tissue. The disclosure of subcellular distribution of these macromolecular nanocarriers is yet another milestone in the complete mechanistic understanding of their pathway of action. However, only further in vivo studies can reveal whether these novel drug-delivery systems will be fully compatible with the immune system and not cause unwanted side effects.

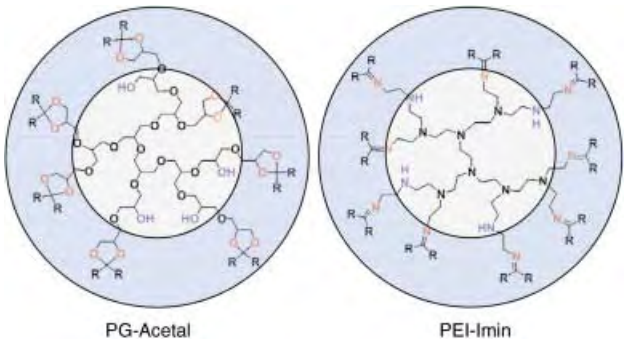


Figure 2. Dendritic core–shell architectures (PG-acetal and PEI-imine) based on commercially available hyperbranched polyglycerol (PG) and poly(ethylene imine) (PEI) with acid-labile shells. Stable supramolecular complexes are formed with various polar guest molecules (dyes, drugs, oligonucleotides). Cleavage of the acetal ($pH < 4$) or imine groups ($pH \leq 6$) release the encapsulated guest molecules. The depicted structures are idealized versions of the polymeric core molecules.

[1] C. A. Lipinski, F. Lombardo, B. W. Dominy, P. J. Feeney, *Adv. Drug Delivery Rev.* **1997**, *23*, 4–25.

[2] a) D. D. Lasic, D. Papahadjopoulos, *Science* **1995**, *267*, 1275–1276; b) L. Zhang, K. Yu, A. Eisenberg, *Science* **1996**, *272*, 1777–1779; c) K. E. Uhrich, *Chem. Rev.* **1999**, *99*, 3181–3198; d) C. Allen, A. Eisenberg, J. Mrsic, D. Maysinger, *Drug Delivery* **2000**, *7*, 139–145; e) R. Langer, *Science* **2001**, *293*, 58–59; f) W. M. Saltzman, *Drug Delivery: Engineering Principles for Drug Therapy*, Oxford University Press, New York, **2001**; g) D. E. Discher, A. Eisenberg, *Science* **2002**, *297*, 967–973; h) V. P. Torchilin, *Adv. Drug Delivery Rev.* **2002**, *54*, 215–225.

[3] K. Kataoka, A. Harada, Y. Nagaski, *Adv. Drug Delivery Rev.* **2001**, *47*, 113–131.

[4] Y. Kakizawa, K. Kataoka, *Adv. Drug Delivery Rev.* **2002**, *54*, 203–222.

[5] J. Kreuter, *Colloidal Drug Delivery Systems*, Marcel Dekker, New York, **1994**.

[6] For a recent reviews, see M. W. P. L. Baars, E. W. Meijer, *Top. Curr. Chem.* **2000**, *210*, 131–182.

[7] For recent reviews, see a) R. Duncan, *Nat. Rev. Drug Discovery* **2003**, *2*, 347–360; b) M. Thanou, R. Duncan, *Curr. Opin. Invest. Drugs* **2003**, *4*, 701–709.

[8] a) L. Deng, M. Mrksich, G. M. Whitesides, *J. Am. Chem. Soc.* **1996**, *118*, 5136–5137; b) I. Szleifer, *Curr. Opin. Solid State Mater. Sci.* **1997**, *2*, 337–344.

[9] K. Kataoka, G. S. Kwon, M. Yokoyama, T. Okano, Y. Sakurai, *J. Controlled Release* **1993**, *24*, 119–132.

[10] Pluronics (BASF) are PEO-b-PPO-copolymers, which are frequently used as pharma additives to solubilize drugs.

[11] S. M. Moghimi, A. C. Hunter, *Pharmacol. Rev.* **2001**, *53*, 283–318.

[12] R. Savic, L. Luo, A. Eisenberg, D. Maysinger, *Science* **2003**, *300*, 615–618.

[13] L. Luo, J. Tam, D. Maysinger, A. Eisenberg, *Bioconjugate Chem.* **2002**, *13*, 1259–1265.

[14] Y. Takakura, M. Hashida, *Crit. Rev. Oncol. Hematol.* **1994**, *18*, 207–231.

[15] F. Yuan, M. Deilian, D. Fukumura, M. Leuning, D. A. Berk, V. P. Torchilin, R. K. Jain, *Cancer Res.* **1995**, *55*, 3752–3756.

[16] Y. Matsumura, H. Maeda, *Cancer Res.* **1986**, *46*, 6387–6392.

[17] H. Maeda, Y. Matsumura, *CRC Crit. Rev. Ther. Drug Carrier Syst.* **1989**, *6*, 193–210.

[18] H. Ringsdorf, *J. Polym. Sci. Polym. Symp.* **1975**, *51*, 135–153.

[19] L. Gros, H. Ringsdorf, H. Schupp, *Angew. Chem.* **1981**, *93*, 311–322; *Angew. Chem. Int. Ed. Engl.* **1981**, *20*, 305–325.

[20] a) F. Kratz, U. Beyer, M. T. Schütte, *Crit. Rev. Ther. Drug Carrier Syst.* **1999**, *16*, 245–288; b) O. L. P. De Jesús, H. R. Ihre, L. Gagne, J. M. J. Fréchet, F. C. J. Szoka, *Bioconjugate Chem.* **2002**, *13*, 453–461.

[21] F. Kratz, R. Müller-Driver, I. Hofmann, J. Drevs, C. Unger, *J. Med. Chem.* **2000**, *43*, 1253–1256.

 © 2004 Wiley-VCH Verlag GmbH & Co. KGaA, Weinheim

[22] a) R. Duncan, P. Kopeckova-Rejmanova, J. Strohalm, I. C. Hume, J. B. Lloyd, J. Kopecek, *Br. J. Cancer* **1988**, *57*, 147 – 156; b) V. Subr, J. Strohalm, K. Ulbrich, R. Duncan, *J. Controlled Release* **1992**, *18*, 123 – 132.

[23] F. Kratz, A. Warnecke, P. C. A. Rodrigues, K. Riebeseel in *Polymeric Biomaterials*, 2nd ed. (Ed.: S. Dumitriu), Marcel Dekker, New York, **2001**, pp. 851 – 894.

[24] Y. Bae, S. Fukushima, A. Harad, K. Kataoka, *Angew. Chem.* **2003**, *115*, 4788 – 4791; *Angew. Chem. Int. Ed.* **2003**, *42*, 4640 – 4643.

[25] An alternative name for adriamycin (ADR) is doxorubicine (DOXO).

[26] L. W. Seymour, Y. Miyamoto, H. Maeda, M. Brereton, J. Strohalm, K. Ulbrich, R. Duncan, *Eur. J. Cancer* **1995**, *31*, 766 – 770.

[27] S.-E. Stiriba, H. Frey, R. Haag, *Angew. Chem.* **2002**, *114*, 1385 – 1390; *Angew. Chem. Int. Ed.* **2002**, *41*, 1329 – 1334.

[28] a) G. R. Newkome, C. N. Moorefield, G. R. Baker, M. J. Saunders, S. H. Grossman, *Angew. Chem.* **1991**, *103*, 1207 – 1209; *Angew. Chem. Int. Ed. Engl.* **1991**, *30*, 1178 – 1180; b) J. F. G. A. Jansen, E. M. M. de Brabander-van den Berg, E. W. Meijer, *Science* **1994**, *266*, 1226 – 1229; c) S. Stevelmans, J. C. M. van Hest, J. F. G. A. Jansen, D. A. F. J. van Boxtel, E. M. M. de Brabander-van den Berg, E. W. Meijer, *J. Am. Chem. Soc.* **1996**, *118*, 7398 – 7399; d) A. P. H. J. Schenning, C. Ellissen-Roman, J.-W. Weener, M. W. P. L. Baars, S. J. van der Gaast, E. W. Meijer, *J. Am. Chem. Soc.* **1998**, *120*, 8199 – 8208; e) V. Chechik, M. Zhao, R. M. Crooks, *J. Am. Chem. Soc.* **1999**, *121*, 4910 – 4911; f) A. Sunder, M. Krämer, R. Hanselmann, R. Mülhaupt, H. Frey, *Angew. Chem.* **1999**, *111*, 3758 – 3761; *Angew. Chem. Int. Ed.* **1999**, *38*, 3552 – 3555; g) C. Kojima, K. Kono, K. Maruyama, T. Takagishi, *Bioconjugate Chem.* **2000**, *11*, 910 – 917; h) M. Liu, K. Kono, J. M. J. Fréchet, *J. Controlled Release* **2000**, *65*, 121 – 131; i) A. W. Kleij, R. van de Coevering, R. J. M. Klein Gebbink, A.-M. Noordman, A. L. Spek, G. van Koten, *Chem. Eur. J.* **2001**, *7*, 181 – 192; j) S.-E. Stiriba, H. Kautz, H. Frey, *J. Am. Chem. Soc.* **2002**, *124*, 9698 – 9699; k) C. Kojima, Y. Haba, T. Fukui, K. Kono, T. Takagishi, *Macromolecules* **2003**, *36*, 2183 – 2186.

[29] J. F. G. A. Jansen, E. W. Meijer, *J. Am. Chem. Soc.* **1995**, *117*, 4417 – 4418.

[30] G. Pistolis, A. Malliaris, D. Tsiourvas, C. M. Paleos, *Chem. Eur. J.* **1999**, *5*, 1440 – 1444.

[31] a) Z. Sideratou, D. Tsiourvas, C. M. Paleos, *Langmuir* **2000**, *16*, 1766 – 1769; b) H. Stephan, H. Spies, B. Johannsen, C. Kauffmann, F. Vögtle, *Org. Lett.* **2000**, *2*, 2343 – 2346.

[32] M. Krämer, J.-F. Stumbé, H. Türk, S. Krause, A. Komp, L. Delineau, S. Prokhorova, H. Kautz, R. Haag, *Angew. Chem.* **2002**, *114*, 4426 – 4431; *Angew. Chem. Int. Ed.* **2002**, *41*, 4252 – 4256.

 © 2004 Wiley-VCH Verlag GmbH & Co. KGaA, Weinheim

Organometallic Reactions

Chiral Tertiary Alcohols Made By Catalytic Enantioselective Addition of Unreactive Zinc Reagents to Poorly Electrophilic Ketones?

*Diego J. Ramón and Miguel Yus**

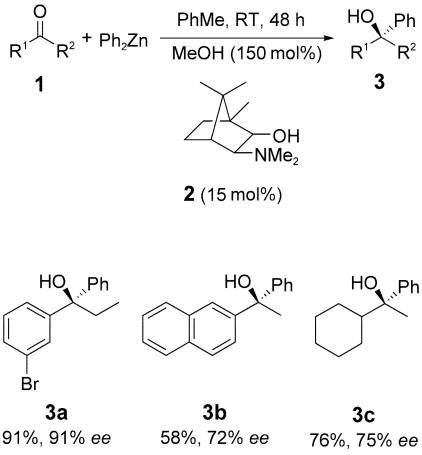
Keywords:
alcohols · asymmetric catalysis · C–C coupling · enantioselectivity · zinc

Nowadays, the generation of tertiary carbon-atom stereocenters can be achieved easily in most cases by using the appropriate chiral auxiliary, reagent, or catalyst. However, the approach to complex compounds bearing quaternary stereocenters, such as tertiary alcohols and related systems, is still a challenge for synthetic organic chemists, and every enantioselective procedure for the construction of a fully substituted carbon center is of great value.[1] Among the different approaches for the synthesis of this type of compound, such as kinetic resolution, enantioselective desymmetrization, oxidation, cyclization, electrophilic alkylation, and nucleophilic addition, those which involve stereoselective C–C bond formation are of particular interest, since one C–C bond and one stereoelement are created in only one synthetic step.

The simplest approach for the preparation of chiral tertiary alcohols is the enantioselective addition of organometallic reagents to a ketone.[2] Although there are several examples of the addition of organolithium[3] and Grignard[4] reagents to ketones, at least one equivalent of a generally expensive and difficult-to-prepare chiral ligand is compulsory in all cases. To reduce the amount of chiral ligand required, an organometallic reagent with lower nucleophilic character is usually considered. However, under these new conditions, and to guarantee the success of the reaction, the chiral system must determine not only the topological course of the reaction but also the chemical reaction itself. This new role of the catalyst system may be achieved by either activating the organometallic reagent or, in the most classical sense, by activating the carbonyl compound. Some catalyst systems are able to activate both the nucleophile and the carbonyl compound at the same time.[5]

Organozinc reagents are the ideal candidates for this type of reaction since their nucleophilic character is very low. In fact, it is well known that they do not add to aldehydes in noncoordinating solvents. This behavior has permitted the development of a plethora of chiral promoters[6] such as amino alcohols, diols, and disulfonamides, these two last type of compounds usually in combination with titanium tetraisopropoxide.[7] In this way the catalyzed enantioselective addition of organozinc reagents to aldehydes has been achieved with excellent enantioselectivity. However, the situation is more complicated when the electrophilic substrate in the reaction is a ketone. Ketones are less reactive electrophiles than aldehydes, and the addition does not take place even when promoters are used and the reaction is conducted at high temperatures. Either the starting ketone is recovered unchanged or products arising from the reduction of the ketone are obtained.[8]

That was the status until the beginning of 1998, when Dosa and Fu published the first catalytic enantioselective addition of a large excess of diphenylzinc to ketones **1** promoted by 3-*exo*-(dimethylamino)isoborneol (daib, **2**) in the presence of methanol to yield the corresponding chiral benzyl alcohols **3** with reasonable enantioselectivity (Scheme 1).[9,10] A simple mechanistic



Scheme 1. Phenylation of ketones according to Dosa and Fu. RT = room temperature.

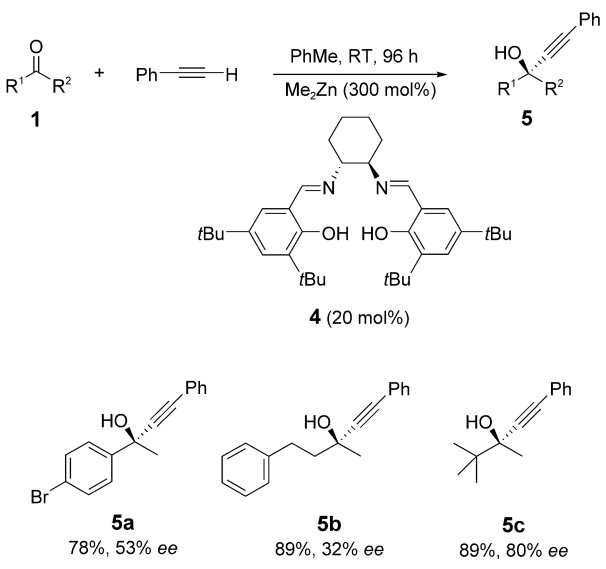
study showed that the catalytic cycle, as well as active species, should be similar to those described for the corresponding aldehyde reaction. A phenyl group is exchanged for a methoxide on the zinc atom of the chiral Lewis acid, and the chiral system activates the ketone and the zinc reagent simultaneously. The success of this reaction was attributed, on the one hand, to the increase of the Lewis acidity of the zinc atom due to the presence of a methoxide moiety, and, on the other hand, to the higher reactivity of diphenylzinc. This reagent does not

[*] Dr. D. J. Ramón, Prof. Dr. M. Yus
Departamento de Química Orgánica
Facultad de Ciencias
Universidad de Alicante
Apdo. 99, 03080-Alicante (Spain)
Fax: (+34) 96-590-3549
E-mail: yus@ua.es

 © 2004 Wiley-VCH Verlag GmbH & Co. KGaA, Weinheim DOI: 10.1002/anie.200301696

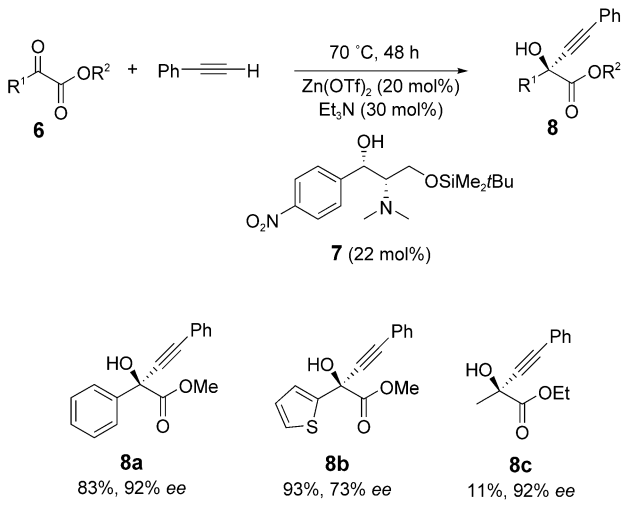
have hydrogen atoms in α-position, and consequently, the formation of zinc hydride and subsequent reduction processes are limited or prevented.

By following this approach Cozzi[11] has been able to perform the alkynylation of ketones with simple acetylene derivatives, excess dimethylzinc, and the chiral salen derivative **4** (Scheme 2). In this case, as previously mentioned, the activation by the active catalytic species takes place on both reagents. The chiral salen **4** is deprotonated to form the corresponding diphenolate–zinc system, which is acidic enough to chelate the ketone effectively. At the same time, one oxygen atom of the chiral ligand can chelate the alkynylzinc reagent, activating it and yielding the postulated catalytic active species.



Scheme 2. Alkynylation of ketones according to Cozzi.

A simpler alkynylation process was developed by Jiang's group.[12] They were able to carry out the alkynylation of α-ketoesters by using different substituted acetylenes as the nucleophile source and simultaneously as the solvent (Scheme 3). In this case, the zinc acetylide is formed as a reactive intermediate in the course of reaction. However, it is still unclear what is activated: the nucleophile, electrophile, or both. Nevertheless, it must be pointed out that the reaction works only for highly electrophilic ketones such as α-ketoesters, providing, in general, excellent results.



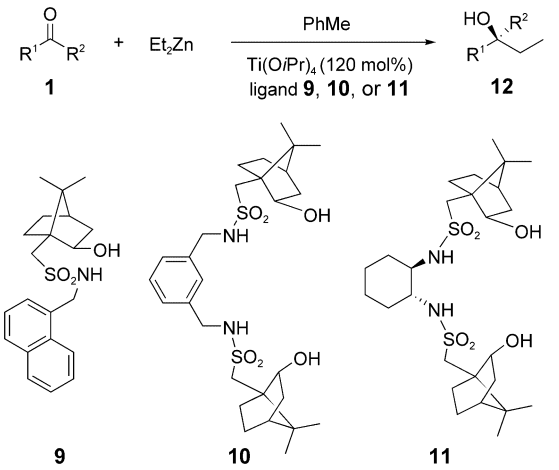
Scheme 3. Alkynylation of α-ketoesters according to Jiang and co-workers. Tf = CF_3SO_2.

Six years ago we found that hydroxycamphorsulfonamide **9** catalyzes the enantioselective addition of different simple dialkylzinc reagents to ketones in the presence of titanium tetraisopropoxide.[13] The reaction yielded the expected tertiary alcohols **12** with good-to-modest yields and enantioselectivities (Scheme 4). A preliminary mechanistic study showed: a) a small nonlinear effect (when a stoichiometric amount of the chiral ligand is used) which disappeared when the reaction was performed with substoichiometric amounts of the chiral ligand; b) the enantioselectivity was independent of chemical yield; and c) the enantioselectivity was highly dependent on the bulk of the ligand. All these facts were similar to those previously described for the known reaction with aldehydes. As a consequence, a similar catalytic cycle and species involved were proposed for this new reaction. In other words, the catalytic species was postulated to be a dinuclear titanium complex, in which one titanium atom bears the chiral ligand and the ketone and the other titanium atom bears the alkyl moiety, and the two metal centers are connected by two isopropoxy bridges.

The assumption of this dinuclear catalytic species calls our attention to the possibility of improving the ligand by eliminating the floppy isopropoxy bridges in the catalytic species. The new ligand would be able to bind to two titanium atoms at the same time. In this way, by playing with the length and angles of the covalent linker, we could approach both titanium atoms and place them at the ideal separation for this addition. In the screening of different diamines as the covalent linker, *o*-xylylendiamine emerged as the best one. The chiral ligand **10** synthesized with this linker led to improved results, and this improvement depended on the reaction conditions.[14] However, the results with ketones were not as good as those with aldehydes, which encouraged further improvement of the chiral system.

The next idea was to use in the system a linker with less conformational freedom such as 1,2-cyclohexanediamine. Walsh's group,[15] coming from another starting point, and we,[16] as result of the aforementioned ideas, both independently synthesized *trans*-1,2-bis(hydroxycamphorsulfonamido)cyclohexane (hocsac, **11**). This ligand is an excellent promoter for the enantioselective addition of dialkylzinc reagents to any kind of ketones, even dialkyl ketones, with titanium tetraisopropoxide. The reaction is the fastest and the conditions are the mildest reported so

 © 2004 Wiley-VCH Verlag GmbH & Co. KGaA, Weinheim



	12a	12b	12c
9 (20 mol%) CaH_2, 4 °C, 96 h	63%, 84% *ee*	72%, 31% *ee*	79%, 76% *ee*
10 (10 mol%) RT, 48 h	75%, 86% *ee*	89%, 86% *ee*	95%, 92% *ee*
11 (10 mol%) RT, 8 h	80%, 98% *ee*	90%, >99% *ee*	70%, 50% *ee*

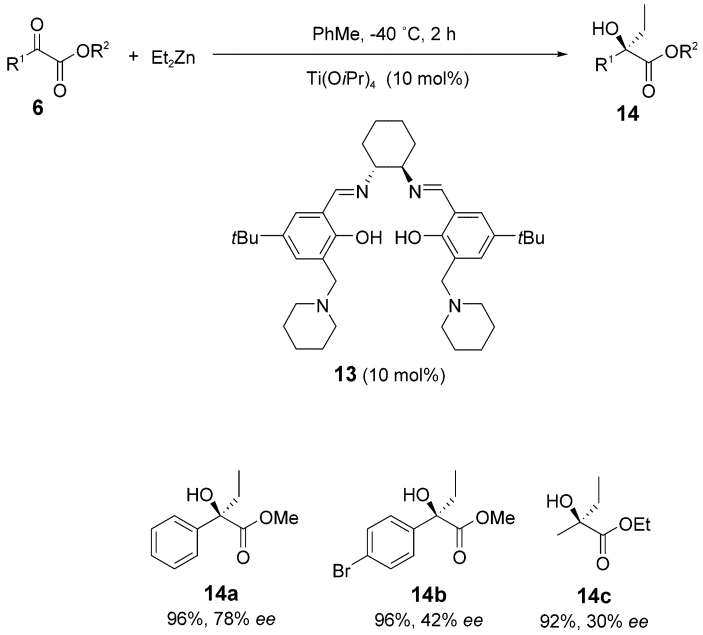
Scheme 4. Alkylation of ketones according to Ramón and Yus.

far. The results obtained were comparable to those for the related addition to aldehydes. For example, this ligand has been used to promote the addition of dimethylzinc to a functionalized α,β-unsaturated ketone (89% *ee*) in the asymmetric key step in the synthesis of (−)-frontalin.[17]

The hocsac ligand **11** works nicely not only for the addition of dialkylzinc reagents to ketones but also for the addition of related arylzinc reagents, and the enantioselectivity remains high (up to 96% *ee*).[18] The high enantioselectivity is maintained even when arylboronic acids were used as starting materials for the preparation of the corresponding arylzinc intermediates in situ.

The final example was reported by DiMauro and Kozlowski, who designed their chiral salen ligand **13** to be able to chelate at the same time one titanium atom, following alkoxy interchange on titanium tetraisopropoxide, and one zinc atom, through coordination of the nitrogen atom by diethylzinc (Scheme 5).[19] In this way the titanium Lewis acid center activates the α-ketoester by coordination to the carbonyl oxygen atom, while the nucleophile is activated at the same time. Although the reaction is described only for α-ketoesters, which are very electrophilic ketones, and the results are still far from excellent, this approach should impel the search for other, better catalytic ligands.

As corollary of the results presented along this short overview on the catalytic enantioselective addition of organozinc reagents to ketones, the answer to the question formulated in the title is now totally positive. The final objective of this article would be achieved if, and only if, it chemists can be motivated to apply this very useful addition to the synthesis of more complicated structures, and also develop new ligands as promoters for this promising reaction.



Scheme 5. Alkylation of α-ketoesters according to DiMauro and Kozlowski.

[1] a) K. Fuji, *Chem. Rev.* **1993**, *93*, 2037–2066; b) E. J. Corey, A. Guzmán-Pérez, *Angew. Chem.* **1998**, *110*, 402–415; *Angew. Chem. Int. Ed.* **1998**, *37*, 388–401; c) J. Christoffers, A. Mann, *Angew. Chem.* **2001**, *113*, 4725–4732; *Angew. Chem. Int. Ed.* **2001**, *40*, 4591–4597; d) J. Christoffers, A. Baro, *Angew. Chem.* **2003**, *115*, 1726–1728; *Angew. Chem. Int. Ed.* **2003**, *42*, 1688–1690.

[2] M. Yus, D. J. Ramón, *Recent Res. Dev. Org. Chem.* **2002**, *6*, 297–378.

[3] A. S. Thompson, E. G. Corley, M. F. Huntington, E. J. J. Grabowski, *Tetrahedron Lett.* **1995**, *36*, 8937–8940; b) A. S. Thompson, E. G. Corley, M. F. Huntington, E. J. J. Grabowski, J. F. Remenar, D. B. Collum, *J. Am. Chem. Soc.* **1998**, *120*, 2028–2038; c) L. Tan, C.-y. Chen, R. D. Tillyer, E. J. J. Grabowski, P. J. Reider, *Angew. Chem.* **1999**, *111*, 724–727; *Angew. Chem. Int. Ed.* **1999**, *38*, 711–712; d) M. A. Huffman, N. Yasuda, A. E. DeCamp, E. J. J. Grabowski *J. Chem. Soc.* **1995**, *60*, 1590–1594; e) G. S. Kauffman, G. D. Harris, R. L. Dorow, B. R. P. Stone, R. L. Parsons, J. A. Pesti, N. A. Magnus, J. M. Fortunak, P. N. Confalone, W. A. Nugent, *Org. Lett.* **2000**, *2*, 3119–3121.

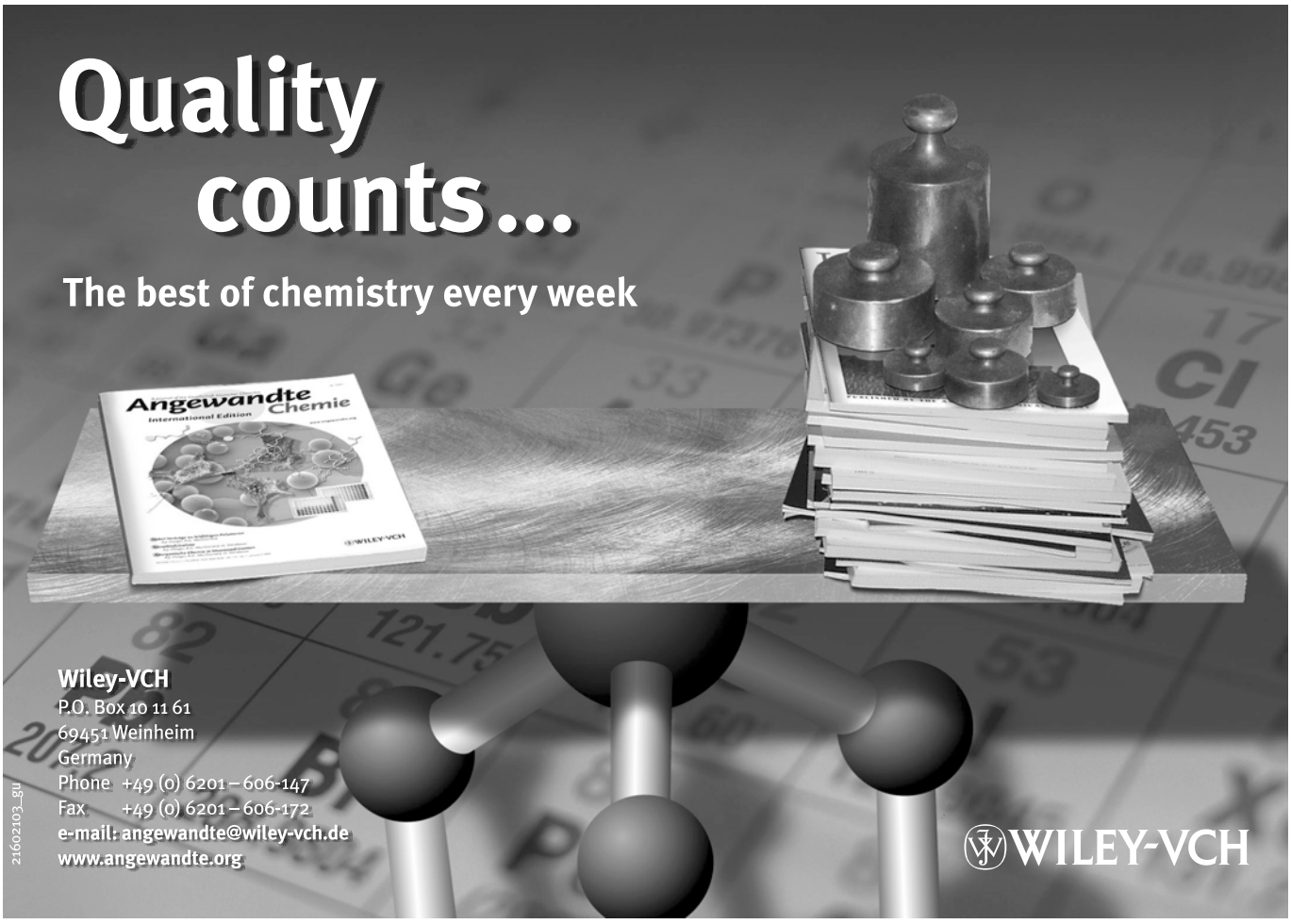
[4] a) B. Weber, D. Seebach, *Angew. Chem.* **1992**, *104*, 96–97; *Angew. Chem. Int. Ed. Engl.* **1992**, *31*, 84–86; b) B. Weber, D. Seebach, *Tetrahedron* **1994**, *50*, 6117–6128.

[5] a) H. Gröger, *Chem. Eur. J.* **2001**, *7*, 5246–5251; b) G. J. Rowlands, *Tetrahedron* **2001**, *57*, 1865–1882; c) S. Woodward, *Tetrahedron* **2002**, *58*, 1017–1050; d) M. Shibasaki, M. Kanai, K. Funabashi, *Chem. Commun.* **2002**, 1989–1999.

[6] a) R. Noyori, M. Kitamura, *Angew. Chem.* **1991**, *103*, 34–55; *Angew. Chem. Int. Ed. Engl.* **1991**, *30*, 49–69; b) K. Soai, T. Shibata in *Comprehensive Asymmetric Catalysis, Vol. II* (Eds.: E. N. Jacobsen, A. Pfaltz, H. Yamamoto), Springer, Berlin, **1999**, pp. 911–922;

 © 2004 Wiley-VCH Verlag GmbH & Co. KGaA, Weinheim

c) L. Pu, H.-B. Yu, *Chem. Rev.* **2001**, *101*, 757 – 824.
[7] D. J. Ramón, M. Yus, *Recent Res. Dev. Org. Chem.* **1998**, *2*, 489 – 523.
[8] a) J. Boersma in *Comprehensive Organometallic Chemistry*, *Vol. 2* (Ed.: G. Wilkinson), Pergamon, Oxford, **1982**, pp. 823 – 862; b) R. Noyori, S. Suga, K. Kawai, S. Okada, M. Kitamura, N. Oguni, T. Kanedo, Y. Matsuda *J. Organomet. Chem.* **1990**, *382*, 19 – 37; c) M. Watanabe, K. Soai, *J. Chem. Soc. Perkin Trans. 1* **1994**, 3125 – 3128; d) P. Knochel in *Encyclopedia of Reagents for Organic Synthesis*, *Vol. 3* (Ed.: L. A. Paquette), Wiley, Chichester, **1995**, pp. 1861 – 1866.
[9] P. I. Dosa, G. C. Fu, *J. Am. Chem. Soc.* **1998**, *120*, 445 – 446.
[10] For a review on catalyzed asymmetric arylation reactions, see: C. Bolm, J. P. Hildebrand, K. Muñiz, N. Hermanns, *Angew. Chem.* **2001**, *113*, 3382 – 3407; *Angew. Chem. Int. Ed.* **2001**, *40*, 3284 – 3308.
[11] P. G. Cozzi, *Angew. Chem.* **2003**, *115*, 3001 – 3004; *Angew. Chem. Int. Ed.* **2003**, *42*, 2895 – 2898.
[12] B. Jiang, Z. Chen, X. Tang, *Org. Lett.* **2002**, *4*, 3451 – 3453.
[13] a) D. J. Ramón, M. Yus, *Tetrahedron Lett.* **1998**, *39*, 1239 – 1242; b) D. J. Ramón, M. Yus, *Tetrahedron* **1998**, *54*, 5651 – 5666.
[14] M. Yus, D. J. Ramón, O. Prieto, *Tetrahedron: Asymmetry* **2003**, *14*, 1103 – 1114.
[15] a) C. García, L. K. LaRochelle, P. J. Walsh, *J. Am. Chem. Soc.* **2002**, *124*, 10970 – 10971; b) S.-J. Jeon, P. J. Walsh, *J. Am. Chem. Soc.* **2003**, *125*, 9544 – 9545.
[16] M. Yus, D. J. Ramón, O. Prieto, *Tetrahedron: Asymmetry* **2002**, *13*, 2291 – 2293.
[17] M. Yus, D. J. Ramón, O. Prieto, *Eur. J. Org. Chem.* **2003**, 2745 – 2748.
[18] a) O. Prieto, D. J. Ramón, M. Yus, *Tetrahedron: Asymmetry* **2003**, *14*, 1955 – 1957; b) During the revision of this Highlight, a report containing more examples of this reaction was published: C. García, P. J. Walsh, *Org. Lett.* **2003**, *5*, 3641 – 3644.
[19] a) E. F. DiMauro, M. C. Kozlowski, *J. Am. Chem. Soc.* **2002**, *124*, 12668 – 12669; b) E. F. DiMauro, M. C. Kozlowski, *Org. Lett.* **2002**, *4*, 3781 – 3784.



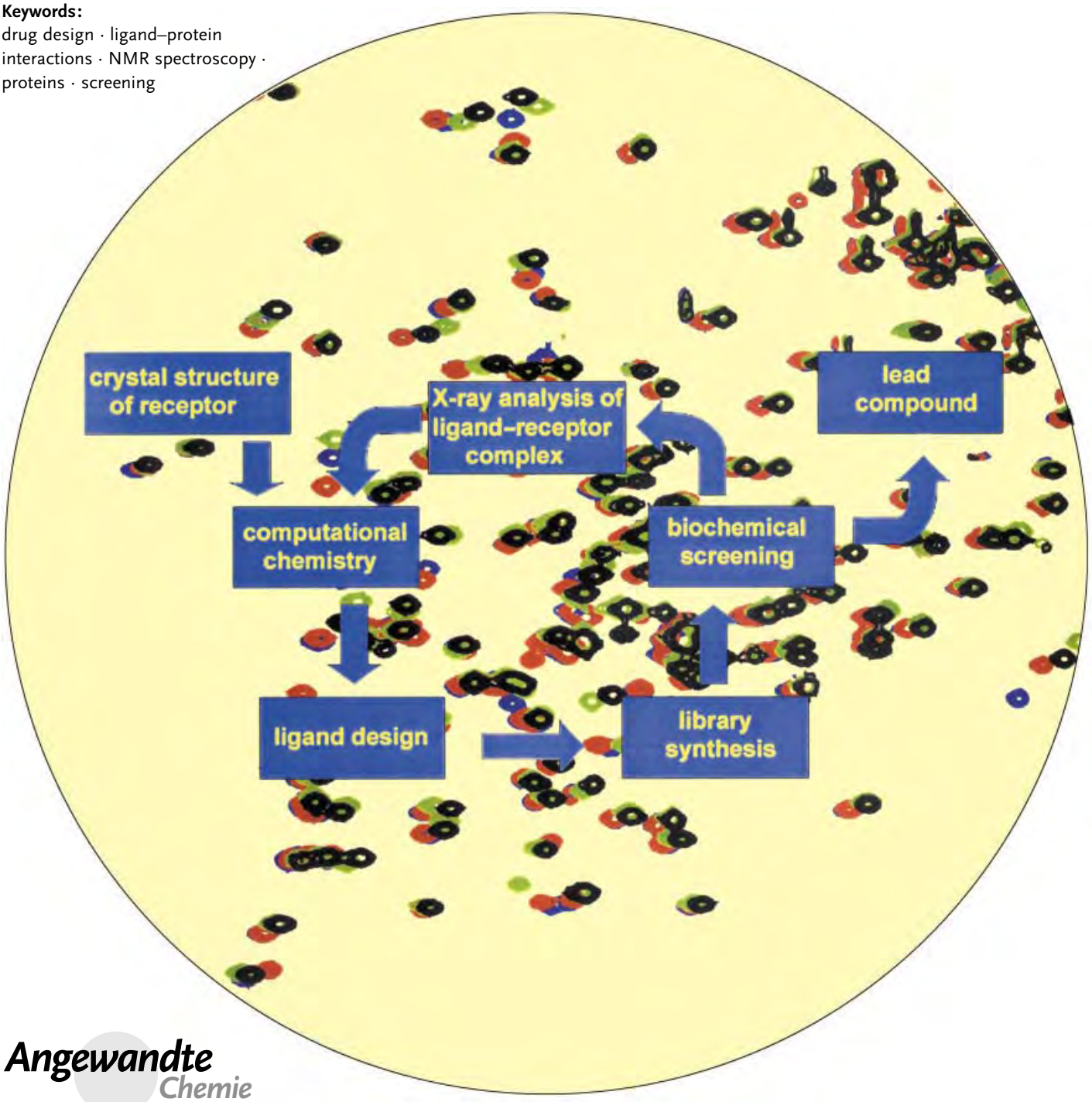
 © 2004 Wiley-VCH Verlag GmbH & Co. KGaA, Weinheim

NMR Spectroscopy of Biomolecules

NMR Spectroscopy Tools for Structure-Aided Drug Design

*Steve W. Homans**

Keywords:
drug design · ligand–protein interactions · NMR spectroscopy · proteins · screening



© 2004 Wiley-VCH Verlag GmbH & Co. KGaA, Weinheim
DOI: 10.1002/anie.200300581

Angewandte Chemie

Biomolecular NMR spectroscopy has expanded dramatically in recent years and is now a powerful tool for the study of structure, dynamics, and interactions of biomolecules. Previous limitations with respect to molecular size are no longer a primary barrier, and systems as large as 900 kDa were recently studied. NMR spectroscopy is already well-established as an efficient method for ligand screening. A number of recently developed techniques show promise as aids in structure-based drug design, for example, in the rapid determination of global protein folds, the structural characterization of ligand–protein complexes, and the derivation of thermodynamic parameters. An advantage of the method is that all these interactions can be studied in solution—time-consuming crystallization is not necessary. This Review focuses on recent developments in NMR spectroscopy and how they might be of value in removing some of the current "bottlenecks" in structure-based drug discovery.

From the Contents

1. Introduction	291
2. Determination of Protein Structure	291
3. Ligand Screening	294
4. Determination of Structures of Complexes	295
5. Molecular Dynamics and Ligand Design	297
6. Summary and Outlook	299

1. Introduction

The Human Genome Sequence project is providing a wealth of information on the products of gene expression, many of which have unknown function. The identification of the roles of these molecules and their interactions in the homeostasis of the cell will offer unprecedented opportunities for therapeutic intervention in disease. Similarly, the increasing numbers of pathogens whose genome sequences have now been described will open new avenues for the development of new antibiotics. This in turn has given rise to a dramatic expansion in the requirement for the 3D structures of proteins. Given the widening gap between the number of protein structures currently solved and the number of available protein sequences, it follows that rapid, robust methods for the determination of protein global folds are urgently required.

From the point of view of structure-based drug design, structure determination is only part of the process that gives rise to suitable lead compounds, as illustrated in the generic iterative cycle of Figure 1. This cycle of design, synthesis, evaluation, and structural analysis involves the determination of the structure of not only the protein target (or ideally the complex of the target with the natural ligand) but also a significant number of ligand–receptor complexes. Moreover, a suitable screening method is required to identify "active ligands", and ideally an understanding of the molecular basis of ligand affinity and specificity is required. It is not surprising given these requirements that a number of "bottlenecks" can occur in this cycle. With the advent of very powerful new methods based on NMR spectroscopy, the possibility now exists to overcome many of these difficulties. Specifically, NMR spectroscopic methods are now well-suited to address the four main aspects of the iterative cycle highlighted in Figure 1. An appraisal of these methods forms the subject of this review, with the focus principally on developments in the last decade. I apologize to those whose substantial earlier contributions are not accredited directly herein but which have already been reviewed adequately elsewhere.[1–8]

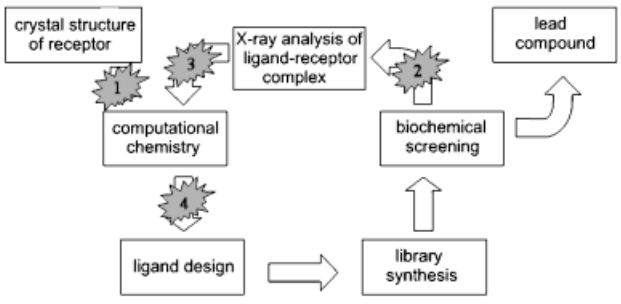


Figure 1. Iterative cycle for the discovery of lead compounds with some "bottlenecks". New NMR-based methods are ideally suited to improve the efficiency of 1) protein-structure determination, 2) ligand screening, 3) structural analysis of ligand–protein complexes, and 4) ligand design.

2. Determination of Protein Structure

2.1. The Problem

Despite a number of very significant advances in both protein crystallography and biomolecular NMR spectroscopy in recent years, the determination of the 3D structures of all but the smallest macromolecules is far from routine. Problems with protein overexpression aside, it is very difficult to predict a timescale for the production of diffraction-quality crystals of a given protein, and in the case of certain membrane proteins it is possible that this cannot be achieved at all in the foreseeable future. Although NMR-based approaches to

[*] Prof. S. W. Homans
School of Biochemistry and Molecular Biology
University of Leeds
Leeds, LS2 9JT (UK)
Fax: (+44) 113-343-3167
E-mail: s.w.homans@leeds.ac.uk

 DOI: 10.1002/anie.200300581 © 2004 Wiley-VCH Verlag GmbH & Co. KGaA, Weinheim

protein-structure determination do not suffer from this limitation, historically there are a number of significant obstacles to the use of this technique in a robust and automated manner. Foremost amongst these is the need to assign a substantial fraction of the resonances observed in NMR spectra in order to generate a list of pairwise nuclear Overhauser effect (NOE) distance restraints with which to determine the 3D structure of the molecule. It is well known that ideally ten or more such restraints per residue (amino acid) are required to obtain a "good" 3D structure. This restraints list will include side-chain- as well as backbone-derived restraints, and thus by definition side-chain resonance assignments are required—a time-consuming task that is not well-suited to automation. However, from the point of view of functional genomics, the determination of the protein global fold is, in principle, sufficient for the assignment of gene function based on 3D structure homology. Whereas a global fold is clearly insufficient for lead optimization, for which atomic-resolution structures are generally required, low-resolution structures may be adequate for "SAR by NMR" type screening, in which the protein is assigned but no 3D structure is available.

2.2. NOE-Based Methods

Given the time-consuming nature of side-chain assignment, it is not surprising that early attempts at the determination of protein global folds focused on the use of NOE restraints from the protein backbone. One of the most successful early attempts was reported by Mal et al.,[9] who used 155 backbone amide NOEs and seven tryptophan indole–backbone amide NOEs to determine the global fold of the Fyn SH3 domain. Importantly, the use of a perdeuterated, uniformly ^{15}N-enriched protein enabled NOE restraints to be measured between amide protons up to 0.7 nm apart, thus giving crucial long-range distance information with which to define the global fold. Despite the fact that only 162 restraints were used in total, a very respectable root mean square deviation (rmsd) for heavy atoms of 0.29 nm was obtained with respect to the crystal structure.

Recognizing that the accuracy of global-fold determination is highly topology-dependent, Kay and co-workers introduced a strategy based on the selective incorporation of protonated methyl groups in otherwise perdeuterated proteins[10] to increase the number of available conformational restraints. This approach with 287 amide–amide, methyl–amide, and methyl–methyl NOE restraints, gave a root mean square deviation (rmsd) of 0.44 nm for heavy atoms of PLCC SH2 domains with respect to the high-resolution solution structure. Overall, however, as indicated by Clore et al.,[11] attempts to define global folds using NOE data alone have been only partially successful, with an attainable accuracy between 0.25 and 0.7 nm for the backbone.

2.3. RDC-Based Methods

Clore et al. also demonstrated[11] that residual dipolar coupling (RDC) measurements can offer a significant improvement in coordinate accuracy when applied as restraints in concert with minimal NOE data sets such as those described in Section 2.2. Unlike NOEs, which provide distance restraints, RDCs provide direct *long-range* angular orientation information.

To see why this is the case, a brief digression into the theory of residual dipolar couplings is necessary. Formally, the dipolar coupling (D_{PQ}) between two nuclei P and Q is given by Equation (1), in which k is a constant that subsumes a

$$D_{PQ}(\theta,\phi) = -\frac{k}{r_{PQ}^3}[A_a(3\cos^2\theta - 1) + \frac{3}{2}A_r \sin^2\theta\cos 2\phi] \quad (1)$$

number of factors that are unimportant for the present discussion, r_{PQ} is the distance between P and Q, A_a and A_r are components of a mathematical function known as the alignment tensor $\boldsymbol{A}$, and θ and ϕ are cylindrical coordinates describing the orientation of the vector P–Q in the principal axis system of $\mathbf{A}$.

The meaning of this equation can be more easily understood by reference to Figure 2. For the purposes of the present discussion, the principal axis system of the alignment tensor can be thought of as an imaginary cartesian coordinate system that lies adjacent to the molecule of interest. If we now define nuclei P and Q as directly bonded NMR-active nuclei, then



Steve Homans obtained his D.Phil. in Biochemistry at the University of Oxford in 1982. He was a postdoctoral fellow with Prof. Raymond Dwek in Oxford, and thereafter relocated to the University of Dundee as a Lecturer in Biochemistry. In 1996 he became Professor of Biophysical Chemistry at the University of St. Andrews, and was elected Fellow of the Royal Society of Edinburgh in 1997. In 1999 he moved to the University of Leeds where he is now Professor of Structural Biology. His research interests include NMR spectroscopy of carbohydrates and proteins, and the dynamics and thermodynamics of protein–ligand interactions.

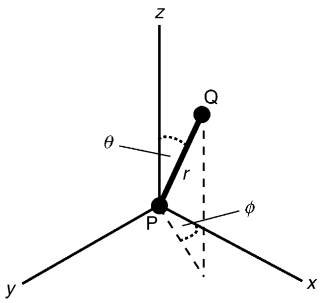


Figure 2. Dependence of the residual dipolar coupling D_{PQ} on the orientation of a bond vector P–Q in terms of cylindrical coordinates (r, θ, ϕ) in the principal axis system (x, y, z) of the orientation tensor.

 © 2004 Wiley-VCH Verlag GmbH & Co. KGaA, Weinheim

the distance r_{PQ} will be known since it is the covalent bond length, and the dipolar coupling D_{PQ} will depend on the orientation of the bond vector in the imaginary coordinate system (Figure 2). We can also determine A_a, A_r, and the orientation of the coordinate frame by using the observed residual dipolar couplings in the molecule.[12,13] Thus if we can measure D_{PQ}, then we can determine the orientation of the bond in the coordinate system. Importantly, the measured dipolar coupling for any NMR-active atom pair will be related to the bond-vector orientation with respect to the same imaginary coordinate system. Thus, bond-vector orientations located at opposite ends of a molecule will be related to each other through a common coordinate system, giving rise to the long-range angular orientation information described above. A minor complication that will be addressed later concerns the fact that more than one orientation of the bond vector can give rise to the same value of D_{PQ}.

The dipolar coupling is manifested in the NMR spectrum as a splitting of the resonance lines, analogous to scalar (J) couplings. However, in isotropic solution, all orientations of the bond vector contribute to the coupling owing to molecular tumbling, and the dipolar coupling averages to zero. In contrast, in the solid state, or under conditions in which the molecule is strongly aligned in some fashion, the dipolar coupling is very strong, and every NMR-active atom in the molecule exhibits a dipolar coupling to every other, despite the r^{-3} dependence of the interaction. The result is a spectrum that is impossible to interpret. Thus, to be of use for macromolecules, a method is required by which the molecule can be *weakly* aligned. Such a system was discovered by Tjandra and Bax, who realized that these dipolar couplings can be measured in dilute liquid-crystalline media.[14] Due to the weak alignment induced by these media, the observed dipolar couplings are a fraction of the strength of those observed in highly aligned systems, and are thus referred to as residual dipolar couplings (RDCs). Since the original observation of Tjandra and Bax, many such media appropriate for biological systems have now been described.[15–22] The availability of more than one medium is very important as the orientation of a given molecule will generally not be the same in two different media. This phenomenon can be used to overcome difficulties with multiple possible orientations of bond vectors mentioned above—it can be shown mathematically that the simultaneous solution of the dipolar coupling equation in two different alignment media (i.e. different alignment tensors) gives rise in general to a single unambiguous vector orientation.[23,24]

As RDCs can be measured in a straightforward fashion from splittings in NMR spectra, it is unsurprising that much attention has been focused in recent years on their use in protein global-fold determination. Mueller et al. developed a methodology for orienting peptide planes by using dipolar couplings, which was utilized to determine the global fold of maltose-binding protein in complex with β-cyclodextrin. This gave rise to pairwise rmsd values between N- and C-terminal domains of the NMR structure and the corresponding regions in the X-ray structure of 0.28 nm and 0.31 nm, respectively.[25,26] Fowler et al.[27] used N_i–H_i^N, H_i^N–H_i^α, H_i^N–$H_{i\pm1}^\alpha$, $H_i^N - H_{i+1}^N$ residual dipolar couplings together with a small number of backbone–side-chain NOEs to determine the backbone fold of the acyl-carrier protein to an rmsd between backbone atoms of 0.3 nm. Moreover, Hus et al.[28] used long-range order restraints available from paramagnetic systems in combination with residual dipolar couplings to define the fold of cytochrome c' in the complete absence of NOE restraints. Recently, the same group determined the global fold of ubiquitin to 0.1 nm rmsd for the backbone (residues 1–71)[29] with respect to the solution structure determined by conventional methods, using restraints derived solely from N_i–H_i^N, C'_{i-1}–N_i, C'_{i-1}–H_i^N, C_i^α–C'_i, C^α–H^α, and C^α–C^β residual dipolar couplings in two independent tensor frames. Excellent results were also obtained by use of residual dipolar couplings in concert with molecular fragment replacement.[30–33] Interesting recent developments include single-step determination of protein substructures[34] from residual dipolar couplings and simultaneous resonance assignment.[35]

Thus it can be seen that use of residual dipolar couplings either alone or in concert with a limited subset of NOE restraints can dramatically increase the accuracy of global-fold determination. Very recently, Giesen et al. demonstrated that it is possible to define the global fold of ubiquitin to an rmsd of 0.14 nm with respect to the crystal structure using only backbone residual dipolar coupling (N_i–H_i^N, N_i–C'_{i-1}, H_i^N–C'_{i-1}) and amide–amide NOE restraints[36] (Figure 3). Importantly, this approach is compatible with both perdeuteration[37] and selective backbone isotopic enrichment[38,39] and thus offers optimal sensitivity for larger proteins. The relative ease with which backbone resonance assignments can be obtained (in contrast to side-chain assignments) suggests that this approach may offer a very rapid route to global-fold determination.



Figure 3. Stereoview of the global fold of human ubiquitin determined by using backbone residual dipolar coupling restraints and long-range amide–amide NOE restraints (black) compared with the crystal structure (grey).[36]

The efficacy of this and other approaches for global-fold determination involving residual dipolar couplings is, however, likely to depend on topology. In proteins that contain a high α-helical content, it is likely that long-range amide NOE restraints will be sparse. In general, long-range NOEs are vital for correct fold determination because they introduce translational position information that is not contained in RDCs (unless all residue positions are defined precisely and uniquely). However, a small number of such NOEs may be sufficient. For example, Prestegard and co-workers[27] were able to derive the global fold of the acyl-carrier protein of

 © 2004 Wiley-VCH Verlag GmbH & Co. KGaA, Weinheim

E. coli by use of residual dipolar coupling measurements together with one backbone–backbone NOE and four backbone–side-chain NOEs. Similarly, the same authors determined the global fold of the NodF protein of *Rhizobium leguminosarum* with five backbone–backbone NOEs.

Clearly, the use of NOEs involving side-chain atoms requires the assignment of the latter, which could, in principle, dramatically increase the time required for the derivation of a global fold. However, since the number of required NOEs would appear to be small, the effort required for assignment can be reduced by careful choice of isotopic-labeling strategies based on residue type, in a manner analogous to that introduced by Kay and co-workers (Section 2.2).[10,40–43] Moreover, the recent demonstration that ^{1}H–^{1}H residual dipolar couplings can provide distance restraints of up to 0.7 nm in ubiquitin[44] suggests an alternative source of long-range restraints for global-fold determination.

2.4. Outlook

The use of residual dipolar couplings in concert with sparse NOE restraints offers a very promising route to the determination of protein structures at low to medium resolution. These structures will be entirely adequate for many structural genomics applications and for NMR-based screening. The barrier to obtaining high-resolution structures using this approach lies in the requirement for additional conformational restraints. This, in turn, dramatically increases the time and effort required to obtain the necessary resonance assignments. In this regard there is clearly significant potential for further optimization of isotopic-labeling strategies to facilitate and ideally automate this process.

3. Ligand Screening

3.1. The Problem

Ligand design is an imprecise art. One reason for this is that, despite enormous advances in techniques for structure determination, our knowledge of the factors that govern affinity and specificity of biomolecular interactions is very rudimentary. Fundamental thermodynamics tells us that the affinity is not governed by structure alone, but is a complex interplay between structure and dynamics (see Section 5). Thus, although a high-resolution structure of the ligand–protein complex is unquestionably thought-provoking in the context of ligand design, the probability that an effective lead compound can be designed on the basis of this structure is very small. One way to overcome this deficiency is to synthesize not one ligand, but many diverse ligands based on a common scaffold, that is, a focused combinatorial library. This gives rise to the need for a suitable screening assay. The NMR chemical shift is an exquisitely sensitive probe of chemical environment and hence biomolecular interaction, and a number of effective NMR-based screening techniques have been described in recent years. These are outlined briefly below. The reader is referred to the recent review of Meyer and Peters for a more detailed account of these methods.[45]

3.2. Methods Based on Protein Resonances

One of the simplest yet most effective NMR-based screening strategies, introduced by Fesik and co-workers, is 2D ^{1}H,^{15}N-heteronuclear single quantum coherence (HSQC) spectroscopy.[46–48] By uniformly enriching the protein with ^{15}N, which is usually straightforward and inexpensive, only the protein resonances are visible in such spectra, and hence the candidate ligand (or ligands, which could be small molecules or other macromolecules) can be included at relatively high concentrations. By comparison of the HSQC spectra of a reference spectrum of the ligand-free protein with a similar spectrum acquired in the presence of ligand(s), information on binding can be obtained from the resonance shifts between the two spectra. A number of candidate ligands, typically ten, can be included in any given sample, and the active ligand can be deconvoluted by further HSQC experiments if a "hit" is obtained. The chemical shifts of protein amide resonances are very sensitive to bound ligands and hence the HSQC approach is a very effective method for the assay of ligands that bind only very weakly ($K_d \leqslant 1$ mM).

Shuker et al.[46] used this method to advantage in a lead-generation approach that effectively covalently links two weakly binding ligands located in adjacent binding sites. Clearly, structural information on the protein is required to apply this technique—in the absence of a crystal structure, an NMR-derived global fold may be sufficient (see Section 2).

Figure 4 illustrates the extreme sensitivity of the HSQC approach. This figure shows a superimposition of the ^{1}H,^{15}N-HSQC spectra of a number of related pyrazine ligands bound to a sample of uniformly ^{15}N-enriched mouse major urinary protein. In this example, both resonance assignments[49] and crystal structures[50,51] are available for the protein, so that it is

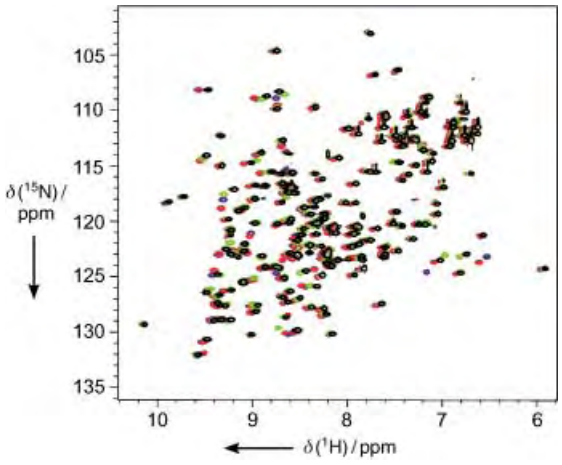


Figure 4. Overlayed ^{1}H,^{15}N-HSQC spectra of uniformly ^{15}N-enriched mouse major urinary protein bound to four related ligands. Blue: 2-methoxypyrazine, red: 2-methoxy-3-methylpyrazine, green: 3-isopropyl-2-methoxypyrazine, black: 3-isobutyl-2-methoxypyrazine.

 © 2004 Wiley-VCH Verlag GmbH & Co. KGaA, Weinheim

a simple matter to identify binding-site residues. By measuring shift differences between spectra,[52] it is also possible to obtain information on the locations of the various aliphatic side chains of the various ligands within the binding site, which agree closely with structural data for related ligands.[51,53]

In terms of simplicity, ease of use, and affordability, the HSQC approach would appear to be a very attractive route to ligand screening. Although this technique is in no way a "high-throughput" approach, it is particularly valuable for screening weakly-binding ligands, which can readily be missed in conventional biochemical assays. Moreover, straightforward measurement of chemical shift changes versus ligand concentration[54] or application of diffusion-based methods[55] enables ligand-binding constants to be measured.

A related approach for ligand screening involves ^{13}C isotopic enrichment of methyl groups on protein side chains. Although ^{13}C isotopic enrichment would typically be considered prohibitively expensive for screening purposes, given the relatively large amounts of protein required, Fesik and co-workers devised an ingenious approach for the selective ^{13}C labeling of side-chain methyl groups by using inexpensive $^{13}CH_3I$.[56] A major advantage of this $^{13}CH_3$-based screening is that $^{1}H,^{13}C$-HSQC is considerably more sensitive than $^{1}H,^{15}N$-HSQC for a given sample concentration. Typically, threefold higher sensitivity is obtained for proteins < 30 kDa, enabling $^{1}H,^{13}C$-HSQC spectra to be acquired on a 50 μM sample of protein in 10 min. Moreover, the use of selective methyl labeling in combination with deuterium enrichment enables screening of protein targets in excess of 100 kDa. The availability of cryoprobe technology at intermediate to high fields promises to widen still further the scope for NMR-based screening, with the possibility of natural-abundance ^{13}C spectroscopy on the horizon.

3.3. Methods Based on Ligand Resonances

While very effective, the approaches described in Section 3.2 do not provide any information on which ligand binds to the target protein, except in trivial cases in which only one ligand is present in a given sample. Moreover, no information is obtained on the "active" chemical groupings of the ligands that are located in and interact with the binding site of the target protein. However, this information can be derived with NMR spectroscopy by using NMR techniques that detect ligand resonances.

One simple approach to detect which ligand (out of a small set of (typically) ten ligands) undergoes binding is to exploit the difference in the relaxation properties or translational diffusion coefficient of the free ligand with when it binds to the target protein. This can be achieved by using simple 1D NMR experiments designed to measure T_2 relaxation times or diffusion coefficients.[57] A related technique exploits the fact that NOEs for bound ligands are typically large and negative whereas for free ligands they are very small.[58] In the fast-exchange regime, that is, relatively weak binding, these so-called transferred NOEs (TRNOEs) can readily be measured by using homonuclear 2D NMR techniques. Importantly, it is not necessary to isotopically enrich either the ligand or the protein in order to record these data. This is because it is possible to work with relatively high ligand/protein ratios (typically 15:1), whereby the relatively narrow ligand resonances can easily observed above the much broader background protein resonances.

To determine the "active" regions of a given ligand, a simple 1D NMR experiment termed saturation transfer difference (STD) can be applied.[59,60] This technique relies on the fact that in large complexes, proton magnetization is very efficiently transferred throughout the molecule or molecules owing to a process known as spin diffusion. Hence, if a region of the NMR spectrum of the complex containing resonances for the protein (but not for the ligand) is saturated (i.e. the magnetization is attenuated) by application of a radiofrequency field, this saturation will be efficiently transferred through the protein and also to resonances of the ligand that are located within the protein-binding site. This technique has proven remarkably successful at mapping the active regions of ligands and can also be used as a simple screening tool.

One situation in which the above approaches might fail concerns ligands that bind strongly to the protein of interest. Under these circumstances, the chemical-exchange phenomena on which the above methods depend are not on the appropriate timescales. However, under these circumstances, NMR reporter screening can be applied. The basis of this approach is quite straightforward: During acquisition of spectra of the free protein and of the protein in the presence of ligand(s), a "reporter-ligand" that is known to bind weakly to the protein is also included. When a ligand that binds more tightly than the reporter ligand is present in the sample, the binding event can be detected by changes in intensity and line-width of the latter—these will change as the fraction of free reporter ligand in solution increases as it is displaced from the binding site of the protein.[61,62]

3.4. Outlook

NMR-based screening is now an established tool in structure-based drug design. One field that is likely to benefit greatly from NMR approaches is "interactome" research, that is, characterization of protein–protein interactions in the genome. With the recent spectacular demonstration by Wuthrich and co-workers that interactions within the 900-KDa complex of GroEL–GroES can be studied[63] by using transverse relaxation optimized spectroscopy (TROSY),[64] molecular size is unlikely to limit the future usefulness of NMR spectroscopy in this application.

4. Determination of Structures of Complexes

4.1. The Problem

The lead discovery and optimization cycle of Figure 1 requires that the structures of a number of candidate ligand–protein complexes are solved. This necessarily must be done

 © 2004 Wiley-VCH Verlag GmbH & Co. KGaA, Weinheim

as rapidly as possible. In this respect X-ray crystallography, although capable of providing high-resolution structures, is not ideal owing to the difficulty in predicting the timescale of crystallization of these complexes. High-resolution NMR spectroscopy offers a useful alternative, not least because it is possible to determine, from simple trial experiments, whether structure determination of a given complex is achievable, and an approximate timescale for the process. However, the NMR approach has in the past suffered from a number of limitations. Described below are a number of recent techniques designed to overcome these challenges.

4.2. NOE-Based Methods

Intuitively, the most obvious approach to structure determination of ligand–protein complexes involves NOE-based distance restraints in a manner analogous to protein-structure determination. However, many of the NOEs are intermolecular in nature and hence a number of useful approaches can be used to simplify the problem of identifying these NOEs from amongst the plethora of intramolecular NOEs from the protein. Essentially, these approaches all rely on the fact that only the protein or the ligand is isotopically enriched. As the former is much easier to achieve by using recombinant DNA technology, the majority of techniques have been designed accordingly.

Early experiments[65,66] utilized ^{15}N-enriched proteins and enabled the selective observation of NOEs between protons attached to ^{15}N and protons attached to ^{14}N, thus suppressing both protein–protein and ligand–ligand NOEs. Whereas the selection of protons attached to ^{15}N or ^{13}C (isotope editing) is very straightforward in a background that contains a natural abundance of ^{15}N or ^{13}C, this is not true for the selection of protons attached to ^{14}N or ^{12}C in a background that is ^{15}N or ^{13}C. The problem derives from the fact that suppression of protons attached to ^{15}N or ^{13}C is achieved by exploiting the scalar one-bond coupling between the proton and the heteronucleus ($^1J_{N,H^N}$ or $^1J_{C,H}$), whereby the magnetization is "nulled" by using a suitable time delay during the sinusoidal evolution of magnetization under the influence of this coupling. Unfortunately, scalar couplings differ between chemical groups, and hence a delay that nulls protons of a given type is only partially effective for protons of another type. The net result is that early isotope-filtration experiments with isotopically-enriched proteins suffered from substantial breakthrough of protein-derived magnetization.

These problems have been largely overcome in a series of 3D NMR experiments described by Kay and co-workers,[67] who used a novel delay period involving frequency-swept ("chirp") refocusing pulses to compensate for nonuniform scalar couplings. These techniques are very effective at enabling even weak ligand–protein NOEs to be observed with practically no interfering protein resonances (Figure 5).

In addition to the measurement of intermolecular NOEs, intramolecular NOEs are useful for the determination of the bound-state conformation of the ligand. The simplest approach for the measurement of these NOEs is to use isotope editing in combination with isotopically enriched ligands.[68–70] However, in all but ideal cases, the synthetic effort and isotope costs involved in the preparation of ^{13}C-enriched ligands is prohibitive. As an alternative, perdeuteration of the protein in combination with homonuclear ^{1}H NMR methods enables interligand NOEs to be observed.[71] Perdeuteration offers the advantage that large complexes can be determined, since the absence of non-exchangeable protons in the protein significantly reduces transverse relaxation of ligand protons.

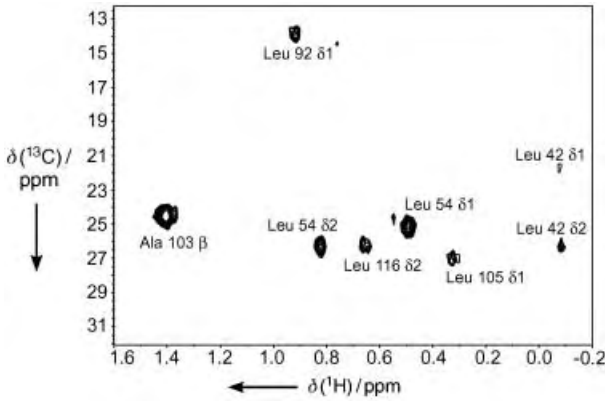


Figure 5. 2D plane from the 3D ^{13}C isotope-filtered NMR spectrum of unlabeled 3-isobutyl-2-methoxypyrazine bound to uniformly ^{13}C-enriched mouse major urinary protein. The slice is taken at the ^{1}H resonance frequency of the magnetically equivalent methyl protons two isobutyl groups. Cross-peaks arise from ^{1}H–^{1}H NOEs between these methyl protons and the indicated side chains of residues within the binding site of the protein.

4.3. RDC-Based Methods

Despite technical advances such as those described in the previous section, it is impossible to obtain sufficient NOE restraints between a protein and a ligand to define the structure of the complex at a resolution competitive with the best crystal structures. However, the use of RDC measurements promises to revolutionize the technique. As mentioned in Section 2, RDC-based restraints provide long-range orientational information. It is thus possible to determine the bound-state conformation of a ligand in the complete absence of ligand–protein or ligand–ligand NOEs.[72–74] Typically, backbone amide ^{15}N–^{1}H RDCs are measured for the protein in a dilute liquid-crystalline medium, and the magnitude and direction of the alignment tensor is determined from these values by using structural coordinates for the protein obtained either by X-ray crystallography or NMR spectroscopy.[13,75] Residual dipolar couplings are then measured for the free ligand under the same conditions to obtain the "inherent" RDCs before binding. These will be typically much smaller than those of the protein owing to the much lower degree of alignment observed for small molecules. In most cases, the measurements of choice for the ligand will be one-bond ^{13}C–^{1}H RDCs. To facilitate their measurement, most studies to date have employed ^{13}C-enriched ligands in combination with isotope editing. Finally, the ligand is combined with the

 © 2004 Wiley-VCH Verlag GmbH & Co. KGaA, Weinheim

protein under the same solution conditions, and the ligand RDCs are remeasured. In the case of weak binding, when the protein is not saturated with ligand, the ligand is titrated with the protein and RDC measurements are taken at different ligand/protein ratios. The effective RDC values for the ligand in the complex are then obtained by extrapolation to 100%-bound ligand, after subtraction of the inherent RDCs for the free ligand. The bound ligand will adopt the alignment tensor of the protein in the complex and hence the orientation of the ligand with respect to the protein can be determined from the latter RDCs.

One limitation of this approach is that the synthesis of ^{13}C-enriched compounds can be time-consuming and costly, and is effectively impossible in any practical lead-discovery and optimization strategy. A further disadvantage of this approach is that in the slow-exchange limit (strong binding, $K_d > 10^{-5}$ M), resonance linewidths become unacceptably large owing to efficient dipolar relaxation between ^{13}C and ^{1}H. Nonetheless, with the availability of cryoprobes for high-field spectrometers, it may be possible to record HSQC spectra of weakly aligned complexes with natural-abundance ^{13}C, thus enabling RDCs to be measured in unlabeled ligands complexed to ^{15}N,^{2}H-enriched proteins.[76]

4.4. Outlook

Given the modest time efficiency of X-ray crystallography for solving multiple ligand–protein complex structures, the NMR approach offers a highly attractive alternative. However, it will be necessary to overcome the current size limitation by judicious use of labeling strategies for the protein, which will necessarily involve substantial deuteration. One area that holds particular promise is the use of homonuclear ^{1}H–^{1}H RDCs[77–79] in a perdeuterated protein background, since protons attached to ^{12}C have workable linewidths under these conditions, even for large complexes.

5. Molecular Dynamics and Ligand Design

5.1. Relevance of Dynamics

Although the crystal structure or NMR-derived structure of a protein is unquestionably thought-provoking in the process of lead discovery, the key to understanding the affinity of a ligand for its receptor lies in the dynamics and thermodynamics of the association rather than in a simple static picture. This can be understood by reference to simple concepts in thermodynamics (Figure 6): The Gibbs energy of binding (ΔG_b) of a ligand to a protein is equal to the difference between the free energies of the free species and the free energy of the complex. As a result of the relation $\Delta G = \Delta H - T\Delta S$, a flexible ligand (higher conformational entropy) will have a lower Gibbs energy than a rigid ligand. As the standard Gibbs energy of binding is related to affinity by the well-known relation $\Delta G^\circ_b = -RT\ln K_a = RT\ln K_d$. It follows that a rigid ligand will bind more tightly than a flexible ligand, all other factors being equal. Exactly the same

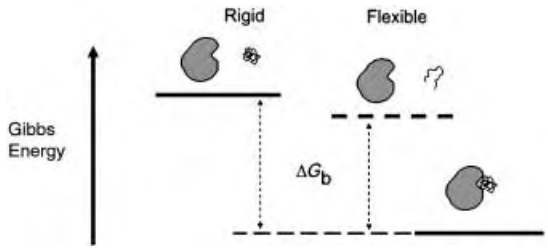


Figure 6. Thermodynamic origin of the difference in affinity between a "rigid" ligand and a "flexible" ligand.

argument can be used with respect to "flexible" side chains in the binding sites of proteins.

It thus follows that we must have information on the dynamics (which determine the entropy) of an interaction as well as structural aspects (which determine enthalpy). In a "real" system we must also consider the solvent. With the advent of new technologies such as isothermal titration calorimetry (ITC), it is possible under ideal circumstances to obtain reliable experimental data on the global thermodynamic parameters that govern a biomolecular association. As an example, Table 1 shows ITC-derived thermodynamic parameters for the binding of a series of pyrazine ligands to the mouse major urinary protein. This table illustrates a number of interesting features: 1) The rank order of binding of the ligands differs depending on whether we consider only enthalpy (i.e. no entropy) or Gibbs energy (i.e. with entropy), which further emphasizes the need to consider both structure and dynamics. 2) The difference in Gibbs energy between micromolar and nanomolar dissociation constants is ≈ 4 kcal mol^{-1}. Thus the difference between a "mediocre" ligand and a "good" ligand equates to approximately one hydrogen bond. 3) These global thermodynamic parameters, while accurately quantifying binding in thermodynamic terms, do not readily tell us why one ligand binds better than another. From the point of view of ligand optimization, it would be of immeasurable benefit to obtain these thermodynamic parameters experimentally on a per-residue rather than on a global basis. In several important recent papers,[80–83] new NMR methodologies are described by which standard Gibbs energies and entropies of binding can be derived on a per-residue basis from NMR relaxation data, thus offering a

Table 1: Thermodynamic parameters for the binding of the listed ligands to the mouse major urinary protein determined from isothermal titration calorimetry experiments.

Ligand	ΔH° [kcal mol^{-1}]	ΔS° [cal K mol^{-1}]	ΔG° [kcal mol^{-1}]	K_d [μM]
3-methylpyrazine	−9.99	−16.4	−5.1	185
2-methoxypyrazine	−10.03	−14.5	−5.7	67
2-methoxy-3-methyl-pyrazine	−8.44	−7.2	−6.3	25
3-isopropyl-2-methoxy-pyrazine	−9.14	−2.0	−8.53	0.56
3-isobutyl-2-methoxy-pyrazine	−11.85	−7.4	−9.65	0.08

 © 2004 Wiley-VCH Verlag GmbH & Co. KGaA, Weinheim

means by which the thermodynamic behavior of ligand–protein interactions can be characterized at a level of detail that has until now not been possible.

5.2. Backbone Dynamics

Isotopic enrichment of proteins enables the measurement of heteronuclear (^{15}N, ^{13}C, or ^{2}H) relaxation times.[84] In general, these heteronuclei are chosen in preference to protons because the latter exhibit very complex relaxation properties under certain circumstances. In particular, uniform ^{15}N enrichment enables straightforward measurement of amide ^{15}N relaxation times, which can be used to probe the dynamics of N–H^N bond vectors in the protein backbone. These relaxation times are referred to as the longitudinal (T_1) and transverse (T_2) relaxation times. The reciprocal values T_1^{-1} and T_2^{-1} are a measure of the rates of decay of the NMR signal along the direction of the applied magnetic field and transverse to this field, respectively. Just as nuclear spins are excited from one energy level to another in NMR spectroscopy by the application of a radiofrequency field at the resonance frequency, relaxation from a higher energy level to the ground state also requires a magnetic field at the appropriate frequency. These fields derive from local dynamic fluctuations within the molecule, such as overall rotational tumbling and internal motions. Thus, by measurement of relaxation times, we can obtain information on the dynamic events that give rise to relaxation.

NMR relaxation times are usually interpreted in terms of the Lipari–Szabo model-free analysis,[85] so named because the relaxation properties can be related to dynamics in a manner that is largely independent of a model for the actual motion. The Lipari–Szabo formalism provides, among others, the square of the so-called generalized order parameter (S^2).[85] This parameter assumes a value of 1 for a bond vector that is completely immobile and a value of 0 for completely isotropic motion. Importantly, Yang and Kay elegantly showed that within certain well-defined approximations, an analytical relationship exists between the S^2 value for a given bond vector and the conformational entropy of that vector.[81] Thus, for example, by measurement of backbone ^{15}N-relaxation parameters for a given protein in the absence and presence of ligands, differences in S^2 values can be estimated as differences in conformational entropy, that is, entropy of binding, on a per-residue basis. In this manner, details of the thermodynamic behavior of ligand binding are available that cannot be obtained by any other technique.

A number of studies have involved the use of this approach in applications ranging from protein–DNA interactions[86] and conformational exchange in calmodulin[87] to protein folding.[81,88] From the perspective of drug design, an interesting example of the application of this approach concerns ligand binding to the major urinary protein described by Stone and co-workers.[89] They observed an increase in protein backbone conformational entropy on ligand binding, and concluded that this term is likely comparable in magnitude to other important Gibbs energy contributions to binding, and may represent a general mechanism in the binding of small ligands to macromolecules. Clearly, information of this kind is completely obscured in simple static pictures of proteins and protein–ligand complexes, yet may be of paramount importance in governing affinity.

5.3. Side-Chain Dynamics

The techniques described in the previous section can similarly be applied to the study of protein side-chain dynamics, with the nucleus of choice being ^{13}C or ^{2}H. In principle, ^{13}C–based measurements offer higher sensitivity,[90] but as discussed at length by Muhandiram et al.,[91] ^{2}H methods are often preferable in terms of ease of interpretation. However, ^{2}H methods do suffer from limitations in terms of molecular mass.[92] Most side-chain studies to date have focused on the dynamics of methyl groups. For technical reasons it is preferable to work with $^{13}CHD_2$ or $^{13}CH_2D$ isotopomers of methyl groups in ^{13}C- and ^{2}H-relaxation studies, respectively, which gives challenging isotopic-enrichment strategies. Partial isotopic enrichment with ^{2}H appears to be the most effective method for obtaining the relevant isotopomers for deuterium-relaxation studies. This can be achieved by overexpression in *E. coli* with uniformly labeled ^{13}C and 50 % ^{2}H enriched glucose as the sole carbon source.[91] Recently, useful methods were described by Torchia and co-workers based on protein overexpression in *E. coli* with ^{13}C,^{2}H-enriched pyruvate as the sole carbon source.[92,93] This approach yields protein samples with high contents of CH_2D and CHD_2 methyl isotopomers of Ala, Val, Leu, and Ile, which is suitable for both ^{2}H- and ^{13}C-relaxation measurements. Indeed, this approach has enabled a favorable comparison of order parameters of the methyl rotation axes obtained with ^{2}H and ^{13}C measurements on the same sample.[92]

A number of studies have employed the above approaches to study side-chain dynamics, with a view to estimating the entropy of rotamer exchange in proteins,[94] correlation of dynamics with local structure,[95] and the measurement of side-chain entropy changes upon formation of a calmodulin–peptide complex.[96] The latter work, discussed in detail by Cavanagh and Akke,[97] is potentially of great relevance to structure-based drug design. Importantly, separation was observed between backbone and side-chain response upon ligand binding—there is little change in the motional characteristics of the backbone, but both increases and decreases in entropy are observed along the side chains. In particular, certain side chains remote from the binding site experience increased entropy upon binding, thus negating, in part, the entropic penalty experienced upon ligand binding by other side chains within the binding site.

5.4. Outlook

Quantitative studies on protein backbone and side-chain entropies with NMR relaxation measurements are still at an early stage, but the results thus far are extremely encouraging. It does appear possible to obtain reasonable estimates of

 © 2004 Wiley-VCH Verlag GmbH & Co. KGaA, Weinheim

protein backbone and side-chain entropy differences upon ligand binding that agree with global thermodynamic data measured by other methods. In this respect, NMR techniques can potentially supply the missing piece in the thermodynamic "jigsaw puzzle" that characterizes ligand binding. The number of such studies is too small as yet to determine whether any patterns will emerge, but given the importance of entropy, or more particularly enthalpy–entropy compensation in biological recognition phenomena,[98–100] further work in this area is certainly warranted.

6. Summary and Outlook

Two decades ago NMR spectroscopy was regarded as a technique restricted to "small" molecules. Since that time, the technique has developed at an enormous pace—structure determinations of proteins in the 30–40-kDa range are becoming routine, and with the advent of higher magnetic fields, cryoprobe technology, and advances in isotopic-enrichment strategies, it is very likely that molecular mass will cease to be the major limitation. As a method that can simultaneously offer a route to determine structure, to screen ligands, and to probe dynamics, it is perhaps surprising that the approach has not been more widely used in the drug-discovery arena. However, many of the advances described in this Review are quite recent, and naturally it will take some time for these to be validated and accepted by the pharmaceutical industry. Of the applications described, the determination of per-residue entropy terms for a given biomolecular interaction is perhaps the most intriguing. Unlike protein crystallography, which can very usefully be applied in parallel to the NMR approach for structure determination and (increasingly) for ligand screening, NMR methods are uniquely able to provide this high-resolution "dynamic" picture of the interaction. Of course, the contribution of solvent is also potentially an important factor that governs affinity, but recent developments in nuclear magnetic relaxation dispersion measurements offer promise in this direction.[101]

The author gratefully acknowledges financial support from the Biotechnology and Biological Sciences Research Council (BBSRC) and the Wellcome Trust.

Received: February 7, 2003 [A581]

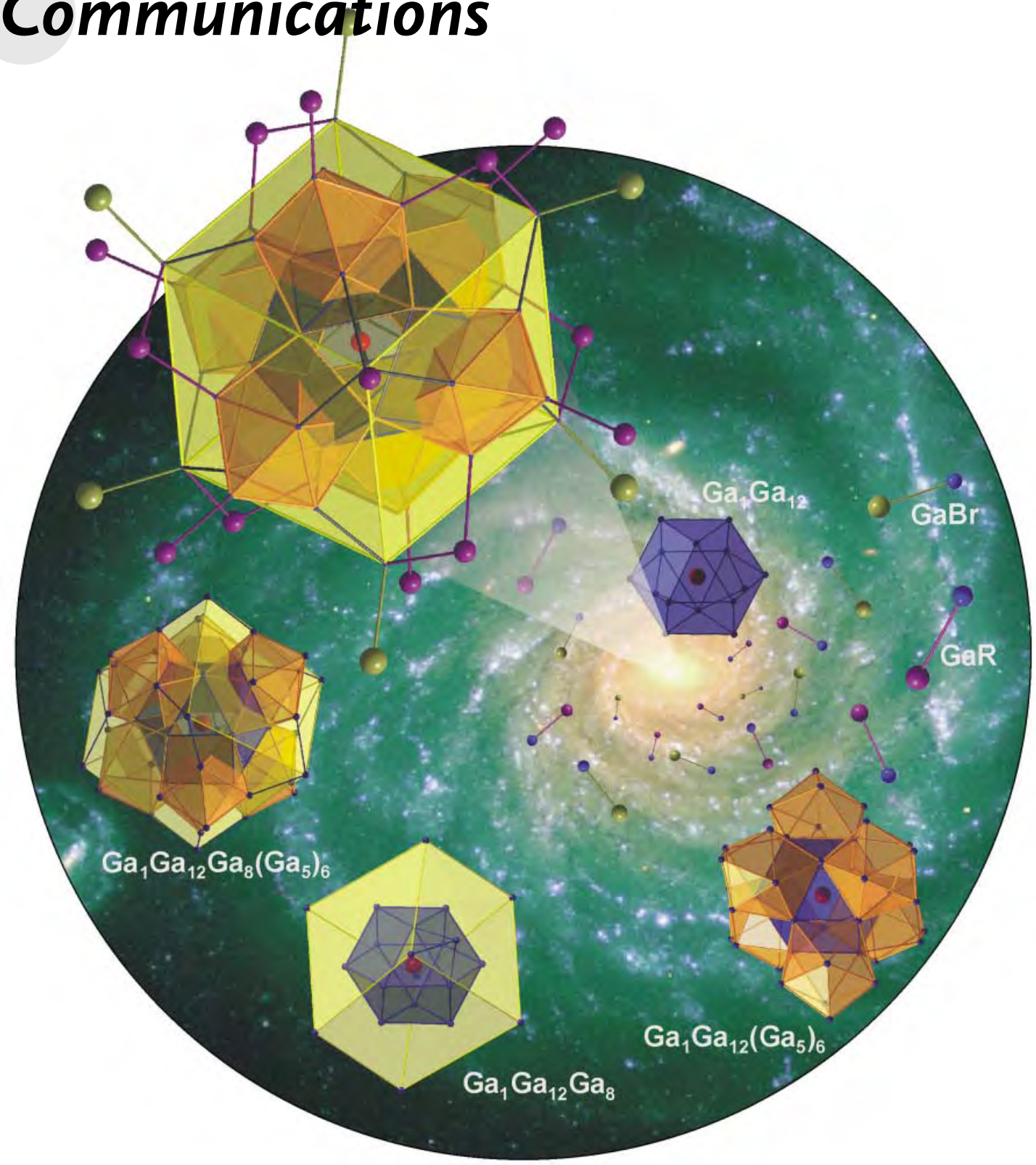
[1] J. H. Prestegard, H. Valafar, J. Glushka, F. Tian, *Biochemistry* **2001**, *40*, 8677.
[2] M. Sattler, J. Schleucher, C. Griesinger, *Prog. Nucl. Magn. Reson. Spectrosc.* **1999**, *34*, 93.
[3] G. M. Clore, A. Gronenborn, *Curr. Opin. Chem. Biol.* **1998**, *2*, 564.
[4] A. M. Gronenborn, G. M. Clore, *Crit. Rev. Biochem. Mol. Biol.* **1995**, *30*, 351.
[5] G. M. Clore, A. M. Gronenborn, *J. Protein Chem.* **1994**, *13*, 441.
[6] A. Bax, S. Grzesiek, *Acc. Chem. Res.* **1993**, *26*, 131.
[7] G. M. Clore, A. M. Gronenborn, *Science* **1991**, *252*, 1390.
[8] M. Pellecchia, D. S. Sem, K. Wüthrich, *Nat. Rev. Drug Discovery* **2002**, *1*, 211.
[9] T. K. Mal, S. J. Matthews, H. Kovacs, I. D. Campbell, J. Boyd, *J. Biomol. NMR* **1998**, *12*, 259.
[10] K. H. Gardner, M. K. Rosen, L. E. Kay, *Biochemistry* **1997**, *36*, 1389.
[11] G. M. Clore, M. R. Starich, C. A. Bewley, M. L. Cai, J. Kuszewski, *J. Am. Chem. Soc.* **1999**, *121*, 6513.
[12] G. M. Clore, A. M. Gronenborn, A. Bax, *J. Magn. Reson.* **1998**, *133*, 216.
[13] J. A. Losonczi, M. Andrec, M. W. F. Fischer, J. H. Prestegard, *J. Magn. Reson.* **1999**, *138*, 334.
[14] N. Tjandra, A. Bax, *Science* **1997**, *278*, 1111.
[15] J. A. Losonczi, J. H. Prestegard, *J. Biomol. NMR* **1998**, *12*, 447.
[16] M. Ottiger, A. Bax, *J. Biomol. NMR* **1998**, *12*, 361.
[17] R. S. Prosser, J. A. Losonczi, I. V. Shiyanovskaya, *J. Am. Chem. Soc.* **1998**, *120*, 11010.
[18] H. Wang, M. Eberstadt, E. T. Olejniczak, R. P. Meadows, S. W. Fesik, *J. Biomol. NMR* **1998**, *12*, 443.
[19] M. Ottiger, A. Bax, *J. Biomol. NMR* **1999**, *13*, 187.
[20] K. Fleming, D. Gray, S. Prasannan, S. Matthews, *J. Am. Chem. Soc.* **2000**, *122*, 5224.
[21] M. Rückert, G. Otting, *J. Am. Chem. Soc.* **2000**, *122*, 7793.
[22] G. M. Clore, M. R. Starich, A. M. Gronenborn, *J. Am. Chem. Soc.* **1998**, *120*, 10571.
[23] B. E. Ramirez, A. Bax, *J. Am. Chem. Soc.* **1998**, *120*, 9106.
[24] H. M. Al-Hashimi, H. Valafar, M. Terrell, E. R. Zartler, M. K. Eidsness, J. H. Prestegard, *J. Magn. Reson.* **2000**, *143*, 402.
[25] G. A. Mueller, W. Y. Choy, D. W. Yang, J. D. Forman-Kay, R. A. Venters, L. E. Kay, *J. Mol. Biol.* **2000**, *300*, 197.
[26] G. A. Mueller, W. Y. Choy, N. R. Skrynnikov, L. E. Kay, *J. Biomol. NMR* **2000**, *18*, 183.
[27] C. A. Fowler, F. Tian, H. M. Al-Hashimi, J. H. Prestegard, *J. Mol. Biol.* **2000**, *304*, 447.
[28] J.-C. Hus, D. Marion, M. Blackledge, *J. Mol. Biol.* **2000**, *298*, 927.
[29] J.-C. Hus, D. Marion, M. Blackledge, *J. Am. Chem. Soc.* **2001**, *123*, 1541.
[30] P. M. Bowers, C. E. M. Strauss, D. Baker, *J. Biomol. NMR* **2000**, *18*, 311.
[31] F. Delaglio, G. Kontaxis, A. Bax, *J. Am. Chem. Soc.* **2000**, *122*, 2142.
[32] M. Andrec, P. Du, R. M. Levy, *J. Biomol. NMR* **2001**, *21*, 335.
[33] C. A. Rohl, D. Baker, *J. Am. Chem. Soc.* **2002**, *124*, 2723.
[34] M. Zweckstetter, A. Bax, *J. Am. Chem. Soc.* **2001**, *123*, 9490.
[35] F. Tian, H. Valafar, J. H. Prestegard, *J. Am. Chem. Soc.* **2001**, *123*, 11791.
[36] A. W. Giesen, S. W. Homans, J. M. Brown, *J. Biomol. NMR* **2003**, *25*, 63.
[37] S. Grzesiek, J. Anglister, H. Ren, A. Bax, *J. Am. Chem. Soc.* **1993**, *115*, 4369.
[38] P. E. Coughlin, F. E. Anderson, E. J. Oliver, J. M. Brown, S. W. Homans, S. Pollak, J. W. Lustbader, *J. Am. Chem. Soc.* **1999**, *121*, 11871.
[39] A. W. Giesen, L. C. Bae, C. L. Barrett, J. A. Chyba, M. M. Chaykovsky, M. C. Cheng, J. H. Murray, E. J. Oliver, S. M. Sullivan, J. M. Brown, F. W. Dahlquist, S. W. Homans, *J. Biomol. NMR* **2001**, *19*, 255.
[40] M. K. Rosen, K. H. Gardner, R. C. Willis, W. E. Parris, T. Pawson, L. E. Kay, *J. Mol. Biol.* **1996**, *263*, 627.
[41] K. H. Gardner, L. E. Kay, *J. Am. Chem. Soc.* **1997**, *119*, 7599.
[42] N. K. Goto, K. H. Gardner, G. A. Mueller, R. C. Willis, L. E. Kay, *J. Biomol. NMR* **1999**, *13*, 369.
[43] N. K. Goto, L. E. Kay, *Curr. Opin. Struct. Biol.* **2000**, *10*, 585.
[44] Z. R. Wu, A. Bax, *J. Am. Chem. Soc.* **2002**, *124*, 9672.
[45] B. Meyer, T. Peters, *Angew. Chem.* **2003**, *115*, 890; *Angew. Chem. Int. Ed.* **2003**, *42*, 864.

 © 2004 Wiley-VCH Verlag GmbH & Co. KGaA, Weinheim

[46] S. B. Shuker, P. J. Hajduk, R. P. Meadows, S. W. Fesik, *Science* **1996**, *274*, 1531.
[47] P. J. Hajduk, R. P. Meadows, S. W. Fesik, *Q. Rev. Biophys.* **1999**, *32*, 211.
[48] P. J. Hajduk, T. Gerfin, J. M. Boehlen, M. Haberli, D. Marek, S. W. Fesik, *J. Med. Chem.* **1999**, *42*, 2315.
[49] F. Abbate, L. Franzoni, F. Lohr, C. Lucke, E. Ferrari, R. T. Sorbi, H. Ruterjans, A. Spinsi, *J. Biomol. NMR* **1999**, *15*, 187.
[50] Z. Böcskei, C. R. Groom, D. R. Flower, C. E. Wright, S. E. V. Phillips, A. Cavaggioni, J. B. C. Findlay, A. C. T. North, *Nature* **1992**, *360*, 186.
[51] D. E. Timm, L. J. Baker, H. Mueller, L. Zidek, M. V. Novotny, *Protein Sci.* **2001**, *10*, 997.
[52] A. Medek, P. J. Hajduk, J. Mack, S. W. Fesik, *J. Am. Chem. Soc.* **2000**, *122*, 1241.
[53] L. Zidek, M. J. Stone, S. M. Lato, M. D. Pagel, Z. S. Miao, A. D. Ellington, M. V. Novotny, *Biochemistry* **1999**, *38*, 9850.
[54] C. Dalvit, P. Floersheim, M. G. M. Zurini, A. Widmer, *J. Biomol. NMR* **1999**, *14*, 23.
[55] J. Fejzo, C. A. Lepre, J. W. Peng, G. W. Bemis, Ajay, M. A. Murcko, J. M. Moore, *Chem. Biol.* **1999**, *6*, 755.
[56] P. J. Hajduk, D. J. Augeri, J. Mack, R. Mendoza, J. G. Yang, S. F. Betz, S. W. Fesik, *J. Am. Chem. Soc.* **2000**, *122*, 7898.
[57] P. J. Hajduk, E. T. Olejniczak, S. W. Fesik, *J. Am. Chem. Soc.* **1997**, *119*, 12257.
[58] B. Meyer, T. Weimar, T. Peters, *Eur. J. Biochem.* **1997**, *246*, 705.
[59] M. Mayer, B. Meyer, *Angew. Chem.* **1999**, *111*, 1902; *Angew. Chem. Int. Ed.* **1999**, *38*, 1784.
[60] H. Takahashi, T. Nakanishi, K. Kami, Y. Arata, I. Shimada, *Nat. Struct. Biol.* **2000**, *7*, 220.
[61] W. Jahnke, P. Floersheim, C. Ostermeier, X. C. Zhang, R. Hemmig, K. Hurth, D. P. Uzunov, *Angew. Chem.* **2002**, *114*, 3570; *Angew. Chem. Int. Ed.* **2002**, *41*, 3420.
[62] A. H. Siriwardena, F. Tian, S. Noble, J. H. Prestegard, *Angew. Chem.* **2002**, *114*, 3604; *Angew. Chem. Int. Ed.* **2002**, *41*, 3454.
[63] J. Fiaux, E. B. Bertelsen, A. L. Horwich, K. Wüthrich, *Nature* **2002**, *418*, 207.
[64] K. Pervushin, R. Riek, G. Wider, K. Wüthrich, *Proc. Natl. Acad. Sci. USA* **1997**, *94*, 12366.
[65] G. Otting, H. Senn, G. Wagner, K. Wüthrich, *J. Magn. Reson.* **1986**, *70*, 500.
[66] G. Otting, K. Wüthrich, *J. Magn. Reson.* **1989**, *85*, 586.
[67] C. Zwahlen, P. Legault, S. J. F. Vincent, J. Greenblatt, R. Konrat, L. E. Kay, *J. Am. Chem. Soc.* **1997**, *119*, 6711.
[68] A. M. Petros, R. T. Gampe, G. Gemmecker, P. Neri, T. F. Holzman, R. Edalji, J. Hochlowski, M. Jackson, J. McAlpine, J. R. Luly, T. Pilotmatias, S. Pratt, S. W. Fesik, *J. Med. Chem.* **1991**, *34*, 2925.
[69] A. M. Petros, G. Gemmecker, P. Neri, E. T. Olejniczak, D. Nettesheim, R. X. Xu, E. G. Gubbins, H. Smith, S. W. Fesik, *J. Med. Chem.* **1992**, *35*, 2467.
[70] D. G. Low, M. A. Probert, G. Embleton, K. Seshadri, R. A. Field, S. W. Homans, J. Windust, P. J. Davis, *Glycobiology* **1997**, *7*, 373.
[71] M. Pellecchia, D. Meininger, Q. Dong, E. Chang, R. Jack, D. S. Sem, *J. Biomol. NMR* **2002**, *22*, 165.
[72] H. Shimizu, A. Donohue-Rolfe, S. W. Homans, *J. Am. Chem. Soc.* **1999**, *121*, 5815.
[73] P. J. Bolon, H. M. Al-Hashimi, J. H. Prestegard, *J. Mol. Biol.* **1999**, *293*, 107.
[74] H. M. Al-Hashimi, P. J. Bolon, J. H. Prestegard, *J. Magn. Reson.* **2000**, *142*, 153.
[75] M. Zweckstetter, A. Bax, *J. Am. Chem. Soc.* **2000**, *122*, 3791.
[76] E. T. Olejniczak, R. P. Meadows, H. Wang, M. L. Cai, D. G. Nettesheim, S. W. Fesik, *J. Am. Chem. Soc.* **1999**, *121*, 9249.
[77] F. Tian, P. J. Bolon, J. H. Prestegard, *J. Am. Chem. Soc.* **1999**, *121*, 7712.
[78] P. J. Bolon, J. H. Prestegard, *J. Am. Chem. Soc.* **1998**, *120*, 9366.
[79] W. Peti, C. Griesinger, *J. Am. Chem. Soc.* **2000**, *122*, 3975.
[80] Z. G. Li, S. Raychaudhuri, A. J. Wand, *Protein Sci.* **1996**, *5*, 2647.
[81] D. W. Yang, L. E. Kay, *J. Mol. Biol.* **1996**, *263*, 369.
[82] D. Yang, Y.-K. Mok, J. D. Forman-Kay, N. Farrow, L. E. Kay, *J. Mol. Biol.* **1997**, *272*, 790.
[83] M. Akke, R. Brüschweiler, A. G. Palmer, *J. Am. Chem. Soc.* **1993**, *115*, 9832.
[84] A. G. Palmer, *Annu. Rev. Biophys. Biomol. Struct.* **2001**, *30*, 129.
[85] G. Lipari, A. Szabo, *J. Am. Chem. Soc.* **1982**, *104*, 4546.
[86] C. Bracken, P. A. Carr, J. Cavanagh, A. G. Palmer, *J. Mol. Biol.* **1999**, *285*, 2133.
[87] J. Evenas, S. Forsen, A. Malmendal, M. Akke, *J. Mol. Biol.* **1999**, *289*, 603.
[88] J. O. Wrabl, D. Shortle, T. B. Woolf, *Proteins Struct. Funct. Genet.* **2000**, *38*, 123.
[89] L. Zidek, M. V. Novotny, M. J. Stone, *Nat. Struct. Biol.* **1999**, *6*, 1118.
[90] A. L. Lee, P. F. Flynn, A. J. Wand, *J. Am. Chem. Soc.* **1999**, *121*, 2891.
[91] D. R. Muhandiram, T. Yamazaki, B. D. Sykes, L. E. Kay, *J. Am. Chem. Soc.* **1995**, *117*, 11536.
[92] R. Ishima, A. P. Petkova, J. M. Louis, D. A. Torchia, *J. Am. Chem. Soc.* **2001**, *123*, 6164.
[93] R. Ishima, J. M. Louis, D. A. Torchia, *J. Biomol. NMR* **2001**, *21*, 167.
[94] D. M. LeMaster, *J. Am. Chem. Soc.* **1999**, *121*, 1726.
[95] A. Mittermaier, L. E. Kay, J. D. Forman-Kay, *J. Biomol. NMR* **1999**, *13*, 181.
[96] A. L. Lee, S. A. Kinnear, A. J. Wand, *Nat. Struct. Biol.* **2000**, *7*, 72.
[97] J. Cavanagh, M. Akke, *Nat. Struct. Biol.* **2000**, *7*, 11.
[98] J. D. Dunitz, *Chem. Biol.* **1995**, *2*, 709.
[99] D. H. Williams, D. P. O'Brien, B. Bardsley, *J. Am. Chem. Soc.* **2001**, *123*, 737.
[100] C. T. Calderone, D. H. Williams, *J. Am. Chem. Soc.* **2001**, *123*, 6262.
[101] V. P. Denisov, K. Venu, J. Peters, H. D. Horlein, B. Halle, *J. Phys. Chem. B* **1997**, *101*, 9380.

 © 2004 Wiley-VCH Verlag GmbH & Co. KGaA, Weinheim

Communications



The bonding patterns of the seven modifications of gallium show the path of the "space molecules" GaBr(GaR) via metalloid gallium clusters—in this case a nanoscale $[Ga_{51}(PtBu_2)_{14}Br_6]$ cluster constrained by GaP units—to the metal. More information on this fascinating chemistry is provided by H. Schnöckel et al. on the following pages.

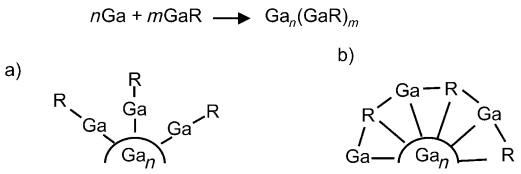
DOI: 10.1002/anie.200352472
© 2004 Wiley-VCH Verlag GmbH & Co. KGaA, Weinheim

Gallium Clusters

$[Ga_{51}(PtBu_2)_{14}Br_6]^{3-}$: An Elementoid Gallium Cluster with Metalloid and Nonmetalloid Structural Elements**

*Jochen Steiner, Gregor Stößer, and Hansgeorg Schnöckel**

We have recently introduced a series of metalloid Ga clusters, in which a core of Ga atoms is surrounded by a shell of GaR units.[1,2] The R groups used so far ($R = N(SiMe_3)_2$, $Si(SiMe_3)_3$, $C(SiMe_3)_3$, $SitBu_3$) were shown to bind to their Ga atoms exclusively through two-center, two-electron (2c2e) bonds (Scheme 1a). In these clusters, the central cores of ligand-free



Scheme 1. Bonding principles in metalloid $Ga_n(GaR)_m$ clusters (see text for details).

Ga atoms were often determined to have topologies corresponding to one of the seven forms of elemental gallium,[1] meaning that coordination numbers typical of both metals (e.g., coordination number 12, as in Ga-III) and nonmetals (e.g., coordination number 1, as in α-Ga, since one short and six long Ga–Ga distances are observed) are found. We previously introduced the concept of metalloid or elementoid clusters[1,3] which seems tailor-made for such Ga clusters. To vary the influence of the outer shell, we recently introduced $PtBu_2$ groups.[4] Steric and electronic influences cause the phosphorus atoms in these groups to form also bridging bonds, which result in their increased interaction with the Ga_n core (Scheme 1b).

In the recently introduced Ga_{16} cluster, the Ga_4 core is so constrained by GaP units that it forms, in comparison to other central Ga_4 units in Ga_nR_m clusters, a particularly compressed Ga_4 tetrahedron.[4] Given these results, we asked ourselves if it would be possible to synthesize larger Ga_n cores in metalloid clusters with surrounding $GaPR_2$ shells by choosing the right conditions. In this case, we would expect centered structures with high coordination numbers for the central gallium atom, as in the fcc packing that was recently found in Ga-IV at high pressures.[5] Herein we describe the synthesis, structure, and bonding relationships in such a metalloid gallium cluster, which, with 51 gallium atoms, is the second largest such cluster characterized to date.

A metastable solution of GaBr in toluene/THF (3:1) was heated from −78 to −35 °C,[1,6] to induce the disproportionation to form metal-rich clusters and $GaBr_3$. Subsequently, a slight excess of $LiPtBu_2$ suspended in toluene was added, and the reaction mixture was heated to 60 °C for 2 h. After several days in a drying oven at about 50 °C, compound **1** crystallizes as black rhombuses, which contain one $[Li_2Br(THF)_6]^+$ and two $[Li(THF)_4]^+$ ions, as well as the anionic cluster $[Ga_{51}(PtBu_2)_{14}Br_6]^{3-}$ (**1a**). The crystal structure analysis[7] shows that **1a** is a metalloid cluster with 31 "naked" and 20 ligand-bearing Ga atoms. The number of cations indicates that the cluster carries a threefold negative charge. Cluster **1a** is depicted in Figure 1.

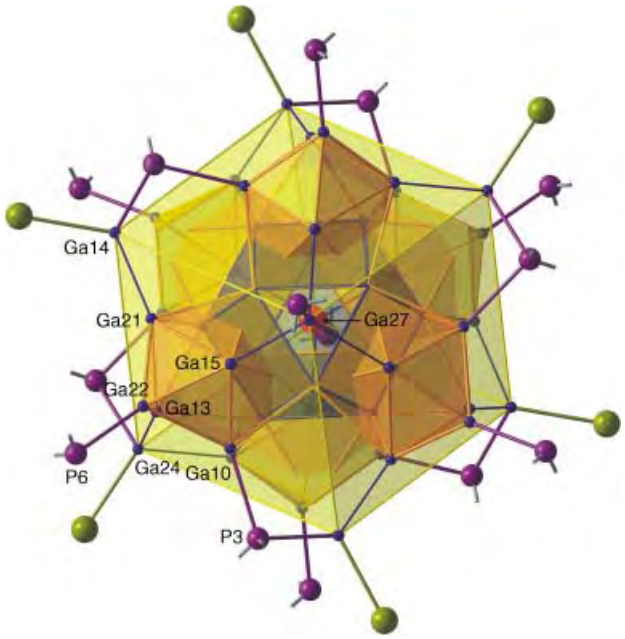


Figure 1. Molecular structure of **1a** in crystals of **1**. For clarity, only the bonds to the α-carbon atoms are shown in the $PtBu_2$ groups. Those atoms discussed in the text are identified by numbers.

The central gallium atom (Ga27, red, Figure 1) is surrounded by twelve more Ga atoms (blue) in a slightly distorted cuboctahedral environment with an average Ga–Ga distance of 284.4 pm (min./max. 276.3 pm/292.2 pm). The Ga–Ga distances depicted in Figure 2 show relatively little variation; in comparison, in the $Ga_{19}R_6^-$ cluster **2** ($R = C(SiMe_3)_3$), which also has a cuboctahedral environment around the central Ga atom and an average bond length of 284.4 pm, the distances range from 272.9 to 295.5 pm.[3] The six slightly distorted square planes of the cubooctahedron in **1a** are capped with Ga_5 units (orange, Figure 1), leading to square antiprismatic units containing a plane capped by a $GaPR_2$ unit (Ga22, P6; assignment according to Figure 1). Two of these six Ga_5 moieties are depicted in Figure 2. Of the four gallium atoms in the distorted square formations (Ga10, Ga13, Ga15, Ga21), two form bonds to Br-atom-bearing Ga

[*] J. Steiner, G. Stößer, Prof. Dr. H. Schnöckel
Institut für Anorganische Chemie der Universität Karlsruhe (TH)
Engesserstrasse 15, Geb. 30.45, 76128 Karlsruhe (Germany)
Fax: (+49) 721-608-4854
E-mail: Hansgeorg.Schnoeckel@chemie.uni-karlsruhe.de

[**] This research was supported by the Deutsche Forschungsgemeinschaft and the Fonds der Chemischen Industrie.

 © 2004 Wiley-VCH Verlag GmbH & Co. KGaA, Weinheim DOI: 10.1002/anie.200352472

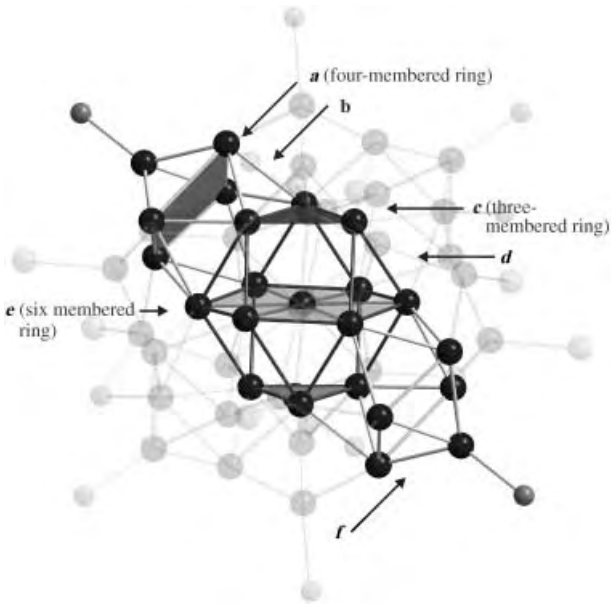


Figure 2. To illustrate the variance of the Ga–Ga distances, a cross-section of **1a** is highlighted (see text). The following distances [pm] are observed: *a* 259.5–295.8, *b* 258.9–278.4, *c* 284.8–286.2, *d* 279.3–295.3, *e* 275.8–278.8, *f* 245.5–268.1.

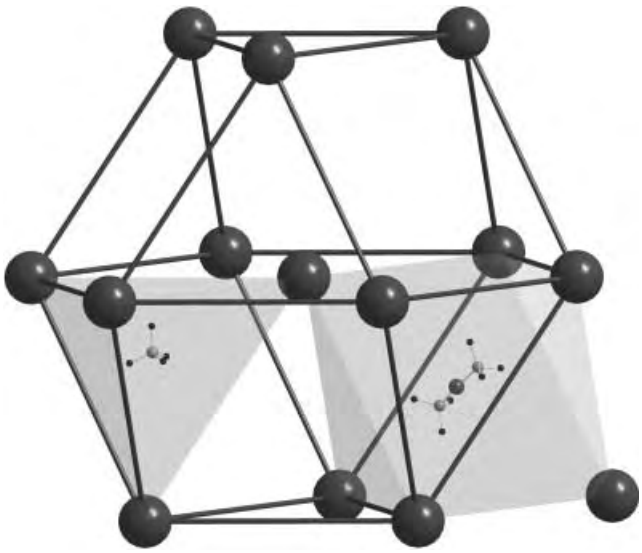


Figure 4. Orientation of the **1a** anions in the crystal. The distances between the anions (in pm) show only a slight variation (min./average/max. 20.495/21.156/21.816). One each of the tetrahedral and octahedral holes containing the $[Li(THF)_4]^+$ or $[Li_2Br(THF)_6]^+$ ions, respectively, is highlighted.

atoms (Ga14, Ga24), one is bound to a gallium atom with a terminal P*t*Bu$_2$ group (Ga27), and the fourth binds directly to a bridging P*t*Bu$_2$ group (P3). The three gallium atoms that are directly bound to these six Ga_4 squares form a distorted Ga_8 cube, which is highlighted in yellow in Figure 1. Six of these eight gallium atoms form bonds to terminal bromine atoms, while two are bonded to terminal P*t*Bu$_2$ groups. Together with the six bridging P*t*Bu$_2$ groups, this results in a pseudo-sixfold axis of rotation, which is made clear by the arrangement of the P and Br atoms in Figure 3.

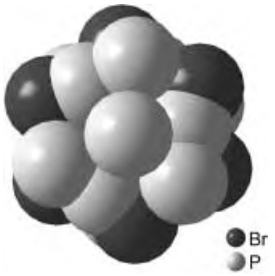


Figure 3. Space-filling model of the P and Br atoms directly bound to the Ga_{51} cluster, depicted in the same orientation of **1a** as in Figure 2.

The arrangement of the $[Ga_{51}(PtBu_2)_{14}Br_6]^{3-}$ cluster anions **1a** in the crystals of **1** is shown in Figure 4. The roughly 2 nm clusters are in a slightly distorted cubic close-packed arrangement, in which all of the tetrahedral holes are filled with $[Li(THF)_4]^+$ ions and all of the octahedral holes with $[Li_2Br(THF)_6]^+$ ions. This is similar to the Li_3Br structure typical of $C_{60}M_3$ fullerides, but the diameter of the cluster anion **1a** is about three times as large as that of the fulleride ion C_{60}^{3-}.

The structure of **1** is unique in cluster chemistry, and merits some discussion and substantiation. The central Ga_{13} unit is very symmetrical and compact. Single-point DFT calculations[8] based on the experimentally determined structural data resulted in a volume of 3071 a_0^3, which, as expected, lies between that of the fcc packing in the recently determined Ga-IV high-pressure modification (2681 a_0^3) and the volume calculated by extrapolation of this high-pressure version to normal pressure (3380 a_0^3).[9] As a result of the coordination number of 12, as in a typical metal, the Ga–Ga distances are larger than those in molecular compounds such as R_2GaGaR_2 (d(Ga–Ga) = 248 pm for R = CH(SiMe$_3$)$_2$).[11] As can be seen in Figure 2, the Ga–Ga distances in **1a** steadily decrease with decreasing coordination number on going from the interior to the exterior; the increasing covalent component of these bonds also becomes clear on moving outward from the center. The Ga_5 units on the square surfaces of the cuboctahedron form square Ga_8 antiprisms, which, by virtue of their bond lengths (Figure 2), differ significantly from those in the similarly structured $Ga_8R_8^{2-}$ cluster (R = $C_{13}H_9$) **3**.[12] The average Ga–Ga distance within the Ga_4 plane in **1a** is thus 280.4 pm, versus 251.9 pm in **3**, whereas the average distance of 266.2 pm between the Ga atoms that lie between the Ga_4 planes in **1a** is somewhat smaller than the corresponding distance of 270.7 pm in **3**. The topology of these square-antiprismatic Ga_8 units on the one hand, and the almost perfect cuboctahedral arrangement around the central Ga atom in **1a** on the other hand resemble the different bonding pattern in modifications of elemental gallium: that is, both nonmetalloid (Ga_8 unit) and metalloid (Ga core) bonding types are present in **1a**.

To back up our topological interpretation of the bonding relationships with a population analysis and calculated NMR

 © 2004 Wiley-VCH Verlag GmbH & Co. KGaA, Weinheim

chemical shifts, DFT calculations[13] were carried out on model compounds in which the P*t*Bu$_2$ group was replaced by either PH$_2$ or P(CH$_3$)$_2$ groups (**1b** and **1c**). These calculations showed that the relationship between the very different distances in **1a** and in the model compounds (**1b** and **1c**) is very well reproduced. However it is evident that the ligands have a strong influence over the absolute values of these distances. This was also true of the calculated ^{71}Ga NMR and ^{31}P NMR chemical shifts and the partial charges calculated from the population analyses. Because reliable calculations are not yet possible with the P*t*Bu$_2$ group, we will refrain from further discussion at this point. However, given the current data, it is possible to conclude that, unlike in the single-shelled C_{60},[14] $B_{12}H_{12}^{2-}$,[15] or Pb_9^{4-}[16] clusters, the ^{71}Ga and ^{31}P NMR chemical shifts for our clusters cannot be simply interpreted through their NICS values and their spherical aromaticity. On the contrary, in these multishelled metalloid clusters we see that the ^{71}Ga signal for the central Ga atom, for example, is shifted significantly (e.g. by 250 ppm for **1c**) downfield relative to the signals for the Ga atoms of the inner cuboctahedron, as in Ga metal. To clarify this, we intend to carry out further calculations as well as solid-state NMR experiments, as **1a** is not soluble in common organic solvents.[17] Such quantum-chemical and experimental investigations should make it possible to draw further conclusions from the topology (distances and coordination numbers) about the metalloid bonding relationships in the center as well as the more covalent bonding in the second shell and periphery of the Ga framework.

Given the recently attained results from the $Ga_{84}R_{20}^{4-}$ cluster (**4**)[18] (metallic conductivity,[19] superconductivity[20]), we are also planning similar investigations for **1**. In addition to the threefold negative charge of **1a**, a partial lower charge (for example 1−), which could be balanced by a dilution in the cationic lattice of the Li_3Bi lattice structure of the Ga_{51} cluster (see Figure 4), is also conceivable for **1**. Since according to latest results, the cluster **4** could be present as both a three- and fourfold negatively charged species in the same crystal,[21] such cluster doping could provide an approach for the clarification of the so far not understood conductivity phenomena.

Experimental Section

Li*t*Bu$_2$ (1 g, 6.57 mmol) was suspended in toluene (50 mL) and cooled to 0 °C in an ice bath. In a second flask, a 0.32 M GaBr solution (17 mL, 5.44 mmol) in toluene/THF (3:1) was warmed from −78 to −35 °C over several hours. The ligand was added to this latter solution through a stainless steel canula, which caused the reaction mixture to warm from −35 to −25 °C. The reaction mixture was warmed to room temperature over 10 h and then held at 60 °C for 2 h. This resulted in a black solution, from which **1** (250 mg, 0.035 mmol) crystallized over several days at 50 °C in the form of black rhombuses.

Received: July 25, 2003 [Z52472]
Published Online: December 9, 2003

Keywords: cluster compounds · gallium · structure elucidation

[1] A. Schnepf, H. Schnöckel, *Angew. Chem.* **2002**, *114*, 6000 – 6021; *Angew. Chem. Int. Ed.* **2002**, *41*, 3533 – 3554.
[2] K. Weiß, H. Schnöckel, *Z. Anorg. Allg. Chem.* **2003**, *629*, 1175 – 1183.
[3] A. Schnepf, G. Stösser, H. Schnöckel, *J. Am. Chem. Soc.* **2000**, *122*, 9178 – 9181.
[4] J. Steiner, G. Stösser, H. Schnöckel, *Angew. Chem.* **2003**, *115*, 2016 – 2019; *Angew. Chem. Int. Ed.* **2003**, *42*, 1971 – 1974.
[5] a) Z. Li, J. S. Tse, *Phys. Rev. B* **2000**, *62*, 9900 – 9902; b) L. Bosio, *J. Chem. Phys.* **1978**, *68*, 1221; c) O. Schulte, W. B. Holzapfel, *Phys. Rev. B* **1997**, *55*, 8122; d) K. Takemura, K. Kobayashi, M. Arai, *Phys. Rev. B* **1998**, *58*, 2482; e) H. G. von Schnering, R. Nesper, *Acta Chem. Scand.* **1991**, *45*, 870; f) U. Häussermann, S. Simak, I. Abrikosov, S. Lidin, *Chem. Eur. J.* **1997**, *3*, 904; g) X. G. Gong, G. Chiarotti, M. Parinello, E. Tosatti, *Phys. Rev. B* **1991**, *43*, 14277.
[6] C. Dohmeier, D. Loos, H. Schnöckel, *Angew. Chem.* **1996**, *108*, 141 – 161; *Angew. Chem. Int. Ed. Engl.* **1996**, *35*, 129 – 149.
[7] Crystal structure data for **1**: $M_r = 7185.02$. Crystal dimensions $0.6 \times 0.1 \times 0.05$ mm, monoclinic, space group $C2/c$, $\beta = 110.26(3)°$, $a = 34.7025(12)$ Å, $b = 21.8163(5)$ Å, $c = 37.5622(14)$ Å, $V = 26677.3(15)$ Å°, $Z = 4$, $\rho_{calcd} = 1.789$ gcm°, $\mu_{Mo} = 6.222$ mm^{-1}, $\theta_{max.} = 25.05(°$, 112878 measured reflections, 23411 independent reflections (R(int.) = 0.1459). Absorption correction: numeric (min./max.-transmission 0.6469/0.9396), $R_1 = 0.0560$, $wR_2 = 0.1295$. STOE-IPDS-diffractometer ($Mo_{K\alpha}$ radiation, $\lambda = 0.71071$ Å), 150 K. The structure was solved by direct methods and refined against F^2 for all observed reflections. Programs used: SHELXS and SHELXTL (G. M. Sheldrick, Universität Göttingen). CCDC-215886 contains the supplementary crystallographic data for this paper. These data can be obtained free of charge via www.ccdc.cam.ac.uk/conts/retrieving.html (or from the Cambridge Crystallographic Data Centre, 12, Union Road, Cambridge CB21EZ, UK; fax: (+44) 1223-336-033; or deposit@ccdc.cam.ac.uk).
[8] The molecular volume was calculated with the GAUSSIAN 98 program package on the SCF level with a 3-21G basis set. We carried out single-point calculations based on the experimentally determined geometry of **1**, in which the ICPM solvation model was used to place a shell of uniform electron density (4×10^{-3} e Å^{-3}) around the Ga_{13} unit. a) IPCM: J. B. Foresman, T. A. Keith, K. B. Wiberg, J. Snoonian, M. J. Frisch, *J. Phys. Chem.* **1996**, *100*, 16098; b) Gaussian 98 (Revision A.7), M. J. Frisch, G. W. Trucks, H. B. Schlegel, G. E. Scuseria, M. A. Robb, J. R. Cheeseman, V. G. Zakrzewski, J. A. Montgomery, R. E. Stratmann, J. C. Burant, S. Dapprich, J. M. Millam, A. D. Daniels, K. N. Kudin, M. C. Strain, O. Farkas, J. Tomasi, V. Barone, M. Cossi, R. Cammi, B. Mennucci, C. Pomelli, C. Adamo, S. Clifford, J. Ochterski, G. A. Petersson, P. Y. Ayala, Q. Cui, K. Morokuma, D. K. Malick, A. D. Rabuck, K. Raghavachari, J. B. Foresman, J. Cioslowski, J. V. Ortiz, B. B. Stefanov, G. Liu, A. Liashenko, P. Piskorz, I. Komaromi, R. Gomperts, R. L. Martin, D. J. Fox, T. Keith, M. A. Al-Laham, C. Y. Peng, A. Nanayakkara, C. Gonzalez, M. Challacombe, P. M. W. Gill, B. G. Johnson, W. Chen, M. W. Wong, J. L. Andres, M. Head-Gordon, E. S. Replogle, J. A. Pople, Gaussian, Inc., Pittsburgh, PA, **2001**.
[9] The volume of the Ga_{13} unit in **2** is 3119 a_0^3, a value of 2955 a_0^3 was calculated for a naked Ga_{13} molecule[10] (see reference [8]).
[10] K. Weiß, R. Köppe, H. Schnöckel, *Int. J. Mass Spectrom.* **2002**, *214*, 383 – 395.
[11] W. Uhl, M. Layh, T. Hildebrand, *J. Organomet. Chem.* **1989**, *364*, 289.
[12] A. Schnepf, G. Stösser, H. Schnöckel, *Z. Anorg. Allg. Chem.* **2000**, *626*, 1676 – 1680.
[13] The ^{69}Ga NMR shifts were first based on the calculated shift for GaCp, and were subsequently set in reference to the usual

 © 2004 Wiley-VCH Verlag GmbH & Co. KGaA, Weinheim

standard ($[Ga(H_2O)_6]^{3+}$). The calculations were carried out in the C_i point group with the PMSHIFT module of the TURBOMOLE program package with DFT (BP 86 functional, SVP basis). TURBOMOLE: a) O. Treutler, R. Ahlrichs, *J. Chem. Phys.* **1995**, *102*, 346; b) Funcional BP 86: A. D. Becke, *Phys. Rev. A* **1998**, *38*, 3098; J. P. Perdew, *Phys. Rev. B* **1996**, *33*, 8822; c) RIDFT: K. Eichkorn, O. Treutler, H. Öhm, M. Häser, R. Ahlrichs, *Chem. Phys. Lett.* **1995**, *242*, 652; K. Eichkorn, F. Weigend, O. Treutler, R. Ahlrichs, *Theor. Chem. Acc.* **1997**, *97*, 119; d) GIAO with DFT: G. Schreckenbach, T. Ziegler, *J. Phys. Chem.* **1995**, *99*, 606; GIAO mit SCF: M. Häser, R. Ahlrichs, H. P. Baron, P. Weiss, H. Horn, *Theor. Chim. Acta* **1992**, *83*, 455.

[14] Z. Chen, H. Jiao, A. Hirsch, P. von R. Schleyer, *Angew. Chem.* **2002**, *114*, 4485 – 4488; *Angew. Chem. Int. Ed.* **2002**, *41*, 4309 – 4312.

[15] P. von R. Schleyer, K. Najafian, *Inorg. Chem.* **1998**, *37*, 3454 – 3470.

[16] a) A. Hirsch, Z. Chen, H. Jiao, *Angew. Chem.* **2001**, *113*, 2916 – 2920; *Angew. Chem. Int. Ed.* **2001**, *40*, 2834 – 2838; b) V. Queneau, S. C. Sevov, *Inorg. Chem.* **1998**, *37*, 1358 – 1360; c) E. Todorov, S. C. Sevov, *Inorg. Chem.* **1998**, *37*, 3889 – 3891; d) J. Campbell, D. A. Dixon, H. P. A. Mercier, G. J. Schrobilgen, *Inorg. Chem.* **1995**, *34*, 5798 – 5809.

[17] NMR experiments with **2** have shown that it has thus far not been possible to reconcile calculated ^{71}Ga NMR chemical shifts with those obtained experimentally. Clearly relativistic effects, among others, play a nontrivial role in the Ga core.

[18] A. Schnepf, H. Schnöckel, *Angew. Chem.* **2001**, *113*, 733 – 737; *Angew. Chem. Int. Ed.* **2001**, *40*, 712 – 715.

[19] O. N. Bakharev, N. Zelders, H. B. Brom, A. Schnepf, H. Schnöckel, L. J. de Jong, *Eur. Phys. J.* **2003**, *D24*, 101 – 104.

[20] J. Hagel, M. T. Kelemen, G. Fischer, B. Pilawa, J. Wosnitza, E. Dormann, H. v. Löhneysen, A. Schnepf, H. Schnöckel, U. Neisel, J. Beck, *J. Low Temp. Phys.* **2002**, *129*, 133 – 142.

[21] A. Schnepf, E. Herrling, B. Pilawa, E. Weckert, A. Meents, B. Jee, H. Schnöckel, *Inorg. Chem.*, in press.

 © 2004 Wiley-VCH Verlag GmbH & Co. KGaA, Weinheim

Giant Silver–Sulfur Clusters

Syntheses and Crystal Structures of the Ag–S Cluster Compounds $[Ag_{70}S_{20}(SPh)_{28}(dppm)_{10}](CF_3CO_2)_2$ and $[Ag_{262}S_{100}(StBu)_{62}(dppb)_6]$**

Dieter Fenske, Claudia Persau, Stefanie Dehnen, and Christopher E. Anson*

Dedicated to Professor Hans Bock on the occasion of his 75th birthday

Numerous reports have described the syntheses and structures of metal-rich compounds. In recent years, research activities in this field have been very successful, especially in the synthesis of heteropolyacids and clusters of main-group and transition-metal elements. Examples include $Na_{48}[H_xMo_{368}O_{1032}(H_2O)_{240}(SO_4)_{46}]$ ($x \approx 16$), $[Pd_{145}(CO)_{60}(PEt_3)_{30}]$, and $[Ga_{84}\{N(SiMe_3)_2\}_{20}Li_6Br_2(thf)_{20}]$.[1–3]

Another area of interest is the preparation of metal chalcogenide clusters.[4] Recently, the synthesis and crystal structure of an ionic compound containing the anion $[Cd_{16}In_{64}S_{134}]^{44-}$ was reported.[5] The size of this structure is within the order of magnitude of nanocrystalline materials.

Metal-rich complexes are also known from chalcogenides of other electron-rich transition-metal elements. Examples include $[NHEt_3]_4[Ag_{50}S_7(SC_6H_4tBu)_{40}]$[6] and other Cu and Ag chalcogenide clusters that were synthesized by using tertiary phosphanes to inhibit the competing formation of the thermodynamically preferred binary metal-chalcogenide phases. Quantum chemical investigations showed that clusters of this type are metastable compounds whose collapse is kinetically prevented.[7]

There is some evidence that selenide and telluride clusters, such as $[Cu_{146}Se_{73}(PPh_3)_{30}]$,[8] $[Ag_{172}Se_{40}(SenBu)_{92}(dppp)_4]$,[9] $[Ag_{38}Te_{13}(TetBu)_{12}(dppe)_6]$[10] and $[Au_{18}Se_8(dppe)_6]Cl_2$[11] (dppp: 1,3-bis(diphenylphosphanyl)propane; dppe: 1,2-bis(diphenylphosphanyl)ethane) are more stable than the respective metal-sulfide clusters. However, some sulfide clusters have already been characterized, such as $[Ag_{70}S_{16}(SPh)_{34}(PhCO_2)_4(triphos)_4]$ (triphos = 1,1,1-tris(diphenylphosphanylmethyl)ethane)and $[Ag_{188}S_{94}(PR_3)_{30}]$ (R = *n*Pr; *n*Bu).[15] These compounds form in high yields upon

[*] Prof. Dr. D. Fenske, Dr. C. Persau, Dr. S. Dehnen, Dr. C. E. Anson
Institut für Anorganische Chemie
Universität Karlsruhe
Engesserstrasse, Geb. 30.45, 76128 Karlsruhe (Germany)
Fax: (+49) 721-608-2086
E-mail: dieter.fenske@aoc1.uni-karlsruhe.de
and
Institut für Nanotechnologie
Forschungszentrum Karlsruhe GmbH
Postfach 3640, 76021 Karlsruhe (Germany)

[**] This work has been supported by the Deutsche Forschungsgemeinschaft (Center for Functional Nanostructures) and the Fonds der Chemischen Industrie. D.F. acknowledges an OVS fellowship provided by St. John's College, Cambridge; (dppm: bis(diphenylphosphanyl)methane, dppb: bis(diphenylphosphanyl)butane).

 DOI: 10.1002/anie.200352351 © 2004 Wiley-VCH Verlag GmbH & Co. KGaA, Weinheim

the reaction of silylated S, Se, or Te derivatives with reactive Cu or Ag salts in the presence of tertiary phosphanes. The organic groups that are bound to the chalcogen and/or phosphorus atoms play a key role in these syntheses as the cluster structures are strongly influenced by the nature of the terminal ligands and also because phosphane chalcogenides always occur as by-products. Initially, various compounds are formed in solution and small amounts of insoluble metal chalcogenides precipitate. However, by means of dynamic light scattering, it was possible to show that after a longer period of time only one species remains, which finally crystallizes. These compounds serve in the study of the transition from molecular clusters—the structural characteristics of which are not related to those of metal chalcogenides in the solid state—to ligand-protected fragments of the binary phases. In $[Cu_{70}Se_{35}(PEt_3)_{22}]$ and $[Cu_{146}Se_{73}(PPh_3)_{30}]$, for example, one observes an arrangement of Cu and Se ions very similar to that in Cu_2Se. In contrast, the molecular structures of smaller compounds that contain fewer Cu centers can be derived from interpenetrating polyhedra of metal or chalcogenide atoms. [12] A similar transition to the solid-state structure of Ag_2Se has been observed with the following compounds: $[Ag_{90}Se_{38}(Se\,t\mathrm{Bu})_{14}(PEt_3)_{22}]$, $[Ag_{112}Se_{32}(Se\,n\mathrm{Bu})_{48}(P\,t\mathrm{Bu}_3)_{12}]$, and $[Ag_{172}Se_{40}(Se\,n\mathrm{Bu})_{92}(dppp)_4]$.[9] This change of structural features leads to a distinct variation of physical properties. This effect can be explained by the dependency of the HOMO–LUMO separation on the number of atoms incorporated in the cluster core, which affects the electronic properties of the compound.[13] The transition towards the characteristics of solid-state structures, discussed above, has not yet been observed for metal sulfide cluster systems.

Herein, we report the syntheses of two Ag–S clusters, one that contains 118 Ag and S atoms (**1**), the other that contains 424 Ag and S atoms (**2**) in their cluster cores.

$[Ag_{70}S_{20}(SPh)_{28}(dppm)_{10}](CF_3CO_2)_2$ **1**

$[Ag_{262}S_{100}(S\,t\mathrm{Bu})_{62}(dppb)_6]$ **2**

Compound **1** is prepared by treating a suspension of silver trifluoroacetate and bis(diphenylphosphanyl)methane (dppm) with a mixture of $S(Ph)SiMe_3$ and $S(SiMe_3)_2$ in dimethoxyethane at −40 °C. The reaction mixture was warmed up to room temperature over one day giving a deep red solution. Upon layering this solution with hexane, red crystals of **1** formed within several days [Eq. (1)].

$$AgCF_3CO_2 + S(Ph)SiMe_3 + S(SiMe_3)_2 + dppm \xrightarrow[-40\,^{\circ}C,\ RT]{DME} \mathbf{1} \qquad (1)$$

In a similar way, black crystals of **2** were obtained from silver benzoate, bis(diphenylphosphino)butane (dppb), and a mixture of $S(t\mathrm{Bu})SiMe_3$ and $S(SiMe_3)_2$ in THF [Eq. (2)].

$$AgPhCO_2 + S(t\mathrm{Bu})SiMe_3 + S(SiMe_3)_2 + dppb \xrightarrow[-20\,^{\circ}C]{THF} \mathbf{2} \qquad (2)$$

According to the X-ray structural analysis,[14] **1** crystallizes in the space group $P2_1/n$ with two molecules in the unit cell. The C_i symmetric cation in **1** is shown in Figure 1. These S atoms are situated on the surface of the egg-shaped core of

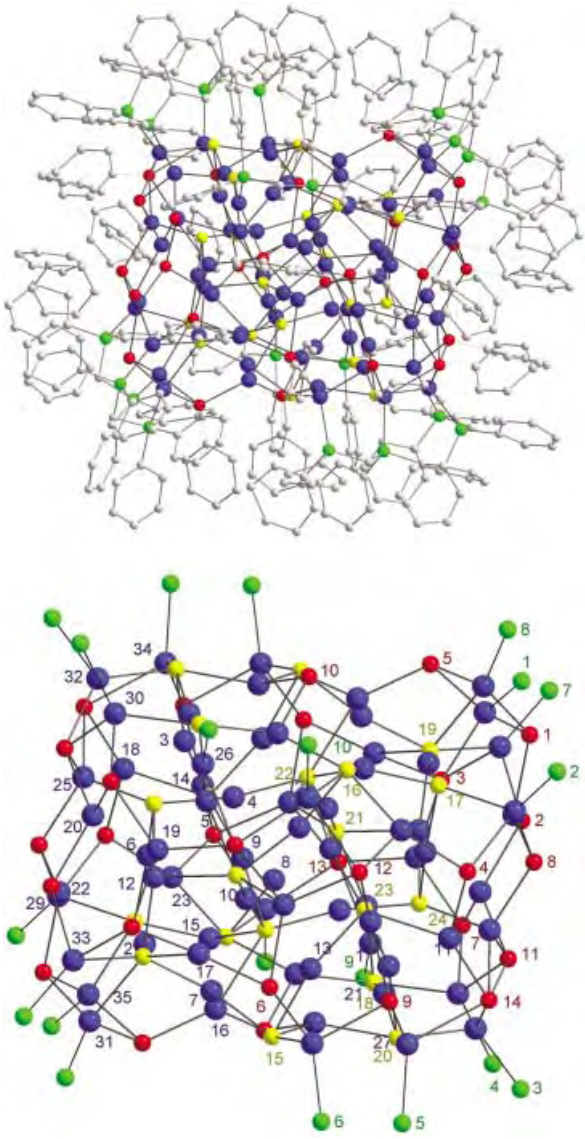


Figure 1. Top: Molecular structure of **1** in the crystal. P atoms green, S^{2-} ligands yellow, S atoms of SPh^- groups red. Bottom: Structure of **1** without organic groups. Atoms of **1** are marked by numbers, the colors of which corresponds to the color of the respective atom type.

the cluster, and are μ_3 bridges (S1–S10) and μ_4 bridges (S11–S14) between Ag atoms (Ag–(μ_3-S): 247.1–277.4(3) pm; Ag–(μ_4-S): 249.2–288.7(3) pm). The 28 S atoms of the SPh group along with a further 12 S atoms (S15–S20) form an outer polyhedron with 40 vertices (Figure 2). S15–S20 are μ_4-, μ_5-, and μ_6-bridging ligands (Ag–(μ_4-S): 239.0–263.4(3); Ag–(μ_5-S): 241.0–266.5(3); Ag–(μ_6-S): 238.6–278.7(3) pm). Within the molecule, the eight remaining S atoms (S21–S24) are arranged in a highly distorted, hexagonal bipyramid. These S atoms are all μ_5 bridges (Ag-(μ_5-S): 239.1–286.2(3) pm).

However, the description of the molecular structure of the cation in **1** based on two S_n polyhedra only provides a simplified view of the real situation: all nonbonding S–S distances within the S_8 or S_{40} polyhedra are above 420 pm and

 © 2004 Wiley-VCH Verlag GmbH & Co. KGaA, Weinheim

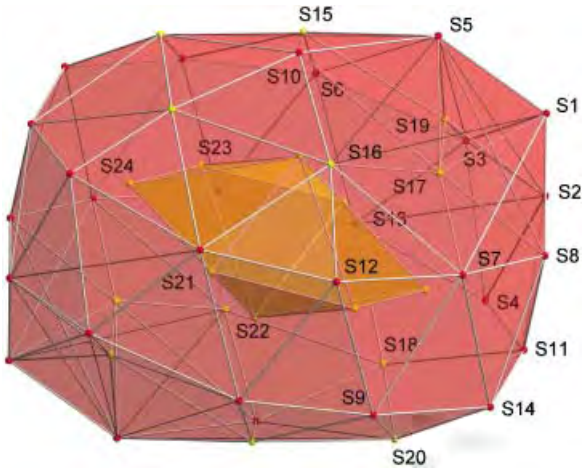


Figure 2. Substructure of S atoms in **1**. The outer polyhedron is shaded red, the inner S_8 polyhedron is shaded yellow. The red balls represent the S atoms of the SPh^- ligands, the yellow balls represent the S^{2-} ligands.

S–S distances between the two polyhedra are about the same values.

An alternative description of the structure is therefore presented in Figure 3. According to this representation, **1** is constructed by a linkage of 22 nearly linear S–Ag–S groups

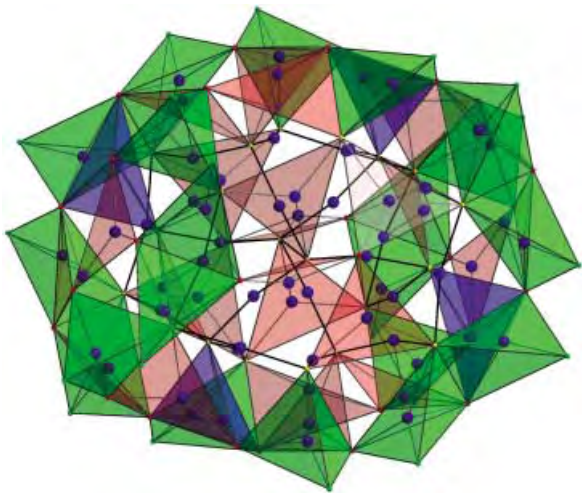


Figure 3. Linkage of the polyhedra that form the heavy-atom framework in **1**. Ag_2S units are highlighted by bold black lines, AgS_3 groups are drawn red, AgS_4 are drawn light blue, and AgS_3P tetrahedra are represented in green.

(bold black lines, Ag1–Ag11; Ag–S: 237.1–246.9(3) pm, S-Ag-S: 161.5–170.2(1)°) with 24 distorted trigonal-planar AgS_3 units (red, Ag12–Ag23; Ag–S: 246.5–288.6(4) pm), four distorted AgS_4 tetrahedra (light blue, Ag24, Ag25; Ag–S: 255.4–275.8(3) pm) and 20 AgS_3P polyhedra (green, Ag26–Ag35; Ag–P: 240.1–247.2(4), Ag–S: 246.9–293.5(3) pm). These building blocks are linked through shared edges or corners.

Many more problems arise with the description of the molecular structure of **2**. These problems are due to the disordering of Ag and S atoms that is observed within a region of about 0.8 nm in diameter around the cluster center. This observation parallels the difficulties that have occurred with the structural determination of other silver-rich complexes. Examples include the Ag–chalcogenide compounds with 90, 112, 172, and 188 Ag atoms that are mentioned above. Possibly, this disorder represents an intrinsic problem of this type of compounds, which has equally been observed for binary silver chalcogenide phases. As a consequence, Ag_2S and Ag_2Se show a relatively high conductivity of Ag^+ ions.[16–18]

For this reason, it is not trivial to assign an exact composition to compound **2**. Considering atomic distances as a restriction (Ag–Ag > 280 pm; S–S > 400 pm) one would obtain the formula $[Ag_{250}S_{94}(StBu)_{62}(dppb)_6]$. Assuming that the region of disordered atoms contains solely Ag_2S, and that the volume of an Ag_2S units amounts to about 54 Å^3,[18] **2** would finally be formulated as $[Ag_{262}S_{100}(StBu)_{62}(dppb)_6]$. The latter is in good agreement with the elemental analysis of **2**.

The results of the X-ray structural analysis show that **2** is a C_2-symmetric, spherical cluster that resembles an oblate ellipsoid. The maximum diameter is about 3.7 nm, which includes the phosphane ligand shell (Figure 4, top) and about 2.6 nm for the Ag–S core (Figure 5); the maximum of the oblate diameter is 2.6 nm, which includes the ligand shell; the corresponding diameter of the Ag–S core amounts to 1.7 nm (Figure 4, bottom). The surface of the cluster is covered by six dppb ligands and 62 $StBu^{1-}$ groups. The S atoms of the latter (S1–S31) act as μ_2-bridges (S1–S6), μ_3-bridges (S7–S29), and μ_4-bridges (S30, S31) between Ag atoms (for clarity, atom labels are omitted in the figures representing **2**; the atom numbers given in the text refer to those in the data that have been deposited with the Cambridge Crystallographic Data Centre). The S atoms of the S^{2-} ligands also show different bridging modes. S32–S47 are μ_4-bridges, S48–S70 are μ_5-bridges, S71–S74 are μ_6-bridges, and S75–S78 are μ_7-bridges. However, as the Ag–S distances vary over a large range, it is difficult to clearly determine interacting distances, and thus to clearly assign the bridging modes. As expected, the average Ag–S distance increases with increasing coordination number of the Ag atoms. These are: (μ_2-S*t*Bu)–Ag: 238.9–258.0(9); (μ_3-S*t*Bu)–Ag: 238.5–290.5(9); (μ_4-S*t*Bu)–Ag: 237.2–289.7(9); (μ_4-S)–Ag: 230.0–275.9(10); (μ_5-S)-Ag: 233.1–292.2(9); (μ_6-S)-Ag: 225.9–290.1(10); (μ_7-S)–Ag: 225.9–296.5(10) pm. These values are, however, of limited significance because of the disorder.

In contrast to the molecular structure of **1**, the cluster core of **2** cannot be described in terms of interpenetrating shells of S ligands. However, neither does it bear a structural relationship to any of the known Ag_2S phases, for example acanthite.[17,18]

As in **1**, the Ag atoms of **2** have various coordination modes. Ag1–Ag77 show nearly linear coordination by two S atoms (Ag–S: 233.4–260.7(10) pm; S-Ag-S: 144.8–179.9(4)°). Ag78–Ag96 have a distortedly trigonal-planar coordination environment of three S neighbors (Ag–S: 242.5–296.8(9) pm;

 © 2004 Wiley-VCH Verlag GmbH & Co. KGaA, Weinheim

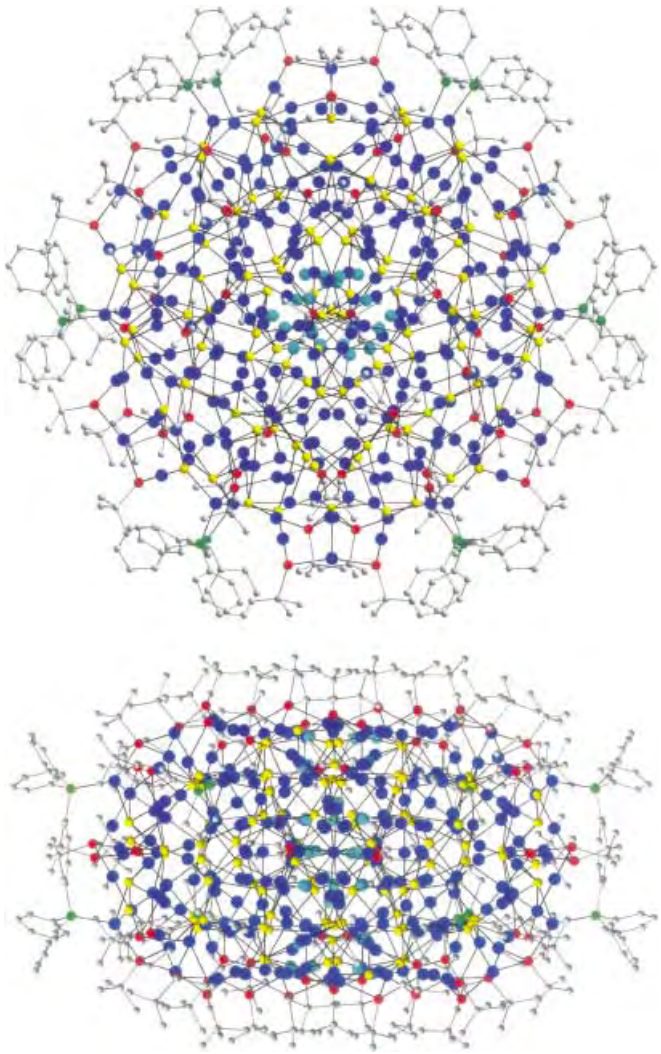


Figure 4. Top: Molecular structure of **2** in the crystal. P atoms green, S^{2-} ligands yellow, S atoms of $StBu^{1-}$ groups red, Ag atoms blue, disordered Ag atoms light blue. Bottom: Molecular structure of **2** rotated about 90° with respect to the upper view.

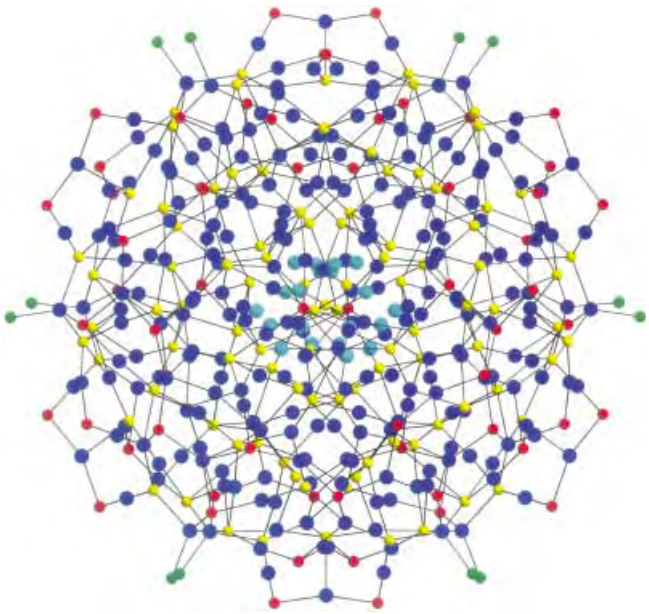


Figure 5. Molecular structure of **2** without organic groups. The disordered Ag atoms (light blue) occupy the center of the cluster.

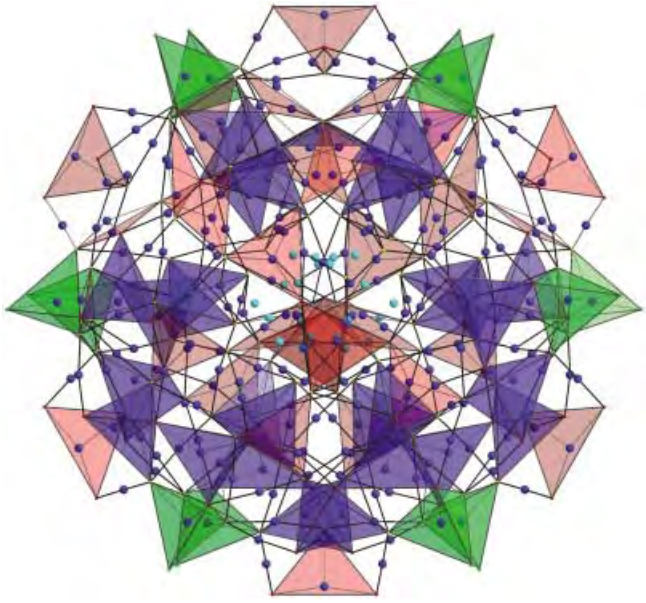


Figure 6. Linkage of the polyhedra that form the heavy atom framework in **1**. Ag_2S units are highlighted by bold black lines, AgS_3 groups are drawn red, AgS_4 and AgS_3P tetrahedra are drawn light blue and green, respectively.

S-Ag-S: 89.5–150.8(4)°; sum of the S-Ag-S angles: 344.0–359.9(4)°). Ag97–Ag116 and Ag117–Ag122 are approximately tetrahedrally coordinated by either four S atoms, or three S atoms and one P atom of a dppb ligand (Ag–S within the AgS_4 tetrahedra: 245.3–289.8(10) pm; within the AgS_3P tetrahedra: 254.8–284.7(9) pm; Ag–P: 243.7–246.2(9) pm). The disordered Ag atomic sites (Ag123–Ag148) cannot be assigned definite coordination polyhedra.

As for **1**, it is possible to alternatively describe the cluster core in **2** as a linkage of AgS_4 tetrahedra (light blue), AgS_3P tetrahedra (green), distorted AgS_3 triangles (red), and approximately linear AgS_2 units (bold black lines; Figure 6). This way, one can see some relation to the solid-state structure of the room temperature phase α-Ag_2S, which has edge-sharing and corner-sharing AgS_4 tetrahedra that are linked by planar AgS_3 groups into the 3D network.[17,18] However, compound **2** still does not represent a structural fragment of this Ag_2S phase.

The molecular structure of **2** again demonstrates the strong influence of phosphane or chalcogenolato ligands on the structure of a cluster. The bidentate dppb ligands, for instance, limit the vertical expansion of the molecule by the size of the organic group between the two P donor atoms. For this reason, one of our current aims is to characterize the species that form from reactions of silylated S derivates with silver salts and bidentate tertiary phosphanes that have a bulkier organic group between the P atoms.

 © 2004 Wiley-VCH Verlag GmbH & Co. KGaA, Weinheim

Experimental Section

All reaction steps were carried out with the exclusion of air and moisture in a purified N_2 atmosphere. Analyses of vacuum-dried crystals of **2** accord to the given fomulae.

1: $AgCF_3CO_2$ (0.229 g, 1.0 mmol) and dppm (0.19 g, 0.5 mmol) were suspended in dimethoxyethane (20 mL). At −40 °C, $S(Ph)SiMe_3$ (0.09 mL, 0.5 mmol) is added. Some minutes later, $S(SiMe_3)_2$ (0.04 mL, 0.25 mmol) were also added. A solution was formed that immediately turned yellow. On warming up to room temperature over a period of one day, the solution turned orange. Layering with hexane led to the formation of red crystals of **1** within several weeks (yield: 40 %).

2: $AgC_6H_5CO_2$ (0.23 g, 1.0 mmol) and dppb (0.213 g, 0.5 mmol) were suspended in THF (20 mL). At room temperature, $S(t\mathrm{Bu})SiMe_3$ (0.18 mL, 1.0 mmol) was added. Initially, a red solution and a fine red precipitate formed. The reaction mixture was cooled to −20 °C and $S(SiMe_3)_2$ (0.08 mL, 0.5 mmol) was added, the precipitate redissolved and the solution turned dark brown solution. The color deepened to become black after another 24 h at room temperature. Black crystals of **2** with formed within several weeks (yield: 50 %). Black, cuboid crystals were also obtained along with **2**; these were, however, shown to be amorphous by X-ray diffraction.

Received: July 10, 2003 [Z52351]
Published Online: December 9, 2003

Keywords: cluster compounds · nanoparticles · silver · structure elucidation · sulfur

[1] A. Müller, E. Beckmann, H. Bögge, M. Schmidtmann, A. Dress, *Angew. Chem.* **2002**, *114*, 1210 – 1215; *Angew. Chem. Int. Ed.* **2002**, *41*, 1162 – 1167.

[2] N. T. Tran, D. R. Powell, L. F. Dahl, *Angew. Chem.* **2000**, *112*, 4287 – 4291; *Angew. Chem. Int. Ed.* **2000**, *39*, 4121 – 4125.

[3] A. Schnepf, H. Schnöckel, *Angew. Chem.* **2001**, *113*, 734 – 737; *Angew. Chem. Int. Ed.* **2001**, *40*, 711 – 715.

[4] a) I. Dance, K. Fisher, *Prog. Inorg. Chem.* **1994**, *41*, 637 – 803; b) M. G. Kanatzidis, S. Huang, *Coord. Chem. Rev.* **1994**, *130*, 509 – 621; c) J. Arnold, *Prog. Inorg. Chem.* **1995**, *43*, 353 – 417.

[5] H. Li, J. Kim, M. O'Keeffe, O. M. Yaghi, *Angew. Chem.* **2003**, *115*, 1863 – 1865; *Angew. Chem. Int. Ed.* **2003**, *42*, 1819 – 1821.

[6] K. Tang, X. Xie, Y. Zhang, X. Zhao, X. Jin, *Chem. Commun.* **2002**, 1024 – 1026.

[7] a) S. Dehnen, A. Schäfer, D. Fenske, R. Ahlrichs, *Angew. Chem.* **1994**, *106*, 786 – 790; *Angew. Chem. Int. Ed. Engl.* **1994**, *33*, 746 – 748; b) A. Schäfer, R. Ahlrichs, *J. Am. Chem. Soc.* **1994**, *116*, 10686 – 10692; c) S. Dehnen, A. Schäfer, R. Ahlrichs, D. Fenske, *Chem. Eur. J.* **1996**, *2*, 429 – 435.

[8] H. Krautscheid, D. Fenske, G. Baum, M. Semmelmann, *Angew. Chem.* **1993**, *105*, 1364 – 1367; *Angew. Chem. Int. Ed. Engl.* **1993**, *32*, 1303 – 1306.

[9] D. Fenske, N. Zhu, T. Langetepe, *Angew. Chem.* **1998**, *110*, 2783 – 2788; *Angew. Chem. Int. Ed.* **1998**, *37*, 2639 – 2644.

[10] T. Langetepe, D. Fenske, *Z. Anorg. Allg. Chem.* **2001**, *627*, 820 – 824.

[11] D. Fenske, T. Langetepe, M. Kappes, O. Hampe, P. Weis, *Angew. Chem.* **2000**, *112*, 1925 – 1928; *Angew. Chem. Int. Ed.* **2000**, *39*, 1857 – 1860.

[12] S. Dehnen, A. Eichhöfer, D. Fenske, *Eur. J. Inorg. Chem.* **2002**, 279 – 317.

[13] a) A. Weller, *Angew. Chem.* **1998**, *110*, 1748 – 1749; *Angew. Chem. Int. Ed.* **1998**, *37*, 1658 – 1659; b) A. P. Alivisatos, *Science*, **1996**, *271*, 933 – 937; c) *Clusters and Colloids. From Theory to Applications* (Ed.: G. Schmid), VCH, Weinheim, **1995**; d) *Physics and Chemistry of Metal Cluster Compounds* (Ed.: L. J. de Jongh), Kluwer, Dordrecht, **1994**.

[14] X-ray analyses: STOE-IPDS 2 diffractometer (**1**) or Bruker SMART Apex CCD diffractometer (**2**), $Mo_{K\alpha}$ radiation, data collection and refinement (SHELX97, SHELXD); empirical absorption correction (habitus). CCDC-214450–214451 contain the supplementary crystallographic data for this paper. These data can be obtained free of charge via www.ccdc.cam.ac.uk/conts/retrieving.html (or from the Cambridge Crystallographic Data Centre, 12 Union Road, Cambridge CB21EZ, UK; fax: (+44) 1223-336-033; or deposit@ccdc.cam.ac.uk). **1**: $C_{412}H_{366}O_4F_6Ag_{70}P_{20}S_{48}$, monoclinic, space group $P2_1/n$ (No. 14), $Z=2$, cell dimensions (100 K): $a=2441.4(5)$, $b=2652.3(5)$, $c=4294.6(8)$ pm, $\beta=105.03(2)°$, $V=26868\times10^6$ pm^3, $\mu(Mo_{K\alpha})=2.77$ mm^{-1}; $2\Theta_{max}=54.3°$, 148260 reflections, 58722 independent reflections of which 32549 with $I>2\sigma(I)$, $R_{int}=0.080$, 1474 parameter (Ag, S, P: anisotropic, C: isotropic), highest differential peak 3 e Å^{-3} near inner Ag atoms (Ag34 and Ag35), $R1=0.076$, $wR2=0.22$, Goof = 1.17. Atoms of the solvent molecules are disordered and could not be assigned atomic sites to. **2**: $C_{416}H_{726}Ag_{262}P_{12}S_{162}$, monoclinic, space group $C2/c$ (No. 15), $Z=4$, cell dimensions (200 K): $a=6149.8(4)$, $b=3620.8(3)$, $c=4749.5(4)$ pm, $\beta=106.875(1)°$, $V=101206\times10^6$ pm^3, $\mu(Mo_{K\alpha})=5.07$ mm^{-1}, $2\Theta_{max}=42.8°$, 95572 reflections, 48428 independent reflections of which 25316 with $I>2\sigma(I)$, $R_{int}=0.083$, 2589 parameter (Ag, P, S: anisotropic; C: isotropic, phenyl groups refined as rigid groups), highest differential peak: 4 e Å^{-3}, $R1=0.108$, $wR2=0.28$. Ag atoms Ag110–Ag128 that are positioned near the cluster center show relatively high displacement parameters as a result of the disorder mentioned in the text. Respective split positions have been given numbers Ag129–Ag148 and S79–S83 and have been refined assuming partial occupation.

[15] X. J. Wang, T. Langetepe, C. Persau, B. S. Kang, G. S. Sheldrick, D. Fenske, *Angew. Chem.* **2002**, *114*, 3972 – 3977; *Angew. Chem. Int. Ed.* **2002**, *41*, 3818 – 3822.

[16] a) G. A. Wiegers, *Am. Mineral.* **1971**, *56*, 1882 – 1888; b) Z. G. Pinsker, C. Chian Ling, R. M. Imamov, E. L. Lapidus, *Sov. Phys. Cristallogr. (Engl. Transl.)* **1965**, *7*, 225 – 233.

[17] a) F. C. Kracek, *Trans. Am. Geophys. Union* **1946**, *27*, 364; b) S. Djurle, *Acta Chem. Scand.* **1958**, *12*, 1427; c) P. Rahlfs, *Z. Phys. Chem. Abt. B* **1936**, *31*, 157 – 194; d) E. Rickert, *Z. Phys. Chem.* **1960**, *24*, 418 – 421; e) A. Böttcher, G. Haase, H. Treupel, *Z. Angew. Phys.* **1955**, *7*, 478 – 487; f) P. Junod, *Helv. Phys. Acta* **1959**, *32*, 567 – 600.

[18] A. J. Früh, *Z. Kristallogr.* **1958**, *110*, 136 – 144.

 © 2004 Wiley-VCH Verlag GmbH & Co. KGaA, Weinheim

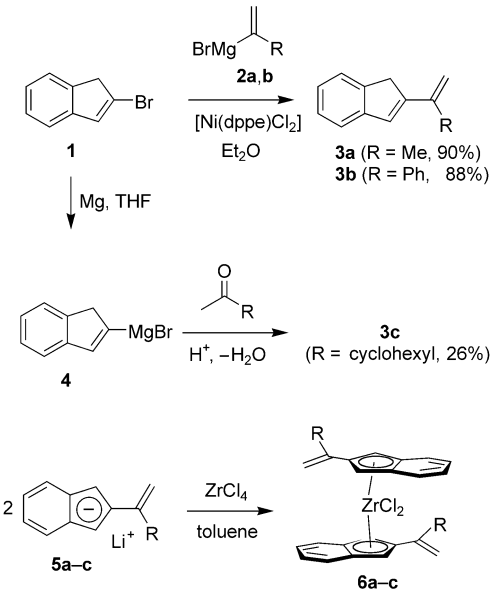
Zirconocene Derivatives

Formation of a Unique *ansa*-Metallocene Framework by Intramolecular Photochemical [2+2] Cycloaddition of Bis(2-alkenylindenyl)zirconium Complexes**

Wan-Li Nie, Gerhard Erker, Gerald Kehr, and Roland Fröhlich*

Developing the chemistry of organic functional groups on bent Group 4 metallocene frameworks and related systems has been notoriously difficult due to the high sensitivity of such organometallic compounds toward the typical reaction conditions used.[1] Noteworthy examples include a Mannich-type carbon–carbon coupling reaction[2] and selective transformations of olefinic substituents attached to the metallocene cyclopentadienyl rings, such as metallacyclic olefin coupling[3] and olefin metathesis reactions.[4] Some time ago we had shown that several bis(alkenylcyclopentadienyl)–$ZrCl_2$ complexes undergo a photochemical [2+2] cycloaddition reaction to yield novel *ansa*-metallocenes. However, many of these systems displayed unfavorable photostationary equilibria.[5] We have now found that bis(2-alkenylindenyl)–$ZrCl_2$ complexes undergo a rapid photochemical olefin [2+2] cycloaddition to produce cyclobutylene-bridged *ansa*-metallocenes in which the annelated indenyl-arene rings are located at the front side of the bent metallocene wedge in a symmetrical fashion above and below the σ-ligand system. A series of typical examples will be described herein.

Two synthetic routes were employed to prepare the ligands.[6] Cross-coupling of 2-bromoindene (**1**) with the alkenyl Grignard reagents **2a** (R = Me) and **2b** (R = Ph) gave the corresponding 2-alkenylindenes **3a**,**b** in about 90% yield each (Scheme 1). The cyclohexyl-substituted 2-alkenylindene was prepared by a complementary route starting from 2-indenyl magnesium bromide (**4**). Addition to cyclohexyl methyl ketone followed by acid-catalyzed dehydration provided both alkene isomers. Chromatographic separation furnished the required compound **3c** in 26% yield. Deprotonation of 2-alkenylindenes **3** was achieved by treatment with *n*-butyl lithium (**3a**,**c**) or LDA (**3b**) in Et_2O at 0°C. Subsequent reaction of the resulting alkenylindenyl lithium reagents (**5a–c**) in toluene with $ZrCl_4$ then yielded the bis(2-alkenylindenyl)–$ZrCl_2$ complexes **6a** (R = Me, 60%), **6b** (R = Ph, 51%), and **6c** (R = cyclohexyl, 27%), respectively.



Scheme 1. Synthesis of bis(2-alkenylindenyl)–$ZrCl_2$ complexes **6a–c**.

In solution, complexes **6a–c** exhibit typical NMR spectra for open, nonbridged metallocenes in rapid conformational equilibrium, even at very low temperatures: complex **6a** (R = Me) displays ^{1}H NMR resonances of symmetry-equivalent CH_2=C(CH_3) substituents at $\delta = 5.41$, 5.17 ppm (=CH_2) and $\delta = 1.94$ ppm (CH_3) [^{13}C NMR: $\delta = 137.8$, 115.3 ppm (C=CH_2), $\delta = 21.2$ ppm (CH_3)]. As expected, only a single indenyl 1-H/3-H signal ($\delta = 6.25$) is observed in addition to a simple AA′XX′ pattern for the 4-H/7-H and 5-H/6-H indene hydrogen resonances ($\delta = 7.56$, 7.22 ppm).

Single crystals for X-ray structure analysis were obtained from the complexes **6a** (R = Me) and **6c** (R = cyclohexyl), in both cases from solutions in toluene/pentane at −20°C. In the crystal **6a** features a "*meso*-like" rotational structure[7] in which the annelated phenylene rings of the two indenyl ligands are oriented toward the same side of the bent metallocene wedge (Figure 1, left). The CH_2=C(CH_3) substituents at the indenyl 2-positions point to the other lateral sector. The CH_2=C(CH_3) substituents are both oriented in the indenyl ligand plane (θ(C9-C1,C10,C11) = −170.6(6)°) with the =CH_2 groups pointing toward the back side of the bent metallocene wedge.

In contrast, the cyclohexyl-substituted complex **6c** attains an approximately C_2-symmetric "*rac*-like" conformation[7,8] in the solid state, with the CH_2=C(cyclohexyl) substituents oriented toward opposite lateral metallocene sectors (Figure 1, right). Again, the alkenyl groups are almost coplanar with the adjacent indenyl rings (θ(C2-C1,C10,C11) = 13.7(5)°). In this case, the =CH_2 moieties point toward the open front side of the bent metallocene wedge.

Complexes **6a–c** provide active homogeneous Ziegler–Natta catalysts when activated with a large excess of methylalumoxane (MAO). They yield atactic polypropylene with typical activities (e.g. 100 g PP mmol^{-1}[Zr] h^{-1} bar^{-1} at

[*] Dr. W.-L. Nie, Prof. Dr. G. Erker, Dr. G. Kehr, Dr. R. Fröhlich[+]
Organisch-Chemisches Institut
Universität Münster
Corrensstrasse 40, 48149 Münster (Germany)
Fax: (+49) 251-833-36503
E-mail: erker@uni-muenster.de

[+] X-ray crystal-structure analysis

[**] Financial support from the Fonds der Chemischen Industrie and the Deutsche Forschungsgemeinschaft is gratefully acknowledged. W.-L. Nie thanks the Alexander-von-Humboldt-Foundation for a fellowship.

 © 2004 Wiley-VCH Verlag GmbH & Co. KGaA, Weinheim DOI: 10.1002/anie.200351886

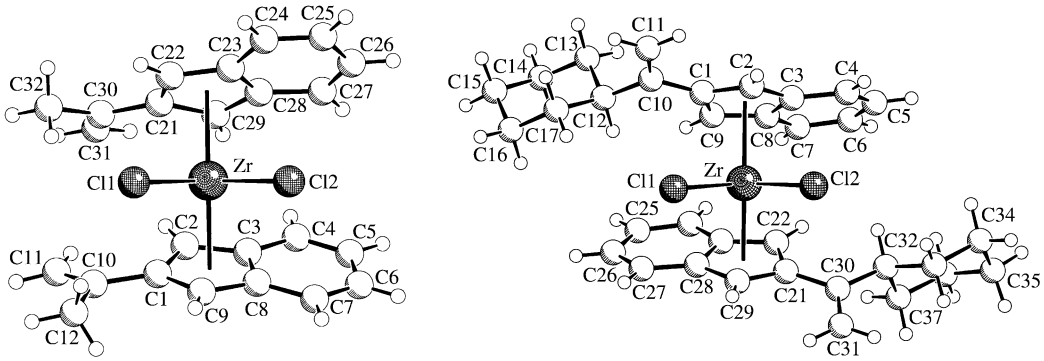
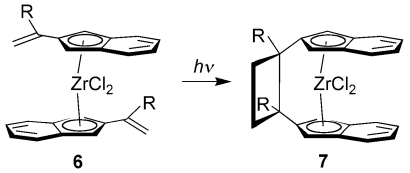


Figure 1. The molecular structure of **6a** (left) and **6c** (right). Selected bond lengths [Å] and angles [°]: **6a**: Zr–Cl1 2.438(2), Zr–Cl2 2.417(2), C1–C10 1.488(8), C21–C30 1.488(8), C10–C11 1.336(9), C30–C31 1.317(8), C10–C12 1.483(8), C30–C32 1.503(9); Cl1-Zr-Cl2 93.6(1), C1-C10-C11 120.1(6), C21-C30-C31 120.9(6), C1-C10-C12 117.1(6), C21-C30-C32 116.6(6), C11-C10-C12 122.5(6), C31-C30-C32 122.6(6). **6c**: Zr–Cl1 2.411(1), Zr–Cl2 2.402(1), C1–C10 1.467(4), C21–C30 1.472(4), C10–C11 1.325(5), C30–C31 1.329(4), C10–C12 1.507(5), C30–C32 1.514(4); Cl1-Zr-Cl2 96.30(3), C1-C10-C11 119.4(3), C21-C30-C31 119.3(3), C1-C10-C12 117.8(3), C21-C30-C32 118.5(3), C11-C10-C12 122.7(3), C31-C30-C32 122.0(3).

0 °C, $M_w = 114000$, $M_w/M_n = 2.1$, mmmm = 11 % for **6a**/MAO, Al:Zr ≈ 2000).

The most remarkable feature of complexes **6** is their behavior upon photolysis. Irradiation of **6a–c** in toluene results in rapid and practically complete conversion into the corresponding 1,2-disubstituted 1,2-cyclobutylene-bridged *ansa*-zirconocenes **7a–c** [Eq. (1)] The [2+2] cycloadditions are complete within 2–3 h, and the conversion **6**→**7** was nearly quantitative, as judged from NMR spectra. The photochemical ring closure takes place stereoselectively to yield **7a–c**, in which the substituents R are in 1,2-*cis* positions at the newly formed four-membered ring. This is evident from the NMR spectra of **7**, which exhibit a right/left differentiation of the indenyl signals (in contrast to the symmetry-equivalent signals of the open, conformationally equilibrated starting materials **6**). The ^{1}H NMR spectrum of **7a** (R = Me) shows equal-intensity pairs of signals for the indenyl protons 1-H/3-H ($\delta = 6.60/6.56$ ppm; ^{13}C NMR: $\delta = 102.7/99.4$ ppm), 4-H/7-H ($\delta = 7.61/7.46$ ppm), and 5-H/6-H ($\delta = 7.21/7.15$ ppm). It also features an AA′XX′ pattern of cyclobutylene proton signals at $\delta = 2.77$ and 2.23 ppm (^{13}C NMR: $\delta = 31.1$ ppm) and a single resonance for the methyl group at $\delta = 1.64$ ppm (^{13}C NMR: $\delta = 25.8$ ppm).



6 **7** (1)

Complex **7c** (R = cyclohexyl) was characterized by X-ray structure analysis (Figure 2).[9] The complex contains a pair of 2-substituted η^5-indenyl ligands with uniformly coordinated annelated five-membered rings (the Zr–C_{Cp} distances range from 2.458(4) Å to 2.608(4) Å). The cyclobutylene bridge that was formed by the photochemical [2+2] cycloaddition is located at the narrow back side of the bent metallocene wedge. Three of the cyclobutane bond lengths are in the typical range [1.548(5) Å (C10–C11), 1.527(5) Å (C11–C31), 1.556(5) Å (C31–C30)] whereas the internal C–C connection is slightly longer [1.628(5) Å (C10-C30)]. This probably indicates a slight strain within the *ansa*-metallocene framework. The four-membered carbocycle in **7c** is slightly puckered (sum of the internal bonding angles: 355.5°; angle between the C11-C10-C30 and C11-C31-C30 planes: 23.0°).

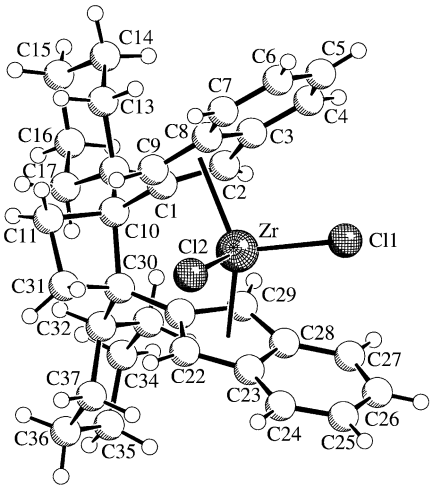


Figure 2. Molecular structure of **7c**. Selected bond lengths [Å] and angles [°]: Zr–Cl1 2.401(1), Zr–Cl2 2.469(1), C1–C10 1.532(5), C21–C30 1.507(5), C10–C30 1.628(5), C10–C11 1.548(5), C30–C31 1.556(5), C10–C12 1.553(5), C30–C32 1.562(5), C11–C31 1.527(5); Cl1-Zr-Cl2 98.19(4), C1-C10-C11 111.2(3), C21-C30-C31 114.3(3), C1-C10-C12 107.8(3), C21-C30-C32 109.1(3), C11-C10-C12 114.3(3), C31-C30-C32 111.0(3), C1-C10-C30 108.2(3), C21-C30-C10 116.0(3), C30-C10-C11 87.4(3), C10-C30-C31 86.7(2), C10-C11-C31 90.6(3), C30-C31-C11 90.8(3).

Upon activation with MAO the *ansa*-metallocenes **7** provide interesting catalysts for ethene/1-octene copolymerization at elevated temperatures.[10] At 60 °C the **7a**/MAO system (Al:Zr ≈ 1150) yields a random ethene/1-octene copolymer. The catalyst activity (ca. 2300 g copolymer mmol^{-1} [Zr] h^{-1} bar^{-1}) and the 1-octene incorporation (ethene:1-

 © 2004 Wiley-VCH Verlag GmbH & Co. KGaA, Weinheim

octene ≈ 5:1) approaches values comparable with those of some "constrained geometry" catalysts;[11] however, the molecular weight of the copolymer obtained with **7a**/MAO is rather low ($M_w = 3800$; $M_w/M_n = 2.0$). Figure 3 shows a ^{13}C NMR spectrum of a typical example.

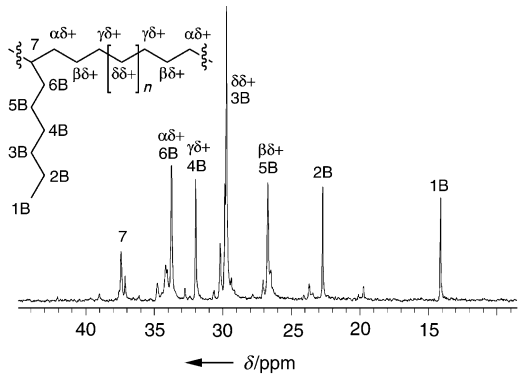
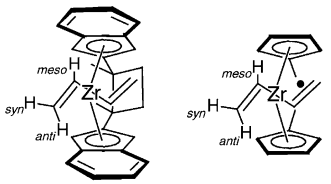


Figure 3. $^{13}C\{^1H\}$ NMR spectrum of an ethene/1-octene copolymer (ca. 5:1) obtained with the **7a**/MAO catalyst at 60 °C (1 bar C_2H_4, Al:Zr ≈ 1150, $M_w \approx 3800$)

The **7a**/MAO catalyst system is still active at 90 °C. However, at this temperature rapid decomposition occurs, which results in darkly colored polymer mixtures as well as lower activities and molecular weights of the ethene/1-octene copolymers (**7a**/MAO, Al:Zr ≈ 1150, 90 °C, activity: ca. 1400, 4.5:1 ethene/1-octene ratio in the copolymer, $M_w \approx 1500$ (bimodal distribution)).

Treatment of many *ansa*-zirconocene dichlorides with butadiene magnesium reagents predominantly (or exclusively) yields the (s-*cis*-η^4-butadiene)zirconocene isomers.[12] In contrast, the reaction of **7a** with $C_4H_6Mg{\cdot}2\,THF$ gives only



s-*trans*-**8** s-*trans*-**9**

s-*trans*-**8**. A comparison of the ^1H NMR spectrum of s-*trans*-**8** (Figure 4) with that of a typical example (e.g. s-*trans*-**9**)[12] reveals a large shift of the butadiene *meso*-H resonances to negative δ values [s-*trans*-**8**: $\delta = -1.45$ (dt, $^3J_{HH(meso,anti)} = {}^3J_{HH(meso,meso)} = 16.2$ Hz, $^3J_{HH(meso,syn)} = 7.2$ Hz), $\delta = -1.55$ (dt, $^3J_{HH} = 16.2$ Hz and 7.1 Hz); s-*trans*-**9**: $\delta = +1.34$]. This indicates that the C–H_{meso} bonds in s-*trans*-**8** are oriented toward the π system of the annelated arene rings. It is likely that the ensuing σ-C–H/π-arene interaction[13] stabilizes s-*trans*-**8** to such an extent that the corresponding s-*cis* isomer can no longer energetically compete under the equilibrium conditions.

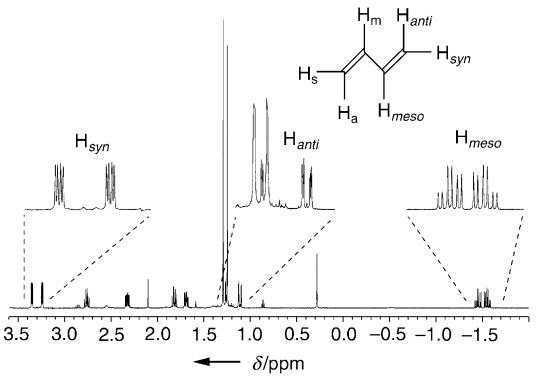


Figure 4. Portion of the ^1H NMR spectrum of s-*trans*-**8** (C_6D_6, 298 K, 600 MHz).

The *ansa*-zirconocene **7** was readily prepared by [2+2] cycloaddition. The remarkable spectroscopic, structural, and chemical features of *ansa*-metallocenes derived from **7** may be regarded as first indications for a unique stereoelectronic environment at the metal center inside the "phenylene π-electron box". We expect that the introduction of reactive ligands into this specific electronic environment will lead to the discovery of additional unusual chemical properties.

Experimental Section

7a: A solution of **6a** (90 mg, 0.19 mmol) in toluene (5 mL) was irradiated for 3 h at ambient temperature in a Schlenk flask with an external Philips HPK 125 UV lamp with a pyrex filter. The solvent was removed in vacuo. The residue was washed with pentane, and the product was collected by filtration to yield **7a** (45 mg, 50 %). Elemental analysis (%) calcd for $C_{24}H_{22}Cl_2Zr$ (472.6): C 61.00, H 4.69; found: C 60.32, H 4.56; ^1H NMR (CD_2Cl_2, 298 K, 599.0 MHz): $\delta = 7.61, 7.46$ (m, each 2H, indenyl 4-H, 7-H), 7.21, 7.15 (m, each 2H, indenyl 5-H, 6-H), 6.60, 6.56 (dd, each 2H, indenyl 1-H, 3-H), 2.77, 2.23 (m, each 2H, cyclobutylene CH_2), 1.64 ppm (s, 6H, CH_3); ^{13}C NMR (CD_2Cl_2, 298 K, 150.6 MHz): $\delta = 147.4$ (indenyl C2), 131.4, 126.8 (indenyl C3a, C7a), 126.5, 125.6 (indenyl C5, C6), 125.7, 125.4 (indenyl C4, C7), 102.7, 99.4 (indenyl C1, C3), 50.3 (cyclobutylene C), 31.1 (cyclobutylene CH_2), 25.8 ppm (CH_3).

7c: The photolysis of **6c** (90 mg, 0.15 mmol) was carried out analogously to yield **7c** (50 mg, 55 %). Single crystals of **7c** were obtained from dichloromethane. Elemental analysis (%) calcd for $C_{34}H_{38}Cl_2Zr{\cdot}0.5\,CH_2Cl_2$ (651.3): C 63.63, H 6.04; found: C 64.39, H 5.94; ^1H NMR (CD_2Cl_2, 298 K, 599.0 MHz): $\delta = 7.64, 7.41$ (m, each 2H, indenyl 4-H, 7-H), 7.24, 7.12 (m, each 2H, indenyl 6-H, 5-H), 6.87, 6.37 (dd, each 2H, indenyl 1-H, 3-H), 2.54, 2.42 (m, each 2H, cyclobutylene CH_2), 2.05 (m, 2H, cyclohexyl CH), 1.90–1.05 ppm (several m, 20H, cyclohexyl CH_2); ^{13}C NMR (CD_2Cl_2, 298 K, 150.6 MHz): $\delta = 144.1$ (indenyl C2), 132.4, 124.0 (indenyl C3a, C7a), 127.0, 125.5 (indenyl C6, C5), 125.31, 125.29 (indenyl C7, C4), 107.3, 99.9 (indenyl C1, C3), 61.2 (butylene C), 47.0 (cyclohexyl CH), 31.4, 29.2, 28.9, 27.5, 27.4, 27.0 ppm (CH_2).

s-*trans* 8: Toluene (30 mL) was added to **7a** (240 mg, 0.51 mmol) and the butadiene magnesium reagent ($C_4H_6Mg{\cdot}2\,THF$, 120 mg, 0.54 mmol) at −78 °C. The mixture was allowed to reach room temperature slowly and stirred overnight. The solvent was removed in vacuo, and the residue was washed with pentane and dried in vacuo to give of **8** (120 mg, 52 %) as a dark red solid. ^1H NMR (C_6D_6, 298 K, 599.0 MHz): $\delta = 6.85, 6.53, 6.49, 6.27, 6.26, 6.13$ (each 1H, $indenyl_A$), 6.84, 6.58, 6.54, 6.47, 6.28, 6.21 (each 1H, $indenyl_B$), 3.35 (dd, $^3J_{HH} =$

 © 2004 Wiley-VCH Verlag GmbH & Co. KGaA, Weinheim

7.2 Hz, $^2J_{HH}=3.2$ Hz) and 3.24 (dd, $^3J_{HH}=7.1$ Hz, $^2J_{HH}=3.1$ Hz) (each 1 H_{syn}, butadiene), 1.28 (dd, $^3J_{HH}=16.2$ Hz, $^2J_{HH}=3.2$ Hz) and 1.11 (dd, $^3J_{HH}=16.2$ Hz, $^2J_{HH}=3.1$ Hz) (each 1 H_{anti}, butadiene), −1.45 (dt, $^3J_{HH}=16.2$ Hz, $^3J_{HH}=7.2$ Hz) and −1.55 (dt, $^3J_{HH}=16.2$ Hz, $^3J_{HH}=7.1$ Hz) (each 1 H_{meso}, butadiene), 2.76/1.69 and 2.32/1.82 (each 1 H, cyclobutylene CH_2), 1.29, 1.25 ppm (each s, each 3 H, CH_3). ^{13}C NMR (C_6D_6, 298 K, 150.6 MHz): $\delta=137.8$, 123.1, 123.5, 122.6, 121.9, 121.6, 119.7, 83.2, 82.8 ($indenyl_B$), 137.2, 123.7, 123.6, 123.3, 122.7, 121.5, 118.0, 83.7, 81.2 ($indenyl_A$), 114.1, 113.5, 73.5, 71.0 (butadiene), 49.1, 48.9, 31.9, 29.9 (cyclobutylene), 27.2, 23.8 ppm (CH_3).

Received: May 13, 2003
Revised: September 8, 2003 [Z51886]

Keywords: indenyl ligands · metallocenes · photolysis · polymerization · zirconium

[1] See, for example: R. D: Rogers, J. L. Atwood, M. D. Rausch, D. W. Macomber, W. P. Hart, *J. Organomet. Chem.* **1982**, *238*, 79; D. W. Macomber, W. P. Hart, M. D. Rausch, *Adv. Organomet. Chem.* **1982**, *21*, 1; M. Oberhoff, L. Duda, J. Karl, R. Mohr, G. Erker, R. Fröhlich, M. Grehl, *Organometallics* **1996**, *15*, 4005 – 4011; K. Klaß, L. Duda, N. Kleigrewe, G. Erker, R. Fröhlich, E. Wegelius, *Eur. J. Inorg. Chem.* **1999**, 11 – 19; J. Wonnemann, M. Oberhoff, G. Erker, R. Fröhlich, K. Bergander, *Eur. J. Inorg. Chem.* **1999**, 1111 – 1120; D. Kunz, G. Erker, R. Fröhlich, G. Kehr, *Eur. J. Inorg. Chem.* **2000**, 409 – 416; D. Hüerländer, R. Fröhlich, G. Erker, *J. Chem. Soc. Dalton Trans.* **2002**, 1513 – 1520.

[2] S. Knüppel, G. Erker, R. Fröhlich, *Angew. Chem.* **1999**, *111*, 2048 – 2051; *Angew. Chem. Int. Ed.* **1999**, *38*, 1923 – 1926; S.-D. Bai, X.-H. Wei, J.-P. Guo, D.-S. Liu, Z.-Y. Zhou, *Angew. Chem.* **1999**, *111*, 2051 – 2054; *Angew. Chem. Int. Ed.* **1999**, *38*, 1926 – 1928.

[3] T. H. Warren, G. Erker, R. Fröhlich, B. Wibbeling, *Organometallics* **2000**, *19*, 127 – 134; L. Lukešová, P. Štěpnička, K. Fejfavrová, R. Gyepes, I. Císařová, M. Horáček, J. Kubišta, K. Mach, *Organometallics* **2002**, *21*, 2639 – 2653; M. Horáček, P. Štěpnička, K. Fejfavrová, R. Gyepes, I. Císařová, J. Kubišta, K. Mach, *J. Organomet. Chem.* **2002**, *642*, 148 – 155; A. I. Licht, H. G. Alt, *J. Organomet. Chem.* **2002**, *648*, 134 – 148.

[4] D. Hüerländer, N. Kleigrewe, G. Kehr, G. Erker, *Eur. J. Inorg. Chem.* **2002**, 2633 – 2642; M. Ogasawara, T. Nagano, T. Hayashi, *J. Am. Chem. Soc.* **2002**, *124*, 9068 – 9069.

[5] G. Erker, S. Wilker, C. Krüger, R. Goddard, *J. Am. Chem. Soc.* **1992**, *114*, 10983 – 10984; G. Erker, S. Wilker, C. Krüger, M. Nolte, *Organometallics* **1993**, *12*, 2140 – 2151.

[6] H. Schumann, D. F. Karasiak, S. H. Muhle, R. L. Halterman, W. Kaminsky, U. Weingarten, *J. Organomet. Chem.* **1999**, *579*, 356 – 372; R. L. Halterman, D. R. Fahey, E. F. Bailly, D. W. Dockter, O. Stenzel, J. L. Shipman, M. A. Khan, S. Dechert, H. Schumann, *Organometallics* **2000**, *19*, 5464 – 5470.

[7] E. Hauptmann, R. M. Waymouth, J. W. Ziller, *J. Am. Chem. Soc.* **1995**, *117*, 11586 – 11587; T. Dreier, G. Erker, R. Fröhlich, B. Wibbeling, *Organometallics* **2000**, *19*, 4095 – 4103; T. Dreier, G. Unger, G. Erker, B. Wibbeling, R. Fröhlich, *J. Organomet. Chem.* **2001**, *622*, 143 – 148; T. Dreier, K. Bergander, E. Wegelius, R. Fröhlich, G. Erker, *Organometallics* **2001**, *20*, 5067 – 5075.

[8] For the general conformational properties of substituted bis(indenyl)$ZrCl_2$ complexes see, for example: M. Knickmeier, G. Erker, T. Fox, *J. Am. Chem. Soc.* **1996**, *118*, 9623 – 9630; T. Jödicke, F. Menges, G. Kehr, G. Erker, U. Höweler, R. Fröhlich, *Eur. J. Inorg. Chem.* **2001**, 2097 – 2106, and references therein.

[9] CCDC 210084–210086 contains the supplementary crystallographic data for this paper. These data can be obtained free of charge via www.ccdc.cam.ac.uk/conts/retrieving.html (or from the Cambridge Crystallographic Data Centre, 12, Union Road, Cambridge CB2 1EZ, UK; fax: (+44) 1223-336-033; or deposit@ccdc.cam.ac.uk). **6a**: $C_{24}H_{22}Cl_2Zr$, monoclinic, space group $P2_1/n$, $a=10.862(1)$, $b=13.507(1)$, $c=14.264(1)$ Å, $\beta=93.23(1)°$, $V=2089.4(3)$ Å^3, $\rho_{calcd}=1.502$ g cm^{-3}, $\mu=7.88$ cm^{-1}, $Z=4$, $T=198$ K, 5775 reflections collected, 3498 independent and 2383 observed, 246 refined parameters, $R=0.056$, $wR^2=0.127$. Due to the small size, the crystal diffracted very weakly. **6c**: $C_{34}H_{38}Cl_2Zr$, orthorhombic, space group $P2_12_12_1$, $a=9.391(1)$, $b=11.494(1)$, $c=26.995(1)$ Å, $V=2913.8(4)$ Å^3, $\rho_{calcd}=1.388$ g cm^{-3}, $\mu=5.82$ cm^{-1}, $Z=4$, $T=198$ K, 20454 reflections collected, 7080 independent and 5824 observed, 334 refined parameters, $R=0.037$, $wR^2=0.067$, Flack parameter −0.06(4). **7c**: $C_{34}H_{38}Cl_2Zr\cdot CH_2Cl_2$, monoclinic, space group $P2_1/n$, $a=10.694(1)$, $b=7.880(1)$, $c=37.258(1)$ Å, $\beta=94.11(1)°$, $V=3131.6(3)$ Å^3, $\rho_{calcd}=1.471$ g cm^{-3}, $\mu=7.16$ cm^{-1}, $Z=4$, $T=198$ K, 11911 reflections collected, 7160 independent, 4785 observed reflections, 362 refined parameters, $R=0.054$, $wR^2=0.156$.

[10] H.-H. Brintzinger, D. Fischer, R. Mülhaupt, B. Rieger, R. M. Waymouth, *Angew. Chem.* **1995**, *107*, 1255 – 1283; *Angew. Chem. Int. Ed. Engl.* **1995**, *34*, 1143 – 1170.

[11] A. L. McKnight, R. M. Waymouth, *Chem. Rev.* **1998**, *98*, 2587 – 2598; K. Kunz, G. Erker, S. Döring, S. Bredeau, G. Kehr, R. Fröhlich, *Organometallics* **2002**, *21*, 1031 – 1041.

[12] M. Dahlmann, G. Erker, R. Fröhlich, O. Meyer, *Organometallics* **2000**, *19*, 2956 – 2967; M. Dahlmann, G. Erker, R. Fröhlich, O. Meyer, *Organometallics* **1999**, *18*, 4459 – 4461.

[13] *The CH/π-Interaction; Evidence, Nature, and Consequences*: M. Nishio, M. Hirota, Y. Umezawa in *Methods in Stereochemical Analysis* (Ed.: A. P. Marchand), Wiley-VCH, New York, **1998**.

 © 2004 Wiley-VCH Verlag GmbH & Co. KGaA, Weinheim

Asymmetric Synthesis

Desymmetrization of Metalated Cyclohexadienes and Application to the Synthesis of Nephrosteranic Acid**

*Florian Schleth and Armido Studer**

The stereoselective nucleophilic addition of allylmetal compounds to carbonyl compounds is a very important C–C bond-forming reaction in modern organic synthesis.[1] Si,[2] Sn,[3] B,[4] Li,[5] and Ti allyl compounds[6] have been used successfully in asymmetric allylations. To the best of our knowledge, no reports on the stereoselective allylation of

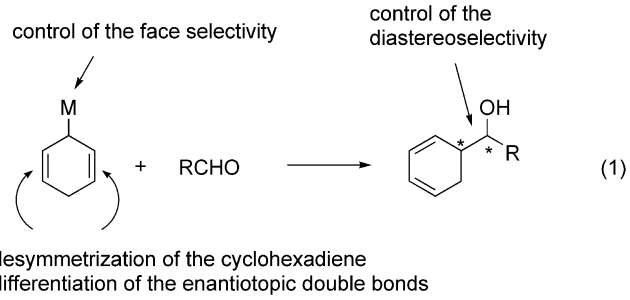
[*] Dipl.-Chem. F. Schleth, Prof. Dr. A. Studer
Fachbereich Chemie der Universität
Hans-Meerwein-Strasse
35032 Marburg (Germany)
Fax: (+49) 6421-2825629
E-mail: studer@mailer.uni-marburg.de

[**] We thank the Deutsche Forschungsgemeinschaft (DFG) for support and Dr. Klaus Harms for the X-ray structure analysis.

Supporting information for this article is available on the WWW under http://www.angewandte.org or from the author.

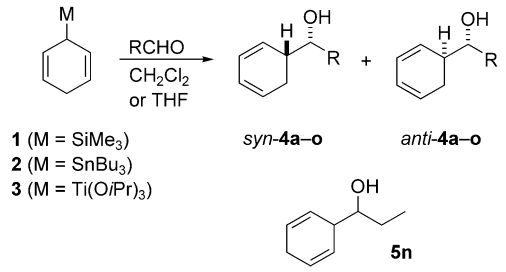
 DOI: 10.1002/anie.200352254 © 2004 Wiley-VCH Verlag GmbH & Co. KGaA, Weinheim

carbonyl compounds using metalated cyclohexadienes [Eq. (1)] have appeared to date. A big challenge is the differentiation of the two enantiotopic double bonds (desymmetrization of the 1,4-cyclohexadiene).[7] The face selectivity



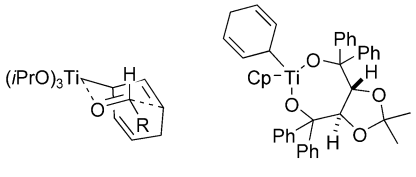
of the electrophilic attack can probably be controlled by the metal (open versus cyclic transition state). Another problem to be solved is the control of the diastereoselectivity. Furthermore, metallotropic 1,3-shifts have to be considered.[1] Herein we describe our first results on the use of metalated cyclohexadienes in highly stereoselective allylation reactions. In addition we present a first application in a highly efficient synthesis of nephrosteranic acid.

The reaction of benzaldehyde with various metalated cyclohexadienes was studied first (Scheme 1). With silylated



Scheme 1. The reaction of cyclohexadienylmetalates with aldehydes (only one enantiomer is shown).

cyclohexadiene **1**[8] and stannylated diene **2** only low diastereoselectivities (< 3:1) were obtained in the presence of different Lewis acids. In contrast, the reaction of the Ti compound **3** with benzaldehyde at −78 °C occurred in excellent yield and with high selectivity (99 %, *syn*/*anti* 9:1).[9,10] The *syn* selectivity can be rationalized by considering a six-membered chair transition state **6**, in which the R group of the aldehyde assumes a pseudo equatorial position .[1]



6 **7**

Encouraged by these first results, we examined the differentiation of the enantiotopic double bonds in cyclohexadienyl Ti compounds. Duthaler et al. have successfully used TADDOL-derived[11] allyltitanium complexes for highly enantioselective allylations.[12] In analogy, we prepared the chiral cyclohexadienyltitanium complex **7**. The reaction of **7** with benzaldehyde (THF, −78 °C) occurred with excellent diastereoselectivity (*syn*/*anti* > 99:1). Furthermore, promising enantioselectivity was measured (e.r. 91:9, chiral GC), however, *syn*-**4a** was formed in low yield (19 %). Most likely some decomposition of **7** occurred at −78 °C. Indeed, the same reaction at lower temperature (−100 to −110 °C, THF/Et_2O) provided *syn*-**4a** in 83 % yield (*syn*/*anti* > 99:1) with high enantioselectivity (e.r. 98:2, Table 1, entry 1).

Table 1: Reaction of **7** with various aldehydes.

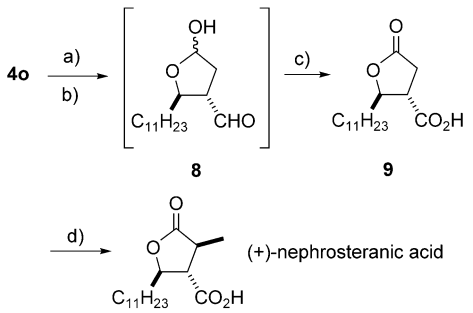
Entry	R	Product	Yield [%]	d.r. (*syn*/*anti*)	e.r.
1	Ph	**4a**	83	> 99:1[a]	98:2[a]
2	4-Me-Ph	**4b**	82	> 99:1[a]	95:5[a]
3	4-MeO-Ph	**4c**	63	> 99:1[b]	> 99:1[b]
4	4-Br-Ph	**4d**	94	> 99:1[a]	97:3[a]
5	3-MeO-Ph	**4e**	58	> 99:1[a]	97:3[b]
6	2-MeO-Ph	**4f**	61	> 99:1[a]	> 99:1[a]
7	2-Me-Ph	**4g**	56	> 99:1[a]	96:4[a]
8	2-Br-Ph	**4h**	92	> 99:1[c]	> 99:1[c]
9	α-naphthyl	**4i**	96	> 99:1[b]	> 99:1[b]
10	β-naphthyl	**4j**	81	> 99:1[b]	90:10[b]
11	furyl	**4k**	72	98:2[a]	93:7[b]
12	PhCH=CH	**4l**	93	> 99:1[b]	90:10[b]
13	PhC≡C	**4m**	86	> 99:1[b]	99:1[b]
14	Et	**4n**	40[d]	> 99:1[a]	91:9[e]

[a] Ratio determined by GC analysis. [b] Ratio determined by HPLC analysis. [c] Determined after transformation to **4a** (*t*BuLi, THF, −78 °C; H_2O) by GC analysis. [d] The 1,4-diene **5n** was formed as a side product and could not be removed (**4n**/**5n** 88:12). [e] Determined after oxidation to (1*R*)-1-phenylpropanol by GC analysis.

The reactions with *para*-, *meta*-, and *ortho*-substituted benzaldehyde derivatives occurred with excellent diastereoselectivity and high enantioselectivity (products **4b**–**h**, entries 2–8). α-Naphthaldehyde and phenylpropargyl aldehyde reacted with complete stereoselectivity, whereas furfural, β-naphthaldehyde, and cinnamaldehyde provided lower but still good enantioselectivity and excellent diastereoselectivity (products **4i**–**m**, entries 9–13). Addition to propanal occurred with high diastereo- but lower enantioselectivity (entry 14), and the 1,4-diene **5n** formed as a side product. The absolute configuration of the major isomers of all the new compounds was assigned based on the rearomatization of **4n** ($Pd(OAc)_2$/$Cu(OAc)_2$, MeOH) to provide (*R*)-1-phenylpropanol (e.r. 91:9). In analogy to the results of Duthaler et al. addition of **7** occurs onto the *Si* face of the aldehyde.

Finally, our new method was applied to the synthesis of nephrosteranic acid.[13] Reaction of **7** with dodecanal afforded **4o** (Scheme 1, R = $C_{11}H_{23}$, 79 %, *syn*/*anti* > 99:1).[14] Double dihydroxylation under Upjohn conditions[15] provided the corresponding pentol, which was directly subjected to diol cleavage ($NaIO_4$, THF/H_2O) to give lactol **8** (Scheme 2).

 © 2004 Wiley-VCH Verlag GmbH & Co. KGaA, Weinheim



Scheme 2. Synthesis of nephrosteranic acid: a) OsO_4 (2%), NMO (3.5 equiv), acetone/H_2O (4:1); b) $NaIO_4$ (3 equiv), THF/H_2O (1:1); c) CrO_3/H_2SO_4, acetone; d) NaHMDS, MeI, THF. HMDS = hexamethyldisilazane, NMO = *N*-methylmorpholine *N*-oxide.

Crude **8** was oxidized under Jones conditions to γ-butyrolactone **9** (19% yield over three steps). Methylation according to a literature procedure[13d] afforded scalemic nephrosteranic acid (60%, $[\alpha]_D^{25} = +22.7$ ($c = 0.78$ in $CHCl_3$); lit.[13a] $[\alpha]_D^{25} = +27.2$ ($c = 1.45$ in $CHCl_3$)).

In conclusion, the easily prepared chiral cyclohexadienyltitanate **7** reacts with aldehydes in highly diastereo- and enantioselective allylations. The resulting functionalized 1,3-cyclohexadienes are highly useful building blocks for the preparation of biologically important γ-butyrolactones, as documented by a short efficient synthesis of nephrosteranic acid.

Received: June 30, 2003
Revised: September 22, 2003 [Z52254]

Keywords: asymmetric synthesis · natural products · synthetic methods · TADDOLs · titanium · total synthesis

[1] *Houben-Weyl*, *Vol. E21b* (Eds.: G. Helmchen, R. W. Hoffmann, J. Mulzer, E. Schaumann), Thieme, Stuttgart, **1995**, pp. 1357–1602; Y. Yamamoto, N. Asao, *Chem. Rev.* **1993**, *93*, 2207.

[2] I. Fleming, A. Barbero, D. Walter, *Chem. Rev.* **1997**, *97*, 2063; "Allylsilanes": E. J. Thomas in *Houben-Weyl*, *Vol. E21b* (Eds.: G. Helmchen, R. W. Hoffmann, J. Mulzer, E. Schaumann), Thieme, Stuttgart, **1995**, p. 1491.

[3] "Allylstannanes": E. J. Thomas in *Houben-Weyl*, *Vol. E21bG* (Eds.: G. Helmchen, R. W. Hoffmann, J. Mulzer, E. Schaumann), Thieme, Stuttgart, **1995**, p. 1508; selected examples: M. Kurosu, M. Lorca, *Tetrahedron Lett.* **2002**, *43*, 1765, and references therein; C.-M. Yu, J.-Y. Lee, B. So, J. Hong, *Angew. Chem.* **2002**, *114*, 169; *Angew. Chem. Int. Ed.* **2002**, *41*, 161, and references therein.

[4] "Allylboron Reagents": W. R. Roush in *Houben-Weyl*, *Vol. E21b* (Eds.: G. Helmchen, R. W. Hoffmann, J. Mulzer, E. Schaumann), Thieme, Stuttgart, **1995**, p. 1410; W. R. Roush, S. Chemler in *Modern Carbonyl Chemistry* (Ed.: J. Otera), Wiley-VCH, Weinheim, **2000**, p. 403.

[5] D. Hoppe, T. Hense, *Angew. Chem.* **1997**, *109*, 2376; *Angew. Chem. Int. Ed. Engl.* **1997**, *36*, 2282.

[6] a) D. Seebach, B. Weidmann, L. Widler, *Mod. Synth. Methods* **1983**, *3*, 217; b) M. T. Reetz, *Organotitanium Reagents in Organic Synthesis*, Springer, Berlin, **1986**; c) "Allyltitanium and Allylzirconium Reagents": D. Hoppe in *Houben-Weyl*, *Vol. E21b* (Eds.: G. Helmchen, R. W. Hoffmann, J. Mulzer, E. Schaumann), Thieme, Stuttgart, **1995**, p. 1551.

[7] For stereoselective dihydroxylations of silylated 1,4-cyclohexadienes see: R. Angelaud, O. Babot, T. Charvat, Y. Landais, *J. Org. Chem.* **1999**, *64*, 9613.

[8] Silylated cyclohexadienes have been used successfully as tin hydride substituents in radical chemistry: A. Studer, S. Amrein, *Angew. Chem.* **2000**, *112*, 3196; *Angew. Chem. Int. Ed.* **2000**, *39*, 3080; A. Studer, S. Amrein, F. Schleth, T. Schulte, J. C. Walton, *J. Am. Chem. Soc.* **2003**, *125*, 5726.

[9] Ti compound **3** was readily prepared from 1,4-cyclohexadiene by lithiation (*s*BuLi, TMEDA, THF, −78°) followed by transmetalation with $Ti(OiPr)_4$.

[10] The major isomer of **4a** was unambiguously assigned as the *syn* isomer based on X-ray structure analysis. All the other compounds were assigned in analogy. CCDC-213624 contains the supplementary crystallographic data for this paper. These data can be obtained free of charge via www.ccdc.cam.ac.uk/conts/retrieving.html (or from the Cambridge Crystallographic Data Centre, 12, Union Road, Cambridge CB21EZ, UK; fax: (+44) 1223-336-033; or deposit@ccdc.cam.ac.uk).

[11] For an excellent review on the use of TADDOLs in asymmetric synthesis see: D. Seebach, A. K. Beck, A. Heckel, *Angew. Chem. Int. Ed.* **2001**, *113*, 96; *Angew. Chem. Int. Ed.* **2001**, *40*, 92.

[12] A. Hafner, R. O. Duthaler, R. Marti, G. Rihs, P. Rothe-Streit, F. Schwarzenbach, *J. Am. Chem. Soc.* **1992**, *114*, 2321.

[13] For recent syntheses of nephrosteranic acid see: a) H. Takahata, Y. Uchida, T. Momose, *J. Org. Chem.* **1995**, *60*, 5628; b) P. A. Jacobi, P. Herradura, *Can. J. Chem.* **2001**, *79*, 1727; c) M. P. Sibi, P. Liu, J. Ji, S. Hajra, J.-x. Chen, *J. Org. Chem.* **2002**, *67*, 1738; d) R. B. Chhor, B. Nosse, S. Sörgel, C. Böhm, M. Seitz, O. Reiser, *Chem. Eur. J.* **2003**, *9*, 260.

[14] The regioisomeric 1,4-diene was formed as a side product and could not be separated (**4o**/**5o** 87:13). Unfortunately, we were not able to determine the enantiomer ratio of the major product **4o**. However, the same reaction with hexanal afforded the major isomer with an enantiomer ratio of 93:7, as determined by GC analysis. We assume that the reaction with dodecanal proceeds with similar selectivity.

[15] V. VanRheenen, R. C. Kelly, D. Y. Cha, *Tetrahedron Lett.* **1976**, 1973.

 © 2004 Wiley-VCH Verlag GmbH & Co. KGaA, Weinheim

Regioselective Epoxide Opening

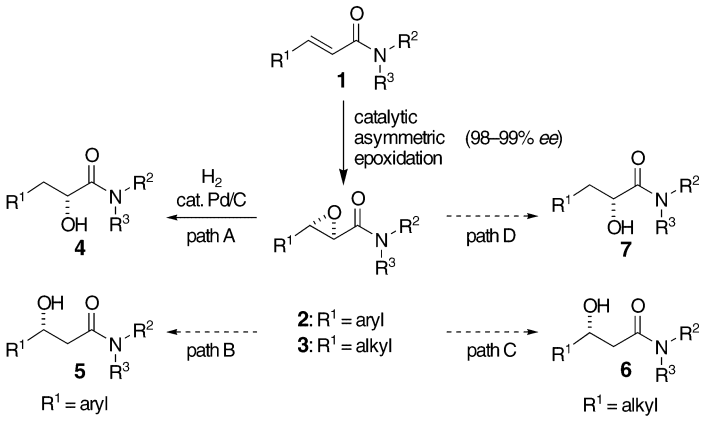
Efficient Synthesis of Chiral α- and β-Hydroxy Amides: Application to the Synthesis of (*R*)-Fluoxetine**

*Hiroyuki Kakei, Tetsuhiro Nemoto, Takashi Ohshima, and Masakatsu Shibasaki**

Chiral α- and β-hydroxy amides are useful building blocks for the synthesis of biologically active compounds.[1] The synthesis of these intermediates in both a regio- and stereoselective manner, however, is difficult. There are only a few methods for the synthesis of such chiral units, and their substrate scope and selectivity remain unsatisfactory.[2] The regioselective epoxide-opening reaction of optically active α,β-epoxy amides is one of the most attractive approaches to this problem. We[3] and Aggarwal's group[4] recently succeeded in developing efficient strategies to obtain α,β-epoxy amides in a highly enantioselective manner. There are no reports, however, on regioselective epoxide-opening reactions of α,β-epoxy amides,[3,5] in contrast to the success with α,β-epoxy ketones.[6] We report herein a new synthesis of nearly enantiomerically pure α- and β-hydroxy amides with high substrate generality, which consists of a novel highly regioselective epoxide opening of both β-alkyl- and β-aryl-substituted α,β-epoxy amides (Scheme 1). An efficient enantioselective synthesis of (*R*)-fluoxetine, using the newly developed method, is also described.

To realize the highly regioselective epoxide-opening reactions of α,β-epoxy amides, it is important to control the relative reactivity of the α- and β-positions, which depends on the β-substituent. Thus, we discuss the reactions of the β-aryl-substituted amide (paths A and B) and of the β-alkyl-substituted amide (paths C and D).

We recently described the highly enantio- and regioselective synthesis of β-aryl α-hydroxy amides using a one-pot, tandem process consisting of catalytic asymmetric epoxidation and a Pd-catalyzed epoxide opening (path A). The selectivity was based on the higher reactivity of the β-position (benzyl position) over that of the α-position.[3] The higher reactivity of the β-position, however, make it difficult to obtain β-hydroxy amides through cleavage of the C_α–O bond (path B). Indeed, the general conditions for selective cleavage of the C_α–O bond in α,β-epoxy ketones, such as SmI_2 and $[Cp_2TiCl_2]/Zn$,[6,7] gave unsatisfactory results (trace amounts) with α,β-unsaturated and -saturated amides as the major



Scheme 1. Strategy to obtain α- and β-hydroxy amides from α,β-epoxy amides by regioselective epoxide opening.

products. To overcome this difficulty, we examined a so-called intramolecular hydride transfer using Red-Al (sodium bis(2-methoxyethoxy)aluminum hydride),[1c,8] which might react with N–H first to produce a N–Al species; the remaining hydride attacks the α-position of the epoxy amide (see Figure 1). As we expected, the reduction of **2a** with Red-Al gave β-hydroxy amide **5a**[7] as the major product in moderate yield (Table 1, entry 1). This result prompted us to optimize the reaction conditions.

To gain insight into the reaction mechanism, especially for the counterion effects, calculations were performed by means of the hybrid density functional method (B3LYP[9]) using a 6-31G(d) basis set. As shown in Figure 1, the coordination of a sodium ion to the epoxide and carbonyl oxygen atoms should weaken the C_β–O bond ($\Delta_\beta = 0.0315$ Å) more effectively than the C_α–O bond ($\Delta_\alpha = 0.0092$ Å).[10] In an attempt to overcome this drawback, we added [15]crown-5 to trap sodium ions. Both regioselectivity and reactivity improved (entries 2–4, and 6). The best selectivity was obtained with a 1:1 ratio of Red-Al and [15]crown-5 (entry 4). The use of [18]crown-6 gave a comparable result (entry 5). Solvents and temperatures were also investigated; the use of dimethoxyethane (DME) and a lower reaction temperature gave much better results (entries 7 and 8).[11] This mixture of reagents, Red-Al and crown ether, was applicable to the selective conversion of various β-aryl α,β-epoxy amides **2b–d** into β-aryl β-hydroxy amides **5b–d** (entries 12–14).[7]

The Red-Al/crown ether strategy was applicable to the regioselective epoxide-opening reaction of β-*alkyl*-substituted amides (Scheme 1, path C). In contrast to β-*aryl*-substituted amides, these substrates have higher reactivity at the α-position than at the β-position, and β-hydroxy amides were obtained with much higher regioselectivity (Table 2, entry 1). Thus, satisfactory selectivity was achieved even when simple reaction reagents, such as DIBAL (diisobutylaluminum hydride, entry 2), were employed. The scope and limitations of this reaction were also examined with various substrates prepared from primary amines **3b**,**c**,**f**,**g** (entries 3, 4, 7, and 8) and α-branched primary amines **3d**,**e** (entries 5 and 6). When two equivalents of DIBAL were used, β-alkyl α,β-epoxy amides were successfully converted into the corre-

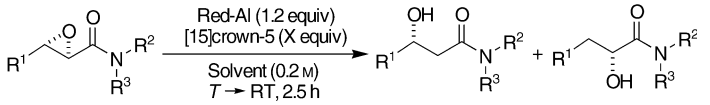
[*] H. Kakei, T. Nemoto, Dr. T. Ohshima, Prof. Dr. M. Shibasaki
Graduate School of Pharmaceutical Sciences
The University of Tokyo, Hongo, Bunkyo-ku, Tokyo 113–0033 (Japan)
Fax: (+81) 3-5684-5206
E-mail: mshibasa@mol.f.u-tokyo.ac.jp

[**] This work was supported by RFTF and by a Grant-in-Aid for the Encouragement of Young Scientists (A) from the Japan Society for the Promotion of Science (JSPS).

Supporting information for this article is available on the WWW under http://www.angewandte.org or from the author.

 DOI: 10.1002/anie.200352431 © 2004 Wiley-VCH Verlag GmbH & Co. KGaA, Weinheim

Table 1: Selective epoxide-opening reaction of β-aryl α,β-epoxy amides (Scheme 1, path B).



2a–d: R^1 = aryl **5a–d** **4a–d**

Entry		Substrate[a] R^1	R^2NR^3	[15]crown-5 [equiv]	Solvent	T [°C]	Yield [%][b]	5:4[c]
1	**2a**	Ph	MeNH	0	DME	4	72	2:1
2	**2a**	Ph	MeNH	0.5	DME	4	78	4:1
3	**2a**	Ph	MeNH	1.0	DME	4	91	7:1
4	**2a**	Ph	MeNH	1.2	DME	4	89	8:1
5	**2a**	Ph	MeNH	1.2[d]	DME	4	86	8:1
6	**2a**	Ph	MeNH	2.0	DME	4	84	8:1
7	**2a**	Ph	MeNH	1.2	DME	−20	87	16:1
8	**2a**	Ph	MeNH	1.2	DME	−40	87	18:1
9	**2a**	Ph	MeNH	1.2	THF	4	80	6:1
10	**2a**	Ph	MeNH	1.2	toluene	4	73	3:1
11	**2a**	Ph	MeNH	1.2	CH_2Cl_2	4	88	3:1
12	**2b**	4-Me-C_6H_4	MeNH	1.2	DME	−20	85	10:1
13	**2c**	4-F-C_6H_4	MeNH	1.2	DME	−20	90	14:1
14[e]	**2d**	Ph	BnNH	1.2	DME	−20	87	5:1

[a] Substrate purity in all cases 99% *ee*. [b] Yield of **4** and **5**. [c] The ratio was determined by ^{1}H NMR analysis of the crude sample. [d] [18]Crown-6 was used instead of [15]crown-5. [e] Reaction time was 5.0 h.

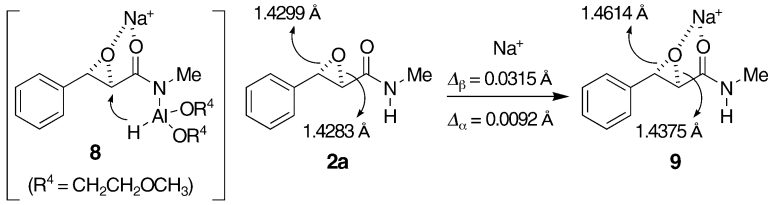
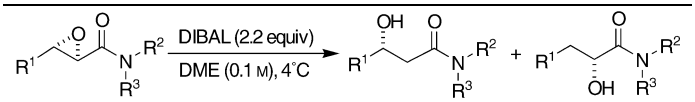


Figure 1. The effects of a sodium ion on the C–O bonds of α,β-epoxy amides **2a** during reduction with Red-Al.

Table 2: Selective epoxide-opening reaction of β-alkyl α,β-epoxy amides (Scheme 1, path C).



3a–g: R^1 = alkyl **6a–g** **7a–g**

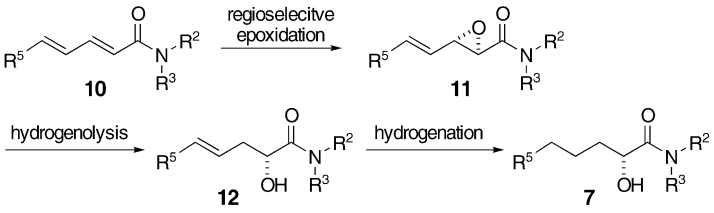
Entry		Substrate[a] R^1	R^2NR^3	t [h]	Yield [%][b]	6:7[c]
1[d]	**3a**	$Ph(CH_2)_2$	MeNH	2.5	95	40:1
2	**3a**	$Ph(CH_2)_2$	MeNH	1.0	94	22:1
3	**3b**	$Ph(CH_2)_2$	BnNH	1.5	88	21:1
4	**3c**	$Ph(CH_2)_2$	AllylNH	1.5	89	20:1
5	**3d**	$Ph(CH_2)_2$	*c*HexNH[e]	1.5	89	28:1
6	**3e**	$Ph(CH_2)_2$	*t*BuNH	1.5	92	>50:1
7	**3f**	$Ph(CH_2)_4$	MeNH	1.5	93	12:1
8	**3g**	*c*Hex[e]	BnNH	1.5	89	11:1

[a] Substrate purity in all cases 99% *ee* except for substrate **3c** (98% *ee*). [b] Yield of **6** and **7**. [c] The ratio was determined by ^{1}H NMR analysis of the crude sample. [d] Red-Al/crown ether conditions shown in Table 1 (entry 6) were used. [e] *c*Hex = cyclohexyl.

sponding β-hydroxy amides **6a–g** in excellent yields and selectivities.[7]

The transformation of β-*alkyl*-substituted α,β-epoxy amides into α-hydroxy amides (Scheme 1, path D) is extremely challenging because the β-position is much less reactive than the α-position. After intensive examination, we obtained α-hydroxy amide **7a** with moderate selectivity (2.7:1) by using $LiAlH_4$.[11] To obtain α-hydroxy amides efficiently, we used a new synthetic strategy with α,β,γ,δ-unsaturated amides, as shown in Scheme 2. In this process, the α,β-selective epoxidation of α,β,γ,δ-unsaturated amides through the intramolecular transfer of peroxide from La to the β-position and hydrogenolysis of the corresponding γ,δ-unsaturated α,β-epoxy amides were key steps.

We first investigated the catalytic asymmetric epoxidation of α,β,γ,δ-unsaturated amides **10a** using Sm–(*S*)-binol–Ph_3As=O (1:1:1) complex **13** (binol = 2,2′-dihydroxy-1,1′-binaphthyl), which is a useful catalyst for the asymmetric epoxidation of α,β-unsaturated amides.[3] The reaction proceeded to afford **11a** with complete α,β-selectivity; however, the reactivity was not satisfactory (Table 3, entry 1). Thus, we further tested a number of other lanthanum complexes.[11] Finally, the Gd–(*S*)-binol–Ph_3As=O complex **14** was determined to be the best in this system (entry 2), and activation of 4-Å molecular sieves was necessary to improve the reactivity (entry 3). This catalytic system was applicable to various α,β-selective epoxidations of α,β,γ,δ-unsaturated amides **10a–f**



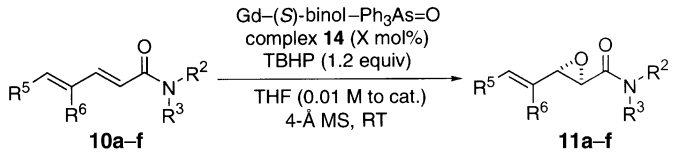
Scheme 2. Strategy to obtain β-alkyl,α-hydroxy amides (Scheme 1, path D)

(entries 5–9). When 10 to 20 mol% of Gd–(*S*)-binol–Ph_3As=O complex **14** was used, amides prepared from primary amines (**10a,b,e,f**), a secondary amine (**10c**), and an α-branched primary amine (**10d**) were epoxidized to afford γ,δ-unsaturated α,β-epoxy amides in good yield and excellent selectivity.[12]

Moreover, these γ,δ-unsaturated α,β-epoxy amides **11a–f** were easily converted into γ,δ-unsaturated α-hydroxy amides **12a–f** via a π-allyl palladium intermediate (Table 4).[13]

 © 2004 Wiley-VCH Verlag GmbH & Co. KGaA, Weinheim

Table 3: Catalytic asymmetric epoxidation of α,β,γ,δ-unsaturated amides.

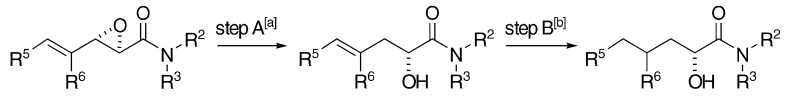


10a–f **11a–f**

Entry		Substrate			Cond.[a]	**14** [mol%]	*t* [h]	Yield [%]	*ee* [%]
		R^5	R^6	R^2NR^3					
1[b]	**10a**	Ph	H	MeNH	A	10	48	48	97
2	**10a**	Ph	H	MeNH	A	10	48	61	99
3	**10a**	Ph	H	MeNH	B	10	48	78	99
4	**10a**	Ph	H	MeNH	B	15	48	85	96
5	**10b**	Ph	H	BnNH	B	10	21	89	99
6	**10c**	Ph	H	MeNMe	B	10	12	90	99
7	**10d**	Ph	H	*c*HexNH	B	15	48	94	99
8	**10e**	Me	H	BnNH	B	20	48	85	99
9	**10f**	-$(CH_2)_4$-		BnNH	B	20	48	76	99

[a] Conditions A: TBHP in decane, 4-Å molecular sieves not dried. Conditions B: TBHP in toluene, 4-Å molecular sieves dried for 3 h at 180°C under reduced pressure. [b] Sm was used as a central metal.

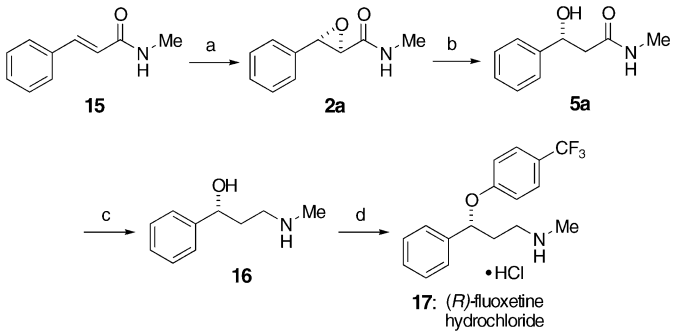
Table 4: Conversion to β-alkyl α-hydroxy amides (Scheme 1, path D).



11a–f **12a–f** **7a–f**

Entry		Substrate			*t* [h]		Yield [%]	
		R^5	R^6	R^2NR^3	step A	step B	step A	step B
1	**11a**	Ph	H	MeNH	1	1	91	95
2	**11b**	Ph	H	BnNH	1	1	90	95
3	**11c**	Ph	H	MeNMe	1	1	87	94
4	**11d**	Ph	H	*c*HexNH	1	1	94	92
5	**11e**	Me	H	BnNH	2	1	94[c]	94
6	**11f**	-$(CH_2)_4$-		BnNH	12	12	94	86

[a] Conditions: $[Pd_2(dba)_3]\cdot CHCl_3$ (2.6 mol%), Bu_3P (2.6 mol%), Et_3N (2 equiv), HCO_2H (5 equiv), THF, RT. [b] Conditions: Pd/C (5 mol%), H_2 (1 atm), THF/MeOH (2:1), RT. [c] A mixture of three olefin isomers was obtained.



Scheme 3. Asymmetric synthesis of (*R*)-fluoxetine hydrochloride (**17**). a) Sm–(S)-binol–Ph_3As=O (**13**) (10 mol%), TBHP (1.2 equiv), THF, 4-Å molecular sieves, RT, 91%, 99% ee; b) Red-Al (1.2 equiv), [15]crown-5 (1.2 equiv), DME (0.2 M), −40°C to RT, 80% (yield of β-OH product isolated), β-OH/α-OH >20:1; c) $LiAlH_4$, THF, reflux, quantitative; d) NaH, DMSO, 4-chlorobenzotrifluoride; HCl, 92% (lit.[14e]). DMSO = dimethyl sulfoxide, RT = room temperature, TBHP = *tert*-butyl hydroperoxide.

Finally, reduction of the C–C double bonds proceeded smoothly with Pd/C and H_2, producing β-*alkyl* α-hydroxy amides **7a–f** efficiently.[7]

To demonstrate the usefulness of our methodology, an asymmetric synthesis of (*R*)-fluoxetine (**17**) was executed on a multigram scale (Scheme 3). Fluoxetine (Prozac, Eli Lilly Co.), marketed as a racemate, is an antidepressant drug and many groups have intensively studied an efficient synthesis of the enantiomerically pure form.[14,15] Catalytic asymmetric epoxidation of **15** (5-g scale) gave enantiomerically pure α,β-epoxy amides **2a** in 91% yield and 99% *ee*. The Red-Al/crown ether strategy was used to convert this epoxide into β-hydroxy amide **5a**.[16] The resulting amide was reduced to the known key intermediate **16** with $LiAlH_4$, and **16** was coupled with 4-chlorobenzotrifluoride to give **17** as the hydrochloride salt.[15d,e]

In summary, regioselective epoxide-opening processes for α,β-epoxy amides to give both α- and β-hydroxy amides have been developed. Moreover, this reaction was successfully applied to an asymmetric synthesis of (*R*)-fluoxetine, demonstrating the power of the newly developed reaction. We are currently investigating more detailed mechanisms of the epoxide-opening reaction and more difficult tasks such as the regioselective epoxide opening of α,β-epoxy amides by carbon nucleophiles and other nucleophiles.

Received: July 21, 2003 [Z52431]

Keywords: asymmetric synthesis · epoxides · regioselectivity · synthetic methods

[1] For reviews, see: a) *Studies in Natural Products Chemistry*, *Vol. 2* (Ed.: Atta-ur-Rahman), Elsevier, **1988**, p. 680; b) α *-Hydroxy Acids in Enantioselective Syntheses* (Eds.: G. M. Coppola, H. F. Schuster), VCH, Weinheim, **1997**; c) S. Masamune, W. Choy, J. S. Petersen, L. R. Sita, *Angew. Chem.* **1985**, *97*, 1–31; *Angew. Chem. Int. Ed. Engl.* **1985**, *24*, 1–30.

[2] a) S. N. Goodman, E. N. Jacobsen, *Angew. Chem.* **2002**, *114*, 4897–4899; *Angew. Chem. Int. Ed.* **2002**, *41*, 4703–4705; b) S. E. Denmark, Y. Fan, *J. Am. Chem. Soc.* **2003**, *125*, 7825–7827.

[3] T. Nemoto, H. Kakei, V. Gnanadesikan, S.-y. Tosaki, T. Ohshima, M. Shibasaki, *J. Am. Chem. Soc.* **2002**, *124*, 14544–14545.

 © 2004 Wiley-VCH Verlag GmbH & Co. KGaA, Weinheim

[4] V. K. Aggarwal, G. Hynd, W. Picoul, J.-L. Vasse, *J. Am. Chem. Soc.* **2002**, *124*, 9964 – 9965.
[5] Recently, the transformation of β-*aryl* substituted α,β-epoxy amides into α-hydroxy amides (path A) using samarium(II) iodide was reported, see: J. M. Concellón, E. Bardales, C. Gómez, *Tetrahedron Lett.* **2003**, *44*, 5323 – 5326.
[6] a) G. A. Molander, G. Hahn, *J. Org. Chem.*, **1986**, *51*, 2596 – 2599; b) M. Miyashita, M. Hoshino, T. Suzuki, A. Yoshokoshi, *Chem. Lett.* **1988**, 507 – 508; c) S. Torii, H. Okumoto, S. Nakayuso, T. Kotani, *Chem. Lett.* **1989**, 1975 – 1978; d) C. Bonini, R. D. Fabio, G. Sotgiu, S. Cavagnero, *Tetrahedron* **1989**, *45*, 2895 – 2904; e) M. Miyashita, T. Suzuki, M. Hoshino, A. Yoshikoshi, *Tetrahedron* **1997**, *53*, 12469 – 12486; f) C. Hardouin, F. Chevallier, B. Rousseau, E. Doris, *J. Org. Chem.* **2001**, *66*, 1046 – 1048; g) C. Lauret, *Tetrahedron: Asymmetry* **2001**, *12*, 2359 – 2383.
[7] Based on the HPLC analysis, there was no racemization in the epoxide-opening process; see the Supporting Information for details.
[8] Red-Al was used for the transformation of allylic alcohol epoxides to 1,3-diols, see: a) P. Ma, V. S. Martin, S. Masamune, K. B. Sharpless, S. M. Viti, *J. Org. Chem.* **1982**, *47*, 1378 – 1380; b) S. M. Viti, *Tetrahedron Lett.* **1982**, *23*, 4541 – 4544; c) J. M. Finan, Y. Kishi, *Tetrahedron Lett.* **1982**, *23*, 2719 – 2722.
[9] a) A. D. Becke, *J. Chem. Phys.* **1993**, *98*, 5648; b) C. Lee, W. Yang, R. G. Parr, *Phys. Rev. B* **1988**, *37*, 785.
[10] The role of counterions in the regioselective opening of 2,3-epoxy alcohol was studied theoretically, see: I. Infante, C. Bonini, F. Leij, G. Righi, *J. Org. Chem.* **2003**, *68*, 3773 – 3780. These results also support our hypothesis.
[11] See the Supporting Information for details.
[12] The absolute configuration of **11a** was determined to be 2*R*,3*S*. See the Supporting Information for details.
[13] M. Oshima, H. Yamazaki, I. Shimizu, M. Nisar, J. Tsuji, *J. Am. Chem. Soc.* **1989**, *111*, 6280 – 6287.
[14] There are marked differences between the two major metabolites (*R*)- and (*S*)-norfluoxetine in regard to their inhibition of 5-HT reuptake, see: a) D. W. Robertson, N. D. Jones, J. K. Swartzendruber, K. S. Yang, D. T. Wong, *J. Med. Chem.* **1988**, *31*, 185 – 189; b) D. W. Robertson, J. H. Krushinski, R. W. Fuller, J. D. Leander, *J. Med. Chem.* **1988**, *31*, 1412 – 1417.
[15] For representative examples of the synthesis of (*R*)-**17**, see: a) M. Srebnik, P. V. Ramachandran, H. C. Brown, *J. Org. Chem.* **1988**, *53*, 2916 – 2920; b) Y. Gao, K. B. Sharpless, *J. Org. Chem.* **1988**, *53*, 4081 – 4084; c) E. J. Corey, G. A. Reichard, *Tetrahedron Lett.* **1989**, *30*, 5207 – 5210; d) A. Kumar, D. H. Ner, S. Y. Dike, *Tetrahedron Lett.* **1991**, *32*, 1901 – 1904; e) T. Koenig, D. Mitchell, *Tetrahedron Lett.* **1994**, *35*, 1339 – 1342; f) J. W. Hilborn, Z.-H. Lu, A. R. Jurgens, Q. K. Fang, P. Byers, S. A. Wald, C. H. Senanayake, *Tetrahedron Lett.* **2001**, *42*, 8919 – 8921.
[16] After the epoxide-opening reaction, [15]crown-5 was recovered in 87% yield. See the Supporting Information. Alternatively, immobilized crown ethers can be applied to this reaction. For an example of the immobilization of crown ethers, see: A. Favre-Réguillon, N. Dumont, B. Dunjic, M. Lemaire, *Tetrahedron Lett.* **1997**, *38*, 1343 – 1360.

 © 2004 Wiley-VCH Verlag GmbH & Co. KGaA, Weinheim

Asymmetric Hydrogenation

Difluorphos, an Electron-Poor Diphosphane: A Good Match Between Electronic and Steric Features**

Séverine Jeulin, Sébastien Duprat de Paule, Virginie Ratovelomanana-Vidal, Jean-Pierre Genêt,* Nicolas Champion, and Philippe Dellis**

The design and synthesis of new chiral ligands, which display high activity and enantioselectivity, is still a significant challenge in the development of transition-metal-catalyzed asymmetric reactions. In recent years, chelating diphosphanes supported by an atropisomeric scaffold, have proved to be among the most active, selective and versatile ligands in this area.[1] Leading diphosphanes such as binap[2] and more recently MeO-biphep[3] have shown excellent results, especially in the field of ruthenium-mediated asymmetric hydrogenation.[4] Many research groups have devoted their efforts toward the discovery of new efficient atropisomeric ligands[5] with unusual stereoelectronic profiles. Both the aryl phosphorus substituents and the biaryl backbone are tunable parts in this family of ligands (Figure 1). Replacing the phenyl

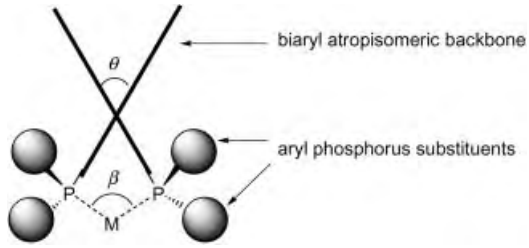


Figure 1. General stereoelectronic tunable features of a C_2-symmetric atropisomeric diphosphane. M = transition metal center, β = bite angle, θ = dihedral angle.

[*] S. Jeulin, Dr. S. Duprat de Paule, Dr. V. Ratovelomanana-Vidal, Prof. Dr. J.-P. Genêt
Laboratoire de Synthèse Sélective Organique et Produits Naturels
Ecole Nationale Supérieure de Chimie de Paris
11, rue Pierre et Marie Curie, 75231 Paris Cedex 05 (France)
Fax: (+33) 144-071-062
E-mail: gvidal@ext.jussieu.fr
genet@ext.jussieu.fr

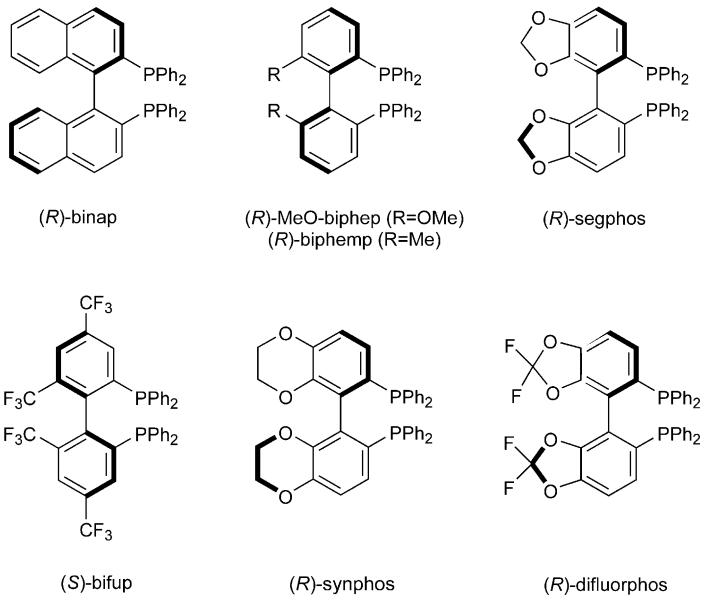
Dr. N. Champion, Dr. P. Dellis
SYNKEM S.A.S., 47, rue de Longvic
21301 Chenôve Cedex (France)
Fax: (+33) 380-447-270
E-mail: p.dellis@fr.fournierpharma.com

[**] CNRS and SYNKEM S.A.S. are gratefully acknowledged for doctoral fellowships (S.J. and S.D.P.). We thank Dr A. Solladié-Cavallo, from the Department of Fine Organic Chemistry (ECPM, Strasbourg, France), for her kind permission to use molecular modeling facilities. We also acknowledge a generous gift of (*R*)- and (*S*)-MeO-biphep from Dr. R. Schmid (Hoffmann-LaRoche).

Supporting information (experimental details and analytical data) for this article is available on the WWW under http://www.angewandte.org or from the author.

 © 2004 Wiley-VCH Verlag GmbH & Co. KGaA, Weinheim DOI: 10.1002/anie.200352453

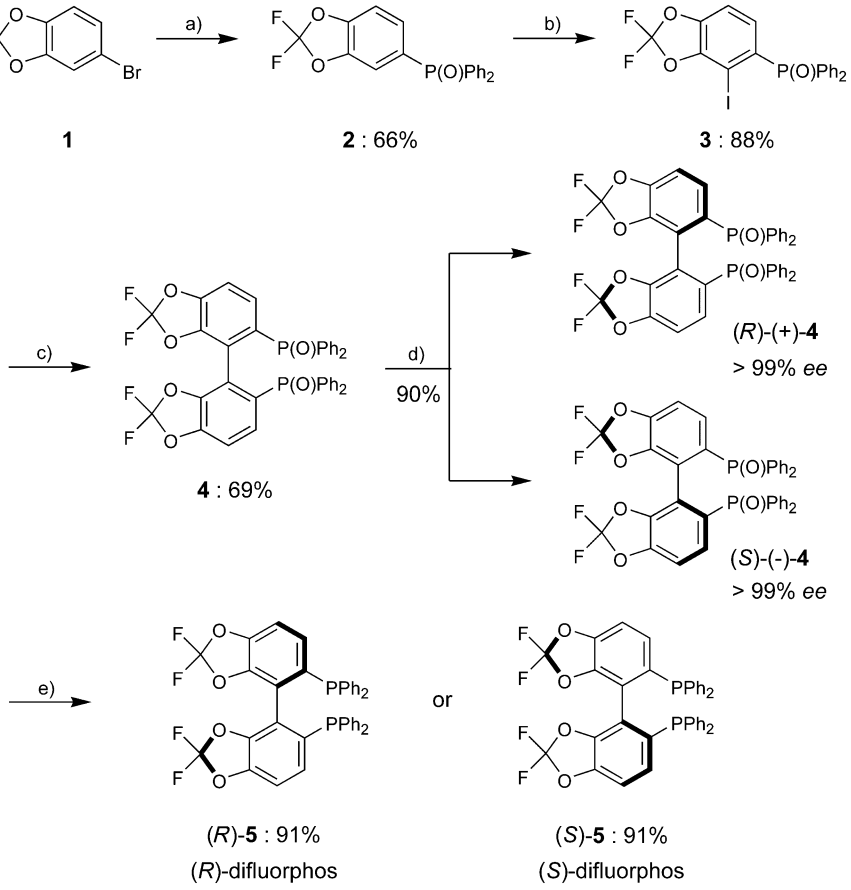
phosphorus substituents by bulkier aromatics (*p*-Tol- binap,[6] DTBM-segphos[7]), electronically modified substituents (*p*-F-binap, Cy-binap)[6] or heteroaromatics (α-furyl-MeO-biphep[3c]), can modify the steric hindrance around the metal and/or the electronic properties of the phosphorus centers and create more selective ligands. Structural variations of the biaryl backbone are at the origin of the wide diversity in the field of atropisomeric diphosphanes. The steric design of the biaryl core has been extensively explored: Cn-TunaPhos[8] by Zhang and co-workers, segphos[7] by Saito and co-workers, and recently synphos[9] by our group have been specially targeted because they displayed a (tunable or) narrow dihedral angle, a steric condition postulated as essential to obtain good enantioselectivities in asymmetric hydrogenation.[7b] However, the electronic design of atropisomeric diphosphanes has been less systematically studied: the more effective ligands designed to date bear an atropisomeric core, which is often electronically richer than that in binap[3,7–9] and there are only few examples of effective electrodeficient atropisomeric diphosphanes. Most of them are based on a biheteroaryl skeleton (binapFu,[10] tetraMe-bitianp[11]) and electron-poor biphenyl-based ligands have rarely displayed satisfactory enantioselectivities (bifup, fupmop).[12] Moreover, in the field of ruthenium-mediated enantioselective hydrogenation, electrodeficiency has sometimes been considered as a drawback for catalytic activity,[12,13] but its influence on enantioselectivity has rarely been underlined.



Scheme 1. Typical diphosphane ligands

Following our interest in ligand design,[9a,14] we report herein the synthesis of a new atropisomeric diphosphane, based on a segphos-like backbone, which has a narrow dihedral angle and electron-withdrawing substituents, hereafter named difluorphos[9a] (Scheme 1). In addition, we describe studies regarding its steric and electronic features. Its performance in ruthenium-mediated asymmetric hydrogenation, compared to other electron-rich atropisomeric diphosphanes, has also been preliminary evaluated.

Our synthetic approach to enantiopure (*R*)- and (*S*)-[4,4′-bi(2,2-difluoro-1,3-benzodioxol)-5,5′-diyl]bis(diphenylphosphane) (**5**; difluorphos) is depicted in Scheme 2. Phosphorylation of commercially available **1** was through the organomagnesium formation, followed by the addition of chlorodiphenylphosphane oxide. Phosphane oxide **2** was obtained in 66% yield. *Ortho*-lithiation of **2** by LDA at −78°C and further iodination with I_2 furnished **3** in 88% yield. Iodide **3** was subjected to an Ullmann-type coupling[15] with copper in DMF at 130°C and afforded the bis(phosphane oxide) **4** in 69% yield. The optical resolution of (*RS*)-**4** was by chiral preparative HPLC using a Chirose C3 Column in 90% yield based on (*RS*)-**4**. (−)-**4** and (+)-**4** were enantiomerically pure (>99% *ee*) according to HPLC (Chiralpak AD column). Reduction of the resolved **4** was performed by heating with an excess of $HSiCl_3$ in xylene in the presence of tributylamine in 91% yields for (*R*)-**5** and (*S*)-**5** ((*R*)-difluorphos and (*S*)- difluorphos).[16] Subsequent oxidation of diphosphanes (*R*)-**5** and (*S*)-**5** with hydrogen



Scheme 2. Reagents and conditions: a) Mg, THF, 60°C→RT; then $ClP(O)Ph_2$, 20°C; b) LDA, THF, −78°C, 2 h; then I_2, −78°C to RT; c) Cu, DMF, 130°C; d) Chiral preparative HPLC, Chirose C3 Column; e) $HSiCl_3$, Bu_3N, xylene, 140°C. LDA = lithium diisopropylamide.

 © 2004 Wiley-VCH Verlag GmbH & Co. KGaA, Weinheim

peroxide showed that no racemization had occurred during the reduction process, in accord with the enantiomeric purities determined by HPLC. Therefore, both enantiomers of this new ligand were obtained on a multigram scale in five steps with an overall yield of 33%.

Having generated a new atropisomeric diphosphane, whose backbone was structurally close to existing electron-rich ligands (synphos or segphos), but with potentially different electronic properties, we performed a preliminary evaluation of its geometric and electronic profiles.

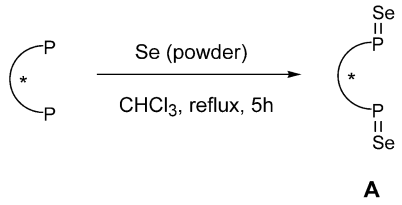
The quantification of steric properties of atropisomeric diphosphanes is conveniently achieved by measuring the dihedral angle (θ) of the biaryl backbone. In transition-metal complexes, this parameter is geometrically related to the bite angle (β)[17] and controls directly the asymmetric spatial environment around the metal center (Figure 1). In asymmetric hydrogenation, the influence of θ on enantioselectivity has only recently been described by Zhang and co-workers,[8] Saito and co-workers[7b] and our group.[18] Based on steric considerations, but not on electronic properties, the narrowest dihedral angle seems to provide the highest selectivities. We used computer modeling to estimate the dihedral angle of difluorphos and five other atropisomeric diphosphanes, binap, biphemp, MeO-biphep, synphos and the closely related segphos (Scheme 1). We took particular care to model all ligands with the same Molecular Mechanics program[19] and parameter set,[20] so as to highlight a correct trend in dihedral angles. As expected, difluorphos and segphos have almost the same dihedral angle (67.6 and 67.2°, respectively), which is the narrowest of the series, followed by synphos (70.7°), MeO-biphep (72.3°), biphemp (74.5°), and then binap (86.2°). These results are in agreement with our previous results[18] and those obtained by Saito and co-workers on minimized structures of Ikariya-type ruthenium complexes.[7b] Therefore the original segphos-modified bi(difluorobenzodioxole) core gives difluorphos, a priori, ideal steric properties for asymmetric hydrogenation, but we expected its electronic profile to differ radically from usual diphosphanes.

A simple way of evaluating the σ-donor ability of a phosphane group is to measure the magnitude of $^1J_{P,Se}$ in the ^{77}Se isotopomer of the corresponding phosphane-selenide.[10,21] Allen and Taylor have reported[21a] that an increase in this coupling constant indicates an increase in the s character of the phosphorus lone-pair orbital (i.e., a less basic phosphane). To estimate the donor ability of phosphorus centers in difluorphos and compare it with other atropisomeric diphosphanes (Table 1), we prepared the corresponding diselenides **A** (Scheme 3) by simply treating

Table 1: ^{31}P–^{77}Se coupling constants in compounds **A**.

Entry	Diphosphane ligand	$^1J_{P,Se}$ in **A** [Hz]
1	binap	738
2	MeO-biphep	742
3	synphos	740
4	segphos[a]	738
5	difluorphos	749
6	PPh_3	732[21a]

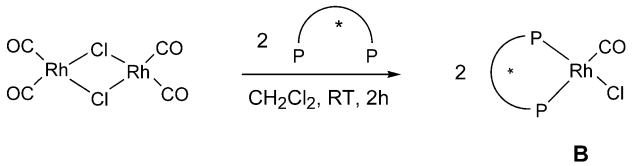
[a] (*R*)-segphos was prepared according to reported procedure.[7]



Scheme 3. Synthesis of diphosphane selenides.

the diphosphanes with elemental selenium in refluxing chloroform. The value for binap (738 Hz, entry 1) is in good agreement with literature.[21a] Atropisomeric diphosphanes of entries 1–5 are less basic than triphenylphosphane (entry 6). Whereas binap, MeO-biphep, synphos, and segphos display equivalent σ-basicities ($^1J_{P,Se}$ around 740 Hz), difluorphos (749 Hz, entry 5) has a significantly lower σ-donor ability.

Electronic donor–acceptor properties of these diphosphanes have also been investigated by studying the carbonyl stretching frequencies of [RhCl(diphosphane)(CO)] complexes **B** which were prepared by the reaction of $[\{RhCl(CO)_2\}_2]$ with diphosphane ligands (Scheme 4).[22] The higher the carbonyl stretching frequency, the higher the π-acidic character of the diphosphane. Results are in Table 2.



Scheme 4. Synthesis of [RhCl(diphosphane)(CO)] complexes **B**.

Table 2: Carbonyl stretching frequencies of [RhCl(diphosphane)(CO)] complexes **B**.

Diphosphane ligand	ν(CO)[a] in **B** [cm^{-1}]
binap	2017
MeO-biphep	2014
synphos	2012
segphos[b]	2016
difluorphos	2023

[a] in $CHCl_3$. [b] (*R*)-segphos was prepared according to the reported procedure.[7]

The five diphosphanes ordered by decreasing π acidity are as follows: difluorphos > binap and segphos > MeO-biphep > synphos. The electron-poor bi(difluorobenzodioxole) backbone of difluorphos is responsible for its higher π-back-donation ability, compared to nonfluorinated analogues, such as segphos or synphos.

Of the five ligands of this electronic comparative study, difluorphos is the poorest σ donor and the best π acceptor. Moreover, if we superimpose steric and electronic scales and line them up on binap (Figure 2), one can observe that oxygenated diphosphanes, such as MeO-biphep, segphos, or synphos, are systematically electron-richer than binap and

 © 2004 Wiley-VCH Verlag GmbH & Co. KGaA, Weinheim

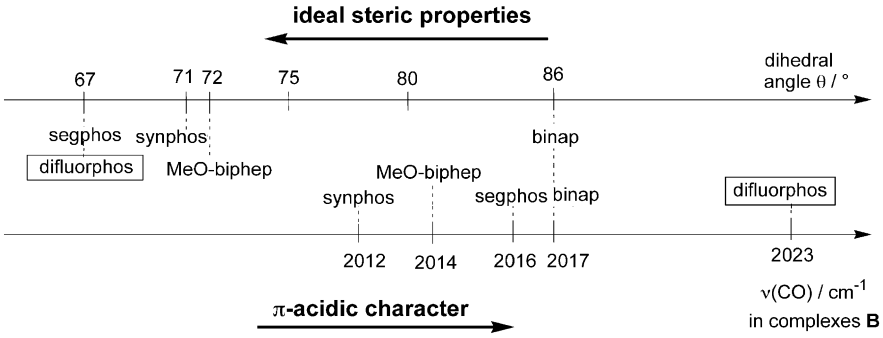
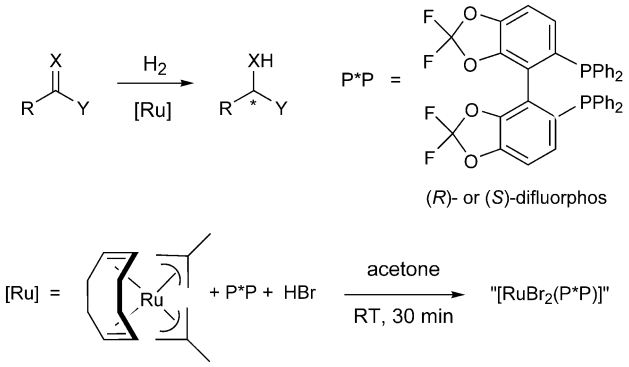


Figure 2. Comparative steric and electronic scales of binap, MeO-biphep, synphos, segphos, and difluorphos.

have narrower dihedral angles. On the contrary, difluorphos does not follow the same trend and is placed at opposite ends of steric and electronic scales, with the narrowest dihedral angle and the most π-acidic character, which confers on it a totally unusual stereoelectronic profile.

To evaluate the performance of difluorphos in ruthenium-mediated asymmetric hydrogenation we followed our convenient procedure,[23] and prepared catalysts from $[(cod)Ru(\eta^3\text{-}(CH_2)_2CCH_3)_2]$ (cod = cyclooctadiene) and difluorphos by addition of a methanolic solution of HBr in acetone (Scheme 5). The hydrogenations were carried out on a 1 mmol scale using 1 mol% catalyst, in a stainless steel autoclave. The conversions were determined by ^{1}H NMR spectroscopy and enantiomeric excesses of the products were determined by chiral GC (Table 3).

In all cases, complete conversion was obtained. The test substrate methyl acetoacetate was reduced in 99% *ee* using the [$RuBr_2$\{(*S*)-difluorphos\}] catalyst under 4 bar of hydrogen at 50°C (entry 1). We were pleased to notice that ethyl benzoylacetate and ethyl (4-fluoro)benzoylacetate were also reduced efficiently (10 bar, 80°C) to afford the corresponding β-hydroxy esters with 92 and 95% *ee*, respectively (entries 2 and 3). In our hands, using the same hydrogenation conditions, [$RuBr_2$\{(*R*)-binap\}] provided only 88% *ee* in the hydrogenation of ethyl benzoylacetate. Interestingly, the difluorphos ligand showed an unexpected efficiency in the Ru-catalyzed hydrogenation of ethyl 4-chloro-acetoacetate, a β-keto ester bearing a chelating substituent (entry 4). Under 10 bar hydrogen, at 110°C, ethyl (3*R*)-hydroxy-4-chloro-butyrate was obtained quantitatively in 97% *ee* using 1 mol% [$RuBr_2$\{(*S*)-difluorphos\}]. This result is in good agreement with work by the Noyori and Saito groups on other biphenyl

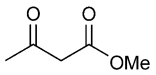
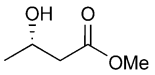
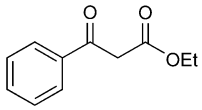
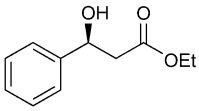
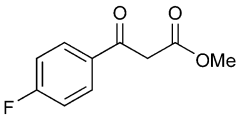
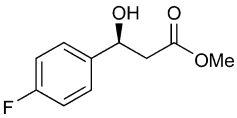
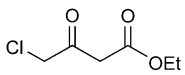
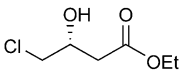


Scheme 5. General procedure for ruthenium-mediated asymmetric hydrogenation reactions using difluorphos.

ligands, such as binap (97% *ee* using [$RuBr_2$\{(*S*)-binap\}] under 100 bar and 100°C)[24,4a] and segphos (98% *ee* using $[\{RuCl[(R)\text{-segphos}]\}_2(\mu\text{-}Cl)_3][NH_2Me_2]$ under 30 bar and 90°C).[7b]

These good results obtained with difluorphos in the hydrogenation of standard substrates encouraged us to investigate more carefully the hydrogenation of "tricky" substrates, especially fluorinated β-functionalized ketones.

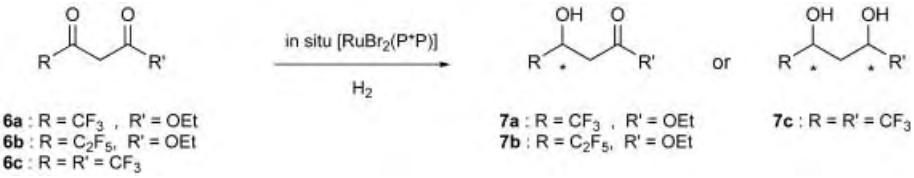
Table 3: Hydrogenation results using the difluorphos ligand.

Entry	Substrate[a]	Ligand[a] Config.	Solvent	pH_2 [bar]	*T* [°C]	*t* [h]	Product[b]	*ee*[c] [%]	Config.
1		*S*	MeOH	4	50	24		99	*S*
2		*R*	EtOH	10	80	24		92	*S*
3		*R*	MeOH	10	80	24		95	*S*
4		*S*	EtOH	10	110	3		97	*R*

[a] Reactions were conducted on a 1-mmol scale, using 1 mol% of in situ prepared[23] [$RuBr_2$\{(*R*)-or (*S*)-difluorphos\}] as catalyst. [b] All conversions were 100%, according to ^{1}H NMR spectroscopy. [c] Enantiomeric excesses were determined by chiral gas chromatography (Lipodex A column).

 © 2004 Wiley-VCH Verlag GmbH & Co. KGaA, Weinheim

We[25] and others[26] have already described low enantioselectivities in the ruthenium-mediated asymmetric hydrogenation of ethyl 4,4,4-trifluoroacetoacetate and ethyl pentafluoropropionylacetate using biphenyl atropisomeric diphosphanes, even at high temperature. Therefore we performed a comparative study between five diphosphanes in the asymmetric hydrogenation of substrates **6a–c** (Scheme 6). We conducted the hydrogenation reactions at least twice under strictly the same conditions for the five diphosphanes: hydrogen pressure, temperature, substrate concentration (0.5 M), substrate/catalyst ratio (S/C = 100; Table 4).



Scheme 6. Asymmetric hydrogenation of fluorinated substrates. P*P = (*S*)-binap, (*S*)-MeO-biphep, (*S*)-synphos, (*R*)-segphos, or (*S*)-difluorphos.

Table 4: Comparative study of difluorphos and other ligands in the ruthenium-catalyzed hydrogenation of fluorinated β-functionalized ketones.

Substrate	Conditions[a]	*ee* [%][b]					Product Config.
		binap	MeO-biphep	synphos	segphos[c]	difluorphos	
6a	10 bar, 110 °C, 1 h, EtOH	23	40	49	59	70	*R*
6b	10 bar, 110 °C, 1 h, EtOH	44	57	63	76	81	*R*
6c	50 bar, 50 °C, 24 h, MeOH	91 (*de* = 77 %)	87 (*de* = 71 %)	85 (*de* = 67 %)	88 (*de* = 71 %)	98 (*de* = 86 %)	*R*,*R*

[a] Reactions were conducted on a 1-mmol scale, using 1 mol % of in situ prepared[23] [$RuBr_2${*S* ligand}] as catalyst. [b] All conversions were 100 %, according to ^1H and ^{19}F NMR spectroscopy. Enantiomeric and diastereomeric excesses were determined by chiral gas chromatography (Lipodex A column). [c] (*R*)-segphos was prepared according to the reported procedure.[7]

Note, for β-keto esters **6a** and **6b**, the enantiomeric excess is lineally related to the dihedral angle of the diphosphane: the narrower the dihedral angle (θ(binap) > θ(MeO-biphep) > θ(synphos) > θ(segphos) = θ(difluorphos)), the better the enantioselectivities (*ee*(binap) < *ee*(MeO-biphep) < *ee*(synphos) < *ee*(segphos) < *ee*(difluorphos)). However, despite the geometric similarity between segphos and difluorphos, the latter provides the best enantiomeric excesses for the three substrates: β-hydroxy esters **7a** and **7b** were obtained in 70 and 81 % *ee*, respectively, and diol **7c** was obtained with very satisfactory diastereo- and enantioselectivity (86 % *de* and 98 % *ee* for the *R*,*R anti* diol). To our knowledge, this is the best reported *ee* values for the ruthenium-catalyzed hydrogenation of **6a**,[27] **6b** and **6c**[28] using biphenyl-based diphosphanes. In this particular case, the superiority of difluorphos over its nonfluorinated analogue segphos lies in the atypical combination of a narrow dihedral angle and a stronger electrodeficient character.

In summary, we have described an efficient synthesis of a new electrodeficient atropisomeric diphosphane, difluorphos. We have shown that its original stereoelectronic structure, based on a bi(difluorobenzodioxole) backbone, displayed a narrow dihedral angle combined with an unusual π-acidity. Comparison of difluorphos with other leading biphenyl-based ligands (binap, MeO-biphep, synphos and segphos) in ruthenium-mediated hydrogenation revealed that its electrodeficiency was crucial in obtaining high levels of enantioselection in the hydrogenation of challenging substrates. Theoretical and experimental studies are currently under investigation in order to rationalize the unusual behavior of difluorphos ligand in asymmetric catalysis.

Experimental Section

Experimental procedures and characterization data for compounds **2**–**5**, **A**, and **B** are given in the Supporting Information.

Typical procedure for asymmetric hydrogenation: (*S*)-difluorphos (7.5 mg, 0.011 mmol) and [(cod)Ru(η^3-$(CH_2)_2CCH_3)_2$] (3.2 mg, 0.01 mmol) were placed in a 10-mL flask, and degassed anhydrous acetone (1 mL) was added dropwise. A methanolic solution of HBr (122 μL, 0.18 M) was added dropwise to the suspension. The reaction mixture was stirred at room temperature for about 30 min and an orange suspension formed. The solvent was removed under vacuum. The orange solid residue was used without further purification as a catalyst for the hydrogenation reaction of the desired substrate (1 mmol) in MeOH or EtOH (2 mL). The reaction vessel was placed in a 500-mL stainless steel autoclave, which was adjusted at the desired pressure and warmed to the desired temperature for 24 h. The solvent was evaporated and the crude product was purified on a short pad of silica gel, eluting with cyclohexane:ethyl acetate (1:1). Conversion and enantiomeric excess were determined by ^1H NMR spectroscopy and chiral GC, respectively.

Received: July 23, 2003 [Z52453]

Keywords: asymmetric catalysis · atropisomerism · fluorinated ligands · hydrogenation · ruthenium

[1] For a review on axially chiral bidentate ligands, see : M. McCarthy, P. J. Guiry, *Tetrahedron* **2001**, *57*, 3809.
[2] a) R. Noyori, H. Takaya, *Acc. Chem. Res.* **1990**, *23*, 345; b) H. Takaya, T. Ohta, R. Noyori, *Catalytic Asymmetric Synthesis* (Ed.: I. Ojima), VCH, New York, **1993**.
[3] a) R. Schmid, M. Cereghetti, B. Heiser, P. Schönholzer, H.-J. Hansen, *Helv. Chim. Acta* **1988**, *71*, 897; b) R. Schmid, J. Foricher, M. Cereghetti, P. Schönholzer, *Helv. Chim. Acta* **1991**, *74*, 370; c) R. Schmid, E. A. Broger, M. Cereghetti, Y. Crameri, J. Foricher, M. Lalonde, R. K. Müller, M. Scalone, G. Schoettel, U. Zutter, *Pure Appl. Chem.* **1996**, *68*, 131.
[4] a) R. Noyori, *Asymmetric Catalysis in Organic Synthesis*, Wiley, New York, **1994**, pp. 1–93; b) "Reductions in Organic Synthesis": J.-P. Genet, *ACS Symp. Ser.* **1996**, *641*, 31–51; c) T. Ohkuma, M. Kitamura, R. Noyori in *Catalytic Asymmetric Synthesis* (Ed.: I. Ojima), **2000**, pp. 1–110; d) R. Noyori, T. Ohkuma, *Angew. Chem.* **2001**, *113*, 41; *Angew. Chem. Int. Ed.* **2001**, *40*, 40; e) J.-P. Genet, *Pure Appl. Chem.* **2002**, *74*, 77; f) H.-

 © 2004 Wiley-VCH Verlag GmbH & Co. KGaA, Weinheim

U. Blaser, C. Malan, B. Pugin, F. Spindler, H. Steiner, M. Studer, *Adv. Synth. Catal.* **2003**, *345*, 103.

[5] For a recent review on new chiral phosphorus ligands for asymmetric hydrogenation, see: W. Tang, X. Zhang, *Chem. Rev.* **2003**, *103*, 3029.

[6] a) K. Mashima, K. Kusano, N. Sato, Y. Matsumura, K. Nozaki, H. Kumobayashi, N. Sayo, Y. Hori, T. Ishizaki, S. Akutagawa, H. Takaya, *J. Org. Chem.* **1994**, *59*, 3064; b) H. Kumobayashi, T. Miura, N. Sayo, T. Saito, X. Zhang, *Synlett* **2001**, 1055.

[7] a) T. Saito, N. Sayo, Z. Xiaoyaong, T. Yokozawa (Takasago International Corporation), EP 0850945, **1998**; b) T. Saito, T. Yokozawa, T. Ishizaki, T. Moroi, N. Sayo, T. Miura, H. Kumobayashi, *Adv. Synth. Catal.* **2001**, *343*, 264.

[8] Z. Zhang, H. Qian, J. Longmire, X. Zhang, *J. Org. Chem.* **2000**, *65*, 6223.

[9] a) S. Duprat de Paule, N. Champion, V. Vidal, J.-P. Genet, P. Dellis (SYNKEM), FR 2830254, **2001**; S. Duprat de Paule, N. Champion, V. Vidal, J.-P. Genet, P. Dellis (SYNKEM), WO 03029259, **2003**. b) See also: C. C. Pai, Y. M. Li, Z. Y. Zhou, A. S. C. Chan, *Tetrahedron Lett.* **2002**, *43*, 2789.

[10] N. G. Andersen, M. Parvez, B. A. Keay, *Org. Lett.* **2000**, *2*, 2817.

[11] a) T. Benincori, E. Brenna, F. Sannicolò, L. Trimarco, P. Antognazza, E. Cesarotti, *J. Chem. Soc. Chem. Commun.* **1995**, 685; b) T. Benincori, E. Brenna, F. Sannicolò, L. Trimarco, P. Antognazza, E. Cesarotti, F. Demartin, T. Pilati, *J. Org. Chem.* **1996**, *61*, 6244.

[12] M. Murata, T. Morimoto, K. Achiwa, *Synlett* **1991**, 827.

[13] T. Benincori, O. Piccolo, S. Rizzo, F. Sannicolò, *J. Org. Chem.* **2000**, *65*, 8340.

[14] a) P. Guerreiro, V. Ratovelomanana-Vidal, J.-P. Genet, P. Dellis, *Tetrahedron Lett.* **2001**, *42*, 3423; b) G. Michaud, M. Bulliard, L. Ricard, J.-P. Genet, A. Marinetti, *Chem. Eur. J.* **2002**, *8*, 3327.

[15] a) F. Ullmann, J. Bielecki, *Ber. Dtsch. Chem. Ges.* **1901**, *34*, 2174; b) J. Hassan, M. Sevignon, C. Gozzi, E. Schulz, M. Lemaire, *Chem. Rev.* **2002**, *102*, 1359.

[16] (+)-(*S*)-difluorphos ((*S*)-**5**): m.p. $>260\,^{\circ}C$; ^{1}H NMR (300 MHz, $CDCl_3$): $\delta = 6.89$ (dt, $J = 1.5$, 8.2 Hz, 2H), 7.02 (d, $J = 8.2$ Hz, 2H), 7.10–7.22 (m, 8H), 7.23–7.35 ppm (m, 12H); ^{31}P NMR (162 MHz, $CDCl_3$, H_3PO_4 (85%)): $\delta = -12.23$ ppm; ^{19}F NMR (376 MHz, $CDCl_3$): $\delta = -49.90$ ppm (dd, $J = 160.8$, 93.4 Hz); MS (EI): m/z: 683 $[M+H]^+$; HR-MS: calculated for $C_{38}H_{25}F_4O_4P_2$ $[M+H]$ 683.1164, found 683.1147; $[\alpha]_D^{20} = +20$ ($c = 0.1$ in benzene). The reduction of (+)-(*R*)-**4** afforded (−)-(*R*)-difluorphos ((*R*)-**5**) in 91% yield as a white solid. All analytical data were identical to the corresponding spectra of (+)-(*S*)-**5**. *R* enantiomer: $[\alpha]_D^{20} = -20$ ($c = 0.1$ in benzene).

[17] a) P. Dierkes, P. W. N. M. van Leeuwen, *J. Chem. Soc. Dalton Trans.* **1999**, 1519; b) P. W. N. M. van Leeuwen, P. C. J. Kamer, J. N. H. Reek, P. Dierkes, *Chem. Rev.* **2000**, *100*, 2741.

[18] a) S. Duprat de Paule, S. Jeulin, V. Ratovelomanana-Vidal, J.-P. Genet, N. Champion, P. Dellis, *Tetrahedron Lett.* **2003**, *44*, 823; b) S. Duprat de Paule, S. Jeulin, V. Ratovelomanana-Vidal, J.-P. Genet, N. Champion, G. Deschaux, P. Dellis, *Org. Process Res. Dev.* **2003**, *7*, 399; c) S. Duprat de Paule, S. Jeulin, V. Ratovelomanana-Vidal, J.-P. Genet, N. Champion, P. Dellis, *Eur. J. Org. Chem.* **2003**, 1931.

[19] CAChe (Computer Aided Chemistry) program.

[20] Force field parameters: MM2; calculation type: structure optimization; optimization method: conjugate gradient for no more than 3000 updates or until convergence to 10^{-4} kcal mol^{-1}.

[21] a) D. W. Allen, B. F. Taylor, *J. Chem. Soc. Dalton Trans.* **1982**, 51; b) A. Suárez, M. A. Mendez-Rojas, A. Pizzano, *Organometallics* **2002**, *21*, 4611.

[22] a) L. Vallarino, *J. Chem. Soc.* **1957**, 2287; b) A. Sanger, *J. Chem. Soc. Dalton Trans.* **1977**, 120; c) K. Mashima, K. Kusano, N. Sato, Y. Matsumura, K. Nozaki, H. Kumobayashi, N. Sayo, Y. Hori, T. Ishizaki, S. Akutagawa, H. Takaya, *J. Org. Chem.* **1994**, *59*, 3064.

[23] a) J.-P. Genet, C. Pinel, V. Ratovelomanana-Vidal, S. Mallart, X. Pfister, M. C. Caño de Andrade, J. A. Laffitte, *Tetrahedron: Asymmetry* **1994**, *5*, 665; b) J.-P. Genet, C. Pinel, V. Ratovelomanana-Vidal, S. Mallart, X. Pfister, L. Bischoff, M. C. Caño de Andrade, S. Darses, C. Galopin, J. A. Laffitte, *Tetrahedron: Asymmetry* **1994**, *5*, 675.

[24] M. Kitamura, T. Ohkuma, H. Takaya, R. Noyori, *Tetrahedron Lett.* **1988**, *29*, 1555.

[25] a) D. Blanc, V. Ratovelomanana-Vidal, J.-P. Gillet, J.-P. Genet, *J. Organomet. Chem.* **2000**, *603*, 128. b) J. Madec, X. Pfister, P. Phansavath, V. Ratovelomanana-Vidal, J.-P. Genet, *Tetrahedron* **2001**, *57*, 2563.

[26] N. Sayo, S. Akutagawa, T. Saito, R. Noyori, H. Kumobayashi, H. Takaya, (Takasago International Corporation), EP 295109, **1988**.

[27] For Ru-catalyzed hydrogenation of ethyl 4,4,4-trifluoro-acetoacetate using biheteroaromatic diphosphanes, see: T. Benincori, E. Cesarotti, O. Piccolo, F. Sannicolò, *J. Org. Chem.* **2000**, *65*, 2043.

[28] Noyori has reported obtaining (*R*,*R*)-1,1,1,5,5,5-hexafluoro-2,3-pentandiol with 70% *de* and 70% *ee* using [Ru{(*S*)-(−)-*p*-Tolbinap}]$(PF_6)_2$ as catalyst: N. Sayo, T. Saito, H. Kumobayashi, S. Akutagawa, R. Noyori, H. Takaya, (Takasago International Corporation), EP 297752, **1989**.

 © 2004 Wiley-VCH Verlag GmbH & Co. KGaA, Weinheim

Iodination

Regioselective Postsynthetic Modification of Phenylalanine Side Chains of Peptides Leading to Uncommon *ortho*-Iodinated Analogues**

Gemma Espuña, Gemma Arsequell, Gregorio Valencia, José Barluenga, Julia M. Alvarez-Gutiérrez, Alfredo Ballesteros, and José M. González*

Interest in therapeutic drugs derived from natural peptides has been steadily increasing as diversity in peptides can be easily implemented by well-established combinatorial

[*] Prof. Dr. J. Barluenga, Dr. J. M. Alvarez-Gutiérrez, Dr. A. Ballesteros, Dr. J. M. González
Inst. Universitario de Química Organometálica "Enrique Moles"
Unidad Asociada al C.S.I.C., Universidad de Oviedo
33071 Oviedo (Spain)
Fax: (+34) 98-5103450
E-mail: Barluenga@sauron.quimica.uniovi.es
Dr. G. Espuña, Dr. G. Arsequell, Dr. G. Valencia
Unit of Glycoconjugate Chemistry, I.I.Q.A.B.-C.S.I.C.
Jordi Girona 18–26, 08034 Barcelona (Spain)
Fax: (+34) 93-2045904

[**] This research was partially supported by the Spanish MCYT (Grant BQU2001-3853) and the Fundación la Caixa (Project Reference 00/010-00 of the IV Program of Grants for Research on Neurodegenarative Diseases of the Fundación La Caixa).

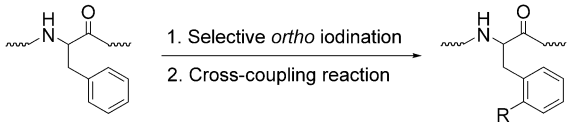
Supporting information for this article (experimental procedures and spectral and chromatographic data for **1**–**6a**, **1**–**2b**, and **7**) is available on the WWW under http://www.angewandte.org or from the author.

 DOI: 10.1002/anie.200352464 © 2004 Wiley-VCH Verlag GmbH & Co. KGaA, Weinheim

chemistry techniques[1] and because effective ways to improve their bioavailability and resistance to metabolic breakdown by peptidomimetic approaches were found.[2] Among the different strategies to facilitate entry to new conformationally restricted peptidomimetic structures and novel ways of diversity generation, selective and efficient manipulation methods of either the backbone[3] or the various side-chain functions[4] of already preformed peptide sequences are being investigated. These postsynthetic modifications of peptides avoid the use of preformed amino acid building blocks and a linear synthesis for every analogue, which has been the basis of many structure–activity relationship (SAR) studies in peptide chemistry.[5] Thus, these newer drug-discovery approaches depart from a single presynthesized peptide sequence that can be conveniently modified (by applying different types of reactions or the same reaction with different substrates) to yield a series of homologous derivatives in a parallel fashion.

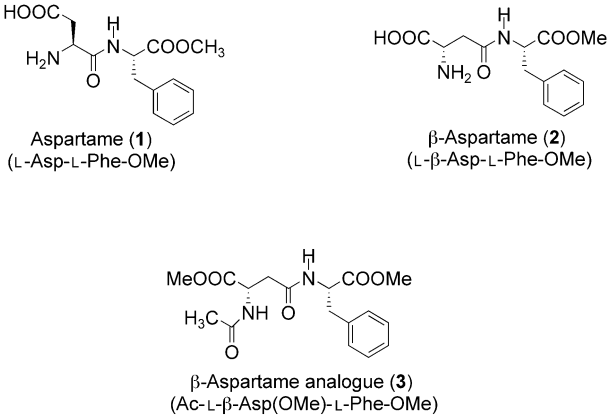
Among the known postsynthetic modifications that could be applied to implement these techniques, the Suzuki, Heck, and Stille type of reactions[6] are especially interesting because Pd^0 catalysis does not compromise peptide stability and is compatible with the multifunctional character of peptides.[7] A common feature among these methods is the need for mainly brominated and iodinated aromatic substrates. To date, general reaction conditions for aromatic electrophilic halogenations of amino acid derivatives and other simple organic molecules are too harsh and result in oxidation and degradation when applied to peptides. This is the main reason for the limited number of methods available for the halogenation of aromatic side chains of presynthesized peptides.[8] In the case of iodination, electrophilic aromatic reagents and milder conditions are only known for the more activated phenolic moiety of Tyr residues, which can be performed, for instance, by the chloramine T method[9] or by the use of the mild and selective iodinating reagent, bis(pyridine) iodonium tetrafluoroborate (IPy_2BF_4),[10] as reported by our group.[11] These iodination methods have never been adapted for the non-activated aromatic side chains of Phe in peptides and direct iodination reactions of such presynthesized peptides have yet to be described. Alternatively, current synthetic methods for halogenated peptides make use of suitable halogenated amino acid building blocks in stepwise linear synthesis protocols. However, the scope of these procedures is restricted by the cost and the number of commercially available halogenated isomeric derivatives of Tyr and Phe. In fact, *ortho*-halogenated Phe derivatives are not commercially available and are also not easy to prepare, as direct electrophilic substitutions always render the *para* derivatives as main reaction products.

Herein we report innovative protocols for the use of IPy_2BF_4 as the first solution for the direct halogenation of phenylalanine-containing peptide sequences and the unusual *ortho* selectivity accompanying this iodination reaction. Furthermore, by overcoming the limitations mentioned above, these results could provide a solution to establish a powerful postsynthetic modification of such peptides with known Pd^0 cross-coupling reactions (Scheme 1).



Scheme 1. Postsynthetic modification of a phenylalanine residue in peptides by sequential iodination/cross-coupling reactions.

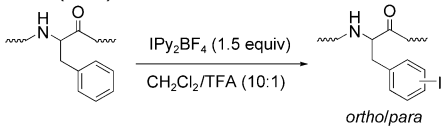
To search for suitable solvents, reaction conditions, peptide/iodonium stoichiometries, and potential acid catalysts, the well-known and readily available dipeptide sweetener aspartame[12] (**1**) and two closely related analogues were selected (Scheme 2). The choice was made to check for possible effects on the iodination reaction of the relative positions of the functional groups in the proximity of the aryl group of Phe.



Scheme 2. Dipeptide models.

We searched for good reaction media that included dichloromethane as the solvent. Trifluoroacetic acid, a broadly used reagent in peptide synthesis, proved to be very valuable as it not only solubilized the peptides, but also provided the required acidic conditions to activate the iodonium reagent. Under these original conditions (Table 1), the reagent is highly effective, and produces the monoiodinated peptide derivatives in short reaction times and preserves peptide integrity. Analysis of crude reaction

Table 1: Monoiodination of model dipeptides promoted by IPy_2BF_4 in the presence of TFA (10%) in CH_2Cl_2.



Dipeptide	*ortho*/*para*[a]	*t* [h]	Conversion [%][b]
1	3:1	0.5	87
2	3:1	0.5	91
3	14:1	0.5	90

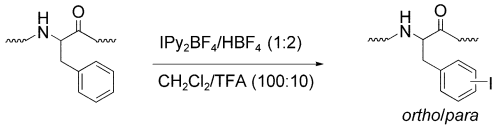
[a] Determined by NMR spectroscopic analysis. [b] Conversion determined by HPLC.

 © 2004 Wiley-VCH Verlag GmbH & Co. KGaA, Weinheim

products by ^{1}H NMR spectroscopy and analytical HPLC showed that mixtures of *ortho*/*para*-iodinated regioisomers (3:1) were obtained as the only reaction products of **1** and **2**. In contrast, the protected analogue **3** gave a 14:1 ratio (Table 1). These results were confirmed by isolation of each isomer by semipreparative HPLC and characterization by ^{1}H and ^{13}C NMR spectroscopy and MALDI-TOF MS techniques. This *ortho* selectivity had not been observed previously in aromatic iodination reactions of simple arene compounds,[13] or even in different protected derivatives of phenylalanine.[11a]

The attractiveness of such a simple entry to the elusive *ortho*-iodo isomer of a phenylalanine derivative prompted us to search for more regioselective reaction conditions. We found that other iodonium-activating acids typically used with IPy_2BF_4 improved the selectivity. The best results were found when we used the same relative amount of TFA (10%) and added the iodonium reagent along with 2 equivalents of HBF_4. Quantitative conversions were observed and the *ortho* isomer was favored over the *para* congener (20:1 in the case of **2**). Most interestingly, the ratio was concentration-dependent: the *ortho*/*para* ratio increased substantially when the reaction was diluted tenfold (Table 2). The proportion of iodonium to HBF_4 (1:2) was very critical to secure high regioselectivity, but did not influence the conversion.[14]

Table 2: Monoiodination of model dipeptides promoted by IPy_2BF_4 in the presence of TFA (10%) in CH_2Cl_2 and HBF_4 (2 equiv).



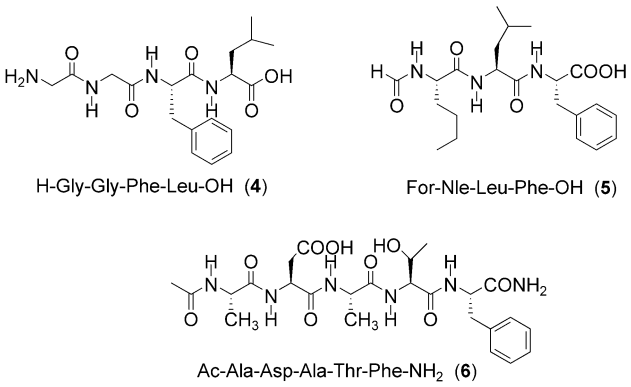
Peptide	*ortho*/*para*[a]	*t* [h]	Conversion [%][b]
1	20:1	0.5	100
2	40:1	0.5	100
3	23:1	0.5	100

[a] Determined by NMR spectroscopic analysis. [b] Conversion determined by HPLC.

The *ortho*/*para* ratio obtained from **2** is twice that obtained from the closely related peptide **1** and from the diprotected analogue **3** (Table 2). This is a good indication of the influence of the structural features surrounding Phe side chains on the regioselectivity of this process.

As mentioned above, *ortho*-iodo derivatives of Phe-containing peptides such as those described herein cannot be prepared by direct iodination or by conventional stepwise peptide elongation methods. Therefore, only *para* analogues are reported in the literature.[15] Furthermore, the potential of running the method on a preparative scale has also been explored. Similar results were observed when the iodination reaction of **2** was performed on a 1-gram scale under the reactions conditions outlined in Table 2 (same ratio, 86% yield).

Because of these encouraging results, three Phe-containing peptides were chosen to test the reaction (Scheme 3): a) **4** is a free tetrapeptide used as an opioid peptide precursor,[16]



Scheme 3. Biologically activity peptides. Nle = norleucine.

b) **5** is a tripeptide that exhibits chemotactic properties,[17] and c) **6** was chosen as a model pentapeptide sequence. All three oligopeptides were synthesized by conventional Fmoc solid-phase protocols. Remarkably, the results observed with these oligopeptides correspond well to those discussed above for the dipeptides (Table 3). In all cases, peptide integrity was preserved, very good conversions were observed, and the peptides yielded mixtures of iodinated isomers as the main reaction products. Again, addition of HBF_4 (method B) was very significant in increasing the *ortho*/*para* ratios. The reaction has proved successful for peptides presenting a single Phe residue. More electron-rich arenes, such as those present in the side chains of Tyr, Trp, and His, are iodinated under these conditions.

Table 3: Monoiodination of biologically active peptides.

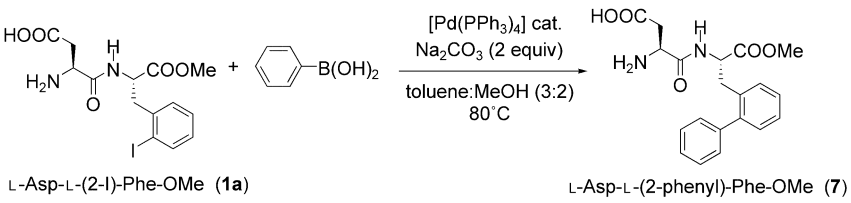
Peptides	Method[a]	*ortho*/*para*[b]	*t* [h]	Conversion [%][c]
5	A	4:1	0.5	100
5	B	7:1	3	100
4	A	3:1	0.5	84
4	B	13:1	3	100
6	A	1:1	0.5	84
6	B	8:1	0.5	90

[a] Method A: 100 mg in CH_2Cl_2/TFA (10:1); IPy_2BF_4 (1.5 equiv). Method B: 100 mg in CH_2Cl_2/TFA (100:10); IPy_2BF_4/HBF_4 (1:2 equiv). [b] Determined by NMR spectroscopic analysis. [c] Conversion based on HPLC.

To illustrate possible applications of these iodinated peptide intermediates, a Pd^0-catalyzed Suzuki-type biphenyl synthesis was attempted (Scheme 4).[7e] The unsually iodinated *ortho* isomer **1a** of aspartame was treated with a simple phenyl boronic acid to yield the constrained *ortho*-phenyl aspartame derivative **7** in good conversion.[18]

In conclusion, a new peptide postsynthetic modification is described. The method provides the first iodination protocol for aromatic side chains of Phe-containing peptides. The procedure is effected by acid-triggered aromatic electrophilic substitution with IPy_2BF_4 to provide *ortho*/*para*-monoiodinated mixtures of peptide analogues mostly quantitatively while preserving peptide integrity. The reaction is sequence- and acid-dependent, a feature that can be used to access the otherwise unavailable *ortho*-iodinated Phe derivatives

 © 2004 Wiley-VCH Verlag GmbH & Co. KGaA, Weinheim



Scheme 4. Suzuki cross-coupling reaction of L-Asp-L-(2-I)-Phe-OMe.

through a highly regioselective procedure. We foresee that this new method will find wide applications in Pd^0 chemistry, particularly for the introduction of novel pharmacologically active functionalities into the Phe side chains of peptides, while preparing large arrays of analogues for SAR studies.

Experimental Section

Typical procedures for the synthesis of β-iodoaspartame derivatives:

Method A: The peptide (100 mg, 0.34 mmol) was dissolved in a mixture of CH_2Cl_2 (10 mL) and TFA (1 mL). IPy_2BF_4 (0.51 mmol) was added (the solution turned dark pink). The reaction mixture was stirred for 0.5 h at room temperature. The solvent was removed in vacuo. The pyridinium salt formed in the reaction was removed by filtration through a short column of silica gel (eluent MeOH/TFA 10:1). The resulting solid was washed with diethyl ether and further purified by reversed-phase HPLC.

Method B: The peptide (100 mg, 0.34 mmol) was dissolved in a mixture of CH_2Cl_2 (100 mL) and TFA (10 mL). HBF_4 (0.75 mmol) was added, followed by addition of IPy_2BF_4 (0.37 mmol) (the solution turned dark pink). The mixture was stirred at room temperature for 0.5 h. The reaction was worked up as described above.

RP-HPLC: C18 (Lichrosorb, 250 × 4 mm). Solvents: A = 0.1% TFA in H_2O, B = 0.1% TFA in CH_3CN. Detection: $\lambda = 214$ nm. Elution gradient for aspartame and its derivatives: from 80 to 20% of A in 25 min.

L-β-Asp-L-(2-I)-Phe-OMe: ^{1}H NMR (400 MHz, CD_3OD): $\delta =$ 2.80 (dd, $^3J(H,H) = 9.3$ Hz, $^2J(H,H) = 8.0$ Hz, 1H), 2.99 (dd, $^2J(H,H) = 8.0$ Hz, $^3J(H,H) = 3.6$ Hz, 1H), 3.11 (dd, $^3J(H,H) =$ 13.9 Hz, $^2J(H,H) = 9.5$ Hz, 1H), 3.35 (dd, $^3J(H,H) = 6.1$ Hz, $^3J(H,H) = 5.9$ Hz, 1H), 3.70 (s, 3H), 4.13 (dd, $^3J(H,H) = 9.3$ Hz, $^3J(H,H) = 3.6$ Hz, 1H), 4.82 (dd, $^2J(H,H) = 9.5$ Hz, $^3J(H,H) = 5.9$ Hz, 1H), 6.97 (t, $^3J(H,H) = 7.7$ Hz, 1H), 7.24 (d, $^3J(H,H) = 7.5$ Hz, 1H), 7.32 (t, $^3J(H,H) = 7.5$ Hz, 1H), 7.86 ppm (d, $^3J(H,H) = 7.7$ Hz, 1H); ^{13}C NMR (100 MHz, CD_3OD): $\delta = 36.1$ (CH_2), 42.7 (CH_2), 50.9 (CH), 53.0 (OCH_3), 54.0 (CH), 101.0 (C-I), 129.6 (CH), 130.1 (CH), 131.9 (CH), 140.6 (C), 141.0 (CH), 169.4 (CO), 172.6 (CO), 172.9 ppm (CO); MALDI-TOF MS: m/z: 442.8 $[M+Na]^+$ (calculated 443.2); retention time): 10.83 min.

L-β-Asp-L-(4-I)-Phe-OMe: ^{1}H NMR (400 MHz, CD_3OD): $\delta =$ 2.69 (dd, $^3J(H,H) = 9.2$ Hz, $^2J(H,H) = 7.9$ Hz, 1H), 2.92 (m, 2H), 3.21 (dd, $^3J(H,H) = 4.0$ Hz, $^3J(H,H) = 5.0$ Hz, 1H), 3.72 (s, 3H), 4.08 (dd, $^2J(H,H) = 9.5$ Hz, $^3J(H,H) = 4.0$ Hz, 1H), 4.71 (dd, $^2J(H,H) = 9.5$ Hz, $^3J(H,H) = 5.0$ Hz, 1H), 7.03 (d, $^3J(H,H) = 8.4$ Hz, 2H), 7.65 ppm (d, $^3J(H,H) = 8.4$ Hz, 2H); ^{13}C NMR (100 MHz, CD_3OD): $\delta = 36.8$ (CH_2), 37.5 (CH_2), 51.3(CH), 53.0 (OCH_3), 55.2 (CH), 93.0 (C-I), 132.3 (2CH), 137.9 (C), 138.9 (2CH), 169.7 (CO), 172.7 (CO), 174.0 ppm (CO); MALDI-TOF MS: m/z: 442.8 $[M+Na]^+$ (calculated 443.2); retention time: 11.99 min

Received: July 24, 2003
Revised: October 14, 2003 [Z52464]

Keywords: amino acids · cross-coupling · iodine · palladium · peptides

[1] a) L. A. Thompson, J. A. Ellman, *Chem. Rev.* **1996**, *96*, 555–600; b) J. S. Fruchtel, G. Jung, *Angew. Chem.* **1996**, *108*, 19–46; *Angew. Chem. Int. Ed. Engl.* **1996**, *35*, 17–42; c) D. V. Patel, E. M. Gordon, *Drug Discovery Today* **1996**, *1*, 134–144; d) N. K. Terrett, *Combinatorial Chemistry*, Oxford University, Oxford, **1998**; e) S. Booth, P. H. H. Hermkens, H. C. J. Otthenheijm, D. C. Rees, *Tetrahedron* **1998**, *54*, 15385–15443.

[2] a) B. Dorner, J. M. Ostresh, S. E. Blondelle, C. T. Dooley, R. A. Houghten, *Adv. Amino Acid Mimetics Peptidomimetics* **1997**, *1*, 109–125; b) J. M. Ahn, N. A. Boyle, M. T. MacDonald, K. D. Janda, *Mini-Rev. Med. Chem.* **2002**, *2*, 463–473.

[3] For illustrative examples of backbone modifications, see: a) D. Ranganathan, N. K. Vaish, K. Shah, *J. Am. Chem. Soc.* **1994**, *116*, 6545–6557; b) M. Davies, M. Bradley, *Tetrahedron* **1999**, *55*, 4733–4746; c) U. Kazmaier, S. Maier, *J. Org. Chem.* **1999**, *64*, 4574–4575; d) S.-I. Murahashi, A. Mitani, K. Kitao, *Tetrahedron Lett.* **2000**, *41*, 10245–10249.

[4] Examples of postsynthetic modifications described for other residues in peptides: Asp/Glu: a) M. Paris, C. Douan, A. Heitz, W. Gibbons, J. Martinez, J. A. Fehrentz, *Tetrahedron Lett.* **1999**, *40*, 5179–5182; Leu: b) M. Mezzeti, E. Mincione, R. Saladino, *Chem. Commun.* **1997**, 1063–1064; c) R. Saladino, M. Mezzeti, E. Mincione, I. Torrini, M. P. Paradisi, G. Mastropietro, *J. Org. Chem.* **1999**, *64*, 8468–8474; Cys: d) J. Cuesta, G. Arsequell, G. Valencia, A. Gonzalez, *Tetrahedron: Asymmetry* **1999**, *10*, 2643–2646e) L. N. Jungheim, T. A. Shepperd, A. J. Baxter, J. Burguess, S. D. Hatch, P. Lubbehusen, M. Wiskerchen, M. A. Muesing, *J. Med. Chem.* **1996**, *39*, 96–108; Met: f) S. E. Blondelle, E. Perez-Payá, G. Alicotti, B. Foored, R. A. Houghten, *Biophys. J.* **1995**, *69*, 604–611g) S. Chowdbury, J. Eshraghi, H. Wolffe, D. Forde, A. G. Hlavac, D. Johnston, *Anal. Chem.* **1995**, *67*, 390–398; Trp: h) S. Ranganathan, D. Ranganathan, D. Bhattacharyya, *J. Chem. Soc. Chem. Commun.* **1987**, 1085–1086; His: i) S. Ranganathan, D. Ranganathan, D. Bhattacharyya, *Tetrahedron Lett.* **1991**, *32*, 5615–5618; j) J. Ueda, T. Ozawa, M. Miyazaki, Y. J. Fujiwara, *J. Inorg. Biochem.* **1994**, *55*, 123–130; Ser: k) J. C. Grammer, J. A. Loo, C. G. Edmons, C. R. Cremo, R. G. Yount, *Biochemistry* **1996**, *35*, 15582–15592; Gly: l) M. Ricci, L. Madariaga, T. Skrydstrup, *Angew. Chem.* **2000**, *112*, 242–252; *Angew. Chem. Int. Ed.* **2000**, *39*, 242–246; m) T. Ooi, E. Tayama, K. Maruoka, *Angew. Chem.* **2003**, *115*, 599–602; *Angew. Chem. Int. Ed.* **2000**, *39*, 242–246; T. Ooi, E. Tayama, K. Maruoka, *Angew. Chem.* **2003**, *115*, 599–602; *Angew. Chem. Int. Ed.* **2003**, *42*, 579–582.

[5] For some examples of SAR studies, see: a) deletion peptides: T. O. Matsunaga, A. M. de Lauro Castrucci, M. E. Hadley, V. J. Hruby, *Peptides* **1989**, *10*, 349–354; b) stereochemical substitutions: V. J. Hruby, *Life. Sci.* **1982**, *31*, 189–199; c) isosteric and other substitutions: M. Bodanszky, V. Vingeaud, *J. Am. Chem. Soc.* **1959**, *81*, 6072–6075; d) constraint: W. F. De Grado, *Adv. Protein Chem.* **1988**, *39*, 51–124; e) Ring size: D. F. Veber, R. M. Freidinger, D. S. Prelow, W. J. Poleveda, F. W. Holly, R. G. Strachan, R. F. Nutt, B. H. Arison, C. Homnick, W. C. Randall, M. S. Glitzer, R. Saperstein, R. Hirchmann, *Nature* **1981**, *292*, 55–57; f) cyclic constraints: T. K. Sawyer, V. J. Hruby, P. S. Darman, M. E. Hadley, *Proc. Natl. Acad. Sci. USA* **1982**, *79*, 1751–1755; g) peptidomimetics: V. J. Hruby, S. Fang, R. Knapp, W. M. Kazmierski, G. K. Lui, H. I. Yamamura, *Int. J. Pept. Protein Res.* **1990**, *35*, 566–573.

[6] a) *Metal-catalyzed Cross-coupling Reactions* (Eds.: F. Diederich, P. Stang), Wiley-VCH, Weinhein, **1998**; b) U. Kazmaier, S. Maier, F. L. Zumpe, *Synlett* **2000**, *11*, 1523–1535.

 © 2004 Wiley-VCH Verlag GmbH & Co. KGaA, Weinheim

[7] From halogenated Phe and Tyr containing peptides, see: a) M. J. Burk, J. R. Lee, J. P. Martínez, *J. Am. Chem. Soc.* **1994**, *116*, 10847 – 10848; b) O. Seitz, H. Kunz, *Angew. Chem.* **1995**, *107*, 901 – 903; *Angew. Chem. Int. Ed. Engl.* **1995**, *34*, 803 – 805; c) J. H. Lai, T. H. Marsilje, S. Choi, S. A. Nair, D. G. Hangauer, *J. Pept. Res.* **1998**, *51*, 271 – 281; d) T. L. Hudgens, K. D. Turnbull, *Tetrahedron Lett.* **1999**, *40*, 2719 – 2722; e) S. Kotha, K. Lahiri, *Bioorg. Med. Chem. Lett.* **2001**, *11*, 2887 – 2890.

[8] Bromination and iodination of Phe side chains can be achieved solely by surrogate indirect methods: a) S. R. Wilson, L. A. Jacob, *J. Org. Chem.* **1986**, *51*, 4833 – 4836; b) S. D. Sharma, G. Toth, V. J. Hruby, *J. Org. Chem.* **1991**, *56*, 4981 – 4983; c) M. Ceusters, D. Tourwé, J. Calaerts, J. Mertens, A. Peter, *J. Org. Chem.* **1995**, *60*, 8324 – 8324.

[9] Used mainly for radiolabelling purposes of peptides and proteins: E. Regoeczi, *Iodine-Labelled Plasma Proteins*, CRS, Boca Raton, FL, **1984**.

[10] a) J. Barluenga, *Pure Appl. Chem.* **1999**, *71*, 431 – 436; b) J. Barluenga, J. M. González in *Current Trends in Organic Synthesis* (Eds.: C. Scolastico, F. Nicotra), Kluwer Academic/Plenum Publishers, New York, **1999**, pp. 145 – 151.

[11] a) J. Barluenga, M. A. García-Martín, J, M. González, P. Clapés, G. Valencia, *Chem. Commun.* **1996**, 1505 – 1506; b) G. Arsequell, G. Espuña, G. Valencia, J. Barluenga, R. Pérez-Carlón, J. M. González, *Tetrahedron Lett.* **1998**, *39*, 7393 – 7396; c) G. Arsequell, G. Espuña, G. Valencia, J. Barluenga, R. Pérez-Carlón, J. M. González, *Tetrahedron Lett.* **1999**, *40*, 7279 – 7282; d) G. Espuña, G. Arsequell, G. Valencia, J. Barluenga, M. Pérez, J. M. González, *Chem. Commun.* **2000**, 1307 – 1308.

[12] a) R. H. Mazur, J. M. Schlatter, A. H. Goldkamp, *J. Am. Chem. Soc.* **1969**, *91*, 2684 – 2691; halogenation seems to enhance the biological properties of sweet compounds: b) A. Heijden, H. Wel, H. G. Peer, *Chem. Senses* **1985**, *10*, 73 – 78.

[13] J. Barluenga, J. M. González, M. A. García-Martín, P. J. Campos, G. Asensio, *J. Org. Chem.* **1993**, *58*, 2058 – 2060.

[14] An example is the case of **1** reacting with iodonium/HBF_4 (1:3), which always yielded 11:1 *ortho*/*para* isomer mixtures in quantitative conversions.

[15] a) Y. Ogata, K. Nakajima, *Tetrahedron* **1964**, 2751 – 2754; b) H. Lei, M. S. Stoakes, K. P. B. Herath, J. Lee, A. W. Schwabacher, *J. Org. Chem.* **1994**, *59*, 4206 – 4210.

[16] In opioid peptides, halogenation may be a new way to modulate the biological activity of parent peptides: a) R. C. Haaseth, T. Zalewska, P. Davis, H. I. Yamamura, F. Porreca, V. J. Hruby, *J. Pept. Res.* **1997**, *50*, 171 – 177; b) C. L. Gentry, R. D. Egleton, T. Gillespie, T. J. Abbruscato, H. B. Bechowski, V. J. Hruby, T. P. Davis, *Peptides* **1999**, *20*, 1229 – 1328; c) R. Guerrini, G. Calo, R. Bigoni, D. Rizzi, M. Zucchini, K. Varani, E. Hashiba, D. G. Lambert, G. Toth, P. A. Borea, S. Salvadori, D. J. Regoli, *J. Med. Chem.* **2001**, *44*, 3956 – 3964.

[17] Chemotactic peptides have been proposed as useful clinical markers of infection and inflammation loci. For new isomeric Phe chemotactic peptide analogues, see: R. J. Freer, A. R. Day, J. A. Radding, E. Schiffmann, S. Aswanikumar, H. J. Showell, E. L. Becker, *Biochemistry* **1980**, *19*, 2404 – 2410.

[18] Incorporation of novel *ortho*-constrained phenylalanine analogues into peptides and peptidomimetics provided fruitful information on the development of peptide and peptidomimetic ligands of use in biologically active melanotropin peptides: W. Wang, M. Cai, C. Xiong, J. Zhang, D. Trivedi, V. J. Hruby, *Tetrahedron* **2002**, *58*, 7365 – 7374.

 © 2004 Wiley-VCH Verlag GmbH & Co. KGaA, Weinheim

Natural Product Analogues

Parallel Fragment Assembly Strategy Towards Multiple-Ether Mimicry of Anticancer Annonaceous Acetogenins**

*Sheng Jiang, Yan Li, Xiao-Guang Chen, Tai-Shan Hu, Yu-Lin Wu, and Zhu-Jun Yao**

The annonaceous acetogenins are naturally occurring polyketides isolated from various species of the plant genus *Annonaceae*. To date, over 400 members of this compound family have been found, most of which have been proven to exhibit high cytotoxic and antitumor activities.[1] The structural features of these acetogenins include several free hydroxy groups with various stereochemistries, variously located oxygenated functional groups, and tetrahydrofuran (THF) ring(s) along the hydrocarbon skeleton. The unique structural features and interesting biological activities of these compounds have rendered them attractive targets for the development of efficient syntheses of both the natural products and functional mimetics.[2,3] In nature, annonaceous acetogenins are believed to block oxidative pathways in complex I in mitochondria,[4] and there is evidence that some members of the family induce apoptosis in cancer cells.[5] In 1994, a group of Japanese chemists first reported NMR studies showing that annonaceous acetogenins can coordinate a calcium cation.[6] Their results prompted us to investigate the biological importance of this property and how it relates to the reported activities of these compounds. On first inspection, the THF ring(s) and flanking hydroxy groups are the structural components most likely to interact with metal cations. Over the past several years, we have successfully developed a series of annonaceous acetogenin mimetics[7–11] in which the THF rings and flanking hydroxy groups have been replaced by an ethylene glycol ether unit. These analogues with simplified structures have proved to be as active as the natural products. More interestingly, we have found that some of these analogues have much better selectivity between

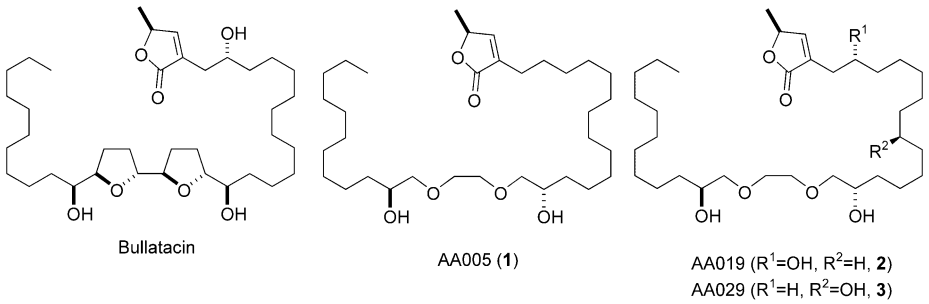
[*] Dr. S. Jiang, Dr. T.-S. Hu, Prof. Y.-L. Wu, Prof. Dr. Z.-J. Yao
State Key Laboratory of Bioorganic
and Natural Products Chemistry
Shanghai Institute of Organic Chemistry
354 Fenglin Road, Shanghai 200032 (China)
Fax: (+86) 2164166128
E-mail: yaoz@mail.sioc.ac.cn
Y. Li, Prof. Dr. X.-G. Chen
Institute of Materia Medica
Chinese Academy of Medical Sciences
1 Xiannongtan Street, Beijing 100050 (China)

[**] This work was supported by the National Natural Science Foundation of China (grant no. 30271531), the Ministry of Science and Technology (MOST) of China (grant no. G2000077502), the Chinese Academy of Sciences (CAS; grant no. KGCX2-SW-209), and the Shanghai Municipal Committee of Science and Technology (grant no. 01QA14049). Dr. Terrence R. Burke, Jr. at the National Cancer Institute (NCI) is thanked for correcting the English text.

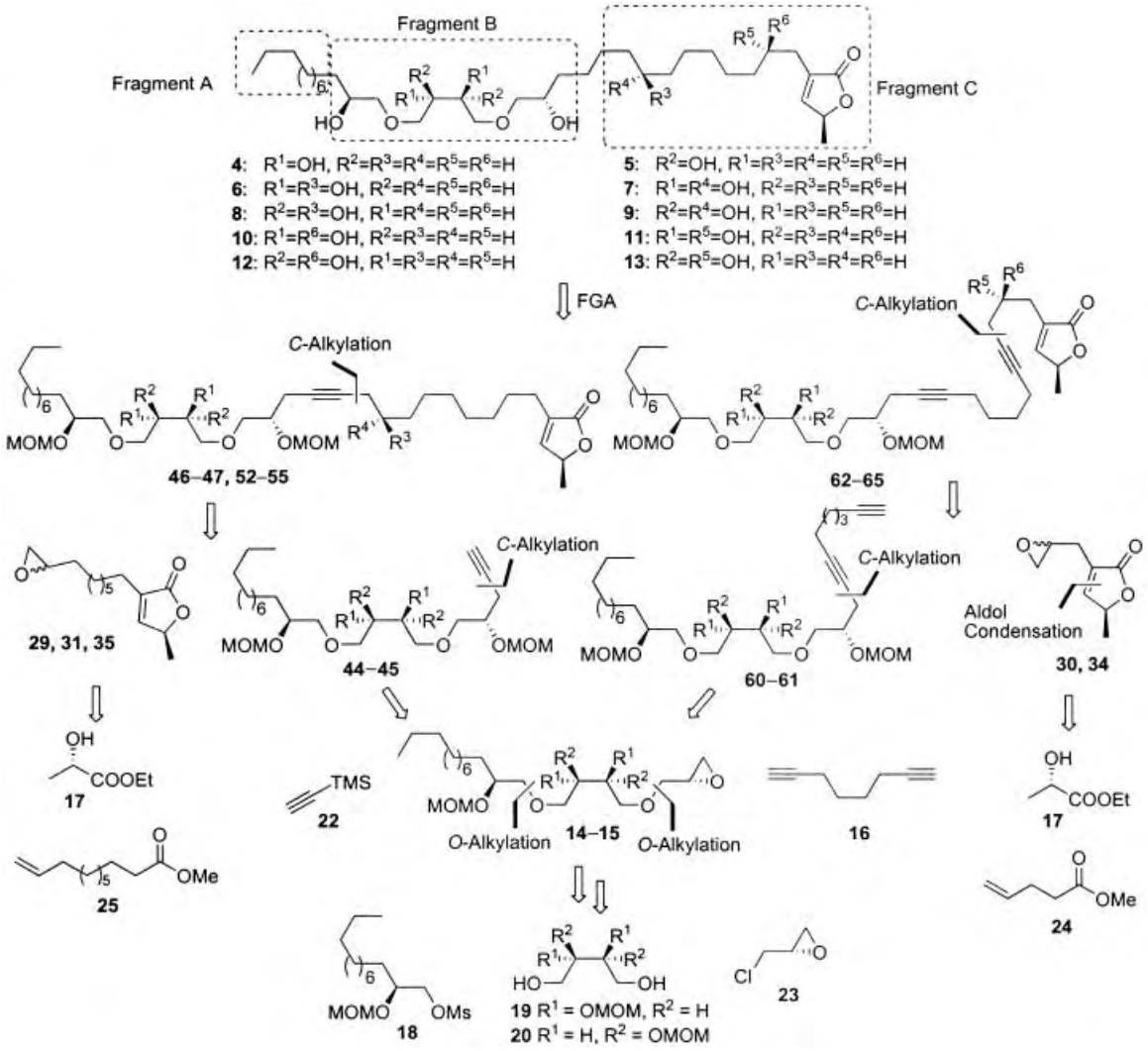
 DOI: 10.1002/anie.200352681 © 2004 Wiley-VCH Verlag GmbH & Co. KGaA, Weinheim

human cancer cells and normal cells.[8] Such selectivity is very difficult to achieve with the naturally occurring counterparts.

In our previous work, bullatacin, a typical acetogenin and one of the most potent, was selected as a template for mimetic design.[12] The first generation of mimetics was obtained by simple modification of the THF region of the molecules and by random syntheses. Individual screening revealed that AA005 (**1**; Scheme 1) is a better agent than bullatacin against several human cancers cells,[9] such as HT-29 and HCT-8. We also recently confirmed that AA005 interacts with the same biological target as do the natural products.[10] A further investigation showed that introduction of a (4*R*)-hydroxy group into AA005 (**1**) raises the potency by up to 15 times (AA019, **2**).[11] Introduction of a (10*R*)-hydroxy group into the AA005 skeleton (AA029, **3**) had little effect on the activity.[8] To accelerate progress in the search for more potent and selective anticancer agents with such modifications and to obtain clearer information on the structure–activity relationship (SAR) of the acetogenins from these mimetics, a systematic organic synthesis strategy involving parallel fragment assembly was developed. By using this strategy, small, focused libraries could be set up efficiently (Scheme 2; these compounds are designated as second-



Scheme 1. Bullatacin and three typical mimetics **1**–**3** produced by random synthesis.



Scheme 2. General fragmentation and retrosynthetic analyses for the acetogenin mimetics **4**–**13**. FGA = functional group addition, MOM = methoxymethyl, TMS = trimethylsilyl, OMs = mesylate.

 © 2004 Wiley-VCH Verlag GmbH & Co. KGaA, Weinheim

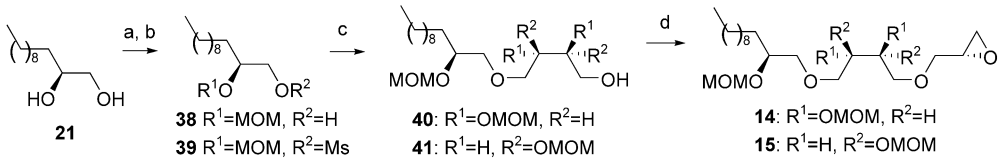
generation mimetics).[13] Herein, we report our initial results from this approach, by which we have synthesized a new class of mimetics. Several of these analogues exhibit good-to-excellent anticancer activity in the low micromolar range.

As shown in Scheme 2, a typical mimetic structure can be broken down into three major fragments A, B, and C, each of which can be synthesized individually or purchased from commercial sources. Assembly of these fragments can be achieved by convergent syntheses. By varying the combination of fragments, ten analogues of the annonaceous acetogenins were obtained by parallel assembly of prefunctionalized units (Scheme 2). The most structurally significant modification in these compounds was made in the middle region (Fragment B), where an L- or D-threotol unit was introduced. In addition, a position-shifting and configuration-variable hydroxy group was introduced into the right-hand portion of the structure (Fragment C).

A retrosynthetic analysis of **4**–**13** is shown in Scheme 2. After a standard FGA treatment of these targets, a key step involved two directional *C*-alkylations of 1,7-octadiyne **16** or trimethylsilylacetylene (**22**) with epoxides **14** or **15** and **29**, **31**, or **35**, or **30** or **34**. To form the ether bonds of the common intermediates **14** and **15**, two successive directional *O*-alkylations were used, which gave precursors **18**, **19** or **20**, and **23**. Compounds **19** and **20** could in turn be prepared easily from L- and D-tartaric acid,[14] respectively. Synthesis of terminal butenolides **30**, **31**, **34**, and **35** could be achieved by a three-step protocol that included an aldol condensation[15] and the hydrolytic kinetic resolution transformation developed by Jacobsen and co-workers.[16]

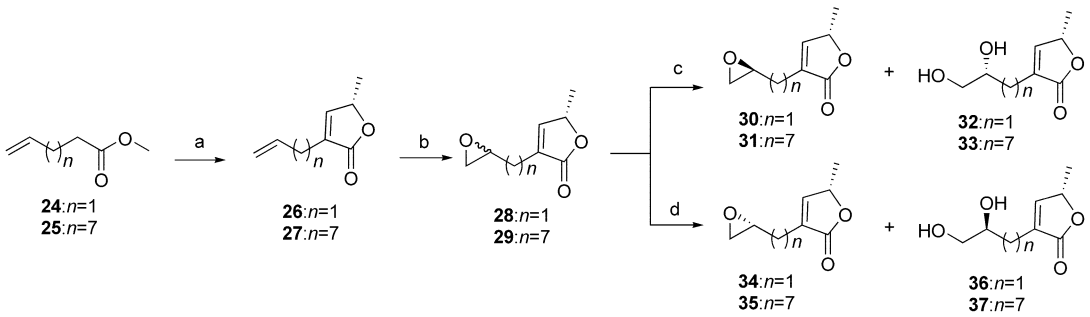
The synthesis of key intermediates **30**, **31**, **34**, and **35** is illustrated in Scheme 3. Compounds **24** and **25** can be prepared easily from the corresponding acids. Appendage of butenolide units onto **24** and **25** to form **26** and **27** involved a three-step sequence: 1) aldol reaction of **24** and **25** with freshly prepared (2*S*)-*O*-tetrahydropyranyl (*O*-THP) lactal, 2) acid-catalyzed deprotection of the *O*-THP group and in situ lactonization, and 3) elimination of a β-hydroxy group by treatment with $(CF_3CO)_2O$ and Et_3N. Regioselective epoxidation of **26** and **27** was achieved by treatment with *m*CPBA to give **28** and **29** in 86% yield. The hydrolytic kinetic resolution of Jacobsen and co-workers was applied to resolve the terminal epoxides.[16b] This reaction was performed in the presence of an (*S*,*S*)-salen–Co(OAc) complex (0.5 mol%) and H_2O (0.55 equiv) to yield **30** and **31** (43%) and diols **32** and **33** (50%) at 4°C. The diastereomeric ratio (d.r.) of **30** and of **31** (>99%) was measured by HPLC, with **28** and **29** as references.[17] Similarly, epoxides **34** and **35** were obtained with high d.r. values (>99%) in the presence of (*R*,*R*)-salen–Co(OAc) (0.5 mol%) and H_2O (0.55 equiv).[17]

The remaining key intermediates **14** and **15** were synthesized as outlined in Scheme 4. Diol **21** was easily prepared from D-mannitol[8] and was regioselectively protected as MOM ether **38** in 90% yield by a two-step procedure.[18] The remaining primary hydroxy group was then masked as a mesylate (**39**, 100% yield). Parallel reaction of mesylate **39** with diols **19** and **20** afforded monoalcohols **40** and **41** in 78% yield. In the presence of a phase-transfer catalyst,[19] further *O*-alkylation of alcohols **40** and **41** by treatment with *R*-(−)-epichlorohydrin **23** led to key intermediates **14** and **15**, respectively, in 78% yield.



Scheme 4. Reagents and conditions: a) 1. $HC(OCH_3)_3$, D-10-camphorsulfonic acid, CH_2Cl_2, 2. diisobutylaluminum hydride in toluene, CH_2Cl_2, 0°C, two steps: 90%. b) MsCl, Et_3N, CH_2Cl_2, 100%. c) **19** or **20** (for **40** and **41**, respectively), NaH, DMF, 130°C, 78%. d) NaOH, H_2O, Bu_4NHSO_4, (*R*)-epichlorohydrin, 78%.

With the functionalized segments described above in hand, a series of parallel assemblies was undertaken that involved the sequential *C*-alkylation of terminal alkynes by the required epoxides. Regioselective opening of epoxides **14** and **15** by treatment with the monolithium salt of trimethylsilylacetylene, followed by protection with MOM and deprotection of the TMS group afforded the "left-hand" segments

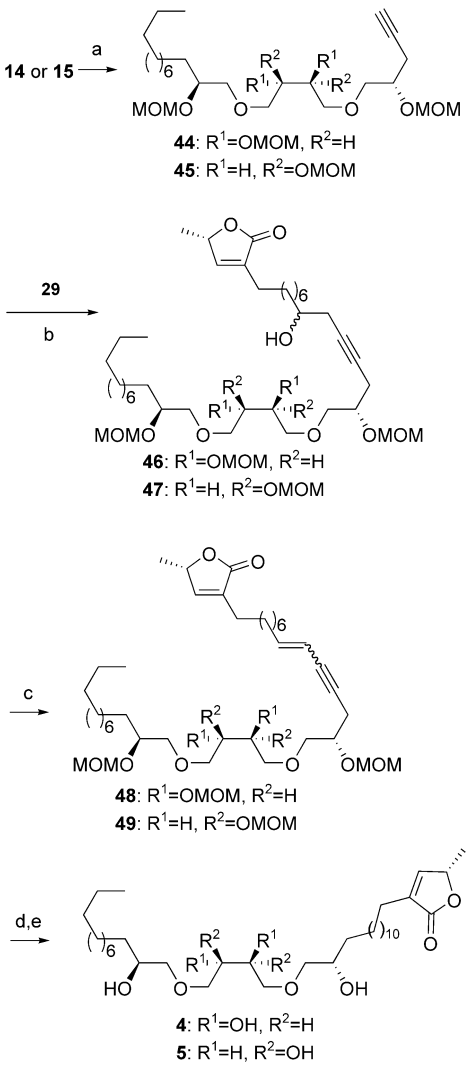


Scheme 3. Reagents and conditions: a) 1. lithium diisopropylamide, THF-hexamethyl phosphoramide, (*S*)-*O*-tetrahydropyranyl lactal, −78°C; 2. 10% H_2SO_4, THF, RT; 3. $(CF_3CO)_2O$, Et_3N, CH_2Cl_2, 60%. b) *meta*-chloroperbenzoic acid (*m*CPBA), CH_2Cl_2, 0°C, 86% yield based on 31% recovery of olefins **26**–**27**. c) (*S*,*S*)-salen–Co(OAc), H_2O, 43% yield for epoxides **30** and **31**. d) (*R*,*R*)-salen–Co(OAc), H_2O, 43% yield for epoxides **34** and **35**.

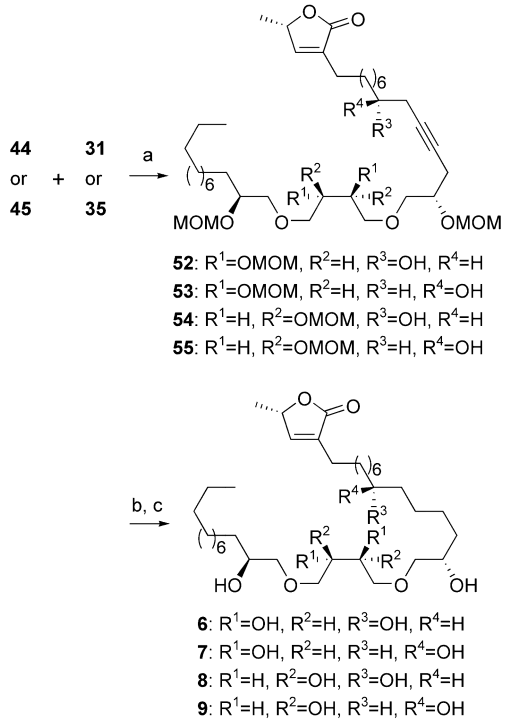
 © 2004 Wiley-VCH Verlag GmbH & Co. KGaA, Weinheim

44 and **45**. Treatment of the terminal alkynes in **44** and **45** with *n*-butyllithium, followed by reaction with epoxide **29** in the presence of BF_3 etherate at −78 °C gave the fully elaborated skeletons **46** and **47** in 70% yield.[20] Elimination of the newly introduced hydroxy groups by treatment with $(CF_3CO)_2O$ and Et_3N (or MsCl and Et_3N) gave **48** and **49**. Selective reduction of the triple and double bonds in the centers of **48** and **49** was achieved by reaction with a diimide. Deprotection of the MOM ethers by treatment with boron trifluoride and dimethylsulfide gave the final products **4** and **5** (Scheme 5).[21]

Treatment of alkynes **44** and **45** with butyllithium and enantiomerically pure epoxides **31** and **35** in different combinations in the presence of BF_3 etherate at −78 °C gave the fully assembled skeletons **52**–**55**. Subsequent selective reduction of the triple bonds and cleavage of the MOM groups in **52**–**55** yielded the final products **6**–**9** (Scheme 6).



Scheme 5. Reagents and conditions: a) 1. *n*BuLi, $BF_3{\cdot}Et_2O$, THF, trimethylsilylacetylene, −78 °C; 2. iPr_2NEt, MOMCl, CH_2Cl_2, 60%. 3. Tetrabutylammonium fluoride, THF, 0 °C, 92%. b) *n*BuLi, $BF_3{\cdot}Et_2O$, THF, −78 °C, 70%. c) $(CF_3CO)_2O$, Et_3N, CH_2Cl_2, 40%, or MsCl, 1,8-diazabicyclo[5.4.0]undec-7-ene, CH_2Cl_2, 60%. d) $TsNHNH_2$, NaOAc, 1,2-dimethoxyethane (DME), reflux, 70%. e) $BF_3{\cdot}Et_2O$, Me_2S, 0 °C, 50%. Ts = tosyl.



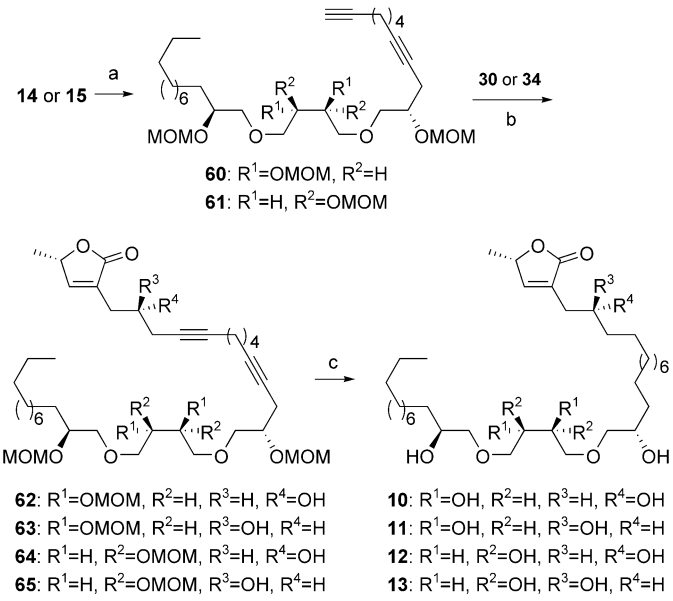
Scheme 6. Reagents and conditions: a) *n*BuLi, $BF_3{\cdot}Et_2O$, THF, −78 °C, 67%. b) $TsNHNH_2$, NaOAc, DME, reflux, 88%. c) $BF_3{\cdot}Et_2O$, Me_2S, 0 °C, 53%.

By analogy to the synthesis described above, reaction of a preformed monolithium salt solution of 1,7-octadiyne (**16**) with epoxides **14** and **15** was performed in parallel in the presence of $BF_3{\cdot}Et_2O$. The newly generated hydroxy group was protected as its MOM ether, which resulted in **60** and **61**. Parallel treatment of **60** and **61** with *n*BuLi, followed by reaction with epoxides **30** and **34** in a variety of combinations afforded **62**–**65**. The triple bonds in **62**–**65** were reduced by treatment with diimide, and deprotection of the MOM ethers afforded targets **10**–**13** (Scheme 7).

Preliminary in vitro measurements gave IC_{50} values in the low micromolar range for the synthetic mimetics (Table 1), except against the Bel-7402 cell line. Compounds **12** and **13** are more potent than **1** against KB cells. It is apparent that activity against Bel-7402 cells is decreased by the introduction of hydroxy groups into the region of the ether bonds in **1**. Such modification improved the selectivity between the KB and Bel-7402 cell lines. This result indicates that the stereochemistry in the vicinity of the ether bonds may provide important contributions to the cytotoxicity towards and selectivity between the various tumor cell lines.

In summary, a new class of multiple-ether-modified analogues (**4**–**13**) of the annonaceous acetogenins was designed based on the structures of mimetics **1** and **2**, and the analogues were synthesized enantioselectively by using a parallel fragment-assembly strategy that involved the combination of prefunctionalized units. This methodology may potentially be applicable to the synthesis of further analogues of this family, as well as other complex, focused libraries. Directional chemo- or regioselective *C*- and *O*-alkylations

 © 2004 Wiley-VCH Verlag GmbH & Co. KGaA, Weinheim



Scheme 7. Reagents and conditions: a) 1. **16**, *n*BuLi, $BF_3{\cdot}Et_2O$, THF, −78 °C; 2. *i*Pr_2NEt, MOMCl, CH_2Cl_2, 66% over two steps. b) *n*BuLi, $BF_3{\cdot}Et_2O$, THF, −78 °C, 48%. c) 1. $TsNHNH_2$, NaOAc, DME, reflux; 2. $BF_3{\cdot}Et_2O$, Me_2S, 0 °C, 49% over two steps.

Table 1: Cytotoxicity data of **1**, **4**–**13**, and adriamycin in vitro.

Compound no. or name	IC_{50} (μM)			
	KB	Bel-7402	HT-29	HCT-8
1[a]	7.65	1.99	0.099	0.11
4	4.02	>10	1.84	3.49
5	13.13	>10	5.72	8.58
6	13.81	>10	7.19	5.71
7	23.30	>10	9.79	10.00
8	9.68	>10	4.56	24.46
9	21.30	>10	7.22	6.14
10	6.75	>10	3.60	3.39
11	6.38	>10	2.36	3.51
12	2.00	>10	1.75	2.00
13	2.35	4.14	1.51	3.46
adriamycin[a]	<0.01	0.95	0.055	0.11

[a] Adriamycin and compound **1** were selected as the positive controls in the screening.

served as key reactions in the synthesis of the target linear assemblies. An aldol-condensation-centered three-step procedure was utilized to form terminal γ-butenolides. The starting materials were all readily availabile and the reagents inexpensive. Biological evaluation of the products showed that introduction of hydroxy groups to the ether-bond region of the compounds results in different selectivities and potencies for different tumor cells. Most importantly, the parallel synthetic strategy presented herein may accelerate discovery of potent and selective antitumor agents. Further SAR information may be forthcoming as additional focused libraries become available.

Received: August 19, 2003
Revised: October 6, 2003 [Z52681]

Keywords: antitumor agents · natural products · parallel synthesis · synthesis design

[1] For reviews, see: a) J. K. Rupprecht, Y. H. Hui, J. L. McLaughlin, *J. Nat. Prod.* **1990**, *53*, 237; b) X. P. Fang, M. J. Rieser, Z. M. Gu, J. L. McLaughlin, *Phytochem. Anal.* **1993**, *4*, 27; c) Z.-J. Yao, Y.-L. Wu, *Chin. J. Org. Chem.* **1995**, *15*, 120; c) L. Zeng, Q. Ye, N. H. Oberlies, G. E. Shi, Z. M. Gu, K. He, J. L. McLaughlin, *Nat. Prod. Rep.* **1996**, 275; d) A. Cave, B. Figadere, A. Laurens, D. Cortes, *Fortschr. Chem. Org. Naturst.* **1997**, *70*, 81; e) F. Q. Alali, X.-X. Liu, J. L. McLaughlin, *J. Nat. Prod.* **1999**, *62*, 504.

[2] Recent examples of total synthesis of annonaceous acetogenins: a) S. Takahashi, A. Kubota, T. Nakata, *Org. Lett.* **2003**, *5*, 1353; b) N. Maezaki, N. Kojima, A. Sakamoto, H. Tominaga, C. Iwata, T. Tanaka, M. Monden, B. Damdinsuren, S. Nakamori, *Chem. Eur. J.* **2003**, *9*, 390.c) S. Takahashi, A. Kubota, T. Nakata, *Tetrahedron Lett.* **2002**, *43*, 8661; d) S. Takahashi, T. Nakata, *J. Org. Chem.* **2002**, *67*, 5739; e) D. J. Dixon, S. V. Ley, D. J. Reynolds, *Chem. Eur. J.* **2002**, *8*, 1621; f) H. Makabe, Y. Hattori, A. Tanaka, T. Oritani, *Org. Lett.* **2002**, *4*, 1083, and references cited therein.

[3] Studies on mimicry of annonaceous acetogenins: a) P. Duret, R. Hocquemiller, J.-C. Gantier, B. Frigadere, *Bioorg. Med. Chem.* **1999**, *7*, 1821; b) S. Hoppen, U. Emde, T. Friedrich, L. Grubert, U. Koert, *Angew. Chem.* **2000**, *112*, 2181; *Angew. Chem. Int. Ed.* **2000**, *39*, 2099; c) S. Arndt, U. Emde, S. Baeurle, T. Friedrich, L. Grubert, U. Koert, *Chem. Eur. J.* **2001**, *7*, 993; d) T. Gallardo, M. C. Zafra-Polo, J. R. Tormo, M. C. Gonzalez, X. Franck, E. Estornell, D. Cortes, *J. Med. Chem.* **2000**, *43*, 4793; e) J. R. Tormo, E. Estornell, T. Gallardo, M. C. Gonzalez, A. Cave, S. Granell, D. Cortes, M. C. Zafra-Polo, *Bioorg. Med. Chem.* **2001**, *11*, 681; f) S. Rodier, Y. L. Huerou, B. Renoux, J. Doyon, P. Renard, A. Pierre, J. P. Gesson, R. Gree, *Anti-Cancer Drug Des.* **2001**, *16*, 109, and refs. [7, 8, 10, 12].

[4] a) J. L. Landolt, K. I. Ahammadsahib, R. M. Hollingworth, R. Barr, F. L. Crane, N. L. Buerck, G. P. McCabe, J. L. McLaughlin, *Chem.-Biol. Interact.* **1995**, *98*, 1; b) R. José, T. Tormo, R. Gallardo, D. Aragón, E. E. Cortes, *Chem.-Biol. Interact.* **1999**, *122*, 171.

[5] H. W. Chih, H. F. Chiu, K. S. Tang, F. R. Chang, Y. C. Wu, *Life Sci.* **2001**, *69*, 1321.

[6] a) S. Sasaki, H. Naito, K. Maruta, E. Kawahara, M. Maeda, *Tetrahedron Lett.* **1994**, *35*, 3337; b) S. Sasaki, K. Maruta, H. Naito, H. Sugihara, K. Hiratani, M. Maeda, *Tetrahedron Lett.* **1995**, *36*, 5571; c) J.-P. Peyrat, J. Mahuteau, B. Figadere, A. Cave, *J. Org. Chem.* **1997**, *62*, 4811.

[7] a) Z.-J. Yao, H.-P. Wu, Y.-L. Wu, *J. Med. Chem.* **2000**, *43*, 2484; b) S. Jiang, Y.-L. Wu, Z.-J. Yao, *Chin. J. Chem.* **2002**, *20*, 1393.

[8] B.-B. Zeng, Y. Wu, S. Jiang, Q. Yu, Z.-J. Yao, Z.-H. Liu, H.-Y. Li, Y. Li, X.-G. Chen, Y.-L. Wu, *Chem. Eur. J.* **2003**, *9*, 282.

[9] B.-B. Zeng, Y. Wu, Q. Yu, Y.-L. Wu, Y. Li, X.-G. Chen, *Angew. Chem.* **2000**, *112*, 2010; *Angew. Chem. Int. Ed.* **2000**, *39*, 1934.

[10] G. Huang, S. Jiang, Y.-L. Wu, Z.-J. Yao, J. Wu, *ChemBioChem* **2003**, *4*, 1216.

[11] S. Jiang, Z.-H. Liu, G. Sheng, B. -B, Zeng, X.-G. Chen, Y.-L. Wu, Z.-J. Yao, *J. Org. Chem.* **2002**, *67*, 3404.

[12] a) Y. H. Hui, J. K. Rupprecht, Y. M. Liu, J. E. Anderson, D. L. Smith, C. J. Chang, J. L. McLaughlin, *J. Nat. Prod.* **1989**, *52*, 463; b) H. W. Chih, H. F. Chiu, Y. M. Hsian, C. H. Tseng, M. J. Wu, Y. C. Wu, *Biochem. Pharmacol.* **2003**, *65*, 319.

[13] For recent reviews on natural-product-based libraries, see: a) R. Breinbauer, I. R. Vetter, H. Waldmann, *Angew. Chem.* **2002**, *114*, 3002; *Angew. Chem. Int. Ed.* **2002**, *41*, 2878; b) P. Arya, R. Joseph, D. T. H. Chou, *Chem. Biol.* **2002**, *9*, 145; c) D. G. Hall, S. Manku, F. Wang, *J. Comb. Chem.* **2001**, *3*, 125.

 © 2004 Wiley-VCH Verlag GmbH & Co. KGaA, Weinheim

[14] a) H. Iida, N. Yamazaki, C. Kibayashi, *Tetrahedron Lett.* **1985**, *26*, 3255; b) H. Iida, N. Yamazaki, C. Kibayashi, *J. Org. Chem.* **1986**, *51*, 1069; c) A. Mccaig, K. P. Meldrum, R. H. Wightman, *Tetrahedron* **1998**, *54*, 9429.
[15] a) Z.-J. Yao, Y.-L. Wu, *Tetrahedron Lett.* **1994**, *35*, 157; b) Z.-J. Yao, Y.-L. Wu, *J. Org. Chem.* **1995**, *60*, 1170.
[16] a) S. E. Schaus, B. D. Brandes, J. F. Larrow, M. Tokunaga, K. B. Hansen, A. E. Gould, E. N. Jacobsen, *J. Am. Chem. Soc.* **2002**, *124*, 1307; b) Q. Yu, Y. Wu, L.-J. Xia, M.-H. Tang, *Chem. Commun.* **1999**, 129.
[17] HPLC conditions for determination of the d.r. values of epoxides **30**, **31**, **34**, and **35**: UV detector (214 nm); Chiralcel AS column; eluent: *i*PrOH/Hexane (2:8); flow rate: 0.7 mL min^{-1}. Retention times: 31.24 min for **30** and 28.74 min for **34**; 67.66 min for **31** and 56.17 min for **35**.
[18] L. L. He, H. S. Byun, R. Bittman, *J. Org. Chem.* **2000**, *65*, 7618.
[19] Y. L. Huerou, J. Doyon, R. L. Gree, *J. Org. Chem.* **1999**, *64*, 6782.
[20] M. Yamaguchi, I. Hirao, *Tetrahedron Lett.* **1983**, *24*, 391.
[21] a) T.-S. Hu, Q. Yu, Y.-L. Wu, Y. Wu, *J. Org. Chem.* **2001**, *66*, 853; b) J. A. Marshall, M. Z. Chen, *J. Org. Chem.* **1997**, *62*, 5996.

 © 2004 Wiley-VCH Verlag GmbH & Co. KGaA, Weinheim

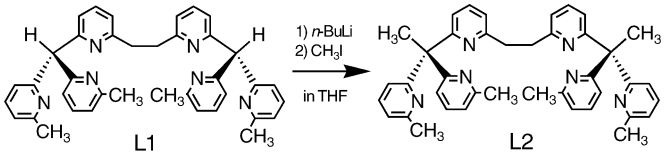
Bioinorganic Chemistry

Synthesis, Structure, and Greatly Improved Reversible O_2 Binding in a Structurally Modulated μ-η^2:η^2-Peroxodicopper(II) Complex with Room-Temperature Stability**

Masahito Kodera, Yuuji Kajita, Yoshimitsu Tachi, Kou Katayama, Koji Kano, Shun Hirota, Shuhei Fujinami, and Masatatsu Suzuki*

Some thermally stable μ-η^2:η^2-peroxodicopper(II) complexes (Cu_2O_2)[1,2] have been reported as models of oxyhemocyanin (oxyHc),[3] and the room-temperature-stable μ-η^2:η^2-Cu_2O_2 complex $[Cu_2(O_2)(L1)](PF_6)_2$ (**1**, where L1 is the sterically hindered hexapyridine ligand 1,2-bis[2-(bis(6-methyl-2-pyridyl)methyl)-6-pyridyl]ethane) is the first example of a μ-η^2:η^2-Cu_2O_2 complex that binds O_2 reversibly in homogeneous solution around room temperature.[2b] However, heating the solution at 80 °C was required for release of O_2 from **1**.[2b] Hence, the next target is to make a functional model of the tense form of oxyHc (low O_2 affinity),[4] which releases O_2 more easily.

It is known that structural modulation of copper complexes by subtle structural perturbation of ligands dramatically affect the Cu/O_2 reactivity.[1] We have synthesized a new sterically hindered hexapyridine ligand having bridgehead methyl groups, namely L2 (Scheme 1), and its μ-η^2:η^2-Cu_2O_2 complexes $[Cu_2(O_2)(L2)](X)_2$ (**3**-X_2, X = PF_6, CF_3SO_3, ClO_4). The structural modulation of the μ-η^2:η^2-Cu_2O_2 complex by the bridgehead methyl groups facilitates release of O_2 and results in an almost perfectly reversible CO/O_2 binding cycle simply by exchanging the gas phase between O_2 and CO. Here, we report greatly improved reversible O_2 binding by **3**, which may provide some insight into the mechanism of Hc, on the basis of the crystal structure and detailed spectral analysis of **3**.



Scheme 1. Synthesis of L2.

Ligand L2 forms Cu^I complexes $[Cu_2(CH_3CN)_2(L2)](X)_2$ (**2**-X_2; X = PF_6, CF_3SO_3, and ClO_4). The structure of **2**-$(CF_3SO_3)_2$ was determined by X-ray analysis[5,7] (Figure 1). The Cu^I ions have a trigonal-pyramidal coordination geometry formed by three pyridyl N atoms of L2 coordinated in a facial mode and a CH_3CN ligand. The Cu···Cu distance in **2** (6.616(1) Å) is large because the CH_2CH_2 spacer connecting the two tripyridyl units adopts an energetically more stable *anti* conformation. The sharp singlet signal of the CH_2CH_2 spacer in the ^{1}H NMR spectrum of **2** (see Experimental Section) indicates free rotation about the C–C single bond in solution.

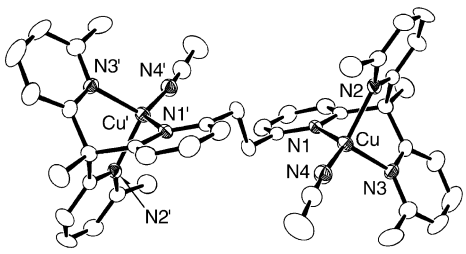


Figure 1. Structure of the cation of **2**-$(CF_3SO_3)_2$ (ORTEP plot, 50% probability; unlabeled open ellipses represent carbon atoms). Selected interatomic distances [Å] and angles [°]: Cu-N1, 2.052(6), Cu-N2, 2.042(7), Cu-N3, 2.070(7), Cu-N4, 1.884(7); Cu···Cu′, 6.616(1), N1-Cu-N2, 88.8(2), N1-Cu-N3, 90.4(3), N1-Cu-N4, 128.9(3), N2-Cu-N3, 93.7(3), N2-Cu-N4, 126.7(3), N3-Cu-N4, 118.1(3).

[*] Prof. Dr. M. Kodera, Y. Kajita, Dr. Y. Tachi, K. Katayama, Prof. Dr. K. Kano
Department of Molecular Science and Technology
Faculty of Engineering
Doshisha University, Kyotanabe, Kyoto 610-0321 (Japan)
Fax: (+81) 774-65-6848
E-mail: mkodera@mail.doshisha.ac.jp
Dr. S. Hirota
Kyoto Pharmaceutical University
Nakauchi-cho, Misasagi, Yamashina-ku, Kyoto 607-8414 (Japan)
Dr. S. Fujinami, Prof. Dr. M. Suzuki
Department of Chemistry, Kanazawa University
Kakuma-machi, Kanazawa 920–1192 (Japan)

[**] This work was supported by the Grant-in-Aid for Scientific Research (A) (14340210) from JSPS and the Aid of Doshisha University's Research Promotion Fund. We thank Prof. Dr. Teizo Kitagawa, Institute for Molecular Science, for permission to use the resonance Raman equipment.

 © 2004 Wiley-VCH Verlag GmbH & Co. KGaA, Weinheim DOI: 10.1002/anie.200352737

The μ-η^2:η^2-Cu_2O_2 complexes **3**-X_2 were prepared by addition of O_2 to dicopper(I) complexes **2**-X_2 in CH_2Cl_2 and isolated as purple crystals by cooling the solution at −30 °C with slow diffusion of $PhCH_3$. Measurements of O_2 uptake with a gas-burette system showed that one equivalent of O_2 is bound to **2**-$(PF_6)_2$ in CH_2Cl_2 at various concentrations and temperatures. Spontaneous decomposition of **3**-$(PF_6)_2$ in solution in CH_2Cl_2, monitored at 350 nm, obeys first-order kinetics with $k = 7.0 \times 10^4\ min^{-1}$ at 25 °C (half-life time $\tau_{1/2}$ = 2.5 h). The thermal stability of **3** is affected by the counteranion: the $\tau_{1/2}$ values of **3**-$(ClO_4)_2$ and **3**-$(CF_3SO_3)_2$ are 3.0 and 3.6 h, respectively.

Reversible binding of O_2 was observed in CH_2Cl_2/acetone (3/0.002) (Figure 2a): **3** releases O_2 under argon simply on heating the solution to 40 °C and is easily regenerated at 0 °C by replacing the gas phase over the solution by O_2. The small amount of acetone assists release of O_2 from **3** by coordination to the copper(I) center. Replacing the O_2 atmosphere with argon is sufficient to release O_2 from **3**. After three cycles of reversible O_2 binding, irreversible decomposition of **3** amounted to less than 10%. Heating at 80 °C in vacuo and addition of a small amount of CH_3CN are necessary for releasing O_2 from **1**. Thus, the reversible O_2 binding of **3** is greatly improved over that of **1**. Moreover, we prepared the CO/L2 complex $[Cu_2(CO)_2(L2)](PF_6)_2$ (**4**-$(PF_6)_2$) and achieved completely reversible O_2/CO binding (Scheme 2) with a solution of **4** in CH_2Cl_2 at 25 °C without addition of any coordinating solvent and without heating (Figure 2b). In this system, **4** is easily converted to **3** by addition of O_2 and regenerated quantitatively when the gas phase is replaced by CO. After several O_2/CO cycles, **4** was quantitatively recovered from the solution. The reason for the greatly improved reversibility is the easy release of O_2 from **3**.

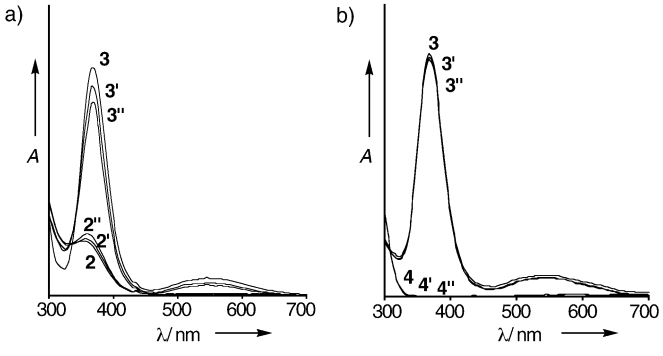


Figure 2. a) Reversible O_2 binding by **2**-$(PF_6)_2$ in CH_2Cl_2/acetone (3/0.002). A solution of **2**-$(PF_6)_2$ was oxygenated at 0 °C under O_2 to give **3**-$(PF_6)_2$ (**2**→**3**). Compound **2**-$(PF_6)_2$ was regenerated from **3**-$(PF_6)_2$ by warming at 40 °C under argon (**3**→**2′**). Three cycles are shown. b) Reversible O_2 binding by **4**-$(PF_6)_2$ in CH_2Cl_2. A solution of **4**·$(PF_6)_2$ was oxygenated at 25 °C under O_2 to form **3**-$(PF_6)_2$ (**4**→**3**). Compound **4**-$(PF_6)_2$ was regenerated form **3**-$(PF_6)_2$ at 25 °C under CO (**3**→**4′**). Three cycles are shown.

The Scheme 2 image contains the following text:

CH_3, CH_3, N, OC—Cu, CH_3, CH_3, Cu—CO, CH_3, CH_3, **4**, $+O_2$, $+CO$, Cu, O, Cu, CH_3, CH_3, CH_3, CH_3, **3**

Scheme 2. Reversible O_2/CO binding by **3**.

The X-ray structure analysis of **3**-$(PF_6)_2$[6,7] revealed two independent molecules **3a** and **3b**, which are similar to each other (Figure 3). Though the overall structure of **3** is similar to that of **1**,[2b] in the former steric repulsion between the bridgehead methyl groups and 3-py H atoms of L2 cause significant structural differences. This so-called pyridine shift[8] enhances the steric hindrance of the 6-Me groups and thus elongates the Cu–O and Cu···Cu distances of **3**. The average Cu–O bond lengths of 1.922 and 1.918 Å and Cu···Cu separations of 3.523 and 3.516 Å for **3a** and **3b**, repectively, are larger than those of 1.910 and 3.477 Å, respectively, for **1**. The Cu–O bond of **3** is the longest of all structurally characterized μ-η^2:η^2-Cu_2O_2 complexes (1.89–1.915 Å[2,9]). The μ-η^2:η^2-Cu_2O_2 core of **3** is more planar than that of **1**; the Cu-O-O′-Cu′ dihedral angles of 168.22 and 168.45° of **3a** and **3b**, respectively, are larger than that of **1** (163.3°). The more planar μ-η^2:η^2-Cu_2O_2 core in **3** may be due to the elongation of the Cu···Cu separation.[10] The copper coordination geometry of **3** is less distorted from square-pyramidal

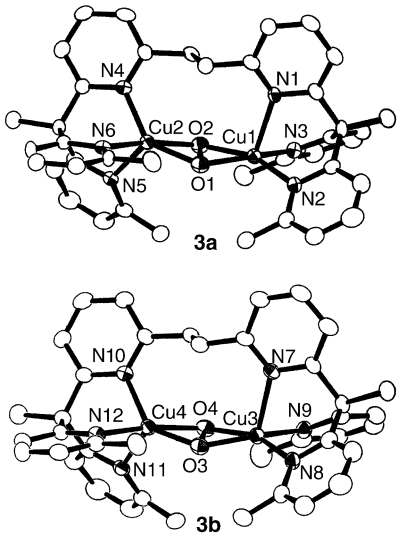


Figure 3. Structures of **3a** and **3b** (ORTEP plots, 50% probability; unlabeled open ellipses represent carbon atoms). Selected interatomic distances [Å] and angles [°]: Cu1-O1, 1.918(4), Cu1-O2, 1.913(3), Cu1-N1, 2.262(4), Cu1-N2, 1.962(4), Cu1-N3, 1.968(4), Cu2-O1, 1.961(4), Cu2-O2, 1.894(4), Cu2-N4, 2.030(4), Cu2-N5, 2.125(4), Cu2-N6, 1.968(4), Cu3-O3, 1.920(4), Cu3-O4, 1.903(4), Cu3-N7, 2.245(4), Cu3-N8, 1.966(4), Cu3-N9, 1.978(4), Cu4-O3, 1.953(4), Cu4-O4, 1.894(4), Cu4-N10, 2.033(4), Cu4-N11, 2.122(4), Cu4-N12, 1.962(4); Cu1···Cu2, 3.523(8), Cu3···Cu4, 3.516(8), O1-O2, 1.491(5), O3-O4, 1.487(5), Cu1-O1-Cu2, 130.5(2), Cu1-O2-Cu2, 135.4(2), Cu3-O3-Cu4, 130.4(2), Cu3-O4-Cu4, 135.7(2); the dihedral angle between the Cu1-O1-O2 and Cu2-O1-O2 planes is 168.22°, and that between the Cu3-O3-O4 and Cu4-O3-O4 planes 168.45.

 © 2004 Wiley-VCH Verlag GmbH & Co. KGaA, Weinheim

than that of **1**; the τ values (τ varies from 0 for an idealized square pyramid to 1 for an idealized trigonal bipyramid)[11] of 0.00 and 0.37 for **3a** and 0.00 and 0.38 for **3b** are smaller than those of 0.16 and 0.44 for **1**. These data suggest that the easy release of O_2 by **3** is due to the elongation of the Cu–O bond and the Cu···Cu distance, and it is not inhibited by the planar structure of the Cu_2O_2 core and by the less distorted copper coordination geometry.[10b]

The resonance Raman spectrum of **3**, obtained with excitation at 514.5 nm, shows a strong band at 765 cm^{-1}, which shifts to 724 cm^{-1} on labeling with ^{18}O and is assigned to the O–O stretch of peroxide bound in a μ-η^2:η^2-mode on the basis of its frequency and isotopic shift (41 cm^{-1}). Solomon et al. reported that the O–O stretch moves to higher energy as the μ-η^2:η^2-Cu_2O_2 core becomes more bent, and the Cu···Cu distance shortens.[10b] In our systems, in contrast, the ν_{O-O} band of **3** is at higher wavenumber than that of **1** (760 cm^{-1}), in spite of the more planar μ-η^2:η^2-Cu_2O_2 core and longer Cu···Cu distance of **3**. The O–O stretch of **3** is the strongest in the range of 713–765 cm^{-1} for μ-η^2:η^2-Cu_2O_2 complexes, including oxyHc, reported so far.[2,9,10b,12] The strong O–O bond may be favorable for release of O_2. The O_2^{2-}–Cu^{II} charge-transfer bands at 360 (24700) and 532 nm (1530 $M^{-1}cm^{-1}$) in **1** shift to slightly lower energy in **3** (366 (24000) and 537 nm (2100 $M^{-1}cm^{-1}$)). This is consistent with the long Cu–O bond of **3** and suggests that the crystal structure of **3** is retained in solution.

In conclusion, **3** is the best model for reversible O_2 binding among all μ-η^2:η^2-Cu_2O_2 complexes reported so far, and the long Cu–O bond, the large Cu···Cu distance, and strong O–O bond of **3** are favorable for easy release of O_2. Structural modulation by the bridgehead methyl groups provides important structural changes that facilitate release of O_2. Therefore, it can be concluded that **3** is a functional model of the tense form of oxyHc.

Experimental Section

L2: Ligand L1 (1.15 g, 2.0 mmol) was dissolved in dry THF (100 mL) and *n*-butyllithium (1.6 M in hexane, 2.63 mL, 4.2 mmol) was added at −78 °C under argon. The mixture was stirred for 3 h at room temperature. Then methyl iodide (0.60 g, 4.2 mmol) was added with stirring at −78 °C, and the mixture was stirred for 2 h at room temperature. Ligand L2 (0.79 g, 66 %) was isolated after purification by column chromatography on silica gel. M.p. 159.2–160.8 °C; elemental analysis (%) calcd for $C_{40}H_{40}N_6$: C 79.44, H 6.67, N 13.90; found: C 78.92, H 6.69, N 13.48; ^{1}H NMR (400 MHz, $CDCl_3$, 25 °C, TMS): δ = 2.24 (s, 6H; CH_3), 2.40 (s, 12H; py-CH_3), 2.99 (s, 4H; CH_2), 6.53 (d, ^3J(H,H) = 7.8 Hz, 4H; py-3), 6.60 (d, ^3J(H,H) = 7.8 Hz, 2H; py′-5), 6.64 (d, ^3J(H,H) = 7.8 Hz, 2H; py′-3), 6.85 (d, ^3J(H,H) = 7.8 Hz, 4H; py-5), 7.21 (t, ^3J(H,H) = 7.8 Hz, 2H; py′-4), 7.28 ppm (t, ^3J(H,H) = 7.8 Hz, 4H; py-4); ^{13}C NMR (100 MHz, $CDCl_3$, 25 °C, TMS), δ = 24.73 (CH_3), 26.87 (py-CH_3), 36.92 (CH_2), 60.24 ($C_{bridgehead}$), 120.28, 120.33, 120.40, 120.91 (py-3, 5, py′-3, 5), 135.53 (py-4, py′-4), 157.06 (py-6), 160.08 (py′-6), 165.36, 165.76 ppm (py-2, py′-2); IR (KBr disk): $\tilde{\nu}$ = 1580, 1565, 1445 cm^{-1} (py ring); FAB MS: *m*/*z*: 605 $[M+H]^+$.

2-$(PF_6)_2$: L2 (120.8 mg, 0.20 mmol) was dissolved in MeCN (10 mL) and added to $[Cu(MeCN)_4](PF_6)$ (149.0 mg, 0.40 mmol) under argon. The mixture was stirred for 1 h at room temperature under argon. On addition of Et_2O (30 mL) to the resultant solution, a pale yellow solid precipitated. The solid was purified by recrystallization from MeCN/Et_2O under Ar. Yield: 183 mg (83 %). Elemental analysis (%) calcd for $C_{44}H_{46}N_8P_2F_{12}Cu_2 \cdot 0.5\,CH_2Cl_2$: C 46.67, H 4.14, N 9.79, Cu 11.00; found: C 46.60, H 4.05, N 9.79, Cu 11.18; ^{1}H NMR (400 MHz, CD_3CN, 25 °C, TMS): δ = 2.48 (s, 6H; CH_3), 2.65 (s, 12H; py-CH_3), 3.45 (s, 4H, CH_2), 7.03 (d, ^3J(H,H) = 7.6 Hz, 2H; py′-5), 7.30 (d, ^3J(H,H) = 7.6 Hz, 4H; py-5), 7.54 (br, 2H; py′-3), 7.65 (br, 4H; py-3), 7.68 (t, ^3J(H,H) = 7.6 Hz, 2H; py′-4), 7.79 ppm (t, ^3J(H,H) = 7.6 Hz, 4H; py-4); IR (KBr disk): $\tilde{\nu}$ = 1590, 1565, 1450 (py ring), 840 cm^{-1} (PF_6); UV/Vis (CH_2Cl_2): λ_{max} (ε) = 257 (15000), 269 (16000), 340 nm (2800 $M^{-1}cm^{-1}$); FAB MS: *m*/*z*: 957 $[M-PF_6]^+$, 749 $[M-2PF_6-2MeCN+H_2O]^+$, 731 $[M-2PF_6-2MeCN]^+$, 667 $[M-2PF_6-2MeCN-Cu]^+$. **2**-$(CF_3SO_3)_2$ and **2**-$(ClO_4)_2$ were obtained by the same method as **2**-$(PF_6)_2$, by using $[Cu(MeCN)_4](CF_3SO_3)$ and $[Cu(MeCN)_4](ClO_4)$, respectively, in place of $[Cu(MeCN)_4](PF_6)$.

3-$(PF_6)_2$ was obtained from **2**·$(PF_6)_2$ as described in the text. Elemental analysis (%) calcd for $C_{40}H_{40}N_6O_2P_2F_{12}Cu_2$: C 45.62, H 3.83, N 7.99, Cu 11.96; found: C 45.35, H 3.79, N 7.78, Cu 11.95; ^{1}H NMR (400 MHz, $(CD_3)_2CO$, −30 °C, TMS): δ = 2.95 (s, 6H; $C_{bridgehead}$–CH_3), 3.24 (s, 12H; py-CH_3), 4.42 (bs, 4H; CH_2), 7.67 (d, ^3J(H,H) = 7.3 Hz, 4H; py-5), 7.84 (d, ^3J(H,H) = 7.3 Hz, 2H; py′-5), 8.13–8.32 ppm (m, 12H; py-3,4, py′-3,4); Resonance Raman (Me_2CO, 25 °C): 765 (^{16}O–^{16}O), 724 cm^{-1} (^{18}O–^{18}O); UV/Vis (CH_2Cl_2, 0 °C): λ_{max} (ε) = 366 (24000), 537 nm (2100 $M^{-1}cm^{-1}$); ESI MS (CH_2Cl_2, 25 °C): *m*/*z*: 909 $\{[Cu_2O_2(L2)](PF_6)\}^+$. ESR: silent in CH_2Cl_2 at 77 K.

4-$(PF_6)_2$: Ligand L2 (120.8 mg, 0.20 mmol) was dissolved in CH_2Cl_2 (10 mL) and $[Cu(MeCN)_4](PF_6)$ (149.0 mg, 0.40 mmol) was added under CO. The mixture was stirred for 2 h at 0 °C under CO. On addition of Et_2O (30 mL), a colorless solid precipitated, which was purified by recrystallization from CH_2Cl_2/Et_2O under CO. Yield: 157 mg (73 %). Elemental analysis (%) calcd for $C_{42}H_{40}N_6O_2P_2F_{12}Cu_2 \cdot 2\,H_2O \cdot 2\,CH_2Cl_2$: C 41.17, H 3.77, N 6.55, Cu 9.9; found: C 41.08, H 3.48, N 6.65, Cu 10.13; ^{1}H NMR (400 MHz, CD_2Cl_2, 25 °C, TMS): δ = 2.63 (s, 6H; CH_3), 2.74 (s, 12H; py-CH_3), 3.58 (s, 4H; CH_2), 6.91 (d, ^3J(H,H) = 7.3 Hz, 2H; py′-5), 7.32 (d, ^3J(H,H) = 7.3 Hz, 4H; py-5), 7.71–7.80 ppm (m, 12H; py-3,4, py′-3,4); IR (KBr disk): $\tilde{\nu}$ = 2083 (CO), 1601, 1570, 1466 (py ring), 833 cm^{-1} (PF_6); UV/Vis (CH_2Cl_2): λ_{max} (ε) = 269 nm (30000 $M^{-1}cm^{-1}$); FAB MS: *m*/*z*: 731 $[M-2PF_6-2CO]^+$.

Received: August 28, 2003 [Z52737]

Keywords: copper · N ligands · O–O activation · peroxo ligands · protein models

[1] a) Z. Tyeklár, K. D. Karlin, *Acc. Chem. Res.* **1989**, *22*, 241; b) N. Kitajima, Y. Moro-oka, *Chem. Rev.* **1994**, *94*, 737; c) E. I. Solomon, F. Tuczek, D. E. Root, C. A. Brown, *Chem. Rev.* **1994**, *94*, 827; d) E. I. Solomon, P. Chen, M. Metz, S.-K. Lee, A. E. Palmer, *Angew. Chem.* **2001**, *113*, 4702; *Angew. Chem. Int. Ed.* **2001**, *40*, 4570; e) P. L. Holland, W. B. Tolman, *Coord. Chem. Rev.* **1999**, *190–192*, 855; f) A. G. Blackman, W. B. Tolman, *Struct. Bonding (Berlin)* **2000**, *97*, 179; g) S. Schindler, *Eur. J. Inorg. Chem.* **2000**, 2311.

[2] a) N. Kitajima, K. Fujisawa, C. Fujimoto, Y. Moro-oka, S. Hashimoto, T. Kitagawa, K. Toriumi, K. Tatsumi, A. Nakamura, *J. Am. Chem. Soc.* **1992**, *114*, 1277; b) M. Kodera, K. Katayama, Y. Tachi, K. Kano, S. Hirota, S. Fujinami, M. Suzuki, *J. Am. Chem. Soc.* **1999**, *121*, 11006; c) Z. Hu, G. N. George, S. M. Gorun, *Inorg. Chem.* **2001**, *40*, 4812.

[3] a) K. A. Magnus, B. Hazes, H. Ton-That, C. Bonaventura, J. Bonaventura, W. G. J. Hol, *Proteins Struct. Funct. Genet.* **1994**, *19*, 302; b) K. A. Magnus, H. Ton-That, J. E. Carpenter, *Chem. Rev.* **1994**, *94*, 727; c) R. H. Holm, P. Kennepohl, E. I. Solomon, *Chem. Rev.* **1996**, *96*, 2239.

 © 2004 Wiley-VCH Verlag GmbH & Co. KGaA, Weinheim

[4] a) E. Antonini, M. Brunori, A. Colosimo, H. A. Kuiper, L. Zolla, *Biophys. Chem.* **1983**, *18*, 117; b) M. Metz, E. I. Solomon, *J. Am. Chem. Soc.* **2001**, *123*, 4938.

[5] X-ray crystallography on **2** was carried out on a Rigaku Mercury CCD area detector. **2**-$(CF_3SO_3)_2$: $C_{46}H_{46}N_8O_6S_2F_6Cu_2$, $M_r = 1112.12$, colorless crystal, $0.10 \times 0.20 \times 0.45$ mm, triclinic, $P\bar{1}$, $a = 8.180(4)$, $b = 12.194(6)$, $c = 13.149(6)$ Å, $\alpha = 79.153(10)$, $\beta = 81.245(13)$, $\gamma = 89.47(1)°$, $V = 1272.8(11)$ Å^3, $Z = 1$, $\rho_{calcd} = 1.451$ g cm^{-}; $2\theta_{max} = 55.0°$, $Mo_{K\alpha}$ radiation ($\lambda = 0.71070$ Å), $T = -50\,°C$, 10440 independent reflections, of which 3475 were used, $R = 0.080$ ($I > 3.00\sigma(I)$), $R_w = 0.102$, GOF = 1.294; $\mu = 9.93$ cm^{-1}; full-matrix, least-squares methods on *F*.

[6] X-ray crystallography on **3** was carried out on a Rigaku RAXIS-IV imaging plate diffractometer. A total of 60 (180.00°) oscillation images were collected, each exposed for 22.0 min. **3**-$(PF_6)_2 \cdot 7\,CH_2Cl_2 \cdot 1.5\,C_6H_5CH_3$: $C_{48.75}H_{53}N_6O_2P_2F_{12}Cu_2Cl_7$, $M_r = 1420.19$, dark violet crystal, $0.25 \times 0.20 \times 0.10$ mm, triclinic, $P\bar{1}$, $a = 19.057(4)$, $b = 21.040(3)$, $c = 14.856(2)$ Å, $\alpha = 93.377(6)$, $\beta = 102.387(6)$, $\gamma = 93.30(1)°$, $V = 5792(1)$ Å^3, $Z = 4$, $\rho_{calcd} = 1.628$ g cm^{-3}; $2\theta_{max} = 51.8°$, $Mo_{K\alpha}$ radiation ($\lambda = 0.71070$ Å), $T = -120\,°C$, 16943 independent reflections, of which 13735 were used, $R = 0.057$ ($I > 3.00\sigma(I)$), $R_w = 0.096$, GOF = 1.67; $\mu = 11.95$ cm^{-1}; full-matrix, least-squares methods on *F*.

[7] CCDC-218413 (**2**) and CCDC-218414 (**3**) contain the supplementary crystallographic data for this paper. These data can be obtained free of charge via www.ccdc.cam.ac.uk/conts/retrieving.html (or from the Cambridge Crystallographic Data Centre, 12, Union Road, Cambridge CB21EZ, UK; fax: (+44) 1223-336-033; or deposit@ccdc.cam.ac.uk).

[8] M. Kodera, Y. Kajita, Y. Tachi, K. Kano, *Inorg. Chem.* **2003**, *42*, 1193.

[9] a) E. Pidcock, S. DeBeer, H. V. Obias, B. Hedman, K. O. Hodgson, K. D. Karlin, E. I. Solomon, *J. Am. Chem. Soc.* **1999**, *121*, 1870; b) B. M. T. Lam, J. A. Halfen, V. G. Young, Jr., J. R. Hagadorn, P. L. Holland, A. Lledós, L. Cucurull-Sánchez, J. J. Novoa, S. Alvarez, W. B. Tolman, *Inorg. Chem.* **2000**, *39*, 4059.

[10] a) N. J. Blackburn, R. W. Strange, A. Farooq, M. S. Haka, K. D. Karlin, *J. Am. Chem. Soc.* **1988**, *110*, 4263; b) E. Pidcock, H. V. Obias, M. Abe, H.-C. Liang, K. D. Karlin, E. I. Solomon, *J. Am. Chem. Soc.* **1999**, *121*, 1299.

[11] A. W. Addison, T. N. Rao, J. V. Reedijk, G. C. Verschoor, *J. Chem. Soc. Dalton Trans.* **1984**, 1349.

[12] J. Ling, L. P. Nestor, R. S. Czernuszewicz, T. G. Spiro, R. Fraczkiewicz, K. D. Sharma, T. M. Loehr, J. Sanders-Loehr, *J. Am. Chem. Soc.* **1994**, *116*, 7682.

 © 2004 Wiley-VCH Verlag GmbH & Co. KGaA, Weinheim

Bio-Analytical Mass Spectrometry

2-Dimethylarsinothioyl Acetic Acid Identified in a Biological Sample: The First Occurrence of a Mammalian Arsinothioyl Metabolite**

*Helle Rusz Hansen, Russell Pickford, Jane Thomas-Oates, Marcel Jaspars, and Jörg Feldmann**

Arsenic is an element with a particularly strong affinity for sulfur; as biological systems are rich in sulfydryl groups it is likely that compounds with this combination of elements are created in vivo. In 1886 it was shown that trialkyl arsine oxides are converted into trialkyl arsine sulfides when treated with hydrogen sulfide in the laboratory.[1] Because of their potential therapeutic applications, many studies on thio-arsenicals were performed in the nineteen thirties.[2–5] Since then, it has been established that thiol groups play an essential role in the enzymatic pathway for biotransformation of arsenic,[6] and that arsenite binds to a variety of sulfur-rich peptides and proteins, such as glutathione (GSH),[7,8] metallothionein,[9] actin and tubulin,[10] galectin I thioredoxin peroxidase II,[11] and other macromolecular constituents of tissues. Despite the fact that arsenic binds to sulfur-rich proteins, As–S and As=S compounds have not been identified in natural samples. Consequently the main focus of arsenic speciation has been on oxo-arsenicals, as these compounds appear to be more abundant in nature. To our knowledge there has only been one report (unpublished) of a thioarsenical (2-dimethylarsinothioyl ethanol) occurring in a natural sample.[12] The response of thio-arsenicals to standard analytical procedures used in the speciation field is unknown, which may result in misleading conclusions. The presence and underestimation of thio-arsenicals in nature has previously been suggested.[13,14]

Herein we report the first characterization of a thio-organoarsenate (2-dimethylarsinothioyl acetic acid (**1**)) compound isolated from a biological source (sheep's urine). Urine samples were obtained from a primitive breed of wild sheep, which lives on the beaches of North Ronaldsay (Orkney

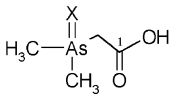
[*] H. R. Hansen, Prof. M. Jaspars, Dr. J. Feldmann
University of Aberdeen
Department of Chemistry
College of Physical Sciences
Meston Walk, Old Aberdeen AB24 3UE, Scotland (UK)
Fax: (+44) 1224-272921
E-mail: j.feldmann@abdn.ac.uk

Dr. J. Feldmann
University of Aberdeen, School of Biosciences
St Machar Drive, Aberdeen AB24 3UE, Scotland (UK)

R. Pickford, Prof. J. Thomas-Oates
Department of Chemistry, University of York
Heslington, York, YO10 3RA, England (UK)

[**] HRH and JF thank BBSRC (1/REI18479) and the University of Aberdeen for financial support. RP and JTO gratefully acknowledge financial support from EPSRC grant no. GR/N08964, the Analytical Chemistry Trust Fund, the RSC Analytical Division and the EPSRC, and ThermoElectron.

 DOI: 10.1002/anie.200352740 © 2004 Wiley-VCH Verlag GmbH & Co. KGaA, Weinheim



Islands, UK) and naturally consumes large amounts of arsenosugars (30 mg As daily) through their major food source, seaweed.[15] Arsenosugars have to date been classified as nontoxic.[16,17] However, as long as the metabolic intermediates are unknown, the real toxicity of a compound cannot be established. The discovery of a thio-organoarsenate compound in the urine samples shows that ingestion of arsenosugars can lead to formation of As–S and As=S compounds in vivo, which may cause interference with metabolic processes.

During the analytical work performed we found **1** very prone to degradation, especially at low pH values. Its elution from chromatographic columns was pH dependent; when using a mobile phase of pH 5.3, the compound was permanently adsorbed on the anion-exchange column. We emphasize the importance of combining a range of complementary analytical methods for the successful structural elucidation of this novel structure.

Urine from North Ronaldsay sheep was analyzed using anion-exchange-HPLC coupled simultaneously to inductively coupled plasma(ICP)-MS and ES-MS. The species giving rise to the main signal in the ES-mass spectrum (*m*/*z* 197), co-eluted with arsenic (giving a signal at *m*/*z* 75) in the ICP-mass spectrum (Figure 1 A, B). Ions giving less intense signals at

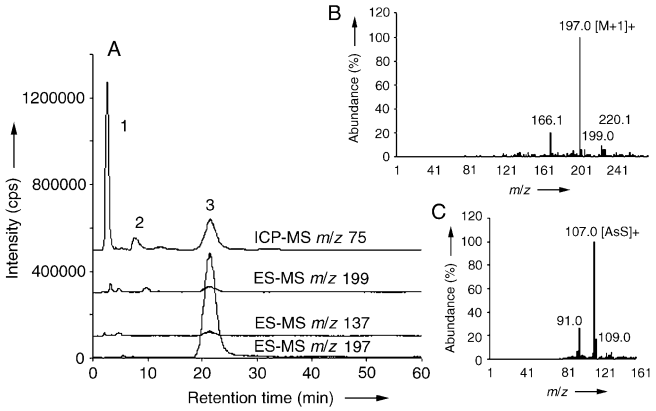


Figure 1. Anion-exchange chromatograms of a urine sample, detected by ICP-MS (*m*/*z* 75) and by ESI-MS (*m*/*z* 199, 198, 137, 197) using scan mode (A). Peak 1 consists mainly of dimethylarsinoyl ethanol, dimethylarsinic acid and dimethylarsinoyl acetic acid, peak 2 and 3 are unknown arsenicals.[20] Mass spectrum of peak 3 at fragmenter voltage B) 100 V and C) 240 V.

m/*z* 199, and 137 were also observed to co-elute (Figure 1 A). When increasing the cone voltage (to 240 V) to induce in-source fragmentation of the ES-generated ions the dominant peak was at *m*/*z* 107 (Figure 1 C). The ICP-MS and ES-MS data provide various clues to the identity of the compound; the relative intensities of the ions at *m*/*z* 197 and 199 were consistent with the isotope pattern of a compound containing one sulfur atom (relative isotopic contributions of ^{32}S and ^{34}S of 95.018 and 4.215%, respectively). Storage and sample treatment slowly resulted in a reduction in the intensity of the ion at *m*/*z* 197 and a concomitant increase in the intensity of an ion at *m*/*z* 181. Dimethylarsinoyl acetic acid (**2**) (which yields a protonated molecule at *m*/*z* 181) has previously been identified as a natural product in shellfish[18,19] and as a breakdown product of arsenosugars in urine.[20] A **2** standard was treated with hydrogen sulfide to produce **1**, which showed matching retention time to the unknown on an anion exchange column, the eluent of which was analyzed by ICP-MS (Figure 2 A), and showed a strong signal at *m*/*z* 197 (Figure 2 B) in the ES mass spectrum. Except for *m*/*z* 166, the ions generated from in-source fragmentation at *m*/*z* 91, 107, and 137 (Figure 1) are consistent with the proposed structure of **1**.

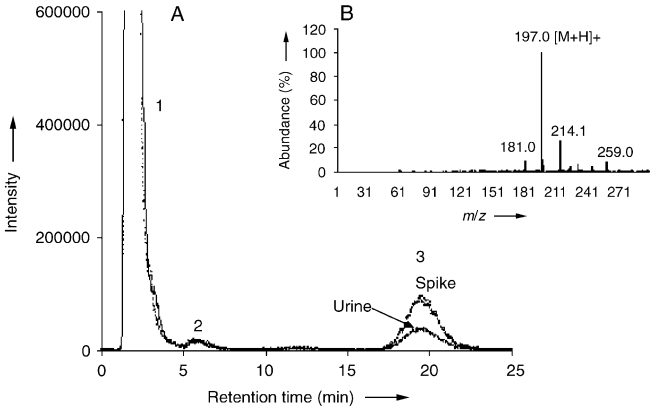


Figure 2. A) Anion-exchange chromatograms with ICP-MS (*m*/*z* 75) detection of a urine sample (solid line) and urine sample spiked with **1** standard (dotted line). Peak 1, 2, and 3 as described in Figure 1. B) Mass spectrum of standard **1** (**2** + hydrogen sulfide).

The urine was subjected to HPLC fractionation, and the fraction containing the unknown arsenical analyzed using ES-IT-MS^n. ES mass spectra obtained from the synthetically prepared **1** (**2** + H_2S) and the fractionated urine contained low-intensity signals at both *m*/*z* 181 and 197. Since the postulated structure contains sulfur, an ion at *m*/*z* 199 corresponding to the ^{34}S isotope is to be expected. However, this species was not obvious above background in the ES mass spectra owing to the low abundance of the parent compound. Collision-induced dissociation (CID) tandem mass spectra of the ions at *m*/*z* 197 in both the synthetically prepared **1** and the fractionated urine were obtained, which yield structurally diagnostic fragment ions (Figure 3). Product ions were observed at *m*/*z* 165, 151, and 137 from both samples. Additionally, the ion at *m*/*z* 197 derived from the urine sample yielded a product ion at *m*/*z* 105. These product ions are consistent with the proposed structure of **1**. Both spectra contain background ions arising from the co-selection and fragmentation of isobaric matrix ions. The structures of the product ions assigned in Figure 3 are supported by the results of further stages of tandem mass spectrometry. The MS^2 ion at *m*/*z* 151 yielded third generation ions at *m*/*z* 123 and 105. The MS^2 ion at *m*/*z* 137 yielded third generation ions at *m*/*z* 121 and 109.

 © 2004 Wiley-VCH Verlag GmbH & Co. KGaA, Weinheim

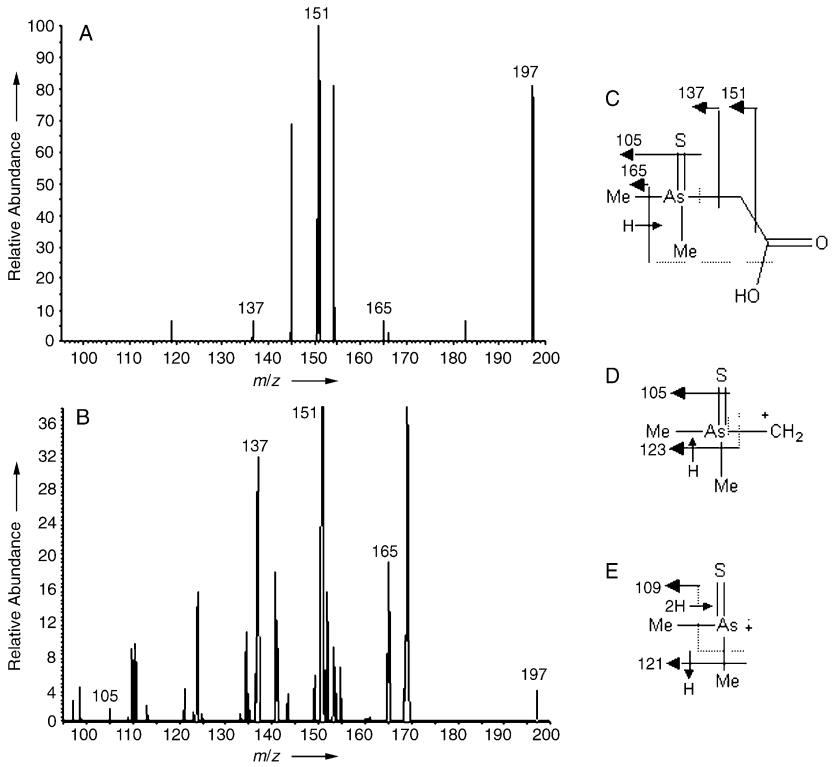


Figure 3. CID MS^2 data obtained from the ion at *m/z* 197 in A) the synthetically prepared **1** and B) the fractionated urine. C) The fragment ions produced from CID MS^2 of the $[M+H]^+$ ion at *m/z* 197, D) The fragment ions produced from CID MS^3 of the MS^2 product ion at *m/z* 151, and E) The fragment ions produced from CID MS^3 of the MS^2 product ion at *m/z* 137.

Despite the fact that the ^{34}S isotopic ion did not stand out above background in the ES mass spectra, structurally diagnostic product ions were obtained from CID tandem mass spectrometric analysis of the ions at *m/z* 199 generated from both samples. The ions are consistent with species containing the ^{34}S isotope of **1** in both samples. Comparison of data obtained from the *m/z* 197 and 199 species facilitated interpretation of the product-ion spectra, particularly localization of the sulfur to the arsenic. The product ions generated from *m/z* 197 previously observed at *m/z* 151 and *m/z* 137 were shifted to *m/z* 153 and *m/z* 139, respectively.

^1H NMR data were obtained on **2** and the **1** standard using a standard presaturation pulse sequence. Owing to the low concentration of the samples, the ^{13}C NMR spectra were obtained indirectly from the HSQC and HMBC spectra (Table 1). In both cases the ^1H methyl singlets correlated in the HSQC to highfield signals in the ^{13}C NMR spectrum. The methylene group in both cases was identified from the 2H integral in the ^1H NMR and correlated in the HSQC to a ^{13}C signal at approximately 40 ppm. The chemical shift of the carboxylate carbon atom at approximately 170 ppm was determined from its HMBC correlation to the methylene proton signal.

Table 1: Chemical shift values [ppm] from ^1H NMR and ^{13}C NMR spectroscopy for **1** and **2**

Group	**1**		**2**	
	δH	δC	δH	δC
C=O	–	170.5	–	172.8
$-CH_2-$	3.19	38.1	2.99	40.0
$-CH_3$	1.87	18.0	1.69	14.0

In conclusion, we report the first characterization of a thio-organoarsenate (2-dimethylarsinothioyl acetic acid (**1**)) compound isolated from a biological source. The finding is novel but not unexpected. We emphasize that more sulfur-containing arsenicals are likely to be found in biological samples in the future—if the right analytical techniques are applied. Since **1** is the first compound of a new class of arsenic metabolites, it indicates that mammalian arsenic metabolism is much more complex than has been claimed for a long time, which opens up new questions about the toxicity of such organoarsenothio(y)l compounds.

Experimental Section

Separation was performed on a PRP-X100 anion-exchange column (150 × 4.6 mm) with a Hamilton PEEK pre-column (11.2 mm, 12–20 μm) from Hamilton Company. The mobile phase used was 30 mM ammonium carbonate (1 mL min^{-1}). Before injection (loop volume 100 μL) onto the HPLC column all samples were filtered through a 0.45-μm nylon filter. For flow injection measurements the sample volume was 20 μL. A HP1100 HPLC system (Agilent Technologies, USA) with cooled autosampler was used throughout the experiments. The autosampler was cooled to 4 °C and the column kept at ambient temperature. Post-column the flow was split in a ratio of 1:4 (1 part into the ICP-MS, 4 parts into the ES-MS) using a microsplitter (Upchurch, UK).

An ICP-MS 7500 ((Agilent Technologies, USA)) was used for element specific detection of arsenic. The instrument was equipped with either a Babington nebulizer or a micro-concentric nebulizer (flow rate < 100 μL min^{-1}) and a peltier cooled spray chamber. The instrument was mostly used in the soft extraction mode without oxygen. The instrument settings were checked daily for arsenic sensitivity and optimized when necessary. The elements monitored were arsenic (*m/z* 75), tellurium (*m/z* 130), sulfur (*m/z* 34), and sulfur oxide (*m/z* 48).

The HP1100 series LC/MSD (quadrupole mass spectrometric detector) instrument (Agilent Technologies, USA) was used as a molecule-specific detector. The MSD was used in the positive-ionization mode from *m/z* 70 to *m/z* 1000 or in the single-ion mode with the API-electrospray head. The settings chosen were: capillary voltage of 4000 V, nebulizer pressure of 40 psi, drying gas flow of 12 L min^{-1} at 350 °C, quadrupole temperature 100 °C, and cone voltage of 100 V or 240 V. The cone voltage set at 100 V allowed the mass spectrometric analysis of intact protonated species, whereas an increased cone voltage of 240 V generated fragments of electrospray-generated ions by collision-induced dissociation with resident atmospheric gases in the source of the mass spectrometer. Mass calibration was controlled regularly and when necessary optimized using the calibration solution supplied by Agilent.

The unknown arsenical in urine samples was isolated by HPLC fractionation (sample treatment and conditions of mobile phase and column as above). The HPLC system consisted of a LKB Bromma

 © 2004 Wiley-VCH Verlag GmbH & Co. KGaA, Weinheim

model 2150 pump with a Rheodyne 6 port sample injector (loop volume of 100 μL). The standard **1** was synthesized when an aqueous solution of standard **2** was purged with gaseous H_2S. The reaction was carried out for 2 h.

Arsenic-containing HPLC fractions were analyzed using a ThermoFinnigan LCQ DECA XP Plus ion-trap mass spectrometer with an electrospray source. Fractions were infused into the source at 1 μL min^{-1} using the built-in syringe driver. The electrospray capillary was held at 5800 V. The buffer gas used was nitrogen. Data were collected over the m/z range 50–200. Collision-induced dissociation (CID) tandem mass spectrometry was performed with a normalized collision energy setting of 30%, activation q setting of 0.250 and an activation time of 30 ms.

Presaturated ^1H, HSQC, and HMBC NMR spectroscopy experiments were recorded on a Varian Unity Inova 400 MHz spectrometer at 299 K in D_2O solution. Chemical shifts are reported in ppm (δ) downfield relative to residual HOD at 4.60 ppm. Samples of compounds (38–48 μg) were prepared in degassed D_2O, capped immediately and used within 2 h of preparation.

Received: August 28, 2003 [Z52740]

Keywords: analytical methods · arsenic · bioinorganic chemistry · mass spectrometry · sulfur

[1] A. Michaelis, U. Paetow, *Justus Liebigs Ann. Chem.* **1886**, *233*, 60.
[2] H. J. Barber, *J. Chem. Soc.* **1929**, 1020.
[3] A. Cohen, H. King, W. I. Strangeways, *J. Chem. Soc.* **1931**, 3043.
[4] A. Cohen, H. King, W. I. Strangeways, *J. Chem. Soc.* **1932**, 2505.
[5] A. Cohen, H. King, W. I. Strangeways, *J. Chem. Soc.* **1932**, 2866.
[6] M. Styblo, D. J. Thomas, *Toxicol. Appl. Pharmacol.* **1997**, *147*, 1.
[7] K. T. Suzuki, B. K. Mandal, Y. Ogra, *Talanta* **2002**, *58*, 111.
[8] G. M. Bogdan, A. Sampayo-Reyes, H. V. Aposhian, *Toxicology* **1993**, *93*, 175.
[9] M. Toyama, M. Yamashita, N. Hirayama, Y. Murooka, *J. Biochem.* **2002**, *132*, 217.
[10] D. B. Menzel, H. K. Hamadeh, E. Lee, D. M. Meacher, V. Said, R. E. Rasmussen, H. Greene, R. N. Roth, *Toxicol. Lett.* **1999**, *105*, 89.
[11] K. N. Chang, T. C. Lee, M. F. Tam, Y. C. Chen, L. W. Lee, S. Y. Lee, P. J. Lin, R. N. Huang, *Biochem. J.* **2003**, *371*, 495.
[12] K. A. Francesconi, **2003**, personal communication.
[13] W. R. Cullen, B. C. McBride, J. Reglinski, *J. Inorg. Biochem.* **1984**, *21*, 45.
[14] W. R. Cullen, B. C. McBride, J. Reglinski, *J. Inorg. Biochem.* **1984**, *21*, 179.
[15] H. R. Hansen, A. Raab, K. A. Francesconi, J. Feldmann, *Environ. Sci. Technol.* **2003**, *37*, 845.
[16] T. Sakurai, T. Kaise, T. Ochi, T. Saitoh, C. Matsubara, *Toxicology* **1997**, *122*, 205.
[17] T. Kaise, Y. Oya-Ohta, T. Ochi, T. Okubu, K. Hanaoka, K. J. Irgolic, T. Sakurai, C. Matsubara, *J. Food Hyg. Soc. Jpn.* **1996**, *37*, 135.
[18] E. H. Larsen, *Fresenius J. Anal. Chem.* **1995**, *352*, 582.
[19] S. McSheehy, J. Spunzar, R. Lobinski, V. Haldys, J. Tortajada, J. S. Edmonds, *Anal. Chem.* **2002**, *74*, 2370.
[20] H. R. Hansen, A. Raab, J. Feldmann, *J. Anal. At. Spectrom.* **2003**, *18*, 474.

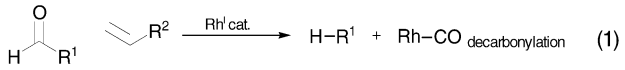
 © 2004 Wiley-VCH Verlag GmbH & Co. KGaA, Weinheim

Hydroacylation of Alkenes

Chelation-Controlled Intermolecular Hydroacylation: Direct Addition of Alkyl Aldehydes to Functionalized Alkenes**

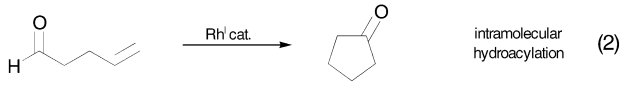
Michael C. Willis, Steven J. McNally, and Paul J. Beswick*

The hydroacylation of alkenes is an example of a growing number of transformations based on C–H bond activation.[1] The transformation has the potential to be a powerful synthetic tool; it is promoted by a number of transition-metal catalysts and is inherently atom-economic.[2] The utility of the reaction is limited by the propensity of the key acyl–metal intermediates to undergo decarbonylation, which results in reduced substrates and inactive catalysts [Eq. (1)].



(1)

Hydroacylation can become competitive with decarbonylation in intramoleculer variants of the process, although the ring size of the product is crucial in determining the success of the reaction [Eq. (2)].[3–6] Intermolecular alkene hydroacylation is a far more demanding transformation and remains a significant synthetic challenge.[7,8] Aside from the cobalt-based method of Brookhart and co-workers,[9] the majority of systems reported require high temperatures (typically 110–200 °C) and/or pressures of CO or ethene and are limited to aromatic aldehydes and simple unfunctionalized alkenes.[10] Of these systems, the method developed by Jun et al., employing the in situ formation of pyridyl imines, is the most synthetically useful, although only unfunctionalized alkenes have been used.[11] Herein we detail a new approach to intermolecular hydroacylation, utilizing chelation-stabi-



(2)

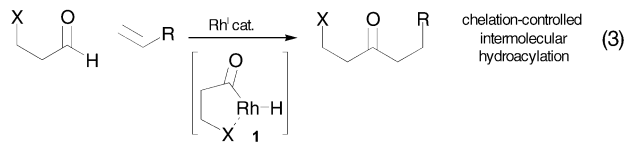
[*] Dr. M. C. Willis, S. J. McNally
Department of Chemistry, University of Bath
Bath, BA2 7AY (UK)
Fax: (+44) 1225-38-6231
E-mail: m.c.willis@bath.ac.uk
Dr. P. J. Beswick
Neurology Centre of Excellence for Drug Discovery
GlaxoSmithKline, Medicines Research Centre
Gunnels Wood Road, Stevenage, SG1 2NY (UK)

[**] This work was supported by the EPSRC, the University of Bath, and GlaxoSmithKline. We also thank the EPSRC Mass Spectrometry service at the University of Wales, Swansea. Dr. A. Weller and Mr. A. Rifat are thanked for their help in the preparation of catalyst **2**.

Supporting information for this article is available on the WWW under http://www.angewandte.org or from the author.

 © 2004 Wiley-VCH Verlag GmbH & Co. KGaA, Weinheim DOI: 10.1002/anie.200352751

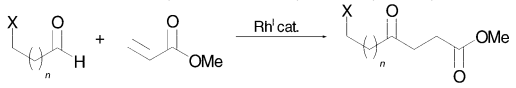
lized acyl–rhodium intermediates, that allows the direct addition of alkyl aldehydes to a range of functionalized alkenes under mild conditions with low catalyst loadings [Eq. (3)].



(3)

We speculated that the use of aldehydes that bear a pendant heteroatom would produce chelated acyl–metal intermediates (such as **1**) that are resistant to decarbonylation but disposed to hydroacylation.[12] The starting point of our investigation was to define appropriate chelating functionality and to identify a suitable catalyst. We recently showed that acrylate esters are excellent substrates in the related hydroiminoacylation reaction and accordingly selected methyl acrylate as a test alkene to evaluate potential aldehydes (Table 1).[13] Reaction of β-benzyloxypropanal with the Wilkinson complex led to decarbonylation (Table 1, entry 1), whereas the use of the cationic catalyst $[Rh(dppe)]ClO_4$ (**2**), which has been used extensively in intramolecular systems, resulted in deactivation of the catalyst (Table 1, entry 2). The analogous β-methoxypropanal produced small amounts of the desired adduct but the major pathway remained decarbonylation (Table 1, entry 3).[14] To obtain a stronger chelating interaction, we next examined sulfide-substituted aldehydes;[15] the reaction of β-methylsulfanyl aldehyde **3** with methyl acrylate at 40 °C produced the hydroacylation adduct in 36% yield along with side product (27%) that originates from a Tischenko-type process (Table 1, entry 4).[16] When dichloroethane was used as solvent and the reaction temperature was raised to 60 °C, the amount of side product decreased to <3% and the conversion into the desired adduct increased to 96% (Table 1, entry 5). Altering the catalyst counterion from perchlorate to triflate had a negligible effect on the efficiency (Table 1, entry 6).[17] Finally, it appears that a five-membered S–Rh chelate is optimal, as both the α- and γ-methylsulfanyl-substituted aldehydes resulted in decarbonylation (Table 1, entries 7 and 8).

Table 1: Evaluation of aldehydes and catalysts in hydroacylation reactions.[a]



Entry	Aldehyde	Catalyst[b]	Solvent	T [°C]	Conversion [%][c]
1	BnO, O, H	$[RhCl(PPh_3)_3]$	PhMe	80	0
2		$[Rh(dppe)]ClO_4$	CH_2Cl_2	40	0
3	MeO, O, H	$[Rh(dppe)]ClO_4$	CH_2Cl_2	40	9
4	MeS, O, H	$[Rh(dppe)]ClO_4$	CH_2Cl_2	40	36[d]
5		$[Rh(dppe)]ClO_4$	$ClCH_2CH_2Cl$	60	96
6	**3**	[Rh(dppe)]OTf	$ClCH_2CH_2Cl$	60	91
7	MeS, O, H	$[Rh(dppe)]ClO_4$	$ClCH_2CH_2Cl$	60	0
8	MeS, O, H, 2	$[Rh(dppe)]ClO_4$	$ClCH_2CH_2Cl$	60	0

[a] Conditions: catalyst (10 mol%), aldehyde (1.0 equiv), alkene (2.5 equiv), 2 h. [b] Catalysts $[Rh(dppe)]ClO_4$ and [Rh(dppe)]OTf were prepared in situ (see Supporting Information for details). [c] Determined by ^{1}H NMR spectroscopic analysis. [d] Together with Tischenko-type adduct (27%; see Supporting Information). Tf = trifluoromethanesulfonyl, dppe = 1,2-bis-(diphenylphosphanyl)ethane.

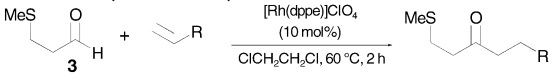
We next explored the scope of the reaction with respect to alkenes (Table 2). A range of functional groups, including esters, amides, and imides, are tolerated well, and the desired hydroacylation adducts are obtained in good yields (Table 2, entries 1–4). The reaction of styrene is slow, presumably due to deactivation of the catalyst. However, the performance of the more-electron-poor 4-cyanostyrene was superior (Table 2, entries 5 and 6). Simple alkyl-substituted alkenes are relatively poor substrates, and decarbonylation becomes competitive (Table 2, entry 7). Dienyl substrates are tolerated, for example, methyl penta-2,4-dienoate delivers the isomerized enone product in moderate yield (Table 2, entry 8). Sulfone functionality is also compatible; hydroacylation of phenyl vinyl sulfone provides the adduct in excellent yield (Table 2, entry 9). Interestingly, the sulfone adduct is obtained exclusively as the more valuable branched regioisomer. Finally, electron-poor alkynes can also be employed: methyl propiolate delivers the enone product in good yield (Table 2, entry 10).

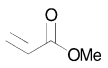
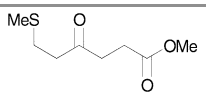
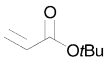
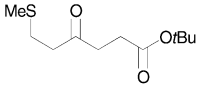
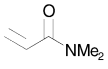
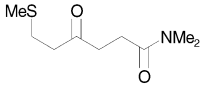
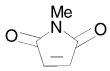
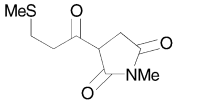
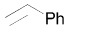
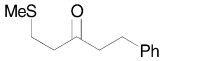
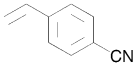
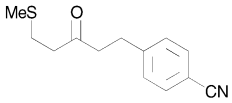
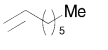
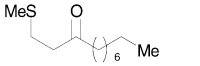
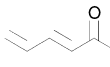
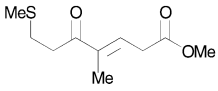
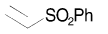
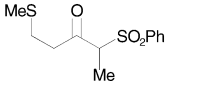
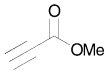
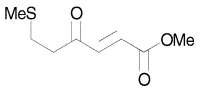
To provide convenient reaction times, all reactions detailed in Table 2 were conducted with 10 mol% of catalyst **2** at 60 °C for 2 h. Modification of these conditions allows lower catalyst loadings to be employed; for example, the reaction between aldehyde **3** and methyl acrylate proceeds with 100% conversion after only 45 min in the presence of 5 mol% of catalyst at 70 °C.[18] The methylsulfanyl substituent was necessary to allow the desired hydroacylation reactions to proceed, but from a synthetic perspective it is important that it can be removed to provide functionality suitable for further manipulation. Towards this end, adduct **4** was treated with MeOTf and $KHCO_3$ to effect elimination of the sulfide and furnish enone **5** in 76% yield (Scheme 1).

In summary, we have described a new method for intermolecular hydroacylation based on the proposed formation of chelation-stabilized acyl–rhodium intermediates. This new approach allows a commercially available methylsulfanyl-substituted aldehyde[19] to be combined directly with a range of commercial, variously functionalized alkenes to produce hydroacylation adducts in good to excellent yields. The reaction uses low catalyst loadings under mild conditions and is tolerant of a variety of functional groups. Studies to explore alternative chelating units, to investigate the regioselectivity further, and to develop asymmetric versions

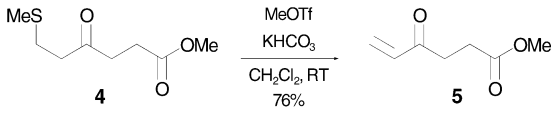
 © 2004 Wiley-VCH Verlag GmbH & Co. KGaA, Weinheim

Table 2: Hydroacylation of aldehyde **3** with representative alkenes.[a]



Entry	Alkene	Product	Regioselectivity[b]	Conversion [%][b]	Yield [%][c]
1			4:1	96	71
2			5:1	95	81
3			>20:1	90	82
4			–	91	73
5			>20:1	64	41
6			>20:1	77	66
7			>20:1	50	33
8			10:1	65	45
9			>20:1	100	84
10			10:1[d]	98	82

[a] Conditions: catalyst (10 mol%), aldehyde (1.0 equiv), alkene (2.5 equiv). [b] Determined by ^{1}H NMR spectroscopic analysis. [c] Yield of isolated pure regioisomer. [d] Geometric isomers.



Scheme 1. Elaboration of sulfide **4**.

of the process are underway and will be reported in due course.

Experimental Section

General procedure: (Bicyclo[2.2.1]hepta-2,5-diene)(1,2-bis(diphenylphosphanyl)ethane) rhodium(I) perchlorate[20] (20 mg, 0.029 mmol) was dissolved in 1,2-dichloroethane (4 mL), and hydrogen gas was bubbled through for 15 min to generate the catalytically active species **2**. The solution was degassed and purged with argon, and the appropriate alkene (0.7 mmol) was then added, followed by aldehyde **3** (30 mg, 0.29 mmol). The reaction mixture was stirred at 60 °C for 2 h then evaporated under reduced pressure. ^{1}H NMR spectroscopic analysis of the crude residue was used to measure the approximate conversion of aldehyde into product (2,5-dimethylfuran was used as a quantitative internal standard).[21] Purification by flash chromatography (silica gel, Et_2O/petroleum ether) provided the pure hydroacylation adducts.

Received: September 1, 2003 [Z52751]

Keywords: aldehydes · alkenes · homogeneous catalysis · hydroacylation · rhodium

[1] For recent reviews on C–H activation, see: a) V. Ritleng, C. Sirlin, M. Pfeffer, *Chem. Rev.* **2002**, *102*, 1731–1769; b) J. A. Labinger, J. E. Bercaw, *Nature* **2002**, *417*, 507–514; c) G. Dyker, *Angew. Chem.* **1999**, *111*, 1808–1822; *Angew. Chem. Int. Ed.* **1999**, *38*, 1699–1712; d) C.-H. Jun, C. W. Moon, D.-Y. Lee, *Chem. Eur. J.* **2002**, *8*, 2423–2428.

[2] B. M. Trost, *Acc. Chem. Res.* **2002**, *35*, 695–705.

[3] For an example of stoichiometric cyclopentanone synthesis, see: K. Sakai, J. Ide, O. Oda, N. Nakamura, *Tetrahedron Lett.* **1972**, 1287–1290.

[4] For selected recent examples of catalytic cyclopentanone synthesis, see: a) K. P. Gable, G. A. Benz, *Tetrahedron Lett.* **1991**, *32*, 3473–3476; b) D. P. Fairlie, B. Bosnich, *Organometallics* **1988**, *7*, 936–945; c) T. Sattelkau, P. Eilbracht, *Tetrahedron Lett.* **1998**, *39*, 9647–9648.

[5] For examples of enantioselective cyclizations, see: a) P. Ducray, B. Rousseau, C. Mioskowski, *J. Org. Chem.* **1999**, *64*, 3800–3801; b) B. Bosnich, *Acc. Chem. Res.* **1998**, *31*, 667–674; c) M. Tanaka, M. Imai, M. Fujio, E. Sakamoto, M. Takahashi, Y. Eto-Kato, X. M. Wu, K. Funakoshi, K. Sakai, H. Suemune, *J. Org. Chem.* **2000**, *65*, 5806–5816, and references therein; d) for an example of intramolecular enantioselective hydroacylation of alkynes, see: K. Tanaka, G. C. Fu, *J. Am. Chem. Soc.* **2002**, *124*, 10296–10297.

[6] For examples of the synthesis of larger rings, see: a) A. D. Aloise, M. E. Layton, M. D. Shair, *J. Am. Chem. Soc.* **2000**, *122*, 12610–12611b) Y. Sato, Y. Oonishi, M. Mori, *Angew. Chem.* **2002**, *114*, 1266–1269; *Angew. Chem. Int. Ed.* **2002**, *41*, 1218–1221.

[7] For Rh-based systems used in combination with CO or ethylene, see: a) J. Schwartz, J. B. Cannon, *J. Am. Chem. Soc.* **1974**, *96*, 4721–4723; b) K. P. Vora, C. F. Lochow, R. G. Miller, *J. Organomet. Chem.* **1980**, *192*, 257–264; c) P. Isnard, B. Denise, R. P. A. Sneeden, J. M. Cognio, P. Dural, *J. Organomet. Chem.* **1982**, *240*, 285–288; d) K. P. Vora, *Synth. Commun.* **1983**, *13*, 99–102; e) T. B. Marder, D. C. Roe, D. Milstein, *Organometallics* **1988**, *7*, 1451–1453.

[8] For Ru-based systems, see: a) T. Kondo, Y. Tsuji, Y. Watanabe, *Tetrahedron Lett.* **1987**, *28*, 6229–6230; b) T. Kondo, M. Akazome, Y. Tsuji, Y. Watanabe, *J. Org. Chem.* **1990**, *55*, 1286–1291; c) T. Kondo, N. Hiraishi, Y. Morisaki, K. Wada, Y. Watanabe, T.-A. Mitsudo, *Organometallics* **1998**, *17*, 2131–2134.

[9] For a Co-based method, see: a) C. P. Lenges, M. Brookhart, *J. Am. Chem. Soc.* **1997**, *119*, 3165–3166; b) C. P. Lenges, P. S. White, M. Brookhart, M. *J. Am. Chem. Soc.* **1998**, *120*, 6965–6979; see also reference [7a].

 © 2004 Wiley-VCH Verlag GmbH & Co. KGaA, Weinheim

[10] The Co system reported by Brookhart and co-workers[9] employs alkyl aldehydes at moderate temperatures for the hydroacylation of terminal vinyl silanes.
[11] For examples of Rh-catalyzed hydroiminoacylation, see reference [1d] and references therein.
[12] a) J. W. Suggs, *J. Am. Chem. Soc.* **1978**, *100*, 640 – 641; b) M. Tanaka, M. Imai, Y. Yamamoto, K. Tanaka, M. Shimowatari, S. Nagumo, N. Kawahara, H. Suemune, *Org. Lett.* **2003**, *5*, 1365 – 1367.
[13] M. C. Willis, S. Sapmaz, *Chem. Commun.* **2001**, 2558 – 2559.
[14] Decarbonylation resulted in stalled reactions and the production of inactive carbonylated catalysts.
[15] For a report of S chelation in intramolecular hydroacylation of alkenes, see: H. D. Bendorf, C. M. Colella, E. C. Dixon, M. Marchetti, A. N. Matukonis, J. D. Musselman, T. A. Tiley, *Tetrahedron Lett.* **2002**, *43*, 7031 – 7034.
[16] For the isolation of similar Tischenko-type products, see: G. A. Slough, J. R. Ashbaugh, L. A. Zannoni, *Organometallics* **1994**, *13*, 3587 – 3593.
[17] For a counterion effect in intramolecular hydroacylation, see reference [6a].
[18] Longer reaction times could also be employed. For example, in the presence of 1.5 mol% of catalyst, 94% conversion was reached at 60°C after 48 h.
[19] 3-(Methylsulfanyl)propanal is available from Sigma-Aldrich Co. Ltd.
[20] R. R. Schrock, J. A. Osborn, *J. Am. Chem. Soc.* **1971**, *93*, 2397 – 2407.
[21] S. W. Gerritz, A. M. Sefler, *J. Comb. Chem.* **2000**, *2*, 39 – 41.

 © 2004 Wiley-VCH Verlag GmbH & Co. KGaA, Weinheim

Cross-Coupling

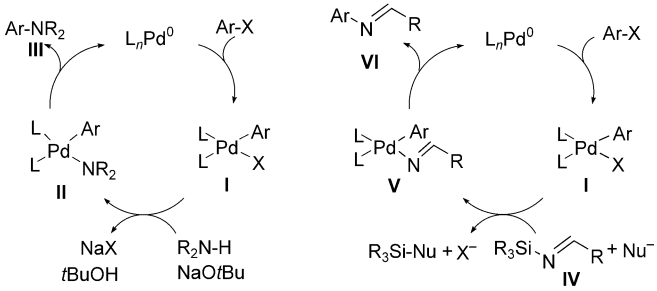
N-Trialkylsilylimines as Coupling Partners for Pd-Catalyzed C–N Bond-Forming Reactions: One-Step Synthesis of Imines and Azadienes from Aryl and Alkenyl Bromides**

José Barluenga, Fernando Aznar, and Carlos Valdés*

The palladium-catalyzed amination of aryl halides, known as the Buchwald–Hartwig reaction, has become a widely employed method in recent years for the synthesis of aryl amines.[1] The broad scope of this C–N bond-forming reaction allows its application with a variety of both reactants, the halide and the nitrogen source. In fact, very efficient catalytic combinations have been uncovered for the coupling of amines with aryl and heteroaryl halides and sulfonates,[2] and also with alkenyl halides.[3] With regard to the nitrogen coupling partner, most NH functional groups can participate in this coupling reaction, including C=N-containing species such as benzophenone imine,[4] and sulfoximines.[5] However, despite the intense development of this reaction in the recent years, the direct preparation of *N*-substituted aldimines by a cross-coupling protocol has not been described yet, probably as a result of the instability of the required NH aldimines. Nevertheless, the one-step transformation of bromides into aldimines is a very interesting reaction indeed, as imines are very versatile starting materials in synthetic organic chemistry, and especially in heterocyclic chemistry. Moreover, aldimines can be hydrolyzed under very mild conditions, therefore the direct synthesis of imines might be a new alternative for the introduction of the -NH_2 group.[6]

Herein we describe the one-step synthesis of aldimines and of 1- and 2-azadienes from aryl and alkenyl bromides and introduce the readily available *N*-trialkylsilyl imines as surrogates for the unstable NH-aldimines in palladium-catalyzed C–N bond-forming reactions.

The palladium-catalyzed aryl amination involves three fundamental steps[7] (Scheme 1, left): 1) oxidative addition of the aryl halide to a Pd^0 complex to form aryl–palladium–halide complex **I**; 2) transformation of **I** into amido complex



Scheme 1. Left: Simplified mechanism of the palladium-catalyzed aryl amination. Right: Proposed mechanism for a cross-coupling reaction involving an *N*-trialkylsilyl imine.

II (this step requires the presence of a base to cleave the N–H bond); 3) reductive elimination to form the aryl amine **III** and to regenerate the Pd^0 catalyst. A similar catalytic cycle could be proposed by replacing the amine with an *N*-trialkylsilyl imine **IV** (Scheme 1, right). In such a case, a proper nucleophilic additive is required to promote the cleavage of the N–Si bond and to form the imido complex **V**.[8] We decided to explore this possibility, which would lead directly to aldimines **VI** from aryl or alkenyl bromides.

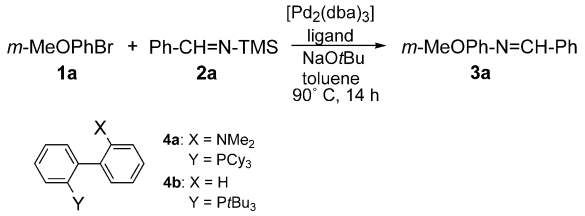
In an initial set of experiments, we studied the reaction of *m*-bromoanisole (**1a**) with the *N*-trimethylsilylimine **2a**[9] (Scheme 2) and chose the Pd^0–binap catalytic system. The reactions were carried out in toluene at 90 °C with Pd (1 mol %) in the presence of different additives. Only the formation of the cross-coupling imine **3a** was observed, although with low conversion (35 %), in the reaction carried out in the presence of NaO*t*Bu. Other basic reagents such as NaOMe and triethylamine furnished unaltered starting

[*] Prof. Dr. J. Barluenga, Prof. Dr. F. Aznar, Dr. C. Valdés
Inst. Universitario de Química Organometálica "Enrique Moles"
Universidad de Oviedo, 33071 Oviedo (Spain)
Fax: (+34) 985-10345
E-mail: barluenga@sauron.quimica.uniovi.es

[**] This research was supported by the DGI (Grant BQU-2001-3853) and the FYCYT (Grant PR-01-GE-09).

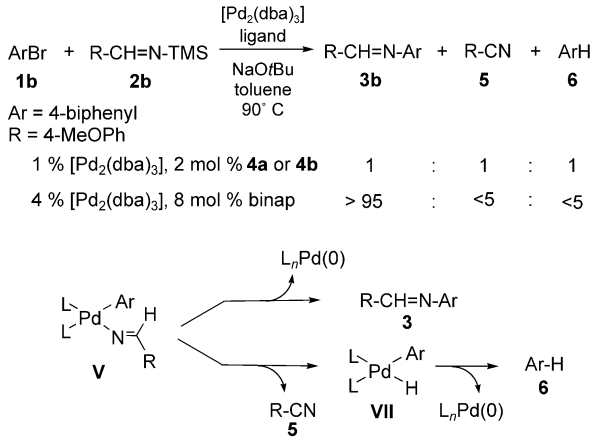
Supporting information for this article is available on the WWW under http://www.angewandte.org or from the author.

 DOI: 10.1002/anie.200352808 © 2004 Wiley-VCH Verlag GmbH & Co. KGaA, Weinheim



Ligand	PPh_3	P(*o*-Tol)$_3$	binap	xantphos	dppf	**4a**	**4b**
Conv. %[a]	<5	<5	35	20	<5	100 (52)	100 (45)

Scheme 2. Influence of the ligand in the coupling of *N*-trimethylsilylbenzaldimine (**2a**) with 3-bromoanisole (**1a**) in the presence of $[Pd_2(dba)_3]$. Reaction conditions: **1a** (1 equiv), **2a** (1.1 equiv), NaO*t*Bu (1.4 equiv), $[Pd_2(dba)_3]$ (1 mol%), ligand (2 mol%), toluene (2 mL/mmol), 90°C, 14 h. dba = dibenzylideneacetone, binap = 2,2′-bis(diphenylphosphanyl)-1,1′-binaphthyl, xantphos = 9,9-dimethyl-4,5-bis-(diphenylphosphanyl)xanthene, dppf = 1,1′-bis(diphenylphosphanyl)ferrocene. [a] Yield of isolated **3a** when **4a** and **4b** were used are indicated in parentheses.



Scheme 3. Influence of the ligand on the ratio of reductive elimination vs β-elimination.

materials. No reaction was observed either with CsF in toluene (probably as a result of solubility problems),[10] and phase-transfer catalysts such as methyltribenzylamonium chloride and tetrabutylammonium fluoride resulted in the decomposition of the silylimine with no coupling product being formed.[11]

The same reaction in the presence of NaO*t*Bu was then studied with a set of different ligands. Only with biphenyl ligands **4a** and **4b** was complete conversion achieved (Scheme 2).[12] However, the yield of pure distilled material did not exceed 52%.

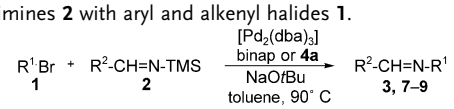
In a different series of experiments with the 4-bromobiphenyl **1b** and silylimine **2b** (Scheme 3), it was observed that the reaction with ligands **4a** and **4b** provided a mixture of coupling product **3b**, 4-methoxybenzonitrile **5**, and biphenyl **6** in a nearly 1:1:1 ratio. This result could be explained by a competing catalytic cycle in which β-elimination in complex **V** would release nitrile **5** and generate hydride complex **VII**. Finally, reductive elimination would give rise to the dehalogenated aromatic hydrocarbon **6** and regenerate the palladium catalyst.[13,14] Apparently, with biphenyls **4** as ligands, both reaction pathways occur to a similar extent. Nevertheless, by using binap and increasing the catalyst loading from 1 to 4 mol%, complete conversions were possible, and interestingly, less than 5% β-elimination was observed.

The reaction was generalized to a range of aryl bromides and silylimines. As represented in Table 1, the coupling proceeds with good to quantitative yields and tolerates electron-donating and -withdrawing groups and some heterocyclic motifs (Table 1, entries 7–9) in both coupling partners. Interestingly, the same reaction allows the synthesis of aldimines **3**, 1-azadienes **7**, 2-azadienes **8**, and even azatrienes **9**, depending on the structure of the coupling partners.

The reaction with vinyl bromides (Table 1, entries 12–14), which constitutes a novel synthesis of electronically neutral 2-azadienes **8** and 2-azatriene **9**, which are very versatile reagents in heterocycloaddition reactions.[15] In this case, the use of ligand **4a** is preferred (method B), as no β-elimination products were formed. Owing to the higher activity of this catalytic system, complete conversions are possible in much shorter times and with lower catalyst loadings.

In summary, we have introduced *N*-trialkylsilylimines **2** as very efficient synthetic equivalents of the unstable and

Table 1: Coupling of silylimines **2** with aryl and alkenyl halides **1**.



Entry	R^1	R^2	Product	Method[a]	*t* [h][b]	Yield [%][c]
1	*m*-MeOPh	*p*-MeOPh	**3c**	A	14	97
2	*p*-ClPh	*p*-MeOPh	**3d**	A	14	86
3	*m*-CNPh	*p*-MeOPh	**3e**	A	20	79
4	*o*-EtPh	*p*-MeOPh	**3f**	A	14	95
5	*m*-CNPh	*p*-ClPh	**3g**	A	14	76
6	*o*-EtPh	*p*-ClPh	**3h**	A	14	96
7	3-Py	*p*-ClPh	**3i**	A	20	86
8	*o*-EtPh	2-Furyl	**3j**	A	14	92
9	*p*-CF_3Ph	2-Furyl	**3k**	A	14	90
10	*p*-ClPh	Ph-CH=CH-	**7a**	A	14	95
11	*m*-MeOPh	Ph-CH=CH-	**7b**	A	20	86
12	Ph-CH=CH-	*p*-ClPh	**8a**	B	2	92
13	Ph-CH=CH-	*p*-MeOPh	**8b**	B	3	90
14	Ph-CH=CH-	Ph-CH=CH-	**9**	B	3	93

[a] Method A: **1** (1 equiv), **2** (1.2 equiv), NaO*t*Bu (1.4 equiv), $[Pd_2(dba)_3]$ (4 mol%), BINAP (8 mol%), toluene (2 mL/mmol), 90°C. Method B: **1** (1 equiv), **2** (1.2 equiv), NaO*t*Bu (1.4 equiv), $[Pd_2(dba)_3]$ (2 mol%), **4a** (4 mol%), toluene (2 mL/mmol), 90°C. [b] Reaction times were not optimized. [c] Yields of isolated product on a 0.5-mmol scale.

 © 2004 Wiley-VCH Verlag GmbH & Co. KGaA, Weinheim

unavailable NH aldimines in palladium-catalyzed cross-coupling reactions. The coupling with aryl bromides allows the one-step synthesis of aldimines, and the reaction with vinyl bromides gives rise to neutral 2-azadienes with excellent yields. Given the easy availability of structurally diverse and functionalized *N*-trialkylsilyl imines[9,16] and the good yields of the coupling reaction, we believe that this transformation may be very useful in heterocyclic chemistry and diversity-oriented organic synthesis. Moreover, these results open the door for the incorporation of *N*-trialkylsilyl imines in other types of metal-catalyzed cross-coupling processes.

Received: September 8, 2003 [Z52808]

Keywords: amination · azadienes · cross-coupling · imines · palladium

[1] For reviews, see: a) J. F. Hartwig in *Modern Amination Methods* (Ed: A. Ricci), Wiley-VCH, Weinheim, **2000**, pp. 195–262; b) A. Muci, S. L. Buchwald, *Top. Curr. Chem.* **2002**, *219*, 131–209; c) J. F. Hartwig in *Handbook of Organopalladium Chemistry for Organic Synthesis* (Ed: E. Negishi), Wiley-Interscience, New York, **2002**, p. 1051.

[2] For representative examples of very efficient catalysts in palladium-catalyzed C–N bond forming reactions, see: a) D. W. Old, J. P. Wolfe, S. L. Buchwald, *J. Am. Chem. Soc.* **1998**, *120*, 9722–9723; b) G. A. Grasa, M. S. Viciu, J. Huang, S. P. Nolan, *J. Org. Chem.* **2001**, *66*, 7729–7737; c) A. Schnyder, A. F. Indolese, M. Studer, H.-U. Blaser, *Angew. Chem.* **2002**, *114*, 3820–3823; *Angew. Chem. Int. Ed.* **2002**, *41*, 3668–3670d) J. P. Stambuli, R. Kuwano, J. F. Hartwig, *Angew. Chem.* **2002**, *114*, 4940–4942; *Angew. Chem. Int. Ed.* **2002**, *41*, 4746–4748; e) X. Huang, K. W. Anderson, D. Zim, L. Jiang, A. Klapars, S. L. Buchwald, *J. Am. Chem. Soc.* **2003**, *125*, 6653–6655.

[3] a) A. Y. Lebedev, V. V. Izmer, D. N. Kazyul'kin, I. P. Beletskaya, A. Z. Voskoboynikov, *Org. Lett.* **2002**, *4*, 623–626; b) J. Barluenga, F. Aznar, M. A. Fernández, C. Valdés, *Chem. Commun.* **2002**, 2362–2363.

[4] J. P. Wolfe, J. Åhman, J. P. Sadighi, R. A. Singer, S. L. Buchwald, *Tetrahedron Lett.* **1997**, *38*, 6367–6370.

[5] C. Bolm, J. P. Hildebrand, *J. Org. Chem.* **2000**, *65*, 169–175.

[6] For other ammonia surrogates in Pd-catalyzed aminations, see: reference [4a] and also: a) K. Hori, M. Mori, *J. Am. Chem. Soc.* **1998**, *120*, 7651–7652; b) S. Jaime-Figueroa, Y. Liu, J. M. Muchowski, D. G. Putman, *Tetrahedron Lett.* **1998**, *39*, 1313–1316; c) C. W. Lim, S. Lee, *Tetrahedron* **2000**, *56*, 5131–5136; d) C. Bolm, J. P. Hildebrand, *Tetrahedron Lett.* **1998**, *39*, 5731–5734; e) X. Huang, S. L. Buchwald, *Org. Lett.* **2001**, *3*, 3417–3419; f) M. C. Harris, X. Huang, S. L. Buchwald, *Org. Lett.* **2002**, *4*, 2885.

[7] a) L. M. Alcazar-Roman, J. F. Hartwig, A. L. Rheingold, L. M. Liable-Sands, I. A. Guzei, *J. Am. Chem. Soc.* **2000**, *122*, 4618–4630; b) U. K. Singh, E. R. Strieter, D. G. Blackmond, S. L. Buchwald, *J. Am. Chem. Soc.* **2002**, *124*, 14104–14114.

[8] The palladium-catalyzed C–C bond formation involving organosilanes (Hiyama coupling) is a well-known reaction: T. Hiyama in *Metal-catalyzed Cross-coupling Reactions* (Eds: F. Diederich, P. J. Stang), Wiley-VCH, New York, **1998**, chap. 10; however, to the best of our knowledge, the analogous C–N bond-forming reaction has not been described previously.

[9] E. W. Colvin, D. McGarry, M. J. Nugent, *Tetrahedron* **1988**, *44*, 4157–4172.

[10] Reactions carried out in the presence of CsF in dioxane as solvent gave rise to the cross-coupling product together with considerable amounts of decomposition materials derived from the imine.

[11] These results indicate that strong nucleophiles tend to promote the N–Si bond cleavage at a much faster rate than the catalytic process itself, giving rise to decomposition of the imine instead of coupling-product formation.

[12] D. W. Old, J. P. Wolfe, S. L. Buchwald, *J. Am. Chem. Soc.* **1998**, *120*, 9722.

[13] The inhibition of the β-elimination pathway was a major challenge in the early work of palladium-catalyzed aryl amination. In fact, catalysts based on chelating ligands such as binap and dppf, so-called second-generation catalysts, favor reductive elimination, thus lowering the amount of β-elimination products: a) J. P. Wolfe, S. Wagaw, S. L. Buchwald, *J. Am. Chem. Soc.* **1996**, *118*, 7215–7216; b) M. S. Driver, J. F. Hartwig, *J. Am. Chem. Soc.* **1996**, *118*, 7217–7218; see also: c) P. W. N. M. van Leeuwen, P. C. J. Kamer, J. N. H. Reek, P. Dierkes, *Chem. Rev.* **2000**, *100*, 2741–2769.

[14] The β-elimination pathway in the presence of a Pd catalyst based on **4b** was recently adapted into a new method for the oxidation of alcohols: A. S. Guram, X. Bei, H. W. Turner, *Org. Lett.* **2003**, *5*, 2485–2487.

[15] a) For a review of the synthetic applications of azadienes, see: S. Jayakumar, M. P. S. Ishar, M. P. Mahajan, *Tetrahedron* **2002**, *58*, 379–471; see also: b) F. Palacios, C. Alonso, P. Amezua, G. Rubiales, *J. Org. Chem.* **2002**, *67*, 1941–1946.

[16] G. Cainelli, D. Giacomini, P. Galletti, A. Gaiba, *Synlett*, **1996**, 657.

 © 2004 Wiley-VCH Verlag GmbH & Co. KGaA, Weinheim

Magnetic Clusters

Mixed Transition-Metal—Lanthanide Complexes at Higher Oxidation States: Heteronuclear Ce^{IV}–Mn^{IV} Clusters**

*Anastasios J. Tasiopoulos, Ted A. O'Brien, Khalil A. Abboud, and George Christou**

High oxidation-state molecular compounds or polymeric oxides of Mn or Ce have a wide range of applications in diverse areas involving inorganic, organic, environmental, and industrial chemistry owing to their ability to oxidize both inorganic and organic substrates.[1–8] The high oxidation-state tetranuclear Mn cluster that is present near photosystem II of

[*] Dr. A. J. Tasiopoulos, Dr. K. A. Abboud, Prof. Dr. G. Christou
Department of Chemistry
University of Florida
Gainesville, FL 32611-7200 (USA)
Fax: (+1) 352-392-8757
E-mail: christou@chem.ufl.edu
Dr. T. A. O'Brien
Department of Chemistry
Indiana University-Purdue University Indianapolis
Indianapolis, IN 46202–3274 (USA)

[**] This work was supported by the U.S. National Science Foundation (Grant CHE-0123603).

 DOI: 10.1002/anie.200352898 © 2004 Wiley-VCH Verlag GmbH & Co. KGaA, Weinheim

green plants is responsible for the oxidation of H_2O to dioxygen.[1,2] As a result, a number of Mn_4 complexes have been made to model its structural and functional properties.[1] Ce^{IV} has also been used in the homogeneous and heterogeneous catalysis by Ru complexes of water oxidation to molecular dioxygen.[2] Similarly, MnO_4^- and Ce^{IV} are commonly employed as oxidants in inorganic synthesis, such as in the formation of Mn^{III} and/or Mn^{IV} clusters, or mixed-valent $Co^{III,IV}$ complexes.[3,4] In addition, compounds such as MnO_4^-, MnO_2, and $(NH_4)_2[Ce(NO_3)_6]$ have a long history as oxidizing agents for a vast variety of organic substrates.[5,6] Further, Mn^{III}, Mn^{IV} and Ce^{IV} oxides have been widely used, either alone or as mixed Mn/Ce oxides, in a number of heterogeneous catalytic oxidation processes.[7,8] For example, Ce^{IV}/Mn^{IV} composite oxides are being widely used in sub- and supercritical catalytic wet oxidations for the treatment of wastewater containing toxic organic pollutants such as ammonia, acetic acid, pyridine, phenol, polyethylene glycol, and others.[8] Mixed Ce^{IV}/Mn^{IV} molecular analogues of these Ce/Mn oxide catalysts have not been available for study, but would likely prove to have interesting oxidative and other properties. We herein report the synthesis, crystallographic characterization and magnetic properties of a novel family of mixed Ce^{IV}/Mn^{IV} complexes with various Ce:Mn ratios. These are also the first crystallographically characterized molecular Mn/Ce complexes in general.

The new compounds described below were all obtained as part of a larger investigation of the oxidation of Mn^{II} reagents by Ce^{IV} under a variety of conditions. The reaction of $Mn(NO_3)_2{\cdot}x\,H_2O$ and 2,2′-bipyridine (bpy) with $(NH_4)_2[Ce(NO_3)_6]$ in a 1:1:2 molar ratio in 25% aqueous acetic acid gave $[Ce^{IV}Mn^{IV}_2O_3(O_2CMe)(NO_3)_4(H_2O)_2(bpy)_2](NO_3){\cdot}2\,H_2O$ (**1**·2 H_2O) in 40% yield. Similarly, the reaction of $[Mn(O_2CMe)_2]{\cdot}4\,H_2O$ and 6-methyl-2-hydroxypyridine (mhpH)[9] with $(NH_4)_2Ce(NO_3)_6$ in a 4:9:6 molar ratio in 30% aqueous acetic acid gave $[Ce_3Mn_2O_6(O_2CMe)_6(NO_3)_2(mhpH)_4]{\cdot}2\,H_2O$ (**2**·2 H_2O) in 24% yield. Finally, the reaction of a solution of $[Mn(O_2CMe)_2]{\cdot}4\,H_2O$ in 50% aqueous acetic acid with $Ce(ClO_4)_4$ (0.5 M solution in $HClO_4$) in a 2:3 molar ratio gave $[Ce^{IV}Mn^{IV}_6O_9(O_2CMe)_9(MeOH)(H_2O)_2](ClO_4){\cdot}3\,H_2O{\cdot}{}^1/_2MeCO_2H$ (**3**·3 $H_2O{\cdot}{}^1/_2MeCO_2H$) in ≈50% yield. Charge considerations, inspection of metric parameters and bond valence sum calculations establish that all the Ce and Mn ions of **1**–**3** are in oxidation state IV.[10]

The structure of the cation of **1** (Figure 1)[11] comprises a $[Mn^{IV}_2(\mu\text{-}O)_2(\mu\text{-}O_2CMe)]^{3+}$ rhomb linked to a Ce^{IV} ion through a linear oxide bridge. The Mn-Mn-Ce angle is 139.6(2)°. The ten-coordinate Ce^{IV} ion is additionally ligated by four bidentate nitrate groups and a water molecule. Octahedral coordination at each Mn is completed by a chelating bpy group and a terminal water molecule at Mn2. The Mn–O and Mn–N bond lengths, and the Mn···Mn separation (2.659 Å) are typical of those in discrete dinuclear complexes containing the $[Mn^{IV}_2(\mu\text{-}O)_2(\mu\text{-}O_2CMe)]^{3+}$ core.[4a] The Ce–O bond lengths (2.44–2.60 Å) are slightly longer than is typical for ten-coordinate Ce^{IV} (Ce–O bond lengths ≈2.3–2.5 Å),[10c] probably as a consequence of the very short Ce^{IV}–O^{2-} bond (Ce–O5 = 1.945 Å), one of the shortest Ce–O

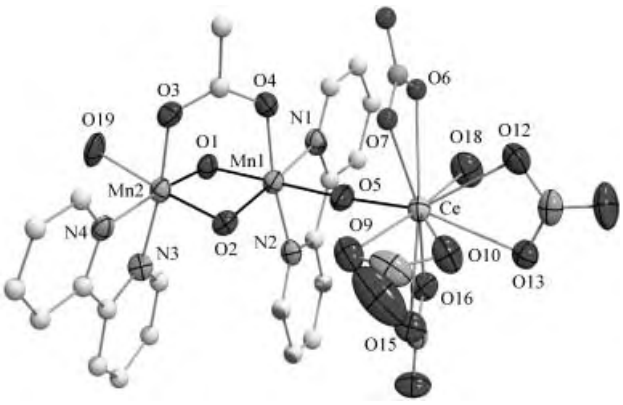


Figure 1. The cation of complex **1,** labeled ORTEP plot (at the 50% probability level) in PovRay format.

bond lengths ever reported. Complex **1** is a new structural type for a mixed Tr/Ln complex (where Tr = transition metal, Ln = lanthanide).

The structure of **2** (Figure 2, top)[11] consists of a Ce^{IV}_3 isosceles triangle, each edge of which is bridged by two μ_3-O^{2-} ions that also bridge to the two Mn^{IV} ions lying one each above and below the Ce^{IV}_3 triangle forming an M_5 trigonal bipyramid (Mn···Mn = 4.818 Å), (Figure 2, bottom).[12] Peripheral ligation is completed by bridging acetate,[12] chelating nitrate and terminal mhpH groups, the latter

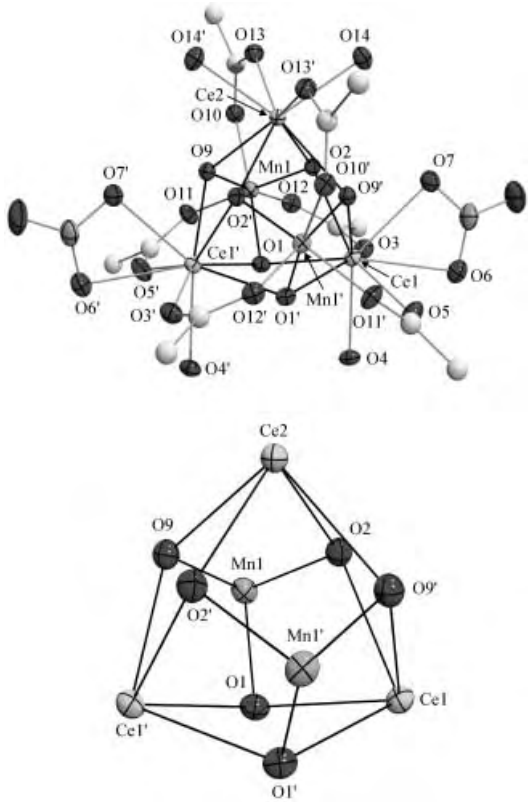


Figure 2. Top: Complex **2**, the methylpyridine groups are omitted, labeled ORTEP plot (at the 50% probability level) in PovRay format. Bottom: The $[Ce^{IV}_3Mn^{IV}_2O_6]^{8+}$ core of **2** emphasizing its trigonal bipyramidal topology.

 © 2004 Wiley-VCH Verlag GmbH & Co. KGaA, Weinheim

protonated at their N atoms and binding only through their O atoms (O4 and O14). The molecule has crystallographically imposed C_{2v} symmetry, the C_2 axis passing through Ce2 and bisecting the O1···O1′ vector. The Ce–O bond lengths are within the expected range for octa- and enneacoordinate Ce^{IV}.[10c] The Ce_3Mn_2 trigonal bipyramidal topology has been observed in mixed 4f/3d chemistry only once before, in a $Nd^{III}{}_3Cr^{III}{}_2$ complex that contains hydroxide bridges, rather than oxide ones as in **2**.[12a]

The structure of **3** (Figure 3, top)[11] contains an unprecedented $Mn^{IV}{}_6$ wheel. Its edges are bridged alternately by (μ_2-O)(μ_3-O)(μ-O_2CMe) and (μ_3-O)(μ-O_2CMe)$_2$ ligand sets, with

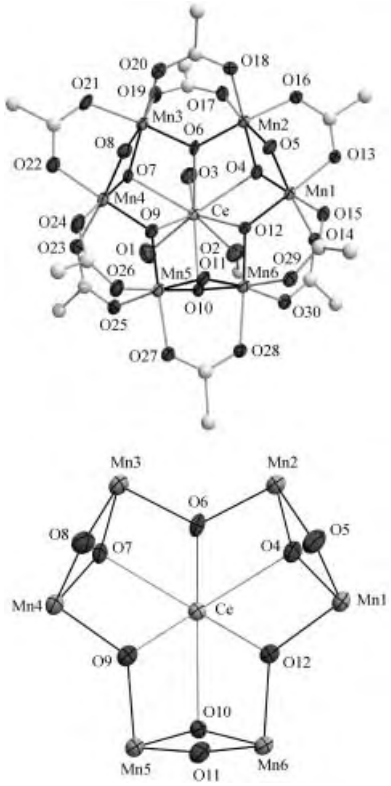


Figure 3. Top: Complex **3,** labeled ORTEP plot (at the 50% probability level) in PovRay format. Bottom: The $[Mn^{IV}{}_6Ce^{IV}O_9]^{10+}$ core of **3**.

Mn···Mn separations of 2.714 and 3.297 Å, respectively. The μ_3-O^{2-} ions are those holding in place the central Ce^{IV} ion,[12] which lies slightly out of the almost planar Mn_6 ring and is also coordinated to one MeOH and two water groups. The Ce–O bond lengths (2.271–2.483 Å) are within the expected range for enneacoordinate Ce^{IV}.[10c] The Mn^{IV}-O^{2-} (1.794–1.863 Å) and Mn–O (acetate) bond lengths (1.931–1.975 Å) are typical of Mn^{IV} values. Apart from being the first $Mn^{IV}{}_6$ wheel, complex **3** is also the first Mn^{IV} complex with only oxide and carboxylate ligands, and its $[M_7O_9]$ core (Figure 2, bottom) is of a structural type never seen before for any metal. In addition it is one of the few known examples of a cyclic Tr_6Ln complex, that is, a wheel of transition-metal ions with a central lanthanide ion.[13]

Solid-state, magnetic susceptibility measurements were carried out on complexes **1**–**3** in the temperature range 5.0–300 K in a 10 kG dc magnetic field. The obtained data are shown as $\chi_M T$ versus T plots (Figure 4; χ_M is the magnetic

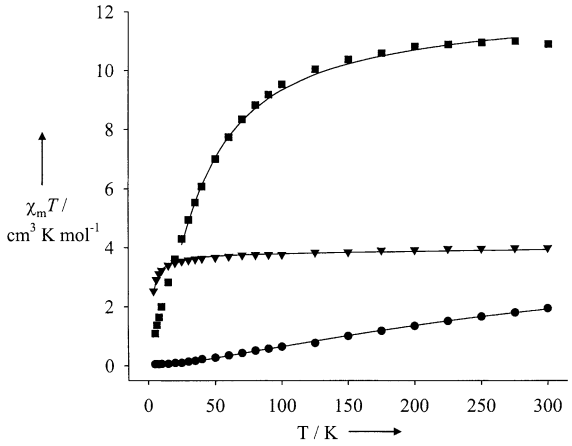


Figure 4. $\chi_M T$ versus T plot for complexes **1** (●), **2** (▼) and **3** (■). The solid lines are the fits of the data; see the text for the fit parameters.

susceptibility). All paramagnetism is associated with the Mn^{IV} ions, since Ce^{IV} is diamagnetic (f^0). The data for **1** and **2** were fit to the theoretical $\chi_M T$ vs. T expression for a d^3–d^3 dimer.[14] The fits (solid lines in Figure 4) gave $J = -45.7\ cm^{-1}$, $\rho = 0.019$, and $g = 1.95$ for **1**, and $J = -0.40\ cm^{-1}$, $\rho = 0.010$, and $g = 2.01$ for **2**, J is the exchange interaction constant, and ρ is the fraction of paramagnetic impurity (assumed to be high-spin Mn^{II}). A temperature independent paramagnetism (TIP) term was held constant at $300 \times 10^{-6}\ cm^3\,mol^{-1}\,K$ for **1**, and $500 \times 10^{-6}\ cm^3\,mol^{-1}\,K$ for **2**.[15] The data for **3** were fit by a matrix diagonalization method described elsewhere.[16] Three exchange constants were used as parameters, J_1 and J_2 for the $[Mn^{IV}{}_2O_2(O_2CMe)]$ and $[Mn^{IV}{}_2O(O_2CMe)_2]$ units, respectively, and J_3 for a uniform next-nearest-neighbor interaction. The preliminary fit (solid line in Figure 4) using data above 25 K to avoid intermolecular interactions gave $J_1 = -5.8\ cm^{-1}$, $J_2 = -0.63\ cm^{-1}$, $J_3 \approx 0$, $\rho = 0.0299$, and $g = 2.07$, with TIP held constant at $700 \times 10^{-6}\ cm^3\,mol^{-1}\,K$.[15]

Complexes **1**–**3** are thus all antiferromagnetically coupled with $S = 0$ ground states. The J value for **1** is in agreement with previously reported values (-24.6 to $-67\ cm^{-1}$) for dinuclear complexes with a $[Mn^{IV}{}_2(\mu\text{-}O)_2(\mu\text{-}O_2CMe)]$ core.[4a,17] The J value for **2** is very weak, as expected for two well separated Mn^{IV} ions interacting through four-bond superexchange pathways. The J_1 value gauging the interaction within the $[Mn^{IV}{}_2O_2(\mu\text{-}O_2CMe)]$ units of **3** is significantly smaller than the lower limit of the above range for dinuclear complexes. This is consistent with the attachment of the strongly Lewis acidic Ce^{4+} ion, which weakens the Mn–O^{2-} bonds that mediate the $Mn^{IV}{}_2$ superexchange interaction. This is reflected in the significantly longer Mn–(μ_3-O^{2-}) bond lengths [av 1.859 Å] and Mn···Mn separations [av 2.714 Å] in this unit in **3**, compared with the Mn–(μ-O^{2-}) bonds of **3** [av 1.813 Å], and the Mn···Mn distances [range 2.58–2.67 Å] of dinuclear

 © 2004 Wiley-VCH Verlag GmbH & Co. KGaA, Weinheim

compounds containing the $[Mn^{IV}_2(\mu\text{-}O)_2(\mu\text{-}O_2CMe)]$ core.[4a] The very small J_2 value can also be rationalized on the basis of the long Mn–(μ_3-O^{2-}) bond lengths [1.83 Å] and Mn···Mn separations [3.297 Å], although discrete dinuclear complexes containing the $[Mn^{IV}_2(\mu\text{-}O)(\mu\text{-}O_2CMe)_2]$ core are currently unknown and thus unavailable for comparison.

The described results establish synthetic access to a new class of mixed $Ce^{IV}/Mn^{IV}/O^{2-}$ molecular clusters. Although there are a few other reported examples of high oxidation state, mixed transition-metal/lanthanide complexes containing early transition-metal ions such as Ti^{IV} or Nb^{V},[12f] compounds **1**–**3** are unique in that both component ions are strong oxidizing agents. The species obtained to date already span a wide range of Ce:Mn ratios, from 3:2 (**2**), 1:2 (**1**), to 1:6 (**3**), and others will undoubtedly be possible. It is interesting that **1**–**3** all contain Ce^{IV} even though Ce^{IV} was used as the oxidant of Mn^{II} in the reaction, and the Mn^{II}:Ce^{IV} reaction ratios were such that all Ce^{IV} was ostensibly reduced to Ce^{III} in generating Mn^{IV}. We believe that this is more than happenstance: The generation of high oxidation state Mn^{IV} is known to favor formation of non-mononuclear products containing bridging O^{2-} ions, but the presence of the hard O^{2-} ions will also in turn favor incorporation of hard Ce^{4+} ions, facilitating formation of Ce^{IV}/Mn^{IV} products, which perhaps involves the participation of atmospheric oxygen. Complexes **1**–**3** have unusual and aesthetically pleasing structures, but they are also soluble in organic solvents, thus making them valuable starting materials for further synthesis and reactivity studies. In particular, their solubility and the high oxidative strength of the metal ions they contain make them very attractive new candidates for catalytic and noncatalytic oxidation of a variety of organic and inorganic substrates.

Experimental Section

1·2H_2O: An orange solution of $(NH_4)_2[Ce(NO_3)_6]$ (5.50 g, 10.03 mmol) in $H_2O/MeCO_2H$ (19 ml/7 ml) was slowly added to a pale yellow-brown solution of $Mn(NO_3)_2{\cdot}x\,H_2O$ (0.90 g, 5.03 mmol) and bpy (0.78 g, 5.00 mmol) in $H_2O/MeCO_2H$ (50 ml/16 ml) resulting in a dark greenish-brown solution. The solution was reduced in volume by ≈60% by rotary-evaporation at 40 °C, and then maintained undisturbed at ambient temperature. After 24 h, dark greenish-brown crystals were collected by filtration, washed with cold acetone (2 × 7 mL) and Et_2O (2 × 15 ml), and dried in vacuo. The yield was 1.06 g (40% based on Mn). Elemental analysis calcd (%) for $C_{22}H_{27}N_9O_{24}CeMn_2$ (**1**·2H_2O): C 25.13, H 2.59, N 11.99; found: C 25.21, H 2.32, N 11.70. Selected IR data (KBr pellet): $\tilde{\nu}$ = 3400(s, br), 1602(m), 1560(w), 1498(m), 1470(m), 1446(s), 1384(s), 1310(s), 1286(m), 1170(w), 1158(w), 1107(w), 1073(w), 1060(w), 1035(m), 825(w), 811(w), 772(s), 738(w), 715(m), 693(w), 670(m), 655(m), 630(s), 592 (m), 419(w) cm^{-1}.

2·2H_2O: An orange solution of $(NH_4)_2[Ce(NO_3)_6]$ (6.78 g, 12.37 mmol) in $H_2O/MeCO_2H$ (9 mL/5 mL) was slowly added to a pale yellow-brown solution of $Mn(O_2CMe)_2{\cdot}4H_2O$ (2.02 g, 8.24 mmol) and mhpH (2.00 g, 18.33 mmol) in $H_2O/MeCO_2H$ (6 mL/1.5 mL) resulting in a dark reddish-brown solution. This was allowed to slowly evaporate at ambient temperature, and after a few days the now dark-red solution had started to produce dark red crystals. After several more days, the formation of large well-shaped red crystals was judged to be complete, and they were collected by filtration, washed with 2 × 6 mL each of cold acetone and Et_2O, and dried in vacuo. The yield was 1.15 g (24% based on Ce). Elemental analysis calcd (%) for $C_{36}H_{50}N_6O_{30}Ce_3Mn_2$ (**2**·2H_2O): C 27.41, H 3.20, N 5.33; found: C 27.60, H 3.00, N 5.05. Selected IR data (KBr pellet): $\tilde{\nu}$ = 3431(s, br), 3256(m), 3100(w), 2931(m), 1635(s), 1618(s), 1542(s), 1417(s), 1384(s), 1349(m), 1292(m), 1165 (m), 1028(m), 1004(m), 804(m), 745(m), 669 (m), 623 (s), 610(s), 578(s), 505(m), 490(m), 438(m) cm^{-1}.

3·3H_2O·0.5HO_2CMe: An orange mixture of a 0.5 M solution in $HClO_4$ of $Ce(ClO_4)_4$ (12.3 mmol, 24.6 mL) and a few drops of MeOH (≈0.2 mL) was slowly added to a colorless solution of $Mn(O_2CMe)_2{\cdot}4H_2O$ (2.02 g, 8.24 mmol) in $H_2O/MeCO_2H$ (4 mL/4 mL). The resulting dark reddish-brown solution was maintained at room temperature for about a week. The black crystals that formed were then collected by filtration, washed with ≈5 mL each of cold acetone and Et_2O, and dried in vacuo. The yield was 0.70 g (49% based on Ce). Elemental analysis calcd (%) for $C_{20}H_{43}O_{38}ClCeMn_6$ (**3**·3$H_2O{\cdot}{}^1/_2MeCO_2H$): C 17.20, H 3.10; found: C 16.90, H 3.00. Selected IR data (KBr pellet): $\tilde{\nu}$ = 3421(s, br), 1635(w), 1555(s), 1493(m), 1421(s), 1352(m), 1144(m), 1110(s), 1090(s), 1046(m), 1030(m), 951(w), 746(m), 693(m), 668(m), 628(s), 500(m) cm^{-1}.

Received: September 17, 2003 [Z52898]

Keywords: cerium · cluster compounds · lanthanides · magnetic properties · manganese · transition metals

[1] a) *Photosynthetic Water Oxidation* (Ed.: J. Nugent), *Biochim. Biophys. Acta* **2001**, *1503*, 1–259 (Special Dedicated Issue); b) V. K. Yachandra, K. Sauer, M. P. Klein, *Chem. Rev.* **1996**, *96*, 2927; c) R. Manchanda, G. W. Brudvig, R. H. Crabtree, *Coord. Chem. Rev.* **1995**, *144*, 1.

[2] a) W. Ruttinger, C. G. Dismukes, *Chem. Rev.* **1997**, *97*, 1; b) M. Yagi, M. Kaneko, *Chem. Rev.* **2001**, *101*, 21.

[3] a) A. J. Tasiopoulos, K. A. Abboud, G. Christou, *Chem. Commun.* **2003**, 580; b) T. Lis, *Acta Crystallogr. Sect. B* **1980**, *36*, 2042.

[4] a) S. Bhaduri, A. J. Tasiopoulos, M. A. Bolcar, K. A. Abboud, W. E. Streib, G. Christou, *Inorg. Chem.* **2003**, *42*, 1483; b) K. R. Reddy, M. V. Rajasekharan, S. Padhye, F. Dahan, J.-P. Tuchagues, *Inorg. Chem.* **1994**, *33*, 428; c) K. R. Reddy, M. V. Rajasekharan, N. Arulsamy, D. J. Hodgson, *Inorg. Chem.* **1996**, *35*, 2283; d) K. Dimitrou, A. D. Brown, T. E. Concolino, A. L. Rheingold, G. Christou, *Chem. Commun.* **2001**, 1284.

[5] a) D. Arndt, *Manganese Compounds as 0xidizing Agents in Organic Chemisty*, Open Court Publishing Company, Illinois, USA, **1981**; b) B. B. Snider, *Chem. Rev.* **1996**, *96*, 339.

[6] a) T.-L. Ho in *Organic Syntheses By Oxidation With Metal Compounds* (Eds.: W. J. Mijs, C. R. H. I. de Jonge), Plenum, New York, **1986**, chap. 11, pp. 569–631; b) V. Nair, J. Mathew, J. Prabhakaran, *Chem. Soc. Rev.* **1997**, *26*, 127.

[7] a) H. Cao, S. L. Suib, *J. Am. Chem. Soc.* **1994**, *116*, 5334; b) M. I. Zaki, M. A. Hasan, L. Pasupulety, K. Kumary, *New J. Chem.* **1998**, *22*, 875; c) A. Trovarelli, *Catal. Rev. Sci. Eng.* **1996**, *38*, 439.

[8] a) Y. I. Matatov-Meytal, M. Sheintuch, *Ind. Eng. Chem. Res.* **1998**, *37*, 309; b) S. Inamura, A. Dol, S. Ishida, *Ind. Eng. Chem. Prod. Res. Dev.* **1985**, *24*, 75; c) S. Hamoudi, K. Belkacemi, F. Larachi, *Chem. Eng. Sci.* **1999**, *54*, 3569; d) S. Hamoudi, K. Belkacemi, A. Sayari, F. Larachi, *Chem. Eng. Sci.* **2001**, *56*, 1275; e) Z. Y. Ding, M. A. Frisch, L. Li, E. F. Gloyna, *Ind. Eng. Chem. Res.* **1996**, *35*, 3257; f) Z. Y. Ding, L. Li, D. Wade, E. F. Gloyna, *Ind. Eng. Chem. Res.* **1998**, *37*, 1707.

[9] This ligand has been employed in the past for the synthesis of other mixed transition metal-lanthanide complexes, for example: a) A. J. Blake, R. O. Gould, C. M. Grant, P. E. Y. Milne, S. Parsons, R. E. P. Winpenny, *J. Chem. Soc. Dalton Trans.* **1997**, 485; b) R. E. P. Winpenny, *Chem. Soc. Rev.* **1998**, *27*, 447.

 © 2004 Wiley-VCH Verlag GmbH & Co. KGaA, Weinheim

[10] a) Bond valence sum (BVS) calculations for the Mn[10b] and Ce[10c] ions of complexes **1**–**3** gave values of: 4.16, 4.08, and 3.98 for Mn1, Mn2 and Ce, respectively, of **1**; 4.06, 3.82 and 3.86 for Mn1, Ce1 and Ce2, respectively, of **2**; 4.07–4.28 for Mn1–Mn6, and 3.84 for Ce of **3**; b) W. Liu, H. H. Thorp, *Inorg. Chem.* **1993**, *32*, 4102; c) P. L. Roulhac, G. J. Palenik, *Inorg. Chem.* **2003**, *42*, 118.

[11] Crystal structure data for **1**·2 H_2O: $C_{22}H_{27}N_9O_{24}CeMn_2$, $M_r = 1051.53$, triclinic, space group $P\bar{1}$, $a = 9.3132(6)$, $b = 12.3866(8)$, $c = 17.4899(12)$ Å, $\alpha = 87.810(2)$, $\beta = 83.871(2)$, $\gamma = 75.134(2)°$, $V = 1938.8(2)$ Å^3, $T = 173$ K, $Z = 2$, $\rho_{calcd} = 1.801$ g cm^{-3}, 17243 reflections collected, 8624 unique ($R_{av} = 0.0868$), $R1 = 0.0806$, w$R2 = 0.1743$, by using 5470 reflections with $I > 2\sigma(I)$. Crystal structure data for **2**·2 H_2O: $C_{36}H_{50}N_6O_{30}Ce_3Mn_2$, $M_r = 1577.04$, orthorhombic, space group Aba2, $a = 22.6707(12)$, $b = 14.8735(8)$, $c = 15.7286(8)$ Å, $V = 5303.6(5)$ Å^3, $T = 173$ K, $Z = 4$, $\rho_{calcd} = 1.970$ g cm^{-3}, 22828 reflections collected, 6051 unique ($R_{av} = 0.0638$), $R1 = 0.0250$, w$R2 = 0.0661$, using 5938 reflections with $I > 2\sigma(I)$. Crystal structure data for **3**·3 H_2O·$^1/_2HO_2CMe$: $C_{20}H_{43}O_{38}ClCeMn_6$, $M_r = 1396.73$, triclinic, space group $P\bar{1}$, $a = 12.2133(7)$, $b = 13.0106(8)$, $c = 16.6337(10)$ Å, $\alpha = 99.056(2)$, $\beta = 101.581(2)$, $\gamma = 111.188(2)°$, $V = 2336.5(2)$ Å^3, $T = 193$ K, $Z = 2$, $\rho_{calcd} = 1.982$ g cm^{-3}, 17436 reflections collected, 8194 unique ($R_{av} = 0.0477$), $R1 = 0.0728$, w$R2 = 0.1594$, using 6724 reflections with $I > 2\sigma(I)$. CCDC 219157–219159 contain the supplementary crystallographic data for this paper. These data can be obtained free of charge via www.ccdc.cam.ac.uk/conts/retrieving.html (or from the Cambridge Crystallographic Data Centre, 12, Union Road, Cambridge CB2 1EZ, UK; fax: (+44) 1223-336-033; or deposit@ccdc.cam.ac.uk).

[12] There are a number of mixed 4f/3d clusters where the transition metal is linked to the lanthanide(III) ion through μ_3-hydroxo or/and bridging carboxylate ligands,[9a,b,12a–d] but only a few containing μ_3-oxide bridges:[12e,f] a) N. Sakagami, M. Tsunekawa, T. Konno, K. Okamoto, *Chem. Lett.* **1997**, 575; b) X.-M. Chen, S. M. J. Aubin, Y.-L. Wu, Y.-S. Yang, T. C. W. Mak, D. N. Hendrickson, *J. Am. Chem. Soc.* **1995**, *117*, 9600; c) Y.-Y. Yang, Y.-L. Wu, L.-S. Long, X.-M. Chen, *J. Chem. Soc. Dalton Trans.* **1999**, 2005; d) Y.-Y. Yang, X.-M. Chen, S. W. Ng, *J. Solid State Chem.* **2001**, *161*, 214; e) C. Benelli, M. Murrie, S. Parsons, R. E. P. Winpenny, *J. Chem. Soc. Dalton Trans.* **1999**, 4125; f) L. G. Hubert-Pfalzgraf, V. Abada, J. Vaissermann, *Polyhedron* **1999**, *18*, 3497.

[13] Y.-J. Zhang, B.-Q. Ma, S. Gao, J.-R. Li, Q.-D. Liu, G.-H. Wen, X.-X. Zhang, *J. Chem. Soc. Dalton Trans.* **2000**, 2249.

[14] a) C. J. O'Connor, *Prog. Inorg. Chem.* **1982**, *29*, 203–283; b) J. H. Van Vleck, *The Theory of Electric and Magnetic Susceptibilities*, Oxford University, London, **1932**.

[15] A value of 100×10^{-6} cm^3 mol^{-1} K per Mn and per Ce was employed, which is a typical value for these ions.[4a,14b]

[16] a) T. A. O'Brien, C. Canada-Vilalta, G. Christou, E. R. Davidson, *J. Phys. Chem. A*, submitted. b) C. Cañada-Vilalta, T. A. O'Brien, M. Pink, E. R. Davidson, G. Christou, *Inorg. Chem.*, in press.

[17] S. Bhaduri, M. Pink, G. Christou, *Chem. Commun.* **2002**, 2352.

 © 2004 Wiley-VCH Verlag GmbH & Co. KGaA, Weinheim

Nanostructures

Micrometer-Sized Hexagonal Tubes Self-Assembled by a Cyclic Peptide in a Liquid Crystal**

Steve Leclair, Pierre Baillargeon, Rachid Skouta, David Gauthier, Yue Zhao, and Yves L. Dory**

Self-assembly of cyclic peptides is an attractive strategy for making hollow tubular structures.[1–4] Stacking of ring-shaped molecules of flat conformation can be stabilized by intermolecular hydrogen bonds formed between the amide groups. Cyclic peptides of rationally designed chemical structures can form nanotubes of different internal diameters and structures, which may find applications in biology and materials sciences.[2,5,6] Generally, the self-assembly process occurs in solution, is often triggered by a change in solubility of the peptide in organic solvents, and results in crystals organized by nanotubes. Herein, we report on the observation of self-assembled structures of a cyclic peptide in a nematic liquid crystal (LC). Hexagonal hollow tubes that have diameters in the order of micrometers and reaching several millimetres in length were observed. Strong experimental evidence suggests the occurrence of a hierarchical and self-similar-structured self-assembly of the cyclic peptide. That is, individual molecules of hexagonal conformation stack up into hexagonal nanotubes, which then self-organize into larger aggregates with the same appearance. Each molecule provides both intra- and intertube H bonding that ensure the molecular stacking within and the packing of nanotubes. To the best of our knowledge, this is the first work exploring the use of liquid crystals for the self-assembly of cyclic peptides, and the results show the surprising impact of the liquid crystalline medium.

Previous work showed that the lipophilic macrolactam cyclo-$(NHCH_2CH{=}CHCH_2CO)_3$ (*E* olefin) is soluble in ethanol and can be crystallized by diffusion of diethyl ether.[4] The crystal structure determined by X-ray crystallography shows the stacking of macrocycles, which have a

[*] S. Leclair, Prof. Y. Zhao
Laboratoire de polymères et cristaux liquides
Département de Chimie
Université de Sherbrooke
Sherbrooke, Qc, J1K 2R1 (Canada)
Fax: (+1) 819-821-8017
E-mail: yue.zhao@usherbrooke.ca

P. Baillargeon, R. Skouta, D. Gauthier, Prof. Y. L. Dory
Laboratoire de Synthèse Supramoléculaire
Département de Chimie
Université de Sherbrooke
Sherbrooke, Qc, J1K 2R1 (Canada)
Fax: (+1) 819-821-8017
E-mail: yves.dory@usherbrooke.ca

[**] This work was supported by NSERC Canada and FQRNT Québec. We thank Drs. S. Jandl and G. Riou, Sherbrooke, for the Raman microspectroscopic measurements.

Supporting information for this article is available on the WWW under http://www.angewandte.org or from the author.

 DOI: 10.1002/anie.200352259 © 2004 Wiley-VCH Verlag GmbH & Co. KGaA, Weinheim

rectangular shape due to one β turn, and the arrangement of the nanotubes into an orthorhombic cell structure. In the study presented herein, the same macrolactam was dissolved in a nematic LC (BL006 from Merck), which is an eutectic mixture mainly composed of biphenyl compounds and has a nematic–isotropic transition at $T_{ni} = 115\,^{\circ}C$. The purpose was to know how the LC medium, which is a fluid but has molecular order, could affect the self-assembly. To prepare the mixture, both compounds were dissolved in ethanol/chloroform 40:60 (w/w), and the solvent was removed. The mixture was flow-filled (at 120 °C) into a glass cell, with a gap of 10 μm. The self-assembly was triggered by a change in temperature; by cooling the mixture from the isotropic phase, in which the peptide is soluble in the LC, to lower temperatures results in aggregation. At a low peptide concentration of 0.5–2 % w/w, the aggregation was observed only in the nematic phase, that is, below 115 °C. Thermally induced self-assembly is a common method used to prepare organogels[7] and liquid-crystal gels.[8]

When the mixture was cooled very slowly, long tube-like aggregates were formed, as is seen from the photomicrograph for a mixture containing 0.5 % peptide and cooled at $0.1\,^{\circ}C\,min^{-1}$ (Figure 1 a). The tubes may be as long as several millimetres and have a diameter of a couple of micrometers. Analyses under crossed polarizers revealed that these tubes retain the LC inside. By dipping the cell in hexane, the LC can be removed slowly. After the cell was opened and dried, the tubes remained intact on the surface of the glass plates. A field emission gun scanning electron microscope was used to examine the tubes. Surprisingly, tubes of various diameters have a hexagonal form (Figure 1 b). Figure 1 c shows a broken tube of larger magnification. The cavity inside is visible and the surface of the tube is smooth. Figure 1 d shows the end of a naturally terminated tube, which is closed but remains highly porous. A very slow aggregation process is key to the formation of large and long tubes, which can also be obtained by isothermally annealing the mixture at a temperature below but close to T_{ni}. Smaller and shorter tubes are formed with an increase in the cooling rate or a decrease in the isothermal-annealing temperature. The striking features in Figure 1 (large cavity and hexagonal form at various diameters) are reminiscent of the concept of self-similar structure, which is used to describe loose and open-structured colloidal aggregates growing with the same appearance at any level of magnification.[9] In what follows, we present a computer modeling and Raman and infrared microspectroscopic analysis that points to a self-assembly mechanism for the observed amplification of the hexagonal form and the hollow structure of the tubes.

The rectangular nanotubes formed in the crystal cannot organize into hexagonal structures that provide the basis for a self-similar-structured growth in diameter of the observed tubular aggregate. We used computer modeling (6.31G* basis set and MM2 force field) to look for possible ways of aggregation for the cyclic peptide to form hexagonal objects. Using ab initio, we found three stable C_3 symmetric conformers[10] with energies of −0.22, 2.56 and 5.09 $kcal\,mol^{-1}$ relative to the crystal conformer.[4] Of the three conformations, the most stable one is unsuitable for stacking through

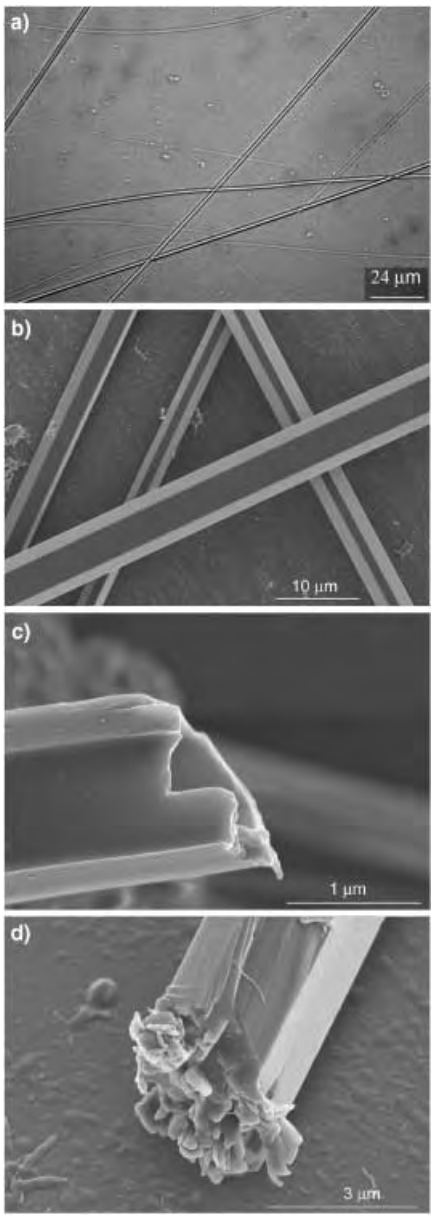


Figure 1. Images of the aggregates: a) Optical microscope; b) to d) scanning electron microscope.

hydrogen bonds, while the stacking of two units of the second stable conformer produced a dimer 12.48 $kcal\,mol^{-1}$ more energetic than the crystal dimer. On the other hand, the less stable conformer gave a parallel dimeric stack and an antiparallel stack (β-sheet description) with relative energies of 5.70 $kcal\,mol^{-1}$ and 6.38 $kcal\,mol^{-1}$, respectively. The lowest-energy dimer, shown in Figure 2 a, has roughly the shape of a hexagonal prism, with a crown of three amide carbonyls at one end, and a crown of three amide NHs at the other end. We then used MM2 force field, which was found to be sufficiently accurate to reproduce the 6.31G* results, to model the stacking and packing of the parallel dimeric stacks. Such hexagonal units can indeed stack on top of each other with the help of three hydrogen bonds to generate a first-generation hexagonal tube that has six alternating lipophilic and hydrophilic faces (Figure 2 b). The polar faces with

 © 2004 Wiley-VCH Verlag GmbH & Co. KGaA, Weinheim

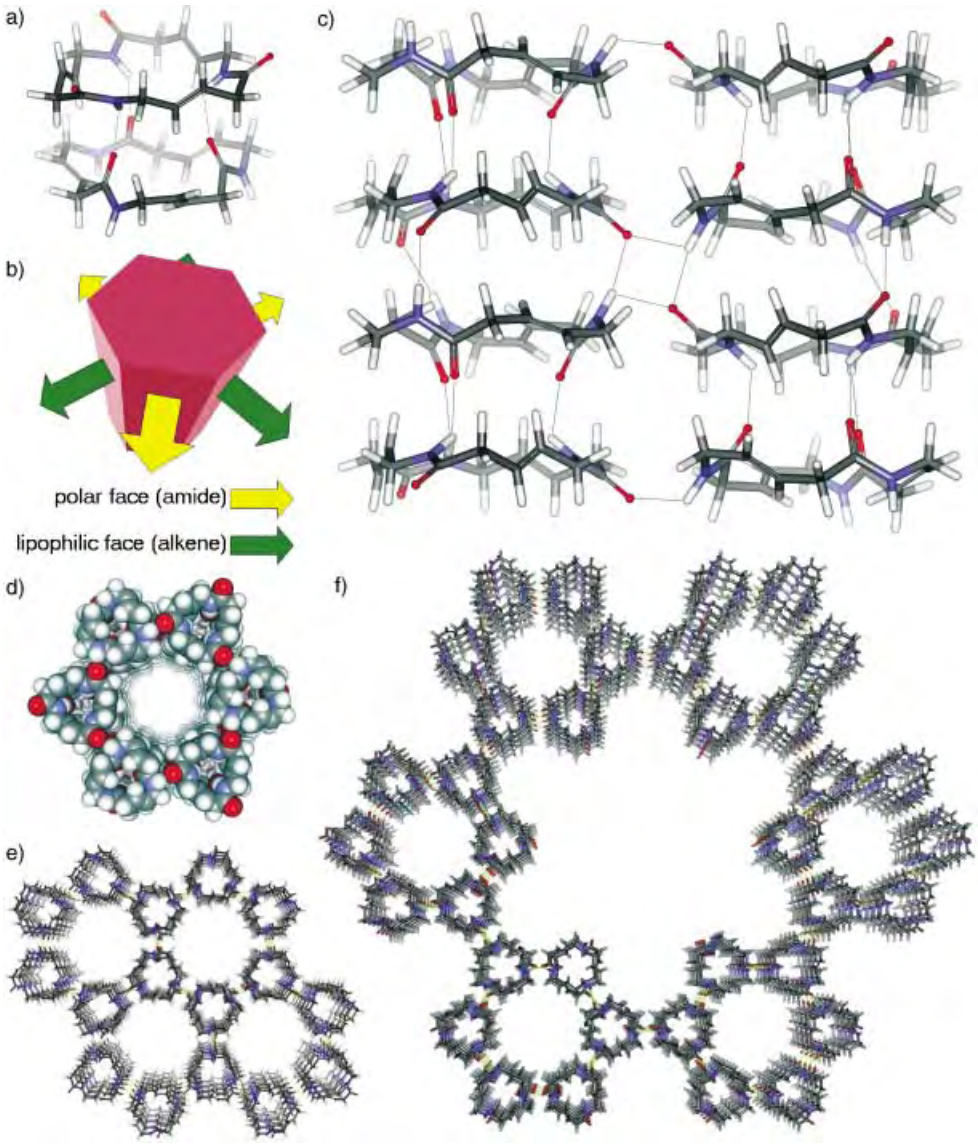


Figure 2. Hierarchical assembly to hollow macrotubes. a) Lowest-energy dimer with three intercycle hydrogen bonds. b) Schematic illustration of the first generation nanotube with intratube hydrogen bonds. c) Lowest-energy packing of two tetramers with intercycle and intertube hydrogen bonds. d) Lowest energy 48-mer as a second generation tube made of a hexagonal pack of six first-generation octameric nanotubes. e) Possible growth by packing of first generation nanotubes. f) Possible growth by packing of second generation tubes. O red, N blue, C gray, H white, H bond green line.

amides can establish interstack hydrogen bonds with neighboring tubes, whereas the hydrophobic faces with alkenes could only interact through van der Waals interactions. Calculations revealed that the most stable way for side-by-side packing of the first generation nanotubes is to have each nanotube with its gross dipole antiparallel to the neighbors. Figure 2c depicts the lowest energy packing of two tetramers showing the nature and orientation of the inter-cycle and intertube hydrogen bonds.

A thorough investigation was further carried out on various oligomeric aggregates that have 2, 4, 6, 8, 12, 24, 36, and 48 units to determine which type of assembly would predominate at each stage. Calculations yielded clues and interesting concepts as regards to the way mesoscopic hexagonal tubes might have formed in liquid crystals.[11] Although stacking of the rectangular crystal conformer is favored up to 12 units, for 24 units the packing of three hexagonal octameric first-generation tubes was preferred. After that point, hexagonal second-generation tubes made of six first-generation tubes become the rule, such as the 48-unit aggregate shown in Figure 2d. This second-generation tube keeps a hexagonal form like its precursor, but the diameter of the interior cavity increases to 10 Å. In contrast with the compact crystal packing that involves only weak van der Waals interactions,[4] the second generation hollow tubular structures may develop stabilizing van der Waals interactions with the lipophilic LC[6] in addition to the hydrogen bonding. In other words, the LC host could act as an active medium sampling C_3 symmetric units[12] and promoting the formation and growth of the hollow structures. From the second generation nanotube, further assembly into the observed micrometer-sized aggregates, while retaining the hexagonal form, may proceed through two mechanisms as illustrated in Figure 2. The first is a uniform packing (Figure 2e), which, however, will give rise to tubes with no large cavities. The second is a self-similar-structured growth. That is, the assembly of six second-generation tubes in the same way as the packing of six first-generation nanotubes will lead to an amplified hexagonal tubular structure with an increased internal cavity (30 Å) (Figure 2f), and the process of assembling the third and higher-generation tubes may go on to end up with the micrometer-scale tubes with a large interior cavity. We cannot rule out the first mechanism, but the observed hexagonal hollow tubes should come from a mechanism close to the second one. What actually happens is probably a combination of both mechanisms, which largely depends on experimental variables such as the cooling rate and the concentration of peptide. We observed that after the tubes were discernible on optical microscope, they grew in

 © 2004 Wiley-VCH Verlag GmbH & Co. KGaA, Weinheim

length over time while their diameters remained unchanged. This suggests that at the earliest stage of aggregation or crystallization, short nanotubes of various generations may self-organize into a sort of stable two-dimensional hexagonal aggregate, which then serves as the seed for further longitudinal growth of the tube.

The key points of the above modeling analysis are that the observed large hexagonal tubes would be built up from nanotubes through a hierarchical and self-similar-structured process, and that both intratube and intertube hydrogen bonding should be involved in the stacking of the cyclic molecules, which form the first generation nanotubes, and the packing of the nanotubes, which ultimately results in the microtubes. Having no access to microbeam X-ray diffraction facility, we used Raman microspectroscopy to probe the structure of the tubes. As is depicted in Figure 3a, the excitation laser beam ($\lambda = 633$ nm), which had a diameter of about 1.5 μm, was focused right on a tube (diameter ≈ 2.5 μm) stayed on the surface of the substrate after removal of the LC. The polarization of the laser beam, which propagated along the *y*-axis of the coordinate system, was set to be parallel and perpendicular, respectively, to the long axis of the tube, that is, along the *z* and *x* axis, and in each case polarized emissions were recorded with the polarization of the analyzer being parallel and perpendicular to the laser polarization, thus yielding Raman spectra of $\boldsymbol{I}_{zz}$, $\boldsymbol{I}_{zx}$, $\boldsymbol{I}_{xx}$ and $\boldsymbol{I}_{xz}$ (the first letter in the subscript indicates the polarization direction of the laser and the second letter is for the polarization of the analyzer). The amide band in the 1600–1700 cm^{-1} region, from the C=O stretching mode, has an anisotropic Raman tensor and can be used to characterize the orientation of hydrogen bonds formed between amide groups in proteins or peptides.[13,14] It is worth noting that in Figure 3a, $\boldsymbol{I}_{xz}$ differs only very slightly from $\boldsymbol{I}_{zx}$, which ensures that the same portion of the tube was excited by the laser during the measurements. Several observations can be made by comparing $\boldsymbol{I}_{zz}$ and $\boldsymbol{I}_{xx}$. First, two C=O bands (amide I) appear at 1664 and 1634 cm^{-1}, thus indicating that there are two types of hydrogen bonds formed between C=O and N–H groups. The hydrogen bonds associated with the 1664 cm^{-1} band are found both along the tube ($\boldsymbol{I}_{zz}$) and normal to the tube ($\boldsymbol{I}_{xx}$). By contrast, the hydrogen bonds associated with the 1634 cm^{-1} band are almost exclusively aligned along the tube, as is indicated by the ratio of the intensities of the bands, $I_{zz}/I_{xx} \approx 10$. Second, the broad band centered at 1424 cm^{-1} arises from CH and CH_2 deformation[13] of the cyclic peptide. The main component of their Raman tensor apparently lies in the plane of the cycle, which leads to more intense emission of $\boldsymbol{I}_{xx}$ than $\boldsymbol{I}_{zz}$ ($I_{xx}/I_{zz} \approx 4$). Third, The band at 1590 cm^{-1}, which is absent for the crystal formed from solution, is assigned to the liquid crystal locked inside the tube. Indeed, polarizing optical microscope observation shows that the LC may be trapped in some tubes or sections after removal of the LC with hexane. The pure LC displays an intense Raman band at 1605 cm^{-1} (in-plane stretching mode of phenyl rings) that has a highly uniaxial Raman tensor.[15] A shift of this band to lower frequency in the tube could occur owing to interactions with the peptide molecules. Since the LC contains mainly biphenyl compounds, the different emissions of $\boldsymbol{I}_{xx}$ and $\boldsymbol{I}_{zz}$ ($I_{zz}/I_{xx} \approx 4$) indicate that the encapsulated LC molecules are aligned along to the tube.

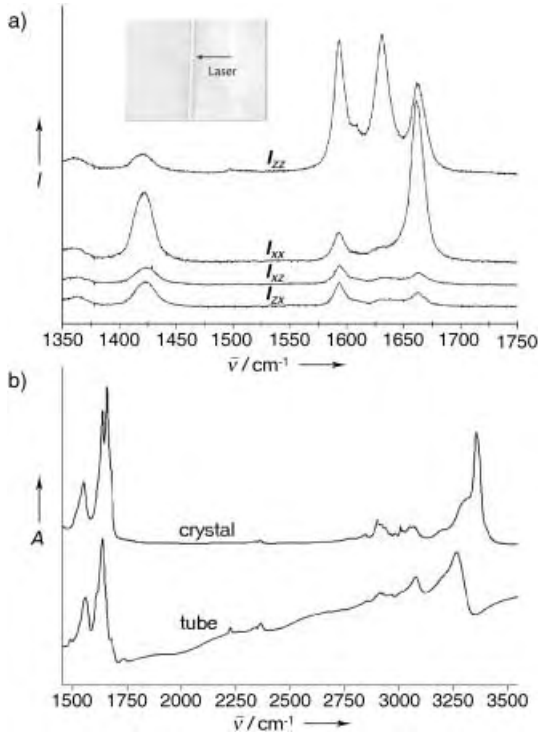


Figure 3. Raman and infrared spectroscopy of the tubes. a) Polarized Raman spectra in the 1350–1750 cm^{-1} region of a self-assembled tube (inset photo). The tube was positioned along the *z* axis and the incident laser beam was directed along the *y*-axis of the coordinate system (*I*: Raman intensity). b) Infrared spectra for the tubes self-assembled in the liquid crystal and the crystal (*A* = absorbance).

The polarized Raman microspectroscopic measurements strongly support the key features emerged from the modeling analyses, which include the stacking of the cyclic molecules along the tube direction and the sharing of intercycle (intratube) and intertube hydrogen bonds. On the one hand, the basic model in Figure 2c reveals indeed two types of hydrogen bonds. The first, formed between one C=O and one N–H, is only intercycle hydrogen bond, which would correspond to the 1634 cm^{-1} band observed only along the tube (Figure 3a). The second involves two C=O and two N–H groups, thus forming four hydrogen bonds (each O atom interacts with two H atoms and vice versa). These are both intercycle and intertube hydrogen bonds, which should be observed in the two directions (along and perpendicular to the tube). On the other hand, the model implies different conformations of the peptide molecules in the tubes and in the crystal, which affects the way they establish and use the hydrogen bonds for self-assembly. This also is qualitatively supported by the microspectroscopic analyses. The Raman spectra recorded with the crystal obtained from solution show the main amide I band shifted to 1680 cm^{-1}, with three other bands at 1669, 1643 and 1630 cm^{-1}. We also used infrared microspectroscopy to confirm the differences between the microtubes and the crystal. Their infrared spectra in the 1500–3500 cm^{-1} region are shown in Figure 3b. For the spectrum of tubes, the incident beam of about 100 μm was directed to an

 © 2004 Wiley-VCH Verlag GmbH & Co. KGaA, Weinheim

area containing several tubes laid randomly on the surface of a CaF_2 window. The major differences can be seen from the hydrogen-bonded N–H stretching bands around the 3200–3300 cm^{-1} region. For the crystal two bands appear at 3358 and 3319 cm^{-1}, while for the tubes they are shifted by about 100 cm^{-1}, to 3266 and 3218 cm^{-1}, respectively. Similar spectral changes can be noticed for the two C=O bands, which shift from 1656 and 1637 cm^{-1} for the crystal, to 1637 and 1614 cm^{-1}, respectively, for the tubes. These results indicate that the tubes formed in the LC have different structures. As a matter of fact, in addition to the hexagonal form and opened structure, the tubes melt at about 203 °C, while no melting could be observed for the crystal before thermal decomposition at about 212 °C.

The formation of micrometer-sized hexagonal hollow tubes, an amplification of the hexagonal conformation of the molecule, is a spectacular manifestation of the effect of the medium on the way the peptide molecules use hydrogen bonding to self-assemble. The modeling and spectroscopic characterization results discussed above show that this is a case of both conformational and packing polymorphism. With respect to the dense crystal structure obtained from solution, the hexagonal hollow structure certainly is not the thermodynamically most stable organization, but is kinetically the most favorable outcome of a slow aggregation process occurred in the nematic LC. As mentioned above, the filling of the LC fluid inside the cavity and the interaction of the LC molecules with the peptide at the interface may stabilize the building of these large hollow tubes. More studies of self-assembly of cyclic peptide in liquid crystals are under way in our laboratories.

Experimental Section

Cooling of the peptide/LC mixture from the isotropic phase was controlled by using the hot stage of a microscope. A Leitz DMR-P polarizing optical microscope was used to examine the tubes in the LC and also after removal of the LC in hexane. The tubes remained on the surface of the substrate were studied by using a Hitachi S-4700 FEG scanning electron microscope as well as Raman and infrared microspectroscopy. Raman spectra of the tubes were recorded on a Jobin Yvon HR800 microspectrophotometer by using the 633 nm excitation from a He–Ne laser. The laser beam, passing through a 100× objective, was positioned on the tube, and the backscattering (360°) was collected. The beam intensity on the tube was about 6.4 mW. The four polarized spectra in Figure 3a were obtained by changing the polarizations of the laser and the analyzer without rotating the tube. The spectral recording was made on several places of the tube, and the results were very much reproducible. The infrared spectra were obtained by using a Nicolet Nic Plan microscope (15×) coupled with a Magna-760 spectrometer.

More computer modeling details, including the Cartesian and mol2 type coordinates of various structures, as well as optical microscopic observations of the tubes are reported in the Supporting Information.

Received: June 30, 2003 [Z52259]

Keywords: liquid crystals · nanostructures · nanotubes · peptides · self-assembly

[1] M. R. Ghadiri, J. R. Granja, R. A. Milligan, D. E. McRee, N. Khazanovich, *Nature* **1993**, *366*, 324.
[2] D. T. Bong, T. D. Clark, J. R. Granja, M. R. Ghadiri, *Angew. Chem.* **2001**, *113*, 1016; *Angew. Chem. Int. Ed.* **2001**, *40*, 988; .
[3] D. Ranganathan, C. Lakshimi, I. L. Karle, *J. Am. Chem. Soc.* **1999**, *121*, 6103.
[4] D. Gauthier, P. Baillargeon, M. Drouin, Y. Dory, *Angew. Chem.* **2001**, *113*, 4771; *Angew. Chem. Int. Ed.* **2001**, *40*, 4635.
[5] M. R. Ghadiri, J. R. Granja, L. K. Buehler, *Nature* **1994**, *369*, 301.
[6] G. M. Whitesides, J. P. Mathias, C. T. Seto, *Science* **1991**, *254*, 1312.
[7] a) P. Terech, R. G. Weiss, *Chem. Rev.* **1997**, *97*, 3133; b) C. Geiger, M. Stanescu, L. Chen, D. G. Whitten, *Langmuir* **1999**, *15*, 2241.
[8] a) L. Guan, Y. Zhao, *Chem. Mater.* **2000**, *12*, 3667; b) L. Guan, Y. Zhao, *J. Mater. Chem.* **2001**, *11*, 1339.
[9] P. Meakin, *Adv. Colloid Interface Sci.* **1988**, *28*, 250.
[10] H. Okamoto, T. Nakanishi, Y. Nagai, M. Kasahara, K. Takeda, *J. Am. Chem. Soc.* **2003**, *125*, 2756.
[11] N. Bowden, I. S. Choi, B. A. Grzybowski, G. M. Whitesides, *J. Am. Chem. Soc.* **1999**, *121*, 5373.
[12] T. D. Clark, L. K. Buehler, M. R. Ghadiri, *J. Am. Chem. Soc.* **1998**, *120*, 651.
[13] M. Tsuboi, Y. Kubo, T. Ikeda, S. A. Overman, O. Osman, G. J. Thomas, Jr., *Biochemistry* **2003**, *42*, 940.
[14] M. Tsuboi, F. Kaneuchi, T. Ikeda, K. Akahane, *Can. J. Chem.* **1991**, *69*, 1752.
[15] H.-M. Liem, P. Etchegoin, K. S. Whitehead, D. C. Bradley, *Adv. Mater.* **2003**, *13*, 66.

 © 2004 Wiley-VCH Verlag GmbH & Co. KGaA, Weinheim

Kinetic Resolution

Palladium-Catalyzed Oxidative Kinetic Resolution with Ambient Air as the Stoichiometric Oxidation Gas**

*Jeffrey T. Bagdanoff and Brian M. Stoltz**

As part of a general program aimed toward developing enantioselective oxidation reactions in the presence of catalytic palladium, we recently reported the oxidative kinetic

[*] J. T. Bagdanoff, Prof. B. M. Stoltz
The Arnold and Mabel Beckman Laboratories of Chemical Synthesis
Division of Chemistry and Chemical Engineering
California Institute of Technology
1200 E. California Blvd., MC 164-30, Pasadena CA 91125 (USA)
Fax: (+1) 626-564-9297
E-mail: stoltz@caltech.edu

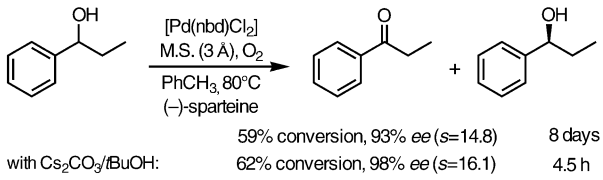
[**] The authors thank the NIH-NIGMS (R01 GM65961-01), the University of California TRDRP (predoctoral fellowship to JTB), the Dreyfus Foundation, Merck Research Laboratories, Research Corporation, Abbott Laboratories, Eli Lilly, GlaxoSmithKline, Johnson and Johnson, Pfizer, and the A. P. Sloan Foundation for generous financial support.

Supporting information for this article is available on the WWW under http://www.angewandte.org or from the author.

 DOI: 10.1002/anie.200352444 © 2004 Wiley-VCH Verlag GmbH & Co. KGaA, Weinheim

resolution of secondary alcohols.[1–3] Our system employed a simple protocol involving a commercially available palladium complex, sparteine, and molecular oxygen. Although our original conditions promoted effective resolutions, several issues restricted the practicality of the method, namely long reaction times and high operating temperatures in flammable mixtures of organic solvents and oxygen. Herein we report a new palladium-catalyzed oxidative kinetic resolution that employs nonflammable solvents, proceeds with excellent levels of enantioselectivity, and for the first time uses ambient air as the stoichiometric oxidation gas.[4]

In the course of our studies, it was determined that the addition of an inorganic exogenous base such as Cs_2CO_3 could accelerate the asymmetric oxidation of secondary alcohols.[1b] Further investigations into the effect of additives on the resolution revealed that the presence of the spectator alcohol *t*BuOH further enhanced reaction rates. The combined effect of these independent additives greatly enhanced the overall reaction rate of the oxidative kinetic resolution of secondary alcohols while preserving the selectivity of the process (Scheme 1).[5,6]

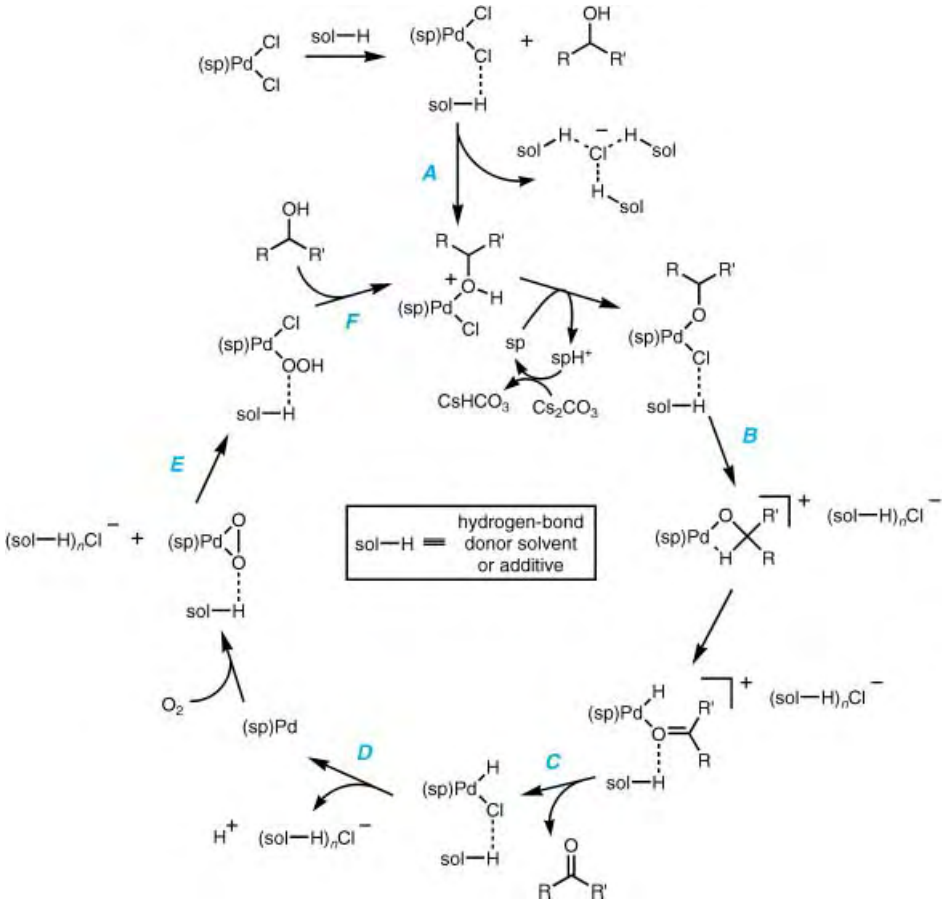


Scheme 1. Cs_2CO_3/*t*BuOH-modified oxidative kinetic resolution.

While the purpose of the carbonate base fit well with our initial mechanistic model for resolution, the effect of *t*BuOH was more subtle. We hypothesized that the exogenous alcohol was affecting reaction rates by forming hydrogen bonds to a number of plausible intermediates along the reaction pathway and/or by aiding in the solvation of halide anions. A number of possibilities are outlined in Scheme 2 and include: A) hydrogen bonding to, or solvation of one chlorine substituent of the [Pd(sparteine)Cl_2] complex to activate the compound toward alcoholysis, B) subsequently aiding in the solvation of another chloride to open a coordination site needed for the β-hydride elimination event, C) assisting in the product exchange, D) facilitating conversion of an [L_nPd(H)Cl] species into a palladium(0) species, E) aiding in the proposed opening of a peroxopalladium species to the corresponding hydroperoxide, and F) participating in the turnover exchange of the palladium hydroperoxide to the bound alcohol complex.[5]

With these hypotheses in mind, we initiated a solvent screen to explore the effect of hydrogen-bond-donating solvents as well as solvents capable of effective chloride anion solvation. Importantly, as part of our screen, we examined solvents that have the capacity to do both, that is, less traditional H-bond-donating halohydrocarbon solvents such as $CHCl_3$ (Table 1). For simplicity, enantiopure (*R*)-(+)-1-phenylethanol was used as the substrate.

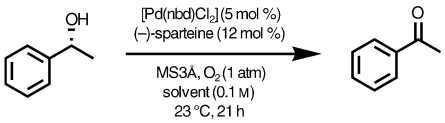
The nonflammable solvent chloroform quickly emerged as a superior solvent for the reaction, supporting rapid reaction rates even at room temperature (Table 1, entry 1).[7] Dichloromethane is also an effective solvent (Table 1, entry 3); however, when applied to the resolution, inferior selectivities are observed. Comparison of the trihalomethanes (Table 1, entries 1 and 2) and dihalomethanes (Table 1, entries 3 and 4) reveals a tendency for more electron-deficient, thus better hydrogen-bonding, halocarbons to accelerate conversion. Furthermore, when CCl_4 is substituted for a protic member of the halogenated hydrocarbon series, conversion is severely impacted (Table 1, entry 6). In accord with our mechanistic hypothesis (Scheme 2), this trend suggests the importance of weak but potential hydrogen-



Scheme 2. Plausible mechanism involving H-bonding species.

 © 2004 Wiley-VCH Verlag GmbH & Co. KGaA, Weinheim

Table 1: Screen with various solvents.



Entry	Solvent	Conversion [%]
1	$CHCl_3$	74
2	$CHBr_3$	68
3	CH_2Cl_2	83
4	CH_2Br_2	73
5	$ClCH_2CH_2Cl$	46
6	CCl_4	2
7	$PhCH_3$	23
8	$PhCH_3$/1 equiv *t*BuOH	39
9	THF	14
10	CH_3CN	3
11	2-propanol	7
12	$PhCH_3$/*t*BuOH (1:1)	29
13	*tert*-amyl alcohol	21
14	H_2O/2-propanol	0
15	pinacolone	21

bond donors as a parameter for efficient resolution.[8a] Having identified chloroform as the most effective solvent for kinetic resolution, we determined that additional *t*BuOH no longer imparted any benefit to the reaction. We reconciled this observation by reasoning that the H-bond-donating solvents may have supplanted the donating effect of the *t*BuOH additive. The carbonate base, however, still enhanced the reaction rate.[8b]

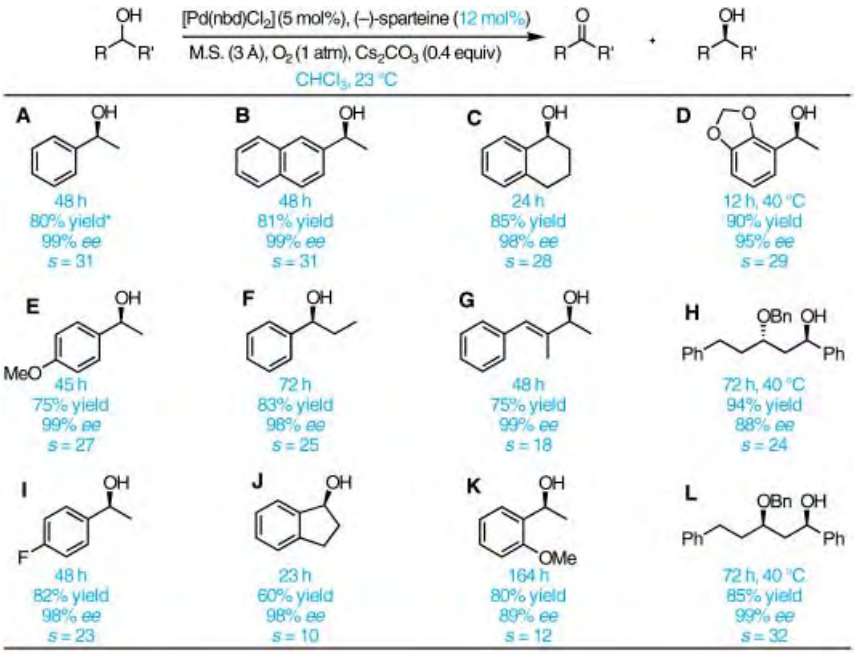
After observing such a dramatic impact on conversion rates and disparate additive effects by simply changing the solvent from toluene to chloroform, it became clear that all other parameters would require reinvestigation. A study of the loading of the sparteine ligand revealed that 12 mol% of sparteine was an optimal concentration for the reaction, in contrast to the 20 mol% previously reported in both toluene and dichloroethane.[1,2] A decrease in the excess sparteine represents a further improvement to the system by conserving our source of chirality in the catalytic system. Evaluation of Cs_2CO_3 stoichiometry revealed that no further benefit to conversion rate was observed beyond 40 mol%.

With the essential parameters optimized, we explored the generality of our modified catalyst system (Scheme 3). Importantly, all previously reported alcohol substrates[1,2] were resolved to high enantiomeric excess when subjected to the new conditions. These resolutions were performed at mild operating temperatures (usually room temperature) and the selectivities for the process also increased, often by a factor of 2.[9]

Particularly striking is the enhancement in selectivity of the non-benzylic alcohol **G**. Previously, this substrate proved to be difficult to resolve to high *ee* values, displaying a low selectivity in the oxidative kinetic resolution process ($s = 6.6$). Under our conditions in chloroform, the resolution proceeds at room temperature to provide the resolved alcohol in 99.0% *ee* with a selectivity factor of 18. The allylic alcohol depicted in **G** may be readily converted into more useful functionality and represents a facile method for the highly enantioselective resolution of less activated secondary alcohols.

Encouraged by the success of our modified reaction conditions and curious to test whether the solvent could influence the post-resolution portion of the proposed mechanism (Scheme 2, C–F), we attempted to resolve secondary alcohols in the presence of the most abundant and inexpensive stoichiometric oxidant conceivable: ambient air.[10] By simply performing the experiments in a reaction vessel equipped with a drying tube open to the air, effective oxidations proceeded to resolve secondary alcohols to high *ee* values, and with high associated selectivity factors (Table 2). Curiously, the time required to conduct the highly selective resolutions was often significantly lower. The subtleties of this effect are currently under investigation.[11]

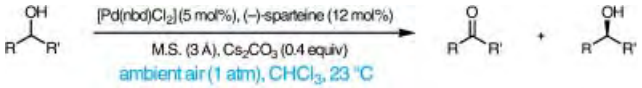
Prompted by concerns over the reproducibility of our results under variable atmospheric concentrations of molecular oxygen, we sought to ascertain the lower limit required for effective resolution. After preparing mixed volumes of nitrogen and oxygen, we found that robust oxidation was consistently supported by as little as 5% O_2. In experiments conducted on enantiopure (*R*)-(+)-1-phenylethanol, it was observed that variable oxygen concentrations in the range of 5–100% had little impact on the conversion (Table 3). For this reason, it is expected that local environmental variability in

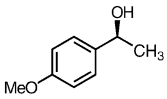
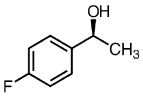
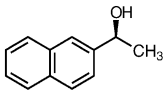
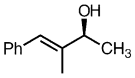
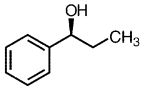


Scheme 3. Modified oxidative kinetic resolution in chloroform. [*] Yields are based on a theoretical maximum of 50%. The total yield was greater than 95% in all cases.

 © 2004 Wiley-VCH Verlag GmbH & Co. KGaA, Weinheim

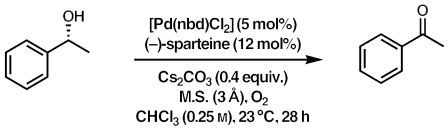
Table 2: Resolutions conducted under ambient air.



Entry	Unreacted alcohol, major enantiomer	Black = O_2, Blue = air t [h]	Conv. [%][a]	*ee* (ROH) [%]	*s*
1		48	62.6	99.9	27.1
		24	62.3	99.8	25.4
2		48	59.3	98.0	23.0
		24	56.7	93.0	19.5
3		48	59.3	99.6	31.1
		24	55.5	98.0	37.3
4		24	57.5	98.0	27.6
		16	60.2	99.6	28.0
5		48	62.6	98.7	17.9
		44	64.7	98.9	15.7
6		72	62.6	98.2	24.4
		48	56.8	94.9	21.7

[a] Conversion was measured by GC on a DB-wax column (see Supporting Information for details)

Table 3: Effect of the concentration of oxygen on the oxidation of secondary alcohols.



Entry	O_2/N_2 [vol %]	Conv. [%]
1	100	75.4
2	25	77.5
3	20	80.3
4	15	76.4
5	10	78.9
6	5	76.9
7	2.5	54.3
8	0	5.3

ambient oxygen concentration will not adversely affect the oxidative kinetic resolution under these conditions.[12] That no decrease in reaction efficiency is observed down to 5% oxygen underscores the power of molecular oxygen to reoxidize palladium(0).

In conclusion, by investigating the role of solvents capable of H-bond donation and chloride ion solvation, we have discovered the most mild and selective conditions for the oxidative kinetic resolution of secondary alcohols by catalytic palladium to date. The features of this catalyst system suggest some interesting mechanistic variations involving H-bonded intermediates: specifically, the activation of the [Pd(sparteine)Cl_2] salt toward attack by an alcohol, and activation of intermediates along the reoxidation pathway. The practical implications of this system include room temperature reactivity in nonflammable solvents and a significant increase in the resolution selectivity. This improvement brings previously poorly resolving, yet synthetically important substrates, namely allylic alcohols, into the synthetically useful range. Furthermore, we have demonstrated the first efficient palladium-catalyzed oxidative kinetic resolution process employing ambient air as the stoichiometric oxidant. Efforts to extend these results to other types of asymmetric dehydrogenation reactions are currently ongoing.[13]

Received: July 22, 2003 [Z52444]

Keywords: asymmetric catalysis · hydrogen bonds · oxidation · oxygen · palladium · solvent effects

[1] a) E. M. Ferreira, B. M. Stoltz, *J. Am. Chem. Soc.* **2001**, *123*, 7725; b) J. T. Bagdanoff, E. M. Ferreira, B. M. Stoltz, *Org. Lett.* **2003**, *5*, 835.

[2] Simultaneous to our publication of reference [1a], a related system was reported: D. R. Jensen, J. S. Pugsley, M. S. Sigman, *J. Am. Chem. Soc.* **2001**, *123*, 7475.

[3] The kinetic resolutions in references [1] and [2] were based on a non-asymmetric oxidation of alcohols employing $Pd(OAc)_2$, pyridine, and O_2: T. Nishimura, K. Ohe, S. Uemura, *J. Org. Chem.* **1999**, *64*, 6750.

[4] For examples of related enzymatic oxidative kinetic resolutions, see: a) K. Faber, *Biotransformations in Organic Chemistry*, 3rd ed., Springer, Berlin, **1997**, pp. 201–205; b) I. J. Jackovac, H. B. Goodbrand, K. P. Lok, J. B. Jones, *J. Am. Chem. Soc.* **1982**, *104*, 4659–4665.

[5] Recently, mechanistic details of related non-asymmetric systems were studied: a) B. A. Steinhoff, S. S. Stahl, *Org. Lett.* **2002**, *4*, 4179; b) B. A. Steinhoff, S. S. Stahl, *J. Am. Chem. Soc.* **2002**, *124*, 766; c) S. S. Stahl, J. L. Thorman, R. C. Nelson, M. A. Kozee, *J. Am. Chem. Soc.* **2001**, *123*, 7188.

[6] For discussions on kinetic resolution, see: a) V. S. Martin, S. S. Woodard, T. Katsuki, Y. Yamada, M. Ikeda, K. B. Sharpless, *J. Am. Chem. Soc.* **1981**, *103*, 6237; b) C.-S. Chen, Y. Fujimoto, G. Girdaukas, C. J. Sih, *J. Am. Chem. Soc.* **1982**, *104*, 7294; c) H. B. Kagan, J. C. Fiaud in *Topics in Stereochemistry*, *Vol. 18* (Ed.: E. L. Eliel), Wiley, New York, **1988**, pp. 249–330.

[7] a) The solubility of O_2 is not a likely factor in disparate reactivities, particularly between toluene and chloroform, in which O_2 is equally soluble. For relevant tables, see: F. Fischer, G. Pfleiderer, *Z. Anorg. Allg. Chem.* **1922**, *124*, 61; b) No correlation between solvent dielectric constant (an estimate of polarity) and conversion is apparent; for relevant tables, see: E. W. Flick in *Industrial Solvents Handbook*, 3rd ed. (Ed.: E. W. Flick), Noyes Data Corp., New Jersey, **1985**, pp. 637–647.

[8] a) No dichlorocarbene was detected under the reaction conditions; b) Exposure of [Pd(sparteine)Cl_2] to Cs_2CO_3 in $CHCl_3$ leads to the production of an interesting [Pd(sparteine)CO_3] complex (see Supporting Information for the solid-state structure). This complex is inactive as a catalyst for kinetic resolution under a variety of conditions.

[9] The selectivity factor (*s*) was determined from the equation: $s = k_{rel}(\text{fast/slow}) = \ln[(1-C)(1-ee)]/\ln[(1-C)(1+ee)]$ (C = conversion).

[10] For an example of a non-asymmetric oxidation of alcohols catalyzed by palladium in the presence of air as the stoichiometric oxidant, see: K. Hallman, C. Moberg, *Adv. Synth. Catal.* **2001**, *343*, 260.

 © 2004 Wiley-VCH Verlag GmbH & Co. KGaA, Weinheim

[11] Spectroscopic grade chloroform (Aldrich) or chloroform stabilized by amylenes was used without further purification. While a drying tube was employed in the reaction setup, no marked effect was observed when wet air was used. Addition of trace amounts of concentrated HCl during the resolution had little effect. Additionally, freshly distilled $CHCl_3$ (washed with H_2O, dried over $CaCl_2$, and distillation from $CaCl_2$) gives identical results. Chloroform stabilized by EtOH must be distilled prior to use.

[12] Oxygen-uptake experiments confirm a 2:1 stoichiometry for substrate/O_2, indicating that $CHCl_3$ is not involved as an oxidant.

[13] We recently reported a number of palladium-catalyzed oxidative hetero- and carbocyclization reactions with molecular oxygen: a) R. M. Trend, Y. K. Ramtohul, E. M. Ferreira, B. M. Stoltz, *Angew. Chem.* **2003**, *115*, 2998 – 3001; *Angew. Chem. Int. Ed.* **2003**, *42*, 2892 – 2895; b) E. M. Ferreira, B. M. Stoltz, *J. Am. Chem. Soc.* **2003**, *125*, 9578 – 9579.

 © 2004 Wiley-VCH Verlag GmbH & Co. KGaA, Weinheim

Surface Chemistry

Reversible Switching between Superhydrophilicity and Superhydrophobicity**

Taolei Sun, Guojie Wang, Lin Feng, Biqian Liu, Yongmei Ma, Lei Jiang, and Daoben Zhu*

Wettability is a very important property that is governed by both chemical composition and surface structure.[1–9] Recently, the control of surface wettability has aroused great interest because of its wide variety of applications. In general, superhydrophobic surfaces[1–6] with a water contact angle (CA) greater than 150° can be obtained by controlling the topography of hydrophobic surfaces, while superhydrophilic surfaces with a CA about 0° can be realized through a 3D[7–8] or 2D capillary effect[9] on hydrophilic surfaces. Stimuli-responsive surfaces[10] make it possible to reversibly control the wettability of the surface and has been demonstrated by various methods, including light-irradiation,[11, 12] use of an electric field,[13, 14] thermal treatment[15] and treatment with solvent.[16] However, reversible switching between superhydrophilicity and superhydrophobicity has never been reported. Herein we show the roughness-enhanced thermally responsive wettability of a poly(*N*-isopropylacrylamide) (PNIPAAm)-modified surface.[17, 18] Reversible switching between superhydrophilicity and superhydrophobicity can be achieved in a narrow temperature range of about 10 °C, which is considered to result from the combined effect of the chemical variation of the surface, and surface roughness. Such switchable surfaces may have wide applications in functional textiles, intelligent microfluidic switching, controllable drug release, and thermally responsive filters.

Surface-initiated atom-transfer radical polymerization[19, 20] was used to fabricate thermally responsive PNIPAAm thin films[21–24] on both a flat and a rough silicon substrate. Results from atomic force microscopy (AFM) and scanning electron microscopy (SEM) showed that the thickness of the PNIPAAm thin film could be well controlled by the polymerization time. Figure 1 a (left) shows a typical SEM image of a rough substrate that has been modified with a PNIPAAm thin film. Compared with the smooth surface (Figure 1 a right) of the flat substrate, the rough substrate exhibits a regular array of square silicon microconvexes (bright squares). The dark lines are microgrooves that are about 6 μm in width and about 5 μm in depth. These microgrooves were generated by a laser cutter (see Experimental Section) on a silicon wafer in a region of about 1 × 1 cm^2. The surface roughness can be adjusted by controlling the spacing between the grooves. In our experiments, different groove spacings of about 31 μm, 18 μm, 8 μm, and 6 μm were selected. The magnified image of the rough surface shows that both microconvexes and microgrooves were also rather rough (Figure 1 b). Further magnified SEM images of the silicon microconvexes before (Figure 1 c) and after (Figure 1 d) PNIPAAm polymerization show that these

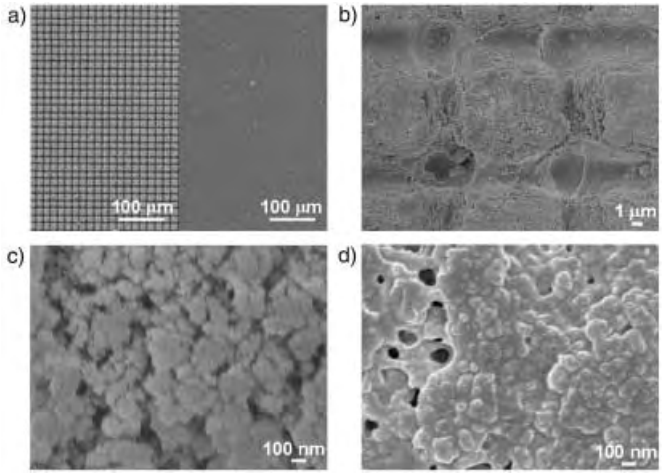


Figure 1. Typical SEM images of a rough substrate with groove spacing of about 8 μm. For all substrates, the width and depth of microgrooves were controlled to about 6 μm and about 5 μm, respectively. The spacing between microgrooves could be varied, thus adjusting the surface roughness of the substrates. Four groove spacings of about 31 μm, 18 μm, 8 μm and 6 μm were selected. a) SEM image for the regular array of silicon microconvexes with PNIPAAm modification (left), compared with that of flat substrate (right). b) Magnified image of the microconvex array in the right of (a). c) Nanostructures on a single microconvex without PNIPAAm modification. d) Nanostructures on a single microconvex with PNIPAAm modification.

[*] Dr. T. Sun, Prof. Dr. G. Wang, Dr. L. Feng, Prof. Dr. B. Liu, Prof. Dr. Y. Ma, Prof. Dr. L. Jiang, Prof. Dr. D. Zhu
Center of Molecular Sciences, Institute of Chemistry, The Chinese Academy of Sciences, Beijing 100080 (P. R. China)
Fax: (+86) 10-8262-7566
E-mail: Jianglei@iccas.ac.cn

[**] This work was supported by the State Key Project for Fundamental Research (G1999064504) and the Special Research Foundation of the National Nature Science Foundation of China (20374054 and 90306011) for continuing financial support.

Supporting information for this article is available on the WWW under http://www.angewandte.org or from the author.

 DOI: 10.1002/anie.200352565 © 2004 Wiley-VCH Verlag GmbH & Co. KGaA, Weinheim

surfaces are composed of many irregular nanoparticles and pores. The nanoparticles were sputtered from adjacent microgrooves and the pores were formed by the aggregation of nanoparticles. Although the nanoporous structure of the surface was partially filled by PNIPAAm polymerization, the micro- and nanostructures of the substrates remained after polymerization.

For the flat substrate, PNIPAAm thin film exhibited thermally responsive switching between hydrophilicity and hydrophobicity. When the temperature changed from 25 °C to 40 °C, the water CA increased from 63.5 ± 2.6° to 93.2 ± 2° (Figure 2a). This effect is explained by the competition

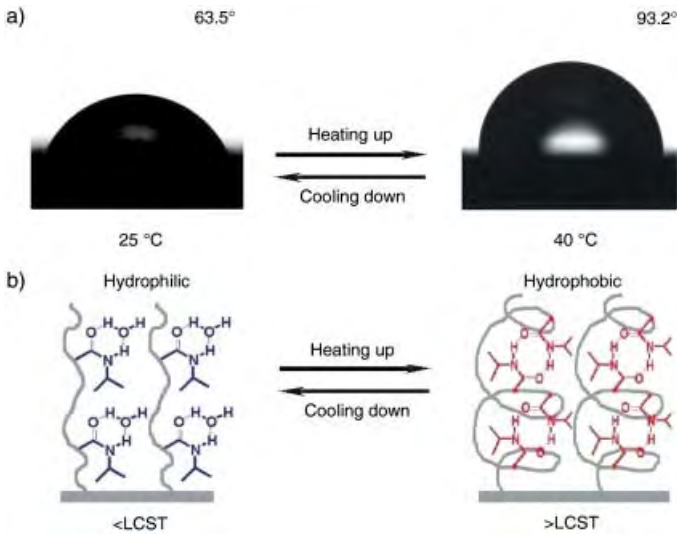


Figure 2. Thermally responsive wettability for a flat PNIPAAm-modified surface. a) Change of water drop profile when temperature was elevated from 25 °C (left) to 40 °C (right) with water CAs of 63.5 ± 2.6° and 93.2 ± 2°, respectively. b) Diagram of reversible formation of intermolecular hydrogen bonding between PNIPAAm chains and water molecules (left) and intramolecular hydrogen bonding between C=O and N-H groups in PNIPAAm chains (right) below and above the LCST, which is considered to be the molecular mechanism of the thermally responsive wettability of a PNIPAAm thin film.

between intermolecular and intramolecular hydrogen bonding below and above the lower critical solution temperature (LCST) of about 32–33 °C (Figure 2b).[25] At temperatures below the LCST, the predominantly intermolecular hydrogen bonding between the PNIPAAm chains and water molecules contributes to the hydrophilicity of PNIPAAm film. At temperatures above the LCST, intramolecular hydrogen bonding between C=O and N−H groups in the PNIPAAm chains results in a compact and collapsed conformation of PNIPAAm chains, which makes it difficult for the hydrophilic C=O and N−H groups to interact with water molecules. Thus, the film exhibits hydrophobicity at high temperatures.

As for the rough substrates with PNIPAAm modification, temperature-dependent experiments indicated that the thermally responsive wettability was greatly enhanced by surface roughness. This is in contrast to the substrates without PNIPAAm grafting, all of which showed superhydrophilicity, with a water CA of about 0°, and were temperature independent. Figure 3a show the relationships between the water CA and the groove spacing, D, at 25 °C and 40 °C for the PNIPAAm-modified substrates. The water CA at 25 °C

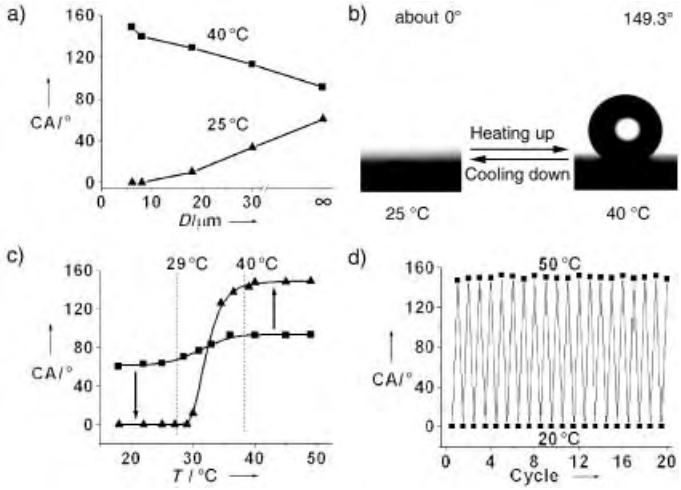


Figure 3. Surface-roughness-enhanced wettability of a PNIPAAm-modified surface. a) The relationships between groove spacing (D) of rough surfaces and the water CAs at low temperature (triangles, 25 °C) and at high temperature (squares, 40 °C). The groove spacing of ∞ represents flat substrate. b) Water drop profile for thermally responsive switching between superhydrophilicity and superhydrophobicity of a PNIPAAm-modified rough surface with groove spacing of about 6 μm, at 25 °C and 40 °C. The water CAs are about 0° and 149.3 ± 2.5°, respectively. c) Temperature (T) dependences of water CAs for PNIPAAm thin films on a rough substrate with groove spacing of about 6 μm (triangles) and on flat substrate (squares). d) Water CA in at two different temperatures for a PNIPAAm-modified rough substrate with groove spacing of 6 μm. Half cycles: 20 °C; and integral cycles: 50 °C.

decreased from 63.5 ± 2.6° for a flat substrate (as denoted by groove spacing of ∞) to 33.5 ± 1.4° (D = 31 μm), 10 ± 0.6° (18 μm), ≈0° (8 and 6 μm). At 40 °C, the water CAs increased from 93.2 ± 2° (flat substrate) to 112.9 ± 2.6° (D = 31 μm), 128.9 ± 1.4° (18 μm), 137.9 ± 2° (8 μm), and 149.3 ± 2.5° (6 μm). These results indicate that thermally responsive switching between superhydrophilicity and superhydropobicity can be realized when the groove spacing of the substrate is small (ca. 6 μm), in other words, when the substrate is sufficiently rough. Figure 3b shows photographs of water drop profile at 25 °C and 40 °C, respectively. The temperature dependences of water CA for the $D \approx 6$ μm rough substrate and the flat substrate was studied in detail and shown in Figure 3c. The superhydrophobic/superhydrophilic switching temperature for flat and rough substrates were almost identical and lay around the LCST, thus indicating that the chemical property of the PNIPAAm thin film did not change with the variation of substrate structure. For the rough substrate, the surface exhibited a water CA of about 0° below 29 °C, whereas it was about 150° above 40 °C, thus indicating a thermally responsive switching between superhydrophilicity and superhydropobicity. We repeatedly cycled the temperature from 20 to 50 °C and recorded the variation of the water CA. The measurements of water CA at high and low

 © 2004 Wiley-VCH Verlag GmbH & Co. KGaA, Weinheim

temperatures were conducted on two sample stages, one set at 50 °C, the other at 20 °C. The results show excellent reversibility for more than 20 cycles (Figure 3d) and a quick transformation between superhydrophilicity and superhydrophobicity as a single cycle lasts only several minutes. This reversibility remained after the samples had been laid aside without special protection for at least three months, which shows that the polymer film is stable. These results suggest that the thermally responsive switching between superhydrophilicity and superhydrophobicity is related to the combination of surface chemical composition and surface roughness. The former provides the thermally responsive chemical change of the surface between hydrophilicity and hydrophobicity, and the latter enhances these properties. Hydrophilicity at low temperatures is increased by surface roughness,[26] which also traps air when it comes into contact with water,[2–4,27] and enhances the hydrophobicity at high temperatures.

At low temperatures, the loosely coiled conformation of PNIPAAm chains and intermolecular hydrogen bonding with water molecules leads to high surface free energy and a small water CA. The film is hydrophilic and water enters the microgrooves beneath the water drop.[7,16] In this situation, surface roughness becomes the dominant factor intensifying the hydrophilicity. The microgroove structure, and the nanostructures on the microconvexes and microgrooves contributes to surface roughness, therefore the increasing hydrophilicity with the decrease of groove spacing can be explained by Wenzel's equation,[26] which describes the amplification effect of surface roughness on wettability. If the water CA on a flat surface is smaller than a critical CA on the rough surface, the imbibition of water will occur on the rough surface as a result of the 3D capillary effect.[7] The critical CA increases with an increase in surface roughness. For the substrates with a groove spacing of about 6 μm, the critical CA is in the range of 71–75° as calculated from surface roughness obtained by AFM measurements. The water CAs for flat PNIPAAm film below 29 °C are all close to or smaller than 71°. According to this study, the surface can exhibit superhydrophilicity below 29 °C (see Supporting Information). At higher temperatures, the compact and collapsed conformation of PNIPAAm chains induced by intramolecular hydrogen bonding between C=O and N–H groups in PNIPAAm chains leads to low surface free energy and large water CAs. The film is hydrophobic and the rough surface traps air. It was reported that the hydrophobicity of a rough surface can be intensified by increasing the air/water interface,[2–4,27] for example, superhydrophobic surfaces with water CAs larger than 170° have been obtained with aligned-nanotube[3] and -nanofiber[4] structures. For the rough surfaces in this study, only the upper part of the microconvexes can make contact with water molecules and thus the size of the air/water interface is controlled by the groove spacing. Therefore water CAs at high temperatures increase with a decrease in groove spacing. The nanostructures on the surfaces of microgrooves and microconvexes also contribute to the increase in the air/water interface and thus further enhance the hydrophobicity of PNIPAAm thin films on rough substrates at high temperatures.

In conclusion, the combination of the change in surface chemistry and surface roughness can enhance stimuli-responsive wettability. Reversible switching between superhydrophilicity and superhydrophobicity, which is a challenging thesis in surface chemistry, can be intelligently controlled through external stimuli. This method can be extended to other stimuli-responsive surfaces. This ability to control the wettability by changing the temperature has applications in a broad range of fields. For example, thermally responsive textiles, controllable drug release,[28] temperature-controlled microfluidic switches,[29] and thermally responsive filters for oil/water separation (see also Supporting Information).

Experimental Section

Synthesis of PNIPAAm thin films on silicon substrates: A clean silicon substrate was immersed in an aqueous NaOH solution (0.1M) for 2 minutes and subsequently in HNO_3 (0.1M) for 10 minutes to generate surface hydroxyl groups. After the substrate had been washed with an excess of water and dried under a flow of nitrogen, it was heated to reflux in toluene that contained 5 wt% aminopropyl trimethoxysilane (ATMS) for at least 6 h to obtain chemically bonded $-NH_2$ groups on the surface. The surface was rinsed with toluene and dichloromethane to remove remaining ATMS, dried under a flow of nitrogen gas, and immersed in dry dichloromethane that contained pyridine (2% w/v). The polymerization initiator bromoisobutyryl bromide was added dropwise into the solvent containing the silicon substrate at 0 °C, and the mixture was left for 1 hour at this temperature then at room temperature for 12 h. The silicon substrate was cleaned with acetone and toluene, and dried under a nitrogen flow. Polymerization of PNIPAAm was achieved by immersing the silicon substrate with the initiator grafted on the surface in a degassed solution of *N*-isopropylacrylamide (25% w/v) in a 1:1 (v/v) mixture of H_2O and MeOH (5 mL) containing CuBr (0.032 g, 0.23 mmol) and pentamethyl diethylene triamine (PMDETA; 0.14 mL) for 100 minutes for all substrates. Under these conditions, the film thickness was about 44.8 ± 4.2 nm.

Laser cutter: The laser cutter used to generate microgrooves on silicon wafer was QuikLaze II (New Wave Research, USA). The wavelength and repetition rate of the laser pulse were 532 nm and 20 Hz, respectively. By adjusting the size of the rectangular laser spot and the intensity of the laser pulse, the width and depth of the microgrooves for rough silicon substrates could be controlled.

SEM and water CA measurements: A field-emission SEM (JSM-6700F, Japan) was used to obtain SEM images of the substrates. Water CAs were measured with a OCA20 machine (DataPhysics, Germany) at saturated humidity. The temperature was controlled by a superthermostat (Julabo F25, Germany).

Received: August 4, 2003
Revised: November 11, 2003 [Z52565]
Published Online: December 19, 2003

Keywords: electron microscopy · hydrophobic effect · nanostructures · polymers · surface chemistry

[1] a) T. Onda, S. Shibuichi, N. Satoh, K. Tsujii, *Langmuir* **1996**, *12*, 2125–2127; b) S. Shibuichi, T. Onda, N. Satoh, K. Tsujii, *J. Phys. Chem.* **1996**, *100*, 19512–19517.

[2] a) W. Chen, A. Y. Fadeev, M. C. Hsieh, D. Öner, J. Youngblood, T. J. McCarthy, *Langmuir* **1999**, *15*, 3395–3399; b) T. J. McCarthy, D. Öner, *Langmuir* **2000**, *16*, 7777–7782; c) J. P. Youngblood, T. J. McCarthy, *Macromolecules* **1999**, *32*, 6800–6806.

 © 2004 Wiley-VCH Verlag GmbH & Co. KGaA, Weinheim

[3] H. Li, X. Wang, Y. Song, Y. Liu, Q. Li, L. Jiang, D. Zhu, *Angew. Chem.* **2001**, *113*, 1793 – 1796; *Angew. Chem. Int. Ed.* **2001**, *40*, 1743 – 1746.
[4] a) L. Feng, S. Li, H. Li, J. Zhai, Y. Song, L. Jiang, D. Zhu, *Angew. Chem.* **2002**, *114*, 1269 – 1271; *Angew. Chem. Int. Ed.* **2002**, *41*, 1221 – 1223; b) L. Feng, Y. Song, J. Zhai, B. Liu, J. Xu, L. Jiang, D. Zhu, *Angew. Chem.* **2003**, *115*, 824 – 826; *Angew. Chem. Int. Ed.* **2003**, *42*, 800 – 802.
[5] L. Feng, S. Li, Y. Li, H. Li, L. Zhang, J. Zhai, Y. Song, B. Liu, L. Jiang, D. Zhu, *Adv. Mater.* **2002**, *14*, 1857 – 1860.
[6] H. Y. Erbil, A. L. Demirel, Y. Avci, O. Mert, *Science* **1977**, *299*, 1377 – 1380.
[7] a) J. Bico, C. Tordeux, D. Quéré, *Europhys. Lett.* **2001**, *55*, 214 – 220; b) J. Bico, U. Thiele, D. Quéré, *Colloids Surf. A* **2002**, *206*, 41 – 46.
[8] S. Herminghaus, *Europhys. Lett.* **2000**, 52, 165 – 170.
[9] R. Wang, K. Hashimoto, A. Fujishima, M. Chikuni, E. Kojima, A. Kitamura, M. Shimohigoshi, T. Watanabe, *Nature* **1997**, *388*, 431 – 432.
[10] T. P. Russell, *Science* **2002**, *297*, 964 – 967.
[11] K. Ichimura, S. Oh, M. Nakagawa, *Science* **2002**, *298*, 1624 – 1626.
[12] C. Feng, Y. J. Zhang, J. Jin, Y. L. Song, L. Y. Xie, G. R. Qu, L. Jiang, D. B. Zhu, *Langmuir* **2001**, *17*, 4593 – 4597.
[13] M. W. J. Prins, W. J. J. Welters, J. W. Weekamp, *Science* **2001**, *291*, 277 – 280.
[14] J. Lahann, S. Mitragotri, T. Tran, H. Kaido, J. Sundaram, I. S. Choi, S. Hoffer, G. A. Somorjai, R. Langer, *Science* **2003**, *299*, 371 – 374.
[15] D. Crevoisier, P. Fabre, J. Corpart, L. Leibler, *Science*, **1999**, *285*, 1246 – 1249.
[16] S. Minko, M. Müller, M. Motornov, M. Nitschke, K. Grundke, M. Stamm, *J. Am. Chem. Soc.* **2003**, *125*, 3896 – 3900.
[17] H. G. Schild, *Prog. Polym. Sci.* **1992**, *17*, 163 – 249.
[18] Z. Hu, Y. Chen, C. Wang, Y. Zheng, Y. Li, *Nature* **1998**, *393*, 149 – 152.
[19] X. Kong, T. Kawai, J. Abe, T. Iyoda, *Macromolecules* **2001**, *34*, 1837 – 1844.
[20] D. M. Jones, W. T. S. Huck, *Adv. Mater.* **2001**, *13*, 1256 – 1259.
[21] Y. G. Takei, T. Aoki, K. Sanui, N. Ogata, Y. Sakurai, T. Okano, *Macromolecules* **1994**, *27*, 6163 – 6166.
[22] a) L. Liang, P. C. Rieke, G. E. Fryxell, J. Liu, M. H. Engelhard, K. L. Alford, *J. Phys. Chem. B* **2000**, *104*, 11667 – 11673; b) L. Liang, P. C. Rieke, J. Liu, G. E. Fryxell, J. S. Young, M. H. Engelhard, K. L. Alford, *Langmuir* **2000**, *16*, 8016 – 8023.
[23] T. Yakushiji, K. Sakai, *Langmuir* **1998**, *14*, 4657 – 4662.
[24] D. M. Jones, J. R. Smith, W. T. S. Huck, C. Alexander, *Adv. Mater.* **2002**, *14*, 1130 – 1134.
[25] S. Lin, K. Chen, R. Liang, *Polymer* **1999**, *40*, 2619 – 2624.
[26] R. N. Wenzel, *Ind. Eng. Chem.* **1936**, *28*, 988 – 994.
[27] A. B. D. Cassie, S. Baxter, *Trans. Faraday Soc.* **1944**, *40*, 546 – 561.
[28] J. R. Robinson, V. H. L. Lee, *Controlled Drug Delivery: Fundamentals and Applications*, 2nd ed., Marcel Dekker, New York, **1987.**
[29] D. J. Beebe, J. S. Moore, Q. Yu, R. H. Liu, M. L. Kraft, B.-H. Jo, C. Devadoss, *Proc. Natl. Acad. Sci. USA* **2000**, *97*, 13488 – 13493.

 © 2004 Wiley-VCH Verlag GmbH & Co. KGaA, Weinheim

Polymer Microcapsules

Photoinduced Vectorial Charge Transfer across Walls of Hollow Microcapsules**

*Lidong Li and Helmuth Möhwald**

In photosynthesis, light is harvested by chromophores and transferred to reaction centers where a photoinduced charge separation and an electron transfer across a membrane of 5-nm thickness is effected. The electrical energy that is created is then converted into chemical energy, that is, products stored on both sides of the membrane.[1] There have been many attempts to mimic this process as photonic energy or information conversion devices.[2] However, to become technically attractive the system must also be sufficiently simple and easy to build up.

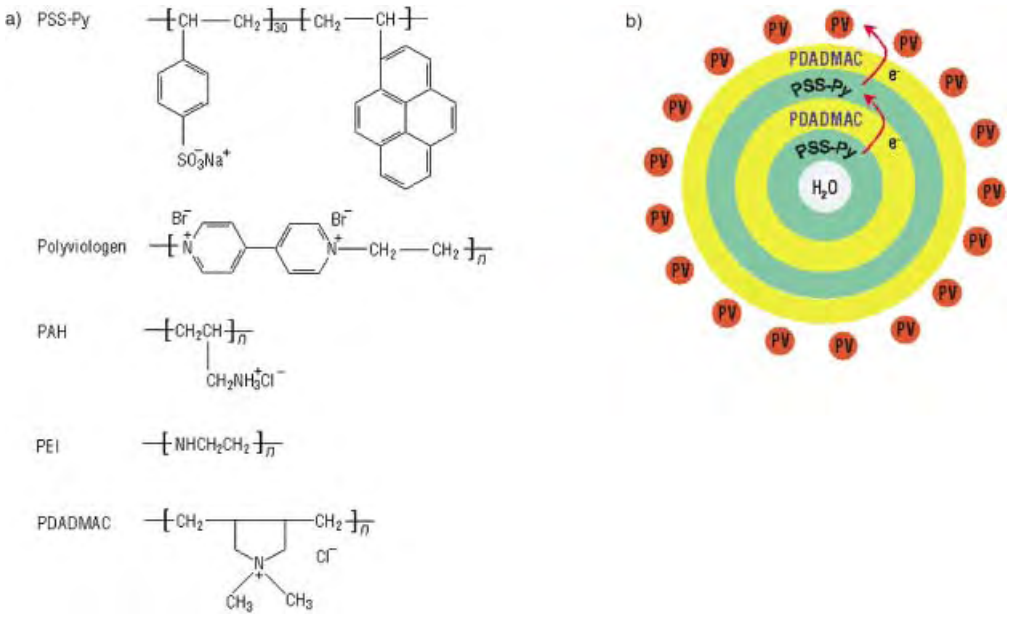
From the viewpoint of system design the electron-transfer chain is most demanding since it requires control of intermolecular distances with nanometer precision. Therefore this work intends to prepare a vectorial electron-transfer chain across a membrane that may later be coupled to a chemical-energy conversion and storage device. The membrane is built up by consecutive adsorption of alternatively charged polyelectrolytes. It exhibits a defined thickness, in most of the samples here of about 10 nm. The membrane represents the shell of a hollow capsule that has been prepared by adsorbing polyelectrolyte multilayers (PEMs) on a colloid that could later be destroyed.[3] We chose this highly versatile system since its constituent compounds and colloidal cores can determine the capsule size, and can also reversibly include macromolecules within the cores. Using appropriate polyelectrolytes, one can also build films with a polarity gradient over nanometer dimensions to direct charge transfer.[4]

We used pyrene as a chromophore in the films because of its well-known photophysical/chemical properties. Many donors and acceptors are known to enable very efficient electron transfer to and from pyrene because of its long excited-state lifetime.[5] We previously reported the synthesis of pyrene with the anionic polyelectrolyte polystyrenesulfonic acid (PSS) in a reasonably high concentration.[6] This should provide the possibility of sufficiently high chromophore density to enable electron transfer between different pyrene units, and indeed adding an oligomeric electron acceptor (polyviologen) allows the fluorescence quenching of pyrene to be observed, even for molecules inside the film. Scheme 1a shows the structures of the polyelectrolytes used in the experiments. Scheme 1b shows the model for electron trans-

[*] L. Li, Prof. H. Möhwald
Max Planck Institute of Colloids and Interfaces
14476 Golm/Potsdam (Germany)
Fax: (+49) 331-567-9202
E-mail: moehwald@mpikg-golm.mpg.de

[**] This work was supported by the Max Planck Society and the Deutsche Forschungsgemeinschaft through SFB 448. L.L. thanks Dr. C. Tedeschi for introducing us to this project. Many thanks to Dr. D. Kurth for supplying the polyviologen.

 © 2004 Wiley-VCH Verlag GmbH & Co. KGaA, Weinheim DOI: 10.1002/anie.200352657



Scheme 1. a) Polymers used to build up the film and electron acceptor in the internal aqueous phase; b) electron transfer between components in the hollow capsule wall. The dimensions are not to scale as the capsule diameter is 1.96 μm and the wall thickness is 6 nm (12 nm in case of the experiment with a polarity gradient).

fer employed in this system. The previous results of pyrene quenching by polyviologen were interpreted as electron transfer, but there remain many unresolved issues:

- The electron acceptor used, polyviologen (PV), did not have a high molecular weight and a broad size distribution. This raises doubts whether a lower-molecular-weight fraction penetrates the film, thus quenching the nearby pyrene emission.
- From the concentration of pyrene in the film, one calculates an average chromophore distance of 2.7 nm.[6] This is rather large for electron transfer.
- Up to now information was basically derived from fluorescence quenching, but the remaining pyrene cation could not be detected. Also, no PV ionic species could be detected in transient absorption spectroscopy, probably due to a short lifetime.

Taking these issues into account, the purpose of this paper is to confirm the previous conclusions and to provide more information on the mechanism. The influence of the local environment is assessed by varying the type of polyelectrolyte and film surface, as well as the chromophore density and film architecture. Having established the mechanism we finally demonstrate the existence of vectorial electron transfer.

Figure 1 shows the emission spectra for pyrene after the addition of PV for a solution of hollow capsules containing PSS-Py in the walls, where the outer surface is either negatively (Figure 1a) or positively charged (Figure 1b). The vibrational structure of the monomer, as well as the shoulder near 480 nm due to the excimer, can be clearly observed. The latter is indicative of a rather high pyrene content because excimer formation is not expected as a result of molecular diffusion, rather only due to dye proximity within the polymer matrix. Both monomer and excimer emission are quenched by PV, and the corresponding intensity change is given in the insets of Figure 1 as a function of PV concentration. In both cases one observes complete quenching, but the amount of PV necessary for this varies by a

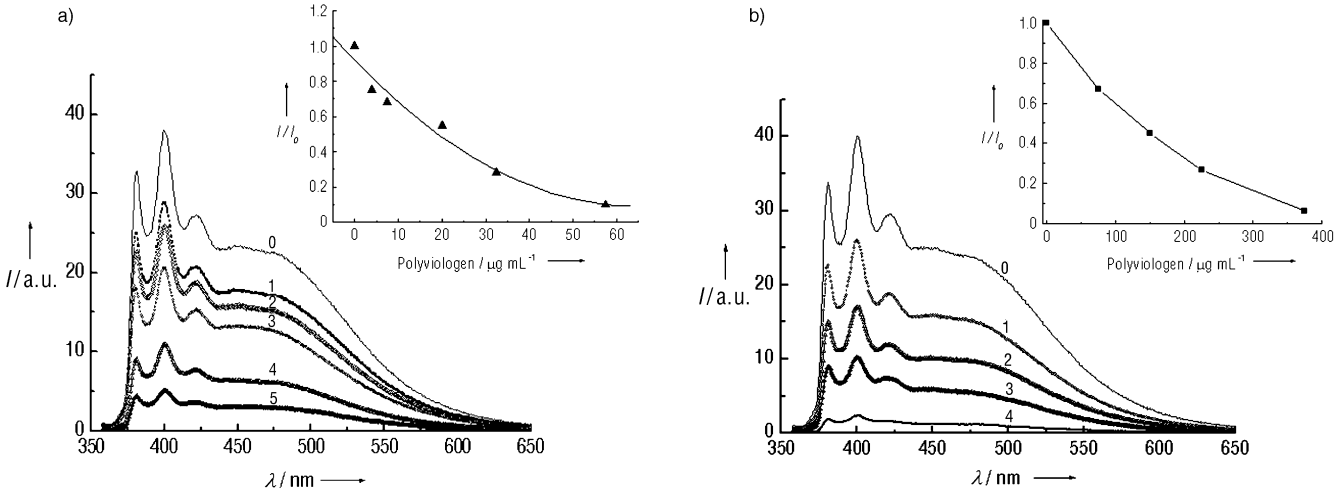


Figure 1. a) Fluorescence spectra of 2-mL hollow capsules (1.96 μm) in water. The shells are composed of $(PSS\text{-}Py/PDADMAC)_3$/PSS-Py. PV concentration: 1) 3.96, 2) 7.5, 3) 20, 4) 32.5, 5) 57.5 μg mL^{-1}; b) Fluorescence spectra of 2-mL hollow capsules (1.96 μm) in water. The shells are composed of $(PSS\text{-}Py/PDADMAC)_3$. PV concentration: 1) 75, 2) 150, 3) , 4) 375 μg mL^{-1}.

 © 2004 Wiley-VCH Verlag GmbH & Co. KGaA, Weinheim

factor of five. This can be qualitatively understood by assuming a PV adsorption equilibrium between the film surface and the bulk. For positively charged PV this equilibrium is shifted towards the bulk if the surface is also positively charged, thus requiring a higher PV concentration for quenching. In the alternate case of PV diffusion into the film, the net surface charge would be less relevant, as previously shown for diffusing low-molecular-weight dyes.[7] We also changed the cationic polymer used for film build-up from poly(diallyldimethylammonium chloride) (PDADMAC) to poly(allylamine hydrochloride) (PAH) and poly(ethylenimine) (PEI). However, the PV concentrations necessary for quenching were very similar, again indicating that the effect is not due to PV in the interior of the film but to PV on the surface. Another strong argument against PV penetrating into the film has been presented by preparing a multilayer architecture with PSS-Py in two double layers interlaced by a pyrene-free double layer. In this case only the outer PSS-Py layer can be quenched.

Having convincingly shown that PV does not penetrate the film the question remains about how the charge transfers to PV after excitation of an arbitrary pyrene unit in the film. There may be energy transfer to a pyrene unit near the surface followed by electron transfer, or electron transfer from the excited molecule. For energy transfer one may envisage two different mechanisms:

Transfer according to a dipolar mechanism (Förster transfer[8]) is highly improbable for this system since it depends on the overlap integral between pyrene absorption and emission spectra; this is essentially zero. In addition the oscillator strength for the longest wavelength absorption is very low.

Transfer according to the Dexter mechanism[9] cannot a priori be ruled out. This mechanism relies on the overlap integral of the wave functions of the excited states and should consequently be of short range. However, it also depends on the overlap of the pyrene absorption and emission spectra, which is very small. Although quantum chemical calculations are not available, the intermolecular distance of 2.7 nm is probably too large for this process to compete with radiative emission with a lifetime of about 100 ns.

The argument against Dexter transfer may also hold against electron transfer because this process also depends on the overlap of wave functions, in this case of anions. However, the relevant time is the lifetime of the pyrene anion, which is much longer in the rather polar PEM. That the transfer mechanism is due to short range interactions of chromophores and that the pyrene density can not be greatly reduced without losing electron-transfer capability can be deduced from the experiment whose results are shown in Figure 2. Here, the build-up of layers was achieved using a mixture of PSS-Py and PSS in varying ratios for the middle of three bilayers and measuring the quenching at saturating PV concentration. The fluorescence intensity as a function of PV concentration (Figure 2a) can be grouped into two types of curves. They either decay towards zero intensity (for high pyrene content) or they decay only to about half the initial intensity. This is displayed more quantitatively in Figure 2b, where the intensity at high PV concentration is plotted versus PSS-Py/PSS-Py + PSS ratio in the middle layer. The two regimes are thus divided more clearly. In films with only one type of polycation, for a PSS-Py content below 70% the transfer chain is interrupted, for higher pyrene content it operates equally well. This means that a pyrene labeling of PSS below 2% would not have been tolerable, and also that the average inter-chromophore distance could not be increased by more than 10%, that is, not above 3 nm. With respect to this dilution experiment, all systems with other polycations are very similar. However, if one prepares a film with a polarity gradient the threshold where the chain is interrupted can be shifted by about 15%. Figure 2b also contains the data for such a film that has been designed to exhibit the highest polarity at the exterior, as previously measured with pyrene probes.[4] Apparently for concentra-

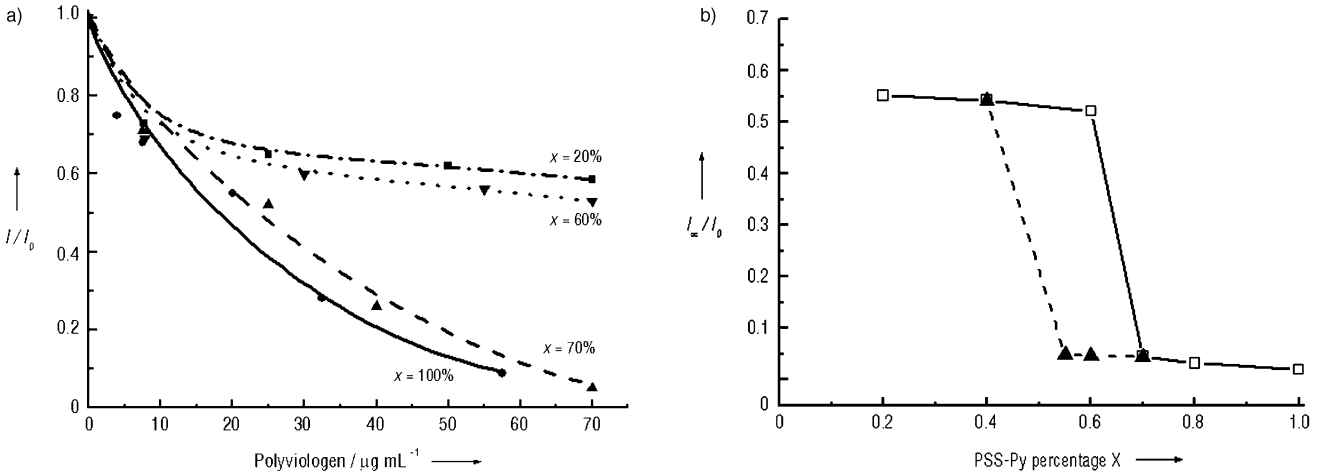
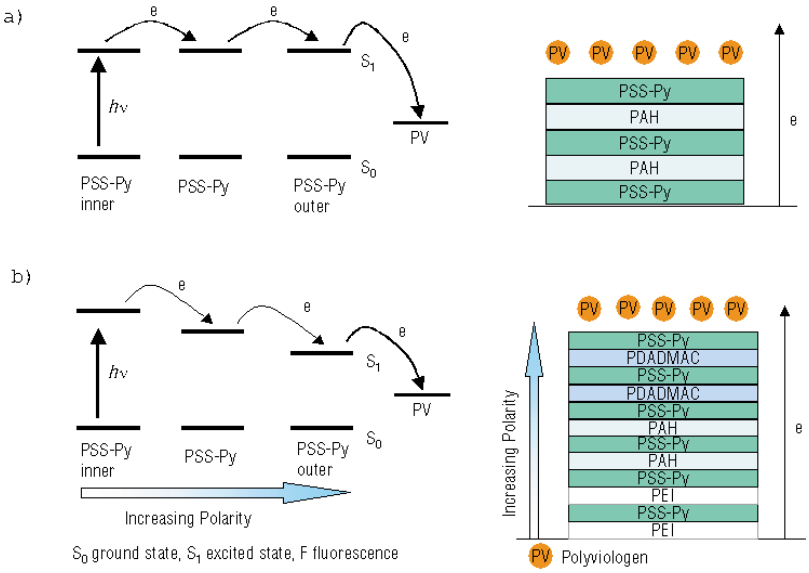


Figure 2. a) Fluorescence intensity as a function of PV concentration for a multilayer with dilution of the pyrene concentration in the middle layer PSS-Py/PDADMAC/$(PSS\text{-}Py)_x$ $(PSS)_{1-x}$/PDADMAC/PSS-Py; b) fluorescence intensity I_∞ measured at high PV concentration as a function of pyrene content x for hollow capsules in water for the system described in a) (full line). The dotted line shows the measurement with a polarity gradient for a film architecture: $(PSS\text{-}Py/PEI)_2$ $[(PSS\text{-}Py)_x$ $(PSS)_{1-x}/PAH)]_2$ $(PSS\text{-}Py/PDADMAC)_2$.

 © 2004 Wiley-VCH Verlag GmbH & Co. KGaA, Weinheim

tions near the threshold ($x \sim 0.6$) the polarity gradient is needed to direct the electron transfer. This is another strong argument in favor of electron transfer versus Dexter transfer.

In conclusion, we have shown the existence of photoinduced vectorial electron transfer from the film to the surface and argued that it is most probably due to electron transfer within the film (Scheme 2). There still remains an unresolved issue concerning the large hopping distance of approximately 3 nm. One possible explanation for this may be a superexchange mechanism, which has been discussed for similar cases involving DNA.[10] In our system the conjugated bonds of polystyrene may be involved, and we plan reference experiments with PEM without conjugation. We could also show that for a suitable composition, electron transfer between identical molecules can be directed by creating a polarity gradient. Hence we have performed experiments on a system that is not defined at the nanometer level but is very versatile and thus provides a means not only for applications but also for further understanding of these interesting mechanisms.



Scheme 2. Left: Energy level scheme for electron transfer in the absence (a) and presence (b) of a polarity gradient. It has been shown[4] by measuring the vibronic structure of pyrene emission that the local polarity is highest for PSS/PDADMAC and lowest for PSS/PEI. However, the numbers cannot unequivocally be converted into a dielectric constant, and therefore we give energy levels only qualititatively; right: architecture corresponding to the energy-level schemes.

Experimental Section

Dispersions of monodisperse weakly cross-linked melamine formaldehyde (MF) particles with a diameter of 1.96 μm were purchased from Microparticles GmbH (Berlin). Poly(diallyldimethylammonium chloride) (PDADMAC, $M_w = 200000$–350000) was purchased from Aldrich Chemical Co. Pyrene-labeled poly(styrenesulfonic acid) (PSS-PY) was synthesized according to the procedure of Tanikawa et al.[11] Polyviologen (PV) was synthesized according to the literature procedure.[12] Solutions of PDADMAC(1 mg mL^{-1}), PEI (1 mg mL^{-1}), PAH (1 mg mL^{-1}), and PSS-Py (5 mg mL^{-1}) in water with NaCl (0.5 M) were prepared in all experiments.

Layer-by-layer self-assembly on colloid particles: Polycation (PDADMAC) and polyanion (PSS-Py) were assembled onto the surface of MF by layer-by-layer adsorption.[3] Excess polyelectrolytes were removed by three repeated centrifugation (3000 rpm, 5 min)/washing/redispersion cycles in each deposition step. After obtaining the desired layers, hollow capsules could be obtained by dissolving the MF core in HCl (0.1 M). The final capsule concentration was 5×10^7 mL^{-1}.

Absorption spectra were measured by a Varian Cary 4E UV-visible spectrophotometer. Steady-state fluorescence spectra were recorded at room temperature using a Spex Fluorolog-2 (model FL-2T2) spectrofluorometer (ISA, Olching, Germany). Some experiments were performed under nitrogen, however, there was no noticeable variation with those experiments carried out in air.

Received: August 15, 2003 [Z52657]

Keywords: electron transfer · fluorescence · microcapsules · nanostructures · pyrene

[1] a) F. Deisenhofer, O. Epp, R. H. Miki, H. Michel, *Nature* **1985**, *318*, 618–624; b) G. J. Kavamos, N. J. Turro, *Chem. Rev.* **1986**, *86*, 401–449; c) D. Gust, T. A. Moore, A. L. Moore, S. J. Lee, E. Bittersman, D. K. Jutrull, A. A. Rehms, J. M. Degraziano, X. C. Ma, F. Gao, R. E. Belford, T. T. Trier, *Science* **1990**, *248*, 199–201.

[2] a) M. R. Wasielewski, *Chem. Rev.* **1992**, *92*, 435–461; b) J. Fan, D. H. Gafney, *J. Phys. Chem.* **1994**, *98*, 13058–13063; c) A. Slama-Schwok, M. Ottolenghi, D. Avnir, *Nature* **1992**, 355, 240–242.

[3] G. Decher, *Science* **1997**, *277*, 1232–1237; b) G. Decher, J. D. Hong, *Macromol. Chem. Macromol. Symp.* **1991**, 46, 321–327; c) E. Donath, G. Sukhorukov, F. Caruso, S. Davis, H. Möhwald, *Angew. Chem.* **1998**, *110*, 2324–2327; *Angew. Chem. Int. Ed.* **1998**, *37*, 2201–2205.

[4] C. Tedeschi, H. Möhwald, S. Kirstein, *J. Am. Chem. Soc.* **2001**, *123*, 954–960.

[5] a) P. K. C. Pillai, M. Goel, *Electrochim. Acta* **1972**, *17*, 1839–1847; b) A, Nakajima, *Bull. Chem. Soc. Jpn.* **1971**, *44*, 3272–3277; c) D. C. Dong, M. A. Winnik, *Photochem. Photobiol.* **1982**, *35*, 17–21; d) A. Tsuchida, Y. Tsujii, M. Ohoka, M. Yamamoto, *J. Phys. Chem.* **1991**, *95*, 5797–5802; e) M. S. Matos, M. H. Gehlen, *Spectrochim. Acta Part A* **1998**, *54*, 1857–1867.

[6] L. Li, C. Tedeschi, H. Möhwald, unpublished results.

[7] R. V. Klitzing, H. Möhwald, *Macromolecules* **1996**, *29*, 6901–6906.

[8] T. Förster, *Ann. Phys.* **1948**, *2*, 55–75.

[9] D. L. Dexter, *J. Chem. Phys.* **1953**, *21*, 836–850.

[10] a) M. Bixon, J. Jortner, M. E. Michel-Beyerle, *Chem. Phys.* **1995**, *197*, 389–404; b) J. Jortner, M. Bixon, T. Langenbacher, M. E. Michel-Beyerle, *Proc. Natl. Acad. Sci. USA* **1998**, *95*, 12759–12765; c) B. Giese, J. Amaudrut, A. K. Koher, M. Spermann, S. Wessely, *Nature* **2001**, *412*, 318–320; d) M. Bixon, J. Jortner, *J. Phys. Chem. B* **2000**, *104*, 3906–3913.

[11] a) K, Tanikawa, T, Ishizuka, K. Suzuki, S. Kusabayashi, H, Mikausa, *Bull. Chem. Soc. Jpn.* **1968**, *41*, 2719–2722; b) R. D. Stramel, C. Nguyen, S. E. Webber, M. A. Rodgers, *J. Phys. Chem. B* **1998**, *102*, 2934–2938.

[12] L. Liang, F. Liu, S. Zhu, Z. Zhou, B. He, *Polym. Adv. Technol.* **1994**, *10*, 60–64.

 © 2004 Wiley-VCH Verlag GmbH & Co. KGaA, Weinheim

Diffusion in Zeolites

Accelerated Diffusion of Long-Chain Alkanes between Nanosized Cavities**

Hervé Jobic, Alain Méthivier, Georg Ehlers, Bela Farago, and Wolfgang Haeussler*

Normally, the mobility of molecules decreases with increasing molecular weight. This is true in liquids and also in porous media, where the transport properties of the liquid have a major influence in various applications such as catalysis and separation. In nanoporous materials, the notion of liquid phase is not applicable, since each adsorbed molecule interacts with the solid. The molecules are geometrically constrained, either by their size or by their orientation. This is the basis of shape-selective catalysis with zeolites. For example, cracking of heavy alkanes in small-pore zeolites such as erionite gives unusual product distributions, with maxima at approximately C_4 and C_{12} and a clear minimum at C_8.[1] This was one of the first examples of what has been termed "product molecular shape selectivity". Gorring studied experimentally the diffusion of several *n*-alkanes in zeolite T (an offretite/erionite intergrowth), in which the less open erionite cages act as bottlenecks for diffusion.[2] He found that molecules in the C_{12} range diffused about two orders of magnitude faster than those in the C_8 range. He proposed that the product distribution in the cracking reaction was due to this anomalous transport phenomenon.[2] The term "window effect" was coined to designate the higher transmittance of the erionite cages for molecules of a given critical length.[2] However, since no other group could find such a periodic variation in diffusivity (e.g., ref. [3]), the existence of the window effect is one of the most controversial topics in zeolite science.

Zeolites are ideal models for microporous materials, because the dimensions of the cages and pores of these crystalline structures are known with accuracy. In NaX zeolite, the framework consists of cages connected by windows with a nominal diameter of 7.4 Å. For a homologous series of *n*-paraffins, a monotonous decrease in the diffusion coefficient with increasing molecular weight was found by pulsed-field gradient NMR (PFG NMR) spectroscopy (Figure 1a). A similar trend was found by quasielastic neutron scattering (QENS) in ZSM-5, the structure of which consists of intersecting channels with a free diameter of about 5.5 Å (Figure 1b). In NaCaA zeolite, the cavities are interconnected by windows with a nominal diameter of 4.1 Å, based on an radius of 1.35 Å for oxygen. The effective radius of oxygen is in fact close to 1 Å, so that the free diameter of the windows is not far from 5 Å, hence the product name zeolite 5A. Zeolite 5A is used in numerous adsorption processes because, like erionite, it adsorbs linear alkanes while rejecting branched ones. Due to the narrow pores, the diffusivities of *n*-alkanes in this structure are too low to be measured by conventional QENS instruments, but they are accessible by the neutron spin echo (NSE) technique.

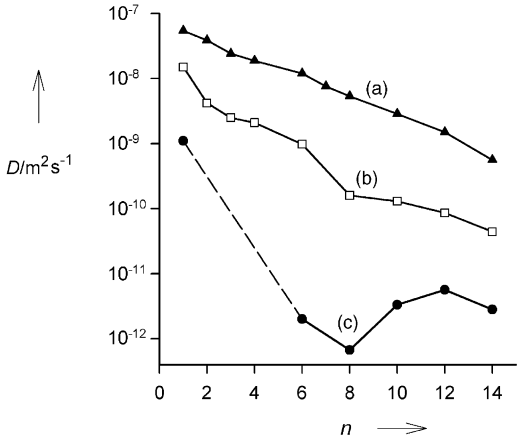


Figure 1. Diffusion coefficients of linear alkanes in various zeolites, obtained by different techniques at 475 K, as a function of the mumber of carbon atoms. a) In NaX zeolite by PFG NMR spectroscopy,[9] b) in ZSM-5 by QENS,[10] and c) in zeolite 5A by NSE. Diffusivities for methane and *n*-hexane are taken from references [11] and [6], respectively. The values from the literature were extrapolated to 475 K by using the reported activation energies. The solid and dashed lines are only guides for the eye.

The NSE technique is unique in the sense that one can measure very small velocity changes for neutrons scattered from the sample (on the order of 10^{-5}). The original idea is based on the determination of the Larmor precession angle of the neutron spin in a strong magnetic field of varying intensity.[4] Small energy changes lead to a decreased polarization, or amplitude, of the echo. The echos are measured for different field integrals, corresponding to varying Fourier times. A recently built NSE spectrometer at the Institut Laue-Langevin[5] is able to probe long times (hundreds of nanoseconds) and it allows the relatively slow diffusivities of long-chain *n*-alkanes in the zeolite 5A structure to be investigated. Measurements were recently performed for *n*-hexane, and good agreement was observed for the results from NSE and PFG NMR spectroscopy.[6]

A characteristic of neutron scattering is the possibility to obtain the self-diffusivity by using hydrogenated molecules,

[*] Dr. H. Jobic
Institut de Recherches sur la Catalyse
CNRS, 2 avenue A. Einstein, 69626 Villeurbanne (France)
Fax: (+33) 472-445-399
E-mail: jobic@catalyse.cnrs.fr
A. Méthivier
Institut Français du Pétrole
BP 311, 92852 Rueil-Malmaison (France)
G. Ehlers,[+] B. Farago, W. Haeussler
Institut Laue-Langevin, BP 156, 38042 Grenoble (France)
[+] Present address:
SNS, Oak Ridge, TN 37830 (USA)

[**] The neutron experiments were performed on the spectrometers IN15 and IN11 at the Institut Laue-Langevin, Grenoble, France. We thank Prof. J. Kärger (Leipzig) and Dr. S. Brandani (London) for discussions. This work is supported by a CNRS-DFG bilateral project.

 © 2004 Wiley-VCH Verlag GmbH & Co. KGaA, Weinheim DOI: 10.1002/anie.200352691

which scatter incoherently, and the transport diffusivity in the case of coherent scatterers, such as deuterated molecules.[7] In NSE, a better signal is obtained with coherent scatterers. This is because spin-polarized neutrons are used, and one wants to recover as far as possible the initial polarization. When the sample contains hydrogen, the spin-incoherent scattering modifies the polarization of the incoming beam from P to $-1/3P$, whereas a coherent scatterer leaves the polarization unchanged. This is the reason why we studied deuterated *n*-alkanes. Another advantage of the microscopic neutron-scattering technique is the possibility of deriving the transport diffusion coefficient, a quantity which is usually obtained from macroscopic measurements. This is because in coherent scattering, the intensity is related to pair correlation functions, so that one has access to density fluctuations in the adsorbed phase. The measured quantity is the normalized intermediate scattering function [Eq. (1)].

$$\frac{I(Q,t)}{I(Q,0)} = \exp(-D(Q)\,Q^2\,t) \qquad (1)$$

The values obtained at different times t are normalized to the value measured at $t=0$. Experimentally, the neutron momentum transfer Q is kept constant, and provided the length scale ($\approx 2\pi/Q$) is large enough, the collective diffusion coefficient $D(Q)$ which is derived becomes the macroscopic transport diffusivity D_t. Normalized intermediate scattering functions measured under the same experimental conditions for several *n*-alkanes at 475 K are shown in Figure 2. The data do not tend to unity at short times because of fast motion within the cages. Since a faster decay corresponds to a larger diffusion coefficient [Eq. (1)], a simple visual inspection of Figure 2 leads to the conclusion that the diffusivity increases with increasing chain length in the sequence $C_8 < C_{10} < C_{12}$. From measurements at two different Q values, and by using a jump diffusion model,[6] the diffusion coefficients of the longer *n*-alkanes could be derived (Figure 1c).

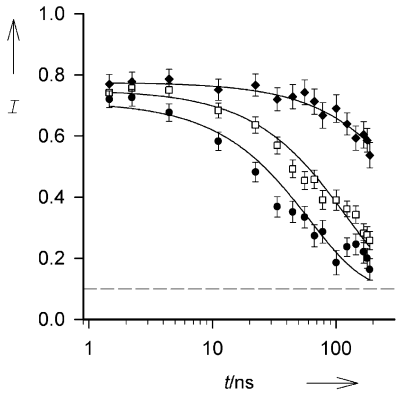


Figure 2. Comparison between experimental and calculated normalized intermediate scattering functions for some *n*-alkanes in zeolite 5A at 475 K: *n*-octane (◆), *n*-decane (□), and *n*-dodecane (●); $Q = 0.2$ Å^{-1}. The dashed line represents the elastic contribution of the zeolite. The concentration of *n*-alkane was similar for all samples in that the number of CD_x groups ($x = 2$ or 3) per cavity was the same (12). This ensures that a similar variation is obtained for the corrected diffusivities, after correcting from the thermodynamic factor, which is related to the driving force.

We find for *n*-alkanes in zeolite 5A that the diffusivity drops to a minimum at C_8, rises for C_{10}, has a maximum at C_{12}, and then decreases again for C_{14}. These experimental data are somewhat in contradiction with recent molecular simulations, which predict a maximum in zeolite 5A only for much longer chains.[8] However, several simplifications must be made in simulations on large systems, so that the computational requirements do not become prohibitive; for example, the cations and electrostatic interactions were ignored in reference [8]. Neutron spin echo measurements are planned on even longer *n*-alkanes to resolve the discrepancy between experiment and simulation.

The activation energies for diffusion were determined from measurements at different temperatures. An Arrhenius plot is shown in Figure 3. C_{12} is more mobile than C_8 by a

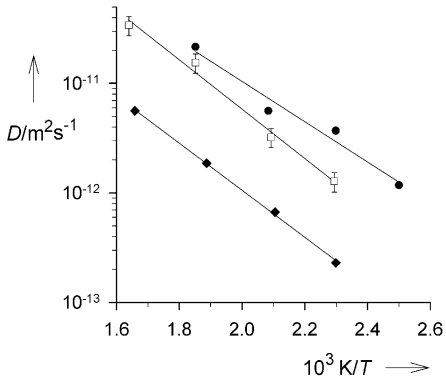


Figure 3. Temperature dependence of the diffusion coefficients determined for some *n*-alkanes in zeolite 5A: *n*-octane (◆), *n*-decane (□), and *n*-dodecane (●). Typical error bars are shown.

factor of 8.4 at 475 K, and by more than one order of magnitude at 436 K. The maximum in the diffusivities should be even more pronounced at 300 K. The finding that E_a for C_8 (41 kJ mol^{-1}) is larger than that of C_{12} (35 kJ mol^{-1}) supports the interpretation of our data in terms of the window effect. Our interpretation is shown schematically in Figure 4: a C_8 chain adopts a conformation that just fits in a cavity and sits in a deep potential well, whereas C_{12} is too long to fit comfortably in a cage and adopts a conformation in which at least one end of the molecule extends through a window. The energy barrier (largely entropic) is thus much easier to cross for the longer molecule, and this leads to a higher diffusivity and lower activation energy. For *n*-alkanes longer than C_{12}, the diffusion coefficient decreases because of the higher molecular weight. Periodicity of diffusivity may exist for even longer *n*-alkanes, with a possible second minimum in the C_{16}–C_{18} range.

This unexpected diffusion effect was not found in NaX zeolite, because the windows are too large (note that the diameters of the large cages in NaX and 5A are very similar). An increase in diffusion occurs in systems for which the sizes of the molecule and of the aperture between cavities are similar, and when the characteristic length scales of the molecule and of the cavity are comparable. In fact, anomalous

 © 2004 Wiley-VCH Verlag GmbH & Co. KGaA, Weinheim

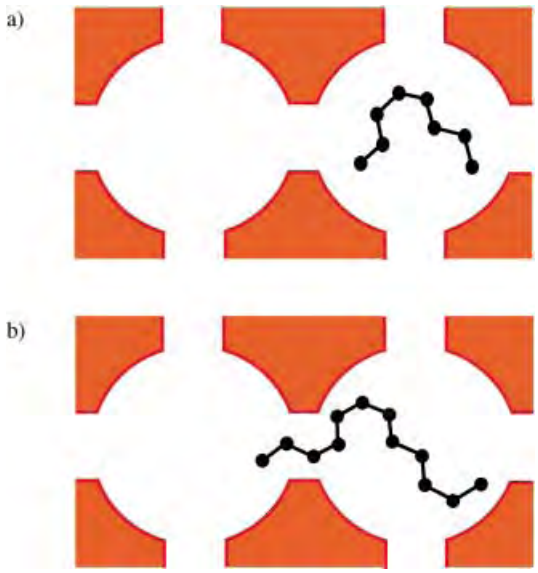


Figure 4. Schematic representation of the configuration of *n*-alkanes in zeolite 5A: *n*-octane just fits into a cavity (a), but one end of *n*-dodecane sits in a window between cages (b).

diffusion is not simply due to the size of the window, it depends both on the cage and window sizes. One could also look for a maximum in the diffusivity of branched alkanes in faujasite zeolites (X or Y), since the dimensions of the molecules and of the windows are comparable. The interplay between cages and windows may also affect the diffusion of molecules in porous materials other than zeolites, for example, in organic or inorganic membranes.

Received: August 21, 2003 [Z52691]

Keywords: alkanes · diffusion · neutron scattering · zeolites

[1] N. Y. Chen, S. J. Lucki, E. B. Mower, *J. Catal.* **1969**, *13*, 329–332.
[2] R. L. Gorring, *J. Catal.* **1973**, *31*, 13–26.
[3] C. L. Cavalcante, M. Eic, D. M. Ruthven, M. L. Occelli, *Zeolites* **1995**, *15*, 293–307.
[4] *Neutron Spin-Echo*, *Lectures Notes in Physics*, *Vol. 128* (Ed.: F. Mezei), Springer, Berlin, **1979**.
[5] P. Schleger, B. Alefeld, J. F. Barthelemy, G. Ehlers, B. Farago, P. Giraud, C. Hayes, A. Kollmar, C. Lartigue, F. Mezei, D. Richter, *Physica B* **1997**, *241*, 164–165.
[6] H. Jobic, H. Paoli, A. Méthivier, G. Ehlers, J. Kärger, C. Krause, *Microporous Mesoporous Mater.* **2003**, *59*, 113–121.
[7] H. Jobic, J. Kärger, M. Bée, *Phys. Rev. Lett.* **1999**, *82*, 4260–4263.
[8] D. Dubbeldam, S. Calero, T. L. M. Maesen, B. Smit, *Phys. Rev. Lett.* **2003**, *90*, 245901/1–245901/4, and references therein.
[9] J. Karger, H. Pfeifer, M. Rauscher, A. Walter, *J. Chem. Soc. Faraday Trans. 1* **1980**, *76*, 717–737.
[10] H. Jobic, *J. Mol. Catal. A* **2000**, *158*, 135–142.
[11] E. Cohen de Lara, R. Kahn, F. Mezei, *J. Chem. Soc. Faraday Trans. 1* **1983**, *79*, 1911–1920.

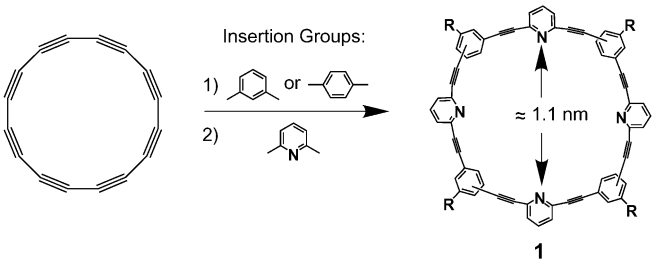
 © 2004 Wiley-VCH Verlag GmbH & Co. KGaA, Weinheim

Light-Emitting Macrocycles

Synthesis and Light-Emitting Characteristics of Doughnut-Shaped π-Electron Systems**

Yoshihiro Yamaguchi, Shigeya Kobayashi, Satoshi Miyamura, Yoshifumi Okamoto, Tateaki Wakamiya, Yoshio Matsubara, and Zen-ichi Yoshida**

Molecular electronics owes its remarkable development in utilization to organic optoelectronic materials, and in particular, to light-emitting devices.[1] To date, many types of organic light-emitting material have been designed and fabricated for this purpose, most of which have a linear molecular shape, such as poly(*p*-phenylene vinylene). In addition to their optoelectronic applications, circular-shaped light-emitting molecules[2] may also be applicable in detecting circular-shaped nanodefects on the surface of materials. These possibilities have inspired us to create the doughnut-shaped light-emitting molecule **1**,[3,4] which is constructed by the formal insertion of pyridine and benzene groups into the single bonds of cyclohexadecayne, and to examine their light-emitting characteristics.



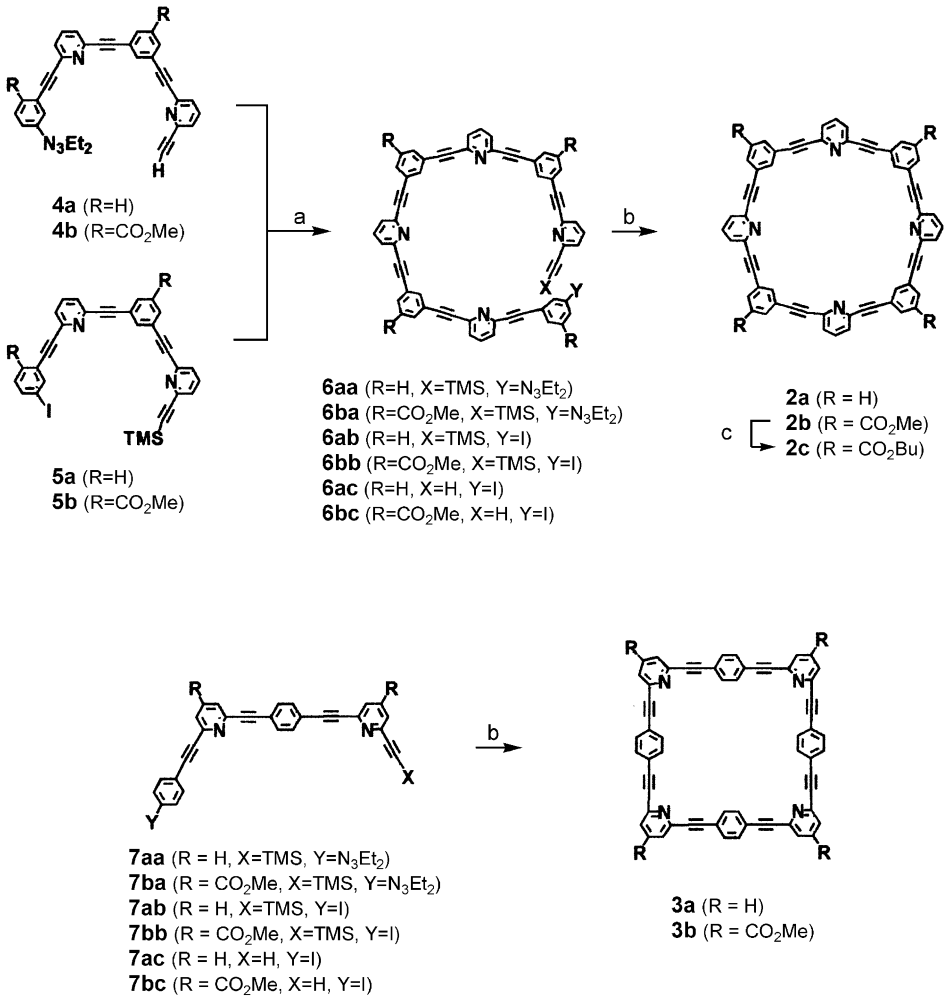
1

Compounds **2** (abbreviated as octakis-*m*-cyclynes) and **3** (abbreviated as octakis-*p*-cyclynes) were synthesized by using the Sonogashira C–C coupling reaction[5] as the key step (Scheme 1). Thus, octakis-*m*-cyclyne **2** was obtained by the intramolecular cyclization of **6ac** (or **6bc**) under high dilution conditions, while octakis-*p*-cyclynes **3** were afforded by the intermolecular cyclization of **7ac** (or **7bc**), which have *p*-phenylethynyl units.

[*] Prof. Dr. Y. Yamaguchi, Dr. S. Kobayashi, S. Miyamura, Y. Okamoto, Prof. Dr. T. Wakamiya, Prof. Dr. Y. Matsubara, Prof. Dr. Z.-i. Yoshida
Faculty of Science and Engineering
Kinki University
Higashi-Osaka, Osaka 577-8502 (Japan)
Fax: (+81) 6-6723-2721
E-mail: yamaguch@chem.kindai.ac.jp
yoshidaz@sc.sumitomo-chem.co.jp

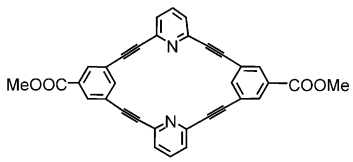
[**] We thank Professor Munakata (Kinki University) for the single-crystal X-ray analysis of Cu^{II} complex **8**. This work was supported by a Grant-in-Aid for Scientific Research (Nos. 13305062 and 14540507) from the Ministry of Education, Science, Sport, and Culture of Japan.

 © 2004 Wiley-VCH Verlag GmbH & Co. KGaA, Weinheim DOI: 10.1002/anie.200352749

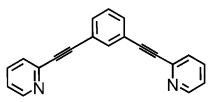


Scheme 1. Reagents and conditions: a) $[PdCl_2(Ph_3P)_2]$, CuI, Et_3N/THF (1:1), 53% (for **6aa**), 62% (for **6ba**); b) i) I_2, CH_2ClCH_2Cl, ii) KOH, MeOH, $CHCl_3$, iii) $[PdCl_2(Ph_3P)_2]$, CuI, Et_3N/THF (1:1), <5% (steps i–iii for **2a**), 35% (steps i–iii for **2b**), 11% (steps i–iii for **3a**), 5% (steps i–iii for **3b**); c) Na, BuOH, $CHCl_3$, 95% (for **2c**). TMS = trimethylsilyl.

Compounds **2** and **3** were fully characterized by ^1H and ^{13}C NMR spectroscopy and mass spectrometry (see Supporting Information). Although the ^1H and ^{13}C chemical shifts of the tetrakis-*m*-cyclynes **9** ($R = CO_2Me$)[4d] (strained system)



9



1,3-PBP

appear at lower field (^1H shift of inner-ring protons: $\delta = 8.67$–8.85 ppm; ^{13}C shift of *sp* carbon atoms: $\delta = 89$–93 ppm) than is usually the case (strain-free system), the chemical shifts of **2** were observed at the same field as those of the acyclic homologue, 1,3-di(pyridylethynyl)benzene (**1,3-PBP**). This suggests **2** to be an almost strain-free system, in accordance with AM1 calculations. The AM1 calculation also suggests that the octakis-*p*-cyclynes **3** are also strain-free. The typical absorption and fluorescence spectra of **2b** and **3b** are shown in Figure 1, which demonstrates that the absorption maximum (λ_{abs}) and fluorescence maximum (λ_{em}) appears at longer wavelength for the *p*-cyclyne **3b** than for the *m*-cyclyne **2b**, although the difference ($\Delta\lambda_{abs} = 51$ nm, $\Delta\lambda_{em} = 49$ nm) is relatively small in spite of the *meta*-fused structure of **2b**.

The photophysical data of **2**[6] and **3** are summarized in Table 1, together with other related systems. The table shows that not only long conjugated octakis-*p*-cyclynes (**3a**, **3b**), but also short conjugated octakis-*m*-cyclynes (**2b** and particularly **2c**) emit an unusually strong fluorescence, in contrast to the acyclic homologue **1,3-PBP**, whose λ_{abs} and λ_{em} values are nonetheless similar. ^1H NMR spectroscopy confirms that compounds **2** and **3** do not aggregate in chloroform solution (10^{-2} M–10^{-4} M). A small Stokes shift is also a characteristic photophysical property of these cyclynes.

It is noteworthy that compound **2b** can include two molecules of $[Cu^{II}(hfac)_2]$ (Hhfac = 1,1,1,5,5,5-hexafluoro-2,4-pentanedione) provide the greenish-blue pentacoordinate Cu^{II} complex **8** upon standing in $CHCl_3$ for a week at room

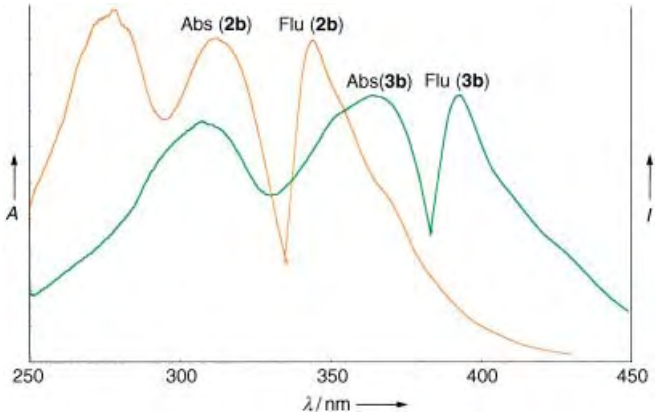


Figure 1. Absorption (Abs) and fluorescence (Flu) spectra of octakis-*m*-cyclyne **2b** and octakis-*p*-cyclyne **3b** in $CHCl_3$ (orange: **2b**; green: **3b**).

 © 2004 Wiley-VCH Verlag GmbH & Co. KGaA, Weinheim

Table 1: Photophysical data of cyclynes and related compounds in $CHCl_3$.

Compound	λ_{abs} [nm]	logε	λ_{em} [nm]	Φ_f[a]	Stokes shift [nm]
2b[b]	315	5.19	344	0.18	29
2c[b]	313	4.92	344	0.37	31
3a[b]	334	5.13	371	0.59	37
3b[b]	366	4.27	393	0.33	27
8[b]	313	5.14	344	0.30	31
9[b]	322	4.64	356	0.11	34
1,3-PBP[b]	307	4.70	329	0.03	22

[a] Quantum yield is calculated relative to quinine ($\Phi_f = 0.55$ in 0.1 M H_2SO_4). [b] λ_{ex} = 312 (**2b**), 311 (**2c**), 333 (**3a**), 364 (**3b**), 313 (**8**), 311 (**9**), and 301 nm (**1,3-PBP**).

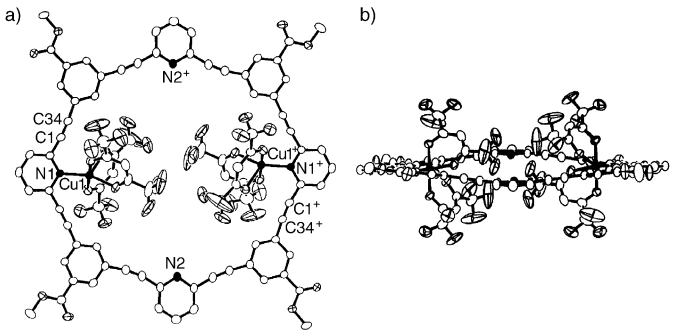


Figure 2. ORTEP representation of the pentacoordinate Cu^{II} complex **8**: a) front view, b) side view.

temperature. Its X-ray crystal structure (Figure 2; see also the Supporting Information) indicates that two opposing pyridine nitrogen atoms of **2b** coordinate to the Cu^{II} ions in $[Cu(hfac)_2]$, and that the cyclyne moiety has a coplanar structure with expected bond lengths and angles. The N···N separation between each Cu-coordinated pyridine ring is 15.56 Å and that between each free pyridine ring is 14.16 Å, while the Cu···Cu distance is 11.58 Å.

The Cu^{II} complex **8** emits remarkably strong fluorescence (Φ_f: 0.30 for **8**, 0.18 for **2b**), which is surprising as Cu^{II} ions are known to quench fluorescence. The reason for this observation is not clear at present. Complex **8** does not disassociate in solution, since the R_f value of complex **8** is quite different from that of parent **2b** in thin-layer chromatography (TLC) analysis with several solvents. Furthermore, the increase of quantum yield in complex **8** is definitive evidence that no dissociation takes place, because the quantum yield decreases in the solution of **2b** and $Cu(OTf)_2$. Therefore, the surprisingly high quantum yield of complex **8** seems to be a consequence of the inhibition of internal conversion, brought about by an increase in the rigidity of the cyclyne ring that stems from the steric-bulk effects of the Cu^{II}-coordinated hfac ligands.

In conclusion, the functionally and structurally interesting octakis-*m*-cyclynes **2** and octakis-*p*-cyclynes **3** are doughnut-shaped π-electron systems that are constructed by the formal insertion of pyridine and benzene groups into the single bonds of cyclohexadecayne. These doughnut-shaped azamacrocycles with cavity dimensions of ≈1 nm have strong light-emitting characteristics. In addition, the pentacoordinate Cu^{II} complex **8** of octakis-*m*-cyclyne **2b** emits remarkably strong fluorescence, contrary to scientific knowledge, which suggests that various transition-metal complexes of octakis-*m*-cyclynes **2** could be utilized to fabricate useful luminescent materials. The optoelectronic properties and other applications of the doughnut-shaped nano-fluorophores will be reported in due course.

Experimental Section

Phenyltriazane deprotection: A sealable flask was charged with the starting material (**6aa**, **6ba** or **7aa**, **7ba**), I_2 (1.2 equiv), and $ClCH_2CH_2Cl$.[7] The solution was degassed, back-filled with Ar, sealed, and stirred at 80 °C for 12 h. The reaction mixture was washed three times with 10% aqueous $Na_2S_2O_3$, dried over $MgSO_4$, and concentrated in vacuo. The residue was purified by column chromatography on SiO_2 (eluent: $CHCl_3$/EtOAc) to give the product (**6ab**, **6bb** or **7ab**, **7bb**).

(Trimethylsilyl)acetylene deprotection**:** The starting material (**6ab**, **6bb** or **7ab**, **7bb**) was dissolved in an approximate 10:1 mixture of $CHCl_3$ and MeOH with 2 M aqueous KOH (≈10 equiv), and the reaction mixture was stirred at room temperature. The reaction was monitored by TLC, and when the reaction was complete the reaction mixture was carefully washed with water. The organic fractions were then dried over $MgSO_4$ and evaporated. Chromatography on SiO_2 (eluent: $CHCl_3$/EtOAc) yielded the product (**6ac**, **6bc** or **7ac**, **7bc**).

Cyclization**:** A Schlenk flask charged with $[PdCl_2(Ph_3P)_2]$ (0.1 equiv) and CuI (0.05 equiv) was evacuated and back-filled with Ar three times. Then dry Et_3N and THF (2:1, v/v) was added to the flask. While the mixture was stirred under Ar at 75 °C, a solution of the sequence precursor (**6ac**, **6bc** or **7ac**, **7bc**) in dry THF was added to the flask by a syringe pump at a rate of ≈8 mL h^{-1}. After addition, the reaction mixture was stirred at the same temperature for 2 h and then the solvent was removed with a rotary evaporator. The product was purified by column chromatography on SiO_2 (eluent: $CHCl_3$/EtOAc and/or benzene/EtOAc) followed by recrystallization from $CHCl_3$. Spectral data of **2a**–**2c**, **3a**, and **3b** can be found in the Supporting Information.

Received: August 29, 2003 [Z52749]

Keywords: alkynes · copper · fluorescence · insertion · macrocycles

[1] For relevant reviews, see: a) S. A. Jenekhe, *Adv. Mater.* **1995**, *7*, 309; b) F. Hide, M. A. Diaz-Garcia, B. J. Schwartz, A. J. Heeger, *Acc. Chem. Res.* **1997**, *30*, 430; c) A. Kraft, A. C. Grimsdale, A. B. Holmes, *Angew. Chem.* **1998**, *110*, 416; *Angew. Chem. Int. Ed.* **1998**, *37*, 402; d) Y. Wada, H. Yamada, K. Matsushige, *Oyo Butsuri* **2001**, *70*, 1395; e) R. L. Carroll, C. B. Gorman, *Angew. Chem.* **2002**, *114*, 4556; *Angew. Chem. Int. Ed.* **2002**, *41*, 4378.

[2] a) *Cyclophane Chemistry for 21st Century* (Ed.: H. Takemura), Research Signpost, Trivandrum, **2002**; b) *Interactions in Molecules, Electronic, and Steric Effects* (Ed.: S. D. Peyerimhoff), Wiley-VCH, Weinheim, **2003**.

[3] For reviews on the synthesis of related carbomacrocycles, see: a) J. S. Moore, *Acc. Chem. Res.* **1997**, *30*, 402; b) D. Zhao, J. S. Moore, *Chem. Commun.* **2003**, 807.

[4] For recent papers on the synthesis of related arene–azaarenecyclynes in which pyridine N atoms are directed inside macrocycles, see: a) Y. Tobe, A. Nagano, K. Kawabata, M. Sonoda, K. Naemura, *Org. Lett.* **2000**, *2*, 3265; b) O. Henz, D. Lentz, A. D. Schlüter, *Chem. Eur. J.* **2000**, *6*, 2362; c) O. Henz, D. Lentz, A.

 © 2004 Wiley-VCH Verlag GmbH & Co. KGaA, Weinheim

Schater, P. Franke, A. D. Schlüter, *Chem. Eur. J.* **2002**, *8*, 357; d) S. Kobayashi, Y. Yamaguchi, T. Wakamiya, Y. Matsubara, K. Sugimoto, Z. Yoshida, *Tetrahedron Lett.* **2003**, *44*, 1469.
[5] For a review, see K. Sonogashira in *Comprehensive Organic Synthesis, Vol. 3* (Eds.: B. M. Trost, I. Fleming), Pergamon, Oxford, **1991**, pp. 521 – 549.
[6] Reliable photophysical data for **2a** are not obtained because of the difficulty of its purification.
[7] Z. Wu, J. S. Moore, *Tetrahedron Lett.* **1994**, *35*, 5539.

 © 2004 Wiley-VCH Verlag GmbH & Co. KGaA, Weinheim

Microcontact Printing

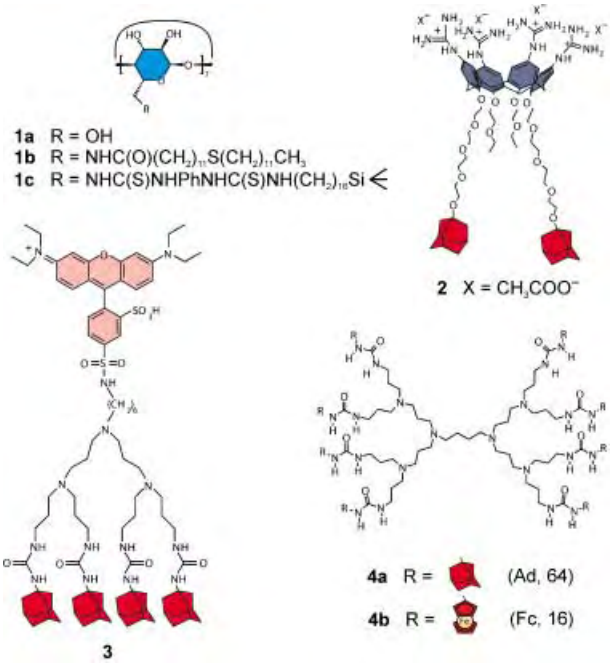
Writing Patterns of Molecules on Molecular Printboards**

Tommaso Auletta, Barbara Dordi, Alart Mulder, Andrea Sartori, Steffen Onclin, Christiaan M. Bruinink, Mária Péter, Christian A. Nijhuis, Hans Beijleveld, Holger Schönherr, G. Julius Vancso, Alessandro Casnati, Rocco Ungaro, Bart Jan Ravoo, Jurriaan Huskens, and David N. Reinhoudt**

Bottom-up nanotechnology has to start with the precise positioning of molecules. For this purpose we are developing molecular printboards, that is, self-assembled monolayers (SAMs) of molecules that have specific recognition sites, for example, molecular cavities, to which molecules can be anchored through specific and directional supramolecular interactions.[1] Such molecular printboards are prepared by the self-assembly of β-cyclodextrin (β-CD) derivatives on gold and silicon oxide surfaces. Herein we describe how to print or write, by microcontact printing (μCP) and dip-pen nanolithography (DPN), respectively, molecular patterns of guest-functionalized calixarene molecules, dendritic wedges labeled by fluorescent groups, and dendrimers on β-CD-terminated printboards. The binding, as well as the desorption of the molecules, can be fine-tuned by chemical design, which allows virtually unlimited flexibility in the chemical functions that can be employed. These structures can be subsequently used to direct the adsorption of different materials, for example, fluorescent dyes.

Microcontact printing has been developed by Whitesides for the preparation of patterns of molecules on bare surfaces by, for example, the transfer of thiols to gold substrates in the contact areas between a soft polymeric stamp and the substrate.[2,3] This has recently been extended by Mirkin and co-workers to writing with molecules on such surfaces by using the DPN approach.[4] Various types of molecules were deposited onto different substrates by DPN which led to arrays of, for example, DNA,[5] proteins,[6] and nanoparticles.[7] Registry capabilities have been demonstrated as well,[8] and a multipen nanoplotter able to produce parallel patterns with different ink molecules has been developed.[9]

β-CD (**1a**, Scheme 1) can act as a host for the binding of a variety of small, organic guest functionalities in water through hydrophobic interactions. We prepared self-assembled monolayers (SAMs) of a β-CD heptathioether adsorbate **1b** (Scheme 1) on gold as described before.[10,11] Such adsorbates form densely packed, well-ordered SAMs with equivalent



Scheme 1. Structures of β-cyclodextrin (β-CD, **1a**) and β-CD adsorbates **1b** and **1c** for attachment to gold and silicon oxide, respectively; bis(adamantyl)-functionalized calixarene (**2**); lissamine-rhodamine B functionalized dendritic wedge (**3**); generic second generation PPI dendrimer with 8 R groups: **4a** has 64 Ad moieties (fifth generation) and **4b** has 16 Fc moieties (third generation).

[*] Dr. T. Auletta, A. Mulder, S. Onclin, C. M. Bruinink, Dr. M. Péter, C. A. Nijhuis, H. Beijleveld, Dr. B. J. Ravoo, Dr. J. Huskens, Prof. Dr. D. N. Reinhoudt
University of Twente, MESA+ Institute for Nanotechnology
Supramolecular Chemistry and Technology
P.O. Box 217, 7500 AE Enschede (The Netherlands)
Fax: (+31) 53-4894645
E-mail: j.huskens@utwente.nl
d.n.reinhoudt@utwente.nl

B. Dordi, Dr. H. Schönherr, Prof. Dr. G. J. Vancso
University of Twente, MESA+ Institute for Nanotechnology
Materials Science and Technology of Polymers
P.O. Box 217, 7500 AE Enschede (The Netherlands)

A. Sartori, Dr. A. Casnati, Prof. Dr. R. Ungaro
Università degli Studi di Parma
Dipartimento di Chimica Organica e Industriale
Parco Area delle Scienze 17A, 43100 Parma (Italy).

[**] The support given by the Netherlands Organization for Scientific Research (NWO; grant 97041), the Applied Science division of the NWO and the Ministry of Economic Affairs (STW; TST 4946), and the MESA+ Institute for Nanotechnology is gratefully acknowledged. Tascon GmbH (Münster, Germany) is gratefully acknowledged for the SIMS measurements.

Supporting information for this article is available on the WWW under http://www.angewandte.org or from the author.

 DOI: 10.1002/anie.200352767 © 2004 Wiley-VCH Verlag GmbH & Co. KGaA, Weinheim

binding sites, the near-hexagonal packing of which can be visualized by AFM.[11]

We have measured the interaction thermodynamics of these β-CD-terminated printboards with several guests, by using a variety of techniques, including AFM dynamic force spectroscopy, which allows the detection of individual rupture forces of host–guest complexes.[12] The binding of small, univalent guest molecules to these SAMs has been studied by surface plasmon resonance (SPR)[13] and electrochemical impedance spectroscopies (EIS).[11] An important finding from these studies was that the interaction strength of such guest molecules with β-CDs on the printboards is identical to the binding strength in solution.[13] The binding of large dendrimers functionalized with adamantyl (Ad) groups through multiple interactions has also been recently discussed.[1]

Multivalency, that is, the use of multiple interactions which are assumed to act in a stepwise, independent assembly process, is of strong current interest[14] for its implications in the design of new ligands and inhibitors for proteins because it offers a tool for fine-tuning overall interaction strengths. It has been, for example, employed in the development of high-affinity vancomycin–peptide systems,[15] which has very recently been extended to the assembly of vancomycin-functionalized polymers at peptide SAMs.[16] Therefore, the use of molecules which allow the formation of *multiple* supramolecular interactions constitutes a tool to tune adsorption and desorption process parameters at surfaces—thermodynamics and kinetics are in principle related in a straightforward manner to the number of interactions and to the strength and kinetics[17] of an individual interaction. Thus, we synthesized the water-soluble calix[4]arene **2** which contains two Ad moieties as the guest motif (Scheme 1). The binding of **2** with β-CD in solution and onto β-CD-terminated SAMs was investigated by microcalorimetry and SPR, respectively. The binding behavior with β-CD in water showed the two Ad groups bound independently[18] to two separate β-CDs, with binding parameters characteristic of Ad–β-CD interactions.[13] The binding constant K obtained for this guest with a β-CD dimer[19] was $1.4\times10^{7}\,\text{M}^{-1}$, based on a 1:1 model.[20] The interaction with the β-CD-terminated SAMs appeared to be much stronger ($K=10^{9}$–$10^{10}\,\text{M}^{-1}$),[21] which is ascribed to the high local concentration of hosts at the surface.[1]

Such interaction strengths are already sufficiently high to apply these molecules in nanofabrication as, for example, in μCP. We employed, for the first time, *supramolecular* μCP, which is the transfer of molecules from a stamp to a surface to give specific host–guest assemblies on the printboards. Patterns were visible directly after printing and remained clearly visible when rinsed with substantial amounts of water or 50 mM aqueous NaCl (Figure 1).[22] Even prolonged washing with β-CD in solution, to promote competition between the host–guest binding in solution and at the printboard, did not completely remove the patterns. The presence of the guest molecules in the contacted areas was also confirmed by secondary ion mass spectrometry (SIMS) imaging, as shown for an image of the molecular ion peak of the calixarene **2** (Figure 1).

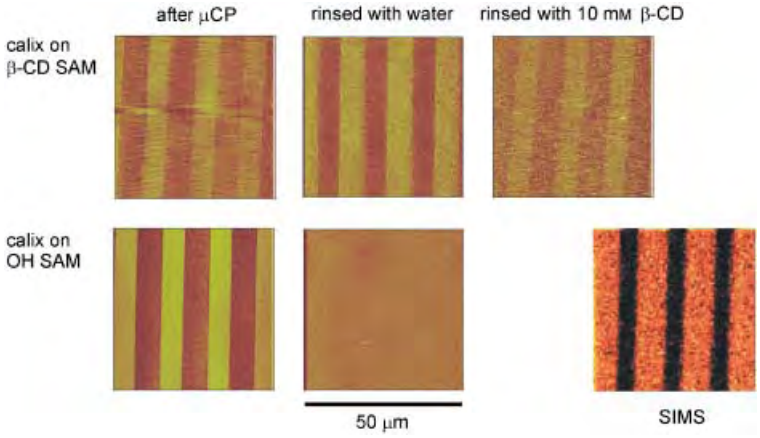


Figure 1. AFM friction force images (acquired in air) of patterns obtained by μCP of the calixarene guest **2** (brighter areas) on β-CD- (top) and OH-terminated SAMs (bottom): before rinsing, after rinsing with Milli-Q water, or after rinsing with 10 mM aqueous β-CD, respectively (image size $50\times50\,\mu\text{m}^2$; friction forces (a.u.) increase from dark to bright contrast). SIMS-TOF image of a β-CD-terminated SAM after printing of **2** (image size: $56\times56\,\mu\text{m}$): the bright areas indicate the presence of the molecular ion peak at $m/z=1418$.

The requirement of specific host–guest interactions for sustained pattern stability is evident when μCP on the β-CD-terminated SAMs is compared to μCP on 11-sulfanyl-1-undecanol SAMs (OH SAMs) on gold (Figure 1). Ink transfer also occurs on the OH SAMs, but patterns were instantly removed upon washing with water or 50 mM aqueous NaCl.

We also employed supramolecular DPN to write local patterns of molecules on the printboard (Figure 2). Silicon nitride AFM tips were dipped into an aqueous solution of the calixarene (**2**) ink and scanned across β-CD- as well as OH-modified SAMs. The transfer of ink was observed for both SAMs, but patterns stable to rinsing were only obtained for the β-CD printboards (Figure 2, left). As a control experiment, a β-CD-terminated SAM was scanned with a bare Si_3N_4 tip under the same experimental conditions reported above for the writing experiment. Subsequent AFM friction force imaging did not show any visible pattern on the surface. This result proves that the structures of Figure 2 do not arise from mechanical forces applied by the tip to the SAM, but rather by the transfer of ink molecules. The resolution that can be attained by this technique is well below 100 nm, as shown by the line patterns in Figure 2 (right). It is likely to be a function of contact time, tip radius, ink concentration, and ink-transfer mechanism, as in traditional DPN.

To widen the scope of the supramolecular patterning approaches described above, we also prepared β-CD printboards on silicon oxide (**1c**, see Supporting Information) because SiO_2 permits fluorescence detection of the assemblies, whereas quenching occurs for SAMs on gold. Microcontact printing of the calixarene guest **2** gave results similar to the β-CD-terminated SAMs on gold, both in regard to ink transfer and pattern stability. The printing of fluorescent dendritic wedge **3** (Scheme 1), which was transferred as the per-β-CD complex, allowed pattern detection by confocal

 © 2004 Wiley-VCH Verlag GmbH & Co. KGaA, Weinheim

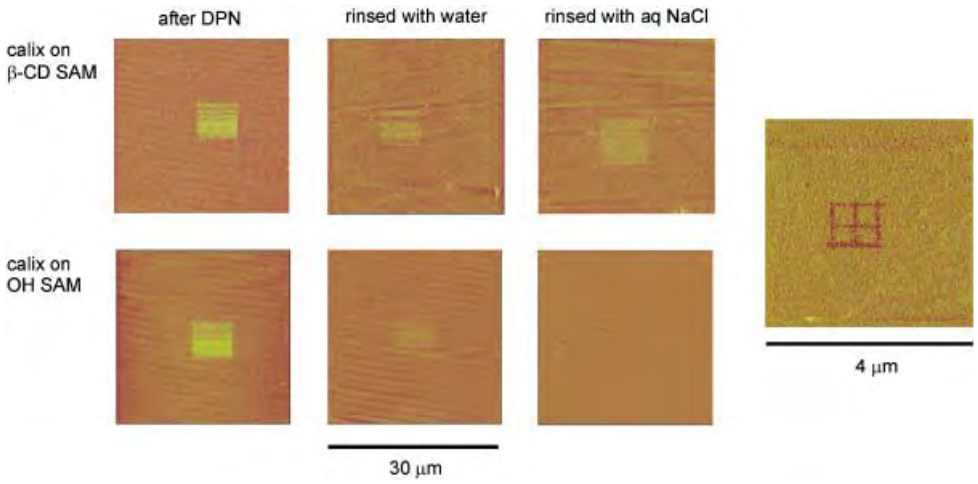


Figure 2. Left: AFM friction force images (friction forces (a.u.) increase from dark to bright contrast) showing, from left to right, patterns produced by DPN on a β-CD-terminated SAM (top) and on an OH-terminated SAM (bottom) using **2** as the ink before rinsing (image acquired in water), after rinsing in situ with Milli-Q water (image acquired in water), and with 50 mM aqueous NaCl (image acquired in aqueous NaCl), respectively. Right: AFM friction force images in air of arrays of lines with mean widths (± standard deviation) of 60 ± 20 nm produced by DPN (friction inversion with respect to the μCP experiments is related to the AFM tip employed in the imaging step, which is the same as in the writing step and thus still covered with the molecular ink). For DPN, cleaned Si_3N_4 tips were coated with the calixarene ink by soaking them for 15 min in a 0.5 mM aqueous solution of **2** and drying, and then scanned twice across a $7\times7\ \mu m^2$ area of a SAM on gold (scan velocity ca. 21 $\mu m\,s^{-1}$, $T = 25\,^{\circ}C$, relative humidity 47 ± 3%). The scan size was then increased to $30\times30\ \mu m^2$, the scan velocity was set to 100–300 $\mu m\,s^{-1}$ and the relative scan angle was adjusted accordingly. The lines were produced by scanning each line for a 40 s period (scan velocity was ca. 2 $\mu m\,s^{-1}$, $T = 25\,^{\circ}C$ and relative humidity 47 ± 3%). The scan size was then increased to $4\times4\ \mu m^2$, and the scan velocity increased to 30 $\mu m\,s^{-1}$. The tip was withdrawn prior to rinsing. The AFM liquid cell was then flushed with 5 mL of Milli-Q water and new images were recorded. Eventually the cell was flushed with 5 mL of 50 mM aqueous NaCl, before new images were recorded.

microscopy (Figure 3, top). Rinsing the surface with a 10 mM aqueous phosphate buffer hardly affected the printed patterns, as witnessed in this case by monitoring fluorescence intensities. Only rinsing with 10 mM β-CD led to a significant reduction of the fluorescence.[23]

Patterns of a fifth generation Ad-terminated poly(propylene imine) dendrimer **4a** (Scheme 1), functionalized with 64 Ad end groups,[24] on β-CD printboards on silicon oxide were created by supramolecular μCP. Such molecules behave as molecular boxes for dyes through electrostatic interactions, both as the free box[25] and as complexes with β-CD in aqueous solution.[24] The dendrimers were printed as the per-β-CD complex. The dendritic boxes were subsequently loaded with two different fluorescent dyes (either fluorescein or rose bengal) by immersing the patterned substrates into aqueous solutions of these dyes (Figure 3, bottom).

We can also use electroactive third generation dendrimers **4b** terminated with ferrocene (Fc; Scheme 1) as the ink (as they also form inclusion complexes with β-CD[26]) to control the desorption of the host–guest assemblies electrochemically. The Fc-functionalized dendrimers were adsorbed from solution onto the β-CD printboards on gold. The known oxidation of the Fc groups to ferrocenium cations that leads to complete loss of the Fc–β-CD interaction[26] provides us with a tool to induce desorption by an external (electrochemical) stimulus in an electrochemical setup where the gold layer of the β-CD printboard acts as the working electrode. Sequential cyclic voltammograms of a monolayer of Fc-modified dendrimer **4b** on the β-CD printboard showed a decrease in the peak current that corresponds to a decrease in the amount of adsorbed material (see the Supporting Information). Peak currents remained constant when the cyclic voltammograms were recorded in the presence of the dendrimer **4b** in solution, which indicates that oxidized and desorbed dendrimers were constantly being replaced by nonoxidized molecules from solution.

In summary, we have shown that molecular printboards allow for versatile nanofabrication schemes of printing and writing that are applicable to various types of substrates and molecules. Their advantages lie in the tunability of the type and number of host–guest motifs and the possibility to erase patterns. Only a limited number of such supramolecular interactions per guest molecule are required for the formation of stable patterns, thus eliminating the need for very complicated synthesis. Molecular printboards will open up ways to fabricate arrays of multiple host–guest systems, to study the formation and dynamics of individual supramolecular assemblies at surfaces, and for the preparation of 3D supramolecular architectures on substrates.

Experimental Section

The synthesis of the β-CD adsorbate **1b** and the preparation of SAMs on Au substrates were reported previously.[10,11] The synthesis of adsorbate **2**, of lissamine–rhodamine B/poly(propylene imine) dendritic wedge **3**, and the preparation of monolayers on silicon oxide are reported in the Supporting Information. The fifth generation adamantane-terminated poly(propylene imine) dendrimer (G5-PPI-$(Ad)_{64}$) **4a**, the third generation ferrocene-terminated poly(propylene imine) dendrimer (G3-PPI-$(Fc)_{16}$) **4b**, and their per-β-CD complexes were synthesised according to literature procedures.[24,27] Microcontact printed substrates were prepared according to literature procedures.[2]

Calorimetric titrations were performed at 25 °C using a Microcal VP-ITC isothermal titration microcalorimeter. Titrations of **2** with native β-CD or a β-CD dimer[19] were performed by adding aliquots of a guest solution to the host solution or vice versa. The titrations were analyzed with a least-squares curve-fitting procedure. Control experiments involved addition of the burette solution to pure water and addition of water to the cell solution.

 © 2004 Wiley-VCH Verlag GmbH & Co. KGaA, Weinheim

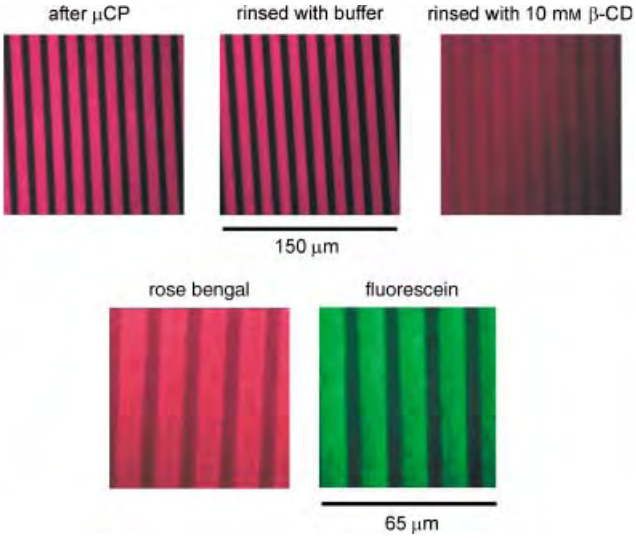


Figure 3. Top: confocal microscopy images after μCP of **3** on β-CD-terminated SAMs on SiO_2. Images shown are after printing, from left to right: without rinsing; after rinsing with ca. 200 mL of an aqueous buffer solution, followed by rinsing with water and drying in a stream of nitrogen; after rinsing with ca. 200 mL of 10 mM β-CD, followed by rinsing with water and drying in a stream of nitrogen. Dendritic wedge **3** was printed as the per-β-CD complex from a 0.1 mM aqueous solution. The oxidized stamp was soaked in the wedge solution, blown dry with nitrogen, and brought into contact with the surface for 1 min without external pressure. Bottom: Confocal microscopy images of μCP of dendrimer **4a** as the per-β-CD complex on a β-CD-terminated SAM on SiO_2, followed by loading with an anionic dye. The dendrimers were printed from a 0.1 mM solution in water for 1 min, without external pressure, and the patterns were washed with ca. 200 mL of 10 mM aqueous phosphate buffer (pH 7) and water to remove physisorbed material. The dendritic boxes were subsequently loaded with rose bengal (left) and fluorescein (right) by dipping the substrates in a 0.1 mM aqueous solution of the dye molecules, followed by rinsing with an aqueous buffer solution, water, and drying in a stream of nitrogen.

SPR measurements were performed in a two-channel vibrating mirror angle scan set-up based on the Kretschmann configuration, as described by Kooyman and co-workers.[28]

SIMS-TOF measurements were performed on an ION-TOF IV spectrometer (Tascon GmbH Münster, Germany) in which an Au_3 gun was employed in a burst alignment mode; target current = 0.02 pA.

XPS measurements were performed on a Physical Electronics Quantum2000 equipped with a spherical sector analyzer and a multichannel plate detector (16 detector elements).

The AFM experiments were carried out with a NanoScope III multimode AFM (Digital Instruments, Santa Barbara, CA, USA) in the contact mode using V-shaped Si_3N_4 cantilevers (Nanoprobes, Digital Instruments) with a spring constant of 0.1 $N\,m^{-1}$. Images were acquired in an ambient atmosphere (ca. 40–50% relative humidity, 25 °C temperature) unless stated otherwise. A standard AFM liquid cell (Digital Instruments) was used for measurements of liquids. The sample was scanned at 90° with respect to the long axis of the cantilever to ensure maximum sensitivity for lateral forces in the friction force images.

Confocal microscopy images were taken on a Carl Zeiss LSM 510. The dendrimer wedge **3** and rose bengal were excited at 543 nm, while fluorescein was excited at 488 nm. The emitted fluorescence was collected on a a PMT Hamamatsu R6357 spectrophotometer.

Electrochemical measurements were performed with an AUTOLAB PGSTAT10 in a custom built three-electrode set-up equipped with a platinum counterelectrode, a mercury sulfate reference electrode ($V_{MSE} = +0.61\,V_{NHE}$), and a screw cap holding the gold working electrode (area exposed to the solution = 0.44 cm^2).

Received: September 2, 2003 [Z52767]
Published Online: December 9, 2003

Keywords: cyclodextrins · host–guest systems · microcontact printing · nanolithography · self-assembly

[1] J. Huskens, M. A. Deij, D. N. Reinhoudt, *Angew. Chem.* **2002**, *114*, 4647–4651; *Angew. Chem. Int. Ed.* **2002**, *41*, 4467–4471.
[2] Y. Xia, G. M. Whitesides, *Angew. Chem.* **1998**, *110*, 568–594; *Angew. Chem. Int. Ed.* **1998**, *37*, 550–575.
[3] B. Michel, A. Bernard, A. Bietsch, E. Delamarche, M. Geissler, D. Juncker, H. Kind, J.-P. Renault, H. Rothuizen, H. Schmid, P. Schmidt-Wenkel, R. Stutz, H. Wolf, *IBM J. Res. Dev.* **2001**, *45*, 697–719.
[4] a) R. D. Piner, J. Zhu, F. Xu, S. Hong, C. A. Mirkin, *Science* **1999**, *283*, 661–663; b) C. A. Mirkin, S. Hong, L. Demers, *ChemPhysChem* **2001**, *2*, 37–39.
[5] a) L. M. Demers, D. S. Ginger, S.-J. Park, Z. Li, S.-W. Chung, C. A. Mirkin, *Science* **2002**, *296*, 1836–1838; b) H. Zhang, Z. Li, C. A. Mirkin, *Adv. Mater.* **2002**, *14*, 1472–1474.
[6] K.-B. Lee, S.-J. Park, C. A. Mirkin, J. C. Smith, M. Mrksich, *Science* **2002**, *295*, 1702–1705.
[7] X. Liu, L. Fu, S. Hong, V. P. Dravid, C. A. Mirkin, *Adv. Mater.* **2002**, *14*, 231–234.
[8] S. Hong, J. Zhu, C. A. Mirkin, *Science* **1999**, *286*, 523–525.
[9] S. Hong, C. A. Mirkin, *Science* **2000**, *288*, 1808–1811.
[10] M. W. J. Beulen, J. Bügler, B. Lammerink, F. A. J. Geurts, E. M. E. F. Biemond, K. G. C. van Leerdam, F. C. J. M. van Veggel, J. F. J. Engbersen, D. N. Reinhoudt, *Langmuir* **1998**, *14*, 6424–6429.
[11] M. W. J. Beulen, J. Bügler, M. R. de Jong, B. Lammerink, J. Huskens, H. Schönherr, G. J. Vancso, B. A. Boukamp, H. Wieder, A. Offenhäuser, W. Knoll, F. C. J. M. van Veggel, D. N. Reinhoudt, *Chem. Eur. J.* **2000**, *6*, 1176–1183.
[12] a) H. Schönherr, M. W. J. Beulen, J. Bügler, J. Huskens, F. C. J. M. van Veggel, D. N. Reinhoudt, G. J. Vancso, *J. Am. Chem. Soc.* **2000**, *122*, 4963–4967; b) S. Zapotoczny, T. Auletta, M. R. de Jong, H. Schönherr, J. Huskens, F. C. J. M. van Veggel, D. N. Reinhoudt, G. J. Vancso, *Langmuir* **2002**, *18*, 6988–6994.
[13] M. R. de Jong, J. Huskens, D. N. Reinhoudt, *Chem. Eur. J.* **2001**, *7*, 4164–4170.
[14] M. Mammen, S.-K. Choi, G. M. Whitesides, *Angew. Chem.* **1998**, *110*, 2908–2953; *Angew. Chem. Int. Ed.* **1998**, *37*, 2754–2794.
[15] a) J. Rao, J. Lahiri, L. Isaacs, R. M. Weis, G. M. Whitesides, *Science* **1998**, *280*, 708–711; b) J. Rao, J. Lahiri, R. M. Weis, G. M. Whitesides, *J. Am. Chem. Soc.* **2000**, *122*, 2698–2710.
[16] S. J. Metallo, R. S. Kane, R. E. Holmlin, G. M. Whitesides, *J. Am. Chem. Soc.* **2003**, *125*, 4534–4540.
[17] The kinetics of β-CD complexes commonly follow diffusion-controlled association (k_f = ca. $10^9\,M^{-1}\,s^{-1}$; J. Szejtli, *Comprehensive Supramolecular Chemistry*, *Vol. 3*, Pergamon, Oxford, **1996**), and thus dissociation rates follow directly from association rates and thermodynamics.
[18] Microcalorimetry gave an intrinsic binding constant for the Ad–β-CD interaction of $5.0\times10^4\,M^{-1}$ and a binding enthalpy of $-7.5\,kcal\,mol^{-1}$ for calixarene guest **2**.
[19] J. J. Michels, J. Huskens, D. N. Reinhoudt, *J. Am. Chem. Soc.* **2002**, *124*, 2056–2064.
[20] The stoichiometry (1:1), the *K* value ($1.4\times10^7\,M^{-1}$), and the binding enthalpy ($-16.2\,kcal\,mol^{-1}$) indicate that both Ad

 © 2004 Wiley-VCH Verlag GmbH & Co. KGaA, Weinheim

groups of the guest interact with both β-CD cavities of the dimer to form a 1:1 complex.
[21] Value obtained for a 1:1 model in which the β-CD SAM is treated as a SAM of dimeric hosts with a concentration of half the β-CD concentration at the surface.
[22] The contrast in the AFM images does not allow any conclusion on the amount of ink present on the patterns directly after printing or after subsequent washing. XPS and EIS measurements showed that: a) three to five monolayers of guest ink are transferred by μCP onto both OH- and β-CD-terminated SAMs; b) approximately one monolayer of guests is present after a first rinsing of the β-CD-terminated SAMs with water; c) submonolayer coverages remain on the β-CD-terminated SAMs upon prolonged washing with water and β-CD solutions (See Supporting Information). A monolayer is defined as a layer of the calixarene guest molecules bound through both Ad groups to two β-CD cavities at the surface.
[23] In contrast, patterns created on a reference polyethyleneglycol monolayer (A. Papra, N. Gadegaard, N. B. Larsen, *Langmuir* **2001**, *17*, 1457 – 1460) were removed easily by rinsing with an aqueous buffer solution.
[24] J. J. Michels, M. W. P. L. Baars, E. W. Meijer, J. Huskens, D. N. Reinhoudt, *J. Chem. Soc. Perkin Trans. 2* **2000**, 1914 – 1918.
[25] a) J. F. G. A. Jansen, E. M. M. de Brabander-van den Berg, E. W. Meijer, *Science* **1994**, *266*, 1226 – 1229b) J. F. G. A. Jansen, H. W. I. Peerlings, E. M. M. de Brabander-van den Berg, E. W. Meijer, *Angew. Chem.* **1995**, *107*, 1321 – 1324; *Angew. Chem. Int. Ed. Engl.* **1995**, *34*, 1206 – 1209.
[26] R. Castro, I. Cuardo, B. Alonso, C. M. Casado, M. Morán, A. E. Kaifer, *J. Am. Chem. Soc.* **1997**, *119*, 5760 – 5761.
[27] I. Cuardo, M. Morán, C. M. Casado, B. Alonso, F. Lobete, B. Carciá, M. Ibisate, J. Losada, *Organometallics* **1996**, *15*, 5278 – 5280.
[28] A. T. M. Lenferink, R. P. H. Kooyman, J. Greve, *Sens. Actuators B* **1991**, *3*, 261 – 265.

 © 2004 Wiley-VCH Verlag GmbH & Co. KGaA, Weinheim

Cover Picture



Klaus Jähnisch,* Volker Hessel,* Holger Löwe, and Manfred Baerns

Microstructured reactors such as the SuperFocus Interdigital micromixer offer an alternative to conventional large-scale techniques. Flow patterns with reduced layer thicknesses lead to enlarged reactive surfaces that result in short mixing times, and thus high-throughput reactions can be achieved. In their review on page 406 ff. K. Jähnisch, V. Hessel, et al. examine the potential of this new and powerful technology.

Contents

Angewandte EarlyView

The following articles are available online (in Wiley InterScience). You can find them at www.angewandte.org, under Full Text, Early View.

G. Mezei, P. Baran, R. G. Raptis:*
Anion Encapsulation by Neutral Supramolecular Assemblies of Cyclic Cu^{II}-Complexes: A Series of Five Polymerization Isomers, $[\{cis\text{-}Cu^{II}(\mu\text{-}OH)(\mu\text{-}pz)\}_n]$, $n = 6, 8, 9, 12$, and 14
DOI: 10.1002/anie.200352636
Published online: December 29, 2003

L. V. Slipchenko, T. E. Munsch, P. G. Wenthold, A. I. Krylov*:*
5-Dehydro-1,3-quinodimethane: A Hydrocarbon with an Open-Shell Doublet Ground State
DOI: 10.1002/anie.200352990
Published online: January 8, 2004

D. Bravo-Zhivotovskii, H. Peleg-Vasserman, M. Kosa, G. Molev, M. Botoshanskii, Y. Apeloig*:*
The Direct Synthesis of a Silene–Organometallic Complex
DOI: 10.1002/anie.200353048
Published online: January 8, 2004

Ž. Tomović, M. D. Watson, K. Müllen:*
Superphenalene-Based Columnar Liquid Crystals
DOI: 10.1002/anie.200352855
Published online: January 8, 2004

Articles judged by the referees or the editor as being either very important or very urgent are immediately edited, proof-read, and electronically published once the manuscript has arrived in the editorial office in final form. As long as there is no page number available these articles should be cited in the following manner:

Author(s) *Angew. Chem. Int. Ed.*, online publication date, DOI.

News

Materials Science: IBM Prize to T. Kato and K. Awaga ____ **392**

Biochemistry: T. Carell Recognized

Chemical Societies: H. Hopf Elected

Books

Methods in Polyphenol Analysis ____ **393** — Celestino Santos-Buelga, Gary Williamson — *reviewed by S. Quideau*

Beyond the Molecular Frontier Challenges for Chemistry and Chemical Engineering ____ **394** — Committee on Challenges for the Chemical Sciences in the 21st Century. Board on Chemical Sciences and Technologies — *reviewed by H. Hopf*

Handbook of Metathesis ____ **395** — Robert H. Grubbs — *reviewed by F. Z. Dörwald*

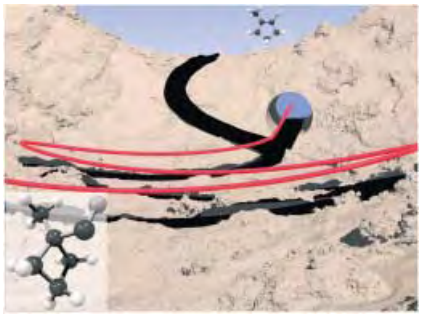
Highlights

A Tunneling Event

R. Berger* ____ **398 – 401**

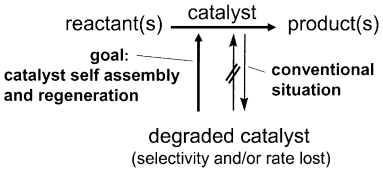
Do Heavy Nuclei See Light at the End of the Tunnel?

The direct route. Low-temperature experiments and calculations on the ring expansion of (1-methylcyclobutyl)fluorocarbene, which involves considerable movement of the heavy nuclei, indicate that tunneling through the barrier is more favorable than the classical route over the "mountain pass" (see picture).



© 2004 Wiley-VCH Verlag GmbH & Co. KGaA, Weinheim

Increased stability of oxidation catalysts results from the self-assembly of the catalysts under near-turnover conditions from oxidatively resistant precursors. The described polyoxometalate epoxidation catalyst uses a green oxidant (H_2O_2), solvent, and separation conditions and is fast, selective, and safe. This self-assembling system is an important step towards truly green catalysis (see scheme).



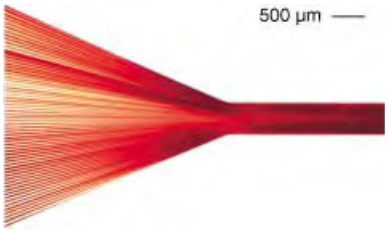
Homogenous Catalysis

C. L. Hill* ——— **402 – 404**

Stable, Self-Assembling, Equilibrating Catalysts for Green Chemistry

Reviews

Good things come in small packages: The reduced dimensions of microstructured reactors offer many advantages in chemistry, particularly with respect to enhanced conversion, selectivity, and safety. This Review presents a discussion of the process parameters and the design of such reactors, which are crucial to their development and optimization.



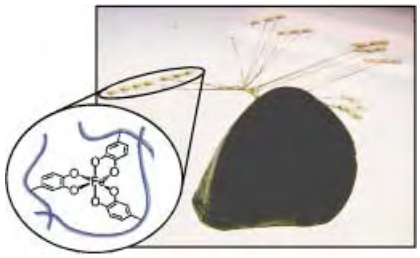
Chemistry in Microreactors

K. Jähnisch,* V. Hessel,* H. Löwe, M. Baerns ——— **406 – 446**

Chemistry in Microstructured Reactors

Communications

Iron muscles into mussels: Marine mussels adhere to rocks with a protein-based glue. An iron complex is the key curing agent in this adhesive, and the iron center is coordinated by three DOPA residues (see picture). These studies present the first identified case in which a transition-metal center is integral to forming a noncrystalline biological material.

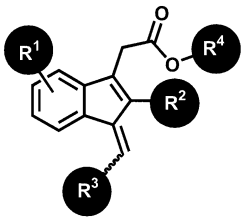


Marine Chemistry

M. J. Sever, J. T. Weisser, J. Monahan, S. Srinivasan, J. J. Wilker* —— **448 – 450**

Metal-Mediated Cross-Linking in the Generation of a Marine-Mussel Adhesive

Blocking the path to cancer: Application of efficient strategy for a phenotype-based screening of compound libraries to a library of sulindac-derived compounds (see scheme) yielded new inhibitors of the tumor-relevant Ras signal transduction pathway with high fidelity (as shown by microscopy). The results underline the advantage of using biologically prevalidated compound classes in chemical biology research.



Drug Discovery I

O. Müller, E. Gourzoulidou, M. Carpintero, I.-M. Karaguni A. Langerak, C. Herrmann, T. Möröy, L. Klein-Hitpaß, H. Waldmann* ——— **450 – 454**

Identification of Potent Ras Signaling Inhibitors by Pathway-Selective Phenotype-Based Screening

For the USA and Canada:
ANGEWANDTE CHEMIE International Edition (ISSN 1433-7851) is published weekly by Wiley-VCH PO Box 191161, D 69451 Weinheim, Germany. Air freight and mailing in the USA by Publications Expediting Inc. 200 Meacham Ave., Elmont, NY 11003. Periodicals postage paid at Jamaica NY 11431. US POSTMASTER: send address changes to *Angewandte Chemie*, Wiley-VCH, 111 River Street, Hoboken, NJ 07030. Annual subscription price for institutions: Europe € 3430.00/3118.00; outside Europe US$ 4499.00/4090.00 (valid for print and electronic/print or electronic delivery); for individuals who are personal members of a national chemical society, or whose institution already subscribes, or who are retired or self-employed consultants, print only: Europe € 248.00/outside Europe US$ 378.00. Postage and handling charges included. All Wiley-VCH prices are exclusive VAT.

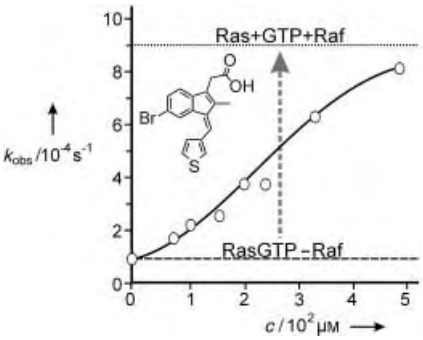
 © 2004 Wiley-VCH Verlag GmbH & Co. KGaA, Weinheim

Contents

Drug Discovery II

H. Waldmann, I.-M. Karaguni, M. Carpintero, E. Gourzoulidou, C. Herrmann, C. Brockmann, H. Oschkinat, O. Müller* ____ **454 – 458**

Sulindac-Derived Ras Pathway Inhibitors Target the Ras–Raf Interaction and Downstream Effectors in the Ras Pathway



Tracking down the target: The biological targets of eight new Ras-pathway inhibitors were investigated. Several of the compounds were shown to inhibit the RasGTP–Raf interaction (see example shown) and NMR data strongly suggest that this inhibition is the result of direct interaction between the inhibitors and the Ras protein. An inhibitor with a target probably downstream of MAP kinase was also found.

Charged Nanocolloids

F. Reincke, S. G. Hickey, W. K. Kegel, D. Vanmaekelbergh* ____ **458 – 462**

Spontaneous Assembly of a Monolayer of Charged Gold Nanocrystals at the Water/Oil Interface

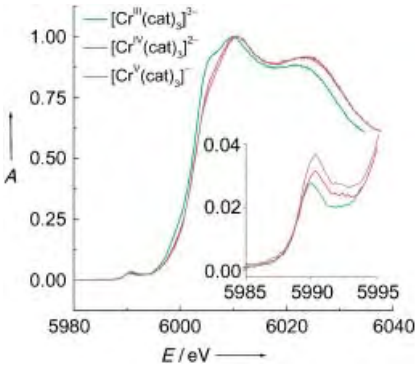
Charge control as a tool for assembly: Dense layers of individual, charged nanocrystals are formed at the aqueous/organic interface upon a slight reduction of the surface charge. The layers are remarkably robust, they creep up the glass (see picture). This method should be widely applicable to a broad range of charged colloids and will lead to the production of new materials.



Oxidation-State Determination

A. Levina, G. J. Foran, D. I. Pattison, P. A. Lay* ____ **462 – 465**

X-ray Absorption Spectroscopic and Electrochemical Studies of Tris(catecholato-(2−))chromate(V/IV/III) Complexes



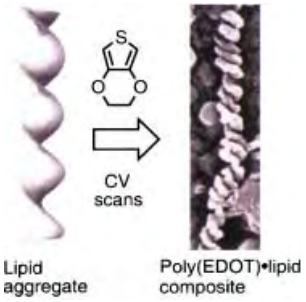
Contrary to popular belief, the redox chemistry of Cr–catecholato complexes $[Cr^{III}(cat)_3]^{3-}$ has been shown by X-ray absorption spectroscopic data to be predominantly metal-based and not ligand-based. The observed increase in the energies of the edge and pre-edge features of the spectra (see picture) and the decrease in the Cr–O bond lengths on oxidation are consistent with the formation of $[Cr^{IV}(cat)_3]^{2-}$ and $[Cr^{V}(cat)_3]^{-}$, both with a strong electron delocalization between the metal ion and the ligands.

Conductive Polymers

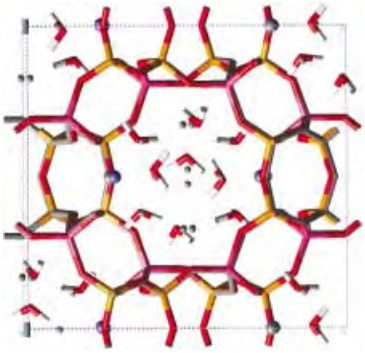
T. Hatano, A.-H. Bae, M. Takeuchi, N. Fujita, K. Kaneko, H. Ihara, M. Takafuji, S. Shinkai* ____ **465 – 469**

Helical Superstructure of Conductive Polymers as Created by Electrochemical Polymerization by Using Synthetic Lipid Assemblies as a Template

A templating method is used to create conductive polymers that have a helical superstructure. The driving force is an electrostatic interaction between the negative charge in a synthetic lipid and the cationic charge generated in the polymers during oxidative electrochemical polymerization of ethylenedioxythiophene (EDOT) and a pyrrole (see picture; CV = cyclic voltammetry).



© 2004 Wiley-VCH Verlag GmbH & Co. KGaA, Weinheim

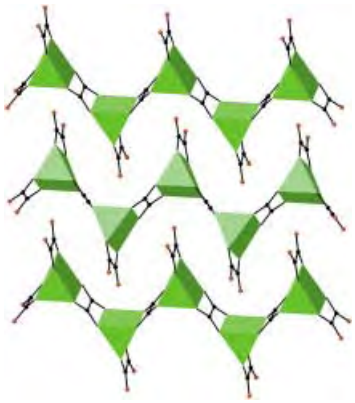


Computer modeling methods predict that the natural zeolite laumontite will undergo pressure-induced hydration. Specifically, the water-poor analogue "leonhardite" transforms to the fully hydrated laumontite structure (see picture), a transformation with significant geochemical impact. The models and methodologies employed are also capable of replicating the observed dehydration behavior of laumontite.

Zeolite Structures

C. L. I. M. White, A. R. Ruiz-Salvador, D. W. Lewis* ——— **469 – 472**

Pressure-Induced Hydration Effects in the Zeolite Laumontite



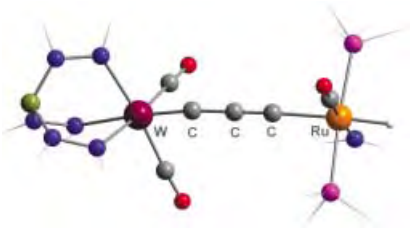
Imprismed metals: Hydrothermal crystallization of Fe and Co oxalates from extremely concentrated KBr solutions yield a coordination network where the paramagnetic metal ions are in rare coordination geometries (see structure). Both materials show a strong 1D magnetic character and for the Fe^{II} derivative no long-range order is seen above 2 K, making it a candidate for a Spin 2 quasi-1D quantum antiferromagnet.

Magnetic Materials

M. B. Hursthouse, M. E. Light, D. J. Price* ——— **472 – 475**

One-Dimensional Magnetism in Anhydrous Iron and Cobalt Ternary Oxalates with Rare Trigonal-Prismatic Metal Coordination Environment

Odd compounds: The study of bimetallic complexes spanned by linear carbon chains was mainly restricted to even-numbered chains. The fluorodesilylation of silylated propargylidynes now provides a range of C_3-spanned heterobimetallic complexes based on Ru and either Mo or W (e.g. see picture).



Polycarbon Bridges

R. D. Dewhurst, A. F. Hill,* M. K. Smith ——— **476 – 478**

Heterobimetallic C_3 Complexes through Silylpropargylidyne Desilylation



A real step-saver! In a one-step procedure for the synthesis of bicyclic amidines, the azido group is used directly as the nucleophile in the ring-forming reaction. Many functionalized and chiral bicyclic amidines were synthesized in good yield under mild reaction conditions.

Nitrogen Heterocycles

N. Kumagai, S. Matsunaga, M. Shibasaki* ——— **478 – 482**

An Efficient Synthesis of Bicyclic Amidines by Intramolecular Cyclization

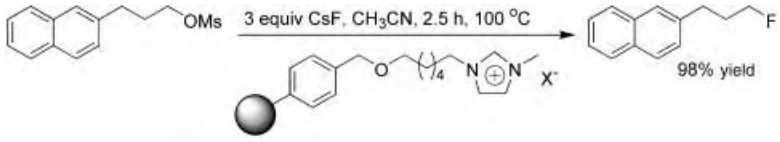
 © 2004 Wiley-VCH Verlag GmbH & Co. KGaA, Weinheim

Contents

Fluorination Catalysts

D. W. Kim, D. Y. Chi* ——— **483 – 485**

Polymer-Supported Ionic Liquids: Imidazolium Salts as Catalysts for Nucleophilic Substitution Reactions Including Fluorinations

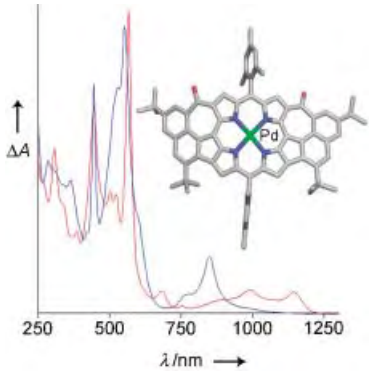


Ionic liquids obtain firm support: Polymer-supported imidazolium salts are shown to be highly efficient catalysts for fluorination and other nucleophilic substitution reactions. The polystyrene-based ionic materials catalyze fluorination reactions (such as that shown in the scheme; $X = BF_4$, OTf) in very high yield, and can be reused for many such reactions.

Small-Bandgap Porphyrins

H. S. Gill, M. Harmjanz, J. Santamaría, I. Finger, M. J. Scott* ——— **485 – 490**

Facile Oxidative Rearrangement of Dispiro-Porphodimethenes to Nonplanar and Sheetlike Porphyrins with Intense Absorptions in the Near-IR Region

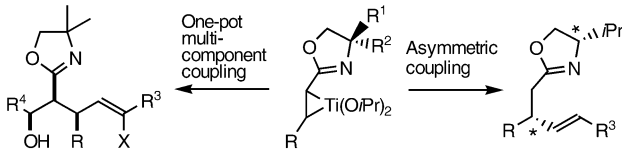


Exceedingly large, planar porphyrin systems composed of 49 non-hydrogen nuclei in highly delocalized π systems display exceptionally low-energy transitions in UV/Vis/NIR spectroscopy and in cyclic voltammetry. The spectra shown are for *cis* palladium complex depicted and the corresponding *trans* isomer

Asymmetric Synthesis

K. Mitsui, T. Sato, H. Urabe,* F. Sato* ——— **490 – 492**

Stereoselective Construction of Acyclic Carbon Chains by a One-Pot Coupling Process Based on Alkenyloxazoline–Titanium Complexes

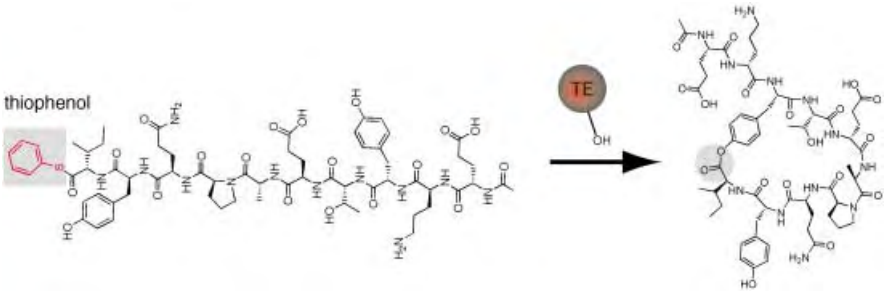


A versatile organometallic intermediate, an alkenyloxazoline–titanium complex, has been developed that enables one-pot multicomponent diastereoselective and asymmetric coupling processes to be achieved in a remarkably efficient manner (see scheme).

Peptide Cyclization

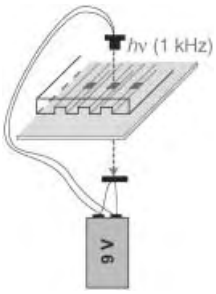
S. A. Sieber, J. Tao, C. T. Walsh, M. A. Marahiel* ——— **493 – 498**

Peptidyl Thiophenols as Substrates for Nonribosomal Peptide Cyclases



Activity-based enzyme acylation: Although small peptides are specifically cyclized by nonribosomal peptide cyclases (thioesterases, TEs) in nature, artificial *N*-acetylcysteamine thioester (SNAC) mimics have often failed to act as substrates for these enzymes in vitro. However, new reactive peptidyl aromatic thioesters solve this problem by selective acylation of the enzyme active site (see scheme).

© 2004 Wiley-VCH Verlag GmbH & Co. KGaA, Weinheim

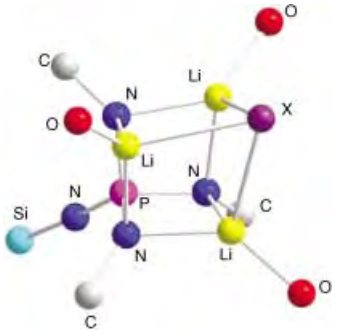


An integrated approach for detecting proteins that is low-cost, portable, battery-operated, and works under field conditions such as direct sunlight has been developed. The "POCKET immunoassay" uses commercially available components, and exhibits an analytical performance approaching that of established bench-top techniques. It may be appropriate for the diagnosis of infectious diseases, such as HIV/AIDS, in developing countries (see picture).

Analytical Methods

S. K. Sia, V. Linder, B. A. Parviz, A. Siegel, G. M. Whitesides* ——— **498 – 502**

An Integrated Approach to a Portable and Low-Cost Immunoassay for Resource-Poor Settings

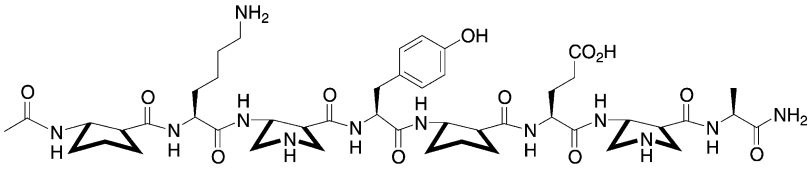


Stable, deep-blue neutral radicals $[(Me_3SiN)P(\mu_3\text{-}NtBu)_3\{\mu_3\text{-}Li(thf)\}_3X]$ (X = Br, I) with distorted cubic structures are obtained by the oxidation of $[\{Li_3[P(NtBu)_3(NSiMe_3)]\}_2]$ with halogens in THF (see picture). The cubes comprise the radical dianion $[P(NtBu)_3(NSiMe_3)]^{\bullet 2-}$, two Li^+ ions, and a molecule of LiX. Solvation in very dilute THF solution releases $(thf)_3LiX$ and generates the cyclic radical monoanion $[(Me_3SiN)(tBuN)P(\mu\text{-}NtBu)_2Li(thf)_2]^{\bullet -}$.

Radicals

A. Armstrong, T. Chivers,* M. Parvez, R. T. Boeré ——— **502 – 505**

Stable Cubic Phosphorus-Containing Radicals

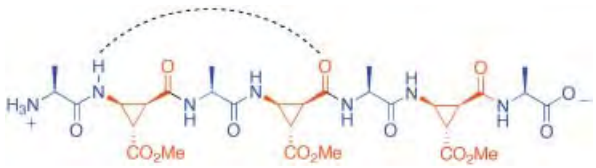


Oligopeptides with heterogeneous backbones, i.e., oligopeptides containing more than one monomer type, may be a fruitful source of new foldamers. This conclusion was suggested by studies on oligomers comprising L-α-amino acid and cyclic β-amino acid residues in a sequentially alternating pattern, which are shown to display helical secondary structure in solution.

Peptide Design I

A. Hayen, M. A. Schmitt, F. N. Ngassa, K. A. Thomasson,* S. H. Gellman* ——— **505 – 510**

Two Helical Conformations from a Single Foldamer Backbone: "Split Personality" in Short α/β-Peptides



With as few as seven residues, acyclic α/β-peptides, which consist of alternating units of (L)-alanine and of *cis*-β-amino-cyclopropanecarboxylic acids (*cis*-β-ACCs, see structure), form stable 3_{13}-helix turns in solution. The configuration of the *cis*-β-ACCs was found to be crucial for the helical structure of this new class of foldamers.

Peptide Design II

S. De Pol, C. Zorn, C. D. Klein, O. Zerbe,* O. Reiser* ——— **511 – 514**

Surprisingly Stable Helical Conformations in α/β-Peptides by Incorporation of *cis*-β-Aminocyclopropane Carboxylic Acids

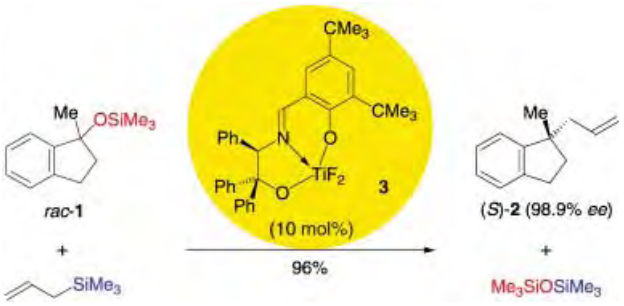
 © 2004 Wiley-VCH Verlag GmbH & Co. KGaA, Weinheim

Contents

Carbon Allylation

M. Braun,* W. Kotter ——— **514 – 517**

Titanium(IV)-Catalyzed Dynamic Kinetic Asymmetric Transformation of Alcohols, Silyl Ethers, and Acetals under Carbon Allylation



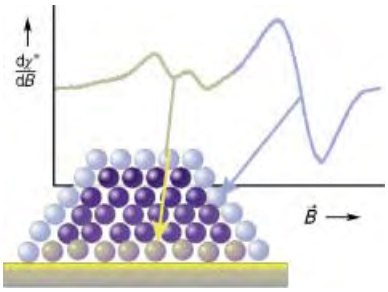
High yields and enantioselectivities are obtained in a dynamic kinetic asymmetric transformation in which the C—O bond of alcohols, silyl ethers, and acetals are substituted by a C—C bond. For example, the racemic indanyl silyl ether **1** is converted into (*S*)-**2** in the presence of the chiral Lewis acidic Ti^{IV} complex **3**.

Ferromagnetic Resonance

T. Risse,* M. Mozaffari-Afshar, H. Hamann, H.-J. Freund ——— **517 – 520**

Structural Changes in Nanoparticle Catalysts as Monitored by Their Magnetic Properties

Interfaces of supported metal nanoparticles, in particular the metal–support interface, are still very difficult to characterize. Since magnetic properties are strongly correlated to structural properties, ferromagnetic resonance spectroscopy can be used (see picture). The high sensitivity of the method is demonstrated for processes at both the particle–gas and the particle–support interface.

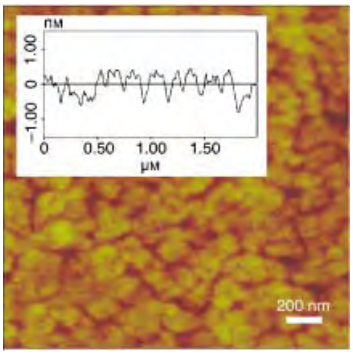


Surface Chemistry

P. Gupta, K. Loos, A. Korniakov, C. Spagnoli, M. Cowman, A. Ulman* ——— **520 – 523**

Facile Route to Ultraflat SAM-Protected Gold Surfaces by "Amphiphile Splitting"

Self-assembled monolayers of both aliphatic and aromatic thiols can be produced with no apparent contact-angle hysteresis by a modified "template-stripping" method. Organothiol solutions serve as splitting reagents for the removal of the mica from the gold surface. These new ultrasmooth SAM surfaces (see the AFM image) provide new information on interfacial properties including wetting and adhesion.



VIP Communications labeled with this symbol have been judged by two referees as being "very important papers".

The publication of Communications labeled with this symbol has been accelerated because of their topical or highly competitive nature.

© 2004 Wiley-VCH Verlag GmbH & Co. KGaA, Weinheim

Looking for outstanding employees?

Do you need another expert for your excellent team?
... Chemists, PhD Students, Managers, Professors, Sales Representatives...

Place an advert in the printed version and have it made available online for 1 month, free of charge!

Angewandte Chemie International Edition
Advertising Sales Department: Marion Schulz
Phone: 0 62 01 - 60 65 65
Fax: 0 62 01 - 60 65 50
E-Mail: MSchulz@wiley-vch.de

Service

Keywords ____ *524*

Authors ____ *525*

Angewandte's Sister Journals *526 – 527*

Preview ____ *529*

Speakers

Steve Adams (UCSD, San Diego)
Philippe Bastiaens (EMBL Heidelberg)
Annette Beck-Sickinger (Leipzig University)
Craig Crews (Yale University, New Haven)
Michael Famulok (Bonn University)
Theodorus Gadella (Amsterdam University)
A. Ganesan (University of Southampton)
Carine Giovannangeli (MNHN, Paris)
Kai Johnson (EPFL Lausanne)
Thomas Mayer (MPI Martinsried)
Tim Mitchison (Harvard Univ., Cambridge)
Peter Nielsen (PI Copenhagen)
Jan-Michael Peters (IMP Vienna)
Greg Petsko (Brandeis University, Waltham)
Orlando Schärer (Zürich University)
Ilme Schlichting (MPI Heidelberg)
Carsten Schultz (EMBL Heidelberg)
Peter Seeberger (ETH Zürich)
Oliver Seitz (Humboldt University, Berlin)
Herbert Waldmann (MPI Dortmund)

Speakers

2nd **EMBO Young Investigator Programme** Symposium

EMBO

Chemistry meets Biology

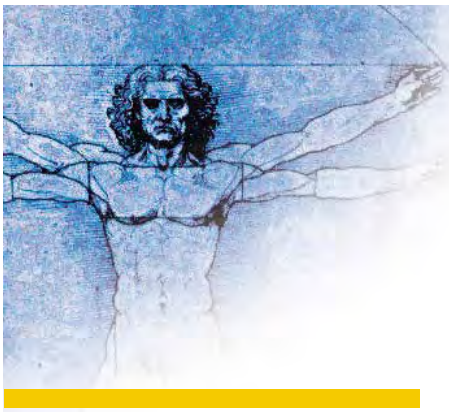
Chemical Approaches to the Study of Biology

5–6 June 2004

EMBL Heidelberg | Germany

For further information and online registration please visit **www.embo.org/projects/yip/chemicalbiologyindex.html** or send an e-mail **yip@embo.org**

 © 2004 Wiley-VCH Verlag GmbH & Co. KGaA, Weinheim



IBM Prize to T. Kato and K. Awaga

Since 1987 the IBM Japan Science Prize has been awarded annually to six scientists for basic research in the fields of physics, chemistry, computer science, and electronics. The recipients must be under 45 years of age and have made significant contributions in their career. In 2003 there were two chemists among the prizewinners.

Takashi Kato (University of Tokyo) was awarded the Prize for his work toward the development of new functional polymers and liquid crystals. After completing his PhD in 1988 at the University of Tokyo, Kato carried out postdoctoral research at Cornell University (Ithaca, NY, USA) on supramolecular, hydrogen-bridge-supported liquid crystals with J. M. J. Fréchet. He then returned to the University of Tokyo, where he is now professor. His research is focused on the development of self-organized, functional materials, such as supramolecular liquid crystals, liquid-crystalline gels, and low-dimensional ion-conducting liquid crystals, and the synthesis of organic–inorganic composite materials by mimicking biomineralization. He recently described "Self-Organized Calcium Carbonate with Regular Surface-Relief Structures" in *Angewandte Chemie*.[1]



T. Kato



K. Awaga

A further IBM Prize went to Kunio Awaga (Nagoya University) in recognition of his work on molecular magnets in three main areas: the synthesis, characterization, and theoretical description of organic ferromagnets, low-dimensional magnets and molecular spin ladders, and the development of functional magnetic materials, in particular materials based on thiazyl radicals. Awaga studied and completed his PhD at the University of Tokyo, became associate professor there in 1992, and in 2001 professor at the University of Nagoya. In his most recent Communication in *Angewandte Chemie* he reported on packing motifs and crystal growth in porphyrazine macrocycles with peripherally annulated thiadiazole rings.[2]

Leibniz Prize to T. Carell

Prizes in the Gottfried Wilhelm Leibniz Program of the Deutsche Forschungsgemeinschaft are awarded annually to outstanding scientists from all research disciplines. At the end of 2003, 11 awards were made, each worth € 1550000.

One of the prizes went to the chemist Thomas Carell. Carell studied chemistry in Münster and Heidelberg (Germany), completed his PhD in 1993 under the guidance of H. A. Staab at the Max-Planck-Institut für medizinische Forschung in Heidelberg, and then went as a postdoctoral researcher to J. Rebek at the Massachusetts Institute of Technology (Cambridge, MA, USA). Following this postdoctoral period he completed his habilitation with F. Diederich at the ETH Zürich (Switzerland). In 2000 he took up a position as full professor at the University of Marburg (Germany) and moved to the Universität München (Germany) in December 2003 to succeed W. Steglich. His research is characterized by two main topics: the repair and mutagenesis of DNA, and the biophysical properties of DNA and hybrid compounds based on DNA or inspired by its structure. His latest Communication in *Angewandte Chemie* is entitled "The Two Main DNA Lesions 8-Oxo-7,8-dihydroguanine and 2,6-Diamino-5-formamido-4-hydroxypyrimidine Exhibit Strongly Different Pairing Properties".[3]



T. Carell

New GDCh President H. Hopf

The Board of the Gesellschaft Deutscher Chemiker (German Chemical Society) has elected Henning Hopf as president for 2004 and 2005. He succeeds Fred-Robert Heiker (Bayer AG). After completing his habilitation in 1972 at the Universität Karlsruhe (Germany), Hopf became professor at the Universität Würzburg. He has held his current position as Professor of Organic Chemistry at the Technische Universität Braunschweig since 1979. His research interests include cyclophanes and highly unsaturated hydrocarbons, such as cumulenes, which feature in his fundamental work "Classics in Hydrocarbon Chemistry" (Wiley-VCH **2000**). His most recent Communication in *Angewandte Chemie* is on liquid-crystalline cyclophane derivatives.[4] Hopf has always been involved in publishing, not only as the author of articles and books, but also as an editor (most recently of "Humoristische Chemie" with Ralf Jakobi, Wiley-VCH **2003**). He played a fundamental role in stimulating the reorganization of the European chemistry journals and is currently chairman of the Editorial Board of the *European Journal of Organic Chemistry*.



H. Hopf

[1] A. Sugawara, T. Ishii, T. Kato, *Angew. Chem.* **2003**, *115*, 5457; *Angew. Chem. Int. Ed.* **2003**, *42*, 5299.

[2] M. Fujimori, Y. Suzuki, H. Yoshikawa, K. Awaga, *Angew. Chem.* **2003**, *115*, 6043; *Angew. Chem. Int. Ed.* **2003**, *42*, 5863.

[3] M. Ober, U. Linne, J. Gierlich, T. Carell, *Angew. Chem.* **2003**, *115*, 5097; *Angew. Chem. Int. Ed.* **2003**, *42*, 4947.

[4] E. L. Popova, V. I. Rozenberg, Z. A. Starikova, S. Keuker-Baumann, H.-S. Kitzerow, H. Hopf *Angew. Chem.* **2002**, *114*, 3561; *Angew. Chem. Int. Ed.* **2002**, *41*, 3411.

 © 2004 Wiley-VCH Verlag GmbH & Co. KGaA, Weinheim

A Tunneling Event

Do Heavy Nuclei See Light at the End of the Tunnel?

*Robert Berger**

Keywords:
carbenes · density functional calculations · IR spectroscopy · matrix isolation · tunneling

The most direct way to the valley on the other side of a ridge passes right through the mountain. This unsurprising insight, however, does not open up new possibilities for classical particles, since they have typically only a single option for surmounting a ridge, namely, to try to climb a suitable mountain pass. Any such attempt will be crowned with success only if the particles are equipped with sufficient energy for overcoming the highest point of the pass. As early as in 1927 Friedrich Hund pointed out,[1] however, that quantum mechanics is in this respect more generous to its particles: Just as if there were horizontal tunnels right through the mountain, quantum-mechanical particles have a nonvanishing probability for reaching the other side of a finite barrier even if their energy is below the threshold energy of the mountain pass. In return, however, particles in the quantum world are plagued by nonclassical reflection at the barrier even at energies above the threshold. Chances for tunneling are usually considered good for light particles like, for instance, electrons or protons, but the probability of a tunneling event is commonly believed to be almost negligible for heavier nuclei. The evidence for significant C nucleus tunneling in a chemical reaction with a sizable barrier reported recently by Zuev et al.[2] contradicts this widely accepted notion and is thus of particular importance for our understanding of quantum effects in chemical processes.

It is due to their wavelike properties that quantum-mechanical particles are able to penetrate finite barriers and have therefore a nonvanishing probability of reaching classical forbidden regions of the coordinate space. This dynamic passage through the barrier is already reflected on the level of the stationary energy eigenstates. If we consider, for instance, a one-dimensional problem, a particle in a bound eigenstate with a corresponding energy below a finite barrier separating two potential wells will not be detected exclusively on one and the same side of the barrier.[3] In the special case of a symmetric potential, moreover, a particle prepared in an energy eigenstate will even be measured with equal probability in each of the two wells, regardless of the particular finite height of the barrier. In the limit of a high barrier, these eigenstates in a symmetric potential come in almost degenerate pairs of a symmetric and an antisymmetric state, which give rise to the well-known tunneling splitting for instance in the microwave and infrared spectra of the prototype system ammonia. Hund realized[3] that tunneling leads apparently to a paradoxical situation for chiral compounds, for which such symmetric (parity-conserving) potentials were assumed. But he argued that once a chiral state of a typical optically active compound has been generated, its interconversion to its mirror-image as a result of tunneling will take a million years or more. Nowadays it is assumed, however, that the fundamental parity-violating interactions destroy this symmetry for chiral systems and induce a slight energy difference between the enantiomers which would have substantial consequences for the dynamics of chiral molecules (see ref. [4] for a review and, for instance, ref. [5] for recent calculations on parity-violating effects in chiral molecules).

The concept of tunneling received particular interest in the nuclear physics community, when Gamov[6] as well as Gurney and Condon[7] proposed quantum-mechanical tunneling to be crucial for the nuclear α-decay process. Gamov demonstrated that the energy-dependent transmission coefficient $T(E)$ in a one-dimensional system can for sufficiently small values of $T(E)$ be approximated with the proportionality relation (1).

$$T(E) \propto \exp[-(4\pi/h)\int_a^b \sqrt{2m\,(V(x)-E)}\,\mathrm{d}x] \quad (1)$$

Here, h is Planck's constant, $V(x)$ the coordinate-dependent potential energy, E the total energy, and m the tunneling mass. For $x=a$ and $x=b$, $E=V(a)=V(b)$. Therefore, the probability for tunneling depends strongly on the width and the height of the barrier as well as on the particle's mass, which underlines the pronounced importance of tunneling for light rather than heavy particles.

In the early stages of the development of the transition-state theory for chemical reactions by Eyring, Evans and Polanyi, and others,[8] (see also ref. [9]), which provides an avenue to the ab initio calculation of absolute rate constants of chemical reactions, it was already recognized that tunneling through the potential barrier should be accounted for. In this context Wigner[10,11] emphasized that tunneling plays a particular role in two distinct cases: Firstly, if molecules have almost enough energy to overcome the potential barrier, and secondly, if the potential barrier is thin

[*] Dr. R. Berger
Institut für Chemie
Technische Universität Berlin
Strasse des 17. Juni 135, 10623 Berlin (Germany)
Fax: (+49) 30-314-21102
E-mail:
Robert.Berger@www.chem.tu-berlin.de

 © 2004 Wiley-VCH Verlag GmbH & Co. KGaA, Weinheim DOI: 10.1002/anie.200301675

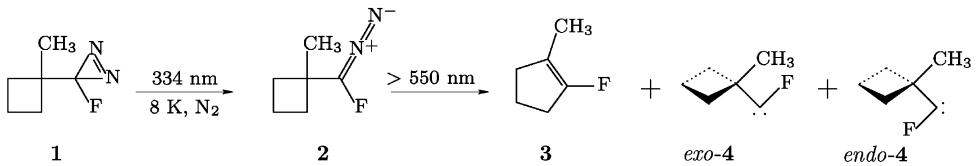
and high and the temperature is very low. In the former situation, tunneling should lead, according to Wigner, only to a correction of the classically calculated rate constants (see, however, for example also ref. [12]). It was concluded that apart from reactions involving hydrogen tunneling, corrections can be neglected at ordinary temperatures.[11] Indeed, for numerous proton-, hydrogen-atom-, and hydride-transfer reactions significant tunneling contributions have been identified.[13]. Experimental evidence for tunneling in these reactions is, apart from measurements of tunneling splittings in infrared or microwave spectra discussed above, generally obtained from nonlinearities in Arrhenius plots ($\ln k$ vs T^{-1} plots), from an unusual ratio of the proton vs the deuterium or the tritium Arrhenius prefactor, or from pronounced and temperature-dependent kinetic isotope effects (see, however, recent results on kinetic isotope effects in multiple-proton-transfer reactions[14]) to name but a few. While in principle all nuclei of a system may contribute to some extent to the tunneling motion and therefore it is often not well justified to attribute the entire process to the tunneling of a single nucleus, reactions for which evidence for significant heavy-nucleus tunneling exist are scarce and even those suggested as potential candidates are contested (see refs. [15–19] for a discussion on heavy-nucleus tunneling in the cyclobutadiene automerization reaction; ref. [20] reports tunneling in isonitrosyl chloride, while ref. [21] gives a more sceptical view and [22–25] discuss other proposals of heavy-nucleus tunneling). Typically, for these systems the second mechanism, which Wigner identified as the prevailing contribution at very low temperatures, is relevant. Thin, high barriers result in only a weak temperature dependence of the reaction rate in the low-temperature regime. Wigner concluded, however, that then the reaction rate is too low to be of practical importance.

Contradicting Wigner's conclusion, Zuev et al.[2] presented recently chemical reactions in matrices at cryogenic temperatures for which the authors ascribed the significant reaction rate to carbon-nucleus tunneling. These authors reported that ultraviolet irradiation ($\lambda = 334$ nm) of 3-(1-methylcyclobutyl)-3-fluorodiazirine (**1**, Scheme 1), which was isolated in an N_2 matrix at 8 K, produced a compound with a strong IR absorption at 2027 cm^{-1}, which was assigned to 1-(diazofluoromethyl)-1-methylcyclopropane (**2**). Upon subsequent irradiation with visible light ($\lambda >$ 550 nm), this compound was transformed partly into 1-fluoro-2-methylcyclopentene (**3**), identified by comparison with the IR spectrum of an authentic sample, and partly into a compound with several intense IR signals around 1100 cm^{-1}. In view of its further chemical reactions as well as by comparison with computed IR and UV/Vis properties this was assigned to (1-methylcyclopropyl)fluorocarbene (**4**), which according to the accompanying quantum-chemical calculations should exist as two isomers, an *exo* and an *endo* form. When **4** was exposed to visible light ($\lambda =$ 436 nm), Zuev et al. observed rapid conversion of the fluorocarbene **4** into the cyclopentene **3**. But even at a temperature of 8 K and in the dark, slow formation of **3** was detected. The kinetics of this interconversion were then studied with the aid of IR spectroscopy by monitoring the change in intensity of two intense IR signals for *exo*- and *endo*-**4** and the increase of the signal corresponding to the C=C stretching fundamental of **3**.

The results of this study were interpreted as follows: At 8 K in the nitrogen matrix, the *endo* form of **4** was essentially unreactive while the *exo* conformer of **4**, which appears to be properly oriented for the intramolecular insertion of a carbene into the C–C σ bond, underwent slow reaction with approximately first-order kinetics and a corresponding rate constant of $k(8\,K) \approx 4 \times 10^{-6}\,s^{-1}$. At 16 K the *exo* conformer disappeared initially 12 times faster than at 8 K but due to deviations from first-order kinetics (a phenomenon that may be caused by varying reaction barriers at different matrix sites[26]) the corresponding rate constant dropped to a value that was only about two times larger than at 8 K. Disappearance of the slower reacting *endo* conformer was also observed at this temperature with an initial rate constant of $6 \times 10^{-6}\,s^{-1}$, which dropped to $1 \times 10^{-6}\,s^{-1}$ after 65% conversion. At 25 K both conformers of **4** disappeared ten times as fast as at 16 K.

In an argon matrix both conformers of **4** reacted already at 8 K with a rate constant for the disappearance of *exo*-**4** of $4 \times 10^{-5}\,s^{-1}$ at 8 K, and the reaction was about twice as fast at 16 K. This relatively modest rise of the reaction constant with doubling the absolute temperature was considered to be inconsistent with a thermally activated process. It was therefore concluded that the ring-expansion reaction of fluorocarbene **4** proceeds by means of carbon-nucleus tunneling. The experimentally observed increase of the rate constant with rising temperature in this low-temperature regime was construed as an environmental effect on the carbene lifetime, for which in particular matrix softening was suggested to be responsible.

The supposition of heavy-nucleus tunneling was supported by accompanying quantum-chemical calculations. The reaction enthalpy of the ring-expansion reaction was computed with density functional theory (modified Perdew–Wang hybrid functional with one parameter adjusted for kinetics (MPW1K), 6-31 + G(d,p) basis set) to amount to $\Delta_r H_0^0 = -328\,kJ\,mol^{-1}$, and the activation enthalpy was obtained as $\Delta^{\neq} H_0^0 = 27\,kJ\,mol^{-1}$. This barrier appears to be too high to be surmounted by thermal activation in the temperature range studied (< 25 K). Indeed, direct



Scheme 1. The photochemical conversion of matrix-isolated **1** leads to *exo*- and *endo*-(1-methylcyclobutyl)fluorocarbene (*exo*- and *endo*-**4**).

 © 2004 Wiley-VCH Verlag GmbH & Co. KGaA, Weinheim

dynamics calculations in the framework of canonical variational transition-state theory[27] predict a low-temperature limit for the rate constant of about $9 \times 10^{-6}\,s^{-1}$ when tunneling contributions are accounted for (here within the small-curvature tunneling approximation, see ref. [28]). Computations with exclusion of tunneling, in contrast, predict a rate constant at 8 K that is smaller by a factor of about 10^{152}. This astounding ratio results, however, plainly as a consequence of the finite low-temperature-limit for the tunneling process as opposed to the vanishing classical barrier-hopping in this limit. Tunneling at 8 K originates according to the calculations nearly exclusively from the vibrational ground state. The tunneling mode's first excited vibrational state contributes to the rate constant by only about 0.04% at this temperature. Figure 1 sketches the vibrational adiabatic ground-state potential curve along the reaction path together with representative molecular structures and with the lowest two vibrational levels in the tunneling mode. Evidently, significant movement of the heavy nuclei is involved in the tunneling processes along this particular path.

As noted by Wigner, due to the tunneling through the barrier the rate constant depends only weakly on the temperature in this temperature range. According to the calculations, for temperatures below 20 K the rate constant deviates by less than 10% from the low-temperature limit. The Arrhenius activation energy E_a increases according to the calculations from $0.3\,J\,mol^{-1}$ at 8 K to $1.2\,kJ\,mol^{-1}$ at 40 K to $23.6\,kJ\,mol^{-1}$ at 150 K. At 216 K the contribution to the rate constant from the classical over-the-barrier and from the quantum-mechanical through-the-barrier processes are equal, and at room temperature the classical process contributes roughly three times more strongly than the tunneling process. This clearly demonstrates that tunneling is also a temperature-activated process since in higher vibrational states the barrier width is typically smaller and tunneling is therefore more likely.

Unless the underlying potential energy hypersurface fails to properly describe the relevant energetics of the reaction, the computations indicate that heavy-nucleus tunneling is the dominating dynamic process of the low-temperature ring expansion of (1-methylcyclopropyl)fluorocarbene. In contrast to most systems for which heavy-nucleus tunneling has been proposed, contributions from electronic triplet states may be neglected for fluorocarbene **4**, since typically the triplet states in fluorocarbenes are energetically well removed. Although a rigorous treatment of tunneling requires in principle the solution of the full-dimensional rovibratoric Schrödinger equation, experience with reaction-path and -surface Hamiltonian treatments shows that main features can often be reproduced successfully (see for instance ref. [29] for calculations on torsional tunneling splittings in hydrogen peroxide).

The reasonable agreement between the computed and the measured orders of magnitude for the rate constant in the present reaction studied by Zuev et al. provides further evidence. A more detailed comparison with the quantum-chemical calculations, which neglect the surrounding medium, requires, however, that experimentally the sources for deviations from first-order kinetics are quantified. Here in particular also the interconversion of *endo*- to *exo*-**4** should be included in an improved modelling. Experiments performed with different matrices will perhaps further substantiate the supposed matrix-softening effect made responsible for the observed temperature-dependence of the rate constant. It will then be particularly interesting to experimentally extend the studied temperature range to above 40 K, where a significant increase of the Arrhenius activation energy is predicted by theory. Some indirect evidence, however, is obtained from the study of the rearrangement of the chloro analogue of **1**. Zuev et al. did not detect the corresponding cyclobutylchlorocarbene. Accompanying computations suggest that in the cyclobutylchlorocarbene the probability of tunneling through the barrier is so large that the rate constant at 8 K is about $1 \times 10^4\,s^{-1}$, and therefore the reaction to 1-chloro-2-methyl-cyclopentene proceeds too fast for the alkylchlorocarbene to be observable in the experiment.

Three-quarters of a century after the concept of tunneling was introduced by Friedrich Hund, it is still one of the most intriguing quantum effects in chemistry. Quantum phenomena in heavier systems are still at the frontier of current research, and they are related to important fundamental questions including the long-term prospect of the prepara-

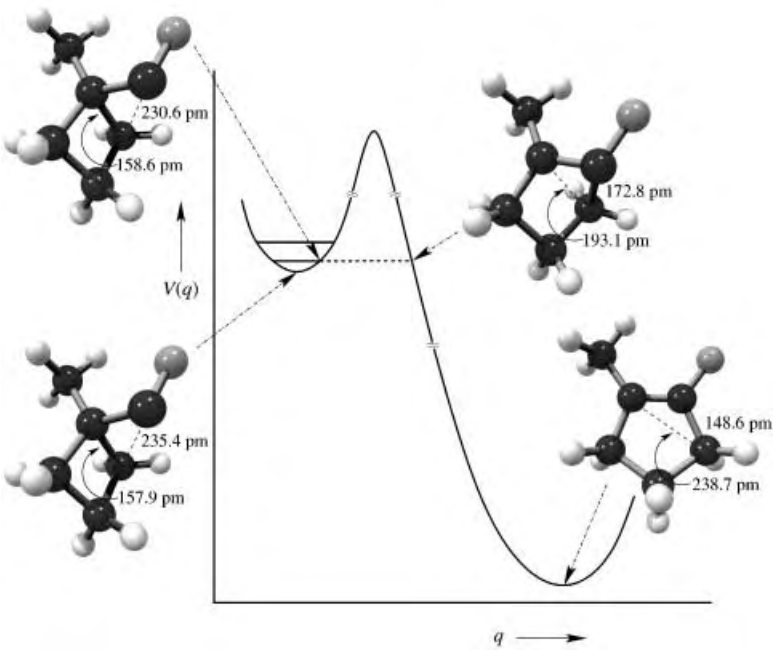


Figure 1. Representative structures along the reaction path *q* for the ring-expansion reaction of (1-methylcyclobutyl)fluorocarbene (**4**). The graph is based on Figure 3 in ref. [2]. Black: C, gray: F, white: H.

 © 2004 Wiley-VCH Verlag GmbH & Co. KGaA, Weinheim

tion of superposition states for heavy or even macroscopic objects. Zuev et al. have indicated that even for heavy nuclei there is light at the end of the tunnel. This work may therefore be an important further step in the direction of a better understanding and control of quantum phenomena in chemistry.

[1] F. Hund, *Z. Phys.* **1927**, *40*, 742 – 764.

[2] P. Zuev, R. Sheridan, T. Albu, D. Truhlar, D. Hrovat, W. Borden, *Science* **2003**, *299*, 867 – 870.

[3] F. Hund, *Z. Phys.* **1927**, *43*, 805 – 826.

[4] a) M. Quack, *Angew. Chem.* **1989**, *101*, 588 – 604; *Angew. Chem. Int. Ed. Engl.* **1989**, *28*, 571 – 586; b) M. Quack, *Angew. Chem.* **2002**, *114*, 4812 – 4825; *Angew. Chem. Int. Ed.* **2002**, *41*, 4618 – 4630.

[5] a) R. Berger, M. Quack, *J. Chem. Phys.* **2000**, *112*, 3148 – 3158; b) R. Berger, M. Quack, *ChemPhysChem* **2000**, *1*, 57 – 60; c) J. Laerdahl, P. Schwerdtfeger, *ChemPhysChem* **2000**, *1*, 60 – 62; d) R. Berger, M. Quack, G. Tschumper, *Helv. Chim. Acta* **2000**, *83*, 1919 – 1950; e) M. Quack, J. Stohner, *Phys. Rev. Lett.* **2000**, *84*, 3807 – 3810; f) J. Laerdahl, P. Schwerdtfeger, H. Quiney, *Phys. Rev. Lett.* **2000**, *84*, 3811 – 3814; g) R. Berger, M. Quack, J. Stohner, *Angew. Chem.* **2001**, *113*, 1716 – 1719; *Angew. Chem. Int. Ed.* **2001**, *40*, 1667 – 1670; h) R. Berger, M. Gottselig, M. Quack, M. Willeke, *Angew. Chem.* **2001**, *113*, 4342 – 4345; *Angew. Chem. Int. Ed.* **2001**, *40*, 4195 – 4198; i) M. Gottselig, D. Luckhaus, M. Quack, J. Stohner, M. Willeke, *Helv. Chim. Acta* **2001**, *84*, 1846 – 1861; j) T. Kitayama, H. Kiyonaga, K. Morihashi, O. Takahashi, O. Kikuchi, *J. Mol. Struct.* **2002**, *589–590*, 183 – 193; k) A. Hennum, T. Helgaker, W. Klopper, *Chem. Phys. Lett.* **2002**, *354*, 274 – 282; l) R. Berger, *Phys. Chem. Chem. Phys.* **2003**, *5*, 12 – 17; m) P. Schwerdtfeger, J. Gierlich, T. Bollwein, *Angew. Chem.* **2003**, *115*, 1331 – 1334; *Angew. Chem. Int. Ed.* **2003**, *42*, 1293 – 1296; n) F. Faglioni, P. Lazzeretti, *Phys. Rev. A* **2003**, *67*, 032101; o) G. Laubender, R. Berger, *ChemPhysChem* **2003**, *4*, 395 – 399; p) A. Soncini, F. Faglioni, P. Lazzeretti, *Phys. Rev. A* **2003**, *68*, 033402.

[6] G. Gamov, *Z. Phys.* **1928**, *51*, 204 – 212.

[7] R. Gurney, E. Condon, *Phys. Rev.* **1929**, *33*, 127 – 140.

[8] a) H. Eyring, *J. Chem. Phys.* **1935**, *3*, 107; b) M. Evans, M. Polanyi, *Trans. Faraday Soc.* **1935**, *31*, 857.

[9] a) K. Laidler, M. King, *J. Phys. Chem.* **1983**, *87*, 2657 – 2664; b) W. Miller, *Faraday Discuss.* **1998**, *110*, 1 – 21; c) G. Petersson, *Theor. Chem. Acc.* **2000**, *103*, 190 – 195; d) B. Garrett, *Theor. Chem. Acc.* **2000**, *103*, 200 – 204 and references therein.

[10] E. Wigner, *Z. Phys. Chem. Abt. B* **1932**, *19*, 203 – 216.

[11] E. Wigner, *Trans. Faraday Soc.* **1938**, *34*, 29 – 41.

[12] J. Troe in *Tunneling*, *Vol. 19* (Eds.: J. Jortner, B. Pullman), Reidel, Dordrecht, **1986**, pp. 149 – 164.

[13] For a recent review on condensed-phase proton- and hydrogen-transfer reactions see: M. Basilevsky, M. Verner, *Russ. Chem. Rev.* **2003**, *72*, 1 – 33.

[14] Z. Smedarchina, W. Siebrand, A. Fernandez-Ramoz, Q. Cui, *J. Am. Chem. Soc.* **2003**, *125*, 243 – 251.

[15] B. Carpenter, *J. Am. Chem. Soc.* **1983**, *105*, 1700 – 1701 and references therein.

[16] A. Orendt, B. Arnold, J. Radziszewski, J. Facelli, K. Malsch, H. Strub, D. Grant, J. Michl, *J. Am. Chem. Soc.* **1988**, *110*, 2648 – 2650.

[17] B. Arnold, J. Radziszewski, A. Campion, S. Perry, J. Michl, *J. Am. Chem. Soc.* **1991**, *113*, 692 – 694.

[18] G. Maier, R. Wolf, H. Kalinowski, *Angew. Chem.* **1992**, *104*, 764 – 766; *Angew. Chem. Int. Ed. Engl.* **1992**, *31*, 738 – 740.

[19] P. Carsky, J. Michl, *Theor. Chim. Acta* **1992**, *84*, 125 – 133.

[20] A. Hallou, L. Schriver-Mazzuoli, A. Schriver, P. Chaquin, *Chem. Phys.* **1998**, *237*, 251 – 264.

[21] G. Maier, H. Reisenauer, M. de Marco, *Chem. Eur. J.* **2000**, *6*, 800 – 808.

[22] H. Frei, G. Pimentel, *J. Phys. Chem.* **1981**, *85*, 3355 – 3360.

[23] M. Sponsler, R. Jain, F. Coms, D. Dougherty, *J. Am. Chem. Soc.* **1989**, *111*, 2240 – 2252.

[24] W. Sander, G. Bucher, F. Reichel, D. Cremer, *J. Am. Chem. Soc.* **1991**, *113*, 5311 – 5322.

[25] S. Buchwalter, G. Closs, *J. Am. Chem. Soc.* **1979**, *101*, 4688 – 4694.

[26] W. Siebrand, T. Wildman, *Acc. Chem. Res.* **1986**, *19*, 238 – 243.

[27] D. Truhlar, B. Garrett, *Annu. Rev. Phys. Chem.* **1984**, *35*, 159 – 189.

[28] Y. Liu, G. Lynch, T. Truong, D. Lu, D. Truhlar, B. Garrett, *J. Am. Chem. Soc.* **1993**, *115*, 2408 – 2415 and references therein.

[29] a) B. Fehrensen, D. Luckhaus, M. Quack, *Z. Phys. Chem.* **1999**, *209*, 1 – 19; b) D. Luckhaus, *J. Chem. Phys.* **2000**, *113*, 1329 – 1347; c) S. Carter, N. Handy, *J. Chem. Phys.* **2000**, *113*, 987 – 993; d) R. Chen, G. Ma, H. Guo, *Chem. Phys. Lett.* **2000**, *320*, 567 – 574; e) V. Benderskii, I. Irgibaeva, E. Vetoshkin, H. Trommsdorff, *Chem. Phys.* **2000**, *262*, 369 – 391; f) J. Koput, S. Carter, N. Handy, *J. Chem. Phys.* **2001**, *115*, 8345 – 8350; g) Y. Guo, D. Thompson, *J. Phys. Chem. A* **2002**, *106*, 8374 – 8377.

 © 2004 Wiley-VCH Verlag GmbH & Co. KGaA, Weinheim

Homogenous Catalysis

Stable, Self-Assembling, Equilibrating Catalysts for Green Chemistry

*Craig L. Hill**

Keywords:
green chemistry · homogeneous catalysis · oxidation · oxygen · self-assembly

The development of catalysts that address most if not all the goals and operating principles in green chemistry remains a topic of considerable intellectual and practical significance.[1] A large number of homogeneous catalysts for selective oxidation of organic substrates under environmentally attractive conditions have been reported recently.[2] Many of these address the oxidation of alcohols to the corresponding carbonyl compounds, and some are operationally very compelling (selective, rapid, use green solvents or no solvent, simple to perform, and safe).[3,4] Some exhibit these attributes and also work with O_2.[3–6] In an ideal case, a catalyst would exhibit these operationally attractive features and also be indefinitely stable so that very high turnover numbers of product could be realized with little or no system modification. Key requisites for stability under oxidizing conditions are the lack of organic ligands, including phase-transfer cations, demonstration that a catalyst can self-assemble under full turnover conditions, and no inactivation from products or by-products.

Neumann and co-workers report a system that embodies and illustrates many of these principles. This work involves an H_2O_2-based oxidation (alcohols to aldehydes and ketones) involving a nontoxic medium (H_2O), a nontoxic catalyst (an early-transition-metal oxygen-anion cluster or polyoxometalate (POM), $Na_{12}[WZnZn_2(H_2O)_2(ZnW_9O_{34})_2]$ (**1**; Figure 1), and facile green workup conditions (separation of the aqueous phase containing the catalyst from the organic-solvent-free aldehyde/ketone phase).[7] It also addresses the overriding issue of catalyst and system stability and thus sustainability.

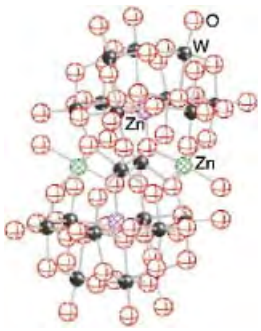


Figure 1. Structure of the polyoxometalate $Na_{12}[WZnZn_2(H_2O)_2(ZnW_9O_{34})_2]$ (**1**), taken from reference [7].

Oxidation processes present the most formidable ensemble of challenges to green yet viable operations, and the collective effort on the part of chemists and engineers in this area parallels the magnitude of these difficulties.[2,8] One challenge is to use the most environmentally and economically attractive oxidants, H_2O_2 and O_2/air. These oxidants and the stoichiometries of their optimal reactions are both green (the only by-product is H_2O) and atom-efficient.[8,9] However, reactivity and selectivity problems abound with these oxidants. H_2O_2 is not sufficiently reactive below its thermal decomposition temperature and therefore a catalyst is usually required for adequate rates to be realized.[10] It is far less reactive than the toxic and carcinogenic stoichiometric oxidants traditionally used for such oxidations (most frequently Cr^{VI} reagents).[1,5] Selectivity is a generic problem in reductant-free O_2-based oxidations. Under these conditions, radical chain oxidation (autoxidation) processes dominate. Except for a couple of special cases in which the structures of the organic substrate and product dictate high selectivity at high conversion (e.g. oxidation of *p*-xylene to terephthalic acid), these reactions are both minimally selective and difficult to control.[9,11] Furthermore, chlorinated hydrocarbons and other environmentally deleterious solvents are conventionally used for homogenous organic oxidation reactions because they simply result in the highest rates and best selectivities.[8] The alternative media for green reactions, including supercritical solvents, ionic liquids, and fluorous biphasic systems, all promise distinct advantages, but each also comes with concerns, (cost, solubility issues, disposal, or other lifetime analysis limitations, etc.).[12] None can match H_2O for ease of use and safety. However, H_2O frequently inhibits catalytic turnover by competing with the substrate and/or key intermediates for vacant coordination sites on the catalyst.

The report of selective and rapid alcohol oxidations by Neumann and coworkers goes beyond the effective use of H_2O_2 in H_2O solvent with facile product separation in that it addresses catalyst stability in a conceptually important way.[7] Catalyst stability dictates sustainability and attendant cost issues, but also has an impact on the key reactivity requisites of a successful catalyst system (rate, selectivity at high conversion, etc.). If a catalyst is degraded during turnover by oxidative, hydrolytic, or other means, selectivity is lost and often

[*] Dr. C. L. Hill
Department of Chemistry, Emory University
1515 Dickey Dr., Atlanta, GA 30322 (USA)
Fax: (+1) 404-727-6076
E-mail: chill@emory.edu

 © 2004 Wiley-VCH Verlag GmbH & Co. KGaA, Weinheim DOI: 10.1002/anie.200301701

the reaction rate also decreases. As a consequence, a great deal of effort has been expended on kinetic stabilization of the organic ligands in homogeneous oxidation catalysts. Electron-withdrawing functional groups on the periphery of the ligand(s), intrinsically unreactive macrocycles such as phthalocyanines, and innovative ligand structures have all been reported repeatedly.[1,8,13–15] Unfortunately all organic ligands remain thermodynamically unstable with respect to oxidation to CO_2 and H_2O. Also, these ligand-modification efforts are generally prohibitively expensive for the resulting catalysts to be practically viable for all processes except those involving the most costly products such as chiral species. Polydentate POM units are the one type of ligand for homogeneous oxidation catalysts that are both thermodynamically stable to oxidative decomposition under turnover conditions and extensively modifiable.[16] Since the initial report of selective homogeneous oxidation (oxygenation of olefins) catalyzed by transition-metal-substituted POMs, their collective attractive properties have inspired considerable ongoing research.[17]

A conceptual step beyond thermodynamically stable ligands for homogeneous oxidation catalysts is the ability of a catalyst to self-assemble from simple, synthetic, oxidatively stable precursors under turnover conditions. The self-assembly of a catalyst under conditions similar to those used in catalysis is not a new concept and has been used in previous studies of homogeneous oxidation catalysts.[3,4] This concept ensures short-term sustainability of a homogeneous catalyst. If the system also contains thermodynamically stable ligands such as many POMs in appropriate pH ranges, longer-term stability should be realized. The next step toward an "immortal" catalyst is to demonstrate that a catalyst system not only self-assembles from stable precursors under full turnover conditions but that it equilibrates under these conditions. In other words, the desired form of the catalyst represents the energy minimum for the dynamic system, and this minimum can be accessed under turnover conditions. Such systems adjust to changing conditions and effectively reassemble should they be damaged during turnover (a crude self-repair capability).[18]

Neumann and co-workers demonstrate that their catalyst **1** self-assembles in their reaction medium, H_2O, and that this self-assembled POM has the same reactivity as **1** prepared and purified separately by conventional means.[7] They do not, however, show that the catalyst both self-assembles and that its components equilibrate with other species present under the catalytic turnover conditions. This would require self-assembly in the presence of H_2O, H_2O_2 oxidant, alcohol substrate, aldehyde/ketone product, and the demonstration of equilibration of the catalyst components. Nonetheless, the combination of the many green attributes noted above and the realization of self-assembly of a homogeneous catalyst under near-turnover conditions from stable precursors makes this report noteworthy.[7] Such innovative efforts should encourage investigators in many subdisciplines of chemistry and chemical engineering, who design and make catalysts and catalytic materials, to consider other aspects of and larger problems associated with this multidisciplinary enterprise.

[1] P. Anastas, J. Warner, *Green Chemistry: Theory and Practice*, Oxford University Press, Oxford, **1998**, p. 160.

[2] For representative recent publications on homogeneous or immobilized homogeneous selective oxidation catalysts, see: a) C. L. Hill, I. A. Weinstock, *Nature* **1997**, *388*, 332; b) R. Neumann, M. Dahan, *Nature* **1997**, *388*, 353; c) R. A. Sheldon, I. W. C. E. Arends, A. Dijksman, *Catal. Today* **2000**, *57*, 157; d) T. Nishimura, Y. Maeda, N. Kaikiuchi, S. Uemura, *J. Chem. Soc. Perkin Trans. 1* **2000**, 4301; e) P. A. Shapley, N. Zhang, J. L. Allen, D. H. Pol, H.-C. Liang, *J. Am. Chem. Soc.* **2000**, *122*, 1079; f) T. Iwahama, Y. Yoshino, T. Ketitoku, S. Sakaguchi, Y. Ishii, *J. Org. Chem.* **2000**, *65*, 6502; g) R. Ben-Daniel, P. Alsters, R. Neumann, *J. Org. Chem.* **2001**, *66*, 8650.h) M. Fabbrini, C. Galli, P. Gentilli, D. Macchitella, *Tetrahedron Lett.* **2001**, *42*, 4551; i) A. Cecchetto, F. Fontana, F. Minisci, F. Rucupero, *Tetrahedron Lett.* **2001**, *42*, 6651; j) A. Dijksman, A. Marino-Gonzalez, I. Mairata, A. Payeras, I. W. C. E. Arends, R. A. Sheldon, *J. Am. Chem. Soc.* **2001**, *123*, 6826; k) N. d'Alessandro, L. Liberatore, L. Tonucci, A. Morvillo, M. Bressan, *J. Mol. Catal. A* **2001**, *175*, 83; l) Y. Ishii, S. Sakaguchi, T. Iwahama, *Adv. Synth. Catal.* **2001**, *343*, 393; m) J. T. Rhule, W. A. Neiwert, K. I. Hardcastle, B. T. Do, C. L. Hill, *J. Am. Chem. Soc.* **2001**, *123*, 12101; n) B. A. Steinhoff, S. R. Fix, S. S. Stahl, *J. Am. Chem. Soc.* **2002**, *124*, 766; o) B. A. Steinhoff, S. S. Stahl, *Org. Lett.* **2002**, *4*, 4179; p) M. Hasan, M. Musawir, P. N. Davey, I. V. Kozhevnikov, *J. Mol. Catal. A* **2002**, *180*, 77; q) A. Wolfson, S. Stijn, D. E. de Vos, I. F. J. Vankelecom, P. A. Jacobs, *Tetrahedron Lett.* **2002**, *43*, 8107; r) G. Ragagnin, B. Betzemeier, S. Quici, P. Knochel, *Tetrahedron* **2002**, *58*, 3985; s) F. Minisci, C. Punta, F. Recupero, F. Fontana, G. F. Pedulli, *Chem. Commun.* **2002**, 688; t) G. Csjernyik, A. H. Éll, L. Fadini, B. Pugin, J. E. Bäckvall, *J. Org. Chem.* **2002**, *67*, 1657; u) N. M. Okun, T. M. Anderson, C. L. Hill, *J. Am. Chem. Soc.* **2003**, *125*, 3194; v) C. Li, P. Zheng, J. Li, H. Zhang, Y. Cui, Q. Shao, X. Ji, J. Zhang, P. Zhao, Y. Xu, *Angew. Chem.* **2003**, *115*, 5217; *Angew. Chem. Int. Ed.* **2003**, *42*, 5063.

[3] O. Bortolini, V. Conte, F. Di Furia, G. Modena, *J. Org. Chem.* **1986**, *51*, 2661.

[4] K. Sato, M. Aoki, J. Takagi, R. Noyori, *J. Am. Chem. Soc.* **1997**, *119*, 12386.

[5] G.-J. ten Brink, I. W. C. E. Arends, R. A. Sheldon, *Science* **2000**, *287*, 1636.

[6] Y. Uozumi, R. Nakao, *Angew. Chem.* **2003**, *115*, 204; *Angew. Chem. Int. Ed.* **2003**, *42*, 194.

[7] D. Sloboda-Rozner, P. L. Alsters, R. Neumann, *J. Am. Chem. Soc.* **2003**, *125*, 5280.

[8] For representative recent reviews on catalytic oxidation, see: a) R. A. Sheldon, J. K. Kochi, *Metal-Catalyzed Oxidations of Organic Compounds*, Academic, New York, **1981**; b) R. A. Sheldon in *Dioxygen Activation and Homogeneous Catalytic Oxidation* (Ed.: L. I. Simandi), Elsevier, Amsterdam, **1991**, p. 573; c) *Catalytic Oxidation: Principles and Applications* (Eds.: R. A. Sheldon, R. A. van Santen), World Sci, Singapore, **1995**; d) A. E. Shilov, G. B. Shul'pin, *Chem. Rev.* **1997**, *97*, 2879; e) R. A. Sheldon, I. W. C. E. Arends, H. E. B. Lempers, *Catal. Today* **1998**, *41*, 387; f) F. Luck, *Catal. Today* **1999**, *53*, 81; g) W. A. Herrmann, J. Fridgen, J. J. Haider, *Peroxide Chemistry*, Wiley-VCH, Weinheim, **2000**, pp. 406–432; h) W. Adam, C. R. Saha-Möller, P. A. Ganeshpure, *Chem. Rev.* **2001**, *101*, 3499; i) D. E. De Vos, B. F. Sels, P. A. Jacobs, *Adv. Catal.* **2001**, *46*, 1–87; j) P. Gamez, P. G. Aubel, W. L. Driessen, J. Reedijk, *Chem. Soc. Rev.* **2001**, *30*, 376; k) W. P. Griffith, *Coord. Chem. Rev.* **2001**, *219–221*, 259; l) J.-M. Brégeault, *Dalton Trans.* **2003**, *17*, 3289.

[9] C. L. Hill, *Nature* **1999**, *401*, 436.

 © 2004 Wiley-VCH Verlag GmbH & Co. KGaA, Weinheim

[10] *Catalytic Oxidations with Hydrogen Peroxide as Oxidant* (Ed.: G. Strukul), Kluwer Academic Publishers, Boston, **1992**, p. 283.
[11] C. A. Tolman, J. D. Druliner, M. J. Nappa, N. Herron in *Activation and Functionalization of Alkanes* (Ed.: C. L. Hill), Wiley, New York, **1989**, p. 303.
[12] *Green Chemistry: Designing Chemistry for the Environment* (Eds.: P. T. Anastas, T. C. Williamson), American Chemical Society, Washington, DC, **1996**, p. 251.
[13] B. Meunier, A. Sorokin, *Acc. Chem. Res.* **1997**, *30*, 470.
[14] B. Meunier, *Chem. Rev.* **1992**, *92*, 1411.
[15] T. J. Collins, *Acc. Chem. Res.* **2002**, *35*, 782.
[16] C. L. Hill in *Activation and Functionalization of Alkanes* (Ed.: C. L. Hill), Wiley, New York, **1989**, p. 243.
[17] For representative reviews, see: a) C. L. Hill, C. M. Prosser-McCartha, *Coord. Chem. Rev.* **1995**, *143*, 407; b) R. Neumann, *Prog. Inorg. Chem.* **1998**, *47*, 317; c) T. Okuhara, N. Mizuno, M. Misono, *Adv. Catal.* **1996**, *41*, 113; d) I. V. Kozhevnikov, *Catalysis by Polyxometalates, Vol. 2*, Wiley, Chichester, **2002**, p. 216.
[18] I. A. Weinstock, E. M. G. Barbuzzi, M. W. Wemple, J. J. Cowan, R. S. Reiner, D. M. Sonnen, R. A. Heintz, J. S. Bond, C. L. Hill, *Nature* **2001**, *414*, 191.

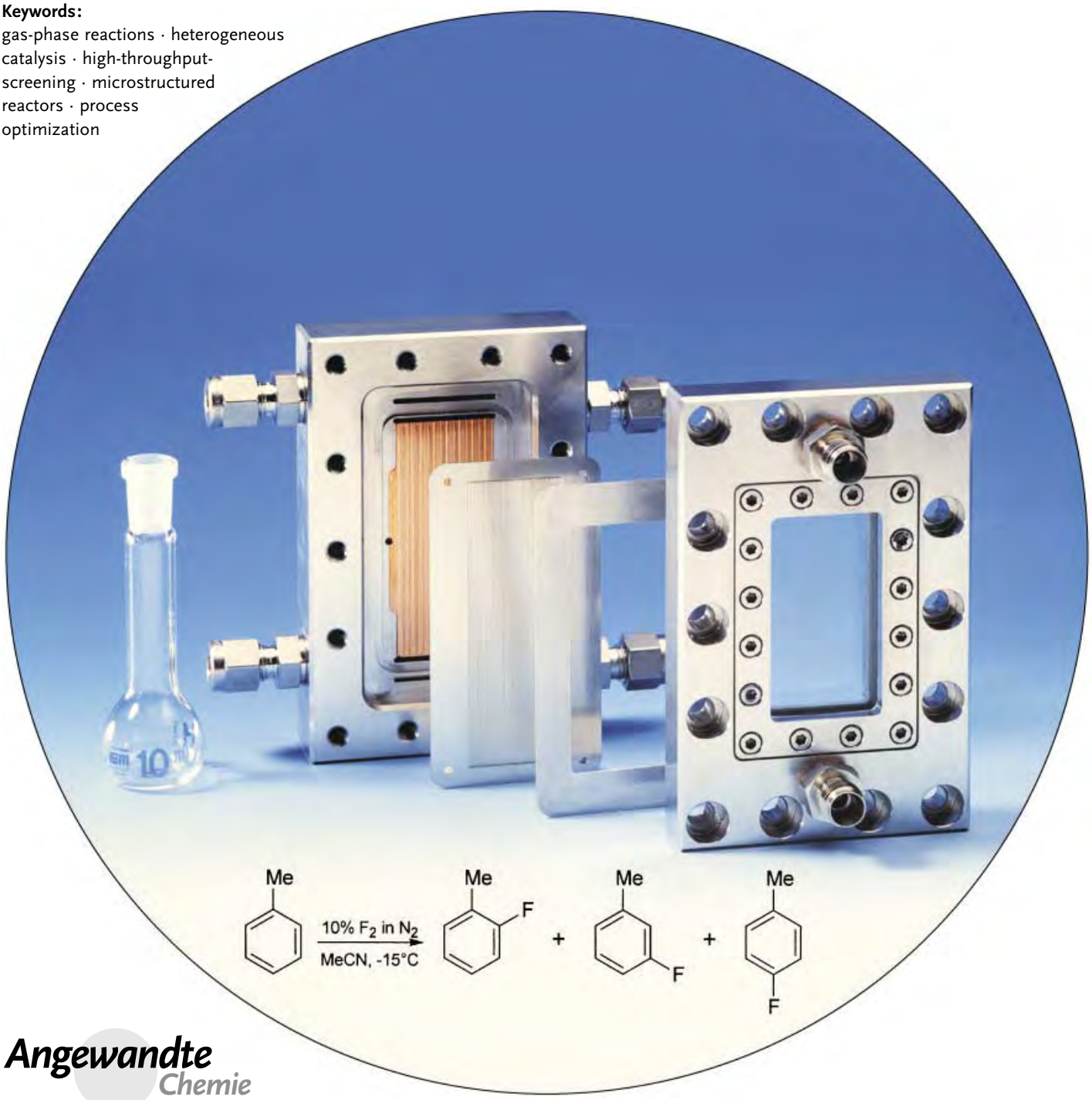
 © 2004 Wiley-VCH Verlag GmbH & Co. KGaA, Weinheim

Chemistry in Microreactors

Chemistry in Microstructured Reactors

Klaus Jähnisch, Volker Hessel,* Holger Löwe, and Manfred Baerns*

Keywords:
gas-phase reactions · heterogeneous catalysis · high-throughput-screening · microstructured reactors · process optimization



© 2004 Wiley-VCH Verlag GmbH & Co. KGaA, Weinheim
DOI: 10.1002/anie.200300577

The application of microstructured reactors in the chemical process industry has gained significant importance in recent years. Companies that offer not only microstructured reactors, but also entire chemical process plants and services relating to them, are already in existence. In addition, many institutes and universities are active within this field, and process-engineering-oriented reviews and a specialized book are available. Microstructured systems can be applied with particular success in the investigation of highly exothermic and fast reactions. Often the presence of temperature-induced side reactions can be significantly reduced through isothermal operations. Although microstructured reaction techniques have been shown to optimize many synthetic procedures, they have not yet received the attention they deserve in organic chemistry. For this reason, this Review aims to address this by providing an overview of the chemistry in microstructured reactors, grouped into liquid-phase, gas-phase, and gas–liquid reactions.

From the Contents

1. Introduction 407
2. Properties of Microstructured Reactors 407
3. Liquid-Phase Reactions 411
4. Gas–Liquid Reactions 417
5. Photochemical and Electrochemical Reactions 420
6. Gas-Phase Reactions 422
7. Industrial Applications of Microstructured Reactors 437
8. Market Prognoses 439
9. Summary and Outlook 439

1. Introduction

Microtechnology is currently an area of rapid growth in many areas of application, and the last seven years have seen the development of microstructured devices for chemical reactions, the advantages of which have been demonstrated most impressively.[1–7]

An original patent from the former East Germany in 1986 contained all of the essential features for how a microstructured system for chemistry should be built.[8] It is noteworthy that the patent presented manufacturing processes for microstructured reactors; under the economic circumstances, however, this knowledge could not be implemented. By 1989, the Forschungszentrum Karlsruhe (Germany) had already built the first micro-heat exchanger, and at an early stage had identified and published its potential for microchemical engineering.[9] Similar pioneering work also began in 1993 at the Pacific Northwest National Laboratory (PNNL, USA), although their work had a particular focus on the energy sector.[10]

The application of microsystems for chemical and biological reactions was discussed at a workshop in 1995 in Mainz (Germany), which can be seen as the starting point for worldwide development.[11] In 1997, the first International Conference for Microtechnology (IMRET 1) took place, which has since been held annually in Europe and the USA, and in 2001 the Industrial Platform of Modular Micro Chemical Technology (MicroChemTec), highlighting the industrial applications of microprocess engineering, was founded in partnership with DECHEMA.

As a consequence of these initiatives, increasing industrial interest, in addition to nationally initiated funding, has led to the publication of approximately 1000 studies on microprocess engineering, albeit mostly in conference proceedings. Thus, the knowledge of chemistry in a small but active area, especially regarding possible applications, is exhibited on a broader base. Meanwhile a wide range of microstructured, and even complete chemical process plants (especially for organic synthesis) are commercially available.[4,12–14] Companies with microstructured devices and services are in the market.[4,13,14] Many institutes devote themselves to this area, universities offer lectures and practical classes,[15] and some process-engineering-orientated reviews,[1–7,16–18] as well as a specialized book[3] are available.

2. Properties of Microstructured Reactors

2.1. Definition of Microstructured Reactors

Microstructured reactors are (generally, but not exclusively) reactors with three-dimensional structures, the inner dimensions of which are under a millimeter in size, and more specifically between ten and a hundred micrometers.[2,3,10] It therefore follows that the main feature of these reactors, in comparison to conventional chemical reactors, is the high surface-area-to-volume ratio. Specific surface areas of micro-

[*] Dr. K. Jähnisch, Prof. Dr. M. Baerns
Institut für Angewandte Chemie Berlin-Adlershof e. V.
Richard-Willstätter-Strasse 12, 12489 Berlin (Germany)
Fax: (+49) 30-6392-4350
E-mail: jaehnisch@aca-berlin.de
Dr. V. Hessel, Prof. Dr. H. Löwe
Institut für Mikrotechnik Mainz GmbH
Carl-Zeiss-Strasse 18–20, 55129 Mainz (Germany)
Fax: (+49) 6131-990-305
E-mail: hessel@imm-mainz.de

 DOI: 10.1002/anie.200300577 © 2004 Wiley-VCH Verlag GmbH & Co. KGaA, Weinheim

structures lie between 10 000 and 50 000 $m^2 m^{-3}$, while those of traditional reactors are generally about 100 $m^2 m^{-3}$ and in rare cases reach 1000 $m^2 m^{-3}$.[19] Since the heat-transfer coefficient is inversely proportional to the channel diameter, a value on the order of 10 $kW m^{-2} K^{-1}$ is obtained,[6,20] which is significantly higher than for traditional heat exchangers. This high heat-exchanging efficiency allows for fast heating and cooling in reaction mixtures within the microstructures whereby reactions under isothermal conditions with exactly defined residence times can be carried out.[20–22] The development of hot spots or the accumulation of reaction heat within microstructures is suppressed so that undesirable side reactions and fragmentations are hindered. The outcome in many cases is higher selectivity, yield, and product quality. Thus, microstructured reactors can be used to great effect for fast and/or strongly exothermic or endothermic chemical reactions.[23]

In addition to heat transport, mass transport is also considerably improved in microstructured reactors. Mixing times in micromixers (down to several milliseconds) are generally smaller than in conventional systems and due to the small dimensions the diffusion times are very short, thus the influence of mass transport on the speed of a reaction can be considerably reduced.[24]

A third aspect of microstructured reactors is the hydrodynamic flow in the microchannels, which is an important feature of microfluidics.[25] The flows are mostly laminar, directed, and highly symmetric.[25,26] In addition, the multiphase flows often exhibit high order[27–31] between the phases. These features are shown to allow the possibility to simulate and model systems to develop microprocess engineering apparatus by rational design. In many cases, basic physical mechanisms[27–31] or intrinsic kinetics can be directly applied. The prediction and confirmation of residence time distributions are of great value to this procedure. Furthermore, "controlled multiphase flow" is due to the dominance of surface and interface forces, as well as tailor-made active areas. Numerous publications are dedicated to conditions such as capillary flow,[32] slug flow,[33–37] segmented flow,[38] or hexagon-flow,[27] to name but a few.

Process parameters such as pressure, temperature, residence time, and flow rate are more easily controlled in reactions that take place in small volumes. The hazard potential of strongly exothermic or explosive reactions can also be drastically reduced.[39,40] Higher safety is also achieved in reactions with toxic substances or higher operating pressures.[24,41] The miniaturization has an immediate effect on the mechanism of explosions, in that radical chains or thermal hold-up are suppressed.[39,40] This allows a drastic broadening of the safe operating range in previous explosive regimes. Indeed, reactions with toxic substances, or at high pressures, have been carried out more safely.[24,41] Veser[40] explains that a relatively fault-tolerant safety level is achieved because of the intrinsic conditions that are available, rather than through safety precautions.

Due to the properties mentioned above, microstructured reactors can be advantageously used as process engineering tools for acquiring information, which allows, in a short time and with greater safety, a process to be transferred to the pilot and production scale. Information from microstructured



Klaus Jähnisch studied chemistry at TH Mersburg, and received his doctorate from the Institut für Organische Chemie, Berlin-Adlerhof, in 1972 with E. Schmitz on the amination of olefins and ketones. From 1980 to 1983, he worked as a group leader at the Cuban Academy of Sciences in Havana. He habilitated in 1991 at TH Mersburg, and since 1994 has been based at the Institut für Angewandte Chemie Berlin-Adlerhof, where his work includes the asymmetric synthesis of amino acid derivatives, and the functionalization of arenes in microstructured reactors.



Volker Hessel studied chemistry at the University of Mainz. He gained his doctorate with H. Ringsdorf in 1993 on supermolecular structures, micelles, and lyotropic liquid crystals. Since 1994, he has worked for the Institut für Mikrotechnik, Mainz GmbH (IMM), becoming a group leader in 1996 and a departmental manager for microreactor technology and chemical processes in 1999. Since 2002, he has been the deputy R&ampD director of IMM. He is the co-author of some 70 publications, a chapter in the Ullmann's Encyclopedia of Industrial Chemistry, and a book about microprocess engineering.



Holger Löwe studied at the University of Leipzig and then worked from 1977 to 1984 as a research-group leader at the film-manufacturing company Wolfen. After graduating at TH Merseburg (1984) he moved to TH Ilmenau, specializing in electrochemistry and galvanotechnics. In 1991 he became group leader and departmental manager at IMM, and in 1999 he became a R&ampD director responsible for chemical microprocess technology, biofluidic simulations, microoptics, LIGA technology, and precision engineering. He is the co-author of more than 250 publications, 30 patents, and a book about microprocess engineering.



Manfred Baerns studied chemistry in Braunschweig and Hannover, and received his doctorate in 1961 on mixing procedures in fluidized-bed reactors. He then worked for two years as a postdoctoral student at the Argonne National Laboratory, USA. After his habilitation at the University of Hannover (1970), he moved to the Krupp chemical plant in Essen. From 1974 to 1995 he was Professor of Technical Chemistry at the Ruhr-Universität Bochum, and since then has been a scientific director of the ACA. He is also an honorary Professor at the Humboldt-Universität Berlin and the TU Berlin. He received the titanium DECHEMA medal in 1999.

 © 2004 Wiley-VCH Verlag GmbH & Co. KGaA, Weinheim

reactors can also be used for optimizing process plants already in operation. This approach has been successfully documented by Wörz et al. (BASF) in many examples from chemical production.[23,42–44]

Microstructured reactors also give opportunities for new production concepts. Depending on demand, more microstructured reactors or such subunits could be connected in parallel ("numbering-up") so that the required intermediate products and end-products can be produced in their required amounts.[45,46] Dimensionalization and capacity utilization problems, such as those witnessed with big plants, would be eliminated. It should be mentioned that these concepts have been, until now, insufficiently implemented from a technical point of view. The reasons for this are partly due to the significant distribution and fouling problems in the complex connected microstructured reactors of the current technology, which still need to be resolved, as well as the hesitation of industry to use this potential. The latter factor, often based on sound principles, results mainly from the complexity of the chemical processes involved, and a reluctance to change from known and reliable procedures (in this case, being batch operation).

Nevertheless, it seems it is only a matter of time until these technical hurdles are tackled. One example is the German, publicly funded, DEMiS project, with partners in both industry and academia. Within the framework of this project a pilot plant for heterogeneously catalyzed gas-phase reactions was founded in Degussa in Hanau. The core of the plant (which is two storeys high) is a microstructured reactor. The aim of this project is to answer key constructive, process, and operational questions and thereby to demonstrate the feasibility of this technology on the industrial scale (Figure 1).

It is evident that multiscale approaches using microstructured reactors will be chosen more often in the future (for example, for process-innovative equipment with different optimum characteristic inner and outer dimensions), rather than "monolithic constructions" for pilot and production operation; this is in line with the motto: "only as small as is necessary".[4] Another aspect of multiscaling is that "the small is part of the big"; that is, the ability to use hybrid substitutes of small reactors next to large reactors or larger process-engineering components[4] (see also for example, the construction of Axiva reactors[3,47–49]). In this sense, in certain cases combined scale-up and numbering-up approaches would also be chosen to combine the best properties of traditional and microprocess engineering operations.[50,51]

All these approaches are thus generally appropriate in assisting a continuous mode of operation. Discontinuous batch reactions could in certain cases be operated through the application of microreactors in an economically advantageous continuous-process mode.[45,46]

2.2. Physical Principles for Chemical Processing in Microstructured Reactors

Microstructured reactors are as a general rule characterized by laminar flow; typical Reynolds numbers lie between 1 and 1000 depending on velocity and channel dimensions.[25]

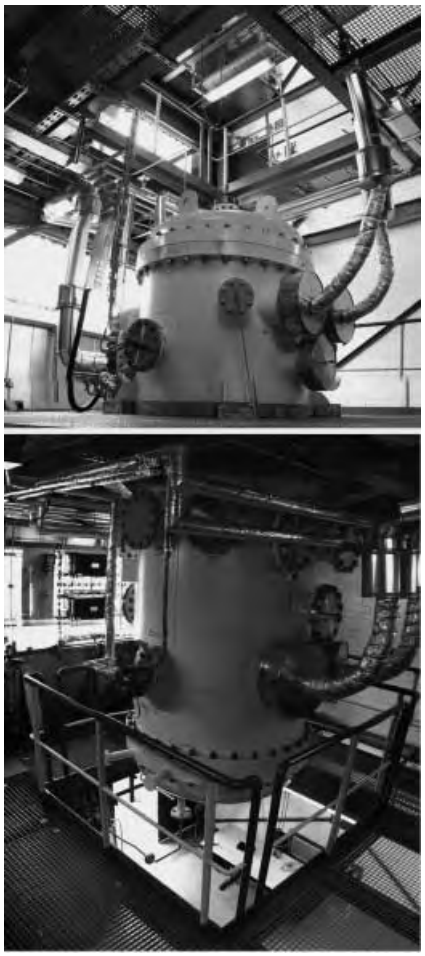


Figure 1. Degussa's experimental reactor for the pilot operation of a gas-phase reaction (source: Degussa, Hanau).

Mixing procedures are thus limited to diffusion and secondary flows. Turbulence-induced mixing procedures, such as agitation, are in general not possible.[52] For this reason, the typical sequence from macro- to micromixing is not observed. Micromixing starts almost exclusively from regular periodical concentration profiles, preferably with steep gradients. Due to this, very short mixing times can be achieved in micromixers;[10,53] for liquids this is typically from a second down to a few milliseconds.[53]

Similarly it is true that very efficient heat transfer is created.[6,10,54] The different contributions to heat conduction in the fluid and the reactor material, as compared to macroscopic apparatus, should be noted. At first sight, it was calculated that glass is superior to copper as a material for counterflow. In glass there is considerably reduced axial heat conduction performance, which negatively affects the temperature profile.[55] In addition to fluid–fluid heat transfer, heat conduction through the material of construction is also directly and advantageously used in microstructured reactors for setting the temperature in the reaction region or to dissipate the heat of reaction.[56] This can, for example, be done through electrical heating.[57] The high wall volume to reaction volume ratio is advantageous for control of the reaction. Complex scenarios, for example, investigating the

 © 2004 Wiley-VCH Verlag GmbH & Co. KGaA, Weinheim

effect of heat conduction of the housing of the microstructure, have also been recently the subject of scientific investigations. Since the assemblies are made of materials with different conductivities, heat management in narrow spaces and at interfaces is rather complex, and requires special methods for heat addition and removal, such as, for example, an asymmetric introduction of cooling fluid flows.[58–60]

The small reaction volume of microreactors is also responsible for advantages in their technical safety.[61] The small inner dimensions not only serve to aid heat removal but can also mechanistically control a reaction where, for example, radical chains are terminated such that the non-explosive region is significantly broader as compared to conventional reactors.[40,62] This arises from the presence of a surface-area reaction of radicals (quenching) on the walls of the microchannels.

The laminar flows cause velocity profiles in the channel to appear typically parabolic in shape, which can lead to a relatively broad residence-time distribution. However, the slip-flow of gases, which occurs at high temperatures, low pressures, and/or narrow channels is a notable exception. The concentration profile for a Hagen–Pousenille distribution also takes a parabolic form when fully developed. Extreme cases exist for flows from species with higher diffusion constants in narrow channels. Axial and radial diffusion can dominate in these cases, which leads to a plug concentration profile with respect to the channel cross section.[63]

The description of single-phase flows in microchannels is significantly older than microprocess engineering itself.[25,64] The effects of heat transport have been thoroughly investigated and possible anomalies and peculiarities that result from miniaturization have been described and questioned.[65–69] Many results referring to these aspects have been challenged by some experts and are thus still the subject of intense discussion.[70] It is generally true that many microfluidic phenomena, which have been known for approximately two decades, still wait to be applied in microprocess engineering investigations.

Multiphase flows in microchannels of microstructured reactors have been documented for liquid–liquid and gas–liquid mixtures.[33,71,72] The Weber number, which is the ratio of inertia to surface forces, is suitable for their description. Weber numbers of flows in microchannels are low, typically less than one. A value of 10^{-3} was determined for flows in a falling-film microreactor.[29] In particular the flow-pattern maps of gas–liquid flows are equivalent to the well documented flows in monoliths, that is, in mesochannels.[71] The first simulation studies were dedicated to describing multiphase flows in microchannels.[28–31] An understanding of droplet and bubble formation in micronozzles, which from the beginnings of micro process engineering had been known about, has found increasing applications in recent times.[30,73] This is also true for the use of internal circulation inside fluid segments within segmented gas–liquid and liquid–liquid flows (capillary flow; slug flow).[32] The first description of pulse operation in single-phase or multiphase flows in microchannels has also recently appeared.[63,74,75]

Several investigations on fluid equidistribution in microchannels have been carried out, which are of special relevance to the numbering-up concept.[76,77] Here, mainly theoretical gas-distribution studies for arrays with various compensation arrangements were presented. Experimental findings for the verification of these predictions are still rare.

2.3. Geometrical Parameters and Process Sizes of Microstructured Reactors

In order to point out the differences between microstructured reactors and conventional equipment, four geometric parameters and three process sizes will be discussed below.

Reactor volume: The internal volume of microstructured reactors can range from significantly below 1 μL up to several μL. Typical large reactors have inner volumes from 100 mL up to several liters. Plant reactors have, for example, a volume of 30 m^3, that is, 30000 L.[23]

Specific reactor surface area: For those reactor volumes mentioned above, microstructured reactors have inner surface areas of several tens of thousands $m^2 m^{-3}$, whilst larger reactors typically only have a surface area of approximately 100 $m^2 m^{-3}$.

Specific phase interface: Depending on the dimensions, flow type, and process parameters, flows in microchannels exhibit specific interfaces from approximately 5000 to 50000 $m^2 m^{-3}$ for liquid–liquid mixtures.[61] The respective values for gas–liquid mixtures are slightly lower. Maximum values of over 20000 $m^2 m^{-3}$ have been determined for a falling-film microreactor. Many conventional apparatus for corresponding applications achieve only limited interfaces, e.g., $\approx 100\ m^2 m^{-3}$. Conventional special apparatus, such as impinging jet reactors for gas–liquid contacting achieve approximately 2000 $m^2 m^{-3}$.

Film thickness: Film thicknesses of ≈ 25 μm have been measured in falling films running through microchannels.[34] These are approximately a factor of ten smaller than for macroscopic falling-film reactors. Even thinner films can exist between Taylor bubbles and channel walls in gas–liquid slug flow, as in the case of annular flows with same-fluid mixtures. Due to experimental difficulties exact values do not exist.

Mixing time: In optimized mixers typical mixing times for liquid mixtures amount to under one second.[53] In some cases, millisecond mixing times have also been proved.[53] This is faster than most conventional stirrers, which have mixing times from one up to several tens of seconds.

Heat transfer: Very high heat-transfer coefficients of up to 25000 $W m^{-2} K^{-1}$ have been measured in micro heat-exchangers for liquid flows.[6] This is significantly higher than the corresponding values for conventional apparatus. The same is true for gas heat exchange (several hundreds of $W m^{-2} K^{-1}$ for microchannels). The power density of the microstructured reactors have also been measured, for example, with values from 2000 $W L^{-1}$ for gas heat exchange, thus increasing significantly the existing state-of-the-art.

Energy: The few investigations available limit themselves to investigating the power input for static mixers. The required energy input in a micromixer and a turbine mixer

 © 2004 Wiley-VCH Verlag GmbH & Co. KGaA, Weinheim

has been measured for the generation of emulsions with equal Sauter diameter.[78] It has been shown under set conditions that the power input for the micromixer is ten times less.

2.4. Perspectives for Reactions in Microstructured Reactors

Thus far, it appears that microtechnology has been noticed mostly by process engineers and less by chemists from the non-industrial research arena. This can be explained by the fact that several years passed until the new technology was available to demonstrate its potential. In the meantime many of the known chemical syntheses, such as the Wittig,[79,80] Knoevenagel,[80] Aldol,[81] Ugi,[80,82] Michael-addition,[80] Hantzsch,[80,83,84] Diels–Alder,[85] Azo-coupling ,[51,86] Suzuki-coupling,[80,87] and Enamin[80,88] reactions, to name but a few, have been carried out successfully, and in most cases with improved results, in microstructured reactors as compared to their macrostructured counterparts.[80] Fluorination,[34,89–93] chlorination,[48] nitration,[32,36,94–97] hydrogenation,[98–101] and oxidation[39,40,56,102–110] reactions have been described in numerous examples. The spectrum of chemical conversions includes many known chemical reaction types, such as additions,[56,102,105,106,111] eliminations,[74,99,112–116] nucleophilic substitutions on aliphatics,[117] electrophilic substitutions on aromatics,[34,91,94–96] cycloadditions,[85] and radical polymerizations[47,49] (For more information, see also Refs. [3,4]). The feasibility of large-volume industrial processes, such as the Andrussov process[118] and the synthesis of ethylene oxide[56,102,105,106,108] could also be demonstrated on a smaller scale.

It has also been shown that enantioselectivities[80,119,120] and isomer selectivities[95,121] (e.g., concerning regio- or *E*/*Z* isomerism) are also modifiable. Reactions can be quenched in milliseconds (e.g., for isolation from intermediate products[86,122]) and thus syntheses that were previously forbidden due to safety reasons are, even in the laboratory, now manageable with relatively low risk.[40,91,107] As new ideas about combinatorial synthesis and material screening arise,[123,124] they naturally generate a demand for small reactors that can vary process parameters quickly and precisely, as well as consume the minimum amounts of materials.[125,126] There are, therefore, many good reasons for the chemist to embrace microtechnology! The aim of this Review is to take such people into consideration by summarizing many activities "from a chemist's point of view".

While published overviews on microtechnology have to date mainly dealt with chemical-process issues,[2–5,7,42,80,127–137] the emphasis of this Review essay lies on typical reaction types, where the advantage of this new reaction technology in comparison to traditional reactors becomes clearer. The details within this Review concentrate on work published since 1995 (with emphasis on the years 2000–2002) and are structured with respect to liquid-phase, gas-phase, and gas–liquid reactions.

3. Liquid-Phase Reactions

3.1. Microstructured Reactors for Liquid-Phase Reactions

The following functions of a reactor must typically be fulfilled for the processing of a chemical reaction:

- Thecomponents must be efficiently mixed,
- time and space for the reaction must be available,
- the heat of reaction must be dissipated, and
- a phase interface must be available for multiphase reactions.

In conventional vessels, components are mixed through intensive stirring, while in microstructures this process is mainly realized through diffusion.[24–26] Despite laminar flows in microstructures, molecules have short paths to overcome so that a nearly complete mixture is achieved within a few seconds, and often as little as a few milliseconds.[24,26,138] Depending on velocity the reaction can be run directly in a flow chamber located after the inlet structures (thus, "in the mixer") or in a connected residence-time module.[53,139,140]

Various principles can be applied for the mixing of liquids. Multilamination[24,26] is a simple and, therefore, frequently applied principle that, for example, in the interdigital mixer of IMM [24,53,117,139–141] (Figure 2) and mgt mikroglas technik AG

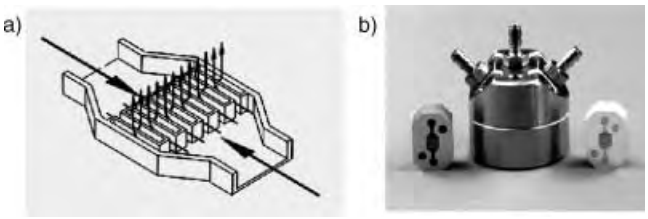


Figure 2. Slit-interdigital micromixer: a) Method of operation; b) construction from metal and stainless steel (source: IMM, Mainz[24]).

(both in Mainz, Germany; Figure 3)[117,142] is employed. With the help of geometrical focusing, mixing times for miscible liquids are possible in the millisecond time regime.[140] Contact between immiscible liquids[117,143–145] or of gases with liquids[27,146] is of a more complex nature. In the example of liquid jet decay, the liquids are combined in the mixing zone and fragmented into droplets. By changing the geometry of the mixing chamber and the wetting properties of the employed microstructured material, it can be determined whether fluid lamellae or fluid cylinders develop. Moreover

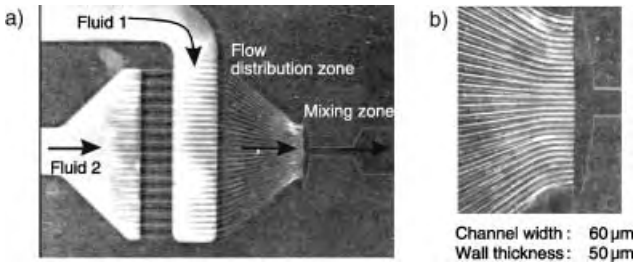


Figure 3. Fluid-introduction system and mixing chamber of a slit-interdigital glass micromixer: a) Overview; b) details of the feeding and mixing zones (source: IMM; microstructure: mgt mikroglas technik AG, Mainz[117]).

 © 2004 Wiley-VCH Verlag GmbH & Co. KGaA, Weinheim

the choice of mixing chamber and fluid flow-rates dictates whether a laminar regime (e.g., with a Rayleigh-plateau fragmentation[27–31]) or a turbulent regime (e.g., with a jet/towing eddy characteristic[78,143]) exists. The droplets formed are either very uniform in size with a certain mean diameter or slightly less uniform and smaller.

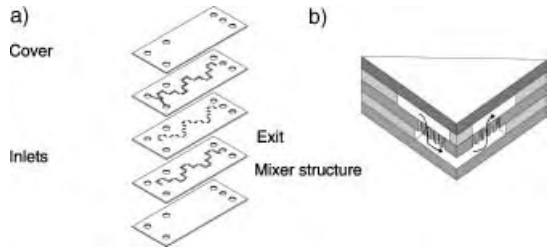


Figure 4. Split–recombine micromixers: a) Explosion diagram; b) fluid flow (source: Little Things Factory, Ilmenau).

Figure 4 shows a mixer built by the Little Things Factory (LTF, Ilmenau, Germany), which operates according to the split–recombine technique. Ideally, multilaminated layers are generated through the repeated splitting and recombining of fluid streams. By many microprocess engineering applications, however, secondary streams up to turbulent operation are induced due to the high fluid velocities in such mixers, so that the majority of relevant practical flows can be categorized as complex, and belonging to an intermediate regime between laminar and turbulent flow. These additional flows are generally advantageous for the mixing process itself, however, they do worsen the residence-time behavior as well as the application of simulation methods used to describe a process. In comparison with the interditigal mixer, the split–recombine mixer type exhibits a lower pressure drop since it has comparably larger inner dimensions. Thus, high flow rates are possible and the operational reliability is less disturbed through the precipitation of particles than in other types of mixers.

Turbulent phenomena are also used for the mixing of liquids in micromixers at higher flow velocities. Figure 5 shows a microjet mixer developed by Synthesechemie (Heusweiler, Germany),[147,148] in which reactants are sprayed as liquid jets through a diamond or sapphire nozzle (with openings between 60 and 350 μm) where they then collide and become intensely mixed. Gas introduced from the side is responsible for removing the reaction mixture from the chamber.

The impinging jet mixer (Figure 6; developed by IMM) functions by using a similar principle.[149–151] Similarly to the impinging jet reactor, the fluids coincide outside of the mixer and become mixed within a short length of time.

The two mixers described above were developed especially for fouling-sensitive reactions. Plugging is here not possible, as reactants do not come into contact with each other within the microchannels but instead in an open space and are transported by an adjustable gas stream.



Figure 6. Design of the impinging jet mixer (source: IMM[149]).

More complex microstructured reactors and complete reactor systems are currently under development. Figure 7 shows a microstructured reactor (mgt mikroglas technik AG), in which a mixer, a residence-time module, and a cooler are integrated.[152] A more complicated microstructured reactor designed and built by IMM for BASF was used for a liquid–liquid two phase reaction.[23,43,44,153] Here, a mixer with a residence-time module and a heat exchanger are assembled in a module composed of four microreactor elements (Figure 8).

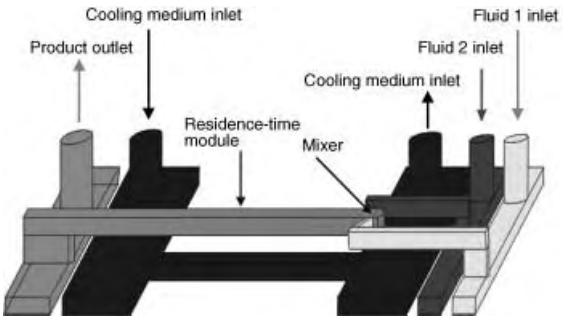


Figure 7. Microstructured reactor with mixer, residence-time module, and heat exchanger (source: mgt mikroglas technik AG).

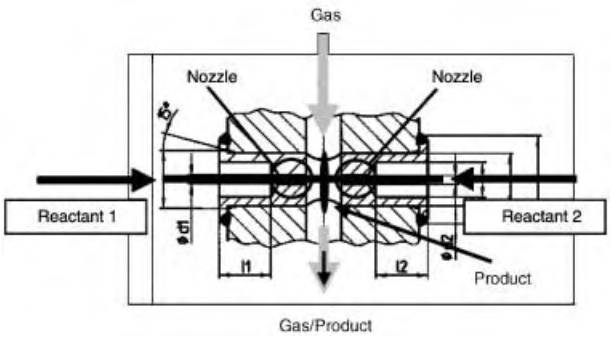


Figure 5. Design of the microjet mixer (source: Synthesechemie GmbH, Heusweiler[147]).

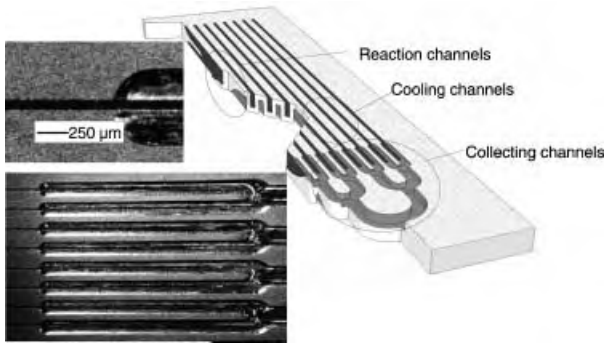


Figure 8. Microstructured reactor with mixer, residence-time module, and heat exchanger (source: IMM[23]).

 © 2004 Wiley-VCH Verlag GmbH & Co. KGaA, Weinheim

Complete reactor process plants are offered by Cellular Process Chemistry Systems GmbH (CPC, Frankfurt), mgt mikroglas technik AG, and IMM, in which pumps, microstructured reactors, residence-time modules, system control, sensors, and online analytical instruments can be integrated. These plants are generally based on the mixer-tube reactor principle and are suited for exploratory investigations of numerous organic syntheses in the laboratory.

For the optimum process operation of a chemical reaction, the microstructured reactor plant for the relevant reaction and mainly for the process function (e.g., increasing the yield) must be individually set. Such special plants are available now and are offered by certain institutes.

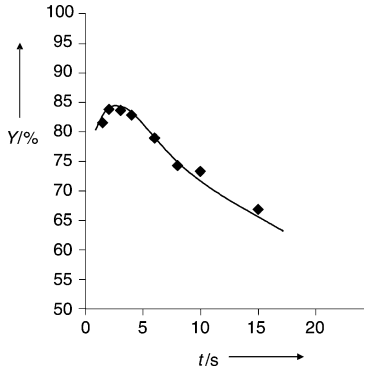


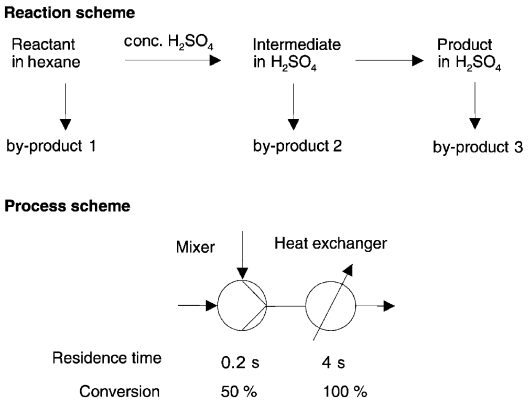
Figure 9. Dependence of yield (Y) on residence time (t) for a microstructured reactor at a reaction temperature of 50 °C.[23]

3.2. Noncatalytic reactions

Wörz et al. described the potential that microstructured reactors possess for the optimization of chemical processes of industrial relevance.[23,43,44,154,155] A very fast exothermic liquid–liquid two-phase reaction, which was used for the industrial production of a vitamin intermediate product, was investigated.

The reactant (dissolved in hexane) and the concentrated sulfuric acid acting as catalyst do not form a miscible phase with each other, and thus the product is found in the acidic phase at the end of the reaction. As with the reactant the intermediate compounds generate fast by-products. In a semi-batch industrial process a yield of 70 % was achieved. The process was later carried out continuously in a mixer/heat exchanger reactor combination (Scheme 1) in which the yield could be increased to 80–85 %. The residence time in the mixer was 0.2 s and 4 s in the heat exchanger.

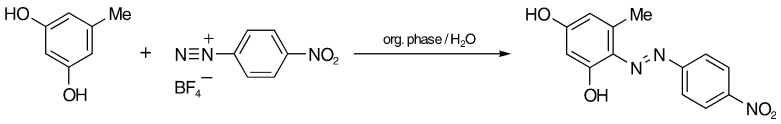
To understand the technical processes involved, investigation of this reaction took place in a microstructured reactor (Figure 8). Figure 9 shows that the yield is strongly dependent on residence time; the optimum time in the reactor combination ($\approx$3 s) lies very near the empirically determined residence time of 4 s. Note that an extension of the residence time by ten seconds leads to a decrease in yield by approximately 17 %.



Scheme 1. Synthesis of an intermediate product in a hexane/sulfuric acid two-phase system.

These investigations led to a better understanding and optimization of the industrial production processes involved. The obtained kinetic information could now be used to run a different temperature–reaction time-window with even better reactor performance. At lower temperatures, with necessarily longer residence times, more careful handling of thermally unstable reactants and intermediate products is possible, e.g., reactions can take place at 20 °C instead of 50 °C, which leads to an increase in yield to 90–95 %. The optimum residence time of 30 s increases the safety of the reaction and enhances the control of the reaction process.

A further example, in which the higher specific phase interface in a microstructured reactor significantly improved the conversion in a two-phase reaction was recently described.[156] The diazo coupling of 5-methylresorcin with 4-nitrobenzoldiazonium tetrafluoroborate took place in an organic phase/water system (Scheme 2). In comparison to



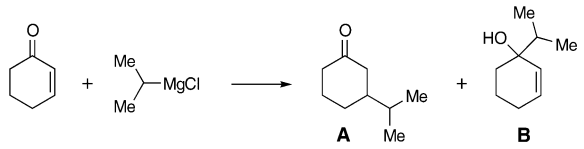
Scheme 2. An example of diazo coupling under phase-transfer conditions in a microstructured reactor.

the macroscopic reaction, where the solution was strongly stirred, the specific phase interface could be doubled through the application of a microstructured reactor. Thus, the conversion was increased from 80 % to $\approx$100 % and the formation of insoluble by-products was reduced.

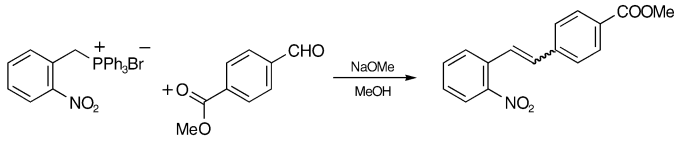
Complete modular microstructured reactor systems operating in a continuous mode are suited for fast screening of reactor parameters such as temperature, time, concentration, concentration ratio, or pH value. Taghavi-Moghadam et al.[157] reported the optimization of a Grignard reaction (Scheme 3). By testing 14 different reaction conditions, the yield of the reaction could be increased from 49 % to 78 % and the ratio of the regioisomers **A**:**B** could be converted from 65:35 to 95:5.

Skelton et al. described a further example of a fast optimization of an organic synthesis (Scheme 4).[158,159] They

 © 2004 Wiley-VCH Verlag GmbH & Co. KGaA, Weinheim



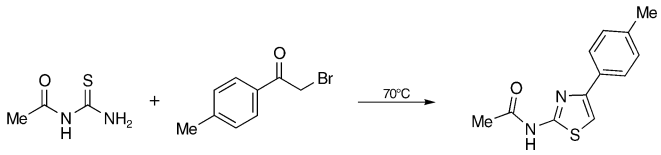
Scheme 3. The reaction of a Grignard reagent and cyclohexanone.



Scheme 4. The Wittig reaction between 2-nitrobenzyl triphenylphosphonium bromide and 4-formyl methylbenzoate.

investigated the Wittig reaction of 2-nitrobenzyl triphenylphosphonium bromide with 4-formyl methylbenzoate in a microstructured reactor made of borosilicate glass with a channel width of 200 μm and channel depth of 100 μm; liquid mixing took place in a microstructure with a T-shaped geometry. Transport of reactant and product solutions occurred by applying a constant and controlled voltage through the electroosmotic flow (EOF).[160,161] It was found that the yield and the *E*/*Z* isomer ratio of the olefin could be optimized through the change of the relative concentration of the reactants and the aimed variation of the concentration gradient. With an aldehyde-to-phosphonium-salt ratio of 2:1 the yield in the microstructured reactor increased from 60% to 70% as compared to a conventional batch synthesis. The *E*/*Z* isomer ratio could be varied between 0.57 and 5.2 in this case (compared with ≈ 3 in a batch operation).

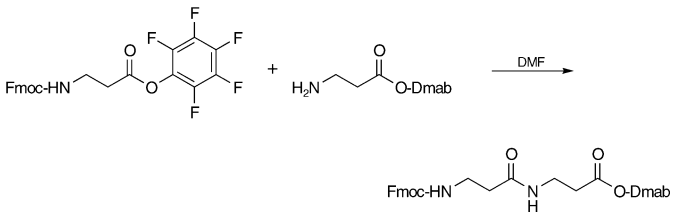
The first continuous, computer-controlled heterocycle synthesis was described by Garcia-Egido et al., who investigated the Hantzsch thiazol synthesis as model reaction (Scheme 5).[83,84] Solutions of 4-methylbromoacetophenone



Scheme 5. The Hantzsch 2-aminothiazol synthesis.

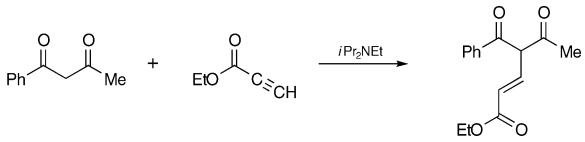
and an *N*-acylated thiourea were pumped through borosilicate-etched microchannels by electroosmosis. The channels were heated to 70°C through a Peltier element. At 500 V, an increase in conversion up to 19% was achieved in the microchannel, compared to conventional batch operation.

Watts et al. carried out the first investigations on the synthesis of peptides in microstructured channels.[80,119,120] To demonstrate the feasibility of such reactions an achiral β-peptide was initially made.[162] It was shown that reaction of an Fmoc-protected pentafluorophenylester of β-alanine with the carboxylic acid protected β-alanine could give the corresponding dipeptide (Scheme 6). Using continuous flows, a quantitative yield of the dipeptide was obtained after 20 min, whereas traditional batch operation only gives 40–50% conversion. The application was expanded to multistep syntheses[120] and was also used for the generation of optically active peptides[163] where it was observed that racemization was reduced by using a microstructured reactor.



Scheme 6. Peptide synthesis in a microstructured reactor. (Dmab = 4-[*N*-1-{(4,4-dimethyl-2,6-dioxocyclohexylidene)-3-methylbutyl}-3-amino]-benzyl; Fmoc = 9-fluorenylmethoxycarbonyl).

Two further examples of organic syntheses in microstructured reactors by Haswell and co-workers employ liquid transport through electroosmosis (Scheme 7),[111] the results



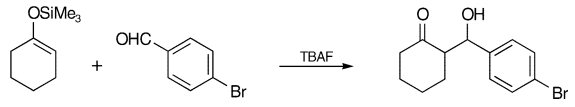
Scheme 7. Addition of enolates to α,β-unsaturated carbonyl compounds.

of which were heavily dependent on the flow path used. During a continuous operating mode a conversion of only 15% was achieved. However, if the flow was stopped after 2.5 s for a duration of 5 s and subsequently switched back on, conversion increased to 34%; this could be increased to 100% by stopping the flow for 10 s. Thus, the conversion was 22% higher than that obtained by batch operation. The authors explain that the increase in conversion occurs because the flow interruption extends the residence time and the mixing is improved through diffusion. This investigation is a good example of the importance of appropriate process procedures in microstructured reactors. The microreactor itself is not a panacea; it is often more difficult to find the optimum operating conditions with these techniques than for conventional stirring reactors.

A significant acceleration of the aldol reaction of silyl enol ethers with aldehydes in the presence of tetrabutylammonium fluoride (TBAF, Scheme 8) was observed in a four-channeled microstructured reactor.[81] Quantitative conversion was achieved after only 20 min, compared to 24 h in conventional systems.

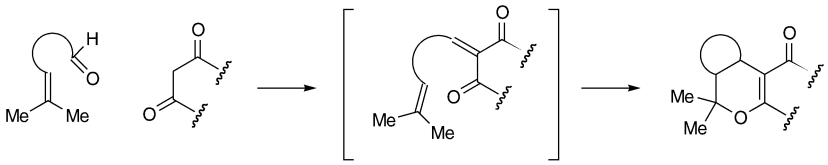
One objective for microstructured reactor applications is to combine many functions, such as synthesis, separation, analysis, and screening within one microdevice to generate compound libraries. It is has been proven that solution

 © 2004 Wiley-VCH Verlag GmbH & Co. KGaA, Weinheim



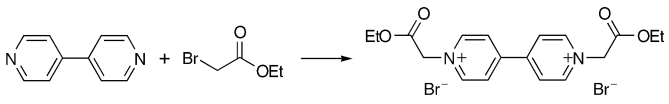
Scheme 8. Aldol reaction of a silyl enol ether with 4-bromobenzaldehyde.

transport for such a task is not favored by electroosmosis, since this is strongly dependent on solvent properties such as pH value and ionic strength, hence the choice of solvent is strongly limited. Fernandez-Suarez et al. recently showed that this disadvantage can be overcome through the use of pumps.[85] A domino reaction was investigated consisting of a Knoevenagel condensation and an intermolecular hetero-Diels–Alder reaction (Scheme 9). The four examples given showed that the results were reproducible without optimization and similar conversions were reached as in a batch reactor.



Scheme 9. Domino reaction: A Knoevenagel condensation and an intermolecular hetero-Diels–Alder reaction. Catalyst = ethylenediamine diacetate (EDDA).

Werner, Hessel, and co-workers described the first application of an impinging jet mixer (Figure 6), which was specially developed for organic syntheses that are prone to fouling. The formation of a quarternary amine from 4,4′-bipyridyl and bromoacetic acid ethyl ester was investigated as model reaction (Scheme 10).[149] It was shown that this solid-forming reaction could be operated up to 8 h continuously with a yield of 75%, a value comparable with the performance of a batch operation. The work describes for the first time a continuous operation for strongly fouling-prone reactions with acceptable reactor efficiency. A "normal" micromixer or other microstructured reactor would be plugged within a few minutes under the same conditions. The impinging jet mixer prevents this and, in a vertical arrangement, can also use straight tubes with suitable dimensions for longer residence-time operation. With this reactor configuration a larger number of solid-sensitive processes can be run.

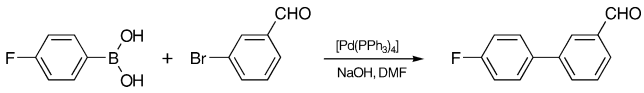


Scheme 10. Formation of a quarternary amine salt of 4,4′-bipyridyl.

Several patents have been published for applications of the microjet mixer (Figure 5).[164–166] Fine particles with a very narrow particle-size distribution can be produced in this reactor through the precipitation of pigments. Thus, the raw pigments are dissolved in concentrated sulfuric acid and pumped through a nozzle of the microjet mixer (e.g., pressure = 50 bar), while water is simultaneously pumped in at the same pressure through a second nozzle. The suspensions evolving after the collision of the jets in the mixing chamber are carried out of the reactor by an air jet, and the produced pigment can be isolated using standard procedures. Using a tetracopper phthalocyanine raw pigment, it was shown that the specific surface area increased from ≈ 13 to $\approx 29\ m^2 g^{-1}$ and the average particle size decreased from 34 to 26 nm. The pressure of the liquids can be increased, as required, up to 3800 bar.

3.3. Catalytic Reactions

The Suzuki reaction (homo- and heterogeneous) was investigated as a rare example of a catalytic liquid-phase reaction in a microstructured reactor. Schwesinger et al. described the conversion of 3-bromobenzaldehyde with 4-fluorophenyl boronic acid in the presence of a dissolved Pd catalyst (Scheme 11).[3,167] Figure 10 shows that through the application of a micromixer/residence-time module combination, the yield could be increased under continuous operation from ≈ 50 to $\approx 90\%$, as compared to the conventional mode.



Scheme 11. An example of a Suzuki reaction in a micromixer/residence-time module combination.

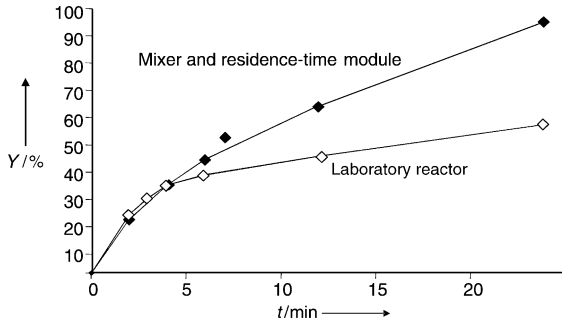
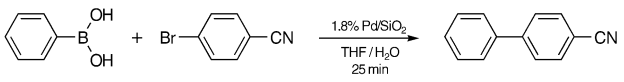


Figure 10. The Suzuki reaction: Comparing the yield (Y) for a laboratory reactor with a micromixer/residence-time module combination.[3,167]

The heterogeneous version of this reaction was recently investigated by Greenway, Skelton, and co-workers,[87,168] who used microstructured borosilicate glass with a channel width of 300 μm and depth of 115 μm. 1.8% Pd/SiO_2 was employed as a catalyst, carried to the surface of the microstructures as a suspension; adhesion was achieved by heating to 100 °C for

 © 2004 Wiley-VCH Verlag GmbH & Co. KGaA, Weinheim

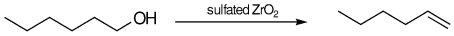
1 h. The reaction of 4-bromobenzonitrile and phenylboronic acid was chosen as a model reaction (Scheme 12). Liquid transport occurred through electroosmosis, with the flow of



Scheme 12. An example of a heterogeneously catalyzed Suzuki reaction in a microstructured reactor.

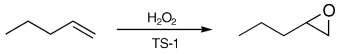
the phenylboronic acid solution being continuous and the bromobenzonitrile solution injected at intervals. After optimization of this procedure, yields were achieved that were 10% higher than those achieved by a conventional batch process.

Wilson et al. described the acidic, heterogeneously catalyzed dehydration of alcohols in microstructured reactors, which were prepared through photolithography and chemical etching of glass. The cover plate, made of polydimethylsiloxane, served as both the heat source and as the carrier of the employed catalyst (sulfated zirconia).[169,170] The dehydration of 1-hexanol to hexene at 155–160 °C was investigated (Scheme 13), in which the liquid transport took place through an injection pump. A conversion of 85–95% was recorded and no by-products were detected. This compares favorably to the 30% conversion achieved by conventional reactors.



Scheme 13. Dehydration of 1-hexanol in a microstructured reactor.

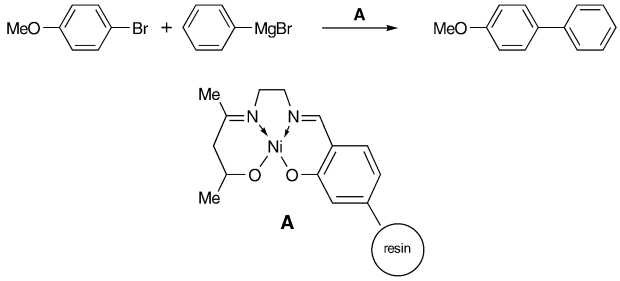
Wan et al. recently reported a series of oxidation reactions over a coating of titanium silicalite 1 (TS-1) in microchannels.[173–175] The silica-etched channels were either 500 or 1000 μm wide and had a depth of 250 μm and a length of 33 mm. Growth of the TS-1 crystals occurred in the open structures, the surfaces of which were initially treated with 3-(trimethoxysilyl)propylthiol to improve the adhesion of TS-1. After the deposition of TS-1 seed crystals a hydrothermal reaction was carried out, which led to a uniform 3-μm thick catalyst coating. The epoxidation of 1-pentene with hydrogen peroxide was then investigated (Scheme 14). The authors



Scheme 14. Epoxidation of 1-pentene with hydrogen peroxide on TS-1 in a microstructured reactor.

found that increasing the surface-area-to-volume ratio (through replacing a 1000 μm channel with a 500 μm channel) approximately doubled the yield due to the higher catalyst concentration. The disadvantage remains that after a continuous operation of more than 100 h catalyst deactivation took place, which could not be reversed even after calcination in air.

Organometallic reactions can also be carried out in microstructured reactors with higher efficiency than in batch reactors, as exemplified by the studies of Haswell, Fletcher, and co-workers,[80,176] who investigated the Kumada–Corriu reaction by reacting 4-bromoanisol with phenylmagnesium bromide in the presence of the Merrifield-resin-immobilized salen-type nickel complex **A** (Scheme 15), which



Scheme 15. An example of a Kumada–Corriu reaction in a microstructured reactor using an immobilized salen-type nickel complex as a catalyst.

in the form of small pellets were packed into capillaries of 1–2 mm diameter; the reagents were then pumped through these microstructures. The reaction rate constant was determined through kinetic measurements, which determined that continuous flow in microchannels led to an increase in the rate by a remarkably large factor of 3.4×10^3 compared to a conventional batch reactor. In other words, the yield obtained in 24 h in a batch reactor could be achieved within a few minutes in a microchannel. This effect was explained as arising from the high pressure through the microstructure, which pushes the reagents deeper into the pores of the resin, and thus a greater number of catalytic sites are reached than in the conventional process.

De Bellefon and co-workers have introduced a new concept for the high-throughput screening (HTS) of homogeneously catalyzed reactions in multiphase systems, by investigating isomerization in a two-phase system (Figure 11).[175–179] The organic phase, substrate, and water were continuously pumped into an interdigital mixer (IMM) and analyzed after flowing through a residence-time module.

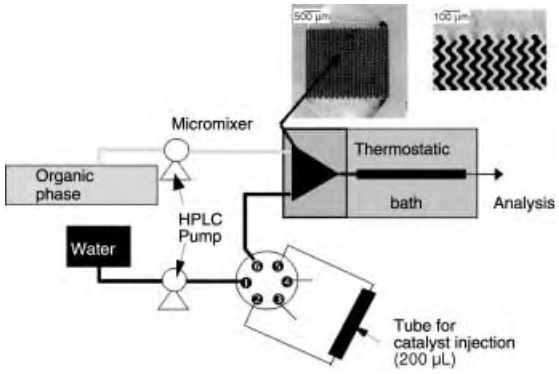
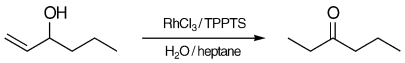


Figure 11. Apparatus for the high-throughput screening of homogeneous catalysts using an interdigital mixer.[177]

 © 2004 Wiley-VCH Verlag GmbH & Co. KGaA, Weinheim

The catalyst solution was injected in pulses through a commercial valve. Complete mixing took place in the micromixer with a residence time of 10^{-2} s, with catalyst amounts of 1–2 μmol being sufficient. This technique is particularly advantageous if the catalysts are available only in small amounts due to difficulties in their synthesis. For example, from a catalyst library, the $RhCl_3$–tris(*m*-sulfonatophenyl)-phosphane (TPPTS) catalyst was found, which catalyzed the isomerization of 1-hexen-3-ol to the desired ethylpropylketone with 53% conversion (Scheme 16).



Scheme 16. Isomerization of 1-hexene-3-ol using a $RhCl_3$/TPPTS catalyst.

4. Gas–Liquid Reactions

Even though gas-phase as well as liquid-phase reactions in microstructured reactors have been described for some time, few investigations on gas–liquid processes have been carried out. Recent years have seen increased interest, however, and in the following section, reactors suitable for such reactions are described along with the associated advantages of applying these microstructured devices for gas–liquid reactions.

4.1. Microstructured Reactors for Gas–Liquid Reactions

Two microstructured reactors suitable for gas–liquid reactions have been developed by IMM and their collaborators.[33,34,91,180–183] Figure 12 shows the design principle of the falling-film microreactor.[33,34,91,180–182] The reactor is built from four components: A bottom housing section with integrated heat exchanger, a reaction plate, a contact-zone mask, and a top housing section with an open space. The central element of this microstructured reactor is the reaction plate on which microchannels with widths from 100 up to 1200 μm and depths from 100 up to 600 μm are arranged. Above the reaction channel, in which the liquid flows downwards due to gravity, a rectangular-shaped open space lies in the top cover of the housing through which the reactant gas flows. The gas inlet is formed in an analogous way to a gas diffuser, thus distributing the gas homogeneously. The dimensions of the cooling channels correspond to the width and depth of the reaction channels. To limit the reaction in the cooled region, contact with the gas in the non-cooled region is prevented by covering with a contact-zone mask.

Figure 13 shows a stainless steel falling-film microreactor with a viewing window. If a quartz window is used, photochemical gas–liquid reactions can be carried out. The high mass- and heat transport achieved in falling-film reactors can be increased further in a falling-film microreactor by the development of a thin liquid film in the microstructured channels. Liquid films up to 15 μm thick correspond to a specific phase interface of up to 20000 $m^2 m^{-3}$, a value which is approximately ten times higher than that of most known commercial systems, such as the impinging jet reactor.

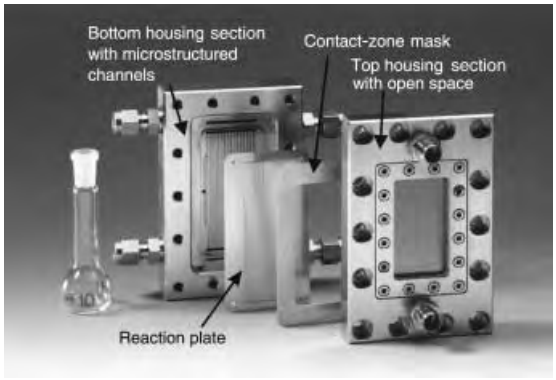


Figure 13. A falling-film microreactor with a viewing window (source: IMM[34,183]).

Similar results have also been achieved with the microbubble column, the principles of which are described in Figure 14.[33,34,71,91,180–182] The central element of the microbubble column is a static microdisperser unit made of a nickel/copper alloy, which is manufactured through a UV-LIGA

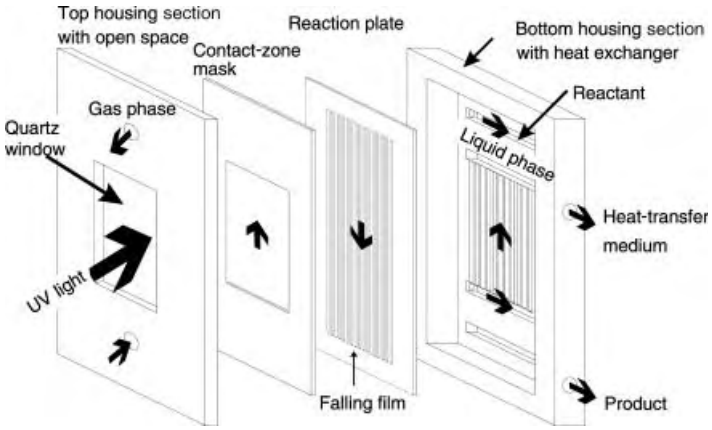


Figure 12. Components of a falling-film microreactor (source: IMM[34]).

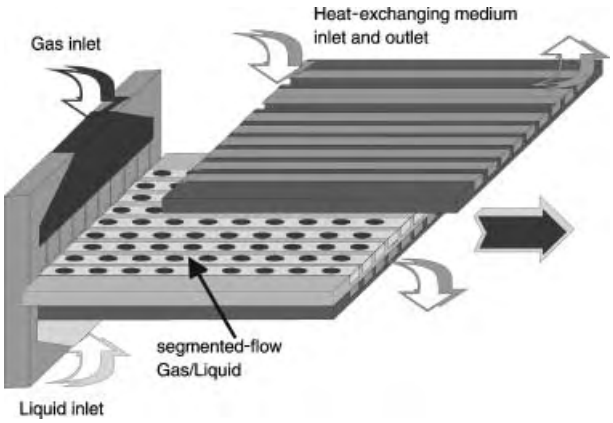


Figure 14. Construction of a microbubble column (source: IMM[34]).

© 2004 Wiley-VCH Verlag GmbH & Co. KGaA, Weinheim

process. Flow distribution of the gas and liquid is achieved through the construction of a pressure barrier in the feed part of the small microdisperser unit, where the gas inlet is no wider than 5 μm and the liquid inlet no wider than 20 μm. The parallel operating reaction channels are arranged on a plate. Effective thermal control is achieved through the use of a heat-transfer medium that flows in small channels in counterflow to the reagents. The reaction channel plate is locked between these heat-transfer channels on each side (the separate parts of the stainless steel microbubble column are shown in Figure 15). The microbubble column is a reactor

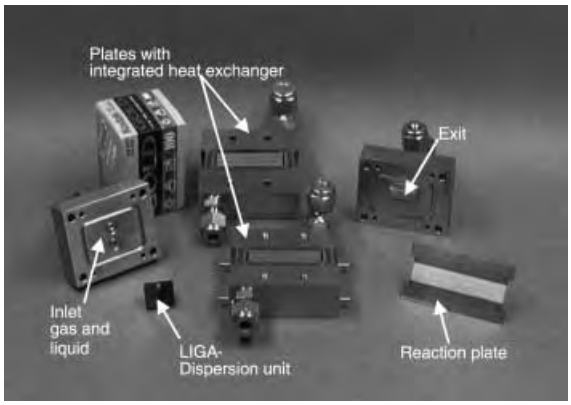


Figure 15. Components of a microbubble column (source: IMM[34]).

designed for short gas–liquid contact time. In addition to the bubble-flow and spray-flow techniques are the slug-flow and the annular-flow regimes, which are set through the appropriate choice of liquid and gas superficial velocities.

Figure 16 shows the gas–liquid–solid microstructured reactor developed at MIT (USA), in which microchannels consist of conventional catalyst-powder fixed beds.[92,185,186] In this way larger inner interfaces are created. This micropacked bed reactor has been successfully employed for the hydrogenation of conjugated olefins and the selective oxidation of benzyl alcohol to benzaldehyde. Of particular note is the numbering-up of ten such reactors. The difficult equidistribution of the gas–liquid flow was realized through specially developed distribution structures.

Figure 17 describes the glass-cyclone mixer, [146] which was built from 11 microstructured stacks which each contain three groups of nozzles. The gas injection nozzle has a width of 30 μm whilst the liquid is dosed through a 50-μm wide opening. The bubble-forming process can be influenced by the arrangement of the gas and liquid injection nozzles (either parallel or vertical). Within the reaction area, spiral patterns of the gas bubbles form in the liquid, similar to a cyclone vortex, which is also employed in liquid–liquid operation. In the large reaction area, clusters of bubbles and foam are formed in addition to isolated bubbles, and these coalesce or deform in smaller microchannels. This reactor type is thus suitable for contacting catalyst slurries to the gas phase, although the nozzle width needs to be widened to 150 μm for this operation.

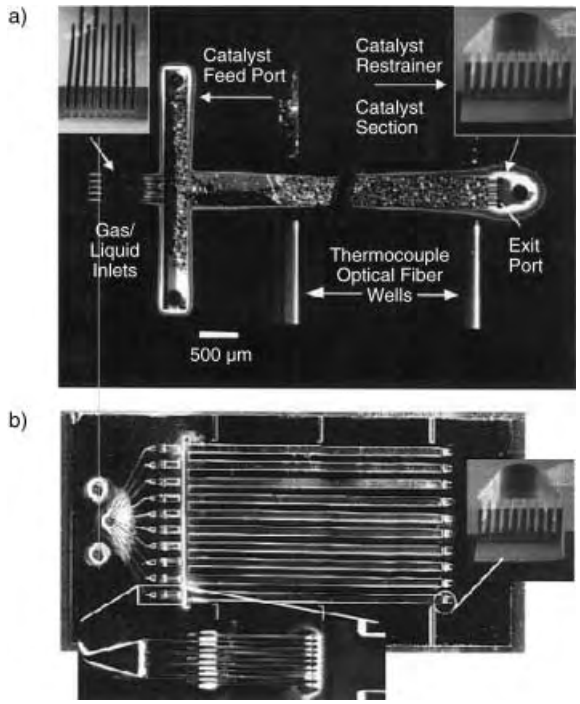


Figure 16. Packed-bed microreactor: a) Single-reactor version; b) ten-reactor version with a flow distribution zone (source: MIT, Cambridge, USA[5]).

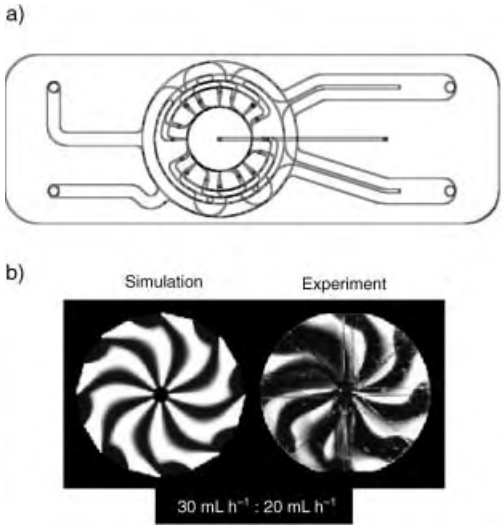


Figure 17. Glass cyclone mixer: a) Construction; b) simulated and experimentally determined liquid–liquid flow patterns (source: IMM; mgt mikroglas AG[146]).

A reactor developed by Chambers et al. is designed specifically for strongly exothermic fluorination using elemental fluorine (Figure 18).[89,90] The liquid and the gas are dosed in a nickel channel at velocities such that an annular flow is exhibited, by which the liquid is distributed as a thin film on the surface of the wall of a microchannel and the gas flows through the center of the channel. Similar flow conditions and well defined gas–liquid contact interfaces are

 © 2004 Wiley-VCH Verlag GmbH & Co. KGaA, Weinheim

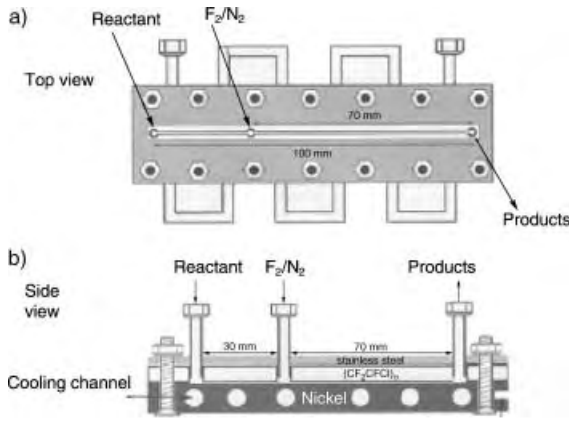


Figure 18. Design of a single-channel reactor (source: University of Durham[89]).

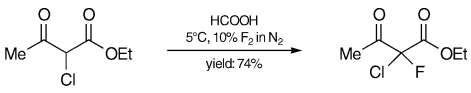
obtained by this method as for a falling-film reactor. Recently this type of reactor was extended to a three-channel reactor.[90] The two-channel silica reactor developed by Jensen et al. functions following an analogous principle where the channel surface is coated with nickel in order to improve chemical resistance.[92]

4.2. Halogenation Reactions

To demonstrate the advantage in using microstructured reactors, the fluorination of organic compounds with elemental fluorine was attempted by many groups.[34,89–93] This reaction is strongly exothermic and is in most cases uncontrollable in conventional reactors. In this way, facile access to fluorine-containing intermediates is provided.

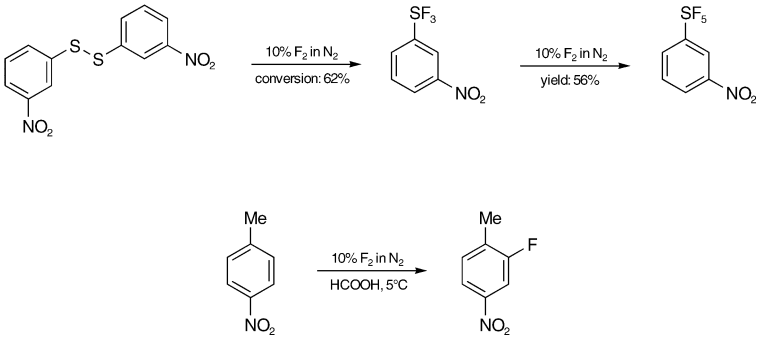
Due to the poor solubility of fluorine in solvents often used for this reaction (e.g., CH_3CN or CH_3OH) the gas–liquid reaction is found to occur at the gas–liquid phase interface where gas–liquid mass transport is the rate-limiting step. Due to the very high specific phase interfaces that serve to form the very thin liquid layer on the surface of the microstructures, both heat transport and mass transport are intensified such that the formation of hot spots is suppressed and the selectivity of the reaction is improved.

The first investigation of this problem was published in 1999 by Chambers and Spink[89] and was discussed in detail later.[90] It was shown that β-dicarbonyl compounds could be converted to respective fluorinated species (in formic acid solution) using 10% F_2 in N_2 by continuous operation. The reaction of ethyl 2-chloroacetoacetate in a three-channel microreactor gave a conversion of 59% and a yield of 74%;[90] conventional methods in batch operation gave a significantly lower conversion and yield.[187] It was further observed that the fluorinated nickel surface in the microchannel led to a catalytic effect through the favored formation of the enol form (Scheme 17). Further examples of the fabrication of pentafluorosulfide compounds and the fluorination of 4-nitrotoluene have been reported, in which conversions up to 77% and yields up to 78% were achieved (Scheme 18).[90]

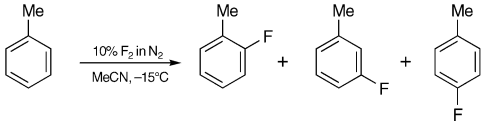


Scheme 17. Fluorination of 2-chloroacetic ester in a three-channel microreactor.

Jähnisch, Hessel, and co-workers showed that both the falling-film microreactor (Figure 13) and the microbubble column (Figure 14) offer advantages over conventional reactors in fluorination reactions with F_2.[34,91] The fluorination of toluene was investigated (using either CH_3CN or CH_3OH as solvent; Scheme 19).The selectivities achievable for the formation of monofluorinated toluene, were determined based on the conversion and were compared to a conventional laboratory-scale bubble column. The selectivity of the formation of monofluorinated toluene in a falling-film micro-



Scheme 18. Fluorination of bis(3-nitrophenyl)disulfide and 4-nitrotoluene in a microstructured reactor.



Scheme 19. The fluorination of toluene was carried out in both a falling-film microreactor and a microbubble column.

reactor is significantly higher than that from a conventional bubble column (Figure 19). A further advantage is the considerably higher space–time yields achievable in microstructured reactors.The results of these studies were taken by de Mas et al. as a benchmark for similar investigations on the same model system in a two-channel reactor made of silica.[92,93] The authors verified the results and, moreover, showed for the first time experimentally that the fluorination with F_2 can be carried out at room temperature.

An improvement in selectivity of the chlorination of acetic acid was recently described in a patent (Scheme 20).[188] Using a falling-film microreactor, a conversion of $>85\%$ to monochloroacetic acid was achieved, and the formation of dichloroacetic acid was reduced from $\approx 3.5\%$ to $<0.1\%$, thus sparing the need for a costly and time consuming separation process.

 © 2004 Wiley-VCH Verlag GmbH & Co. KGaA, Weinheim

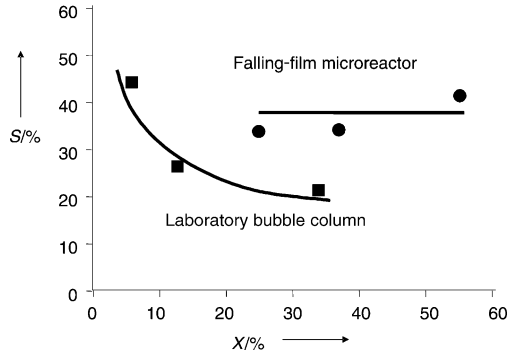
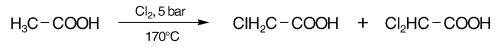


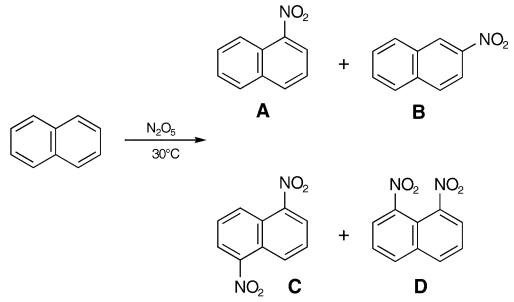
Figure 19. Conversion (*X*) and selectivity (*S*) in the fluorination of toluene in a falling-film microreactor and in a laboratory bubble column (source: ACA, Berlin[91]).



Scheme 20. The chlorination of acetic acid, optimized in a falling-film microreactor.

4.3. Nitrations

Loebbecke, Antes, and co-workers developed a continuous process for the nitration of aromatics in microstructured reactors, which was shown to significantly increase selectivity through their improved heat- and mass transport properties.[94,95,121,189] The strongly exothermic nitration of naphthalene using N_2O_5 in both the gas phase (in situ production from N_2O_4 and O_3) and the liquid phase was investigated (Scheme 21). The modes of operation of the interdigital

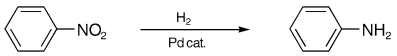


Scheme 21. Nitration of naphthalene in a microstructured reactor.

mixers (using the multilamination principle) as well as the microstructures (working according to the split–recombine technique) were studied. Nitration in conventional batch operation requires temperatures from −50 to −20 °C, while the same reactions can be carried out in microstructures under continuous processing at 30 °C with a flow rate of 1 mL min^{-1} at a residence time of 3 s. The preferred mononitro derivatives **A** and **B** are formed, as well as the dinitro compounds **C** and **D**, while the formation of higher nitrated products was quantitatively suppressed. Interestingly, through varying the reaction conditions and the choice of reactor geometry, not only could the level of nitration be set but also the isomer ratio could be changed considerably. In macroscopic batch reactors the isomer ratio **C**:**D** is invariably around 1:3.6, while applying microstructures allows greater access to the 1,5-dinitro compound **C** (**C**:**D** ≈1:2.8). The isomer ratio of mononitro naphthalene products could also be changed (20:1 for **A**:**B** in the industrial process, compared with 32:1 for the microstructured reactor).

4.4. Catalytic Hydrogenation of Nitrobenzene

Yeong et al. described the heterogeneously catalysed exothermic hydrogenation of nitrobenzene to aniline (Scheme 22) in a falling-film microreactor (Figure 13).[190]



Scheme 22. Heterogeneously catalyzed hydrogenation of nitrobenzene to aniline in a falling-film microreactor.

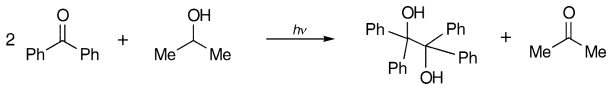
Pd catalysts were deposited by sputtering onto the microstructured plates via the decomposition of $Pd(OAc)_2$ with UV light, impregnation of γ-Al_2O_3 with palladium nitrate, or through the incipient wetness method, and hydrogenation was carried out at 60 °C and 1–4 bar H_2. Catalysts prepared by the latter two methods gave the best results (82 % conversions). However, considerable deactivation occurred through the deposition of organic compounds, which could be reversed by oxidation at 130 °C. In addition, deactivation through the loss of palladium could be counteracted by increasing the Pd concentration. These investigations were the first to utilize a three-phase (gas–liquid–solid) system in a microstructured reactor, and highlighted the advantages of microtechnology for improved heat- and mass transport in optimizing heterogeneous catalysis.

5. Photochemical and Electrochemical Reactions

Few studies describing the application of microstructured reactors for photochemical and electrochemical reactions have been carried out. Jensen and co-workers have developed a single-channel silica reactor in which a miniature UV lamp, as well as in situ UV spectroscopic analysis was integrated.[191–193] The main advantage in applying microstructures in photochemical reactions is that the thin layers allow extensive penetration of the solution and thus a more efficient use of the energy due to light. The large specific phase interfaces give rise to high heat-transfer rates, which make isothermal reaction processes a possibility.

Jensen et al. investigated the radical formation of pinacol from benzophenone and 2-propanol (Scheme 23). Technical reaction data, such as the dependence of the flow velocity on conversion and quantum-yield values were determined, and online analysis of the reaction mixture was achieved. The results of these studies provide a tool with which the intrinsic

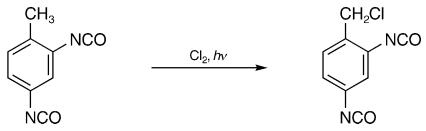
 © 2004 Wiley-VCH Verlag GmbH & Co. KGaA, Weinheim



Scheme 23. Photochemical reductive coupling of benzophenone in a single-channeled microstructured silica reactor.

reaction kinetics of photochemical reactions can be determined without the influence of mass transport.

Jähnisch, Ehrich, et al. reported that a falling-film microreactor (Figure 13) can be used for photochemically induced gas–liquid reactions, such as the photochlorination of toluene-2,4-diisocyanate (Scheme 24).[194] The reaction was carried



Scheme 24. An example of photochlorination in a falling-film microreactor.

out under continuous operation using both a nickel and an iron reaction plate. Figure 20 shows how these systems compare with a conventional batch reactor (a mercury vapor lamp submerged in a reaction flask). The results show

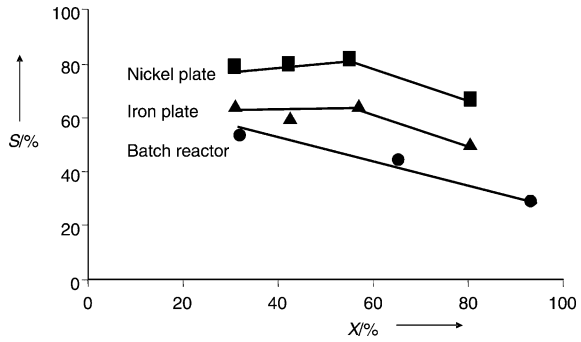
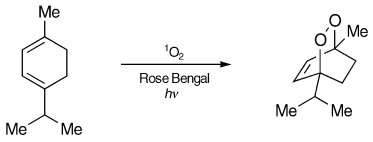


Figure 20. Selectivity (*S*) for the formation of 1-chloromethyl-2,4-diisocyanatobenzene with respect to the conversion (*X*) of toluene-2,4-diisocyanate (source: ACA[194]).

that with similar conversions a significant increase in selectivity is observed in the falling-film microreactor compared to conventional working methods. The application of a nickel plate gives the highest selectivity, while the iron plate exhibited catalytic activity that favored ring substitution as a side reaction.

The advantage of microstructured reactors, in terms of selectivity and space–time yield, stems from the better penetration of photons and the higher mass-transfer rates in the thinner liquid films. Chlorine radicals are located over the total film volume and high local radical concentrations, which lead to recombination, are avoided. In a conventional reactor, the radical concentration near the light source is high while, in contrast, it is very low at the center of the reactor. As a result the selectivity of the desired side-chain chlorinated derivatives decreases, since without photochemical induction chlorination prefers to take place at the aromatic core.

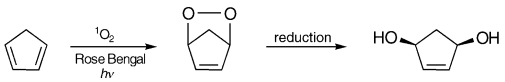
Another interesting field of application for microstructured reactors are reactions in which explosive or toxic compounds are formed. Due to the small volumes involved, the hazard potential can be greatly reduced in such reactions. Wootton et al. recently described the production of singlet oxygen through the photochemical stimulation of oxygen in the presence of catalytic amounts of Rose Bengal in a single-channeled glass reactor;[86] a [4+2]-cycloaddition of α-terpinene led to the formation of ascaridole (Scheme 25). This



Scheme 25. The reaction of α-terpinene and singlet oxygen to give ascaridole.

process could be run continuously, which avoided the enrichment of the explosive endoperoxide ascaridole and delivered very high conversions after an exposure of only 5 s. In this example, light penetration through the liquid layer plays an important role as the dissolved photosensitizer Rose Bengal possesses a large extinction coefficient and all of the light is absorbed over a rather short distance.

Jähnisch et al. showed that the falling-film microreactor (Figure 13) is also suitable for the continuous photochemical generation of singlet oxygen in the presence of dissolved Rose Bengal. For example, a [4+2] cycloaddition reaction of cyclopentadiene with singlet oxygen was investigated (Scheme 26).[195] The explosive endoperoxide, which appears as an intermediate, was reduced with thiourea to give 2-cyclopenten-1,4-diol, which is of pharmaceutical importance.[196]



Scheme 26. Photooxygenation of cyclopentadiene in a falling-film microreactor.

Löwe et al. developed an electrochemical microstructured reactor that was suitable for electroorganic syntheses (Figure 21).[197] The main component of this reactor is a microstructured electrically nonconducting layer, which is sandwiched by the electrodes. The microchannels have a width of 80 μm, a depth of 25 μm, and a length of 64 mm, and are operated at a flow rate of 6 $mL\,h^{-1}$ and a pressure drop of 1.1 bar. An integrated cooling element ensures an effective control of temperature.

In this reactor, the technically important oxidation reaction of 4-methoxytoluene to 4-methoxybenzaldehyde was investigated (Scheme 27). Best results were achieved at

 © 2004 Wiley-VCH Verlag GmbH & Co. KGaA, Weinheim

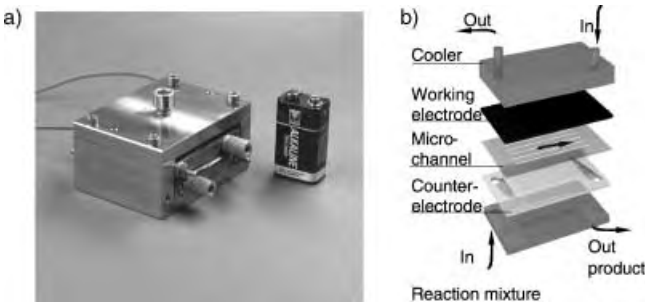
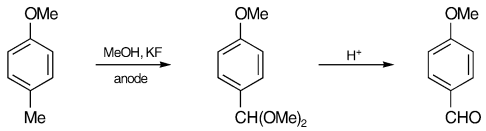


Figure 21. a) Microstructured reactor with an integrated cooler for electrochemical processes; b) explosion diagram (source: IMM[197]).



Scheme 27. The anodic oxidation of 4-methoxytoluene in an electrochemical microstructured reactor.

a voltage of 4.5 V (Figure 22), where a selectivity of 86% at a conversion of 88% was recorded. In contrast with conventional processes, it was also possible to perform the reaction

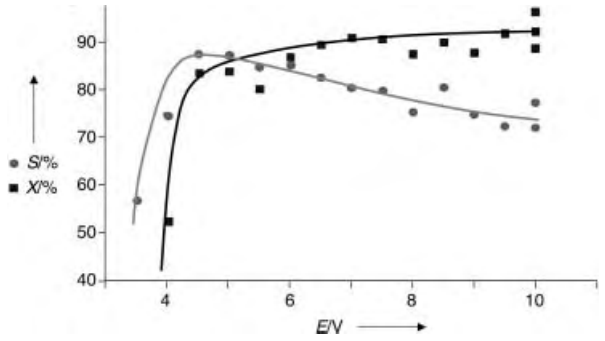
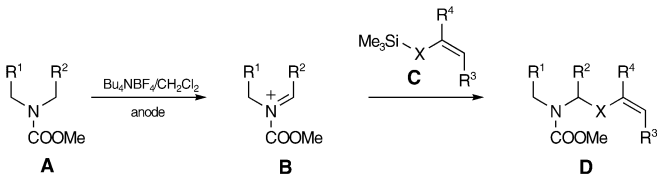


Figure 22. Dependence of conversion (*X*) and selectivity (*S*) on the electrode potential (*E*) in the electrochemical oxidation of 4-methoxytoluene (source: IMM[197]).

without a conducting salt, and selectivity up to 98% was achieved with small concentrations, compared to ≈85% for the conventional process. The increase in selectivity can be explained by the fact that both the short distance between the electrodes and the nature of running a reaction in microchannels leads to intense mass- and heat transport. In addition, over short residence times, a homogeneous current density and velocity distribution existed such that the electrochemical reaction could be run under precisely defined operating conditions.

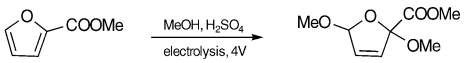
Suga et al. developed the so-called "cation-flow" method for the continuous production of very reactive acyliminium ions **B** in microreactors, which were immediately converted in a C–C bond formation reaction to substituted derivative **D** using various nucleophiles **C** such as allylsilanes or enol silyl ethers (Scheme 28).[198,199] The reaction takes place over short residence times and is suitable for combinatorial synthesis



Scheme 28. Electrochemical synthesis of highly-functionalized derivative **D** in an electrochemical microstructured reactor using the "cation-flow" method. (R^1, R^2 = alkyl, cycloalkyl; R^3, R^4 = H, alkyl, cycloalkyl; X = O, CH_2).

where the flow of the reactants can be controlled. A carbon-fiber anode and a platinum-wire cathode was employed, and Bu_4NBF_4 was used as the conducting salt. The *N*-acyliminium ions **B** were detected by in situ IR spectroscopy.

Menegaud, Ferrigno, and co-workers recently described the coupling of a ceramic electrochemical microstructured reactor with a mass spectrometer.[200–203] In their study the electrochemical dimethoxylation of furan-2-carboxylic acid methylester was investigated (Scheme 29). This combination allows mechanistic studies of electrochemical reactions and identification of unstable intermediate steps.



Scheme 29. Electrochemical dimethoxylation of furan-2-carboxylic acid methylester.

6. Gas-Phase Reactions

Apart from organic liquid-phase reactions, gas-phase reactions are the most frequently investigated processes in microstructured reactors. Aside from the economic and scientific value of such investigations, microstructured reactors seem technologically well suited to such reactions. According to Wörz,[23] processes with high reaction rates together with a high release of heat should be investigated in microstructured reactors, especially if the reactions take place in different phases.

The former aspect is true for several gas-phase reactions, such as oxidations, which can be completed in several milliseconds, mainly at significantly high temperatures. Most gas-phase reactions are carried out over a catalyst, and these two-phase (solid and gas) reactions are especially suited to microprocess engineering. Many industrial and laboratory gas-phase processes are carried out in flow-through reactors, which are, at least, a formal equivalent to a microstructured reactor.

While microstructured reactors and conventional reactors for gas-phase reactions resemble each other in their process operation, they are often different in terms of catalyst technology. Conventional reactors mainly use catalyst in the form of pellets (fixed-bed technology) or fine, agitated powders (fluidized-bed technology). The use of thin catalyst layers on the reactor walls is almost exclusively used in microstructured reactors. Washcoats, such as those applied in

 © 2004 Wiley-VCH Verlag GmbH & Co. KGaA, Weinheim

exhaust-gas cleaning in automobiles, as well as in monolith reactors, are often applied as a carrier on the microchannel wall. Then, for example, wet-chemical impregnation can be carried out. Beds in microstructured reactors are generally not employed as they cause a large pressure drop and a change the laminar flow.

6.1. Microstructured Reactors for Gas-Phase Reactions

6.1.1. Multiplate-Stacked Microstructured Reactors

One of the more frequently used reactor types contains a stack of plates, each of which possesses parallel microchannels.[9,48,56,60,74,100,101,105–107] Such stacks are either welded together externally (Figure 23),[48,204] encased by a cover

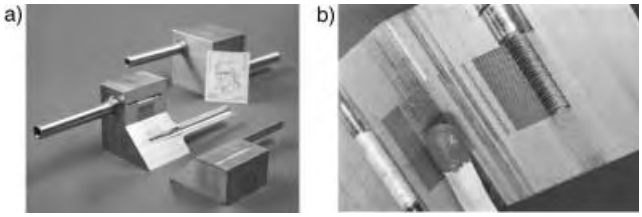


Figure 23. Overview (a) and more detailed view (b) of an externally welded multiplate-stacked reactor (source: IMM).

(Figure 24),[9,100,101,205,206,212,213] have end plates containing fluidic connections (Figure 25),[74,207,208] or are directly inserted into a two-part housing unit with a pocket (Figure 26).[56,60,105–107] If required, graphite gaskets (or other materials) divide single fluidic areas on the plates and isolate the plates from each other.[74,207] The housing is often sealed with screws, resulting in an even pressing of the surface of the plates. Tightening of the housing parts is possible also without internal sealing of the plates using graphite or similar foils,

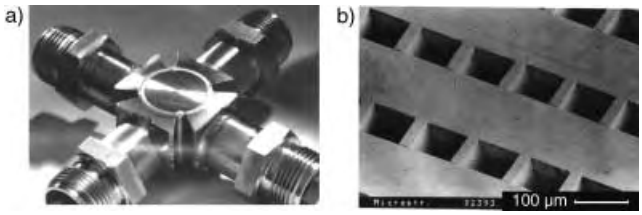


Figure 24. Overview (a) and more detailed view (b) of a diffusion-bonded multiplate-stacked reactor (source: Forschungzentrum Karlsruhe[205]).

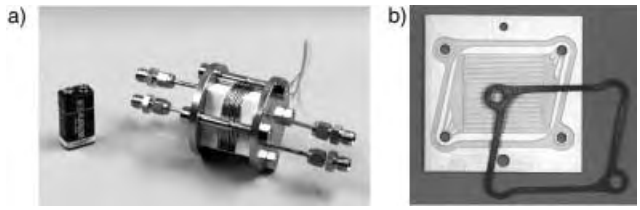


Figure 25. A multiplate-stacked reactor with an end plate: a) Overview, b) single plate with gasket (source: IMM[184]).

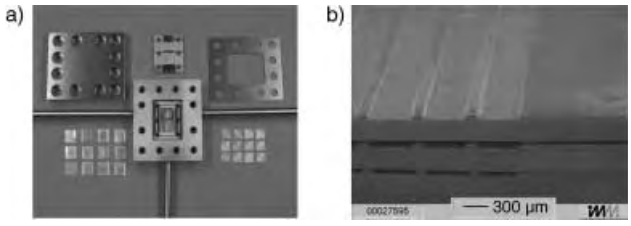


Figure 26. Multiplate-stacked reactor with a two-part housing: a) Component parts, b) detailed view of a stack of plates (source: IMM[3]).

simply by means of surface pressure.[56] However, the microstructured plates can also be irreversibly connected, for example, through laser welding[48,204] or through diffusion bonding.[100,101,212,213] Diffusion-bonded plates are also surrounded by a housing. The compactness of such configurations can be optimized, thus giving large active areas for a given volume.

Examples of housed microstructured stacks include those prepared by Schouten et al., which is a manufactured reactor for the investigation the oxidation of ammonia,[60,214] and those of Richter and Cominos et al., which are designed for the synthesis of ethylene oxide[56,105] and for methanol steam reforming, respectively.[215,216] Schubert and co-workers have optimized the diffusion bonding of microstructured stacks, which also exhibit excellent heat transfer despite being uncoated.[6,9,20,205,206,217,218] In addition, a range of reactors exists that are available for flow rates of a few 10s of $L\,min^{-1}$ for liquids and of a few 10s of $m^3\,min^{-1}$ for gases.[6,20,205,219]

6.1.2. Multiplate-Stacked Microstructured Reactors for Parallel Catalyst Testing

A special form of multiplate-stacked reactors are those consisting of similar plates but with different catalysts.[125,220,221] A multiplate-stacked reactor (35 plates) was designed and constructed by Zech and Hönicke, together with co-workers from IMM.[125,220] The central component of the process plant that surrounds the microstructured reactor is a 300-µm-wide aligned capillary, which automatically collects samples from each plate (Figure 27). Later Kolb et al. constructed a 10-fold stacked reactor to carry out two

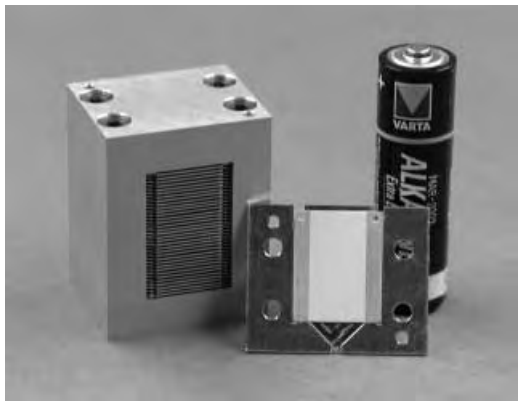


Figure 27. Microstructured reactor module with 35 stacked frame plates (source: Universiät Chemnitz; IMM[220]).

© 2004 Wiley-VCH Verlag GmbH & Co. KGaA, Weinheim

functions.[221] Depending on the end plates used, a parallel or serial operation can be carried out using the same reactor core. Primary screening and catalyst optimization are thus possible within the same reactor set-up without changing the channel geometry.

6.1.3. Single-Plate and Single-Channeled Microstructured Reactors

Single-plate reactors have the advantage that problematic fluid distribution is limited to the microchannels.[222] A special case is the single-channeled reactor, a simply built example of which was designed by Veser et al.[39,40] Two plates, one with a channel and wire, and the other with cover plate, were sandwiched together.

Ajmera et al. described a single-channeled microstructured reactor that incorporates catalyst powder or particles (Figure 28).[223,224] To compensate for local differences in the particle-size distribution, the channel has a specific length, which achieves a uniform flow distribution from both sides by applying a bifurcated cascade.

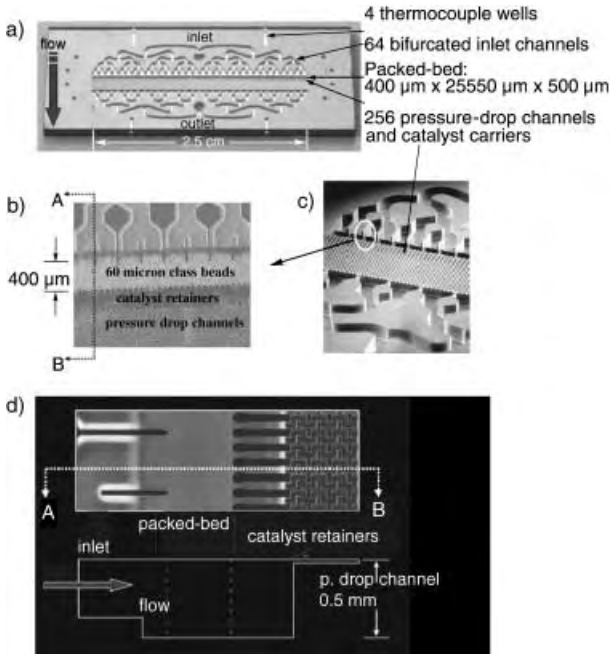


Figure 28. a) Cross-flow microstructured reactor chip made of silicon; b) microstructured reactor packed with 50 µm glass beads; c) SEM image of a microstructured reactor; d) inlet region and pressure barrier (source: MIT[223]).

6.1.4. Membrane-Microstructured Reactors

Franz et al.[54,225] and Jensen et al.[226–228] introduced a single-channeled microstructured reactor which incorporated numerous pressure and temperature sensors along the reaction zone.[229,230] The microstructured reactor is closed from above by a thin impermeable membrane which contains a Pt thin-film catalyst (Figure 29). Depending on the strength and material of this membrane, and thus its ability to allow heat to dissipate, numerous operating modes are available for certain reactions, such as ammonia oxidation.

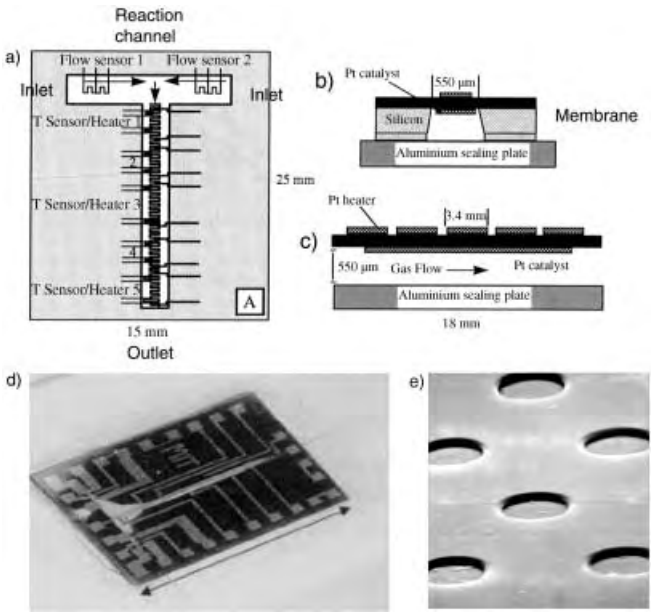


Figure 29. A T-shaped membrane-based microstructured reactor: a) view from above; b) cross section through a reaction channel; c) longitudinal section through a reaction channel; d) photo of the microreactor; e) regularly arranged free-standing Pd membranes (source: MIT Cambridge[5,228,231]).

Membrane-microstructured reactors with permeable membranes can be used for the coupling and separation of a reaction, which through permanent product removal increases the conversion, according to the law of mass action.[116,231–233] Thin membranes are therefore fitted over the opening of a plate, which serves to separate the reactant and product gas streams from each other.[231]

6.1.5. Two-Channeled Microstructured Reactors with Counter-Current Flow

Two-channeled microstructured reactors can be used for counter-current flow operation.[22,60,107,207] Thus, an exothermic reaction can heat up its own reactant stream.[22] It is also possible to couple exothermic and endothermic reactions in this way.[207]

6.1.6. Chip-Microstructured Reactors

Many gas-phase microstructured reactors are designed by using the silicon micromachining technology of microelectronics. Chip systems are mostly formed of two or more joined silicon (or glass) wafers,[54,225–230,234] but occasionally relatively complex multiplate systems, which can have several functions in every layer, are employed.[21] A groundbreaking silicon chip, designed by MIT and DuPont, was fabricated with such an architecture (Figure 30).[21]

6.1.7. Microreactors Without Microchannel Feeding Systems

A microreactor without microchannel guidance was recently described by Wolfrath et al.,[233] in which filaments

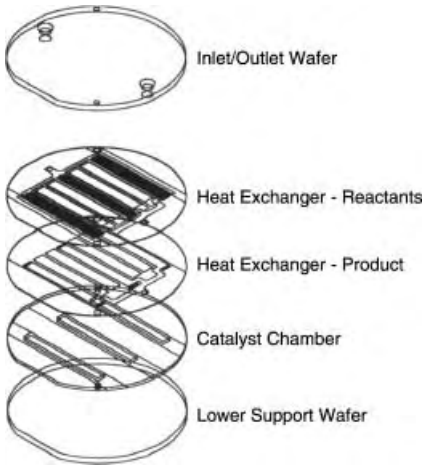


Figure 30. Explosion diagram of an integrated microstructured reaction system made of silicon (source: DuPont, Delaware[21]).

were inserted into the product stream and miniature active areas were produced.

It is likely that many similar microreactors will find future applications, simply due to costs. They will always be advantageous as long as the fundamental elements of microprocess operation technology are fully understood in advance. This knowledge then also allows alternative solutions to be found, and optimal process operations to be applied. The target factor to be achieved always has priority in process development and optimization. Thus, the manufacture of microstructured elements is no longer based purely upon the criterion of a supposedly necessary, partly exaggerated structural precision. On the contrary, there is room for compromised solutions where the dimensions of the structures are not so accurately defined as in microtechnological manufacturing processes.

6.2. Catalyst/Carrier Systems for Gas-Phase Reactions In Microchannels

Catalysts and their carriers are applied onto microchannels in different forms using various coating methods. In a simple variant, the material of the microstructured reactor forms the catalyst itself without requiring a carrier.[56,118,206] The microchannel walls act as the catalyst surface, so that only small specific surface areas are available. Applications thus remain limited to fast reactions, or more generally to process operations with low flow rates.

With the development and optimization of methods, particularly for microchannel coatings, catalyst/carrier layers with thicknesses of 1–50 μm are often applied. Thus, diversity is possible with respect to porosity, material, consistency, size, form, and (crystal) structure.[292] In the design of catalyst/carrier systems onto microchannels, surface forces naturally play an important role such that non-optimized coatings in rectangular or semicircular channels often lead to V-shaped profiles. In some cases, the surfaces of semicircular channels can be almost uniformly coated so that the catalyst surfaces possess semicircular profiles.[184]

In a conventional form, catalyst powder or particles are introduced in a channel as miniature fixed beds.[223] Alternative or more complex catalyst forms also find applications such as catalyst filaments,[233] wires,[40] and membranes.[116,231]

Most coatings in microchannels are prepared by the washcoat route with subsequent wet-chemical impregnation.[74,207,235] Zeolites are another class of industrially used catalysts that can be directly grown into microchannels.[173,174,236] The anodic oxidation of aluminum channels is frequently used in order to generate nanoporous carrier layers.[213] Thin-film technologies such as CVD[207] and PVD (especially sputtering[231]) can be used to generate compact, thin catalyst films. Other types of catalyst/carrier systems can be prepared through aerosol techniques,[225] sol–gel techniques,[237] plasma electrochemical processes,[238] or electrolysis.[239]

Detailed descriptions of prepared catalyst/carrier systems in microchannels can be found for both washcoat systems[74,235] and for zeolite growth[173,174,236]. The so-called "Fill in/Wipe off" method is a typical procedure for catalyst preparation using washcoats.[74,207]

Few review papers to date have appeared that are dedicated entirely to the subject of catalyst/carrier systems and especially their basic characterization (e.g., with respect to morphology, porosity, consistency). Even so, many reports contain useful information regarding heterogeneously catalyzed gas-phase reactions. In particular, SEM imaging documents the macro- and microstructure of catalysts.[56,105] In many cases, analysis of cross-sectional profiles (perpendicular to the flow direction) show that a nonuniform layer thickness exists (Figure 31). Large differences in layer thickness have been found, especially in the lower half of channels.[225,237,240]

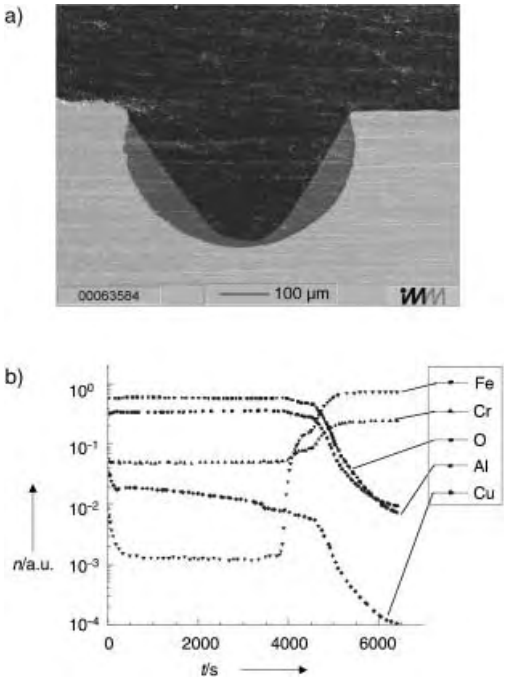


Figure 31. a) SEM image of a cross section of a semicircular microchannel with a γ-alumina washcoat layer (Source: IMM[184]); b) depth profile of catalyst, carrier, and microstructure concentration (source: Universität Kaiserslautern[292]).

 © 2004 Wiley-VCH Verlag GmbH & Co. KGaA, Weinheim

In one case, the simulation of temperature profiles inside an alumina layer was performed.[60]

6.3. Oxidations

6.3.1. Ammonia Oxidation

Rebrov et al. initially compared three reactor systems with microscale flow chambers (based on parallel plates, monolith, and microstructured plate stack concepts) with respect to the oxidation of ammonia to nitrogen dioxide (N_2O); later the work was completed with the investigation of a microstructured reactor/heat exchanger (Scheme 30).[60,214]

$$NH_3 \xrightarrow[\text{Pt cat.}]{O_2} N_2O + NO + N_2 + H_2O$$

Scheme 30. The oxidation of ammonia over a Pt catalyst.

In this system an external jacket provided fast heating and cooling inside the module. Microstructured reactors of various forms could be positioned inside the space formed.

A kinetic model for the oxidation of ammonia was coupled with a hydrodynamic description and analysis of heat development.[214] Using regression analysis, reaction rates and selectivites for all products at equilibrium were predicted. Experiments proved that with optimum reactor designs, N_2O selectivities up to 50% were achieved with complete NH_3 conversions in a temperature range of 300–380 °C (Figure 32). Complete conversion at the lowest temperature was achieved by the microstructured stacked plate reactor, which incorporated the highest Pt loading. Normalization of the activities based on a single catalyst atom divides the investigated reactors into distinct two groups, suggesting the existence of either Pt clusters or single atoms dependent upon Pt loading. Numerical simulations have suggested that isothermal behavior in optimized microstructured designs can be achieved under conditions that correspond to an adiabatic temperature increase of up to 1400 °C.

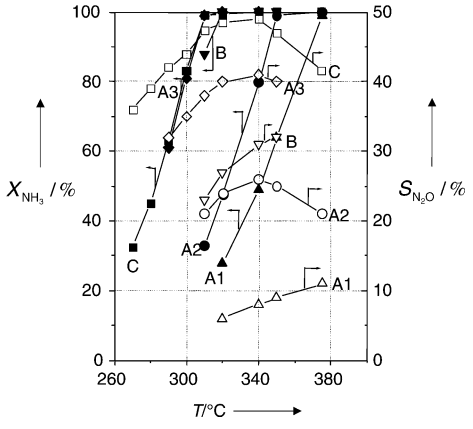


Figure 32. NH_3 conversion (X_{NH_3}) and N_2O selectivity (S_{N_2O}) for the Pt-catalyzed oxidation of ammonia in various multiplate-stacked microstructured reactors (parallel-plate (**A**), monolith (**B**), and multiplate-stacked microreactor (**C**)) with respect to reactor temperature. 0.022–0.543 mg Pt/Al_2O_3; 6 vol% NH_3, 88 vol% O_2, balance He; 600 (**A1**), 1175 (**A2**), 4430 (**A3**), 580 (**B**), and 4290 $cm^3 min^{-1}$ (**C**) under standard temperature and pressure (STP). Reactors **A**–**C** differ in their microchannel geometries and in the amount of catalyst carrier Al_2O_3. Reactors **A1**–**A3** differ in the amount of loaded Pt, with similar internal dimensions of the microflow (source: University of Eindhoven[60]).

Further studies by Rebrov et al. showed that the material that carries the catalyst also has an influence on the selectivity achieved. When, for example, platinum is used instead of aluminum, N_2O selectivity is reduced to 20%.[60] The lower thermal conductivity of platinum leads to a greater temperature difference within the microstructured reactor.

Jensen et al. carried out the same reaction, but used a silicon chip microstructured reactor in which an etched channel was covered by a thin membrane.[54,225–230,234] The membrane held the catalyst at its base (exposed to the microchannel) as a thin layer while its top side incorporated heating elements and temperature sensors. Through the thermal conductivity of the materials used and the thickness of the membrane the reaction temperature could be controlled as heat was dissipated exclusively through convection, which occurs over the membrane and out towards the Si walls.

Oxidation reactions with ammonia usually have an ignition/extinction mechanism that governs autothermal behavior. At a fixed temperature the reaction starts (if the heat added exceeds the heat dissipation of the reactor). The temperature suddenly increases through heat production up to a state where the heat input and output are stabilized. The reaction can now proceed without additional external heating, that is autothermally. As the microstructured reactor now has a dramatically superior heat output compared to conventional reactors, it is possible for the reaction to be investigated in temperature regions that otherwise would not be accessible (Figure 33). This behavior was exhibited in the study of Franz et al. for three different membranes (1 μm SiN_x, and 1.5 and 2.6 μm Si).[225] While the 1 μm membrane exhibited ignition behavior up to 570 °C at low power and autothermal operation up to 500 °C thereafter, the 2.6 μm membrane showed opposite behavior. Over a wide power range, a gradual increase in temperature was observed followed by only a small increase in temperature through ignition (from ≈ 270 to ≈330 °C). In contrast to conventional reactors, an ignition–extinction hysteresis did not truly occur. The 1.5 μm Si membranes show intermediate behavior; a fast increase up to ≈520 °C with a developed hysteresis.

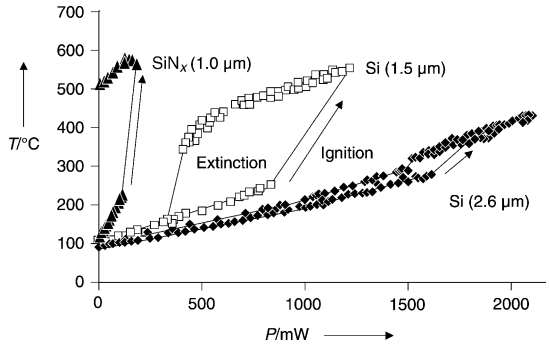


Figure 33. Ignition and extinction curves for the oxidation of ammonia over Pt in various membrane-based silicon-chip microstructured reactors with respect to heating output (*P*) (source: MIT[225]).

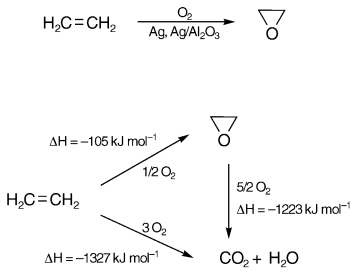
 © 2004 Wiley-VCH Verlag GmbH & Co. KGaA, Weinheim

What use is the precise temperature control exhibited by microstructured reactors through the choice of membrane type and heating power input? The selectivity of exothermic, high-temperature reactions, such as the oxidation of ammonia, responds to the operating temperature. Yet, due to the above-mentioned reasons, this temperature control was not available for conventional reactors; this is now possible with microstructured reactors. Besides the N_2O/N_2 slectivity, the NO/N_2 selectivity is also a sensitive parameter that increases with increasing reaction temperature. In a chip-microstructured reactor an increase of the latter parameter is observed from 0.5 to $\approx$2.5 in the temperature region of 340–570 °C. Note also that the microstructured reactor allows investigations in the temperature region below 340 °C for the first time. Here an increase in NO/N_2 selectivity is surprisingly found, which is an indication of an altered mechanistic behavior.[225]

Thus, the investigations of Franz et al. show that chip-microstructured reactors with precise temperature control can be used to carry out reactions with better, and especially well-controlled selectivity. It is possible to operate previously high-temperature reactors at lower temperatures. Even though the oxidation of ammonia to NO is achieved at lower yields, these operations pave the way for future partial oxidations of hydrocarbons to other valuable products, such as anhydrides, ketones, or alcohols. Aspects of industrial relevance allow such microstructured reactors to investigate over large operating windows (here, over a wide temperature range). They are already a vital tool for improving the accuracy and applicability of kinetic studies in heterogeneous catalysis.

6.3.2. *Oxidation of Ethylene to Ethylene Oxide*

Kestenbaum, Schüth, and co-workers have carried out a very detailed investigation of the oxidation of ethylene to ethylene oxide in a microstructured reactor, where good temperature control and the ability to conduct nonhazardous work in a generally explosive synthetic area are the fundamental motives of their work.[56,105] The reaction enthalpy of the total oxidation to carbon dioxide and water is more than ten times greater than that of the partial oxidation (Scheme 31). Thus, very high local temperature regions (hot-spots) with negative consequences for the course of the reaction can occur.



Scheme 31. Above: Oxidation of ethylene to ethylene oxide in a microstructured reactor. Below: Enthalpies of epoxidation and total oxidation.

To begin their study, Kestenbaum et al. used a multiplate-stacked microstructured reactor made of polycrystalline silver foil (Figure 34) in which they achieved selectivities up to 49 % at a conversion of 12 %.[56,105] Since pure oxygen was used for their experiments, safe-working limits in the explosive regime could be documented shortly afterwards. Using polycrystalline silver the selectivity increased to 65 % without the use of industial promoters, such as 1,2-dichloroethane.[56] This level of selectivity is considerably better than that found elsewhere in the literature for this unpromoted catalyst; best values achieved elsewhere were 69 % with promoters, and 80 % with a combination of promoters and another catalyst, Ag/Al_2O_3.

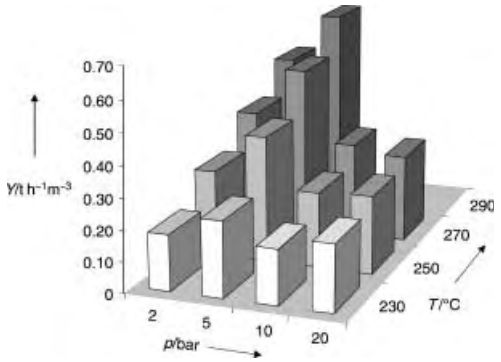


Figure 34. Space–time yield (Y) for the synthesis of ethylene oxide in a multiplate-stacked microstructured reactor, with respect to pressure and temperature (0.235–2.350 s; 15 % ethylene, 85 % oxygen; 1 $L h^{-1}$; source: MPI-Kohlenforschung, Mülheim[56]).

Remarkably, the space–time yield for a microstructured reactor ($0.78\ t\,h^{-1}\,m^{-3}$) exceeds that of an industrial reactor ($0.13–0.26\ t\,h^{-1}\,m^{-3}$), at least if one defines the reactor volume to be only that of the microchannel, that is, the inner reaction volume. By considering the plate volume and thus also the external dimensions of the reactor, a maximum value of $0.13\ t\,h^{-1}\,m^{-3}$ is obtained, which is still within reach of the industrial performance. Schüth et al. carried out further studies on the influence of microtechnological manufacturing processes (especially regarding the roughness of the microchannel), the residence time, the temperature and pressure, and the partial pressures of ethylene and oxygen in the ethylene oxide process (Table 1).

Even though results are very encouraging, industry has yet to apply such reactors. Prior to this taking place, the selectivity must be increased to above 80 % as the cost of ethylene makes up 80 % of the cost of the overall process. In addition, further production demands (whether in small or in large levels) have to be taken into account, for example, reliability, process control, and many other factors.

Kursawe and Hönicke have also investigated the ethylene oxide synthesis, working at high conversions up to 60 %.[102,108] Within the limits of their investigated process window, Ag/Al_2O_3 was found to be better suited than Ag/Al layers, despite a slightly lower selectivity. The thickness of the Ag coating on Al had a strong influence on the conversion and selectivity behavior (Figure 35).[108] In this case, selectivities up to 60 % were achieved at a conversion window between 5 and $\approx$30 %.

 © 2004 Wiley-VCH Verlag GmbH & Co. KGaA, Weinheim

Table 1: Operating parameters and reactor performance for the ethylene oxide synthesis (Scheme 31) in three multiplate-stacked microstructured reactors that differ in the choice of microstructured plates. The values are compared to those of industrial processes.[56]

	Industrial process	Microreactor (Laser-LIGA)	Microreactor (etched)	Microreactor (Aluchrom)
C_2H_4 concentration [vol%]	15–40	1.5–6	3–15	15
O_2 concentration [vol%]	5–9	10–41	5–85	85
CH_4 concentration [vol%]	1–60			
Temperature [°C]	220–275	240–290	240–290	270
Pressure [bar]	10–22	5	2–20	5
Residence time [s]	0.9–1.8	0.1–0.2	0.1–1.5	1.2
C_2H_4 conversion [%]	7–15	2–15	5–20	2–6
Selectivity [%]	80	44–69	38–69	42–58
Space—time yield [$t\,h^{-1}\,m^{-3}$]	0.13–0.26[a]	0.01–0.07[b] 0.14–0.78[c]	0.03–0.13[b] 0.18–0.67[c]	0.01–0.06[b] 0.08–0.36[c]

[a] Reactor. [b] Plate. [c] Channels.

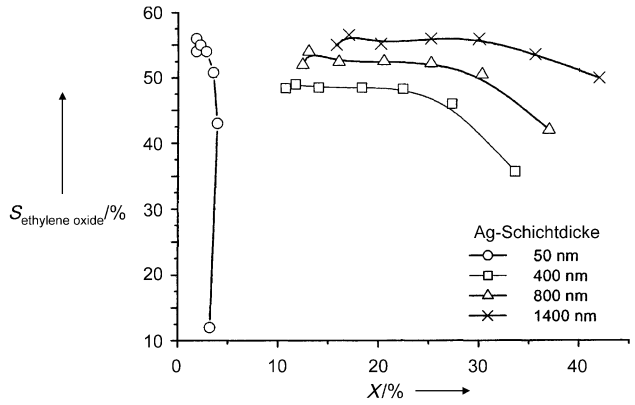


Figure 35. Selectivity (S) and conversions (X) for a Ag/Al microstructured reactor, as a function of the Ag-layer thickness. (250 °C; 3 bar; 20 vol% ethylene in oxygen; 0.23–2 s. Source: Universität Chemnitz[108]).

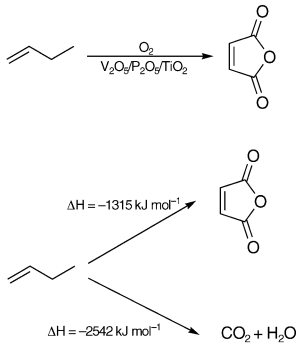
Furthermore, safe working within the explosion regime has be proven for ethylene oxide synthesis in a microstructured reactor.[108] Sputtered silver, as well as sol–gel-grown Al_2O_3/silver layers on microstructures made of an aluminium alloy (AlMg3) were investigated. Neither explosions nor flames were observed. The cross sections of the microchannels were $200 \times 200\ \mu m^2$ and $700 \times 300\ \mu m^2$.

6.3.3. *Oxidation of 1-Butene to Maleic Anhydride*

Kah et al. carried out the oxidation of 1-butene to maleic anhydride in a multiplate-stacked microstructured reactor over a $V_2O_5/P_2O_5/TiO_2$ catalyst (Scheme 32).[103] Selectivities of $\approx 33\%$ were achieved at conversions between 73–85%. An increase in the space–time yield by a factor of five compared to a fixed-bed reactor was achieved (Figure 36). These reactions were carried out safely within the explosive regime.

6.3.4. *Oxidation of Alcohols to Aldehydes*

Wörz et al. investigated the partial oxidation of a substituted alcohol over a silver catalyst, which led to the corresponding aldehyde (Scheme 33).[19,23,43,154,241] Since then, BASF have successfully used an analogous formaldehyde synthesis from methanol with high conversions. It was expected that the synthesis of substituted aldehydes would also present few problems. The new reactions, carried out with a reliable pan-like reactor (pan diameter: 5 cm), gave results that were initially satisfying. At 50% conversion, a selectivity of 90% was achieved. When a production reactor with a diameter of 3 m was used, the results were rather sobering; at 50% conversion now only a selectivity of 40% was achieved. The reason seemed clear; due to the large heat build-up (as a result of the heat of reaction) an increase in temperature occurred (a hot



Scheme 32. Above: Oxidation of 1-butene to maleic anhydride in a multiplate-stacked microstructured reactor. Below: Enthalpies of synthesis and total oxidation.[102]

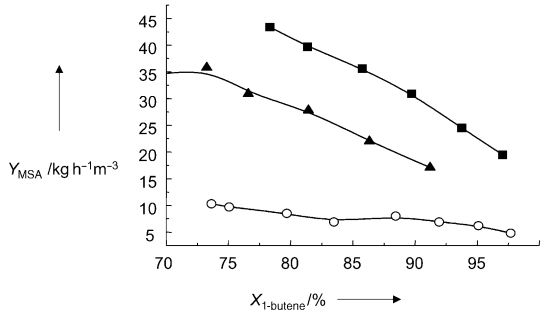
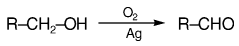


Figure 36. Space–time yield (Y) of maleic anhydride (MA) as a function of 1-butene conversion (X) in two microstructured reactors (■ and ▲), which differ in both their dimensions and the number of parallel operating plates, and in a fixed-bed reactor (○). (400 °C; 0.4% 1-butene in air; 0.1 MPa).[103]



Scheme 33. Oxidation of an alcohol to an aldehyde in a microstructured reactor.

 © 2004 Wiley-VCH Verlag GmbH & Co. KGaA, Weinheim

spot exceeding the reaction temperature by 160 K) that overshot the set operating temperature. In the formaldehyde synthesis this was marginal, while for the aldehyde synthesis both the reactants and products were unstable, and a result, thermally induced side reactions took place.

With this in mind, the actions needed to be taken were obvious: a decrease in hot spots, a decrease in the overall operating temperature and, at best, a significantly reduced contact time. The ideal combination of all these requirements can only be set in a microstructured reactor. Wörz et al. successfully obtained a selectivity to 96% at a conversion of 55% (without a hot spot). However, all conventional solutions that take one aspect into account above the other, show results that are superior to a panlike reactor, but inferior to a microstructured reactor (Figures 37 and 38). Thus, a

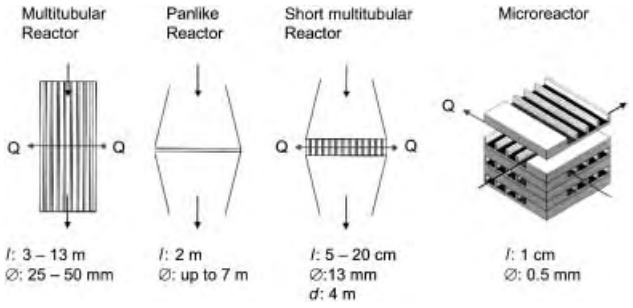


Figure 37. Various reactor configurations for the selective oxidation of an alcohol to an aldehyde in the gas phase (source: BASF, Ludwigshafen[19]).

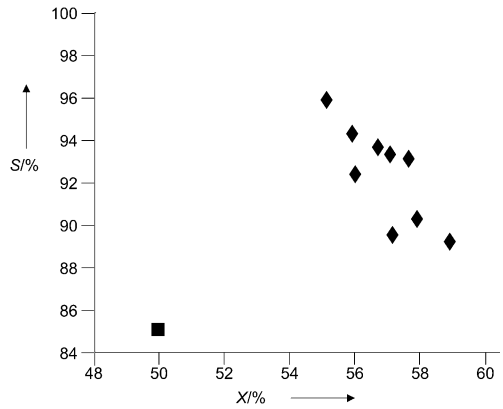
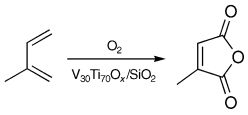


Figure 38. Comparison of the reactor performance of a short multitubular reactor (■) and a multiplate-stacked microstructured reactor (◆) in the selective oxidation of an alcohol to an aldehyde (source: BASF[23]).

single-tube reactor can be operated almost isothermally, yet its considerably long residence time reduces selectivity. A multitubular reactor with many short tubes can, in comparison, achieve significantly shorter residence times with acceptable heat transfer (conversion 50%; selectivity 85%; hot spot 60 °C). Again, a microstructured reactor gives superior results for both of the measured parameters.

6.3.5. Oxidation of Isoprene to Citraconic Anhydride

Citraconic anhydride is currently manufactured using complex synthetic methods. An alternative to these methods could exist through the heterogeneous catalytic oxidation of a suitable hydrocarbon, such as maleic or phthalic anhydride. In this context Liauw, Walter, and co-workers investigated the partial gas-phase oxidation of isoprene in a microstructured reactor (Scheme 34).[207,240] The excellent heat-transfer properties of microstructured reactors are essential in this case, since these reaction release large amounts of heat ($\approx 1000\ kJ\,mol^{-1}$). When overheating occurs, total oxidation to water and carbon dioxide can dominate in the reaction.



Scheme 34. Oxidation of isoprene to citraconic anhydride.

The same authors showed that selectivities (up to 28%) and conversions (up to 100%) comparable to operation in a fixed-bed reactor were achieved in a microstructured reactor, however the microstructured reactor achieved its maximum performance at 400 °C, whilst the fixed bed delivered optimum results at 360 °C (Figure 39). This illustrates the excellent heat dissipation in the microstructured reactor. In the fixed-bed reactor the catalyst temperature lies ≈40 °C higher that in the set reactor temperature, which was proven by placing a thin thermocouple in the reactor bed. The catalyst from the fixed-bed experiments ($V_{30}Ti_{70}O_x$) was inserted in the microchannels in the form of a silicic acid suspension. Although, the chemical composition was slightly modified ($V_{30}Ti_{70}O_x/SiO_2$), this had no influence on the

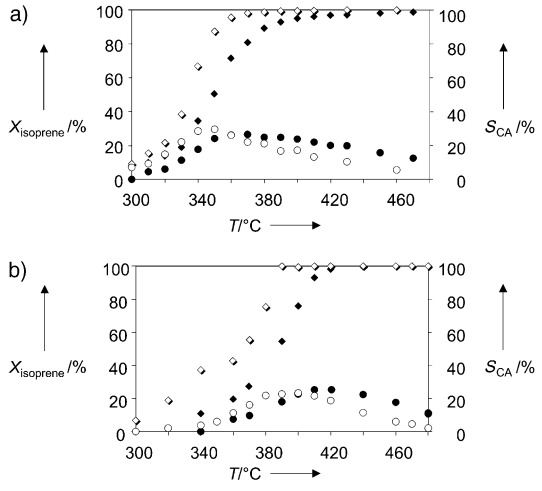


Figure 39. Isoprene conversion ($X_{isoprene}$) and citraconic anhydride selectivity (S_{CA}) in the partial oxidation of isoprene at various flow rates in a) a fixed-bed reactor, and b) a microstructured reactor. ($\diamond = X_{isoprene}$ (120 ml min^{-1}), $\blacklozenge = X_{isoprene}$ (300 ml min^{-1}), $\circ = S_{CA}$ (120 ml min^{-1}), $\bullet = S_{CA}$ (300 ml min^{-1}); 0.6 vol% isoprene, 20 vol% oxygen; 1.2 bar; $V_{30}Ti_{70}O_x$ (fixed bed); $V_{30}Ti_{70}O_x/SiO_2$ (microstructured reactor; source: Universität Erlangen[240]).

 © 2004 Wiley-VCH Verlag GmbH & Co. KGaA, Weinheim

catalyst properties in the fixed-bed experiments. In comparison to the (ceramic) fixed-bed reactor the yield found in the (metallic) microstructured reactor was slightly reduced, due to the blind activity of the total oxidation in the microstructured reactor that results from, among other things, the high surface-to-volume ratio.

6.3.6. *Partial Oxidation of Methane (Production of Syngas)*

Mayer, Fichtner, and co-workers have investigated the manufacture of syngas (a mixture of carbon monoxide and hydrogen) through the partial oxidation of methane over a rhodium catalyst at temperatures between 1090 °C und 1190 °C (Scheme 35).[206,242] The conversion of methane to syngas is part of a strategy where the gases in subsequent process steps are converted to liquid products such as methanol which are easier to transport.

$$CH_4 \xrightarrow[\text{Rh cat.}]{O_2} CO + 2\,H_2$$

Scheme 35. Manufacture of syngas through the partial oxidation of methane in a microstructured reactor.

A microstructured reactor was used whose structure consisted of a solid Rh monolith with 120 μm microchannels. In comparison to laboratory fixed-bed reactors or conventional extruded monoliths, which are coated with the catalyst, microstructured reactor monoliths differ mainly in their decreased dimensions, the decreased pressure drop through the optimized flow paths, and the application of a solid catalyst material. A good heat distribution over the microchannels is achieved. As a result, the conversion and the hydrogen and carbon monoxide selectivities are higher than corresponding laboratory reactors (Figure 40). In combination with the lower pressure drop, a higher space–time yield is obtained. A study of the influence of parameters such as temperature, total pressure, CH_4/O_2 ratio, space velocity, and inert gas dilution was also presented. These studies highlighted the influence of the elementary reactions (total oxidation and reforming) and carbon deposits on the catalyst during the course of the reaction.

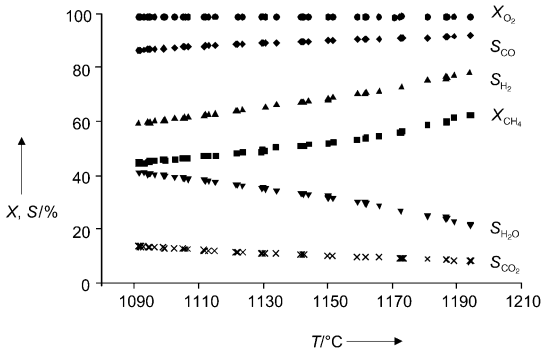


Figure 40. Syngas production: CH_4 and O_2 conversions (X), as well as CO, CO_2, and H_2 selectivites (S) at various temperatures for a Rh multiplate-stacked microstructured reactor (CH_4/O_2: 2; 0.12 MPa; 0.2–3 ms; 7.8×10^5 L h^{-1} (STP); source: Forschungszentrum Karlsruhe[206]).

6.3.7. *The Andrussov Reaction*

Hessel et al. have investigated the Andrussov synthesis, in which hydrogen cyanide is formed from methane, ammonia, and oxygen, by using a microstructured reactor with a mixer, and a structured catalyst foil with microchannels and a heat exchanger (Scheme 36).[118] It is noteworthy that temperatures exceeding 1000 °C were recorded in parts of the catalyst structure. With increasing temperature, yields of hydrogen cyanide up to 31 % (approximately half the value found in the industrial process) were obtained with a near complete conversion of methane. The ammonia selectivity of 62 % is within the region of the industrial process, however, methane selectivity (30 %) is considerably lower because total oxidation reactions take place in addition to the formation of hydrogen cyanide (Figure 41).

$$CH_4 + NH_3 \xrightarrow[\text{Pt cat.}]{O_2} HCN + 3\,H_2O$$

Scheme 36. The Andrussov reaction to form hydrogen cyanide.

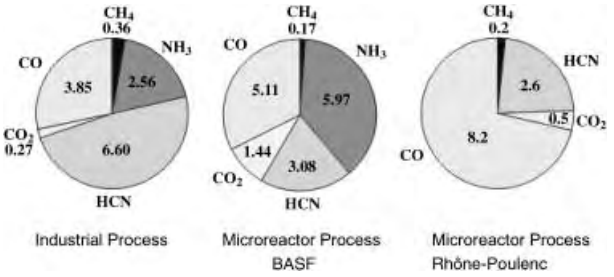


Figure 41. The Andrussov process: Comparison of products from a complex microstructured reactor and an optimized industrial plant (source: IMM[118]).

When one compares the yield with that of laboratory reactors (e.g., monoliths), microstructured reactors are shown to be superior to laminar operating systems, exhibiting only a slightly lower performance than a monolith under turbulent operation (yield 38 %). Although results from the microstructured reactor do not approach industrial levels, the feasibility of an industrial three-component reaction at very high temperatures was demonstrated. A six-party industrial consortium was established and measurements were carried out at BASF and Rhodia (Lyon, France). It can also be argued that these results demonstrate that microstructured reactors does not suit every chemical process.

6.3.8. *Oxyhydrogen Gas Reaction*

The reaction between hydrogen and oxygen was investigated by Hagendorf et al. as a basic study of the technical process,[107] and by Veser as a detailed mechanistic analysis[39,40] (Scheme 37). Both investigations proved that this reaction, which lies in the explosive regime (for most p, T, and c values), could be handled safely in microstructured reactors. Veser speaks of an intrinsic safety when working under

 © 2004 Wiley-VCH Verlag GmbH & Co. KGaA, Weinheim

$$H_2 + O_2 \xrightarrow{Pt,\ Pd,\ or\ Pt/Al_2O_3} H_2O$$

Scheme 37. Catalyzed oxyhydrogen reaction in a microstructured reactor.

atmospheric pressure as soon as sub-millimeter dimensions are attained.[40] Hagendorf et al. showed that complete conversion is achievable and thus that the corresponding reaction mixtures can exist outside of the explosive regime.[107] At high mass flows, a large amount of heat is naturally released that cannot be completely dissipated, even in good microheat exchangers (Figure 42). The device heats up in certain areas, as proved by thermographic analysis.

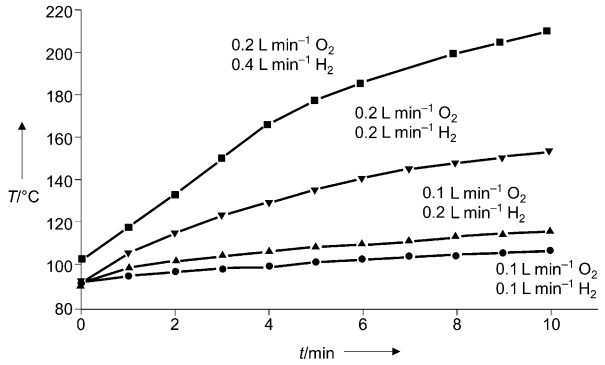


Figure 42. Reaction temperature of an oxyhydrogen reaction in a multiplate-stacked microstructured reactor at various residence times and reactant flows (source: MPI-Kohlenforschung[105]).

A quartz microstructured reactor could function at temperatures above 1000 °C without degrading the microdevice.[40] Veser achieved this by increasing the amount of hydrogen in steps at a given synthetic air flow rate. A second reactor with improved thermal-loss properties and a Pt contact showed no evidence of homogeneous reactions, for example in the form of flames or explosions. Kinetic analysis based on a radical-chain mechanism determined the three explosion limits of the oxyhydrogen reaction as a function of the characteristic diameter. By decreasing the diameter from 1 m down to between 1 mm and 100 μm, a shift in these limits was observed. Therefore, previously explosive regimes could now be handled safely.

While the first explosion limit is affected mainly by the diffusion path length, the third explosion limit (which is responsible for many explosions under normal pressure) has a complex dimensional dependency due to a complex interaction of elementary reactions. Investigations showed that a kinetic quenching of the radical-chain mechanism is responsible for the suppression of explosive behavior, and not a thermal quenching due to significantly higher heat-transfer rates (Figure 43). This means that reactors with slightly poorer heat transfer (e.g., due to an increase in productivity through more compact construction of many parallel reactors) should also be intrinsically safe. This result also shows that similar effects can be achieved for other radical-chain reactions.

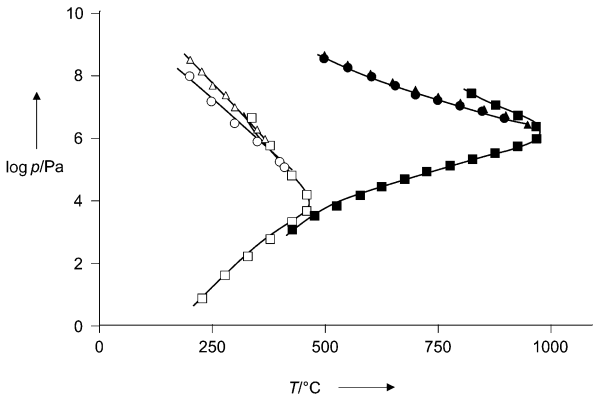


Figure 43. Shift of the kinetic (□, ■) and thermal explosion limits (○, ● for $T_{wall} = RT$; △, ▲ for $T_{wall} = T_{reaction}$) for the reaction of hydrogen and oxygen for a conventional reactor (1 m; □, ○, △) and a microstructured reactor (300 μm; ■, ●, ▲; source: MPI-Kohlenforschung[40]).

Franz et al. carried out the oxyhydrogen reaction in a Pd-membrane-microstructured reactor to investigate the possibility of combined reaction and separation.[231] A hydrogen/nitrogen flow runs parallel to a flow of oxygen, with both streams separated by a membrane, which can withstand a pressure of 5 bar; water was shown to form by this process.

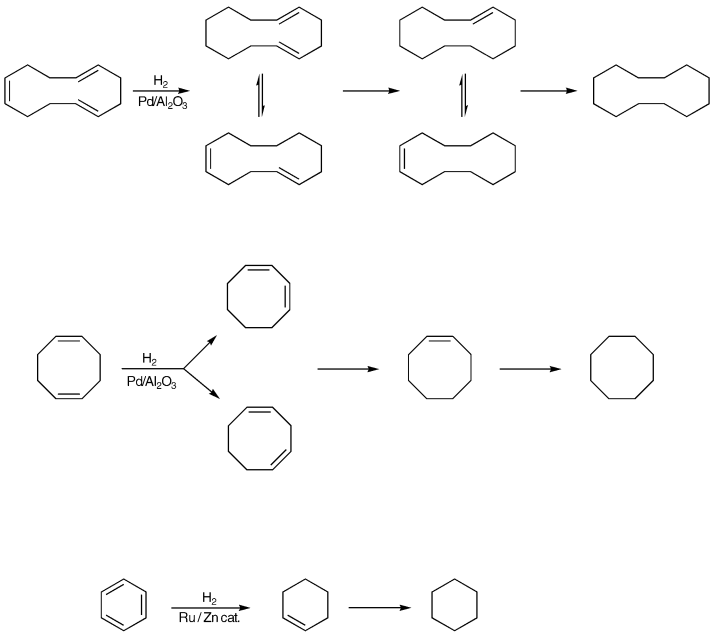
6.4. Hydrogenation

6.4.1. Hydrogenation of Polyenes and Arenes

Wießmeier, Hönicke, and co-workers have investigated the hydrogenation of *cis*,*trans*,*trans*-1,5,9-cyclododecatriene, 1,5-cyclooctadiene, and benzene in an Al multiplate-stacked reactor that was anodically oxidized at the microchannel surface to create nanopores,[100,101,213,243–245] which were subsequently impregnated with a Pd salt (Scheme 38). All of the above-mentioned substrates possess several double bonds and thus can undergo several hydrogenation steps. However, technically useful and valuable products are not always the end products, but unsaturated intermediates such as cyclododecene, cycloctene, and cyclohexene. Microstructured reactors were investigated in order to establish whether their good mass- and heat transport, and their well-defined residence time would increase the selectivity of the partial hydrogenation.

In a very illustrative experiment the hydrogenation of *cis*,*trans*,*trans*-1,5,9-cyclododecatriene was attempted using a conventional grain-shaped catalyst in both a fixed-bed reactor and in a microstructured housing with fitted microchanneled plates (Figure 44).[244] As an intermediate step, cut wires and aluminum foil were investigated as a fixed bed, which had the same nanoporous structure as the microstructured reactor; the conventional catalyst, on the other hand, had a less regular pore structure. The difference between the fixed beds and the microstructured reactor was most notable in terms of the flow, which followed either a path through various voids and dead volumes, or along a direct and regular route in the microchannel. The difference between the fixed-bed reactors is in the administration of the catalyst: "conventional" or

 © 2004 Wiley-VCH Verlag GmbH & Co. KGaA, Weinheim



Scheme 38. Catalyzed hydrogenation of polyenes and arenes in microstructured reactors.

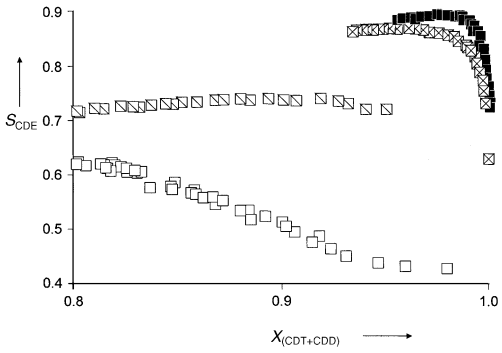


Figure 44. Selectivity(*S*)–conversion(*X*) diagram for the hydrogenation of *cis*,*trans*,*trans*-1,5,9-cyclododecatriene (CDT) to cyclododecene (CDE) in a conventional Pd/Al_2O_3 (□) fixed-bed compared with fixed beds wires (▨) and small cut foils (⊠), which act as an anodically modified microstructure. Also shown are results for a microstructural reactor (■). (source: Universität Chemnitz[244]).

"wire/foil" catalysts both have a locally ordered nanoporous structure. The difference between the fixed-bed "wire" and "foil" is only in the density of their packing; the administration of the catalyst is the same.

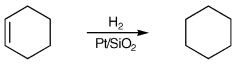
The reactors were compared in terms of their selectivity/conversion ratio. The selectivity for the conventional fixed bed decreased from 62% to 44% in the investigated conversion window (80–100% conversion, respectively). In contrast a selectivity of 73% was found for the foil-fixed bed. The more densely packed wire-fixed bed gave even better results. For microstructured reactors, the best results gave a selectivity of 84% with complete conversion.

The selective hydrogenation of cyclooctadiene to cyclooctene gives even better conversion in microstructured reactors.[245] A selectivity of 98% at total conversion was found, thus giving a yield of 98% (116 ms; 150°C; 110 kPa). The best results were achieved by increasing the hydrogen partial pressure and adding CO.

The hydrogenation of benzene in a microstructured reactor with a Pd catalyst does not proceed immediately, and increasing the hydrogen partial pressure leads to the undesired formation of cyclohexane.[245] Thus, a Rh/Zn catalyst was used and methanol was added in order to hinder the readsorption of cyclohexene (the desired product) at the catalyst, and the partial hydrogenation reaction could proceed. The conversion decreased from an initial value of 90% to ≈10% within 4 h; the catalyst however became more selective. Whilst only cyclohexane was generated initially, a cyclohexene selectivity of 36% was eventually achieved.

6.4.2. *Hydrogenation of Cyclohexene*

Besser's group have carried out a detailed study of the hydrogenation of cyclohexene to cyclohexane over a Pt catalyst (Scheme 39).[99,112] This reaction serves as model reaction for understanding important industrial gas-phase processes (e.g., hydrotreatment in petrochemistry and hydrogen extraction by fossil-fuel processing). Dehydrogenation to benzene also occurs as a competitive reaction, depending on the reaction temperature.



Scheme 39. Catalyzed hydrogenation of cyclohexene in a microstructured reactor.

A microstructured reactor with a fresh catalyst achieved a conversion of 50% with a selectivity of 60% (cyclohexane) or 40% (benzene) at room temperature. However, the reaction behavior was transient, that is, the selectivity shifed with time towards the hydrogenation reaction. This transience was reduced by conditioning the catalyst through increased chemisorption with cyclohexene and hydrogen. In such a stable state at 120°C, cyclohexene selectivity was increased to 100% at a conversion of 95%. On raising the temperature to 200°C, however, conversion was found to decrease again in favor of dehydrogenation to benzene, which can achieve a selectivity of nearly 80% (Figure 45).

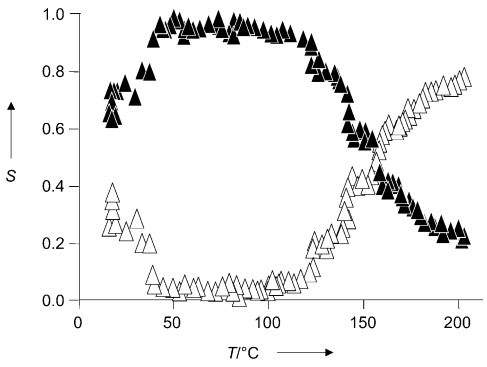


Figure 45. Selectivity (*S*) of the Pt-catalyzed hydrogenation/dehydrogenation of cyclohexene to benzene (△) and cyclohexane (▲), with respect to the temperature of a silicon-chip-based microstructured reactor (source: Stevens Institute, Hoboken[99]).

 © 2004 Wiley-VCH Verlag GmbH & Co. KGaA, Weinheim

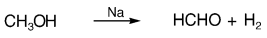
In addition, the H_2/cyclohexene partial pressure ratio and the residence time were varied, and through the application of Pt on a porous layer the influence of the porosity was investigated. The specific surface area was increased approximately by a factor of two compared to the planar Pt catalyst coating. Here, no differences in the maximum activity could be seen unless the H_2/cyclohexene partial pressure ratio was varied.

Perhaps the most important and striking result from these studies was the ability to use only small quantities of reagents by using silicon-chip reactors. For example, a 140 h experiment required only 3.1 g (≈ 4 mL) of cyclohexene.

6.5. Dehydrogenation

6.5.1. Dehydrogenation of Methanol to Formaldehyde

The endothermic dehydrogenation of methanol to formaldehyde is a high-temperature reaction (700–900 °C) with a contact time in the region of milliseconds (Scheme 40).



Scheme 40. Dehydrogenation of methanol to formaldehyde in a microstructured reactor.

Alépée et al. carried out theoretical investigations to optimize the fluid path and develop suitable heating and cooling concepts in microstructured reactors.[22] As a result, a double-sided, heated microstructured design was developed, which made use of counter-flow paths for reactant and product gases to give a superior heat balance. As well as allowing ultra-short contact times to be set exactly, heating and cooling processes could be carried out in less than 0.5 ms (at rates of ≈ 1000 K ms^{-1}).

In addition, Maurer et al. investigated the dehydrogenation of methanol to formaldehyde at 700–800 °C by homogeneous catalysis with sodium steam.[114] The process was investigated using a multiplate-stacked microstructured reactor system consisting of a mixer, reactor, and heat exchanger. Preliminary investigations indicated a strong influence of mixing on selectivity. Depending on the form of the flow path during mixing, differences between 15 % and 70 % in selectivity were obtained (Figure 46).

The same process, although as an oxidative dehydrogenation, was also investigated by Cao et al.[113] A microstructured reactor manufactured using deep-etching technology (Deep Reactive Ion Etching, DRIE) in silicon has two layouts; one with 70-μm and one with 130-μm-deep channels (both 600 μm wide). A silver catalyst was applied by sputtering through a shadow mask. The structured silicon wafers were enclosed with pyrex glass wafers.

Investigations between 430 and 530 °C showed methanol conversions of 60–75 % with selectivities of around 90 % (12–91.5 vol % pure oxygen, 8.5 vol % methanol, helium as the remainder). Conversions and selectivities were comparable to industrial processes but were achieved at lower temperatures in the microstructured reactor. The use of high oxygen

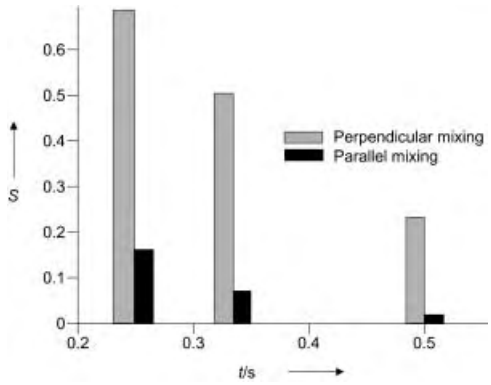


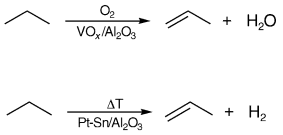
Figure 46. The influence of mixing (in methanol and sodium steam flow paths) on the formaldehyde selectivity (*S*) in the Na-catalyzed dehydrogenation of methanol, with respect to residence time (source: EPFL Lausanne[22]).

concentrations (91.5 %) was also possible without danger, and had no detrimental influence on methanol conversion or formaldehyde selectivity. In addition, an increase in the residence time, accompanied by an increase in conversion from 57 % to 72 % for the 130 μm microstructured reactor, did not decrease the selectivity.

These experimental results correspond well to a simple reactor model that was proposed by Gobby et al. for a catalyst-wall plate microreactor.[246] The reaction constant *k* was determined from an Arrhenius plot. By using an approximation, which took into account the Peclet and Damköhler numbers, as well as the microchannel aspect ratio, the conversion values were calculated.

6.5.2. Dehydrogenation of Propane to Propene

Baerns, Steinfeldt, et al. have compared a multiplate-stacked microstructured reactor and a fixed-bed reactor for the oxidative dehydrogenation of propane to propene over a VO_x/Al_2O_3 catalyst (Scheme 41). For both reactors the gas



Scheme 41. Dehydrogenation of propane to propene in a microstructured reactor.

composition ($C_3H_8/O_2/Ne$), temperature (733–800 K), and gas flow rate (50–150 mL min^{-1}) were varied. Both reactor systems exhibited similar selectivity/conversion behavior in isothermal operation.[247] The same VO_x/Al_2O_3/boehmite suspension was used as a starting material for catalyst preparation in both cases. It was clear that a similar catalyst wall coating was generated in the microstructured reactor and as the packing in a fixed-bed reactor. This was proved by characterization of the catalyst surface with XRD, BET, TEM, and ICP-OES measurements.

 © 2004 Wiley-VCH Verlag GmbH & Co. KGaA, Weinheim

These studies assessed the correlation between the hot spot of the reaction and reactor performance (in terms of conversion and selectivity by measuring fixed-bed axial temperature gradients and temperatures at the inlet and outlet of the plates of the microstructured reactor against propane and oxygen conversion (Figure 47). Depending on

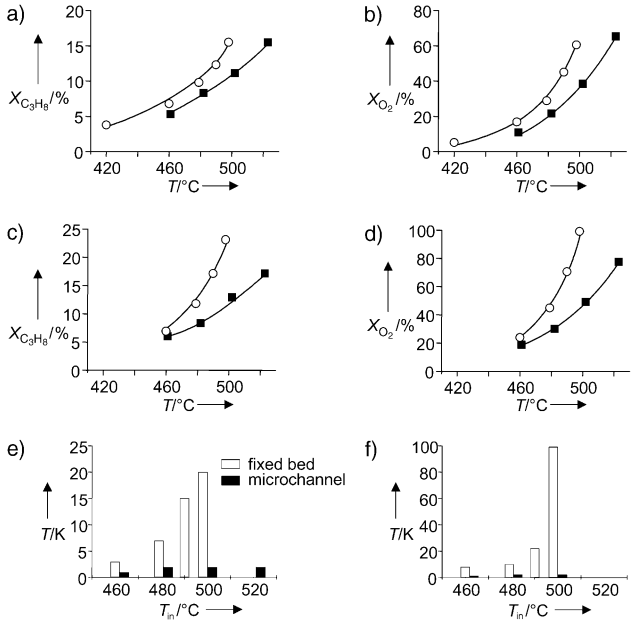


Figure 47. Dehydrogenation of propane: C_3H_8 (a,c), O_2 (b,d) conversion (X), and temperature gradients $\Delta T = T_{max} - T_{in}$ (e,f) as a function of reactor inlet temperature (T_{in}) for a fixed-bed reactor (○) and a microstructured reactor (■). a), b), e): $C_3H_8/O_2/Ne = 0.3/0.15/0.55$, $F_{tot} = 150\ mL\,min^{-1}$; c), d), f): $C_3H_8/O_2/Ne = 0.5/0.25/0.25$, $F_{tot} = 120\ mL\,min^{-1}$ (source: ACA, Berlin[247]).

reaction conditions, temperature gradients up to 100 K were achieved in the fixed-bed reactor, while the differences in the microreactor were a maximum of 3 K. No variation in propane and oxygen conversion was observed under isothermal conditions, while with increasing temperature gradient, conversions for both gases increased more rapidly in the fixed-bed reactor. The results showed that (strongly exothermic) reactions in microstructured reactors can be achieved without axial temperature gradients, and the experimental data obtained under isothermal operation could be used as a basis for kinetic modeling.

Wolfrath et al. carried out the thermal dehydrogenation of propane over a Pt-Sn/γ-Al_2O_3 catalyst filament (3–10 μm in diameter).[233] A structured catalytic bed was obtained, which resulted in laminar flows similar to those obtained in microstructured channels. The filaments, arranged concentrically, were grouped into two zones. In the first zone, dehydrogenation over the catalyst took place. The second zone, separated from the first by a hydrogen-permeable Pd/Ag membrane, removed hydrogen from the reaction mixture and burned it through the introduction of oxygen (Figure 48). Propane conversion up to 30% and selectivities up to 96% were achieved and the pressure drop was lower than an equivalent fixed-bed packing consisting of spherical particles.

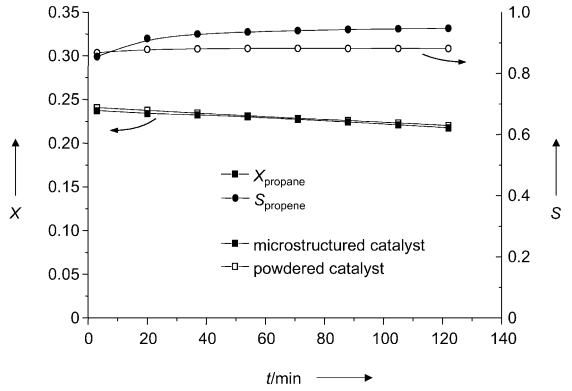
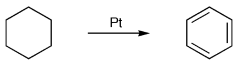


Figure 48. Dehydrogenation of propane: Propane conversion (X; □, ■) and propene selectivity (S; ○, ●) for a filament-based catalyst (■, ●) and a conventional powder catalyst (□, ○) as a function of time (t). (550°C; 0.14 MPa; space velocity: 1161 h^{-1}; 3.1 s; source: EPFL Lausanne[233]).

6.5.3. *Dehydrogenation of Cyclohexane to Benzene*

Ciu et al. have recently designed a microstructured reactor for the dehydrogenation of cyclohexane to benzene over a Pt catalyst in the presence of a hydrogen-permeable Pd membrane.[112] Experimental results have not yet been presented (Scheme 42).



Scheme 42. Dehydrogenation of cyclohexane to benzene in a microstructured reactor.

6.6. *Extraction of Hydrogen and Other Fuels*

Fuel processing, with an aim of extracting hydrogen, continues to gain in importance. Consequently, there have been numerous investigations on this subject that have been carried out in microstructured reactors.[206,209–211,215,216,222,242,248–267] These reactions are often a complex network of many elementary reactions. The reactions are generally assessed in terms of the amount of hydrogen obtained (corresponding to the stored energy), which is typically then fed into a fuel cell to produce energy. Due to the importance of mobile applications (e.g., in cars) the weight and size of the systems used play an important role. Very good heat exchange is essential to couple exothermic reactions with endothermic reactions. Because of these factors, the performance of a hydrogen-generating system cannot be fixed purely on the individual parameters of the respective reactions (e.g., selectivity) but instead must achieve an overall balance.

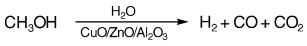
It is clear that a overview of hydrogen-generating reactions would fall outside the remit of this Review. Therefore, only three examples will be briefly discussed.

6.6.1. *Methanol and Propane Steam Reforming*

The interested reader is referred to the important studies by the groups of Schubert,[222,252] Wegeng,[249,255,256] and

Renken[253,254] to obtain a more detailed insight into this area of research.

Cominos et al. investigated methanol steam reforming at 200–300 °C in a multiplate-stacked microstructured reactor over a $CuO/ZnO/\gamma\text{-}Al_2O_3$ catalyst (Scheme 43).[215,216] A power density of 1.8 $W\,cm^{-3}$ and a hydrogen content of 50 vol % in the product gases were obtained. The process was designed for a potential 100 W fuel-cell system.



Scheme 43. Steam reforming of methanol in a microstructured reactor.

Kolb et al. extended these investigations through the detailed screening of CuO/Cr_2O_3 and CuO/Mn_2O_3 catalysts on various aluminum oxide washcoats, such as corundum, boehmite, and γ-alumina (Figure 49).[184] A 10-fold parallel-screening reactor was used, in which each plate was coated with a different catalyst.[221] It was observed that the catalyst on boehmite showed the highest activity.

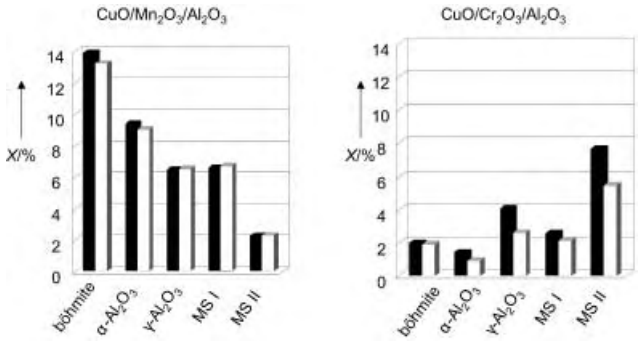
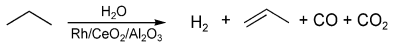


Figure 49. Methanol steam reforming: Comparison of the activities of CuO/Mn_2O_3 and CuO/Cr_2O_3 catalysts with various aluminium oxide washcoats (source: IMM[184]). MS = mixed systems. First measurement: black; second measurement (displaying catalyst deactivation): white.

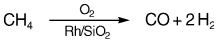
Kolb et al. carried out the propane steam reforming process at 650–800 °C in a two-plate sandwich-microstructured reactor (Scheme 44).[184] Screening tests on Rh, Pt, Pd, Rh/Pt, and commercially available Ni catalysts loaded on γ-alumina were operated in series. The Rh sample was shown to exhibit the highest activity. Also, impregnation of the Rh, Pt, and Rh/Pt catalysts with CeO_2 increased both activity and CO_2 selectivity, yet decreased the selectivity of CO and propene, which are the main by-products that arise when short residence times are employed. Complete conversion to CO_2, CO, and H_2 (with no by-products) was achieved with a $Rh/Pt/CeO_2/\gamma\text{-}Al_2O_3$ catalyst at 750 °C with a residence time less than 10 ms and a steam-to-carbon ratio of three, without observing significant deactivation.



Scheme 44. Steam reforming of propane in a microstructured reactor.

6.6.2. *Partial Oxidation of Methane*

Tonkovich et al. investigated the partial oxidation of methane at 700 °C in a microstructured reactor over a Rh catalyst on a silica carrier (Scheme 45; residence time: 50 ms).[267] Their investigations concentrated mainly on determining selectivity under different operating conditions, and using catalysts at different positions on the microchanneled plate. First, the catalyst powder was allowed into the microchannels, thus forming something similar to a micro fixed-bed reactor. Measurements under non-equilibrium conditions show CO selectivities up to 70 % and a H_2 selectivity over 50 %. The first set of values lie partly over equilibrium, while the second set reside below. Both sets tend to increase with increasing temperature. Future investigations should offer even better selectivities if, for example, operation up to 900 °C is possible.



Scheme 45. Partial oxidation of methane in a microstructured reactor.

If the catalyst is packed at the inlet region of a microstructured reactor, different results are obtained. Selectivities become constant over the entire temperature range and correspond to values that are obtained in the micro fixed-bed reactor at operating temperatures of 700 °C and above. This indicates significant local overheating due to the heat of the reaction. Even with an external reactor temperature of 300 °C, temperatures of 700 °C exist at the inlet (Figure 50) because of the large volumes used and the less well-directed flow path in the inlet. Both experiments highlight the importance of a microchannel inlet feed path. In addition, they show that almost no carbon is deposited. It should be noted that this work describes one of the first examples of an exothermic high-temperature reaction with a contact time less than 10 ms, and is truly pioneering work in microstructured reactor technology.

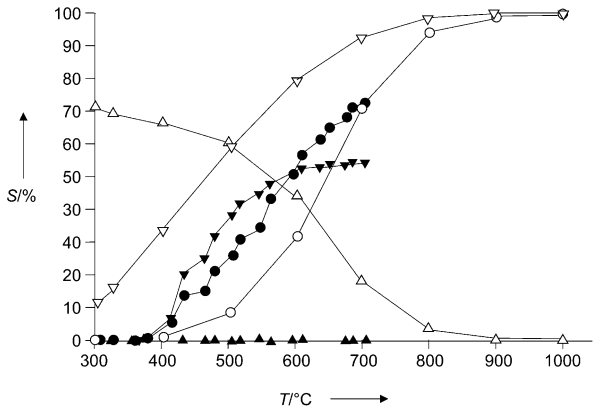
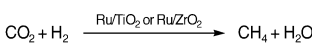


Figure 50. Partial oxidation of methane in a multiplate-stacked microstructured reactor with a Rh contact. Comparison of experimental selectivities (S_{exp}) for CO (●), $C_{(s)}$ (▲), and H_2 (▼) under nonequilibrium conditions, and at equilibrium (CO (○, $C_{(s)}$ (△), and H_2 (▽); source: PNNL, Richland[267]).

 © 2004 Wiley-VCH Verlag GmbH & Co. KGaA, Weinheim

6.6.3. The Sabatier Reaction

The Sabatier reaction is a process for generating methane from hydrogen and carbon dioxide at temperatures around 400 °C (Scheme 46).[268,269] Initially, one fuel is converted into



Scheme 46. Sabatier reaction in a microstructured reactor.

another, however using hydrogen instead of methane is advantageous in terms of energy density, and thus also in terms of freight weight in the case of mobile applications and transportation. Thus, Wegeng et al. are investigating applications of the Sabatier reaction for unmanned missions to Mars.[269] The carbon dioxide present in the atmosphere of Mars could be converted into methane using the transported hydrogen.

Tonkovich, Wegeng, and co-workers have investigated these and further reversible exothermic reactions, such as the water-gas-shift (WGS) reaction, both experimentally and theoretically.[210] All these processes have in common the fact that with reaction rates increase with increasing temperature, but also exhibit a lower equilibrium conversion. Thus, the temperature determines the interaction between kinetic and chemical equilibrium in the reaction chamber (Figure 51).

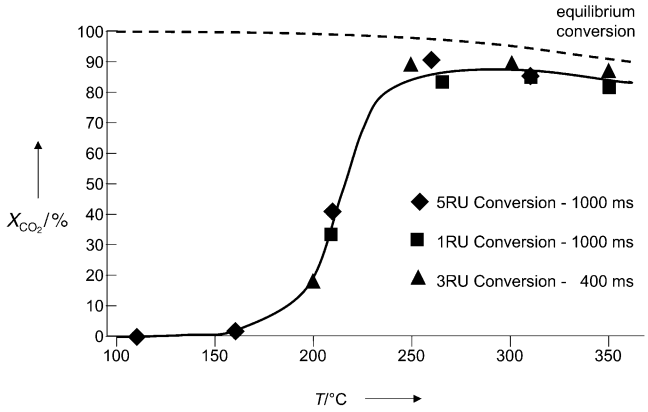


Figure 51. The Sabatier reaction: The influence of temperature on CO_2 conversion (X_{CO_2}) with a fixed-bed catalyst. -----= equilibrium conversion; 1RU: 1 wt% Ru/61-80 (United Catalysts); 3RU: 3 wt% Ru/TiO_2 (Degussa); 5RU: 5 wt% (Engelhard). Source: PNNL, Richland.[269]

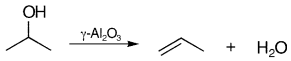
They have been able to control productivity and, thus, the necessary catalyst loading of the reactors. Optimized temperature trajectories are demanded for reversible exothermic reactions in compact systems. Whilst this problem has been challenged so far with adiabatic reactors and heat exchangers connected in series, or fixed-bed reactors with tube-heat exchangers, microprocess technology apparatus can offer entirely new possibilities.

This has been impressively proved by the experiments and simulations of Tonkovich et al.[210] The Sabatier reaction was carried out in a microchanneled reactor with counter-current flow cooling (through N_2 gas heat transfer) to remove the heat of reaction (165 kJ mol^{-1} at 25 °C). Operating under isothermal conditions, conversions up to 85% at a selectivity of 99.4% were obtained (60–450 ms; 400 °C; 20% CO_2, 80% H_2). This represents significant enhancement of the process compared to adiabatic operation which under the given conditions leads to a temperature increase up to 625 °C; conversion is limited to 66% and the selectivity decreases to 41.6%.

6.7. Eliminations

6.7.1. Dehydration of 2-propanol to Propene

Rouge et al. have carried out the elimination reaction of 2-propanol to propene over a γ-alumina catalyst at 200 °C and 1.3 bar, which can lead to a bimolecular side reaction to give diisopropyl ether (Scheme 47).[74]



Scheme 47. Dehydration of 2-propanol in a microstructured reactor.

Theoretical predictions, as well as investigations with a laboratory fixed-bed reactor, proved that periodic operation at varying concentration leads to an increase in the product concentration in the gas mixture and the overall yield, respectively (Figure 52). This improvement in reaction performance, which occurs through setting the flow rate of the reactants to zero, is considered to be a "stop effect", and is due to altered adsorption/desorption behavior on the active sites of the catalyst during periodic operation. From periodic measurements with the laboratory reactor, kinetic data were obtained that led to a model to be used with microstructured reactors.

Periodic operations in a microstructured reactor benefit mainly from a smaller volume of reagents and a narrower residence-time distribution, which allows for operations at higher frequencies compared to conventional reactors. The results of a periodic operation in a multiplate-stacked micro-

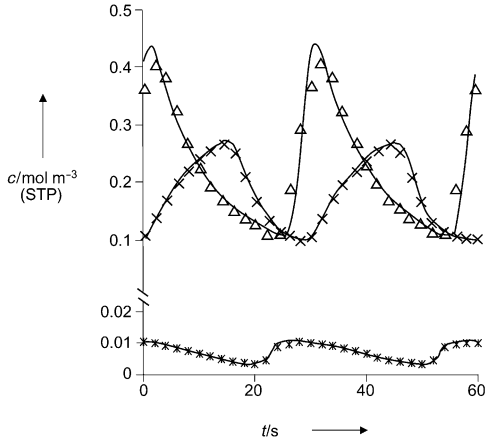


Figure 52. The concentration of 2-propanol (△), propene (×), and diisopropyl ether (✱) in the periodically operated dehydration of 2-propanol to propene in a multiplate-stacked microstructured reactor over a γ-alumina catalyst (change in 2-propanol concentration of 0.86 mol m^{-3} at STP to 0 (av 0.43 mol m^{-3} 2-propanol); 200 °C; 1.3 bar; 0.175 s; source: EPFL Lausanne[74]).

 © 2004 Wiley-VCH Verlag GmbH & Co. KGaA, Weinheim

structured reactor compared very well to the model predictions. A 30 s cycle was carried out, during which the amount of propene in the reaction mixture increased from 0.1 to ≈ 0.27 mol m^{-3} (at standard temperature and pressure).

6.8. Catalyst Screening

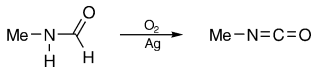
Most of the studies concerning catalyst screening for gas-phase reactions in microstructured reactors have dealt mainly with the discovery of good new catalyst materials and less often with the reaction itself.[125,220,221,270–275] Catalyst screening is an individual and broad discipline which would exceed the scope of this Review.

7. Industrial Applications of Microstructured Reactors

7.1. Process Development on the Laboratory Scale

1995 witnessed the beginning of concentrated microstructured reactor research activities, coming in the same year that scientists met for the first time at a workshop to discuss results in microprocess technology. The same year saw the development of two important processes, both carried out in industrial chemical laboratories. Wörz et al. described the partial oxidation of an alcohol to an aldehyde; a process that BASF carried out on the production scale (see Section 5.3.4.).[19,23,43,154,241]

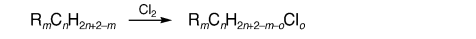
Lerou et al. carried out a number of catalytic gas-phase reactions in microstructured reactors, which were subsequently analyzed extensively by DuPont in their investigations into high-temperature, dangerous, catalytic, and photochemical gas-phase processes. The microstructured reactor composed of a stack of silica wafers based on typical silicon-chip architectures.[21] Each wafer had a specific function, for example, as a heat exchanger or a catalyst room. The catalyst was introduced in the form of solid particles, that is, as a miniature fixed bed. For the synthesis of methyl isocyanate from methyl formamide, similar conversions as conventional synthesis could be obtained, albeit at lower selectivities (Scheme 48).[21] One reason for this is seen in the non-ideal temperature profiles within the reaction zone of the microstructured reactor packing.



Scheme 48. Synthesis of methyl isocyanate from methyl formamide in a microstructured reactor.

Numerous industrial laboratory investigations have since been carried out. However, many of these studies have not been published, which illustrates their increasing interest and industrial relevance. Economic benefits from these studies are expected, which is reflected by the ever-increasing number of pending industrial patents in microprocess technology.[49,276–286] Almost every chemical company has a small, or perhaps larger unit that is dedicated to issues in microprocess technology. In particular, fine chemicals companies have turned their attention to this technology, and the subject is expected to be one of the key themes of future chemical industry.[287] Oroskar et al. have provided a description of the potential of microstructured reactors from the industrial point of view.[61,288]

A recent example of a successful industrial investigation based on micro heat-exchangers was presented by Bayer et al. (Siemens Axiva, Hoechst, Germany) based on the chlorination of alkanes. (Scheme 49).[48] Conventional tube reactors



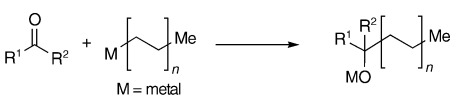
Scheme 49. Industrial chlorination of alkanes in a micromodule.

for such processes exhibit slow temperature ramping and thermal overshooting. Externally heated micro heat-transfer modules allow for a suitable choice of operating temperature, with a steep temperature increase possible. Such microheater modules, which are several times smaller than the combination of a long tube reactor and a surrounding oven, allow reactants to be heated up to ten times faster.

Although preheating was carried out with a microdevice, a conventional tube reactor was still used for the reaction itself, since no process improvement was expected in this region. In addition, it was preferred due to the pressure drop and to its operating reliability compared to the microstructured reactor. With this hybrid system configuration a significant increase in conversion by about 25% and an increase of space–time yield of ≈240 to ≈430 g h^{-1} L^{-1} was achieved. The key to this process enhancement is fast and uniform initial radical formation, which stems from better thermal control of the process.

7.2. Production of Organic Chemicals

It is difficult to estimate how present investigations are divided into the various industrial areas of laboratory, pilot, and production scale, for the reason that the disclosure of results in industry is the exception rather than the rule. Thus, only few examples are available for discussion. Krummradt, Stoldt, and co-workers (Merck) provided the first industrial example of the use of small-structured reactors, reporting an increase in yield by 25% for an organometallic reaction that used an interdigital mixer rather than a batch process (Scheme 50, Figure 53).[50]Their studies were not limited to laboratory scale. Since 1998 a plant at Merck has produced fine chemicals using five parallel-connected mini-mixers, which have replaced the conventional stirred tank. Equidis-



Scheme 50. An organometallic reaction in a mictrostructured reactor that is carried out on the production scale.

 © 2004 Wiley-VCH Verlag GmbH & Co. KGaA, Weinheim

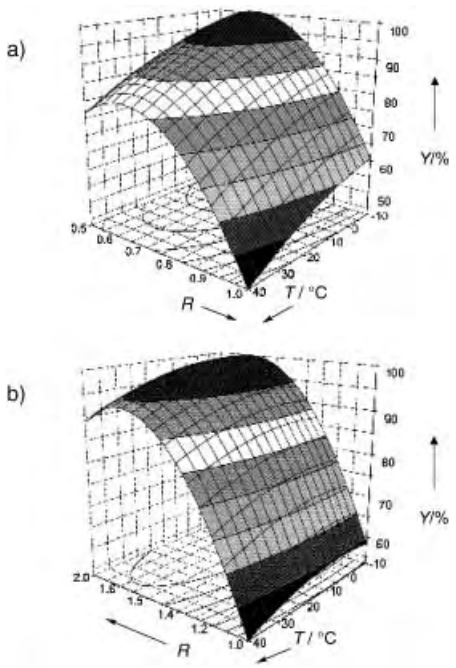


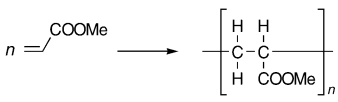
Figure 53. The search for the optimal temperature and gas composition (*R*) for an organometallic reaction in an interdigital micromixer tube reactor using statistical methods. a) flow rate = 0.4 L h^{-1}, b) flow rate = 2.0 L h^{-1} (source: Merck[50]).

tribution to the mini-mixer units is technically challenging and thus significant efforts in terms of process control are required.

Recently Hessel (IMM), Wehle (Clariant), and co-workers described the development of a laboratory process that is fast, strongly exothermic, and sensitive to mixing.[289] The original batch process was very slow, with several parallel and secondary ractions decreasing the yield to 65% during production. Initially, a yield of 85% was obtained by using an interdigital micromixer tube reactor, which increased to 90% with optimized reaction conditions. Similarly to the example from Merck mentioned above, an increase in the internal dimensions of the micromixer achieved adequately high flow rates for pilot-plant investigations. A so-called caterpillar mixer[24] is the central unit of a pilot plate, which is currently being tested for production applications.

7.3. Production of Polymers and Pigments

Investigations by Bayer, Pysall, and co-workers (Siemens Axiva) have proved that significantly reduced fouling of the radical solution in the polymerization of acrylates is achieved by using interdigital mixers (Scheme 51).[47,49] Since in-line



Scheme 51. Radical polymerization of acrylates in interdigital micromixers.

static mixers in continuous operation tend to plug, the change in fluid dynamics throughout the mixer leads to varying concentration distributions of all the participating active species, the result being that insoluble high-molecular polymers are no longer prepared. Micromixers operate mostly plug-free, even though the inner dimensions are much smaller than conventional static mixers. A process with only 28 parallel-connected micromixers fulfilled the demands of industrial production (Figure 54).

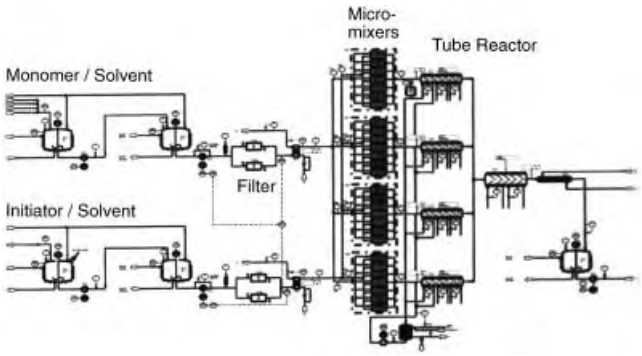
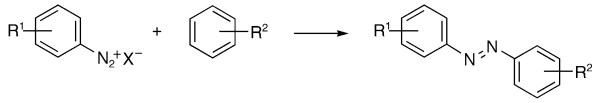


Figure 54. Plan of a production plant (2000 tonnes per year) for the radical polymerization of acrylates in solution (source: Siemens-Axiva, Frankfurt[47]).

Wille et al. (Clariant) described the first production applications for producting pigments in microstructured reactors.[51] Two industrially relevant azo-coupling processes were carried out that are distinguished by the coupling agent and the diazonium salt used (Scheme 52). The azo coupling is



Scheme 52. Azo coupling as part of a pigment synthesis, carried out in a microstructured reactor.

only one step of a three-step pigment synthesis (diazotization, azo coupling, and pigmentation). Initially, the two azo couplings were successfully carried out in a laboratory microstructured reactor at flow rates up to 80 mL min^{-1} (equivalent to one tonne per year). While in the first synthesis a diazonium salt solution could be used, the success of the second synthesis showed that suspensions could also be handled in microstructured reactors.

The pigments obtained showed a 20–40% higher color strength compared to standard pigments obtained through stirred-reactor synthesis. In addition, their brightness and transparency are 5–6 levels better than the standard. The second synthesis was also carried out on a pilot-plant scale (flow: 500 mL min^{-1}, equivalent to 10 tonnes per year). The microstructured reactor simultaneously used three principles to achieve higher flow rates. Initially the inner dimensions were increased by a small amount (scale-up). Then three

 © 2004 Wiley-VCH Verlag GmbH & Co. KGaA, Weinheim

microstructured reactors were operated in parallel and within these units were in addition several reactor plates connected in parallel (internal and external numbering-up). The pigment obtained using this pilot plant has a 50% higher color strength compared to the conventional technology. Brightness and transparency are equivalent to the good levels of the laboratory reactor. The d_{50} value is 90 nm and the standard deviation, $s = 1.5$ (conventional: $d_{50} = 600$ nm, $s = 2.0$; Figure 55). This example is encouraging in the sense that it proves that a microstructured reactor can be used for processes where difficult fluid transportation, such as with suspensions, is necessary, even on a pilot-plant scale.

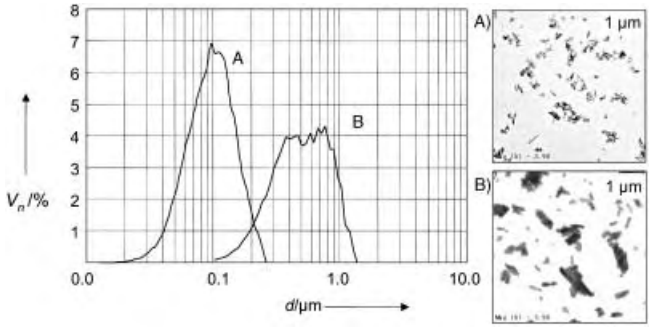


Figure 55. Particle-size distribution (left) and TEM image (right 14000 ×) of a pigment on an azo-dye basis. A) Product from a pilot-plant microstructured reactor; B) product from a conventional stirred reactor: $d_{50} \approx 600$ nm (source: Clariant, Frankfurt[51]).

8. Market Prognoses

Prognoses for the number and volume of microstructured devices are regularly published within the framework of a NEXUS study. It is, however, striking that in none of these studies do microstructured reactors appear. Thus, only a short market study by Yole Developpement and IMM will be mentioned here.[290,291] The study states that by 2002 the market volume for sales of microstructured reactors and related services were approximately $35 million per year. It is hence no surprise that a small number of middle-sized enterprises define microstructured reactors as their core business while larger companies and chemical-plant manufacturers do not have them in their portfolio but still observe the market segment intensely.

The study, based on interviews with about 100 selected companies (≈70%), institutes, and universities, predicted a small increase in worldwide turnover, based on general economic development. At the same time, however, increasing acceptance and a significant improvement of the technical suitability of microstructured reactors (e.g., for the chemical production) could lead to an amplification in increased market turnover over the short term. The positive market expectations highlighted by this study were reinforced in an attached interview.

9. Summary and Outlook

Approximately 1000 publications regarding the applications of microstructured devices paint a comprehensive picture for their possibilities in chemistry. The *number* of improvements achieved is impressive. The *quality* of the publications and thus the *expertise* shown has improved significantly. Initially feasibility studies have been superceded by detailed mechanistic descriptions and reviews dedicated to specific themes, such as organic chemistry in microstructured reactors.[80] In addition, the *variety* of the studies undertaken has also improved: from pure liquid- and gas-phase chemistry, through multiphase processes, up to photo- and electrochemical experiments on the microscale. Furthermore, both catalytic and noncatalytic applications have been described. The result of this development is increasing *scientific recognition*; regular contributions to this field now appear in all of the big peer-reviewed journals. In particular, *Analytical Chemistry* and *Lab on a Chip* are rich sources of such publications.

Until now these practices have been strongly influenced by process engineers. Increasing, for example, the yield of one structural isomer over another or the enantioselectivity of a reaction (despite there being only a few examples to date) should be motivation enough for chemists to become interested in microstructured reactors. Ultrafast metalorganic syntheses, asymmetric syntheses, and reactions with highly active reactants are but three more examples of areas that could be exploited by chemists. It is hoped that this Review will contribute to new discoveries and the continued development of this most fascinating area of research.

Received: February 5, 2003 [A577]

[1] A. Gavriilidis, P. Angeli, E. Cao, K. K. Yeong, Y. S. S. Wan, *Trans. Inst. Chem. Eng. Part A* **2002**, *80*, 3.
[2] W. Ehrfeld, V. Hessel, V. Haverkamp, *Ullmann's Encyclopedia of Industrial Chemistry*, 6th ed., Wiley-VCH, Weinheim, **1999**.
[3] a) W. Ehrfeld, V. Hessel, H. Löwe, *Microreactors*, Wiley-VCH, Weinheim, **2000**; b) V. Hessel, S. Hardt, H. Löwe, *Chemical Micro Process Engineering*, Wiley-VCH, Weinheim, **2004**.
[4] V. Hessel, H. Löwe, *Chem. Ing. Tech.* **2002**, *74*, 185.
[5] K. F. Jensen, *Chem. Eng. Sci.* **2001**, *56*, 293.
[6] K. Schubert, J. Brandner, M. Fichtner, G. Linder, U. Schygulla, A. Wenka, *Microscale Thermophys. Eng.* **2001**, *5*, 17.
[7] A. de Mello, R. Wootton, *Lab Chip* **2002**, *2*, 7N.
[8] W. Löhder, L. Bergann (Akademie der Wissenschaften der DDR), DD 246257, **1986**.
[9] K. Schubert, W. Bier, G. Linder, D. Seidel, *Chem. Ing. Tech.* **1989**, *61*, 172.
[10] R. W. Wegeng, C. J. Call, M. K. Drost, *American Institute of Chemical Engineers Spring National Meeting* (New Orleans, USA, **1996**), p. 1.
[11] W. Ehrfeld, *DECHEMA-Monographs*, DECHEMA, Frankfurt, **1995**, p. 132.
[12] V. Hessel, H. Löwe, T. Stange, *Lab Chip* **2002**, *2*, 14N.
[13] K. Golbig, S. Taghavi-Moghadam, P. Born, *IMRET 6: 6th International Conference on Microreaction Technology* (New Orleans, USA, **2002**), American Institute of Chemical Engineers Pub. No. 164, p. 131.

 © 2004 Wiley-VCH Verlag GmbH & Co. KGaA, Weinheim

[14] A. Freitag, T. R. Dietrich, *IMRET 4: 4th International Conference on Microreaction Technology* (Atlanta, USA, **2000**), American Institute of Chemical Engineers Topical Conference Proceedings, p. 48.
[15] B. Ondruschka, P. Scholz, R. Gorges, W. Klemm, K. Schubert, A. Halbritter, H. Löwe, *Chem. Ing. Tech.* **2002**, *74*, 1577.
[16] V. Hessel, H. Löwe, *Chem. Eng. Technol.* **2003**, *26*, 13.
[17] V. Hessel, H. Löwe, *Chem. Eng. Technol.* **2003**, *26*, 391.
[18] V. Hessel, H. Löwe, *Chem. Eng. Technol.* **2003**, *26*, 531.
[19] K. P. Jäckel, *Microsystem Technology for Chemical and Biological Microreactors, DECHEMA Monographs*, *Vol. 132* (Ed.: W. Ehrfeld), VCH, Weinheim, **1996**, p. 29.
[20] K. Schubert, W. Bier, J. Brandner, M. Fichtner, C. Franz, G. Linder, *Process Miniaturization—IMRET 2: 2nd International Conference on Microreaction Technology* (New Orleans, USA, **1998**), *Topical Conference Preprints* (Eds.: W. Ehrfeld, I. H. Rinard, R. S. Wegeng), American Institute of Chemical Engineers, p. 88.
[21] J. J. Lerou, M. P. Harold, J. Ryley, J. Ashmead, T. C. O'Brien, M. Johnson, J. Perrotto, C. T. Blaisdell, T. A. Rensi, J. Nyquist, *Microsystem Technology for Chemical and Biological Microreactors, DECHEMA Monographs*, *Vol. 132* (Ed.: W. Ehrfeld), VCH, Weinheim, **1996**, p. 51.
[22] C. Alépée, L. Vulpescu, P. Cousseau, P. Renaud, R. Maurer, A. Renken, *IMRET 4: 4th International Conference on Microreaction Technology* (Atlanta, USA, **2000**), American Institute of Chemical Engineers Topical Conference Proceedings, p. 71.
[23] O. Wörz, K. P. Jäckel, T. Richter, A. Wolf, *Chem. Eng. Technol.* **2001**, *24*, 138.
[24] H. Löwe, W. Ehrfeld, V. Hessel, T. Richter, J. Schiewe, *IMRET 4: 4th International Conference on Microreaction Technology* (Atlanta, USA, **2000**), American Institute of Chemical Engineers Topical Conference Proceedings, p. 31.
[25] P. Gravesen, J. Branjeberg, O. S. Jensen, *Micro Mechanics Europe, MME'93* (Neuchatel, Switzerland, **1993**), p. 143.
[26] J. Branebjerg, P. Gravesen, J. P. Krog, C. R. Nielsen, *IEEE-MEMS'96* (San Diego, USA, **1996**), p. 441.
[27] V. Hessel, W. Ehrfeld, K. Golbig, V. Haverkamp, H. Löwe, T. Richter, *Process Miniaturization—IMRET 2: 2nd International Conference on Microreaction Technology* (New Orleans, USA, **1998**), *Topical Conference Preprints* (Eds.: W. Ehrfeld, I. H. Rinard, R. S. Wegeng), American Institute of Chemical Engineers, p. 259.
[28] S. Hardt, F. Schönfeld, F. Weise, C. Hofmann, V. Hessel, W. Ehrfeld, *Computational Methods for Multiphase Flow*, (Orlando, USA, **2001**), p. 217.
[29] S. Hardt, F. Doffing, H. Pennemann, *5th International Conference on Modeling and Simulation*, Springer, San Juan, Puerto Rico, **2002**, p. 54.
[30] S. Hardt, F. Schönfeld, F. Weise, C. Hofmann, W. Ehrfeld, *International Conference on Modeling and Simulations of Microsystems* (Hilton Head Island, USA, **2001**).
[31] S. Hardt, F. Schönfeld, *5th World Congress on Computional Mechanics, WCCM* (Vienna, Austria, **2002**), http://wccm.tuwien.ac.at.
[32] "CAMURE IV Conference on Multiphase Catalysis; 4th International Symposium on Catalysis in Multiphase Reactors": G. Dummann, U. Quitmann, L. Gröschel, D. W. Agar, O. Wörz, K. Morgenschweis, *Catal. Today* **2002**, *78–79*, 433.
[33] V. Haverkamp, G. Emig, V. Hessel, M. A. Liauw, H. Löwe, *Microreaction Technology—IMRET 5: Proceedings of the 5th International Conference on Microreaction Technology* (Eds.: M. Matlosz, W. Ehrfeld, J. P. Baselt), Springer, Berlin, **2001**, p. 202.
[34] V. Hessel, W. Ehrfeld, K. Golbig, V. Haverkamp, H. Löwe, M. Storz, C. Wille, A. Guber, K. Jähnisch, M. Baerns, *Microreaction Technology—IMRET 3: Proceedings of the 3rd International Conference on Microreaction Technology* (Ed.: W. Ehrfeld), Springer, Berlin, **2000**, p. 526.
[35] J. R. Burns, C. Ramshaw, A. J. Bull, P. Harston, *Microreaction Technology—IMRET 1: Proceedings of the 1st International Conference on Microreaction Technology* (Ed.: W. Ehrfeld), Springer, Berlin, **1997**, p. 127.
[36] J. R. Burns, C. Ramshaw, P. Harston, *Process Miniaturization—IMRET 2: 2nd International Conference on Microreaction Technology* (New Orleans, USA, **1998**), *Topical Conference Preprints* (Eds.: W. Ehrfeld, I. H. Rinard, R. S. Wegeng), American Institute of Chemical Engineers, p. 39.
[37] J. R. Burns, C. Ramshaw, *Lab Chip* **2001**, *1*, 10.
[38] N. Jongen, M. Donnet, P. Bowen, J. Lemaitre, H. Hofmann, R. Schenk, C. Hofmann, M. Aoun-Habbache, S. Guillemet-Fritsch, J. Sarrias, A. Rousset, M. Viviani, M. T. Buscaglia, V. Buscaglia, P. Nanni, A. Testino, J. R. Herguijuela, *Chem. Engin. Trans.* **2002**, 807.
[39] G. Veser, G. Friedrich, M. Freygang, R. Zengerle, *Microreaction Technology—IMRET 3: Proceedings of the 3rd International Conference on Microreaction Technology* (Ed.: W. Ehrfeld), Springer, Berlin, **2000**, p. 674.
[40] G. Veser, *Chem. Eng. Sci.* **2001**, *56*, 1265.
[41] W. Ehrfeld, V. Hessel, S. Kiesewalter, H. Löwe, T. Richter, J. Schiewe, *Microreaction Technology—IMRET 3: Proceedings of the 3rd International Conference on Microreaction Technology* (Ed.: W. Ehrfeld), Springer, Berlin, **2000**, p. 14.
[42] O. Wörz, *Microreaction Technology—IMRET 5: Proceedings of the 5th International Conference on Microreaction Technology* (Eds.: M. Matlosz, W. Ehrfeld, J. P. Baselt), Springer, Berlin, **2001**, p. 377.
[43] O. Wörz, K. P. Jäckel, T. Richter, A. Wolf, *Chem. Ing. Tech.* **2000**, *72*, 460.
[44] T. Richter, A. Wolf, K. P. Jäckel, O. Wörz, *Chem. Ing. Tech.* **1999**, *71*, 973.
[45] I. H. Rinard, *Process Miniaturization—IMRET 2: 2nd International Conference on Microreaction Technology* (New Orleans, USA, **1998**), *Topical Conference Preprints* (Eds.: W. Ehrfeld, I. H. Rinard, R. S. Wegeng), American Institute of Chemical Engineers, p. 299.
[46] N. Saha, I. H. Rinard, *IMRET 4: 4th International Conference on Microreaction Technology* (Atlanta, USA, **2000**), American Institute of Chemical Engineers Topical Conference Proceedings, p. 327.
[47] T. Bayer, D. Pysall, O. Wachsen, *Microreaction Technology—IMRET 3: Proceedings of the 3rd International Conference on Microreaction Technology* (Ed.: W. Ehrfeld), Springer, Berlin, **2000**, p. 165.
[48] T. Bayer, H. Heinichen, I. Leipprand, *VDE World Microtechnologies Congress, MICRO.tec 2000*, *Vol. 2*, VDE, Berlin, **2000**, p. 493.
[49] D. Pysall, O. Wachsen, T. Bayer, S. Wulf (Aventis Research & Technologies GmbH & Co KG), DE 19816886, **1998**.
[50] H. Krummradt, U. Kopp, J. Stoldt, *Microreaction Technology—IMRET 3: Proceedings of the 3rd International Conference on Microreaction Technology* (Ed.: W. Ehrfeld), Springer, Berlin, **2000**, p. 181.
[51] C. Wille, V. Autze, H. Kim, U. Nickel, S. Oberbeck, T. Schwalbe, L. Unverdorben, *IMRET 6: 6th International Conference on Microreaction Technology* (New Orleans, USA, **2002**), American Institute of Chemical Engineers Pub. No. 164, p. 7.
[52] G. B. Tatterson, *Scaleup and Design of Industrial Mixing Processes*, McGraw-Hill, New York, **1994**.
[53] V. Hessel, S. Hardt, H. Löwe, F. Schönfeld, *AIChE J.* **2003**, *49*, 566.
[54] A. J. Franz, D. J. Quiram, R. Srinivasan, I.-M. Hsing, S. L. Firebaugh, K. F. Jensen, M. A. Schmidt, *Process Miniaturiza-*

tion—IMRET 2: 2nd International Conference on Microreaction Technology (New Orleans, USA, **1998**), *Topical Conference Preprints* (Eds.: W. Ehrfeld, I. H. Rinard, R. S. Wegeng), American Institute of Chemical Engineers, p. 33.

[55] T. Stief, O.-U. Langer, *IMRET 4: 4th International Conference on Microreaction Technology* (Atlanta, USA, **2000**), American Institute of Chemical Engineers Topical Conference Proceedings, p. 215.

[56] H. Kestenbaum, A. Lange de Olivera, W. Schmidt, F. Schüth, W. Ehrfeld, K. Gebauer, H. Löwe, T. Richter, *Ind. Eng. Chem. Res.* **2000**, *41*, 710.

[57] J. Brandner, M. Fichtner, K. Schubert, *Microreaction Technology—IMRET 3: Proceedings of the 3rd International Conference on Microreaction Technology* (Ed.: W. Ehrfeld), Springer, Berlin, **2000**, 607.

[58] P. van Male, M. H. J. M. de Croon, R. M. Tiggelaar, A. van den Berg, J. C. Schouten, *Int. J. Heat Mass Transfer* **2004**, *47*, 87.

[59] E. V. Rebrov, S. A. Duinkerke, M. H. J. M. de Croon, J. C. Schouten, *Chem. Eng. J.* **2003**, *91*, 1.

[60] E. V. Rebrov, M. H. J. M. de Croon, J. C. Schouten, *Catal. Today* **2001**, *69*, 183.

[61] A. R. Oroskar, K. VandenBussche, S. F. Abdo, *Microreaction Technology—IMRET 5: Proceedings of the 5th International Conference on Microreaction Technology* (Eds.: M. Matlosz, W. Ehrfeld, J. P. Baselt), Springer, Berlin, **2001**, p. 153.

[62] S. Chattopadhyay, G. Veser, *ChemConn-2001* (Chennai, India, **2001**), p. 1.

[63] S. Walter, M. Liauw, *IMRET 4: 4th International Conference on Microreaction Technology* (Atlanta, USA, **2000**), American Institute of Chemical Engineers Topical Conference Proceedings, p. 209.

[64] G. E. Karniadakis, A. Beskok, *Micro Flows—Fundamentals and Simulation*, Springer, New York, **2002**.

[65] X. F. Peng, G. P. Peterson, B. X. Wang, *Exp. Heat Transfer* **1994**, *7*, 249.

[66] J. M. Commenge, L. Falk, J. P. Corriou, M. Matlosz, *VDE World Microtechnologies Congress, MICRO.tec 2000*, *Vol. 1*, VDE, Berlin, **2000**, p. 375 (EXPO Hannover).

[67] X. F. Peng, B. X. Wang, *Int. J. Heat Mass Transfer* **1995**, *38*, 127.

[68] X. F. Peng, G. P. Peterson, *Int. J. Heat Mass Transfer* **1995**, *38*, 755.

[69] S. B. Choi, R. F. Barron, R. O. Warrington, *Micromechanical Sensors, Actuators, and Systems*, *Vol. 32*, American Society of Mechanical Engineering, **1991**, p. 123.

[70] L. A. Luo, U. D'Ortana, D. Tondeur, *Microreaction Technology—IMRET 3: Proceedings of the 3rd International Conference on Microreaction Technology* (Ed.: W. Ehrfeld), Springer, Berlin, **2000**, p. 556.

[71] V. Haverkamp, Dissertation, Universität Erlangen-Nürnberg, **2002**.

[72] N. de Mas, A. Günther, M. A. Schmidt, K. F. Jensen, *Ind. Eng. Chem. Res.* **2003**, *42*, 698.

[73] S. Sugiura, M. Nakajima, M. Seki, *Microreaction Technology—IMRET 5: Proceedings of the 5th International Conference on Microreaction Technology* (Eds.: M. Matlosz, W. Ehrfeld, J. P. Baselt), Springer, Berlin, **2001**, p. 252.

[74] A. Rouge, B. Spoetzl, K. Gebauer, R. Schenk, A. Renken, *Chem. Eng. Sci.* **2001**, *56*, 1419.

[75] H. Pennemann, V. Hessel, H.-J. Kost, H. Löwe, C. de Bellefon, *AIChE J.* **2004**, in press.

[76] J. M. Commenge, L. Falk, J. P. Corriou, M. Matlosz, *AIChE J.* **2000**, *48*, 345.

[77] S. Walter, G. Frischmann, R. Broucek, M. Bergfeld, M. Liauw, *Chem. Ing. Tech.* **1999**, *71*, 447.

[78] T. Bayer, H. Heinichen, T. Natelberg, *IMRET 4: 4th International Conference on Microreaction Technology* (Atlanta, USA, **2000**), American Institute of Chemical Engineers Topical Conference Proceedings, p. 167.

[79] V. Skelton, G. M. Greenway, S. J. Haswell, P. Styring, D. O. Morgan, B. H. Warrington, S. Wong, *IMRET 4: 4th International Conference on Microreaction Technology* (Atlanta, USA, **2000**), American Institute of Chemical Engineers Topical Conference Proceedings, p. 78.

[80] P. D. I. Fletcher, S. J. Haswell, E. Pombo-Villar, B. H. Warrington, P. Watts, S. Y. F. Wong, X. Zhang, *Tetrahedron* **2002**, *58*, 4735.

[81] C. Wiles, P. Watts, S. J. Haswell, E. Pombo-Villar, *Lab Chip* **2001**, *1*, 100.

[82] V. Skelton, S. J. Haswell, P. Styring, B. H. Warrington, S. Wong, *Micro Total Analysis Systems* (Eds.: J. M. Ramsey, A. van den -Berg), Kluwer, Dordrecht, **2001**, p. 589.

[83] E. Garcia-Egido, S. Y. F. Wong, *Micro Total Analysis Systems* (Eds.: J. M. Ramsey, A. van den Berg), Kluwer, Dordrecht, **2001**, p. 517.

[84] E. Garcia-Egido, S. Y. F. Wong, B. H. Warrington, *Lab Chip* **2002**, *2*, 31.

[85] M. Fernandez-Suarez, S. Y. F. Wong, B. H. Warrington, *Lab Chip* **2002**, *2*, 170.

[86] R. C. R. Wootton, R. Fortt, A. J. de Mello, *Org. Process Res. Dev.* **2002**, *60*, 187.

[87] V. Skelton, G. M. Greenway, S. J. Haswell, P. Styring, D. O. Morgan, *Microreaction Technology—IMRET 3: Proceedings of the 3rd International Conference on Microreaction Technology* (Ed.: W. Ehrfeld), Springer, Berlin, **2000**, p. 235.

[88] M. Sands, S. J. Haswell, S. M. Kelly, V. Skelton, D. Morgan, P. Styring, B. H. Warrington, *Lab Chip* **2001**, *1*, 64.

[89] R. D. Chambers, R. C. H. Spink, *Chem. Commun.* **1999**, 883.

[90] R. D. Chambers, D. Holling, R. C. H. Spink, G. Sandford, *Lab Chip* **2001**, *1*, 132.

[91] K. Jähnisch, M. Baerns, V. Hessel, W. Ehrfeld, W. Haverkamp, H. Löwe, C. Wille, A. Guber, *J. Fluorine Chem.* **2000**, *105*, 117.

[92] N. de Mas, R. J. Jackman, M. A. Schmidt, K. F. Jensen, *Microreaction Technology—IMRET 5: Proceedings of the 5th International Conference on Microreaction Technology* (Eds.: M. Matlosz, W. Ehrfeld, J. P. Baselt), Springer, Berlin, **2001**, p. 60.

[93] N. de Mas, *IMRET 6: 6th International Conference on Microreaction Technology* (New Orleans, USA, **2002**), American Institute of Chemical Engineers Pub. No. 164, p. 184.

[94] J. Antes, T. Tuercke, E. Marioth, F. Lechner, M. Scholz, F. Schnürer, H. H. Krause, S. Löbbecke, *Microreaction Technology—IMRET 5: Proceedings of the 5th International Conference on Microreaction Technology* (Eds.: M. Matlosz, W. Ehrfeld, J. P. Baselt), Springer, Berlin, **2001**, p. 446.

[95] J. Antes, T. Tuercke, E. Marioth, K. Schmid, H. Krause, S. Loebbecke, *IMRET 4: 4th International Conference on Microreaction Technology* (Atlanta, USA, **2000**), American Institute of Chemical Engineers Topical Conference Proceedings, p. 194.

[96] J. R. Burns, C. Ramshaw, *IMRET 4: 4th International Conference on Microreaction Technology* (Atlanta, USA, **2000**), American Institute of Chemical Engineers Topical Conference Proceedings, p. 133.

[97] J. R. Burns, C. Ramshaw, *Trans. Inst. Chem. Eng. Part A* **1998**, *77*, 206.

[98] R. Födisch, W. Reschetilowski, D. Hönicke, *DGMK-Conference on the Future Role of Aromatics in Refining and Petrochemistry* (Erlangen, **1999**), p. 231.

[99] H. Surangalikar, R. S. Besser, *IMRET 6: 6th International Conference on Microreaction Technology* (New Orleans, USA, **2002**), American Institute of Chemical Engineers Pub. No. 164, p. 248.

[100] G. Wießmeier, D. Hönicke, *Ind. Eng. Chem. Res.* **1996**, *35*, 4412.

[101] G. Wießmeier, D. Hönicke, *J. Micromech. Microeng.* **1996**, *6*, 285.

 © 2004 Wiley-VCH Verlag GmbH & Co. KGaA, Weinheim

[102] A. Kursawe, D. Hönicke, *IMRET 4: 4th International Conference on Microreaction Technology* (Atlanta, USA, **2000**), American Institute of Chemical Engineers Topical Conference Proceedings, p. 153.
[103] S. Kah, D. Hönicke, *Microreaction Technology—IMRET 5: Proceedings of the 5th International Conference on Microreaction Technology* (Eds.: M. Matlosz, W. Ehrfeld, J. P. Baselt), Springer, Berlin, **2001**, p. 397.
[104] A. Kursawe, E. Dietzsch, S. Kah, D. Hönicke, M. Fichtner, K. Schubert, G. Wießmeier, *Microreaction Technology—IMRET 3: Proceedings of the 3rd International Conference on Microreaction Technology* (Ed.: W. Ehrfeld), Springer, Berlin, **2000**, p. 213.
[105] H. Kestenbaum, A. Lange de Oliveira, W. Schmidt, F. Schüth, K. Gebauer, H. Löwe, T. Richter, *Microreaction Technology—IMRET 3: Proceedings of the 3rd International Conference on Microreaction Technology* (Ed.: W. Ehrfeld), Springer, Berlin, **2000**, p. 207.
[106] H. Kestenbaum, A. Lange de Olivera, W. Schmidt, H. Schüth, W. Ehrfeld, K. Gebauer, H. Löwe, T. Richter, *Stud. Surf. Sci. Catal.* **2000**, *130*, 2741.
[107] U. Hagendorf, M. Janicke, F. Schüth, K. Schubert, M. Fichtner, *Process Miniaturization—IMRET 2: 2nd International Conference on Microreaction Technology* (New Orleans, USA, **1998**), *Topical Conference Preprints* (Eds.: W. Ehrfeld, I. H. Rinard, R. S. Wegeng), American Institute of Chemical Engineers, p. 81.
[108] A. Kursawe, D. Hönicke, *Microreaction Technology—IMRET 5: Proceedings of the 5th International Conference on Microreaction Technology* (Eds.: M. Matlosz, W. Ehrfeld, J. P. Baselt), Springer, Berlin, **2001**, p. 240.
[109] K. Haas-Santo, O. Görke, K. Schubert, J. Fiedler, H. Funke, *Microreaction Technology—IMRET 5: Proceedings of the 5th International Conference on Microreaction Technology* (Eds.: M. Matlosz, W. Ehrfeld, J. P. Baselt), Springer, Berlin, **2001**, p. 313.
[110] M. Kraut, A. Nagel, K. Schubert, *IMRET 6: 6th International Conference on Microreaction Technology* (New Orleans, USA, **2002**), American Institute of Chemical Engineers Pub. No. 164, p. 352.
[111] C. Wiles, P. Watts, S. J. Haswell, E. Pombo-Villar, *Lab Chip* **2002**, *2*, 62.
[112] T. Ciu, J. Fang, J. Maxwell, J. Gardner, R. Besser, B. Elmore, *IMRET 4: 4th International Conference on Microreaction Technology* (Atlanta, USA, **2000**), American Institute of Chemical Engineers Topical Conference Proceedings, p. 488.
[113] E. Cao, K. K. Yeong, A. Gavriilidis, Z. Cui, D. W. K. Jenkins, *IMRET 6: 6th International Conference on Microreaction Technology* (New Orleans, USA, **2002**), American Institute of Chemical Engineers Pub. No. 164, p. 76.
[114] R. Maurer, C. Claivaz, M. Fichtner, K. Schubert, A. Renken, *IMRET 4: 4th International Conference on Microreaction Technology* (Atlanta, USA, **2000**), American Institute of Chemical Engineers Topical Conference Proceedings, p. 100.
[115] N. Steinfeldt, N. Dropka, D. Wolf, *Microreaction Technology—IMRET 5: Proceedings of the 5th International Conference on Microreaction Technology* (Strasbourg, France, **2001**).
[116] A. Zheng, F. Jones, J. Fang, T. Cui, *IMRET 4: 4th International Conference on Microreaction Technology* (Atlanta, USA, **2000**), American Institute of Chemical Engineers Topical Conference Proceedings, p. 284.
[117] T. Herweck, S. Hardt, V. Hessel, H. Löwe, C. Hofmann, F. Weise, T. Dietrich, A. Freitag, *Microreaction Technology—IMRET 5: Proceedings of the 5th International Conference on Microreaction Technology* (Eds.: M. Matlosz, W. Ehrfeld, J. P. Baselt), Springer, Berlin, **2001**, p. 215.
[118] V. Hessel, W. Ehrfeld, K. Golbig, C. Hofmann, S. Jungwirth, H. Löwe, T. Richter, M. Storz, A. Wolf, O. Wörz, J. Breysse, *Microreaction Technology—IMRET 3: Proceedings of the 3rd International Conference on Microreaction Technology* (Ed.: W. Ehrfeld), Springer, Berlin, **2000**, p. 152.
[119] P. Watts, C. Wiles, S. J. Haswell, E. Pombo-Villar, P. Styring, *Microreaction Technology—IMRET 5: Proceedings of the 5th International Conference on Microreaction Technology* (Eds.: M. Matlosz, W. Ehrfeld, J. P. Baselt), Springer, Berlin, **2001**, p. 508.
[120] P. Watts, C. Wiles, S. J. Haswell, E. Pombo-Villar, *Tetrahedron* **2002**, *58*, 5427.
[121] S. Löbbecke, J. Antes, T. Türcke, E. Marioth, K. Schmid, H. Krause, *31th Int. Annu. Conf. ICT; Energetic Materials—Analysis, Diagnostics and Testing* (Karlsruhe, **2000**).
[122] D. Bökenkamp, A. Desai, X. Yang, Y.-C. Tai, E. M. Marzluff, S. L. Mayo, *Anal. Chem.* **1998**, *70*, 232.
[123] B. Jandeleit, D. J. Schaefer, T. S. Powers, H. W. Turner, W. H. Weinberg, *Angew. Chem.* **1999**, *111*, 2648; *Angew. Chem. Int. Ed.* **1999**, *38*, 2494.
[124] F. Balkenhohl, C. von dem Bussche-Hünnefeld, A. Lansky, C. Zechel, *Angew. Chem.* **1996**, *108*, 2436; *Angew. Chem. Int. Ed. Engl.* **1996**, *35*, 2288.
[125] T. Zech, D. Hönicke, A. Lohf, K. Golbig, T. Richter, *Microreaction Technology—IMRET 3: Proceedings of the 3rd International Conference on Microreaction Technology* (Ed.: W. Ehrfeld), Springer, Berlin, **2000**, p. 260.
[126] A. Müller, K. Drese, H. Gnaser, M. Hampe, V. Hessel, H. Löwe, S. Schmitt, R. Zapf, *Catalysis Today* **2002**, *81*, 377.
[127] V. Hessel, H. Löwe, *Chem. Ing. Tech.* **2002**, *74*, 381.
[128] V. Hessel, H. Löwe, *Chem. Ing. Tech.* **2002**, *74*, 17.
[129] O. Wörz, *Chem. Unserer Zeit* **2000**, *34*, 24.
[130] T. Schwalbe, V. Autze, G. Wille, *Chimia* **2002**, *56*, 636.
[131] S. deWitt, *Curr. Opin. Chem. Biol.* **1999**, *3*, 350.
[132] H. Löwe, W. Ehrfeld, *Electrochim. Acta* **1999**, *44*, 3679.
[133] K. Golbig, M. Hohmann, T. Schwalbe, *VDE World Microtechnologies Congress, MICRO.tec 2000*, *Vol. 1*, VDE, Berlin, **2000**, p. 361 (EXPO Hannover).
[134] H. Okamoto, *J. Synth. Org. Chem. (Jpn.)* **1999**, 805.
[135] S. J. Haswell, R. J. Middleton, B. O'Sullivan, V. Skleton, P. Watts, P. Styring, *Chem. Commun.* **2001**, 391.
[136] K. Kanno, M. Fujii, *Yuki Gosei Kagaku Kyokaishi* **2002**, *60*, 701.
[137] A. Mainz, J. C. T. Eijkel, *Pure Appl. Chem.* **2001**, *73*, 1555.
[138] V. Autze, K. Golbig, A. Kleemann, S. Oberbeck, *Nachr. Chem.* **2000**, *48*, 683.
[139] S. Hardt, F. Schönfeld, *AIChE J.* **2003**, *49*, 578.
[140] V. Hessel, T. Dietrich, A. Freitag, S. Hardt, C. Hofmann, H. Löwe, H. Pennemann, A. Ziogas, *IMRET 6: 6th International Conference on Microreaction Technology* (New Orleans, USA, **2002**), American Institute of Chemical Engineers Pub. No. 164, p. 297.
[141] W. Ehrfeld, K. Golbig, V. Hessel, H. Löwe, T. Richter, *Ind. Eng. Chem. Res.* **1999**, *38*, 1075.
[142] A. Freitag, T. R. Dietrich, R. Scholz, *VDE World Microtechnologies Congress, MICRO.tec 2000*, *Vol. 1*, VDE, Berlin, **2000**, p. 355 (EXPO Hannover).
[143] V. Haverkamp, W. Ehrfeld, K. Gebauer, V. Hessel, H. Löwe, T. Richter, C. Wille, *Fresenius J. Anal. Chem.* **1999**, *364*, 617.
[144] V. Hessel, W. Ehrfeld, V. Haverkamp, H. Löwe, J. Schiewe, *Dispersion Techniques for Laboratory and Industrial Production*, *Vol. 42* (Eds.: R. H. Müller, B. H. L. Böhm), Wissenschaftliche Verlagsgesellschaft mbH, Stuttgart, **2001**, p. 45.
[145] J. Schiewe, W. Ehrfeld, V. Haverkamp, V. Hessel, H. Löwe, C. Wille, M. Altvater, R. Rietz, R. Neubert, *IMRET 4: 4th International Conference on Microreaction Technology* (Atlanta, USA, **2000**), American Institute of Chemical Engineers Topical Conference Proceedings, p. 467.

[146] S. Hardt, T. Dietrich, A. Freitag, V. Hessel, H. Löwe, C. Hofmann, A. Oroskar, F. Schönfeld, K. VandenBussche, *IMRET 6: 6th International Conference on Microreaction Technology* (New Orleans, USA, **2002**), American Institute of Chemical Engineers Pub. No. 164, p. 329.
[147] B. Penth, WO 00/61275, **1999**.
[148] B. Penth, *Microreaction Technology—IMRET 5: Proceedings of the 5th International Conference on Microreaction Technology* (Strasbourg, France, **2001**).
[149] B. Werner, M. Donnet, V. Hessel, C. Hofmann, N. Jongen, H. Löwe, R. Schenk, A. Ziogas, *IMRET 6: 6th International Conference on Microreaction Technology* (New Orleans, USA, **2002**), American Institute of Chemical Engineers Pub. No. 164, p. 168.
[150] R. Schenk, V. Hessel, B. Werner, A. Ziogas, C. Hofmann, M. Donnet, N. Jongen, *Chem. Engin. Trans.* **2002**, *1*, 909.
[151] R. Schenk, M. Donnet, V. Hessel, C. Hofmann, N. Jongen, H. Löwe, *Microreaction Technology—IMRET 5: Proceedings of the 5th International Conference on Microreaction Technology* (Eds.: M. Matlosz, W. Ehrfeld, J. P. Baselt), Springer, Berlin, **2001**, p. 489.
[152] S. Loebbecke, J. Antes, T. Tuercke, D. Boskovich, W. Schweikert, E. Marioth, F. Schnuerer, H. H. Krause, *IMRET 6: 6th International Conference on Microreaction Technology* (New Orleans, USA, **2002**), American Institute of Chemical Engineers Pub. No. 164, p. 37.
[153] A. Wolf, W. Ehrfeld, H. Lehr, F. Michel, T. Richter, H. Gruber, O. Wörz, *F&M, Feinwerktech. Messtech.* **1997**, *105*, 436.
[154] O. Wörz, K. P. Jäckel, T. Richter, A. Wolf, *Process Miniaturization—IMRET 2: 2nd International Conference on Microreaction Technology* (New Orleans, USA, **1998**), *Topical Conference Preprints* (Eds.: W. Ehrfeld, I. H. Rinard, R. S. Wegeng), American Institute of Chemical Engineers, p. 183.
[155] O. Wörz, K. P. Jäckel, T. Richter, A. Wolf, *Microtechnologies and Miniaturization, Tools, Techniques, and Novel Applications for the Biopharmaceutical Industry*, IBC Global Conferences Limited, London, **1998**.
[156] H. Hisamoto, T. Saito, M. Tokeshi, A. Hibara, T. Kitamori, *Chem. Commun.* **2001**, 2662.
[157] S. Taghavi-Moghadam, A. Kleemann, S. Overbeck, *VDE World Microtechnologies Congress, MICRO.tec 2000*, *Vol. 2*, VDE, Berlin, **2000**, p. 489 (EXPO Hannover).
[158] V. Skelton, G. M. Greenway, S. J. Haswell, P. Styring, D. O. Morgan, B. H. Warrington, S. Y. F. Wong, *Analyst* **2001**, *126*, 11.
[159] V. Skelton, G. M. Greenway, S. J. Haswell, P. Styring, D. O. Morgan, B. H. Warrington, S. Y. F. Wong, *Analyst* **2001**, *126*, 7.
[160] P. D. I. Fletcher, S. J. Haswell, V. N. Paunow, *Analyst* **1999**, *124*, 1273.
[161] H. Salimi-Moosavi, T. Tang, D. J. Harrison, *J. Am. Chem. Soc.* **1997**, *119*, 8716.
[162] P. Watts, C. Wiles, S. J. Haswell, E. Pombo-Villar, P. Styring, *Chem. Commun.* **2001**, 990.
[163] P. Watts, C. Wiles, S. J. Haswell, E. Pombo-Villar, *Lab Chip* **2002**, *2*, 141.
[164] E. Dietz, J. Weber, D. Schnaitmann, C. Wille, L. Unverdorben, B. Brychcy, EP 1195413A1, **2001**.
[165] E. Dietz, J. Weber, D. Schnaitmann, C. Wille, L. Unverdorben, B. Brychcy, EP 1195414A1, **2001**.
[166] E. Dietz, J. Weber, D. Schnaitmann, C. Wille, L. Unverdorben, B. Brychcy, EP 1195415A1, **2001**.
[167] N. Schwesinger, O. Marufke, F. Qiao, R. Devant, H. Wurziger, *Process Miniaturization—IMRET 2: 2nd International Conference on Microreaction Technology* (New Orleans, USA, **1998**), *Topical Conference Preprints* (Eds.: W. Ehrfeld, I. H. Rinard, R. S. Wegeng), American Institute of Chemical Engineers, p. 124.
[168] G. M. Greenway, S. J. Haswell, D. O. Morgan, V. Skelton, P. Styring, *Sens. Actuators B* **2000**, *63*, 153.
[169] N. G. Wilson, T. McCreedy, *Microreaction Technology—IMRET 3: Proceedings of the 3rd International Conference on Microreaction Technology* (Ed.: W. Ehrfeld), Springer, Berlin, **2000**, p. 346.
[170] N. G. Wilson, T. McCreedy, *Chem. Commun.* **2000**, 733.
[171] Y. S. S. Wan, J. L. H. Chau, A. Gavriilidis, K. L. Yeung, *Chem. Commun.* **2002**, 878.
[172] Y. S. S. Wan, J. L. H. Chau, A. Gavriilidis, K. L. Yeung, *Microporous Mesoporous Mater.* **2001**, *42*, 157.
[173] Y. S. S. Wan, J. L. H. Chau, A. Gavriilidis, K. L. Yeung, *Microreaction Technology—IMRET 5: Proceedings of the 5th International Conference on Microreaction Technology* (Eds.: M. Matlosz, W. Ehrfeld, J. P. Baselt), Springer, Berlin, **2001**, p. 94.
[174] S. J. Haswell, B. O'Sullivan, P. Styring, *Lab Chip* **2001**, *1*, 164.
[175] C. de Bellefon, N. Pestre, T. Lamouille, P. Grenouillet, *Adv. Synth. Catal.* **2003**, *345*, 190.
[176] C. de Bellefon, R. Abdallah, T. Lamouille, N. Pestre, S. Caravieilhes, P. Grenouillet, *Chimia* **2002**, *56*, 621.
[177] C. de Bellefon, N. Tanchoux, S. Caravieilhes, P. Grenouillet, V. Hessel, *Angew. Chem.* **2000**, *112*, 3584; *Angew. Chem. Int. Ed.* **2000**, *39*, 3442.
[178] S. Caravieilhes, C. de Bellefon, N. Tanchoux, *Catal. Today* **2001**, *66*, 145.
[179] C. de Bellefon, S. Caravieilhes, P. Grenouillet, *Microreaction Technology—IMRET 5: Proceedings of the 5th International Conference on Microreaction Technology* (Eds.: M. Matlosz, W. Ehrfeld, J. P. Baselt), Springer, Berlin, **2001**, p. 408.
[180] H. Löwe, W. Ehrfeld, K. Gebauer, K. Golbig, O. Hausner, V. Haverkamp, V. Hessel, T. Richter, *Process Miniaturization—IMRET 2: 2nd International Conference on Microreaction Technology* (New Orleans, USA, **1998**), *Topical Conference Preprints* (Eds.: W. Ehrfeld, I. H. Rinard, R. S. Wegeng), American Institute of Chemical Engineers, p. 63.
[181] V. Hessel, W. Ehrfeld, T. Herweck, V. Haverkamp, H. Löwe, J. Schiewe, C. Wille, T. Kern, N. Lutz, *IMRET 4: 4th International Conference on Microreaction Technology* (Atlanta, USA, **2000**), American Institute of Chemical Engineers Topical Conference Proceedings, p. 174.
[182] C. Wille, W. Ehrfeld, T. Herweck, V. Haverkamp, V. Hessel, H. Löwe, N. Lutz, K.-P. Möllmann, F. Pinno, *VDE World Microtechnologies Congress, MICRO.tec 2000*, VDE, Berlin, **2000**, p. 349 (EXPO Hannover).
[183] C. Wille, Dissertation, Technische Universität Clausthal **2002**.
[184] IMM, unpublished results.
[185] M. W. Losey, M. A. Schmidt, K. F. Jensen, *Microreaction Technology—IMRET 3: Proceedings of the 3rd International Conference on Microreaction Technology* (Ed.: W. Ehrfeld), Springer, Berlin, **2000**, p. 277.
[186] M. W. Losey, S. Isogai, M. A. Schmidt, K. F. Jensen, *IMRET 4: 4th International Conference on Microreaction Technology* (Atlanta, USA, **2000**), American Institute of Chemical Engineers Topical Conference Proceedings, p. 416.
[187] R. D. Chambers, M. P. Greenhall, J. Hutchings, *Tetrahedron* **1996**, *52*, 1.
[188] D. Wehle, M. Dejmek, J. Rosenthal, H. Ernst, D. Kampmann, S. Trautschold, R. Pechatschek, DE 10036603A1, **2000**.
[189] C. S. Loebbecke, W. Schweikert, T. Tuercke, J. Antes, E. Marioth, H. Krause, *VDE World Microtechnologies Congress, MICRO.tec 2000*, *Vol. 2*, VDE, Berlin, **2000**, p. 789 (EXPO Hannover).
[190] K. K. Yeong, A. Gavriilidis, R. Zapf, V. Hessel, *Catal. Today* **2003**, *81*, 641.
[191] R. J. Jackman, T. M. Floyd, R. Ghodssi, M. A. Schmidt, K. F. Jensen, *J. Micromech. Microeng.* **2001**, *11*, 263.
[192] H. Lu, M. A. Schmidt, K. F. Jensen, *Lab Chip* **2001**, *1*, 22.

 © 2004 Wiley-VCH Verlag GmbH & Co. KGaA, Weinheim

[193] H. Lu, M. A. Schmidt, K. F. Jensen, *Microreaction Technology—IMRET 5: Proceedings of the 5th International Conference on Microreaction Technology* (Eds.: M. Matlosz, W. Ehrfeld, J. P. Baselt), Springer, Berlin, **2001**, p. 175.
[194] H. Ehrich, D. Linke, K. Morgenschweis, M. Baerns, K. Jähnisch, *Chimia* **2002**, *56*, 647.
[195] K. Jähnisch, M. Baerns, DD 10257239.9, **2002**.
[196] F. Theil, S. Ballschuh, H. Schick, M. Haupt, H. Häfner, S. Schwarz, *Synthesis* **1988**, 540.
[197] A. Ziogas, H. Löwe, M. Küpper, W. Ehrfeld, *Microreaction Technology—IMRET 3: Proceedings of the 3rd International Conference on Microreaction Technology* (Ed.: W. Ehrfeld), Springer, Berlin, **2000**, p. 136.
[198] S. Suga, M. Okajima, K. Fujiwara, J.-I. Yoshida, *J. Am. Chem. Soc.* **2001**, *123*, 7941.
[199] S. Suga, M. Okajima, K. Fujiwara, J. Yoshida, *IMRET 6: 6th International Conference on Microreaction Technology* (New Orleans, USA, **2002**), American Institute of Chemical Engineers Pub. No. 164, p. 29.
[200] V. Mengeaud, J. Josserand, H. H. Girault, *Anal. Chem.* **2002**, *74*, 4279.
[201] R. Ferrigno, V. Reid, H. H. Girault, *Microreaction Technology—IMRET 3: Proceedings of the 3rd International Conference on Microreaction Technology* (Ed.: W. Ehrfeld), Springer, Berlin, **2000**, p. 294.
[202] V. Menegaud, O. Bagel, R. Ferrigno, H. H. Girault, A. Haider, *Lab Chip* **2002**, *2*, 39.
[203] V. Mengeaud, R. Ferrigno, J. Josserand, H. H. Girault, *Microreaction Technology—IMRET 5: Proceedings of the 5th International Conference on Microreaction Technology* (Eds.: M. Matlosz, W. Ehrfeld, J. P. Baselt), Springer, Berlin, **2001**, p. 350.
[204] H. Heinichen, *Chem. Tech.* **2001**, *30*, 89.
[205] "DSC-Microstructures, Sensors, and Actuators": W. Bier, W. Keller, G. Linder, D. Seidel, K. Schubert, *Am. Soc. Mech. Eng. Pap.* **1990**, *19*, 189.
[206] M. Fichtner, J. Mayer, D. Wolf, K. Schubert, *Ind. Eng. Chem. Res.* **2001**, *40*, 3475.
[207] M. Liauw, M. Baerns, R. Broucek, O. V. Buyevskaya, J.-M. Commenge, J. P. Corriou, L. Falk, K. Gebauer, H. J. Hefter, O.-U. Langer, H. Löwe, M. Matlosz, A. Renken, A. Rouge, R. Schenk, N. Steinfeld, S. Walter, *Microreaction Technology—IMRET 3: Proceedings of the 3rd International Conference on Microreaction Technology* (Ed.: W. Ehrfeld), Springer, Berlin, **2000**, p. 224.
[208] D. W. Matson, P. M. Martin, D. C. Steward, A. L. Y. Tonkovich, M. White, J. L. Zilka, G. L. Roberts, *Microreaction Technology—IMRET 3: Proceedings of the 3rd International Conference on Microreaction Technology* (Ed.: W. Ehrfeld), Springer, Berlin, **2000**, p. 62.
[209] A. L. Y. Tonkovich, D. M. Jimenez, J. L. Zilka, M. J. LaMont, J. Wang, R. S. Wegeng, *Process Miniaturization—IMRET 2: 2nd International Conference on Microreaction Technology* (New Orleans, USA, **1998**), *Topical Conference Preprints* (Eds.: W. Ehrfeld, I. H. Rinard, R. S. Wegeng), American Institute of Chemical Engineers, p. 186.
[210] A. L. Tonkovich, J. L. Zilka, M. J. LaMont, Y. Wang, R. Wegeng, *Chem. Eng. Sci.* **1999**, *54*, 2947.
[211] A. L. Tonkovich, S. P. Fitzgerald, J. L. Zilka, M. J. LaMont, Y. Wang, D. P. VanderWiel, R. Wegeng, *Microreaction Technology—IMRET 3: Proceedings of the 3rd International Conference on Microreaction Technology* (Ed.: W. Ehrfeld), Springer, Berlin, **2000**, p. 364.
[212] D. Hönicke, G. Wießmeier, *Microsystem Technology for Chemical and Biological Microreactors*; *DECHEMA Monographs, Vol. 132* (Ed.: W. Ehrfeld), VCH, Weinheim, **1996**, p. 93.
[213] G. Wießmeier, K. Schubert, D. Hönicke, *Microreaction Technology—IMRET 1: Proceedings of the 1st International Conference on Microreaction Technology* (Ed.: W. Ehrfeld), Springer, Berlin, **1997**, p. 20.
[214] E. V. Rebrov, M. H. J. M. de Croon, J. C. Schouten, *Microreaction Technology—IMRET 5: Proceedings of the 5th International Conference on Microreaction Technology* (Eds.: M. Matlosz, W. Ehrfeld, J. P. Baselt), Springer, Berlin, **2001**, p. 49.
[215] V. Cominos, S. Hardt, V. Hessel, G. Kolb, H. Löwe, M. Wichert, R. Zapf, *Chem. Eng. Comm.* **2004**, in press.
[216] V. Cominos, S. Hardt, V. Hessel, G. Kolb, H. Löwe, M. Wichert, R. Zapf, *IMRET 6: 6th International Conference on Microreaction Technology* (New Orleans, USA, **2002**), American Institute of Chemical Engineers Pub. No. 164, p. 113.
[217] T. Schaller, W. Bier, G. Linder, K. Schubert, *KFK-Nachr.* **1995**, *5670*, 45.
[218] K. Schubert, W. Bier, G. Linder, D. Seidel, *Ind. Diamond Rev.* **1990**, *50*.
[219] W. Bier, W. Keller, G. Linder, D. Seidel, K. Schubert, H. Martin, *Chem. Eng. Process.* **1993**, *32*, 33.
[220] T. Zech, D. Hönicke, *IMRET 4: 4th International Conference on Microreaction Technology* (Atlanta, USA, **2000**), American Institute of Chemical Engineers Topical Conference Proceedings, p. 379.
[221] G. Kolb, V. Cominos, K. Drese, V. Hessel, C. Hofmann, H. Löwe, O. Wörz, R. Zapf, *IMRET 6: 6th International Conference on Microreaction Technology* (New Orleans, USA, **2002**), American Institute of Chemical Engineers Pub. No. 164, p. 61.
[222] P. Pfeifer, M. Fichtner, K. Schubert, M. A. Liauw, G. Emig, *Microreaction Technology—IMRET 3: Proceedings ot the 3rd International Conference on Microreaction Technology* (Ed.: W. Ehrfeld), Springer, Berlin, **2000**, p. 372.
[223] S. K. Ajmera, C. Delattre, M. A. Schmidt, K. F. Jensen, *Microreaction Technology—IMRET 5: Proceedings of the 5th International Conference on Microreaction Technology* (Eds.: M. Matlosz, W. Ehrfeld, J. P. Baselt), Springer, Berlin, **2001**, p. 414.
[224] S. K. Ajmera, C. Delattre, M. A. Schmidt, K. F. Jensen, *Sens. Actuators A* **2002**, *82*, 297.
[225] A. J. Franz, S. K. Ajmera, S. L. Firebaugh, K. F. Jensen, M. A. Schmidt, *Microreaction Technology—IMRET 3: Proceedings of the 3rd International Conference on Microreaction Technology* (Ed.: W. Ehrfeld), Springer, Berlin, **2000**, p. 197.
[226] K. F. Jensen, S. L. Firebaugh, A. J. Franz, D. Quiram, R. Srinivasan, M. A. Schmidt, *Micro Total Analysis Systems* (Eds.: J. Harrison, A. van den Berg), Kluwer, Dordrecht, **1998**, p. 463.
[227] K. F. Jensen, *AIChE J.* **1999**, *45*, 2051.
[228] K. F. Jensen, I.-M. Hsing, R. Srinivasan, M. A. Schmidt, M. P. Harold, J. J. Lerou, J. F. Ryley, *Microreaction Technology—IMRET 1: Proceedings of the 1st International Conference on Microreaction Technology* (Ed.: W. Ehrfeld), Springer, Berlin, **1997**, p. 2.
[229] R. Srinivasan, I.-M. Hsing, P. E. Berger, K. F. Jensen, S. L. Firebaugh, M. A. Schmidt, M. P. Harold, J. J. Lerou, J. F. Ryley, *AIChE J.* **1997**, *43*, 3059.
[230] D. J. Quiram, I.-M. Hsing, A. J. Franz, K. F. Jensen, M. A. Schmidt, *Chem. Eng. Sci.* **2000**, *55*, 3065.
[231] A. J. Franz, K. J. Jensen, M. A. Schmidt, *Microreaction Technology—IMRET 3: Proceedings of the 3rd International Conference on Microreaction Technology* (Ed.: W. Ehrfeld), Springer, Berlin, **2000**, p. 267.
[232] S. V. Karnik, M. K. Hatalis, M. V. Kothare, *Microreaction Technology—IMRET 5: Proceedings of the 5th International Conference on Microreaction Technology* (Eds.: M. Matlosz, W. Ehrfeld, J. P. Baselt), Springer, Berlin, **2001**, p. 295.
[233] O. Wolfrath, L. Kiwi-Minsker, A. Renken, *Microreaction Technology—IMRET 5: Proceedings of the 5th International*

Conference on Microreaction Technology (Eds.: M. Matlosz, W. Ehrfeld, J. P. Baselt), Springer, Berlin, **2001**, p. 192.

[234] D. J. Quiram, I.-M. Hsing, A. J. Franz, R. Srinivasan, K. F. Jensen, M. A. Schmidt, *Process Miniaturization—IMRET 2: 2nd International Conference on Microreaction Technology* (New Orleans, USA, **1998**), *Topical Conference Preprints* (Eds.: W. Ehrfeld, I. H. Rinard, R. S. Wegeng), American Institute of Chemical Engineers, p. 205.

[235] P. Pfeifer, O. Görke, K. Schubert, *IMRET 6: 6th International Conference on Microreaction Technology* (New Orleans, USA, **2002**), American Institute of Chemical Engineers Pub. No. 164, p. 281.

[236] E. V. Rebrov, G. B. F. Seijger, H. P. A. Calis, M. H. J. M. de Croon, C. M. van den Bleek, J. C. Schouten, *Appl. Catal. A* **2001**, *206*, 125.

[237] S. Zhao, R. S. Besser, *IMRET 6: 6th International Conference on Microreaction Technology* (New Orleans, USA, **2002**), American Institute of Chemical Engineers Pub. No. 164, p. 289.

[238] R. Gorges, J. Kässbohrer, G. Kreisel, S. Meyer, *IMRET 6: 6th International Conference on Microreaction Technology* (New Orleans, USA, **2002**), American Institute of Chemical Engineers Pub. No. 164, p. 186.

[239] K. Kusakabe, D. Miyagawa, Y. Gu, H. Maeda, S. Morooka, *Microreaction Technology—IMRET 5: Proceedings of the 5th International Conference on Microreaction Technology* (Eds.: M. Matlosz, W. Ehrfeld, J. P. Baselt), Springer, Berlin, **2001**, p. 78.

[240] S. Walter, E. Joannet, M. Schiel, I. Boullet, R. Philipps, M. A. Liauw, *Microreaction Technology—IMRET 5: Proceedings of the 5th International Conference on Microreaction Technology* (Eds.: M. Matlosz, W. Ehrfeld, J. P. Baselt), Springer, Berlin, **2001**, p. 387.

[241] O. Wörz, K. P. Jäckel, *Chem. Tech.* **1997**, *26*, 130.

[242] J. Mayer, M. Fichtner, D. Wolf, K. Schubert, *Microreaction Technology—IMRET 3: Proceedings of the 3rd International Conference on Microreaction Technology* (Ed.: W. Ehrfeld), Springer, Berlin, **2000**, p. 187.

[243] G. Wießmeier, D. Hönicke, *Process Miniaturization—IMRET 2: 2nd International Conference on Microreaction Technology* (New Orleans, USA, **1998**), *Topical Conference Preprints* (Eds.: W. Ehrfeld, I. H. Rinard, R. S. Wegeng), American Institute of Chemical Engineers, p. 152.

[244] G. Wießmeier, D. Hönicke, *Process Miniaturization—IMRET 2: 2nd International Conference on Microreaction Technology* (New Orleans, USA, **1998**), *Topical Conference Preprints* (Eds.: W. Ehrfeld, I. H. Rinard, R. S. Wegeng), American Institute of Chemical Engineers, p. 24.

[245] E. Dietzsch, D. Hönicke, M. Fichtner, K. Schubert, G. Wießmeier, *IMRET 4: 4th International Conference on Microreaction Technology* (Atlanta, USA, **2000**), American Institute of Chemical Engineers Topical Conference Proceedings, p. 89.

[246] D. Gobby, I. Eames, A. Gavriilidis, *Microreaction Technology—IMRET 5: Proceedings of the 5th International Conference on Microreaction Technology* (Eds.: M. Matlosz, W. Ehrfeld, J. P. Baselt), Springer, Berlin, **2001**, p. 141.

[247] N. Steinfeldt, O. V. Buyevskaya, D. Wolf, M. Baerns, *Stud. Surf. Sci. Catal.* **2001**, *136*, 185.

[248] J. Find, J. A. Lercher, C. Cremers, U. Stimming, O. Kurtz, K. Crämer, *IMRET 6: 6th International Conference on Microreaction Technology* (New Orleans, USA, **2002**), American Institute of Chemical Engineers Pub. No. 164, p. 99.

[249] S. P. Fitzgerald, R. S. Wegeng, A. L. Y. Tonkovich, Y. Wang, H. D. Freeman, J. L. Marco, G. L. Roberts, D. P. VanderWiel, *IMRET 4: 4th International Conference on Microreaction Technology* (Atlanta, USA, **2000**), American Institute of Chemical Engineers Topical Conference Proceedings, p. 358.

[250] Y. Gonjo, M. Sato, T. Sugimoto, *2nd Intenational Fuel Cell Conference*, **1996**, p. 359.

[251] A. V. Pattekar, M. V. Kothare, S. V. Karnik, M. K. Hatalis, *Microreaction Technology—IMRET 5: Proceedings of the 5th International Conference on Microreaction Technology*, (Strasbourg, France, **2001**), p. 332.

[252] P. Pfeifer, K. Schubert, M. Fichtner, M. A. Liauw, G. Emig, *IMRET 6: 6th International Conference on Microreaction Technology* (New Orleans, USA, **2002**), American Institute of Chemical Engineers Pub. No. 164, p. 125.

[253] P. Reuse, P. Tribolet, L. Kiwi-Minsker, A. Renken, *Microreaction Technology—IMRET 5: Proceedings of the 5th International Conference on Microreaction Technology* (Eds.: M. Matlosz, W. Ehrfeld, J. P. Baselt), Springer, Berlin, **2001**, p. 322.

[254] P. Reuse, A. Renken, *IMRET 6: 6th International Conference on Microreaction Technology* (New Orleans, USA, **2002**), American Institute of Chemical Engineers Pub. No. 164, p. 73.

[255] G. A. Whyatt, W. E. TeGrotenhuis, R. S. Wegeng, L. R. Pederson, *Microreaction Technology—IMRET 5: Proceedings of the 5th International Conference on Microreaction Technology* (Strasbourg, France, **2001**), p. 303.

[256] G. A. Whyatt, C. M. Fischer, J. M. Davis, *IMRET 6: 6th International Conference on Microreaction Technology* (New Orleans, USA, **2002**), American Institute of Chemical Engineers Pub. No. 164, p. 85.

[257] E. A. Daymo, D. P. VanderWiel, S. P. Fitzgerald, Y. Wang, R. T. Rozmiarek, M. J. LaMont, A. L. Y. Tonkovich, *IMRET 4: 4th International Conference on Microreaction Technology* (Atlanta, USA, **2000**), American Institute of Chemical Engineers Topical Conference Proceedings, p. 364.

[258] J. Holladay, E. Jones, M. Phelps, J. Hu, *IMRET 6: 6th International Conference on Microreaction Technology* (New Orleans, USA, **2002**), American Institute of Chemical Engineers Pub. No. 164, p. 107.

[259] E. Jones, J. Holladay, S. Perry, R. Orth, B. Rozmiarel, J. Hu, M. Phelps, C. Guzman, *Microreaction Technology—IMRET 5: Proceedings of the 5th International Conference on Microreaction Technology* (Eds.: M. Matlosz, W. Ehrfeld, J. P. Baselt), Springer, Berlin, **2001**, p. 277.

[260] D. W. Matson, P. M. Martin, A. L. Y. Tonkovich, G. L. Roberts, *SPIE Conference on Micromachined Devices and Components IV, Vol. 3514* (Santa Clara, USA, **1998**), Society of Photographic Instrumentation Engineers, p. 386.

[261] L. Mex, J. Müller, *Microreaction Technology—IMRET 3: Proceedings of the 3rd International Conference on Microreaction Technology* (Ed.: W. Ehrfeld), Springer, Berlin, **2000**, p. 402.

[262] L. Mex, M. Sussiek, J. Müller, *IMRET 4: 4th International Conference on Microreaction Technology* (Atlanta, USA, **2000**), American Institute of Chemical Engineers Topical Conference Proceedings, p. 370.

[263] D. Palo, R. Rozmiarek, P. Steven, J. Holladay, C. Guzman, Y. Wang, J. Hu, R. Dagle, E. Baker, *Microreaction Technology—IMRET 5: Proceedings of the 5th International Conference on Microreaction Technology* (Eds.: M. Matlosz, W. Ehrfeld, J. P. Baselt), Springer, Berlin, **2001**, p. 359.

[264] R. Peters, H.-G. Düsterwald, B. Höhlein, J. Meusinger, U. Stimming, *Microreaction Technology—IMRET 1: Proceedings of the 1st International Conference on Microreaction Technology* (Ed.: W. Ehrfeld), Springer, Berlin, **1997**, p. 27.

[265] W. Schütz, K. Schubert, *IMRET 6: 6th International Conference on Microreaction Technology* (New Orleans, USA, **2002**), American Institute of Chemical Engineers Pub. No. 164, p. 105.

[266] J. Zilka-Marco, A. L. Y. Tonkovich, M. J. LaMont, S. P. Fitzgerald, D. P. VanderWiel, R. S. Wegeng, *IMRET 4: 4th International Conference on Microreaction Technology* (Atlanta, USA,

 © 2004 Wiley-VCH Verlag GmbH & Co. KGaA, Weinheim

2000), American Institute of Chemical Engineers Topical Conference Proceedings, p. 301.
[267] A. L. Y. Tonkovich, J. L. Zilka, M. R. Powell, C. J. Call, *Process Miniaturization—IMRET 2: 2nd International Conference on Microreaction Technology* (New Orleans, USA, **1998**), *Topical Conference Preprints* (Eds.: W. Ehrfeld, I. H. Rinard, R. S. Wegeng), American Institute of Chemical Engineers, p. 45.
[268] W. E. TeGrotenhuis, D. L. King, K. P. Brooks, B. J. Holladay, R. S. Wegeng, *IMRET 6: 6th International Conference on Microreaction Technology* (New Orleans, USA, **2002**), American Institute of Chemical Engineers Pub. No. 164, p. 18.
[269] D. P. VanderWiel, J. L. Zilka-Marco, Y. Wang, A. Y. Tonkovich, R. S. Wegeng, *IMRET 4: 4th International Conference on Microreaction Technology* (Atlanta, USA, **2000**), American Institute of Chemical Engineers Topical Conference Proceedings, p. 187.
[270] T. Zech, D. Hönicke, J. Klein, S. Schunk, D. Demuth, *Microreaction Technology—IMRET 5: Proceedings of the 5th International Conference on Microreaction Technology* (Strasbourg, France, **2001**).
[271] T. Zech, S. Schunk, J. Klein, D. Demuth, *IMRET 6: 6th International Conference on Microreaction Technology* (New Orleans, USA, **2002**), American Institute of Chemical Engineers Pub. No. 164, p. 32.
[272] C. Hoffmann, A. Wolf, F. Schüth, *Angew. Chem.* **1999**, *111*, 2971; *Angew. Chem. Int. Ed.* **1999**, *38*, 2800.
[273] C. Hoffmann, H.-W. Schmidt, F. Schüth, *J. Catal.* **2001**, *198*, 348.
[274] M. Orschel, J. Klein, H.-W. Schmidt, W. F. Maier, *Angew. Chem.* **1999**, *111*, 2961; *Angew. Chem. Int. Ed.* **1999**, *38*, 2791.
[275] U. Rodemerck, P. Ignaszewski, M. Lucas, P. Claus, M. Baerns, *Microreaction Technology—IMRET 3: 3rd International Conference on Microreaction Technology* (Ed.: W. Ehrfeld), Springer, Berlin, **2000**, p. 287.
[276] G. Hildebrand, J. Tack, S. Harnisch (Schering AG), WO 00/72955, **1999**.
[277] A. Beirau, F. Schwarz, M. Schmelz, J. Stoldt (Merck GmbH), DE 19746581, **1997**.
[278] J. Stoldt, F. Schwarz, M. Schmelz (Merck GmbH), DE 19746584, **1997**.
[279] A. Flink, E. Herrmann, L. Weismantel, G. Wießmeier, K. Schubert, M. Fichtner (Bayer AG, Forschungszentrum Karlsruhe GmbH), DE 19800529, **1998**.
[280] K. Schubert, W. Bier, G. Linder, D. Seidel, T. Menzel, B. Koglin, H.-J. Preisigke, E. Herrmann (Bayer AG, Leverkusen, Forschungszentrum Karlsruhe), EP 0758981, **1994**.
[281] K. Schubert, W. Bier, G. Linder, E. Herrmann (Bayer AG, Leverkusen, Forschungszentrum Karlsruhe GmbH), DE 19703779, **1997**.
[282] R. Schütte, T. Balduf, C. Becker, I. Hemme, B. Bertsch-Frank, W. Wildner, J. Rollmann, G. Markowz (Degussa AG, Düsseldorf), DE 10042746, **2000**.
[283] M. Weber, U. Tanger, W. Kleinloh (Phenolchemie GmbH & Co. KG), WO 01/30732, **1999**.
[284] N. Schwesinger, T. Frank (Merck Patent GmbH, Darmstadt), WO 96/30113, **1995**.
[285] F. Eisenbeiss, J. Kinkel (Merck Patent GmbH, Darmstadt), DE 19920794, **1999**.
[286] J. zur Lage, H.-J. Driller, J. Bünger, A. Wagner (Merck Patent GmbH, Darmstadt), DE 19911777, **1999**.
[287] U.-H. Felcht, *Chem. Eng. Technol.* **2002**, *25*, 345.
[288] A. R. Oroskar, K. VandenBussche, G. Towler, *VDE World Microtechnologies Congress, MICRO.tec 2000*, *Vol. 1*, VDE, Berlin, **2000**, p. 385 (EXPO Hannover).
[289] V. Hessel, H. Löwe, C. Hofmann, F. Schönfeld, D. Wehle, B. Werner, *IMRET 6: 6th International Conference on Microreaction Technology* (New Orleans, USA, **2002**), American Institute of Chemical Engineers Pub. No. 164, p. 39.
[290] S. Kiesewalter, *Chem. Rundsch.* **2002**.
[291] S. Kiesewalter, K. M. Russow, T. Stange, C. Balsalobre, P. Boulon, M. Provence, *IMRET 6: 6th International Conference on Microreaction Technology* (New Orleans, USA, **2002**), American Institute of Chemical Engineers Pub. No. 164, p. 135.
[292] R. Zapf, C. Becker-Willinger, K. Berresheim, H. Holz, H. Graser, V. Hessel, G. Kolb, P. Löb, A.-K. Pannwitt, A. Ziogas, *TransIChemE* **2003**, *81*, 721.

Communications



Marine mussels affix themselves to surfaces with a protein-based, cross-linked adhesive. Studies with mussel glue, extracted protein, and peptide models show an $Fe(DOPA)_3$ cross-link, which is key for the generation of this common biological material. For more information, see the Communication by J. J. Wilker and co-workers following pages.

DOI: 10.1002/anie.200352759
© 2004 Wiley-VCH Verlag GmbH & Co. KGaA, Weinheim

Marine Chemistry

Metal-Mediated Cross-Linking in the Generation of a Marine-Mussel Adhesive**

*Mary J. Sever, Jaime T. Weisser, Jennifer Monahan, Shalini Srinivasan, and Jonathan J. Wilker**

Mariners have been contending with the tenacious holdfasts of barnacles and mussels for over 4000 years. These protein-based adhesives exhibit striking materials properties still unmatched by human technology. Such hardened matrices are formed by extensive cross-linking of protein precursors.[1–3] This cross-linking approach to biomaterial synthesis is shared by glues from mussels, limpets, and kelp, cements from barnacles, oysters, and polychaete worms, coral skeletons, and skate egg shell cases.[2,3] In none of these systems, however, is there available a detailed picture of the bonding schemes employed for material construction. For mussel adhesive plaques (Figure 1), posttranslational incorporation of 3,4-dihydroxyphenylalanine (DOPA) into the protein (Scheme 1) is essential for subsequent cross-linking and proper adhesion.[1–3] Other interesting properties of the mussel glues include a transition-metal-ion content (e.g., copper, iron, and zinc)[4,5] up to 100 000 times that found in open ocean waters.[6] Recently we have shown that metal ions, in particular Fe^{III}, bring about curing of adhesive precursors extracted from mussels.[7] To gain insights on bonding of marine adhesives, we present data on mussel glues and related systems indicating that metal–protein interactions participate in the generation of these materials.

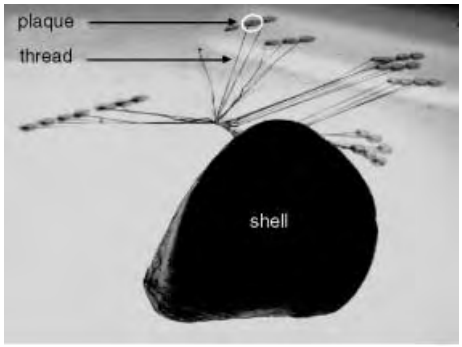
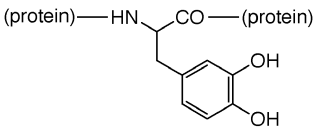


Figure 1. Photograph of a marine mussel adhering to a glass sheet.



Scheme 1. Protein-bound 3,4-dihydroxyphenylalanine (DOPA).

Common blue mussels (*Mytilus edulis*) were collected from coastal Maine and placed on glass sheets in salt water tanks (deionized water and Marine Environment salt) at 6 °C. After deposition of adhesive (Figure 1), mussels and threads were cut free, the adhesive plaques were scraped from the glass, washed with deionized water, and dried under vacuum. Collected plaques were examined by electron paramagnetic resonance spectroscopy (EPR, Figure 2a) at 15 K. This spectrum showed the conspicuous presence of high-spin Fe^{III} centers ($g = 4.239$, 1531 G; $g = g$ factor) and an organic radical ($g = 1.997$, 3249 G), possibly accompanied by weak signals for Cu^{II} or low-spin Fe^{III} centers (2615, 2734, 2904, 3070 G).[8,9]

The DOPA-containing proteins Mefp-1 and Mefp-2, soluble precursors to cured mussel adhesive,[2,3] were extracted from mussel feet prior to cross-linking.[10] A frozen solution of mussel precursor proteins in 10% glycerol showed neither a significant Fe^{III}-ion signal nor any evidence of an organic radical when examined by EPR spectroscopy (Figure 2a). Addition of aqueous iron ions (e.g., $Fe(NO_3)_3$ or $FeCl_3$ at 500 mM, pH ≈ 1.5) to a solution of the soluble adhesive precursor proteins (DOPA concentration of 0.5 mM, pH ≈ 1.5) brought about immediate precipitation of a beige solid which was isolated, washed, and dried. Examination of this solid by EPR spectroscopy displayed signals for an Fe^{III} ion and an organic radical, which showed this spectrum to resemble that of adhesive plaques from live mussels (Figure 2a). Aqueous solutions of $Fe(NO_3)_3$ or $FeCl_3$ showed EPR spectra distinct from all other samples. The radical found in plaques and the iron–protein solid thus appears to arise from Fe^{III}-ion-dependent oxidation of the protein. The highly reactive properties of radical species may provide a pathway to organic cross-links such as a di-DOPA moiety[11] or enable coupling to surfaces and formation of adhesive bonds.

Adhesive plaques were pressed into a KBr pellet for examination by infrared spectroscopy (IR, Figure 2b). Bands for amide I and II (≈1656 and ≈1534 cm^{-1}) were visible along with a cluster (1458–1439 cm^{-1}) attributable to DOPA.[12] Soluble adhesive precursor protein[10] was lyophilized into a colorless solid and investigated by IR spectroscopy (Figure 2b). Similar features were observed when compared to the plaques, however, the protein showed one prominent DOPA band (1456 cm^{-1}). The iron–protein solid exhibited a DOPA band split to 1456 and 1437 cm^{-1}. Such splitting is indicative of metal binding as exemplified by the case of enterobactin, a tris (1,2-dihydroxybenzene) ("catechol") ligand employed in bacterial iron transport.[13] The enterobactin catechol band at 1460 cm^{-1} splits into 1460 and

[*] M. J. Sever, J. T. Weisser, J. Monahan, S. Srinivasan, Prof. J. J. Wilker
Department of Chemistry, Purdue University
560 Oval Drive
West Lafayette, Indiana 47907-2084 (USA)
Fax: (+1) 765-494-0239
E-mail: wilker@purdue.edu

[**] We thank Mark Nilges and Joshua Telser for experimental assistance and valuable discussions regarding EPR. J.J.W. appreciates the generous support provided by an Arnold and Mabel Beckman Foundation Young Investigator Award, a National Science Foundation Faculty Early Career Development (CAREER) Award, and an Alfred P. Sloan Foundation Research Fellowship.

Supporting information for this article is available on the WWW under http://www.angewandte.org or from the author.

 © 2004 Wiley-VCH Verlag GmbH & Co. KGaA, Weinheim DOI: 10.1002/anie.200352759

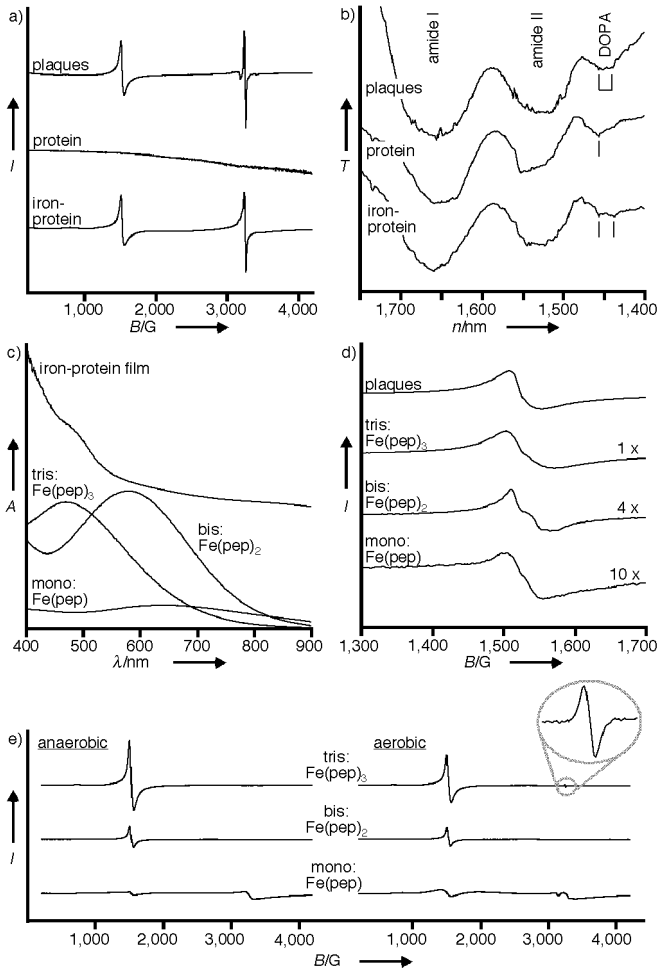


Figure 2. Spectroscopic characterization of marine mussel adhesive plaques and related systems: a) EPR spectra of intact mussel plaques, adhesive precursor protein, and precursor protein precipitated from solution with $Fe(NO_3)_3$. b) IR spectra of plaques, lyophilized precursor protein, and iron–protein solid. c) UV/Vis spectra of an adhesive film prepared from precursor protein reacted with $Fe(NO_3)_3$ and solutions of mono, bis, and tris Fe-AdopaTP peptide complexes, $[Fe(pep)_n]$. The solid spectrum was obtained by overlapping four films. d) EPR spectra of plaques with tris, bis, and mono $[Fe(pep)_n]$ peptide complexes. Vertical scale on spectra were adjusted as indicated to aid comparisons. e) EPR spectra of tris, bis, and mono $[Fe(pep)_n]$ complexes prepared anaerobically and aerobically. An expansion is provided for the radical region of aerobic $[Fe(pep)_3]$, the only sample to exhibit a radical.[15]

1440 cm^{-1} upon binding iron.[13] Thus, the single DOPA band for adhesive precursor protein contrasts with the split bands of the iron-protein solid and whole plaques, which indicates metal binding in the latter two samples.

UV/Vis absorption spectroscopic studies with the DOPA-containing peptide models Ac-Ala-DOPA-Thr-Pro-$CONH_2$ ("AdopaTP") and Ac-Asn-DOPA-Arg-Gly-$CONH_2$ ("NdopaRG")[14] showed strong binding of the DOPA catechol-like side chain to Fe^{III}, but no interaction with Cu^{II}, Zn^{II}, or any other divalent transition-metal ion.[15] In addition to bringing about a focus on iron chemistry, such model studies provide complexes for spectral comparisons with the whole plaque and protein systems. Although poor optical quality of whole plaques prevented us from obtaining a suitable UV/Vis spectrum, the reaction of mussel protein[10] with $Fe(NO_3)_3$ on silanized glass yielded a uniform adhesive film that exhibits absorption at $\approx$470 nm (Figure 2c).[15] A comparison with UV/Vis spectra of peptide models indicated $[Fe(DOPA)_3]$ coordination within this material (Figure 2c). Control experiments with protein alone, $Fe(NO_3)_3$ alone, or bovine serum albumin with $Fe(NO_3)_3$ did not form an adhesive film or show visible-light absorption.

EPR spectra of anaerobic $[Fe(AdopaTP)_n]$ models in 10% glycerol displayed Fe^{III} signals for mono ($n=1$), bis ($n=2$), and tris ($n=3$) complexes, with splitting observed in the bis, $\{Fe(AdopaTP)_2\}$, case ($g\approx4.205$, $\approx$1538 G, Figure 2d). This splitting was also present in the EPR spectra of bis, $\{Fe(L)_2\}$, models prepared with the ligands L = catechol or NdopaRG, but not in tris, $[Fe(L)_3]$, complexes.[15] A lack of such splitting in the EPR spectra of whole plaques and iron–protein solid indicates that bis, $\{Fe(DOPA)_2\}$, cross-links are not present in these samples (Figure 2d). A mono coordination environment in the plaques and iron–protein solid is also unlikely owing to an inability to bring about protein–metal–protein interactions.

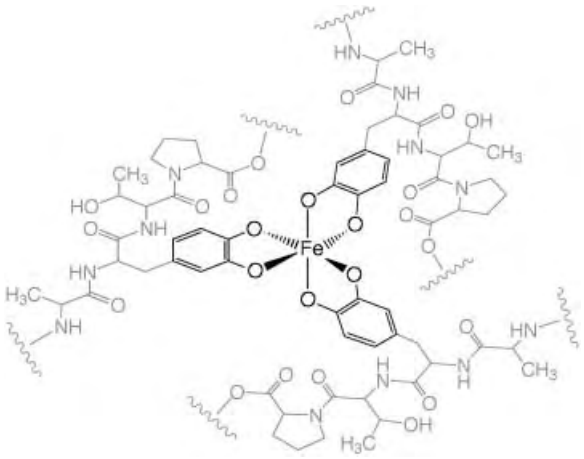
When $[Fe(AdopaTP)_n]$ models were prepared in air, a radical signal was observed ($g=1.989$, 3251 G) in the EPR spectrum of the tris, $[Fe(AdopaTP)_3]$, complex (Figure 2e).[15] No evidence was seen for radical formation in the mono, $\{Fe(AdopaTP)\}$, or bis, $\{Fe(AdopaTP)_2\}$, species in air.[15] Similar results were found when the models were prepared from solutions with excess peptide. Observed peptide oxidation by oxygen and iron from an $[Fe(DOPA)_3]$ complex, as opposed to the bis or mono analogues, is consistent with a greater degree of Fe^{III}- and less Fe^{II}-ion character in the tris coordination environment.[16] Radical generation in the aerobic $[Fe(AdopaTP)_3]$ complex coincided with an Fe^{III}-ion signal ($g=4.209$, 1537 G) of decreased intensity relative to the anaerobic sample (Figure 2e). These data suggest the occurrence of a redox reaction in which ligand oxidation is accompanied by a $Fe^{III} \rightarrow Fe^{II}$-ion reduction. Such intramolecular redox processes are known to occur in metal–catecholate systems.[17]

Although enterobactin and other siderophores have been known for quite some time,[18] metal–catecholate interactions are becoming increasingly conspicuous in biology. Recent findings on the extradiol[19] and intradiol[20,21] catechol dioxygenases may provide further insights on adhesive synthesis. A proposed mechanism for the intradiol catechol dioxygenases begins with an Fe^{III}–catecholate followed by valence tautomerism to a Fe^{II}–semiquinone.[20,21] Subsequent reactivity with oxygen yields a ligand-based radical species for further chemistry.[20,21]

In summary, EPR and IR spectroscopies provide evidence for metal–DOPA interactions in mussel adhesive plaques. An adhesive film was produced by iron curing of extracted protein. Iron in the presence of air oxidized both extracted protein and peptide models to yield products that contain organic radicals. More specifically, insights upon the coordination environment of iron were gained from EPR data in which the Fe^{III} of plaques did not resemble bis, $\{Fe(DOPA)_2\}$, bonding. The adhesive film prepared by reaction of iron and

 © 2004 Wiley-VCH Verlag GmbH & Co. KGaA, Weinheim

protein displayed a UV/Vis spectrum similar to that of the tris, [Fe(AdopaTP)$_3$], model. Finally, only the tris, [Fe(AdopaTP)$_3$], complex underwent oxidation to yield a radical upon exposure to air. When coupled with results showing that Fe^{III} brings about curing of adhesive extracts more than other ions,[7] these data implicate iron to be the key reagent in protein cross-linking for adhesive synthesis. Thus, we propose that the iron center in mussel plaques cross-links three DOPA residues as shown in Scheme 2. Subsequent reaction of this



Scheme 2. Proposed mussel adhesive metal-protein cross-link.

[Fe(DOPA)$_3$] and oxygen brings about protein oxidation, generation of a reactive radical species, and a potential means of coupling to a surface for adhesive bond formation. Mussel glues present the first identified case in which transition metals play an integral role in the generation of a noncrystalline biological material. The impressive properties derived from metal-protein interactions may prove to be a prevalent theme in marine biomaterials such as those of coral reef structures, kelp adhesives, and barnacle cements.

Received: September 1, 2003
Revised: October 10, 2003 [Z52759]

Keywords: bioinorganic chemistry · functional materials · peptidomimetics · proteins · transition metals

[1] T. J. Deming, *Curr. Opin. Chem. Biol.* **1999**, *3*, 100 – 105.
[2] L. M. Rzepecki, J. H. Waite in *Bioorganic Marine Chemistry*, *Vol. 4* (Ed.: P. J. Scheuer), Springer, New York, **1991**, pp. 120 – 148.
[3] J. H. Waite, *Comp. Biochem. Physiol. Part B* **1990**, *97*, 19 – 29.
[4] T. L. Coombs, P. J. Keller, *Aquat. Toxicol.* **1981**, *1*, 291 – 300.
[5] S. G. George, B. J. S. Pirie, T. L. Coombs, *J. Exp. Mar. Biol. Ecol.* **1976**, *23*, 71 – 84.
[6] J. R. Donat, K. W. Bruland in *Trace Elements in Natural Waters* (Eds.: B. Salbu, E. Steinnes), CRC, Ann Arbor, MI, **1995**, pp. 247 – 282.
[7] J. Monahan, J. J. Wilker, *Chem. Commun.* **2003**, 1672 – 1673.
[8] A. Avdeef, S. R. Sofen, T. L. Begante, K. N. Raymond, *J. Am. Chem. Soc.* **1978**, *100*, 5362 – 5370.
[9] A. Gergely, T. Kiss, *Inorg. Chim. Acta* **1976**, *16*, 51 – 59.
[10] J. H. Waite, *Methods Enzymol.* **1995**, *258*, 1 – 20.
[11] L. M. McDowell, L. A. Burzio, J. H. Waite, J. Schaefer, *J. Biol. Chem.* **1999**, *274*, 20293 – 20295.
[12] P. A. Suci, G. G. Geesey, *Langmuir* **2001**, *17*, 2538 – 2540.
[13] V. L. Pecoraro, W. R. Harris, G. B. Wong, C. J. Carrano, K. N. Raymond, *J. Am. Chem. Soc.* **1983**, *105*, 4623 – 4633.
[14] M. J. Sever, J. J. Wilker, *Tetrahedron* **2001**, *57*, 6139 – 6146.
[15] See Supporting Information.
[16] H. K. J. Powell, M. C. Taylor, *Aust. J. Chem.* **1982**, *35*, 739 – 756.
[17] C. G. Pierpont, *Coord. Chem. Rev.* **2001**, *216–217*, 99 – 125.
[18] K. N. Raymond, G. Müller, B. F. Matzanke, *Top. Curr. Chem.* **1984**, *123*, 49 – 102.
[19] T. D. H. Bugg, G. Lin, *Chem. Commun.* **2001**, 941 – 952.
[20] D. D. Cox, L. Que, Jr., *J. Am. Chem. Soc.* **1988**, *110*, 8085 – 8092.
[21] H. G. Jang, D. D. Cox, L. Que, Jr., *J. Am. Chem. Soc.* **1991**, *113*, 9200 – 9204.

 © 2004 Wiley-VCH Verlag GmbH & Co. KGaA, Weinheim

Drug Discovery I

Identification of Potent Ras Signaling Inhibitors by Pathway-Selective Phenotype-Based Screening**

*Oliver Müller, Eleni Gourzoulidou, Mercedes Carpintero, Ioanna-Maria Karaguni, Anette Langerak, Christian Herrmann, Tarik Möröy, Ludger Klein-Hitpaß, and Herbert Waldmann**

Phenotype-based screening of compound libraries utilizes chemistry and biology together at a very early phase of a chemical biological research program and identifies both potential biological targets and hit compounds in one step.[1] The power of the combination of this approach with modern chemistry and biology research techniques was recently demonstrated in the context of chemical genetics research.[2]

[*] Dipl.-Chem. E. Gourzoulidou, Dr. M. Carpintero, C. Herrmann, Prof. Dr. H. Waldmann
Max-Planck-Institut für molekulare Physiologie
Abteilung Chemische Biologie
Otto-Hahn-Strasse 11, 44227 Dortmund (Germany)
and
Universität Dortmund
Fachbereich 3, Organische Chemie
Fax: (+49) 231-133-2499
E-mail: herbert.waldmann@mpi-dortmund.mpg.de
Priv.-Doz. Dr. Dr. O. Müller, I.-M. Karaguni, A. Langerak
Max-Planck-Institut für molekulare Physiologie
Abteilung Strukturelle Biologie, Dortmund (Germany)
Prof. Dr. T. Möröy, Priv.-Doz. Dr. L. Klein-Hitpaß
Institut für Zellbiologie (Tumorforschung)
Universitätsklinikum Essen
Virchowstrasse 173, 45122 Essen (Germany)

[**] We thank Alfred Wittinghofer for his support. This study was supported by the Fonds der Chemischen Industrie and the European Union (Marie Curie Fellowship to M.C.).

Supporting information for this article is available on the WWW under http://www.angewandte.org or from the author.

 © 2004 Wiley-VCH Verlag GmbH & Co. KGaA, Weinheim DOI: 10.1002/anie.200352587

The use of phenotypic change in entire organisms or unbiased cellular systems as a readout may render the identification of the biological target a complicated and laborious endeavor. The study of the reversal or change of the phenotype of a well-defined cellular system carrying known genomic lesions that directly correlate with a particular change in the microscopic phenotype should significantly improve the process of target identification. This improvement should be particularly evident if the genomic lesion affects a protein that acts at a prominent position of a multifaceted and branched signal transduction pathway. Pathway selectivity can be ensured by counterscreening two cell lines carrying lesions in different signaling pathways. In addition, an increase in efficiency can be expected if the compound class to be screened can be regarded as biologically prevalidated and if links from this compound class to the pathways of interest are known. The particular organism or cell type chosen should allow conclusive identification of the biological target while leaving room for identification of additional target proteins. Ideally, the biologically prevalidated compound classes should be based on "privileged structures," that is, structures that mediate binding to multiple biological targets.[3] If these prerequisites are fulfilled, one can expect that even a fairly small compound library will deliver hits with an appreciable rate.[4] Hits from such screens are expected to be of high quality because they have already been through a first round of biological validation. In addition, the library might yield hits for more than one target in a given pathway of interest, and possibly for targets in all pathways screened.

Herein we report the validation of this approach by employment of a phenotypic screen with a cell line activated in the Ras pathway for primary screening, and a cell line activated in the Wnt pathway for counterscreening (Figure 1).

The mutationally activated proto-oncoprotein Ras plays a significant role in the establishment of more than 30% of all human tumors. The development of small molecules that interfere with Ras signaling activity is a promising approach that is being pursued intensively in anticancer drug research.[5]

Antagonization of the interaction between Ras and its downstream effector Raf in the Ras signaling pathway poses a particularly challenging and difficult problem since this prototypical protein–protein interaction covers a large surface area.[5] Despite the attempts made in various intensive screening studies (including high-throughput screening approaches), inhibitors of the Ras–Raf interaction could only be identified in two cases.[6,7] In one of these cases, the metabolite **2** of the nonsteroidal antiinflammatory drug (NSAID) sulindac (**1**; see Table 1) was shown to be a Ras–Raf inhibitor. A compound derived from **1** was found to interfere with the Ras pathway as well, although its molecular target remained unidentified.[6]

Sulindac and its metabolites also influence various other biological phenomena, such as the inflammation-relevant cyclooxygenase pathway, an apoptosis-inducing pathway, and the tumor-relevant Wnt pathway (Figure 1).[8]

The established link between sulindac and the Ras pathway, and the ability of sulindac-derived compounds to interact with different proteins led us to synthesize a compound library with the underlying structure of this NSAID as a guiding scaffold. We analyzed the library for potential inhibitors of the Ras signal transduction pathway by using the phenotype-based strategy delineated above as the primary screen.

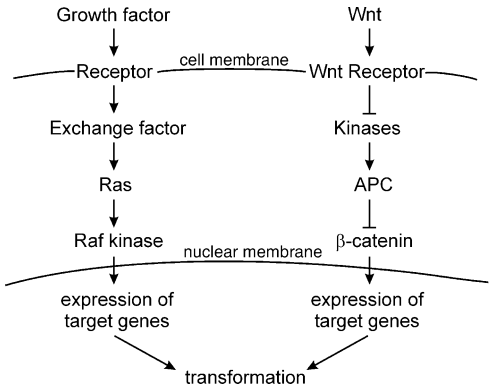
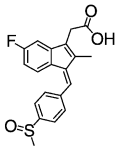
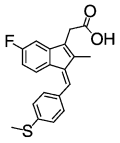
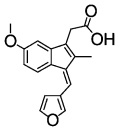
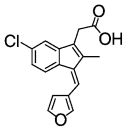
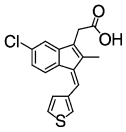
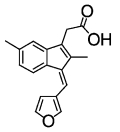
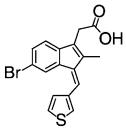
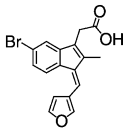
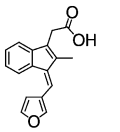
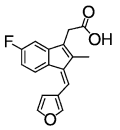


Figure 1. Schematic representation of the Ras (left) and the Wnt (right) pathways. Both pathways start outside the cell with the binding of a signaling protein to a transmembrane receptor. In the case of Ras, this binding leads, through a so-called exchange factor, to the activation of the Ras protein, which itself activates several kinases through the effector Raf kinase. The activation of the Wnt receptor leads to the activation, that is, the negative inhibition of the key signaling protein β-catenin through the action of several kinases and the tumor suppressor protein adenomatous polyposis coli (APC). The two pathways are formed by different proteins and are based in part on different biochemical principles. Nevertheless, both pathways lead to similar cellular effects: activation of target gene expression and transformation, that is, the transition from a normal cell into a tumor cell. By using suitable cell-culture models such as those used in the study described herein, cell transformation can be visualized by light microscopy.

The sulindac-derived compound library was synthesized on a solid support as shown in Scheme 1. Variously substituted indenylacetic acids **3**[9] were attached to 2-chlorotrityl chloride resin (obtained from Calbiochem–Novabiochem, loading 1.08 mmol g^{-1}, or from CBL–Patras, loading 1.6 mmol g^{-1}). Application of the Wang linker led to undesired cleavage of the indenylacetic acids under the basic conditions of the subsequent steps (see below). Resin-bound intermediates **4** were subjected to a Knoevenagel condensation with aromatic aldehydes to yield 188 sulindac analogues **5** in overall yields of 47–98% (calculated based on the initial loading of the resin) after release from the resin under acidic conditions. Critical to the successful execution of the Knoevenagel reaction is the choice of the base, which must be strong enough to mediate the condensation yet must not induce cleavage of the ester. Use of $(i\mathrm{Pr})_2\mathrm{NEt}$ or piperidine in DMF or toluene at up to 100 °C did not induce condensation. In the presence of sodium or potassium *tert*-butoxide the condensation proceeded, but the ester was also cleaved. DBU was used as the base of choice. In the presence of 10 equivalents DBU in DMF or toluene at 60 °C the desired products are formed without unwanted cleavage of the ester. The library was further expanded by subjecting immobilized indenylacetic acids **4** containing a bromine or an iodine atom in the aromatic ring to a Heck, Suzuki, or Sonogashira coupling, followed by the Knoevenagel condensation under

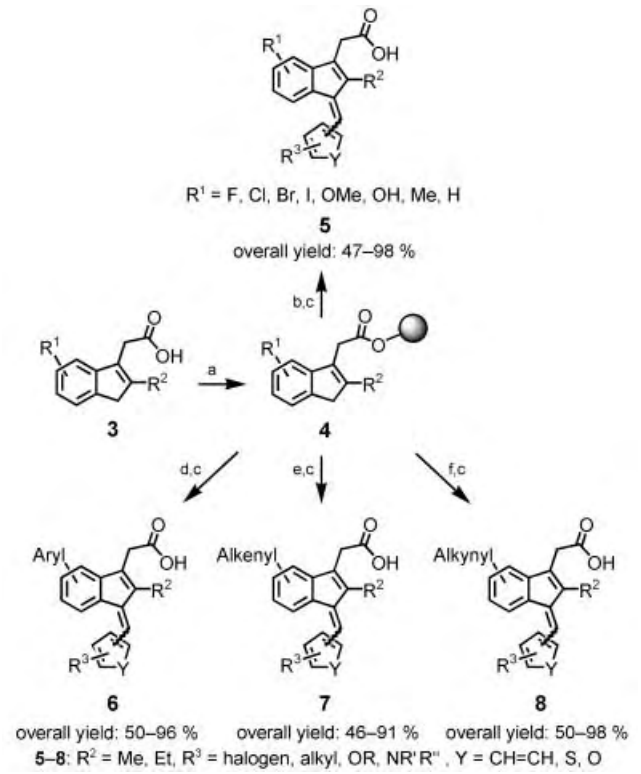
 © 2004 Wiley-VCH Verlag GmbH & Co. KGaA, Weinheim

Table 1: Summary of the major results of the MTT assay and of analysis of cell biological parameters.[a] Data for sulindac (**1**) and its physiological sulfide metabolite **2** are shown for comparison.[6,12]

No.	Compound	Effects on MDCK-F3 cells	IC_{50} MDCK-F3 [μM]	IC_{50} ratio MDCK/MDCK-F3	IC_{50} ratio C57MG-Wnt-1/MDCK-F3
1		no effect	320	1/1	n.a.
2		no effect	200	1/1	n.a.
5a		phenotype reversion, induction of apoptosis	50	10/1	6/1
5b		phenotype reversion, induction of apoptosis	90	3/1	2/1
5c		phenotype reversion	50	2/1	4/1
5d		phenotype reversion, induction of apoptosis	50	4/1	6/1
5e		phenotype reversion	10	30/1	28/1
5f		phenotype reversion, induction of apoptosis	40	2.5/1	6/1
5g		phenotype reversion, induction of apoptosis	50	3/1	6/1
5h		phenotype reversion	50	6/1	9/1

[a] Micromolar concentrations leading to a 50% decrease of the number of living cells are shown. The cell biological effects of 100 μM of each substance are shown. MTT = 3-(4,5-dimethylthiazol-2-yl)-2,5-diphenyltetrazolium bromide; n.a. = not applicable.

the conditions described above (Scheme 1). The conditions of the Pd-catalyzed reactions had to be optimized to obtain high yields. After substantial experimentation it was found that the



Scheme 1. a) 2-Chlorotrityl chloride resin, CH_2Cl_2, $(iPr)_2NEt$, 2 h, 21 °C; b) DBU, DMF or toluene, 60 °C, 16–48 h, aromatic aldehyde R^3CHO; c) 2% CF_3COOH in CH_2Cl_2; d) alkene (5 equiv), $[Pd_2(dba)_3]$ (0.5 equiv), P(*o*-tol)$_3$ (2 equiv), Et_3N/dioxane (1:1), Bu_4NBr (5 equiv), 85 °C, 20 h; e) boronic acid (10 equiv), $[Pd(PPh_3)_4]$ (0.35 equiv); $K_3PO_4 \cdot H_2O$ (20 equiv), DMF, 82 °C, 22 h; f) alkyne (20 equiv), CuI (0.3 equiv), DMF/Et_3N (1:1), PPh_3 (0.5 equiv), $[Pd(PPh_3)_4]$ (0.5 equiv), 85 °C, 20 h. DBU = 1,8-diazabicyclo[5.4.0]undec-7-ene, DMF = dimethylformamide; dba = *trans*,*trans*-dibenzylideneacetone.

Heck reaction proceeded best if $[Pd_2(dba)_3]$ was employed together with P(*o*-tol)$_3$ and nBu_4NBr as the catalyst system and the reaction was carried out in NEt_3/dioxane (1:1) at 85 °C. The Suzuki reaction proceeded efficiently at 82 °C in DMF in the presence of $[Pd(PPh_3)_4]$, and the Sonogashira reaction gave satisfactory results if $[Pd(PPh_3)_4]$ was used as the catalyst in DMF/NEt_3 (1:1) at 85 °C. It was necessary to use an alkene, alkyne, or boronic acid in 5–20-fold excess and to run the reactions for approximately 20 h to obtain acceptable results.

Knoevenagel condensation of the coupling products with different aromatic aldehydes followed by release from the solid support by treatment with acid led to sulindac analogues **6–8**, which have an aromatic substituent, an alkene or an alkyne, attached to the former indene benzene ring (Scheme 1). The desired sulindac analogues **6–8** were obtained in overall yields ranging from around 50% to over 90% by using these reaction sequences. The compounds had a purity in most cases of over 80% immediately after cleavage. Crude products with a purity of less than 80% were purified by flash chromatography on silica gel with ethyl acetate/cyclohexane (1:12 (v/v)) and 1% acetic acid as eluent to increase the purity to more than 80%. In total, 239 compounds were prepared.

 © 2004 Wiley-VCH Verlag GmbH & Co. KGaA, Weinheim

NMR spectroscopic investigation with NOE techniques revealed that, in general, *Z* isomers were predominantly formed in the Knoevenagel reactions, with *Z*/*E* ratios of more than 9/1. The corresponding ethylene glycol esters of selected compounds were prepared (see the Supporting Information).

Phenotype-based screening of the library for in vivo effects was performed with the Madine–Darby canine kidney (MDCK) cell line for primary screening. MDCK cells are immortalized epithelial cells with a large and round phenotype. They grow in a monolayer, attached to each other by regular cell-to-cell contacts (Figure 2). MDCK cells can be

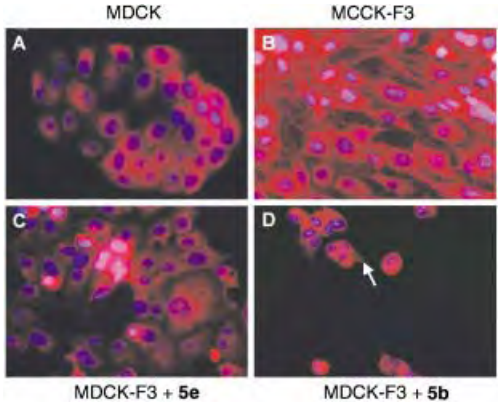


Figure 2. Representative results of the cell biological phenotype assays. Cellular morphology was visualized microscopically by immunostaining of intracellular F-actin fibers (red) and by staining nuclei with the DNA dye 4,6-diamidino-2-phenylindole (blue). A) MDCK cells have a round and regular phenotype. These cells grow attached to each other in epithelium-like, monolayer accumulations. B) MDCK-F3 cells show a spindle-shaped, longitudinal phenotype without regular cell contacts. C) MDCK-F3 cells treated with compound **5e** display a round morphology resembling that of the MDCK mother cells, but the treated cells form cell contacts. This change can be assigned to the reversion of the H-Ras-induced transformation. D) MDCK-F3 cells treated with compound **5b** show morphological signs of apoptosis, such as swollen, round cell bodies, condensed DNA, and apoptotic vesicles (arrow).

transformed by transfection with the H-Ras oncogene. The resulting F3 cells are long and spindlelike and grow in multiple layers without regular cell-to-cell contacts.[10] Since the H-Ras oncogene causes such a significant morphological alteration, cellular morphology can be used as a parameter for measuring the effects of a compound on the activated H-Ras pathway.[6] The specificity of the results obtained in the MDCK/MDCK-F3 assays was evaluated by counterscreening for the effects of all compounds on two cell lines. C57MG cells are murine epithelial mammary gland cells with a round and large phenotype. The transfection of C57MG cells with the Wnt-1 oncogene leads to similar morphological changes as the H-Ras transfection of MDCK cells described above: C57MG cells turn into spindle-shaped C57MG/Wnt-1 cells that grow without any contact inhibition.[11] Three parameters were investigated after incubation of cells with the compounds: In addition to detailed comparative analysis of the morphologies of treated and untreated cells, the influence of each compound on cell proliferation and cell survival was analyzed. These parameters were quantified by using a colorimetric proliferation assay with 3-(4,5-dimethylthiazol-2-yl)-2,5-diphenyltetrazolium bromide (MTT) as an indicator of the number of living cells.[12,13] Cells were also screened for signs of apoptosis. Swollen and vesicle-forming cell bodies and fragmented nuclei were taken as signs of apoptosis. To confirm the apoptotic effects of the compounds, cells were stained with annexin V, which binds to phosphatidylserine on the outer plasma membrane leaflet of cells in the early phases of apoptosis.[14,15]

In total, 189 compounds were subjected to the primary screen and analyzed for their ability to return the phenotype of MDCK-F3 cells to the phenotype of MDCK cells (Figure 2) and to induce apoptosis, as well as for their effect on the survival of Ras-transformed MDCK-F3 cells and C57MG/Wnt-1 cells in the MTT assay relative to the survival of the untransformed parent cell lines.

Compounds were scored as positive hits and selected for further analysis if they a) induced the reversion of the transformed phenotype of MDCK-F3 cells to the phenotype of MDCK cells or induced apoptosis, b) decreased the number of living cells by 50% at a concentration at least two–threefold lower when applied to MDCK-F3 cells than that required for MDCK cells, and c) showed at least two–threefold lower cytoxicity with both C57MG/Wnt-1 and C57MG cells than with MDCK and MDCK-F3 cells (Table 1; Figure 3).

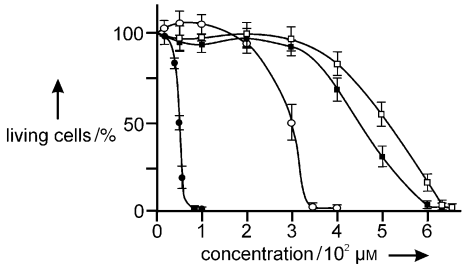


Figure 3. Representative cell survival and proliferation assay. The curves show the dependence of the percentage of living cells on the concentration of compound **5h**. H-Ras-transformed MDCK-F3 cells (filled circles) are more sensitive to compound **5h** than untransformed MDCK cells (open circles), which indicates that the compound affects the H-Ras pathway. C57MG-Wnt1 (filled squares) and C57MG cells (open squares), which were used for counterscreening in a control experiment, showed even lower sensitivity to **5h**.

Of all the tested compounds, 23 fulfilled the above criteria. The most promising compounds were **5a**–**5h** (see Table 1 and Figure 3). Closer inspection of the screening results reveals an initial structure–activity relationship for the compounds that fulfil the biological criteria. The most active compounds, **5a**–**5h**, carry a small substituent in the 5- or 6-position of the indenylacetic acid part of the molecule and a methyl group on the five-membered ring. The arylidene substituent should preferably be a five-membered electron-rich aromatic ring. Only carboxylic acids were active.

Taken together, the results demonstrate that phenotype-based pathway-selective screening provides new small-mole-

 © 2004 Wiley-VCH Verlag GmbH & Co. KGaA, Weinheim

cule inhibitors of tumor-relevant pathways with high fidelity. Only a fairly small compound collection, one screen, and one counterscreen were employed in our investigation. The cell-biological screening and analysis of the sulindac-derived compound library yielded eight compounds with the desired profile. This result amounts to a hit rate of above 4%, a value that is entirely acceptable. The most active compound **5e** had an IC_{50} value of 10 μM in the cellular cytotoxicity assay and was 30 times more active than the parent molecule sulindac.

The results recorded for the phenotypic screen certainly reflect the fact that the underlying structure chosen for the compound library was based on that of sulindac, a compound whose influence on the Ras pathway had already been established and that can be regarded as biologically prevalidated. These results reinforce the notion forwarded above that biologically prevalidated compound classes should be used preferentially in chemical biology investigations in general, and in phenotype-based screens in particular, to obtain high hit rates.

In addition to high hit rates and hit compounds with significantly higher cellular activity than is often obtained with other methods, our results prove that phenotype screening based on a branched signaling pathway can deliver compounds that affect the pathway by acting on different targets. In the following paper,[16] we demonstrate that the majority of the compounds shown in Table 1 interfere with the Ras–Raf interaction. Such a screen may additionally yield compounds that target the pathway employed for counterscreening,[17] which renders the entire library synthesis, as well as the biological and biochemical investigations, very efficient.

Received: August 7, 2003 [Z52587]

Keywords: bioorganic chemistry · combinatorial chemistry · library screening · medicinal chemistry · signal transduction

[1] Review: B. R. Stockwell, *Neuron* **2002**, *36*, 559–562.
[2] See, for example, a) T. U. Mayer, T. M. Kapoor, S. J. Haggarty, R. W. King, S. L. Schreiber, T. J. Mitchison, *Science* **1999**, *286*, 971–974; b) S. Hotha, J. C. Yarrow, J. G. Yang, S. Garrett, K. V. Renduchintala, T. U. Mayer, T. M. Kappor, *Angew. Chem.* **2003**, *115*, 2481–2484; *Angew. Chem. Int. Ed.* **2003**, *42*, 2379–2382.
[3] B. E. Evans, K. E. Rittle, M. G. Bock, R. M. DiPardo, R. M. Freidinger, W. L. Whitter, G. F. Lundell, D. F. Veber, P. S. Anderson, R. S. L. Chang, V. J. Lorri, D. J. Cerino, T. B. Chen, P. J. Kling, K. A. Kunkel, J. P. Sprinter, J. Hirshfield, *J. Med. Chem.* **1988**, *31*, 2235–2246.
[4] R. Breinbauer, I. R. Vetter, H. Waldmann, *Angew. Chem.* **2002**, *114*, 3002–3015; *Angew. Chem. Int. Ed.* **2002**, *41*, 2879–2890.
[5] Reviews: a) H. Waldmann, A. Wittinghofer, *Angew. Chem.* **2000**, *112*, 4360–4383; *Angew. Chem. Int. Ed.* **2000**, *39*, 4192–4214; b) J. Downward, *Nat. Rev. Cancer* **2002**, *3*, 11–22.
[6] a) C. Herrmann, C. Block, C. Geisen, K. Haas, C. Weber, G. Winde, T. Moroy, O. Müller, *Oncogene* **1998**, *17*, 1769–1776; b) I. M. Karaguni, P. Herter, P. Debruyne, S. Chtarbova, A. Kasprzynski, U. Herbrand, M. R. Ahmadian, K. H. Glusenkamp, G. Winde, M. Mareel, *Cancer Res.* **2002**, *62*, 1718–1723.
[7] J. Kato-Stankiewicz, I. Hakimi, G. Zhi, J. Zhang, I. Serebriiskii, L. Guo, H. Edamatsu, H. Koide, S. Menon, R. Eckl, S. Sakamuri, Y. Lu, Q.-Z. Chen, S. Agarwal, W. R. Baumbach, E. A. Golemis, F. Tamanoi, V. Khazak, *Proc. Natl. Acad. Sci. USA* **2002**, *99*, 14398–14403.
[8] a) M. J. Thun, S. J. Henley, C. Patrono, *J. Natl. Cancer Inst.* **2002**, *94*, 252–266; b) E. T. Goluboff, *Expert Opin. Invest. Drugs* **2001**, *10*, 1875–1882; c) I.-M. Karaguni, M. Carpintero, E. Gourzoulidou, L. Klein-Hitpaß, T. Möröy, H. Waldmann, O. Müller, unpublished work.
[9] a) T.-Y. Shen, B. E. Witzel, H. Jones, B. O. Linn, R. B. Greenwald (Merck and Co.), DE 2039426, **1971** [*Chem. Abstr.* **1971**, *74*, 141379]; b) A. Bhattacharya, B. Segmuller, A. Ybarra, *Synth. Commun.* **1996**, *26*, 1775–1784.
[10] J. Behrens, M. M. Mareel, F. M. Van Roy, W. Birchmeier, *J. Cell Biol.* **1989**, *108*, 2435–2447.
[11] H. Shimizu, M. A. Julius, M. Giarre, Z. Zheng, A. M. Brown, J. Kitajewski, *Cell Growth Differ.* **1997**, *8*, 1349–1358.
[12] I. M. Karaguni, K. H. Glusenkamp, A. Langerak, C. Geisen, V. Ullrich, G. Winde, T. Möröy, O. Müller, *Bioorg. Med. Chem. Lett.* **2002**, *12*, 709–713.
[13] F. Denizot, R. Lang, *J. Immunol. Methods* **1986**, *89*, 271–277.
[14] S. J. Martin, C. P. Reutelingsperger, A. J. McGahon, J. A. Rader, R. C. van Schie, D. M. LaFace, D. R. Green, *J. Exp. Med.* **1995**, *182*, 1545–1556.
[15] M. van Engeland, L. J. Nieland, F. C. Ramaekers, B. Schutte, C. P. Reutelingsperger, *Cytometry* **1998**, *31*, 1–9.
[16] H. Waldmann, I. M. Karaguni, M. Carpintero, E. Gourzoulidou, C. Herrmann, C. Brockmann, H. Oschkinat, O. Müller, *Angew. Chem.* **2004**, *116*, 460; *Angew. Chem. Int. Ed.* **2004**, *43*, 454 (following article in this issue).
[17] H. Waldmann, O. Müller, unpublished results.

 © 2004 Wiley-VCH Verlag GmbH & Co. KGaA, Weinheim

Drug Discovery II

Sulindac-Derived Ras Pathway Inhibitors Target the Ras–Raf Interaction and Downstream Effectors in the Ras Pathway**

*Herbert Waldmann, Ioanna-Maria Karaguni, Mercedes Carpintero, Eleni Gourzoulidou, Christian Herrmann, Christoph Brockmann, Hartmut Oschkinat, and Oliver Müller**

In the preceding article[1] we introduced a method to synthesize a library of compounds structurally based on the nonsteroidal antiinflammatory drug (NSAID) sulindac (**1**,

[*] Dr. I.-M. Karaguni, Prof. Dr. C. Herrmann, Priv.-Doz. Dr. O. Müller
Max-Planck-Institut für molekulare Physiologie
Abteilung Strukturelle Biologie
Otto-Hahn-Strasse 11, 44227 Dortmund (Germany)
Fax: (+49) 231-133-2199
E-mail: oliver.mueller@mpi-dortmund.mpg.de
Prof. Dr. H. Waldmann, Dr. M. Carpintero,
Dipl.-Chem. E. Gourzoulidou
Max-Planck-Institut für molekulare Physiologie
Abteilung Chemische Biologie, Dortmund (Germany)
Dr. C. Brockmann, Prof. Dr. H. Oschkinat
Forschungsinstitut für molekulare Pharmakologie
Berlin (Germany)

[**] We thank Alfred Wittinghofer for his support. This study was supported by the Fonds der Chemischen Industrie and the European Union (Marie Curie Fellowship to M.C.).

 © 2004 Wiley-VCH Verlag GmbH & Co. KGaA, Weinheim DOI: 10.1002/anie.200353089

Table 1). Phenotype-based pathway-selective screening revealed that several members of the library affect the Ras signaling pathway.

In the study described herein, we investigated whether the identified compounds directly affect the Ras protein and its major activities, with the aim of determining the biochemical mechanism responsible for the measured cellular effects.

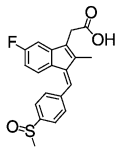
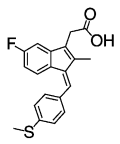
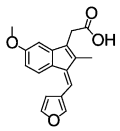
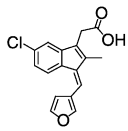
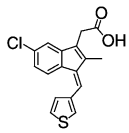
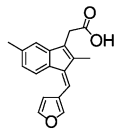
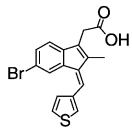
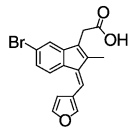
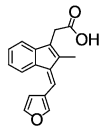
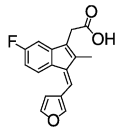
The eight library members with the highest differences between the effective concentration for activity on MDCK-F3 (MDCK = Madine–Darby canine kidney) cells and the effective concentration with MDCK cells were tested to investigate their level of inhibition of the Ras pathway and of the Ras protein in further detail (Table 1). We performed biochemical assays to determine whether these compounds inhibit the interaction of the Ras protein with its major effector Raf. We carried out an NMR analysis of the most active compound and found that this substance does inhibit the Ras–Raf interaction by direct binding to the Ras protein. Next, we showed that four of the new compounds inhibit the activation of the effector protein MAP kinase, which is located downstream of the Ras protein in the signaling pathway.

The oncogenic Ras protein cycles between a bound inactive guanine diphosphate (GDP) and a bound active guanine triphosphate (GTP) state (Figure 1). Active RasGTP can bind and activate the main effector Raf kinase. The activated Raf kinase phosphorylates, and thereby activates, other downstream kinases, of which MAP kinase is the most prominent. This cascade leads to the known cellular effects of the Ras protein, that is, activation of cell proliferation and cell transformation.

To identify potential inhibitors of the Ras–Raf interaction we tested the compounds in a quantitative biochemical assay. This assay is based on the finding that Raf binding lowers the dissociation rate of the RasGTP complex (Figure 1).[2] This so-called guanine nucleotide dissociation (GDI) effect can be quantified spectroscopically by using fluorescently labeled nucleotides. The GDI effect was measured in the presence of the active compounds to look for hints of a possible influence of the compounds on the binding of Raf to RasGTP. Compounds that lower the GDI effect are regarded as inhibitors of the interaction between Raf and RasGTP (Figure 2). Six compounds were found in this assay to inhibit the RasGTP–Raf interaction. Compound **5g** had no effect. Compound **5a** absorbs light at the wavelength applied for fluorescence excitation, which renders its influence on the Ras–Raf interaction undetectable. This compound could therefore not be investigated. The concentrations of the other compounds leading to half maximal inhibition (IC_{50}) ranged between 100 μM and 450 μM, with one exception: compound **5h** inhibited the RasGTP–Raf interaction with an IC_{50} value of 30 μM, which indicates that it has the strongest effect of the tested compounds.

We analyzed the direct interaction of the Ras protein bound to nonhydrolyzable GppNHp (p = phoshpate) with sulindac sulfide (**2**) and **5h** by NMR spectroscopy. ^{15}N HSQC spectra of 50-μM solutions of the protein were recorded in the absence of ligand and with a 300 μM solution of **2** or 290 μM solution of **5h**. HSQC assignments were taken from the study of Ito et al.[3] The binding of **2** was detected by line broadening in the 1D ^{1}H NMR spectrum of a 300 μM solution of the compound in the presence of a 50 μM solution of the protein, compared to the spectrum in the absence of protein (Figure 3A). Few changes in the ^{15}N HSQC spectrum of the

Table 1: Properties of the eight compounds found in the previous cellular screens to have the strongest activity.

No.[a]	Compound	IC_{50} Ras–Raf interaction[b] [μM]	MAPK phosphorylation[c]
1		no effect	no effect
2		210	inhibited
5a		not detectable (absorption by compound)	no effect
5b		180	inhibited
5c		100	inhibited
5d		160	inhibited
5e		220	n.a.[d]
5f		450	n.a.[d]
5g		no effect	n.a.[d]
5h		30	inhibited

[a] The compounds are numbered according to the numbering in the accompanying article.[1] [b] IC_{50} values for inhibition of the RasGTP–Raf interaction. [c] MAPK = mitogen-activated protein kinase. [d] n.a. = not analyzed.

 © 2004 Wiley-VCH Verlag GmbH & Co. KGaA, Weinheim

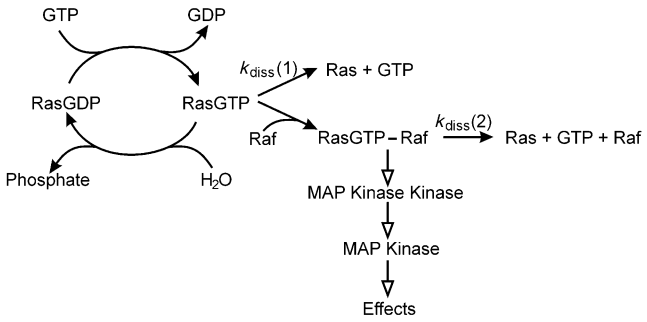


Figure 1. Simplified scheme of the Ras signaling pathway. The Ras protein is activated by the exchange of the bound guanine nucleotide GDP for GTP, and inactivated by the hydrolysis of the bound GTP. Active RasGTP can bind to the effector kinase Raf. The RasGTP–Raf complex activates the downstream effector MAP kinase kinase by phosphorylation (open arrowheads). MAP kinase kinase itself phosphorylates and thereby activates MAP kinase. Phosphorylated MAP kinase can phosphorylate further downstream effectors, which finally leads to the known effects of Ras signaling, such as cell proliferation and transformation. Remarkably, binding of Raf to RasGTP stabilizes the binding of GTP to Ras, which results in a dissociation rate $k_{diss}(2)$ of the RasGTP–Raf complex that is significantly lower than the dissociation rate $k_{diss}(1)$ of RasGTP. This effect is known as the guanine nucleotide dissociation inhibition effect of Raf. We measured the dissociation rates by using fluorescently labeled guanine nucleotides and used the results to identify new inhibitors of the interaction between RasGTP and Raf.

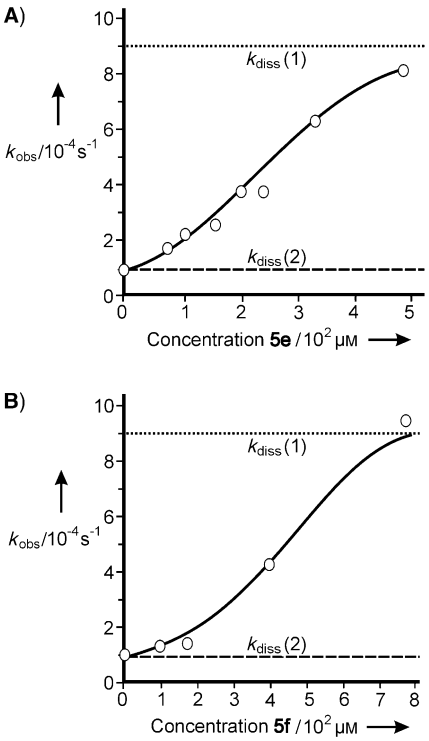


Figure 2. Representative data showing the influence of the new compounds on the RasGTP–Raf interaction. The graphs show the dissociation rate constant of the RasGTP–Raf complex (k_{obs}) as a function of the concentrations of compounds **5e** (A) or **5f** (B), respectively. The nucleotide dissociation rate constant $k_{diss}(1)$ for RasGTP (dotted line) is significantly higher than the dissociation rate constant for RasGTP–Raf ($k_{diss}(2)$, dashed line). The dissociation rate of the RasGTP–Raf complex increases with increasing concentrations of the test compounds. At concentrations higher than 500 μM **5e** or 700 μM **5f**, k_{obs} reaches the value of the dissociation rate constant of RasGTP (dotted line). At these concentrations, only the dissociation rate of RasGTP is measured since the interaction of Raf with RasGTP is inhibited almost completely.

protein could be observed upon addition of ligand (Figure 3B). Small, but significant, shifts were observed for the resonances corresponding to amino acids K16, V29, and Y40. The position of K16, which is located close to the GppNHp nucleotide bound in the active site of Ras, is shown in Figure 3D. The chemical shift of the signal of I163 depends on the concentration of dimethylsulfoxide used (data not shown). Previous structural studies have shown that the Raf-binding site of Ras is close to its GTP-binding site and includes the switch I region (amino acid (aa) 30–37).[4] The switch I and switch II (aa 59–63) regions of Ras do not produce signals in the ^{15}N HSQC spectrum.[3] From our observation by ^{1}H NMR spectroscopy of the binding of **2** and the small changes in the ^{15}N HSQC spectrum for signals of residues close to switch I upon binding, we conclude that the binding occurs almost exclusively in the switch regions of Ras. The binding is thus poor but still observable by HSQC spectroscopy. The same situation occurs with compound **5h** (Figure 3C), which we thus expect to bind to a similar region of the protein to that bound by **2**. The direct binding of the two compounds to the Raf-binding site in the Ras protein further supports the model in which their effects on the Ras signaling pathway are the result of direct interference with the RasGTP–Raf interaction.

Next we investigated whether compounds **5a–5d** and **5h** affect the activation of one of the major downstream targets of Ras. We incubated H-Ras-transfected MDCK-F3 cells with the compound to be tested and analyzed the level of MAP kinase phosphorylation. We measured the level of phosphorylated MAP kinase by immunoblot using an antibody specific for phosphorylated MAP kinase. In a parallel control experiment the total amount of MAP kinase was visualized by using an antibody that detects MAP kinase independently of its phosphorylation status. Remarkably, **5b–5d** and **5h** decreased the amount of activated phosphorylated MAP kinase (Figure 4). Application of compound **5a** did not lead to a significant decrease in the level of phosphorylated MAP kinase.

In this study the biochemical targets of the newly discovered Ras pathway inhibitors were narrowed down to a few possibilities. In the light of the suggestion that sulindac (**1**) itself influences the Ras pathway by interfering with the interaction between Ras and its downstream effector Raf kinase, the compounds were subjected to an assay that monitors inhibition of the RasGTP–Raf interaction. Six of the eight compounds under investigation inhibited the interaction. In addition, NMR data strongly suggest that this inhibition is a result of direct interaction of the compounds with the Ras protein. While sulindac (**1**) itself showed no inhibitory activity and sulindac sulfide (**2**) showed only very weak activity ($IC_{50} = 210$ μM), the most efficient inhibitor **5h** was significantly more active than the parent compound. Ras interacts with the Raf kinase in a prototypical protein–protein

 © 2004 Wiley-VCH Verlag GmbH & Co. KGaA, Weinheim

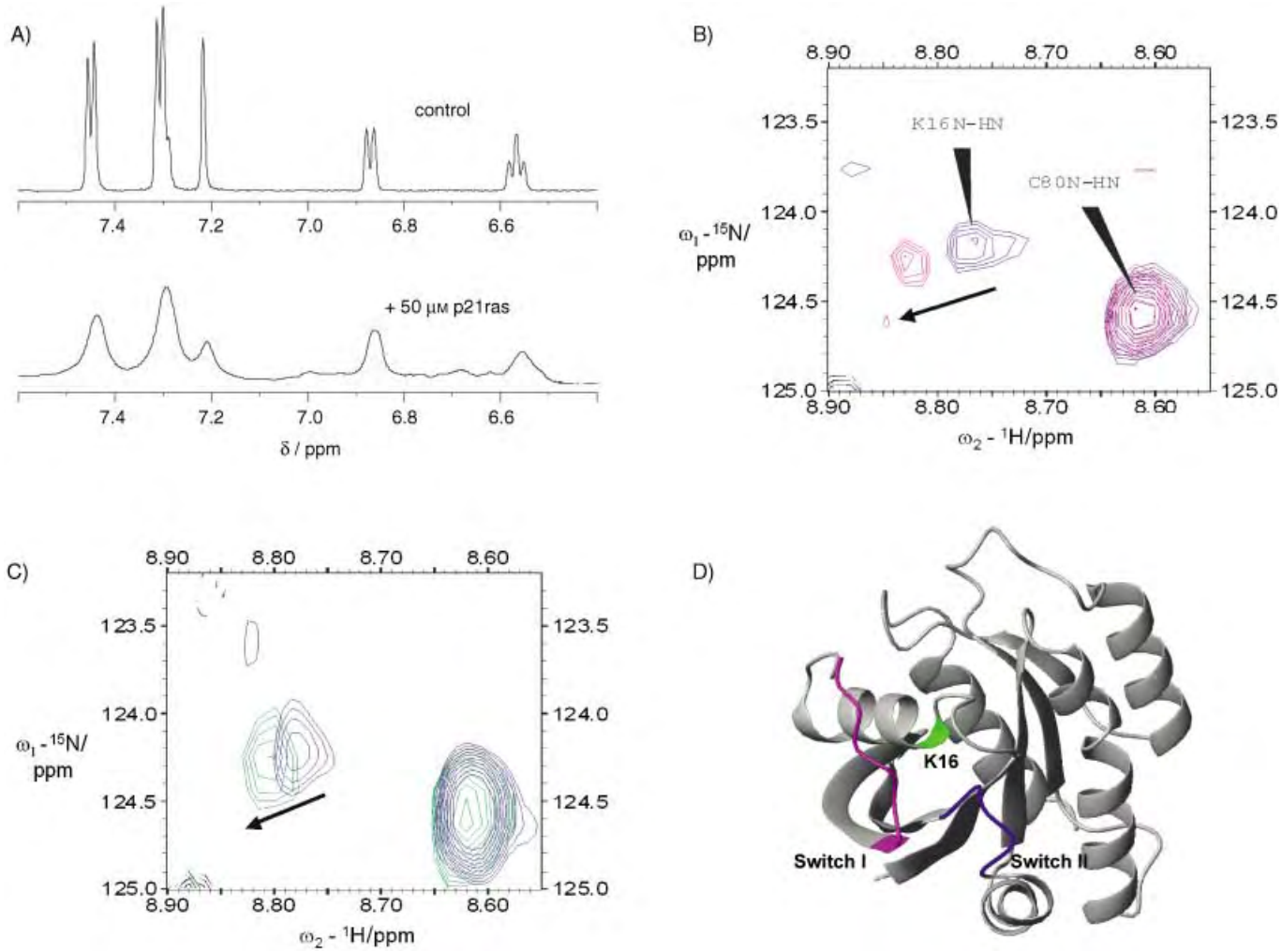


Figure 3. Sulindac sulfide (**2**) and **5h** bind directly to Ras. A) Part of the ^{1}H NMR spectrum of 300 μM **2** in the absence (control) and presence of 50 μM Ras. The significant line broadening in the presence of the protein indicates strong binding. B) Parts of the HSQC spectra of Ras with and without **2**. The reference spectrum of 50 μM Ras without ligand is shown in blue. The spectrum plotted in magenta was recorded in the presence of 300 μM **2**. C) Parts of the HSQC spectra of Ras with and without **5h**. The spectrum plotted in green was recorded in the presence of 290 μM **5h**. D) Spatial relationship of the switch regions I (magenta) and II (blue) in Ras, which are not observable in the HSQC spectra, to the location of K16 (green). The structure was taken from Pai et al.[6]).

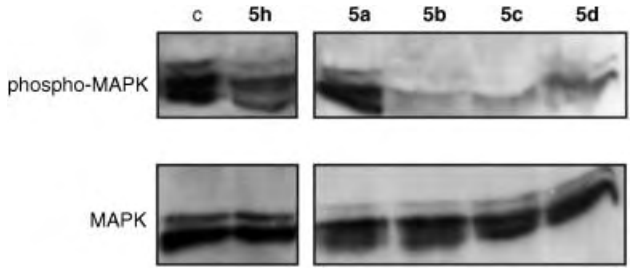


Figure 4. Immunoblot analysis of the levels of phosphorylated MAP kinase (phospho-MAPK) and of total MAPK (bottom) carried out by using an antibody specific for phospho-MAPK and one that binds all MAPK, respectively. The intensities of the bands correlate with the protein levels. The tested compounds do not influence the total level of MAPK. Compounds **5b**, **5c**, **5d**, and **5h** reduce the level of phospho-MAPK. Lysates from MDCK-F3 cells treated with the indicated compound (100 μM) were used for analysis; lysates from untreated MDCK-F3 cells were used as a control (c).

interaction over a very large contact region. Thus, interference with the RasGTP–Raf interaction by using a small molecule is expected to be very difficult. Only very recently was success in this area reported.[5] Our findings may open up a new avenue of research in this area. The results were confirmed in a structural analysis of the interaction between compound **5h** and Ras. NMR data show that **5h** binds to a region of Ras that is important for the interaction with Raf. Finally, we showed that four of the six compounds that inhibit the interaction between Ras and Raf kinase decrease the intracellular level of phosphorylated MAP kinase significantly. Compound **5a** did not decrease MAP kinase phosphorylation. Nevertheless, this compound reverses Ras-induced transformation, which indicates that its cellular target might be a protein located downstream of MAP kinase.

Together with the data detailed in the previous paper, the results of our investigation prove that phenotype-based

 © 2004 Wiley-VCH Verlag GmbH & Co. KGaA, Weinheim

pathway-selective screening followed by detailed biochemical validation provides new small-molecule inhibitors of a tumor-relevant pathway with high fidelity. Only a fairly small compound collection, two cellular screens, and two biochemical experiments were employed in our investigation. This very limited screening effort, however, led to the identification of new inhibitors of the Ras–Raf interaction that are up to 30-fold more active than the parent structure of the compound library, and to a new Ras-pathway inhibitor with a target potentially located downstream of MAP kinase. Our results open up new avenues for research in which signaling pathways are addressed through chemical–biological or medicinal–chemical investigations. The application of similar strategies to other compound classes should reveal new inhibitors of other signal transduction pathways.

Received: August 7, 2003 [Z53089]

Keywords: bioorganic chemistry · medicinal chemistry · NMR spectroscopy · Ras proteins · signal transduction

[1] O. Müller, E. Gourzoulidou, M. Carpintero, I. M. Karaguni, A. Langerak, C. Herrmann, T. Möröy, H. Waldmann, *Angew. Chem.* **2004**, *116*, 456; *Angew. Chem. Int. Ed.* **2004**, *43*, 450.

[2] Herrmann, G. A. Martin, A. Wittinghofer, *J. Biol. Chem.* **1995**, *270*, 2901 – 2905.

[3] Y. Ito, K. Yamasaki, J. Iwahara, T. Terada, A. Kamiya, M. Shirouzu, Y. Muto, G. Kawai, S. Yokoyama, E. D. Laue, M. Walchli, T. Shibata, S. Nishimura, T. Miyazawa, *Biochemistry* **1997**, *36*, 9109 – 9119.

[4] T. Terada, Y. Ito, M. Shirouzu, M. Tateno, K. Hashimoto, T. Kigawa, T. Ebisuzaki, K. Takio, T. Shibata, S. Yokoyama, B. O. Smith, E. D. Laue, J. A. Cooper, *J. Mol. Biol.* **1999**, *286*, 219 – 232.

[5] J. Kato-Stankiewicz, I. Hakimi, G. Zhi, J. Zhang, I. Serebriiskii, L. Guo, H. Edamatsu, H. Koide, S. Menon, R. Eckl, S. Sakamuri, Y. Lu, Q. Z. Chen, S. Agarwal, W. R. Baumbach, E. A. Golemis, F. Tamanoi, V. Khazak, *Proc. Natl. Acad. Sci. USA* **2002**, *99*, 14398 – 14403.

[6] E. F. Pai, U. Krengel, G. A. Petsko, R. S. Goody, W. Kabsch, A. Wittinghofer, *EMBO J.* **1990**, *9*, 2351 – 2359.

 © 2004 Wiley-VCH Verlag GmbH & Co. KGaA, Weinheim

Charged Nanocolloids

Spontaneous Assembly of a Monolayer of Charged Gold Nanocrystals at the Water/Oil Interface

*Francois Reincke, Stephen G. Hickey, Willem K. Kegel, and Daniel Vanmaekelbergh**

Novel materials based on 2D and 3D arrays of nanocrystalline building blocks can be prepared from colloidal suspensions by controlled processing. There is a large effort in this field due to the exciting electrical,[1–3] magnetic[4,5] and optical[6,7] properties of such systems, which can be tuned by the size of the building blocks and the interactions between them. Ordered arrays of uncharged, sterically stabilized nanocrystals have been successfully obtained by a subtle destabilization of the suspension[8] or by assembly at a liquid/air[9–11] or liquid/liquid interface.[12] There is, however, an important class of suspensions that are stable owing to the nanocrystal surface charge. Assembly of uncapped, charged nanocrystals into arrays is considerably more difficult as destabilization of a suspension usually leads to uncontrolled coagulation.[13] Herein, we report surprising results that may lead to novel routes for the controlled fabrication of materials from charge-stabilized nanocrystal colloids. We have observed that gold nanocrystals spontaneously form a monolayer at the water/oil interface if the surface charge of the nanocrystals is gradually reduced. The separation between the nanocrystals in the layer is smaller than the width of the diffuse electrical double layer. Nevertheless, coagulation of the particles into clumps does not occur. The monolayers are remarkably robust and can be easily transferred to substrates, opening the way to technological applications. The spontaneous 2D assembly of charged nanocrystals is qualitatively described in terms of a reduction of the water/oil interfacial energy upon particle adsorption counteracted by electrostatic repulsion in the film.

Suspensions of sterically stabilized and supposedly uncharged gold nanocrystals have been used as model systems for the study of self-assembly. A wealth of gold nanocrystal structures have been reported[9,11,14] and their optoelectrical properties are still under investigation. The synthesis of charge-stabilized gold sols is well established. The processing of such sols has been focused on the capping of charged nanocrystals with organic molecules to allow transfer to a

[*] F. Reincke, Dr. S. G. Hickey,[+] Prof. Dr. D. Vanmaekelbergh
Physics and Chemistry of Condensed Matter
Debye Institute, Utrecht University, 3508 TA Utrecht
(The Netherlands)
Fax: (+31) 30-253-2403
E-mail: daniel@phys.uu.nl
Dr. W. K. Kegel
van't Hoff Laboratory for Physical and Colloid Chemistry
Debye Institute, Utrecht University, 3508 TA Utrecht The Netherlands)
[+] Present address:
Institut für Physikalische Chemie, Universität Hamburg
Bundesstrasse 45, 20146 Hamburg (Germany)

 © 2004 Wiley-VCH Verlag GmbH & Co. KGaA, Weinheim DOI: 10.1002/anie.200352339

nonaqueous phase. In addition, the assembly of these nanocrystals into molecular-like structures, covalently linked by organic bridges[15] or DNA strands[16] have been reported. Herein, we report the formation of an interfacial monolayer of charged gold nanocrystals from an aqueous gold sol upon gradual reduction of the surface charge.

Aqueous suspensions of charge-stabilized gold nanocrystals with diameters between 8 and 40 nm were prepared according to the method of Frens.[17] The gold nanocrystals in the suspension have a negative surface charge due to the adsorption of citrate and gold-chloride anions.[18] We determined the surface-charge density by measuring of the nanocrystal diffusion coefficient with an ac-electrophoresis method (Figure 1a). The as-prepared gold nanocrystals have a surface-charge density of about $-0.010\ C\,m^{-2}$. It can be seen in Figure 1a that the addition of ethanol to the sol gradually decreases the surface charge, very likely because of competitive adsorption of ethanol molecules,[19] which displace the citrate or gold-chloride anions from the gold surface. About half the original charge density is preserved upon further addition of ethanol, and the gold sol remains stable. However, when a layer of heptane is introduced above this solution, gold nanocrystals quickly adsorb at the water/heptane interface. A vial containing the alcohol-free aqueous gold sol (pink) covered with an immiscible layer of heptane (colorless) is shown in Figure 1b (left). Upon addition of ethanol to the gold sol, a blue layer with a metallic aspect is immediately formed at the water/oil interface (Figure 1b, centre and

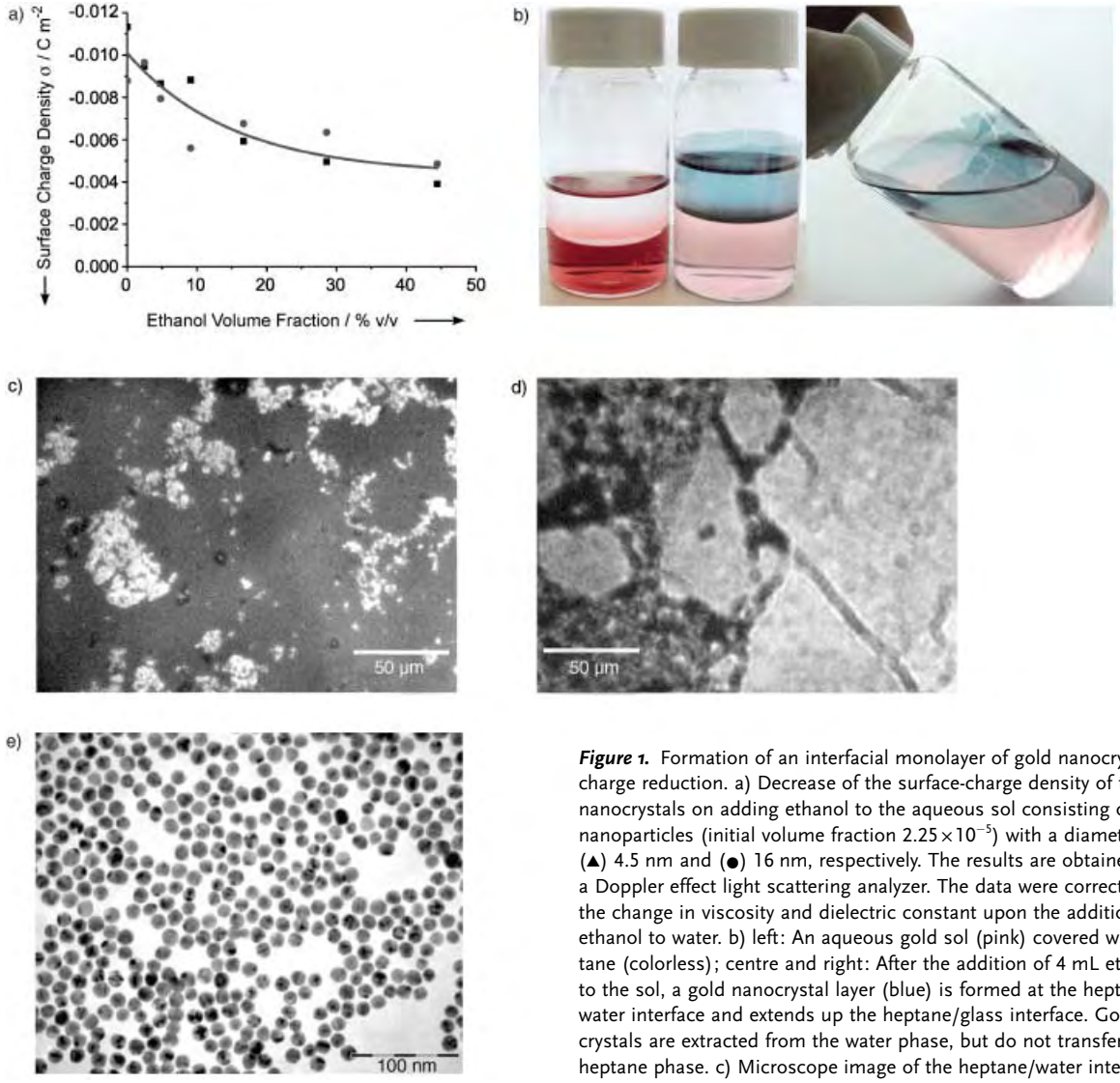


Figure 1. Formation of an interfacial monolayer of gold nanocrystals by charge reduction. a) Decrease of the surface-charge density of the gold nanocrystals on adding ethanol to the aqueous sol consisting of Au nanoparticles (initial volume fraction 2.25×10^{-5}) with a diameter of (▲) 4.5 nm and (●) 16 nm, respectively. The results are obtained with a Doppler effect light scattering analyzer. The data were corrected for the change in viscosity and dielectric constant upon the addition of ethanol to water. b) left: An aqueous gold sol (pink) covered with heptane (colorless); centre and right: After the addition of 4 mL ethanol to the sol, a gold nanocrystal layer (blue) is formed at the heptane/water interface and extends up the heptane/glass interface. Gold nanocrystals are extracted from the water phase, but do not transfer to the heptane phase. c) Microscope image of the heptane/water interface after addition of 1.7 mL ethanol to 10 mL of gold sol covered with 5 mL of heptane: the coverage is low and islands of gold nanocrystals are visible. d) Microscope image of the heptane/water interface after addition of 3.8 mL of ethanol to 10 mL of gold sol: the gold nanocrystals form large domains (>50 μm) that consist of a dense layer of nanocrystals. e) TEM image of a layer with maximum coverage (65%) collected from the heptane/water interface by a Langmuir–Blodgett technique showing that the layer does not contain 3D aggregates, the voids have a typical size equivalent to 1–10 nanocrystals; the space between particles is 1–4 nm.

 © 2004 Wiley-VCH Verlag GmbH & Co. KGaA, Weinheim

right). The nanocrystal coverage of the water/oil interface increases gradually with the decrease of the surface charge density on the gold nanocrystals. Figure 1c and 1d shows in situ optical microscope pictures of the nanocrystal layer after addition of 17 and 38 volume % of ethanol, respectively. Upon the addition of 17% of ethanol, islands of gold nanocrystals form (Figure 1c); they extend and coalesce to a coherent monolayer as the ethanol content increases (Figure 1d). The monolayers do not collapse into multilayers nor are the gold nanocrystals transferred to the heptane phase. Instead, the layer creeps up the glass wall of the vial (see Figure 1b, centre and right). This indicates that there is a strong driving force for the formation of an interfacial monolayer. The films are remarkably robust if one considers that the monolayer reaches up the vertical wall of the vial to a height of a few centimeters without breaking into pieces (see Figure 1b, centre and right). The interfacial nanocrystal layers could be transferred to a glass or mica substrate as a Langmuir–Blodgett film, and studied by atomic force microscopy (AFM) and transmission electron microscopy (TEM); a typical TEM image is presented in Figure 1e. In all cases we found monolayers of gold nanocrystals; coagulation of the gold nanocrystals into 3D aggregates and the spontaneous collapse of the film into multilayers was not observed. We checked that the structure of the interfacial gold nanocrystal layer is not disturbed by the transfer procedure, which is commonly the case for Langmuir–Blodgett transfer.[9] The nanocrystal coverage of the water/oil interface saturates at around 65% for 16 nm particles. Similar results were obtained for gold crystals with a diameter in the range 8 to 40 nm. The typical distance between the nanocrystal surfaces was between 1 and 4 nm (Figure 1e). This is smaller than twice the width of the electrical double layer around the gold nanocrystals in the sol (2×5 nm). The layers are not ordered, which may arise from the size dispersion of the nanocrystals being about 10%. The layers have voids equivalent to, typically, between one and ten nanocrystals. The metallic sheen of the monolayer is due to electronic coupling between the uncapped nanocrystals.[20,21]

Adsorption of a charged gold nanocrystal at the water/oil interface must be driven by a reduction of the interfacial energy; the repulsion between the charged nanocrystals in the monolayer forms a counteracting force. We conjecture that the reduction of the charge density on the gold nanocrystals is a prerequisite for the formation of the nanocrystal monolayers at the water/oil interface. This is supported by experiments in which hydrochloric or sulfuric acid was added to the sol to lower the pH from about 5.8 to 2.0. As a result, the charge on the gold surface decreases by protonation of the adsorbed citrate ions. As for ethanol addition, monolayers of gold nanocrystals were formed at the water/oil interface. Again, coagulation does not occur. In contrast, a decrease in the thickness of the diffuse electrical double layer by adding salt to the gold sol leads to coagulation in the bulk solution. Thus, a decrease in the charge density of the nanocrystals leads to the controlled formation of a monolayer of gold nanocrystals at the water/oil interface, while reduction of the width of the diffuse double layer leads to conventional destabilization[14] of the suspension.

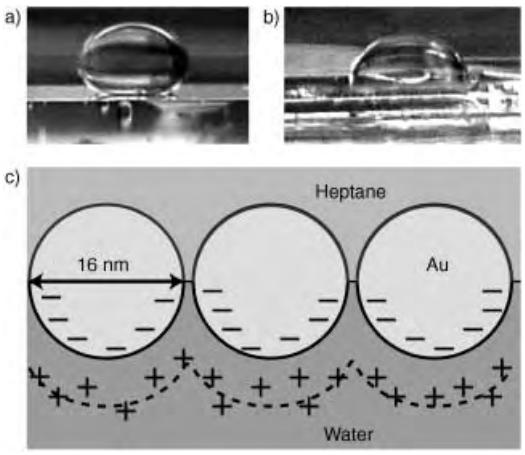


Figure 2. Wetting of an uncharged and charged gold surface with a drop of a mixture of water and ethanol covered with a heptane phase. a) A water + 37% ethanol droplet immersed in heptane shows a negative contact angle with flame-annealed gold, which shows that heptane has a stronger affinity for uncharged gold than the water droplet. b) As in (a) but now with a gold surface on which citrate has been adsorbed (the gold substrate has been immersed in an aqueous solution of 1% v/v trisodium citrate for 1 hour): the water + ethanol droplet shows a contact angle of 90°, which indicates a similar affinity of the water mixture and heptane phase for charged, citrate-covered gold. c) Schematic representation of the nanocrystals at the heptane/water interface, derived from the experiment described by (b), and TEM and AFM characterization. The charged gold nanocrystals are half in the water and half in the heptane phase. Most charge is located at the water side, but charge remaining at the gold/oil interface determines the degree of Coulomb repulsion, see text.

The energy of the layer of charged gold nanocrystals adsorbed at the water/heptane interface is decided by three quantities; a) the interfacial energy due to surface tension, b) the electrostatic energy and c) van der Waals attraction between the nanocrystals. These contributions are discussed below.

a) The first contribution is related to the surface tension of the water/oil ($\chi_{w/o}$), nanocrystal/water ($\chi_{c/w}$) and nanocrystal/oil ($\chi_{c/o}$) interface. The microscopic structure of the interfacial nanocrystal layer is of key importance for a valuable estimation of this contribution. We, therefore, studied the wetting of the (charged gold/water and ethanol/heptane) three-phase system, see Figure 2. With flame-annealed gold the contact angle is negative (Figure 2a), thus showing that heptane has a stronger affinity for hydrophobic gold than the drop of water and ethanol. This changed significantly when citrate was adsorbed on the gold. We found that the contact angle θ between heptane at a charged gold substrate and a drop of a mixture of water and ethanol is close to 90 degrees (Figure 2b). According to the Young–Dupré equation $\cos\theta = (\chi_{c/o} - \chi_{c/w})/\chi_{w/o}$ thus $\chi_{c/o} \cong \chi_{c/w}$, in which c represents the charged gold, w represents the aqueous phase, o represents the oil phase, and these / represents the interface. This means that the gold particles are half in the oil and half in the water phase (Figure 2c). Adsorption of a gold particle at the water/oil interface leads to a reduction in the interfacial energy related to the surface

 © 2004 Wiley-VCH Verlag GmbH & Co. KGaA, Weinheim

tension of roughly $-\pi R^2 \chi_{w/o}$, R is the radius of the gold nanocrystal. For example, with gold nanocrystals with a diameter of 16 nm and $\chi_{w/o}$ being 5 mN m^{-1}, this amounts to -240 kT per adsorbed particle. This contribution is independent of the nanocrystal interfacial coverage.

b) The main force counteracting layer formation is electrostatic repulsion between the negatively charged nanocrystals in the layer. This depends strongly on the distribution of the charge over the surface of the gold nanocrystal, which is half in the water and half in the oil phase. Very probably, there is a considerable redistribution of the remaining surface charge when the particle is adsorbed at the interface. In addition, the diffuse ion cloud at the water side could become considerably deformed. Residual charges at the oil side of the water/oil interface lead to unscreened Coulombic repulsion between the adsorbed particles.[22]

c) The third contribution to the total energy is due to van der Waals interactions between the gold nanocrystals. This contribution becomes more important with increasing nanocrystal coverage, and thus counteracts the effect of Coulombic repulsion to a certain extent. We remark that van der Waals interactions are not the main driving force for layer formation. If van der Waals interactions were predominant, 3D coagulation would prevail.

A quantitative model for adsorption of charged nanocrystals at the water/oil interface will be presented in detail elsewhere. Here we show the nanocrystal coverage of the water/oil interface as a function of the decreasing effective charge density on the nanocrystals calculated on the basis of the contributions discussed above (Figure 3). The interfacial coverage is small at the maximum charge density (no ethanol added) and increases gradually with a reduction of the charge density. Thus, the crude model is in agreement with our observation that, although layer formation is not observed with the as-prepared gold sol, a decrease of the charge density on the gold nanocrystals by a factor of two leads to the formation of an interfacial layer with a significant nanocrystal coverage (about 65%). The model also explains layer formation in a qualitatively similar way for a wide range of particle sizes as observed experimentally. The inhomogeneous microscopic structure of the nanocrystal monolayer is more difficult to explain: it is not clear yet why dense 2D domains coexist with relatively large voids. Possibly, the van der Waals interactions which favor dense layers compete, on a scale of 100 nanometer, with Coulombic repulsion; this may lead to 2D aggregates of a limited lateral size coexisting with voids, in a similar way as has been shown in the 3D case.[23]

Charged colloidal nanocrystals have considerable technological relevance. Many preparation methods lead to charge-stabilized sols. Furthermore, it has become clear that even sterically stabilized colloids in nonaqueous solvents can carry residual charge.[24] The preparation of monolayers of such charged colloids would form an important step forwards in the route to the fabrication of 2D and 3D materials for optoelectrical or magnetic applications. We have shown that charged gold nanocrystals self-assemble at the water/oil interface upon gradual reduction of the surface charge density. As charge reduction can be accomplished in various ways, this method of assembly does not depend on the details of the surface chemistry and should thus be widely applicable. Our discovery of spontaneous monolayer formation of charged gold nanocrystals at the water/oil interface forms a new impetus to research devoted to the controlled 2D assembly of charged nanocrystals.

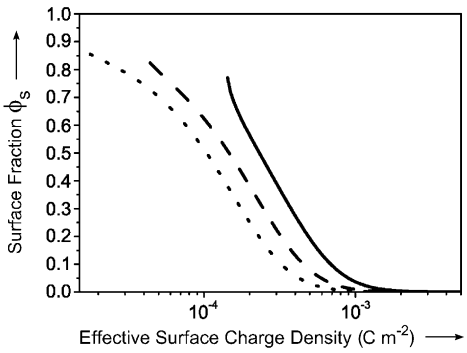


Figure 3. The gold nanocrystal coverage of the water/oil interface as a function of the effective charge density on the nanocrystals. The results are obtained from a model that accounts for the reduction of the water/oil surface tension, and the repulsion and van der Waals attraction between the charged nanocrystals (see text). The equilibrium coverage increases with decreasing surface-charge density for all sizes of nanocrystals (full line: 16 nm diameter; dashed line: 40 nm diameter, dotted line: 80 nm diameter). Details of the model will be presented elsewhere.

Received: July 9, 2003
Revised: October 22, 2003 [Z52339]

Keywords: colloids · electrostatic interactions · interfaces · nanostructures · self-assembly

[1] M. Brust, D. Bethell, D. J. Schiffrin, C. J. Kiely, *Adv. Mater.* **1995**, *7*, 795.
[2] R. Parthasarathy, X. M. Lin, H. M. Jaeger, *Phys. Rev. Lett.* **2001**, *87*, 186807.
[3] A. L. Roest, J. J. Kelly, D. Vanmaekelbergh, E. A. Meulenkamp, *Phys. Rev. Lett.* **2002**, *89*, 36801.
[4] H. Zeng, J. Li, J. P. Liu, Z. L. Wang, S. H. Sun, *Nature* **2002**, *420*, 395.
[5] C. B. Murray, S. H. Sun, W. Gaschler, H. Doyle, T. A. Betley, C. R. Kagan, *IBM J. Res. Dev.* **2001**, *45*, 47.
[6] C. R. Kagan, C. B. Murray, M. Nirmal, M. G. Bawendi, *Phys. Rev. Lett.* **1996**, *76*, 1517.
[7] S. A. Crooker, J. A. Hollingsworth, S. Tretiak, V. I. Klimov, *Phys. Rev. Lett.* **2002**, *89*, 186802.
[8] C. B. Murray, C. R. Kagan, M. G. Bawendi, *Science* **1995**, *270*, 1335.
[9] J. R. Heath, C. M. Knobler, D. V. Leff, *J. Phys. Chem. B* **1997**, *101*, 189.
[10] R. P. Andres, J. D. Bielefeld, J. I. Henderson, D. B. Janes, V. R. Kolagunta, C. P. Kubiak, W. J. Mahoney, R. G. Osifchin, *Science* **1996**, *273*, 1690.
[11] C. J. Kiely, J. Fink, M. Brust, D. Bethell, D. J. Schiffrin, *Nature* **1998**, *396*, 444.

 © 2004 Wiley-VCH Verlag GmbH & Co. KGaA, Weinheim

[12] Y. Lin, H. Skaff, T. Emrick, A. D. Dinsmore, T. P. Russell, *Science* **2003**, *299*, 226.
[13] E. J. W. Verwey, J. T. G. Overbeek, *Theory of the Stabiliy of Lyophobic Colloids*, Dover, New York, **1999**.
[14] J. Fink, C. J. Kiely, D. Bethell, D. J. Schiffrin, *Chem. Mater.* **1998**, *10*, 922.
[15] J. P. Novak, D. L. Feldheim, *J. Am. Chem. Soc.* **2000**, *122*, 3979.
[16] J. J. Storhoff, C. A. Mirkin, *Chem. Rev.* **1999**, *99*, 1849.
[17] G. Frens, *Nature* **1973**, *241*, 20.
[18] M. K. Chow, C. F. Zukoski, *J. Colloid Interface Sci.* **1994**, *165*, 97.
[19] F. Reincke, S. G. Hickey, J. J. Kelly, T. W. Braam, L. W. Jenneskens, D. Vanmaekelbergh, *J. Electroanal. Chem.* **2002**, *522*, 2.
[20] C. P. Collier, R. J. Saykally, J. J. Shiang, S. E. Henrichs, J. R. Heath, *Science* **1997**, *277*, 1978.
[21] G. Markovich, C. P. Collier, J. R. Heath, *Phys. Rev. Lett.* **1998**, *80*, 3807.
[22] R. Aveyard, B. P. Binks, J. H. Clint, P. D. I. Fletcher, T. S. Horozov, B. Neumann, V. N. Paunov, J. Annesley, S. W. Botchway, D. Nees, A. W. Parker, A. D. Ward, A. N. Burgess, *Phys. Rev. Lett.* **2002**, *88*, 246102.
[23] J. Groenewold, W. K. Kegel, *J. Phys. Chem. B* **2001**, *105*, 11702.
[24] L. N. Donselaar, A. P. Philipse, J. Suurmond, *Langmuir* **1997**, *13*, 6018.

 © 2004 Wiley-VCH Verlag GmbH & Co. KGaA, Weinheim

Oxidation-State Determination

X-ray Absorption Spectroscopic and Electrochemical Studies of Tris(catecholato(2−))chromate(VI/V/III) Complexes**

*Aviva Levina, Garry J. Foran, David I. Pattison, and Peter A. Lay**

Complexes of transition-metal ions with redox-active catecholato ligands have been studied extensively as potential conductive or magnetic molecular materials[1] and as biologically active substances.[2] In particular, chromium–catecholato complexes have been considered among the possible reactive species in Cr^{VI}-induced genotoxicity.[3] There has been a recent debate[3,4] over the involvement of the Cr center in the redox reactions of such complexes. Pierpont[1,4] has suggested, on the basis of X-ray crystallographic and magnetic studies, that these reactions are exclusively ligand-centered and lead to interconversions of catecholato, *o*-semiquinonato, and *o*-quinone forms of the ligands, while the metal ion remains in the Cr^{III} state. Our research group[3c] has previously assigned the metal oxidation state in $[Cr(3,5\text{-dtbcat})_3]^-$ (dtbcat = di-*tert*-butylcatecholato(2−)) as Cr^{V} (with a strong electron delocalization between the Cr ion and the ligands), based on X-ray absorption spectroscopic (XAS) and EPR spectroscopic data. Herein, definitive evidence for the

[*] Dr. A. Levina, Dr. D. I. Pattison, Prof. P. A. Lay
Centre for Heavy Metals Research
School of Chemistry, University of Sydney
Sydney, NSW 2006 (Australia)
Fax: (+61) 2-93513329
E-mail: p.lay@chem.usyd.edu.au
Dr. G. J. Foran
Australian Nuclear Science and Technology Organisation
PMB 1, Menai, NSW 2234 (Australia)

[**] Financial support of this work was provided by an Australian Research Council (ARC) grant (to P.A.L.) and an ARC grant for the fluorescence detector at ANBF. This work was supported by the Access to Major Facilities Program funded by the Department of Industry, Science and Resources and managed by the Australian Nuclear Science and Technology Organisation. X-ray absorption spectroscopy was performed partially at the ANBF, with support from the Australian Synchrotron Research Program, which is funded by the Commonwealth of Australia under the Major National Research Facilities program, and partially at the Stanford Synchrotron Radiation Laboratory, a national user facility operated by Stanford University on behalf of the US, Department of Energy, Office of Basic Energy Sciences. The SSRL Structural Molecular Biology Program is supported by the National Institutes of Health, National Centre for Research Resources, Biomedical Technology Program, and by the Department of Energy, Office of Biological and Environmental Research. We thank Dr. Peter Barnard and Mr Jack Zylmans (University of Sydney) for contributions to the design and construction of the electrochemical XAS cell, and Ms Jade Aitken (University of Sydney) and Dr. Britt Hedman, Dr. Matthew Latimer, and Dr. Alison Soo Hoo (SSRL) for their help in XAS data collection.

Supporting information for this article is available on the WWW under http://www.angewandte.org or from the author.

 © 2004 Wiley-VCH Verlag GmbH & Co. KGaA, Weinheim DOI: 10.1002/anie.200352418

formation of Cr^{IV}– and Cr^{V}–catecholato complexes by sequential one-electron oxidations of $[Cr^{III}(cat)_3]^{3-}$ (cat = catecholato(2−)) has been obtained by electrochemical XAS studies of a redox series ($[Cr(cat)_3]^{n-}$ ($n = 1$–3)).

Solutions of chromium–catecholato complexes in DMF, used for the electrochemical generation of $[Cr(cat)_3]^{n-}$ ($n = 1$–3), were prepared by aerial oxidation of $K_3[Cr(cat)_3]$ (synthesized by a known method).[5] Three reversible one-electron oxidation/reduction steps (with $E_{1/2} = -296$, -89, and $+396$ mV versus Ag/AgCl; or -831, -624, and -139 mV versus the ferrocenium/ferrocene couple; $\Delta E_p = 58$–64 mV at 295 K)[6] were observed by cyclic voltammetric analysis of such solutions containing an excess of free ligand and $(n\mathrm{Bu_4N})BF_4$ as a supporting electrolyte (Figure 1). To our

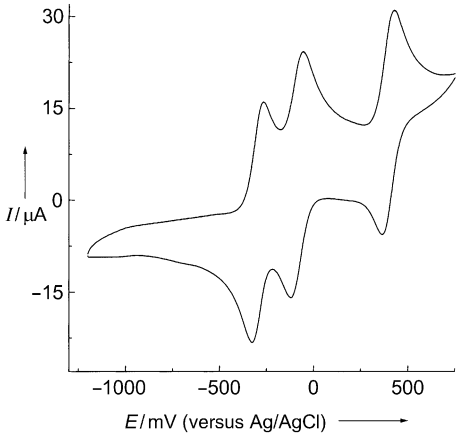


Figure 1. A typical cyclic voltammogram of the air-oxidized (saturated with Ar after oxidation) solution of $K_3[Cr(cat)_3]$ (10 mM) in DMF in the presence of $catH_2$ (20 mM) and $(n\mathrm{Bu_4N})BF_4$ (0.10 M) at a glassy carbon electrode: scan rate 100 mVs^{-1}; 100% internal resistance compensation.

knowledge, these are the first reported reversible electron-transfer reactions for a Cr^{III} complex with unsubstituted catechol (similar electrochemical behavior has been observed for Cr^{III} complexes of catechol derivatives).[7] Bulk electrolysis of the air-oxidized (dark red, mainly $[Cr(cat)_3]^{2-}$) solution at $E = -600$ mV led to a green air-sensitive solution of $[Cr(cat)_3]^{3-}$. Two sequential one-electron oxidation steps, starting from the green solution, led to a dark-red solution of $[Cr(cat)_3]^{2-}$ ($E = -190$ mV), then to a dark-violet solution of $[Cr(cat)_3]^{-}$ ($E = +200$ mV). One-electron oxidations at -190 and $+200$ mV were confirmed by coulometric measurements (experimental error ±10%), while the electrolysis at $+600$ mV was slow and nonstoichiometric, which is indicative of oxidative degradation of $[Cr(cat)_3]^{-}$. Electronic and EPR spectra of the electrogenerated species (see the Supporting Information) were in agreement with nearly quantitative (ca. 90–95%) formation of $[Cr(cat)_3]^{n-}$ complexes with $n = 3$, 2, or 1 at -600, -190, and $+200$ mV, respectively, and with the oxidative degradation at $+600$ mV (by comparison with the published data for Cr complexes of substituted catechols).[3,7,8] EPR spectroscopic analysis also revealed a significant decomposition of the electrochemically generated $[Cr(cat)_3]^{-}$ ($E = +200$ mV) in the absence of added free ligand (see the Supporting Information). Solutions of the $[Cr(cat)_3]^{n-}$ complexes ($n = 1$–3) for XAS studies contained excess ligand, and were either generated directly in the XAS cell (in situ spectroelectrochemistry at 295 K), or frozen in liquid N_2 for the XAS studies at 10 K.

Typical changes in X-ray absorption near-edge structure (XANES) in the spectra of the $[Cr(cat)_3]^{n-}$ complexes ($n = 1$–3) during the in situ electrochemical XAS (295 K) are shown in Figure 2. Small, but significant, increases in the edge

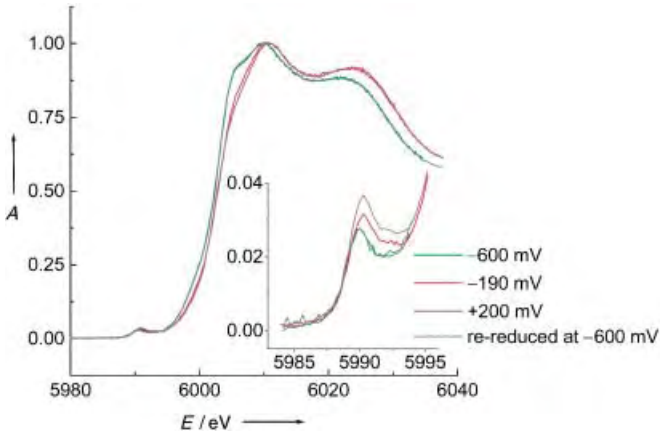


Figure 2. XANES spectra of the $[Cr(cat)_3]^{n-}$ ($n = 1$–3) solutions, generated in situ (295 K) by bulk electrolysis of a solution of $[Cr(cat)_3]^{n-}$ (10 mM), $catH_2$ (20 mM), and $(n\mathrm{Bu_4N})BF_4$ (0.10 M) in DMF.

energies (6002.9 versus 6002.4 eV) and in the intensities of pre-edge peaks for $[Cr(cat)_3]^{2-/1-}$ (relative to $[Cr(cat)_3]^{3-}$) point to an increase in the Cr oxidation state in the former complexes to greater than Cr^{III}.[3c] A shift in the edge position by about 0.5 eV is similar to that observed for related Cr^{III}/Cr^{IV} couples,[3c] and is consistent with the redox chemistry being predominantly metal-centered. The changes in the XANES spectra were fully reversible, as shown by bulk electrolysis at -600 mV, followed by oxidation at $+200$ mV, and re-reduction at -600 mV (Figure 2). Very similar changes in the XANES spectra were observed for a series of frozen solutions of $[Cr(cat)_3]^{n-}$ ($n = 1$–3) at 10 K (see the Supporting Information).

Changes in the Cr–O bond lengths in the $[Cr(cat)_3]^{n-}$ complexes ($n = 1$–3) were determined by multiple scattering (MS) analyses of X-ray absorption fine structure (XAFS) spectra (Table 1; full details of MS XAFS analyses are given in the Supporting Information). The MS XAFS models included all the non-H atoms in $[Cr(cat)_3]^{n-}$ and led to excellent fits (goodness-of-fit parameter, $R = 14$–16%; fits with $R < 20\%$ are considered acceptable)[9] for both frozen solutions and the solutions obtained by electrolysis in situ (see the Supporting Information). The optimized bond lengths and angles from the MS XAFS calculations for $[Cr(cat)_3]^{3-}$ agreed, within the experimental errors, to those determined from the crystal structure of $K_3[Cr(cat)_3]$ (see the Supporting Information).[5b] Analyses of systematic errors of MS XAFS calculations (see the Supporting Information) have shown

 © 2004 Wiley-VCH Verlag GmbH & Co. KGaA, Weinheim

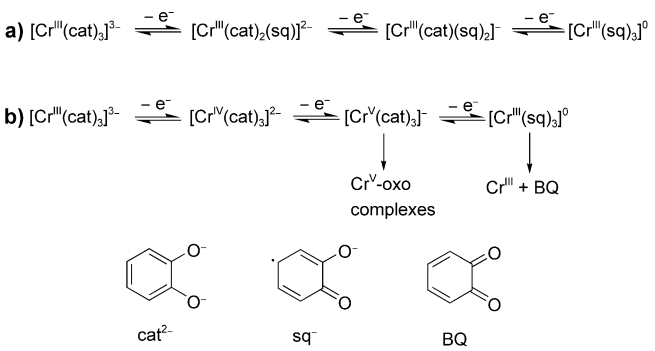
that significant increases in the R value ($\geq 0.5\,\%$) were caused by small deviations from the optimum (≤ 0.005 Å) in the Cr–O bond lengths, or by much larger deviations (0.02–0.04 Å) in the bond lengths within the ligands. Errors in the bond lengths, which arise from the noise in the data (determined by Monte–Carlo analysis),[9] did not exceed 0.002 Å for the Cr–O bonds and 0.01 Å for the bonds within the ligands. No significant changes were detected in the bond lengths within the ligands or in the bond angles of $[Cr(cat)_3]^{n-}$ ($n = 1$–3; see the Supporting Information). In addition, good single-scattering (SS) XAFS fits of the first coordination shells (six equal Cr–O bonds) were obtained for all samples (see the Supporting Information), and the calculated average Cr–O bond lengths were the same (within 0.001–0.006 Å), as the corresponding values obtained by MS calculations (see Table 1 and the Supporting Information).

Table 1: Average Cr–O bond lengths in $[Cr(cat)_3]^{n-}$ complexes.[a]

n	T [K]	Cr–O [Å][b]
3[c]	295[e]	1.980[f]
2[c]	295[e]	1.943
1[c]	295[e]	1.937
3[d]	10	1.986
2[c]	10	1.966
1[c]	10	1.952

[a] Determined by MS XAFS analyses (see the Supporting Information). [b] Errors in the determination of the bond lengths did not exceed 0.005 Å (see the Supporting Information). [c] Solutions of $[Cr(cat)_3]^{n-}$ (10 mM), $catH_2$ (20 mM), and $(nBu_4N)BF_4$ (0.10 M) in DMF generated by bulk electrolysis (at −600, −190, and +200 mV for $n = 3$, 2, and 1, respectively). [d] Solution of $K_3[Cr(cat)_3]$ (10 mM) in aqueous NaOH (0.10 M). [e] Determined by in situ spectroelectrochemistry. [f] Values determined by X-ray crystallography: 1.97–2.00 Å.[5b]

The most important feature revealed by XAFS analyses was a significant decrease in the Cr–O bond length with decreasing n value (increasing oxidation state of the complex) in the $[Cr(cat)_3]^{n-}$ series ($n = 1$–3) in two independent sets of experiments at either 295 or 10 K, as determined by either MS or SS XAFS analyses (see Table 1 and the Supporting Information). This finding is inconsistent with the dominant opinion[1,4] that the oxidation of Cr^{III}–catecholato complexes is exclusively ligand-based (Scheme 1 a). If this was the case, the decreased donor ability of the *o*-semiquinonato(1−) versus catecholato(2−) ligands would lead to an increase in the Cr–O bond lengths.[3c,10] Decreases in the metal–oxygen bond lengths as the oxidation state of the metal ion increases, similar to those found in the $[Cr(cat)_3]^{n-}$ series ($n = 1$–3, Table 1), were observed in a series of crystallographically characterized catecholato complexes of V^{III}, V^{IV}, and V^{V}.[11] On the other hand, oxidation of $[Cr^{III}(tren)(3,6\text{-dtbcat})]^{+}$ to $[Cr^{III}(tren)(3,6\text{-dtbsq})]^{2+}$ (tren = tris(2-aminoethyl)amine, 3,6-dtbcat = 3,6-di-*tert*-butylcatecholato(2−), and 3,6-dtbsq = 3,6-di-*tert*-butylsemiquinonato(1−)) was accompanied by an increase in the average Cr–O bond length of 0.015 Å (determined by X-ray crystallography).[12] Thus, the results of MS XAFS analyses, together with the XANES data (see Figure 2 and the Supporting Information), strongly support the suggestion[3c] that the effective oxidation states of Cr in $[Cr(cat)_3]^{2-/1-}$ are higher than in $[Cr(cat)_3]^{3-}$, and that the former species can be considered as Cr^{IV} or Cr^{V} complexes with a significant degree of Cr–O π bonding.



Scheme 1. Redox sequences of the electronic isomers formed during the oxidation of $[Cr(cat)_3]^{3-}$: a) as assumed by most authors[1,4] and b) as proposed in the current work.

Further oxidation of $[Cr(cat)_3]^{-}$ at $E = +600$ mV (in situ electrochemical XAS experiments, 295 K) led to an increase in the average Cr–O bond length from 1.939(2) to 1.958(2) Å (as determined by SS XAFS analysis of the first coordination shells, see the Supporting Information). Attempts to apply MS analysis to the XAFS spectrum of the reaction mixture, oxidized at $E = +600$ mV, led to poor fits (R = ca. 25 %) and to unreasonably high Debye–Waller factor values (> 0.02 Å^2) for the second and further coordination shells. These features are in agreement with the oxidative degradation of $[Cr^{V}(cat)_3]^{-}$ at $E = +600$ mV, probably via unstable $[Cr^{III}(sq)_3]^{0}$ (sq = semiquinonato (1−)), since Cr^{VI} is too strong an oxidant to be stabilized by three catecholato(2−) ligands. Fast ligand exchange of $[Cr^{V}(cat)_3]^{-}$ with trace amounts of water in DMF at $E = +200$ mV in the absence of excess ligand leads to Cr^{V}–oxo complexes (as shown by EPR spectroscopy; see the Supporting Information). This observation is in agreement with the kinetically labile nature of all d^1 complexes of the first transition series with bidentate ligands (including Cr^{V}),[13] and contradicts the assignment of the former species as d^3 $[Cr^{III}(cat)(sq)_2]^{-}$ (Scheme 1 a),[1,4] which would be kinetically inert.[13] These observations are consistent with a sequence of redox reactions of Cr–catecholato complexes in Scheme 1 b.

The Cr^{V} complex $[Cr(cat)_3]^{-}$ is a rare example of a structurally characterized (by MS XAFS modeling, see the Supporting Information) Cr^{V} species without an oxo or nitrido ligand, and the Cr^{IV} complex $[Cr(cat)_3]^{2-}$ is a very rare example of a moderately stable and structurally characterized Cr^{IV} complex.[13] This is also the first example of the structural characterization of all three oxidation states (Cr^{III}–Cr^{V}) in complexes with the same coordination environment, and the first application of electrochemical XAS to the studies of redox reactions in metal complexes with non-innocent ligands. Such studies are not only of fundamental importance in assigning the oxidation states of the metal and the ligand, but are also essential in understanding the reactivities of these complexes, which has wide applications

 © 2004 Wiley-VCH Verlag GmbH & Co. KGaA, Weinheim

in bioinorganic chemistry and in the design of magnetic materials.[1–3]

Experimental Section

Full details of the used reagents, preparation of reaction solutions, instrumental techniques, and XAS data collection and analysis are given in the Supporting Information.

Received: July 18, 2003 [Z52418]

Keywords: bioinorganic chemistry · chromium · electrochemistry · redox-active ligands · X-ray spectroscopy

[1] For a recent review, see C. G. Pierpont, *Coord. Chem. Rev.* **2001**, *219–221*, 415 – 433, and references therein.
[2] a) F. L. Meyskens, Jr., P. Farmer, J. P. Fruehauf, *Pigm. Cell Res.* **2001**, *14*, 148 – 154; b) W. R. Humphries (Rowett Research Services Ltd., UK), WO 9909050, **1999** [*Chem. Abstr.* **1999**, *130*, 205114].
[3] a) D. I. Pattison, P. A. Lay, M. J. Davies, *Inorg. Chem.* **2000**, *39*, 2729 – 2739; b) D. I. Pattison, M. J. Davies, A. Levina, N. E. Dixon, P. A. Lay, *Chem. Res. Toxicol.* **2001**, *14*, 500 – 510; c) D. I. Pattison, A. Levina, M. J. Davies, P. A. Lay, *Inorg. Chem.* **2001**, *40*, 214 – 217.
[4] C. G. Pierpont, *Inorg. Chem.* **2001**, *40*, 5727 – 5728.
[5] a) S. S. Isied, G. Kuo, K. N. Raymond, *J. Am. Chem. Soc.* **1976**, *98*, 1763 – 1767; b) K. N. Raymond, S. S. Isied, L. D. Brown, F. R. Fronczek, J. H. Nibert, *J. Am. Chem. Soc.* **1976**, *98*, 1767 – 1774.
[6] In the following text, the values of the redox potentials are given versus the Ag/AgCl reference electrode.
[7] a) S. R. Sofen, D. C. Ware, S. R. Cooper, K. N. Raymond, *Inorg. Chem.* **1979**, *18*, 234 – 239; b) H. H. Downs, R. M. Buchanan, C. G. Pierpont, *Inorg. Chem.* **1979**, *18*, 1736 – 1740.
[8] a) C. G. Pierpont, H. H. Downs, *J. Am. Chem. Soc.* **1976**, *98*, 4834 – 4838; b) S. P. Solodovnikov, K. Sarbasov, B. L. Tumansky, A. I. Prokof'ev, V. B. Vol'eva, N. N. Bubnov, M. I. Kabachnik, *Izv. Akad. Nauk SSSR Ser. Khim.* **1984**, *8*, 1789 – 1794; c) M. Branca, M. Fruianu, S. Sau, M. A. Zoroddu, *J. Inorg. Biochem.* **1996**, *62*, 223 – 230.
[9] A. M. Rich, R. S. Armstrong, P. J. Ellis, H. C. Freeman, P. A. Lay, *Inorg. Chem.* **1998**, *37*, 5743 – 5753.
[10] R. M. Wood, K. A. Abboud, R. C. Palenik, G. J. Palenik, *Inorg. Chem.* **2000**, *39*, 2065 – 2068.
[11] a) S. R. Cooper, Y. B. Koh, K. N. Raymond, *J. Am. Chem. Soc.* **1982**, *104*, 5092 – 5102; b) M. E. Cass, N. R. Gordon, C. G. Pierpont, *Inorg. Chem.* **1986**, *25*, 3962 – 3967.
[12] J. H. Rodriguez, D. E. Wheeler, J. K. McCusker, *J. Am. Chem. Soc.* **1998**, *120*, 12051 – 12068.
[13] For a review, see a) R. P. Farrell, P. A. Lay, *Comments Inorg. Chem.* **1992**, *13*, 133 – 175; b) R. Codd, C. T. Dillon, A. Levina, P. A. Lay, *Coord. Chem. Rev.* **2001**, *216–217*, 533 – 577.

 © 2004 Wiley-VCH Verlag GmbH & Co. KGaA, Weinheim

Conductive Polymers

Helical Superstructure of Conductive Polymers as Created by Electrochemical Polymerization by Using Synthetic Lipid Assemblies as a Template**

*Tsukasa Hatano, Ah-Hyun Bae, Masayuki Takeuchi, Norifumi Fujita, Kenji Kaneko, Hirotaka Ihara, Makoto Takafuji, and Seiji Shinkai**

Poly(ethylenedioxythiophene) (poly(EDOT)) and poly(pyrrole) are conductive polymers easily obtained by electrochemical polymerization or chemical synthesis of the corresponding monomers.[1] In spite of the convenience of the preparation method and the cheapness of the monomers, the applications have been rather limited.[1–3] This limitation is due to the difficulty in the structural control arising from their hardness and low solubility. So far, several attempts have been made to overcome this difficulty: for example, deposition of monomers in the oriented environments such as LB membranes,[4] surfactant aggregates,[5,6] liquid crystals,[7] or self-assembly of chemically modified monomers.[8,9] It is known, however, that in these systems the prediction of the resultant superstructures and the fine tuning of the molecular assemblies are nearly impossible.

Recently, we and others have explored a new method to transcribe a variety of organic superstructures into inorganic materials by a sol–gel reaction of metal alkoxides ("templating sol–gel reaction"), by which one can control the morphology of inorganic compounds and create various new superstructural inorganic materials.[10–18] The driving force operating in this templating sol–gel reaction is considered to be electrostatic and/or hydrogen-bonding interactions between silica nanoparticles and organic assemblies acting as templates.[16] Thus, it occurred to us that the morphology of these conductive polymers would be also controllable by applying the concept of the templating method to the electrochemical polymerization process: that is, as oxidative polymerization of these monomers produces cationic intermediates, the anionic assemblies should act as a potential template owing to the

[*] T. Hatano, A.-H. Bae, Dr. M. Takeuchi, Dr. N. Fujita, Prof. Dr. S. Shinkai
Department of Chemistry and Biochemistry
Graduate School of Engineering
Kyushu University, Fukuoka 812-8581 (Japan)
Fax: (+81) 092-642-3611
E-mail: seijitcm@mbox.nc.kyushu-u.ac.jp
Prof. Dr. K. Kaneko
HVEM Laboratory, Kyushu University
Fukuoka 812-8581 (Japan)
Prof. Dr. H. Ihara, Dr. M. Takafuji
Department of Materials and Life Science, Graduate School of Science and Technology, Kumamoto University, Kumamoto 860–8555 (Japan)

[**] We would like to thank the referees for their fruitful comments on our manuscript.

Supporting information for this article is available on the WWW under http://www.angewandte.org or from the author.

 DOI: 10.1002/anie.200351749 © 2004 Wiley-VCH Verlag GmbH & Co. KGaA, Weinheim

mutual electrostatic attractive force. More recently, we found that [60]fullerene encapsulated in *p*-sulfonatocalix[8]arene and J aggregates of 5,10,15,20-tetrakis(4-sulfonatophenyl)-porphyrin are readily deposited on the indium–tin oxide (ITO) electrode by electrochemical polymerization of these monomers.[19] Observation by SEM established that the resulting conductive polymeric assemblies have superstructures similar to those of the original organic templates. This finding prompted us to apply this concept to some anionic organic template that bears a helical superstructure. Here, we synthesized amphiphile **2** from **1**, which is already known as a helix-forming amphiphile (Scheme 1).[20] We confirmed from the TEM and SEM images (prepared from [**2**] = 0.3 mM, 10% MeOH aqueous solution) that **2** forms a fibrous structure with a left-handed helical motif (see Supporting Information). Oxidative polymerization of EDOT and pyrrole was carried out by using this helical superstructure as a template. Interestingly, we have found that electrochemical polymerization results in polymeric superstructures such as a helical-tape superstructure. This is the first example of a helical superstructure that is composed of conductive polymers designed by a templating method.

Compound **2** (2.1 mg, 2.9 μmol) EDOT (13 mg, 92 μmol) and $NaClO_4$ (61 mg, 0.5 mmol) of were dissolved in a 10% MeOH aqueous solution (10 mL). The cell consisted of an ITO electrode as the working electrode (working area = 2.2 cm^2), a Pt counter electrode, and an Ag/AgCl reference electrode. The redox cycle was repeated in a voltage range of −0.5–0.9 V (versus Ag/AgCl) with a scan rate of 0.05 V s^{-1} at 25 °C. In the electrochemical polymerization, the value of electric current increased during the successive potential sweeping in the presence of **2** (Figure 1 a). The oxidized and reduced states of an obtained poly(EDOT) film deposited on ITO electrode was characterized by UV/Vis spectroscopy. The oxidized state showed a weak absorption band in the visible region and a strong absorption band in the near-IR region, whereas the reduced state showed a broad absorption band at 587 nm because of the π–π* electronic transition (Figure 1 b). The cyclic voltammetry (CV) waves and UV/Vis spectral change were very similar to those reported for the EDOT/SDS (anionic micelle; SDS = sodium dodecyl sulphate) system.[21] This result indicates that the poly(EDOT)·amphiphile composite film is deposited on the ITO electrode. After the electrode had been washed, we carried out a further five redox cycles in 50 mM $NaClO_4$ aqueous solution in the absence of EDOT and **2**.

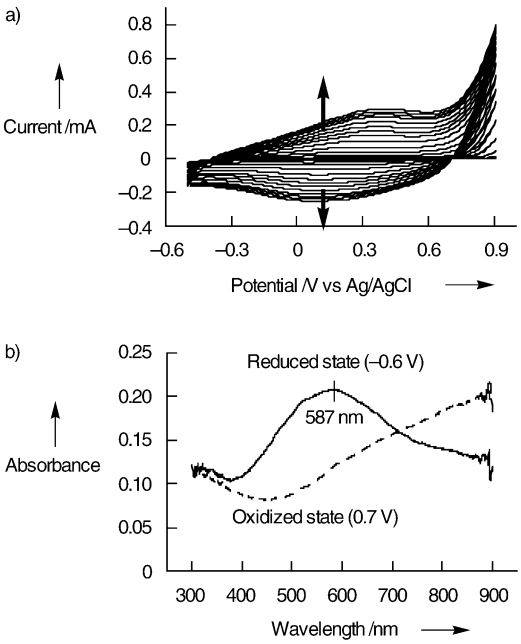
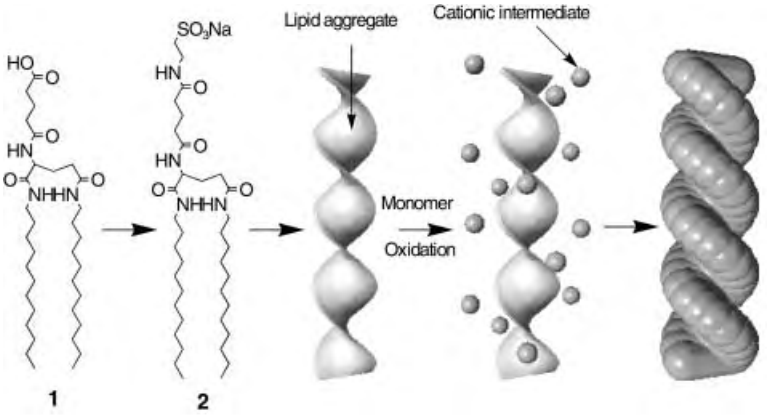


Figure 1. a) Cyclic voltammograms for EDOT obtained on an ITO electrode and b) UV/Vis absorption spectra of a poly(EDOT) film at reduced (——) and oxidized (-----) states electrodeposited on an ITO electrode from a tamplating method.



Scheme 1. Structure of a synthetic lipid **1** and **2** bearing an L-glutamic segment and schematic illustration of a templating oxidative polymerization.

The attenuated total reflection (ATR) IR spectra of the modified ITO electrode were measured (see Supporting Information). One can recognize a new peak at 1641 cm^{-1} (shown by an arrow mark), which is not present in the film of poly(EDOT) obtained in the absence of **2**. This result shows that **2** is deposited on the poly(EDOT) film. Figure 2 shows the SEM images of this composite film.

Electrochemical polymerization of EDOT in the presence of **2** results in a left-handed helical superstructure. In contrast, the same treatment in the absence of **2** results in a film with a smooth surface covered by pebblelike masses (see Supporting Information). As evidenced from a

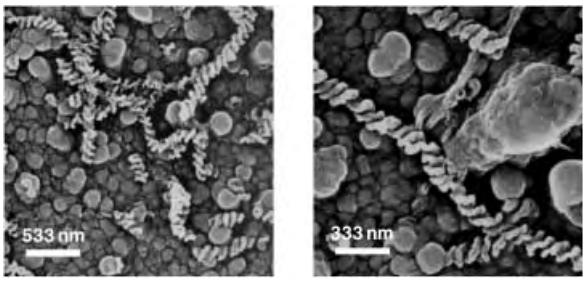


Figure 2. SEM images of poly(EDOT)·**2** composite film obtained by a templating method.

 © 2004 Wiley-VCH Verlag GmbH & Co. KGaA, Weinheim

TEM image of the poly(EDOT)·**2** composite prepared by chemical oxidation with ammonium peroxodisulfate (APS) (Figure 3), this poly(EDOT) has a tubular structure, which indicates that the lipid fiber acts as a template.[22]

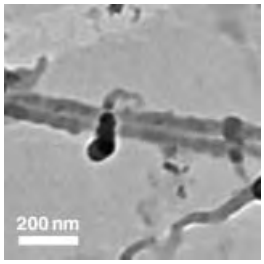


Figure 3. TEM image of poly(EDOT)·**2** composite prepared by chemical oxidation with APS.

Pt coated interdigitated microelectrodes were used for in situ conductance measurements[23,24] of the poly(EDOT)·**2** composites. The polymers were electrosynthesized under the same conditions as those used for the ITO electrode. As shown in AFM images of poly(EDOT)·**2** composites electrochemically deposited on interdigitated microelectrodes (Figure 4). The bridge between two electrodes is attained only by helical fibers. It is also seen from Figure 4 that poly(EDOT) dots generated without the presence of template are adsorbed onto the surface of the microelectrodes, but do not bridge the two electrodes.

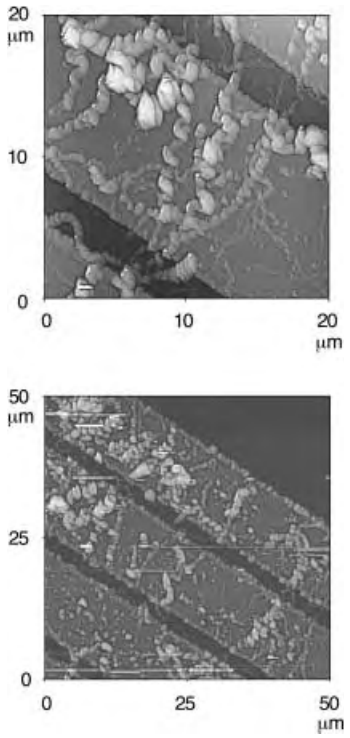


Figure 4. AFM images of poly(EDOT)·**2** composites electrochemically deposited on interdigitated microelectrodes by a templating method.

The conductance measurement of the poly(EDOT) polymer was carried out in 50 mM $NaClO_4$ aqueous solution. The conductivity was estimated by holding one Pt line at fixed potential, Vg, versus Ag/AgCl and the other at Vg+20 mV. The potential difference between the electrodes results in a current flow (drain current). The drain current was scarcely observed under −0.5 V, then increased above −0.5 V, and reached a plateau at +0.1 V (Figure 5).[25] This result is similar to that reported in reference[24] and indicates that the observed conductivity is due to the poly(EDOT)·**2** fiber composites.

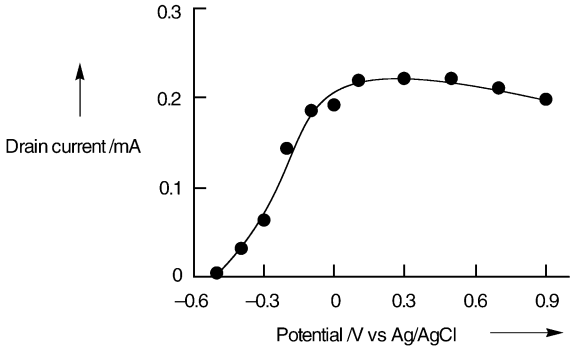


Figure 5. Drain current vs gate voltage (Vg) plot for poly(EDOT)·**2** composite.

It occurred to us that electrochemical polymerization of pyrrole, the mechanism of which is basically similar to that of EDOT, would also proceed under the template effect. The poly(pyrrole) film is more rigid than the poly(EDOT) film and if it is once formed, it is scarcely soluble in any solvent. This means that the morphology-controlled poly(pyrrole) synthesis is highly significant. The electrochemical polymerization was carried out with [pyrrole] = 14 mM, [$NaClO_4$] = 50 mM, and [**2**] = 0.3 mM. After 60 redox cycles (between −0.50 and 0.8 V versus Ag/AgCl) in the polymerization solution and five redox cycles in the 50 mM $NaClO_4$ solution (for washing the electrode in the absence of pyrrole and **2**), the poly(pyrrole) film was observed by SEM. In the SEM studies (Figure 6a), one can see a left-handed helical superstructure similar to that observed for the poly(EDOT)·**2** composites.[26] As shown in a TEM image of poly(pyrrole)·**2** composites prepared by chemical oxidation with APS (Figure 6b), this poly(pyrrole) has a hollow structure with a helical motif, indicating that the lipid fiber acts as a template.[22]

In conclusion, this study demonstrates, for the first time to the best of our knowledge, that the morphology of the poly(EDOT) and poly(pyrrole) films obtained by electrochemical polymerization of EDOT and pyrrole, respectively, can be controlled by using anionic synthetic lipid assemblies as a template. Therefore, one may regard this process as a novel templating of anionic templates to oxidizable monomers through electrochemical polymerization. Until now, it was believed that in the electrochemical polymerization of these monomers, the easiness in the preparation method is an

 © 2004 Wiley-VCH Verlag GmbH & Co. KGaA, Weinheim

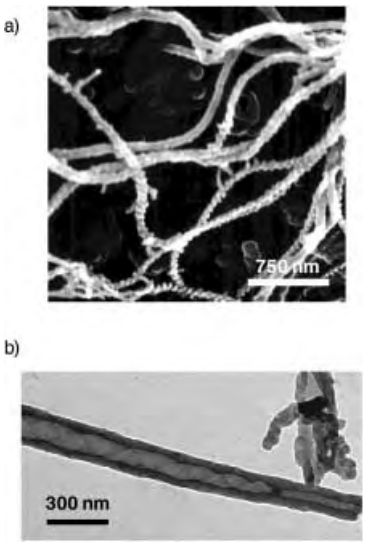


Figure 6. a) SEM image of poly(pyrrole)·**2** composite film electropolymerized on an ITO electrode and b) TEM image of poly(pyrrole)·**2** composite prepared by chemical oxidation with APS.

advantage, whereas the difficulty in the morphology control is a serious disadvantage. This disadvantage, which has outweighed the benefits, has hampered the broad application of these conductive polymers as functional materials. Therefore, we now believe that as this problem of morphology control has been solved (at least partially) and this study will stimulate further use of these polymers as new functional materials. We now consider that, in principle, the various polymeric superstructures can be created from poly(EDOT) and poly(pyrrole) as long as the appropriate "anionic" assemblies suitable for the template exist.

Experimental Section

The synthesis of **1** was reported previously.[20]

The synthesis of **2**: **1** (0.15 g, 0.25 mmol) and a few drops of triethylamine were added to DMF (10 mL). Benzotriazol-1-yloxy-tris(dimethylamino)phosphonium hexafluorophosphate (BOP) reagent (0.22 g, 0.5 mmol, 2.0 equiv) was added and the resultant reaction mixture was allowed to react for a few minutes. 2-Aminoethanesulfonic acid (63 mg, 0.5 mmol, 2 equiv) was dissolved into 50% DMF aqueous solution containing a few drops of triethylamine and this solution was subsequently added to the reaction mixture. This mixture was stirred for one day at room temperature and then evaporated under reduced pressure. The residue was dissolved into water and an excess of octyltrimethylammonium bromide was added. The ion-paired product of lipid·octyltrimethylammonium was extracted with CH_2Cl_2 and the organic layer was separated and dried over Na_2SO_4. An addition of a solution of $NaClO_4$ in MeCN into the organic layer resulted in a white precipitate. The precipitate was recovered by filtration and washed with CH_2Cl_2 and MeCN in that order. This operation gave the white solid **2** (100 mg, 55%): mp decomposed at 230 °C; ^{1}H NMR (600 MHz, [D$_6$]DMSO): $\delta = 0.85$ (t, 6H, $J = 6.72$ Hz), 1.20–1.28 (br d, 36H), 1.30–1.40 (br d, 4H), 1.62–1.81 (m, 4H), 1.99 (t, 2H, $J = 7.07$ Hz), 2.05–2.14 (m, 4H), 2.53–2.61 (m, 2H), 2.92–3.01 (br d, 4H), 3.24–3.30 (m, 2H), 4.11–4.15 (m, 1H), 7.77–7.80 (m, 2H), 7.85 (t, 1H, $J = 5.64$ Hz), 8.02 ppm (d, 1H, $J = 7.92$ Hz); IR (ATR): $\tilde{\nu}_{max} = 1639, 1177, 1060$ cm^{-1}; MALDI-TOF MS found m/z 726([M+H]$^+$), 748([M+Na]$^+$); calcd for $C_{36}H_{69}N_4O_7SNa$ m/z 726([M+H]$^+$), 748([M+Na]$^+$).

Pyrrole (Tokyo Kasei Kogyo) was used after distillaion. Ethylenedioxythiophene (Aldrich), and Sodium perchlorate (Tokyo Kasei Kogyo) were used as received. CV experiments were performed with a one-compartment, three-electrode electrochemical cell driven by an electrochemical analyzer (Autolab PGSTAT12 potentiostat/galvanostat) in aqueous solution containing supporting electrolyte ($NaClO_4$, 50 mM) and 10% MeOH. The oxidative polymerization of ethylenedioxythiophene was carried out in a CV cell with an ITO electrode as the working electrode, a Pt counter electrode and an Ag/AgCl reference electrode. The redox was repeated in a voltage range of −0.5–0.9 V (versus Ag/AgCl) with scan rate 0.05 mV s^{-1} at 25 °C. The oxidative polymerization of pyrrole was carried out in a CV cell by using an ITO electrode as the working electrode, a Pt counter electrode and an Ag/AgCl reference electrode. The redox was repeated in a voltage range of −0.5–0.8 V (versus Ag/AgCl) with scan rate 0.05 V s^{-1} at 25 °C. After polymerization, five redox cycles in the corresponding range were performed in 50 mM $NaClO_4$ aqueous solution to wash the film. Conductivity measurements were carried out Autolab PGSTAT12 with BIPOT bipotentiostat. Atomic force microscopy (AFM) studies were carried out on a Topometrix TMX-2100 (noncontact mode). SEM studies were carried out on a Hitachi S-5000. Transmission electron microscopy TEM studies were carried out on a JEOL JEM-2010. ATR IR spectra were recorded with a PerkinElmer Spectrum One.

Received: April 25, 2003
Revised: October 24, 2003 [Z51749]

Keywords: conducting materials · helical structures · lipids · polymerization · template synthesis

[1] D. T. McQuade, A. E. Pullen, T. M. Swager, *Chem. Rev.* **2000**, *100*, 2537–2574.
[2] E. Pringsheim, E. Terpetschnig, S. A. Piletsky, O. S. Wolfbeis, *Adv. Mater.* **1999**, *11*, 865–868.
[3] E. Shoji, M. S. Freund, *J. Am. Chem. Soc.* **2001**, *123*, 3383–3384.
[4] T. Iyoda, M. Ando, T. Kaneko, A. Ohtani, T. Shimizu, K. Honda, *Langmuir* **1987**, *3*, 1169–1170.
[5] W. Wernet, M. Monkenbusch, G. Wegner, *Macromol. Rapid Commun.* **1984**, *5*, 157–164.
[6] a) M. Kanungo, A. Kumar, A. Q. Contractor, *J. Electroanal. Chem.* **2002**, *528*, 46–56; b) Z. Zhong, M. Wan, *Synth. Met.* **2002**, *128*, 83–89; c) Z. Zhong, M. Wan, *Adv. Mater.* **2002**, *14*, 1314–1317; d) L. Qu, G. Shi, *Chem. Commun.* **2003**, 206–207; e) Z. Wei, M. Wan, T. Lin, L. Dai, *Adv. Mater.* **2003**, *15*, 136–139.
[7] J. F. Hulvat, S. I. Stupp, *Angew. Chem.* **2003**, *115*, 802–805; *Angew. Chem. Int. Ed.* **2003**, *42*, 778–781.
[8] J. H. Georger, A. Singh, R. R. Price, J. M. Schnur, P. Yager, P. E. Schoen, *J. Am. Chem. Soc.* **1987**, *109*, 6169–6175.
[9] a) M. Ikegame, K. Tajima, T. Aida, *Angew. Chem.* **2003**, *115*, 2204–2207; *Angew. Chem. Int. Ed.* **2003**, *42*, 2154–2157; b) G. Li, S. Bhosale, T. Wang, Y. Zhang, H. Zhu, J. H. Fuhrhop, *Angew. Chem.* **2003**, *115*, 3948–3951; *Angew. Chem. Int. Ed.* **2003**, *42*, 3818–3821.
[10] a) J. H. Jung, Y. Ono, K. Hanabusa, S. Shinkai, *J. Am. Chem. Soc.* **2000**, *122*, 5008–5009; b) J. H. Jung, Y. Ono, K. Sakurai, M. Sano, S. Shinkai, *J. Am. Chem. Soc.* **2000**, *122*, 8648–8653; c) Y. Ono, K. Nakashima, M. Sano, J. Hojo, S. Shinkai, *J. Mater. Chem.* **2001**, *11*, 2412–2419.
[11] S. Kobayashi, N. Hamasaki, M. Suzuki, M. Kimura, H. Shirai, K. Hanabusa, *J. Am. Chem. Soc.* **2002**, *124*, 6550–6551, and references therein.

 © 2004 Wiley-VCH Verlag GmbH & Co. KGaA, Weinheim

[12] A. M. Seddon, H. M. Patel, S. L. Burkett, S. Mann, *Angew. Chem.* **2002**, *114*, 3114 – 3117; *Angew. Chem. Int. Ed.* **2002**, *41*, 2988 – 2991, and references therein.
[13] K. Katagiri, R. Hamasaki, K. Ariga, J. Kikuchi, *J. Am. Chem. Soc.* **2002**, *124*, 7892 – 7893.
[14] J. H. Jung, S. Shinkai, T. Shimizu, *Nano Lett.* **2002**, *2*, 17 – 20.
[15] K. Sugiyasu, S. Tamaru, M. Takeuchi, D. Berthier, I. Huc, R. Oda, S. Shinkai, *Chem. Commun.* **2002**, 1212 – 1213.
[16] For recent reviews see a) G. J. de A. A. Soler-Illia, C. Sanchez, B. Lebean, J. Patorin, *Chem. Rev.* **2002**, *102*, 4093 – 4138; b) K. J. C. van Bommel, A. Friggeri, S. Shinkai, *Angew. Chem.* **2003**, *115*, 1010 – 1030; *Angew. Chem. Int. Ed.* **2003**, *42*, 980 – 999.
[17] a) Y. Ono, K. Nakashima, M. Sano, Y. Kanekiyo, K. Inoue, J. Hojo, S. Shinkai, *Chem. Commun.* **1998**, 1477 – 1478; b) J. H. Jung, Y. Ono, S. Shinkai, *Chem. Eur. J.* **2000**, *6*, 4552 – 4557.
[18] The helical structure of CdS has been also created; E. D. Sone, E. R. Zubarev, S. I. Stupp, *Angew. Chem.* **2002**, *114*, 1781 – 1785; *Angew. Chem. Int. Ed.* **2002**, *41*, 1705 – 1709.
[19] a) T. Hatano, M. Takeuchi, A. Ikeda, S. Shinkai, *Chem. Commun.* **2003**, 342 – 343; b) T. Hatano, M. Takeuchi, A. Ikeda, S. Shinkai, *Chem. Lett.* **2003**, 314 – 315; c) T. Hatano, M. Takeuchi, A. Ikeda, S. Shinkai, *Org. Lett.* **2003**, *5*, 1395 – 1398.
[20] For compound **1** see H. Hachisako, Y. Murata, H. Ihara, *J. Chem. Soc. Perkin Trans. 2* **1999**, 2569 – 2577. For the helical structure of lipid molecules see N. Nakashima, S. Asakuma, T. Kunitake, *J. Am. Chem. Soc.* **1985**, *107*, 509 – 510.
[21] N. Sakmeche, S. Aeiyah, J. J. Aaron, M. Jouini, L. C. Lacroix, P. C. Lacaze, *Langmuir* **1999**, *15*, 2566 – 2574.
[22] TEM pictures were taken without staining treatment. Therefore, the observed contrast is due to the formation of conductive polymers.
[23] G. Schiavon, S. Sitran, G. Zotti, *Synth. Met.* **1989**, *32*, 209 – 217.
[24] K. Krishnamoorthy, A. V. Ambade, S. P. Mishra, M. Kanungo, A. Q. Contractor, A. Kumar, *Polymer* **2002**, *43*, 6465 – 6470.
[25] Since the interdigitated microelectrode gaps were not filled with helical fibers, it was difficult to transfer the observed drain current to conductance.
[26] In the electrochemical polymerization, the value of electric current increased during the successive potential sweeping in the presence of **2** (see Supporting Information).

 © 2004 Wiley-VCH Verlag GmbH & Co. KGaA, Weinheim

Zeolite Structures

Pressure-Induced Hydration Effects in the Zeolite Laumontite**

*Catherine L. I. M. White, A. Rabdel Ruiz-Salvador, and Dewi W. Lewis**

The hydration level of minerals is an important indicator of the conditions prevailing during their formation and during any subsequent geological transformation. The precise water content of mineral zeolites, often highly sensitive to pressure and temperature due to their microporous structure, is particularly key in estimating rock porosity. The presence of the mineral zeolite laumontite near petroleum deposits, for example, can significantly reduce rock permeability, which may limit the production potential of the reservoir.[1] However, since laumontite readily partially dehydrates at ambient conditions[1,2] the exact composition during formation and subsequent diagenesis remains a key question. Neuhoff and Bird[1] postulated that laumontite ($Ca_4Si_{16}Al_{18}O_{48}\cdot 18H_2O$) actually forms as "leonhardite" ($Ca_4Si_{16}Al_{18}O_{48}\cdot 14H_2O$)[3] and only becomes fully hydrated at elevated pressures. Lee et al.[4–6] recently showed that another natural zeolite, natrolite, undergoes pressure-induced overhydration. As a consequence, it is imperative that we can determine the structure of such zeolites at nonambient conditions if we are to understand, not only their geochemistry, but also to assess the impact of extreme conditions on their suitability as, for example, nuclear-waste-containment and barrier materials. Here, we show using computational methods that laumontite can transform from the low-water "leonhardite" composition to the fully hydrated structure under the influence of pressure.

Laumontite (LAU·$18H_2O$; Figure 1) is one of the more common natural zeolites. The structure comprises channels bounded by eight tetrahedral units, parallel to the *c* axis, that contain Ca^{2+} ions coordinated to the framework and water (labeled[2] W2 and W8), together with an additional hydrogen-bonded water network (W1 and W5). At ambient conditions the water molecules labeled W1 are readily lost (reversibly) to give $Ca_4Si_{16}Al_{18}O_{48}\cdot 14H_2O$ (LAU·$14H_2O$). Indeed, typical samples of laumontite have $\approx 16H_2O$ molecules per unit cell and the fully hydrated material can only be obtained by prolonged immersion in water.[2,7,8] Furthermore, laumontite often occurs with a composition of Ca_4Si_{16}-

[*] C. L. I. M. White, Dr. D. W. Lewis
Centre for Theoretical and Computational Chemistry
Department of Chemistry, University College London
20 Gordon Street, London WC1H 0AJ (UK)
Fax: (+44) 20-7679-7463
E-mail: d.w.lewis@ucl.ac.uk
A. R. Ruiz-Salvador
Zeolite Engineering Laboratory, IMRE—Faculty of Physics University of Havana, Havana 10400 (Cuba)

[**] The EPSRC is acknowledged for funding of this work.

Supporting information for this article is available on the WWW under http://www.angewandte.org or from the author.

 DOI: 10.1002/anie.200352364 © 2004 Wiley-VCH Verlag GmbH & Co. KGaA, Weinheim

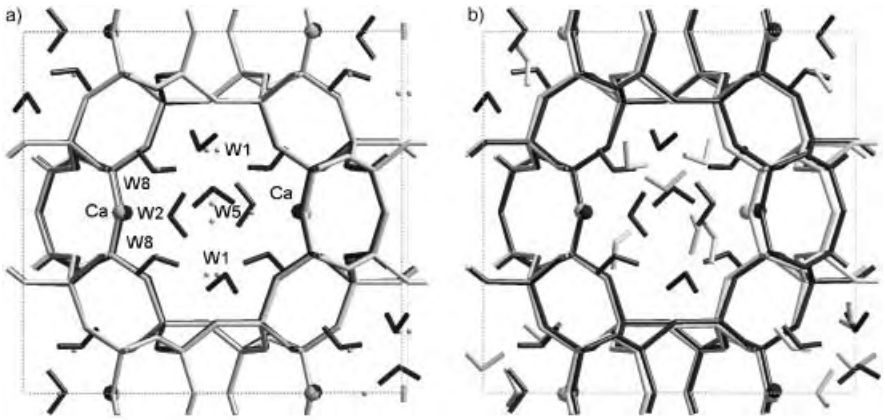


Figure 1. a) Comparison of calculated LAU·18 H_2O (black) with the experimental structure (gray) of Fridriksson et al.[8] Note that all possible partially occupied experimental water sites (O only) are shown. For example, only one of the adjacent W1 sites can be occupied, as is the case for the W5 site; b) comparison of the calculated LAU·14 H_2O structure (gray) obtained by dehydration of the calculated LAU·18 H_2O structure (black). Note the loss of the W1 water molecules and the increase in disorder (also see Supporting Information).

$Al_{18}O_{48}$·14 H_2O, commonly referred to as "leonhardite",[3] particularly in mineral deposits that are geothermal in nature (i.e., near the earth's surface). However, the water content of laumontite in deeper deposits cannot be determined accurately, due to the facile loss of water at ambient conditions. Here, we have constructed models for LAU·18 H_2O and LAU·14 H_2O phases and performed energy minimization calculations to simulate the dehydration behavior and then determine the relative stability and structure of these phases to the application of external pressure.

Computer modeling of zeolitic materials has enjoyed considerable success over the past couple of decades, driven in no small degree by their application as catalysts. Consequently, most studies have focused on acidic, high-silica (uncommon in natural zeolites) materials in their dehydrated state. Furthermore, modeling of hydrated systems is notoriously difficult, often failing to accurately reproduce experimental observations.[9] However, we believe that we have made significant progress in this field recently, demonstrating that we are both able to reproduce experimental structures and also to provide thermochemical mechanisms for cation and framework compositions.[10,11] The simulations are based on the classical Born model of solids with interatomic potentials describing the forces between the atoms. Energy minimizations were performed with the GULP program,[12] by using the potential parameters described by Jackson and Catlow[13] and de Leeuw et al.,[14,15] with minor modifications by Lewis et al.[11] We have already successfully modeled a number of hydrated calcium-bearing zeolites[10,11] using these parameters and methods.

Optimized models of the unit cell of fully hydrated laumontite (LAU·18 H_2O) were constructed that compared very favorably (Figure 1) with the latest crystallographic study by Fridriksson et al.[8] A number of alternative models have also been optimized that give a similar quality of fit and differ only by the relative orientations of the hydrogen-bonded water molecule in the center of the channel. The largest deviation from experiment is ≈2%, mainly due to the Ca–OH_2 bond lengths being underestimated by ≈5%.

A stepwise dehydration[11] of the structure was performed, similar in some respects to that used by Ferey and co-workers[16,17] to simulate the removal of templates from zeolites by calcination. Each unique water molecule is removed in turn, with each of the structures obtained being then optimized, before removing a further water molecule from the lowest-energy structure; a procedure repeated until all the water is removed (Figure 2). At the "leonhardite" (LAU·14 H_2O) composition, only water from the W1 site had been lost, with the W5 water molecules being the next to be lost: the same as found experimentally,[2,8] which confirms the accuracy of the potentials in modeling the energetics of the system. The calculated average enthalpy of dehydration of the first four water molecules (75 kJ mol^{-1}) is significantly lower than that of the remaining water molecules (102 kJ mol^{-1}), corroborating the experimental observation[2,7,8] of facile dehydration at ambient conditions, particularly to give a composition with ≈16 H_2O. The total dehydration enthalpy of LAU·18 H_2O and LAU·14 H_2O is calculated to be 96 and 102 kJ mol^{-1} per water molecule, respectively, which compares remarkably well with experimental values of 80 and 84 kJ mol^{-1}.[18] The changes in unit-cell dimensions (Figure 2; see also the Supporting Information) are also in excellent agreement with those measured during in situ diffraction studies of dehydration,[2] with major changes noted when the water content reduces to 14 H_2O

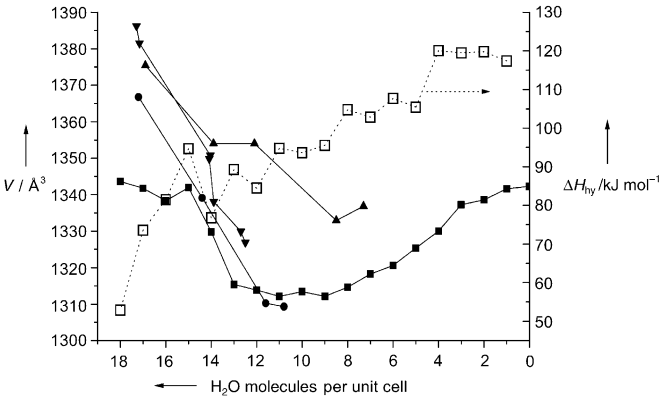


Figure 2. Calculated dehydration profile of laumontite: Dehydration enthalpies, δH_{hy} (----, □, right axis), for each of the water molecules (each is relative to vapor-phase water) and calculated (■) unit-cell volumes, *V*, compared with the experimental values of Stahl et al.[2] (▲), Armbruster and Kohler[7] (●), and Fridriksson et al.[8] (▼), on the left axis. Experimentally, water is lost at four distinct temperatures. Full dehydration is not possible experimentally without transformation to wairakite (note that our model would not allow such a structural transformation). Stahl et al.[2] report that eight H_2O molecules remain up to 600 °C, which corresponds to the increase to higher dehydration energies at such a composition observed in our calculations.

 © 2004 Wiley-VCH Verlag GmbH & Co. KGaA, Weinheim

molecules per unit cell. We find that the β angle in the cell increases initially before decreasing and there is a rapid decrease in b and c when the hydrogen-bonded water molecules are removed, whilst a decreases more gradually (Supporting Information, Figure 1).

Structurally, the same trends in water-site occupation are observed as in experiments, that is, W1 water molecules being lost first followed by W5. In addition, after the W1 water molecule is lost, disorder is introduced at the W8 site, which concurs with the smearing of electron density at this site that was found by Fridriksson et al.[8] Similarly, it was found that below a composition of LAU·12 H_2O, (corresponding to the loss of all the original hydrogen-bonded water molecules) the remaining water is further disordered with often little distinction between the W2 and W8 sites. Such disorder is a consequence of the remaining water having to satisfy both the coordination sphere of Ca^{2+} and maintain the structural integrity of the pore. This provides an explanation of why, experimentally, the structure undergoes a phase transformation to wairakite when the water content drops to $\approx 8\,H_2O$.[2]

Both the LAU·18 H_2O and LAU·14 H_2O structures were then subjected to optimization at pressures of 0–15 GPa (Figure 3). LAU·14 H_2O undergoes volume contraction,

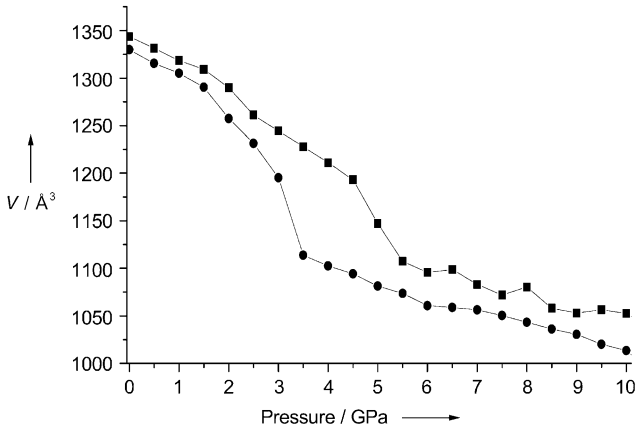


Figure 3. Calculated unit-cell volume V as a function of pressure: LAU·18 H_2O (■) and LAU·14 H_2O (●) undergo a phase transformation between 4–5.5 GPa and 3–3.5 GPa, respectively.

which becomes more severe as the pressure increases (between 2–3 GPa) and then undergoes a dramatic phase transformation at 3.5 GPa (Figure 4 a). In contrast, the rate of change of cell volume with pressure for the fully hydrated structure (LAU·18 H_2O) does not increase significantly until it also undergoes a phase transition at ≈ 5.5 GPa (Figure 4 b). However, the perturbation to the water structure is much more severe in LAU·18 H_2O when it undergoes this phase transformation (compared to that calculated for LAU·14 H_2O); evidence that at such pressures a complete structural rearrangement may occur. We note that wairakite is found in deeper deposits than laumontite[19] and that a phase

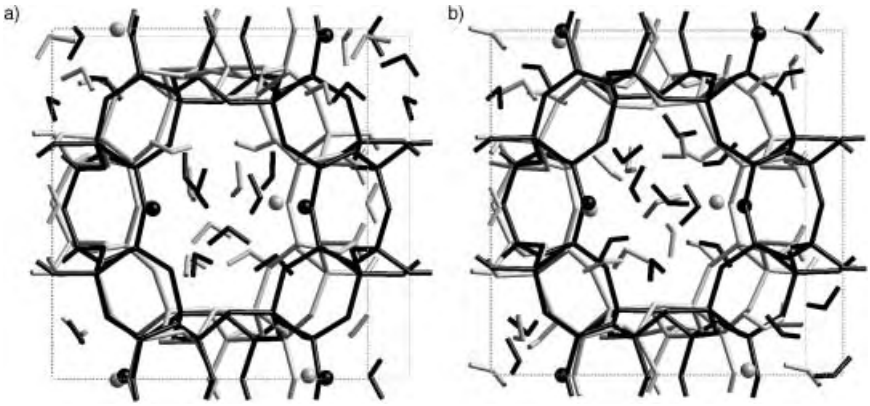


Figure 4. Phase transformations at high pressure: a) LAU·14 H_2O at 3.5 GPa (gray) compared to 2.5 GPa (black); b) LAU·18 H_2O at 5.5 GPa (gray) compared to 0.01 GPa (black). Also see Supporting Information.

transformation to wairakite occurs on the thermal dehydration of laumontite.

A convergence in the enthalpies of the two systems (LAU·18 H_2O compared with LAU·14 H_2O + 4 H_2O) is observed; although the exact crossover point is dependant on the phase of water we choose. However, since these calculations do not include entropic contributions, we would not wish to rely solely on an energetic argument of stability. Nevertheless, it is quite clear that structurally, LAU·14 H_2O begins to collapse at ≈ 1.5–2.0 GPa and becomes increasingly unstable above 3.5 GPa. In contrast, LAU·18 H_2O remains stable to higher pressures. Indeed (assuming that the uptake of water is not kinetically controlled), it may be expected that LAU·14 H_2O would transform to LAU·18 H_2O once the cell volumes become comparable (≈ 1.5–2 GPa). Experimentally, the overhydration of the zeolite natrolite occurs at ≈ 1.2 GPa,[5] whilst in a separate study on the natrolite family[20] we calculated that the overhydrated phase was not favored up to a pressure of ≈ 4 GPa. Thus, given such a discrepancy between experiment and calculation (which is relatively small, in this context[20]) we expect "leonhardite" to be fully transformed to laumontite below 1 GPa, and may transform at significantly lower pressures. Such pressures correspond to depths of up to ≈ 10 km, where laumontite is typically found.

We note that the methods used here make many simplifications (e.g., by being a static representation at 0 K), but their suitability is clear, not only from the reproduction of experimental observations (structure and dehydration behavior), but also from their general applicability, robustness, and low computational cost. Furthermore, we are able to simulate our materials at conditions inaccessible to experimentation, such as the "leonhardite" composition at high pressures. Other (more costly) methods provide further detail of the mechanisms, for example, librations of the water molecules[21] but the methods used here are clearly appropriate for the modeling of phase changes.

Our simulations clearly show that when pressure is applied, the structural stability of the laumontite framework is enhanced by the presence of a fully occupied water

 © 2004 Wiley-VCH Verlag GmbH & Co. KGaA, Weinheim

network. Conversely, since the W1 water molecule is only loosely bound, we do not consider it necessary for the water network to be fully occupied during the formation of the laumontite structure. Indeed, a number of other calcium zeolites form with little or no water that is not directly coordinated to the calcium ions. Our results, therefore, support the postulate of Neuhoff and Bird[1] that laumontite formation at the earth's surface results in a material with the "leonhardite" ($LAU{\cdot}14H_2O$) composition and that subsequent application of pressure, as a result of burial, leads to diagenesis to the fully hydrated phase ($LAU{\cdot}18H_2O$). Thus, fully hydrated laumontite can be considered to be a pressure-induced overhydrated phase of the "as-formed" material. Since we predict that the transformation to the $LAU{\cdot}18H_2O$ structure will occur at (or below) pressures of ≈ 1 GPa, we suggest that laumontite should be treated as being fully hydrated when considering its impact on rock porosity and petrology. Work is underway to determine if there is scope for any higher levels of hydration, analogous to the overhydration of natrolite.[4]

Received: July 14, 2003 [Z52364]

Keywords: computer chemistry · geochemistry · high-pressure chemistry · phase transitions · zeolites

[1] P. S. Neuhoff, D. K. Bird, *Mineral. Mag.* **2001**, *65*, 59.
[2] K. Stahl, G. Artioli, J. C. Hanson, *Phys. Chem. Miner.* **1996**, *23*, 328.
[3] Note, the mineral name "leonhardite" has been discredited as a unique mineral phase (since it merely differs from laumontite in water content) by the International Mineralogical Association (see D. S. Coombs, A. Alberti, T. Armbruster, G. Artioli, C. Colella, E. Galli, J. D. Grice, F. Liebau, J. A. Mandarino, H. Minato, E. H. Nickel, E. Passaglia, D. R. Peacor, S. Quartieri, R. Rinaldi, M. Ross, R. A. Sheppard, E. Tillmanns, G. Vezzalini, *Eur. J. Mineral.* **1998**, *10*, 1037). However, we retain the terminology here for convenience.
[4] Y. Lee, J. A. Hriljac, T. Vogt, J. B. Parise, G. Artioli, *J. Am. Chem. Soc.* **2001**, *123*, 12732.
[5] Y. Lee, T. Vogt, J. A. Hriljac, J. B. Parise, G. Artioli, *J. Am. Chem. Soc.* **2002**, *124*, 5466.
[6] Y. Lee, T. Vogt, J. A. Hriljac, J. B. Parise, J. C. Hanson, S. J. Kim, *Nature* **2002**, *420*, 485.
[7] T. Armbruster, T. Kohler, *Neues Jahrb. Mineral. Monatsh.* **1992**, 385.
[8] T. Fridriksson, D. L. Bish, D. K. Bird, *Am. Mineral.* **2003**, *88*, 277.
[9] J. R. Hill, A. R. Minihan, E. Wimmer, C. J. Adams, *Phys. Chem. Chem. Phys.* **2000**, *2*, 4255.
[10] N. Almora-Barrios, A. Gómez, A. R. Ruiz-Salvador, M. Mistry, D. W. Lewis, *Chem. Commun.* **2001**, 531.
[11] D. W. Lewis, A. R. Ruiz-Salvador, N. Almora-Barrios, A. Gomez, M. Mistry, *Mol. Simul.* **2002**, *28*, 649.
[12] J. D. Gale, *J. Chem. Soc. Faraday Trans.* **1997**, *93*, 629.
[13] R. A. Jackson, C. R. A. Catlow, *Mol. Simul.* **1988**, *1*, 207.
[14] N. H. de Leeuw, S. C. Parker, *Phys. Rev. B* **1998**, *58*, 13901.
[15] N. H. de Leeuw, S. C. Parker, *J. Am. Ceram. Soc.* **1999**, *82*, 3209.
[16] T. Loiseau, C. Mellot-Draznieks, C. Sassoye, S. Girard, N. Guillou, C. Huguenard, F. Taulelle, G. Ferey, *J. Am. Chem. Soc.* **2001**, *123*, 9642.
[17] S. Girard, A. Tuel, C. Mellot-Draznieks, G. Ferey, *Angew. Chem.* **2002**, *114*, 1014; *Angew. Chem. Int. Ed.* **2002**, *41*, 972.
[18] I. Kiseleva, A. Navrotsky, I. A. Belitsky, B. A. Fursenko, *Am. Mineral.* **1996**, *81*, 658.
[19] M. Utada in *Natural Zeolites: Occurance, Properties, Applications, Vol. 45* (Eds.: D. L. Bish, D. W. Ming), The Mineralogical Society of America, Washington, DC, **2001**, pp. 277.
[20] T. Gibbs, D. W. Lewis, unpublished results.
[21] E. Fois, A. Gamba, G. Tabacchi, S. Quartieri, G. Vezzali, *Phys. Chem. Chem. Phys.* **2001**, *3*, 4158.

 © 2004 Wiley-VCH Verlag GmbH & Co. KGaA, Weinheim

Magnetic Materials

One-Dimensional Magnetism in Anhydrous Iron and Cobalt Ternary Oxalates with Rare Trigonal-Prismatic Metal Coordination Environment**

*Michael B. Hursthouse, Mark E. Light, and Daniel J. Price**

Solid-state coordination chemistry of oxalate (ox) compounds continues to receive much attention, with new structure types being reported for even the simplest binary oxalates.[1] In anhydrous materials complex network structures are formed owing to the high degree of ox^{2-} coordination (bridging up to six metal ions). In contrast hydrates and materials containing additional noncoordinating cations[2] tend have reduced oxalate coordination, linking only two metals with the symmetric bischelating mode as the dominant bridging motif in the network structure. While there are a great many hydrated ternary oxalates very few anhydrous salts are known.[3] Most ternary oxalates are formed at high ox^{2-}:M^{n+} ratios (M = metal center) resulting in simple discrete anionic complexes with $[M(ox)_{2-4}]^{m-}$ compositions although in a few cases the $[M_q(ox)_r]^{m-}$ component forms an extended network structure.[4]

The oxalate dianion is well known to mediate a significant antiferromagnetic exchange interaction when it bridges paramagnetic ions, and transition-metal oxalates[5] have played a key role in the development of molecular-based magnetism. New oxalate-bridged transition-metal networks are likely to provide many new and useful model magnetic systems.

We have used hydrothermal synthesis to produce a new anhydrous ternary metal oxalate; $K_2M(ox)_2$ which comprises

[*] Prof. Dr. M. B. Hursthouse, Dr. M. E. Light, Dr. D. J. Price
School of Chemistry
University of Southampton
Highfield, Southampton, SO17 1BJ (UK)
Fax: (+44) 238-059-6805
E-mail: daniel.price@soton.ac.uk

[**] D.J.P. gratefully acknowledges financial support in the form of an Advance Research Fellowship from the EPSRC of the UK. We thank Dr. H. J. Blythe (University of Sheffield) for his assistance with magnetization measurements and Dr. A. L. Hector (University of Southampton) for TGA measurements.

Supporting information for this article is available on the WWW under http://www.angewandte.org or from the author.

 © 2004 Wiley-VCH Verlag GmbH & Co. KGaA, Weinheim DOI: 10.1002/anie.200352406

a network structure in which chains of Fe^{II} or Co^{II} ions are coordinated in a rare trigonal-prismatic environment.

Hydrothermal reaction of mixtures containing MCl_2 (M = Fe, Co), K_2ox, KBr, and H_2O (in an approximately 1:2:25:200 molar ratio) yield crystals of $K_2M(ox)_2$ (M = Fe (**1**), Co (**2**)), and KBr on cooling from 225 °C. Addition of water to the cooled reaction mixture results in the decomposition of the ternary oxalate and the precipitation of $Mox(H_2O)_2$. Experiments show that a minimum potassium-ion concentration of approximately 6 Molar is required to from these products. This situation implies that the chemical potential of potassium ions in these materials is very high, and that neither of these compounds can be crystallized from a solution containing the components in the same stoichiometry as in the solid phases.

Compounds **1** and **2** are isostructural, crystallizing[6] in the space group *P*2/*c*. The asymmetric unit contains one Fe^{II}/Co^{II} ion, three potassium cations and three crystallographically distinct oxalate anions (Figure 1). Each transition-metal center is coordinated by three oxalate ligands in the usual chelating mode. The M^{II} ion has a rare trigonal-prismatic coordination geometry. The O···O separations along the triangular face of the prism fall between 2.776–3.005 Å for **1** and 2.711–2.935 Å, for **2**, while the O···O distances between these triangular faces are constrained by the oxalate anions and lie in the narrow range 2.643–2.677 Å for both compounds. The degree of distortion from trigonal-prismatic geometry can be characterized by the twist angle φ ($\varphi = 0°$ for a trigonal prism, $\varphi = 30°$ for a trigonal antiprism), we determine $\varphi = 1.68$ and 1.75° for **1** and **2**, respectively. The

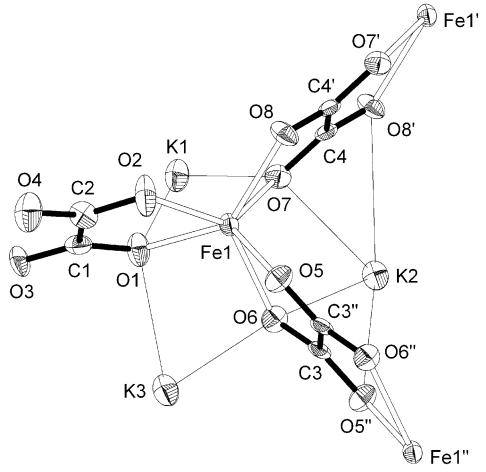


Figure 1. The asymmetric unit of $K_2M(ox)_2$; M = Fe (**1**) and selected symmetry equivalent atoms, showing the trigonal-prismatic coordination of the transition-metal ion and the bridging coordination of two of the oxalate dianions. Thermal ellipsoids are set at 90% probability. Selected bond lengths [Å] an angles [°] for **1** (M = Fe)/**2** (M = Co): M1-O1 2.091(4)/2.059(3), M1-O2 2.107(5)/2.071(3), M1-O5 2.141(7)/2.121(3), M1-O6 2.174(6)/2.151(3), M1-O7 2.138(6)/2.115(3), M1-O8 2.159(6)/2.137(3); O1-M1-O2 78.02(11)/79.87(12), O1-M1-O5 131.36(11)/132.47(12), O1-M1-O6 84.51(10)/84.14(13), O1-M1-O7 90.56(10)/89.36(13), O1-M1-O8 140.94(11)/141.86(12), O2-M1-O5 88.28(11)/87.40(13), O2-M1-O6 139.93(11)/140.74(13), O2-M1-O7 135.08(11)/135.97(13), O2-M1-O8 85.24(11)/84.99(13), O5-M1-O6 76.70(10)/77.47(13), O5-M1-O7 128.52(10)/128.23(13), O5-M1-O8 82.56(10)/80.95(12), O6-M1-O7 80.17(10)/78.90(13), O6-M1-O8 127.97(10)/126.88(13), O7-M1-O8 76.83(10)/77.66(13).

three potassium environments show considerable variation in their coordination; K3 is six coordinate in a distorted octahedral environment, K1 occupies a distorted square antiprism, and K2 is in an irregular nine-coordinate geometry.

The structure can be considered as infinite chains of transition-metal oxalate, with the formula $[M^{II}(ox)_2]_n^{2n-}$ separated from each other by the potassium cations (Figure 2). These anionic chains contain the two distinct types of oxalate ion, one of which is simply coordinated to a single M ion, while the others bridge two M ions in the common bischelating mode (Figure 1). This results in a zigzag chain running along the *a* axis with M···M separations of 5.570(15) for **1** and 5.512(2) Å for **2**.

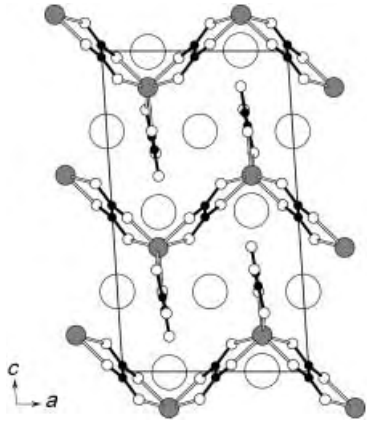


Figure 2. Packing diagram of **1**, viewed along the *b* axis, showing the interdigitation of the $[M(ox)_2]_n^{2n-}$ chains and the relative positions of the potassium counter ions. K large open circles, Fe gray circles, O small open circles, C black circles.

The $[M(ox)_2]_n^{2n-}$ chains pack with the capping oxalate from adjacent chains being interdigitated, which results in layers in the *ac* plane.

The trigonal-prismatic geometry for Fe^{II} and Co^{II} centers is rare. A few examples of high spin $M^{II}O_6$ coordination are known[7,8] but in most cases the M^{II} cation is also found in other coordination geometries within the crystal structure. While both Fe^{II} and Co^{II} stand to lose considerable crystal-field stabilization energy (CFSE) by not adopting an octahedral geometry, repulsion-energy calculations favor a geometry between trigonal-prism and trigonal-antiprism for trischelated metal ions.[9] On these electrostatic arguments we expect the normalized ligand bites (defined as the ratio of the distance between donor atoms on a chelating ligand and the average metal-to-donor-atom separation) of 1.248 and 1.263 for **1** and **2** to have corresponding twist angles of approximately 22°. It is clear that the observed coordination geometry is only formed under exceptional conditions. In this case packing forces in $K_2M(ox)_2$ are responsible for stabilizing the MO_6 trigonal-prismatic geometry in the solid state.

Another unusual feature of these materials is the transition-metal-oxalate chain motif. While a number of "zigzag" oxalate chains are known,[10] in most cases a bidentate amine has been used to cap two *cis*-related coordination sites on the metal center, which prevents further oxalate coordination and

 © 2004 Wiley-VCH Verlag GmbH & Co. KGaA, Weinheim

a more extensive structure. Only one other example of a chain where an oxalate has a capping function has been reported; $[C_6N_2H_{14}][Zn(ox)_2](H_2O)_3$.[11]

The magnetic susceptibility of **1** shows three distinct features (Figure 3): an abrupt step-like transition at 117(3) K, a broad maximum centered at 18.5(5) K and a "paramagnetic tail" at the lowest experimental temperatures. The transition at 117 K is due to the Verwey transition[12] in magnetite, a common minor impurity from hydrothermal methods[13] (in this case we estimate the magnetite impurity at $\approx 0.4\,\%$). The broad maximum at 18 K is characteristic of the low-dimensional antiferromagnetic behavior[14] expected for **1**, while the "paramagnetic tail" at the lowest temperatures is normally associated with a low level of paramagnetic impurity. In this case defects in the chain may result in paramagnetic-like behavior from "chain ends".[15] The precise behavior of magnetite in the vicinity of the Verwey transition is very sample dependent,[16] being influenced by particle size, purity, crystal orientation and applied field strength. Consequently we exclude the region between 90–120 K from our analysis. At first we attempted to model the observed behavior as a sum of three components; a contribution from the magnetite impurity, a component from a simple linear antiferromagnetically coupled chain[17] plus a small contribution from a paramagnetic impurity. Data below the broad maximum is not well described by this model as the susceptibility is observed to decrease more rapidly than expected. A better fit is obtained by excluding the data below 12 K and fitting with just the 1D antiferromagnetic model plus a magnetite contribution (Figure 3). This approach gives an oxalate-mediated exchange coupling of "$2J/k_B$" $= -4.65(5)$ K and a g value of 2.24(2) for a high spin $S = 2$ electronic configuration. The interaction strength is a little weaker compared with other similarly bridged Fe^{II} compounds[18] which range from -7 to -11 K. The low-temperature deviation of the susceptibility could signify either a transition to a long-range ordered antiferromagnetic state (which is not evident in the powder susceptibility measurement) or more interestingly, unusual quantum phase behavior. In particular integer-spin antiferromagnetic chains are predicted to show a "Haldane" gap[19] between a nonmagnetic quantum ground state and the first excited triplet state. While there are several convincing examples of $S = 1$ Haldane materials,[20] $S = 2$ examples remain unknown. In addition advances in theory now suggest[21] a fundamental difference exists between the ground-state quantum-order of odd and even integer 1D antiferromagnets.

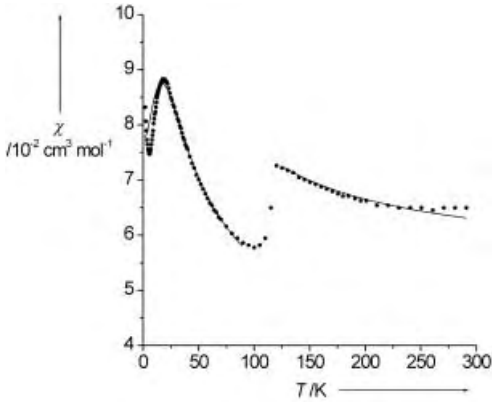


Figure 3. The magnetic susceptibility of **1** showing the three distinct features described in the main text, and the best fit to the data.

The magnetism of **2** (Supporting Information) is not complicated by impurities. On cooling **2** shows a broad maximum in χ at 47(2) K followed by a discontinuity at 37 K. The data above 120 K is well described by the Curie–Weiss law with $C = 3.66(2)\ \mathrm{cm^{-3}\,K\,mol^{-1}}$ and $\theta = -41(1)$ K. The room temperature moment of $5.04\,\mu_B$ is large compared to the spin only expectation for a high-spin configuration, which signifies a substantial orbital contribution. This contribution can be parameterized in an effective g value of 2.60. All the data in the paramagnetic regime above 37 K is very well described by the antiferromagnetic chain model[17] with $S = 3/2$, least-squares analysis give a coupling constant "$2J/k_B$" $= -19.5(1)$ K. This value is considerably larger than for comparable oxalate-bridged $Co^{II}O_6$ octahedra.[18a,22] It appears that at 37 K the sample undergoes a magnetic phase transition, to an ordered, essentially 3D antiferromagnetic state. Interchain interactions and single ion anisotropy are likely to be responsible for this dimensionality crossover.

In summary we have demonstrated the synthesis of an uncommon anhydrous ternary oxalate from very concentrated aqueous potassium-ion solutions. The transition-metal environment in these materials is a rare trigonal-prismatic geometry. From a magnetic perspective the simple structure makes these materials good 1D model systems. In particular **1** may be the first serious candidate in which to find the much prized Spin 2 Haldane quantum antiferromagnetic behavior at low temperatures. More sophisticated magnetic studies are underway to establish this latter point.

Experimental Section

Optimal synthesis of $K_2Fe(ox)_2$ (**1**): $FeCl_2(H_2O)_4$ (0.419 g, 2.12 mmol), $K_2ox(H_2O)$ (0.960 g, 5.02 mmol), KBr (5.97 g, 50.2 mmol), and distilled water (7 mL, 390 mmol) were placed in a 23-mL capacity Teflon-lined autoclave and heated to 225 °C for 4 h then cooled back to room temperature over 14 h. The solvent was decanted and ethanol added to the mixture resulting in the precipitation of KBr. Repeated sonication in ethanol and removal of the flocculent precipitate by decanting the fine suspension left a mixture of the product and large crystals of KBr. This mixture of solids was collected by filtration and dried under suction. Glycerol (80 mL) was added to the mixture of solids, and heated to 100 °C, dissolving the KBr. The orange crystalline product was collected by filtration, washed with methanol, and dried in air. (Yield 0.4239 mg, 1.48 mmol, 70 %) Magnetization studies (see main text) show Fe_3O_4 impurity at $\approx 4\,\%$. IR diff. refl., KBr matrix: $\tilde{\nu} =$ 3432 m, 3229 w, 3190 w, 3114 w, 3040 w, 2949 w, 2902 w, 2940 w, 2841 w, 2818 w, 2696 w, 2612 w, 2559 w, 1928 w, 1836 w, 1777 m, 1668 s, 1624 s, 1425 m, 1388 m, 1337 m, 1285 m, 892 w, 801 m, 783 m, 520 m, 504 m, 415 w, 386 $\mathrm{cm^{-1}}$ w. UV, diff. refl., $BaSO_4$ matrix, λ $\mathrm{nm^{-1}}$ (abs/relative) 2392 (0.073), 2211 (0.065), 1798 (0.080) sh, 1625 (0.088), 1353 (0.087) sh, 1123 (0.092), 412 (0.17), 301 (0.11) sh. Elemental analysis (%) calcd for $K_2FeC_4O_8$: C 15.49; found: C 15.39. Thermogravimetric analysis (TGA; 60 % O_2, 40 % N_2, 10 °C $\mathrm{min^{-1}}$) single-step decomposition, onset 406 °C, mass lost 29.1 %. Expected loss for decomposition to $K_2CO_3 + 0.5(Fe_2O_3)$, 29.7 %.

 © 2004 Wiley-VCH Verlag GmbH & Co. KGaA, Weinheim

Optimal synthesis of $K_2Co(ox)_2$ (**2**): As for **1** but with the following reagent quantities: $CoCl_2(H_2O)_6$ (0.29 g,1.2 mmol), $K_2ox(H_2O)$ (0.59 g, 3.2 mmol), KBr (15.96 g, 134.1 mmol), and distilled water (5 mL, 280 mmol). (Yield 123 mg, 33 %) IR diff. refl., KBr matrix: $\tilde{\nu}$ = 3436 m, 3230 w, 3206 w, 3157 w, 3122 w, 3080 w, 3042 w, 2940 w, 2900 w, 2829 w, 2699w, 2620 w, 2561 w, 2512 w, 2427 w, 2376 w, 1931 w, 1672 s, 1626 s, 1428 m, 1385 m, 1340 m, 1285 m, 1135 br m, 894 w, 806 m, 783 m, 518 m, 505 m, 420 cm^{-1} w. UV, diff. refl., $BaSO_4$ matrix, λ nm^{-1} (abs/relative) 1805 (0.055) sh, 1614 (0.062), 1350 (0.072) sh, 1095 (0.088), 549 (0.10), 496 (0.080) sh, 293 (0.12). Elemental analysis (%) calcd for $K_2CoC_4O_8$: C 15.34; found: C 15.07. TGA (60 % O_2, 40 % N_2, 10 °C min^{-1}) single-step decomposition, onset 353 °C, mass lost 28.6 %. Expected loss for decomposition to K_2CO_3 + 0.333 (Co_3O_4), 30.3 %.

Field-cooled magnetic-susceptibility measurements were performed between 2 and 290 K in applied fields of 200 and 1000 G. A diamagnetic correction of -92×10^{-6} cm^3mol^{-1} was estimated from Pascal's constants.[23]

Received: July 17, 2003 [Z52406]

Keywords: chain structures · hydrothermal synthesis · iron · magnetic properties · O ligands

[1] a) R. E. Dinnebier, S. Vensky, M. Panthöfer, M. Jansen, *Inorg. Chem.* **2003**, *42*, 1499 – 1507; b) E. Jeanneau, N. Audebrand, D. Louër, *Acta Crystallogr. Sect. C* **2001**, *57*, 1012 – 1013; c) D. J. Price, A. K. Powell, P. T. Wood, *Polyhedron* **1999**, *18*, 2499 – 2503; d) D. Yu. Naumov, A. Virovets, N. V. Podberezskaya, E. V. Boldyreva, *Acta Crystallogr. Sect. C* **1995**, *51*, 60 – 62; e) A. N. Christensen, P. Norby, J. C. Hanson, *Z. Kristallogr.* **1994**, *209*, 874 – 877.

[2] a) W. Ollendorf, F. Weigel, *Inorg. Nucl. Chem. Lett.* **1969**, *5*, 263 – 269; b) S. Natarajan, R. Vaidhyanathan, C. N. R. Rao, S. Ayyappan, A. K. Cheetham, *Chem. Mater.* **1999**, *11*, 1633 – 1639; c) R. Vaidhyanathan, S. Natarajan, A. K. Cheetham, C. N. R. Rao, *Chem. Mater.* **1999**, *11*, 3636 – 3642; d) H. Hernandez-Molina, F. Lloret, C. Ruiz-Perez, M. Julve, *Inorg. Chem.* **1998**, *37*, 4131 – 4135.

[3] a) M. Jaber, R. Faure, H. Loiseleur, *Acta Crystallogr. Sect. B* **1978**, *34*, 429 – 431; b) J. D. Donaldson, M. T. Donoghue, C. H. Smith, *Acta Crystallogr. Sect. B* **1976**, *32*, 2098 – 2101; c) J.-C. Trombe, P. Thomas, C. Brouca-Cabarrecq, *Solid State Sci.* **2001**, *3*, 309 – 319.

[4] a) D. J. Price, A. K. Powell, P. T. Wood, *J. Chem. Soc. Dalton Trans.* **2000**, 3566 – 3569; b) C. Boudaren, J. P. Auffredic, M. Louër, D. Louër, *Chem. Mater.* **2000**, *12*, 2324 – 2333; c) T. Bataille, D. Louër, *Acta Crystallogr. Sect. C* **1999**, *55*, 1760 – 1762.

[5] a) C. Mathoniere, C. J. Nuttall, S. G. Carling, P. Day, *Inorg. Chem.* **1996**, *35*, 1201 – 1206; b) G. de Munno, R. Ruiz, F. Lloret, J. Faus, R. Sessoli, M. Julve, *Inorg. Chem.* **1995**, *34*, 408 – 411; c) S. Decurtins, H. W. Schmalle, P. Schneuwly, H. R. Oswald, *Inorg. Chem.* **1993**, *32*, 1888 – 1892; d) M. Julve, M. Verdaguer, A. Gleizes, M. Philochelevisalles, O. Kahn, *Inorg. Chem.* **1984**, *23*, 3808 – 3818.

[6] Unit cell parameters and data for **1** and **2** were collected on a Bruker Nonius Kappa CCD diffractometer mounted at the window of a rotating anode generator following standard procedures. Structures were solved by direct methods and refined by a full-matrix least-squares on F^2. All atoms were refined anisotropically. Crystal data for **1**, $K_2Fe(C_2O_4)_2$, 120(2) K, monoclinic, *P*2/*c* (no. 13), a = 8.5207(3), b = 6.8846(2), c = 14.6912(6) Å, β = 93.8105(16)°, V = 859.90(5) $Å^3$, Z = 4, ρ_{cald} = 2.419 g cm^{-3}, θ_{max} = 27.48°, μ(0.71073 Å) = 3.274 mm^{-1}. 4840 reflections collected, 1508 unique reflections [1446 $I > 2\sigma(I)$] were used in the refinement. Final R values: R (all data/2$\sigma(I)$) 0.0346/0.0333, *wR*2 (all data/2$\sigma(I)$) 0.0847/0.842 for 138 parameters. Largest residual peak (hole) 0.879 (−0.496) e $Å^{-3}$. For **2**, $K_2Co(C_2O_4)_2$, 120(2) K, monoclinic, *P*2/*c* (no. 13), a = 8.4505(2), b = 6.9084(2), c = 14.6600(4) Å, β = 93.3359(8)°, V = 854.39(4) $Å^3$, Z = 4, ρ_{cald} = 2.171 g cm^{-3}, θ_{max} = 25.02°, μ(0.71073 Å) = 3.663 mm^{-1}. 4364 reflections collected, 1008 unique reflections [924 $I > 2\sigma(I)$] were used in the refinement. Final R values: R (all data/2$\sigma(I)$) 0.0383/0.0342, *wR*2 (all data/2$\sigma(I)$) 0.0705/0.0693 for 138 parameters. Largest residual peak (hole) 0.324 (−0.337) e $Å^{-3}$. CCDC-215206 (**1**) and CCDC-215207 (**2**) contains the supplementary crystallographic data for this paper. These data can be obtained free of charge via www.ccdc.cam.ac.uk/conts/retrieving.html (or from the Cambridge Crystallographic Data Centre, 12 Union Road, Cambridge CB21EZ, UK; fax: (+44) 1223-336-033; or deposit@ccdc.cam.ac.uk).

[7] For Fe^{II}; M. Ijjaali, G. Venturini, R. Gerardin, B. Malaman, C. Gleitzer, *Eur. J. Solid State Inorg. Chem.* **1991**, *28*, 983 – 998.

[8] For Co^{II}; a) J. Darriet, L. Elcoro, A. El Abed, E Gaudin, J. M. Perez-Mato, *Chem. Mater.* **2002**, *14*, 3349 – 3363; b) M.-H. Whangbo, H.-J. Koo, K.-S. Lee, O. Gourdon, M. Evain, S. Jobic, R. Brec, *J. Solid State Chem.* **2001**, *160*, 239 – 246; c) H.-C. zur Loye, K. E. Stitzer, M. D. Smith, A. El Abed, J. Darriet, *Inorg. Chem.* **2001**, *40*, 5152 – 5156.

[9] D. L. Kepert, *Inorganic Stereochemistry*, Springer, Berlin, **1982**.

[10] a) J.-H. Luo, M.-C. Hong, Y.-C. Liang, R. Cao, *Acta Crystallogr. Sect. E* **2001**, *57*, m361-m362; b) J. Y. Lu, T. J. Schroeder, A. M. Babb, M. Olmstead, *Polyhedron* **2001**, *20*, 2445 – 2449; c) D. Deguenon, G. Bernardinelli, J.-P. Tuchages, P. Castan, *Inorg. Chem.* **1990**, *29*, 3031 – 3037.

[11] R. Vaidhyanathan, S. Natarajan, C. N. R. Rao, *J. Chem. Soc. Dalton Trans.* **2001**, 699 – 706.

[12] F. Walz, *J. Phys. Condens. Matter* **2002**, *14*, R285-R340.

[13] M. Molinier, D. J. Price, P. T. Wood and A. K. Powell, *J. Chem. Soc. Dalton Trans.* **1997**, 4061 – 4068.

[14] L. J. de Jongh, A. R. Miedema, *Adv. Phys.* **2001**, *50*, 947 – 1170.

[15] K. Kojima, A. Keren, L. P. Le, G. M. Luke, W. D. Wu, Y. J. Uemura, K. Kiyono, S. Miyasaka, H. Takagi, S. Uchida, *Phys. Rev. Lett.* **1995**, *74*, 3471 – 3474.

[16] a) V. A. M. Brabers, F. Walz, H Kronmüller, *Phys. Rev. B* **1998**, *58*, 14163 – 14166; b) J. M. Honig, *J. Alloys Compd.* **1995**, *229*, 24 – 39.

[17] W. Hiller, J. Strähle, A. Datz, M. Hanack, W. E. Hatfield, L. E. ter Haar, P. Gütlich, *J. Am. Chem. Soc.* **1984**, *106*, 329 – 335.

[18] a) J. Glerup, P. A. Goodson, D. J. Hodgson, K. Michelsen, *Inorg. Chem.* **1995**, *34*, 6255 – 6264; b) D. Armentano, G. de Munno, F. Lloret, M. Julve, J. Curély, A. M. Babb, J. Y. Lu, *New J. Chem.* **2003**, *27*, 161 – 165.

[19] a) F. D. Haldane, *Phys. Lett. A* **1983**, *93*, 464 – 468; b) F. D. Haldane, *Phys. Rev. Lett.* **1983**, *50*, 1153 – 1156.

[20] a) W. J. L. Buyers, R. M. Morra, R. L. Armstrong, M. J. Hogan, P. Gerlach, K. Hirakawa, *Phys. Rev. Lett.* **1986**, *56*, 371 – 374; b) Y. Ajiro, T. Goto, H. Kikuchi, T. Sakakibara, T. Inami, *Phys. Rev. Lett.* **1989**, *63*, 1424 – 1427; c) N. Metoki, Y. Koike, Y. Matsuoka, T. Kobayashi, M. Yamashita, *J. Magn. Magn. Mater.* **2001**, *226–230*, 414 – 416.

[21] a) M. A. Ahrens, A. Schadschneider, J. Zittartz, *Europhys. Lett.* **2002**, *59*, 889 – 895; b) U. Schollwock, O. Golinelli, T. Jolicoeur, *Phys. Rev. B* **1996**, *54*, 4038 – 4051; c) T. Kennedy, H. Tasaki, *Phys. Rev. B* **1992**, *45*, 304 – 307.

[22] a) V. B. Kursigerski, V. V. Spasojeviæ, N. Dj. Lazarov, D. S. Markoviæ, V. M. Matić, S. P. Sovilij, M. Guillot, *Solid State Commun.* **2003**, *126*, 319 – 322; b) O. Castillo, A. Luque, P. Román, F. Lloret, M. Julve, *Inorg. Chem.* **2001**, *40*, 5526 – 5535.

[23] See for example: O. Kahn, *Molecular Magnetism*, VCH, Weinheim, **1993**.

 © 2004 Wiley-VCH Verlag GmbH & Co. KGaA, Weinheim

Polycarbon Bridges

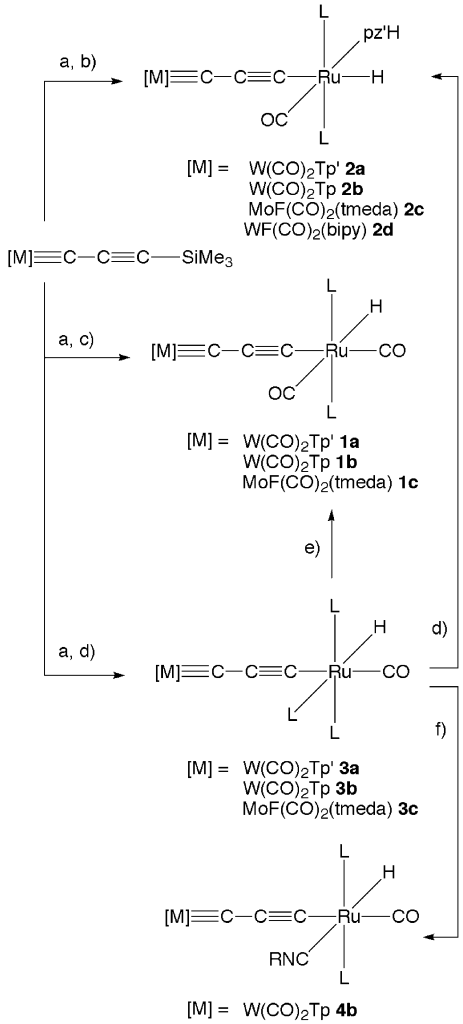
Heterobimetallic C_3 Complexes through Silylpropargylidyne Desilylation

Rian D. Dewhurst, Anthony F. Hill, and Matthew K. Smith*

Dedicated to Professor Michael I. Bruce on the occasion of his 65th birthday

Although the chemistry of bimetallic compounds bridged by linear polycarbon ligands, $L_nM(C_x)ML_n$, has grown at an enormous pace,[1] there remains a hiatus for odd-numbered examples ($x = 3, 5, 7\ldots$). It would be premature to attribute this to any inherent instability, though this may well eventually prove to be a contributing factor.[2] Rather, at present, it is a reflection of the majority of synthetic strategies that commence with free polyynes $R(C_2)_{x/2}R$ ($R = H$, $SiMe_3$) or metal poly(ynyls) $L_nM(C_2)_{x/2}R$, each of which by necessity lead to even-numbered carbon chains. Bimetallic compounds spanned by linear C_3 ligands are limited to: 1) $[(\eta\text{-}C_5Me_5)(NO)(PPh_3)Re\text{-}C{\equiv}C{-}C{\equiv}ML_n]$ ($ML_n = \{Fe(CO)_4\}^+$; $\{Mn(CO)_2(\eta\text{-}C_5H_mCl_{5-m})\}^+$ $m = 0, 1, 5$; $W(OtBu_3)_3$), which arise from Fischer-type carbyne syntheses commencing with $[(\eta\text{-}C_5Me_5)(NO)(PPh_3)Re\text{-}C{\equiv}C\text{-}Li]$ and the appropriate metal carbonyl,[3a,b] or alkyne metathesis of the diynyl complexes $[(\eta\text{-}C_5Me_5)(NO)(PPh_3)Re\text{-}C{\equiv}C{-}C{\equiv}CR]$ ($R = H$, Me) with $[W_2(OtBu)_6]$,[3c] as described by Gladysz and co-workers; and 2) $[Tp'(CO)_2M{\equiv}C{-}C{\equiv}C\text{-}M'(=O)_2Tp']$ (M, M′ = Mo, W; Tp′ = hydrotris(3,5-dimethylpyrazolyl)borate) obtained by Templeton and Woodworth through deprotonation of $[Tp'(CO)_2M{\equiv}C\text{-}CH_2C{\equiv}M'(CO)_2Tp']$ under aerobic conditions.[4] Whilst these were each ground-breaking in establishing the viability of this class of compound, the routes at present lack generality and the metal centers involved are inert to substitution. Herein we report two synthetic strategies for the construction of a range of $L_nMC_3ML_n$ complexes which offer scope for extension to many metals.

We previously described convenient synthetic routes to a range of propargylidyne complexes of the Group 6 metals, $L_nM{\equiv}C{-}C{\equiv}CCMe_3$ (M = Mo, W).[5] Fischer and co-workers recently extended this protocol to include silylated examples $L_nM{\equiv}C{-}C{\equiv}CSiMe_3$ and suggested that they might be prone to desilylation.[6] As fluorodesilylation of alkynyl silanes is a widely employed synthetic protocol, we envisaged that silylpropargylidynes might serve as suitable reagents for constructing $L_nM{\equiv}C{-}C{\equiv}C\text{-}ML_n$ linkages. Towards this end, the reaction of $[Tp'(CO)_2W{\equiv}C{-}C{\equiv}CSiMe_3]$[6a] with $[Bu_4N]F$ was investigated in the presence of $[Ru(CO)_2(PPh_3)_3]$, a complex that is known to oxidatively add terminal alkynes.[7] From this reaction, the bimetallic complex $[Tp'(CO)_2W{\equiv}C{-}C{\equiv}C\text{-}RuH(CO)_2(PPh_3)_2]$ (**1a**) was readily isolated in modest yield, implicating the intermediacy of the parent propargylidyne complex $[Tp'(CO)_2W{\equiv}C{-}C{\equiv}CH]$ (Scheme 1) consistent with the suggestion of Fischer and co-workers.[6a]



Scheme 1. L = PPh_3, R = 2,4,6 $Me_3C_6H_2$, [M] = $W(CO)_2Tp$, $W(CO)_2Tp'$, $MoF(CO)_2$(tmeda), $WF(CO)_2$(bipy) (not all combinations). a) $[Bu_4N]F$; b) $[RuHCl(CO)(Hpz')L_2]$; c) $[Ru(CO)_2L_3]$; d) $[RuH(NCMe)_2(CO)L_2]BF_4$ or $[RuHCl(CO)L_3]$; e) CO; f) Hpz′; g) CNR. tmeda = tetramethylethylenediamine, bipy = bipyridyl.

As an alternative to the oxidative addition approach, the possibility of deploying nucleophilic anions $[L_nM{\equiv}C{-}C{\equiv}C][Bu_4N]$, generated in situ, for halide metathesis reactions was investigated, although no attempt was made to isolate these intermediate species. Treatment of a range of silylpropargylidynes with $[Bu_4N]F$ in the presence of the hydrido complex $[RuHCl(CO)(Hpz')(PPh_3)_2]$ (Hpz′ = 3,5-dimethylpyrazole)[8] provided the bimetallic complexes $[L_nM{\equiv}C{-}C{\equiv}C\text{-}RuH(CO)(Hpz')(PPh_3)_2]$ ($L_nM = W(CO)_2Tp'$ (**2a**), $W(CO)_2Tp$ (**2b**, Tp = hydrotris(pyrazolyl)borate), $MoF(CO)_2$(tmeda)

[*] R. D. Dewhurst, Prof. Dr. A. F. Hill, Dr. M. K. Smith
Institute of Advanced Studies, Australian National University
Canberra, A.C.T. (Australia)
Fax: (+61) 261-253-216
E-mail: a.hill@anu.edu.au

Supporting information for this article is available on the WWW under http://www.angewandte.org or from the author.

 © 2004 Wiley-VCH Verlag GmbH & Co. KGaA, Weinheim DOI: 10.1002/anie.200352693

(**2c**), WF(bipy)$(CO)_2$ (**2d**)). Notably, when trifluoroacetato complexes [Mo(≡C−C≡C$SiMe_3$)$(O_2CCF_3)(CO)_2$(tmeda)] and [W(≡C−C≡C$SiMe_3$)$(O_2CCF_3)(CO)_2$(bipy)] were employed, CF_3CO_2/F metathesis also occurred at the Group 6 metal center. The complex [RuHCl$(CO)(PPh_3)_3$][9] has been shown to react with LiC≡C*t*Bu to provide [RuH(C≡C*t*Bu)-$(CO)(PPh_3)_3$],[10] and the related set of C_3-bridged complexes [L_nM≡C−C≡CRuH$(CO)(PPh_3)_3$] (L_nM = W$(CO)_2$Tp′ (**3a**), W$(CO)_2$Tp (**3b**), MoF$(CO)_2$(tmeda) (**3c**)) were readily prepared by reaction of the appropriate silylpropargylidyne with [Bu_4N]F and [RuHCl$(CO)(PPh_3)_3$]. Unexpectedly, we first observed these same products spectroscopically from similar treatment of the [RuH$(NCMe)_2(CO)(PPh_3)_2$]BF_4 salt, presumably via phosphane redistribution. The lability of one phosphane ligand could be demonstrated by reactions with CO, Hpz′, or 2,4,6-Me_3-CNC_6H_2 to provide [L_nM≡C−C≡C-RuH(CO)(L)$(PPh_3)_2$] (L = CO (**1**), Hpz′ (**2**), 2,4,6-Me_3-CNC_6H_2 (**4**)). The complex [RuHCl$(CO)(PPh_3)_3$] readily hydrometallates alkynes,[11] diynes,[12] and phosphaalkynes,[13] and so it is noteworthy that halide metathesis occurs instead under the present reactions.

The hydride ligand in these complexes serves as a useful "reporter" ligand for NMR spectroscopic analysis, reinforcing the assignments for the MC_3Ru spines. Thus, ^1H,^{13}C-HMBC NMR spectra acquired for the complexes indicate coupling between the hydride nucleus and the three carbon nuclei. This is illustrated for the complex **1b** (Figure 1) for which correlations are observed for a) W≡C−C≡C-Ru, b) and c) Ru$(CO)_2$, d) W≡C−C≡C-Ru, e) $C^1(PC_6H_5)$, f) $C^{2,6}(PC_6H_5)$, and g) W≡C−C≡C-Ru. The chemical shifts of the three bridging carbon nuclei, namely $\delta = 260.6$ (W≡C−C≡C-Ru), 138.6 (W≡C−C≡C-Ru) and 118.7 ppm (W≡C−C≡C-Ru) are consistent with a somewhat localized W≡C−C≡C-Ru bonding description.

The complex **2a** was the subject of a crystallographic study,[14] the results of which are summarized in Figure 2. The molecular structure confirms the pseudooctahedral geometries at both the tungsten and ruthenium centers and establishes the *trans*-HRuC≡C stereochemistry, the hydride ligand having been located and satisfactorily refined. Interest focuses on the essentially linear W(sp-C)$_3$Ru spine, the geometric parameters of which conform to a W≡C−C≡C-Ru valence bond description akin to that suggested for {(η-C_5Me_5)(NO)(PPh_3)Re-C≡C−C≡W$(OtBu)_3$}$_2$[3b] rather than the more cumulenic salt {(η-C_5Me_5)(NO)(PPh_3)Re=C=C=C=Mn$(CO)_2$(η-C_5H_5)]BF_4.[3c] Thus, the W≡C separation of 1.848(5) Å is typical of those observed for tungsten alkylidynes,[15] and the Ru1-C3 bond length of 2.096(5) Å falls within the range noted for ruthenium alkynyls.[16] The C2-C3 [1.230(7)] and C2-C1 [1.373(7) Å] lengths correspond to essentially localized triple and single bonds between two coordinated carbon centers.

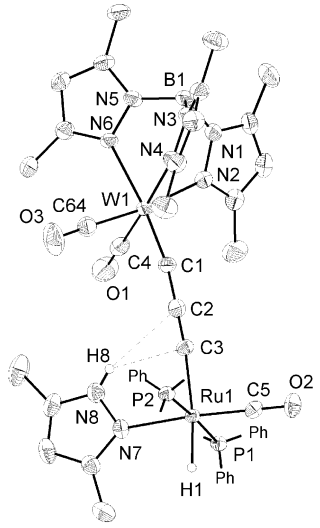


Figure 2. Molecular geometry of **2a** (phenyl groups omitted). Selected distances [Å] and angles [°]: Ru1-C3 2.096(5), C3-C2 1.230(7), C2-C1 1.373(7), W1-C1 1.848(5), W1-N4 2.230(4), W1-N2 2.206(4), W1-N6 2.300(4), Ru1-H 1.56(6), H8-C3 2.28(5), H8-C2 2.59(5), W1-Ru1 6.515(2), Ru1-C3-C2 175.0(4), C1-C2-C3 178.9(5), W1-C1-C2 171.2(4).

In summary, we have shown that silylpropargylidynes can serve as useful precursors for the construction of linear C_3-bridged bimetallic compounds through two complementary routes: 1) in situ generation of terminal propargylidyne complexes for subsequent oxidative addition (≡C-H activation) or 2) in situ generation of propargylidynyl nucleophiles for metathesis with metal halides. Although a dozen new examples of linear C_3-bridged bimetallic complexes have resulted, they all contain M≡C−C≡C-Ru (M = Mo, W) spines. Accordingly, we are currently exploring the generality of this protocol with respect to extension to other metal centers.

Received: August 21, 2003 [Z52693]

Keywords: alkynes · carbynes · multiple bonds · ruthenium · tungsten

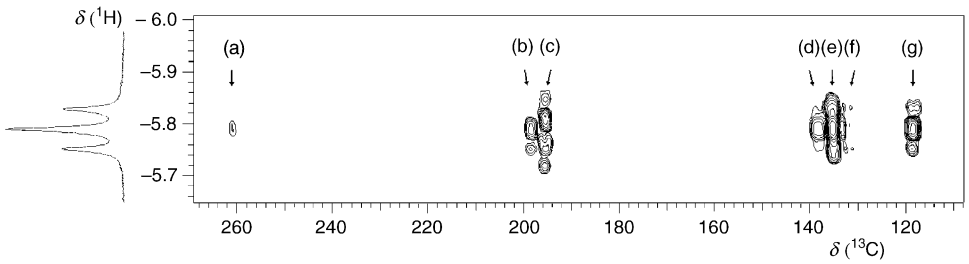


Figure 1. ^{13}C,^1H-HMBC NMR spectrum ($\delta < 0$) for [Tp$(CO)_2$W≡C−C≡C-RuH$(CO)_2(PPh_3)_2$] (**1b**) optimized for 2 Hz ^1H–^{13}C coupling.

 © 2004 Wiley-VCH Verlag GmbH & Co. KGaA, Weinheim

[1] For a review of $L_nM(C_x)R$ and $L_nM(C_x)ML_n$ complexes, respectively, see: a) P. J. Low, M. I. Bruce, *Adv. Organomet. Chem.* **2002**, *48*, 71; b) M. I. Bruce, P. J. Low, *Adv. Organomet. Chem.* **2004**, *50*, in press.

[2] For a theoretical study of odd-numbered carbon complexes, see: H. Jiao, J. A. Gladysz, *New J. Chem.* **2001**, *25*, 551.

[3] a) W. Weng, J. A. Ramsden, A. M. Arif, J. A. Gladysz, *J. Am. Chem. Soc.* **1993**, *115*, 3824; b) T. Bartik, W. Weng, J. A. Ramsden, S. Szafert, S. B. Falloon, A. M. Arif, J. A. Gladysz, *J. Am. Chem. Soc.* **1998**, *120*, 11071; c) R. Deminski, S. Szafert, P. Haquette, T. Lis, J. A. Gladysz, *Organometallics* **1999**, *18*, 5438.

[4] B. E. Woodworth, J. L. Templeton, *J. Am. Chem. Soc.* **1996**, *118*, 7418.

[5] I. J. Hart, A. F. Hill, F. G. A. Stone, *J. Chem. Soc. Dalton Trans.* **1989**, 2261.

[6] a) B. Schwenzer, J. Schleu, N. Burzlaff, C. Karl, H. Fischer, *J. Organomet. Chem.* **2002**, *641*, 134; b) B. Schwenzer, H. Fischer, *J. Organomet. Chem.* **2003**, *667*, 16.

[7] a) B. E. Cavit, K. R. Grundy, W. R. Roper, *J. Chem. Soc. Chem. Commun.* **1972**, 60; b) B. E. Cavit, M.Sc. Thesis, University of Auckland, **1972**.

[8] A. Romero, A. Vegas, A. Santos, A. M. Cuadro, *J. Chem. Soc. Dalton Trans.* **1987**, 183.

[9] L. Vaska, *J. Am. Chem. Soc.* **1964**, *86*, 1943.

[10] Y. Wakatsuki, H. Yamazaki, N. Kumegawa, T. Satoh, J. Y. Satoh, *J. Am. Chem. Soc.* **1991**, *113*, 9604.

[11] M. R. Torres, A. Vegas, A. Santos, *J. Organomet. Chem.* **1986**, *309*, 169.

[12] A. F. Hill, R. P. Melling, *J. Organomet. Chem.* **1990**, *396*, C22; b) A. F. Hill, R. P. Melling, A. R. Thompsett, *J. Organomet. Chem.* **1991**, *402*, C8; c) A. F. Hill, M. C. J. Harris, R. P. Melling, *Polyhedron* **1992**, *11*, 781.

[13] R. B. Bedford, A. F. Hill, C. Jones, *Angew. Chem.* **1996**, *108*, 587; *Angew. Chem. Int. Ed. Engl.* **1996**, *35*, 547; b) R. B. Bedford, A. F. Hill, C. Jones, J. D. E. T. Wilton-Ely *Organometallics* **1998**, *17*, 4744.

[14] Crystal data for **2a**: $C_{64}H_{65}BCl_4N_8O_3P_2RuW$, $M_w = 1493.7$, triclinic, $P\bar{1}$ (no. 2), $a = 9.788(1)$, $b = 15.125(1)$, $c = 22.850(1)$ Å, $\alpha = 72.050(1)$, $\beta = 88.365(1)$, $\gamma = 88.699(1)°$, $V = 3216.5(4)$ Å^3, $Z = 2$, $T = 200(2)$ K, $\rho_{cald} = 1.542\ g\,cm^{-3}$, $Mo_{K\alpha}$ radiation, $\mu = 2.289\ mm^{-1}$, yellow rod $0.36 \times 0.15 \times 0.05\ mm^3$; 14738 independent measured reflections, F^2 refinement, $R_1 = 0.046$, $wR_2 = 0.107$, 11888 independent observed absorption-corrected reflections ($I > 2\sigma(I)$), $2\theta = 55.1°$], 778 parameters. CCDC-217762 contains the supplementary crystallographic data for this paper. These data can be obtained free of charge via www.ccdc.cam.ac.uk/conts/retrieving.html (or from the Cambridge Crystallographic Data Centre, 12, Union Road, Cambridge CB21EZ, UK; fax: (+44) 1223-336-033; or deposit@ccdc.cam.ac.uk).

[15] a) A. Mayr, H. Hoffmeister, *Adv. Organomet. Chem.* **1991**, 32, 227; b) H. P. Kim, R. J. Angelici, *Adv. Organomet. Chem.* **1987**, 27, 51.

[16] A. F. Hill in *Comprehensive Organometallic Chemistry II*, *Vol. 7* (Ed.: E. W. Abel, F. G. A. Stone, G. Wilkinson), Pergamon, Oxford, **1995**.

 © 2004 Wiley-VCH Verlag GmbH & Co. KGaA, Weinheim

Nitrogen Heterocycles

An Efficient Synthesis of Bicyclic Amidines by Intramolecular Cyclization**

*Naoya Kumagai, Shigeki Matsunaga, and Masakatsu Shibasaki**

Bicyclic amidines and guanidines are organic superbases utilized in various synthetic transformations. Recently, chiral guanidines have been widely explored as non-metal-containing bases in asymmetric synthesis[1] as well as in asymmetric phase-transfer catalysis.[1d,2] In spite of great success in catalysis with chiral guanidine derivatives, asymmetric reactions with chiral derivatives of bicyclic amidines[3] have not been widely studied, possibly because of the difficulty of synthesizing chiral bicyclic amidines. The nucleophilic character of bicyclic amidines[3c,4] further broadens their utility as catalysts. Considering the potency of chiral bicyclic amidines as organocatalysts, the development of an efficient protocol for the synthesis of these compounds would greatly contribute toward the progress in this area.[5]

For the formation of a bicyclic amidine, the starting material should have two nitrogen-containing functionalities that can assemble intramolecularly to form an amidine core at the ring junction. Previous reports[3,6] indicate that the intramolecular attack of a free amino group on a lactam in the presence of a strong acid (*p*-toluenesulfonic acid or $TiCl_4$)[6a] in refluxing xylene, and the intramolecular attack of a Boc-protected amino group (Boc = *t*-butoxycarbonyl) to a thiolactam under acidic conditions[3a,b,6c] are reliable (Scheme 1). However, the former method requires harsh reaction conditions, and the latter, too many steps from readily available organic materials although the reaction conditions are mild. We report a concise synthetic procedure for bicyclic amidines starting from readily available tethered azido lactams by means of an intramolecular cyclization (Scheme 1), which provides easy access to various achiral and chiral bicyclic amidines under mild reaction conditions. The direct use of an azido function, instead of an amino group, plays a key role in our reaction design. We also describe mechanistic aspects of the reaction based on an in situ IR study.

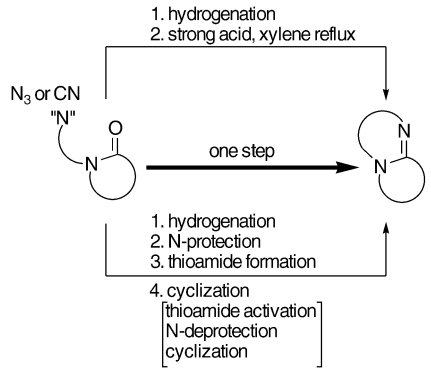
We focused on the use of an azido group as the nucleophile in the intramolecular cyclization.[7,8] Although

[*] N. Kumagai, S. Matsunaga, Prof. Dr. M. Shibasaki
Graduate School of Pharmaceutical Sciences
The University of Tokyo, Hongo, Bunkyo-ku, Tokyo 113-0033 (Japan)
Fax: (+81) 3-5684-5206
E-mail: mshibasa@mol.f.u-tokyo.ac.jp

[**] This work was supported in part by RFTF and by a Grant-in-Aid for the Encouragement of Young Scientists (B) (for S.M.) from JSPS. N.K. is the recipient of a JSPS Research Fellowship for Young Scientists. We thank Prof. S. Kobayashi and R. Matsubara at the University of Tokyo for their help with the in situ IR study. We thank Prof. H. Kotsuki at Kochi University for helpful discussions.

Supporting information for this article is available on the WWW under http://www.angewandte.org or from the author.

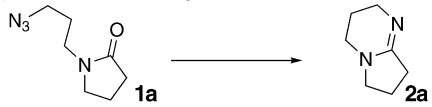
 © 2004 Wiley-VCH Verlag GmbH & Co. KGaA, Weinheim DOI: 10.1002/anie.200352750



Scheme 1. Strategies for the formation of bicyclic amidines. Top: An amino group serves as the nucleophile; cyclization under harsh conditions. Middle: An azido group functions directly as the nucleophile in a mild and efficient, one-step conversion. Bottom: The lengthy reaction sequence features thioamide formation and protection–deprotection of the amino group.

the intramolecular aza-Wittig reaction of an azido group on an imide carbonyl under Staudinger conditions has been reported,[9] the conditions were not effective for the simple amide carbonyl **1a**.[10] The cyclized product **2a** was obtained in less than 10% yield, and the iminophosphorane was the main product when either triphenylphosphane or tributylphosphane were employed (Table 1, entries 1 and 2).[11] To overcome the intrinsic low reactivity of the amide, chemoselective activation was necessary. Unlike the thiolactam method,[12] direct use of an azido group enables chemoselective activation of the amide because the azido unit is not affected by many kinds of electrophilic reagents. In this design, the azido group serves as a nucleophile[7] or a 1,3-dipole[8] that undergoes cyclization with an activated amide moiety, followed by the extrusion of molecular nitrogen to afford the bicyclic amidine.

Table 1: Bicyclic-amidine-forming reaction with azido lactam **1a**.



Entry	Reagent	Solvent	T [°C]	t [h]	Yield [%]
1	Ph_3P	xylene	reflux[a]	24	<10
2	Bu_3P	xylene	reflux[a]	24	<10
3	$POCl_3$	CH_2Cl_2	RT	24	32
4	PCl_5	CH_2Cl_2	RT	24	<5
5	$(COCl)_2$	CH_2Cl_2	0 to RT[b]	24	81
6	$(COCl)_2$	$(CHCl)_2$	0 to RT[b]	24	76
7	$(COCl)_2$	THF	0 to RT[b]	24	<10
8	$(COCl)_2$	toluene	0 to RT[b]	24	11
9	$(COCl)_2$	CH_3CN	0 to RT[b]	24	37
10	$(COBr)_2$	CH_2Cl_2	0 to RT[b]	4	68
11	$(COBr)_2$	$(CHCl)_2$	0 to RT[b]	4	92

[a] The reagent was added at room temperature (RT), and the reaction mixture was stirred at the same temperature for the first hour before it was heated to reflux. [b] Reagent was added at 0°C, and the reaction mixture was stirred at this temperature for the first hour before it was allowed to warm to room temperature.

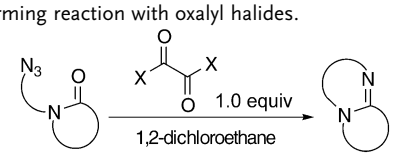
Initially, various reagents were screened in reactions with the achiral substrate **1a** to determine if they activate the amide moiety. Phosphorus oxytrichloride (entry 3) and phosphorus pentachloride (entry 4), common reagents for Vilsmeier's salt formation, resulted in low yields. Among the other reagents tested, oxalyl chloride (1 equiv) was effective for the formation of a chloroiminium intermediate, leading to clean formation of 1,5-diazabicyclo[4.3.0]non-5-ene (DBN, **2a**) in 81% yield at room temperature (Table 1, entry 5). At the initial stage of the reaction, it was essential to keep the reaction temperature at 0°C for 1 h, otherwise a side reaction occurred triggered by enamine formation[13] from the chloroiminium intermediate, and the reaction mixture became complicated. Among the solvents investigated, CH_2Cl_2 and 1,2-dichloroethane gave the best results (entries 5–8). The use of oxalyl bromide in 1,2-dichloroethane was the most effective, and **2a** was obtained in 92% yield within 4 h after workup with anisole/MeOH (entry 11).

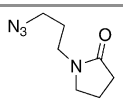
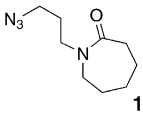
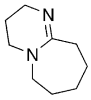
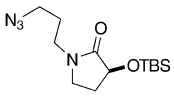
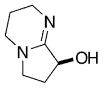
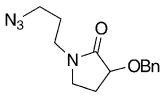
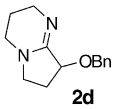
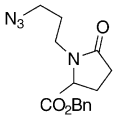
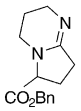
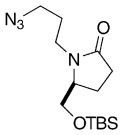
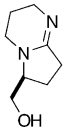
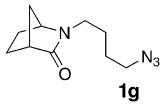
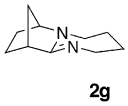
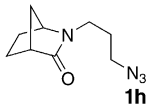
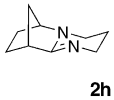
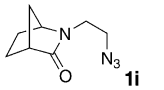
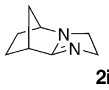
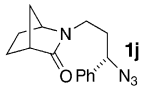
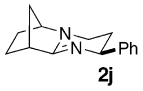
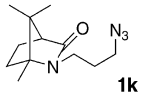
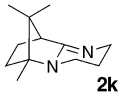
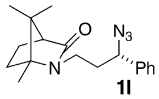
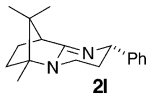
We then applied these optimized conditions to the synthesis of various achiral and chiral bicyclic amidines from tethered azido lactams (Table 2). The substrates for this amidine-forming reaction were easily prepared by S_N2 substitution of azidoalkyl tosylate with the parent lactam.[14] The present bicyclic-amidine-forming reaction has broad substrate generality. Bicyclo[4.3.0] (entries 1, 2, and 4–8), bicyclo[5.4.0] (entry 3), and polycyclic amidine ring systems (entries 9–15) were obtained in good yield. Oxalyl bromide gave better results than oxalyl chloride, especially for the less reactive substrates. For example, the reaction of **1g** with oxalyl bromide afforded **2g** in 82% yield after 4 h (entry 10), while the use of oxalyl chloride gave **2g** in only 18% yield (entry 9).[15] The formation of five- and seven-membered rings required more forcing conditions than the formation of six-membered rings (entry 11 vs entries 9, 10, and 12). The ester functionality was tolerated under these reaction conditions (entry 7). The phenyl group at the position α to the azido group did not interfere with the cyclization; the desired cyclic amidines were obtained in good yield without halogenation of the aromatic ring (entries 13 and 15). Thus, functionalized achiral bicyclic amidines **2d** and **2e** (entries 5–7), functionalized chiral bicyclic amidines **2c** and **2f** (entries 4, 8), and chiral polycyclic amidines **2g**–**2l** (entries 9–15) were synthesized efficiently under mild conditions. Preparation of the polycyclic amidine **2k** from the same substrate **1k** by the thiolactam method[3a] required four steps, and **2k** was obtained in 43% overall yield.[16] It is noteworthy that our method accomplished the same conversion in a single step with 88% yield after simple extraction (entry 14).

Having achieved an efficient process for the formation of bicyclic amidines, we performed several model experiments to gain mechanistic insight into the reaction. Considering the smooth reaction of the bicyclic substrates **1g**–**1l** (Table 2, entries 9–15), in which based on Bredt's rule[17] enamine formation should not occur, the involvement of an enamine intermediate was rationally excluded. In situ IR spectroscopy with **1a** illustrated the possible reaction course (Figure 1a–d).[18] As shown in Figure 1a, the addition of oxalyl bromide to **1a** in 1,2-dichloroethane at 0°C caused the chemoselective transformation of the lactam ($\tilde{\nu} = 1683\ cm^{-1}$, C=O stretch)

 © 2004 Wiley-VCH Verlag GmbH & Co. KGaA, Weinheim

Table 2: Bicyclic-amidine-forming reaction with oxalyl halides.



Entry	Substrate	Product	Reagent [X]	T [°C]	t [h]	Yield [%]
1[a]	 **1a**	 **2a**	Cl	RT	24	81
2			Br	RT	4	92
3	 **1b**	 **2b**	Br	RT	6	87
4[b]	 **1c**	 **2c**	Br	50	4	84
5[a]	 **1d**	 **2d**	Cl	RT	24	78
6			Br	RT	6	88
7	 **1e**	 **2e**	Cl	RT	24	86
8[b]	 **1f**	 **2f**	Br	RT	4	91
9	 **1g**	 **2g**	Cl	70	48	18
10			Br	70	4	82
11	 **1h**	 **2h**	Cl	RT	24	94
12[c]	 **1i**	 **2i**	Br	60	4	77
13	 **1j**	 **2j**	Br	RT	4	80
14[a]	 **1k**	 **2k**	Cl	50	24	88
15[c]	 **1l**	 **2l**	Br	50	3	92

[a] CH_2Cl_2 was used as solvent. [b] TBS = tert-butyldimethylsilyl. [c] Reaction was conducted with 1.5 equiv reagent.

into the bromoiminium intermediate ($\tilde{\nu} = 1644\ cm^{-1}$, C=O stretch)[19] without affecting the azido group ($\tilde{\nu} = 2104\ cm^{-1}$, N=N stretch). When the reaction mixture was warmed from 0 °C to 25 °C (Figure 1b), the peaks derived from the bromoiminium intermediate and azido function diminished gradually, accompanied by evolution of N_2 gas. Two new peaks appeared at $\tilde{\nu} = 1679\ cm^{-1}$ and $\tilde{\nu} = 1637\ cm^{-1}$, which were assigned to **2a**·HBr (C=N stretch) and **2a**·Br_2 (C=N stretch), respectively.[20] To test the validity of this assignment, the following experiments were performed. As shown in Figure 1c, model substrate **1m**, which lacks an azido group, was treated with oxalyl bromide and followed by in situ IR spectroscopy. Although the bromoiminium intermediate ($\tilde{\nu} = 1644\ cm^{-1}$) formed smoothly at 0 °C, it remained unchanged even after the reaction mixture had been warmed from 0 °C to 25 °C. Therefore, the new peaks in Figure 1b ($\tilde{\nu} = 1679,\ 1637\ cm^{-1}$) were not derived from the hydrolysis of the bromoiminium intermediate nor from oxalyl bromide. As shown in Figure 1d, **2a**·Br_2 prepared from **2a** and Br_2 was easily solvolyzed to **2a**·HBr within 10 min by the addition of MeOH at 25 °C. The result suggested that **2a**·HBr ($\tilde{\nu} = 1679\ cm^{-1}$) in Figure 1b arises from the hydrolysis of **2a**·Br_2 ($\tilde{\nu} = 1637\ cm^{-1}$) by moisture under the conditions of the in situ IR study. Under strictly anhydrous conditions the final product in the reaction mixture was expected to be **2a**·Br_2.[21] This assumption was supported by the following observation. After the reaction was complete, the addition of anisole to the reaction mixture resulted in the smooth formation of 4-bromoanisole in equimolar amout to **1a**, which implied that some brominating agent, such as **2a**·Br_2, was present in the reaction mixture.[22]

On the basis of the above results, the plausible reaction mechanism is outlined as in Scheme 2. First, bromoiminium intermediate **3a** is formed cleanly by the action of oxalyl bromide on **1a** without affecting the azido group. The involvement of the enamine intermediate **4a** was excluded as mentioned above, and two possibilities for the cyclization step remain. One possibility is the intramolecular 1,2-addition of the azido group to give the bicyclic intermediate **5a**, followed by a 1,2-shift of Br and extrusion of molecular nitrogen (Scheme 2, pathway a). The other possibility is the intramolecular [3+2] cycloaddition to afford tetrazolium intermediate **6a**, and subsequent retro-[3+2] reaction with a concomitant 1,2-shift of Br (Scheme 2, pathway b). Considering the nature of azido functionality as a 1,3-dipole and previous reports concerning the [3+2] cycloaddition of azides,[7] pathway b is assumed to be more favorable for the

 © 2004 Wiley-VCH Verlag GmbH & Co. KGaA, Weinheim

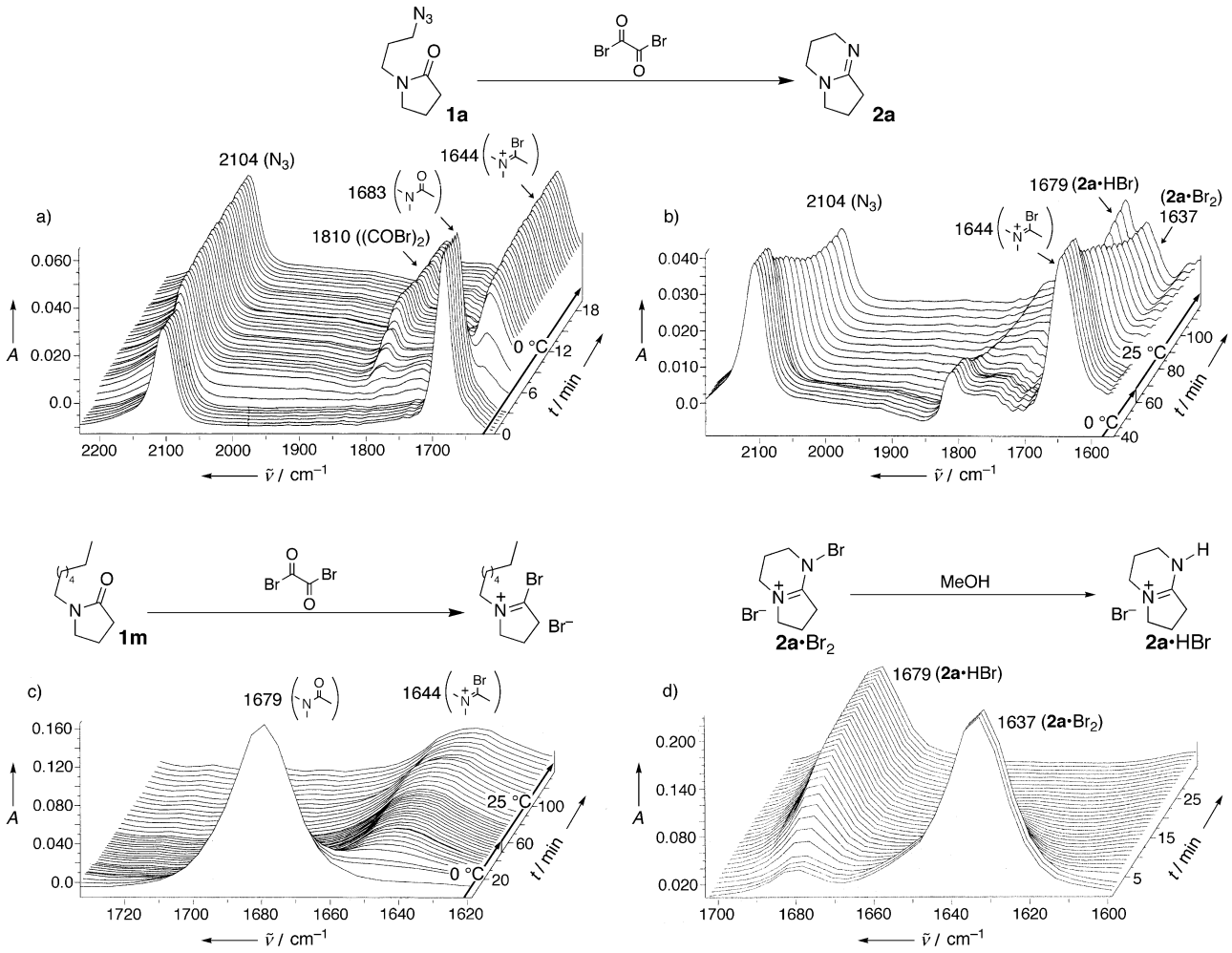
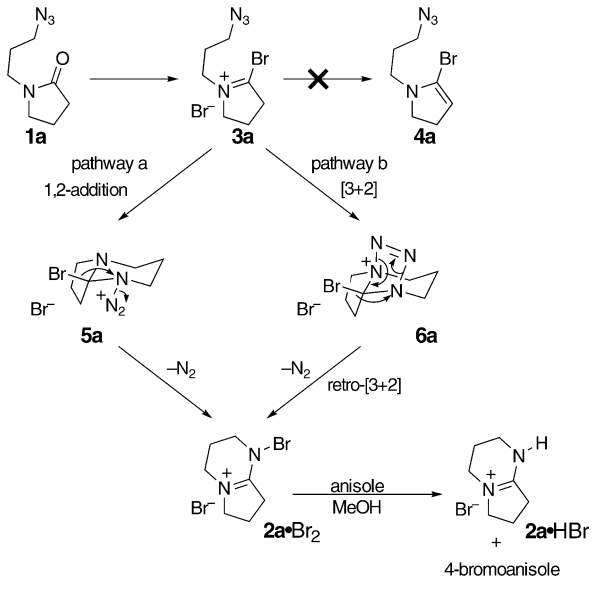


Figure 1. In situ IR study of the amidine-forming reactions in 1,2-dichloroethane as shown. Reaction temperatures: a) 0 °C, b) 60 min at 0 °C then 25 °C, c) 50 min at 0 °C then 25 °C, d) 25 °C.



Scheme 2. Plausible reaction mechanism.

present bicyclic-amidine-forming reaction. In our in situ IR study, neither intermediate **5a** nor **6a** was observed. Thus, the possibility of pathway a cannot be excluded. The resulting brominating species **2a**·Br_2 in the reaction mixture was scavenged with anisole.

In summary, we have developed an efficient method for the synthesis of bicyclic amidines by the intramolecular attack of an azido group on a lactam function. The present reaction conditions allow for facile cyclization without unmasking the azido group to give the amine. This enables the synthesis of various achiral and chiral bicyclic amidines under mild conditions and with a small number of steps compared with the previous methods. Mechanistic studies using in situ IR spectroscopy shed light on the possible reaction pathway. The application of chiral bicyclic amidines to asymmetric catalysis is in progress.

Experimental Section

Representative procedure for the synthesis of bicyclic amidines: To a solution of azido lactam **1a** (103.3 mg, 0.612 mmol, 0.1M) in 1,2-

 © 2004 Wiley-VCH Verlag GmbH & Co. KGaA, Weinheim

dichloroethane (6.1 mL) under an Ar atmosphere was added a solution of oxalyl bromide in dichloromethane (306 μL, 2.0 M, 0.612 mmol) dropwise at 0 °C. After the reaction mixture was stirred at 0 °C for 1 h, it was warmed to room temperature and stirred for 4 h at the same temperature. The resulting mixture was quenched with anisole (133 μL, 1.22 mmol) and MeOH (1.2 mL) at 0 °C and stirred for 30 min at room temperature. The resulting mixture was concentrated to half of the original volume and extracted with 1 M aq HCl. The aqueous extract was washed with CH_2Cl_2 and concentrated under reduced pressure. The resulting residue was passed through Amberlite IRA 400 (OH^-) with MeOH as the eluent. Evaporation of the organic solvent gave the pure amidine **2a** (70.2 mg, 0.565 mmol, 92% yield).

Received: August 29, 2003 [Z52750]

Keywords: azides · chirality · cyclization · nitrogen heterocycles

[1] a) M. S. Iyer, K. M. Gigstad, N. D. Namdev, M. Lipton, *J. Am. Chem. Soc.* **1996**, *118*, 4910; b) E. J. Corey, M. J. Grogan, *Org. Lett.* **1999**, *1*, 157; c) T. Ishikawa, T. Isobe, *Chem. Eur. J.* **2002**, *8*, 553, and references therein; d) T. Kita, A. Georgieva, Y. Hashimoto, T. Nakata, K. Nagasawa, *Angew. Chem.* **2002**, *114*, 2956; *Angew. Chem. Int. Ed.* **2002**, *41*, 2832; e) for an early example, see R. Chinchilla, C. Nájera, P. Sánchez-Agulló, *Tetrahedron: Asymmetry* **1994**, *5*, 1393.

[2] For a recent review, see: K. Maruoka, T. Ooi, *Chem. Rev.* **2003**, *103*, 3013.

[3] a) H. Kotsuki, A. Sugino, H. Sakai, H. Yasuoka, *Heterocycles* **2000**, *53*, 2561; b) M. Ostendorf, J. Dijkink, F. P. J. T. Rutjes, H. Hiemstra, *Eur. J. Org. Chem.* **2000**, 115; c) A. E. Taggi, A. M. Hafez, T. Dudding, T. Lectka, *Tetrahedron* **2002**, *58*, 8351.

[4] a) R. Reed, R. Réau, F. Dahan, G. Bertrand, *Angew. Chem.* **1993**, *105*, 464; *Angew. Chem. Int. Ed. Engl.* **1993**, *32*, 399; b) V. K. Aggarwal, A. Mereu, *Chem. Commun.* **1999**, 2311.

[5] For reviews, see: a) E. R. Jarvo, S. J. Miller, *Tetrahedron*, **2002**, *58*, 2481; b) B. List, *Tetrahedron*, **2002**, *58*, 5573.

[6] a) H. Yamamoto, K. Maruoka, *J. Am. Chem. Soc.* **1981**, *103*, 4186; b) M. A. Convery, A. P. Davis, C. J. Dunne, J. W. MacKinnon, *Tetrahedron Lett.* **1995**, *36*, 4279; c) J. Dijkink, K. Eriksen, K. Goubitz, M. N. A. Van Zanden, H. Hiemstra, *Tetrahedron: Asymmetry* **1996**, *7*, 515; d) M. Alajarín, P. Molina, A. Vidal, F. Tovar, *Tetrahedron* **1997**, *53*, 13449.

[7] For recent selected examples of nucleophilic reactions of azides, see: a) P. G. Reddy, B. Vahghese, S. Baskaran, *Org. Lett.* **2003**, *5*, 583; b) K. Sahasrabudhe, V. Gracias, K. Furness, B. T. Smith, C. E. Katz, D. S. Reddy, J. Aubé, *J. Am. Chem. Soc.* **2003**, *125*, 7194; c) S. Lang, A. R. Kennedy, J. A. Murphy, A. H. Payne, *Org. Lett.* **2003**, *5*, 3655; d) D. S. Reddy, W. R. Judd, J. Aubé, *Org. Lett.* **2003**, *5*, 3899.

[8] For recent selected examples of 1,3-dipolar cycloadditions of azides, see: a) F. Himo, Z. P. Demko, L. Noodleman, K. B. Sharpless, *J. Am. Chem. Soc.* **2002**, *124*, 12210, and references therein; b) S. Kamijo, T. Jin, Z. Huo, Y. Yamamoto, *J. Am. Chem. Soc.* **2003**, *125*, 7786, and references therein; c) N. Shangguan, S. Katukojvala, R. Greenberg, L. J. Williams, *J. Am. Chem. Soc.* **2003**, *125*, 7754, and references therein; d) for a related reaction of azides bearing an electron-withdrawing functional group and a highly strained enamine to afford amidines, see: J. K. Crandall, L. C. Crawley, J. B. Komin, *J. Org. Chem.* **1975**, *40*, 2045.

[9] For a review, see: a) P. Molina, M. J. Vilaplana, *Synthesis* **1994**, 1197. For an application to total synthesis, see: b) F. He, B. M. Foxman, B. B. Snider, *J. Am. Chem. Soc.* **1998**, *120*, 6417.

[10] For examples of aza-Wittig cyclizations at an amide carbonyl, usually suffering from low yields, see: a) Y. G. Gololobov, N. I. Gusar, M. P. Chaus, *Tetrahedron*, **1985**, *41*, 1823; b) P. Molina, M. Alajarín, C. López-Leonardo, I. Madrid, C. Foces-Foces, F. H. Cano, *Tetrahedron* **1989**, *45*, 1823; c) J. Kurita, T. Iwata, S. Yasuike, T. Tsuchiya, *J. Chem. Soc. Chem. Commun.* **1992**, 81; d) M. Alajarín, P. Molina, Á. Vidal, F. Tovar, *Synlett* **1998**, 1288.

[11] Confirmed by TLC and LC-MS analysis.

[12] In the thiolactam method, as illustrated in Scheme 1, at least four steps are required including nonproductive protection–deprotection reactions because of the high reactivity of the amino functionality (see refs. [3a], [3b], and [6c] for details).

[13] W. Müller, W. Dorsch, F. Effenberger, *Chem. Ber.* **1987**, *120*, 55.

[14] For the preparation of starting material, see the Supporting Information.

[15] When oxalyl chloride was used, formation of the chloroiminium intermediate was confirmed by ^1H and ^{13}C NMR spectroscopy. Therefore, the cyclization step would be faster when oxalyl bromide is used.

[16] Synthetic procedure reported by Kotsuki et al. (in ref. [3a]) was as follows; 1. hydrogenation of the azide, 2. Boc protection of the resulting amine, 3. thioamide formation with Lawesson's reagent, 4. activation of thioamide (MeI) followed by Boc deprotection and cyclization (trifluoroacetic acid).

[17] For reviews, see: a) G. Köbrich, *Angew. Chem.* **1973**, *85*, 494; *Angew. Chem. Int. Ed. Engl.* **1973**, *12*, 464; b) K. J. Shea, *Tetrahedron* **1980**, *36*, 1683.

[18] In situ IR spectra were recorded on a ReactIR 4000 instrument from ASI Applied Systems.

[19] The value was in good agreement with that from a similar compound: B. A. Phillips, G. Fodor, J. Gal, F. Letourneau, J. J. Ryan, *Tetrahedron* **1973**, *29*, 3309.

[20] The IR spectra of **2a**·HBr and **2a**·Br_2 prepared from **2a** were measured in 1,2-dichloroethane for the reference. **2a**·HBr showed $\tilde{\nu} = 1679\ cm^{-1}$ and **2a**·Br_2 showed $\tilde{\nu} = 1637\ cm^{-1}$ as a characteristic absorption. See the Supporting Information.

[21] **2a**·Br_2 was also detected with an electrospray ionization mass spectrometer by directly sampling the reaction mixture. The peak at $m/z = 203$, 205 ([$\mathbf{2a}^+ + Br$]) derived from **2a**·Br_2 was detected although its relative intensity was weak compared to the peak at $m/z = 125$ ([$\mathbf{2a}^+ + H$]) derived from **2a**·HBr.

[22] Oxalyl bromide alone did not brominate anisole.

 © 2004 Wiley-VCH Verlag GmbH & Co. KGaA, Weinheim

Fluorination Catalysts

Polymer-Supported Ionic Liquids: Imidazolium Salts as Catalysts for Nucleophilic Substitution Reactions Including Fluorinations**

*Dong Wook Kim and Dae Yoon Chi**

Although nucleophilic substitutions that use metal salts as nucleophiles are crucial synthetic transformations, these reactions, especially fluorinations,[1] often proceed sluggishly because of the limited solubility and low nucleophilicity of metal salts in organic solvents.[2] Phase-transfer catalysts such as crown ethers[3] and quaternary ammonium or phosphonium salts[4] have been used to enhance the solubility and nucleophilicity of the metal salt in organic solvent systems, consequently accelerating the reaction rate.[3,4] However, phase-transfer catalysts are ineffective when the metal and nuclelophile form a tight ion pair, and some quaternary ammonium salt catalysts are thermally unstable.[5] There are many reports in which catalysts of this nature are immobilized (so-called triphase catalysts) to facilitate product isolation and enable catalyst recovery by simple filtration.[5,6] However, nucleophilic displacements using such solid-supported phase-transfer catalysts generally proceed at slower rates than those using the corresponding nonimmobilized catalysts.[5]

Due to their unique physical and chemical properties, ionic liquids containing imidazolium cations and their counteranions have currently received much attention as alternative reaction media for conducting various chemical processes.[7] Recently, we reported highly efficient nucleophilic fluorination and other substitution reactions[8] using alkali-metal salts in the presence of ionic liquids. In these transformations, the ionic liquid not only significantly enhanced the reactivity of the alkali-metal salts, but they also reduced by-product formation compared to the use of conventional protocols.[1,8a] However, we encountered problems when the product was polar and contained many heteroatoms, because it became difficult to extract it from the ionic liquid.

To overcome this drawback of ionic liquids, we have designed a polymer-supported ionic liquid (Figure 1) that can be used for nucleophilic displacements. There have been some recent efforts to prepare immobilized ionic liquids. Mehnert et al. reported an ionic liquid supported on the surface of silica gel.[9] However, they used a nonimmobilized ionic liquid to carry out their reaction, and the silica framework is also unstable against fluoride ions, water, and acids. In this report, we introduce a new polystyrene-based polymer-supported ionic-liquid system, which we term a "polymer-supported imidazolium salt" (PSIS), as a highly efficient catalyst for nucleophilic fluorination and for other nucleophilic substitution reactions. These PSISs have the advantage of significantly enhancing the nucleophilicity of the metal salts compared with conventional methods. Furthermore, PSISs can be reused many times without decomposition and loss of activity.

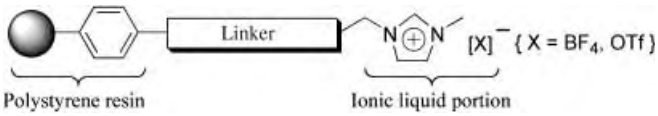
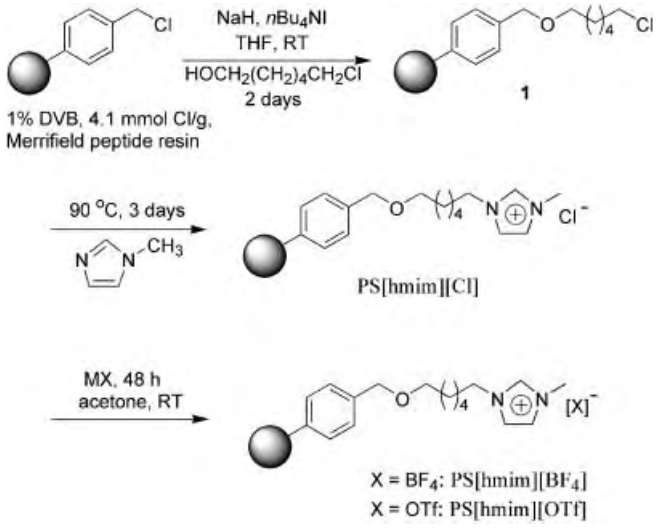


Figure 1. Polystyrene-supported ionic liquids: polymer-supported imidazolium salts.

The PSISs PS[hmim][X] (PS = polymer support; hmim = 1-*n*-hexyl-3-methylimidazolium cation; X = BF_4, OTf) were prepared by the procedure shown in Scheme 1. We have prepared many PSISs with different linkers. The physical and chemical properties of the PSISs depend on the length as well as type of linker employed. In this report, the most promising polymer-supported imidazolium system are described. Merrifield resin[10] (divinylbenzene (1%), Cl (4.5 mmol g^{-1})) was reacted with 6-chloro-1-hexanol in the presence of NaH in THF to obtain resin **1**. PS[hmim][Cl] was prepared by the direct reaction of resin **1** and 1-methylimidazole at 90 °C for 3 days. Further treatment of PS[hmim][Cl] with either $NaBF_4$ or KOTf in acetone for 48 h provides PS[hmim][BF_4] (2.2 mmol of ionic liquid per gram of polymer-supported product obtained) or PS[hmim][OTf] (2.1 mmol of ionic



Scheme 1. Preparation of the polymer-supported imidazolium salts PS[hmim][BF_4] and PS[hmim][OTf]. DVB = divinylbenzene; hmim = 1-*n*-hexyl-3-methylimidazolium cation; MX = $NaBF_4$, KOTf; PS = polymer support.

[*] D. W. Kim, Prof. Dr. D. Y. Chi
Department of Chemistry
Inha University
253 Yonghyundong Namgu, Inchon 402-751 (Korea)
Fax: (+82) 32-867-5604
E-mail: dychi@inha.ac.kr

[**] This work was supported by the National Research Laboratory Program. We thank Professor J. A. Katzenellenbogen and Dr. C. E. Song for helpful discussions.

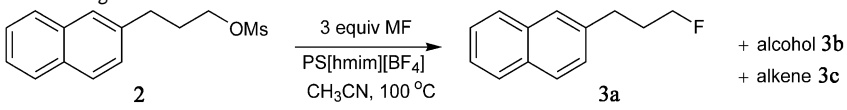
Supporting information for this article is available on the WWW under http://www.angewandte.org or from the author.

 DOI: 10.1002/anie.200352760 © 2004 Wiley-VCH Verlag GmbH & Co. KGaA, Weinheim

liquid). The PSISs were characterized by ^{1}H, ^{13}C, and ^{19}F NMR (solid-state) spectroscopy, and by elemental analysis.

Table 1 concerns the nucleophilic fluorination of the model compound 2-(3-methanesulfonyloxypropyl)naphthalene (**2**) with various alkali-metal fluorides in the presence of the PSISs under various reaction conditions. Whereas the fluorination of mesylate **2** with 3 equiv of CsF in CH_3CN at 100 °C barely proceeded after 2 h (entry 5), the same reaction in the presence of 2.2 or 1.1 equiv of PSIS PS[hmim][BF_4] was complete within 2 h, affording the fluoroalkane **3a** (97 and 98 %, entries 1 and 2). Moreover, the fact that the use of less than one equiv (0.55 or 0.28 equiv in entries 3[11] and 4) of PS[hmim][BF_4] also greatly accelerated the fluorination demonstrates that PS[hmim][BF_4] is likely to be a good catalyst for this reaction. Interestingly, fluorination using PS[hmim][BF_4] as an immobilized catalyst (entry 3) proceeds much faster than that using the same amount of ionic liquid as the phase-transfer catalytic system (entry 6),[5] or by using [18]crown-6 (entry 7). An alternative PSIS (PS[hmim][OTf]; entry 8) with a different anion shows slightly lower catalytic activity compared with PS[hmim][BF_4] in affording the fluoroalkane **3a** (91 %). The results of entries 3, 9, and 10 indicate that even with the PSIS, the rate of fluorination still depends on the nature of the metal cation.

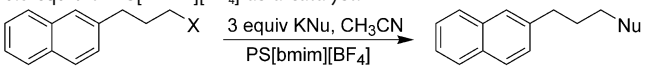
Table 1: Fluorinations of mesylate **2** with alkali-metal fluorides (MF) using PS[hmim][BF_4] or the stated alternative reagents.[a]



Entry	PS[hmim][BF_4] [mg] (equiv[b])	MF	CH_3CN [mL]	*t* [h]	Yield of product [%]			
					2	**3a**	**3b**	**3c**
1	1000 (2.2)	CsF	12	1.5	–	97	–	trace
2	500 (1.1)	CsF	6	2	–	98	–	–
3	250 (0.55)	CsF	3	2.5	–	98	–	–
4	125 (0.28)	CsF	3	4	trace	95	trace	–
5	–	CsF	3	2	91	trace	–	–
6	[bmim][BF_4] (0.55)	CsF	3	3	27	68	–	–
7	[18]crown-6 (2)	CsF	6	5	trace	88	–	7[c]
8	PS[hmim][OTf] (0.55)	CsF	3	5	trace	91	6[c]	–
9	250 (0.55)	RbF	3	9	–	94	5[c]	–
10	250 (0.55)	KF[d]	3[e]	24	–	66	31	–

[a] All reactions were carried out on a 1.0 mmol reaction scale of mesylate **2** using 3 mmol of CsF at 100 °C. [b] Equivalent amount of the ionic liquid portion, not PS[hmim][BF_4]. [c] Determined by NMR spectroscopy (see Supporting Information). [d] 5 equiv of KF was used. [e] CH_3CN containing 5 % H_2O.

Table 2: Nucleophilic substitutions with various potassium salts using 0.5 equiv of PS[hmim][BF_4] as a catalyst.[a]



2: X = OMs, **4**: X = Br — Nu = Cl, Br, I, OAc, CN

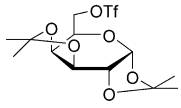
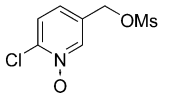
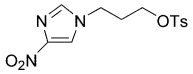
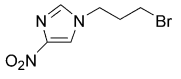
Entry	Substrate	KNu	*T* [°C]	*t* [h]	Yield [%]
1	**2**	KCl	100	6	97
2	**2**	KBr	100	0.8	99
3	**2**	KI	100	0.5	99
4	**4**	KOAc	90	1	99
5	**4**	KCN	100	3	97

[a] Mesylate **2** or bromoalkane **4** (1.0 mmol), KNu (3 mmol), and 0.5 equiv of the ionic liquid portion of PS[bmim][BF_4] were used in 3 mL of CH_3CN.

To investigate how many times PS[hmim][BF_4] could be reused, we carried out the fluorination repeatedly under the conditions given in entry 2 in Table 1. It was observed that PS[hmim][BF_4] could indeed be reused repeatedly without the loss of its catalytic activity; in each cycle, product **3a** was obtained in high yield (96–99 %).

Nucleophilic substitutions with various potassium salts in the presence of 0.5 equiv of PS[hmim][BF_4] were also attempted (Table 2). Entries 1, 2, and 3 show that the halogenation of mesylate **2** proceeds nearly quantitatively (in 97, 99, and 99 % yield, respectively). In entries 4 and 5, the acetoxylation and nitrile substitution of bromoalkane **4** also proceeded in high yield (99 and 97 %, respectively).

Table 3: Fluorination or acetoxylation of various substrates in the presence of PS[bmim][BF_4].[a]

Entry	Compound	Metal salt	Reaction time [min]	*T* [°C]	Yield [%]
1		CsF	90	80	94
2		CsF	60	80	63
3		CsF	60	90	80
4		KOAc	50	90	96

[a] 1.0 mmol of each compound with 3 mmol of the metal salt and 0.5 equiv of the ionic liquid portion of PS[hmim][BF_4] in 3 mL of CH_3CN.

Table 3 illustrates the fluorination of polar substrates, which can only be extracted from ionic liquids with great difficulty because of their high solubility in the liquid salts. Reaction of these substrates with 0.5 equiv of PS[hmim][BF_4] not only proceeded in high yield, but also allowed products to be isolated and purified easily. A fluorosugar was synthesized under mild conditions in

 © 2004 Wiley-VCH Verlag GmbH & Co. KGaA, Weinheim

94% yield in 1.5 h by fluorination of the corresponding sugar triflate (entry 1). The fluorination of 6-chloro-α-mesyloxy-3-picoline *N*-oxide afforded the corresponding fluorinated product in relatively good yield compared with that from an earlier method (entry 2).[12] 1-(3-Fluoropropyl)-4-nitroimidazole was produced in good yield by the fluorination of the corresponding tosylate (entry 3). In the final example, acetoxylation of 1-(3-bromopropyl)-4-nitroimidazole afforded the acetoxy product in 96% (entry 4).

In summary, we have prepared new polymer-supported imidazolium salts (PSIS) that act as highly efficient catalysts for nucleophilic fluorination and other substitutions, which convert various haloalkanes and sulfonyloxyalkanes to their corresponding fluorinated products. The PSIS itself has many practical merits: product recovery and purification is simple and catalyst recovery and reuse is practical. These factors are technically attractive for considering the use of these materials in industrial chemical processes. Furthermore, these PSISs enhance the reactivity of the alkali-metal salts significantly. In particular, PS[hmim][BF_4] shows much higher catalytic activity than the free ionic liquid. Further studies on the development of more efficient PSISs through structural modifications and the application of these unusual catalysts to other reactions, such as the rapid labeling of radiopharmaceuticals with the short-lived positron-emitting radionuclide fluorine-18, are in progress in our laboratories.

Received: September 1, 2003 [Z52760]
Published Online: December 18, 2003

Keywords: fluorination · heterogeneous catalysis · ionic liquids · nucleophilic substitution · polymers

[1] For reviews on nucleophilic fluorination, see: a) M. R. C. Gerstenberger, A. Haas, *Angew. Chem.* **1981**, *93*, 659–681; *Angew. Chem. Int. Ed. Engl.* **1981**, *20*, 647–667; b) O. A. Mascaretti, *Aldrichimica Acta* **1993**, *26*, 47–58.

[2] See: M. D. Smith, J. March, *Advanced Organic Chemistry*, 5th ed., Wiley InterScience, New York, **2001**, pp. 389–674.

[3] a) G. W. Gokel, *Crown Ethers and Cryptands*. Royal Society of Chemistry, Cambridge, **1991**; b) C. J. Pedersen, *J. Am. Chem. Soc.* **1967**, *89*, 7017–7036; c) C. L. Liotta, H. P. Harris, *J. Am. Chem. Soc.* **1974**, *96*, 2250–2252; d) D. J. Sam, H. E. Simmons, *J. Am. Chem. Soc.* **1974**, *96*, 2252–2253.

[4] a) E. V. Dehmlow, S. S. Dehmlow, *Phase Transfer Catalysis*, 3rd ed., VCH, New York, **1993**; b) E. V. Dehmlow, *Angew. Chem.* **1977**, *89*, 521–533; *Angew. Chem. Int. Ed. Engl.* **1977**, *16*, 493–505; c) C. M. Starks, *J. Am. Chem. Soc.* **1971**, *93*, 195–199; d) C. M. Starks, R. M. Owens, *J. Am. Chem. Soc.* **1973**, *95*, 3613–3617.

[5] a) M. Cinquini, S. Colonna, H. Molinari, F. Montanari, P. Tundo, *J. Chem. Soc. Chem. Commun.* **1976**, 394–396; b) H. Molinari, F. Montanari, P. Tundo, *J. Chem. Soc. Chem. Commun.* **1977**, 639–641.

[6] a) S. L. Regen, D. P. Lee, *J. Am. Chem. Soc.* **1974**, *96*, 294–296; b) S. L. Regen, *J. Am. Chem. Soc.* **1975**, *97*, 5956–5957.

[7] For recent reviews on ionic liquids, see: a) H. Zhao, S. V. Malhotra, *Aldrichimica Acta* **2002**, *35*, 75–83; b) R. Sheldon, *Chem. Commun.* **2001**, 2399–2407; c) P. Wasserscheid, W. Kein, *Angew. Chem.* **2000**, *112*, 3926–3945; *Angew. Chem. Int. Ed.* **2000**, *39*, 3772–3789; d) T. Welton, *Chem. Rev.* **1999**, *99*, 2071–2083; e) C. C. Tzschucke, C. Markert, W. Bannwarth, S. Roller, A. Hebel, R. Haag, *Angew. Chem.* **2002**, *114*, 4136–4173; *Angew. Chem. Int. Ed.* **2002**, *41*, 3964–4000.

[8] a) D. W. Kim, C. E. Song, D. Y. Chi, *J. Am. Chem. Soc.* **2002**, *124*, 10278–10279; b) D. W. Kim, C. E. Song, D. Y. Chi, *J. Org. Chem.* **2003**, *68*, 4281–4285; c) D. W. Kim, Y. S. Choe, D. Y. Chi, *Nucl. Med. Biol.* **2003**, *30*, 345–350.

[9] C. P. Mehnert, R. A. Cook, N. C. Dispenziere, M. Afeworki, *J. Am. Chem. Soc.* **2002**, *124*, 12932–12933.

[10] R. B. Merrifield, *J. Am. Chem. Soc.* **1963**, *85*, 2149–2154.

[11] In a typical experiment, CsF (454 mg, 3 mmol) was added to a mixture of mesylate **2** (264 mg, 1.0 mmol) and PS[hmim][BF_4] (250 mg, 0.55 mmol) in acetonitrile (3 mL). This mixture was stirred for 2.5 h at 100 °C and then filtered through a short flash-chromatography column (20% EtOAc/hexanes). The filtrate afforded 184 mg (98%) of 2-(3-fluoropropoxy)naphthalene (**3a**).

[12] K. C. Lee, D. Y. Chi, *J. Org. Chem.* **1999**, *64*, 8576–8581.

 © 2004 Wiley-VCH Verlag GmbH & Co. KGaA, Weinheim

Small-Bandgap Porphyrins

Facile Oxidative Rearrangement of Dispiro-Porphodimethenes to Nonplanar and Sheetlike Porphyrins with Intense Absorptions in the Near-IR Region**

*Hubert S. Gill, Michael Harmjanz, Javier Santamaría, Isaac Finger, and Michael J. Scott**

The spectroscopy, redox potentials, spin states, and axial coordination chemistry of metalloporphyrins, chlorins, and related compounds can be modulated through distortions in planarity or the presence of exocyclic ring systems fused to the periphery of the macrocycle. In biological systems, the reactivity and properties of tetrapyrrolic macrocycles are often tuned through subtle combinations of these two factors.[1] To help elucidate the origins resulting from modifications to the porphyrin frame, nonplanar porphyrins with

[*] H. S. Gill, Dr. M. Harmjanz, I. Finger, Prof. M. J. Scott
Department of Chemistry and Center for Catalysis
University of Florida
P.O. Box 117200, Gainesville, FL 32611-7200 (USA)
Fax: (+1) 352-392-3255
E-mail: mjscott@chem.ufl.edu
Dr. J. Santamaría
Instituto Universitario de Química Organometálica "Enrique Moles"
Unidad Asociada al CSIC, Universidad de Oviedo
Julián Clavería 8, 33071-Oviedo (Spain)

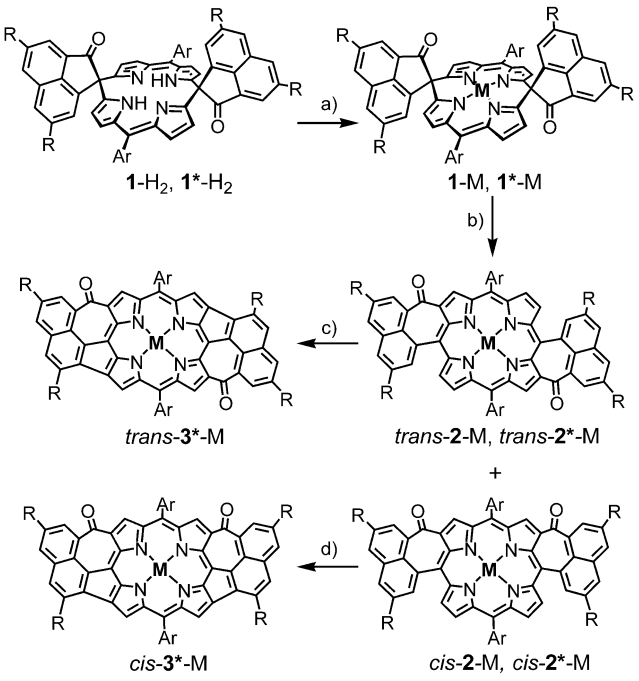
[**] We thank the Deutsche Forschungsgemeinschaft (postdoctoral fellowship for M. Harmjanz), the Research Corporation (Research Innovation Award), and the Alfred P. Sloan Foundation for providing financial support for this work. Support from the National Science Foundation (CAREER Award - 9874966) is also gratefully acknowledged.

Supporting information for this article is available on the WWW under http://www.angewandte.org or from the author.

 DOI: 10.1002/anie.200352762 © 2004 Wiley-VCH Verlag GmbH & Co. KGaA, Weinheim

unusual symmetries, as well as porphyrins exhibiting π-electron delocalization with extremely low-energy electronic transitions and multiple interacting ring systems, continue to be desirable synthetic targets.[2] Along with providing theoretical insight into these biologically relevant but still poorly understood phenomena,[3] synthetic porphyrins with small bandgaps may find practical utility as novel optical, electronic, or therapeutic materials,[4] while nonplanar porphyrins with engineered deformations exhibit enhanced properties for a variety of applications in catalysis[5] and host–guest chemistry.[6] Herein, we present a straightforward oxidative-rearrangement method for the conversion of metalloporphodimethenes to intrinsically nonplanar porphyrins with two exocyclic naphthocycloheptanone ring systems. Further oxidative dehydrogenation generates exceedingly large, almost perfectly planar porphyrins, bearing bis(naphthoazulenone) ring systems, in high yield, and to the best of our knowledge, these compounds exhibit the longest absorption wavelength reported for monomeric metalloporphyrins.

Presumably due to their predisposition to form the fully aromatic porphyrin, the porphodimethene macrocycle, a two-electron reduced form of the porphyrin macrocycle with sp^3 carbons at two *trans meso* positions, has yet to be found in nature. Until only very recently,[7] porphodimethenes such as **1**-H_2 (Scheme 1) have been difficult to prepare in the laboratory.[8,9] Reasoning that the conversion from porphodimethenes to porphyrins is a 2e, $2H^+$ process, and given the considerable driving force for forming the aromatic macrocycle, we undertook electrochemical investigations of **1**-H_2 and several of the metalated derivatives. In these experiments, irreversible oxidations were observed, with the free ligands having higher oxidation potentials than the metalated derivatives by 0.5 ± 0.2 V.[10] Treatment of **1**-H_2 under various oxidative conditions resulted in either no reaction or complex mixtures of often insoluble products. Reactions of **1**-Cu and **1**-Pd under the same sets of conditions led to green products and/or sparingly soluble dark red products. By using light and an excess of DDQ under anhydrous conditions, we optimized the conversions of **1**-Cu and **1**-Pd to the *cis* and *trans* isomer pairs of **2**-Cu and **2**-Pd to produce high combined yields of the two isomers (Scheme 1). Photolysis experiments with UV/Vis monitoring and initial photophysical measurements indicate photolytic cleavage, likely a Norrish Type I process, for the initiation of the reaction, but a donor–acceptor adduct with the oxidant may be the initial step in this pathway.[11] The use of excess DDQ to rapidly drive the oxidative processes, as well as the rigorous exclusion of water and alcohols, was necessary to avoid competitive reactions.[12]



Scheme 1. Synthetic methodology: a) for M = Cu: $Cu(OAc)_2$, $CHCl_3$/MeOH, Δ, 1 h; for M = Pd: $[(C_6H_5CN)_2PdCl_2]$, THF, Δ, 2.5 h; b) *hν*, DDQ (2×1.2 equiv), CH_2Cl_2, RT, 25–120 min; c) DDQ (7.2 equiv), $FeCl_3 \cdot 6H_2O$ (20 equiv), CH_2Cl_2, Δ, 5–6 h; d) DDQ (4.8 equiv), $FeCl_3 \cdot 6H_2O$ (10 equiv), CH_2Cl_2, Δ, 15 min. DDQ = 2,3-dichloro-5,6-dicyano-1,4-benzoquinone, RT = room temperature. *Implies R = *t*Bu, otherwise, R = H.

The Soret bands in the UV/Vis spectra of these unusual porphyrins appear at lower energy than those of tetraphenylporphyrin and range from 466 nm (*trans*-**2**-Pd) to 490 nm (*cis*-**2***-Cu). The low-energy electronic transitions for these porphyrins are also quite red-shifted (652 nm for *cis*-**2**-Pd; 705 nm for *trans*-**2***-Cu) as well as broad and intense ($\lg \varepsilon = 4.6$) in comparison to the Q bands found for typical metalloporphyrins. In the solid-state (Figure 1),[13] the *trans* nonplanar porphyrin, *trans*-**2**-Pd, adopts an *anti* configuration with respect to the carbonyl groups of the cycloheptanone moieties. Steric clash of naphthyl (at C22, C33) and pyrrolic hydrogens (at C7, C17) induces a distortion in the macrocycle, resulting in a mean deviation of 0.32 Å for the 20 carbon atoms in the porphyrin core from the average plane defined by the four nitrogen atoms. The macrocycle exhibits a ruffled B_{1u} deformation with the *meso*-carbon atoms displaced alternately above and below this N-normal plane. Both the nonplanar distortion and the delocalization of electron density through the fused naphthocycloheptanone ring systems likely contribute to the bathochromic shifts observed for porphyrins of the type **2**-M and **2***-M.

In addition to multiple reductive currents and one reversible oxidative wave, cyclic voltammograms of *cis*-**2**-Cu and *trans*-**2**-Cu exhibit irreversible oxidations at 1.36 and 1.30 V vs Ag/AgCl, respectively. Chemical treatment of these porphyrins with oxidants produces poorly soluble products similar to those obtained from the treatment of **1**-Cu and **1**-Pd with strong oxidants. In order to enhance the solubility of the products, *t*Bu groups were introduced at the 4- and 7-positions of the acenaphthenequinone precursor, and **1***-H_2 was prepared in the same way as **1**-H_2 and other dispiroporphodimethenes.[9] Although both the *syn*- and *anti*-porphodimethenes react analogously, the *anti* isomer was used exclusively for all reactions reported herein, because **1***-H_2 is easy to isolate.

Metalation of **1***-H_2 with Cu or Pd and oxidation to the corresponding nonplanar butylated cycloheptanone porphyrins proceed as expected. Chromatographic separation of the isomers for both palladium and copper results in the *cis* and *trans* porphyrins in an approximately 2:1 ratio, as observed for

 © 2004 Wiley-VCH Verlag GmbH & Co. KGaA, Weinheim

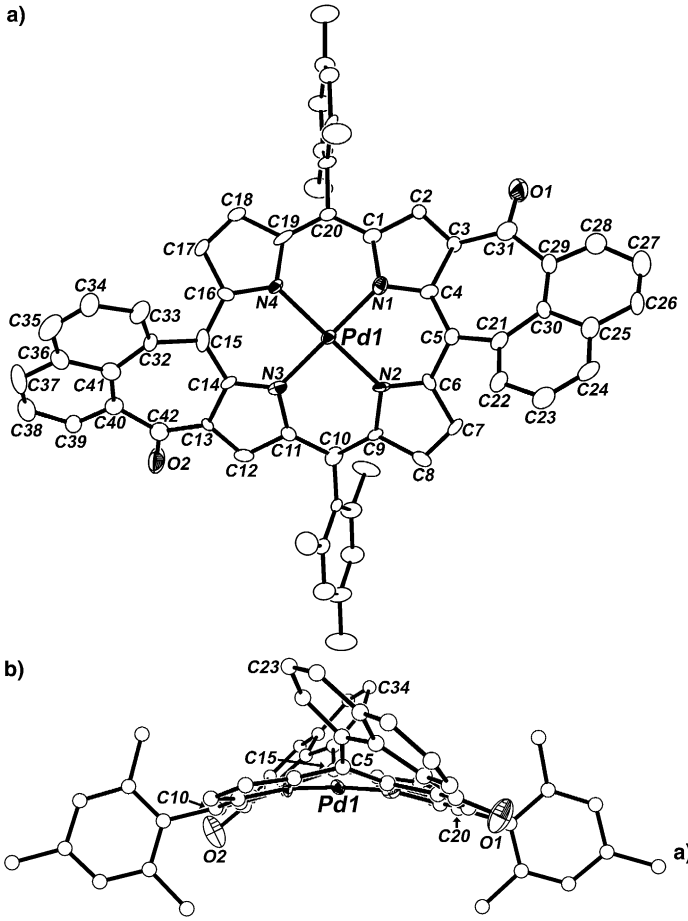


Figure 1. a) X-ray structure of *trans*-**2**-Pd (ellipsoids at 30% probability). Hydrogen atoms have been omitted for clarity. Only one of the two symmetry-inequivalent porphyrins found in the asymmetric unit is depicted. Selected bond lengths [Å] and angles [°]: Pd1-N1 1.990(6), Pd1-N2 1.986(7), Pd1-N3 2.005(7), Pd1-N4 2.002(6), N1-Pd1-N2 88.4(2), N1-Pd1-N3 175.7(2), N1-Pd1-N4 91.2(2). b) Side view of *trans*-**2**-Pd (arbitrary radii for carbon atoms) illustrating the ruffled deformation of the macrocycle.

the conversion of **1**-M to *cis*- and *trans*-**2**-M porphyrins. Reaction of *cis*-**2***-M with an excess of both DDQ and $FeCl_3 \cdot 6H_2O$ in refluxing CH_2Cl_2, followed by aqueous workup and filtration over silica produces the *cis*-bisnaphthoazuleneone porphyrins, *cis*-**3***-M. The flat *trans* isomer, *trans*-**3***-M, can be generated similarly from *trans*-**2***-M. Compared to the conversion of the *cis* isomers, however, reaction times are longer,[14] and the procedure requires additional equivalents of oxidants and a reductive aqueous workup. The two oxidative processes can be performed in one pot, generating a mixture of *cis*- and *trans*-**3***-M directly from **1***-M, but chromatographic resolution of the isomer pairs is considerably easier for the **2***-M porphyrins than for the **3***-M compounds. While oxidative biaryl-coupling reactions utilizing $FeCl_3$ or DDQ as an oxidant are common, it seems the only report of their use in combination involved the deprotection of methoxy phenyl methyl esters using catalytic amounts of DDQ with excess $FeCl_3$. In this system, Fe^{III} regenerates the active oxidant from its reduced form (H_2DDQ).[15] DDQ in conjunction with other metals such as $Sc(OTf)_3$ will induce the oxidative coupling of triarylporphyrins to generate coplanar diporphyrins,[16] and although the $Sc(OTf)_3$/DDQ procedure was not attempted for the oxidation of **2***-M to **3***-M, numerous other reagents and conditions were tested. None of these trials produced the desired products in yields as high as those achieved with the $FeCl_3$/DDQ procedures described herein, and the isolation of the porphyrins was often more problematic.

Slow diffusion of diethyl ether into a saturated CH_2Cl_2 solution of *cis*-**3***-Cu produced single crystals as purple plates with a green metallic luster. Structure analysis by X-ray diffraction reveals a relatively planar porphyrin interior, with a mean deviation of only 0.08(6) Å for the 20 carbon atoms in the porphyrin core from the average plane defined by the four nitrogens (Figure 2). The naphthyl moieties at the periphery of the ring system deviate slightly from this nitrogen plane with a mean deviation of 0.27(16) Å for the 22 carbon atoms in the two naphthyl groups (max. deviation 0.53 Å for C26). These minor deviations are likely induced by packing forces in the solid state. Interestingly, the largest displacement (0.78 Å) from the N_4 plane in the macrocyclic core is found at one of the carbonyl oxygens, O2. Many unusual bond angles are found in this ring system, which, discounting *t*Bu and mesityl aryl groups, contains 49 non-hydrogen nuclei arranged as eight six-, six five-, and two seven-membered

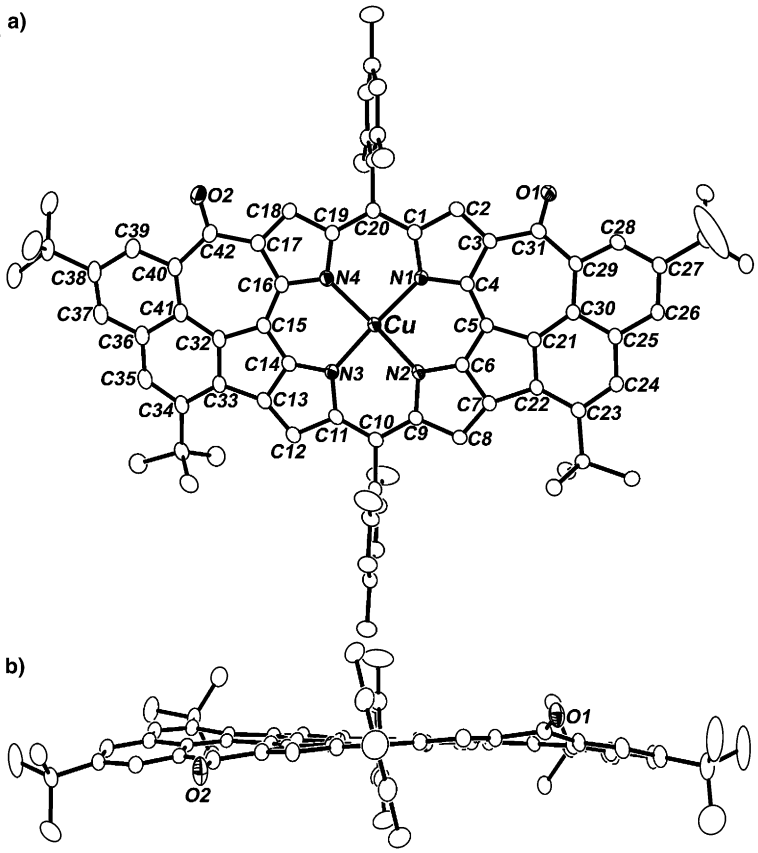


Figure 2. a) Top view and b) side view of the X-ray structure of *cis*-**3***-Cu (30% ellipsoids). Hydrogen atoms have been omitted for clarity. Selected bond lengths [Å] and angles [°]: Cu-N1 2.002(2), Cu-N2 1.952(2), Cu-N3 1.949(2), Cu-N4 1.997(2), N1-Cu-N2 92.33(8), N1-Cu-N3 176.86(9).

 © 2004 Wiley-VCH Verlag GmbH & Co. KGaA, Weinheim

rings, interlocked in a highly delocalized π system, with two carbonyls in the plane of hybridization. Among the 42 sp^2 carbons in the porphyrin plane, 17 have a bond angle of 110° or less, and 9 have a bond angle of 130° or more, with extremes represented at the C7 and C13 vertices (C8-C7-C6: 104.5°(2); C8-C7-C22: 149.8°(2)). The distance between the two furthest separated sp^2 carbon atoms (C27, C38) in the sheetlike macrocycle is 1.69 nm.

The UV/Vis/NIR spectra of these porphyrins display numerous exceptional features, including low-energy (Q-type) absorptions with dramatic bathochromic shifts relative to the absorptions of typical Cu and Pd porphyrins (Figure 3).

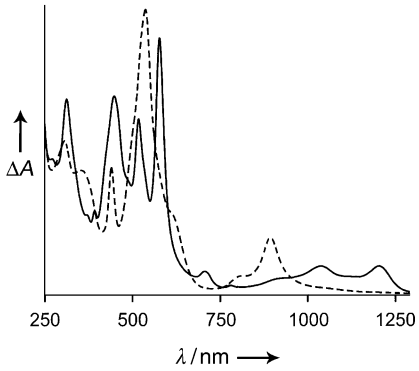


Figure 3. UV-Vis/NIR spectra of the sheetlike copper porphyrins *trans*-**3***-Cu (——) and *cis*-**3***-Cu (-----).

All porphyrins of the type **3***-M have a band at ≈450 nm; the location of the other transitions is metal dependant, with copper species having spectra further red-shifted than those of their palladium analogues. Otherwise, the shapes of the spectra are very similar for each isomer, regardless of the metal incorporated. For both the *cis* and *trans* isomers, the most intense absorption band ($\lg\varepsilon = 4.9$) occurs in the visible region ($\lambda = 540$–579 nm), and these bands approach the record low-energy Soret absorption of $\lambda = 625$ nm noted by Lash and co-workers.[17] In addition to the aforementioned high-energy bands, the *cis* isomers exhibit a rather intense ($\lg\varepsilon = 4.2$), Q-like band at $\lambda = 850$ nm for *cis*-**3***-Pd and at $\lambda =$ 894 nm for *cis*-**3***-Cu. While the *trans* isomers have visible spectra that are only slightly red-shifted relative to the spectra of their *cis* counterparts, their Q-like bands exhibit extreme bathochromic shifts and are split into two less intense transitions in the near-IR region. For *trans*-**3***-Pd these low-energy bands are found at $\lambda = 994$ nm and 1145 nm, and for *trans*-**3***-Cu they are found at $\lambda = 1038$ nm and 1204 nm. Although the absorptions of triply fused, multiporphyrin tapes have been shown to reach further into the IR region,[16b,18] the extremely red-shifted transitions observed for *trans*-**3***-Cu are, to the best of our knowledge, the lowest energy electronic transitions ever observed for a *monomeric* porphyrin species.

In light of the spectral features in the NIR region indicating very small band-gaps, cyclic voltammetric studies of compounds *cis*-**3***-Cu and *trans*-**3***-Cu were carried out in benzonitrile. As expected based upon their spectrophotometry, the first oxidation potential was less positive and the first reduction potential less negative for *trans*-**3***-Cu ($ox_1 =$ 0.73 V, $red_1 = -0.44$ V) than for *cis*-**3***-Cu ($ox_1 = 0.87$ V, $red_1 = -0.46$ V). Special attention was paid to the difference in the first 1 e oxidation and 1 e reduction potentials for the macrocycles in comparison to the potentials for simple porphyrins such as Cu^{II} tetramesitylporphyrin (CuTMP). Relative to CuTMP ($ox_1 = 1.18$ V, $red_1 = -1.36$ V), the separation between the first reduction and oxidation potentials are quite small for both *cis*-**3***-Cu and *trans*-**3***-Cu (Figure 4). Even the second reversible 1 e reductions for both *trans*-**3***-Cu (−0.85 V) and *cis*-**3***-Cu (−0.89 V) occur at potentials far less negative than the first 1 e reduction for CuTMP.

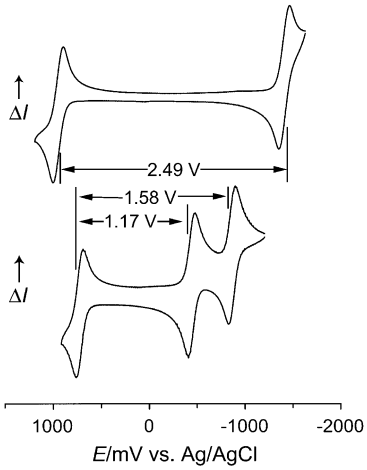


Figure 4. Cyclic voltammogram of *trans*-**3***-Cu (bottom) compared to that of CuTMP (top).

With their tendency to form fully aromatic porphyrins, dispiro-porphodimethene macrocycles are excellent synthons for the preparation of distorted porphyrins bearing two naphthocycloheptanones fused to the macrocycle core as well as 1.69-nm wide, planar porphyrins with two naphthoazulen-8-one moieties. These unusual, soluble macrocycles can be isolated in high yields in one- or two-pot procedures from metalloporphodimethenes, allowing for the preparation of large quantities of material. Detailed investigations into the reactivity and photochemistry of the macrocycles, as well as the extension of the rearrangement and coupling procedures to other dispiro-porphodimethenes and biaryl systems, respectively, are underway.

Experimental Section

Complete experimental details including MS, NMR, and elemental data for all compounds are available in the Supporting Information. General procedure for the preparation of bis(naphthocycloheptanone) porphyrins **2**-M and **2***-M: Metalloporphodimethenes **1**-M or **1***-M were treated under an inert atmosphere, with excess DDQ in anhydrous, degassed CH_2Cl_2. The solution was irradiated from a distance of 10 cm with a 20-W halogen light source fitted with a UV filter. Reaction times varied from 25 min (**2**-Cu) to 2 h (**2***-Pd). Reaction mixtures were subsequently diluted with CH_2Cl_2, washed with water, and dried over Na_2SO_4, and the solvents removed. In the separation by silica gel column chromatography the *trans* isomers

 © 2004 Wiley-VCH Verlag GmbH & Co. KGaA, Weinheim

eluted as the first major green bands. *trans*-**2**-Cu: 36% yield; UV/Vis (CH_2Cl_2): λ_{max} ($\lg\varepsilon$) = 470 (5.2), 700 (4.5) nm. *cis*-**2**-Cu: 59% yield; UV/Vis (CH_2Cl_2): λ_{max} ($\lg\varepsilon$) = 488 (5.2), 678 (4.5) nm. *trans*-**2***-Cu: 32% yield; UV/Vis (CH_2Cl_2): λ_{max} ($\lg\varepsilon$) = 473 (5.3), 705 (4.6) nm. *cis*-**2***-Cu: 57% yield; UV/Vis (CH_2Cl_2): λ_{max} ($\lg\varepsilon$) = 490 (5.3), 681(4.6) nm; *trans*-**2**-Pd: 37% yield; UV/Vis (CH_2Cl_2): λ ($\lg\varepsilon$) = 466 (5.3), 674 (4.6) nm; *cis*-**2**-Pd: 59% yield (88 mg); UV/Vis (CH_2Cl_2): λ ($\lg\varepsilon$) = 483 (5.4), 652 (4.6) nm. *trans*-**2***-Pd: 32% yield; UV/Vis (CH_2Cl_2): λ_{max} ($\lg\varepsilon$) = 470 (5.4), 678 (4.7) nm. *cis*-**2***-Pd: 62% yield; UV/Vis (CH_2Cl_2): λ_{max} ($\lg\varepsilon$) = 486 (5.4), 656 (4.6) nm.

General procedures for the preparation of bis(naphthoazulenone) porphyrins **3***-M: *trans* Isomers: A solution of *trans*-**2***-M in CH_2Cl_2 was treated with an excess of both DDQ and $FeCl_3{\cdot}6H_2O$. The mixture was heated at reflux for 6 h, allowed to cool to room temperature, and decanted. Freshly prepared aqueous $NaBH_4$ was added to the solution, and the resulting biphasic mixture was stirred. After dilution with CH_2Cl_2 and water, the organic phase was separated, washed with water, dried over Na_2SO_4, and filtered over silica (4 × 4-cm, $CHCl_3$). The solvents were removed, and the residue was redissolved in *o*-$C_6H_4Cl_2$. Addition of hexanes to this solution causes the precipitation of *trans*-**3***-M as a metallic, red-gray powder. *cis* Isomers: The *cis* isomers, *cis*-**2***-M, were treated in analogy to the *trans* isomers, but the reaction times were considerably shorter (15–20 min) and less of the oxidant mixture was required. Filtration over silica (6 × 4-cm, CH_2Cl_2/hexanes 1:1) and slow removal of the solvents afforded *cis*-**3***-M as purple-green microcrystalline solids. Normally, for convenience sake, the reactions were run on scales to produce the products in approximately 50-mg quantities, but the synthetic procedures allow for the isolation of the materials in amounts over a gram. *trans*-**3***-Cu: 90% yield; UV/Vis (CH_2Cl_2): λ_{max} ($\lg\varepsilon$) = 314 (4.8), 449 (4.8), 519 (4.7), 579 (4.9), 706 (3.8), 1038 (3.9), 1204 (3.9) nm. *cis*-**3***-Cu: 98% yield; UV/Vis (CH_2Cl_2): λ_{max} ($\lg\varepsilon$) = 308 (4.6), 441 (4.6), 540 (4.9), 894 (4.2) nm. *trans*-**3***-Pd: 92% yield; UV/Vis (CH_2Cl_2): λ_{max} ($\lg\varepsilon$) = 307 (4.6), 445 (4.7), 502 (4.5), 522 (4.5), 567 (4.9), 682 (3.8), 994 (3.8), 1145 (3.8) nm. *cis*-**3***-Pd: 96% yield; UV/Vis (CH_2Cl_2): λ_{max} ($\lg\varepsilon$) = 285 (4.6), 445 (4.8), 553 (4.9), 850 (4.2) nm.

Received: September 1, 2003 [Z52762]

Keywords: fused-ring systems · photochemistry · porphyrinoids · rearrangements · redox chemistry

[1] a) P. D. Smith, B. R. James, D. H. Dolphin, *Coord. Chem. Rev.* **1981**, *39*, 31; b) M. H. Barley, D. Dolphin, B. R. James, *J. Chem. Soc. Chem. Commun.* **1984**, 1499; c) M. W. Renner, R. J. Cheng, C. K. Chang, J. Fajer, *J. Phys. Chem.* **1990**, *94*, 8508; d) C. J. Medforth, M. O. Senge, K. M. Smith, L. D. Sparks, J. A. Shelnutt, *J. Am. Chem. Soc.* **1992**, *114*, 9859; e) W. Jentzen, E. Unger, X. Z. Song, S. L. Jia, I. Turowska-Tyrk, R. Schweitzer-Stenner, W. Dreybrodt, W. R. Scheidt, J. A. Shelnutt, *J. Phys. Chem. A* **1997**, *101*, 5789; f) J. A. Shelnutt, X. Z. Song, J. G. Ma, S. L. Jia, W. Jentzen, C. J. Medforth, *Chem. Soc. Rev.* **1998**, *27*, 31; g) M. O. Senge, *J. Porphyrins Phthalocyanines* **1998**, *2*, 107; h) S. L. Jia, W. Jentzen, M. Shang, X. Z. Song, J. G. Ma, W. R. Scheidt, J. A. Shelnutt, *Inorg. Chem.* **1998**, *37*, 4402; i) T. J. Neal, B. S. Cheng, J. G. Ma, J. A. Shelnutt, C. E. Schulz, W. R. Scheidt, *Inorg. Chim. Acta* **1999**, *291*, 49; j) M. O. Senge in *The Porphyrin Handbook*, *Vol. 1* (Eds.: K. M. Kadish, K. M. Smith, R. Guilard), Academic, San Diego, **2000**, p. 239; k) K. M. Barkigia, M. W. Renner, J. Fajer, *J. Porphyrins Phthalocyanines* **2001**, *5*, 415,l) M. W. Renner, K. M. Barkigia, D. Melamed, J. P. Gisselbrecht, N. Y. Nelson, K. M. Smith, J. Fajer, *Res. Chem. Intermed.* **2002**, *28*, 741; m) D. J. Nurco, K. M. Smith, J. Fajer, *Chem. Commun.* **2002**, 2982; n) L. N. Todd, M. Zimmer, *Inorg. Chem.* **2002**, *41*, 6831; o) O. S. Finikova, A. V. Cheprakov, P. J. Carroll, S. Dalosto, S. A. Vinogradov, *Inorg. Chem.* **2002**, *41*, 6944; p) E. Sigfridsson, U. Ryde, *J. Biol. Inorg. Chem.* **2003**, *8*, 273.

[2] a) L. Barloy, D. Dolphin, D. Dupre, T. P. Wijesekera, *J. Org. Chem.* **1994**, *59*, 7976; b) H. J. Callot, R. Ocampo in *The Porphyrin Handbook*, *Vol. 1* (Eds.: K. M. Kadish, K. M. Smith, R. Guilard), Academic, San Diego, **2000**, p. 349; c) T. D. Lash in *The Porphyrin Handbook*, *Vol. 2* (Eds.: K. M. Kadish, K. M. Smith, R. Guilard), Academic, San Diego, **2000**; d) S. Richeter, C. Jeandon, R. Ruppert, H. J. Callot, *Tetrahedron Lett.* **2001**, *42*, 2103; e) H. Aihara, L. Jaquinod, D. J. Nurco, K. M. Smith, *Angew. Chem.* **2001**, *113*, 3547; *Angew. Chem. Int. Ed.* **2001**, *40*, 3439; f) S. Richeter, C. Jeandon, J. P. Gisselbrecht, R. Ruppert, H. J. Callot, *J. Am. Chem. Soc.* **2002**, *124*, 6168.

[3] a) A. Forman, M. W. Renner, E. Fujita, K. M. Barkigia, M. C. W. Evans, K. M. Smith, J. Fajer, *Isr. J. Chem.* **1989**, *29*, 57; b) M. O. Senge, *J. Photochem. Photobiol. B* **1992**, *16*, 3; c) T. D. Lash, *J. Porphyrins Phthalocyanines* **2001**, *5*, 267; d) H. Ryeng, A. Ghosh, *J. Am. Chem. Soc.* **2002**, *124*, 8099; e) R. E. Haddad, S. Gazeau, J. Pecaut, J. C. Marchon, C. J. Medforth, J. A. Shelnutt, *J. Am. Chem. Soc.* **2003**, *125*, 1253.

[4] a) J. G. Moser, A. Ruck, H. J. Schwarzmaier, C. Westphalfrosch, *Opt. Eng.* **1992**, *31*, 1441; b) J. H. Chou, H. S. Nalwa, M. E. Kosal, N. A. Rakow, S. S. Suslick in *The Porphyrin Handbook*, *Vol. 6* (Eds.: K. M. Kadish, K. M. Smith, R. Guilard), Academic, San Diego, **2000**, p. 43; c) R. K. Pandey, G. Zheng in *The Porphyrin Handbook*, *Vol. 6* (Eds.: K. M. Kadish, K. M. Smith, R. Guilard), Academic, San Diego, **2000**, p. 157; d) A. Wiehe, H. Stollberg, S. Runge, A. Paul, M. O. Senge, B. Roder, *J. Porphyrins Phthalocyanines* **2001**, *5*, 853.

[5] S. Gazeau, J. Pecaut, R. Haddad, J. A. Shelnutt, J. C. Marchon, *Eur. J. Inorg. Chem.* **2002**, 2956.

[6] a) M. Mazzanti, J. C. Marchon, M. Y. Shang, W. R. Scheidt, S. L. Jia, J. A. Shelnutt, *J. Am. Chem. Soc.* **1997**, *119*, 12400; b) S. Gazeau, J. Pecaut, J. C. Marchon, *Chem. Commun.* **2001**, 1644.

[7] a) J. W. Buchler, L. Puppe, *Liebigs Ann. Chem.* **1974**, 1046b) A. Botulinski, J. W. Buchler, K. L. Lay, J. Ensling, H. Twilfer, J. Billecke, H. Leuken, B. Tonn, *Adv. Chem. Ser.* **1982**, 253.

[8] a) V. Král, J. L. Sessler, R. S. Zimmerman, D. Seidel, V. Lynch, B. Andrioletti, *Angew. Chem.* **2000**, *112*, 1097; *Angew. Chem. Int. Ed.* **2000**, *39*, 1055; b) L. Bonomo, E. Solari, R. Scopelliti, C. Floriani, N. Re, *J. Am. Chem. Soc.* **2000**, *122*, 5312.c) M. O. Senge, S. Runge, M. Speck, K. Ruhlandt-Senge, *Tetrahedron* **2000**, *56*, 8927; d) J. L. Sessler, R. S. Zimmerman, C. Bucher, V. Král, B. Andrioletti, *Pure Appl. Chem.* **2001**, *73*, 1041; e) D. H. Burns, Y. H. Li, D. C. Shi, T. M. Caldwell, *J. Org. Chem.* **2002**, *67*, 4536.

[9] a) M. Harmjanz, M. J. Scott, *Chem. Commun.* **2000**, 397; b) M. Harmjanz, H. S. Gill, M. J. Scott, *J. Org. Chem.* **2001**, *66*, 5374; c) M. Harmjanz, I. Bozidarevic, M. J. Scott, *Org. Lett.* **2001**, *3*, 2281.

[10] We measured a reversible oxidation at 0.94 V for the Cu(calix[4]phyrin) prepared by Sessler and co-workers (ref. [8a]).

[11] O. L. Chapman, D. S. Weiss in *Organic Photochemistry*, *Vol. 3*, (Ed.: O. L. Chapman), Dekker, New York, **1973**, p. 197.

[12] Details of some of these competitive reactions will be published in an upcoming paper.

[13] Crystal structure data for *trans*-**2**-Pd·2$CHCl_3{\cdot}{}^1/_4C_5H_{12}$: monoclinic, space group $P2_1/c$, a = 12.085(3), b = 31.100(8), c = 28.596(7) Å, β = 98.472(4)°, V = 10630(4) Å^3, T = 193 K, Z = 8, ρ_{cald} = 1.555 g cm^{-3}, $\mu(Mo_{K\alpha})$ = 0.702 mm^{-1}, 50631 reflections collected, 16688 unique, of which 8508 with $I > 2\sigma$ were used in the refinement. R_1 = 0.0700 [$I > 2\sigma(I)$], wR_2 = 0.1543, GOF = 0.902 for 1307 parameters. Crystal structure data for *cis*-**3***-Cu·2$CH_2Cl_2{\cdot}{}^1/_2Et_2O$: monoclinic, space group $C2/c$, a = 29.5740(14), b = 12.4738(6), c = 41.109(2) Å, β = 100.309(1)°, V = 14920.3(12) Å^3, T = 193 K, Z = 8, ρ_{cald} = 1.193 g cm^{-3}, $\mu(Mo_{K\alpha})$ = 0.484 mm^{-1}, 45023 reflections collected, 14679

 © 2004 Wiley-VCH Verlag GmbH & Co. KGaA, Weinheim

unique, of which 10048 with $I > 2\sigma$ were used in the refinement. $R_1 = 0.0558$ [$I > 2\sigma(I)$], $wR_2 = 0.1550$, GOF = 1.098 for 811 parameters. CCDC-218523 (*trans*-**2**-Pd) and CCDC-218524 (*cis*-**3***-Cu) contain the supplementary crystallographic data for this paper. These data can be obtained free of charge via www.ccdc.cam.ac.uk/conts/retrieving.html (or from the Cambridge Crystallographic Data Centre, 12, Union Road, Cambridge CB21EZ, UK; fax: (+44)1223-336-033; or deposit@ccdc.cam.ac.uk).

[14] For the *trans* isomers, the partially oxidized ($2H^+$, $2e^-$) species with one naphthocycloheptanone and one naphthoazulenone peripheral group have been isolated. The details of the synthesis of these intermediates and their properties are forthcoming.

[15] S. Chandrasekhar, G. Sumithra, J. S. Yadav, *Tetrahedron Lett.* **1996**, *37*, 1645.

[16] a) M. D. Watson, A. Fechtenkötter, K. Müllen *Chem. Rev.* **2001**, *101*, 1267; b) M. Kamo, A. Tsuda, Y. Nakamura, N. Aratani, K. Furukawa, T. Kato, A. Osuka, *Org. Lett.* **2003**, *5*, 2079.

[17] J. D. Spence, T. D. Lash, *J. Org. Chem.* **2000**, *65*, 1530.

[18] a) A. Tsuda, A. Osuka, *Science* **2001**, *293*, 79; b) H. S. Cho, D. H. Jeong, S. Cho, D. Kim, Y. Matsuzaki, K. Tanaka, A. Tsuda, A. Osuka, *J. Am. Chem. Soc.* **2002**, *124*, 14642; c) D. H. Yoon, S. B. Lee, K. H. Yoo, J. Kim, J. K. Lim, N. Aratani, A. Tsuda, A. Osuka, D. Kim, *J. Am. Chem. Soc.* **2003**, *125*, 11062.

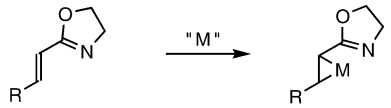
 © 2004 Wiley-VCH Verlag GmbH & Co. KGaA, Weinheim

Asymmetric Synthesis

Stereoselective Construction of Acyclic Carbon Chains by a One-Pot Coupling Process Based on Alkenyloxazoline–Titanium Complexes**

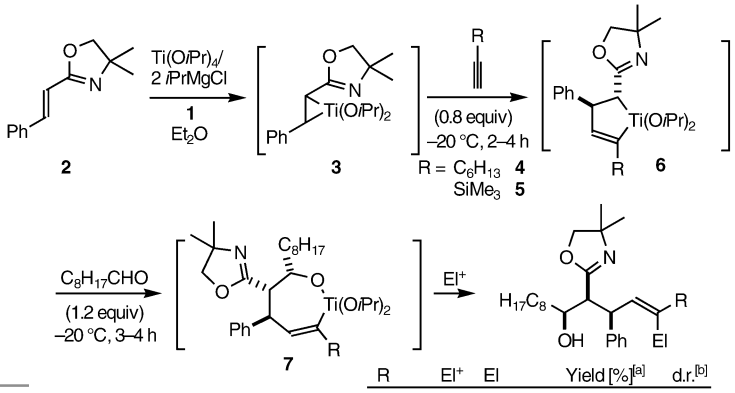
Kazuhisa Mitsui, Takayuki Sato, Hirokazu Urabe, and Fumie Sato**

Oxazoline is known as a versatile functional group in organic synthesis for the activation of substrates and for asymmetric synthesis.[1] Complexation of organic compounds having this group with transition metals may lead to the development of unique synthetic transformations,[2] but an olefin complex such as the one in Scheme 1 (M = metal)[3] has not been investigated. We report here that titanation of alkenyloxazolines proceeds nicely to give novel olefin–titanium complexes (Scheme 1, M = Ti(O*i*Pr)$_2$), which subsequently allow for a diastereoselective multicomponent coupling process and an asymmetric coupling reaction.



Scheme 1. Generation of the olefin–metal complex.

Treatment of alkenyloxazoline **2**[4] with a titanium(II) alkoxide reagent **1** formed from Ti(O*i*Pr)$_4$ with two equivalents of *i*PrMgCl,[5] generates olefin complex **3**,[6] which underwent a coupling reaction with 1-octyne (**4**) to give titanacycle **6** (R = C_6H_{13}; Scheme 2). Intermediates **3** and **6** were identified by deuteriolysis.[7] The carbon–titanium bond α to the oxazoline (rather than the vinyl–titanium bond) of **6** selectively reacted with the octanal to give, after hydrolytic work-up, a single regioisomer **8** having exclusively an *E*-olefinic bond. Surprisingly, the crude reaction mixture contained this adduct **8** together with a very small amount of one of the four possible diastereoisomers (d.r. = 96:4) arising from the three consecutive stereogenic centers. Compound **8** could be readily separated from this minor isomer[8] by flash chromatography on silica gel to give a pure sample in 66% yield. The stereochemistry of **8** was determined (as depicted) by derivatization.[7] A stereochemical course from **2** to **8** is proposed in the Supporting Information.[7] Analogously, the sequential treatment of **2** with silylacetylene **5** and nonanal



R	El$^+$	El		Yield [%][a]	d.r.[b]
C_6H_{13}	H^+	H	**8**	66	96:4
$SiMe_3$	H^+	H	**9**	73	93:7
$SiMe_3$	D^+	D	**10**	73[c]	93:7
$SiMe_3$	I_2	I	**11**	52	93:7

[a] Pure sample. [b] In a crude mixture.
[c] 96% incorporation of deuterium.

Scheme 2. Four-component coupling process.

[*] K. Mitsui, T. Sato, Prof. H. Urabe
Department of Biological Information
Graduate School of Bioscience and Biotechnology
Tokyo Institute of Technology
4259 Nagatsuta-cho, Midori-ku, Yokohama
Kanagawa 226-8501 (Japan)
Fax: (+81) 45-924-5826
E-mail: hurabe@bio.titech.ac.jp
Prof. F. Sato
Department of Biomolecular Engineering
Graduate School of Bioscience and Biotechnology
Tokyo Institute of Technology
4259 Nagatsuta-cho, Midori-ku, Yokohama
Kanagawa 226-8501 (Japan)
Fax: (+81) 45-924-5826
E-mail: fsato@bio.titech.ac.jp

[**] We thank the Japan Society for the Promotion of Science and Kurata Foundation (to H.U.) for financial support and Professor Munetaka Akita of this institute for the X-ray crystallographic analysis.

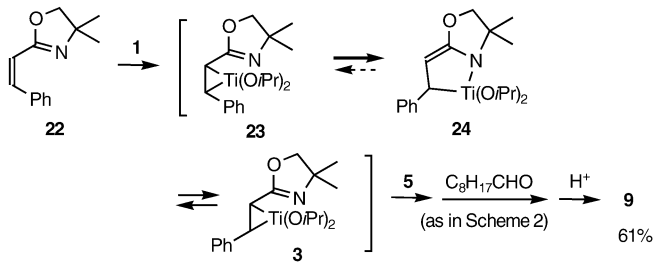
Supporting information for this article is available on the WWW under http://www.angewandte.org or from the author.

 © 2004 Wiley-VCH Verlag GmbH & Co. KGaA, Weinheim DOI: 10.1002/anie.200352769

afforded the adduct **9** in good yield. In place of the simple hydrolysis, deuteriolysis or iodinolysis of the remaining vinyl–titanium bond in the intermediate **7** ($R = SiMe_3$) gave deuterium-labeled and iodinated products **10** and **11**, respectively. Thus, the four-component coupling of the unsaturated oxazoline, acetylene, aldehyde, and an electrophile proceeded in one pot with nearly complete regio-, olefinic stereo-, and diastereoselectivities to give an acyclic carbon chain of the defined structure.[9] This and the following transformations were made possible by the collaboration of the aforementioned feature of oxazolines and the behavior of the olefin–metal complex.

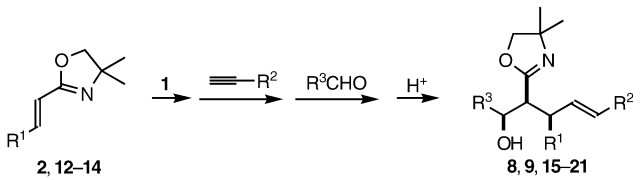
More results regarding the transformation of Scheme 2 are summarized in Table 1. The combination of oxazoline **2**, acetylene **4** or **5**, and a variety of aldehydes always showed high diastereoselectivities (entries 1–6). The structure of product **18** (entry 6) was also confirmed by X-ray crystallographic analysis.[7,10] The aryl-substituted vinyloxazolines **12** and **13** also participated in the reaction (entries 7 and 8). Entry 9 illustrates the diastereoselective preparation of functionalized allylsilane **21**[11] from (silylvinyl)oxazoline **14**.[12]

While all reactions described above started with *E*-alkenyloxazolines, *Z*-alkenyloxazolines such as **22**[13] in Scheme 3 gave the same product **9** previously obtained from the *E*-oxazoline **2** (see Scheme 2). Rapid isomerization of the initially formed olefin complex **23** to less sterically congested **3** via the azatitanacyclopentene **24** should account for this phenomenon. The *E*-olefinic oxazolines are more readily available than the *Z* isomers, and hence the former are, synthetically, the substrates of choice.



Scheme 3. Stereochemistry of the starting alkenyloxazoline.

Table 1: Diastereoselective coupling reaction of oxazolines, acetylenes, and aldehydes according to Scheme 2.

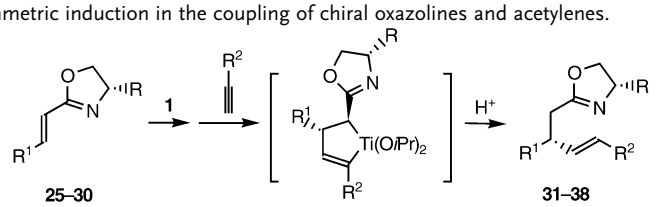


Entry	Oxazoline		Acetylene		Aldehyde		Product	
	R^1		R^2		R^3		Yield [%][a]	d.r.[b]
1	Ph	**2**	C_6H_{13}	**4**	C_8H_{17}	**8**	66	96:4
2	Ph	**2**	C_6H_{13}	**4**	(*E*)-$C_5H_{11}CH{=}CH-$	**15**	54	88:12
3	Ph	**2**	C_6H_{13}	**4**	Ph	**16**	68	92:8
4	Ph	**2**	$SiMe_3$	**5**	C_8H_{17}	**9**	73	93:7
5	Ph	**2**	$SiMe_3$	**5**	*i*Pr	**17**	72	90:10
6	Ph	**2**	$SiMe_3$	**5**	Ph	**18**	70	95:5
7	*p*-ClC_6H_4	**12**	$SiMe_3$	**5**	C_8H_{17}	**20**	62	96:4
8	1-$C_{10}H_7$[c]	**13**	$SiMe_3$	**5**	C_8H_{17}	**21**	60	95:5
9	$SiMe_3$	**14**	$SiMe_3$	**5**	C_8H_{17}	**8**	48	89:11

[a] Yield of the isolated pure major isomer after chromatographic separation on silica gel. [b] Diastereoselectivity of a crude sample. Two stereoisomers were detected in the crude reaction mixture. [c] 1-Naphthyl.

Oxazoline is a potential chiral auxiliary,[1] so we next pursued the possibility of an asymmetric coupling reaction between the oxazoline–titanium complex and acetylene (Table 2). Oxazolines **25**–**27**[4] (R = Et, *t*Bu, and *i*Pr groups, respectively) were used in the reaction (entries 1–3) to evaluate the chiral induction by the oxazoline substituent R. Of these substrates, oxazoline **27** (R = *i*Pr) prepared from (*S*)-valinol showed the most satisfactory result (entry 3). High chiral induction of 92:8–96:4 was uniformly observed with the valinol-derived oxazolines **27**–**30** to give coupling products **34**–**38** in good yields (entries 4–8).[14] The stereochemistry of the products **31** and **33** was unambiguously determined as depicted by derivatization to a known compound.[7] Optically active allylsilane **38**[11] was easily prepared

Table 2: Asymmetric induction in the coupling of chiral oxazolines and acetylenes.



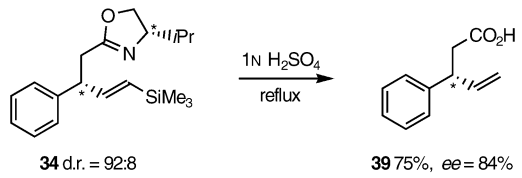
Entry	R	Oxazoline R^1		Acetylene R^2		Product	Yield [%][a]	d.r.[b]
1	Et	Ph	**25**	C_6H_{13}	**4**	**31**	65	75:25[b,c]
2	*t*Bu	Ph	**26**	C_6H_{13}	**4**	**32**	52	92:8[d]
3	*i*Pr	Ph	**27**	C_6H_{13}	**4**	**33**	72	93:7[b]
4	*i*Pr	Ph	**27**	$SiMe_3$	**5**	**34**	73	92:8[b,d]
5	*i*Pr	*p*-ClC_6H_4	**28**	C_6H_{13}	**4**	**35**	67	96:4[d]
6	*i*Pr	*p*-ClC_6H_4	**28**	$SiMe_3$	**5**	**36**	74	94:6[d]
7	*i*Pr	1-$C_{10}H_7$[e]	**29**	$SiMe_3$	**5**	**37**	54	95:5[d]
8	*i*Pr	$SiMe_3$	**30**	$SiMe_3$	**5**	**38**	63	95:5[d]

[a] Yield of isolated product. [b] Enantioselectivity of the carboxylic acid produced after hydrolysis of the oxazoline. [c] In practice, the antipode of **25** was used. [d] Diastereoselectivity of a crude sample. [e] 1-Naphthyl.

 © 2004 Wiley-VCH Verlag GmbH & Co. KGaA, Weinheim

from (silylvinyl)oxazoline **30** with a high chiral induction (entry 8).

The oxazoline moiety of the above products should be useful for further transformations.[1] For example, hydrolysis of **34** with dilute aqueous acid effected concomitant desilylation (Scheme 4) to give a 3-aryl-4-pentenoic acid **39**, which is a known precursor for the synthesis of neurokinin receptor antagonists.[15]



34 d.r. = 92:8 **39** 75%, *ee* = 84%

Scheme 4. Synthetic application.

In conclusion, the novel alkenyloxazoline–titanium complexes proved to be a versatile template for diastereoselective and asymmetric coupling reactions. Further investigation on the utility of these functionalized olefin–titanium complexes and the synthetic application of the products obtained here is in progress.

Received: September 2, 2003 [Z52769]

Keywords: asymmetric synthesis · C-C coupling · diastereoselectivity · metallacycles · oxazolines

[1] For reviews, see: a) K. A. Lutomski, A. I. Meyers in *Asymmetric Synthesis*, *Vol. 3*, *Part B* (Ed.: J. D. Morrison), Academic, Orlando, **1984**, pp. 213–274; b) T. G. Gant, A. I. Meyers, *Tetrahedron* **1994**, *50*, 2297–2360; c) A. I. Meyers, *J. Heterocycl. Chem.* **1998**, *35*, 991–1002.

[2] Aryloxazoline–transition metal complexes have found useful applications; see ref. [1b] and A. R. Pape, K. P. Kaliappan, E. P. Kündig, *Chem. Rev.* **2000**, *100*, 2917–2940.

[3] The olefin complex could be depicted by a few limiting structures involving **24**, but all of these are represented by the general form of the metallacyclopropane shown in Scheme 1.

[4] For their preparation, see: M. C. Elliott, E. Kruiswijk, *J. Chem. Soc. Perkin Trans. 1* **1999**, 3157–3166.

[5] F. Sato, H. Urabe in *Titanium and Zirconium in Organic Synthesis* (Ed.: I. Marek), Wiley-VCH, Weinheim, **2002**, pp. 319–354; F. Sato, S. Okamoto, *Adv. Synth. Catal.* **2001**, *343*, 759–784; J. J. Eisch, *J. Organomet. Chem.* **2001**, *617–*618, 148–157; F. Sato, H. Urabe, S. Okamoto, *Chem. Rev.* **2000**, *100*, 2835–2886; O. G. Kulinkovich, A. de Meijere, *Chem. Rev.* **2000**, *100*, 2789–2834.

[6] For reviews on olefin complexes of Group 4 metals, see: ref. [5]; E. Negishi, T. Takahashi, *Acc. Chem. Res.* **1994**, *27*, 124–130; E. Negishi in *Comprehensive Organic Synthesis*, *Vol. 5* (Eds.: B. M. Trost, I. Fleming), Pergamon, Oxford, **1991**, pp. 1163–1184; and S. L. Buchwald, R. B. Nielsen, *Chem. Rev.* **1988**, *88*, 1047–1058.

[7] For details, see the Supporting Information.

[8] The stereochemistry of the minor isomer has not been determined.

[9] Multicomponent coupling of the ethylene—Group 4 metal complex, acetylene, and aldehyde (or ketone) was reported: B. H. Lipshutz, M. Segi, *Tetrahedron* **1995**, *51*, 4407–4420; C. Copéret, E. Negishi, Z. Xi, T. Takahashi, *Tetrahedron Lett.* **1994**, *35*, 695–698; C. Zhao, T. Yu, Z. Xi, *Chem. Commun.* **2002**, 142–143; M. G. Thorn, J. E. Hill, S. A. Waratuke, E. S. Johnson, P. E. Fanwick, I. P. Rothwell, *J. Am. Chem. Soc.* **1997**, *119*, 8630–8641. However, in these cases, the notion of diastereoselective synthesis is not applicable. In contrast, (*internal* olefin)–metal complexes could be used for diastereoselective transformations as described in the text, but their generation and the subsequent reactions appear to be retarded because of the enhanced steric hindrance around the olefin portion. Indeed, few examples of their generation and monoaddition to ketones were reported, and the double addition has not been achieved: D. Enders, M. Kroll, G. Raabe, J. Runsink, *Angew. Chem.* **1998**, *110*, 1770–1773; *Angew. Chem. Int. Ed.* **1998**, *37*, 1673–1675; J. Scholz, S. Kahlert, H. Görls, *Organometallics* **1998**, *17*, 2876–2884; J. Scholz, M. Nolte, C. Krüger, *Chem. Ber.* **1993**, *126*, 803–809. See also: B. H. Edwards, R. D. Rogers, D. J. Sikora, J. L. Atwood, M. D. Rausch, *J. Am. Chem. Soc.* **1983**, *105*, 416–426; J. M. Davis, R. J. Whitby, A. Jaxa-Chamiec, *J. Chem. Soc. Chem. Commun.* **1991**, 1743–1745; S. Kahlert, H. Görls, J. Scholz, *Angew. Chem.* **1998**, *110*, 1958–1962; *Angew. Chem. Int. Ed.* **1998**, *37*, 1857–1861.

[10] CCDC-218515 contains the supplementary crystallographic data for this paper. These data can be obtained free of charge via www.ccdc.cam.ac.uk/conts/retrieving.html (or from the Cambridge Crystallographic Data Centre, 12 Union Road, Cambridge CB21EZ, UK; fax: (+44) 1223-336-033; or deposit@ccdc.cam.ac.uk).

[11] For reviews, see: T. K. Sarkar in *Science of Synthesis*, *Vol. 4*, *Organometallic Compounds of As*, *Sb*, *Bi and Si* (Ed.: I. Fleming), Georg Thieme, Stuttgart, **2002**, pp. 837–925; I. Fleming, A. Barbero, D. Walter, *Chem. Rev.* **1997**, *97*, 2063–2192; T. K. Sarkar, *Synthesis* **1990**, 969–983; T. K. Sarkar, *Synthesis* **1990**, 1101–1111.

[12] When the aryl or silyl substituent of vinyloxazolines is replaced with an alkyl group, the desired coupling product was not formed. For silicon-assisted stabilization of olefin–titanium alkoxide complexes, see R. Mizojiri, H. Urabe, F. Sato, *Tetrahedron Lett.* **1999**, *40*, 2557–2560; R. Mizojiri, H. Urabe, F. Sato, *J. Org. Chem.* **2000**, *65*, 6217–6222.

[13] The pure *Z* isomer was prepared by the treatment of the (phenylethynyl)oxazoline with **1** followed by hydrolysis. The generation and utility of the intermediate alkynyloxazoline–titanium alkoxide complex will be reported in due course.

[14] The further addition of benzaldehyde to the intermediate titanacyclopentene generated according to entry 4 in Table 2 afforded most likely an 82:13:5 mixture of three isomeric products in 67% yield, which nearly appears to be the sum of the observations of Tables 1 and 2.

[15] N.-Y. Shih, M. Albanese, J. C. Anthes, N. I. Carruthers, C. A. Grice, L. Lin, P. Mangiaracina, G. A. Reichard, J. Schwerdt, V. Seidl, S.-C. Wong, J. J. Piwinski, *Bioorg. Med. Chem. Lett.* **2002**, *12*, 141–145.

 © 2004 Wiley-VCH Verlag GmbH & Co. KGaA, Weinheim

Peptide Cyclization

Peptidyl Thiophenols as Substrates for Nonribosomal Peptide Cyclases**

*Stephan A. Sieber, Junhua Tao, Christopher T. Walsh, and Mohamed A. Marahiel**

Natural small peptide molecules such as cyclosporin, vancomycin, and penicillin have attracted much attention in the past because of their exceptional pharmacological and biological activities. A common feature of all these compounds is their constrained structure, which ensures the precise functionality that is important for interaction with the dedicated molecular target. In many cases, rigidity is achieved by cyclization of the peptide backbone, which leads to diverse macrolactams and macrolactones. Since peptide cyclization can be a difficult task in chemical synthesis, there has been significant interest in exploring enzymatic cyclization mechanisms to develop new synthesis routes for the production of modified natural cyclic peptides.[1] Nature achieves the synthesis of linear peptide precursors and their subsequent cyclization by using large multienzyme complexes referred to as nonribosomal peptide synthetases (NRPS).[2] These multimodular enzymes contain all the catalytic units necessary for the assembly of the linear peptide sequence. In addition, a peptide cyclase domain referred to as the thioesterase domain (TE) is present at the end of the assembly line and catalyzes the release of the cyclic product. Recent research on excised tyrocidine and surfactin peptide cyclases provided insights into their substrate tolerance and cyclization mechanism, and allowed a chemoenzymatic approach to be used to generate a library of novel products.[3–5]

Characterization of these enzymes requires translation between the biological and chemical languages. Linear peptide precursors were produced by solid-phase peptide synthesis and subsequently coupled to an analogue of the natural cofactor. In the multienzyme complex, the linear peptide is tethered to a phosphopantetheine (ppan) arm on the peptidyl carrier protein (PCP) through a thioester bond. To retain the enzymatic recognition elements associated with this natural cofactor, the last part of the phosphopantetheine arm, *N*-acetylcysteamine thioester (SNAC), was used as a mimic for the natural PCP ppan arm and attached to the C-terminal end of the synthetic linear peptide substrate.[6] In contrast to the surfactin and tyrocidine peptide cyclases, many cyclases from other NRPS systems, such as fengycin, mycosubtilin, and syringomycin, were found to be inactive with peptidyl SNAC substrates (data not shown). We recently overcame this limitation for the fengycin cyclase by using 4′-phosphopantetheine transferase (Sfp) to catalyze the loading of peptidyl coenzyme A (CoA) onto the invariant serine residue of the PCP domain of a recombinant apo PCP–TE didomain.[7] Cyclization and hydrolysis products were observed when this approach was used, which indicates that precise presentation of the substrate by ppan-PCP is essential for recognition and catalysis by the cyclase. After product release, the cofactor ppan remains attached to the PCP–TE didomain and blocks Sfp-catalyzed transfer of additional peptidyl CoAs onto ppan-PCP and limits this approach to a single turnover. We have now developed a new strategy to force multiple turnover cycles and expand the utility of this method. This strategy is based on a thioester exchange reaction between the free ppan-PCP thiol group and a soluble thioester peptide substrate that should ensure chemical reloading of the substrate onto the ppan-PCP–TE didomain.[8,9]

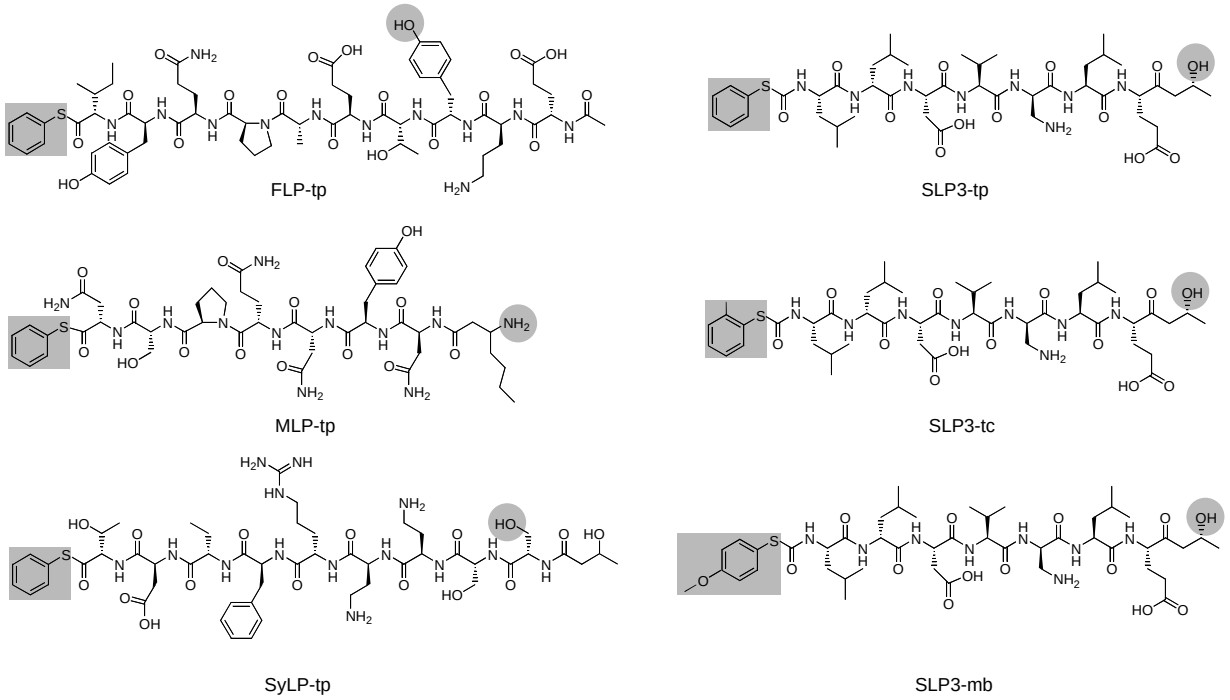
We report herein a new chemoenzymatic route to cyclic compounds through activity-based TE enzyme acylation with reactive thioester leaving groups (thiophenol). This method has allowed biochemical characterization of fengycin, mycosubtilin, and syringomycin peptide cyclases, which are not active with SNAC substrates. The potency of reactive thioester leaving groups attached to surfactin in cyclization reactions was evaluated in comparison with data obtained previously for SNAC substrates.

Our initial aim was to achieve a thioester exchange reaction between the free thiol group of ppan in the fengycin bidomainal fragment ppan-PCP–TE[7] and synthetic fengycin thiophenol (FLP-tp; Scheme 1). Surprisingly, control reactions of FLP-tp with apo PCP–TE, which lacks the free thiol group, revealed hydrolysis and cyclization activity not observed with SNAC substrates (Scheme 2 and Figure 1 A). A control reaction with a fengycin cyclase containing a Ser-to-Ala mutation in the active site showed that this mutation abolishes the activity. The identities of all substrates (Table 1) and products (Table 2) were verified by HPLC-MS. No increase in product turnover was observed with holo PCP–TE, which indicates that the thiophenol substrate efficiently directly acylates the serine residue in the active-site of the TE enzyme. Thiophenol has excellent leaving group properties as a result of delocalization of the thiolate electrons throughout the aromatic ring. In contrast, no such stabilization is possible with the mimic SNAC. The results emphasize that, for these peptidyl thioester substrates, the chemical reactivity of the

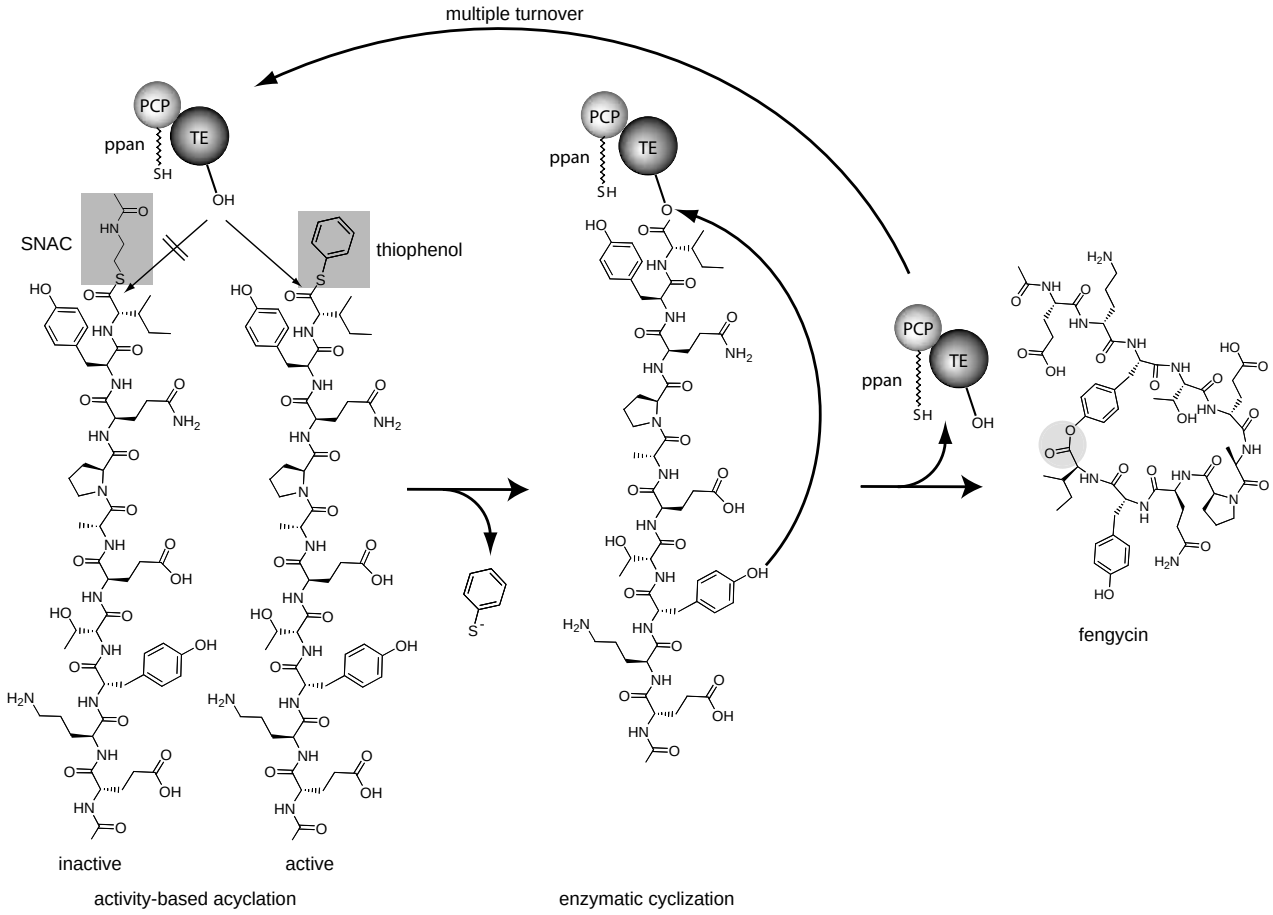
[*] S. A. Sieber, Prof. M. A. Marahiel
Fachbereich Chemie/Biochemie
Philipps-Univerität Marburg
Hans-Meerwein-Strasse, 35032 Marburg (Germany)
Fax: (+49) 6421-2822191
E-mail: marahiel@chemie.uni-marburg.de
Prof. C. T. Walsh
Department of Biological Chemistry
and Molecular Pharmacology
LHRRB 309, Harvard Medical School
Boston, MA 02115 (USA)
Dr. J. Tao
Pfizer Inc.
4215 Sorrento Valley Boulevard
San Diego, CA 92121 (USA)

[**] We gratefully acknowledge the Studienstiftung des deutschen Volkes (S.A.S.), Deutsche Forschungsgemeinschaft (M.A.M.), and National Institutes of Health (grant no. GM20011; C.T.W.). We thank Dirk Schwarzer for helpful comments, Uwe Linne for MS/MS sequencing, Christina Dauth for her help with the synthesis, and Antje Schäfer for technical assistance. J.T. thanks Kim Albizati, Van Martin, and Shanghui Hu for their generous support of his Pfizer secondment.

 DOI: 10.1002/anie.200352787 © 2004 Wiley-VCH Verlag GmbH & Co. KGaA, Weinheim



Scheme 1. Structures of peptidyl aryl thioester substrates. Leaving groups are indicated by boxes and nucleophiles for enzymatic intramolecular cyclization are indicated by circles.



Scheme 2. Activity-based enzyme acylation. The active-site serine residue of the fengycin peptide cyclase (TE) is selectively acylated by a reactive peptidyl thiophenol substrate. The acyl-enzyme intermediate is then captured by an intramolecular nucleophilic attack by Tyr3 to give the cyclic peptidolactone fengycin. No activity is observed with a peptidyl SNAC substrate previously believed to be important for enzyme recognition.

 © 2004 Wiley-VCH Verlag GmbH & Co. KGaA, Weinheim

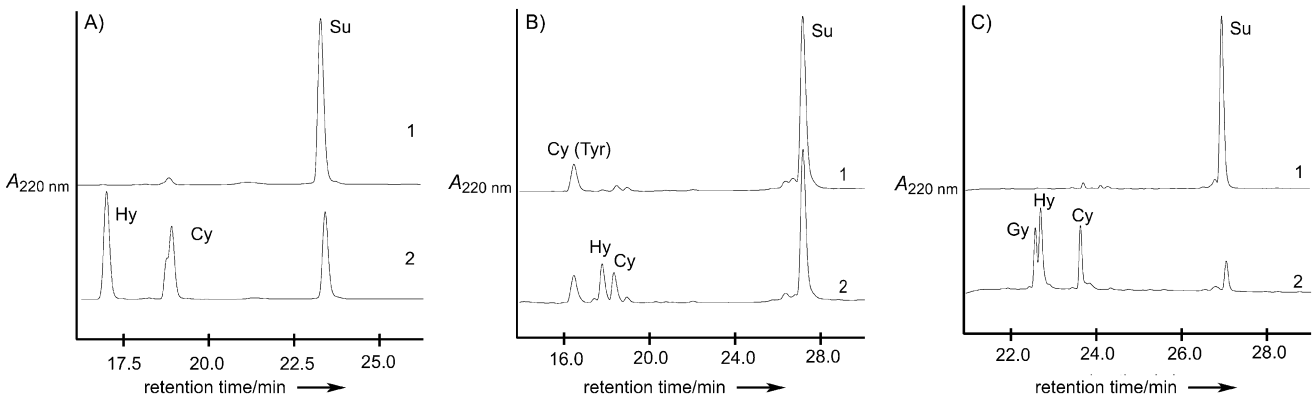


Figure 1. HPLC traces of peptide cyclases (SNAC inactive) incubated with peptidyl thiophenol substrates. A) Fengycin cyclase incubated with FLP-tp for 1.5 h (trace 2). Trace 1 was obtained after incubation of the substrate with a cyclase in which the active-site Ser residue is mutated to Ala. B) Mycosubtilin cyclase incubated with MLP-tp for 5 min (trace 2). Trace 1 shows incubation of the substrate without enzyme. Uncatalyzed cyclization through Tyr3 [Cy(Tyr)] is observed. C) Syringomycin cyclase incubated with SyLP-tp for 30 min (trace 2). Trace 1 shows substrate incubation without enzyme. Su = substrate, Hy = hydrolyzed product, Cy = cyclized product, Gy = glycerol adduct.

Table 1: Characterization of substrates by ESI MS.

Compound	Observed (calculated) mass for $[M+H]^+$ [Da]
FLP-tp	1361.4 (1361.6)
SLP-tp	965.4 (965.5)
MLP-tp	1055.5 (1055.5)
SyLP-tp	1175.6 (1175.5)
SLP-tc	979.4 (979.5)
SLP-mb	995.4 (995.5)

Table 2: Characterization of products by ESI MS.

Compound	Observed (calculated) mass for $[M+H]^+$ [Da] cyclized product	hydrolyzed product	Cy/Hy ratio
FLP-tp	1251.4 (1251.6)	1269.4 (1269.6)	0.85/1
SLP-tp	855.4 (855.5)	873.4 (873.5)	0.78/1
MLP-tp	945.4 (945.4)	963.4 (963.5)	0.85/1
SyLP-tp	1065.3 (1065.5)	1083.6 (1083.5)	0.65/1
SLP-tc	855.4 (855.5)	873.4 (873.5)	0.73/1
SLP-mb	855.4 (855.5)	873.4 (873.5)	0.64/1

thiophenol leaving group is more important for enzyme acylation than recognition of SNAC, the cofactor analogue. Kinetic data for the cyclization of FLP-tp (catalytic rate constant $k_{cat} = 0.33\ min^{-1}$, Michaelis constant $K_M = 461\ \mu M$, Cy/Hy ratio = 0.85/1) indicate saturation kinetics and suggest sufficient catalytic efficiency for preparative-scale reactions.

Surfactin cyclase (Srf TE), which was previously characterized with SNAC substrates,[4] was incubated with surfactin thiophenol to evaluate the general utility of thiophenol leaving groups in substrates for other peptide cyclases (SLP3-tp; Scheme 1). HPLC analysis revealed enzyme-catalyzed cyclization and hydrolysis activity, with $K_M = 126\ \mu M$, and $k_{cat} = 5.66\ min^{-1}$ and $11.33\ min^{-1}$ for cyclization and hydrolysis, respectively (Figure 2A). Comparison of the catalytic cyclization efficiency for SLP3-tp ($k_{cat}/K_M = 44.9\ mM^{-1}min^{-1}$) with that for SLP3-SNAC ($2.9\ mM^{-1}min^{-1}$)[4] revealed a 15-fold higher activity for the thiophenol substrate, with a Cy/Hy ratio of 0.78/1 for thiophenol and 0.54/1 for SNAC. These results are consistent with a common acyl enzyme intermediate for the two

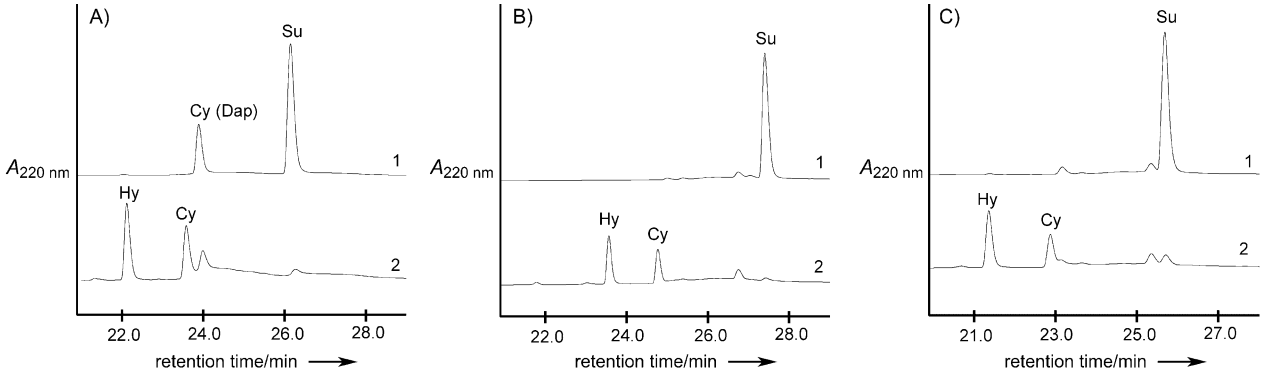


Figure 2. HPLC traces of surfactin cyclase (SNAC active) incubated with aromatic thioester substrates. A) Incubation of surfactin cyclase with SLP-tp for 10 min (trace 2). Trace 1 shows incubation of the substrate without enzyme. Uncatalyzed cyclization through a diaminopropionic acid residue at position 3 [Cy(Dap)] is observed. B) Incubation of surfactin cyclase with SLP-tc for 10 min (trace 2). Trace 1 shows substrate incubation without enzyme. C) Incubation of surfactin cyclase with SLP-mb for 10 min (trace 2). Trace 1 shows substrate incubation without enzyme. Su = substrate, Hy = hydrolyzed product, Cy = cyclized product.

 © 2004 Wiley-VCH Verlag GmbH & Co. KGaA, Weinheim

substrates, and breakdown of this intermediate may be rate-determining for the SLP3-tp reaction. However, the greater thermodynamic activation of the peptide effected by thiophenol seems to facilitate nonenzymatic cyclization, as observed in the surfactin control reaction without enzyme (Figure 2A). MS/MS sequencing of the cyclic species obtained (minus Srf TE) showed that the uncatalyzed cyclization occurs through a diaminopropionic acid (Dap) residue at position three (Table 3). Such nonenzymatic cyclization of peptides is an intrinsic property of some peptide sequences, as has been reported before for the tyrocidine series.[10] To suppress unspecific nonenzymatic cyclization of the thiophenol peptides through their side chains, the reactivity of the leaving group was decreased by substitution of the aromatic ring. Substituents with a positive inductive or mesomeric effect (methyl and methoxy groups) were introduced onto the aromatic thiophenol ring at the *ortho*, *meta*, or *para* positions. Each of the six new aryl thiol leaving groups was coupled to the free carboxylic acid moiety of the surfactin peptide, which was subsequently incubated with surfactin cyclase. Replacement of thiophenol with *o*-thiocresol (SLP3-tc) or *p*-methoxybenzenethiol (SLP3-mb) gave the best suppression of unspecific background cyclization, while enzyme-catalyzed substrate cyclization and hydrolysis rates remained constant (Table 2, Scheme 1, Figure 2B and C). The attachment of substituents to the aromatic ring can therefore adjust the activity as desired for any peptidyl thioester substrate. Substitution in the *ortho* and *para* positions seems to be preferred, probably because of the destabilizing impact on the thiophenolate anion. Srf TE directs cyclization towards the β-OH group of the fatty acyl chain rather than the DAP residue, which undergoes amide formation in nonenzymatic cyclization.

Table 3: MS/MS fragmentation data for autocatalytic cyclization products.

Compound	Species	Observed mass of fragments (calculated mass) [Da]		
		cyclization through Dap3	cyclization through Tyr2	cyclization through Ser6
SLP3 cycle[a]	$[M+H]^+$	527.316 (527.319)		
SLP3 cycle[b]	$[M+H]^+$	n.d. (510.293)		
MLP cycle[a]	$[M+H]^+$		704.278 (704.300)	n.d. (202.083)
MLP cycle[b]	$[M+H]^+$		687.254 (687.274)	n.d. (185.056)

[a] Fragmentation of the peptide bond at the proposed cyclization position. [b] Fragmentation of the adjacent NH–CH bond. N/D = not detected.

The observed catalytic activity of the fengycin and surfactin peptide cyclases on peptidyl thiophenol substrates encouraged us to investigate other peptide cyclases with this new technology. Mycosubtilin PCP–TE and syringomycin TE were cloned from their multimodular synthetases, overexpressed, and purified as soluble proteins.[11,12] Both enzymes failed to show any activity with peptidyl SNAC substrates (data not shown). Thiophenol was therefore attached to peptide sequences derived from those of mycosubtilin (MLP-tp) and syringomycin (SyLP-tp; Scheme 1). The peptide analogue of syringomycin differs from the wild-type peptide[13] for synthetic reasons: the 4-Cl-threonine residue at position 9 was replaced by threonine, dehydrobutyrine by aminobutyric acid, and β-hydroxy aspartate by aspartate, and the long fatty acid moiety was replaced by a shorter β-hydroxy fatty acyl chain to improve the solubility. In syringomycin, cyclization occurs through a serine side chain, whereas the fatty acid chain seems to be important in the mycosubtilin sequence, since macrolactamization occurs through the β-amino fatty acid moiety (Scheme 1). The natural fatty acid chain of mycosubtilin was replaced by a C_4-β-aminoacyl chain, which was synthesized chemically (see the Experimental section). Incubation of mycosubtilin peptide cyclase with MLP-tp led to enzyme-catalyzed hydrolysis and cyclization (Figure 1B). Cyclization occured with a k_{cat} value of 2.16 min^{-1}, a K_M value of 3991 μM, and a Cy/Hy ratio of 0.85/1. The high K_M value could be the result of the absence of enzymatic recognition elements in the artificial cofactor thiophenol. As was observed for surfactin, autocatalytic self-cyclization of MLP-tp ocurred in a control reaction without enzyme. The identity of the new species was investigated by MS/MS sequencing and cyclization was shown to occur through the tyrosine residue at position two (Table 3), again a distinct regiospecificity from that imposed during enzymatic cyclization. Incubation of syringomycin peptide cyclase with SyLP-tp produced both cyclized and hydrolyzed products (Figure 1C). A glycerol adduct was also formed because 5% glycerol had to be added to stabilize syringomycin peptide cyclase. Saturation behavior was observed and the k_{cat} and K_M values of the cyclization determined ($k_{cat} = 0.32$ min^{-1} and $K_M = 28$ μM, Cy/Hy ratio = 0.65/1). Previously recorded data show that in vivo cyclization of syringomycin occurs through the L-serine residue at position one[13] and not at the adjacent D-serine residue at position two, which raised the question of whether a change in stereochemistry at positions one and two could alter the product formed. Two new thiophenol substrates were made, one with D-serine at position one and L-serine at position two, and the other with L-serine at positions one and two. Incubation of these substrates with syringomycin cyclase only led to hydrolysis in both cases, which demonstrates the importance of Ser1,2 stereochemistry for enzymatic cyclization (data not shown).

Activity-based enzyme acylation with soluble thiophenol-based peptide substrates is a powerful method to obtain enzymatic catalysis by NRPS peptide cyclases. This methodology led to the formation of cyclic peptidolactone or -lactam products of the fengycin, mycosubtilin, and syringomycin cyclases, enzymes that were inactive when peptidyl SNACs were used as potential substrates. Typical yields of macrocyclic products ranged from 96–40%. As expected, undesired hydrolytic by-products are formed in this in vitro system because the substrate presentation and enzyme environment are unnatural. The ratio of cyclization to hydrolysis could be increased by providing natural unmodified thiophenol substrates that fit precisely into the active site of the enzyme.

While we and others have previously used SNAC leaving groups as ppan surrogates on the assumption that the structure is important for enzyme recognition and activity, we report herein that the potential of the leaving group for

 © 2004 Wiley-VCH Verlag GmbH & Co. KGaA, Weinheim

chemical acylation seems to be a more crucial determinant of reactivity than cofactor recognition. Peptides with thiophenol and other aromatic leaving groups will allow the characterization of new NRPS peptide cyclases and will therefore overcome a major limitation of past research in this area. Libraries of peptide and hybrid polyketide–peptide[14] analogues can be synthesized easily and screened for altered or increased biological activity. Selective acylation of enzymes by titration with aromatic thioesters could also be important for many other enzymatic systems, such as polyketide synthases or serine hydrolases.

Experimental Section

Cloning, expression, and purification of mycosubtilin PCP–TE and syringomycin TE: The mycosubtilin (ATCC 6633) and syringomycin (DSMZ B-301D) gene fragments encoding Myc PCP–TE and Syr TE were amplified from chromosomal DNA by the polymerase chain reaction (PCR) with Pfu polymerase (Stratagene) and the following oligonucleotides: Myc PCP–TE, 5′-AAA AAC ATA TGG CTG CTC CCC GAA CGT TGA TT-3′ and 5′-AAA AAC TCG AGT GTT CGA TCA GAT TTT GTG CGA CTC-3′; Syr TE, 5′-AAA AAC ATA TGG GCC AGG CAC GCC CC-3′ and 5′-AAA AAC TCG AGC TCA GCT GGC GCG GTT ATC-3′. The PCR products were cloned into the *NdeI*/*XhoI* site of a pET37b vector (Novagene). *Escherichia coli* TOP 10 (Novagen) was used for preparation of recombinant plasmids. The identities of all constructs were confirmed by sequencing. The plasmids were used to produce proteins with a C-terminal hexahistidine tag.

Recombinant proteins were overproduced in *E. coli* BL21 cells (Novagen) by using standard protocols.[15] Purification of the proteins was carried out as described previously[16] and the products were analyzed by electrophoresis on sodium dodecylsulfate polyacrylamide gel. After dialysis against standard assay buffer (25 mM *N*-(2-hydroxyethyl)piperazine-*N*′-2-ethanesulfonic acid (HEPES) and 50 mM NaCl, pH 7.0), all proteins were shock-frozen in liquid nitrogen. 5% Glycerol was added to the Syr TE buffer. The concentrations ($mg\,mL^{-1}$) of the purified proteins were determined photometrically at 280 nm by using calculated extinction coefficients (Myc PCP–TE, $0.83\ mol^{-1}\,dm^3\,cm^{-1}$; Syr TE, $0.80\ mol^{-1}\,dm^3\,cm^{-1}$). Cloning and expression of Srf TE,[17] Fen PCP–TE, and the Ser-to-Ala mutant Fen PCP–TE[7] was described previously.

Synthesis of *N*-*tert*-butoxycarbonyl-3-amino-heptanoic acid: General:[18] All commercially available reagents were used without further purification unless otherwise noted. All organic solvents used were anhydrous, were bought from Aldrich, and were of the highest purity available. All reactions were performed in a dry N_2 or Ar atmosphere unless otherwise indicated. All reactions were monitored by analytical thin-layer chromatography performed with the indicated solvent onsilica gel 60 F_{254} plates (E. Merck; 0.25 mm) unless otherwise indicated. Compounds were visualized under UV light (λ = 254 nm). Flash column chromatography was performed in the indicated solvent on silica gel 60 (E. Merck, 40–63 m). NMR spectra (^1H, ^{13}C) were recorded on a Bruker spectrometer (300 MHz). LC-MS was carried out by using ESI positive and negative modes. LC chromatography runs were performed on a Tuna C18 column (3μ, 30 × 4.6 mm) with ACN/H_2O (containing 0.1% formic acid) as the mobile phases, a gradient of 10–90% ACN in 3.5 min then isocratic for 1 min, a flow rate of $0.8\ mL\,min^{-1}$, and detection at 220 nm and 254 nm.

Synthesis of 3-amino ester **2:** β-ketoester **1** (1 g, 5.8 mmol) was dissolved in MeOH (15 mL) and ammonium acetate (4.7 g, 60 mmol) was added. The mixture was stirred at RT for 17 h and LC-MS showed that the the reaction was complete. After rotary evaporation of MeOH, the crude product was dissolved in EtOAc (50 mL), and 1N NaOH (30 mL) was added. The organic layer was separated from the mixture, washed with brine (50 mL), and dried over Na_2SO_4. Rotary evaporation gave the desired product **2** (943 mg, 95%): ESI MS: *m*/*z*: $[M+H]^+$ 172.20. ^1H NMR (300 MHz, $CDCl_3$): $\delta = 0.91$ (t, $J = 7.1$ Hz, 3H), 1.25 (t, $J = 7.1$ Hz, 3H), 1.37 (m, 2H), 1.51 (m, 2H), 2.12 (t, $J = 7.9$ Hz, 2H), 4.09 (q, $J = 7.1$ Hz, 2H), 4.53 ppm (s, 1H). ^{13}C NMR (75 MHz, $CDCl_3$): $\delta = 14.0$, 14.9, 22.5, 30.3, 36.4, 58.8, 83.6, 164.3, 170.8 ppm.

Synthesis of 3-amino ester **3**: Compound **2** (400 mg, 2.34 mmol) was added to a mixture of HOAc (5 mL) and $NaBH(OAc)_3$ (992 mg, 4.68 mol) at 10°C. The reaction was monitored by LC-MS. After 1 h, the mixture was dissolved in methyl *tert*-butyl ether (10 mL) and washed with 10% Na_2CO_3 (10 mL × 2). The organic layer was separated from the mixture and dried over Na_2SO_4. Rotary evaporation gave the desired product **3** (304 mg, 75%): ESI MS: *m*/*z*: $[M+H]^+$ 174.20. ^1H NMR (300 MHz, $CDCl_3$): $\delta = 0.89$ (t, $J = 7.6$ Hz, 3H), 1.25 (t, $J = 7.0$ Hz, 3H), 1.28–1.60 (m, 6H), 2.19–2.47 (m, 2H), 3.14–3.19 (m, 1H), 4.13 ppm (q, $J = 7.6$ Hz, 2H). ^{13}C NMR (75 MHz, $CDCl_3$): $\delta = 14.3$, 14.6, 23.0, 28.3, 37.7, 43.1, 48.7, 60.6, 173.0 ppm.

Synthesis of *N*-*tert*-butoxycarbonyl 3-amino-heptanoic acid (**4**): $(Boc)_2O$ (Boc, *tert*-butoxycarbonyl; 440 mg, 1.96 mmol, 2 equiv) was added to a solution of **3** (170 mg, 0.98 mmol) in 1N NaOH (4 mL) and dioxane (4 mL). The mixture was stirred at RT for 24 h, adjusted to pH 3.0, and extracted with CH_2Cl_2 (10 mL × 2). The organic layer was dried over Na_2SO_4. Rotary evaporation gave the desired product **4** (304 mg, 75%): ESI MS: *m*/*z*: $[M-H]^+$ 244.10. ^1H NMR (300 MHz, $CDCl_3$): $\delta = 0.81$ (t, $J = 7.5$ Hz, 3H), 1.23–1.50 (m, 6H), 1.36 (s, 9H), 2.31 (d, $J = 6.6$ Hz, 2H), 3.76 ppm (m, 1H). ^{13}C NMR (75 MHz, $CDCl_3$) $\delta = 14.37$, 23.8, 29.2, 29.7, 35.9, 41.3, 80.3, 158.3, 175.6 ppm.

Synthesis of peptidyl thiophenol substrates: All linear peptides were produced by solid-phase peptide synthesis as described previously.[17] Protected amino acids were purchased from Novabiochem and Bachem Bioscience. All other compounds were purchased from Sigma–Aldrich. The general procedure for the synthesis of peptidyl thiophenol substrates is based on the synthesis of peptidyl SNACs described previously.[6] Thiophenol or a thiophenol derivative (10 equiv), *N*,*N*′-dicyclohexylcarbodiimide (2 equiv), and 1-hydroxy-1*H*-benzotriazole (2 equiv) in tetrahydrofuran were added to the protected peptide (1 equiv). The mixture was agitated for 3 h and after 30 min potassium carbonate (4 equiv) was added. The solvent was removed and acid-labile side-chain protecting groups were cleaved by incubation with triflouracetic acid (TFA)/triflourethanol/water (95:2.2:2.5). The deprotected peptidyl thiophenol was purified by preparative HPLC on an Äkta purifier (Pharmacia) HPLC system with a reversed-phase C18 Nucleodur column (Macherey and Nagel). The identities of the peptidyl thiophenol substrates were verified by HPLC-MS.

Assays: Reactions were carried out in 2-[4-(2-hydroxyethyl)-1-piperazinyl]ethanesulfonic acid (HEPES, 25 mM) and NaCl (50 mM) at pH 7.0 in a total volume of 50 μL. The substrate concentration was 100 μM for standard reactions and varied in the kinetic investigations. Reactions were initiated by addition of enzyme to final concentrations of 5 μM for Fen PCP–TE, 1 μM for Srf TE, 30 μM for Myc PCP–TE, and 15 μM for Syr TE. Reactions were quenched at various time points by addition of 4% TFA/H_2O (35 μL), and the products were analyzed by HPLC-MS on a reversed-phase C_{18} Nucleodur column (Macherey and Nagel, 250/3, pore diameter 100 Å, particle size, 3 μm) under the following conditions: Fen PCP–TE: 0–35 min, 30–60% acetonitrile/0.1% TFA in water/0.1% TFA, $0.4\ mL\,min^{-1}$, 40°C; Srf TE: 0–40 min, 20–55% acetonitrile/0.1% TFA in water/0.1% TFA, $0.4\ mL\,min^{-1}$, 40°C; Myc PCP–TE: 0–40 min, 5–50% acetonitrile/0.1% TFA in water/0.1% TFA, $0.4\ mL\,min^{-1}$, 40°C; Syr TE: 0–40 min, 10–50% acetonitrile/0.1% TFA in water/0.1% TFA, $0.4\ mL\,min^{-1}$, 40°C. The identities of the products were confirmed by ESI-MS and cyclic by-products were additionally analyzed by MS/MS to verify the connection regiospecificity (API Qstar Pulsar I, Applied Biosystems). The concentrations of the peptidyl thiophenol

 © 2004 Wiley-VCH Verlag GmbH & Co. KGaA, Weinheim

thioesters were calculated by using experimentally determined extinction coefficients at 220 nm and the coefficients were assumed to be the same for the cyclized and hydrolyzed products. Kinetic characterization of the cyclization and hydrolysis reactions was carried out by determining the initial reaction rates at 5–7 substrate concentrations. At each concentration, measurements were taken at two time points within the linear region of the enzyme-catalyzed reactions, as determined by recording the reaction time courses.

Received: September 4, 2003 [Z52787]

Keywords: antibiotics · biomimetic synthesis · cyclization · enzyme catalysis · peptides

[1] R. M. Kohli, C. T. Walsh, *Chem. Commun.* **2003**, 297.
[2] C. T. Walsh, *Antibiotics: Actions, Origins, Resistance*, ASM, Washington, DC, **2003**.
[3] J. W. Trauger, R. M. Kohli, C. T. Walsh, *Biochemistry* **2001**, *40*, 7092.
[4] C. C. Tseng, S. D. Bruner, R. M. Kohli, M. A. Marahiel, C. T. Walsh, S. A. Sieber, *Biochemistry* **2002**, *41*, 13350.
[5] R. M. Kohli, C. T. Walsh, M. D. Burkart, *Nature* **2002**, *418*, 658.
[6] J. Trauger, R. Kohli, H. Mootz, M. Marahiel, C. Walsh, *Nature* **2000**, *407*, 215.
[7] S. A. Sieber, C. T. Walsh, M. A., Marahiel, *J. Am. Chem. Soc.* **2003**, in press.
[8] T. W. Muir, D. Sondhi, P. A. Cole, *Proc. Natl. Acad. Sci. USA* **1998**, *95*, 6705.
[9] P. E. Dawson, M. J. , Churchill, M. R. Ghadiri, S. B. H. Kent, *J. Am. Chem. Soc.* **1997**, *119*, 4325.
[10] X. Bu, X. Wu, G. Xie, Z. Guo, *Org. Lett.* **2002**, *4*, 2893.
[11] E. H. Duitman, L. W. Hamoen, M. Rembold, G. Venema, H. Seitz, W. Saenger, F. Bernhard, R. Reinhardt, M. Schmidt, C. Ullrich, T. Stein, F. Leenders, J. Vater, *Proc. Natl. Acad. Sci. USA* **1999**, *96*, 13294.
[12] E. Guenzi, G. Galli, I. Grgurina, D. C. Gross, G. Grandi, *J. Biol. Chem.* **1998**, *273*, 32857.
[13] A. Segre, R. C. Bachmann, A. Ballio, F. Bossa, I. Grgurina, N. S. Iacobellis, G. Marino, P. Pucci, M. Simmaco, J. Y. Takemoto, *FEBS Lett.* **1989**, *255*, 27.
[14] R. M. Kohli, M. D. Burke, J. Tao, C. T. Walsh, *J. Am. Chem. Soc.* **2003**, *125*, 7160.
[15] J. Sambrook, E. F. Fritsch, T. Maniatis, *Molecular Cloning: A Laboratory Manual*, Cold Spring Harbor Laboratory Press, Cold Spring Harbor, NY, **1989**.
[16] T. Stachelhaus, H. D. Mootz, V. Bergendahl, M. A. Marahiel, *J. Biol. Chem.* **1998**, *273*, 22773.
[17] R. M. Kohli, J. W. Trauger, D. Schwarzer, M. A. Marahiel, C. T. Walsh, *Biochemistry* **2001**, *40*, 7099.
[18] G. Neyer, J. Achatz, B. Danzer, I. Ugi, *Heterocycles* **1990**, *30*, 863.

 © 2004 Wiley-VCH Verlag GmbH & Co. KGaA, Weinheim

Analytical Methods

An Integrated Approach to a Portable and Low-Cost Immunoassay for Resource-Poor Settings**

*Samuel K. Sia, Vincent Linder, Babak Amir Parviz, Adam Siegel, and George M. Whitesides**

The development of technology for use in resource-poor countries encounters a specific type of challenge not ordinarily faced in academic science: the technology must be inexpensive and it must work with minimal infrastructure. This challenge is particularly severe when the problems being solved are, by their nature, ones that require high-technology solutions. For these kinds of problems, the elegance of the solutions must lie in the use of science to guide the assembly of readily available components into a simple, workable, and well-integrated package. In this paper, we describe an integrated approach to a miniaturized immunoassay called a "POCKET immunoassay" ("POCKET" is short for *po*rtable and *c*ost-*e*ffec*t*ive). This immunoassay has, we believe, the potential to be inexpensive and operable with minimal equipment and technical skills, and shows an analytical performance approaching that of enzyme-linked immunosorbent assays (ELISA) performed in a bench-top format in clinical laboratories.

A top priority for improving health in developing countries is technology for simple, affordable diagnosis of infectious diseases.[1] Immunoassays such as ELISA are the most reliable and widely used methods for detecting antigens and antibodies, but they require expensive and bulky instruments for optical detection, hours of incubation for diffusion-limited reactions on the surface, and many steps of pipetting.[2,3] These constraints prevent the use of ELISA in settings that require low-cost or compact equipment, and in environments that lack electricity or trained personnel. One application with these requirements is the detection of infectious diseases in the field in developing countries;[1,4,5] other potential uses include point-of-care diagnostics by first responders and in health clinics,[6] and detection of biological warfare agents in the field.[2,7] Immunochromatographic assays (also known as "strip tests" and "lateral-flow

[*] Dr. S. K. Sia, Dr. V. Linder, Dr. B. A. Parviz, A. Siegel, Prof. G. M. Whitesides
Department of Chemistry and Chemical Biology
Harvard University
Cambridge, MA 02138 (USA)
Fax: (+1) 617-495-9857
E-mail: gwhitesides@gmwgroup.harvard.edu

[**] This research was supported by DARPA/NSF (ECS-0004030) and NIH (GM 65364), and used the MRSEC shared facilities supported by the NSF under Award No. DMR-9809363. V.L. was a recipient of a postdoctoral fellowship from the Swiss National Science Foundation. A.S. was a recipient of a Howard Hughes Medical Institute Predoctoral Fellowship. We thank Tyler Aldredge of the Center for Genomics Research for technical assistance.

Supporting information for this article is available on the WWW under http://www.angewandte.org or from the author.

 © 2004 Wiley-VCH Verlag GmbH & Co. KGaA, Weinheim DOI: 10.1002/anie.200353016

assays") are simple to operate, rapid, and commercially available, but they are less sensitive than ELISA, and give primarily yes/no results;[8] current work focuses on improving their sensitivity and capacity for quantitative analysis.[8–10] Moreover, although they are less expensive than many tests, they are still too costly for widespread use in developing countries, and for applications that require high-throughput analysis such as screening of blood samples.[4] As such, an immunoassay that is portable, rapid and simple to operate (like immunochromatographic assays), and that offers parallel, quantitative analysis and a strong, reliable analytical performance (like bench-top ELISA), will be a useful tool of detection in settings for which neither strip tests nor conventional ELISA are appropriate.

We take a comprehensive approach to the design of the assay by miniaturizing and integrating both the immunoassay and the detection device. The immunoassay in this study is performed in an inexpensive, miniaturized platform (made by soft lithography) that is compatible with microfluidics. Microfluidic immunoassays offer several advantages relative to microwell plates, which include kinetically rapid reactions at the surface, and the potential for automated fluid delivery and analysis of many samples in parallel.[11–14] The use of ELISA in microfluidics, however, poses two problems: The generation by enzymes of freely diffusible products makes detection difficult under conditions of continuous flow, and the small cross-sectional path length in microchannels limits the sensitivity of assays using simple optical detection. We address both of these problems in our approach for the immunoassay (Figure 1): instead of enzyme-conjugated secondary antibodies, we add antibodies conjugated to 10 nm gold colloids, followed by a solution containing silver nitrate and hydroquinone (as reducing agent). The gold colloids catalyze the reduction of silver ions to silver atoms; in turn, the solid silver catalyzes the further reduction of silver ions.[15] The resultant silver film, whose opacity is a function of the concentration of the analyte, partially blocks the transmission of light through the transparent polystyrene plate. Because the opaque silver product is attached to the surface, reduction of silver may be an effective method of amplification for microfluidic devices that operate under continuous-flow conditions, and may overcome the limitation of a small path length for optical detection of molecules in microchannels.

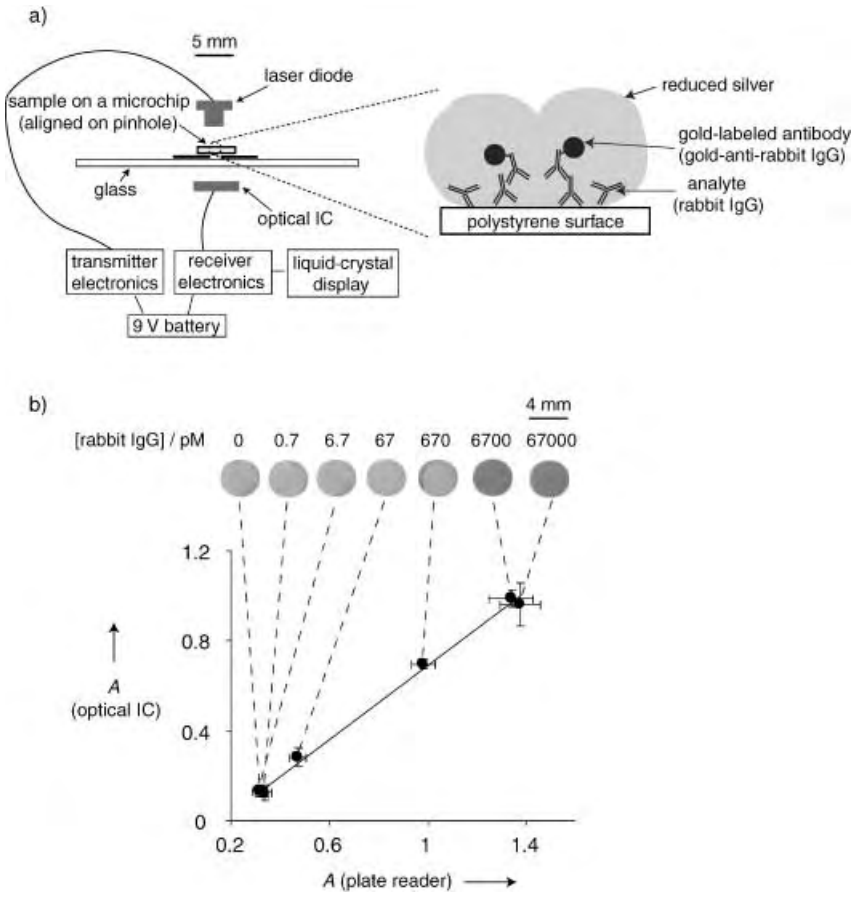


Figure 1. Schematic representation of the POCKET immunoassay, and performance of the optical detection device. a) Red light from the laser diode passed through the silver-coated microwell containing the sample to the optical IC. A pinhole was used to block stray light that did not pass through the sample. The laser diode and the optical IC were driven by the same circuit, which also had an integrated liquid-crystal display that showed the measured transmittance value; b) an immunoassay using silver reduction was performed on a 96-well plate that detected rabbit IgG. Optical micrographs of the silver films on microwells are shown for each sample. The apparent absorbance of each microwell was measured by an optical IC, and compared to its reading by a UV/Vis plate reader; both measurements were made at 654 nm. The best-fit line by linear regression has a correlation coefficient of 0.989, slope of 1.12, and intercepts the *y* axis at 0.16.

A detector for use in the field should be compact, low-cost, battery-powered, and if possible, reusable. Ideally, it should operate under different conditions in the field, such as direct sunlight. We designed and built a detector that satisfies these requirements, by measuring the transmission of light through the silver film. The detector consisted of an InGaAlP red semiconductor laser diode (654 nm) as the light source, and an optical integrated circuit (IC; which contains a photodiode, an amplifier, and a voltage regulator; it has a peak sensitivity wavelength of 700 nm) as the photodetector. To enhance the utility of the detector in direct sunlight, we used pulse modulation of the optical signal at 1 kHz to filter out noise from ambient light (most of which is at 0 Hz). This feature permitted measurements to be made under ambient light in the laboratory (as were all measurements shown in this report); neither shining a flashlight onto the detector nor bringing the device outdoors in daylight produced a change in the background signal. (We believe that, in the future, other types of modulation can be used to further increase the signal-to-noise ratio.) The entire detector was powered using a single 9 V battery (for over three hours of continuous usage), making it suitable for transportation and use in the field in conditions without ground electricity. We also connected the optical IC to a liquid-crystal display to obviate the need for a multimeter. The components for this reusable and portable detector were bought from commercial vendors for $45. (See

 © 2004 Wiley-VCH Verlag GmbH & Co. KGaA, Weinheim

Supporting Information for the details of the circuit design.)[16]

We first characterized the performance of silver reduction with optical detection by the portable detector by performing an immunoassay of a model antigen in microwell plates. The concentration of rabbit IgG was determined in an immunoassay featuring a series of dilutions that spanned five orders of magnitude in concentrations (Figure 1b). The opacities of the samples were measured by the optical IC and by a bench-top UV/Vis absorbance plate reader. For comparison with the data from the plate reader, transmittance values reported by the optical IC were converted to apparent absorbance values (which accounted for both absorption and reflection of the incoming light by the silver film). The optical IC produced readings in excellent agreement with those of the plate reader (correlation coefficient of 0.996). The imperfect agreement between the two measurement methods may have resulted from inhomogeneous silver deposition.[16]

We compared the analytical performance of our method of detection (silver reduction with the low-cost, portable detector) to that of ELISA using the most common reporting systems with bench-top plate readers: absorbance, fluorescence, and chemiluminescence (Figure 2a). For this comparison, we used ELISA substrates that are highly sensitive. The titration data were fitted to sigmoidal curves, the best-fit curves of all methods were normalized to between 0 and 1, and the sensitivities and limits of detection were calculated [16] For an immunoassay detecting rabbit IgG, the most sensitive to the least sensitive method (as defined by the slope of the titration curve in the middle of the linear range of detection, in normalized units per 100 pM) is: chemiluminescence (0.19), fluorescence (0.12), silver (0.08), and absorbance (0.04). For limits of detection, the assays with the lowest limit to the highest limit were: chemiluminescence (22 pM), absorbance (55 pM), silver (89 pM), and fluorescence (163 pM). Immunoassays using silver reduction showed an average overall standard deviation of 7% (for multiple independent measurements of the same concentration of analyte) when measured by the plate reader, and 13% when measured by the optical IC, compared to 9–15% for the ELISA measurements. Thus, the overall analytical performance (sensitivity, limit of detection, and reproducibility) of the POCKET immunoassay in the microwell format approaches that of bench-top ELISA.

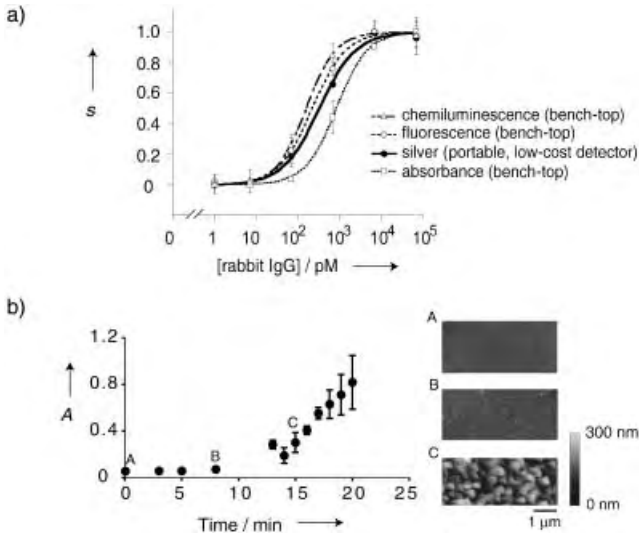


Figure 2. Performance of the POCKET immunoassay. a) Comparison of the POCKET immunoassay using detection by silver reduction and optical IC with detection by absorbance (pNPP substrate), fluorescence (AttoPhos substrate), and chemiluminescence (Supersignal ELISA Femto, a derivative of luminol, as substrate). Standard deviations of triplicates in a single experiment are shown as error bars (see Supporting Information for the procedure for normalizing the signal for different assays). In concentration units, 6.7 pM corresponds to 1 ng mL^{-1}. S = normalized signal; b) kinetics of silver deposition in an immunoassay (for all samples, the concentration of rabbit IgG was 67 nM, and the dilution of gold-labeled anti-rabbit IgG was 1:100). The microwells were incubated in silver enhancement solutions for the indicated times, the reaction was quenched with sodium thiosulfate, and the apparent absorbances of the silver films were measured by a UV/Vis plate reader. AFM images of samples at three different time points are shown. Standard deviations of triplicates in a single experiment are shown as error bars.

We characterized the process of silver deposition by performing an immunoassay for rabbit IgG in microwells, and stopping the silver reduction at various time points. As determined by UV/Vis spectroscopy, after incubation with the silver enhancement solution, silver reduction exhibited an initial slow-growth phase, and then proceeded rapidly at an approximately linear rate (Figure 2b). Analysis of the same samples by atomic force microscopy (AFM) confirmed that the increase in opacity of the surface correlated with the growth of silver particles (Figure 2b). In our assays, quenching the reaction after 10–20 min (see Supporting Information for specific times for each assay) resulted in reproducible amounts of silver that were formed for triplicates in a single experiment. A normalization procedure, such as the one described in Figure 2a (or other methods for running calibration curves) can be used to account for day-to-day fluctuations in the rate of silver deposition (due to an increase in temperature, for example, which increases the rate of silver deposition).

We developed the immunoassay in a microfluidic format by quantifying anti-HIV-1 antibodies in the sera of HIV-1-infected patients (Figure 3). The microfluidic device was fabricated in poly(dimethylsiloxane) (PDMS) using soft lithography.[17] For comparison, we also performed the same immunoassay in the microwell format. In both formats, the opacity of the silver film was measured using the portable detector. Incubation times required for each reagent were 10 min in the microfluidic device, and 1–3 h in the microwells (that is, a 6- to 18-fold reduction in the time required for this part of the assay). The POCKET immunoassay, in both the microwell and microfluidic format, can reliably distinguish the sera of HIV-1-infected patients from those of noninfected patients (Figure 3). Moreover, the assay in both formats can detect quantitative differences in the amount of anti-gp41 in the sample (Figure 3). At high concentrations of serum (low dilutions), the lower signals of the negative controls in the microfluidic device compared to microwells may have resulted from better washing of antibodies that were nonspecifically bound to the surface. We believe that in the

 © 2004 Wiley-VCH Verlag GmbH & Co. KGaA, Weinheim

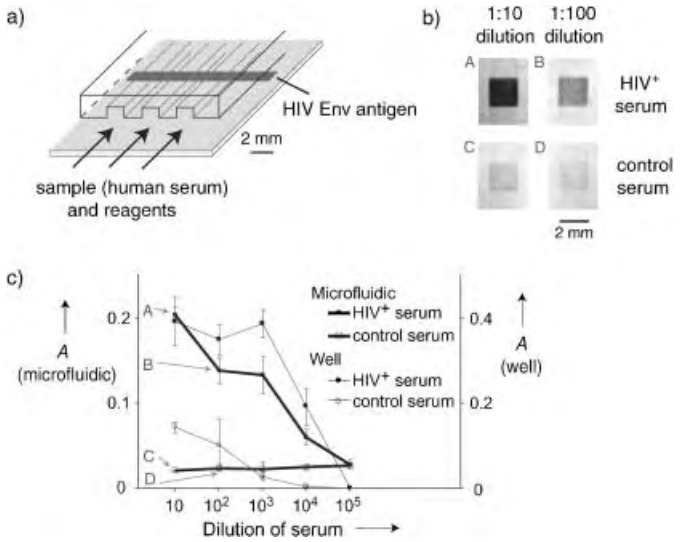


Figure 3. Detection of anti-HIV-1 antibodies in human-patient sera using the POCKET immunoassay. a) Schematic representation of a microfluidic device that detects anti-HIV-1 antibodies. The HIV Env antigen is patterned onto a polystyrene surface as a stripe, and a slab of PDMS with microchannels is placed orthogonally to the stripe. A sequence of reagents (blocking buffer, human serum sample, gold-labeled anti-human IgG, and the silver enhancement solution) is added to the microchannels using pressure-driven flow. Analysis of many dilutions was achieved in parallel by adding a different dilution of the human serum sample to each microchannel; b) photographs of the detection areas with reduced silver films; c) apparent absorbance values from an immunoassay detecting different dilutions of sera from HIV-positive (HIV^+) patients and control patients. For comparison, the assay was also performed in a 96-well plate. Standard deviations of triplicates in a single experiment are shown as error bars. The apparent absorbance values of the samples shown in b) are shown in this graph.

future, the pipetting steps of ELISA in microwells can be automated in the microfluidic device, although we have not implemented this feature yet in our device.

This study offers an alternative approach to other efforts for miniaturizing immunoassays for portable use. Methods for analysis of biomolecules on microchips include electrochemical detection,[12] electrical detection,[18] and integrated on-chip optical detection.[7,19,20] Compared to the detection of colorimetric and fluorescent substrates in solution, detection of silver reduction catalyzed on gold colloids (a method that has been used in other applications to analyze proteins[15,19,21,22] and DNA[23–26]) offers a number of advantages: 1) It is an effective method of signal amplification under conditions of continuous flow in microfluidics; 2) it circumvents the problem of a small path length in microchannels; 3) silver film, unlike fluorescent substrates, does not photobleach; 4) silver, unlike solutions of optically active molecules, is stable for months, which allows results of immunoassays to be kept for long-term use (after 23 days of storage in ambient laboratory conditions, the absorbance readings changed by 1.5%); 5) silver films block light at a broad spectrum of wavelengths (the absorbance of silver showed a maximum variation of 20% from 400 to 1000 nm), whereas chromophores and fluorophores are active only at specific wavelengths. With silver reduction, a wide variety of laser diodes and photodetectors (of any wavelength) can be used in the detection device.

Overall, the integrated POCKET immunoassay has several advantages: 1) It is low-cost and portable, and therefore is appropriate for use in the field; 2) the reporter method of silver reduction is compatible with the use of microfluidics under continuous flow conditions, which decreases the time required for the assay and makes possible a simplified delivery of reagents; 3) the optical detector is battery-powered, reusable, and, with pulse modulation, operable under field conditions such as direct sunlight; 4) the analytical performance of this integrated miniaturized device approaches that of ELISA using relatively expensive benchtop equipment. The POCKET immunoassay may therefore be appropriate for applications in resource-poor settings, including the diagnosis of infectious diseases in developing countries.

Received: October 6, 2003 [Z53016]

Keywords: analytical methods · colloids · immunoassays · microfluidics · proteins

[1] A. S. Daar, H. Thorsteinsdottir, D. K. Martin, A. C. Smith, S. Nast, P. A. Singer, *Nat. Genet.* **2002**, *32*, 229.
[2] J. R. Crowther, *The ELISA Guidebook*, *Vol. 149* (Ed.: J. M. Walker), Humana Press Inc., Totawa, New Jersey, **2001**.
[3] *The Immunoassay Handbook*, 2nd ed. (Ed.: D. Wild), Nature Press, **2001**.
[4] I. V. Jani, G. Janossy, D. W. G. Brown, F. Mandy, *Lancet Infect. Dis.* **2002**, *2*, 243.
[5] A. Alwan, B. Modell, *Nat. Rev. Genet.* **2003**, *4*, 61.
[6] A. Hatch, A. E. Kamholz, K. R. Hawkins, M. S. Munson, E. A. Schilling, B. H. Weig, P. Yager, *Nat. Biotechnol.* **2001**, *19*, 461.
[7] D. N. Stratis-Cullum, G. D. Griffin, J. Mobley, A. A. Vass, T. Vo-Dinh, *Anal. Chem.* **2003**, *75*, 275.
[8] P. E. Andreotti, G. V. Ludwig, A. H. Peruski, J. J. Tuite, S. S. Morse, L. F. Peruski Jr. , *Biotechniques* **2003**, *35*, 850.
[9] J. Hampl, M. Hall, N. A. Mufti, Y. M. Yao, D. B. MacQueen, W. H. Wright, D. E. Cooper, *Anal. Biochem.* **2001**, *288*, 176.
[10] R. Shyu, H. Shyu, H. Liu, S. Tang, *Toxicon* **2002**, *40*, 255.
[11] A. Bernard, B. Michel, E. Delamarche, *Anal. Chem.* **2001**, *73*, 8.
[12] J. S. Rossier, H. H. Girault, *Lab Chip* **2001**, *1*, 153.
[13] R. F. Ismagilov, J. M. K. Ng, P. J. A. Kenis, G. M. Whitesides, *Anal. Chem.* **2001**, *73*, 5207.
[14] X. Jiang, J. M. K. Ng, A. D. Stroock, S. K. W. Dertinger, G. M. Whitesides, *J. Am. Chem. Soc.* **2003**, *125*, 5294.
[15] G. R. Newman, B. Jasani, *J. Pathol.* **1998**, *186*, 119.
[16] Supporting Information includes experimental protocols, a schematic of the electronic circuit for optical detection, and a comparison of absorbance readings from of a solution product using the portable detector and a UV/Vis spectrophotometer.
[17] D. C. Duffy, J. C. McDonald, O. J. A. Schueller, G. M. Whitesides, *Anal. Chem.* **1998**, *70*, 4974.
[18] T. Aytur, P. R. Beatty, B. Boser, M. Anwar, T. Ishikawa, *Solid-State Sensor, Actuator and Microsystems Workshop*, Hilton Head Island, South Carolina, **2002**, pp. 126.
[19] S. Koch, H. Wolf, C. Danapel, K. A. Feller, *Biosens. Bioelectron.* **2000**, *14*, 779.
[20] M. L. Chabinyc, D. T. Chiu, J. C. McDonald, A. D. Stroock, J. F. Christian, A. M. Karger, G. M. Whitesides, *Anal. Chem.* **2001**, *73*, 4491.

 © 2004 Wiley-VCH Verlag GmbH & Co. KGaA, Weinheim

[21] B. F. Rocks, M. P. Bailey, V. M. R. Bertram, *PCT Int. Appl.* WO9101003, **1991**.
[22] J. M. Nam, C. S. Thaxton, C. A. Mirkin, *Science* **2003**, *301*, 1884.
[23] S. Park, T. A. Taton, C. A. Mirkin, *Science* **2002**, *295*, 1503.
[24] T. A. Taton, C. A. Mirkin, R. L. Letsinger, *Science* **2000**, *289*, 1757.
[25] O. D. Velev, E. W. Kaler, *Langmuir* **1999**, *15*, 3693.
[26] R. Moller, A. Csaki, J. M. Kohler, W. Fritzsche, *Langmuir* **2001**, *17*, 5426.

 © 2004 Wiley-VCH Verlag GmbH & Co. KGaA, Weinheim

Radicals

Stable Cubic Phosphorus-Containing Radicals**

Andrea Armstrong, Tristram Chivers, Masood Parvez, and Rene T. Boeré*

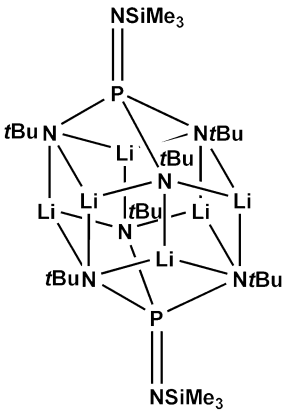
The study of radicals of the heavier main-group elements is an area of significant current interest.[1] Many of the so-called stable radicals[2] are obtained as charged species, that is, ionic radicals. Examples of stable neutral radicals are less common, but several have been structurally characterized recently in the solid state by X-ray crystallography, for example, $CB_{11}Me_{12}^{\bullet}$,[3] [M(dbdab)$_2$] (M = Al, Ga; dbdab = 1,4-di-*tert*-butyl-1,4-diazabutadiene),[4] [R_2MMR]$^{\bullet}$ (M = Ga, Al; R = Si*t*Bu$_3$),[5–7] $R_3SiSi(tBu)_2^{\bullet}$ [R = SiMe(*t*Bu)$_2$],[8] [R_3E]$^{\bullet}$ (E = Si, Ge; R = SiMe(*t*Bu)$_2$),[9] and [Ge($C_6H_3Mes_2$-2,6)]$^{\bullet}$ (Mes = 2,4,6-$(CH_3)_3C_6H_2$).[10] The structure of the phosphorus-centered radical $:P[CH(SiMe_3)_2]_2^{\bullet}$ has been determined in the gas phase by electron diffraction.[11] The diphosphanyl radical [Mes*(Me)PPMes*]$^{\bullet}$ (Mes* = 2,4,6-*t*Bu$_3C_6H_2$) has been stabilized by doping into single crystals of Mes*(Me)PP(Me)Mes*.[12]

An intriguing feature of the chemistry of the lithium derivatives of polyimido anions of p-block elements [13] is the formation of deeply colored persistent radicals[2] upon oxidation of the chalcogen-centered clusters [{Li_2[E(N*t*Bu)$_3$]}$_2$] (E = S, Se).[14] The solution EPR spectra of these radicals consist of a septet of dectets, which is attributed to coupling of the unpaired electron with three equivalent ^{14}N nuclei (I = 1, $a \approx 5.5$ G) and three equivalent ^{7}Li nuclei (I = 3/2, $a \approx 0.8$ G).[15,16] Their solid-state structures have not been determined.

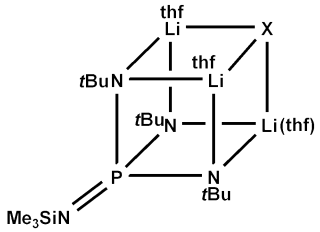
[*] A. Armstrong, Prof. T. Chivers, Dr. M. Parvez
Department of Chemistry
University of Calgary
Calgary, AB T2N 1N4 (Canada)
Fax: (+1) 403-289-9488
E-mail: chivers@ucalgary.ca
Prof. R. T. Boeré
Department of Chemistry and Biochemistry
University of Lethbridge
Lethbridge, AB T1K 3M4 (Canada)

[**] The authors gratefully acknowledge financial support from the Natural Sciences and Engineering Research Council (Canada)

The first tetrakisimidophosphate was obtained as the solvent-separated ion pair [Li(thf)$_4$][(thf)$_2$Li(μ-Nnaph)$_2$P(μ-Nnaph)$_2$Li(thf)$_2$] (naph = 1-naphthyl) by Wright and coworkers in 1997.[17] However, no reactions of this important member of the family of p-block polyimido anions have been reported. Our recent discovery of a simple and versatile route to tetrakisimidophosphates, for example, [{Li_3[P(N*t*Bu)$_3$(NSiMe$_3$)]}$_2$] (**1**),[18] has facilitated investigations of the



1



2a: X = Br
2b: X = I

chemistry of these isoelectronic analogues of the orthophosphate PO_4^{3-} ion. We describe here the synthesis of the stable, neutral radicals [$Me_3SiNP(\mu_3\text{-}NtBu)_3\{\mu_3\text{-}Li(thf)\}_3X$]$^{\bullet}$ (**2a**, X = Br; **2b**, X = I) obtained by the oxidation of **1** with halogens. The derivative **2b** has been structurally characterized in the solid state by X-ray crystallography. The solution behavior of these novel radical systems has been investigated by EPR and UV/Vis spectroscopies.

The reactions of the dimer **1** with one equivalent of bromine or iodine in a mixture of toluene and THF at 295 K produce deep blue solutions immediately. Removal of the solvents gives **2a** or **2b**, respectively, as blue powders in good yields. Crystals of **2b** suitable for an X-ray structural determination[19] were grown from a supersaturated syrup in THF at 295 K. The molecular structure and pertinent structural parameters for **2b** are depicted in Figure 1. The crystal was composed of **2b** (75%) cocrystallized with the diamagnetic seco-cube [{$Me_3SiNP(\mu_3\text{-}NtBu)_3[\mu_3\text{-}Li(thf)]_3$}] (25%), that is, a trisolvated monomeric unit of **1**. The molecule has a highly distorted cubic structure similar to that reported by Stalke et al. for the colorless, diamagnetic sulfur(IV) complex {$S(\mu_3\text{-}NtBu)_3[\mu_3\text{-}Li(thf)]_3I$}, which contains the trisimidosulfite dianion [$S(NtBu)_3$]$^{2-}$.[15] The absence of iodine in 25% of the molecules in **2b** leads to a more compact lattice compared to the analogous sulfur(IV) complex,[15] as evidenced by several contacts between iodine and THF hydrogen atoms that are less than the sum of the van der Waals radii. The blue, paramagnetic complex **2b** is comprised of the radical dianion [$P(NtBu)_3(NSiMe_3)$]$^{2-\bullet}$ (formed by the one-electron oxidation of the [$P(NtBu)_3(NSiMe_3)$]$^{3-}$ trianion in **1**), two Li^+ counterions and a molecule of lithium iodide. Each of the three Li^+ ions is solvated by one THF molecule. The mean bond lengths in the PN_3Li_3I cube are 1.66 (P–N),

 © 2004 Wiley-VCH Verlag GmbH & Co. KGaA, Weinheim DOI: 10.1002/anie.200353108

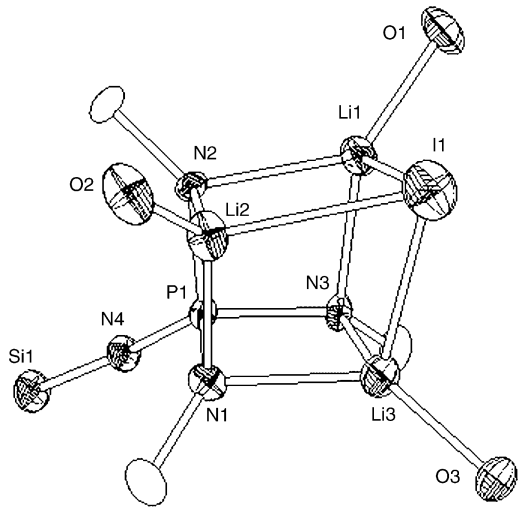


Figure 1. X-ray crystal structure of **2b**. Only the O atoms of THF ligands are shown. Selected bond lengths [Å] and bond angles [°]. Li1-I1 2.704(13), Li2-I1 2.790(13), Li3-I1 2.776(14), P1-N1 1.667(5), P1-N2 1.647(5), P1-N3 1.665(5), P1-N4 1.546(5), Li1-N2 2.046(13), Li1-N3 2.093(14), Li2-N1 2,090(14), Li2-N2 2.071(14), Li3-N1 2.086(13), Li3-N3 2.089(13), Si1-N4 1.650(5); P1-N4-Si1 176.0(4).

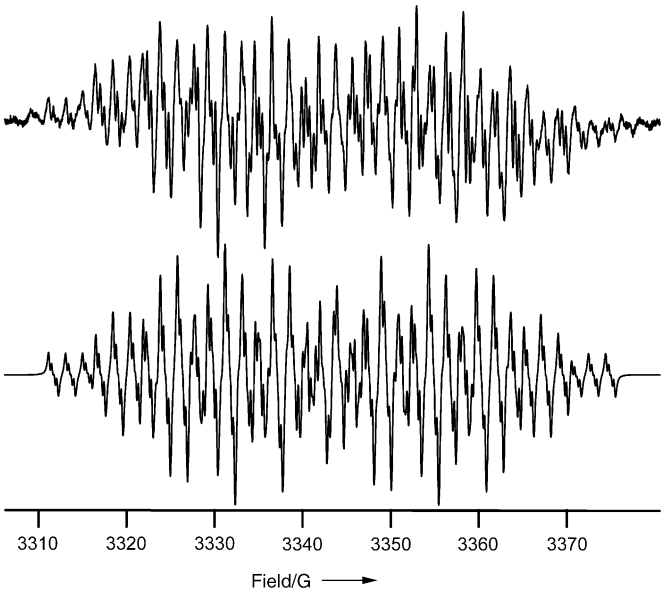
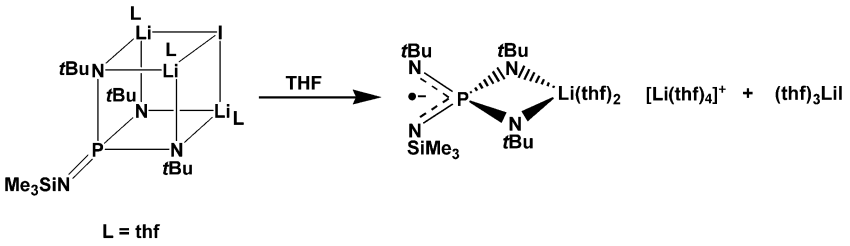


Figure 2. Experimental (top) and simulated (bottom) EPR spectra of a very dilute THF solution of **2b** under vacuum at 295 K.

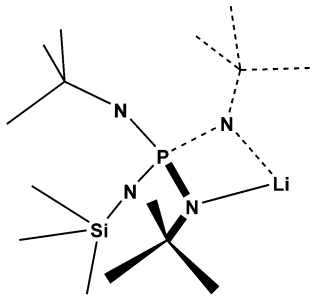
2.08 (Li–N), and 2.75 Å (Li–I). The Li–I bond length is ≈0.19 Å shorter than the corresponding bond in the analogous sulfur(IV) complex.[15] The exocyclic P–N bond length is 1.542(4) Å, and the P-N-Si arrangement in **2b** is almost linear (176.5°), as was found for **1**.[18]

The radicals **2a** and **2b** dissolve in THF to give intensely blue solutions that persist for several weeks at room temperature. In other solvents, for example hexane, the blue color disappears rapidly. Finely powdered **2b** was dissolved in THF in a T-shaped tube sealed under vacuum, and EPR spectra were recorded as functions of temperature and concentration. A similar study was performed for **2a** and both compounds were found to exhibit similar behavior. Complex spectra with many hyperfine lines that were strongly dependent on both concentration and temperature were obtained. Under high dilution ($<10^{-4}$ M) at 295 K, the spectrum of **2b** stabilized to a limiting pattern (Figure 2). This spectrum could be reasonably well simulated as a monolithium species with the following hyperfine coupling (hfc) values (G): $a_N = 1.93$ to one ^{14}N, $a_N = 5.38$ to two equivalent ^{14}N, $a_N = 7.38$ to one ^{14}N, $a_P = 23.1$ to one ^{31}P, and $a_{Li} = 0.30$ to one ^{7}Li nucleus. We propose that upon dissolution in THF, the cubic cage structure of **2b** is ruptured with the release of solvated lithium iodide and the formation of a solvent-separated ion pair $[Li(thf)_4][(Me_3SiN)(tBuN)P(\mu\text{-}NtBu)_2Li(thf)_2]$ (**3**) (Scheme 1).



Scheme 1. Solvation of lithium ions in **2b** in very dilute THF solutions.

Confirmation of the dissociation of the cube was provided by the isolation of the by-product $(thf)_3LiI$, which was identified by determination of the unit-cell parameters.[20] We have probed possible structures for the radical monoanion in **3** by using AM1 calculations on the corresponding dianion. A reasonable geometry was obtained with $\Delta H_f = -200$ kJ mol^{-1} in the gas phase for the monocyclic structure **3′**, in which two *t*BuN groups chelate the single Li^+ ion, while the third (noncoordinated) *t*BuN group carries the greater portion of the unpaired spin density. The local C_s symmetry of



3'

this cyclic structure is consistent with the EPR spectra of extremely dilute solutions of **2b** described above.[21] The transformation depicted in Scheme 1 implies that the breakdown of the cubic structures of **2a** and **2b** in THF solution will lead to the formation of the same radical species. Indeed, the EPR spectrum of **2a** in very dilute THF solution shows

 © 2004 Wiley-VCH Verlag GmbH & Co. KGaA, Weinheim

similar features to that of **2b**, and the *g* values are 2.00638 (**2a**) and 2.00632 (**2b**). In addition, the UV/Vis spectra of **2a** and **2b** in THF are essentially identical with broad absorption maxima at $\approx$640 nm. At higher concentrations, the room-temperature EPR spectra are very complex, but contain components with considerably higher symmetry. At lower temperatures the spectra are simpler, and the EPR spectrum of a solution of **2a** ($\approx 10^{-2}$ M) recorded in a THF gel at 173 K (Figure 3) fits well to a simulation with the following hfc

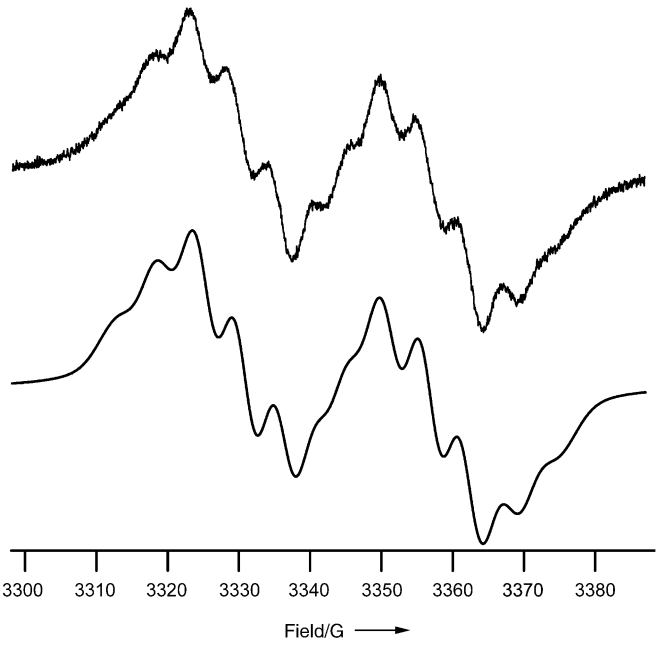


Figure 3. Experimental (top) and simulated (bottom) EPR spectra of **2b** in a THF gel at 173 K.

values (G): $a_N = 5.36$ to three equivalent ^{14}N and $a_P = 26.0$ to one ^{31}P nucleus. This spectrum is consistent with the structure of **2b** (local C_3 symmetry) if the hfc to the three Li-bonded nitrogen atoms is significantly larger than that to the unique nitrogen atom that is bonded to the silicon center. Alternative structures containing two (or even one) Li^+ ion can be envisaged, but line broadening obscures potentially informative smaller hfcs. EPR spectra of solid **2a** and **2b** are featureless singlets with no detectable hfc.

Surprisingly, the NMR spectra of concentrated, deep-blue solutions of **2a** and **2b** in [D$_8$]THF at room temperature exhibit narrow resonances with normal chemical shifts. The ^{1}H, ^{7}Li, and ^{31}P chemical shifts are essentially identical for **2a** and **2b** and only very minor changes in the shifts are observed over the concentration range 0.05–0.16 M. The ^{1}H NMR spectra show two resonances for the *t*BuN groups with relative intensities of 2:1, in addition to the resonance for the SiMe$_3$ group. These observations indicate the formation of a diamagnetic species with local C_s or C_2 symmetry, presumably by dimerization of the radical monoanion in **3** at these concentrations. Apparently the presence of the radical monoanions in these solutions (deep-blue color) does not have a significant effect on the NMR spectra of the diamagnetic species.

The discovery of the radical dianion [P(N*t*Bu)$_3$(NSiMe$_3$)]$^{2-\bullet}$ provides a cogent example of the different behavior of polyimido anions of the p-block elements compared to that of the isoelectronic oxo anions.[22] This radical dianion is stabilized in a distorted cubic framework by two lithium counterions and a molecule of lithium halide. The stability of these deep-blue, neutral radicals is attributed to a combination of electron delocalization over the nitrogen centers within the cube and the steric protection provided by the three N*t*Bu and one NSiMe$_3$ groups. In THF solution, solvation of the lithium centers results in the disruption of the cube with the release of an LiX (X = Br, I) molecule and the formation of [(Me$_3$SiN)(*t*BuN)P(μ-N*t*Bu)$_2$Li(thf)$_2$]$^{-\bullet}$, a monolithium derivative of the radical dianion.

Experimental Section

All reactions and the manipulations of products were carried out under anaerobic and anhydrous conditions using Schlenk techniques and an inert-atmosphere (argon) glove box. EPR spectra were recorded on a Bruker EMX 113 spectrometer equipped with a variable-temperature accessory. A pure Lorentzian line shape and a line width of 0.23 G were employed in the simulation shown in Figure 2 using WINEPR SimFonia, v. 1.25, Bruker Analytische Messtechnik GmbH. A Lorentzian (60%)/Gaussian (40%) line shape and a line width of 5.5 G were used for the simulation shown in Figure 3.

2a: A solution of Br_2 in toluene (3.7 mL, 0.113 M, 0.419 mmol) was added to a colorless solution of [{Li$_3$[P(N*t*Bu)$_3$(NSiMe$_3$)]}$_2$] (0.295 g, 0.419 mmol) in toluene/THF (5 mL/1 mL) at 295 K, resulting in a deep-blue solution. After 5 min, the solvents were removed via dynamic vacuum to leave **2a** as a bright-blue powder (0.387 g, 0.594 mmol, 71%). UV/Vis (THF): λ_{max} 638 nm (br); ^{1}H NMR ([D$_8$]THF): $\delta = 1.26$ (s, N*t*Bu, 18H), 1.18 (s, N*t*Bu, 9H), −0.05 ppm (s, SiMe$_3$, 9H); ^{7}Li NMR ([D$_8$]THF): $\delta = 0.74$ ppm (s); ^{31}P{^{1}H} NMR ([D$_8$]thf): $\delta = 6.37$ ppm (s).

2b: A solution of I_2 in toluene (4.80 mL, 0.071 mmol, 0.342 mmol) was added to a colorless solution of {Li$_3$[P(N*t*Bu)$_3$(NSiMe$_3$)]}$_2$ (0.239 g, 0.339 mmol) in toluene/THF (5 mL/0.5 mL) at 295 K, resulting in a deep-blue solution. After 10 min, solvents were removed via dynamic vacuum to leave **2b** as a bright-blue powder (0.339 g, 0.488 mmol, 72%). Elemental analysis calcd (%) for $C_{27}H_{60}ILi_3N_4O_3PSi$: C 46.62, H 8.69, N 8.06; found: C 44.21, H 8.96, N, 8.57; UV/Vis (THF): λ_{max} 640 nm (br); ^{1}H NMR ([D$_8$]THF): $\delta =$ 1.24 (s, N*t*Bu, 18H), 1.16 (s, N*t*Bu, 9H), −0.06 ppm (s, SiMe$_3$, 9H); ^{7}Li NMR ([D$_8$]THF): $\delta = 0.75$ ppm (s); ^{31}P NMR ([D$_8$]THF): $\delta =$ 6.55 ppm (s). X-ray quality crystals of **2b** were obtained from an extremely concentrated THF solution at 295 K.

Received: October 17, 2003 [Z53108]
Published Online: December 18, 2003

Keywords: cubanes · lithium · main group elements · phosphorus · radicals

[1] For a recent review, see P. P. Power, *Chem. Rev.* **2003**, *103*, 789–809.
[2] As defined in ref. [1], the term "stable", as applied to radicals, is taken to indicate "a species that can be isolated and shows no sign of decomposition under an inert atmosphere at room

 © 2004 Wiley-VCH Verlag GmbH & Co. KGaA, Weinheim

temperature", whereas a "persistent" radical has "a relatively long lifetime under the conditions it is generated".

[3] B. T. King, B. C. Noll, A. J. McKinley, J. Michl, *J. Am. Chem. Soc.* **1996**, *118*, 10902 – 10903.

[4] W. Kaim, W. Matheis, *J. Chem. Soc. Chem. Commun.* **1991**, 597 – 598.

[5] N. Wiberg, K. Amelunxen, H. Nöth, W. Kaim, A. Klein, T. Scheiring, *Angew. Chem.* **1997**, *109*, 1258 – 1261; *Angew. Chem. Int. Ed. Engl.* **1997**, *36*, 1213 – 1215.

[6] N. Wiberg, T. Blank, W. Kaim, B. Schwerderski, G. Lintl, *Chem. Eur. J.* **2000**, 1475 – 1481.

[7] N. Wiberg, T. Blank, K. Amelunxen, H. Nöth, J. Knozek, T. Habereden, W. Kaim, M. Wanner, *Eur. J. Inorg. Chem.* **2001**, 1719 – 1727.

[8] A. Sekiguchi, T. Matsuno, M. Ichinoke, *J. Am. Chem. Soc.* **2001**, *123*, 12436 – 12437.

[9] A. Sekiguchi, T. Fukawa, M. Nakamoto, V. Y. Lee, M. Ichinoke, *J. Am. Chem. Soc.* **2002**, *124*, 9865 – 9869.

[10] M. M. Olmstead, L. Pu, R. S. Simons, P. P. Power, *Chem. Commun.* **1997**, 1595 – 1596.

[11] S. L. Hinchley, C. A. Morrison, D. W. H. Rankin, C. L. B. MacDonald, R. J. Wiacek, A. H. Voigt, A. H. Cowley, M. F. Lappert, G. Gundersen, J. A. C. Clyburne, P. P. Power, *J. Am. Chem. Soc.* **2001**, *123*, 9045 – 9053.

[12] S. Loss, A. Magistrato, L. Cataldo, S. Hofmann, M. Geoffroy, U. Röthlisberger, H. Grützmacher, *Angew. Chem.* **2001**, *113*, 749 – 751; *Angew. Chem. Int. Ed.* **2001**, *40*, 723 – 726.

[13] For recent reviews, see: a) J. K. Brask, T. Chivers, *Angew. Chem.* **2001**, *113*, 4082 – 4098; *Angew. Chem. Int. Ed.* **2001**, *40*, 3961 – 3976; b) G. M. Aspinall, M. C. Copsey, A. P. Leedham, C. A. Russell, *Coord. Chem. Rev.* **2002**, *227*, 217 – 232.

[14] For reviews, see: a) R. Fleischer, D. Stalke, *Coord. Chem. Rev.* **1998**, *176*, 431 – 450; b) D. Stalke, *Proc. Indian Acad. Sci. Chem. Sci.* **2000**, *112*, 155 – 170.

[15] R. Fleischer, S. Freitag, D. Stalke, *J. Chem. Soc. Dalton Trans.* **1998**, 193 – 197.

[16] J. K. Brask, T. Chivers, B. McGarvey, G. Schatte, R. Sung, R. T. Boeré, *Inorg. Chem.* **1998**, *37*, 4633 – 4636.

[17] P. R. Raithby, C. A. Russell, A. Steiner, D. S. Wright, *Angew. Chem.* **1997**, *109*, 670 – 671; *Angew. Chem. Int. Ed. Engl.* **1997**, *36*, 649 – 650.

[18] A. Armstrong, T. Chivers, M. Krahn, M. Parvez, G. Schatte, *Chem. Commun.* **2002**, 2332 – 2333.

[19] Crystal data for **3b**: $C_{27}H_{60}I_{0.75}Li_3N_4O_3PSi$, $M_r = 663.85$, monoclinic, space group $P2_1/c$, $a = 9.860(2)$, $b = 18.206(4)$, $c = 21.261(6)$ Å, $\beta = 96.431(10)°$, $V = 3792.6(16)$ Å^3, $Z = 4$, $\rho_{calcd} = 1.218\ g\,cm^{-3}$, $F(000) = 1407$, $T = 173(2)$ K. Data were collected on a Nonius Kappa CCD diffractometer on a blue block-shaped crystal ($0.20 \times 0.16 \times 0.14\ mm^3$) coated with Paratone 8277 oil and mounted on a glass fiber. Of the 24850 reflections collected, 6717 were unique ($R_{int} = 0.056$) and 4546 were observed [$I \leq 2.00\sigma(I)$] and used to refine 373 parameters. The structure was solved by direct methods (SIR92) expanded with Fourier techniques (DIRDIF94). The non-hydrogen atoms were refined anisotropically. Refinement of the site occupancy factor for I indicated only 75% electron population at that location. The carbon atoms of one THF ligand were disordered over two sites with equal site-occupancy factors. Refinement by least-squares calculations (SHELXL97) converged at $R_1 = 0.061$ and $wR_2 = 0.153$ [$I \leq 2.00\sigma(I)$]. CCDC-221735 contains the supplementary crystallographic data for this paper. These data can be obtained free of charge via www.ccdc.cam.ac.uk/conts/retrieving.html (or from the Cambridge Crystallographic Data Centre, 12, Union Road, Cambridge CB21EZ, UK; fax: (+44) 1223-336-033; or deposit@ccdc.cam.ac.uk).

[20] H. Nöth, R. Waldhor, *Z. Naturforsch. B* **1998**, *54*, 1525 – 1528.

[21] The normal mechanism for hfc operates through the valence s-orbital components of the singly occupied molecular orbital (SOMO). An AM1 caculation on the cyclic radical monoanion **3′** gave the expected small s coefficients from the nitrogen atoms in the SOMO, as these are predominantly p functions. By using the isotropic hfcs of J. R. Morton, K. F. Preston, *J. Magn. Reson.* **1978**, *30*, 577 – 58, as reported in J. A. Weil, J. R. Bolton, J. E. Wertz, *Electron Paramagnetic Resonance*, Wiley, New York, **1994**, p. 534, reasonable agreement between calculated and experimental hfcs was obtained. In particular, the large coupling to phosphorus in these systems reflects the approximately fivefold higher intrinsic coupling to ^{31}P compared to ^{14}N for a unit s-orbital contribution to the SOMO.

[22] A phosphorus-containing radical formed from single crystals of $K[H_2PO_4]$ upon irradiation by X-rays has been detected by EPR spectroscopy at 77 K; this radical is unstable at 130 K.W. E. Hughes, W. G. Moulton, *J. Chem. Phys.* **1963**, *39*, 1359 – 1360.

 © 2004 Wiley-VCH Verlag GmbH & Co. KGaA, Weinheim

Peptide Design I

Two Helical Conformations from a Single Foldamer Backbone: "Split Personality" in Short α/β-Peptides**

Ahlke Hayen, Margaret A. Schmitt, Felix N. Ngassa, Kathryn A. Thomasson, and Samuel H. Gellman**

Oligomers that adopt predictable conformations ("foldamers") are subjects of increasing interest from the perspectives of both fundamental research and applications.[1] The study of unnatural oligomers that display secondary structures analogous to those of proteins or nucleic acids provides new insight on the parameters that influence the "foldability" of a backbone, e.g., the relationships between conformational stability and number of residues or residue flexibility. As the rules that govern shape are elucidated for new backbones, this

[*] Dr. A. Hayen,[+] M. A. Schmitt,[+] Prof. Dr. S. H. Gellman
Department of Chemistry
University of Wisconsin
1101 University Avenue, Madison, WI 53706 (USA)
Fax: (+1) 608-265-4534
E-mail: gellman@chem.wisc.edu

F. N. Ngassa, Prof. Dr. K. A. Thomasson
Department of Chemistry
University of North Dakota
Grand Forks, ND 58202 (USA)

[+] These authors contributed equally.

[**] This research was supported by the NSF (CHE-0140621). A.H. was supported in part by a postdoctoral fellowship from the DAAD (German Academic Exchange Service), M.A.S. in part by an NIH Molecular Biophysics Training grant, and F.N.N. in part by a North Dakota EPSCoR Doctoral Dissertation Fellowship. NMR spectrometers were purchased with partial support from the NSF and the NIH.

Supporting information for this article is available on the WWW under http://www.angewandte.org or from the author.

 DOI: 10.1002/anie.200352125 © 2004 Wiley-VCH Verlag GmbH & Co. KGaA, Weinheim

information can be applied to create foldamers with interesting functions.[2] Most unnatural foldamers reported so far have homogeneous backbones, i.e., they are constructed from building blocks of a single class (e.g., α- or β-amino acids), as is also the case for biological foldamers.[1] Heterogeneous backbones, composed of two or more residue types, can also display well-defined folding behavior, although this strategy for foldamer design has received relatively little attention to date.[3] The exploration of heterogeneous backbones is important because mixing monomer classes leads to an exponential increase in the range of potential foldamers. Increasing the number of distinct shapes that can be predictably achieved should enhance opportunities to endow foldamers with desirable activities.

Here we show that combining α-amino acid and cyclic β-amino acid residues in a sequentially alternating pattern can lead to helix formation within relatively short heterooligomers.[4] Structural data suggest that these foldamers have a "split personality," simultaneously populating two different helical conformations. Both helices contain backbone C=O···H–N hydrogen bonds with N→C directionality, but they differ in the sequential spacing between C=O and H–N ($i,i+3$ in one case, $i,i+4$ in the other). This behavior parallels closely the split personality observed among peptides composed exclusively of α-amino acid residues, which frequently populate both α- and 3_{10}-helical conformations in solution.[5] Our α/β-peptides differ from α-peptides, however, in that folding is observed with fewer residues in the former than in the latter. The different monomer types in the heterogeneous α/β-peptide backbone offer complementary benefits to the new foldamers we have identified: the constrained β-residues provide conformational preorganization, while the α-residues allow facile introduction of specific side chains at specific positions.

Initial two-dimensional NMR studies[6] were conducted with diastereomeric hexamers **1a**,**b** in CD_3OH (Figure 1). Both contain (*S*,*S*)-*trans*-2-aminocyclopentanecarboxylic acid (ACPC)[7] residues in the β-amino acid positions. The two lysine residues were selected to promote solubility in polar media, and the central tyrosine residue was placed to promote ^{1}H NMR resonance dispersion (by means of the magnetic anisotropic effects of the aromatic side chain). Proteinogenic L-α-residues (*S* configuration) were used for **1a**, while D-α-residues were used for **1b**. The signals in the ^{1}H NMR spectrum of oligomer **1a** were moderately dispersed, and a number of NOEs were detected between residues that are not

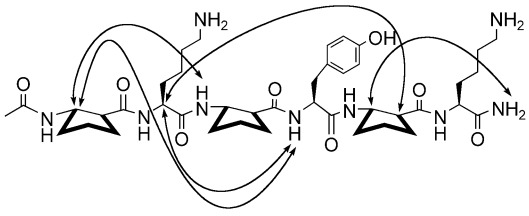


Figure 1. Graphical summary of unambiguously assigned NOEs involving sequentially nonadjacent residues for α/β-peptide **1a** in CD_3OH. α/β-Peptide **1b** is the diastereomer in which all α-residues have the opposite configuration (not shown); no nonsequential NOEs were detected for **1b**.

adjacent in sequence. Nonsequential NOEs of this type are strong evidence that the oligomer adopts a compact conformation, or perhaps multiple compact conformations, for at least part of the time. (Interconversion between folded and unfolded states, and between alternative folded states, is presumably rapid on the NMR timescale.) No nonsequential NOEs could be detected for **1b**, which suggests that this diastereomer has little propensity to fold under these conditions.

Five nonsequential NOEs could be assigned with certainty for **1a** (Figure 1); several other nonsequential NOEs were present but of ambiguous identity because of resonance overlap. The unambiguous nonsequential NOEs were consistent with formation of helices involving backbone hydrogen bonds from carbonyl groups to amide protons in the C-terminal direction. Each of the ambiguous nonsequential NOEs had a possible assignment that was consistent with this type of helix.[8] The same hydrogen-bond directionality is observed in the two most common helices formed by homogeneous L-α-residue backbones, the α-helix (13-membered-ring hydrogen bonds, C=O(i)···H–N($i+4$)) and the 3_{10}-helix (10-membered-ring hydrogen bonds, C=O(i)···H–N($i+3$)), and in the 12-helix[9] formed by homooligomers of (*S*,*S*)-ACPC (12-membered-ring hydrogen bonds, C=O(i)···H–N($i+3$)).

Structural conclusions based on the data for **1a** are tentative because relatively few nonsequential NOEs could be confidently assigned. Prior to the design of a second generation of α/β-peptides related to **1a**, intended to display greater NMR resonance dispersion, we used an ACPC/alanine dodecamer for computational modeling[10] of three helical conformations that contain backbone C=O···H–N hydrogen bonds with N→C directionality (Figure 2). These helices are named based on the characteristic hydrogen-bond ring size: 11-helix, 14/15-helix, and 18-helix (Figure 3). The model structures suggest that some nonsequential NOEs (or lack thereof) might allow distinctions to be drawn among the alternative helices (Table 1). For example, α-residue $H^{\alpha}(i)$/α-residue NH($i+2$) NOEs are expected for the 11-helix (3.8 Å average interproton distance predicted), but not for the 14/15- or 18-helix (>5 Å). In **1a**, one of the two possible NOEs of this class was observed. On the other hand, α-residue $H^{\alpha}(i)$/β-residue $H^{\alpha}(i+3)$ NOEs are expected for the 14/15-helix (3.0 Å) and the 18-helix (4.3 Å), but not for the 11-helix (>5 Å). In **1a**, the only possible NOE of this type was observed. (The other unambiguous NOEs observed for **1a** were two β-residue $H^{\beta}(i)$/β-residue NH($i+2$) NOEs and one β-residue $H^{\beta}(i)$/α-residue NH($i+3$) NOE, which the models indicate to be possible in all three helices). Model structures were constructed also for helices defined by hydrogen bonds with the opposite directionality, from carbonyl groups to amide protons in the N-terminal direction (the 9-, 12/13-, and 16-helices; not shown). This set of helical conformations could be ruled out because the NOEs predicted for these structures, mostly NH of residue i to H^{α} or H^{β} of residue $i+2$, $i+3$, or $i+4$, were not detected for **1a** or the oligomers discussed below.

α/β-Peptides **2** and **3** (Figure 4) were prepared in an effort to search for the $i,i+3$, $i,i+4$, and $i,i+5$ NOE patterns that

 © 2004 Wiley-VCH Verlag GmbH & Co. KGaA, Weinheim

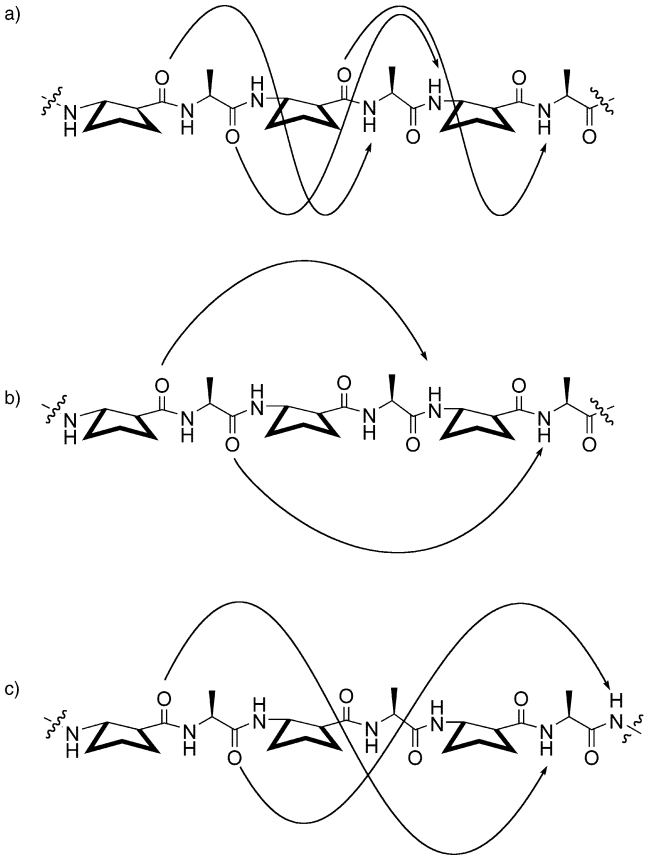


Figure 2. Hydrogen-bond patterns that define the helical secondary structures of the α/β-peptides considered here, with hydrogen bonds from carbonyl groups to amide protons in the C-terminal direction; a) 11-helix, b) 14/15-helix, c) 18-helix.

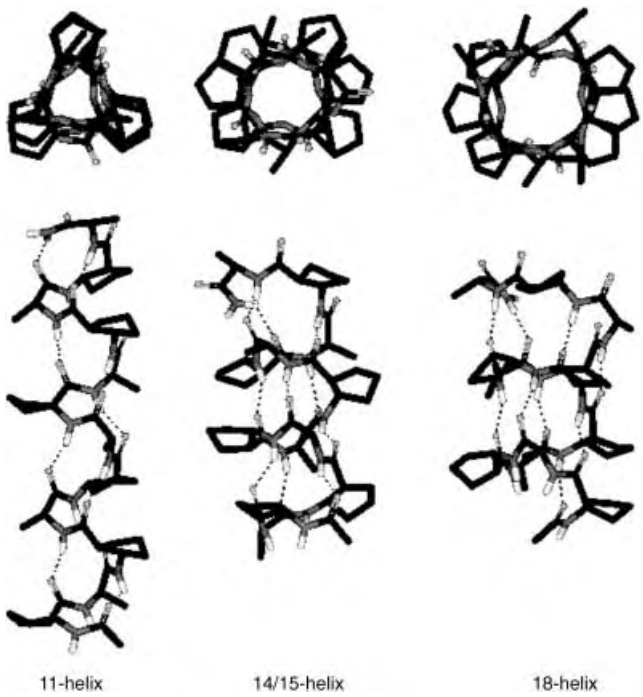


Figure 3. Model helices generated in SYBYL to examine possible conformations of α/β-peptides. Dotted gray lines indicate hydrogen bonds. The upper views are along the helical axis; the lower views are perpendicular to the helical axis.

would aid in identifying the helical conformation(s) adopted by this type of heterogeneous backbone. These new compounds contain eight residues, rather than the six in **1a**. They are stereochemical analogues of **1a**, but two of the β-residues are (3*R*,4*S*)-*trans*-3-aminopyrrolidine-4-carboxylic acid ((3*R*,4*S*)-APC) rather than (*S*,*S*)-ACPC. Four different L-α-residues were employed. Oligomers **2** and **3** differ only in the placement of the Lys and Glu residues.[11]

Oligomer **2** in CD_3OH displayed the best ^1H NMR resonance dispersion among the α/β-peptides we examined, although there was still some overlap. Eight of the 14 possible $i,i+2$ NOEs between backbone protons could be unambiguously identified (Table 2), including two of the four possible α-residue $H^{\alpha}(i)$/α-residue $NH(i+2)$ NOEs. As pointed out above, this type of NOE is suggested by our simple modeling to be consistent with only the 11-helix. Modeling suggests that three $i,i+3$ NOE patterns would be most likely among backbone protons in the three helical secondary structures considered: 1) β-residue $H^{\beta}(i)$/α-residue $NH(i+3)$, 2) α-residue $H^{\alpha}(i)$/β-residue $NH(i+3)$, and 3) α-residue $H^{\alpha}(i)$/β-residue $H^{\alpha}(i+3)$. Among these three patterns, the third is not expected for the 11-helix, but is consistent with the other two helices, as discussed above; two of the three possible NOEs of this type were observed for **2**. Our second predicted NOE pattern is consistent with the 11-helix (3.6 Å average interproton distance predicted) and the 14/15-helix

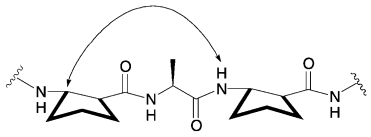
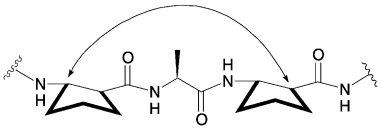
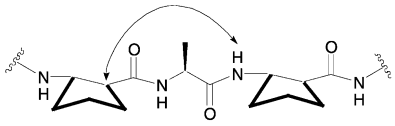
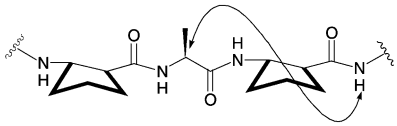
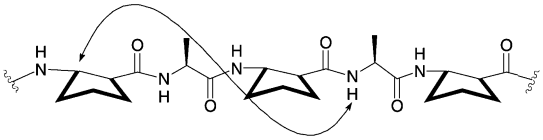
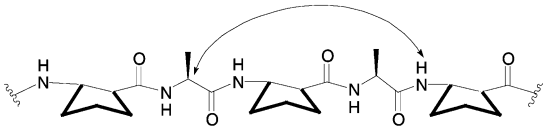
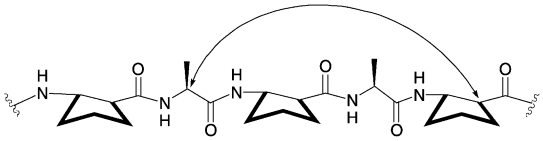
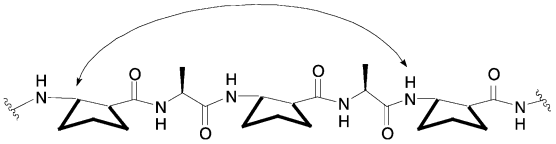
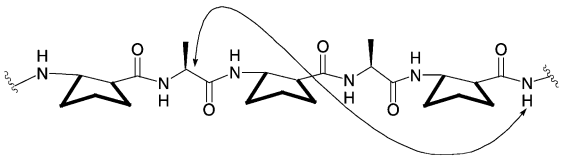
Table 1: Average interproton distances [Å] measured from model helices.[a]

NOE type	11-helix	14/15-helix	18-helix
β-residue $H^{\beta}(i)$/β-residue $NH(i+2)$	3.3	3.9	4.6
β-residue $H^{\beta}(i)$/β-residue $H^{\alpha}(i+2)$	2.4	3.7	4.5
β-residue $H^{\alpha}(i)$/β-residue $NH(i+2)$	4.3	4.1	3.8
α-residue $H^{\alpha}(i)$/α-residue $NH(i+2)$	3.8	–	–
β-residue $H^{\beta}(i)$/α-residue $NH(i+3)$	3.1	2.3	4.3
β-residue $H^{\beta}(i)$/α-residue $H^{\alpha}(i+3)$	–	4.6	–
α-residue $H^{\alpha}(i)$/β-residue $NH(i+3)$	3.6	4.3	–
α-residue $H^{\alpha}(i)$/β-residue $H^{\alpha}(i+3)$	–	3.0	4.3
β-residue $H^{\beta}(i)$/β-residue $NH(i+4)$	–	3.0	3.4
β-residue $H^{\alpha}(i)$/β-residue $H^{\alpha}(i+4)$	–	–	4.8
β-residue $H^{\beta}(i)$/β-residue $H^{\alpha}(i+4)$	–	–	2.4
α-residue $H^{\alpha}(i)$/α-residue NH(i+4)	–	4.0	3.1
β-residue $H^{\beta}(i)$/α-residue $NH(i+5)$	–	–	3.7
α-residue $H^{\alpha}(i)$/β-residue $NH(i+5)$	–	–	3.7

[a] Measurements less than 5 Å were used for predicting expected NOEs. "–" indicates that all distances were greater than 5 Å and no NOEs would be expected.

 © 2004 Wiley-VCH Verlag GmbH & Co. KGaA, Weinheim

Table 2: Summary of NOEs involving nonsequentially adjacent residues for α/β-peptides **2** and **3** in CD_3OH.[a]

NOE type and residues	Oligomer **2**	Oligomer **3**	Structure
i_β $H^\beta \rightarrow i+2_\beta$ HN			
1→3	Yes*	?	
3→5	Yes	?	
5→7	Yes*	Yes	
7→9	Yes	Yes	
i_β $H^\beta \rightarrow i+2_\beta$ H^α			
1→3	Yes*	Yes*	
3→5	Yes	Yes	
5→7	Yes*	No	
i_β $H^\alpha \rightarrow i+2_\beta$ HN			
1→3	Yes	Yes*	
3→5	Yes	No	
5→7	Yes	No	
7→9	No	No	
i_α $H^\alpha \rightarrow i+2_\alpha$ HN			
0→2	Yes	No	
2→4	Yes	No	
4→6	No	No	
6→8	No	No	
i_β $H^\beta \rightarrow i+3_\alpha$ HN			
1→4	?	?	
3→6	Yes	Yes	
5→8	?	Yes	
i_α $H^\alpha \rightarrow i+3_\beta$ HN			
0→3	Yes	?	
2→5	Yes	?	
4→7	Yes	Yes	
6→9	Yes	Yes	
i_α $H^\alpha \rightarrow i+3_\beta$ H^α			
0→3	No	No	
2→5	Yes	No	
4→7	Yes	No	
i_β $H^\beta \rightarrow i+4_\beta$ HN			
1→5	No	?	
3→7	No	Yes	
5→9	No	?	
i_α $H^\alpha \rightarrow i+4_\alpha$ HN			
0→4	No	?	
2→6	No	?	
4→8	No	Yes	

[a] "Yes" indicates that an NOE was observed that had only one possible assignment. "Yes*" indicates that an NOE was observed that had two or more possible assignments, one of which was consistent with the indicated nonsequential NOE. Other assignments for this NOE were not consistent with other probable nonsequential NOEs. "No" indicates that no NOE was observed, but that the indicated NOE would have been observed if it had been present. "?" indicates that an NOE was observed, but that it could not be assigned because of overlap with either a sequential or intraresidue NOE, or that more than one probable nonsequential assignment for the NOE was possible.

 © 2004 Wiley-VCH Verlag GmbH & Co. KGaA, Weinheim

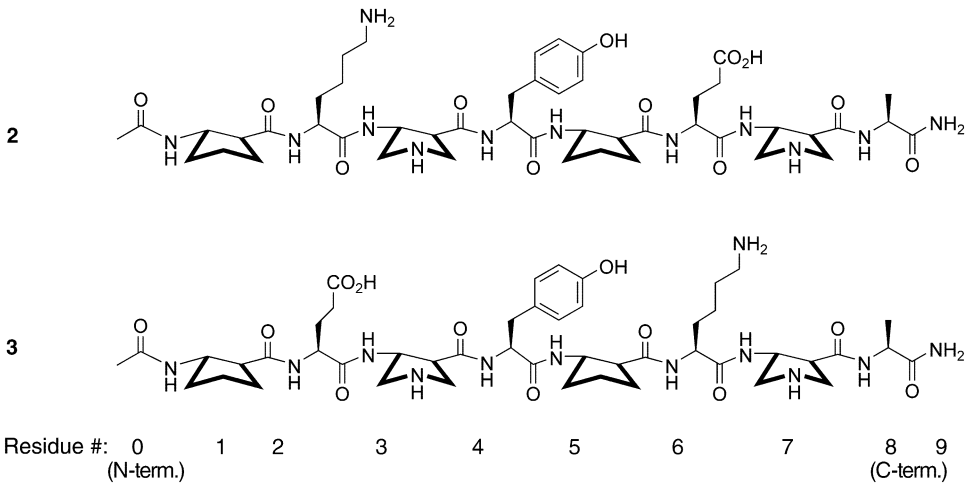


Figure 4. α/β-Peptides **2** and **3** shown with residue numbering used in Table 2.

(4.3 Å), but not with the 18-helix. All four of the possible NOEs of this type were observed for **2**.

Oligomer **3** displayed poorer ^{1}H NMR resonance dispersion than did isomer **2**, particularly in the N-terminal region, but it was nevertheless possible to identify ten unambiguous nonsequential NOEs (Table 2). These included two of the four possible α-residue $H^{\alpha}(i)$/β-residue NH($i+3$) NOEs (pattern #2 above), expected for the 11- and 14/15-helices but not the 18-helix. Also observed was a β-residue $H^{\beta}(i)$/β-residue NH($i+4$) NOE, which is consistent with the 14/15-helix (3.0 Å average interproton distance predicted), and the 18-helix (3.4 Å), but not with the 11-helix, and an α-residue $H^{\alpha}(i)$/α-residue NH($i+4$) NOE, which is consistent with the 14/15-helix (4.0 Å) and the 18-helix (3.1 Å), but not with the 11-helix.

The observed NOE data can be explained by proposing that α/β-peptides like **2** adopt both the 11-helix and the 14/15-helix, which interconvert rapidly and give rise to averaged NMR data.[12] Significant population of the 18-helix can be ruled out based on missing nonsequential NOEs. Specifically, modeling suggests that three types of nonsequential NOEs should be unique to the 18-helix among the secondary structures we considered: 1) β-residue $H^{\beta}(i)$/β-residue $H^{\alpha}(i+4)$ (2.4 Å average interproton distance predicted), 2) β-residue $H^{\beta}(i)$/α-residue NH($i+5$) (3.7 Å), and 3) α-residue $H^{\alpha}(i)$/β-residue NH($i+5$) (3.7 Å). None of these NOEs was observed for **2** or **3**, in which two of each type could have occurred, even though most of the NOEs could have been readily detected (no sequence overlap for 7 of the 12 diagnostic NOEs in **2** and **3**).

As a further probe of the folding preferences of α/β-peptides, we examined the analogue of **2** containing (*S*,*S*)-*trans*-2-aminocyclohexanecarboxylic acid (ACHC)[13] in place of ACPC, and the diastereomer containing (*S*,*S*)-ACHC and D-α-residues. Neither octamer displayed any nonsequential NOEs in methanol; thus, ACHC does not support α/β-peptide helix formation, in contrast to ACPC. This stark difference between these two types of β-amino acids, with five- and six-membered rings, may arise because homogeneous ACHC backbones favor a helix containing C=O···H–N hydrogen bonds with C→N directionality,[14] which is opposite to the hydrogen-bond directionality in the α-helix, the β-peptide 12-helix, and the α/β-peptide helices detected in this work.

The data reported here demonstrate a strong propensity for helical secondary structure among short oligomers with heterogeneous backbones of alternating proteinogenic α- and cyclic β-amino acid residues. This folding is noteworthy since peptides of similar length composed exclusively of proteinogenic α-amino acids do not adopt helical conformations in methanol.[15] The apparent rapid interconversion between two alternative helical conformations is particularly interesting because of parallels with behavior that is well-documented among peptides containing exclusively α-amino acid residues.[5] We are currently trying to identify residue and sequence design strategies that will favor the 11-helix relative to the 14/15-helix and vice versa; some success has been achieved with analogous efforts to disentangle the α- and 3_{10}-helices among α-peptides.[5] At a general level, our findings suggest that heterogeneous oligomers containing two or more types of amino acid residues will be fruitful sources of new foldamers.

Received: June 12, 2003 [Z52125]

Keywords: α-amino acids · β-amino acids · foldamers · helical structures · NMR spectroscopy

[1] a) S. H. Gellman, *Acc. Chem. Res.* **1998**, *31*, 173; b) D. J. Hill, M. J. Mio, R. B. Prince, T. S. Hughes, J. S. Moore, *Chem. Rev.* **2001**, *101*, 3893.

[2] Examples: a) M. Werder, H. Hauser, S. Abele, D. Seebach, *Helv. Chim. Acta* **1999**, *82*, 1774; b) Y. Hamuro, J. P. Schneider, W. F. DeGrado, *J. Am. Chem. Soc.* **1999**, *121*, 12200; c) E. A. Porter, X. Wang, H.-S. Lee, B. Weisblum, S. H. Gellman, *Nature* **2000**, *404*, 565; d) D. Liu, W. F. DeGrado, *J. Am. Chem. Soc.* **2001**, *123*, 7553; e) E. A. Porter, B. Weisblum, S. H. Gellman, *J. Am. Chem. Soc.* **2002**, *124*, 7324; f) K. Gademann, T. Kimmerlin, D. Hoyer, D. Seebach, *J. Med. Chem.* **2001**, *44*, 2461; g) U. Arnold, M. P. Hinderaker, B. L. Nilsson, B. R. Huck, S. H. Gellman, R. T. Raines, *J. Am. Chem. Soc.* **2002**, *124*, 8522; h) T. L. Raguse, E. A.

 © 2004 Wiley-VCH Verlag GmbH & Co. KGaA, Weinheim

Porter, B. Weisblum, S. H. Gellman, *J. Am. Chem. Soc.* **2002**, *124*, 12774.

[3] Selected examples: a) M. Hagihara, N. J. Anthony, T. J. Stout, J. Clardy, S. L. Schreiber, *J. Am. Chem. Soc.* **1992**, *114*, 6568; b) R. S. Lokey, B. L. Iverson, *Nature* **1995**, *375*, 303; c) Y. Hamuro, S. J. Geib, A. D. Hamilton, *J. Am. Chem. Soc.* **1996**, *118*, 7529; d) B. R. Huck, J. D. Fisk, S. H. Gellman, *Org. Lett.* **2000**, *2*, 2607; e) B. Gong, H. Q. Zeng, J. Zhu, L. H. Yua, Y. H. Han, S. Z. Cheng, M. Furukawa, R. D. Parra, A. Y. Kovalevsky, J. L. Mills, E. Skrzypczak-Jankun, S. Martinovic, R. D. Smith, C. Zheng, T. Szyperski, X. C. Zeng, *Proc. Natl. Acad. Sci. USA* **2002**, *99*, 11583.

[4] α/β-Peptides designed to mimic neuropeptide Y have recently been shown to bind selectively to the Y_1 receptor:N. Koglin, C. Zorn, R. Beumer, C. Cabrele, C. Bubert, N. Sewald, O. Reiser, A. G. Beck-Sickinger, *Angew. Chem.* **2003**, *115*, 212; *Angew. Chem. Int. Ed.* **2003**, *42*, 202.

[5] A. K. Bolin, G. L. Millhauser, *Acc. Chem. Res.* **1999**, *32*, 1027, and references therein.

[6] COSY: W. P Aue, E. Bartholdi, R. R. Ernst, *J. Chem. Phys.* **1976**, *64*, 2229; TOCSY: A. Bax, D. G. Davis, *J. Magn. Reson.* **1985**, *65*, 355; ROESY: A. A. Bothner-By, R. L. Stephens, J. Lee, C. D. Warren, R. W. Jeanloz, *J. Am. Chem. Soc.* **1984**, *106*, 811.

[7] P. L. LePlae, N. Umezawa, H.-S. Lee, S. H. Gellman, *J. Org. Chem.* **2001**, *66*, 5629.

[8] Ambiguous NOEs were assigned by using the program DYANA (P. Guntert, C. Mumenthaler, K. Wuthrich, *J. Mol. Biol.* **1997**, *273*, 283) in an iterative process. Each ambiguous NOE had one assignment that was consistent with all other nonsequential NOEs.

[9] a) D. H. Appella, L. A. Christianson, D. A. Klein, D. R. Powell, X. Huang, J. J. Barchi, S. H. Gellman, *Nature* **1997**, *387*, 381; b) D. H. Appella, L. A. Christianson, D. A. Klein, M. R. Richards, D. R. Powell, S. H. Gellman, *J. Am. Chem. Soc.* **1999**, *121*, 7574.

[10] Alternative helices were generated for an ACPC-Ala dodecamer using SYBYL (Tripos, St. Louis, MO) by imposing distance constraints for hydrogen bonds between appropriate C=O/H–N pairs. These structures were minimized using a continuum dielectric constant of 32.6, to simulate methanol, with the MMFF94s force field (T. A. Halgren, *J. Comput. Chem.* **1999**, *20*, 720.). Each of the resulting helical structures was taken to represent a possible local minimum in conformational energy for the dodecamer.

[11] It seemed possible that this design might bias each oligomer into either an 11- or 14/15-helical conformation based upon charge–charge interactions between side chains, allowing us to use rational principles to design α/β-oligomers with specific conformational preferences. A potential salt bridge between APC3 and Glu6 in **2** may preferentially stabilize an 11-helical conformation (helical wheel diagrams are included in the Supporting Information). In contrast, an interaction between APC3 and Lys6 in **3** may destabilize the 11-helical conformation, possibly favoring the 14/15-helical conformation. Complete evaluation of this hypothesis was not possible because of the severe resonance overlap observed for **2** and **3** in aqueous solution. In methanol, we do not expect the Glu side chain to be significantly deprotonated, minimizing the chance that salt-bridge formation would influence conformational preferences. Oligomers **2** and **3** show slightly different NOE patterns, suggesting that one helical conformation may be slightly more populated in one oligomer than in the other. Further investigations are under way to explore these possibilities.

[12] A helical conformation containing three-center backbone hydrogen bonds, simultaneous 11-membered ring and 14/15-membered ring hydrogen-bonding patterns, could also explain the nonsequential NOEs observed for the α/β-peptides described here. NOE-restrained analysis with the program DYANA (P. Guntert, C. Mumenthaler, K. Wuthrich, *J. Mol. Biol.* **1997**, *273*, 283) suggests that a helix containing three-center hydrogen bonds could explain the NMR data. The DYANA-generated structures resemble this "hybrid" helix in shape; however, hydrogen bonds are not observed in these structures. As pointed out in the text, a rapidly interconverting mixture of 11- and 14/15-helices can also explain the NOE data. We do not favor the helix with three-center hydrogen bonds because there is little precedent for analogous hydrogen bonds in α-peptide helices and none for β-peptide helices. Three-center hydrogen bonds in which an amide proton interacts simultaneously with two acceptor groups, such as oxygen atoms, are rare in proteins: E. N. Baker, R. E. Hubbard, *Prog. Biophys. Mol. Biol.* **1984**, *44*, 97. For crystallographic detection of a single three-center hydrogen bond at the transition point between α- and 3_{10}-helical domains in a synthetic α-peptide, see: V. Pavone, E. Benedetti, B. Di Blasio, C. Pedone, A. Santini, A. Bavoso, C. Toniolo, M. Crisma, L. Sartore, *J. Biomol. Struct. Dyn.* **1990**, *7*, 1321. It has been shown in one system that a three-center C=O···H···O=C interaction is higher in energy than an alternative two-center C=O···H hydrogen bond: J. Yang, S. H. Gellman, *J. Am. Chem. Soc.* **1998**, *120*, 9090.

[13] a) A. Berkessel, K. Glaubitz, J. Lex, *Eur. J. Org. Chem.* **2002**, *17*, 2948; b) M. Schinnerl, J. K. Murray, J. M. Langenhan, S. H. Gellman, *Eur. J. Org. Chem.* **2003**, *4*, 721.

[14] a) D. H. Appella, L. A. Christianson, I. L. Karle, D. R. Powell, S. H. Gellman, *J. Am. Chem. Soc.* **1996**, *118*, 13071; b) D. H. Appella, L. A. Christianson, I. L. Karle, D. R. Powell, S. H. Gellman, *J. Am. Chem. Soc.* **1999**, *121*, 6206.

[15] D. Seebach, M. Overhand, F. N. M. Kühnle, B. Martinoni, L. Oberer, U. Hommel, H. Widmer, *Helv. Chim. Acta* **1996**, *79*, 913.

 © 2004 Wiley-VCH Verlag GmbH & Co. KGaA, Weinheim

Peptide Design II

Surprisingly Stable Helical Conformations in α/β-Peptides by Incorporation of *cis*-β-Aminocyclopropane Carboxylic Acids**

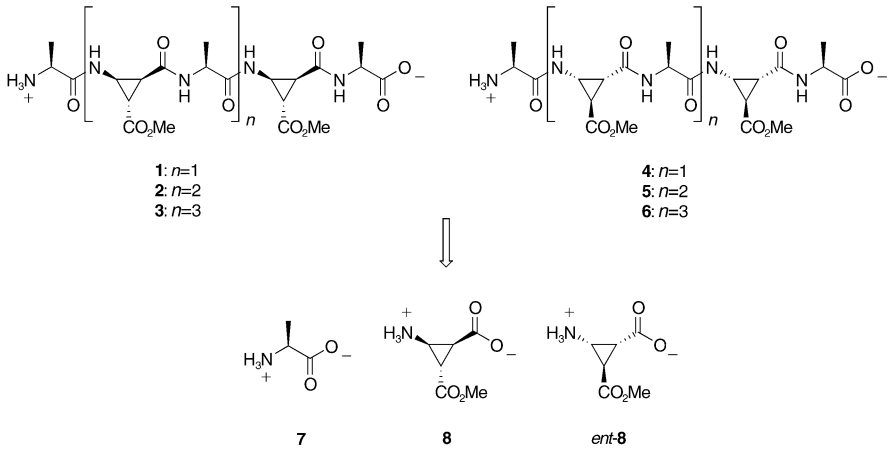
Silvia De Pol, Chiara Zorn, Christian D. Klein, Oliver Zerbe, and Oliver Reiser**

The development of structurally defined peptide units is an important prerequisite for protein design. The search for oligopeptides having stable conformations in solution, so-called foldamers,[1] is therefore an active area of bioorganic chemistry. Most foldamers are homooligopeptides, but some examples of foldamers containing two or more different residues have been also reported.[2] Peptides constructed from the naturally occurring α-amino acids must typically have a length of at least 12 units in order to adopt a stable conformation in solution. In contrast, oligopeptides composed of β-amino acids assume surprisingly stable secondary structures even in short oligomers of five to eight units.[3] The stabilization of turn structures in cyclic peptides composed of mainly α-amino acids by incorporation of β-amino acids has also been recognized.[4]

We could recently show that alternating α-amino acids with *cis*-β-aminocyclopropanecarboxylic acids (*cis*-β-ACCs)[5] resulted in surprisingly short acyclic α/β-peptides that bind selectively and with high affinity to the Y_1 receptor of neuropeptide Y.[6] In order to gain insight on whether α/β-peptides form especially stable secondary structures, we investigated oligopeptides **1**–**6**, which consist of (L)-alanine **7** and either enantiomer of *cis*-β-aminocyclopropanecarboxylic acid, that is, **8** and *ent*-**8** (Scheme 1).[7] Here, we report that oligomers with this motif as short as pentapeptides adopt defined conformations even in polar solvents like methanol. Moreover, extension of this sequence to peptides composed of seven or nine residues results in helical structures.

While structure determination of smaller globular proteins is well-established, particular care must be taken with smaller peptides. In this class of molecules folded conformations are possibly in (fast) exchange with extended forms, or differently folded forms may rapidly interconvert. We have therefore tried to monitor a number of parameters in order to determine whether a single, well-folded conformation predominates. The following approach was used in order to determine predominant structures of the peptides **1**–**6** in methanol and to quantify to what extent these peptides are folded. Structures were calculated according to conventional methodology using NOE-derived distance restraints as the sole source of (upper) distance limits. We assume that a peptide adopts a well-folded form predominantly when the following three criteria are fulfilled: 1. No consistent violations of the distant restraints are found. 2. A uniform calibration (NOE volume integral–distance conversion) can be used, and known distances adopt reasonable values. 3. All distances shorter than 3.5 Å that occur in more than half of the low-energy DYANA structures (DYANA = NMR-restrained MD calculations in dihedral-angle space) give rise to crosspeaks in the NOESY spectrum. We found the third criterion to be particular useful to determine whether a single conformer predominates. If NOE-derived distance restraints are due to two different conformers, the calculated structure representing only a single conformer usually displays short distances for which no NOEs can be found in the spectra.

To further verify that the proposed conformers are realistic we have conducted molecular-dynamics (MD) simulations. The NMR structures were subjected to extensive temperature cycling in order to extensively screen conformational space and to perform statistical analysis on the resulting



Scheme 1. Structures of oligopeptides **1**–**6**, which consist of alternating units of (*S*)-alanine (**7**) and **8** or *ent*-**8**.

[*] Dipl.-Chem. S. De Pol, Dr. C. Zorn, Prof. Dr. O. Reiser
Institut für Organische Chemie
Universität Regensburg
Universitätsstrasse 31, 93053 Regensburg (Germany)
Fax: (+49) 941-943-4121
E-mail: oliver.reiser@chemie.uni-regensburg.de
Dr. O. Zerbe
Institut für Organische Chemie
Universität Zürich (Schweiz)
Fax: (+41) 1-635-6833
E-mail: oliver.zerbe@oci.unizh.ch
Dr. C. D. Klein
Pharmazeutische und Medizinische Chemie
Universität des Saarlandes, Saarbrücken (Germany)

[**] This work was supported by the Deutsche Forschungsgemeinschaft (RE-948-4/2 and GRK 760), the International Quality Network Medicinal Chemistry (DAAD/BMBF), and the Fonds der Chemischen Industrie.

Supporting information for this article is available on the WWW under http://www.angewandte.org or from the author.

 DOI: 10.1002/anie.200352267 © 2004 Wiley-VCH Verlag GmbH & Co. KGaA, Weinheim

low-energy structures. For the structures that fulfill the above-described criteria, well-folded conformers resulted that were in agreement with the NMR data.

All the peptides investigated display helical conformations, as is apparent from the presence of NOEs between sequential amide protons. However, they largely differ in the extent to which they are *uniquely* folded. To summarize, peptides **1**–**3**, which contain β-ACC amino acids of type **8**, are less subject to conformational averaging, i.e., they are likely not to exist as equilibrium mixtures of conformers. Amongst all investigated peptides, the heptapeptide **2** and nonapeptide **3** are the structurally best defined. A representative conformer of **2** from the ensemble of low-energy NMR structures computed from the NOESY data with the program DYANA is displayed in Figure 1.

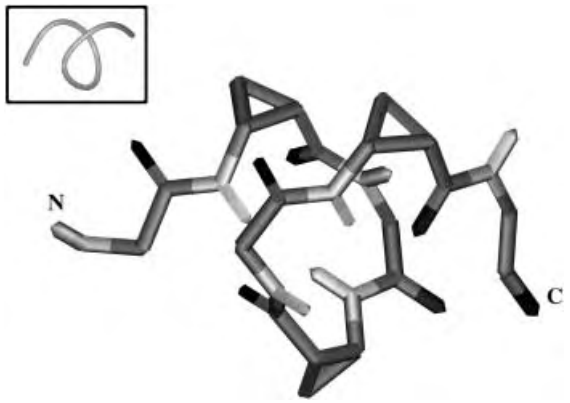


Figure 1. One low-energy conformer of **2**. The side-chain atoms and all but the amide hydrogen atoms have been omitted for clarity. The small insert schematically outlines the backbone conformation.

The backbone of **2** forms a left-handed 3_{13}-helix, and hydrogen bonds occur between the amide proton of the β-ACC in position 2 and the carbonyl oxygen of the β-ACC in position 4, as well as between the amide proton and the carbonyl oxygen of the β-ACC in position 6,[8] in most of the low-energy structures. The structure is surprisingly well-defined for a noncyclic heptapeptide without disulfide bonds or other constraints. The helical fold[9] is supported by a larger number of medium-range NOEs, in particular by a number of $i,i+3$ contacts (see Table A in the Supporting Information). Moreover, in **2** the $^3J_{H^NH^\alpha}$ scalar coupling constants are less than 4.2 Hz. In comparison, values of 7.6–8.1 Hz are measured for analogous Xxx-ACC dipeptides (measured in $CDCl_3$). All NOESY crosspeaks due to interresidual distances smaller than 3.5 Å in the 20 low-energy DYANA structures of **2** were found in the NOESY spectrum. In the spectra no $i,i+1$-H^α,H^α peaks were found, which indicates the absence of *cis* Xxx-ACC bonds. This is in contrast to the spectra from other peptides in this study. In order to detect possible aggregation effects and to exclude intermolecular NOEs from the analysis, the sample was diluted to approximately 0.8 mM. Chemical shifts remained constant during dilution, and the same NOE crosspeaks were observed in the NOESY spectrum at the lower concentration. Moreover, we would like to emphasize that all the proton signals for peptides **1**–**6** were sufficiently separated so that all the NOESY crosspeaks could be assigned unambiguously.

In contrast, the conformation of heptapeptide **5**, which differs from **2** by having *ent*-**8** instead of **8** in its sequence, is less well-defined. Although a number of medium-range NOE correlations can be found in the spectra (see Table 1 and the Supporting Information) and structures of reasonable energy may be computed from the NMR data, a large number of crosspeaks corresponding to distances between protons from nonadjacent residues that are less than 3.5 Å apart are actually missing in the NMR spectra. This indicates that the NOEs are not due to a single, predominant conformation but arise from a set of conformers, which rapidly interconvert on the NMR timescale. This view is supported by the magnitude of the vicinal H^N,H^α coupling constants, which, for all residues except for the β-ACC in position 2, adopts values in the range of 6–7 Hz, indicative of rotationally averaged ϕ backbone angles. Considering that most medium-range contacts are found in the first half of the sequence and that rather strong NOEs occur between sequential amide protons, a likely scenario is that predominantly helical portions interconvert locally with extended conformations such that the full helix does not persist. This view is related to the observation that medium-range NOEs such as $\alpha(i)$,$\beta(i+3)$ correlations are required to distinguish stably folded α-helixes from nascent helices.[9]

Table 1: Vicinal coupling constants for H^N, H^α in CD_3OH.

Residue	Peptide	^3J [Hz]	Peptide	^3J [Hz]
2	**1**	3.4	**4**	4.4
3		6.4		6.3
4		5.5		7.0
5		6.9		7.5
2	**2**	3.4	**5**	4.6
3		6.4		6.2
4		3.4		6.3
5		6.0		6.5
6		4.2		7.2
7		7.2		8.0
2	**3**	3.9	**6**	4.5
3		6.0		5.3
4		3.4		6.8
5		5.9		5.8
6		3.5		6.9
7		6.7		6.3
8		5.6		7.3
9		6.8		7.4

The trend seen in the different conformational preferences of the heptapeptides **2** and **5** is also found for the pentapeptides **1** and **4** and for the nonapeptides **3** and **6**. Again, the structure calculation of **1** converges to a helically folded peptide, and many more medium-range NOEs are detected for **1** than for **4**. Some characteristic correlations observed for **2** are also seen for **1**, for example, the NOE between the α-protons of the alanine residues in positions 1

 © 2004 Wiley-VCH Verlag GmbH & Co. KGaA, Weinheim

and 5. In addition, the $^3J_{H^N,H^\alpha}$ coupling constants are low for all ACC residues in **1**, but not in **4**. Moreover, **4** contains a noticeable number of *cis* Ala-ACC peptide bonds, which is reflected in the occurrence of H^α,H^α NOEs for adjacent residues. As a result, a larger number of consistent distance violations remain in the structure calculation. This is consistent with the view that **4** exists as an equilibrium of both folded and extended conformations.

As a further check we have compared spectra of **1** and **4** measured in aqueous solution to those measured in methanol. In water, the peptides are largely unstructured, as seen from the absence of correlations between adjacent amide protons. Whereas little differences in the chemical shifts for amide and α-protons were found for **4**, differences as large as ± 0.5 ppm were observed for **3**, indicating that for the latter the difference in the structures adopted in the two solvent systems is more substantial. The helical fold displayed by **3** is similar to that seen in **2**, and no indications for significant conformational averaging in **3** are found. Low scalar couplings and a high number of medium-range NOEs indicate that this peptide is well-structured. The nonapeptide **6**, which is isomeric to **3**, is again less well-defined, as is evident from higher values of the scalar couplings and a lower number of medium-range NOEs.

The NMR technique delivers static pictures in which NMR-related parameters such as distances and dihedral angles are time-averaged during the mixing time (NOE) or acquisition times (couplings). In order to gain insight into possible conformational transitions, an MD simulation over 2 ns was performed with the program AMBER.[10] We employed a simulation protocol with repeated cycles of heating and cooling. The coordinates of the low-energy conformers were used for further analysis. The coordinates were superimposed and sorted into families of conformations with positions that deviated from the corresponding mean by less than 1 Å in a cluster analysis. The results from the MD trajectories calculated for **1** and **4** were distinctly different: The calculation for **1** revealed two highly populated families (Figure 2A), one of which closely resembles the NMR-derived ensemble, whereas the other family was similarly helical, but with right-handed helices instead.

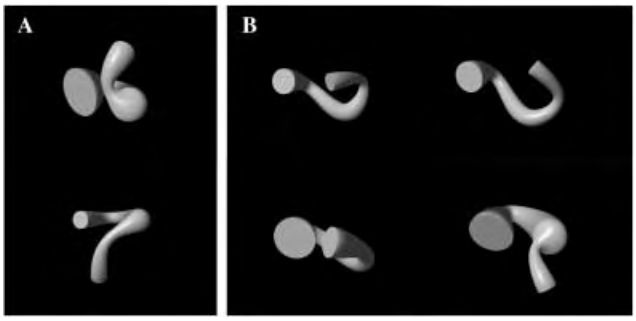


Figure 2. The conformational space sampled by backbone atoms of conformers of **1** (A) and **4** (B) is represented as a spline function through the C^α-positions. This results from the 2-ns MD trajectory, in which electrostatics were calculated using a distance-dependent dielectric constant. The most highly populated clusters are presented (see text).

In contrast, the MD trajectory of **4** revealed four families of conformers (see Figure 2B) that differed largely, some of them adopting a more extended, nonhelical conformation. Equilibria between helical and extended conformations lead to the simultaneous observation of strong NOEs for αH^N and H^N-H^N of adjacent residues, as was the case for **4**. The MD simulations therefore support the view that mixed α/β-peptides incorporating **8** give rise to a better defined structure than their counterparts derived from the (*ent*)-**8** units.

Our structural data indicate that peptides with alternating α- and β-amino acids display conformational preferences unknown in shorter noncyclic peptides containing only α-amino acids, thus further extending the range of foldamers.[11] Like the peptides solely containing β-peptides, theses peptides prefer helical conformations. The relative *cis* stereochemistry of the backbone strands at the cyclopropane moiety obviously leads to steric interactions, and we speculate that the extent of these interactions is primarily governed by the influence of the side chains of the adjacent α-amino acids. From the molecules investigated the picture emerges that alternating peptides composed of (L)-Ala and β-ACC **8** adopt helical backbone conformations, while similar peptides with β-ACC (*ent*)-**8** lead to equilibrium mixtures of conformers.

Received: July 1, 2003 [Z52267]

Keywords: α/β-peptides · β-amino acids · foldamers · helical structures · NMR spectroscopy

[1] a) D. J. Hill, M. J. Mio, R. B. Prince, T. S. Hughes, J. S. Moore, *Chem. Rev.* **2001**, *101*, 3893; b) S. H. Gellman, *Acc. Chem. Res.* **1998**, *31*, 173; c) D. Seebach, J. L. Matthews, *Chem. Commun.* **1997**, 2015.

[2] Selected examples: a) B. Gong, H. Q. Zeng, J. Zhu, L. H. Yua, Y. H. Han, S. Z. Cheng, M. Furukawa, R. D. Parra, A. Y. Kovalevsky, J. L. Mills, E. Skrzypczak-Jankun, S. Martinovic, R. D. Smith, C. Zheng, T. Szyperski, X. C. Zeng, *Proc. Natl. Acad. Sci. USA* **2002**, *99*, 11583; b) B. R. Huck, J. D. Fisk, S. H. Gellman, *Org. Lett.* **2000**, *2*, 2607; c) Y. Hamuro, S. J. Geib, A. D. Hamilton, *J. Am. Chem. Soc.* **1996**, *118*, 7529; d) R. S. Lokey, B. L. Iverson, *Nature* **1995**, *375*, 303; e) M. Hagihara, N. J. Anthony, T. J. Stout, J. Clardy, S. L. Schreiber, *J. Am. Chem. Soc.* **1992**, *104*, 6568.

[3] Recent examples: a) E. A. Porter, B. Weisblum, S. H. Gellman, *J. Am. Chem. Soc.* **2002**, *124*, 7324; b) U. Arnold, M. P. Hinderaker, B. L. Nilsson, B. R. Huck, S. H. Gellman, R. T. Raines, *J. Am. Chem. Soc.* **2002**, *124*, 8522; c) T. L. Raguse, E. A. Porter, B. Weisblum, S. H. Gellman, *J. Am. Chem. Soc.* **2002**, *124*, 12774; d) D. Liu, W. F. DeGrado, *J. Am. Chem. Soc.* **2001**, *123*, 7553; e) K. Gademann, T. Kimmerlin, D. Hoyer, D. Seebach, *J. Med. Chem.* **2001**, *44*, 2461; f) E. A. Porter, X. Wang, H.-S. Lee, B. Weisblum, S. H. Gellman, *Nature* **2000**, *404*, 565; g) M. Werder, H. Hausre, S. Abele, D. Seebach, *Helv. Chim. Acta* **1999**, *82*, 1774; h) Y. Hamuro, J. P. Schneider, W. F. DeGrado, *J. Am. Chem. Soc.* **1999**, *121*, 12200.

[4] a) V. Pavone, A. Lombardi, X. Yang, C. Pedone, B. D. Blasio, *Biopolymers* **1990**, *30*, 189; b) V. Pavone, A. Lombardi, G. D'Auria, M. Saviano, F. Nastri, L. Paolillo, B. D. Blasio, C. Pedone, *Biopolymers* **1992**, *32*, 173; c) B. D. Blasio, A. Lombardi, X. Yang, C. Pedone, V. Pavone, *Biopolymers* **1991**, *31*, 1181; d) V. Pavone, A. Lombardi, C. A. Maggi, L. Quartara, C. Pedone, *J. Pept. Sci.* **1995**, *1*, 236; e) A. Lombardi, M. Saviano, F.

 © 2004 Wiley-VCH Verlag GmbH & Co. KGaA, Weinheim

Nastri, O. Maglio, M. Mazzeo, C. Isernia, L. Paolillo, V. Pavone, *Biopolymers* **1996**, *38*, 693.
[5] Review: F. Gnad, O. Reiser, *Chem. Rev.* **2003**, *103*, 1603 – 1624.
[6] N. Koglin, C. Zorn, R. Beumer, C. Cabrele, C. Bubert, N. Sewald, O. Reiser, A. G. Beck-Sickinger, *Angew. Chem.* **2003**, *115*, 212; *Angew. Chem. Int. Ed.* **2003**, *42*, 202.
[7] Synthesis and special peptide coupling techniques for **8** and *ent*-**8** have been reported: a) C. Zorn, F. Gnad, S. Salmen, T. Herpin, O. Reiser, *Tetrahedron Lett.* **2001**, *42*, 7049; b) R. Beumer, C. Bubert, C. Cabrele, O. Vielhauer, M. Pietzsch, O. Reiser, *J. Org. Chem.* **2000**, *65*, 8960.
[8] The IR spectra of simple amides derived from **7** ($CONEt_2$ instead of CO_2Me, *N*-Ac instead of *N*-Boc) in solution indeed indicate the presence of complete intramolecular hydrogen bonding between CO and NH in *cis* position. In contrast, the analogous β-alanine derivative does not show any hydrogen bonding, cf. G. P. Dado, S. H. Gellman, *J. Am. Chem. Soc.* **1994**, *116*, 1054.
[9] Dyson and Wright have established criteria by which partially folded shorter peptides can be identified: H. J. Dyson, M. Rance, R. A. Houghton, R. A. Lerner, P. E. Wright, *J. Mol. Biol.* **1988**, *201*, 161; H. J. Dyson, P. E. Wright, *Annu. Rev. Biophys. Biophys. Chem.* **1991**, *20*, 519. NOEs between sequential amide protons indicate significant ϕ,ψ population in the helical part of the Ramachandran plot but medium-range (mainly $i,i+2$ and $i,i+3$) connectivities are required to unambiguously prove the presence of a helix and thereby distinguish it from interconverting, turnlike structures. Small temperature dependencies of the amide proton chemical shift have also been used as an indication that the amide proton is involved in a hydrogen bond, but it has been argued recently that low-temperature coefficients indicate folding upon temperature lowering instead: H. A. Andersen, J. W. Neidigh, S. M. Harris, G. M. Lee, Z. Liu, H. Tong, *J. Am. Chem. Soc.* **1997**, *119*, 8547.
[10] D. A. Case, D. A. Pearlman, J. W. Caldwell, T. E. Cheatham III, J. Wang, W. S. Ross, C. Simmerling, T. Darden, K. M. Merz, R. V. Stanton, A. Cheng, J. J. Vincent, M. Crowley, V. Tsui, H. Gohlke, R. Radmer, Y. Duan, J. Pitera, I. Massova, G. L. Seibel, U. C. Singh, P. Weiner, P. A. Kollman, *AMBER 7*, University of California, San Francisco, **2002**.
[11] See also: A. Hayen, M. A. Schmitt, F. N. Ngassa, K. A. Thomasson, S. H. Gellman, *Angew. Chem.* **2004**, *116*, 511; *Angew. Chem. Int. Ed.* **2004**, *43*, 505.

 © 2004 Wiley-VCH Verlag GmbH & Co. KGaA, Weinheim

Carbon Allylation

Titanium(IV)-Catalyzed Dynamic Kinetic Asymmetric Transformation of Alcohols, Silyl Ethers, and Acetals under Carbon Allylation**

Manfred Braun and Wolfgang Kotter*

Dedicated to Professor Reinhard W. Hoffmann on the occasion of his 70th birthday

Reactions that allow the complete conversion of an achiral starting material into an enantiomerically pure product are in accord with the principle of "chiral economy".[1] Comparable efficiency and utility is provided by reactions in which both enantiomers of a racemic substrate are converted into a single, enantiomerically pure product. Such processes, which are particularly advantageous when they are combined with the formation of a carbon–carbon bond, rely on either kinetically[2] or thermodynamically[3] controlled dynamic resolutions. The large majority of the hitherto known dynamic resolutions are mediated by enzymes,[2c,e] and their scope was enhanced in the 1990s by combining enzymatic conversions with transition-metal catalysis.[2e,4] The relatively rare non-enzymatic methods rely partly on stoichiometric amounts of chiral auxiliaries[5] or co-solvents[3,6] and partly on transition-metal catalysts.[7]

Only very few dynamic resolutions have been disclosed that lead to concomitant carbon–carbon bond formation at a stereogenic center and do not require an auxiliary reagent in stoichiometric amounts.[7e] A prerequisite for both enantiomers of a racemic starting material to be converted into an enantiomerically pure product is an in situ racemization. The term "dynamic kinetic asymmetric transformation" (DYKAT)[2d,7g] has been proposed for such cases in which the racemization occurs as a result of the configurational lability of organometallic intermediates, which subsequently react to give the final products. Herein we describe a novel, titanium(IV)-catalyzed substitution of a carbon–oxygen bond by a carbon–carbon bond, a method that relies on a dynamic kinetic conversion and leads to products that result from a carbon allylation in a highly enantioselective manner.

The carbon allylation of tertiary alcohols, a transformation that opens a simple possibility for the formation of quaternary carbon centers,[8] was observed in the course of the geminal dialkylation of ketones;[9] it takes place upon treatment with allylic silanes and is mediated by stoichiometric amounts of strong Lewis acids.[10] Accordingly, treatment of indanol **1a**[11] with allyltrimethylsilane in the presence of

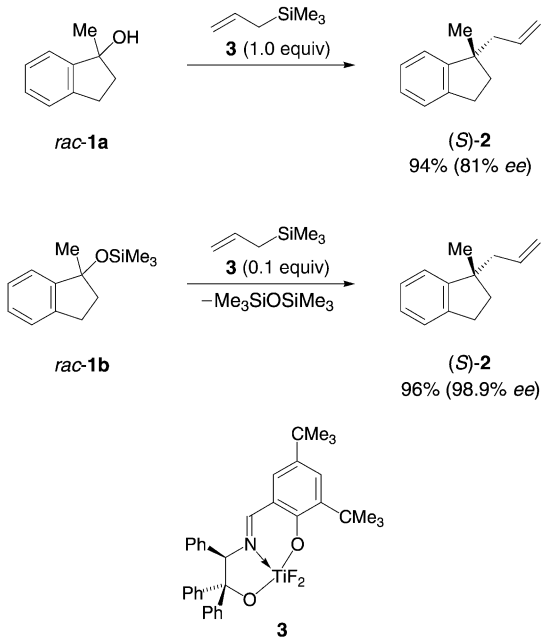
[*] Prof. Dr. M. Braun, Dipl.-Chem. W. Kotter
Institut für Organische und Makromolekulare Chemie
Heinrich-Heine-Universität Düsseldorf
Universitätsstrasse 1, 40225 Düsseldorf (Germany)
Fax: (+49) 211-81-15079
E-mail: braunm@uni-duesseldorf.de

[**] This work was supported by the Deutsche Forschungsgemeinschaft and the Fonds der Chemischen Industrie.

 © 2004 Wiley-VCH Verlag GmbH & Co. KGaA, Weinheim DOI: 10.1002/anie.200352128

titanium tetrafluoride results in the carbon-allylation product *rac*-**2**, which features a quaternary carbon center (Scheme 1). As a stereoselective variant of the carbon allylation of tertiary alcohols was unknown, we first studied whether racemic alcohols such as **1a** can be converted stereoselectively into nonracemic allylation products when the reaction is mediated by a chiral Lewis acid. The difluorotitanium complex **3**,[12] accessible from (*R*)-2-amino-1,1,2-triphenylethanol, seemed to be a suitable chiral reagent with sufficient Lewis acidity (Scheme 1).

First, the racemic alcohol *rac*-**1a** was allowed to react with allyltrimethylsilane in the presence of a stoichiometric amount of the titanium complex **3** (Scheme 1). The alkene

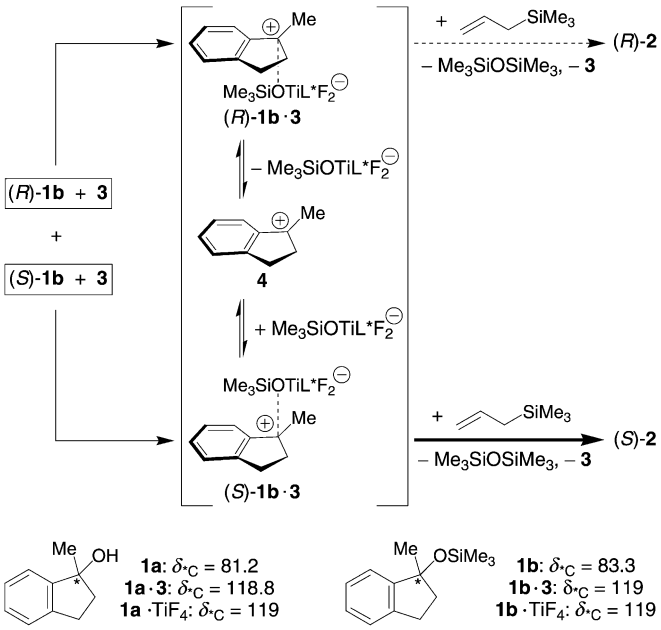


Scheme 1. Conversion of racemic **1a** or **1b** into (*S*)-alkene **2**.

(*S*)-**2** was thus obtained with 81% *ee*. The fact that its chemical yield amounted to 94% clearly shows that both enantiomers of the starting material had been converted. Therefore, the reaction cannot be a simple kinetic resolution. Presumably, owing to the protic substrate **1a**, the Lewis acid **3** is consumed in the course of the reaction. Thus, stoichiometric amounts of the titanium complex are necessary—clearly an unfavorable situation with respect to the "chiral economy" of the reaction. In the search for a solution to this problem, the hydroxy group in the substrate *rac*-**1a** was replaced by a different leaving group.

When the silyl ether *rac*-**1b**, readily available by protection of *rac*-**1a** according to standard procedures,[13] was submitted to a reaction with allyltrimethylsilane, it turned out that just 0.1 equivalents of the titanium compound **3** was sufficient to bring about a 96% yield of (*S*)-**2**. Furthermore, the enantiomeric excess was enhanced to 98.9% *ee*, a clear improvement over the reaction with **1a**. In this catalytic variant of the reaction, the titanium complex **3** is evidently not blocked by the silyloxy leaving group. Instead, the latter is found in the $Me_3SiOSiMe_3$ by-product, whose formation was proven by gas chromatography by comparison with an authentic sample.

The essentially complete conversion of the racemic substrate *rac*-**1b** into the allylation product (*S*)-**2** with high enantiomeric excess is rationalized as a dynamic kinetic asymmetric transformation (Scheme 2): It is assumed that,



Scheme 2. Dynamic kinetic asymmetric carbon allylation of racemic **1b** into (*S*)-**2**, mediated by the titanium(IV) complex **3**. ^{13}C NMR chemical shift values for the carbinyl carbon atoms of **1a** and **1b** as well as of **1a** und **1b** in the presence of equimolar amounts of **3** and TiF_4 (solvent: CD_3CN).

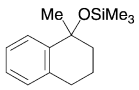
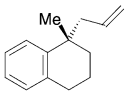
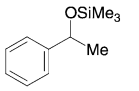
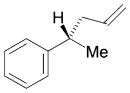
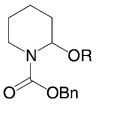
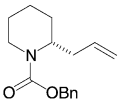
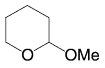
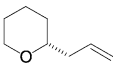
first, the chiral Lewis acid **3** and both enantiomers of the silyl ether **1b** form two diastereomeric contact ion pairs, (*R*)-**1b**·**3** and (*S*)-**1b**·**3**. They rapidly equilibrate via the planar, achiral carbenium ion **4**. In the subsequent reaction with allyltrimethylsilane, one of the ion pairs, (*S*)-**1b**·**3**, is postulated to react distinctly faster than its diastereomer (*R*)-**1b**·**3**. Presumably, the allyl residue attacks the indanyl cation from the face that is not occupied by the titanium.[14]

The ^{13}C NMR spectra of 1:1 mixtures formed from the substrates **1a** or **1b** and the titanium complex **3** in CD_3CN give an indication of a significant partial positive charge at the carbinyl carbon atom—clearly as a result of a strongly polarized carbon–oxygen bond. Both the alcohol **1a** and the silyl ether **1b** display substantial downfield shifts of the signals for the carbinyl carbon atom. As shown in Scheme 2, comparable downfield shifts also result when the substrates **1a** or **1b** are measured in the presence of equimolar amounts of titanium tetrafluoride.[15]

To check the scope of this enantioselective carbon allylation procedure, a series of further substrates **5**–**8** were allowed to react with allyltrimethylsilane in the presence of the chiral Lewis acid **3** (Table 1). In the case of the tetrahydronaphthyl ether **5**, a slightly lower enantiomeric

 © 2004 Wiley-VCH Verlag GmbH & Co. KGaA, Weinheim

Table 1: Carbon allylation of ethers **5** and **6** as well as of the N,O- and O,O-acetals **7** and **8** into alkenes **9**–**12**.

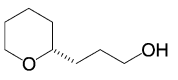
Substrate	Alkene	Yield [%]	*ee* [%]	Conditions
		96	93	[a]
rac-**5**	(*S*)-**9**			
		62	90	[a]
rac-**6**	(*S*)-**10**			
		82	56	[a]
rac-**7a**: R = Me *rac*-**7b**: R = $SiMe_3$	(*R*)-**11**			
		75 82	54 79	[b] [c]
rac-**8**	(*R*)-**12**			

[a] **3**: 10 mol%. [b] **3**: 10 mol%, TiF_4: 90 mol%. [c] **3**: 200 mol%.

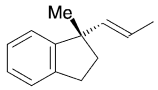
excess was observed in the alkene **9** relative to the corresponding indanyl derivative. Furthermore, the silyl ether **6** derived from 1-phenylethanol was used as a substrate to find out whether the method is limited to substrates whose stereogenic center is incorporated in a carbocycle or heterocycle. Evidently, this limitation does not apply: The allylation product (*S*)-**10** was also obtained with an enantiomeric excess of 90%. This result also shows that the method is not restricted to the silyl ethers of tertiary alcohols. Finally, heterocyclic substrates were also used. The benzyloxycarbonyl-protected[16] piperidines **7a**[17a] and **7b**[17b] yielded the expected carbon-allylation product **11** when treated with allyltrimethylsilane. In the presence of 0.1 equivalents of the chiral Lewis acid **3**, the alkene (*R*)-**11** was obtained with 56% *ee* from either N/O-acetal **7a** or **7b**.

In all the carbon-allylation reactions described so far, the titanium(IV) complex **3** was used in substoichiometric amounts, usually 0.1 equivalents. However, when these conditions were applied to the tetrahydropyranyl ether **8**, the allylation product was obtained in only 9%. It seems that the chiral Lewis acid **3** is bound irreversibly to the tetrahydropyran **8**. To enforce the substoichiometric use of the alkoxyimine titanium(IV) complex **3**, a mixture of the Lewis acid **3** and titanium tetrafluoride (1:9) was employed. Indeed, these conditions, which aimed at an in situ regeneration of the chiral titanium complex **3**, led to the formation of the alkene **12** in 75% yield. The moderate enantioselectivity (54% *ee*) could be enhanced to 79% *ee* when a larger amount of the chiral Lewis acid **3** (2.0 equivalents) was used.

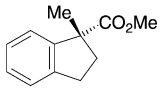
The *ee* values for the carbon-allylation products **2** and **9**–**11** were determined in each case by HPLC on a chiral column (chiracel OJ). The enantiomeric ratio of the tetrahydropyran derivative **12** could only be determined by HPLC after its conversion into the alcohol **13** (by means of hydroboration with 9-BBN). The absolute configurations of the alkene **10** and the carbamate **11** were assigned by comparison of their



(*R*)-**13**



(*S*)-**14**



(*R*)-**15**

optical rotations with the corresponding data described in the literature.[18] The indanyl derivative **2** was converted into the ester **15**, whose configuration is known:[19] A rhodium(III) chloride catalyzed shift of the carbon–carbon double bond[20] delivered the alkene **14**, whose ozonolysis and subsequent oxidative workup gave the corresponding carboxylic acid, which was finally esterified by treatment with diazomethane to yield (*R*)-**15**. Its configuration was determined by the comparison of the optical rotations.[19] Bearing in mind the formal inversion of the configuration owing to a change of priorities in the course of the transformation, the *S* configuration was assigned to **2**. By analogy, the tetrahydronaphthalene derivative **9** is assumed to have the same configuration.

By means of the chiral titanium(IV) complex **3**, the substitution of a hydroxy, silyloxy, or alkoxy group by an allylic residue is possible, for the first time, in a dynamic kinetic asymmetric transformation. Substrates that carry leaving groups in strongly activated positions are suitable starting materials, and the method allows the generation of quaternary carbon centers in a highly enantioselective manner. The procedure is not restricted to substrates whose stereogenic carbon center is incorporated in a cyclic skeleton.

Experimental Section

(*S*)-1-(2-Propenyl)-1-methylindane [(*S*)-**2**]: In a 50-mL two-necked flask, equipped with a magnetic stirrer, a septum, and a connection to a combined nitrogen/vacuum line, a solution of the titanium complex **3** (0.021 g, 0.035 mmol) in absolute CH_2Cl_2 (12 mL) was stirred at −78°C under nitrogen. In a second 25-mL two-necked flask with the same setup, siloxyindane **1b** (0.077 g, 0.35 mmol) was dissolved in absolute CH_2Cl_2 (3 mL) and subsequently added dropwise through a cannula to the solution of the titanium complex **3**. Allyltrimethylsilane (0.048 g, 0.42 mmol) was then injected by syringe. The mixture was allowed to warm to 0°C over 12 h, and stirring was continued for another 6 h at the same temperature. After the addition of a saturated aqueous solution of NH_4F (15 mL), the organic layer was separated, and the aqueous phase was extracted with CH_2Cl_2 (3 × 15 mL). The combined organic layers were washed with a saturated aqueous solution of NaF (10 mL) and dried with Na_2SO_4. The solvent was removed on a rotary evaporator, and the oily residue was purified by distillation to yield (*S*)-**2** (0.058 g, 94%). B.p. 118°C/12 mbar; HPLC (Chiracel OJ; Daicel Chemical Industries; *n*-hexane/2-propanol, 96:4): (*S*)-**2**: t_R = 8.2 min, (*R*)-**2**: t_R = 9.4 min; 98.9% *ee*; ^{1}H NMR (500 MHz, $CDCl_3$, TMS): δ = 1.24 (s, 3H; CH_3), 1.81 (dt, J_d = 12.6 Hz, J_t = 7.6 Hz, 1H; 2-H_a), 2.05 (dt, J_d = 12.6 Hz, J_t = 7.6 Hz, 1H; 2-H_b), 2.29 (m, 2H; CH_2CH=), 2.87 (t, J = 7.6 Hz, 2H; 3-H), 5.01 (d, J_{cis} = 10.0 Hz, 1H; C*H*H=CH), 5.01 (d, J_{trans} = 17.0 Hz, 1H; CH*H*=CH), 5.72 (m, 1H; CH_2=C*H*), 7.15 ppm (m, 4H; aromatic H); ^{13}C NMR (125 MHz, $CDCl_3$, TMS): δ = 26.6, 30.1, 38.2, 45.7, 47.2, 117.1, 122.6, 124.3, 125.7, 126.1, 135.7, 143.2, 151.0 ppm; GC/MS (70 eV; t_R = 9.28 min): *m*/*z* (%): 172 (7) [M^+], 170 (38) [M^+ − 2H], 155 (100)

 © 2004 Wiley-VCH Verlag GmbH & Co. KGaA, Weinheim

$C_{12}H_{11}$; elemental analysis: calcd for $C_{13}H_{16}$ (172.27): C 90.64, H 9.36; found C 90.62, H 9.38.

Received: June 12, 2003 [Z52128]

Keywords: allylation · asymmetric catalysis · C–C coupling · Lewis acids · nucleophilic substitution

[1] A. Fischli, *Chimia* **1976**, *30*, 4.
[2] Reviews: a) R. S. Ward, *Tetrahedron: Asymmetry* **1995**, *6*, 1475; b) R. Noyori, M. Tokunaga, M. Kitamura, *Bull. Chem. Soc. Jpn.* **1995**, *68*, 36; c) H. Stecher, K. Faber, *Synthesis* **1997**, 1; d) E. J. Ebbers, G. J. A. Ariaans, J. P. M. Houbiers, A. Bruggink, B. Zwanenburg, *Tetrahedron* **1997**, *53*, 9417; e) U. T. Strauss, U. Felfer, K. Faber, *Tetrahedron: Asymmetry* **1999**, *10*, 107; f) S. Caddick, K. Jenkins, *Chem. Soc. Rev.* **1996**, *25*, 447; g) F. F. Huerta, A. B. E. Minidis, J.-E. Bäckvall, *Chem. Soc. Rev.* **2001**, *30*, 321.
[3] Review: P. Beak, D. R. Anderson, M. D. Curtis, J. M. Laumer, D. J. Pippel, G. A. Weisenburger, *Acc. Chem. Res.* **2000**, *33*, 715.
[4] P. M. Dinh, J. A. Howarth, A. R. Hudnott, J. M. J. Williams, W. Harris, *Tetrahedron Lett.* **1996**, *37*, 7623; J. V. Allen, J. M. J. Williams, *Tetrahedron Lett.* **1996**, *37*, 1859; M. T. Reetz, K. Schimossek, *Chimia* **1996**, *50*, 668; A. L. E. Larsson, B. A. Persson, J.-E. Bäckvall, *Angew. Chem.* **1997**, *109*, 1256; *Angew. Chem. Int. Ed. Engl.* **1997**, *36*, 1211; R. Stürmer, *Angew. Chem.* **1997**, *109*, 1221; *Angew. Chem. Int. Ed. Engl.* **1997**, *36*, 1173, and references therein.
[5] S. G. Davies, D. Middlemiss, A. Naylor, M. Wills, *J. Chem. Soc. Chem. Commun.* **1990**, 797; R. W. Hoffmann, T. Rühl, F. Chemla, T. Zahneisen, *Liebigs Ann. Chem.* **1992**, 719; D. S. Matteson, H.-W. Man, *J. Org. Chem.* **1994**, *59*, 5734; D. Enders, R. Maaßen, J. Runsink, *Tetrahedron: Asymmetry* **1998**, *9*, 2155; R. N. Ben, T. Durst, *J. Org. Chem.* **1999**, *64*, 7700; A. Kubo, H. Kubota, M Takahashi, K. Nunami, *J. Org. Chem.* **1997**, *62*, 5830; P. N. Devine, U.-H. Dolling, R. M. Heid, Jr., D. M. Tschaen, *Tetrahedron Lett.* **1996**, *37*, 2683; T. Rein, R. Kreuder, P. von Zezschwitz, C. Wulff, O. Reiser, *Angew. Chem.* **1995**, *107*, 1099; *Angew. Chem. Int. Ed. Engl.* **1995**, *34*, 1023.
[6] T. Heinl, S. Retzow, D. Hoppe, G. Fraenkel, A. Chow, *Chem. Eur. J.* **1999**, *5*, 3464.
[7] a) R. Noyori, T. Ohkuma, *Angew. Chem.* **2001**, *113*, 41; *Angew. Chem. Int. Ed.* **2001**, *40*, 40; b) E. Coulon, M. C. C. de Andrade, V. Ratovelomanana-Vidal, J.-P. Genêt, *Tetrahedron Lett.* **1998**, *39*, 6467; c) J. M. Ready, E. N. Jacobsen, *J. Am. Chem. Soc.* **1999**, *121*, 6086; d) B. M. Trost, F. D. Toste, *J. Am. Chem. Soc.* **1999**, *121*, 3543; e) G. C. Lloyd-Jones, C. P. Butts, *Tetrahedron* **1998**, *54*, 901; f) J. Liang, J. C. Ruble, G. C. Fu, *J. Org. Chem.* **1998**, *63*, 3154.
[8] Reviews: E. J. Corey, A. Guzman-Perez, *Angew. Chem.* **1998**, *110*, 403; *Angew. Chem. Int. Ed.* **1998**, *37*, 388; J. Christoffers, A. Mann, *Angew. Chem.* **2001**, *113*, 4725; *Angew. Chem. Int. Ed.* **2001**, *40*, 4591.
[9] Review: M. T. Reetz, *Top. Curr. Chem.* **1982**, *106*, 1.
[10] T. Seitz, Dissertation, Universität Marburg, **1988**.
[11] E. C. Friedrich, D. B. Taggart, *J. Org. Chem.* **1978**, *43*, 805.
[12] R. Fleischer, H. Wunderlich, M. Braun, *Eur. J. Org. Chem.* **1998**, 1063.
[13] T. W. Greene, P. G. M. Wuts, *Protective Groups in Organic Synthesis*, Wiley, New York **1991**, p. 68–73.
[14] See: H. Sakurai, *Pure Appl. Chem.* **1982**, *54*, 1; I. Fleming, J. Dunoguès, R. Smithers, *Org. React.* **1989**, *37*, 57.
[15] The downfield shift of more than 35 ppm measured in this case is distinctly larger than that observed upon complexation of ketones with $TiCl_4$ or CH_3TiCl_3 (approximately 11 ppm); see: M. T. Reetz, M. Hüllmann, T. Seitz, *Angew. Chem.* **1987**, *99*, 478; *Angew. Chem. Int. Ed. Engl.* **1987**, *26*, 477, and references therein.
[16] A. Giovannini, D. Savoia, A. Umani-Ronchi, *J. Org. Chem.* **1989**, *54*, 228.
[17] a) O. Okitsu, R. Suzuki, S. Kobayashi, *J. Org. Chem.* **2001**, *66*, 809; b) prepared by silylation of N-Cbz-protected 2-hydroxypiperidine.[13]
[18] a) **10**: L. Lardicci, P. Salvadori, A. M. Caporusso, R. Menicagli, E. Belgodere, *Gazz. Chim. Ital.* **1972**, *102*, 64; b) **11**: T. Yasuo, A. Kumiko, T. Kentaro, A. Mitoshi, K. Hye-Sook, W. Yusuke, H. Takahashi, *Tetrahedron* **2001**, *57*, 1213.
[19] H. des Abbayes, M. A. Boudeville, *Tetrahedron Lett.* **1976**, 2137.
[20] See: M. Ando, N. Kataoka, M. Yasunami, K. Takase, N. Hirata, Y. Yanagi, *J. Org. Chem.* **1987**, *52*, 1429.

 © 2004 Wiley-VCH Verlag GmbH & Co. KGaA, Weinheim

Ferromagnetic Resonance

Structural Changes in Nanoparticle Catalysts as Monitored by Their Magnetic Properties**

Thomas Risse, Mohsen Mozaffari-Afshar, Heiko Hamann, and Hans-Joachim Freund*

Scanning probe microscopies, transmission electron microscopy, and other spectroscopic techniques have been successfully applied to accumulate structural information on nanoparticle catalysts.[1–5] Even though these methods provide data at the atomic level, it has not been possible so far to unravel all details necessary to establish structure–reactivity relationships. One problem is the presence of several interfaces in such systems, that is, the particle–gas and the particle–support interfaces. As a result, the search for analytical tools with sufficient sensitivity is ongoing. It has long been recognized that small changes in the structure influence the magnetic properties drastically (see, for example, reference [6,7]). Therefore, monitoring magnetic properties of these systems could help to provide deeper insight into structure–reactivity relationships. Some processes in nanoparticle catalysts that can be probed by the magnetic properties of the system are illustrated schematically in Figure 1.

The adsorption of molecules is the primary step of a surface reaction. Although ferromagnetism is a bulk property, it will be shown that the magnetic properties are extremely sensitive to the adsorption process (Figure 1, route A). In addition, the method provides access to properties of the particle–substrate interface (route B). It can be used, for

[*] Dr. T. Risse, Dr. M. Mozaffari-Afshar, Dr. H. Hamann, Prof. Dr. H.-J. Freund
Fritz-Haber-Institut der Max-Planck Gesellschaft
Abteilung Chemische Physik
Faradayweg 4–6, 14195 Berlin (Germany)
Fax: (+49) 30-8413-4316
E-mail: risse@fhi-berlin.mpg.de

[**] Financial support by the DFG (SFB 290, TP A9) and the Max Planck Society are gratefully acknowledged. We thank Walter Wachsmann for technical assistance.

 DOI: 10.1002/anie.200352107 © 2004 Wiley-VCH Verlag GmbH & Co. KGaA, Weinheim

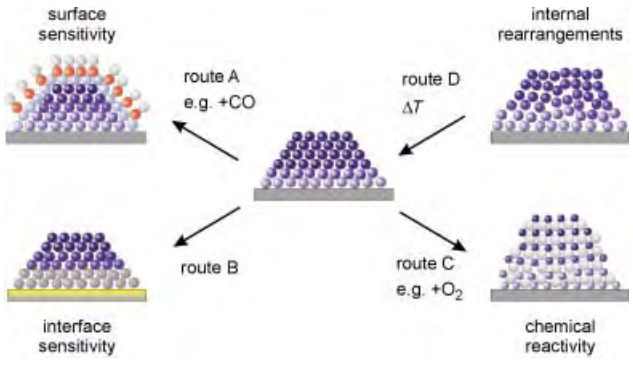


Figure 1. Schematic representation of different processes monitored by magnetic properties.

example, to monitor chemical reactions between the supported metal particle and the substrate. More generally, chemical modifications of the particles caused by reactions with a gas atmosphere can be identified by changes in the magnetic properties (route C). In dispersed catalytic systems, thermal stability of the nanoparticles is an important factor. Besides a sintering of particles—that is, a redistribution of atoms between particles at elevated temperatures—internal rearrangements such as a crystallization of the particles may be important (route D). It has been shown for model catalysts that structural characteristics determine important properties such as the adsorption sites of molecules from the gas phase.[8] Both effects, namely, interparticle as well as intraparticle redistributions, can be studied. Given that magnetic properties can be recorded in situ, the sensitivity to these processes provides unique opportunities in catalytic research.

Electron spin resonance (EPR) spectroscopy (usually called ferromagnetic resonance (FMR) in the case of ferromagnetic systems) has proved to be a valuable tool for both powder catalysts and single crystal surfaces.[9–12] It was used under ultrahigh-vacuum (UHV) conditions to characterize the ferromagnetic properties of Ni and Co nanoparticles on well-defined Al_2O_3 surfaces. In the following we want to focus the discussion on the interfacial sensitivity of this method. The sensitivity to adsorption of molecules at the metal–vacuum interface as well as the sensitivity towards the metal–substrate interface will be shown by two examples. In particular, the latter interface is difficult to access with other methods.

Nickel particles with a lateral size of 60–250 nm and an average height of 9 nm, based on scanning electron microscopy (SEM; Figure 2), were prepared by depositing the equivalent of a 14-Å thick Ni layer onto an α-Al_2O_3 $(11\bar{2}0)$ surface at room temperature and subsequent annealing to 900 K. The low-energy electron diffraction pattern shows hexagonal spots of Ni crystallites in the (111) orientation as well as rectangular spots of the underlying $(11\bar{2}0)$ surface. The (111) facets exhibit the lattice spacing of bulk Ni, indicating a relaxation of the uniaxial lattice mismatch of 11% along the $(1\bar{1}00)$ direction of the α-Al_2O_3 crystal in the top layers of the Ni particles (the lattice constant in the (0001) direction of the α-Al_2O_3 surface fits almost perfectly to Ni(111)).[13]

The prepared surface was exposed to CO. The diagram on the left-hand side of Figure 2 shows the positions of the three signals in the FMR spectra as a function of CO dosage. The measurements were made with the static magnetic field perpendicular to the surface. Owing to the overlap of the three signals the resonance positions of the two low-field signals were determined by assuming a symmetric line shape. The weak signal at 5500 G was assigned on the basis of temperature-dependent measurements, which clearly reveal a doublet of lines. Above 0.4 L of CO (1 L = 10^{-6} torr s) this line

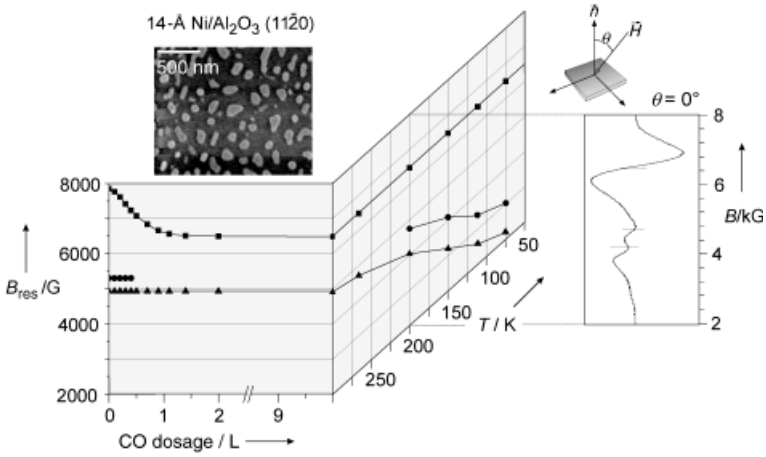


Figure 2. Left: Resonance positions measured for 14-Å Ni on an α-Al_2O_3 $(11\bar{2}0)$ surface as a function of CO dosage. Right: Resonance positions for the CO-saturated state as a function of the substrate temperature. The measurements were made at normal incidence of the static magnetic field. The spectrum shown was measured at 200 K. Inset: an SEM image of the sample (1.8×1.5 μm^2).

overlaps with the intense high-field absorption; this prevents a reliable determination of the resonance position. Although the proportion of surface atoms in particles of this size is relatively low, the high-field resonance exhibits a strong dependence of the resonance position on CO adsorption. In contrast to the high-field resonance the two resonances at lower field are unaffected within the resolution of the experiment. The shift of the high-field line renders the sensitivity range from approximately 0.05 L up to saturation coverage at 1 L. After desorption of CO at elevated temperatures the resonance position of the pristine particles is restored, which proves this process to be reversible. It should be noted that adsorption of hydrogen has the same effect as CO adsorption.

The situation is exactly reversed if the temperature dependence is considered. With decreasing temperature the two low-field resonances shift strongly towards lower fields, whereas the resonance at high field is basically unaffected (Figure 2, right diagram). The observation of three resonances for a system with a broad but smooth and monomodal particle-size distribution is surprising, since simple ferromagnetic resonance theory predicts one uniform precession mode.

 © 2004 Wiley-VCH Verlag GmbH & Co. KGaA, Weinheim

However, for systems with an inhomogeneous magnetization, as expected for well-faceted nanocrystals with a large lattice mismatch at the particle–support interface,[14] the excitation of other spin states becomes possible.[15,16] The high-field resonance, whose position strongly depends on gas adsorption, can be attributed to a surface mode, which is very sensitive to changes in the boundary conditions at the surface of the particle. The intensity of this resonance decreases strongly if the orientation of the static magnetic field deviates from the perpendicular orientation with respect to the surface. The two other modes behave as conventional uniform precession modes. Both show a smooth variation of the resonance position with the angle of the incident static magnetic field (data not shown). An analysis of the angle dependence indicates an additional anisotropy component, which can be assigned to interface contributions. The lack of sensitivity of the resonance position to changes at the metal–vacuum interface (e.g. molecular adsorption or metal oxidation) indicates that the particle–substrate interface is the origin of this extra contribution. The temperature dependence of the signal corroborates this assignment, which also agrees with earlier studies with thin Ni films on metals.[11] The splitting of the resonance into two lines may be a consequence of the uniaxial distortion of the nickel lattice along the $(1\bar{1}00)$ direction of the α-Al_2O_3 $(11\bar{2}0)$ surface.

The particle–substrate interface plays an important role for the understanding of deposited-metal systems. The situation is complicated by the fact that this interface can rarely be described as a static system, especially at elevated temperatures and under reactive conditions. In the following we will show that magnetic properties can be used to monitor the interface reaction between an Al_2O_3 surface and Co and Ni particles at elevated temperatures.

Co (2 Å) was deposited at room temperature on a thin Al_2O_3 film grown on a NiAl(110) surface. The normalized intensity of the FMR spectra measured for this system was used as the reference (where the red curve crosses the *y* axis in Figure 3). Subsequently, the Co particles were oxidized with 30 L of oxygen at 300 K, resulting in complete loss of the FMR signal. Upon heating to 530 K the signal intensity was restored to 55% of its original value. As indicated by the scanning tunneling microscopy (STM) images taken under identical conditions, this procedure does not alter the morphology of the particles to a measurable extent. Upon repeating the procedure several times, the recovery of the FMR intensity decreased for subsequent cycles, indicating that the process becomes less effective. Based on this observation and the STM result, a simple thermal decomposition of the oxide phase can be ruled out. The observation can be explained by assuming that annealing to 530 K leads to a reduction of the Co oxide phase to metallic Co, caused by a concomitant oxidation of the NiAl substrate. The oxidation of NiAl increases the thickness of the alumina film progressively; similar results were obtained for Pd particles.[17] This factor limits, most likely because of kinetic effects, the efficiency of the redox process, thus explaining the progressive drop of efficiency for subsequent cycles.

This type of solid-state reaction is not restricted to thin films. A similar effect was observed on an α-Al_2O_3 single crystal. Ni (4 Å) was deposited at 300 K on the reconstructed (12×4) α-Al_2O_3 $(11\bar{2}0)$ surface and subsequently annealed to 900 K. The intensity observed after oxidation with 300 L of oxygen at room temperature and subsequent annealing to 900 K is shown in Figure 3 (black trace). The FMR intensity exhibits the same oscillatory behavior observed for the thin film. In this case the α-Al_2O_3 single crystal acts as a reducing agent because the reconstructed surface suffers from an oxygen deficiency in the top layers.[18] However, the reduction capacity of the surface is limited because of the restriction of the oxygen deficiency to the few top layers, which explains the strong decrease in the efficiency of this process after several cycles.

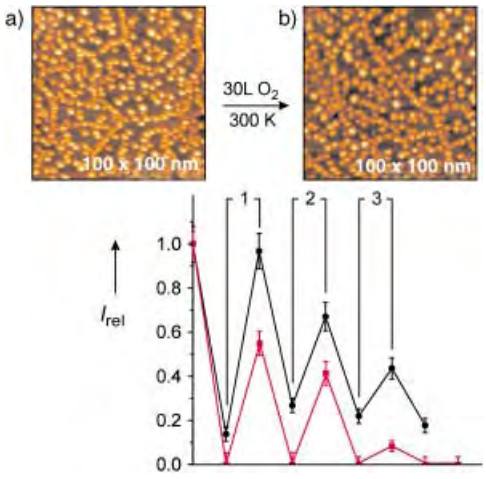


Figure 3. Top: STM pictures for 2-Å Co deposited at 300 K on a thin alumina film on NiAl(110):[21] a) pristine deposits, b) after oxidation with 30 L of oxygen at 300 K. Diagram: Intensity of the FMR signals during the oxidation–heating cycles (see text). Black trace: 4-Å Ni deposited at 300 K on a (12×4) reconstructed α-Al_2O_3 $(11\bar{2}0)$ surface and subsequently annealed to 900 K; red trace: 2-Å Co deposited at 300 K on a thin alumina film on NiAl(110).

In summary, we have shown that the magnetic properties of supported nanoparticles can be used to probe changes in the structure as well as the chemical environment of the particles. This has been demonstrated not only for adsorption and reaction with molecules from the gas phase but also for a reaction at the metal–support interface. Although all experiments described herein were carried out under UHV conditions, it is also possible to work at ambient pressure with FMR and ESR spectroscopy. The latter has been utilized for in situ model studies of Ziegler–Natta catalysts.[19]

Experimental Section

The FMR experiments were carried out in a specially designed UHV apparatus, which has been previously described.[20] The spectra were recorded with a commercial EPR spectrometer (Bruker, B-ER 420), which had been modified with an improved microwave bridge (Bruker, ECS 041 XK) and a new lock-in amplifier (Bruker, ER 023M) to improve the signal-to-noise ratio. A commercial electron beam evaporator (EFM3 Focus/Omicron) was used to deposit the metals. A deposition rate of 1 Å min^{-1}, as calibrated by a quartz microbalance, was used for all experiments. The sample was biased to the voltage of the evaporation material to avoid an

 © 2004 Wiley-VCH Verlag GmbH & Co. KGaA, Weinheim

acceleration of metal ions onto the surface. The pressure during metal evaporation never rose above 1.5×10^{-10} mbar, and the base pressure in the apparatus was better than 5×10^{-11} mbar. The coverage is given as an average height of a hypothetical, homogeneous film. Clean (1×1) and (12×4) reconstructed α-Al_2O_3 ($11\bar{2}0$) surfaces (Crystec GmbH and Crystal GmbH, both Berlin) were prepared by annealing the sample several times for 20 min to 1200 K and 1500 K, respectively. The clean surface showed neither carbon nor other impurities within the sensitivity of Auger spectroscopy. The reconstruction of the surface after this treatment was verified by low-energy electron diffraction (LEED). The thin alumina film on the NiAl(110) single-crystal surface was prepared according to a procedure described in the literature.[8]

Received: June 10, 2003 [Z52107]

Keywords: EPR spectroscopy · magnetic properties · nanostructures · supported catalysts · surface chemistry

[1] C. R. Henry, *Surf. Sci. Rep.* **1998**, *31*, 235.
[2] C. T. Campbell, *Surf. Sci. Rep.* **1997**, *27*, 1.
[3] O. Dulub, W. Hebenstreit, U. Diebold, *Phys. Rev. Lett.* **2000**, *84*, 3646.
[4] H.-J. Freund, *Angew. Chem.* **1997**, *109*, 444; *Angew. Chem. Int. Ed. Engl.* **1997**, *36*, 452.
[5] H.-J. Freund, *Surf. Sci.* **2002**, *500*, 271.
[6] S. P. Li, W. S. Lew, J. A. C. Bland, L. Lopez-Diaz, C. A. F. Vaz, M. Natali, Y. Chen, *Phys. Rev. Lett.* **2002**, *88*, 7202.
[7] D. Sander, *Rep. Prog. Phys.* **1999**, *62*, 809.
[8] M. Bäumer, H.-J. Freund, *Prog. Surf. Sci.* **1999**, *61*, 127.
[9] M. Sterrer, T. Berger, O. Diwald, E. Knözinger, *J. Am. Chem. Soc.* **2003**, *125*, 195.
[10] G. Pinarello, C. Pisani, A. D'Ercole, M. Chiesa, M. C. Paganini, E. Giamello, O. Diwald, *Surf. Sci.* **2001**, *494*, 95.
[11] M. Farle, *Rep. Prog. Phys.* **1998**, *61*, 755.
[12] H. Schlienz, M. Beckendorf, U. J. Katter, T. Risse, H.-J. Freund, *Phys. Rev. Lett.* **1995**, *74*, 761.
[13] G. Beitel, J. Markert, J. Wiecherts, J. Hrbek, R. J. Behm in *Adsorption on Ordered Surfaces of Ionic Solids and Thin Films* (Eds.: E. Umbach, H.-J. Freund), Springer, Berlin, **1993**.
[14] R. I. Joseph, E. Schlömann, *J. Appl. Phys.* **1965**, *36*, 1579.
[15] A. R. Ferchmin, H. Puszkarski, *J. Appl. Phys.* **2001**, *90*, 5335.
[16] W. N. Wang, Z. S. Jiang, Y. W. Du, *J. Appl. Phys.* **1995**, *78*, 6679.
[17] S. Shaikhutdinov, M. Heemeier, J. Hoffmann, I. Meusel, B. Richter, M. Bäumer, H. Kuhlenbeck, J. Libuda, H. J. Freund, R. Oldman, S. D. Jackson, C. Konvicka, M. Schmid, P. Varga, *Surf. Sci.* **2002**, *501*, 270.
[18] T. Becker, A. Birkner, G. Witte, C. Wöll, *Phys. Rev. B* **2002**, *65*, 5401.
[19] T. Risse, J. Schmidt, H. Hamann, H.-J. Freund, *Angew. Chem.* **2002**, *114*, 1587; *Angew. Chem. Int. Ed.* **2002**, *41*, 1517.
[20] M. Beckendorf, U. J. Katter, H. Schlienz, H. J. Freund, *J. Phys. Condens. Matter* **1993**, *5*, 5471.
[21] A. F. Carlsson, M. Naschitzki, M. Bäumer, personal communication.

 © 2004 Wiley-VCH Verlag GmbH & Co. KGaA, Weinheim

Cover Picture

David Scheschkewitz, Hideki Amii, Heinz Gornitzka, Wolfgang W. Schoeller, Didier Bourissou, and Guy Bertrand*



A motion picture of chemical transformation can be pieced together only from femtosecond spectroscopic techniques. The Communication by G. Bertrand and co-workers on page 585 ff. describes how the reaction profile corresponding to the inversion of bicyclo[1.1.0]butane, which involves the stretching of the B–B bond as symbolized by the tugging men, can be modeled by series of analogues that contain the boron–phosphorus ring.

Contents

Angewandte EarlyView

The following articles are available online (in Wiley InterScience). You can find them at www.angewandte.org, under Full Text, Early View.

A. E. C. Palmqvist, B. B. Iversen, E. Zanghellini, M. Behm, G. D. Stucky:*
A Crystalline Microporous Narrow-Bandgap Semiconductor
DOI: 10.1002/anie.200351284
Published online: January 8, 2004

Articles judged by the referees or the editor as being either very important or very urgent are immediately edited, proof-read, and electronically published once the manuscript has arrived in the editorial office in final form. As long as there is no page number available these articles should be cited in the following manner:

Author(s) *Angew. Chem. Int. Ed.*, online publication date, DOI.

Web Sites

http://www.johnkyrk.com ——— **542**	The Living Cell	*Georg Pohnert*

Books

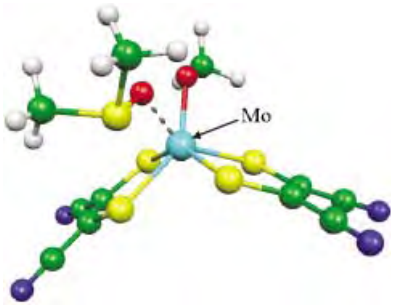
Quasicrystals ——— **543**	Hans-Rainer Trebin	*reviewed by G. Kreiner*
Hydrolysis in Drug and Prodrug Metabolism ——— **544**	Bernard Testa, Joachim M. Mayer	*reviewed by V. Wehner*

Highlights

Reaction Mechanisms

M. Kaupp* ——— **546–549**

Trigonal Prismatic or not Trigonal Prismatic? On the Mechanisms of Oxygen-Atom Transfer in Molybdopterin-Based Enzymes



Nature is versatile and can make use of even seemingly exotic bonding situations. Recent quantum chemical evidence suggests trigonal-prismatic intermediates and transition states occur in oxygen-atom transfer catalysis of molybdopterin-based enzymes from the DMSO reductase family (see structure, green C, yellow S, blue N, red O, white H). This Highlight presents the fascinating theoretical and experimental findings within the general framework of "non-VSEPR" structures of d^0–d^2 transition metal complexes.

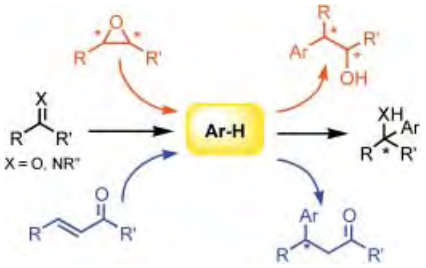
Minireviews

Stereoselective Alkylations

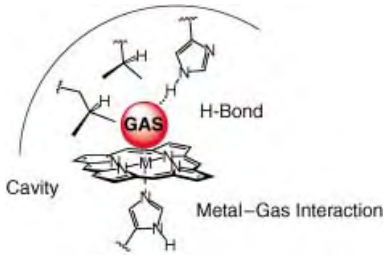
M. Bandini,* A. Melloni, A. Umani-Ronchi* ——— **550–556**

New Catalytic Approaches in the Stereoselective Friedel–Crafts Alkylation Reaction

Still going strong after 125 years: The development of new catalytic systems for the enantioselective construction of benzylic stereocenters is a significant goal for the chemical community. Recently numerous chiral metal-based and metal-free, homogeneous and heterogeneous catalysts have been reported that control the stereochemical course of Friedel–Crafts alkylations of electron-rich aromatic systems (see scheme).



Reviews



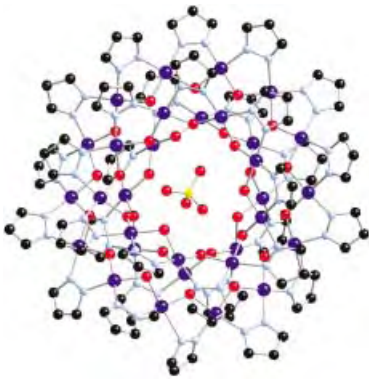
The ins and outs of gases: A deeper understanding into the interaction of gases with biological molecules is obtained by using the principles and techniques of supramolecular chemistry (see schematic representation). This approach not only provides knowledge about the structure and dynamics of receptor–analyte complexes on a molecular level, it also allows for the synthesis of more-selective and sensitive receptors for gas sensing, storage, and controlled release.

Gas–Receptor Complexes

D. M. Rudkevich* ——— **558 – 571**

Emerging Supramolecular Chemistry of Gases

Communications

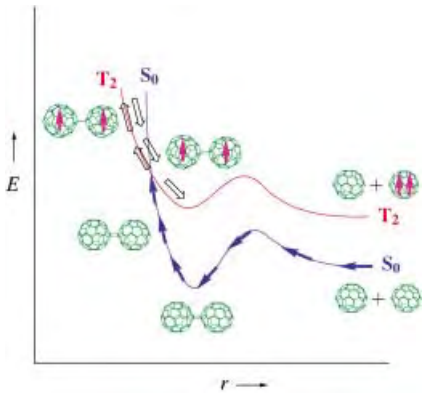


Concentric circles: The interplay of metal-coordination geometry, dipolar interactions, and hydrogen bonding orchestrate the complex supramolecular assembly of three or four neutral metallacycles of [{*cis*-Cu(μ-OH)(μ-pz)}$_n$] $n = 6$, 8, 9, 12, 14, that encapsulate anions (encapsulated SO_4^{2-} depicted; Cu blue; O red; N light blue; C black; S yellow) by multiple hydrogen bonding. This orchestration of several chemical forces for the accomplishment of a specific task imitates the strategies of Nature for similar purposes.

Host–Guest Chemistry

G. Mezei, P. Baran, R. G. Raptis* ——— **574 – 577**

Anion Encapsulation by Neutral Supramolecular Assemblies of Cyclic Cu^{II} Complexes: A Series of Five Polymerization Isomers, [{*cis*-Cu^{II}(μ-OH)(μ-pz)}$_n$], $n = 6$, 8, 9, 12, and 14



Magnetism in polymeric rhombohedral C_{60} phases was studied by ab initio calculations. Compression of C_{60} leads to the formation of C_{60}–C_{60} bonds in the S_0 state, and with increasing pressure the S_0 and T_2 curves meet (see picture), and some of the bonds can cross to the magnetically active T_2 state. When the pressure is released these follow the T_2 curve and remain magnetically active at ambient pressure. r = interfullerene distance.

Magnetism in Compressed Fullerenes

J. Ribas-Ariño, J. J. Novoa* ——— **577 – 580**

The Origin of the Magnetic Moments in Compressed Crystals of Polymeric C_{60}

For the USA and Canada:
ANGEWANDTE CHEMIE International Edition (ISSN 1433-7851) is published weekly by Wiley-VCH PO Box 191161, D 69451 Weinheim, Germany. Air freight and mailing in the USA by Publications Expediting Inc. 200 Meacham Ave., Elmont, NY 11003. Periodicals postage paid at Jamaica NY 11431. US POSTMASTER: send address changes to *Angewandte Chemie*, Wiley-VCH, 111 River Street, Hoboken, NJ 07030. Annual subscription price for institutions: Europe € 3430.00/3118.00; outside Europe US$ 4499.00/4090.00 (valid for print and electronic/print or electronic delivery); for individuals who are personal members of a national chemical society, or whose institution already subscribes, or who are retired or self-employed consultants, print only: Europe € 248.00/outside Europe US$ 378.00. Postage and handling charges included. All Wiley-VCH prices are exclusive VAT.

 © 2004 Wiley-VCH Verlag GmbH & Co. KGaA, Weinheim

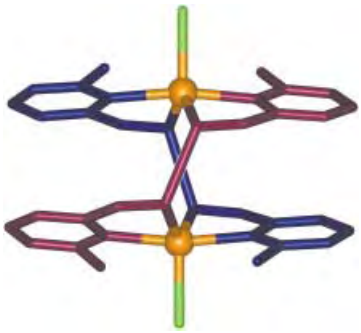
Contents

Helicates

S. G. Telfer,* T. Sato, R. Kuroda* ——— 581 – 584

Noncovalent Ligand Strands for Transition-Metal Helicates: The Straightforward and Stereoselective Self-Assembly of Dinuclear Double-Stranded Helicates Using Hydrogen Bonding

A genuinely supramolecular approach to transition-metal helicates is presented in which eight simple components (four ions and four small molecules) self-assemble to form dinuclear double helicates, where the ligand strands are built up through hydrogen-bonding interactions (see picture). The self-assembly process was found to be highly stereoselective.



Main-Group Chemistry

D. Scheschkewitz, H. Amii, H. Gornitzka, W. W. Schoeller, D. Bourissou, G. Bertrand* ——— 585 – 587

σ-Bond Stretching: A Static Approach for a Dynamic Process



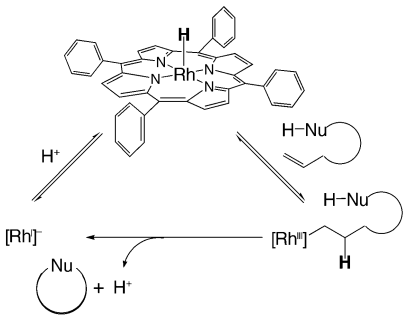
Ring stretching: The reaction profile corresponding to the inversion of bicyclo[1.1.0]butane derivatives, including the cyclobutane-1,3-diyl transition state, has been modeled by the preparation of a series of boron–phosphorus-containing analogues (see picture: P red; B blue). These differ only in the substituents around the B_2P_2 core, yet a variation of 40% in the boron–boron separation is observed.

Alkene Functionalization

M. S. Sanford, J. T. Groves* ——— 588 – 590

Anti-Markovnikov Hydrofunctionalization of Olefins Mediated by Rhodium–Porphyrin Complexes

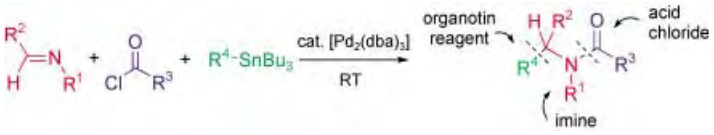
A rationally designed mechanistic approach to anti-Markovnikov olefin hydrofunctionalization and its application to the synthesis of heterocycles are described. Porphyrin–rhodium complexes have been shown to exhibit remarkable reactivity and selectivity for each step of the proposed catalytic cycle (see scheme). A critical step of this reaction sequence is a new, facile, and remarkably general carbon–heteroatom bond-forming reductive elimination.



Imines in Stille Reactions

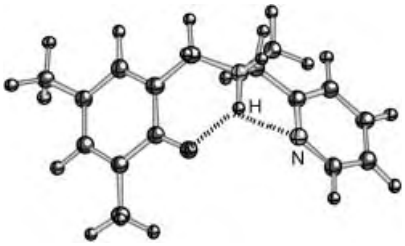
J. L. Davis, R. Dhawan, B. A. Arndtsen* ——— 590 – 594

Imines in Stille-Type Cross-Coupling Reactions: A Multicomponent Synthesis of α-Substituted Amides



An alternative to nucleophilic chemistry for the construction of α-substituted amides and amine derivatives from imines is provided by the Stille-type coupling of imines with organotin reagents and acid chlorides (see scheme). This Pd-catalyzed reaction is suitable for components with a range of functional groups and has been extended into a four-component-coupling reaction with carbon monoxide. dba = dibenzylideneacetone, RT = room temperature.

© 2004 Wiley-VCH Verlag GmbH & Co. KGaA, Weinheim

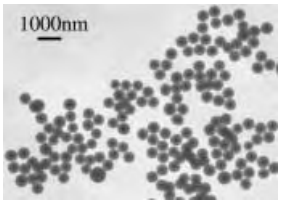


Hydrogen-bonded phenoxyl radicals are made and the strength of the hydrogen bond between the O(phenoxyl) and the H(ammonium) atoms strongly affects their stability. The rate constants for the intramolecular proton-migration process in these systems are reported and a bifurcated hydrogen-bonded system has been characterized (see model). Investigations show that the proton transfer from the phenoxyl-radical cation to the tertiary amine is assisted by a neighboring nitrogen atom.

Proton/Electron Transfer

F. Thomas,* O. Jarjayes, H. Jamet, S. Hamman, E. Saint-Aman, C. Duboc, J.-L. Pierre _____ **594 – 597**

How Single and Bifurcated Hydrogen Bonds Influence Proton-Migration Rate Constants, Redox, and Electronic Properties of Phenoxyl Radicals

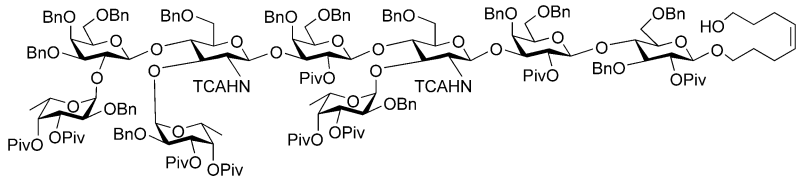


All wrapped up: Carbon-encapsulated metal nanoparticles, carbon microspheres decorated with metal nanoparticles, and particles with layered structures are all accessible by means of a method based on hydrothermal treatment of glucose, which produces monodisperse colloidal carbon microspheres with reactive surfaces. The picture shows silver-cored carbon spheres obtained by using silver nanoparticles as seeds.

Nanoparticles

X. Sun, Y. Li* _____ **597 – 601**

Colloidal Carbon Spheres and Their Core/Shell Structures with Noble-Metal Nanoparticles



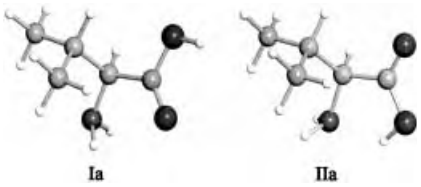
Speedy synthesis: The development of a novel linker and monitoring each glycosylation reaction during automated solid-phase synthesis allows the rapid assembly of three Lewis-type cell-surface oligosaccharides. The synthesis of the protected tumor-marker Le^y–Le^x (see structure; Bn = benzyl, Piv = pivaloyl, TCA = trichloroacetyl) from monosaccharide building blocks was achieved in just 23 h, while the syntheses of Lewis X and Lewis Y required only 12 and 14 h, respectively.

Automated Synthesis

K. Routenberg Love, P. H. Seeberger* _____ **602 – 605**

Automated Solid-Phase Synthesis of Protected Tumor-Associated Antigen and Blood Group Determinant Oligosaccharides

Jet-cooled rotational spectroscopy with laser ablation has enabled two conformers of neutral valine to be observed in the gas phase. The most stable conformer (**Ia**) exhibits a bifurcated amine-to-carbonyl (NH···O=C) intramolecular hydrogen bond, while the second conformer (**IIa**) presents a hydrogen bond between the lone pair of electrons on the nitrogen atom and the hydroxy group (N···O–H).



The isopropyl side chain adopts a similar staggered arrangement in both conformers.

Conformational Analysis

A. Lesarri, E. J. Cocinero, J. C. López, J. L. Alonso* _____ **605 – 610**

The Shape of Neutral Valine

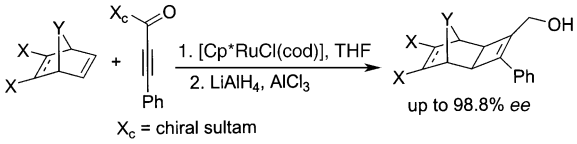
 © 2004 Wiley-VCH Verlag GmbH & Co. KGaA, Weinheim

Contents

Asymmetric Cycloadditions

K. Villeneuve, W. Tam* ——— **610 – 613**

Asymmetric Induction in Ruthenium-Catalyzed [2+2] Cycloadditions between Bicyclic Alkenes and a Chiral Acetylenic Acyl Sultam

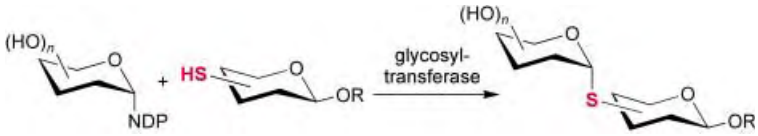


Cyclobutene tricyclic products were isolated in good yields (44–99%) from Ru-catalyzed [2+2] cycloadditions between bicyclic alkenes and a chiral acetylenic acyl sultam (see scheme). The cycloadditions occurred with high stereoselectivity (only *exo* cycloadducts were formed) and high levels of asymmetric induction (67–98.8% *ee* after removal of the chiral auxiliary). X = H, CH_2OMe, Br; X–X = Ar; Y = CH_2, O, CHPh; Cp* = 1,2,3,4,5-pentamethylcyclopentadiene; COD = 1,5-cyclooctadiene.

Thiosugar Synthesis

J. R. Rich, A. Szpacenko, M. M. Palcic, D. R. Bundle* ——— **613 – 615**

Glycosyltransferase-Catalyzed Synthesis of Thiooligosaccharides

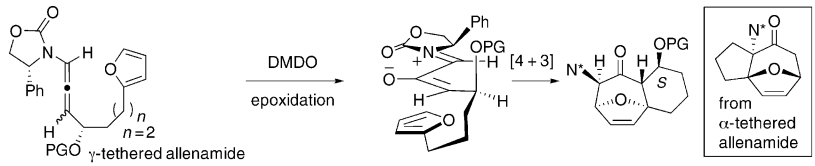


An alternative to chemical synthesis: thiooligosaccharides can be prepared from appropriate carbohydrate thiols and sugar nucleotide donors by incubation with glycosyltransferases. The products of these reactions are stable towards glycosylhydrolases and may serve as antigens with extended in vivo availability.

Stereoselective Cycloaddition

C. Rameshkumar, R. P. Hsung* ——— **615 – 618**

A Tandem Epoxidation/Stereoselective Intramolecular [4+3] Cycloaddition Reaction Involving Nitrogen-Stabilized Oxyallyl Cations Derived from Chiral Allenamides



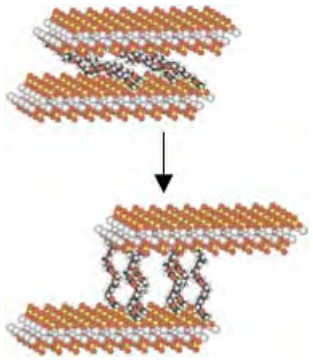
Tandem cycling: Nitrogen-stabilized chiral oxyallyl cation intermediates are generated by chemoselective epoxidation of allenamides tethered to either the α or γ carbon atom of dienes. The stereoselectivity of the subsequent [4+3] cycloaddition step of the tandem reaction shown in the scheme depends on the length of the tether and the chiral auxiliary (N*) on the allenamide. DMDO = dimethyl dioxirane, PG = protecting group.

Crystal Engineering

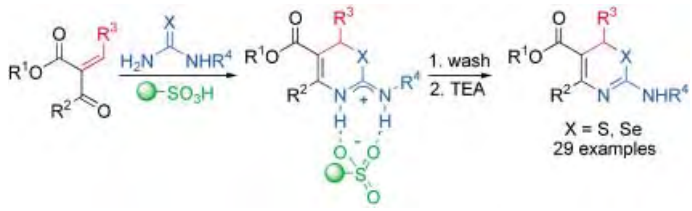
E. Brunet,* M. J. de la Mata, O. Juanes, J. C. Rodríguez-Ubis ——— **619 – 621**

Solid-State Reshaping of Crystals: Flash Increase in Porosity of Zirconium Phosphate-Hypophosphite That Contains Polyethylenoxa Diphosphonate Pillars

Shape shifting: A novel pillared, solid organic–inorganic phase is prepared by stepwise double topotactic exchange of γ-zirconium phosphate with pentaethylenglycol-derived diphosphonic acid and hypophosphite. The interlayer distance of the title material sharply increases when treated with methylamine. This enormous sensitivity of microcrystalline porosity towards intercalation of small molecules has no precedent.



© 2004 Wiley-VCH Verlag GmbH & Co. KGaA, Weinheim

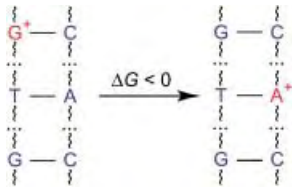


A dual role: The supported sulfonic acid reagent promotes the ring closure of the thiazine products and also binds them in situ as ion pairs (see scheme). The nonbasic by-products and excess reagents can be removed by filtration and the products subsequently released on treatment with triethylamine (TEA).

Compound Libraries

G. A. Strohmeier, C. O. Kappe* ——— 621 – 624

Combinatorial Synthesis of Functionalized 1,3-Thiazine Libraries Using a Combined Polymer-Supported Reagent/Catch-and-Release Strategy



The relative energies of radical cation states on nucleobases in DNA are considerably affected by the local distribution of water molecules and counterions. In fact, fluctuations of ΔG are large enough to render electron-hole transfer from G^+ to A energetically feasible, thus allowing a changeover from the generally accepted G-hopping mechanism to A-hopping (see picture).

Electronic Interactions in DNA

A. A. Voityuk, K. Siriwong, N. Rösch* ——— 624 – 627

Environmental Fluctuations Facilitate Electron-Hole Transfer from Guanine to Adenine in DNA π Stacks



Making Waves: Low-temperature CuCN has a curious wave structure (see picture Cu purple, C/N blue). Interconversion of this and the high-temperature, highly disordered form can be achieved at room-temperature via a novel zeolitic intermediate which is also structurally characterized.

Polymorphs of CuCN

S. J. Hibble,* S. G. Eversfield, A. R. Cowley, A. M. Chippindale* ——— 628 – 630

Copper(I) Cyanide: A Simple Compound with a Complicated Structure and Surprising Room-Temperature Reactivity



Selective cyclizations of selenium electrophiles lead to either tetrahydrofurans or lactones (see scheme), depending on the counterions and additives. Modification of the selenium electrophiles allow selective cyclizations, irrespective of the reaction conditions applied.

Cyclizations

S. S. Khokhar, T. Wirth* ——— 631 – 633

Selenocyclizations: Control by Coordination and by the Counterion

The size and the shape of micelles can be determined with a new fluorescence dye (see picture blue N, turquoise C, red O). The fluorescence lifetime of this new porphyrin derivative is about 10 ns, which is in the order of the rotation time of a micelle. The size of the dye (diameter ca. 37 Å) ensures that it perfectly fits into most micelles. It is the first fluorescent probe that reflects only the rotation of the micelles without the disturbing internal motions of the dye.



Porphyrin Dyes

J. Duschl, M. Michl, W. Kunz* 634 – 636

A Porphyrin Dye with Monoexponential Fluorescence Intensity and Anisotropy Decay Behavior in Spherical Micelles

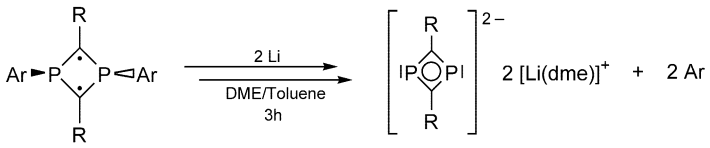
 © 2004 Wiley-VCH Verlag GmbH & Co. KGaA, Weinheim

Contents

Phosphorus Heterocycles

M. Sebastian, M. Nieger, D. Szieberth, L. Nyulászi,* E. Niecke* ——— **637 – 641**

Synthesis and Structure of a 1,3-Diphosphacyclobutadienediide: An Aniomesolytic Fragmentation of a 1,3-Diphosphetane-2,4-diyl in Solution



1 **2**

Stepwise reduction of the 1,3-diphosphetane-2,4-diyl **1** by alkali metals (Li, K) leads to the 1,3-diphoshacyclobutadiendiide salts **2** by aniomesolytic fragmentation. DFT calculations provide insight into the reaction pathway.

Communications labeled with this symbol have been judged by two referees as being "very important papers".

The publication of Communications labeled with this symbol has been accelerated because of their topical or highly competitive nature.

The issues for January 2004 appeared online on the following dates
Issue 1: December 17, 2003 · Issue 2: December 19, 2003 · Issue 3: December 29, 2003 · Issue 4: January 14, 2004.

Sources

Product and Company Directory

You can start the entry for your company in "Sources" in any issue of *Angewandte Chemie*.

If you would like more information, please do not hesitate to contact us.

Wiley-VCH Verlag – Advertising Department
Tel.: 0 62 01 - 60 65 65
Fax: 0 62 01 - 60 65 50
E-Mail: MSchulz@wiley-vch.de

Service

Keywords ——— *642*

Authors ——— *643*

Sources ——— *A7*

Preview ——— *645*

Corrigendum

In the Communication "Synthesis and Biological Evaluation of an Indomethacin Library Reveals a New Class of Angiogenesis-Related Kinase Inhibitors" by A. Giannis, H. Waldmann et al. (*Angew. Chem. Int. Ed.* **2004**, *43*, 224–228) the address information was given incorrectly. The correct information is as follows:

Prof. Dr. H. Waldmann, Dr. C. Rosenbaum
Max-Planck-Institut für molekulare Physiologie
Abteilung Chemische Biologie
Otto-Hahn-Strasse 11, 44227 Dortmund (Germany)
and
Universität Dortmund, Fachbereich 3, Organische Chemie
Fax: (+49) 231-133-2499
E-mail: herbert.waldmann@mpi-dortmund.mpg.de

Dr. R. Matzitschek, Dipl.-Chem. P. Baumhof, Prof. Dr. A. Giannis
Universität Leipzig
Institut für Organische Chemie
Johannisallee 29, 04103 Leipzig (Germany)
Fax: (+49) 341-9736-599
E-mail: giannis@chemie.uni-leipzig.de

© 2004 Wiley-VCH Verlag GmbH & Co. KGaA, Weinheim

Reaction Mechanisms

Trigonal Prismatic or not Trigonal Prismatic? On the Mechanisms of Oxygen-Atom Transfer in Molybdopterin-Based Enzymes **

*Martin Kaupp**

Keywords:
bioinorganic chemistry · molybdenum · oxotransferase enzymes · reaction mechanisms · transition metal complexes

In two recent quantum chemical studies, the mechanisms of oxygen-transfer reactions in suitable model complexes for the active sites of enzymes from the dimethyl sulfoxide reductase (DMSOR) family have been investigated.[1,2] In some, but not in all of the systems studied, six-coordinate reactive intermediates and associated transition states have been identified that are best described as trigonal prismatic. Furthermore they resemble some of the active-site structures found crystallographically for the oxidized Mo^{VI} form of enzymes from the DMSOR family. The aim of this article is to discuss the truly remarkable results of these theoretical and experimental studies from a general perspective, based on the underlying principles of "non-VSEPR" (valence-shell electron-pair repulsion) structural preferences in d^0–d^2 transition-metal complexes.[3]

Mononuclear Molybdenum and Tungsten Enzymes

With the exception of the molybdenum-containing nitrogenase, the main role of molybdenum and tungsten in biology is as redox-active centers in a series of mononuclear oxo-transferase enzymes which has been extensively studied (while the majority of these enzymes indeed catalyze oxygen-atom transfer, others are better described as hydroxylases).[4,5] The entire set of enzymes shares the common feature of a pyranopterin ligand (cofactor) which has apparently evolved specifically for this purpose, and which is frequently called molybdopterin (Figure 1). The ligand coordinates the metal center in a dithiolene-type chelating fashion. The appreciable number of known enzymes of this type (often termed "moco" enzymes because of the molybdopterin cofactor) has been classified into three distinct families, based on sequence-homology, active-site structure, and function:[4] the xanthine oxidase, sulfite oxidase, and DMSO reductase (DMSOR) families, respectively. Of these, the DMSOR family stands out, as two molybdopterin ligands occupy four metal coordination sites (Figure 1), whereas in the other two families of enzymes two sites are occupied by one ligand. It is thought that in most cases the mechanism of reduction of a substrate by the reduced form of the enzyme involves the direct transfer of an oxygen atom from the substrate to the metal center (and vice versa for an oxidative half reaction).[6]

Computational Evidence for Approximately Trigonal-Prismatic Intermediates and Transition States

The two recent computational studies[1,2] employed somewhat different model complexes and computational methods. Their results agree, but they

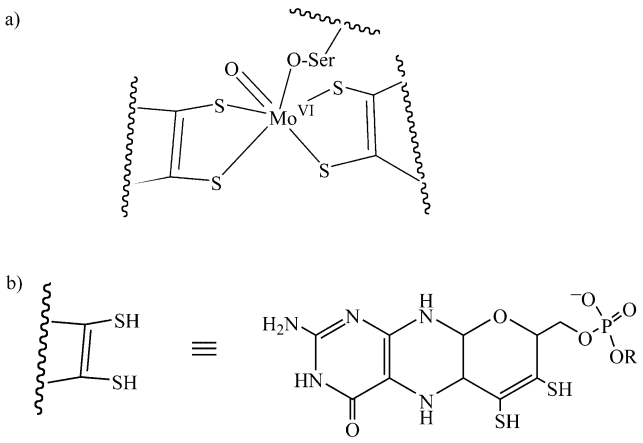


Figure 1. a) The presumed coordination environment of molybdenum in the oxidized form of DMSOR. b) The pyranopterin cofactor.

[*] Prof. Dr. M. Kaupp
Institut für Anorganische Chemie
Universität Würzburg
Am Hubland, 97074 Würzburg (Germany)
Fax: (+49) 931-888-7135
E-mail: kaupp@mail.uni-wuerzburg.de

[**] The author's work in the field has been funded by Deutsche Forschungsgemeinschaft and by Fonds der Chemischen Industrie.

 © 2004 Wiley-VCH Verlag GmbH & Co. KGaA, Weinheim DOI: 10.1002/anie.200301690

are to some extent also complementary. In the initial study, Webster and Hall[1] used two $[Me_2C_2S_2]^{2-}$ (mdt) ligands as dithiolene (dt) component, in an attempt to model the reaction of a synthetic functional model of DMSOR.[7] They employed hybrid density functional theory (DFT) methods and started with an approximately square-pyramidal $[Mo(mdt)_2OMe]^-$ complex as a model for the reduced (formally Mo^{IV})[8] form of the enzyme (cf. **I** in Figure 2 with Me instead of CN).[1] The overall reduction of DMSO to dimethyl sulfide (DMS) transferred the oxygen atom from DMSO to the metal center, to give a distorted octahedral Mo^{VI} complex[8] $[Mo(mdt)_2(O)OMe]^-$ (cf. **V** in Figure 2). Remarkably, however, the intermediate $[Mo(mdt)_2(DMSO)OMe]^-$ with attached DMSO (cf. **III** in Figure 2), as well as the transition state for oxygen-atom transfer from DMSO to the metal (cf. **IV** in Figure 2), were found to be close to trigonal prismatic. Moreover, Webster and Hall pointed out[1] that the bond angles around the metal in the intermediate and in the transition state were close to the structural parameters of the oxidized state of the active site in a variety of structurally characterized enzymes.[6a,9] This observation led these authors to suggest[1] that the structural constraints of the enzyme active site are less favorable for the preferably square-pyramidal educt and preferably distorted octahedral product than for the trigonal-prismatic transition state. This situation should lower the activation barrier relative to the constrained educt state, consistent with the idea of an entatic principle.[10] It was also suggested that the product state is destabilized, particularly by the deformation from a distorted octahedral structure in the free model complex to an approximately trigonal-prismatic structure in the enzyme active site. This destabilization should reduce the exothermicity of the reduction reaction.

In their subsequent computational study, Thapper et al. used maleonitrile-1,2-dithiolate, $[(CN)_2C_2S_2]^{2-}$ (mnt), as the dt component and employed local and gradient-corrected DFT methods to investigate a somewhat wider set of reactions.[2] Their results for the reduction of DMSO by $[Mo(mnt)_2OMe]^-$ (Figure 2) were very similar to those of Webster and Hall,[1] with slightly different energetics (which is understandable in view of the different model ligands and computational levels). The main additional aspect in this study was the determination of another nearly trigonal-prismatic transition state, in this case for DMSO binding (**II** in Figure 2).[2] Note that the scheme of Thapper et al.[2] (Figure 2) and the work of Webster and Hall[1] both favor oxygen-atom transfer as rate-determining step of the overall reaction, and not substrate binding. This is not unequivocally accepted,[7a] and it may well be that different rate-determining steps are involved in enzymes and models. Notably, however, both transition states **II** and **IV** (Figure 2) involve a distorted trigonal-prismatic metal coordination environment.

In other enzyme structures, the Mo^{IV} state already contains one oxo ligand and the final Mo^{VI} state is suggested to have two oxo ligands; one such example is the Me_3NO reductase from *R. capsulatus*.[11] Thapper et al. used $[Mo^{IV}(mnt)_2(O)]^{2-}$ to model the reduction of Me_3NO and of DMSO by Me_3NO reductase. The reduction of Me_3NO by this model complex was computed to proceed via a distorted octahedral intermediate with bound substrate, and via two related transition states for substrate binding and oxygen-atom abstraction, which were also described as distorted octahedral.[2] The reduction was calculated to be exothermic, and the activation barriers were around 70 kJ mol^{-1} relative to the initial state, similar to the above-mentioned reduction of DMSO by $[Mo(mnt)_2OMe]^-$. This result agrees with experimental data for the same model $[Mo^{IV}(mnt)_2(O)]^{2-}$ complex.[7] In contrast, when the same model was employed in a simulation of the reduction of DMSO,

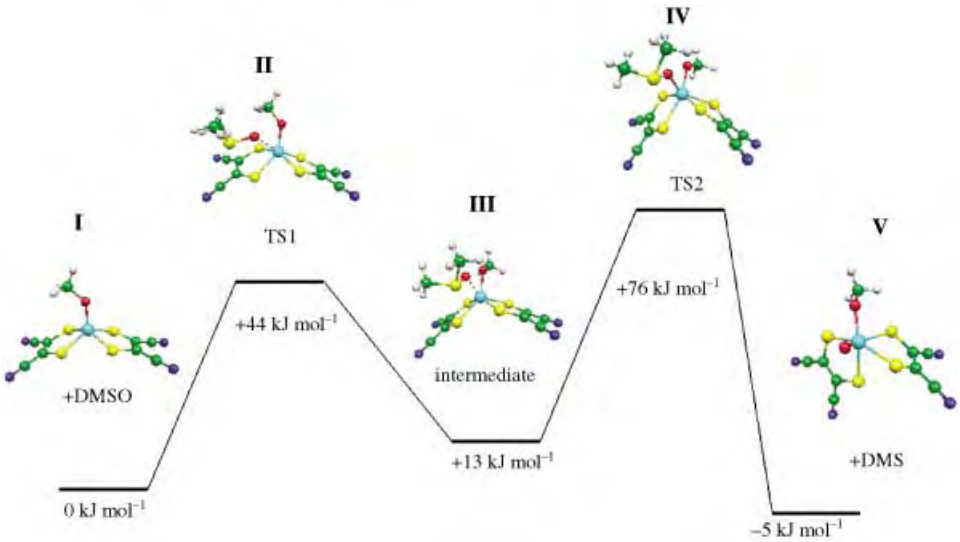


Figure 2. Optimized structures of stationary points along the pathway of oxygen-atom transfer from DMSO to a dithiolene molybdenum complex in a simplified molecular model system. Structural data and energies have been taken from the computational study of Thapper et al.:[2] **I** educt $[Mo^{IV}(mnt)_2OMe]^-$, **II** transition state for DMSO binding, **III** intermediate with bonded DMSO, **IV** transition state for oxygen-atom abstraction, **V** product $[Mo^{VI}(mnt)_2(O)OMe]^-$.

 © 2004 Wiley-VCH Verlag GmbH & Co. KGaA, Weinheim

no intermediate structure was found. The reaction proceeded over a very high barrier of approximately 150 kJ mol^{-1} and was computed to be endothermic, consistent with experimental observation.[2] It appears thus, that a [Mo^{IV}-(dt)$_2$(O)]$^{2-}$-type model is able to reduce the "easier target" Me_3NO but not DMSO, whereas [Mo(dt)$_2$OMe]$^-$ is able to reduce also DMSO.

Electronic Factors that Control the Preference for Trigonal-Prismatic over Octahedral Structures in d^0 and d^2 Complexes

The significance of trigonal-prismatic transition states and reactive intermediates in these model reactions, together with the apparently trigonal-prismatic coordination found for a number of enzyme active-site structures in their final oxidized M^{VI} form, should not be underestimated! As suggested by Webster and Hall,[1] the preforming of a trigonal-prismatic environment by the constraints of the pterin ligands, and of the additional coordinated amino acid ligand (serine in DMSOR, cystein or selenocystein in related cases[4,5]), appears to lower the activation barrier. Furthermore, the constraints of the protein apparently reduce the exothermicity of the reaction and thereby make it more reversible, in agreement with experimental observation.

These results suggest that nature makes good use of the preference of intermediate **III** and of its two associated transition states **II** and **IV** (Figure 2) for an approximately trigonal-prismatic metal coordination environment. It is thus important to understand why such trigonal-prismatic structures appear to be favorable in DMSOR and related active sites with an amino acid ligand at the metal center, whereas they do not appear in systems such as Me_3NO reductase, in which even the reduced Mo^{IV} state has an oxo ligand (see above).

Formally,[8] the oxidized Mo^{VI} and reduced Mo^{IV} states of DMSOR may be considered d^0 and d^2 systems, respectively. Under certain circumstances, which have been discussed in detail in a recent review,[3] hexacoordinate d^0 or d^2 systems may prefer "non-VSEPR" structures that are derived from a trigonal prism. While σ bonding involving metal d orbitals favors prismatic structures, π bonding tends to stabilize octahedral metal coordination. The main prerequisite for prismatic structures is thus a ligand donor set that contains no strong π-donor ligands. For example, prototype organometallic d^0 systems, such as hexamethyl tungsten or -molybdenum, which have only σ-donating ligands, are known to have trigonal-prismatic structures that are even often distorted further characteristically towards a C_{3v} skeleton. Corresponding d^1 systems, such as hexamethyl rhenium are regular trigonal prismatic, and the d^2 system hexamethyl osmium has also been computed to be a regular trigonal prism.[12]

This extreme situation with exclusively σ-donor ligands is restricted to specific, extremely reactive organometallic complexes, or to recently characterized hydrides in matrix isolation.[13] However, dithiolene ligands provide the closest equivalent: When viewed as dianionic dithiolates,[8] they may be considered single-sided π donors. But owing to the partial delocalization of the corresponding π orbital on sulfur into the unsaturated backbone, dithiolenes are particularly weak π donors.[3] Indeed, the remarkably poor π-donor ability could be one of the properties that led to the evolution of the specialized molybdopterin ligands for moco enzymes. Even before the nature of the molybdopterin ligand had been established, tris(dithiolene) systems were the first molecular complexes with trigonal-prismatic structures to be discovered, and many tris(dithiolene) and related compounds have been structurally characterized.[3] Computations show that in electron-poor transition-metal systems, the unsaturated dithiolenes, owing to reduced π bonding abilities, provide a significantly larger electronic preference for prismatic arrangements than their saturated thiolate analogues.[3]

As had already been pointed out,[3] the bonding of two weakly π donating dithiolene ligands to the metal in the active sites of enzymes from the DMSOR family (or of related tungsten-based enzymes that also feature bis(dithiolene) coordination[5]) makes trigonal-prismatic arrangements much more likely in these enzymes than in any of the two other known families, in which only one of the two pterin ligands is bonded to the metal. Indeed, crystallographic characterization of enzymes in, and model complexes for, the Xanthine Oxidase or Sulfite Oxidase families have never provided any indication of trigonal-prismatic structures. In all of these cases, strongly π-donating oxo or sulfido coligands were present, and hexacoordinate complexes were always found to be distorted octahedral. Even with four coordination sites occupied by dithiolene sulfur atoms, the presence of an oxo or sulfido ligand will lead to an electronic preference for distorted octahedral structures. This tendency may be seen clearly for synthetic M^{VI} product model complexes,[7] as well as for computationally determined structures of [M(dt)$_2$(O)L]-type intermediates (L being the substrate).[1,2] As pointed out by Webster and Hall,[1] this shows clearly that the distorted trigonal-prismatic structures found crystallographically for the [Mo^{VI}(dt)$_2$(O)X]$^-$-type product states (X = serine, cystein, selenocystein) in a number of enzymes from the DMSOR family,[4,7] as well as for the structurally characterized tungsten enzymes,[5] must be a result of the constraints imposed by the protein scaffold, to which both the pterin ligands and the amino acid coligand X are fixed. It is even conceivable that an important purpose of the characteristic ring closure of the pyran ring in the pterin ligand[4,5] could be to provide a rigid tricyclic skeleton that transmits the constraints of the protein framework to the metal coordination environment.

Concluding Remarks

Recent computational findings,[1,2] together with crystallographic evidence for both enzyme active sites and synthetic model complexes,[4–7,9–11] provide clear evidence that the "non-VSEPR" preferences of d^0 and d^2 complexes with weak π-donor sets[3] are used in an appreciable number of enzymes of the DMSOR family to provide low activation barriers, and probably also thermochemical reversibility of the oxygen-atom transfer reaction. In contrast, in those examples from the DMSOR fam-

 © 2004 Wiley-VCH Verlag GmbH & Co. KGaA, Weinheim

ily that do already feature an oxo ligand in the Mo^{IV} reduced state (and thus two oxo ligands in the Mo^{VI} product), this type of stabilization by trigonal-prismatic intermediates is not possible. The same holds for the xanthine oxidase and sulfite oxidase families of enzymes. In these cases, the role of the oxo (or sulfido) "spectator ligands" is thought[1] to involve a variability of π bonding at different stages of the reaction,[14] to provide a fine tuning of the electron deficiency at the metal center, and to thereby lower the activation barriers. We note in passing that the poor π-donor abilities and the delocalized nature of bonding with dithiolene ligands is also thought to contribute generally to the adjustment of the redox potential of the enzyme active site.[4,5]

The different enzymes are specific for different reactions with different overall thermochemistry. For example, oxygen abstraction from DMSO is much more difficult than from Me_3NO or from nitrate. This is related to the strength of the bond to be broken, as well as to the basicity of the reduced product fragment.[7] Apparently, the catalytic abilities of the different oxotransferase enzymes are carefully adjusted by the different ligands. Stabilization of transition states by either 1) forcing a trigonal-prismatic ligand scaffold in the absence of oxo or sulfido ligands or by 2) employing the π-electron buffer abilities of oxo or sulfido ligands seem to be two major strategies in the adjustment of kinetics and thermochemistry of the different reactions. The π-donor abilities of the amino acid coligands may also adjust the redox potentials, as suggested by the fact that O, S, and Se donor atoms from serine, cystein, and selenocystein, respectively, are employed in different systems, to catalyze different reactions.[4,5]

An additional strategy that should be mentioned is a change of the metal center. Compared to its 4d homologue molybdenum, the 5d metal tungsten stabilizes the M^{VI} relative to the M^{IV} state and thereby modifies not only the thermochemistry but also the kinetics of the redox reaction. This effect may have played a role in evolution. For example, tungsten is employed almost exclusively in an anaerobic environment (the W^{IV} species tend to be oxidized by molecular oxygen), for reactions with rather low redox potentials, and typically at high temperatures of operation (in particular in hyperthermophilic bacteria).[5] Interestingly, the differences between the relative stabilities of the M^{VI} and M^{IV} oxidation states for 5d compared to 4d metals are largely a result of the much larger relativistic effects for the former. The effects of special relativity expand and destabilize 5d orbitals much more than 4d orbitals and thereby enhance the bond ionicity and stabilize higher oxidation states.[3,15]

Finally, it is worth mentioning, that "non-VSEPR" distortions of d^0–d^2 systems are not only of biological importance but also play an important role in many extended solids of relevance for materials sciences. Examples are ferroelectric, distorted perovskites, or the various, important allotropes of ZrO_2.[3] In these solids the various electronic preferences of metal coordination[3] are also further modulated by the environment, in these cases by the constraints of the extended crystal.[16]

[1] C. E. Webster, M. B. Hall, *J. Am. Chem. Soc.* **2001**, *123*, 5820.

[2] S. Thapper, R. J. Deeth, E. Nordlander, *Inorg. Chem.* **2002**, *41*, 6695.

[3] M. Kaupp, *Angew. Chem.* **2001**, *113*, 3642; *Angew. Chem. Int. Ed.* **2001**, *40*, 3534 and references therein.

[4] R. Hille, *Chem. Rev.* **1996**, *96*, 2757.

[5] M. K. Johnson, D. C. Rees, W. W. Adams, *Chem. Rev.* **1996**, *96*, 2817.

[6] a) H. Schindelin, C. Kisker, J. Hilton, K. V. Rajagopalan, D. C. Rees, *Science* **1996**, *272*, 1615; b) S. D. Garton, J. Hilton, H. Oku, B. R. Crouse, K. V. Rajgopalan, M. K. Johnson, *J. Am. Chem. Soc.* **1997**, *119*, 12906; c) B. E. Schultz, R. Hille, R. H. Holm, *J. Am. Chem. Soc.* **1995**, *117*, 827.

[7] a) K.-M. Sung, R. H. Holm, *J. Am. Chem. Soc.* **2002**, *124*, 4312; b) B. S. Lim, R. H. Holm, *J. Am. Chem. Soc.* **2001**, *123*, 1920; c) B. S. Lim, K.-M. Sung, R. H. Holm, *J. Am. Chem. Soc.* **2000**, *122*, 7410.

[8] The formal designations of Mo oxidation states and d configurations used herein are based on the presumption of a dianionic $[R_2C_2S_2]^{2-}$ form of the dithiolene ligand. It is important to note that this conventional oxidation-state formalism is not expected to be a very faithful representation for the true electronic situation of the molybdenum complex in question, owing to extensive delocalization.

[9] H.-K. Li, C. Temple, K. V. Rajagopalan, H. Schindelin, *J. Am. Chem. Soc.* **2000**, *122*, 7573; J. C. Boyington, V. N. Gladyshev, S. V. Khangulov, T. C. Stadtman, P. D. Sun, *Science* **1997**, *275*, 1305; M. K. Chan, S. Mukund, A. Kletzin, M. W. W. Adams, D. C. Rees, *Science* **1995**, *267*, 1463.

[10] B. L. Valee, R. J. P. Williams, *Proc. Natl. Acad. Sci. USA* **1968**, *59*, 498; R. J. P. Willliams, *Eur. J. Biochem.* **1995**, *234*, 363.

[11] M. Czizek, J.-P. Dos Santos, J. Pommier, G. Giordane, V. Méjean, R. Haser, *J. Mol. Biol.* **1998**, *284*, 435.

[12] M. Kaupp, *Chem. Eur. J.* **1998**, *4*, 1678.

[13] X. Wang, L. Andrews, *J. Am. Chem. Soc.* **2002**, *124*, 5637; X. Wang, L. Andrews, *J. Phys. Chem. A* **2002**, *106*, 6720.

[14] A. K. Rappé, W. A. Goddard III, *J. Am. Chem. Soc.* **1982**, *104*, 3287.

[15] See, for example: P. Pyykkö, *Chem. Rev.* **1988**, *88*, 563.

[16] M. Kunz, I. D. Brown, *J. Solid State Chem.* **1995**, *115*, 395.

 © 2004 Wiley-VCH Verlag GmbH & Co. KGaA, Weinheim

Stereoselective Alkylations

New Catalytic Approaches in the Stereoselective Friedel–Crafts Alkylation Reaction**

Marco Bandini, Alfonso Melloni, and Achille Umani-Ronchi**

Keywords:
alkylation · aromatic substitution · asymmetric catalysis · Lewis acids · synthesis design

After more than 125 years, the Friedel–Crafts alkylation is still one of the most studied and most utilized reactions in organic synthesis. What is the secret of this astonishing success? Perhaps the great versatility in scope and applicability continues to justify its crucial role in the synthesis of more and more complex molecules. However, it has taken more than a century for asymmetric catalytic versions of this reaction to be developed and subsequently extended to a range of aromatic compounds and alkylating agents. Herein we review recent developments in the design and use of catalytic and stereoselective strategies for the alkylation of aromatic systems and synthesis of a wide range of polyfunctionalized enantiomerically enriched compounds.

1. Introduction

The Friedel–Crafts (F–C) reaction is one of the oldest organic transformations to employ Lewis acids as promoters, and since the pioneering study by Charles Friedel and James M. Crafts[1] it has been one of the most powerful C–C bond-forming processes in organic synthesis.[2] The original procedure (for which stoichiometric amounts of a Lewis acid were required) has subsequently been replaced by milder and more environmentally friendly conditions.[3] The ever-increasing number of catalytic procedures reported in the literature over the past decade for the catalytic alkylation and acylation of aromatic and heteroaromatic compounds is striking (Figure 1).[4]

In the mid-1980s the first examples of the asymmetric addition of aromatic C–H bonds to carbonyl compounds appeared in the literature.[5] Since then the synthetic relevance of the formation of benzylic carbon stereocenters prompted several groups to develop new stereoselective and catalytic strategies.[6] Herein, a brief overview of the most recent asymmetric protocols of the metal- and organocatalyzed electrophilic alkylation of aromatic compounds is presented. We found it convenient to gather the F–C alkylations into three sections: ring-opening reactions of epoxides by aromatic compounds (Scheme 1 a), enantioselective 1,2-

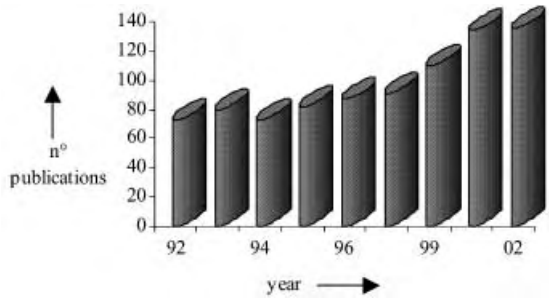
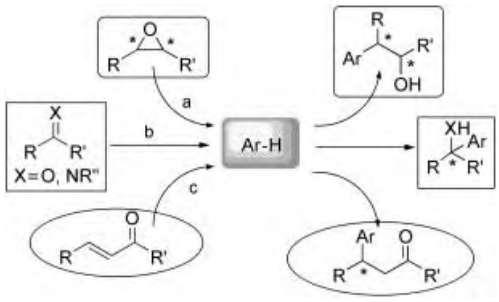


Figure 1. The increasing number of catalytic Friedel–Crafts procedures published from 1991 to date.



Scheme 1. Possible approaches in the asymmetric Friedel–Crafts alkylation of aromatic compounds.

[*] Dr. M. Bandini, A. Melloni, Prof. Dr. A. Umani-Ronchi
Dipartimento di Chimica "G. Ciamician", Università di Bologna
Via Selmi, 2, 40126 Bologna (Italy)
Fax: (+39) 051-209-9456
E-mail: marco.bandini@unibo.it
umani@ciam.unibo.it

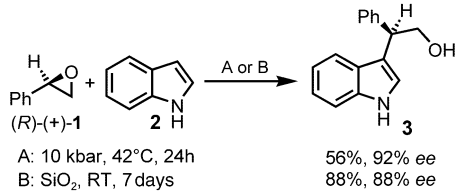
[**] We thank "Progetti FIRB", Consorzio C.I.N.M.P.I.S. (Bari), M.U.R.S.T. (Rome) "Progetto Stereoselezione in Chimica Organica. Metodologie ed Applicazioni", and the University of Bologna (funds for selected research topics) for the financial support of this research.

© 2004 Wiley-VCH Verlag GmbH & Co. KGaA, Weinheim
DOI: 10.1002/anie.200301679

additions of aromatic systems to carbonyl groups (Scheme 1b), and 1,4-conjugate additions of aromatic systems to α,β-unsaturated carbonyl compounds (Scheme 1c).

2. Catalytic Stereocontrolled Ring-Opening of Epoxides by Aromatic Compounds

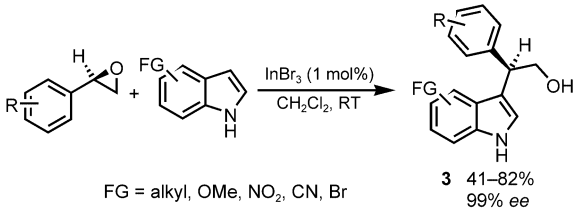
The ring-opening of epoxides by aromatic compounds in the presence of Lewis acids, bases, and solid acids is widely recognized as an effective step in the synthesis of polyfunctionalized compounds.[7] Moreover, the ready availability of enantioenriched *cis* and *trans* epoxides by means of various stereoselective epoxidations makes this approach an attractive candidate for use as a tool in the synthesis of optically active aromatic compounds. The main drawbacks encountered in this strategy are the occurrence of polyalkylation and the frequent absence of regioselectivity. Only a few examples involving enantiomerically enriched epoxides have been described. In particular, Kotsuki et al. reported the regio- and stereoselective alkylation of indole (**2**) with (*R*)-(+)-styrene oxide (**1**) promoted by high pressure or catalyzed by silica gel (Scheme 2).[8] Although both approaches guaranteed satisfactory yields of **3**, partial racemization of the enantiomerically pure starting epoxide was observed (high pressure: 92% *ee*, SiO_2: 88% *ee*).



Scheme 2. High-pressure and silica-gel-catalyzed stereoselective ring-opening of (*R*)-(+)-styrene oxide.

The use of Lewis acids represents a valuable way to promote and control the reactivity of oxiranes toward nucleophiles. Furthermore, the electronic features of the Lewis acid must be considered carefully to prevent the formation of carbocation intermediates. In this context, the mild Lewis acidity of indium(III) salts and their relatively low oxophilicity[9] make them suitable candidates for the promotion of stereoselective alkylations of aromatic compounds by the ring-opening of enantiomerically pure epoxides.

Our research group reported a highly stereoselective alkylation of functionalized indoles with enantiomerically pure aryl epoxides in the presence of anhydrous $InBr_3$ (1 mol%).[10] The reaction, which proceeds exclusively through a regio- and stereoselective S_N2-type pathway at the benzylic position of the epoxide, allows a number of β-3-indolyl alcohols **3** to be isolated in high yields and with 99% *ee* (Scheme 3).



Scheme 3. Regio- and stereoselective ring-opening of optically active epoxides catalyzed by $InBr_3$.

As a natural extension of the ring-opening of enantiomerically pure epoxides, we recently developed the first catalytic asymmetric resolution of racemic internal aromatic oxiranes through a carbon–carbon bond-forming reaction. It was found that 2-methylindole reacts smoothly and regioselectively with (±)-styrene oxide (**1**) in the presence of a catalytic amount (5 mol%) of the commercially available [Cr(salen)Cl] complex **4a** (salen = *N*,*N*′-bis(3,5-di-*tert*-butylsalicylidene)-1,2-cyclohexanediamine) to afford both the unreacted styrene oxide and the indolyl derivative **5** with moderate enantiomeric excess (55 and 56% *ee*, respectively, Scheme 4a).[11] By careful tuning of the conversion of the kinetically controlled step, the protocol allowed functionalized internal *cis* and *trans* epoxides to be prepared in enantiomerically pure form (up to 99% *ee*) and in moderate yields (Scheme 4b). Moreover, the [Cr(salen)Cl] **4a** was also found able to promote the desymmetrization of *meso* stilbene oxide in the presence of variously substituted indoles. The desired β-indolyl alcohols **5**′ were isolated in excellent chemical yields and optical purities (up to 98% yield, up to 98% *ee*, Scheme 5).

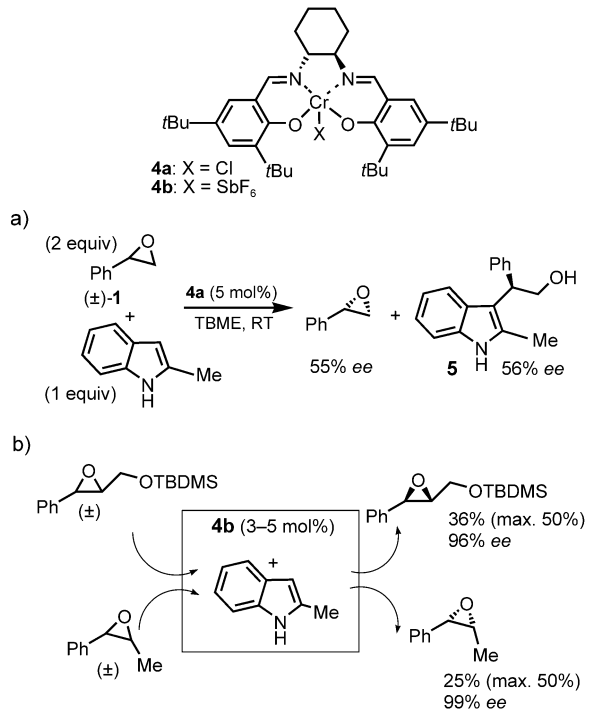


Marco Bandini was born in Faenza (Italy) in 1973. He received his BSc degree (Laurea) in 1997 from the University of Bologna. In 1999 he spent a period in the research group of Prof. M. R. Gagné at North Carolina University, Chapel Hill. In 2000 he received his PhD under the supervision of Prof. Umani-Ronchi and was appointed assistant professor at the University of Bologna. He was the recipient of the G.I.C.O. Junior Award of the Italian Chemical Society in 2002. His current scientific interests are focused on asymmetric synthesis mediated by homogeneous organometallic catalysts.



Alfonso Melloni, born in Padova (Italy) in 1973, received his BSc in chemistry from the University of Bologna in 1999. In 2000 he joined Prof. P. Bravo (Politecnico of Milan), working on the total synthesis of fluorinated pheromones. He is currently a PhD student in the research group of Prof. A. Umani-Ronchi. His research is focused on the synthesis of optically active compounds by employing chiral organometallic catalysts.

© 2004 Wiley-VCH Verlag GmbH & Co. KGaA, Weinheim



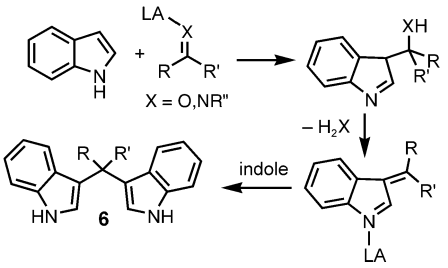
Scheme 4. Asymmetric kinetic resolution of *cis* and *trans* epoxides catalyzed by [Cr(salen)X] complexes. TBDMS = *tert*-butyldimethylsilyl, TBME = *tert*-butyl methyl ether.



Scheme 5. Enantioselective desymmetrization of *meso* stilbene oxide catalyzed by [Cr(salen)X] complexes.

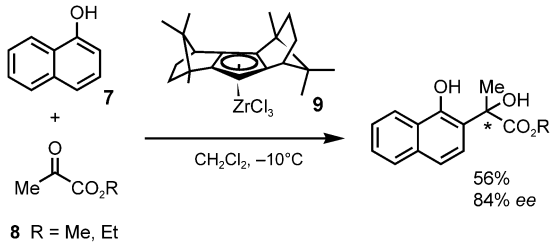
3. Catalytic Asymmetric Addition of Aromatic Compounds to C=O and C=NR Groups

The addition of electron-rich aromatic compounds to aldehydes, ketones, and imines leads to the formation of versatile functionalized compounds.[12] However, because of the intrinsic instability of many aminomethyl and hydroxymethyl aromatic systems, polysubstitution reactions to give bisaryl compounds of the type **6** are commonly encountered both under homogeneous and heterogeneous catalysis (Scheme 6).[13] After the first catalytic asymmetric addition



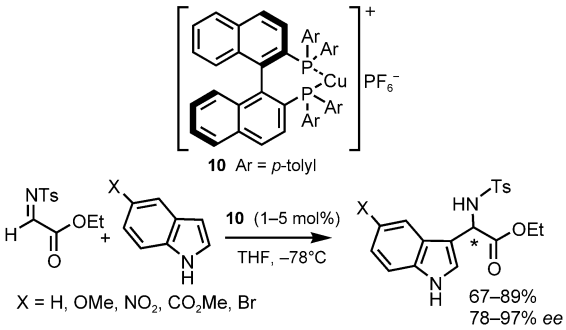
Scheme 6. Bisindolyl compounds **6** as side products in Lewis acid (LA) mediated additions of indoles to carbonyl compounds.

of 1-naphthol (**7**) to pyruvic esters **8** mediated by the chiral zirconocene complex **9** (Scheme 7),[5b] a considerable breakthrough in this area was made independently by Johannsen[14a]



Scheme 7. The use of a chiral zirconocene complex **9** as the catalyst for the addition of 1-hydroxynaphthalene (**7**) to the pyruvic esters **8**.

and Mikami and co-workers.[14b] They described the synthesis of heteroaromatic *N*-tosyl-α-amino acids catalyzed by tol-binap/$CuPF_6$ (the Lectka catalyst (**10**), Scheme 8) and the preparation of organofluoro compounds by the addition of electron-rich arenes to fluoral (**11**) in the presence of a chiral substituted binol–titanium complex **12** (Scheme 9), respec-

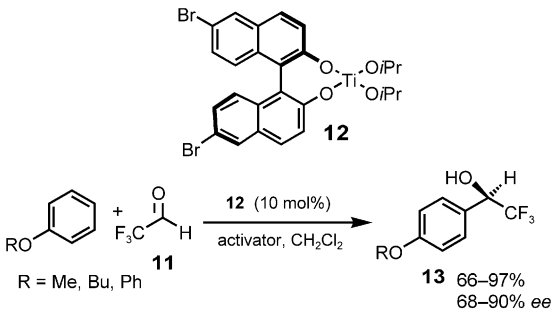


Scheme 8. Enantioselective Friedel–Crafts alkylation of indoles catalyzed by the tol-binap–Cu^{I} complex **10**. Ts = *p*-toluenesulfonyl, tol-binap = bis[2,2′-(di-*p*-tolylphosphanyl)-1,1′-naphthyl].



Achille Umani-Ronchi graduated in chemistry in 1960 from the University of Rome. He was an assistant at the Politecnico of Milan (Italy) from 1961 to 1969, then an assistant professor at the University of Bari. He spent one year (1964–65) as a postdoctoral fellow at the ETH in Zürich (Prof. D. Arigoni) and six months as a postdoctoral fellow at the University of Cambridge (Prof. J. Lewis). Since 1980 he has been a full professor of organic chemistry at the University of Bologna. In 2002 he received the Award of the Italian Chemical Society for his contributions to organic synthesis.

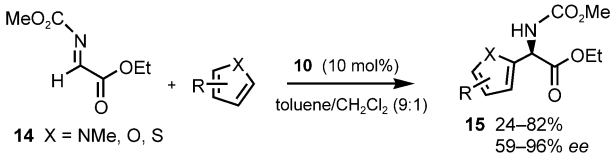
 © 2004 Wiley-VCH Verlag GmbH & Co. KGaA, Weinheim



Scheme 9. Use of a binol–titanium complex **12** as the catalyst for the asymmetric addition of electron-rich arenes to fluoral (**11**). binol = 1,1′-bis(2-naphthol).

tively. In the latter case, a notable improvement in the catalytic effectiveness was observed when biphenols were added as activators (asymmetric activation) to the chiral titanium-based Lewis acid.[15]

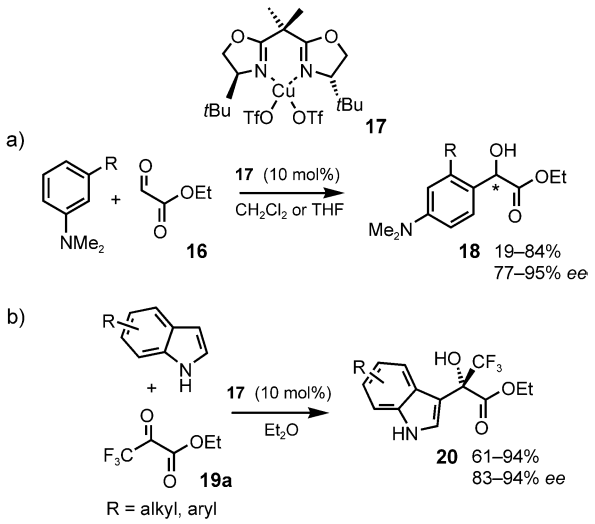
The range of accessible enantiomerically enriched α-heteroarene α-amino acids, starting from a variety of substituted benzenes and furans, was improved remarkably by utilizing the catalytic system **10** and α-imine esters **14** as electrophiles.[16] In this study, several N-protecting groups were tested, and the highest chemical yields and *ee* values were observed when a readily removable *N*-carbamate group was used (Scheme 10).



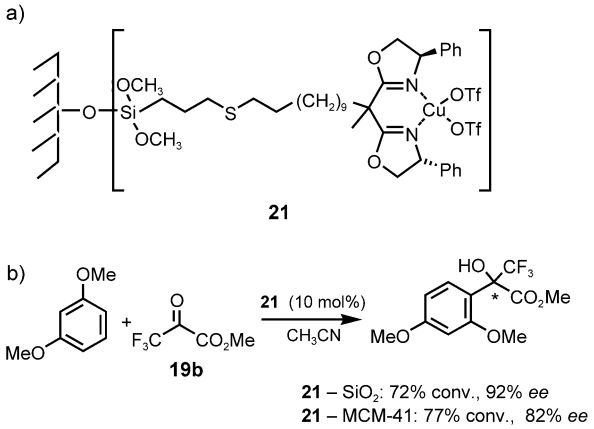
Scheme 10. Enantioselective addition of electron-rich aromatic compounds to imines catalyzed by **10**.

The synthetic versatility of the catalytic F–C alkylation was further emphasized by Jørgensen and co-workers, who were able to obtain aromatic mandelic esters **18**[17a] and heteroaromatic hydroxytrifluoromethyl esters **20**[17b] by asymmetric F–C reactions of aromatic compounds to ethyl glyoxylate (**16**, Scheme 11 a) and ethyl trifluoropyruvate (**19 a**, Scheme 11 b), respectively. The cationic *t*Bu-box–copper(II) triflate complex **17** (box = bisoxazoline) and chelating substrates were used in these catalytic approaches to give high stereoselectivity. Under these conditions aromatic amines, anisoles, and heteroaromatic compounds were all found to undergo highly enantioselective F–C reactions, thus showing the wide applicability of the catalytic system. However, less-reactive substituted furans required a higher catalyst loading (40 mol %) for satisfactory chemical yields to be observed.[18]

Corma et al. recently studied the first example of heterogeneous catalytic asymmetric F–C alkylation, in the reaction of 1,3-dimethoxybenzene with methyl 3,3,3-trifluoropyruvate (**19 b**) in the presence of a chiral Ph-box–copper(II) complex covalently anchored to silica or mesoporous MCM-41 (**21**, Scheme 12).[19] The use of supported catalysts furnished the



Scheme 11. Stereoselective syntheses of substituted mandelic esters and heteroaromatic trifluoromethyl-substituted esters through F–C alkylations catalyzed by box–Cu^{II} complexes.



Scheme 12. Chiral copper catalyst anchored to solid supports (silica, MCM-41) as a mediator of the asymmetric alkylation of 1,3-dimethoxybenzene. conv. = conversion.

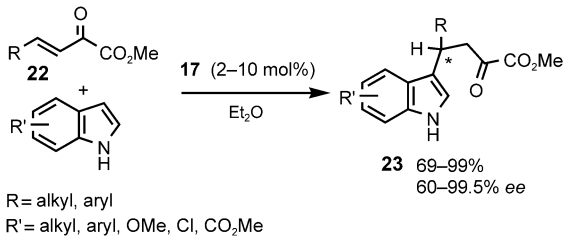
same levels of stereoselectivity (82–92 % *ee*, 72–77 % conversion) as observed in the homogeneous process (86 % *ee*),[17a] and the heterogeneous catalysts could be recovered easily by filtration. The reusability of the chiral catalyst **21**–MCM-41 was also investigated, and the second catalytic reaction afforded the same level of enantioselectivity (84 % *ee*) and only a slight decrease in conversion (73 %).

4. Catalytic Asymmetric Michael-Type Addition of Aromatic Compounds to α,β-Unsaturated Carbonyl Compounds

α,β-Unsaturated carbonyl compounds are suitable substrates for F–C alkylations, and in fact numerous acid-catalyzed Michael-type additions of aromatic compounds have been described.[20] Nevertheless, stereoselective variants have been less explored. The first example of highly

 © 2004 Wiley-VCH Verlag GmbH & Co. KGaA, Weinheim

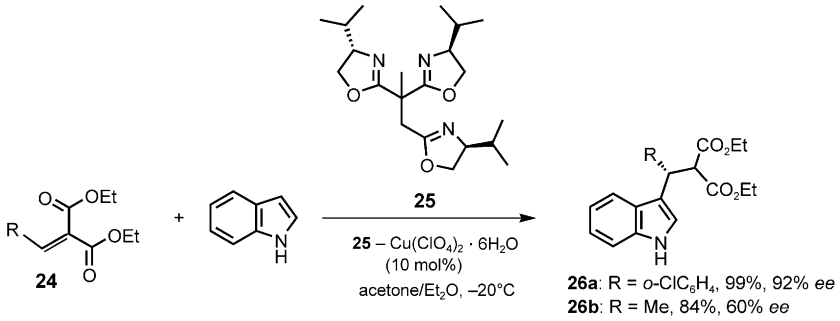
enantioselective catalytic 1,4-addition of electron-rich aromatic compounds to β,γ-unsaturated-α-keto esters **22**, in the presence of the chiral box-copper(II) complex **17**, was described by Jørgensen et al. (Scheme 13).[21] Later, Zhou and Tang demonstrated the effectiveness of the pseudo-C_3-



Scheme 13. Enantioselective conjugate addition of indoles to β,γ-unsaturated α-ketoesters in the presence of the cationic *t*Bu-box–copper(II) complex **17**.

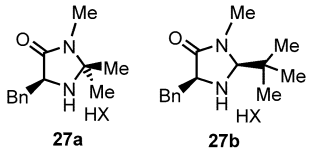
symmetric trisoxazoline **25** complexed with $Cu(ClO_4)_2 \cdot 6H_2O$ in promoting (both under anhydrous and non-anhydrous conditions) the enantioselective addition of indole to arylidene malonates **24** (R = Ar) at −20 °C (Scheme 14).[22] The data collected by the authors show that the presence of an aromatic group bonded to the malonate C–C double bond is crucial for high enantioselectivity to be observed. When the F–C reaction was carried out with an alkylidene malonate (**24**, R = Me), the enantioselectivity dropped to 60 % *ee* for the product **26b**. Comparison of the results obtained in the analogous reaction by Jørgensen and co-workers with the classic bidentate C_2-symmetric *t*Bu-box ligand (maximum *ee* value: 69 %)[23] shows the influence of the sidearm present in the tridentate ligand **25**.

The use of chelating substrates in combination with chiral cationic Lewis acids is a well-known strategy to ensure high levels of stereoselectivity. However, it also represents a significant restriction in applicability. A Michael-type reaction between aromatic compounds and nonchelating α,β-unsaturated carbonyl compounds was first reported by the research group of MacMillan,[24] and more recently by our research group.[25] MacMillan and co-workers elegantly designed and employed the chiral tailored benzyl imidazo-

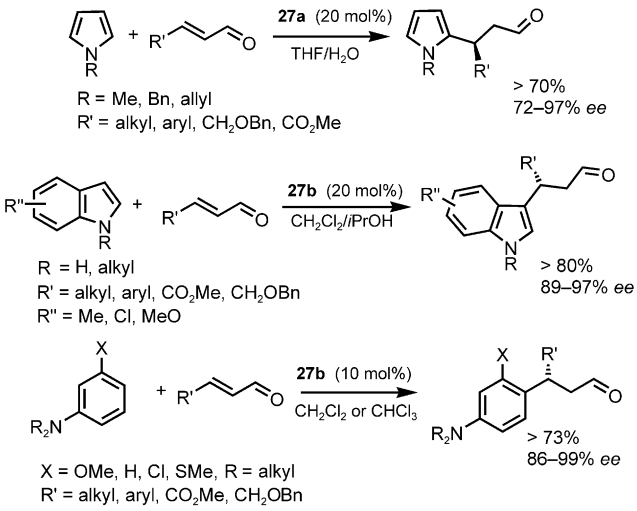


Scheme 14. Versatility of new chiral trisoxazoline ligands in the Michael addition of indole to alkylidene and arylidene malonates. The sidearm effect.

lidinone·HX salts **27a**,**b** derived from L-phenylalanine as organic catalysts for the 1,4-addition of pyrroles, indoles, and



aniline derivatives to α,β-unsaturated aldehydes (Scheme 15). The LUMO-lowering activation of aldehydes by reversible formation of chiral intermediate iminium salts **28**

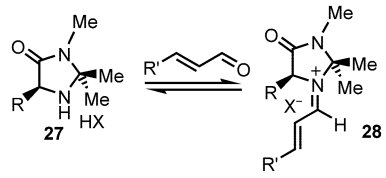


Scheme 15. Examples of enantioselective organocatalyzed Friedel–Crafts Michael-type addition of pyrroles, indoles, and anilines to α,β-unsaturated aldehydes.

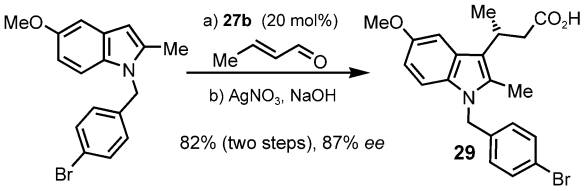
(Scheme 16) is responsible for the modulation of both reactivity and stereoselectivity in these F–C reactions. This new metal-free approach for the catalytic and stereoselective alkylation of electron-rich arenes proved to be general in scope, and polyalkylation, which is the main type of side reaction in the metallocatalyzed addition of arenes to aldehydes, was not observed. Finally, the stereoselective 1,4-addition of indoles to crotonaldehyde in the presence of **27b** led to a very useful synthetic application of this strategy, allowing the synthesis of indolobutyric acid **29** (COX-2 inhibitor) in good yield and good optical purity (Scheme 17).

The aforementioned organocatalysis protocol is ineffective toward the stereoselective addition of aromatic compounds to α,β-unsaturated ketones, which are less reactive than the corresponding aldehydes. We recently investigated the use of the chiral [Al(salen)Cl] complex **31** in the presence 2,6-lutidine as the catalyst for the first enantioselective addition of indoles to α,β-unsaturated aryl ketones (up to 89 % *ee*, Scheme 18). Experimental evidence suggests that a new catalytic species, formed by

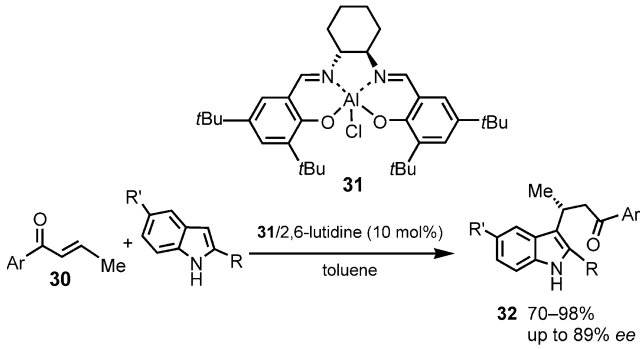
 © 2004 Wiley-VCH Verlag GmbH & Co. KGaA, Weinheim



Scheme 16. The LUMO-lowering activation of α,β-unsaturated aldehydes by formation of chiral iminium salts **28**.



Scheme 17. Organocatalyzed Friedel–Crafts alkylation for the synthesis of the COX-2 inhibitor **29**.



Scheme 18. Enantioselective Michael-type addition of indoles to α,β-unsaturated aryl ketones catalyzed by an [Al(salen)Cl]/2,6-lutidine complex.

complexation of the aluminum complex with the amine, operates in the enantiodiscrimination step of the F–C alkylation.

5. Summary and Outlook

As we have seen herein, the design and development of new catalytic and stereoselective strategies for the alkylation of aromatic compounds have received a great deal of attention in recent years. These strategies, which overcome the historical drawbacks of a lack in regio- and chemoselectivity associated with Friedel–Crafts alkylations, allow easy access to several classes of polyfunctionalized enantiomerically enriched compounds, which are valuable building blocks in organic synthesis.[26] These reactions are undergoing continuous development. The attempt to extend the applicability of catalytic stereoselective protocols to less reactive aromatic compounds is only one of the challenges that engage researchers on a daily basis in one of the oldest reactions of modern organic synthesis.

Received: July 10, 2003 [M1679]

[1] a) C. Friedel, J. M. Crafts, *C. R. Hebd. Seances Acad. Sci.* **1877**, *84*, 1392; b) C. Friedel, J. M. Crafts, *C. R. Hebd. Seances Acad. Sci.* **1877**, *84*, 1450.

[2] a) G. A. Olah in *Friedel-Crafts and Related Reactions*, Wiley, New York, **1963**; b) G. A. Olah in *Friedel-Crafts Chemistry*, Wiley, New York, **1973**.

[3] a) T. Tsuchimoto, K. Tobita, T. Hiyama, S. Fukuzawa, *J. Org. Chem.* **1997**, *62*, 6997–7005; b) S. Gmouh, H. Yang, M. Vaultier, *Org. Lett.* **2003**, *5*, 2219–2222.

[4] Based on a survey of the SciFinder Scholar (ACS), CARPLUS, and MEDLINE databases.

[5] a) F. Bigi, G. Casiraghi, G. Casnati, G. Sartori, *J. Org. Chem.* **1985**, *50*, 5018–5022; b) G. Erker, A. A. H. van der Zeijden, *Angew. Chem.* **1990**, *102*, 562–565; *Angew. Chem. Int. Ed. Engl.* **1990**, *29*, 512–514.

[6] For a recent overview of asymmetric F–C reactions, see: Y. Wang, K. Ding, L. Dai, *Chemtracts* **2001**, *14*, 610–615.

[7] For representative examples of Lewis acid catalyzed F–C alkylations, see: a) S. K. Taylor, S. A. May, E. S. Stansby, *J. Org. Chem.* **1996**, *61*, 2075–2080; b) R. Reddy, J. B. Jaquith, V. R. Neelagiri, S. Saleh-Hanna, T. Durst, *Org. Lett.* **2002**, *4*, 695–697; c) S. Nagumo, I. Miyoshi, H. Akita, N. Kawahara, *Tetrahedron Lett.* **2002**, *43*, 2223–2226.

[8] H. Kotsuki, K. Hayashida, T. Shimanouchi, H. Nishizawa, *J. Org. Chem.* **1996**, *61*, 984–990.

[9] a) B. C. Ranu, *Eur. J. Org. Chem.* **2000**, 2347–2356; b) K. K. Chauhan, C. G. Frost, *J. Chem. Soc. Perkin Trans. 1* **2000**, 3015–3019.

[10] M. Bandini, P. G. Cozzi, P. Melchiorre, A. Umani-Ronchi, *J. Org. Chem.* **2002**, *67*, 5386–5389.

[11] M. Bandini, P. G. Cozzi, P. Melchiorre, A. Umani-Ronchi, *Angew. Chem.* **2004**, *116*, 86–89; *Angew. Chem. Int. Ed.* **2004**, *43*, 84–87.

[12] G. A. Olah, R. Khrisnamurti, G. K. Surya Prakash, *Comprehensive Organic Synthesis*, *Vol. 3*, 1st ed., Pergamon, New York, **1991**, pp. 293–339.

[13] For homogeneous catalysis, see: a) J. S. Yadav, B. V. Subba Reddy, Ch. V. S. R. Murthy, G. Mahesh Kumar, Ch. Madan, *Synthesis* **2001**, 783–787; b) J. Hao, S. Taktak, K. Aikawa, Y. Yusa, M. Hatano, K. Mikami, *Synlett* **2001**, 1443–1445; for heterogeneous catalysis, see: C. Ramesh, J. Banerjee, R. Pal, B. Das, *Adv. Synth. Catal.* **2003**, *345*, 557–559.

[14] a) M. Johannsen, *Chem. Commun.* **1999**, 2233–2234; b) A. Ishii, V. A. Soloshonok, K. Mikami, *J. Org. Chem.* **2000**, *65*, 1597–1599.

[15] K. Mikami, S. Matsukawa, *Nature* **1997**, *385*, 613–615.

[16] a) S. Saaby, X. Fang, N. Gathergood, K. A. Jørgensen, *Angew. Chem.* **2000**, *112*, 4280–4282; *Angew. Chem. Int. Ed.* **2000**, *39*, 4114–4116; b) S. Saaby, P. Bayón, P. S. Aburel, K. A. Jørgensen, *J. Org. Chem.* **2002**, *67*, 4352–4361.

[17] a) N. Gathergood, W. Zhuang, K. A. Jørgensen, *J. Am. Chem. Soc.* **2000**, *122*, 12517–12522; b) W. Zhuang, N. Gathergood, R. G. Hazell, K. A. Jørgensen, *J. Org. Chem.* **2001**, *66*, 1009–1013.

[18] Very recently an interesting stereoselective tandem oxa-Michael addition/Friedel–Crafts alkylation was reported for the synthesis of functionalized chromanes: H. L. van Lingen, W. Zhuang, T. Hansen, F. P. J. T. Rutjes, K. A. Jørgensen, *Org. Biomol. Chem.* **2003**, *1*, 1953–1958.

[19] A. Corma, H. García, A. Moussaif, M. J. Sabater, R. Zniber, A. Redouane, *Chem. Commun.* **2002**, 1058–1059.

[20] For examples, see: a) P. E. Harrington, M. A. Kerr, *Synlett* **1996**, 1047–1048; b) K. Manabe, N. Aoyama, S. Kobayashi, *Adv. Synth. Catal.* **2001**, *343*, 174–176; c) M. Bandini, P. G. Cozzi, M. Giacomini, P. Melchiorre, S. Selva, A. Umani-Ronchi, *J. Org. Chem.* **2002**, *67*, 3700–3704; d) M. Bandini, P. Melchiorre, A.

 © 2004 Wiley-VCH Verlag GmbH & Co. KGaA, Weinheim

Melloni, A. Umani-Ronchi, *Synthesis* **2002**, 1110 – 1114; e) M. Bandini, M. Fagioli, A. Melloni, A. Umani-Ronchi, *Synthesis* **2003**, 397 – 402; f) N. Srivastava, B. K. Banik, *J. Org. Chem.* **2003**, *68*, 2109 – 2114.

[21] K. B. Jensen, J. Thorhauge, R. G. Hazell, K. A. Jørgensen, *Angew. Chem.* **2001**, *113*, 164 – 167; *Angew. Chem. Int. Ed.* **2001**, *40*, 160 – 163.

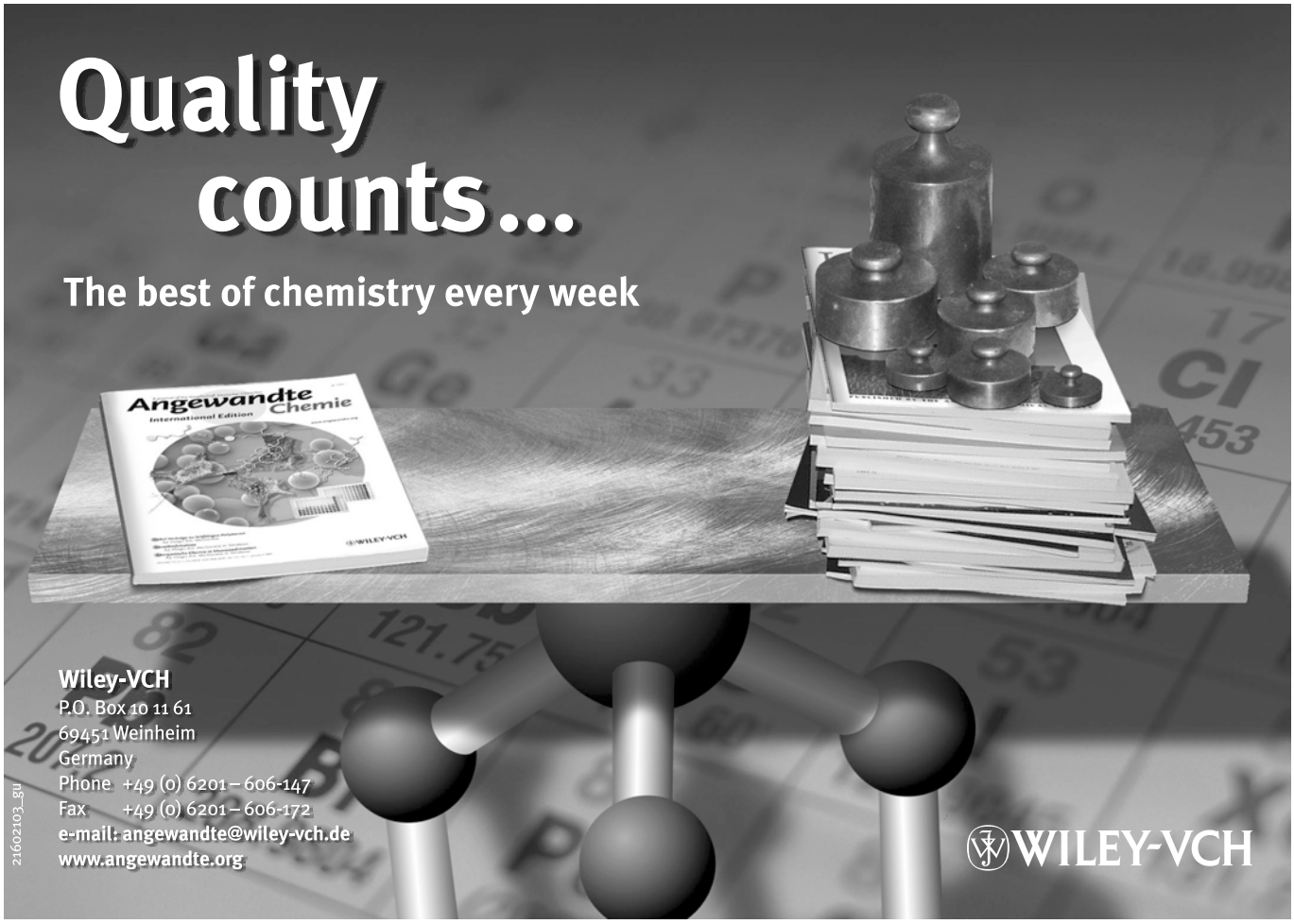
[22] J. Zhou, Y. Tang, *J. Am. Chem. Soc.* **2002**, *124*, 9030 – 9031.

[23] W. Zhuang, T. Hansen, K. A. Jørgensen, *Chem. Commun.* **2001**, 347 – 348.

[24] a) N. A. Paras, D. W. C. MacMillan, *J. Am. Chem. Soc.* **2001**, *123*, 4370 – 4371; b) J. A. Austin, D. W. C. MacMillan, *J. Am. Chem. Soc.* **2002**, *124*, 1172 – 1173; c) N. A. Paras, D. W. C. MacMillan, *J. Am. Chem. Soc.* **2002**, *124*, 7894 – 7895.

[25] M. Bandini, M. Fagioli, P. Melchiorre, A. Melloni, A. Umani-Ronchi, *Tetrahedron Lett.* **2003**, *44*, 5846 – 5849.

[26] Some β-indolyl esters and β-indolyl aldehydes are currently commercially available in enantiomerically pure form; see: www.materia-inc.com.



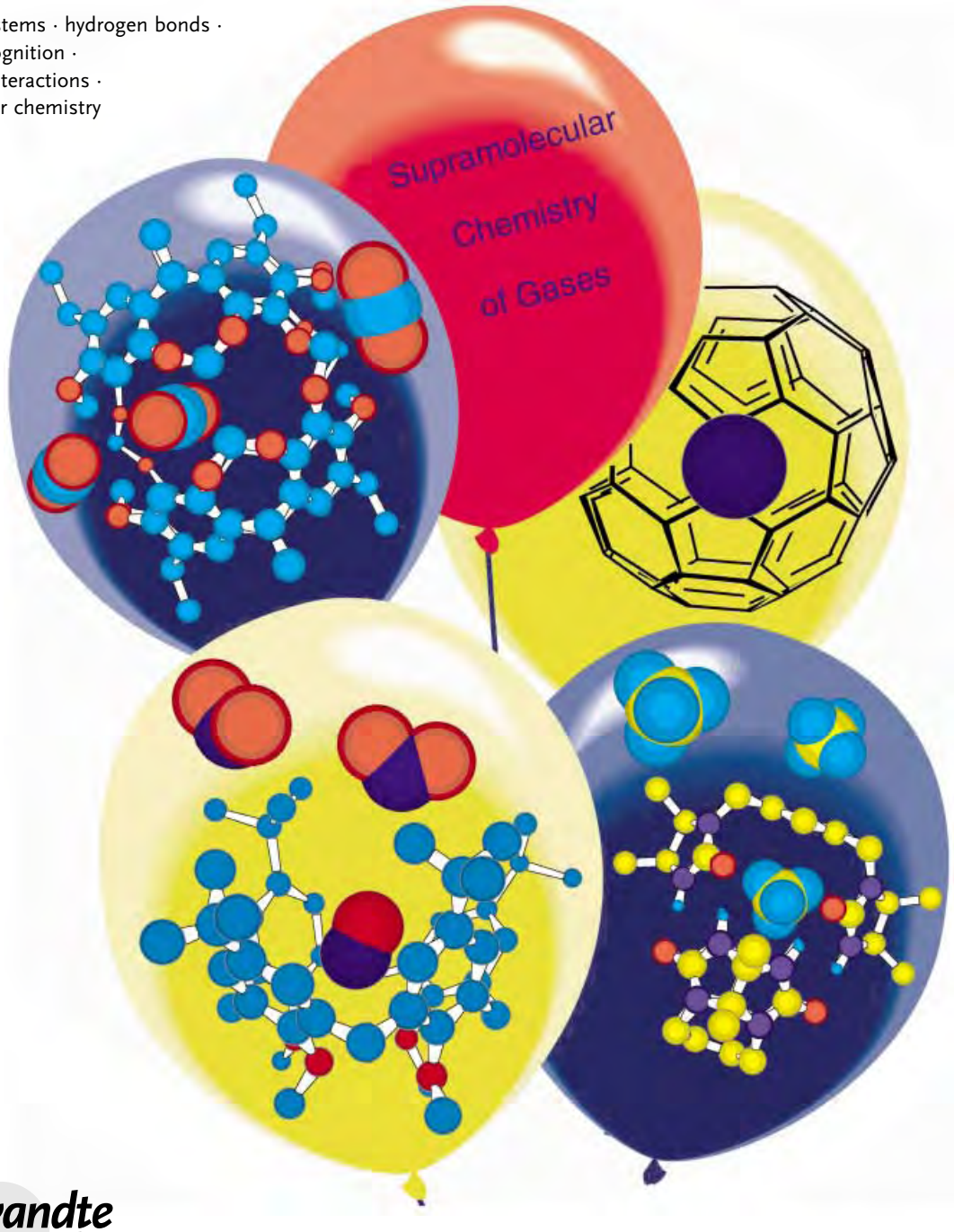
 © 2004 Wiley-VCH Verlag GmbH & Co. KGaA, Weinheim

Gas–Receptor Complexes

Emerging Supramolecular Chemistry of Gases

*Dmitry M. Rudkevich**

Keywords:
host–guest systems · hydrogen bonds · molecular recognition · noncovalent interactions · supramolecular chemistry



© 2004 Wiley-VCH Verlag GmbH & Co. KGaA, Weinheim
DOI: 10.1002/anie.200300606

Molecular recognition of gases is an emerging area of chemistry. Supramolecular chemistry helps us to understand how gases interact with biological molecules and offers delicate insights into the mechanisms of their physiological activity. Principles of molecular recognition have been used for gas sensing, and have provided fundamental knowledge about the structure and dynamics of receptor–analyte complexes, and novel materials for gas sensing and storage have been developed. Supramolecular chemistry is also enabling us to learn how to transform gases into synthetically useful reagents. The rational design of novel catalysts for gas conversion and, more recently, encapsulation complexes with gases open novel directions in preparative synthetic chemistry.

From the Contents

1. Introduction	559
2. Lessons from Nature	560
3. Hydrogen Bonding of Gases	561
4. Lewis Acid–Base Interactions: From Receptors to Materials	562
5. Encapsulation of Gases	565
6. Summary and Outlook	569

1. Introduction

Molecular chemistry is based on the covalent bond, while weaker, noncovalent forces define the field of molecular recognition and supramolecular chemistry. Accordingly, supramolecular chemistry relies on intermolecular interactions and assembly of molecules.[1] Within the last three decades revolutionary advances in supramolecular chemistry have resulted in the successful complexation and sensing of ions and neutral organic molecules.[2] Somewhat surprising, however, is that the molecular recognition of gases is still at an early stage. Gases comprise the atmosphere of the Earth and also occupy a central position in biomedicine, science, technology, and agriculture.

Oxygen (O_2) is of great importance in such diverse areas as medicine and steel making, while nitrogen (N_2) is utilized in space technology and in the production of ammonia (NH_3). Chemical, biomedical, and food industries widely use O_2, carbon dioxide (CO_2), N_2, NH_3, chlorine (Cl_2), and ethylene (C_2H_4). CO_2 and nitrous oxide (N_2O) are major greenhouse gases and huge amounts of CO_2 are released into the air upon the burning of fuels, such as oil, coal, wood, and natural gas. As a result, CO_2 is accumulating faster in the atmosphere than the Earth's natural processes—plants and aqueous resources—can absorb it.[3] The excessive emission of N_2O into the atmosphere is caused by the widespread use of nitrogenous fertilizers and the industrial manufacturing of nylon.[4] CO_2 and N_2O are also involved in a number of biochemical processes and are called blood gases. N_2O is heavily used in anesthesia. Another crucial group of gases is NO_x, which comprises nitric oxide (NO), nitrogen dioxide (NO_2), N_2O_3, dinitrogen tetroxide (N_2O_4), and N_2O_5. NO has multiple roles in the human organism:[5] It serves as an important messenger in signal-transduction processes in smooth muscle cells and neurons and it is also the key intermediate in global denitrification. Other NO_x gases are extremely toxic pollutants derived from fossil-fuel combustion, power plants, and large-scale industrial processes. NO_x gases participate in the formation of ground-level ozone, global warming, and they also form toxic chemicals, nitrate particles, and acid rain/aerosols. NO_x gases are aggressively involved in damaging nitrosation processes in biological tissues.[6] The so-called SO_x gases SO_2 and SO_3 as well as hydrogen sulfide (H_2S)[7] also contribute significantly to the production of smog and acid rain.

Such an extensive circulation of gases necessitates the development of novel methods for their sensing under a variety of conditions. Another, still unresolved, issue is their chemical fixation in environmentally benign processes. Surprisingly, the application of principles and techniques of supramolecular chemistry and molecular recognition for these purposes is only at the very beginning. Rules governing reversible gas–receptor interactions, which are responsible for binding selectivity and biochemical action, and usually precede the covalent fixation, are still poorly understood. The gases that surround us, however, are not "ideal gases" and they interact with other molecules, and thus their recognition/complexation remains a great challenge. Furthermore, gases are technically more difficult to handle than liquids and solids. In addition, their molecules are neutral, and electrostatic binding interactions are much less effective than they would be for similar-sized cations and anions, although a number of gas molecules have dipole or quadruple moments. Furthermore, gases are small molecules with a size of 2–4 Å and very close contacts with receptor sites are needed to achieve their binding. The limited polarizability, dimensions, and geometries of the gas molecules necessitates a high degree of design in the receptor to achieve complementarity, and often a combination of different binding forces is necessary. Solvation may well compete with the recognition event, and while some gases are soluble in water some are lipophilic.

The supramolecular chemistry and molecular recognition of gases definitely deserve attention. Here, an overview of the general principles towards the design and synthesis of receptor molecules for gases is given. The possibilities of hydrogen bonding and Lewis acid–base interactions, dipole–

[*] Prof. Dr. D. M. Rudkevich
Department of Chemistry & Biochemistry
University of Texas at Arlington
Arlington, TX 76019-0065 (USA)
Fax: (+1) 817-272-3808
E-mail: rudkevich@uta.edu

 DOI: 10.1002/anie.200300606 © 2004 Wiley-VCH Verlag GmbH & Co. KGaA, Weinheim

dipole attractions, as well as encapsulation will be discussed and experimental progress in this direction will be analyzed. Furthermore, existing approaches towards studying supramolecular complexes with gases will be reviewed. Published thermodynamic and kinetic parameters of these interactions will be presented, as well as the data concerning the geometry and stereochemistry of the complexes. This knowledge should allow for the development of more specific/selective receptors and molecular containers for gases, potentially useful chemical processes and catalysts for their utilization, novel gas sensors, and chemically modified materials for detection and purification. It will be shown that the application of principles of molecular recognition for gas sensing, storage, and chemistry may lead to conceptually new discoveries and inventions.

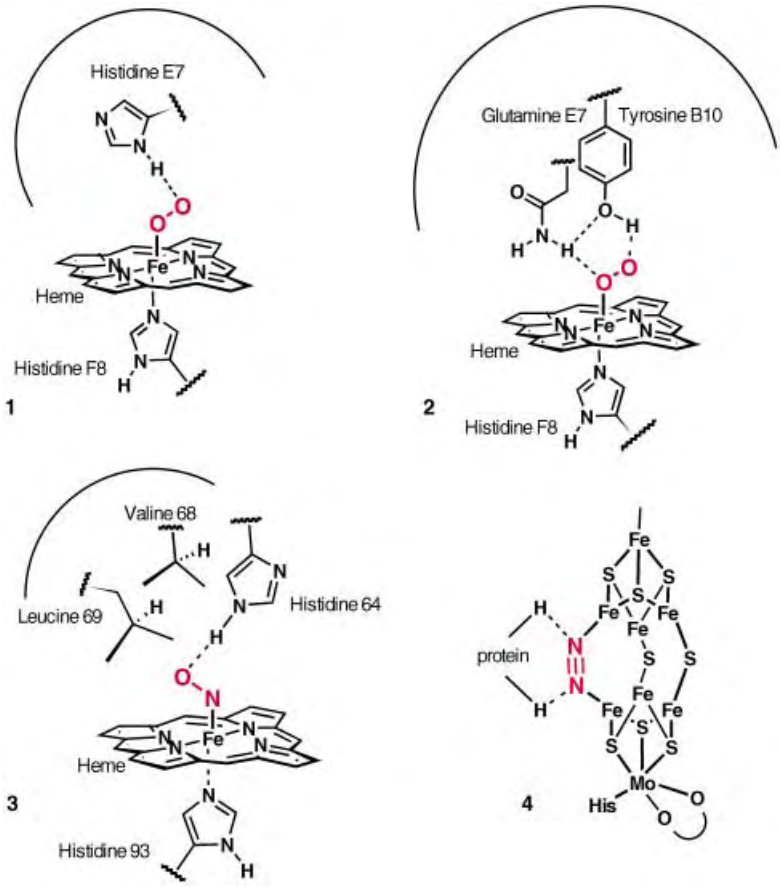
2. Lessons from Nature

Nature employs molecular recognition for effectively discriminating between blood gases, with differences in the O_2/CO binding by heme molecules being the most spectacular example.[8] In addition to the iron–gas interaction, the histidine residue on the distal porphyrin face of hemoglobin and myoglobin is involved in hydrogen bonding with O_2 (**1**, Scheme 1), as evident from EPR, X-ray, and neutron-diffraction studies. Such hydrogen-bonding interactions not only affects oxygen affinity, but may also stabilize the oxy form and prevent autooxidation. The distal cavity is also important, particularly the polarity of the walls, the functional composition, and the 3D arrangement.

In oxygen-avid *Ascaris* hemoglobin, glutamine and tyrosine residues participate in hydrogen bonding with O_2 (**2**, Scheme 1).[9] The crystal structure of complex **2** shows the tyrosine hydroxy group to be perfectly positioned to make a strong hydrogen bond with the distal atom of the complexed O_2, and the glutamine forms a somewhat weaker hydrogen bond to the oxygen atom coordinated to the iron center.



Dmitry M. Rudkevich studied chemistry at the Institute of Organic Chemistry, National Academy of Sciences of the Ukraine. He completed his PhD in the laboratory of Prof. David N. Reinhoudt at the University of Twente in the Netherlands in 1995. In 1996 he joined the research group of Prof. Julius Rebek, Jr. and was a Research Assistant Professor of the Skaggs Institute for Chemical Biology at Scripps (1997–2001). He is currently an Assistant Professor of Chemistry at the University of Texas at Arlington. His research interests focus on molecular recognition.



Scheme 1. Molecular recognition of gases in nature.

There is also a hydrogen bond between the tyrosine and glutamine fragments. Such a hydrogen-bonding network is believed to be responsible for the K_d values for O_2 being four orders of magnitude greater than that of human hemoglobin.

The crystal structures of complexes of heme protein with NO also suggest that the distal cavity is important in gas binding. Such cavities are rather hydrophobic and possibly help to exclude the noncoordinated H_2O molecule prior to the complexation of NO. The X-ray structure of the ferrous–nitric oxide complex of native sperm whale myoglobin **3** (Scheme 1) shows a Fe–NO interaction as well as the formation of a hydrogen bond between the gas molecule and the histidine 64 residue on the distal porphyrin face of the myoglobin.[10] Overall, the NO binding event takes place in a tight cavity formed by the lipophilic leucine 69 and valine 68 fragments as well as histidine 64.

It is believed that upon atmospheric N_2 fixation by enzymes, the NH nitrogen–metal intermediates **4** participate in hydrogen-bonding interactions with the amino acid residues of the enzyme (Scheme 1).[11]

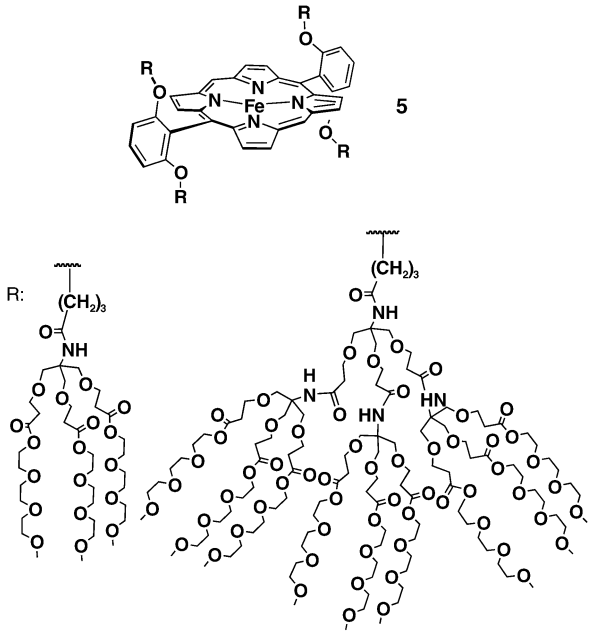
These examples offer great inspiration for designers of artificial receptors for gases. They directly point out the binding forces to employ and explore: a) hydrogen bonding, b) metal–gas interactions, and c) cavity effects.

 © 2004 Wiley-VCH Verlag GmbH & Co. KGaA, Weinheim

3. Hydrogen Bonding of Gases

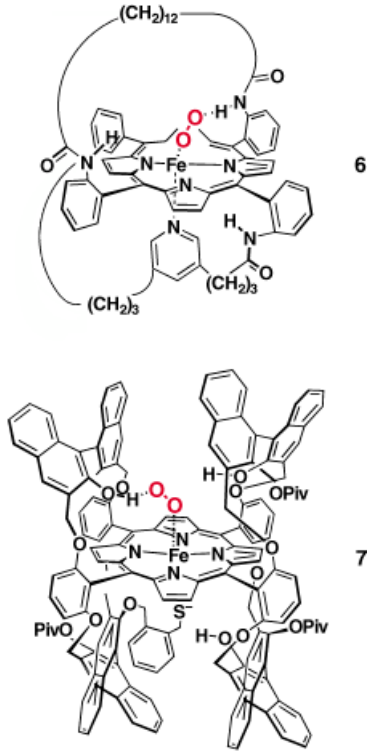
Hydrogen bonding is one of the most important interactions utilized by nature and is responsible for biotic self-assembly and the selectivity of enzymes. As seen in the previous section, it readily works for both gases and heme proteins. In addition to the natural examples, other information on hydrogen bonds with gases comes from gas-phase adducts of acidic HF, HCl, HBr, and HCN with N_2, CO, CO_2, and OCS.[12] The geometry of the B···H–X (B = N, O, S, etc.; X = halogen) complexes was deduced from ab initio calculations and also from advanced spectroscopic measurements, such as molecular beam FT microwave spectroscopy, vibration spectroscopy, and photoelectron spectroscopy. Zero-electron kinetic energy (ZEKE) photoelectron spectroscopy and resonance-enhanced multiphoton ionization (REMPI) spectroscopy proved to be very useful for characterizing the Aryl-OH···gas (gas = Ar, N_2, CO) molecular clusters.[13] Much less is known about hydrogen bonding of gases in solution.

A wide variety of heme models have been prepared which are based on sterically hindered "picket fence", "picnic basket", "capped", "strapped", "hanging base", and other "superstructured" metalloporphyrins.[14] In some cases, the increased affinity of these porphyrins towards O_2 was interpreted by favorable hydrogen-bonding interactions between the complexed O_2 molecule and the hydrogen-donating fragment within the porphyrin structure.[14] In a most recent impressive effort, dendritic iron porphyrins **5** (Scheme 2) have been introduced that possess highly protected gas-binding pockets. These also exhibited increased affinity towards O_2, for which hydrogen bonding between the coordinated O_2 and the C(O)NH function of the dendritic arms has been proposed.[15]



Scheme 2. Dendritic porphyrins **5** prepared by Diederich and co-workers.[15]

Spectroscopy offered direct proof of the presence of hydrogen-bonding interactions. In the early ^{1}H NMR studies with the O_2 complexes of amide-functionalized, "basket-handle" porphyrins **6** (Scheme 3) a pronounced downfield



Scheme 3. Superstructured porphyrins **6** and **7** and their dioxygen complexes.[16,17] Piv = pivaloyl = trimethylacetyl.

shift of the signal for the amide C(O)NH proton was observed in apolar solvents, thus indicating the presence of a C(O)NH···O_2 hydrogen-bonding interaction.[16] This hydrogen bond, however, must be rather weak, since the estimated nitrogen–O_2 distance is approximately 4 Å.

Recently, Naruta and co-workers presented Raman spectroscopic evidence for the presence of hydrogen bonding in the complex of "twin-coronet" porphyrin **7** and O_2 (Scheme 3).[17] Specifically, the hydrogen bond formed between the bound dioxygen and the OH groups of the binaphthyl moieties was studied through H/D exchange experiments. Deuteration of the OH groups in **7** resulted in the frequencies of the ν(O–O) bands being shifted by 2 cm^{-1} to a higher wavenumber. The estimated distances between the binaphthyl oxygen atoms and the bound O_2 are small, in the range of 3 Å.

Direct evidence of a hydrogen bond in oxyhemoglobin was recently obtained by echo–anti-echo (^{1}H, ^{15}N) heteronuclear multiple quantum coherence (HMQC) NMR experiments.[18] Analysis of the pattern of cross-peaks for the distal histidine residues in the HMQC spectrum showed that the histidine NH hydrogen atom in the dioxygen complex is stabilized against solvent exchange through formation of a hydrogen bond with O_2.

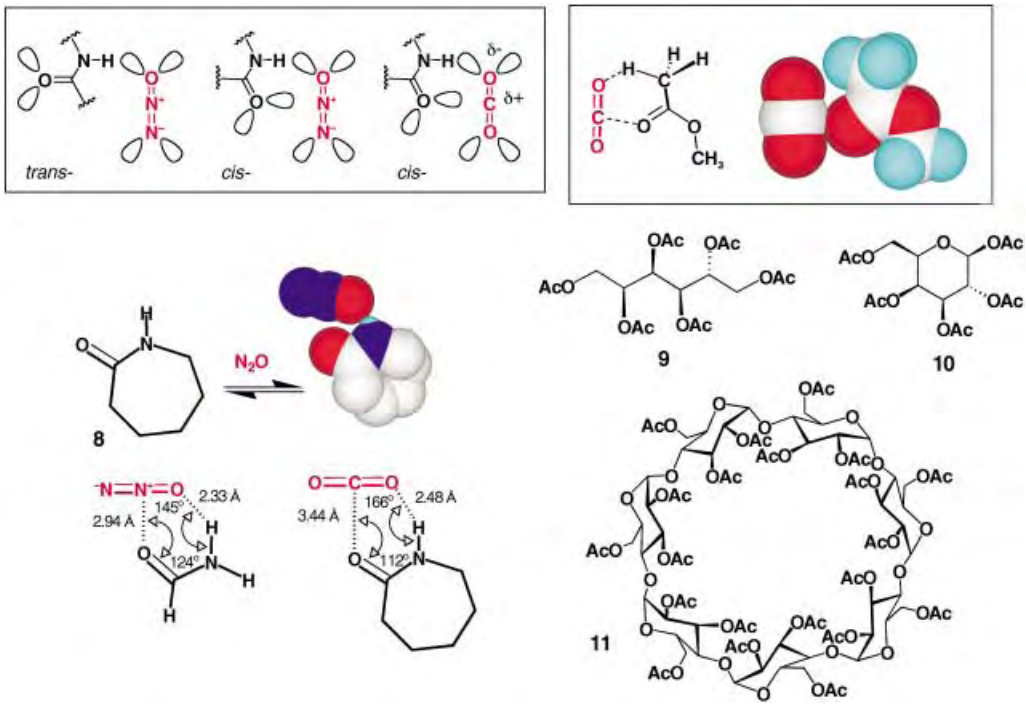
© 2004 Wiley-VCH Verlag GmbH & Co. KGaA, Weinheim

Studies with CO_2 and N_2O have also been reported. These gases frequently circulate in biological fluids, however, the possibility of their involvement in hydrogen-bonding interactions with proteins and enzymes had been routinely ignored. Only recently, it was found that secondary *cis*-amides, for example, ε-caprolactam (**8**), interact with N_2O and CO_2 in apolar solutions (Scheme 4).[19] Saturation of a solution of **8** with N_2O in $CDCl_3$ and [D_6]benzene at room temperature resulted in the singlet corresponding to the NH proton being shifted upfield by $\Delta\delta \approx 0.25$ ppm. Ab initio calculations of the complex formed between simple formamide ($HC(O)NH_2$), which possesses a *cis*-amide arrangement, and N_2O confirm that a hydrogen bond can form between the amide NH hydrogen atom and the partially negatively charged oxygen atom of the gas molecule. A N–H–O=N^+=$N^:$$^-$ distance of 2.33 Å was obtained, which places the basic amide C=O oxygen atom right in front of the central, electron-deficient nitrogen atom of the N_2O molecule. There is an electrostatic attraction between the lone pair of electrons and the latter partial positive charge, and a C=O–N^+ distance of 2.94 Å was calculated. These results taken together indicate that a two-point noncovalent interaction occurs, which is not possible for *trans*-amides. Semi-empirical calculations with **8** and N_2O yielded similar results. As saturation with N_2O disrupts the dimerization of *cis*-amides ($K_D \leq 5\,M^{-1}$), this sets the lower limit for the described N_2O complexation to be $\Delta G^{295} \approx 0.9$ kcal mol^{-1}, which is typical for weak interactions in apolar solution. Analogous conclusions were obtained from molecular modeling studies, calculations, and ^1H NMR measurements with CO_2, which is isoelectronic to N_2O.

Similar two-point interactions between a $C(O)CH_3$ acetyl group and CO_2 were proposed for complexes of peracetylated carbohydrates **9**–**11** and CO_2.[20] This situation involves both the acetate C=O···CO_2 electrostatic and C–H···O_2C hydrogen-bonding interactions (Scheme 4). Derivatives **9**–**11** have an enhanced solubility in supercritical CO_2, and in general, the Lewis basic C=O group is known as a CO_2-phile. Ab initio calculations on complexes formed between CO_2 and simple carbonyl compounds were performed, and gave binding energy values of 2.69 kcal mol^{-1} per complex. The Raman spectra of the complexes formed between acetaldehyde and CO_2 showed the maximum red-shift of the acetaldehyde carbonyl band to be from 1746.0 to 1743.5 cm^{-1} and the maximum blue-shift of the aldehyde CH proton band to be from 2717.0 to 2718.3 cm^{-1}. Both observations were consistent with the computer-predicted structures.

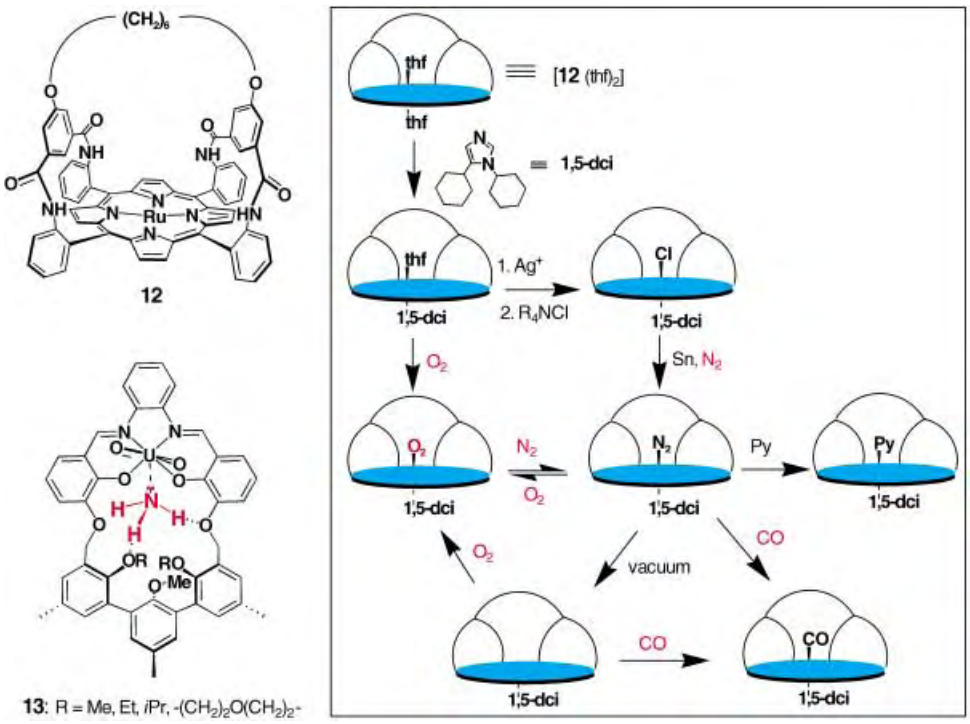
4. Lewis Acid–Base Interactions: From Receptors to Materials

Inorganic and organometallic compounds are widely known to react with N_2, NO, N_2O, CO, CO_2, O_2, and other gases through formation of a metal–gas bond. Some of these processes are reversible and can be described as supramolecular in nature. Irreversible chemistry between metals and gases has been effectively employed in catalysis and also in photo and redox processes which are used in industrial, environmental, and biomedical gas sensing and monitoring. This has been thoroughly described in numerous reviews and original papers.[21] Here, we discuss the most characteristic advances related to molecular recognition of gases. Molecular recognition is usually defined by the delicate balance of energy and chemical information involved in the binding and selection processes.[1]



Scheme 4. Involvement of N_2O and CO_2 in hydrogen-bonding and electrostatic interactions during their complexation with *cis*-amides and acetates.[19,20]

 © 2004 Wiley-VCH Verlag GmbH & Co. KGaA, Weinheim



Scheme 5. Exchange experiments with gases in "picnic-basket" porphyrin **12** as well as the structure of **13**.[22] Py = pyridine.

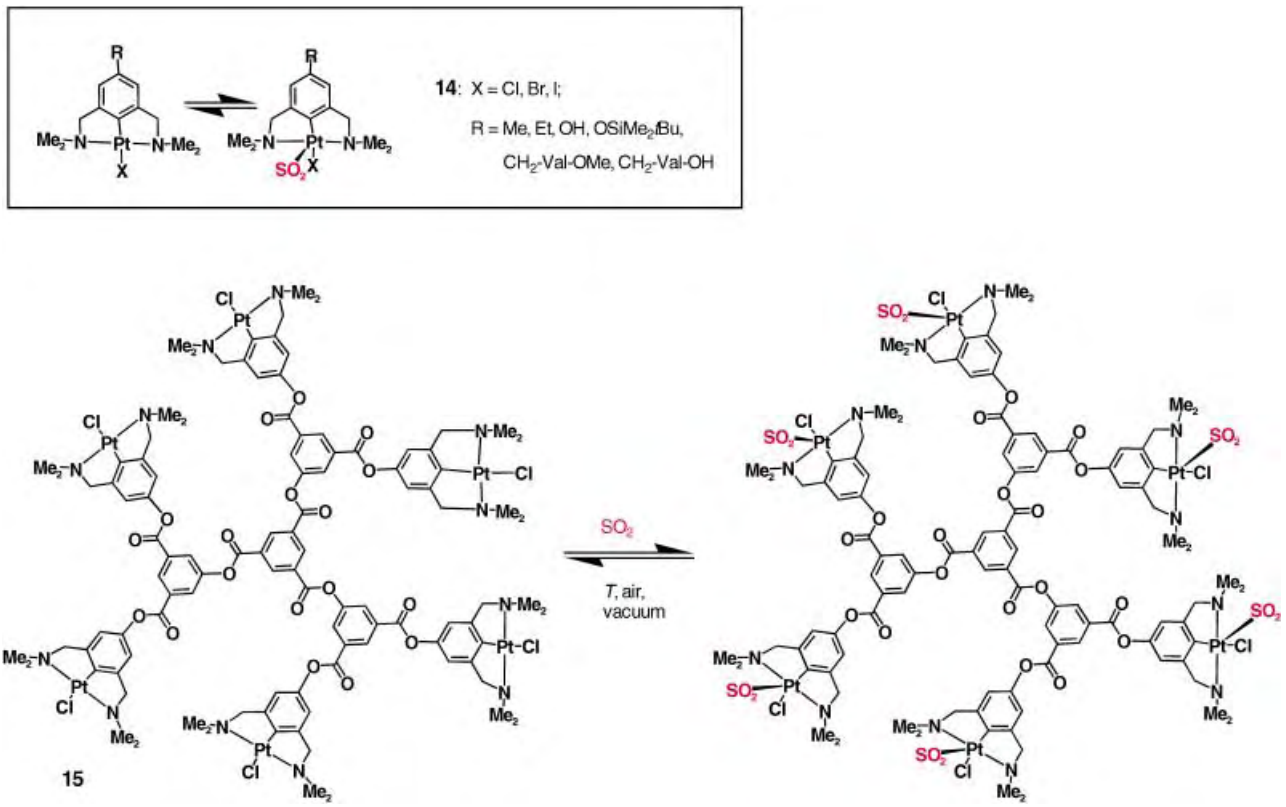
Collman et al. identified controlled gas exchange within the cavity of ruthenium "picnic-basket" porphyrins **12** (Scheme 5).[22] The Ru^{II}–gas interactions were the driving force for these processes, but the cavity also played a crucial role, especially in the kinetics and regioselectivity. First, the so-called bis-solvent complex [**12**$(thf)_2$] was prepared by photolysis of the corresponding carbonyl derivative [**12**(CO)(thf)]. Treatment of this complex with bulky 1,5-dicyclohexylimidazole (1,5-DCI) resulted in formation of [**12**$(thf)_{in}$(1,5-dci)$_{out}$], with the thf molecule coordinated inside the cavity. Dry O_2 quantitatively replaced the internally coordinated thf molecule in toluene solution, and this processes was shown to be reversible. Furthermore, the introduction of N_2 enabled reversible exchange between the corresponding dioxygen [**12**$(O_2)_{in}$(1,5-dci)$_{out}$] and dinitrogen [**12**$(N_2)_{in}$(1,5-dci)$_{out}$] complexes to be achieved. Dinitrogen complex [**12**$(N_2)_{in}$(1,5-dci)$_{out}$] was also converted into the carbon monoxide analogue [**12**$(CO)_{in}$(1,5-dci)$_{out}$] simply by exposure to CO gas, and also to the gas-free derivative [**12**(1,5-dci)$_{out}$]. This latter complex was readily converted into [**12**$(O_2)_{in}$(1,5-dci)$_{out}$] by exposure to O_2. The gas-exchange processes were effectively monitored by visible, IR, and ^{1}H NMR spectroscopies.

The combination of a metal center and hydrogen-bonding sites was also employed for the recognition of other gases. For example, preorganized and rigid UO_2-containing macrocycles **13** were shown to selectively bind NH_3 over primary alkyl amines (Scheme 5).[23] K_{ass} values of 3×10^2 to $1\times10^3\,M^{-1}$ were obtained for NH_3 in $CDCl_3$ solution, which is more than an order of magnitude higher than for amines RNH_2 (R = Me, Et, *n*Pr, Bz). In addition to the binding of the lone pair of electrons on the NH_3 nitrogen atom to the Lewis acidic UO_2 cation, several N–H···O hydrogen bonds may be formed between the gas molecule and the phenolic oxygen atoms on the receptor. Furthermore, the preorganized macrocycle apparently introduced steric restrictions in binding larger guests.

In a series of thorough papers, van Koten and co-workers reported on square-planar N,C,N-terdentate pincer Pt^{II} complexes **14** for the reversible sensing of sulfur dioxide (SO_2)[24] in which SO_2 is directly bound to the metal center. In the presence of SO_2, complexes **14** spontaneously adsorbed the gas and formed pentacoordinate, square-pyramidal adducts [**14**(SO_2)] (Scheme 6). The process is fast and reversible, both in apolar solution (CH_2Cl_2, $CHCl_3$, $C_2F_4Br_2$, and toluene) and in the solid state. Importantly, a characteristic color change of the complex from colorless to bright orange occurred upon entrapment of SO_2. The exchange of SO_2 is fast at room temperature, but can be slowed down and studied by conventional ^{1}H NMR spectroscopy at 167–188 K (in $C_2F_4Br_2$). For example, the rate constants for exchange are $k=(1.5\pm0.5)\times10^8\,s^{-1}$ at 298 K and $k=(2.34\pm0.08)\times10^3\,s^{-1}$ at 174 K. Variable-temperature NMR analysis of the equilibrium constant between complex **14** and adduct [**14**(SO_2)] (X = I) gave $\Delta H^\circ=-36.6\pm0.8\,kJ\,mol^{-1}$, $\Delta S^\circ=-104\pm3\,J\,K^{-1}\,mol^{-1}$, and $K_{298}=9\pm4\,M^{-1}$.

Reactions of **14** and SO_2 in the crystalline-state produced orange-colored, reversible adducts, which may be used for gas storage and switchable optoelectronic devices. Compound **14** was also covalently linked to the amino acid valine (Val) through the N-terminus to form a compound that may act as a diagnostic peptide-labeling tool for biomedical applications. Indeed, such organoplatinum-labeled peptides may be traced

 © 2004 Wiley-VCH Verlag GmbH & Co. KGaA, Weinheim



Scheme 6. Reversible binding of SO_2 by pincer Pt^{II} complexes **14** and **15** prepared by van Koten and co-workers.[24]

and located specifically in biological systems by "highlighting" the platinum site with SO_2 gas.

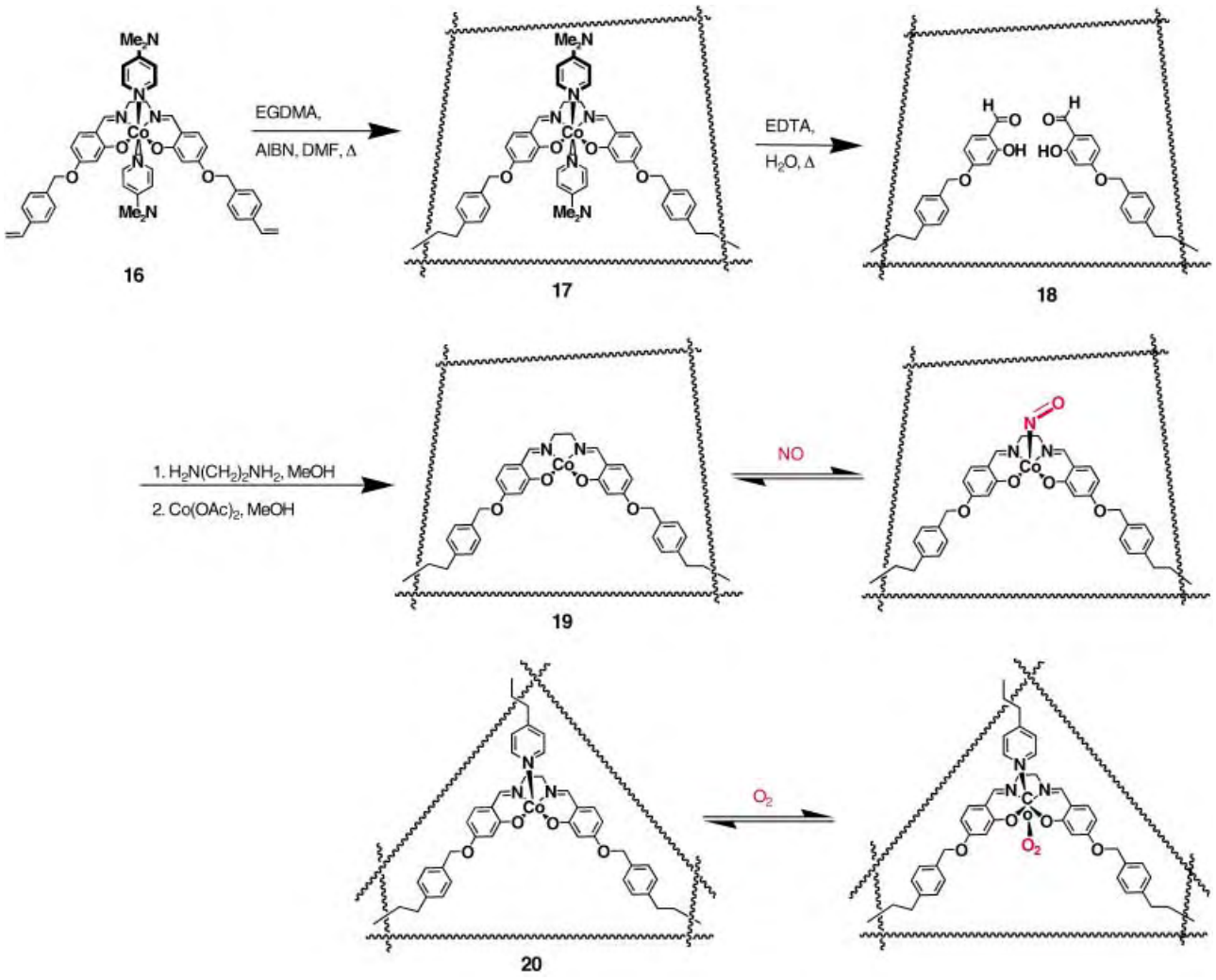
Dendritic organoplatinum(II) complexes **15** were prepared as reusable SO_2-sensing and -storing materials (Scheme 6). Such dendrimers offer monodisperse, globular nanostructures with defined size and shape that satisfy the new challenges of chemistry to build macromolecular entities composed of many identical components, which are arranged to function as receptors for given binding units or ligands. Multiple, multivalent interactions enable macromolecular receptors **15** to display an increased affinity towards the gas substrate.

A dendritic model of hemocyanin was prepared which is capable of storing oxygen.[25] Hemocyanin proteins are known to bind O_2 at a site containing two copper atoms directly ligated by protein side chains. A multi-oxygen complex was obtained from the synthesized Cu^I dendrimer with 10–11 molecules of O_2 per one dendritic molecule. It was shown that 60–70 % of the Cu^I centers were involved in the binding of oxygen. The high local concentration of oxygenating equivalents in such a dendrimer represents an exciting promise for synthetic chemistry.

Borovik and co-workers developed porous organic materials for the reversible binding of CO, O_2, and NO (Scheme 7). Templated co-polymerization was employed for the immobilization of metal centers. For example, template complex **16**, along with cross-linking agent EGDMA, and solvent, which served as the porogen during the radical polymerization process, was used for NO gas.[26] The preformed kinetically inert Co^{III}–4-dimethylaminopyridine (DMAP) complex **17** contains the styrene-modified salen ligand (salen = *N*,*N*′-bis(salicylidene)ethylenediamine dianion), which is covalently attached to the porous methacrylate host. The Co^{III} ions and DMAP were removed under acidic conditions to afford **18**. The two immobilized salicylaldehyde moieties in **18** further reacted with ethylenediamine to reform the immobilized tetradentate salen ligand. The resulting polymer now readily binds Co^{II} ions to form **19** which contains immobilized four-coordinate Co^{II} centers, with the cobalt concentration ranging from 180 to 230 mol g^{-1} and an average pore diameter of 25 Å. Polymer **19** binds NO in toluene solution and even at the air–solid interphase, but it is relatively inert toward other biologically important gases such as O_2, CO_2, and CO. Moreover, NO is slowly released from **19** under ambient conditions. It was shown that approximately 80 % of the NO was lost from **19** after 30 days and heating the sample accelerated the gas release. Such controlled, slow release of NO is important for medical applications.[5]

The NO-binding properties of **19** differ from those of the corresponding monomolecular analogues, and this is attributed to the presence of the porous polymethacrylate host in these materials. The pronounced color change resulting from the conversion of **19** into [**19**(NO)] suggests potential use in the detection of NO. The polymer can be recycled, retains a high binding affinity for NO, and works equally well in the solid state or as a suspension in a liquid. Similar results have been obtained for O_2-binding polymers **20** which are made by template copolymerization methods (Scheme 7).[27]

 © 2004 Wiley-VCH Verlag GmbH & Co. KGaA, Weinheim



Scheme 7. Formation of porous organic materials **19** and **20** for reversible binding of NO and O_2.[26,27] EGDMA = ethylene glycol dimethacrylate, AIBN = azobisisobutyronitrile, EDTA = ethylenediaminetetraacetate.

5. Encapsulation of Gases

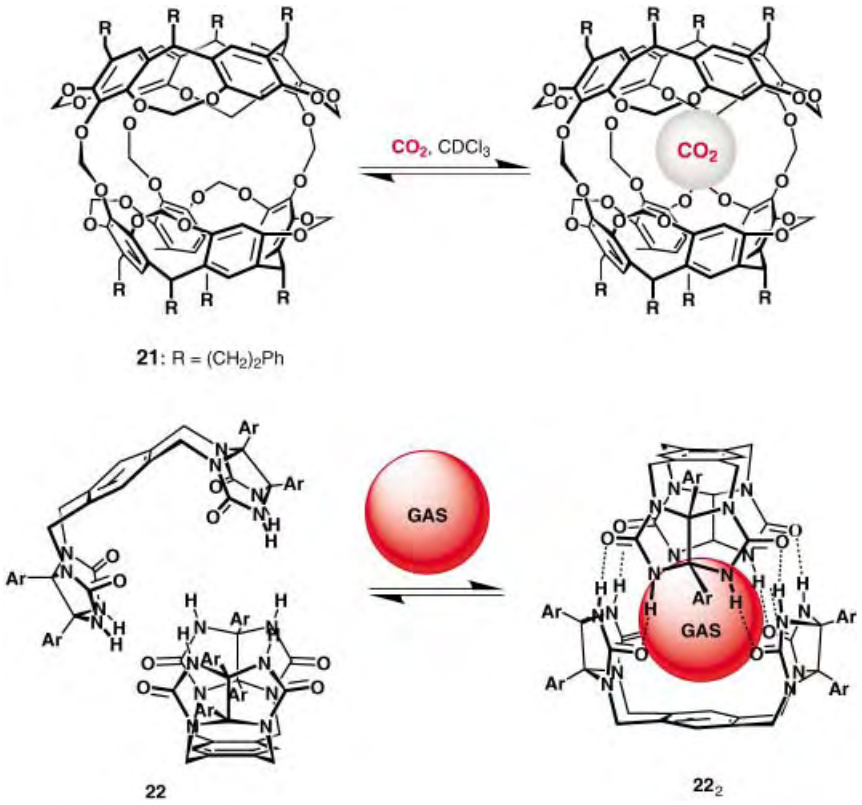
It has been known for several decades that low-molecular-weight hydrocarbons, N_2, O_2, Cl_2, CO_2, N_2O, H_2S, SO_2, and PH_3 can be encapsulated within self-assembled $(H_2O)_n$ lattices in the solid state.[28] Caged zeolites have recently been shown to reversibly incarcerate NO_x.[29] Early experiments on gas encapsulation within organic cavities were performed with cyclodextrins in the 1950s.[30] α-Cyclodextrin, for example, interacted with Cl_2, Kr, Xe, O_2, CO_2, C_2H_4, CH_4, C_2H_6, C_3H_8, and n-C_4H_{10} in water with the formation of stable clathrates. The corresponding CO_2⊂cyclodextrin complex can be isolated simply through precipitation, and this process is used for the purification of the cyclodextrin itself.[31]

Over the years, the desirability of controlling the size, shape, and dynamics of the cavity led to the synthesis of various molecular containers, such as cavitands, carcerands, and capsules. These days, chemists focus on nanoscale cavities, which are capable of complexing two or even more guest molecules or a single guest with a size of up to 15–20 Å.[32] However, much more modest dimensions are required for gas complexation, and closer contacts with the inner walls of the cavity are needed. Additional binding sites may also be desirable.

Hemicarcerand **21**—covalently sealed molecular containers with aromatic walls—prepared by Cram et al. encapsulated O_2, N_2, CO_2, and Xe (Scheme 8).[33] The exchange between the free and occupied hemicarcerand was slow on the NMR time-scale, with association constants K_{ass} of 180 M^{-1} (N_2), 44 M^{-1} (O_2), and 200 M^{-1} (Xe) being obtained in $CDCl_3$ at 22 °C, assuming a 1:1 stoichiometry. The volume of the inner cavity in **21** is relatively large (ca. 120 $Å^3$) compared to the gas molecules (ca. 40 $Å^3$). Hemicarcerand **21** can probably accommodate more than one gas molecule, but this has not been investigated.

The "tennis balls" **22** developed by Rebek and co-workers self-assembled through the formation of hydrogen bonds around a molecule of CH_4, ethylene, or Xe in $CDCl_3$ solution (Scheme 8).[34] The volumes of the gas molecules are 28, 40, and 42 $Å^3$, respectively, and the inner cavity of **22** is approximately 50 $Å^3$. Similar to **21**, the exchange between the free and occupied capsule was slow on the ^1H NMR time-

 © 2004 Wiley-VCH Verlag GmbH & Co. KGaA, Weinheim



Scheme 8. Encapsulation of gases within hemicarcerand **21**[33] and self-assembling capsule $\mathbf{22}_2$.[34]

scale. The same was true for the guest species: uncomplexed CH_4 exhibited a singlet at $\delta = 0.24$ ppm, while the encapsulated species gave a signal at $\delta = -0.91$ ppm; both signals could be seen simultaneously. For this gas, $\Delta H = -9$ kcal mol^{-1}, $\Delta S = -20\,J\,K^{-1}\,mol^{-1}$, and $K^{273} = 300\,M^{-1}$ were estimated in $CDCl_3$. Clearly, the inclusion of the gas involved a large entropic cost, as was seen for complexes **14**.

Cryptophane-A (**23**, Scheme 9) developed by Collet and co-workers possesses an inner cavity of 95 Å^3 and was shown to encapsulate CH_4 with $K_{ass} = 130\,M^{-1}$ and Xe with $K_{ass} \approx 3000\,M^{-1}$ in $(CDCl_2)_2$.[35] The gas molecules were clearly better guests for receptors **21**–**23** than bulky (> 70 Å^3) solvent molecules, which are too big to enter and/or occupy the interiors. In general, this provides a strong driving force for the entrapment of the gas.

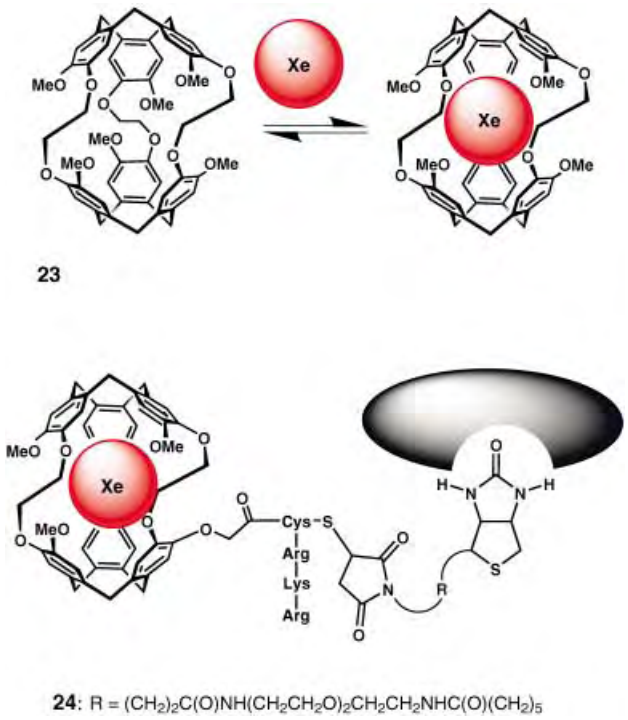
Gas encapsulation within molecular containers is still in its infancy, but may lead to important applications. For example, studies with cyclodextrins showed that it is possible to use ^{129}Xe NMR spectroscopy to obtain quantitative information about complexation processes. Xenon is highly polarizable, but inert and hydrophobic. Two isotopes are easily accessible to NMR spectroscopy: ^{129}Xe ($I = 1/2$, natural abundance of 26 %) and ^{131}Xe ($I = 3/2$, abudance 21 %). The NMR parameters of these isotopes are very sensitive to the environment in which Xe is located, and this can be used to probe structural and dynamic properties of host–guest complexes, both in the solid state and in solution.

Specifically, protein NMR studies have shown that weak Xe–protein interactions influence the ^{129}Xe chemical shift depending on the accessible protein surface, and allow the protein void space and conformations to be monitored. Recently, Pines and co-workers attached cryptophane-A (**23**) to biotin and used ^{129}Xe NMR spectroscopy to detect biotin–avidin binding (Scheme 9).[36]

Free Xe in water generates a signal at $\delta =$ 193 ppm, while the signal for Xe⊂**24** is located at $\delta \approx 70$ ppm. Addition of avidin results in the appearance of a third signal 2.3 ppm downfield of the Xe⊂**24** signal, which was assigned to the protein-bound Xe⊂**24** complex. The intensity of this signal increased when the concentration of avidin was increased. The proposed methodology offers the capability of attaching different ligands to different cages, thus forming Xe sensors that show distinct chemical shifts upon encapsulation.

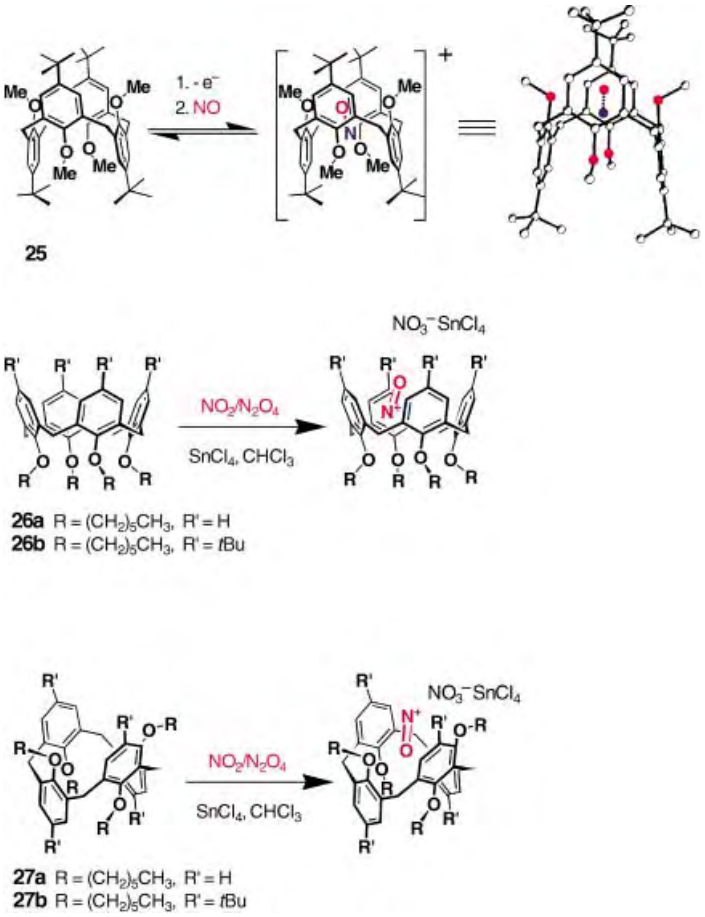
Recently, Kochi and co-workers demonstrated the encapsulation of NO by 1,3-*alternate* calix[4]arene **25** (Scheme 10).[37] Initially, calixarene **25** was oxidized to its radical cation, which then complexed NO gas with the formation of the calix–nitrosonium species NO^+⊂**25**.

Strong charge-transfer interactions between NO^+ and the π surface of the calixarene placed the gas molecule at a distance of 2.4 Å from the cofacial aromatic rings, which is much shorter than the typical van der Waals contact (3.2 Å). An association constant of $K_{ass} > 5 \times 10^8\,M^{-1}$ was estimated. However, NO^+ was easily released from the cavity upon addition of Cl^- ions, as a



Scheme 9. Cryptophane-A (**23**) and its complexes with Xe.[35] Biotinylated cryptophan-A (**24**) for binding to proteins.[36]

 © 2004 Wiley-VCH Verlag GmbH & Co. KGaA, Weinheim



Scheme 10. Encapsulation complexes of NO_x gases with calix[4]arenes **25**–**27**; formation of NO^+⊂calixarene complexes.[37,38]

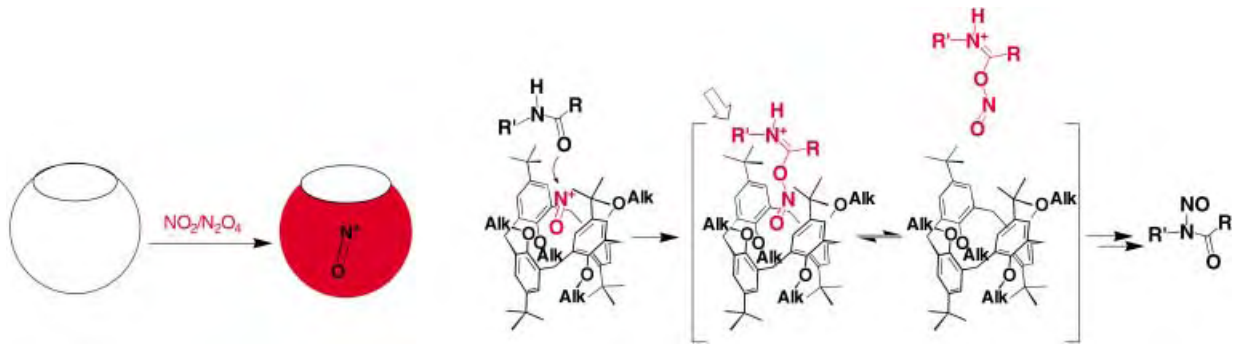
result of the formation of nitrosyl chloride (NOCl). The complexation can also be controlled by redox and/or temperature changes. The charge-transfer complex NO^+⊂**25** is deeply colored and thus can be used for colorimetric NO sensing.

More recently calix[4]arenes were employed to visually detect and chemically transform NO_2/N_2O_4 gases.[38] The tetrakis-*O*-alkylated calix[4]arenes **26** and **27** reversibly interacted with NO_2/N_2O_4 and entrapped the highly reactive NO^+ ion within their cavities (Scheme 10). NO^+ is generated from N_2O_4, which is known to disproportionate to $NO^+NO_3^-$ upon exposure to aromatic compounds. Stable nitrosonium complexes NO^+⊂**26** and NO^+⊂**27** were quantitatively isolated upon addition of a stabilizer—Lewis acidic $SnCl_4$. Only one NO^+ ion was found per cavity. These interactions are reversible. The addition of H_2O or alcohols resulted in the dissociation of the complexes NO^+⊂**26** and NO^+⊂**27** and the recovery of **26** and **27**. The complex with **27** (R′ = H) decomposes instantly, but it takes several minutes for complex **26b** (R′ = *t*Bu) to break up. Bulky *t*Bu groups at the upper rim of **26b** protect the encapsulated NO^+ ion. Such stability of the arene–NO^+ complex is without precedent.

Dramatic color changes result from the charge transfer. Moreover, these interactions are specific. The detection of NO_2 in the presence of gases such as H_2O, O_2, HCl, HBr, SO_x, NH_3, and neat NO can be fully expected, since none of these vapors/gases undergoes reactions with calixarenes. All this may be of interest for sensing technology.

Complexes NO^+⊂**26** and NO^+⊂**27** may release NO^+, which acts as an encapsulated nitrosating species (Scheme 11). Thus, secondary amides were quite reactive towards complex NO^+⊂**27b** (R′ = *t*Bu) and showed remarkable selectivity.[39] Amides with NCH_3 substituents reacted smoothly with NO^+ (298 K, $CHCl_3$; 50–95 %), however, bulkier amides did not react because of steric hindrance: N substituents larger than CH_3 do not allow the substrate to enter the cavity. Such stability and selectivity cannot be easily achieved for the existing nitrosating agents NO^+ salts, $NaNO_2/H_2SO_4$, NO/O_2, N_2O_3, and NO_2/N_2O_4.

Simple solids held together by van der Waals forces may also be used for gas storage, processing, and controlled release. Recently, Atwood et al. elegantly demonstrated that CH_4, CF_4, C_2F_6, CF_3Br, and other low-boiling halogenated C_1-alkanes can be reversibly entrapped and retained within the lattice voids of a crystalline calix[4]arene framework.[40] Such gas-storing crystals appeared to be extremely stable and release their guests only at rather elevated temperatures—hundreds of °C above their boiling points.



Scheme 11. Left: transformation of NO_2/N_2O_4 into NO^+⊂calixarene complexes—encapsulated nitrosating reagents. Right: proposed mechanism of amide nitrosation within the calixarene cavity.[39] The dimensions and shape of the R′ substituent are crucial. The amide substrate approaches the cavity facing the carbonyl oxygen atom, which places the NR′ alkyl group in proximity to the bulky groups on the calixarene. This situation could be sterically unfavorable for sizeable R′ groups so that the substrate C=O and the encapsulated NO^+ ion would not reach each other.

 © 2004 Wiley-VCH Verlag GmbH & Co. KGaA, Weinheim

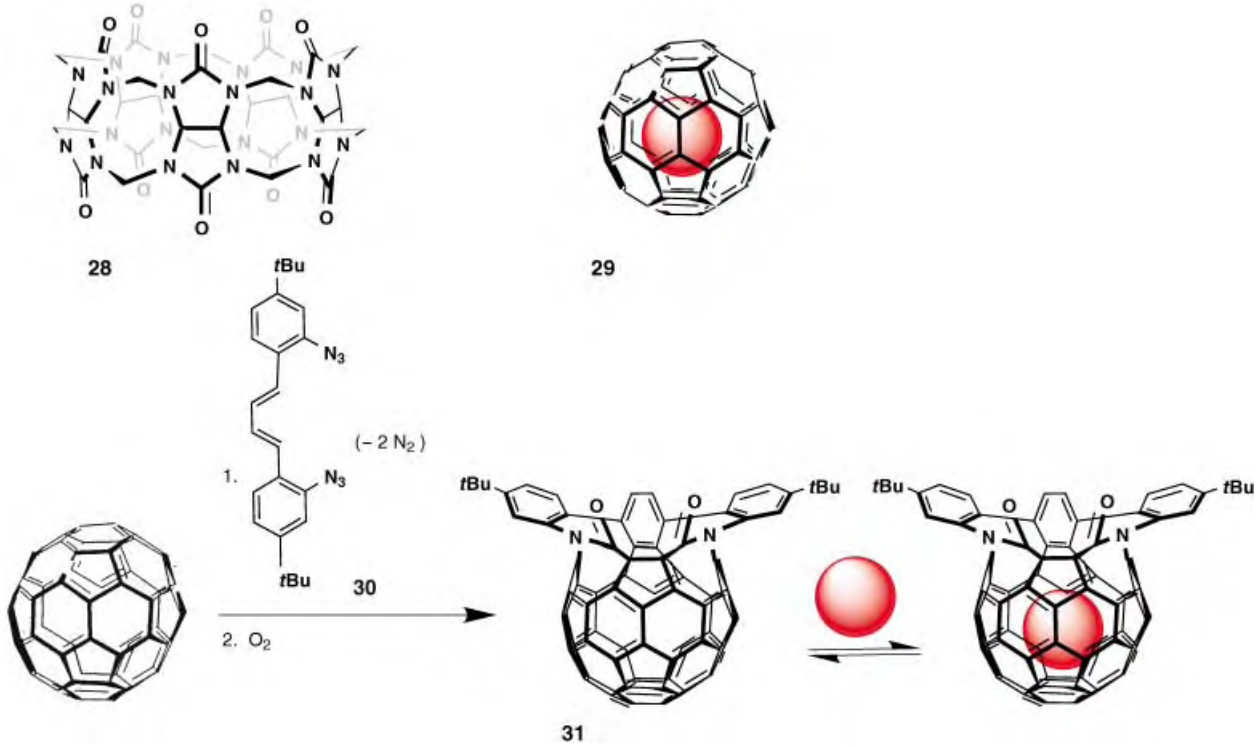
An interesting approach to encapsulate gases, which is based on the delicate interplay between hydrophilic and lipophilic interactions, was demonstrated for decamethylenecucurbit[5]uril **28** (Scheme 12). Water-soluble molecular container **28**—a smaller relative of cucurbituril—was found to entrap a large variety of lipophilic gases (H_2, He, Ne, Ar, N_2, O_2, N_2O, NO, CO, CO_2, CH_4, and acetylene) within its interior.[41] The encapsulation of the gases was studied by single-crystal X-ray analysis and also by NMR spectroscopy in D_2O. For example, the encapsulated CH_4 singlet appeared at $\delta = -0.87$ ppm (^{1}H NMR), the weak resonance at $\delta =$ 127.4 ppm (^{13}C NMR) for the dissolved CO_2 transformed into a rather strong signal at $\delta = 127.1$ ppm (^{13}C NMR) upon encapsulation, and likewise, the typically insoluble acetylene produced signals at $\delta = 1.02$ ppm (^{1}H NMR) and $\delta =$ 73.6 ppm (^{13}C NMR) in the presence of **28**. Most of the gases were encapsulated upon bubbling them through the solution of **28** in D_2O at room temperature. Larger gases (for example, CH_4, Kr, and Xe), however, required heating to 80 °C. Most probably, competition with earlier encapsulated water molecules was responsible for this behavior.

Circulating air through **28** powder resulted in a decrease in the level of CO_2 from 5% to 0.01%. Although **28** has a lower capacity for CO_2 than 5-Å molecular sieves, it has a lower regeneration temperature of 110 °C (versus 350 °C) and a lower affinity to water.

Much attention is currently focused on fullerenes and nanotubes for fabricating nanoscale structures for potential biomedical and materials applications. Fullerenes are known to permanently trap noble gases (for example, **29**, Scheme 12). Heating fullerenes at 650 °C and at 2000–3000 atm pressures of noble gases leads to incorporation of He, Ne, Ar, Kr, and Xe within the C_{60} and C_{70} interiors. Even though the conditions are extreme, the fractional occupational levels are typically about 0.1%.[42] It was proposed that the noble gas enters through a "window" formed by the reversible breaking of one or more carbon–carbon bonds. Theoretical barriers for He to penetrate the benzene rings of fullerene were calculated to be ≥ 200 kcal mol^{-1}. At the same time, the encapsulated gases can be released by the breaking of one or more carbon–carbon bonds upon heating under a vacuum.

Fullerenes can also be "opened through molecular surgery".[43] Thus, reaction of C_{60} with bis-azide **30** affords open-neck bislactam **31**, which encapsulates gases much more easily (Scheme 12). Calculated insertion barriers for He and H_2 are 24.5 and 41.4 kcal mol^{-1}, respectively, which corresponds to insertion temperatures of 124 and 397 °C, respectively. Experimentally, ^{3}He gas was inserted into **31** at 475 atm and approximately 300 °C over 7.5 h (1.5% maximal yield), while for H_2, it took 100 atm, 400 °C, and 48 h (5% yield). Both complexes were studied by NMR spectroscopy. Thus, the helium complex showed a ^{3}He NMR signal at $\delta =$ -10.10 ppm, relative to the free ^{3}He gas at $\delta = 0$ ppm. The encapsulated H_2 was seen at $\delta = -5.43$ ppm in the ^{1}H NMR spectrum.[44]

Recent studies have revealed that some industrially and biologically important gases can be adsorbed and stored inside single-walled carbon nanotubes (SWNTs). The initial synthesis of SWNTs typically produces sealed structures, which prevents adsorption of the gas within the interiors. Chemical treatments, for example, oxidation, leads to open-



Scheme 12. Top: decamethylenecucurbit[5]uril (**28**) and fullerene **29** provides enclosed inner cavities for gases.[41,42] Bottom: "molecular surgery" on C_{60} allows opening of the fullerene to form bislactam **31**, which complexes with gases.[43]

 © 2004 Wiley-VCH Verlag GmbH & Co. KGaA, Weinheim

ended SWNTs. In addition to the interiors, gases may also be adsorbed on the outside surfaces, in groove sites, and in the interstitial sites of nanotubes. Calculations showed that the interiors of SWNTs are energetically more favorable for absorption than their surfaces.[45] Entrapping isotopes of noble gases by SWNTs may improve their use in medical imaging, where it would be desirable to confine the gas physically before injection.[46] SWNTs also trap N_2, O_2, NO, and CF_4 within their interiors.[47] They have been shown to effectively sense O_2, NH_3, and NO_2 through a dramatic change in the electrical resistance of the nanotubes.[48] Storage of H_2 in single-walled carbon nanotubes is extremely promising in the design of energy-rich fuel-cell electric devices. This area is currently a subject of extensive study.[49]

6. Summary and Outlook

The chemistry of gases dates back to the 18th century, when most of them were discovered and described in detail. Experimental studies of gases by Joseph Black, Henry Cavendish, Joseph Priestley, Carl Scheele, and others, coupled with the revolutionary ideas of Antoine Laurent Lavoisier, prepared the groundwork for modern chemistry.[50] Supramolecular chemistry of gases emerged almost 300 years later. Chemists have reached a molecular-level understanding of the forces that bind gases, trap them, fix them in time and in space, and further chemically transform them. This understanding, of course, required inspiration and lessons from nature, which indeed had offered a number of superb examples of gas binding and storing by heme proteins. After this, synthetic receptors, which mimicked the natural systems, were guaranteed to succeed.

It is clear now, that Lewis acid–base, dipole–dipole interactions, hydrogen bonding, van der Waals forces, constrictive encapsulation within enclosed spaces, and a smart combination of all these are most likely to work for gas recognition. Some important receptor/sensing systems, which function through these intermolecular forces, have already been constructed.

Despite the tiny dimensions and simple atomic composition, each gas is different in its physical and chemical properties and requires an individual approach. However, it is possible to rationalize the kinetics, thermodynamics, and selectivity of molecular hosts for gases on the basis of electronic and geometrical complementary between the receptor and substrate. It is also clear that widely accepted concepts of ion coordination and neutral host–guest chemistry, such as the preorganization, multiplication of binding sites, and encapsulation, are applicable to gases. As for all other areas of supramolecular chemistry, spectroscopic techniques and molecular modeling studies are crucial for elucidating the specific contributions of various binding forces, as well as solvent effects.

Supramolecular chemistry provides deeper understanding in biomimetic areas of how gases interact with biological molecules—peptides, enzymes, nucleic acids—and tissues. This may offer some insight into the mechanisms of the physiological activity of gases. The principles and techniques of molecular recognition can be used for gas sensing. In contrast to conventional, mostly electrochemical sensors, this approach provides fundamental knowledge about the structure and dynamics of receptor–analyte complexes on a molecular level, thus opening the way for desirable detection selectivity and sensitivity through the development of novel materials and membranes for gas sensing, storage, and controlled release. Finally, supramolecular chemistry may and will find ways to chemically transform gases into synthetically useful reagents.[51] The rational design of novel catalysts for gas conversion remains a mainstream area of research. However, "molecule-within-molecule" or encapsulation complexes with gases also offer a promising breakthrough as they can entrap and release guest species at will, under subtle chemical or physical control. Most excitingly, however, is that this is just the beginning of much bigger developments.

Financial support is acknowledged from the University of Texas at Arlington and the Donors of The Petroleum Research Fund, administered by the American Chemical Society. D.M.R. is an Alfred P. Sloan Research Fellow. Special thanks are also due to the D.M.R. research group and Prof. R. A. Paselk and the Robert A. Paselk Scientific Instrument Museum (Humboldt State University).

Received: April 11, 2003 [A606]

[1] J.-M. Lehn, *Supramolecular Chemistry. Concepts and Perspectives*, VCH, Weinheim, **1995**.
[2] *Compr. Supramol. Chem.* **1996**, *1*; *Compr. Supramol. Chem.* **1996**, *2*.
[3] a) D. S. Schimel, J. I. House, K. A. Hibbard, P. Bousquet, P. Ciais, P. Peylin, B. H. Braswell, M. J. Apps, D. Baker, A. Bondeau, J. Canadell, G. Churkina, W. Cramer, A. S. Denning, C. B. Field, P. Friedlingstein, C. Goodale, M. Heimann, R. A. Houghton, J. M. Melillo, B. Moore III, D. Murdiyarso, I. Noble, S. W. Pacala, I. C. Prentice, M. R. Raupach, P. J. Rayner, R. J. Scholes, W. L. Steffen, C. Wirth, *Nature* **2001**, *414*, 169–172; b) X. Xiaoding, J. A. Moulijn, *Energy Fuels* **1996**, *10*, 305–325; c) N. H. Batjes, *Biol. Fertil. Soils* **1998**, *27*, 230–235.
[4] a) A. V. Leont'ev, O. A. Fomicheva, M. V. Proskurnina, N. S. Zefirov, *Russ. Chem. Rev.* **2001**, *70*, 91–104; b) W. C. Trogler, *Coord. Chem. Rev.* **1999**, *187*, 303–327.
[5] a) L. J. Ignarro, *Angew. Chem.* **1999**, *111*, 2002–2013; *Angew. Chem. Int. Ed.* **1999**, *38*, 1882–1892; b) S. Pfeiffer, B. Mayer, B. Hemmens, *Angew. Chem.* **1999**, *111*, 1824–1841; *Angew. Chem. Int. Ed.* **1999**, *38*, 1714–1731; c) A. R. Butler, D. L. H. Williams, *Chem. Soc. Rev.* **1993**, *22*, 233–241.
[6] a) M. T. Lerdau, J. W. Munger, D. J. Jacob, *Science* **2000**, *289*, 2291–2293; b) M. Kirsch, H.-G. Korth, R. Sustmann, H. de Groot, *Biol. Chem.* **2002**, *383*, 389–399.
[7] a) L. A. Komarnisky, R. J. Christopherson, T. K. Basu, *Nutrition* **2003**, *19*, 54–61; b) O. Herbarth, G. Fritz, P. Krumbiegel, U. Diez, U. Franck, M. Richter, *Environ. Toxicol.* **2001**, *16*, 269–276; c) C. N. Hewitt, *Atmos. Environ.* **2001**, *35*, 1155–1170.
[8] B. A. Springer, S. G. Sligar, *Chem. Rev.* **1994**, *94*, 699–714.
[9] D. E. Goldberg, *Chem. Rev.* **1999**, *99*, 3371–3378.
[10] E. A. Brucker, J. S. Olson, M. Ikeda-Saito, G. N. Phillips, Jr., *Proteins Struct. Funct. Genet.* **1998**, *30*, 352–356.
[11] D. Sellmann, *Angew. Chem.* **1993**, *105*, 67–70; *Angew. Chem. Int. Ed. Engl.* **1993**, *32*, 64–67.

 © 2004 Wiley-VCH Verlag GmbH & Co. KGaA, Weinheim

[12] A. C. Legon, *Angew. Chem.* **1999**, *111*, 2850 – 2880; *Angew. Chem. Int. Ed.* **1999**, *38*, 2686 – 2714.

[13] C. E. H. Dessent, K. Müller-Dethlefs, *Chem. Rev.* **2000**, *100*, 3999 – 4022.

[14] a) M. Momenteau, C. A. Reed, *Chem. Rev.* **1994**, *94*, 659 – 698; b) G. E. Wuenschell, C. Tetreau, D. Lavalette, C. A. Reed, *J. Am. Chem. Soc.* **1992**, *114*, 3346 – 3355; c) J. P. Collman, X. Zhang, K. Wong, J. I. Brauman, *J. Am. Chem. Soc.* **1994**, *116*, 6245 – 6251; d) C. K. Chang, Y. Liang, G. Aviles, *J. Am. Chem. Soc.* **1995**, *117*, 4191 – 4192.

[15] a) A. Zingg, B. Felber, V. Gramlich, L. Fu, J. P. Collman, F. Diederich, *Helv. Chim. Acta* **2002**, *85*, 333 – 351; b) B. Felber, C. Calle, P. Seiler, A. Schweiger, F. Diederich, *Org. Biomol. Chem.* **2003**, 1090 – 1093, and references therein.

[16] J. Mispelter, M. Momenteau, D. Lavalette, J.-M. Lhoste, *J. Am. Chem. Soc.* **1983**, *105*, 5165 – 5166; see also ref. [14a].

[17] a) F. Tani, M. Matsu-ura, S. Nakayama, M. Ichimura, N. Nakamura, Y. Naruta, *J. Am. Chem. Soc.* **2001**, *123*, 1133 – 1142; b) S. Nakayama, F. Tani, M. Matsu-ura, Y. Naruta, *Chem. Lett.* **2002**, 496 – 497.

[18] J. A. Lukin, V. Simplaceanu, M. Zou, N. T. Ho, C. Ho, *Proc. Natl. Acad. Sci. USA* **2000**, *97*, 10354 – 10358.

[19] G. V. Zyryanov, E. M. Hampe, D. M. Rudkevich, *Angew. Chem.* **2002**, *114*, 4010 – 4013; *Angew. Chem. Int. Ed.* **2002**, *41*, 3854 – 3857.

[20] a) P. Raveendran, S. L. Wallen, *J. Am. Chem. Soc.* **2002**, *124*, 7274 – 7275; b) P. Raveendran, S. L. Wallen, *J. Am. Chem. Soc.* **2002**, *124*, 12590 – 12599; c) M. A. Blatchford, P. Raveendran, S. L. Wallen, *J. Am. Chem. Soc.* **2002**, *124*, 14818 – 14819; see also: V. K. Potluri, J. Xu, R. Enick, E. Beckman, A. D. Hamilton, *Org. Lett.* **2002**, *4*, 2333 – 2335.

[21] Oxygen transfer: Y. Moro-oka, *Catal. Today* **1998**, *45*, 3 – 12; dinitrogen fixation: S. Gambarotta, *J. Organomet. Chem.* **1995**, *500*, 117 – 126; catalysis with CO_2: P. G. Jessop, T. Ikariya, R. Noyori, *Chem. Rev.* **1995**, *95*, 259 – 272; P. Braunstein, D. Matt, D. Nobel, *Chem. Rev.* **1988**, *88*, 747 – 764; catalysis with NO_x: M. C. Kung, H. H. Kung, *Top. Catal.* **2000**, *10*, 21 – 26; catalysis with N_2O: J. T. Groves, J. S. Roman, *J. Am. Chem. Soc.* **1995**, *117*, 5594 – 5595; sensing: A. L. Linsebigler, G. Lu, J. T. Yates, Jr., *Chem. Rev.* **1995**, *95*, 735 – 758; O. S. Wolfbeis, *Anal. Chem.* **2000**, *72*, 81R – 89R; K. J. Franz, N. Singh, S. J. Lippard, *Angew. Chem.* **2000**, *112*, 2194 – 2197; *Angew. Chem. Int. Ed.* **2000**, *39*, 2120 – 2122; see also refs. [3b, 4b].

[22] J. P. Collman, J. I. Brauman, J. P. Fitzgerald, J. W. Sparapani, J. A. Ibers, *J. Am. Chem. Soc.* **1988**, *110*, 3486 – 3495.

[23] F. C. J. M. van Veggel, H. G. Noorlander-Bunt, W. L. Jorgensen, D. N. Reinhoudt, *J. Org. Chem.* **1998**, *63*, 3554 – 3559.

[24] a) M. Albrecht, R. A. Gossage, M. Lutz, A. L. Spek, G. van Koten, *Chem. Eur. J.* **2000**, *6*, 1431 – 1445; b) M. Albrecht, R. A. Gossage, U. Frey, A. W. Ehlers, E. J. Baerends, A. E. Merbach, G. van Koten, *Inorg. Chem.* **2001**, *40*, 850 – 855; c) M. Albrecht, G. Rodriguez, J. Schoenmaker, G. van Koten, *Org. Lett.* **2000**, *2*, 3461 – 3464; d) M. Albrecht, G. van Koten, *Adv. Mater.* **1999**, *11*, 171 – 174; e) M. Albrecht, M. Lutz, A. L. Spek, G. van Koten, *Nature* **2000**, *406*, 970 – 974.

[25] R. J. M. K. Gebbink, A. W. Bosman, M. C. Feiters, E. W. Meijer, R. J. M. Nolte, *Chem. Eur. J.* **1999**, *5*, 65 – 69.

[26] K. M. Padden, J. F. Krebs, C. E. MacBeth, R. C. Scarrow, A. S. Borovik, *J. Am. Chem. Soc.* **2001**, *123*, 1072 – 1079.

[27] A. C. Sharma, A. S. Borovik, *J. Am. Chem. Soc.* **2000**, *122*, 8946 – 8955.

[28] G. A. Jeffrey, *An Introduction to Hydrogen Bonding*, Oxford University Press, Oxford, **1997**.

[29] A. Sultana, R. Loenders, O. Monticelli, C. Kirschhock, P. A. Jacobs, J. A. Martens, *Angew. Chem.* **2000**, *112*, 3062 – 3066; *Angew. Chem. Int. Ed.* **2000**, *39*, 2934 – 2937.

[30] a) F. Cramer, F. M. Henglein, *Chem. Ber.* **1957**, *90*, 2572 – 2575; b) F. D. Cramer, *Rev. Pure Appl. Chem.* **1955**, *5*, 143 – 146; c) F. Cramer, *Angew. Chem.* **1952**, *64*, 437 – 447.

[31] E. Fenyvesi, L. Szente, N. R. Russel, M. McNamara, *Compr. Supramol. Chem.* **1996**, *3*, 305 – 366.

[32] a) D. M. Rudkevich, *Bull. Chem. Soc. Jpn.* **2002**, *75*, 393 – 413; b) A. Jasat, J. C. Sherman, *Chem. Rev.* **1999**, *99*, 931 – 967; c) F. Hof, S. L. Craig, C. Nuckolls, J. Rebek, Jr., *Angew. Chem.* **2002**, *114*, 1556 – 1578; *Angew. Chem. Int. Ed.* **2002**, *41*, 1488 – 1508.

[33] D. J. Cram, M. E. Tanner, C. B. Knobler, *J. Am. Chem. Soc.* **1991**, *113*, 7717 – 7727.

[34] a) N. Branda, R. Wyler, J. Rebek, Jr., *Science* **1994**, *263*, 1267 – 1268; b) N. Branda, R. M. Grotzfeld, C. Valdes, J. Rebek, Jr., *J. Am. Chem. Soc.* **1995**, *117*, 85 – 88.

[35] a) K. Bartik, M. Luhmer, J.-P. Dutasta, A. Collet, Reisse, *J. Am. Chem. Soc.* **1998**, *120*, 784 – 791; b) T. Brotin, A. Lesage, L. Emsley, A. Collet, *J. Am. Chem. Soc.* **2000**, *122*, 1171 – 1174; c) T. Brotin, J.-P. Dutasta, *Eur. J. Org. Chem.* **2003**, 973 – 984.

[36] M. M. Spence, S. M. Rubin, I. E. Dimitrov, E. J. Ruiz, D. E. Wemmer, A. Pines, S. Q. Yao, F. Tian, P. G. Schultz, *Proc. Natl. Acad. Sci. USA* **2001**, *98*, 10654 – 10657.

[37] a) R. Rathore, S. V. Lindeman, K. S. S. Rao, D. Sun, J. K. Kochi, *Angew. Chem.* **2000**, *112*, 2207 – 2211; *Angew. Chem. Int. Ed.* **2000**, *39*, 2123 – 2127; b) S. V. Rosokha, J. K. Kochi, *J. Am. Chem. Soc.* **2002**, *124*, 5620 – 5621; c) S. V. Rosokha, S. V. Lindeman, R. Rathore, J. K. Kochi, *J. Org. Chem.* **2003**, *68*, 3947 – 3957; d) Review on NO^+ and its complexes: G. I. Borodkin, V. G. Shubin, *Russ. Chem. Rev.* **2001**, *70*, 211 – 230.

[38] a) G. V. Zyryanov, Y. Kang, S. P. Stampp, D. M. Rudkevich, *Chem. Commun.* **2002**, 2792 – 2793; b) G. V. Zyryanov, Y. Kang, D. M. Rudkevich, *J. Am. Chem. Soc.* **2003**, *125*, 2997 – 3007.

[39] G. V. Zyryanov, D. M. Rudkevich, *Org. Lett.* **2003**, *5*, 1253 – 1256.

[40] J. L. Atwood, L. J. Barbour, A. Jerga, *Science* **2002**, *296*, 2367 – 2369; for a highlight, see B. C. Gibb, *Angew. Chem.* **2003**, *115*, 1724 – 1725; *Angew. Chem. Int. Ed.* **2003**, *42*, 1686 – 1687.

[41] Y. Miyahara, K. Abe, T. Inazu, *Angew. Chem.* **2002**, *114*, 3146 – 3149; *Angew. Chem. Int. Ed.* **2002**, *41*, 3020 – 3023.

[42] a) M. Saunders, H. A. Jimenez-Vazquez, J. R. Cross, S. Mroczkowski, M. L. Gross, D. E. Giblin, R. J. Poreda, *J. Am. Chem. Soc.* **1994**, *116*, 2193 – 2194; b) M. Saunders, R. J. Cross, H. A. Jimenez-Vazquez, R. Shimshi, A. Khong, *Science* **1996**, *271*, 1693 – 1697.

[43] Y. Rubin, T. Jarrosson, G.-W. Wang, M. D. Bartberger, K. N. Houk, G. Schick, M. Saunders, R. J. Cross, *Angew. Chem.* **2001**, *113*, 1591 – 1594; *Angew. Chem. Int. Ed.* **2001**, *40*, 1543 – 1546.

[44] Quantitative (100%) encapsulation of molecular H_2 was very recently achieved for C_{60} fullerene with a wider opening, see Y. Murata, M. Murata, K. Komatsu, *J. Am. Chem. Soc.* **2003**, *125*, 7152 – 7153.

[45] J. Zhao, A. Buldum, J. Han, J. P. Lu, *Nanotechnology* **2002**, *13*, 195 – 200.

[46] G. E. Gadd, M. Blackford, S. Moricca, N. Webb, P. J. Evans, A. M. Smith, G. Jacobsen, S. Leung, A. Day, Q. Hua, *Science* **1997**, *277*, 933 – 936.

[47] a) O. Byl, P. Kondratyuk, S. T. Forth, S. A. FitzGerald, L. Chen, J. K. Johnson, J. T. Yates, Jr., *J. Am. Chem. Soc.* **2003**, *125*, 5889 – 5896; b) O. Byl, P. Kondratyuk, J. T. Yates, Jr., *J. Phys. Chem. B* **2003**, *107*, 4277 – 4279; c) A. Fujiwara, K. Ishii, H. Suematsu, H. Kataura, Y. Maniwa, S. Suzuki, Y. Achiba, *Chem. Phys. Lett.* **2001**, *336*, 205 – 211.

[48] a) J. Kong, N. R. Franklin, C. Zhou, M. G. Chapline, S. Peng, K. Cho, H. Dai, *Science* **2000**, *287*, 622 – 625; b) P. G. Collins, K. Bradley, M. Ishigami, A. Zettl, *Science* **2000**, *287*, 1801 – 1804; c) S. Peng, K. Cho, *Nanotechnology* **2000**, *11*, 57 – 60.

[49] See, for example, a) A. C. Dillon, K. M. Jones, T. A. Bekkedahl, C. H. Kiang, D. S. Bethune, M. J. Heben, *Nature* **1997**, *386*, 377 – 379; b) C. Liu, Y. Y. Fan, M. Liu, H. T. Cong, H. M. Cheng, M. S.

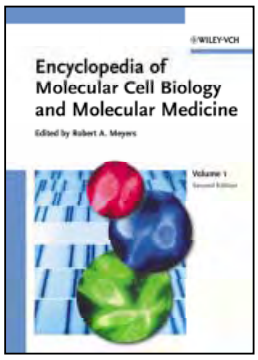
 © 2004 Wiley-VCH Verlag GmbH & Co. KGaA, Weinheim

Dresselhaus, *Science* **1999**, *286*, 1127 – 1129; c) H. Cheng, G. P. Pez, A. C. Cooper, *J. Am. Chem. Soc.* **2001**, *123*, 5845 – 5846; d) W.-F. Du, L. Wilson, J. Ripmeester, R. Dutrisac, B. Simard, S. Denommee, *Nano Lett.* **2002**, *2*, 343 – 346; d) M. Volpe, F. Cleri, *Chem. Phys. Lett.* **2003**, *371*, 476 – 482.

[50] J. R. Partington, *A Short History of Chemistry*, 3rd ed., Dover Publicatons, New York, **1989**.

[51] The use of reversible covalent chemistry between CO_2 and amines has led to the development of novel sensing systems and materials—thermally reversible organogels and imprinting polymers; see a) E. M. Hampe, D. M. Rudkevich, *Chem. Commun.* **2002**, 1450 – 1451; b) M. George, R. G. Weiss, *J. Am. Chem. Soc.* **2001**, *123*, 10393 – 10394; c) C. D. Ki, C. Oh, S.-G. Oh, J. Y. Chang, *J. Am. Chem. Soc.* **2002**, *124*, 14838 – 14839.

The Nucleus of Knowledge



2005. Approx. 10,000 pages.
Hardcover.
ISBN 3-527-30542-4
Prepublication price
approx. € 4144.-
valid until March 31, 2004
thereafter approx. € 4944.-

Publication dates:
volumes 1-5 Jan 2004
volumes 6-10 Aug 2004
volumes 11 –16 May 2005

ROBERT A. MEYERS, Ramtech Ltd., Tarzana, CA, USA (ed.)
Encyclopedia of Molecular Cell Biology and Molecular Medicine
16 Volume Set

"*This series is a classic...*" -
Molecular Medicine Today/Trends in Molecular Medicine

The insight of 10 Nobel laureates

The second edition of the bestselling "Encyclopedia of Molecular Biology and Molecular Medicine" provides a one-stop working library of the molecular basis of life, disease diagnosis and therapy with a new focus on the cell level.

It was designed in collaboration with a founding board of 10 Nobel laureates. The encyclopedia is published in 16 volumes containing approximately 425 articles. Each article presents an in-depth treatment accompanied by a key word list with definitions and an extensive bipartite bibliography of primary and secondary papers.

Save € 800,- until March 31st, 2004

http://meyers-emcbmm.de

Register now for the free
WILEY-VCH Newsletter!
www.wiley-vch.de/home/pas

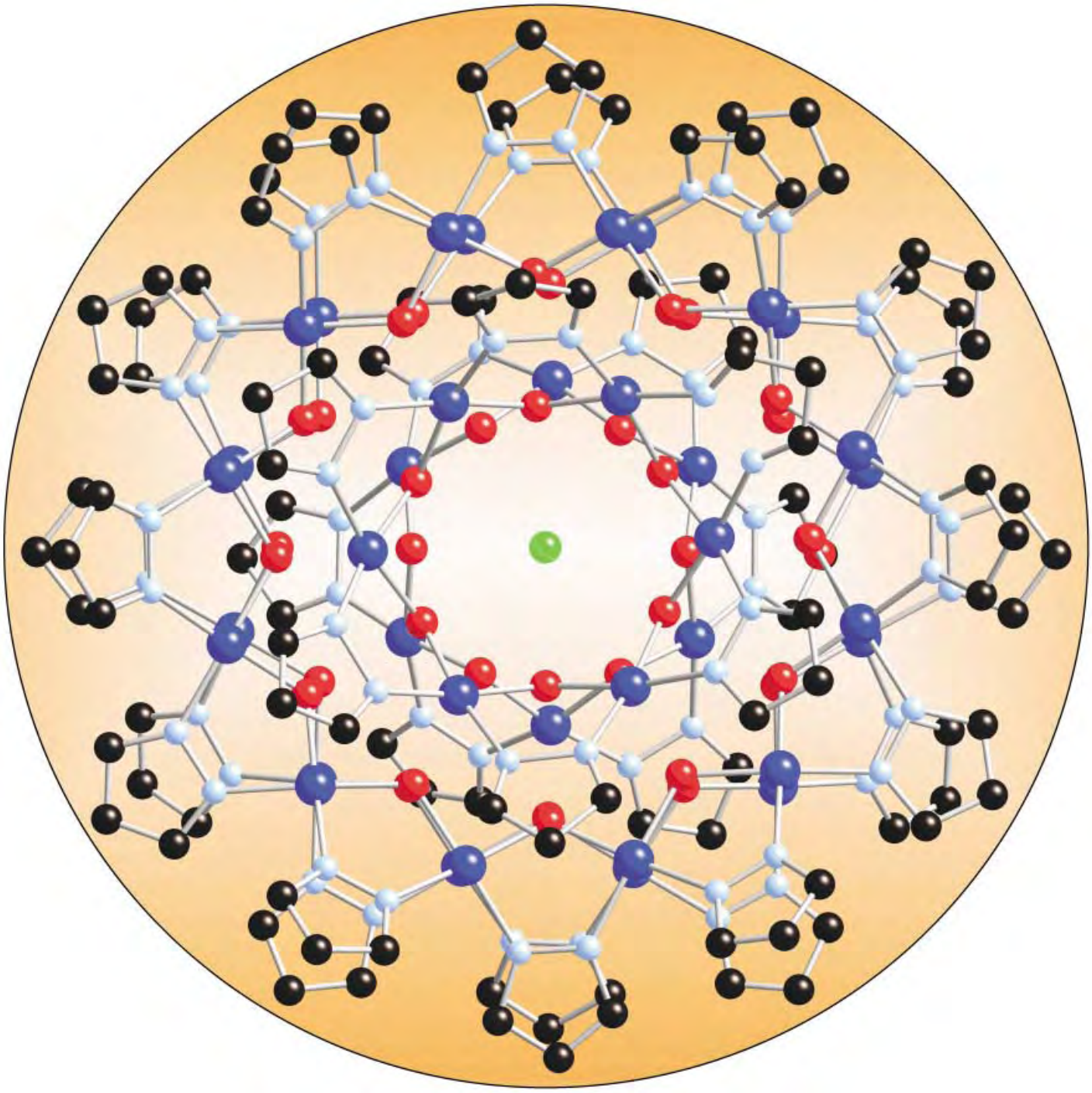
WILEY-VCH • P.O. Box 11 11 61 • D-69451 Weinheim, Germany • Fax: +49 (0) 62 01 - 60 61 84
e-mail: service@wiley-vch.de • www.wiley-vch.de

WILEY-VCH

57503052_kn

 © 2004 Wiley-VCH Verlag GmbH & Co. KGaA, Weinheim

Communications



Three or four neutral metallacycles ([{*cis*-Cu(μ-OH)(μ-pz)}$_n$], $n = 6$, 8, 9, 12, 14) self-assemble with their lipophilic pyrazoles (pz) oriented towards the outer surface and their hydrophilic OH groups towards an encapsulated anion at the inner cavity of the assembly. For more information, see the Communication by R. G. Raptis and co-workers on the following pages.

DOI: 10.1002/anie.200352636
© 2004 Wiley-VCH Verlag GmbH & Co. KGaA, Weinheim

Host–Guest Chemistry

Anion Encapsulation by Neutral Supramolecular Assemblies of Cyclic Cu^{II} Complexes: A Series of Five Polymerization Isomers, [{*cis*-Cu^{II}(μ-OH)(μ-pz)}$_n$], $n = 6, 8, 9, 12$, and 14**

*Gellert Mezei, Peter Baran, and Raphael G. Raptis**

In memory of Leigh Christopher Porter

We describe herein the characterization of three novel supramolecular anion-encapsulating assemblies, where neutral covalently-bound host units converge around the anionic guests, thus forming an elaborate set of host–guest and host–host H bonds. The organization of their architecture mimics the strategy of Nature in constructing ion carriers and channels.

The design and synthesis of biomimetic molecules has developed into a central theme of supramolecular chemistry.[1] Anion recognition and encapsulation[2] is an active research area of biomimetic chemistry that relates to the mechanism of hydrophilic anion transport across hydrophobic cell membranes by various translocases.[3,4] Considerable effort has been devoted to the synthesis of artificial specific anion-recognition agents and several organic and inorganic systems, often cationic macrocyclic and polycyclic cages, are known.[5–9] Several of the synthetic anion-binding hosts are polynuclear metal complexes, in which coordinatively unsaturated metal atoms are preorganized around the space designed to receive a guest anion.[10] In contrast, only few of the biologically relevant, neutral anion-binding agents have been prepared to date.[11–18]

We report preliminary studies of the synthesis of a five-membered series of metallacyclic [{*cis*-Cu^{II}(μ-OH)(μ-pz)}$_n$] polymerization isomers (pz = pyrazolato anion, $C_3H_3N_2^-$), $n = 6, 8, 9, 12$ and 14. The X-ray crystal structures of anion-specific supramolecular assemblies of three or four [{*cis*-Cu^{II}(μ-OH)(μ-pz)}$_n$] rings—$[PPN^+][Cl^-\subset\{[Cu(\mu\text{-}OH)(\mu\text{-}pz)]_{6+12}\}_2]$ (**1**), $[Bu_4N^+][Cl^-\subset\{[Cu(\mu\text{-}OH)(\mu\text{-}pz)]_{6+12}\}_2]$ (**2**), $[Bu_4N^+]_2[CO_3^{2-}\subset\{Cu(\mu\text{-}OH)(\mu\text{-}pz)\}_{6+12+9}]$ (**3**) and $[PPN^+]_2[SO_4^{2-}\subset\{Cu(\mu\text{-}OH)(\mu\text{-}pz)\}_{8+14+9}]$ (**4**) (PPN^+ = bis(triphenylphosphoranylidene)ammonium cation) are presented.[19] The assemblies **1** and **4** were found cocrystallized in a single crystal structure.

The supramolecules **1** and **4** were originally prepared serendipitously in a reaction involving the removal of chlorides from the complex $[PPN]_2[Cu_3(\mu_3\text{-}O)(\mu\text{-}pz)_3Cl_3]$, followed evidently by ring-opening, oligomerization, and ring-closing of the Cu–pz backbone in a wet solvent.[20] A similar procedure employing $(Bu_4N)_2[Cu_3(\mu_3\text{-}Cl)_2(\mu\text{-}pz)_3Cl_3]$ yielded **3**. Subsequently, **2** was prepared in a rational procedure from the reaction of $Cu(OH)_2$ and pzH, in the presence of Bu_4NCl (Supporting Information). The unusually high solubility of **1**–**4** in organic solvents has not allowed the development of a facile crystallization procedure to date and long periods of standing have been necessary for the growth of single crystals.

The [{*cis*-Cu^{II}(μ-OH)(μ-pz)}$_n$] rings (Figure 1) all consist of distorted square-planar Cu^{II}-centers connected by μ-pz ligands at the outer-and μ-OH ligands at the inner surface of a

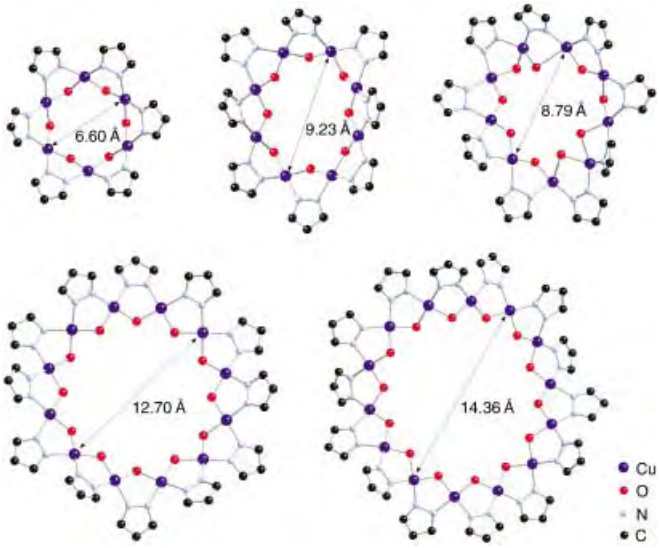


Figure 1. Ball-and-stick representations of the [*cis*-Cu(μ-OH)(μ-pz)]$_n$ rings, $n = 6, 8, 9, 12, 14$; hydrogen atoms not shown. Bond length [Å] and angle [°] ranges: Cu···Cu = 3.130(2)–3.381(2), Cu-N = 1.91(1)–2.08(2), Cu-OH = 1.894(8)–2.013(14), N-Cu-N = 93.8(5)–101.4(5), O-Cu-O = 87.5(3)–95.3(2), and O-Cu-N = 82.4(4)–102.5(4).

toroid.[21] In all four aggregates, **1**–**4**, the larger rings act as hosts (O donors) for one or two smaller rings, binding them by multiple, weak O···Cu interactions. In this arrangement, the OH groups of both rings are directed to the center of the assembly and the pyrazoles to the periphery, thus defining hydrophilic and hydrophobic domains, respectively.

In the 12-membered [{Cu(μ-OH)(μ-pz)}$_{12}$] rings of **1** and **2**, pyrazoles alternate in approximately in-plane and out-of-plane orientations (Figure 2). The out-of-plane pyrazoles direct their two *trans* OH groups (also out-of-plane) to the opposite side, while the in-plane pyrazoles point their respective trans-OH groups (also in-plane) to the center of the ring. In contrast, the six-membered rings adopt a crown shape with all atoms defining the conical surface. In the [{Cu(μ-OH)(μ-pz)}$_{6+12}$] assemblies, the six inward-pointing hydroxyl groups of the outer ring are appropriately oriented to interact with all six Cu-centers of the inner six-membered ring at the axial positions of what become square-pyramidal Cu-centers. The inter-ring Cu···O distances of 2.399(6) to 2.464(6) Å are significantly longer than the intraring Cu–(μ-

[*] G. Mezei, Dr. P. Baran, Prof. Dr. R. G. Raptis
Department of Chemistry, University of Puerto Rico
San Juan, PR 00931–3346 (USA)
Fax: (+1) 787-756-8242
E-mail: raphael@adam.uprr.pr

[**] G.M. acknowledges a NSF–EPSCoR doctoral (Grant No. EPS-9874782).

Supporting information for this article is available on the WWW under http://www.angewandte.org or from the author.

 © 2004 Wiley-VCH Verlag GmbH & Co. KGaA, Weinheim DOI: 10.1002/anie.200352636

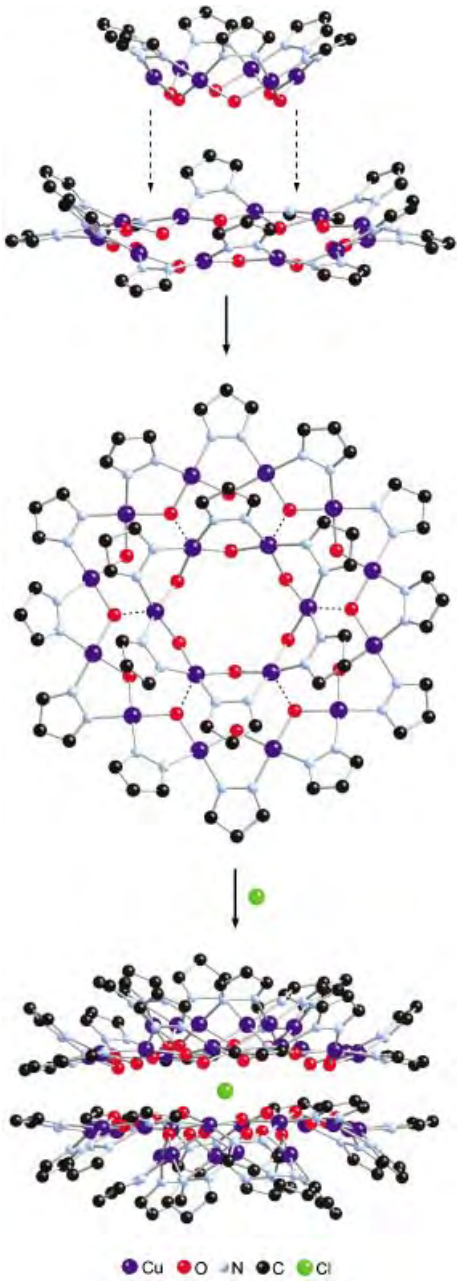


Figure 2. Scheme of ball-and-stick diagrams showing stepwise the assembly of $[Cl^-\subset\{[Cu(\mu\text{-}OH)(\mu\text{-}pz)]_{6+12}\}_2]$ in **1** and **2**; H-atoms not shown. Twelve H-bonded Cl···O distances of 3.306(7)–3.698(7) Å between all six OH-groups of the two $[\{Cu(\mu\text{-}OH)(\mu\text{-}pz)\}_6]$ rings and the encapsulated chloride. Twelve H-bonded O···O distances of 2.754(9)–2.995(9) Å between all twenty four OH-groups of the two $[\{Cu(\mu\text{-}OH)(\mu\text{-}pz)\}_{12}]$ rings—six in-plane HO's of one 12-membered ring and six out-of-plane OH's of the other, and vice versa.

OH) bonds of 1.894(8) to 1.982(8) Å within either the six- or twelve-membered rings. However, the cumulative effect of six such weak Cu···O interactions between the two rings may account for the formation of this "Russian doll" assembly. The neutral $[\{Cu(\mu\text{-}OH)(\mu\text{-}pz)\}_{6+12}]$ assembly has segregated hydrophilic (hydroxyl) and hydrophobic (pyrazole) groups in a structure resembling a metal-containing calixarene.

Two face-to-face $[\{Cu(\mu\text{-}OH)(\mu\text{-}pz)\}_{6+12}]$ units sandwich a chloride ion between their hydrophilic sides; the chloride ion is held by weak H bonds to twelve OH groups, six on each side, which belong to the six-membered rings forming the $Cl^-\subset[\{[Cu(\mu\text{-}OH)(\mu\text{-}pz)]_{6+12}\}_2]$ assembly (Figure 2). The assembly is further supported by a picket fence of twelve H bonds (not shown in Figure 2) formed between pairs of OH groups, one each from the two 12-membered rings. At the opposite side of the encapsulated chloride, either a phenyl (**1**) or a butyl group (**2**) of the PPN^+ and Bu_4N^+ counterions, respectively, dips into the hydrophobic bowl formed by the pyrazoles of the inner $[\{Cu(\mu\text{-}OH)(\mu\text{-}pz)\}_6]$ ring.

The $\{Cu(\mu\text{-}OH)(\mu\text{-}pz)\}_{6+12}$ unit is also present in the structure of **3**, in which a carbonate ion is encapsulated between this unit and a nine-membered ring (Figure 3). Each carbonate O atom is in H-bonding distance to all hydroxyl

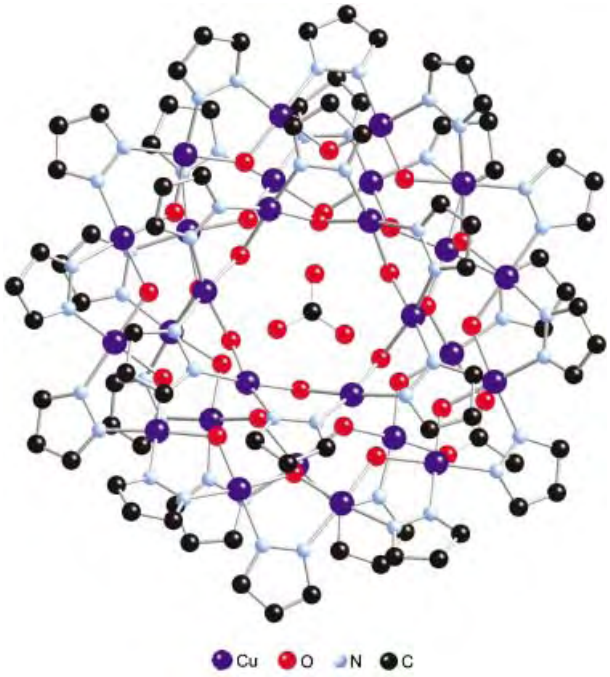


Figure 3. Ball-and-stick diagram of **3**. Each carbonate O-atom has four H-bonds— O···O distances of 2.73(1)–2.97(1) Å, and two longer interactions, 3.27(1)–3.52(1) Å, with OH-groups of the 6- and 9-membered rings. Six Cu···O inter-ring (6- and 12-membered rings) contacts of 2.390(8)–2.577(8) Å, and three more, 2.354(8)–2.428(8) Å, between Cu-atoms of the 9-membered ring and O-atoms of the 12-membered one. Six additional H-bonds between the 9- and the 12-membered rings: O···O distances, 2.75(1)–2.93(1) Å.

groups of the nine- and six-membered rings on either side, with O–O interatomic distances as short as 2.734(9) Å. Additional H bonds and O···Cu interactions between rings on either side of the carbonate plane are contributing to the assembly. A similar but more irregular H bonding and O···Cu interaction pattern is seen in the structure of **4** (Figure 4). The 14-membered ring acts as a host, binding to the Cu-atoms of the eight- and nine-membered rings, which, in turn, bind the encapsulated sulfate ion. While the H bonds holding the chloride, carbonate, and sulfate anions at the hydrophilic

 © 2004 Wiley-VCH Verlag GmbH & Co. KGaA, Weinheim

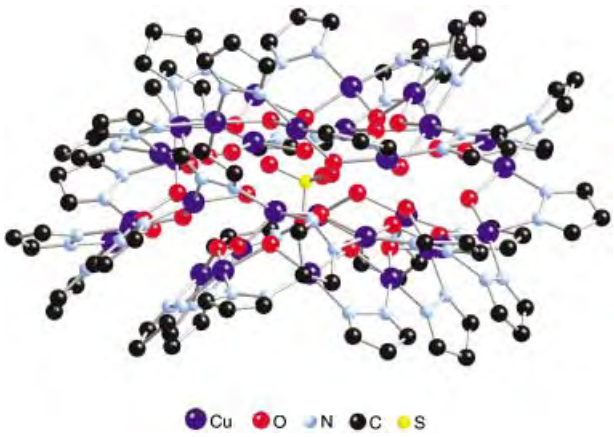


Figure 4. Ball-and-stick diagram of **4**. The sulfate O-atoms form eighteen O···O contacts of 2.83(1)–3.37(1) Å, with OH-groups of the 8- and 9-membered rings. Seven Cu···O contacts of 2.376(6)–2.736(6) Å between O-atoms of the 14-membered ring and Cu-atoms of the 8-membered one and six more, 2.392(6)–2.855(6) Å, with those of the 9-membered ring. Six additional H-bonds between the 14-membered ring and each of the 8- and 9-membered ones: O···O distances, 2.732(9)–3.018(9) Å.

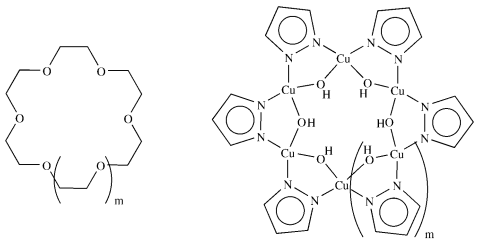
pockets of **1**–**4** are weak, they are also numerous and their cumulative effect should amount to significant overall stability.

Several transition metals and bridging ligands have been employed in the synthesis of a variety of metallacyclic rings, including a [{*trans*-Cu(μ-OH)(μ-3,5-Me_2-pz)}$_8$] ring and a [{Zn_2(μ-5-Me-3-Ph-pz)$_2$(μ-OCH_2CH_2S)}$_6$] ring.[24,25] Yet, there are only a few examples of polymerization isomers—complexes of the same empirical formula—in this group of compounds.[10,26–31] The characterization in a single crystal structure (containing the assemblies **1** and **4**) of all five ring sizes reported here, implies that there are only small, entropy-controlled differences in the Gibbs free energy between rings of different sizes, thus allowing all five to coexist. As only a part of the reaction products has been isolated in crystalline form, while a major part remained in solution, it is possible that rings of different sizes other than the five described here are still present in the mother liquor, but lack the appropriate anions for their crystallization.

The metallacyclic ring sizes are not dependent on the nature of the encapsulated anion; six-membered rings are part of the structures of **1** (and **2**) and **3**, while nine-membered rings are encountered in **3** and **4**. In contrast, the aggregation of metallacycles is specific to the encapsulated anion; the smaller chloride finds a snug fit between two six-membered rings of **1** and **2**, the planar carbonate requires a six- and a nine-membered ring in **3**, while the tetrahedral sulfate is encapsulated among an eight-, a nine- and a fourteen-membered rings in **4**. Two different cations, PPN^+ and Bu_4N^+, have been found associated with the same host–guest anion in **1** and **2**, which suggests that the counterions do not play a determining role in this chemistry. Several metallacycles may be present in solution and the availability of anions determines which metallacycles aggregate to form the neutral supramolecular hosts. Different combinations of metallacycles may also be required for the encapsulation of anions other than chloride, carbonate, or sulfate.

Four levels of self-organization are manifested in the structures of the three anion-encapsulating aggregates described here: First, the approximately square-planar coordination preference of the Cu^{II}-cations, coupled with the availability of only pyrazole and hydroxyl ligands, favor the formation of one-dimensional Cu(μ-OH)(μ-pz) chains, which eventually close into metallacyclic rings. Second, the residual positive charges of the Cu-centers and the partial negative charges associated with the μ-OH ligands make possible the formation of two-, or three-ring assemblies through Cu···OH interactions. Third, hydrogen bonds, between the encapsulated anions and the μ-OH ligands of the neutral host, orient the latter towards the center of the supramolecular ensemble and wrap the metallacycles around the guest anions. Fourth, a complement of peripheral H bonds between rings add to the stability of the assemblies. The interplay of covalent coordination algorithms, H bonding and weak dipolar interactions in orchestrating the formation of complex assemblies of highly specific function is imitating the strategies employed by Nature for similar purposes. None of the above chemical properties are unique to copper or pyrazole, thus raising the possibility that structures **1**–**4** are only the frontrunners of a new class of supramolecular anion-encapsulating agents.

The structures of the series of metallacycles [{*cis*-Cu(μ-OH)(μ-pz)}$_n$], $n = 6, 8, 9, 12, 14$ (Figure 1), resemble those of crown ethers and natural ionophores and can be considered as fully protonated, copper-containing crowns; metallacrowns. However, while crown ethers and ionophores function as cation binders by virtue of their inward oriented oxygen electron lone pairs, the copper metallacrowns show an inverted function, namely anion binding through the cooperative H bonding to all μ-OH groups. Work is underway to



determine the effects of temperature, concentration, solvent, and the nature of the anion on the composition and structure of the supramolecular assemblies.

Received: August 13, 2003
Revised: October 14, 2003 [Z52636]
Published Online: December 29, 2003

Keywords: copper · host–guest systems · hydrogen bonds · self-assembly · supramolecular chemistry

[1] J.-M. Lehn, *Science* **2002**, *295*, 2400–2403.
[2] P. D. Beer, P. A. Gale, *Angew. Chem.* **2001**, *113*, 502–532; *Angew. Chem. Int. Ed.* **2001**, *40*, 486–516.

 © 2004 Wiley-VCH Verlag GmbH & Co. KGaA, Weinheim

[3] R. Dultzler, E. B. Campbell, M. Cadene, B. T. Chait, R. MacKinnon, *Nature* **2002**, *415*, 287 – 294.
[4] R. Dutzler, E. B. Campbell, R. MacKinnon, *Science* **2003**, *300*, 108 – 112.
[5] F. P. Schmidtchen, M. Berger, *Chem. Rev.* **1997**, *97*, 1609 – 1646.
[6] P. D. Beer, D. K. Smith, *Prog. Inorg. Chem.* **1997**, *46*, 1 – 96.
[7] P. A. Gale, *Coord. Chem. Rev.* **2000**, *199*, 181 – 233.
[8] P. A. Gale, *Coord. Chem. Rev.* **2001**, *213*, 79 – 128.
[9] J. J. Bodwin, A. D. Cutland, R. G. Malkani, V. L. Pecoraro, *Coord. Chem. Rev.* **2001**, *216–217*, 489 – 512.
[10] E. Cadot, F. Sécheresse, *Chem. Commun.* **2002**, 2189 – 2197.
[11] M. M. G. Antonisse, D. N. Reinhoudt, *Chem. Commun.* **1998**, 443 – 448.
[12] S. Mason, T. Clifford, L. Seib, K. Kuczera, K. Bowman-James, *J. Am. Chem. Soc.* **1998**, *120*, 8899 – 8900.
[13] Md. A. Hossain, J. M. Llinares, D. Powell, K. Bowman-James, *Inorg. Chem.* **2001**, *40*, 2936 – 2937.
[14] A. Szumna, J. Jurczak, *Eur. J. Org. Chem.* **2001**, 4031 – 4039.
[15] R. Herges, A. Dikmans, U. Jana, F. Köhler, P. G. Jones, I. Dix, T. Fricke, *Eur. J. Org. Chem.* **2002**, 3004 – 3014.
[16] S. Kubik, R. Kirchner, D. Nolting, J. Seidel, *J. Am. Chem. Soc.* **2002**, *124*, 12752 – 12760.
[17] J.-H. Liao, C.-T. Chen, J.-M. Fang, *Org. Lett.* **2002**, *4*, 561 – 564.
[18] D.-W. Yoon, H. Hwang, C.-H. Lee, *Angew. Chem.* **2002**, *114*, 1835 – 1837; *Angew. Chem. Int. Ed.* **2002**, *41*, 1757 – 1759.
[19] X-ray crystal structure analysis of **1**+**4**: crystal dimensions $0.20\times0.10\times0.04$ mm; $T=302$ K; triclinic, space group $P\bar{1}$; $a=21.240(3)$ Å, $b=30.420(4)$ Å, $c=35.863(5)$ Å, $\alpha=98.447(3)°$, $\beta=91.774(3)°$, $\gamma=99.056(3)°$, $V=22601(6)$ Å^3, $Z=2$; $\rho_{calcd}=1.709$ g cm^{-3}; $\mu=3.181$ mm^{-1}; $3.1<2\theta<46.6°$; of 64863 unique reflections, 30064 were observed $[I>2\sigma(I)]$; 4818 parameters; $R_1=0.0559$, $wR_2=0.1217$ for $I>2\sigma(I)$; GOF = 0.936. X-ray crystal structure analysis of **2**: crystal dimensions $0.20\times0.18\times0.05$ mm; $T=300$ K; monoclinic, space group $P2_1/n$; $a=17.545(2)$ Å, $b=34.275(4)$ Å, $c=36.036(5)$ Å, $\beta=90.541(3)°$, $V=21669(5)$ Å^3, $Z=4$; $\rho_{calcd}=1.714$ g cm^{-3}; $\mu=3.531$ mm^{-1}; $2.3<2\theta<46.6°$; of 31296 unique reflections, 13276 were observed $[I>2\sigma(I)]$; 2346 parameters; $R_1=0.0585$, $wR_2=0.1384$ for $I>2\sigma(I)$; GOF = 0.915. X-ray crystal structure analysis of **3**: crystal dimensions $0.28\times0.18\times0.10$ mm; $T=303$ K; monoclinic, space group $P2_1/n$; $a=34.796(5)$ Å, $b=26.036(4)$ Å, $c=38.820(6)$ Å, $\beta=95.337(3)°$, $V=35016(9)$ Å^3, $Z=4$; $\rho_{calcd}=1.716$ g cm^{-3}; $\mu=3.276$ mm^{-1}; $3.3<2\theta<46.6°$; of 50472 unique reflections, 20614 were observed $[I>2\sigma(I)]$; 3651 parameters; $R_1=0.0656$, $wR_2=0.1425$ for $I>2\sigma(I)$; GOF = 0.979. Refinement details can be found as Supporting Information. CCDC-212810 (**1**+**4**), CCDC-212812 (**2**) and CCDC-212811 (**3**) contains the supplementary crystallographic data for this paper. These data can be obtained free of charge via www.ccdc.cam.ac.uk/conts/retrieving.html (or from the Cambridge Crystallographic Data Centre, 12 Union Road, Cambridge CB21EZ, UK; fax: (+44) 1223-336-033; or deposit@ccdc.cam.ac.uk).
[20] P. A. Angaridis, P. Baran, R. Boca, F. Cervantes-Lee, W. Haase, G. Mezei, R. G. Raptis, R. Werner, *Inorg. Chem.* **2002**, *41*, 2219 – 2228.
[21] The 6- through to 14-membered isomers depicted in Figure 1 can also be described as inverse metallacrowns:[22,23] *inv*(OH)$_6$[18-MC$_{Cu^{2+}N,N(pz)}$-6], *inv*(OH)$_8$[24-MC$_{Cu^{2+}N,N(pz)}$-8], *inv*(OH)$_9$[27-MC$_{Cu^{2+}N,N(pz)}$-9], *inv*(OH)$_{12}$[36-MC$_{Cu^{2+}N,N(pz)}$-12] and *inv*(OH)$_{14}$[42-MC$_{Cu^{2+}N,N(pz)}$-14], respectively.
[22] A. J. Stemmler, J. W. Kampf, V. L. Pecoraro, *Inorg. Chem.* **1995**, *34*, 2271 – 2272.
[23] V. L. Pecoraro, A. J. Stemmler, B. R. Gibney, J. J. Bodwin, H. Wang, J. W. Kampf, A. Barwinski, *Prog. Inorg. Chem.* **1997**, *45*, 83 – 177.
[24] G. A. Ardizzoia, M. A. Angaroni, G. La Monica, F. Cariati, S. Cenini, M. Moret, M. Masciocchi, *Inorg. Chem.* **1991**, *30*, 4347 – 4353.
[25] D. T. Puerta, S. Cohen, *Chem. Commun.* **2003**, 1278 – 1279.
[26] R. W. Saalfrank, I. Bernt, E. Uller, F. Hampel, *Angew. Chem.* **1997**, *109*, 2596 – 2599; *Angew. Chem. Int. Ed. Engl.* **1997**, *36*, 2482 – 2485.
[27] J. D. Higgins III, J. W. Suggs, *Inorg. Chim. Acta* **1988**, *145*, 247 – 252.
[28] S. A. Ivanov, M. A. Kozee, W. A. Merrill, S. Agarwal, L. F. Dahl, *Dalton Trans.* **2002**, 4105 – 4115.
[29] F. Köhler, A. Schell, B. Weber, *Chem. Eur. J.* **2002**, *8*, 5219 – 5227.
[30] B. Hasenknopf, J.-M. Lehn, N. Boumediene, A. Dupont-Gervais, A. Van Dorsselaer, B. Kneisel, D. Fenske, *J. Am. Chem. Soc.* **1997**, *119*, 10956 – 10962.
[31] H. Nierengarten, J. Roho, E. Leize, J.-M. Lehn, A. Van Dorsselaer, *Eur. J. Inorg. Chem.* **2002**, 573 – 579.

 © 2004 Wiley-VCH Verlag GmbH & Co. KGaA, Weinheim

Magnetism in Compressed Fullerenes

The Origin of the Magnetic Moments in Compressed Crystals of Polymeric C_{60}**

*Jordi Ribas-Ariño and Juan J. Novoa**

Makarova et al.[1] reported that the rhombohedral phases of polymeric C_{60} (*rh*-C_{60}) exhibit the typical properties of ferromagnets (magnetization hysteresis loops, saturation magnetization) up to 500 K, and this is a remarkable and puzzling performance for a purely organic molecular magnet (the previous highest critical temperature at atmospheric pressure was 36 K,[2] which increased to 65 K on applying a pressure of 16 kilobars[3]). These findings were later confirmed by Wood et al.[4] on pristine C_{60} at 9 GPa and 800 K. The origin of magnetism in *rh*-C_{60} still lacks a solid explanation based on evidence, although the original authors suggested some possibilities. Here, on the basis of results from quantum-mechanical calculations, it is shown that under pressure the lowest energy state for a pair of 2+2 covalently linked C_{60} molecules is a triplet T_2 state with only one

[*] J. Ribas-Ariño, Prof. J. J. Novoa
Departament de Química Física
Facultat de Química and CER Química Teòrica
Parc Cientific, Universitat de Barcelona
Av. Diagonal 647, 08028-Barcelona (Spain)
Fax: (+34) 93-402-1231
E-mail: novoa@qf.ub.es

[**] This work was sponsored by the CEPBA-IBM Research Institute, as one of its cooperative research projects. We also thank the Spanish "Ministerio de Ciencia y Teconología", and the Catalan CIRIT for grants which made this work possible (projects BQU2002-04587-C02-02 and 2001SGR-0044, respectively). J.R. also acknowledges Universitat de Barcelona and "Ministerio de Educación Cultura y Deportes" for the award of a Ph.D. grant.

Supporting information for this article is available on the WWW under http://www.angewandte.org or from the author.

 DOI: 10.1002/anie.200352118 © 2004 Wiley-VCH Verlag GmbH & Co. KGaA, Weinheim

interfragment C–C bond, in which the C_{60} molecules are doublets. Once formed at high pressure/temperature, the T_2 state is stable at ambient pressure, and radical centers can be found in the solid. When enough activated bonds are present in the solid, it can exhibit macroscopic magnetic properties.

At room temperature, the nonmagnetic *rh*-C_{60} phases form stacks of hexagonal planes (Figure 1).[6,7] In each plane

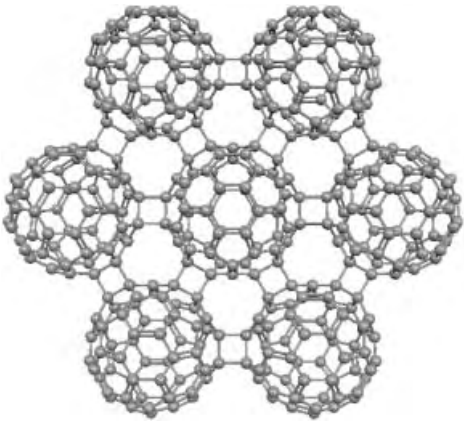


Figure 1. Structure of the planes of rhombohedral polymeric C_{60}.

the C_{60} molecules are joined to six neighboring C_{60} molecules by two C–C single bonds with a length of 1.68 Å.[6] Each pair of bonds results from a [2+2] cycloaddition involving one [6,6] bond (at the junction of two hexagons) in each C_{60} molecule.[8–10] No precise structural information is available on the structure of *rh*-C_{60} samples under pressure and at high temperature, although all evidence supports preservation of the C_{60} units and the presence of a layered structure.[1,4]

The origin of the magnetic interactions[11] in compressed *rh*-C_{60} is puzzling. Experimental data excluded that magnetism is due to O_2 adsorbed on the samples or the presence of small amounts of impurities.[1,4,12] Recent experimental data[4] also ruled out that the magnetic properties could be due to radical fragments formed by rupture of C_{60} molecules under the external pressure (the experiments showed that the formation of magnetic *rh*-C_{60} phases does not damage the C_{60} molecules). Therefore, we are left with what was considered by Palacio[13] to be "the most basic and obvious question": where do the magnetic moments in compressed *rh*-C_{60} come from? Some proposals were put forward by the original authors,[1,4] without giving any solid evidence for their validity. This prompted us to carry out a systematic exploration, using quantum-chemical methods, of the changes undergone by C_{60}–C_{60} bonds when they are compressed, by searching for stable open-shell states.

Our main line of approach was that, at the macroscopic level, compression decreases the macroscopic volume, which, at the microscopic level, translates into a shortening of the intermolecular C_{60}–C_{60} bonds. Therefore, the possible structural and electronic changes induced by the external pressure in these bonds can be investigated by studying the shape of the potential energy curve of the C_{60}–C_{60} bonds in the short-distance region. In a first approach, we can explore the changes in the simplest model representing C_{60}–C_{60} bonds of the *rh*-C_{60} planes, namely, the unsubstituted C_{60}–C_{60} dimer. These calculations were performed with the B3LYP density functional,[14] as implemented in a parallel version of GAMESS.[15]

The existence of magnetic interactions requires the presence of thermally accessible open-shell states. Therefore, we explored the shape of the potential energy curves for the most stable singlet (S_0), triplet (T_1), and quintet (Q_1) states (the geometry of the dimer was fully optimized at each point; in the S_o T_1 and Q_1 states the two C–C interfragment bonds are forced to be equal). To lower the computational cost we explored the curves in two steps: a full search was performed for a "half-ball" model of the C_{60}–C_{60} dimer; then, selective calculations on the whole C_{60}–C_{60} dimer were carried out on the physically relevant regions of the curves. The half-ball model is a $C_{32}H_{10}$–$C_{32}H_{10}$ dimer obtained by removing one hemisphere from each ball of the C_{60}–C_{60} dimer along the equator and adding C–H bonds to equatorial C atoms where C–C bonds were present before the cut. It is designed to mimic the electronic structure in the [6,6] C atoms participating in the [2+2] cycloaddition (the optimum geometry of both dimers exhibit the same distribution of double and single bonds around the [6,6] C atoms, and the distances are similar (see Supporting Information). Both dimers were oriented as in the *rh*-C_{60} planes, the preferred orientation for the [2+2] cycloaddition of two C_{60} molecules.[16,17]

Figure 2 shows the shape of the lowest energy singlet (S_0), triplet (T_1), and quintet (Q_1) potential energy curves calculated for the $C_{32}H_{10}$–$C_{32}H_{10}$ dimer by using the B3LYP functional and the 3-21G basis set. The curves range from a longest C–C interfragment distance of 4 Å to a distance of 1.1 Å, for which the interaction energy is on the order of 300 kcal mol^{-1}. The compression of two isolated half-balls in their singlet S_0 ground state leads to formation of a doubly

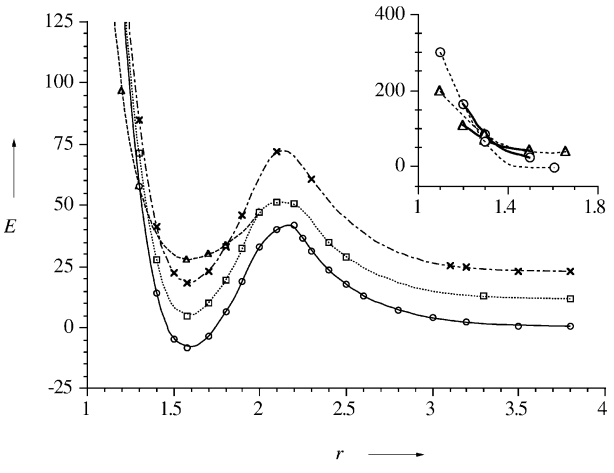


Figure 2. Potential energy curves for the $C_{32}H_{10}$–$C_{32}H_{10}$ dimer in the singlet S_0 (circles), triplet T_1 (squares), triplet T_2 (triangles), and quintet Q_1 states (crosses). Inset: S_0 and T_2 curves for the C_{60} dimer in the region of S_0–T_2 crossing, calculated at the B3LYP/3-21G and BLYP/plane wave levels (broken and solid lines, respectively). The energy *E* is given in kcal mol^{-1}, and the C–C interfragment distance *r* in angstroms.

 © 2004 Wiley-VCH Verlag GmbH & Co. KGaA, Weinheim

C–C covalently linked $C_{32}H_{10}$–$C_{32}H_{10}$ dimer after overcoming an activation barrier of about 40 kcal mol^{-1} (the structure of the $C_{32}H_{10}$–$C_{32}H_{10}$ dimer and the activation barrier are similar to those found for compression of two C_{60} molecules[18,19]). Each half of the $C_{32}H_{10}$–$C_{32}H_{10}$ dimer (Figure 3) has the

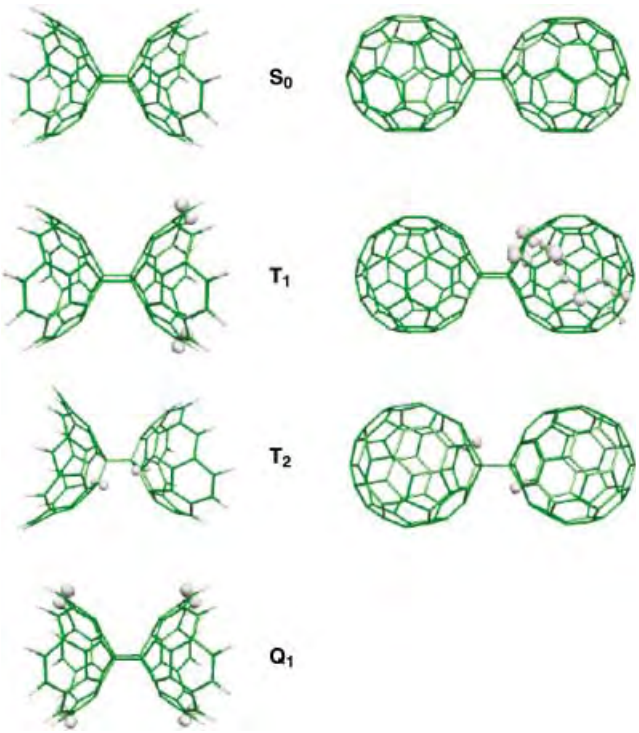


Figure 3. Optimum geometry of the S_0, T_1, T_2, and Q_1 states of the $C_{32}H_{10}$–$C_{32}H_{10}$ and C_{60}–C_{60} dimers. The spin distribution of some states is also shown (the 0.045 a.u. surface, a region of high spin distribution).

electronic structure of an isolated $C_{32}H_{10}$(singlet), with alternating single and double bonds, with the exception of the [6,6] bonds involved in the [2+2] cycloaddition. When higher pressure is applied, the $C_{32}H_{10}$–$C_{32}H_{10}$ dimer is forced to climb the repulsive wall of the S_0 curve, where it crosses the curve of the triplet T_2 state, but not the T_1 or Q_1 curves.

The lowest energy triplet (T_1) and quintet (Q_1) states are obtained by taking the S_0 state and converting C=C double bonds to C–C bonds without destroying the topology of the balls (T_1 dissociates into a $C_{32}H_{10}$(triplet) and a $C_{32}H_{10}$(singlet) fragment, while Q_1 dissociates into two $C_{32}H_{10}$(triplet) fragments). The T_1 and Q_1 curves are nearly parallel to the S_0 curve at interfragment distances larger than the minimum, and their minimums lie at similar C–C interfragment distances (1.586, 1.586, and 1.587 Å, for the S_0, T_1, and Q_1 states, respectively). This is an indication of similar electronic structures of the $C_{32}H_{10}$(singlet) and $C_{32}H_{10}$(triplet) fragments in the region of the [6,6] bonds involved in the [2+2] cycloaddition. As the S_0, T_1, and Q_1 curves never cross (Figure 2) the T_1 and Q_1 states cannot be responsible for the existence of magnetic interactions in compressed pristine C_{60} crystals.

The state responsible for the presence of magnetic interactions in the half-ball dimers is the T_2 triplet state. It is obtained when one of the two interfragment C–C bonds present in the S_0 state is broken and its two electrons are placed in a triplet disposition, one in each fragment (each $C_{32}H_{10}$ fragment of the T_2 state is a doublet). The T_2 triplet has a minimum at an interfragment C–C bond length of 1.590 Å (see Figure 2). There are two minimum-energy conformations: one in which the four [6,6] atoms involved in the [2+2] cycloaddition (C_1–C_4) are in a *trans* disposition (C1-C2-C3-C4 ca. 180°), and another in which they are in a *gauche* arrangement (C_1-C2-C3-C4 ca. 60°). In both minima the T_2 state is less stable than the S_0, T_1, or Q_1 minima (Figure 2). The transition from T_2 to S_0, T_1, or Q_1 is forbidden by the Frank–Condon principle, since the T_2 state has a rotational maximum for the C1-C2-C3-C4 dihedral angle where the S_0, T_1, and Q_1 have minima (C1-C2-C3-C4 0°). Consequently, overlap of the vibrational functions of T_2 with these of S_0, T_1, or Q_1 is negligible. The T_2 state becomes the ground state when the interfragment C–C distance is shorter than 1.3 Å, a fact that can be interpreted by stating that the energy required to compress the two fragments of the dimer is smaller when they are linked by one C–C bond than when they are linked by two. The T_2 and T_1 curves dissociate into the same fragments, that is, $C_{32}H_{10}$(singlet) and a $C_{32}H_{10}$(triplet).

Having determined the shape of the half-dimer curves, we then calculated the required points in the S_0 and T_2 curves of the C_{60}–C_{60} dimer to show the presence of a minimum in these curves and T_2–S_0 curve crossing (the minimum obtained by full optimization; the crossing by single-point B3LYP/STO-3G optimization at three points, followed by a B3LYP/3-21G calculation of the energy). The optimum geometry and spin density for the S_0, T_1, and T_2 states of the C_{60}–C_{60} dimer are shown in Figure 3. The B3LYP/3-21G C_{60}–C_{60} S_0 and T_2 curves are shown in the inset of Figure 2. We found that 1) the S_0 and T_2 curves have a minimum, 2) the optimum geometries of the C_{60}–C_{60} dimers (Figure 3) are similar to those calculated for the half-ball model (in the S_0 state the optimum interfragment C–C distance is 1.611 Å in the half-ball dimer and 1.633 Å in the C_{60}–C_{60} dimer), 3) the T_2 and S_0 curves cross around 1.3 Å, and 4) the electronic structures of the T_2 states of the C_{60}–C_{60} and half-ball dimers are similar (Figure 3). We also found that the T_2 state has two minima, for C1-C2-C3-C4 angles around 60° and 180° (the *trans* is 3.5 kcal mol^{-1} more stable than the *gauche* conformation). The existence of T_2–S_0 curve crossing was also found in DFT calculations with plane-wave basis[20] on these C_{60}–C_{60} curves around the crossing region (see inset in Figure 2). Consequently, the magnetically active species in the C_{60}–C_{60} dimers are C_{60} molecules covalently connected by one C–C interfragment bond, in which each C_{60} molecule is a doublet coupled in a ferromagnetic fashion.

The previous results can now be used to understand the generation of magnetic interactions in compressed polymeric *rh*-C_{60} phases. As the structure of these phases is not currently known, we will only perform a qualitative analysis with the help of Figure 4. After an initial pressure is applied to pristine C_{60}, C_{60}–C_{60} bonds are formed in the S_0 state (light arrows in Figure 4). All electrons are paired, so these bonds are diamagnetic. When higher pressure is applied to the solid,

 © 2004 Wiley-VCH Verlag GmbH & Co. KGaA, Weinheim

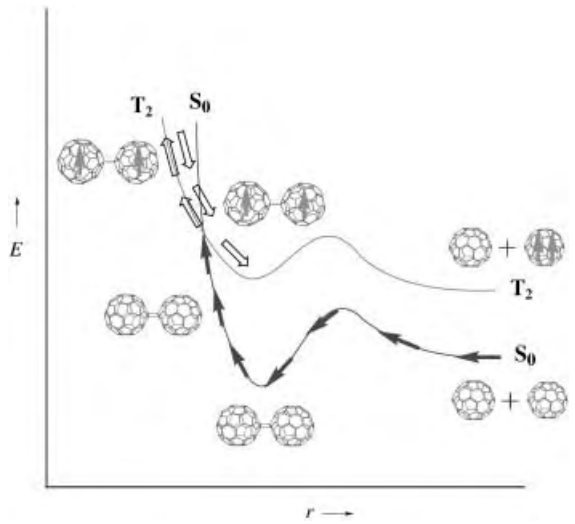


Figure 4. Graphical representation of the electronic and structural changes which take place when two C_{60} molecules in their ground state are compressed (follow the arrows). The molecules initially are on the diamagnetic S_0 surface (dark arrows). When enough pressure is applied they reach the S_0–T_2 crossing point. There, some dimers cross to the ferromagnetic T_2 state (light arrows). When the pressure decreases, these ferromagnetic dimers go back to the S_0–T_2 crossing point. Some remain on the ferromagnetic T_2 surface and reach the T_2 minimum. These bonds are magnetically active.

the C_{60}–C_{60} bonds are forced into the repulsive wall. At some point, the S_0 and T_2 curves cross, and thus some of the bonds can cross to the T_2 state and become magnetically active (dark arrows in Figure 4). Increasing the temperature makes it easier to reach the crossing point at lower pressures (by populating the appropriate excited vibrational states). When the pressure and temperature of the T_2 activated bonds is released they go down the T_2 curve. A percentage of them will remain in the T_2 state after passing through the S_0–T_2 crossing point, and thus remain magnetically active, until they reach the T_2 minimum. The percentage of molecules in the T_2 state versus the S_0 state is small, a fact that agrees with the small density of magnetic moments in these solids. The molecules can remain in the T_2 state because jumping to the T_1 or S_0 states by emission of a photon is vibrationally forbidden (the latter is also spin-forbidden).

If enough bonds remain in the T_2 state, they allow the presence of continuous paths of T_2 magnetically active bonds, and macroscopic magnetic behavior is observed. We calculated the nature of the magnetic coupling for two adjacent C_{60}–C_{60} bonds in a C_{60}–C_{60}–C_{60} trimer in which the two end C_{60} fragments are doublet radicals, and the central one is a diradical). The ground state is a quintet or a singlet, depending on the *orto*, *meta*, or *para* position of the lateral fragments, that is, adjacent T_2 bonds can couple ferro- or antiferromagnetically.[21] Studies are underway to evaluate the probability of each type of coupling and the magnitude of the magnetic interaction.

In summary, ab initio calculations on C_{60}–C_{60} dimers indicate that the magnetically active species in compressed *rh*-C_{60} solids are C_{60} molecules participating in C_{60}–C_{60} bonds that are in their T_2 state. In this T_2 state the C_{60} molecules are doublets covalently connected by one C–C interfragment bond. When enough C_{60}–C_{60} bonds are in this T_2 state, the magnetic interaction can propagate through the solid. Adjacent T_2 bonds can couple ferro- or antiferromagnetically, depending on their relative positions.

Received: June 11, 2003 [Z52118]

Keywords: ab initio calculations · fullerenes · magnetic properties

[1] T. L. Makarova, B. Sundqvist, R. Hohne, P. Esquinazi, Y. Kopelevich, P. Scharff, V. A. Davydov, L. S. Kasherova, A. V. Rakhmanina, *Nature* **2001**, *413*, 716–718.
[2] F. Palacio, G. Antorrena, M. Castro, R. Burriel, J. Rawson, J. N. B. Smith, N. Bricklebank, J. J. Novoa, C. Ritter, *Phys. Rev. Lett.* **1997**, *79*, 2336–2339.
[3] M. Mito, T. Kawae, K. Takeda, S. Takagi, Y. Matsushita, H. Deguchi, J. M. Rawson, F. Palacio, *Polyhedron* **2001**, *20*, 1509–1512.
[4] R. A. Wood, M. H. Lewis, M. R. Lees, S. M. Bennington, M. G. Cain, N. Kitamura, *J. Phys. Condens. Matter* **2002**, *14*, L385–L391.
[5] B. Sundqvist, *Adv. Phys.* **1999**, *48*, 1–134.
[6] M. Núñez-Regueiro, L. Marques, J.-L. Hodeau, O. Béthoux, M. Perroux, *Phys. Rev. Lett.* **1995**, *74*, 278–281.
[7] C. H. Xu, G. E. Scuseria, *Phys. Rev. Lett.* **1995**, *74*, 274–277.
[8] M. Prato, *J. Mater. Chem.* **2002**, *7*, 1097–1109.
[9] *The Physics of Fullerene-Based and Fullerene-Related Materials* (Ed.: W. Andreoni), Kluwer, Dordrecht, **2000**.
[10] *Acc. Chem. Res.* **1992**, *25*, 98–175, special issue on fullerenes.
[11] For a good introduction to the magnetism of molecule-based materials, see: J. S. Miller, A. J. Epstein, *Angew. Chem.* **1994**, *106*, 399; *Angew. Chem. Int. Ed. Engl.* **1994**, *33*, 385–415.
[12] R. Höhne, P. Esquinazi, *Adv. Mater.* **2002**, *14*, 753–756.
[13] F. Palacio, *Nature* **2001**, *413*, 690–691.
[14] B3LYP is a density functional obtained by taking the three-parameter nonlocal exchange funcional of Becke and the nonlocal correlation functional of Lee–Yang–Parr: A. D. Becke, *J. Chem. Phys.* **1993**, *98*, 5648–5652; C. Lee, W. Yang, R. G. Parr, *Phys. Rev. B* **1988**, *37*, 785–789.
[15] GAMESS, Revision 2000, M. W. Schmidt, K. K. Baldridge, J. A. Boatz, S. T. Elbert, M. S. Gordon, J. H. Jensen, S. Koseki, N. Matsunaga, K. A. Nguyen, S. J. Su, T. L. Windus, M. Dupuis, J. A. Montgomery, *J. Comput. Chem.* **1993**, *14*, 1347–1363.
[16] J. Kürti, K. Németh, *Chem. Phys. Lett.* **1996**, *256*, 119–125.
[17] G. E. Scuseria, *Chem. Phys. Lett.* **1996**, *257*, 583–586.
[18] Experimental data: D. V. Konarev, S. S. Khasanov, A. Otsuka, G. Saito, *J. Am. Chem. Soc.* **2002**, *124*, 8520–8521.
[19] Theoretical data on C_{60} and derivatives is reviewed in W. Andreoni, *Annu. Rev. Phys. Chem.* **1998**, *49*, 405–439.
[20] These calculations were carried out on isolated C_{60}–C_{60} dimers by using CPMD-3.5.2 (J. Hutter et al., Copyright IBM Zurich Research Laboratory and MPI für Festkörperforschung, **1995**–**2001**) with the BLYP functional. The cutoff value was 35 Ry. The dimer was placed in a box large enough to avoid interaction between dimers. Full details of this calculation will be given elsewhere.
[21] J. Ribas-Ariño, J. J. Novoa, *J. Phys. Chem. Solids*, accepted.

 © 2004 Wiley-VCH Verlag GmbH & Co. KGaA, Weinheim

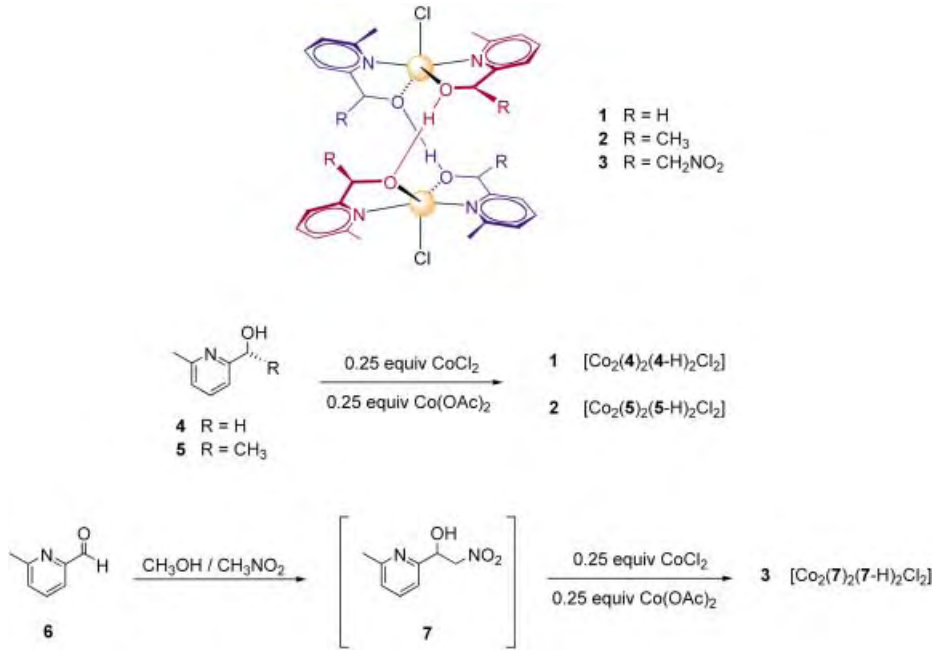
Helicates

Noncovalent Ligand Strands for Transition-Metal Helicates: The Straightforward and Stereoselective Self-Assembly of Dinuclear Double-Stranded Helicates Using Hydrogen Bonding**

Shane G. Telfer, Tomohiro Sato, and Reiko Kuroda**

Transition-metal helicates have played a central role in supramolecular chemistry for many years.[1–3] The synthetic approach to these structures typically follows a two-step process: 1) The synthesis of a covalent organic ligand using classical methods prior to 2) the reaction of this ligand with suitable metal ions to assemble the desired helicate. The first step in this process is often rather laborious and inefficient, especially compared to the second step which, in general, takes advantage of the kinetic lability of metal–ligand bonds to ensure that the most thermodynamically stable product is formed rapidly and in high yield. Given the obvious advantages of this noncovalent self-assembly step, it is somewhat surprising that noncovalent approaches to step 1, the construction of the ligand strands, have been reported only rarely. In these few cases metal ions were used as structural units in the ligand strands of triple helicates[4] and mesocates.[5,6] In the present paper we would like to report on a novel, noncovalent strategy for the construction of ligand strands for a series of dinuclear double helicates. This strategy utilizes hydrogen bonding between simple pyridine-alcohol precursors to build up the ligand backbone, and we show that the self-assembly of these helicates proceeds with high stereoselectivity.

Helicate **1** self-assembles upon mixing commercially available 6-methylpyridine-2-methanol (**4**) with 0.25 equivalents each of cobalt(II) chloride and cobalt(II) acetate in methanol (Scheme 1). Crimson-colored crystals of the complex were obtained in high yield by layering this solution with dioxane. Helicate **2** was prepared from *R*-6-methylpyridine-2-ethanol (**5**) in an analogous fashion. This chiral starting material was obtained in 93% *ee* by the asymmetric reduction of 2-acetyl-6-methylpyridine using the general method of Ikariya and co-workers.[7] 6-Methylpyridine-2-nitromethanol (**7**), which serves as the precursor to helicate **3**, was generated in situ by the by the Henry reaction[8,9] of 6-methylpyridine-2-carboxaldehyde (**6**) with nitromethane. This reaction is probably catalysed by the acetate ions that are present as $Co(OAc)_2$. Details of all experimental procedures are given in the Supporting Information.



Scheme 1. The straightforward synthetic route to helicates **1**–**3**. Compound **7**, which serves as a precursor to helicate **3**, is prepared in situ. The cobalt(II) centers of the helicates are colored orange and the ligand strands are shown in different colors for emphasis.

The three helicates **1**–**3** were characterized in the solid state by X-ray crystallography (discussed below), elemental analysis, UV/Vis and IR spectroscopy, and, in the case of **2**, solid-state circular dichroism (CD) spectroscopy (see Supporting Information for details). The yield of helicate **1** is high (71%), however the yields of **2** (27%) and **3** (18%) are more modest. Monitoring of the self-assembly process of **2** in solution indicates quantitative formation of the helicate,[10] thus it appears that the crystallization step is responsible for the low yield, and we are currently exploring a variety of methods to improve upon this. It is noteworthy that the presence of a methyl substituent at the 6-position of the pyridine ring appears to be essential for the assembly of the helicates (all experiments performed using unsubstituted pyridyl starting materials led to the formation of other products).

The crystal structure of **1** (Figure 1) reveals that a pair of pyridine-methanol molecules **4** are hydrogen-bonded via their oxygen atoms to form a bisbidentate ligand strand.

[*] Dr. S. G. Telfer, T. Sato, Prof. Dr. R. Kuroda
JST ERATO Kuroda Chiromorphology Project
Park Building, 4-7-6 Komaba, Meguro-ku
Tokyo 153-0041 (Japan)
Fax: (+81) 3-5465-0104
E-mail: shane.telfer@chiromor2.erato.rcast.u-tokyo.ac.jp
ckuroda@mail.ecc.u-tokyo.ac.jp

[**] We thank Dr. T. Harada for help with the spectropolarimetry measurements and Dr Y. Imai for performing the HPLC analyses. The Japan Society for the Promotion of Science (JSPS) provided a post-doctoral fellowship to S.G.T.

Supporting information for this article is available on the WWW under http://www.angewandte.org or from the author.

 DOI: 10.1002/anie.200352833 © 2004 Wiley-VCH Verlag GmbH & Co. KGaA, Weinheim

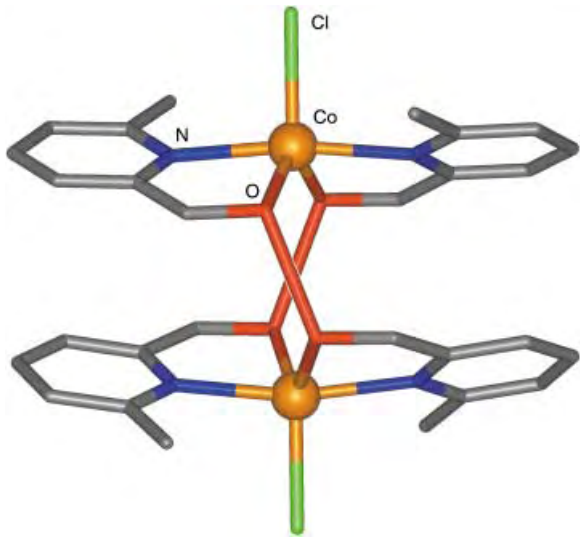


Figure 1. The X-ray crystal structure of the *P* enantiomer of helicate **1**. The hydrogen bonds between the oxygen atoms, which are used to build up the ligand strands, are shown in red. The other hydrogen atoms have been omitted for clarity.

Two such strands wrap around an axis defined by two cobalt(II) ions to give a dinuclear double-stranded helicate. A chloride ion completes the coordination sphere of each metal center. One proton has been lost from each ligand strand so the hydrogen bonds are of the alkoxide–alcohol type[11] and overall the helicate is neutrally charged. The separation of the two oxygen atoms is 2.42 Å, which indicates a very strong bonding interaction.[12] The use of hydrogen bonding as a construction element for the ligand strands represents the unique feature of these helicates. This truly supramolecular approach is simple, rapid, and high yielding. It also renders the covalent synthesis of a ligand strand unnecessary, and provides access to ligands that may be impossible to synthesize via conventional means.

The solid-state structures of **2** and **3** have also been determined by X-ray crystallography (Table 1). All three helicates have similar overall structures. In all cases, the pentacoordinate cobalt(II) centers adopt a distorted trigonal-bipyramidal geometry and the internuclear separations fall in the range 4.33–4.43 Å. All three helicates possess approximate D_2 symmetry, however only one twofold axis is crystallographically imposed in each structure. The alignment of this crystallographic axis determines whether the "upper and lower" (**2**) or "left and right" (**1** and **3**) halves of the helicates are symmetry related. Two pyridine rings belonging to different ligand strands and coordinated to different metal centers are found to be nearly parallel, with a separation of around 3.55 Å. This indicates a stabilizing π–π interaction and is highlighted by the space-filling model of **1** (Figure 2). Figure 3 presents a diagram of **2** and a view down the Co···Co axis (the structure of **3** is included as Supporting Information).

Table 1: Selected crystallographic data for helicates **1**–**3**.

	1	**2**	**3**
Selected separations [Å]			
Co–Co	4.38	4.33	4.43
O–O	2.42	2.42–2.44	2.42
Co–N	2.14–2.15	2.13–2.15	2.14–2.17
Co–O	1.99–2.00	1.96–2.00	2.00
Co–Cl	2.31–2.34	2.34	2.30–2.31
Selected angles [°]			
N-Co-N	168.8 (av)	170.1	170.3 (av)
O-Co-O	115.8 (av)	120.9	115.4 (av)
O-H-O	173.3	179.9	177.0
crystallographic C_2 axis	Co–Co axis	⊥ to Co–Co axis	Co–Co axis

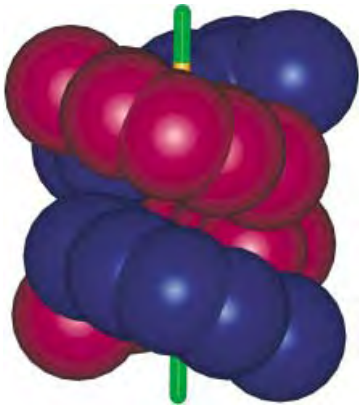


Figure 2. Space-filling diagram of the *P* enantiomer of helicate **1**. The ligand strands are colored differently for emphasis.

Helicates are intrinsically chiral and can be assigned the stereochemical descriptors *P* or *M* depending on whether the ligand strands describe a right- or left-handed helix. This helicity can be directly correlated with the absolute configurations of the metal centers, and in the case of helicates **1**–**3** the *Λ*,*Λ* configuration gives rise to a *P* helix. As the ligand strands of helicate **1** are achiral, this complex exists as a simple mixture of *P* (*Λ*,*Λ*) and *M* (Δ,Δ) enantiomers. On the other hand, the ligand strands of helicates **2** and **3** each feature two asymmetric carbon centers. These can have either *R* or *S* stereochemistry, therefore there are seven potential ligand sets for these helicates: ligand strand A/ligand strand B = *RR*/*RR*, *SS*/*SS*, *RR*/*RS*, *RS*/*SS*, *RR*/*SS*, *RS*/*RS*, and *RS*/*SR*. As each ligand set could lead to either a *P* helicate or an *M* helicate, there are seven pairs of enantiomers for each helicate. It is also possible that a mesocate structure may form, in which the two metal centers have opposite absolute configurations. There are a further ten distinct mesocate stereoisomers (four pairs of enantiomers and two achiral stereoisomers) which means that there is a total of 24 stereoisomers of helicates **2** and **3**.

In the synthesis of helicate **3**, the precursor compound **7** is formed in situ and will be present as a racemic mixture of *R* and *S* isomers. The X-ray crystal structure shows that the self-assembly reaction is remarkably stereoselective as only one

 © 2004 Wiley-VCH Verlag GmbH & Co. KGaA, Weinheim

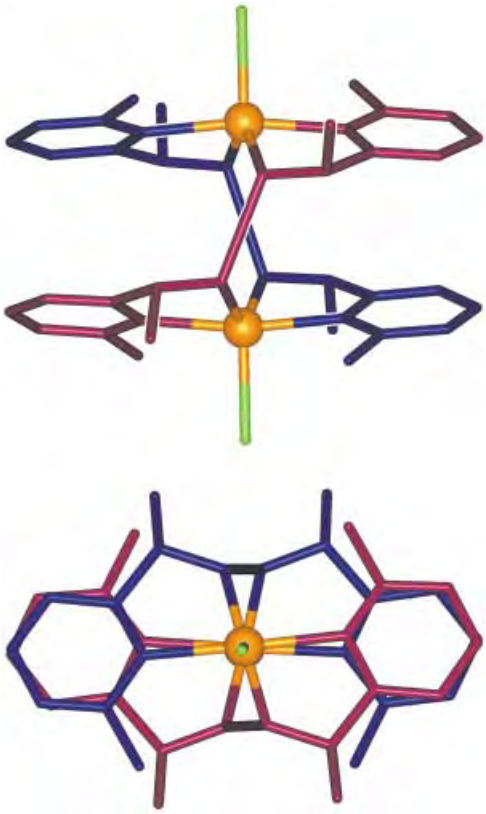


Figure 3. Two views of the X-ray crystal structure of helicate **2**. Above: The overall structure highlighting the orientations of the methyl groups of the ligand strands; below: a view along the Co···Co axis. The hydrogen atoms have been omitted for clarity.

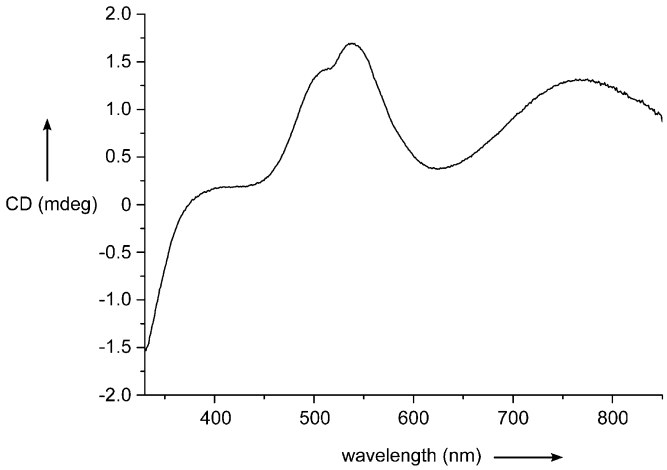


Figure 4. The CD spectrum of **2** in the visible region, measured in the solid state as a KBr disc.

pair of enantiomers, namely, Δ,Δ-(*SS*/*SS*) and *Λ*,*Λ*-(*RR*/*RR*), is actually observed. This demonstrates that 1) homochiral ligand sets are favored over heterochiral ligand sets, and 2) that the absolute configurations of the cobalt(II) centers are "predetermined" by the chirality of the ligands.[13] With respect to observation 1), similar self-sorting processes based on chirality have been reported for other helicates[14] and for mononuclear complexes.[15] Observation 2) is readily explained on steric grounds; a model of **3** shows that the *Λ*,*Λ*-*SS*/*SS* diastereomer (which does not form) would have the nitromethyl arms of one ligand strand pointing directly towards one of the pyridine rings of the other ligand strand.

In the case of helicate **2**, the sample of compound *R*-**5** that was used for its synthesis had an *ee* of 93%. Therefore, statistically the *RR*/*RR* ligand set will be highly favored and indeed the enantiopure *RR*/*RR*-**2** helicate was observed in the X-ray crystal structure. As expected on the basis of the results discussed above for helicate **3**, this ligand set induces the *Λ* configuration at both metal centers. A sample of compound *R*-**5** that was extracted from crystals of **2** had an *ee* of 100%, as indicated by chiral HPLC analysis. Thus the assembly of **2** functions as method of providing an enantiopure form of this compound, albeit a rather inefficient one due to the modest yield of the helicate. The solid-state CD spectrum[16,17] of helicate **2** is presented in Figure 4.

These observations raise some interesting questions regarding the mechanisms of the self-assembly of these helicates and of the homochiral ligand-sorting process. Given the noncovalent nature of the ligand strand, it is likely that their mechanism of self-assembly differs considerably from conventional helicates. One intuitive hypothesis is that a stepwise assembly route is followed, in which precursor mononuclear complexes, for example, [CoL(L−H)Cl] (L = **4**, **5**, or **7**), are formed initially. Dimerization of such complexes would produce the observed helicates. We speculate that the observed self-sorting of the homochiral ligand may result from the stereospecific dimerization of homochiral monomers. The precise nature of the assembly process is likely to be of interest in the context of hierarchical self-assembly and we hope to report more details in the near future.

In summary, we have presented a novel and straightforward approach to transition-metal helicates by employing hydrogen bonding as a construction element for the ligand strands. The helicates self-assemble from eight simple components (four ions and four small molecules) and are stabilized by a range of supramolecular interactions: coordination bonds, hydrogen bonds, and π–π interactions. This genuinely supramolecular approach to the synthesis of transition-metal helicates has obvious advantages over traditional methods, which often require the tedious synthesis of covalent ligands. Furthermore, the self-assembly process exhibits remarkable stereoselectivity: only homochiral ligand sets are observed and the chirality of these ligands efficiently predetermines the absolute configuration of the metal centers. The present paper compliments other recent advances in the fields of catalysis,[18] coordination polymers,[19,20] and other supramolecular assemblies,[21–24] which benefit from a fruitful combination of coordination and hydrogen bonding. Due to the labile nature of the chloro ligands these helicates have great promise as building blocks for metal–organic coordination networks; an avenue of research we are actively pursuing.

 © 2004 Wiley-VCH Verlag GmbH & Co. KGaA, Weinheim

Experimental Section

Crystal data: CCDC 219398–219400 contain the supplementary crystallographic data for this paper. These data can be obtained free of charge via www.ccdc.cam.ac.uk/conts/retrieving.html (or from the Cambridge Crystallographic Data Centre, 12, Union Road, Cambridge CB2 1EZ, UK; fax: (+44) 1223-336-033; or deposit@ccdc.cam.ac.uk).

1·2 H_2O ($C_{28}H_{34}Cl_2Co_2N_4O_4$·2 H_2O, $M_r = 715.38$), $0.50 \times 0.25 \times 0.10$ mm, orthorhombic, *Pbcn*, $a = 14.4508(7)$, $b = 15.1817(8)$, $c = 13.5843(7)$ Å, $\alpha = \beta = \gamma = 90°$, $V = 2980.2(3)$ Å^3, $Z = 4$, $\rho_{calcd} = 1.594$ mg m^{-3}, $F(000) = 1480$, radiation $\lambda(Mo_{K\alpha}) = 0.71073$ Å, $T = 135$ K, reflections collected/unique: 17654/3495, $R_{int} = 0.025$. Data acquired with Lorentzian, polarization, and absorption corrections ($\mu = 1.342$ mm^{-1}, $T_{min} = 0.55$, $T_{max} = 0.88$). Structure solved by direct methods (SHELXS-97) and refined by a full-matrix least-squares method on $|F|^2$ using anisotropic displacement parameters for all non-hydrogen atoms (SHELXL-97). The hydrogen atom involved in hydrogen bonding (H19) was found on the electron-density difference map. All other hydrogen atoms were placed in calculated positions. Final R factor for 3495 reflections ($I > 2\sigma(I)$) with 193 parameters was 0.050 ($R_w = 0.15$). GOF = 1.20, max./min. residual electron density = 1.94/−0.93 Å^{-3}.

2·2 CH_3OH ($C_{32}H_{42}Cl_2Co_2N_4O_4$·2 CH_3OH, $M_r = 799.54$), $0.25 \times 0.20 \times 020$ mm, orthorhombic, $P2_12_12$, $a = 11.4404(15)$, $b = 17.704(2)$, $c = 9.4371(12)$) Å, $\alpha = \beta = \gamma = 90°$, $V = 1911.4(4)$ Å^3, $Z = 2$, $\rho_{calcd} = 1.39$ mg m^{-3}, $F(000) = 836$, radiation $\lambda(Mo_{K\alpha}) = 0.71073$ Å, $T = 100$ K, reflections collected/unique: 11411/4315, $R_{int} = 0.031$. Data acquired with Lorentzian, polarization, and absorption corrections ($\mu = 1.054$ mm^{-1}, $T_{min} = 0.78$, $T_{max} = 0.82$). Structure solved by direct methods (SHELXS-97) and refined by a full-matrix least-squares method on $|F|^2$ using anisotropic displacement parameters for all non-hydrogen atoms (SHELXL-97). The hydrogen atoms involved in hydrogen bonding (H9 and H19) were found on the electron-density difference map. All other hydrogen atoms were placed in calculated positions. Final R factor for 4315 reflections ($I > 2\sigma(I)$) with 224 parameters was 0.065 ($R_w = 0.14$). GOF = 1.19, max./min. residual electron density = 0.81/−1.10 Å^{-3}, Flack parameter = 0.09(3).

3·2 CH_3NO_2 ($C_{34}H_{38}Cl_2Co_2N_8O_8$·2 CH_3NO_2, $M_r = 1037.55$), $0.20 \times 0.12 \times 0.06$ mm, monoclinic, $C2/c$, $a = 19.6707(13)$, $b = 14.4567(10)$, $c = 16.7018(11)$ Å, $\beta = 110.7210(10)°$, $V = 4442.3(5)$ Å^3, $Z = 4$, $\rho_{calcd} = 1.551$ mg m^{-3}, $F(000) = 2136$, radiation $\lambda(Mo_{K\alpha}) = 0.71073$ Å, $T = 120$ K, reflections collected/unique: 13742/5130, $R_{int} = 0.048$. Data acquired with Lorentzian, polarization, and absorption corrections ($\mu = 0.95$ mm^{-1}, $T_{min} = 0.83$, $T_{max} = 0.95$). Structure solved by direct methods (SHELXS-97) and refined by a full-matrix least-squares method on $|F|^2$ using anisotropic displacement parameters for all non-hydrogen atoms (SHELXL-97). The hydrogen atom involved in hydrogen bonding (H9) was found on the electron-density difference map. All other hydrogen atoms were placed in calculated positions. Final R factor for 4154 reflections ($I > 2\sigma(I)$) with 298 parameters was 0.056 ($R_w = 0.12$). GOF = 1.14, max./min. residual electron density = 0.85/−1.09 Å^{-3}.

Received: September 10, 2003 [Z52833]

Keywords: enantioselectivity · helical structures · noncovalent interactions · self-assembly · supramolecular chemistry

[1] C. Piguet, G. Bernardinelli, G. Hopfgartner, *Chem. Rev.* **1997**, *97*, 2005.
[2] M. Albrecht, *Chem. Rev.* **2001**, *101*, 3457.
[3] A. F. Williams, *Chem. Eur. J.* **1997**, *3*, 15.
[4] M. H. W. Lam, S. T. C. Cheung, K.-M. Fung, W.-T. Wong, *Inorg. Chem.* **1997**, *36*, 4618.
[5] X. Sun, D. W. Johnson, D. L. Caulder, R. E. Powers, K. N. Raymond, E. H. Wong, *Angew. Chem.* **1999**, *111*, 1386; *Angew. Chem. Int. Ed.* **1999**, *38*, 1303.
[6] X. Sun, D. W. Johnson, D. L. Caulder, K. N. Raymond, E. H. Wong, *J. Am. Chem. Soc.* **2001**, *123*, 2752.
[7] K. Okano, K. Murata, T. Ikariya, *Tetrahedron Lett.* **2000**, *41*, 9277.
[8] L. Henry, *C. R. Hebd. Seances Acad. Sci.* **1895**, *120*, 1265.
[9] R. S. Varma, R. Dahiyal, S. Kumar, *Tetrahedron Lett.* **1997**, *38*, 5131.
[10] S. G. Telfer, unpublished results.
[11] G. A. Jeffrey, *An Introduction to Hydrogen Bonding*, Oxford University, New York, **1997**.
[12] J. Emsley, *Chem. Soc. Rev.* **1980**, *9*, 91.
[13] U. Knof, A. von Zelewsky, *Angew. Chem.* **1999**, *111*, 312; *Angew. Chem. Int. Ed.* **1999**, *38*, 303.
[14] M. A. Masood, E. J. Enemark, T. D. P. Stack, *Angew. Chem.* **1998**, *110*, 973; *Angew. Chem. Int. Ed.* **1998**, *37*, 928.
[15] S. G. Telfer, A. F. Williams, G. Bernardinelli, *Chem. Commun.* **2001**, 1498.
[16] R. Kuroda in *Circular Dichroism*, 2nd ed. (Eds.: N. Berova, K. Nakanishi, R. W. Woody), Wiley-VCH, New York, **2000**, p. 159.
[17] R. Kuroda, T. Harada, Y. Shindo, *Rev. Sci. Instrum.* **2001**, *72*, 3802.
[18] B. Breit, W. Seiche, *J. Am. Chem. Soc.* **2003**, *125*, 6608.
[19] R. Sekiya, S. Nishikiori, *Chem. Commun.* **2001**, 2612.
[20] A. M. Beatty, *Coord. Chem. Rev.* **2003**, *246*, 131.
[21] T. B. Norsten, K. Chichak, N. R. Branda, *Chem. Commun.* **2001**, 1794.
[22] M. H. Al-Sayah, N. R. Branda, *Chem. Commun.* **2002**, 178.
[23] T. D. Hamilton, G. S. Papaefstathiou, L. R. MacGillivray, *J. Am. Chem. Soc.* **2002**, *124*, 11606.
[24] Z. Qin, M. C. Jennings, R. J. Puddephatt, *Chem. Commun.* **2001**, 2676.

 © 2004 Wiley-VCH Verlag GmbH & Co. KGaA, Weinheim

Main-Group Chemistry

σ-Bond Stretching: A Static Approach for a Dynamic Process**

*David Scheschkewitz, Hideki Amii, Heinz Gornitzka, Wolfgang W. Schoeller, Didier Bourissou, and Guy Bertrand**

The understanding of chemical transformations has been considerably improved by the direct observation of short-lived intermediates or through the synthesis of stable versions of these species.[1–5] However, since chemical bonds form, break, and change geometrically with awesome rapidity, only femtosecond spectroscopic techniques[6] can give a "motion picture" of chemical transformations by "freezing" molecular structures as reactions unfold and pass through their transition states. Herein, we demonstrate that it is possible to mimic the dynamic process corresponding to one of the simplest chemical reaction: the stretching and eventual rupture of a σ bond to afford two single-electron species, together with the reverse bond-forming process.

One of the archetypal examples of this type of reaction is the inversion of bicyclo[1.1.0]butanes **A**,[7] which occurs via singlet cyclobutane-1,3-diyls **B** in the transition state (Figure 1).[8] Two different types of 1,3-diradicals, related to **A**, have been recently isolated by taking advantages of the unique properties of the heteroelements.[9] The groups of Niecke and Yoshifuji have reported the synthesis of 2,4-diphosphacyclobutane-1,3-diyls **D**,[10,11] confined by a transannular antibonding π overlap, which makes the thermal ring closure into **C** forbidden. In marked contrast, 1,3-dibora-2,4-diphosphoniocyclobutane-1,3-diyls **F**[12,13] feature a transannular bonding π overlap, which allows for the thermal ring closure into **E** (Figure 2). Therefore, a variation of the phosphorus and boron substituents was expected to strongly influence the ground-state structure of compounds **E** and **F** and thus offered an opportunity not only to isolate the structural extremes, as reported for **C** and **D**,[14] but also to mimic the whole reaction profile for the inversion of **E**.

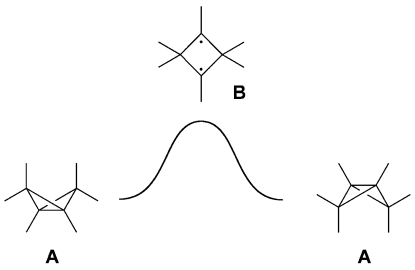


Figure 1. Schematic representation for the reaction profile between bicyclo[1.1.0]butanes **A**, and cyclobutane-1,3-diyls **B**.

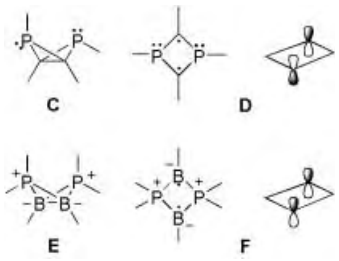
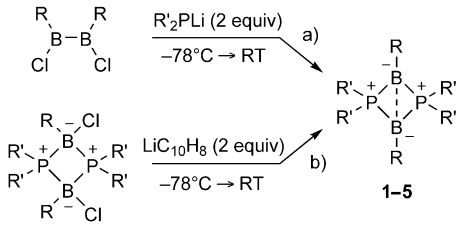


Figure 2. Structure of the heteroatom-containing analogues **C**, **D**, **E**, and **F** and schematic representations of the HOMO orbitals for **D** and **F**.

Compounds **2**–**4** were obtained by the synthetic route used previously for the preparation of **1**[12]: the reaction of the appropriate lithium phosphide (two equiv) with 1,2-dichlorodiborane. As the 1,2-diphenyl-1,2-dichlorodiborane is known to be highly unstable,[15] derivative **5** was synthesized by the reduction of the corresponding 1,3-dichloro-1,3-diborata-2,4-diphosphoniocyclobutane[16] with two equivalents of lithium naphthalenide in toluene solution. The compounds **2**–**5** were isolated in moderate to good yields as very air-sensitive, but thermally highly stable crystalline materials (Scheme 1).



1: R=*t*Bu, R'=*i*Pr, 68% yield; mp = 212°C; yellow (a)
2: R=Dur, R'=*i*Pr, 72% yield; mp = 224°C; colorless (a)
3: R=*t*Bu, R'=Ph, 71% yield; mp = 228°C; colorless (a)
4: R=Dur, R'=Et, 58% yield; mp = 213°C; colorless (a)
5: R=Ph, R'=Ph, 47% yield; mp = 181°C; colorless (b)

Scheme 1. Synthesis and physical properties of derivatives **1**–**5**.

[*] Dr. D. Scheschkewitz, Prof. G. Bertrand
UCR-CNRS Joint Research Chemistry Laboratory (UMR 2282)
Department of Chemistry
University of California
Riverside, CA 92521-0403 (USA)
Fax: (+1) 909-787-2725
E-mail: gbertran@mail.ucr.edu
Dr. D. Scheschkewitz, Dr. H. Amii, Dr. H. Gornitzka, Dr. D. Bourissou, Prof. G. Bertrand
Laboratoire Hétérochimie Fondamentale et Appliquée du CNRS (UMR 5069)
Université Paul Sabatier
118, route de Narbonne, 31062 Toulouse Cedex 04 (France)
Prof. W. W. Schoeller
Fakultät für Chemie
Universität Bielefeld
Postfach 10 01 31, 33615 Bielefeld (Germany)

[**] We are grateful to the NSF (CHE 0213510), the CNRS, the DFG and RHODIA for financial support of this work, and to the Alexander von Humboldt Foundation for a grant to D.S. We thank Mr. Christian Pradel for his help in generating the cover illustration.

Supporting information for this article is available on the WWW under http://www.angewandte.org or from the author.

 DOI: 10.1002/anie.200352944 © 2004 Wiley-VCH Verlag GmbH & Co. KGaA, Weinheim

The impact of the substituents on the boron atoms upon structure was first investigated by replacing the *tert*-butyl groups of **1** by duryl rings (duryl = 2,3,5,6-tetramethylphenyl), while retaining the *iso*-propyl groups on the phosphorus atoms. Single-crystal X-ray diffraction analysis[17] (Figure 3) revealed that **2** adopts a very different structure to that observed for **1**. The BPBP core deviates from planarity (interplanar angle between the two PBB units 130°), the B–B distance is significantly shortened (2.24 Å). Steric hindrance probably does not favor a coplanar arrangement of the duryl rings and BPBP core of **2**, thereby preventing efficient stabilization of the radical centers through π delocalization.[18]

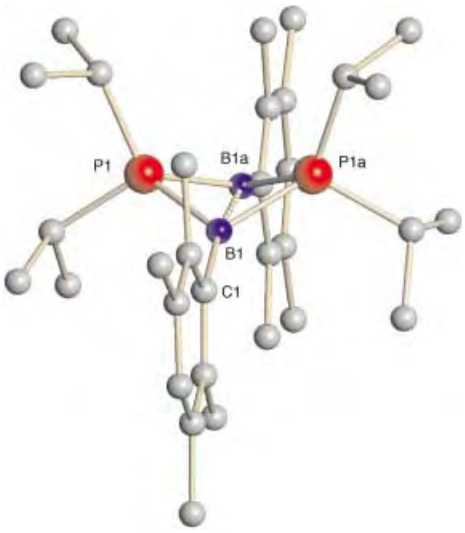


Figure 3. Molecular view of **2** in the solid state. Selected bond lengths and angles are as follows: P1-B1, 1.8879 ± 10 Å; P1-B1a, 1.8891 ± 11 Å; B1-C1, 1.5984 ± 13 Å; B1-P1-B1a, 72.77 ± 5°, P1-B1-P1a, 95.35 ± 5°, P1-B1-C1, 132.33 ± 7°; P1a-B1-C1, 130.83 ± 7°.

The influence of the substituents on the phosphorus atoms was then studied by replacing the *iso*-propyl substituents of **1** by phenyl rings. The B–B distance of **3** is noticeably shortened again (1.99 Å), while the BPBP core deviates further from planarity (interplanar angle 118°) (Figure 4). This result suggests that the less sterically demanding substituents on the phosphorus atoms favor the folded structure by decreasing the 1,3-diaxial interactions. This hypothesis was confirmed by comparing the solid-state structures of compounds **4** (B–B = 1.89 Å; interplanar angle 115°) and **2**, both featuring duryl groups on the boron atoms, but ethyl (**4**) and *iso*-propyl (**2**) substituents on the phosphorus atoms.

Lastly, the most folded structure (interplanar angle 114°) was obtained for the perphenylated derivative **5**, for which the B–B distance (1.83 Å) is in the range typical for B–B single bonds, and about 40% shorter than in **1**. The geometric parameters observed for **5** are very similar to those calculated for the parent bicyclic compound **E*** (hydrogen atom on the boron and phosphorus and phosphorus atoms), while the data for **1** are very close to those predicted for the parent diradical **F***, which is the transition state for the inversion of **E***.[12] Therefore, in the solid state, derivatives **2**–**4** adopt intermediate structures between those of **E** and **F**.

Variable-temperature NMR studies give some information on the dynamic behavior of each of the individual derivatives **2**–**5** (Figure 4). All of these compounds invert rapidly at room temperature as shown by the magnetic equivalence of the axial and equatorial phosphorus substituents. The shortening of the B–B bond from **2** to **5** was

compound	**1** ($iPr_2PBtBu)_2$	**2** ($iPr_2PBDur)_2$	**3** ($Ph_2PBtBu)_2$	**4** ($Et_2PBDur)_2$	**5** ($Ph_2PBPh)_2$
δ ^{31}P (ppm)[a]	+3	−26	−56	−55	−54
δ ^{11}B (ppm)[a]	+25	−13	−12	−19	−13
B–B (Å)	2.57	2.24	1.99	1.89	1.83
τ (°)	180	130	118	115	114
top view [b]					
side view [b]					

Figure 4. ^{11}B and ^{31}P NMR chemical shifts at room temperature in solution, X-ray data and molecular structure of compounds **1**–**5**. a) ^{11}B and ^{31}P NMR chemical downfield chemical shifts are expressed with a positive sign, in parts per million, relative to external $BF_3.OEt_2$ and 85% H_3PO_4, respectively. b) For clarity the substituents are omitted.

 © 2004 Wiley-VCH Verlag GmbH & Co. KGaA, Weinheim

expected to strengthen the inversion barrier of the bicyclic form **E** via the diradical **F**. Indeed, the inversion process could be frozen at low temperature for **4**, but not for the less folded derivative **2** even at −95 °C. The coalescence temperature ($T_c = -81$ °C) observed in solution for the ^{13}C NMR signal of the CH_2 ethyl group of **4** corresponds to an inversion barrier $\Delta G^{\neq}$ of about 8.5 kcal mol^{-1}, which is about half of that predicted for the parent derivative **E*** (16.4 kcal mol^{-1}).[12]

Snapshots on the reaction profile between **E** and **F** are obtained by varying the substituents around the BPBP framework. Besides this static approach that makes use of different derivatives, the characterization of bond-stretch isomers for a single compound remains a challenging project.

Experimental Section

All reactions and manipulations were carried out under an atmosphere of dry argon by using standard Schlenk techniques.

Route a: A solution of R'_2PLi, which was prepared by adding *n*BuLi (3.75 mL, 1.6 M, hexane) to R'_2PH (6 mmol) in diethyl ether (10 mL) at −80 °C and subsequent stirring at room temperature for 2 h, was added dropwise to 3 mmol of the desired 1,2-dichlorodiborane in diethyl ether (20 mL) at −80 °C. The reaction mixture was warmed to room temperature within 1 h and the solvents were removed under vacuum. Toluene (20 mL) was added, the salts were removed by filtration and the remaining product was washed with toluene (2 × 3 mL). Crystals of compounds **2**–**4** were obtained by cooling saturated boiling toluene solutions to room temperature.

Route b: A freshly prepared solution of lithium naphthalenide (6.4 mL, 0.8 M, THF) was added dropwise to the desired 1,3-dichloro-2,4-diphospha-1,3-diboretane (2.5 mmol) in toluene (15 mL) at −80 °C. The reaction mixture was warmed to room temperature and stirring was maintained for about 30 minutes. The solvents were removed in vacuo and the residue was dissolved in pentane (30 mL). The salts were removed by filtration and the pentane was removed in vacuo. Naphtalene was sublimed by heating to 80 °C in vacuo for 30 minutes. Crystals of compound **5** were obtained by cooling saturated pentane solutions to −30 °C.

Received: September 24, 2003 [Z52944]
Published Online: January 8, 2004

Keywords: boron · heterocycles · phosphorus · radicals · substituent effects

[1] For example, stable versions of carbocations,[2] radicals,[3] triplet[4] and singlet carbenes[5] have been described and reviewed.
[2] G. A. Olah, *Angew. Chem.* **1995**, *107*, 1517; *Angew. Chem. Int. Ed. Engl.* **1995**, *34*, 1393.
[3] C-Radikale in *Methoden der Organischen Chemie (Houben-Weyl)*, *Vol. E19a* (Eds.: M. Regitz, B. Giese), Thieme, Stuttgart, **1989**.
[4] H. Tomioka, *Acc. Chem. Res.* **1997**, *30*, 315.
[5] D. Bourissou, O. Guerret, F. P. Gabbaï, G. Bertrand, *Chem. Rev.* **2000**, *100*, 39.
[6] A. H. Zewail, *Angew. Chem.* **2000**, *112*, 2688; *Angew. Chem. Int. Ed.* **2000**, *39*, 2587.
[7] For recent work on carbon-based 1,3-diradicals, see: M. Abe, W. Adam, T. Minamoto, Y. Ino, M. Nojima, *J. Org. Chem.* **2003**, *68*, 1796, and references therein.
[8] K. A. Nguyen, M. S. Gordon, J. A. Boatz, *J. Am. Chem. Soc.* **1994**, *116*, 9241.
[9] H. Grützmacher, F. Breher, *Angew. Chem.* **2002**, *114*, 4178; *Angew. Chem. Int. Ed.* **2002**, *41*, 4006.
[10] a) E. Niecke, A. Fuchs, F. Baumeister, M. Nieger, W. W. Schoeller, *Angew. Chem.* **1995**, *107*, 640; *Angew. Chem. Int. Ed. Engl.* **1995**, *34*, 555; b) O. Schmidt, A. Fuchs, D. Gudat, M. Nieger, W. Hoffbauer, E. Niecke, W. W. Schoeller, *Angew. Chem.* **1998**, *110*, 995; *Angew. Chem. Int. Ed.* **1998**, *37*, 949; c) W. W. Schoeller, C. Begemann, E. Niecke, D. Gudat, *J. Phys. Chem. A* **2001**, *105*, 10731.
[11] H. Sugiyama, S. Ito, M. Yoshifuji, *Angew. Chem.* **2003**, *115*, 3932; *Angew. Chem. Int. Ed.* **2003**, *42*, 3802.
[12] D. Scheschkewitz, H. Amii, H. Gornitzka, W. W. Schoeller, D. Bourissou, G. Bertrand, *Science* **2002**, *295*, 1880.
[13] a) M. Seierstad, C. R. Kinsinger, C. J. Cramer, *Angew. Chem.* **2002**, *114*, 4050; *Angew. Chem. Int. Ed.* **2002**, *41*, 3894; b) W. W. Schoeller, A. Rozhenko, D. Bourissou, G. Bertrand, *Chem. Eur. J.* **2003**, *9*, 3611; c) Y. Jung, M. Head-Gordon, *ChemPhysChem* **2003**, *4*, 522; d) M. J. Cheng, C. H. Hu, *Mol. Phys.* **2003**, *101*, 1319.
[14] E. Niecke, A. Fuchs, M. Nieger, *Angew. Chem.* **1999**, *111*, 3213; *Angew. Chem. Int. Ed.* **1999**, *38*, 3028.
[15] H. Hommer, H. Nöth, J. Knizek, W. Ponikwar, H. Schwenk-Kircher, *Eur. J. Inorg. Chem.* **1998**, 1519.
[16] M. S. Lube, R. L. Wells, P. S. White, *Inorg. Chem.* **1996**, *35*, 5007.
[17] Crystal data for **2**: $C_{32}H_{54}B_2P_2$, $M_r = 522.31$, monoclinic, space group $C2/c$, $a = 21.8891(4)$, $b = 8.8609(2)$, $c = 16.9297(3)$ Å, $\beta = 107.800(1)°$, $V = 3126.45(11)$ Å^3, $Z = 4$, $\mu(Mo_{K\alpha}) = 0.158$ mm^{-1}, crystal size $0.5 \times 0.6 \times 0.8$ mm^3, 21139 reflections collected (5525 independent, $R_{int} = 0.0210$), 171 parameters, $R1$ $[I > 2\sigma(I)] = 0.0392$, $wR2$ [all data] = 0.1140, largest electron density residue: 0.549 e Å^{-3}. **3**: $C_{16}H_{19}BP$, $M_r = 253.09$, orthorhombic, space group $Pccn$, $a = 10.2223(6)$, $b = 13.7704(8)$, $c = 21.0047(13)$ Å, $V = 2956.7(3)$ Å^3, $Z = 8$, $\mu(Mo_{K\alpha}) = 0.166$ mm^{-1}, crystal size $0.1 \times 0.4 \times 0.5$ mm^3, 16514 reflections collected (3026 independent, $R_{int} = 0.0386$), 166 parameters, $R1$ $[I > 2\sigma(I)] = 0.0360$, $wR2$ [all data] = 0.0995, largest electron density residue: 0.281 e Å^{-3}. **4**: $C_{14}H_{23}BP$, $M_r = 233.10$, tetragonal, space group $P4_32_12$, $a = 8.5915(5)$, $b = 8.5915(5)$, $c = 37.445(3)$ Å, $V = 2764.0(3)$ Å^3, $Z = 8$, $\mu(Mo_{K\alpha}) = 0.171$ mm^{-1}, crystal size $0.4 \times 0.6 \times 0.8$ mm^3, 17302 reflections collected (3571 independent, $R_{int} = 0.0625$), 151 parameters, $R1$ $[I > 2\sigma(I)] = 0.0410$, $wR2$ [all data] = 0.1054, largest electron density residue: 0.277 e Å^{-3}. **5**: $C_{18}H_{15}BP$, $M = 273.08$, triclinic, space group $P\bar{1}$, $a = 10.180(3)$, $b = 10.846(3)$, $c = 15.558(5)$ Å, $\alpha = 90.628(6)°$, $\beta = 108.642(5)°$, $\gamma = 113.071(6)°$, $V = 1479.0(8)$ Å^3, $Z = 4$, $\mu(Mo_{K\alpha}) = 0.171$ mm^{-1}, crystal size $0.1 \times 0.4 \times 0.5$ mm^3, 8522 reflections collected (4251 independent, $R_{int} = 0.0714$), 361 parameters, $R1$ $[I > 2\sigma(I)] = 0.0514$, $wR2$ [all data] = 0.0951, largest electron density residue: 0.360 e Å^{-3}. Data for all structures were collected at 193(2) K using an oil-coated shock-cooled crystal on a Bruker-AXS CCD 1000 diffractometer ($\lambda = 0.71073$ Å). Semi-empirical absorption corrections were employed.[19] The structures were solved by direct methods (SHELXS-97),[20] and refined by using the least-squares method on F^2.[21] CCDC-224340 (**2**), 224341 (**3**), 224342 (**4**) and 224343 (**5**) contain the supplementary crystallographic data for this paper. These data can be obtained free of charge via www.ccdc.cam.ac.uk/conts/retrieving.html (or from the Cambridge Crystallographic Data Centre, 12 Union Road, Cambridge CB2 1EZ, UK; fax: (+44) 1223-336-033; or deposit@ccdc.cam.ac.uk).
[18] A. C. Goren, D. A. Hrovat, M. Seefelder, H. Quast, W. T. Borden, *J. Am. Chem. Soc.* **2002**, *124*, 3469.
[19] SADABS, Program for data correction, Bruker-AXS.
[20] G. M. Sheldrick, *Acta Crystallogr. Sect. A* **1990**, *46*, 467.
[21] SHELXL-97, Program for Crystal Structure Refinement, G. M. Sheldrick, University of Göttingen, **1997**.

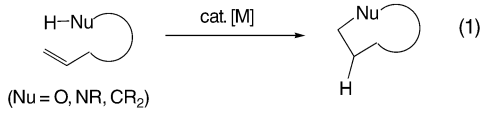
 © 2004 Wiley-VCH Verlag GmbH & Co. KGaA, Weinheim

Alkene Functionalization

Anti-Markovnikov Hydrofunctionalization of Olefins Mediated by Rhodium–Porphyrin Complexes**

*Melanie S. Sanford and John T. Groves**

The development of catalysts for the anti-Markovnikov addition of H-Nu (H-Nu = H-NR_2, H-OR) to olefins could provide an atom-economical approach to amines, ethers, and heterocyclic compounds [Eq. (1)].[1] These products are of



(1)

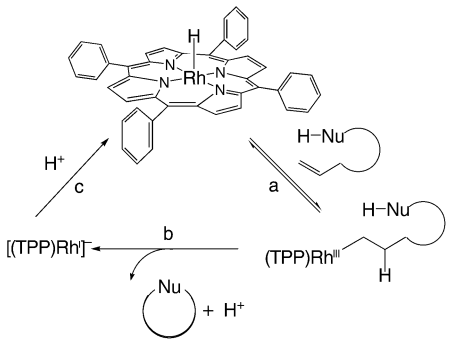
significant utility to both the chemical and pharmaceutical industries, and as a result the development of new catalysts for this type of transformation has been identified as one of the "top ten challenges for catalysis".[2] However, despite considerable effort in this area over the past two decades,[3–5] general and selective processes and catalysts for such transformations have remained elusive. This report describes the rational design of a new mechanistic pathway, which offers a potentially general solution to anti-Markovnikov olefin hydrofunctionalization.

We envisaged a three-step catalytic cycle for intramolecular anti-Markovnikov olefin hydrofunctionalization involving: a) olefin insertion into a [Rh]–H bond, b) intramolecular functionalization of the resulting σ-alkyl adduct, and c) protonation of the resulting $[Rh^I]^-$ species to regenerate the starting [Rh]-H complex (Scheme 1). We anticipated that the regioselectivity of the reaction would be dictated by the olefin-insertion step, which should favor the less-substituted metal σ-alkyl species[6] and thereby selectively provide the anti-Markovnikov product. We report herein that (TPP)Rh-H (TPP = tetraphenylporphyrin) efficiently mediates each step of this postulated catalytic cycle to afford heterocyclic products with extremely high (>97%) anti-Markovnikov regioselectivity. The functionalization step serves as a rare and unusually general example of direct $C(sp^3)$–heteroatom bond-forming reductive elimination.[7,8]

[*] Dr. M. S. Sanford, Prof. J. T. Groves
Department of Chemistry, Princeton University
Princeton, NJ 08544 (USA)
Fax: (+1) 626-564-9297
E-mail: jtgroves@princeton.edu

[**] This research was supported by the National Science Foundation (CHE 9814301). M.S.S. also thanks the NIH for a postdoctoral fellowship (GM64158-02).

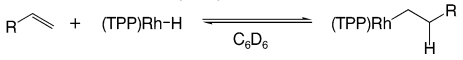
Supporting information for this article is available on the WWW under http://www.angewandte.org or from the author.

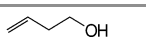
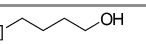
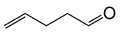
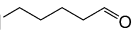
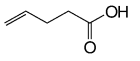
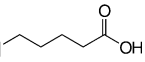
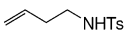
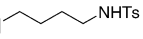
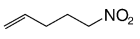
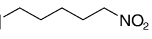


Scheme 1. Rhodium–porphyrin-mediated olefin hydrofunctionalization.

The first step of the process involves a reversible olefin insertion into (TPP)Rh-H to produce a σ-alkyl rhodium complex (Scheme 1, step a).[9] As summarized in Table 1, the desired reaction proceeded efficiently (within 1 h at 25 °C) to

Table 1: Olefin insertion into (TPP)Rh-H.[a]



Entry	Substrate	Product	Yield [%][b]
1			88
2			74
3			91
4			76
5			83

[a] Conditions: 25 °C; 12 h; [Rh] ~ 0.01 M; [olefin] ~ 0.10 M. In all cases the yield of the reaction was >90% as measured by ^{1}H NMR spectroscopy. [b] Yield of isolated product.

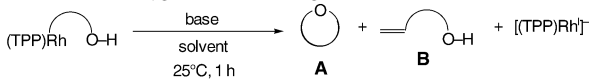
afford a variety of stable rhodium–alkyl products.[10] This transformation was highly regioselective, and in all cases the less-substituted metal–alkyl species was the only insertion product observed by ^{1}H NMR spectroscopy.[10] Furthermore, yields remained excellent in the presence of a diverse array of functional groups, including alcohols, aldehydes, carboxylic acids, sulfonamides, and nitroalkanes (Table 1, entries 1–5). This extraordinary functional-group tolerance is particularly notable because the insertion mechanism involves reactive Rh^{II} radicals as intermediates.[9,11]

The second step involves reaction of the σ-alkyl–rhodium species with an internal nucleophile (Nu; Scheme 1, step b). C–Nu bond-forming reductive elimination reactions are extremely rare, particularly when the α carbon atom is sp^3 hybridized and/or β hydrogen atoms are present.[6,7,12] We note several previous examples of this transformation that involve methyl–rhodium–porphyrin complexes (e.g., Nu = PPh_3[12a] or Rh^I[12b]).

Initial investigations focused on the intramolecular cyclization of (TPP)Rh$(CH_2)_4$OH to produce THF (Table 2, entries 1-3). The pendant alcohol was not sufficiently nucleophilic to cleave the Rh–alkyl bond under neutral conditions. However, the addition of base led to rapid C–O

 © 2004 Wiley-VCH Verlag GmbH & Co. KGaA, Weinheim DOI: 10.1002/anie.200351941

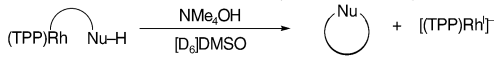
Table 2: Carbon–oxygen bond-forming reductive elimination.[a]



Entry	Substrate	Solvent	Base	Yield [%] A	B
1[b]	[Rh]–OH	C_6D_6	KO*t*Bu	29	71
2[b]	[Rh]–OH	[D$_6$]DMSO	KO*t*Bu	60	40
3[c]	[Rh]–OH	[D$_6$]DMSO	NMe4OH	78	22
4[c]	[Rh]–OH	[D$_6$]DMSO	NMe4OH	70	30
5[b,d]	[Rh]–OH	C_6D_6	KO*t*Bu	>97	<3
6[c,e]	[Rh]–OH	[D$_6$]DMSO	NMe_4OH	<3	>97
7[c]	[Rh]–OH	[D$_6$]DMSO	NMe_4OH	<3	>97

[a] Reactions were quantitative by ^{1}H NMR spectroscopy and were characterized by integration of the ratio of the two organic products. Unless noted, Rh–alkyl substrates were prepared by insertion of the corresponding olefin into (TPP)Rh-H. [b] Conditions: [Rh] = 8.1 mM; [KO*t*Bu] = 16 mM; [[18]crown-6] = 16 mM. [c] Conditions: [Rh] = 8.1 mM; [NMe_4OH] = 24 mM. [d] Substrate prepared according to reference [13]. [e] Substrate prepared by alkylation of (TPP)Rh with $Br(CH_2)_3OH$.

Table 3: Formation of O and N heterocycles and nitropentane.[a]



Entry	Substrate	Product	Yield [%]
1[b]	[Rh]–OH	O	73
2[b]	[Rh]–OH	O	>95
3[b]	[Rh]–HO	O	>95
4[c]	[Rh]–NO_2	O_2N–	69
5[b,d]	[Rh]–HO	O	53
6[c]	[Rh]–NHTs	Ts–N	83
7[c]	[Rh]–NHTs	Ts–N	92
8[c]	[Rh]–NHTs	Ts–N	>95

[a] Reactions were monitored by ^{1}H NMR spectroscopy and proceeded quantitatively to give a mixture of the cyclized product and the elimination product (olefin). Yields were determined by integration of the ^{1}H NMR spectrum of the crude reaction mixture. Rh–alkyl substrates were prepared by insertion of the corresponding olefin into (TPP)Rh-H. [b] Conditions: 25 °C; 1 h; [Rh] = 8.1 mM; [NMe_4OH] = 24 mM. [c] Conditions: 70 °C; 12 h; [Rh] = 8.1 mM; [NMe_4OH] = 24 mM. [d] The elimination product was allylphenol.

bond-forming reductive elimination. THF was produced in 78% yield under optimized conditions ([D$_6$]DMSO, NMe_4OH (3 equiv); Table 2, entry 3). The only other organic product identified was 3-buten-1-ol, which is readily recycled under the hydrofunctionalization conditions. The Rh–porphyrin complex was converted into [(TPP)Rh^{I}]$^{-}$ quantitatively. The cyclization of β-hydroxyalkyl–Rh^{III} derivatives to produce epoxides also proceeded in high yield (>97%; Table 2, entry 5).[13] However, attempts to prepare four- and six-membered oxygen heterocycles by using this methodology were unsuccessful. Instead the corresponding olefins were the only organic products formed (Table 2, entries 6 and 7).[14]

Several pieces of evidence suggest that these unusual reductive eliminations, which involve the formation of a C–O bond, proceed by an S_N2 mechanism. First, the furan/olefin product ratio increased dramatically upon changing the solvent from C_6D_6 to [D$_6$]DMSO (Table 2, entries 1 and 2). Furthermore, modification of the nucleophile from a primary to a secondary alkoxide (Table 2, entries 3 and 4) led to a significant decrease in the ratio of the cyclic product to the 3-buten-1-ol. Both results are indicative of competing S_N2 and E_2 reactions, whereby the S_N2 transition state is favored in more polar solvents[15] and with less sterically hindered nucleophiles. Han has also shown that the cyclization of (TPP)Rh(CDH)CH(CH)$_3$OH (a deuterated analogue of the substrate in Table 2, entry 5) produces [D$_1$]propylene oxide with 100% inversion of stereochemistry at the α carbon atom.[13] This experiment clearly implicates an S_N2 mechanism that proceeds by backside attack at the carbon atom bonded to Rh (as opposed to precoordination of the alkoxide to the Rh center).[7] Importantly, the proposed mechanism is consistent with that of a closely related Rh^{III}/Rh^{I} alkyl-exchange reaction, which proceeds through an S_N2 pathway.[12b]

As summarized in Tables 2 and 3, C(sp^3)–Nu reductive elimination is extremely general in this system and could be applied to the formation of the C–O, C–N, and C–C bonds of a diverse range of cyclic compounds. Once again, the only organic products observed were the desired heterocycle (or carbocycle in the case of Table 3, entry 4) and the corresponding olefin. The Rh complex was quantitatively converted into [(TPP)Rh^{I}]$^{-}$. For example, α-, β-, and γ-substituted Rh–alkyl intermediates with pendant alcohol groups underwent cyclization to produce the corresponding tetrahydrofurans within 1 h at 25 °C (Table 3, entries 1–3). A phenol-substituted rhodium complex underwent facile cyclization at room temperature to give 2,3-dihydro-2-methylbenzofuran (Table 3, entry 5). The modest yield (53%) observed for this system is probably due to the S_N2 mechanism, which requires nucleophilic attack at a sterically hindered tertiary carbon center. Finally, the C–C bonds of cyclopentane (Table 3, entry 4) and C–N bonds of pyrrolidine derivatives (Table 3, entries 6–8) were also constructed readily by using this methodology. Although harsher conditions (70 °C, 12 h) were required relative to the analogous C–O bond-forming reactions, the yields and S_N2/E_2 product ratios remained excellent.

The final step of the catalytic cycle involves protonation of [(TPP)Rh^{I}]$^{-}$ to regenerate the (TPP)Rh-H catalyst (Scheme 1, step c). Nelson and Dimagno recently reported that the pK_a value of (TPP)Rh-H is approximately 11;[12a] therefore, as expected, the addition of excess trifluoroacetic acid to the crude reaction mixtures resulted in quantitative regeneration of (TPP)Rh-H.[16] This transformation com-

 © 2004 Wiley-VCH Verlag GmbH & Co. KGaA, Weinheim

pletes the proposed catalytic cycle and makes it possible to recycle the expensive rhodium porphyrin.

In summary, we have developed and implemented a new, rational mechanistic approach to the design of catalysts for the anti-Markovnikov hydrofunctionalization of olefins. We have shown that (TPP)Rh-H mediates each step of the proposed catalytic cycle with high selectivity, and have demonstrated a new and remarkably general carbon–heteroatom bond-forming reductive elimination reaction. The reactions described herein do not yet constitute a working catalytic cycle. Preliminary attempts to carry out these transformations under catalytic conditions (e.g., with several phenol-based substrates and a variety of weak bases) have thus far been hampered by the incompatibility of step a with the polar solvents required for steps b and c. However, the reactions as performed do allow for the facile recycling of the valuable porphyrin–Rh-H complex. Additionally, we anticipate that the design principles presented herein will serve as a valuable foundation for the development of a new generation of regioselective olefin-hydrofunctionalization catalysts. Current efforts in our laboratories are aimed at improving these systems in terms of catalytic turnover through modification of the solvent system, as well as by steric or electronic perturbation of the porphyrin ligands. Efforts to circumvent reaction-medium limitations through the use of solid-supported Rh catalyst systems are also in progress.

Received: May 21, 2003
Revised: October 24, 2003 [Z51941]

Keywords: alkenes · hydroamination · porphyrinoids · reductive elimination · rhodium

[1] B. M. Trost, *Science* **1991**, *254*, 1471 – 1477.
[2] J. Haggin, *Chem. Eng. News* **1993**, *71(22)*, 23.
[3] a) C. M. Jensen, W. C. Trogler, *Science* **1986**, *233*, 1069 – 1071; b) D. Ramprasad, H. J. Yue, J. A. Marsella, *Inorg. Chem.* **1988**, *27*, 3151 – 3155.
[4] a) M. Utsunomiya, R. Kuwano, M. Kawatsura, J. F. Hartwig, *J. Am. Chem. Soc.* **2003**, *125*, 5608 – 5609; b) M. Beller, C. Breindl, M. Eichberger, C. G. Hartung, J. Seayad, O. R. Thiel, A. Tillack, H. Trauthwein, *Synlett*, **2002**, *10*, 1579 – 1594; c) M. Beller, O. R. Thiel, H. Trauthwein, C. G. Hartung, *Chem. Eur. J.* **2000**, *6*, 2513 – 2522; d) M. Beller, H. Trauthwein, M. Eichberger, C. Breindl, T. E. Muller, *Eur. J. Inorg. Chem.* **1999**, 1121 – 1132; e) M. Beller, H. Trauthwein, M. Eichberger, C. Breindl, J. Herwig, T. E. Muller, O. R. Thiel, *Chem. Eur. J.* **1999**, *5*, 1306 – 1319.
[5] For an alternative approach, see: A. Seayad, M. Ahmed, H. Klein, R. Jackstell, T. Gross, M. Beller, *Science* **2002**, *297*, 1676 – 1678.
[6] R. H. Crabtree, *The Organometallic Chemistry of the Transition Metals*, 2nd ed., Wiley, New York, **2001**, chap. 7.
[7] For recent examples of direct carbon–heteroatom bond-forming reductive elimination under mild conditions, see: a) B. S. Williams, K. I. Goldberg, *J. Am. Chem. Soc.* **2001**, *123*, 2576 – 2587; b) J. F. Hartwig, *Acc. Chem. Res.* **1998**, *31*, 852 – 860; c) S. S. Stahl, J. A. Labinger, J. E. Bercaw, *Angew. Chem.* **1998**, *110*, 2298 – 2311; *Angew. Chem. Int. Ed.* **1998**, *37*, 2181 – 2192.
[8] Reductive elimination induced by oxidation is more common; for a recent example, see: a) B. L. Lin, C. R. Clough, G. L. Hillhouse, *J. Am. Chem. Soc.* **2002**, *124*, 2890 – 2891.
[9] The mechanism of this reaction (involving $[L]Rh^{II}$· intermediates) has been studied, but its scope and functional-group tolerance have not been reported. a) X. F. Fu, L. Basickes, B. B. Wayland, *Chem. Commun.* **2003**, 520 – 521; b) K. W. Mak, F. Xue, T. C. W. Mak, K. S. Chan, *J. Chem. Soc. Dalton Trans.* **1999**, 3333 – 3334; c) D. J. Anderson, R. Eisenberg, *Organometallics* **1996**, *15*, 1697 – 1706; d) R. S. Paonessa, N. C. Thomas, J. Halpern, *J. Am. Chem. Soc.* **1985**, *107*, 4333 – 4334;
[10] Products were identified by ^{1}H NMR spectroscopy based on ^{1}H–Rh coupling and on upfield shifts of the alkyl resonances.[9] The linear product was formed in situ in $>90\%$ yield, whereas the branched isomer was not detected; thus, the lower limit of regioselectivity corresponds to $\sim 97\%$.
[11] a) K. J. Delrossi, X. X. Xhang, B. B. Wayland, *J. Organomet. Chem.* **1995**, *504*, 47 – 56; b) B. B. Wayland, S. J. Ba, A. E. Sherry *J. Am. Chem. Soc.* **1991**, *113*, 5305 – 5311.
[12] a) A. P. Nelson, S. G. Dimagno, *J. Am. Chem. Soc.* **2000**, *122*, 8569 – 8570; b) J. P. Collman, J. I. Brauman, A. M. Madonik, *Organometallics* **1986**, *5*, 215 – 218.
[13] H.-Z. Han, Ph.D. Thesis, Princeton University, 1992.
[14] The origin of this effect is currently under investigation.
[15] K. A. Cooper, M. L. Dhar, E. D. Hughes, C. K. Ingold, B. J. MacNulty, L. I. Woolf, *J. Chem. Soc.* **1948**, 2043 – 2049.
[16] The addition of an excess of trifluoroacetic acid (~5 equiv relative to the base) to the crude cyclization reaction mixtures in C_6D_6 (e.g., Table 2, entry 1) or $[D_7]$DMF resulted in quantitative regeneration of (TPP)Rh-H. The analogous reaction in $[D_6]$DMSO produced a complex mixture of (TPP)Rh products owing to the apparent instability of (TPP)Rh-H in this medium.

 © 2004 Wiley-VCH Verlag GmbH & Co. KGaA, Weinheim

Imines in Stille Reactions

Imines in Stille-Type Cross-Coupling Reactions: A Multicomponent Synthesis of α-Substituted Amides**

*Jason L. Davis, Rajiv Dhawan, and Bruce A. Arndtsen**

Palladium-catalyzed cross-coupling processes such as the Stille reaction have emerged as some of the more important methods for the construction of carbon–carbon bonds.[1–3] A useful feature of the Stille coupling is its use of nonpolar organostannanes, rather than nucleophilic agents, in reactions with organic halides. Organotin reagents are generally air- and moisture-stable, and they can be prepared with a diverse range of transferrable substituents, many of which are less readily formed, or unavailable, within nucleophilic reagents

[*] J. L. Davis, R. Dhawan, Prof. B. A. Arndtsen
Department of Chemistry, McGill University
801 Sherbrooke Street West
Montreal, Quebec H3A 2K6 (Canada)
Fax: (1) 514-398-3797
E-mail: bruce.arndtsen@mcgill.ca

[**] This work was supported by NSERC (Canada) and FQRNT (Quebec). R.D. thanks NSERC for a graduate scholarship.

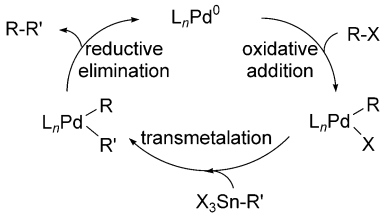
Supporting information for this article is available on the WWW under http://www.angewandte.org or from the author.

 © 2004 Wiley-VCH Verlag GmbH & Co. KGaA, Weinheim DOI: 10.1002/anie.200352123

(e.g. Grignard, organozinc, and organolithium reagents). In addition, the lower reactivity of organotin reagents makes them easily handled and compatible with most functional groups, allowing their use on substrates without prior functional-group protection.[1]

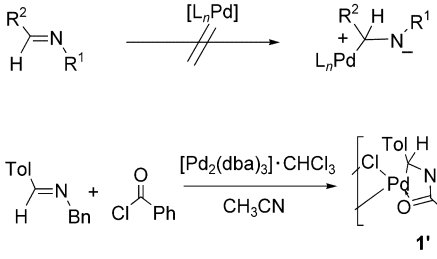
While Stille couplings with organotin reagents have been performed extensively with electrophilic compounds RX (organic halides and triflates, and related σ-bonded substrates),[1] one traditional limitation of this process is its inability to mediate similar reactions with a second important class of electrophiles: multiply bonded substrates $R_2C{=}X$ such as imines.[4] Carbon–carbon bond formation with imines is typically performed with nucleophilic agents and provides a useful method to construct α-substituted amines.[5] However, these reactions lack many of the features detailed above in the complementary Stille cross-coupling reactions. This limitation is of relevance, since α-substituted amines and amides are among the more common units in biologically relevant molecules, including α-amino acids, peptides, peptidomimetics, and β-lactam antibiotics.[6] We report below the development of a method to utilize multiply bonded substrates such as imines in cross-coupling reactions. This provides a palladium-catalyzed alternative to nucleophilic chemistry for the preparation of α-substituted amides, protected amines, and α-amino acid derivatives by a Stille-type coupling of imines with organotin reagents.[7]

Analysis of a generalized mechanism for palladium-catalyzed cross-coupling reactions (Scheme 1) reveals why



Scheme 1. General mechanism of Stille couplings.

imines and related substrates (aldehydes, ketones) have remained inappropriate as cross-coupling partners: imines have no demonstrated propensity to add directly to palladium to generate a Pd–C bond. This is likely due to the lack of stabilization of either the nitrogen anion or palladium cation shown in Equation (1a). This analysis suggests, however, that the addition of substrates that could neutralize the nitrogen anionic charge might provide a route to activate imines towards this transformation.[8] Indeed, we have recently observed that imines can undergo a catalyzed coupling with carbon monoxide and acid chlorides to generate 1,3-oxazolium-5-oxides (Münchnones),[9] a process that was postulated to proceed by formation of palladium-chelated amides.[10] This indicates that the addition of acid chlorides to imines can convert the latter into a substrate capable of oxidative addition.[11,12] This is clearly demonstrated in stoichiometric control experiments [Eq. (1b)], where the mixing of Tol(H)C=NBn (Tol = 4-$CH_3C_6H_4$), PhCOCl, and $[Pd_2(dba_3)]{\cdot}CHCl_3$ (dba = dibenzylideneacetone) leads to the quantitative formation of chelated product **1′**. Notably,



the ^{1}H NMR spectrum reveals reduction of the imine C=N bond upon addition to palladium ($\delta = 5.06$ ppm (s, C*H*Tol)), and ^{13}C NMR data indicates that amide chelation has occurred to form a five-membered metallacycle ($\delta =$ 182.3 ppm (*C*OPh)).[13,14] Mass spectrometric data is consistent with the dimeric structure of **1′**, likely formed through bridging chloro ligands to generate a pseudo-square-planar 16-electron palladium complex.

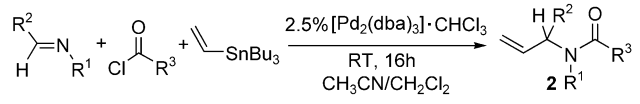
The oxidative addition chemistry in Equation (1b) suggested that this process might also be employed with imines in palladium-catalyzed carbon–carbon bond-forming reactions, provided the palladium–carbon-bonded intermediate **1** can be intercepted with transmetalation. This does turn out to be the case. The reaction of a solution of Tol(H)C=NEt, PhCOCl, and $Bu_3Sn(CH{=}CH_2)$ with 2.5 mol% $[Pd_2(dba_3)]{\cdot}CHCl_3$ results in the rapid disappearance of starting materials at ambient temperature. Workup of the reaction solution reveals that the clean coupling of the three reactants has occurred to form the vinyl-substituted amide **2a** in 82% yield (Table 1, entry 1).

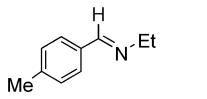
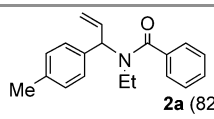
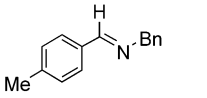
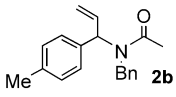
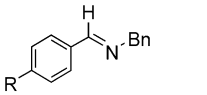
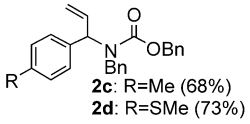
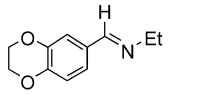
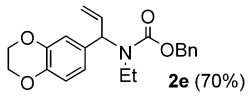
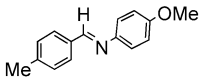
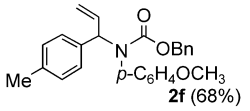
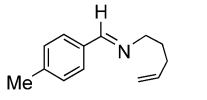
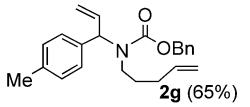
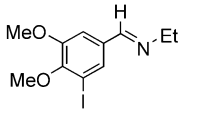
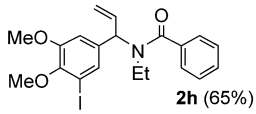
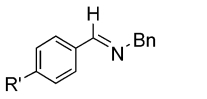
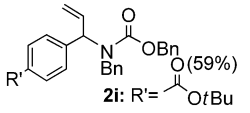
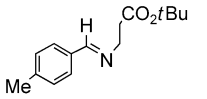
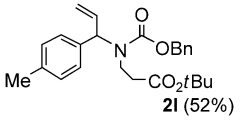
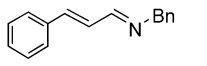
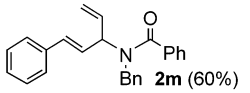
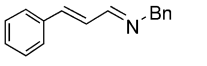
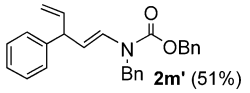
This palladium-catalyzed three-component coupling occurs under mild conditions and with high selectivity, considering that acid chlorides themselves are known to undergo cross-coupling reactions.[1] In examining the plausible mechanism (Scheme 2), we can attribute this selectivity to the equilibrium reaction of imine and acid chloride strongly favoring *N*-acyl iminium salt/α-chloroamide (**3**) formation, which undergoes selective addition to Pd^0.[12] This is facilitated by the ability of **3** to chelate to give **1**, allowing catalysis to proceed in the absence of the ligands often required to aid in oxidative addition.[1] Indeed, the addition of ligands significantly inhibits this coupling,[15] consistent with reports that suggest that an empty coordination site can facilitate transmetalation from tin.[16] As such, reaction with the organotin reagent can occur directly with the three-coordinate complex **1** to form **4**,[17] which yields products by reductive elimination. Overall, these multiple mechanistic steps create what is to our knowledge a unique method to utilize palladium-catalyzed cross-coupling chemistry to convert imines into α-substituted amides.

Further investigation of this catalytic reaction shows it to have a good degree of generality. Thus both aryl and alkyl acid chlorides (Table 1, entry 2) can be employed to generate vinyl-substituted amides. Alternatively, acid chlorides can be replaced with chloroformates. This is somewhat surprising, since the iminium salt of a chloroformate does not oxidatively add to Pd^0 to form a stable product. This provides a catalytic method to convert imines directly into N-protected, α-substituted amine building blocks. As anticipated, the cata-

 © 2004 Wiley-VCH Verlag GmbH & Co. KGaA, Weinheim

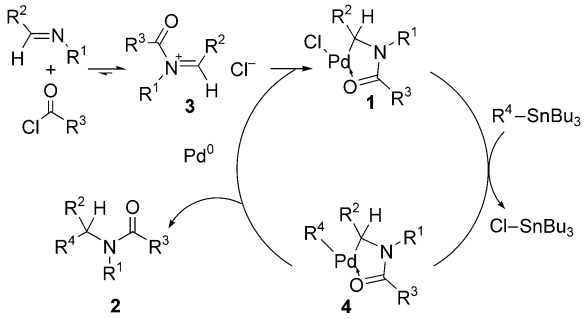
Table 1: Palladium-catalyzed synthesis of amides.[a]



Entry	Imine	Acid chloride	Product (yield)
1		PhCOCl	 **2a** (82%)
2		MeCOCl	 **2b** (78%)
3		BnOCOCl	 **2c**: R=Me (68%) **2d**: R=SMe (73%)
4		BnOCOCl	 **2e** (70%)
5		BnOCOCl	 **2f** (68%)
6		BnOCOCl	 **2g** (65%)
7		PhCOCl	 **2h** (65%)
8		BnOCOCl	 **2i:** R'= (59%)
9		BnOCOCl	 **2l** (52%)
10		PhCOCl	 **2m** (60%)
11[b]		BnOCOCl	 **2m'** (51%)

[a] Reaction conditions: 0.75 mmol imine, 0.75 mmol acid chloride, 0.75 mmol tributylvinyltin, 2.5 mol% $[Pd_2(dba_3)]\cdot CHCl_3$ for 16 h in 20 mL CH_3CN/CH_2Cl_2 (1:1). [b] In the presence of 0.75 mmol Bu_4NBr.

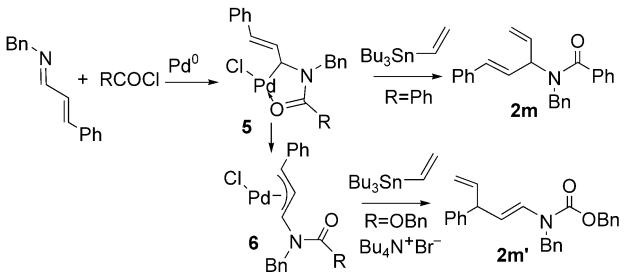
lytic reaction shows tolerance to various functional groups (e.g. ethers, thioethers, and esters; entries 3–5, 8, 9), although enolizable C-alkyl imines are not compatible with these coupling conditions.[18] This process is also amenable to substrates capable of undergoing other palladium-catalyzed reactions. Imines with terminal alkene substituents, which can undergo Heck couplings with acid chlorides,[19] react exclusively at the imine carbon to form α-substituted carbamates



Scheme 2. Postulated mechanism for the palladium-catalyzed three-component coupling.

(entry 6). Similarly, imines containing standard Stille coupling groups such as aryl bromides and electron-rich aryl iodides undergo preferential coupling as the iminium salt (entries 7 and 8). This selectivity can be attributed to the stabilizing effect of amide chelation in the product arising from oxidative addition of the iminium salt, which leads to the favored generation of **1** for transmetalation and coupling.

In addition to imines of aromatic aldehydes, α,β-unsaturated imines react with benzoyl chloride and tributylvinyltin to form α-substituted amides (**2m**, entry 10). Interestingly, replacement of the acid chloride with benzylchloroformate results in the generation of the Michael addition product **2m′** as well as **2m** (ca. 1:1 ratio). Based on the mechanism of this reaction, this would appear to result from the rearrangement of a chelated amide intermediate **5** to the π-allylic structure **6**, which can reductively eliminate at the remote carbon (Scheme 3). The addition of a weakly coordinating bromide

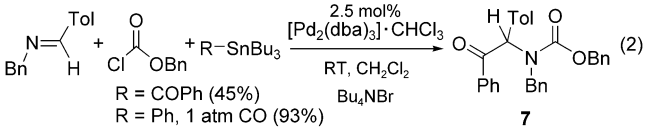


Scheme 3. Palladium-catalyzed vinylation of α,β-unsaturated imines.

source ($Bu_4N^+Br^-$), which can presumably accelerate an associative rearrangement mechanism relative to transmetalation,[20] results in the favored formation of the 1,4-addition product **2m′** (entry 11). This provides a useful catalyst-based method to control the regioselectivity of the addition to unsaturated imine substrates as opposed to nucleophilic approaches, which typically rely upon variation of the actual vinyl-transfer substrate.[21]

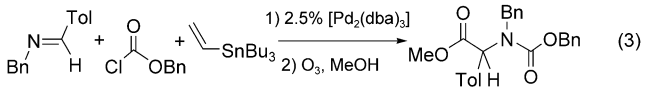
The use of organotin reagents also provides a route to incorporate substrates into the α-position beyond those accessible from nucleophilic sources. This is illustrated in Equation (2), where the palladium-catalyzed reaction of benzoyltributyltin[22] with imine and chloroformate leads to transfer of the benzoyl unit to the imine carbon and formation of **7**. Even more simplified, the intermediacy of Pd–C-bonded

 © 2004 Wiley-VCH Verlag GmbH & Co. KGaA, Weinheim



complexes suggests the possibility of incorporating insertion substrates into the overall catalytic process.[1] Thus, the catalytic coupling of Tol(H)C=NBn, BnOCOCl, and phenyltributyltin under one atmosphere of carbon monoxide yields the same product **7** in 51% yield.[10] Examination of the crude mixture revealed that the only starting materials present were free imine and phenyltributyltin. The addition of excess chloroformate (4 equiv) can thus be used to drive conversion of the imine into **7** in 93% yield.[23] This represents a rare example of a selective four-component cross-coupling reaction, in this case from imine, chloroformate, phenyltin, and carbon monoxide, and allows the construction of α-amido ketones. The latter are useful components for the synthesis of heterocycles[24] and as enzyme inhibitors.[25]

In conclusion, this study describes a convenient and general one-pot synthesis of α-substituted amides and N-protected amines by a palladium-catalyzed three-component-coupling of imines, acid chlorides or chloroformates, and organotin reagents. Mechanistically, this process provides an oxidative addition/reductive elimination-based alternative to nucleophilic approaches to C–C bond formation with imines, in which the imines are activated towards addition to palladium by RCOCl. Considering the utility of imine-reduction products, as well as the generality and mild features of tin couplings, this chemistry could prove useful in the preparation of a range of α-substituted amine derivatives. One illustration of this is in Equation (3), where the



palladium-catalyzed reaction of Tol(H)C=NBn, BnOCOCl, and tributylvinyltin followed by ozonolysis of the vinylic group under Marshall conditions[26] provides a simple two-step route to diprotected α-arylglycine derivatives from air-stable reagents and a commercially available catalyst. Studies directed towards the extension of this process to other general classes of cross-coupling reactions, as well as the incorporation of asymmetry into the reaction products, are currently underway.

Experimental Section

All reactions were carried out under an N_2 atmosphere using a Vacuum Atmospheres 553-2 drybox or by standard Schlenk techniques.

Synthesis of **2**: Imine (0.75 mmol) and acid chloride or chloroformate (0.75 mmol) were dissolved in CH_3CN (10 mL) and stirred for 1 h. To this solution was added $[Pd_2(dba)_3]\cdot CHCl_3$ (20 mg, 0.019 mmol). Tributylvinyltin (238 mg, 0.75 mmol) in CH_2Cl_2 (10 mL) was added, and the resulting solution was stirred at ambient temperature for 16 h. The solvent was removed in vacuo, the residue was dissolved in ethyl acetate (50 mL) and added to a saturated KF solution (25 mL). The white precipitate was filtered off and extracted water/ethyl acetate, and the organic layers were dried over $MgSO_4$. Product **2** was isolated by column chromatography (silica gel 60, hexanes/ethyl acetate).

Received: June 11, 2003 [Z52123]

Keywords: amides · imines · multicomponent reactions · palladium · Stille reaction

[1] a) J. K. Stille, *Angew. Chem.* **1986**, *98*, 504–520; *Angew. Chem. Int. Ed. Engl.* **1986**, *25*, 508–523; b) V. Farina, V. Krishnamurthy, W. J. Scott, *Org. React.* **1997**, *50*, 1–652; c) T. N. Mitchell in *Metal-Catalyzed Cross-Coupling Reactions* (Eds.: F. Diederich, P. J. Stang), Wiley-VCH, New York, **1998**, chap. 4.

[2] For product-diversity applications: B. A. Lorsbach, M. J. Kurth, *Chem. Rev.* **1999**, *99*, 1549–1581.

[3] For examples in natural product synthesis: a) K. C. Nicolaou, N. Winssinger, J. Pastor, F. Murphy, *Angew. Chem.* **1998**, *110*, 2677–2680; *Angew. Chem. Int. Ed.* **1998**, *37*, 2534–2537; b) L. Alcaraz, G. Macdonald, J. Ragot, N. J. Lewis, R. J. K. Taylor, *Tetrahedron* **1999**, *55*, 3707–3716.

[4] Certain reactive tin species (allyl, allenyl, cyano, etc.) undergo addition to multiply bonded substrates by alternative mechanisms.: a) Y. Yamamoto, N. Asao, *Chem. Rev.* **1993**, *93*, 2207; b) H. Yamamoto in *Comprehensive Organic Synthesis*, *Vol. 2* (Ed.: B. M. Trost), Pergamon, Oxford, **1991**, chap. 1; c) J. A. Marshall, *Chem. Rev.* **1996**, *96*, 31; d) H. Ishitani, S. Komiyama, Y. Hasegawa, S. Kobayashi, *J. Am. Chem. Soc.* **2000**, *122*, 762–766.

[5] S. Kobayashi, H. Ishitani, *Chem. Rev.* **1999**, *99*, 1069–1094.

[6] a) *Chemistry and Biochemistry of the Amino Acids* (Ed.: G. C. Barrett), Chapman and Hall, London, **1985**; b) A. E. Taggi, A. M. Hafez, T. Leckta, *Acc. Chem. Res.* **2003**, *36*, 10–19, and references therein.

[7] The palladium-catalyzed α-arylation of ketones to form amino acids has been reported recently: a) J. F. Hartwig, S. Lee, N. A. Beare, *J. Am. Chem. Soc.* **2001**, *123*, 8410–8411; b) S. L. Buchwald, J. L. Rutherford, M. P. Rainka, *J. Am. Chem. Soc.* **2002**, *124*, 15168–15169.

[8] For the oxidative addition of protonated imines: C. R. Baar, L. P. Carbray, M. C. Jennings, R. J. Puddephatt, *Organometallics* **2001**, *20*, 408–417.

[9] a) R. Dhawan, R. Dghaym, B. A. Arndtsen, *J. Am. Chem. Soc.* **2003**, *125*, 1474–1475; b) R. D. Dghaym, R. Dhawan, B. A. Arndtsen, *Angew. Chem.* **2001**, *113*, 3328–3330; *Angew. Chem. Int. Ed.* **2001**, *40*, 3228–3230.

[10] Palladium-catalyzed amidocarbonylations are postulated to proceed by a similar process. For a review: M. Beller, M. Eckert, *Angew. Chem.* **2000**, *112*, 1026; *Angew. Chem. Int. Ed.* **2000**, *39*, 1010.

[11] Structurally, this can be considered to arise from stabilization of the nitrogen anion by acylation and the palladium cation by chloride coordination.

[12] For a review of the oxidative addition chemistry of iminium salts: K. Severin, R. Bergs, W. Beck, *Angew. Chem.* **1998**, *110*, 1722–1743; *Angew. Chem. Int. Ed.* **1998**, *37*, 1634–1654.

[13] R. D. Dghaym, K. J. Yaccato, B. A. Arndtsen, *Organometallics* **1998**, *17*, 46–48.

[14] For characterization of compounds **1**, **2**, and **7** see the Supporting Information.

[15] The addition of 2,2′-bipyridyl resulted in no appreciable coupling under similar conditions.

[16] a) J. Louie, J. F. Hartwig, *J. Am. Chem. Soc.* **1995**, *117*, 11598–11599; b) C. Gennari, S. Ceccarelli, U. Piarulli, *J. Org. Chem.*

 © 2004 Wiley-VCH Verlag GmbH & Co. KGaA, Weinheim

2000, *65*, 6254 – 6256; c) A. L. Casado, P. Espinet, A. M. Gallego, *J. Am. Chem. Soc.* **2000**, *122*, 11 771 – 11 782.
[17] The three-coordinate complexes **1** and **4** are likely solvent-stabilized in acetonitrile solution.
[18] These imines rapidly generate enamides with acid chlorides.
[19] I. P. Beletskaya, A. V. Cheprakov, *Chem. Rev.* **2000**, *100*, 3009 – 3066.
[20] Isomerization on square-planar complexes can be facilitated by ligating species: R. H. Crabtree, *The Organometallic Chemistry of the Transition Metals*, 3rd ed., Wiley, New York, **2001**.
[21] a) L. N. Pridgen, M. K. Mokhallalati, M.-J. Wu, *J. Org. Chem.* **1992**, *57*, 1237 – 1241; b) K. Tomioka, Y. Shioya, Y. Nagaoka, K. Tamada, *J. Org. Chem.* **2001**, *66*, 7051 – 7054.
[22] G. Reginato, A. Faggi, *J. Org. Chem.* **1989**, *54*, 2966 – 2968.
[23] Interestingly, phenyltributyltin does not undergo direct coupling to generate α-phenyl-substituted amides. We are currently investigating this selectivity.
[24] a) J. A. Murry, D. E. Frantz, A. Soheili, R. Tillyer, E. J. Grabowski, P. J. Reider, *J. Am. Chem. Soc.* **2001**, *123*, 9696 – 9697; b) R. R. Gupta, M. Kumar, V. Gupta in *Heterocyclic Chemistry*, Springer, Berlin, **1998**, chap. 2.
[25] a) A. Lee, L. Huang, J. Ellman, *J. Am. Chem. Soc.* **1999**, *121*, 9907 – 9914; b) T. A. Rano, T. Timkey, E. P. Peterson, J. Rotonda, D. W. Nicholson, J. W. Becker, K. T. Chapman, N. A. Thornberry, *Chem. Biol.* **1997**, *4*, 149 – 155.
[26] J. A. Marshall, A. W. Garofalo, *J. Org. Chem.* **1993**, *58*, 3675.

 © 2004 Wiley-VCH Verlag GmbH & Co. KGaA, Weinheim

Proton/Electron Transfer

How Single and Bifurcated Hydrogen Bonds Influence Proton-Migration Rate Constants, Redox, and Electronic Properties of Phenoxyl Radicals

Fabrice Thomas, Olivier Jarjayes, Hélène Jamet, Sylvain Hamman, Eric Saint-Aman, Carole Duboc, and Jean-Louis Pierre*

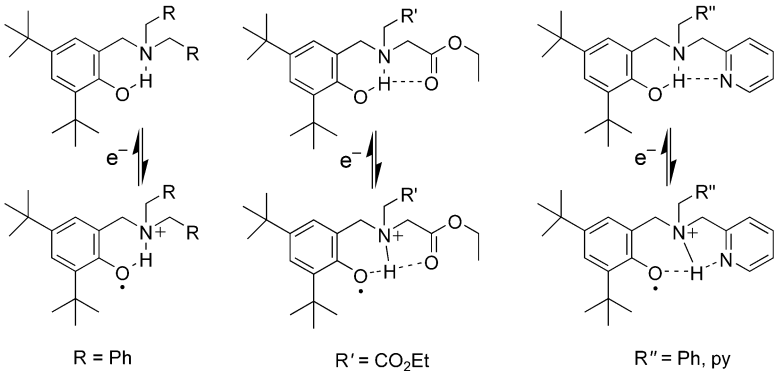
Tyrosine/tyrosyl radical redox systems are involved in many biological processes.[1] Among tyrosyl-radical enzymes, interest has been mainly focused on photosystem II,[2] prostaglandin H synthase,[3] galactose oxidase[4] and ribonucleotide reductase.[5] The phenolic (or phenolate) oxygen may be either bonded to a metal center (as in galactose oxydase) or hydrogen bonded to an appropriately orientated acidic residue of the protein. Despite the crucial role of hydrogen bonding on free radical properties,[6] only two pioneering works have appeared recently in the literature concerning simple biomimetic models of hydrogen bonded phenoxyl radicals.[7] The single intramolecular hydrogen-bonded phenoxyl radicals were evidenced through the reversibility of the phenol/phenoxyl redox couple, but unfortunately no rate constants for the proton transfer were reported. To better understand the way in which single and bifurcated hydrogen bonds influence the properties of phenoxyl-radical cations and phenoxyl radicals, we have synthesized and characterized several ortho-substituted 4,6-di(*tert*-butyl)-phenols in which the phenolic hydrogen atom is involved in hydrogen bonding with the nitrogen atom of a tertiary amine (Scheme 1). The strength of this hydrogen bond is modulated through the substituants of the amine. These compounds incorporate: 1) ester and pyridine groups that can establish weak or strong additional hydrogen bonds with the ammonium proton and 2) benzylic hydrogen atoms between the phenol group and the tertiary amine to obtain geometric information about the radical structure from EPR.

The electrochemical behavior of these substituted phenols has been studied in the nonpolar solvent CH_2Cl_2 + 0.1 M tetra *n*-butyl ammonium perchlorate (TBAP) by cyclic voltammetry (CV): On scanning towards the positive potentials, an electrochemical signal is observed at E_p^a, which corresponds to the oxidation of the phenol into a phenoxyl radical cation. On the reverse scan the cathodic peak at E_p^c is observed at a much lower potential ($\Delta E_p > 0.3$ V at 100 mV s^{-1}, 298 K), which suggests that a chemical reaction, attributed to a proton-migration process, is associated with the electron transfer (Scheme 2).[8] Similar potential values (referred to the Fc/Fc$^+$ system) were measured for HL^{Benz} ($E_p^a = +0.72$ V, $E_p^c = +0.32$ V, Figure 1 insert), HL^{Benzpy} ($E_p^a = +0.67$ V, $E_p^c = +0.30$ V) and HL^{py} ($E_p^a = +0.62$ V, $E_p^c = +0.32$ V). All these values are low compared to that obtained for the 2,4,6-tri(*tert*-butyl)phenol ($E_p^a = +1.20$ V): the hydrogen bonding increases the electron density on the phenolic oxygen making it easier to be oxidized. The rate constants of the proton-migration process were obtained from simulation and best fitting of the CV curves (see Supporting Information for details) recorded at several scan rates according to Scheme 2. The determined rate constants are: $k_1 = 10^{7.4\pm0.5}$ s^{-1}, $k_{-1} = 10^{4.1\pm0.7}$ s^{-1}, $k_2 = 10^{5.3\pm0.1}$ s^{-1}, and $k_{-2} = 10^{2.3\pm0.1}$ s^{-1} in the case of HL^{Benz}, with $E_1^0 = +0.65$ V, $E_2^0 = +0.28$ V. For HL^{Benzpy}, with $E_1^0 = +0.67$ V and $E_2^0 = +0.23$ V, these values are $k_1 = 10^{9.6\pm0.4}$ s^{-1}, $k_{-1} = 10^{5.1\pm0.4}$ s^{-1}, $k_2 = 10^{6.2\pm0.2}$ s^{-1}, $k_{-2} = 10^{3.4\pm0.1}$ s^{-1}.[10] The proton transfer from the phenoxyl cation to the tertiary amine is thus assisted, kinetically and thermodynamically, by the pyridine nitrogen atom as reflected by higher k_1 and K_1 (equilibrium constant) values obtained for HL^{Benzpy} relative to HL^{Benz}. Interestingly, in the presence of tetrabutylammonium hydroxide an irreversible signal corresponding to the phenolate/phenoxyl couple is observed for HL^{Benz} and HL^{Benzpy} at

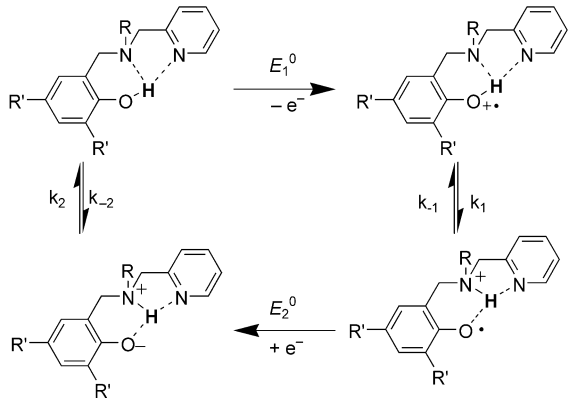
[*] Dr. F. Thomas, Dr. O. Jarjayes, Dr. S. Hamman, Prof. Dr. J.-L. Pierre
Laboratoire de Chimie Biomimétique
LEDSS, UMR CNRS 5616, ICMG FR CNRS 2607
Université J. Fourier, BP 53, 38041 Grenoble cedex 9 (France)
Fax: (+33) 4-76-51-48-36
E-mail: Fabrice.Thomas@ujf-grenoble.fr
Dr. H. Jamet
Laboratoire de Chimie Théorique
LEDSS, UMR CNRS 5616, ICMG FR CNRS 2607
Université J. Fourier, BP 53, 38041 Grenoble cedex 9 (France)
Prof. Dr. E. Saint-Aman
LEOPR, UMR CNRS 5630, ICMG FR CNRS 2607
Université J. Fourier, BP 53, 38041 Grenoble Cedex 9 (France)
Dr. C. Duboc
High Magnetic Field Laboratory of Grenoble
CNRS-MPI UPR 5021, BP 166, 38042 Grenoble Cedex 9 (France)

Supporting information for this article is available on the WWW under http://www.angewandte.org or from the author.

 © 2004 Wiley-VCH Verlag GmbH & Co. KGaA, Weinheim DOI: 10.1002/anie.200352368



Scheme 1. Phenol derivatives HL^{Benz} (R = Ph), HL^{est} (R′ = CO_2Et), HL^{Benzpy} (R″ = Ph) and HL^{py} (R″ = py) and their corresponding hydrogen-bonded phenoxyl radicals.



Scheme 2. Minimum proton-migration process during electron transfer; $K_1 = k_1/k_{-1}$ and $K_2 = k_2/k_{-2}$.

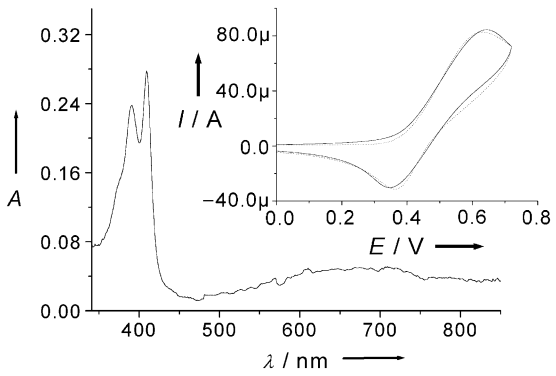
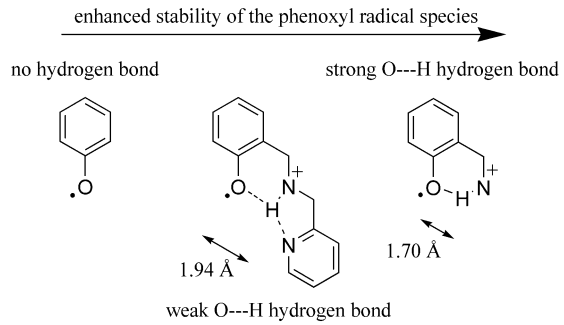


Figure 1. Electronic spectrum of the electrogenerated $HL^{Benz\bullet+}$ 0.32 mM recorded in CH_2Cl_2 0.01 M TBAP at 233 K (path length $l = 1$ cm); Inset: CV curve of HL^{Benz}, 2.4 mM in CH_2Cl_2 0.1 M TBAP at 298 K; Scan rate: 0.1 Vs^{-1}, solid line: experimental, dotted line: simulation by using the parameters given in the text. (A = absorption, arbitrary units; I = electrical current).

−0.48 V: the non-hydrogen bonded phenoxyl-radical species thus degrade at the time scale of the experiment.

Upon one-electron electrochemical oxidation at 233 K, the colorless solutions of the phenolic compounds turn deep-green. Their UV/Vis spectra exhibit π–π* transitions typical of a phenoxyl radical at around 400 nm and a weaker band at 650 nm (Figure 1).[9] Under similar electrolysis conditions, in CH_2Cl_2, the 2,4,6-tri(*tert*-butyl)phenoxyl-radical species was too unstable to be characterized, thus attesting that hydrogen bonds are of prime importance to stabilize a phenoxyl radical electrochemically generated from a phenol. The electrochemically generated-radical species are moderately stable at 298 K. $HL^{py\bullet+}$ and $HL^{Benzpy\bullet+}$ are less stable ($k_{dec} > 5\ min^{-1}$) than $HL^{est\bullet+}$ and $HL^{Benz\bullet+}$ ($k_{dec} = 1.20\ min^{-1}$ and $0.18\ min^{-1}$ respectively). An additional hydrogen bond in $HL^{py\bullet+}$, $HL^{Benzpy\bullet+}$ and $HL^{est\bullet+}$ decreases the strength of the O(phenoxyl)–H(ammonium) hydrogen bond, thus destabilizing the phenoxyl radical (Scheme 3).[10] The effect is more pronounced in $HL^{py\bullet+}$and $HL^{Benzpy\bullet+}$ than in $HL^{est\bullet+}$ according to the strength of the O(phenoxyl)–H(ammonium) hydrogen bond.



Scheme 3. Stability of phenoxyl radical species (O–H distances were obtained from DFT calculations, see text) under our experimental conditions.

The X-Band EPR spectra of the electrochemically oxidized species recorded at 213 K in CH_2Cl_2 (0.1 M TBAP) show an isotropic signal typical of an organic radical (Figure 2a). It is dominated by a large hyperfine coupling constant (hfc) of the spin with one benzylic hydrogen (A_H ranging from 0.51 to 0.80 mT). This is a signature of a rigid conformation of the phenoxyl radical arising from a six-membered ring involving hydrogen bonding. Assuming that the distance d (O(phenoxyl)–H(ammonium)) depends only on θ and the validity of a Mc Connell-type angle-dependent relationship between the hfc and the benzylic hydrogens, the magnitude of A_H is correlated to $\cos^2\theta$ and consequently to d (Figure 3a). The strongest hfc (lowest θ value) obtained for $HL^{Benz\bullet+}$ suggests a shorter d distance. The lowest hfc values were obtained for the compounds bearing one or two pyridines, in which the additional hydrogen bond established between the nitrogen atom of the pyridine and the ammonium proton displaces the latter farther from the oxygen.

Density functional theory (DFT) calculations were performed on two model systems, namely the *N*,*N*-dimethyl-2-

 © 2004 Wiley-VCH Verlag GmbH & Co. KGaA, Weinheim

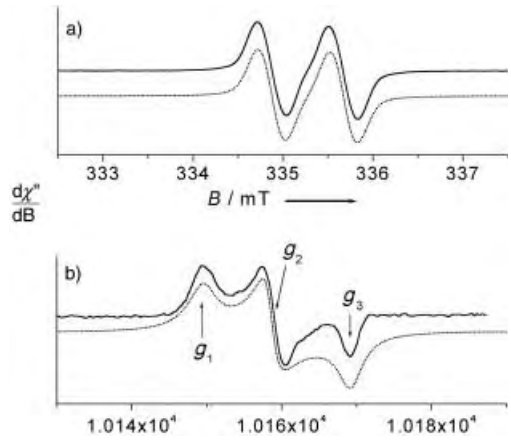


Figure 2. EPR spectra of electrochemically oxidized $HL^{Benz\bullet+}$ radical species recorded in CH_2Cl_2 solution (0.1 M TBAP): a) isotropic X-band spectrum at 213 K (modulation: 100 KHz, 0.0393 mT, Frequency: 9.4103 GHz, 10 mW, $[HL^{Benz\bullet+}] = 1.6$ mM); b) 285 GHz spectrum at 5 K ($[HL^{Benz\bullet+}] = 5$ mM); solid lines: experimental spectrum, dotted lines: simulation by using the parameters given in the Supporting Information. (B = magnetic-flux density).

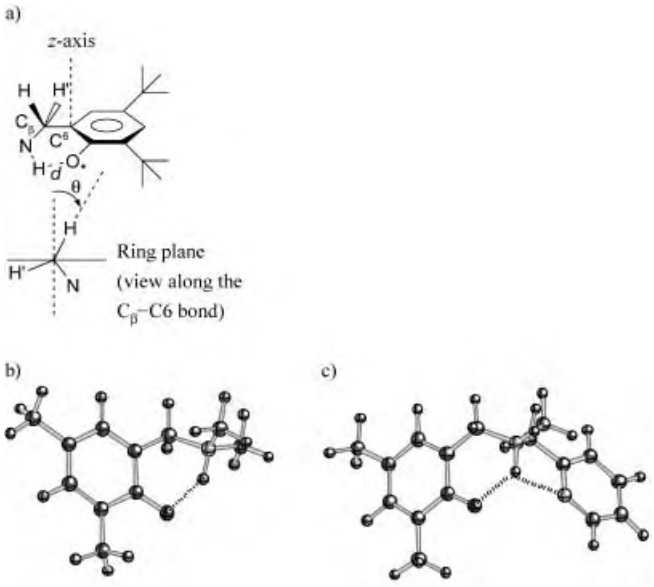
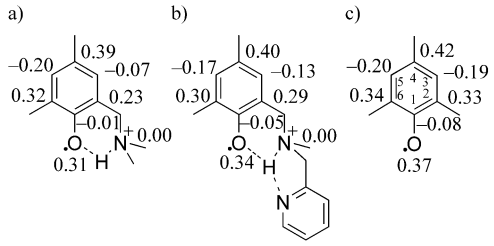


Figure 3. a) Model for the hydrogen bonded phenoxyl radicals; b) (U)B3LYP6-31g* optimized structure of a single hydrogen bonded phenoxyl-radical model system; c) (U)B3LYP6-31g* optimized structure of a bifurcated hydrogen bonded phenoxyl-radical model system.



Scheme 4. Spin density in a a) single hydrogen bonded phenoxyl-radical model system b) bifurcated hydrogen bonded phenoxyl-radical model system and c) "free" 2,4,6 tri(methyl)phenoxyl radical.

methylammonium-4,6-di(methyl)phenoxyl radical ($L^{Me2\bullet+}$, Scheme 4a) and the *N*-(pyrid-2-ylmethyl)-*N*-methyl-2-methylammonium-4,6-di(methyl)phenoxyl radical ($L^{Mepy\bullet+}$, Scheme 4b).[11] All calculations were performed by using the B3LYP hybrid density functional. The efficiency of this method to describe geometries of radical complexes has been recently illustrated.[12] The proton-transferred (phenoxyl–ammonium) and non-proton-transferred (phenoxyl cation–amine) forms were first considered. No non-proton-transferred form could be finally found on the potential energy surface, in agreement with the electrochemical and high field EPR (HFEPR) (see below) data. The optimized structures (Figure 3b,c) of the proton-transferred forms confirmed that the benzylic hydrogen atoms are not equivalent. In $L^{Mepy\bullet+}$ (Figure 3c) the pyridine nitrogen interacts with the ammonium proton, as reflected by a N(pyridine)···H(ammonium) distance of 2.25 Å. Consequently the ammonium proton is displaced farther from the phenoxyl oxygen than in $L^{Me2\bullet+}$: the O(phenoxyl)···H(ammonium) distance is 1.70 Å in $L^{Me2\bullet+}$ (single hydrogen bonded), while it is 1.94 Å in $L^{Mepy\bullet+}$ (bifurcated hydrogen bonded). The spin-density distributions were compared with the values of the "free" 2,4,6 tri(methyl)phenoxyl radical (Scheme 4c). A redistribution of spin density from the oxygen atom to the carbon atom that bears the O atom arises from the presence of the hydrogen bond. Spin density is lost at the C2 atom position and increases at the C3 position. The effect is more pronounced in $L^{Me2\bullet+}$ in agreement with a stronger O···H hydrogen bond. Similar redistribution has been previously reported for a phenol–imidazole hydrogen bonded complex.[12b]

This particular spin distribution, suggested to be responsible for the persistency of phenoxyl radicals in solution,[7a] is reflected by the g_1-tensor value determined by HFEPR experiments[2d,13] (within the molecular frame chosen by van Dam et al.).[5c] The 285 GHz EPR spectra recorded at 5 K exhibit a $S = 1/2$ signal (Figure 2b). The g_2 and g_3 values are known to be independent of the surrounding of the tyrosyl radical. The relatively low g_1 values, 2.0061, 2.0064 and 2.0066 for $HL^{Benz\bullet+}$, $HL^{Benzpy\bullet+}$, $HL^{est\bullet+}$ respectively,[14] are far from that of a "free" tyrosyl radical (usually 2.009). This further confirms that an intramolecular hydrogen bond is established between the phenoxyl-radical oxygen atom and the ammonium proton in our model compounds. These are within the range of that reported (2.0067) for the strongly hydrogen bonded γ-irradiated tyrosine HCl crystals,[15] HSV1 ribonucleotide reductase, prostaglandin synthase tyrosyl radicals (2.0075)[3] or the hydrogen bonded Photosystem II $TyrD^{\bullet}$ (2.0076).[2a]

The stability of phenoxyl radicals is thus correlated to the presence (preventing formation of a phenoxyl radical cation) and strength of an intramolecular hydrogen bond established between the phenoxyl oxygen and an adjacent ammonium proton. The proton-coupled electron transfer from the phenoxyl cation to the tertiary amine is assisted kinetically and thermodynamically by a neighboring hydrogen acceptor: the induced multiple hydrogen-bond network makes the proton move farther and faster. Such processes could play a crucial role in biological systems.[16]

 © 2004 Wiley-VCH Verlag GmbH & Co. KGaA, Weinheim

Experimental Section

Starting materials were obtained commercially. *N*-benzyl-*N*-(2-methylpyridine)[17] and HL^{py}[8] were prepared according to the reported procedures.

2,4-di-*tert*-butyl phenol (5 mmol) and the corresponding amine (5 mmol) were dissolved in methanol (40 mL). Aqueous formaldehyde solution (2 mL, 37%) were then added and the mixture was refluxed for two days. The resulting white suspension was filtered, washed with cold methanol and dried under vacuum.

HL^{Benz}: Yield: 65%. ^{1}H NMR (300 MHz, $CDCl_3$): $\delta = 10.71$ (s, 1H), 7.36–7.22 (m, 10H), 7.19 (d, 1H), 6.84 (d, 1H), 3.71 (s, 2H), 3.60 (s, 4H), 1.43 (s, 9H), 1.26 ppm (s, 9H); MS (DCI, NH_3/isobutane): *m*/*z* (%) 416 (100) $[M+H]^+$; elemental analysis calcd (%) for $C_{29}H_{37}NO$: C 83.81, H 8.97, N 3.37; found: C 83.42, H 8.95, N 3.12.

HL^{est}: Yield: 40%. ^{1}H NMR (300 MHz, $CDCl_3$): $\delta = 9.22$ (s, 1H), 7.24 (d, 1H), 6.82 (d, 1H), 4.20 (q, 4H), 3.97 (s, 2H), 3.53 (s, 4H), 1.42 (s, 9H), 1.24–1.22 ppm (m, 15H); MS (DCI, NH_3/isobutane) : *m*/*z* (%) 408 (100) $[M+H]^+$; elemental analysis calcd (%) for $C_{23}H_{37}NO_5$: C 67.78, H 9.15, N 3.44; found: C 67.21, H 9.29, N 3.39.

HL^{Benzpy}: Yield: 51%. ^{1}H NMR (300 MHz, $CDCl_3$): $\delta = 10.66$ (s, 1H), 8.56 (d, 1H), 7.70–7.61 (m, 1H), 7.37–7.13 (m, 9H), 6.86 (d, 1H), 3.78 (s, 4H), 3.69 (s, 2H), 1.45 (s, 9H), 1.26 ppm (s, 9H); MS (DCI, NH_3/isobutane): *m*/*z* (%) 417 (100) $[M+H]^+$; elemental analysis calcd (%) for $C_{28}H_{36}N_2O$: C 80.73, H 8.71, N 6.72; found: C 80.60, H 8.59, N 6.60.

Received: July 14, 2003 [Z52368]

Keywords: electron transfer · EPR spectroscopy · hydrogen bonds · proton transfer · radicals

[1] J. Stubbe, W. A. van der Donk, *Chem. Rev.* **1998**, *98*, 705.
[2] a) P. Dorlet, A. W. Rutherford, S. Un, *Biochemistry* **2000**, *39*, 7826; b) Y.-N. Wang, L. A. Eriksson, *Int. J. Quantum Chem.* **2001**, *83*, 220; c) B. A. Diner, D. A. Force, D. W. Randall, R. D. Britt, *Biochemistry* **1998**, *37*, 17931; d) S. Un, M. Atta, M. Fontecave, A. W. Rutherford, *J. Am. Chem. Soc.* **1995**, *117*, 10713.
[3] P. Dorlet, S. A. Seibold, G. T. Babcock, G. J. Gerfen, W. L. Smith, A. L. Tsai, S. Un, *Biochemistry* **2002**, *41*, 6107.
[4] a) J. W. Whittaker in *Advances in Protein Chemistry, Vol. 60* (Ed.: F. M. Richards, D. S. Eisenberg, J. Kuriyan), Academic, Elsevier, **2002**, pp. 1–49; b) J. W. Whittaker, *Chem. Rev.* **2003**, *103*, 2347.
[5] a) P. Nordlund, B.-M. Sjöberg, H. Eklund, *Nature* **1990**, *345*, 593; b) P. P. Schmidt, K. K. Andersson, A.-L. Barra, L. Thelander, A. Graslünd, *J. Biol. Chem.* **1996**, *271*, 23615; c) P. J. Van Dam, J. P. Willems, P. P. Schmidt, S. Pötsch, A. L. Barra, W. R. Hagens, B. M. Hoffman, K. K. Andersson, A. Gräslund, *J. Am. Chem. Soc.* **1998**, *120*, 5080.
[6] D. M. Chipman, *J. Phys. Chem. A* **2000**, *104*, 11816.
[7] a) T. Maki, Y. Araki, Y. Ishida, O. Onomura, Y. Matsumura, *J. Am. Chem. Soc.* **2001**, *123*, 3371; b) M. Lucarini, V. Muguaini, G. F. Pedulli, M. Guerra, *J. Am. Chem. Soc.* **2003**, *125*, 8318.
[8] This contrasts with the fully reversible ($\Delta E_p = 0.06$ V) anodic wave characteristic of the electrochemical behavior of the Cu^{II} complex with HL^{py} in which no intramolecular proton transfer can occur (see A. Philibert, F. Thomas, C. Philouze, S. Hamman, E. Saint-Aman, J.-L. Pierre, *Chem. Eur. J.* **2003**, *9*, 3803).
[9] a) L. Benisvy, A. J. Blake, D. Collison, E. S. Davies, C. D. Garner, E. J. L. McInnes, J. McMaster, G. Whittaker, C. Wilson, *Chem. Commun.* **2001**, 1824; b) P. Chaudhuri, K. Wieghardt, *Prog. Inorg. Chem.* **2001**, *50*, 151c) F. Thomas, G. Gellon, I. Gautier-Luneau, E. Saint-Aman, J.-L. Pierre, *Angew. Chem.* **2002**, *114*, 3173; *Angew. Chem. Int. Ed.* **2002**, *41*, 3044.
[10] The electronic effect of the ammonium substituents are negligible: the radical compound described by Maki et al.[7a] bearing two methyl groups instead of the two benzyl moieties of $HL^{Benz\bullet+}$ presents a similar stability ($k_{dec} = 0.21$ min^{-1} at 298 K, Figure S8)
[11] In these model compounds, the *tert*-butyl or the benzyl groups were replaced by methyl groups to obtain reasonable calculation times.
[12] a) P. J. O'Malley, *J. Am. Chem. Soc.* **1998**, *120*, 11732; b) F. Himo, *Chem. Phys. Lett.* **2000**, *328*, 270; c) D. J. Henry, C. J. Parkinson, P. M. Mayer, L. Radom, *J. Phys. Chem. A* **2001**, *105*, 6750.
[13] S. Un, X. Tang, B. A. Diner, *Biochemistry* **1996**, *35*, 679.
[14] It was not possible to generate $HL^{py\bullet+}$ in sufficient amount to record a well resolved HFEPR spectrum.
[15] E. L. Fasanella, W. Gordy, *Proc. Natl. Acad. Sci. USA* **1969**, *62*, 299.
[16] J. Stubbe, D. G. Nocera, C. S. Yee, M. C. Y. Chang, *Chem. Rev.* **2003**, *103*, 2167.
[17] B. Chabut, Ph.D thesis, Université Joseph Fourier, Grenoble, France, **1997**.

 © 2004 Wiley-VCH Verlag GmbH & Co. KGaA, Weinheim

Nanoparticles

Colloidal Carbon Spheres and Their Core/Shell Structures with Noble-Metal Nanoparticles**

*Xiaoming Sun and Yadong Li**

Colloidal micro- and nanospheres have been of continuous research interest, since their intrinsic properties can be finely tuned by changing parameters such as diameter, chemical composition, bulk structure, and crystallinity. Up to now, they have found a broad range of applications in fields such as drug delivery, biodiagnostics, combinatorial synthesis, and photonic band-gap crystals (PBG).[1–3] The success of these applications strongly depends on the availability of colloidal spheres with tightly controlled size and surface properties.[1,2] However, until now, only amorphous silica and some colloidal polymer spheres can be routinely prepared with satisfactorily narrow size distributions.[4] As-prepared colloidal nano- and microspheres usually have relatively inert surfaces, which make surface modification almost unavoidable before use as supports or templates.[3,5]

[*] X. Sun, Prof. Dr. Y. Li
Department of Chemistry
Tsinghua University
Beijing, 100084 (P.R. China)
The Key Laboratory of Atomic & Molecular Nanosciences (Ministry of Education)
Fax: (+86) 10-6278-8765
E-mail: ydli@mail.tsinghua.edu.cn

[**] This work was supported by the NSFC (20025102, 50028201, 20151001), the Foundation for the Author of National Excellent Doctoral Dissertation of P.R. China, and the State Key Project of Fundamental Research for nanomaterials and nanostructures.

 DOI: 10.1002/anie.200352386 © 2004 Wiley-VCH Verlag GmbH & Co. KGaA, Weinheim

Coating the spheres with noble-metal nanoparticles (NMNPs), oxide nanoparticles, or semiconductor quantum dots could endow the spheres with specific catalytic, magnetic, electronic, optical, or optoelectronic properties and greatly widen their utility in fields such as electronics, magnetism, optics, and catalysis.[3,5–13] For instance, the immobilization of transition-metal nanoparticles (TMNPs) on these spheres could allow them to retain high catalytic or biocatalytic activity on recycling, enhance their pH and temperature stability, and enable easy separation from reaction media for reuse.[10,11] In previous reports, immobilization was achieved by two main methods: "layer-by-layer" coating with organic ligands or polyelectrolytes as "glue",[5–8] and "in situ" formation by dispersion copolymerization of styrene and a polyamine in the presence of metal salts.[11] These methods clearly suffer through elaborate surface compositions, manipulation of complex experimental parameters, and/or time-consuming steps for immobilization. We have developed a convenient and controllable hydrothermal synthetic route to hollow ZnSe microspheres.[14] Herein we report an approach to monodisperse colloidal carbon spheres in the size range 150–1500 nm which inherit the reactivity and hydrophilicity of the starting material.

To investigate the chemical reactivity of as-prepared carbon spheres, noble-metal (Ag, Au, Pd, Pt) nanoparticles were loaded onto or encapsulated in carbon spheres to form hybrid structures. A layered structure integrating differently sized noble-metal nanoparticles was obtained when a combination of both synthetic strategies was utilized.

The carbon spheres were prepared from glucose under hydrothermal conditions at 160–180 °C, which is higher than the normal glycosidation temperature and leads to aromatization and carbonization.[15–17] The narrow size distributions of the final products were demonstrated by TEM and SEM observation. Figure 1 a and b show typical TEM and SEM images of such colloidal carbon nanospheres with diameters of 200 and 1500 nm, respectively. Some spheres in Figure 1 a formed hexagonal contacts with one other, and this suggests potential use in construction of photonic crystals or other nanodevices.

The diameters of the carbon spheres were influenced by reaction time, temperature, and concentration of starting material, of which the first-named was dominant. At constant concentration and temperature (e.g., 0.5 M, 160 °C), as the time increased from 2 to 4, 6, 8, and 10 h, the diameter grew from 200 to 500, 800, 1100, and 1500 nm.

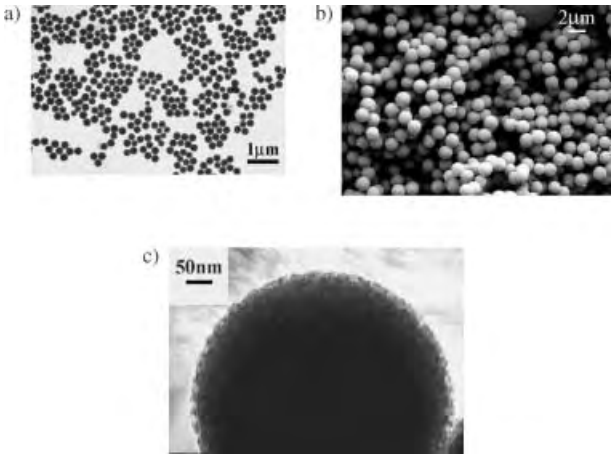


Figure 1. a) SEM image of 200-nm carbon spheres prepared at 0.5 M, 160 °C, 3.5 h, b) TEM image of 1500-nm carbon spheres prepared at 1 M, 180 °C, 10 h, c) Magnified TEM image of an individual carbon sphere.

Various chemical reactions of glucose can take place under hydrothermal conditions and result in a complex mixture of organic compounds,[14,15] and this makes it difficult to determine the exact chemical reaction in the sealed vessel. According to our experimental results, the growth of carbon spheres seems to conform to the LaMer model,[18] shown schematically in Figure 2. No carbon spheres formed when a 0.5 M glucose solution was hydrothermally treated below 140 °C or for less than 1 h. However, the orange or red color and increased viscosity of the resulting solutions indicate that some aromatic compounds and oligosaccharides are formed,[15] in what has been denoted the "polymerization" step. When the solution reached a critical supersaturation (e.g., 0.5 M, 160 °C, 3 h), a short single burst of nucleation resulted. This carbonization step may arise from cross-linking induced by intermolecular dehydration of linear or branchlike oligosaccharides, or other macromolecules formed in prior

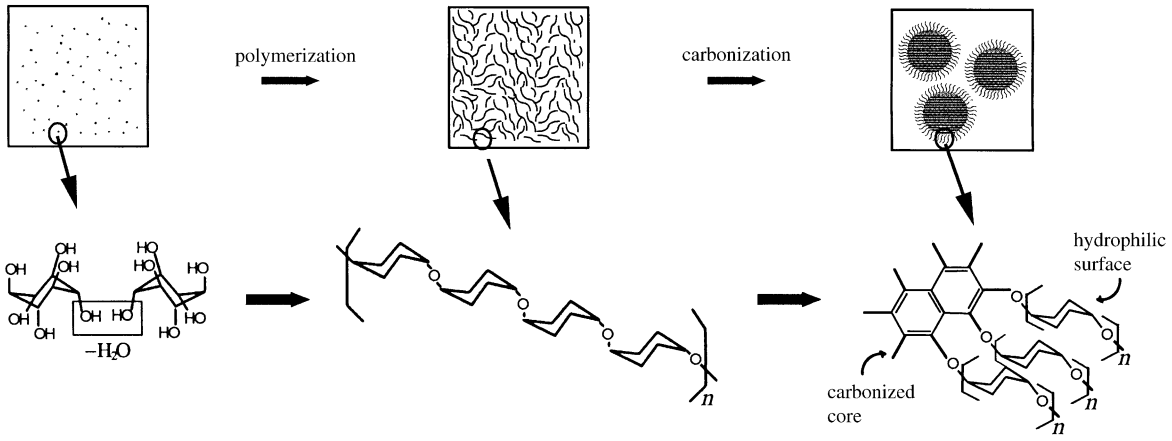


Figure 2. Schematic growth model for carbon spheres (in the final step, the carbonized core and the hydrophilic surface formed by dehydration are schematically represented by aromatic rings and polysaccharides, respectively).

 © 2004 Wiley-VCH Verlag GmbH & Co. KGaA, Weinheim

step. The resulting nuclei then grew uniformly and isotropically by diffusion of solutes toward the particle surfaces until the final size was attained. The diameters of these nanospheres could thus be tuned in the range from 150 nm (the initial core size, and the smallest size we attained) to 1500 nm by controlling the growth parameters. The TEM image of an individual sphere (Figure 1c) showed some nanosized pores distributed uniformly on the surface, which could caused by removal of residual organic compounds, such as oligosaccharides from the surface by washing with water and alcohol. These pores could not only increase the surface area, but also aid penetration of reactive species. In comparison to the synthesis of polymer or silica spheres, two features become apparent: 1) our approach is an absolutely "green" method. The monodisperse colloidal nanospheres were obtained in aqueous glucose solutions, and no toxic reagents were used. 2) The synthetic procedure involves none of the organic solvents, initiators, or surfactants which are commonly used for preparation of polymer micro- or nanospheres. This ensures that the as-prepared nanoparticles are nontoxic enabling their used in biochemistry or biodiagnostics.

Dehydration and aromatization are usually regarded as a process of decreasing the number of functional groups.[15] The FTIR spectrum (Figure 3a) was used to identify the functional groups present after hydrothermal treatment. The bands at $\tilde{\nu} = 1710$ and 1620 cm^{-1}, attributed to C=O and C=C vibrations, respectively, support the concept of aromatization of glucose during hydrothermal treatment. The bands in the range $\tilde{\nu} = 1000$–1300 cm^{-1}, which include the C–OH stretching and OH bending vibrations, imply the existence of large numbers of residual hydroxy groups. Partially dehydrated residues in which reductive OH or CHO groups are covalently bonded to the carbon frameworks improve the hydrophilicity and stability of the microspheres in aqueous systems, and greatly widen their range of applications in biochemistry, diagnostics, and drug delivery, and as templates for hybrid core/shell structures or hollow/porous materials. For instance, they could be covalently bonded to biomacromolecules and used as a hydrophilic drug-delivery system,[19] or react with metal ions to form metal nanoparticles, which could be used as probes for detection of molecules by surface-enhanced raman scattering (SERS).

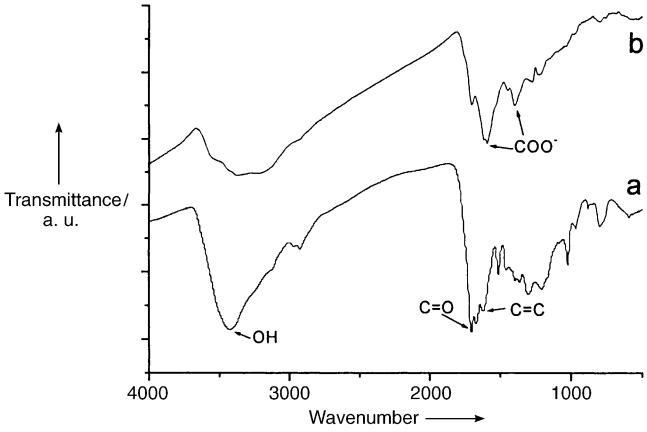


Figure 3. FTIR spectra of carbon spheres: a) sample unloaded with noble metal, and b) sample loaded with silver nanoparticles.

To demonstrate the reactivity of as-prepared carbon microspheres, silver and palladium nanoparticles were loaded onto their surfaces by room-temperature surface reduction or by the reflux method. Figure 4a shows silver-loaded carbon spheres prepared at room temperature by ultrasonication in 1M $AgNO_3$ solution. Thanks to the moderate synthesis conditions, the silver nanoparticles decorating the carbon nanospheres were usually no larger than 15 nm (Figure 4b). Energy dispersive X-ray analysis (EDXA) of the spherical core/shell structure revealed the elemental constitution of the noble-metal-loaded spheres (Figure 4c): two major peaks, corresponding to carbon and silver, and one weak peak (≈0.8 keV) indicating the presence of oxygen. The effectiveness of the reflux method was demonstrated by loading palladium nanoparticles onto the surfaces of carbon spheres, which occurs at a far lower concentration (0.1→0.02 M). After 20 min under reflux, the carbon spheres were covered by a uniform shell of 10–20-nm palladium nanoparticles (Figure 4d,e).

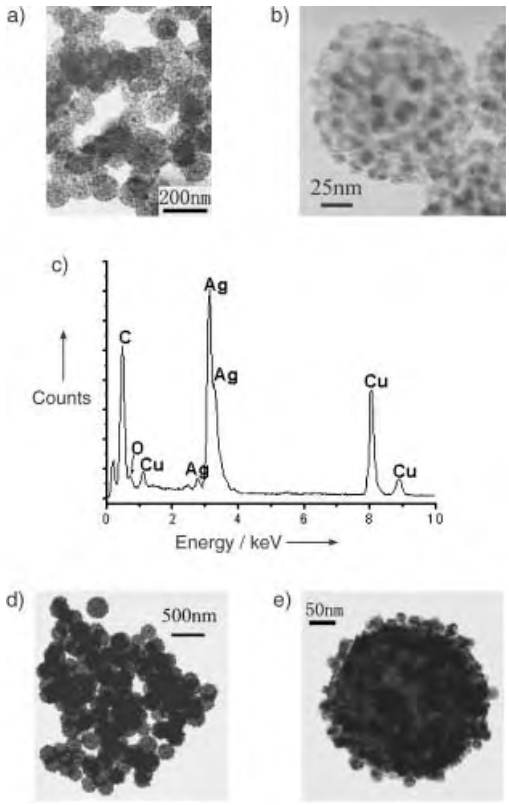


Figure 4. a, b) Carbon spheres loaded with silver nanoparticles at room temperature. c) EDXA spectrum of silver-loaded carbon spheres. d, e) Carbon spheres loaded with palladium nanoparticles by the reflux method.

The surface redox reactions decreased the number of reducing organic functional groups, as revealed by the FTIR spectrum (Figure 3 trace b). The O–H stretching band

 © 2004 Wiley-VCH Verlag GmbH & Co. KGaA, Weinheim

centered at 3500 cm^{-1} was weakened. Two major peaks centered at 1590 and 1390 cm^{-1} could be attributed to asymmetric and symmetric stretching vibrations of COO^- groups,[20] respectively, and this suggested that the final products of oxidation were carboxylates.

A surprising feature of these carbon spheres is their ability to encapsulate nanoparticles in their cores with retention of the surface functional groups. Nanoparticles of gold and silver could be encapsulated in carbon by in situ hydrothermal reduction of noble-metal ions with glucose, or by using silver nanoparticles as nuclei for subsequent formation of carbon spheres. The latter is a more general method that can be used for the encapsulation of various colloidal nanoparticles, such as metals, oxides, and chalcogenides. Figure 5a shows micro-

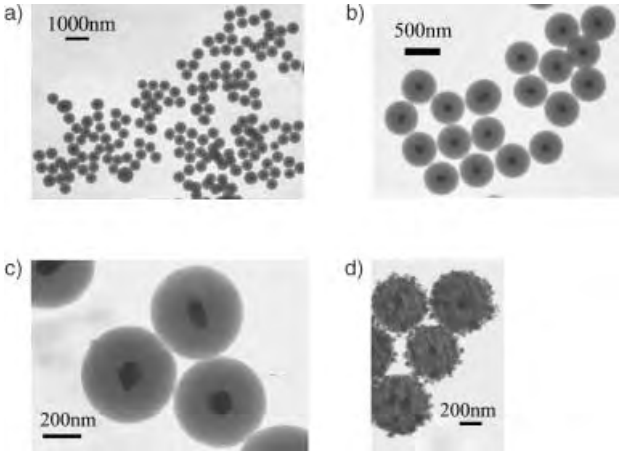


Figure 5. NMNP-encapsulated carbon spheres prepared in different ways: a) Au-cored carbon spheres from hydrothermal reduction and encapsulation method, b, c) silver-cored carbon spheres from encapsulation of silver nanoparticle seeds, and d) layered structure with an silver core, a platinum shell, and a carbon interlayer, formed by seed-based encapsulation followed by the reflux method.

graphs of gold-cored carbon spheres prepared by the former method. Carbon spheres containing one or two metal nanoparticle cores were obtained. The samples for TEM observation were tilted by $\pm 25°$ to check whether the nanoparticles were always encapsulated at the centers of the carbon spheres rather than attached to the surface. Figure 5b shows carbon spheres containing silver nanoparticles prepared by the latter method. Silver nanoparticles with different morphologies were encapsulated in the carbon spheres (Figure 5c). The diameter of the noble-metal nanoparticles could be manipulated in the range of 8–50 nm. This procedure protects the silver nanoparticles with carbon and retains the surface functional groups for loading other functional groups, enzymes, antigens, or other nanoparticles.

The ability of the retained functional groups to load nanoparticles was demonstrated by reductive loading of platinum nanoparticles onto silver-cored carbon spheres. A layered structure consisting of an Ag core about 60 nm in size, a platinum shell composed of 10–20-nm platinum nanoparticles, and a carbon interlayer was prepared in this way (Figure 5d). The layered structure should be of interest to physicists and material scientists, since the optical (including Raman and IR), electronic, and catalytic properties of NMNPs are size-dependent,[21,22] and this kind of structure integrates differently sized NMNPs in a single system. In fact, the silver and other metal nanoparticles generated by our method could be replaced by each other, and this opens an avenue to tailoring the structures and hence the properties of these hybrid structures, as well as exploring the distinct properties of noble metal nanoparticles. Furthermore, the silver-loaded carbon nanoparticles could be transformed into hollow structures by ion-exchange and thus form more complex structures.[23]

The stability of colloids was affected by the decoration and encapsulation of noble-metal nanoparticles on/in the carbon spheres. Colloidal suspensions of spheres with diameters of 200 and 500 nm were stable for one month and 10 days, respectively. While for the noble-metal-loaded spheres (e.g., the sample shown in Figure 5c), the time decreased to 3–5 days. However, when the mixtures were shaken or ultrasonicated for 5 s, a homogeneous suspension was formed at once.

A SERS analysis of unloaded carbon spheres showed no clear peaks (Figure 6 trace a) owing to their poor crystallinity in the as-formed state. In contrast, silver-loaded spheres showed two strong peaks at 1585 cm^{-1} and 1390 cm^{-1} (Figure 6 trace b), which were attributed to in-plane vibra-

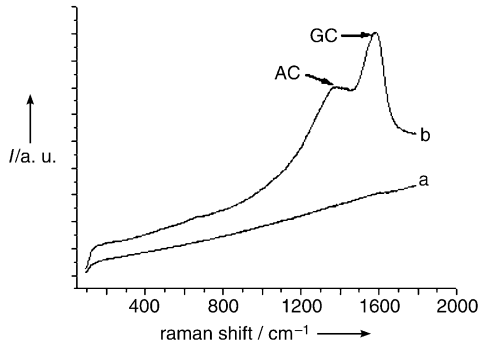


Figure 6. Raman spectra of carbon spheres: a) unloaded with noble metal, and b) loaded with Ag nanoparticles. GC: graphitic carbon, AC: amorphous carbon.

tions of crystalline graphite and disordered amorphous carbon, respectively.[24] The greatly increased signal-to-noise ratio suggested promising applications of this kind of noble-metal-loaded carbon spheres in developing convenient and sensitive methods for trace analysis and studying adsorption behavior, etc.[25] Since spherical objects are easily packed and assembled into arrays,[1,9] and biomacromolecules such as proteins can be adsorbed on NMNPs,[9] our method provides new basic units for the construction of nanodevices for use in biochemical detection. Furthermore, since carbon is far more stable than polymers with respect to high-temperature stability and resistance to acids, bases, and solvents, these hybrid structures should have clear advantages over NMNP-decorated polymer spheres in fields such as catalysis or detection.

 © 2004 Wiley-VCH Verlag GmbH & Co. KGaA, Weinheim

In summary, monodisperse colloidal carbon microspheres were prepared from aqueous glucose solutions by hydrothermal synthesis, and encapsulated nanoparticles were also obtained by this procedure. The synthesis is convenient, and the as-formed colloidal spheres inherit functional groups from the starting material and have reactive surfaces, which facilitate loading with NMNPs and make it possible to integrate differently sized NMNPs in layered structures. Furthermore, the synthetic strategy can be transferred to other systems such as oxides, chalcogenides, and nitrides for the formation of hybrid, hollow, or porous structures. Thus, the synthesis of these carbon spheres opens an avenue to tailoring the structure, composition, and morphology for use in fields such as drug delivery, porous ceramics, adsorbents, and catalysis.

Experimental Section

Carbon nanospheres: Glucose (4–8 g, analytical purity, Beijing Chemical Reagent Factory) was dissolved in water (40 mL) to form a clear solution, which was placed in a 40-mL teflon-sealed autoclave and maintained at 160–180 °C for 4–20 h. The black or puce products were isolated by centrifugation, cleaned by three cycles of centrifugation/washing/redispersion in water and in alcohol, and oven-dried at 80 °C for more than 4 h.

Loading silver nanoparticles onto carbon spheres: Newly prepared nanocarbon spheres were dispersed in water with the aid of ultrasonication to give a 0.5 wt % suspension. 1 mL of this suspension was added to 1 M $AgNO_3$ (10 mL) solution drop by drop with vigorous stirring. The mixture was supersonicated for 10 min, aged for 1 h, and subjected to four centrifugation/water wash/redispersion cycles to remove silver ions. The resulting powder was centrifuged, redispersed in alcohol, and deposited on a copper grid for TEM observation.

Reflux method: 5 mL $\approx$0.2 wt % of an aqueous suspension of carbon spheres was heated under reflux for 5 min and then 0.1 M $PdCl_2$ was added drop by drop under vigorous stirring until the final Pd ion concentration reached 0.02 M. The suspension was refluxed for 20 min before sampling and rinsing.

Encapsulation of Au and Ag nanoparticles: A solution of $HAuCl_4$ (1 mL, 0.02 M) or freshly prepared silver colloid[26] (1 mL, ca. 10^{13} mL^{-1}) was added to a glucose solution (40 mL, 0.5 M) with stirring to form clear solutions. The subsequent procedures were the same as described above for the synthesis of carbon spheres.

Synthesis of layered structures: A suspension (5 mL) of carbon spheres (ca. 50 nm) encapsulating Ag nanoparticles was heated under reflux for 5 min, and then 0.02 M K_2PtCl_6 solution was added until the Pt concentration reached 0.005 M. The suspension was heated under reflux for a further 20 min before sampling and rinsing.

Characterization: All the samples were characterized by TEM (Hitachi H800, acceleration voltage 200 kV), SEM (Leo 1530), Raman spectroscopy (Renishaw RM1000 Raman spectrometer, excitation wavelength 514 nm), and FTIR spectroscopy (Perkin-Elmer Spectrum GX).

Received: July 15, 2003 [Z52386]

Keywords: carbon · colloids · layered structures · nanostructures · noble metals

[1] Y. N. Xia, B. Gates, Y. D. Yin, Y. Lu, *Adv. Mater.* **2000**, *12*, 693–713, and references therein.
[2] W. Schärtl, *Adv. Mater.* **2000**, *12*, 1899–1908.
[3] F. Caruso, *Top. Curr. Chem.* **2003**, *227*, 145–168.
[4] P. Jiang, J. F. Bertone, V. L. Colvin, *Science* **2001**, *291*, 453.
[5] a) F. Caruso, R. A. Caruso, H. Möhwald, *Science* **1998**, *282*, 1111; b) F. Caruso, *Adv. Mater.* **2001**, *13*, 11–22; c) D. Y. Wang, A. L. Rogach, F. Caruso, *Nano Lett.* **2002**, *2*, 857–861; d) Q. Wang, H. Li, L. Q. Chen, X. J. Huang, *Carbon* **2001**, *39*, 2211–2214.
[6] a) S. J. Oldenburg, R. D. Averitt, S. L. Westcott, N. J. Halas, *Chem. Phys. Lett.* **1998**, *288*, 243; b) A. Dokoutchaev, J. T. James, S. C. Koene, S. Pathak, G. K. S. Prakash, M. E. Thompson, *Chem. Mater.* **1999**, *11*, 2389–2399; c) A. G. Dong, Y. J. Wang, Y. Tang, N. Ren, W. L. Yang, Z. Gao, *Chem. Commun.* **2002**, 350–351.
[7] a) L. M. Liz-Marzan, M. Giersig, P. Mulvaney, *Langmuir* **1996**, *12*, 4329–4335; b) Y. Kobayashi, V. Salgueirino-Maceira, L. M. Liz-Marzan, *Chem. Mater.* **2001**, *13*, 1630.
[8] a) O. D. Velev, E. W. Kaler, *Langmuir* **1999**, *15*, 3694–4698; b) C. Graf, A. van Blaaderen, *Langmuir* **2002**, *18*, 524–534.
[9] J. Zhou, Y. Zhou, S. L. Ng, H. X. Zhang, W. X. Que, Y. L. Lam, Y. C. Chan, C. H. Kam, *Appl. Phys. Lett.* **2000**, *76*, 3337–3339.
[10] S. Phadtare, A. Kumar, V. P. Vinod, C. Dash, D. V. Palaskar, M. Rao, P. G. Shukla, S. Sivaram, M. Sastry, *Chem. Mater.* **2003**, *15*, 1944–1949.
[11] a) C. W. Chen, M. Q. Chen, T. Serizawa, M. Akashi, *Adv. Mater.* **1998**, *10*, 1122–1126; b) C. W. Chen, T. Serizawa, M. Akashi, *Chem. Mater.* **2002**, *14*, 2232–2239.
[12] H. Li, Q. Wang, L. H. Shi, L. Q. Chen, X. J. Huang *Chem. Mater.* **2002**, *14*, 103–108.
[13] F. Goutfer-Wurmser, H. Konno, Y. Kaburagi, K. Oshida, M. Inagaki, *Synthetic Metals* **2001**, *118*, 33–38.
[14] Q. Peng, Y. J. Dong, Y. D. Li, *Angew. Chem.* **2003**, *115*, 3135–3138; *Angew. Chem. Int. Ed.* **2003**, *42*, 3027–3030.
[15] T. Sakaki, M. Shibata, T. Miki, H. Hirosue, N. Hayashi, *Bioresour. Technol.* **1996**, 58, 197–202.
[16] G. C. A. Luijkx, F. van Rantwijk, H. van Bekkum, M. J. Antal, Jr., *Carbonhydrate Res.* **1995**, *272*, 191–202.
[17] Q. Wang, H. Li, L. Q. Chen, X. J. Huang, *Solid State Ionics* **2002**, *152*–153, 43–50.
[18] V. K. LaMer, *Ind. Eng. Chem.* **1952**, *44*, 1270.
[19] M. L. Hans, A. M. Lowman, *Curr. Opin. Solid State Mater. Sci.* **2002**, 6, 319–327.
[20] W. Tian, L. M. Yang, Y. Z. Xu, S. F. Weng, J. G. Wu, *Carbohydr. Res.* **2000**, *324*, 45–52.
[21] S. R. Emory, W. E. Haskins, S. M. Nie, *J. Am. Chem. Soc.* **1998**, *120*, 8009–8010.
[22] U. Heiz, F. Vanolli, A. Sanchez, W. D. Schneider, *J. Am. Chem. Soc.* **1998**, *120*, 9668–9671.
[23] Y. G. Sun, B. T. Mayers, Y. N. Xia, *Nano Lett.* **2002**, *2*, 481–485.
[24] A. Ilie, C. Durkan, W. I. Milne, M. E. Welland, *Phys. Rev. B* **2002**, *66*, 045412.
[25] a) S. W. Joo, W. J. Kim, W. S. Yoon, I. S. Choi, *J. Raman Spectrosc.* **2003**, *34*, 271–275; b) L. L. Bao, S. M. Mahurin, C. D. Liang, S. Dai, *J. Raman Spectrosc.* **2003**, *34*, 394–398.
[26] Y. D. Li, X. F. Duan, Y. T. Qian, L. Yang, H. W. Liao, *J. Colloid Interface Sci.* **1999**, *209*, 347–349.

 © 2004 Wiley-VCH Verlag GmbH & Co. KGaA, Weinheim

Automated Synthesis

Automated Solid-Phase Synthesis of Protected Tumor-Associated Antigen and Blood Group Determinant Oligosaccharides**

*Kerry Routenberg Love and Peter H. Seeberger**

The Lewis blood group oligosaccharides are a family of fucosylated, ceramide-containing glycosphingolipids decorating the exterior of healthy and disease-derived cells.[1] These complex carbohydrates consist of a reducing-end lactose β-(1→3) linked to a central *N*-acetyl glucosamine unit. Members of this family of structures differ in the arrangement of galactose and fucose residues around the glucosamine core. Lewis-type penta- and hexasaccharides are part of the inflammatory cascade[2] and have been implicated in bacterial and viral infection,[3] as well as autoimmune diseases.[4] The Lewis Y hexasaccharide and dimeric combinations of Lewis antigens, including the Le^y–Le^x nonasaccharide, are tumor markers currently being explored as cancer vaccines.[5]

The biological importance of the Lewis antigens has rendered them targets of intense examination. Since the microheterogeneity of carbohydrates limits the amount of pure oligosaccharides that may be isolated from natural sources, chemical synthesis is essential to procure appreciable quantities of material for biological study. Owing to their significance and complexity, the Lewis blood group determinants have served as synthetic targets for the development of new methods for oligosaccharide synthesis in solution,[6–11] on soluble polymeric supports,[12] and on solid support.[13]

Our strategy for the synthesis of these branched carbohydrates differs markedly from previous routes where maximum convergence was desired. Typically, a series of block couplings specific to each target has been used to combine di- and trisaccharide portions of the molecule. The Le^y–Le^x nonasaccharide has been constructed twice in heroic solution-phase total syntheses.[14,15] To simplify the synthesis of such structures, we present here a general method utilizing a small number of common building blocks for a sequential synthesis, by adding one monomer at a time to a growing oligosaccharide chain. With this strategy, access to the entire family of Lewis antigens may be achieved.

Our initial work on automated oligosaccharide assembly demonstrated that relatively simple carbohydrates could be prepared on a machine that executes a coupling cycle, including steps for glycosylation and deprotection.[16] Further fundamental advances are required to expand this methodology to include structures containing a variety of residues and linkages and to simplify the synthetic process.

Initially we identified the monosaccharide building blocks found in the protected Lewis X pentasaccharide **1**, Lewis Y hexasaccharide **2**, and Le^y–Le^x nonasaccharide **3** (Scheme 1). Five monomers are sufficient for the construction of the three target structures, which each contain five different glycosidic bonds. Each monosaccharide unit must contain appropriate temporary protecting groups to establish the required connections in the target and be synthetically readily accessible. Additionally, we were interested in monitoring the progress of the solid-phase assembly in real time. The success of individual couplings is routinely monitored during automated oligopeptide and oligonucleotide synthesis.

The differentially protected monosaccharide building blocks were rapidly prepared from glycals by using a one-pot procedure.[17] Glycosyl phosphates **4**, **5**, and **8** were synthesized for the placement of glucose and galactose residues. Glucosamine phosphate **6** was selected based on solution-phase studies. Fucosyl phosphate **7** showed excellent selectivity in creating the difficult α-(1→2-*cis*) and α-(1→3-*cis*) fucose linkages common to the Lewis antigens.[9,17]

For each monosaccharide, a protecting-group pattern that allowed for selective unveiling of a single hydroxy group was selected. We chose the Fmoc group for the temporary protection of the hydroxy groups because it is completely stable under the acidic glycosylation conditions, it is readily cleaved by mildly basic amines,[18] and it facilitates monitoring of protecting-group removal by UV/Vis spectroscopy.[19] Analysis of Fmoc deprotection provided a qualitative assay for the efficiency of each glycosylation and deprotection cycle during automated assembly (Scheme 2). While real-time analysis is common in automated oligopeptide and oligonucleotide synthesis, analogous monitoring of solid-phase glycosylation reactions had not been demonstrated in automated carbohydrate synthesis.[20]

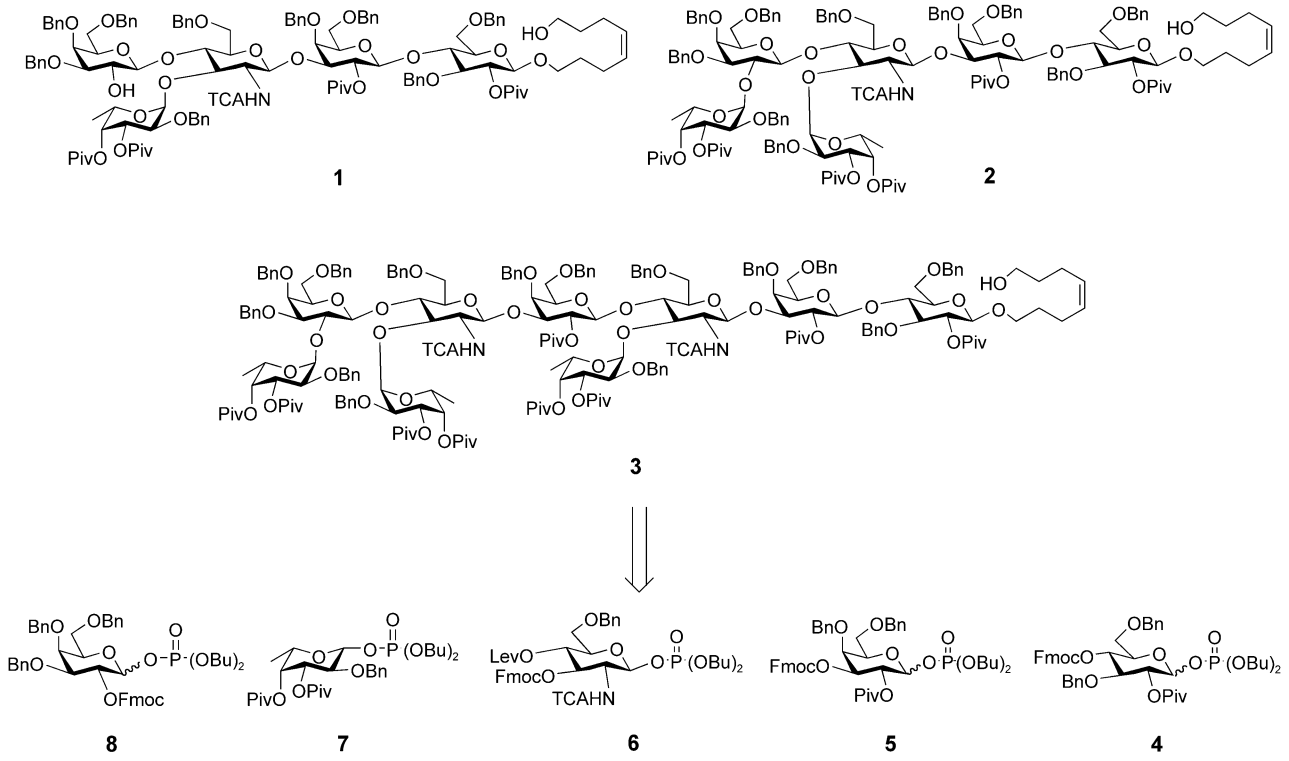
To account for branching connections through both the C3 and C4 positions of the glucosamine units in targets **1**–**3**, an additional temporary protecting group was installed in monomer **6**. The levulinoyl ester was selected, as it is easily removed with hydrazine and is completely orthogonal to the Fmoc group. The use of temporary protecting groups that require only mildly basic conditions for removal allowed the improvement of another feature of previous automated syntheses: the lengthy cleavage of the product from the solid support following assembly. Condensation of the previously employed octenediol linker[21] with carboxy-terminated polystyrene resin resulted in an ester linkage, which was rapidly cleaved with strong base at the end of the synthesis.

[*] Prof. Dr. P. H. Seeberger
Laboratorium für Organische Chemie
ETH-Hönggerberg, 8093, Zürich (Switzerland)
Fax: (+41) 1633-1235
E-mail: seeberger@org.chem.ethz.ch
K. Routenberg Love, Prof. Dr. P. H. Seeberger
Department of Chemistry, Massachusetts Institute of Technology
Cambridge, Massachusetts 02139 (USA)

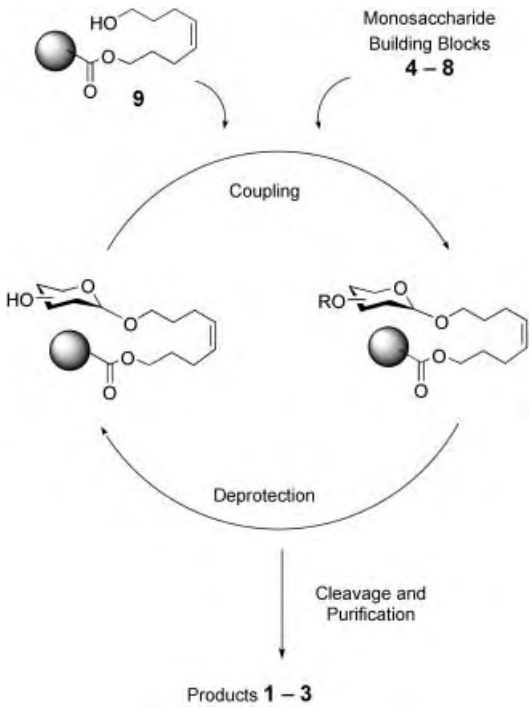
[**] Financial support from the Alfred P. Sloan Foundation (Fellowship to P.H.S.), GlaxoSmithKline (Scholar Award to P.H.S.), Merck, and the National Institutes of Health (NIH; Biotechnology Training Grant Fellowship to K.R.L.) is gratefully acknowledged. Funding for the MIT-DCIF Varian 500 MHz NMR spectrometer was provided by the National Science Foundation (NSF; Award CHE-9808061). Funding for the MIT-DCIF Avance (DPX) 400 MHz NMR spectrometer was provided by the NIH (Award 1S10RR13886-01). Funding for the MIT-DCIF Varian 300 MHz NMR spectrometer was provided by the NSF (Award DBI-9729592). We thank the members of the MIT DCIF for help with the analysis of the reaction products.

Supporting information for this article is available on the WWW under http://www.angewandte.org or from the author.

 © 2004 Wiley-VCH Verlag GmbH & Co. KGaA, Weinheim DOI: 10.1002/anie.200352539



Scheme 1. Retrosynthesis of the protected Lewis X pentasaccharide **1**, Lewis Y hexasaccharide **2**, and Le^y–Le^x nonasaccharide **3** indicates monosaccharide building blocks **4**–**8**. Bn = benzyl, Bu = butyl, Fmoc = 9-fluorenylmethoxycarbonyl, Lev = levulinoyl, Piv = pivaloyl, TCA = trichloroacetamide.



Scheme 2. Automated oligosaccharide synthesis with glycosyl phosphates. Initial glycosylation of resin-bound acceptor **9** produces a coupling product that may be subsequently deprotected. Iteration of coupling and deprotection cycles with phosphate donors **4**–**8** followed by cleavage of the resin-bound oligosaccharides and purification gives **1**–**3**.

The internal double bond remains a functional handle for further chemistry[21] and can be cross-linked to a variety of olefins by metathesis.

To accommodate real-time monitoring and further increase coupling and deprotection efficiency, new coupling cycles were devised for use on the automated oligosaccharide synthesizer (Table 1). Activation of the phosphate donors was conducted at −15 °C with a solution of TMSOTf. Two sets of deprotection conditions were programmed to effect removal of the Fmoc and levulinoyl ester groups. Fmoc cleavage was achieved by three exposures to piperidine (20 % in DMF). Following each exposure, the solution from the reaction vessel was collected for UV analysis; this enabled determi-

Table 1: General cycle used with glycosyl phosphates for the construction of **1**–**3**.[a]

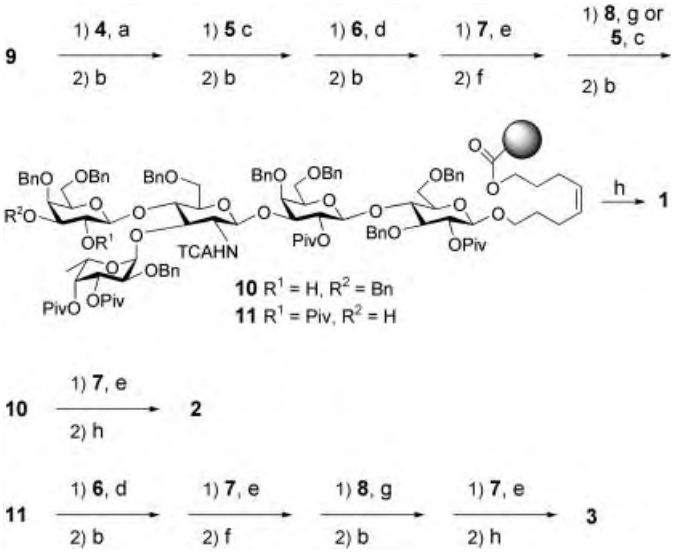
Step	Function	Reagent	*t* [min]
1	coupling	donor (5 equiv), TMSOTf (5 equiv)	21
2	washing	dichloromethane	9
3	coupling	donor (5 equiv), TMSOTf (5 equiv)	21
4	washing	DMF	9
5	deprotection	3 × piperidine (175 equiv) in DMF or 5 × hydrazine (10 equiv) in DMF	34 or 80
6	washing	DMF	9
7	washing	0.2 M acetic acid in tetrahydrofuran	9
8	washing	tetrahydrofuran	9
9	washing	dichloromethane	9

[a] TMSOTf = trimethylsilyl trifluoromethanesulfonate, DMF = *N*,*N*-dimethylformamide.

 © 2004 Wiley-VCH Verlag GmbH & Co. KGaA, Weinheim

nation of the amount of Fmoc-protected oligomer bound to the solid support at each step. The efficiency of the coupling and Fmoc-removal steps together was resolved qualitatively by using this data, thus allowing termination or correction of syntheses that indicated unproductive coupling steps. Removal of the C4 levulinate group from the glucosamine residue of a resin-bound trisaccharide initially proved to be difficult and required modification of the initial conditions to improve the deprotection efficiencies. The levulinoyl group was removed by five washes with a solution of hydrazine (10% in DMF). A series of washing steps was conducted before and after each deprotection to swell the resin or purge any remaining basic residues in preparation for the next glycosylation cycle.

Protected Lewis X pentasaccharide **1** was constructed in just 12 hours[22] (Scheme 3) by utilizing the reported coupling



Scheme 3. Automated synthesis of pentasaccharide **1**, hexasaccharide **2**, and nonasaccharide **3** on the 25-mmol scale, that is, with 25 mmol of resin (45 mg, 0.56 mmol g^{-1} loading) for each synthesis. a) Donor **4** (5 equiv), TMSOTf (5 equiv), repeated 2 times for 15 min each; b) 20% piperidine in DMF (2.2 mL), repeated 3 times for 10 min each; c) donor **5** (5 equiv), TMSOTf (5 equiv), repeated 2 times for 15 min; d) donor **6** (3.5 equiv), TMSOTf (3.5 equiv), repeated 3 times for 15 min each; e) donor **7** (5 equiv), TMSOTf (5 equiv), repeated 2 times for 15 min each; f) 10% N_2H_4 in DMF (2.5 mL), repeated 5 times for 15 min each; g) donor **8** (5 equiv), TMSOTf (5 equiv), repeated 2 times for 15 min each; h) NaOMe (10 equiv) in $MeOH/CH_2Cl_2$ (1:4), repeated 4 times for 90 min each.

cycles (Table 1). Initial glycosylation of linker **9** with glucose monomer **4** was followed by removal of the Fmoc group and iterative addition of monomers **5**–**8** to form the resin-bound pentasaccharide **10**. Cleavage from the support was achieved by repeated treatment with a solution of sodium methoxide over a period of six hours. Pentasaccharide **1** was isolated in 12.6% yield after HPLC purification.

Following our success in synthesizing Lewis X, the reaction sequence was modified to include a coupling cycle for the addition of a fucose residue to the terminal galactose (Scheme 3). In this manner, protected Lewis Y hexasaccharide **2** was synthesized in 14 hours with a yield of 9.9%. The assembly of pentamer **1** and hexamer **2** not only provided access to biologically relevant oligosaccharides but also demonstrated the preparation of important portions of the protected Le^y–Le^x nonasaccharide **3**.

The first four monosaccharides of **3** were installed in an identical fashion to the assembly of the Lewis X hexasaccharide **1**. Galactose building block **5** enabled the formation of the additional glucosamine-β(1→3)-galactose linkage. The assembly of **3** (Scheme 3) was completed by addition of glucosamine **6** followed by the final three residues of the Lewis Y hexamer. The solid-phase synthesis of nonasaccharide **3** was finished after 23 hours; cleavage from the solid support and HPLC purification produced **3** as the major product in 6.5% yield.

Two technical advances provided the foundation for rapid access to these complex oligosaccharides of biological importance: monitoring of the monosaccharide installation and a novel linker system. Fmoc analysis proved instrumental in the development of the coupling cycles for all syntheses. Unproductive steps were easily identified and glycosylations or deprotection conditions were modified accordingly to develop successful coupling cycles. Facile removal of the oligosaccharide from the resin by using a base-labile linker enabled swift analysis of the final products. The fully protected Lewis X and Lewis Y oligosaccharides and the Le^y–Le^x dimer were all produced in overall yields comparable to or better than previous solution-phase syntheses and in a fraction of the time previously required. Each of these syntheses was completed without initial solution-phase exploration of the synthetic route; monomer reactivity and electronic compatibility with the generated acceptors was tested solely during the course of the automated solid-phase assembly.

Automation of oligosaccharide assembly has the potential to revolutionize the biological understanding of complex oligosaccharides as nonspecialists gain access to a variety of structures. Automated assembly of the Le^y–Le^x tumor marker and the Lewis X and Lewis Y blood group antigens by a stepwise monosaccharide approach serves as a first example of our ability to make a host of structures of biological significance. The adaptation of coupling cycles to include Fmoc protection and the introduction of linker strategies to enable base cleavage bring automated methods of oligosaccharide synthesis a step closer to the existing protocols for peptide synthesis. Additional research to expand the diversity of structures accessible through automation, to increase overall yields and to decrease assembly times is on-going.

Received: August 4, 2003
Revised: November 3, 2003 [Z52539]

Keywords: automation · carbohydrates · Lewis antigens · oligosaccharides · synthetic methods

[1] S. Hakomori, Y. Zhang, *Chem. Biol.* **1997**, *4*, 97.
[2] E. E. Simanek, G. J. McGarvey, J. A. Jablonowski, C. H. Wong, *Chem. Rev.* **1998**, *98*, 833.

 © 2004 Wiley-VCH Verlag GmbH & Co. KGaA, Weinheim

[3] K. A. Karlsson, *Curr. Opin. Struct. Biol.* **1995**, *5*, 622.
[4] M. Chmiela, T. Wadstrom, H. Folkesson, I. P. Malecka, E. Czkwianianc, T. Rechcinski, W. Rudnicka, *Immunol. Lett.* **1998**, *61*, 119.
[5] G. Ragupathi, P. P. Deshpande, D. M. Coltart, H. M. Kim, L. J. Williams, S. J. Danishefsky, P. O. Livingston, *Int. J. Cancer* **2002**, *99*, 207.
[6] For a recent review on glycosphingolipid synthesis, see: Y. D. Vankar, R. R. Schmidt, *Chem. Soc. Rev.* **2000**, *29*, 201.
[7] For a recent review on the synthesis of glycopeptide antigens, see: C. Brocke, H. Kunz, *Bioorg. Med. Chem.* **2002**, *10*, 3085.
[8] K.-K. T. Mong, C.-H. Wong, *Angew. Chem.* **2002**, *114*, 4261 – 4264; *Angew. Chem. Int. Ed.* **2002**, *41*, 4087.
[9] K. R. Love, R. B. Andrade, P. H. Seeberger, *J. Org. Chem.* **2001**, *66*, 8165.
[10] L. Lay, L. Manzoni, R. R. Schmidt, *Carbohydr. Res.* **1998**, *310*, 157.
[11] M. R. E. Aly, E. S. I. Ibrahim, E. S. H. El Ashry, R. R. Schmidt, *Carbohydr. Res.* **1999**, *316*, 121.
[12] T. Zhu, G. J. Boons, *Chem. Eur. J.* **2001**, *7*, 2382.
[13] C. S. Zheng, P. H. Seeberger, S. J. Danishefsky, *Angew. Chem.* **1998**, *110*, 831 – 834; *Angew. Chem. Int. Ed.* **1998**, *37*, 786.
[14] G. Hummel, R. R. Schmidt, *Tetrahedron Lett.* **1997**, *38*, 1173.
[15] P. P. Deshpande, S. J. Danishefsky, *Nature* **1997**, *387*, 164.
[16] O. J. Plante, E. R. Palmacci, P. H. Seeberger, *Science* **2001**, *291*, 1523.
[17] O. J. Plante, E. R. Palmacci, R. B. Andrade, P. H. Seeberger, *J. Am. Chem. Soc.* **2001**, *123*, 9545.
[18] G. Fields, Z. Tian, G. Barany in *Synthetic Peptides* (Ed.: G. Grant), W. H. Freeman, New York, **1992**.
[19] L. A. Carpino, G. Y. Han, *J. Org. Chem.* **1972**, *37*, 3404.
[20] S. Manabe, Y. Ito, *J. Am. Chem. Soc.* **2002**, *124*, 12638.
[21] R. B. Andrade, O. J. Plante, L. G. Melean, P. H. Seeberger, *Org. Lett.* **1999**, *1*, 1811.
[22] The total time given for the construction of each Lewis oligosaccharide does not include the time required for the synthesis of each monomer building block. While this time cannot be neglected, it should be noted that monomers may be prepared on a large scale and are generally useful in the synthesis of many carbohydrate structures.

 © 2004 Wiley-VCH Verlag GmbH & Co. KGaA, Weinheim

Conformational Analysis

The Shape of Neutral Valine**

*Alberto Lesarri, Emilio J. Cocinero, Juan C. López, and José L. Alonso**

Nowadays there is growing interest in the study of biomolecules under isolation conditions in the gas phase. Although the gas phase represents far from in situ conditions of the condensed medium in which biological reactions take place, important intramolecular properties of bare molecules are manipulated by the environment and it is difficult to distinguish in condensed phases which properties are intrinsically intramolecular.[1] Solid amino acids exhibit a bipolar zwitterionic structure[2] ($^{+}NH_3CH(R)COO^{-}$) far from that of the neutral structure present in the polypeptide chain as a result of intermolecular interactions. Therefore, the investigation of the neutral structure of amino acids must be conducted in the gas phase. The problem arises from the fact that most amino acids have high melting points and extremely low vapor pressures and quickly decompose under the classical heating methods of vaporization. Thus, only a limited number of studies on amino acids have been carried out in the gas phase.[1a–b] Relevant structural aspects concerning these building blocks of life are as yet unknown.

The amino acids have many possible degrees of freedom which result in a corrugated potential energy surface with many conformational minima, and the population can be spread over more than one minimum. Their conformational preferences are controlled by a delicate balance between the covalent forces and the noncovalent interactions, mainly intramolecular hydrogen bonding. The use of the collisionless environment of a supersonic jet expansion[3] constituted a major step forward in the isolation and detection of the existing conformers in the gas phase. The supersonic cooling quenches the population into the zero-point levels of each of the individual conformers if the potential-energy barriers separating them are sufficiently high. Thus, although the molecules are rotationally and vibrationally cooled, their conformational distribution is not necessarily so. Hence, conformers can be independently detected in the supersonic expansion and their individual structures can be obtained.

[*] Prof. Dr. A. Lesarri, E. J. Cocinero, Prof. Dr. J. C. López, Prof. Dr. J. L. Alonso
Grupo de Espectroscopía Molecular
Departamento de Química Física
Facultad de Ciencias, Universidad de Valladolid
Prado de la Magdalena s/n, E-47005 Valladolid (Spain)
Fax: (+34) 983-423204
E-mail: jlalonso@qf.uva.es

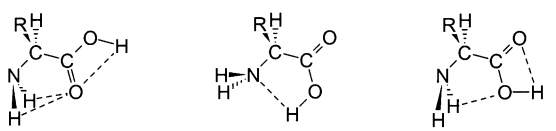
[**] We would like to thank the Ministerio de Ciencia y Tecnología (grant BQU2000-0869), the Junta de Castilla y León (grants VA017/01 and VA087/03), and the Fundación Ramón Areces for financial support.

Supporting information for this article is available on the WWW under http://www.angewandte.org or from the author.

 DOI: 10.1002/anie.200352543 © 2004 Wiley-VCH Verlag GmbH & Co. KGaA, Weinheim

Two experimental approaches are mainly being used in the spectroscopic studies of amino acids and biological molecules in the gas phase.[1] Jet-cooled electronic spectroscopy (laser-induced fluorescence (LIF),[4,5] resonant two-photon ionization spectroscopy[6,7] (R2PI), and UV/UV or UV/IR "hole-burning"[8,9] double-resonance methods) has been applied to the three aromatic natural amino acids of phenylalanine,[4,8] tyrosine,[4,7] and tryptophan[5,6,9] since strong UV chromophoric absorptions facilitate the detection of the electronic spectrum corresponding to each conformer. Another experimental approach is based on microwave spectroscopy. Rotational studies of supersonically cooled amino acids provide detailed structural information for each of the individual conformations that are present in significant populations in the adiabatic expansion. Thermal heating has only enabled the study of the aliphatic natural amino acids glycine[10] (m.p. 240 °C) and alanine[11] (m.p. 315 °C), either in static samples[10a–c] or in supersonic jets.[10d–f,11] Laser-ablation and -desorption techniques[12] constitute an alternative way to overcome the problem caused by the low vapor pressures of the amino acids. Since the first experiment was carried out by Levy and co-workers,[13] this method of vaporization has been applied successfully in combination with laser spectroscopy techniques[14] for the study of neutral molecules of biological interest. Suenram and co-workers[10d] reported the first trial of the use of a laser ablation device in the analysis of the rotational spectrum of glycine in the microwave region. No improvement was observed over that obtained with the usual heating method. We have recently developed a new instrument based on a laser ablation system in combination with Fourier transform microwave spectroscopy in a supersonic jet (laser-ablation molecular-beam Fourier transform microwave, LA-MB-FTMW). This system has been successfully applied to the structural study of the natural amino acid proline (m.p. 228 °C), and two conformers were observed in the supersonic jet.[15]

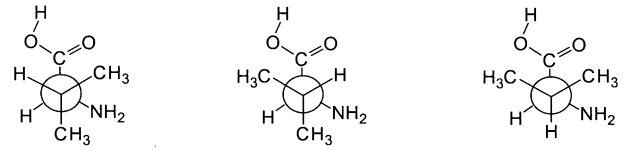
Valine (m.p. 295–300 °C) is an aliphatic natural α-amino acid ($NH_2CH(R)COOH$) with a lateral isopropyl chain (R = $CH(CH_3)_2$). Like glycine[10] (R = H) and alanine[11] (R = CH_3), the conformational behavior of valine should reflect the stabilizing effects from the *cis*-carboxylic functional group and the potential formation of the three intramolecular hydrogen bonds shown in Scheme 1. Configuration **I** is stabilized by a bifurcated amine-to-carbonyl (N–H···O=C) hydrogen bond, while configuration **II** exhibits an intramolecular hydrogen bond between the hydrogen atom of the hydroxy group and the lone pair of electrons on the nitrogen atom (N···H–O). A third plausible form **III** exhibits an intramolecular hydrogen bond between the amine group and the oxygen atom of the hydroxy group (N–H···O–H). Configurations **I** and **II** have been observed by rotational spectroscopy in glycine[10] and alanine,[11] with configuration **I** being the most stable one.



I (N-H···O=C and *cis*-COOH) **II** (N···H-O) **III** (N-H···O-H and *cis*-COOH)

Scheme 1. Intramolecular hydrogen bonds and α-amino acid backbone configurations.

Additionally, the presence of a bulky lateral isopropyl group in valine could generate much greater steric demands compared to the methyl group of alanine, which could affect the conformation of the amino acid backbone of the molecule. Three unstrained staggered orientations of the isopropyl side chain "a", "b", and "c" (Scheme 2) can be considered for each of the three configurations above. Ab initio molecular orbital calculations[16] predict different energies for for the side-chain orientations.



Conformer **Ia** Conformer **Ib** Conformer **Ic**

Scheme 2. Possible conformations for configuration **I** of valine.

No previous experimental studies of valine in the gas phase have been reported. The application of our LA-MB-FTMW technique to valine will provide the first information on the conformation and structure of the neutral form of this natural amino acid. The results will help to understand how the intramolecular interactions govern the conformational behavior.

The experimental spectroscopic searches were initially guided by simple structural models and theoretical predictions. We focused our attention on the previously predicted nine lowest energy conformers[16] (Figure 1) and ab initio calculations were conducted using second-order Møller–Plesset perturbation theory (MP2) with a standard 6-311++G(d,p) basis set[17] to predict values of relevant molecular properties such as rotational constants, the ^{14}N nuclear quadrupole coupling parameters, and the components of the electric dipole moment (Table 1). After long scans around the regions where the most intense transitions were predicted, a set of R-branch μ_a-type transitions of a near-prolate asymmetric rotamer were readily assigned. The experimental measurements were completed with R-branch μ_b-type transitions, but no μ_c-type transitions were observed. In addition to the Doppler splitting (see Experimental Section), all the transitions exhibited ^{14}N nuclear quadrupole hyperfine structure (Figure 2), thus confirming the presence of a single nitrogen atom. The measured rotational frequencies were fitted[18] to a Hamiltonian given by $H_R^{(A)} + H_Q$, where $H_R^{(A)}$ represents the Watson *A*-reduced semirigid rotor Hamiltonian[19] and H_Q is a nuclear quadrupole coupling interaction term,[20] to give the rotational parameters of Table 2. At first glance, the predicted rotational constants of Table 1 indicated the presence of conformer **IIa** in the supersonic expansion. However, a definitive argument came from the excellent

 © 2004 Wiley-VCH Verlag GmbH & Co. KGaA, Weinheim

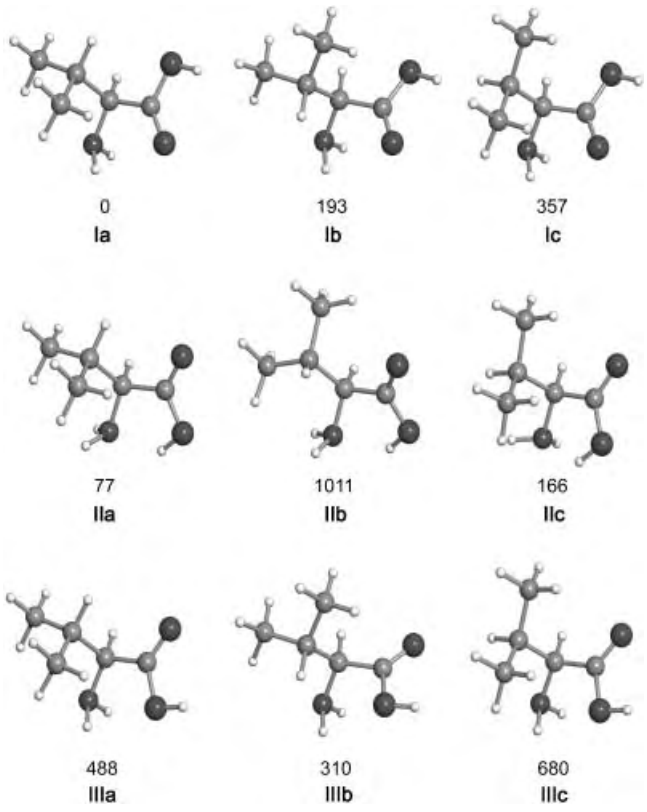


Figure 1. Conformers of valine and predicted relative energies in cm^{-1}.

agreement between the experimental and predicted values of the nuclear quadrupole coupling constants χ_{aa}, χ_{bb}, and χ_{cc} for conformer **IIa** in Tables 1 and 2. These parameters depend on the electronic environment around the amine nitrogen atom and are very sensitive to molecular conformation,[21] thus it is a precious tool for discriminating between the different conformers. The microwave power required for optimum polarization of the μ_a-and μ_b-type transitions is also consistent with the predicted values of the electric dipole moments for conformer **IIa**. The isotopic frequency shifts for the ^{15}N isotopomer were predicted on the basis of the assignment of the parent species. Transitions were found near the predicted values for an enriched sample, and they were readily recognized from the absence of nuclear quadrupole coupling hyperfine structure associated with a ^{15}N nucleus (see Figure 2). This is a further corroboration of the existence of conformer **IIa** in gaseous valine.

Wide frequency searches for transitions belonging to the other plausible conformers were carried out using the ^{15}N-enriched sample because the absence of hyperfine structure on the nuclear quadrupole coupling produces an enhancement in the spectrum signal. After rejecting the lines corresponding to conformer **IIa**, weak R-branch transitions of μ_a, μ_b, and μ_c types of a second rotamer were identified. After the rotational spectrum of the ^{15}N species had been analyzed, the weaker transitions of the ^{14}N species, split by nuclear quadrupole coupling effects (Figure 3), were also analyzed. Rotational parameters for the parent and ^{15}N species shown in Table 2 were obtained following the same procedure described for the conformer **IIa**. The notable agreement between the experimental rotational and quadrupole coupling constants in Table 2 and those predicted for the **Ia** conformer in Table 1 reveals that this newly detected conformer undoubtedly corresponds to the **Ia** conformer. The intensities of the different types of rotational transitions are in accordance with the predicted magnitudes of the electric dipole moment components. No transitions attributable to other plausible conformers remained in the spectrum. All the measured frequencies for conformers **Ia** and **IIa** are given in the Supporting Information.

Some information on the relative stability of the two observed conformers of neutral valine can be obtained from a comparison of the intensities of the rotational transitions.[22] The fact that the μ_b-type transitions are of comparable intensity in both conformers while the predicted μ_b values are about three times larger in conformer **IIa** clearly indicates that conformer **Ia** corresponds to the global minimum. The energy difference between conformers **Ia** and **IIa** can be estimated to be about 100 cm^{-1}.

Table 1: Ab initio molecular properties of valine.

	MP2/6-311++G(d,p)								
	Ia	**Ib**	**Ic**	**IIa**	**IIb**	**IIc**	**IIIa**	**IIIb**	**IIIc**
relative energy [kJ mol^{-1}]	0.0	2.3	4.3	0.9	12.1	2.0	5.8	3.7	8.1
[cm^{-1}]	(0.0)	(193)	(357)	(77)	(1011)	(166)	(488)	(310)	(680)
	rotational constants								
A [MHz]	2939	2800	2380	3026	3000	2454	2977	2828	2385
B [MHz]	1442	1586	1806	1488	1584	1811	1430	1562	1787
C [MHz]	1338	1240	1436	1274	1107	1450	1336	1260	1449
	^{14}N nuclear quadrupole coupling parameters								
χ_{aa} [MHz]	−4.58	−4.15	−2.99	−3.75	−3.97	0.17	−4.42	−4.03	−2.30
χ_{bb} [MHz]	2.89	2.55	2.55	2.10	2.40	2.62	2.76	2.35	1.86
χ_{cc} [MHz]	1.69	1.60	0.44	1.65	1.57	−2.78	1.66	1.68	0.44
	electric dipole moment								
μ_a [D][a]	0.4	0.5	0.5	4.3	3.6	2.4	0.6	0.2	0.5
μ_b [D]	1.0	0.7	1.1	3.2	3.5	4.2	1.0	0.3	0.8
μ_c [D]	0.6	0.8	0.5	0.0	0.5	1.9	0.8	1.4	1.0
μ_T [D]	1.3	1.2	1.3	5.3	5.1	5.2	1.5	1.5	1.4

[a] 1 D = ca. 3.3356×10^{-30} C m.

 © 2004 Wiley-VCH Verlag GmbH & Co. KGaA, Weinheim

Table 2: Rotational parameters of valine.

	Conformer **II a**		Conformer **I a**	
	parent	[^{15}N]valine	parent	[^{15}N]valine
A [MHz][a]	3038.25151 (41)[f]	2983.53453 (65)	2944.58890 (42)	2892.03823 (19)
B [MHz]	1476.84596 (13)	1476.73942 (20)	1445.21281 (27)	1444.32066 (26)
C [MHz]	1261.22035 (13)	1251.74423 (19)	1326.37063 (22)	1315.45400 (20)
Δ_J [kHz][b]	0.2090 (20)	0.2132 (31)	0.2248 (42)	0.2185 (40)
Δ_{JK} [kHz]	0.408 (15)	0.387 (14)	0.562 (26)	0.5129 (72)
Δ_K [kHz]			−0.118 (30)	[−0.118]
δ_J [kHz]			0.0251 (42)	0.0182 (31)
δ_K [kHz]	0.533 (43)	[0.533][g]		
χ_{aa} [MHz][c]	−3.5387 (28)		−4.2053 (40)	
χ_{bb} [MHz]	1.9203 (46)		2.7421 (41)	
χ_{cc} [MHz]	1.6183 (46)		1.4632 (41)	
σ [kHz][d]	1.7	1.8	2.3	1.7
N[e]	63	17	59	28

[a] A, B, and C represent the rotational constants. [b] Δ_J, Δ_{JK}, Δ_K, δ_J, and δ_K are the quartic centrifugal distortion constants. [c] χ_{aa}, χ_{bb}, and χ_{cc} are ^{14}N nuclear quadrupole coupling parameters. [d] rms deviation of the fit. [e] Number of fitted transitions. [f] Standard error in parenthesis in units of the last digit. [g] Parameters in square brackets were kept fixed in the fit.

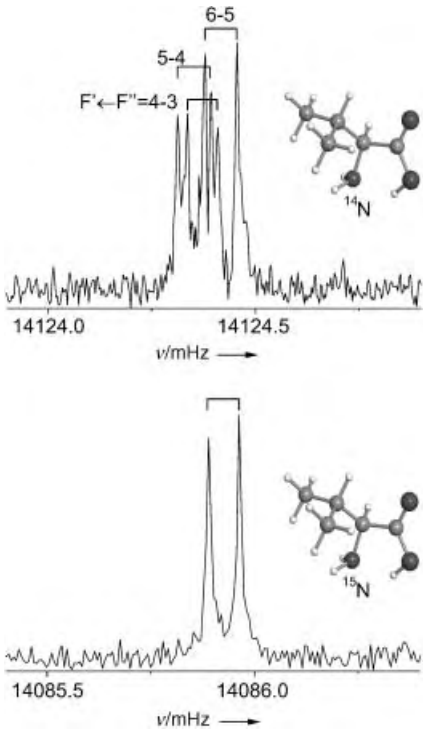


Figure 2. The $5_{1,4}$–$4_{1,3}$ rotational transition of conformer **II a** for the parent ^{14}N (upper trace) and the ^{15}N isotopomer (lower trace) of valine. The hyperfine components of the ^{14}N isotopomer ($F'\leftarrow F''$) are labeled by the quantum numbers $F = I + J$. Each component appears as a doublet (⊓) as a result of the Doppler effect (see Experimental Section).

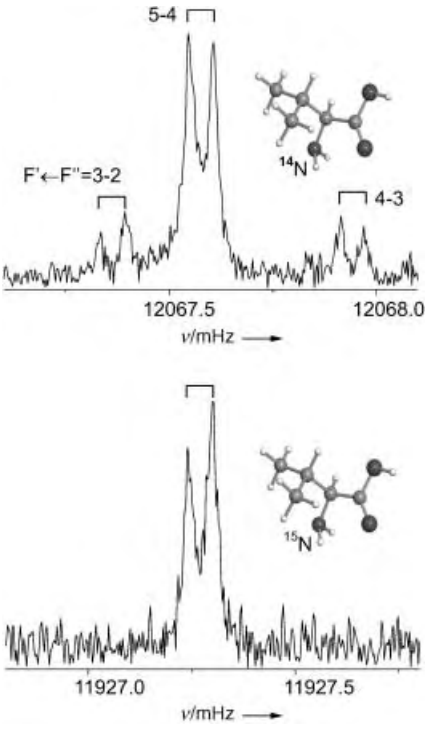


Figure 3. The $4_{1,4}$–$3_{0,3}$ rotational transition of conformer **I a** for the parent ^{14}N (upper trace) and the ^{15}N isotopomer (lower trace) of valine. The hyperfine components of the ^{14}N isotopomer ($F'\leftarrow F''$) are labeled by the quantum numbers $F = I + J$. Each component appears as a doublet (⊓) as a result of the Doppler effect (see Experimental Section).

The conformational behavior of valine is in close agreement with that observed for the smaller aliphatic natural α-amino acids glycine[10] and alanine.[11] Affixing an isopropyl side chain to the α-amino acid backbone does not alter the relative energies of the lowest energy conformers. This observation indicates that the relative stabilities of the amino acid skeleton are controlled by intramolecular hydrogen bonding. The bifurcated amine-to-carbonyl hydrogen bond (N–H···O=C) gives rise to the most stable conformer in the three amino acids. This fact has been attributed to the cooperative stabilizing effect caused by the *cis* arrangement of the carboxylic acid.[23] Although the nitrogen-to-hydroxy (N···H–O) intramolecular hydrogen bond is predicted to have a larger stabilization effect,[23b] it gives rise to the second

 © 2004 Wiley-VCH Verlag GmbH & Co. KGaA, Weinheim

stable conformer since the carboxylic acid group is forced to adopt a *trans* arrangement. The preferred orientation for the isopropyl side chain is "a" in both conformers, which seems to minimize the steric strains in the molecule.

The absence of some of the conformational species shown in Figure 1 which are predicted to fall in the group of lowest energy deserves some comments. This problem of "missing conformers"[24] is associated with the fact that some conformers may relax to the most stable forms in the supersonic expansion if the barrier to interconversion is low enough. It is accepted that this event takes place by collisions with the noble carrier gas in the adiabatic expansion. This phenomenon has been observed in systems involving only one degree of freedom such as torsional isomerism[25] and axial/equatorial relaxation in hydrogen-bonded complexes[26] when energy barriers are less than about 400 cm^{-1}. Studies on systems with multiple degrees of freedom have proposed barrier heights below 1000 cm^{-1}.[27] In this context, Godfrey et al.[24] estimated barriers below 400 cm^{-1} for the interconversion between conformer **III** and conformer **I** in glycine[10] and alanine,[11] and proposed that conformational relaxation was the origin of the absence of conformer **III** in the supersonic expansion. The same can be argued for the absence of the type **III** conformations in valine. Relaxation of **Ib** or **Ic** to **Ia** and **IIb** or **IIc** to **IIa** by a rotation around the $^{\beta}C-^{\alpha}C$ bond, which can also take place in the side chain of valine, may justify the observation of only the **Ia** and **IIa** forms. It must be taken into consideration that the observations in the expansion reflect both the relative energies of the conformers and the barriers hindering the interconversion between them.[27a] In any case, the two observed conformers of valine are the most stable forms, even if relaxation takes place.

The present work consolidates the use of the LA-MB-FTMW technique as a very important tool for the generation of isolated neutral amino acids, thus making possible the analysis of their rotational structure. The interpretation of the experimental data, coupled with high-level ab initio computations, is making it possible to begin the determination of the conformational landscapes of relevant biological molecules. Valine represents an intermediate step for the future studies of more complicated amino acids.

Experimental Section

Commercial samples of DL-valine (99%, Aldrich) and ^{15}N L-valine (98%, Cambridge Isotope Labs.) were used in this study. The laser-ablation molecular-beam Fourier transform microwave spectrometer, operating in the frequency region 6–18 GHz, has been briefly described previously.[15] Pressed sample rods of 6-mm diameter and 1–2-cm long were vaporized with the green line (532 nm) of a Nd:YAG laser, with energy pulses of ca. 50 mJ. Neon at stagnation pressures of about 5 bar was used as the carrier gas (gas pulses of 0.4–0.7 ms), with polarization pulses of 0.2–0.5 μs (1–300 mW). The delays between the gas, laser ablation, and microwave pulses were optimized for maximum signals. The free-induction decay in the time-domain signal was recorded in 40 ns intervals, which is equivalent to a frequency resolution of ca. 3 kHz. Frequency accuracy is better than 5 kHz. Each rotational transition is split by the Doppler effect because of the coaxial orientation of the supersonic jet and resonator axes, so the rotational frequencies are taken as the arithmetic mean of the two components of the Doppler doublet.

Received: August 1, 2003
Revised: October 10, 2003 [Z52543]

Keywords: amino acids · conformational analysis · hydrogen bonds · rotational spectroscopy · structure elucidation

[1] a) E. G. Robertson, J. P. Simons, *Phys. Chem. Chem. Phys.* **2001**, *3*, 1; b) R. Weinkauf, J.-P. Schermann, M. S. de Vries, K. Kleinermans, *Eur. Phys. J. D* **2002**, *20*, 309; c) T. S. Zwier, *J. Phys. Chem. A* **2001**, *105*, 8827.
[2] M. F. Jarrold, *Annu. Rev. Phys. Chem.* **2000**, *51*, 179.
[3] D. H. Levy, *Annu. Rev. Phys. Chem.* **1980**, *31*, 197.
[4] S. J. Martinez III, J. C. Alfano, D. H. Levy, *J. Mol. Spectrosc.* **1992**, *156*, 421.
[5] T. R. Rizzo, Y. D. Park, D. H. Levy, *J. Chem. Phys.* **1986**, *85*, 6945.
[6] a) T. R. Rizzo, Y. D. Park, L. A. Peteanu, D. H. Levy, *J. Chem. Phys.* **1985**, *83*, 4819; b) T. R. Rizzo, Y. D. Park, L. A. Peteanu, D. H. Levy, *J. Chem. Phys.* **1986**, *84*, 2534.
[7] a) L. I. Grace, R. Cohen, T. M. Dunn, D. M. Lubman, M. S. de Vries, *J. Mol. Spectrosc.* **2002**, *215*, 204; b) R. Cohen, B. Brauer, E. Nir, L. Grace, M. S. De Vries, *J. Phys. Chem. A* **2000**, *104*, 6351.
[8] L. C. Snoek, E. G. Robertson, R. T. Kroemer, J. P. Simons, *Chem. Phys. Lett.* **2000**, *321*, 49.
[9] a) F. Piuzzi, L. Dimicoli, M. Mons, B. Tardivel, Q. Zhao, *Chem. Phys. Lett.* **2000**, *320*, 282; b) L. C. Snoek, R. T. Kroener, M. R. Hockridge, J. P. Simons, *Phys. Chem. Chem. Phys.* **2001**, *3*, 1819.
[10] a) R. D. Brown, P. D. Godfrey, J. W. V. Storey, M. P. Bassez, *J. Chem. Soc. Chem. Commun.* **1978**, *547*; b) R. D. Suenram, F. J. Lovas, *J. Mol. Spectrosc.* **1978**, *72*, 372; c) R. D. Suenram, F. J. Lovas, *J. Am. Chem. Soc.* **1980**, *102*, 7180; d) F. J. Lovas, Y. Kawashima, J.-U. Grabow, R. D. Suenram, G. T. Fraser, E. Hirota, *Astrophys. J.* **1995**, *455*, L201; e) P. D. Godfrey, R. D. Brown, *J. Am. Chem. Soc.* **1995**, *117*, 2019; f) S. J. McGlone, P. S. Elmes, R. D. Brown, P. D. Godfrey, *J. Mol. Struct.* **1999**, *485*, 225.
[11] P. D. Godfrey, S. Firth, L. D. Hatherley, R. D. Brown, A. P. Pierlot, *J. Am. Chem. Soc.* **1993**, *115*, 9687.
[12] a) R. J. Levis, *Annu. Rev. Phys. Chem.* **1994**, *45*, 483; b) *Chem. Rev.* **2002**, *103* (special issue).
[13] J. R. Cable, M. J. Tubergen, D. H. Levy, *J. Am. Chem. Soc.* **1988**, *110*, 7349.
[14] a) E. Nir, K. Kleinermanns, M. S. de Vries, *Nature* **2000**, *408*, 949;b) M. Mons, I. Dimicoli, F. Piuzzi, B. Tardivel, M. Elhanine, *J. Phys. Chem. A* **2002**, *106*, 5088.
[15] A. Lesarri, S. Mata, E. J. Cocinero, S. Blanco, J. C. López, J. L. Alonso, *Angew. Chem.* **2002**, *114*, 4867; *Angew. Chem. Int. Ed.* **2002**, *41*, 4673.
[16] a) L. Schäfer, S. Q. Kulp-Newton, K. Siam, V. J. Klimkowski, C. J. Van Alsenoy, *J. Mol. Struct.* **1990**, *209*, 373; b) S. Shirazian, S. Gronert, *J. Mol. Struct.* **1997**, *397*, 107; c) S. G. Stepanian, I. D. Reva, E. D. Radchenko, L. Adamowicz, *J. Phys. Chem. A* **1999**, *103*, 4404.
[17] Gaussian 98 (Revision A.7), M. J. Frisch, G. W. Trucks, H. B. Schlegel, G. E. Scuseria, M. A. Robb, J. R. Cheeseman, V. G. Zakrzewski, J. A. Montgomery, R. E. Stratmann, J. C. Burant, S. Dapprich, J. M. Millam, A. D. Daniels, K. N. Kudin, M. C. Strain, O. Farkas, J. Tomasi, V. Barone, M. Cossi, R. Cammi, B. Mennucci, C. Pomelli, C. Adamo, S. Clifford, J. Ochterski, G. A. Petersson, P. Y. Ayala, Q. Cui, K. Morokuma, D. K. Malick, A. D. Rabuck, K. Raghavachari, J. B. Foresman, J. Cioslowski, J. V. Ortiz, B. B. Stefanov, G. Liu, A. Liashenko, P. Piskorz, I. Komaromi, R. Gomperts, R. L. Martin, D. J. Fox, T. Keith, M. A.

 © 2004 Wiley-VCH Verlag GmbH & Co. KGaA, Weinheim

Al-Laham, C. Y. Peng, A. Nanayakkara, C. Gonzalez, M. Challacombe, P. M. W. Gill, B. G. Johnson, W. Chen, M. W. Wong, J. L. Andres, M. Head-Gordon, E. S. Replogle, J. A. Pople, Gaussian, Inc., Pittsburgh, PA, **1998**.
[18] H. M. Pickett, *J. Mol. Spectrosc.* **1991**, *148*, 371.
[19] J. K. Watson in *Vibrational Spectra and Structure*, *Vol. 6* (Ed.: J. R. Durig), Elsevier, Amsterdam, **1977**, p. 1.
[20] W. Gordy, R. L. Cook, *Microwave Molecular Spectra*, Wiley, New York, **1984**.
[21] J. C. López, A. de Luis, S. Blanco, A. Lesarri, J. L. Alonso, *J. Mol. Struct.* **2002**, *612*, 287.
[22] G. T. Fraser, R. D. Suenram, C. L. Lugez, *J. Phys. Chem. A* **2000**, *104*, 1141.
[23] a) C.-H. Hu, M. Shen, H. F. Schaefer III, *J. Am. Chem. Soc.* **1993**, *115*, 2923; b) A. G. Császár, *J. Phys. Chem.* **1996**, *100*, 3541; c) A. G. Császár, W. D. Allen, H. F. Schaefer III, *J. Chem. Phys.* **1998**, *108*, 9751.
[24] P. D. Godfrey, R. D. Brown, F. M. Rodgers, *J. Mol. Struct.* **1996**, *376*, 65.
[25] R. S. Ruoff, T. D. Klots, T. Emilson, H. S. Gutowski, *J. Chem. Phys.* **1990**, *93*, 3142.
[26] a) S. Antolínez, J. C. López, J. L. Alonso, *Angew. Chem.* **1999**, *111*, 1889; *Angew. Chem. Int. Ed.* **1999**, *38*, 1772; b) S. Antolínez, J. C. López, J. L. Alonso, *ChemPhysChem* **2001**, *2*, 114; c) M. E. Sanz, A. Lesarri, J. C. López, J. L. Alonso, *Angew. Chem.* **2001**, *113*, 961; *Angew. Chem. Int. Ed.* **2001**, *40*, 935; d) M. E. Sanz, J. C. Lopez, J. L. Alonso, *Chem. Eur. J.* **2002**, *8*, 4265.
[27] a) G. M. Florio, R. A. Christie, K. D. Jordan, T. S. Zwier, *J. Am. Chem. Soc.* **2002**, *124*, 10236; b) P. D. Godfrey, R. D. Brown, *J. Am. Chem. Soc.* **1998**, *120*, 10724.

 © 2004 Wiley-VCH Verlag GmbH & Co. KGaA, Weinheim

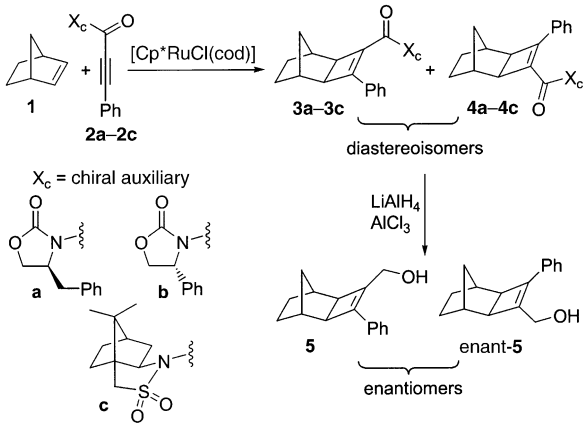
Asymmetric Cycloadditions

Asymmetric Induction in Ruthenium-Catalyzed [2+2] Cycloadditions between Bicyclic Alkenes and a Chiral Acetylenic Acyl Sultam**

*Karine Villeneuve and William Tam**

Cycloaddition reactions of unactivated alkenes, alkynes, and dienes usually require extreme reaction conditions, such as high temperature and high pressure, for the cycloadducts to be formed in good yields. Transition-metal catalysts provide new opportunities for highly selective cycloaddition reactions, as the complexation of the metal to an alkene, alkyne, or diene significantly modifies the reactivity of this moiety, thus opening up possibilities for enhanced reactivity and novel reactions.[1] One of the most important consequences of complexation to a transition metal is the temporary polarization and activation of an otherwise unreactive species. The rate enhancements observed in the presence of the metal catalyst, and the potential to carry out asymmetric transformations by the use of chiral ligands or chiral auxiliaries are among the most attractive features of this strategy.

Recent developments in transition-metal-catalyzed [2+2+1],[2] [4+2],[3] [5+2],[4] [4+4],[5] and [6+2][6] cycloadditions have provided efficient methods for the construction of five- to eight-membered rings. We and others have studied various aspects of transition-metal-catalyzed [2+2] cycloadditions between alkenes and alkynes for the synthesis of cyclobutene rings, including the development of novel catalysts, studies on the reactivity of the reaction partners, and investigations into regioselectivity with unsymmetrical substrates.[7–10] However, to the best of our knowledge, no asymmetric version of transition-metal-catalyzed [2+2] cycloadditions between alkenes and alkynes has been reported in the literature. Herein, we report our first results of studies on asymmetric induction in ruthenium-catalyzed [2+2] cycloadditions of bicyclic alkenes with alkynes that bear a chiral auxiliary (Scheme 1). The cycloaddition of a bicyclic alkene



Scheme 1. Ruthenium-catalyzed [2+2] cycloaddition of norbornene (**1**) with chiral alkynes.

with an alkyne could give rise to two stereoisomers (*exo* or *endo* cycloadducts). However, based on our previous studies on ruthenium-catalyzed [2+2] cycloadditions of bicylic alkenes with alkynes[10] we anticipated that only *exo* cycloadducts would be formed. The cycloaddition of norbornene (**1**) with a chiral alkyne **2** could result in the formation of two *exo* diastereoisomers **3** and **4**. Removal of the chiral auxiliary would provide **5** and its enantiomer.

We first prepared the chiral acetylenic acyl carbamates **2a** and **2b** and the chiral acetylenic acyl sultam **2c** from the oxazolidinones of Evans and the sultam of Oppolzer.[11b] These chiral alkynes showed a high level of asymmetric

[*] K. Villeneuve, Prof. Dr. W. Tam
Guelph-Waterloo Centre for Graduate Work in Chemistry and Biochemistry
Department of Chemistry and Biochemistry, University of Guelph
Guelph, Ontario N1G 2W1 (Canada)
Fax: (+1) 519-766-1499
E-mail: wtam@uoguelph.ca

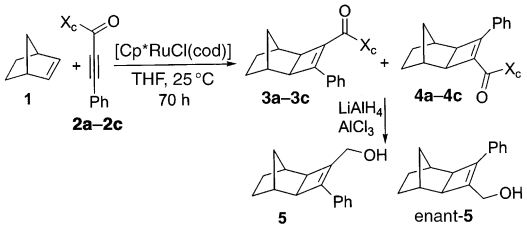
[**] This work was supported by NSERC (Canada) and Boehringer Ingelheim (Canada) Ltd. W.T. thanks Boehringer Ingelheim (Canada) Ltd. for a Young Investigator Award, and K.V. thanks NSERC and FCAR for postgraduate scholarships. We thank Professor France-Isabelle Auzanneau of our department for allowing us to use her HPLC system.

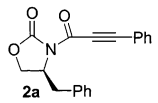
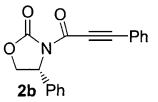
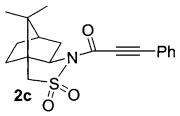
Supporting information for this article is available on the WWW under http://www.angewandte.org or from the author.

 © 2004 Wiley-VCH Verlag GmbH & Co. KGaA, Weinheim DOI: 10.1002/anie.200352555

induction in cobalt-mediated Pauson–Khand [2+2+1] cycloadditions.[11] The results of our ruthenium-catalyzed [2+2] cycloadditions of **2a–c** with **1** are shown in Table 1. As observed previously,[10] these cycloadditions were found to be

Table 1: Ruthenium-catalyzed [2+2] cycloadditions between **1** and alkynes with different chiral auxiliaries.[a]



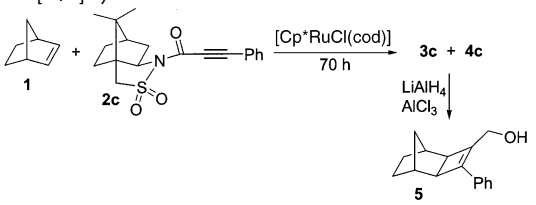
Entry	Alkyne	Yield[b] [%]	d.r.[c] (**3**/**4**)	*ee* (**5**)[d] [%]
1	 **2a**	97	1.3:1	nd[e]
2	 **2b**	80	1.3:1	nd[e]
3	 **2c**	94	131:1	98.5

[a] All reactions were carried out with 3 equivalents of **1** (with respect to the alkyne) and 5–10 mol% of [Cp*RuCl(cod)]. [b] Yield of isolated products (**3c+4c**). [c] The diastereomeric ratio was determined by NMR (400 MHz) or HPLC. [d] The *ee* value of **5** was determined by HPLC on a chiral phase (Chiralcel OJ-H column); see Supporting Information for details. [e] Not determined.

completely stereoselective for the *exo* cycloadducts, but high yielding only in the presence of excess norbornene (**1**; 3 equiv). Although the chiral alkynes **2a** and **2b**, which bear Evans oxazolidinones, gave a low level of asymmetric induction in the cycloadditions, the ruthenium-catalyzed [2+2] cycloadditions of **1** with the chiral acetylenic acyl sultam **2c** were found to be highly diastereoselective and to give the two diastereoisomers **3c** and **4c** in a 131:1 ratio. Upon removal of the recoverable chiral auxiliary (the camphorsultam of Oppolzer), compound **5** was formed with 98.5% *ee*. We believe that the exceptionally high level of asymmetric induction observed in the ruthenium-catalyzed [2+2] cycloadditions of **1** with **2c** (but not with the chiral acetylenic acyl carbamates **2a** and **2b**) may arise from coordination of the sulfone oxygen atom of the sultam with the ruthenium metal center.[12]

The effect of the temperature and the solvent on the asymmetric induction in the ruthenium-catalyzed [2+2] cycloadditions of **1** with **2c** was studied (Table 2). When the cycloadditions were carried out in THF, an increase in the temperature from 25 to 50°C led to a decrease in the diastereoselectivity from d.r. 131:1 to 64:1. No further decrease in the diastereoselectivity was observed when the

Table 2: Effect of the temperature and of the solvent in the ruthenium-catalyzed [2+2] cycloaddition of **1** with **2c**.[a]



Entry	Solvent[b]	*T* [°C]	Yield [%][c]	d.r. (**3c**/**4c**)[d]	*ee* (**5**) [%][e]
1	THF	25	95	131:1	98.5
2	THF	50	95	64:1	nd[f]
3	THF	80	99	64:1	nd[f]
4	THF/Et_3N (1:1)	25	95	114:1	98
5	DME	25	76	132:1	nd[f]
6	diglyme	25	90	126:1	nd[f]

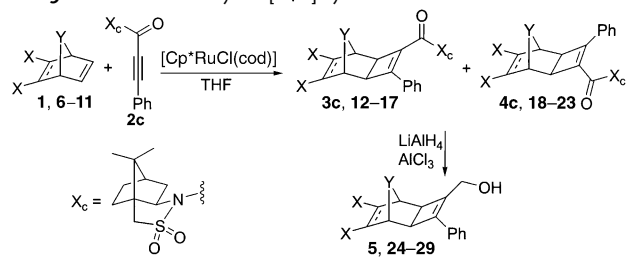
[a] All reactions were carried out with 3 equivalents of **1** (with respect to the alkyne) and 5–10 mol% of [Cp*RuCl(cod)]. [b] The use of other solvents, such as DMSO, DMF, toluene, hexanes, and 1,2-dichloroethane, led to very low yields. [c] Yield of isolated products (**3c+4c**). [d] The diastereomeric ratio was determined by HPLC. [e] The *ee* value of **5** was determined by HPLC on a chiral phase (Chiralcel OJ-H column; see Supporting Information for details). [f] Not determined.

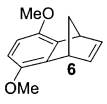
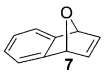
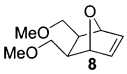
temperature was increased to 80°C (Table 2, entries 1–3). Ethereal solvents (THF, 1,2-dimethoxyethane (DME), and diglyme) were found to be the most effective in the cycloadditions in terms of the yields and levels of asymmetric induction observed. The use of other solvents, such as dimethyl sulfoxide (DMSO), dimethyl formamide (DMF), toluene, hexanes, and 1,2-dichloroethane, led to very low yields ($<20\%$).[10a]

To test the generality of the asymmetric induction in the ruthenium-catalyzed [2+2] cycloaddition, we studied the reactions of various bicyclic alkenes (**6–11**) with **2c** (Table 3; for detailed experimental procedures, compound characterization data, and HPLC traces, see Supporting Information). All the bicyclic alkenes were found to undergo completely stereoselective cycloaddition reactions to give only the *exo* cycloadducts. The cycloadditions of 2,3-dibromonorbornadiene (**10**) and 7-phenylnorbornadiene (**11**) were also completely regioselective (Table 3, entries 6 and 7) and only occurred at the less-hindered, less-substituted double bond. Similar to with norbornene (**1**) (Table 3, entry 1), both the yield and the diastereoselectivity observed in the cycloaddition of **6** with **2c** were very high (98% yield, d.r. 163:1; Table 3, entry 2). Removal of the chiral auxiliary provided compound **24** with 98.8% *ee*. This is the highest *ee* value we have observed in ruthenium-catalyzed [2+2] cycloadditions with **2c**. High levels of asymmetric induction were also observed with the 7-oxanorbornenes **7** and **8** (94 and 95% *ee* after removal of the chiral auxiliary), although the yields were only moderate (78% and 73%, respectively; Table 3, entries 3 and 4). The levels of asymmetric induction observed in the cycloadditions of norbornadiene (**9**) and its derivatives **10** and **11** were significantly lower (Table 3, entries 5–7) than those observed for **1** and its derivatives (usually $>94\%$ *ee*; Table 3, entries 1–4). Whereas **9** reacted with **2c** to give the diastereomeric cycloadducts with d.r. 8:1 at 25°C and d.r. 5:1

 © 2004 Wiley-VCH Verlag GmbH & Co. KGaA, Weinheim

Table 3: Ruthenium-catalyzed [2+2] cycloadditions of **2c** with alkenes.[a]



Entry	Alkene	T [°C]	t [h]	Yield[b] [%]	d.r.	ee[c] [%]
1	 **1**	25	70	94	131:1[d]	98.5
2	 **6**	25	70	98	163:1[e]	98.8
3	 **7**	25	70	78	33:1[f]	94
4	 **8**	25	168	73	35:1[f]	95
5	 **9**	25	168	27[g]	8:1[f]	75
		65	168	89	5:1[e]	67
6	 **10**	25	70	85	10:1[f]	83
7	 **11**	25	168	44[g]	24:1[f]	90

[a] All reactions were carried out with 3 equivalents of the alkene (with respect to the alkyne) and 5–10 mol% of [Cp*RuCl(cod)]. [b] Yield of isolated cycloadducts. [c] The *ee* values of **5** and **24**–**29** were determined by HPLC on a chiral phase (Chiralcel OJ-H column; see Supporting Information for details). [d] The diastereomeric ratio of the cycloadducts was determined by HPLC. [e] The diastereomeric ratio of the cycloadducts was determined indirectly from the *ee* value of the product obtained upon removal of the auxiliary. [f] The diastereomeric ratio of the cycloadducts was determined by ^{1}H NMR spectroscopy (400 MHz). [g] The cycloaddition did not proceed to completion and starting materials were recovered.

at 65 °C, 2,3-dibromonorbornadiene (**10**) and 7-phenylnorbornadiene (**11**) reacted with **2c** to provide the corresponding diastereomeric cycloadducts with d.r. 10:1 and 24:1, respectively.

In conclusion, we have demonstrated asymmetric induction in ruthenium-catalyzed [2+2] cycloadditions between alkenes and alkynes. The cycloadditions were found to be highly stereo- and regioselective, and excellent levels of asymmetric induction (up to 98.8% *ee* after removal of the recoverable chiral auxiliary) were observed. This method is a mild and simple procedure for the asymmetric construction of cyclobutene ring systems. Further investigations into the source of the asymmetric induction in the cycloadditions, the scope of the reaction, and the application of this method to the asymmetric synthesis of four-membered-ring-containing natural products are currently in progress in our laboratory.

Experimental Section

Typical procedure: A mixture of **1** (27.1 mg, 0.288 mmol), **2c** (30.6 mg, 0.089 mmol), and THF (0.4 mL) in an oven-dried vial was added through a cannula to an oven-dried screw-cap vial containing [Cp*RuCl(cod)] (weighed out from a dry box, 4.4 mg, 0.012 mmol; Cp* = 1,2,3,4,5-pentamethylcyclopentadiene) under nitrogen. The residue in the first vial was then dissolved in THF (0.1 mL) and added through a cannula to the reaction mixture. The reaction mixture was stirred in the dark at 25 °C for 70 h. The crude product was purified by column chromatography (EtOAc/hexanes 1:9) to give an inseparable mixture of the cycloadducts **3c** and **4c** (14.8 mg, 0.052 mmol, 95%, d.r. 131:1 (determined by HPLC)) as a white solid (m.p. 155–158 °C, hexanes/CH_2Cl_2). $R_f = 0.44$ (EtOAc/hexanes 3:7); HPLC (C-18 column, 1 mL min^{-1}, 20% acetonitrile/water, 254 nm): t_R (major diastereomer): 11.85 min, t_R (minor diastereomer): 8.59 min; IR (CH_2Cl_2): $\tilde{\nu} = 3054$ s, 2987 m, 2966 m, 2875 w, 1669 w, 1422 m, 1266 vs, 1167 w, 1059 cm^{-1} w; ^{1}H NMR ($CDCl_3$, 400 MHz, major diastereomer): $\delta = 7.84$–7.86 (m, 2H), 7.26–7.36 (m, 3H), 4.11 (m, 1H), 3.50 (d, $J = 13.6$ Hz, 1H), 3.43 (d, $J = 13.6$ Hz, 1H), 3.29 (br d, $J = 2.9$ Hz, 1H), 2.85 (br d, $J = 3.1$ Hz, 1H), 2.28 (br s, 1H), 2.19 (br s, 1H), 2.06–2.14 (m, 2H), 1.87–1.96 (m, 3H), 1.60–1.62 (m, 2H), 1.36–1.48 (m, 3H), 1.26 (s, 3H), 1.19–1.26 (m, 2H), 1.03 (d, $J = 10.9$ Hz, 1H), 1.00 ppm (s, 3H); ^{13}C NMR (APT, $CDCl_3$, 100 MHz, major diastereomer): $\delta = 162.9$, 157.0, 132.7, 129.91, 129.86, 128.5, 128.2, 65.8, 53.7, 48.2, 48.1, 47.7, 47.0, 45.2, 38.8, 35.6, 34.4, 33.3, 30.8, 28.2, 28.1, 26.4, 21.3, 19.9 ppm; elemental analysis calcd (%) for $C_{26}H_{31}NO_3S$: C 71.36, H 7.14; found: C 71.48, H 7.01.

A solution of a mixture of **3c** and **4c** (20.0 mg, 0.0457 mmol) in THF (0.7 mL) was added through a cannula to an oven-dried vial containing a suspension of $LiAlH_4$ (2.5 mg, 0.065 mmol) and $AlCl_3$ (1.8 mg, 0.014 mmol) in THF (0.3 mL) under nitrogen at 0 °C. The reaction mixture was stirred at 0 °C for 45 min, then quenched with water. Ethyl acetate was added, and the layers were separated. The aqueous phase was extracted twice with ethyl acetate, and the combined organic layers were washed with brine, dried over anhydrous $MgSO_4$, and concentrated to dryness. The crude product was purified by column chromatography (EtOAc/hexanes 1:7) to give **5** (9.1 mg, 0.040 mmol, 88%) as a white solid (m.p. 57–60 °C, hexanes/CH_2Cl_2). $R_f = 0.30$ (EtOAc/hexanes 3:7); $[\alpha]_D^{23} = -20.3$ ($c = 0.35$, $CHCl_3$, 98.5% *ee*); HPLC (OJ-H column, 1 mL min^{-1}, 10% *i*PrOH/hexane, 254 nm): t_R (major enantiomer): 5.69 min, t_R (minor enantiomer): 7.84 min; IR (CH_2Cl_2): $\tilde{\nu} = 3445$ br, s, 3060 w, 3028 w, 2947 s, 2871 s, 1448 m, 737 m, 696 cm^{-1} m; ^{1}H NMR ($CDCl_3$, 400 MHz): $\delta =$ 7.31–7.36 (m, 4H), 7.21–7.25 (m, 1H), 4.48 (d, $J = 14.0$ Hz, 1H), 4.40 (d, $J = 14.0$ Hz, 1H), 2.73 (br d, $J = 3.2$ Hz, 1H), 2.59 (br d, $J = 3.3$ Hz, 1H), 2.20 (br s, 1H), 2.14 (br s, 1H), 1.58–1.66 (m, 2H), 1.44 (d, $J =$ 10.2 Hz, 1H), 1.37 (br s, 1H), 1.12–1.22 (m, 2H), 1.02 ppm (d, $J =$ 10.2 Hz, 1H); ^{13}C NMR (APT, $CDCl_3$, 100 MHz): $\delta = 140.6$, 140.1, 134.3, 128.4, 127.2, 126.5, 59.0, 46.4, 46.3, 34.5, 34.2, 30.6, 28.5, 28.1 ppm; HRMS calcd for $C_{16}H_{18}O$: *m/z* 226.1358; found: *m/z* 226.1345.

Received: August 4, 2003 [Z52555]

Keywords: alkenes · alkynes · asymmetric synthesis · cycloaddition · ruthenium

[1] For reviews on transition-metal-catalyzed cycloadditions, see: a) M. Lautens, W. Klute, W. Tam, *Chem. Rev.* **1996**, *96*, 49; b) L. S. Hegedus, *Coord. Chem. Rev.* **1997**, *161*, 129; c) P. A. Wender, J. A. Love in *Advances in Cycloaddition, Vol. 5*, JAI, Greenwich, **1999**, pp. 1–45.

[2] For recent reviews on transition-metal-catalyzed [2+2+1] cycloadditions, see: a) M. A. Pericas, J. Balsells, J. Castro, I. Marchueta, A. Moyano, A. Riera, J. Vazquez, X. Verdaguer, *Pure Appl.*

Chem. **2002**, *74*, 167; b) T. Sugihara, M. Yamaguchi, M. Nishizawa, *Chem. Eur. J.* **2001**, *7*, 1589; c) K. M. Brummond, J. L. Kent, *Tetrahedron* **2000**, *56*, 3263; d) S. L. Buchwald, F. A. Hicks in *Comprehensive Asymmetric Catalysis I–III, Vol. 2* (Eds.: E. N. Jacobsen, A. Pfaltz, H. Yamamoto), Springer, Berlin, **1999**, pp. 491–510; e) Y. Keun Chung, *Coord. Chem. Rev.* **1999**, *188*, 297.

[3] a) P. A. Wender, T. E. Jenkins, *J. Am. Chem. Soc.* **1989**, *111*, 6432; b) R. S. Jolly, G. Luedtke, D. Sheehan, T. Livinghouse, *J. Am. Chem. Soc.* **1990**, *112*, 4965; c) P. A. Wender, T. E. Jenkins, S. Suzuki, *J. Am. Chem. Soc.* **1995**, *117*, 1843; d) D. J. R. O'Mahoney, D. B. Belanger, T. Livinghouse, *Synlett* **1998**, 443; e) M. Murakami, M. Ubukata, K. Itami, Y. Ito, *Angew. Chem.* **1998**, *110*, 2362; *Angew. Chem. Int. Ed.* **1998**, *37*, 2248; f) S.-J. Paik, S. U. Son, Y. K. Chung, *Org. Lett.* **1999**, *1*, 2045.

[4] a) P. A. Wender, H. Takahashi, B. Witulski, *J. Am. Chem. Soc.* **1995**, *117*, 4720; b) P. A. Wender, H. Rieck, M. Fuji, *J. Am. Chem. Soc.* **1998**, *120*, 10976; c) B. M. Trost, H. Shen, *Angew. Chem.* **2001**, *113*, 2375; *Angew. Chem. Int. Ed.* **2001**, *40*, 2313; d) P. A. Wender, T. J. Williams, *Angew. Chem.* **2002**, *114*, 4732; *Angew. Chem. Int. Ed.* **2002**, *41*, 4550.

[5] a) P. A. Wender, N. C. Ihle, *J. Am. Chem. Soc.* **1986**, *108*, 4678; b) P. A. Wender, J. M. Nuss, D. B. Smith, A. Suarez-Sobrino, J. Vagberg, D. Decosta, J. Bordner, *J. Org. Chem.* **1997**, *62*, 4908.

[6] P. A. Wender, A. G. Correa, Y. Sato, R. Sun, *J. Am. Chem. Soc.* **2000**, *122*, 7815.

[7] B. M. Trost, M. Yanai, K. Hoogsteen, *J. Am. Chem. Soc.* **1993**, *115*, 5294.

[8] T. Mitsudo, H. Naruse, T. Kondo, Y. Ozaki, Y. Watanabe, *Angew. Chem.* **1994**, *106*, 595; *Angew. Chem. Int. Ed. Engl.* **1994**, *33*, 580.

[9] a) D.-J. Huang, D. K. Rayabarapu, L.-P. Li, T. Sambaiah, C.-H. Cheng, *Chem. Eur. J.* **2000**, *6*, 3706; b) K. C. Chao, D. K. Rayabarapu, C.-C. Wang, C.-H. Cheng, *J. Org. Chem.* **2001**, *66*, 8804.

[10] a) R. W. Jordan, W. Tam, *Org. Lett.* **2000**, *2*, 3031; b) R. W. Jordan, W. Tam, *Org. Lett.* **2001**, *3*, 2367; c) R. W. Jordan, W. Tam, *Tetrahedron Lett.* **2002**, *43*, 6051.

[11] a) S. T. Ingate, J. Marco-Contelles, *Org. Prep. Proced. Int.* **1998**, *30*, 121; b) S. Flonquerna, A. Moyano, M. A. Pericas, A. Riera, *J. Am. Chem. Soc.* **1997**, *119*, 10225.

[12] The coordination of a sulfone oxygen atom with a ruthenium metal center has been proposed to explain the regioselectivity in ruthenium-catalyzed ring-closing metathesis (RCM) reactions; see: L. A. Paquette, F. Fabris, J. Tae, J. C. Gallucci, J. E. Hofferberth, *J. Am. Chem. Soc.* **2000**, *122*, 3391.

 © 2004 Wiley-VCH Verlag GmbH & Co. KGaA, Weinheim

Thiosugar Synthesis

Glycosyltransferase-Catalyzed Synthesis of Thiooligosaccharides**

*Jamie R. Rich, Adam Szpacenko, Monica M. Palcic, and David R. Bundle**

S-Linked oligomers are metabolically stable mimics of their naturally occurring counterparts, since the rate of hydrolysis of the thioglycosidic bond by glycosylhydrolases is several orders of magnitude slower than that of the corresponding O-glycosides.[1] In addition, the conformational space sampled by thioglycosides is similar to that of O-glycosides. These properties suggest that S-linked carbohydrates may be attractive antigens with extended in vivo activity,[2] and the ability of glycosyltransferases to create such linkages has significant potential.

Considerable attention has been focused on the synthesis of complex oligosaccharides containing S-linked residues, and a variety of chemical approaches are available to construct this linkage.[1,3] Most thiooligosaccharide syntheses take advantage of the reduced basicity and enhanced nucleophilicity of sulfur compared to oxygen, employing a sugar thiol or thiolate anion in a reaction with another carbohydrate bearing an electrophilic leaving group.[4] Other commonly employed methods include glycosylation of thiosugar acceptors with activated glycosyl donors such as trichloroacetimidates,[5] and Michael addition of anomeric thiolates to α,β-unsaturated systems.[6] Recently active-site mutants of glycosylhydrolases, termed thioglycoligases, have been shown to transfer a glycosyl residue to appropriate sugar thiols.[7]

The chemical synthesis of oligosaccharides and their analogues is a laborious pursuit. Glycosyltransferases, which catalyze the formation of glycosidic bonds in nature, are now indispensable tools in synthetic carbohydrate chemistry, both for the production of natural and nonnatural oligosaccharides.[8,9] Since glycosyltransferases establish glycosyl linkages without the need for protecting groups, their use constitutes an obvious advantage over traditional chemical synthesis of

[*] J. R. Rich, Dr. A. Szpacenko, Prof. Dr. M. M. Palcic, Prof. Dr. D. R. Bundle
Alberta Ingenuity Center for Carbohydrate Science
Department of Chemistry
University of Alberta
Edmonton, AB. T6G 2G2 (Canada)
Fax: (+1) 780-492-7705
E-mail: dave.bundle@ualberta.ca

[**] We would like to thank Dr. Irma van Die for supplying the β1,3-*N*-acetylglucosaminyl transferase clone and Dr. Angie Morales-Izquierdo for acquiring mass spectra. J.R. thanks the Natural Sciences and Engineering Research Council of Canada (NSERC) and the Alberta Heritage Foundation for Medical Research (AHFMR) for graduate fellowships. Funding for this work was received from the NSERC (D.R.B., M.M.P.) and the Alberta Ingenuity Centre for Carbohydrate Science (D.R.B, M.M.P.).

Supporting information for this article is available on the WWW under http://www.angewandte.org or from the author.

 DOI: 10.1002/anie.200352606 © 2004 Wiley-VCH Verlag GmbH & Co. KGaA, Weinheim

oligosaccharides. Increasingly, a growing interest in glycobiology and advances in biotechnology and molecular biology are making glycosyltransferases available to the synthetic chemist in multiunit quantities. The ready availability of these enzymes not only facilitates carbohydrate synthesis but also contributes to an increased understanding of these biocatalysts.

Herein we report a new enzymatic method for the synthesis of thiooligosaccharides. In summary, our approach employs glycosyltransferases to catalyze the transfer of a monosaccharide residue from an activated sugar nucleotide donor to a thiol-bearing carbohydrate acceptor. We have examined the ability of two enzymes, a recombinant bovine α1,3-galactosyltransferase (α1,3GalT) and a β1,3-*N*-acetylglucosaminyltransferase (β1,3GlcNAcT) from *Neisseria menigitidis*, to catalyze glycosyl transfer to a 3′-thiolactose acceptor.[10,11] The formation of thioglycoside products is facilitated by addition of a reducing agent such as dithiothreitol (DTT) to the reaction mixture, which serves to maintain a pool of the reactive thiol acceptor for consumption in the reaction.

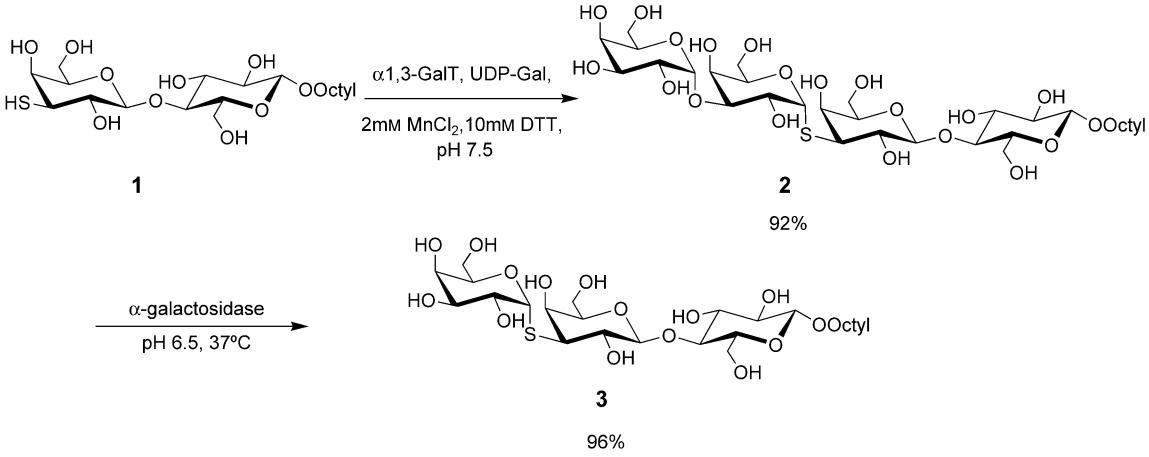
The development of an enzymatic approach to the synthesis of thiooligosaccharides does not obviate the considerable effort required for the construction of thiosugar acceptors. However, this method demonstrates the high yields and stereo- and regioselectivities characteristic of glycosyltransferase-catalyzed oligosaccharide synthesis, renders a final deprotection step unnecessary, and may be more suitable than chemical methods for the formation of thioglycosidic linkages in molecules containing sensitive functionalities. In addition the incorporation of a reducing agent into the reaction mixture, uncommon in traditional chemical approaches to thiooligosaccharide synthesis, prevents the loss of valuable carbohydrate thiols resulting from disulfide formation.

Octyl-β-D-lactose is a substrate for bovine α1,3-GalT, and the product of this reaction is easily purified by solid-phase extraction on C_{18} silica gel. In order to establish whether the analogous S-linked trisaccharide could be synthesized by the same enzyme, octyl β-D-3′-thiolactoside **1** (Scheme 1) was prepared. Beginning with known (2,6-di-O-acetyl-β-D-galactopyranosyl)-(1→4)-1,2,3,6-tetra-O-acetyl β-D-glucopyranose,[12] a linear synthesis was devised affording the thiol acceptor **1** after five steps in 26% overall yield (see the Supporting Information).

The α1,3-GalT-catalyzed galactosylation of **1** is outlined in Scheme 1. Unexpectedly, incubation of a mixture of the thiol and its disulfide (~3:1) with UDP-Gal and unit quantities of α1,3GalT in the presence of DTT afforded the thio-linked tetrasaccharide **2** in 92% yield after passage through a SepPak C18 cartridge. Thus, following the initial transfer of a galactosyl residue to the thiol acceptor, a second glycosyl transfer occurred. The second reaction is not without precedent, as Wang has reported the galactosylation of an α-linked galactosyl residue by α1,3-GalT, albeit at a rate lower than that of the reaction of the β-linked substrate.[13] Treatment of octyl β-D-lactose under the same conditions yielded the trisaccharide as the major product and a second compound which was identified as the tetrasaccharide by analysis of the high-resolution mass and ^{1}H NMR spectra of the mixture.

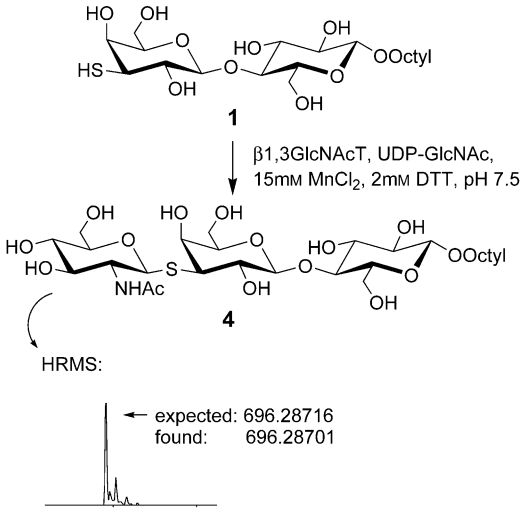
Fortunately, the marked difference in stability between O-glycosyl and S-glycosyl bonds could be exploited, and the desired trisaccharide **3**, an analogue of the *Clostridium difficile* toxin A binding ligand, was obtained in near-quantitative yield following treatment with an α-galactosidase from green coffee beans (Scheme 1). This synthetic sidetrack inadvertently reinforced the rationale for the synthesis of thiooligosaccharides.

Encouraged by the successful glycosyl transfer to a sugar thiol acceptor, we hoped to test the generality of our approach. β-Lactosides are known acceptors of a β-1,3-*N*-acetylglucosaminyltransferase from *Neisseria meningitidis*, which has recently been cloned and expressed in *E. coli*.[11] It was thus expected that this enzyme would catalyze the transfer of an *N*-acetylglucosaminyl residue to thiol acceptor **1**, resulting in the formation of the trisaccharide **4** as outlined in Scheme 2. In fact, our initial results confirm that this reaction takes place, and we have established the successful formation of the thioglycoside product by high-resolution mass spectrometry(HRMS). Owing to the significant instability of our enzyme preparation and the slow rate of reaction,



Scheme 1. α1,3-Galactosyltransferase (E.C. 2.4.1.151) catalyzed synthesis of a thiotetrasaccharide **2** and selective hydrolysis of the terminal O-glycosidic linkage by α-galactosidase (E.C. 3.2.1.22) to give thiotrisaccharide **3**.

 © 2004 Wiley-VCH Verlag GmbH & Co. KGaA, Weinheim



Scheme 2. β1,3-*N*-acetylglucosaminyl transferase catalyzes glycosyl transfer to thiol **1**. Product formation is confirmed by high-resolution mass spectrometry.

we have not yet generated sufficient product for full characterization by other means.

Standard radiochemical assays,[14] as well as the formation of a tetrasaccharide product (Scheme 1) suggest a substantial decrease in the rate of glycosyl transfer to the 3′-thiolactose acceptor **1** relative to β-octyl lactose. Kinetic analysis showed that the V_{max} for **1** was 0.2 % of that for β-octyl lactose; there was also an effect on K_M which increased from 5 mM to 15 mM. Trisaccharide **3** is a better substrate than **1** with a V_{max} 17 % of the parent lactoside and a K_M of 7 mM, accounting for the preferential formation of tetrasaccharide **2**. In light of the similarity of the K_M values for acceptor **1** and β-octyl lactose, and the substantially diminished rate of transfer to the thiol compound, it seems evident that the nucleophilicity of the thiol is modulated in the enzyme active site.

We have demonstrated here a new method for the synthesis of thiooligosaccharides using glycosyltransferases. Although the observed rate of glycosyl transfer to carbohydrate thiols is diminished relative to unmodified acceptors, the availability of cloned glycosyltransferases makes this a viable method for preparative synthesis. We anticipate that analogous glycosylations of carbohydrate thiols will be observed with a variety of glycosyltransferases. Further, as our understanding of the structure–activity relationships of the active site of these enzymes increases, the development of active site mutants should permit the creation of redesigned glycosyltransferases with improved kinetics for the synthesis of S-linked oligosaccharides.

Received: August 8, 2003 [Z52606]

Keywords: enzyme catalysis · glycosylation · oligosaccharides · thiooligosaccharides

[1] For a reviews of the use of thiooligosaccharides as nonhydrolyzable substrate analogues in glycobiology, see: J. Defaye, J. Gelas in *Studies in Natural Products Chemistry* (Ed: Atta-ur-Rahman), Elsevier, Amsterdam, **1991**, pp. 315–357; H. Driguez, *Chembiochem* **2001**, *2*, 311–318.

[2] H. N. Yu. Doctoral Thesis, University of Alberta, **2002**.

[3] J. K. Fairweather, H. Driguez in *Carbohydrates in Chemistry and Biology, Vol. 1* (Eds.: B. Ernst, G. W. Hart, P. Sinaÿ), Wiley-VCH, **2000**, pp. 531–564; H. Driguez, *Top. Curr. Chem.* **1997**, *187*, 85–116.

[4] M. Blanc-Muesser, J. Defaye, H. Driguez, *Tetrahedron Lett.* **1976**, *17*, 4307–4310; M. Blanc-Muesser, J. Defaye, H. Driguez, *Carbohydr. Res.* **1978**, *67*, 305–328.

[5] R. R. Schmidt, M. Stumpp, *Liebigs Ann. Chem.* **1983**, 1249–1256; T. Eisele, A. Toepfer, G. Kretzschmar, R. R. Schmidt, *Tetrahedron Lett.* **1996**, *37*, 1389–1392.

[6] Z. J. Witczak, J. M. Sun, R. Mielguj, *Bioorg. Med. Chem. Lett.* **1995**, *5*, 2169–2174.

[7] M. Jahn, J. Marles, R. A. J. Warren, S. G. Withers, *Angew. Chem.* **2003**, *115*, 366–368; *Angew. Chem. Int. Ed.* **2003**, *42*, 352–354.

[8] X. Qian, K. Sujino, M. M. Palcic, R. M. Ratcliffe, *J. Carbohydr. Chem.* **2002**, *21*, 911–942.

[9] R. Ohrlein, *Top. Curr. Chem.* **1999**, *200*, 227–254.

[10] Y. R. Fang, K. Sujino, A. Lu, J. Gregson, R. Yeske, V. P. Kamath, R. M. Ratcliffe, M. J. Shur, W. W. Wakarchuk, M. M. Palcic in *Carbohydrate Bioengineering, Interdisciplinary Approaches* (Eds.: T. T. Teeri, B. Svensson, H. J. Gilbert, T.Feizi), Royal Society of Chemistry, London, **2002**, pp. 127–134

[11] O. Blixt, I. van Die, T. Norberg, D. H. van den Eijnden, *Glycobiology* **1999**, *9*, 1061–1071.

[12] H. H. Baer, S. A. Abbas, *Carbohydr. Res.* **1980**, *84*, 53–60.

[13] J. Fang, X. Chen, W. Zhang, A. Janczuk, P. G. Wang, *Carbohydr. Res.* **2000**, *329*, 873–878.

[14] M. M. Palcic, L. D. Heerze, M. Pierce, O. Hindsgaul, *Glycoconjugate J.* **1988**, *5*, 49–63.

 © 2004 Wiley-VCH Verlag GmbH & Co. KGaA, Weinheim

Stereoselective Cycloaddition

A Tandem Epoxidation/Stereoselective Intramolecular [4+3] Cycloaddition Reaction Involving Nitrogen-Stabilized Oxyallyl Cations Derived from Chiral Allenamides**

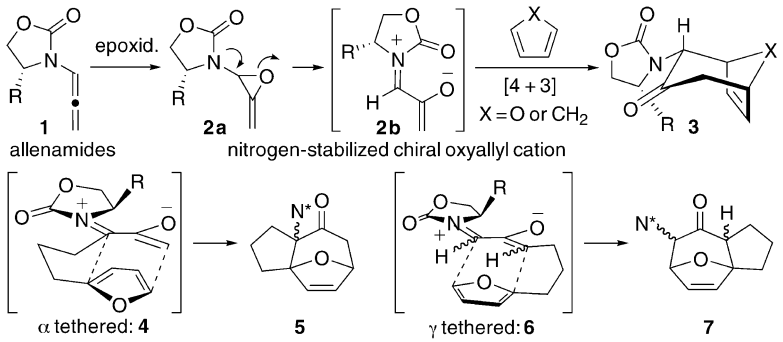
*Challeppan Rameshkumar and Richard P. Hsung**

We recently reported that allenamides **1** can be epoxidized to give nitrogen-stabilized chiral oxyallyl cations **2b**,[1] which can be made to participate in highly stereoselective [4+3] cycloadditions with dienes (Scheme 1).[2] 1,3-Dipolar cycloadditions of oxyallyl cations represent a powerful synthetic tool

[*] C. Rameshkumar, Prof. R. P. Hsung
Department of Chemistry
University of Minnesota
Minneapolis, MN 55455 (USA)
Fax: (+1) 612-626-7541
E-mail: hsung@chem.umn.edu

[**] This work was supported by the National Science Foundation (Grant no. CHE-0094005). R.P.H. is a recipient of the 2001 Camille Dreyfus Teacher-Scholar and McKnight Faculty Awards

 DOI: 10.1002/anie.200352632 © 2004 Wiley-VCH Verlag GmbH & Co. KGaA, Weinheim



Scheme 1. Epoxidation of allenamides **1** produces nitrogen-stabilized chiral oxyallyl cations, which undergo a stereoselective [4+3] cycloaddition to yield **3**. Tethered allenamides **4** and **6** undergo intramolecular [4+3] cycloaddition.

for constructing complex carbo- and heterocycles.[3] Heteroatoms such as oxygen[4] and sulfur,[5] as well as halogen-substituted[6] oxyallyl cations have become very attractive intermediates for developing not only highly regioselective, but also stereoselective [4+3] cycloadditions.[7]

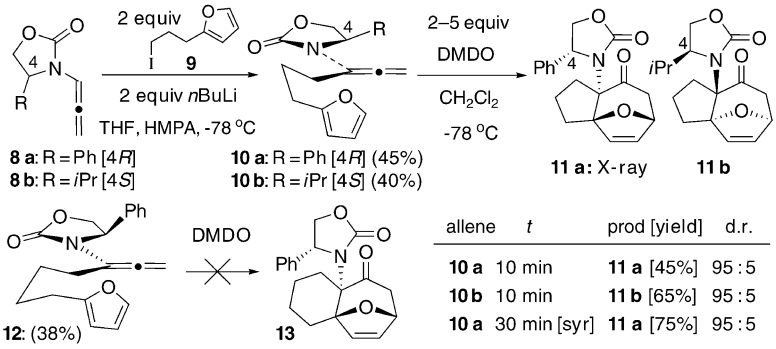
Nitrogen-substituted oxyallyl cations, however, had received less attention[8] until studies were reported recently by Myers and Barbay[9] and Harmata et al.,[10] in addition to work from our own research group.[2,11] The trivalency of the nitrogen atom provides flexibility by allowing the tethering of a chiral auxiliary and presents a valuable platform on which to achieve highly stereoselective oxyallyl cycloadditions, which remain a challenge.[3,7,12] As part of our ongoing efforts to develop stereoselective methods using allenamides,[13–15] we have been exploring intramolecular [4+3] oxyallyl cycloaddition[16] in α-tethered (**4**) and γ-tethered allenamides (**6**; Scheme 1). We report herein the first tandem epoxidation/stereoselective intramolecular [4+3] cycloaddition reactions involving nitrogen-stabilized chiral oxyallyl cations.

To establish the feasibility of intramolecular [4+3] cycloaddition of α-tethered allenamides, we prepared allenamides **10a** and **10b**,[17] tethered with the furan units from **8a** and **8b**, respectively, by our α-alkylation protocol[14c] (Scheme 2). Epoxidation of **10a** and **10b** by treatment with 2–5 equivalents of dimethyl dioxirane (DMDO) at −78 °C gave satisfactory yields, and the ensuing cycloadditions gave **11a** and **11b** in 45 and 65% yield, respectively. The products were obtained as single diastereomers containing a quaternary stereocenter and the stereochemistry was assigned based on X-ray analysis of **11a**.

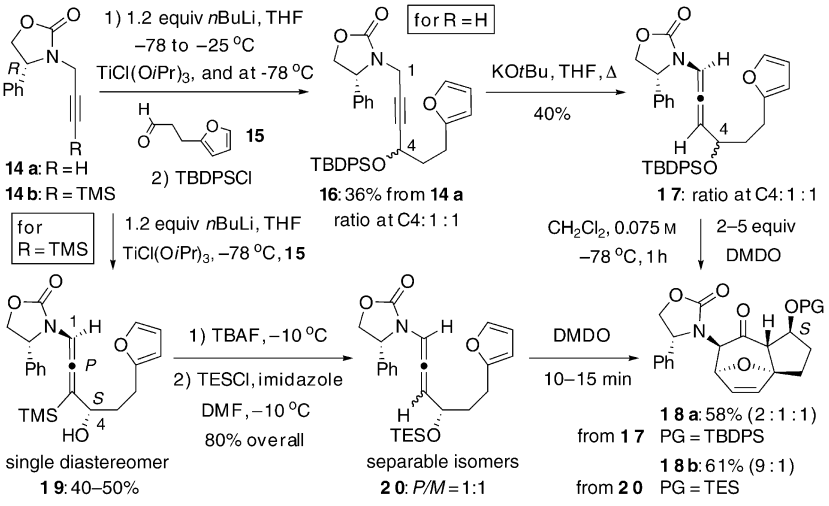
These cycloadditions were much more facile than intermolecular reactions,[2] with the intramolecular reactions completed in 10 min at lower temperatures. A prolonged reaction time actually led to a much lower yield. Addition of DMDO By syringe pump was found to improve the yield of **11a** to 75%, although it was not a procedure that was frequently used in these reactions. Allenamide **12**, which contains one additional carbon atom within the tether compared to **10a** and **10b**, failed to provide cycloadduct **13**.

Once we had established the feasibility of this cycloaddition, we turned to γ-tethered allenamides, whose syntheses featured Seebach's elegant γ lithiation and asymmetric aldol addition,[15a] as shown in Scheme 3.

γ-Tethered allenamide **17** was prepared by an unusual regio- and stereoselective base-induced isomerization[14b,e,18] of the propargyl amide **16**[15a] (1:1 ratio of stereoisomers with a chiral center at C4). Propargyl amide **16** was prepared by addition of the lithium acetylide of **14a** to aldehyde **15** in the presence of $TiCl(OiPr)_3$[15a] followed by protection with TBDPSCl. Cycloaddition of **17** under standard conditions provided cycloadduct **18a** as a mixture of three isomers. The major isomer, shown in Scheme 3, was assigned by correlation with the X-ray structure of a related cycloadduct.



Scheme 2. Synthesis of tethered allenamides **10a** and **10b**, their epoxidation, and the subsequent cycloaddition reactions. syr, syringe-pump addition of DMDO.



Scheme 3. Sythesis and reaction of γ-tethered allenamides. Imid, imidazole; TMS, *tert*-butyldimethylsilyl; TBDPS, *tert*-butylphenylsilyl; TBAF, tetrabutylammonium fluoride; TES, triethylsilyl.

 © 2004 Wiley-VCH Verlag GmbH & Co. KGaA, Weinheim

Since the C4 stereochemistry in **17** could have eroded the selectivity of the cycloaddition, we prepared **19** as a single diastereomer[19] in 40–50% yield from **14b** by using Seebach's protocol for γ-lithiation and asymmetric aldol addition.[15a] However, **19** did not undergo cycloaddition even when the secondary hydroxy group was protected with TESCl or AcCl.

We then removed the TMS group by treatment with TBAF, but this desilylation led to scrambling of the allenic axial stereocenter and afforded **20** as a 1:1 isomeric mixture (*P*/*M*) after protection with TESCl. Cycloaddition of **20** as a mixture of isomers was facile in the presence of DMDO at −78 °C and gave **18b** in 61% yield, with a 9:1 ratio of major and minor isomers that match the two major components obtained from **17**.

The scope and stereoselectivity of cycloadditions of γ-tethered allenamides are summarized in Table 1. Reaction of the cleanly separated isomers (*P*)-**20** and (*M*)-**20** (entries 1 and 2) provided **18b** in 60 and 75% yield, respectively, in a 90:10 ratio in favor of the same major isomer in both cases. These results suggest that the chirality of the allene does not have an impact on the stereoselectivity of the cycloaddition.

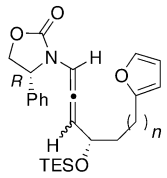
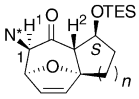
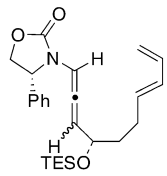
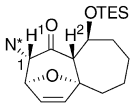
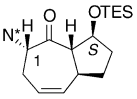
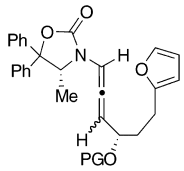
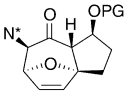
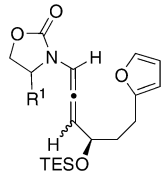
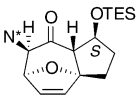
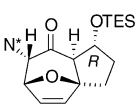
Unlike α-tethered allenamides, γ-tethered allenamides with various lengths of tether were found to be suitable for cycloaddition: **23** ($n=2$) and **24** ($n=3$) led to cycloadducts **25** (X-ray structure) and **26**, respectively, in good yields and with high stereoselectivity (entries 3 and 4, Table 1).[20] Intriguingly, the stereochemistry was completely reversed at C1 in **26**, which resulted in a major isomer (assigned by NOE measurements) that corresponds to the minor isomer of **18b** or **25** (entry 4). Butadienes **27** can also be utilized in this intramolecular cycloaddition to give cycloadduct **28** as a single diastereomer, again with reversal of stereochemistry at C1 (entries 5 and 6), although in lower yields.

Various chiral auxiliaries were examined (Entries 7–12). The *P* and *M* isomers of **36** ($R^1=i$Pr) provided **37** with the best diastereomeric ratio (entries 11 and 12) achieved in our experiments. The protecting group can be either a silyl or an acyl group (entries 7 and 8). Allenamide **35** led to *ent*-**18b** as expected (entry 10).

Oxyallyl cation intermediates are known to prefer W configuration **A** (with respect to the nitrogen group in the compounds discussed herein) over sickle configurations **B** and **C**, whilst the U-cation **D** configuration is the least stable because it possesses the most $A^{1,3}$ strain (Scheme 4).[1,2,21] One W configuration is possible for α-tethered oxyallyl cation **38**, and *endo* (or compact[21]) addition would lead to the observed major isomers of **11a** or **11b**. In contrast, it appears that both W configuration **A** and sickle configurations **B** and **C** could play a role for γ-tethered oxyallyl cations **39** and **40**. Since H1 and H2 can be assigned as *anti* in cycloadducts **18b** and **25**, the oxyallyl cation probably assumed either sickle configuration **B** through *endo* addition (**39a**), or sickle configuration **C** by *exo* (extended[21]) addition (**39b**) to give the observed major isomer. For cycloadducts **26** and **28**, the W configuration **A** of the cation is likely to be favored, as shown for γ-tethered oxyallyl cation **40**. This configuration would lead to placement of H1 and H2 *syn* to one another by *exo* (extended[21]) addition. These assessments can rationalize the stereochemical outcomes of the cycloadditions, but we are currently investigating the origin of this configuration switch.

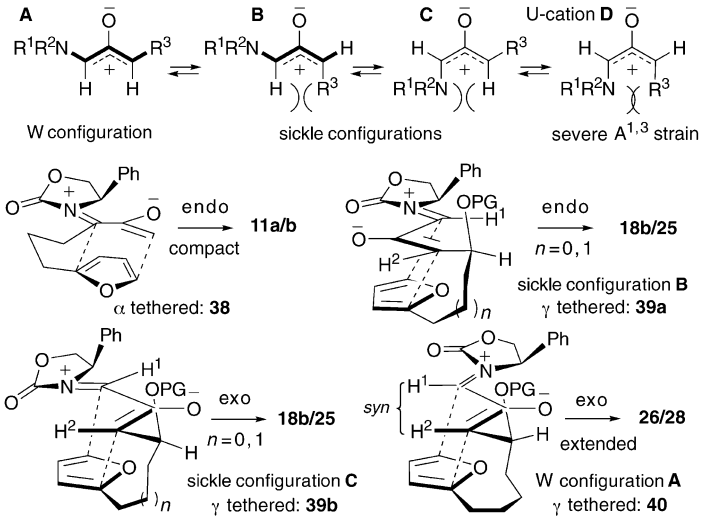
We have herein described a novel tandem epoxidation/stereoselective intramolecular [4+3] cycloaddition involving nitrogen-stabilized chiral oxyallyl cations derived from allenamides. These complex polycyclic manifolds could be useful in the synthesis of natural products. Efforts

Table 1: The scope and stereoselectivity of cycloadditions of γ-tethered allenamides.

Entry	Allenamides[a]	Cycloadducts[b]		Yield [%][c]	Ratio[d]
1			**18b**	60	90:10
2	(*M*)-**20**: $n=1$		**18b**	75	90:10
3	**23**: $n=2$; $P/M=1:1$		**25**[e]	65	93:7
4			**26**	55	≤5:95
5	(*M*)-**27**		**28**	30	≤5:95
6	(*P*)-**27**		**28**	34	≤:95
7			**31**	78	86:14
8	**30**: PG = Ac: $P/M=2.5:1$		**32**	83	90:10
9			**34**	65	71:29
10	**35**: $R^1=$ (*S*)-Ph; $P/M=1:1$ $R^1=$ (*S*)-*i*Pr; $P/M=2:1$		*ent*-**18b**[f]	60	90:10
11	(*P*)-**36**		**37**	60	95:5
12	(*M*)-**36**		**37**	60	95:5

[a] Details of the syntheses of the allenamides are given in the Supporting Information. All reactions were carried out in Ch_2Cl_2 (conc. ca. 0.075 M) at −78 °C; DMDO (2.5 equiv) was added as a solution in acetone and Ch_2Cl_2 was added at −78 °C through a cannula. The reaction was complete after 5–15 min. [b] N* denotes the corresponding chiral auxiliary. [c] Yields of isolated products. [d] Ratios of isomers determined by ^{1}H and/or ^{13}C NMR spectroscopy. [e] The X-ray structure was obtained. [f] Assigned by NOE measurements.

 © 2004 Wiley-VCH Verlag GmbH & Co. KGaA, Weinheim



Scheme 4. The configurations of the oxyallyl cation intermediates can be used to rationalize the mechanism of the cycloaddition reaction.

are currently underway to apply the compounds in such syntheses.

Received: August 12, 2003 [Z52632]

Keywords: chiral allenamides · cycloaddition · epoxidation · nitrogen · stereoselectivity

[1] C. Rameshkumar, H. Xiong, M. R. Tracey, C. R. Berry, L. J. Yao, R. P. Hsung, *J. Org. Chem.* **2002**, *67*, 1339.

[2] H. Xiong, R. P. Hsung, C. R. Berry, C. Rameshkumar, *J. Am. Chem. Soc.* **2001**, *123*, 7174.

[3] For recent reviews, see a) M. Harmata, P. Rashatasakhon, *Tetrahedron* **2003**, *59*, 2371; b) H. M. L. Davies in *Advances in Cycloaddition*, *Vol. 5* (Ed.: M. Harmata), JAI, Greenwich, **1998**, p. 119; c) M. Harmata in *Advances in Cycloaddition*, *Vol. 4* (Ed. M. Lautens), JAI, Greenwich, **1997**, p. 41; d) F. G. West in *Advances in Cycloaddition*, *Vol. 4* (Ed.: M. Lautens), JAI, Grennwich, **1997**, pp. 1–40; e) J. H. Rigby, F. C. Pigge, *Org. React.* **1997**, *51*, p. 351; f) A. Padwa, A. Schoffstall in *Advances in Cycloaddition*, *Vol. 2* (Ed.: D. P. Curran, JAI, Greenwich, CT, **1990**, p. 1; g) A. Padwa, *1,3-Dipolar Cycloaddition Chemistry* (Ed.: A. Padwa), Wiley-Interscience, New York, **1984**.

[4] For some examples of oxygen-substituted oxyallyls, see a) R. L. Funk, R. A. Aungst, *Org. Lett.* **2001**, *3*, 3553; b) J. C. Lee, S.-J. Jin, J. K. Cha, *J. Org. Chem.* **1998**, *63*, 2804; c) M. Harmata, U. Sharma, *Org. Lett.* **2000**, *2*, 2703; d) B. Föhlisch, D. Krimmer, E. Gehrlach, D. Kashammer, *Chem. Ber.* **1988**, *121*, 1585.

[5] For examples of sulfur-substituted oxyallyls, see a) M. Harmata, K. W. Carter, *ARKIVOC* **2002**, *8*, 62; b) M. Harmata, M. Kahraman, *Tetrahedron Lett.* **1998**, *39*, 3421; c) M. Harmata, D. E. Jones, *Tetrahedron Lett.* **1996**, *37*, 783; d) K. Masuya, K. Domon, K. Tanino, I. Kuwajima, *J. Am. Chem. Soc.* **1998**, *120*, 1724.

[6] K. Lee, J. K. Cha, *Org. Lett.* **1999**, *1*, 523.

[7] For a recent review on heteroatom-stabilized oxyallyls in [4+3] cycloadditions, see M. Harmata, *Recent Res. Dev. Org. Chem.* **1997**, *1*, 523–535.

[8] For oxidopyridinium ions, see a) M. J. Sung, H. I. Lee, Y. Chong, J. K. Cha, *Org. Lett.* **1999**, *1*, 2017; b) N. Dennis, B. Ibrahim, A. R. Katritzky, *J. Chem. Soc. Perkin Trans. 1* **1976**, *1*, 2307; for phthalimide-substituted systems, see c) M. A. Walters, H. R. Arcand, *J. Org. Chem.* **1996**, *61*, 1478, and references cited therein.

[9] A. G. Myers, J. K. Barbay, *Org. Lett.* **2001**, *3*, 425.

[10] M. Harmata, S. K. Ghosh, X. Hong, S. Wacharasindu, P. Kirchhoefer, *J. Am. Chem. Soc.* **2003**, *125*, 2058.

[11] H. Xiong, R. P. Hsung, L. Shen, J. M. Hahn, *Tetrahedron Lett.* **2002**, *43*, 4449.

[12] For recent elegant stereoselective approaches to [4+3] cycloadditions, see a) R. S. Grainger, R. B. Owoare, P. Tisselli, J. W. Steed, *J. Org. Chem.* **2003**, *68*, 7899; b) K. T. Meilert, M.-E. Schwenter, Y. Shatz, S. R. Dubbaka, P. Vogel, *J. Org. Chem.* **2003**, *68*, 2964; c) A. M. Montaña, P. M. Grima, *Tetrahedron* **2002**, *58*, 4769; d) H. Beck, C. B. W. Stark, H. M. R. Hoffmann, *Org. Lett.* **2000**, *2*, 883, and references cited therein; e) C. B. W. Stark, U. Eggert, H. M. R. Hoffmann, *Angew. Chem.* **1998**, *110*, 1337; *Angew. Chem. Int. Ed.* **1998**, *37*, 1266; f) M. Harmata, D. E. Jones, M. Kahraman, U. Sharma, C. L. Barnes, *Tetrahedron Lett.* **1999**, *40*, 1831; g) S. Y. Cho, J. C. Lee, J. K. Cha, *J. Org. Chem.* **1999**, *64*, 3394.

[13] For a review on allenamides, see a) R. P. Hsung, L.-L. Wei, H. Xiong, *Acc. Chem. Res.* **2003**, *36*, 773; for reviews on allenes, see b) R. W. Saalfrank, C. J. Lurz, *Methoden der Organischen Chemie (Houben-Weyl)*, *Vol. E8*, **1993**, p. 3093; c) H. E. Schuster, G. M. Coppola, *Allenes in Organic Synthesis*, Wiley, New York, **1984**.

[14] a) C. R. Berry, C. Rameshkumar, M. R. Tracey, L.-L. Wei, R. P. Hsung, *Synlett* **2003**, 791; b) C. Rameshkumar, R. P. Hsung, *Synlett* **2003**, 1241; c) L.-L. Wei, J. A. Mulder, H. Xiong, C. A. Zificsak, C. J. Douglas, R. P. Hsung, *Tetrahedron* **2001**, *57*, 459; d) H. Xiong, R. P. Hsung, L.-L. Wei, C. R. Berry, J. A. Mulder, B. Stockwell, *Org. Lett.* **2000**, *2*, 2869; e) L.-L. Wei, R. P. Hsung, H. Xiong, J. A. Mulder, N. T. Nkansah, *Org. Lett.* **1999**, *1*, 2145; f) L.-L. Wei, H. Xiong, C. J. Douglas, R. P. Hsung, *Tetrahedron Lett.* **1999**, *40*, 6903.

[15] For recent elegant studies using allenamides, see a) C. Gaul, D. Seebach, *Helv. Chim. Acta* **2002**, *85*, 963; b) Y. Kozawa, M. Mori, *Tetrahedron Lett.* **2002**, *43*, 1499; c) Y. Horino, M. Kimura, S. Tanaka, T. Okajima, Y. Tamaru, *Chem. Eur. J.* **2003**, *9*, 2419; d) S. S. Kinderman, J. H. van Maarseveen, H. E. Schoemaker, H. Hiemstra, F. P. T. Rutjes, *Org. Lett.* **2001**, *3*, 2045; e) R. Grigg, I. Köppen, M. Rasparini, V. Sridharan, *Chem. Commun.* **2001**, 964, and references cited therein; f) Y. Horino, M. Kimura, Y. Wakamiya, T. Okajima, Y. Tamaru, *Angew. Chem.* **1999**, *111*, 123; *Angew. Chem. Int. Ed.* **1999**, *38*, 121; g) M. Kimura, Y. Horino, Y. Wakamiya, T. Okajima, Y. Tamaru, *J. Am. Chem. Soc.* **1997**, *119*, 10869.

[16] For excellent reviews on intramolecular [4+3] cycloadditions, see a) M. Harmata, *Acc. Chem. Res.* **2001**, *34*, 595; b) M. Harmata, *Tetrahedron* **1997**, *53*, 6235.

[17] All new compounds were identified and characterized by ^{1}H NMR, ^{13}C NMR, and FTIR spectroscopies, $[\alpha]_D^{20}$ measurements, and by LRMS.

[18] J. Huang, H. Xiong, R. P. Hsung, C. Rameshkumar, J. A. Mulder, T. P. Grebe, *Org. Lett.* **2002**, *4*, 2417.

[19] The allene stereochemistry in **19** was assigned based on the report by Gaul and Seebach.[15a] The C4 stereochemistry was later confirmed by the X-ray structure of cycloadduct **25**.

[20] When we extended the tether with another carbon atom ($n = 4$), the cycloaddition reaction did not proceed under these conditions.

[21] For a review on Hoffmann's notations, see a) H. M. R. Hoffmann, *Angew. Chem.* **1973**, *85*, 877; *Angew. Chem. Int. Ed. Engl.* **1973**, *12*, 819; see also: b) H. M. R. Hoffmann, D. R. Joy, *J. Chem. Soc. B* **1968**, 1182.

 © 2004 Wiley-VCH Verlag GmbH & Co. KGaA, Weinheim

Crystal Engineering

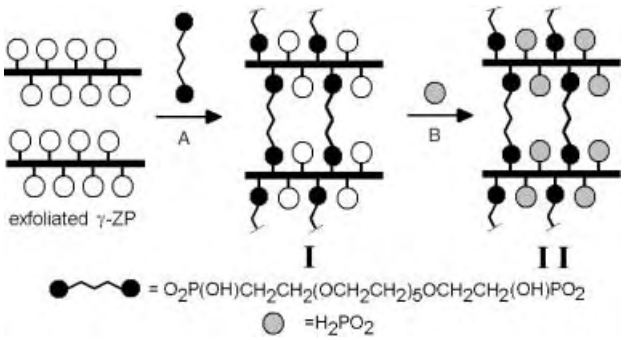
Solid-State Reshaping of Crystals: Flash Increase in Porosity of Zirconium Phosphate-Hypophosphite That Contains Polyethylenoxa Diphosphonate Pillars**

Ernesto Brunet, María José de la Mata, Olga Juanes, and Juan Carlos Rodríguez-Ubis*

Engineering of crystals and solids[1] is an active area of research that intertwines the concepts of supramolecular chemistry[2] and materials science.[3] The supramolecular construction of nanoporous solids[4] with ample, open voids that can be freely accessed by other molecular species is quite a difficult task and pursued by a vast number of research groups.[5] One common approach is the spontaneous aggregation of dissolved small-molecular building blocks. However, its success is rather limited because for the self-aggregation to render useful architectures, one should posses a profound predictive knowledge of the involved intermolecular forces, which implies the proposition and preparation of molecules ("aggregons") with suitable geometries and functionalities. Yet, worse, once the crystal or solid is formed, there are few opportunities, if any, to further manipulate its structure.

Layered γ-zirconium phosphate (γ-ZP) is a versatile and well-known structure[6] in which the phosphates that reside in the surfaces of the lamellae are topotactically replaceable by phosphonates[7] and diphosphonates,[8] the latter leading to pillared, porous solids. Layered γ-ZP can be thus used as a carving board in which appropriate organic molecules could be orderly grafted at a controlled, low density. Therefore, size and shape of interpillar spaces may be tuned by simply choosing organic moieties of appropriate length and flexibility and by controlling the degree of pillaring.[9] Moreover, one may select a suitable chemical response of interpillar spaces by including sophisticated functionalities in the organic chain.[10] These facts, together with the possibility of replacing all remaining superficial phosphates by other phosphorous functions of different polarity,[11] make the prospects of this building-block combination to be limited only by the imagination of the researcher.

We report herein that the chemical response to a simple acid–base reaction induces fast, sharp porosity changes in the microcrystals of the inorganic–organic material created by stepwise, double topotactic exchange of γ-ZP by pentaethylenglycol derived diphosphonic acid and hypophosphite (see Scheme 1).



Scheme 1. Synthesis of **I** and **II**.

Treatment of exfoliated γ-ZP in 1:1 water/acetone at 80 °C with the diphosphonic acid in the appropriate molar ratio (step A) led to the pillared material **I** of empirical formula $ZrPO_4[O_2P(OH)_2]_{0.74}[O_2P(OH)\text{-}R\text{-}(OH)PO_2]_{0.13}\cdot n\,H_2O$, R = $CH_2CH_2(OCH_2CH_2)_5OCH_2CH_2$. Careful neutralization of **I** with methylamine followed by treatment with hypophosphorous acid (Scheme 1 step B; see Experimental Section) yielded a new material **II**. Elemental and thermogravimetric analyses for **II** gave the empirical formula $Zr(PO_4)(O_2PH_2)_{0.74}(C_{14}H_{30}P_2O_{12})_{0.13}\cdot 0.8\,H_2O$, thus showing that all exchangeable phosphates of **I** were replaced by hypophosphite without appreciable loss of diphosphonate. A sample of material **II**, dissolved in HF/D_2O, gave a ^{31}P NMR spectrum with signals at 0.0, 8.9, and 25.3 ppm attributable to phosphoric, hypophosphorous, and phosphonic acids, respectively. Their relative intensity (3.97:2.91:1) was in excellent agreement with the calculated ratios (3.84:2.85:1) for the empirical formula obtained from the other techniques. FTIR of **II** showed the expected stretching P–H band at 2403 cm^{-1} while solid-state MAS ^{31}P NMR revealed the presence of the nonexchangeable phosphates at −27.9 and the complete disappearance of the signal at −13.6 ppm arising from exchangeable phosphates of the starting material **I**. Both hypophosphite and phosphonate groups gave a broad signal at about 10 ppm, whose intensity heavily increased under cross-polarization conditions (contact time 2 ms). X-ray powder diffraction of **II** showed a reasonable degree of crystallinity and an interlayer distance of 1.28 nm, which was independent of the degree of humidity of the sample.

The unexpectedly fast swelling of material **II** occurred when it reacted with a very small amount of methylamine. A comparative study of the titration of **I** and **II** with methylamine is depicted in Figure 1 a. While **I** gradually increases its interlayer distance with increasing pH (see powder XRD patterns in Figure 1 b), **II** shows a remarkable, sharp swelling from 1.28 nm to 2.14 nm in a very narrow pH range (ca. 4.2 to 5.0) corresponding to the addition of solely 0.2 equivalents of amine. It should be noted that **II** suffers extensive oxidation at pH > 7. Solid-state ^{31}P NMR and elemental analysis indicate that phase **II** completely transforms into phase **I** at pH 9.

The forces governing the piling of γ-ZP and γ-ZP/hypophosphite (γ-ZPH) layers are very different. In γ-ZP the outer layer of exchangeable phosphates form a network of

[*] Prof. Dr. E. Brunet, Dr. M. J. de la Mata, Prof. Dr. O. Juanes, Prof. Dr. J. C. Rodríguez-Ubis
Departamento de Química Orgánica
Facultad de Ciencias C-I
Universidad Autónoma de Madrid, 28049-Madrid (Spain)
Fax: (+34) 91-397-3966
E-mail: ernesto.brunet@uam.es

[**] This work was supported by MCYT of Spain under grants PB98-0103 and MAT2002-03243. We also thank FYSE-ERCROS S.A. (Aranjuez, Spain) for generous indirect funding.

 DOI: 10.1002/anie.200352711 © 2004 Wiley-VCH Verlag GmbH & Co. KGaA, Weinheim

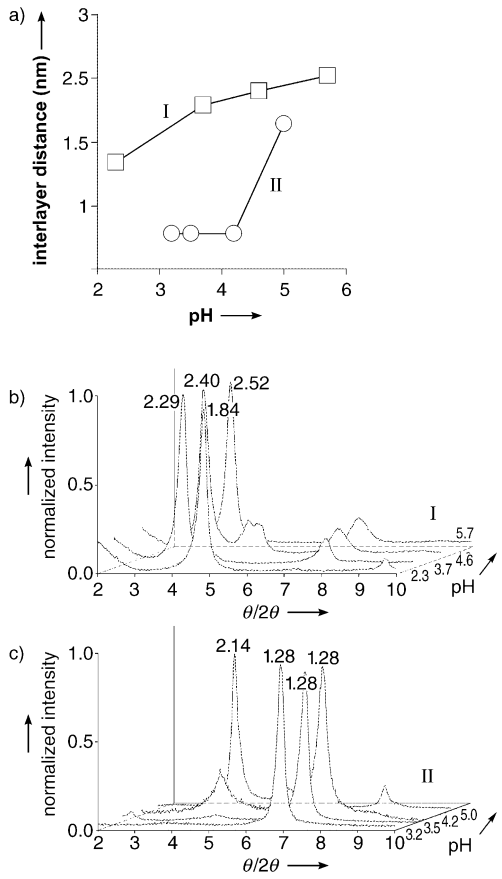


Figure 1. a) Variation of interlayer distance of materials **I** and **II** with pH (methylamine titration; see text). Relevant powder XRD patterns for **I** (b) and **II** (c).

hydrogen bonding interactions between consecutive lamellae in which several molecules of interlayer water are involved.[12] In appropriate conditions of polarity and temperature, γ-ZP can be easily exfoliated, each lamella being surrounded by water molecules and thus effectively solvated. However, the γ-ZPH phase does not have polar exchangeable phosphates, the layer surfaces are carpeted by a grid of nonpolar PH_2 groups that glue the lamellae one another by sturdy hydrophobic, van der Waals forces. γ-ZPH phase lacks interlamellae water molecules and its interlayer distance is thus very short (0.88 nm) as compared to that of γ-ZP (1.22 nm). As a consequence, the γ-ZPH phase cannot be exfoliated in water or any other common organic solvent.[13] Besides, the very low acidic character of hypophosphite PH_2 bonds avoid phase swelling by the action of acid–base processes in the same way as those that take place in the γ-ZP intercalation of amines.

In material **I**, the acidity and polarity of the remaining superficial phosphoric groups and the relatively large initial interlayer distance (1.8 nm) allows for the methylammonium ions and the water molecules to move somewhat freely in the interlayer space, the hydrogen-bonding network is gradually disrupted and the material progressively swells.

In the case of **II**, the hydrophobic forces governing the behavior of the pure γ-ZPH phase are still much at work. The fact that the starting interlayer distance of **II** is very short (1.28 nm) and humidity independent should be manifestations of this behavior. Molecular modeling shows that at this interlayer distance, the organic chains have to lie parallel to the layers, somewhat compressed along the channels left along the hypophosphite grid. Yet in **II** every organic phosphonate still has an acidic OH and hence amine intercalation is now possible. In the highly nonpolar interlayer region of **II** there should be few opportunities for the ammonium ions to be stabilized but instead form tight ion pairs with phosphonates. Consequently, the bulky organic cations should rest very close to the organic chains and act as a wedge that makes the pillars stand up. The lamellae of γ-ZP and γ-ZPH phases are known to be very rigid. Once a few amine molecules have diffused into the interlayer region, the van der Waals forces are quickly disrupted and the material swells very abruptly. The interlayer distance is then almost doubled in the narrow gap of 0.2 equivalents of added amine. To the best of our knowledge, this enormous sensitivity of microcrystalline porosity towards the intercalation of small molecules has no precedent.

This work shows that by selecting the appropriate functionality of both organic and inorganic moieties in γ-ZP pillared materials, shape, porosity, and functionality can be selected beforehand. But more interestingly, those properties can be remodeled afterwards in the solid state by processes as simple as small-molecule intercalation. Such reactions at the edges of the microcrystals can induce a cascade of conformational changes that remotely and sharply affect the entire structure, thus leading to a phenomenon that could be named supramolecular allostery.

Experimental Section

The synthesis of pentaethylenglycol diphosphonic acid, and the pillaring procedure were previously described.[14] Material **I** (0.3 g) was dispersed in a 0.1M water solution (30 mL) of methylammonium chloride. An aqueous solution of methylamine (0.1M) was then added by means of an automatic titroprocessor until the pH reached 7. The suspension was centrifuged, washed with water (25 × 3 mL) and dried at 100°C for 4 h. The resulting solid (0.3 g) was dispersed into a solution containing 3.8 g of 50% wt H_3PO_2 in water/acetone (1:1, 30 mL) under argon. The mixture was maintained at 80°C overnight, centrifuged and the solid washed with water (25 × 3 mL). The resulting white solid, **II**, was dried at 100°C for 4 h and conditioned at 90% relative humidity ($BaCl_2$) for at least 24 h.

Received: August 25, 2003 [Z52711]

Keywords: crystal engineering · layered compounds · supramolecular chemistry · topochemistry · zirconium

[1] a) G. R. Desiraju, *J. Indian Chem. Soc.* **2003**, *80*, 151–155; in *Crystal Engineering: The Design of Organic Solids*, Elsevier, Amsterdam, **1989**; D. Braga, G. R. Desiraju, J. S. Miller, A. G. Orpen, S. L. Price, *Cryst. Eng.* **2002**, *4*, 500–509.

[2] J. M. Lehn, *Angew. Chem.* **1990**, *102*, 1347; *Angew. Chem. Int. Ed. Engl.* **1990**, *29*, 1304; J. M. Lehn, *Supramolecular Chemistry: Concepts and Perspectives*, VCH, Weinheim, **1995**.

[3] *Perspectives in Supramolecular Chemistry. The Crystal as a Supramolecular Entity* (Ed.: G. R. Desiraju), Wiley, Chichester, UK, **1996**; *Comprehensive Supramolecular Chemistry, Vol. 11*

 © 2004 Wiley-VCH Verlag GmbH & Co. KGaA, Weinheim

(Eds.: J. L. Atwood, J. E. D. Davies, D. D. MacNicol, F. Voegtle), Pergamon, Oxford, **1996**.
[4] A. Lerf in *Handbook of Nanostructured Materials and Nanotechnology*, *Vol. 5* (Ed.: H. S. Nalwa), Academic, New York, **2000**, pp. 1 – 166.
[5] M. D. Ward, *Science* **2003**, *300*, 1104 – 1105; J. A. Hubbell, *Science* **2003**, *300*, 595 – 596; B. L. Chen, M. Eddaoudi, S. T. Hyde, M. Okeeffe, O. M. Yaghi, *Science* **2001**, *291*, 1021 – 1023; Y. Diskin-Posner, S. Dahal, I. Goldberg, *Angew. Chem.* **2000**, *112*, 1344 – 1348; *Angew. Chem. Int. Ed.* **2000**, *39*, 1288 – 1292.
[6] D. M. Poojary, A. Clearfield, *Acc. Chem. Res.* **1997**, *30*, 414 – 422, and references therein.
[7] E. Brunet, M. Huelva, J. C. Rodríguez-Ubis *Tetrahedron Lett.* **1994**, *35*, 8697 – 8700.
[8] A. Clearfield, Z. Wang, *J. Chem. Soc. Dalton Trans.* **2002**, 2937 – 2947G. Alberti in *Comprehensive Supramolecular Chemistry*, *Vol. 7* (Ed.: J. M. Lehn), Pergamon, **1996**, chap. 5.
[9] E. Brunet *Chirality* **2002**, *14*, 135 – 143.
[10] E. Brunet, M. Alonso, M. J. de la Mata, S. Fernández, O. Juanes, O. Chavanes, J. C. Rodríguez-Ubis, *Chem. Mater.* **2003**, *15*, 1232 – 1234.
[11] E. Brunet, M. Huelva, R. Vázquez, O. Juanes, J. C. Rodríguez-Ubis, *Chem. Eur. J.* **1996**, *12*, 1578 – 1584.
[12] D. M. Poojary, B. Shpeizer, A. Clearfield, *J. Chem. Soc. Dalton Trans.* **1995**, 111 – 113.
[13] G. Alberti, M. Casciola, R. K. Biswas, *Inorg. Chim. Acta* **1992**, *201*, 207 – 212.
[14] G. Alberti, E. Brunet, C. Dionigi, O. Juanes, M. J. de la Mata, J. C. Rodiguez-Ubis, R. Vivani, *Angew. Chem.* **1999**, *111*, 3548 – 3551; *Angew. Chem. Int. Ed.* **1999**, *38*, 3351 – 3353.

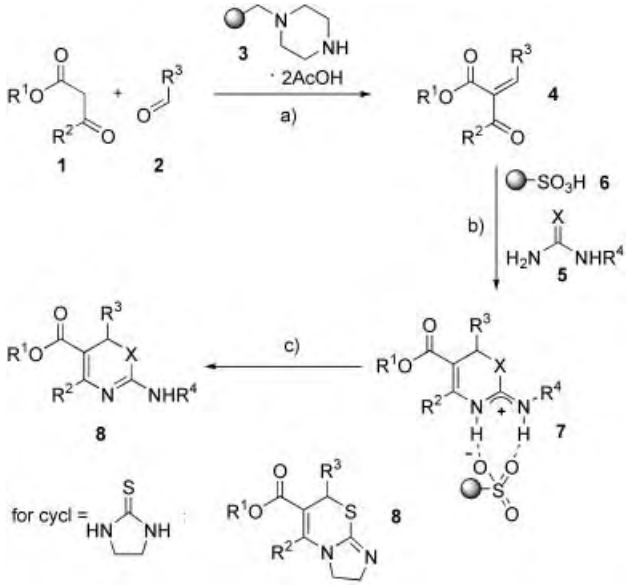
 © 2004 Wiley-VCH Verlag GmbH & Co. KGaA, Weinheim

Compound Libraries

Combinatorial Synthesis of Functionalized 1,3-Thiazine Libraries Using a Combined Polymer-Supported Reagent/Catch-and-Release Strategy**

*Gernot A. Strohmeier and C. Oliver Kappe**

Combinatorial chemistry has emerged as a highly valuable and powerful method in medicinal chemistry, catalyst discovery, and materials science over the past few years.[1] Driven by the force to discover and develop new molecules with tailored properties more efficiently and in increasingly shorter times, scientists have developed several highly successful concepts. Combinatorial methods focusing on small organic molecules are mainly dominated by two strategies: solid-phase synthesis[2] and with increasing importance solution-phase protocols with the aid of scavenger resins and polymer-bound reagents.[3] A special concept in solution-phase synthesis is the "catch-and-release" strategy, where the formed target molecule is selectively bound (covalently or by means of an ionic bond) to a resin. After excess reagents, unreacted starting materials, catalysts, etc. are removed by simple washings, the product is released from the polymer support. One could envision that in an ideal case such catch-and-release methods could be incorporated in the synthesis step. Appropriately functionalized polymeric resins could be utilized that not only mediate a specific chemical reaction but at the same time selectively remove the desired product from the reaction mixture. However, examples for such one-pot, in situ synthesis/catch-and-release protocols are extremely rare.[4] Herein we report on the generation of libraries of densely functionalized (five diversity points) 1,3-thiazines of type **8**, employing a resin-bound sulfonic acid that acts simultaneously as reaction promoter in a cyclocondensation step and as a selective sequester of the final basic thiazine products (Scheme 1).



Scheme 1. Synthesis of thiazines **8**. a) 10 mol% **3**, chlorobenzene, 115°C, 5 h; b) 0.6 equiv **5**, 0.5 equiv **6**, dioxane, 90°C, 18 h; c) washing, then MeOH/TEA 3:1. TEA = triethylamine.

The 2-amino-1,3-thiazine-5-carboxylate scaffold **8** has hitherto received scant attention,[5,6] despite its close structural similarity to the dihydropyrimidinones (DHPMs), which are privileged structures with heterocyclic cores[7] and well-documented pharmacological properties.[8] The overall strategy for the generation of a library of thiazines **8** utilizing the tandem ring-closure/resin-capture approach is outlined in Scheme 1.

Our synthesis started with the Knoevenagel condensation of β-keto esters **1** with aldehydes **2** under open-vessel conditions to facilitate the removal of water formed during

[*] Dr. G. A. Strohmeier, Prof. Dr. C. O. Kappe
Institute of Chemistry, Organic and Bioorganic Chemistry
Karl-Franzens University Graz
Heinrichstrasse 28, A-8010 Graz (Austria)
Fax: (+43) 316-380-9840
E-mail: oliver.kappe@uni-graz.at

[**] We are indebted to BASF AG, Ludwigshafen (Germany), and the Austrian Science Fund (FWF, P-15582) for financial support.

Supporting information for this article is available on the WWW under http://www.angewandte.org or from the author.

 DOI: 10.1002/anie.200352731 © 2004 Wiley-VCH Verlag GmbH & Co. KGaA, Weinheim

the reaction. A slight excess of the aldehyde was required to ensure good conversion in this step. We found the polymer-bound piperazine diacetate **3** to be a very effective catalyst for this reaction.[9] Not only is the catalyst itself easily removed, this method also removes the basic 2-amino-1,3-cyclohexadiene by-products formed by known catalyst-derived side reactions.[10,11] Importantly, these basic by-products must be removed so they do not interfere with the subsequent catch-and-release of the thiazine products (**4**→**7**→**8**). After filtration from the catalyst the crude enones were used directly in the subsequent ring-closing reaction. In the second step, the enones **4** (in excess) were treated with the appropriate thioureas and the polymer-bound sulfonic acid **6**[12,13] at 90 °C in inert dioxane, which proved superior to other solvents tested. Since the formed 1,3-thiazines are the only basic molecules in the reaction system, they are selectively captured by the supported sulfonic acid, presumably as tightly coordinated ion pairs with the strongly basic amidine-like isothiourea moiety.[14] Here, the polymer-bound sulfonic acid acts as an acidic mediator to facilitate the thiazine ring-closure and subsequently as a selective sequester for the desired basic thiazine products (see Scheme 1). Finally, by filtration and multiple washing steps, reagents, excess starting materials, solvents, and by-products (see below) are removed. The desired products are cleaved from the resin by displacement with triethylamine, which is a significantly stronger base than the 1,3-thiazines **8**.

This approach was used to prepare 28 1,3-thiazines and one 1,3-selenazine[15] in general good to excellent purities and overall yields from good to moderate over the two reaction steps (Table 1). It is evident that aldehyde building blocks **2** without or with little steric hindrance lead to generally higher yields. For aromatic aldehydes, substituents in *ortho* position, in particular if they are electron withdrawing, lower the yields significantly, although not the purities. Aliphatic substituents in position 4 of 1,3-thiazines (see R^2 in Table 1) are important for the success of the method. Despite the effects of the substituents on the efficiency of the thiazine ring-closure, it is important to note that even in cases of low yields (10–15 %) the purity of products is still high (72–98 %). This clearly demonstrates the success of the tandem ring-closure/catch-and-release strategy, since incomplete conversions—presumably as a result of the reduced reactivity of some building blocks—do not result in the propagation of impurities. The efficacy of the concept is clearly illustrated by HPLC monitoring at different stages of the synthesis.[16]

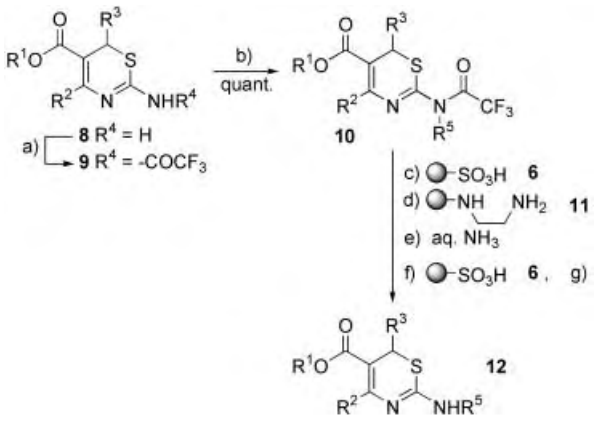
In order to synthesize more diverse derivatives of the parent scaffold, we envisioned a selective and flexible functionalization of the amino group in position 2 of the 1,3-thiazines **8**. This is of particular importance because the number of thioureas successfully applied in the ring-closure sequence **4**+**5**→**8** is limited. Therefore, we developed a protocol for the selective alkylation of the 2-amino group on the thiazine ring utilizing the Mitsunobu reaction as the diversity-generating method and again employing polymer-supported sequesteration reagents (Scheme 2).[17]

We found that activation of the amino group as a trifluoroacetamide was an effective method to provide an acidic nitrogen prone to undergo Mitsunobu alkylation.[18]

Table 1: Solution-phase synthesis of 1,3-thiazines **8**.

Entry	R^1	R^2	R^3	R^4	X	Yield [%][a]	Purity [%][b]
1	Et	Me	Ph	NH_2	S	78	93
2	Et	Me	Ph	NHMe	S	97	>98
3	Et	Me	Ph	NHPh	S	72	93
4	Et	Me	Ph	cycl[c]	S	71	96
5	Et	Me	2-CF_3-Ph	NHMe	S	18	>98
6	Me	Et	2-CF_3-Ph	NH_2	S	10	80
7	Me	Et	2-CF_3-Ph	NHBn	S	51	94
8	Et	Me	2,3-Cl-Ph	NHMe	S	89	>98
9	Et	Pr	2,3-Cl-Ph	NH_2	S	45	94
10	Et	Pr	2,3-Cl-Ph	NH_2	Se	11	90
11	Et	Pr	2-Cl-Ph	NH_2	S	35	94
12	Bn	Me	2-Cl-Ph	NHMe	S	30	98
13	Et	Pr	2-Cl-Ph	NHBn	S	70	98
14	Bn	Me	2-Cl-Ph	NH-Mes	S	42	87
15	Et	Me	2-thienyl	NH_2	S	56	96
16	Et	Me	2-thienyl	NHMe	S	15	>98
17	Et	Me	2-thienyl	cycl[c]	S	15	90
18	Et	Pr	C_5H_{11}	NH_2	S	26	85
19	Et	Me	3-OH-Ph	NH_2	S	24	84
20	Et	Me	3-OH-Ph	NHMe	S	36	90
21	*i*Pr	Me	3-Cl-Ph	NH_2	S	78	98
22	*i*Pr	Me	3-Cl-Ph	NHMe	S	75	96
23	Et	Pr	3-NO_2-Ph	NH_2	S	22	89
24	Et	Pr	3-NO_2-Ph	NHMe	S	46	78
25	Bn	Me	3-NO_2-Ph	cycl[c]	S	13	72
26	Me	Et	4-Cl-Ph	NH_2	S	32	97
27	Me	Et	4-Cl-Ph	NHPh	S	66	95
28	*i*Pr	Me	2,5-MeO-Ph	NH_2	S	43	91
29	*i*Pr	Me	2,5-MeO-Ph	NHMe	S	67	92

[a] Yields calculated on the basis of the experimentally determined loading of **6** (4.18 mmol g^{-1}) over two reaction steps. [b] Purity determined by LC-MS. [c] Imidazolidine-2-thione (see Scheme 1).

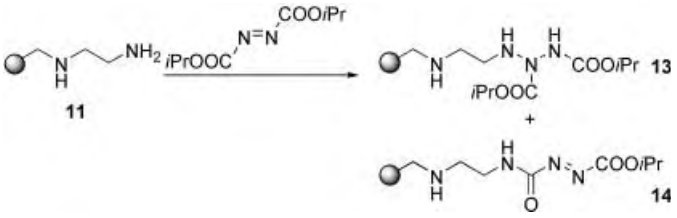


Scheme 2. Scaffold decoration of thiazine libraries by Mitsunobu alkylation. a) 2 equiv TFAA, dichloromethane, RT, 30 min; b) 4 equiv DIAD, 4 equiv TPP, 4 equiv R^5OH, THF, RT, 12 h; c) 5 equiv **6**, RT, 10 min; d) 2 equiv **11**, RT, 12 h; e) aq NH_3, RT, 3 h; f) 2 equiv **6**, RT, 10 min; g) MeOH/TEA 3:1. DIAD = diisopropyl azodicarboxylate, RT = room temperature, TEA = triethylamine, TFAA = trifluoroacetic anhydride, TPP = triphenylphosphane.

This intermediate (**9**) was easy to generate, and the trifluoroacetate was easy to remove at the end of the synthesis by treatment with aqueous ammonia. The alkylation sequence started with the standard acetylation of 2-aminothiazines **8**

 © 2004 Wiley-VCH Verlag GmbH & Co. KGaA, Weinheim

($R^4 = H$) with trifluoroacetic anhydride and subsequent concentration to dryness to produce pure nonbasic trifluoroacetamides **9**. This change of basicity upon acylation also plays a critical role in the subsequent purification. Mitsunobu alkylation with primary alcohols was performed under classical conditions using a combination of diisopropyl azodicarboxylate (DIAD) and triphenylphosphane as well as the appropriate alcohol.[18] It should be noted that the application of a polymer-bound Mitsunobu reagent[19] did not result in useful conversions. Since the alkylated thiazine **10** remains nonbasic, it is possible to remove excess Mitsunobu reagent and the reduced *N*,*N*′-diacylhydrazide by-product by treating the reaction mixture with polymer-supported sulfonic acid **6**. In order to completely sequester all of the Mitsunobu reagent we also added a resin-bound amine base (**11**) that effectively sequestered the azodicarboxylate by forming either the polymer-bound triazene or monoamide (Scheme 3).[20,21] To the best of our knowledge this propensity



Scheme 3. Polymer-supported scavenging mechanisms for DIAD.[22]

of polymer-supported amines to react with azodicarboxylates constitutes a new strategy for the removal of Mitsunobu reagents. Procedures previously published applied tagged or polymer-supported phosphanes,[22,23] acid-labile ester groups (*tert*-butyl) for the selective degradation of Mitsunobu reagents,[23] and ROMP-based sequestration.[24] Finally the trifluoroacetate is cleaved with aqueous ammonia to yield thiazine **12** in its basic form. This recovery of basicity now allows for a catch-and-release strategy at the end using sulfonic acid resin **6** to produce pure monoalkylated thiazine products. The final purification effectively removes the excess triphenylphosphane and the formed triphenylphosphane oxide. It must be pointed out that the manipulations required for the sequence **8**→**12** consist solely of evaporation and polymer-assisted steps, and the sequence is therefore applicable to parallel synthesis.

Selective N-monoalkylation was accomplished in acceptable yield and products the were obtained with good purity over three reaction steps and subsequent catch-and-release purification (Table 2). In all cases the Mitsunobu reactions went to completion; the moderate yields were a consequence of incomplete sequestration of the product from the complex reaction mixture.

In summary, we have presented a concept for the construction of diverse libraries of 1,3-thiazines based on the dual action of a polymer-bound sulfonic acid as the mediator of a ring-closure reaction and the concomitant scavenger of the desired product. Five diversity points are addressed in the synthesis and subsequent scaffold decoration, with yields up to 97% and good to excellent purities.

Table 2: Solution-phase N-alkylation of 1,3-thiazines under Mitsunobu conditions to give products **12**.

Entry	R^1	R^2	R^3	R^5	Yield [%]	Purity [%][a]
1	Et	Me	Ph	3-Me-butyl	38	95
2	Et	Me	2,3-Cl-Ph	2-EtO-ethyl	41	80
3	Et	Me	2-thienyl	2-EtO-ethyl	52	94
4	Et	Me	C_5H_{11}	3-F-benzyl	19	75
5	Et	Me	3-Cl-Ph	hexyl	24	96
6	Me	Et	4-Cl-Ph	propyl	19	94

[a] Purity determined by LC-MS.

Experimental Section

Typical procedure for the Knoevenagel condensation (outlined for the enone leading to thiazine **8**, entry 1 in Table 1: Benzaldehyde (110 mg, 1.04 mmol), ethyl acetoacetate (118 mg, 0.91 mmol), and polymer-supported piperazine (as the diacetate) (90 mg, 10 mol%) were placed in a glass vial containing chlorobenzene (1 mL) and heated at 115 °C for 5 h under open-vessel conditions. After filtration and washing with dry dioxane (2 × 0.8 mL) the combined filtrates (approximately 2 mL) were directly subjected to the subsequent reaction.

A solution of the appropriate enone and thiourea (38 mg, 500 μmol) were added to dry DOWEX 50X2 **6** (102 mg, 426 μmol, 4.18 mmol g^{-1} as experimentally determined) in a Teflon frit (ACT Synthesizer PLS 6x4) and heated at 90 °C for 18 h. After cooling, the resin was washed (dioxane, MeOH, water, MeOH, dichloromethane), and the product was released by addition of triethylamine (500 μL) and methanol (1.5 mL). After the cocktail had been shaken for 20 min, it was filtered and the resin washed twice with 10% triethylamine in methanol (1.5 mL). The combined filtrates were evaporated to dryness, redissolved in dichloromethane, and filtered through a 1-cm plug of silica gel (eluent: ethyl acetate/petroleum ether 3:1) yielding 92.4 mg (334 μmol, 78% based on experimentally determined loading of the ion-exchange resin) of compound **8** (entry 1 in Table 1).

Received: August 28, 2003 [Z52731]

Keywords: combinatorial chemistry · heterocycles · molecular recognition · polymer-bound reagents · scavenger resins

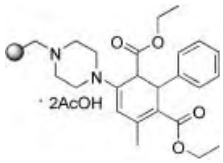
[1] a) *Handbook of Combinatorial Chemistry* (Eds.: K. C. Nicolaou, R. Hanko, W. Hartwig), Wiley-VCH, Weinheim, **2002**; b) *Combinatorial Chemistry: Synthesis, Analysis, Screening* (Ed.: G. Jung), Wiley-VCH, Weinheim, **1999**; c) *Combinatorial Chemistry: A Practical Approach* (Eds.: W. Bannwarth, E. Felder), Wiley-VCH, Weinheim, **2000**.

[2] F. Zaragoza Dörwald, *Organic Synthesis on Solid Phase*, *Vol. 2*, Wiley-VCH, Weinheim, **2002**.

[3] a) S. V. Ley, I. R. Baxendale, R. N. Bream, P. S. Jackson, A. G. Leach, D. A. Longbottom, M. Nesi, J. S. Scott, R. I. Storer, S. J. Taylor, *J. Chem. Soc. Perkin Trans. 1* **2000**, 3815–4196; b) S. V. Ley, I. R. Baxendale, *Nat. Rev. Drug Discovery* **2002**, *1*, 573–586; c) A. Kirschning, H. Monenschein, R. Wittenberg, *Angew. Chem.* **2001**, *113*, 670–701; *Angew. Chem. Int. Ed.* **2001**, *40*, 650–679; d) C. C. Tzschucke, C. Markert, W. Bannwarth, S. Roller, A. Hebel, R. Haag, *Angew. Chem.* **2002**, *114*, 4136–4173; *Angew. Chem. Int. Ed.* **2002**, *41*, 3964–4000.

 © 2004 Wiley-VCH Verlag GmbH & Co. KGaA, Weinheim

[4] a) B. A. Kulkarni, A. Ganesan, *Angew. Chem.* **1997**, *109*, 2565 – 2567; *Angew. Chem. Int. Ed. Engl.* **1997**, *36*, 2454 – 2455; b) B. A. Kulkarni, A. Ganesan, *Chem. Commun.* **1998**, 785 – 786; c) T. L. Graybill, S. Thomas, M. A. Wang, *Tetrahedron Lett.* **2002**, *43*, 5305 – 5309.
[5] K. S. Atwal, B. C. O'Reilly, J. Z. Gougoutas, M. F. Malley, *Heterocycles* **1987**, *26*, 1189 – 1192.
[6] C. O. Kappe, *J. Org. Chem.* **1997**, *62*, 7201 – 7204.
[7] a) C. O. Kappe, *Acc. Chem. Res.* **2000**, *33*, 879 – 888;b) C. O. Kappe, *QSAR Comb. Sci.* **2003**, *22*, 630 – 645.
[8] For a review, see C. O. Kappe, *Eur. J. Med. Chem.* **2000**, *35*, 1043 – 1052.
[9] a) J. Simpson, D. L. Rathbone, D. C. Billington, *Tetrahedron Lett.* **1999**, *40*, 7031 – 7033; b) J. S. Yadav, M. Syamala, *Chem. Lett.* **2002**, 688 – 689.
[10] a) K. Take, K. Okumura, K. Takimoto, M. Kato, M. Ohtsuka, Y. Shiokawa, *Chem. Pharm. Bull.* **1991**, *39*, 2915 – 2923; b) H. Nitta, K. Takimoto, I. Ueda, *Chem. Pharm. Bull.* **1992**, *40*, 858 – 863; c) K. Take, K. Okumura, K. Takimoto, M. Ohtsuka, Y. Shiokawa, *Chem. Pharm. Bull.* **1992**, *40*, 899 – 906.
[11] The compound shown here is an example of the basic 2-amino-1,3-cyclohexadiene side-product in the Knoevenagel condensation of benzaldehyde and ethyl acetoacetate (entry 1 in Table 1).



[12] For applications of polymer-bound sulfonic acid in catch-and-release strategies, see the following: a) D. L. Flynn, J. Z. Crich, R. V. Devraj, S. L. Hockerman, J. J. Parlow, M. S. South, S. Woodard, *J. Am. Chem. Soc.* **1997**, *119*, 4874 – 4881; b) C. Blackburn, B. Guan, P. Fleming, K. Shiosaki, S. Tsai, *Tetrahedron Lett.* **1998**, *39*, 3635; c) J. Habermann, S. V. Ley, J. S. Scott, *J. Chem. Soc. Perkin Trans. 1* **1999**, 1253 – 1256; d) R. I. Storer, T. Takemoto, P. S. Jackson, S. V. Ley, *Angew. Chem.* **2003**, *115*, 2625 – 2629; *Angew. Chem. Int. Ed.* **2003**, *42*, 2521 – 2525; e) T. Mukade, D. R. Dragoli, J. A. Ellman, *J. Comb. Chem.* **2003**, *5*, 590 – 596.
[13] A low crosslinking of 2% DVB (DOWEX 50X2) is absolutely necessary. Application of macroporous DOWEX 50X8 (8% DVB) led to yields $<1\%$ under otherwise identical reaction conditions.
[14] a) M. G. Hutchings, M. C. Grossel, D. A. S. Merckel, A. M. Chippendale, M. Kenworthy, G. McGeorge, *Cryst. Growth Des.* **2001**, *1*, 339 – 342; b) A. Cherouana, N. Benali-Cherif, L. Bendjeddou, *Acta Crystallogr. Sect. E* **2003**, *59*, 180 – 182.
[15] For selected publications on 1,3-selenazines see: a) D. Dubreuil, J. P. Pradere, N. Giraudeau, *Tetrahedron Lett.* **1995**, *36*, 237 – 240; b) F. Purseigle, D. Dubreuil, A. Merchand, J. P. Pradere, M. Goli, L. Toupet, *Tetrahedron* **1998**, *54*, 2545 – 2562; c) M. Koketsu, H. Ishihara, W. Wu, K. Murakami, I. Saiki, *Eur. J. Pharm. Sci.* **1999**, *9*, 157 – 161; d) M. Koketsu, T. Senda, K. Yoshimura, H. Ishihara, *J. Chem. Soc. Perkin Trans. 1* **1999**, 453 – 456.
[16] For a graphical representation see the Supporting Information.
[17] O. Mitsunobu, *Synthesis* **1981**, 1 – 28.
[18] T. C. Norman, N. S. Gray, J. T. Koh, P. G. Schultz, *J. Am. Chem. Soc.* **1996**, *118*, 7430 – 7431.
[19] L. D. Arnold, H. I. Assil, J. C. Vederas, *J. Am. Chem. Soc.* **1989**, *111*, 3973 – 3976.
[20] a) O. Diels, P. Fritzsche, *Ber. Dtsch. Chem. Ges.* **1911**, *44*, 3018 – 3027; b) O. Diels, *Ber. Dtsch. Chem. Ges.* **1922**, *55*, 1524 – 1528; c) K. E. Cooper, E. H. Ingold, *J. Chem. Soc.* **1926**, 1894 – 1896; d) G. W. Kenner, R. J. Stedman, *J. Chem. Soc.* **1952**, 2089 – 2094; e) N. Egger, L. Hoesch, A. S. Dreiding, *Helv. Chim. Acta* **1983**, *66*, 1416 – 1426.
[21] For an on-bead FTIR analysis of the reaction of diisopropyl azodicarboxylate (DIAD) with scavenger resin **11** see the Supporting Information.
[22] a) M. v. Itzstein, M. Mocerino, *Synth. Commun.* **1990**, *20*, 2049 – 2057; b) A. R. Tunoori, D. Dutta, G. I. Georg, *Tetrahedron Lett.* **1998**, *39*, 8751 – 8754; c) P. Lan, J. A. Porco, Jr., M. S. South, J. J. Parlow, *J. Comb. Chem.* **2003**, *5*, 660 – 669.
[23] a) G. W. Starkey, J. J. Parlow, D. L. Flynn, *Bioorg. Med. Chem. Lett.* **1998**, *8*, 2385 – 2390; b) M. Kiankarimi, R. Lowe, J. R. McCarthy, J. P. Whitten, *Tetrahedron Lett.* **1999**, *40*, 4497 – 4500; c) J. C. Pelletier, S. Kincaid, *Tetrahedron Lett.* **2000**, *41*, 797 – 800.
[24] A. G. M. Barrett, R. S. Roberts, J. Schröder, *Org. Lett.* **2000**, *2*, 2999 – 3001.

 © 2004 Wiley-VCH Verlag GmbH & Co. KGaA, Weinheim

Electronic Interactions in DNA

Environmental Fluctuations Facilitate Electron-Hole Transfer from Guanine to Adenine in DNA π Stacks**

*Alexander A. Voityuk, Khatcharin Siriwong, and Notker Rösch**

Long-range hole migration along the π stack of DNA currently receives much experimental and theoretical attention.[1] Charge displacements of up to 200 Å[2–5] can occur by propagating radical cation states between guanine bases (G) mediated by tunneling through intervening bridges of AT base pairs ("G-hopping"). This G-hopping mechanism[6,7] was analyzed in detail[8–10] and successfully used to interpret many experiments on charge transport through DNA.[1,11–13] A-hopping, which involves radical cation states on adenine bases (A),[14] was postulated as an additional mechanism because the G-hopping model failed to rationalize several recent experimental findings.[14–17] Yet A-hopping cannot be well described using the energetics estimated from the redox potentials of nucleobases in water,[18] which find the radical cation state G^+ on guanine more stable than the state A^+ by $\Delta = 0.4$ eV (radical states C^+ and T^+ are considerably higher in energy than G^+, with an energy gap of ≈ 1 eV,[18] and therefore are highly unlikely to accept an electron hole in DNA). Long-range hole transport over $(AT)_n$ bridges ($n > 4$) in DNA was suggested to occur[6,19] via thermally induced hole excitation from G^+ to A, followed by hole hopping to neighboring adenine bases. The Boltzmann factor

[*] Dr. A. A. Voityuk, K. Siriwong, Prof. N. Rösch
Institut für Physikalische und Theoretische Chemie
Technische Universität München
85747 Garching (Germany)
Fax: (+49) 89-2891-3468
E-mail: roesch@ch.tum.de

[**] This work was supported by Deutsche Forschungsgemeinschaft (SFB 377), Volkswagen Foundation, and Fonds der Chemischen Industrie.

 © 2004 Wiley-VCH Verlag GmbH & Co. KGaA, Weinheim DOI: 10.1002/anie.200352824

$\exp(-\Delta/kT)$ for thermally induced hopping from G^+ to A^+, implied by the energy gap of 0.4 eV, is 10^{-7}; it is very sensitive to variations of Δ. In this work, by using results of hybrid quantum mechanics/molecular dynamics (QM/MD) modeling,[20] we studied the variation of the relative energy Δ of G^+ and A^+ radical states due to fluctuations (on a time scale of 0.3–0.4 ns) of the electrostatic interaction between DNA and its electrolyte environment, and we explored the possibility for near degeneracy of the G^+ and A^+ states.

Thus far, redox potentials of nucleobases in the interior of a DNA double helix have not been measured. Clearly, estimates derived for individual nucleosides in aqueous solution[18] disregard the possible influence of neighboring base pairs and the sugar–phosphate backbone, as well as the effect of a structured environment.

In DNA, guanine triplets $(GC)_3$ are stronger hole acceptors than single GC pairs embedded in AT runs.[5,21] This significant result demonstrated that hole trapping by guanine is significantly affected by neighboring base pairs. The stabilizing effect of neighboring pairs on radical cation states in the DNA π stacks was systematically studied using quantum-chemical calculations.[22] Hole trapping by a base B in the duplex sequence 5′-XBY-3′ was shown to be considerably affected by the subsequent base pair Y (with is relatively shifted up to 0.3 eV), whereas the effect of the preceding base pair X turned out to be rather small. In addition, recent modeling led to the conclusion that the localization and energetics of an electron-hole state in a DNA strand can be strongly affected by the configuration of neighboring sodium cations.[23,24] Therefore, among other factors, the surrounding electrolyte has to be considered as a source for changes in the electrostatic potential created in the interior of DNA that can influence the charge transfer.

Thermal structural fluctuations of DNA and its environment play an important role for charge transfer (CT) through the double helix. In particular, electronic coupling between neighboring base pairs is extremely sensitive to conformational changes in DNA.[25–27] Molecular dynamics (MD) simulations provide a detailed microscopic description of the structure and motion of DNA and its environment.[28] Here, we focus on how structural fluctuations of DNA and its surroundings affect the CT energetics between nucleobases, based on long-time ($\approx$12 ns) MD simulations[29] of various duplexes. Along the trajectories, we monitored the energetics of hole transfer in the 5′→3′ direction from G to neighboring bases A and G. For this purpose, we estimated the corresponding reaction free energy ΔG of hole transfer along the trajectories with a quantum-chemical method that takes the instantaneous atomic configuration of the environment into account (that is, snapshots at every picosecond).[34] As the estimated ΔG values correspond to an ensemble of nuclear configurations, their standard deviations include three contributions, due to: 1) the nuclear vibrations of the nucleobases, 2) the conformational changes of DNA, and 3) the fluctuations of the solvent environment.

As an example, we present results for the 14-mer duplex 5′-$TTG_3(T)_8G_{12}$TT-3′ in an aqueous solution, which includes 26 Na^+ counterions. Table 1 lists the relative energies of hole states localized on purine nucleobases. As expected, the average free energy of the A^+ hole states is positive, about 0.4 eV; guanine is a stronger hole acceptor than adenine. As the standard deviations of the ΔG values are $\approx$0.3–0.4 eV, configurations of the system should exist where a radical cation state A^+ is more stable than G^+ and, thus, hole transfer from G^+ to A is energetically feasible.[37] The nucleobases G_3 and G_{12} in the duplex have similar surroundings (however, they are not equivalent) and, therefore, the CT driving force between them is close to zero on average.

Table 1: Relative energies ΔG of radical cation states in the duplex 5′-$TTG_3T_4T_5T_6T_7T_8T_9T_{10}T_{11}G_{12}$TT-3′ and its modified neutral derivative[a] calculated for an MD trajectory of 12 ns. The occupation[b] of the states corresponding to the equilibrium distribution of hole states is also given, measured as the fraction of time (along the trajectory) where the corresponding state has the lowest energy.

	Normal DNA		Modified DNA[a]	
Base	ΔG [eV]	Occupation [%][b]	ΔG [eV]	Occupation [%][b]
G_3		50.7		36.7
A_4	0.38 ± 0.28	1.8	0.30 ± 0.23	0.8
A_5	0.43 ± 0.32	1.3	0.31 ± 0.26	0.8
A_6	0.44 ± 0.35	1.0	0.30 ± 0.29	1.0
A_7	0.45 ± 0.37	0.7	0.29 ± 0.30	1.2
A_8	0.46 ± 0.39	0.6	0.29 ± 0.32	0.9
A_9	0.44 ± 0.40	0.5	0.28 ± 0.33	1.0
A_{10}	0.41 ± 0.42	0.6	0.26 ± 0.35	1.0
A_{11}	0.40 ± 0.45	0.8	0.23 ± 0.36	1.1
G_{12}	0.06 ± 0.49	42.0	-0.12 ± 0.40	55.5

[a] Negatively charged phosphates are replaced by neutral methylphosphonate groups. [b] In view of the hole transfer from site G_3 to site G_{12}, the distribution was normalized for the whole range between the donor to the acceptor sites. Each $(TA)_2$ unit at either end of the duplex beyond the G sites would contribute about 5% (in absolute terms).

Figure 1 describes the fluctuations of the CT energy between the bases G_3 and A_6 as a function of time. The characteristic time of such relevant fluctuations is 0.3–0.4 ns.[38] Analysis of QM/MD results obtained for the present duplex and other systems[20] suggests that fluctuations of the CT driving force are mainly due to two contributions: 1) molecular vibrations of the donor and acceptor sites, and 2) correlated motion of counterions and water molecules. The conformational dynamics of DNA, that is, the relative motion of adjacent nucleobases, plays only a minor role in the CT energetics, however, it substantially affects the electronic coupling between base pairs.[25] Because the vibrations of nucleobases occur on the femtosecond time scale, they are not pertinent to the charge migration process that occurs on a time scale ranging from several tens of picoseconds to several nanoseconds.[39]

Counterions in the vicinity of nucleobases have been suggested to strongly affect the energetics of radical cation states; the consequences for electron transfer have been referred to as an "ion-gating" mechanism.[23,24] Counterions are solvated and their motion is correlated by their hydration shell, which partially screens their long-range Coulombic

 © 2004 Wiley-VCH Verlag GmbH & Co. KGaA, Weinheim

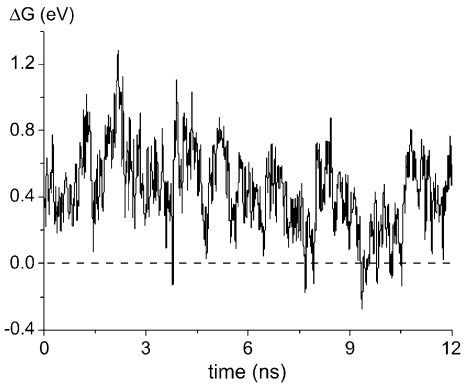


Figure 1. Fluctuations of the relative energy ΔG for hole transfer from G_3 to A_6 in the duplex 5′-$TTG_3T_4T_5T_6T_7T_8T_9T_{10}T_{11}G_{12}TT$-3′, calculated along a MD trajectory of 12 ns.

effect. To estimate directly the role of environmental fluctuations in modulating the value of ΔG for hole transfer, we considered a model system where only environmental fluctuations were accounted for, namely the rigid oligomer 5′-$(T)_5G(T)_2G(T)_5$-3′.[20] Standard deviations of ΔG for hole transfer in such a rigid system (≈ 0.15 eV) do not differ significantly from the standard deviations obtained for the corresponding system with a flexible DNA (≈ 0.19 eV), which confirms the key role of movement in the environment for modulating the hole-state energetics.

To quantify the effect of the counterions directly, we modeled a modified DNA duplex {5′-$(T)_2G(T)_8G(T)_2$-3′} where the negatively charged phosphate groups of the DNA backbone were replaced by neutral methylphosphonate groups.[23] Unlike the highly charged original duplex ($26e^-$), the modified duplex is neutral and, therefore, was modeled without counterions. The energy difference between G^+ and A^+ in modified DNA is reduced to $\Delta \approx 0.3$ eV (Table 1). Analysis of the radical ion state energies shows that on going from modified (neutral) DNA to normal DNA, the stabilization of the cations due to the phosphates is not quite compensated by the hydrated counterions, and an overall stabilization of the cation states results. Therefore, the reduced energy gap Δ of modified DNA implies that, on average, the A^+ states are better stabilized than the G^+ states. Thus, the possibility for hole hopping onto the A sites of the bridge should increase. Also, the standard deviations of the relative energies of modified DNA were calculated to be only $\approx 20\%$ smaller than for normal DNA. Apparently, the movement of the water molecules is responsible for the major contribution ($\approx 80\%$) to the energy variation of the hole states.

Changes in the energies of the hole states on different sites of a duplex were correlated. The correlation coefficients between energies of neighboring pairs of unmodified DNA (≈ 0.5) rapidly decreased with distance to 0.30, 0.11, and 0.02 for the second, third, and fourth neighbors, respectively. However, energies of states on remote sides tend to be negatively related; for instance, the correlation coefficients between hole states at G_3 on the one hand and A_8, A_{10}, and G_{12} on the other were -0.12, -0.20, and -0.31, respectively. The corresponding correlations for the modified duplex are somewhat weaker, -0.02, -0.16, and -0.29. Negative correlations are due to changes in the part of the environment between the sites; for instance, the rotation of the dipole of a water molecule directed along the DNA axis to G_3 by 180° will stabilize a hole state at G_3 and concomitantly destabilize a hole state at G_{12}. Also, the movement of counterions along DNA located between the considered sites contributes to the negative correlation.

Finally, we addressed the distribution of the hole states for CT from the donor site G_3 to the acceptor site G_{12} in the 14-mer duplex 5′-$TTG_3(T)_8G_{12}TT$-3′ and its methylphosphonate derivative (Table 1). This distribution was estimated as the fraction of time (along trajectories of 12 ns) when the corresponding hole state has the lowest energy compared to all other sites under consideration. The longest time interval for a hole resting on one of the G sites (i.e., when this hole state is lower than the cation states at all other sites) is about 100 ps, whereas this resting time is at most 12 ps on a $(TA)_8$ bridge. Non-negligible probabilities ($\approx 1\%$) were determined for events where an electron hole is localized on adenine bases. The total fractions of preferred bridge sites of unmodified and modified DNA (7–8%) are similar, but the distributions over the bridge sites differ in a characteristic way.[20] Thus, the dynamics of water molecules and counterions considerably modulates the relative redox potentials of the nucleobases. As a result, fluctuations of the environment can render hole-transfer processes from an GC base pair to an AT pair in a DNA duplex energetically feasible.

Analysis of our QM/MD simulations supports the recently proposed ion-gated mechanism for CT in DNA.[23] Note, however, that the thermal movement of the water molecules significantly dominates the variation of the hole-state energies in DNA. The fluctuations of relative energies of radical cation states are significant even in the absence of counterions, as in the case of a modified duplex with methylphosphonate groups instead of phosphates in the backbone. Our results suggest that adenine bases can also act as intermediates of electron-hole transfer. Thermal fluctuations of counterions and water molecules around DNA are responsible for configurations where the free energy of CT from a guanine to an adenine is negative. Such configurations are implied in the recently suggested A-hopping mechanism or, in a wider sense, in a domain mechanism, as recently inferred on the basis of experimental data.[14,15] Clearly, fluctuations of the CT driving force should be accounted when estimating the CT rate constants within the thermally induced hole-hopping model.[19] Further experiments probing the role of environmental fluctuations in a quantitative way are highly desirable for gaining further understanding of the CT mechanism in DNA.

Received: September 9, 2003
Revised: October 27, 2003 [Z52824]

Keywords: charge transfer · DNA · electron holes · quantum mechanical calculations

 © 2004 Wiley-VCH Verlag GmbH & Co. KGaA, Weinheim

[1] Long-Range Charge Transfer in DNA: *Topics in Current Chemistry* (Ed.: G. B. Schuster), Springer, Berlin, **2004**, in press.
[2] D. B. Hall, R. E. Holmlin, J. K. Barton, *Nature* **1996**, *382*, 731.
[3] S. M. Gasper, G. B. Schuster, *J. Am. Chem. Soc.* **1997**, *119*, 12762.
[4] B. Giese, S. Wessely, M. Spormann, U. Lindemann, E. Meggers, M. E. Michel-Beyerle, *Angew. Chem.* **1999**, *111*, 1050; *Angew. Chem. Int. Ed.* **1999**, *38*, 996.
[5] I. Saito, T. Nakamura, K. Nakatani, Y. Yoshioka, K. Yamaguchi, H. Sugiyama, *J. Am. Chem. Soc.* **1998**, *120*, 12686.
[6] D. Ly, Y. Kan, B. Armitage, G. B. Schuster, *J. Am. Chem. Soc.* **1996**, *118*, 8747.
[7] M. Bixon, B. Giese, S. Wessely, T. Langenbacher, M. E. Michel-Beyerle, J. Jortner, *Proc. Natl. Acad. Sci. USA* **1999**, *96*, 11713.
[8] M. Bixon, J. Jortner, *J. Phys. Chem. B* **2000**, *104*, 3906.
[9] Y. A. Berlin, A. L. Burin, M. A. Ratner, *J. Phys. Chem. A* **2000**, *104*, 443.
[10] F. C. Grozema, Y. A. Berlin, L. D. Siebbeles, *J. Am. Chem. Soc.* **2000**, *122*, 10903.
[11] B. Giese, *Acc. Chem. Res.* **2001**, *34*, 159.
[12] F. D. Lewis, R. L. Letsinger, M. R. Wasielewski, *Acc. Chem. Res.* **2001**, *34*, 159.
[13] K. Nakatani, C. Dohno, I. Saito, *J. Am. Chem. Soc.* **2000**, *122*, 5893.
[14] B. Giese, J. Amaudrut, A. K. Köhler, M. Spormann, S. Wessely, *Nature*, **2001**, *412*, 318.
[15] T. T. Williams, D. T. Odom, J. K. Barton, *J. Am. Chem. Soc.* **2000**, *122*, 9048.
[16] M. Pascaly, J. Yoo, J. K. Barton, *J. Am. Chem. Soc.* **2002**, *124*, 9083.
[17] K. Kawai, T. Takada, S. Tojo, T. Majima, *J. Am. Chem. Soc.* **2003**, *125*, 6842.
[18] S. Steenken, S. V. Jovanovic, *J. Am. Chem. Soc.* **1997**, *119*, 617.
[19] a) M. Bixon, J. Jortner, *J. Am. Chem. Soc.* **2001**, *123*, 12556; b) M. Bixon, J. Jortner, *Chem. Phys.* **2002**, *281*, 393.
[20] K. Siriwong, A. A. Voityuk, N. Rösch, unpublished results. Here, we describe in detail the computational method for estimating the energetics of electron-hole states in DNA and provide an in-depth analysis of the role of different dynamical factors. We considered several DNA models with different bridges, namely the duplexes 5′-$(T)_5G(T)_nG(T)_5$-3′ ($n=1$–4), 5′-$(T)_3G(T)_6G(T)_3$-3′, and 5′-$(T)_2G(T)_8G(T)_2$-3′; the environment effect on the charge-transfer energetics is very similar in these models, which comprise $(AT)_n$ bridges ($n=1$–8).
[21] I. Saito, M. Takayama, H. Sugiyama, K. Nakatani, A. Tsuchida, M. Yamamoto, *J. Am. Chem. Soc.* **1995**, *117*, 6406.
[22] A. A. Voityuk, J. Jortner, M. Bixon, N. Rösch, *Chem. Phys. Lett.* **2000**, *324*, 430.
[23] R. N. Barnett, C. L. Cleveland, A. Joy, U. Landman, G. B. Schuster, *Science* **2001**, *294*, 567.
[24] R. N. Barnett, C. L. Cleveland, U. Landman, E. Boone, S. Kanvah, G. B. Schuster, *J. Phys. Chem. A* **2003**, *107*, 3525.
[25] A. A. Voityuk, K. Siriwong, N. Rösch, *Phys. Chem. Chem. Phys.* **2001**, *3*, 5421.
[26] A. A. Voityuk, N. Rösch, *J. Chem. Phys.* **2002**, *117*, 5607.
[27] A. Troisi, G. Orlandi, *J. Phys. Chem. B* **2002**, *106*, 2093.
[28] T. E. Cheatham III, P. A. Kollman, *Ann. Rev. Phys. Chem.* **2000**, *51*, 435.
[29] MD simulations were performed with the AMBER 6 program[30] and the force field of Cornell et al.,[31] following a standard protocol.[32] In line with that protocol, the dielectric constant $\varepsilon=1$ was used. Because of the small number of ions compared to water molecules and their very long residence time (0.1–1 ns) around DNA, long simulation times (of the order of 10 ns) are essential for a statistically meaningful representation of ion distributions.[33]
[30] D. A. Case, D. A. Pearlman, J. W. Caldwell, T. E. Cheatham III, W. S. Ross, C. L. Simmerling, T. A. Darden, K. M. Merz, R. V. Stanton, A. L. Cheng, J. J. Vincent, M. Crowley, V. Tsui, R. J. Radmer, Y. Duan, J. Pitera, I. Massova, G. L. Seibel, U. C. Singh, P. K. Weiner, P. A. Kollman, *AMBER 6*, University of California, San Francisco, **1999**.
[31] W. D. Cornell, P. Cieplak, C. I. Bayly, I. R. Gould, K. M. Merz, D. M. Ferguson, D. C. Spellmeyer, T. Fox, J. W. Caldwell, P. A. Kollman, *J. Am. Chem. Soc.* **1995**, *117*, 5179.
[32] T. E. Cheatham III, P. A. Kollman, *J. Mol. Biol.* **1996**, *259*, 434.
[33] M. Feig, B. M. Pettitt, *Biophys. J.* **1999**, *77*, 1769.
[34] The model assumes that the ensemble of radical cation states can be approximately characterized by data obtained for the corresponding non-ionized duplex; reorganization effects on the structure of DNA and its solvation shell are neglected. The driving force for hole transfer between two sites was estimated as being the difference of vertical ionization potentials calculated along MD trajectories of DNA fragments. The ionization energies were determined with the semiempirical NDDO-G method,[35] which is specially parameterized for calculating ionization and excitation energies of organic molecules. This procedure reproduces experimental ionization potentials of nucleobases in the gas phase with an average deviation of 0.09 eV,[35] and is thus well suited for estimating the value of ΔG for hole transfer between nucleobases. Because the reorganization energies connected with the formation of cation hole states of guanine and adenine bases are very similar, the corresponding contributions cancel when one estimates energy differences of such states. Thus, differences of vertical (instead of adiabatic) ionization energies can be used to estimate ΔG. The electrostatic effects of the surroundings were accounted for by approximating all atoms in the MD simulation box (26 Na^+ ions and 3936 water molecules) as point charges with values according to the force field;[31] the effective dielectric constant of the medium was chosen to be 2, which corresponds to fast electronic polarization.[36]
[35] A. A. Voityuk, M. C. Zerner, N. Rösch, *J. Phys. Chem. A* **1999**, *103*, 4553.
[36] a) K. A. Sharp, B. Honig, *Annu. Rev. Biophys. Biophys. Chem.* **1990**, *19*, 301; b) K. Siriwong, A. A. Voityuk, M. D. Newton, N. Rösch, *J. Phys. Chem. B* **2003**, *107*, 2595.
[37] In line with experimental data,[1,18] radical states T^+ and C^+ lie considerably higher (1.4 and 1.2 eV, respectively) and cannot serve as hole acceptors in DNA.
[38] Characteristic times were estimated from the Fourier transform of the autocorrelation function of ΔG; they decrease from 380 ps for hole transfer $G_3 \rightarrow A_4$ to 304 ps for $G_3 \rightarrow G_{12}$.
[39] Pertinent CT time scales can be illustrated by rates for hole transfer in DNA. DNA hairpins linked by stilbene dicarboxamide imply characteristic times ranging from 30 ps to 5 ns for bridges of 1 to 3 AT base pairs.[12] Similar estimates from 10 to 200 ps were received for hole transfer from an acridine derivative as chromophore to 7-deazaguanine as acceptor, separated by one and two intermediate AT pairs.[40] Direct fluorescence probing of the dynamics of water around DNA with femtosecond resolution yielded mean residence times and reorientation times of water molecules at 3–6 ps.[41] MD simulations identified three characteristic time scales (120 ps, 280 ps, and 960 ps) for the dynamics of sodium ions near DNA.[33]
[40] W. B. Davis, S. Hess, I. Naydenova, R. Haselsberger, A. Ogrodnik, M. D. Newton, M. E. Michel-Beyerle, *J. Am. Chem. Soc.* **2002**, *124*, 2422.
[41] S. K. Pal, L. Zhao, A. H. Zewail, *Proc. Natl. Acad. Sci. USA* **2003**, *100*, 8113.

 © 2004 Wiley-VCH Verlag GmbH & Co. KGaA, Weinheim

Polymorphs of CuCN

Copper(I) Cyanide: A Simple Compound with a Complicated Structure and Surprising Room-Temperature Reactivity**

Simon J. Hibble, Sharon G. Eversfield, Andrew R. Cowley, and Ann M. Chippindale**

The structural chemistries of CuCN, AgCN, and AuCN are much more complex than might be anticipated for compounds of such simple formulae. This is particularly true for the first member of the group, CuCN, for which the situation has been complicated by the existence of more than one polymorph and the mistaken identification in the literature of copper(I) cyanide hydrates as additional polymorphs. The structure of solid CuCN has long been presumed to consist of -Cu–CN–Cu–CN- chains, by analogy with the structures of the other group 11 cyanides[1–3] and with supporting evidence from a wide range of techniques including NMR spectroscopy,[4] nuclear quadrupole resonance (NQR),[4] extended X-ray absorption fine-structure spectroscopy (EXAFS)[5] and vibrational spectroscopy.[3] However, it was not until 2002 that the structure of what is now known to be the high-temperature form of CuCN (HT-CuCN) was determined.[6–8] This phase can, under certain conditions, be prepared at room temperature[8] and is also formed irreversibly from the low-temperature polymorph (LT-CuCN) at 563 K. HT-CuCN is isomorphous with AgCN[3,9] and structurally related to AuCN,[3,10] and consists of hexagonally packed infinite linear -(Cu–CN)- chains with adjacent chains displaced by $\pm 1/3$ along the chain axis. Although the basic structures of all three materials are simple, disorder, which includes large static and thermal displacements of the chains and "head-to-tail disorder" of the CN groups (that is, NC versus CN), made the structure determinations problematical. Nevertheless, using total diffraction[8–10] and NMR spectroscopy experiments,[4,11] the average and local structures of these three cyanides has now been well determined.

Surprisingly, the structure of LT-CuCN, which is sold as "copper(I) cyanide" by chemical companies, such as Fluka and Aldrich, has so far proved elusive, even though a report of the preparation of single crystals appeared as long ago as 1957.[12] Herein we report for the first time the structure of LT-CuCN and the interconversion of LT- and HT- forms at room temperature via an isolable intermediate phase, $KCu_2(CN)_2Br{\cdot}H_2O$. The relationship between all three structures is discussed.

Single crystals of LT-CuCN were grown from polycrystalline LT-CuCN under hydrothermal conditions at 433 K employing KCN as a mineralizer.[13] The structure is curious and consists of infinite CuCN chains, each containing five crystallographically distinct Cu atoms, which form waves with a repeat corresponding to nine CuCN units (Figure 1).

Refinement of C and N occupancies was possible and indicated "head-to-tail" disorder of the cyanide groups, as observed in related materials.[4,10,11] The bond lengths appear reasonable (Cu–C/N 1.839(9)–1.872(12) Å, C≡N 1.148(12)–1.177(13) Å) and are in good agreement with those found in HT-CuCN.[8] Unlike in HT-CuCN, where the bond angles are fixed by symmetry at 180°, in LT-CuCN they deviate slightly from linearity (N/C-Cu-C/N 176.7(3)–179.0(5)°, C-N-Cu 174.0(8)–179.3(7)°). The combination of these small local deviations leads to significant divergence from linearity for the chain as a whole. The chains stack parallel to each other with the waves "in phase" to form layers lying in the *ac* plane. The chain axes in adjacent layers are rotated by 49° (Figure 2a and b). As the local geometries (i.e. the bond lengths and angles around the Cu, C, and N atoms) in LT-CuCN are very similar to those in HT-CuCN,[7,8] the infrared and Raman spectra are therefore almost identical. A notable feature of LT-CuCN is that it shows negative thermal expansion of the *a* axis reflecting the strength and nature of the bonding within the chains. We have observed similar effects in HT-CuCN, AgCN, and AuCN.[10,17] It is a curiosity that the cell volumes per CuCN unit are, within experimental error, identical over the temperature range 150–300 K, which is in contrast to the assumption that the more thermodynamically stable phase will have the lower volume.

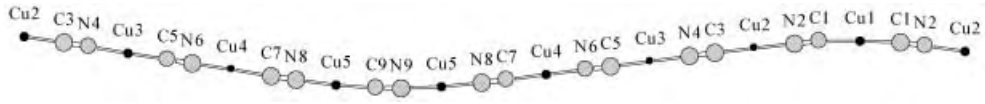


Figure 1. A portion of a single -(Cu–CN)- chain in LT-CuCN showing the repeat distance of the wave. In reality there is "head-to-tail" disorder of C≡N groups and one possible arrangement is shown.

[*] Dr. S. J. Hibble, S. G. Eversfield, Dr. A. M. Chippindale
School of Chemistry
University of Reading
Whiteknights, Reading, Berks RG6 6AD (UK)
Fax: (+44) 118-378-6331
E-mail: s.j.hibble@reading.ac.uk
a.m.chippindale@reading.ac.uk
Dr. A. R. Cowley
Chemical Crystallography Laboratory
9 Parks Rd, Oxford OX1 3PD (UK)

[**] AMC thanks the Leverhulme Trust for a Research Fellowship.
Supporting information for this article is available on the WWW under http://www.angewandte.org or from the author.

The conversion of the LT-CuCN into HT-CuCN requires a major reorganization of the structure to make all the -(Cu–CN)- chains lie parallel and can be achieved by heating above 563 K.[6,7] Interestingly, this transformation can also be carried out at room temperature by stirring polycrystalline LT-CuCN in concentrated aqueous KBr (or NH_4Br) followed by washing with copious amounts of cold water (Scheme 1). Limiting the amount of water used in washing leads to recovery of CuCN predominantly in the low-temperature form. The reactions proceed without dissolution of the CuCN containing species via an intermediate, highly crystalline powdered phase, which undergoes immediate flocculation on

 © 2004 Wiley-VCH Verlag GmbH & Co. KGaA, Weinheim DOI: 10.1002/anie.200352844

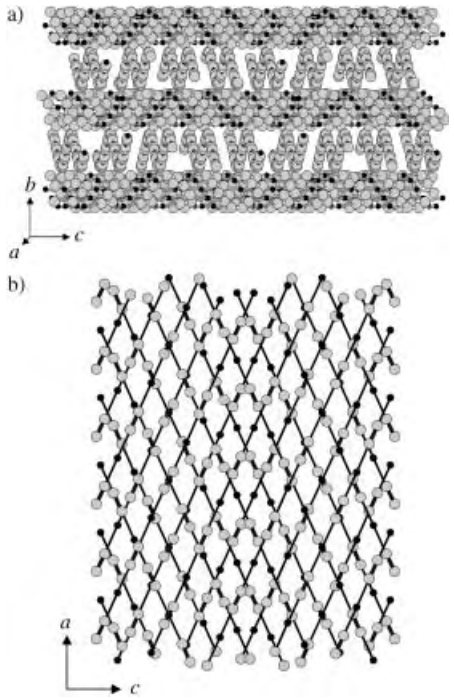
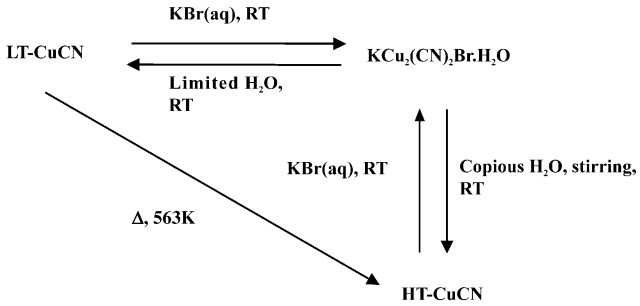


Figure 2. a) A view showing layers of -(Cu–CN)- chains, which lie in the [150] direction. Small black circles represent Cu and large gray circles disordered C/N atoms. b) A view along the *b* axis showing that the -(Cu–CN)- chains in the layers shown in Figure 2a are identical, but are rotated by 49° between adjacent layers (key as in Figure 2a).



Scheme 1. Interconversion of LT- and HT-CuCN.

treatment with water. Stirring HT-CuCN with concentrated aqueous KBr (or NH_4Br) produces the same intermediate. It has proved possible to grow single crystals of the intermediate by heating either HT- or LT-CuCN in concentrated aqueous KBr under hydrothermal conditions at 433 K for a few hours and it has the formula $KCu_2(CN)_2Br{\cdot}H_2O$. The reclamation of CuCN after reactions with aqueous KBr and KI has been studied previously by Bowmaker et al.,[18] but neither the polymorphs of CuCN, nor the nature of the intermediates, were identified. The phase of CuCN that is formed is clearly sensitive to reaction conditions. The work of Wang et al.[6] shows that LT-CuCN is the thermodynamically stable phase below 563 K. In that work[6] it is also shown that HT-CuCN does not convert back into LT-CuCN on cooling. This is not surprising as we can prepare both forms at room temperature. As might be expected more rapid formation of CuCN from $KCu_2(CN)_2Br{\cdot}H_2O$ produces the more highly disordered HT-CuCN form of CuCN.

$KCu_2(CN)_2Br{\cdot}H_2O$ is structurally interesting in its own right for its zeolite-like framework[19] (Figure 3) as well as for its role in the interconversion of LT- and HT-CuCN. The

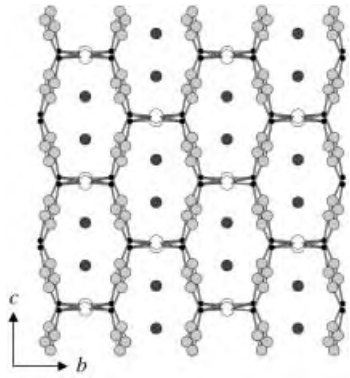


Figure 3. View along the *a* axis of $KCu_2(CN)_2Br{\cdot}H_2O$ showing the open 3D structure generated by linking of -(Cu–CN)- chains (key as in Figure 2) by Br atoms (open circles). K^+ ions (large black circles), and water (not shown) reside in the pores.

-(Cu–CN)- chains observed in both forms of CuCN are retained in this intermediate compound and similarly exhibit "head-to-tail" disorder in the cyanide groups (Cu–C/N 1.892(3) and 1.884(4) Å, C≡N 1.158(5) Å). Additional bonding to two bromine atoms gives rise to distorted tetrahedral coordination around the Cu atom (Cu–Br 2.6643(6) and 2.7014(6) Å, Br-Cu-Br′ 88.564(14)°) and severe bending of the -(Cu–CN)- chains (N/C-Cu-C/N 147.10(15)°; Figure 4). The bromine atoms serve to link adjacent -(Cu–CN)- chains together to generate a 3D framework of formula $[Cu_2(CN)_2Br]^-$ containing pores in which K^+ and H_2O reside. The K^+ ion is coordinated by two water molecules (K···O 2.803(5) and 2.896(5) Å) and one framework bromine atom (K···Br 3.299(1) Å), with additional rather weak interactions to nitrogen (K···N separations lie in the range 3.272(3)–3.387(4) Å). Given the rather poor coordination around the K^+ ion, it is not too surprising that this ion can be "washed out" together, by necessity, with the Br^- ion. Remarkably, it appears that the -(Cu–CN)- chains are retained during this process.

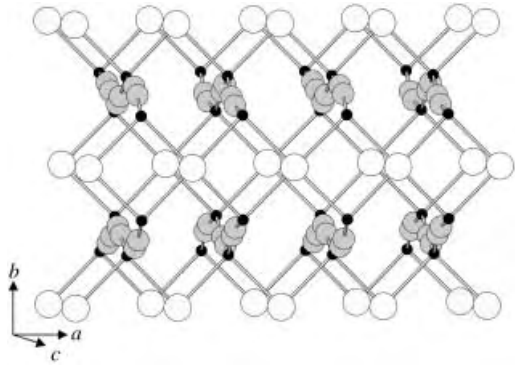


Figure 4. A view of the CuCNBr framework of $KCu_2(CN)_2Br{\cdot}H_2O$ showing the -(Cu–CN)- chains and the square planar arrangement of Cu atoms around each Br atom (key as in Figure 3).

 © 2004 Wiley-VCH Verlag GmbH & Co. KGaA, Weinheim

In summary, the structure of the most commonly occurring form of CuCN has been solved. The chemical interconversion between this and the high-temperature disordered form of CuCN has been achieved at room temperature using aqueous KBr and the structure of the open framework intermediate, $KCu_2(CN)_2Br.H_2O$, determined. Further work will include using total neutron diffraction to determine whether dynamic wavelike motions of -(Cu–CN)- chains, similar in form to the static waves found in LT-CuCN, account for the negative thermal expansion in the chain direction in HT-CuCN.[7]

Experimental Section

LT-CuCN. Small colorless crystals (too small for X-ray analysis) were obtained on heating CuCN (0.5 g, 55 mmol, polycrystalline LT-CuCN, Fluka) with KCN (0.02 g, 0.3 mmol) in H_2O (10 mL) in a Teflon liner in an autoclave at 433 K for 6 days. Addition of further KCN (0.02 g) and reheating for 14 days produced a mixture of products including colorless blocks. These blocks were very fragile and broke into plates when touched with a steel needle. One of these plates was used for the single-crystal X-ray study.[13] The powder X-ray pattern generated from this structural study is in excellent agreement with the pattern measured for both commercial and laboratory-prepared polycrystalline LT-CuCN (see Supporting Information).

Vibrational spectra for polycrystalline samples of copper cyanide: LT-CuCN. IR (Nujol): ν(CN) 2166(vs), 2118 cm^{-1} (m); Raman: ν(CN) 2177(vs), 2114 (vvw); δ(MCN) 332 (vw, sh), 321 cm^{-1} (w); HT-CuCN. IR (Nujol): ν(CN) 2167(vs), 2120 cm^{-1} (m, sh); Raman: ν(CN) 2177(vs), 2121(vvw); δ(MCN) 332(vw, sh), 321 cm^{-1} (w).

$KCu_2(CN)_2Br{\cdot}H_2O$. Single crystals of $KCu_2(CN)_2Br{\cdot}H_2O$ were obtained from either LT- or HT-CuCN under hydrothermal conditions. CuCN (0.19 g, 21 mmol) was added to a KBr solution (10 mL, 3.2 M) and heated in an autoclave at 433 K for 24 h. The sample was collected by filtration and allowed to dry without washing. The solid product consisted of colorless hexagonal plates of $KCu_2(CN)_2Br{\cdot}H_2O$, suitable for diffraction studies[19] as the majority phase. Beige polycrystalline samples, were prepared by stirring CuCN (0.75 g, 82 mmol, LT- or HT-) in a KBr solution (25 mL, 3.2 M) for 2 h, at room temperature, filtering, and washing with further KBr solution. Powder X-ray patterns could be fully indexed on the basis of the unit cell determined in the single-crystal study[19] with additional lines from KBr confirming that the products from LT- or HT-CuCN are identical (see Supporting Information); IR (Nujol): $\tilde{\nu} = \nu$(OH) 3580(w), 3553(vw); ν(CN) 2112(s); $\delta(OH_2)$ 1607(s); $\rho(OH_2)$ 524 cm^{-1} (s).

Received: September 11, 2003
Revised: October 15, 2003 [Z52844]

Keywords: copper · cyanide · hydrothermal synthesis · polymorphism · structure elucidation

[1] A. G. Sharpe, *The Chemistry of Cyano Complexes of the Transition Metals*, Academic, London, **1976**, p. 265.
[2] A. F. Wells, *Structural Inorganic Chemistry*, 5th ed., Clarendon, Oxford, **1984**, p. 1104.
[3] G. A. Bowmaker, B. J. Kennedy, J. C. Reid, *Inorg. Chem.* **1998**, *37*, 3968 – 3974.
[4] S. Kroeker, R. E. Wasylishen, J. V. Hanna, *J. Am. Chem. Soc.* **1999**, *121*, 1582 – 1590.
[5] T. L. Stemmler, T. M. Barnhart, J. E. Penner-Hahn, C. E. Tucker, P. Knochel, M. Bohme, G. Frenking, *J. Am. Chem. Soc.* **1995**, *117*, 12489 – 12497.
[6] J. Wang, M. F. Collins, G. P. Johari, *Phys. Rev. B* **2002**, *65*, 180103.
[7] O. Reckeweg, C. Lind, A. Simon, F. J. DiSalvo, *Z. Naturforsch. B* **2003**, *58*, 155 – 158.
[8] S. J. Hibble, S. M. Cheyne, A. C. Hannon, S. G. Eversfield, *Inorg. Chem.* **2002**, *41*, 4990 – 4992.
[9] S. J. Hibble, S. M. Cheyne, A. C. Hannon, S. G. Eversfield, *Inorg. Chem.* **2002**, *41*, 1042 – 1044.
[10] S. J. Hibble, A. C. Hannon, S. M. Cheyne, *Inorg. Chem.* **2003**, *42*, 4724 – 4730.
[11] D. L. Bryce, R. E. Wasylishen, *Inorg. Chem.* **2002**, *41*, 4131 – 4138.
[12] D. T. Cromer, R. M. Douglass, E. Staritzky, *Anal. Chem. B* **1957**, *29*, 316.
[13] Crystal Data for LT-CuCN: $C_9Cu_9N_9$, $M_r = 806.13$, $\rho_{calcd} = 2.988\ mg\,m^{-3}$, orthorhombic, $C\ 222_1$, $Z = 4$, $a = 7.9024(5)$, $b = 12.6403(8)$, $c = 17.9364(13)$ Å, $V = 1791.6$ Å^3 at 150 K (Cell parameters at 293 K: $a = 7.8418(6)$, $b = 12.8045(10)$, $c = 18.1450(14)$ Å, $V = 1821.6$ Å^3). X-ray data collected at 150 K for a colorless rectangular plate (dimensions: $0.03 \times 0.08 \times 0.20$ mm) using an Enraf Nonius Kappa CCD diffractometer (graphite monchromated $Mo_{K\alpha}$ radiation, $\lambda = 0.71073$ Å). The data were processed using DENZO/SCALEPACK[14] and a multi-scan absorption correction applied (data range: $(5.160 < \theta < 27.459)°$, 2027 measured reflections, 2017 independent, $T_{min} = 0.38$, $T_{max} = 0.73$). The structure was solved by direct methods[15] and the model refined by full-matrix least-squares analysis.[16] "Head-to-tail" disorder of the C and N atoms of each cyanide group was included in the refinement. 128 parameters were refined, including anisotropic temperature factors for all atoms and the Flack parameter (0.44(7), racemic twin) ($R(F) = 0.0365$ $wR(F) = 0.0416$ using 1391 reflections with $I > 3\sigma(I)$). Further details on the crystal structure investigations may be obtained from the Fachinformationszentrum Karlsruhe, 76344 Eggenstein-Leopoldshafen, Germany (fax: (+49) 7247-808-666; e-mail: crysdata@fiz-karlsruhe.de), on quoting the depository number CSD-391243.
[14] Z. Otwinowski, W. Minor in *Methods in Enzymology*, *Vol. 276* (Eds.: C. W. Carter, R. M. Sweet), Academic Press, New York, **1997**, pp. 307 – 326.
[15] A. Altomare, G. Cascarano, C. Giacovazzo, A. Guagliardi, M. C. Burla, G. Polidori, M. Camalli, *J. Appl. Crystallogr.* **1994**, *27*, 435.
[16] D. J. Watkin, C. K. Prout, J. R. Carruthers, P. W. Betteridge, R. I. Cooper, *CRYSTALS*, Issue 11, Chemical Crystallography Laboratory, Oxford, UK, **2001**.
[17] S. M. Cheyne, PhD Thesis, University of Reading, UK, **2003**.
[18] G. A. Bowmaker, H. Hartl, V. Urban, *Inorg. Chem.* **2000**, *39*, 4548 – 4554.
[19] Crystal Data for $KCu_2(CN)_2Br{\cdot}H_2O$: $C_2H_2BrCu_2KN_2O$, $M_r = 316.16$, $\rho_{calcd} = 2.887\ mg\,m^{-3}$, orthorhombic, *Pnma*, $Z = 4$, $a = 7.4699(5)$, $b = 10.3199(5)$, $c = 9.4336(5)$ Å, $V = 727.2$ Å^3 at 150 K (Cell parameters at 293 K: $a = 7.5522(4)$, $b = 10.4461(5)$, $c = 9.3825(5)$ Å, $V = 740.2$ Å^3). X-ray data collection and processing as above[13] for a colorless hexagonal plate (dimensions: $0.01 \times 0.08 \times 0.10$ mm, data range: $(5.112 < \theta < 27.473)°$, 1652 measured reflections, 875 independent, $T_{min} = 0.33$, $T_{max} = 0.89$). The hydrogen atom of the water molecule was located in a difference Fourier map. "Head-to-tail" disorder of the C and N atoms of each cyanide group was modeled in the refinement. 51 parameters, including anisotropic temperature factors for all non-hydrogen atoms, were refined ($R(F) = 0.0316$ $wR(F) = 0.0355$ using 671 reflections with $I > 3\sigma(I)$). Further details on the crystal structure investigations may be obtained from the Fachinformationszentrum Karlsruhe, 76344 Eggenstein-Leopoldshafen, Germany (fax: (+49) 7247-808-666; e-mail: crysdata@fiz-karlsruhe.de), on quoting the depository number CSD-413310.

 © 2004 Wiley-VCH Verlag GmbH & Co. KGaA, Weinheim

Cyclizations

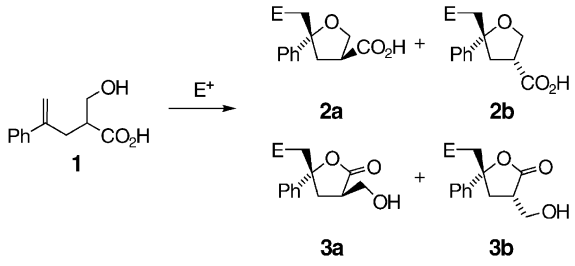
Selenocyclizations: Control by Coordination and by the Counterion**

*Shaista S. Khokhar and Thomas Wirth**

Electrophilic selenenylation reactions of alkenes have been used successfully to functionalize inactivated carbon–carbon double bonds.[1] Stereoselective variants of this reaction with chiral selenium electrophiles have been performed by numerous research groups.[2,3] These reagents can also be employed in cyclization reactions for the stereoselective synthesis of different heterocyclic compounds.[4] This reaction continues to draw attention, both from a methodological and synthetic perspective, for the elaboration of highly functionalized heterocyclic compounds. Different electrophilic selenium reagents and a variety of reaction conditions have been employed and recent reviews have highlighted the scope of this general process.[3,5]

The effect of counterions in selenenylations[2c,6] and the interactions of selenium electrophiles with nearby heteroatoms have been reported previously,[7] but these observations do not yet allow for a conclusive picture. We recently observed interesting effects of external nucleophiles on the course of selenenylation reactions.[8] In order to probe in which way different nucleophiles, solvents, and counterions affect selenocyclizations, we synthesized alkene **1**, which contains two competing nucleophiles, an alcohol group, and a carboxylic acid function.[9] We describe herein how the interactions of nucleophiles, solvents, and counterions with selenium electrophiles affect the direction of cyclization and how selective cyclizations can be achieved.

Electrophilic 5-*exo*-cyclization of **1** can lead to either tetrahydrofurans **2** or to lactones **3**, depending on the attacking nucleophile (Scheme 1). Unfortunately, NOE experiments could not clarify the relative stereochemistry because of overlapping signals in **2** and **3**, which are both obtained as mixtures of *cis* (**2a**, **3a**) and *trans* isomers (**2b**, **3b**). Only an X-ray crystallographic analysis of **3a** (E = I) allowed an unambiguous assignment.[10] The radical deiodination led to the same compound **3a** (E = H) as the radical deselenation of **3a** with E = SePh. The ratios **2a**/**2b** and **3a**/**3b** in all experiments described herein were determined by integration of characteristic ^{1}H NMR signals.



Scheme 1. Electrophilic cyclization of **1** to tetrahydrofurans **2** and lactones **3**.

We observed that small amounts of additives can influence the course of selenenylation reactions.[11] The results of selenocyclizations with phenylselenenyl triflate as electrophile in different solvents and with different additives are shown in Table 1. Two main interactions influence the cyclization. First, the selenium electrophile can interact with the internal nucleophile of the unsaturated substrate, with the alcohol group, or with the acid function. Second, there are interactions between the electrophile and the external nucleophile/additive or the solvent. Both interactions are additionally influenced by the counterion.

Table 1: Cyclizations of **1** with phenylselenenyl triflate (E = PhSe) and additives.

Entry	Solvent	Additive (10 equiv)	**2a**/**2b**	**3a**/**3b**	**2**/**3**[a]	Yield [%]
1	Et_2O	–	49:51	72:28	75:25	83
2	Et_2O	MeOH	13:87	81:19	63:37	67
3	Et_2O	BnOH[b]	27:73	64:36	89:11	76
4	Et_2O	H_2O	0:100	77:23	27:73	58[c]
5	CH_2Cl_2	MeOH	33:67	73:28	43:57	85
6	MeCN	MeOH	46:54	50:50	84:16	90
7	Et_2O	$PhCO_2H$	53:47	100:0	88:12	69
8	Et_2O	AcOH	47:53	–	100:0	90
9	CH_2Cl_2	AcOH	41:59	76:24	75:25	92
10	MeCN	AcOH	49:51	65:35	63:37	88

[a] Tetrahydrofuran/lactone ratio. [b] Bn = benzyl. [c] This reaction was very slow and $(PhSe)_2$ was isolated in 25% yield.

An alcohol has a higher nucleophilicity than a carboxylic acid, and the selenium electrophile coordinates to the hydroxy group rather than to the carboxylic acid moiety of the substrate. This interaction can, however, be dramatically influenced by additives, as shown in Table 1 and is partially overridden in cyclizations involving the triflate counterion. In these latter cyclizations, the formation of the tetrahydrofurans **2** is favored over the formation of the lactones **3**. Only if the electrophile–hydroxy group interaction is disturbed by the addition of water, is **3** formed preferentially (Table 1, entry 4). On the other hand, acetic acid, as a weakly coordinating additive, tunes the reactivity of the electrophile and the tetrahydrofurans **2** are formed highly selectively (Table 1, entry 8). This seems to be a quite unique combination, as benzoic acid (Table 1, entry 7) or other additional solvents (Table 1, entries 9 and 10) lead to the formation of a considerable amount of lactones **3**. In these examples, there seems to be almost no coordination of the electrophile to the carboxylic acid moiety of the substrate, because the *cis* and *trans* isomers of the tetrahydrofuran **2** are formed in similar amounts. A coordination to the carboxylic acid moiety should have led to a preferred formation of the *cis* isomer **2a**.[12]

[*] S. S. Khokhar, Prof. Dr. T. Wirth
Department of Chemistry, Cardiff University
PO Box 912, Cardiff, CF10 3TB (UK)
Fax: (+44) 29-2087-6968
E-mail: wirth@cf.ac.uk

[**] This work was supported by the EPSRC.

 DOI: 10.1002/anie.200352884 © 2004 Wiley-VCH Verlag GmbH & Co. KGaA, Weinheim

The outcome of the competitive selenocyclizations is different when other counterions are involved. Whereas the phenylselenenyl bromide and triflate yield mixtures of tetrahydrofurans **2** and lactones **3** (Table 2, entries 1–3), the corresponding hexafluorophosphate (Table 2, entry 5) or sulfate (Table 2, entry 8) can be used to synthesize exclusively the lactone **3** under the standard reaction conditions. Prolonged reaction times with phenylselenenyl hexafluorophosphate lead to the formation of small amounts of tetrahydrofuran **2b** (Table 2, entry 6). The addition of methanol (10 equiv) in these reactions is important as its replacement with acetic acid (10 equiv) leads to the formation of a mixture of **2** and **3** in very low yield (Table 2, entry 7). As already mentioned, the coordination of the selenium electrophile to the hydroxy group of the substrate is stronger than to the carboxylic acid moiety. Irrespective of the additive used, this behavior is reflected in the *cis*/*trans* ratio (**3a**/**3b**) as coordination to the alcohol moiety of **1** leads to the *cis* lactone **3a** as the major isomer.

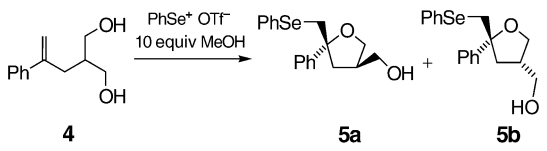
Table 2: Selenocyclizations with the phenylselenenyl electrophile in diethyl ether with different counterions.

Entry	Reagent	Additive (10 equiv)	**2a**/**2b**	**3a**/**3b**	**2**/**3**[a]	Yield [%]
1	PhSeBr	–	20:80	63:37	54:46	74
2	PhSeOTf	–	49:51	72:28	75:25	83
3	PhSeOTf	MeOH	13:87	81:19	63:37	67
4	$PhSeBF_4$	MeOH	0:100	84:16	14:86	70
5	$PhSePF_6$	MeOH	–	78:22	0:100	50
6	$PhSePF_6$[b]	MeOH	0:100	73:27	30:70	85
7	$PhSePF_6$	AcOH	42:58	100:0	92:8	11
8	$(PhSe)_2SO_4$[c]	MeOH	–	67:33	0:100	42

[a] Tetrahydrofuran/lactone ratio. [b] Reaction time 5.5 h instead of 2.5 h. [c] This reaction was slow owing to the insolubility of Ag_2SO_4, and starting material **1** (40%) was recovered. Tf = trifluoromethanesulfonyl.

We have developed conditions for highly selective cyclizations with the phenylselenenyl electrophile. The exclusive formation of the tetrahydrofuran **2** can be achieved with the triflate counterion with additional acetic acid (Table 1, entry 8), whereas the cyclization can be also directed towards complete formation of lactone **3** with the hexafluorophosphate or sulfate counterion with additional methanol (Table 2, entries 5 and 8).

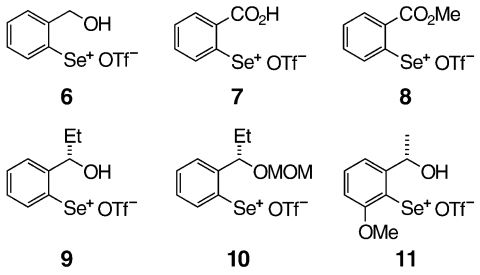
The cyclization of substrate **4**[13] with phenylselenenyl triflate in the presence of methanol (10 equiv) generates the diastereomers **5a** and **5b** (60:40) albeit in lower yield (36%). A preference for the *cis* isomer **5a** is again observed (Scheme 2).



4 **5a** **5b**

Scheme 2. Cyclization of the alkene **4** to *cis* and *trans* tetrahydrofurans **5a** and **5b**.

Forcing the additive to coordinate to the selenium electrophile can be achieved in an intramolecular fashion, which we already investigated theoretically.[7b] The selenium electrophiles **6**–**10**, generated from the corresponding diselenides,[14] were employed in the cyclization of **1** with and without additional additives (Table 3). Using these modified reagents, the additive now seems to have almost no influence on the course of the cyclization, undoubtedly because of the efficient coordination of the internal oxygen atoms in **6**–**8** to the selenium electrophile. The *cis*/*trans* ratio (**3a**/**3b**) is consistent in these reactions (Table 3, entries 1–9), indicating again some interaction with the hydroxy group of **1**. Electrophiles **6** and **9** have very strong internal selenium–oxygen coordination, which allows an exclusive synthesis of the corresponding lactones **3**, even with the triflate counterion and irrespective of any additive (Table 3, entries 1–3, 10).



6 **7** **8** **9** **10** **11**

Table 3: Selenocyclizations with different selenium electrophiles.

Entry	Electrophile	Additive (10 equiv)	**2a**/**2b**	**3a**/**3b**	**2**/**3**[a]	Yield [%]
1	**6**	–	–	80:20	0:100	51[b]
2	**6**	MeOH	–	80:20	0:100	40[b]
3	**6**	AcOH	–	80:20	0:100	45[b]
4	**7**	–	32:68	82:18	46:54	89
5	**7**	MeOH	33:67	84:16	52:48	99
6	**7**	AcOH	52:48	83:17	49:51	45
7	**8**	–	50:50	82:18	41:59	74
8	**8**	MeOH	25:75	81:19	44:56	79
9	**8**	AcOH	24:76	84:16	50:50	91
10	**9**	MeOH	–	79[c]:21[d]	0:100	40[b]
12	**10**	MeOH	–	82[e]:18[f]	0:100	68
11	**11**	MeOH	30[g]:70[g]	85[h]:15[i]	50:50	77

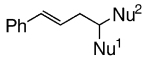
[a] Tetrahydrofuran/lactone ratio. [b] This reaction was slow and a considerable amount (24–27%) of diselenide was formed. [c] 69:31 d.r. [d] 78:22 d.r. [e] 79:21 d.r. [f] 88:22 d.r. [g] d.r. not determined. [h] 88:12 d.r. [i] 89:11 d.r.

The coordination of the acid and ester moieties in **7** and **8**, respectively, is weaker, and mixtures of **2** and **3** are formed. Chiral selenium electrophiles can also be used. With the sterically less-hindered electrophile **9**, exclusively lactone formation was observed (Table 3, entry 10). The additional methoxy group in **11** leads, as established earlier, to slightly higher stereoselectivities, but also to a mixture of **2** and **3** owing to steric interactions.[15] There is a distinct difference in the diastereoselectivities of the *cis* and *trans* isomers, which was determined by radical cleavage of the selenium moiety and subsequent analysis by HPLC. This further proves that

 © 2004 Wiley-VCH Verlag GmbH & Co. KGaA, Weinheim

the differential coordination of the alcohol or acid moiety of the substrate **1** to the electrophile influences the face selectivity of the reaction with the double bond.

Attempts to synthesize compound **12a** failed because of decomposition during selective reduction of **12b**;[16] only a



12

12a: $Nu^1 = CH_2OH$, $Nu^2 = CO_2H$
12b: $Nu^1 = CO_2Me$, $Nu^2 = CO_2H$
12c: $Nu^1 = Nu^2 = CH_2OH$

complete reduction to **12c** was successful. Various electrophiles (I^+, $PhSe^+$, **9**) led to cyclization products of **12c** in yields between 45 and 79% with *cis*/*trans* rations of about 10:90.

In conclusion, we were able to develop conditions for nucleophile-selective electrophilic cyclizations. We have shown that the cyclization can be dramatically influenced and directed by the counterion and additives to the phenylselenenyl electrophile, or by internal coordination with hydroxy moieties.

Experimental Section

Cyclization with selenium electrophiles:[4] In an inert atmosphere, the diselenide (0.085 mmol) was dissolved in diethyl ether (3.5 mL), cooled to −78 °C, and treated with bromine (0.085 mmol, 0.085 mL of a 1 M solution in CCl_4). After 10 min, a solution of silver triflate (0.24 mmol, 61 mg) in methanol (2 mmol, 80 μL) (or the corresponding amount of a silver salt dissolved in 10 equiv of the additive used) was added at −78 °C and stirred for 10 min. The mixture was treated with the substrate (0.17 mmol) and stirred at −78 °C for 3 h followed by 1 h at room temperature. The mixture was treated with *sym*-collidine (0.13 mmol, 17 μL) and then with water (20 mL). After extraction with *tert*-butyl methyl ether, the organic extracts were combined, dried with $MgSO_4$, and the solvent was evaporated to produce a crude product, which was purified by flash column chromatography on silica gel (*tert*-butyl methyl ether/petroleum ether eluent).

Received: September 16, 2003 [Z52884]

Keywords: alkenes · electrophiles · heterocycles · selenium · stereoselective synthesis

[1] a) *Organoselenium Chemistry* (Ed.: T. G. Back), Oxford University, Oxford, **1999**; b) *Topics in Current Chemistry*, *Vol. 208* (Ed.: T. Wirth), Springer, Berlin, **2000**.

[2] a) R. Déziel, E. Malenfant, G. Bélanger, *J. Org. Chem.* **1996**, *61*, 1875 – 1876; b) R. Déziel, E. Malenfant, C. Thibault, *Tetrahedron Lett.* **1998**, *39*, 5493 – 5496; c) K.-I. Fujita, K. Murata, M. Iwaoka, S. Tomoda, *Tetrahedron* **1997**, *53*, 2029 – 2048; d) S. Fukuzawa, K. Takahashi, H. Kato, H. Yamazaki, *J. Org. Chem.* **1997**, *62*, 7711 – 7716; e) S. Uemura, *Phosphorus Sulfur Relat. Elem.* **1998**, *136–138*, 219 – 234; f) T. G. Back, S. Nan, *J. Chem. Soc. Perkin Trans. 1* **1998**, 3123 – 3124; g) T. G. Back, B. P. Dyck, S. Nan, *Tetrahedron* **1999**, *55*, 3191 – 3208; h) T. G. Back, Z. Moussa, *Org. Lett.* **2000**, *2*, 3007 – 3009; i) M. Tiecco, L. Testaferri, C. Santi, C. Tomassini, F. Marini, L. Bagnoli, A. Temperini, *Tetrahedron: Asymmetry* **2000**, *11*, 4645 – 4650; j) M. Tiecco, L. Testaferri, C. Santi, C. Tomassini, F. Marini, L. Bagnoli, A. Temperini, *Chem. Eur. J.* **2002**, *8*, 1118 – 1124; k) T. G. Back, Z. Moussa, M. Parvez, *J. Org. Chem.* **2002**, *67*, 499 – 509; l) M. Tiecco, L. Testaferri, C. Santi, C. Tomassini, F. Marini, L. Bagnoli, A. Temperini, *Angew. Chem.* **2003**, *115*, 3239 – 3241; *Angew. Chem. Int. Ed.* **2003**, *42*, 3131 – 3133.

[3] Reviews: a) M. Tiecco, *Top. Curr. Chem.* **2000**, *208*, 7 – 54; b) T. Wirth, *Angew. Chem.* **2000**, *112*, 3890 – 3900; *Angew. Chem. Int. Ed.* **2000**, *39*, 3742 – 3749.

[4] G. Fragale, T. Wirth, *Eur. J. Org. Chem.* **1998**, 1361 – 1369.

[5] a) P. L. Beaulieu, R. Déziel in *Organoselenium Chemistry* (Ed.: T. G. Back), Oxford University, Oxford, **1999**, pp. 35 – 66; b) N. Petragnani, H. A. Stefani, C. J. Valduga, *Tetrahedron* **2001**, *57*, 1411 – 1448.

[6] M. Gruttadauria, C. Aprile, R. Noto, *Tetrahedron Lett.* **2002**, *43*, 1669 – 1672.

[7] a) H. Komatsu, M. Iwaoka, S. Tomoda, *Chem. Commun.* **1999**, 205 – 206; b) M. Spichty, G. Fragale, T. Wirth, *J. Am. Chem. Soc.* **2000**, *122*, 10914 – 10916; c) C. Aprile, M. Gruttadauria, M. E. Amato, F. D'Anna, P. Lo Meo, S. Riela, R. Noto, *Tetrahedron* **2003**, *59*, 2241 – 2251.

[8] L. Uehlin, G. Fragale, T. Wirth, *Chem. Eur. J.* **2002**, *8*, 1125 – 1133.

[9] Alkene **1** was synthesized by reaction of 3-bromo-2-phenylpropene with the enolate of methyl 3-hydroxypropionate and subsequent hydrolysis of the ester.

[10] CCDC-214760 contains the supplementary crystallographic data for this paper. These data can be obtained free of charge via www.ccdc.cam.ac.uk/conts/retrieving.html (or from the Cambridge Crystallographic Data Centre, 12, Union Road, Cambridge CB21EZ, UK; fax: (+44) 1223-336-033; or deposit@ccdc.cam.ac.uk).

[11] G. Fragale, T. Wirth, *Chem. Eur. J.* **1997**, *3*, 1894 – 1902.

[12] The energies of the tetrahydrofurans **2a** and **2b** and of the lactones **3a** and **3b** are almost identical, as shown by ab initio calculations at different levels (6-31G*, 6-311G*).

[13] Alkene **4** was synthesized by reduction of **1** with lithium aluminum hydride in 85% yield.

[14] a) 2,2′-diselenobisbenzyl alcohol: M. Iwaoka, S. Tomoda, *Phosphorus Sulfur Relat. Elem.* **1992**, *67*, 125 – 130; b) 2,2′-diselenobisbenzoic acid: H. Rosenmund, *Ber. Dtsch. Chem. Ges.* **1920**, *53*, 2238; c) methyl 2,2′-diselenobisbenzoate: T. Onami, M. Ikeda, S. S. Woodard, *Bull. Chem. Soc. Jpn.* **1996**, *69*, 3601 – 3605; d) (*S*,*S*)-bis[2-(1-hydroxypropyl)-phenyl] diselenides;[11] e) (*S*,*S*)-bis-2-(1-methoxymethoxypropyl)phenyl] diselenide;[8] f) (*S*,*S*)-bis[2-(1-hydroxyethyl)-6-methoxyphenyl] diselenides.[8]

[15] Although not yet determined, we assume, in analogy to earlier experiments, that the structures shown in Scheme 1 represent the absolute configurations of the major diastereomers.

[16] Compound **12b** was synthesized by addition of carbon dioxide to the enolate of methyl 5-phenyl-4-pentenoate.

 © 2004 Wiley-VCH Verlag GmbH & Co. KGaA, Weinheim

Porphyrin Dyes

A Porphyrin Dye with Monoexponential Fluorescence Intensity and Anisotropy Decay Behavior in Spherical Micelles**

*Josef Duschl, Martin Michl, and Werner Kunz**

The size of a micelle is usually determined with scattering techniques, especially neutron and X-ray scattering.[1] In principle fluorescence measurements could provide the same information, to date this technique has suffered from a lack of appropriate dyes. The chromophores used so far to probe the size of micelles were acridine orange,[2] rhodamine B, octadecylrhodamine B,[3] various porphyrin dyes,[4] merocyanine 540,[5] nile red, cresyl violet and a cyanine dye (DODCl).[6] Even in spherical micelles all of these fluorophores exhibited a biexponential or more complex decay of the fluorescence anisotropy. This situation very much complicated or even inhibited the modeling of micelles.

As the fluorophores used to date were much smaller than a whole micelle they could not reflect exclusively the global rotation of a micellar aggregate. Instead, intensity and anisotropy decay measurements revealed their distribution within different locations of a micelle and their complex self-rotation inside the aggregates.

The ideal probe should have a fluorescence lifetime in the order of the rotation time of micelles, about 10 ns. In this case time-resolved anisotropy decay measurements reflect the average angular displacement during the excited state of the chromophore. The fundamental anisotropy at the excitation wavelength should also be reasonably high. Furthermore, it should be possible to excite the dye at wavelengths easily accessible with commercial light sources. The dye must not be soluble in the continuous phase, but completely incorporated into the micelle and tightly fixed there so that its rotation only reflects the rotation of the micelle.

Pyrenes, aminonaphthalene sulfonates and porphyrins are promising candidates. However, different pyrene dyes, synthesized in our laboratory, all exhibit lifetimes shorter than 1 ns. Aminonaphthalene sulfonates show a partition equilibrium between the head-group region and the central part of the micelles. Such a partition results in a biexponential intensity decay and a multiexponential anisotropy decay behavior.[7]

Herein we present a newly synthesized porphyrin derivative, P4D, as a micellar probe which fulfils all the requirements mentioned before. It is a tetraphenylporphyrin dye with four di(isopropylene glycol) methyl ether residues (Figure 1).

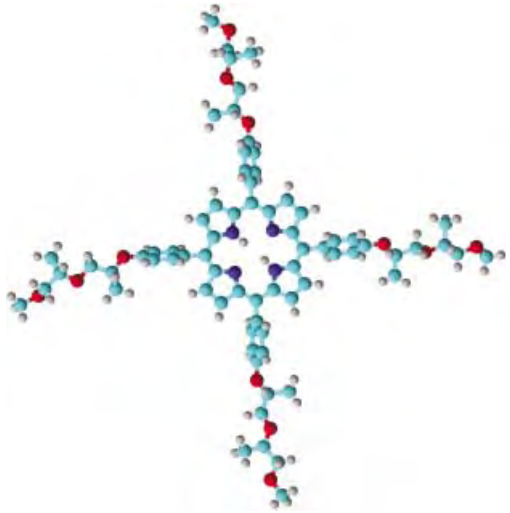


Figure 1. Structure of the new chromophore P4D; blue N, turquoise C, red O.

The porphyrin P4D has been prepared according to a synthesis developed by Bonar-Law (Scheme 1).[8] The multistep reaction starts with the preparation of the benzaldehyde **3** with a *p*-di(isopropylene glycol) methyl ether substituent. This compound is condensed with pyrrole in aqueous sodium dodecylsulfate (SDS) solution in the presence of hydrochloric acid. The formed porphyrinogen is irreversibly oxidized by *p*-chloranil to give P4D.

Figure 2 shows the absorption spectrum and the emission spectrum of P4D in 0.22 M SDS solution. The Soret band maximum is at 423 nm and Q-band maxima are at 521, 559, 593, and 649 nm. The emission maxima are at 662 and 719 nm. Also shown is the excitation anisotropy spectrum of the immobilized porphyrin in propylene glycol at −70 °C.

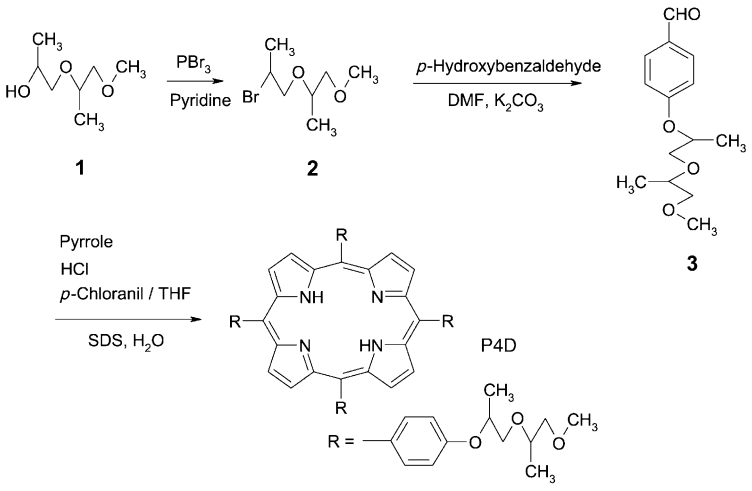
The diameter of the planar porphyrin ring is approximately 1.1 nm while the diameter of the water-insoluble P4D molecule with its four flexible side chains is around 3.7 nm. This size is about the dimension of a micelle and about three-times bigger than typical rhodamine fluorophores used to probe micelle size. The di(isopropylene glycol) methyl ether molecules forming the side chains are good cosurfactants so that tight incorporation into the surfactant layer of the micelle can be expected. To test this hypothesis, fluorescence intensity decays of P4D in various anionic and cationic surfactant solutions were measured. The surfactants were sodium octylsulfate (NaOS), sodium decylsulfate (NaDS), sodium dodecylsulfate (SDS) and dodecyltrimethylammonium bro-

[*] J. Duschl, Prof. W. Kunz
Institut fur Physikalische und Theoretische Chemie
Universität Regensburg
93040 Regensburg (Germany)
Fax: (+49) 941-943-4532
E-mail: werner.kunz@chemie.uni-regensburg.de
M. Michl
Department of Physical Electronics
Czech Technical University in Prague
V Holesovickach 2, 180 00 Praha 8 (Czech Republic)

[**] J.D. thanks the Department of Physical Electronics of the Technical University in Prague for financial support (from research project No. J04/98.210000022 of MSMT CR) during his stay in Prague. We thank Simon Schrödle and Peter Fuchs for the development of a data-processing algorithm.

Supporting information for this article (experimental details) is available on the WWW under http://www.angewandte.org or from the author.

 © 2004 Wiley-VCH Verlag GmbH & Co. KGaA, Weinheim DOI: 10.1002/anie.200351773



Scheme 1. Synthesis of P4D.

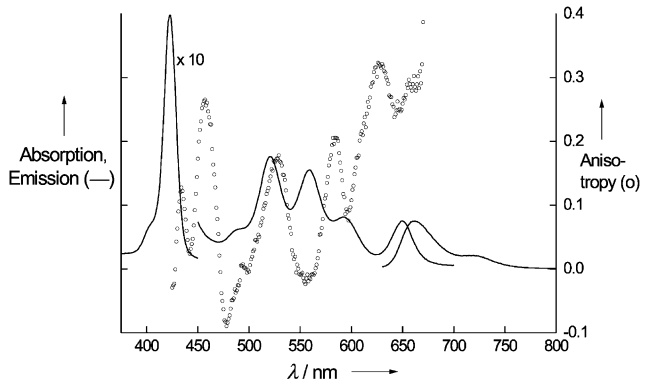


Figure 2. Excitation anisotropy spectrum of the porphyrin dye in propylene glycol at −70 °C (○). Absorption and emission spectrum of 8.3×10^{-5} M P4D (in arbitrary units) in 0.22 M SDS solution.

mide (DTAB). The critical micellar concentration cmc, the aggregation number N_{agg}, and the analytical surfactant concentration [S] of the systems considered are given in Table 1. The concentration of the micelles [M] is calculated according to Equation (1). To exclude the possibility of an alteration of

$$[M] = ([S]-cmc)/N_{agg} \quad (1)$$

the micelles in the presence of the probe, measurements of the surface tension in the SDS and DTAB systems with and without added porphyrin were carried out. These measurements did not show any significant change in the cmc values of the surfactant solutions.

Table 1: Critical micellar concentration cmc, aggregation number N_{agg}, analytical concentration [S], concentration of micelles [M], and concentration of porphyrin [P] in the fluorescence experiments.

surfactant	cmc [mmol L^{-1}][9]	N_{agg}	[S] [mmol L^{-1}]	[M] [mmol L^{-1}]	[P]/[M]
NaOS	133	20[10]	430	14.9	1:178
NaDS	33	50[11]	347	6.28	1:75.4
SDS	8.3	64[12]	220	3.31	1:39.7
DTAB	15.6	55[12]	204	3.43	1:41.1

Figure 3 displays typical fluorescence lifetime decay data for the porphyrin dye dissolved in 0.22 M SDS solution and a corresponding fit to a monoexponential decay function. The parameters for the monoexponential decay are $\tau = 9.12$ ns and $\chi^2 = 1.003$. In all the measured surfactant solutions the best fits were obtained by monoexponential decay functions. In no case was the quality of the fit significantly improved by using a biexponential or higher multiexponential fitting function.

Anisotropy measurements were performed on a frequency domain fluorimeter. The measured data were analyzed with the freely available program DIFANL (global frequency domain anisotropy differential phase and modulation analysis) from the Center of Fluorescence Spectroscopy, University of Maryland, USA. The data were fitted

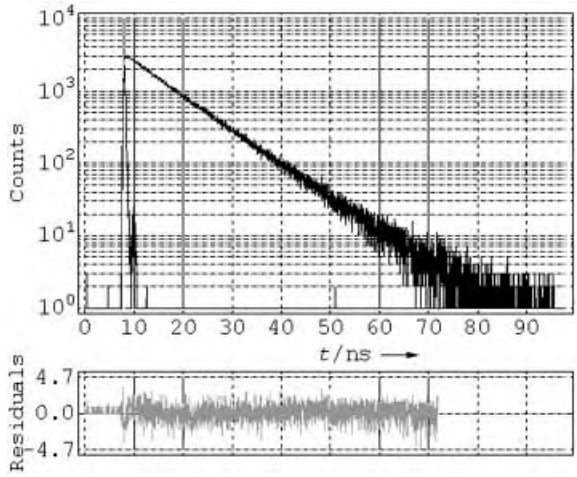


Figure 3. Top: Time-dependent fluorescence decay data of 8.3×10^{-5} mol L^{-1} porphyrin P4D in aqueous 0.22 M SDS solution and corresponding fit to a monoexponential decay function. The fitted lifetime for the monoexponential decay is $\tau = 9.12$ ns and χ^2 is 1.003. Bottom: Distribution of the weighed residuals for the monoexponential fit of the fluorescence decay. The porphyrin dye was excited at 405 nm and the emission was collected at 670 nm.

to a monoexponential anisotropy decay. A fit of the data to an assumed biexponential anisotropy decay function resulted in a worse fit. Table 2 shows the fitted rotational correlation times θ_m of the fluorophore P4D in various aqueous surfactant solutions. From these correlation times the micellar radii r_m were calculated with the Debye–Stokes–Einstein equation [Eq. (2)] with "stick" boundary conditions, where η is the shear viscosity of water (0.89 cP at 25 °C), k_B the Boltzmann constant and $T = 298$ K).

$$\theta_m = \frac{4\pi r_m^3 \eta}{3 k_B T} \quad (2)$$

The micellar radius can be estimated as the sum of the length

 © 2004 Wiley-VCH Verlag GmbH & Co. KGaA, Weinheim

Table 2: Lifetimes τ, fundamental anisotropies r_0 and rotational correlation times θ_m of the P4D in NaOS, NaDS, SDS, and DTAB. Experimental values of the volumes V, radii r_m, and literature values of the radii of the modeled micelles are given.

surfactant	τ [ns]	r_0	θ_m [ns]	Volume [nm$_3$]	r_m [nm]	$r_m^{[ref.]}$ [nm]
NaOS	10.88	0.344	3.60 ± 0.04	16.61 ± 0.21	1.583 ± 0.006	1.553[15]
NaDS	10.53	0.313	4.80 ± 0.04	22.15 ± 0.20	1.743 ± 0.005	1.982, [15] 1.26 (core)[16,17]
SDS	9.12	0.317	5.76 ± 0.02	26.61 ± 0.09	1.852 ± 0.002	2.520,[15] 1.7,[18] 1.88,[19] 1.57[16,17]
DTAB	10.18	0.321	5.72 ± 0.08	26.40 ± 0.40	1.847 ± 0.009	2.21[20]

of the head group and the alkyl chain, which is given by the Tanford equation [Eq. (3)][13] where λ_{max} is the length of the chain in nm and n_c is the number of carbon atoms in the chain minus one.

$$\lambda_{max} = 0.15 + 0.1265\, n_c \quad (3)$$

For the octyl chain, λ_{max} is 1.04 nm, for the decyl chain 1.29 nm and for the dodecyl chain 1.55 nm. To the length of the alkyl chain the length of the sulfate head group is added which is 0.47 nm.[14] The measured micellar radii are close to the theoretical length of the surfactant molecules and are in good agreement with values inferred from scattering experiments (Table 2).

In a recent study in our group, DTAB/1-hexanol mixed micelles were investigated both by small-angle neutron (SANS) and small-angle X-ray (SAXS) scattering.[21] For mixtures with a molar surfactant:alcohol ratio of 1:1 a prolate shape was found with semi-axes of 1.7 and 4.3 nm for surfactant concentrations of 0.11M. In the present study for this system a triexponential anisotropy decay was assumed to describe the two rotational diffusion coefficients of an ellipsoid of revolution. The measured biexponential anisotropy decay in the DTAB/1-hexanol system provided a short and a long rotational correlation time. From these two correlation times and neglecting a third correlation time, which could not be measured, the volume of the micelle and the axial ratio was modeled. The result is a prolate ellipsoid with semi-axes of 1.2 nm and 3.8 nm which is in close agreement with the scattering data. Furthermore, it was checked that the detected concentration thresholds at which the micelles begin to deviate from a spherical shape were very similar from both scattering and fluorescence measurements.

In summary, the novel fluorophore P4D is the first fluorophore that shows a monoexponential decay both in fluorescence intensity and in anisotropy in solutions of spherical micelles. The micellar radii deduced with the help of this fluorophore are in excellent agreement with values inferred from scattering experiments. It should be stressed that the experiments are rapid to carry out. It is to be expected that this new dye will make fluorescence spectroscopy even more useful in colloid chemistry, allowing the size of liquid nanostructures to be characterized, rapidly and simply.

Received: April 29, 2003
Revised: September 22, 2003 [Z51773]

Keywords: dyes · fluorescence spectroscopy · micelles · porphyrinoids

[1] J. Kalus, U. Schmelzer, *Trends Phys. Chem.* **1992**, *3*, 299–325.
[2] S.-H. Chou, M. J. Wirth, *J. Phys. Chem.* **1989**, *93*, 7694–7698.
[3] A. J. W. G. Visser, K. Vos, A. van Hoek, J. S. Santema, *J. Phys. Chem.* **1988**, *92*, 759–765.
[4] N. C. Maiti, S. Mazumdar, N. Periasamy, *J. Phys. Chem.* **1995**, *99*, 10708–10715.
[5] E. L. Quitevis, A. H. Marcus, M. D. Fayer, *J. Phys. Chem.* **1993**, *97*, 5762–5769.
[6] N. C. Maiti, M. M. G. Krishna, P. J. Britto, N. Periasamy, *J. Phys. Chem. B* **1997**, *101*, 11051–11060.
[7] S. Matzinger, D. M. Hussey, M. D. Fayer, *J. Phys. Chem. B* **1998**, *102*, 7216–7224.
[8] R. P. Bonar-Law, *J. Org. Chem.* **1996**, *61*, 3623–3634.
[9] P. Mukerjee, K. J. Mysels, NSRDA-NBS-36, US-Government Printing Office, Washington, DC.
[10] E. Hutchinson, J. C. Melrose, *Z. Phys. Chem. (Muenchen Ger.)* **1954**, *2*, 363–374.
[11] H. V. Tartar, A. L. M. Lelong, *J. Phys. Chem.* **1955**, *59*, 1185–1190.
[12] P. Lianos, R. Zana, *J. Colloid Interface Sci.* **1981**, *84*, 100–107.
[13] C. Tanford, *The Hydrophobic Effect: Formation of Micelles and Biological Membranes*, Wiley, New York, **1980**, p. 75.
[14] H. Pilsl, H. Hoffmann, S. Hofmann, J. Kalus, A. W. Kencono, P. Lindner, W. Ulbricht, *J. Phys. Chem.* **1993**, *97*, 2745–2754.
[15] P. J. Missel, N. A. Mazer, G. B. Benedek, M. C. Carey, *J. Phys. Chem.* **1983**, *87*, 1264–1277.
[16] S. Vass, *J. Phys. Chem. B* **2001**, *105*, 455–461.
[17] S. Vass, T. Gilany, S. Borbely, *J. Phys. Chem. B* **2000**, *104*, 2073–2081.
[18] *Intermolecular and Surface Forces*, *Vol 250*, J. N. Israelachvili, Academic Press, London, **1992**.
[19] F. Bockstahl, G. Duplatre, *Phys. Chem. Chem. Phys.* **1999**, *1*, 2767–2772.
[20] S. Berr, R. R. M. Jones, J. S. Johnson Jr. , *J. Phys. Chem.* **1992**, *96*, 5611–5614.
[21] H. Preu, C. Schirmer, M. Tomsic, M. Bester Rogac, A. Jamnik, L. Belloni, W. Kunz, *J. Phys. Chem.*, submitted.

 © 2004 Wiley-VCH Verlag GmbH & Co. KGaA, Weinheim

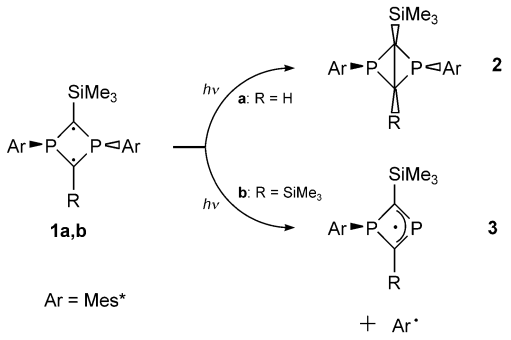
Phosphorus Heterocycles

Synthesis and Structure of a 1,3-Diphosphacyclobutadienediide: An Aniomesolytic Fragmentation of a 1,3-Diphosphetane-2,4-diyl in Solution**

Manuel Sebastian, Martin Nieger, Dénes Szieberth, László Nyulászi, and Edgar Niecke**

Dedicated Professor Bernt Krebs on the occasion of his 65th birthday

1,3-diphosphetane-2,4-diyls[1] have a biradicaloid electronic structure with a small singlet–triplet gap,[2] and a low excitation energy.[3,4] Their stability significantly depends on the substitution pattern. Thermally they undergo ring opening with generation of phosphanylcarbenes.[5] As was demonstrated recently, **1a** (R = H) isomerizes easily in a photochemical reaction to *gauche*-2,4-diphosphabicyclo[1.1.0]butane **2** (Scheme 1).[6] The formation of the bicyclic compound, however, can be suppressed by introducing sterically demanding substituents at both ring carbon atoms (**1b**; R = $SiMe_3$) thus resulting in a homolytic cleavage of one P–C_{aryl} bond, with generation of 1,3-diphosphetane-2-yl **3**.[7]



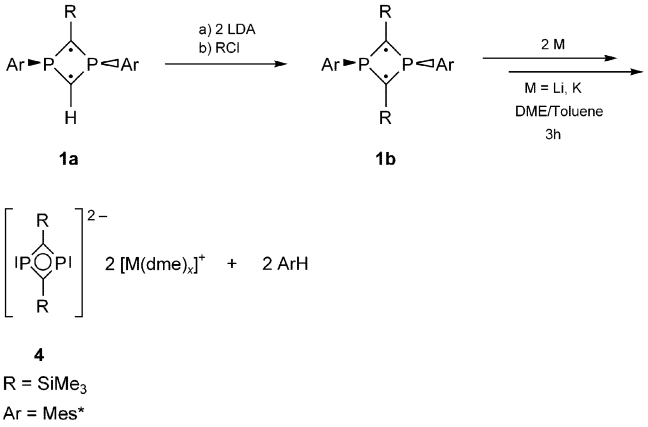
Scheme 1. Different photochemical behavior of **1a** and **1b**; Mes* = 2,4,6-$tBu_3(C_6H_2)$.

[*] Dr. D. Szieberth, Prof. Dr. L. Nyulászi
Department of Inorganic Chemistry
Technical University of Budapest
Gellért tér 4, 1521 Budapest (Hungary)
E-mail: nyulaszi.inc@chem.bme.hu
Dipl.-Chem. M. Sebastian, Dr. M. Nieger, Prof. Dr. E. Niecke
Institut für Anorganische Chemie
Rheinische Friedrich-Wilhelms-Universität
Gerhard-Domagk Strasse 1, 53121 Bonn (Germany)
Fax: (+49) 228-73-53-27
E-mail: e.niecke@uni-bonn.de

[**] This work was supported by the Deutsche Forschungsgemeinschaft and the Fonds der Chemischen Industrie. Generous allocation of computer time from NIIF/Hungary, and support from OTKA T 034675 is also gratefully acknowledged. The term aniomesolytic refers to a reaction in which a radical anion is split into a radical and an anion.

The cleavage of the P–C_{aryl} bond in the photochemical reaction indicates that a radical anion formed from **1**, through reaction with alkali metals, will undergo aniomesolytic cleavage,[8] thus finally giving the 1,3-diphosphacyclobutadienediide **4** (Scheme 2). Herein we report the synthesis of **4**, the crystal structure of the dilithium complex **4**$[Li(dme)]_2$ and the mechanism of its formation.

The 1,3-diphosphetane-2,4-diyl **1a**[6] is easily converted into the bis(trimethylsilyl) derivative **1b**. The reaction of **1b** with two equivalents of lithium proceeds with a color change from orange to red (Scheme 2). Analysis of the NMR



Scheme 2. Synthesis of the diphosphacyclobutadienediides **4**; LDA = lithium diisopropyl amide.

spectroscopic data of the reaction mixture indicates the formation of two new products, in a ratio of 2:1, and identified as 1,3,5-tri-*tert*-butylbenzene and the dilithium salt **4**$[Li(dme)]_2$. The analogous reaction of **1b** with potassium led to the dipotassium species **4**$[K(dme)_2]_2$. Both species were isolated as highly air and moisture sensitive yellow solids.

The molecular structure[9] of **4**$[Li(dme)]_2$ (Figure 1) shows a monomer consisting of a planar, C_i-symmetric four-membered P_2C_2-ring ($\sphericalangle$(PCP) = 83.8(1)°, $\sphericalangle$(CPC) = 96.2(1)°). The two lithium ions located 206.6(2) pm above and below the ring center are each coordinated by one molecule of DME. The P–C bonds are equivalent within the experimental error (179.7(1), 180.0(1) pm) and are comparable to those in similar complexes of d- and p-block elements.[10,11] The silicon atoms of the $SiMe_3$ substituents lie in the four-membered ring plane and the methyl groups of the two $SiMe_3$ units adopt a staggered conformation. The Si–C(P_2) bonds (181.9(1) pm) are comparable to the Si–C bond lengths in silyl substituted cyclobutadiene dianions (183–186 pm).[12] These relatively short bond lengths have been attributed[12] to an effective p(C)→σ*(Si) electron transfer ("negative hyperconjugation").

The constitution of complex **4**$[Li(dme)]_2$ in solution is unequivocally assigned on the basis of multinuclear NMR spectroscopic investigations. The characteristic deshielding of the atoms in the central P_2C_2 unit indicates a PC π-bonding system ($\delta^{31}P = 200.3$, $\delta^{13}C_{Ring} = 126.0$ ppm (t, $^2J_{C,P} = 59.2$ Hz)). These resonance signals lie in the range typical for cyclic π-delocalized phospha-aromatics, such as $P_2(tBuC)_3$·[K(thf)]

 DOI: 10.1002/anie.200352746 © 2004 Wiley-VCH Verlag GmbH & Co. KGaA, Weinheim

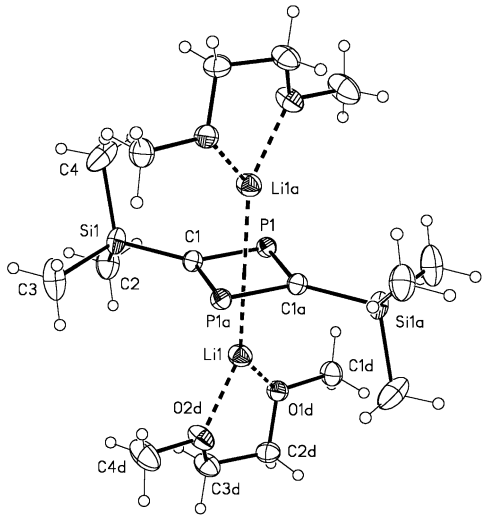


Figure 1. ORTEP plot of **4**[Li^+(dme)]$_2$ (thermal ellipsoids set at 50% probability) with representative bond lengths [pm] and angles [°] (ring center = Z). P1-C1 180.0(1), P1-C1a 179.7(1), C1-Si1 181.9(1), C1-Li1 239.1(3), Li1-P1 245.8(2), Li1-Z 206.6(2); C1-P1-C1a 83.8(1), P1-C1-P1a 96.2(1).

($\delta^{31}P = 187.6$ ppm)[13] and(tBuC)$_3$P$_3$ ($\delta^{31}P =$ 232.6, $\delta^{13}C = 218$ ppm, $^1J_{P,C} = 77$ Hz).[14] The shielding of the silicon atoms of the $SiMe_3$ group ($\delta^{29}Si = -17.3$ ppm (t, $^2J_{Si,P} =$ 18.3 Hz)) supports the interpretation of a "negative hyperconjugation" in accord with the X-ray analysis. The DME solvation of the lithium atoms is demonstrated by the results of the 2D ^{7}Li, ^{1}H HOESY experiment.

The shielding of the ^{7}Li nucleus ($\delta^7Li =$ −4.6 ppm) indicates a diatropic ring current which has also been proposed for dilithium complexes of silylated cyclobutadienediides.[12] No $^2J_{Li,P}$ coupling is observed in the ^{31}P or the ^{7}Li NMR spectrum of **4**[Li(dme)]$_2$. Comparison of a series of ^{7}Li spectra recorded between 30 °C and −90 °C revealed that the line width gradually decreases (30 °C: $b_{1/2} = 50$ Hz, −30 °C: $b_{1/2} = 12$ Hz),[15] while the line width of the ^{31}P signal remains nearly unchanged. These findings suggest an intermolecular [Li(dme)]$^+$ exchange at higher temperatures.

The possible aromaticity of the cyclobutadienediides deserves special attention.[16] As phosphorus can conjugate to carbon in π systems,[17] one can expect the aromaticity of the 1,3-diphosphacyclobutadienediide to be comparable to that of the related carbon system. Calculation[18] of the NICS(0) value for **4**[Li(dme)]$_2$[19] gives −7 ppm (B3LYP6-311 + G**//B3LYP6-31 + G*) which is somewhat lower than the −9.2 ppm obtained for [Li(dme)]$_2$[($CSiMe_3$)$_4$] at the same level of theory. Schleyer and co-workers have obtained larger negative values (−22.0 to −23.7 ppm) for the doubly Li^+ capped (CR)$_4$ dianions (R = H, Me, tBu).[20] The difference might be attributed to the effect of the silyl substituents, which decrease the π electron density in the ring. Since the calculated NICS(0) values are apparently influenced by the shielding of the σ system,[21] we also calculated the Li NMR shifts. While for **4**[Li(dme)]$_2$ the calculated shift is $\delta^7Li =$ −4.7 ppm, for [Li(dme)]$_2$[($CSiMe_3$)$_4$] values of $\delta^7Li = -3.9$ and −6.4 ppm were obtained (reference LiCl·5 H_2O; it should be noted that the optimized structure is not fully symmetric resulting in different shielding of the Li atoms).

The comparison of the ^{31}P and ^{29}Si NMR data of **4**[Li(dme)]$_2$ with **4**[K(dme)$_2$]$_2$ ($\delta^{31}P = 217.3$, $\delta^{29}Si =$ −22.5 ppm, $^2J_{Si,P} = 20.7$ Hz) reveals that in the latter the phosphorus atoms are considerably more deshielded and the silicon atoms are more shielded, which reflects a stronger charge separation $P^{\delta+}/Si^{\delta-}$ in the potassium salt.

To clarify the mechanism of the reaction described above, DFT calculations were carried out.[18] Since the calculations on the real molecule were an excessively demanding computational task, both *para-tert*-butyl groups of the 2,4,6-tri-*tert*-butylphenyl substituents have been neglected, and the thus simplified molecule **Ib** was considered as a model system (Figure 2). This simplification maintains the flattening effect of the substituents on the tricoordinate phosphorus atoms (which influences the availability of the phosphorus lone pairs

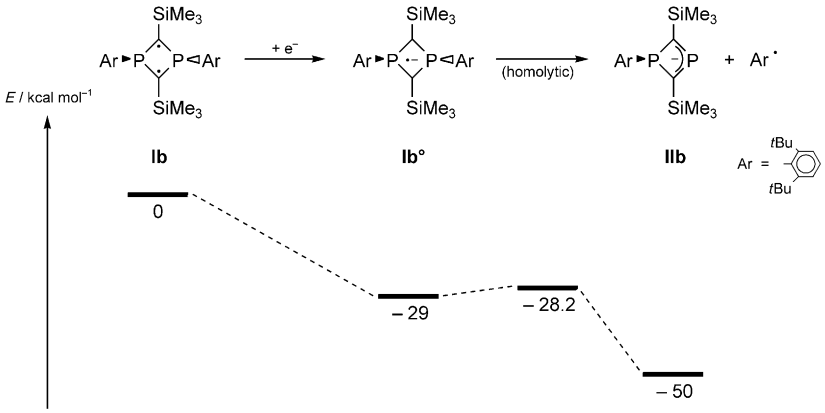


Figure 2. Calculated (gas phase) energy diagram of the reaction **Ib**→**Ib°**→**IIb**.

for the π-system), and also preserves the steric congestion about the reaction center.

First we considered the radical anion **Ib°** which is formed from **Ib**, and turns out to be stable against electron loss. The structural features of **Ib** and **Ib°** resemble each other, however the bond lengths in **Ib°** are somewhat lengthened, as expected for anions. Noteworthy is the large elongation of the P–C_{aryl} bond to 194 pm, which indicates an easy cleavage of this bond. This elongation is easily understood if the SOMO of the radical anion, that is essentially identical to the LUMO of **Ib**, is considered (Figure 3). This orbital is localized mainly on the ring atoms,[2] but also has a considerable antibonding (σ^*_{PC}) character. Populating this orbital by an electron weakens the σ bond between phosphorus and the aryl residue.[22]

The DFT calculations show that **Ib°** is more stable than **Ib** by 29 kcal mol^{-1} and they reveal a low-lying transition state (+0.8 kcal mol^{-1} with respect to **Ib°**) for the loss of the aryl

 © 2004 Wiley-VCH Verlag GmbH & Co. KGaA, Weinheim

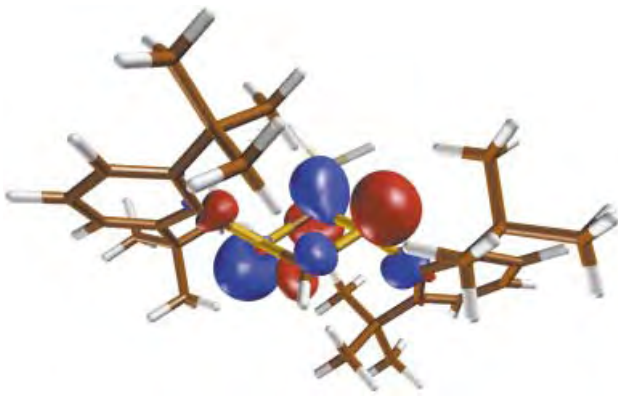
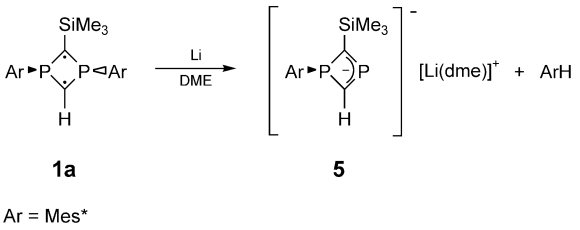


Figure 3. SOMO of the radical anion **Ia°**[Li(dme)].

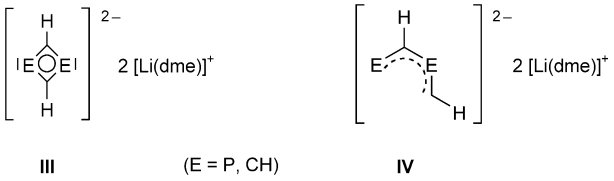
moiety. The state of the anionic intermediate **IIb** and the 2,6-di-*tert*-butylphenyl radical, is more stable than **Ib°** by 21.1 kcal mol^{-1} (Figure 2). Because it can be anticipated that the counterion and the donor solvent influence the stability of the anion and also take part in the reaction progress, calculations were performed taking into consideration the presence of the Li ion and the solvent (DME). The complex **Ia°**[Li(dme)] proved to be a local minimum with similar structural features to **Ia°** , for example, the significant extension of the P–C_{aryl} bond (Figure 4). A calculation of the transition state (**Ia°**[Li(dme)])‡ corresponding to the loss of the aryl moiety resulted in a first-order saddle point, which is 5.1 kcal mol^{-1} less stable than the lithium complex **Ia°**[Li(dme)] (B3LYP6-31 + G*//B3LYP3-21G(*)). The products of the first fragmentation step **IIa**[Li(dme)] intermediate and 2,6-di-*tert*-butylphenyl radical are finally 7.7 kcal mol^{-1} (B3LYP6-31 + G*) more stable than **Ia°**[Li(dme)]. This relative stability increases to 25.5 kcal mol^{-1} in terms of Gibbs free energy, due to the entropy contribution at room temperature.

A controlled investigation of reacting **1a** with one equivalent of lithium, was followed by ^{31}P NMR spectroscopy and experimentally verified the proposed mechanism, including the formation of the cyclic phosphaallyl anion **5**[Li(dme)] as an intermediate (Scheme 3).[23] The data for this reaction product (yield > 80%), **5**[Li(dme)] are in accord with a cyclic structure (25 °C, DME) $\delta^{31}P = -25.0$, 269.3 ppm; $^{2}J_{P,P} = 129.7$ Hz, $^{2}J_{P,H} = 18.5$ Hz).



Scheme 3. Synthesis of **5**[Li(dme)].

A comparison of the relative stability of the dilithium complexes of cyclobutadienediides **III** with their open chain analogues **IV** is also of interest. At the B3LYP6-31 + G* level



III is more stable than its acyclic analogue **IV** for E = P by 25.6 kcal mol^{-1}, while for E = CH **III** is less stable than **IV** by 10.9 kcal mol^{-1}. An apparent reason for this enhanced stability of the cyclic form **III** with E = P is the relief of the ring strain by the phosphorus atoms in the four-membered ring, compared to the all-carbon analogue.

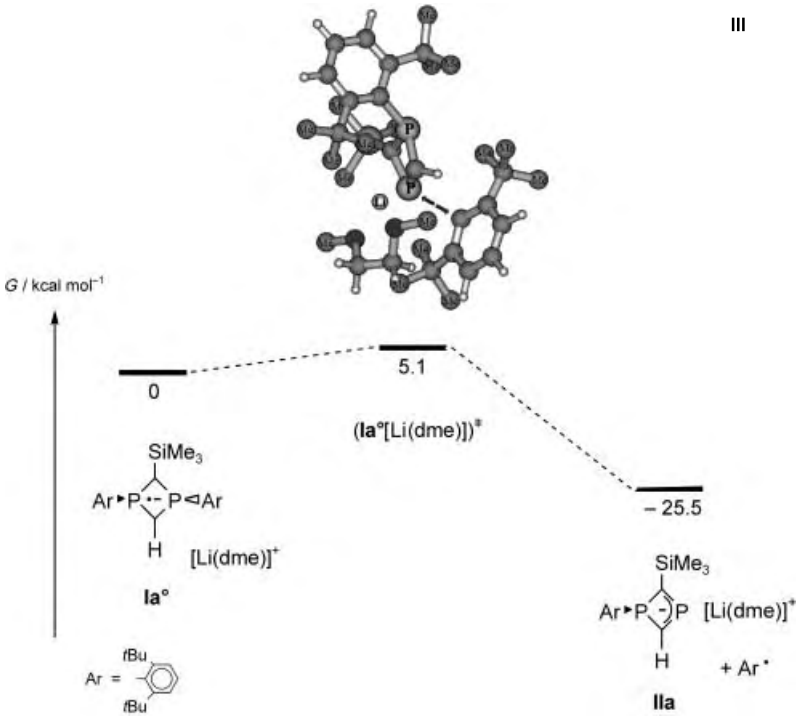


Figure 4. Calculated (gas phase) energy diagram of the reaction **Ia°**[Li(dme)]→(**Ia°**[Li(dme)])‡→**IIa**[Li(dme)].

Experimental Section

1b: To a solution of **1a** (0.325 g, 0.5 mmol) in THF (10 mL) LDA (lithium diisopropyl amide) (1.0 mmol) was added, and the reaction mixture was stirred for 3 h. After this time, Me_3SiCl (0.6 mmol) was added, dropwise, to the dark red solution. An orange precipitate soon formed which was isolated from the mother-liquor, and dried in vacuo. Yield 315 mg (87%); NMR ($CDCl_3$, 25 °C): ^{31}P NMR: $\delta = 0.5$ ppm (s); ^{1}H NMR: $\delta = -0.28$ (s, $Si(CH_3)_3$); ^{13}C NMR: $\delta = 2.0$ (t, $^{3}J_{C,P} = 2.6$ Hz, $Si(CH_3)_3$), 118.9 ppm (t, PCP); ^{29}Si NMR: $\delta = -16.4$ ppm (t, $^{2}J_{Si,P} = 5.6$ Hz, $Si(CH_3)_3$). MS (40 eV,

 © 2004 Wiley-VCH Verlag GmbH & Co. KGaA, Weinheim

EI) m/z (%): 722 (0.5) [M^+], 649 (0.35) [M^+−$Si(CH_3)_3$], 477 (54) [M^+−Mes*], 73 (100) ($Si(CH_3)_3^+$).

4[Li(dme)]$_2$: An orange suspension of **1b** (0.72 g, 1.0 mmol) in DME (15 mL) and lithium (0.07 g, 10.0 mmol) were stirred at room temperature for 3 h, forming a light red solution. The reaction mixture was filtered to remove residual metal, and the solvent was removed in vacuo. Yield 396 mg (93%); NMR ([D$_8$]THF, 25°C): ^{31}P NMR: $\delta = 200.3$ ppm (s); ^{1}H NMR: $\delta = 0.0$ (s, $Si(CH_3)_3$), 1.3 (s, Mes*), 3.4 (s, DME), 3.5 (s, DME), 7.3 ppm (s, Mes*); ^{7}Li NMR: $\delta = -4.6$ ppm (s); ^{13}C NMR: $\delta = 0.0$ (t, $^3J_{C,P} = 2.4$ Hz, $Si(CH_3)_3$), 56.3 (s, DME), 69.4 (s, DME), 126.0 ppm (t, $^1J_{C,P} = 59.2$ Hz, P*C*P); ^{29}Si NMR: $\delta = -17.3$ ppm (t, $^2J_{Si,P} = 18.3$ Hz, $Si(CH_3)_3$). The pale yellow solid was then dissolved in a mixture of hexane (5 mL) and DME (0.2 mL) and the solution was stored at −30°C. Yellow crystals of **4**[Li$^+$(dme)]$_2$ formed over a period of 2 days.

4[K(dme)$_2$]$_2$: Potassium (0.39 g, 10.0 mmol) was added to an orange suspension of **1b** (0.72 g 1.0 mmol) in DME (15 mL), and the mixture was stirred for 3 h at room temperature. The solution became dark red, as the reaction proceeded. The reaction mixture was filtered to remove residual metal, and the solvent was then removed in vacuum. The residue was washed with hexane (20 mL). Yield: 471 mg (96%); NMR ([D$_8$]THF, 25°C): ^{31}P NMR: $\delta = 217.3$ ppm (s); ^{1}H NMR: $\delta = 0.0$ (s, $Si(CH_3)_3$), 1.4 (s, Mes*), 3.3 (s, DME), 3.4 (s, DME), 7.4 ppm (s, Mes*); ^{13}C NMR: $\delta = 0.0$ (t, $^3J_{C,P} = 2.6$ Hz, $Si(CH_3)_3$), 55.5 (s, DME), 69.4 (s, DME), 125.5 ppm (s, P*C*P); ^{29}Si NMR: $\delta = -22.5$ ppm (t, $^2J_{Si,P} = 20.7$ Hz, $Si(CH_3)_3$).

Received: August 29, 2003 [Z52746]

Keywords: density functional calculations · dianions · fragmentation · phosphorus heterocycles · radical anions

[1] A. Fuchs, F. Baumeister, M. Nieger, W. W. Schoeller, E. Niecke, *Angew. Chem.* **1995**, *107*, 640–642; *Angew. Chem. Int. Ed. Engl.* **1995**, *34*, 555.

[2] W. W. Schoeller, C. Begemann, E. Niecke, D. Gudat, *J. Phys. Chem. A* **2001**, *105*, 10731.

[3] Very recently a stable 1,3-diphosphetane-2,4-diyl was obtained exhibiting a large red shift: H. Sugiyama, S. Ito, M. Yoshifuji, *Angew. Chem.* **2003**, *115*, 3932; *Angew. Chem. Int. Ed.* **2003**, *42*, 3802.

[4] Similar biradicaloid features have been demonstrated for a 1,3-diphospha-2,4-diboracyclobutane-2,4-diyl: D. Scheschkewitz, H. Amii, H. Gornitzka, W. W. Schoeller, D. Bourissou, G. Bertrand, *Science* **2002**, *295*, 1880.

[5] a) A. Fuchs, O. Schmidt, D. Gudat, M. Nieger, W. Hoffbauer, W. W. Schoeller, E. Niecke, *Angew. Chem.* **1998**, *110*, 995; *Angew. Chem. Int. Ed.* **1998**, *37*, 949; b) A. Fuchs, M. Sebastian, O. Schmidt, M. Nieger, L. Nyulászi, E. Niecke, unpublished results.

[6] A. Fuchs, M. Nieger, E. Niecke, *Angew. Chem.* **1999**, *111*, 3213; *Angew. Chem. Int. Ed.* **1999**, *38*, 3028.

[7] a) Presented at the 10th International Symposium on Inorganic Ring Systems: M. Sebastian, M. Nieger, L. Nyulaszi, E. Niecke (Vermont, USA, August **2003**); b) M. Sebastian, O. Schmidt, M. Nieger, L. Nyulászi, E. Niecke, unpublished results.

[8] P. Maslak, *Top. Curr. Chem.* **1993**, *168*, 1; J.-M. Savéant, *Acc. Chem. Res.* **1993**, *26*, 455.

[9] X-ray structure analysis of **4**[Li(dme)]$_2$: $C_{16}H_{38}Li_2O_4P_2Si_2$: yellowish crystals, crystal dimension $0.15 \times 0.20 \times 0.50$ mm^3; $M_r = 426.46$; monoclinic, space group $P2_1/n$ (No. 14), $a = 11.1755(2)$, $b = 10.9568(2)$, $c = 11.1966(2)$ Å, $\beta = 105.786(1)°$, $V = 1319.29(4)$ Å^3, $Z = 2$, $\mu(Mo_{K\alpha}) = 0.270$ mm^{-1}, $T = 123(2)$ K, $F(000) = 460$. 26387 reflection up to $2\theta_{max.} = 50°$ were measured on a Nonius KappaCCD diffractometer with $Mo_{K\alpha}$ radiation, 2329 of which were independent and used for all calculations. The structure was solved by direct methods and refined to F^2 anisotropically, the H atoms were refined with a riding model. The final quality coefficient $wR2(F^2)$ for all data was 0.0750, with a conventional $R(F) = 0.0258$ for 118 parameters. CCDC-216013 (**4**[Li(dme)]$_2$) contains the supplementary crystallographic data for this paper. These data can be obtained free of charge via www.ccdc.cam.ac.uk/conts/retrieving.html (or from the Cambridge Crystallographic Data Centre, 12 Union Road, Cambridge CB2 1EZ, UK; fax: (+44) 1223-336-033; or deposit@ccdc.cam.ac.uk).

[10] a) P. Binger, R. Milczarek, R. Mynott, M. Regitz, W. Rösch, *Angew. Chem.* **1986**, *98*, 645; *Angew. Chem. Int. Ed. Engl.* **1986**, *25*, 644; b) P. B. Hitchcock, M. J. Maah, J. F. Nixon, *J. Chem. Soc. Chem. Commun.* **1986**, 737.

[11] a) J. Lynam, M. Copsey, M. Green, J. Jeffery, J. McGrady, C. Russell, J. Slattery, A. Swain, *Angew. Chem.* **2003**, *115*, 2884; *Angew. Chem. Int. Ed.* **2003**, *42*, 2778; b) M. D. Francis, P. B. Hitchcock, *Chem. Commun.* **2002**, 86; c) G. Anderson, J. C. Green, M. D. Francis, *Organometallics* **2003**, *22*, 2897.

[12] a) A. Sekiguchi, T. Matsuo, H. Watanabe, *J. Am. Chem. Soc.* **2000**, *122*, 5652; b) A. Sekiguchi, M. Tanaka, T. Matsuo, H. Watanabe, *Angew. Chem.* **2001**, *113*, 1721; *Angew. Chem. Int. Ed.* ***2001***, *40*, 1675; c) A. Sekiguchi, T. Matsuo, M. Tanaka, *Organometallics* **2002**, *21*, 1072.

[13] F. G. N. Cloke, P. B. Hitchcock, J. F. Nixon, D. J. Wilson, *Organometallics* **2000**, *19*, 219.

[14] F. Tabellion, C. Peters, U. Fischbeck, M. Regitz, F. Preuss, *Chem. Eur. J.* **2000**, *6*, 4558.

[15] Further cooling to −90° results in a signal broadening because of quadrupolar relaxation: O. Howarth in *Multinuclear NMR Spectroscopy*, (Ed.: J. Mason), Plenum, New York, **1987**, pp. 133.

[16] The aromatic character of the cyclobutadiene dianion together with other possibly aromatic dianions has recently been studied in detail. a) T. Sommerfeld, *J. Am. Chem. Soc.* **2002**, *124*, 1119; b) S. Feuerbacher, A. Dreuw, L. S. Cederbaum, *J. Am. Chem. Soc.* **2002**, *124*, 3163; c) S. Feuerbacher, L. S. Cederbaum, *J. Am. Chem. Soc.* **2003**, *125*, 9531; d) A. Dreuw, L. S. Cederbaum, *Chem. Rev.* **2002**, *102*, 181. The interesting conclusion of these studies is that the increasing conjugation destabilizes the dianions against electron loss, thus reducing their lifetimes. Note that these conclusions do not refer to the ion-pair-stabilized anions.

[17] L. Nyulászi, T. Veszprémi, J. Réffy, *J. Phys. Chem.* **1993**, *97*, 4011.

[18] Calculations were carried out by using the Gaussian 98 package. (Gaussian 98 (Revision A.7), M. J. Frisch, G. W. Trucks, H. B. Schlegel, G. E. Scuseria, M. A. Robb, J. R. Cheeseman, V. G. Zakrzewski, J. A. Montgomery, R. E. Stratmann, J. C. Burant, S. Dapprich, J. M. Millam, A. D. Daniels, K. N. Kudin, M. C. Strain, O. Farkas, J. Tomasi, V. Barone, M. Cossi, R. Cammi, B. Mennucci, C. Pomelli, C. Adamo, S. Clifford, J. Ochterski, G. A. Petersson, P. Y. Ayala, Q. Cui, K. Morokuma, D. K. Malick, A. D. Rabuck, K. Raghavachari, J. B. Foresman, J. Cioslowski, J. V. Ortiz, B. B. Stefanov, G. Liu, A. Liashenko, P. Piskorz, I. Komaromi, R. Gomperts, R. L. Martin, D. J. Fox, T. Keith, M. A. Al-Laham, C. Y. Peng, A. Nanayakkara, C. Gonzalez, M. Challacombe, P. M. W. Gill, B. G. Johnson, W. Chen, M. W. Wong, J. L. Andres, M. Head-Gordon, E. S. Replogle, J. A. Pople, Gaussian, Inc., Pittsburgh, PA, **1998**. Unless otherwise stated the geometries were optimized first at the B3LYP3-21G(*) level of theory, and at the optimized structures second derivatives were calculated to show, whether minimum (positive eigenvalues only) or transition structure (a single negative eigenvalue of the hessian matrix) has been obtained. Further optimization was performed at the B3LYP6-31 + G* level of the theory. Magnetic shieldings were calculated by using the GIAO method, at the B3LYP6-311 + G**//B3LYP6-31 + G* level. To calculate the thermodynamic functions the B3LYP3-21G(*)

harmonic frequencies were used. Correction for internal rotations was not considered.

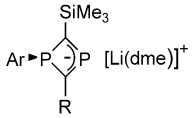
[19] Since the dianions are unstable against electron loss (for details see ref. [16]) computation of the uncomplexed dianion by standard ab initio methods might provide misleading results. Therefore we have calculated the bis[Li(dme)]$^+$ complexed forms of the dianions. The calculated structural characteristics are essentially the same as those obtained from the crystal structure of **4**[Li(dme)]$_2$.

[20] M. Balci, M. L. McKee, P. von R. Schleyer, *J. Phys. Chem. A* **2000**, *104*, 1246.

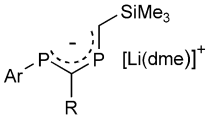
[21] The paratropic effect of the σ framework in cyclobutane has been analyzed recently. D. Moran, M. Manoharan, T. Heine, P. von R. Schleyer, *Org. Lett.* **2003**, *5*, 23.

[22] This behavior of a radical anion is particularly noteworthy, since radical anions are usually formed from aromatic systems. (For a recent work on a mesolytic fragmentation see L. Pisano, M. Farriol, X. Asensio, I. Gallardo, A. Gonzalez-Lafont, J. M. Lluch, J. Marquet *J. Am. Chem. Soc.* **2002**, *124*, 4708.) A subsequent cleavage of the radical anion to a radical and an anion requires the electron to be transferred from the aryl π* orbital into the σ* orbital of the bond to be broken. In the present case the extra electron of the radical anion is captured in an orbital already having σ* character.

[23] The DFT calculations also show that in the second fragmentation step the intermediate **II a**[Li(dme)] is first attacked by another [Li(dme)]$^+$ ion, to form a stable radical dianion **II a°**[Li(dme)]$_2$. This species has a long P–C$_{aryl}$ bond (195.1 pm, B3LYP6-31 + G*), similar to complex **I a°**[Li(dme)], again indicating the ease with which this bond can be broken. The transition state corresponding to the loss of the second aryl moiety is less stable than the complex **II a°**[Li(dme)]$_2$ by 4.2 kcal mol^{-1} (B3LYP6-31 + G*). The energy difference between the [Li(dme)]$^+$ complexes of *cis*-1,3-diphosphabutadienyl anions **V**[Li(dme)] and the corresponding 1,3-diphos-



II



V

phetene-2-ides **II**[Li(dme)] have been calculated (B3LYP6-31 + G*//B3LYP3-21G(*)) and the acyclic forms **V**[Li(dme)] (R = H, SiMe$_3$) are found to be 7 kcal mol^{-1} less stable than the cyclic ones. The formation of an acyclic species, [MeP=C(Mes*)P=CMes*]$^{2-}$, was proposed for the reaction product in the 2:1 molar reaction of the phospha-alkyne, Mes*CP, and methyl lithium: A. Arif, A. Barron, A. Cowley, S. Hall, *J. Chem. Soc. Chem. Commun.* **1988**, 171. However, the ^{31}P NMR data of this product fit well with those observed for **5**[Li(dme)]. The B3LYP6-311 + G**//B3LYP6-31 + G* chemical shifts of the [Li(dme)]$^+$ complex of the acyclic anion are 382.2 and 295.9 ppm for the two phosphorus atoms. Also Yoshifuji and co-workers have postulated a cyclic anionic intermediate.[24]

[24] S. Ito, H. Sugiyama, M. Yoshifuji, *Chem. Commun.* **2002**, 1744.

 © 2004 Wiley-VCH Verlag GmbH & Co. KGaA, Weinheim

Cover Picture



Lyudmila V. Slipchenko, Tamara E. Munsch, Paul G. Wenthold,* and Anna I. Krylov*

Contrary to the accepted guidelines for the occupancy of orbitals (such as Hund's rule or the Aufbau principle), three unpaired electrons are coupled antiferromagnetically in the 5-dehydro-*m*-xylylene triradical. This first example of an organic molecule with an "open-shell" doublet ground state is described by P. G. Wenthold, A. I. Krylov, and co-workers on page 742 ff. The cover pictures shows the singly occupied orbitals in the triradical and highlights the correlation between theoretical and experimental results.

Contents

Angewandte EarlyView

The following articles are available online (in Wiley InterScience). You can find them at www.angewandte.org, under Full Text, Early View.

K. Ohkubo, H. Kotani, J. Shao, Z. Ou, K. M. Kadish, G. Li, R. K. Pandey,* M. Fujitsuka, O. Ito,* H. Imahori,* S. Fukuzumi*:*
Production of an Ultra-Long-Lived Charge-Separated State in a Zinc Chlorin–C_{60} Dyad by One-Step Photoinduced Electron Transfer
DOI: 10.1002/anie.200352870
Published online: January 22, 2004

A. Srinivasan, T. Ishizuka, H. Furuta:*
Doubly N-Fused Pentaphyrin
DOI: 10.1002/anie.200352946
Published online: January 22, 2004

D. P. Gamblin, P. Garnier, S. van Kasteren, N. J. Oldham, A. J. Fairbanks, B. G. Davis:*
Glyco-SeS: Selenenylsulfide-Mediated Protein Glycoconjugation—A New Strategy in Post-Translational Modification
DOI: 10.1002/anie.200352975
Published online: January 21, 2004

Y. Tachibana, G. L. Fletcher, N. Fujitani, S. Tsuda, K. Monde, S.-I. Nishimura:*
Antifreeze Glycoproteins: Elucidation of the Structural Motifs That Are Essential for Antifreeze Activity
DOI: 10.1002/anie.200353110
Published online: January 22, 2004

I. Lévêque, M. Cusack, S. A. Davis, S. Mann:*
Promotion of Fluorapatite Crystallization by Soluble-Matrix Proteins from *Lingula anatina* Shells
DOI: 10.1002/anie.200353115
Published online: January 22, 2004

Articles judged by the referees or the editor as being either very important or very urgent are immediately edited, proof-read, and electronically published once the manuscript has arrived in the editorial office in final form. As long as there is no page number available these articles should be cited in the following manner:

Author(s) *Angew. Chem. Int. Ed.*, online publication date, DOI.

News

Organic Synthesis: K. C. Nicolaou honored — **658**

Medicinal Chemistry: R. Langer receives prize

Catalysis: D. Blackmond on the move

Books

Chemical Metallurgy Principles and Practice — **659**
Chiranjib Kumar Gupta
reviewed by G. Sauthoff

Introduction to Green Chemistry
Green Chemistry for Schools and Colleges
Green Chemistry — **660**
American Chemical Society, Royal Society of Chemistry, Gesellschaft Deutscher Chemiker
reviewed by J. O. Metzger

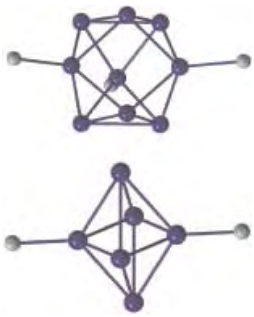
Computer-Aided Structure Elucidation — **661**
Ernö Pretsch, Gábór Tóth, Morton E. Munk, Martin Badertscher
reviewed by W. Bauer, A. H. C. Horn

Highlights

Carbon-Group Elements

A. Schnepf* — **664 – 666**

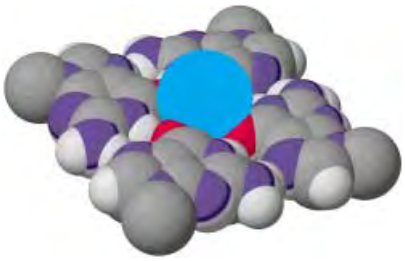
Novel Compounds of Elements of Group 14: Ligand-Stabilized Clusters with "Naked" Atoms



Naked Facts: Recently, cluster compounds that contain both ligand-bound and unsubstituted atoms of Group 14 have been described. The general formula M_nR_m, where $m < n$ (see picture) can be assigned to these compounds. More recent developments in this area, the bonding situation within these compounds, and their possible significance for nanotechnology are discussed.

© 2004 Wiley-VCH Verlag GmbH & Co. KGaA, Weinheim

Reviews



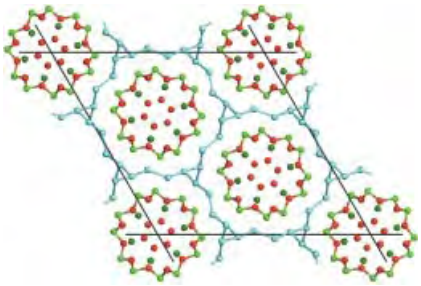
Mononucleotides in water, lipophilic nucleosides in organic solvents, or G-rich DNA in the chromosome: Cation-templated self-assembly of guanosine gives supramolecular structures based on the G-quartet (see picture). These structures have a wide range of potential functions in areas as diverse as cancer biology, separations chemistry, and biomaterials.

Supramolecular Chemistry

J. T. Davis* ——— **668 – 698**

G-Quartets 40 Years Later: From 5′-GMP to Molecular Biology and Supramolecular Chemistry

Communications

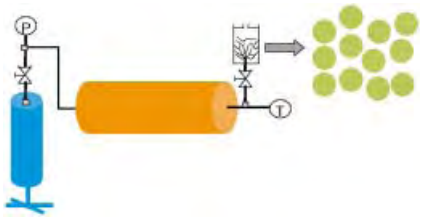


A crystalline microporous semiconductor $|(|K_6(H_2O)_6|[Sb_{12}O_{18}])_3|[Te_{36}]$ (denoted SBC-1) has been prepared, which consists of 24-ring tubular tellurium units that host 12-ring $\{Sb_{12}O_{18}\}$ tubular units, which in turn act as hosts for K^+ ions and H_2O molecules (see picture). An example of a second-order zeoate, it has a narrow bandgap of 0.25 eV and exhibits highly anisotropic electrical conductivity.

Semiconductors

A. E. C. Palmqvist,* B. B. Iversen, E. Zanghellini, M. Behm, G. D. Stucky ——— **700 – 704**

A Crystalline Microporous Narrow-Bandgap Semiconductor



Nanoparticles of a fluoropolymer, which is soluble in supercritical carbon dioxide, can be recovered from a liquid solvent after a rapid expansion process (see scheme). Nanoparticles with an average diameter less than 50 nm were initially obtained, however many strategies led to aggregation and the formation of agglomerates. Sodium dodecyl sulfate was found to be most effective in stabilizing the polymeric nanoparticles in aqueous suspension.

Polymer Nanoparticles

M. J. Meziani, P. Pathak, R. Hurezeanu, M. C. Thies, R. M. Enick, Y.-P. Sun* ——— **704 – 707**

Supercritical-Fluid Processing Technique for Nanoscale Polymer Particles

For the USA and Canada:
ANGEWANDTE CHEMIE International Edition (ISSN 1433-7851) is published weekly by Wiley-VCH PO Box 191161, D 69451 Weinheim, Germany. Air freight and mailing in the USA by Publications Expediting Inc. 200 Meacham Ave., Elmont, NY 11003. Periodicals postage paid at Jamaica NY 11431. US POSTMASTER: send address changes to *Angewandte Chemie*, Wiley-VCH, 111 River Street, Hoboken, NJ 07030. Annual subscription price for institutions: Europe € 3430.00/3118.00; outside Europe US$ 4499.00/4090.00 (valid for print and electronic/print or electronic delivery); for individuals who are personal members of a national chemical society, or whose institution already subscribes, or who are retired or self-employed consultants, print only: Europe € 248.00/outside Europe US$ 378.00. Postage and handling charges included. All Wiley-VCH prices are exclusive VAT.

 © 2004 Wiley-VCH Verlag GmbH & Co. KGaA, Weinheim

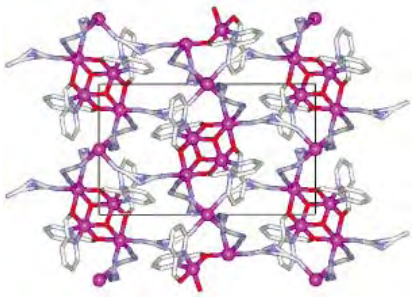
Contents

Three-Dimensional Networks

H. Miyasaka,* K. Nakata, K.-i. Sugiura, M. Yamashita, R. Clérac* —— **707 – 711**

A Three-Dimensional Ferrimagnet Composed of Mixed-Valence Mn_4 Clusters Linked by an $\{Mn[N(CN)_2]_6\}^{4-}$ Unit

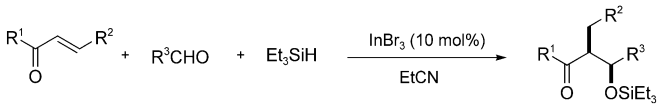
A ferrimagnet with a 3D molecular network (depicted) has been synthesized and characterized. The compound is composed of units of mixed-valence Mn_4 clusters, a unit that is well known for its single-molecule magnet properties, and Mn^{II} paramagnetic units. Both building blocks are linked by a dicyanamide bridging ligand to form a covalently bonded three-dimensional network. The compound becomes a ferrimagnet at 4.1 K that exhibits a spin-flip phenomenon under the influence of a magnetic field.



Reductive Aldol Reaction

I. Shibata,* H. Kato, T. Ishida, M. Yasuda, A. Baba* —— **711 – 714**

Catalytic Generation of Indium Hydride in a Highly Diastereoselective Reductive Aldol Reaction



A one-pot synthesis of β-hydroxyketones has been achieved by the reductive aldol reaction of enones and aldehydes in the presence of Et_3SiH and a catalytic amount of $InBr_3$ (see scheme). The reaction is highly diastereoselective and no reduction of the starting aldehydes occurs. This method is superior to conventional reductive aldol reactions in terms of applicability to a wide range of enones and aldehydes.

Ring Rearrangements

R. E. Bulo, H. Jansen, A. W. Ehlers, F. J. J. de Kanter, M. Schakel, M. Lutz, A. L. Spek, K. Lammertsma* — **714 – 717**

The Circumambulation of a Phosphirane: Taking 9-Phenyl-9-phosphabicyclo[6.1.0]-nona-2,4,6-triene for a "Walk"

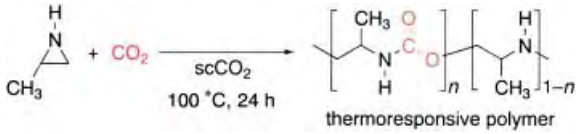
Walking rings: At room temperature, the P-R entity of a bicyclic phosphirane (see picture) "walks" along the perimeter of the larger ring. Although this concerted rearrangement is similar to that of its hydrocarbon analogue, the additional 1,5-sigmatropic shift follows a different mechanism.



Thermoresponsive Polymers

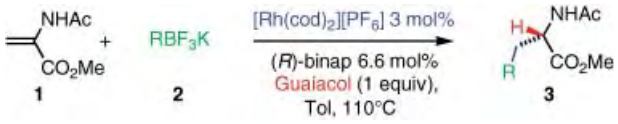
O. Ihata, Y. Kayaki,* T. Ikariya* **717 – 719**

Synthesis of Thermoresponsive Polyurethane from 2-Methylaziridine and Supercritical Carbon Dioxide



Under pressure: Temperature-dependent optical transmission in aqueous solution is exhibited by polyurethanes that are obtained by copolymerization of 2-methylaziridine and supercritical CO_2 ($scCO_2$; see scheme). The transmittance drops sharply at the lower critical solution temperature (LCST). The molecular weight, content of urethane linkages, and LCST value of the polyurethanes are controllable simply by changing the CO_2 pressure.

© 2004 Wiley-VCH Verlag GmbH & Co. KGaA, Weinheim



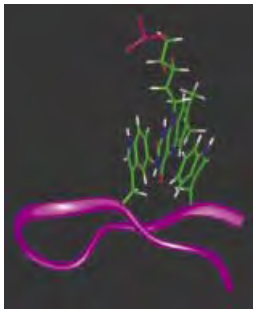
Conjugate addition of potassium trifluoro(organo)borates **2** (R = aryl, alkenyl) to 2-acetamidoacrylate **1** mediated by a chiral rhodium catalyst and with in situ enantioselective protonation afforded a variety of α-amino acids **3** with high yields and *ee* values up to 90% (see scheme, cod = cycloocta-1,5-diene, binap = 2,2′-bis(diphenylphosphanyl)-1,1′-binaphthyl). Among the tested chiral ligands and proton sources, binap in combination with 2-methoxyphenol (guaiacol), an inexpensive and nontoxic phenol, afforded the highest asymmetric inductions.

Asymmetric Catalysis

L. Navarre, S. Darses,*
J.-P. Genet* ——— **719 – 723**

Tandem 1,4-Addition/Enantioselective Protonation Catalyzed by Rhodium Complexes: Efficient Access to α-Amino Acids

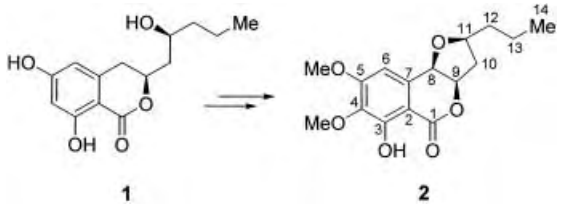
Pinning down flavoproteins: A designed β-hairpin peptide binds flavin mononucleotide (FMN) in water through noncovalent interactions involving Trp and Lys residues on one face of the β hairpin (see model). Reduction of FMN is disfavored in the complex as a result of favorable π–π stacking interactions between Trp side chains and the oxidized flavin ring. This system mimicks the function of naturally occurring flavoproteins.



Peptidomimetics

S. M. Butterfield, C. M. Goodman,
V. M. Rotello, M. L. Waters* — **724 – 727**

A Peptide Flavoprotein Mimic: Flavin Recognition and Redox Potential Modulation in Water by a Designed β Hairpin

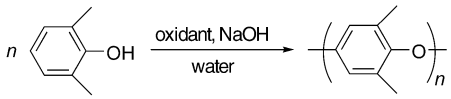


Enzyme essential: Feeding studies with *Dreschlera ravenelii* show that labeled dihydroisocoumarin **1** is metabolized into monocerin (**2**) in exceptionally high levels. These results provide evidence for the role of **1** as the first enzyme-free intermediate in the monocerin biosynthesis pathway and, thus, as the final product of the polyketide synthase (PKS) catalyzed part of the pathway. Compound **1** may therefore be of use in further studies to isolate and sequence the monocerin PKS gene.

Monocerin Biosynthesis

L. C. Axford, T. J. Simpson,*
C. L. Willis ——— **727 – 730**

Synthesis and Incorporation of the First Polyketide Synthase Free Intermediate in Monocerin Biosynthesis



Green polymerization: The simple stirring of 2,6-dimethylphenol with an excess of oxidant or a catalytic amount of a copper complex in an alkaline aqueous solution yields poly(2,6-dimethyl-1,4-phenyleneoxide), a commercially important polymer (see scheme). The formed polymer was easily separated as an off-white powder by filtration.

Polymerization

K. Saito, T. Tago, T. Masuyama,
H. Nishide* ——— **730 – 733**

Oxidative Polymerization of 2,6-Dimethylphenol To Form Poly(2,6-dimethyl-1,4-phenyleneoxide) in Water

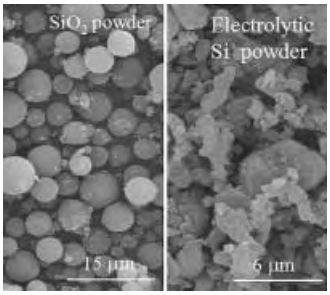
© 2004 Wiley-VCH Verlag GmbH & Co. KGaA, Weinheim

Contents

Electrochemical Synthesis

X. B. Jin, P. Gao, D. H. Wang, X. H. Hu, G. Z. Chen* ——— **733 – 736**

Electrochemical Preparation of Silicon and Its Alloys from Solid Oxides in Molten Calcium Chloride

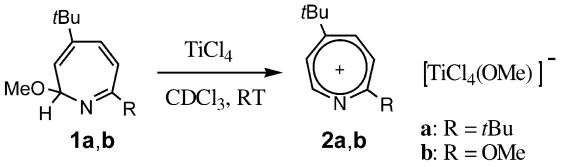


Electroreduction, or electrodeoxidation, of pelleted SiO_2 powder (left image) or its mixture with other metal oxide powders in molten $CaCl_2$ produces pure Si powder (right image), or the respective silicon alloy powder. Being advantageous by simplicity and resulting in less CO_2 emission, the electrochemical approach has an energy consumption that is below 13 kWh (kg of Si)$^{-1}$.

Aromaticity

K. Satake,* Y. Kubota, C. E. J. Cordonier, H. Okamoto, M. Kimura ——— **736 – 738**

Synthesis of a Delocalized Azepinium Ion and Investigation of Its Electrophilic Character

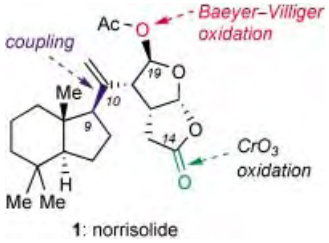


An isolated example: The first π-delocalized azepinium ions **2** were generated from 2*H*-azepines **1** and fully characterized by NMR spectroscopy. The stability of the ions was investigated by ab initio calculations. Reaction with nucleophiles led to further support of the characterization of the ions by the selective formation of 2-substituted 2*H*-azepines.

Natural Products Synthesis

T. P. Brady, S. H. Kim, K. Wen, E. A. Theodorakis* ——— **739 – 742**

Stereoselective Total Synthesis of (+)-Norrisolide

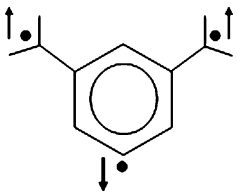


In a convergent approach to the marine natural product (+)-norrisolide (**1**) the two bicyclic ring systems are coupled through the C9–C10 bond to assemble the carbon framework in a late stage of the synthesis. Other highlights of the synthetic strategy include the formation of the unusual fused γ-lactone–γ-lactol motif of **1** through a sequence of oxidation reactions.

Radicals

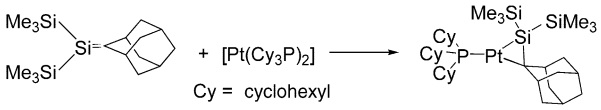
L. V. Slipchenko, T. E. Munsch, P. G. Wenthold,* A. I. Krylov* **742 – 745**

5-Dehydro-1,3-quinodimethane: A Hydrocarbon with an Open-Shell Doublet Ground State



Theory predicts an open-shell doublet ground state for the 5-dehydro-1,3-quinodimethane triradical (see picture), with three low-spin coupled electrons in three singly occupied molecular orbitals. The bond dissociation enthalpy for formation of the triradical from *meta*-xylylene, measured by MS indicates an interaction of (1 ± 4) kcal mol^{-1} between the unpaired electrons in the σ and π systems in the triradical.

© 2004 Wiley-VCH Verlag GmbH & Co. KGaA, Weinheim



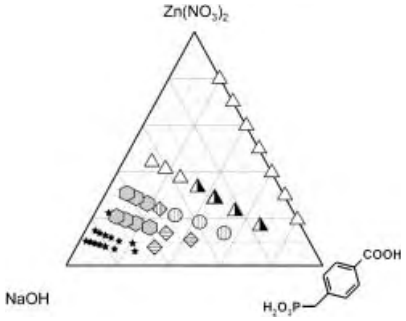
1

σ or π? The direct synthesis and the molecular and electronic structures of a novel η^2-silene platinum complex, **1**, is reported (see scheme). The nature of bonding in **1** was studied by using geometrical and electronic structure criteria, and the results suggested that **1** is best described as an hybrid between a π complex and a σ-cyclopropane structure with a more dominant π-complex character than in a related disilene complex.

Silene–Organometallic Complexes

D. Bravo-Zhivotovskii,*
H. Peleg-Vasserman, M. Kosa, G. Molev,
M. Botoshanskii, Y. Apeloig* _ **745 – 748**

The Direct Synthesis of a
Silene–Organometallic Complex

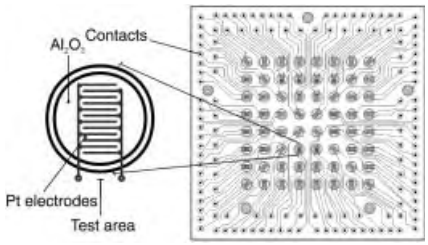


A new phase in combinatorial chemistry: High-throughput methods for hydrothermal reactions including automated solid-dosing and pH-measurement capabilities have been applied to the synthesis of five novel zinc phosphonocarboxylates and seven novel metal tetraphosphonates. This automated combinatorial synthesis and characterization method allows a large parameter space to be explored rapidly (see phase diagram) and has great potential for materials science.

Hybrid Compounds

N. Stock,* T. Bein* _____ **749 – 752**

High-Throughput Synthesis of
Phosphonate-Based Inorganic–Organic
Hybrid Compounds under
Hydrothermal Conditions



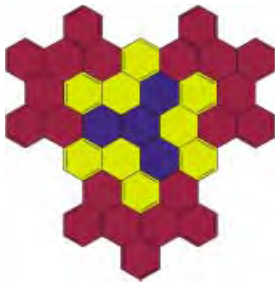
A combinatorial work flow for the rapid synthesis and testing of thick oxide films for the development of new gas sensors with improved sensitivity and selectivity involves the synthesis and deposition of mixed-oxide films of variable composition. The library is based on the sol–gel synthesis of mixed oxides on an array of 8×8 interdigitated electrodes. For the characterization of the sensor arrays, test gas sequences and sensor temperatures were varied.

Sensor Screening

A. Frantzen, J. Scheidtmann, G. Frenzer,
W. F. Maier,* J. Jockel, T. Brinz, D. Sanders,
U. Simon* _____ **752 – 754**

High-Throughput Method for the Impedance Spectroscopic Characterization of
Resistive Gas Sensors

Liquid crystals from large graphitic segments: Discotic compounds based on substituted superphenalenes were prepared by a surprisingly simple synthesis and processed to give soft and highly soluble columnar liquid-crystalline materials. The regiospecific synthesis leads to compounds with pinwheel-type C_3 symmetry.



Liquid Crystals

Ž. Tomović, M. D. Watson,
K. Müllen* _____ **755 – 758**

Superphenalene-Based Columnar
Liquid Crystals

Communications labeled with this symbol have been judged by two referees as being "very important papers".

The publication of Communications labeled with this symbol has been accelerated because of their topical or highly competitive nature.

 © 2004 Wiley-VCH Verlag GmbH & Co. KGaA, Weinheim

Deadline for recruitment adverts

11/2004	February 19	Publication date:	March 05
12/2004	February 26	Publication date:	March 12

Angewandte Chemie International Edition
Advertising Sales Department:
Marion Schulz
Phone: 0 62 01 – 60 65 65
Fax: 0 62 01 – 60 65 50
E-Mail: MSchulz@wiley-vch.de

Place an advert in the printed version
and have it made available online for 1 month, free of charge!

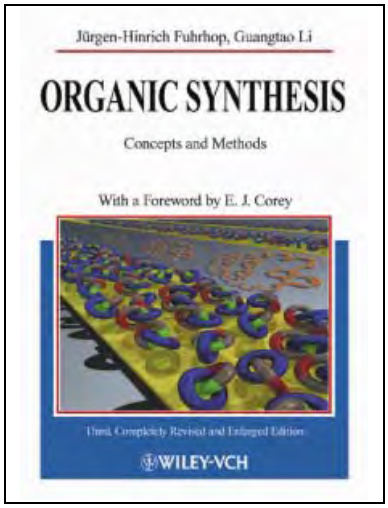
Service

Keywords ____ *760*

Authors ____ *761*

Preview ____ *763*

A Bestseller in its 3rd Edition



ISBN 3-527-30272-7 Hbk.
€ 95,- / sFr 140,-
ISBN 3-527-30273-5 Pbk.
€ 55,- / sFr 81,-

JÜRGEN-HINRICH FUHRHOP and GUANGTAO LI, both of FU Berlin, Germany

Organic Synthesis
Concepts and Methods
3rd completely revised and enlarged edition
2003. XVI, 517pp Hbk

Every student of organic chemistry will need to cover this topic at some point, and this third edition of a well-proven textbook is specially written for advanced undergraduates and graduates. 50% of the text is new and includes chapters on combinatoric chemistry, non-covalent molecular assemblies and using the Web for searching chemical compounds. The authors have chosen the methods for their efficiency, elegance, and didactic value and have highlighted important reactions within the text, making this equally useful for research chemists.

From reviews of the second edition:

'The text is very readable, and the authors are especially gifted at explaining complex concepts clearly and succinctly...This book is highly recommended reading for anyone wishing to gain an overview of organic synthesis.'
J. Am. Chem. Soc.

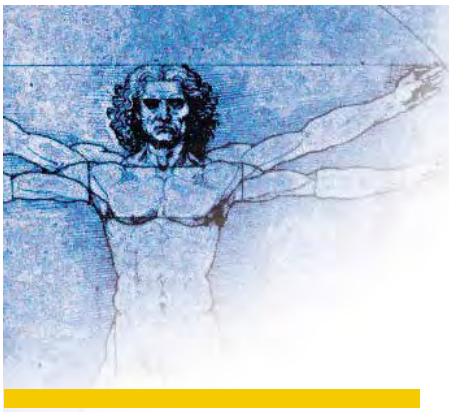
Wiley-VCH Verlag
Fax: +49 (0)6201 606 184
e-Mail: service@wiley-vch.de
www.wiley-vch.de

Register now for the free
WILEY-VCH Newsletter!
www.wiley-vch.de/home/pas

WILEY-VCH

50503032_kn

 © 2004 Wiley-VCH Verlag GmbH & Co. KGaA, Weinheim



K. C. Nicolaou Receives Honorary Doctorate

In the year of its 700th anniversary, the University of Rome "La Sapienza", Italy, has awarded an honorary doctorate in Chemistry and Pharmaceutical Technology to K. C. Nicolaou for his creativity in drug design.

Kyriacos C. Nicolaou was born in Cyprus and educated in England and the USA. He is currently Chairman of the Department of Chemistry at The Scripps Research Institute in La Jolla, CA (USA) where he holds the Darlene Shiley Chair in Chemistry and the Aline W. and L. S. Skaggs Professorship in Chemical Biology. He is also a Professor of Chemistry at the University of California, San Diego. His impact on chemistry, biology, and medicine flows from his works in organic synthesis described in numerous publications and patents.



K. C. Nicolaou

The research in his group is devoted to the art and science of total synthesis[1a] by means of asymmetric synthesis, and in particular of natural products. His book on "Classics in Total Synthesis" has already become a classic itself (co-author: E. Sorensen). Part II, which he co-authored with S. Snyder, has just appeared.[1b] The most recent of his many Communications in *Angewandte Chemie* details the "Total Synthesis of 1-*O*-Methyllateriflorone".[1c]

Nicolaou is a recipient of numerous honors and awards, which include honorary doctorates from universities around the Mediterranean: Cyprus, Athens (Greece), and Alcala (Spain). He is a member of the International Advisory Board of *Angewandte Chemie* and the Editorial Board of *ChemBioChem*.

R. Langer Honored

Robert S. Langer, Professor of Chemical and Biomedical Engineering at the Massachusetts Institute of Technology (MIT, Cambridge, USA), received the Heinz Award for Technology, the Economy and Employment worth US$ 250 000. The prize is given annually in five categories in memory of US Senator John Heinz (1938–1991). Langer was selected for his achievements in a variety of areas on the interface between chemistry and medicine, such as controlled drug delivery in general, by means of magnets or ultrasound in particular, and the design of three-dimensional polymer scaffolds for human-tissue growth.[2a] Recently, he reported on the "Semi-Automated Synthesis and Screening of a Large Library of Degradable Cationic Polymers for Gene Delivery"[2b] in a Communication in *Angewandte Chemie*.



R. Langer

Before joining MIT, Langer studied Chemical Engineering to earn Bachelor and PhD degrees from Cornell University and MIT, respectively. He served as a member and chairman of the Science Board of the US Food and Drug Administration and received honorary doctorates from the ETH Zurich (Switzerland), Technion and Hebrew University (Israel), and the Université Catholique de Louvain (Belgium). He is a member of the International Advisory Board of *Angewandte Chemie*.

D. Blackmond Moves to Imperial College

Donna G. Blackmond has quite an international career. She started as an Assistant and Associate Professor at the University of Pittsburgh, PA (USA), then joined Merck Inc. in Rahway, NJ (USA) as an Associate Director. From 1996 to 1999, she was a group leader at the Max-Planck-Institut für Kohlenforschung in Mülheim (Germany). In 1999, she was appointed Professor of Physical Chemistry at the University of Hull (UK). Now, she is moving to Imperial College London (UK) to assume a joint chair in catalysis in the Departments of Chemistry and Chemical Engineering.



D. Blackmond

Her research is focused on kinetic aspects of catalytic organic reactions and the understanding of complex reaction mechanisms, particularly for asymmetric catalytic reactions. Recently, she described "… the Condition for Asymmetric Amplification in Autocatalytic Reactions".[3] A Communication from her group on "Physical and Chemical Rationalization for Asymmetric Amplification in Autocatalytic Reactions" will be published in *Angewandte Chemie* soon.

Photo (DB): N. Miles, IC (London)

[1] a) K. C. Nicolaou, Y.-L. Zhong, P. S. Baran, *Angew. Chem.* **2000**, *112*, 46; *Angew. Chem. Int. Ed.* **2000**, *39*, 44, b) K. C. Nicolaou, S. A. Snyder, *Classics in Total Synthesis II*, Wiley-VCH, Weinheim, **2003**, c) K. C. Nicolaou, P. K. Sasmal, H. Xu, K. Namoto, A. Ritzén, *Angew. Chem.* **2003**, *115*, 4357; *Angew. Chem. Int. Ed.* **2003**, *42*, 4225.

[2] a) A. N. Zelikin, D. M. Lynn, J. Farhadi, I. Martin, V. Shastri, R. Langer, *Angew. Chem.* **2003**, *115*, 149; *Angew. Chem. Int. Ed.* **2003**, *41*, 141, b) D. G. Anderson, D. M. Lynn, R. Langer, *Angew. Chem.* **2003**, *115*, 3261; *Angew. Chem. Int. Ed.* **2003**, *42*, 3153.

[3] D. G. Blackmond, *Adv. Synth. Catal.* **2002**, *344*, 156.

 © 2004 Wiley-VCH Verlag GmbH & Co. KGaA, Weinheim

Carbon-Group Elements

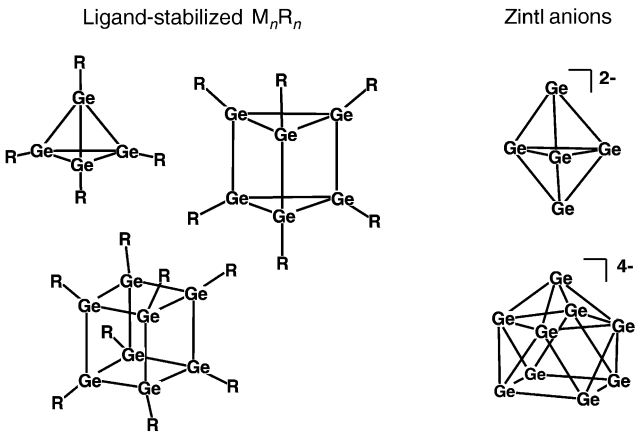
Novel Compounds of Elements of Group 14: Ligand-Stabilized Clusters with "Naked" Atoms

*Andreas Schnepf**

Keywords:
cluster compounds · germanium · group 14 elements · nanostructures · tin

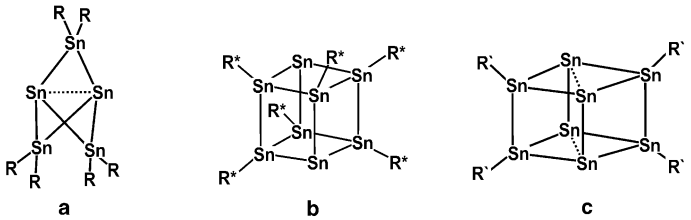
Molecular cluster compounds of the heavier elements of group 14 (Si–Pb) have been known for some time. They can be divided roughly into two large classes (Scheme 1): the Zintl anions, such as $[M_5]^{2-}$ or $[M_9]^{n-}$ (M = Si, Ge, Sn, Pb, n = 2–4),[1] and the ligand-stabilized cluster compounds of the general formula $[M_nR_n]$ (M = Ge, Si, n = 4,6,8; M = Sn, n = 6,8,10)[2] which contain solely ligand-bearing metal atoms. Some Zintl anions can be solubilized from the respective Zintl phases with ethylenediamine and subsequently crystallized with cryptand molecules as isolated molecular units. The ligand-stabilized cluster compounds are usually prepared by reductive dehalogenation of the corresponding REX_3 halogen compounds (e.g. $n\,RMX_3 + 3n\,Na \rightarrow (RM)_n + 3n\,NaX$).

In addition to these well-defined compounds, which are mainly characterized by crystal-structure analysis, numerous silicon and germanium nanoparticles are known. These species exhibit interesting optical properties and are of considerable interest for the investigation of quantum size effects.[3] The nanoparticles are prepared by controlled pyrolysis of SiH_4 and GeH_4, respectively.[4] Germanium nanoparticles are also formed in the reduction of $Si_nGe_{1-n}O_2$ mixed oxides with elemental hydrogen.[5] These nanoparticles are obtained, however, as a mixture with a certain size distribution and consequently are structurally only poorly characterized. Particularly for small particles (< 2 nm) no experimental information on their structure is available,[6] although these particles exhibit especially good photoluminescence properties.[5b]



Scheme 1. Selected structural formulae of group 14 ligand-stabilized cluster compounds (left) and Zintl anions (right).

Light could be shed on this structural darkness by cluster compounds of the general formula $[M_mR_n]$, where $n < m$, which, in addition to ligand-bearing metal atoms also contain metal atoms which are only bonded to other metal atoms, and which are referred to as "naked" metal atoms in the following.[7] Group 14 compounds of this type were, until recently, unknown. First results came from tin chemistry reported by Sita and Bickerstaff. They were successful in preparing for the first time a ligand-stabilized cluster containing naked tin atoms ($[Sn_5R_6]$, R = 2,6-$Et_2C_6H_3$; Scheme 2a).[8] In this cluster the number of metal atoms is still smaller than that of the ligands, but even in this case it was demonstrated that such compounds exhibit interesting bonding situations. Above all the question whether a bond exists between the two bridgehead atoms in the propellane $[Sn_5R_6]$—and



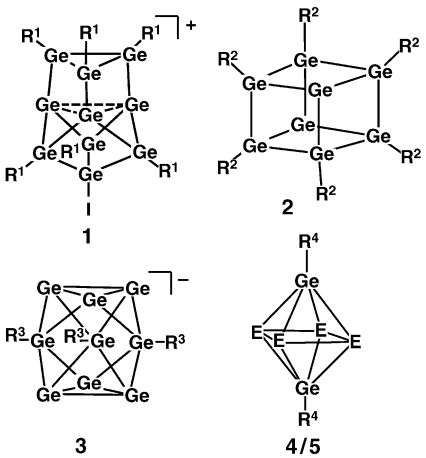
Scheme 2. Structural formulae of the tin compounds a) $[Sn_5R_6]$, b) $[Sn_8R^*_6]$, c) $[Sn_8R'_4]$. R = 2,6-$Et_2C_6H_3$; R* = Si*t*Bu_3; R′ = 2,6-$Mes_2C_6H_3$, Mes = 2,4,6-$Me_3C_6H_2$.

[*] Dr. A. Schnepf
Institut für Anorganische Chemie
Universität Karlsruhe (TH)
Engesserstrasse, Geb.30.45
76128 Karlsruhe (Germany)
Fax: (+49) 721-608-4854
E-mail: schnepf@aoc2.uni-karlsruhe.de

 © 2004 Wiley-VCH Verlag GmbH & Co. KGaA, Weinheim DOI: 10.1002/anie.200301706

if yes, how strong it is—has been discussed in depth.[9] A few years later Wiberg et al.[10] and Power et al.[11] synthesized the first tin compounds which fulfilled the aforementioned criteria, namely $[Sn_8(SitBu_3)_6]$ and $[Sn_8R_4]$($R = 2,6\text{-}Mes_2C_6H_3$, $Mes = 2,4,6\text{-}Me_3C_6H_2$), respectively (Scheme 2b and c). Structurally these two tin clusters may be derived from the cubic compound $[Sn_8R_8]$[12] by elimination of two and four ligands, respectively. In $[Sn_8(SitBu_3)_6]$ the cubic geometry is hardly distorted, whereas in the $[Sn_8R_4]$ compound a strongly distorted $\{Sn_8\}$ cube is present with two additional Sn–Sn contacts, 310 pm in length (broken line in Scheme 2c).[11]

In the case of germanium, which is of considerable interest in nanotechnology several syntheses of corresponding cluster compounds have been developed in recent years. Sekiguchi et al. synthesized the cationic germanium cluster compound $[Ge_{10}(SitBu_3)_6I]^+$ (**1**) containing three naked germanium atoms (Scheme 3) by mild thermolysis (50 °C, several weeks) of a mixture of $[Ge_3(SitBu_3)_3I]$ and KI/K^+TTFBP^- ($TTFBP^- = B(C_6F_4H)_4^-$) in toluene which gave **1** in 37% yield.[13] The occurrence of naked germanium atoms can be attributed to a reductive elimination of $SitBu_3I$ which is obtained as a byproduct of the reaction. In addition, we have been able to prepare the cluster compounds $[Ge_8\{N(SiMe_3)_2\}_6]$ (**2**)[14] and $[Ge_9\{Si(SiMe_3)_3\}_3]^-$ (**3**)[15] with two and six naked germanium atoms, respectively, by disproportionation of a subvalent Ge^I halide (GeBr).



Scheme 3. Structural formulae of the cluster compounds $[Ge_{10}(SitBu_3)_6I]^+$ (**1**), $[Ge_8\{N(SiMe_3)_2\}_6]$ (**2**), $[Ge_9\{Si(SiMe_3)_3\}_3]^-$ (**3**), $[Ge_6R_2]$(**4**; E = Ge) and $[Ge_2Sn_4R_2]$ (**5**; E = Sn) where $R = 2,6\text{-}Dipp_2C_6H_3$; $Dipp = 2,6\text{-}iPr_2C_6H_3$).

Recently Power et al. introduced a further, highly promising possibility for the synthesis of cluster compounds with naked metal atoms of group 14 which gave the cluster compounds $[Ge_6R_2]$ (**4**) and $[Ge_2Sn_4R_2]$ (**5**) ($R = 2,6\text{-}Dipp_2C_6H_3$; $Dipp = 2,6\text{-}iPr_2C_6H_3$).[16] In this approach RGeCl was reductively coupled in the presence of $GeCl_2$ or $SnCl_2$ with the aid of C_8K. The naked germanium or tin atoms originate from the dihalides since without their addition to the reaction mixture only the compound $[(GeR)_2]$ was isolated.[17] At the first glance the yields of **4** (40%) and **5** (20%) appear low, but considering the complex reaction course taking place during the formation of the octahedral compounds **4** and **5** from monomeric units the yields are surprisingly high. With these compounds prepared by Power the family of ligand-stabilized germanium cluster compounds with naked germanium atoms already includes four members (**1**–**4**).

Common to the cluster compounds **1**–**4** is that some of the Ge–Ge bonds in the cluster core are much longer than a normal Ge–Ge single bond (ca. 244 pm[18]). For example, the Ge–Ge separation between the naked germanium atoms in **1** is 325 pm,[13] and consequently the presence of a significant bonding interaction appears questionable. Quantum chemical calculations on the model compound $[Ge_{10}H_7]^+$ (**1′**) show, however, that in spite of the very large Ge–Ge separation a three-center, two-electron bond between the three naked germanium atoms is present. The occurrence of a bonding interaction in **1′** emerges from a comparison with the model compound $[Ge_{10}H_{10}]$, without naked metal atoms, for which an unambiguous nonbonding Ge–Ge separation of 379 pm was calculated. Furthermore, the quantum chemical calculations showed that a homoaromatic system is present in **1′** since an aromatic stabilization energy of $-19.2\ kJ\,mol^{-1}$ and a nucleus-independent chemical shift (NICS) of −26.4 ppm were calculated.[13]

The occurrence of multicenter bonding components could also be demonstrated for compounds **2** and **3**. Thus quantum chemical calculations on the model compounds $[Ge_8(NH_2)_6]$ (**2′**)and $[Ge_9H_3]^-$ (**3′**) gave three-center bonding components with an SEN (shared electron number) of 0.13 for **2′** and 0.32 for **3′**.[14,15] However, the bonding situations in this case are more complicated than in **1** since no isolated multicenter bond (as in **1′**) is found. Rathermore, molecular orbitals are present which extend over the whole cluster core and thus can be classified as delocalized cluster MOs.[19]

These findings confirm that owing to the additional electrons which are available to the cluster core through the naked germanium atoms delocalization of the bonding electrons occurs in the cluster core.[20] The bonding situation in the clusters **1**–**4** thus resembles that in the Zintl anions, in which the bonding electrons are also delocalized. In the case of the Zintl anions it is also found, however, that the germanium atoms with the higher coordination number form, as expected, longer Ge–Ge contacts. In contrast—in the compounds **3** (triply capped trigonal prism) and **4** (octahedral) which are structurally most closely related to the Zintl anions—the germanium atoms with the higher coordination number form shorter Ge–Ge bonds. Thus a bonding situation is presented which has not been previously observed in germanium cluster compounds.

The bonding situation found in this new group of complexes can also be interpreted as follows: starting from the fully substituted germanium clusters $[(GeR)_n]$, the bonding situation of which can be described by localized two-center two-electron bonds in the cluster core. The formal introduction of germanium atoms causes delocalization of the bonding electrons in the cluster core (analogous to **1**–**4**). Further insertion of germanium atoms leads next to nanoparticles and finally to the solid phase of elemental germanium in which the bonding situation for the germanium atoms can again be described simply by localized two-center two-electron bonds.

What effects this interaction between localized and delocalized bonding electrons has for the physical and chemical properties of the compounds have to be explored in future experimental and theoretical studies. Moreover, the syn-

 © 2004 Wiley-VCH Verlag GmbH & Co. KGaA, Weinheim

thesis strategies introduced need to be extended to prepare larger cluster systems.[21]

[1] J. D. Corbett, *Angew. Chem.* **2000**, *112*, 682; *Angew. Chem. Int. Ed.* **2000**, *39*, 670.

[2] A. Sekiguchi, H. Sakurai, *Adv. Organomet. Chem.* **1995**, *37*, 1.

[3] "Nanotechnology—Molecularly Designed Materials": M. S. El-Shall, S. Li, D. Graiver, U. Pernisz, *ACS Symp. Ser.* **1996**, 622.

[4] C. R. Gorla, S. Liang, G. S. Tompa, W. E. Mayo, Y. Lu, *J. Vac. Sci. Technol. A* **1997**, *15*, 860; A. Bapat, C. R. Perrey, S. A. Campbell, C. B. Carter, U. Kortshagen, *J. Appl. Phys.* **2003**, *94*, 1969.

[5] a) D. C. Paine, C. Caragianis, T. Y. Kim, Y. Shigesato, *Appl. Phys. Lett.* **1993**, *62*, 2842; b) H. Yang, X. Wang, H. Shi, S. Xie, F. Wang, X. Gu, X. Yao, *Appl. Phys. Lett.* **2002**, *81*, 5144.

[6] D. K. Yu, R. Q. Zhang, S. T. Lee, *Phys. Rev. B* **2002**, *65*, 245417.

[7] "Naked" here does not mean isolated, that is interaction-free, but is merely a linguistic simplification to distinguish the different types of metal atoms in these clusters. Alternatively the metal atoms could also be termed ligand-free. However, this description is equally inexact since bonded metal atoms can also be classified as ligands.

[8] L. R. Sita, R. D. Bickerstaff, *J. Am. Chem. Soc.* **1989**, *111*, 6454.

[9] By means of comprehensive ab initio calculations on the model compounds $[E_5H_6]$ of the [1.1.1]propellane type (E = C, Si, Ge, Sn) it was possible to show that the bond strength between the two bridgehead atoms decreases from carbon to tin. Furthermore, in these calculations only in the case of the carbon compound can a bond critical point between the two bridgehead atoms be calculated, which is necessary for a classical covalent bond. In contrast, in the case of the higher homologues the bonding electrons are not directly localized along the nuclear bonding axis. M. S. Gordon, K. A. Nguyen, M. T. Carroll, *Polyhedron* **1991**, *10*, 1247; H. Grützmacher, F. Breher, *Angew. Chem.* **2002**, *114*, 4178; *Angew. Chem. Int. Ed.* **2002**, *41*, 4006.

[10] N. Wiberg, H.-W. Lerner, S. Wagner, H. Nöth, T. Seifert, *Z. Naturforsch. B* **1999**, *54*, 877.

[11] B. E. Eichler, P. P. Power, *Angew. Chem.* **2001**, *113*, 818; *Angew. Chem. Int. Ed.* **2001**, *40*, 796.

[12] L. R. Sita, I. Kinoshita, *Organometallics* **1990**, *9*, 2865.

[13] A. Sekiguchi, Y. Ishida, Y. Kabe, M. Ichinohe, *J. Am. Chem. Soc.* **2002**, *124*, 8776.

[14] A. Schnepf, R. Köppe, *Angew. Chem.* **2003**, *115*, 940; *Angew. Chem. Int. Ed.* **2003**, *42*, 911.

[15] A. Schnepf, *Angew. Chem.* **2003**, *115*, 2728; *Angew. Chem. Int. Ed.* **2003**, *42*, 2624.

[16] A. F. Richards, H. Hope, P. P. Power, *Angew. Chem.* **2003**, *115*, 4205; *Angew. Chem. Int. Ed.* **2003**, *42*, 4071.

[17] M. Stender, A. D. Phillips, R. J. Wright, P. P. Power, *Angew. Chem.* **2002**, *114*, 1863; *Angew. Chem. Int. Ed.* **2002** *41*, 1785.

[18] A. F. Wells, *Structural Inorganic Chemistry*, 5th ed., Oxford, **1984**, p. 1279.

[19] Such a delocalization of the bonding electrons is also to be expected in the compounds **4** and **5** described by Power et al. since the Ge–Ge and Sn–Sn separations in the four-membered ring of naked Ge/Sn atoms are very large at 286 and 312 pm, respectively.

[20] a) Thus no multiple bonds are formed that would lead to a shortening of the Ge–Ge bond as in the series germane (244 pm)—germene (230 pm in $[Ge_2R_4]$; R = 2,6-*i*Pr$_2$C$_6$H$_3$)[20b]—germine (228 pm in $[Ge_2R_2]$; R = 2,6-Dipp$_2$C$_6$H$_3$, Dipp = 2,6-*i*Pr$_2$C$_6$H$_3$).[17] b) J. Park, S. A. Batcheller, S. Masamune, *J. Organomet. Chem.* **1989**, *367*, 39.

[21] A coupling of the individual clusters to larger aggregates which has already led to interesting compounds with the Zintl anions would also be a plausible route.T. F. Fässler, *Angew. Chem.* **2001**, *113*, 4289; *Angew. Chem. Int. Ed.* **2001**, *40*, 4161.

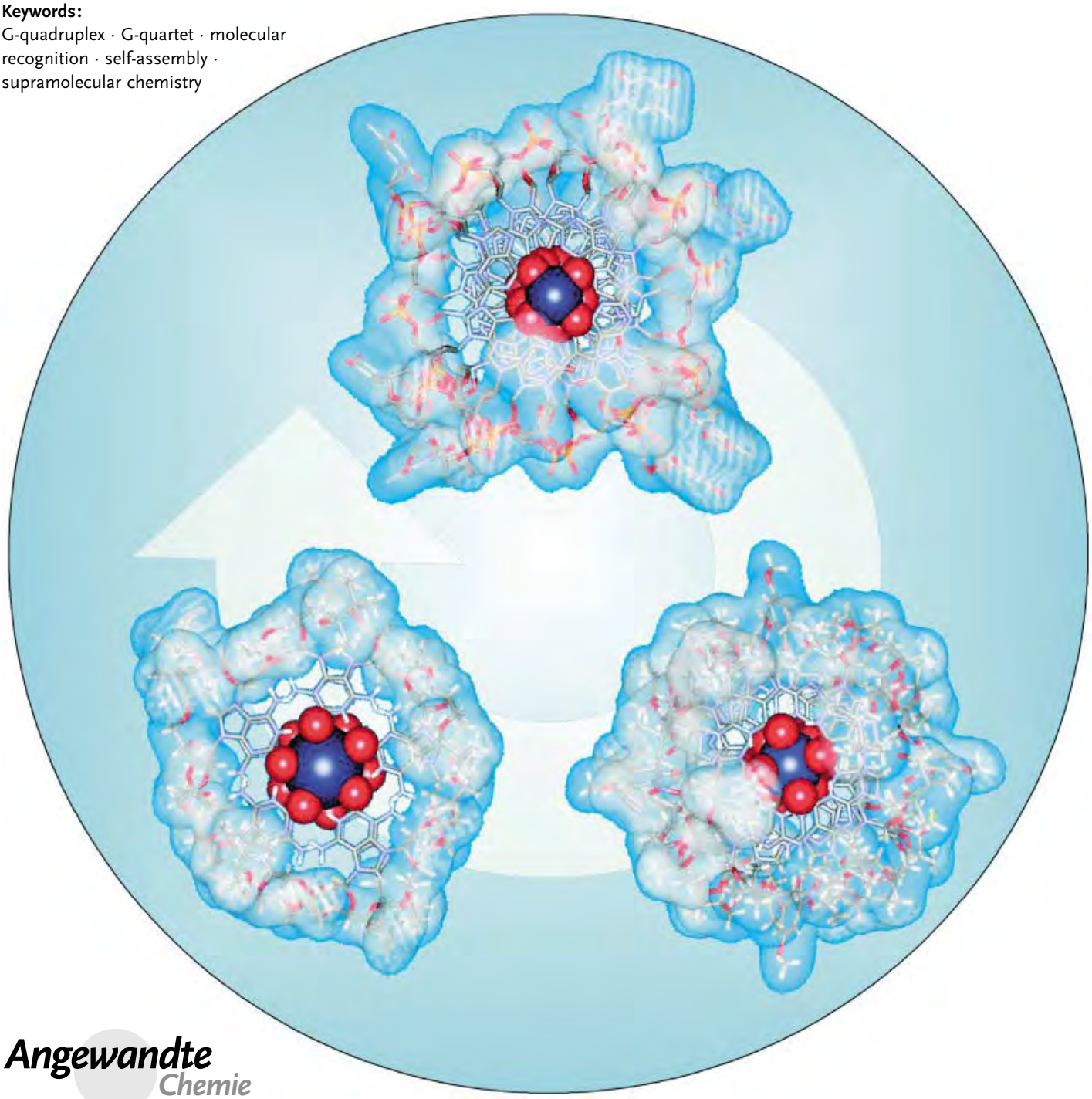
 © 2004 Wiley-VCH Verlag GmbH & Co. KGaA, Weinheim

Supramolecular Chemistry

G-Quartets 40 Years Later: From 5′-GMP to Molecular Biology and Supramolecular Chemistry

*Jeffery T. Davis**

Keywords:
G-quadruplex · G-quartet · molecular recognition · self-assembly · supramolecular chemistry



© 2004 Wiley-VCH Verlag GmbH & Co. KGaA, Weinheim

DOI: 10.1002/anie.200300589

Molecular self-assembly is central to many processes in both biology and supramolecular chemistry. The G-quartet, a hydrogen-bonded macrocycle formed by cation-templated assembly of guanosine, was first identified in 1962 as the basis for the aggregation of 5′-guanosine monophosphate. We now know that many nucleosides, oligonucleotides, and synthetic derivatives form a rich array of functional G-quartets. The G-quartet surfaces in areas ranging from structural biology and medicinal chemistry to supramolecular chemistry and nanotechnology. This Review integrates and summarizes knowledge gained from these different areas, with emphasis on G-quartet structure, function, and molecular recognition.

From the Contents

1. Introduction 669

2. The Early Studies on the Self-Assembly of 5′-Guanosine Monophosphate 671

3. Nucleic Acid G-Quadruplexes: Structure and Molecular Recognition 673

4. Lipophilic G-Quadruplexes: Structural Models for DNA, Self-Assembled Ionophores and Other Structural Motifs 682

5. Guanosine Self-Assembly in Materials Science, Biosensor Design, and Nanotechnology 689

6. Summary and Outlook 693

1. Introduction

In 1990 Guschlbauer, Chantot, and Thiele published the review article "Four-Stranded Nucleic Acid Structures 25 Years Later: From Guanosine Gels to Telomer DNA."[1] In that paper, they pointed out the emerging importance of the G-quartet, a hydrogen-bonded ionophore first identified in 1962 (Figure 1).[2] Renewed attention to the G-quartet in the late 1980s was generated by intriguing proposals that the motif, when formed in DNA, might be biologically relevant.[3,4] Today, interest in G-quartet structures remains unabated. Thousands of reports on some aspect of G-quartet structure or function have since appeared, including some excellent reviews.[5–14] G-quartet structures now surface in areas ranging from structural biology and medicinal chemistry to supramolecular chemistry and nanotechnology.

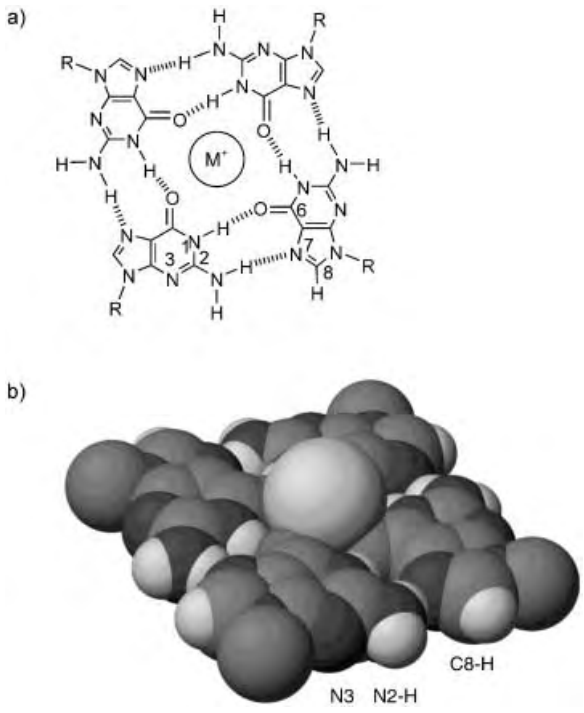


Figure 1. a) The G-quartet; b) space-filling model from the crystal structure of $[\mathbf{1}]_{16}\cdot 3\,K^+/Cs^+\cdot 4\,pic^-$ showing a G-quartet with a K^+ ion bound above the planar assembly.[29] The riboses have been removed for clarity.

The G-quartet, a hydrogen-bonded complex that binds cations, fits particularly well with contemporary studies in molecular self-assembly and noncovalent synthesis.[15–26] The activities in molecular self-assembly can be divided into three areas: 1) biomimetic studies, 2) basic studies of noncovalent interactions, and 3) synthesis of new assemblies; Figure 2 indicates the connections between these divisions. Molecular self-assembly is a hallmark of many natural and synthetic systems and good models for understanding self-assembly often come from inspecting nature (pathway A in Figure 2).[27] A model aims to simplify a complex system, thus allowing one to focus on specific interactions that are important for the self-assembly (B). Fundamental information from model studies may be used to either better

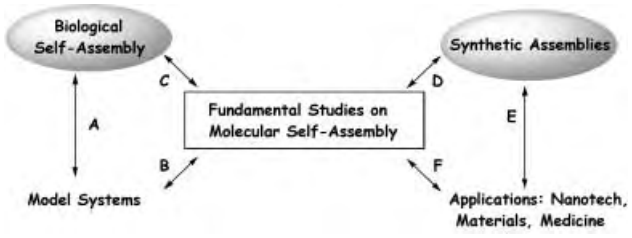


Figure 2. Noncovalent interactions are central to both biological self-assembly and to the synthesis of new supramolecular structures.

[*] Prof. Dr. J. T. Davis
Department of Chemistry and Biochemistry
University of Maryland
College Park, MD 20742 (USA)
Fax: (+1) 301-314-9121
E-mail: jd140@umail.umd.edu

 DOI: 10.1002/anie.200300589 © 2004 Wiley-VCH Verlag GmbH & Co. KGaA, Weinheim

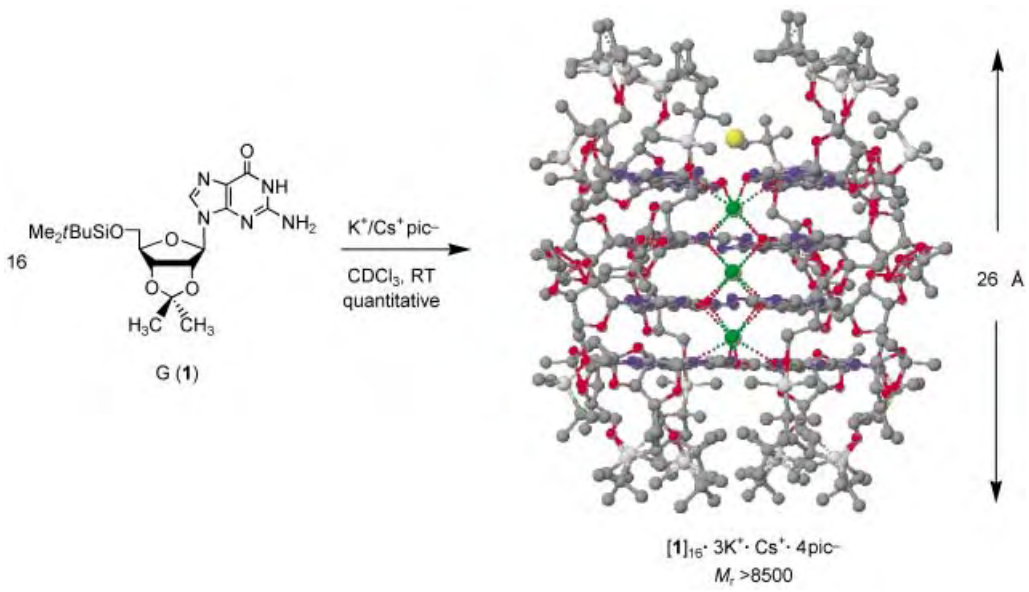


Figure 3. The cation-templated self-assembly of 16 equivalents of 5′-silyl-2′,3′-*O*-isopropylidene guanosine (G, **1**) gives a lipophilic G-quadruplex $[\mathbf{1}]_{16}\cdot 3\,K^+/Cs^+\cdot 4\,pic^-$ in the solid state and in solution (green K, yellow Cs, blue N, red O).[29] This G-quadruplex, with four stacked G-quartets, is prepared quantitatively by extracting salts from water with a solution of **1** in $CHCl_3$.

understand the parent system (C) or to build and apply new synthetic systems (D–F).[27,28] As discussed below, the G-quartet serves as an excellent model to learn about the fundamentals and utility of molecular self-assembly.

1.1. An Introductory Example: Stabilization of Lipophilic G-Quadruplexes by Noncovalent Interactions

An example from our research introduces some of the key structural features of the G-quartet and also highlights the different noncovalent interactions that drive the self-assembly of guanosine. In the presence of templating cations 5′-silyl-2′, 3′-*O*-isopropylidene guanosine (G, **1**) forms a lipophilic G-quadruplex that is stable in nonpolar solvents and that also gives single crystals with long-range order. A G-quadruplex is defined as a structure built from the vertical stacking of multiple G-quartets. Over the past few years Fettinger and co-workers have solved the crystal structures of a number of lipophilic G-quadruplexes.[29–33] The G-quadruplex depicted in Figure 3, with a formula of $[\mathbf{1}]_{16}\cdot 3\,K^+\cdot Cs^+\cdot 4\,pic^-$, illustrates the synthetic potential of self-assembly. Upon mixing in an organic solvent, 24 components organize into a single diastereomer with dimensions of $26\times 30\times 30$ Å and a molecular weight of over 8500.[29] The lipophilic G-quadruplex $[\mathbf{1}]_{16}\cdot 4\,M^+\cdot 4\,pic^-$ is also functional: it is a self-assembled ionophore that can extract salts from water into organic solvents.



Jeff Davis, born and raised in Western Massachusetts, received his B.A. in 1981 from Colby College in Waterville, Maine. He earned his Ph.D. from MIT in 1987 under the guidance of Professor Satoru Masamune. After three years at Genzyme Co. in Boston, he continued his training with Professor Brian Reid at the University of Washington in Seattle as an NIH post-doctoral fellow. In 1993 he joined the faculty in the Department of Chemistry and Biochemistry at the University of Maryland in College Park. He was promoted to Professor in 2003. His research interests concern problems in molecular self-assembly and molecular recognition.

While the noncovalent interactions that enable formation of a G-quadruplex are certainly interconnected, the structure can be dissected into three organizational levels (Figure 4). In the first level, four molecules of G(**1**) use self-complementary hydrogen bonds to form a planar G-quartet. As shown in level II, the G-quartets stack with a separation of 3.3 Å between individual layers. An octacoordinate cation, which forms cation–dipole interactions with eight separate molecules of **1** and located between two G-quartets, stabilizes hydrogen-bonded quartets and enhances base-stacking interactions to provide a C_4-symmetric $G_8\cdot K^+$ octamer. In level III, four picrate anions hydrogen bond to amino groups projecting from the G-quartets. These nucleobase–anion hydrogen bonds link the two inner G-quartets in the D_4-symmetric hexadecamer $[\mathbf{1}]_{16}\cdot 4\,M^+\cdot 4\,pic^-$, a structure that is stable in the solid state and solution.[29–32] One remarkable feature of this structure is the four colinear cations, spaced 3.3 Å apart, that are arranged down a central channel. The electrostatic repulsion that might be expected between the channel cations is clearly minimized by the G-quartet oxygen atoms and aromatic rings.

There is also a stereochemical consequence to the cation-templated self-assembly of **1**. A G-quartet with chiral sugars attached to each nucleobase has two diasterotopic faces: a

 © 2004 Wiley-VCH Verlag GmbH & Co. KGaA, Weinheim

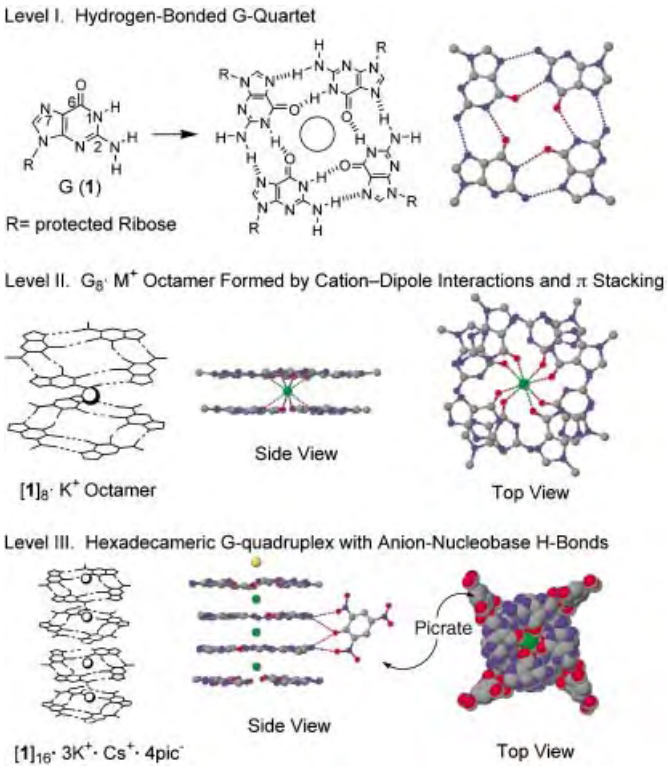


Figure 4. Schematic representation of hierarchical self-assembly processes that occur to give the lipophilic G-quadruplex $[\mathbf{1}]_{16}\cdot 3\,K^+/Cs^+\cdot 4\,pic^-$.[29] The structure is held together by nucleobase hydrogen bonds, cation–dipole interactions, stacking interactions, and hydrogen bonds between the nucleobase and anion. The ribose units have been omitted for clarity.

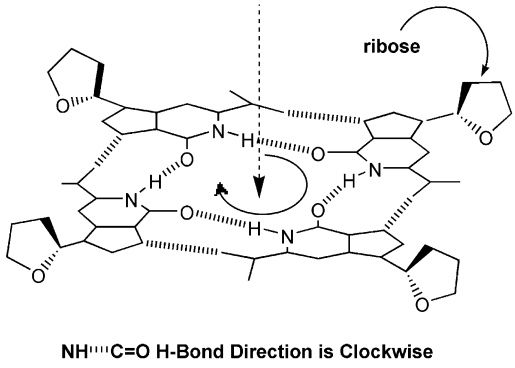


Figure 5. The attached sugars result in the chiral G-quartet having diastereotopic faces, a "head" and a "tail". The "head" of the G-quartet is that face with clockwise rotation of the NH to C=O hydrogen bonds.[34]

"head" and a "tail" (Figure 5).[34] In this way the nucleoside sugars transfer and amplify their chirality upon the supramolecular organization of chiral G-quartets. Although there are 16 stacking permutations for a 4-layered G-quadruplex, only a single diastereomer of $[\mathbf{1}]_{16}\cdot 4\,M^+\cdot 4\,pic^-$ is observed.[29] This selectivity for this noncovalent assembly of formula $[\mathbf{1}]_{16}\cdot 4\,M^+\cdot 4\,pic^-$ is striking since, unlike in DNA, there is no covalent backbone connecting the G subunits to induce supramolecular helicity. Various noncovalent interactions (hydrogen bonds, cation–dipole interactions, and van der Waals interactions) work together to fix the structure and stereochemistry of these lipophilic G-quadruplexes. The cooperativity of these noncovalent forces is a hallmark of guanosine self-assembly in biology and synthetic chemistry.

1.2. The Review's Organization

After this Introduction, a review of early studies on guanosine self-association is given in Section 2. This work provided the foundation for later structural biology and supramolecular studies. Section 3 discusses G-quadruplexes in molecular biology and medicinal chemistry. In particular, structural and recognition studies have been highlighted that might appeal to chemists looking to learn about self-assembly from nature. Section 4 gives a review of the self-assembly of lipophilic nucleosides. Here, assemblies that are models for DNA structure and that also provide inspiration for new supramolecular forms and functions are discussed. Section 5 focuses on applications of guanosine self-association in materials science and nanotechnology. Section 6 provides a summary and an outlook.

2. The Early Studies on the Self-Assembly of 5′-Guanosine Monophosphate

The self-association of guanine occurs in many settings. Some spiders have cells known as guanocytes that are filled with crystalline plates of guanine (Figure 6). When disturbed, these spiders change color instantly by retracting the guanocytes from their surface.[35] The eyes of certain deep-sea fish contain layered guanine crystals that focus light to the photoreceptors.[36]

Guanosine derivatives are notoriously intractable in the laboratory.[37] The review by Guschlbauer et al. tabulated 30 different G derivatives that gel in water.[1] It is not surprising that guanosine self-associates: its edges have self-complementary hydrogen-bond donors and acceptors, and its polarizable aromatic surface, with a strong molecular dipole,[38] is ideal for stacking. This basis for self-association was established over 40 years ago, when Gellert et al. reported that 3′-GMP (**2**) and 5′-GMP (**3**) form layers of hydrogen-bonded tetramers.[2] Their model, developed from fiber diffraction studies, had the N1-H and N2-H donor atoms of one guanine molecule pairing with the N7 and O6 atoms of a neighboring guanine molecule. The resulting G-quartet is a planar macrocycle held together by eight hydrogen bonds. The authors proposed that G-quartets stacked 3.25 Å apart formed a helix, which was consistent with later diffraction data obtained for guanosine analogues and polyguanylic acid.[39–41] Shortly after the report by Gellert et al., Fresco and Massoulie reported that polyguanylic acid also formed a multistranded helix in solution.[42] They, too, correctly proposed that stacking hydrogen-bonded G-quartets stabilized the polyguanylate assemblies.

In the 1970s and 1980s two key discoveries were made concerning the self-association of guanosine. First, 5′-GMP

 © 2004 Wiley-VCH Verlag GmbH & Co. KGaA, Weinheim

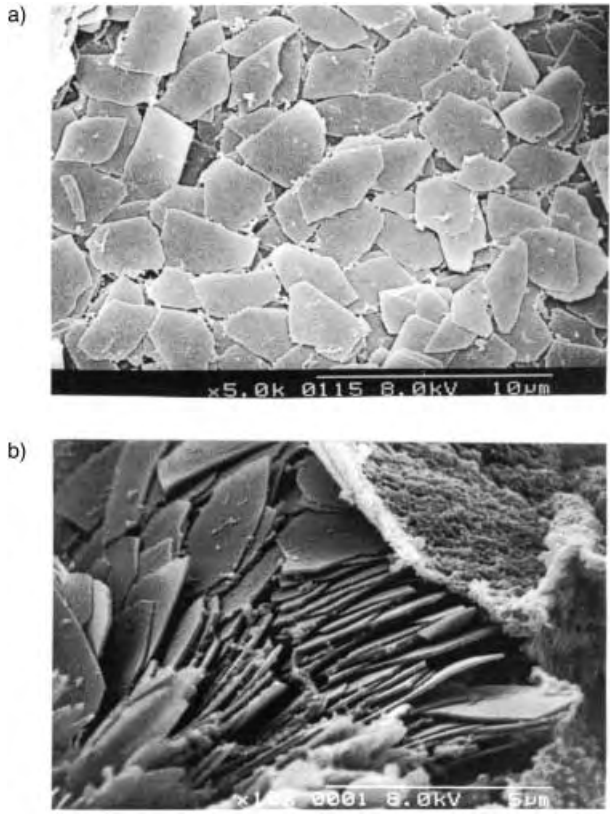
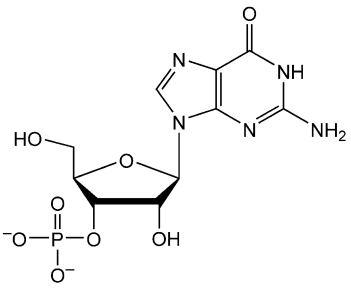


Figure 6. Crystalline guanine deposits from the spider *Tetragnatha polychromata*.[35b] a) Surface view of crystalline guanine plates (approximately 4×2 µm). b) Side view of the same crystals showing the thinness and stacking of the guanine plates. The photographs were supplied by Harriet Mitchell.

(**3**) did not always give gels. At basic pH values, where it is dianionic, 5′-GMP (**3**) formed smaller assemblies that could be studied by NMR spectroscopy.[43] Second, alkali-metal cations, particularly K^+ and Na^+, stabilized these complexes.[44] Cation binding is understandable, since a G-quartet has four oxygen atoms clustered in its center. Without a bound cation, this cyclic arrangement would be electronically unfavorable,[45] and so, the cation is essential for templation and stabilization of the G-quartet. Discrete cation-bound octamers of the type $G_8{\cdot}M^+$ were proposed to be the building blocks for extended columns of stacked G-quartets (Figure 7). Despite different conclusions about stoichiometry and stereochemistry,[46,47] it was clear that G-quartets were the foundation for the self-assembly of guanosine. The basics of guanosine self-assembly were confirmed by dynamic light scattering, single-crystal X-ray, electrospray mass spectrometric, and solid-state NMR spectroscopic studies.[48–53]

These early G-quartet studies remain timely, as they are pertinent to themes that surround supramolecular chemistry today. For example, dynamic combinatorial chemistry is a powerful method for generating molecular receptors.[54–57] The findings that 5′-GMP (**3**) self-associates only with certain cations[44] and that G-C base pairs give way to G-quartets upon addition of K^+ ions[58] exemplify the shift in equilibrium that is the basis of dynamic combinatorial chemistry. Whereas template experiments with Li^+ and Cs^+ ions showed no effect, the addition of Na^+ or K^+ ions to 5′-GMP (**3**) gave G-quartet-based structures, and prompted the conclusion: *"We believe this to be the first demonstration of the ability of alkali metal ions to direct structure formation of a nucleotide through a size-selective coordination mechanism"*.[44] Pinnavaia et al. suggested that K^+ ions were too large to be coplanar and fit



3′-GMP (**2**)

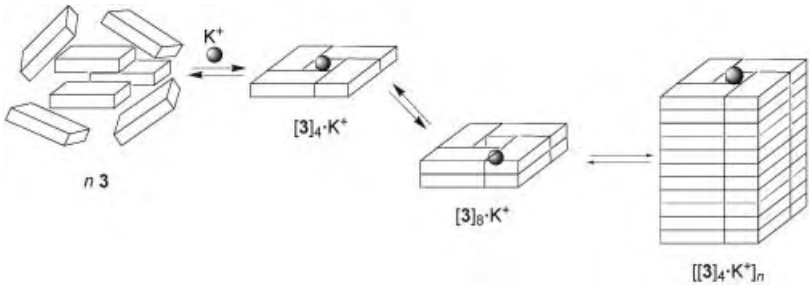
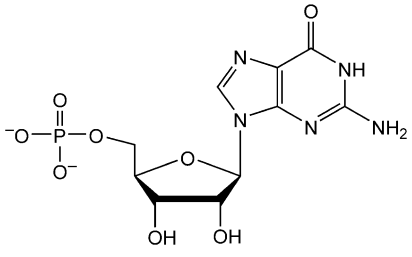


Figure 7. Equilibria involved in the self-association of 5′-GMP (**3**). Poorly defined aggregates are formed in the absence of cations. Cations template the formation of the planar G-quartets, which can give discrete $[\mathbf{3}]_8{\cdot}M^+$ octamers or helical G-quadruplex stacks.



5′-GMP (**3**)

between G-quartets to give a $G_8{\cdot}K^+$ octamer. The estimated K–O distance in the octamer matched bond lengths for known octacoordinate K^+ complexes. The authors summarized this key feature: *"We suggest that cavity complexation as described contributes stability to the complex, and that it is a necessary condition for self-structure formation by neutral GMP"*.[44] Crystal structures of the lipophilic G-quadruplex $[\mathbf{1}]_{16}{\cdot}3K^+/Cs^+{\cdot}4pic^-$ and of the DNA G-quadruplex $[d(GGGGTTTTGGGG)]_4$ later showed K^+ ions sandwiched between G-quartets.[29,59,60]

 © 2004 Wiley-VCH Verlag GmbH & Co. KGaA, Weinheim

The NMR spectrum of the assembly also raised issues about supramolecular stereochemistry, an area intensely studied today.[61–63] Stacking two chiral G-quartets can give at least six possible diastereomers for a $G_8{\cdot}M^+$ octamer, depending on the stacking orientation and relative rotation about the central axis.[46] The NMR spectra for 5′-GMP·Na^+ indicated, however, the presence of only two stable diastereomers, thus indicating a high stereoselectivity in this self-assembly process.

Another important finding concerned the stability of the assembly towards dissociation. The ^{1}H NMR spectra of 5′-GMP·Na^+ showed separate signals for the monomer and the assembly.[43,44] This slow exchange was remarkable since such kinetically stable systems are rare, especially in water. Hydrogen-bonded assemblies and their components are usually in fast exchange and give averaged NMR signals. The self-assembly of 5′-GMP **3** is also relevant today, since obtaining discrete noncovalent assemblies that are thermodynamically and kinetically stable in water is still challenging.[64–67]

Another topical area of supramolecular chemistry involves the mechanisms of assembly and disassembly.[68] Again, the early studies with GMP were also concerned with such issues. Multinuclear NMR studies by Laszlo, Detellier, and co-workers were especially insightful.[47,69,70] Analysis by ^{23}Na NMR spectroscopy revealed that the Na^+ ions moved in and out of the $[\mathbf{3}]_8{\cdot}Na^+$ octamer 10^4–10^8 times per second, which is orders of magnitude faster than ligand exchange.[69] These assemblies did not need to fully dissociate to release their guests, which suggests that such systems might be useful for mediating cation exchange. The ^{1}H NMR data also provided thermodynamic constants for the formation of the octamer $[\mathbf{3}]_8{\cdot}K^+$ ($\Delta H = -17 \pm 2$ kcal mol^{-1} and $\Delta S = -51 \pm 6$ cal mol^{-1} K^{-1}) that indicated an enthalpic process: *"Self-assembly of the 5′-GMP nucleotides does not occur because of release of water. Self-assembly of 5′-GMP, unlike a normal stacking interaction is not determined predominantly by hydrophobic forces. Cation binding plays an important role, together with and reinforcing the hydrogen bonding of the guanines into planar tetramers."*[47]

Finally, one active area in supramolecular chemistry involves the self-organization of noncovalent assemblies, which is important in materials science and nanoscience.[71] The G-quartet system based on 5′-GMP (**3**) provides a nice example of this self-assembly/self-organization paradigm.[72–74] It was shown that GMP oligomers—from mononucleotide 5′-GMP **3** to the d(GGGGGG) hexanucleotide—formed liquid crystals in water (Figure 8).[72,73] The CD and X-ray diffraction data of these oligomers were consistent with the formation of helical rods containing stacked G-quartets. At increasing concentration these compounds formed a hexagonal liquid crystalline phase by lateral association of G columns (Figure 8c). The finding that self-assembled G-quadruplexes could self-organize into liquid crystals with long range order was important for later applications in materials science and nanotechnology (see Section 5).

In retrospect, these early studies on the self-association of 5′-GMP (**3**) involved much of what motivates studies in supramolecular chemistry today, namely structure and stereochemistry, mechanism, and function. However, recognition of the name G-quartet really developed in the late 1980s, when it was proposed that G-quartets might be biologically functional.[3,4,75,76] In particular, Sen and Gilbert suggested that G-quartets were involved in chromosome association during meiosis.[75] Sundquist and Klug proposed that the G-quadruplex was an important secondary structure that regulated biochemical processes in the telomeric region of the chromosome.[76] A research explosion on G-quadruplexes followed.

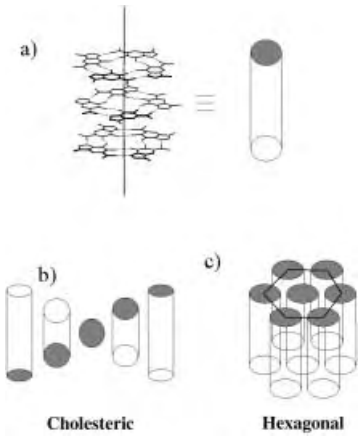


Figure 8. Formation of liquid crystals by G derivatives. a) G-quartets stack to give a columnar structure. b) The relative arrangements of the G-quartet columns in the cholesteric phase and c) in the hexagonal liquid-crystalline phase. Reprinted in a modified form from ref. [7]

3. Nucleic Acid G-Quadruplexes: Structure and Molecular Recognition

G-quadruplexes are formed in vitro by DNA and RNA oligonucleotides with sequences that occur in chromosomal telomeres, gene promoter regions, recombination sites, RNA packaging sites, and RNA dimerization domains.[12–14] For many years there has been debate as to whether these structures have any functional roles in living cells. Many papers contain the qualifier that the role of the G-quartet in vivo is yet to be proven, but evidence is now mounting that DNA and RNA G-quadruplex structures do indeed have in vivo relevance. For example, the most common form of mental retardation, fragile X syndrome, is caused by a mutation to the fragile X mental retardation protein (FMRP), which transports messenger RNA. One theory is that fragile X syndrome results when mutant FMRP doesn't properly bind mRNA.[77] Darnell et al. recently discovered that FMRP binds particularly tightly to G-quadruplex RNA.[78a] They concluded that… *"(T)hese data demonstrate that G quartets serve as physiologically relevant targets for FMRP and identify mRNAs whose dysregulation may underlie human mental retardation."* In an accompanying study, Warren and co-workers used antibodies to pull out FMRP and its bound RNAs from mouse brains.[78b] Seventy percent of the several hundred mRNAs identified were proposed to form the RNA G-quadruplex.

 © 2004 Wiley-VCH Verlag GmbH & Co. KGaA, Weinheim

Other major developments occurred in 2002 when Hurley and co-workers reported in vivo evidence for the structure and function of G-quadruplex in a gene-promoter region within human cells.[79] This intramolecular G-quadruplex, made up of a 20–30 base-pair region, was specifically targeted and stabilized by a small molecule, which resulted in transcription repression of the oncogenic c-myc protein. Furthermore, Riou et al. reported that another small molecule designed to stabilize G-quadruplex DNA impairs telomerase activity in cancer cells.[80] Reports of controlling gene expression and in vivo enzyme activity by targeting G-quadruplexes will certainly fuel more investigations into characterizing and controlling these nucleic acid structures.

3.1. Overview of Oligonucleotide G-Quadruplex Structure

In the past decade there have been many NMR studies and a growing number of X-ray structures of G-quadruplexes (see Table 1), and the topic of structure has been reviewed in many articles.[8–10,13]

Oligonucleotide G-quadruplexes differ in their chain number and orientation (Figure 9). Quadruplexes are always stabilized by cations and can form from four separate strands, from two pieces, or from a single chain. NMR spectroscopic analysis has shown that oligonucleotides with a single sequence of G residues form quadruplexes with four parallel strands (Figure 9a).[81–82] A crystal structure of $[d(TGGGGT)]_4$ with bound Na^+ ions is shown in Figure 10.[83,84] Two separate helices, each containing four G-quartets, stack with the 5′ ends in the same orientation to give a column of eight G-quartets. The four-stranded DNA, with seven colinear Na^+ ions, looks much like an ion channel, and very much resembles the lipophilic G-quadruplex $[\mathbf{1}]_{16}\cdot 3\,K^+\cdot Cs^+\cdot 4\,pic^-$ shown in Figures 3 and 4.[29] The Na^+ ions in this parallel DNA tetraplex are either sandwiched between G-quartets or coplanar with a G-quartet.

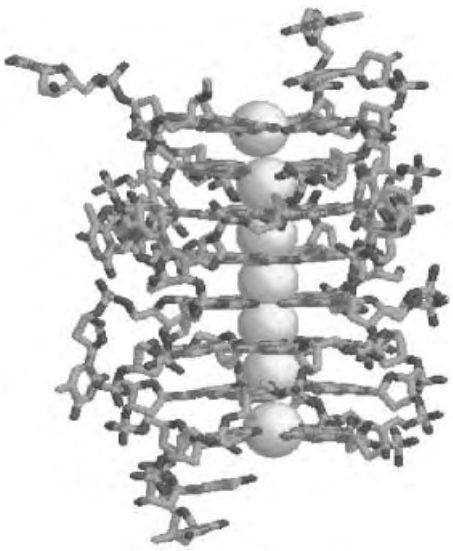


Figure 10. Crystal structure of the Na^+ form of the parallel-stranded G-quadruplex $[d(TGGGGT)]_4$.[84] The seven colinear Na^+ ions give the impression of an ion channel. PDB code for this structure: 352D.

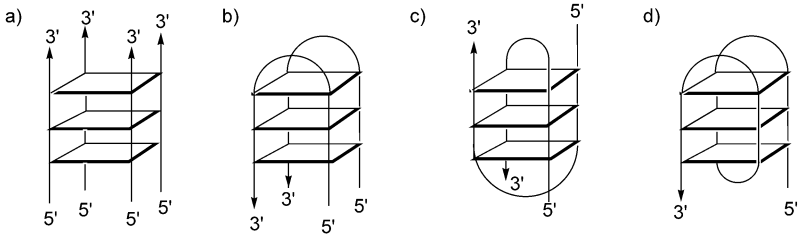


Figure 9. Different G-quadruplex DNA structures. a) A parallel stranded tetraplex; b) a bimolecular complex formed from hairpin dimerization with "edgewise" loops; c) a bimolecular complex with "diagonal" loops; and d) a unimolecular G-quadruplex.

Electrostatic repulsion between such tightly packed cations must be diminished by coordination to the oxygen atoms of the G-quartet. Ab initio calculations show charge transfer from the G-quartet oxygen atoms to the bound cation.[85] Other calculations conclude that the carbonyl–cation enthalpies provide more stabilization than either hydrogen bonding or stacking interactions.[86] Furthermore, molecular dynamics simulations indicate that G-quadruplex DNA is stable only when Na^+ ions are bound;[87] removal of the cations from the channel results in structural collapse.

An oligonucleotide with two G-rich regions can fold into a hairpin held together by G-G Hoogsteen

Table 1: X-ray crystal Structures of G-Quadruplexes.

Structure	Comment	Year	PDB entry	Ref.
Oxytricha $d(G_4T_4G_4)_2$	K^+-bound bimolecular G-quadruplex	1992	1D59	[91]
thrombin binding aptamer and thrombin	protein–DNA complex	1993	1HUT	[129]
		1996	1HAP	[130]
d(TGGGGT) with Na^+	parallel four-stranded G-quadruplex	1994	244D	[83]
		1997	352D	[84]
$[\mathbf{1}]_{16}\cdot 3\,K^+/Cs^+\cdot 4\,pic^-$	first lipophilic G-quadruplex	2000		[29]
$r(UGGGGU)_4$ with Sr^{2+}	RNA G-quadruplex with base octad	2001	1J8G	[126]
$d(G_4T_4G_4)_2$ and *Oxytricha* telomere binding protein	DNA–protein complex with bimolecular G-quadruplex	2001	1JB7	[59]
human telomeric DNA sequences	parallel bimolecular G-quadruplex with fold-back loops	2002	1K8P	[95]
Oxytricha $d(G_4T_4G_4)_2$	K^+-bound bimolecular quadruplex	2002	1JPQ	[60]
			1JRN	
Oxytricha $d(G_4T_4G_4)_2$ with **9**	first DNA-quadruplex-drug complex	2003	1L1H	[190]
$d(TGGGGT)_4$ with daunomycin trimer	DNA-quadruplex-drug complex	2003	1O0K	[191]

 © 2004 Wiley-VCH Verlag GmbH & Co. KGaA, Weinheim

pairs (Figure 9b,c). Dimerization of a hairpin structure then provides a bimolecular G-quadruplex with two loops. These loops can orient in two ways to give different folds: "edgewise" loops connect adjacent antiparallel chains, whereas "diagonal" loops cross over the G-quadruplex to connect antiparallel chains. In the early 1990s studies on the telomere repeat unit $d(G_4T_4G_4)$ of *Oxytricha* suggested that this sequence adopted different structures with different cations.[88] The NMR solution structure with Na^+ ions showed a bimolecular G-quadruplex with diagonal loops,[89,90] whereas a crystal structure of the K^+ form of $[d(G_4T_4G_4)]_2$ had "edgewise" loops.[91] The significance of these differences has been diminished by more recent crystal structures of the K^+ form of $[d(G_4T_4G_4)]_2$ that, like the NMR structures,[92] also show a bimolecular quadruplex with diagonal loops.[59,60] The secondary structure of the G-quadruplex can be used to template the synthesis of other unusual DNA topologies. For example, Chan et al. took advantage of the shape of bimolecular G-quadruplexes to carry out a phosphodiester ligation on a single stranded DNA to provide circular oligonucleotides (Figure 11).[93]

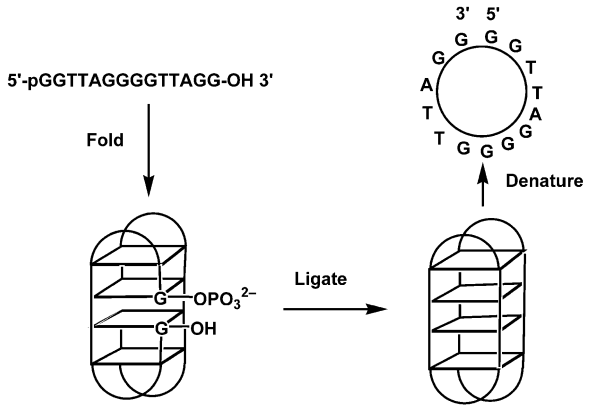


Figure 11. Synthesis of circular DNA oligonucleotides using a bimolecular G-quadruplex as template.[93] A cation-promoted folding of the DNA single strand is followed by chemical ligation and denaturation to give the circular DNA.

Unimolecular G-quadruplexes, with three loops, form from a single strand (Figure 9d).[94] Usually the loops constrain the G-quadruplex chains to be all antiparallel. Crystal structures of oligonucleotides containing the human telomeric sequence d(TTAGGG) in their K^+-bound form add another loop geometry to the G-quadruplex family.[95] The 22-mer $d(AGGG(TTAGGG)_3)$ forms an intramolecular G-quadruplex in which all three TTA loops undergo a "double-chain-reversal" to give a unimolecular G-quadruplex with four parallel chains. These TTA loops extend far from the G-quartet core, thus providing potential sites for protein recognition (Figure 12). Furthermore, this structure, with its extended loops and exposed G-quadruplex core, suggests how different TTAGGG repeats might pack within the chromosome.[96]

G-quadruplexes are cation-dependent and are stabilized by alkali and alkaline-earth cations. K^+ and Na^+ ions are

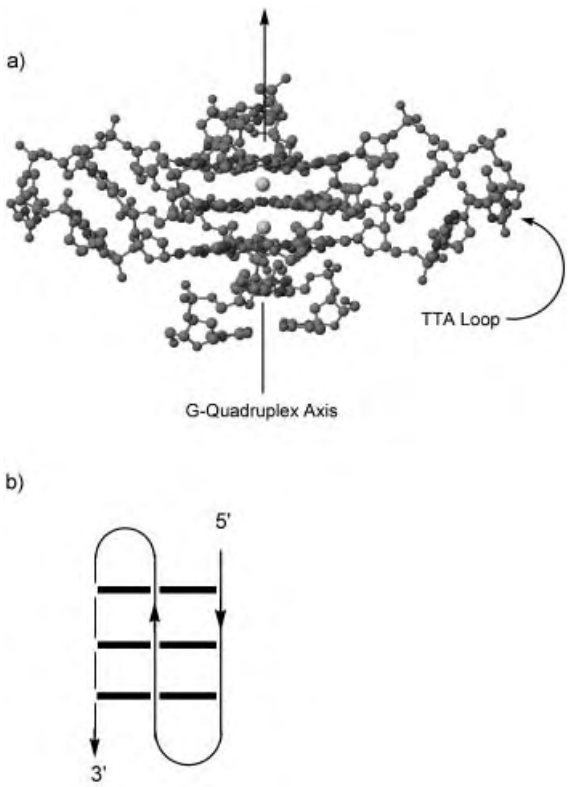


Figure 12. Crystal structure of an oligonucleotide $d(AGGG(TTAGGG)_3)$ containing the human telomeric sequence.[95] a) Side view of the G-quadruplex showing the extended TTA loops. b) Schematic representation showing the "double-chain-reversal" that occurs within the TTA loops. PDB code for this structure: 1K8P.

prevalent in the cell, and thus these cations have received most attention.[97] In general, DNA/RNA G-quadruplexes bind K^+ over Na^+ ions. This selectivity is often attributed to the better fit of K^+ ions into a G_8-octamer cage. Ross and Hardin, however, concluded that the "optimal fit" proposal did not fully explain the K^+/Na^+ selectivity of the G_8-octamer and suggested electronic factors must be important.[98] Later, Hud et al. provided evidence that the hydration energy of the cations was the major determinant of K^+/Na^+ selectivity.[99] While both cations fit between G-quartets, it is easier to dehydrate K^+ ions. Calculations support this ion dehydration argument.[100]

In addition to oligonucleotides, polymers with modified backbones also form G-quadruplexes. Peptide nucleic acids (PNA) are nucleic acid mimics where the charged backbone is replaced by uncharged *N*-(2-aminoethyl)glycine linkages.[101] Unlike DNA, hybridization and self-association of neutral PNA is not destabilized by electrostatic repulsion between the strands. Complementary C-rich PNA can invade and unfold intramolecular G-quadruplexes.[102–104] Recently, Armitage and co-workers reported that G-rich PNA can also participate directly in four-stranded structures.[105] They showed by using CD and fluorescence resonance energy transfer (FRET) that 1:1 mixtures of homologous DNA and PNA sequences assemble to form a stable hybrid PNA_2:DNA_2 G-quadruplex (Figure 13). Their findings

 © 2004 Wiley-VCH Verlag GmbH & Co. KGaA, Weinheim

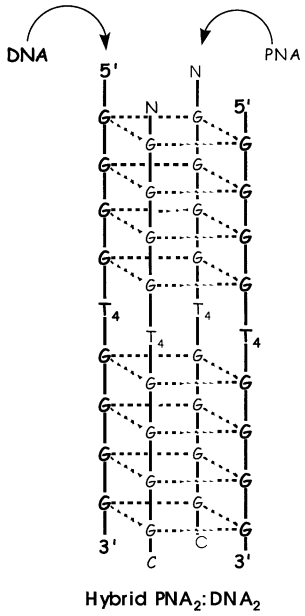
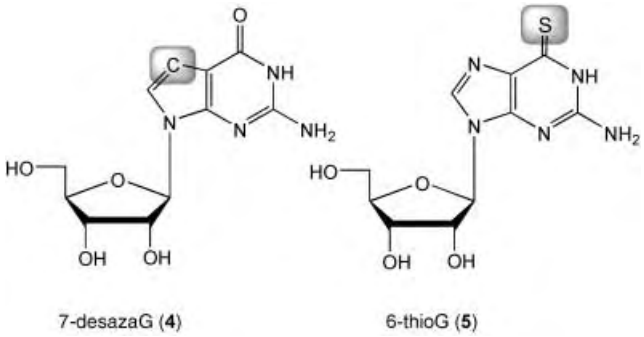


Figure 13. Proposed structure for a PNA_2-DNA_2 hybrid G-quadruplex, with the DNA (bold) and PNA strands diagonally opposed to each other.[105]

expand the scope of PNA in molecular recognition processes and also suggest that PNA deserves consideration as a potential therapeutic toward targeting G-quadruplexes.

Sometimes G-rich DNA forms unwanted secondary structures. For example, DNA sequencing and polymerase chain reaction (PCR) amplification of G-rich sequences is often challenging because of extensive self-association. Modified nucleobases that can form G-C Watson–Crick base pairs, but that can't self-associate, have been used to circumvent such problems. Mizusawa et al. showed that 7-deazaG (**4**) enables accurate nucleotide sequencing of G-rich



DNA.[106] Later, Seela and Mersmann demonstrated that disaggregation of the RNA G-quadruplex $[r(UGGGGU)]_4$ could be effected by sequentially replacing G with 7-deazaG (**4**),[107,108] which indicates that removal of the N(7) atom of guanosine gives a system that does not form stable G-quadruplexes. A decreased propensity to form G-quadruplexes was also observed for oligonucleotides containing 6-thioG (**5**).[109] The molecular basis for this effect may be a consequence of the significantly larger van der Waals radius of the sulfur atom, as well as its poorer hydrogen-bonding and cation binding abilities. Molecular dynamics of DNA containing 6-thioG (**5**) supported the hypothesis that a sulfur atom at C6 is just too big to form a G-quartet.[110]

3.2. G-Quartets Stabilize Stacking of Nucleobase Triads and Tetrads

As shown in Figure 14 and Table 2, there are different ways in which molecules can interact with G-quadruplexes: by face recognition, edge recognition, loop recognition, or by simultaneous binding to the surface of the G-quartet and an adjacent loop or groove.

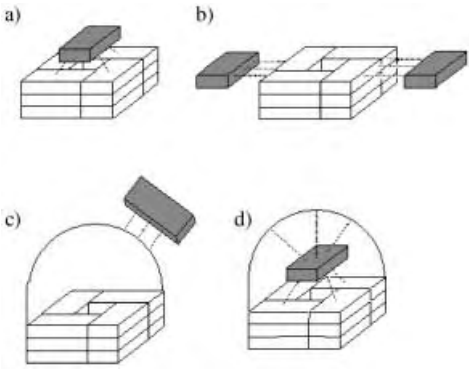


Figure 14. Schematic representation showing some of the ways that other molecules recognize a bimolecular G-quadruplex. a) "Face" recognition is achieved by stacking interactions, either on the terminal G-quartet or by intercalating between G-quartet layers; b) "edge" recognition occurs with the exposed N3, N2-H, and C8-H atoms on the G-quartet; c) binding of molecules to single-stranded loops connected to the G-quadruplex core; d) simultaneous "end" stacking and interaction of molecules with adjacent loop or groove regions.

Table 2: Molecular recognition of G-quadruplexes.

face recognition through stacking:
- nucleobase triads and tetrads
- aromatic molecules/telomerase inhibitors

edge recognition through hydrogen bonding:
- hydrogen bonding of other nucleobases
- protein recognition: edge interactions with amino acids
- water–nucleobase interactions

loop recognition through hydrogen bonding and electrostatic interactions:
- protein interactions: electrostatic phosphate–ammonium interactions
- small molecules and water

groove recognition through hydrogen bonding and electrostatic interactions
- water interactions with the hydration spine
- side-chain interactions with stacked aromatic molecules

 © 2004 Wiley-VCH Verlag GmbH & Co. KGaA, Weinheim

Within the context of nucleic acids, there are two major ways for adjacent nucleobases to recognize a G-quartet: either by stacking on its surface or by hydrogen bonding to an exposed edge. Furthermore, neighboring loops in bimolecular and unimolecular G-quadruplexes are also molecular recognition sites, particularly for proteins and small molecules.[59] One emerging theme from biophysical studies is that the G-quartet provides a platform on which to stabilize other hydrogen-bonded motifs.[9] Cheong and Moore first showed this with $[r(UG_4U)]_4$.[111] From the NMR spectrum they deduced a structure that featured a hydrogen-bonded U_4-quartet stacked above the G-quadruplex. They suggested that the U_4-quartet forms because it was *"… in the special context provided at the end of a tetra G stack, not because it is an intrinsically stable structure"*.[111] Patel and co-workers have used the G-quartet to template formation of base triplets and quartets,[112–116] and emphasize that stacking interactions stabilize these hydrogen-bonded arrangements. One example that illustrates the concept is the 12-mer $d(A_2G_2T_4A_2G_2)$, which dimerizes in the presence of Na^+ ions to give a diamond structure, with symmetry-related G-quartets at its core.[114] The diamond features progressive stacking of a G-quartet, a T-[A-A] base triplet, a mismatched dimer, and a single base (Figure 15). These studies highlight the ability of the G-quartet to expand the structural diversity of DNA. Unusual structures, such as this diamond, should be prime candidates for binding small molecules and proteins.

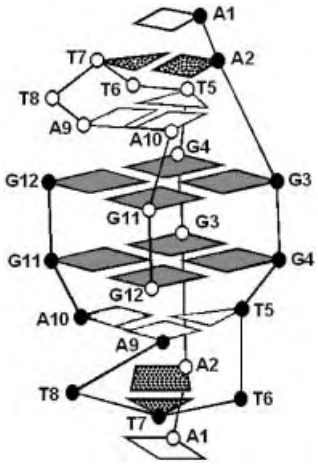


Figure 15. NMR spectroscopically derived "diamond" structure formed upon bimolecular association of the oligonucleotide $d(A_2G_2T_4A_2G_2)$ in the presence of Na^+ ions. The G-quartet core acts as a platform on which to stabilize adjacent T-[A-A] base triads.[114] The T residues are depicted as triangles and the G/A residues as rectangles.

Base tetrads, such as U_4, T_4, and A_4, can cap G-quadruplexes.[111,117,118] Stable mixed tetrads with more than one nucleobase type also form above the G-quartet. Patel et al. showed that $d(GCGGT_3GCGG)$ dimerizes in solution to give a quadruplex with G:C:G:C tetrads stacked above the G-quartets.[119] These mixed G:C:G:C tetrads are dimers of Watson–Crick G:C base pairs which switch between distinct geometries (Figure 16) depending on the ionic conditions.

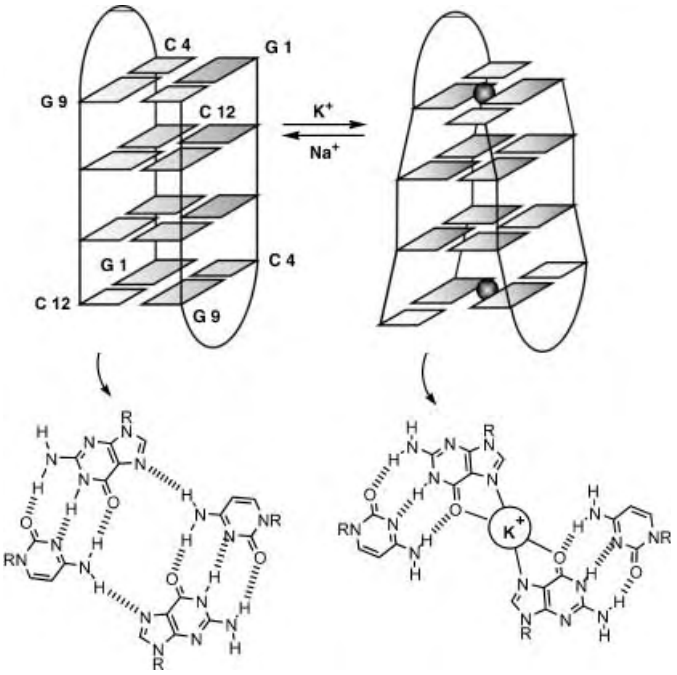


Figure 16. A cation-templated conformational change for the bimolecular G-quadruplex formed by $d(GGGCT_4GGGC)$. A G:C:G:C tetrad with directly opposed G-C base pairs is stacked above a G-quartet in Na^+ solution. These four bases adopt a "slipped" alignment of the G-C pairs upon complexation of K^+ by the N7 and O6 atoms of the guanosine.[120–122] The organization of the G:C:G:C tetrad is shown below the schematic diagrams.

NMR studies of $d(GGGCT_4GGGC)$ in Na^+ solution showed a G:C:G:C tetrad with directly opposed G-C pairs.[119] Transition to a slipped alignment of G-C pairs occurred upon addition of K^+ ions, presumably as a result of cation chelation by the N7 and O6 atoms of the guanosine.[120] Both ab initio and molecular dynamics calculations reproduced this K^+-induced transformation between the "closed" and "sheared" forms of the G:C:G:C tetrad.[121,122] Both G:C:G:C geometries show extensive overlap of their aromatic surfaces onto the flanking G-quartet. Extensive base stacking along the length of this G-quadruplex undoubtedly stabilizes its fold. These studies show that DNA quadruplexes don't need to be entirely composed of G-quartets. Furthermore, the propensity of G-rich sequences to template formation of base tetrads and triads also greatly increases the structural variability of DNA.

3.3. Molecular Recognition of the G-Quartet Edges

Hydrogen-bond donor (N2-H and C8-H) and acceptor (N3) atoms on the exposed edges of the G-quartet are also molecular recognition sites (see Figure 1 b). These sites, which are located along the floor of a groove running the length of the G-quadruplex, can bind water, ions, amino acid side chains, and other nucleobases. For example, some G-quartets form "sheared" G-A hydrogen bonds with a local adenine residue. NMR studies have identified hexad and heptad

 © 2004 Wiley-VCH Verlag GmbH & Co. KGaA, Weinheim

motifs, where two or three adenine nucleobases hydrogen bond to a single G-quartet.[123–126]

Uesugi and co-workers found in an NMR study of r(GGAGGUUUUGGAGG) that one RNA molecule folds into a quadruplex containing a G:G:G:G tetrad and a G:G(:A):G:G(:A) hexad.[125] As depicted in Figure 17, expansion of the lower G-quartet into a hydrogen-bonded hexad also increases the surface area available for stacking interactions, and two r(GGAGGUUUUGGAGG) molecules dimerize in solution using this hexad–hexad interface. The extensive base-stacking and hydrogen-bonding interactions contribute to the high thermodynamic stability of this particular RNA quadruplex. A crystal structure of a Sr^{2+}-bound RNA showed the ultimate in base expansion: an octad, with one G:U pair formed for every member of a G-quartet.[126] These studies indicate that recognition of a G-quartet edge may be an important theme in nucleic acid folding.

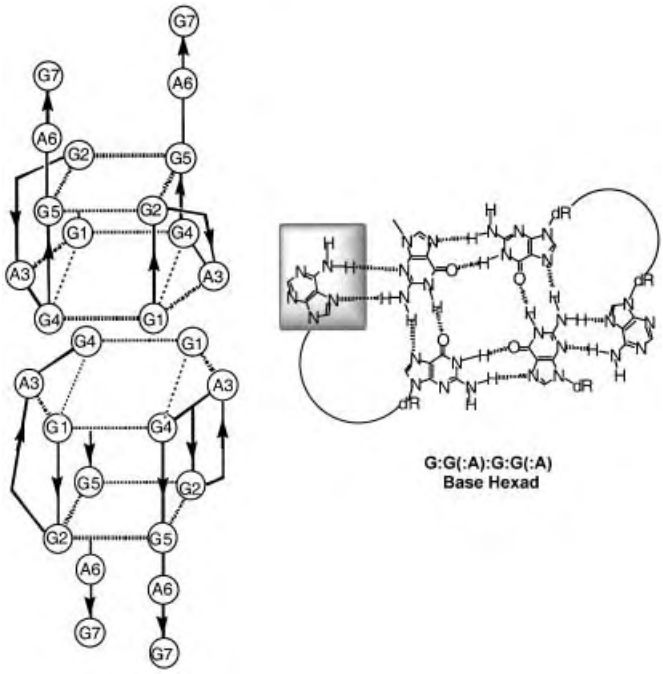


Figure 17. Edge recognition of a G-quartet through formation of hydrogen bonds between nearby adenine units to the exposed face of the quartet. One molecule of r(GGAGGUUUUGGAGG) folds into a G-quadruplex containing a G:G:G:G tetrad and a G:G(:A):G:G(:A) hexad. Two such RNA molecules dimerize in solution using this hexad–hexad interface.[125]

3.4. Molecular Recognition of G-Quadruplexes by Water

Crystal structures provide a wealth of information about the molecular recognition of G-quadruplexes.[59,60,84] In particular, these structures indicate that water helps maintain the structural integrity of DNA. A G-quadruplex has four grooves on its surface and the floors of these grooves consist of the C8-H, N2-H, and N3 atoms. Above these floors, the grooves are lined on both sides by the oxygen atoms of phosphate and sugar groups. All these atoms, on the floor and along the edges, can form hydrogen bonds with water molecules and there are, indeed, many different combinations of cross-connections possible.[59,60,84] Horvath and Schultz observed that hydrogen bonds involving C8-H are a key feature of G-quartet hydration in the *Oxytricha* structure, with 7 of 25 bound water molecules forming hydrogen bonds to the aromatic C8-H proton.[59] Water molecules make extensive hydrogen-bonding interactions with the edges of the guanine units and with the sugar-phosphate backbone to provide well-ordered hydration spines in the grooves of the G-quadruplex. An example of a hydration spine, from the $[d(TG_4T)]_4$ structure, is shown in Figure 18.[84]

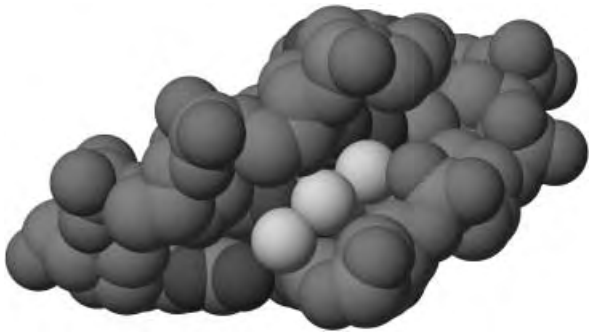


Figure 18. View of a hydration spine filling one of the grooves in the Na^+ form of the G-quadruplex $[d(TGGGGT)]_4$.[84] The light-colored atoms are the water oxygen atoms. PDB file for this structure: 352D.

Neidle and co-workers detailed the hydration pattern of this bimolecular G-quadruplex in their study of *Oxytricha* DNA.[60] Again, all the grooves had water clusters that bridged adjacent DNA strands. In addition, the G-quadruplex loops were also extensively hydrated, and water molecules connected the loops to the terminal K^+ ion and to the hydration spines running along the grooves. Water-mediated bridges between domains surely help to stabilize the loop conformations.

3.5. Molecular Recognition of G-Quadruplexes by Proteins

DNA and RNA oligonucleotides called aptamers have been selected by in vitro selection to bind molecular targets.[127] These targets are often proteins. One well-known aptamer is the thrombin binding aptamer (TBA), a DNA 15 mer that inhibits clotting.[128] Crystallographic[129,130] and NMR[131–134] spectroscopic studies have shown that TBA forms a unimolecular G-quadruplex with two G-quartets and three loops. The structure and biological activity of TBA are K^+-dependent. NMR spectroscopic, calorimetric, and ESI-MS studies have shown, however, that TBA is even more stable with divalent Pb^{2+}, Sr^{2+}, and Ba^{2+} ions.[135–137] Related DNA aptamers are inhibitors of human HIV integrase with IC_{50} values in the nM region[138,139] and adopt a unimolecular

G-quadruplex similar to TBA.[140,141] An intermolecular G-quadruplex aptamer that bound the V3 loop of HIV reverse transcriptase was formed by a 17-mer phosphorothioate oligonucleotide.[142] Like many G-quadruplexes, this phosphorothioate aptamer was extremely stable and had a dissociation half-life of 60 days.[143] Thus, it remained active even at μM concentrations. Many other protein-binding aptamers have been proposed to form G-quadruplexes as part of their bioactive structure.[144–148]

Although many proteins, including aptamers, oncogenic factors,[149a] antibodies,[150] and telomeric proteins,[12–14] all bind G-quadruplexes, there are few molecular details known about quadruplex–protein interactions.[12] The crystal structure of TBA bound to thrombin showed some ion pairs between the phosphate groups in the loops of the aptamer and Lys and Arg side chains.[129,130] A crystal structure of the telomeric protein of *Oxytricha nova* complexed to $d[G_4T_4G_4]_4$ is particularly valuable.[59] As in the DNA solution structures, the bimolecular quadruplex in this complex has diagonal loops. Most of the DNA–protein contacts take place with these loops, rather than with the quadruplex core.

The major DNA–protein interactions include: 1) electrostatic interactions, wherein the surface formed by three symmetry-related proteins provides a deep, electropositive cavity to hold the folded DNA; 2) van der Waals interactions, such as where the aromatic rings of Tyr 142 and Phe 141 pack against the G-4 sugar; 3) water mediated hydrogen bonds, wherein one of the T_4 loops forms an extensive network of water-mediated hydrogen bonds with the protein; 4) nucleobase–peptide packing interactions, wherein the T6 residue of the other loop contacts the protein using both van der Waals and H-bond interactions. This T6 nucleobase packs between a Leu side chain and the polarized Asp 437–Gly 438 peptide bond, while simultaneously hydrogen bonding with atoms of the protein side chain and main chain.

In both cases where crystal structures are available, for the *Oxytricha* and for the thrombin systems,[59,129,130] there are few direct interactions between the protein and the G-quadruplex core. Instead, the G-quadruplex seems to function as a scaffold on which loops are displayed for molecular recognition. Certainly, the crystal structure of the unimolecular G-quadruplex formed from the human telomeric sequence d(TTAGGG) suggests that the extended loops provide ideal protein-binding sites.[95] Wen and Gray have also proposed that g5p—a protein that binds single-stranded DNA—may prefer to bind constrained loops, as opposed to random coils, to reduce its entropic binding cost. This might be best accomplished by having a G-quadruplex core constrain the conformation and dynamics of nearby loops.[147] In time, as more structural information becomes available, we should learn if a preference to bind loops is general for G-quadruplex–protein interactions.[149]

3.6. G-Quadruplex Aptamers: Recognition by Small Molecules

Small molecules can also generate DNA and RNA aptamers, and G-quartets often appear as part of the aptamer structure.[151,152] Porphyrins and G-quartets have similar surface areas, and many biophysical and biochemical studies have demonstrated stacking interactions between porphryins and G-quadruplexes.[79,153–158] Sen and co-workers as well as other research groups have described some oligonucleotide aptamers that bind to porphyrins.[159–164] On the basis of optical spectroscopy and chemical protection evidence it was proposed that these aptamers folded into G-quadruplexes in the presence of the porphyrin. These studies went beyond demonstrating ligand–receptor binding: some aptamers, selected with transition-state analogue *N*-methylmesoporphyrin (NMM), catalyzed the Cu^{2+} and Zn^{2+} metalation of porphyrins (Figure 19).[161] This catalytic DNA, which

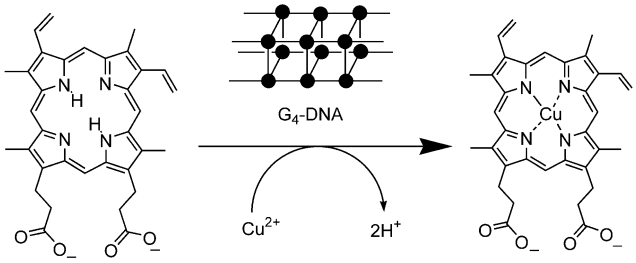


Figure 19. Porphyrin metalation catalyzed by a DNA G-quadruplex.[161]

requires K^+ ions for activity, may bind the porphyrins either by external stacking or by intercalation between G-quartets. Li and Sen concluded that the DNA chelatases used substrate binding energy to distort the planar conformation of the porphyrin, thus making the porphyrin more basic and easier to metalate.[163] They suggested that the G-quartet is sufficiently rigid to enable such a substrate distortion.[164]

Sen and co-workers also identified DNA aptamers that catalyze another reaction.[165,166] Some DNA–hemin complexes had enhanced peroxidase activity relative to the heme cofactor alone. They concluded that the folded DNA activates the bound heme.[165] A G-quadruplex with a heme intercalated between G-quartets was proposed to explain the enhanced peroxidase activity of the aptamers.[166] These studies underscore the potential of DNA to function as a catalyst, in addition to its information storage role.

By using in vitro selection Isalen et al. discovered Zn^{2+} finger peptides that bind G-quadruplexes.[167] High affinity peptides ($K_a = 25$ nM) containing three helices bound the human telomeric sequence d(GGTTAG). These Zn^{2+} fingers were G-quadruplex-specific; duplex DNA with the same sequence was not bound. The Zn^{2+} fingers contained high amounts of certain amino acids, and the authors speculated that Glu/Asp side chains might form hydrogen bond with the N2 amino groups of the guanosine while His groups could stack on the G-quartet.

3.7. Telomerase Inhibitors: Small Molecules that Stabilize DNA G-Quadruplexes

The telomere is a protective nucleoprotein complex located at the ends of chromosomes.[168–171] In humans,

 © 2004 Wiley-VCH Verlag GmbH & Co. KGaA, Weinheim

telomeric DNA is a 5000–15000 base section of 5′-TTAGGG-3′ repeats bound by an array of proteins. Since 50–500 TTAGGG units are lost with each replication, the telomere is slowly whittled away and the cell dies. Tumor cells evade this fate by expressing telomerase, a reverse transcriptase with a RNA template for telomere extension.[172–174] Telomeres are proposed to be involved in cancer, based in part on the finding that in vitro telomerase induction can transform healthy cells into malignant ones.[175] Furthermore, telomerase inhibition can kill cancer cells, "*… validating human telomerase … as an important target for anti-neoplastic therapies.*"[176]

One approach to inhibit telomerase is to block the enzyme–substrate interaction. Whereas single-stranded DNA is a telomerase substrate, G-quadruplex DNA is not. The single stranded overhang of 5′-TTAGGG-3′ repeats in the human telomere has been proposed to fold into an intramolecular G-quadruplex, and ionic conditions that stabilize G-quadruplexes inhibit telomerase. Cech and co-workers reported that the telomerase activity of *Oxytricha nova* dropped significantly in the presence of K^+ ions: "*… (f)olding of telomeric DNA into G-quartet structures seems to influence the extent of telomere elongation in vitro and might therefore act as a negative regulator of elongation in vivo.*"[177]

Telomerase inhibition depends on shifting the equilibrium between the single-strand and quadruplex towards the folded form. One strategy is to stabilize the G-quadruplex form by binding high-affinity small molecules. A number of reviews describe well how drug design and screening efforts have identified compounds that bind G-quadruplexes and inhibit telomerase.[178–183] As shown by the structural formulas **6**–**15**, most telomerase inhibitors are aromatic compounds with electron-deficient rings suited for stacking with the electron-rich G-quartet. Ethidium bromide (**6**), a well-known duplex intercalator, binds DNA quadruplexes,[184] but its surface area doesn't quite cover a G-quartet, and it was reasoned that larger aromatic compounds would be better inhibitors.

The first report of a small molecule, anthraquinone derivative **7**, that binds G-quadruplex DNA and inhibits telomerase came in 1997.[185] Since then, hundreds of telomerase inhibitors have appeared.[178–183] There is debate about how the aromatic inhibitors interact with G-quadruplex DNA. Some suggest that they intercalate between G-quartets,[186] while others argue that the compounds end-stack on terminal G-quartets.[155] The few known quadruplex–ligand structures, obtained from NMR spectroscopic,[187,188] fiber diffraction,[189] and single-crystal X-ray crystallographic analysis,[190,191] indicate that telomerase inhibitors end-stack rather than intercalate (Figure 20). In their recent X-ray study of

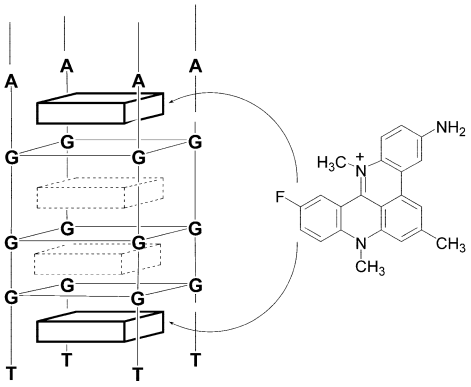
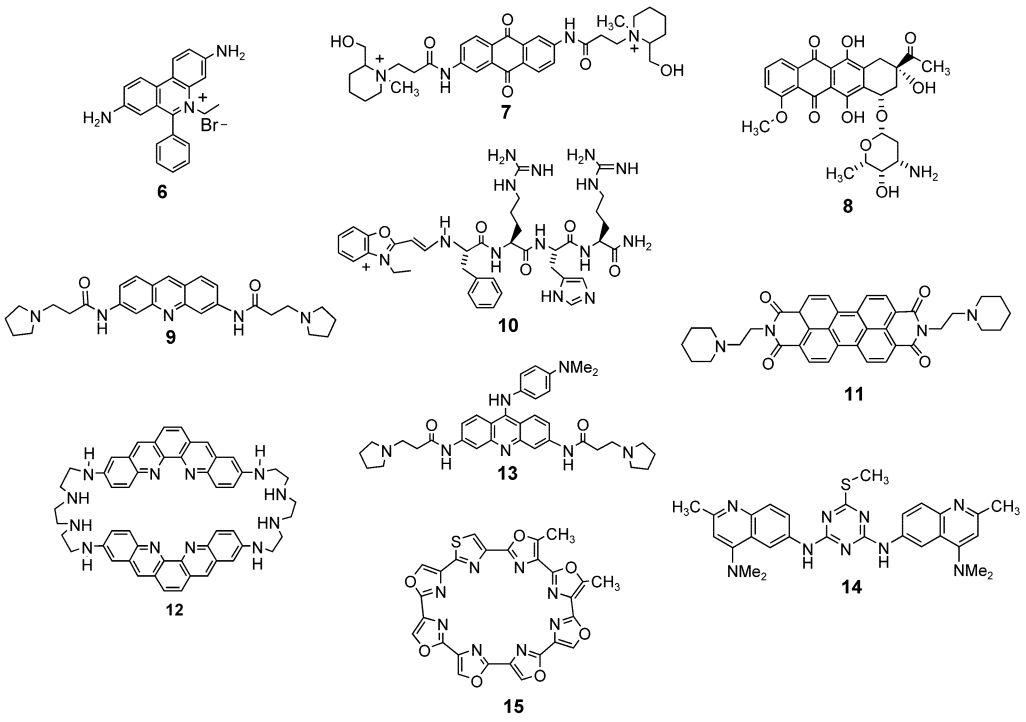


Figure 20. Interaction of the aromatic inhibitor with G-quadruplex DNA: NMR data show the drug stacking on ends of the G-quadruplex (bold), as opposed to intercalation between the G-quartet layers (dotted).[188]



interactions between G-quadruplex and daunomycin (**8**) Clark et al. noted that intercalation of drugs between G-quartet layers should be energetically more costly than end stacking, as intercalation requires unstacking of the tetrad and unwinding of the helix.[191] In addition, end stacking of aromatic drugs, as opposed to intercalation, would allow stabilizing cations to remain coordinated within the G-quadruplex core. In another crystal structure of a G-quadruplex–drug complex, the drug **9** not only end-stacks on the terminal G-quartet, it also simultaneously binds the adjacent loop with its side chains to secure its position.[190]

Structure-based design and activity-based screening have both identified telomerase inhibitors. For example, Shafer and co-workers used computer modeling to screen "virtual" libraries for compounds that might interact with G-quadruplexes. These efforts identified a carbocyanine dye that binds bimolecular G-quadruplexes.[192] Recently, a carbocyanine–peptide conjugate **10**, identified by combinatorial selection, was shown to bind G-quadruplex DNA with high affinity and quadruplex/duplex selectivity.[193]

In another modeling approach, Fedorov, Hurley, and co-workers designed and synthesized the quadruplex interactive compound PIPER (**11**), which was a potent telomerase inhibitor.[187] The slow NMR exchange between DNA-bound and free PIPER (**11**), along with ligand–DNA NOE interactions, allowed determination of the drug's location when bound to G-quadruplex DNA. The conclusion was that PIPER (**11**) end-stacked over a terminal G-quartet. Significantly, this perylene derivative is also a molecular chaperone, as it accelerated the formation rate of a bimolecular G-quadruplex by 100-fold.[194] Salazar and co-workers took advantage of this affinity in designing a PIPER conjugate, perylene-[Fe^{II}(edta)] for cleavage of G-quadruplex DNA.[195] They used NMR spectroscopy to establish that the Fe-free perylene stacked on the terminal G-quartet. They then demonstrated that perylene-[Fe^{II}(edta)] selectively cleaved G-quadruplex DNA without damaging duplex DNA. Compounds that selectively destroy G-quadruplex DNA could be useful structural probes.

Recent work suggests that G-quadruplexes, themselves self-assembled structures, also interact with aggregated ligands. These findings are reasonable, when the extensive surface area provided by a planar G-quartet is considered. Although the structural basis is unclear, Kerwin and co-workers showed that the binding selectivity of the tetraplex is greatly enhanced when PIPER (**11**) is aggregated.[196,197]

A crystal structure illustrates this remarkable self-assembly feature of G-quadruplex:drug interactions. Clark et al. showed that daunomycin (**8**) self-assembles into a noncovalent trimer $[\mathbf{8}]_3$ when interacting with four-stranded $[d(TG_4T)]_4$ (Figure 21). The daunomycin trimers are held together by van der Waals interactions. In this crystal, two daunomycin trimers stack between the 5′-G-quartets that make up the G-quadruplex.[191] There are also extensive stacking interactions between the terminal G-quartet and the daunomycin trimer. In addition, sugars on the three daunomycin molecules extend into the grooves where they hydrogen bond with the G-quadruplex core.

Competition dialysis experiments recently showed that the dimeric macrocycle BOQ (**12**), unlike its monomeric analogue, selectively binds G-quadruplex DNA.[198] Compound **12** is also a potent telomerase inhibitor. The selectivity of the dimeric macrocycle, relative to the monomeric form, is attributed to its enhanced stacking and hydrophobic interactions with G-quadruplex DNA.

Read et al. have shown how structure-based design can be used to obtain improved telomerase inhibitors.[199] Molecular modeling studies suggested that addition of a properly positioned third side chain to an existing acridine drug **9** (to give **13**) would increase the affinity of the G-quadruplex. They reasoned that additional contacts between the side chains and grooves would further stabilize the folded DNA, and thus lead to more telomerase inhibition. A comparison of the properties of acridines **9** and **13** showed that attachment of this third side chain improved the drug's affinity to bind with the G-quadruplex, it's quadruplex–duplex selectivity, and it's telomerase inhibitory activity.

Promising telomerase inhibitors have also come from combinatorial screening strategies. The research groups of Mergny and Hélène used a FRET-based assay to identify triazine compounds such as **14** that induce a DNA oligonucleotide to fold into a G-quadruplex.[200,201] Some of these triazines were inhibitors of human telomerase at nanomolar concentrations. Such combinatorial screens can lead to active compounds that might not have been considered in structure-based design.

Finally, the most potent and selective telomerase inhibitor, telomestatin (**15**), is a natural product isolated from *Streptomyces anulatus* during an activity screen.[202] NMR and modeling studies indicate that telomestatin stacks on a G-quartet, which again suggests that telomerase inhibition derives from an ability to stabilize the G-quadruplex form of telomeric DNA.[203]

3.8. Summary of Interactions Important for G-Quadruplex Structure and Molecular Recognition

As for most supramolecular systems, different noncovalent interactions work in concert to provide a G-quadruplex. Both experiment and calculations show that cation–dipole interactions are essential for the hydrogen bonding and base stacking that is characteristic of G-quadruplex structures. Cation binding presumably reduces the repulsion of the four central oxygen atoms of the hydrogen-bonded quartet, enhances hydrogen-bond strength, and stabilizes G-quartet stacking.

Stacking interactions are also clearly important in controlling the structure and molecular recognition of G-quadruplex DNA. Base stacking is driven by electrostatic and dispersive (van der Waals) interactions.[204,205] The G-quartet provides an extended surface for interactions with aromatic compounds, be they other nucleobase assemblies or small molecule ligands. While there is debate over the relative importance of the forces that drive aromatic-stacking interactions,[204] both calculations and experiment suggest that the

 © 2004 Wiley-VCH Verlag GmbH & Co. KGaA, Weinheim

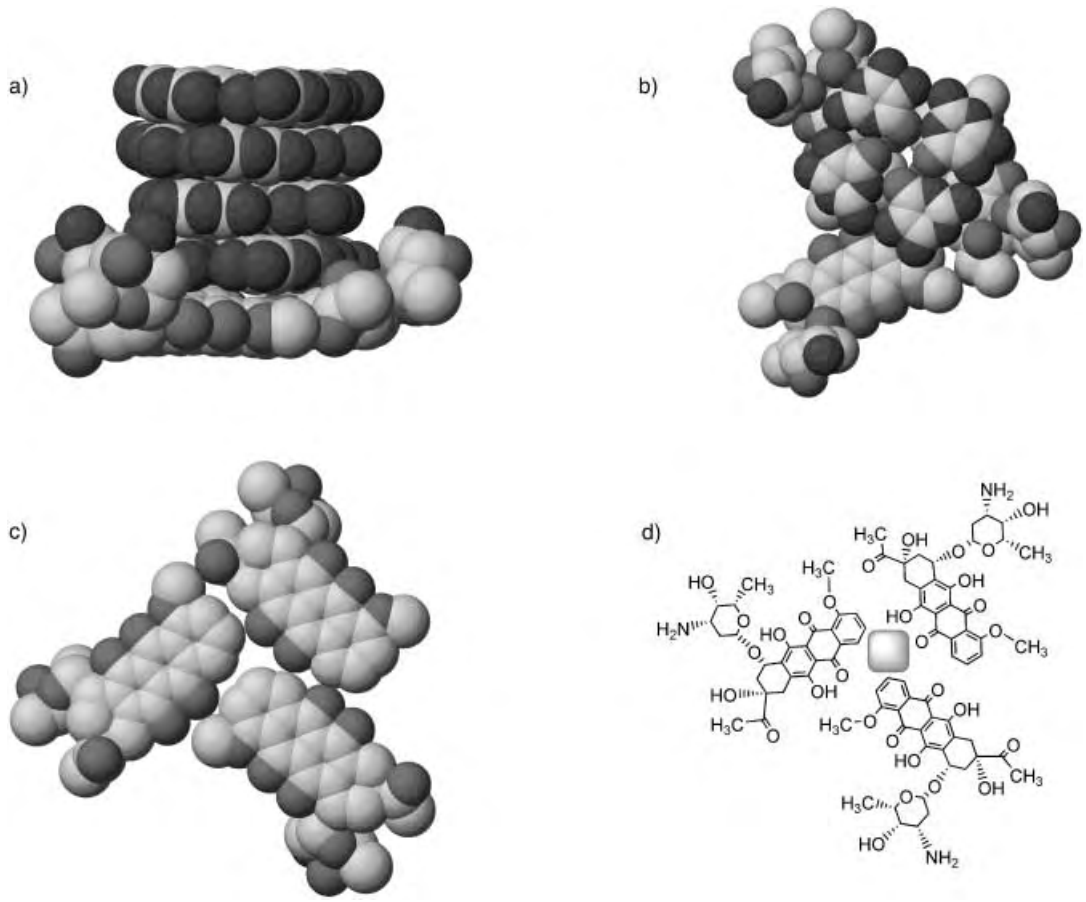


Figure 21. Depictions of the crystal structure showing a self-assembled daunomycin trimer $[\mathbf{8}]_3$ bound to the four-stranded G-quadruplex $[d(TG_4T)]_4$.[191] a) The G-quartet core stacked on top of $[\mathbf{8}]_3$; b) a top view of the terminal G-quartet stacked on trimer $[\mathbf{8}]_3$; c) bottom view of the daunomycin trimer held together by van der Waals interactions; d) the structural formula of the daunomycin trimer $[\mathbf{8}]_3$. PDB code for this crystal structure: 1O0K.

nonclassical hydrophobic effect can explain such stacking interactions.[205] For example, Spöner and co-workers calculated that van der Waals interactions between two G-quartets are strongly attractive, with $\Delta H = -49$ kcal mol^{-1}, while the electrostatic component was repulsive, with $\Delta H = +28$ kcal mol^{-1}, which gives an overall stacking energy of $\Delta H = -21$ kcal mol^{-1}, even in the absence of the templating cation.[87] This enthalpy for quartet stacking ($\Delta H = -21$ kcal mol^{-1}) is greater than the enthalpies of $\Delta H = -10$ to -15 kcal mol^{-1} calculated for stacking interactions within duplex DNA. Calorimetry measurements on G-quadruplex–ligand interactions also show the hallmarks of the "nonclassical" hydrophobic effect, with $\Delta H \ll 0$ and $T\Delta S \ll 0$.[186] This effect arises from the enthalpic gain of stacking large aromatic surfaces containing polarizable atoms.[205] There is also an enthalpic gain when weakly bound water is released from these aromatic surfaces to the bulk.

Finally, hydration spines within the grooves and the water molecules that link the loops to the G-quartet core also help control G-quadruplex structure, dynamics, and function.

4. Lipophilic G-Quadruplexes: Structural Models for DNA, Self-Assembled Ionophores and Other Structural Motifs

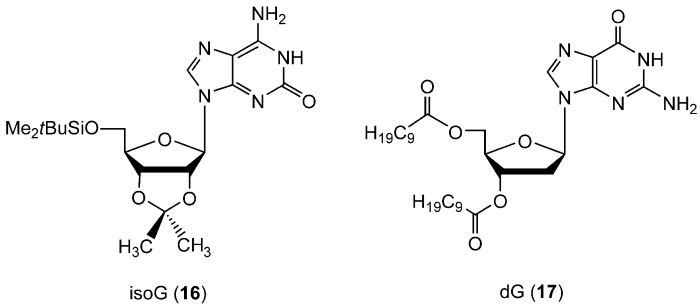
In the 1990 review by Guschlbauer et al. it was stated that "*(w)ater appears to be an indispensable solvent for the autoassociation of guanosine … organic solvents give rise to poorly organized aggregates*".[1] At that time, the analogues and conditions needed to form G-quadruplexes in organic solvents had not yet been identified. Since then it has been found that lipophilic nucleosides do indeed form stable, well-ordered species in organic solvents. These lipophilic G nucleosides are used as models for DNA G-quadruplexes, as the basis for studying noncovalent interactions, and as the inspiration for synthetic molecular assemblies.

4.1. Early Intermediates in Guanosine Self-Assembly: Discrete $G_8{\cdot}K^+$ Octamers in Organic Solvents

While exploring base pairing in organic solvents, it was observed that lipophilic G (**1**) and its isoguanosine isomer

 © 2004 Wiley-VCH Verlag GmbH & Co. KGaA, Weinheim

(isoG, **16**), both self-associate in the presence of cations.[206,207] Concurrently, Gottarelli et al. reported the K^+-templated self-assembly of 3′,5′-didecanoyl-2′-dG (**17**) in $CDCl_3$.[208] Depending on conditions, dG (**17**) can extract K^+ picrate from water into $CDCl_3$ to give either a discrete octamer, $[\mathbf{17}]_8 \cdot K^+$, or a polymer, $([\mathbf{17}]_4)_n \cdot (K^+)_m$. Lateral self-organization of the stacked $([\mathbf{17}]_4)_n \cdot (K^+)_m$ columns in hydrocarbon solvents gives hexagonally packed liquid crystals.[209]



To better understand the transition from molecule to defined aggregate to ordered phase in organic solvents, we collaborated with Gottarelli et al. to determine the NMR structure of the octamer $[\mathbf{17}]_8 \cdot K^+ \cdot I^-$ in $CDCl_3$, the first detectable intermediate in self-assembly and self-organization of dG (**17**).[210] Remarkably, the NMR data indicated that this octamer was a single diastereomer. In one G-quartet, all dG units had a *syn*-glycosidic conformation, while the other tetramer had an "all-*anti*" conformation. NOE interactions indicated a "head-to-tail" orientation of the "all-*anti*" G-quartet stacked on the "all-*syn*" G-quartet, with a 30° twist about the central axis. Small angle neutron scattering and NMR data later showed that the $([\mathbf{17}]_4)_n \cdot (K^+)_m$ polymer had the same G-quartet geometry and organization as did this discrete $[\mathbf{17}]_8 \cdot K^+$ octamer.[211] This NMR study firmly established that discrete G-quartet structures exist in organic solvents. The study also showed that self-assembly of dG (**17**), followed by domain self-organization, was promising for building nanostructures (see Section 5). Structural characterization of discrete species such as $[\mathbf{17}]_8 \cdot K^+ \cdot I^-$ provided a better understanding of self-assembly, and also generated ideas for new supramolecular designs.

4.2. Crystal Structures of Lipophilic G-Quadruplexes: Models for Locating Ions in DNA

Besides X-ray crystallography, there are few methods to directly locate cations in DNA G-quadruplexes. ^{15}N NMR has provided insight into NH_4^+ binding, and ^{205}Tl NMR showed how a K^+ surrogate stabilizes the $[d(T_2G_4T_2)]_4$ quadruplex.[212,213] Although ^{23}Na NMR spectroscopy in solution provides dynamic information, it gives no structural insight.[214] There is a need, therefore, for techniques that detect DNA-bound metals. The high-resolution crystal structures of lipophilic G-quadruplexes synthesized from G (**1**)[29–33] have helped validate such new methods, namely solid-state ^{23}Na and ^{39}K NMR spectroscopy and extended X-ray absorption fine structure (EXAFS).

Solid-state ^{23}Na NMR spectra were previously obtained for the DNA quadruplex $[d(TG_4T)]_4$,[215] but assignment of the G-quartet-bound Na^+ ion was compromised by atmospheric Na^+ ions bound to the DNA phosphates. The lipophilic G-quadruplex $[\mathbf{1}]_{16} \cdot 3\,Na^+/Cs^+ \cdot 4\,pic^-$ was an ideal model for circumventing such problems; it has three crystallographically distinct channel Na^+ ions and no phosphate-bound Na^+ ions to complicate the NMR analysis. Wu and co-workers used 2D ^{23}Na MQMAS NMR spectroscopy (MQMAS = multiple quantum magic angle spinning) to determine the isotropic chemical shifts and other parameters for the three Na^+ sites within $[\mathbf{1}]_{16} \cdot 3\,Na^+/Cs^+ \cdot 4\,pic^-$.[33] The unambiguous detection of Na^+ ions within the channel firmly established these lipophilic G-quadruplexes as excellent models for DNA G-quadruplexes.

Wu et al. also used solid-state ^{39}K NMR spectroscopy to identify K^+ ions within the lipophilic G-quadruplex $[\mathbf{1}]_{16} \cdot 3\,K^+/Cs^+ \cdot 4\,pic^-$.[216] The quartet-bound K^+ ions provided a distinctive ^{39}K NMR signal at $\delta = -45$ ppm. Importantly, the ^{39}K chemical shift for this model then enabled the authors to distinguish different K^+ ions in the 5′-GMP quadruplex; both the G-quartet-bound and phosphate-bound K^+ ions were identified. This solid-state ^{39}K NMR study, the first spectroscopic detection of biologically relevant K^+ ions, bodes well for studies of DNA-$(G_4)_n \cdot K^+$ quadruplexes.

Shafer and co-workers described the first use of EXAFS to characterize DNA–metal ion binding in solution.[217] EXAFS provides coordination numbers and quantitative internuclear distances for the bound metal. The authors determined the location of the Pb^{2+} ions and the Pb-O distances for the thrombin binding aptamer $d(G_2T_2G_2TGTG_2T_2G_2)$ (TBA). They had previously shown that this unimolecular G-quadruplex binds Pb^{2+} ions tightly,[218] but is was unclear as to whether the Pb^{2+} ions were bound between the two G-quartets of the TBA, or coordinated to the terminal G-quartet and adjacent loop (Figure 22).[219,220] The lipophilic G-quadruplex $[\mathbf{1}]_{16} \cdot 2\,Pb^{2+} \cdot 4\,pic^-$ helped resolve this structural issue. The crystal structure had previously shown that an octacoordine Pb^{2+} ion was sandwiched between two G-quartets.[30] The EXAFS Pb-O distances for the model G-quadruplex

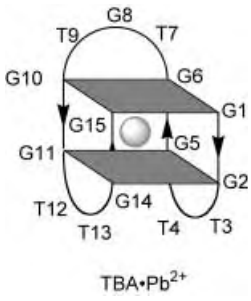


Figure 22. The thrombin binding aptamer (TBA) with a bound Pb^{2+} ion. Comparison of the EXAFS data for the lipophilic G-quadruplex $[\mathbf{1}]_{16} \cdot 2\,Pb^{2+}$ and for Pb^{2+}·TBA helped identify the cation binding site.[217]

 © 2004 Wiley-VCH Verlag GmbH & Co. KGaA, Weinheim

$[\mathbf{1}]_{16}\cdot 2\,Pb^{2+}\cdot 4\,pic^-$ matched well with the Pb-O distances determined by crystallography. Both coordination numbers and EXAFS Pb-O distances for $[\mathbf{1}]_{16}\cdot 2\,Pb^{2+}\cdot 4\,pic^-$ and Pb^{2+}·TBA were identical, thus providing evidence that the Pb^{2+} ion was located between the two G-quartets in Pb^{2+}·TBA. This study not only established EXAFS as a method for providing quantitative information about binding between DNA and metal ions, it also again demonstrated the value of using lipophilic G-quadruplexes containing G (**1**) as models for locating metal ions in the analogous DNA structures.

4.3. G-Quartets and IsoG Pentamers: Controlling the Self-Assembly through the Nucleobase Structure and the Cation Template

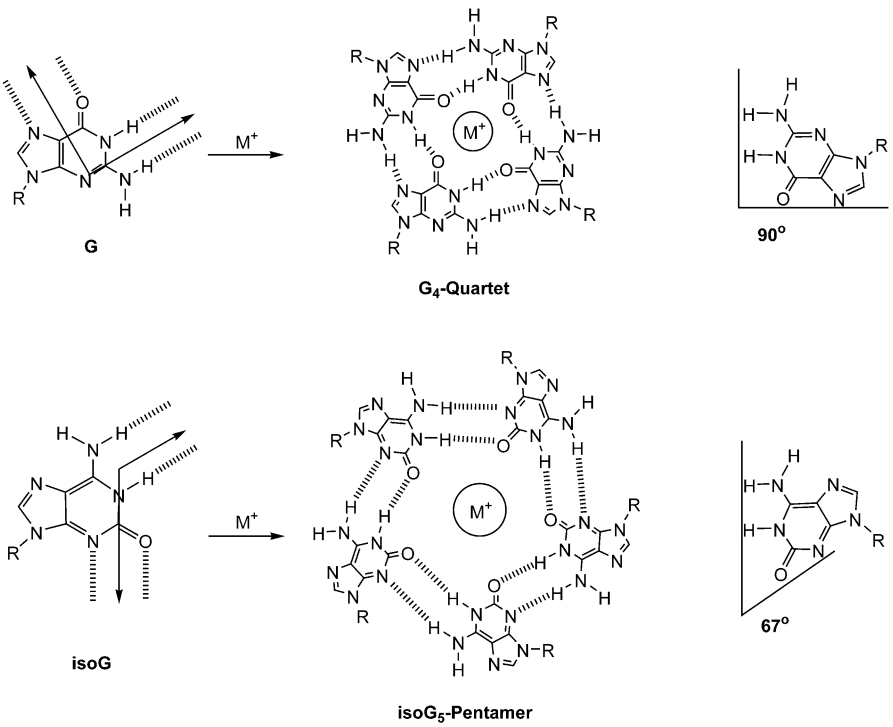


Figure 23. Self-association of G (**1**) and isoG (**16**) in the presence of cations to give hydrogen-bonded G_4-quartets or $isoG_5$-pentamers, respectively. The relative orientation of the hydrogen-bond donor and acceptor groups on the nucleoside determines the size of the assembly formed. The van der Waals angle of 67° for IsoG favors pentamers, whereas the 90° angle in G favors a quartet.[223]

The outcome of self-assembly is determined by the information programmed into the components. Even small perturbations to those building blocks can dramatically alter supramolecular structure. Consider G (**1**) and isoG (**16**): These isomers differ only in the location of an oxygen and nitrogen atom, yet they self-assemble much differently. Crystal structures show that G (**1**) forms a hexadecameric G-quadruplex, $[\mathbf{1}]_{16}\cdot 4\,M^+$,[29–33] whereas isoG (**16**) gives a decamer, $[\mathbf{16}]_{10}\cdot Cs^+$, in which hydrogen-bonded pentamers sandwich a Cs^+ ion.[221,222] Comparative studies of G (**1**) and isoG (**16**) have led to two conclusions: 1) the size of the self-assembled macrocycle depends on the nucleoside's hydrogen bonding pattern and 2) a cation is needed to stabilize these synthetic macrocycles.

In accord with our studies on nucleosides in organic solvents, the research groups of Switzer and Seela have found that the nucleobase and cation play a similar role in the self-assembly of DNA. Thus, DNA oligonucleotides with d-isoG sequences form five-stranded structures in the presence of Cs^+ ions.[223–225] Chaput and Switzer rationalized[223] that the size of the hydrogen-bonded macrocycle is influenced by the relative location of the hydrogen bond donors and acceptors in the nucleobase (Figure 23). G-quartets form because the G donor and acceptor units are 90° to each other, thus ensuring the formation of a planar tetramer with linear hydrogen bonds. The ability of isoG to form a hydrogen-bonded pentamer, particularly in the presence of a large templating cation, was proposed to originate from the 67° angle between the van der Waals surfaces of the hydrogen bonding faces of the isoG. This angle is close to a cyclic pentamer's optimum angle of 72° (360°/5).[223]

In agreement with these above arguments, the identity of the cation is critical in controlling the self-assembly of isoG-DNA. Thus, the same sequences that form pentaplexes with Cs^+ ions assemble into four-stranded structures with the smaller (and more charge dense) K^+ and Na^+ ions.[223–228] Seela and Kröschel showed that addition of Cs^+ ions to $d(T_2isoG_4T_2)$ gave only the pentaplex, whereas only the tetraplex was identified in the presence of Na^+ ions. Remarkably, both the four-stranded and five-stranded DNA exist together in a solution containing Rb^+ ions, an ion intermediate in size between Na^+ and Cs^+.[225] Recent calculations have confirmed that formation of isoG quartets and isoG pentamers depends on the size of the templating cation.[229] Since isoG and G are self-complementary,[230,231] it is also possible that G and isoG may be able to form mixed assemblies.[232]

In addition to the ligand and the cation, the anion may also affect the self-assembly of lipophilic nucleosides. In our early studies, we concluded that isoG (**16**) self-assembled into tetramers in the presence of potassium picrate.[233] In retrospect, the coordinating picrate anion may have compromised the determination of the stoichiometry. Crystal structures and NMR data later obtained with the noncoordinating Ph_4B^- ion were consistent with isoG (**16**) forming hydrogen-bonded pentamers with alkali-metal cations in organic solvents.[221,222,234,235]

Both G (**1**) and isoG (**16**) require a cation for self-assembly. This was demonstrated in ^1H NMR and ESI-MS experiments carried out during the study of the "self-sorting" of **1** and **16**.[236] A 1:1 ratio of G (**1**) and isoG (**16**) in CD_2Cl_2 without cations gave a mixture of ill-defined hydrogen-

bonded complexes. Addition of $Ba(pic)_2$ to the nucleoside mixture resulted in formation of the discrete complexes $[\mathbf{1}]_{16}{\cdot}2\,Ba^{2+}$ and $[\mathbf{16}]_{10}{\cdot}Ba^{2+}$ (Figure 24). The separate aggregation of the isomers in these experiments demonstrated the central role of the cation in expressing the hydrogen-bonding and base-stacking information embedded in these nucleosides. This self-sorting experiment with G (**1**) and isoG (**16**) provides an example of the shifting equilibrium essential for dynamic combinatorial chemistry.[237] Wu and Isaacs have recently shown that cation-templated self-sorting of G (**1**) and isoG (**16**) even occurs in mixtures containing six other potentially competitive hydrogen-bonded assemblies.[238]

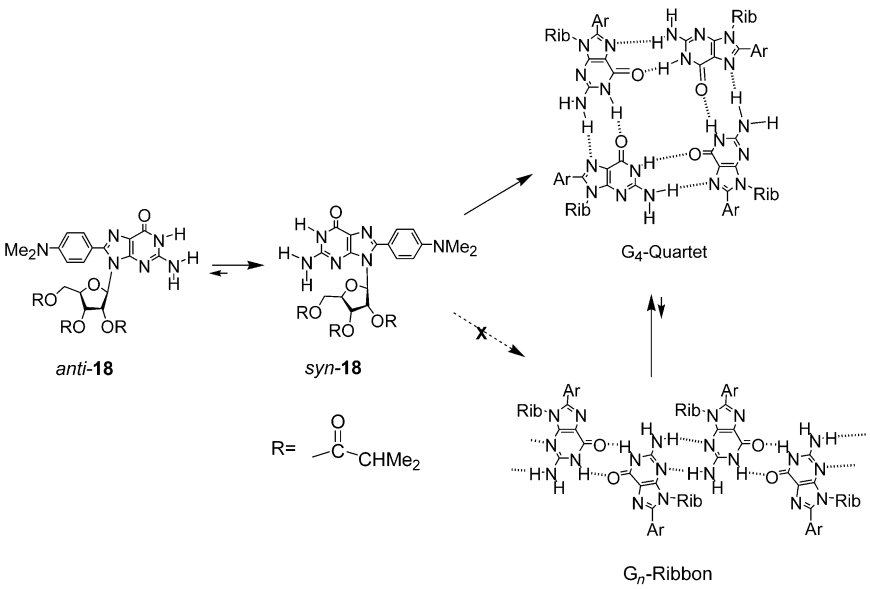


Figure 25. The conformationally constrained guanosine **18** forms a G-quartet without the need for a cation template.[45]

4.4. Empty Quartets. Guanosine Self-Assembly Without a Cation

While the dogma seems to be that a cation is needed to stabilize the G-quartet, Sessler et al. have shown otherwise:[45] A crystal structure of a G analogue **18**, modified with a large C8 substituent, revealed a hydrogen-bonded G-quartet with an empty cavity. Solution NMR spectroscopy in CD_2Cl_2 also showed characteristic signals for a stable G-quartet. The critical feature needed to obtain an "empty" G-quartet is a conformationally constrained monomer. In the absence of a cation, unconstrained guanosine derivatives self-associate to give ribbon structures by using the N3 position as a hydrogen-bond acceptor. In **18**, the dimethylaniline substituent at C8 forces the nucleoside into a *syn* conformation, where the sugar blocks the N3 position, thus preventing ribbon formation (Figure 25). Consequently, the Hoogsteen pairing that results in the G-quartet is the only option available to **18**. This study illustrates that control over monomer conformation can dramatically influence the self-assembly of guanosine.

More recently, Sessler et al. have prepared another cyclic hydrogen-bonded assembly from the lipophilic dinucleoside **19** (Figure 26).[239a] This guanosine–cytosine conjugate associates through self-complementary Watson–Crick hydrogen bonds to form a cyclic trimer $(\mathbf{19})_3$. The use of modified nucleobases to control self-assembly, expands on efforts that have used synthetic CG analogues to build such elegant structures as Janus molecules, self-assembling dendrimers, and helical rosettes.[239b]

4.5. Enantiomeric Self-Recognition of Lipophilic Nucleosides: Formation of Homochiral Hydrogen-Bonded Assemblies

Although not directly involved in the G-quartet hydrogen bonds, the sugar can modulate nucleoside self-assembly. We

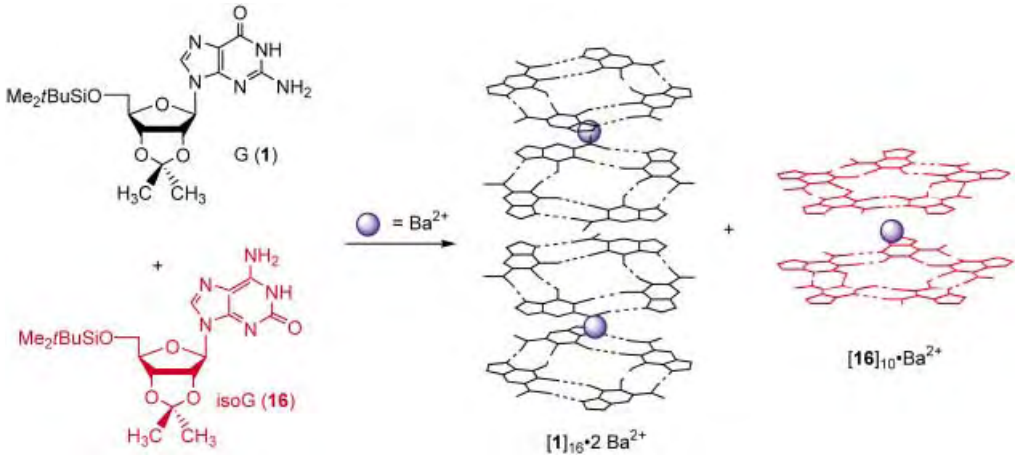


Figure 24. The isomers G (**1**) and isoG (**16**) "self-sort" in the presence of barium picrate to give the discrete complexes $[\mathbf{1}]_{16}{\cdot}2\,Ba^{2+}{\cdot}4\,pic^-$ and $[\mathbf{16}]_{10}{\cdot}Ba^{2+}{\cdot}2\,pic^-$.[236]

 © 2004 Wiley-VCH Verlag GmbH & Co. KGaA, Weinheim

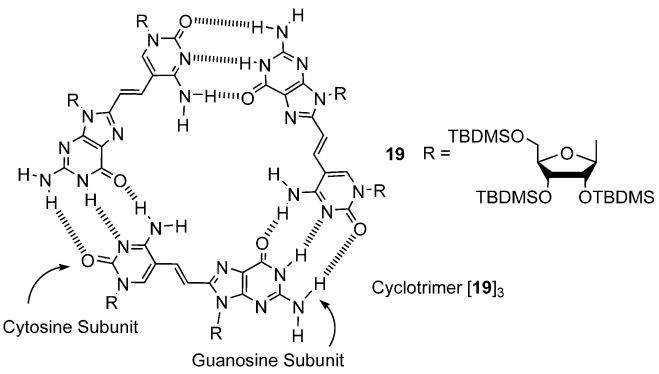


Figure 26. Self-assembly of the lipophilic dinucleoside **19** into cyclotrimer $(\mathbf{19})_3$.[239a] TBDMS = *tert*-butyldimethylsilyl.

have shown that sugar chirality influences the self-assembly of guanosine. Racemic nucleosides D,L-G (**1**) and D,L-isoG (**16**) undergo highly enantioselective self-recognition.[31,222] In both cases, an achiral metal ion triggers the stereoselective assembly.

The X-ray structure of $[\text{D-}\mathbf{16}]_{10}\cdot Cs^{+}\cdot Ph_4B^{-}$ showed nucleobase–sugar hydrogen bonds between neighboring isoG units within a pentamer.[222] We postulated that these sugar–base hydrogen bonds, besides contributing to the outstanding Cs^+ selectivity of the ionophore,[240] might also transmit information from one sugar to its base-paired neighbor. Indeed, a subsequent crystal structure confirmed that D,L-isoG (**16**) underwent enantiomeric self-recognition in the presence of $CsPh_4B$. The resulting "*meso*" decamer, $[\text{D-}\mathbf{16}]_5\cdot Cs^{+}\cdot[\text{L-}\mathbf{16}]_5\cdot Ph_4B^{-}$ had one pentamer composed of only D-**16** and the other pentamer made up entirely of L-**16** (Figure 27).[222] The Cs^+ ion was sandwiched by the two homochiral pentamers. This "*meso*" diastereomer was also the major species in solution. We proposed that the enthalpy provided by the additional five sugar–nucleobase hydrogen bonds helps overcome the negative entropy associated with enantiomeric self-association.

Later, we identified an even more impressive example of enantiomeric self-recognition: formation of a homochiral assembly containing 16 nucleosides. In the presence of barium picrate D,L-**1** formed homochiral G-quadruplexes $[\text{D-}\mathbf{1}]_{16}\cdot 2\,Ba^{2+}\cdot 4\,pic^{-}$ and $[\text{L-}\mathbf{1}]_{16}\cdot 2\,Ba^{2+}\cdot 4\,pic^{-}$,[31] while in the presence of potassium picrate a diastereomeric mixture was obtained. Since Ba^{2+} and K^+ have similar ionic radii, the cation's charge is clearly crucial for the high levels of enantiomeric self-recognition obtained with Ba^{2+} ions (Figure 28). This result again argues that the enthalpic contribution from self-assembly of G (**1**) around the divalent Ba^{2+} ion (with a corresponding increase in cation–dipole, hydrogen bond, and stacking energies relative to K^+) compensates for the entropic cost of enantiomeric separation. We envision that such homochiral assemblies may be used for enantioselective separations and catalysis.

4.6. Binding of Anions to Lipophilic G-Quadruplexes to Form Ion-Pair Receptors

While it is generally appreciated that G-quartets coordinate cations, less attention has been paid to the role of the

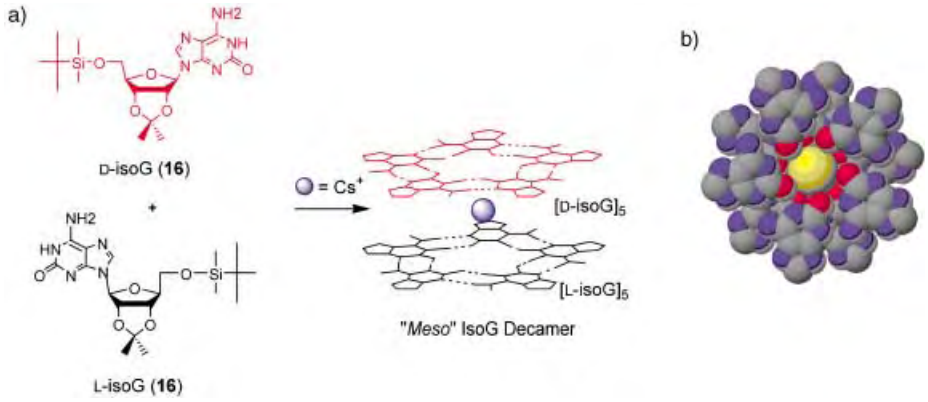


Figure 27. a) Enantiomeric self-association: the addition of Cs^+ ions to racemic (D,L)-isoG (**16**) resulted in formation of homochiral hydrogen-bonded pentamers. The major species in solution and in the solid state is the "*meso*" decamer $[\text{D-}\mathbf{10}]_5\cdot Cs^{+}\cdot[\text{L-}\mathbf{16}]_5$. b) Top view of the crystal structure of $[\text{D-}\mathbf{10}]_5\cdot Cs^{+}\cdot[\text{L-}\mathbf{16}]_5$.[222]

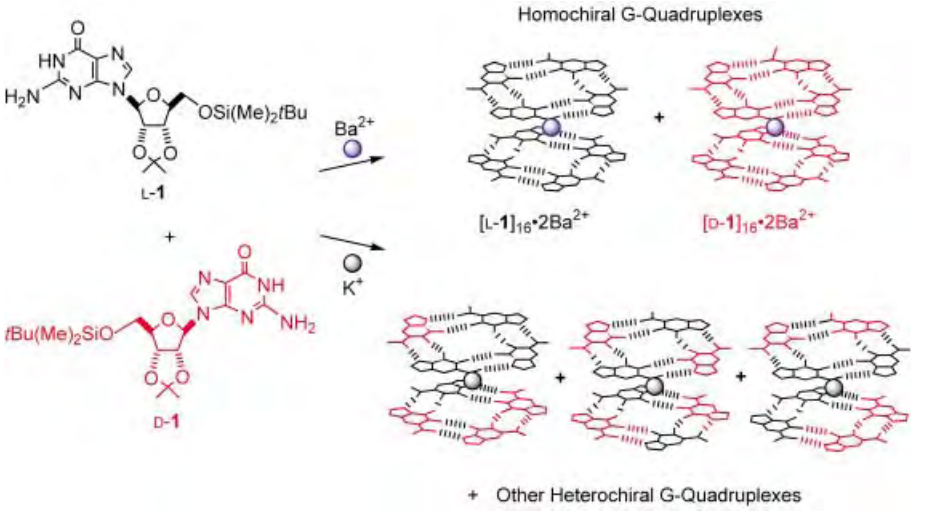
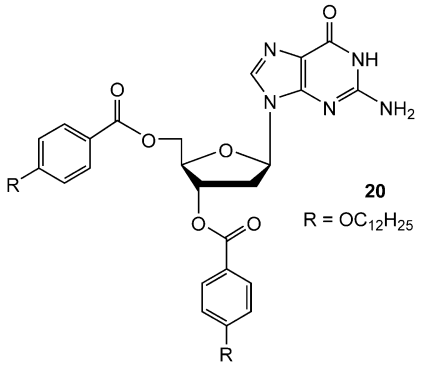


Figure 28. Cation-dependant enantiomeric self-association of G (**1**). Racemic (D,L)-G (**1**) self-assembles in the presence of Ba^{2+} ions to give homochiral G-quadruplexes $[\text{D-}\mathbf{1}]_{16}\cdot 2\,Ba^{2+}\cdot 4\,pic^{-}$ and $[\text{L-}\mathbf{1}]_{16}\cdot 2\,Ba^{2+}\cdot 4\,pic^{-}$. The addition of K^+ ions to G (**1**) gave a diastereomeric mixture of heterochiral assemblies.[31]

 © 2004 Wiley-VCH Verlag GmbH & Co. KGaA, Weinheim

anion in self-assembly. For nucleotides and oligonucleotides the hydrogen-bonding ligand carries an anionic phosphate group. This is not so for nucleosides, where a counterion is needed for the G-quartet-bound cation. Our studies of lipophilic G-quadruplexes in organic solvents indicate that anions can indeed significantly influence the properties of G-quartets.

Gottarelli and co-workers discovered that the lipophilic deoxyguanosine derivative **20** extracted a K^+ salt of *N*-



dinitrophenyl-L-tryptophan from water into $CDCl_3$ with a 3:1 enantioselectivity over the D-Trp enantiomer.[241] This result indicated that there were attractive interactions between anions and the chiral G-quadruplex made from **20** and K^+.

We also found that lipophilic G-quadruplexes bind anions. Self-assembly of G (**1**) provides a structure that we regard as an ion-pair receptor.[32,242] Most ion-pair receptors are ditopic, that is, single molecules with prefabricated cation and anion binding sites.[243] In contrast, the allosteric ion-binding sites within the G-quadruplex are generated by a network of noncovalent interactions.[244] Cations template G-quartets that stack so that their N2 amino groups generate hydrogen-bonding sites for anions. Much of the stability of the G-quadruplex arises from the four picrate anions that clip these inner G-quartets together (Figure 29). Moreover, the picrate ions remain bound to the G-quadruplex in solution and the anion can greatly modulate the kinetic stability of the structure. Thus, NMR experiments have shown that the anion controls the rate of rearrangement of $[\mathbf{1}]_8{\cdot}M^{2+}$ octamers between two different hexadecamers. For example, the formation of the "mixed" hexadecamer $[\mathbf{1}]_8{\cdot}Ba^{2+}{\cdot}[\mathbf{1}]_8{\cdot}Sr^{2+}{\cdot}4\,pic^-$ from a 1:1 ratio of the Ba^{2+} and Sr^{2+} G-quadruplexes occurred 100-times slower when the anion was picrate than when the anion was SCN^-.[32] The tridentate picrate maintains a stronger hydrogen-bonding network with the exocyclic N2 amino groups of the G-quadruplex than does a monodentate thiocyanate anion.

The rearrangement of octamers $[\mathbf{1}]_8{\cdot}M^{2+}$ can be halted altogether by increasing the basicity of the anion. Thus, with 2,6-dinitrophenolate (2,6-DNP), a much more basic anion than picrate, no isomerization product $[\mathbf{1}]_8{\cdot}Ba^{2+}{\cdot}[\mathbf{1}]_8{\cdot}Sr^{2+}{\cdot}4\,(2,6\text{-DNP})^-$ was observed even two months after combining the Ba^{2+} and Sr^{2+} G-quadruplexes in CD_2Cl_2.[242] These studies show that noncovalent assemblies can be locked in place with other peripheral noncovalent interactions, a feature that should enable regioselective modification of G-quadruplexes.

4.7. Dynamic Exchange in Self-Assembled Ionophores

The building blocks and bound guests in noncovalent assemblies exchange with "free" components in solution (Figure 30).[245] Quantifying such dynamic processes are important for determining self-association mechanisms.[68] Such mechanistic insight, when coupled with structural knowledge, will surely guide the design of improved self-assembling systems.

We used ^1H-^1H and ^7Li-^7Li EXSY NMR (EXSY = exchange spectroscopy) as well as ^{133}Cs NMR spectroscopy to probe the dynamic properties of the decamers $[\mathbf{16}]_{10}{\cdot}M^+$ in organic solvents.[235,236] While the $[\mathbf{16}]_{10}{\cdot}Cs^+$ decamer is thermodynamically stable, it is kinetically labile toward Cs^+ exchange. This dynamic ion exchange is desirable if one wants to use these complexes for ion separations and transport. A study of the exchange processes for $[\mathbf{16}]_{10}{\cdot}Cs^+$ in $CDCl_3$ by ^{133}Cs and ^1H NMR spectroscopy showed that the Cs^+ guest exchanges with free Cs^+ 40000 times faster than the exchange between bound and "free" isoG **16**. This clear difference in the rates of exchange indicates that cation exchange occurs without complete dissociation of the hydrogen-bonded complex. The strength of the hydrogen bond in the isoG decamer in the series $[\mathbf{16}]_{10}{\cdot}M^+$ (M = Li, Na, K, Rb, and Cs) also depends on the identity of the cationic guest. Thus, exchange of isoG (**16**) between bound and free sites was 10–100-times slower for the Cs^+ decamer $[\mathbf{16}]_{10}{\cdot}Cs^+$ than decamers containing the other alkali-metal ions. This result also highlights the extensive cooperativity of forces that exist in these self-assembled ionophores; thus, the bound Cs^+ ion increased the kinetic stability of the assembly by strengthening the hydrogen-bonding network.[235]

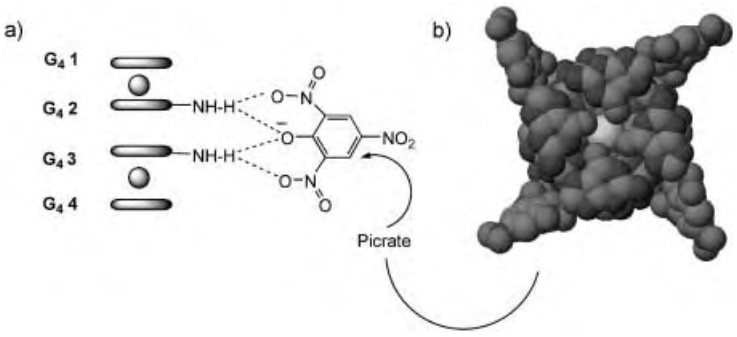


Figure 29. a) Hydrogen bonds between the nucleobase and picrate in the hexadecamer $[\mathbf{1}]_{16}{\cdot}2\,Sr^{2+}{\cdot}4\,pic^-$.[32] The amino protons are derived from the exocyclic N2 groups on the guanine. b) Top view of the G-quadruplex, with the sugars removed. The hydrogen bonds between the nucleobase and the anion result in four picrate anions forming an anionic belt around the G-quadruplex between G-quartet layers two and three.

 © 2004 Wiley-VCH Verlag GmbH & Co. KGaA, Weinheim

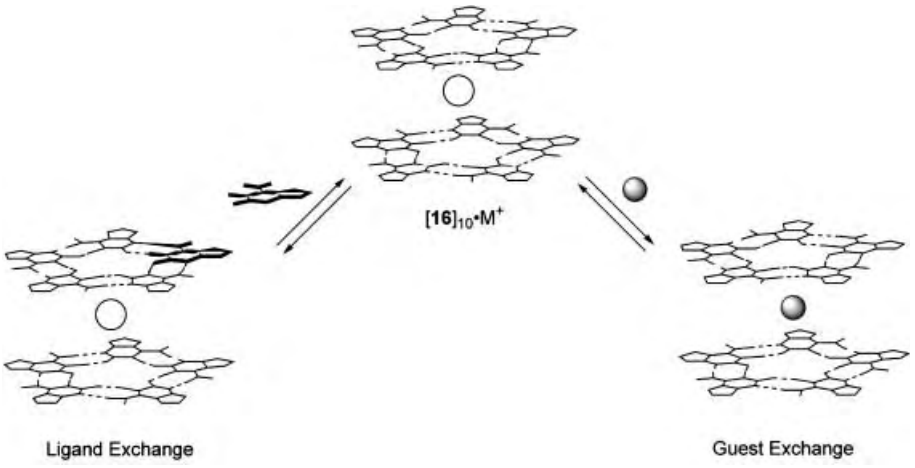


Figure 30. Dynamic exchange processes in the decamer $[\mathbf{16}]_{10}\cdot Cs^+$. Both the isoG ligand **16** and the cationic guest Cs^+ exchange with free species in solution. NMR data shows that Cs^+ exchange is over 40000 faster than exchange of the ligand isoG (**16**).[235]

4.8. Why Build Self-Assembled Ionophores?

Covalent ionophores such as crown ethers and calixarenes have binding sites already built into their frameworks.[246,247] While preorganization may enable strong ion binding, the synthetic effort needed to fix the conformation is often considerable. Alternatively, noncovalent interactions can be used to synthesize self-assembled ionophores more efficiently.[206,208,240] In addition to improved synthetic accessibility, self-assembled ionophores have other potential advantages over their covalent counterparts. In particular, it should be easy to reversibly assemble and disassemble these dynamic structures by altering the solvent, temperature, or pH.

The radionuclide $^{137}Cs^+$ is a major contaminant in nuclear waste.[248] One challenge in $^{137}Cs^+$ separation is achieving sufficient selectivity, as the waste contains more Na^+ and K^+ than Cs^+ ions. The selective extraction of Cs^+ ($r = 1.67$ Å) in the presence of Na^+ ($r = 0.97$ Å) and K^+ ions ($r = 1.33$ Å) is challenging because of it's large size. The larger crown ethers ([21]crown-7 and [24]crown-8 derivatives) usually have only modest Cs^+ selectivity because of their flexibility.[249–252] Better results are obtained using more rigid macrocycles such as the calix[4]arene–crown ethers.[253,254] While their Cs^+ binding constants and Cs^+/M^+ selectivity are often impressive, these macrocycles can be expensive to synthesize. As mentioned above, isoG (**16**) can bind Cs^+ with high affinity and selectivity with the formation of a hydrogen-bonded decamer $[\mathbf{16}]_{10}\cdot Cs^+$ in the solid state and in solution (Figure 31).[221,222] In competition experiments the self-assembling isoG (**16**) was able to quantitatively remove bound Cs^+ ions from a calix[4]arene–crown ether.[240] The self-assembled ionophore formed from isoG (**16**) is one of the strongest and most selective Cs^+ ionophore identified to date.

The lipophilic decamer $[\mathbf{16}]_{10}\cdot Cs^+$ also enables selective transport of Cs^+ ions across organic membranes. Lamb and coworkers showed that this assembly transports $CsNO_3$ across bulk liquid membranes (BLM) and polymer inclusion membranes (PIM) with excellent Cs^+ selectivity and Cs^+ transport rates (Table 3).[255] The Cs^+/Na^+ transport selectivity for isoG (**16**) in the PIM experiments was consistently above 5000:1, and approached 10000:1 with 6 mM concentrations of $[\mathbf{16}]_{10}\cdot Cs^+$. In addition, both the Cs^+ transport rate and selectivity of the self-assembled decamer $[\mathbf{16}]_{10}\cdot Cs^+$ were competitive with calix[4]arene—crown ethers, compounds which are currently being evaluated as extractants for nuclear waste remediation.[255,256] These membrane transport results with $[\mathbf{16}]_{10}\cdot Cs^+$ are certainly encouraging for the use of self-assembled ionophores in environmental separations and waste remediation.

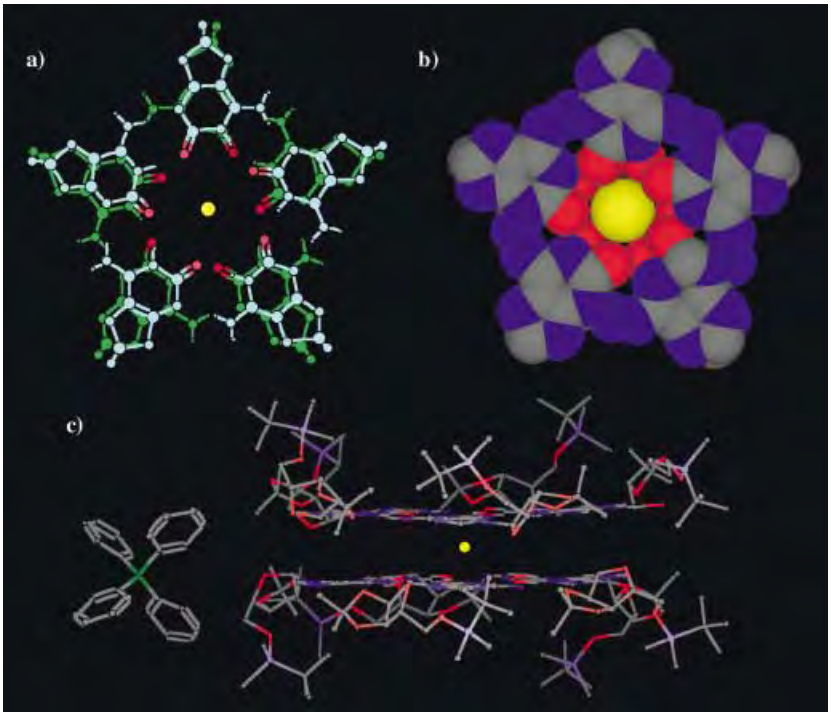


Figure 31. Crystal Structure of $[\mathbf{16}]_{10}\cdot Cs^+\cdot Ph_4B^-$: a) Top view (the sugars have been removed for clarity); one isoG pentamer is shown in blue and the other in green. b) Space-filling model; the Cs^+ ion is bound to 10 carbonyl oxygen atoms, with a mean $d_{Cs\cdot O} = 3.40$ Å. C) Side view (some of ribose atoms have been removed for clarity); this view shows the two planar isoG pentamers sandwiching the encapsulated Cs^+ ion.[221]

 © 2004 Wiley-VCH Verlag GmbH & Co. KGaA, Weinheim

Table 3: Cs^+ selective ionophore. Percentage and permeability of transported cations and selectivity (Cs^+/Na^+) through polymer inclusion membranes containing precomplexed $[\mathbf{16}]_{10}{\cdot}CsBPh_4$.[a,b]

$c[\mathbf{16}]_{10}$ [mM]	Transport [%]		Permeability [$m\,s^{-1}$]		Selectivity
	Cs^+	Na^+	Cs^+	Na^+	(Cs^+/Na^+)
1.1	16.5	0.002	2.1×10^{-7}	2.8×10^{-11}	7500
2.1	31	0.004	4.4×10^{-7}	8.3×10^{-11}	5300
4.1	44.5	0.004	6.4×10^{-7}	8.3×10^{-11}	7700
6.2	53	0.004	8.0×10^{-7}	8.3×10^{-11}	9600

[a] Transport conditions: Source phase: 1.0 mM $CsNO_3$ + 50 mM $NaNO_3$ in water. Carrier: $[\mathbf{16}]_{10}$. Receiving phase: 0.5 M HNO_3. Total transport time 24 h. [b] Values taken from reference [255].

4.9. Toward Synthetic Ion Channels

Lipophilic G-quartets are promising scaffolds on which to build functional assemblies. With an eye toward artificial photosynthesis, Masiero et al. described a lipophilic guanosine carrying a porphyrin chromophore.[257] They obtained CD and NMR evidence for the formation of a supramolecular complex containing a $G_8{\cdot}K^+$ octamer with an array of eight porphyrins.

Our research group is interested in using the G-quadruplex to build transmembrane ion channels. NMR studies have shown that base pairs in DNA G-quadruplexes open slowly and G-quadruplex dissociation is often quite slow, taking days or weeks. Yet, K^+ ions are bound for only milliseconds.[258] These results suggest that ions move without disruption of the G-quartet, thus making the G-quadruplex analogous to an ion channel. For example, Feigon and coworkers showed that NH_4^+ ions enter and exit through the ends of a G-quadruplex, which prompted the authors to also suggest that such structures mimic ion channels.[212]

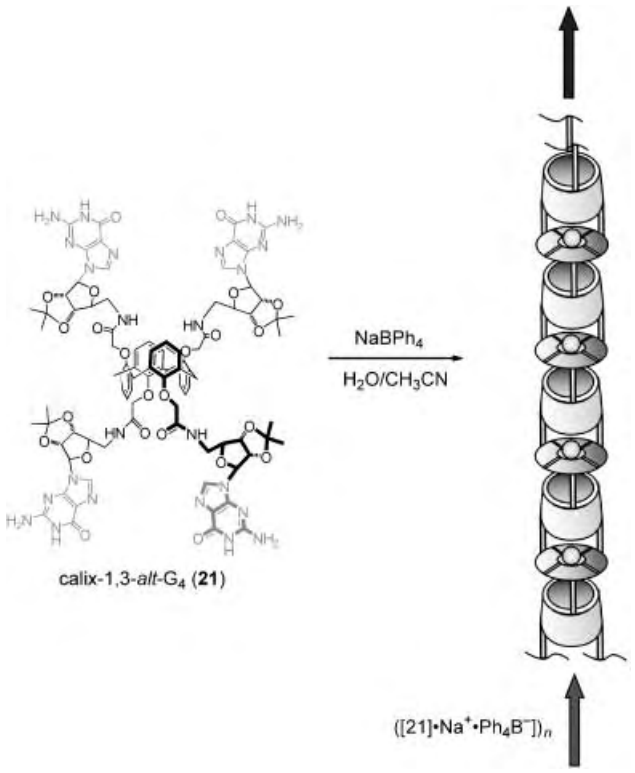


Figure 32. The guanosine–calix[4]arene-1,3-*alt* **14** self-associates in the presence of alkali-metal cations to form a 1D nanotube, presumably formed by a G-quartet-based polymer.[263]

Among various designs,[259–261] the G-quartet has been proposed as a scaffold on which to build synthetic ion channels.[29,262,263] Our efforts involved self-assembly of **21**, a calix[4]arene with four attached guanosine moieties (Figure 32).[263] The 1,3-alternate conformation of the calixarene orients orthogonal pairs of G nucleosides for intermolecular G-quartet formation upon addition of a cation. We reasoned that a tubular structure, with a channel of alternating G-quartets and calixarene macrocycles, would result if the G units on both sides of **21** were to self-associate upon cation templation. The addition of $NaBPh_4$ to a solution of **21** gave a noncovalent polymer that precipitated from solution. Electron microscopy studies showed that the solid consisted of micrometer-long strands and bundles (with diameters of 3 and 50 nm, respectively). Since a G-quartet has a diameter of 2.5 nm,[29] the single strands had dimensions approaching that of a G-quartet. This noncovalent polymer dissolved upon heating or acidification, thus indicating that 1) hydrogen-bond assembly can control long-range organization and 2) self-association of **21** is reversible. We are currently testing whether **21** and analogues can act as synthetic ion channels.

5. Guanosine Self-Assembly in Materials Science, Biosensor Design, and Nanotechnology

> *"Quadruplexes show promise as components for nanowires, ion channels, and building blocks for directing the assembly of nanoscale components into sophisticated structures."*
> M. Keniry[10]

The burgeoning field of nanotechnology depends on controlled positioning of molecules on the nanometer to micrometer scale. The four-stranded G-quadruplex seems ideal for ordering material over such distances. Self-assembly is a powerful way to arrange molecules into specific patterns and DNA has been used to construct nanoscale devices.[264,265] Efforts in using guanosine derivatives to build supramolecular structures with new properties are described below.

5.1. DNA Nanostructures: G-Wires, Frayed Wires, and Synapses

Fiber diffraction studies on crystalline GMP and poly(guanylic acid) had shown that these compounds self-assem-

 © 2004 Wiley-VCH Verlag GmbH & Co. KGaA, Weinheim

ble into rods of stacked G-quartets.[2,39–41] It was later discovered that DNA superstructures formed from sequences with 3′-terminal dG residues. Sen and Gilbert reported that $d(A_4G_4)$ gave stable assemblies that were much larger than expected for a four-stranded G-quadruplex $[d(A_4G_4)]_4$.[266] Although the authors noted that the sequences could aggregate in different ways, the G-quartet cores favored a head to tail orientation to give a continuous polymer, with poly-A tails radiating from the core. Guo and co-workers also observed the formation of superstructures upon cation-templated aggregation of $d(A_4G_4)$.[267]

In the mid-1990s, the research groups of both Henderson and Sheardy further established that G-rich DNA formed nanometer assemblies.[268–271] They showed by using gel electrophoresis that $d(G_4T_2G_4)$, in the presence of K^+ and Mg^{2+} ions formed high molecular weight assemblies that were well resolved from the smaller G-quadruplex $[d(G_4T_2G_4)]_4$. The polymers were extraordinarily stable; heating at 80 °C or dissolving in 8 M urea did not denature them. Marsh and Henderson coined the term "G-wires" to describe the continuous, parallel-stranded DNA superstructures formed when the 5′-end of one DNA duplex with G-G pairs associates with the 3′-end of a similar duplex (Figure 33).[268] Atomic

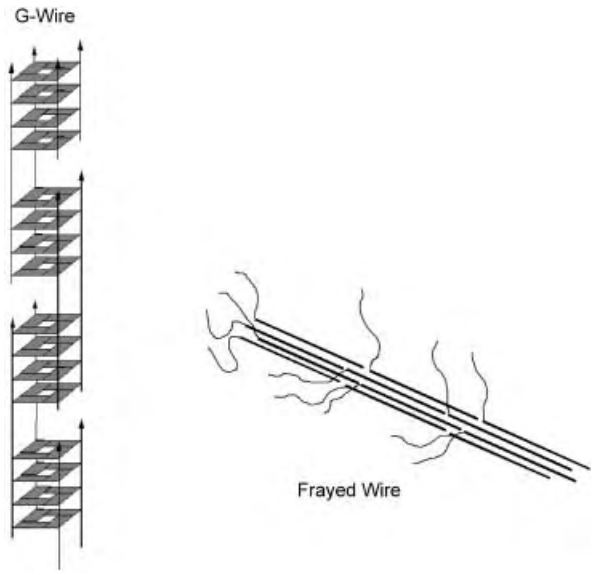


Figure 33. Superstructures formed by G-rich oligonucleotides. "G-wires" are formed by association of $d(G_4T_2G_4)$[263] while "frayed wires" are formed by association of $d(G_{15}A_{15})$. The G residues make up the core, while the A_{15} arms radiate from the core.[273]

force microscopy showed that G-wires formed from $d(G_4T_2G_4)$ were 10–1000 nm in length and 18–25 Å in width, which is consistent with the 25-Å diameter of the G-quartet.[269] The influence of the cation on polymer structure and stability was also consistent with formation of a G-quartet, as addition of Na^+ ions gave longer G-wires that were much less compressible than duplex DNA on mica. Marsh and Henderson proposed that G-wires could be useful in nanotechnology, nanoelectronics and biosensor development. Chen showed that certain G/C sequences formed cross-linked G-wires under acidic conditions.[272] He proposed that the sequence CGG used C-CH^+ base pairs to bridge G-wires into a dendrimeric structure.

MacGregor and co-workers identified DNA sequences, $d(A_{15}G_{15})$ and $d(T_{15}G_{15})$, that give extended structures in the presence of K^+ ions.[273–277] They called these structures "frayed wires" to distinguish them from G-wires (Figure 33). The unique feature of frayed wires is the flexible A_{15}/T_{15} strands that radiate from a guanine core (akin to barbed wire). The fact that the N7 position of guanosine can be alkylated without loss of structure suggests that typical G-quartets do not form the core. Extensive 2D aggregation was observed by AFM when the single-stranded T_{15} complement was added to a solution of frayed $d(A_{15}G_{15})$ wires.[278] One experiment that shows potential applications for frayed wires involved attachment of enzymes to the A_{15} arms. A network formed by the noncovalent attachment of avidin-conjugated peroxidase to the frayed wires with biotinylated arms retained its structure and enzyme activity.[278]

Sen and co-workers described a method to build nanostructures based on the synapsis between two DNA duplexes.[279–281] Each duplex contained "synaptic domains", that is, repeating G-G base pairs engineered to facilitate formation of a G-quartet upon dimerization of the duplex (Figure 34). An attractive feature of synapsis is that it doesn't require annealing. The addition of cations to a DNA duplex triggers G-quartet-mediated dimerization to give the nanostructures. The yields of synapsed DNA follow the trend typically observed for cationic G-quartet stabilization ($K^+ > Rb^+ > Na^+ > Li^+, Cs^+$ and $Sr^{2+} > Ba^{2+} > Ca^{2+} > Mg^{2+}$), which led to the statement: *"Guanine-mediated synapsis … provides a means for the self-recognition and supramolecular assembly by intact, unmelted DNA double helices under conditions of low temperature and physiological salt."*[280]

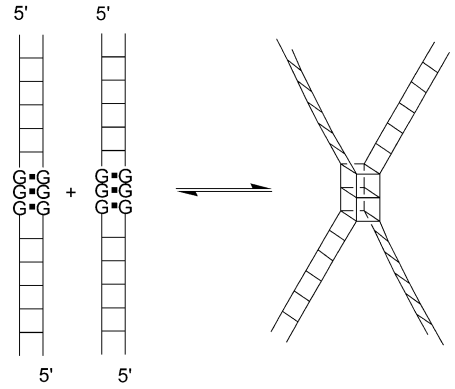


Figure 34. "Synapsed" DNA formed from G-quartet structures between duplex DNA strands containing G-G mismatches.[280]

5.2. Formation of Biosensors and Nanomachines with G-Quadruplex DNA

While DNA aptamers have potential as therapeutics and diagnostics (see Sections 3.6 and 3.7), they also have appli-

 © 2004 Wiley-VCH Verlag GmbH & Co. KGaA, Weinheim

cations in bioanalytical chemistry. Small molecules and proteins can be separated by using G-quadruplex DNA as stationary phases in chromatography or electrophoresis. McGown and co-workers found that G-quadruplex DNA based on the TBA sequence can bind nontarget compounds with useful selectivity.[282–284] The authors noted that these DNA aptamers are attractive stationary phase materials, as a consequence of their ease of synthesis and surface attachment as well as their ability to change binding affinities by sequence modification. These G-quadruplex aptamers effected baseline separation of the enantiomers of D,L-Trp and D,L-Tyr, as well as an aromatic hydrocarbon mixture.[282] In another study, DNA aptamers featuring an intramolecular G-quadruplex served as the stationary phase for the separation of the isomeric dipeptides Trp–Arg and Arg–Trp.[283] In addition to the separation of small molecules, a G-quadruplex aptamer was used for electrochromatographic separation of bovine β-lactoglobulins A and B, proteins that vary by just 2 of 162 amino acids.[284]

DNA G-quadruplex aptamers labeled with fluorescent dyes have also served as a prototype for biosensors.[285–289] In particular, FRET has been used to study the secondary structure of G-rich DNA oligonucleotides.[290,291] FRET is a distance-dependent method for detecting conformational changes over distances of 10–100 Å. Fluorescence is quenched when a donor fluorophore and an acceptor chromophore are close in space, but when the distance between the donor and acceptor increases, as a result of a conformational change, there is a corresponding increase in fluorescence. Intramolecular folding of an oligonucleotide into its G-quadruplex form leads to FRET between donor and acceptor dyes that are attached to the 5′ and 3′ ends. This sensitive technique allows the effect of cations, ligands, nucleic acids, and proteins on the equilibria of unfolded and G-quadruplex DNA to be monitored. For example, Takenaka and co-workers showed that a single-stranded DNA folded into an intramolecular G-quadruplex can detect K^+ ions in water at submicromolar concentrations.[292]

FRET has also been used to monitor the formation of molecular "nanomotors" from single-stranded DNA.[293,294] Li and Tan used FRET to monitor in real time the conformational switching between a double-stranded duplex and a folded G-quadruplex caused an extension and shrinking motion.[293] In a closely related study, Alberti and Mergny also reported that the conformational equilibrium between DNA duplex and quadruplex defines a nanomolecular machine.[294] The conformational states of a 21-mer DNA with a 5′-fluorescein donor and a 3′-rhodamine acceptor were detected by FRET (Figure 35). The switching between the folded unimolecular G-quadruplex and a duplex conformation caused a displacement of 5–6 nm. The machine was cycled between its closed G-quadruplex state and open duplex state by sequential addition of other DNA strands: a "C-fuel" and a "G-fuel". The C-fuel unfolds the unimolecular G-quadruplex to generate a duplex, while the G-fuel is used to liberate the labeled 21-mer so that it refolds into a G-quadruplex.

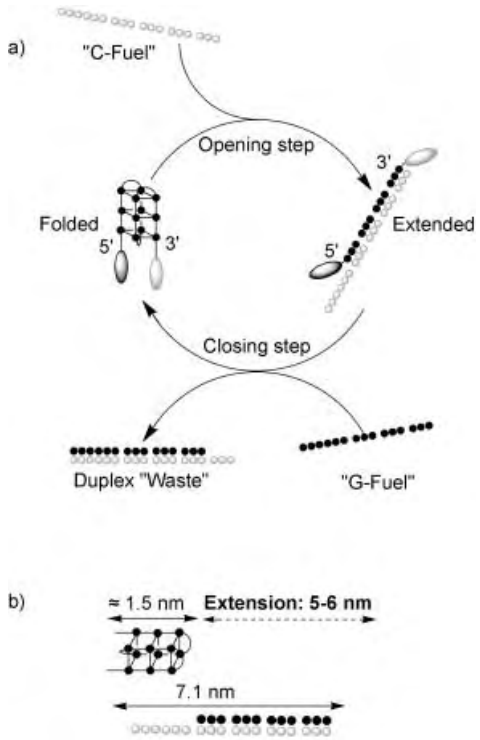


Figure 35. A G-quadruplex nanomachine.[294] The experimental design is similar to a system described by Li and Tan.[293] a) Switching between an intramolecular quadruplex (left) and a duplex (right). Folding of a G-rich oligonucleotide gives an intramolecular quadruplex that undergoes efficient FRET between bound fluorescein and rhodamine groups (ovals). The "C-fuel" strand is complementary to the G-rich sequence. b) Induced movement upon G-quadruplex folding and unfolding.

5.3. Dynamic Materials from Guanosine and Folate Self-Assembly

In addition to G-rich oligonucleotides, smaller guanosine derivatives also show promise for nanotechnology and materials applications. In particular, lipophilic guanosine and folate analogues form dynamic liquid crystals and gels whose morphologies can be controlled by varying the ionic conditions, solvent, or temperature.

The research groups of Rabe and Gottarelli used scanning force microscopy to show that surface changes modulate the structure of the hydrogen-bonded assembly.[295,296] Lipophilic dG (**17**) formed films with the signature of cyclic G-quartets on mica containing bound K^+ ions. However, if the K^+ ions were washed off the surface, dG (**17**) formed extended ribbons consistent with hydrogen-bond patterns observed previously in solution and the crystalline state.[297,298] It was shown that without cations lipophilic guanosines such as dG (**17**) form liquid crystals and gels in organic solvents. The authors showed by using electrospray mass spectrometry, solution NMR spectroscopic, and single crystal X-ray analysis that these guanosine derivatives adopt two different hydrogen-bonded ribbons (Figure 36).[295,296] One of the hydrogen-bonded structures has an overall dipole (ribbon A), while the other hydrogen-bonding arrangement gives a 2D structure without a molecular dipole (ribbon B). The type of ribbon

 © 2004 Wiley-VCH Verlag GmbH & Co. KGaA, Weinheim

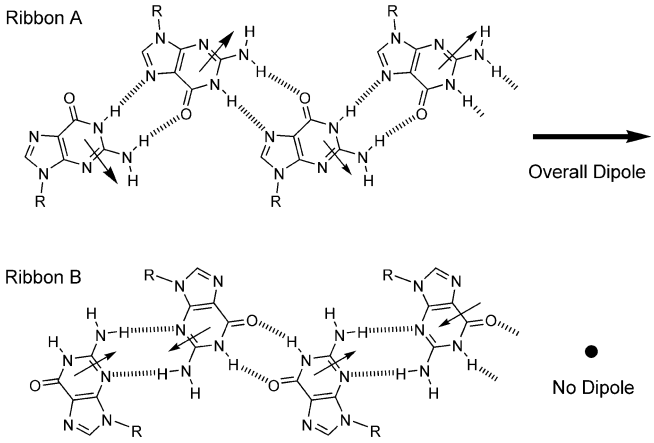
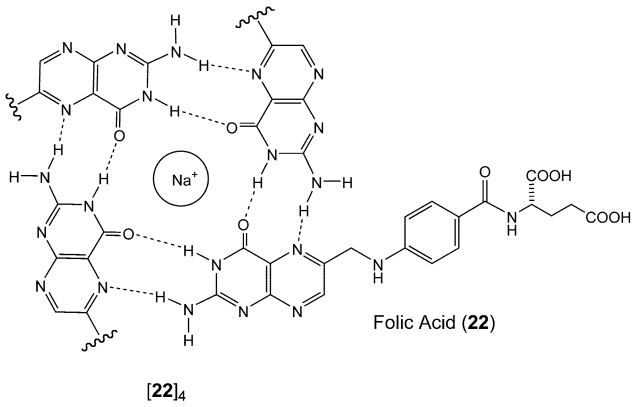


Figure 36. Two different H-bonded ribbons formed by self-assembly of lipophilic dG (**17**). Ribbon A has a dipole moment, whereas ribbon B does not.[295,296] R = modified deoxyribose.

formed (ribbon A versus ribbon B) can be controlled by the sugar unit on the nucleoside and by the solvent. Some of these lipophilic guanosine derivatives are promising gelators, which are able to immobilize organic solvents at critical concentrations as low as 2–4 wt %.[299]

Folic acid **22** and guanosine have similar hydrogen-bonding patterns, so it was expected that



$[\mathbf{22}]_4$

folates would also form cyclic tetramers. Over 10 years ago Gottarelli and co-workers demonstrated that folic acid underwent a cation-dependent assembly in water.[300] Potassium folate formed liquid crystals that were hexagonally packed columns of stacked folate tetramers even at concentrations as low as 1 wt %.[301,302] Kato and co-workers further investigated the cation-templated assembly of lipophilic folates in organic solvents in which they focused on controlling their dynamic assembly and their materials properties.[303,304]

A liquid crystal is a fluid somewhere between the ordered crystal and the disordered liquid.[305] Materials that form liquid crystals without solvent are thermotropic liquid crystals, and phase transitions occur with temperature changes. Most thermotropic liquid crystals arise from rod-shaped compounds with an aromatic core and flexible side chains. These materials form different types of liquid crystals, such as the nematic, smectic, and discotic phases. The nematic phase is a fluid with one-dimensional order along a single molecular axis, but is otherwise disordered. In smectic phases, ordered molecules are arranged in layers and there is short-range positional order within these layers. Discotic liquid crystals have even longer range positional ordering of the cyclic cores. In particular, hydrogen-bonded assemblies have been used to generate discotic liquid crystals.[306,307]

Kato and co-workers found that temperature and cations induce a phase change in folate-derived liquid crystals. X-ray diffraction and IR spectroscopy studies indicated that lipophilic folates with 2-(3,4-dialkoxyphenyl)ethyl substituents formed thermotropic liquid crystals (Figure 37).[308] Two liquid-crystal phases are formed depending on the conditions: a smectic and a columnar discotic phase. Similar to dG (**17**), the pterin rings of the folate hydrogen bond to give a self-

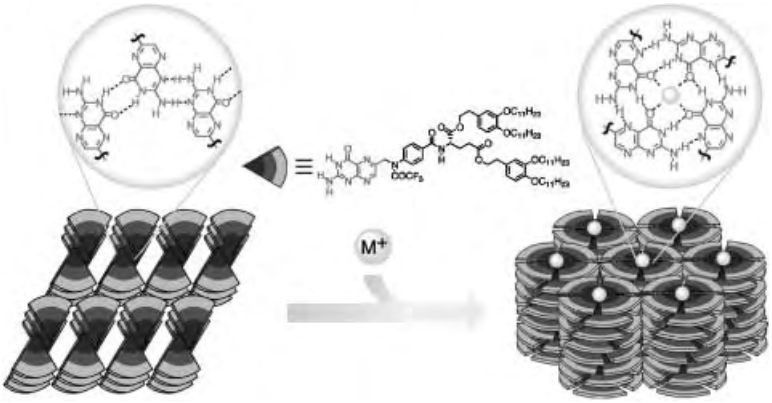


Figure 37. Self-assembly/self-organization of lipophilic folate derivatives.[303] Ion-responsive self-assembled liquid crystals are formed on reaction with ions. The ribbon structures of a folic acid derivative undergo an ion-templated transformation to discotic tetramers.

associated ribbon structure, which is the basis for the smectic phase. Alternatively, the folate ring forms a cyclic tetramer in the presence of a cation, which leads to a columnar discotic liquid crystal. The smectic phase was transformed into the hexagonal discotic phase upon addition of alkali-metal salts.[309] The solvent polarity also induced a reorganization of the liquid crystal from ribbons to disks, as less polar solvents favor the cyclic hydrogen-bonded form.[310] The finding that cations and solvent can trigger rearrangement from an H-bonded ribbon to cyclic tetramer indicates that folate-derived liquid crystals are dynamic materials, which are able to change their structure and properties in response to an external stimulus.

5.4. Organic Semiconductors from Hydrogen-Bonded Guanosines

In 1975 Aviram and Ratner proposed that organic molecules could conduct charge.[311] Today, with the minia-

turization of semiconductor components, the potential of molecular electronics is even clearer.[312] Recent experiments with DNA suggest that biomolecular self-organization is a viable strategy for electron transport.[313,314]

Guanine derivatives are attractive candidates for electron transport. Guanine has the lowest oxidation potential of the nucleobases and it forms a variety of ordered structures. Rinaldi et al. recently fabricated a semiconductor device with dG (**17**) bridging electrodes.[315] Atomic force microscopy showed that evaporation of a solution of dG (**17**) in $CHCl_3$ gave hydrogen-bonded ribbons on the surface of the device which were consistent with previous AFM and diffraction data. Current–voltage (*I-V*) measurements on this device revealed high conductivity when the electrode spacing was less than 100 nm.[315,316] Asymmetric *I-V* curves, which are characteristic of molecular rectification, were attributed to the dipole of the hydrogen-bonded ribbon upon self-association of dG (**17**; ribbon A in Figure 36). Ab initio calculations indicated that conduction through dG (**17**) occurs by orbital overlap of stacked ribbons and not through the intermolecular hydrogen bonds.[317,318] A major challenge is to orient these crystalline materials so that they can conduct current over longer distances. Molecular self-assembly of lipophilic dG analogues could then be coupled with lithography to form useful devices.

6. Summary and Outlook

This Review has touched on diverse areas in chemistry where the G-quartet motif is important. Three decades after its identification in 5′-GMP gels, the G-quartet really gained visibility because of the biological implications of G-quadruplex DNA. Consequently, structural characterization of nucleic acid G-quadruplexes has accelerated over the past decade. In 1992 the Protein Data Bank showed just two entries for G-quadruplexes. Ten years later, there are more than 35 deposited G-quadruplex structures, including 9 crystal structures. This data provides a wealth of information about the noncovalent interactions that drive self-assembly of G-rich nucleic acids. More structures of G-quadruplex–protein and quadruplex–ligand complexes are needed in the future; indeed, the first three examples were published in just the last year.[59,190,191] Detailed information about protein and ligand complexes with G-quadruplexes will help us better understand G-quadruplex molecular recognition and further enhance drug design.

The most prominent role of the G-quartet relates to its potential to mediate crucial in vivo processes, particularly those associated with telomere structure and function. Telomerase is a key anticancer target and research is intense. A citation search of the Web of Science showed just 7 references to this enzyme in 1990, whereas more than 750 references to telomerase occurred in 2002. The development of G-quadruplex interactive drugs to inhibit telomerase will surely continue. The major challenge to getting candidates into clinical trials will be to identify nontoxic drugs that are truly selective for the G-quadruplex.[178]

There are also many nonmedicinal aspects of G-quartets. Supramolecular chemistry has taught us much about using noncovalent interactions to build large and functional assemblies. As nanotechnology develops there will be a growing interest in using such noncovalent structures for specific functions. Of course, nature often provides useful blueprints. The G-quartet is a prime example of a natural system that is amenable to synthetic modifications and which can be used to study the structure and dynamics of molecular self-assembly. It can also inspire the design of new and useful synthetic assemblies. The use of the G-quartet and related motifs to form self-assembled ionophores, synthetic channels, dynamic liquid crystals, noncovalent polymers, nanomachines, biosensors, therapeutic aptamers, chromatography supports, new PNA assemblies, and molecular electronic devices demonstrates how concepts from biology and supramolecular chemistry can merge quite nicely.

I thank my fellow group members, Sampath Tirumala, Allison Marlow, Mangmang Cai, Scott Forman, Mike Shi, Frank Kotch, and Vladimir Sidorov for all their efforts and enthusiasm in studying the self-assembly of guanosine. I thank Dr. Jim Fettinger for his determination and skill in solving the crystal structures of these large, noncovalent assemblies. I thank Prof. Giovanni Gottarelli and his co-workers at the University of Bologna for a fruitful collaboration over the years. I thank Prof. David Reinhoudt and his research group at the University of Twente for hosting me during a sabbatical, during which time I wrote this Review. I thank Prof. Frank Seela (Osnabrück) and the reviewers for helpful comments that improved the manuscript. I thank Fijs van Leeuwen (Twente) and Frank Kotch (Maryland) for preparing the figures and Professor Geoff Oxford (York) for the photos of the guanine crystals in Figure 6. I thank the US Department of Energy (BES, Separations and Analysis), the Dreyfus Foundation, and the State of Maryland's TEDCO Program for support.

Received: February 19, 2003 [A589]

[1] W. Guschlbauer, J. F. Chantot, D. Thiele, *J. Biomol. Struct. Dyn.* **1990**, *8*, 491 – 511.
[2] M. Gellert, M. N. Lipsett, D. R. Davies, *Proc. Natl. Acad. Sci. USA* **1962**, *48*, 2013 – 2018.
[3] E. Henderson, C. C. Hardin, S. K. Walk, I. Tinoco, E. H. Blackburn, *Cell* **1987**, *51*, 899 – 908.
[4] J. R. Williamson, M. K. Raghuraman, T. R. Cech, *Cell* **1989**, *59*, 871 – 880.
[5] J. R. Williamson, *Curr. Opin. Struct. Biol.* **1993**, *3*, 357 – 362.
[6] J. R. Williamson, *Annu. Rev. Biophys. Biomol. Struct.* **1994**, *23*, 703 – 730.
[7] G. Gottarelli, G. P. Spada, A. Garbesi in *Comprehensive Supramolecular Chemistry, Vol. 9* (Eds.: J.-P. Sauvage, M. W. Hossieni), Elsevier, Rugby, **1996**, p. 483.
[8] D. E. Gilbert, J. Feigon, *Curr. Opin. Struct. Biol.* **1999**, *9*, 305 – 314.
[9] J. Sühnel, *Biopolymers* **2001**, *56*, 32 – 51.
[10] M. Keniry, *Biopolymers* **2001**, *56*, 123 – 146.
[11] C. G. Hardin, A. G. Perry, K. White, *Biopolymers* **2001**, *56*, 147 – 194.
[12] I. Smirnov, R. H. Shafer, *Biopolymers* **2001**, *56*, 209 – 227.
[13] T. Simonsson, *Biol. Chem.* **2001**, *382*, 621 – 628.

 © 2004 Wiley-VCH Verlag GmbH & Co. KGaA, Weinheim

[14] H. Arthanari, P. H. Bolton, *Chem. Biol.* **2001**, *8*, 221 – 230.
[15] J. S. Lindsey, *New J. Chem.* **1991**, *15*, 153 – 180.
[16] D. S. Lawrence, T. Jiang, M. Levett, *Chem. Rev.* **1995**, *95*, 2229 – 2260.
[17] D. Philp, J. F. Stoddart, *Angew. Chem.* **1996**, *108*, 1242 – 1286; *Angew. Chem. Int. Ed. Engl.* **1996**, *35*, 1154 – 1196.
[18] S. C. Zimmerman, P. S. Corbin, *Struct. Bonding (Berlin)* **2000**, *96*, 63 – 94.
[19] T. Kato, *Struct. Bonding (Berlin)* **2000**, *96*, 95 – 146.
[20] S. Leininger, B. Olenyuk, P. J. Stang, *Chem. Rev.* **2000**, *100*, 853 – 907.
[21] M. Fujita, *Struct. Bonding (Berlin)* **2000**, *96*, 177 – 201.
[22] L. Brunsveld, B. J. B. Folmer, E. W. Meijer, R. P. Sijbesma, *Chem. Rev.* **2001**, *101*, 4071 – 4097.
[23] G. M. Whitesides, E. E. Simanek, J. P. Mathias, C. T. Seto, D. N. Chin, M. Mammen, D. M. Gordon, *Acc. Chem. Res.* **1995**, *28*, 37 – 44.
[24] L. J. Prins, D. N. Reinhoudt, P. Timmerman, *Angew. Chem.* **2001**, *113*, 2446 – 2492; *Angew. Chem. Int. Ed.* **2001**, *40*, 2383 – 2426.
[25] D. N. Reinhoudt, M. Crego-Calama, *Science* **2002**, *295*, 2403 – 2407.
[26] J. F. Stoddart, H. R. Tseng, *Proc. Natl. Acad. Sci. USA* **2002**, *99*, 4797 – 4800.
[27] a) L. M. Greig, D. Philp, *Chem. Soc. Rev.* **2001**, *30*, 287 – 302; b) R. Fiammengo, M. Crego-Calama, D. N. Reinhoudt, *Curr. Opin. Chem. Biol.* **2001**, *5*, 660 – 673.
[28] V. Balzani, A. Credi, F. M. Raymo, J. F. Stoddart, *Angew. Chem.* **2000**, *112*, 3484 – 3530; *Angew. Chem. Int. Ed.* **2000**, *39*, 3348 – 3391.
[29] K^+: S. L. Forman, J. C. Fettinger, S. Pieraccini, G. Gottarelli, J. T. Davis, *J. Am. Chem. Soc.* **2000**, *122*, 4060 – 4067.
[30] Pb^{2+}: F. W. Kotch, J. C. Fettinger, J. T. Davis, *Org. Lett.* **2000**, *2*, 3277 – 3280.
[31] Ba^{2+}: X. D. Shi, J. C. Fettinger, J. T. Davis, *J. Am. Chem. Soc.* **2001**, *123*, 6738 – 6739.
[32] Sr^{2+}: X. Shi, J. C. Fettinger, J. T. Davis, *Angew. Chem.* **2001**, *113*, 2909 – 2913; *Angew. Chem. Int. Ed.* **2001**, *40*, 2827 – 2831.
[33] Na^+: A. Wong, J. C. Fettinger, S. L. Forman, J. T. Davis, G. Wu, *J. Am. Chem. Soc.* **2002**, *124*, 742 – 743.
[34] The "head" of the G-quartet is the face that shows a clockwise rotation when moving from the H-bond donor NH to the carbonyl acceptor C=O: F. W. Smith, F. W. Lau, J. Feigon, *Proc. Natl. Acad. Sci. USA* **1994**, *91*, 10546 – 10550.
[35] a) G. S. Oxford, R. G. Gillespie, *Annu. Rev. Entomol.* **1998**, *43*, 619 – 643; b) G. S. Oxford, *Proc. 17th Europ. Colloq. Arachnology* (Ed.: P. A. Seldon), **1998**, pp. 121–131.
[36] R. H. Douglas, J. C. Partridge, N. J. Marshall, *Prog. Retinal Eye Res.* **1998**, *17*, 597 – 636.
[37] I. Bang, *Biochem. Z.* **1910**, *26*, 293 – 296.
[38] A. Calzolari, R. Di Felice, E. Molinari, A. Garbesi, *Phys. E* **2002**, *13*, 1236 – 1239.
[39] P. Tougard, J.-F. Chantot, W. Guschlbauer, *Biochim. Biophys. Acta* **1973**, *308*, 9 – 16.
[40] S. B. Zimmerman, G. H. Cohen, D. R. Davies, *J. Mol. Biol.* **1975**, *92*, 181 – 192.
[41] S. B. Zimmerman, *J. Mol. Biol.* **1976**, *106*, 663 – 672.
[42] J. Fresco, J. Massoulie, *J. Am. Chem. Soc.* **1963**, *85*, 1352 – 1353.
[43] T. J. Pinnavaia, H. T. Miles, E. D. Becker, *J. Am. Chem. Soc.* **1975**, *97*, 7198 – 7200.
[44] T. J. Pinnavaia, C. L. Marshall, C. M. Mettler, C. L. Fisk, H. T. Miles, E. D. Becker, *J. Am. Chem. Soc.* **1978**, *100*, 3625 – 3627.
[45] For a G-quartet without a cation: J. L. Sessler, M. Sathiosatham, K. Doerr, V. Lynch, K. A. Abboud, *Angew. Chem.* **2000**, *112*, 1356 – 1359; *Angew. Chem. Int. Ed.* **2000**, *39*, 1300 – 1303.
[46] E. Bouhoutsos-Brown, C. L. Marshall, T. J. Pinnavaia, *J. Am. Chem. Soc.* **1982**, *104*, 6576 – 6584.
[47] M. Borzo, C. Detellier, P. Laszlo, A. Paris, *J. Am. Chem. Soc.* **1980**, *102*, 1124 – 1134.
[48] W. Eimer, T. Dorfmuller, *J. Phys. Chem.* **1992**, *96*, 6790 – 6800.
[49] A. A. Lipanov, J. Quintana, R. E. Dickerson, *J. Biomol. Struct. Dyn.* **1990**, *8*, 483 – 489.
[50] K. J. Koch, T. Aggerholm, S. C. Nanita, R. G. Cooks, *J. Mass Spectrom.* **2002**, *37*, 676 – 686.
[51] T. Aggerholm, S. C. Nanita, K. J. Koch, R. G. Cooks, *J. Mass Spectrom.* **2003**, *38*, 87 – 97.
[52] G. Wu, A. Wong, *Chem. Commun.* **2001**, 2658 – 2659.
[53] A. Wong, G. Wu, *J. Phys. Chem. A* **2003**, *107*, 579 – 586.
[54] J.-M. Lehn, *Chem. Eur. J.* **1999**, *5*, 2455 – 2463.
[55] G. R. L. Cousins, S. A. Poulsen, J. K. M. Sanders, *Curr. Opin. Chem. Biol.* **2000**, *4*, 270 – 279.
[56] O. Ramstrom, J.-M. Lehn, *Nat. Rev. Drug Discovery* **2002**, *1*, 26 – 36.
[57] S. J. Rowan, S. J. Cantrill, G. R. L. Cousins, J. K. M. Sanders, J. F. Stoddart, *Angew. Chem.* **2002**, *114*, 938 – 993; *Angew. Chem. Int. Ed.* **2002**, *41*, 898 – 952.
[58] J. A. Walmsley, B. L. Sagan, *Biopolymers* **1986**, *25*, 2149 – 2172.
[59] M. P. Horvath, S. C. Schultz, *J. Mol. Biol.* **2001**, *310*, 367 – 377.
[60] S. Haider, G. N. Parkinson, S. Neidle, *J. Mol. Biol.* **2002**, *320*, 189 – 200.
[61] B. L. Feringa, R. A. van Delden, *Angew. Chem.* **1999**, *111*, 3624 – 3645; *Angew. Chem. Int. Ed.* **1999**, *38*, 3419 – 3438.
[62] L. J. Prins, J. Huskens, F. de Jong, P. Timmerman, D. N. Reinhoudt, *Nature* **1999**, *398*, 498 – 502.
[63] L. J. Prins, F. de Jong, P. Timmerman, D. N. Reinhoudt, *Nature* **2000**, *408*, 181 – 184.
[64] J. H. K. K. Hirschberg, L. Brunsveld, A. Ramzi, J. A. J. M. Vekemans, R. P. Sijbesma, E. W. Meijer, *Nature* **2000**, *407*, 167 – 170.
[65] T. Kawasaki, M. Tokuhiro, N. Kimizuka, T. Kunitake, *J. Am. Chem. Soc.* **2001**, *123*, 6792 – 6800.
[66] H. Fenniri, B.-L. Deng, A. E. Ribbe, K. Hallenga, J. Jacob, P. Thiyagarajan, *Proc. Natl. Acad. Sci. USA* **2002**, *99*, 6487 – 6492.
[67] L. Brunsveld, J. A. J. M. Vekemans, J. H. K. K. Hirschberg, R. P. Sijbesma, E. W. Meijer, *Proc. Natl. Acad. Sci. USA* **2002**, *99*, 4977 – 4982.
[68] A. V. Davis, R. M. Yeh, K. N. Raymond, *Proc. Natl. Acad. Sci. USA* **2002**, *99*, 4793 – 4796.
[69] A. Delville, C. Detellier, P. Laszlo, *J. Magn. Reson.* **1979**, *34*, 301 – 315.
[70] C. Detellier, P. J. Laszlo, *J. Am. Chem. Soc.* **1980**, *102*, 1135 – 1141.
[71] J.-M. Lehn, *Science* **2002**, *295*, 2400 – 2403.
[72] P. Mariani, C. Mazabard, A. Garbesi, G. P. Spada, *J. Am. Chem. Soc.* **1989**, *111*, 6369 – 6373.
[73] S. Bonazzi, M. Capobianco, M. M. De Morais, A. Garbesi, G. Gottarelli, P. Mariani, M. G. P. Bossi, G. P. Spada, L. Tondelli, *J. Am. Chem. Soc.* **1991**, *113*, 5809 – 5816.
[74] a) G. Gottarelli, G. Proni, G. P. Spada, S. Bonazzi, A. Garbesi, F. Ciuchi, P. Mariani, *Biopolymers* **1997**, *42*, 561 – 574; b) G. Gottarelli, G. Proni, G. P. Spada, *Liq. Cryst.* **1997**, *22*, 563 – 566; c) G. P. Spada, S. Bonazzi, A. Garbesi, S. Zanella, F. Ciuchi, P. Mariani, *Liq. Cryst.* **1997**, *22*, 341 – 348.
[75] D. Sen, W. Gilbert, *Nature* **1988**, *334*, 364 – 366.
[76] W. I. Sundquist, A. Klug, *Nature* **1989**, *342*, 825 – 829.
[77] a) H. Moine, J. L. Mandel, *Science* **2001**, *294*, 2487 – 2488; b) C. Schaffer, B. Bardoni, J. L. Mandel, B. Ehresmann, C. Ehresmann, H. Moine, *EMBO J.* **2001**, *20*, 4803 – 4813.
[78] a) J. C. Darnell, K. B. Jensen, P. Jin, V. Brown, S. T. Warren, R. B. Darnell, *Cell* **2001**, *107*, 489 – 499; b) V. Brown, P. Jin, S. Ceman, J. C. Darnell, W. T. O'Donnell, S. A. Tenenbaum, X. K. Jin, Y. Feng, K. D. Wilkinson, J. D. Keene, R. B. Darnell, S. T. Warren, *Cell* **2001**, *107*, 477 – 487.

 © 2004 Wiley-VCH Verlag GmbH & Co. KGaA, Weinheim

[79] a) A. Siddiqui-Jain, C. L. Grand, D. J. Bearss, L. H. Hurley, *Proc. Natl. Acad. Sci. USA* **2002**, *99*, 11593 – 11598; b) for an earlier suggestion that in vivo G-quadruplexes regulate c-myc gene expression, see T. Simonsson, P. Pecinka, M. Kubista, *Nucleic Acids Res.* **1998**, *26*, 1167 – 1172.
[80] J.-F. Rioui, L. Guittat, P. Mailliet, A. Laoui, E. Renou, O. Petitgenet, F. Megnin-Chanet, C. Helene, J.-L. Mergny *Proc. Natl Acad. Sci. USA* **2002**, 99, 2672 – 2677.
[81] Y. Wang, D. J. Patel, *Biochemistry* **1992**, *31*, 8112 – 8119.
[82] a) F. Aboul-ela, A. I. H. Murchie, D. M. J. Lilley, *Nature* **1992**, *360*, 280 – 282; b) F. Aboul-ela, A. I. H. Murchie, D. G. Norman, D. M. J. Lilley, *J. Mol. Biol.* **1994**, *243*, 458 – 471.
[83] G. Laughlan, A. I. H. Murchie, D. G. Norman, M. H. Moore, P. C. E. Moody, D. M. J. Lilley, B. Luisi, *Science* **1994**, *265*, 520 – 524.
[84] K. Phillips, Z. Dauter, A. I. H. Murchie, D. M. J. Lilley, B. Luisi, *J. Mol. Biol.* **1997**, *273*, 171 – 182.
[85] M. Meyer, T. Steinke, M. Brandl, J. Sühnel, *J. Comput. Chem.* **2001**, *22*, 109 – 124.
[86] J. Gu, J. Leczczynski, M. Bansal, *Chem. Phys. Lett.* **1999**, *311*, 209 – 214.
[87] N. Spackova, I. Berger, J. Spöner, *J. Am. Chem. Soc.* **1999**, *121*, 5519 – 5534.
[88] M. Frank-Kamenetskii, *Nature* **1992**, *356*, 105.
[89] F. W. Smith, J. Feigon, *Nature* **1992**, *356*, 164 – 168.
[90] F. W. Smith, J. Feigon, *Biochemistry* **1993**, *32*, 8682 – 8692.
[91] C. Kang, X. H. Zhang, R. Ratliff, R. Moyzis, A. Rich, *Nature* **1992**, *356*, 126 – 131.
[92] P. Schultze, N. V. Hud, F. W. Smith, J. Feigon, *Nucleic Acids Res.* **1999**, *27*, 3018 – 3028.
[93] J. Chen, D. S. Liu, A. H. F. Lee, J. Y. Qi, A. S. C. Chan, T. H. Li, *Chem. Commun.* **2002**, 2686 – 2687.
[94] Y. Wang, D. J. Patel, *Structure* **1993**, *1*, 263 – 282.
[95] G. N. Parkinson, M. P. H. Lee, S. Neidle, *Nature* **2002**, *417*, 876 – 880.
[96] D. J. Patel, *Nature* **2002**, *417*, 807 – 808.
[97] D. Sen, W. Gilbert, *Nature* **1990**, *344*, 410 – 414.
[98] W. S. Ross, C. C. Hardin, *J. Am. Chem. Soc.* **1994**, *116*, 6070 – 6080.
[99] N. V. Hud, F. W. Smith, F. A. L. Anet, J. Feigon, *Biochemistry* **1996**, *35*, 15383 – 15390.
[100] J. D. Gu, J. Leszczynski, *J. Phys. Chem. A* **2002**, *106*, 529 – 532.
[101] P. E. Nielsen, M. Egholm, R. H. Berg, O. Buchardt, *Science* **1991**, *254*, 1497 – 1500.
[102] B. Datta, B. A. Armitage, *J. Am. Chem. Soc.* **2001**, *123*, 9612 – 9619.
[103] J. J. Green, L. M. Ying, D. Klenerman, S. Balasubramanian, *J. Am. Chem. Soc.* **2003**, *125*, 3763 – 3767.
[104] B. A. Armitage, *Drug Discovery Today* **2003**, *8*, 222 – 228.
[105] B. Datta, C. Schmitt, B. A. Armitage, *J. Am. Chem. Soc.* **2003**, *125*, 4111 – 4118.
[106] S. Mizusawa, S. Nishimura, F. Seela, *Nucleic Acids Res.* **1986**, *14*, 1319 – 1324.
[107] F. Seela, K. Mersmann, *Helv. Chim. Acta* **1993**, *76*, 1435 – 1449.
[108] F. Seela, Y. M. Chen, C. Mittelbach, *Helv. Chim. Acta* **1998**, *81*, 570 – 583.
[109] a) T. S. Rao, R. H. Durland, D. M. Seth, M. A. Myrick, V. Bodepudi, G. P. Revankar, *Biochemistry* **1995**, *34*, 765 – 772; b) V. M. Marathias, M. J. Sawicki, P. H. Bolton, *Nucleic Acids Res.* **1999**, *27*, 2860 – 2867.
[110] R. Stefl, N. Spackova, I. Berger, J. Koca, J. Spöner, *Biophys. J.* **2001**, *80*, 455 – 468.
[111] C. J. Cheong, P. B. Moore, *Biochemistry* **1992**, *31*, 8406 – 8414.
[112] A. Kettani, S. Bouaziz, W. Wang, R. A. Jones, D. J. Patel, *Nat. Struct. Biol.* **1997**, *4*, 382 – 389.
[113] V. Kuryavyi, A. Majumdar, A. Shallop, N. Chernichenko, E. Skripkin, R. Jones, D. J. Patel, *J. Mol. Biol.* **2001**, *310*, 181 – 194.
[114] V. Kuryavyi, A. Kettani, W. M. Wang, R. Jones, D. J. Patel, *J. Mol. Biol.* **2000**, *295*, 455 – 469.
[115] A. Kettani, G. Basu, A. Gorin, A. Majumdar, E. Skripkin, D. J. Patel, *J. Mol. Biol.* **2000**, *301*, 129 – 146.
[116] H. M. Al-Hashimi, A. Majumdar, A. Gorin, A. Kettani, E. Skripkin, D. J. Patel, *J. Am. Chem. Soc.* **2001**, *123*, 633 – 640.
[117] P. K. Patel, R. V. Hosur, *Nucleic Acids Res.* **1999**, *27*, 2457 – 2464.
[118] a) P. K. Patel, A. S. R. Koti, R. V. Hosur, *Nucleic Acids Res.* **1999**, *27*, 3836 – 3843; b) E. Gavathiotis, M. S. Searle, *Org. Biomol. Chem.* **2003**, *1*, 1650 – 1656.
[119] A. Kettani, S. Bouaziz, A. Gorin, H. Zhao, R. Jones, D. J. Patel, *J. Mol. Biol.* **1998**, *282*, 619 – 636.
[120] S. Bouaziz, A. Kettani, D. J. Patel, *J. Mol. Biol.* **1998**, *282*, 637 – 652.
[121] J. D. Gu, J. Leszczynski, *J. Phys. Chem. A* **2000**, *104*, 7353 – 7358.
[122] N. Spakova, I. Berger, J. Spöner, *J. Am. Chem. Soc.* **2001**, *123*, 3295 – 3307.
[123] A. Kettani, A. Gorin, A. Majumdar, T. Hermann, E. Skripkin, H. Zhao, R. Jones, D. J. Patel, *J. Mol. Biol.* **2000**, *297*, 627 – 644.
[124] A. Matsugami, K. Ouhashi, M. Kanagawa, H. Liu, S. Kanagawa, S. Uesugi, M. Katahira, *J. Mol. Biol.* **2001**, *313*, 255 – 269.
[125] H. Liu, A. Matsugami, M. Katahira, S. Uesugi, *J. Mol. Biol.* **2002**, *322*, 955 – 970.
[126] J. P. Deng, Y. Xiong, M. Sundaralingam, *Proc. Natl. Acad. Sci. USA* **2001**, *98*, 13665 – 13670.
[127] M. Famulok, *Curr. Opin. Chem. Biol.* **1999**, *9*, 324 – 329.
[128] L. C. Bock, L. C. Griffin, J. A. Latham, E. H. Vermaas, J. J. Toole, *Nature* **1992**, *355*, 564 – 566.
[129] K. Padmanabhan, K. P. Padmanabhan, J. D. Ferrara, J. E. Sadler, A. Tulinsky, *J. Biol. Chem.* **1993**, *268*, 17651 – 17654.
[130] K. Padmanabhan, A. Tulinsky, *Acta Crystallogr. Sect. D* **1996**, *52*, 272 – 282.
[131] K. Y. Wang, S. McCurdy, R. G. Shea, S. Swaminathan, P. H. Bolton, *Biochemistry* **1993**, *32*, 1899 – 1904.
[132] R. F. Macaya, P. Schultze, F. W. Smith, J. A. Roe, J. Feigon, *Proc. Natl. Acad. Sci. USA* **1993**, *90*, 3745 – 3749.
[133] P. Schultze, R. F. Macaya, J. Feigon, *J. Mol. Biol.* **1994**, *235*, 1532 – 1547.
[134] J. A. Kelly, J. Feigon, T. O. Yeates, J. *Mol. Biol.* **1996**, *256*, 417 – 422.
[135] I. Smirnov, R. H. Shafer, *Biochemistry* **2000**, *39*, 1462 – 1468.
[136] B. I. Kankia, L. A. Marky, *J. Am. Chem. Soc.* **2001**, *123*, 10799 – 10804.
[137] M. Vairamani, M. L. Gross, *J. Am. Chem. Soc.* **2003**, *125*, 42 – 43.
[138] A. Mazumder, N. Neamati, J. O. Ojwang, S. Sunder, R. F. Rando, Y. Pommier, *Biochemistry* **1996**, *35*, 13762 – 13771.
[139] N. J. Jing, R. F. Rando, Y. Pommier, M. E. Hogan, *Biochemistry* **1997**, *36*, 12498 – 12505.
[140] N. J. Jing, M. E. Hogan, *J. Biol. Chem.* **1998**, *273*, 34992 – 34999.
[141] N. J. Jing, C. Marchand, J. Liu, R. Mitra, M. E. Hogan, Y. Pommier, *J. Biol. Chem.* **2000**, *275*, 21460 – 21467.
[142] J. R. Wyatt, T. A. Vickers, J. L. Roberson, R. W. Buckheit, Jr., T. Klimkait, E. DeBaets, P. W. Davis, B. Rayner, J. L. Imbach, D. J. Ecker, *Proc. Natl. Acad. Sci. USA* **1994**, *91*, 1356 – 1360.
[143] J. R. Wyatt, P. W. Davis, S. W. Freier, *Biochemistry* **1996**, *35*, 8002 – 8008.
[144] Y. Lin, A. Padmapriya, K. M. Morden, S. D. Jayasena, *Proc. Natl. Acad. Sci. USA* **1995**, *92*, 11044 – 11048.
[145] Y. Lin, S. D. Jayasena, *J. Mol. Biol.* **1997**, *271*, 100 – 111.
[146] J.-D. Wen, C. W. Gray, D. M. Gray, *Biochemistry* **2001**, *40*, 9300 – 9310.
[147] J.-D. Wen, D. M. Gray, *Biochemistry* **2002**, *41*, 11438 – 11448.
[148] a) M. L. Andreola, F. Pileur, C. Calmels, M. Ventura, L. Tarrago-Litvak, J. J. Toulme, S. Litvak, *Biochemistry* **2001**, *40*, 10087 – 10094; b) V. R. de Soultrait, P. Y. Lozach, R. Altmeyer,

 © 2004 Wiley-VCH Verlag GmbH & Co. KGaA, Weinheim

L. Tarrago-Litvak, S. Litvak, M. L. Andreola, *J. Mol. Biol.* **2002**, *324*, 195 – 203.
[149] a) Miller and co-workers have described antiproliferative activity of some G-quadruplex oligonucleotides in human cancer cells. They suggested that the quartet core, rather than the loops, interacts with the target proteins: V. Dapic, P. J. Bates, J. O. Trent, A. Rodger, S. D. Thomas, D. M. Miller, *Biochemistry* **2002**, *41*, 3676 – 3685; b) models have also been proposed for the interaction of polyinosine tetraplex DNA with triple helical peptides. In these models lysine-rich helical peptides bind the grooves of the four-stranded DNA and to make ammonium–phosphate electrostatic interactions: S. E. Meilewczyk, K. J. Breslauer, R. B. Anachi, B. Brodsky, *Biochemistry* **1996**, *35*, 11396 – 11402.
[150] C. Shaffitzel, I. Berger, J. Postberg, J. Hanes, H. J. Lipps, A. Plückthun, *Proc. Natl. Acad. Sci. USA* **2001**, *98*, 8572 – 8577.
[151] D. E. Huizenga, J. W. Szostak, *Biochemistry* **1995**, *34*, 656 – 665.
[152] C. T. Lauhon, J. W. Szostak, *J. Am. Chem. Soc.* **1995**, *117*, 1246 – 1257.
[153] N. V. Anantha, M. Azam, R. D. Sheardy, *Biochemistry* **1998**, *37*, 2709 – 2714.
[154] H. Arthanari, S. Basu, T. L. Kawano, P. H. Bolton, *Nucleic Acids Res.* **1998**, *26*, 3724 – 3728.
[155] H. Y. Han, D. R. Langley, A. Rangan, L. H. Hurley, *J. Am. Chem. Soc.* **2001**, *123*, 6485 – 6495.
[156] R. T. Wheelhouse, D. K. Sun, H. Y. Haiyong, F. X. G. Han, L. H. Hurley, *J. Am. Chem. Soc.* **1998**, *120*, 3261 – 3262.
[157] J. S. Ren, J. B. Chaires, *Biochemistry* **1999**, *38*, 16067 – 16075.
[158] D. F. Shi, R. T. Wheelhouse, D. Y. Sun, L. H. Hurley, *J. Med. Chem.* **2001**, *44*, 4509 – 4523.
[159] Y. F. Li, C. R. Geyer, D. Sen, *Biochemistry* **1996**, *35*, 6911 – 6922.
[160] Y. F. Li, D. Sen, *Nat. Struct. Biol.* **1996**, *3*, 743 – 747.
[161] Y. F. Li, D. Sen, *Biochemistry* **1997**, *36*, 5589 – 5599.
[162] N. Sugimoto, T. Toda, T. Ohmichi, *Chem. Commun.* **1998**, 1533 – 1534.
[163] Y. F. Li, D. Sen, *Chem. Biol.* **1998**, *5*, 1 – 12.
[164] C. R. Geyer, D. Sen, *J. Mol. Biol.* **2000**, *299*, 1387 – 1398.
[165] P. Travascio, Y. F. Li, D. Sen, *Chem. Biol.* **1998**, *5*, 505 – 517.
[166] P. Travascio, P. K. Witting, A. G. Mauk, D. Sen, *J. Am. Chem. Soc.* **2001**, *123*, 1337 – 1348.
[167] M. Isalan, S. D. Patel, S. Balasubramanian, Y. Choo, *Biochemistry* **2001**, *40*, 830 – 836.
[168] D. Rhodes, R. Giraldo, *Curr. Opin. Struct. Biol.* **1995**, *5*, 311 – 322.
[169] E. H. Blackburn, *Cell* **2001**, *106*, 661 – 673.
[170] T. M. Bryan, T. R. Cech, *Curr. Opin. Struct. Biol.* **1999**, *11*, 318 – 324.
[171] T. R. Cech, *Angew. Chem.* **2000**, *112*, 34 – 44; *Angew. Chem. Int. Ed.* **2000**, *39*, 34 – 43.
[172] M. J. McEachern, A. Krauskopf, E. H. Blackburn, *Annu. Rev. Genet.* **2000**, *34*, 331 – 358.
[173] C. W. Greider, *Annu. Rev. Biochem.* **1996**, *65*, 337 – 357.
[174] K. Collins, *Curr. Opin. Cell Biol.* **2000**, *12*, 378 – 383.
[175] W. C. Hahn, C. M. Counter, A. S. Lundberg, R. L. Beijersbergen, M. W. Brooks, R. A. Weinberg, *Nature* **1999**, *400*, 464 – 468.
[176] W. C. Hahn, S. A. Stewart, M. W. Brooks, S. G. York, E. Eaton, A. Kurachi, R. L. Beijersbergen, J. H. M. Knoll, M. Meyerson, R. A. Weinberg, *Nat. Med.* **1999**, *5*, 1164 – 1170.
[177] A. M. Zahler, J. R. Williamson, T. R. Cech, D. M. Prescott, *Nature* **1991**, *350*, 718 – 720.
[178] S. Neidle, G. Parkinson, *Nat. Rev. Drug Discovery* **2002**, *1*, 383 – 393.
[179] H. Y. Han, L. H. Hurley, *Trends Pharmacol. Sci.* **2000**, *21*, 136 – 142.
[180] P. J. Perry, J. R. P. Arnold, T. C. Jenkins, *Expert Opin. Invest. Drugs* **2001**, *10*, 2141 – 2156.
[181] S. M. Kerwin, *Curr. Pharm. Des.* **2000**, *6*, 441 – 471.
[182] L. H. Hurley, R. T. Wheelhouse, D. Sun, S. M. Kerwin, M. Salazar, O. Y. Federoff, F. X. Han, H. Y. Han, E. Izbicka, D. D. Von Hoff, *Pharmacol. Ther.* **2000**, *85*, 141 – 158.
[183] Z. Chen, D. R. Corey, *Adv. Cancer Res.* **2003**, *87*, 31 – 58.
[184] Q. Guo, M. Lu, L. A. Marky, N. R. Kallenbach, *Biochemistry* **1992**, *31*, 2451 – 2455.
[185] D. Y. Sun, B. Thompson, B. E. Cathers, M. Salazar, S. M. Kerwin, J. O. Trent, T. C. Jenkins, S. Neidle, L. H. Hurley, *J. Med. Chem.* **1997**, *40*, 2113 – 2116.
[186] I. Haq, J. O. Trent, B. Z. Chowdhry, T. C. Jenkins, *J. Am. Chem. Soc.* **1999**, *121*, 1768 – 1779.
[187] O. Yu. Fedoroff, M. Salazar, H. Han, V. V. Chemeris, S. M. Kerwin, L. H. Hurley, *Biochemistry* **1998**, *37*, 12367 – 12374.
[188] E. Gavathiotis, R. A. Heald, M. F. G. Stevens, M. S. Searle, *Angew. Chem.* **2001**, *113*, 4885 – 4887; *Angew. Chem. Int. Ed.* **2001**, *40*, 4749 – 4751.
[189] M. A. Read, S. Neidle, *Biochemistry* **2000**, *39*, 13422 – 13432.
[190] S. M. Haider, G. N. Parkinson, S. Neidle, *J. Mol. Biol.* **2003**, *326*, 117 – 125.
[191] G. R. Clark, P. D. Pytel, C. J. Squire, S. Neidle, S. *J. Am. Chem. Soc.* **2003**, *125*, 4066 – 4067.
[192] Q. Chen, I. D. Kuntz, R. H. Shafer, *Proc. Natl. Acad. Sci. USA* **1996**, *93*, 2635 – 2639.
[193] J. A. Schouten, S. Ladame, S. J. Mason, M. A. Cooper, S. Balasubramanian, *J. Am. Chem. Soc.* **2003**, *125*, ASAP April 17.
[194] H. Han, C. L. Cliff, L. H. Hurley, *Biochemistry* **1999**, *38*, 6981 – 6986.
[195] W. Tuntiwechapikul, T. L. Jeong, M. Salazar, *J. Am. Chem. Soc.* **2001**, *123*, 5606 – 5607.
[196] S. M. Kerwin, G. Chen, J. T. Kern, P. W. Thomas, *Bioorg. Med. Chem. Lett.* **2002**, *12*, 447 – 450.
[197] J. T. Kern, P. W. Thomas, S. M. Kerwin, *Biochemistry* **2002**, *41*, 11379 – 11389.
[198] M.-P. Teulade-Fichuo, C. Carrasco, L. Guittat, C. Bailly, P. Alberti, J.-L. Mergny, A. David, J.-M. Lehn, W. D. Wilson, *J. Am. Chem. Soc.* **2003**, *125*, 4732 – 4740.
[199] M. Read, R. J. Harrison, B. Romagnoli, F. A. Tanious, S. H. Gowan, A. P. Reszka, W. D. Wilson, L. R. Kelland, S. Neidle, *Proc. Natl. Acad. Sci. USA* **2001**, *98*, 4844 – 4849.
[200] J.-L. Mergny, L. Lacroix, M.-P. Teulade-Fichou, C. Hounsou, L. Guittat, M. Hoarau, P. B. Arimondo, J.-P. Vigneron, J.-M. Lehn, J.-F. Riou, T. Garestier, C. Helene, *Proc. Natl. Acad. Sci. USA* **2001**, *98*, 3062 – 3067.
[201] F. Koeppel, J. F. Riou, A. Laoui, P. Mailliet, P. B. Arimondo, D. Labit, O. Petitgenet, C. Helene, J.-L. Mergny, *Nucleic Acids Res.* **2001**, *29*, 1087 – 1096.
[202] K. Shin-ya, K. Wierzba, K. Matsuo, T. Ohtani, Y. Yamada, K. Furihata, Y. Hayakawa, H. Seto, *J. Am. Chem. Soc.* **2001**, *123*, 1262 – 1263.
[203] M. Y. Kim, H. Vankayalapati, S. Kazuo, K. Wierzba, L. H. Hurley, *J. Am. Chem. Soc.* **2002**, *124*, 2098 – 2099.
[204] The stabilization resulting from aromatic stacking has been attributed to dispersion forces, electrostatic interactions, and the hydrophobic effect. For a review on aromatic π-π interactions in organic model systems, see M. L. Waters, *Curr. Opin. Chem. Biol.* **2002**, *6*, 736 – 741; b) for a review discussing DNA base stacking, see E. T. Kool, *Annu. Rev. Biophys. Biomol. Struct.* **2001**, *30*, 1 – 22.
[205] For a review on aromatic interactions in chemistry and biology that discusses the "nonclassical" hydrophobic effect, see E. A. Meyer, R. K. Castellano, F. Diederich, *Angew. Chem.* **2003**, *115*, 1244 – 1287; *Angew. Chem. Int. Ed.* **2003**, *42*, 1210 – 1250.
[206] J. T. Davis, S. Tirumala, J. Jenssen, E. Radler, D. Fabris, *J. Org. Chem.* **1995**, *60*, 4167 – 4176.

 © 2004 Wiley-VCH Verlag GmbH & Co. KGaA, Weinheim

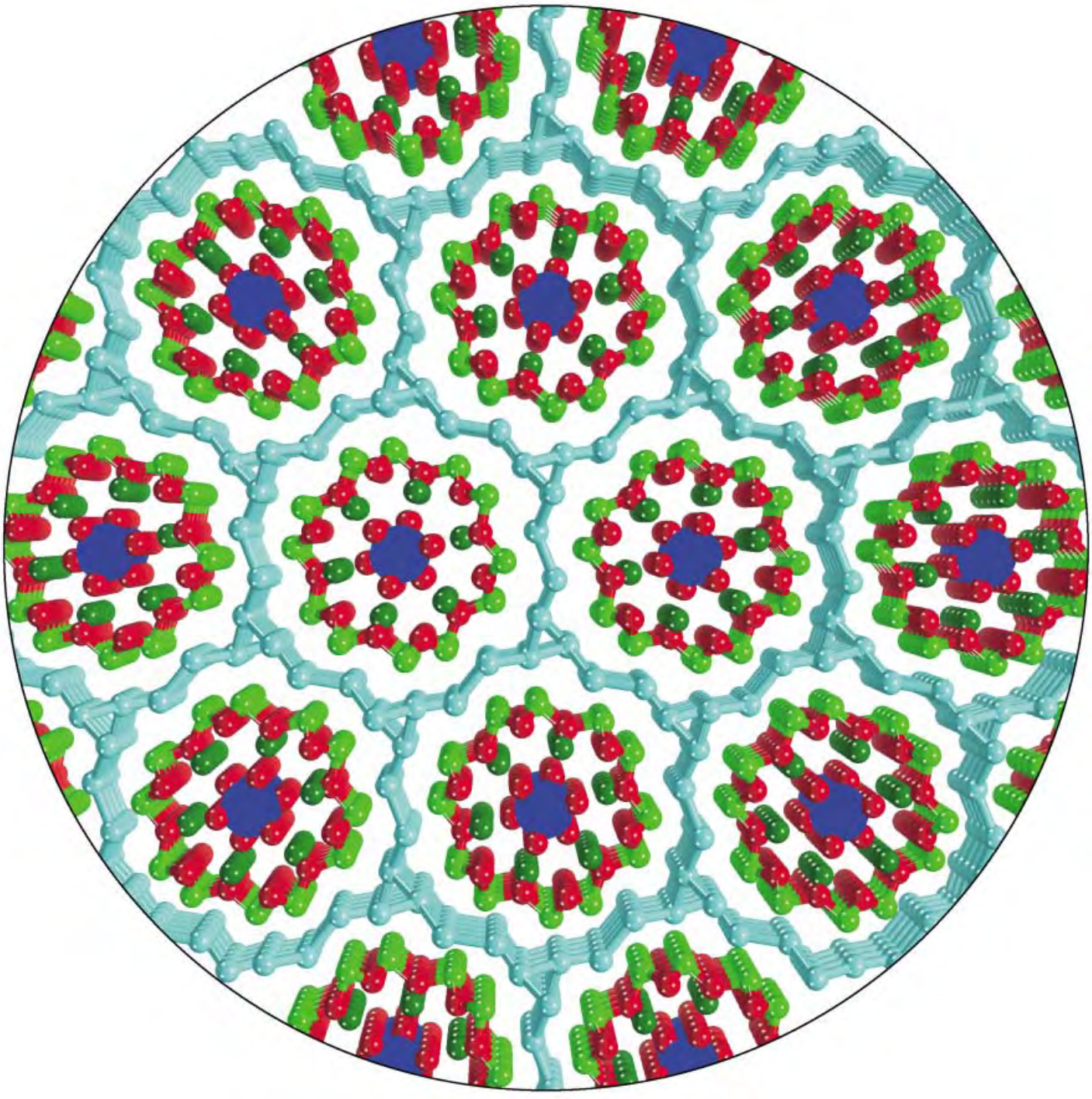
[207] Poly(isoG) aggregates more strongly than poly(G): T. Golas, M. Fikus, Z. Kazimierczuk, D. Shugar, *Eur. J. Biochem.* **1976**, *65*, 183 – 192.
[208] G. Gottarelli, S. Masiero, G. P. Spada, *J. Chem. Soc. Chem. Commun.* **1995**, 2555 – 2557.
[209] S. Pieraccini, G. Gottarelli, P. Mariani, S. Masiero, L. Saturni, G. P. Spada, *Chirality* **2001**, *13*, 7 – 12.
[210] A. L. Marlow, E. Mezzina, G. P. Spada, S. Masiero, J. T. Davis, G. Gottarelli, *J. Org. Chem.* **1999**, *64*, 5116 – 5123.
[211] E. Mezzina, P. Mariani, R. Itri, S. Masiero, S. Pieraccini, G. P. Spada, F. Spinozzi, J. T. Davis, G. Gottarelli, *Chem. Eur. J.* **2001**, *7*, 388 – 395.
[212] N. V. Hud, P. Schultze, V. Sklenar, J. Feigon, *J. Mol. Biol.* **1999**, *285*, 233 – 243.
[213] S. Basu, A. A. Szewczak, M. Cocco, S. A. Strobel, *J. Am. Chem. Soc.* **2000**, *122*, 3240 – 3241.
[214] H. Deng, W. H. Braunlin, *J. Mol. Biol.* **1996**, *255*, 476 – 483.
[215] D. Rovnyak, M. Baldus, G. Wu, N. V. Hud, J. Feigon, R. G. Griffin, *J. Am. Chem. Soc.* **2000**, *122*, 11 423 – 11 429.
[216] G. Wu, A. Wong, Z. Gan, J. T. Davis, *J. Am. Chem. Soc.* **2003**, *125*, 7182 – 7183.
[217] I. V. Smirnov, F. W. Kotch, I. J. Pickering, J. T. Davis, R. H. Shafer, *Biochemistry* **2002**, *41*, 12 133 – 12 139.
[218] I. Smirnov, R. H. Shafer, *J. Mol. Biol.* **2000**, *296*, 1 – 5.
[219] V. M. Marathias, P. H. Bolton, *Biochemistry* **1999**, *38*, 4355 – 4364.
[220] V. M. Marathias, P. H. Bolton, *Nucleic Acids Res.* **2000**, *28*, 1969 – 1977.
[221] M. Cai, A. L. Marlow, J. C. Fettinger, D. Fabris, T. J. Haverlock, B. A. Moyer, J. T. Davis, *Angew. Chem.* **2000**, *112*, 1339 – 1341; *Angew. Chem. Int. Ed.* **2000**, *39*, 1283 – 1285.
[222] X. D. Shi, J. C. Fettinger, M. M. Cai, J. T. Davis, *Angew. Chem.* **2000**, *112*, 3254 – 3257; *Angew. Chem. Int. Ed.* **2000**, *39*, 3124 – 3127.
[223] a) J. C. Chaput, C. Switzer, *Proc. Natl. Acad. Sci. USA* **1999**, *96*, 10 614 – 10 619; b) J. C. Chaput, C. Switzer, *Methods* **2001**, *23*, 141 – 148.
[224] F. Seela, C. F. Wei, A. Melenewski, E. Feiling, *Nucleosides Nucleotides* **1998**, *17*, 2045 – 2052.
[225] F. Seela, R. Kröschel, *Bioconjugate Chem.* **2001**, *12*, 1043 – 1050.
[226] F. Seela, C. F. Wei, A. Melenewski, *Nucleic Acids Res.* **1996**, *24*, 4940 – 4945.
[227] F. Seela, C. F. Wei, A. Melenewski, *Origins Life Evol. Biosphere* **1997**, *27*, 601 – 608.
[228] F. Seela, C. F. Wei, *Chem. Commun.* **1997**, 1869 – 1870.
[229] M. Meyer, J. Sühnel, *J. Phys. Chem. A* **2003**, *107*, 1025 – 1031.
[230] K. Groebke, J. Hunziker, W. Fraser, L. Peng, U. Diederichsen, K. Zimmermann, A. Holzner, C. Leumann, A. Eschenmoser, *Helv. Chim. Acta* **1998**, *81*, 375 – 474.
[231] M. F. H. Hoffmann, A. M. Bruckner, T. Hupp, B. Engels, U. Diederichsen, *Helv. Chim. Acta* **2000**, *83*, 2580 – 2593.
[232] C. Roberts, J. C. Chaput, C. Switzer, *Chem. Biol.* **1997**, *4*, 899 – 908.
[233] S. Tirumala, J. T. Davis, *J. Am. Chem. Soc.* **1997**, *119*, 2769 – 2776.
[234] A. L. Marlow, J. T. Davis, *Tetrahedron Lett.* **1999**, *40*, 3539 – 3542.
[235] M. M. Cai, V. Sidorov, Y.-F. Lam, R. A. Flowers III, J. T. Davis, *Org. Lett.* **2000**, *2*, 1665 – 1668.
[236] M. M. Cai, X. D. Shi, V. Sidorov, D. Fabris, Y.-F. Lam, J. T. Davis, *Tetrahedron* **2002**, *58*, 661 – 671.
[237] Such equilibrium shifting was also demonstrated using mass spectrometry. A synthetic napthyridine, designed to base-pair with G, destroyed a dG_4-K^+ quartet: S. Sakamoto, K. Nakatani, I. Saito, K. Yamaguchi, *Chem. Commun.* **2003**, 788 – 789.
[238] A. X. Wu, L. Isaacs, *J. Am. Chem. Soc.* **2003**, *125*, 4831 – 4835.
[239] a) J. L. Sessler, J. Jayawickramarajah, M. Sathiosatham, C. L. Sherman, J. S. Brodbelt, *Org. Lett.* **2003**, *5*, 2627 – 2630; b) for examples of synthetic assemblies constructed from GC hybrid compounds, see A. Marsh, M. Silvestri, J.-M. Lehn, *Chem. Commun.* **1996**, 1527 – 1528; M. Mascal, N. M. Hext, R. Warmuth, M. H. Moore, J. P. Turkenburg, *Angew. Chem.* **1996**, *108*, 2204 – 2206; *Angew. Chem. Int. Ed. Engl.* **1996**, *35*, 2348 – 2350; Y. G. Ma, S. V. Kolotuchin, S. C. Zimmerman, *J. Am. Chem. Soc.* **2002**, *124*, 13 757 – 13 769; H. Fenniri, B.-L. Deng, A. E. Ribbe, *J. Am. Chem. Soc.* **2002**, *124*, 11 064 – 11 074.
[240] J. T. Davis, S. Tirumala, A. L. Marlow, *J. Am. Chem. Soc.* **1997**, *119*, 5271 – 5272.
[241] V. Andrisano, G. Gottarelli, S. Masiero, E. H. Heijne, S. Pieraccini, G. P. Spada, *Angew. Chem.* **1999**, *111*, 2543 – 2544; *Angew. Chem. Int. Ed.* **1999**, *38*, 2386 – 2388.
[242] X. Shi, K. M. Mullaugh, J. C. Fettinger, Y. Jiang, S. A. Hofstadler, J. T. Davis, *J. Am. Chem. Soc.* **2003**, *125*, 10 830 – 10 831.
[243] For a review on ditopic receptors, see G. J. Kirkovits, J. A. Shriver, P. A. Gale, J. L. Sessler, *J. Inclusion Phenom. Macrocyclic Chem.* **2001**, *41*, 69 – 75.
[244] For another family of self-assembled ionophores, see H. Piotrowski, K. Polborn, G. Hilt, K. Severin, *J. Am. Chem. Soc.* **2001**, *123*, 2699 – 2700.
[245] Examples: a) S. H. M. Söntjens, R. P. Sijbesma, M. H. P. van - Genderen, E. W. Meijer, *J. Am. Chem. Soc.* **2000**, *122*, 7487 – 7493; b) S. Y. Chang, J. S. Choi, K. S. Jeong, *Chem. Eur. J.* **2001**, *7*, 2687 – 2697; c) F. Hof, C. Nuckolls, S. L. Craig, T. Martin, J. Rebek, *J. Am. Chem. Soc.* **2000**, *122*, 10 991 – 10 996.
[246] X. X. Zhang, R. M. Izatt, J. S. Bradshaw, K. E. Krakowiak, *Coord. Chem. Rev.* **1998**, 174, 179 – 189.
[247] R. M. Izatt, K. Pawlak, J. S. Bradshaw, R. L. Bruening, *Chem. Rev.* **1995**, *95*, 2529 – 2586.
[248] J.-F. Dozol in *New Separation Chemistry Techniques for Radioactive Waste and Other Applications* (Eds.: L. Cecille, M. Casati, L. Pietrelli), Elsevier, Amsterdam, **1991**, pp. 163 – 172.
[249] J. W. McDowell, G. N. Case, J. A. McDonough, R. A. Bartsch, *Anal. Chem.* **1992**, *64*, 3013 – 3017.
[250] Y. P. Deng, R. A. Sachleben, B. A. Moyer, *J. Chem. Soc. Faraday Trans.* **1995**, *91*, 4215 – 4222.
[251] R. A. Sachleben, Y. Deng, D. R. Bailey, B. A. Moyer, *Solvent Extr. Ion Exch.* **1996**, *14*, 995 – 1015.
[252] a) J. C. Bryan, R. A. Sachleben, B. P. Hay, *Inorg. Chim. Acta* **1999**, *290*, 86 – 94; b) J. C. Bryan, K. Kavallieratos, R. A. Sachleben, *Inorg. Chem.* **2000**, *39*, 1568 – 1572.
[253] A. Casnati, A. Pochini, R. Ungaro, F. Ugozzoli, F. Arnaud, S. Fanni, M. J. Schwing, R. J. M. Egberink, F. De Jong, D. N. Reinhoudt, *J. Am. Chem. Soc.* **1995**, *117*, 2767 – 2777.
[254] F. Arnaud-Neu, Z. Asfari, B. Souley, J. Vicens, *New J. Chem.* **1996**, *20*, 453 – 463.
[255] S. C. Lee, J. D. Lamb, M. M. Cai, J. T. Davis, *J. Inclusion Phenom. Macrocyclic Chem.* **2001**, *40*, 51 – 57.
[256] a) T. G. Levitskaia, J. D. Lamb, K. L. Fox, B. A. Moyer, *Radiochim. Acta* **2002**, *90*, 43 – 52; b) T. J. Haverlock, P. V. Bonnesen, R. A. Sachleben, B. A. Moyer, *J. Inclusion Phenom. Macrocyclic Chem.* **2000**, *36*, 21 – 37.
[257] S. Masiero, G. Gottarelli, S. Pieraccini, *Chem. Commun.* **2000**, 1995 – 1996.
[258] Q. W. Xu, H. Deng, W. H. Braunlin, *Biochemistry* **1993**, *32*, 13 130 – 13 137.
[259] J. M. Boon, B. D. Smith, *Curr. Opin. Chem. Biol.* **2002**, *6*, 749 – 756.
[260] G. W. Gokel, A. Mukhopadhyay, *Chem. Soc. Rev.* **2001**, *30*, 274 – 286.
[261] T. M. Fyles, *Curr. Opin. Chem. Biol.* **1997**, *1*, 497 – 505.

 © 2004 Wiley-VCH Verlag GmbH & Co. KGaA, Weinheim

[262] For an early proposal to build synthetic ion channels from G-quartets, see L. Chen, N. Sakai, S. T. Moshiri, S. Matile, *Tetrahedron Lett.* **1998**, *39*, 3627 – 3630.
[263] V. Sidorov, F. W. Kotch, M. El-Kouedi, J. T. Davis, *Chem. Commun.* **2000**, 2369 – 2370; see also F. W. Kotch, V. Sidorov, K. J. Kayser, Y. F. Lam, M. S. Kaucher, J. T. Davis, J. Am. Chem. Soc. **2003**, *125*, 15140 – 15150.
[264] C. M. Niemeyer, *Angew. Chem.* **2001**, *113*, 4254 – 4287; *Angew. Chem. Int. Ed.* **2001**, *40*, 4128 – 4158.
[265] C. M. Niemeyer, M. Adler, *Angew. Chem.* **2002**, *114*, 3779 – 3783; *Angew. Chem. Int. Ed.* **2002**, *41*, 3779 – 3783.
[266] D. Sen, W. Gilbert, *Biochemistry* **1992**, *31*, 65 – 70.
[267] M. Lu, Q. Guo, N. R. Kallenbach, *Biochemistry* **1992**, *31*, 2455 – 2459.
[268] T. C. Marsh, E. Henderson, *Biochemistry* **1994**, *33*, 10718 – 10724.
[269] T. C. Marsh, J. Vesenka, E. Henderson, *Nucleic Acids Res.* **1995**, *23*, 696 – 700.
[270] T.-Y. Dai, S. P. Marotta, R. D. Sheardy, *Biochemistry* **1995**, *34*, 3655 – 3662.
[271] S. P. Marotta, P. A. Tamburri, R. D. Sheardy, *Biochemistry* **1996**, *35*, 10484 – 10492.
[272] F.-M. Chen, *J. Biol. Chem.* **1995**, *270*, 23090 – 23096.
[273] E. Protozanova, R. B. Macgregor, Jr., *Biochemistry* **1996**, *35*, 16638 – 16645.
[274] E. Protozanova, R. B. Macgregor, Jr., *Biophys. Chem.* **1998**, *75*, 249 – 257.
[275] E. Protozanova, R. B. Macgregor, Jr., *Biophys. J.* **1998**, *75*, 982 – 989.
[276] K. Poon, R. B. Macgregor, Jr., *Biophys. Chem.* **2000**, *84*, 205 – 216.
[277] K. Poon, R. B. Macgregor, Jr., *Biopolymers* **1998**, *45*, 427 – 434.
[278] M. A. Batalia, E. Protozanova, R. B. Macgregor, Jr., D. A. Erie, *Nano Lett.* **2002**, *2*, 269 – 274.
[279] E. A. Venczel, D. Sen, *J. Mol. Biol.* **1996**, *257*, 219 – 224.
[280] R. P. Fahlman, D. Sen, *J. Mol. Biol.* **1998**, *280*, 237 – 244.
[281] R. P. Fahlman, D. Sen, *J. Am. Chem. Soc.* **1999**, *121*, 11079 – 11085.
[282] R. B. Kotia, L. J. Li, L. B. McGown, *Anal. Chem.* **2000**, *72*, 827 – 831.
[283] J. A. M. Charles, L. B. McGown, *Electrophoresis* **2002**, *23*, 1599 – 1604.
[284] M. A. Rehder, L. B. McGown, *Electrophoresis* **2001**, *22*, 3759 – 3764.
[285] I. German, D. D. Buchanan, R. T. Kennedy, *Anal. Chem.* **1998**, *70*, 4540 – 4545.
[286] R. A. Potyrailo, R. C. Conrad, A. Ellington, G. M. Heiftje, *Anal. Chem.* **1998**, *70*, 3419 – 3425.
[287] N. Hamaguchi, A. Ellington, M. Stanton, *Anal. Biochem.* **2001**, *294*, 126 – 131.
[288] J. W. J. Li, X. H. Fang, W. H. Tan, *Biochem. Biophys. Res. Commun.* **2002**, *292*, 31 – 40.
[289] R. Nutiu, Y. F. Li, *J. Am. Chem. Soc.* **2003**, *125*, 4771 – 4778.
[290] T. Simonsson, R. Sjoback, *J. Biol. Chem.* **1999**, *274*, 17379 – 17383.
[291] J.-L. Mergny, J.-C. Maurizot, *ChemBioChem* **2001**, *2* 124 – 132.
[292] H. Ueyama, M. Takagi, S. Takenaka, *J. Am. Chem. Soc.* **2002**, *124*, 14286 – 14287.
[293] J. W. J. Li, W. H. Tan, *Nano Lett.* **2002**, *2*, 315 – 318.
[294] P. Alberti, J.-L. Mergny, *Proc. Natl. Acad. Sci. USA* **2003**, *100*, 1569 – 1573.
[295] G. Gottarelli, S. Masiero, E. Mezzina, S. Pieraccini, J. P. Rabe, P. Samori, G. P. Spada, *Chem. Eur. J.* **2000**, *6*, 3242 – 3248.
[296] P. Samori, S. Pieraccini, S. Masiero, G. P. Spada, G. Gottarelli, J. P. Rabe, *Colloids Surf. B* **2002**, *23*, 283 – 288.
[297] T. Giorgi, F. Grepioni, I. Manet, P. Mariani, S. Masiero, E. Mezzina, S. Pieraccini, L. Saturni, G. P. Spada, G. Gottarelli, *Chem. Eur. J.* **2002**, *8*, 2143 – 2152.
[298] G. Gottarelli, S. Masiero, E. Mezzina, G. P. Spada, P. Mariani, M. Recanatini, *Helv. Chim. Acta* **1998**, *81*, 2078 – 2092.
[299] G. Gottarelli, S. Masiero, E. Mezzina, S. Pieraccini, G. P. Spada, P. Mariani, *Liq. Cryst.* **1999**, *26*, 965 – 971.
[300] F. Ciuchi, G. Dinicola, H. Franz, G. Gottarelli, P. Mariani, M. G. P. Bossi, G. P. Spada, *J. Am. Chem. Soc.* **1994**, *116*, 7064 – 7071.
[301] S. Bonazzi, M. M. Demorais, G. Gottarelli, P. Mariani, G. P. Spada, *Angew. Chem.* **1993**, *105*, 251 – 254; *Angew. Chem. Int. Ed. Engl.* **1993**, *32*, 248 – 250.
[302] G. Gottarelli, E. Mezzina, G. P. Spada, F. Carsughi, G. DiNicola, P. Mariani, A. Sabatucci, S. Bonazzi, *Helv. Chim. Acta* **1996**, *79*, 220 – 234.
[303] T. Kato, *Science* **2002**, *295*, 2414 – 2418.
[304] T. Kato, N. Mizshita, K. Kanie, *Macromol. Rapid Commun.* **2001**, *22*, 797 – 814.
[305] R. P. Lemieux, *Acc. Chem. Res.* **2001**, *34*, 845 – 853.
[306] M. Suarez, J.-M. Lehn, S. C. Zimmerman, A. Skoulios, B. Heinrich, *J. Am. Chem. Soc.* **1998**, *120*, 9526 – 9532.
[307] M. Gallant, M. T. P. Viet, J. D. Wuest, *J. Am. Chem. Soc.* **1991**, *113*, 721 – 723.
[308] K. Kanie, T. Yasuda, S. Ujiie, T. Kato, *Chem. Commun.* **2000**, *19*, 1899 – 1900.
[309] K. Kanie, T. Yasuda, M. Nishii, S. Ujiie, T. Kato, *Chem. Lett.* **2001**, *6*, 480 – 481.
[310] K. Kanie, M. Nishii, T. Yasuda, T. Taki, S. Ujiie, T. Kato, *J. Mater. Chem.* **2001**, *11*, 2875 – 2886.
[311] A. Aviram, M. Ratner, *Chem. Phys. Lett.* **1974**, *29*, 277 – 283.
[312] C. Joachim, J. K. Gimzewski, A. Aviram, *Nature* **2000**, *408*, 541 – 548.
[313] H. W. Fink, C. Schönenberger, *Nature* **1999**, *398*, 407 – 410.
[314] D. Porath, A. Bezryadin, S. de Vries, C. Dekker, *Nature* **2000**, *403*, 635 – 638.
[315] R. Rinaldi, E. Branca, R. Cingolani, S. Masiero, G. P. Spada, G. Gottarelli, *Appl. Phys. Lett.* **2001**, *7*, 3541 – 3546.
[316] R. Rinaldi, G. Maruccio, A. Biasco, V. Arima, R. Cingolani, T. Giorgi, S. Masiero, G. P. Spada, G. Gottarelli, *Nanotechnology* **2002**, *13*, 398 – 403.
[317] R. Di Felice, A. Calzolari, E. Molinari, A. Garbesi, *Phys. Rev. B* **2001**, *65*, 045104.
[318] A. Calzolari, R. Di Felice, E. Molinari, A. Garbesi, *Appl. Phys. Lett.* **2002**, *80*, 3331 – 3333.

 © 2004 Wiley-VCH Verlag GmbH & Co. KGaA, Weinheim

Communications



A crystalline microporous narrow-bandgap semiconductor that exhibits highly anisotropic conductivity consists of a framework of tellurium channels that host antimony(III) oxide channels, which in turn enclose potassium ions and water molecules. For more information, see the Communication by A. E. C. Palmqvist et al. on the following pages.

DOI: 10.1002/anie.200351284
© 2004 Wiley-VCH Verlag GmbH & Co. KGaA, Weinheim

Semiconductors

A Crystalline Microporous Narrow-Bandgap Semiconductor**

Anders E. C. Palmqvist, Bo B. Iversen, Ezio Zanghellini, Mårten Behm, and Galen D. Stucky*

Crystalline microporous solids are of great importance and interest for many chemical and physical applications, due to their ordered arrangements of monodisperse channels, cavities, and cages in the molecular size regime where quantum effects occur. The best known group of these so-called molecular-sieve materials are the zeolites and zeolite-type metal oxides, which have applications in, for example, catalysis, adsorption, and ion-exchange processes. Zeolites are insulators due to their chemical composition, and although much effort have been made over the past 15 years to prepare semiconducting zeolite analogues, it was not until recently that an ordered $2\times2\times1$ superstructure of the crystalline microporous mineral cetineite[2] with the composition $|K_3(H_2O)_3|[Sb_7O_9Se_3]$ was found to be a photo-semiconductor with a bandgap of 2.06 eV.[3] The optical bandgap of the cetineite-type phases was found to depend on the elemental composition and is, for example, 2.5 eV in $|Na_6(H_2O)_6|[Sb_{14}O_{18}S_6]$.[4]

Apparently, tellurium does not form the cetineite structure,[5] but we have found that by using a different synthesis approach, a new microporous semiconductor can be prepared.[6] The structure, referred to as SBC-1 (SBC = Santa Barbara–Chalmers), includes the potassium and water-containing $\{Sb_{12}O_{18}\}$ tubes found in cetineite but in addition SBC-1 has a unique tubular tellurium structural unit replacing the $\{SbSe_3\}$ pyramids present in cetineite, and a bandgap of merely 0.25 eV. This is a very narrow bandgap for microporous materials compared with, for example, 1.32 eV reported by Hanko and Kanatzidis for $RbCuSb_2Se_4\cdot H_2O$.[7] To our knowledge this is the first crystalline microporous antimony(III) oxide telluride. In addition, SBC-1 appears to be the first example of a second-order "zeoate" according to the definitions given in the most recent microporous materials nomenclature.[1] The new class of SBC-1 materials opens up a wide field of potential applications that are unique to the domain of microporous narrow-bandgap semiconductors.

Black SBC-1 needlelike crystals of a few millimeters in length and a diameter of approximately 0.1 mm were formed during the solvothermal treatment of a mixture of *n*-propylamine, aqueous KOH, Te, and Sb (trigonal space group $R\bar{3}$ (no. 148); hexagonal axes $a=b=27.3361(11)$, $c=5.6909(3)$ Å at 293 K). The crystal structure of SBC-1, as solved by single crystal XRD, is presented in Figure 1 with the hydrogen atoms in the water molecules (O_w) removed for clarity. The structure contains the characteristic 12-ring $\{Sb_{12}O_{18}\}$ tubular unit, with a ring width of 6.70×6.76 Å (assuming a van der Waals radius $r(O)=1.35$ Å). The unit is built up from pyramidal $\{SbO_3\}$ groups linked together via common oxygen atoms, and hosts potassium ions and water molecules. The walls of the $\{Sb_{12}O_{18}\}$ tube consist of $\{Sb_6O_6\}$ rings with a ring width of $2.73\times2.88\times2.99$ Å ($r(O)=1.35$ Å). These 6-rings coordinate the potassium ions in a manner similar to crown ethers, with the six distances between the potassium ion and the oxygen atoms ranging from 2.77 to 3.03 Å. In addition, the potassium ions coordinate four water molecules at potassium–oxygen separations of 3.03 to 3.35 Å.

The most conspicuous feature of the SBC-1 structure is, however, the 24-ring tellurium tubular unit hosting the $\{Sb_{12}O_{18}\}$ tubes. The 24-ring has a ring width of 10.99 Å assuming a van der Waals radius $r(Te)=2.06$ Å. The tellurium unit can be viewed as a tubular sheet or net of tellurium atoms folded around the $\{Sb_{12}O_{18}\}$ tube, where the tellurium tubes are in a hexagonal packing arrangement with the individual tubes connected to its six neighboring tellurium tubes through wall sharing (Figure 1a). Although unique in its overall structure the tellurium tube is built up from well-known tellurium building blocks, that is, the "dreier chains" found in elementary tellurium, and the Te_2^{2-} dumbbells found in, for example, the two tellurides $BaSbTe_3$ and $BaBiTe_3$.[8] There are also structures known to contain flat nets of Te^- ions, for example, $SrSbTe_3$, and $KBa_2[Ag_3Te_3(Te_3)]$, and further structures that contain T-shaped $TeTe_3^{n-}$ units, for example, $NaTe_3$,[9] and $CsTe_4$.[10]

Each tellurium tube in SBC-1 thus consists of six parallel dreier single chains running along the *c* axis connected to each other through the (001) plane via Te_2^{2-} dumbbells. The tellurium atoms in the dumbbells (Te(1)) are bound to two neighboring Te atoms: one to the other Te(1) atom in the dumbbell (Te(1)–Te(1): 2.78 Å) and the other to an atom denoted Te(2) in the dreier chain (Te(1)–Te(2): 3.18 Å).

[*] Dr. A. E. C. Palmqvist
Department of Materials and Surface Chemistry
and Competence Centre for Catalysis
Chalmers University of Technology
412 96 Göteborg (Sweden)
Fax: (+46) 31-160062
E-mail: anders.palmqvist@surfchem.chalmers.se
Dr. B. B. Iversen
Department of Chemistry
University of Aarhus, 8000 Aarhus (Denmark)
Dr. E. Zanghellini
Department of Physics and Engineering Physics
Chalmers University of Technology, 412 96 Göteborg (Sweden)
Dr. M. Behm
Department of Chemical Engineering and Technology
Applied Electrochemistry
Royal Institute of Technology, 100 44 Stockholm (Sweden)
Prof. G. D. Stucky
Department of Chemistry and Biochemistry, Materials Department
University of California, Santa Barbara, CA 93106 (USA)

[**] In reviewing this manuscript, Prof. F. Liebau pointed out that there was no accepted current nomenclature for the new structure presented. This situation has now been addressed and the authors gratefully acknowledge fruitful discussions with Prof. Liebau.[1] Financial support of this work from the Swedish Foundation for International Cooperation in Research and Higher Education (STINT), ONR, Carl Trygger Foundation, and The Swedish Research Council (VR) is greatly appreciated. The authors would like to thank the beam personnel for assistance in the use of beamline X18B at NSLS, which is supported by the U.S. Dept. of Energy, Division of Materials Sciences, under contract No. DE-AC02-98CH10886.

 © 2004 Wiley-VCH Verlag GmbH & Co. KGaA, Weinheim DOI: 10.1002/anie.200351284

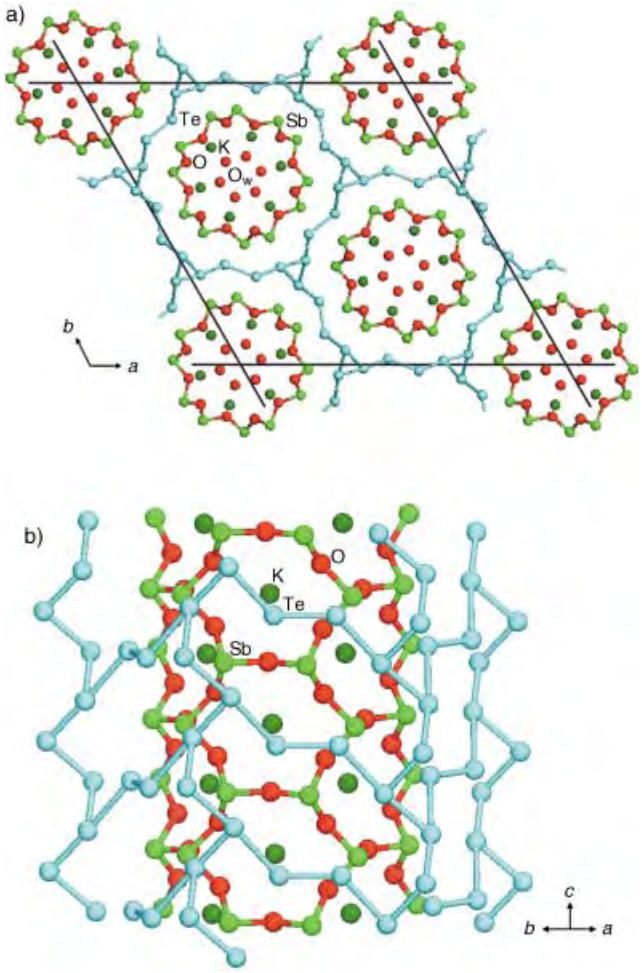


Figure 1. Structure of SBC-1: a) Projection onto the (001) plane showing the 24-ring tubular tellurium unit that hosts the 12-ring $\{Sb_{12}O_{18}\}$ tubular unit, which in turn hosts potassium ions and water molecules (represented by the oxygen O_w); b) a view of one set of tubes with water molecules omitted for clarity.

Interestingly, the Te(1) atoms are located on the opposite side of the $\{Sb_6O_6\}$ rings of the $\{Sb_{12}O_{18}\}$ tube walls from the potassium ions, at a separation of 4.05 Å. However, the Te(1) atom is located away from the center of the 6-ring, with separations between the Te(1) atoms and the six Sb atoms in the ring ranging from 3.40 to 5.51 Å. There are also three Sb atoms located in the neighboring $\{Sb_{12}O_{18}\}$ tube at distances between 3.54 and 4.36 Å from the Te(1) atom. The Te(2) atoms in the dreier chains bond to three tellurium neighbors: two Te(2) atoms within the chain (Te(2)–Te(2): 2.88 Å) besides the one to Te(1) in the Te_2^{2-} dumbbell. These Te–Te distances are comparable to those in elemental tellurium (2.84 Å).[8] The walls of the 24-ring tube consist of six tellurium 12-rings per channel segment (Figure 1b). There are potentially additional weak secondary bonds between Te(1) and Te(2) atoms, which are separated by 3.66 and 4.07 Å. If one considers the shorter distance to be a weak bond, the 12-ring becomes a 10-ring and two 3-rings. Assuming a van der Waals radius $r(\mathrm{Te}) = 2.06$ Å, the ring dimensions are $2.21 \times 2.22 \times 2.71$ Å, which makes the 12-ring non-permeable to H_2O and K^+, and gives a one-dimensional pore system.

Since tellurium and antimony have similar scattering cross sections for X-rays it is difficult to unambiguously distinguish between the two using only X-ray diffraction. For this reason EXAFS analysis of the local structure of antimony was performed to firmly establish the position of these two elements in the structure. Figure 2 shows the experimentally

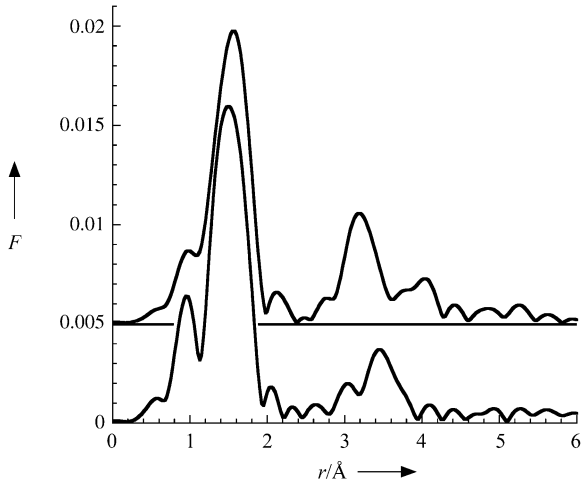


Figure 2. Experimental EXAFS spectra of the Sb K-edge of SBC-1 (bottom) compared to Sb_2O_3 (top) confirming the structure of SBC-1 as presented in Figure 1. F = Fourier transform $F(\chi(k)\,k^2)$; r = radial distance.

determined local structure of antimony in SBC-1 compared to that of antimony in Sb_2O_3, in the form of the Fourier transform of the EXAFS signal. The local structure of antimony in SBC-1 was found to be similar to that of antimony in Sb_2O_3, and the antimony and tellurium sites in SBC-1 were confirmed as being those shown in Figure 1.

To better understand the oxidation state of the host elements in the SBC-1 structure, XANES analyses were performed at the antimony and tellurium K-edges. Figure 3a presents the antimony K-edge XANES spectrum of SBC-1 compared to that of Sb_2O_3. The oxidation state of antimony in SBC-1 is the same as that in Sb_2O_3 (+3), which confirms that the $\{Sb_{12}O_{18}\}$ tubes are charge neutral. Figure 3b shows the experimental and theoretical tellurium K-edge XANES spectrum of SBC-1 compared to the experimentally determined spectrum of TeO_2 and the theoretically calculated spectra of TeO_2 and Sb_2Te_3. It is clear that tellurium in SBC-1 is not oxidized, but instead, on average, is present in a slightly reduced form. Simple electron-counting arguments suggest a mixed tellurium oxidation state with an average of −0.5. Mixed oxidation states of tellurium in polytellurides have been frequently observed, and there are examples where the average tellurium oxidation state is −0.5 and where the structure is an open framework, for example, in $[Cr(en)_3Te_6]$ (en = ethylene diamine).[11] In other examples the oxidation state of tellurium is between 0 and −0.5 and the structure is layered (e.g., Cs_3Te_{22}[12]) or has an open framework (e.g., Cs_4Te_{28}[13]). These polytelluride structures are clathrates according to the suggested nomenclature definitions,[1,14] whereas SBC-1 is a zeoate.

 © 2004 Wiley-VCH Verlag GmbH & Co. KGaA, Weinheim

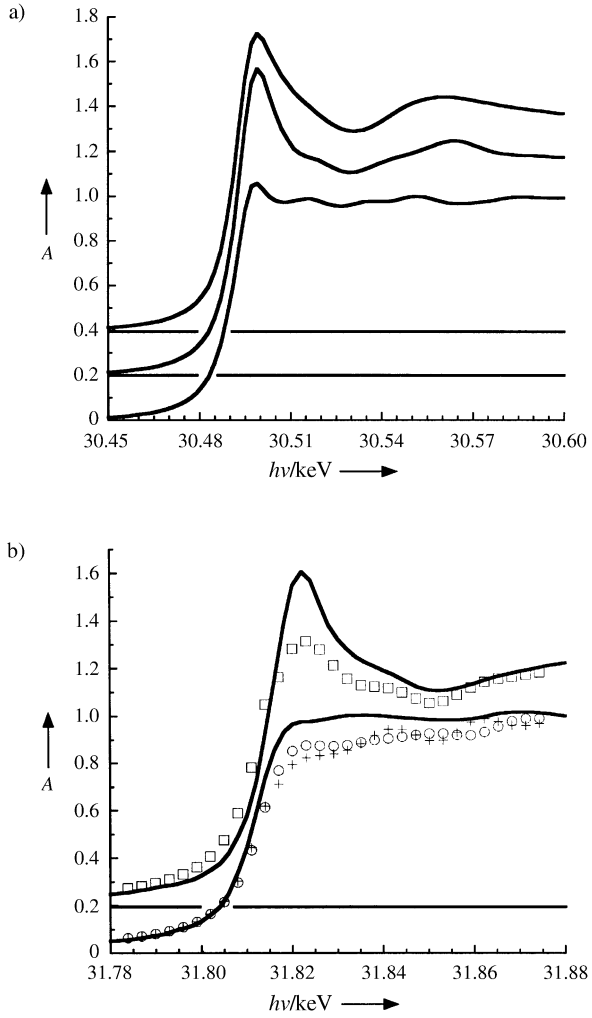


Figure 3. a) Experimental XANES spectra of the Sb K-edge of SBC-1 (top) compared to Sb (bottom) and Sb_2O_3 (middle); b) experimental (solid lines) and theoretical (symbols) XANES spectra of the Te K-edge of SBC-1 (bottom line and ○) compared to Sb_2Te_3 (+) and TeO_2 (top line and □) confirming that the antimony oxide tube is charge neutral and the tellurium is slightly reduced. *A* = normalized absorption.

SBC-1 can thus be described as a microporous polytelluride with neutral antimony(III) oxide tubular guests, which themselves host potassium ions and water molecules. In our attempt to give the proper crystal chemical formula of SBC-1, following the most recent 2001 IUPAC nomenclature for microporous materials,[15] we were informed that there was no current nomenclature for SBC-1. This situation has now been addressed for the suggested nomenclature of microporous materials of n^{th} order,[1] according to which SBC-1 is a second-order zeoate and its strongly reduced crystal chemical formula is written thus:

$$|(|K_6(H_2O)_6|\,[Sb_{12}O_{18}])_3|\,[Te_{36}]$$

Based on the structural similarities and differences with the cetineite family, SBC-1 was expected to have interesting semiconducting properties. Figure 4 shows the reflectance spectrum of SBC-1 and displays its transparency below

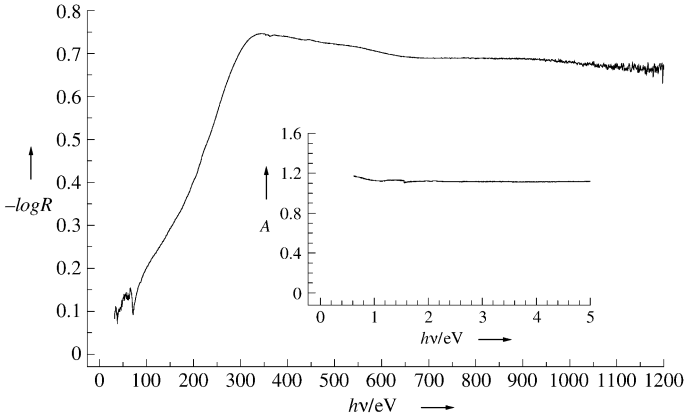


Figure 4. Diffuse reflectance FTIR spectra of a collection of ≈200 single crystals of SBC-1 showing a sharp absorption edge corresponding to an optical bandgap of 0.25 eV. The spectrum represents the logarithm of the inversion of the diffuse reflection from the sample. The inset shows the featureless response in the range 0.8–5 eV. The units on the ordinate axes are arbitrary.

0.25 eV as well as its high absorptivity there above. The inset shows that no other features appear up to at least 5 eV. The transition between these two opposite situations is characterized by a rise of absorptivity that spans about 120 meV. This rise is associated with the Urbach tail below the energy gap and with the energy dependence of the photon absorption coefficient above the gap.

Although the logarithm of the inverse reflection ($-\log R$) is not exactly equivalent to the absorption spectrum, the former is the best estimate of the latter that could be obtained from the available sample with conventional techniques. To estimate the actual energy gap (E_g) from the data, the derivative of the $-\log R$ spectrum with respect to energy was taken. It has been shown that this technique can be applied to estimate the actual value of E_g of both direct- and indirect-bandgap semiconductors directly from the absorption spectrum, within an approximation of about 5 meV.[16] This derivative spectrum presents a single peak centered at about 0.25 eV, with an almost triangular shape and a full-width at half-maximum (FWHM) value of about 120 meV. The presence of a single peak means that SBC-1 is quite probably direct-bandgap semiconductor.

Measurements of the electrical conductivity of SBC-1 were performed on single crystals oriented with a micromanipulator. Figure 5 shows the complex impedance spectra of SBC-1 along its crystallographic *c* direction and in its (001) plane. The measurements give semicircles, and from their low-frequency minima, the dc resistance *R*, and the specific conductivity were extracted. SBC-1 was found to have a highly anisotropic conductivity of $5.9\times10^{-3}\,S\,cm^{-1}$ in the *c* direction and $2.6\times10^{-6}\,S\,cm^{-1}$ in the (001) plane.

The value for the *c* direction is roughly 10^5 times higher than the corresponding values reported for the cetineite family, and since the two structures have the potassium containing $\{Sb_{12}O_{18}\}$ tubular unit in common, we attribute the higher conductivity and narrower bandgap of SBC-1 to its unique tellurium arrangement. The large anisotropy found suggests that conduction takes place in the proximity of the

 © 2004 Wiley-VCH Verlag GmbH & Co. KGaA, Weinheim

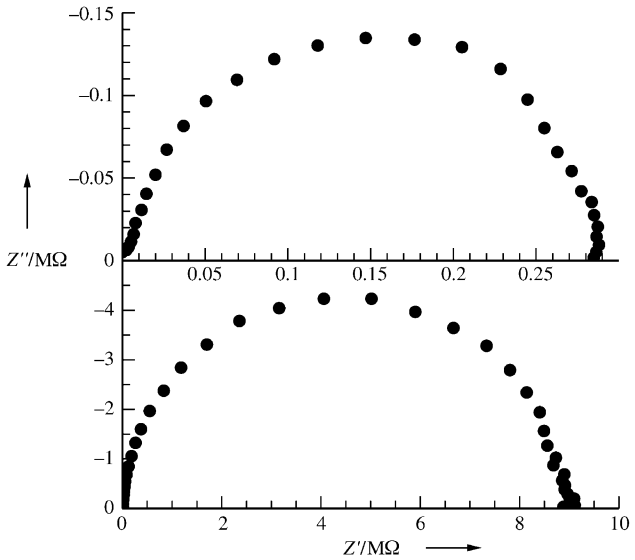


Figure 5. Impedance spectroscopy measurements of the electrical resistance of SBC-1 showing, when recalculated, that the electrical conductivity is highly anisotropic and equal to 2.6×10^{-6} S cm^{-1} in the (001) plane, and 5.9×10^{-3} S cm^{-1} in the *c* direction.

dreier chains rather than the dumbbells of the tellurium tube. The bandgap of SBC-1 is narrower than the 0.33 eV of elementary tellurium, which probably is due to the interaction between the $\{Sb_{12}O_{18}\}$ tubes and the tellurium chains. Clearly the conduction is confined to the *c* direction and thus the SBC-1 structure may be an example of a low-dimensional semiconductor. Band-structure calculations are currently underway to investigate these aspects in more detail.

The SBC-1 structure does not undergo any phase transitions in the temperature range between 100 K and 300 K, and from thermogravimetric and differential thermal analysis it was found to be stable in air up to at least 600 K at atmospheric pressure. At higher temperatures in air SBC-1 appears less stable.

In conclusion, a potentially very useful new material has been prepared by a solvothermal procedure, whose structure was established by a combination of X-ray diffraction and absorption techniques. The material (SBC-1) is a microporous narrow-bandgap semiconductor. It represents a new class of antimony(III) oxide tellurides and is the first example of a second-order zeoate structure.[1] Its narrow bandgap of 0.25 eV, high anisotropy, relatively high conductivity, and microporous structure present possibilities for SBC-1 in new applications, for example, in the fields of chemical sensors, catalysts, membranes, adsorbents, ion exchangers, electro-optics, thermoelectrics, and low-dimensional electronics.

Experimental Section

Crystallization of SBC-1 was effected by solvothermal treatment over 7 days at 453 K in a teflon-lined autoclave using a mixture of Te, Sb, KOH, *n*-propylamine, and water in a molar ratio of 1.00:0.682:1.548:0.68:18.57. The product obtained typically consisted of approximately 40–50 vol % SBC-1, mixed with varying amounts of Sb_2Te_3 and unreacted Te. The synthesis of SBC-1 is sensitive to a number of variables and a more elaborate study concerning this issue is currently underway and will be presented elsewhere.

The crystal structure of SBC-1 was determined at 293 K and 100 K using a Siemens SMART CCD single-crystal X-ray diffractometer ($Mo_{K\alpha}$). Data collection and integration was carried out using the SMART software. Averaging and absorption corrections were done using SADABS. Structure solution and refinement was performed with the SHELX-97 software. SBC-1: trigonal, $R\bar{3}$ (no. 148), $a=b=27.3361(11)$, $c=5.6909(3)$ Å at 293 K (27.282(9) and 5.662(2) Å at 100 K), $V=3682.9(3)$ Å^3, $27\times55\times400$ μm, $\rho_{calcd}=4.901$ g cm^{-3}, $2\theta_{max}=56.52°$, $\lambda=0.7107$ Å, $\mu=14.05$ mm^{-1}; no. of measured reflections = 7584, no. of unique reflections included in refinement = 1948, least-squares refinement, $N_{par}=89$, hydrogen atoms were constrained to have $U_{iso}=1.2\times$ equivalent U_{iso} of the oxygen atom to which they bond, O–H distances were refined with the restraint that they be equal within 0.02 Å, $R(int)=0.0329$, $R(\sigma)=0.0289$, $R1=0.0257$ refined against $|F|$, $wR2=0.0761$ and GOF = $S=1.262$ refined against $|F^2|$. Further details on the crystal structure investigations may be obtained from the Fachinformationszentrum Karlsruhe, 76344 Eggenstein-Leopoldshafen, Germany (fax: (+49) 7247-808-666; e-mail: crysdata@fiz-karlsruhe.de), on quoting the depository number CSD-413484.

Tellurium and antimony K-edge XANES and EXAFS measurements were performed at the X18B beamline of NSLS at Brookhaven National Laboratory, New York, on a powdered sample of SBC-1 smeared onto a Scotch tape, which was folded 24 times to ensure the absence of pinholes. Data were treated using the WinXAS 2.1 software.[17] Theoretical calculations of XANES spectra were carried out using the FEFF 8.10 software.[18]

FTIR spectroscopy data were collected in a diffuse reflectance (DR) geometry using a Grasseby Specac unit, model Selector, and a Bruker IFS 66v/S FTIR spectrometer equipped with an MCT detector and a KBr beam-splitter for the MIR, and an InGaAs detector and quartz beam-splitter for the NIR spectral ranges. A set of about 200 hand-picked single crystals was disposed at random on a flat metallic surface. The configuration of the DR unit avoids light reflected from the support surface to reach the detector and the measured radiation comes both from specular reflection at the surfaces of the sample crystals and from diffuse reflectance. The data result from the mean of 100 scans. Special care was taken to ensure that no impurity phases were present during these measurements.

The absorption of SBC-1 in the UV/Vis spectral range was measured in transmission mode through a coarse powder of ground single crystals of SBC-1, placed on a good quality, highly transparent, scotch tape using a Cary 500 UV/Vis/NIR spectrometer.

The electrical conductivity was analyzed on selected single crystals of SBC-1 using impedance spectroscopy in the frequency range of 1 Hz to 10 MHz with a Solartron 1255 HF Frequency Response Analyzer and a Solartron 1296 Dielectric Interface. In the crystallographic *c* direction of SBC-1, impedance measurements were carried out on free-standing freshly cleaved single crystals mounted with a micromanipulator between a sticky copper film and a gold wire. A droplet of silver paste was applied and left to dry between SBC-1 and the gold wire to ensure good electric contact. In the (001) plane the measurements were carried out on single crystals pressed against a gold foil by a gold wire.

Received: February 26, 2003
Revised: November 5, 2003 [Z51284]
Published Online: January 8, 2004

Keywords: antimony · microporous materials · semiconductors · tellurium · zeolite analogues

[1] F. Liebau, unpublished results; F. Liebau, personal communication.
[2] C. Sabelli, I. Nakai, S. Katsura, *Am. Mineral.* **1988**, *73*, 398–404.

 © 2004 Wiley-VCH Verlag GmbH & Co. KGaA, Weinheim

[3] U. Simon, F. Schüth, S. Schunk, X. Wang, F. Liebau, *Angew. Chem.* **1997**, *109*, 1138 – 1140; *Angew. Chem. Int. Ed. Engl.* **1997**, *36*, 1121 – 1124.
[4] F. Starrost, E. E. Krasovskii, W. Schattke, J. Jockel, U. Simon, X. Wang, F. Liebau, *Phys. Rev. Lett.* **1998**, *80*, 3316 – 3319.
[5] X. Wang, F. Liebau, *Eur. J. Solid State Inorg. Chem.* **1998**, *35*, 27 – 37.
[6] A. E. C. Palmqvist, B. B. Iversen, G. D. Stucky, Recent research reports of the 13th International Zeolite Conference (July 8 – 13, Montpellier, France), **2001**.
[7] J. A. Hanko, M. G. Kanatzidis, *Angew. Chem.* **1998**, *110*, 354 – 356; *Angew. Chem. Int. Ed.* **1998**, *37*, 342 – 344.
[8] W. S. Sheldrick, M. Wachhold, *Coord. Chem. Rev.* **1998**, *176*, 211 – 322, and references therein.
[9] P. Böttcher, R. Keller, *Z. Anorg. Allg. Chem.* **1986**, *542*, 144 – 152.
[10] P. Böttcher, U. Kretschmann, *Z. Anorg. Allg. Chem.* **1985**, *523*, 145 – 152.
[11] C. Reisner, W. Tremel, *Chem. Commun.* **1997**, 387 – 388.
[12] W. S. Sheldrick, M. Wachhold, *Angew. Chem.* **1995**, *107*, 490; *Angew. Chem. Int. Ed. Engl.* **1995**, *34*, 450 – 451.
[13] W. S. Sheldrick, M. Wachhold, *Chem. Commun.* **1996**, 607 – 608.
[14] F. Liebau, *Microporous Mesoporous Mater.* **2003**, *58*, 15 – 72.
[15] L. B. McCusker, F. Liebau, G. Engelhardt, *Pure Appl. Chem.* **2001**, *73*, 381 – 394.
[16] W. Z. Shen, *Int. J. Infrared Millimeter Waves* **2002**, *23*, 61 – 69.
[17] T. Ressler, *J. Synchrotron Radiat.* **1998**, *5*, 118 – 122.
[18] A. L. Ankudinov, B. Ravel, J. J. Rehr, S. D. Conradson, *Phys. Rev. B* **1998**, *58*, 7565 – 7576.

 © 2004 Wiley-VCH Verlag GmbH & Co. KGaA, Weinheim

Polymer Nanoparticles

Supercritical-Fluid Processing Technique for Nanoscale Polymer Particles**

*Mohammed J. Meziani, Pankaj Pathak, Razvan Hurezeanu, Mark C. Thies, Robert M. Enick, and Ya-Ping Sun**

It remains a challenge to develop reliable and versatile techniques for the production of well-dispersed organic and polymeric nanoparticles (that is, particles of 100 nm or less) for various applications (e.g., drug delivery).[1,2] Several supercritical-fluid processing methods have been identified as being promising for such a purpose.[3–7] In particular, particle formation via the rapid expansion of a supercritical solution (RESS) has been studied extensively.[8–23] In traditional RESS, the solute is dissolved in a supercritical fluid to form a solution, followed by the rapid expansion of the solution across an orifice or a capillary nozzle into ambient air. The high degree of supersaturation accompanying the rapid pressure reduction in the expansion results in homogenous nucleation and thereby the formation of well-dispersed particles.[24,25] Results from mechanistic studies of different model solutes by the RESS process indicate that both nanometer- and micrometer-sized particles are present in the expansion jet, though microparticles are generally obtained as primary products.[9,17,18,24,25]

We have made a simple but significant modification to the traditional RESS process by expanding the supercritical solution into a liquid solvent instead of ambient air, or the *r*apid *e*xpansion of a supercritical solution into a liquid *solv*ent (RESOLV).[7,26] The liquid solvent apparently suppresses the particle growth in the expansion jet, thus making it possible to obtain primarily nanosized particles. We have applied RESOLV to the preparation of small nanoparticles (less than 10 nm) with relatively narrow size distributions from a variety of inorganic materials, which include nanoscale semiconductors, metals, and metal oxides.[7,26–32] In addition, a unique feature of the RESOLV method is that it requires no nanoscale templating agents for nanoparticle formation because the templating effect is provided by the "supercritical fluid rapid expansion process", thus offering a clean way to directly couple the nanoparticles with biological species.[31,32]

In this paper we report the application of RESOLV to the preparation of nanoscale (on average less than 50 nm) polymeric particles. The selected polymer poly(heptadecafluorodecylacrylate) (PHDFDA) is highly soluble in supercritical CO_2 (under various conditions such as a pressure of 130–210 bar and a temperature of 35 °C) but insoluble in water, amenable to the RESOLV processing by rapidly expanding a supercritical CO_2 solution of the polymer into an aqueous medium. The results from characterizations of the polymeric nanoparticles produced under various experimental conditions are presented and discussed.

A RESOLV setup for the preparation of polymeric nanoparticles is shown in Figure 1. In a typical experiment, a CO_2 solution of the polymer PHDFDA (0.3 wt %) was pressurized in a syringe pump and pushed through the heating unit (a copper block wrapped with a stainless steel tube) to attain the desired supercritical temperature (35 °C) before reaching the expansion nozzle. The expanded solution (pre-expansion pressure of 207 bar) was passed through the nozzle (fused silica capillary hosted in stainless steel tubing) into a chamber containing ambient water. Since the polymer is insoluble in water, it precipitated to form nanoscale particles. The expansion of the supercritical CO_2 solution (60 mL) took about 30 min. In the first 5 min of the rapid expansion, the aqueous nanoparticle suspension appeared clear and stable. An aliquot of the clear suspension was used to prepare a specimen for scanning electron microscopy (SEM) analysis.

[*] M. J. Meziani, P. Pathak, R. Hurezeanu, Prof. Dr. Y.-P. Sun
Department of Chemistry
Clemson University, Clemson, South Carolina 29634 (USA)
Fax: (+1) 864-656-5007
E-mail: syaping@clemson.edu
M. C. Thies
Department of Chemical Engineering
Clemson University, Clemson, South Carolina 29634 (USA)
R. M. Enick
Department of Chemical Engineering
University of Pittsburgh
Pittsburgh, Pennsylvania 15261 (USA)

[**] Financial support from the National Science Foundation through the Center for Advanced Engineering Fibers and Films (an Engineering Research Center at Clemson University, EEC-9731680) and the EPSCoR program (EPS-0132573) is gratefully acknowledged.

 © 2004 Wiley-VCH Verlag GmbH & Co. KGaA, Weinheim DOI: 10.1002/anie.200352834

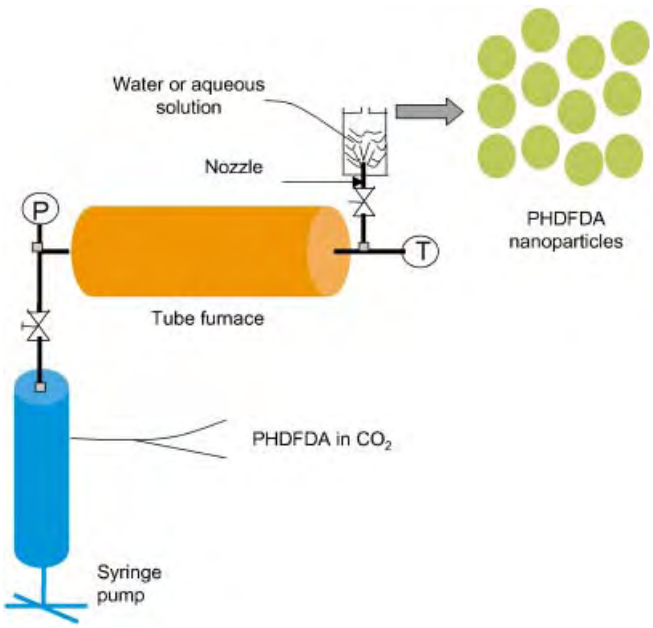


Figure 1. Experimental setup for the preparation of polymeric nanoparticles using the RESOLV process. PHDFDA = poly(heptadecafluorodecylacrylate)

The SEM image thus obtained exhibits dispersed small aggregates of nanoparticles (Figure 2). The result from an energy dispersive X-ray (EDX) analysis of the specimen confirms the presence of C, O, and F in compositions consistent with those of PHDFDA. As the rapid expansion progressed (about 15 min and longer), larger objects were seen to form in the aqueous suspension. According to SEM analyses, these suspended objects are larger aggregates of PHDFDA nanoparticles (Figure 2). It seems reasonable to suggest that the RESOLV process intrinsically produces small PHDFDA nanoparticles suspended in water and that these initially produced nanoparticles of high surface areas agglomerate to form larger aggregates in the absence of any stabilization agents in the aqueous suspension.

In an effort to prevent agglomeration of the initially formed PHDFDA nanoparticles, an aqueous NaCl solution (0.5 M) was used instead of water at the receiving end in the rapid expansion process. The increased ionic strength in the initially formed nanoparticle suspension had some stabilization effect, slowing down the agglomeration process by some degree. As shown in Figure 3, the initially formed PHDFDA nanoparticles have an average diameter of 43 nm, with a standard deviation of 8.5 nm. However, even in the presence of NaCl, the nanoparticles began to agglomerate to form visible larger aggregates during the RESOLV process. An SEM image of the nanoparticle aggregates is also shown in Figure 3.

A highly basic aqueous solution of NaOH (pH ≈ 11–12) was also evaluated for use at the receiving end in the rapid expansion process. The purpose was to test an idea, taken from inorganic nanoparticle research, of attaching OH^- ions to the surfaces of the initially formed PHDFDA nano-

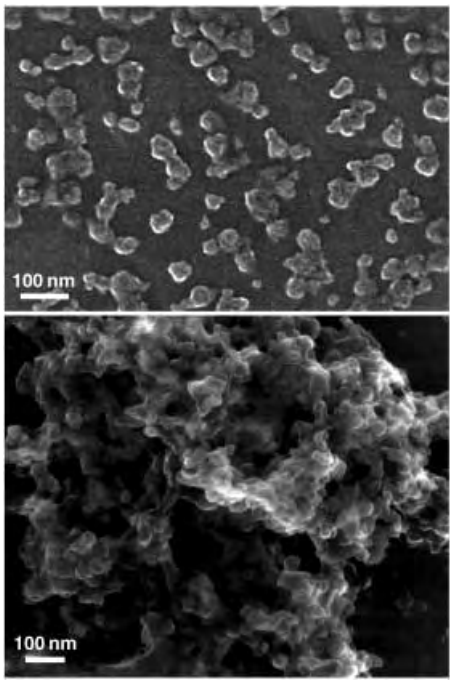


Figure 2. SEM images of PHDFDA nanoparticle specimens from aqueous suspension, obtained about 5 min (top) and 15 min (bottom) after the start of the rapid expansion process.

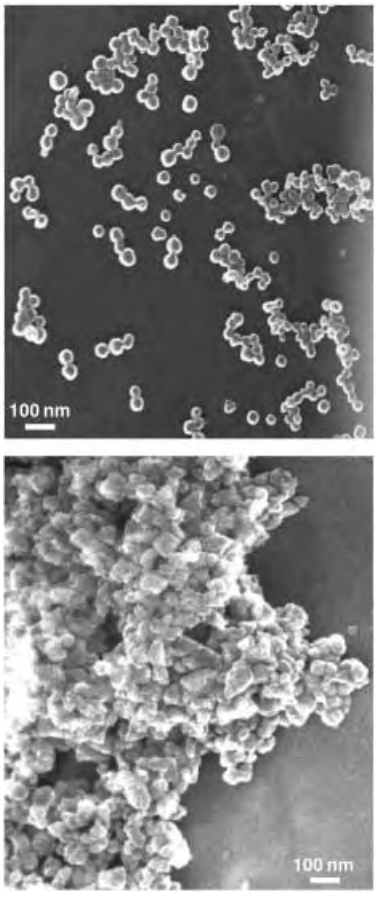


Figure 3. SEM images of PHDFDA nanoparticle specimens prepared from an aqueous suspension containing NaCl (0.5 M), obtained about 5 min (top) and 15 min (bottom) after the start of the rapid expansion process.

 © 2004 Wiley-VCH Verlag GmbH & Co. KGaA, Weinheim

particles, to prevent agglomeration due to attractive interparticle interactions. Experimentally, however, the high pH value did not stabilize the initially formed nanoparticles to a greater degree than with NaCl, as discussed above.

The PHDFDA nanoparticles formed in the RESOLV process could be protected from agglomeration by adding a surfactant such as sodium dodecyl sulfate (SDS) to a basic aqueous solution (pH ≈ 11) at the receiving end in the rapid expansion process. In the presence of SDS (20 mM), the aqueous suspension of PHDFDA nanoparticles remained stable for an extended period of time (at least several days). The dispersion of the nanoparticles in a stabilized aqueous suspension was confirmed by SEM analyses (Figure 4). SEM

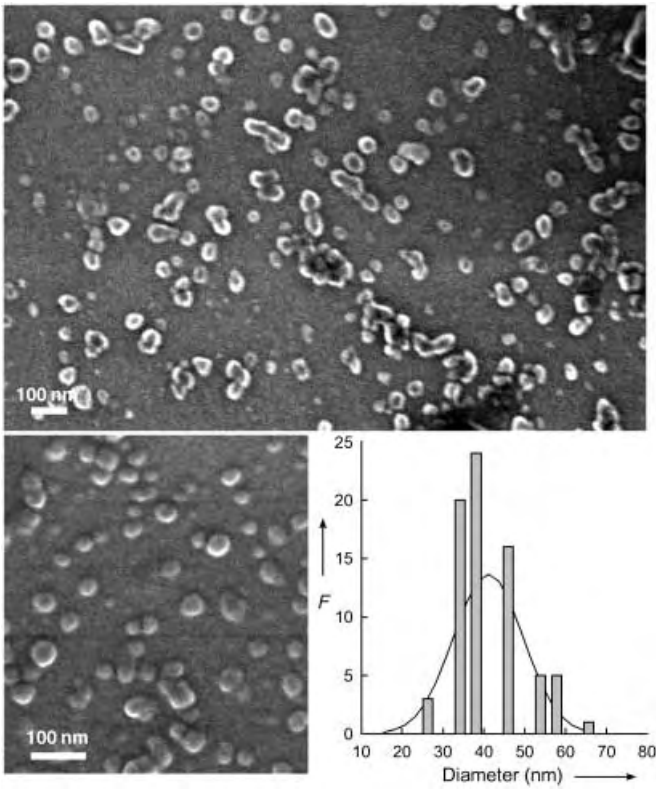


Figure 4. SEM images of a PHDFDA nanoparticle specimen prepared from a basic (pH ≈ 11) aqueous suspension containing SDS (20 mM) as a stabilization agent. A statistical analysis of the particle sizes is shown (bottom right; *F* = frequency).

images of the specimen prepared from the suspension following the RESOLV experiment exhibit no large nanoparticle aggregates. The result from an EDX analysis of the sample indicates the presence of C, F, O, S, and Na, consistent with the SDS protection of PHDFDA nanoparticles. According to a statistical analysis of the SEM images, these nanoparticles have an average diameter of 41 nm when approximated as spheres, with a standard deviation of 8.5 nm.

The results presented here show that the RESOLV process yields nanoscale polymer particles of less than 50 nm and that the nanoparticles can be obtained as primary products if the subsequent agglomeration of the nanoparticles is suppressed or eliminated.[33] According to reported modeling efforts on RESS,[25] the rapid expansion process itself should intrinsically produce small nanoparticles. Theoretical calculations have predicted the formation of nanoparticles much less than 50 nm in diameter for RESS (upstream of the Mach disk in the supersonic free-jet region).[25] The experimental observation of primarily micrometer-sized particles in traditional RESS has been attributed to the particle growth processes of condensation and coagulation during the rapid expansion (downstream of the Mach disk in the transonic and subsonic free-jet regions).[19,20,24] In this context, the use of a liquid at the receiving end of the rapid expansion process in RESOLV probably interferes or disrupts condensation and coagulation in the expansion jet, thus effectively quenching rapid particle-growth processes. After the initial formation of polymeric nanoparticles in RESOLV, the observed agglomeration of nanoparticles in aqueous suspension occurs over a longer time scale. This agglomeration process is absent in traditional RESS because there the particles are in the solid state following the expansion. While it presents a different set of technical challenges to protect the as-formed polymeric nanoparticles in RESOLV, many methods for stabilizing nanoparticle suspensions are already available.[1,2] One such method is the use of surfactant molecules, as demonstrated in this work on the effective protection of the PHDFDA nanoparticles by SDS to form a stable aqueous suspension. Thus, it is safe to conclude that RESOLV, coupled with a post-nanoparticle-formation strategy, should be further developed to become a reliable and versatile technique for the production of well dispersed polymeric and organic nanoparticles.

Experimental Section

Carbon dioxide (high-purity SFC grade) was supplied by Air Products. The monomer 3,3,4,4,5,5,6,6,7,7,8,8,9,9,10,10,10-heptadecafluorodecyl acrylate was obtained from Aldrich. PHDFDA was prepared from the monomer via solution polymerization, as reported elsewhere.[34] The polymer is semicrystalline, with a melting point of 78 °C, no glass-transition observed above room temperature, and stable up to 275 °C. According to results from gel permeation chromatography (hexafluoroisopropanol with 0.1 M sodium trifluoroacetate as mobile phase), the polymer has an average molecular weight M_W of 254000 g mol^{-1} and a polydispersity index of ≈ 3.

A Hitachi HD-2000 STEM system was used in the SEM mode for the imaging of the polymeric nanoparticles. The specimen for the SEM imaging was prepared by depositing a few drops of a dilute nanoparticle aqueous suspension onto a carbon-coated copper grid, followed by drying under ambient conditions. Energy dispersive X-ray (EDX) analysis was performed in situ on the same STEM system.

Received: September 10, 2003
Revised: November 5, 2003 [Z52834]

Keywords: aggregation · electron microscopy · nanostructures · polymers · supercritical fluids

[1] J. Rieger, D. Horn, *Angew. Chem.* **2001**, *113*, 4460; *Angew. Chem. Int. Ed.* **2001**, *40*, 4330.
[2] G. Zhang, A. Niu, S. Peng, M. Jiang, Y. Tu, M. Li, C. Wu, *Acc. Chem. Res.* **2001**, *34*, 249.
[3] a) P. York, *Pharm. Sci. Tech. Today* **1999**, *2*, 430; b) S. Palakodaty, P. York, R. Sloan, A. Kordikowski in *Supercritical Fluid*

 © 2004 Wiley-VCH Verlag GmbH & Co. KGaA, Weinheim

Technology in Materials Science and Engineering: Syntheses, Properties, and Applications (Ed.: Y.-P. Sun), Marcel Dekker, New York, **2002**, p. 439.
[4] J. Jung, M. Perrut, *J. Supercrit. Fluids*, **2001**, *20*, 179.
[5] T. L. Rogers, K. P. Johnston, R. O. Williams III, *Drug Dev. Ind. Pharm.* **2001**, *27*, 1003.
[6] L. A. Stanton, F. Dehghani, N. R. Foster, *Aust. J. Chem.* **2002**, *55*, 443.
[7] Y.-P. Sun, H. W. Rollins, J. Bandara, M. J. Meziani, C. E. Bunker in *Supercritical Fluid Technology in Materials Science and Engineering: Synthesis, Properties, and Applications* (Ed.: Y.-P. Sun), Marcel Dekker, New York, **2002**, p. 491.
[8] D. W. Matson, J. L. Fulton, R. C. Petersen, R. C. Smith, *Ind. Eng. Chem. Res.* **1987**, *26*, 2298.
[9] "Supercritical Fluid Science and Technology": R. S. Mohamed, D. S. Halverson, P. G. Debenedetti, R. K. Prud'homme, *ACS Symp. Ser.* **1989**, *406*, 355.
[10] C. J. Chang, A. D. Randolph, *AIChE J.* **1989**, *35*, 1876.
[11] A. K. Lele, A. D. Shine, *AIChE J.* **1992**, *38*, 742.
[12] E. Reverchon, G. Donsi, D. Gorgoglione, *J. Supercrit. Fluids* **1993**, *6*, 241.
[13] P. G. Debenedetti in *Supercritical Fluids: Fundamentals for Application*, Kluwer, Boston, **1994**, p. 719.
[14] S. Mawson, K. P. Johnston, J. R. Combes, J. M. DeSimone, *Macromolecules* **1995**, *28*, 3182.
[15] G.-T. Liu, K. Nagahama, *Ind. Eng. Chem. Res.* **1996**, *35*, 4626.
[16] A. Alessi, A. Cortesi, I. Kikic, N. R. Foster, S. J. MacNaughton, I. Colombo, *Ind. Eng. Chem. Res.* **1996**, *35*, 4718.
[17] C. Domingo, E. Berends, G. M. Van Rosmalen, *J. Supercrit. Fluids* **1997**, *10*, 39.
[18] H. Kröber, U. Teipel, H. Krause, *Chem. Eng. Technol.* **2000**, *23*, 763.
[19] B. Helfgen, M. Türk, K. Schaber, *Powder Technol.* **2000**, *110*, 22.
[20] M. Türk, P. Hils, B. Helfgen, K. Schaber, H.-J. Martin, M. A. Wahl, *J. Supercrit. Fluids* **2002**, *22*, 75.
[21] Y. Chernyak, F. Henon, R. B. Harris, R. D. Gould, R. K. Franklin, J. R. Edwards, J. M. DeSimone, R. G. Carbonell, *Ind. Eng. Chem. Res.* **2001**, *40*, 6118.
[22] R. K. Franklin, J. R. Edwards, Y. Chernyak, R. D. Gould, F. Henon, R. G. Carbonell, *Ind. Eng. Chem. Res.* **2001**, *40*, 6127.
[23] T. J. Young, S. Mawson, K. P. Johnston, I. B. Henriksen, G. W. Pace, A. K. Mishra, *Biotechnol. Prog.* **2000**, *16*, 402.
[24] D. M. Ginosar, W. D. Swank, R. D. McMurtery, W. J. Carmack, Proceedings of 5th International Symposium on Supercritical Fluids (April 8–12, Atlanta), **2000**.
[25] M. Weber, M. C. Thies in *Supercritical Fluid Technology in Materials Science and Engineering: Syntheses, Properties, and Applications* (Ed.: Y.-P. Sun), Marcel Dekker, New York, **2002**, p. 387.
[26] Y.-P. Sun, H. W. Rollins, *Chem. Phys. Lett.* **1998**, *288*, 585.
[27] Y.-P. Sun, H. W. Rollins, R. Guduru, *Chem. Mater.* **1999**, *11*, 7.
[28] Y.-P. Sun, R. Guduru, F. Lin, T. Whiteside, *Ind. Eng. Chem. Res.* **2000**, *39*, 4663.
[29] Y.-P. Sun, P. Atorngitjawat, M. J. Meziani, *Langmuir* **2001**, *17*, 5707.
[30] "Supercritical Carbon Dioxide Separations and Processes": M. J. Meziani, P. Pathak, L. F. Allard, Y.-P. Sun, *ACS Symp. Ser.* **2003**, *860*, 309.
[31] M. J. Meziani, H. W. Rollins, L. F. Allard, Y.-P. Sun, *J. Phys. Chem. B* **2002**, *106*, 11178.
[32] M. J. Meziani, Y.-P. Sun, *J. Am. Chem. Soc.* **2003**, *125*, 8015.
[33] Expansion into ambient air in traditional RESS under similar experimental conditions resulted in micro- and submicro-sized PHDFDA particles.
[34] A. Blasig, C. M. Shi, R. M. Enick, M. C. Thies, *Ind. Eng. Chem. Res.* **2002**, *41*, 4976.

 © 2004 Wiley-VCH Verlag GmbH & Co. KGaA, Weinheim

Three-Dimensional Networks

A Three-Dimensional Ferrimagnet Composed of Mixed-Valence Mn_4 Clusters Linked by an $\{Mn[N(CN)_2]_6\}^{4-}$ Unit**

Hitoshi Miyasaka, Kazuya Nakata, Ken-ichi Sugiura, Masahiro Yamashita, and Rodolphe Clérac**

In the field of molecule-based magnetism, tremendous effort has been devoted to the design of magnetic materials that exhibit spontaneous magnetization.[1] The molecular approach offers a unique opportunity to choose beforehand the properties of precursors and magnetic bridges to obtain magnets with desired physical properties. This strategy has already led to fascinating compounds that exhibit multifunctional physical properties.[2–4] Among the available building blocks, single-molecule magnets (SMMs) are one of the most appealing. SMMs have a large spin ground state together with a strong uniaxial anisotropy, which leads to a slow relaxation of their magnetization.[5] Therefore, these clusters can be seen as monodisperse superparamagnetic particles capable of storing information at the molecular level. Recently, Wernsdorfer et al. reported a new material composed of antiferromagnetically coupled dimeric units of SMMs.[6] They discovered that the presence of weak magnetic interactions between SMMs allows a fine tuning of the quantum properties. Their conclusions open new perspectives on the design of new magnetic materials by using SMM clusters as the building block to create more complicated architectures. In this vein, a 3D network of magnetically coupled SMMs could lead to new magnetic behavior induced by the intrinsic properties carried by these magnetic units (such as high spin state, Ising type anisotropy, quantum effects). Herein, we present the first example of such 3D magnetic materials, $[Mn_4(hmp)_4(OH)_2Mn(dcn)_6]\cdot 2\,MeCN\cdot 2\,THF$ (**1**) (Hhmp = hydroxymethylpyridine, Hdcn = dicyanamine), built on a well-known Mn_4 SMM, reported by Hendrickson, Christou,

[*] Dr. H. Miyasaka, K. Nakata, Prof. K.-i. Sugiura, Prof. M. Yamashita[+]
Department of Chemistry, Graduate School of Science
Tokyo Metropolitan University
1-1 Minami-Ohsawa, Hachioji, Tokyo 192-0397 (Japan)
and "Structural Ordering and Physical Properties"
PRESTO, Japanese science and technology agency
4-1-8 Honcho Kawaguchi, Saitama 332-0012 (Japan)
Fax: (+81) 426-77-2525
E-mail: miyasaka@comp.metro-u.ac.jp
Dr. R. Clérac
Centre de Recherche Paul Pascal, CNRS UPR 8641
115 avenue du Dr. A. Schweitzer, 33600 Pessac (France)
Fax: (+33) 5-56-84-56-00
E-mail: clerac@crpp-bordeaux.cnrs.fr
[+] CREST, Japanese science and technology agency
4-1-8 Honcho Kawaguchi, Saitama 332-0012 (Japan)

[**] This work was supported by PRESTO (H.M.) and CREST (M.Y.), Japanese science and technology agencies. R.C. would like to thank the CNRS, the Université de Bordeaux I and the Conseil Regional d'Aquitaine for financial support. We thank Prof. Claude Coulon for fruitful discussions.

 DOI: 10.1002/anie.200353093 © 2004 Wiley-VCH Verlag GmbH & Co. KGaA, Weinheim

and co-workers,[7] linked by dicyanamide $N(CN)_2^-$ to paramagnetic Mn^{II} centres.

Compound **1** has been obtained by a self-assembly reaction in a basic MeCN/THF solution that contained $[Mn(H_2O)_2](ClO_4)_x$, hmp^- ions, and $NaN(CN)_2$ in a molar ration of 1:2:1, respectively. The resulting solution was then filtered and single crystals suitable for X-ray diffraction were obtained by slow diffusion of THF. The crystal-structure analysis of **1** revealed a covalently bonded 3D structure that crystallizes in monoclinic space group, $P2_1/n$ ($Z = 2$). The 3D network is composed of two basic units: a mixed-valence $Mn_4^{II,III}$ cationic complex, $\{Mn_4(hmp)_4(\mu_3\text{-}OH)_2\}^{4+}$, and an octahedral Mn^{II} anionic moiety, $\{Mn[N(CN)_2]_6\}^{4-}$, in a 1:1 ratio (Figure 1). The Mn_4 cluster unit has a rhombic core quasi-identical to one observed for $[Mn_4(hmp)_6Br_2(H_2O)_2]Br_2\cdot 4H_2O$.[7] The four Mn ions are hexacoordinated and arranged in a double-cuboidal fashion. Two different sites of Mn ions can be identified. The Mn(2) sites (Mn(2) and Mn(2*)) are individually chelated by two hmp^- ligands, which are *cis* to each other, and are interconnected by two hydroxy O(1) bridges to form a $\{(hmp)_2Mn(2)\text{–}(OH)_2\text{–}Mn(2^*)(hmp)_2\}$ motif lying on an inversion center (* symmetry operation: $-x$, $-y$, $-z$). This moiety is connected to the two Mn(1) centers (Mn(1) and Mn(1*)) by the hydroxy oxygen atom (μ_3-O(1)), and alkoxy oxygen atoms arising from the hmp^- ligands (μ_2-O(2) and O(3)), thus forming the Mn_4 cluster core, $\{Mn_4(hmp)_4(\mu_3\text{-}OH)_2\}^{4+}$ (Figure 1). The octahedral coordination sphere of Mn(1) ion is completed by three nitrogen atoms of $N(CN)_2^-$ ligands. The other side of each $N(CN)_2^-$ is connected to a monomeric Mn^{II} ion, Mn(3). Six $N(CN)_2^-$ bridging ligands make the coordination sphere of Mn(3) octahedron and finally form a $\{Mn[N(CN)_2]_6\}^{4-}$ unit. Each of these $\{Mn_4(hmp)_4(\mu_3\text{-}OH)_2\}^{4+}$ and $\{Mn[N(CN)_2]_6\}^{4-}$ units is linked to six different neighbors with opposite charge to form the 3D network of **1** shown in Figure 2. The oxidation states of the three Mn ion sites, Mn(1) and Mn(2) ions in the cluster moiety and Mn(3) ion of $\{Mn[N(CN)_2]_6\}^{4-}$ unit, can be easily assigned as divalent, trivalent, and divalent, respectively, based on charge balance consideration, bond valence sum calculation,[8] and the presence on Mn(2) of Jahn–Teller elongation axis (N(2)–Mn(2)–O(1*); Figure 1). As expected for typical Mn^{II} ions, bond lengths around Mn(1) and Mn(3) are found in the range of 2.174(4) to 2.278(5) Å. On the other hand, bond lengths around the Mn(2) are significantly longer in the axial position (N(2)-Mn(2) = 2.213(5) Å and O(1*)-Mn(2) = 2.220(3) Å) than in the equatorial plane (average value of 1.961 Å), thus revealing a Jahn–Teller distortion. On a particular Mn_4 cluster, Jahn–Teller axes on Mn(2) and Mn(2*) are parallel to each other and individually slightly bent N(2)-Mn(2)-O(1*) = 159.6(1)°.

The temperature dependence of the magnetic susceptibility was measured on a nujol-restrained polycrystalline

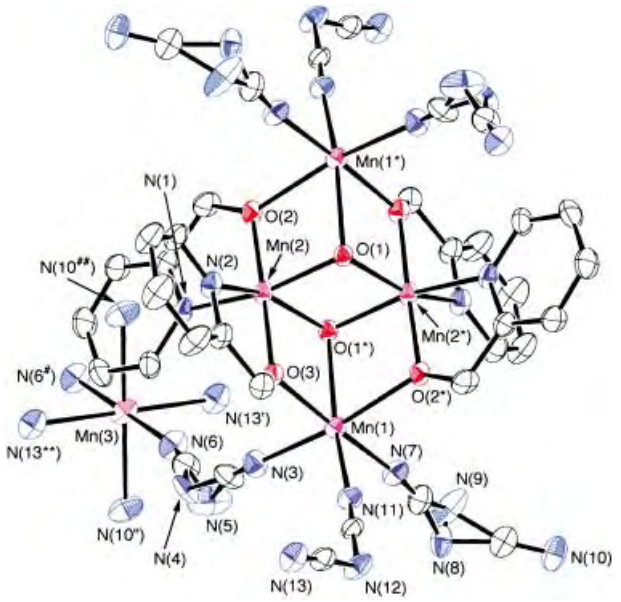


Figure 1. Structure of the repeating unit in **1** with thermal ellipsoids set at 30% probability. Hydrogen atoms and crystallization solvents are omitted for clarity.

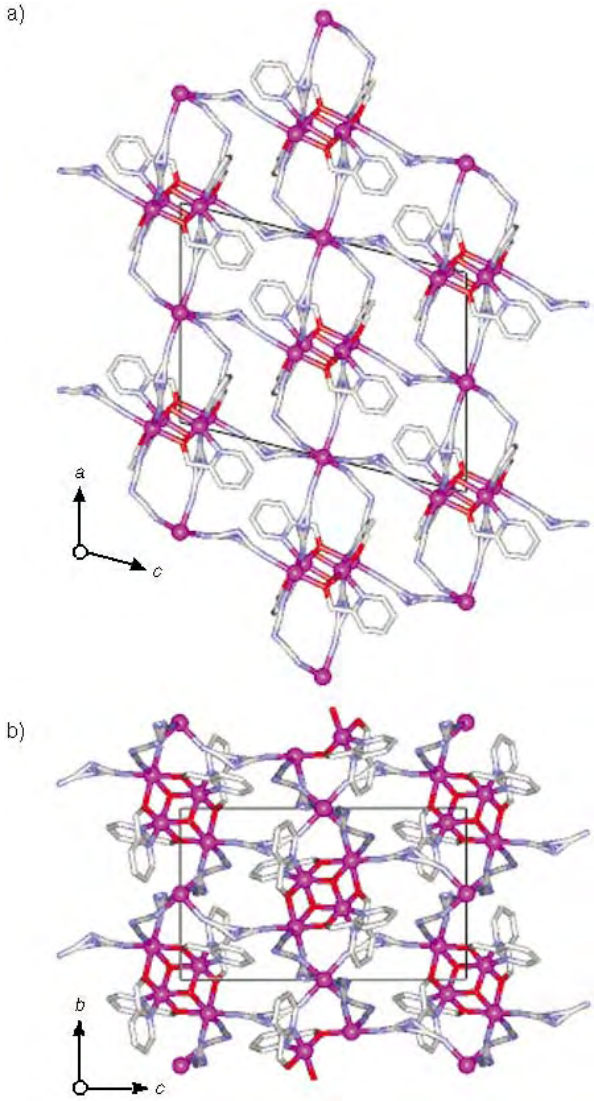


Figure 2. Perspective views of 3D packing of **1** in the *ac* (a) and *bc* (b) planes; C gray; N blue; O red; Mn purple.

 © 2004 Wiley-VCH Verlag GmbH & Co. KGaA, Weinheim

sample of **1** in the temperature range of 1.8 K to 300 K under 1 kOe.[9] Above 100 K, the $1/\chi$ product (χ is the magnetic suscepitibility) obeys the Curie-Weiss law with $C = 18.15\ cm^3\,K\,mol^{-1}$ and $\theta = +20.2$ K; C is the Curie constant, θ is the Weiss constant.[10] Based on the interaction mediated by dicyanamide being relatively small,[11] the positive Weiss constant indicates that ferromagnetic exchange interactions are dominant in the Mn_4 unit. With lowering temperature, the χT product (19.38 $cm^3\,K\,mol^{-1}$ at 300 K) increases gradually in the temperature range of 300 to 30 K and then abruptly to reach a maximum of 186.2 $cm^3\,K\,mol^{-1}$ at 3.7 K (Figure 3). At

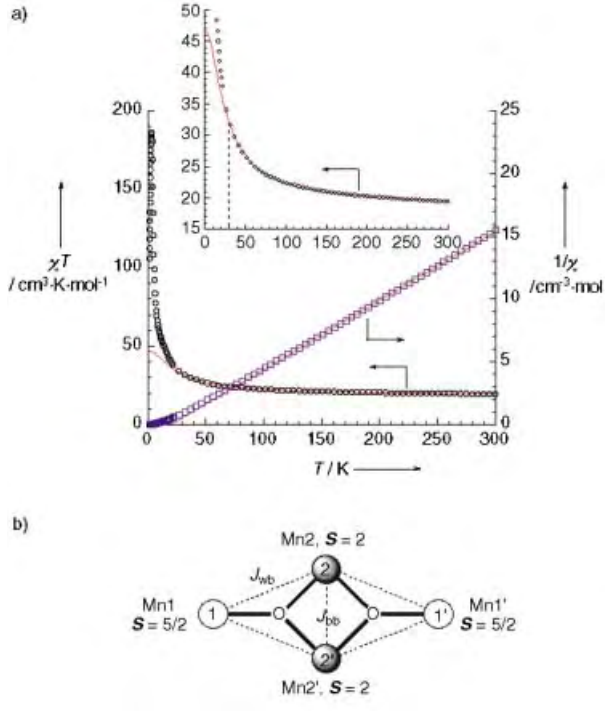


Figure 3. a) Temperature dependence of the χT product and $1/\chi$ measured on a Nujol-restrained polycrystalline sample of **1** under 1 kOe. The solid line represents a best-fitting simulation using a Kambe model to describe the Mn_4 unit susceptibility (see text). b) Schematic representation of the exchange coupling in the Mn_4 core of **1** with principal exchange pathways J_{wb} and J_{bb}.

lower temperatures, the χT decreases to 105.6 $cm^3\,K\,mol^{-1}$ at 1.8 K. It should be noted here that if a Curie contribution ($S = 5/2$, $g = 2$; S is the spin angular momentum, g is the g factor) of the $\{Mn[N(CN)_2]_6\}^{4-}$ unit is removed, the magnetic behavior of **1** above 50 K can be almost overlapped to the one observed for $[Mn_4(hmp)_6Br_2(H_2O)_2]Br_2{\cdot}4\,H_2O$.[7] Therefore, a similar analysis of the magnetic data has been performed by using the Kambe vector-coupling method.[12] Based on the structure analysis, the number of magnetic interactions can be reduced significantly: $J_{1'2} = J_{1'2'} = J_{12} = J_{12'} = J_{wb}$, $J_{22'} = J_{bb}$ (see Figure 3b; J = magnetic exchange interactions), hence the Hamiltonian can be written: [Eq (1)]

$$\mathscr{H} = \{-J_{wb}(\boldsymbol{S}_T^2 - \boldsymbol{S}_A^2 - \boldsymbol{S}_B^2) - J_{bb}(\boldsymbol{S}_A^2 - \boldsymbol{S}_1^2 - \boldsymbol{S}_{1'}^2) + g_{av}\,\mu_B\,\boldsymbol{S}_T\,\boldsymbol{H}\} + g_{Mn^{II}}\,\mu_B\,\boldsymbol{S}_{Mn^{II}}\,\boldsymbol{H} \quad (1)$$

in which $\boldsymbol{S}_A = \boldsymbol{S}_1 + \boldsymbol{S}_{1'}$, $\boldsymbol{S}_B = \boldsymbol{S}_2 + \boldsymbol{S}_{2'}$, $\boldsymbol{S}_T = \boldsymbol{S}_A + \boldsymbol{S}_B$ (the spin operators $\boldsymbol{S}$ are given in Figure 3b) g_{av} is the average g value of the Mn_4 unit. In Equation (1), the first term is modeling the magnetic behavior of the Mn_4 core and the latter is related to the Mn^{II} paramagnetic center of $\{Mn[N(CN)_2]_6\}^{4-}$ unit. Fitting of the experimental data between 30 and 300 K leads to $g_{av} = 1.95$, $g_{Mn^{II}} = 2.00$, $J_{wb}/k_B = +1.5$ K, $J_{bb}/k_B = +7.1$ K, TIP $= 600 \times 10^{-6}\ cm^3\,mol^{-1}$ (fixed; TIP = temperature-independent paramagnetism, and k_B is the Boltzmann constant). The estimated values of intracluster magnetic exchange interactions, J_{wb} and J_{bb} are similar to the values reported for $[Mn_4(hmp)_6Br_2(H_2O)_2]Br_2{\cdot}4\,H_2O$, and associated with an $S = 9$ spin ground state for the Mn_4 unit in **1**. Below 30 K, the magnetic interaction (J_{3D}) mediated by dicyanamide bridges between $\{Mn_4(hmp)_4(\mu_3\text{-}OH)_2\}^{4+}$ and $\{Mn[N(CN)_2]_6\}^{4-}$ units becomes relevant and the previous model cannot reproduce the experimental data.

As shown in Figure 4, in-phase ac magnetic susceptibility, χ', exhibits a peak located around 4 K and out-of-phase ac susceptibility, χ'', leaves from zero at 4.1 K. This behavior was found to be independent on the ac frequency used, which indicates the presence of a 3D magnetic ordering at about 4.1 K.

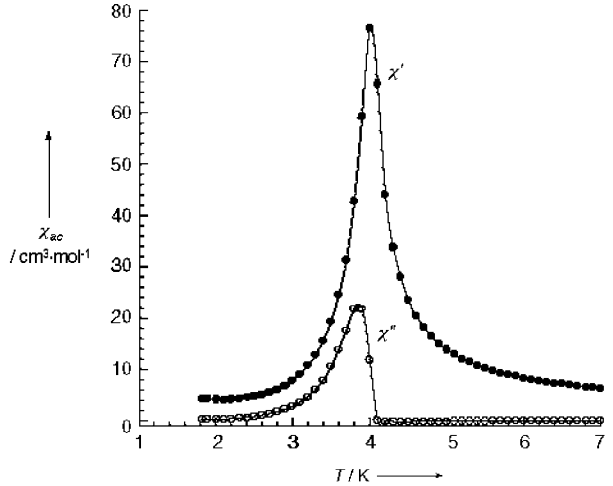


Figure 4. Temperature dependence of ac susceptibilities, in-phase (χ') and out-of-phase (χ'') measured on a Nujol-restrained polycrystalline sample of **1** at 1200 Hz (in zero applied dc field and 3 Oe oscillating ac field).

A hysteresis loop of the magnetization is observed as a function of external field at 1.9 K with a small coercive field of 28 Oe (Figure 5a). This feature disappears when the temperature reaches about 4.1 K, which indicates a long-range magnetic transition at this temperature. The magnetization was also measured up to 7 T (Figure 5b, at 1.9 K). At low fields, as expected for a magnet, the magnetization abruptly rises up to around 11 μ_B at 2 kOe. This magnetization is close to the expected value of 13 μ_B ($g = 2$) for an ordered ferrimagnetic phase in which the $S = 9$ Mn_4 units are antiferromagnetically coupled with the $S = 5/2$

 © 2004 Wiley-VCH Verlag GmbH & Co. KGaA, Weinheim

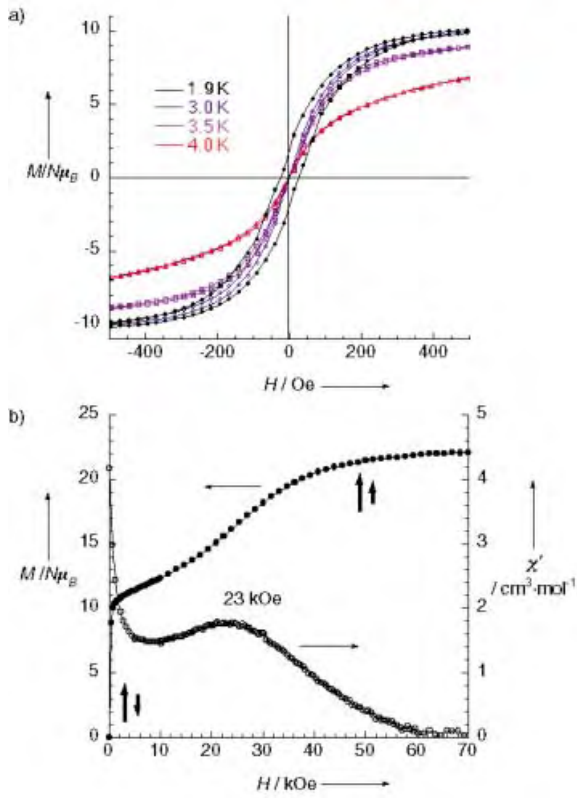


Figure 5. a) Field dependence of magnetization (hysteresis loops) measured on a Nujol-restrained polycrystalline sample of **1** below 4.0 K in the field of ±500 Oe and b) field dependence of magnetization and the in-phase ac susceptibility at 1.9 K (ac frequency, 10 Hz; oscillating ac field, 3 Oe and zero applied dc field).

$\{Mn[N(CN)_2]_6\}^{4-}$ units. When the field is further increased, the magnetization gradually reaches 22 μ_B (at 7 T), value close to the one expected for all parallel oriented spins (23 μ_B with $g=2$). This field-induced behavior is expected for ferrimagnetic systems[13,14] when the strength of the magnetic interaction between spin carriers is overcome by an applied magnetic field (H_c). The sigmoidal shape of the magnetization or the maximum observed on the χ' versus H plot is a characteristic feature associated with a spin flipping of one of the two ferrimagnetic sublattices. Because of the strong uniaxial anisotropy of the Mn_4 unit, the field-induced transition is expected to be of first order like the spin-flip transition in a metamagnetic material and related to the flipping of the moment carried by the $\{Mn[N(CN)_2]_6\}^{4-}$ units. The temperature dependence of χ' versus H plots allows the monitoring of the spin-flip transition up to about 4.1 K and confirms the critical temperature previously determined by ac susceptibility and the field dependence of the magnetization. In a simple mean-field model that treats Mn_4 units as classical Ising spins and $\{Mn[N(CN)_2]_6\}^{4-}$ units as Heisenberg spins, it is possible to estimate J_{3D}/k_B at −0.030 K from the value of the critical field ($H_C=23$ kOe, $J_{3D}/k_B=-g\,\mu_B H_c/(2\,z\,k_B S_{Mn_4})$,[13a] in which z is the number of neighbors, that is, $z=z_{Mn_4}=z_{Mn}=6$ in this system). A rough estimation of J_{3D} can also be done based on the critical temperature (4.1 K): $J_{3D}/k_B=-3\,T_c/(2\,z\sqrt{S_{Mn_4}(S_{Mn_4}+1)\,S_{Mn}(S_{Mn}+1)})$.[15] The J_{3D}/k_B is found to be −0.037 K, which is in excellent agreement with the above estimation from the critical field H_c and published values.[10]

In summary, we have reported a unique 3D ferrimagnet ($T_C=4.1$ K) composed of the SMM Mn_4 building blocks ($S=9$) and paramagnetic Mn^{II} bridges ($S=5/2$). The strong uniaxial anisotropy of the Mn_4 unit and its magnetic coupling through magnetic linkage induces a spin-flip transition at 23 kOe and leads at higher fields to the parallel alignment of the two magnetic sublattices. To the best of our knowledge, this material is the first example in which an SMM complex has been used to design 3D ordered magnets. The enhancement of the magnetic inter-SMM interaction combined with the intrinsic properties of the SMM building block could open new perspectives in the design of high temperature anisotropic magnets.

Experimental Section

$\{Mn_4(hmp)_4(OH)_2Mn(dcn)_6\}\cdot 2MeCN\cdot 2THF$ (**1**): Hydroxymethylpyridine (218 mg, 2 mmol) and NEt_4OH with 20% water (736 mg, 1 mmol) was added to an acetonitrile solution (20 mL) containing $Mn(ClO_4)_2\cdot 6H_2O$ (362 mg, 1 mmol). The mixture was gently stirred at room temperature for one hour, then solid $NaN(CN)_2$ (89 mg, 1 mmol) was added. After the mixture had been stirred for a further hour, it was filtered, and the filtrate was carefully diffused in THF (40 mL) in a narrow glass tube ($\phi=6$ mm) to form brown block crystals of **1** (Yield: 31% based on Mn). Elemental analysis calcd for $C_{48}H_{48}N_{24}O_8Mn_5$: C 42.27, H 3.55, N 24.65; found: C 42.13, H 3.47, N 24.95. IR (KBr): $\tilde{\nu}=2299$ (s), 2241 (s), 2167 (s), 1606 (s), 1569 (m), 1481 (s), 1440 (s), 1359 (s), 1286 (m), 1253 (w), 1224 (w), 1157 (m), 1070 (s), 1047 (s), 914 (w), 889 (w), 823 (w), 765 cm^{-1} (s).

X-ray crystallographic analysis of **1**: Data collections were made on a Rigaku CCD diffractometer (Saturn70) with a graphite monochromated $Mo_{K\alpha}$ radiation ($\lambda=0.71069$ Å). The structures were solved by a direct method (SIR92)[16] and expanded by using Fourier techniques.[17] The non-hydrogen atoms were refined anisotropically, while hydrogen atoms were introduced as fixed contributors. Full-matrix least-squares refinements on F^2 based on 9108 unique reflections were employed, where the unweighted and weighted agreement factors of $R=\Sigma\,||F_o|-|F_c||/\Sigma\,|F_o|$ and $wR=[\Sigma w(F_o^2-F_c^2)^2/\Sigma w(F_o^2)^2]^{1/2}$ ($I>3.00\sigma(I)$) were used. A Sheldrick weighting Scheme was used. Plots of $\Sigma w(F_o^2-F_c^2)^2$ versus F_o^2, reflection order in data collection, $\sin\theta/\lambda$ and various classes of indices showed no unusual trends. Neutral atom scattering factors were taken from Cromer and Waber.[18] Anomalous dispersion effects were included in F_{calcd}; the values $\Delta f'$ and $\Delta f''$ were those of Creagh and McAuley.[19] The values for the mass attenuation coefficients are those of Creagh and Hubbel.[20] All calculations were performed by using the CrystalStructure crystallographic program.[21] Crystal data of **1**: $C_{48}H_{48}N_{24}O_8Mn_5$, $M_r=1363.75$, monoclinic $P2_1/n$ (no. 14), $T=160\pm 1$ K, $\lambda=0.71069$ Å, $a=14.386(5)$, $b=11.232(4)$, $c=19.251(7)$ Å, $\beta=103.704(5)°$, $V=3022.2(18)$ Å^3, $Z=2$, $\rho_{calcd}=1.499$ g cm^{-3}, $F_{000}=1386.00$. Final $R=0.066$, $wR=0.146$, GOF = 1.250 for 415 parameters and a total of 9108 reflections, 4292 unique ($R_{int}=0.035$) with $I>3.00\sigma(I)$; equivalent reflections were merged. The linear absorption coefficient, μ, for $Mo_{K\alpha}$ radiation is 1.086 mm^{-1}. An empirical absorption correction was applied which resulted in transmission factors ranging from 0.702 to 0.805. The data were corrected for Lorentz and polarization effects. Maximum positive and negative peaks in ΔF map were found to be $\rho_{max}=0.71$ e Å^{-3} and $\rho_{min}=-0.56$ e Å^{-3}.

CCDC-221351 contains the supplementary crystallographic data for this paper. These data can be obtained free of charge via www.ccdc.cam.ac.uk/conts/retrieving.html (or from the Cambridge

 © 2004 Wiley-VCH Verlag GmbH & Co. KGaA, Weinheim

Crystallographic Data Centre, 12 Union Road, Cambridge CB2 1EZ, UK; fax: (+44) 1223-336-033; or deposit@ccdc.cam.ac.uk).

Received: October 15, 2003 [Z53093]

Keywords: cluster compounds · coordination modes · coordination polymers · magnetic properties · manganese

[1] a) J. Larionova, O. Kahn, S. Golhen, L. Ouahab, R. Clérac, *J. Am. Chem. Soc.* **1999**, *121*, 3349 – 3356; b) M. Ohba, N. Usuki, N. Fukita, H. Okawa, *Angew. Chem.* **1999**, *111*, 1911 – 1914 ; *Angew. Chem. Int. Ed.* **1999**, *38*, 1795 – 1798; c) J. S. Miller, *Adv. Mater.* **2002**, *14*, 1105 – 1110; d) J. R. Galán-Mascarós, K. R. Dunbar, *Angew. Chem.* **2003**, *115*, 2391 – 2395 ; *Angew. Chem. Int. Ed.* **2003**, *42*, 2289 – 2293; e) H. Miyasaka, H. Ieda, N. Matsumoto, K. Sugiura, M. Yamashita, *Inorg. Chem.* **2003**, *42*, 3509 – 3515.

[2] E. Coronado, J. R. Galán-Mascarós, C. J. Gómez-Garcia, V. Laukhin, *Nature* **2000**, *408*, 447 – 449.

[3] O. Sato, T. Iyoda, A. Fujishima, K. Hashimoto, *Science* **1996**, *272*, 704 – 705.

[4] Magnetism: A Supramolecular Function: Ed.: O. Kahn, *Nato ASI Ser. C* **1996**.

[5] Review: D. Gatteshi, R. Sessoli, *Angew. Chem.* **2003**, *115*, 278 – 309; *Angew. Chem. Int. Ed.* **2003**, *42*, 268 – 297, and references therein.

[6] W. Wernsdorfer, N. Aliaga-Alcalde, D. N. Hendrickson, G. Christou, *Nature* **2002**, *416*, 406 – 409.

[7] a) E. K. Brechin, J. Yoo, M. Nakano, J. C. Huffman, D. N. Hendrickson, G. Christou, *Chem. Commun.* **1999**, 783 – 784; b) J. Yoo, E. K. Brechin, A. Yamaguchi, M. Nakano, J. C. Huffman, A. L. Maniero, L.-C. Brunel, K. Awaga, H. Ishimoto, G. Christou, and D. N. Hendrickson, *Inorg. Chem.* **2000**, *39*, 3615 – 3623.

[8] I. D. Brown, D. Altermatt, *Acta Crystallogr. Sect. B* **1985**, *41*, 244 – 247.

[9] The polycrystalline samples for all magnetic measurements were restrained in nujol to avoid the partial reorientation of the crystals during magnetic measurements.

[10] The Curie constant is in good agreement with the value of 19.1 $cm^3 K mol^{-1}$ expected for three $S = 5/2$ Mn^{II} and two $S = 2$ Mn^{III} ions (with $g = 2$).

[11] a) S. R. Batten, P. Jensen, B. Moubaraki, K. S. Murray, R. Robson, *Chem. Commun.* **1998**, 439 – 440; b) M. Kurmoo, C. J. Kepert, *New J. Chem.* **1998**, *22*, 1515 – 1524; c) J. L. Manson, C. R. Kmety, Q. Z. Hunang, J. W. Lynn, G. M. Bendele, S. Pagola, P. W. Stephens, L. M. Liablesands, A. L. Rheingold, A. J. Epstein, J. S. Miller, *Chem. Mater.* **1998**, *10*, 2552 – 2560; d) J. L. Manson, C. D. Incarvito, A. L. Rheingold, J. S. Miller, *J. Chem. Soc. Dalton Trans.* **1998**, 3705 – 3706; e) P. Jensen, S. R. Batten, G. D. Fallon, B. Moubaraki, K. S. Murray, D. J. Price, *Chem. Commun.* **1999**, 177 – 178; f) J. L. Manson, C. R. Kmety, A. J. Epstein, J. S. Miller, *Inorg. Chem.* **1999**, *38*, 2552 – 2553; g) J. L. Manson, A. M. Arif, C. D. Incarvito, L. M. Liable-Sands, A. L. Rheingold, J. S. Miller, *J. Solid State Chem.* **1999**, *145*, 369 – 378; h) S. R. Marshall, C. D. Incarvito, J. L. Manson, A. L. Rheingold, J. S. Miller, *Inorg. Chem.* **2000**, *39*, 1969 – 1973; i) A. Escuer, F. A. Mautner, N. Sanz, R. Vicente, *Inorg. Chem.* **2000**, *39*, 1668 – 1673; j) I. Dasna, S. Golhen, L. Ouahab, O. Peña, J. Guillevic, M. Fettouhi, *J. Chem. Soc. Dalton Trans.* **2000**, 129 – 132; k) H. Miyasaka, R. Clérac, C. S. Campos-Fernández, K. R. Dunbar, *Inorg. Chem.* **2001**, *40*, 1663 – 1671.

[12] K. Kambe, *J. Phys. Soc. Jpn.* **1950**, *5*, 48.

[13] a) S. Chikazumi, *Physics of Ferromagnetism*, Clarendon Press, Oxford Science Publications, Oxford, **1997**, p. 521; b) A. Herpin, *Théorie du Magnétisme*, Blibliothèque des Sciences et Techniques Nucléaires, Presses Universitaires de France, Paris, **1968**, p. 620.

[14] a) M. Matsuura, Y. Okuda, M. Morotomi, H. Mollymoto, M. Date, *J. Phys. Soc. Jpn.* **1979**, *46*, 1031 – 1032; b) A. E. Clark, A. Callen, *J. Appl. Phys.* **1968**, *39*, 5972 – 5982.

[15] S. Ohkoshi, T. Iyoda, *Phys. Rev. B* **1997**, *56*, 11642 – 11652.

[16] SIR92: A. Altomare, M. C. Burla, M. Camalli, M. Cascarano, C. Giacovazzo, A. Guagliardi, G. Polidori, *J. Appl. Crystallogr.* **1994**, *27*, 435.

[17] DIRDIF99: P. T. Beurskens, G. Admiraal, G. Beurskens, W. P. Bosman, R. de Gelder, R. Israel, J. M. M. Smits, The DIRDIF99 program system, Technical Report of the Crystallography Laboratory, University of Nijmengen, The Netherlands, **1999**.

[18] D. T. Cromer, J. T. Waber, *International Tables for Crystallography* Vol IV, The Kynoch Press, Birmingham, England, **1974**, Table 2.2A.

[19] D. C. Creagh, W. J. McAuley, *International Tables for Crystallography*, *Vol. C* (Ed.: A. J. C. Wilson), Kluwer Academic Publishers, Boston, **1992**, pp. 219 – 222, Table 4.2.6.8.

[20] D. C. Creagh, J. H. Hubbell, *International Tables for Crystallography*, *Vol. C* (Ed.: A. J. C. Wilson), Kluwer Academic Publishers, Boston, **1992**, pp. 200 – 206, Table 4.2.4.3.

[21] CrystalStructure 3.15: Crystal structure analysis program, Rigaku and Rigaku/MSC, 9009 New Trails Dr. The Woodlands TX 77381, USA, **2000–2002**.

 © 2004 Wiley-VCH Verlag GmbH & Co. KGaA, Weinheim

Reductive Aldol Reaction

Catalytic Generation of Indium Hydride in a Highly Diastereoselective Reductive Aldol Reaction**

Ikuya Shibata, Hirofumi Kato, Tatsuya Ishida, Makoto Yasuda, and Akio Baba**

The reductive aldol reaction of metal hydrides, enones, and aldehydes is a valuable route to β-hydroxyketones because it is a convenient one-pot method without the need to synthesize metal enolates. However, a difficulty of this reaction is that aldehydes are more sensitive than enones to

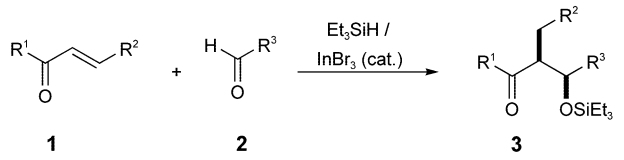
[*] Dr. I. Shibata, H. Kato, T. Ishida, Dr. M. Yasuda, Prof. Dr. A. Baba
Department of Molecular Chemistry
Science and Technology Center for Atom, Molecules and Ions Control
Graduate School of Engineering, Osaka University
2-1 Yamadaoka, Suita, Osaka 565-0871 (Japan)
Fax: (+81) 66879-7387
E-mail: shibata@chem.eng.osaka-u.ac.jp
baba@chem.eng.osaka-u.ac.jp

[**] This research was carried out at the Strategic Research Base "Handai Frontier Research Center" supported by the Japanese Government's Special Coordination Fund for Promoting Science and Technology, and was partially supported by a Grant-in-Aid for Scientific Research from the Ministry of Education, Science, Sports, and Culture.

Supporting information for this article is available on the WWW under http://www.angewandte.org or from the author.

 DOI: 10.1002/anie.200352738 © 2004 Wiley-VCH Verlag GmbH & Co. KGaA, Weinheim

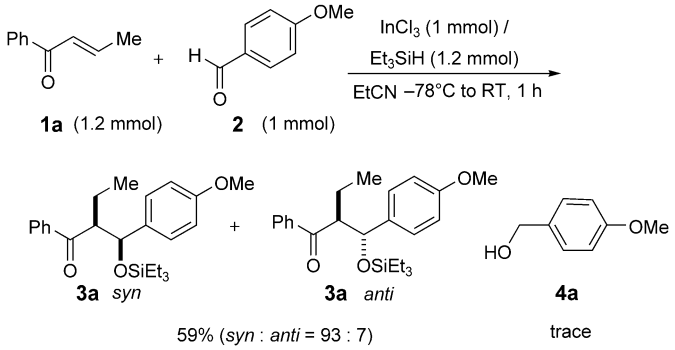
conventional metal hydrides.[1] Furthermore, reagents that achieve high diastereoselectivity have scarcely been reported. We have already reported the initiation of reductive aldol reactions by dihaloindium hydrides (Cl_2InH and Br_2InH), generated by transmetalation of nBu$_3$SnH and In^{III} halides InX_3.[2] However, since indium hydrides should be generated prior to the addition of enones or aldehydes, equimolar amounts of InX_3 must be treated with nBu$_3$SnH before the reaction.[3,4] Here we report a superior method in which no presynthesis of indium hydrides is required and where nBu$_3$SnH is not used. In particular, the catalytic use of $InBr_3$ was acieved (Scheme 1).



Scheme 1. Reductive aldol reaction.

We focused on hydrosilanes as hydride sources instead of nBu$_3$SnH. Active metal hydrides such as $NaBH_4$ and $LiAlH_4$ are not appropriate as they readily reduce aldehydes in the absence of InX_3. Trialkyl silanes are stable liquids that are easy to handle and have low toxicity.[5] They have no reactivity towards carbonyl compounds in the absence of additives.[5b] When transmetalation with InX_3 occurs, only indium hydrides could act as reactive species in reactions with electrophiles.

Initially, we applied the $Et_3SiH/InCl_3$ system to the reductive aldol reaction. Thus, 1-phenyl-2-buten-1-one (**1a**, 1.2 mmol) and *p*-methoxybenzaldehyde (**2**, 1 mmol) were added in one portion to a solution of $InCl_3$ (1 mmol) and Et_3SiH (1.2 mmol) in THF, but only a trace of silyl aldolate **3a** was obtained. However, when the reaction was performed in EtCN, the yield of **3a** was increased to 59% based on **2** (Scheme 2).



Scheme 2. Reductive aldol reaction with an equimolar amount of $InCl_3$.

For the nBu$_3$SnH/InX_3 system, we earlier reported the formation of thermodynamically stable *anti*-aldol adducts under aprotic conditions.[2] Furthermore, a serious problem was the reduction of the starting aldehydes, which gave **4** as an unavoidable side product. In contrast, the hydrosilane-promoted reaction in Scheme 2 has opposite diastereoselectivity and gives *syn*-aldolate **3a** even under aprotic conditions. Moreover, the result given in Scheme 2 is noteworthy because the reduction of aldehyde scarcely occurred.

Next, we investigated the generation of indium hydride by transmetalation. $Et_3SiH/InCl_3$ was chosen for comparison with our previously reported generation of Cl_2InH from nBu$_3$SnH/$InCl_3$.[6] When $InCl_3$ and Et_3SiH were mixed in CD_3CN at −10 °C for 5 min, ^{1}H NMR analysis showed a new peak at $\delta = 6.6$ ppm besides the Et_3SiH peak at $\delta = 3.6$ ppm.[6a] The peak at $\delta = 6.6$ ppm is consistent with our previously reported value for Cl_2InH generated from the nBu$_3$SnH/$InCl_3$ system, for which transmetalation occurred smoothly at −78 °C in THF. After stirring the solution of $Et_3SiH/InCl_3$ at −10 °C for 20 min, the peak of Cl_2InH gradually decreased because of its instability, while the peak of Et_3SiH still remained. When the ^{1}H NMR analysis was performed in [D$_8$]THF, no peaks other than that of Et_3SiH were observed. Although the transmetalation was slow compared with the nBu$_3$SnH/$InCl_3$ system, it was found that Cl_2InH was generated from $Et_3SiH/InCl_3$ in nitrile solvents.

Thus, the effective reaction shown in Scheme 2 is explainable: Indium hydride generated in situ promotes 1,4-reduction of enone **1a** to the indium enolate, which gives aldolate **3** by reaction with aldehyde **2**. The formation of *syn*-aldolates **3a** indicates that immediate trapping of kinetically controlled *syn*-indium aldolate would occur by Et_3SiH. This result suggests the possibility of using indium halides as catalysts, because the silicon trapping agent generates indium hydride.

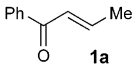
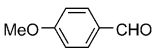
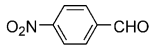
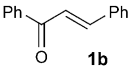
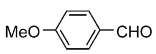
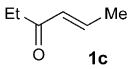
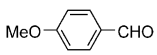
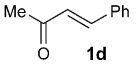
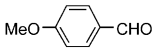
Next we investigated the catalytic use of indium halides. As shown in Table 1, the use of $InCl_3$ (10 mol%) resulted in an unsatisfacory yield of silyl aldolate **3a** (entry 1). However, **3a** was obtained in 75% yield when $InBr_3$ was used as the catalyst (entry 2). *p*-Nitrobenzaldehyde and benzaldehyde gave **3b** and **3c**, respectively (entries 3 and 4). Aliphatic aldehydes were also applicable to give **3d–f** (entries 5–7). It is noteworthy that no reduction of aldehydes **2** took place in these cases. Thus, the present system exhibits high chemo- and regioselectivity for enones. As mentioned previously, these results represent an advantage over the nBu$_3$SnH/$InBr_3$ system, which is seriously limited to the reaction with *p*-anisaldehyde because the system could not prevent the reduction of electrophilic aldehydes such as *p*-nitrobenzaldehyde. Enones bearing aromatic and aliphatic substituents were also reactive (entries 8–12).

A plausible catalytic cycle for $InBr_3$ is shown in Scheme 3. Initially, Br_2InH is generated by the slow transmetalation of $InBr_3$ with Et_3SiH. The generated Br_2InH next undergoes 1,4-addition with enone **1** to give indium enolate A. In this step, Br_2InH does not reduce the coexistent aldehydes **2**. The absence of aldehyde reduction is due to the low concentration of Br_2InH from the slow transmetalation. In contrast, in the case of nBu$_3$SnH/$InBr_3$, Br_2InH is formed in high concentration because of the easy transmetalation of nBu$_3$SnH with $InBr_3$ and the equimolar reaction, which was accompanied by partial reduction of the aldehydes. (*Z*)-Indium enolate A can be considered to be generated initially because of the preferred 1,4-addition of indium hydride to the *s-cis* form of enone **1**.[7] Indium enolate A reacts with **2** via a Zimmerman–

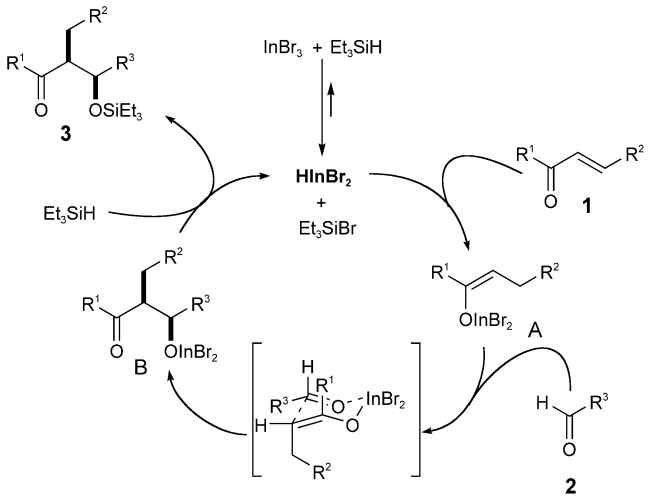
 © 2004 Wiley-VCH Verlag GmbH & Co. KGaA, Weinheim

Table 1: Diastereoselective reductive aldol reactions.[a]

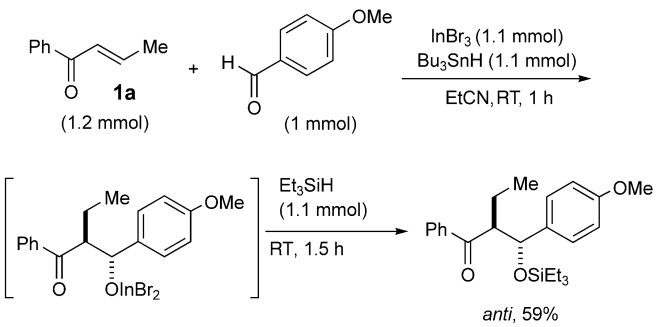


Entry	Enone **1**	Aldehyde **2**	Product	Yield [%]	*syn*:*anti*
1	 **1a**		**3a**	33[b]	>99:1
2			**3a**	75	90:10
3			**3b**	59	>99:1
4		PhCHO	**3c**	78	92:8
5		$PhCH_2CHO$	**3d**	40	>99:1
6		*t*BuCHO	**3e**	73	>99:1
7		Et_2CHO	**3f**	87	90:10
8	 **1b**		**3g**	82	>99:1
9		PhCHO	**3h**	65[c]	78:22
10	 **1c**		**3i**	61	>99:1
11		PhCHO	**3j**	40	>99:1
12	 **1d**		**3k**	46	>99:1

[a] Conditions: Et_3SiH (1.2 mmol), $InBr_3$ (0.1 mmol), enone **1** (1 mmol), EtCN (1 mL). [b] $InCl_3$ was used instead of $InBr_3$. [c] Product was isolated as desilylated aldol adduct.



Scheme 3. Plausible catalytic cycle.



Scheme 4. Trapping of indium aldolate by a trialkyl silane.

Traxler six-membered cyclic transition state[8] to form *syn*-indium aldolate B, which is immediately trapped by Et_3SiH. Thus, *syn*-silyl aldolate **3** is obtained with regenation of Br_2InH. In this step, there is the possibility of trapping of indium aldolate B with Et_3SiBr to regenerate $InBr_3$, because Et_3SiBr is produced by the initial transmetalation step. However, we consider that the trapping of indium aldolate A by Et_3SiH is plausible considering the initial concentrations of Et_3SiH and Et_3SiBr. Moreover, it was confirmed that the Et_3SiBr-free indium aldolate generated by $nBu_3SnH/InBr_3$[2] is easily trapped by Et_3SiH (Scheme 4).

In summary, the Et_3SiH-promoted diastereoselective reductive aldol reaction has been established by using $InBr_3$ as a catalyst. This three-component reaction afforded only silyl aldolates as products without any side reactions. The silicon compounds, including the Et_3SiH starting material, could be easily removed by evaporation after the reaction. The *syn* selectivity obtained here is higher than that of any other reductive aldol reaction, including those promoted by tin hydride.

Received: August 28, 2003 [Z52738]

Keywords: aldol reaction · diastereoselectivity · hydroxyketones · indium · silanes

[1] a) I. Matsuda, K. Takahashi, S. Sato, *Tetrahedron Lett.* **1990**, *31*, 5331–5334; b) E. J. Enholm, Y. Xie, K. A. Abboud, *J. Org. Chem.* **1995**, *60*, 1112–1113; c) T. Kawakami, M. Miyatake, I. Shibata, A. Baba, *J. Org. Chem.* **1996**, *61*, 376–379; d) T. Ooi, K. Doda, D. Sakai, K. Maruoka, *Tetrahedron Lett.* **1999**, *40*, 2133–2136; e) S. J. Taylor, M. O. Duffey, J. P. Morken, *J. Am. Chem. Soc.* **2000**, *122*, 4528–4529.

[2] K. Inoue, T. Ishida, I. Shibata, A. Baba, *Adv. Synth. Catal.* **2002**, *344*, 283–287.

[3] The potential of indium compounds in the field of organic synthesis has been intensively studied. Barbier-type allylation: a) S. Araki, H. Ito, Y. Butsugan, *J. Org. Chem.* **1988**, *53*, 1831–1833; b) C. J. Li, T. H. Chan, *Tetrahedron Lett.* **1991**, *32*, 7017–7020; c) C. J. Li, T. H. Chan, *Tetrahedron* **1999**, *55*, 11149–11176; d) C. J. Li, *Tetrahedron Lett.* **1995**, *36*, 517–518; e) M. B. Isaac, T. H. Chan, *Tetrahedron Lett.* **1995**, *36*, 8957–8960; f) L. A. Paquette, T. M. Mitzel, *J. Org. Chem.* **1996**, *61*, 8799–8804; Pd-catalyzed allylation: g) S. Araki, T. Kamei, T. Hirashita, H. Yamamura, M. Kawai, *Org. Lett.* **2000**, *2*, 847–849. Pinacol coupling h) H. J. Lim, G. Keum, S. B. Kang, B. Y. Chung, Y. Kim, *Tetrahedron Lett.* **1998**, *39*, 4367–4368; Transmetalation: i) J. A. Marshall, K. W. Hinkle, *J. Org. Chem.* **1995**, *60*, 1920–1921; j) J. A. Marshall, K. W. Hinkle, *J. Org. Chem.* **1996**, *61*, 105–108; k) M. Yasuda, T. Miyai, I. Shibata, R. Nomura, H. Matsuda, A.

 © 2004 Wiley-VCH Verlag GmbH & Co. KGaA, Weinheim

Baba, *Tetrahedron Lett.* **1995**, *36*, 9497 – 9500; l) T. Miyai, K. Inoue, M. Yasuda, A. Baba, *Synlett* **1997**, 699 – 700.

[4] Although several indium hydrides have been reported, they have scarcely been used in organic synthesis. $LiPh_nInH_{4-n}$ ($n = 0$–2): a) M. Yamada, K. Tanaka, S. Araki, Y. Butsugan, *Tetrahedron Lett.* **1995**, *36*, 3169 – 3172; b) M. Yamada, T. Horie, M. Kawai, H. Yamamura, S. Araki, *Tetrahedron* **1997**, *53*, 15685 – 15690; $InH_3[CN(Mes)C_2H_2N(Mes)]$ and $InH_3[P(C_6H_{11})_3]$: c) C. D. Abernethy, M. L. Cole, A. J. Davies, C. Jones, *Tetrahedron Lett.* **2000**, *41*, 7567 – 7570.

[5] a) N. Greeves in *Comprehensive Organic Synthesis*, *Vol. 8* (Eds.: B. M. Trost, I. Fleming), Pergamon, Oxford, **1991**, p. 1; b) L. Fry, M. Orfanopoulos, M. G. Adlington, W. R. Dittman, S. B. Silverman, *J. Org. Chem.* **1978**, *43*, 374 – 375.

[6] We reported the first generation of Cl_2InH, which showed a ^1H NMR peak at $\delta = 6.5$ ppm in THF. a) T. Miyai, K. Inoue, M. Yasuda, I. Shibata, A. Baba, *Tetrahedron Lett.* **1998**, *39*, 1929 – 1932; b) K. Inoue, M. Yasuda, I. Shibata, A. Baba, *Tetrahedron Lett.* **2000**, *41*, 113 – 116; c) K. Inoue, A. Sawada, I. Shibata, A. Baba, *Tetrahedron Lett.* **2001**, *42*, 4661 – 4663.

[7] a) G. P. Boldrini, F. Mancini, E. Tagliavini, C. Trombini, A. Umani-Ronchi, *J. Chem. Soc. Chem. Commun.* **1990**, 1680 – 1681; b) G. P. Boldrini, M. Bortolotti, F. Mancini, E. Tagliavini, C. Trombini, A. Umani-Ronchi, *J. Org. Chem.* **1991**, *56*, 5820 – 5826.

[8] H. E. Zimmerman, M. D. Traxler, *J. Am. Chem. Soc.* **1957**, *79*, 1920 – 1923.

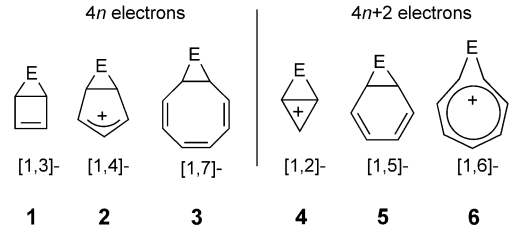
 © 2004 Wiley-VCH Verlag GmbH & Co. KGaA, Weinheim

Ring Rearrangements

The Circumambulation of a Phosphirane: Taking 9-Phenyl-9-phosphabicyclo[6.1.0]nona-2,4,6-triene for a "Walk"**

*Rosa E. Bulo, Helen Jansen, Andreas W. Ehlers, Fransiscus J. J. de Kanter, Marius Schakel, Martin Lutz, Anthony L. Spek, and Koop Lammertsma**

Degenerate rearrangements are among the most captivating features of bicyclic hydrocarbons with three-membered rings.[1] These bishapto circumambulations are referred to as "walks", with the cyclopropane ring moving around the perimeter of the other ring in a series of [1,*n*]-sigmatropic shifts. When 4*n* electrons participate (Scheme 1, **1**–**3**), the



Scheme 1. Circumambulating 4*n* and 4*n*+2 systems.

Woodward–Hoffmann (WH) rules for concerted pericyclic processes predict the migrating group to invert,[2] causing the structure to remain unaltered (Figure 1a). With $4n+2$ electrons involved, (Scheme 1, **4**–**6**) the migrating group should retain its configuration, causing rearrangements between two isomeric structures that reflect a non-least motion pathway (Figure 1b), but such systems often follow a symmetry-forbidden stereochemical path with diradical character.[3]

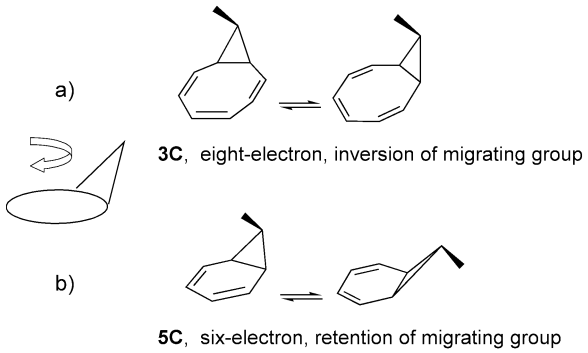


Figure 1. "Walk" rearrangement for a) six-electrons and b) eight-electron hydrocarbons.

"Walk" rearrangements are also known for **1**, **2**, and **5**, with sulfur, nitrogen, or oxygen as the migrating atom,[1] but not with phosphorus, though a degenerate rearrangement along part of a ring has been reported for a triphospha analogue of **1**, with a weak phosphorus–phosphorus bond.[4] Whereas thio,[5] oxa,[6] amino,[7] and phospha analogues[8] of **3** are known, the potential for "walk" activity has not been recognized for any. Herein we present the first such bishapto eight-electron phosphirane circumambulation for **3P** (E = PPh).

The reaction of the cyclooctatriene dianion with dichlorophenylphosphane affords exclusively *exo*-**3P**, the crystal structure of which is shown in Figure 2. The ^{1}H NMR spectrum of **3P** does not display noticeable line broadening at 300 K, but on selective inversion (by a DPFGE (double-pulsed field-gradient spin echo) sequence)[9] of one of the ring

[*] Dr. R. E. Bulo, H. Jansen, Dr. A. W. Ehlers, Dr. F. J. J. de Kanter, Dr. M. Schakel, Prof. Dr. K. Lammertsma
Vrije Universiteit, FEW, Department of Chemistry
De Boelelaan 1083, 1081 HV Amsterdam (The Netherlands)
Fax: (+31) 20-444-7488
E-mail: lammert@chem.vu.nl
Dr. M. Lutz, Prof. Dr. A. L. Spek
Bijvoet Center for Biomolecular Research
Department of Crystal and Structural Chemistry
Utrecht University (The Netherlands)

[**] We are very grateful to Prof. Dr. S. Grimme, University of Münster, for sharing the information on the SCS-MP2 method[2] prior to publication. This work was supported by The Netherlands Foundation for Chemical Sciences (CW) and by the National Computing Facilities Foundation (NCF) for the use of supercomputing facilities, both with financial support from the Netherlands Organization for Scientific Research (NWO).

Supporting information for this article is available on the WWW under http://www.angewandte.org or from the author.

 © 2004 Wiley-VCH Verlag GmbH & Co. KGaA, Weinheim DOI: 10.1002/anie.200351855

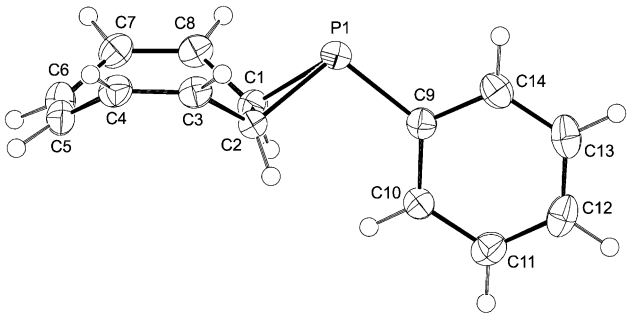


Figure 2. Displacement ellipsoid plot (50% probability level) of **3P**. Selected bond lengths [Å], angles [°], and torsion angles [°]: C1-C2 1.4954(18), P1-C2 1.8731(13), C2-C3 1.4819(18), C3-C4 1.332(2), C4-C5 1.454(2), C5-C6 1.334(2), P1-C9 1.8313(13), C1-P1-C2 47.18(6), C1-C2-P1 66.09(7), C8-C3-C4-C5 36.53(17). The angle between the phenyl ring and the C1-C2 bond is 81.10(8)°.

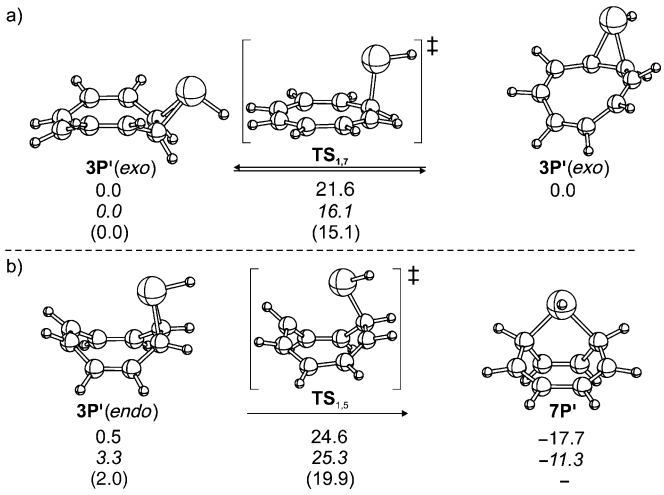


Figure 3. Relative SCS-MP2/cc-pVTZ, B3LYP6-31G* (in italics), and CASPT2(10,10)/6-31G* (in parenthesis) enthalpies at 298 K (in kcal/mol) for a) the "walk" rearrangement of **3P′** and b) its 1,5-sigmatropic shift.

protons (with a mixing time of 1 s) subsequent magnetization transfer occurs to all the other ring protons, the transfer rate to the nearest protons being strongest. This is indicative of interconversion of the ring hydrogen atoms and thus of circumambulation. Clearly, at room temperature in solution, the PPh group *walks* around the hydrocarbon ring. An activation enthalpy $\Delta H^{\neq}$ of 20 kcal mol^{-1} was deduced for this dynamic process by ^{31}C NMR spectroscopy line-shape analysis over a temperature range of 300–332 K (Table 1).

The nature of the "walk", during which the migrating group inverts with each step

Table 2: Relative enthalpies[a] for the **7C** and **7P′** conformers, transition states, and products.

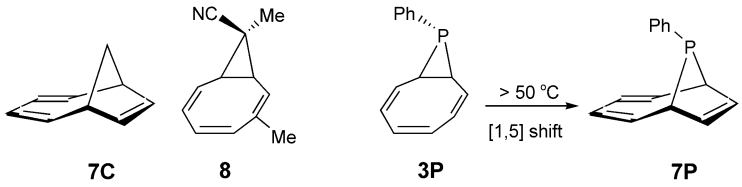
3	Method	*exo*	$TS_{1,7}$	TS_{inv}	*endo*	$TS_{1,5}$	7
3C	UB3LYP[b]	0.0	33.0	5.8	3.7	38.2/35.9	−18.1
3C	CASPT2(8,8)[b,c]	0.0	34.3	7.8	1.1	40.0/39.2	–
3P′	B3LYP[b]	0.0	16.1	3.6	3.3	25.3	−11.3
3P′	CASPT2(10,10)[b,d]	0.0	15.1	–	2.0	19.9	–
3P′	SCS-MP2[d–f]	0.0	21.6	3.5	0.5	24.6	−17.7

[a] B3LYP6-31G* zero-point energy and temperature corrections included. [b] The 6-31G* basis set was used. [c] Reference [13]. [d] The B3LYP geometry was used. [e] Basis set: cc-pVTZ. [f] Reference [11].

Table 1: Kinetic data for the circumambulation of **3P**.

T [K]	k [s^{-1}]	T [K]	k [s^{-1}]
300	1.0	308	1.8
313	4.0	318	7.5
323	11.5	328	19.0
332	23.0		

(**3P′**→**TS**$_{1,7}$→**3P′** in Figure 3a), was also inspected theoretically[10]for the parent organophosphorus compound **3P′** (E = PH) and related to that for hydrocarbon **3C** (E = CH_2, Table 2). $\Delta H^{\neq}$ values of 16.1 and 15.0 kcal mol^{-1} were obtained at the B3LYP6–31G* and CASPT2(10,10)/6-31G* levels of theory,[11] respectively, and 21.5 kcal mol^{-1} with the improved second-order Møller–Plesset perturbation SCS-MP2/cc-pVTZ method of Grimme.[12] This method is a simple modification of MP2 theory and gives improved reaction energies, particularly when aromatic systems are involved. The [1,7] shift of **3P′** reflects such behavior, and, indeed, the agreement with the experimental value for **3P** (E = PPh) is excellent. A modestly lower barrier for **3P** should be expected, resulting from conjugation of the phenyl substituent with the p orbital on the phosphorus atom in the transition state (**TS**$_{1,7}$). Hydrocarbon **3C** has a much higher "walk" barrier, that is, 32.5, 31.5, and 34.2 kcal mol^{-1} at the SCS-MP2/cc-pVTZ, B3LYP6-31G*, CASPT2(8,8)//CASSCF(8,8)/6-31G*[13] levels of theory, respectively, but experimental verification is absent as ring opening to *cis,trans,cis,cis*-cyclonona-1,3,5,7-tetraene is favored instead. The closest comparison is between the calculated $\Delta H^{\neq}$ value of 27.3 kcal mol^{-1} (CASPT2(8,8)) for 9,9-$(CN)_2$-**3C** and the experimental $\Delta G^{\neq}$ value of 29 kcal mol^{-1} for **8** (Scheme 2).[14]



Scheme 2.

Heating **3P** above 50 °C yields only **7P**, which is the WH-allowed product for a [1,5] shift. An enthalpy barrier $\Delta H^{\neq}$ of 24 kcal/mol was obtained for this process from a kinetic ^{31}P NMR spectroscopic study (**3P**: δ = 179 ppm; **7P**:[15] δ = −79 ppm) over a temperature range of 323–363 K (Table 3). The barrier of 24.1 kcal/mol calculated at the SCS-MP2 level of theory for **3P′** (**3P′**→**TS**$_{1,5}$→**7P′** in Figure 3b) is in excellent agreement with the experimentally determined value; the small difference may reflect modest steric congestion by the phenyl substituent. B3LYP gives a slightly

 © 2004 Wiley-VCH Verlag GmbH & Co. KGaA, Weinheim

Table 3: Kinetic data for the 1,5-phosphorus rearrangement of **3P**.

T [K]	$k\,10^7$ [s^{-1}]	T [K]	$k\,10^7$ [s^{-1}]
323	72	333	226
343	667	353	1940
358	3425	363	4683

smaller barrier (22.0 kcal mol^{-1}), and CASPT2(10,10) a much lower value (17.9 kcal mol^{-1}). The [1,5]-rearrangement is pericyclic without diradical character for transition state $\mathbf{TS}_{1,5}$. In sharp contrast, the more-demanding conversion of hydrocarbon **3C** into **7C** occurs in a diradical manner, as inferred from the ^{15}N/N scrambling during the [1,5] shift of singly ^{15}N-labeled 9,9-$(CN)_2$-**3C**.[13] The reaction path for **3C** was reported to have two similar high-lying transition states ($\mathbf{TS}_{1,5}$(a) 40.0 and $\mathbf{TS}_{1,5}$(b) 39.2 kcal mol^{-1} at the CASPT2(8,8)[13] level of theory) without an intermediate (Figure 4), enabling both retention and inversion of configuration of the migrating carbon atom. Similar barriers of 37.8 ($\mathbf{TS}_{1,5}$(a)) and 35.9 kcal mol^{-1} ($\mathbf{TS}_{1,5}$(b)) are predicted at the UB3LYP level of theory using a spin-projection method to obtain proper open-shell singlet energies.[16,17] The origin of the diradical [1,5] shift for the hydrocarbons has been attributed to the too long distance between the migrating methylene carbon and the opposite ring carbon to allow for a pericyclic process.[13] Evidently, the longer C–P bonds and the more diffuse character of phosphorus underlie the *pericyclic* nature of the [1,5]-rearrangement of **3P** into **7P**.

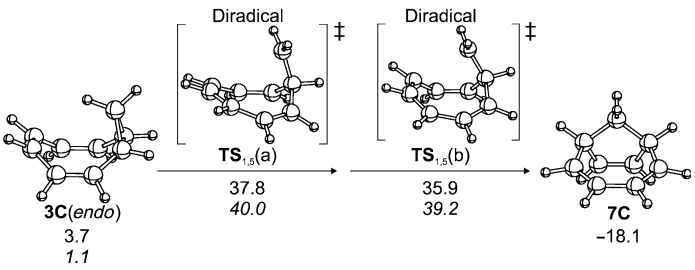


Figure 4. Relative (U)B3LYP6-31G* and CASPT2(8,8)[13] (in italics) enthalpies at 298 K (in kcal mol^{-1}) for the [1,5] shift of hydrocarbon **3C**.

The *exo* conformer of **3P′**, which shows excellent agreement with the X-ray structure of **3P**, readily inverts to the less-stable (0.5 kcal mol^{-1}) *endo* form (**3P′**(*exo*)→$\mathbf{TS}_{inv}$→**3P′**(*endo*) SCS-MP2, Figure 3b) via a low-energy (3.5 kcal mol^{-1}), planar, eight-membered ring form (as does **3C**), indicating conformational fluxional behavior of the hydrocarbon frame.

In conclusion, we have demonstrated that 9-phenyl-9-phospha-bicyclo[6.1.0]nona-2,4,6-triene (**3P**) is a dynamic molecule that undergoes a perpetual degenerate [1,7] sigmatropic shift in solution and a pericyclic [1,5]-rearrangement at temperatures above 50 °C.

Experimental Section

3P: The cyclooctatrienyl dianion was treated with dichlorophenylphosphane.[18] Recrystallization from methanol at −78 °C gave light-yellow crystals (2.07 g, 34 %); m.p. 42–43 °C. ^{31}P NMR (250 MHz, $CDCl_3$): $\delta = 179$ ppm; ^{1}H NMR (250 MHz, $CDCl_3$): $\delta = 3.65$ (d, ^2J(H,P) = 2.7 Hz; H1), 5.95 (s; H4), 6.05 (d, ^3J(H,H) = 11.6 Hz; H 3), 6.40 (dd, ^3J(H,P) = 8.2 Hz, ^3J(H,H) = 11.6 Hz; H2), 7.25–7.35 (m; *m*-H_{Ar} and *p*-H_{Ar}), 7.39–7.50 ppm (m, *p*-H_{Ar}); IR (KBr): $\tilde{\nu} = 696.4$, 665.5 cm^{-1} (w, P-C).

Crystal data for **3P**: $C_{14}H_{13}P$, $F_w = 212.21$, colorless cubic crystal, $0.36 \times 0.30 \times 0.15$ mm^3, orthorhombic, $P2_12_12_1$ (no. 19), $a = 8.9692(1)$, $b = 10.6590(1)$, $c = 11.8322(2)$ Å, $V = 1131.19(3)$ Å^3, $Z = 4$, $D_x = 1.246$ g cm^{-3}, $\mu = 0.205$ mm^{-1}; 15794 reflections were measured on a Nonius Kappa CCD diffractometer with rotating anode ($\lambda = 0.71073$ Å) at a temperature of 150(2) K up to a resolution of $(\sin\theta/\lambda)_{max} = 0.65$ Å^{-1}; 2593 reflections were unique ($R_{int} = 0.036$); an absorption correction was not considered necessary. The structure was solved with direct methods (SHELXS-97)[19] and refined with SHELXL-97[20] against F^2 of all reflections. Non-hydrogen atoms were refined freely with anisotropic displacement parameters. H atoms of the phenyl ring were refined as rigid groups; all other H atoms were refined freely with isotropic displacement parameters; 168 refined parameters, no restraints. Flack *x* parameter[21]: −0.06(7); *R* values [$I > 2\sigma(I)$]: $R1 = 0.0255$, $wR2 = 0.0618$. *R* values [all reflections]: $R1 = 0.0292$, $wR2 = 0.0634$. GoF = 1.062. Residual electron density between −0.17 and 0.19 e Å^{-3}. Molecular illustration, structure checking, and calculations were performed with the PLATON package.[22] CCDC 205388 contains the supplementary crystallographic data for this paper. These data can be obtained free of charge via www.ccdc.cam.ac.uk/conts/retrieving.html (or from the Cambridge Crystallographic Data Centre, 12, Union Road, Cambridge CB2 1EZ, UK; fax: (+44) 1223-336-033; or deposit@ccdc.cam.ac.uk).

Received: May 9, 2003
Revised: October 6, 2003 [Z51855]

Keywords: density functional calculations · phosphorus heterocycles · sigmatropic rearrangement

[1] Review: a) R. F. Childs, *Tetrahedron* **1982**, *38*, 567–608; b) F.-G. Klärner, *Top. Stereochem.* **1984**, *15*, 1.
[2] R. B. Woodward, R. Hoffmann, *The Conservation of Orbital Symmetry*, Academic, New York, **1970**.
[3] a) A. Kless, M. Nendel, S. Wilsey, K. N. Houk, *J. Am. Chem. Soc.* **1999**, *121*, 4524–4525; b) A. A. Jarzecki, J. Gajewski, E. R. Davidson, *J. Am. Chem. Soc.* **1999**, *121*, 6928–6935.
[4] a) S. M. Bachrach, V. Caliman, J. F. Nixon, *J. Chem. Soc. Chem. Commun.* **1995**, 2395–2396; b) V. Caliman, P. B. Hitchcock, J. F. Nixon, *Chem. Commun.* **1998**, *15*, 1537–1538.
[5] L. D. Quin, N. S. Rao, J. Szewczyk, *Tetrahedron Lett.* **1985**, *26*, 6293–6296.
[6] A. C. Cope, B. D. Tiffany, *J. Am. Chem. Soc.* **1951**, *73*, 4158–4161.
[7] G. C. Tustin, C. E. Monken, W. H. Okamura, *J. Am. Chem. Soc.* **1972**, *94*, 5112–5113.
[8] W. J. Richter, *Chem. Ber.* **1985**, *118*, 97–106.
[9] K. Stott, J. Stonehouse, J. Keeler, T.-L. Hwang, A. J. Shaka, *J. Am. Chem. Soc.* **1995**, *117*, 4199–4200.
[10] Gaussian 98 (Revision A.7), M. J. Frisch, G. W. Trucks, H. B. Schlegel, G. E. Scuseria, M. A. Robb, J. R. Cheeseman, V. G. Zakrzewski, J. A. Montgomery, R. E. Stratmann, J. C. Burant, S. Dapprich, J. M. Millam, A. D. Daniels, K. N. Kudin, M. C. Strain, O. Farkas, J. Tomasi, V. Barone, M. Cossi, R. Cammi, B. Mennucci, C. Pomelli, C. Adamo, S. Clifford, J. Ochterski, G. A. Petersson, P. Y. Ayala, Q. Cui, K. Morokuma, D. K. Malick, A. D. Rabuck, K. Raghavachari, J. B. Foresman, J. Cioslowski, J. V. Ortiz, B. B. Stefanov, G. Liu, A. Liashenko, P. Piskorz, I. Komaromi, R. Gomperts, R. L. Martin, D. J. Fox, T. Keith, M. A.

 © 2004 Wiley-VCH Verlag GmbH & Co. KGaA, Weinheim

Al-Laham, C. Y. Peng, A. Nanayakkara, C. Gonzalez, M. Challacombe, P. M. W. Gill, B. G. Johnson, W. Chen, M. W. Wong, J. L. Andres, M. Head-Gordon, E. S. Replogle, J. A. Pople, Gaussian, Inc., Pittsburgh, PA, **1998**. All stationary points were optimized at the B3LYP6-31G* level of theory.
[11] MOLCAS, Version 5, University of Lund, Lund, Sweden, **2000**.
[12] S. Grimme, *J. Chem. Phys.* **2003**, *118*, 9095 – 9102.
[13] M. B. Reyes, E. B. Lobkovsky, B. K. Carpenter, *J. Am. Chem. Soc.* **2002**, *124*, 641 – 651.
[14] a) F.-G. Klärner, M. Wette, *Chem. Ber.* **1978**, *111*, 282 – 298; b) H. Günther, *Tetrahedron Lett.* **1970**, *11*, 5173 – 5176.
[15] a) G. Märkl, B. Alig, *J. Organomet. Chem.* **1984**, *273*, 1 – 29; b) L. D. Quin, N. S. Rao, *J. Org. Chem.* **1983**, *48*, 3754 – 3759.
[16] E. Goldstein, B. Beno, K. N. Houk, *J. Am. Chem. Soc.* **1996**, *118*, 6036 – 6043.
[17] T. L. Cottrell, *The Strengths of Chemical Bonds*, 2nd ed., Butterworths, London, **1958**.
[18] E. W. Turnblom, T. J. Katz, *J. Am. Chem. Soc.* **1973**, *95*, 4292 – 4311.
[19] G. M. Sheldrick, SHELXL-97, Program for crystal structure solution, University of Göttingen, Göttingen (Germany), **1997**.
[20] G. M. Sheldrick, SHELXL-97, Program for crystal structure refinement, University of Göttingen, Göttingen (Germany), **1997**.
[21] H. D. Flack, *Acta Crystallogr. Sect. A* **1983**, *39*, 876 – 881.
[22] A. L. Spek, PLATON, A multipurpose crystallographic tool, Utrecht University, The Netherlands, **2002**.

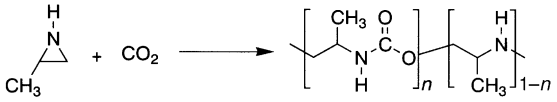
 © 2004 Wiley-VCH Verlag GmbH & Co. KGaA, Weinheim

Thermoresponsive Polymers

Synthesis of Thermoresponsive Polyurethane from 2-Methylaziridine and Supercritical Carbon Dioxide**

Osamu Ihata, Yoshihito Kayaki, and Takao Ikariya**

Utilization of CO_2 as an abundant C_1 feedstock is of environmental importance and a synthetic challenge.[1] Chemical fixation of CO_2 in functionalized polymers with long lifetimes is one of the most viable large-scale approaches.[2] Metal-catalyzed copolymerization of epoxides and CO_2 to give polycarbonates has been investigated as a potential method for CO_2 fixation.[3,4] Analogously, aziridines have been reported to react with CO_2 to give cyclic urethanes[5a] and polymers[5b] consisting of urethane and amine units (Scheme 1). However, the fraction of urethane linkages in the polymer products did not exceed 0.3, mainly because homopolymerization of aziridines competes with copolymerization with CO_2.[5b] The use of supercritical CO_2 ($scCO_2$) as reaction medium and reactant offers the opportunity to manipulate the outcome of reactions, including the polymer structure, this is thanks to the easy tunability of the properties of $scCO_2$ by means of pressure and temperature.[6,7] Herein we describe the reaction of 2-methylaziridine (**1**) and CO_2 under supercritical conditions to give polymer products with a high content of urethane units and unique temperature-sensitive phase transitions in water.



Scheme 1. Copolymerization of **1** with CO_2.

We examined the reactivity of **1** towards CO_2 under supercritical conditions by high-pressure NMR spectroscopy.[8] In the early stages of the reaction the aziridine was completely miscible with $scCO_2$ (Figure 1), but disappearance of the signals of **1** after 17 h suggested that CO_2-insoluble compounds would form under these conditions. Separate experiments showed that polymeric products were obtained by treatment of **1** with 3.0–22 MPa of CO_2 in a stainless steel

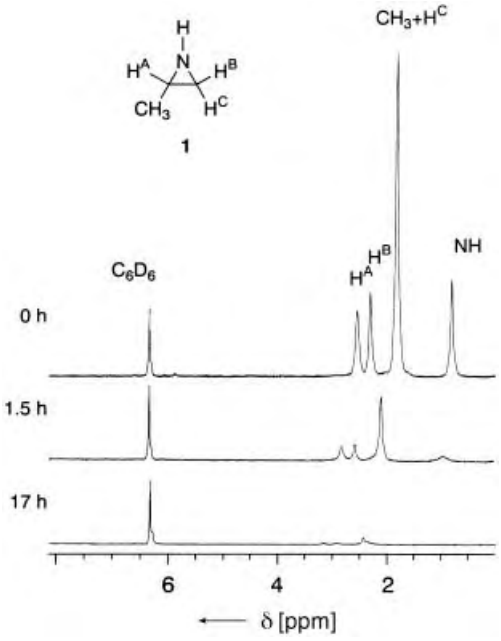


Figure 1. ^1H NMR spectra of **1** in $scCO_2$ (40 °C, 8.0 MPa). C_6D_6 in a sealed capillary tube was used as lock.

[*] Dr. O. Ihata, Dr. Y. Kayaki
PRESTO
Japan Science and Technology Agency
2-12-1 O-okayama, Meguro-ku, Tokyo, 152-8552 (Japan)
Fax: (+81) 3-5734-2637
E-mail: ykayaki@o.cc.titech.ac.jp
Prof. T. Ikariya
Graduate School of Science and Engineering and
Frontier Collaborative Research Center
Tokyo Institute of Technology
2-12-1 O-okayama, Meguro-ku, Tokyo, 152-8552 (Japan)

[**] This work was financially supported by a Grant-in-Aid from the Ministry of Education, Science, Sports and Culture of Japan (No 14078209, Reaction Control of Dynamic Complexes). This work was partly supported by the 21st Century COE Program. We thank Mr. S. W. Choi, Dr. Y. Sato, and Prof. A. Maruyama at Tokyo Institute of Technology for useful discussions and performing SEC-MALLS analysis and temperature-controlled UV/Vis spectroscopy.

 DOI: 10.1002/anie.200352215 © 2004 Wiley-VCH Verlag GmbH & Co. KGaA, Weinheim

autoclave at 100 °C, and **1** was completely consumed in the reaction. Reprecipitation by adding a solution of the reaction mixture in methanol to diethyl ether afforded a white powderlike material. The yields and properties of the obtained polymers **2**–**5** are listed in Table 1. In the absence of CO_2, no polymerized product was obtained, and the starting material was recovered completely. An increase in CO_2 pressure caused a marked improvement in the yield.

Table 1: Physical data on the product polymers prepared from **1** and CO_2.[a]

Entry	Product	p [MPa]	CO_2 density [g cm^{-3}]	Yield [%]	Urethane content[b] [unit ratio]	M_w
1		0	0.0	0.0	–	–
2	**2**	3	4.9×10^{-2}	14.2	0.32	6.5×10^{3}
3	**3**	10	2.0×10^{-1}	17.9	0.47	1.5×10^{5}
4	**4**	16	3.6×10^{-1}	22.1	0.53	1.4×10^{5}
5	**5**	22	5.2×10^{-1}	27.1	0.62	2.7×10^{4}

[a] 50-mL stainless autoclave, [**1**] = 8.8 mmol, 100 °C, 24 h. [b] Calculated on the basis of elemental analyses.

The ^{1}H and ^{13}C NMR spectra of the polymers showed signals arising from the NH protons and the carbonyl carbon atom of the urethane structure (−NHCOO−) at around δ = 4.0 and 158 ppm, respectively. Elemental analysis revealed that the urethane content of the products increased to 0.62 when the CO_2 pressure was increased to 22 MPa. An increase in the content of urethane units could also be confirmed by ^{1}H NMR spectroscopy. Analysis of **2**–**5** by size-exclusion chromatography coupled with multiangle laser light scattering (SEC-MALLS) revealed that the weight-average molecular weights M_w of the products obtained under supercritical conditions were significantly higher than that of **2** obtained at 3.0 MPa. The reaction of 2-ethylaziridine with $scCO_2$ at 22 MPa of CO_2 also gave the corresponding copolymer with a urethane content of 0.62, as observed in the reaction of **1**. These results indicate that the use of $scCO_2$ results in effective copolymerization of aziridines and CO_2 without any additives.

The outcome of the reaction proved to be strongly influenced by the phase behavior of the reaction system.[9] High-pressure NMR spectra of the reaction mixture indicated that the polymeric products formed an independent phase by precipitation from the reaction phase. Addition of appropriate co-solvents would allow easy manipulation of the rate of the reaction and the product properties by enhancing the solubility of the reaction mixture in $scCO_2$.[10] In fact, the reaction in the presence of *N*,*N*-dimethylacetamide (DMAc) at 22 MPa led to a marked improvement in the molecular weight of the polymers, and the urethane content of the product increased to 0.74 (Table 2). Visual inspection of the reaction mixture containing DMAc in a reactor equipped with a window confirmed that a homogeneous phase formed at 22 MPa. At lower CO_2 pressure, phase separation took place, and polymerization was strongly retarded. Thus, this phase behavior of the reaction mixture is a crucial factor in controlling the product properties.

Table 2: Effect of DMAc co-solvent on the polymerization of **1** and CO_2.[a]

p [MPa]	DMAc [wt%]	Phase	Yield [%]	Urethane content[b] [unit ratio]	M_w
12	7.2	biphasic	11.3	0.56	4.8×10^{3}
16	5.0	transient	22.0	0.63	2.8×10^{4}
22	3.6	homogeneous	30.7	0.74	2.1×10^{5}

[a] 50 mL stainless autoclave, [**1**] = 8.8 mmol, 100 °C, 24 h, 11 mmol DMAc. [b] Calculated on the basis of elemental analyses.

The copolymerization products of **1** and CO_2 exhibit thermally induced reversible transitions in water around the lower critical solution temperatures (LCSTs).[11] This unique thermal property of polymers, such as poly(*N*-isopropylacrylamide)s, in water has attracted increasing attention in the fields of drug-delivery systems,[12a] protein–ligand recognition,[12b] tissue-engineering applications,[12c] separation,[12d] and catalysis.[12e] Since the dissolution/precipitation transition in aqueous solution is attributed to the cleavage of the hydrogen-bonding network involving water and the polymers, as well as hydrophobic aggregation of the polymers, a suitable balance of hydrophilic and hydrophobic moieties in the polymer structure should essentially determine the thermoresponsive properties.[13]

Figure 2 shows the temperature dependence of the light transmittance of 2.0 wt% aqueous polymer solutions. The thermoresponsive properties of the products were delicately influenced by reaction conditions such as CO_2 pressure and the nature of the aziridine monomer. The transmittance of the solution of **2**, prepared at 3.0 MPa of CO_2, decreased gradually above 80 °C, while products **3**–**5**, obtained under supercritical conditions, exhibited a sharp drop in transmittance at their LCSTs. The effect of CO_2 pressure on the LCST is presumably due to the urethane content of the products. The increased urethane content of polymers obtained under supercritical conditions results in a decrease in their LCSTs, possibly because of the decreased hydrophilicity of the polymers. The molecular weight of the

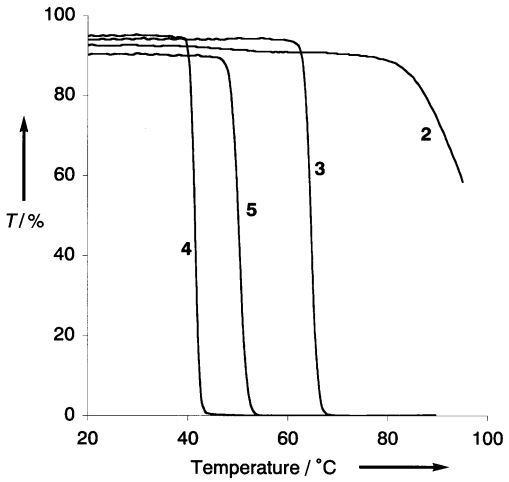


Figure 2. Temperature dependence of transmittance for aqueous solutions of **2**–**5** (LCSTs: **2**: 85 °C; **3**: 64 °C; **4**: 41 °C; **5**: 48 °C).

 © 2004 Wiley-VCH Verlag GmbH & Co. KGaA, Weinheim

copolymer also influences the LCST, as was observed for copolymers **4** and **5** (Table 1 and Figure 2). An inverse dependence of LCST on molecular weight was reported in other polymer systems.[14] The copolymer obtained from 2-ethylaziridine and CO_2 under supercritical conditions was not sufficiently soluble in water and therefore showed no marked thermoresponsive behavior in water.

In conclusion, we have demonstrated a novel synthetic procedure for obtaining thermoresponsive polyurethanes from **1** and CO_2 under supercritical conditions. The copolymers exhibit LCST in aqueous solution, with a sharp phase transition over a wide range of 41–85 °C.

Experimental Section

Caution: Since high gas pressures are involved, appropriate safety precautions must be taken.

Typical procedure for copolymerization: The reaction was carried out in a 50-mL stainless steel autoclave. The autoclave was filled with argon gas, and **1** (8.8 mmol) was introduced by syringe. Then the vessel was charged with CO_2 through a cooling apparatus with an HPLC pump. After stirring at 100 °C for 24 h, the reaction was stopped by cooling the autoclave in a dry ice/methanol bath. CO_2 was vented and the autoclave was slowly warmed to room temperature. The crude reaction product was then dissolved in the methanol. The polymeric product was purified by reprecipitation by adding the methanol solution to diethyl ether to remove low-molecular-weight products and drying in vacuo.

The molar mass distributions of the products were determined by SEC-MALLS measurements, which were carried out at 40 °C on Shodex OHpak SB-804HQ and SB-806MHQ columns at a polymer concentration of 10 mg mL^{-1}. All samples were filtered through Millipore Milex-LG (0.20 μm) before analysis. An aqueous solution of 0.2 M Na_2SO_4/0.5 M CH_3COOH was used as eluent. The MALLS device was a DAWN model DSP-F (Wyatt Technology Co.) in which a laser beam of wavelength of 632.8 nm was focused on the flow cell. LCSTs of the polymers were measured by monitoring the absorbance at 500 nm at a heating rate of 2 °C min^{-1} with a variable-temperature Shimadzu UV-1600PC UV/Vis spectrometer.

Received: June 24, 2003
Revised: September 3, 2003 [Z52215]

Keywords: carbon dioxide fixation · copolymerization · polyurethanes · supercritical fluids

[1] a) M. M. Halmann, *Chemical Fixation of Carbon Dioxide. Methods for Recycling CO_2 into Useful Products*, CRC, Boca Raton, **1993**; b) *Carbon Dioxide Chemistry: Environmental Issues* (Eds.: J. Paul, C. M. Pradier), The Royal Society of Chemistry, Cambridge, **1994**; c) W. Leitner, *Angew. Chem.* **1995**, *107*, 2391–2405; *Angew. Chem. Int. Ed. Engl.* **1995**, *34*, 2207–2221.

[2] E. J. Beckman, *Science* **1999**, *283*, 946–947.

[3] S. Inoue, H. Koinuma, T. Tsuruta, *J. Polym. Sci. Part B* **1969**, *7*, 287–292.

[4] Recent reviews on the polymerization of epoxides and CO_2: W. Kuran, *Prog. Polym. Sci.* **1998**, *23*, 919–992; M. Super, E. J. Beckman, *Trends Polym. Sci.* **1997**, *5*, 236–240.

[5] a) K. Soga, S. Hosoda, H. Nakamura, S. Ikeda, *J. Chem. Soc. Chem. Commun.* **1976**, *16*, 617; b) K. Soga, W. Y. Chiang, S. Ikeda, *J. Polym. Sci. Polym. Chem. Ed.* **1974**, *12*, 121–131.

[6] a) P. G. Jessop, T. Ikariya, R. Noyori, *Science* **1995**, *269*, 1065–1069; b) P. G. Jessop, T. Ikariya, R. Noyori, *Chem. Rev.* **1999**, *99*, 475–494; c) S. L. Wells, J. DeSimone, *Angew. Chem.* **2001**, *113*, 534–544; *Angew. Chem. Int. Ed.* **2001**, *40*, 518–529; d) R. S. Oakes, A. A. Clifford, C. M. Rayner, *J. Chem. Soc. Perkin Trans. 1* **2001**, 917–941.

[7] *Chemical Synthesis Using Supercritical Fluids* (Eds: P. G. Jessop, W. Leitner), Wiley-VCH, Weinheim, **1999**.

[8] Y. Kayaki, T. Suzuki, Y. Noguchi, S. Sakurai, M. Imanari, T. Ikariya, *Chem. Lett.* **2002**, 424–425.

[9] J. Ke, B. Han, M. W. George, H. Yan, M. Poliakoff, *J. Am. Chem. Soc.* **2001**, *123*, 3661–3670.

[10] a) J.-L. Xiao, S. C. A. Nefkens, P. G. Jessop, T. Ikariya, R. Noyori, *Tetrahedron Lett.* **1996**, *37*, 2813–2816; b) S. Lange, A. Brinkmann, P. Trautner, K. Woelk, J. Bargon, W. Leitner, *Chirality* **2000**, *12*, 450–457.

[11] a) I. Y. Galaev, B. Mattiasson, *Trends Biotechnol.* **1999**, *17*, 335–340; b) M. Heskins, J. E. Guillet, *J. Macromol. Sci. Chem.* **1968**, *A2*, 1441–1445; c) Y. Tachibana, M. Kurisawa, H. Uyama, T. Kakuchi, S. Kobayashi, *Chem. Commun.* **2003**, 106–107.

[12] a) A. Kikuchi, T. Okano, *Adv. Drug Delivery Rev.* **2002**, *54*, 53–77; b) P. S. Stayton, T. Shimobji, C. Long, A. Chilkoti, G. Chen, J. M. Harris, A. S. Hoffman, *Nature* **1995**, *378*, 472; c) K. Y. Lee, D. J. Mooney, *Chem. Rev.* **2001**, *101*, 1869–1880; d) T. Yakushiji, K. Sakai, A. Kikuchi, T. Aoyagi, Y. Sakurai, T. Okano, *Anal. Chem.* **1999**, *71*, 1125–1130; e) D. E. Bergbreiter, *Chem. Rev.* **2002**, *102*, 3345–3384.

[13] L. D. Taylor, L. D. Cerankowski, *J. Polym. Sci. Polym. Chem. Ed.* **1975**, *13*, 2551–2570.

[14] D. G. Lessard, M. Ousalem, X. X. Zhu, *Can. J. Chem.* **2001**, *79*, 1870–1874.

 © 2004 Wiley-VCH Verlag GmbH & Co. KGaA, Weinheim

Asymmetric Catalysis

Tandem 1,4-Addition/Enantioselective Protonation Catalyzed by Rhodium Complexes: Efficient Access to α-Amino Acids**

Laure Navarre, Sylvain Darses, and Jean-Pierre Genet**

The 1,4-addition of organometallic reagents (Michael-type additions) to electron-deficient alkenes catalyzed by transition metals has emerged as a powerful tool in organic synthesis for constructing carbon–carbon bonds.[1] Efficient asymmetric versions of this reaction have been developed in which a chiral ligand complexed to a transition metal allows efficient enantioselective introduction of a chiral center in the β position of the unsaturated substrate.[2] Useful examples

[*] L. Navarre, Dr. S. Darses, Prof. J.-P. Genet
Laboratoire de Synthèse Sélective Organique (UMR 7573, CNRS)
Ecole Nationale Supérieure de Chimie de Paris
11 rue P&M Curie, 75231 Paris cedex 05 (France)
Fax: (+33) 144-071-062
E-mail: darses@ext.jussieu.fr
genet@ext.jussieu.fr

[**] This work was supported by the Centre National de la Recherche Scientifique (CNRS). L.N. thanks the Ministère de L'Education et de la Recherche for a grant.

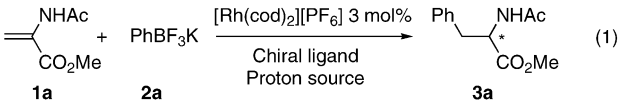
 DOI: 10.1002/anie.200352518 © 2004 Wiley-VCH Verlag GmbH & Co. KGaA, Weinheim

include the asymmetric 1,4-addition of organozinc reagents catalyzed by chiral copper complexes[2,3] and of organoboronic acids and derivatives catalyzed by chiral rhodium complexes.[4] Such carbometalation transformations generate a transient metal enolate, which can further react with electrophiles in a tandem process[5] or more commonly in a two-step process that requires the introduction of the electrophilic partner subsequent to generation of the enolate by carbometalation.[6] It is believed that in these processes the stereochemistry of the generated α center is generally governed by the stereochemistry of the β center. Examples are rare of catalytic asymmetric transformations where the stereochemical outcome is determined at the quenching step of the generated oxa-π-allylmetal intermediate, not at the insertion step of the organometallic reagent[5a,d] (Scheme 1).

Herein we show that conjugate addition of organometallic reagents to *N*-acylamidoacrylate mediated by a chiral rhodium catalyst together with in situ enantioselective protonation[7–10] using achiral phenol derivatives furnishes a variety of α-amino acid derivatives[11] with good to excellent efficiency. A similar approach, but based on radical chemistry, has recently been described by Sibi et al. for radical conjugate additions to α-aminoacrylates[12a] and α-methacrylate[12b] followed by hydrogen atom transfer.

We chose potassium trifluoro(organo)borates as organometallic partners for this tandem 1,4-addition/enantioselective protonation because of their high stability and ease of preparation and purification.[13] Moreover, such compounds have proven to be highly reactive in transition-metal-catalyzed reactions such as cross-coupling reactions[14] and asymmetric 1,4-additions.[15] In particular, we have shown that potassium trifluoro(organo)borates added efficiently to dehydroamino esters to afford racemic non-natural α-amino esters.[16]

We initially tested the feasibility of tandem 1,4-addition/enantioselective protonation by the addition of potassium trifluoro(phenyl)borate (**2a**) to methyl 2-acetylamidoacrylate (**1a**) in the presence of a catalytic amount of the cationic rhodium complex $[Rh(cod)_2][PF_6]$ (cod = cycloocta-1,5-diene) and a chiral ligand [Eq. (1)] using different protonating agents.

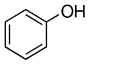
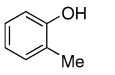
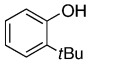
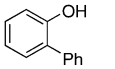
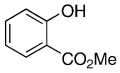
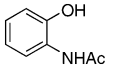
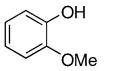
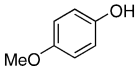
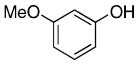


(1)

Disappointing results were obtained using water as the protonating agent of the in situ generated oxa-π-allylrhodium intermediate.[17] The *ee* values were usually below 28%, irrespective of the chiral ligand tested[18] (Table 1, entry 1). Moreover, results were not always reproducible with respect to the level of asymmetric induction obtained. From these results it appeared that water was not able to protonate one face of the rhodium enolate selectively when common chiral ligands were used.[8,9]

Thus, we investigated the use of more-hindered proton sources in this transformation. It appeared that carboxylic acids or sulfonic acids were not suitable and resulted in a blocking of the catalytic cycle,[19] with no Michael addition product observed (entries 2 and 3). However, quantitative conversions were achieved and more significant *ee* values were observed in the presence of phenol derivatives. For example, the α-amino ester **3a** was obtained in 81% yield and 18% *ee* using phenol and (S)-2,2′-bis(diphenylphosphanyl)-1,1′-binaphthyl ((*S*)-binap) as the chiral ligand (entry 4). Encouraged by this result, a large variety of phenol derivatives were screened to improve the asymmetric induction achieved during the protonation step. It appeared that the *ee* values were highly dependent on the structure of the protonating phenol (Table 1).

Table 1: Effect of the proton source in the 1,4-addition/enantioselective protonation.[a]

Entry	Proton source	Conv. [%][b]	Yield [%][c]	*ee*[d] [%]
1	H_2O	100	quant.	0–28[18]
2	$(Ph)_2CHCO_2H$	0		
3	CSA[e]	0		
4		88	81	18
5		100	63	37
6		39	28	44
7		100	77	69
8		57	36	26
9		69	23	3
10		100	91	83
11		77	75	45
12		100	84	51

[a] Reactions conducted using 0.5 mmol of **1a** and 2 equiv of **2a** with 3 mol% of $[Rh(cod)_2][PF_6]$, and 3.3 mol% of (*S*)-binap in toluene at 110°C for 20 h. [b] Determined by GC analysis. [c] Yields of isolated products. [d] Determined by HPLC analysis using a Daicel Chiralcel OD-H chiral column. [e] Camphor sulfonic acid.

Higher *ee* values were generally achieved with *ortho*-substituted phenols.[20] Moreover, increasing steric hindrance in this position generally resulted in an increase in the *ee* value (entries 4–6). Even though we cannot rationalize the relation between the electronic nature of the *ortho* substituent and the level of asymmetric induction at present, it appeared that the highest *ee* values were generally obtained using moderately chelating substituents (compare entries 7 and 10 with 8 and 9). The reaction was not complete and the *ee* values were generally low when better complexing *ortho* substituents such as CO_2Me (entry 8) or NHAc (entry 9) were used. The highest *ee* values were achieved using inexpensive and nontoxic 2-methoxyphenol (guaiacol), which resulted in

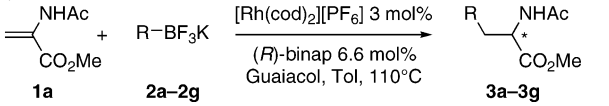
 © 2004 Wiley-VCH Verlag GmbH & Co. KGaA, Weinheim

the highly reproducibile formation of α-amino ester **3a** in 91% yield and 83% *ee* (entry 10). Once again the other isomers of methoxyphenol gave a lower level of asymmetric induction, even if they were efficient proton sources (entries 11 and 12).

Despite further optimizations by the screening of various chiral ligands and solvents, no improvements were observed for either the *ee* values or yields; the highest *ee* values were achieved using binap as the chiral ligand and toluene (or dioxane) as the solvent. However, a slight improvement in the *ee* values could be obtained by using two equivalents of chiral diphosphane to one equivalent of rhodium (89.5% *ee* compared to 83% *ee* with 1.1 equivalents of binap).

We tested the generality of the reaction under these optimized conditions ($[Rh(cod)_2][PF_6]$ and 2.2 equivalents of (*R*) or (*S*)-binap as the catalyst precursor in the presence of one equivalent of guaiacol) by treating substrate **1a** with various potassium trifluoro(organo)borates (Table 2).

Table 2: Tandem 1,4-addition/enantioselective protonation of RBF_3K to dehydroamino esters.[a]



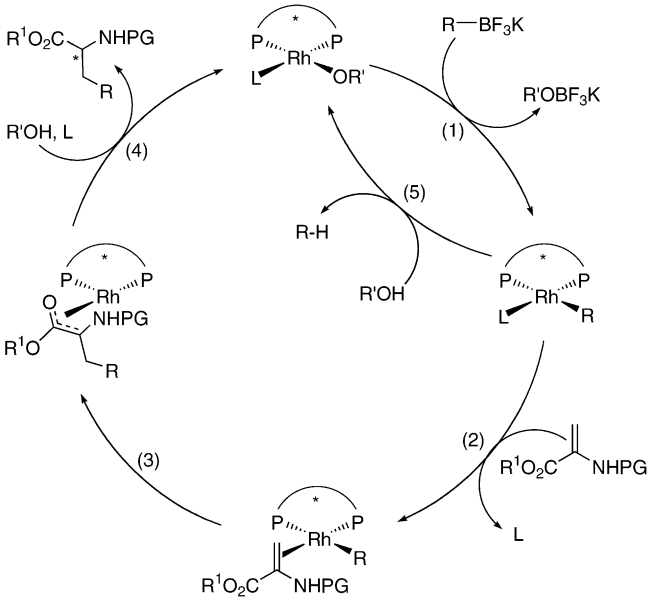
1a **2a–2g** **3a–3g**

Entry	RBF_3K	Product	Yield [%]	*ee*[b] [%]
1	**2a**	**3a**	89	89.5 (*S*)
2	**2b**	**3b**	89	89.5 (*S*)
3	**2c**	**3c**	88	86.5 (*S*)
4	**2d**	**3d**	82	83 (*S*)
5	**2e**	**3e**	75	81 (*S*)
6	**2f**	**3f**	68	81 (*S*)
7	**2g**	**3g**	96[c]	88 (*S*)

[a] Reactions conducted using 0.5 mmol of **1a**, 2 equiv of **2a**, 1 equiv of guaiacol, and 1 equiv of guaiacol with 3 mol% of $[Rh(cod)_2][PF_6]$ and 6.6 mol% of (*R*)-binap in toluene at 110°C for 20 h. [b] Determined by HPLC analysis using a Daicel Chiralcel OD-H column. The absolute configuration was determined by the sign of the optical rotation or HPLC retention time, and is given in parentheses. [c] Isolated as an inseparable mixture with 30% of the 3,4-isomer.

From these preliminary results it appeared that a great variety of aryl alanine derivatives are accessible using this tandem carbometalation/enantioselective protonation process[21] (Table 2). Enantioselectivity ranging from 81 to nearly 90% *ee* was generally achieved. Heterocyclic (entry 6) and functionalized (entry 5) derivatives are also accessible using this strategy; the latter can undergo further cross-coupling reactions to introduce higher diversity. It appeared that alkenyl-substituted alanine derivatives are produced efficiently with good *ee* values and yields from potassium alkenyltrifluoroborates (entry 7), although some isomerization of the double bond was observed, presumably through rhodium-catalyzed double-bound migration. This result represents an interesting feature of this carbometalation since these substrates are not easily accessible,[22] even from efficient asymmetric hydrogenation processes.[23] The absolute configuration of the carbometalation adducts were established by comparison of the sign of the optical rotation or chiral HPLC retention time with those of configurationally assigned compounds. From these results it appeared that products with an *S* configuration were obtained using (*R*)-binap, that is, protonation of the rhodium enolate intermediate takes place on the *Re* face of the amidoacrylate (Scheme 1).

Some general features concerning the mechanism of this transformation may be postulated on the basis of recent work carried out by Hayashi et al.[17] (Scheme 1). The initial step (step 1) should consist of the transmetalation of the organoboron reagent, but we have no evidence that potassium trifluoro(organo)borates directly transmetalate Rh^I species. Preferential coordination of one face of the amidoacrylate (eventually involving a second coordination of the NHAc group), followed by insertion of the R substituent then affords an oxa-π-allylrhodium intermediate (steps 2 and 3). In the last



Scheme 1. Proposed reaction mechanism. PG = protecting group.

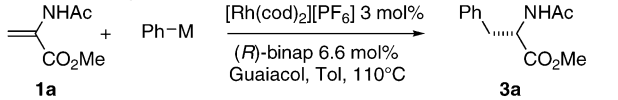
 © 2004 Wiley-VCH Verlag GmbH & Co. KGaA, Weinheim

step (step 4), that is, protonation of the rhodium enolate, proton transfer can occur either by H-transfer from the rhodium center or by external protonation of the enolate, but it is quite evident that steric hindrance and/or coordination of the *ortho* substituent on the phenol plays a key role. Deuterium-labeling as well as computational studies are currently underway to get insights into this protonation step.

Overall, it is important to note that in all the reactions examined, the phenol derivatives not only allowed high *ee* values to be reached but that no reduction of the boron derivative was observed, which is very often a competitive process on protonation with water[4] (Scheme 1, path 5). Moreover, this phenol is easily and quantitatively recovered at the end of the reaction by simple acidification/extraction procedures.

The scope of the present tandem 1,4-additon/enantioselective protonation was further extended by studying the organometallic partner that could carbometalate dehydroamino ester **1a**. Indeed, we tested some other organometallic reagents, such as tin, silicon, and other boron derivatives, under the previously described conditions and using guaiacol as the proton source (Table 3). Of the organoboron compounds tested (entries 1–3) it appeared that only potassium trifluoro(organo)borates were able to transfer their organic moiety with high yields and *ee* values. The 1,4-addition was not efficient (42% yield) with phenylboronic acid **2b** because of competitive reduction (Scheme 1, path 5) and the *ee* value was surprisingly low. This lower asymmetric induction may be explained by the fact that boronic acids can act as competitive proton sources relative to guaiacol and are not able to induce enantiofacial discrimination (Scheme 1). On the other hand, pinacol ester derivative **2c** (entry 3) does not transmetalate rhodium under these conditions, and no 1,4-addition adduct was observed.

Table 3: Other organometallic reagents used in the tandem 1,4-addition/enantioselective protonation.[a]



1a **3a**

Entry	Ph-M	Yield [%]	*ee*[b] [%]
1	$PhBF_3K$ **2a**	89	89.5
2	$PhB(OH)_2$ **2b**	42	42
3	PhBpin[c] **2c**	0	
4	Ph_2SiCl_2 **2d**	0	
5	**2d**/NaF[d]	0	
6	$PhSnBu_3$ **2e**	52	88
7	$PhSnMe_3$ **2f**	89	71

[a] Reactions were conducted using 0.5 mmol of **1a** and 2 equiv of RM with 3 mol% of $[Rh(cod)_2][PF_6]$ and 6.6 mol% of (*R*)-binap in toluene at 110–115°C for 20 h. [b] Determined by HPLC analysis using a Daicel Chiralcel OD-H or OJ column. [c] Bpin: pinacolborane. [d] 1 equiv of NaF was used.

Organosilane **2d** did not react at all, even in the presence of fluoride ions[24] (entries 4 and 5), which are known to favor transmetalation of silicon derivatives to transition metals.[25] In contrast to organoboronic acid derivatives, organostannanes[26] also proved to be suitable in this reaction (entries 5 and 6) and provided α-amino acids in good yields and high enantioselectivities, which were comparable to potassium trifluoro(organo)borates.

We have shown that the concept of rhodium-catalyzed tandem carbometalation/enantioselective protonation is a highly efficient process for the introduction of an organic substituent in the β position of an electron-deficient alkene with concomitant control of the chirality of the α center. In this tandem process, the use of phenol derivatives, and particularly nontoxic and inexpensive guaiacol, as the proton source was crucial for achieving satisfactory levels of enantioselectivity and for the reproducibility of the reaction. This proton source may be easily recovered and completely suppresses the competitive reduction of the organometallic reagent that is usually observed in these rhodium-catalyzed reactions.[4] Application of dehydroamino esters in this reaction allowed access to diversely substituted α-amino esters in high yields and *ee* values (up to 90%) using binap as the chiral ligand.

Received: July 30, 2003
Revised: September 24, 2003 [Z52518]

Keywords: amino acids · asymmetric catalysis · borates · protonation · rhodium

[1] For reviews on 1,4-addition reactions, see a) B. A. Rossiter, N. M. Swingle, *Chem. Rev.* **1992**, *92*, 771–806; b) P. Perlmutter, *Conjugate Addition Reaction in Organic Synthesis*, Pergamon, Oxford, **1992**.

[2] For recent reviews on asymmetric 1,4-additions, see a) A. Alexakis, *Transition Metal Catalyzed Reactions* (Eds.: S.-I. Murahashi, S. G. Davies), IUPAC Blackwell Science, Oxford, **1999**, pp. 303–316; b) K. Tomioka, Y. Nagoka, *Comprehensive Asymmetric Catalysis* (Eds.: E. N. Jacobsen, A. Pfaltz, H. Yamamoto), Springer, New York, **2000**, pp. 1105–1120; c) M. P. Sibi, S. Manyem, *Tetrahedron* **2000**, *56*, 8033–8061; d) N. Krause, A. Hoffmann-Röder, *Synthesis* **2001**, 171–196.

[3] Review: A. Alexakis, C. Benhaim, *Eur. J. Org. Chem.* **2002**, 3221–3236.

[4] Y. Takaya, M. Ogasawara, T. Hayashi, M. Sakai, N. Miyaura, *J. Am. Chem. Soc.* **1998**, *120*, 5579–5580; reviews: T. Hayashi, *Synlett* **2001**, 879–887; T. Hayashi, K. Yamasaki, *Chem. Rev.* **2003**, *103*, 2829–2844.

[5] For examples of asymmetric tandem catalytic enone conjugate addition/aldol trapping, see a) S. J. Taylor, M. O. Duffey, J. P. Morken, *J. Am. Chem. Soc.* **2000**, *122*, 4528–4529; b) L. A. Arnold, R. Naasz, A. J. Minnaard, B. L. Feringa, *J. Am. Chem. Soc.* **2001**, *123*, 5841–5842; c) H. Mizutani, S. J. Degrado, A. H. Hoveyda, *J. Am. Chem. Soc.* **2002**, *124*, 779–781; d) K. Yoshida, M. Ogasawara, T. Hayashi, *J. Am. Chem. Soc.* **2002**, *124*, 10984–10985; e) D. F. Cauble, J. D. Gipson, M. J. Krische, *J. Am. Chem. Soc.* **2003**, *125*, 1110–1111.

[6] For recent examples of catalytic enantioselective enone conjugate addition followed by enolate traping, see a) M. Kitama, T. Miki, K. Nakano, R. Noyori, *Tetrahedron Lett.* **1996**, *37*, 5141–5144; b) B. L. Feringa, M. Pineschi, L. A. Arnold, R. Imbos, A. H. M. de Vries, *Angew. Chem.* **1997**, *109*, 2733–2736; *Angew. Chem. Int. Ed. Engl.* **1997**, *36*, 2620–2623; c) S. J. Degrado, H. Mizutani, A. H. Hoveyda, *J. Am. Chem. Soc.* **2001**, *123*, 755–756; d) A. Alexakis, G. P. Trevitt, G. Bernardinelli, *J. Am. Chem.*

 © 2004 Wiley-VCH Verlag GmbH & Co. KGaA, Weinheim

Soc. **2001**, *123*, 4358 – 4359; e) K. Yoshida, M. Ogasawara, T. Hayashi, *J. Org. Chem.* **2003**, *68*, 1901 – 1905.

[7] For a first example of the enantioselective protonation of a rhodium enolate intermediate (18% *ee*), see S. H. Bergens, B. Bosnich, *J. Am. Chem. Soc.* **1991**, *113*, 958 – 967.

[8] When we started our studies only one example was described of such a transformation in which the 1,4-addition of phenylboronic acid to methyl α-acetamidoacrylate catalyzed by a rhodium complex chelated with a binol-based diphosphonite chiral ligand furnished the phenylalanine derivative in 77% *ee* on protonation with water, but using excess NaF as an additive: M. T. Reetz, D. Moulin, A. Gosberg, *Org. Lett.* **2001**, *3*, 4083 – 4085.

[9] During the refereeing process a related reaction was published using aryl boronic acids as organometallic partners and water as the proton source with *ee* values ranging from 37 to 72%: C. J. Chapman, K. J. Wadsworth, C. G. Frost, *J. Organomet. Chem.* **2003**, *680*, 206 – 211.

[10] For enantioselective protonation of enolates, see a) L. Duhamel, J.-C. Plaquevent, *J. Am. Chem. Soc.* **1978**, *100*, 7415 – 7416; reviews: b) L. Duhamel, P. Duhamel, J.-C. Launay, J.-C. Plaquevent, *Bull. Soc. Chim. Fr.* **1984**, 421 – 430; c) C. Fehr, *Angew. Chem.* **1996**, *108*, 2726 – 2748; *Angew. Chem. Int. Ed. Engl.* **1996**, *35*, 2566 – 2587; d) A. Yanagisawa, K. Ishihara, H. Yamamoto, *Synlett* **1997**, 411 – 420; e) J. Eames, N. Weerasooriya, *Tetrahedron: Asymmetry* **2001**, *12*, 1 – 24.

[11] For examples of non-asymmetric 1,4-additions of organometallic reagents to dehydroamino esters catalyzed by rhodium(I) complexes, see a) T.-S. Huang, C.-J. Li, *Chem. Commun.* **2001**, 2348 – 2349; b) T.-S. Huang, C.-J. Li, *Org. Lett.* **2001**, *3*, 2037 – 2039; c) C. J. Chapman, C. G. Frost, *Adv. Synth. Catal.* **2003**, *345*, 353 – 355.

[12] a) M. P. Sibi, Y. Asano, J. B. Sausker, *Angew. Chem.* **2001**, *113*, 1333 – 1336; *Angew. Chem. Int. Ed.* **2001**, *40*, 1293 – 1296; b) M. P. Sibi, J. B. Sausker, *J. Am. Chem. Soc.* **2002**, *124*, 984 – 991.

[13] For a review on potassium trifluoro(organo)borate chemistry, see S. Darses, J. P. Genet, *Eur. J. Org. Chem.* **2003**, 4313 – 4327.

[14] For selected examples, see a) S. Darses, J.-L. Brayer, J.-P. Demoute, J.-P. Genet, *Tetrahedron Lett.* **1997**, *38*, 4393 – 4396; b) S. Darses, G. Michaud, J.-P. Genet, *Eur. J. Org. Chem.* **1999**, 1875 – 1883; c) R. A. Batey, T. D. Quach, *Tetrahedron Lett.* **2001**, *42*, 9099 – 9103; d) G. A. Molander, B. W. Katona, F. Machrouki, *J. Org. Chem.* **2002**, *67*, 8416 – 8423; e) G. A. Molander, B. Biolatto, *J. Org. Chem.* **2003**, *68*,4302 – 4314; f) G. A. Molander, C.-S. Yun, M. Ribagorda, B. Biolatto, *J. Org. Chem.* **2003**, *68*, 5534 – 5539.

[15] For a racemic version, see R. A. Batey, A. N. Thadani, D. V. Smil, *Org. Lett.* **1999**, *1*, 1683 – 1686; for asymmetric 1,4-additions, see M. Pucheault, S. Darses, J.-P. Genet, *Tetrahedron Lett.* **2002**, *43*, 6155 – 6157; M. Pucheault, S. Darses, J.-P. Genet, *Eur. J. Org. Chem.* **2002**, 3552 – 3557.

[16] L. Navarre, S. Darses, J.-P. Genet, *Eur. J. Org. Chem.* **2003**, in press.

[17] Such complexes have been shown to be intermediates in 1,4-additions of organometallic reagents (particularly organoboronic acids) to enones: T. Hayashi, M. Takahashi, Y. Takaya, M. Ogasawara, *J. Am. Chem. Soc.* **2002**, *124*, 5052 – 5058.

[18] Maximum *ee* values obtained with selected ligands: (*S*)-binap (16%), (*S*)-6,6′-dimethoxy-2,2′-bis(diphenylphosphanyl)-1,1′-biphenyl (MeOBiphep, 28%), (*R*,*S*)-(−)-1-[2-(diphenylphosphanyl)ferrocenyl]ethyldicyclohexylphosphane (josiphos, 28%), (*S*)-6,6′-dimethoxy-2,2′-bis[di(4-dimethylaminophenyl)-phosphanyl)-1,1′-biphenyl ((*S*)-pDMA-MeObiphep, 11%), (*R*)-6,6′-dimethoxy-2,2′-bis[di(2-furyl)phosphanyl)-1,1′-biphenyl ((*R*)-2-furylMeObiphep, 18%), (*S*,*R*)-1-[2-(dicyclohexylphosphanyl)ferrocenyl]ethyldiphenylphosphane ((*S*,*R*)-Cy_2PFPPh_2, 10%), (*R*)-6,6′-dimethoxy-2,2′-bis[di(3,5-di-*tert*-butylphenyl)-phosphanyl)-1,1′-biphenyl ((*R*)-3,5-*t*BuMeOBiphep, 9%).

[19] An inhibitory effect was observed upon the addition of acids in the rhodium-catalyzed 1,4-addition of organoboronic acids: S. Sakuma, N. Miyaura, *J. Org. Chem.* **2001**, *66*, 8944 – 8946.

[20] *Ortho*-substituted phenols that are capable of forming chelate complexes have been used successfully in the diastereoselective protonation of enolate intermediates: N. Krause, *Angew. Chem.* **1994**, *106*, 1845 – 1847; *Angew. Chem. Int. Ed. Engl.* **1994**, *33*, 1764 – 1765; review: N. Krause, S. Ebert, A. Haubrich, *Liebigs Ann.* **1997**, 2409 – 2418.

[21] Typical procedure: A septum-capped vial equipped with a magnetic stirring bar was charged with dehydroamino ester **1a** (0.5 mmol, 71.6 mg), potassium (4-bromophenyl)trifluoroborate **2e** (2 equiv, 1 mmol, 263 mg), $[Rh(cod)_2][PF_6]$ (3 mol%, 6.9 mg), and (*R*)-binap (6.6 mol%, 20.6 mg). The vial was closed and evacuated under vacuum and then placed in an argon atmosphere. Degassed toluene (2 mL) and distilled guaiacol (1 equiv, 0.5 mmol, 55 μL) were added and the mixture was stirred in a preheated oil bath at 110–115 °C for 20 h. After cooling the vessel to room temperature, the reaction mixture was purified by column chromatography (ethyl acetate/cyclohexane 3:2) on silica gel to afford **3e** as a white solid (113 mg, 75% yield). $[\alpha]_D^{25} = +79$ ($c = 1.03$, $CHCl_3$). HPLC (M. J. Burk, J. E. Feaster, W. A. Nugent, R. L. Harlow, *J. Am. Chem. Soc.* **1993**, *115*, 10125 – 10138): Daicel Chiralcel OJ, hexane/propan-2-ol 90/10, 0.5 mL min^{-1}, 215 nm, $t_R = 25.3$ (*S*) and 29.2 min (*R*).

[22] M. J. Burk, J. G. Allen, W. F. Kiesman, *J. Am. Chem. Soc.* **1998**, *120*, 657 – 663.

[23] For reviews on asymmetric hydrogenation, see a) R. Noyori, *Asymmetric Catalysis In Organic Synthesis*, Wiley, New York, **1994**; b) "Reductions in Organic Synthesis: Recent Advances and Practical Applications": J.-P. Genet, *ACS Symp. Ser.* **1996**, *641*, 31 – 51; c) M. J. Burk, *Chemtracts: Org. Chem.* **1998**, *11*, 787 – 802; d) T. Ohkuma, M. Kitama, R. Noyori, *Catalytic Asymmetric Synthesis* (Ed.: I. Ojima), VCH, Weiheim, **2000**, chap. 1.4; e) R. Noyori, T. Ohkuma, *Angew. Chem.* **2001**, *113*, 40 – 75; *Angew. Chem. Int. Ed.* **2001**, *40*, 40 – 73; f) J. P. Genet, *Acc. Chem. Res.* **2003**, in press.

[24] For 1,4-additions of organosilanes catalyzed by rhodium(I) complexes, see a) S. Oi, M. Moro, Y. Inoue, *Organometallics* **2001**, *20*, 1036 – 1037; b) T. S. Huang, C.-J. Li, *Chem. Commun.* **2001**, 2348 – 2349; c) A. Mori, Y. Danda, T. Fujii, K. Hirabayashi, K. Osakada, *J. Am. Chem. Soc.* **2001**, *123*, 10774 – 10775; d) T. Koike, X. Du, A. Mori, F. Osakada, *Synlett* **2002**, 301 – 303; e) S. Oi, Y. Honma, Y. Inoue, *Org. Lett.* **2002**, *4*, 667 – 669; f) S. Oi, A. Taira, Y. Honma, Y. Inoue, *Org. Lett.* **2003**, *5*, 97 – 99.

[25] a) K. Tamao, K. Kobayashi, Y. Ito, *Tetrahedron Lett.* **1989**, *30*, 6051 – 6054; b) ref. [11b]; c) Y. Hatanaka, K. Goda, Y. Okahara, T. Hiyama, *Tetrahedron* **1994**, *50*, 8301 – 8316; d) T. Hiyama, Y. Hatanaka, *Pure Appl. Chem.* **1994**, *66*, 1471 – 1478.

[26] For 1,4-additions of organostannanes catalyzed by rhodium(I) complexes, see a) S. Oi, M. Moro, S. Ono, Y. Inoue, *Chem. Lett.* **1998**, 83 – 84; b) T. S. Huang, C.-J. Li, *Org. Lett.* **2001**, *3*, 2037 – 2039; c) T. Huang, Y. Meng, S. Venkatraman, D. Wang, C.-J. Li, *J. Am. Chem. Soc.* **2001**, *123*, 7451 – 7452.

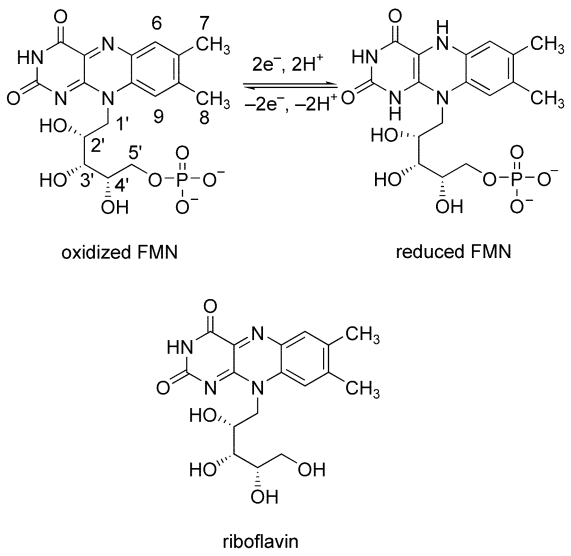
 © 2004 Wiley-VCH Verlag GmbH & Co. KGaA, Weinheim

Peptidomimetics

A Peptide Flavoprotein Mimic: Flavin Recognition and Redox Potential Modulation in Water by a Designed β Hairpin**

*Sara M. Butterfield, Catherine M. Goodman, Vincent M. Rotello, and Marcey L. Waters**

The design of miniature proteins that demonstrate both structure and function is an important goal with chemical and biomedical implications.[1] Redox systems are particularly attractive targets for these studies, because of the diversity and importance of redox-mediated processes. In the field of de novo protein design, much effort has gone into the development of designed proteins that bind metals and hemes as metalloenzyme mimics for catalytic applications.[1a] Designed proteins and peptides that incorporate cofactors including pyridoxal, thiamine, nicotinamide, and flavin functionalities have also been developed, but all of these systems feature covalent attachment to the polypeptide.[1b] Although covalent incorporation of cofactors has led to novel functional properties in designed systems, recent studies suggest that protein binding of a cofactor plays a more significant role than simply bringing it in proximity to the substrate. For example, studies of flavoenzymes have shown that noncovalent interactions are essential not only for regulating cofactor recognition, but also for tuning the redox properties of the flavin cofactor and thus controlling the overall catalytic activity of the enzyme.[2] The shift in reduction potential of flavin mononucleotide (FMN) upon binding to flavodoxin is believed to result in part from stacking interactions between the flavin ring and aromatic side chains in the protein; these interactions disfavor the two-electron reduction to the hydroquinone form of the cofactor (Scheme 1).[2a–c] This shift to a more negative potential has been described in synthetic model systems[2e,f] and counteracts the effects of hydrogen bonding, which has been shown to increase flavin reduction potentials.[2d] In addition, the presence of charged residues has been shown to influence the redox potential of FMN. For example, basic residues in the FMN binding pocket of flavodoxin have been shown to stabilize the anionic hydroquinone.[2a]



Scheme 1. Structures of the flavin cofactors and the two-electron reduction of FMN.

Given the interplay between noncovalent interactions and flavoprotein redox activity, an ideal designed flavoenzyme would incorporate a binding site for a flavin cofactor, thereby allowing modulation of the flavin redox properties through specific interactions with preorganized side chains. To this end, we have designed a 12-residue β-hairpin peptide that binds FMN strongly in water and demonstrates many of the same features as are seen in flavoproteins, including modulation of the flavin redox potential.

The recently reported peptide receptor **1**[3] has been shown to be a well-folded β hairpin.[4] The peptide sequence incorporates two Trp residues in a diagonal orientation on one face of the β hairpin; this forms a binding cleft for aromatic guests. In addition, two Lys residues were incorporated on the same face of the hairpin to allow favorable electrostatic interactions with FMN.

Ac-Arg-**Trp**-Val-**Lys**-Val-Asn-Gly-Orn-**Trp**-Ile-**Lys**-Gln-NH_2
Peptide **1**
(Bold lettering indicates the residues on the binding face of the *β*-hairpin)

Titration of peptide **1** with FMN, monitored by using NMR, UV/Vis, and fluorescence spectroscopy, demonstrates that the flavin ring intercalates between the two Trp residues. The addition of approximately ten equivalents of FMN to peptide **1** produced a 0.3 ppm upfield shift of the signals for the H-5 protons of both Trp residues of the hairpin in the NMR spectra; this result indicates a stacking interaction involving both Trp side chains.[5] Furthermore, the signals for the nonexchangeable flavin aromatic ring protons were upfield shifted substantially in the presence of the hairpin, thus supporting the participation of stacking interaction in

[*] S. M. Butterfield, Prof. M. L. Waters
Department of Chemistry, CB 3290
University of North Carolina
Chapel Hill, NC 27599 (USA)
Fax: (+1) 919-962-2388
C. M. Goodman, Prof. V. M. Rotello
Department of Chemistry
Department of Polymer Science and Engineering
Program in Molecular and Cell Biology
University of Massachusetts
Amherst, MA 01003 (USA)

[**] We gratefully acknowledge the University of North Carolina College of Arts and Sciences for startup funds. This work was supported in part by a National Science Foundation Career Award (CHE-0094068, to M.W.) and the National Institutes of Health (GM GM59249, to V.R.). We thank W. John Cooper and Robert M. Hughes for the molecular modeling studies.

Supporting information for this article is available on the WWW under http://www.angewandte.org or from the author.

 © 2004 Wiley-VCH Verlag GmbH & Co. KGaA, Weinheim DOI: 10.1002/anie.200352527

binding (Figure 1). Upfield shifting of the FMN sugar proton signals was also observed and could be indicative of CH–π interactions with the Trp rings. However, the magnitude of the shift of the sugar proton signal decreases with increasing

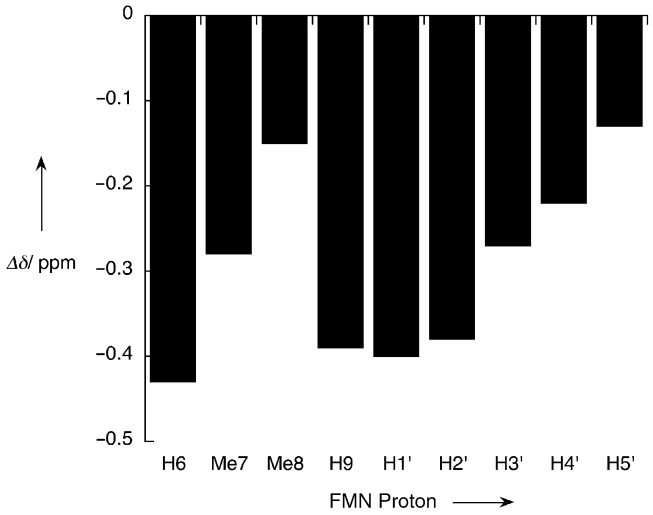


Figure 1. Change in the chemical shift values of the signals for nonexchangeable FMN protons in the presence of one equivalent of peptide **1**.

distance from the flavin ring; this suggests that the shift is a consequence of its proximity to the flavin intercalation site.

In the UV/Vis spectrum, the FMN band at 373 nm is blue-shifted by approximately 4 nm at binding saturation, which indicates that the flavin ring is in a more hydrophobic environment when it is bound by the peptide.[6] The flavin band at 446 nm also demonstrates hypochromicity in the presence of peptide **1**, as has been observed for other flavins participating in π–π stacking interactions.[7] In addition, quenching of the FMN fluorescence upon titration with peptide **1** also denotes an interaction between the Trp side chains and the flavin ring (Figure 2).[8]

NMR studies indicate that FMN is bound to the peptide in its folded state. Cross-strand NOE interactions are apparent in peptide **1** in the presence and absence of FMN, thus indicating that the peptide maintains a β-hairpin structure when FMN is bound (Figure 3a). In addition, the chemical-shift difference between the glycine diastereotopic protons in the turn is unchanged in the presence of FMN ($\Delta\delta$Gly = 0.74 ppm for both free and complexed peptide **1**); this suggests that no significant structural change occurs upon binding.[9] Upfield shifts of the signals for the α protons of peptide **1** were observed upon FMN binding, presumably because of the proximity of the flavin ring as opposed to destabilization of the β hairpin,[10] since cross-strand NOE interactions and $\Delta\delta$Gly values indicate that the peptide is well-folded in the presence of FMN. Moreover, the greater shifting of the signals for the Trp and Lys side-chain protons in the presence of excess FMN as compared to those for other residues suggests that FMN binds on this face of the β hairpin (Figure 3b). Taken together, these results indicate that FMN is binding to the peptide in the folded conformation, and the

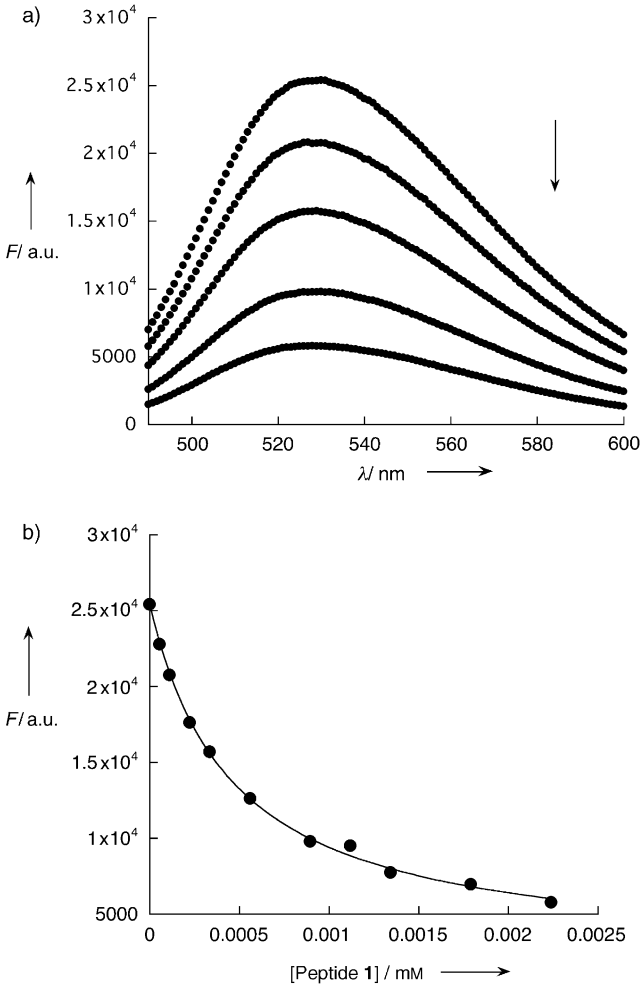


Figure 2. a) FMN fluorescence quenching in the presence of increasing concentrations of peptide **1** in 10 mM acetate buffer (pH 5.0) at 25 °C ([FMN] = 37 μM, [peptide] = 0–2.25 mM). The arrow indicates the direction of change in fluorescence intensity with increasing peptide concentration. b) FMN fluorescence at 530 nm versus the concentration of peptide **1** ([FMN] = 37 μM). The line through the data represents the best fit to a 1:1 binding equation. a.u. = arbitrary units.

cofactor interacts directly with both Trp residues on one face of the hairpin.

The binding affinity of FMN was quantified by using fluorescence quenching of the flavin. Fitting of the fluorescence quenching data as a function of peptide concentration to a 1:1 binding equation gave an association constant (K_{assoc}) of 2200 M^{-1} (Table 1), with a 1:1 binding ratio demonstrated by a Job plot by NMR spectroscopy. Variation of the FMN concentration by a factor of ten does not significantly influence the observed association constant, which suggests that higher order aggregates are unlikely. The designed hairpin and FMN therefore exhibit a strong interaction in water through noncovalent interactions of FMN with the side-chains of the peptide in the folded state.[11]

The difference in binding affinities between FMN and riboflavin (K_{assoc} = 315 M^{-1}; Table 1) indicates that electrostatic interactions involving the FMN phosphate group contribute approximately −1 kcal mol^{-1} to FMN binding,

 © 2004 Wiley-VCH Verlag GmbH & Co. KGaA, Weinheim

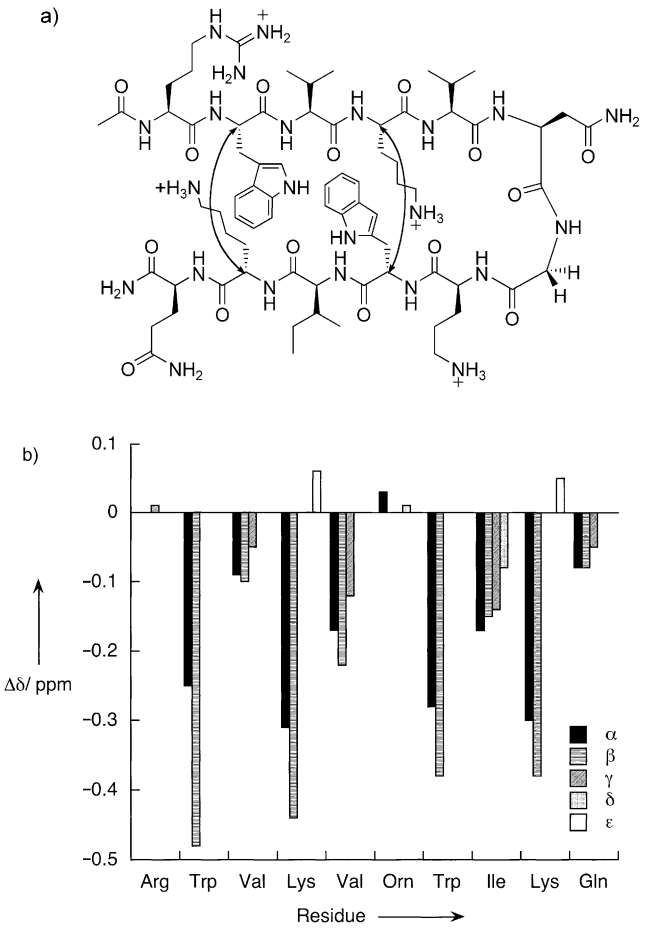


Figure 3. a) Cross-strand NOE interactions observed in the presence of ten equivalents of FMN. b) Change in side-chain proton chemical shifts for peptide **1** in the presence of ten equivalents of FMN, with turn residues (Asn–Gly) omitted ($\Delta\delta H_\alpha = \delta H_{\alpha,10FMN} - \delta H_{\alpha,0FMN}$). Measurements were made in 10 mM [D_3]acetate buffer (pH 5.0, uncorrected) at 25 °C. α–ε indicate the position on the sidechains. The γ and δ protons on Lys4 and Lys9 could not be unambiguously.

Table 1: Association and dissociation constants (K_{assoc} and K_d) for flavin recognition by peptide **1**.[a]

Flavin substrate	[KCl] [mM]	K_{assoc} [M^{-1}]	K_d [mM]	$\Delta G_{binding}$ (error) [kcal mol^{-1}][b]
FMN	0	2200	0.45	−4.6 (0.1)
riboflavin	0	310	3.2	−3.4 (0.1)
FMN[c]	100	720	1.4	−3.9 (0.1)
$FMNH_2$[c]	100	40	25	−2.2

[a] In 10 mM acetate buffer (pH 5.0) at 25 °C, determined by fluorescence titrations unless otherwise stated. [b] Errors determined by the average deviation between two to three separate titration experiments. [c] In 10 mM phosphate buffer with 100 mM KCl (pH 5.0) at 25 °C. The association constant for $FMNH_2$ was determined from electrochemical measurements (see Supporting Information).

which is in agreement with electrostatic contributions to adenosine triphosphate (ATP) recognition by peptide **1**.[3] The electrostatic contribution probably arises from interactions between the FMN phosphate group and the Lys side chains. If the recognition of riboflavin by peptide **1** is driven by aromatic interactions alone (that is, in the absence of hydrogen bonds or CH–π interactions), then the flavin–tryptophan interaction contributes approximately −3.4 kcal mol^{-1} to FMN recognition, which is nearly twice the strength of the adenine–tryptophan interaction ($\Delta G = -1.8$ kcal mol^{-1}) estimated previously for ATP recognition by peptide **1**.[3] The strength of the flavin–tryptophan interaction in our system is similar in magnitude to previously measured π–π stacking interactions involving flavin rings in water.[7a] The strong aromatic interaction between flavin and the Trp side chains is not surprising given the large π surface area of flavin, but can also be attributed to favorable electrostatic overlap between the electron-rich Trp side chains with the electron-poor flavin ring.

Electrochemical studies were performed to determine the influence of peptide binding on the FMN reduction potential. Square wave voltammetry measurements show a shift of FMN reduction potentials to more negative values with increasing peptide concentration (Figure 4). At binding

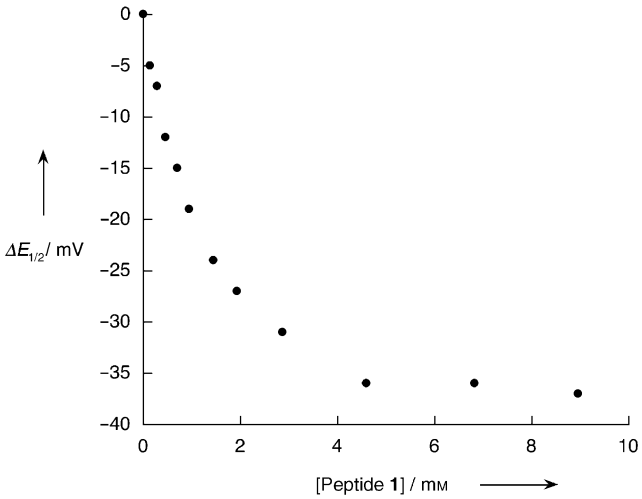


Figure 4. Change in reduction potential (*E*) with added peptide ($\Delta E_{1/2} = E_{FMN,bound} - E_{FMN,free}$).

saturation, $\Delta E_{1/2}$ is −38 mV, which indicates that the bound flavin ring is more difficult to reduce to the $FMNH_2$ hydroquinone by 1.7 kcal mol^{-1}, relative to unbound FMN. This result is consistent with previous investigations of the influence of aromatic interactions on the reduction potential of flavin. McCormick and co-workers have shown that peptides with intramolecular stacking interactions between flavin and Trp show slowed rates of FMN reduction compared to uncomplexed flavin,[12] while Breinlinger and Rotello have shown that flavin stacking with anthracene shifts the potential by −63 mV in chloroform.[2e] The contribution of aromatic stacking is substantial in peptide **1**, as a cationic environment has been shown to *increase* the redox potential of FMN, thereby counteracting the modulation provided by the stacking interactions.[1b] Although the perturbation of the FMN redox potential can be of the order of hundreds of millivolts in naturally occurring flavoproteins, stacking interactions typically only contribute a fraction of the shift, with the rest

 © 2004 Wiley-VCH Verlag GmbH & Co. KGaA, Weinheim

resulting from solvent exclusion as well as proximity to several negatively charged side chains in the binding site.[2] The magnitude of the negative potential shift in our system is substantial given that it results solely from aromatic interactions at a solvent-exposed location in a cationic peptide.

From the change in reduction potential of FMN in the presence of peptide **1**, the binding affinity of the reduced FMN is calculated[13] to be $40\,\text{M}^{-1}$ in 100 mM KCl, a approximately 18-fold drop from the $720\,\text{M}^{-1}$ value observed for the oxidized flavin under the same conditions (Table 1). This finding further emphasizes the role of the electrostatic component of aromatic–aromatic interactions in regulating flavin redox processes. Favorable interactions exist between the electron-poor oxidized flavin and the electron-rich Trp side chains. These interactions are attenuated upon reduction of the flavin to the electron-rich hydroquinone form, thereby reducing the strength of the peptide–flavin interaction. The observation of an electrostatic effect on FMN binding indicates that electrostatics are a major contributor to aromatic stacking interactions, even in water.[14]

This is the first report of a designed, structured peptide with a noncovalent flavin binding site. Our results indicate that diagonal Trp residues in the non-hydrogen-bonding sites of a model β hairpin create a pre-organized recognition cleft for flavin cofactors. The electrostatic nature of the stacking interactions in the peptide–FMN complex perturbs the flavin reduction potential such that two-electron reduction to the reduced hydroquinone is disfavored relative to free FMN, as observed in many flavoenzymes. While synthetic receptors have been shown to both complex flavin and shift its redox potential, to our knowledge there have been no reports of designed systems that accomplish both of these feats in water. Catalysis by this redox-active miniature protein with a bound FMN cofactor will be explored in the future.

Received: July 31, 2003
Revised: October 27, 2003 [Z52527]

Keywords: flavins · molecular recognition · peptidomimetics · protein models · redox chemistry

[1] a) L. Baltzer, *Top. Curr. Chem.* **1999**, *202*, 39 – 76; b) B. Imperiali, K. A. McDonnell, M. Shrogren-Knaak, *Top. Curr. Chem.* **1999**, *202*, 1 – 38.

[2] a) R. P. Swenson, G. D. Krey, *Biochemistry* **1994**, *33*, 8505 – 8514; b) Z. Zhou, R. P. Swenson, *Biochemistry* **1995**, *34*, 3183 – 3192; c) Z. Zhou, R. P. Swenson, *Biochemistry* **1996**, *35*, 15980 – 15988; d) E. Breinlinger, A. Niemz, V. M. Rotello, *J. Am. Chem. Soc.* **1995**, *117*, 5379 – 5380; e) E. C. Breinlinger, V. M. Rotello, *J. Am. Chem. Soc.* **1997**, *119*, 1165 – 1166; f) E. C. Breinlinger, C. J. Keenan, V. M. Rotello, *J. Am. Chem. Soc.* **1998**, *120*, 8606 – 8609.

[3] S. M. Butterfield, M. L. Waters, *J. Am. Chem. Soc.* **2003**, *125*, 9580 – 9581.

[4] For reviews on β-hairpin peptides as models for β-sheet proteins, see: a) S. H. Gellman, *Curr. Opin. Chem. Biol.* **1998**, *2*, 717 – 725; b) M. S. Searle, *J. Chem. Soc. Perkin Trans. 2* **2001**, 1011 – 1020.

[5] A shift is apparent at other Trp aromatic-ring protons as well, but extensive peak overlap prevented accurate determination of changes in the chemical shift values.

[6] D. L. Pavia, G. M. Lapman, G. S. Kriz, *Introduction to Spectroscopy*, 3rd ed., Harcourt College Publishers, Fort Worth, TX, **2001**.

[7] a) E. M. Seward, R. B. Hopkins, W. Sauerer, S. W. Tam, F. Diederich, *J. Am. Chem. Soc.* **1990**, *112*, 1783 – 1790; b) T. Ishida, M. Itoh, M. Horiuchi, S. Yamashita, M. Doi, M. Inoue, Y. Mizunoya, Y. Tona, A. Okada, *Chem. Pharm. Bull.* **1986**, *34*, 1853 – 1864.

[8] J. B. Burk, *Photophysics of Aromatic Molecules*, Wiley-Interscience, New York, **1970**.

[9] a) S. R. Griffiths-Jones, A. J. Maynard, M. S. Searle, *J. Mol. Biol.* **1999**, *292*, 1051 – 1069; b) C. D. Tatko, M. L. Waters, *J. Am. Chem. Soc.* **2002**, *124*, 9372 – 9373.

[10] D. S. Wishart, B. D. Sykes, F. M. Richards, *Biochemistry* **1992**, *31*, 1647 – 1651.

[11] Select examples of synthetic nucleotide receptors in water: a) C. Jasper, T. Schrader, J. Panitsky, F. G. Klärner, *Angew. Chem.* **2002**, *114*, 1411 – 1415; *Angew. Chem. Int. Ed.* **2002**, *41*, 1355 – 1358; b) H. J. Schneider, T. Blatter, B. Palm, U. Pfingstag, V. Rüdiger, I. Theis, *J. Am. Chem. Soc.* **1992**, *114*, 7704 – 7708; c) Y. Shi, H. J. Schneider, *J. Chem. Soc. Perkin Trans. 2* **1999**, 1797 – 1803.

[12] F. Y. H. Wu, R. E. MacKenzie, D. B. McCormick, *Biochemistry* **1970**, *9*, 2219 – 2224.

[13] a) A. Niemz, V. M. Rotello, *Acc. Chem. Res.* **1999**, *32*, 44 – 52; b) A. E. Kaifer, *Acc. Chem. Res.* **1999**, *32*, 62 – 71.

[14] For recent reviews discussing electrostatic contributions to aromatic interactions, see: a) C. A. Hunter, K. R. Lawson, J. Perkins, C. J. Urch, *J. Chem. Soc. Perkin Trans. 2* **2001**, 651 – 669; b) E. A. Meyer, R. K. Castellano, F. Diederich, *Angew. Chem.* **2003**, *115*, 1244 – 1287; *Angew. Chem. Int. Ed.* **2003**, *42*, 1210 – 1250.

 © 2004 Wiley-VCH Verlag GmbH & Co. KGaA, Weinheim

Monocerin Biosynthesis

Synthesis and Incorporation of the First Polyketide Synthase Free Intermediate in Monocerin Biosynthesis**

Lorraine C. Axford, Thomas J. Simpson, and Christine L. Willis*

Monocerin (**5**) is a polyketide fungal metabolite that exhibits antifungal, insecticidal, and plant pathogenic properties. It has been isolated from several fungal species, including *Dreschlera monoceras*,[1] *D. ravenelii*,[2] *Exserohilum turcum*,[3] and, along with the related fusarentin ethers, for example, **4**, from *Fusarium larvarum*.[4] Polyketide metabolites are pro-

[*] L. C. Axford, Prof. T. J. Simpson, Prof. C. L. Willis
School of Chemistry
University of Bristol
Cantock's Close, Bristol, BS8 1TS (UK)
Fax: (+44) 117-9298611
E-mail: tom.simpson@bristol.ac.uk

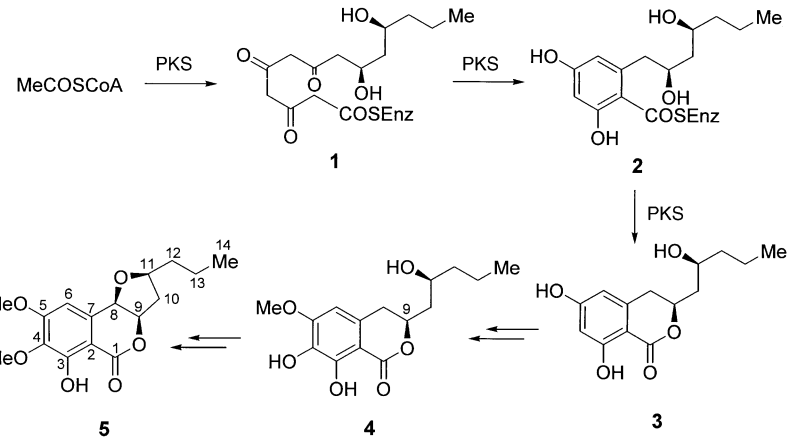
[**] We thank the Engineering and Physical Sciences Research Council for support (GR/N21352) and for a research studentship (L.C.A.), and Dr. M. P. Crump for a 600 MHz NMR spectrum.

 DOI: 10.1002/anie.200352652 © 2004 Wiley-VCH Verlag GmbH & Co. KGaA, Weinheim

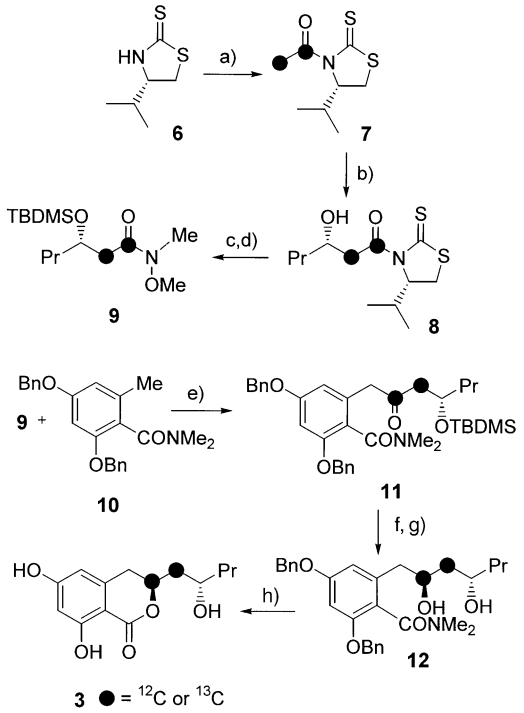
duced via linear, highly functionalized "polyketide" intermediates that are assembled from simple acyl coenzyme A (CoA) precursors by multifunctional enzyme complexes—polyketide synthases (PKSs)—the exact nature of which varies according to the source: bacteria, fungi, or higher plants.[5] In fungi, all PKSs characterized to date belong to the Type I class and consist of a single multidomain protein encoded by a single gene,[6] but the isolation and characterization of fungal PKSs remains a significant challenge. To investigate this problem we have developed a polymerase chain reaction (PCR) based method that uses oligonucleotide primers designed on consensus sequences from the keto-synthase or methyl-transferase domains of known PKS genes.[7] A complication with fungi, however, is that they frequently contain several polyketide pathways and so isolation of the desired PKS gene may still require a reverse genetics approach. Ideally, this would involve an assay based on the product of the PKS of interest, which is not usually the same as the product isolated from fungal fermentations. The isolated metabolite will almost always contain functionality introduced during PKS-catalyzed assembly and cyclization and also structural modifications effected by post-assembly "tailoring" enzymes.[5] As these modifications are not necessarily readily distinguishable, the exact structure of the PKS-derived intermediate is often uncertain.

In the case of monocerin (**5**), stable-isotope labeling studies[2] suggest that the immediate PKS-derived product should be the dihydroisocoumarin **3**. This would be formed as shown in Scheme 1 by cyclization of the linear heptaketide **1** to give the enzyme-bound orsellinate analogue **2**. Lactonization by intramolecular displacement of the thioester linkage to the PKS by the 9-hydroxy group would give **3** as the first enzyme-free intermediate in monocerin biosynthesis. There is much current interest in the engineering and heterologous expression of PKS genes from different sources to permit the rational production of novel structures.[6,8] The monocerin PKS is likely to be of particular interest in this context as it produces an intermediate, **1**, with an initial high level of reductive modification and ending with a more classical poly-β-ketide moiety. Thus, a synthesis of **3** was required for two reasons: first, in isotopically labeled form for incorporation studies to establish its obligate intermediacy on the monocerin biosynthetic pathway, and second as a standard for an assay (for example, HPLC) to facilitate detection of monocerin PKS activity in cell-free extracts of monocerin-producing cultures. Subsequent isolation and purification of the PKS protein will allow partial peptide sequencing and design of specific oligonucleotide probes for isolation of the monocerin PKS gene.

Dihydroisocoumarin **3** was prepared as shown in Scheme 2 by modification of our previously described convergent route[9] with coupling of the Weinreb amide **9** and the benzylic anion derived from benzamide **10** as the key carbon–carbon bond-forming step. To obtain **3** with vicinal ^{13}C labels for incorporation studies, sodium [$^{13}C_2$]acetate was converted



Scheme 1. Proposed biosynthesis of monocerin (**5**) via PKS-bound and post-assembly intermediates.



Scheme 2. Synthesis of dihydroisocoumarin **3**. Reagents and conditions: a) $NaN(SiMe_3)_2$, THF, −78 °C; then $MeCO_2COCMe_3$, 5 h, 35%; b) $Sn(OTf)_2$, 1-ethylpiperidine, CH_2Cl_2, −40 °C, 4.5 h; then butanal, −78 °C, 20 min, 88%; c) Et_3N, MeNHOMe, CH_2Cl_2, 25 °C, 72 h, 92%; d) TBDMSOTf, 2,6-lutidine, CH_2Cl_2, −25 °C, 1 h; then −25 °C→RT, 12 h, 98%; e) *sec*-BuLi, THF, −72 °C, 15 min; then **9**, −72 °C, 1.25 h, 45%; f) HCl/EtOH (1%), 25 °C, 5 h, 87%; g) AcOH, $Me_4N{\cdot}B(OAc)_3H$, MeCN, 6.25 h, −10 °C, 92%; h) 3 N HCl/dioxane (1:1), reflux, 48 h, 83%. Bn = benzyl, TBDMS = *tert*-butyldimethylsilyl Tf = triflate = trifluoromethanesulfonyl, THF = tetrahydrofuran.

with pivaloyl chloride into the mixed anhydride,[10] which was then used to acetylate the sodium salt of the thiazolidinethione **6**. A stereoselective aldol reaction[11] of the acetylated auxiliary **7** with butanal in the presence of tin triflate and 1-ethylpiperidine gave alcohol **8** as a single diastereoisomer. Displacement of the auxiliary with *N*,*O*-dimethylhydroxylamine and triethylamine[11] followed by TBDMS protection of the secondary alcohol gave the required Weinreb amide **9**.

 © 2004 Wiley-VCH Verlag GmbH & Co. KGaA, Weinheim

The benzylic anion, formed by treatment of a rigorously deoxygenated THF solution of benzamide **10**[12] with *sec*-butyllithium under argon, was treated with **9** to give ketone **11** in 45% optimized yield. Deprotection of the silyl ether and stereoselective reduction[13] of the resultant β-hydroxyketone gave the *anti* diol **12** as a single diastereoisomer. Lactone formation and removal of the benzylic ethers were effected in a single step by refluxing in 3 N HCl.

Preliminary fermentation studies showed that monocerin production in *D. ravenelii* commenced after about five days and increased steadily to give a yield of approximately 200 mg L^{-1} after a total of 14 days growth. [9,10-$^{13}C_2$]-Labeled **3** was pulse fed (30 mg in 0.6 mL of dimethyl sulfoxide (DMSO), three aliquots at 2 h intervals) to three flasks of fresh culture after 96 h. After a further 144 h, the cultures were worked up and monocerin (**5**) was isolated by flash column chromatography and further purified by HPLC. Initial analysis of the isolated metabolite by ^{1}H NMR spectroscopy showed that exceptionally high-level (60%) incorporation of intact isotopic label from **3** had occurred. The signal assigned to the proton 9-H shows the normal (natural abundance) multiplet at $\delta = 5.06$ ppm flanked by corresponding multiplets due to one-bond ^{13}C–^{1}H coupling ($^1J = 159$ Hz) from the incorporation of the ^{13}C label from **3** at C-9. Similar ^{1}H–^{13}C couplings are seen for the signals due to the diastereotopic methylene protons centered at $\delta = 2.52$ and 2.09 ppm ($^1J = 130$ and 135 Hz, respectively; Figure 1). In addition to the one-bond coupling, the latter signal also shows a clear two-bond ^{1}H–^{13}C coupling ($^2J = 6$ Hz) to the vicinal ^{13}C label incorporated at C-9. The high specific incorporation of **3** into monocerin was confirmed in the ^{13}C NMR spectrum ($\delta_C = 39.1$ and 81.2 ppm, $^1J = 37$ Hz) and the mass spectrum ([M^+] 308 (73%), [$M+2$] 310 (100%)).

We have analyzed the fermentation extracts for **3**, but within the limits of sensitivity of HPLC we were not able to demonstrate its presence. Initially this may be surprising, but given the remarkable efficiency with which **3** is incorporated into monocerin, we would not expect it to be present in observable quantities in the cultures. The rate of conversion must be so high that on release from the PKS it is immediately further converted into monocerin, and so the steady-state concentration of **3** will be negligible.

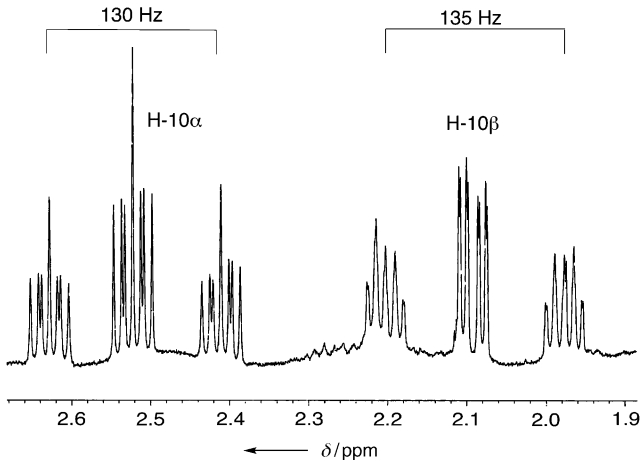


Figure 1. 600 MHz ^{1}H NMR spectrum showing the 10-H_2 signals of monocerin (**5**) enriched from incorporation of [9,10-$^{13}C_2$]-labeled dihydroisocoumarin **3**.

The results of this feeding study demonstrate that an exceptionally high level of incorporation of dihydroisocoumarin **3** into monocerin occurs, and this provides compelling evidence for the role of **3** as an essential intermediate. The level of incorporation, taken along with the previous stable-isotope labeling experiments[2] is entirely consistent with the proposed role of **3** as the first enzyme-free intermediate on the pathway and, thus, the final product of the PKS-catalyzed part of the pathway. This work has paved the way for the use of **3** in further studies to isolate and sequence the monocerin PKS gene. These are in progress.

Experimental Section

[9,10-$^{13}C_2$]-Labeled **3**: This was prepared according to the route shown in Scheme 2 from sodium [1,2-$^{13}C_2$]acetate (1.50 g, 17.86 mmol) to give dihydroisocoumarin **3** as an oil (169 mg); $[\alpha]_D^{25} = +15.6$ (MeOH, $c = 0.8$); IR (film): $\tilde{\nu}_{max} = 3285, 1629, 1465, 1378, 1255, 1165$ cm^{-1}; ^{1}H NMR (400 MHz, $CDCl_3$): $\delta = 10.98$ (s, 1H, 3-OH), 8.35 (br s, 1H, 5-OH), 6.28 (d, $J = 2.2$ Hz, 1H, ArH), 6.14 (br s, 1H, ArH), 4.78 (dm, $J = 140$ Hz, 1H, 9-H), 4.05 (br s, 1H, 11-OH), 4.05 (m, 1H, 11-H), 2.82 (m, 1H, 8-*H*H), 2.71 (dm, $J = 13.9$ Hz, 1H, 8-H*H*), 1.94 (dm, $J = 140$ Hz, 1H, 10-*H*H), 1.69 (dm, $J = 140$ Hz, 1H, 10-H*H*), 1.30–1.55 (m, 4H, 12-H_2 and 13-H_2), 0.92 (t, $J = 6.8$ Hz, 3H, 14-H_3) ppm; ^{13}C NMR (100 MHz, $CDCl_3$), enriched signals only: $\delta =$ 76.4 (d, $J = 40$ Hz, C-9), 41.8 (d, $J = 40$ Hz, C-10) ppm; MS (CI): *m*/*z* (%): 269 [$M^+ + 1$] (40%), 251 (100), 233 (16), 196 (22), 178 (15), 83 (29); HRMS (CI): calcd for $C_{12}{}^{13}C_2H_{19}O_5$ [$M^+ + 1$]: 269.1300; found: 269.1288.

Isolation of monocerin (**5**): *Dreschlera ravenelii* (CBS 200.29) was stored as a spore suspension in 20% glucose solution at −78 °C. Potato dextrose agar plates were inoculated with spore suspension (200 μL), spread with a glass spreader, and incubated upside down at 28 °C for seven days. A spore suspension prepared from this plate was used to inoculate further potato dextrose agar plates and, after growth, was stored in the dark at 4 °C. *D. ravenelii* was observed as fluffy pale gray mycelia with a dark underside. A spore suspension was made from two agar plates with sterile water (15 mL) and filtered through glass wool. This was used to inoculate liquid culture medium (100 mL) in five Erlenmeyer flasks (500 mL). The liquid medium was made from D-fructose (50.0 g), mycological peptone (2.0 g), sodium nitrate (2.0 g), potassium dihydrogen phosphate (1.0 g), potassium chloride (0.5 g), magnesium sulfate heptahydrate (0.5 g), and iron(II) sulfate heptahydrate (0.01 g) dissolved in MilliQ purified water (1000 mL). The fungus was grown as a static culture at 25 °C for 14 days. The mycelial mat was filtered through Merck filter paper and washed with distilled water. The filtrate was extracted into ethyl acetate (4 × volume), the organic phases were combined and dried over $MgSO_4$, and the solvent was removed in vacuo to yield an orange oil. This was purified by column chromatography on silica, with a gradient eluent of 20→50% EtOAc in petrol, to give monocerin (**5**; 98 mg from 5 Erlenmeyer flasks, corresponding to 196 mg L^{-1}) as a yellow oil; $R_f = 0.31$ (silica gel, EtOAc/petroleum ether 40–60 (1:1)); $[\alpha]_D^{21} = +48.2$ (MeOH, $c = 1.1$), literature value[14] $= +53$ (MeOH, $c =$ 0.85); IR (film): $\tilde{\nu}_{max} = 2928, 2856, 2253, 1664, 1375, 1274, 1120, 787, 731$ cm^{-1}; ^{1}H NMR (400 MHz, $CDCl_3$): $\delta = 11.29$ (s, 1H, ArOH), 6.60 (s, 1H, 6-H), 5.06 (ddd, $J = 6.2, 3.3, 1.0$ Hz, 1H, 9-H), 4.55 (d, $J =$ 3.3 Hz, 1H, 8-H), 4.12 (m, 1H, 11-H), 3.95 (s, 3H, OCH_3), 3.89 (s, 3H, OCH_3), 2.60 (ddd, $J = 14.6, 8.6, 6.0$ Hz, 1H, 10-*H*H), 2.16 (ddd, $J =$ 14.6, 6.2, 1.0 Hz, 1H, 10-H*H*), 1.71 (m, 1H, 12-*H*H), 1.57 (m, 1H, 12-H*H*), 1.40 (m, 2H, 13-H_2), 0.92 (t, $J = 7.3$ Hz, 3H, 14-H_3) ppm; ^{13}C NMR (100 MHz, $CDCl_3$): $\delta = 167.8$ (C-1), 158.8 (C-5), 157.5 (C-

 © 2004 Wiley-VCH Verlag GmbH & Co. KGaA, Weinheim

3), 137.0 (C-4), 131.2 (C-7), 104.5 (C-6), 101.9 (C-2), 81.3 (C-9), 78.8 (C-11), 74.5 (C-8), 60.7 (CH_3O), 56.3 (CH_3O), 39.1 (C-10), 38.1 (C-12), 19.2 (C-13), 14.0 (C-14) ppm; MS (EI): *m*/*z* (%): 308 [M^+] (100%), 265 (52), 209 (30).

Feeding study: Culture medium (100 mL) in four Erlenmeyer flasks (500 mL) was inoculated with spore suspension (1.2 mL) obtained from one agar plate (with 5 mL of sterile water) and grown as a static culture at 25 °C. After 96 h, the cultures in three flasks were fed with ^{13}C-labeled compound **3** (30 mg) in DMSO (0.6 mL, divided equally between the three flasks). The feeding was pulsed into three batches, with each culture receiving 67 μL every two hours. After a further 144 h, the mycelia were filtered and extracted into ethyl acetate as usual. The organic extract was purified by column chromatography, with a gradient eluent of 20→50% EtOAc in petrol, to give a mixture of [$^{13}C_2$]-labeled monocerin and **3**. This mixture was then dissolved in ethyl acetate/hexane (ca. 1:1) and purified further by preparative HPLC on a Luna 5μ silica normal-phase column (250 × 21.20 mm) at 254 nm with an ethyl acetate/hexane gradient. [9,10-$^{13}C_2$]-Monocerin was isolated as a pale oil (4 mg); ^{1}H NMR (400 MHz, $CDCl_3$): $\delta = 11.28$ (s, 1H, ArOH), 6.59 (s, 1H, 6-H), 5.06 (ddd, $J = 6.1$, 3.4, 1.2 Hz, 0.40H, and ddd, $J = 159$, 5.6, 2.9 Hz, 0.60H, 9-H), 4.55 (m, 1H, 8-H), 4.12 (m, 1H, 11-H), 3.95 (s, 3H, OCH_3), 3.90 (s, 3H, OCH_3), 2.60 (ddd, $J = 14.7$, 8.7, 6.1 Hz, 0.40H, and dddd, $J = 130$, 14.7, 8.7, 6.1 Hz, 0.60H, 10-H*H*), 2.16 (ddd, $J = 14.7$, 6.6, 1.0 Hz, 0.40H, and dddd, $J = 135$, 14.7, 6.6, 6.0 Hz, 0.60H, 10-*H*H), 1.71 (m, 1H, 12-H*H*), 1.59 (m, 1H, 12-*H*H), 1.38 (m, 2H, 13-H_2), 0.92 (t, $J = 7.3$ Hz, 3H, 14-H_3) ppm; ^{13}C NMR (100 MHz, $CDCl_3$), enriched signals only: $\delta = 81.2$ (d, $J = 37$ Hz, C-9), 39.1 (d, $J = 37$ Hz, C-10) ppm; MS (EI): *m*/*z* (%): 310 [*M*+2] (100), 308 [M^+] (73), 267 [*M*+2−C_3H_7] (62), 265 [M^+−C_3H_7] (40), 209 (63), 83 (43); HRMS (EI): calcd for $C_{14}{}^{13}C_2H_{20}O_6$ [M^+]: 310.1327; found: 310.1328.

Received: August 14, 2003 [Z52652]

Keywords: biosynthesis · fungal metabolites · monocerin · polyketide synthases · polyketides

[1] D. C. Aldridge, W. B. Turner, *J. Chem. Soc. C* **1970**, 2598–2600.
[2] F. E. Scott, T. J. Simpson, L. A. Trimble, J. C. Vederas, *J. Chem. Soc. Chem. Commun.* **1984**, 756–758.
[3] D. J. Robeson, G. A. Strobel, *Agric. Biol. Chem.* **1982**, *46*, 2681–2683.
[4] J. F. Grove, M. Pople, *J. Chem. Soc. Perkin Trans. 1* **1979**, 2048–2051.
[5] J. Staunton, K. J. Weissman, *Nat. Prod. Rep.* **2001**, *18*, 380–430.
[6] I. Fujii, A. Watanabe, U. Sankawa, Y. Ebizuka, *Chem. Biol.* **2001**, *8*, 189–197.
[7] L. E. H. Bingle, T. J. Simpson, C. M. Lazarus, *Fungal Genet. Biol.* **1999**, *26*, 209–223; T. P. Nicholson, C. M. Lazarus, B. A. M. Rudd, M. J. Dawson, T. J. Simpson, R. J. Cox, *Chem. Biol.* **2001**, *8*, 151–178.
[8] C. Khosla, *J. Org. Chem.* **2000**, *65*, 8127–8133.
[9] C. McNicholas, T. J. Simpson, N. J. Willett, *Tetrahedron Lett.* **1996**, *37*, 8053–8056.
[10] N. M. Kelly, R. G. Reid, C. L. Willis, P. L. Winton, *Tetrahedron Lett.* **1995**, *36*, 8315–8318.
[11] N. Murakami, M. Sugimoto, M. Kobayashi, *Bioorg. Med. Chem.* **2001**, *9*, 57–67.
[12] P. Watts, PhD Thesis, University of Bristol, **1999**; L. C. Axford, T. J. Simpson, D. M. Smith, P. Watts, C. L. Willis, unpublished results.
[13] R. F. Cunico, L. Bedell, *J. Org. Chem.* **1980**, *45*, 4797–4798; D. A. Evans, K. T. Chapman, E. M. Carreira, *J. Am. Chem. Soc.* **1988**, *110*, 3560–3578.
[14] K. Mori, H. Takaishi, *Tetrahedron* **1989**, *45*, 1639–1646.

 © 2004 Wiley-VCH Verlag GmbH & Co. KGaA, Weinheim

Polymerization

Oxidative Polymerization of 2,6-Dimethylphenol To Form Poly(2,6-dimethyl-1,4-phenyleneoxide) in Water**

*Kei Saito, Takahiro Tago, Toru Masuyama, and Hiroyuki Nishide**

One of the critical factors in realizing a green chemical reaction process involves the choice of water as the reaction solvent,[1] particularly for polymer production on a large scale. The oxidative polymerization of 2,6-dimethylphenol (**1**; DMP), reported in 1959 by A. S. Hay and his GE group,[2] provides a convenient and industrial method to prepare poly(2,6-dimethyl-1,4-phenyleneoxide) (**2**; PPO), an important plastic in engineering. This polymerization proceeds at room temperature and is an ideal atom-economical reaction that does not require any leaving groups (Scheme 1). However, the polymerization is carried out in organic solvents such as toluene and benzene under oxygen. Therefore, both a solvent-recovery process and an antiexplosive reactor are needed for the industrial production. Herein we report the first oxidative polymerization of DMP to form PPO in water as a green chemical process.

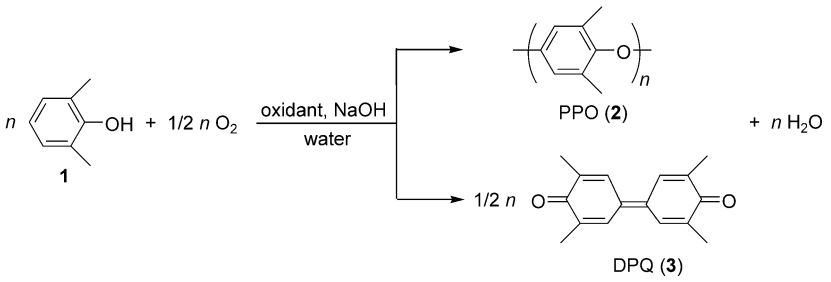
Although the preparation of PPO has been studied in detail,[3–5] there has been no report in which water was used as the polymerization solvent, except for a few studies in aqueous–organic biphasic solvents.[6,7] The oxidation of DMP in water is well-known to give predominantly DPQ (**3**), which is formed by the C–C coupling of two monomeric phenols (Scheme 1).[6,8] There is another unsolved problem associated with polymerization in water: The dimer of DMP is insoluble, even in an alkaline aqueous solution, and the molecular weight of the formed PPO remains very low. We have now succeeded in oxidatively polymerizing DMP to form high-molecular-weight PPO in water. DMP was vigorously stirred in an alkaline aqueous solution with an oxidant in air. In this reaction, the DMP monomer was insoluble in water but it dissolved in water when an equimolar amount of base (NaOH) was added.[9] The formed dimer and the following oligomers and polymers were insoluble in the alkaline aqueous solution, and the reaction mixture became heterogeneous immediately after the addition of the oxidant (see a photograph of the polymerization in water in the Supporting Information). The precipitated product could be

[*] K. Saito, T. Tago, T. Masuyama, Prof. Dr. H. Nishide
Department of Applied Chemistry, Waseda University
Tokyo 169-8555 (Japan)
Fax: (+813) 3209-5522
E-mail: nishide@waseda.jp

[**] This work was partially supported by Grants-in-Aid for Scientific Research (No. 13450384) and for the 21COE Research "Practical Nano-Chemistry" from MEXT, Japan. We thank Dr. Kenichi Oyaizu for productive discussions.

Supporting information for this article is available on the WWW under http://www.angewandte.org or from the author.

 © 2004 Wiley-VCH Verlag GmbH & Co. KGaA, Weinheim DOI: 10.1002/anie.200352764



Scheme 1. Oxidative polymerization of 2,6-dimethylphenol in water.

separated as an off-white powder from the reaction mixture by simple filtration after the polymerization, and the recovered alkaline aqueous solution could be used repeatedly for the polymerization. The product was identified as PPO by ^{1}H-, ^{13}C NMR, and IR spectroscopy. The 10%-thermal-degradation temperature ($T_{d10\%}$) and glass-transition temperature (T_g) were determined to be 401 °C and 208 °C, respectively,[10] by TG and DSC and were found to be comparable with those of the commercial values.[11]

Some examples of the polymerization are given in Table 1. The control reaction (Table 1, entry 1) showed that the oxidation of DMP did not proceed without the addition of base. Another control reaction (Table 1, entry 2) revealed that the oxidation of DMP with an equal amount of base and potassium ferricyanide in water predominantly gave DPQ and a small amount of the phenyleneoxide oligomer ($M_n = 4.0\times10^2$, $M_w/M_n = 1.5$) as previously reported.[6,8] We found that the oxidation of DMP resulted in polymerization at an optimal temperature of 50 °C in the presence of excess base (relative to the monomer) (Table 1, entry 5);[12] significantly, DPQ formation was suppressed to less than 0.4%.[13] The addition of a surfactant as an emulsifier was effective: High-molecular-weight PPO ($M_n > 10^4$) was obtained almost quantitatively (98%) by the addition of sodium *n*-dodecyl sulfate (Table 1, entry 6). Upon addition of the surfactant, the reaction mixture became a latex, but the polymer could also be separated by a simple filtration after being salted out.

The use of potassium ferricyanide as an oxidant is not adequate from the point of view of a green process. However, DMP was also oxidatively polymerized to give PPO in the presence of a copper catalyst (e.g. [Cu(tmeda)]; Table 1, entry 7) and oxygen or an excess of a metal oxide (e.g., MnO_2; Table 1, entry 8) without the formation of DPQ in the same alkaline medium at 50 °C. The former catalytic reaction could be improved by tuning the conditions.

Phenol derivatives such as 2,6-diphenylphenol were also polymerizable in the basic solution to form the corresponding PPO derivatives such as poly(2,6-diphenyl-1,4-phenyleneoxide) (Table 1, entry 9).

One of the reasons for using alkaline water as the solvent is a significant decrease in the oxidation potential of phenols. The pH value of the aqueous phase of the reaction mixture was 13.5 ([NaOH] = 0.5 M). Cyclic voltammograms in the alkaline aqueous solution (Figure 1, inset) showed irreversible oxidation peaks of the phenol groups of DMP and 4-(2,6-dimethylphenoxy)-2,6-dimethylphenol (dimer), and their oxidative potentials were estimated to be 0.26 and 0.12 V

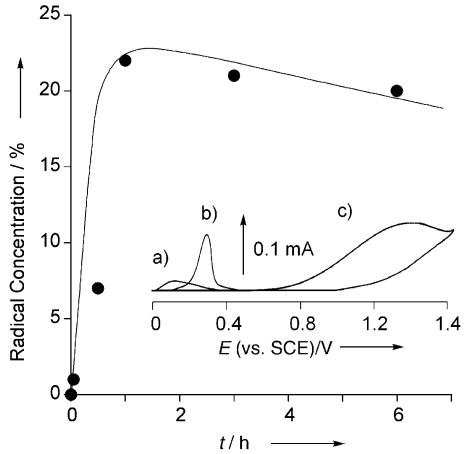


Figure 1. Radical concentration determined by SQUID. Inset: Cyclic voltammograms a) DMP in water with sodium hydroxide (0.5 M), b) dimer of DMP in water with sodium hydroxide (0.5 M), and c) DMP in CH_2Cl_2 with pyridine (3.0 M). Phenol concentration: 0.01 M; scan rate: 25 mV s^{-1}.

Table 1: Oxidative polymerization of 2,6-dimethylphenol in water.[a]

Entry	ArOH [mmol][b]	Oxidant or catalyst	[mmol]	NaOH [mmol]	SDS [mmol][c]	*T* [°C]	Yield [%] DPQ[d]	PPO	PPO M_n [/10^3]	PPO M_w/M_n[e]
1	50	$K_3[Fe(CN)_6]$	100	0	0	RT	0.1	0		
2	50	$K_3[Fe(CN)_6]$	100	50	0	RT	74	23	0.4	1.5
3	50	$K_3[Fe(CN)_6]$	100	250	0	RT	66	32	1.6	1.6
4	1.0	$K_3[Fe(CN)_6]$	2.0	50	0	RT	24	74	3.9	2.3
5	1.0	$K_3[Fe(CN)_6]$	2.0	50	0	50	0.4	76	3.5[g]	2.0
6	1.0	$K_3[Fe(CN)_6]$	2.0	50	0.1	50	0.4	98	13	1.8
7	50	$[Cu(tmeda)]Cl_2$[f]	5.0	50	5.0	50	0.2	67	2.9	1.7
8	1.0	MnO_2	10	50	0	50	0	24	5.0	4.0
9	0.5	$K_3[Fe(CN)_6]$	1.0	50	0.5	70	0.9	96	6.9	1.8

[a] All the polymerizations were carried out in water (100 mL) under air (except entry 7, which was carried out under oxygen), 6 h. [b] DMP, except entry 9, which was studied with 2,6-diphenylphenol. [c] Sodium *n*-dodecyl sulfate. [d] Determined by UV/Vis absorption at $\lambda_{max} = 421$ nm. [e] Determined by gel-permeation chromatography relative to polystyrene standards in chloroform. [f] tmeda = *N*,*N*,*N*′,*N*′-tetramethylethylenediamine. [g] The molecular weight was determined to be 3.4×10 by NMR spectroscopic analysis (terminal phenolic group content).

 © 2004 Wiley-VCH Verlag GmbH & Co. KGaA, Weinheim

(vs. SCE), respectively. The former value is much lower than that of DMP (1.31 V) in a basic organic solvent such as dichloromethane involving pyridine as the base. The oxidative potential for the dimer was lower than that of the DMP monomer, suggesting that the oxidation potential of the terminal phenolic group becomes lower as the polymerization progresses.

The ESR spectrum of the polymerization mixture was recorded: The signal at $g = 2.0044$ was ascribed to the organic phenoxyl radical. After filtering the powder product from the mixture and quickly washing with alkaline water, it was transferred to the capsule of a SQUID magnetometer to determine the radical concentration of the powder product.[14] The radical concentration in the polymerization reaction (Figure 1) was maintained at approximately 20% per polymer molecule or per polymer terminal phenolic group.[15] The polymerization mechanism of DMP in the water is described below.

DMP is dissolved in the basic aqueous phase to form the phenolate anion, and is oxidized to the phenoxyl radical. The C–O coupling of two phenoxyl radicals gives the dimer. The formed dimer and oligomer are insoluble in the alkaline aqueous solution, and the reaction mixture becomes heterogeneous. However, the terminal phenolic groups located at the water interface are oxidized to give the polymeric phenoxyl radicals, which are redistributed to the high-molecular-weight polymer in the solid that precipitates from the water.

In summary, we have described the polymerization of DMP to form PPO in water. The oxidative polymerization of phenols in alkaline water has the potential to become a convenient green polymerization procedure.

Experimental Section

Oxidative polymerization DMP in water with $K_3[Fe(CN)_6]$ (Table 1, entry 6): DMP (0.122 g, 1 mmol) was dissolved in water (100 mL) containing sodium hydroxide (2.00 g, 50 mmol) and sodium *n*-dodecyl sulfate (29 mg, 0.1 mmol). Potassium ferricyanide (0.658 g, 2 mmol) was added to the solution, and the mixture was vigorously stirred (3000 rpm) under air at 50 °C for 6 h. The polymer was obtained as an off-white powder (98%) by filtration after salting out by the addition of sodium chloride (5.84 g, 0.25 mol) and by washing with water. ^{1}H NMR: (500 MHz, $CDCl_3$, TMS): $\delta = 6.44$ (2H, s; H_{Ar}), 2.09 ppm (s, 6H; CH_3); ^{13}C NMR: (125 MHz, $CDCl_3$, TMS): $\delta = 16.8$, 114.5, 132.5, 145.4, 154.7 ppm; IR (KBr): $\tilde{\nu}_{C\text{-}O\text{-}C} = 1186\ cm^{-1}$. The reactions described in Table 1, entries 1–5, 8, and 9 were carried out analogously.

Oxidative polymerization of DMP in water with [Cu(tmeda)] (Table 1, entry 7): A solution [Cu(tmeda)] (0.250 g, 5 mmol) in water (10 mL) was added to a solution of DMP (6.10 g, 50 mmol), sodium hydroxide (2.00 g, 50 mmol), and sodium *n*-dodecyl sulfate (1.45 g, 5 mmol) in water (90 mL). The mixture was then vigorously stirred (3000 rpm) in oxygen at 50 °C for 6 h. After salting out with sodium chloride (29.2 g, 1 mol), the product was obtained by filtration. The reprecipitation from chloroform to methanol gave an off-white polymer (67%). The ^{1}H, ^{13}C NMR, and IR spectra were similar to those described above.

UV/Vis spectral detection of DPQ: A sample of the filtered product (1.2 mg) was removed and dissolved in toluene (10 mL). This solution gave a UV/Vis absorption with the maximum at 421 nm, which was ascribed to DPQ. The molar extinction coefficient ε was determined to be $54000\ M^{-1}cm^{-1}$ in toluene using pure DPQ. The amount of formed DPQ is given as a percentage of the feed amount of DMP.

SQUID magnetic measurement: The magnetization and static magnetic susceptibility were measured with a Quantum Design MPMS-7 SQUID magnetometer. Powder samples for the measurement were prepared as follows: The polymerizations of DMP with potassium ferricyanide were carried out as described above for 0.05, 0.5, 1, 3, and 6 h. After these reaction times, the powder product was filtered, quickly washed with alkaline water, and transferred to the capsule of the SQUID magnetometer. The magnetization was measured from 0.5 to 7 T at 1.8, 2, 2.5, 3, 5, 20, and 200 K. The static magnetic susceptibility was measured from 1.8 to 200 K in a field of 0.5 T.

Received: September 2, 2003 [Z52764]

Keywords: green chemistry · oxidation · polymerization · radicals · water chemistry

[1] a) C.-J. Li, T.-H. Chan, *Organic Reactions in Aqueous Media*, Wiley, New York, **1997**; b) P. Tundo, P. Anastas, D. S. Black, J. Breen, T. Collins, S. Memoli, J. Miyamoto, M. Polyakoff, W. Tumas, *Pure Appl. Chem.* **2000**, *72*, 1207–1228; c) J. M. Desimone, *Science* **2002**, *297*, 799–803.

[2] a) A. S. Hay, H. S. Blanchard, G. F. Endres, J. W. Eustance, *J. Am. Chem. Soc.* **1959**, *81*,6335–6336; b) A. S. Hay, *J. Polym. Sci.* **1962**, *58*, 581–591; c) A. S. Hay, *Macromolecules* **1969**, *2*, 107–108; d) A. S. Hay, *J. Polym. Sci. Part A* **1998**, *36*, 505–517.

[3] a) E. Tsuchida, M. Kaneko, H. Nishide, *Makromol. Chem.* **1972**, *151*, 221–234; b) E. Tsuchida, H. Nishide, *Makromol. Chem.* **1975**, *176*, 1349–1358; c) E. Tsuchida, H. Nishide, *Adv. Polym. Sci.* **1977**, *24*,1–87; d) K. Oyaizu, Y. Kumaki, K. Saito, E. Tuschida, *Macromolecules* **2000**, *33*, 5766–5769.

[4] D. Aycock, V. Abolins, D. M. White, *Encyclopedia of Polymer Science and Engineering*, *Vol. 13*, 2nd ed., Wiley, New York, **1986**, pp. 1–30.

[5] a) W. Koch, W. Risse, W. Heitz, *Makromol. Chem. Suppl.* **1985**, *12*, 105–123; b) E. Tuschida, F. Suzuki, E. Shouji, K. Yamamoto, *Macromolecules* **1994**, *27*, 1057–1060; c) P. J. Baesjou, W. L. Driessen, G. Challa, J. Reedijk, *J. Am. Chem. Soc.* **1997**, *119*, 12590–12594; d) H. A. M. van Aert, M. H. P. van Gendersen, G. J. M. L. van Steenpaal, L. Nelissen, E. W. Meijer, *Macromolecules* **1997**, *30*, 6056–6066; e) H. Higashimura, K. Fujisawa, Y. Moro-oka, M. Kubota, A. Shiga, A. Terahara, H. Uyama, S. Kobayashi, *J. Am. Chem. Soc.* **1998**, *120*, 8529–8530.

[6] a) G. D. Staffin, C. C. Price, *J. Am. Chem. Soc.* **1960**, *82*, 3632–3634; b) C. C. Price, N. S. Chu, *J. Polym. Sci.* **1962**, *61*, 135–141.

[7] a) H. Komoto, K. Ohmura, *Makromol. Chem.* **1973**, *166*, 57–68; b) V. Percec, T. D. Shaffer, *J. Polym. Sci. Polym. Lett. Ed.* **1986**, *24*, 439–446; c) K. Mühlbach, V. Percec, *J. Polym. Sci. Polym. Chem. Ed.* **1987**, *25*, 2605–2627; d) R. Ikeda, J. Sugihara, H. Uyama, S. Kobayashi, *Macromolecules* **1996**, *29*, 8702–8705; e) H. Yonami, H. Uyama, S. Kobayashi, *J. Macromol. Sci., Pure Appl. Chem.* **1999**, *36*, 719–730; f) Y. M. Chung, W. S. Ahn, P. K. Lim, *J. Mol. Catal. A* **1999**, *148*, 117–126.

[8] C. G. Haynes, A. H. Turner, W. A. Waters, *J. Chem. Soc.* **1956**, 2823–2831.

[9] The solubility of DMP in aqueous NaOH (0.5 M) is $< 61\ g\,L^{-1}$.

[10] $T_{d10\%}$ and T_g were for the polymer described in Table 1, entry 6.

[11] F. E. Karasz, H. E. Bair, J. M. O'Reilly, *J. Polym. Sci. Part A-2* **1968**, *6*, 1141–1148.

[12] The formation of DPQ in water was hardly affected by temperature, in contrast to the case in organic solvents. G. F. Endres, A. S. Hay, J. W. Eustance, *J. Org. Chem.* **1963**, *28*, 1300–1305.

 © 2004 Wiley-VCH Verlag GmbH & Co. KGaA, Weinheim

[13] The yield of DPQ was determined by the UV/Vis absorption at $\lambda_{max} = 421$ nm. The formation of DPQ was suppressed dramatically. By comparison, conventional polymerization methods (e.g., catalyzed by a copper–amine complex in toluene at room temperature) give DPQ in 3–5% yield. a) F. J. Viersen, G. Challa, *Recl. Trav. Chim. Pays-Bas* **1990**, *109*, 97–102; b) F. J. Viersen, J. Renkema, G. Challa, J. Reedijk, *J. Polym. Sci. Part A* **1992**, *30*, 901–911.

[14] Normalized plots of magnetization versus the ratio of the magnetic field and effective temperature for the powder product obeyed a theoretical curve corresponding to the $S = {}^1/_2$ Brillouin function (S = spin quantum number). This showed no contribution of the contaminants such as the potassium ferricyanide oxidant to the measurement of the radical concentration.

[15] The half-life of the phenoxyl radical was determined to be approximately 4 min by ESR spectroscopic analysis of the powder sample.

 © 2004 Wiley-VCH Verlag GmbH & Co. KGaA, Weinheim

Electrochemical Synthesis

Electrochemical Preparation of Silicon and Its Alloys from Solid Oxides in Molten Calcium Chloride**

*Xianbo Jin, Pei Gao, Dihua Wang, Xiaohong Hu, and George Z. Chen**

Silicon plays essential roles in the fabrication of solar cells, silicon chips, optical fibres, silicones, and is important as an element in lighter and stronger alloys, as well as hundreds of other advanced applications.[1,2] The industrial production of silicon is at present mainly through the carbothermic reduction of SiO_2 at 1700 °C, in which the oxygen is removed by the generation of CO_2.[3,4] This old-fashioned charcoal technology should be replaced by a more advanced process from the viewpoint of an environmentalist, in that the earth's climate is gradually becoming worse owing to the emission of greenhouse gases.[5] The world production of silicon in 2002 was about 4.1×10^6 tonnes,[6] equivalent to about 6.5×10^6 tonnes of CO_2 entering the atmosphere. A desired method of producing silicon may be the electrochemical reduction of SiO_2 in which the use of carbon reductant can be avoided and hence less environmental damage. In fact, electrolytic production of silicon began in 1854,[7] and silicon of 99.999 % in purity was later claimed[8] upon electrolysis of fluorosilicates in molten fluorides. DeMattei et al. in 1982 suggested[9] that the ideal raw material for silicon production should be SiO_2, and silicon metal with a purity of 99.97 % was produced in the $BaO/SiO_2/BaF_2$ system with the cell temperature being around 1450 °C. Recently, in molten $CaCl_2$ at about 900 °C, electrochemical deoxygenation of metals was investigated.[10–12] It was reported more recently[13–17] that when solid metal oxides are made into an electrode, regardless of their electron conductivities, they can be electroreduced (or electrodeoxidised) directly to the respective metals or alloys. This leads to a great possibility for the production of silicon directly from solid SiO_2. However, until now, there is only one relevant report that concerns the electroreduction of solid SiO_2, and only partial reduction of the SiO_2 electrode (quartz plate) was achieved.[18]

Herein, we report the fast, complete, and low energy electroreduction of a porous electrode prepared from SiO_2 powder. We also report an experimental observation that might indicate the existence of an optimal thickness of an insulating solid oxide, for example, SiO_2, through which the electroreduction can progress "quickly" to completion. Furthermore, two examples of silicon alloys have also been produced by the same electroreduction method.

Recently, Nohira et al. succeeded in removing oxygen from the surfaces of solid SiO_2 plates (quartz) in a molten $CaCl_2$ electrolyte at 850 °C.[18] Similar results were also obtained in our laboratory by using a different electrode design. In the experiments, a tungsten wire of 300 μm in diameter was sealed in a quartz tube by using a gas flame. The end face of the tungsten wire was revealed by grinding. The SEM image showed a very intimate contact between the quartz and the W wire (Figure 1 a). This W–SiO_2 electrode was then inserted into molten $CaCl_2$ at 850 °C and cyclic voltammetry was carried out by using a Pt wire and a graphite rod as the pseudoreference and counter electrodes, respectively. As shown in Figure 2 a, the reduction of SiO_2 began at −0.85 V, which led to a sharp increase in the current that reached a peak of about −12.5 mA at −1.0 V. The current then went through a slightly inclined plateau on which a couple of small peaks can be seen (Figure 2 a). These peaks are thought to correspond to the formation of the calcium and silicon compounds.[18,19] Upon reversing the potential sweep the current formed a typical stripping peak. When the sweep reached more positive potentials, a large poorly defined anodic peak occurred at about −0.7 V, thus suggesting that the reoxidation process may involve both pure and compounded forms of Si. A further study of the reaction mechanism is ongoing.

Figure 1 a–d shows the SEM images of the W-SiO_2 electrode before and after the first potential sweep cycle. After this sweep the central W disc was surrounded by a ring of porous product of about 200 μm in breadth (Figure 1 b).

[*] Dr. X. B. Jin, P. Gao, Dr. D. H. Wang, Dr. X. H. Hu
College of Chemistry and Molecular Science
Wuhan University, Wuhan, 430072 (P. R. China)
Fax: (+86) 27-87210319
E-mail: mel@chem.whu.edu.cn
Dr. G. Z. Chen
Specially Invited Professor
College of Chemistry and Molecular Science
Wuhan University, Wuhan, 430 072 (P.R. China)
and
School of Chemical, Environmental and Mining Engineering
University of Nottingham
University Park, Nottingham NG7 2RD (UK)
Fax: (+44) 115-9514171
E-mail: george.chen@nottingham.ac.uk

[**] The authors are grateful to the Ministry of Education of China and the Natural Science Foundation of China for financial support.

 DOI: 10.1002/anie.200352786 © 2004 Wiley-VCH Verlag GmbH & Co. KGaA, Weinheim

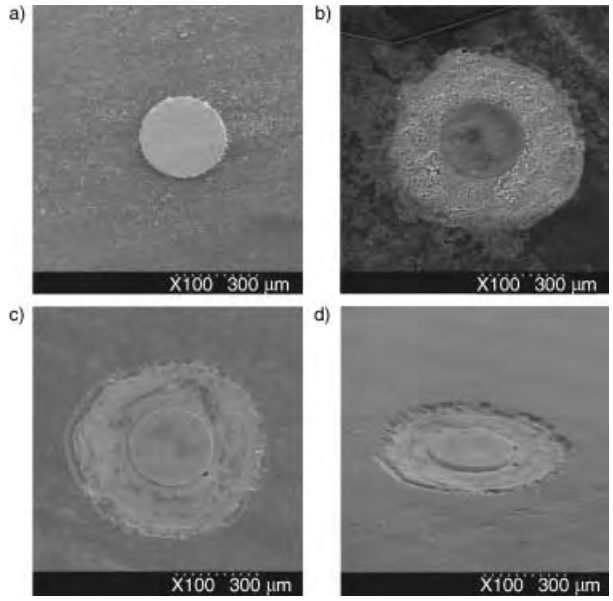


Figure 1. SEM images of the W–SiO2 electrode a) before and b) after one cycle of potential sweep between 0.5 and −1.7 V, and c) after washing the electrode shown in (b) in an ultrasonic water bath. d) A side view of the situation in (c).

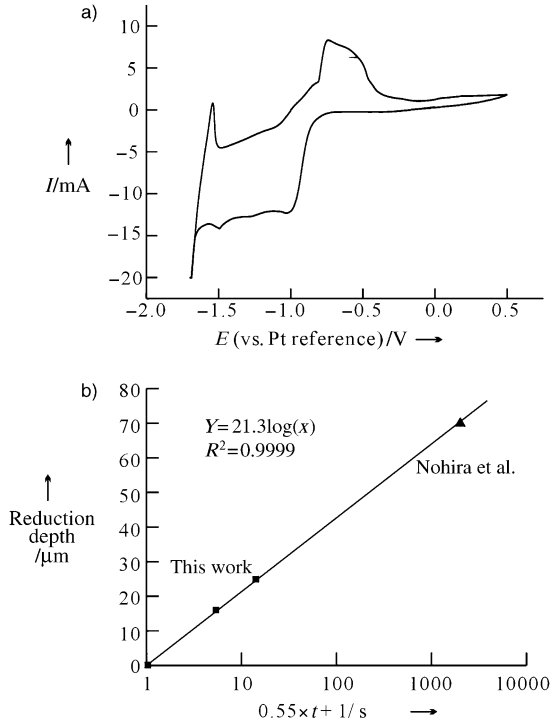


Figure 2. a) Cyclic voltammogram of the W–SiO_2 electrode in molten $CaCl_2$ (200 $mV s^{-1}$, 850 °C), b) the relationship between the depth and time of reduction of solid SiO_2.

The product was removed by immersing the electrode in an ultrasonic water bath, thus resulting in a circular cave in the shape of a flat-bottom pan. By using the depth (16 μm), the top (200 μm) and bottom breadths (150 μm) of the cave (Figure 1c, d), the volume of the reacted SiO_2 was estimated to be about 4.2×10^{-6} cm^3. Considering the density of quartz (2.2 $g cm^{-3}$)[19] and the molecular mass of SiO_2 (60 g/mol), we estimate that about 1.54×10^{-7} moles of SiO_2 were reduced, which is equivalent to a total charge of about 59.4 mC if four electrons were transferred. This value can be compared with the total charge of about 61.5 mC passed during the negative and positive sweep between −0.85 V and −1.7 V (Figure 2a). The good agreement between the two charge values is strong evidence that the reduction product between −0.85 and −1.7 V was mainly silicon.

By using the average current of the plateau between −1.0 V and −1.7 V, the reaction rate was estimated to be higher than 80 $A cm^{-2}$ with reference to the revealed side surface of the tungsten wire, which is 1.41×10^{-4} cm^2 (Figure 1d). This value is even higher than that usually observed in the electrodeposition of metals from liquid electrolytes. Such a high current density suggests a great potential of the electroreduction of solid SiO_2 for the industrial production of silicon. However, it should be pointed out that this high reaction rate was observed at the very beginning of the electroreduction, and the affected volume of the quartz was very small. The question is whether this high reaction rate could be achieved if the volume of quartz were significantly increased.

It was proposed that the electroreduction of insulating solid oxides could proceed at the three-phase boundary linking the conductor, oxide and electrolyte.[14] This principle was advocated and demonstrated with an elegantly designed experiment for the reduction of a quartz plate.[18] In our experiment, before reduction had occurred, there was a W/SiO_2/$CaCl_2$ three-phase boundary at the edge of the central W disc (end of wire). Upon electron transfer, the SiO_2 next to the W disc was converted into silicon which has a reasonably high electronic conductivity (50 $\Omega^{-1} cm^{-1}$).[20] Therefore, further reduction may occur at the newly formed Si/SiO_2/$CaCl_2$ three-phase boundary. In theory, the continuation of this change should lead to the propagation of the three-phase boundary in a 3D manner. However, Figure 1c, d tells a different story and shows a transverse reaction width of 200 μm, but a reaction depth of only 16 μm. While this is an indication of a greater reaction resistance along the depth direction than the transverse direction, the phenomenon may be broadly understood by the accessibility of the molten salt to the reaction sites that are directly in touch with the molten salt along the transverse direction, but in a different situation along the depth direction.

However, if the volume remains the same, the removal of oxygen from SiO_2 should result in a porosity of about 56.2 % if the density difference between SiO_2 and Si is considered (2.2 and 2.33 $g cm^{-2}$,[19] respectively). Therefore, the transverse propagation of the Si/SiO_2/$CaCl_2$ three-phase boundary opens up the solid phase by creating pores/channels for the molten salt to access the SiO_2 phase behind the porous Si layer.[18] This explanation agrees well with the porous product shown in Figure 1b. Nonetheless, it can be reasonably considered that the mass transfer within the formed porous silicon layer is slower than that at the SiO_2/molten salt interface, thus leading to a slower reaction rate along the depth direction than the transverse direction.

 © 2004 Wiley-VCH Verlag GmbH & Co. KGaA, Weinheim

The observation of a flat bottom in the cave (Figure 1c) suggests that the electroreduction of the insulating SiO_2 might be limited to a certain distance in the depth direction, which is less dependent on the time of the applied potential. This depth limit as shown in Figure 1d may be mainly attributed to the limit of mass transfer through the porous silicon layer formed on the surface.

We would like to highlight the practical significance of this finding of different reaction rates along the transverse and depth directions. For industrial production, the use of bulk solid quartz as the electrode is obviously not practical. Instead, a process is likely to involve the use of readily available SiO_2 powder to fabricate a porous SiO_2 electrode, on the analogy of the reports by Chen and co-workers.[13,14] However, it can be anticipated that, if the oxide particles are too large, the same situation would occur to the individual oxide particles, as observed in our electroreduction of the bulk solid quartz electrode. That is, within a practically tolerable time, the reduction would take place only on the surface of the oxide particle with the inner part being unaffected. To the best of our knowledge, there has not been any report in the literature giving an accurate account, either experimental or theoretical, of the effect of powder particle size on the efficiency of the electro-reduction. On the basis of our findings and that of Nohira et al.,[18] a logarithm relation could be approximated between the reduction depth and time (see Figure 2b). It can then be estimated that, for example, the complete reduction takes place within 0.1 s, 1.3 s and 403 s of three SiO_2 particles of 1 μm, 10 μm and 100 μm in diameter, respectively.

The above estimation was found to agree broadly with the result from the electrolysis of the SiO_2 powder, with particle sizes ranging from 2 to 7 μm (Figure 3a). The powder was manually pressed into a porous pellet (1.3 cm in diameter,

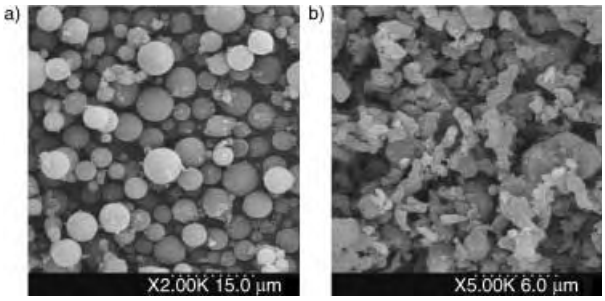


Figure 3. SEM images showing a) the SiO_2 powder electroreduced in molten $CaCl_2$ (2.8 V, 850 °C, 4 hrs) into b) the Si powder.

0.5 cm in thickness, 1.5 g in weight). A manually operated press was used for making the pellets and hence the actual pressure was unknown but was sufficient to form a strong pellet. After sintering at 1000 °C, the pellet was pressed and sandwiched between two porous nickel foils. Then, constant-voltage (2.8 V) electrolysis was performed, under argon, on the assembled cathode in molten $CaCl_2$ at 850 °C with a graphite rod as the anode. The recorded current was very high (about 4 A) during the first few minutes but declined thereafter (within 2 h) to the background value, ≈0.2 A. After electrolysis, which usually lasted for 4 h to ensure complete reduction, the cathode was removed from the molten salt. Upon washing the cathode (pellets) in distilled water in an ultrasonic bath, a grey powder was collected.

The obtained powder was dried and analyzed by XRD (Figure 4), thus confirming the product to be dominated by pure silicon. In addition to the pure silicon phase, the XRD spectrum also exhibited some small but distinguishable sundry peaks which are likely due to $MgSiO_3$. This was tracked down to an $MgCl_2$ impurity (about 0.3%) contained in the $CaCl_2$ used in this work.

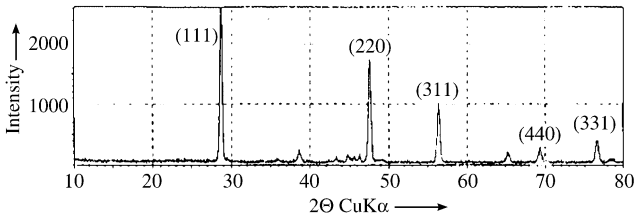


Figure 4. The XRD spectrum of the Si powder obtained from the electroreduction of pellets of the SiO_2 powder in $CaCl_2$ molten salts.

When inspected under SEM (Figure 3b), the silicon powder particles were observed to be 1–3 μm in diameter, which is in accordance with the theoretical prediction from the density difference between Si and SiO_2. Because both SiO_2 and Si are almost insoluble in $CaCl_2$, the output rate should be very high. These results prove that the silicon powder can be mass produced from the SiO_2 powder by the electroreduction method. It is worth mentioning that in our experiments complete reduction of the SiO_2 pellets took a much shorter time than the reduction of TiO_2 (≈15 h) under similar conditions as reported in literature.[13] This difference may be due to the fact that oxygen is highly soluble in solid titanium but not in solid silicon.

By mixing powders of different metal oxides, alloys can be produced by the electroreduction method. [13,14,21] Because fine powders of oxides can be prepared easily and mixed uniformly, the electroreduction of such a mixture leads to an alloy, the composition of which is precisely controlled. Indeed, in our experiments, Si–Fe and Si–Cr alloy powders with a particle size of 2–3 μm were also prepared.

In conclusion, we have demonstrated, for the first time, that porous pellets of the SiO_2 powder or its mixture with other metal oxide powders can be electroreduced to pure silicon or the respective silicon alloy powders in molten $CaCl_2$. Furthermore, cyclic voltammetry revealed that the electroreduction of SiO_2 could proceed very quickly, with the current density reaching beyond 80 A cm^{-2} with reference to the surface area of the conducting substrate. Although such a high current density may be difficult to achieve on an industrial scale, it may be used as a fundamental reference for the design of an industrial process for the mass production of silicon powder by electrolysis. Furthermore, we found that the relation between the reduction depth and time of solid SiO_2 may be approximated by the logarithm law. This finding may be used to select the particles sizes of the SiO_2 powder so

 © 2004 Wiley-VCH Verlag GmbH & Co. KGaA, Weinheim

that complete reduction of the electrode prepared from the SiO_2 powder can be achieved within a practically tolerable time. This work shows that when the particle size is in the range of 2–7 μm, complete reduction of a 0.5 mm thick porous pellet at 2.8 V and 850 °C could be less than 4 h with the energy consumption being within 13 kWh (kg of Si)$^{-1}$ which is expected to decrease further upon optimization. This can be compared with the energy consumption, 13–16 kWh (kg of Si)$^{-1}$, of the carbothermic method used by the industry in China.[22]

Received: September 4, 2003 [Z52786]

Keywords: electrochemistry · green chemistry · high-temperature chemistry · silicon

[1] B. Mazumder, *Silicon and It's Compounds*, Science publishers, USA, **2001**.
[2] A. Shah, P. Torres, R. Tscharner, N. Wyrsch, H. Keppner, *Science* **1999**, *285*, 692 – 698.
[3] N. Nagamuri, I. Malinsky, A. Claveau, *Metall. Trans. B* **1986**, *17*, 503 – 514.
[4] W. Zulehner, B. Elvers, S. Hawkin, W. Russey G. Schulz, *Ullmann's Encyclopedia of Industrial Chemistry*, *Vol. A23*, 5th ed., VCH, Weinheim, **1995**, pp. 721 – 748.
[5] J. T. Houghton, *Climate Change 1995: The Science of Climate Change*, Cambridge, University Press, Cambridge, **1996**.
[6] U.S. Geological Survey, *Mineral Commodity Summaries*, *Silicon*, **2003**, pp. 150–151.
[7] H. St. C. Deville, *Ann. Chim. Phys.* **1854**, *43*,31.
[8] G. M. Rao, D. Elwell, R. S. Feigelson, *J. Electrochem. Soc.* **1980**, *127*, 1940 – 1946.
[9] R. C. DeMattei, D. Elwell, R. S. Feigelson, *J. Electrochem. Soc.* **1981**, *128*, 1712 – 1714.
[10] T. H. Okabe, T. Oishi, K. Ono, *Metall. Trans. B* **1992**, *23*, 583 – 588.
[11] T. H. Okabe, M. Nakamura, T. Oishi, K. Ono, *Metall. Trans. B* **1993**, *24*, 449 – 455.
[12] K. Hirota, T. H. Okabe, F. Saito, Y. Waseda, K. T. Jacob, *J. Alloys Compd.* **1999**, *282*, 101 – 108.
[13] G. Z. Chen, D. J. Fray, T. W. Farthing, *Nature* **2000**, *407*, 361 – 364.
[14] G. Z. Chen, D. J. Fray in *Proceedings of 6th International Symposium on Molten Salt Chemistry and Technology*, (Eds.: N. Y. Chen, Z. Y. Qiao), Shanghai University, Shanghai, China, **2001**, pp. 79 – 85.
[15] G. Z. Chen, D. J. Fray, *J. Electrochem. Soc.* **2002**, *149*, E455-E467.
[16] K. Ono, R. O. Suzuki, *JOM* **2002**, *54*, 59 – 61.
[17] R. O. Suzuki, K. Teranuma, K. Ono, *Metall. Mater. Trans. B* **2003**, *34*, 287 – 295.
[18] T. Nohira, Y. Kasuda, Y. Ito, *Nat. Mat.* **2003**, *2*, 397 – 401.
[19] X. Y. Fang in *Series of Inorganic Chemistry*, *Vol. 3* (Ed.: Q. L. Zhang), Sience publishers, Beijing, **1998**, pp. 105 – 238 (in Chinese).
[20] L. C. Burton, A. H. Madjid, *Phys. Rev.* **1969**, *185*, 1127 – 1132.
[21] A. J. Muir Wood, R. C. Copcutt, G. Z. Chen, D. J. Fray, *Adv. Eng. Mater.* **2003**, *5*, 650 – 653.
[22] L. X. Nie, W. F. Zhang, *Light Met.* **1999**, *10*, 43 – 46 (in Chinese).

 © 2004 Wiley-VCH Verlag GmbH & Co. KGaA, Weinheim

Aromaticity

Synthesis of a Delocalized Azepinium Ion and Investigation of Its Electrophilic Character**

Kyosuke Satake, Yasuhiro Kubota, Christopher E. J. Cordonier, Hideki Okamoto, and Masaru Kimura*

The aromatic azepinium ion **1** is a topic of fundamental interest in connection to its isoelectronic hydrocarbon analogue, the tropylium ion **2** (Scheme 1). Theoretical investigations predict that azepinium ions should be a stable aromatic ion rather than a species with a triplet state,[1,2] however, to date, the synthesis of the heterocyclic ion has not been reported. So far, evidence for the azepinium ion is limited to the MS fragment ions of anilines,[3] isoquinoline derivatives[4] and phenyl azides.[5] The formation of the ion has also been deduced from the electrode reaction of a 3*H*-azepine derivative by inspection of its cyclic voltammogram.[6] On the other hand, cycloheptatriene (CHT; **2H**) was observed to react with an equivalent of bromine or a trityl cation to give **2**,[7] the high stability and low electrophilic reactivity of which has been rationalized by resonance energy.[8] Our similar approach using 3*H*-azepine derivatives to generate the azepinium ion by the action of bromine or trityl cation was unsuccessful. The result suggests that **1** is unstable compared to the hydrocarbon analogue **2**. In studying the chemistry of 3*H*-azepines, we established a new procedure for the synthesis of 2-methoxy-2*H*-azepine derivatives from 3*H*-azepine derivatives.[9] Since 2*H*-azepine is considered to be another good precursor for an azepinium ion, generation of the ionic species by acid-promoted ether bond cleavage was examined. Herein, we report evidence for the formation of an azepinium ion from the reaction between a 2-methoxy-2*H*-azepine derivative and titanium tetrachloride ($TiCl_4$).



1 **2**

Scheme 1. The azepinium ion **1** and the tropylium ion **2**.

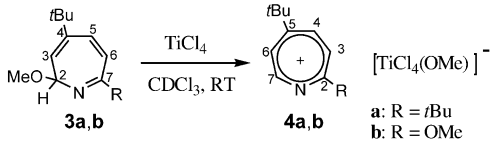
When an excess of $TiCl_4$ was added to a $CDCl_3$ solution of 4,7-di-*tert*-butyl-2-methoxy-2*H*-azepine (**3a**, see Scheme 2) in an NMR sample tube, all the resonance signals attributed to **3a** vanished and new signals that indicate four ring protons ($\delta = 8.10$, 8.11, 8.78, and 9.24 ppm), two *tert*-butyl groups ($\delta =$ 1.48 and 1.55 ppm), and $[TiCl_4(OMe)]^-$ ($\delta = 4.8$ ppm) were observed. This spectral change suggests that all the ring

[*] Dr. K. Satake, Y. Kubota, C. E. J. Cordonier, Dr. H. Okamoto, Prof. Dr. M. Kimura
Department of Chemistry, Faculty of Science
Okayama University
3-1-1 Tsushima-Naka, Okayama 700-8530 (Japan)
Fax: (+81) 86-251-7841
E-mail: satake@cc.okayama-u.ac.jp

[**] We thank the SC-NMR Laboratory of Okayama University for the ^1H and ^{13}C NMR measurements.

 © 2004 Wiley-VCH Verlag GmbH & Co. KGaA, Weinheim DOI: 10.1002/anie.200352794

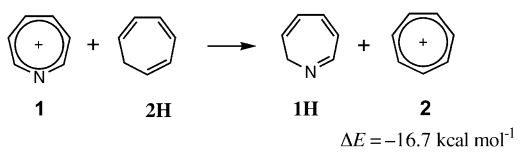
carbon atoms are sp^2 hybridized. This assumption was confirmed by the measurement of C–H coupling constants ($^1J_{C,H}$) for the ring carbon atoms resonating at $\delta = 133.1$ ($J =$ 169 Hz), 133.7 ($J = 166$ Hz), 150.0 ($J = 160$ Hz), and 158.6 ppm ($J = 191$ Hz). The NMR spectroscopic data supports the formation of the ionic species **4a** by Lewis acid promoted demethoxylation. Treatment of 4-*tert*-butyl-2,7-dimethoxy-2*H*-azepine (**3b**) with $TiCl_4$ showed a similar change in the NMR spectrum, which suggests the formation of ionic species **4b** (Scheme 2). Attempts to isolate the salt failed owing to its instability, thus detection of the ion was



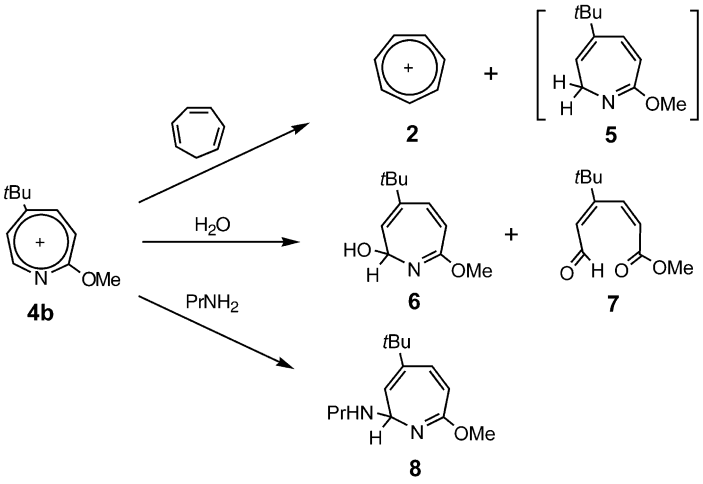
Scheme 2. Generation of azepinium ions (**4a,b**) from 2*H*-azepine derivatives (**3a,b**).

limited to the solution in which it was generated. Complete assignment of ^1H and ^{13}C NMR spectra were performed by heteronuclear correlation spectroscopy using HMQC[10] and HMBC[11] techniques (Table 1). Interestingly, despite two asymmetrically located substituents, the β- and β′-positions (3- and 6-positions) of ion **4a** give rise to resonance signals with almost the same ^1H and ^{13}C NMR chemical shifts. If the positive charge is delocalized, these positions must be equivalent when the ring has no substituents. As the electronic perturbation of *tert*-butyl group is considered to be small, the NMR spectral data attained for **4a** suggests the induced positive charge is delocalized.

Displacement of an sp^2 carbon atom with a more electronegative sp^2 nitrogen atom is expected to destabilize the conjugated system. To rationalize this expectation, ab initio energy analysis of an isodesmic reaction (Scheme 3) between **1** and **2H** (CHT) was performed at a level of B3LYP[12] with the 6-31G(d) basis set using the Gaussian 98[13] program. Calculated energies for **1**, **1H**, **2**, and **2H** were −286.6891, −287.5468, −270.6786, and −271.5096 a.u., respectively. The hydride affinity of **1** is greater than that of **2** by 16.7 kcal mol^{-1} reflecting the decrease in the aromatic resonance energy, that is, the increase in electrophilicity. To confirm the relative hydride affinity between **4b** and **2**, demethoxylation of **3b** (→ **4b**) was performed in the presence of CHT in an NMR tube (Scheme 4). The reaction mixture showed a complex spectrum, however, a prominent singlet at $\delta = 9.38$ ppm was



Scheme 3. An isodesmic reaction between **1** and cycloheptatriene (**2H**) giving 2*H*-azepine (**1H**) and **2**.



Scheme 4. Observed reactions of 5-*tert*-butyl-2-methoxyazepinium (**4b**) with cycloheptatriene, water, and propylamine.

observed in place of the set of peaks attributed to **4b**, which suggests the formation of **2** based on the reported chemical shift of $\delta = 9.33$ ppm in CD_3CN.[14] This result explains that the azepinium **4b** is a stronger electrophile and has decreased resonance energy in comparison to **2**, however, clear spectral evidence for the expected product **5** was not found under these conditions. To obtain more evidence for the structure assignment of the azepinium ion, a GIAO ^{13}C chemical shift calculation[15] (B3LYP6-311 + G(2d,p)) based on the optimized geometry of **1** was performed. Calculated δ_C values for Cα, Cβ, and Cγ were 184.3, 148.1, and 164.0 ppm, respectively. Although overestimation of experimental δ_C values by 15–25 ppm resulted, this calculation and experimental data agree that the minimum shielding in the ring is at Cα and the maximum shielding is at Cβ.

The tropylium ion **2** typically reacts as an electrophile with basic nucleophiles to give the correspondingly substituted cycloheptatriene derivatives.[16] When freshly generated **4b** was quenched with an excess of water, 4-*tert*-butyl-7-

Table 1: Observed ^{13}C and ^1H chemical shifts, and selected coupling constants ($^1J_{C,H}$ and $^3J_{H,H}$) for the ring carbon atoms and ring protons of azepinium ion **4a** and **4b** in $CDCl_3$.

Compound	^{13}C Chemical shifts [ppm] ($^1J_{C,H}$ [Hz])						^1H Chemical shifts [ppm]				$^3J_{H,H}$ [Hz]		
	C2	C3	C4	C5	C6	C7	C3-H	C4-H	C6-H	C7-H	$J_{3,4}$	$J_{4,6}$	$J_{6,7}$
4a	187.5	133.1	150.0	180.0	133.7	158.6	8.11	8.78	8.10	9.24	11.1.	2.4	4.7
	–	(168.5)	(160.4)	–	(166.2)	(190.7)							
4b	176.0	131.0	150.8	181.2	134.5	170.2	7.81	8.61	8.19	9.36	11.7	2.1	6.0
	–	(170.7)	(161.4)	–	(163.8)	(185.6)							

 © 2004 Wiley-VCH Verlag GmbH & Co. KGaA, Weinheim

methoxy-2*H*-azepin-2-ol (**6**)[17] was isolated in 45% yield along with hydrolyzed methyl 4-*tert*-butyl-6-oxo-hexa-2Z,4E-dienoate (**7**)[18] in 24% yield (see Scheme 4). A pattern of signals for four ring protons similar that of **3b** and the appearance of a new signal attributed to an alcoholic proton (D_2O exchangeable) at $\delta = 2.65$ ppm supports the 2-hydroxy-2*H*-azepine structure of **6**. When propylamine was used in place of water, 4-*tert*-butyl-7-methoxy-2-propylamino-2*H*-azepine (**8**)[19] was obtained in 85% yield as a single product. The highfield shift of the resonance signal of C2-H by 0.93 ppm compared to **6** indicates the replacement of the hydroxy by the propylamino group connected to the 2-position of the 2*H*-azepine ring. Regioslectivity of the reaction can be explained by the frontier molecular orbital interaction[20] between a nucleophile and the ion **4b**. The most important orbital is considered to be the π_{LUMO} of **4b**, for which AM1[21] calculated orbital profiles are illustrated in Figure 1. Selective formation of 2-substituted 2*H*-azepine can be explained by an effective mutual interaction between the nucleophile and the carbon atom with the largest orbital coefficient.

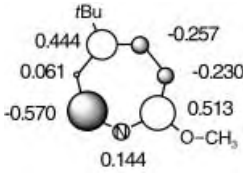


Figure 1. AM1 calculated π_{LUMO} for azepinium ion **4b**. Values indicate the orbital coefficients of each ring atom.

Proposed NMR spectral data and the results of nucleophilic reactions suggest the formation of a hitherto unknown azepinium ion, which is less stable than tropylium.

Received: September 4, 2003
Revised: October 29, 2003 [Z52794]

Keywords: ab initio calculations · aromaticity · azepinium · heterocycles · tropylium

[1] D. A. Smith, J. Bitar, *J. Org. Chem.* **1993**, *58*, 6.
[2] M. Di Stefano, M. Rosi, A. Sgamellotti, D. Ascenzi, D. Bassi, P. Franceschi, P. Tosi, *J. Chem. Phys.* **2003**, *119*, 1978.
[3] A. V. Robertson, C. Djerassi, *J. Am. Chem. Soc.* **1968**, *90*, 6992.
[4] M. Marx, C. Djerassi, *J. Am. Chem. Soc.* **1968**, *90*, 678.
[5] R. A. Abramovitch, E. P. Kyba, E. F. V. Scriven, *J. Org. Chem.* **1971**, *36*, 3796; T. A. Brown, P. R. Lowe, C. H. Schwalbe, M. F. G. Stevens, *J. Chem. Soc. Perkin Trans. 1* **1983**, 2485.
[6] S. Batori, R. Gompper, J. Meier, H.-U. Wagner, *Tetrahedron* **1988**, *44*, 3309.
[7] W. von E. Doering, L. H. Knox, *J. Am. Chem. Soc.* **1954**, *76*, 3203; H. J. Dauben, Jr., F. A. Gadecki, K. M. Harmon, D. L. Pearson, *J. Am. Chem. Soc.* **1957**, *79*, 4557; H. J. Dauben, Jr., L. R. Honnen, K. M. Harmon, *J. Org. Chem.* **1960**, *25*, 1442.
[8] R. Breslow, H. Höver, H. W. Chaug, *J. Am. Chem. Soc.* **1962**, *84*, 3168.
[9] K. Satake, Y. Tawada, H. Okamoto, M. Kimura, *J. Chem. Soc. Perkin Trans. 1* **1997**, 2015; K. Satake, C. Cordonier, Y. Kubota, Y. Jin, M. Kimura, *Heterocycles* **2003**, *60*, 2211.
[10] L. Müller, *J. Am. Chem. Soc.* **1979**, *101*, 4481.
[11] A. Bax, M. F. Summers, *J. Am. Chem. Soc.* **1986**, *108*, 2093.
[12] A. D. Becke, *J. Chem. Phys.* **1993**, *98*, 5648.
[13] Gaussian 98 (Revision A.7), M. J. Frisch, G. W. Trucks, H. B. Schlegel, G. E. Scuseria, M. A. Robb, J. R. Cheeseman, V. G. Zakrzewski, J. A. Montgomery, R. E. Stratmann, J. C. Burant, S. Dapprich, J. M. Millam, A. D. Daniels, K. N. Kudin, M. C. Strain, O. Farkas, J. Tomasi, V. Barone, M. Cossi, R. Cammi, B. Mennucci, C. Pomelli, C. Adamo, S. Clifford, J. Ochterski, G. A. Petersson, P. Y. Ayala, Q. Cui, K. Morokuma, D. K. Malick, A. D. Rabuck, K. Raghavachari, J. B. Foresman, J. Cioslowski, J. V. Ortiz, B. B. Stefanov, G. Liu, A. Liashenko, P. Piskorz, I. Komaromi, R. Gomperts, R. L. Martin, D. J. Fox, T. Keith, M. A. Al-Laham, C. Y. Peng, A. Nanayakkara, C. Gonzalez, M. Challacombe, P. M. W. Gill, B. G. Johnson, W. Chen, M. W. Wong, J. L. Andres, M. Head-Gordon, E. S. Replogle, J. A. Pople, Gaussian, Inc., Pittsburgh, PA, **1998**.
[14] H. Volz, M. V. Lecea, *Justus Liebigs Ann. Chem.* **1971**, *750*, 136.
[15] K. Wolinski, J. F. Hilton, P. Pulay, *J. Am. Chem. Soc.* **1990**, *112*, 8251; J. R. Cheeseman, G. W. Trucks, T. A. Keith, M. J. Frisch, *J. Chem. Phys.* **1996**, *104*, 5497.
[16] W. von E. Doering, L. H. Knox, *J. Am. Chem. Soc.* **1957**, *79*, 352; K. Conrow, *J. Am. Chem. Soc.* **1959**, *81*, 5461; N. L. Bauld, Y. S. Rim, *J. Am. Chem. Soc.* **1967**, *89*, 6763; H. J. Dauben, D. F. Rhoades, *J. Am. Chem. Soc.* **1967**, *89*, 6764.
[17] Selected data for **6**: ^{1}H NMR (500 MHz, $CDCl_3$): $\delta = 1.11$ (s, 9H), 2.65 (brs, 1H), 3.70 (s, 3H), 4.68 (d, $J = 4.2$ Hz, 1H), 5.79 (dd, $J = 4.2$, 1.0 Hz, 1H), 6.47 (d, $J = 12.0$ Hz, 1H), 6.96 ppm (dd, $J = 12.0$, 1.0 Hz, 1H); ^{13}C NMR (150 MHz, $CDCl_3$): $\delta = 29.5$, 34.4, 53.8, 80.6, 124.6, 130.4, 139.6, 144.9, 158.5 ppm; IR (neat): $\tilde{\nu} = 3370$ cm^{-1} (O-H); UV/Vis (EtOH): λ_{max} (log ε) 277 nm (3.03); MS (FAB): *m*/*z* 196 $[M+H]^+$.
[18] Selected data for **7**: ^{1}H NMR (500 MHz, $CDCl_3$): $\delta = 1.19$ (s, 9H), 3.66 (s, 3H), 6.05 (dd, $J = 7.5$, 1.5 Hz, 1H), 6.23 (d, $J = 12.5$ Hz, 1H), 6.74 (dd, $J = 12.5$, 1.5 Hz, 1H), 9.69 ppm (d, $J = 7.5$ Hz, 1H); ^{13}C NMR (150 MHz, $CDCl_3$): $\delta = 28.8$, 37.5, 51.5, 125.1, 125.4, 139.1, 165.0, 168.0, 193.1 ppm; IR (neat): $\tilde{\nu} = 1734$, 1676 cm^{-1} (C=O); UV/Vis (EtOH): λ_{max} (log ε) 236 nm (4.02); MS (FAB): *m*/*z* 197 $[M+H]^+$.
[19] Selected data for **8:** m.p. 75.5–77.0°C; ^{1}H NMR (600 MHz, $CDCl_3$): $\delta = 0.95$ (t, $J = 7.2$ Hz, 3H), 1.07 (s, 9H), 1.50–1.60 (m, 2H), 1.70 (brs, 1H), 2.51–2.57 (m, 1H), 2.93–2.99 (m, 1H), 3.66 (s, 3H), 3.75 (d, $J = 4.8$ Hz, 1H), 5.62 (d, $J = 4.8$ Hz, 1H), 6.46 (d, $J = 12.0$ Hz, 1H), 6.92 ppm (d, $J = 12.0$ Hz, 1H); ^{13}C NMR (150 MHz, $CDCl_3$): $\delta = 12.0$, 23.4, 29.6, 34.5, 48.0, 53.4, 70.3, 124.5, 128.9, 139.0, 145.8, 159.5 ppm; IR (KBr): $\tilde{\nu} = 3260$ cm^{-1} (N-H); UV/Vis (EtOH): λ_{max} (log ε) 276 nm (3.07); MS (FAB): *m*/*z* 237 $[M+H]^+$.
[20] K. Fukui, *Acc. Chem. Res.* **1971**, *4*, 57, and references therein.
[21] M. J. S. Dewar, E. G. Zoebisch, E. F. Healy, J. J. P. Stewart, *J. Am. Chem. Soc.* **1985**, *107*, 3902.

 © 2004 Wiley-VCH Verlag GmbH & Co. KGaA, Weinheim

Natural Products Synthesis

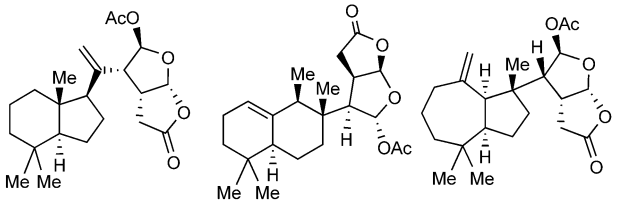
Stereoselective Total Synthesis of (+)-Norrisolide**

*Thomas P. Brady, Sun Hee Kim, Ke Wen, and Emmanuel A. Theodorakis**

In memory of David J. Faulkner

Nudibranch molluscs are known to harvest a variety of chemical metabolites from sponges and use them for their own defense.[1,2] In an effort to understand this behavior from a chemical perspective, Faulkner and co-workers isolated a novel diterpene named norrisolide (**1**) from the skin extracts of the dorid nudibranch *Chromodoris norrisi*.[3] Further studies led to the isolation of **1** from different species of sponges that support the feeding patterns of these molluscs.[4]

From a structural standpoint, norrisolide belongs to a family of marine diterpenes that also includes macfarlandin C (**2**) and dendrillolide A (**3**; Scheme 1).[5] These natural



Scheme 1. Representative natural products with a fused tetrahydrofuran–γ-lactone ring system

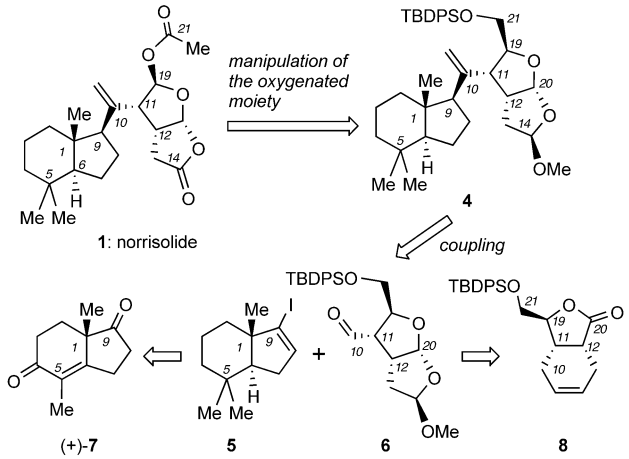
products share a common structural motif characterized by a fused γ-lactone–γ-lactol ring system attached to a hydrophobic bicyclic core. The unusual pattern of functionalities encountered in this highly oxygenated system confers to these molecules a high degree of chemical reactivity, the biological significance of which remains largely unexplored.[6] Herein we describe a stereoselective synthesis of (+)-norrisolide (**1**). Not only have our studies led to the first synthesis of any member of this family of diterpenes, but they have also established the absolute configuration of **1** to be that shown in Scheme 1.[7,8]

[*] T. P. Brady, S. H. Kim, K. Wen, Prof. E. A. Theodorakis
Department of Chemistry and Biochemistry
University of California, San Diego
9500 Gilman Drive, MC, 0358 La Jolla, CA 92093-0358 (USA)
Fax: (+1) 858-822-0386
E-mail: etheodor@chem.ucsd.edu

[**] Financial support from the NIH (CA 086079) is gratefully acknowledged. We also thank Dr. L. N. Zakharov and Dr. P. Gantzel (UCSD, X-Ray Facility) for the crystallographic studies reported and Professor D. J. Faulkner (Scripps Institute of Oceanography) for a sample of natural norrisolide.

Supporting information for this article is available on the WWW under http://www.angewandte.org or from the author.

Our retrosynthetic strategy towards norrisolide (**1**) is illustrated in Scheme 2. As we were concerned about the potential reactivity of the fused γ-lactone–γ-lactol motif

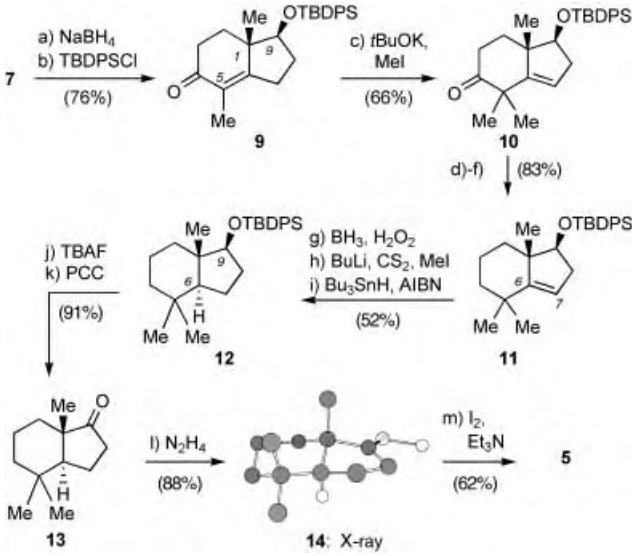


Scheme 2. Strategic bond disconnections of **1**. TBDPS = *tert*-butyldiphenylsilyl.

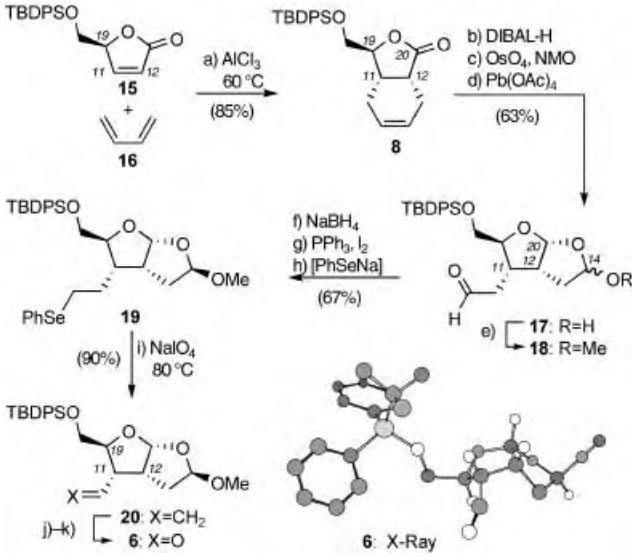
towards nucleophilic attack, we attempted the synthesis of **1** via the less-oxygenated and more-stable precursor **4**.[9] In the forward direction, we envisaged that **4** could be converted into the natural product through oxidation at C14 and subsequent insertion of an oxygen atom between the C19 and C21 centers. The latter manipulation would be possible, in principle, by a Baeyer–Villiger oxidation, which was expected to proceed in a regio- and stereoselective manner.[10] Disconnection at the C9–C10 bond in **4** unveils components **5** and **6**, which could be connected in the desired manner by a nucleophilic reaction at the aldehyde in **6**. It was planned to construct the bicyclic framework of **6** from the lactone **8**, which contains the desired *cis* stereochemistry at the C11 and C12 centers. The *trans*-fused hydrindane motif of **5** could be formed from the enantiomerically enriched enone (+)-**7**. Our efforts to bring this plan to fruition are highlighted in the schemes that follow.

Our synthetic approach began with the optically pure enone **7**, which was available through an L-phenylalanine-mediated asymmetric Robinson annulation (55–65% yield, >95% *ee* after a single recrystallization).[11] Selective reduction at the more reactive C9 carbonyl group, followed by protection of the resulting alcohol, afforded the silyl ether **9** in 76% yield over the two steps (Scheme 3).[12] Methylation of the extended enolate of **9** at the C5 center produced ketone **10** (66% yield), the reduction and radical deoxygenation of which led to the alkene **11** in 83% yield (from **10**). Several methods were examined for the conversion of the alkene **11** into the *trans*-fused bicycle **12**.[13] The best results were obtained by hydroxylation of the double bond (ratio at C6: *trans*/*cis* 2.5:1) and subsequent reduction of the resulting alcohol (52% yield from **11**). The use of the bulky TBDPS group to protect the C9 hydroxy group was found to be crucial in terms of the diastereomeric outcome of the hydroxylation reaction.[11d] Fluoride-induced desilylation of **12** followed by

 DOI: 10.1002/anie.200352868 © 2004 Wiley-VCH Verlag GmbH & Co. KGaA, Weinheim



Scheme 3. Reagents and conditions: a) $NaBH_4$ (0.33 equiv), EtOH, −25 °C, 0.5 h, 99%; b) imidazole (2.5 equiv), TBDPSCl (2.0 equiv), DMAP (0.1 equiv), DMF, 25 °C, 4 h, 77%; c) *t*BuOK, MeI, DMF, 25 °C, 1 h, 66%; d) $NaBH_4$ (1.2 equiv), MeOH, 0 °C, 1 h, 100%; e) *n*BuLi (1.2 equiv), 0 °C, 0.5 h, CS_2 (10 equiv), 2 h, then MeI (3.0 equiv), THF, 0.5 h, 95%; f) nBu_3SnH (2.5 equiv), AIBN (0.1 equiv), toluene, 120 °C, 0.25 h, 87%; g) BH_3·THF (3.0 equiv), THF, 0 °C, 12 h, then aqueous NaOH (3 M, 20 equiv), H_2O_2 (20 equiv), 25 °C, 12 h, 80% (56% *trans*, 24% *cis*); h) *n*BuLi (1.2 equiv), 0 °C, 0.5 h, CS_2 (10 equiv), 2 h, then MeI (3.0 equiv), THF, 0 °C, 0.5 h; i) nBu_3SnH (2.5 equiv), AIBN (0.1 equiv), toluene, 120 °C, 0.25 h, 92% (over two steps); j) TBAF (3.0 equiv), THF, 60 °C, 8 h, 99%; k) PCC (4.5 equiv), celite, CH_2Cl_2, 25 °C, 1 h, 92%; l) N_2H_4·H_2O (30 equiv), Et_3N (4.0 equiv), EtOH, reflux, 5 h, 88%; m) I_2 (until N_2 evolution has ceased), Et_3N (10 equiv), THF, 25 °C, 0.25 h, 62%. AIBN = azobisisobutyronitrile, DMAP = 4-dimethylaminopyridine, DMF = *N*,*N*-dimethylformamide, PCC = pyridinium chlorochromate TBAF = tetrabutylammonium fluoride.



Scheme 4. Reagents and conditions: a) $AlCl_3$ (0.33 equiv), CH_2Cl_2, 60 °C, 6 days, 85%; b) DIBAL-H (1.2 equiv), CH_2Cl_2, −78 °C, 0.5 h, 98%; c) OsO_4 (0.01 equiv), NMO (1.1 equiv), pyridine (3 drops), acetone/H_2O (10:1), 25 °C, 8 h; d) $Pb(OAc)_4$ (1.2 equiv), CH_2Cl_2, 0 °C, 0.5 h, 64% (over two steps); e) MeOH (1.2 equiv), amberlyst 15, molecular sieves (3 Å), Et_2O, 25 °C, 10 h, 77% (**18**α/**18**β 1:1); f) $NaBH_4$ (1.5 equiv), MeOH, 25 °C, 0.5 h; g) imidazole (2.2 equiv), PPh_3 (1.1 equiv), I_2 (1.2 equiv), THF, 25 °C, 0.5 h, 93% (over two steps); h) $(PhSe)_2$ (0.55 equiv), $NaBH_4$ (1.5 equiv), EtOH, 25 °C, 0.5 h, 92%; i) $NaIO_4$ (1.6 equiv), MeOH/H_2O (5:2), 25 °C, 1 h, then Et_3N/PhH (1:1), reflux, 0.5 h, 90%; j) OsO_4 (0.05 equiv), NMO (1.1 equiv), pyridine (3 drops), acetone/H_2O (10:1), 25 °C, 10 h; k) $Pb(OAc)_4$ (1.2 equiv), CH_2Cl_2, 0 °C, 0.5 h, 94% (over two steps). DIBAL-H = diisobutylaluminum hydride, NMO = 4-methylmorpholine *N*-oxide.

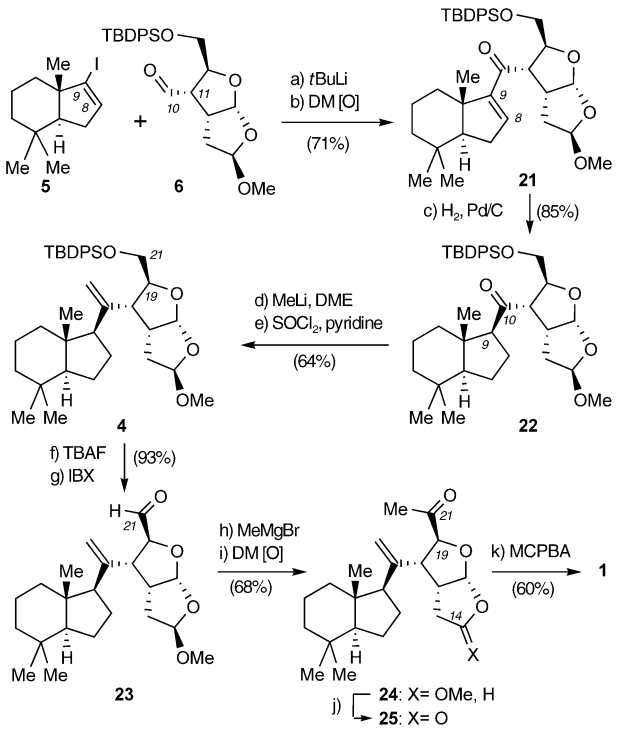
PCC oxidation provided the ketone **13** in 91% yield.[14] The treatment of **13** with hydrazine then produced the hydrazone **14**. Single-crystal X-ray diffraction analysis of **14** showed the *trans* junction of the bicycle unambiguously.[15] Finally, treatment of **14** with I_2/Et_3N led to the formation of the desired vinyl iodide **5** (62% yield).[16]

The construction of aldehyde **6** is highlighted in Scheme 4. The C11 and C12 centers were connected by a Diels–Alder reaction between the butenolide **15**[17] and butadiene (**16**). Under Lewis acid catalysis this cycloaddition proceeded exclusively from the opposite face to that with the bulky TBDPS group to afford **8** as a single isomer (85% yield).[18] Reduction of the lactone unit at C20, followed by oxidative cleavage of the alkene in the other ring, produced the fused lactol **17** in 63% yield as a 1:1 mixture of isomers at C14. These compounds were separated[19] after conversion into the corresponding methyl ether **18**.[20] The aldehyde **18** (β isomer with respect to C14) was then converted into the selenide **19**, which underwent oxidation and elimination to give the alkene **20** (61% from **18**).[21] Osmylation of **20**, followed by oxidative cleavage of the resulting diol, furnished the aldehyde **6** (two steps, 94% yield). The aldehyde **6** was crystalline and its structure was confirmed unambiguously by X-ray crystallographic analysis.[15]

The remaining steps in the synthesis of **1** are illustrated in Scheme 5. Lithiation of the vinyl iodide **5**, followed by addition of the aldehyde **6** and oxidation of the resulting alcohol, afforded the enone **21** in 71% yield. Hydrogenation of the C8–C9 double bond proceeded exclusively from the more accessible α face of the bicyclic core to form the ketone **22** in 75% yield. Standard olefination procedures (Wittig, Peterson) failed to convert **22** into **4**, presumably as a result of the steric hindrance at the C10 carbonyl group. This obstacle was circumvented by implementing a two-step procedure that included methylation of the ketone **22** (MeLi, DME) and treatment of the resulting alcohol with $SOCl_2$ in the presence of pyridine.[22] This manipulation produced the alkene **4** in 64% yield from **22**.

With substrate **4** in hand the stage was now set for the final functionalization of the oxygenated bicycle (Scheme 5). The silyl ether at C21 was cleaved (99% yield), and the resulting alcohol was then oxidized to the aldehyde **23**[23] and subsequently converted into the ketone **24** (MeMgBr, then Dess–Martin oxidation, 68% yield). Treatment of **24** with CrO_3 in aqueous acetic acid produced the lactone **25** in 80% yield.[24] Finally, Baeyer–Villiger oxidation of **25** (MCPBA, $NaHCO_3$, 60% yield) led to insertion of the oxygen atom as desired between the C19 and C21 centers with complete retention of

 © 2004 Wiley-VCH Verlag GmbH & Co. KGaA, Weinheim



Scheme 5. Reagents and conditions: a) **5** (1.5 equiv), *t*BuLi (3.0 equiv), THF, −78→−40°C, 0.5 h, then **6**, THF, −78°C, 1 h, 75%; b) Dess–Martin periodinane (8.0 equiv), CH_2Cl_2, 25°C, 10 h, 95%; c) 10% Pd/C, H_2, MeOH, 25°C, 10 h, 85%; d) MeLi (5.0 equiv), THF/DME (1:3), 0°C, 0.5 h, 75%; e) $SOCl_2$ (10.0 equiv), pyridine (20.0 equiv), CH_2Cl_2, 0°C, 0.5 h, 85%; f) TBAF (2.0 equiv), THF, 25°C, 8 h, 99%; g) IBX (3.0 equiv), MeCN, 80°C, 2 h, 96%; h) MeMgBr (10.0 equiv), THF, 0°C, 0.5 h, 72%; i) Dess–Martin periodinane (2.5 equiv), CH_2Cl_2, 25°C, 6 h, 94%; j) CrO_3 (10 equiv), $AcOH/H_2O$ (2:1), 25°C, 6 h, 80%; k) MCPBA (2.5 equiv), $NaHCO_3$ (2.5 equiv), CH_2Cl_2, 0°C, 4 h, 60%. DME = dimethoxyethane, DM[O] = Dess–Martin oxidation, IBX = 1-hydroxy-1,2-benziodoxol-3(1*H*)-one 1-oxide, MCPBA = *m*-chloroperbenzoic acid.

configuration[10] to produce norrisolide (**1**). Synthetic **1** was spectroscopically and analytically identical to natural norrisolide (**1**).

In conclusion, we have presented herein a synthesis of (+)-norrisolide (**1**) that also establishes its absolute stereochemistry. Our strategy is highlighted by the union of fragments **5** and **6** to produce the natural product after manipulations of the oxygenated bicyclic moiety. The synthetic approach paves the way for the preparation of analogues of **1** and will be helpful for the evaluation of the biological potential of norrisolide and related metabolites.

Received: September 15, 2003 [Z52868]

Keywords: alkylation · Diels–Alder reaction · natural products · synthetic methods · total synthesis

[1] For selected reviews, see: a) D. J. Faulkner in *Biomedical Importance of Marine Organisms, Vol. 13* (Ed.: D. G. Fautin), Memoirs California Academy of Sciences, San Francisco, CA, **1988**, pp. 29–36; b) P. Karuso in *Bioorganic Marine Chemistry* (Ed.: P. J. Scheuer), Springer, Berlin, **1987**, pp. 31–60; c) D. J. Faulkner, *Nat. Prod. Rep.* **1984**, *1*, 251–280; d) T. E. Thompson, *J. Mar. Biol. Assoc. U. K.* **1960**, *39*, 115–122.

[2] For selected natural products isolated from nudibranchs, see: a) B. J. Burreson, P. J. Scheuer, J. Finer, J. Clardy, *J. Am. Chem. Soc.* **1975**, *97*, 4763–4764; b) E. J. Dumbei, E. D. de Silva, R. J. Andersen, M. I. Choudhary, J. Clardy, *J. Am. Chem. Soc.* **1989**, *111*, 2712–2713; c) B. Carte, D. J. Faulkner, *J. Chem. Ecol.* **1986**, *12*, 795–804; d) G. Cimino, S. De Rosa, S. De Stefano, G. Sodano, G. Villani, *Science* **1983**, *219*, 1237–1238; e) M. Tischler, R. J. Andersen, *Tetrahedron Lett.* **1989**, *30*, 5717–5720.

[3] J. E. Hochlowski, D. J. Faulkner, G. K. Matsumoto, J. Clardy, *J. Org. Chem.* **1983**, *48*, 1141–1142.

[4] a) B. Sullivan, D. J. Faulkner, *J. Org. Chem.* **1984**, *49*, 3204–3206; b) A. Rudi, Y. Kashman, *Tetrahedron* **1990**, *46*, 4019–4022.

[5] a) S. C. Bobzin, D. J. Faulkner, *J. Org. Chem.* **1989**, *54*, 5727–5731; b) T. F. Molinski, D. J. Faulkner, *J. Org. Chem.* **1986**, *51*, 4564–4567.

[6] For recent biological data on related metabolites, see: M. Arno, L. Betancur-Galvis, M. A. Gonzalez, J. Sierra, R. J. Zaragoza, *Bioorg. Med. Chem.* **2003**, *11*, 3171–3177.

[7] For synthetic studies toward **1**, see: a) C. Kim, R. Hoang, E. A. Theodorakis, *Org. Lett.* **1999**, *1*, 1295–1297; b) R. L. Casaubon, M. L. Snapper, *224th ACS Natl. Meeting*, Boston, USA, **2002**.

[8] For selected syntheses of related metabolites, see: a) A. D. Lebsack, L. E. Overman, R. J. Valentekovich, *J. Am. Chem. Soc.* **2001**, *123*, 4851–4852; b) A. Abad, M. Arno, M. L. Marin, R. J. Zaragoza, *J. Org. Chem.* **1992**, *57*, 6861–6864; c) M. Arno, M. A. Gonzalez, R. J. Zaragoza, *J. Org. Chem.* **2003**, *68*, 1242–1251.

[9] For a catalytic asymmetric Diels–Alder approach to a related tricyclic γ-lactone–γ-lactol ring system, see: E. J. Corey, M. A. Letavic, *J. Am. Chem. Soc.* **1995**, *117*, 9616–9617.

[10] For selected reports on the Baeyer–Villiger reaction, see: a) M. Hudlicky in *Oxidations in Organic Chemistry*, American Chemical Society, Washington, DC, **1990**, pp. 186–195; b) K. Mislow, J. Brenner, *J. Am. Chem. Soc.* **1953**, *75*, 2318–2322; c) R. M. Goodman, Y. Kishi, *J. Am. Chem. Soc.* **1998**, *120*, 9392–9393.

[11] a) U. Eder, G. Sauer, R. Wiechert, **1971**, *83*, 492–493; b) Z. G. Hajos, D. R. Parrish, (Hoffmann-La Roche, Inc.), US 70–96597, **1976** [*Chem. Abstr.* **1977**, 86, 89274]; c) H. Hagiwara, J. Uda, *J. Org. Chem.* **1988**, *53*, 2308–2311; d) H. Hagiwara, H. Sakai, T. Uchiyama, Y. Ito, N. Morita, T. Hoshi, T. Suzuki, M. Ando, *J. Chem. Soc. Perkin Trans. 1* **2002**, 583–591.

[12] All new compounds exhibited satisfactory spectroscopic and analytical data (see Supporting Information). Yields refer to spectroscopically and chromatographically homogeneous materials.

[13] All hydrogenation conditions produced a mixture of *cis* (major product) and *trans* bicycles, which were difficult to separate by using standard chromatographic techniques.

[14] For an alternative synthetic route to **13**, see: a) L. Paquette, H.-L. Wang, *Tetrahedron Lett.* **1995**, *36*, 6005–6008; b) L. Paquette, H.-L. Wang, *J. Org. Chem.* **1996**, *61*, 5352–5357.

[15] CCDC-216393 (**14**) and CCDC-216394 (**6**) contain the supplementary crystallographic data for this paper. These data can be obtained free of charge via www.ccdc.cam.ac.uk/conts/retrieving.html (or from the Cambridge Crystallographic Data Centre, 12, Union Road, Cambridge CB21EZ, UK; fax: (+44) 1223-336-033; or deposit@ccdc.cam.ac.uk).

[16] a) D. H. R. Barton, R. E. O'Brien, S. Sternhill, *J. Chem. Soc. Perkin Trans. 1* **1962**, 470–476. b) A. Fernandez-Mateos, G. P. Coca, R. R. Gonzalez, C. T. Hernandez, *Tetrahedron* **1996**, *52*, 4817–4828.

[17] Compound **15** is readily available from D-mannitol by the procedures reported in the following publications: a) C. R. Schmid, J. D. Bryant, M. Dowlatzedah, J. L. Phillips, D. E. Prather, R. D. Shantz, N. L. Sear, C. S. Vianco, *J. Org. Chem.*

 © 2004 Wiley-VCH Verlag GmbH & Co. KGaA, Weinheim

1991, *56*, 4056 – 4058; b) J. Mann, A. Weymouth-Wilson, *Carbohydr. Res.* **1991**, *216*, 511 – 515; c) F. Fazio, M. P. Scheider, *Tetrahedron: Asymmetry* **2000**, *11*, 1869 – 1876**.**

[18] M. G. B. Drew, J. Mann, A. Thomas, *J. Chem. Soc. Perkin Trans. 1* **1986**, 2279 – 2285.

[19] In principle, both C14 isomers can be used for the synthesis of **1**. Nonetheless, to facilitate the spectroscopic characterization of the synthetic intermediates the strategy was evaluated with the β isomer (with respect to the substituent at C14).

[20] F. Petit, R. Furstoss, *Synthesis* **1995**, 1517 – 1520.

[21] P. J. Kocienski, P. Raubo, C. Smith, F. T. Boyle, *Synthesis* **1999**, 2087 – 2095.

[22] E. J. Corey, M. Ohno, R. B. Mitra, P. A. Vatakencherry, *J. Am. Chem. Soc.* **1964**, *86*, 478 – 485.

[23] J. D. Moore, N. S. Finney, *Org. Lett.* **2002**, *4*, 3001 – 3003.

[24] Y. Lin, Y. Kuo, Y. Chen, *Chem. Pharm. Bull.* **1989**, *37*, 2191 – 2193.

 © 2004 Wiley-VCH Verlag GmbH & Co. KGaA, Weinheim

Radicals

5-Dehydro-1,3-quinodimethane: A Hydrocarbon with an Open-Shell Doublet Ground State**

Lyudmila V. Slipchenko, Tamara E. Munsch, Paul G. Wenthold, and Anna I. Krylov**

We report experimental and theoretical studies of the organic triradical, 5-dehydro-1,3-quinodimethane (5-dehydro-*m*-xylylene, DMX, Figure 1), a hydrocarbon with an unprecedented electronic ground state of three low-spin coupled unpaired electrons, that is, an "open-shell doublet." Although low-spin, open-shell states occur in molecules containing transition metals, the ground states of organic molecules are rarely of this type. Organic biradicals can have open-shell singlet ground states, depending on the orbital structure,[1] but DMX is the first example of an organic triradical with an open-shell doublet ground state.

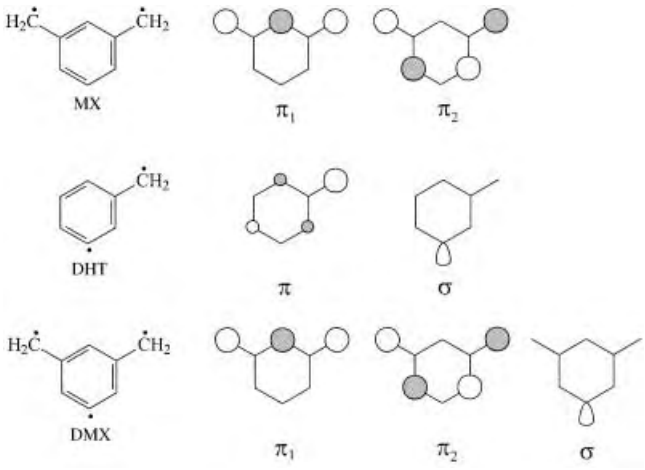


Figure 1. Nonbonding molecular orbitals in MX, DHT, and DMX.

Qualitatively, the preference for the open-shell doublet ground state in DMX can be understood by considering the electronic structures in *m*-xylylene (MX) and α,3-dehydrotoluene (DHT). The MX biradical has a triplet ground state[2–4] with two ferromagnetically coupled electrons in two π molecular orbitals (Figure 1). DHT, also shown in Figure 1, is a $\sigma^1\pi^1$ biradical[5] with singlet-coupled unpaired electrons, a result of spin polarization that favors antiferromagnetic coupling.[5,6] The features responsible for the MX and DHT ground state multiplicities are also present in DMX. The π system is similar to that of MX, such that it should contain two ferromagnetically coupled electrons. Likewise, the interaction between the σ and π systems resembles that in DHT, and should therefore have a preference for antiferromagnetic coupling. The net result is a hydrocarbon with a $\sigma^1\pi^1\pi^1$, open-shell doublet, ground state configuration (Figure 1).

More rigorously, the electronic structure of triradicals is described by the three-electrons-in-three-orbitals model.[7] Different occupations of three nearly degenerate triradical orbitals result in one quartet and eight doublet low-lying states.[7] The eight lowest energy electronic states of DMX are shown in Figure 2. Orbital near-degeneracies in the triradical result in multiconfigurational wave functions for most of the

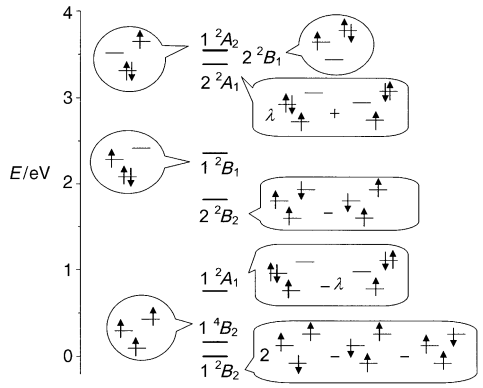


Figure 2. Vertical state ordering in DMX calculated at the SF-CCSD/6-311G** level at the equilibrium geometry of the ground $X\,^2B_2$ state. The orbital ordering is as follows: the lowest orbital is σ, the middle one is π_1, and the upper one is π_2 orbital from Figure 1.

[*] T. E. Munsch, Prof. P. G. Wenthold
Department of Chemistry
Purdue University
560 Oval Drive, West Lafayette, IN 47907-2084 (USA)
Fax: (+1) 765-494-0239
E-mail: pgw@purdue.edu
L. V. Slipchenko, Prof. A. I. Krylov
Department of Chemistry
University of Southern California
3620 McClintock Avenue, Los Angeles, CA 90089-0482 (USA)
Fax: (+1) 213-740-3972
E-mail: krylov@usc.edu

[**] This work was funded by the National Science Foundation (P.G.W.: CHE-0137627; A.I.K.: CAREER CHE-0094116). Additional support was provided by the Petroleum Research Fund, administered by the American Chemical Society (P.G.W. and A.I.K.), and the Camille and Henry Dreyfus New Faculty Awards and Alfred P. Sloan Programs (A.I.K.).

Supporting information for this article is available on the WWW under http://www.angewandte.org or from the author.

 © 2004 Wiley-VCH Verlag GmbH & Co. KGaA, Weinheim DOI: 10.1002/anie.200352990

low-lying electronic states, which greatly complicates electronic structure calculations. Fortunately, the recently introduced spin–flip (SF) approach,[8–10] wherein the target electronic states are described as spin–flipping excitations from a high-spin reference state, is well-suited for these calculations. Unlike low-spin states, the high-spin states are not affected by orbital degeneracies and can be accurately described by a single-reference method. In the case of triradicals we employ the high-spin component of the quartet state as a reference and describe the doublets and the low-spin component of the quartet as "excited" states in the space of the single spin–flipping excitations as shown in Equation (1), in which

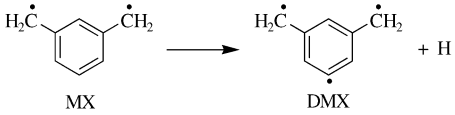
$$\Psi^{d,q}_{M_S=1/2} = \hat{R}_{M_S=-1}\tilde{\Psi}^{q}_{M_S=3/2} \quad (1)$$

M_S is the projection of the total spin, $\tilde{\Psi}^{q}_{M_S=3/2}$ is the $\alpha\alpha\alpha$ component of the quartet reference state, $\Psi^{d,q}_{M_S=1/2}$ represents the wave functions of the final doublet and quartet states, and $\hat{R}_{M_S=-1}$ is an excitation operator that flips the spin of one electron.

Because all the Slater determinants present in triradical wave functions from Figure 2 are formally single spin–flipping excitations, a balanced and accurate description of all the triradical states can be obtained within the SF scheme,[7,11] similar to the way that problematic singlet states of biradicals can be well-described as spin–flipping excitations from the high-spin triplet reference. As demonstrated in the comprehensive benchmark study of 15 biradicals, the SF models describe open-shell systems with an accuracy comparable to that achieved by traditional single reference methods in the case of well-behaved closed-shell molecules.[11] Most of the results presented in this work are obtained by the SF model in which the reference state is described by the coupled-cluster method with single and double substitutions (CCSD), and the excitation operator $\hat{R}$ consisting of single- and double-excitation operators involving the flip of the spin of one electron (SF-CCSD). For this method, the typical errors in the singlet–triplet gaps in biradicals are about 1 kcal mol^{-1}.[11] All SF calculations were performed by using the Q-CHEM 2.1 electronic structure package.[12]

The multistate nature of the SF approach allows the calculation of an entire manifold of low-lying electronic states of DMX. In agreement with the qualitative, spin-polarization-based predictions, the ground state of DMX is the open-shell doublet 1^2B_2 state (Figure 2). The counterpart of the 1^2B_2 state, the 1^4B_2 quartet, is 0.16 eV higher in energy. Equilibrium geometries of these two states are similar. Interestingly, the 1^2B_1 state that results from sequential electron addition (an "aufbau" approach) is more than 2 eV higher in energy than the open-shell 1^2B_2, as transferring an electron between spatially separated π and σ systems leads to an anionic state with negative charge at the C5 position. Similar considerations also explain the high excitation energy of the 2^2A_1 state. The lowest energy closed-shell type doublet (i.e., doublet with one of the triradical orbitals being occupied by a pair of electrons) is the 1^2A_1 state, which resembles the lowest-energy singlet in MX.[4] The net conclusion is that state-of-the-art calculations carried out by using the SF approach confirm the prediction of the open-shell doublet ground state for DMX.

We have carried out an experimental determination of the heat of formation of the DMX triradical by measuring the bond dissociation enthalpy, DH_{298}, at the C5 position of MX, as shown in Equation (2). The value of DH_{298} was obtained



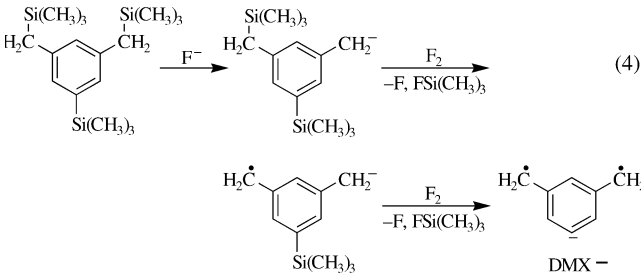
(2)

from the gas-phase acidity of the C5 position of MX ($\Delta_{acid}H_{298}$(5-MX)), the electron affinity (EA) of DMX, and the ionization energy (IE) of the hydrogen atom according to the relationship shown in Equation (3). The gas-phase acidity

$$DH_{298}(\mathrm{MX}) = \mathrm{EA}(\mathrm{DMX}) + \Delta_{acid}H_{298}(\mathrm{MX}) - \mathrm{IE}(\mathrm{H}) \quad (3)$$

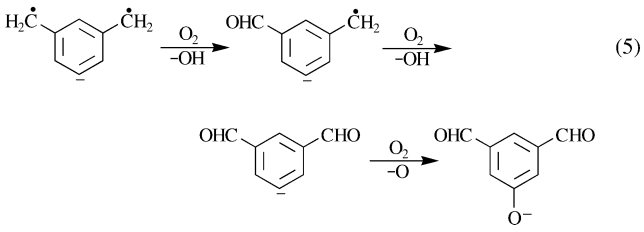
and electron affinity values were obtained from studies of DMX^- anion.[13]

The synthesis of DMX^- involves sequential reaction of 5,α,α′-*tris*-trimethylsilyl-*m*-xylene with F^- and two equivalents of F_2 [Eq. (4)] results in formation of an ion with *m*/*z* 103, $C_8H_7^-$, which is deduced on the basis of reactivity studies



(4)

to be DMX^-. Reaction of the ion with O_2 leads to a product that has the same mass-to-charge ratio and collision-induced dissociation spectrum as 3,5-*bis*-formylphenoxide ion [Eq. (5)]. The formation of the phenoxide ion can be



(5)

attributed to oxygen atom abstraction from O_2 by DMX^- and sequential oxidation of the benzylic radicals. Oxidation of benzylic radicals in distonic biradical anions with O_2 has been observed previously by Hu and Squires.[14] The formation of the phenoxide from reaction of DMX^- with oxygen confirms the dehydro-*m*-xylylene structure of the ion.

The gas-phase acidity at the C5 position in MX was determined by bracketing the proton affinity of DMX^-.

 © 2004 Wiley-VCH Verlag GmbH & Co. KGaA, Weinheim

Proton transfer bracketing results,[15] summarized in Table 1, indicate a proton affinity very close to that of phenyl anion, and we assign a value of 392 ± 3 kcal mol^{-1} for $\Delta_{acid}G_{298}$ of the C5 position of MX. The quantity $\Delta_{acid}H_{298}$ is calculated from the measured $\Delta_{acid}G_{298}$ by using $\Delta H = \Delta G + T\Delta S$. The value of $\Delta_{acid}\Delta S_{298}$ is calculated from the B3LYP/6-311+G* frequencies for DMX^- and MX to be 29.0 cal mol^{-1} K^{-1}, giving a value of 401 ± 3 kcal mol^{-1} for the 298 K acidity of the C5 position of MX.

Table 1: Proton transfer bracketing results for DMX^-.

Reference acid	$\Delta_{298}G_{acid}$[a]	Is proton transfer observed?[b]
iPrNH$_2$	389.9 ± 3.0	Yes
nPrNH$_2$	391.0 ± 3.0	Yes
EtNH$_2$	391.7 ± 0.7	No
DMF	392.0 ± 4.0	No
C_6H_6	392.3 ± 0.1	Yes
MeNH$_2$	395.7 ± 0.7	No
NH$_3$	396.0 ± 0.2	No

[a] Acidity values taken from reference [15], in kcal mol^{-1}. [b] A "Yes" indicates that proton transfer is observed with this acid, and "No" indicates that proton transfer is not observed.

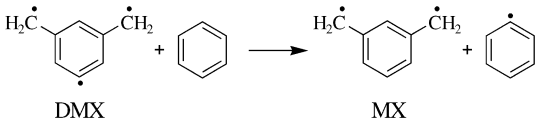
The EA of DMX was determined by using the kinetic method developed by Cooks, and co-workers.[16] The experiment involves the measurement of the branching ratio for collision-induced dissociation of the SO_2 adducts of DMX^- [Eq. (6)][17] prepared by direct addition of DMX^- with SO_2. In

$$DMXSO_2^- \rightarrow \begin{cases} DMX^- + SO_2 \\ DMX + SO_2^- \end{cases} \quad (6)$$

this work, we have used the extended form of the kinetic method that incorporates the entropy differences in the competing dissociation channels.[17,18] The experimental procedures and representative data plots are provided in the Supporting Information. From our measurements, we obtain EA(DMX) $= 24.9 \pm 2.0$ kcal mol^{-1}, similar to that for phenyl radical, 25.3 ± 0.1 kcal mol^{-1}.[19] Combination of the measured EA and $\Delta_{acid}H_{298}$ values according to Equation (3) gives a C–H DH_{298} of 112 ± 4 kcal mol^{-1}, indistinguishable from the DH_{298} of benzene, 112.9 ± 0.5 kcal mol^{-1}.[20] By using the measured DH_{298} along with the previously reported heat of formation of MX, 80.8 ± 2.4 kcal mol^{-1},[21] the heat of formation of DMX is found to be 141 ± 5 kcal mol^{-1}.

We have previously described the "triradical stabilization energy" (TSE)[22] as the energy required to separate a radical into radical and biradical components. The TSE for DMX corresponds to the energy change for the reaction shown in Equation (7), where DMX and MX are in their ground doublet and triplet states, respectively. From the experimental results, the TSE of DMX is calculated to be 1 ± 4 kcal mol^{-1}, thus indicating little measurable interaction between the σ and π electrons in this open-shell doublet triradical.

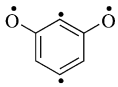
The experimentally determined TSE can be compared to that obtained from ab initio calculations. To achieve a balanced description of all species involved in Equation (7),



DMX MX (7)

we first calculate the TSE for the quartet state (TSE_Q) at the CCSD with perturbative triples corrections [CCSD(T)] level. Since all species involved in the high-spin reaction are well described by single-reference methods, the calculated TSE_Q is expected to be very accurate (within 1 kcal mol^{-1}). The TSE for the doublet state is obtained by adding the quartet-doublet energy difference ΔE_{QD}, calculated at the SF-CCSD level, to TSE_Q. Basis set effects were estimated by calculating the difference in ΔE_{QD} in double- and triple-ζ basis sets at the lower level of theory as described previously.[11] Our best estimate for TSE_Q is 0.35 kcal mol^{-1}, which, when combined with $\Delta E_{QD} = 2.54$ kcal mol^{-1} for DMX, gives TSE = 2.89 kcal mol^{-1} for the ground state triradical. Thus, the calculated TSE indicates a weak but stabilizing interaction between σ and π radical centers in DMX, in agreement with the experimental result.

The presence of a weak electronic interaction between the σ and π electrons in DMX is consistent what has been found previously in other organic systems such as the dehydrotoluenes[5] and the dehydrophenylnitrenes.[23] On the other hand, recently reported computational studies by Clark and Davidson[24] suggest a strong interaction between the σ and π systems in 2,6-dehydro-*m*-quinone (DMQ), somewhat surprising for electrons in formally orthogonal regions of space. These results indicate a myriad of mechanisms for the interactions between electrons in open-shell systems, a factor that will become more important as their size continues to grow.[25]



DMQ

Received: October 1, 2003 [Z52990]
Published Online: January 8, 2004

Keywords: ab initio calculations · radicals · spin–flip method · thermochemistry · triradicals

[1] L. Salem, C. Rowland, *Angew. Chem.* **1972**, *84*, 86; *Angew. Chem. Int. Ed. Engl.* **1972**, *11*, 92.
[2] G. Kothe, K. H. Denkel, W. Summermann, *Angew. Chem.* **1970**, *82*, 935; *Angew. Chem. Int. Ed. Engl.* **1970**, *9*, 906.
[3] G. R. Luckhurst, G. F. Pedulli, *J. Chem. Soc. B* **1971**, 329.
[4] P. G. Wenthold, J. B. Kim, W. C. Lineberger, *J. Am. Chem. Soc.* **1997**, *119*, 1354.
[5] P. G. Wenthold, S. G. Wiershke, J. J. Nash, R. R. Squires, *J. Am. Chem. Soc.* **1994**, *116*, 7378.
[6] W. T. Borden, E. R. Davidson, *J. Am. Chem. Soc.* **1977**, *99*, 4587.
[7] L. V. Slipchenko, A. I. Krylov, *J. Chem. Phys.* **2003**, *118*, 9614.
[8] A. I. Krylov, *Chem. Phys. Lett.* **2001**, *338*, 375.
[9] A. I. Krylov, C. D. Sherrill, *J. Chem. Phys.* **2002**, *116*, 3194.
[10] Y. Shao, M. Head-Gordon, A. I. Krylov, *J. Chem. Phys.* **2003**, *118*, 4791.
[11] L. V. Slipchenko, A. I. Krylov, *J. Chem. Phys.* **2002**, *117*, 4694.
[12] J. Kong, C. A. White, A. I. Krylov, D. Sherrill, R. D. Adamson, T. R. Furlani, M. S. Lee, A. M. Lee, S. R. Gwaltney, T. R. Adams, C. Ochsenfeld, A. T. B. Gilbert, G. S. Kedziora, V. A. Rassolov,

 © 2004 Wiley-VCH Verlag GmbH & Co. KGaA, Weinheim

D. R. Maurice, N. Nair, Y. Shao, N. A. Besley, P. E. Maslen, J. P. Dombroski, H. Daschel, W. Zhang, P. P. Korambath, J. Baker, E. F. C. Byrd, T. V. Voorhis, M. Oumi, S. Hirata, C.-P. Hsu, N. Ishikawa, J. Florian, A. Warshel, B. G. Johnson, P. M. W. Gill, M. Head-Gordon, J. A. Pople, *J. Comput. Chem.* **2000**, *21*, 1532.

[13] P. J. Marinelli, J. A. Paulino, L. S. Sunderlin, P. G. Wenthold, J. C. Poutsma, R. R. Squires, *Int. J. Mass Spectrom. Ion Processes* **1994**, *130*, 89.

[14] J. Hu, R. R. Squires, *J. Am. Chem. Soc.* **1996**, *118*, 5816.

[15] J. E. Bartmess in *NIST Chemistry WebBook*, *NIST Standard Reference Database Number 69*, March 2003 ed. (Eds.: W. G. Mallard, P. J. Linstrom), National Institute of Standards and Technology, Gaithersburg, MD, 20899, **March 2003**.

[16] R. G. Cooks, P. S. H. Wong, *Acc. Chem. Res.* **1998**, *31*, 379.

[17] H. A. Lardin, R. R. Squires, P. G. Wenthold, *J. Mass Spectrom.* **2001**, *36*, 607.

[18] P. B. Armentrout, *J. Am. Soc. Mass Spectrom.* **2000**, *11*, 371.

[19] R. F. Gunion, M. K. Gilles, M. L. Polak, W. C. Linenberger, *Int. J. Mass Spectrom. Ion Processes* **1992**, *117*, 601.

[20] K. M. Ervin, V. F. DeTuri, *J. Phys. Chem. A* **2002**, *106*, 9947.

[21] L. A. Hammad, P. G. Wenthold, *J. Am. Chem. Soc.* **2000**, *122*, 11203.

[22] H. A. Lardin, J. J. Nash, P. G. Wenthold, *J. Am. Chem. Soc.* **2002**, *124*, 12612.

[23] H. F. Bettinger, W. Sander, *J. Am. Chem. Soc.* **2003**, *125*, 9726.

[24] A. E. Clark, E. R. Davidson, *J. Org. Chem.* **2003**, *68*, 3387.

[25] A. Rajca, J. Wongsriratanakul, S. Rajca, *Science* **2001**, *294*, 1503.

 © 2004 Wiley-VCH Verlag GmbH & Co. KGaA, Weinheim

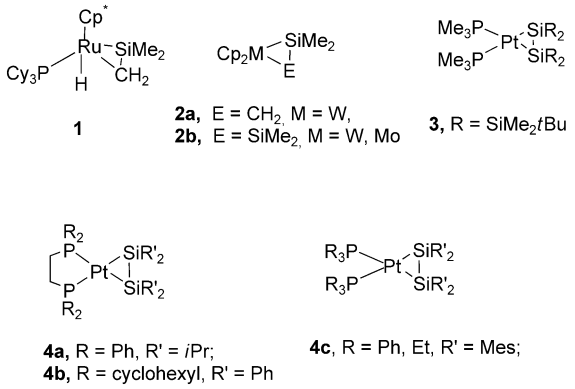
Silene–Organometallic Complexes

The Direct Synthesis of a Silene–Organometallic Complex**

Dmitry Bravo-Zhivotovskii, Hanan Peleg-Vasserman, Monica Kosa, Gregory Molev, Mark Botoshanskii, and Yitzhak Apeloig**

Dedicated to Professor Henry F. Schaefer III on the occasion of his 60th birthday

The first stable compounds with doubly bonded silicon atoms were reported in 1981 and since then vast progress has been made in this field,[1] including the synthesis of several transition-metal complexes of silenes and disilenes such as compounds **1**–**4**.[2–6] However, while numerous olefin–organometallic complexes were synthesized directly from the corresponding olefins, all known silene complexes were synthesized by indirect processes. For example, **1**,[3] **2a**,[4] **2b**,[5] **3**,[6] **4a** and **4b**[7a,b] were all obtained by cyclization reactions. Only **4c** was synthesized by a direct reaction of a disilene with an organometallic reagent, but its molecular structure was not determined by X-ray crystallography (Mes = $C_6H_2Me_3$).[7b]



1

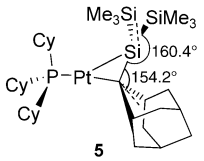
2a, E = CH_2, M = W,
2b, E = $SiMe_2$, M = W, Mo

3, R = $SiMe_2t$Bu

4a, R = Ph, R' = *i*Pr;
4b, R = cyclohexyl, R' = Ph

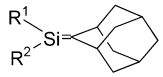
4c, R = Ph, Et, R' = Mes;

We report herein the synthesis and the molecular and electronic structure of a novel platinum η^2-silene complex, **5**, the first silene complex synthesized by a direct reaction of a silene (**6**) and an organometallic reagent $Pt(PCy_3)_2$.



5

Cy = cyclohexyl



6, $R^1=R^2=Me_3Si$
7, $R^1 = Me_3Si$, $R^2 = tBuMe_2Si$
8, $R^1 = R^2 = Me_3SiMe_2Si$

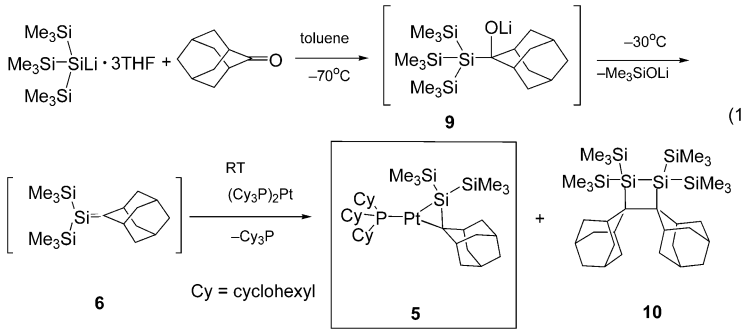
Our initial attempts to obtain a silene–platinum complex by a reaction of $Pt(PCy_3)_2$[8] and the stable silenes **7**[9] and **8**[10] failed, thus leading to a complex mixture of products. Molecular models reveal that the double bond in **7** and **8** is so effectively protected by the very bulky R^1 and R^2 substituents that the desired complex cannot be formed. A less heavily substituted silene was required and we chose **6**, which is obtained as a short lived intermediate.[11] Reaction of $(Me_3Si)_3SiLi\cdot 3THF$ with 2-adamantanone in toluene at −70 °C yields the isolable addition adduct **9**.[12] On warming of the reaction mixture (or warming of **9** directly) to −30 °C the transient silene **6** was formed and its formation was monitored by ^{29}Si NMR (the NMR chemical shifts of **6** are very similar to those of the stable **7**[9]).[12] The warming of this reaction mixture to room temperature yielded dimer **10**, thus supporting the presence of silene **6**. Warming of the toluene reaction mixture from −30 °C to room tempretature in the presence of $Pt(PCy_3)_2$ led to the formation of **5** (31 %). A

[*] D. Bravo-Zhivotovskii, H. Peleg-Vasserman, M. Kosa, G. Molev, M. Botoshanskii, Y. Apeloig
Department of Chemistry and
the Lise Meitner-Minerva Center for Computational Quantum Chemistry
Technion-Israel Institute of Technology
Haifa 32000 (Israel)
Fax: (+972) 4823-3735
E-mail: chrbrzh@tx.technion.ac.il
chrapel@tx.technion.ac.il

[**] This research was supported by the Israel Science Foundation administrated by the Israel Academy of Sciences and Humanities. We are grateful to Dr. Miriam Karni and Dr. Thomas Müller for helpful discussions. D.B.-Z. is grateful to the Ministry of Immigrant Absorption, State of Israel, for a Kamea scholarship.

 DOI: 10.1002/anie.200353048 © 2004 Wiley-VCH Verlag GmbH & Co. KGaA, Weinheim

higher yield (40%) of the desired silene–platinum complex **5** (together with **10**, 37%) was obtained when $Pt(PCy_3)_2$ was added to a toluene solution of **9** at −70°C and the solution was warmed to room temperature [Eq. (1)]. These experiments support strongly the conclusion that **5** is obtained by a direct reaction between the transient silene **6** and $Pt(PCy_3)_2$ as shown in Equation (1). Compound **5** was obtained as pale pink crystals and its molecular structure was determined by X-ray crystallography.[13]



The molecular structure of **5** (Figure 1) reveals the surprising presence of a tricoordinated Pt atom. Thus, the reaction of silene **6** with $Pt(PCy_3)_2$ involves a ligand substitution reaction at the dicoordinated Pt center at which one of the PCy_3 ligands is displaced to allow coordination with the sterically bulky silene. To our best knowledge this ligand exchange reaction is unprecedented in dicoordinated Pt compounds. Another unusual feature of the structure of **5** is the near colinearity of the C25-Pt1-P1 atoms (bond angle 177.7°).

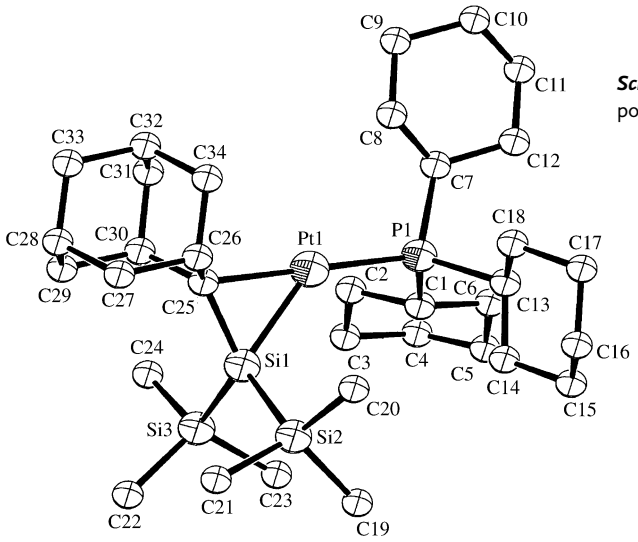
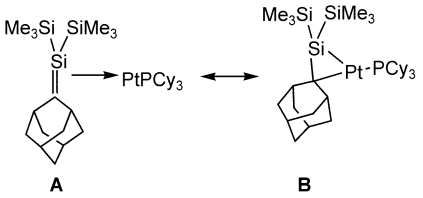


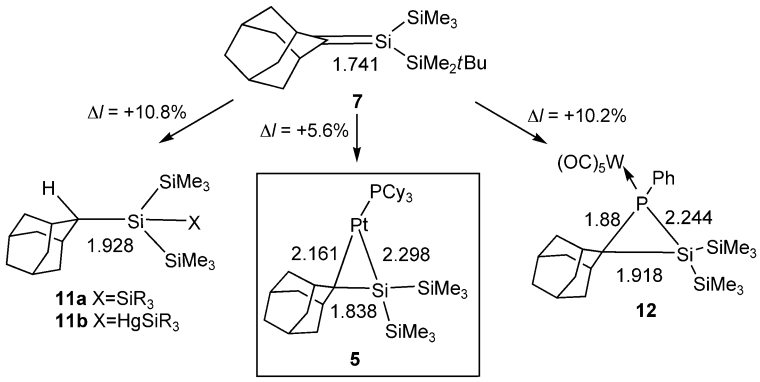
Figure 1. ORTEP diagram of the η^2-silene–platinum complex **5**. Hydrogen atoms are omitted for clarity. Selected bond lengths [Å] and angles [°]: Si1-C25 1.838(12), Pt-Si1 2.298(3), Pt-C25 2.161(11), Pt-P 2.268(3), Si1-Si2 2.344(5), P-C7 1.861(11), C25-Pt-Si1 48.6(3), Pt-Si1-C25 61.8(3), Pt-C25-Si1 69.6(4), P-Pt-C25 177.7(3), P-Pt-Si 131.24(11), Pt-Si1-Si2 116.21(15), C25-Si1-Si2 119.5(4), C25-Si1-Si3 122.1(4), Si2-Si1-Si3 112.22(18), P-Pt-Si1-C25 177.0(4), C25-Pt-Si1-Si2 111.0(4), P-Pt-Si1-Si2 72.0(2).

The NMR spectrum is consistent with the molecular structure of **5**. The NMR signals of ^{29}Si1 ($\delta = 6.8$ ppm) and of ^{13}C25 ($\delta = 137.8$ ppm) of **5** are shifted upfield, as expected, compared to silenes (e.g., $\delta(^{29}Si) = 51.7$ ppm, $\delta(^{13}C) = 196.8$ ppm in **7**). The ^{31}P signal in **5** of $\delta = 21.5$ ppm is similar to that in $Pt(PMe_3)_3$.

Is **5** better described as a π-complex (**A**) or as a σ-bonded cyclopropane-type compound (**B**)?



One criterion to answer this question is the structure of **5**, most importantly the Si–C bond length and the degree of bending around the complexed Si=C bond.[14] Structural data for comparison with model compounds is given in Scheme 1.



Scheme 1. A comparison of Si–C bond lengths (Å) in several organosilicon compounds.

The Si=C bond of silene **7** (a close model for **6**) is elongated (Δl) by 5.6%, from 1.741 Å in **7** to 1.838 Å in **5**. This bond elongation is similar to that found in **1, 2a**, and **3**, compared to the corresponding Si=E bonds ($\Delta l = +5.8\%$, $+6.4\%$ and $+5.4\%$, respectively). However, the l(Si–C) bond in **5** is significantly shorter than in related singly bonded compounds; e.g., 1.928 Å in **11a** and **11b**; [10b] thus Δl in **11a** and **11b** is almost twice as large as in **5** (Scheme 1). The closest available comparison is between **5** and **12**,[15] as both have a three-membered ring; l(Si–C) in **5** is 0.08 Å shorter than in **12.**[16] The bending angles in **5** at Si1 and C25 of 160.4° and 154.2°, respectively, are larger than those of analogous angles in **3** (150.7°[6]). The sum of the angles around Si1 and C25 are 353.8° and 353.1° respectively. In conclusion, the geometrical parameters indicate that **5** is best described as a hybrid between π complex (**A**) and σ-bonded compound (**B**),as **5** has a higher π-complex character than the disilene complex **3**.[6]

The difference Fourier (DF) electronic map of **5** was studied experimentally at −70°C and a cut through the main

 © 2004 Wiley-VCH Verlag GmbH & Co. KGaA, Weinheim

molecular plane is shown in Figure 2. Three main regions of accumulation of nonnuclear electron density are observed: (a) between Pt and the Si1 and C25 atoms, with significant density overlap at the center of the PtSiC ring and being polarized towards the Pt–C internuclear region (b) between the Si1 and C25 atoms—a maximum which is shifted outwards of the three-membered ring and towards the C atom, and (c) along the Pt–P bond, corresponding to a Pt–P σ bond.

Natural bond orbital (NBO)[17] calculations[18–20] for the model complex **13** reveal that on complexation 0.15 electrons are transferred from the organometallic fragment to the silene. In the complex, the π orbital of the silene ($(H_3Si)_2Si{=}C(CH_3)_2$), is depopulated to 1.64 electrons while the π*(C=Si) orbital is populated by 0.42 electrons. The σ* (Pt–P) antibonding orbital, which is located mainly on Pt, is populated with 0.31 electrons. According to the calculated second-order perturbation interaction energies[18b] the strongest orbital interaction in complex **13** (and thus in **5**) is interaction **14a**, between the polarized π(Si=C) orbital and the σ*(Pt–P) orbital. This interaction is also evident in the observed (Si–C), (Pt–Si) and (Pt–C) electron-density peaks. The strong polarization of π(Si=C) towards C and the good acceptor ability of phosphorous dictates the near linearity of the P-Pt-C angle. The energy difference between optimized **13** (∢ P-Pt-Si = 129.6°, P–Pt–C = 180°) and its constrained isomer, in which ∢ P-Pt-Si = 180° is 15.9 kcal mol^{-1}. The second strongest interaction is **14b** between the filled Pt(d_{xy}) orbital and the empty π*(Si=C) orbital, which is polarized towards the Si atom. In general, the NBO calculations produce the classical Dewar–Chatt–Duncanson model.[21]

In summary, the silene—platinum complex **5** is best described as an hybrid between a π complex (**A**) and a σ-cyclopropane structure (**B**), which has a more pronounced π-complex character than the disilene complex **3**. We are currently studying the chemistry of **5** and using similar strategies to prepare other silene and disilene organometallic complexes.

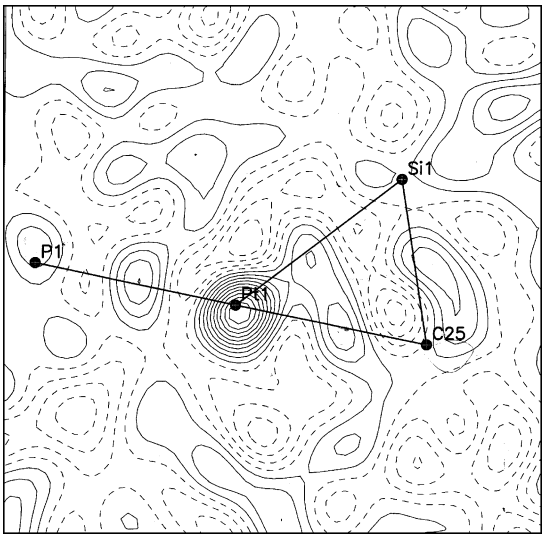
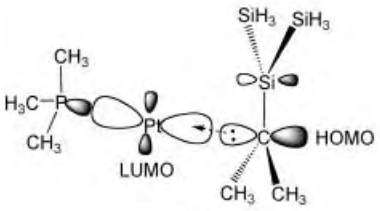


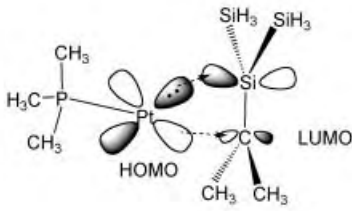
Figure 2. Difference Fourier electronic map of **5** at −70 °C, showing a cut through the main molecular plane.



13



14a



14b

Experimental Section

Standard Schlenk techniques were used for the syntheses and sample manipulations.

A toluene solution of $(Me_3Si)_3SiLi{\cdot}3\,THF$ (0.123 g, 0.26 mmol; 10 mL) was added to a toluene solution of 2-adamantanone (0.038 g, 0.25 mmol; 10 mL), which was kept at −70 °C under vacuum. After the reaction mixture had been stirred for 30 min, a toluene solution of $Pt(PCy_3)_2$[8] (0.2 g, 0.26 mmol; 20 mL) was added and the mixture allowed to reach room temperature and maintained at this temperature overnight. The solvent was removed by evaporation and the crude product was crystallized from hexane (0.083 g, 0.1 mmol; 40 % yield), of pale pink crystals suitable for X-ray crystallization of **5** were obtained. ^{1}H NMR (C_6D_6): $\delta = 0.174$ (18 H s, $SiMe_3$), 1.2–2.4 ppm (14 H m, Ad, 33 H m, PCy_3); ^{13}C NMR (C_6D_6): $\delta = 137.8$ (1 C PtC(Ad)Si), 4.1 (6 C $SiMe_3$), 44.1, 43.0, 41.0, 35.9, 34.0, 32.7, 32.1, 31.9, 31.5, 29.1, 28.0, 26.9, 25.6 ppm (9 C Ad, 18 C PCy_3); ^{29}Si NMR (C_6D_6): $\delta = 6.8$ (1 Si PtSiAd), −14.67 ppm (2 Si $SiMe_3$); ^{31}P NMR (C_6D_6): $\delta = 21.5$ (1 P t $^1J_{Pt,P} = 1475$ Hz, PCy_3); MS(CI) *m*/*z* 756.3 (*M*−2 Me).

Received: October 9, 2003 [Z53048]
Published Online: January 8, 2004

Keywords: bond theory · platinum · Si ligands · transition metals

[1] T. Müller, W. Ziche, N. Auner, *The Chemistry of Organic Silicon Compounds*, *Vol. 2* (Eds.: Z. Rappoport, Y. Apeloig), Wiley, Chichester, **1998**, chap. 16.
[2] T. D. Tilley, *The Silicon-Heteroatom Bond* (Eds.: S. Patai, Z. Rappoport) **1991**, chap. 10, p. 330.
[3] a) B. K. Campion, R. H. Heyn, T. D. Tilley, *J. Am. Chem. Soc.* **1988**, *110*, 7558; b) B. K. Campion, R. H. Heyn, T. D. Tilley, *J. Am. Chem. Soc.* **1990**, *112*, 4079.
[4] T. S. Koloski, P. J. Carroll, D. H. Berry, *J. Am. Chem. Soc.* **1990**, *112*, 6405–6406.
[5] J. H. Chey, P. J. Carroll, H. S. Zipin, D. H. Berry, *J. Am. Chem. Soc.* **1990**, *112*, 452–453.
[6] H. Hashimoto, Y. Sekiguchi, T. Iwamoto, C. Kabuto, M. Kira, *Organometallics* **2002**, *21*, 454–456.

 © 2004 Wiley-VCH Verlag GmbH & Co. KGaA, Weinheim

[7] a) E. K. Pham, R. West, *J. Am. Chem. Soc.* **1989**, *111*, 7667–7668; b) E. K. Pham, R. West, *Organometallics* **1990**, *9*, 1517.
[8] R. Yoshida, S. Otsuka, *Inorg. Synth.* **1979**, *19*, 105.
[9] Y. Apeloig, M. Bendikov, M. Yuzefovich, M. Nakash, D. Bravo-Zhivotovskii, D. Bläser, R. Boese, *J. Am. Chem. Soc.* **1996**, *118*, 12228–12229.
[10] a) M. Bendikov, MSc thesis, Technion-Israel Institute of Technology, **1996;**b) N. Sigal, MSc thesis, Technion-Israel Institute of Technology, **2001**.
[11] D. Bravo-Zhivotovskii, V. Braude, A. Stanger, M. Kapon, Y. Apeloig, *Organometallics* **1992**, *11*, 2326.
[12] D. Bravo-Zhivotovskii, G. Korogodsky, Y. Apeloig, *J. Organomet. Chem.* **2003**, *686*, 58.
[13] X-ray structure data: Nonius Kappa CCD diffractometer; phi-scans; $Mo_{K\alpha}$ radiation ($\lambda = 0.7107$); $T = 220$ K; semiempirical absorption correction; the structure were solved by direct methods with SHELXS-97 and refined against F^2 with SHELXL-97. The hydrogen atoms were generated with idealized geometry. Crystal structure data: Pt1 P1 Si3 C34 H65; $M_r = 784.18$; crystal size $0.14 \times 0.125 \times 0.038$ mmmonoclinic space group $P21/n$, $a = 13.455(3)$ Å, $b = 19.568(4)$ Å, $c = 14.818(3)$ Å, $\beta = 106.15(3)$, $V = 3747(1)$ Å^3, $Z = 4$, $\rho_{calcd} = 1.39$, $\mu(Mo_{K\alpha}) = 3.904$ mm^{-1}, $F(000) = 1616.0$, $2\theta_{max} = 50.04$, 24189 reflections measured, 6587 unique reflections ($R_{int} = 0.098$), final $R_1 = 0.0623$ for 3782 reflections [$I > 2\sigma(I)$], $R_w = 0.1142$(all data), residual maximum electron density 1.714 e$^-$ Å^3. CCDC-220373 contains the supplementary crystallographic data for this paper. These data can be obtained free of charge via www.ccdc.cam.ac.uk/conts/retrieving.html (or from the Cambridge Crystallographic Data Centre, 12 Union Road, Cambridge CB2 1EZ, UK; fax: (+44) 1223-336-033; or deposit@ccdc.cam.ac.uk).
[14] J. Uddin, S. Dapprich, G. Frenking, B. F. Yates, *Organometallics* **1999**, *18*, 457–465.
[15] M. J. M. Vlaar, A. W. Ehlers, F. J. J. de Kanter, M. Schakler, A. L. Spek, M. Lutz, N. Sigal, Y. Apeloig, K. Lammertsma, *Angew. Chem.* **2000**, *112*, 4296–4299; *Angew. Chem. Int. Ed.* **2000**, *39*, 4127–4129.
[16] l(Pt–C) in **5** of 2.161 Å is within the range found in a bisolefin platinum monophosphane complex (2.154–2.185 Å),[16a] but it is shorter than l(Ru–C) and l(W–C) in **1** and **2a** of 2.250 Å and 2.329 Å, respectively. l(Pt–Si) in **5** of 2.298 Å is at the shorter end of reported l(Pt–Si) distances (2.255–2.444 Å[16b]), but it is significantly shorter than in **3** (2.43 Å). a) G. Chandra, P. Y. Lo, P. B. Hitchcock, M. F. Lappert, *Organometallics* **1987**, *6*, 191–192; b) J. Y. Corey, J. Braddock-Wilking, *Chem. Rev.* **1999**, *99*, 175.
[17] A. E. Reed, L. A. Curtiss, F. Weinhold, *Chem. Rev.* **1988**, *88*, 899–926.
[18] The fully optimized geometry of **13** is similar to that of **5.** All calculations were performed with the Gaussian 98 program[18a] with implementation of NBO version 5.0;[18b] a) Gaussian 98 (Revision A.11.3), M. J. Frisch, G. W. Trucks, H. B. Schlegel, G. E. Scuseria, M. A. Robb, J. R. Cheeseman, V. G. Zakrzewski, J. A. Montgomery, R. E. Stratmann, J. C. Burant, S. Dapprich, J. M. Millam, A. D. Daniels, K. N. Kudin, M. C. Strain, O. Farkas, J. Tomasi, V. Barone, M. Cossi, R. Cammi, B. Mennucci, C. Pomelli, C. Adamo, S. Clifford, J. Ochterski, G. A. Petersson, P. Y. Ayala, Q. Cui, K. Morokuma, D. K. Malick, A. D. Rabuck, K. Raghavachari, J. B. Foresman, J. Cioslowski, J. V. Ortiz, B. B. Stefanov, G. Liu, A. Liashenko, P. Piskorz, I. Komaromi, R. Gomperts, R. L. Martin, D. J. Fox, T. Keith, M. A. Al-Laham, C. Y. Peng, A. Nanayakkara, C. Gonzalez, M. Challacombe, P. M. W. Gill, B. G. Johnson, W. Chen, M. W. Wong, J. L. Andres, M. Head-Gordon, E. S. Replogle, J. A. Pople, Gaussian, Inc., Pittsburgh, PA, **2002**.; b) NBO 5.0. E. D. Glendening, J. K. Badenhoop, A. E. Reed, J. E. Carpenter, J. A. Bohmann, C. M. Morales, F. Weinhold, Theoretical Chemistry Institute, University of Wisconsin, Madison, WI, **2001**; http://www.chem.wisc.edu/~nbo5.
[19] All calculation used the B3LYP/6-31G(d) level of theory for all atoms, except for Pt for which B3LYP/SDD was used.
[20] For previous theoretical studies on Pt–silene complexes see: a) T. R. Cundari, M. S. Gordon, *THEOCHEM* **1994**, 47; b) S. Sakaki, M. Ieki, *Inorg. Chem.* **1991**, *30*, 4218.
[21] a) M. J. S. Dewar, *Bull. Soc. Chim. Fr.* **1951**, *18*, C79; b) J. Chatt, L. A. Duncanson, *J. Chem. Soc.* **1953**, 2929.

 © 2004 Wiley-VCH Verlag GmbH & Co. KGaA, Weinheim

Hybrid Compounds

High-Throughput Synthesis of Phosphonate-Based Inorganic–Organic Hybrid Compounds under Hydrothermal Conditions**

Norbert Stock and Thomas Bein**

High-throughput methods applied to materials discovery have attracted much attention over the last few years.[1,2] The high efficiency of high-throughput methods, allows the systematic investigation of the reaction parameter space, that is, compositional and process parameters. The first investigations regarding the discovery and optimization of solid-state materials were based on thin-film techniques or high-temperature oxide chemistry. The introduction of high-throughput methods incorporating hydrothermal synthesis has been particularly challenging. Employing a varying degree of miniaturization and automation, the proof of concept was first given through the investigation of known microporous materials[3–6] but recently also new zinc phosphates[7] and a new manganese arsenate[8] have been obtained. All these studies were limited by the necessity of using only soluble or liquid starting materials which can be automatically dispensed by liquid-handling robots. Nevertheless, for a large number of compounds that are obtained under hydrothermal conditions, solid starting materials are mandatory and a challenge lies in the automated weighing of these compounds in mg quantities. The incorporation of solid-dosing capabilities into the workflow of high-throughput methods would also open up this methodology to other fields, such as classical high-temperature solid-state chemistry.

One variable that has a profound impact on the product formation of hydrothermal syntheses is the pH value of the reaction mixture. Therefore automated pH measurements of the reaction mixtures would deliver valuable information on reaction conditions and permit a better understanding of reaction processes.

The use of carboxylic, phosphonic, and phosphonocarboxylic acids in the synthesis of three-dimensional (3D) framework structures has attracted much interest over the last few years.[9–11] We have focused our attention on the use of polyphosphonic and phosphonocarboxylic acids as organic building units; herein we present results on the use of the tetraphosphonic acid, $(H_2O_3PCH_2)_2N(CH_2)_4N(CH_2PO_3H_2)_2\cdot 2H_2O$ ($H_8L^1\cdot 2H_2O$),[12] and the aromatic phosphonocarboxylic acid, p-$H_2O_3PCH_2C_6H_4COOH$ (H_3L^2),[13] in the synthesis of inorganic–organic hybrid compounds.

For the investigation of the system $Zn(NO_3)_2/H_3L^2$/NaOH, two experiments were designed. A discovery library was set up, in which the water content was kept constant and the molar ratios of the three starting materials varied accordingly (Figure 1). Under basic conditions (pH > 9) the formation of ZnO is observed. In addition, five new phases are discovered, three of which are obtained as single-crystalline compounds $Zn(HO_3PCH_2C_6H_4COOH)_2$[14,15] (**1**), $Zn(O_3PCH_2C_6H_4COOH)$[16] (**2**) and $Zn_3(HO_3PCH_2C_6H_4COO)_2\cdot 3H_2O$[17] (**3**). Automated pH measurements showed that a decrease in the H^+ ion concentration leads to higher condensed structures. While isolated columns are observed in **1** (pH ≈ 0), layers that are connected by hydrogen bonds are found in **2** (pH ≈ 1), and in **3** (pH ≈ 6) a 3D framework structure is observed. In the second experiment a focused library was set up to investigate the influence of the water content in the synthesis of **1** while keeping constant the molar ratio $Zn(NO_3)_2$:H_3L^2:NaOH. This investigation led to the new zinc phosphonocarboxylate $Zn(HO_3PCH_2C_6H_4COOH)_2\cdot 4H_2O$ (**4**) under very dilute conditions (99 mol% H_2O).[18] It is possible to adjust the ratio for the products **1**:**4** by varying the water content between 98–99.84 mol%.

Based on results on the corresponding Mn compound,[19] the system $M^{2+}/H_8L^1\cdot 2H_2O$ with M = Mg, Ca, Sr, Ba, Mn, Fe, Co, Ni, Zn, Cd, Sn, Pb was investigated in two experiments. A discovery library was set up in which the water content was kept constant at 95.7 mol and the $M^{2+}/H_8L^1\cdot 2H_2O$ molar ratio varied (Figure 2). The formation of microcrystalline products was observed for M = Mg, Ca, Mn, Fe, Co, Ni, Zn, Cd. Comparison of the X-ray powder diagrams showed that the compounds are isostructural. The evaluation of the ionic radii indicates that only divalent ions with a radius between 88 pm (Mg^{2+}) and 114 pm (Ca^{2+}) are incorporated. Based on energy dispersive X-ray microanalysis (EDX) measurements, the molar ratios M:P of 1:4 were found in all crystalline products.

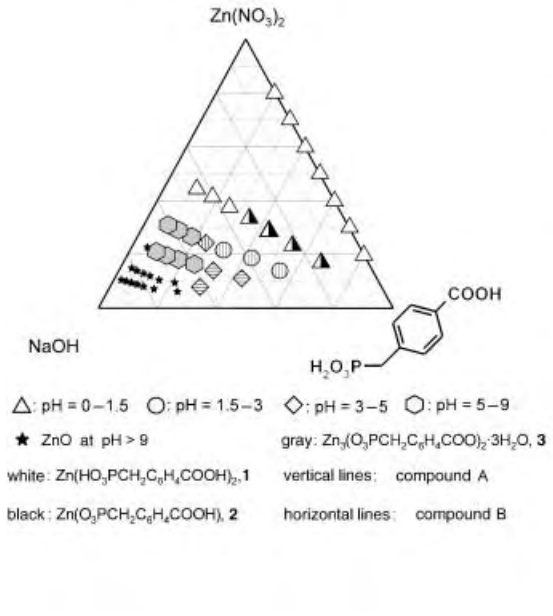
Thus in a second, focused library, using only elements leading to microcrystalline metal tetraphosphonates, the growth of products having larger crystallite sizes, suitable for single-crystal X-ray diffraction, was investigated. For this purpose, the molar ratio M^{2+}:H_8L^1 was kept constant at 1:1, and the concentration of the starting material was changed by varying the water content between 98–99.84 mol%. This approach led to the formation of single-crystalline products $M(H_6L^1)$ with M = Mg, Mn, Co, Ni, Cd, Zn (Figure 3).[20] For M = Ca and Fe, single crystals could only be obtained using conventional reactors and very dilute conditions as well as using a diffusion-controlled set-up and CaO/Fe as starting materials. The 3D structure of the metal tetraphosphonates $M(H_6L^1)$ is composed of M^{2+} ions and zwitter ions $[(HO_3PCH_2)_2(H)N(CH_2)_4N(H)(CH_2PO_3H)_2]^{2-}$ where each phosphonate group and each N atom is protonated by one H atom. The M^{2+} ions are surrounded by six phosphonate groups in the second coordination sphere. Thus 8-rings are formed by alternating MO_6 and PO_3C polyhedra leading to layers in the a,b plane (Figure 4). These layers are connected

[*] Dr. N. Stock, Prof. Dr. T. Bein
Department Chemie
Ludwig-Maximilians-Universität München
Butenandtstrasse 5–13 (Haus E), 81377 Munich (Germany)
Fax: (+49) 89-2180-7622
E-mail: norbert.stock@cup.uni-muenchen.de
tbein@cup.uni-muenchen.de

[**] We thank the BMBF for the support of this work through the grant 03C0309D, Chemspeed for the use of the solid-dosing station and P. Mayer for the single-crystal X-ray measurements. N.S. wishes to thank the "Fonds der Chemischen Industrie" for financial support.

Supporting information for this article is available on the WWW under http://www.angewandte.org or from the author.

 DOI: 10.1002/anie.200351718 © 2004 Wiley-VCH Verlag GmbH & Co. KGaA, Weinheim



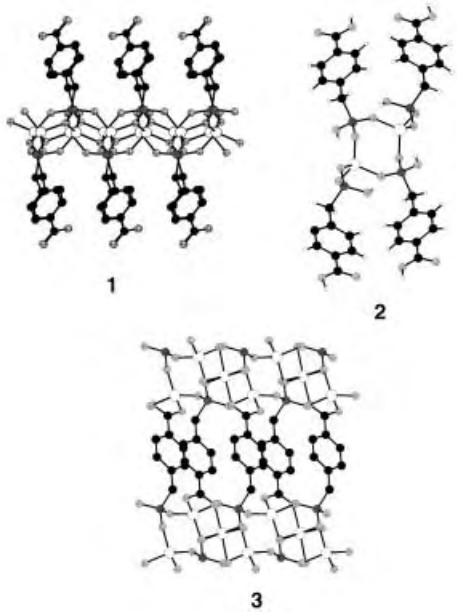


Figure 1. Left: Crystallization diagram of observed phases in the system $Zn(NO_3)_2/H_3L^2/NaOH$. In addition to **1**, **2**, and **3** two unidentified compounds (A and B) were formed (lattice constants for B: $a = 898.9(1)$, $b = 1095.6(1)$, $c = 831.3(1)$ pm, $\alpha = 127.0(1)$, $\beta = 93.8(1)$, $\gamma = 107.6(1)°$). Right: sections of the structures of **1**, **2**, and, **3**; Zn: white, C: black, P: dark gray, O: light gray.

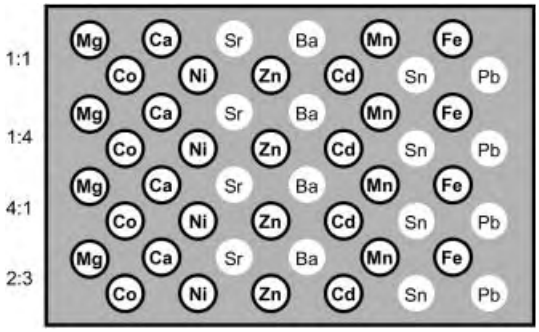


Figure 2. Discovery library and the results of the reaction between different metal salts and the tetraphosphonic acid $H_8L^1 \cdot 2H_2O$ using the molar ratios M^{2+}:$H_8L^1 = 1{:}1$, 1:4, 4:1, and 2:3, respectively. Bold letters indicate crystalline products, normal letters X-ray amorphous products.

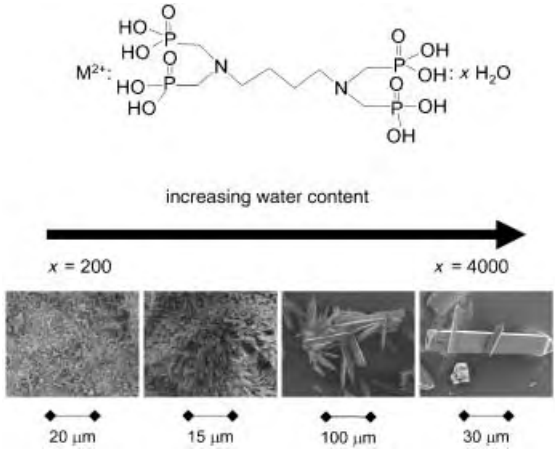


Figure 3. Influence of the water content on the product crystallinity of $M(H_6L^1)$. Shown M = Zn.

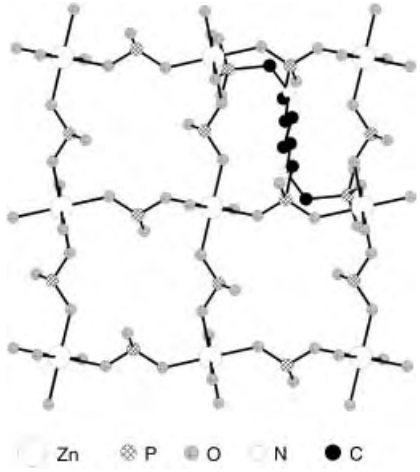


Figure 4. In $M(H_6L^1)$ with M = Mg, Ca, Mn, Fe, Co, Ni, Cd, Zn, the metal ions are surrounded by six hydrogenphosphonate groups. Shown M = Zn.

in a diagonal fashion by the organic groups, $(CH_2)_2N(CH_2)_4N(CH_2)_2$ thus blocking the 8-ring apertures.

Our method demonstrates the power of high-throughput approaches for the hydrothermal synthesis of new compounds. Using inert rectors and a direct dosing system for liquids as well as for solids, the automated synthesis and characterization of 48 individual products is achieved without the manipulation of individual samples. Furthermore, the automated measurement of the H^+ ion concentration of the starting and the final reaction mixtures has been demonstrated. Low reagent consumption and the possibility to work under identical conditions allows us to scan a larger part of the parameter space than would normally be possible. We

 © 2004 Wiley-VCH Verlag GmbH & Co. KGaA, Weinheim

have shown that the method can be applied to the discovery of new phosphonate-based compounds under hydrothermal conditions.

Experimental Section

The detailed description of the high-throughput methodology as well as the exact amounts of starting materials and the measured pH-values are given in the Supporting Information.

Hydrothermal syntheses: For the synthesis of the zinc phosphonocarboxylates **1**–**4**, H_3L^2 was dispensed as a solid.[21] The two starting solutions, 2 M NaOH and 2 M $Zn(NO_3)_2$, were successively added and the water content was adjusted by adding distilled water. For the discovery library the final water content was set to 95.5 mol%. The focused library was designed to keep the molar ratio $Zn(NO_3)_2$:H_3L^2:NaOH constant at 2.5:5:1.5 and varying the water content between 98–99.84 mol%. A total volume of 200 μL solution was used per reactor. The reaction mixtures were homogenized by stirring for 30 min using small stirring bars, followed by aging at room temperature for 12 h. The multiclave was then placed in an oven for 48 h at 130 °C.

$M(H_6L^1)$ with M = Mg, Ca, Mn, Fe, Co, Ni, Zn, Cd: The phosphonic acid $H_8L^1{\cdot}2H_2O$ was dispensed as a solid and the metal salts $MgCl_2{\cdot}6H_2O$, $CaCl_2{\cdot}2H_2O$, $SrCl_2$, $Ba(NO_3)_2$, $MnCl_2{\cdot}4H_2O$, $FeSO_4{\cdot}7H_2O$, $CoCl_2{\cdot}6H_2O$, $Ni(OOCCH_3)_2{\cdot}4H_2O$, $Zn(OOCCH_3)_2{\cdot}2H_2O$, $CdCl_2{\cdot}H_2O$, $Pb(NO_3)_2$, or $SnCl_2$ were added as 2 M or 1 M solutions. For the discovery library the water content was adjusted by adding distilled water to a final water content of 95.7 mol%. For the focused library the molar ratio M:$H_8L^1{\cdot}2H_2O$ was kept at 1:1 and the water content adjusted to 98, 98.5, 99, 99.2, 99.5, 99.8 mol% H_2O. A total volume of 200 μL solution was used per reactor. The reaction mixtures were homogenized by stirring for 30 min using small stirring bars. Then the multiclave was placed in an oven for 48 h at 150 °C.

The 48 products were isolated in parallel as an array by a custom-designed centrifuge apparatus and washed using a custom-designed filtration apparatus. The sample array was collected on filter paper in a metal frame which was transferred to a sample holder for automated X-ray analysis which was carried out using a newly developed STOE powder diffraction instrument for high-throughput measurements in transmission geometry and equipped with an image-plate detector system. The data collection time was 2–6 min per sample.

Received: April 22, 2003
Revised: August 12, 2003 [Z51718]

Keywords: combinatorial chemistry · high-throughput methods · organic–inorganic hybrid compounds · phosphonates · structure elucidation

[1] T. Bein, *Angew. Chem.* **1999**, *111*, 335; *Angew. Chem. Int. Ed.* **1999**, *38*, 323.
[2] P. J. Cong, R. D. Doolen, Q. Fan, D. M. Giaquinta, S. H. Guan, E. W. McFarland, D. M. Poojary, K. Self, H. W. Turner, W. H. Weinberg, *Angew. Chem.* **1999**, *111*, 508; *Angew. Chem. Int. Ed.* **1999**, *38*, 483.
[3] D. E. Akporiaye, I. M. Dahl, A. Karlsson, R. Wendelbo, *Angew. Chem.* **1998**, *110*, 629; *Angew. Chem. Int. Ed. Engl.* **1998**, *37*, 3369.
[4] J. Klein, C. W. Lehmann, H. W. Schmidt, W. F. Maier, *Angew. Chem.* **1998**, *110*, 3557; *Angew. Chem. Int. Ed.* **1998**, *37*, 3369.
[5] K. Choi, D. Gardner, N. Hilbrandt, T. Bein, *Angew. Chem.* **1999**, *111*, 3070; *Angew. Chem. Int. Ed.* **1999**, *38*, 2891.
[6] R. Lai, B. S. Kang, G. R. Gavalas, *Angew. Chem.* **2001**, *113*, 422; *Angew. Chem. Int. Ed.* **2001**, *40*, 408.
[7] Y. Song, J. Yu, G. Li, Y. Li, Y. Wang, R. Xu, *J. Chem. Soc. Chem. Commun.* **2002**, 1720.
[8] N. Stock, T. Bein, *Solid State Sci.* **2003**, *5*, 1207.
[9] a) N. Stock, S. Frey, G. D. Stucky, A. K. Cheetham, *J. Chem. Soc. Dalton Trans.* **2000**, 4292; b) N. Stock, G. D. Stucky, A. K. Cheetham, *Chem. Commun.* **2000**, 2277; c) N. Stock, *Solid State Sci.* **2002**, *4*, 1089; d) N. Stock, T. Bein, *J. Solid State Chem.* **2002**, *167*, 330.
[10] a) N. L. Rosi, M. Eddaoudi, J. Kim, M. O'Keeffe, O. M. Yaghi, *Angew. Chem.* **2002**, *114*, 294; *Angew. Chem. Int. Ed.* **2002**, *41*, 284; b) M. Eddaoudi, D. B. Moler, H. Li, B. Chen, T. M. Reineke, M. O'Keeffe, O. M. Yaghi, *Acc. Chem. Res.* **2001**, *34*, 319.
[11] F. Millange, C. Serre, G. Ferey, *Chem. Commun.* **2002**, 822; K. Barthelet, J. Marrot, D. Riou, G. Ferey, *Angew. Chem.* **2002**, *114*, 291; *Angew. Chem. Int. Ed.* **2002**, *41*, 281.
[12] $H_8L^1{\cdot}2H_2O$ was synthesized by a Mannich-type reaction starting from 1,4-diaminobutane, according to: K. Modritzer, R. R. Irani, *J. Org. Chem.* **1966**, *31*, 1603.
[13] H_3L^2 was synthesized by a classical Arbuzov reaction followed by acidic hydrolysis according to: M. M. Taqui Khan, A. E. Martell, *Inorg. Chem.* **1975**, *14*, 676.
[14] CCDC-208389 (**1**), CCDC-208390 (**4**), CCDC-208391 (**3**) contains the supplementary crystallographic data for this paper. These data can be obtained free of charge via www.ccdc.cam.ac.uk/conts/retrieving.html (or from the Cambridge Crystallographic Data Centre, 12 Union Road, Cambridge CB2 1EZ, UK; fax: (+44) 1223-336-033; or deposit@ccdc.cam.ac.uk). The following numbers have been assigned to the metal tetraphosphonates $M(H_6L^1)$: CCDC-206624 (M = Mn), CCDC-208382 (M = Ca), CCDC-208383(M = Cd), CCDC-208384 (M = Co), CCDC-208385(M = Fe), CCDC-208386(M = Mg), CCDC-208387 (M = Ni), CCDC-208388(M = Zn).
[15] Crystal data for $Zn(HO_3PCH_2C_6H_4COOH)]_2$ (**1**) 495.6 g mol^{-1}: triclinic, $P\bar{1}$, $a = 5.3512(2)$, $b = 11.3828(4)$, $c = 15.8307(5)$ Å, $\alpha = 99.338(2)$, $\beta = 92.850(2)$, $\gamma = 95.350(2)°$, $V = 945.28(6)$ Å^3, $Z = 2$, $\rho_{calcd} = 1.741$ g m^{-3}. $\mu(Mo_{K\alpha}) = 1.523$ mm^{-1}, $2\theta_{max} = 27.52$, 19481 measured reflections, 4270 independent reflections giving 3242 unique reflections with $I > 2\sigma(I)$ ($R_{int} = 0.066$). The final discrepancy indices were $R1 = 0.039$ and $wR2 = 0.081$.
[16] Since up to now only very thin crystal plates of the compound have been obtained only the preliminary crystal data for **2** can be presented: $Zn(O_3PCH_2C_6H_4COOH)$ 279.48 g mol^{-1}: triclinic, $P\bar{1}$, $a = 5.1888(2)$, $b = 10.5838(5)$, $c = 17.3514(10)$ Å, $\alpha = 81.139(2)$, $\beta = 88.525(2)$, $\gamma = 89.389(3)°$, $V = 941.18(8)$ Å^3, $Z = 4$, $\rho_{calcd} = 1.972$ g m^{-3}, $\mu(Mo_{K\alpha}) = 2.775$ mm^{-1}, $2\theta_{max} = 27.49$, 12409 measured reflections, 4235 independent reflections giving 3174 unique reflections with $I > 2\sigma(I)$ ($R_{int} = 0.0834$). The final discrepancy indices were $R1 = 0.1398$ and $wR2 = 0.3875$.
[17] Crystal data for $Zn_3(O_3PCH_2C_6H_4COO)_2{\cdot}3H_2O$ (**3**) 676.35 g mol^{-1}: monoclinic, $P2_1/a$, $a = 10.7950(2)$, $b = 9.3322(2)$, $c = 21.6181(4)$, $\beta = 91.584(1)$, $V = 2177.0(1)$, $Z = 4$, $\rho_{calcd} = 2.064$ g m^{-3}, $\mu(Mo_{K\alpha}) = 3.494$ mm^{-1}, $2\theta_{max} = 27.49$, 28743 measured reflections, 4916 independent reflections giving 3040 unique reflections with $I > 2\sigma(I)$ ($R_{int} = 0.0581$). The final discrepancy indices were $R1 = 0.04$ and $wR2 = 0.097$.
[18] Crystal data for $Zn(HO_3PCH_2C_6H_4COOH)_2{\cdot}4H_2O$ (**4**) 567.66 g mol^{-1}: triclinic, $P\bar{1}$, $a = 4.7633(2)$, $b = 6.9325(4)$, $c = 16.5314(9)$ Å, $\alpha = 83.236(3)$ $\beta = 89.669(3)$, $\gamma = 83.006(2)°$, $V = 538.04(5)$ Å^3, $Z = 1$, $\rho_{calcd} = 1.752$ g m^{-3}, $\mu(Mo_{K\alpha}) = 1.363$ mm^{-1}, $2\theta_{max} = 27.57$, 8881 measured reflections, 2444 independent reflections giving 1708 unique reflections with $I > 2\sigma(I)$ ($R_{int} = 0.0764$). The final discrepancy indices were $R1 = 0.046$ and $wR2 = 0.096$.

 © 2004 Wiley-VCH Verlag GmbH & Co. KGaA, Weinheim

[19] N. Stock, M. Rauscher, T. Bein, *J. Solid State Chem.*, in press.
[20] The crystal data for the Zn compound are given as representative of the seven metal tetraphosphonates $M(H_6L^1)$ with M = Mg, Ca, Fe, Co, Ni, Cd, Zn: $Zn(H_6L^1)$ 527.53 $g\,mol^{-1}$: monoclinic, $P2_1/a$, $a = 9.5077(2)$, $b = 9.0102(3)$, $c = 10.5520(3)$ Å, $\beta = 104.7744(1)$,° $V = 874.10(4)$ $Å^3$, $Z = 2$, $\rho_{calcd} = 2.004$ $g\,m^{-3}$, $\mu(Mo_{K\alpha}) = 1.838$ mm^{-1}, $2\theta_{max} = 27.43$, 9330 measured reflections, 1982 independent reflections giving 1609 unique reflections with $I > 2\sigma(I)$ ($R_{int} = 0.0584$). The final discrepancy indices were $R1 = 0.039$ and $wR2 = 0.093$.
[21] Accelerator Dual Dosing Station, Chemspeed Ltd., Augst, Switzerland.

 © 2004 Wiley-VCH Verlag GmbH & Co. KGaA, Weinheim

Sensor Screening

High-Throughput Method for the Impedance Spectroscopic Characterization of Resistive Gas Sensors**

Andreas Frantzen, Jens Scheidtmann, Gerald Frenzer, Wilhelm F. Maier, Jörg Jockel, Thomas Brinz, Daniel Sanders, and Ulrich Simon**

Sensors and sensor arrays are increasingly being used for process control, environmental protection, in medical applications, as well as in automotive and domestic applications. The development of rapid and sensitive gas sensors with low cross-sensitivity is the subject of intensive studies. However, the majority of the research activity is restricted to simple modification and improvement of known systems and is not directed towards the search for alternative sensor materials. The biggest problems with known materials are high cross-sensitivity and insufficient long-term stability.[1] The demand for more selective and stable sensors for a wide range of applications is therefore very high. Despite the increasing demand, the commercially used resistive sensor materials are confined to a few inorganic semiconductors such as titanium dioxide or tin dioxide. For sensor applications, the doped oxide is deposited as a thick film on a ceramic support. This film is electrically connected to a measuring device and a separate heating unit. The relatively complex setup aggravates the rapid screening of potential sensor materials.

The application of combinatorial methods in materials research promises significant acceleration, especially in the area of material and parameter optimization, as well as in the discovery of new materials.[2] Several reports of successful studies of oxide layers for electric or electronic applications were made. Already in 1999, the automated electrochemical analysis of library plates of an array of 64 electrodes on a silicon waver was published.[3] A comparable technology for the electrochemical deposition and characterization of samples of similarly designed library plates was reported by Symyx Technologies in a patent application.[4] The preparation of gradient libraries has been used for the discovery of transparent transistors based on ZnO[5] as well as for the discovery of transparent ferromagnetic mixed oxides (Co-doped TiO_2).[6] Procedures for the discovery of new microwave dielectrics have also been reported.[7] It is striking that in all these applications, the library was prepared exclusively with the help of PVD (physical vapor deposition) and CVD (chemical vapor deposition) methods. Such materials libraries are not suitable for the investigation of resistive-sensor properties. On the one hand, a variable homogeneous doping below one atom percent is difficult to achieve. On the other hand, porosity and microstructure of the desired sensor materials is dependent on the preparation procedure and is of fundamental importance for the sensor properties.[8,9] Herein we report the use of liquid-phase deposition methods in the search for new sensor materials based on optimized sol–gel synthesis procedures.

Specially developed thin ceramic aluminum oxide plates with printed interdigitated structures of platinum were used as substrate materials instead of the commonly used Si-wafers (Figure 1).[10] The sensor array is composed of a square arrangement of 64 interdigitated electrodes (see magnification in Figure 1).

The contact of the electrodes is positioned at the rim of the library plate. The variably doped sensor layers were deposited in a reactor, whose design was borrowed from combinatorial catalysis research (Figure 2).[11] The top of the reactor consists of a mask with 64 drill holes positioned

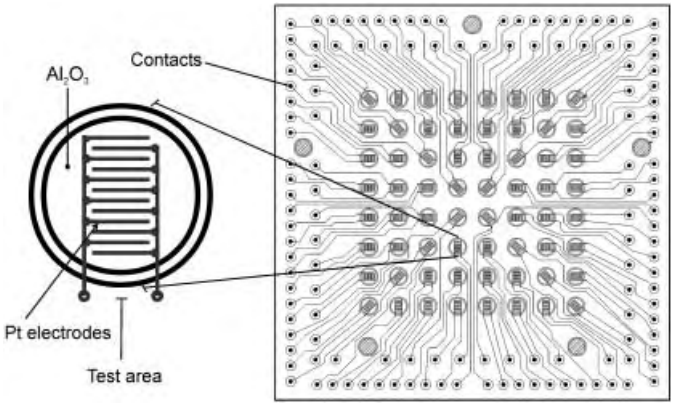


Figure 1. Library plate with an 8×8 interdigitated electrode array.[10]

[*] Dr. A. Frantzen, Dipl.-Phys. J. Scheidtmann, Dr. G. Frenzer, Prof. Dr. W. F. Maier
Universität des Saarlandes
Postfach 151150, 66041 Saarbrücken (Germany)
Fax: (+49) 681-302-2343
E-mail: w.f.maier@mx.uni-saarland.de
D. Sanders, Prof. Dr. U. Simon
RWTH Aachen
Professor-Pirlet-Strasse 1, 52056 Aachen (Germany)
Fax: (+49) 241-80-99003
E-mail: ulrich.simon@ac.rwth-aachen.de
Dr. J. Jockel, Dr. T. Brinz
Robert Bosch GmbH
Zentralbereich Forschung und Vorausentwicklung
Forschung 1, Angewandte Chemie und Energietechnik (Germany)

[**] This work was supported by the German Federal Ministry for Education and Research (BMBF, PID 03C0305D) as project "KOMBISENS".

 © 2004 Wiley-VCH Verlag GmbH & Co. KGaA, Weinheim DOI: 10.1002/anie.200352424

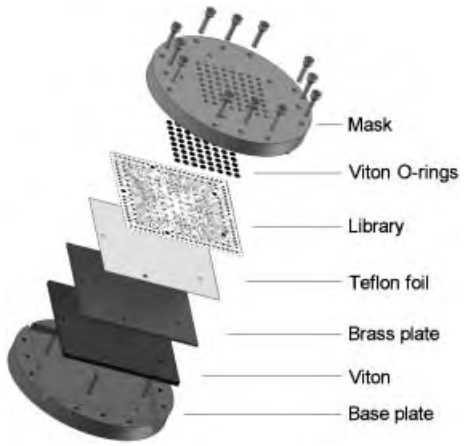


Figure 2. Setup of the reactor for direct materials synthesis on the library plate.

according to the library design. Viton fittings (O-rings) are positioned on the bottom of the mask. Both the library plate (aluminum oxide) and the mask are screwed to a metal base plate. A viton foil, a metal plate, and a teflon foil between the library plate and the metal base plate distribute the pressure from the screws more evenly. It was of interest to sample the sensor properties of sol–gel materials, because sol–gel procedures have rarely been used in the preparation of solid sensor materials. Sol–gel procedures are especially well-suited for automated synthesis through pipetting robots. The development of suitable sol–gel recipes for the preparation of mixed-oxide films has been carried out conventionally in laboratories. Before their application to libraries, the sol–gel recipes were optimized for good adhesion and to avoid the formation of cracks on the library plates. The procedure was transferred to a pipetting robot, which introduced the sol mixtures directly into the openings of the library reactor. Doping was achieved by the addition of appropriate salt solutions in the reactor. After gelation and drying, the reactor was opened and the library plate was removed. After a visual inspection, the plate was calcined at 700 °C.

The base material of the library shown here is a tungsten(VI) oxide doped with tantalum (0.5 atom %). The surface of the potential sensor layers was doped by impregnation with various chloride-free metal salt solutions.

The sensor characterization was carried out by high-throughput impedance spectroscopy (HT-IS). The setup of the HT-IS consists of a measuring head in which the library plate is positioned. Each individual electrode on the library plate is electrically connected. The measuring head is positioned in an oven, which allows electrical measurements at temperatures up to 800 °C in a controlled atmosphere, prepared by proper mixing of analytical gas mixtures and reference gases with the help of mass flow controllers. The experimental flow and data accumulation are controlled by special software.[12]

The measurements discussed herein start with synthetic air (20 % O_2, 80 % N_2) as reference, which is also the carrier gas of the test gases. The experimental sequence of test gases is 50 ppm H_2, synthetic air, 50 ppm CO, synthetic air, 5 ppm NO, synthetic air, 5 ppm NO_2, synthetic air, 50 ppm propene, synthetic air, synthetic air. All gas mixtures have a relative humidity of 45 % at 25 °C. The measurements in this example were carried out at 350 °C. The measurements were started 15 minutes after a constant gas flow has been reached. The test gases flow through the reactor (volume $\approx$ 45 mL) at a flow rate of 100 mL s^{-1}. Accordingly, 2560 measurements are made per library plate, which results from 64 samples, ten different gas-flow compositions, and four temperatures.

The materials on the libraries were electrically analyzed with an impedance analyzer (Agilent 4192A) within a frequency range from 10 to 10^7 Hz and a measurement voltage of 100 mV under variation of temperature and gas composition. The impedance spectra show typical electric *RC* responses, which allow automated data fitting by the associated circuit equivalent. This allows the evaluation of the total frequency response of the samples to be restricted to a few parameters, such as resistance *R*, capacitance *C*, and the related relaxation time τ. Figure 3 shows the complex impedance plot of a typical measurement (Argand plot) as well as the associated parallel *RC* circuit equivalent. In this case $R = 2.49 \times 10^6\ \Omega$ and $C = 6.1 \times 10^{-12}$ F.

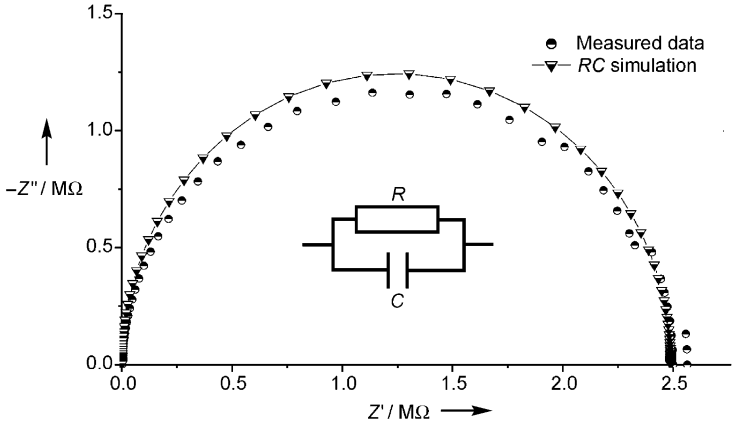


Figure 3. Complex impedance (Argand plot) of a typical measurement on the library and its automated fit with the circuitry model (parallel *RC* couple).

For the description of the response properties towards various test gases, the sensitivity *S* was defined as $S = \pm(R_{max} - T_{min})/R_{max}$, with R_{max} as the maximum resistance and R_{min} as the minimum resistance resulting from data fitting by the parallel *RC* element. The minus sign (−) indicates an increase in resistance and the plus sign (+) indicates a decrease in resistance upon contact with gas.

The sensitivities towards the various test gases are presented as a Manhattan plot. This presentation provides characteristic fingerprints of the individual materials tested (Figure 4). Upon exposure to H_2, CO, and propene, a decrease in resistance relative to that of the reference synthetic air atmosphere is observed, while the material responds to exposure to NO_2 with a small increase in resistance. After each exposure to a test gas, the measurement in the reference gas atmosphere shows the reversibility of the observed response during the time of the experiment (15 min).

 © 2004 Wiley-VCH Verlag GmbH & Co. KGaA, Weinheim

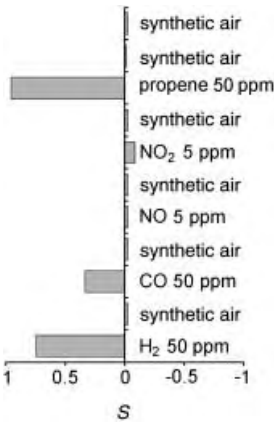


Figure 4. Fingerprint of the library position 6-6: WO_3; bulk dopant Ta (0.5 atom%), surface dopant Au (0.5 atom%).

Figure 5 shows the fingerprints of the complete library plate. The surface doping elements are labeled below the plots. Empty plots indicate library positions whose electric properties were identified as pure capacitance by the automated data fitting. Such empty diagrams can be explained by insufficient electrical contact of the materials on the library.

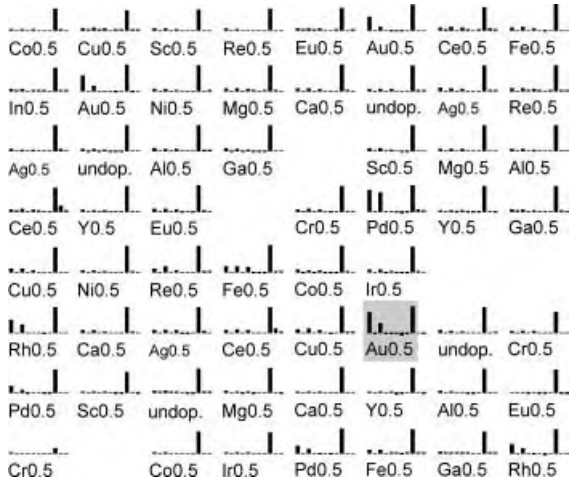


Figure 5. Sensor characteristics of the materials on the tungsten oxide library. See text for details. The shaded (gray) fingerprint corresponds to the position used in Figure 4.

The multiple deposition of individual samples as well as the spatial distribution of identical doping elements on the library are used to compensate for gradients in gas concentration, which result from catalytic conversion of test gases, such as CO. Especially with CO, a concentration decrease from the center to the outer plate was noted.

Most of the materials in these studies show a distinct sensitivity for 50 ppm propene in the form of a decrease in resistance. They also show a low cross-sensitivity against the other test gases. Exceptions are the materials impregnated with gold, rhodium, and palladium. Besides the response to propene, these materials also show a decrease in resistance upon exposure to H_2 (50 ppm) and CO (50 ppm). The significant sensitivity deviation of identical materials, as observed with the palladium-doped positions, is associated with a concentration gradient of the test gases.

These measurements have shown that the presented combination of high-throughput materials synthesis on multielectrode arrays with an interdigitated capacitor structure and high-throughput impedance spectroscopy is a useful technique for the rapid screening for new sensor materials for gas-sensing applications. This is the first method that allows the investigation of a large number of new potential sensor materials. The multiple deposition described herein was used to compensate for concentration gradients and will not be necessary in future applications, since an improved method for the introduction of the test gas has been developed.[12] This technology allows new materials and applications to be tested, which previously would have required time-consuming tests for individual sensors. This technology can also be used for the discovery of new materials in the areas of electrocatalysis, ferroelectrics, and dielectrics.

Received: July 21, 2003 [Z52424]

Keywords: combinatorial chemistry · high-throughput screening · impedance spectroscopy · sensors · sol–gel processes

[1] N. Barsan, M. Schweizer-Berberich, W. Göpel, *Fresenius J. Anal. Chem.* **1999**, *365*, 287.
[2] B. Jandeleit, D. J. Schaefer, T. S. Powers, H. W. Turner, W. H. Weinberg, *Angew. Chem.* **1999**, *111*, 2648; *Angew. Chem. Int. Ed.* **1999**, *38*, 2494.
[3] M. G. Sullivan, H. Utomo, P. J. Fagan, M. D. Ward, *Anal. Chem.* **1999**, *71*, 4369.
[4] C. J. Warren, R. C. Haushalter, L. Matsiev, US 6187164 B1, **2001** [*CAplus AN* **2001**, 110095].
[5] J. Nishii, F. M. Hossain, T. Aita, Y. Ohmaki, S. Kishimoto, T. Fukumura, Y. Ohno, H. Ohno, S. Takagi, K. Saikusa, I. Ohkubo, A. Ohtomo, F. Matsukura, H. Koinuma, M. Kawasaki, *Jpn. J. Appl. Phys.* **2003**, *42*, 347.
[6] Y. Matsumoto, M. Murakami, T. Hasegawa, T. Fukumura, M. Kawasaki, P. Ahmet, K. Nakajima, T. Chikyow, H. Koinuma, *Appl. Surf. Sci.* **2002**, *189*, 344.
[7] H. Chang, X.-D. Xiang, *Integr. Ferroelectr.* **2000**, *28*, 113.
[8] J. F. McAleer, P. T. Moseley, J. O. Norris, D. E. Williams, *J. Chem. Soc. Faraday Trans.* **1987**, *83*, 1323.
[9] J. F. McAleer, P. T. Moseley, J. O. Norris, D. E. Williams, *J. Chem. Soc. Faraday Trans.* **1988**, *84*, 411.
[10] U. Simon, D. Sanders, J. Jockel, C. Heppel, T. Brinz, *J. Comb. Chem.* **2002**, *4*, 511.
[11] J. Scheidtmann, P.-A. Weiß, W. F. Maier, *Appl. Catal. A* **2001**, *222*, 79–89.
[12] U. Simon, D. Sanders, J. Jockel, unpublished results.

 © 2004 Wiley-VCH Verlag GmbH & Co. KGaA, Weinheim

Liquid Crystals

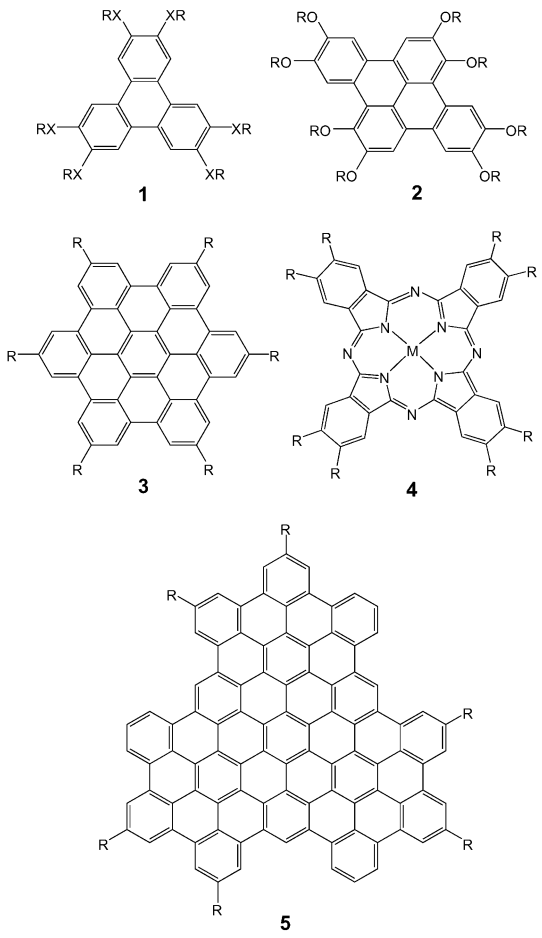
Superphenalene-Based Columnar Liquid Crystals**

*Željko Tomović, Mark D. Watson, and Klaus Müllen**

Solution-processable oligomers are complementary alternatives to polymers and crystalline small-molecule organic semiconductors in the burgeoning field of molecular electronics.[1] While crystalline small molecules can be purified readily by sublimation and processed, liquid-crystalline materials should also be inexpensive to process in solution. The resulting materials display good film formation, can be aligned by standard techniques, and are capable of self-healing.[2] In linear conjugated systems, precise control over regioregularity and the use of well-defined oligomers have in some cases led to superior transistor performance, which is attributed to enhanced supramolecular order.[3] Alternatively, one can consider discrete soluble two-dimensional fused-ring systems with specific substitution patterns and oligomeric sizes. Disk size has been increased by, for example, covalently fusing units to phthalocyanines[4a–d] or by noncovalent assembly of disk segments.[4e,f]

Well-defined benzenoid polycyclic aromatic hydrocarbons (BPAHs)[5] with a broad range of sizes and shapes may be prepared in a straightforward manner.[6] Appropriately functionalized planar disks (Scheme 1) are not only suitable for testing theoretical modeling of the properties of graphitic segments,[7] they can also self-assemble into columnar (liquid)-crystalline phases.[8] Because of their electronic and optoelectronic properties, triphenylenes **1**, dibenzopyrenes **2**, and hexa-*peri*-hexabenzocoronenes (HBC) **3**, as well as non-BPAH columnar discotic phthalocyanines **4**, have potential applications in photovoltaic devices, field-effect transistors (FETs), and other molecular electronic devices.[9–12]

Larger disk cores should lead to liquid crystals with increased columnar stability and order and to materials with higher charge-carrier mobilities.[13] At some critical size, new types of mesophases should be obtained, in which the tendency of smaller disks to tilt against the columnar axes will be replaced by a simple lateral offset (graphite-like stacking adopted to optimize orbital interactions). It may at first appear challenging to synthesize larger soluble graphitic subunits[14] with discrete sizes, symmetry, and substitution patterns, all of which may critically affect device performance.



Scheme 1. Molecular structures of selected discotic liquid crystals.

We focused our attention on superphenalene **5a**[15] (in which the BPAH core is around six times larger than triphenylene and between 2.5–3 times bigger than HBC), because its symmetry (D_{3h}) and straightforward regiospecific (C_3-symmetric) functionalization on the periphery could lead to helical bulk phases and chiral expression during 2D surface patterning.[16] Highly efficient face-to-face stacking in the bulk should be realized from such a truncated near-triangular shape, unperturbed by tethered side chains located near its apexes. With 96 core carbons (34 fused benzene rings), these molecular materials lie somewhere in the gap between small-molecule and polymeric organic electronics.

The simple synthesis of the hexasubstituted C_{96} disks **5b–f** (Scheme 2), based on our general route to large PAHs, can be completed in two steps from readily available starting materials. The Diels–Alder reaction of commercially available 1,3,5-triethynylbenzene (**6**) with excess (3.6 equiv) cyclopentadienones **7b–f** in o-xylene at 170 °C gave the corresponding polyphenylene compounds **8b–f** in nearly quantitative yields (Scheme 2).[17] All were readily soluble in organic solvents, and their structures and purities were unequivocally confirmed by ^{1}H and ^{13}C NMR spectroscopy, MALDI-TOF mass spectrometry, and elemental analysis.

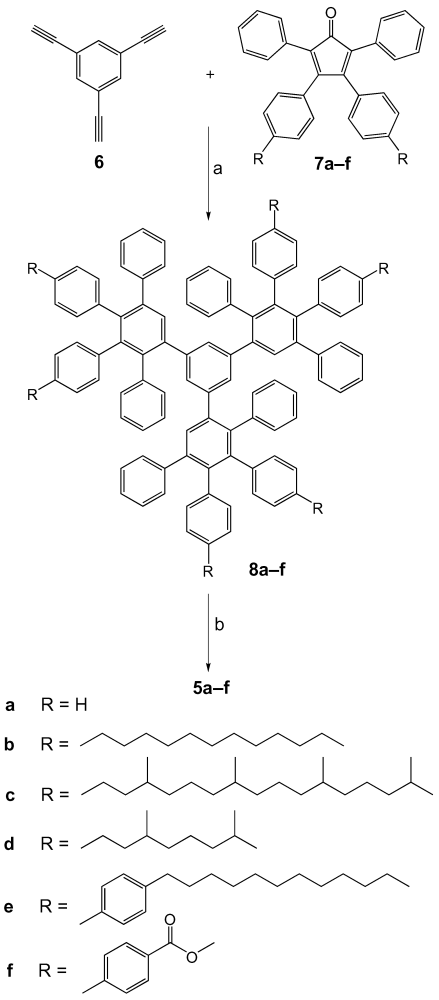
The final, key step is the oxidative cyclodehydrogenation of polyphenylene precursors under Lewis acidic conditions.[18]

[*] Ž. Tomović, Dr. M. D. Watson, Prof. Dr. K. Müllen
Max Planck Institute for Polymer Research
Ackermannweg 10, 55128 Mainz (Germany)
Fax: (+49) 6131-379100
E-mail: muellen@mpip-mainz.mpg.de

[**] This work was supported by the Zentrum für Multifunktionelle Werkstoffe und Miniaturisierte Funktionseinheiten (BMBF 03N 6500) and by the EU projects DISCEL (G5RD-CT-2000-00321) and MAC-MES (GRD2-2000-30242).

Supporting information for this article is available on the WWW under http://www.angewandte.org or from the author.

 DOI: 10.1002/anie.200352855 © 2004 Wiley-VCH Verlag GmbH & Co. KGaA, Weinheim



Scheme 2. a) *o*-Xylene, 170 °C, 18 h, 97%; b) $FeCl_3$, CH_3NO_2, CH_2Cl_2, 15 h, ≈70%.

For example, **8b** was dissolved in CH_2Cl_2 and planarization was achieved with a solution of $FeCl_3$ (90 equiv, i.e. 2.5 equiv per hydrogen to be removed) in CH_3NO_2. Longer reaction times and greater amounts of oxidant were required to obtain the near-quantitative conversions typically realized in HBC synthesis. A deep red-brown solid was precipitated with methanol from the reaction mixture, dried, and purified by column chromatography (first column: water/THF; second column: toluene) to remove residual inorganic impurities and partially fused products.[19] The low solubilities of **5d** and **5e** have so far precluded preparative chromatography.

Compounds **5b–f** were identified by MALDI-TOF mass spectrometry (see the Supporting Information),[20,21] proving the loss of exactly 36 hydrogen atoms during the formation of 18 new carbon–carbon bonds. Although a hexaphenylbenzene carrying the same functionality as **8f** resists cyclodehydrogenation to give the analogous HBC, **5f** was obtained under standard conditions. Soluble **5f** is a novel functionalized mesogenic building block, which, owing to the ester groups, offers new possibilities for post-synthesis chemical modification, for example, by the attachment of polymer arms or additional electronic components for columnar "double cables."[22]

In all the ^{1}H NMR spectra of compounds **5**, regardless of the solvent and temperature (up to 170 °C), resonances arising from the mobile alkyl side chains could be resolved, but not those of the protons on the aromatic core, because of their low mobility and the multitude of local environments associated with dynamic aggregation.[23] Compound **5b** aggregates so strongly in solution that analysis by gel-permeation chromatography gives a bimodal molecular weight distribution (THF, polystyrene standards) extending to 200 kDa. When the sample was diluted by an order of magnitude and heated just prior to measurement, a monomodal elution profile resulted with a maximum of approximately 2 kDa, clearly indicating dynamic aggregation.

The UV/Vis absorption spectrum of **5b** in THF (Figure 1) shows a broad, featureless profile ($\lambda_{max} \approx 460$ nm) with a low-energy tail extending to roughly 700 nm. A good correlation between the size of all-benzenoid PAHs and their absorption

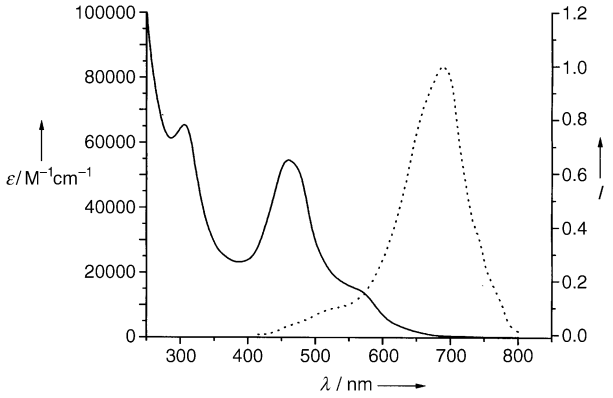


Figure 1. UV/Vis absorption (solid line) and fluorescence (dotted line) spectra of **5b** in THF (6.3×10^{-6} M).

λ_{max} values has been put forth,[6b] and the values for the C_{96} compounds fit nicely onto this curve. The maximum absorption is shifted, relative to HBC ($\lambda_{max} \approx 360$ nm), to a position within the visible spectrum that could lead to more effective photovoltaic performance.[24]

The solubility behaviors of compounds **5** have been completely unpredictable so far. Derivatives **5b**, **5c**, and **5f** readily dissolve in common organic solvents at room temperature, despite their large aromatic core, and do not precipitate upon concentration to lyotropic phases. This is in marked contrast to the significantly smaller HBC-C_{12} (**3**, R = *n*-$C_{12}H_{25}$), which precipitates virtually completely from heated organic solvents upon cooling to room temperature, even at concentrations lower than micromolar! Under suitable conditions, **5b** slowly precipitates—or can be solvent-cast—to form soft films,[25] unlike the analogous HBC-C_{12}, which rapidly self-assembles to micro- and nanofibers and gels the mother liquor.[26] In compounds **5d** and **5e** the side chains that induce high solubility in HBC lead to very low solubility regardless of solvent and temperature. Counterintuitively, the short 4-methoxycarbonylphenylene side chains of **5f** induce

 © 2004 Wiley-VCH Verlag GmbH & Co. KGaA, Weinheim

very high solubility while long flexible 4-*n*-$C_{12}H_{25}$-phenylene side chains in **5e** lead to very poor solubility. Solubility is clearly a function of side-chain space-filling and packing, (strong solution aggregation indicates that dissolution occurs by the penetration of solvent between rather within the columns) though no clear correlation can be derived as yet. Hydrolysis of the ester groups of **5f** to give carboxylic acids (not shown) imparts high solubility in alkaline water, most by formation of columnar micelles.

Solid samples of **5b–f** were characterized by differential scanning calorimetry (DSC), polarized optical microscopy (POM), and wide-angle X-ray diffraction (WAXD). Surprisingly, **5b** is a soft waxy material at room temperature, in contrast to HBC-C_{12}[27] which is a microcrystalline powder, due to crystallization (tilting) of the disks within their columns and partial crystallization of the side chains. While **5c–f** show no thermal transitions (DSC) in the interval from −100 °C to 250 °C, **5b** gives a single, reversible first order endotherm at 38 °C on heating. The liquid-crystalline character of **5b** was confirmed by the observation of birefringent, shearable thin films between crossed-polars, but no sharp changes with temperature were seen. Instead, we noted a steady increase in birefringence and the development of some as yet unassignable textures while annealing at 150 °C. This birefringence persists, that is, the sample does not become isotropic, up to the experimentally accessible maximum, 550 °C (cf. HBC-C_{12}: $T_{\text{isotropization}} \approx 410$–420 °C).

Fibers with coincident columnar and fiber axes were produced from **5b** and **5c** by extrusion through a 0.7-mm orifice.[27] Compounds **5d–f** could not be forced through the extruder even at temperatures as high as 200 °C. 2D-WAXD diffractograms from **5b** and **5c** (Figure 2) reveal hexagonally packed columnar mesophases with disk planes perpendicular to the columnar axes, based on the three main features: 1) equatorial reflections with relative reciprocal spacings of 1, $\sqrt{3}$, $\sqrt{4}$, etc., which indicates a hexagonal packing, 2) diffuse halo arising from liquid-like side chains, and 3) intense symmetric arcs on the meridian at $d = 0.34$ nm, typical for π–π stacking. The broadness and low relative intensity of the higher order equatorial reflections may reflect the electron-density profile (large disk cross-section with "thin" alkyl mantel), or may indicate short-range order lateral to the columns, again pointing to the high solubility in spite of very strong stacking.

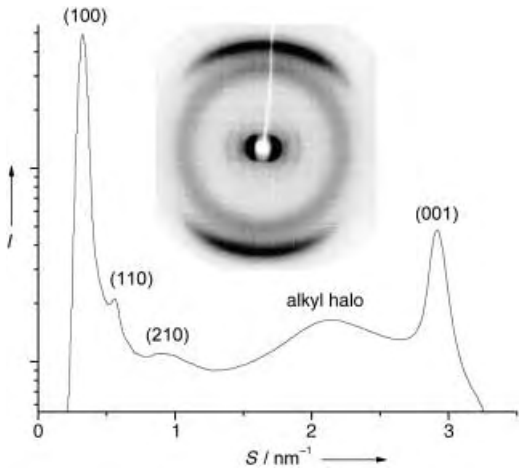


Figure 2. 2D X-ray diffraction pattern of an extruded fiber of **5b** and its integrated intensity distribution (room temperature after annealing at 150 °C for 12 h). In the diffratogram the fiber/column axes are vertical.

The meridianal reflexes ($d = 0.34$ nm, labeled 001) are relatively intense, suggesting long-range intracolumnar order. "Crystallization" (tilting) of the cores, often observed in columnar discotics and planar π-systems in general,[28] is completely suppressed at room temperature in the case of **5b**. In concord with POM observations, there was no abrupt change in the diffraction pattern with temperature, but instead all peaks became sharper and more intense after the sample was annealed at 150 °C for 12 h.

When **5b** is cooled well below its endothermic transition and then measured at room temperature, reversible reorganization to a superstructure superimposed on the hexagonal columnar arrangement is evident. Additional weak smaller-angle meridianal/equatorial reflexes and off-meridianal reflexes flanking the original ≈0.34-nm reflex appear while selected equatorial arcs split with minima at the equator (see the Supporting Information). Initial solid-state NMR and rheological measurements indicate cessation of disk mobility and development of a more rigid phase below the endothermic transition (DSC). We will describe this in detail later along with a more specific assignment of the superstructure.[29] These effects are ascribed to the predicted helical stacking and/or formation of a "plastic"[30a] or "glassy"[30b] mesophase promoted by the "pinwheel" substitution pattern and the extended BPAH core. Smaller discotic π-systems become immobile and tilt to optimize intermolecular orbital interactions,[28b] a thermodynamic contribution that is overwhelmed at higher temperature. In the absence of tilting, which we have also observed for other as yet unreported large BPAHs, favorable orbital interactions might be achieved instead by a lateral disk offset (graphite-like stacking).

In conclusion, we have expanded the scope of our straightforward synthetic approach to columnar discotic liquid crystals based on larger BPAHs, which now are comparable in size to promising linear organic semiconductors. The remarkable solubility of derivatives **5b** and **5c** and their good film-forming properties at room temperature can be explained by inefficient side-chain packing around self-assembled columns, which are otherwise well developed. The shape and substitution pattern could eventually result in symmetry-breaking chiral 2D assemblies at surfaces and to bulk helical columnar superstructures, as is indicated by WAXD. We are currently focusing on the synthesis and phase-behavior of larger alkylated BPAH derivatives with 114, 132, and 222 core carbon atoms.

Received: September 12, 2003 [Z52855]
Published Online: January 8, 2004

Keywords: cyclodehydrogenation · Diels–Alder reaction · graphite · liquid crystals · polycycles

 © 2004 Wiley-VCH Verlag GmbH & Co. KGaA, Weinheim

[1] F. Garnier, *Acc. Chem. Res.* **1999**, *32*, 209 – 215.
[2] M. O'Neill, S. M. Kelly, *Adv. Mater.* **2003**, *15*, 1135 – 1146.
[3] a) C. D. Dimitrakopoulos, P. R. L. Malenfant, *Adv. Mater.* **2002**, *14*, 99 – 117; b) D. Fichou, *J. Mater. Chem.* **2000**, *10*, 571 – 588; c) F. Garnier, *Chem. Phys.* **1998**, *227*, 253 – 262.
[4] a) B. Mohr, G. Wegner, K. Ohta, *J. Chem. Soc. Chem. Commun.* **1995**, 995 – 996; b) J. M. Fox, T. J. Katz, S. V. Elshocht, T. Verbiest, M. Kauranen, A. Persoons, T. Thongpanchang, T. Krauss, L. Brus, *J. Am. Chem. Soc.* **1999**, *121*, 3453 – 3459; c) A. N. Cammidge, H. Gopee, *Chem. Commun.* **2002**, 966 – 967; d) C. F. van Nostrum, S. J. Picken, A. J. Schouten, R. J. M. Nolte, *J. Am. Chem. Soc.*, **1995**, *117*, 9957 – 9965; e) R. P. Sijbesma, E. W. Meijer, *Chem. Commun.* **2003**, 5 – 16; f) V. Percec, M. Glodde, T. K. Bera, Y. Miura, I. Shiyanovskaya, K. D. Singer, V. S. K. Balagurusamy, P. A. Heiney, I. Schnell, A. Rapp, H. W. Spiess, S. D. Hudsonk, H. Duank, *Nature* **2002**, *419*, 384 – 387.
[5] a) E. Clar, *Polycyclic Hydrocarbons*, Academic Press and Springer Verlag, Berlin, **1964**; b) E. Clar, *The Aromatic Sextet*, Wiley, London, **1972**; c) J. R. Dias, *Handbook of Polycyclic Hydrocarbons—Part A: Benzenoid Hydrocarbons*, Elsevier, Amsterdam, **1987**; d) I. Gutman, S. J. Cyvin, *Introduction to the Theory of Benzenoid Hydrocarbons*, Springer, Berlin, **1989**; e) M. Zander, *Polycyclische Aromaten-Kohlenwasserstoffe und Fullerene*, Teubner, Stuttgart, **1995**.
[6] a) F. Dötz, J. D. Brand, S. Ito, L. Ghergel, K. Müllen, *J. Am. Chem. Soc.* **2000**, *122*, 7707 – 7717; b) M. D. Watson, A. Fechtenkötter, K. Müllen, *Chem. Rev.* **2001**, *101*, 1267 – 1300; c) M. Lee, J.-W. Kim, S. Peleshenko, K. Larsen, Y.-S. Yoo, D. Vaknin, S. Markutsya, V. V. Tsukruk, *J. Am. Chem. Soc.* **2002**, *124*, 9121 – 9128; d) R. Rathore, C. L. Burns, *J. Org. Chem.* **2003**, *68*, 4071 – 4074.
[7] a) D. Moran, F. Stahl, H. F. Bettinger, H. F. Schäfer III, P. von R. Schleyer, *J. Am. Chem. Soc.* **2003**, *125*, 6746 – 6752; b) M. Randić, X. F. Guo, *New J. Chem.* **1999**, *23*, 251 – 260; c) I. Gutman, V. Ivanov-Petrović, J. R. Dias, *Polycyclic Aromat. Compd.* **2000**, *18*, 221 – 229; d) F. Negri, C. Castiglioni, M. Tommasini, G. Zerbi, *J. Phys. Chem. A* **2002**, *106*, 3306 – 3317.
[8] a) S. Chandrasekhar, B. K. Sadashiva, K. A. Suresh, *Pramana* **1977**, *7*, 471 – 480; b) R. J. Bushby, O. R. Lozman, *Curr. Opin. Colloid Interface Sci.* **2002**, *7*, 343 – 354; c) R. J. Bushby, O. R. Lozman, *Curr. Opin. Solid State Mater. Sci.* **2003**, *6*, 569 – 578.
[9] a) D. Adam, P. Schuhmacher, J. Simmerer, L. Häussling, K. Siemensmeyer, K. H. Etzbach, H. Ringsdorf, D. Haarer, *Nature* **1994**, *371*, 141 – 143; b) E. O. Arikainen, N. Boden, R. J. Bushby, J. Clements, B. Movaghar, A. Wood, *J. Mater. Chem.* **1995**, *5*, 2161 – 2165; c) N. Boden, R. J. Bushby, J. Clements, B. Movaghar, K. J. Donovan, T. Kreouzis, *Phys. Rev. B* **1995**, *52*, 13274 – 13280; d) N. Boden, R. J. Bushby, J. Clements, B. Movaghar, *J. Mater. Chem.* **1999**, *9*, 2081 – 2086.
[10] S. Kumar, J. Naidu, D. S. S. Rao, *J. Mater. Chem.* **2002**, *12*, 1335 – 1341.
[11] a) A. Stabel, P. Herwig, K. Müllen, J. P. Rabe, *Angew. Chem.* **1995**, *107*, 1768 – 1770; *Angew. Chem. Int. Ed. Engl.* **1995**, *34*, 1609 – 1611; b) A. M. van de Craats, J. M. Warman, A. Fechtenkötter, J. D. Brand, M. A. Harbison, K. Müllen, *Adv. Mater.* **1999**, *11*, 1469 – 1472; c) L. Schmidt-Mende, A. Fechtenkötter, K. Müllen, E. Moons, R. H. Friend, J. D. MacKenzie, *Science* **2001**, *293*, 1119 – 1122; d) A. M. van de Craats, N. Stutzmann, O. Bunk, M. M. Nielsen, M. Watson, K. Müllen, H. D. Chanzy, H. Sirringhaus, R. H. Friend, *Adv. Mater.* **2003**, *15*, 495 – 499; e) C.-Y. Liu, A. Fechtenkötter, M. D. Watson, K. Müllen, A. J. Bard, *Chem. Mater.* **2003**, *15*, 124 – 130.
[12] a) P. G. Schouten, J. M. Warman, M. P. de Haas, C. F. van Nostrum, G. H. Gelinck, R. J. M. Nolte, M. J. Copyn, J. W. Zwikker, M. K. Engel, M. Hanack, Y. H. Chang, W. T. Ford, *J. Am. Chem. Soc.* **1994**, *116*, 6880 – 6894; b) C. F. van Nostrum, A. W. Bosman, G. H. Gelinck, P. G. Schouten, J. M. Warman, A. P. M. Kentgens, M. A. C. Devillers, A. Meijerink, S. J. Picken, U. Sohling, A. J. Schouten, R. J. M. Nolte, *Chem. Eur. J.* **1995**, *1*, 171 – 182; c) H. Eichhorn, *J. Porphyrins Phthalocyanines* **2000**, *4*, 88 – 102.
[13] A. M. van de Craats, J. M. Warman, *Adv. Mater.* **2001**, *13*, 130 – 133.
[14] a) V. S. Iyer, K. Yoshimura, V. Enkelmann, R. Epsch, J. P. Rabe, K. Müllen, *Angew. Chem.* **1998**, *110*, 2843 – 2846; *Angew. Chem. Int. Ed.* **1998**, *37*, 2696 – 2699.
[15] V. S. Iyer, M. Wehmeier, J. D. Brand, M. A. Keegstra, K. Müllen, *Angew. Chem.* **1997**, *109*, 1675 – 1679; *Angew. Chem. Int. Ed. Engl.* **1997**, *36*, 1604 – 1607.
[16] See, for example, 1,7,13-substituted decacyclenes: a) C. Li, Q. Zeng, P. Wu, S. Xu, C. Wang, Y. Qiao, L. Wan, C. Bai, *J. Phys. Chem. B* **2002**, *106*, 13262 – 13267; b) E. Keinan, S. Kumar, R. Moshenberg, R. Ghirlando, E. J. Wachtel, *Adv. Mater.* **1991**, *3*, 251 – 254.
[17] a) M. A. Ogliaruso, M. G. Romanelli, E. I. Becker, *Chem. Rev.* **1965**, *65*, 261 – 367; b) S. Ito, M. Wehmeier, J. D. Brand, C. Kübel, R. Epsch, J. P. Rabe, K. Müllen, *Chem. Eur. J.* **2000**, *6*, 4327 – 4342; c) F. Morgenroth, K. Müllen, *Tetrahedron*, **1997**, *53*, 15349 – 15366; d) F. Morgenroth, E. Reuther, K. Müllen, *Angew. Chem.* **1997**, *109*, 647 – 649; *Angew. Chem. Int. Ed. Engl.* **1997**, *36*, 631 – 634; e) U. M. Wiesler, A. J. Berresheim, F. Morgenroth, G. Lieser, K. Müllen, *Macromolecules* **2001**, *34*, 187 – 199.
[18] P. Kovacic, M. B. Jones, *Chem. Rev.* **1987**, *87*, 357 – 379.
[19] We thank Beate Müller of the Max Planck Institut for Polymer Research for HPLC experiments.
[20] a) L. Przybilla, J. D. Brand, K. Yoshimura, H. J. Räder, K. Müllen, *Anal. Chem.* **2000**, *72*, 4591 – 4597; b) K. Yoshimura, L. Przybilla, S. Ito, J. D. Brand, M. Wehmeier, H. J. Räder, K. Müllen, *Macromol. Chem. Phys.* **2001**, *202*, 215 – 222.
[21] MALDI-TOF mass spectra were calibrated with samples of C_{60} and C_{70} fullerenes. The matrix for the MALDI-TOF measurement was 7,7,8,8-tetracyanoquinodimethane (TCNQ); MALDI-TOF = matrix-assisted laser desorption/ionization time of flight.
[22] N. Tchebotareva, M. D. Watson, D. Felder, J. F. Nierengarten, K. Müllen, submitted.
[23] Alkylated disks with ≤ 60 core carbons provide resolved spectra, while larger ones do not. K. Müllen, unpublished results.
[24] Initial evaluation by pulse-radiolysis time-resolved microwave conductivity (PR-TRMC) measurements of charge-carrier mobilities and lifetimes are comparable to or better than for HBCs; M. Debije, Ž. Tomović, M. D. Watson, K. Müllen, J. Warman, unpublished results.
[25] These films are in fact meshes of intertwined, meandering nanofibers (AFM visualization); P. Samori, M. Palma, Ž. Tomović, M. D. Watson, K. Müllen, unpublished results.
[26] A. Tracz, D. Wostek, I. Kucinska, J. K. Jeszka, M. Watson, K. Müllen, T. Pakula in *NATO Sci. Ser. II* **2002**, *59*, 315 – 318.
[27] I. Fischbach, T. Pakula, P. Minkin, A. Fechtenkötter, K. Müllen, H. W. Spiess, K. Saalwächter, *J. Phys. Chem. B* **2002**, *106*, 6408 – 6418.
[28] a) G. R. Desiraju, A. Gavezotti, *Acta Crystallogr. Sect. B* **1989**, *45*, 473 – 482; b) C. A. Hunter, K. R. Lawson, J. Perkins, C. J. Urch, *J. Chem. Soc. Perkin. Trans. 2* **2001**, 651 – 669.
[29] We thank Ingrid Fischbach and Prof. Tadeusz Pakula of the Max Planck Institute for Polymer Research for the NMR and rheological measurements, respectively.
[30] a) B. Glüsen, A. Kettner, J. H. Wendorff, *Mol. Cryst. Liq. Cryst. Sci. Technol. Sect. A* **1997**, *303*, 115 – 120; b) N. Boden, R. J. Bushby, A. N. Cammidge, A. El-Mansoury, P. S. Martin, Z. Lu, *J. Mater. Chem.* **1999**, *9*, 1391 – 1402.

 © 2004 Wiley-VCH Verlag GmbH & Co. KGaA, Weinheim